



Proceedings  
PRO 121



# Syner '18 Crete

24-26 October 2018, Funchal, Portugal

## **Interdisciplinary Approaches for Cement-based Materials and Structural Concrete: Synergizing Expertise and Bridging Scales of Space and Time**

Final Conference of COST Action TU1404

**Electronic Version of Proceedings: Volume 1&2**

Edited by Miguel Azenha, Dirk Schlicke, Farid Benboudjema,  
Agnieszka Jędrzejewska

**SynerCrete'18: Interdisciplinary  
Approaches for Cement-based Materials  
and Structural Concrete:  
Synergizing Expertise and Bridging  
Scales of Space and Time  
Vol. 1 & 2**

This is an electronic version of the proceedings of SynerCrete'18. It keeps the same page numbering of the two printed volumes, whereas the blank pages in the printed volumes are omitted.

Published by RILEM Publications S.A.R.L.  
4 avenue du Recteur Poincaré 75016 Paris - France  
Tel : + 33 1 42 24 64 46 Fax : + 33 9 70 29 51 20  
<http://www.rilem.net> E-mail: [dg@rilem.net](mailto:dg@rilem.net)  
© 2018 RILEM – Tous droits réservés.  
ISBN Vol. 1:978-2-35158-211-4 ISBN Vol. 2: 978-2-35158-212-1  
ISBN Vol. 1&2: 978-2-35158-202-2 e-ISBN Vol. 1&2: 978-2-35158-203-9  
DOI: 10.5281/zenodo.1405563  
Printed by Canto Redondo / VASP DPS <http://www.cantoredondo.eu>  
Cover design by: Boutik Studio <http://boutik.pt/>

**Publisher's note:** *this book has been produced from electronic files provided by the individual contributors. The publisher makes no representation, express or implied, with regard to the accuracy of the information contained in this book and cannot accept any legal responsibility or liability for any errors or omissions that may be made.*

*All titles published by RILEM Publications are under copyright protection; said copyrights being the property of their respective holders. All Rights Reserved.*

*No part of any book may be reproduced or transmitted in any form or by any means, graphic, electronic, or mechanical, including photocopying, recording, taping, or by any information storage or retrieval system, without the permission in writing from the publisher.*

RILEM, The International Union of Laboratories and Experts in Construction Materials, Systems and Structures, is a non-profit-making, non-governmental technical association whose vocation is to contribute to progress in the construction sciences, techniques and industries, essentially by means of the communication it fosters between research and practice. RILEM's activity therefore aims at developing the knowledge of properties of materials and performance of structures, at defining the means for their assessment in laboratory and service conditions and at unifying measurement and testing methods used with this objective.

RILEM was founded in 1947, and has a membership of over 900 in some 70 countries. It forms an institutional framework for co-operation by experts to:

- optimise and harmonise test methods for measuring properties and performance of building and civil engineering materials and structures under laboratory and service environments,
- prepare technical recommendations for testing methods,
- prepare state-of-the-art reports to identify further research needs,
- collaborate with national or international associations in realising these objectives.

RILEM members include the leading building research and testing laboratories around the world, industrial research, manufacturing and contracting interests, as well as a significant number of individual members from industry and universities. RILEM's focus is on construction materials and their use in building and civil engineering structures, covering all phases of the building process from manufacture to use and recycling of materials.

RILEM meets these objectives through the work of its technical committees. Symposia, workshops and seminars are organised to facilitate the exchange of information and dissemination of knowledge. RILEM's primary output consists of technical recommendations. RILEM also publishes the journal *Materials and Structures* which provides a further avenue for reporting the work of its committees. Many other publications, in the form of reports, monographs, symposia and workshop proceedings are produced.

SynerCrete'18:  
Interdisciplinary Approaches for Cement-based Materials  
and Structural Concrete: Synergizing Expertise and  
Bridging Scales of Space and Time  
Vol. 1 & 2

Funchal, Madeira, Portugal  
24-26 October 2018

Edited by  
Miguel Azenha  
Dirk Schlicke  
Farid Benboudjema  
Agnieszka Jędrzejewska

SynerCrete'18 International Conference on Interdisciplinary Approaches  
for Cement-based Materials and Structural Concrete

24-26 October 2018, Funchal, Madeira Island, Portugal

### National Support (Portugal)



### International Support



### Sponsors



## RILEM Publications

The following list is presenting the global offer of RILEM Publications, sorted by series. Each publication is available in printed version and/or in online version.

### RILEM PROCEEDINGS (PRO)

- PRO 1:** Durability of High Performance Concrete (ISBN: 2-912143-03-9); *Ed. H. Sommer*
- PRO 2:** Chloride Penetration into Concrete (ISBN: 2-912143-00-04);  
*Eds. L.-O. Nilsson and J.-P. Ollivier*
- PRO 3:** Evaluation and Strengthening of Existing Masonry Structures (ISBN: 2-912143-02-0);  
*Eds. L. Binda and C. Modena*
- PRO 4:** Concrete: From Material to Structure (ISBN: 2-912143-04-7); *Eds. J.-P. Bournazel and Y. Malier*
- PRO 5:** The Role of Admixtures in High Performance Concrete (ISBN: 2-912143-05-5);  
*Eds. J. G. Cabrera and R. Rivera-Villarreal*
- PRO 6:** High Performance Fiber Reinforced Cement Composites - HPFRCC 3  
(ISBN: 2-912143-06-3); *Eds. H. W. Reinhardt and A. E. Naaman*
- PRO 7:** 1st International RILEM Symposium on Self-Compacting Concrete (ISBN: 2-912143-09-8); *Eds. Å. Skarendahl and Ö. Petersson*
- PRO 8:** International RILEM Symposium on Timber Engineering (ISBN: 2-912143-10-1);  
*Ed. L. Boström*
- PRO 9:** 2nd International RILEM Symposium on Adhesion between Polymers and Concrete ISAP '99 (ISBN: 2-912143-11-X); *Eds. Y. Ohama and M. Puterman*
- PRO 10:** 3rd International RILEM Symposium on Durability of Building and Construction Sealants (ISBN: 2-912143-13-6); *Eds. A. T. Wolf*
- PRO 11:** 4th International RILEM Conference on Reflective Cracking in Pavements (ISBN: 2-912143-14-4); *Eds. A. O. Abd El Halim, D. A. Taylor and El H. H. Mohamed*
- PRO 12:** International RILEM Workshop on Historic Mortars: Characteristics and Tests (ISBN: 2-912143-15-2); *Eds. P. Bartos, C. Groot and J. J. Hughes*
- PRO 13:** 2nd International RILEM Symposium on Hydration and Setting (ISBN: 2-912143-16-0); *Ed. A. Nonat*
- PRO 14:** Integrated Life-Cycle Design of Materials and Structures - ILCDES 2000 (ISBN: 951-758-408-3); (ISSN: 0356-9403); *Ed. S. Sarja*
- PRO 15:** Fifth RILEM Symposium on Fibre-Reinforced Concretes (FRC) - BEFIB'2000 (ISBN: 2-912143-18-7); *Eds. P. Rossi and G. Chanvillard*
- PRO 16:** Life Prediction and Management of Concrete Structures (ISBN: 2-912143-19-5); *Ed. D. Naus*
- PRO 17:** Shrinkage of Concrete – Shrinkage 2000 (ISBN: 2-912143-20-9);  
*Eds. V. Baroghel-Bouny and P.-C. Aïtcin*

- PRO 18:** Measurement and Interpretation of the On-Site Corrosion Rate (ISBN: 2-912143-21-7);  
*Eds. C. Andrade, C. Alonso, J. Fullea, J. Polimon and J. Rodriguez*
- PRO 19:** Testing and Modelling the Chloride Ingress into Concrete (ISBN: 2-912143-22-5);  
*Eds. C. Andrade and J. Kropp*
- PRO 20:** 1st International RILEM Workshop on Microbial Impacts on Building Materials (CD  
02) (e-ISBN 978-2-35158-013-4); *Ed. M. Ribas Silva*
- PRO 21:** International RILEM Symposium on Connections between Steel and Concrete  
(ISBN: 2-912143-25-X); *Ed. R. Eligehausen*
- PRO 22:** International RILEM Symposium on Joints in Timber Structures  
(ISBN: 2-912143-28-4); *Eds. S. Aicher and H.-W. Reinhardt*
- PRO 23:** International RILEM Conference on Early Age Cracking in Cementitious Systems  
(ISBN: 2-912143-29-2); *Eds. K. Kovler and A. Bentur*
- PRO 24:** 2nd International RILEM Workshop on Frost Resistance of Concrete  
(ISBN: 2-912143-30-6); *Eds. M. J. Setzer, R. Auberg and H.-J. Keck*
- PRO 25:** International RILEM Workshop on Frost Damage in Concrete  
(ISBN: 2-912143-31-4); *Eds. D. J. Janssen, M. J. Setzer and M. B. Snyder*
- PRO 26:** International RILEM Workshop on On-Site Control and Evaluation of Masonry Structures  
(ISBN: 2-912143-34-9); *Eds. L. Binda and R. C. de Vekey*
- PRO 27:** International RILEM Symposium on Building Joint Sealants (CD03); *Ed. A. T. Wolf*
- PRO 28:** 6th International RILEM Symposium on Performance Testing and Evaluation of Bituminous Materials - PTEBM'03 (ISBN: 2-912143-35-7; e-ISBN: 978-2-912143-77-8); *Ed. M. N. Partl*
- PRO 29:** 2nd International RILEM Workshop on Life Prediction and Ageing Management of  
Concrete Structures (ISBN: 2-912143-36-5); *Ed. D. J. Naus*
- PRO 30:** 4th International RILEM Workshop on High Performance Fiber Reinforced Cement  
Composites - HPFRCC 4 (ISBN: 2-912143-37-3); *Eds. A. E. Naaman and H. W. Reinhardt*
- PRO 31:** International RILEM Workshop on Test and Design Methods for Steel Fibre Reinforced  
Concrete: Background and Experiences (ISBN: 2-912143-38-1); *Eds. B. Schnütgen and L. Vandewalle*
- PRO 32:** International Conference on Advances in Concrete and Structures 2 vol.  
(ISBN (set): 2-912143-41-1); *Eds. Ying-shu Yuan, Surendra P. Shah and Heng-lin Lü*
- PRO 33:** 3rd International Symposium on Self-Compacting Concrete  
(ISBN: 2-912143-42-X); *Eds. Ö. Wallevik and I. Nielsson*
- PRO 34:** International RILEM Conference on Microbial Impact on Building Materials  
(ISBN: 2-912143-43-8); *Ed. M. Ribas Silva*
- PRO 35:** International RILEM TC 186-ISA on Internal Sulfate Attack and Delayed Ettringite  
Formation (ISBN: 2-912143-44-6); *Eds. K. Scrivener and J. Skalny*
- PRO 36:** International RILEM Symposium on Concrete Science and Engineering – A Tribute to  
Arnon Bentur (ISBN: 2-912143-46-2); *Eds. K. Kovler, J. Marchand, S. Mindess and J. Weiss*
- PRO 37:** 5th International RILEM Conference on Cracking in Pavements – Mitigation, Risk Assessment and Prevention  
(ISBN: 2-912143-47-0); *Eds. C. Petit, I. Al-Qadi and A. Millien*
- PRO 38:** 3rd International RILEM Workshop on Testing and Modelling the Chloride Ingress into  
Concrete (ISBN: 2-912143-48-9); *Eds. C. Andrade and J. Kropp*

- PRO 39:** 6th International RILEM Symposium on Fibre-Reinforced Concretes - BEFIB 2004 (ISBN: 2-912143-51-9); *Eds. M. Di Prisco, R. Felicetti and G. A. Plizzari*
- PRO 40:** International RILEM Conference on the Use of Recycled Materials in Buildings and Structures (ISBN: 2-912143-52-7); *Eds. E. Vázquez, Ch. F. Hendriks and G. M. T. Janssen*
- PRO 41:** RILEM International Symposium on Environment-Conscious Materials and Systems for Sustainable Development (ISBN: 2-912143-55-1); *Eds. N. Kashino and Y. Ohama*
- PRO 42:** SCC'2005 - China: 1st International Symposium on Design, Performance and Use of Self-Consolidating Concrete (ISBN: 2-912143-61-6); *Eds. Zhiwu Yu, Caijun Shi, Kamal Henri Khayat and Youjun Xie*
- PRO 43:** International RILEM Workshop on Bonded Concrete Overlays (e-ISBN: 2-912143-83-7); *Eds. J. L. Granju and J. Silfwerbrand*
- PRO 44:** 2nd International RILEM Workshop on Microbial Impacts on Building Materials (CD11) (e-ISBN: 2-912143-84-5); *Ed. M. Ribas Silva*
- PRO 45:** 2nd International Symposium on Nanotechnology in Construction, Bilbao (ISBN: 2-912143-87-X); *Eds. Peter J. M. Bartos, Yolanda de Miguel and Antonio Porro*
- PRO 46:** ConcreteLife'06 - International RILEM-JCI Seminar on Concrete Durability and Service Life Planning: Curing, Crack Control, Performance in Harsh Environments (ISBN: 2-912143-89-6); *Ed. K. Kovler*
- PRO 47:** International RILEM Workshop on Performance Based Evaluation and Indicators for Concrete Durability (ISBN: 978-2-912143-95-2); *Eds. V. Baroghel-Bouny, C. Andrade, R. Torrent and K. Scrivener*
- PRO 48:** 1st International RILEM Symposium on Advances in Concrete through Science and Engineering (e-ISBN: 2-912143-92-6); *Eds. J. Weiss, K. Kovler, J. Marchand, and S. Mindess*
- PRO 49:** International RILEM Workshop on High Performance Fiber Reinforced Cementitious Composites in Structural Applications (ISBN: 2-912143-93-4); *Eds. G. Fischer and V.C. Li*
- PRO 50:** 1<sup>st</sup> International RILEM Symposium on Textile Reinforced Concrete (ISBN: 2-912143-97-7); *Eds. Josef Hegger, Wolfgang Bramehuber and Norbert Will*
- PRO 51:** 2<sup>nd</sup> International Symposium on Advances in Concrete through Science and Engineering (ISBN: 2-35158-003-6; e-ISBN: 2-35158-002-8); *Eds. J. Marchand, B. Bissonnette, R. Gagné, M. Jolin and F. Paradis*
- PRO 52:** Volume Changes of Hardening Concrete: Testing and Mitigation (ISBN: 2-35158-004-4; e-ISBN: 2-35158-005-2); *Eds. O. M. Jensen, P. Lura and K. Kovler*
- PRO 53:** High Performance Fiber Reinforced Cement Composites - HPRFCC5 (ISBN: 978-2-35158-046-2); *Eds. H. W. Reinhardt and A. E. Naaman*
- PRO 54:** 5<sup>th</sup> International RILEM Symposium on Self-Compacting Concrete (ISBN: 978-2-35158-047-9); *Eds. G. De Schutter and V. Boel*
- PRO 55:** International RILEM Symposium Photocatalysis, Environment and Construction Materials (ISBN: 978-2-35158-056-1); *Eds. P. Baglioni and L. Cassar*
- PRO56:** International RILEM Workshop on Integral Service Life Modelling of Concrete Structures (ISBN 978-2-35158-058-5); *Eds. R. M. Ferreira, J. Gulikers and C. Andrade*
- PRO57:** RILEM Workshop on Performance of cement-based materials in aggressive aqueous environments (e-ISBN: 978-2-35158-059-2); *Ed. N. De Belie*
- PRO58:** International RILEM Symposium on Concrete Modelling - CONMOD'08 (ISBN: 978-2-35158-060-8); *Eds. E. Schlangen and G. De Schutter*



- PRO 59:** International RILEM Conference on On Site Assessment of Concrete, Masonry and Timber Structures - SACoMaTiS 2008 (ISBN set: 978-2-35158-061-5); *Eds. L. Binda, M. di Prisco and R. Felicetti*
- PRO 60:** Seventh RILEM International Symposium on Fibre Reinforced Concrete: Design and Applications - BEFIB 2008 (ISBN: 978-2-35158-064-6); *Ed. R. Gettu*
- PRO 61:** 1<sup>st</sup> International Conference on Microstructure Related Durability of Cementitious Composites 2 vol., (ISBN: 978-2-35158-065-3); *Eds. W. Sun, K. van Breugel, C. Miao, G. Ye and H. Chen*
- PRO 62:** NSF/ RILEM Workshop: In-situ Evaluation of Historic Wood and Masonry Structures (e-ISBN: 978-2-35158-068-4); *Eds. B. Kasal, R. Anthony and M. Drdácáký*
- PRO 63:** Concrete in Aggressive Aqueous Environments: Performance, Testing and Modelling, 2 vol., (ISBN: 978-2-35158-071-4); *Eds. M. G. Alexander and A. Bertron*
- PRO 64:** Long Term Performance of Cementitious Barriers and Reinforced Concrete in Nuclear Power Plants and Waste Management - NUCPERF 2009 (ISBN: 978-2-35158-072-1); *Eds. V. L'Hostis, R. Gens, C. Gallé*
- PRO 65:** Design Performance and Use of Self-consolidating Concrete - SCC'2009 (ISBN: 978-2-35158-073-8); *Eds. C. Shi, Z. Yu, K. H. Khayat and P. Yan*
- PRO 66:** 2<sup>nd</sup> International RILEM Workshop on Concrete Durability and Service Life Planning - ConcreteLife'09 (ISBN: 978-2-35158-074-5); *Ed. K. Kowler*
- PRO 67:** Repairs Mortars for Historic Masonry (e-ISBN: 978-2-35158-083-7); *Ed. C. Groot*
- PRO 68:** Proceedings of the 3<sup>rd</sup> International RILEM Symposium on 'Rheology of Cement Suspensions such as Fresh Concrete (ISBN 978-2-35158-091-2); *Eds. O. H. Wallevik, S. Kubens and S. Oesterheld*
- PRO 69:** 3<sup>rd</sup> International PhD Student Workshop on 'Modelling the Durability of Reinforced Concrete (ISBN: 978-2-35158-095-0); *Eds. R. M. Ferreira, J. Gulikers and C. Andrade*
- PRO 70:** 2<sup>nd</sup> International Conference on 'Service Life Design for Infrastructure' (ISBN set: 978-2-35158-096-7, e-ISBN: 978-2-35158-097-4); *Ed. K. van Breugel, G. Ye and Y. Yuan*
- PRO 71:** Advances in Civil Engineering Materials - The 50-year Teaching Anniversary of Prof. Sun Wei' (ISBN: 978-2-35158-098-1; e-ISBN: 978-2-35158-099-8); *Eds. C. Miao, G. Ye, and H. Chen*
- PRO 72:** First International Conference on 'Advances in Chemically-Activated Materials - CAM'2010' (2010), 264 pp, ISBN: 978-2-35158-101-8; e-ISBN: 978-2-35158-115-5, *Eds. Caijun Shi and Xiaodong Shen*
- PRO 73:** 2<sup>nd</sup> International Conference on 'Waste Engineering and Management - ICWEM 2010' (2010), 894 pp, ISBN: 978-2-35158-102-5; e-ISBN: 978-2-35158-103-2, *Eds. J. Zh. Xiao, Y. Zhang, M. S. Cheung and R. Chu*
- PRO 74:** International RILEM Conference on 'Use of Superabsorbent Polymers and Other New Additives in Concrete' (2010) 374 pp., ISBN: 978-2-35158-104-9; e-ISBN: 978-2-35158-105-6; *Eds. O.M. Jensen, M.T. Hasholt, and S. Laustsen*
- PRO 75:** International Conference on 'Material Science - 2nd ICTRC - Textile Reinforced Concrete - Theme 1' (2010) 436 pp., ISBN: 978-2-35158-106-3; e-ISBN: 978-2-35158-107-0; *Ed. W. Brameshuber*

- PRO 76:** International Conference on 'Material Science - HetMat - Modelling of Heterogeneous Materials - Theme 2' (2010) 255 pp., ISBN: 978-2-35158-108-7; e-ISBN: 978-2-35158-109-4; *Ed. W. Brameshuber*
- PRO 77:** International Conference on 'Material Science - AdIPoC - Additions Improving Properties of Concrete - Theme 3' (2010) 459 pp., ISBN: 978-2-35158-110-0; e-ISBN: 978-2-35158-111-7; *Ed. W. Brameshuber*
- PRO 78:** 2<sup>nd</sup> Historic Mortars Conference and RILEM TC 203-RHM Final Workshop – HMC2010 (2010) 1416 pp., e-ISBN: 978-2-35158-112-4; *Eds J. Válek, C. Groot, and J. J. Hughes*
- PRO 79:** International RILEM Conference on Advances in Construction Materials Through Science and Engineering (2011) 213 pp., e-ISBN: 978-2-35158-117-9; *Eds Christopher Leung and K.T. Wan*
- PRO 80:** 2<sup>nd</sup> International RILEM Conference on Concrete Spalling due to Fire Exposure (2011) 453 pp., ISBN: 978-2-35158-118-6, e-ISBN: 978-2-35158-119-3; *Eds E.A.B. Koenders and F. Dehn*
- PRO 81:** 2<sup>nd</sup> International RILEM Conference on Strain Hardening Cementitious Composites (SHCC2-Rio) (2011) 451 pp., ISBN: 978-2-35158-120-9, e-ISBN: 978-2-35158-121-6; *Eds R.D. Toledo Filho, F.A. Silva, E.A.B. Koenders and E.M.R. Fairbairn*
- PRO 82:** 2<sup>nd</sup> International RILEM Conference on Progress of Recycling in the Built Environment (2011) 507 pp., e-ISBN: 978-2-35158-122-3; *Eds V.M. John, E. Vazquez, S.C. Angulo and C. Ulsen*
- PRO 83:** 2<sup>nd</sup> International Conference on Microstructural-related Durability of Cementitious Composites (2012) 250 pp., ISBN: 978-2-35158-129-2; e-ISBN: 978-2-35158-123-0; *Eds G. Ye, K. van Breugel, W. Sun and C. Miao*
- PRO 85:** RILEM-JCI International Workshop on Crack Control of Mass Concrete and Related issues concerning Early-Age of Concrete Structures – ConCrack 3 – Control of Cracking in Concrete Structures 3 (2012) 237 pp., ISBN: 978-2-35158-125-4; e-ISBN: 978-2-35158-126-1; *Eds F. Toutlemonde and J.-M. Torrenti*
- PRO 86:** International Symposium on Life Cycle Assessment and Construction (2012) 414 pp., ISBN: 978-2-35158-127-8, e-ISBN: 978-2-35158-128-5; *Eds A. Ventura and C. de la Roche*
- PRO 87:** UHPFRC 2013 – RILEM-fib-AFGC International Symposium on Ultra-High Performance Fibre-Reinforced Concrete (2013), ISBN: 978-2-35158-130-8, e-ISBN: 978-2-35158-131-5; *Eds F. Toutlemonde*
- PRO 88:** 8<sup>th</sup> RILEM International Symposium on Fibre Reinforced Concrete (2012) 344 pp., ISBN: 978-2-35158-132-2, e-ISBN: 978-2-35158-133-9; *Eds Joaquim A.O. Barros*
- PRO 89:** RILEM International workshop on performance-based specification and control of concrete durability (2014) 678 pp, ISBN: 978-2-35158-135-3, e-ISBN: 978-2-35158-136-0; *Eds. D. Bjegović, H. Beushausen and M. Serdar*
- PRO 90:** 7<sup>th</sup> RILEM International Conference on Self-Compacting Concrete and of the 1<sup>st</sup> RILEM International Conference on Rheology and Processing of Construction Materials (2013) 396 pp, ISBN: 978-2-35158-137-7, e-ISBN: 978-2-35158-138-4; *Eds. Nicolas Roussel and Hela Bessaies-Bey*

**PRO 91:** CONMOD 2014 - RILEM International Symposium on Concrete Modelling (2014), ISBN: 978-2-35158-139-1; e-ISBN: 978-2-35158-140-7; *Eds. Kefei Li, Peiyu Yan and Rongwei Yang*

**PRO 92:** CAM 2014 - 2nd International Conference on advances in chemically-activated materials (2014) 392 pp., ISBN: 978-2-35158-141-4; e-ISBN: 978-2-35158-142-1; *Eds. Caijun Shi and Xiadong Shen*

**PRO 93:** SCC 2014 - 3rd International Symposium on Design, Performance and Use of Self-Consolidating Concrete (2014) 438 pp., ISBN: 978-2-35158-143-8; e-ISBN: 978-2-35158-144-5; *Eds. Caijun Shi, Zhihua Ou, Kamal H. Khayat*

**PRO 94 (online version):** HPFRCC-7 - 7th RILEM conference on High performance fiber reinforced cement composites (2015), e-ISBN: 978-2-35158-146-9; *Eds. H.W. Reinhardt, G.J. Parra-Montesinos, H. Garrecht*

**PRO 95:** International RILEM Conference on Application of superabsorbent polymers and other new admixtures in concrete construction (2014), ISBN: 978-2-35158-147-6; e-ISBN: 978-2-35158-148-3; *Eds. Viktor Mechtcherine, Christof Schroefl*

**PRO 96 (online version):** XIII DBMC: XIII International Conference on Durability of Building Materials and Components (2015), e-ISBN: 978-2-35158-149-0; *Eds. M. Quattrone, V.M. John*

**PRO 97:** SHCC3 - 3rd International RILEM Conference on Strain Hardening Cementitious Composites (2014), ISBN: 978-2-35158-150-6; e-ISBN: 978-2-35158-151-3; *Eds. E. Schlangen, M.G. Sierra Beltran, M. Lukovic, G. Ye*

**PRO 98:** FERRO-11 - 11th International Symposium on Ferrocement and 3rd ICTRC - International Conference on Textile Reinforced Concrete (2015), ISBN: 978-2-35158-152-0; e-ISBN: 978-2-35158-153-7; *Ed. W. Brameshuber*

**PRO 99 (online version):** ICBBM 2015 - 1st International Conference on Bio-Based Building Materials (2015), e-ISBN: 978-2-35158-154-4; *Eds. S. Amziane, M. Sonebi*

**PRO 100:** SCC16 - RILEM Self-Consolidating Concrete Conference (2016), ISBN: 978-2-35158-156-8; e-ISBN: 978-2-35158-157-5

**PRO 101 (online version):** III Progress of Recycling in the Built Environment (2015), e-ISBN: 978-2-35158-158-2; *Eds I. Martins, C. Ulsen and S. C. Angulo*

**PRO 102 (online version):** RILEM Conference on Microorganisms-Cementitious Materials Interactions (2016), e-ISBN: 978-2-35158-160-5; *Eds. Alexandra Bertron, Henk Jonkers, Virginie Wiktor*

**PRO 103 (online version):** ACESC'16 - Advances in Civil Engineering and Sustainable Construction (2016), e-ISBN: 978-2-35158-161-2

**PRO 104 (online version):** SSCS'2015 - Numerical Modeling - Strategies for Sustainable Concrete Structures (2015), e-ISBN: 978-2-35158-162-9

**PRO 105:** 1st International Conference on UHPC Materials and Structures (2016), ISBN: 978-2-35158-164-3, e-ISBN: 978-2-35158-165-0

**PRO 106:** AFGC-ACI-fib-RILEM International Conference on Ultra-High-Performance Fibre-Reinforced Concrete - UHPFRC 2017 (2017), ISBN: 978-2-35158-166-7, e-ISBN: 978-2-35158-167-4; *Eds. François Toutlemonde & Jacques Resplendino*

**PRO 107 (online version):** XIV DBMC – 14th International Conference on Durability of Building Materials and Components (2017), e-ISBN: 978-2-35158-159-9; *Eds. Geert De Schutter, Nele De Belie, Arnold Janssens, Nathan Van Den Bossche*

**PRO 108:** MSSCE 2016 - Innovation of Teaching in Materials and Structures (2016), ISBN: 978-2-35158-178-0, e-ISBN: 978-2-35158-179-7; *Ed. Per Goltermann*

**PRO 109 (two volumes):** MSSCE 2016 - Service Life of Cement-Based Materials and Structures (2016), ISBN Vol. 1: 978-2-35158-170-4, Vol. 2: 978-2-35158-171-4, Set Vol. 1&2: 978-2-35158-172-8, e-ISBN : 978-2-35158-173-5; *Eds. Miguel Azenha, Ivan Gaborjel, Dirk Schlicke, Terje Kanstad and Ole Mejlhede Jensen*

**PRO 110:** MSSCE 2016 - Historical Masonry (2016), ISBN: 978-2-35158-178-0, e-ISBN: 978-2-35158-179-7; *Eds. Inge Rörig-Dalgaard and Ioannis Ioannou*

**PRO 111:** MSSCE 2016 - Electrochemistry in Civil Engineering (2016), ISBN: 978-2-35158-176-6, e-ISBN: 978-2-35158-177-3; *Ed. Lisbeth M. Ottosen*

**PRO 112:** MSSCE 2016 - Moisture in Materials and Structures (2016), ISBN: 978-2-35158-178-0, e-ISBN: 978-2-35158-179-7; *Eds. Kurt Kielsgaard Hansen, Carsten Rode and Lars-Olof Nilsson*

**PRO 113:** MSSCE 2016 - Concrete with Supplementary Cementitious Materials (2016), ISBN: 978-2-35158-178-0, e-ISBN: 978-2-35158-179-7; *Eds. Ole Mejlhede Jensen, Konstantin Kovler and Nele De Belie*

**PRO 114:** MSSCE 2016 - Frost Action in Concrete (2016), ISBN: 978-2-35158-182-7, e-ISBN: 978-2-35158-183-4; *Eds. Marianne Tange Hasholt, Katja Fridh and R. Doug Hooton*

**PRO 115:** MSSCE 2016 - Fresh Concrete (2016), ISBN: 978-2-35158-184-1, e-ISBN: 978-2-35158-185-8; *Eds. Lars N. Thrane, Claus Pade, Oldrich Svec and Nicolas Roussel*

**PRO 116:** BEFIB 2016 – 9th RILEM International Symposium on Fiber Reinforced Concrete (2016), ISBN: 978-2-35158-187-2, e-ISBN: 978-2-35158-186-5;

**PRO 117:** 3rd International RILEM Conference on Microstructure Related Durability of Cementitious Composites (2016), ISBN: 978-2-35158-188-9, e-ISBN: 978-2-35158-189-6; *Eds. Changwen Miao, Wei Sun, Jiaping Liu, Huisu Chen, Guang Ye and Klaas van Breugel*

**PRO 118 (4 volumes):** International Conference on Advances in Construction Materials and Systems (2017), ISBN Set: 978-2-35158-190-2, Vol. 1: 978-2-35158-193-3, Vol. 2: 978-2-35158-194-0, Vol. 3: ISBN:978-2-35158-195-7, Vol. 4: ISBN:978-2-35158-196-4, e-ISBN: 978-2-35158-191-9; *Ed. Manu Santhanam*

**PRO 119 (online version):** ICBBM 2017 - Second International RILEM Conference on Bio-based Building Materials, (2017), e-ISBN: 978-2-35158-192-6; *Ed. Sofiane Amziane*

**PRO 120 (2 volumes):** EAC-02 - 2nd International RILEM/COST Conference on Early Age Cracking and Serviceability in Cement-based Materials and Structures, (2017), Vol. 1: 978-2-35158-199-5, Vol. 2: 978-2-35158-200-8, Set: 978-2-35158-197-1, e-ISBN: 978-2-35158-198-8; *Eds. Stéphanie Staquet and Dimitrios Aggelis*

## **RILEM REPORTS (REP)**

**Report 19:** Considerations for Use in Managing the Aging of Nuclear Power Plant Concrete Structures (ISBN: 2-912143-07-1); *Ed. D. J. Naus*

**Report 20:** Engineering and Transport Properties of the Interfacial Transition Zone in Cementitious Composites (ISBN: 2-912143-08-X); *Eds. M. G. Alexander, G. Arliguie, G. Ballivy, A. Bentur and J. Marchand*

**Report 21:** Durability of Building Sealants (ISBN: 2-912143-12-8); *Ed. A. T. Wolf*

**Report 22:** Sustainable Raw Materials - Construction and Demolition Waste (ISBN: 2-912143-17-9); *Eds. C. F. Hendriks and H. S. Pietersen*

**Report 23:** Self-Compacting Concrete state-of-the-art report (ISBN: 2-912143-23-3); *Eds. Å. Skarendahl and Ö. Petersson*

**Report 24:** Workability and Rheology of Fresh Concrete: Compendium of Tests (ISBN: 2-912143-32-2); *Eds. P. J. M. Bartos, M. Sonebi and A. K. Tamimi*

**Report 25:** Early Age Cracking in Cementitious Systems (ISBN: 2-912143-33-0); *Ed. A. Bentur*

**Report 26:** Towards Sustainable Roofing (Joint Committee CIB/RILEM) (CD 07) (e-ISBN 978-2-912143-65-5); *Eds. Thomas W. Hutchinson and Keith Roberts*

**Report 27:** Condition Assessment of Roofs (Joint Committee CIB/RILEM) (CD 08) (e-ISBN 978-2-912143-66-2); *Ed. CIB W 83/RILEM TC166-RMS*

**Report 28:** Final report of RILEM TC 167-COM 'Characterisation of Old Mortars with Respect to Their Repair' (ISBN: 978-2-912143-56-3); *Eds. C. Groot, G. Ashall and J. Hughes*

**Report 29:** Pavement Performance Prediction and Evaluation (PPPE): Interlaboratory Tests (e-ISBN: 2-912143-68-3); *Eds. M. Partl and H. Piber*

**Report 30:** Final Report of RILEM TC 198-URM 'Use of Recycled Materials' (ISBN: 2-912143-82-9; e-ISBN: 2-912143-69-1); *Eds. Ch. F. Hendriks, G. M. T. Janssen and E. Vázquez*

**Report 31:** Final Report of RILEM TC 185-ATC 'Advanced testing of cement-based materials during setting and hardening' (ISBN: 2-912143-81-0; e-ISBN: 2-912143-70-5); *Eds. H. W. Reinhardt and C. U. Grosse*

**Report 32:** Probabilistic Assessment of Existing Structures. A JCSS publication (ISBN 2-912143-24-1); *Ed. D. Diamantidis*

**Report 33:** State-of-the-Art Report of RILEM Technical Committee TC 184-IFE 'Industrial Floors' (ISBN 2-35158-006-0); *Ed. P. Seidler*

**Report 34:** Report of RILEM Technical Committee TC 147-FMB 'Fracture mechanics applications to anchorage and bond' Tension of Reinforced Concrete Prisms – Round Robin Analysis and Tests on Bond (e-ISBN 2-912143-91-8); *Eds. L. Elfgren and K. Noghabai*

**Report 35:** Final Report of RILEM Technical Committee TC 188-CSC 'Casting of Self Compacting Concrete' (ISBN 2-35158-001-X; e-ISBN: 2-912143-98-5); *Eds. Å. Skarendahl and P. Billberg*

**Report 36:** State-of-the-Art Report of RILEM Technical Committee TC 201-TRC 'Textile Reinforced Concrete' (ISBN 2-912143-99-3); *Ed. W. Brameshuber*

**Report 37:** State-of-the-Art Report of RILEM Technical Committee TC 192-ECM 'Environment-conscious construction materials and systems' (ISBN: 978-2-35158-053-0); *Eds. N. Kashino, D. Van Gemert and K. Imamoto*

**Report 38:** State-of-the-Art Report of RILEM Technical Committee TC 205-DSC 'Durability of Self-Compacting Concrete' (ISBN: 978-2-35158-048-6); *Eds. G. De Schutter and K. Audenaert*

**Report 39:** Final Report of RILEM Technical Committee TC 187-SOC 'Experimental determination of the stress-crack opening curve for concrete in tension' (ISBN 978-2-35158-049-3); *Ed. J. Planas*

**Report 40:** State-of-the-Art Report of RILEM Technical Committee TC 189-NEC ‘Non-Destructive Evaluation of the Penetrability and Thickness of the Concrete Cover’ (ISBN 978-2-35158-054-7);

*Eds. R. Torrent and L. Fernández Luco*

**Report 41:** State-of-the-Art Report of RILEM Technical Committee TC 196-ICC ‘Internal Curing of Concrete’ (ISBN 978-2-35158-009-7); *Eds. K. Kovler and O. M. Jensen*

**Report 42:** ‘Acoustic Emission and Related Non-destructive Evaluation Techniques for Crack Detection and Damage Evaluation in Concrete’ - Final Report of RILEM Technical Committee 212-ACD (e-ISBN: 978-2-35158-100-1); *Ed. M. Ohtsu*

**Report 45:** Repair Mortars for Historic Masonry - State-of-the-Art Report of RILEM Technical Committee TC 203-RHM (e-ISBN: 978-2-35158-163-6); *Eds. Paul Maurenbrecher and Caspar Groot*

**Report 46:** Surface delamination of concrete industrial floors and other durability related aspects guide - Report of RILEM Technical Committee TC 268-SIF ( e-ISBN: 978-2-35158-201-5); *Ed. Valérie Pollet*

## Conference Chairs

Miguel Azenha, Dirk Schlicke

## Scientific Committee Chairs

Farid Benboudjema, Agnieszka Jędrzejewska

## National Organizing Committee

Paulo Lobo, José Sena Cruz, Eduardo Júlio, Rui Faria, Manuel Pipa, Romeu Vicente

## COST Organizing Committee

Violeta Bokan-Bosiljkov, Laurie Lacarrière, Terje Kanstad, Sreejith Nanukuttan, Emmanuel Rozière, Marijana Serdar, Stéphanie Staquet, François Toutlemonde, Mateusz Wyrzykowski

## Scientific Committee

Farid Benboudjema (Chair)	Eduardus Koenders	Marijana Serdar
Agnieszka Jędrzejewska (Chair)	Barbara Klemczak	Carlos Serra
Ouali Amiri	Laurie Lacarrière	Ioannis Sfikas
Sofiane Amziane	Paulo B. Lourenço	Paulo Silva Lobo
Shingo Asamoto	Ippei Maruyama	Mohammed Sonebi
Miguel Azenha	Kyuichi Maruyama	Carlos Sousa
Nele de Belie	Enrico Masoero	Tayfun Altuğ Söylev
Violeta Bokan Bosiljkov	Hadi Mazaheripour	Maria Stefanidou
Alexandra Bourdot	Sreejith Nanukuttan	Stéphanie Staquet
Matthieu Briffaut	Małgorzata Pająk	Aljoša Šajna
Tomo Cerovšek	Arnaud Perrot	Vít Šmilauer
Özlem Cizer	Bernhard Pichler	Luping Tang
Gianluca Cusatis	Manuel Pipa	Katrin Turner
Aveline Darquennes	John Provis	Jean-Michel Torrenti
Szymon Dawczyński	Vlastimir Radonjanin	François Toutlemonde
Eduardo Fairbairn	Marta Roig	Jörg F. Unger
Rui Faria	Emmanuel Rozière	Neven Ukrainczyk
Ivan Gabrijel	Mercedes Sanchez Moreno	Mateusz Wyrzykowski
Erez Gal	Ryoichi Sato	Guang Ye
Dariusz Gawin	José Sena-Cruz	Ismail Yurtdas
Ole Jensen	Dirk Schlicke	Xiangming Zhou
Joachim Juhart	Geert De Schutter	Mariusz Zych
Terje Kanstad	Giuseppe Sciumè	

## Preface

The focus of the conference is set to communicating, discussing and arousing progress in research, development and application of Cement-based Materials and Structural Concrete, which have been attained through combination of expertise from distinct fields of knowledge. Indeed, in the words of Federico Capasso, a renowned Physicist who was one of the inventors of the quantum cascade laser:

*“... we must not think of science in a disciplinary way, by making boxes. Nature does not know what physics, chemistry or biology is! It is a question of putting an end to the positivist philosophy of Auguste Comte, fortunately in decline of speed, which classified the disciplines and despised the experimental activity.”*

The intent of this conference was therefore to provide added value through collaboration and by bringing together researchers and practitioners with similar views in regard to interdisciplinary approaches in the fields of Cement-based Materials and Structural Concrete: it is about **Synergizing** expertise on the ultimate goal of Structural Conc**Crete**, hence the acronym **SynerCrete**, was chosen for the conference. Exciting fields of research such as performance-based design, 3D modelling for analysis/design, Building Information Modelling and even robotics (e.g. digital fabrication or robotics design) were included, while retaining focus on multi-scale approaches at time and spatial levels.

SynerCrete'18 also marks the end of COST Action TU1404 “Towards the next generation of standards for service life of cement-based materials and structures” ([www.tu1404.eu](http://www.tu1404.eu)), offering a final forum to the discussions raised during the funded period of the Action, that started 4 years ago in 2014. The conference is an opportunity for the 304 COST Action members to deepen their collaboration and to focus on activities that allow the continuation of the networking which was established by the Action. A sense of accomplishment is felt by all the members of the Action, in the view of the important achievements of networking tools that were brought about by the extended Round Robin Testing Programme (RRT+), the Numerical Benchmarking Activities and 24 Short Term Scientific Missions (STSMs). Indeed, a remarkable number of papers that have been published in the two volumes of these Conference Proceedings are directly a result of one of the aforementioned networking tools.

The conference has consisted of 8 key-note speakers and 180 regular papers presented over 3 days. It is also relevant to emphasize the collaboration of another COST Action in SynerCrete: COST Action CA15202 “Self-healing As preventive Repair of CONcrete Structures – SARCOS”, which has an important contribution to the purposes of COST TU1404.

A further remark in regard to the wide international institutional support that this conference attained, is about the direct support of RILEM, fib, JCI and ACI. Specifically, with regard to the Japanese Concrete Institute, a mention is given to the special session dedicated to the most recent version of “JCI Guidelines for Control of Cracking of Mass Concrete”, as it was indeed one of the most inspiring documents that influenced the genesis of COST Action TU1404.



A final word is given in regard to the location of the conference which combines implicit symbolisms. Firstly, this is the only event of COST Action TU1404 taking place in Portugal, which is the home country of the Grant Holder and Chairman of the Action. Secondly, the conference venue is the island of Madeira, therefore not in mainland Portugal, putting attention to one of the remotest regions of Europe, officially classified as one of the eight ultra-peripheral regions of the European Union.

**Miguel Azenha     Dirk Schlicke     Farid Benboudjema     Agnieszka Jędrzejewska**

October 2018, Funchal, Portugal

## Acknowledgements

This publication is based upon work from COST Action TU1404 ‘Towards the next generation of standards for service life of cement-based materials and structures’, supported by COST (European Cooperation in Science and Technology).

COST (European Cooperation in Science and Technology) is a pan-European intergovernmental framework. Its mission is to enable break-through scientific and technological developments leading to new concepts and products and thereby contribute to strengthening Europe’s research and innovation capacities. It allows researchers, engineers and scholars to jointly develop their own ideas and take new initiatives across all fields of science and technology, while promoting multi- and interdisciplinary approaches. COST aims at fostering a better integration of less research intensive countries to the knowledge hubs of the European Research Area. The COST Association, an International not-for-profit Association under Belgian Law, integrates all management, governing and administrative functions necessary for the operation of the framework. The COST Association has currently 37 Member Countries.



Funded by the Horizon 2020 Framework Programme  
of the European Union

[www.tu1404.eu](http://www.tu1404.eu)  
[www.cost.eu](http://www.cost.eu)

**VOLUME 1**

**KEYNOTE LECTURES**

INNOVATION IN RESEARCH ON NEW BINDERS John Provis	3
UNDERSTANDING OF MATERIAL DEPENDENT STRUCTURAL BEHAVIOR FOR AGING MANAGEMENT OF CONCRETE STRUCTURES Ippei Maruyama	11
INNOVATIVE WAYS IN CONDITION ASSESSMENT OF CONCRETE BRIDGE DECKS: DATA COLLECTION USING ROBOTICS, AND ADVANCED DATA INTERPRETATION AND VISUALIZATION Nenad Gucunski, Jinyoung Kim, Kien Dinh, Jie Gong, Fei Liu, Seong-Hoon Kee, Basily Basily	21
DEMONSTRATION PROJECTS WITH SELF-HEALING CAPSULE-BASED AND BACTERIA- BASED CONCRETE Nele De Belie, Maria Araujo, Tim Van Mullem, Elke Gruyaert	29
 <b>COST ACTION TU1404 - RRT+, NUMERICAL BENCHMARKING AND RECOMMENDATIONS</b>	
COMPILED COST ACTION RRT+ RESULTS FROM NTNU: DETERMINATION OF PARAMETERS REQUIRED FOR EARLY AGE CRACK ASSESSMENT Anja Estensen Klausen, Terje Kanstad, Emmanuel Rozière	41
MECHANICAL PROPERTIES OF CEMENT BASED MATERIALS – EXTENDED ROUND ROBIN TEST OF COST ACTION TU 1404 Violeta Bokan Bosiljkov, Marjeta Kramar Fijavž, Marijana Serdar	47
STRENGTH AND ELASTIC PROPERTIES OF CEMENT BASED MATERIALS – CONTRIBUTION OF UNIVERSITY OF LJUBLJANA TO THE RRT+ OF COST ACTION TU 1404 Martin Klun, Lucija Strmšek, Violeta Bokan Bosiljkov	55
VOLUME STABILITY OF CEMENT-BASED MATERIALS: ROUND-ROBIN TESTING WITHIN COST ACTION TU1404 Emmanuel Roziere, Marijana Serdar, Stéphanie Staquet, Dirk Schlicke, Miguel Azenha, Ahmed Zakarya Bendimerad, Brice Delsaute, Vinciane Dieryck, Jacek Gołaszewski, José Granja, Terje Kanstad, Anja Klausen, Zhenming Li, Elica Marušić, Martina Pezer, Antonio Ribeiro, Sofia Ribeiro, Aljoša Šajna, François Toutlemonde, Guang Ye, Behzad Zahabizadeh	61
BENCHMARK NUMERICAL SIMULATION IN MICRO-LEVEL WITHIN THE COST ACTION 1404 Peng Gao, Hua Dong, Jiayi Chen, Guang Ye	67
COMPARISON BETWEEN THE EXPERIMENTAL MEASUREMENT RESULTS AND THE MICROMECHANICAL MODELLING ON THE AGEING BASIC CREEP OF VERCORS CONCRETE Shun Huang, Julien Sanahuja, Luc Dormieux, Benoit Bary, Eric Lemarchand, Laurent Charpin, Romain Thion	73
MACROSCOPIC HYGRO-MECHANICAL MODELING OF RESTRAINED RING TEST - RESULTS FROM COST TU1404 BENCHMARK Vít Šmilauer, Tobias Gasch, Arnaud Delaplace, David Bouhjiti, Fragkoulis Kanavaris, Miguel Azenha, Laurie Lacarrière	79
BACKGROUND FOR A NEW EUROCODE 2-ANNEX: EVALUATION OF EARLY-AGE AND LONG-TERM CRACKING DUE TO RESTRAINED DEFORMATIONS Terje Kanstad, Anja Klausen	85

**CONCRETE TECHNOLOGY AND ADVANCED MATERIAL TESTING**

A CONCRETE HOME FOR MARINE MICRO INHABITANTS Atteyeh S. Natanzi, Ciaran McNally	93
AMINO-ALCOHOLS AS CORROSION INHIBITORS AGAINST SULPHATE-INDUCED CORROSION OF MILD STEEL REINFORCEMENT IN FRESH CALCIUM SULPHOALUMINATE BASED CEMENTITIOUS MATERIALS: PRELIMINARY STUDIES Yegor Morozov, Simone Pellegrini, Sergio Lorenzi, Fátima Montemor	99
ASPECTS OF ACTIVATED FLY ASH: A COMPARATIVE STUDY OF DIFFERENT MECHANICAL TREATMENTS Alexander Mezhov, Ursula Pott, Dietmar Stephan, Konstantin Kovler	105
ASSESSMENT OF INTERNAL RELATIVE HUMIDITY AND TEMPERATURE OF CEMENT- BASED MATERIALS – PARALLEL STUDY USING TWO SENSOR SYSTEMS Martin Klun, Violeta Bokan Bosiljkov, Samo Beguš, Slaven Ranogajec, Zvonko Jagličić	111
CARBONATION RESISTANCE OF HIGH-VOLUME FLY ASH (HVFA) MORTAR: EFFECT OF APPLIED CO <sub>2</sub> CONCENTRATION Philip Van den Heede, Didier Snoeck, Tim Van Mullem, Nele De Belie	117
CHARACTERISATION OF CONCRETE PUMPING BEHAVIOUR Egor Secieru, Viktor Mechtcherine	123
CHLORIDE DIFFUSION RESISTANCE OF LIMESTONE CALCINED CLAY CEMENT (LC3) CONCRETE Quang Dieu Nguyen, Mohammad Khan, Arnaud Castel	129
COMPARISON OF STANDARD CONCRETE AND ECO-CONCRETE IN RESPECT TO TECHNICAL, ENVIRONMENTAL AND DURABILITY PERFORMANCE Joachim Juhart, Rok Bregar, Gheorge David, Markus Krüger	135
COMPRESSIVE STRENGTH DEVELOPMENT OF FLY ASH CONCRETES CURED UNDER DIFFERENT CONDITIONS Tayfun Altuğ Söylev, Turan Özturan	141
DEVELOPMENT OF A HEATING MORTAR BLOCK SYSTEM FOR SNOW MELTING THROUGH QUASI MICROWAVES Yosuke Ito, Shinji Kawabe	147
DURABILITY PROPERTIES OF AUTOCLAVED AERATED AND HIGH PERFORMANCE FOAMED CONCRETE Genadijs Sahmenko, Aleksandrs Korjakins, Eva Namsone	153
EFFECT OF INITIAL CURING ON CORROSION BEHAVIOR ON STEEL BARS IN FA CONCRETE UNDER DRY AND WET ACTIONS Wakako Sugino, Keiyuu Kawai, Isao Ujike	159
EFFECT OF MARBLE POWDER WASTE ON THE PROPERTIES OF SELF COMPACTING CONCRETE Ali M. Mansor, Asaad A. Elshab, Ruben P. Borg, Ahmed M. M. Hamed	165
ESTIMATING THE STRESS DEVELOPMENT IN EARLY AGE CONCRETE WITH MINERAL ADDITIONS FROM COUPLED MEASUREMENTS Jérôme Carette, Brice Delsaute, Stéphanie Staquet	171
EVALUATION OF STRENGTH OF REINFORCED CONCRETE SLABS OPERATING UNDER THE CHANGING WATER LEVEL Raimondas Šadzevičius, Rosita Norvaišienė, Edita Smetonaitė	177

SynerCrete'18 International Conference on Interdisciplinary Approaches  
for Cement-based Materials and Structural Concrete  
24-26 October 2018, Funchal, Madeira Island, Portugal

EXPERIMENTAL INVESTIGATION OF ACCELERATORS IN FLOOR CONCRETE MIXTURE UNDER COLD CLIMATIC CONDITIONS Themistoklis Tsalkatidis, Even Solbraa	183
EXPERIMENTAL INVESTIGATION OF NEW CEMENT COMPOSITES LONG-TERM PROPERTIES Andina Sprince, Leonids Pakrastinsh, Liga Radina	189
EXPERIMENTAL PROCEDURES FOR DETERMINING THE LEVEL OF SEGREGATION OF LIGHTWEIGHT CONCRETES Afonso Miguel Solak, Antonio José Tenza-Abril, Francisco Baeza-Brotons, Victoria Eugenia García-Vera, Marcos Lanzón	195
EXPOSITION TO ACID ATTACK OF MORTARS WITH NANOSILICA, ZINC STEARATE AND ETHYL SILICATE COATING Victoria García-Vera, Antonio Tenza-Abril, Marcos Lanzón, Afonso Miguel Solak	201
GAS DIFFUSION IN CEMENTITIOUS MATERIALS: TEST METHODS REVIEW Fabien Gendron, Mouna Boumaaza, Philippe Turcry, Bruno Huet, Abdelkarim Aït-Mokhtar	207
HEAT OF HYDRATION OF TERNARY-, QUATERNARY-BLENDED CEMENTS Arnaud Delaplace, Denis Garcia, Marie Bayle, Quentin Favre-Victoire	213
HYDRATION PROCESS OF NATURAL HYDRAULIC LIME BLENDED CEMENT MORTARS Reda Jaafri, Emmanuel Rozière, Syed Yasir Alam, Ahmed Loukili	219
IMPROVEMENT OF MICROWAVE ABSORPTION CHARACTERISTICS BY SINTERING SLAG AS AGGREGATE Haruki Taguchi, Yosuke Ito, Shinji Kawabe	225
INFLUENCE OF RECYCLED AGGREGATE AND RECYCLED SAND ON THE DEVELOPMENT OF THE EARLY AGE PROPERTIES OF CONCRETE SINCE SETTING Brice Delsaute, Stéphanie Staquet	231
INFLUENCE OF SELECTED FACTORS ON UNCERTAINITY OF RHEOLOGICAL MEASUREMENT OF FRESH MORTARS Jacek Gołaszewski, Grzegorz Cygan, Małgorzata Gołaszewska	237
INFLUENCE OF THE MIXTURE COMPOSITION OF CEMENTITIOUS PASTES WITH OPTIMIZED PACKING DENSITY ON SETTING AND HARDENING STUDIED BY ULTRASOUND INVESTIGATION Markus Krüger, Rok Bregar, Gheorghe Alexandru David, Joachim Juhart	243
INFLUENCE OF UGANDAN VOLCANIC SCORIA AS AGGREGATES IN CONCRETE Stephen O. Ekolu, Kgashane T. Moila, Mikaash Bhagwager, Harry Quainoo	249
INVESTIGATION, ASSESSMENT AND REALTIME READJUSTMENT OF THE RHEOLOGICAL PROPERTIES OF SELF COMPACTING CONCRETE Ivan Parić, Wolfgang Kusterle	255
MACRO- AND MICRO-STRUCTURE EVALUATIONS OF RECYCLED POST-CONSUMER GLASS CEMENTITIOUS MATERIAL FOR CONCRETE Marija Krstic, Julio F. Davalos	261
MONITORING FRESH CEMENTITIOUS MATERIAL BY DIGITAL IMAGE CORRELATION (DIC) Evin Dildar Dzaye, Geert De Schutter, Dimitrios Aggelis	267

NEW INSIGHTS ON THE SEGREGATION DUE TO MANUFACTURE CONDITIONS OF LIGHTWEIGHT AGGREGATE CONCRETES Afonso Miguel Solak, Antonio José Tenza-Abril, Francisco Baeza-Brotons, Victoria Eugenia García-Vera, Marcos Lanzón	273
PARTICLE-MATRIX PROPORTIONING OF HIGH STRENGTH LIGHTWEIGHT AGGREGATE CONCRETE Elisabeth Leite Skare, Jelena Zivkovic, Stefan Jacobsen, Jan Arve Øverli	279
PHOTOCATALYTIC NOVEL CONCRETE MATERIAL APPLICATION AND ITS LIFE TIME STANDARD TESTING František Peterka	285
PHYSICAL EVOLUTION OF THE INTERFACE OF FRESH CONCRETE/FORMWORK FROM PLACEMENT TO SETTING TIME Typhanie Craipeau, Arnaud Perrot, Fabrice Toussaint, Thibaut Lecompte	291
PROPERTIES OF CEMENT WITH INCREASED LITHIUM CONTENT Theodor Staněk, Alexandra Rybová, Anežka Zezulová, Martin Boháč	297
PROPOSAL OF A TEST SETUP FOR SIMULTANEOUS APPLICATION OF AXIAL RESTRAINT AND VERTICAL LOADS TO SLAB-LIKE SPECIMENS: SIZING PRINCIPLES AND APPLICATION José Gomes, Miguel Azenha, José Granja, Rui Faria, Carlos Sousa, Behzad Zahabizadeh, Ali Edalat-Behbahani, Dirk Schlicke	303
RESISTANCE TO SULFATE AND ACID ATTACK OF SELF-COMPACTING CONCRETE WITH RECYCLED AGGREGATES Said Kenai, Mohamed Omrane	309
SELF-COMPACTING CONCRETE WITH RECYCLED CONCRETE AGGREGATE AS ECOLOGICAL MATERIAL Iva Despotovic, Ksenija Jankovic, Dragan Bojovic, Marko Stojanovic	315
STANDARD AND INNOVATIVE CHARACTERIZATION OF STRENGTH, STIFFNESS, AND NON-AGING CREEP OF CONCRETE AT EARLY AGES Mario Ausweger, Eva Binder, Olaf Lahayne, Roland Reihnsner, Gerald Maier, Martin Peyerl, Bernhard Pichler	321
STRESS DISTRIBUTION IN RESTRAINED RING TEST DUE TO DRYING AND AUTOGENOUS SHRINKAGE Semion Zhutovsky	327
STUDY ON CHARACTERISTICS OF TENSILE STRENGTH OF CONCRETE CONSIDERING TEMPERATURE DEPENDENCE IN MASS CONCRETE STRUCTURES Hiroki Izumi, Jun-ichi Arai, Toshiaki Mizobuchi	333
SULPHATE-INDUCED CORROSION OF STEEL REINFORCEMENT IN FRESH CALCIUM SULPHOALUMINATE BINDERS: PRELIMINARY STUDIES Yegor Morozov, Simone Pellegrini, Sergio Lorenzi, Fátima Montemor	339
THE DEVELOPMENT OF THE EARLY-AGE ELASTIC MODULUS IN CEMENT-MATERIALS WITH DIFFERENT WATER COEFFICIENT Romana Halamová, Dalibor Kocáb, Barbara Kucharczyková, Petr Daněk	345
THE USE OF ACOUSTIC METHODS TO DESCRIBE THE BEHAVIOUR OF CEMENT PASTES IN THE EARLY STAGE OF AGEING Michaela Hoduláková, Libor Topolář, Barbara Kucharczyková, Dalibor Kocáb	351

TIME DEPENDENT OF YOUNG'S MODULUS OF CONCRETE IN VERY EARLY AGE Tatsuya Usui, Takeda Hitoshi, Hiroshi Murata, Takuya Tani	357
UTILISING EXCAVATED ROCK MATERIAL FROM TUNNEL BORING MACHINES (TBMS) FOR CONCRETE Torjus Berdal, Pål Drevland Jakobsen, Stefan Jacobsen	363
WATER ABSORPTION CHANGES IN MORTARS WITH CRYSTALLINE ADMIXTURE EXPOSED TO ACID ENVIRONMENT Victoria Eugenia García-Vera, Antonio José Tenza-Abril, Marcos Lanzón, Afonso Miguel Solak, Concepción Pla, David Benavente	369
X-RAY MICROTOMOGRAPHIC IMAGES OF FIBRE CONCRETE COMPOSITES FABRICATED USING DIFFERENT METHODS Zbigniew Ranachowski, Marcin Lewandowski, Krzysztof Schabowicz, Tomasz Gorzelańczyk, Stanislav Kudela Jr, Tomas Dvorak	375
<b>GEOPOLYMERS AND ALKALI-ACTIVATED MATERIALS</b>	
ACOUSTIC EMISSION PARAMETERS OF ALKALI ACTIVATED FLY ASH SPECIMENS WITH HEMP FIBRES UNDER STATIC LOADING Libor Topolář, Hana Šimonová, Barbara Kucharczyková	383
ALKALI ACTIVATED MATERIALS: REVIEW OF CURRENT PROBLEMS AND POSSIBLE SOLUTIONS Adeyemi Adesina	389
ALKALI-ACTIVATED BLEND OF CALCINED LATERITIC SOIL AND WASTE MARBLE SLURRY Luca Valentini, Ludovico Mascarin, Enrico Garbin, Maria Chiara Dalconi	395
CHARACTERIZATION OF THE SELF-HEALING EFFECT THROUGH PORE STRUCTURE AND DURABILITY OF ALKALI-ACTIVATED CEMENT CONCRETE Pavel Krivenko, Igor Rudenko, Oleh Petropavlovskiy, Oles' Lastivka	401
DURABILITY OF CALCIUM SULFOALUMINATE – PORTLAND CEMENT BLENDS Gultekin Ozan Ucal, Mehmet Kemal Ardoga, Melike Sucu, Tughan Delibas, Ismail Ozgur Yaman	407
EARLY-AGE CRACKING TENDENCY OF ALKALI-ACTIVATED SLAG BINDERS COMPARED TO ORDINARY PORTLAND CEMENT Farah Rifai, Aveline Darquennes, Benoist Muzeau, Lavinia Stefan, Farid Benboudjema	413
EFFECT OF BAUXITE CONTENT AND FINENESS ON COMPRESSIVE STRENGTH OF VOLCANIC ASH-BASED GEOPOLYMER MORTARS Léonel N. Tchadjié, Stephen O. Ekolu	419
EFFECT OF COMPACTING PRESSURE AND CARBONATION DURATION ON CARBON DIOXIDE ACTIVATED BINDERS. Pedro Humbert, João Castro Gomes	425
EFFECT OF GREEN ACTIVATORS ON THE PROPERTIES OF ALKALI ACTIVATED MATERIALS: A REVIEW Adeyemi Adesina	431
EFFECT OF TEMPERATURE ON RHEOLOGICAL PROPERTIES OF ALKALI ACTIVATED BRICK POWDER BASED PASTES Martin Vyšvařil, Pavla Rovnaníková	437

EXPERIMENTAL STUDY OF THE CHEMICAL DEFORMATION OF METAKAOLIN BASED GEOPOLYMER Zhenming Li, Guang Ye	443
FLEXURAL BEHAVIOR AND STRENGTHENING OF GEOPOLYMER CONCRETE BEAMS REINFORCED WITH GFRP BARS USING CRPP SHEETS Abdalla Elbana, M Talha Junaid, Salah Altoubat	449
HYBRID ALKALI-ACTIVATED PORTLAND CEMENTS Lukáš Kalina, Vlastimil Bílek Jr., Lada Bradová, Radoslav Novotný, Tomáš Opravil, František Šoukal	455
INFLUENCE OF SODIUM HYDROXIDE CONCENTRATION ON MECHANICAL PARAMETERS OF FLY ASH-BASED GEOPOLYMER Natalia Paszek, Marcin Górski	461
INVESTIGATION ON STRENGTH DEVELOPMENT IN GEOPOLYMER MADE OF POWER PLANT FLY ASH SUSPENSION Szymon Dawczyński, Anita Kajzer, Marcin Górski	467
SELF-SENSING PROPERTIES OF ALKALI-ACTIVATED SLAG COMPOSITE WITH CARBON NANOTUBES Pavel Rovnaník, Míková Maria, Ivo Kusák, Pavel Schmid, Libor Topolář	473
SOLIDIFICATION/STABILIZATION OF PORT SEDIMENTS CONTAMINATED BY HEAVY METALS AND TBT USING SLAG-BASED BINDERS Tanya Gutsalenko, Alexandra Bourdot, Peter Seymour, Laurent Frouin, Mohend Chaouche	479
<b>BIO-BASED MATERIALS</b>	
ALGANITE-BACILLUS SUBTILIS BASED REPAIR MATERIALS FOR SEALING CRACKS IN CONCRETE Masahiko Ide, Keiyuu Kawaai, Isao Ujike	487
EFFECT OF ANISOTROPY ON THERMAL AND HYGRIC PROPERTIES OF HEMP COMPOSITE Florence Collet, Sylvie Pretot, Brahim Mazhoud, Christophe Lanos	493
EVALUATION OF THE POTENTIAL OF CORN AND SUNFLOWER BARK PARTICLES AS BIO-AGGREGATES FOR LIGHTWEIGHT CONCRETE Alexandra Bourdot, Camille Magniont, Méryl Lagouin, Guillaume Lambaré, Laurent Labonne, Philippe Evon	499
EVOLUTION OF HEMP CONCRETE PROPERTIES EXPOSED TO DIFFERENT TYPES OF ENVIRONMENTS Guillaume Delannoy, Sandrine Marceau, Philippe Glé, Etienne Gourlay, Marielle Guéguen-Minerbe, Sofiane Amziane, Fabienne Farcas	505
INFLUENCE OF FILLER EFFECT AND POZZOLANIC REACTION OF BIOMASS ASHES ON MECHANICAL PROPERTIES OF CEMENT MORTARS Vlastimir Radonjanin, Mirjana Malešev, Slobodan Šupić, Miroslava Radeka	511
IN-PLANE RACKING STRENGTH OF TIMBER WALLS FILLED WITH HEMP CONCRETE Husam Wadi, Sofiane Amziane, Evelyne Toussaint, Mustapha Taazount	517
LIFE CYCLE ASSESSMENT OF BIO-BASED CONSTRUCTION PANELS WITH MAGNESIUM BINDER Maris Sinka, Aleksandrs Korjakins, Diana Bajare, Genadijs Sahmenko	523

MARKET POTENTIAL OF WOOD BIOMASS ASH UTILISATION IN CEMENT COMPOSITIES - CROATIAN CASE STUDY	529
Nina Štirmer, Ivana Carević, Bojan Milovanović, Ana Baričević	
MECHANICAL PERFORMANCE, SHRINKAGE AND WEATHERING OF TREATED HEMP CONCRETE	535
Mohammed Sonebi, C. Sentenac, Sofiane Amziane	
MECHANICAL PREDICTION OF W.C.C. PROPERTIES: EXPERIMENTAL STUDY AND ANALYTICAL MODELING	541
Jean Gérard Ndong Engone, Ahmed El-Moumen, Chafika Djelal, Abdellatif Imad, Yannick Vanhove	
RISK ASSESSMENT OF MOLD GROWTH IN HEMP CONCRETE	547
Dmytro Kosiachevskiy, Kamilia Abahri, Mohend Chaouche, Evelyne Prat, Anne Daubresse, Cécile Bousquet	

## **VOLUME 2**

### **MULTI-PHYSICS SIMULATION AND STRUCTURAL DESIGN**

CONCRETE CASTING AND LIFETIME CONDITIONS IMPACT ON HIGH TEMPERATURE RESISTANCE	555
Giuseppe Sciumè, Stefano Dal Pont, Dorjan Dauti	
DAMAGE INVESTIGATION AND ANALYTICAL INVESTIGATION OF PILOTIS-TYPE RC BUILDING IN THE 2016 KUMAMOTO EARTHQUAKE	561
Masaru Shimazu	
EFFECT OF HUMIDITY AND ELEVATED TEMPERATURE ON THE MECHANICAL BEHAVIOR OF CONCRETE	567
Laurie Lacarrière, Ponleu Chhun, Alain Sellier	
EFFECT OF PARTIAL RESTRAINING CONDITIONS AND POISSON'S RATIO IN BOTTOM-RESTRAINED WALLS	573
Dirk Schlicke, Lýdia Matiašková, Július Šoltész	
GAMMA AND X RADIATION ABSORPTION CHARACTERISTICS OF SPECIALLY SELECTED TYPES OF CONCRETE	579
Srboljub Stankovic, Ksenija Jankovic	
HYDRO-MECHANICAL MODELLING OF SELF INDUCED STRESSES: IMPACT OF DRYING GRADIENTS ON DAMAGE	585
Francois Soleilhet, Farid Benboudjema, Xavier Jourdain, Fabrice Gatuingt	
NUMERICAL MODELING OF POROUS MEDIA FREEZING PROCESS BY MEANS OF A NON-EQUILIBRIUM APPROACH	591
Dariusz Gawin, Francesco Pesavento	
NUMERICAL SIMULATION OF THE EARLY-AGE CONCRETE BEHAVIOUR OF AN ARCH DAM	597
Noemí Leitão, Eloísa Castilho	
NUMERICAL STUDY OF CHLORIDE INGRESS IN CONCRETE: EFFECT OF EXPOSURE CONCENTRATION	603
Mohamad Achour, Ouali Amiri, François Bignonnet, Emmanuel Rozière, Mahdi Haidar	



PARAMETRIC STUDY OF THE MINIMUM REQUIRED REINFORCEMENT FOR CRACKING CONTROL IN THICK RESTRAINED RC MEMBERS BASED ON THERMO-HYGRO-MECHANICAL FE ANALYSES	609
Carlos Sousa, Miguel Azenha, Cláudio Ferreira, Rui Faria	
PARAMETRIC STUDY ON DAMAGES AND STRENGTH BEHAVIOURS OF POST-TENSIONED GIRDERS IN DECHATIWONG BRIDGES	615
Nat Hanwiboonwat, Tidarut Jirawattanasomkul, Songpol Charuvisit, Nattamet Wuttiwannasak, Nuttapon Kongwang, Chinapat Banluelap, Tawan Norsakul	
PARAMETRIC STUDY ON DAPPED-END OF PRESTRESSED CONCRETE GIRDER IN DECHATIWONG BRIDGE USING FINITE ELEMENT ANALYSIS	621
Nuttapon Kongwang, Tidarut Jirawattanasomkul, Wanakorn Prayoonwet, Songpol Charuvisit	
PREDICTION OF THE IMPACT OF SHRINKAGE ON CONCRETE STRENGTH WITH THE BEAM-PARTICLE APPROACH	627
Nicolas Chan, Cécile Oliver-Leblond, Farid Benboudjema, Frédéric Ragueneau, Francois Soleilhet	
THERMOMECHANICAL MODELLING FOR THE ESTABLISHMENT OF A NEW BUILDING METHOD FOR BASEMENTS OF CONVENTIONAL HOUSINGS	633
Dirk Schlicke, Thomas Hochgatterer, Martin Zabern, Alexander Glebe, Alexander Reinisch	
<b>MULTI-SCALE IN TIME AND SPACE MODELLING AND EXPERIMENTS</b>	
A NEW CREEP TEST METHOD FOR REINFORCED CONCRETE TENSION MEMBERS UNDER CONSTANT LOADING	641
Eugenijus Gudonis, Pui-Lam Ng, Shao-Hua Chu, Aleksandr Sokolov	
AN EXPERIMENT-BASED FE APPROACH TO ANALYZE EARLY-AGE TEMPERATURE AND STRAIN DISTRIBUTION IN LARGE-DIMENSION CONCRETE WALL	647
Yan Geng, Suduo Xue, Xiongyan Li, Jinguang Li	
ASSESSING THE CO <sub>2</sub> -BINDING OF CONCRETE DURING ITS SERVICE LIFE	653
Andreas Leemann, Fritz Hunkeler, Heiner Widmer	
CREEP PROPERTIES OF POLYMER PARTICLES IN POLYMER-MODIFIED CEMENT PASTES, QUANTIFIED BY MEANS OF MULTISCALE MODELING	659
Luise Göbel, Markus Königsbeger, Andrea Osburg, Bernhard Pichler	
DEVELOPMENT OF PORE-SCALE MODEL FOR INGRESS OF CO <sub>2</sub> BRINE THROUGH CEMENT PASTE	665
Ravi A. Patel, Nikolaos Prasianakis	
EARLY AGE MECHANICAL PROPERTIES AND SHRINKAGE OF BLENDED CEMENT CONCRETE CONTAINING SLAG	671
Tahsin Alper Yikici, Egemen Kesler, Yılmaz Akkaya	
EARLY-AGE EVOLUTION OF ELASTIC STIFFNESS AND COMPRESSIVE STRENGTH OF RECYCLED CONCRETE: INSIGHTS FROM MULTISCALE MICROMECHANICS MODELING	677
Markus Königsberger, Stéphanie Staquet	
EFFECT OF HIGH TEMPERATURE AT EARLY AGE ON INTERFACIAL TRANSITION ZONE AND MATERIAL PROPERTIES OF CONCRETE	683
Shingo Asamoto, Ryosuke Yuguchi, Isao Kurashige, Pang-jo Chun	

EFFECT OF THE MATURATION PRESSURE ON MECHANICAL AND HYDRAULIC PROPERTIES OF OILWELL CEMENT PASTE Issam Takla, Nicolas Burlion, Jian-Fu Shao, Thomas Rougelot	689
ESTIMATION OF SETTING TIME IN CONCRETE THROUGH MODELLING OF ULTRASONIC PARAMETERS Ivan Gabrijel, Mario Pintar	695
EULERIAN TWO-PHASE COMPUTATIONAL FLUID DYNAMICS MODEL OF A CONCRETE SCREW MIXER Nicolò Beccati, Cristian Ferrari	701
FROM DISORDERED TO ORDERED PACKINGS: A NEW PACKING MODEL FOR UHPC? Gerard Roquier	707
HOW DOES THE SIZE OF AGGREGATES AFFECT PERMEABILITY OF DAMAGED CONCRETE? Marta Choinska, Stéphanie Bonnet, Aurélie Fabien, Hayder Al-Khazraji, Abdelhafid Khelidj	713
IMPACT OF DRYING RATE ON DELAYED STRAINS IN CEMENT-BASED MATERIALS Justin Kinda, Laurent Charpin, Jean-Luc Adia, Farid Benboudjema, Sylvie Michel-Ponnelle	719
INFLUENCE OF THE FLEXIBILITY OF CALCIUM SILICATE HYDRATES LAYERS ON THE MESOTEXTURE: COARSE GRAINED SIMULATIONS ACCOUNTING FOR THREE-BODY INTERACTIONS Tulio Honorio	725
INTERACTIONS BETWEEN CRYSTALLINE CALCIUM SILICATE HYDRATES: GRAND CANONICAL SIMULATION OF PRESSURE AND TEMPERATURE EFFECTS Tulio Honorio	731
MICROSTRUCTURAL CHARACTERISATION OF CEMENT-BASED MATERIALS (CBM) USING THE NUMERICAL SIMULATION OF ULTRASONIC PROPAGATION José Vicente Fuente, Sreejith Nanukuttan, Jorge Gosalbez, Neil Campbell	737
MICROSTRUCTURE-BASED PREDICTION OF THERMAL PROPERTIES OF CEMENT PASTES AT EARLY AGES Hadi Mazaheripour, Amin Abrishambaf, Rui Faria, Miguel Azenha, Ye Guang	743
MULTI-SCALE MODELING AND NON DESTRUCTIVE TESTING: ASSESSING WATER CONTENT OF CONCRETE Vincent Guihard, Jean-Luc Adia, Julien Sanahuja	749
NUMERICAL ANALYSIS OF THE DRYING KINETICS IN 3D CONCRETE SPECIMENS OF DIFFERENT SIZE Benoit Bary, Stéphane Poyet	755
NUMERICALLY ACCELERATED CHEMICAL EVOLUTION IN CEMENTITIOUS SYSTEMS Janez Perko, Diederik Jacques	761
PARTICLE MODEL FOR THE PREDICTION OF LONG-TERM DEFORMABILITY PROPERTIES OF DAM CONCRETE Carlos Serra, Nuno Monteiro Azevedo, António Lopes Batista	767
SCALE EFFECT ON ALKALI-SILICA REACTION Jacques Jabbour, Aveline Darquennes, Loic Divet, Rachid Bennacer, Jean-Michel Torrenti, Georges Nahas	773

SMALL SCALE FRACTURE PROPERTIES OF CEMENT PASTE AND ALKALI-ACTIVATED FLY ASH	779
Jiri Němeček, Jitka Němečková, Jiri Němeček, Jan Maňák	
STRUCTURAL PERFORMANCE OF REINFORCED CONCRETE SLAB SUBJECTED TO FIRE AND EXPLOSION	785
Jianpeng Shu, Terje Kanstad, Max Hendriks, Jan Arve Øverli, Assis Barenys	
THE IMPACT OF C-S-H NANOSTRUCTURE ON AUTOGENOUS SHRINKAGE AND SORPTION ISOTHERMS	791
Enrico Masoero, Giovanni Di Luzio, Gianluca Cusatis	
<b>BIM AND STRUCTURAL CONCRETE</b>	
BIM FOR PRECAST	799
Peter Karlsson	
COST-OPTIMAL ANALYSIS OF CONCRETE SOLUTIONS FOR SINGLE-FAMILY NZEBs APPLYING AN OPEN BIM WORKFLOW	805
Afonso Solak, Javier Pereiro-Barceló	
INTEGRATED APPLICATION OF ADVANCED SURVEYING TECHNIQUES AND BIM FOR INSPECTION AND ASSET MANAGEMENT OF REINFORCED CONCRETE BRIDGES	811
Miguel Azenha, Gabriel Sousa, José Matos, José Sena-Cruz, Vitor Brito	
STRUCTURAL DESIGN WITH OPENBIM: FROM THE ARCHITECTURAL MODEL TO THE STRUCTURAL ANALYSIS WITH A STATE-OF-THE-ART CALCULATION ENGINE	817
Javier Pereiro-Barceló, Afonso Miguel Solak	
THE ROAD TO SENSOR-DRIVEN CLOUD-BASED INFRASTRUCTURE MANAGEMENT	823
Carlos Gil Berrocal, Ignasi Fernandez, Rasmus Rempling	
<b>DIGITAL FABRICATION AND ROBOTICS</b>	
A 3D PRINTER OF CEMENT MORTARS BASED ON INITIAL DEPOSITION OF DRY MATERIALS	831
Miguel Azenha, Caetano Monteiro, Ricardo Morais	
RESEARCH AND DEVELOPMENT OF INFRASTRUCTURE DIAGNOSTIC ROBOT SYSTEM (ALP) BY CONCRETE WALL MOVING MECHANISM USING VACUUM SUCTION PAD	837
Junichiro Nojima, Toshiaki Mizobuchi	
THE ROLE OF VARIOUS AGGREGATES ON RHEOLOGY OF FRESH 3D PRINTING CONCRETE	843
Martin Boháč, Bohdan Nešpor, Theodor Staněk	
<b>ON-SITE MONITORING AND STRUCTURAL CONDITION ASSESSMENT</b>	
AN INVESTIGATION OF APPROPRIATE CURING REGIMES FOR PRECAST CONCRETE STRUCTURAL ELEMENTS WITH GGBS USING MATURITY FUNCTIONS	851
Fragkoulis Kanavaris, Marios Soutsos, Jian-Fei Chen, Sreejith Nanukuttan	

DETECTION, ASSESSMENT AND MONITORING OF COMMON ANOMALIES IN CONCRETE DAMS João Conde Silva	857
DETERIORATION DIAGNOSIS TECHNIQUE OF POLYMER CEMENT WATERPROOFING MEMBRANES BY DIFFERENCE IN THERMAL CHARACTERISTICS OF CONSTITUENT MATERIALS USING ACTIVE THERMOGRAPHY Masayuki Tsukagoshi, Hiroki Toyoda, Takao Ueda, Masashi Ishikawa	863
EVALUATION OF THE MATERIAL EMBEDDED IN CONCRETE BY ULTRASONIC AND GPR IMAGES Sofia Aparicio, José Vicente Fuente, Dalmay Lluveras, Miguel Angel García Izquierdo, Margarita González, José Javier Anaya Velayos	869
INCREASE CONCRETE QUALITY DURING DESIGN AND EXECUTION PHASE Stefan Scheuchelbauer, Massimo Maffezzoli, Alexander Reinisch	875
INSPECTION AND MAINTENANCE OF CONCRETE BRIDGES: INVESTIGATION OF MOST SIGNIFICANT DAMAGE MECHANISMS VS. LOCATIONS R.M. Chandima Ratnayake, Yousef Saad, Kamshan Karunaharan, Samindi M.K. Samarakoon	881
OVERVIEW ON THE MULTI-DECADE DATABASE OF PORTUGUESE LARGE CONCRETE DAMS MONITORING DATA António Tavares de Castro, José Barateiro, Carlos Serra	887
LOAD-BEARING PERFORMANCE SIMPLE EVALUATION SYSTEM OF RC ROAD BRIDGE DETERIORATED CAUSED BY SALT DAMAGE Hitoshi Ito, Toshiaki Mizobuchi	893
<b>SCIENTIFIC INSIGHTS VS. STANDARDIZATION</b>	
A COMPARISON OF TWO MAJOR APPROACHES USED FOR CONCRETE STRENGTH PREDICTION FOR DIFFERENT CONCRETE TYPES Seda Yesilmen, Sinan Kefeli	901
A SIMPLIFIED 1D STRESS APPROACH FOR CRACKING RISK PREDICTION Luis Ebensperger	907
EXPERIMENTAL SETUP FOR THE CHARACTERIZATION OF THE LONG TERM BOND AND CRACK WIDTHS IN RC TIES UNDER CONSTANT AXIAL FORCE Carlos Sousa, Mário Pimentel, Amin Abrishambaf, Rui Faria, Miguel Azenha	913
INFLUENCE OF CARBONATION AND CONCRETE SPECIMEN SIZE ON GAS DIFFUSION COEFFICIENT Mouna Boumaaza, Bruno Huet, Philippe Turcry, Christoph Gehlen, Abdelkarim Aït-Mokhtar, Detlef Heinz	919
INFLUENCE OF PRESTRESS LOSSES ON THE DYNAMIC OVER STATIC CAPACITY RATIOS OF RAILWAY CONCRETE SLEEPERS Chayut Ngamkhanong, Sakdirat Kaewunruen	925
THE INFLUENCE OF SLAG CHEMISTRY ON BLENDED CEMENTS MADE WITH IRON-RICH SLAG Vincent Hallet, Jos Denissen, Remus Iacobescu, Yiannis Pontikes	931

**FIBRE-REINFORCED CONCRETE AND NON-METALLIC REINFORCEMENT**

A NUMERICAL MODEL FOR PREDICTING CRACKING OF FIBRE REINFORCED CONCRETE RINGS IN RESTRAINED SHRINKAGE TEST Wei Dong, Xiaoyu Zhao, Xiangming Zhou, Wenyan Yuan	939
BRITTLINESS OF HIGH-STRENGTH LIGHTWEIGHT AGGREGATE CONCRETE Jelena Zivkovic, Mladena Lukovic, Jan Arve Øverli, Dick Hordijk	945
COST-OPTIMAL DESIGN OF FLEXURAL CONCRETE BEAM REINFORCED WITH FRP REINFORCEMENTS Sigbjørn Tveit, Martin Wilhelmsen, Vlad Aleksander Lundeland, Mahdi Kioumars	951
DURABILITY OF HEMP FIBRE REINFORCED CEMENTITIOUS MORTARS BY MEANS OF FIBRE PROTECTION AND CEMENT SUBSTITUTION WITH METAKAOLIN Bojan Poletanović, Katalin Kopecskó, Ildiko Merta	957
INFLUENCE OF MICRO-CRACKING ON CAPILLARY WATER ABSORPTION OF AN UHPFRC Ana Mafalda Matos, Sandra Nunes, José L. Barroso Aguiar	963
INFLUENCE OF THE ALKALINE TREATMENT ON THE TENSILE PROPERTIES OF JUTE FIBERS AND ON THE FIBER-MATRIX BONDING Yasmim Gabriela dos Santos Mendonça, Bartosz Zukowski, Romildo Dias Toledo Filho	969
NUMERICAL SIMULATION OF REINFORCED CONCRETE CUT-OFF WALL WITH STEEL FIBRES UNDER DAM Homa Kazemi, Mohammad Mahdi Kioumars, Mohsen Zarghani, Hamed Sarkardeh	975
PERFORMANCE OF RECYCLED AND COMMERCIAL FIBRE REINFORCED CONCRETE BEAMS IN COMBINED ACTION WITH CONVENTIONAL REINFORCEMENT Katerina Bernhoft, Samindi Samarakoon, Luis Evangelista, Bjarne Mikalsen	981
PROBABILISTIC NUMERICAL MODEL FOR DESIGNING STEEL FIBRE REINFORCED CONCRETE STRUCTURES Pierre Rossi, Jean-Louis Tailhan	987
RHEOLOGICAL BEHAVIOUR OF FLEXIBLE FIBER-REINFORCED CEMENTITIOUS MATERIALS Fariza Sultangaliyeva, Hélène Carré, Christian La Borderie, Nicolas Roussel	993
STRAIN HARDENING CHARACTERISTICS OF BLENDED ALKALI ACTIVATED BINDERS CURED AT AMBIENT TEMPERATURES M. Talha Junaid, Mohamed Maalej	999
STRAIN RATE EFFECT ON THE TENSILE BEHAVIOUR OF ULTRA-HIGH PERFORMANCE STEEL FIBER REINFORCED CONCRETE Veronika Goglin, Götz Hüsken, Hans-Carsten Kühne, H.J.H. Brouwers	1005
STRAIN RESILIENT CEMENTITIOUS COMPOSITES MADE WITH CALCAREOUS FLY ASH AND POLYPROPYLENE FIBERS: THE EFFECT OF TEMPERATURE AND FREEZE-THAW ON FLEXURAL TENSION Souzana Tastani, Ioannis Savvidis	1011
STUDY ON TEMPERATURE DEPENDENCE OF PROPERTIES OF HIGH STRENGTH MORTAR USING HIGH ALITE CEMENT AND FINE POZZOLANIC POWDER Hirokazu Kiriya, Eiji Maruya, Kenji Kawai, Ryoichi Sato	1017
TENSION STIFFENING MODEL FOR SERVICEABILITY ANALYSIS OF STEEL AND FRP REINFORCED CONCRETE BEAMS Gintaris Kaklauskas, Pui-Lam Ng, Aleksandr Sokolov	1023

USING INTELLIGENT SYSTEM APPROACH FOR SHEAR STRENGTH FORECASTING OF STEEL FIBER-REINFORCED CONCRETE BEAMS Ali Kheyroddin, Masoud Ahmadi, Mahdi Kioumars	1029
<b>SELF-HEALING AND REPAIR OF CONCRETE STRUCTURES (COST CA15202 - SARCOS)</b>	
A METHOD FOR INDUCING CONTROLLED CRACKS IN CONCRETE AND MEASURING THE EFFICIENCY OF SELF-HEALING AGENTS Amir Sidiq, Syed Adil Amzar Bin Syed Amerruddin, Rebecca Gravina, Sujeeva Setunge, Filippo Giustozzi	1037
A PRELIMINARY STUDY ON THE SELF-HEALING POTENTIAL OF BACTERIA-MODIFIED FIBERS IN CONCRETE Kira Weise, Henk Jonkers, Eddie Koenders	1043
ACTIVE MINERAL ADDITIVES AND THEIR CONTRIBUTION TO NATURAL SELF-HEALING ABILITY OF CONCRETE Pavel Reiterman	1049
APPLICATION OF LYSINIBACILLUS SPHAERICUS FOR CONCRETE CRACK HEALING USING DIFFERENT CALCIUM SOURCES Christine Farrugia, Ruben Paul Borg, Joseph Buhagiar, Liberato Ferrara	1053
BIOTREATED CONVENTIONAL CONCRETE AND CDW-CONCRETE BY USE OF MICROBIAL MIXED CULTURES BIOPRODUCTS Julia García-González, André Freches, Pedro Vaz, Paulo C. Lemos, Alice S. Pereira, Andrés Juan-Valdés, Paulina Faria	1059
CHARACTERIZATION AND MONITORING OF THE CRACK SELF-HEALING ABILITY OF BIO-MORTAR Bojan Miljevic, Francesco Lo Monte, Snazana Vucetic, Olja Sovljanski, Ivan Ristic, Branka Pilic, Sinisa Markov, Liberato Ferrara, Jonjaua Ranogajec	1065
EFFECT OF FLY ASH AND SUPERABSORBENT POLYMER OPTIMIZATION ON SELF-HEALING CAPABILITY OF CONCRETE Pattharaphon Chindasiriphan, Hiroshi Yokota, Paponpat Pimpakan	1071
EFFECTIVENESS OF SELF-HEALING TECHNOLOGIES IN CEMENT BASED MATERIALS: CONCEPT FOR AN INTER-LABORATORY EXPERIMENTAL EVALUATION BY MULTIPLE TEST METHODS. A PROPOSAL BY COST ACTION CA 15202 SARCOS Liberato Ferrara, Tim Van Mullem, Estefania Cuenca, Henk M. Jonkers, Francesco Lo Monte, Mercedes Sanchez, Nele De Belie, Anthony Jefferson	1077
EXTENDING THE SERVICE LIFE OF POLYMER INDUSTRIAL FLOOR COATINGS BY IMPROVING ITS ADHESION TO CEMENT-BASED SUBSTRATES Łukasz Sadowski, Agnieszka Chowaniec	1085
IMPROVEMENT OF SELF-HEALING EFFICIENCY IN ENGINEERED CEMENTITIOUS COMPOSITES BY ADDITION OF FOREST BIOMASS ASH Gloria Perez, Jose Luis García Calvo, Pedro Carballosa, Ana Guerrero	1091
NANO-SCALE TAILORING OF ENGINEERED CEMENTITIOUS COMPOSITES FOR SIMULTANEOUS ACHIEVEMENT OF ENHANCED SELF-HEALING AND SELF-SENSING ATTRIBUTES Oğuzhan Öztürk, Gürkan Yıldırım, Anıl Kul, Ülkü Sultan Keskin, Mustafa Şahmaran	1097

SELF-HEALING AND STRENGTH RECOVERY EVALUATION OF SUPER ABSORBENT POLYMERS CONCRETE MIXES UNDER CONTROLLED DAMAGE Amir Sidiq, Rebecca Gravina, Sujeeva Setunge, Filippo Giustozzi	1103
SELF-HEALING OF CEMENT SLURRY FOR OIL WELLS CONTAINING CRYSTALLINE ADMIXTURE: EARLY RESULTS Aline de Souza Oliveira, Romildo Dias Toledo Filho, Eduardo de Moraes Rego Fairbairn, Otávio da Fonseca Martins Gomes	1109
STRESS REDISTRIBUTION MECHANISM IN CONCRETE ELEMENTS WITH POLYMER FLEXIBLE JOINT: EXPERIMENTAL RESULTS Łukasz Zdanowicz, Marcin Tekieli, Arkadiusz Kwiecień	1115
SURFACE TREATMENTS AS REPAIR METHODS FOR PROTECTING REBARS FROM CORROSION Mercedes Sanchez, Fabiano Tavares	1121
THE EFFECTS OF CONTINUED HYDRATION OF UNDAMAGED MATERIAL ON APPARENT HEALING INDICES IN CEMENTITIOUS MATERIALS Robert Davies, Cristina De Nardi, Anthony Jefferson	1127
THE ROLE OF NANO-PARTICLES IN SELF HEALING PROCESS OF CEMENTITIOUS MATERIALS Maria Stefanidou, Eirini-Chrysanthi Tsardaka, Evangelia Tsampali	1133
UTILIZATION OF QUARTZ QUARRY DUST IN ENGINEERED CEMENTITIOUS COMPOSITES PRODUCTION Olkan Ilter Taş, Süleyman Bahadır Keskin, Özlem Kasap Keskin, Mustafa Sahmaran	1139

# **KEYNOTE LECTURES**



## **INNOVATION IN RESEARCH ON NEW BINDERS**

**John L. Provis**<sup>(1)</sup>

(1) University of Sheffield, Sheffield S1 3JD, UK

### **Abstract**

The development and uptake of new cementitious binders is always a slow process, in a global industry which is both very large and necessarily very conservative. However, the drivers for diversification of the world's "toolkit" of cements are growing stronger, as we appreciate that it is not possible to meet the construction and infrastructure needs of global society with a "one-size-fits-all" material solution, as we seek sustainable development at both local and worldwide levels. This is fundamentally because human society is the sum (not the average) of a very diverse set of local scenarios, each with its own particular set of needs, and each with its own portfolio of resources. If we were to consider the average, there would potentially be a single best option that is valid worldwide - but this is not the case, and a technology (cement, concrete or any other material) which is sustainable and optimal in one location will often not be appropriate in another. This leads to the absolute requirement for development of a toolkit of cements, each of which is sustainable and fit for purpose in its own scenario and context. This presentation will give some examples of such cements, with a particular focus on alkali-activated binders, and will outline how innovation in materials science research is intrinsically interlinked with innovation in use and uptake of new materials.

### **1. The role of alternative binders in the future cements landscape**

As global society seeks sustainability in every aspect of its activities, following international treaties, commitments and pledges to protect the planet for future generations, the construction materials industry faces deep and fundamental challenges. As the largest-volume manufactured product worldwide other than drinking water, Portland cement is used almost ubiquitously, and is valued for its technical characteristics (strength and durability), its ease of use, and most of all its versatility and robustness. This brings the ability to 'mistreat' a material in many practical senses through improper formulation, mixing, casting and curing,

yet still obtaining sufficient technical performance for general usage in non-structural applications. However, as society aims to reduce anthropogenic influence on the global environment, and thus the intrinsic carbon dioxide emissions profile of Portland cement receives increasing scrutiny, it is increasingly becoming clear that there are important roles to play within a broader construction materials ‘toolkit’, for alternative materials that can offer sufficient (or outstanding) technical characteristics in specified applications, without these necessarily needing to be as broadly applicable or universally available as is Portland cement.

Examples of attractive members of this cements toolkit include calcium aluminate cements [1, 2], various magnesia-based cements (silicates, phosphates, carbonates, oxysalts, and others) [3-7], and alternative clinker types including those containing hydraulic calcium sulfoaluminate or sulfosilicate phases [8-10], as well as those which more closely resemble the chemistry of conventional Portland cement, such as belitic clinkers [11-13] and high-volume blends of latent hydraulic or pozzolanic supplementary cementitious materials (SCMs) with Portland cement [14-18]. In the early period of cement usage through the 1800s – and before Portland cement became established as the near-universal cement deployed in construction – there was a much broader range of cement types available [19], and it is in fact debatable whether the first “Portland cements” (including those described by the 1824 patent of Aspdin) bear any real resemblance to those which were produced even 100 years later [20], let alone those used in current engineering practice.

Having seen the global growth and domination of Portland cement extend to every part of the globe in the past decades, with over 100 million tonnes of cement and clinker now transported internationally by ship per annum (and at least a similar quantity transported domestically by ship) [21], there is growing emphasis on “local solutions to local needs” as a pathway to reducing the environmental impact of the global construction materials industry. Much of the long-distance transport of cements is required because local production facilities are not sufficient to meet demand – for example, in parts of sub-Saharan Africa which import cement – but many of these regions do have locally-available mineral or by-product resources which can be eminently suited to the production of non-Portland cements. A particular example of this is the tropical belt of lateritic clay soils, which are found in locations such as western Africa and northern Brazil which have high demand for construction and relatively low levels of industrialisation, have been used effectively in the development of alkali-activated binders [22, 23]. Similarly, nations such as South Africa and Australia which have very high levels of fly ash generation from coal combustion provide obvious and attractive scope for the use of alkali-activation in valorising this material [24, 25].

The utilisation of local resources offers the possibility for large-scale improvement in the selection and use of construction materials in local contexts, through diversification and the adoption of a materials toolkit approach. The value of such an approach becomes particularly evident when we consider what is really meant by the “global construction industry”. Most national and international roadmapping and planning exercises are conducted on the basis of averaging across local situations, with weighting factors applied as needed, to distil a large and complex body of data into readily comprehensible information. However, such an approach will inevitably lead to recommendations of a one-size-fits-all approach, as local variations are smoothed out, and the apparent ‘best’ overall solution for a globally averaged

calculation is unlikely to be locally optimal in regions which have very different needs and materials availability. The alternative approach – and the one which is likely to strongly highlight the value of the toolkit approach to materials selection – is to change the methodology by which local scenarios are aggregated: instead of considering the *average* of all local scenarios, it is better to consider their *sum*. So, rather than attempting to homogenise all of the details and special circumstances which prevail locally, these can be considered and an appropriate toolkit designed and made available to account for them. Using the strengths, opportunities and resources in each location, to make available appropriate and fit-for-purposes materials and processes, also opens the possibility for vernacular expertise and skills to be fully incorporated into future sustainable development paradigms, rather than an externally-driven, externally-imposed, uniform solution.

It should also be noted that there is a strong possibility that such a local analysis will result in the recommendation that a particular material (e.g. an alkali-activated binder) turns out not to be the most appropriate selection for a particular location. This raises a further point around the design of a materials toolkit approach: it is essential that advocates of sustainable construction as a whole, can decouple this from the (often financially based) drive to advocate a single material above all others regardless of context. An attitude shift is needed: instead of asking “*can* this material be used in this application?”, a more valuable question to ask (and far more difficult to answer holistically) is “*should* this material be used in this application?”. This question requires a combination of technical or scientific insight (to be addressed in the following section), linked with economic, social and environmental insights, to generate an answer which can realistically be used as the basis of decision-making in materials selection at a large scale. This is generally not something that can be achieved by a single researcher, specifier, producer, designer, engineer, technologist or policy-maker, but requires multi-disciplinary combinations of insight to justify and support materials selection which is technically sound, environmentally responsible, and economically feasible.

## **2. The importance of materials science in developing and validating new cements**

The development of a deeper understanding of the materials science of cements – both Portland and non-Portland based – is fundamental and essential to proving their serviceability and durability [26-28]. This is particularly important in applications where very long term durability is critical, and where the timescales of importance are far beyond those which are accessible in the laboratory; for example, in major infrastructure projects in demanding environments which are designed for a service life of centuries or more [26, 29, 30], and in the long-term storage and disposal of nuclear waste, which may require cementitious materials to serve their designed purpose for hundreds of millennia in preventing the release of contaminants [31-33]. The particular needs of this latter application are one of the reasons why so much of the fundamental science of cements has been developed and published by organisations and research programmes linked to the nuclear energy sector, but the availability of this information brings obvious and essential benefits in other usages of cements as well.

The work of cement chemists (and cement materials scientists more broadly) has on occasion been criticised for being apparently esoteric in nature, and not always fully connected to civil engineering applications [34]. While this is certainly true in some instances, with high-profile research programmes having generated (and widely disseminated) research outputs which are demonstrably incorrect regarding, for example, the fundamental science and chemical nature of cement hydrate gels, alkali-activated binders, and solid-fluid reaction processes, this should not be extended to discarding the essential – and correct – research findings of those who have conducted careful and detailed research to generate new physicochemical insight from advanced modelling and experimental investigations. Rather, any apparent mis-steps that may appear in the scientific record need to be openly discussed (see e.g. documents such as [35, 36], as well as numerous ‘Discussion’ or ‘Letter to the Editor’ documents published in journals, although at a decreasing rate in recent years compared to the historical practice), any useful information that can be gleaned from the work extracted in any case, and the results used to build ‘more correct’ theoretical foundations for our understanding. The field of cements science is – fortunately – one in which fundamental and important questions remain the topic of evolving discussion, analysis and improvement [29]; there are many key scientific advances still remaining to be made in this field, and many points upon which leading experts have not yet reached consensus regarding the underlying chemical and physical processes and molecular structures that control the reactivity and performance of cementitious materials, both novel and “traditional”.

This also raises the need for advances in the application of modern materials science characterisation techniques to the study of cements [37, 38]. Cementitious binders are almost invariably complex in chemical and mineralogical characteristics, often dominated by crystallographically disordered phases, and are dynamic materials which evolve significantly as a function of time (unless hydration is halted – which is a potentially intrusive procedure in and of itself). The presence of water in most cement reaction products raises additional difficulty in applying techniques that may require vacuum conditions for analysis, e.g. surface-sensitive spectroscopic and many microscopic techniques, the binder phases are often prone to atmospheric carbonation during sample preparation, transfer and analysis, and the brittle and porous nature of cementitious specimens can also make sample preparation challenging. However, through appropriately careful sample preparation, the application of advanced analytical techniques can bring insight, understanding and advancement in the field which more than justifies the difficulties involved in obtaining, analysing and interpreting the data. There are certainly cases where the application of highly advanced analytical approaches brings essentially the same information as can be obtained from more ‘everyday’ experimentation – and often in a more time-consuming and expensive manner – leading to criticisms that researchers are seeking a “beautiful answer to a stupid question”. However, if experimental campaigns are more intelligently designed to make use of the unique capabilities of specific tools, techniques and instruments, some truly unique (and valuable) scientific studies, and important engineering insight, can certainly be gained.

### 3. Conclusions

The value that can be derived from the broader uptake and use of innovative types of cements, as a component of a future sustainable global built environment, must be motivated by a real industrial or societal demand. Technology push will never be enough to bring a new cement into large scale use; something which appears to be a solution in search of a problem is much less attractive than the ability to develop a tailored solution to solve a clearly identified problem. In some cases, the problem must first be highlighted as end-users are not necessarily aware that the performance of the existing material or design solution is below desirable levels, but there are many cases – for example, related to the need to reduce global carbon emissions, or to improve the acid resistance of concrete sewer pipes – where the problem is well understood and the industry is actively seeking a solution (or set of solutions). In such cases, it is extremely valuable for a scientist, engineer or technologist to hold a ‘toolkit’ of materials, understanding the strengths and limitations of each, to enable them to generate and validate recommendations for the selection of the best material for each task. In current practice, the ‘best’ is generally assumed to be Portland cement, simply because it is the ubiquitous answer to almost every question of cement selection. However, in a sustainable future society where a materials toolkit is truly available, this need not always be the case. Portland cement, and its blends, will certainly continue to play a major role in global construction for the foreseeable future. However, the availability of a validated toolkit of fit-for-purpose alternative cements will add value and bring outstanding opportunities to improve technical, environmental and economic performance in the industry, and this more than justifies the continued effort in research, development and deployment of alternative cements.

### Acknowledgements

The research leading to these results has received funding from the European Research Council under the European Union's Seventh Framework Programme (FP7/2007-2013)/ ERC grant agreement n° 335928 “GeopolyConc”, and from the Engineering and Physical Sciences Research Council (UK), grants EP/M003272/1 and EP/P013171/1.

### References

- [1] K.L. Scrivener, J.-L. Cabiron, R. Letourneux, High-performance concretes from calcium aluminate cements, *Cem Concr Res*, 29 (1999) 1215-1223.
- [2] C. Evju, S. Hansen, Expansive properties of ettringite in a mixture of calcium aluminate cement, Portland cement and  $\beta$ -calcium sulfate hemihydrate, *Cem Concr Res*, 31 (2001) 257-261.
- [3] S.A. Walling, J.L. Provis, Magnesia based cements – a journey of 150 years, and cements for the future?, *Chem Rev*, 116 (2016) 4170-4204.
- [4] C. Roosz, S. Grangeon, P. Blanc, V. Montouillout, B. Lothenbach, P. Henocq, E. Giffaut, P. Vieillard, S. Gaboreau, Crystal structure of magnesium silicate hydrates (M-S-H): The relation with 2:1 Mg–Si phyllosilicates, *Cem Concr Res*, 73 (2015) 228-237.
- [5] S. Sorel, Sur un nouveau ciment magnésien (On a new magnesium cement), *C R Hebd Acad Sci (Paris)*, 65 (1867) 102-104.

- [6] T. Zhang, L.J. Vandeperre, C.R. Cheeseman, Magnesium-silicate-hydrate cements for encapsulating problematic aluminium containing wastes, *J Sust Cem-Based Mater*, 1 (2012) 34-45.
- [7] A.S. Wagh, *Chemically Bonded Phosphate Ceramics*, Elsevier, Oxford, UK, 2004.
- [8] E. Gartner, T. Sui, Alternative cement clinkers, *Cem Concr Res*, (2018) in press, DOI 10.1016/j.cemconres.2017.1002.1002.
- [9] T. Hanein, I. Galan, F.P. Glasser, S. Skalamprinos, A. Elhoweris, M.S. Imbabi, M.N. Bannerman, Stability of ternesite and the production at scale of ternesite-based clinkers, *Cem Concr Res*, 98 (2017) 91-100.
- [10] F. Bullerjahn, D. Schmitt, M. Ben Haha, Effect of raw mix design and of clinkering process on the formation and mineralogical composition of (ternesite) belite calcium sulphoaluminate ferrite clinker, *Cem Concr Res*, 59 (2014) 87-95.
- [11] C.D. Popescu, M. Muntean, J.H. Sharp, Industrial trial production of low energy belite cement, *Cem Concr Compos*, 25 (2003) 689-693.
- [12] L. Kacimi, A. Simon-Masseron, S. Salem, A. Ghomari, Z. Derriche, Synthesis of belite cement clinker of high hydraulic reactivity, *Cem Concr Res*, 39 (2009) 559-565.
- [13] J.J. Thomas, S. Ghazizadeh, E. Masoero, Kinetic mechanisms and activation energies for hydration of standard and highly reactive forms of  $\beta$ -dicalcium silicate (C2S), *Cem Concr Res*, 100 (2017) 322-328.
- [14] E. Gartner, H. Hirao, A review of alternative approaches to the reduction of CO<sub>2</sub> emissions associated with the manufacture of the binder phase in concrete, *Cem Concr Res*, 78 (2015) 126-142.
- [15] M.C.G. Juenger, R. Siddique, Recent advances in understanding the role of supplementary cementitious materials in concrete, *Cem Concr Res*, 78 (2015) 71-80.
- [16] B. Lothenbach, K. Scrivener, R.D. Hooton, Supplementary cementitious materials, *Cem Concr Res*, 41 (2011) 1244-1256.
- [17] R. Snellings, G. Mertens, J. Elsen, Supplementary cementitious materials, *Rev Miner Geochem*, 74 (2012) 211-278.
- [18] K. Scrivener, F. Martirena, S. Bishnoi, S. Maity, Calcined clay limestone cements (LC3), *Cem Concr Res*, (2018) in press, DOI 10.1016/j.cemconres.2017.1008.1017.
- [19] G.R. Redgrave, C. Spackman, *Calcareous Cements: Their Nature, Manufacture, and Uses, with some Observations upon Cement Testing* (2nd Ed.), Charles Griffin & Company, London, 1905.
- [20] A.C. Davis, *A Hundred Years of Portland Cement, 1824-1924*, Concrete Publications Limited, London, 1924.
- [21] A. Ligthart, Cement and clinker trade and risk of a Chinese slowdown, *Global Cement*, <http://www.globalcement.com/magazine/articles/995-cement-and-clinker-trade-and-risk-of-a-chinese-slowdown>, 2016.
- [22] P.N. Lemougna, A.B. Madi, E. Kamseu, U.C. Melo, M.-P. Delplancke, H. Rahier, Influence of the processing temperature on the compressive strength of Na activated lateritic soil for building applications, *Contr Build Mater*, 65 (2014) 60-66.
- [23] K.C. Gomes, G.S.T. Lima, S.M. Torres, S. De Barros, I.F. Vasconcelos, N.P. Barbosa, Iron distribution in geopolymer with ferromagnetic rich precursor, *Mater Sci Forum*, 643 (2010) 131-138.

- [24] J. Shekhovtsova, I. Zhernovsky, M. Kovtun, N. Kozhukhova, I. Zhernovskaya, E. Kearsley, Estimation of fly ash reactivity for use in alkali-activated cements - A step towards sustainable building material and waste utilization, *J Cleaner Prod*, 178 (2018) 22-33.
- [25] Beyond Zero Emissions, Zero Carbon Industry Plan - Rethinking Cement, Melbourne, 2017.
- [26] M. Alexander, M. Thomas, Service life prediction and performance testing — Current developments and practical applications, *Cem Concr Res*, 78 (2015) 155-164.
- [27] R.D. Hooton, J.A. Bickley, Design for durability: The key to improving concrete sustainability, *Constr Build Mater*, 67C (2014) 422-430.
- [28] H.M. Jennings, J.W. Bullard, From electrons to infrastructure: Engineering concrete from the bottom up, *Cem Concr Res*, 41 (2011) 727-735.
- [29] J.J. Biernacki, J.W. Bullard, G. Sant, K. Brown, Fredrik P. Glasser, S. Jones, T. Ley, R. Livingston, L. Nicoleau, J. Olek, F. Sanchez, R. Shahsavari, P.E. Stutzman, K. Sobolev, T. Prater, Cements in the 21st century: challenges, perspectives, and opportunities, *J Am Ceram Soc*, 100 (2017) 2746-2773.
- [30] J.R. Clifton, Predicting the service life of concrete, *ACI Mater J*, 90 (1993) 611-617.
- [31] A.S. Aloy, J.R. Harbour, E.W. Holtzscheiter, C.A. Langton, Evaluation of durability of mortars and concretes used in ancient structures, *MRS Symp Proc*, 1107 (2008).
- [32] N.B. Milestone, Reactions in cement encapsulated nuclear wastes: Need for toolbox of different cement types, *Adv Appl Ceram*, 105 (2006) 13-20.
- [33] F.P. Glasser, Mineralogical aspects of cement in radioactive waste disposal, *Miner Mag*, 65 (2001) 621-633.
- [34] A.M. Neville, *Neville on Concrete* (2nd Ed), Booksurge, Charleston, SC, 2006.
- [35] I.G. Richardson, The importance of proper crystal-chemical and geometrical reasoning demonstrated using layered single and double hydroxides, *Acta Cryst B*, 69 (2013) 150-162.
- [36] J.L. Provis, On the use of the Jander equation in cement hydration modelling, *RILEM Techn Lett* 1 (2016) 62-67.
- [37] J.L. Provis, A. Hajimohammadi, C.E. White, S.A. Bernal, R.J. Myers, R.P. Winarski, V. Rose, T.E. Proffen, A. Llobet, J.S.J. van Deventer, Nanostructural characterization of geopolymers by advanced beamline techniques, *Cem Concr Compos*, 36 (2013) 56-64.
- [38] S.R. Chae, J. Moon, S. Yoon, S. Bae, P. Levitz, R. Winarski, P.J.M. Monteiro, Advanced nanoscale characterization of cement based materials using X-ray synchrotron radiation: A review, *Int J Concr Struct Mater*, 7 (2013) 95-110.

## **UNDERSTANDING MATERIAL-DEPENDENT STRUCTURAL BEHAVIOUR FOR THE AGING MANAGEMENT OF CONCRETE STRUCTURES**

**Ippei Maruyama**<sup>(1)</sup>

(1) Nagoya University, Nagoya, Japan

### **Abstract**

The structural performance of concrete structures constantly changes due to the chemical and physical reactions of concrete components in a given environment. For the long-term use of concrete structures, such aging phenomena should be understood and controlled. Herein, the most common environmental drying impacts on concrete structures are discussed with regards to the cement paste, aggregate and their mutual interactions; the roles of these elements on structural performance are clarified. The alteration of calcium silicate hydrate in Portland cement paste during the first drying significantly impacts the strength and shrinkage of cement paste and concrete. The rock-forming mineral composition of the aggregate used plays a significant role in the volume stability. Damage caused by an imbalance of volumetric change between aggregates and cement paste significantly contributes to the compressive strength and Young's modulus of concrete. Structural performance changes of a shear reinforced concrete wall due to drying are explained by examining the roles of concrete components.

### **1. Introduction**

For the continuous use of concrete structures after disasters, the monitoring of the health of concrete structures by using sensors is one of the promising technologies. Recently, many public buildings have been installed with accelerators and velocimeters. These sensors can evaluate the dynamic motion of building structures; the accelerator results as a function of deformation (obtained by the second-order integration of the accelerator) represent the relationship between force and deformation. Based on this relationship, the structural damage can be obtained by a difference of tangents. As is shown in Fig. 1, all the concrete structures showed natural frequency changes with time [1]. These trends are not yielded during mid- or



small- earthquakes, instead they take place during in-between earthquakes [2]. The general environmental condition, namely, drying, mostly likely has an impact on concrete and concrete structures.

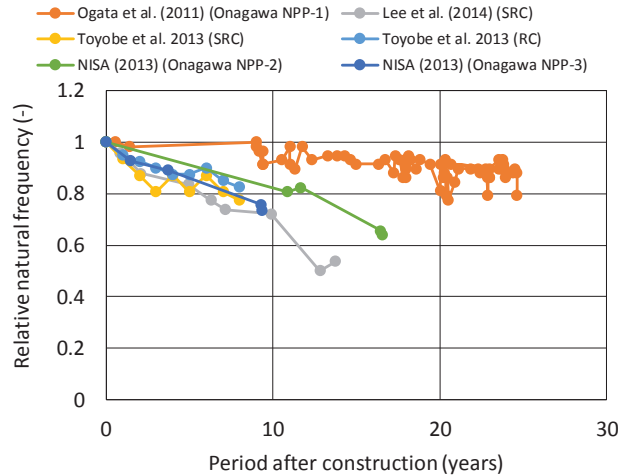


Figure 1: Natural frequency changes of concrete buildings [1].

## 2. Hardened cement paste

Hardened cement paste (hcp) is considered a porous and colloidal material [3]. The colloidal nature has been confirmed by sorption measurements [4,5], small-angle scattering measurements [6,7], and visual observations [8]. To understand the nature of hcp, especially for the first desorption process, the physical properties [10], microstructure [10, 11] as well as shrinkage behaviour [10, 12] have been studied. As shown in Figure 2, the bending strength and Young's modulus of matured hcp showed dramatic changes under different relative humidity (RH) conditions. At the same time, the microstructure of hcp changed during this drying process, as shown in Figure 3. Due to the colloidal nature of calcium silicate hydrate (C-S-H), which is the major hydrate of Portland cement paste, the capillary pores in hcp increased during the drying; therefore, the trend of decreasing general strength has been confirmed, especially from 90% to 40% RH, due to the stress concentration mechanism caused by an increase in capillary pores. At the same time, the solid portion agglomerated [11] and the interlayer distance of C-S-H reduced when the RH was less than or equal to 40% RH [11]. The strength and Young's modulus of C-S-H increased by this solid phase alteration in the corresponding RH range, as shown in Figure 2. Interestingly, as confirmed by the leftmost inset in Figure 3, in the case of the 11% RH condition, meso-pores, which are pores corresponding to the water sorption from 40% RH to 95% RH, were re-created; these meso-pores were minimized at the drying condition of 40% RH.

On the contrary, the shrinkage of hardened cement paste occurred largely between 80% and 40% RH, and the incremental shrinkage from 40% RH to 11% RH was not large [12]. This behaviour also reflects the microstructural changes during drying, as shown in Figure 4. The hcp samples dried at different RH conditions were tested for short-term length-change isotherms by using a thermal mechanical analyser coupled with a RH generator. When the sample was dried, the total shrinkage tended to be small. As shown in the rightmost inset of Figure 4, the incremental strain from 40% RH to 98% RH reduced when the drying condition

for the samples changed from 90% RH to 40% RH.

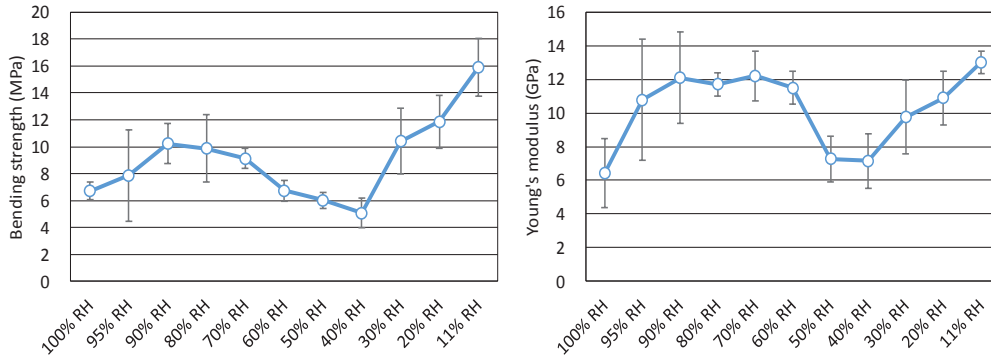


Figure 2: Change of bending strength (left) and Young's modulus (right) of matured hardened cement paste under different equilibrium relative humidity conditions [9].

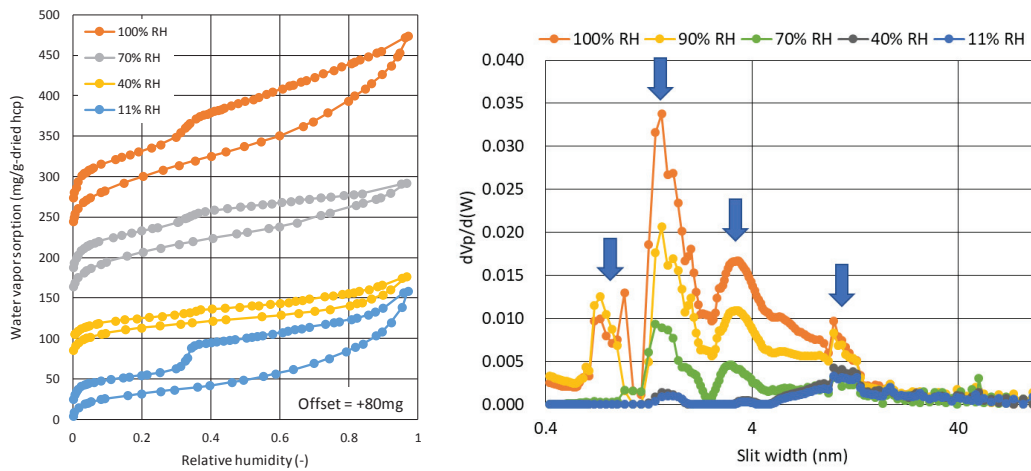


Figure 3: Microstructural changes of matured hardened cement under different equilibrium relative humidity conditions through water vapour sorption isotherms at 293 K (left) and slit size distribution obtained by the Grand Canonical Monte Carlo method (GCMC) for nitrogen sorption isotherms at 77 K.

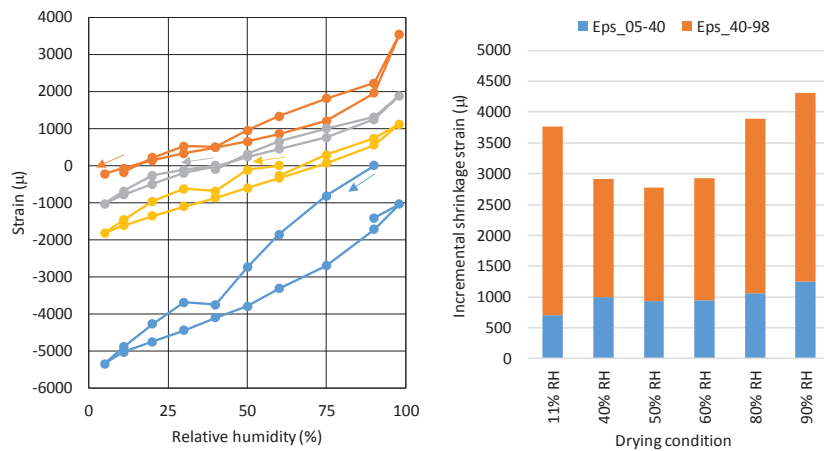


Figure 4: Shrinkage of hcp dried at different RH conditions (left [12]) and incremental shrinkage of hcp (right [12]).

Therefore, the microstructural changes during the first desorption are very crucial factors of the physical properties of hcp.

### 3. Concrete

The physical properties of concrete change with drying. Figure 5 shows an example of the compressive strength ratio (normalized to the compressive strength for the sealed condition) of concrete and mortar after reaching an equilibrium at different RH conditions as well as the bending strength ratio (normalized to the bending strength at the 95% RH condition) of hcp. The basic trend of the strength ratio was similar: a slight increase from the sealed condition to 80% RH, a decrease from 80% RH to 40% RH, and an increase from 40% RH to more intense drying conditions. Based on this figure, it can be concluded that compressive strength change of concrete is determined by the nature of hcp. It should be noted that the compressive strength of concrete was initiated from the failure of hcp under the compressive-shear mechanism, and this failure mode is close to the tensile strength (or the bending strength) rather than the compressive strength of hcp. In addition, when the type of coarse aggregate is changed for the same volumetric mixture proportion, the behaviour of the compressive strength ratio changes. When a low shrinkage aggregate was used, the reduction ratio increased. Therefore, it was elucidated experimentally that the nature of the aggregate also influences the compressive strength change due to drying. When the concrete was dried, there was a difference in the volumetric stability of the aggregate and cement paste, and the aggregate restrained the shrinkage of the cement paste. Consequently, damage due to the inhomogeneous shrinkage of aggregate and cement paste was reduced when a shrinking aggregate was used in the concrete. The example of crack development, visualized with the digital image correlation method, during drying is shown in Fig. 6 (right).

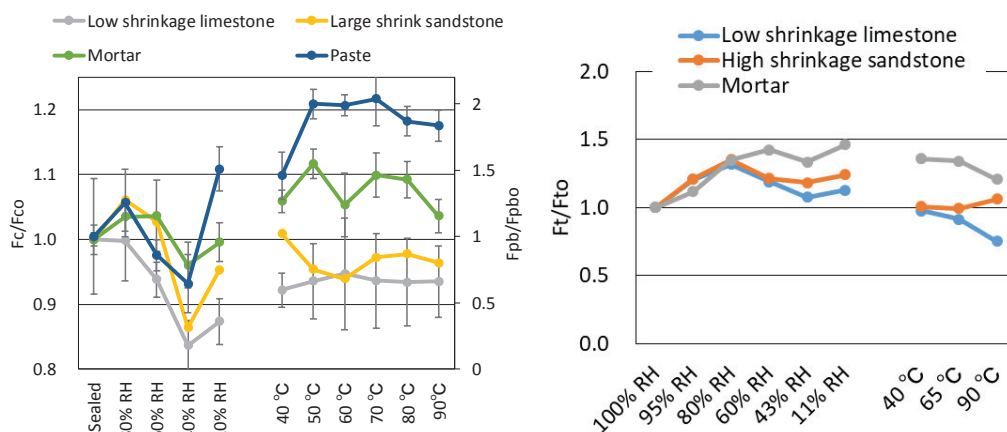


Figure 5: Compressive strength (left [9, 13]) and splitting tensile strength (right [14]) of matured concrete after reaching equilibrium at different RH conditions.

A similar trend was confirmed for tensile cracking, as shown in Fig. 5 (right). The splitting tensile strength of mortar, concrete with high shrinkage sandstone and concrete with low

shrinkage limestone were compared. Like the compressive strength, the strength increased from the high RH range to 80% RH. Then, the tensile strength decreased in cases of concrete. However, the decreasing trend is affected by the coarse aggregate; in cases where the concrete contains high-shrinkage sandstone coarse aggregate, the reduction becomes small. This also suggests that the inhomogeneous shrinkage behaviour between aggregate and hcp and the resultant cracking around aggregates impact the reduction of the change in splitting tensile strength.

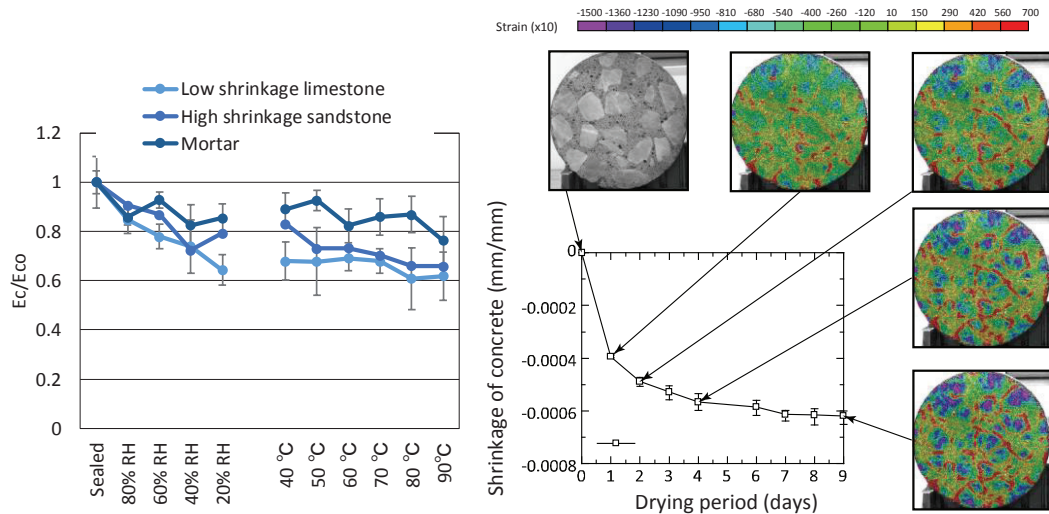


Figure 6: Young's modulus of matured concrete after reaching equilibrium at different RH conditions (left [9, 13]) and cracking around aggregates in concrete under drying conditions [15].

Young's modulus of concrete decreases when the concrete dries, as confirmed in the leftmost inset of Fig. 6. This reduction trend is also determined by the type of aggregate. When a low-shrinkage aggregate was used in the concrete, a large decrease in Young's modulus was observed. This result reveals that the inhomogeneous shrinkage behaviour between the aggregate and hcp as well as the opening of cracks around aggregates cause stress concentration, which reduces Young's modulus.

When the concrete shrinkage is restrained, the restraining role of the aggregate in terms of the shrinkage of hcp is changed. The crack development behaviours of concrete with high or low shrinkage coarse aggregates were confirmed experimentally (experimental setup is shown in the leftmost inset of Fig. 7) by using the digital image correlation method, as shown in the rightmost inset of Fig. 7.

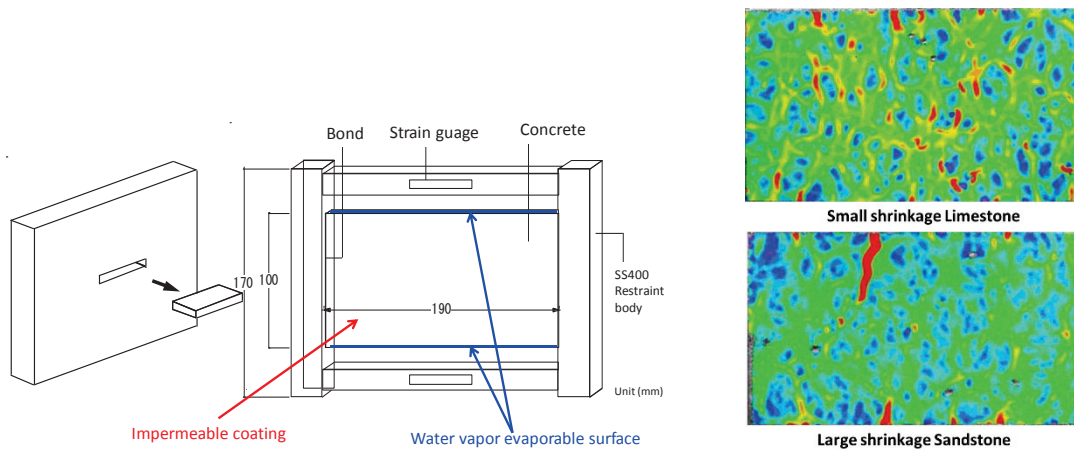


Figure 7: Restrained condition of concrete (left) and cracking behaviour of concrete with small shrinkage limestone (top right) and large shrinkage sandstone (bottom right) [16].

In the case of low-shrinkage limestone aggregate, when the concrete surface cracked due to water evaporation and the resultant shrinkage of the surface region occurred, the cracks did not propagate inwards because of the high bond strength between the aggregate and cement paste and the low shrinkage property of the aggregate. Softening due to this small crack was trivial and subsequent multiple small cracks occurred in other surface regions. Small cracks gradually proceeded into the inner part. On the contrary, when large-shrinkage sandstone was used, the small crack at the surface was connected to the surface cracking on the aggregate surface, and the first small crack abruptly proceeded internally. This is due to the smaller bond strength between the aggregate and cement paste, and the large shrinkage nature of the coarse aggregate, which contributes to the opening of cracks. Therefore, this crack propagation released the accumulated stress in other parts of the concrete; subsequently, one large (and probably visible) crack occurred in concrete, which became a through crack. Therefore, it was concluded that surface properties and the shrinkage nature of aggregate has a large influence on the concrete cracking.

#### 4. Reinforced concrete member

The shrinkage of concrete induces stiffness changes of reinforced concrete structures [17]; it decreases in the flexural cracking moment and increases in the curvature and maximum crack width of beams [18-21]. This has been explained by the tensile stress of concrete induced by the restraining shrinkage and strain differences before and after the cracking of concrete. In this regard, the creep strain of concrete in RC columns under axial compressive loads plays the same role as that of shrinkage [22]. Creep strain and shrinkage strain in columns cause the re-distribution of stress among concrete and rebars, and in the case of the un-loading process, such as in seismic response, cracks are easily produced in tension [22]. This re-distribution of stress caused by shrinkage also reduces the moment capacity when the failure of covering concrete occurs [23].

For the shear cracking and shear failure, the diagonal cracking moment of the RC beam as well as the shear capacity of the RC beam is affected by shrinkage [24-26]. This is simply

because the stress, position and direction of diagonal cracking are altered by the shrinkage-induced stress and the enlarged crack width. The wider diagonal cracks also affect the performance of the RC column; the loading capacity in the cyclic loading process after the formation of diagonal cracking is decreased by the width of diagonal cracks [27]. Aoyama [29] concluded that self-induced stress will not affect the ultimate strength of reinforced concrete members if the failure mode is not changed.

The impact on drying of the reinforced concrete shear wall has been experimentally investigated recently [29]. The specimen details are shown in the leftmost inset of Figure 8. The specimens were well cured for about 3 months, and one was investigated. The other specimen was then subjected to drying for about a year, and after confirming that the shrinkage strain of the dummy wall specimen reached an equilibrium state (Figure 8, top right), the specimen was investigated. The comparison of the envelope of the load–deformation relationship is summarized in the bottom right inset of Figure 8.

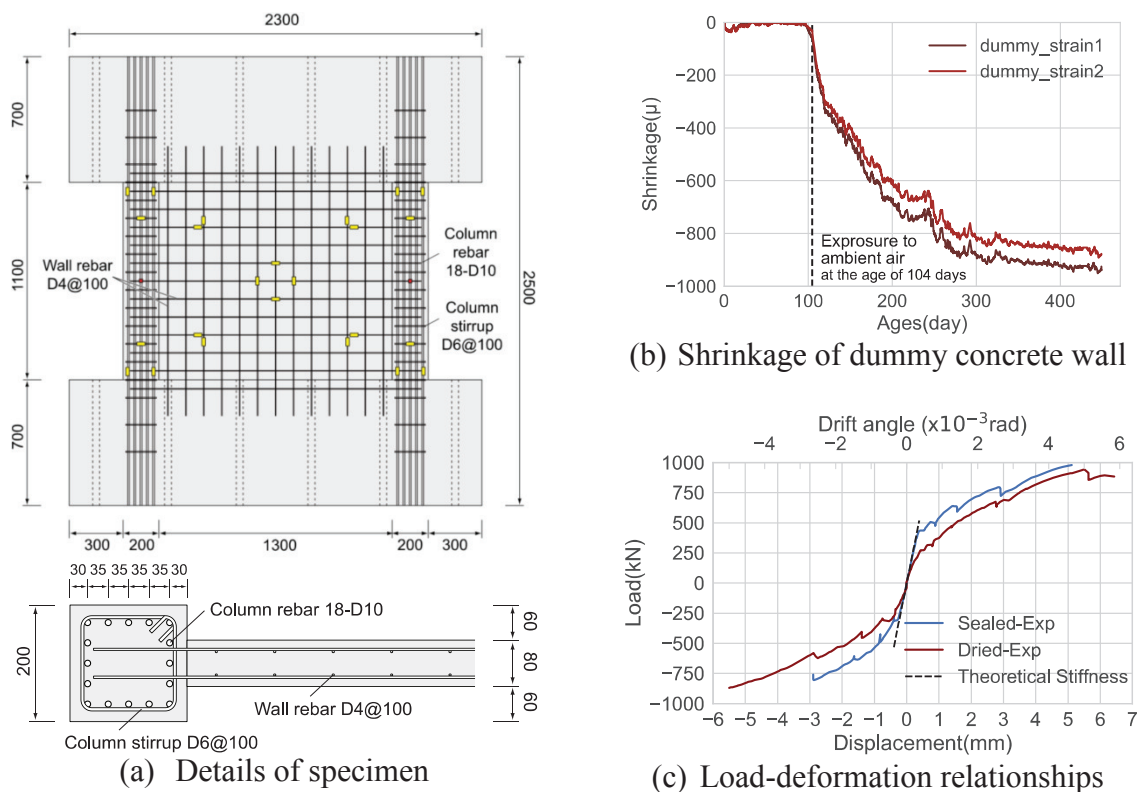


Figure 8: Experimental results of the impact of drying on the structural performance of reinforced concrete shear wall: (a) details of the specimen, (b) shrinkage of concrete, and (c) load–deformation relationship of shear walls before and after drying [17].

One of the remarkable results was that the initial stiffness of the concrete wall after drying became about half that of the non-dried state. This value is quite consistent to the value obtained in Fig. 1. This means that this stiffness change of the reinforced structure needs special attention, especially for the earthquake response of high-rise buildings and vibration

resonance between buildings and installed equipment, from a viewpoint of aging management.

The other point worth mentioning is that the ultimate strength of the shear wall was not affected by drying, even though the deformation at the failure was increased by 25%. However, considering this difference in the ultimate strength using numerical analysis, it was found that this is attained by an increase in the material strength (about a 10% increase of the compressive strength for cylinder specimen) and a decrease in the structural concrete strength due to cracks opening normal to the strut compressive load in the wall, which can be analysed using the equation proposed by Vecchio and Collins [30]. As the compressive strength can be reduced by 15% due to drying and this behaviour is not monotonic, there is a risk of the ultimate shear strength of the concrete wall changing due to drying; RH conditions, the water-to-cement ratio of concrete and the type of coarse aggregate greatly influence this phenomenon. The risks of the ultimate shear strength change are also determined by the shape of the wall and reinforcement ratio.

## 5. Conclusion

The physical property changes of concrete during the first drying cannot be ignored from the viewpoint of the aging management of concrete structures. Structural stiffness changes and the potential ultimate strength of reinforced concrete members are crucial and determined by environmental conditions as well as material properties. This contribution has exhibited a research pathway from the material knowledge to the structural response. Now, a multiscale experimental campaign based on an appropriate research strategy would contribute to evaluating the current performance, and predict and control the future performance of concrete structures.

## Acknowledgements

The experimental results shown in this contribution were supported by JSPS-KAKENHI 18H03804, 16H06363, 15H04077, and a research project of the Japanese Nuclear Regulatory Authority (JAMPSS). The author wishes to express his sincere gratitude to Prof. M. Teshigawa (Nagoya University), Dr A. Nakamura (Japanese Housing Authority), Dr G. Igarashi (Tohoku university), Ms. Y. Nishioka (Takenaka co.), Mr. H. Sasano, Mr. R. Kurihara, Mr. Jiri Rymes and Mr. H. Sugimoto (Nagoya University) for their contributions to the experiments and fruitful discussions.

## References

- [1] Maruyama, I., Multi-scale Review for Possible Mechanisms of Natural Frequency Change of Reinforced Concrete Structures under an Ordinary Drying Condition, *J Adv Conc Tech* 14(11) (2016), 691-705
- [2] Li, L. et al, Earthquake damage evaluation of an 8-story steel-reinforced concrete building using Sa-Sd curves, *J Struct Constr Eng* 79(702) (2014), 1107-1115
- [3] Jesser, L., *Kolloide Chemische Reaktionen des Tonerdezementmörtels*, *Zement* 16 (1927), 741

- [4] Tomes, A. et al, Some Factors Affecting the Surface Area of Hydrated Portland Cement as Determined by Water-Vapor and Nitrogen Adsorption, *Journal of Research of the National Bureau of Standards* 59(6) (1957), 357-364
- [5] Hunt, M. et al, Some Effects of Aging on the Surface Area of Portland Cement Paste, *Journal of Research of the National Bureau of Standards* 64A(2) (1960), 163-169
- [6] Kropp, J. et al, Characterization of the microstructure of hydrated cement paste by small angle X-ray scattering. In: Arrowsmith JW, editor. *Principles and Applications of Pore Structural Characterization*, Bristol (1985), 83-96
- [7] Völkl, J. et al, The specific surface of hardened cement paste by small-angle X-ray scattering effect of moisture content and chlorides, *Cem Conc Res* 17(1) (1987), 81-88
- [8] Fonseca, P., and Jennings, H., The effect of drying on early-age morphology of C-S-H as observed in environmental SEM, *Cem Conc Res* 40(12) (2010), 1673-1680
- [9] Maruyama, I., et al., Development of Soundness Assessment Procedure for Concrete Members Affected by Neutron and Gamma-Ray Irradiation, *J Adv Conc Tech* 15(9) (2017), 440-523
- [10] Maruyama, I., et al., Microstructural and bulk property changes in hardened cement paste during the first drying process, *Cem Conc Res* 58 (2014), 20-34
- [11] Maruyama, I., et al., Microstructural changes in white Portland cement paste under the first drying process evaluated by WAXS, SAXS, and USAXS, *Cem Conc Res* 91 (2016), 24-32
- [12] Maruyama, I., et al., Bimodal behavior of C-S-H interpreted from short-term length change and water vapor sorption isotherms of hardened cement paste, *Cem Conc Res* 73 (2015), 158-168
- [13] Maruyama, I., et al., Strength and Young's modulus change in concrete due to long-term drying and heating up to 90°C, *Cem Conc Res* 66 (2014), 48-63
- [14] Lin, M., et al., Mechanism of Change in Splitting Tensile Strength of Concrete during Heating or Drying up to 90°C, *J Adv Conc Tech* 13(2) (2015), 94-102
- [15] Maruyama, I. and Sasano, H., Strain and crack distribution in concrete during drying, *Mater Struct* 47(3) (2014), 517-532
- [16] Maruyama, I., et al., Impact of aggregate properties on the development of shrinkage-induced cracking in concrete under restraint conditions. *Cem Conc Res* 85 (2016), 82-101
- [17] Sasano, H., et al., Impact of drying on structural performance of reinforced concrete shear walls, *J Adv Conc Tech* 16(5) (2018), 210-232
- [18] Okada, T., et al., Model tests for evaluation of restoring force characteristics of reactor buildings. Part 6: Scale effect test, *Summaries of technical papers of Annual Meeting Architectural Institute of Japan. B, Structures I*, 1986, 1089-1090 (in Japanese)
- [19] Rusch, H. et al., *Creep and shrinkage*, New York, Springer-Verlag (1983)
- [20] Bischoff, H., Effects of shrinkage on tension stiffening and cracking in reinforced concrete, *Can J Civil Eng* 28(3) (2001), 363-374
- [21] Iso, M., et al., Experimental study on bending-shear behavior of reinforced concrete columns after subjected to seismic load, *Proc. JCI* (1993), 15(2), 525-530 (in Japanese)
- [22] Tanimura, M. et al, Serviceability performance evaluation of RC flexural members improved by using low-shrinkage high-strength concrete, *J Adv Conc Tech* 5(2) (2007), 149-160
- [23] Komuro, T., et al., Study on long term performance of reinforced concrete columns using high strength concrete, *Proc. JCI* (2008), 30(3) 223-228, (in Japanese)



- [24] Collins, et al., Structural design considerations for high-strength concrete, *Conc Int* 15(5) (1993), 27-34
- [25] Maruta, M. and Yamazaki, M., Study on the shear behavior of RC beams subjected to high temperature for long time, *Proc. JCI* (1990), 12(1), 603-608 (in Japanese)
- [26] Sato, R. and Kawakane, H., A new concept for the early age shrinkage effect on diagonal cracking strength of reinforced HSC beams, *J Adv Conc Tech* 6(1) (2008), 45-67
- [27] Nakarai, K., et al., Shear Strength of Reinforced Concrete Beams: Concrete Volumetric Change Effects. *J Adv Conc Tech* 14(5) (2016), 229-244
- [28] Maruyama, I. et al., Effect of autogenous shrinkage on the structural performance of short rc column., *Proc. AIJ, C-2, Structures IV*, 107-108 (in Japanese)
- [29] Aoyama, H., Impact of self-induced stress of reinforced concrete buildings (translated), PhD Thesis, University of Tokyo (1960)
- [29] Sasano, H., et al., Impact of drying on structural performance of reinforced concrete shear walls, *J Adv Conc Tech* 16(5) (2018), 210-232
- [30] Vecchio, F.J. and Collins, M.P., The modified compression-field theory for reinforced concrete elements subjected to shear, *ACI J* March-April (1986), 219-231

## **INNOVATIVE WAYS IN CONDITION ASSESSMENT OF CONCRETE BRIDGE DECKS: DATA COLLECTION USING ROBOTICS, AND ADVANCED DATA INTERPRETATION AND VISUALIZATION**

**Nenad Gucunski<sup>(1)</sup>, Jinyoung Kim<sup>(2)</sup>, Kien Dinh<sup>(3)</sup>, Jie Gong<sup>(1)</sup>, Fei Liu<sup>(1)</sup>, Seong-Hoon Kee<sup>(4)</sup>, Basily Basily<sup>(1)</sup>**

(1) Rutgers University, Piscataway, New Jersey, USA

(2) Ajou University, Suwon-si, Gyeonggi-do, Republic of Korea

(3) Marshall University, Huntington, West Virginia, USA

(4) Dong-A University, Busan, Republic of Korea

### **Abstract**

Concrete bridge decks deteriorate faster than other bridge components due to their direct exposure to traffic and environmental loads. Therefore, the ability to assess their condition and deterioration progression in a reliable and consistent manner is essential for implementation of appropriate maintenance and rehabilitation strategies and, ultimately, their economic management. A fully automated system named RABIT (Robotics Assisted Bridge Inspection Tool) integrates multiple nondestructive evaluation (NDE) technologies for a comprehensive and rapid assessment of concrete bridge decks. The system concentrates on the characterization of internal deterioration and damage, in particular three most common deterioration types in concrete bridge decks: rebar corrosion, delamination, and concrete degradation. RABIT implements four NDE technologies: electrical resistivity (ER), impact echo (IE), ultrasonic surface waves (USW) and ground-penetrating radar (GPR). ER enables characterization of the concrete's corrosive environment, while IE detection and characterization of delamination in the deck. The USW test concentrates on the assessment of concrete quality by measuring the concrete elastic modulus. Finally, GPR provides a qualitative assessment of concrete deck deterioration, mapping of rebars and measurement of concrete cover. The NDE technologies are used in a complementary way to enhance the overall condition assessment and certainty regarding the detected deterioration. The benefits stemming from periodical NDE surveys, along with several innovative ways of data interpretation and visualization are presented.

## 1. RABIT description and data collection

RABIT is a robotic system that can fully autonomously collect bridge deck data. The system was developed at Rutgers University with the support from Federal Highway Administration's (FHWA's) Long Term Bridge Performance (LTBP) Program. The system's NDE, imaging and navigation components are shown in Fig. 1. On the front end of RABIT there are two acoustic arrays and four Wenner type ER probes. Acoustic arrays are used in detection and characterization of delamination by impact echo (IE) method [1], and concrete quality through the modulus measurement using ultrasonic surface waves (USW) method [2]. Each of the acoustic arrays incorporates multiple solenoid type impact sources and receivers (accelerometers). Individual impact sources and nearby receivers are used in IE testing, while single sources and sets of nearby sensor pairs are used in USW measurements. The ER probes are used in the characterization of the concrete's corrosive environment by measuring electrical resistivity of concrete. The ER results can be correlated to the anticipated corrosion rates [3]. Two GPR arrays, placed in the rear of the robotic platform, provide a qualitative deck assessment [4]. Each array contains eight pairs of GPR antennas of dual polarization. Finally, two cameras on the front end are taking images of the deck surface, which are later stitched into high resolution images of larger deck sections.

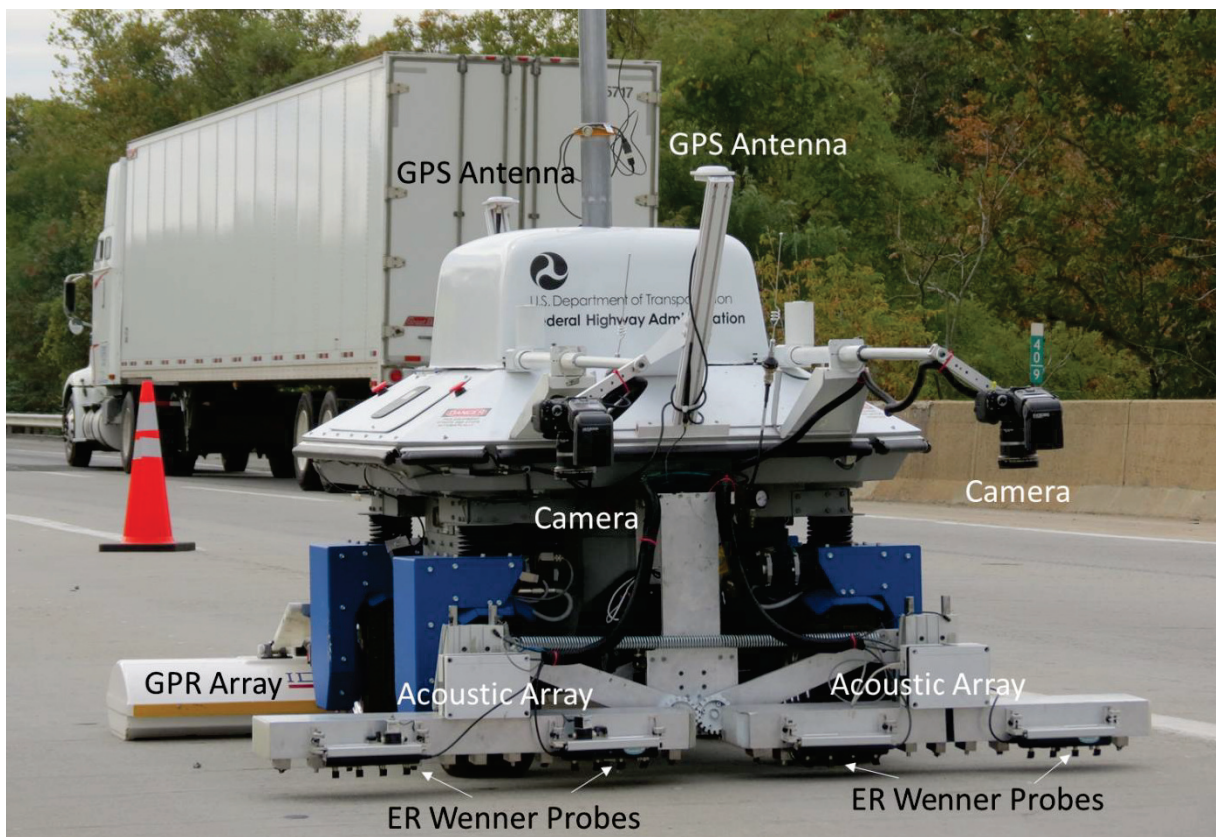


Figure 1: RABIT and NDE, imaging and navigation components.

Accurate and reliable robot localization and navigation is achieved through a fusion of three navigation systems. The first system is the differential global positioning system (DGPS) with

real-time kinematic (RTK) correction. The DGPS consists of a base-station GPS receiver, placed at any point on or near the bridge, and two GPS receivers located at the front and back of the robot (Fig. 1). After very precise GPS coordinates are obtained for the base station, a small portable cart with a GPS antenna is used to take GPS coordinates at three points on the deck. Those will be sufficient to fully define the path of RABIT data collection. The second navigation component is an inertial measurement unit (IMU), which are measuring the rotational position. Finally, the third system is wheel odometry that enables accurate distance measurement. The information coming from the three navigation components is fused using an extended Kalman filter (EKF) [5]. RABIT collects data at production rates of about 350 m<sup>2</sup> of deck area per hour.

## 2. Deck condition data presentation

The results from NDE RABIT surveys are presented in terms of condition maps and condition indices. As an example, delamination, concrete modulus and electrical resistivity maps obtained from three NDE technologies: IE, USW and ER, respectively, are shown in Fig. 2. Hot and warm colours indicate detected defects or deterioration, or lower material properties. In the case of delamination, the serious condition describes a fully developed delamination, while fair and poor conditions describe signs of delamination development. In the case of ER measurement, the resistivity results are correlated to the anticipated corrosion rates [6].

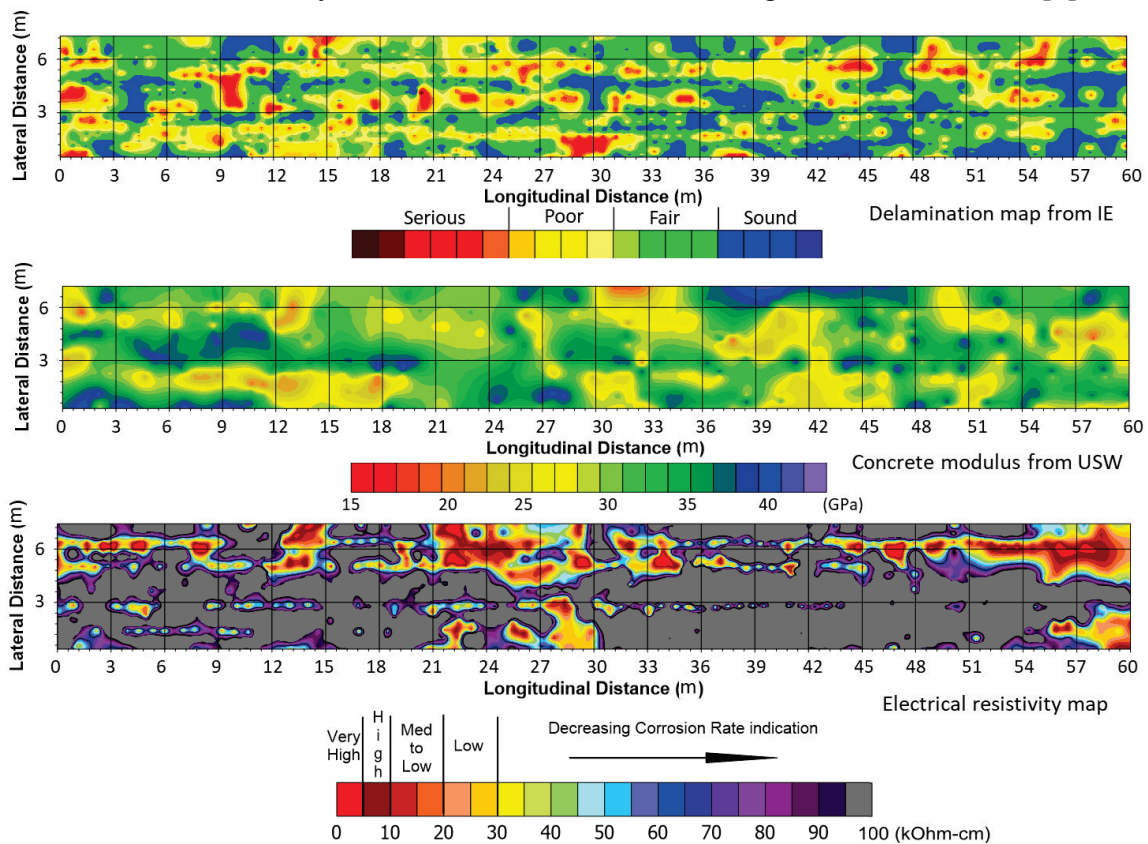


Figure 2: Delamination (top), concrete modulus (middle) and electrical resistivity maps (bottom) for Bridge no. 1328153, New Jersey.

Condition indices are used to present the overall condition of a deck. The condition index for each individual technology represents a weighted average of percentages of deck area in various states/conditions. The condition index (CI) is on a scale of 0 to 100, where 0 represents a fully deteriorated condition, and 100 a perfectly sound condition. The weight for any of the states are assigned based on their significance in the agency's decision making. For example, the FHWA's LTBP Program uses the following formula for the delamination CI:

$$\text{Delamination Index (IE)} = \frac{A_{\text{Sound}} \times 100 + A_{\text{Fair}} \times 50 + A_{\text{Poor}} \times 50 + A_{\text{Serious}} \times 0}{A_{\text{Total}}} \quad (1)$$

where  $A_{\text{Sound}}$ ,  $A_{\text{Fair}}$ ,  $A_{\text{Poor}}$ , and  $A_{\text{Serious}}$  are the areas in "Sound", "Fair", "Poor", and "Serious" conditions. A 100 weight factor is given to the sound condition, 50 to fair and poor, and a 0 weight factor to the serious state. Table 1 summarizes the results for three delamination surveys for the same bridge conducted in 2013, 2015 and 2017.

Table 1: Delamination CI and percentages of deck area in various states for Bridge no. 1328153.

Year	Condition Index	Distribution (%)			
		Sound	Fair	Poor	Serious
2013	74.1	56	30	5	8
2015	65.9	44	32	9	13
2017	59.4	34	31	20	15

Images taken by the front end cameras are stitched into images of larger sections of the deck surface and become permanent "visual inspection" records. An example of a section of a stitched deck image is shown in Fig. 3. The image represents a record of the joint condition of a skewed bridge, which in this case is clearly filled with debris. Looking into the future, comparisons of images from multiple years will provide an insight into progression of visible deterioration and defects, and repairs conducted during the same period.

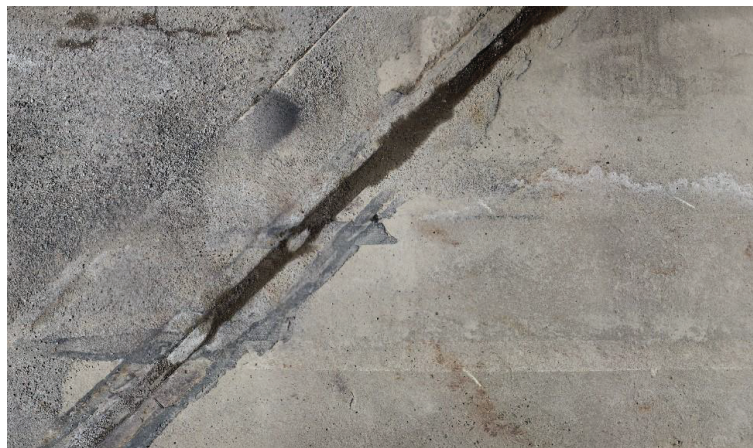


Figure 3. Image of a deck section around the joint of a bridge over Pohatcong River, Pohatcong Township, New Jersey.

### 3. Complementary forms of data presentation

The results from NDE surveys by RABIT can be merged with results from other technologies and data presentation platforms to provide a more intuitive presentation of the results. An example of one of approaches is merging of LiDAR (Light Detection and Ranging) point cloud data and a GPR condition map image from a RABIT survey is shown in Fig. 4. Condition maps from different NDE technology surveys, and for different years of surveys, can be superimposed on the LiDAR map and easily reviewed from different viewing positions.

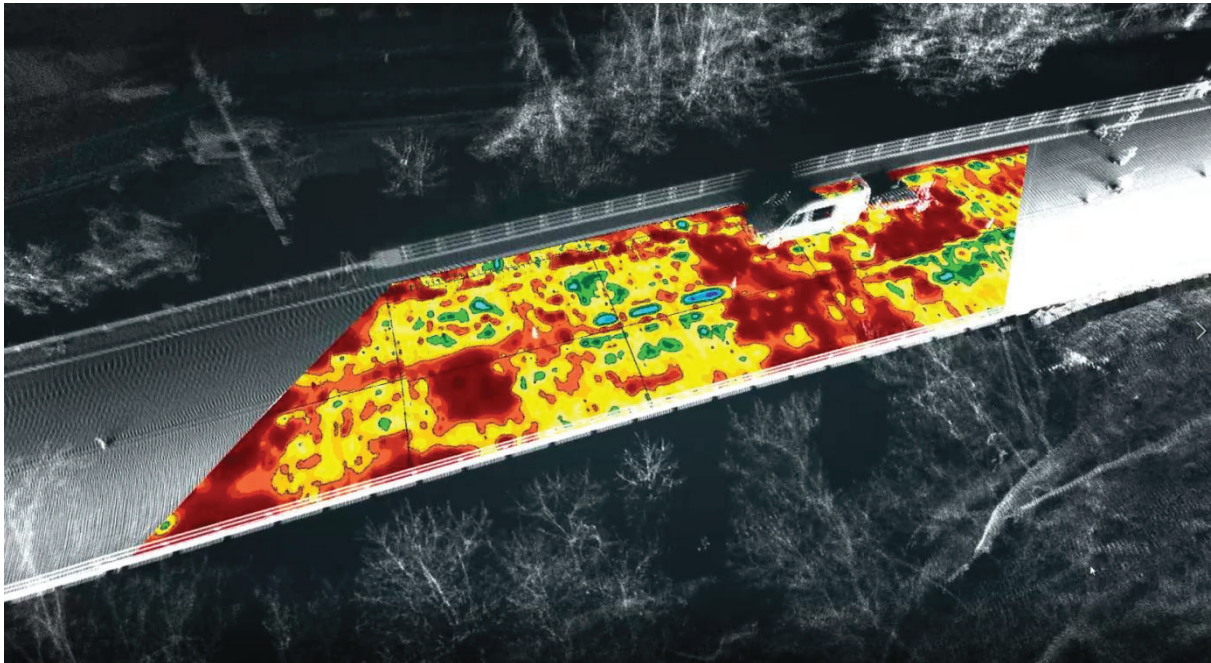


Figure 4: GPR condition map for Pohatcong Bridge superimposed on the LiDAR map.

Similarly, the NDE condition maps can be displayed in Google Earth. An example of it are the ER maps for a deck of the bridge on State Route 15 over Interstate 66 in Haymarket, Virginia, shown in Figure 5. The bridge was surveyed four times using manual NDE technologies, and once by RABIT, between 2009 and 2015. As it can be clearly observed, there was significant progression, in the size of the area affected and aggressiveness, of the concrete's corrosive environment. Similar to the ER results, results from other NDE technologies for any of the four surveys can be invoked.

### 4. Deterioration and predictive modeling using NDE results

Very important benefits from NDE surveys are stemming from the quantitative nature of the NDE results, which can be used in the development of more realistic deterioration and predictive models. As described earlier and illustrated in Tab. 1, the condition of a bridge deck can be quantified and expressed in terms of a condition index (CI) for a particular

deterioration or defect type. The indices in Tab. 1 for the assessments between 2013 and 2017 clearly point to a worsening of condition with respect to delamination.

A more comprehensive example of the use of CIs in describing progression of deterioration is shown in Fig. 6 for the Haymarket Bridge. Results for four NDE technologies: IE, ER, GPR and half-cell potential (HCP) are presented. The HCP is used to assess the probability of active corrosion in the deck reinforcement. Results from all four technologies describe a rapid progression of deterioration during the four year period.

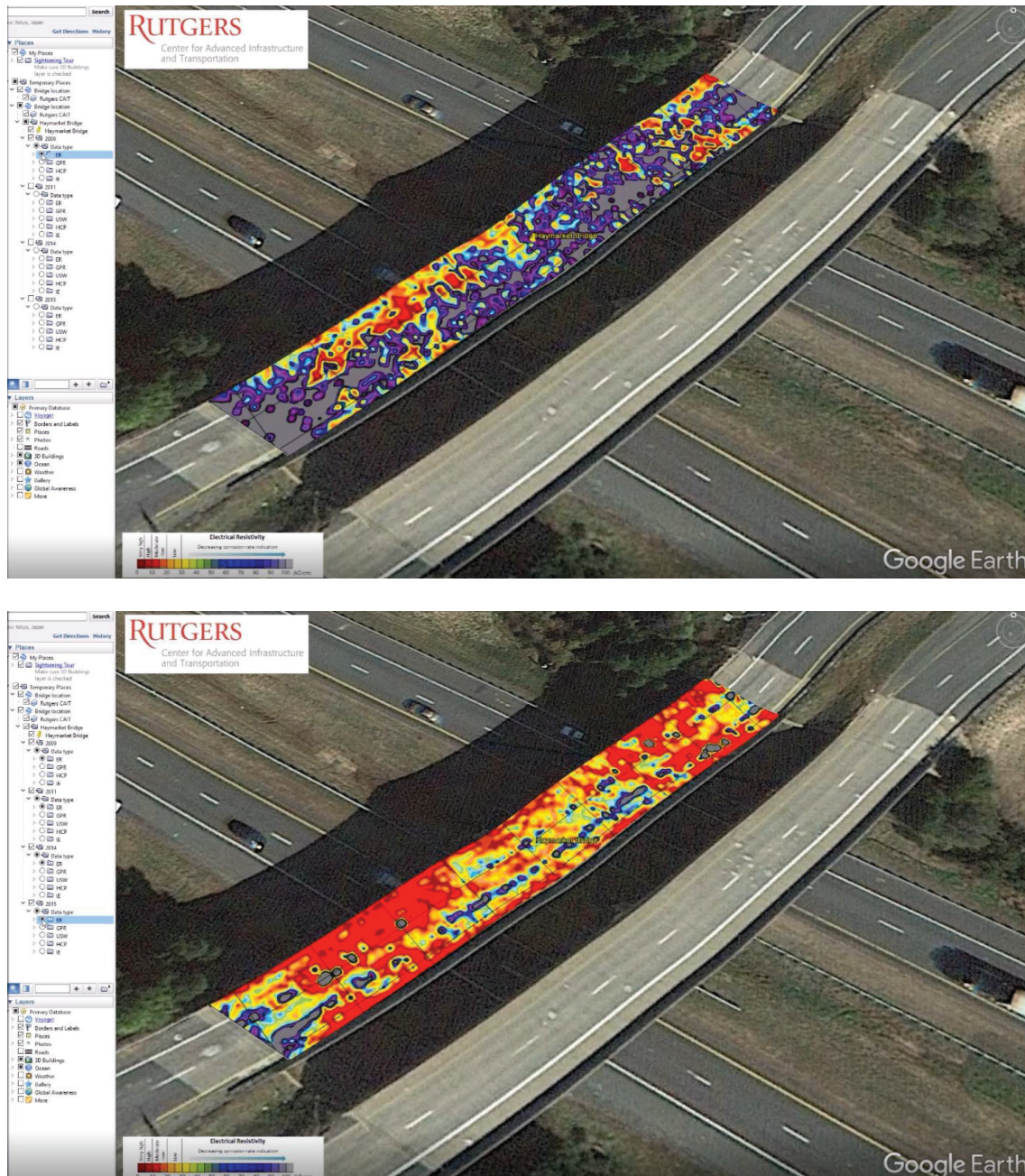


Figure 5: ER maps for 2009 (top) and 2015 (bottom) for State Route 15 over Interstate 66 bridge in Haymarket, Virginia.

In addition to the individual NDE technology indices, a combined condition index is also presented in the figure. In this case, the combined CI was calculated as a simple average of the four technology indices. In practice, the combined CI should be calculated as a weighted average of multiple technology indices based on the significance of a deterioration type in the deck maintenance decision making. Finally, to emphasize the benefit of the NDE evaluation in capturing deterioration progression, the condition rating from the National Bridge Inventory, which is based on the visual inspection, is presented in the same graph. As shown, the condition rating did not change during the same period. In fact, the data show that it did not change since 1992.

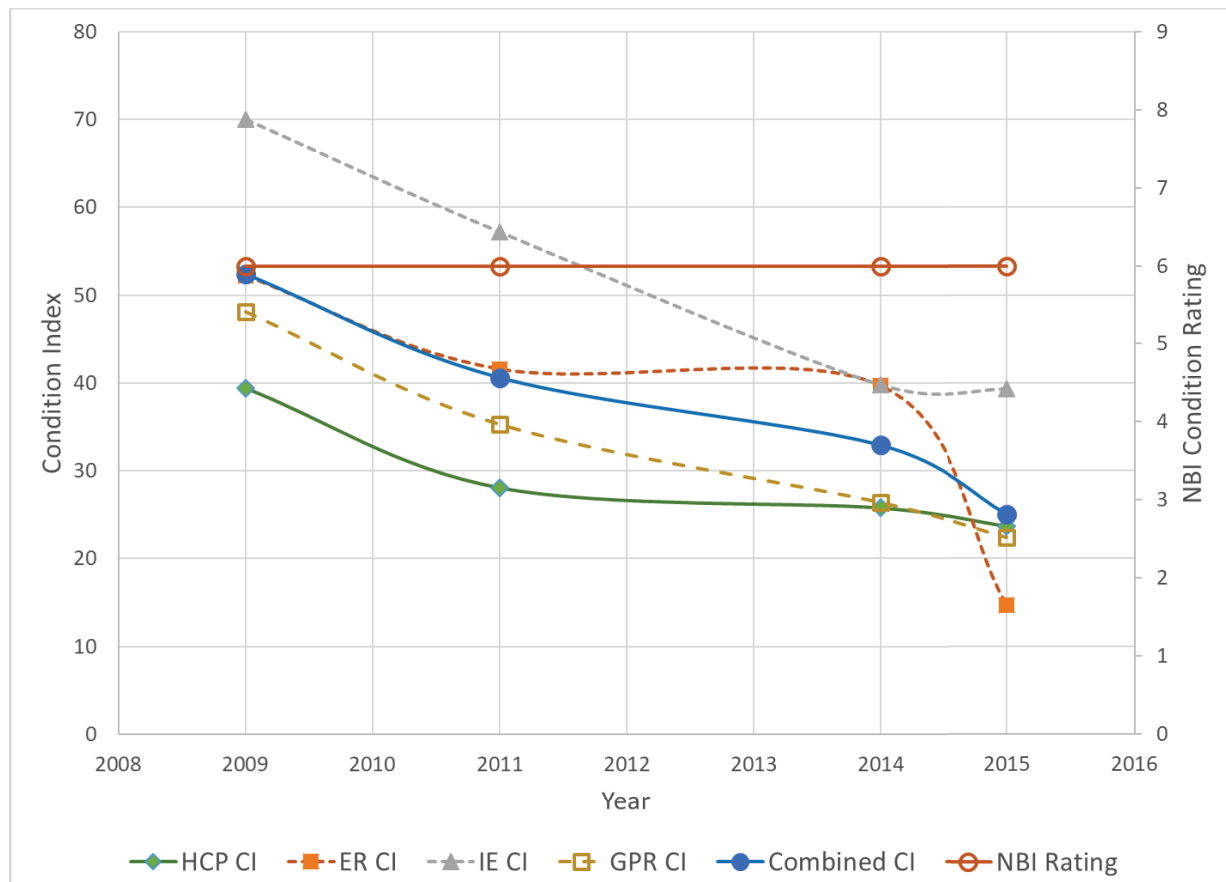


Figure 6: NDE condition indices and NBI condition ratings for the Haymarket Bridge for a period 2009-2015.

## 5. Conclusions

Accurate condition assessment of concrete bridge decks is essential for an effective bridge management. The robotic platform RABIT builds on the best practices of NDE and visual inspection for concrete bridge decks to improve the speed and cost of data collection, and accuracy of the obtained results. The improvements stem from the deployment of a large number of sensors and sensor arrays, and fully autonomous RABIT motion. Multi NDE technology data collection, including imaging, enables detection and characterization of all



primary deterioration types, and improves correlation between those to identify the primary causes of deterioration. Periodically collected data open opportunities for the development of more realistic deterioration and predictive models. Ultimately, it is expected that all the described advances will encourage bridge owners to pursue robotic bridge inspections on the network level.

## References

- [1] Sansalone, M., Impact-echo: The complete story. *ACI Materials Journal*, 94(6), (1997), 777-786.
- [2] Nazarian, S., M. R. Baker, Crain, K., Report SHRP-H-375: Development and testing of a Seismic Pavement Analyzer, Report, Transportation Research Board, National Research Council, Washington, D.C. (1993).
- [3] Gowers, K. R., Millard, S. G.: Measurement of concrete resistivity for assessment of corrosion severity of steel using Wenner technique." *ACI Materials Journal*, 96(5), (1999), 536-542.
- [4] Barnes, C. L., Trottier, J.-F.: Ground penetrating radar for network level concrete deck repair management. *Journal of Transportation Engineering, ASCE*, 126(3), (2000), 257-262.
- [5] Gucunski, N., Basily, B., Kim, J., Dinh, K., Duong, T., Kee, S.H., and Maher, A., RABIT: Implementation, performance validation and integration with other robotic platforms for improved management of bridge decks, *International Journal of Intelligent Robotics and Applications*, 1(3), (2017), 271-286.
- [6] Pailes, B.M. and Gucunski, N., Understanding multi-modal nondestructive testing data through the evaluation of twelve deteriorating reinforced concrete bridge decks, *Journal of Nondestructive Testing*, 34(4), (2015), 34: 30.

## **DEMONSTRATION PROJECTS WITH SELF-HEALING CAPSULE-BASED AND BACTERIA-BASED CONCRETE**

**Nele De Belie<sup>(1)</sup>, Maria Araujo<sup>(1)</sup>, Tim Van Mullem<sup>(1)</sup>, Elke Gruyaert<sup>(2)</sup>**

(1) Ghent University, Ghent, Belgium

(2) KU Leuven, Ghent, Belgium

### **Abstract**

To reduce downtime, costs and labour for repair of concrete structures, self-healing concrete has been proposed as a solution. Over the last decade, the efficiency of different self-healing mechanisms has been tested at laboratory scale. Lately, the first demonstrators have been made in order to test the self-healing efficiency at real scale and in actual service conditions.

At the one hand our team has cast real-scale concrete beams, containing previously selected polymeric capsules. As capsule wall material, poly(methyl methacrylate) (PMMA) was chosen due to its high chemical stability in contact with concrete, high survival ratio during the concrete mixing process and ability to rupture when crossed by cracks of small width. The self-healing efficiency of the concrete elements with randomly dispersed PMMA capsules was determined after crack creation by 3-point-bending tests.

Secondly, an in situ demonstration project was established with microbial self-healing concrete. A mixed ureolytic culture of bacterial spores (MUC+) and the nutrients urea and calcium nitrate were mixed into the concrete in a real concrete plant. With this self-healing concrete the roof plate of a sewer inspection pit was cast. From the same batch of concrete, prisms were taken to the laboratory for crack creation and evaluation of the self-healing efficiency. For cracks with an average width of 348  $\mu\text{m}$ , created after 6 weeks of curing, a sealing efficiency against water flow of more than 90% was measured after 24 weeks of water immersion.

### **1. Introduction**

While natural materials such as bone or skin are able to heal themselves in an autonomous manner after mechanical damage, traditional man-made materials generally lack this intrinsic capacity for self-healing. In 1969, self-healing properties were for the first time built-in inside

polymeric materials [1] and in the following decades publications about self-healing in thermoplastic and cross-linked systems and concrete appeared [2]. Nevertheless, it was only in 2001, through an article about self-healing in polymer based materials published in Nature, that research in the field of self-healing materials was really triggered [3]. By restoring their functional properties autonomously after damage, self-healing materials would offer tremendous advantages over traditional materials in many application areas.

An extensive review on self-healing in cementitious materials was published in 2013 [2]. This has been updated recently in three review publications by the members of the COST action CA15202 SARCOS “Self-healing as preventive repair of concrete structures”. The first paper of this series [4] focuses on the methodologies to realize self-healing concrete for damage management of structures. The second paper [5] gives insights in the experimental characterization of the self-healing capacity of cement based materials and its effects on the material performance, while the third paper [6] deals with research progress on numerical models for self-healing cementitious materials. The previously mentioned review [4] provides a state-of-the-art of recent developments of self-healing concrete, covering autogenous or intrinsic healing of traditional concrete followed by stimulated autogenous healing via use of mineral additions, crystalline admixtures or (superabsorbent) polymers, and subsequently autonomous self-healing mechanisms, i.e. via application of micro-, macro- or vascular encapsulated polymers, minerals or bacteria. The (stimulated) autogenous mechanisms are generally limited to healing crack widths of about 100-150  $\mu\text{m}$ , take several weeks or even months to heal cracks completely and heavily rely on the environmental conditions (mainly presence of water). In contrast, most autonomous self-healing mechanisms can heal cracks of 300  $\mu\text{m}$ , even sometimes up to more than 1 mm, and usually act faster (complete healing obtained in a time span of 1 day up to 3-4 weeks depending on the system). Two of these techniques, being polymeric macro-capsules with healing agent and mixed cultures of ureolytic bacteria, have been developed in our laboratory up to a level where they could be incorporated in concrete demonstration elements.

In recent years, self-healing of concrete cracks using macro-encapsulated healing agents has attracted quite some attention. However, most of the research has mainly been performed at a laboratory scale using small-scale mortar samples. Furthermore, the experiments using this self-healing approach generally involve manual placement of the capsules in the concrete matrix in strategic locations to ensure crack propagation through the capsules. The self-healing efficiency of concrete with randomly dispersed capsules is seldom investigated and it is limited to a few studies. Van Tittelboom et al. [7] evaluated the crack healing efficiency of concrete containing randomly distributed capsules filled with polyurethane. The authors concluded that a higher amount of capsules is needed to obtain the same probability of cracks hitting capsules compared to other placement methods in which capsules were strategically positioned (i.e. ideally positioned compared to the crack orientation). Although in this study some attempts have been made to increase the chance that the glass and ceramic capsules survive casting and mixing, it was observed that half of the capsules broke during mixing. In his PhD, Feiteira [8] has prepared self-healing concrete with randomly dispersed glass capsules (filled with polyurethane) with a wall thickness of 0.8 mm and a length of 3 cm. It was found that when a capsule dosage of 13 capsules per liter was used, the amount of capsules intersected by a crack was 4. This value was doubled by increasing the capsule dosage up to 36 capsules per liter. Higher dosage of capsules (up to 50 capsules per liter) are

suggested in order to achieve consistent healing efficiencies. Hilloulin et al. [9] investigated the potential of using brittle polymeric materials with a relatively low glass transition temperature ( $T_g$ ) as protection materials in self-healing concrete and found that the capsule survival probability could be improved if the capsules were heated (above  $T_g$ ) prior to mixing. Gruyaert et al. [10] explored the use of ethyl cellulose capsules containing different plasticizers to increase the survival of the capsules during concrete mixing. These plasticizing agents would make the capsules more flexible in an early stage and increase the resistance of the capsules during the mixing. Then, due to leaching out of the plasticizers, the capsules would become more brittle during concrete hardening and break more easily when a crack would form. The tested capsules could survive the concrete mixing; however, they did not break when cracks with a width of 0.4 mm were created.

In our latest work, poly(methyl methacrylate) (PMMA) with a low molecular weight was selected as the polymeric encapsulation material to test in real-scale concrete elements, based on previous results regarding the durability of the polymeric capsules in different environments (demineralized water, salt water and simulated concrete pore solution) and their compatibility with various healing agents and survival tests [11, 12]. Positive results with regard to strength regain and regain in liquid-tightness using encapsulated one-component polyurethane were obtained in lab-scale proof-of-concept tests [13]. Since compatibility tests showed that PMMA capsules are compatible with PU, this healing agent seemed to be the preferential choice. However, when capsules were filled with a polyurethane pre-polymer, it was noticed that the healing agent cured prematurely inside the capsules within a few days. The reason is that the polyurethane pre-polymer polymerizes in the presence of moisture/air and the capsules are not completely impermeable. Therefore, a water repellent agent finally was selected as agent to be encapsulated in the PMMA tubes for the larger scale experiments. A water repellent agent will not physically block the cracks, but will prevent ingress of water containing aggressive agents into the concrete matrix. Hence the main goal of self-healing concrete, i.e. to restore the durability of the concrete element after cracking, can be reached.

Based on the results of the EC FP7 project HEALCON, a second demonstrator was cast in situ, incorporating a bacterial healing agent. The HEALCON project, which was completed at the end of 2016, aimed to bring the self-healing concrete one step closer to the market. The most promising self-healing agents were further developed and upscaled, applied in large-scale concrete elements and tested with regard to the self-healing performance [14]. In 2017, one of the upscaled healing agents, a mixed ureolytic culture ( $MUC^+$ ) developed by the HEALCON partner Avecom, was incorporated in a roof plate of an inspection pit. This inspection pit is part of the preparatory works for the Oosterweel link in the city of Antwerp, Belgium.  $MUC^+$  consists of a mixture of MUC (mixed ureolytic culture derived from microbial biomass from a vegetable treatment plant with high ureolytic activity and no need of encapsulation [14]) and anaerobic granular bacteria with high  $CO_2$  production and  $CaCO_3$  precipitation capability. In comparison to axenic cultures, these non-axenic cultures can be produced at a low cost. Through their metabolism, ureolytic bacteria enzymatically transform the urea that is provided as nutrient into ammonium and carbonate ions and the latter will combine with calcium from the concrete matrix and/or an added calcium source to form calcium carbonate which heals formed cracks.

## 2. Materials and methods

### 2.1 Concrete beam with macro-capsule based self-healing system

The poly(methyl methacrylate) (PMMA) was supplied by Evonik Performance Materials (Plexiglas 8909,  $M_n = 38000$  g/mol). Hollow tubes were extruded on a Bradender extruder equipped with a single screw and a tubular die (OD: 10 mm; ID: 8 mm). The processing temperature was 225-235 °C and the screw speed was 10 min<sup>-1</sup>. The wall thickness of the tubes was controlled by adjusting the conveyor speed (0.2 – 1 m/min):  $\varnothing_{\text{outer}} = 6.5$  mm, wall thickness = 0.7 mm. The capsules used in the large scale experiments were filled with a water repellent agent (WRA, Sikagard 750L) supplied by Sika Belgium nv [12].

Two real-scale concrete beams (250 cm × 40 cm × 20 cm) were made with self-compacting concrete. One of them contained PMMA capsules, another one was a reference beam without capsules. All mixes had the same composition (853 kg/m<sup>3</sup> sand 0/5, 370 kg/m<sup>3</sup> gravel 2/8, 328 kg/m<sup>3</sup> gravel 8/16, 300 kg/m<sup>3</sup> CEM I 52.5 N, 300 kg/m<sup>3</sup> limestone filler, 165 l/m<sup>3</sup> water and 2.5 l/m<sup>3</sup> superplasticizer). For the beam with self-healing properties, PMMA capsules were added during the last minutes of the mixing process. A vertical shaft mixer (200 L) with a rotating pan was used to mix all components. As PMMA capsules tend to float due to their relatively low density, the concrete was cast in 2 layers. First, a concrete mix containing the capsules (approximately 22 capsules per liter of concrete) was prepared and poured into the mould (layer of 12 cm). Then, another mix (without capsules) was made and placed into the mould on top of the previous layer (Fig. 1).

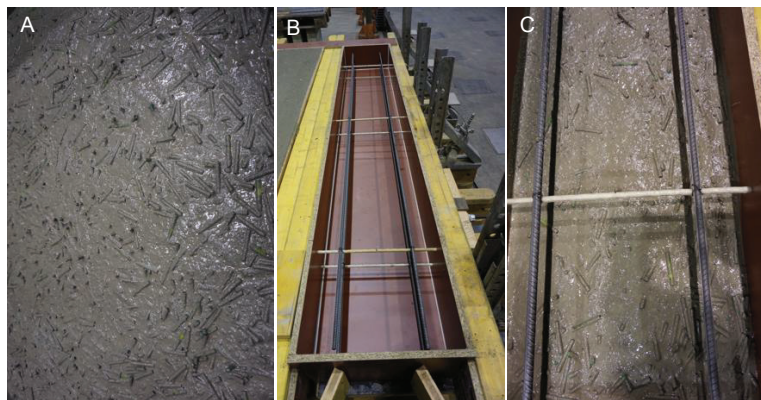


Figure 1: Concrete beam with self-healing properties. (A) Concrete mix with dispersed PMMA capsules; (B) Position of the reinforcement bars within the mould; (C) Concrete mix with randomly dispersed capsules poured into the mould, forming a layer of 12 cm.

At the age of 14 days, 6 cracks with varying crack widths (0.3 till 0.6 mm) were created in each beam by means of consecutive 3-point-bending tests. To create localized cracks, a notch was sawn at the corners of the beam in the middle of the span for the 3-point bending. One crack per day was created by moving the 3-point-bending set-up along the length of the beam. Immediately after cracking, the notches were filled with a shrinkage-free repair mortar to fix the crack opening. The load was only removed after sufficient hardening of the repair mortar. The final crack widths of each crack were measured at 6 positions using an optical microscope.

The self-healing efficiency of the concrete beams was evaluated by determining the resistance of the self-healed concrete against chloride ingress. The beams were positioned slightly tilted with the cracks in the upper surface and a 3 wt% NaCl solution was flown over the beams during 24 uninterrupted hours per week (Fig. 2). This 1 day wet – 6 days dry cycle was repeated during 6 consecutive weeks. Prior to exposure, all sides of the beams except the top and bottom surfaces were covered with a waterproof aluminium foil so that only the top surface was exposed to the chloride solution.

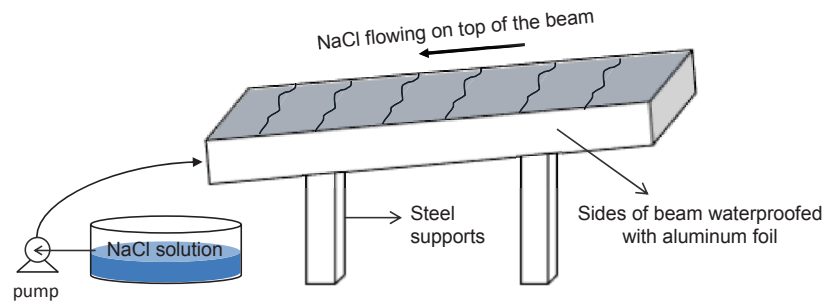


Figure 2: Schematic representation of a concrete beam exposed to 3 wt% NaCl solution.

To determine the chloride ingress, 2 cores with a diameter of 150 mm, with a crack inside, were extracted from each beam. Subsequently, each core was split along the crack surface and one half was then used to measure the chloride ingress. This was done by grinding off material at various depths (5, 25, 50 and 85 mm) in 2 mm layers perpendicular to the crack face. In addition, material was ground from the exposed surface downwards. Concrete powders were collected from ten layers for each zone and dried in an oven at 95 °C for at least 7 days. The total chloride concentration per ground layer was determined by an acid-soluble extraction in a nitric acid ( $\text{HNO}_3$ ) solution followed by a potentiometric titration against silver nitrate. More details about the test procedure can be found in [15].

## 2.2 Concrete slab with self-healing properties through incorporation of mixed ureolytic bacterial cultures

Bacterial self-healing concrete was produced at a concrete plant in Merksem, nearby the location of the inspection pit in which the concrete would be applied. A cement type CEM III/B 42.5N was used ( $430 \text{ kg/m}^3$ ) and a water-to-cement ratio of 0.46. The self-healing agent,  $\text{MUC}^+$  provided in powder form, was added in a dosage of 1% vs. cement mass in the concrete mix. Additionally, a precipitation precursor (urea) and a calcium source (calcium nitrate tetrahydrate), which function as bacterial nutrients, were added to the concrete mixture in a dosage of 1 m% vs. cement mass. These products were dissolved in a part of the mixing water and were separately added to the concrete mix, together with the  $\text{MUC}^+$ , via an inspection opening above the mixer. About  $3.5 \text{ m}^3$  of this bacterial self-healing concrete was produced. The fresh concrete properties measured at the mixing plant showed that the slump amounted to 90 mm and the air content was 4.5%.

The roof plate (Fig. 3) was prefabricated on the construction site near the inspection pit and installed on the pit 5 weeks after fabrication. Visual inspection 6 months after casting (and before filling of the pit with earth) showed that the surface was at that time still free of cracks.



Figure 3: Inspection pit (left) and roof plate made of self-healing concrete with MUC+ (right)

In order to test the sealing capacity of the concrete, 5 prisms (150 x 150 x 550 mm) were cast on site. These prisms contained 2 reinforcement bars ( $\varnothing$  6 mm) located at 30 mm from the bottom side and 3 glass tubes ( $\varnothing$  10 mm) located at 60 mm from the top side. After 6 weeks of curing the beams were cracked in a three point bending setup with a span of 450 mm aiming at a final crack width around 350  $\mu$ m. After sealing the cracks at the sides of the specimens, the prisms were saturated for 5 days in tap water, after which an initial water flow test was performed (see [8] for a more detailed description). In short, one side of the glass tubes was sealed, while the other side was connected to a water reservoir under 1 bar pressure. Water would flow from the reservoir to the broken glass tubes, into the crack and leak out at the bottom side of the cracks. The water leakage in function of healing time was quantified by capturing the water over a 15 minutes test duration in a container on a scale with automatic logging. Water flow measurements were performed on the initially unhealed specimens (immediately after crack formation) and then once every 3 weeks during the healing period. During this period the specimens were submersed in tap water and measurements were taken until a 24 weeks healing period was reached. The sealing efficiency SE after different healing times can then be calculated based on Eq. (1).

$$SE = \frac{WF_{initial} - WF_t}{WF_{initial}} \cdot 100\% \quad (1)$$

in which  $WF_{initial}$  is the initial water flow (g/min) and  $WF_t$  is the water flow after t weeks of healing.

### 3. Results

#### 3.1 Concrete beam with macro-capsule based self-healing system

During loading of the beams containing encapsulated healing agent, leaking of the healing agent was detected, indicating that some capsules were crossed by the crack and broke. From previous results the PMMA capsules are expected to rupture when crossed by cracks of around 100  $\mu$ m in width [16].

While exposing the concrete beams to the chloride solution, spots where the WRA leaked out could be clearly identified on the concrete beams, as shown in Fig. 4. This also confirms that some of the randomly dispersed capsules broke during crack formation and release their content. A reduction in the ingress of aggressive liquids is therefore expected for the concrete beams with self-healing properties.

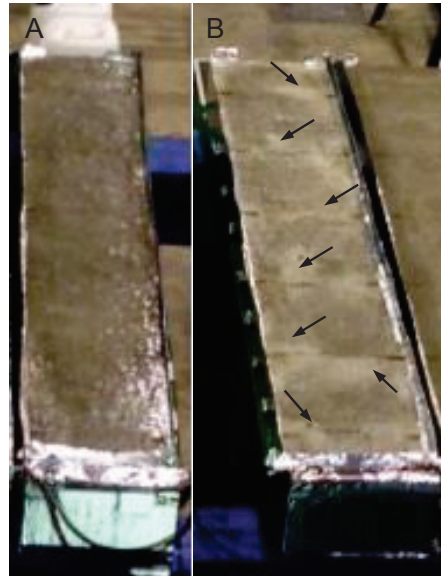


Figure 4: Concrete beams exposed to the chloride solution: (A) Reference beam without capsules; (B) Beam with self-healing properties provided by PMMA capsules. Arrows indicate the spots where leakage of WRA was visible.

The experimentally determined chloride profiles for all cracked (REF) and healed (PMMA) samples in the crack zone, when drilling down from the exposed surface, are shown in Fig. 5.

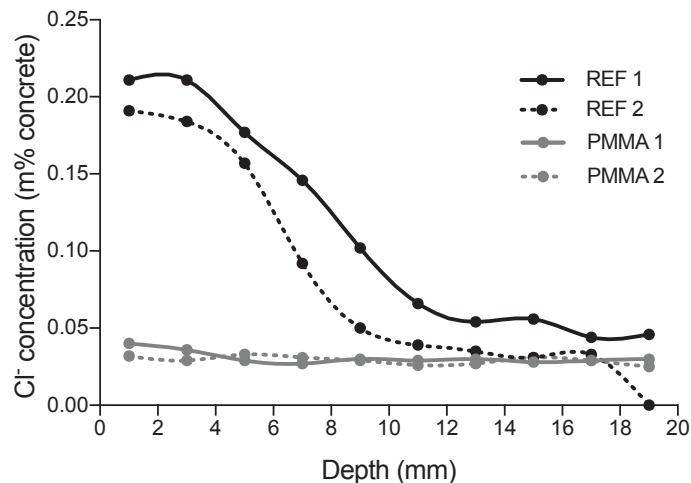


Figure 5: Chloride profiles taken near the cracks after 6 weeks of wet-dry cycles including 5 days dry period and 1 day exposure to a 3 wt% NaCl solution.



For the samples taken from the beam with PMMA capsules, the chloride concentration is approximately constant at every depth. When comparing with cracked concrete it is clear that the chloride content is considerably reduced due to release of healing agent from the capsules. For the reference samples, the highest chloride concentrations at every depth are found near the exposed surface. The chlorides have not only penetrated from the surface, but also through and perpendicular to the crack. The chloride profiles taken perpendicular to the crack face can be found in [17]. Here it is obvious that for the specimens containing PMMA capsules, the chloride concentration in the layer at 5 mm below the exposed surface may be more elevated, while the profiles taken deeper down (at 25, 50 and 85 mm from the exposed surface) show low chloride concentrations. For the reference cracked concrete, however, it was clear that the chloride concentration increased when approaching the crack wall. These results show that the ingress of chlorides is considerably reduced in areas where WRA was released from the capsules. This stresses the importance of having a uniform distribution of the capsules to achieve the highest possible sealing efficiencies.

### 3.2 Concrete slab with self-healing properties through incorporation of mixed ureolytic bacterial cultures

The results of the crack width measurements performed prior to saturation of the prisms that were cast alongside the slab, as well as the water flow results are given in Tab. 1. The average crack width of the specimens is equal to 348  $\mu\text{m}$  with a coefficient of variance of 6.7%. During the healing period deposition of  $\text{CaCO}_3$  crystals was noticed at the crack mouth. Evaluation of the crack widths and the initial water flows in Tab. 1 makes clear that the internal geometry of the cracks will have a large effect on the water flow. Specimens 3 and 5 for instance have the same mean crack width, however they show clearly different water flow values. Tab. 1 indicates that some healing is already obtained after 3 weeks in submersed conditions (average SE above 50%). The healing keeps increasing with time and the SE reaches an average value of 96% after 24 weeks.

Table 1: Overview of water flow and initial crack width measurements, as well as the calculated sealing efficiency after 3, 12 and 24 weeks submersed healing.

	Mean crack width [ $\mu\text{m}$ ]	Initial water flow [g/min]	SE after 3 wk healing [-]	SE after 12 wk healing [-]	SE after 24 wk healing [-]
1	335	60.9	39%	65%	97%
2	320	33.4	49%	97%	100%
3	352	45.7	74%	81%	98%
4	383	26.9	50%	73%	86%
5	352	7.1	72%	100%	100%
<b>Mean</b>	348		57%	83%	96%

#### 4. Conclusions

Two demonstrators were prepared to evaluate the self-healing efficiency of two different self-healing methodologies for concrete.

First a real-scale concrete beam (250 cm × 40 cm × 20 cm) was made with self-compacting concrete containing PMMA macro-capsules filled with a water repellent agent. Since PMMA capsules tend to float, the concrete was cast in 2 layers. At the age of 14 days, 6 cracks of 0.3-0.6 mm in width were created. When exposing the beams to a 3 wt% NaCl solution it was clear that WRA was released from the capsules and made also part of the concrete surface water repellent. When comparing the self-healing beam with a reference beam it was clear that the chloride ingress was considerably reduced due to release of WRA from the capsules.

Secondly, a mixed ureolytic culture of bacteria (MUC<sup>+</sup>) was incorporated in a roof plate of an inspection pit in a dosage of 1% vs. cement mass. Additionally, urea and calcium nitrate tetrahydrate were added to the concrete mixture in a dosage of 1 m% vs. cement mass. Visual inspection 6 months after casting showed that the surface of the plate was at that time still free of cracks. Water flow tests were executed on prisms (150 x 150 x 550 mm) cast on site and cracked in a three point bending setup aiming at a final crack width around 350 µm. This allowed to illustrate that, if cracks appear, some healing is already obtained after 3 weeks in submersed conditions (average SE above 50%), and reaches on average values of 96% after 24 weeks.

#### Acknowledgements

The research leading to these results has received funding from the European Union Seventh Framework Programme (FP7/2007-2013) under grant agreement n° 309451 (HEALCON) and from VLAIO (Flanders Innovation & Entrepreneurship) for the project “Encapsulation of polymeric healing agents in self-healing concrete: capsule design”. T. Van Mullem acknowledges the grant (17SCIP-B103706-03) from the Construction Technology Research Program funded by Ministry of Land, Infrastructure and Transport of Korean Government.

#### References

- [1] Malinskii, Y.M. et al, Investigation of self-healing of cracks in polymers, *Mekhanika Polim.* 2 (1969), 271-275
- [2] Van Tittelboom, K. and De Belie, N., Self-healing in cementitious materials - a review, *Materials* 6 (2013), 2182-2217
- [3] White, S.R. et al, Autonomic healing of polymer composites, *Nature* 409 (2001), 794-797
- [4] De Belie, N. et al, A review of self-healing concrete for damage management of structures. *Advanced Materials Interfaces* (2018), 1800074, in press
- [5] Ferrara, L. et al, Experimental characterization of the self-healing capacity of cement based materials and its effects on the material performance: A state of the art report by COST Action SARCOS WG2, *Construction and building materials* 167 (2018), 115-142.
- [6] Jefferson, A.D. et al, Research progress on numerical models for self-healing cementitious materials. *Advanced Materials Interfaces* (2018), 1701378, 19 p

- [7] Van Tittelboom K, et al, The efficiency of self-healing concrete using alternative manufacturing procedures and more realistic crack patterns. *Cement and Concrete Composites* 57 (2015),142-152
- [8] Feiteira, J., Self-healing concrete encapsulated polymer precursors as healing agents for active cracks, PhD thesis, Ghent University (2017)
- [9] Hilloulin, B. et al, Design of polymeric capsules for self-healing concrete. *Cement and Concrete Composites* 55 (2015), 298-307
- [10] Gruyaert, E. et al, Capsules with evolving brittleness to resist the preparation of self-healing concrete. *Materials de Construcción* 66 (323) (2016), e092, 13 p
- [11] Gruyaert, E. et al, Test method to assess the survival probability of capsules in self-healing concrete, 6th International Conference on Self-Healing Materials. Graf-Zeppelin-Haus, Friedrichshafen, Germany (2017)
- [12] Araújo, M. et al, Design and testing of tubular polymeric capsules for self-healing of concrete, 3rd International conference “Innovative Materials, Structures and Technologies” IMST2017, Riga, Latvia (2017). *Journal of Physics: IOP Conference Series: Material Science Engineering* 251, 012003.
- [13] Van Tittelboom, K et al, Self-healing efficiency of cementitious materials containing tubular capsules filled with healing agent. *Cement and Concrete Composites*, 33(4) (2011), 497-505
- [14] Gruyaert, E. et al, Evaluation of the performance of self-healing concrete at small and large scale under laboratory conditions, *Proceeding of the XIV DBMC - 14th International Conference on durability of building materials and components*, PRO 107, Ghent (2017), 203-204, paper 203, 12 p
- [15] Araújo, M. Design of novel polymeric healing agents and cylindrical capsules for self-healing concrete, PhD thesis, Ghent University (2018)
- [16] Šavija, B. et al, Simulation aided design of tubular carriers for self-healing concrete. *Materials* 10 (10) (2017), 13 p
- [17] Araújo, M. et al, Poly(methyl methacrylate) capsules as an alternative to the “proof-of-concept” glass capsules used in self-healing concrete, *Cement and concrete composites*, 89 (2018), 260-271.

## **COST ACTION TU1404**

**RRT<sup>+</sup>, NUMERICAL BENCHMARKING AND RECOMMENDATIONS**

## **COMPILED COST ACTION RRT<sup>+</sup> RESULTS FROM NTNU: DETERMINATION OF PARAMETERS REQUIRED FOR EARLY AGE CRACK ASSESSMENT**

**Anja Estensen Klausen<sup>(1)</sup>, Terje Kanstad<sup>(1)</sup>, Emmanuel Roziere<sup>(2)</sup>**

(1) Norwegian University of Science and Technology (NTNU), Trondheim, Norway

(2) CENTRALE NANTES, Nantes, France

### **Abstract**

Volume changes of concrete in the hardening phase and the associated cracking risk can be predicted by using calculation methods to assess the early age structural behaviour of the concrete. Based on such calculations and corresponding material parameters determined from laboratory experiments, proper choice of concrete type, mineral additives and execution methods on-site can be taken to minimize or avoid cracking. The current article constitutes a compilation of the Cost Action TU1404 RRT results from NTNU, and it aims to provide a set of parameters necessary to perform early age crack assessment of the investigated concrete. A vital part of the current test program was the Temperature-Stress Testing Machine (TSTM) at NTNU, which measures the restrained stress development of concrete through the hardening phase.

### **1. Introduction**

Concrete in the hardening phase is subjected to volume changes caused by thermal dilation (TD) and autogenous deformation (AD). If these volume changes are restrained, they may lead to cracking and further to functionality, durability, and esthetical issues. The volume changes of concrete and the associated cracking risk can be predicted by using calculation methods to assess the early age structural behaviour of the concrete. Based on such calculations and corresponding material parameters determined from laboratory experiments, proper choice of concrete type, mineral additives and execution methods on-site can be taken to minimize or avoid cracking.

An extensive RRT program was initiated by the Cost Action TU1404 [1], and involved testing of properties of concrete by various European laboratories using both standardised and non-

standardised methods. The current article constitutes a compilation of the RRT results from NTNU, and aims to provide a set of parameters necessary to perform early age crack assessment of the investigated concrete. A vital part of the current test program was the Temperature-Stress Testing Machine (TSTM) at NTNU [2].

## 2. Experimental set-up

### 2.1 Property development

Compressive strength, direct uniaxial tensile strength and E-modulus in compression were tested under 20 °C isothermal conditions.

Compressive strength tests were performed on  $\varnothing 100 \times 200$  mm cylinders according to NS-EN 12390-3:2009.

Uniaxial tensile tests were performed by the standard method at SINTEF/NTNU in Norway: a uniaxial load was applied the  $100 \times 100 \times 600$  mm specimen until it developed failure in tension. During testing, the deformation was measured over the 100 mm mid-section by two displacement transducers placed on opposite side of the prism. The strain rate was approximately  $100 \times 10^{-6}$  per min.

Modulus of elasticity in compression tests were performed on  $\varnothing 100 \times 200$  cylinders according to the Norwegian standard NS3676.

### 2.2 TSTM-System

The Temperature-Stress Testing Machine (TSTM) System at NTNU consists of a Dilation Rig and a TSTM, Fig. 1. The Dilation Rig measures free deformation, i.e. thermal dilation (TD) and autogenous deformation (AD), while the TSTM is constructed to measure the stress generation of concrete through the hardening phase. The TSTM-system is temperature controlled, i.e. it is possible to prescribe and apply realistic or isothermal temperature histories to the two concrete specimens.

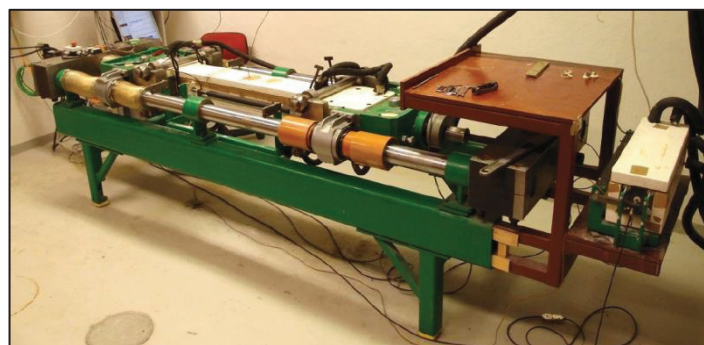


Figure 1: The TSTM-system at NTNU

The TSTM is both deformation-controlled and load-controlled. By applying a given degree of restraint and a chosen temperature history, the TSTM can directly simulate the stress development in a selected section of a concrete structure. During testing, a comprehensive stress-strain relation for each TSTM regulation is obtained. This stress-strain relation provides

an incremental E-modulus development (i.e. obtained from incremental loading) over time for the concrete in question. The stress development from the TSTM tests was also used to determine the start time for stress calculations,  $t_0$  [2]. After testing, temperature steps of  $\pm 3$  °C around an initial temperature of 20 °C was applied to the TSTM-system to determine the Coefficient of Thermal Expansion (CTE).

### 3. Materials and experimental program

All tests were performed on the ordinary concrete mixture (OC) as defined by TU1404 [1]. The mix design is presented in Tab. 1 a), and the test program is given in Tab. 1 b). During the realistic-temperature TSTM test, the concrete was subjected to a temperature history provided by Vercors project [1], Fig. 2.

Table 1: a) Concrete mix-design and b) Test program

a)		b) Test method	Test age [Days]
Cement CEM I 52,5 N-SR3	320	Compressive strength	7, 28
Sand 0-4	830	Tensile strength	7, 28
Gravel 4-11	449	E-modulus in compression	7, 28
Gravel 8-16	564	TSTM – isothermal, $R = 1.0^*$	0 - 62
Admixture	1.44	TSTM – realistic temp., $R = 0.5^*$	0 - 15
Added water	172.4		

*\*) R = degree of restraint*

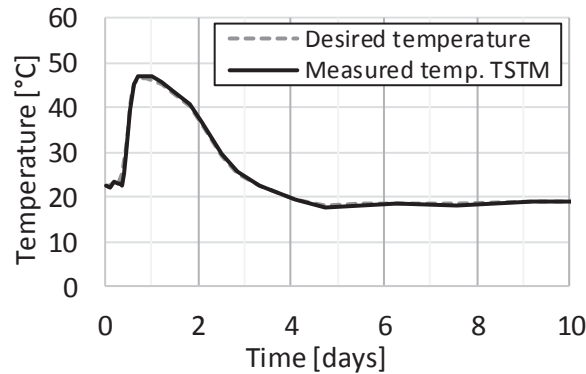


Figure 2: Temperature in the TSTM during testing

### 4. Material models and stress development calculations

The compressive strength, tensile strength and E-modulus were modelled by Eq. 1, which is a modified version of the CEB-FIP MC 1990-model, see [3] and [4]. The  $s$ -parameter is the

same for all properties, while the  $n$ -parameter is varying. The 28-days properties as well as the curve-fitting parameters were determined by parallel mechanical testing.

$$X(t_e) = X(28) \cdot \left\{ \exp \left[ s \cdot \left( 1 - \sqrt{\frac{672 - t_0}{t_e - t_0}} \right) \right] \right\}^n \quad (1)$$

where  $X(t_e)$  is the property as a function of maturity  $t_e$ .  $X(28)$  is the property at 28 days,  $s$  and  $n$  are curve-fitting parameters, and  $t_0$  is the start time for stress development [maturity time]

The stress development measured in the TSTM was also calculated by a calculation routine in Excel and Visual Basic. The stress calculations were based on linear viscoelasticity with age adjusted effects, using the degree of restraint, the measured temperature and free deformation from the dilation rig as input data [2].

## 5. Test results and discussion

Material parameters for the OC was determined by fitting the material model described in the previous section to the results from the mechanical test series by using the method of least squares. The  $s$ -parameter was determined based on the measured incremental E-modulus development during the realistic TSTM-test, while the  $n$ -parameters and the property values at 28 days were found from the 7-day and 28-day values determined by the test program, see Tab. 2. The creep parameters were estimated based on previous experience, and then adjusted by fitting the calculated stress development to the measured stress development. The obtained model parameters are presented in Tab. 3.

Measured and modelled property developments are presented in Fig. 3. The two E-modulus test set-ups, i.e. the TSTM and the mechanical tests, provided good agreement.

Table 2: Test results, average values

Time [Days]	$f_c^*$ [MPa]	$f_t$ [MPa]	$E_c$ [GPa]	$E_{TSTM}$ [GPa]	$t_0$ [h]	CTE [MPa]
7	34.0	2.9	30.5	30.4	-	-
28	48.4	3.8	31.9	33.0	-	-
-	-	-	-	-	10.3	8.9**

\*) Cylinder strength

\*\*\*) Average value of 15.8 days (CTE = 8.7) and 62.5 days (CTE = 9.1)

Table 3: Deduced model parameters (where  $f_{c28}$  = cylinder strength)

Property development						Deduced creep parameters		
$s$	$n_t$	$n_E$	$f_{c28}$ [MPa]	$f_{t28}$ [MPa]	$E_{28}$ [GPa]	$\Phi_0$	$p$	$d$
0.342	0.754	0.321	48.4	3.8	33.0	0.65	0.20	0.40



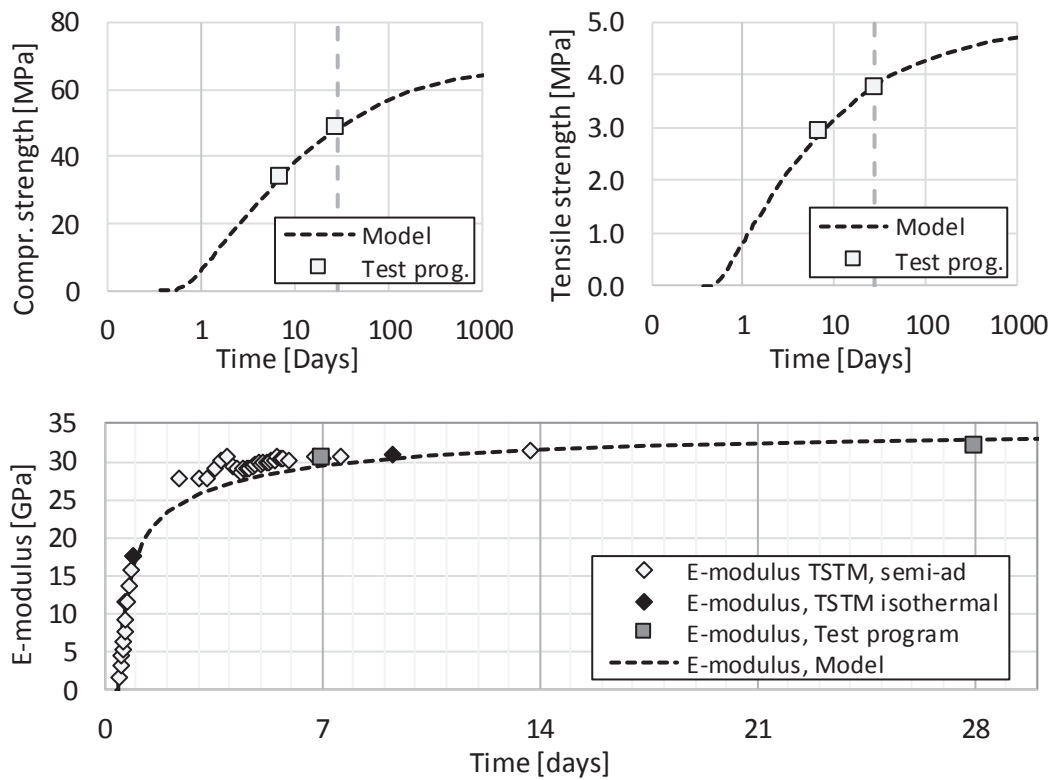


Figure 3: Property development

The AD developments were deduced by subtracting the TD from the total measured free deformation. The results are presented in Fig. 4a, and show that the concrete experiences a rather limited AD development under both isothermal and realistic temperature curing conditions.

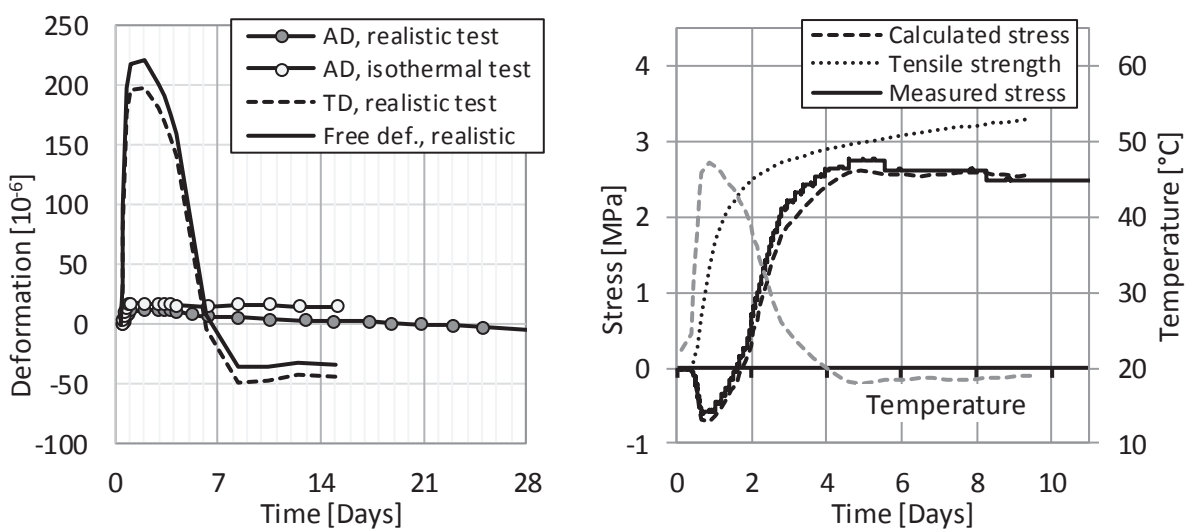


Figure 4: a) Measured deformation b) Measured and calculated stress development

The measured and calculated stress developments for the TSTM-test at realistic temperature conditions and a degree of restraint of 50% are presented in Fig. 4b. The agreement between measured and calculated stress is obviously good, as the creep parameters were deduced by fitting the calculated stress curve to the measured stress development. No dedicated creep tests were included in the current test program, however, previous experience has shown good agreement between creep parameters deduced from 1) stress development tests in the TSTM and 2) dedicated creep tests in the TSTM [2, 5].

## 6. Summary and conclusion

The current article constitutes a compilation of the Cost Action TU1404 RRT results from NTNU. Based on these results, the article proposes a set of parameters necessary to perform early age crack assessment of the investigated concrete. By using these model parameters combined with dedicated calculation methods to assess the early age structural behavior of the concrete, the volume changes of the concrete and the associated cracking risk can be predicted. Based on such calculations, proper choice of concrete type, mineral additives and execution methods on-site can be taken to minimize or avoid early age cracking.

## Acknowledgements

The article is based on work performed in the User-driven Research-based Innovation project DaCS (Durable advanced Concrete Solutions, 2015 - 2019) and the COST Action TU1404 ([www.tu1404.eu](http://www.tu1404.eu)).

## References

- [1] Cost Action TU1404, RRT+, Main phase of the Extended Round Robin Testing programme for TU1404, TESTING PROTOCOLS, 2016.
- [2] Anja Estensen Klausen, Early age crack assessment of concrete structures: experimental determination of decisive parameters, PhD Thesis, ISBN 978-82-326-1850-7 [printed ver.], ISBN 978-82-326-1851-4 [electronic ver.], Norwegian University of Science and Technology (NTNU), Trondheim, Norway, 2016.
- [3] Terje Kanstad, Tor Arne Hammer, Øyvind Bjøntegaard, Erik J. Sellevold, Mechanical properties of young concrete: Part II: Determination of model parameters and test program proposals, *Materials and Structures* 36 (2003) pp. 226-230.
- [4] Jan-Erik Jonasson, Peter Fjellström, Henrik Bäckström, Inverkan av variabel härdningstemperatur på betongens hållfasthetsutvikling (The influence of variable curing temperature on the strength development of concrete - only available in Swedish), *Bygg & Teknik* (2010)
- [5] Anja Estensen Klausen, Terje Kanstad, Øyvind Bjøntegaard, Erik J. Sellevold, Comparison of tensile and compressive creep of fly ash concretes in the hardening phase, *Cement and Concrete Research* 95 (2017) pp. 188-194.

## **MECHANICAL PROPERTIES OF CEMENT BASED MATERIALS – EXTENDED ROUND ROBIN TEST OF COST ACTION TU 1404**

**Violeta Bokan Bosiljkov <sup>(1)</sup>, Marjeta Kramar Fijavž <sup>(1)</sup>, Marijana Serdar <sup>(2)</sup>**

(1) University of Ljubljana, Faculty of Civil and Geodetic Engineering, Slovenia

(2) University of Zagreb, Faculty of Civil Engineering, Croatia

### **Abstract**

The Extended Round Robin Testing program (RRT+) of COST ACTION TU1404 is the main activity within Working Group 1 (WG 1): Testing of cement-based materials (CBMs). In its Main Experimental Phase the RRT+ program is divided into six group priorities, among which group priority 1d (GP1d) deals with mechanical properties and creep of CBMs across several scales: hardened cement paste, mortar and concrete. One of the aims of the RRT+ as a whole is to extensively characterize a set of predefined CBMs and support the development and validation of material models in WG2 - modelling and benchmarking. At the end of the Main Experimental Phase of RRT+, results of 15 laboratories were available for analyses in the scope of GP1d. This paper focuses on statistical analysis of reported test results. The analysis was carried out for properties at 7 and 28 days, where the number of reported test results was high enough. For the compressive strength, observations of the mortar and concrete scale are given. For the tensile strength and unloading E-modulus, only the results at concrete scale are presented and discussed.

### **1. Introduction**

The Extended Round Robin Testing program (RRT+) of COST ACTION TU1404 European project is the main activity within Working Group 1 (WG 1): Testing of cement-based materials (CBMs) [1]. The Main Experimental Phase of the RRT+ started in November 2016, after detailed guidelines for the test protocols [2] had been made available on the Action web site [1]. Test protocols under group priority 1d (GP1d) of WG1 can be broadly divided into two stages. The first stage includes the determination of the basic mechanical properties of hardened cement paste, mortar and concrete, which are compressive strength, splitting tensile strength and unloading E-modulus from compression (with Poisson's ratio) and dynamic

characterization of isotropic elasticity by ultrasound test [3]. The foreseen testing ages of specimens are 24, 30, 36, 48 and 72 hours, and 7 and 28 days. It is aimed at providing input testing parameters for the second stage of the tests. The second stage includes tests of creep behaviour of CBMs and advanced test methods.

A total of 25 laboratories expressed interest to participate in the testing of CBMs' properties in the framework of GP1d [3]. At the end of the Main Experimental Phase results of 15 laboratories were available for analyses in the scope of the first stage tests. The number of tests and the extent of testing campaign (scale of testing, testing age, shape of specimen, etc.) vary considerably between different laboratories. The majority of 15 laboratories reported only the results of compressive strength measured on the OC and MOC concrete at 7 and 28 days.

This paper focuses on statistical analysis of the reported test results. In case of compressive strength at least 3 laboratories reported results for the mortar and concrete scale, at 7 and 28 days. Therefore, the determination of correlation between concrete and the corresponding mortar compressive strength is possible for the two ages. For the tensile strength and the unloading E-modulus only the results for concrete compositions, at 7 and 28 days, were reported by a significant number of laboratories, which allows us to carry out statistical analysis of the test results.

## 2. Materials and test methods

Compositions of the CBMs under consideration, ordinary mortar (OM), modified ordinary mortar (MOM), ordinary concrete (OC) and modified ordinary concrete (MOC), are given in [2]. OM and MOM present "identical" mixtures on the mortar scale, in relation to the concrete compositions: OC and MOC, respectively. The main difference between the concrete compositions is the w/c ratio, which is 0.52 for the OC (and for the associated OM) and 0.42 for the MOC (and for the associated MOM). Reduction in the w/c for the modified compositions was obtained by increasing cement content of the mixture (considerably), its water content (slightly) and by increasing the content of active component of superplasticizer (amount of the SP – water) from 0.09% to 0.17% in relation to the cement mass.

Protocols described in [2] were followed for the mixture preparation and determination of compressive strength ( $f_c$ ), splitting tensile strength ( $f_{st}$ ) and unloading E-modulus from compression ( $E_s$ ). These are standard tests that are performed routinely in most of the participating laboratories. Although prismatic (preferably 100 mm x 100 mm x 200 mm) or cylindrical (preferably 150 mm x 300 mm) shapes of the specimens were proposed for the compressive tests, beside cubic one (150 mm cube), in order to obtain relevant data for the creep tests in the second stage of the GP1d program, the majority of laboratories decided to carry out compressive tests on the cubic specimens only. As a rule, 3 replicates were used to determine a particular property of the CBMs, for compressive strength. However, 6 replicates were used by a limited number of laboratories. All reported results were considered in the statistical analyses. Since the majority of 15 laboratories reported concrete compressive strengths for the 150 mm cube, conversion factor 1.25 was used to estimate the 150 mm cube strength for the laboratories that measured compressive strength on standard cylinder (150

mm x 300 mm or 100 mm x 200 mm) or 100 mm x 100 mm x 200 mm prism. For the tensile strength results, the shape of the specimen was not considered as influencing parameter. Moreover, results of direct tensile strength reported by one laboratory were added to the analysed results.

For the statistical analysis of the reported test results Wolfram Mathematica computing system [5] was used. The normality of the data was tested graphically (ProbabilityPlot) as well as by performing a goodness-of-fit test (DistributionFitTest). In reality, however, we do not have enough samples for any test to be appropriate; therefore we will not address this issue. In order to show particularity of individual laboratory results, they are presented using a boxplot, also called a box and whisker plot, in order to show the spread and centres of each data set. Measures of spread include the interquartile range, with minimum and maximum value of the considered property. Measures of centre include the mean value (i.e., the average), presented by a black line, and the median (the middle of a data set), presented by a white line. The general mean of the whole group is reported only for the results of compressive strength. The analysis of variance tests (ANOVA) were carried out to compare mean values of different laboratories (labs). Mandel's h and k statistics were calculated to track the possible outliers, following the standard ISO 5725-2 [6].

### 3. Results and discussion

#### 3.1 Compressive strength

Compressive strength is one of the most important performance indicators to assess the similarity of concrete mixtures. In Fig. 1 the results for the OC and MOC concretes are given for 7 (OC7, MOC7) and 28 days (OC28, MOC28). 11 labs reported results for the OC concrete. General mean for the compressive strength of the group is 37 MPa and 50 MPa for 7 and 28 days, respectively. Values are lower than reported in the Initial Experimental Phase of the RRT<sup>+</sup>, where general mean at 7 days was 40 MPa (30 labs) and 52 MPa at 28 days (26 labs) [4]. This is a consequence of higher spread of the reported results in the Main Experimental Phase, due to low compressive strengths reported by labs 3 and 4. However, despite these low compressive strengths, all the reported values for OC28 are higher than 37 MPa, which means that all OC mixtures prepared in different laboratories comply with the same concrete class of C30/37. Two labs reported 6 results for the OC composition (lab 10 and 15) at 7 and 28 days, and lab 10 reported 6 results also for the MOC composition at both ages. However, these two labs used 150 x 300 mm cylinder to determine compressive strength. Thus, correction factor of 1.25 was used to estimate the 150 mm cube compressive strength. Comparison of results between the OC and the MOC for the particular laboratory that reported both results reveal, as a rule, considerably higher spread of test results for the MOC composition. We can also see (Fig. 1) that for the MOC composition only lab 7 and lab 8 reported compressive strength results at 7 and 28 days. General mean of the group regarding MOC compressive strength is 51 MPa at 7 days and 67 MPa at 28 days. All MOC mixtures prepared in different laboratories comply with the concrete class of C45/55.

We calculated Mandel's h and k coefficients for the OC7, OC28, MOC7, and MOC28 results of compressive strength and compared them to the critical values of these statistics (presented

by red dashed lines in Fig. 1) for the significance level 0.05 according to ISO 5725-2 [6]. The tests show that the results obtained by different laboratories are consistent. No outliers were identified (Fig. 1).

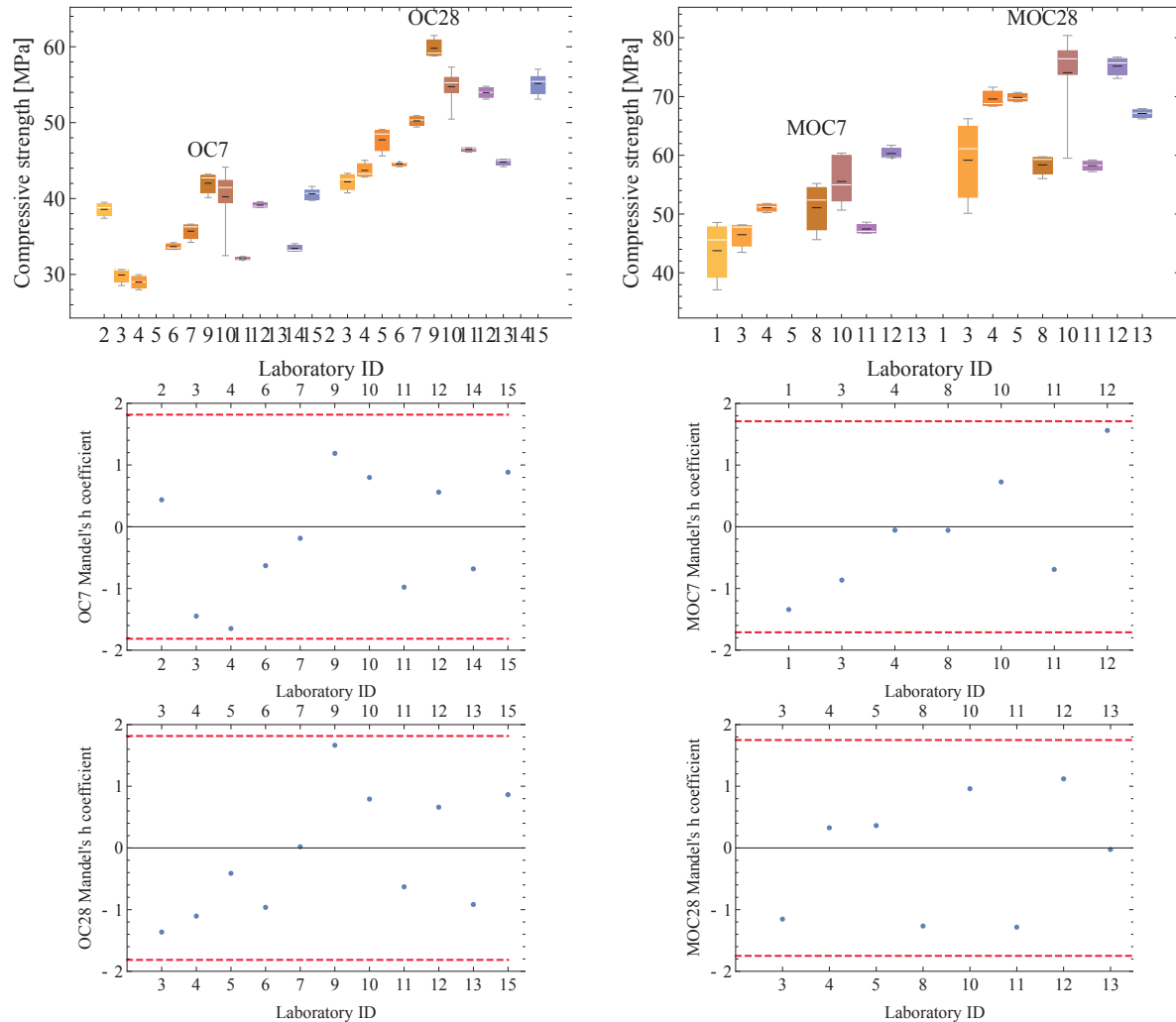


Figure 1: Concrete compressive strength boxplots of individual laboratory measured on the 150 mm cube for the OC and MOC, and Mandel's h coefficient

Only 3 labs reported results on the mortar scale, for the MOM7, OM7 and OM28. For the MOM composition, lab 1 reported the highest spread of test results, using 6 replicates to determine its compressive strength, and lab 2 reported the lowest spread of test results (on 3 replicates). Mean compressive strengths of the two labs, on the other hand, do not differ significantly (62 MPa for the lab 1 and 64.5 MPa for the lab 2). Mean compressive strength of lab 3 is 35.5 MPa, which is not a realistic value. Since this strength is lower than that of the OM7 reported by the same lab, where w/c ratio is considerably higher, it is highly likely that mistakes were made during the processing of the test results, or possible formation of micro cracks, due to autogenous shrinkage [7], reduced the OM7 compressive strength considerably. General mean of the group regarding OM compressive strength is 43 MPa and 59 MPa for 7

and 28 days, respectively. In relation to the OC compressive strengths, the obtained values are higher, which was expected.

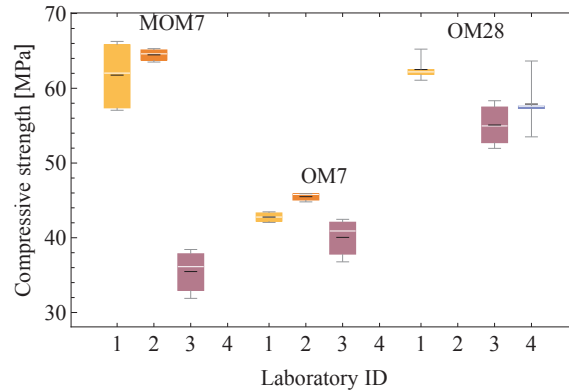


Figure 2: Mortars compressive strength boxplots of individual laboratory measured on 40 mm cube (half of 40 mm x 40 mm x 160 mm prism)

According to Pearson's correlation test with significance level 0.05 all the tested pairs of OM-OC and MOM-MOC samples are linearly independent. The test was carried out only for laboratories that reported measurements for identical compositions on mortar and concrete scale, with the same number of test results (3). The analysis of variance tests for every mixture (OM, MOM, OC and MOC) and age of specimens (7 and 28 days) with significance level 0.01 show that, with the only exception of OM7, the means of the compressive strengths between different laboratories all differ significantly.

### 3.2 Tensile strength

By the analysis of variance tests with significance level 0.01 all the means differ significantly for the concrete tensile strength. Therefore, the reported results were compared to the interval of the tensile strengths calculated from the mean compressive strength for individual laboratory by using modified MC2010 expressions [8]:

$$\text{lower bound value: } f_{st,min} = 0.7 \cdot 0.3 \cdot (f_{cm})^{2/3},$$

$$\text{upper bound value: } f_{st,max} = 1.3 \cdot 0.3 \cdot (f_{cm})^{2/3},$$

where  $f_{cm}$  stands for the mean compressive strength measured on cylinder 150 mm x 300 mm. Wherever individual lab reported 150 mm cube compressive strengths, conversion factor 0.8 was used to determine the  $f_{cm}$ .

From the results in Fig. 3 it is evident that lab 10 stands out with high values of the mean tensile strength for all compositions and ages, and with high spread of the test results for the OC composition at 28 days. At the same time, all reported tensile strength data are much higher than the calculated upper bound value of lab 10, for the OC and MOC composition. Therefore, results of lab 10 will be excluded from the discussion. At the OC composition the lowest values were reported by lab 4 (mean values of 2.11 MPa and 3.24 MPa for 7 and 28 days, respectively), where 80/300 mm cylinder was used to determine the splitting tensile strength of concrete. However, all the data of lab 4 are inside its calculated interval of tensile strengths. The highest mean tensile strength at 7 days was reported by lab 15 (3.63 MPa on 100/100/200 mm prism), and at 28 days by lab 6 (4.47 MPa on 150/300 mm cylinder), while

lab 15 reported the mean value of 4.21 MPa. All the data of lab 15 are inside its calculated intervals of tensile strengths. Lab 6, on the other hand, measured higher tensile strengths than estimated by the calculated interval, which is true also for lab 5. For the rest of the labs that reported results for the OC composition, all data are inside the calculated intervals. We calculated lower and upper bound value of the OC tensile strength interval also from the general mean compressive strength of the group, for 7 days ( $f_{st,min}$  2 MPa,  $f_{st,max}$  2.7 MPa) and 28 days ( $f_{st,min}$  2.5 MPa,  $f_{st,max}$  4.6 MPa). With the exception of lab 10, mean tensile strengths of all labs lie inside the appropriate calculated intervals.

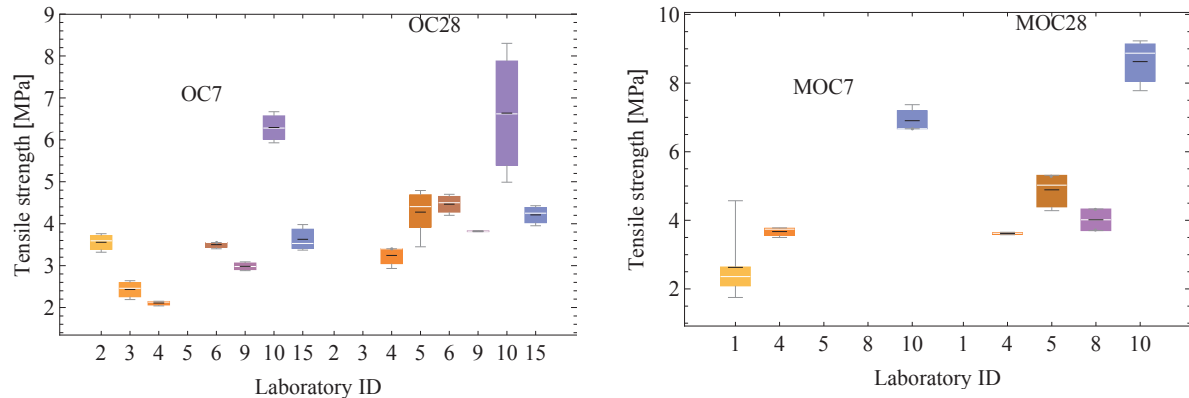


Figure 3: Concrete tensile strength boxplots of individual laboratory for the OC and MOC

For the MOC composition only a few labs reported results as presented in Fig. 3. The data reported by labs 4, 5 and 8 are all inside the calculated intervals for the particular lab. They are also inside the tensile strength intervals calculated from the general mean compressive strength of the group, for 7 days ( $f_{st,min}$  2.5 MPa,  $f_{st,max}$  4.6 MPa) and 28 days ( $f_{st,min}$  3 MPa,  $f_{st,max}$  5.5 MPa). For lab 1, on the other hand, only 3 out of 6 results lie inside the calculated interval of the lab, while the lowest two (1.75 MPa and 2.09 MPa) and the highest (4.17 MPa) value are outside.

### 3.3 Unloading modulus of elasticity

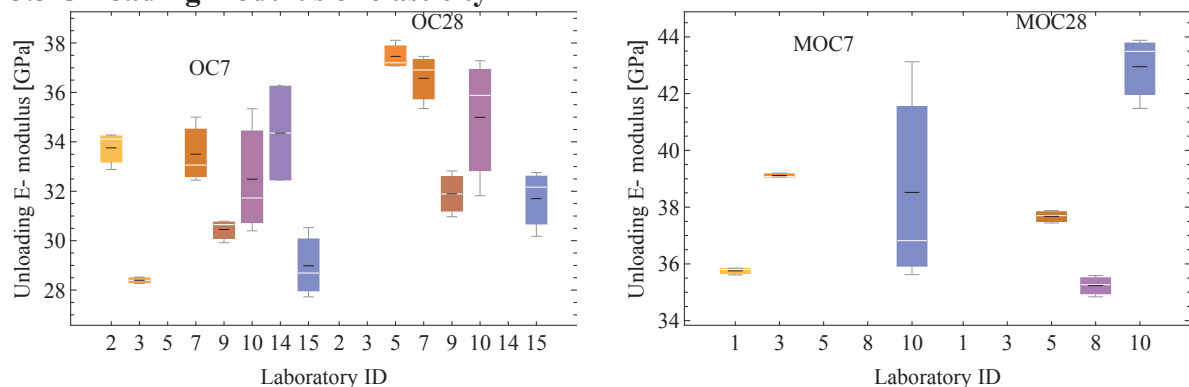


Figure 4: Unloading modulus of elasticity boxplots of individual laboratory for the OC and MOC

By the analysis of variance tests with significance level 0.01, only the means of MOC at 7 days do not differ significantly. Therefore, the reported results were compared to the interval



of the E-modulus calculated from the mean compressive strength for individual lab by using MC2010 expressions [8]:

$$\text{lower bound value: } E_{s,\min} = 21.5 \cdot 10^3 \cdot 0.9 \cdot (f_{cm}/10)^{1/3},$$

$$\text{upper bound value: } E_{s,\max} = 21.5 \cdot 10^3 \cdot 1 \cdot (f_{cm}/10)^{1/3},$$

where  $f_{cm}$  stands for the mean compressive strength measured on cylinder 150 mm x 300 mm. Wherever individual lab reported 150 mm cube compressive strengths, conversion factor 0.8 was used to determine the  $f_{cm}$ . The lower limit belongs to limestone aggregates and the upper one to quartzite aggregates. The actual aggregate used for the OC and MOC compositions contains silicates and limestone [2], which justifies the selection of the interval limits for E-modulus.

Results for the unloading E-modulus are presented in Fig. 4. By comparing experimental OC7 results of individual laboratory to its calculated  $E_s$  interval we can conclude that only for labs 3 and 9 all the reported data lie inside the interval, and for lab 15 the mean value lies inside the interval. The rest of the labs reported higher values of the E-modulus, with mean values between 3 % and 15 % higher than appropriate upper bound value of the calculated  $E_s$ . At the OC28, the mean values of lab 10 and lab 15 lie inside the interval, the mean E-modulus of lab 9 is 2.4 % lower and that of lab 5 and lab 7 is 15 % and 7 % higher, respectively, compared to the appropriate bound value of the calculated  $E_s$  interval.

By comparing the experimental MOC7 results of individual laboratory to its calculated  $E_s$  interval, we can conclude that the measured values are all considerably higher than the upper bound value of the appropriate interval, by 10 %, 17 % and 9 % for labs 1, 3 and 10, respectively. When the same comparison is carried out for the MOC28, all results are considerably higher than the upper bound value of the appropriate  $E_s$  interval only for lab 10 (11 % higher mean value). Data of labs 5 and 8, which did not report the MOC7 results, lie all inside the calculated  $E_s$  interval of the particular lab.

#### 4. Conclusions

This paper presents and discusses results of statistical analyses performed on the data of CBMs mechanical properties, gathered during the Main Experimental Phase of the RRT<sup>+</sup>, in the framework of group priority 1d. At the end of the Main Experimental Phase results of 15 laboratories were available for analyses. The number of experimental tests and the extent of testing campaign (scale of testing, testing age, shape of specimen, etc.) vary considerably between different laboratories. Therefore, statistical analyses were carried out only for compressive strength (mortar and concrete scale), tensile strength (concrete scale) and unloading E-modulus (concrete scale), measured at 7 and 28 days, where significant number of laboratories reported the obtained results. The main conclusions are as follows:

- Comparison of the results of compressive strengths between the OC and the MOC, as well as between the OM and the MOM, for the particular laboratory that reported both results, reveal considerably higher spread of test results for the modified compositions.
- Results of the OC compressive strengths reported by different laboratories indicate the same reproducibility of experimental results as in the Initial Phase of the RRT<sup>+</sup>.

- For laboratories that reported compressive strengths for identical compositions on mortar and concrete scale, with the same number of test results, the tested pairs of OM-OC and MOM-MOC samples are linearly independent.
- The analysis of variance tests for every mixture (OM, MOM, OC and MOC) and age of specimens (7 and 28 days) shows that the means of the compressive strengths, tensile strengths and unloading E-modulus from compression between different laboratories all differ significantly. The only exceptions are compressive strength of the OM and E-modulus of the MOC at 7 days.
- With the exception of one laboratory, tensile strengths reported by different laboratories are inside the limits calculated using the MC2010 expressions.
- Unloading E-moduli reported by different laboratories indicate high scatter of results for this property and, especially for measurements at 7 days, the reported results are higher than estimated by relevant MC2010 expressions.

### Acknowledgements

The authors would like to acknowledge networking and dissemination support by the COST Action TU1404 (<http://www.tu1404.eu/>). The research performed within the RRT+ program of the COST Action is on volunteering basis, since there is no budget foreseen for research activities. Therefore, the authors would like to express their sincere gratitude to all participating laboratories for their dedicated work within this experimental campaign. The authors also acknowledge financial support of EDF, France, CEVA Logistics, Austria and Germany, OeBB Infra, Austria, Staten Vegvesen, Norway and Schleibinger Gerate, Germany. This work was partially supported by Slovenian Research Agency through Programme P2-0185 and Research Project J2-8194.

### References

- [1] COST Action TU 1404, <http://www.tu1404.eu/> (accessed in June 2018)
- [2] Staquet, S. et al., RRT+ Main phase of the Extended Round Robin Testing programme for TU1404, Testing protocols, Ver. 22th November 2016, (2016), 57p.
- [3] Bokan-Bosiljkov, V. et al., Progress on Testing of Mechanical Properties of Cement Based Materials - Extended Round Robin Test of Cost Action TU 1404, RILEM Proceedings PRO 118 from International Conference on Advances in Construction Materials and Systems, India (2017), 171-178.
- [4] Serdar M., Staquet S., Schlicke D., Rozière E., Trtnik G., Nanukuttan S., Azenha M., "Extended Round Robin test RRT+ Initial Phase – Results and lessons learned", presentation at the COST TU1404 Zagreb meeting, March 2016, 34p
- [5] Wolfram Research, Inc., Mathematica, Version 11.1, Champaign, IL (2017).
- [6] Wilrich, P., Critical values of Mandel's h and k, the Grubbs and the Cochran test statistic, AStA Advances in Statistical Analysis. 97 (2013), 1-10.
- [7] Klun, M., Strmšek, L., Bokan-Bosiljkov, V., Strength and elastic properties of cement based materials – contribution of University of Ljubljana to the RRT+ of COST Action TU 1404, Proceedings of the SynerCrete'18 International Conference (2018), 6p.
- [8] Model Code 2010, Final draft, Volume 1, FIB Bulletin 65, March 2012.

## **STRENGTH AND ELASTIC PROPERTIES OF CEMENT BASED MATERIALS – CONTRIBUTION OF UNIVERSITY OF LJUBLJANA TO THE RRT+ OF COST ACTION TU 1404**

**Martin Klun <sup>(1)</sup>, Lucija Strmšek <sup>(2)</sup>, Violeta Bokan Bosiljkov <sup>(1)</sup>**

(1) University of Ljubljana, Faculty of Civil and Geodetic Engineering, Slovenia

(2) STRABAG, Slovenia

### **Abstract**

Research group at the University of Ljubljana carried out extensive test campaign in the framework of the Extended Round Robin Testing program (RRT+) of COST ACTION TU1404. In this paper the first phase test results are given and discussed. The tests were carried out on modified cement paste, ordinary mortar and modified ordinary mortar, at the ages of 24, 30, 36, 48, 72 hours and 7 and 28 days. Hardened properties were evaluated by destructive standard tests and by measurements of compressive and shear ultrasonic waves. The obtained results show big influence of high content of SP with retarding effect on the properties of the modified cement paste and modified ordinary mortar. The age of samples of 2 days was estimated as the time when the retarding effect of the SP stops to act. Formation of micro cracks, due to autogenous shrinkage of the cement paste in the modified compositions, was seen as the source of tensile strength decrease observed at specimens' age of 7 days.

### **1. Introduction**

The Extended Round Robin Testing program (RRT+) of COST ACTION TU1404 European project is the main activity within Working Group 1 (WG 1): Testing of cement-based materials (CBMs) [1]. The RRT+ program is divided into six group priorities, among which group priority 1d (GP1d) deals with mechanical properties and creep of CBMs across several scales – hardened cement paste, mortar and concrete [2].

Research group at the University of Ljubljana (UL FGG) carried out extensive test campaign in the framework of the RRT+, by focusing mainly on the hardened properties of CBMs in within GP1d. The tests of hardened properties were divided in two phases. In the first phase tests were carried out on modified cement paste (MCP), ordinary mortar (OM) and modified

ordinary mortar (MOM) aged 24, 30, 36, 48, 72 hours and 7 and 28 days. Due to unexpected test results showing drop of the CBMs flexural and tensile strength at certain ages of the specimens, the tests were repeated (second phase tests) on the MCP and MOM, and additional tests were carried out on modified ordinary concrete (MOC). In this way mechanical and elastic properties of CBMs across several scales were determined in the same laboratory. In this paper only results of the first test phase are presented and discussed.

## 2. Materials

Compositions of the MCP, MOM and OM are given in [3]. They present “identical” mixtures on the mortar and paste scale, in relation to two reference concrete compositions: ordinary concrete (OC) and modified ordinary concrete (MOC) [3]. The main difference between the concrete compositions is the w/c ratio, which is 0.52 for the OC (and for the associated OM) and 0.42 for the MOC (and for the associated MOM and MCP). Reduction in the w/c for the modified compositions was obtained by increasing cement content of the mixture (considerably), its water content (slightly) and by increasing the SP content by factor around 2.5. Ordinary cement paste with the w/c ratio of 0.52 is not stable enough at the fresh state (bleeding) and is thus problematic for the accurate assessment of the mechanical properties on the paste scale. That is why only the MCP was kept in the main experimental phase of the RRT+.

## 3. Test methods and testing

Protocols described in [3] were followed for the mixture preparation, with some deviations. For the MCP mixing the EN 163-1 standard blade was used, because special blade required in the Testing protocol [3] is not available in the UL FGG laboratory. At the same time, temperature in the laboratory in which specimens were prepared and tested differed from the required temperature of  $(20 \pm 2)^\circ\text{C}$ .

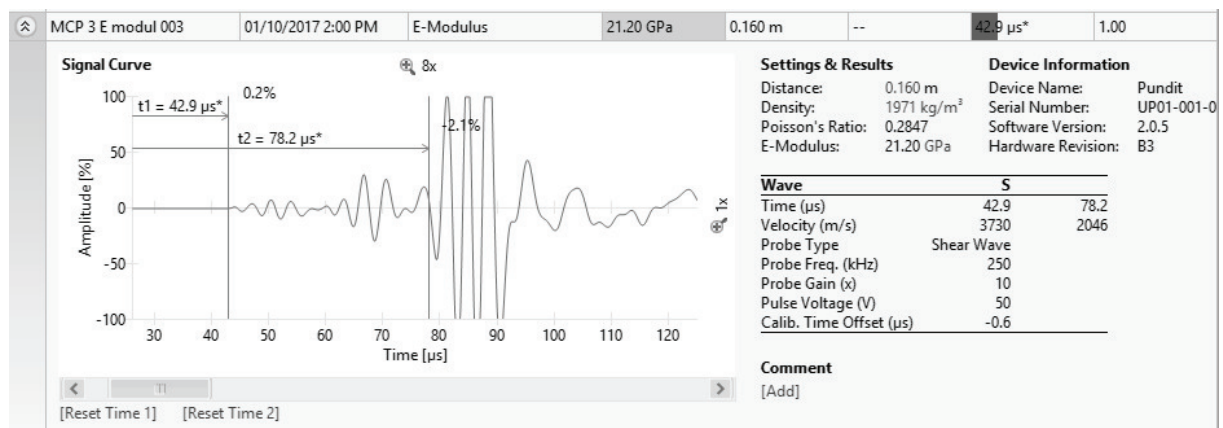


Figure 1: Determination of the dynamic elastic properties using the Pundit device.

Protocols of the GP1d [3] were followed when hardened properties of the CBMs, compressive strength ( $f_c$ ), splitting tensile strength ( $f_{st}$ ) and unloading elastic modulus from compression ( $E_s$ ) were determined. Additionally, flexural strength ( $f_{ft}$ ) and static Poisson's ratio from compression ( $\nu_s$ ), and ultrasonic pulse velocity (UPV) measurements were carried out. The Pundit PL-200 equipment was used in order to determine dynamic elastic parameters of CBMs, such as dynamic elastic modulus ( $E_d$ ), dynamic shear modulus ( $G_d$ ) and dynamic Poisson's ratio ( $\nu_d$ ) (Fig. 1). For the measurements of compressive and shear waves, P-wave and S-wave transducers of 150 kHz and 250 kHz were applied, respectively.

The tests were carried out on specimens aged 24, 30, 36, 48 and 72 hours and 7 and 28 days.

## 4. Test results and discussion

### 4.1 Fresh properties

In December 2016, CBMs mixtures were prepared to cast 40 mm x 40 mm x 160 mm prisms in order to determine dynamic elastic properties and compressive, flexural and splitting tensile strengths of MCP, MOM and OM. In January 2017 additional mixtures were prepared to cast 40 mm x 40 mm x 80 mm prisms in order to determine the static elastic modulus and Poisson's ratio of MCP, MOM and OM. Due to lower temperature of the laboratory in December 2016, initial temperature of particular mixture was much lower than required [3], although all materials were stored at  $(20 \pm 1)$  °C for at least 7 days prior the mixing. Properties of the MCP, MOM and OM in fresh state are given in Tab. 1. The MCP was stable and without evidence of bleeding.

Table 1: Fresh properties of tested CBMs

	December 2016			January 2017		
	T [°C]	Flow value [mm]	Density [kg/m <sup>3</sup> ]	T [°C]	Flow value [mm]	Density [kg/m <sup>3</sup> ]
MCP	14.7	267	1919	18.1	283	1926
MOM	15.1	220	2262	17.8	219	2262
OM	15.2	226	2214	18.3	203	2186

The results in Tab. 1 lead to the conclusion that the difference in the fresh mixture temperature, due to low temperature of the air in the laboratory during mixing, did not have any important influence on the fresh properties of the MCP and MOM, that is on the CBMs with very high content of SP.

### 4.2 Hardened properties

Fig. 2 presents the results of CBMs' compressive tests. Logarithmic scale was used to distinguish between values at ages up to 2 days. The results show that, despite much lower w/c ratio at the MOM (0.4), its compressive strength up to 30 hours is the same as for the OM (w/c 0.52). Observed behaviour is most probably due to much higher content of SP in the MOM and its retarding effect, which was observed also at demoulding of the MOM and MCP specimens after 24 hours. Both specimens looked as if their final setting time was close to 24 hours. For the MCP this observation is supported by the results of the setting time test (EN

196-3) reported by the TU Graz [4], where initial and final setting time was equal to 23.5 and 26.6 hours, respectively. However, at the TU Graz, laboratory mixing blade and laboratory environment were according to set requirements [3]. Similar influence of SP with retarding effect to the mechanical properties of SCC mixtures was observed at the UL FGG earlier [5]. For the CBMs under consideration the age of 2 days seems to represent the time when retarding effect of SP stops to act. Retarding effect is much lower for the OM, due to considerably lower dosage of SP than in case of the MCP and MOM. Compressive strength of the MCP is lower than at the MOM from 1.5 days on. Higher number of micro cracks inside the MCP specimens, due to autogenous shrinkage, is most probable reason for the observed behaviour.

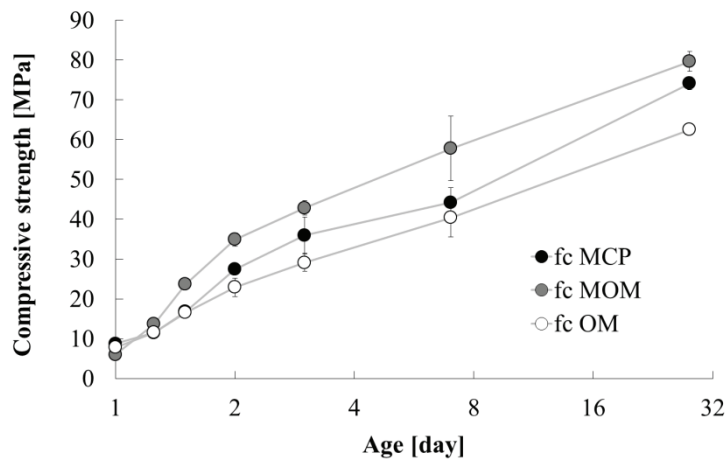


Figure 2: Compressive strength development with specimen's age.

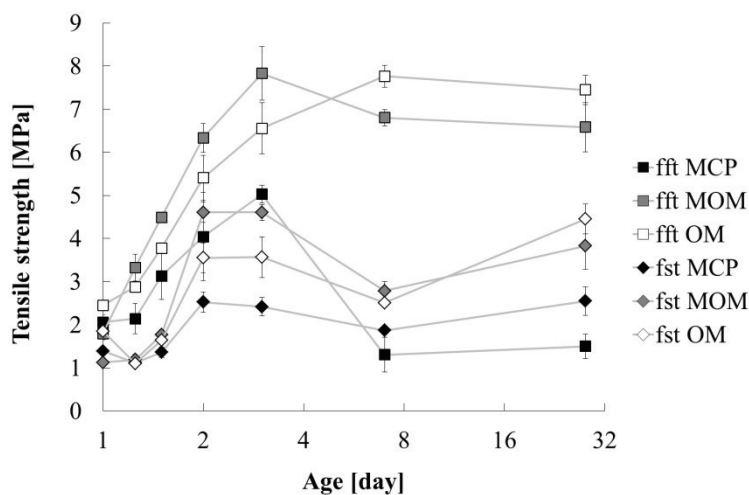


Figure 3: Flexural and splitting tensile strength development with specimen's age.

Fig. 3 shows results of CBMs flexural ( $f_{ft}$ ) and splitting ( $f_{st}$ ) tensile strength. When calculating tensile strength, validity of elastic theory was adopted. However, at the ages of 24, 30 and 36 hours impress of loading pieces and loading rollers into specimens was observed at splitting and flexural test, respectively, for the MCP and MOM specimens. Therefore, the results in Fig. 3 may not present realistic values of tensile strength at very early age. We can see (Fig. 3) that  $f_{ft}$  of the MCP and MOM is increasing with age up to 3 days, and at the age of

7 days drop in  $f_{ft}$  was obtained. Decrease of  $f_{ft}$  was extreme for the MCP and much lower for the MOM. This is in agreement with the compressive strength at 7 days (Fig. 2), where the average value obtained for the MCP is much lower than expected. At 28 days  $f_{ft}$  of the MCP and MOM is the same as at 7 days. Because also in the second phase test similar behaviour of MCP and MOM was observed, we can conclude that the presence of micro cracks inside the specimens is responsible for the observed behaviour. Autogenous shrinkage of the cement paste can be responsible for the micro crack formation. Results of splitting tensile test do not follow the pattern observed for the flexural strengths, since  $f_{st}$  increases only up to 2 days, stays the same until 3 days and after that drop in the strength was obtained at 7 days. However, the decrease in  $f_{st}$  for the MCP is much lower, compared to the decrease of  $f_{ft}$ . On the other hand, the MOM shows much higher relative drop of  $f_{st}$ , compared to  $f_{ft}$ . At the age of 28 days all specimens show higher  $f_{st}$  than at 7 days.

Fig. 4 shows the results of unloading elastic modulus in compression ( $E_s$ ), measured on prisms 40 mm x 40 mm x 80 mm, and dynamic modulus of elasticity ( $E_d$ ), determined by the UPV measurement. We can see that also these results confirm retarding action of SP up to 2 days, since  $E_s$  is higher than or equal to  $E_d$  at age lower than 2 days. From 2 days on elastic moduli increase with the specimen's age and the ratio between  $E_d$  and  $E_s$  stays constant and equal to 1.21, 1.26 and 1.11 for the MCP, MOM and OM, respectively.

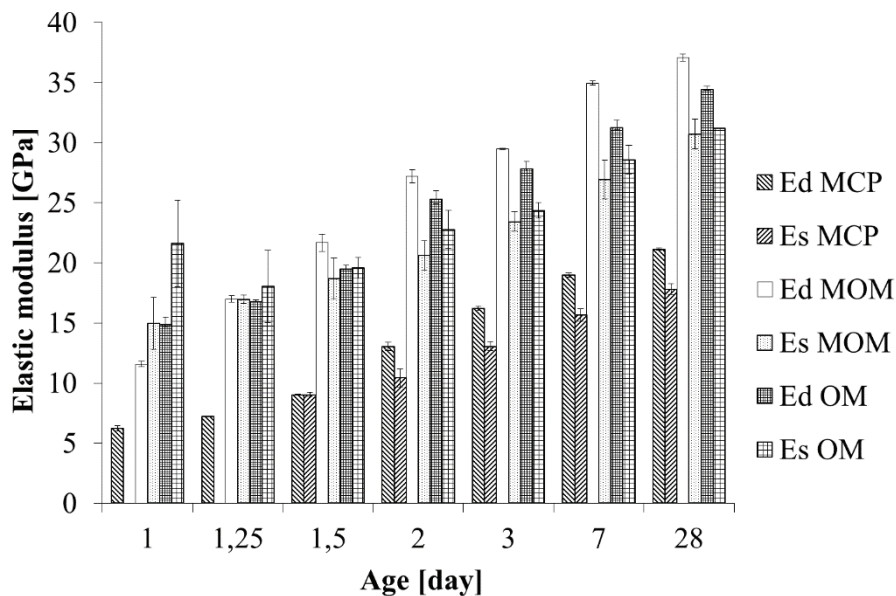


Figure 4: Static and dynamic elastic modulus of CBMs.

Based only on the results of dynamic shear modulus (Fig. 5), retarding effect of SP is clearly evident only up to the age of 30 hours, where the values of  $G_d$  are the same for the MOM and OM, despite much lower w/c ratio at the MOM. Only correlation between the shear moduli of the MCP and MOM reveals that the behaviour is also for this elastic property different for ages lower than 2 days, compared to that at the age of 2 days or higher.

For the MCP the values of Poisson's ratios  $\nu_d$  and  $\nu_s$  are around 0.3 and 0.25, respectively, and for the MOM around 0.27 and 0.19, respectively. In case of the OM,  $\nu_d$  and  $\nu_s$  are around 0.27 and 0.20, respectively. For the modified compositions, the  $\nu_d$  values show decreasing tendency as the function of the specimen's age, and the  $\nu_s$  values show increasing tendency.

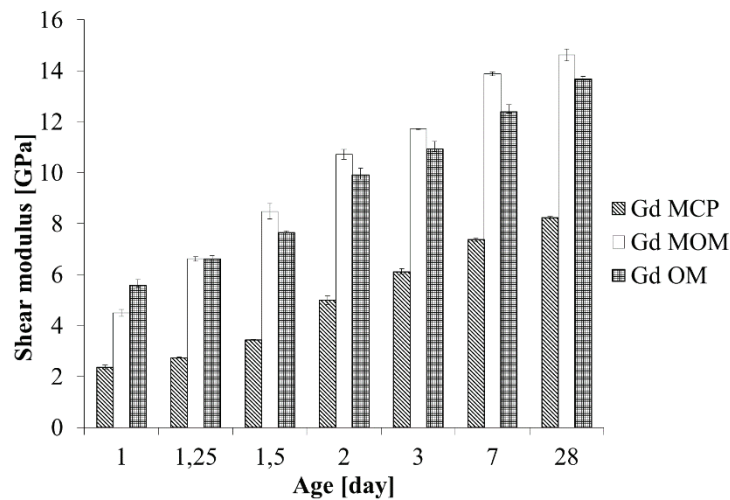


Figure 5: Dynamic shear modulus of CBMs.

## 5. Conclusions

Test results presented in the paper show that by using combination of destructive standard tests and non-destructive UPV measurements, when evaluating properties of hardened CBMs, realistic explanation of the test results that do not confirm “common knowledge” in the area of the CBMs is possible. However, additional microstructural analyses are needed to finally confirm our observation.

## Acknowledgements

This work was financially supported by the Slovenian Research Agency through Programme Group P2-0185, Research Project J2-8194 and PhD project of Martin Klun. The authors acknowledge networking support by the COST Action TU1404.

## References

- [1] Serdar, M. et al., COST Action TU1404 : recent advances of the Extended Round Robin Test RRT+, RILEM Proceedings PRO 120 from 2nd International RILEM/COST Conference on Early Age Cracking and Serviceability in Cement-based Materials and Structures, Belgium (2017), 63-70
- [2] Bokan-Bosiljkov, V. et al., Progress on Testing of Mechanical Properties of Cement Based Materials - Extended Round Robin Test of Cost Action TU 1404, RILEM Proceedings PRO 118 from International Conference on Advances in Construction Materials and Systems, India (2017), 171-178.
- [3] Staquet, S. et al., RRT+ Main phase of the Extended Round Robin Testing programme for TU1404, Testing protocols, Ver. 22<sup>th</sup> November 2016, (2016) 57p
- [4] Bregar, R. et al., Main experimental phase RRT+ COST TU 1404 – Supplementary report of the TU Graz to Excel data sheets, Austria (2017), 25p
- [5] Bokan-Bosiljkov, V. et al., New type of superplasticizer for SCC mixtures with increased robustness, RILEM PRO 90 from International Conference on Rheology and Processing of Construction Materials, France (2013), 6p.



## **VOLUME STABILITY OF CEMENT-BASED MATERIALS: ROUND-ROBIN TESTING WITHIN COST ACTION TU1404**

**Emmanuel Roziere<sup>(1)</sup>, Marijana Serdar<sup>(2)</sup>, Stéphanie Staquet<sup>(3)</sup>, Dirk Schlicke<sup>(4)</sup>, Miguel Azenha<sup>(5)</sup>, Ahmed Zakarya Bendimerad<sup>(1)</sup>, Brice Delsaute<sup>(3)</sup>, Vinciane Dieryck<sup>(6)</sup>, Jacek Golaszewski<sup>(7)</sup>, José Granja<sup>(5)</sup>, Terje Kanstad<sup>(8)</sup>, Anja Klausen<sup>(8)</sup>, Zhenming Li<sup>(9)</sup>, Elica Marušić<sup>(10)</sup>, Martina Pezer<sup>(2)</sup>, Antonio Ribeiro<sup>(11)</sup>, Sofia Ribeiro<sup>(11)</sup>, Aljoša Šajna<sup>(13)</sup>, François Toutlemonde<sup>(12)</sup>, Guang Ye<sup>(9)</sup>, Behzad Zahabizadeh<sup>(5)</sup>**

(1) GeM, Ecole Centrale de Nantes, Nantes, France

(2) Faculty of Civil Engineering, University of Zagreb, Zagreb, Croatia

(3) BATir, Université Libre de Bruxelles ULB, Brussels, Belgium

(4) Graz University of Technology, Institute of Structural Concrete

(5) Department of Civil Engineering, University of Minho (ISISE), Guimarães, Portugal

(6) Belgian Building Research Institute, Limelette, Belgium

(7) Silesian University of Technology, Gliwice, Poland

(8) Norwegian University of Science and Technology (NTNU), Trondheim, Norway

(9) Faculty of Civil Engineering and Geosciences, TU Delft, Netherlands

(10) Institut IGH, Split, Croatia

(11) LNEC, Lisboa, Portugal

(12) IFSTTAR, France

(13) Slovenian National Building and Civil Engineering Institute, Slovenia

### **Abstract**

Advanced experimental techniques and modelling are necessary to predict the evolution of existing structures and design more sustainable materials and structural systems. An Extended Round Robin Testing program (RRT+) has been designed within COST Action TU 1404 “Towards the next generation of standards for service life of cement-based materials and structures”. The RRT+ program provides a platform to compare non-standardized techniques. The results presented in this paper are related to “Volume stability” with a focus on autogenous deformation. 11 laboratories were actually involved in the testing program. They used different measuring techniques but the preliminary results showed good overall agreement. A deeper analysis requires data related to hydration and hardening kinetics. The tested concrete mixtures showed relatively low shrinkage magnitudes. The evolution of autogenous deformations is discussed taking into account their stress-inducing potential.

## 1. Introduction

COST Action TU1404 is entitled “Towards the next generation of standards for service life of cement-based materials and structures”, as it gives a special attention to the issue of analysing serviceability under the combined effect of imposed deformations (namely, due to thermal and hygral effects) together with applied loads, with due account for viscoelasticity and cracking effects [1]. Such analysis requires advanced models and measuring techniques to take into account the main phenomena and determine the input parameters. Among the three main working groups (WG) of the Action, the WG1 designed an Extended Round Robin Testing program (RRT+) with two stages: the Initial Phase and the Main Phase. The objective of the Initial Phase was to define procedures for preconditioning, mixing and curing of concrete well enough so that laboratories could prepare a comparable concrete. The Main phase provided a platform to compare non-standardized or advanced testing procedures [2]. Since a vast range of properties were targeted, the experimental work and analysis was divided into Group Priorities (GP) focusing on different groups of properties. This paper presents some of the methods and results of GP1e on “Volume stability” [3]. This gathers advanced tests to characterize the causes (hygral and thermal changes) and consequences (shrinkage-induced cracking) of volumes changes, from fresh state to long-term behaviour. Preliminary results shown in this paper are mainly related to autogenous deformations.

## 2. Materials and methodology

### 2.1 Reference mixtures

The “Ordinary” concrete mixture (OC) and “Modified” concrete mixture (MOC) were designed by working group 1 (WG1) of COST Action TU1404 [4] and their compositions are given in RRT+ documents [5]. The mix-design of OC is based on Vercors Project [6], which aims at reproducing nuclear reactor containment building at the scale of one third. Note that OC differs from Vercors concrete in terms of cement type and plasticizer content. Namely, in RRT+ CEM I 52.5 N-SR3 CE PM-CP2 NF HRC cement was used, instead of CEM I 52.5 N CE CP2 NF with a higher C<sub>3</sub>A amount used in the Vercors project.

Table 1: Concrete mixtures, amounts [kg/m<sup>3</sup>].

	OC	MOC
<b>Cement</b> , CEM I 52,5 N-SR3 Gaurain	320	439
<b>Dry sand</b> , 0-4 mm, REC GSM LGP1	830	772
<b>Fully saturated gravel</b> ,		
4-11mm, R GSM LGP1	449	525
8-16 mm, R Balloy	564	424
<b>Admixtures</b> , Plasticizer SIKAPLAST Techno 80	1.44	3.73
<b>Added water</b>	180.7	178.4
<b>W<sub>eff</sub>/C</b>	0.52	0.40

The MOC mixture is derived from the OC mixture. The modifications are namely a decreased W/C ratio as well as the corresponding necessary changes in regard to the plasticizer and paste volume to achieve different properties of fresh and hardened material when compared to OC. In terms of volume stability (GP1e), MOC is expected to show higher thermal and autogenous deformations. Cement paste (MCP) and mortar mixtures (OM, MOM) were derived from OC and MOC mixtures [2]. The paste and mortar mixtures were designed to allow multiscale modelling performed in the WG2. Some measuring techniques are actually based on smaller specimens but these volumes should remain representative of the tested materials.

## 2.2 Methodology

15 COST Action members initially committed to participate in the part of RRT+ program dedicated to Volume stability. 11 Laboratories were actually involved in testing activities; the corresponding laboratory numbers are given in Table 2. The research within the COST Action is performed on volunteering basis, since there is no budget foreseen for research activities. The experimental program was relatively wide, from early-age to long-term behaviour, with and without restraint.

Table 2: COST Action members involved in experimental program.

	OC	MOC
Chemical shrinkage	9 (OCP, OM)	
Early age (0-24h) autogenous shrinkage	1, 2, 3, 6, 8, 11, 12, (OCP, OM), 9 (OM)	1, 2, 5, 9 (MCP)
Early age (0-24h) plastic shrinkage	1, 7	
Restrained shrinkage, TSTM	8	8
Drying shrinkage, weight loss	1, 6, 10, 11 (OM), 9	1, 6, 9
Restrained shrinkage, ring test	1, 5, 9, 13	1
Thermal dilation	3, 5, 8	

RRT+ provides a platform to compare the different methods and to discuss the degree to which the experimental procedure or the data analysis should be standardized to obtain consistent results. This is the case for free shrinkage measurements for instance, as these data are used as input data of models. The measurement of autogenous shrinkage has been a major concern for the last decades but there is still no consensus on the geometry of the specimens [7] and the time when deformations should be initialized [8]. Laboratories #1, 2, 6, 8 performed horizontal measurements with rigid prismatic moulds (from 70x70 to 100x100 mm<sup>2</sup> cross-section), Laboratories #9 and 11 used the corrugated tubes method, and Laboratories #3 and 12 used BTJADE system with vertical corrugated mould [7].

Some experimental techniques are not meant to be standardized; they were used in connection with WG2 activities such as benchmarks and validation of models before upscaling. Temperature Stress Testing Machine (TSTM) allows the measurement of deformations from

the casting of concrete specimen, in controlled temperature conditions [9]. The specimen can move freely until a deformation threshold is reached. An additional load is then applied to cancel the deformation. As a consequence a TSTM system can provide restraint by applying loads, in tension or compression. The determination of stresses and strains at each increase of load allows the assessment of elastic modulus. The comparison between cumulated stresses and tensile strength provides the evolution of the risk of cracking. The TSTM system allows investigating free and restrained shrinkage, mechanical properties, and creep in compression and tension [10-11] from early age.

### 3. Preliminary results

#### 3.1 Autogenous deformation

Autogenous deformation was measured in quasi isothermal controlled conditions. 8 laboratories participated in this part of the RRT+. They provided the evolution of deformations from fresh to hardened state. During the first hours, several phenomena take place in fresh concrete such as thermal dilation/contraction, settlement, etc. The induced volume changes are not of interest as they do not have stress-inducing potential until the material starts to harden. The monitoring of other properties is necessary to determine “time-zero” and provide the relevant shrinkage curve. As such information was not systematically provided by the participating laboratories, the first derivative (with respect to time) was used to analyse the deformation data. For all the laboratories its values were relatively low from the ages of 16 and 18 hours for OC and MOC respectively. These times were chosen to initialize the curves, except for Lab#9. They monitored the setting of OM and MCP using Vicat needle and obtained final setting times of 14.5 and 25.5 hours respectively. Their curves were initialized at these times (Figs. 1 and 2).

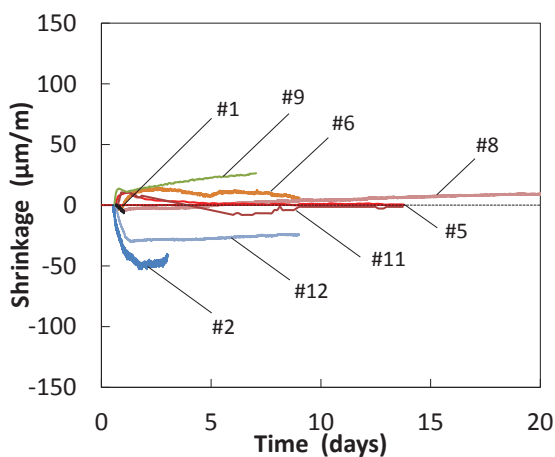


Fig. 1: OC shrinkage from fresh state

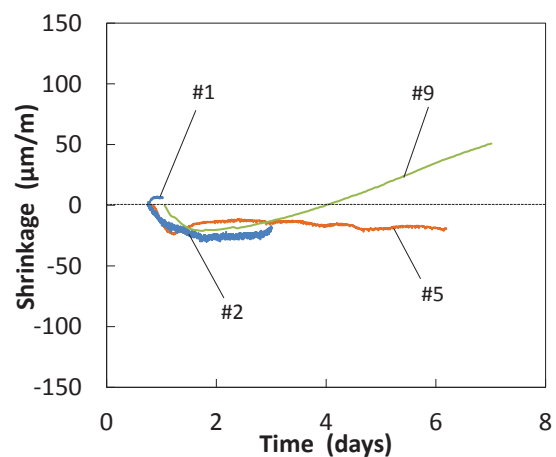


Fig. 2: MOC shrinkage from fresh state

Figure 1 shows discrepancies between the 8 data series, but the magnitudes are consistent with the relatively high water-to-cement ratio of ordinary concrete (0.52). For a given experimental absolute uncertainty, the relative uncertainty increases with a decrease in shrinkage magnitude. High performance concrete generally show autogenous deformations of

hundreds of  $\mu\text{m/m}$  [7], whereas normal strength concrete such as OC studied here show significantly lower shrinkage magnitudes in sealed conditions. Another cause of discrepancies is the determination of “time-zero”. Additional information is needed to assess this time and a common methodology should be used to analyse the results; however the participating have different procedures to determine setting time or time-zero and some do not have any equipment.

The four shrinkage curves of MOC specimens are plotted on Figure 2. Most of evolutions show swelling between 16 and 36 hours. This behaviour has already been reported in previous studies of autogenous deformations [12]. In spite of significantly lower water-to-cement ratio of 0.40, MOC show slightly higher shrinkage magnitude (Fig. 2).

### 3.2 Restrained shrinkage – TSTM

TSTM test was performed on OC in quasi-isothermal conditions for a significant time period (Fig. 3). The control started at 6.7 hours and the deformation threshold triggering load increment was  $6 \mu\text{m/m}$ . Between two subsequent load increments, the stress was kept constant through load control. The strain curve represents the cumulated strain assessed by adding the strains between two load increments. During the first days a moderate swelling was observed thus compressive stresses developed, then concrete progressively shrank. This result confirms the behaviour observed by several laboratories in dilation rigs (Fig. 1). The first load increment occurred at 22.3 hours and reached 0.15 MPa in compression. This time can be compared to the initialization time chosen for the analysis of free autogenous deformation (3.1). After more than 60 days, the stress remained relatively low. The upcoming TSTM tests will be performed with realistic temperature histories as the studied concrete mixtures showed significant hydration heat.

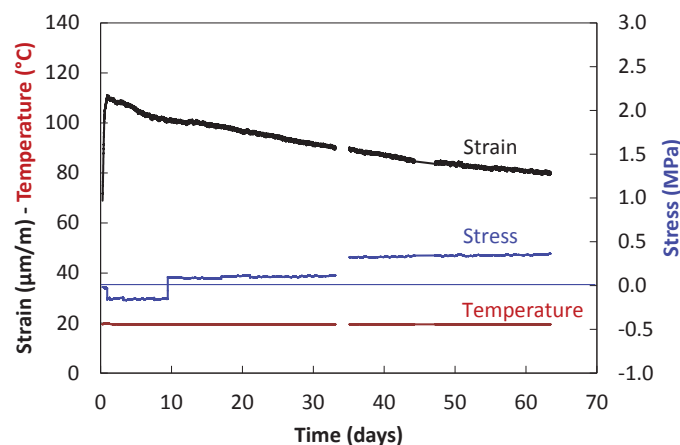


Fig. 3: TSTM test at NTNU on OC under controlled  $20^{\circ}\text{C}$  temperature.

## 4. Conclusion

Eleven European laboratories were involved in volume stability testing, mainly free and restrained shrinkage. The experimental program targeted early-age as well as long-term behaviour, in sealed and drying conditions. The tests were performed on concrete, mortar, or paste, depending on the available test rigs. In the framework of COST Action TU1404, the

same raw materials have been sent to all the participants and a very detailed mixing procedure has been defined in Extended Round-Robin Testing (RRT+) to limit the scatter of results due to materials and their preconditioning. Autogenous deformations showed discrepancies, which are related to two main issues. First both studied concrete mixtures were characterized by relatively high water-to-cement ratios, thus low shrinkage magnitudes, which emphasizes the influence of experimental uncertainties. Second the determination of time-zero was not satisfying and further analyses are required. This paper only presents a part of available results. Experimental campaign yielded satisfactory results, as several laboratories provided consistent data even if the measuring procedures were not standardized. The evolution of other properties is often needed to perform deeper analysis of volume changes. The obtained data are also being used to design benchmarks and update models, thus they actually contribute in reaching the goals of COST Action TU1404.

## References

- [1] COST Action TU 1404, <http://www.tu1404.eu/>
- [2] Serdar M., Staquet S., Gabrijel I., Cizer O., Nanukuttan S., Bokan-Bosiljkov V., Rozière E., Šajna A., Schlicke D., Azenha M., COST Action TU1404: recent advances of the Extended Round Robin Test RRT<sup>+</sup>, 2<sup>nd</sup> International RILEM/COST Conference on Early Age Cracking and Serviceability in Cement-based Materials and Structures - EAC2, 12–14 September 2017, ULB-VUB, Brussels, Belgium, 10 p.
- [3] Bjøntegaard, Ø., Martius-Hammer, T.A., Krauss, M., Budelmann, H. Recommendation for Test Methods for AD and TD of Early Age Concrete Round Robin Documentation Report: Program, Test Results and Statistical Evaluation, RILEM, 2015
- [4] Staquet S., Serdar M., Delsaute B., Rozière E., Schlicke D., Nanukuttan S., Azenha M., Further works on concrete at early age coordinated within COST TU1404 European project, JCI-RILEM International Workshop CONCRACK5, 10 p.
- [5] RRT+, Main phase of the Extended Round Robin Testing programme for TU1404, <http://www.tu1404.eu/rrt/current-status-of-rrt-and-deadlines/>
- [6] <http://fr.amianto.com/EDF-vercors-project.html>
- [7] Roziere E., Delsaute B., Loukili A., and Staquet S., Experimental Assessment of Autogenous Shrinkage, CONCREEP10, 2015, Vienna, Austria, 983-992
- [8] Huang, H., Ye, G. Examining the “time-zero” of autogenous shrinkage in high/ultra-high performance cement pastes, Cement and Concrete Research, Volume 97, 2017, 107–114
- [9] Staquet S., Delsaute B., Darquennes A., Espion B., Design of revisited TSTM system for testing concrete since setting time under free and restraint conditions. Proceedings of the RILEM-JCI International Workshop CONCRACK 3, 15-16 March 2012, Paris, France
- [10] Estensen Klausen, A., Kanstad, T., Bjøntegaard, Ø. Sellevold, E. Comparison of tensile and compressive creep of fly ash concretes in the hardening phase, Cement and Concrete Research, Volume 95, 2017, 188-194
- [11] B. Delsaute, C. Boulay, S. Staquet, Creep testing of concrete since setting time by means of permanent and repeated minute-long loadings, Cem. Concr. Compos., 73 (2016), pp. 75-88
- [12] Lura P. Autogenous deformation and internal curing of concrete, DTU, The Netherlands, PhD thesis; 2003. 180p.

## **BENCHMARK NUMERICAL SIMULATION IN MICRO-LEVEL WITHIN THE COST ACTION 1404**

**Peng Gao<sup>(1,2)</sup>, Hua Dong<sup>(1)</sup>, Jiayi Chen<sup>(1)</sup>, Guang Ye<sup>(1)</sup>**

(1) Delft University of Technology, Delft, The Netherlands

(2) South China University of Technology, Guangzhou, China

### **Abstract**

This paper aims to present an example of the benchmark numerical simulation for cement-based materials in Micro-level within COST Action 1404 by using numerical tools developed at Delft University of Technology. In the benchmark, the Portland cement paste with water-to-cement ratio 0.4 at temperature 20 °C was used. The input parameters included the chemical and mineral composition, the density, the specific surface and the particle size distribution of Portland cement. The hydration process and microstructure development of Portland cement paste were simulated with HYMOSTRUC3D model. The water permeability and chloride diffusivity of Portland cement paste were simulated with Lattice Boltzmann method based on simulated microstructure. The mechanical properties of Portland cement paste, including load-displacement curve, elastic modulus, tensile strength and cracking pattern were simulated with a 3D lattice finite element fracture model.

### **1. Introduction**

The benchmark numerical simulation in Micro-level of cementitious materials was launched within the COST Action 1404. Delft University of Technology, as one of the participants, has joint the benchmark numerical simulation. Fig. 1 shows the outline of the simulation performed by Delft University of Technology. The mineral composition, particle size distribution and density of PC, and the water to cement (w/c) of cement paste, etc., were taken as input parameters. HYMOSTRUC3D model [1-3] was used to simulate the hydration process and microstructure development of cement paste. With HYMOSTRUC3D model, the overall degree of hydration of PC, degree of hydration of minerals of PC, heat release, capillary porosity, pore size distribution, chemical shrinkage and compressive strength of PC paste were simulated. Using the Lattice Boltzmann method [4] the water permeability and

chloride diffusivity of cement paste were simulated, in which the microstructure of PC paste simulated by HYMOSTRUC3D model was taken as input. The mechanical properties including load-displacement curve, elastic modulus, tensile strength and cracking pattern of cement paste were simulated with the lattice finite element fracture analysis method [5], in which the microstructure of cement paste simulated with HYMOSTRUC3D model was also taken as input.

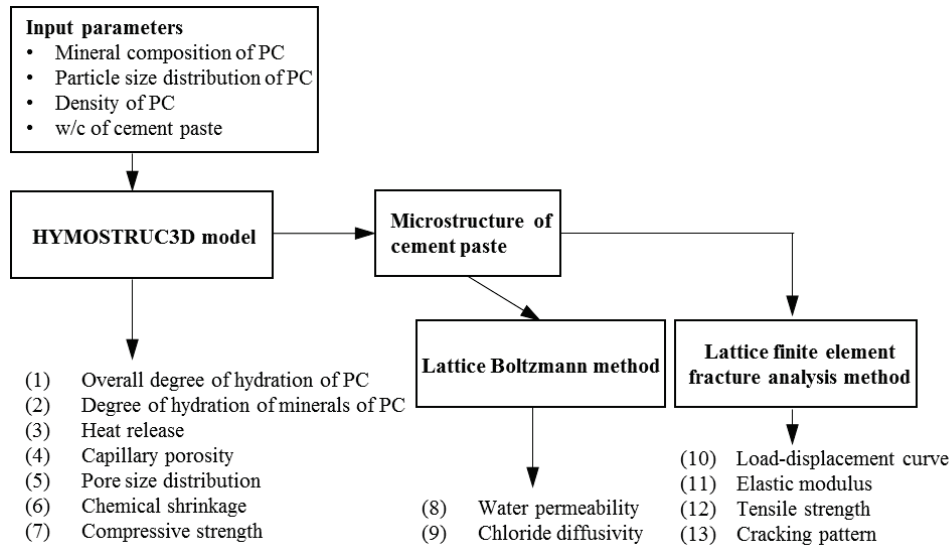


Figure 1: Outline of the simulation performed by using numerical tools developed by Delft University of Technology

## 2. The properties of raw materials

The mineral composition of PC measured with Quantitative X-Ray Diffraction method (Q-XRD) is: 58.3%  $C_3S$ , 20.7%  $C_2S$ , 3.6%  $C_3A$ , 7.3%  $C_4AF$  and 2.4% gypsum. The density of PC is  $3.20 \text{ g/cm}^3$ . Figure 2 shows the particle size distribution of PC measured with laser diffraction particle size analyser. The measured particle size distribution of PC follows the Rosin Rammler Bennett (RRB) distribution, viz.:  $G(x) = 1 - \exp(-bx^n)$ .  $G(x)$  is the cumulative weight,  $x$  is the particle diameter,  $n$  and  $b$  are fitting parameters. The water-to-cement ratio (w/c) of the PC paste is 0.4.

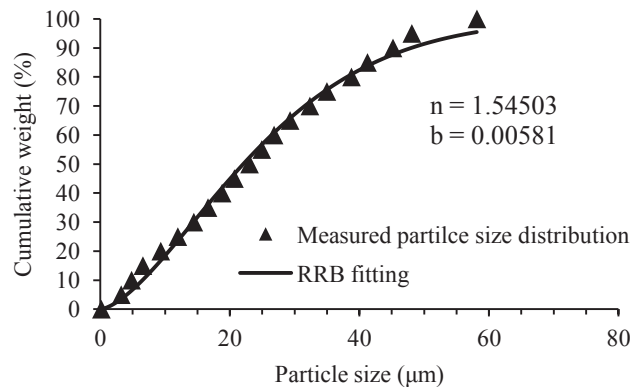


Figure 2: Measured and fitted particle size distribution of PC



### 3. Modelling approach

#### 3.1 Simulation with HYMOSTRUC3D model

$K_0$  and  $\delta_{tr}$  are two important modelling parameters of HYMOSTRUC3D model.  $K_0$  is the initial penetration rate of the reaction front of hydrating PC-components, viz.,  $C_3S$ ,  $C_2S$ ,  $C_3A$ ,  $C_4AF$ .  $\delta_{tr}$  is the transition thickness when the hydration mechanism of  $C_3S$ ,  $C_2S$ ,  $C_3A$ ,  $C_4AF$  change from *phase boundary reaction* to *diffusion-controlled reaction*. Both the values of  $K_0$  and  $\delta_{tr}$  are calculated according to [6]. The calculated values of  $K_0$  of the reaction fronts of  $C_3S$ ,  $C_2S$ ,  $C_3A$  and  $C_4AF$  are 0.111, 0.007, 0.055 and 0.027 [ $\mu\text{m}/\text{h}$ ], respectively, and the values of  $\delta_{tr}$  for the reaction fronts of  $C_3S$ ,  $C_2S$ ,  $C_3A$  and  $C_4AF$  are 4.339, 3.904, 4.365 and 1.441 [ $\mu\text{m}$ ], respectively. Based on the modelling parameters, the hydration process and microstructure of PC paste were simulated with HYMOSTRUC3D. The microstructure of hydrating cement paste consists of inner and outer hydration products, calcium hydroxide, unhydrated cement and capillary pores. To simulate the transport and mechanical properties the microstructure of PC paste was digitized to a dimension of  $100 \times 100 \times 100 \mu\text{m}^3$  (resolution =  $1 \mu\text{m}/\text{voxel}$ ).

#### 3.2 Simulation with Lattice Boltzmann method

##### a. Modelling parameters for the simulation of water permeability

With the method described in [4] (D3Q19 model was used), the water permeability of PC paste was simulated.

##### b. Modelling parameters for the simulation of chloride diffusivity

To simulate the chloride diffusivity of cement paste, specific diffusion coefficients of chloride were assigned to water ( $2.032\text{E-}9 \text{ m}^2/\text{s}$ ), inner product ( $1.0\text{E-}12 \text{ m}^2/\text{s}$ ) and outer product ( $9.0\text{E-}12 \text{ m}^2/\text{s}$ ). Then extra 3 liquid layers were added to two ends at direction of simulation. The concentration at the start layer was set at constant and the concentration gradient between the last two layers was set at zero. The boundary condition was set as bounce-back at the surface of unhydrated cement particle and calcium hydroxide. D3Q19 model was also used.

#### 3.3 Simulation with lattice finite element fracture analysis method

The bulk elastic modulus of the cement paste was simulated with the lattice finite element fracture analysis method as reported by Qian et al. [5]: The bottom voxels of PC paste are fixed. An incremental tensile displacement was given at each top voxel of PC paste. Correspondingly, the response stress at the top surface nodes was simulated with the lattice finite element fracture analysis method. The bulk elastic modulus of PC paste was calculate from the tensile displacement and the response stress.

### 4. Simulation results

The simulated properties of PC paste, like the capillary porosity, compressive strength and water permeability of PC paste at specific ages, viz., 1, 3, 7 and 28 days are given in Table 1. This will be convenience for the validation with experiments. However, to present the simulation results, like the degree of hydration of different minerals of PC, the pore size

distribution of PC paste, the water flow in PC paste, etc., more directly, these simulation results are plotted in figures.

Table 1: Simulated properties of PC and PC paste at different ages

Simulated properties	Unit	1day	3days	7days	28days
Overall degree of hydration	$[\alpha]$	0.36	0.58	0.68	0.79
Heat release of PC	[J/g]	171.2	277.8	326.6	370.4
Capillary porosity		0.38	0.28	0.24	0.18
Chemical shrinkage	[mL/100g]	2.10	3.87	4.60	5.37
Compressive strength	[MPa]	2.9	14.1	20.4	28.5
Water permeability	[m <sup>-2</sup> ]	1.29E-13	4.06E-14	2.62E-14	1.08E-14
Chloride diffusion coefficients	[m <sup>2</sup> /s]	4.63E-11	2.25E-11	1.67E-11	9.36E-12
Elastic modulus	[GPa]	2.12	6.16	8.25	13.12
Tensile strength	[MPa]	4.13	10.63	15.38	29.45

Figure 3 shows the degree of hydration of different minerals of PC simulated with HYMOSTRUC3D in comparison with the experimental results. The experimental results were provided by COST Action. Figure 3 shows that the simulation results of C<sub>3</sub>S and C<sub>2</sub>S phases are in good agreement with experiments but C<sub>3</sub>A and C<sub>4</sub>AF shows discrepancy. The pore size distribution of PC paste simulated with HYMOSTRUC3D is shown in Figure 4.

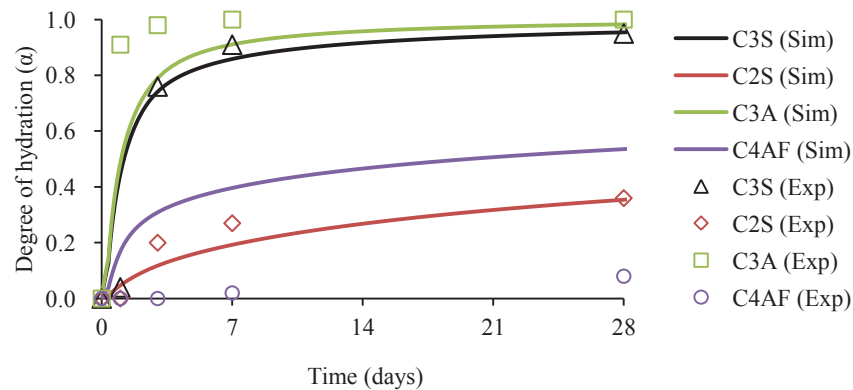


Figure 3: Simulated and measured degree of hydration of different minerals of PC

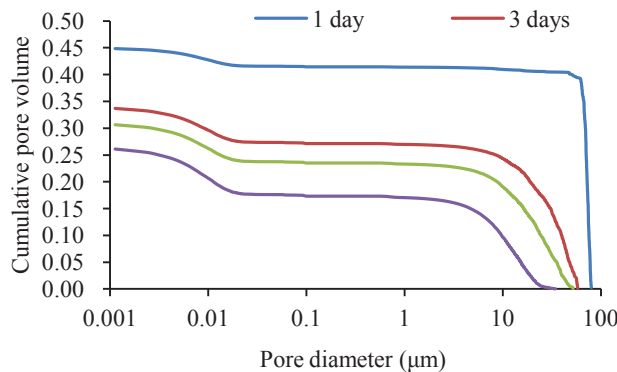
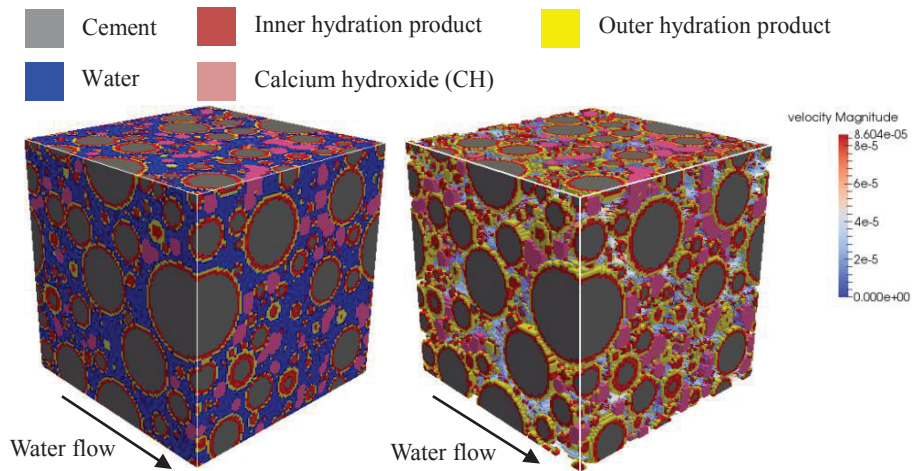


Figure 4: Simulated pore size distribution of cement paste

Figure 5 illustrates the streamline of water flow through the PC paste at hydration age of 1 day and Figure 6 shows the simulated concentration field of chloride in PC paste at curing age of 7 days.



(a) Simulated microstructure at 1 day (b) Streamline of water flow  
Figure 5: Simulated water flow in a 1 day-old PC paste ( $w/c = 0.4$ )

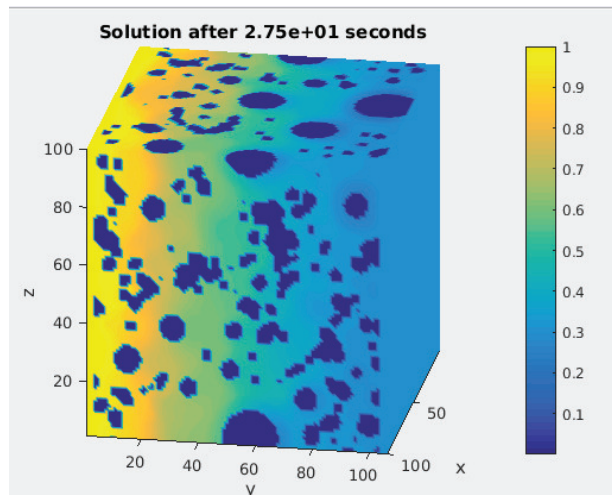
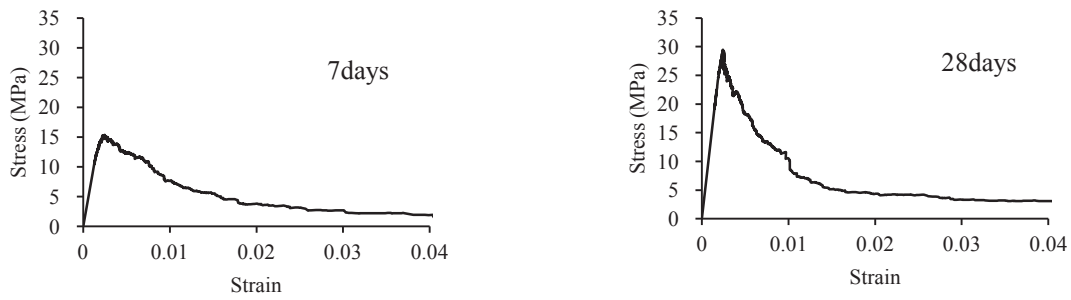


Figure 6: Simulated concentration field of chloride in PC paste (time = 7 days)

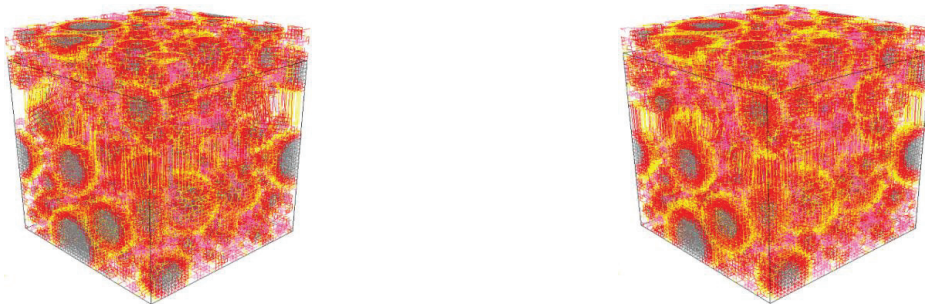
Figure 7 presents the simulated load-displacement curve of PC paste at different ages. The maximum stress from 15 MPa increases to 29 MPa when curing age change from 7 days to 28 days. In Figure 8 the simulated cracking pattern of PC paste at curing age of 7 days and 28 ages are illustrated.



(a) time = 7 days

(b) time = 28 days

Figure 7: Simulated load-displacement curve of cement paste at different ages



(a) time = 7 days

(b) time = 28 days

Figure 8: Simulated cracking pattern of PC paste at different ages

## 5. Conclusions

This study presents the benchmark numerical simulation results for cement-based materials in Micro-level performed by using numerical tools developed at Delft University of Technology. In further study, the simulated properties of PC and PC paste will be used to compare the experimental data, and compare the simulation results from different research groups.

## References

- [1] Van Breugel, K, Simulation of hydration and formation of structure in hardening cement-based materials, PhD Thesis, Delft University of Technology (1991)
- [2] Koenders, E. A. B., Simulation of volume changes in hardening cement-based materials, PhD Thesis, Delft University of Technology (1997)
- [3] Ye, G., Experimental Study and Numerical Simulation of the Development of the microstructure and permeability of cementitious materials, PhD Thesis, Delft University of Technology (2003)
- [4] Zhang, M., Multiscale lattice Boltzmann-finite element modelling of transport properties in cement-based materials, PhD Thesis, Delft University of Technology (2013)
- [5] Qian, Z. W., Schlangen, E., Ye, G. et al. Prediction of mechanical properties of cement paste at microscale. *Materiales de Construccion* 60 (2010) 7-18
- [6] Nguyen V.T. Rice husk ash as a mineral admixture for ultra high performance concrete PhD Thesis, Delft University of Technology (2011)

## **COMPARISON BETWEEN THE EXPERIMENTAL MEASUREMENT RESULTS AND THE MICROMECHANICAL MODELLING ON THE AGEING BASIC CREEP OF VERCORS CONCRETE**

**Shun Huang**<sup>(1)(2)(3)</sup>, **Julien Sanahuja**<sup>(1)</sup>, **Luc Dormieux**<sup>(2)</sup>, **Benoit Bary**<sup>(3)</sup>, **Eric Lemarchand**<sup>(2)</sup>, **Laurent Charpin**<sup>(1)</sup> and **Romain Thion**<sup>(1)</sup>

(1) EDF lab, Site des Renardieres, Route de Sens, Ecuelles, 77250 Moret sur Loing, France

(2) École Nationale des Ponts et Chaussées, 77455 Marne-la-Vallée, France

(3) CEA, DEN, DPC, SECR, Laboratoire d'Etude du Comportement des Bétons et des Argiles, F-91191 Gif-sur-Yvette, France

### **Abstract**

The concrete creep is critical for the prestressed containment building of nuclear power plants, since creep yields prestress relaxation. To develop a model of material behaviour incorporating the ageing creep, given the multi-scale and multi-physics nature of concrete, the creep experiments and the micro-mechanical modelling approach are attractive on the study of the VeRCoRs concrete, which is a typical formulation for the construction of the containment building.

The experimental campaign is carried out to characterize the ageing basic creep at different scales and at different ages of loading with the formulation of the VeRCoRs concrete. The purpose of the experiments is to describe the basic creep behaviour on cement paste, mortar and concrete. The ageing viscoelastic part (the basic creep) of the experimental results are concerned in the comparison. Moreover, for each specimen loaded, a complete unloading is performed to highlight the effect of creep recovery. The basic creep strain rate decreases with the increase of the age of loading (corresponds to an increase of the hydration degree).

A direct confrontation between the experimental results and the modelling results is also performed. The ageing basic creep behaviour is compared with the application of mean-field homogenisation schemes.

### **1. Experimental study of the creep of cement paste, mortar and concrete with the formulations derived from the materials for the VeRCoRs mock-up**

The purpose of the experiments is to describe the characterization experiments of autogenous shrinkage, and basic creep under uni-axial compression at 20 °C and 50% RH at the different

ages of loading (1 day, 2 days, 3 days, 7 days, 28 days, 3 months and potentially 1 year in 2018) on cylindrical samples of cement paste, mortar and concrete, to validate the aging viscoelastic model. The mix design of cement paste, mortar and concrete was derived from the materials of the VeRCoRs mock-up in EDF for the construction of the containment building (at the scale of the corresponding mortar, the cement paste is the matrix; at the scale of the VeRCoRs concrete, the corresponding mortar is the matrix). These characterization experiments were carried out on two geometries: small cylindrical specimens with the diameter of 3.6 cm and the height of 18 cm for cement paste and mortar, and big cylindrical specimens with the diameter of 8 cm and the height of 29 cm for concrete. The non-drying shrinkage and creep experiments are carried out at different times. For this reason, it was decided to use 3 layers of self-adhesive aluminium tape on the shaft and the ends of the sample to perform the seal. This requires the preparation of different pieces of tape for each sample. There has been assessment of the effectiveness of the adhesive aluminium tape. For example, the mass loss of the specimens during 370 days has been 0.37g, so that the relative mass loss is only 0.051% of the mass of the sample. This assessment confirms the feasibility of claiming sealed conditions

For each loading time, the constant load is calculated to be lower than 1/3 of the compressive strength, and controlled, to keep the creep behaviour in the linear regime.

Until now, the creep experiments at the scale of cement paste, of mortar and of the VeRCoRs concrete have been carried out with the ages of loading at 1 day, 2 days, 3 days, 7 days, 28 days and 3 months. The creep experiments at the scale of cement paste and of mortar with the age of loading at 1 year is ongoing. In addition, the experiments at the scale of cement paste are performed at 2 different water–cement ratio ( $w/c=0.525$  and  $w/c=0.400$ ).

2 samples from the same batch are tested for each loading time. The axial displacement sensors are placed at 120° vertically. The loading is performed by imposing a constant stress. The temperature evolution in the lab is controlled around 20°C. But the continuous monitoring of the sample temperature, done during the measurements in order to take into account the effect of temperature on the hydration process, reveals that several abrupt temperature changes was caused by the air conditioning unit issues. For example, the temperature in the lab has rose from 20°C to 34°C during 1 day on 08/28/2017 and the abrupt temperature changes larger than 1°C have happened 6 times until now, which make it more feasible and necessary to adopt a method to take into account the accelerating effect of a given temperature history to experiments.

An equivalent time  $t_{eq}$  is thus computed with the Eq (1) proposed by Freiesleben Hansen and Pedersen in [1].

$$t_{eq}(t, T) = \sum_0^t \exp\left(-\frac{E_a}{R}\left(\frac{1}{273 + T} - \frac{1}{273 + T_{ref}}\right)\right) \Delta t \quad (1)$$

Where:

- T is the temperature, in °C
- $T_{ref}$  is the reference temperature, generally 20°C
- R is the universal gas constant, 8.314J/mol/K
- $E_a$  is the apparent activation energy, in J/mol

This equation models the accelerating effect of a given temperature history  $T$  in comparison with a reference temperature  $T_{ref}$  (when  $T > T_{ref}$ ). The apparent activation energy  $E_a$  is determined from the curve fitting of the experimental data with respect to the compliance model for basic creep described as follows:

In the light of recent developments, the compliance data can be fitted using a creep law reworked by Torrenti [2] based on ideas arising from an analysis of experimental tests. Indeed, this law showed that the derivative of the compliance  $dJ/dt$  tends to  $1/Ct$  when  $t$  was large. Based on the compliance data from the experiments on VeRCoRs materials, the value of  $C$  for a given material depends on the age of loading  $t_0$ . But this compliance function underestimate the compliance value in the range of  $10^{-2} - 10^0$  days. So a Kelvin unit with the retardation time  $\tau_{Kelvin} = 10^{-2}$  day is added in the compliance function to correct the error value in the range of  $10^{-2} - 10^0$  days.

The ageing compliance model for basic creep is thus the following:

$$J(t, t_0) = \frac{1}{E(t_0)} + \frac{1}{C(t_0)} \text{Log} \left( 1 + \frac{t - t_0}{\tau(t_0)} \right) + \frac{1}{E_{Kelvin}(t_0)} \left( 1 - e^{-\frac{t-t_0}{\tau_{Kelvin}}} \right) \quad (2)$$

Where:

- $E(t_0)$  is the Young's modulus at the age of loading, in GPa
- $C(t_0)$  is a variable depending on mix design and the age of loading, describing the long term creep, in GPa
- $\tau(t_0)$  is a kinetic constant depending on the age of loading, in day.

The Eq (2) describes only the compliance reaction to a step of load, but the loading period (about 20 seconds) is ignored. To consider the loading period, the Eq (2) is improved to the Eq (3) with the application of the Laplace-Carson transform [3]:

$$J(t, t_0) = \left( \frac{t_{load} - (t - t_0)}{E(t_0)t_{load}} - \frac{(t - t_0 + \tau(t_0)) \ln \left( \frac{t - t_0 + \tau(t_0)}{\tau(t_0)} \right)}{C(t_0)t_{load} \ln(10)} + \frac{t_{load} - t}{C(t_0)t_{load}} \right) \text{Heaviside}(t - t_{load}) \quad (3)$$

$$+ \frac{t}{E(t_0)t_{load}} + \frac{(t + \tau(t_0)) \ln \left( \frac{t + \tau(t_0)}{\tau(t_0)} \right)}{C(t_0)t_{load} \ln(10)} - \frac{t}{C(t_0)t_{load}} + \frac{1}{E_{Kelvin}(t_0)} \left( 1 - e^{-\frac{t-t_0}{\tau_{Kelvin}}} \right)$$

Where  $t_{load}$  is the loading period in day.

With the nonlinear least squares optimization between the Eq (3) and the experimental results, the value of  $E(t_0)$ ,  $C(t_0)$ ,  $\tau(t_0)$  and  $E_a$  can be identified for each experiment with a given age of loading and a given material.

The experimental evolution of the strain/stress ratio of basic creep strain is presented in Fig. 1 (autogenous strains have been subtracted). For each sample loaded, a complete unloading is performed to highlight the effect of creep recovery. As expected, from the scale of cement paste to that of mortar, then to that of concrete, the compliance of basic creep is lower and lower. Moreover, the basic creep strain rate decreases with the increase of the age of loading (which corresponds to an increase of the hydration degree). The curves are used to compare with the modelling behaviour results.

## 2. Micromechanical model (Example dedicated to mortar scale)

With the parameters identified from the experiments, micromechanical model can be developed to perform the multi-scale homogenization model.

### 2.1 Identification of parameters

There are three steps to finish the processes of the identification of parameters.

Firstly, the Eq (1) and the Eq (3) are applied in the nonlinear optimization to calculate the correct apparent activation energy  $E_a(t_0)$  considering the effect of temperature on the hydration process, with which the equivalent time  $t_{eq}(t_0)$  can be calculated for each experiment. The correct  $E_{Kelvin}(t_0)$  is optimized in this step, too.

Secondly, the compliance results during the loading period (about 20 seconds) in the equivalent time  $t_{eq}$  are used the nonlinear optimization with the Eq (3) to define the correct Young's modulus at the age of loading  $E(t_0)$ .

Thirdly, with the correct  $E(t_0)$ , a least squares polynomial fit process is performed with the end of the compliance results. The derivative of the compliance  $dJ/dt$  tends to  $1/C(t_0)$  when  $t$  was large, which aides to calculate  $C(t_0)$ .

Fourthly, with the correct  $E(t_0)$  and the least squares polynomial fit line,  $\tau(t_0)$  is calculated.

With this method, the analytical solution of the compliance for each material and each age of loading is calculated with the form of the Eq (3). An example is presented in the Fig. 2.

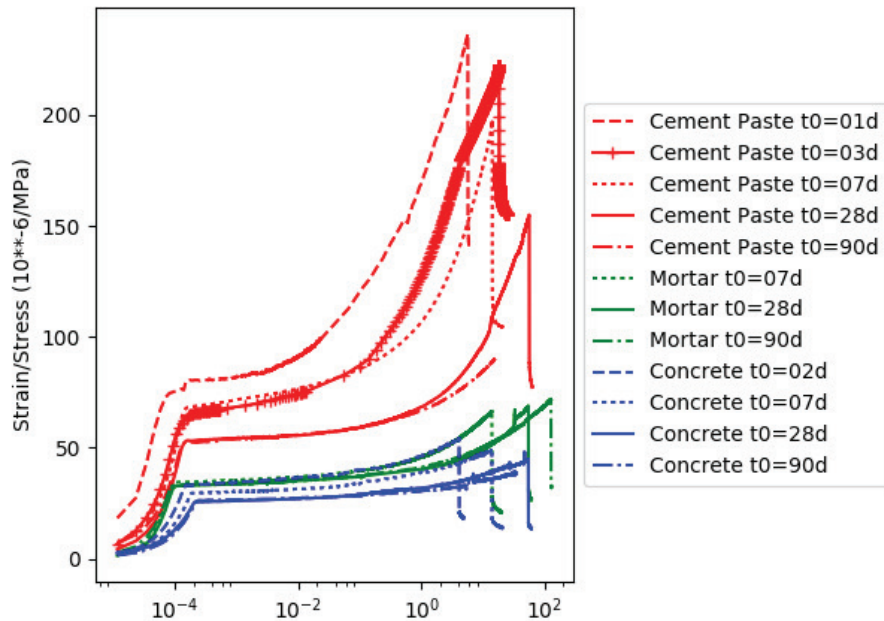


Figure 1:  $\varepsilon/\sigma$  evolution: loading age effect ( $t_0$  = age of end of loading).

$E(t_0)$ ,  $C(t_0)$ ,  $\tau(t_0)$ ,  $E_a(t_0)$ ,  $E_{Kelvin}(t_0)$  and  $t_{eq}(t_0)$  for each age of loading can be calculated with this method. And  $E(t_0)$ ,  $C(t_0)$ ,  $\tau(t_0)$  and  $E_{Kelvin}(t_0)$  can be described as follows:

$$f(t_0) = A + B(1 - e^{-\frac{t_0}{D}}) \quad (4)$$



The method of optimization is applied with the Eq (4) to calculate the proper parameter A, B and D for  $E(t_0)$ ,  $C(t_0)$ ,  $\tau(t_0)$  and  $E_{Kelvin}(t_0)$  for  $t_0$  varies from 1 day to 1 year.

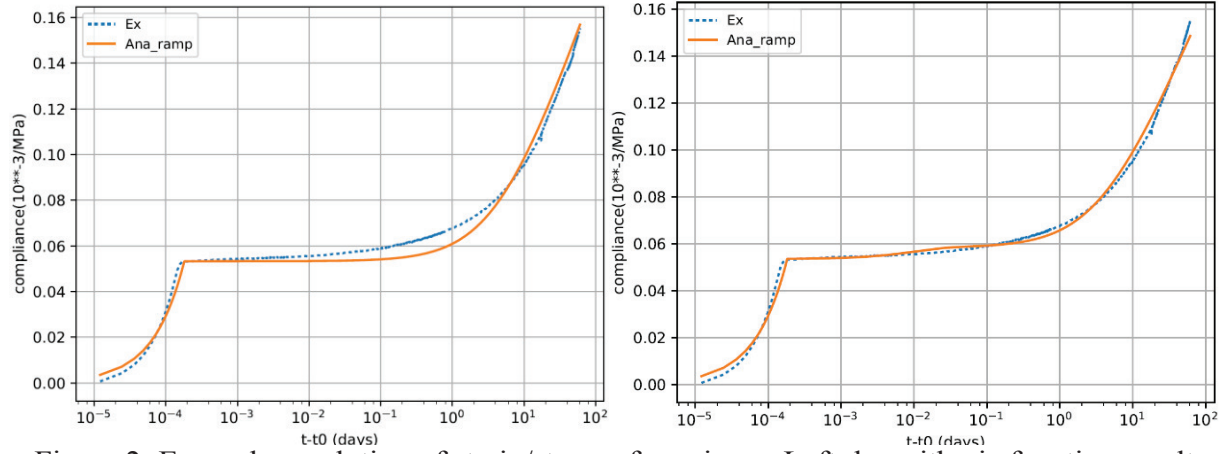


Figure 2: Example: evolution of strain/stress of specimen. Left: logarithmic function result (solid line), Right: model result (solid line), cement paste with age of loading = 28 days.

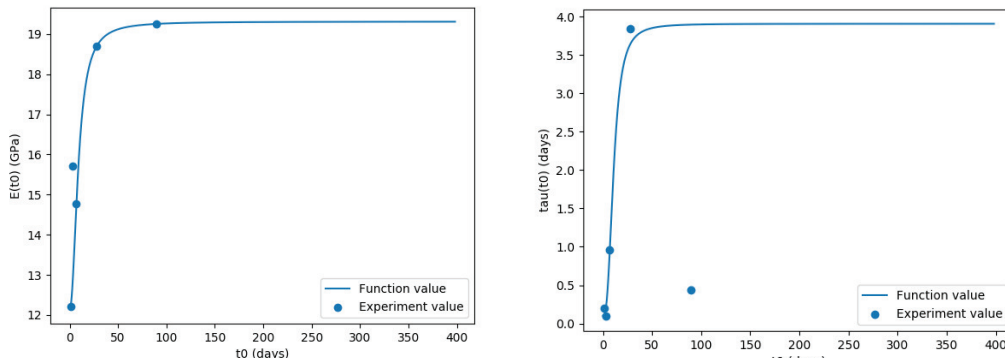


Figure 3: Experimental value (dots) and model (plain line) of  $E(t_0)$  (left) and  $\tau(t_0)$  (right).

## 2.2 Upscaling using homogenization

This part proposes a semianalytical approach to estimate the effective aging viscoelastic behaviour characterized by the compliance tensors as functions of two time variables ( $t, t_0$ ) [3]. The Mori–Tanaka homogenization scheme and the self-consistent homogenization schemes is then applied to upscale the ageing viscoelastic behaviour from the scale of cement paste to the scale of mortar (with cement paste as the ageing viscoelastic matrix and sand as the inclusion), and from the scale of mortar to the scale of concrete (with mortar as the ageing viscoelastic matrix and coarse aggregate as the inclusion). The mechanical behaviour of sand and coarse aggregate are supposed to be elastic.

For the upscaling from the scale of cement paste to that of mortar, the volume fraction of sand is obtained by the mix design of the mortar samples:  $f_{sand} = 0.54$ . With the same principle, for the upscaling from the scale of mortar to that of concrete, the volume fraction of the phase of coarse aggregate is obtained by the mix design of the concrete samples:  $f_{aggregate} = 0.39$ . In the VeRCORs concrete, the mechanical properties of aggregates are as in the Table 1. The effective aging uniaxial compliance function is plotted in Fig. 4 as continuous lines with the method mentioned in [4].

### 3. Conclusion and prospects

Homogenization modelling results underestimate the compliance and this underestimation is more evident at the early age. However, the model shows the tendency to underestimate the experimental results. It thus opens to us new ways for improving the quality of the model by: 1. Taking into account the cement paste/aggregate interface (ITZ); 2. Developing the microcracking of the VER during hydration; 3. The Poisson's Ratio of the matrix can also be regarded as a variable of time  $\vartheta(t_0)$  to improve the model.

Table 1: Mechanical properties of materials of different scales for the VeRCoRs concrete.

	Sand	Coarse aggregate	Cement paste	Mortar
Young's Modulus (GPa)	50	55		
Poisson's ratio	0.27	0.27	0.23	0.24

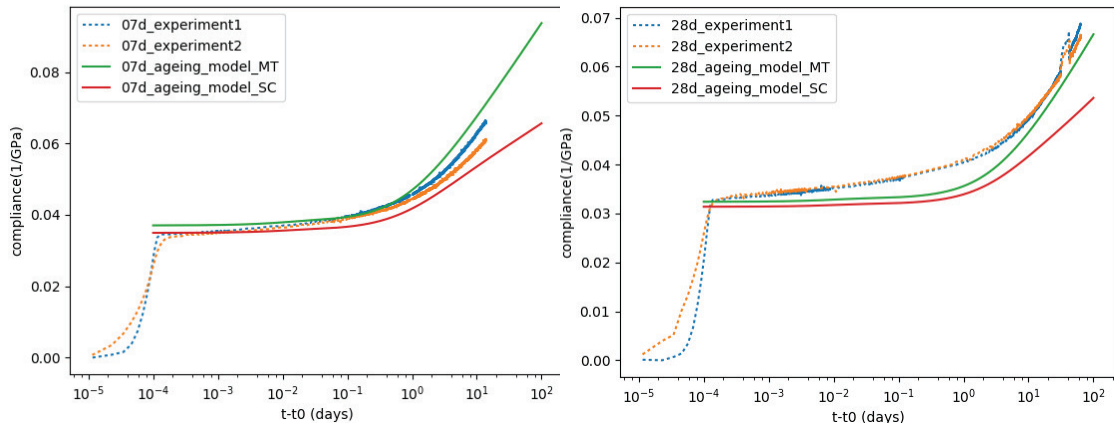


Figure 4: Effective uniaxial compliance [5] functions of mortar ( $w/c=0.525$ ), plotted for various ages of loading  $t_0 = 7 \text{ days}, 28 \text{ days}$ . Comparison between the experimental results (2 dotted lines) and the upscaling using Mori–Tanaka and the self-consistent homogenization scheme from the scale of cement paste to the scale of mortar (continuous line).

### References

- [1] Freiesleben Hansen, Pedersen EJ (1977) "Maturity Analysis by Computer for Controlled Curing and Hardening of Concrete," Nord Betong, no. 1, pp. 21-25.
- [2] Torrenti JM, Le Roy R (2015) Analysing and modelling basic creep. In Concreep-10 conference, Vienna
- [3] Sanahuja, J (2014). "Homogenization of solidifying random porous media: Application to ageing creep of cementitious materials." RILEM Symp. on Concrete Modelling, Beijing.
- [4] Sanahuja J, Huang S (2017) Mean-Field Homogenization of Time-Evolving Microstructures with Viscoelastic Phases: Application to a Simplified Micromechanical Model of Hydrating Cement Paste. Journal of Nanomechanics and Micromechanics.7:4016011.
- [5] Salençon J., Salencon J., & SpringerLink (Online service). (2001). Handbook of continuum mechanics: General concepts thermoelasticity. Berlin/Heidelberg: Springer Berlin Heidelberg. doi:10.1007/978-3-642-56542-7

## **MACROSCOPIC HYGRO-MECHANICAL MODELING OF RESTRAINED RING TEST - RESULTS FROM COST TU1404 BENCHMARK**

**Vít Šmilauer<sup>(1)</sup>, Tobias Gasch<sup>(2)</sup>, Arnaud Delaplace<sup>(3)</sup>, David Bouhjiti<sup>(4)</sup>,  
Fragkoulis Kanavaris<sup>(5)</sup>, Miguel Azenha<sup>(6)</sup>, Laurie Lacarrière<sup>(7)</sup>**

- (1) Czech Technical University in Prague, Czech Republic
- (2) KTH Royal Institute of Technology, Stockholm, Sweden
- (3) LafargeHolcim Research Center, Isle d'Abeau, France
- (4) Chair PERENITI – 3SR, Laboratory, University of Grenoble Alpes, France
- (5) Previously in University of Minho, currently in Arup, London, UK
- (6) ISISE, University of Minho, Portugal
- (7) INSA, Toulouse, France

### **Abstract**

The restrained ring test under constant temperature is used for estimating cracking tendency of pastes, mortar or concrete. This test induces hygro-mechanical interactions, with intricate interplay of several phenomena such as autogenous shrinkage, drying shrinkage, basic and drying creep, as well as evolution of tensile strength and fracture energy. The benchmark described in this paper relies on extensive experimental data sets obtained through the extended Round Robin Testing programme (RRT+) of COST Action TU1404. Five teams took part with their simulation models. A series of outputs were produced, starting from mass loss of a prism through its axial deformation up to stress/strain evolution in the ring. Three teams quantified also damage due to drying and stress concentration around a ring's notch. All models showed excellent performance on mass loss while strain validation showed higher scatter and influence of several other factors. The benchmark demonstrated high capability of used models and emphasized strong role of calibration with regards to available experimental data.

### **1. Introduction**

The restraint ring shrinkage test is a well-established method for testing cementitious binders for crack resistance during early ages, adopted further in e.g. ASTM C1581 or AASHTO T334. R. Carlson used the test already in 1942 [1] and a strong correlation with concrete

surface cracking after 53 years was found. Several papers were published afterwards for optimizing binders and models using the ring, as shown in the review of reference [2]. COST Action TU1404 “Towards the next generation of standards for service life of cement-based materials and structures” has set up this benchmark to simulate experimental results on a reference concrete (labelled as ‘OC’) and to test different modelling approaches. Interested participants received input experimental data and they knew experimental results in advance in order to calibrate further their models if needed. The participants were free to use their modelling approaches and models, however, several intermediate steps were required to validate their partial data. Five participants took part in the benchmark:

1. Arup+University of Minho, (ARUP+UMinho)
2. CTU in Prague (CTU)
3. KTH Royal Institute of Technology, Stockholm (KTH)
4. LafargeHolcim Research Center, Isle d'Abeau (LafargeHolcim)
5. Chair Pereniti-3SR Lab, Grenoble (Pereniti)

Experimental methods were defined in the documentation of the Extended Round Robin testing programme (RRT+) of COST TU1404 [3], including the restrained ring shrinkage test. Since deformation of the ring is driven dominantly by drying, the benchmark had two consecutive stages: hygro-mechanical simulation of drying prisms  $100 \times 100 \times 400$  mm and hygro-mechanical simulation of the ring. Fig. 1 shows ring geometry, whereas Table 1 presents the composition of OC concrete mix used in the experiment.

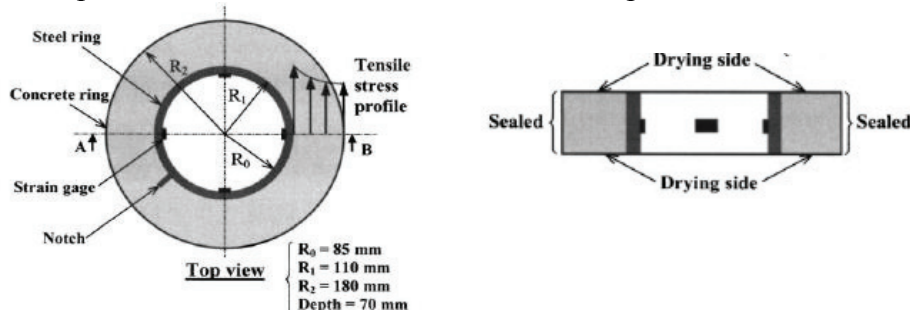


Figure 1: Geometry of the ring test

Table 1: Composition of OC concrete mix [3].

Basic Material	Type of the material	Amount [ $\text{kg}/\text{m}^3$ ]
Cement	CEM I 52.5 N-SR3 CE PM-CP2 NF HRC Gaurain	320
Dry sand	0-4 mm, REC GSM LGP1 (13 % of CaO and 72 % of SiO <sub>2</sub> )	830
Fully saturated gravel	4-11 mm, R GSM LGP1 (rounded, containing silicate and limestone)	449
	8-16 mm, R Balloy (rounded, containing silicate and limestone)	564
Admixtures	Plasticizer SIKAPLAST Techno 80	1.44
Added water	Water that needs to be added to the mixer	172.4
$w_{\text{eff}}/c$		0.52

## 2. Description of models used by participants

Participants used different governing equations and constitutive models for hygro-mechanical coupled simulations, as shown in Table 2. Four models for moisture transport were based on

single-phase balance equations with humidity or moisture field as the unknowns. The KTH model used mass balance of a gas-phase and a liquid-phase based on the thermodynamically constrained averaging theory. All moisture models used non-constant diffusivity, decreasing with lowering relative humidity. Some participants took advantage of desorption isotherm which was known from a similar mature Vercors concrete [4] with calibrated saturation from TU1404 data. Total water content at the full saturation of mature concrete was found as 165.3 kg/m<sup>3</sup>. Only KTH model considered water consumption during hydration and its effect on decreasing evaporable water content during hydration.

All participants used small strain decomposition and incremental stress-strain relationship to account for creep. The most advanced models used the following incremental constitutive law

$$\Delta\varepsilon = E''(\Delta\varepsilon - \Delta\varepsilon'' - \Delta\varepsilon_{as} - \Delta\varepsilon_{ds} - \Delta\varepsilon_f) \quad (1)$$

where  $\varepsilon_{as}$  is the autogenous shrinkage strain,  $\varepsilon_{ds}$  is the drying shrinkage strain and  $\varepsilon_f$  stands for fracturing strain. Except KTH, the participants assumed linear relation between drying shrinkage strain rate and relative humidity/moisture rate using a shrinkage factor. Four participants used fracture material model for crack initiation and propagation, usually in the framework of isotropic damage model.

Table 2: Summary of used equations, material models, software and computation times.

	<b>Arup+UMinho</b>	<b>CTU</b>	<b>KTH</b>	<b>LafargeHolcim</b>	<b>Pereniti</b>
Equation for moisture transport	Humidity balance, h	Humidity balance, h	Gas-phase and liquid-phase, water, dry air	Water balance, w	Water balance, w
Material model for creep	Double-power law	Calibrated B3/B4	Calibrated B3 with MPS theory	Two ageing Kelvin units	Burger model
Material model for fracture	Multidirectional fixed crack model	Isotropic damage model	Isotropic damage model	-	Stochastic isotropic damage model
Software	iDiana, Diana, Matlab	OOFEM	COMSOL	Aster	Aster
Computation time - prism	20 min	8 min	3.5 min	2 min	3.5 min
Computation time - ring	20 min	20 min	10 min	5 min	21 min

### 3. Results and discussion

#### 3.1 Prism

The first part considered simulation of a prism 100×100×400 mm which started drying at 50 % RH after 1 day of sealed hydration. For this test, the mass loss in Fig. 2 and the total strain in Fig. 4 were measured in RRT+. Total strain is used for the identification of the parameter managing the moisture transport (through the measurement of mass loss) and for the shrinkage coefficient in models using linear relation between the moisture rate and the drying strain.

Drying shrinkage tests were held for 22 days and the asymptotic value at very long time was deduced from tests performed on smaller 70×70×280 mm specimens for which the hydric

equilibrium is reached faster ( $-450 \mu\epsilon$  and  $89.2 \text{ kg/m}^3$  of water loss for drying shrinkage at 50%RH and  $-50 \mu\epsilon$  for autogenous shrinkage) [3].

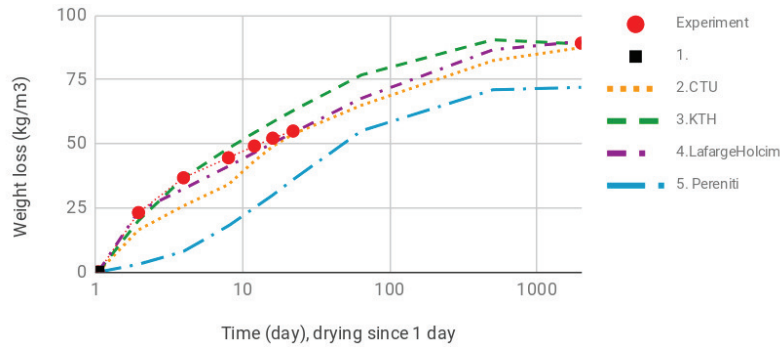


Figure 2: Weight loss of a prism  $100 \times 100 \times 400 \text{ mm}$ .

Fig. 3 shows models calibration to E-modulus and basic creep at  $t'=1$  day. It is noted that the team of Arup+UMinho have used data for E-modulus from a distinct source within the RRT (data from EMM-ARM method measured at UMinho on the same concrete). Fig. 4 then provides the simulated total shrinkage (autogenous and drying) on the axis of the prism. It can be seen that the identification of the shrinkage models allows a good reproduction of the results. Criteria for fracture initiation used splitting tensile strength 1.4 MPa at 2 days, 3.5 MPa at 7 days and 4.5 MPa at 28 days.

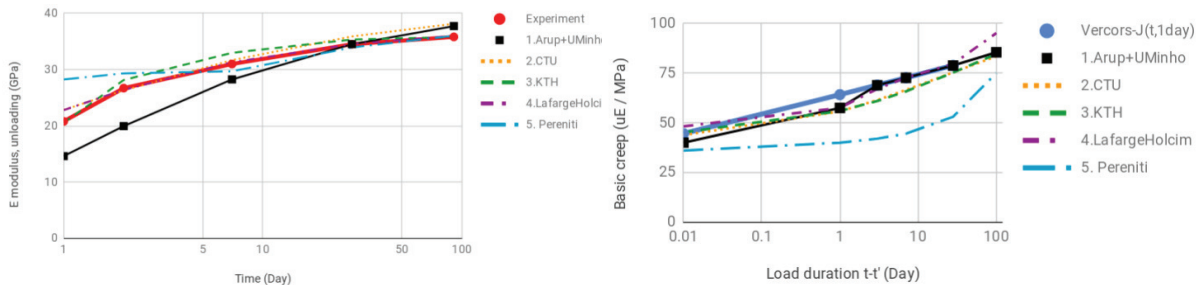


Figure 3: Calibration for E modulus and basic creep at  $t'=1$  day.

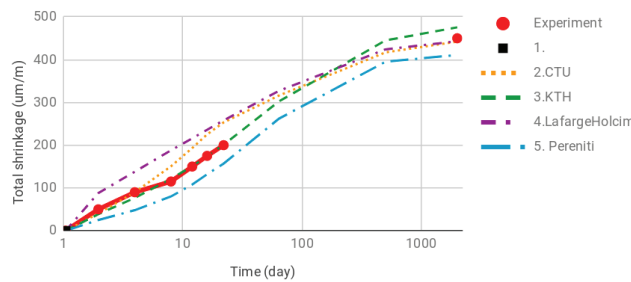


Figure 4: Total shrinkage on prism's axis.

### 3.2 Ring

Once the drying kinetics were validated on the prism, simulation of ring test took place using the same constitutive laws for moisture transport. All participants used a 3D model except LafargeHolcim who used axisymmetric model without any damage. Fig. 5 shows meshes in hygro-mechanical models.

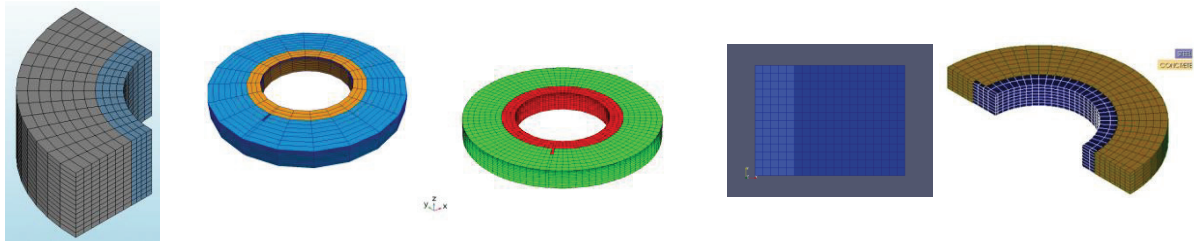


Figure 5: Meshes used in hygro-mechanical simulations of the ring.

First, the models validated steel strain, as shown Fig. 6. Except for the results from Pereniti, where strain localization occurs earlier than observed in the selected reference ring test, the participants have all simulated the experimentally measured strain rather well up to the maximum strain. Damage occurs immediately after the drying on dried horizontal surfaces up to a few mm, further damage occurs after approximately 10 days around steel, breaking up standard linear creep law. This is probably the main cause of slow strain decrease after the strain peak at  $70 \mu\epsilon$  at 50 days.

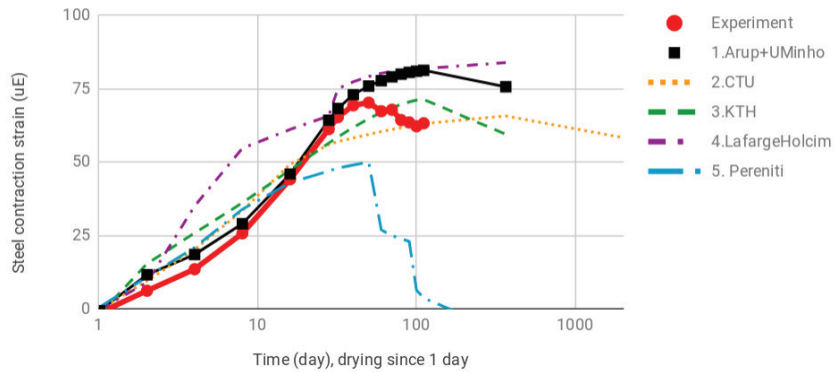


Figure 6: Validation of hoop steel strain.

Two material points are interesting for stress evolution; proximal point close to steel ring and distal point close to vertical exterior. Hoop stresses testify non-constant stress distribution across the ring as known even from analytical elastic solution [2]. Models provided blind prediction which is summarized in Fig. 7. The notch in the ring created small stress concentration but, due to stress gradient, it did not propagate to a visible crack even after experimental 111 days (except in the case of Pereniti team where visible cracks are obtained within 51 days). Fig. 8 shows non-validated and blind weight loss predictions of the ring.

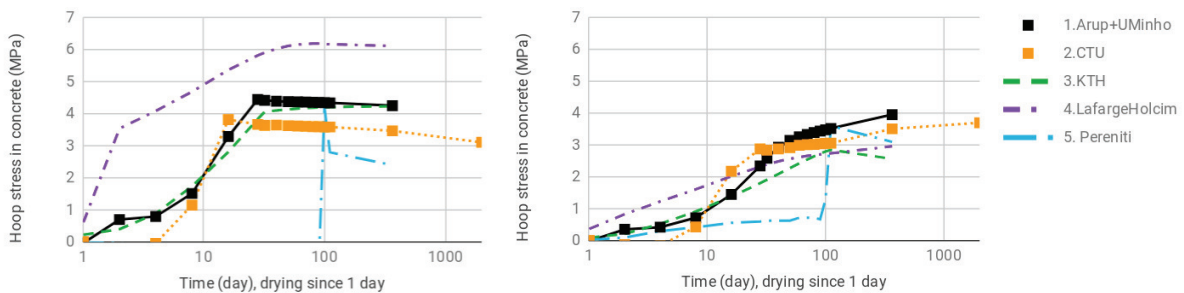


Figure 7: Proximal and distal hoop stress in concrete, blind prediction.

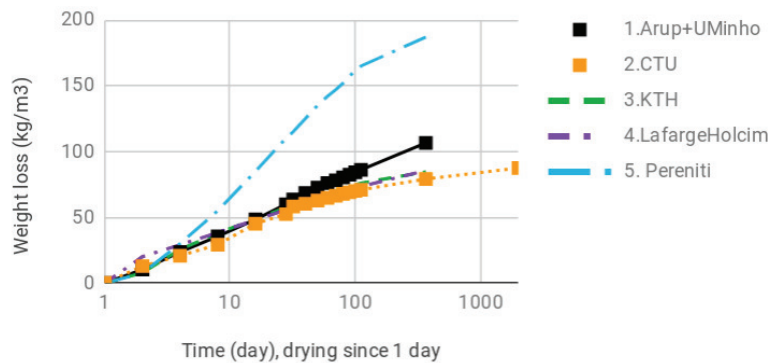


Figure 8: Blind prediction of ring's weight loss.

#### 4. Conclusions

This benchmark extensively used available experimental data generated in the RRT+ programme of COST Action TU1404. Selection of feasible and reasonable data was a prerequisite for successful macroscopic validation of the ring test. The results from five participants showed:

- Drying shrinkage presents the main driving strain and mass loss needs validation. Data on prisms  $100 \times 100 \times 400$  mm with asymptotic values served for this purpose.
- Ageing creep with correct evolution of E-modulus represents sensitive constitutive law for stress evolution, damage and potential macro-crack formation.
- Hygro-mechanical models performed generally well. Nonlinear creep occurring close to tensile strength would likely improve strain evolution after its maximum. The variability of results is both due to calibration on limited data sets and models' limitations.

#### Acknowledgements

The authors would like to acknowledge networking support by the COST Action TU1404 ([www.tu1404.eu](http://www.tu1404.eu)). Czech Technical University acknowledges support of Technology Agency of the Czech Republic in the project TH03020404. The team of UMinho acknowledges the support of FCT/FEDER(COMPETE2020) through the research project IntegraCrete PTDC/ECM-EST/1056/2014 (POCI-01-0145-FEDER-016841).

#### References

- [1] Burrows, R. W., The visible and invisible cracking of concrete, ACI monograph, 1998
- [2] Turcry, P., Loukili, A., Haidar, K, Pijaudier-Cabot, G., Belarbi, A., Cracking Tendency of Self-Compacting Concrete Subjected to Restrained Shrinkage: Experimental Study and Modeling, Journal of Materials in Civil Engineering (2006), 46-54
- [3] COST TU1404, RRT+ Main phase of the extended round robin testing programme for TU1404, testing protocols, (2016).
- [4] EDF. Projet VeRCoRs. (2015-2021). <https://www.conference-service.com/EDF-VeRCoRs-Benchmark-2018/welcome.cgi>



## **BACKGROUND FOR A NEW EUROCODE 2-ANNEX: EVALUATION OF EARLY-AGE AND LONG-TERM CRACKING DUE TO RESTRAINED DEFORMATIONS**

**Terje Kanstad <sup>(1)</sup>, Anja Estensen Klausen <sup>(1)</sup>**

(1) Norwegian University of Science and Technology (NTNU), Trondheim, Norway

### **Abstract**

It is agreed within the relevant CEN-committees that Eurocode 2 should give regulations that clearly describe how imposed deformations including early age effects can be accounted for in structural serviceability limit state design. This paper aims to give background for some of the proposed methods and text in a new annex including literature references, verifications and explanations of the applied methods and parameters. A new equation for development of mechanical properties is included as basis for stress calculation. It is accounting particularly for the time right after setting, and can also be applied for general reference ages between 28 and 91 days. A simplified approach based on the age adjusted effective E-modulus, which has been proven to work well also at early ages is included. It applies an effective E-modulus accounting both for aging and creep. The most recent draft of the annex considers the largest tensile stress for two particular stages, at temperature equilibrium at early ages, and at the design life. The crack strain is described, while the crack spacing is found in the main SLS-chapter as for ordinary loads, and thus the surface crack width may be calculated.

### **1. Introduction**

Cracking may impair the performance of concrete structures due to aesthetics, durability, and tightness. The consequences are related to economy and sustainability, and it is important that Eurocode 2 gives regulations that clearly describe how and when cracking shall be accounted for in the structural design. The new proposed Annex D is entitled "Evaluation of early-age and long-term cracking due to restraint [1], and considers the effects of temperature changes due to the concrete's hardening process and basic shrinkage in combination with imposed deformations occurring at later ages. The main objective of the proposed methods is to evaluate the cracking risk, and provide guidance on crack calculations if cracking is expected to occur. The major focus is on through-cracks, which may span over the whole thickness of

the concrete member, and occur in the cooling phase of the hardening process, typically between 2 and 30 days after casting depending mainly on the dimension of the structural member and the binder type. Possible measures to reduce the amount of through-cracking are to use concretes with low heat production, concretes with low coefficient of thermal expansion, cooling pipes in the hardening concrete, heating cables in the restraining concrete, reduced fresh concrete temperature, or to reduce the degree of restraint for the hardening concrete member. The measures may be expensive, and as the significance of early age cracking is case-dependent, it is important that the measures are reflecting the criticality of cracking. The typical temperature and stress histories at early ages are illustrated in Figure 1, where  $T_{ci}$  is the fresh concrete temperature,  $T_{c,max}$  the maximum concrete temperature due to hydration heat,  $T_0$  the temperature of the restraining structure, while  $\Delta T_{min}$  is an additional temperature drop which might be due to daily or seasonal temperature variations. The most unfavourable moment in time for early-age cracking is denoted  $t_{crit}$ , corresponding to the moment when temperature equilibrium with the restraining structure is achieved (within 2°C). It might be relevant to consider crack-control in the following three states: (1) At temperature-equilibrium between the recently cast concrete structural member and the restraining structure. (2) At commissioning of the structure. (3) During the design service life. In the two latter cases, the temperature reduction  $\Delta T_{min}$  and drying shrinkage must be added to the early age effects. In the present draft of the annex the formulations are particularly directed towards (1) and (3). If particular demands are related to tightness, durability or appearance, the cumulative impact of early age effects, load effects and later imposed deformations must be considered in the crack control. Otherwise, the crack control of these states can be verified separately. To restrict cracking either crack prevention or crack limitation may be used. The latter may be achieved either by minimum reinforcement for crack limitation as explained in section 9 of the Eurocode [1], or by calculations.

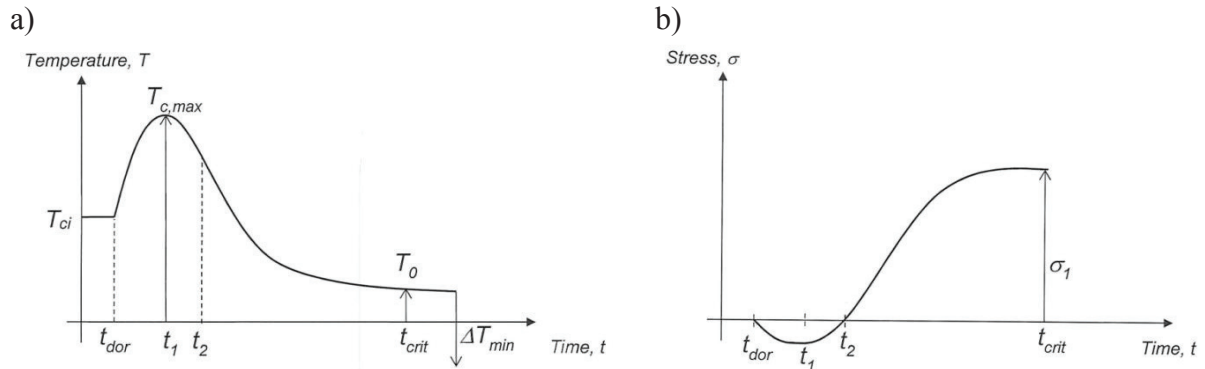


Figure 1: Typical temperature (a) and stress (b) histories due to early age effects [1]

## 2. Time-development of mechanical properties

The time-development of the compressive strength, for  $t < 91$  days, is described as:

$$f_{c,eq}(t) = \beta f_{c28} \quad \beta = \exp \left\{ s \left( 1 - \sqrt{\frac{t_{ref} - t_{dor}}{t_{eq} - t_{dor}}} \right) \sqrt{\frac{28 - t_{dor}}{t_{ref} - t_{dor}}} \right\} \quad (1)$$

Default values for the material parameters are presented in Table 1 reflecting two novel points: Introduction of the parameter  $t_{dor}$  (Figure 1, “end of the dormant phase”) that defines when stiffness and strength start to be significant. This is a decisive parameter to include thermal dilation and basic shrinkage in a consistent way because both effects may develop very fast at early ages, and typically, it varies between 8 and 13 maturity hours. The parameter may be strongly affected by admixtures, and it is important that the choice of the parameter is consistent with basic shrinkage and temperature development. The modification of the equation with the last square root-sign term including the term  $t_{ref}$ , which can vary between 28 and 91 days, makes it possible to utilize the strength increase after 28 days which may be significant for low heat and more environmentally friendly concretes. Default values for  $s$  and  $t_{dor}$  are given in Table 1 below, which is based on experimental results in [2,3,4,5].

Table 1: Parameters for strength development

Cement Strength	High early strength [R]		Ordinary strength (N)		Low early strength (S)	
	$s$	$t_{dor}(d)$	$s$	$t_{dor}(d)$	$s$	$t_{dor}(d)$
<C35	0,3	0,35	0.35	0,45	0.4	0,5
C40-C55	0.2	0,3	0.25	0,4	0.35	0,45
>C60	0.1	0,3	0.17	0,35	0,3	0,4

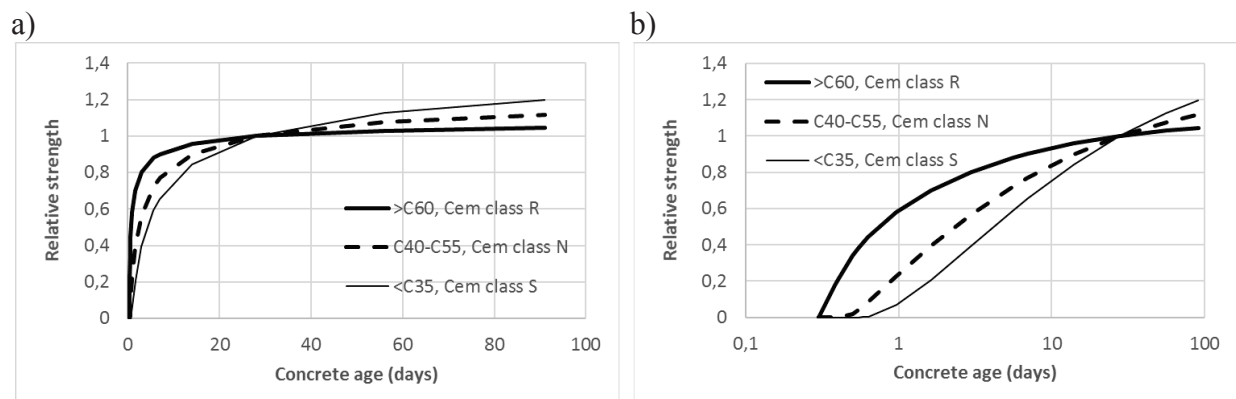


Figure 2 – Time development of compressive strength

### 3. Stress calculation

This section is mainly meant for verification of if cracking will occur or not. Obviously nonlinear finite element analysis are often used for such stress calculations, but still it is found useful to include a simplified method based on the effective E-modulus method. Such method can give the solution for a specified position in a structural member at a specific time. The simplified approach is based on the well-known age adjusted effective E-modulus method (Troost–Bazant), which has been proven to work well also at early ages [6,7] as illustrated in Figure 3. The method is based on uncracked concrete cross sections and applies an effective

E-modulus accounting for aging and creep. Using parameters described in Table 1 and Figure 1, the tensile stress in a predefined position, including cumulative impacts, can be determined.

$$\sigma_I(t) = (\Delta\varepsilon_T(t-t_2) + \varepsilon_{cbs}(t-t_2))E_1 R_1 + \alpha_T \Delta T_{min} E_2 R_2 + \varepsilon_{cds}(t-t_2) E_3 R_3 \quad (2)$$

Where  $t_2$  is the time when the stress changes sign. For early age problems the time  $t$  should be set equal to  $t_{crit}$  as defined in Figure 1, while if cumulative impacts are included  $t$  is the relevant design service life.  $\Delta\varepsilon_T(t-t_2) = k_1(T_{max} - T_0)\alpha_T$  represents the part of the temperature causing tensile stresses and  $\varepsilon_{cbs}(t-t_2)$  is the part of the basic shrinkage occurring in the cooling phase and  $\varepsilon_{cds}$  is the drying shrinkage strain.  $E_1 = E_c(t_{2eq}) / (1 + k_2 * \varphi(t, t_{2eq}))$  is the effective E-modulus representing the cooling phase. Default values based on Scandinavian practice [6,7] are  $k_1 = 0,9$  and  $k_2 = 0,8$ . The parameters  $E_2$  and  $E_3$  are corresponding longterm E-modules representative for the additional effects. Three different values for the degree of restraint are used in expression (2). This is because this parameter will vary with the concrete age and the time period considered, and because the structural system may change with time.

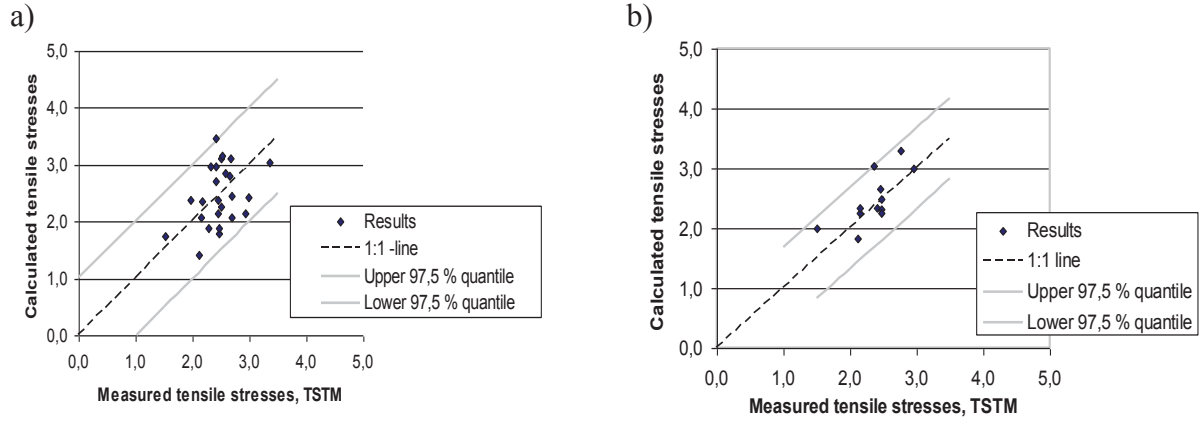


Figure 3: Verification of stress calculation methods, (a) Age adjusted effective E-modulus method, (b) Linear viscoelasticity for aging materials [6].

The most recent draft of Eurocode 2 [1] modifies equation (2) for two particular stages, but a verification corresponding to [6,7] still remains. At temperature equilibrium ( $t_{crit}$ ), and for longterm analysis at the design life ( $t$ ), the expressions are:

$$\sigma_1(t_{crit}) = R_1 \frac{E_c(t_{crit})}{1 + \chi\varphi_{st}} (k_1 \alpha_T (T_{c,max} - T_0) + \varepsilon_{cbs}(t_{crit})) \quad (3)$$

$$\sigma_1 = R_1 \frac{E_{c28}}{1 + \chi\varphi(t, t_{crit})} (k_1 \alpha_T (T_{c,max} - T_0) + \varepsilon_{cbs}(t)) + R_2 E_{c28} \alpha_T \Delta T_{min} + R_3 \frac{E_{c28}}{1 + \chi\varphi(t, t_s)} \varepsilon_{cds} \quad (4)$$

$R_1$ ,  $R_2$  and  $R_3$  are representative restraint factors as described previously.  $\chi\varphi_{st}$  accounts for short term creep, and its value may be estimated as 0.55.  $\chi$  is the aging coefficient (corresponding to  $k_2$  in equation (2)) which may be taken as 0.8.  $E_{c,28}$  is the tangent modulus of elasticity of concrete at an age of 28 days.

#### 4. Crack width calculation

The annex [1] describes the crack strain, while the crack spacing is found in the main SLS-chapter as for ordinary loads, and thus crack width at the concrete surface may be calculated as:

$$w_{calc} = S_{r,max} \cdot (\varepsilon_{sm} - \varepsilon_{cm} + \eta_r \varepsilon_{cs}) \quad (5)$$

where  $w_{calc}$  is the surface crack width,  $S_{r,max}$  the maximum crack spacing,  $\varepsilon_{sm}$  and  $\varepsilon_{cm}$  are the mean strains in the reinforcement and the concrete, respectively. The parameter  $\eta_r$  is 0 for short-term loading and long-term loading in the crack formation stage and equal to 1.0 in other cases while  $\varepsilon_{cs}$  is the shrinkage strain

For elements subjected to restrained imposed strains and which are restrained at the edges (typically walls on foundations),  $(\varepsilon_{sm} - \varepsilon_{cm} + \eta_r \varepsilon_{cs})$  in Equation (5) may be calculated as:

$$\varepsilon_{sm} - \varepsilon_{cm} + \eta_r \varepsilon_{cs} = R \varepsilon_{free} - k_t \cdot \frac{f_{ct,ef}}{E_{cm}} \quad (6)$$

where  $R$  is the restraint factor,  $\varepsilon_{free}$  is the imposed strain,  $k_t$  is a coefficient dependent on the nature and duration of the load,  $f_{ct,ef}$  is the mean value of the tensile strength of the concrete at the time when the cracks are expected to occur while  $E_{cm}$  is the modulus of elasticity.

For elements restrained at the edges, the annex [1] states that  $(R \varepsilon_{free})$  in Equation (6) can be taken as  $\varepsilon_r$ :

$$\varepsilon_r = R_1 [k_1 \alpha_T (T_{max} - T_0) + \varepsilon_{cbs} (t_{crit} - t_2)] + R_2 \alpha_T \Delta T_{min} + R_3 \varepsilon_{c ds} \quad (7)$$

where the parameter  $k_1 = 0.9$  takes into account that the tensile stress development starts slightly after the maximum temperature (due to the initial thermal expansion),  $\alpha_T$  is the coefficient of thermal expansion,  $\varepsilon_{cbs}$  is basic shrinkage,  $\varepsilon_{c ds}$  drying shrinkage, while  $t_{crit}$ ,  $t_2$ ,  $\Delta T_{min}$  and  $R_1$ ,  $R_2$ ,  $R_3$  are parameters described previously in this paper.

#### 5. Concluding remarks

This paper presents parts of the background for the new Eurocode 2 Annex D entitled “Evaluation of early-age and long-term cracking due to restraint”. The Annex has been elaborated for some years by the technical group CENTC250/SC2/WG1/TG7, where the authors did the main part of the writing. However, it is now published by CEN/TC 250/SC 2/WG1/PT1 as a final draft [1]. However, the work on this Annex will continue, and it might therefore be changed before the final version of the next Eurocode 2 is published. Presently this is scheduled for 2023.

#### References

- [1] CEN/TC 250/SC 2/WG 1 PT1prEN 1992-1-1: Eurocode 2: Design of concrete structures – Part 1-1: General rules, rules for buildings, bridges and civil engineering structures, Annex D pp 234-239. Report N 1358, June 2018.

- [2] Kanstad, T.; Hammer, T.A.; Bjøntegaard, Ø.; Sellevold, E. J. Mechanical Properties of Young Concrete: Part I - Experimental Results related to Test Methods and Temperature Effects. *Materials and Structures* 2003 ;Volume 36. p. 218-225
- [3] Klausen, A.; Early age crack assessment of concrete structures: experimental investigation of decisive parameters. Trondheim: NTNU,2016 (ISBN 978-82-326-1850-7) PhD-thesis.
- [4] Neville, A.M.; *Properties of concrete*, Pitman, London, 1975.
- [5] Graf, O., et al; *Die eigenschaften des betons*. Springer Verlag, Berlin, 1960.
- [6] Kanstad, T. Verification of three different calculation methods for early age concrete. In: *Crack Risk Assessment of Hardening Concrete Structures*. The Nordic Concrete Federation 2006 ISBN 82-91341-97-4. p. 101-110
- [7] Larson, M.; Estimation of crack risk in early age concrete, simplified methods for practical use, Licentiate thesis, Luleå technical university, Sweden 2000:10, ISSN 1402-1757.

**CONCRETE TECHNOLOGY  
AND  
ADVANCED MATERIAL TESTING**

## **A CONCRETE HOME FOR MARINE MICRO INHABITANTS**

**Atteyeh S. Natanzi <sup>(1)</sup>, Ciaran McNally <sup>(1)</sup>**

(1) School of Civil Engineering - University College Dublin (UCD), Dublin, Ireland

### **Abstract**

In the last decades, the prevalence of artificial marine structures along natural shorelines has increased significantly. In some parts of the world, more than half of the available natural shoreline has been covered by these structures. Epibiotic diversity has been shown to decrease significantly on submerged artificial structures due to the reduced environmental heterogeneity of artificial environments. Natural rocky shores provide microhabitats through their rough surfaces, pits, rock pools and crevices. In contrast, modern building materials typically fail to provide many of these features. The ecological value of artificial coastal infrastructure could be increased through careful design of pre-fabricated ecological engineering units. Material selection is a crucial parameter in the design of these units. Reinforced concrete plays an important role in the design process due to its ease of production, relatively low cost and its suitability for mass construction.

To maximise the potential of concrete to support biodiversity and natural capital, binder composition, aggregate type, and texture are considered to be important parameters. To investigate these parameters, an experimental programme has been developed which is focusing on a number of different concrete designs. Key engineering parameters, such as strength, chloride diffusion coefficient, and their ecological colonisation performance are evaluated.

### **1. Introduction**

In the last 40 years, the number of urban dwelling people has nearly doubled, with urbanized areas quadrupling in size [1]. Almost two thirds of the world's population is now estimated to live in coastal areas [2]. As the population has increased in coastal areas, more pressure has been put on coastal ecosystems through habitat conversion, increased pollution and more demand for marine resources [3]. These types of marine developments are always associated with fragmentation and loss of natural habitats, damaged seascapes and reduced biodiversity [4]. This irreversible alteration, often from natural to urban infrastructure development, is



considered to be one of the main threats to coastal ecosystem and sustainability [5]. Natural habitats provide microhabitats through their rough surfaces, pits, rock pools and crevices. In contrast, modern building materials typically fail to provide many of these features, with a notable impact on the organisms that would seek to colonise these surfaces. Artificial marine structures could support more invasive non-indigenous species and less diverse communities than natural habitats [5, 6]. The ecological value of artificial coastal infrastructure could be increased through careful design of pre-fabricated ecological engineering units. Material selection is a crucial parameter in the design of these units. Reinforced concrete plays an important role in the design process due to its ease of production, relatively low cost and its suitability for mass construction. Concrete composition plays a significant role in biodiversity enhancement of marine structures [7]. More than half of marine infrastructures are made using Portland cement concrete, and this has been shown to provide a good support for colonising organisms as calcareous skeletons deposit calcium carbonate onto the surface in the biogenic build-up process [8]. Concrete, however, has a high surface alkalinity (pH 12-13 compared to 8 for seawater), and this could reduce settlement of marine organisms and result in communities dominated by a few alkotolerant taxa such as barnacles [9]. The addition of pozzolanic materials such as GGBS to the concrete mix could reduce the alkalinity of the concrete and create more suitable surfaces for colonisation by marine species [10]. As chloride ingress in reinforced concrete structures in marine environments is one of the most challenging forms of degradation, replacement of Portland cement by pozzolanic materials such as GGBS could improve concrete durability and delay the reinforcement corrosion [11]. Chloride ions exist in seawater and can destroy the passive layer at the rebar surface when the chloride concentration at the cover depth is greater than the critical chloride concentration ( $C_{cr}$ ). Previous research [12,13] has shown that as the GGBS content increases, the possibility of steel corrosion decreases. Other factors such as surface texture, holes, crack pits and pools have been also investigated and are found to have a significant and direct effect on increasing biodiversity on artificial marine infrastructures [14].

Although some research has been conducted to use concrete as a new habitat for marine microhabitants, they rarely consider the engineering side and focus mainly on ecological issues. Here, the alternative possibility of using coastal infrastructures as a habitat for epibiota is exploring. The service life that may be expected from these different mix designs is also examined and show how they are being assessed in the field.

## 2. Materials and Methods

A number of concrete mixes were designed with a view to assessing their engineering performance, as well as their ability to support marine life. A number of specimens were cast for each mix, including:

- 8 reinforced concrete tiles of dimension 200 x 200 x 40 mm which would be installed in a marine environment;
- 3 concrete cylinders of diameter 100mm and height 200mm for assessing resistance to chloride ingress;
- 6 concrete cubes of dimension 100mm to confirm concrete strength at 7 and 28 days.

As the concrete tiles would be subject to corrosion arising from sea-borne chlorides, the exposure class was considered to be XS3. This also corresponds to the tidal zone, as the

samples will not be fully submerged, and subjected to spray and inter-tidal conditions. For this particular exposure class, the Irish National Annex to EN206 requires a minimum cement content of  $360 \text{ kg/m}^3$ , a maximum water/binder ratio of 0.5 and a minimum strength class of C35/45. Nine different concrete compositions were designed in this study, and parameters of interest were binder type, aggregate type and influence of plasticiser. Two binder compositions were used: 100% CEM I, and a 50% blend of CEM I and GGBS. This was selected as it was considered that it would provide a higher chloride resistance, as well as a significant change in concrete alkalinity that could influence marine colonisation. Plasticiser was also added as a variable and the selected dosage was 0.8% of cement content. It is not expected to have any major influence on the engineering performance, but its influence on colonisation behaviour is completely unknown. Finally, the coarse aggregates chosen were limestone and granite. Limestone is the dominant aggregate type in Ireland and significant quantities of concrete are manufactured using this. Granite was also chosen, as anecdotal experience has shown that marine organisms are often attracted to materials with the reddish colour of coralline algae. As such, the granite colouring is of interest to us and will be used as a variable for the field testing. A final mix (mix 9) was added to the testing programme as an initial assessment of the influence of concrete texture, whereby a rough surface was obtained by removing the concrete surface as the material was setting. A full list of the selected mixes is described in Tab. 1.

Table 1: Concrete mix design compositions.

Mix	Binder	Aggregate	Reinforcement	Plasticiser
1	CEM I	Limestone	Steel mesh	No
2	CEM I	Limestone	Steel mesh	Yes
3	CEM I + GGBS	Limestone	Steel mesh	No
4	CEM I + GGBS	Limestone	Steel mesh	Yes
5	CEM I	Granite	Steel mesh	No
6	CEM I	Granite	Steel mesh	Yes
7	CEM I + GGBS	Granite	Steel mesh	No
8	CEM I + GGBS	Granite	Steel mesh	Yes
9	CEM I	Limestone	Steel mesh	Yes

## 2.1 Concrete Characterisation

Compressive strength of the concrete cubes was obtained by testing according to EN 12390-3 [15]. The chloride resistance was determined by use of a chloride migration test, and the particular method used was the non-steady state migration test according to NordTest NT BUILD 492 [16]. The test involves driving chloride ions through a concrete section of 100mm diameter and 50mm thickness under the action of the electric field. The catholyte solution is 10% NaCl by mass in tap water and anolyte solution is 0.3M NaOH in distilled water. A voltage, typically of the order of 30 V is applied for 24 hours, after which the concrete sample is removed and split. The depth of chloride penetration is visually determined by spraying 0.1 M silver nitrate solution on the freshly split concrete section. To determine the chloride concentration at the depth, X, for a service life of  $t=50$  years, Cranks solution to Ficks Law was used:

$$C(x, t) = C_{sn} \left[ 1 - \operatorname{erf} \left( \frac{X}{2\sqrt{D_m t}} \right) \right] \quad (1)$$

where  $C_{sn}$  is surface chloride concentration and  $D_m$  is the mean chloride diffusion coefficient for the exposure time  $t$  and calculated from Eq. (2) and (3).

$$D_m(t) = \frac{1}{t} \int_0^t D(\tau) \cdot d\tau \quad (2)$$

$$D(\tau) = D_R \left( \frac{t_R}{\tau} \right)^m \quad (3)$$

For this study, the surface chloride concentration was taken as 0.8% by mass of binder. This is based on research by Poulsen and Sørensen [17] who assessed 34 year old concrete bridges in a marine environment. It is recognised that this is a time and material dependent parameter, but the use of a fixed value is considered appropriate for comparative purposes. The parameter  $m$  is an age factor, and based on the work of Attari et al. [18] is taken as 0.17 for 100% OPC binders and 0.3 for binders containing 50% GGBS,  $t_R$  is reference time (in this case 81 days). Determination of effective diffusion coefficients from migration testing is as described by Tang and Nilsson [19].

### 3. Results and Discussion

#### 3.1 Compression test

The results of the compression testing are presented in Tab. 2. It can be seen that the use of a 50% GGBS replacement level resulted in almost no change to the strength. The most significant change was in the early strength of the concrete samples manufactured using granite aggregate, but this appears to be reduced at 28 days. All samples comfortably achieve the minimum strength of exposure class XS3 (C35/45).

Table 2: Concrete compressive strength results.

Mix	Average 7 days compressive strength (MPa)	Average 28 days compressive strength (MPa)
1	41.30	50.24
2	40.78	45.13
3	35.79	50.12
4	31.72	49.94
5	34.78	47.46
6	32.93	41.92
7	26.32	47.42
8	26.40	45.74

#### 3.2 Chloride Migration

Results of the chloride migration testing are shown in Tab. 3. The required service life was 50 years, and as such the data was manipulated using equations 1, 2 and 3 so as to produce the time dependent diffusion coefficient for this period. This is then used to determine the

chloride content at a selected concrete cover depth of 50mm. Corrosion is typically accepted to be initiated when the chloride concentration reaches a critical value of 0.4% by mass of binder.

In all cases it can be seen that the critical variable is the use of GGBS; without this, the required service life of 50 years cannot be achieved. This is supported by other research in this area [20]. The influence of the other parameters (plasticiser, aggregate) is found to be much lower, and these can be utilised without compromising performance of the concrete.

Table 3: Results of chloride resistance tests.

Mix	$D_{nssm}$ ( $\times 10^{-12}$ m <sup>2</sup> /s)	$D_R$ ( $\times 10^{-12}$ m <sup>2</sup> /s)	$D_m$ ( $\times 10^{-12}$ m <sup>2</sup> /s)	C(5,50)
1	17.08	13.00	3.66	0.51
2	21.46	16.61	4.67	0.54
3	3.52	2.39	0.44	0.14
4	3.34	2.25	0.41	0.13
5	17.40	13.26	3.73	0.52
6	18.05	13.75	3.87	0.52
7	3.00	1.96	0.36	0.11
8	3.13	2.06	0.38	0.12

The next strand in this work is the ecological assessment of the concrete mixes, and the 200mm concrete tiles were deployed on a breakwater on Ireland's east coast in April 2018 (Fig.1). Samples are attached to the exposed and sheltered surfaces on this rocky breakwater and are fully submerged during high tide. They will remain in this intertidal environment for 12 months to evaluate the influence of concrete mix design on colonisation behaviour. Quadrat sampling will determine if different concrete mixes can lead to improved substrates for marine life. This strand of the work will be reported at a later stage.



Figure 1: Concrete tiles installation and deployment.

#### 4. Conclusions

Corrosion of reinforced concrete is the main threat to marine structures. The results of our service life prediction showed that the addition of GGBS plays a significant role in achieving

the required service life and that if this is included then other parameters can be included without issue. Concrete mixes with limestone aggregate were also shown to be slightly stronger than mixes with granite aggregate. The connection between these engineering parameters and the marine colonisation behaviour will be monitored with interest over the next 12 months.

## References

- [1] Seto, K.C. et al, A meta-analysis of global urban land expansion, *PloS one* 6(8) (2011), e23777
- [2] Creel L. *Ripple effects: population and coastal regions*, Washington, DC: Population Reference Bureau, (2003)
- [3] Airoidi L. and Beck MW., *Loss, status and trends for coastal marine habitats of Europe*, In *Oceanography and marine biology*, CRC Press, (2007), 357-417
- [4] Dugan, J.E. et al, 8.02-Estuarine and coastal structures: environmental effects, a focus on shore and nearshore structures, *Treatise on estuarine and coastal science* 8 (2011), 17-41
- [5] Glasby, T. and Connell, S., *Urban structures as marine habitats*, *Ambio* 28 (1999), 595-598
- [6] Mineur, F. et al, *Changing coasts: marine aliens and artificial structures*, *Oceanography And Marine Biology: An Annual Review* 50 (2012), 1027-1051
- [7] Dennis, H.D. et al, *Reefcrete: Reducing the environmental footprint of concretes for eco-engineering marine structures*, *Ecological Engineering* (2017)
- [8] Risinger, J.D., *Biologically dominated engineered coastal breakwaters*, PhD Thesis, Louisiana State University and Agricultural and Mechanical College (2012)
- [9] Guilbeau, B.P. et al, *Algae attachment on carbonated cements in fresh and brackish waters—preliminary results*, *Ecological Engineering* 20(4) (2003), 309-319
- [10] Bertos, M.F. et al, *A review of accelerated carbonation technology in the treatment of cement-based materials and sequestration of CO<sub>2</sub>*, *Journal of Hazardous Materials* 112(3) (2004), 193-205
- [11] Pacheco-Torgal, F. and Jalali, S., *Cementitious building materials reinforced with vegetable fibres: A review*, *Construction and Building Materials* 25(2) (2011), 575-581
- [12] Pack, S.W. et al, *Prediction of time dependent chloride transport in concrete structures exposed to a marine environment*, *Cement and Concrete Research* 40(2) (2010), 302-312
- [13] Cheewaket, T. et al, *Long term performance of chloride binding capacity in fly ash concrete in a marine environment*, *Construction and Building Materials* 24(8) (2010), 1352-1357
- [14] Evans, A.J. et al, *Drill-cored rock pools: an effective method of ecological enhancement on artificial structures*, *Marine and Freshwater Research*, 67(1) (2016), 123-130
- [15] National Standards Authority of Ireland, *EN 12390-3: Testing hardened concrete: compressive strength of test specimens*, (2012)
- [16] NordTest, *NTBuild 492. Method for chloride migration coefficient from non-steady state migration experiments in concrete, mortar, and cement-based repair materials* (1999)
- [17] Poulsen, S.L. and Sørensen, H.E., *Chloride ingress in old Danish bridges*. In *Proceedings 2nd International Congress on Durability of Concrete (ICDC)*, New Delhi, India(2014)
- [18] Attari, A., McNally, C. and Richardson, M.G., *A probabilistic assessment of the influence of age factor on the service life of concretes with limestone cement/GGBS binders*, *Construction and Building Materials* 111(2016), 488-494
- [19] Luping, T. and Nilsson, L.O., *Rapid determination of the chloride diffusivity in concrete by applying an electric field*, *Materials Journal* 89(1) (1993), 49-53
- [20] McNally, C. and Sheils, E., *Probability-based assessment of the durability characteristics of concretes manufactured using CEM II and GGBS binders*, *Construction and Building Materials* 30 (2012), 22-29

## **AMINO-ALCOHOLS AS CORROSION INHIBITORS AGAINST SULPHATE-INDUCED CORROSION OF MILD STEEL REINFORCEMENT IN FRESH CALCIUM SULPHOALUMINATE BASED CEMENTITIOUS MATERIALS: PRELIMINARY STUDIES**

**Yegor Morozov<sup>(1)</sup>, Simone Pellegrini<sup>(2)</sup>, Sergio Lorenzi<sup>(3)</sup>, Fátima Montemor<sup>(1)</sup>**

(1) Centro de Química Estrutural, Instituto Superior Técnico, Universidade de Lisboa,  
Lisbon, Portugal

(2) Security Building Service S.R.L., Via Santi Filippo e Giacomo, Covo (Bergamo), Italy

(3) Department of Engineering, University of Bergamo, Bergamo, Italy

### **Abstract**

Calcium sulphoaluminate cements (CSA) are unique in properties and application. However, despite numerous advantages, the corrosion of mild steel reinforcement in fresh CSA mortars and concretes at early stages of binder hydration, caused by the combination of low pH and high concentration of dissolved sulphates, is their greatest limitation. Thus, the elimination of rebar corrosion is the indispensable requirement for wide market acceptance and successful application of CSA in construction practice. In this regard, the use of corrosion inhibitors seems to be the most promising solution, considering cumulatively the ease of their introduction into existing construction practice, expected corrosion prevention efficiency, and costs, supported by the fact that they would be required only for short periods.

The performance of corrosion inhibitors of amino-alcohol family was briefly assessed by electrochemical impedance spectroscopy in simulating alkaline solutions containing sulphates. In this paper 2-aminoethanol (MHEA), diethanolamine (DHEA) and triethanolamine (THEA) as well as commercial corrosion inhibitor blends – Sika<sup>®</sup> FerroGard<sup>®</sup>901 (SF901) and Sika<sup>®</sup> FerroGard<sup>®</sup>903 (SF903) were tested as preventive repair measure. Highly preliminary results suggested that MHEA and SF903 eliminated sulphate-induced depassivation of steel, providing long-lasting protection of reinforcement, thus they should be addressed in the future for detailed and versatile studies.

## 1. Introduction

Calcium sulphoaluminate cements are unique. They are in focus as an alternative hydraulic binder with low environmental impact, one tonne of which is accompanied by the release of just 340 kg of CO<sub>2</sub>. CSA are perfect for pre-cast construction due to high early strength and rapid hardening [1], which together with high frost resistance of fresh binders make them attractive for cold weather construction. CSA mortars and concretes evidence limited shrinkage in shrinkage-compensating formulations, or could be used to make self-stressing concrete [1-3]. However, the principal difference with respect to ordinary Portland cement (OPC) is the intrinsic immunity of CSA-based materials against sulphate attack [4], which together with lower porosity [5], can result in improved durability and higher performance. In addition, CSA binders are less alkaline compared to OPC, being suitable for glass-fibre cement composites [1]. However, CSA concretes could be more susceptible to carbonation with an adverse effect on the passivation of steel reinforcement, as it has been proven for blended cements. Long-term durability of CSA in terms of steel reinforcement corrosion is not well documented yet [1]. Therefore in our previous work, the behaviour of mild steel was studied in simulating solutions of wide pH-sulphate combinations to obtain sulphate – pH corrosion diagram, over which reported ranges of pore solution composition for pure CSA and OPC binders estimated after 30 minutes and 85 days after initiation of hydration [2, 6-8] were superimposed.

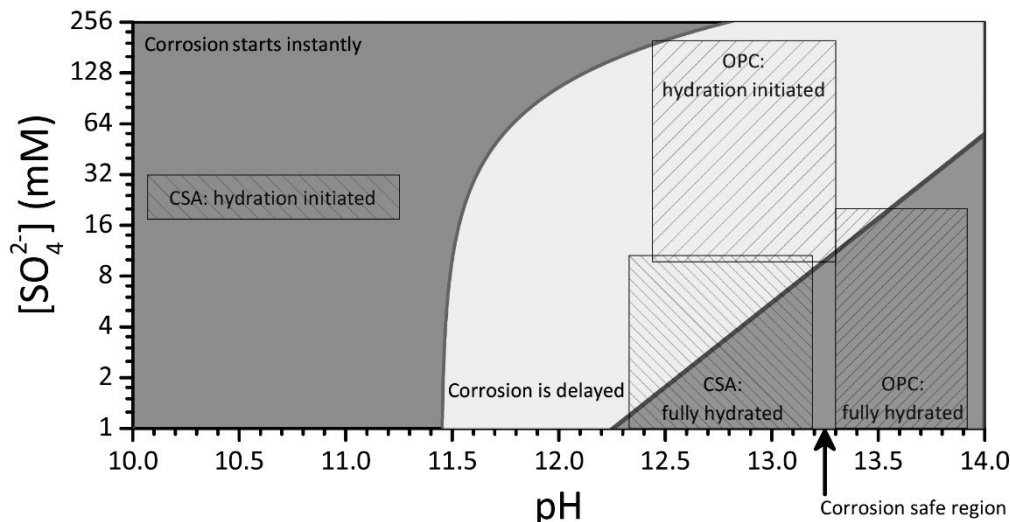


Figure 1: Schematic sulphate - pH corrosion diagram of mild steel

Previous preliminary findings suggest that the sulphate-induced corrosion of common mild steel reinforcement is very likely to happen and will start instantly in pure CSA binder at early stages of hydration (Fig. 1), though the conditions found in fully hydrated state are favourable for steel passivation, unlike to OPC-based mortars and concretes. In addition, it has been proven that once initiated, the corrosion of steel reinforcement proceeded further, and repassivation could not be observed even after favourable conditions were met.

Therefore, despite numerous advantages, the corrosion of mild steel reinforcement in fresh CSA mortars and concretes, caused by the combination of low pH and high concentration of dissolved sulphates, is their greatest limitation. Therefore, preventive or corrective solutions are of the greatest demand, since the elimination steel reinforcement corrosion in CSA-based

cementitious materials during binder hydration is the indispensable requirement for wide market acceptance, and successful application of CSA in construction practice.

Among various preventive repair approaches to diminish the risk of concrete cracking and extend the service life of CSA-based reinforced structures, the use of corrosion inhibitors to stop sulphate-induced corrosion of plain low carbon steel seems to be a promising solution, considering cumulatively the costs, the ease of their introduction into existing construction practice, expected corrosion prevention efficiency. Supported by the fact that inhibitors would be required just for short periods of initial binder hydration, they could be used in smaller quantities. Previously amino-alcohols were reported to be effective corrosion inhibitors against chloride-induced corrosion of steel reinforcement, as they create protective adsorption layer on steel surface, thereby competing with chloride ions that cause passive oxide film thinning and disruption followed by pitting corrosion propagation [9-13]. Thus, we aim to study several amino-alcohols (Fig. 2), such as 2-aminoethanol (MHEA), diethanolamine (DHEA) and triethanolamine (THEA), as well as commercial blends Sika® FerroGard®901 (SF901) and Sika® FerroGard®903 (SF903), as corrosion inhibitors against sulphate-induced corrosion in alkaline solutions, that simulate liquid phase of CSA binder at early hydration stage.

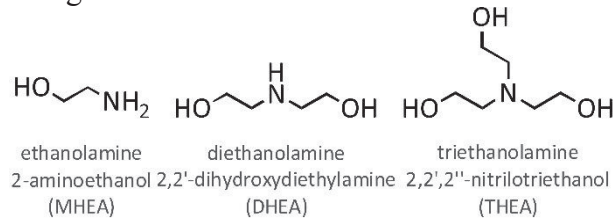


Figure 2: Chemical structures of corrosion inhibitors

## 2. Materials and experimental procedures

Low carbon steel CK45K reinforcement rebar (in wt.%: C 0.4, Mn 0.7, Si 0.2, S max. 0.05, P max. 0.05, balance – Fe) of 1.2 cm in diameter was cut perpendicularly to the axis with a water-cooled circular sand saw. Copper wire was attached to the inner side of steel piece with a silver paint, and the pieces were embedded into epoxy resin. Samples were polished under water using SiC papers up to 1000 grit at 500 rpm, rinsed with deionized water and ethanol, dried with compressed air. Finally, 3M™ Scotchrap™ 50 tape was applied over polished surface, defining the exposed area of 0.24 cm<sup>2</sup>. At least three identical samples were prepared for all the tests and conditions.

Corrosion tests were performed in 0.316 mM NaOH solution, containing 10.0 mM of K<sub>2</sub>SO<sub>4</sub> and corrosion inhibitors – MHEA, DHEA or THEA of 50 mM; or 12 kg/m<sup>3</sup> of SF901 or SF903. MHEA, DHEA, and THEA were purchased from Sigma-Aldrich, while SF901 and SF903 were kindly provided by Sika Portugal. All reagents were used without further modification.

The corrosion behaviour of steel samples in the presence of inhibitors was studied mainly by electrochemical impedance spectroscopy (EIS) [10, 13-15]. EIS tests were performed in three-electrode arrangement (Pt wire as a counter electrode, saturated calomel electrode as a reference electrode, and steel sample as a working electrode) using Autolab PGSTAT302N by applying single sinusoidal potential perturbations of 10 mV (rms) versus open circuit potential within frequency range 50 kHz to 5 mHz. The EIS data were fitted by ZView 3.5a software.



### 3. Results and discussion

As expected from our previous findings, the corrosion of mild steel started instantly when it was placed into sulphate-rich media, as evidenced by low impedance values. Both  $|Z|_{5\text{mHz}}$ , proportional to polarization resistance,  $R_p$ , and  $|Z|_{1-10\text{Hz}}$ , proportional to passive film resistance,  $R_{PF}$ , decreased with time, and bode phase angle plot suggested the depression of capacitive response of the passive film. On the other hand, in the presence of 50 mM MHEA (Fig. 3), initial (1 h)  $|Z|_{5\text{mHz}}$  was  $182 \text{ k}\Omega\cdot\text{cm}^2$  compared to  $3.7 \text{ k}\Omega\cdot\text{cm}^2$  for the reference sample. They values increased with immersion time, after 50 hours reaching  $\text{M}\Omega\cdot\text{cm}^2$  – a level normally observed for mild steel in passive state, and stabilizing at 1.5-1.6  $\text{M}\Omega\cdot\text{cm}^2$  after 15 days of immersion. Middle frequency impedance values also increased with time, reaching  $4.3 \text{ k}\Omega\cdot\text{cm}^2$  (3.15 Hz) on 23<sup>rd</sup> day. Thus, progressive development of the passive film and its capacitive behaviour, evidenced from phase angle Bode plot (Fig. 3), was clearly observed. However, pH of the solution was higher (11.32), when compared to the reference sample (pH 10.44), and this had to be considered in evaluation of corrosion inhibition efficiency [18]. Therefore, steel exposed to 3.16 mM NaOH (pH 11.46) solution containing 10.0 mM of  $\text{K}_2\text{SO}_4$  was tested. It was found that rebars were subjected to severe corrosion, and EIS spectra were close to 0.316 mM NaOH, suggesting that in the case of MHEA a specific metal-inhibitor interaction is responsible for corrosion protection.

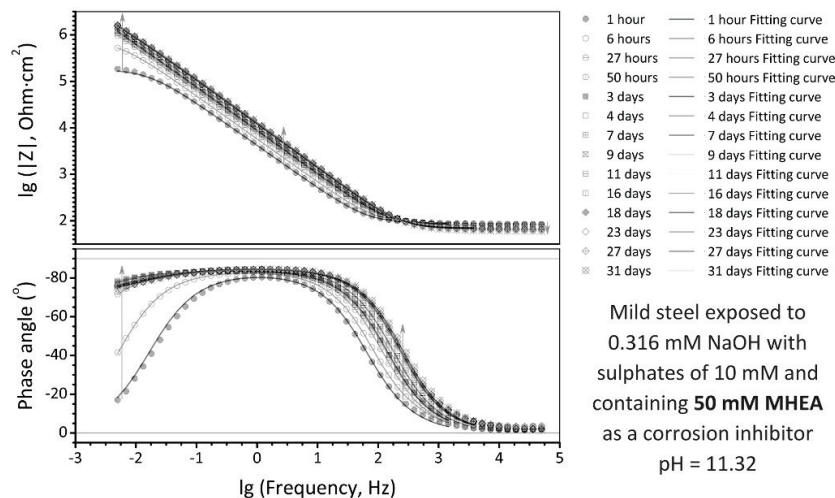


Figure 3: EIS spectra of mild steel exposed to sulphates in the presence of 50 mM MHEA

Like MHEA, DHEA showed similar behaviour in the beginning, evidenced by high  $|Z|_{5\text{mHz}}$  values – 240 and  $646 \text{ k}\Omega\cdot\text{cm}^2$  after 1 and 6 hours, but after 7 hours values decreased abruptly till  $2.3 \text{ k}\Omega\cdot\text{cm}^2$ , suggesting corrosion onset, as passive film disrupted, indicated by  $|Z|_{1-10\text{Hz}}$ . Since depassivation occurred earlier than 3 days of immersion, as it is required for favourable conditions to reach naturally during hydration, DHEA could not be used. The addition of THEA, on the other hand, did not show any improvement at all. In particular, observed  $|Z|_{5\text{mHz}}$  were 1.77, 1.45 and  $1.15 \text{ k}\Omega\cdot\text{cm}^2$ , when compared to 2.87, 1.29 and  $1.26 \text{ k}\Omega\cdot\text{cm}^2$  for blank sample after 6 hours, 1 and 2 days. Same behaviour was observed in middle frequency range.

Sika<sup>®</sup> FerroGard<sup>®</sup> 901 and Sika<sup>®</sup> FerroGard<sup>®</sup> 903 are commercial products initially designed to prevent chloride-induced corrosion of steel reinforcement. SF901 is a concrete admixture, i.e.

added during fresh concrete preparation ( $12 \text{ kg/m}^3$ ), being therefore more suitable for the intended application under consideration. SF903, on the other hand, is an impregnating solution, which is applied over concrete surface ( $0.5 \text{ kg/m}^2$ ), thus the dosage to be tested was unclear, but  $12 \text{ kg/m}^3$  was fixed for both.

Regardless of high expectations, SF901 was not able to provide neither short- nor long-term protection of steel reinforcement against sulphate-induced corrosion even at relatively high dosage.  $|Z|_{5\text{mHz}}$  values were close to ones observed for the reference sample, being 1.60, 1.71 and  $1.36 \text{ k}\Omega\cdot\text{cm}^2$  after 6, 23 and 46 hours of immersion. SF903, on the other hand, showed perfect protection against sulphate-induced corrosion (Fig. 4), similarly to MHEA (Fig. 3). Both  $|Z|_{5\text{mHz}}$  and  $|Z|_{3.15\text{Hz}}$  increased with time, reaching stable values after ca. 11 - 16 days. In particular, observed  $|Z|_{5\text{mHz}}$  (Fig. 4) values were 0.182, 0.758, 0.99, 1.43 and  $1.51 \text{ MOhm}\cdot\text{cm}^2$  after 1 hour, 1, 2, 12 and 31 days, indicating no corrosion of steel, highly capacitive response pointed out the existence and development of intact passive film. Such high corrosion protection performance, despite pH of 9.69 (Fig. 4), lower than that for the reference sample tested in the absence of corrosion inhibitor, confirming specific metal-inhibitor interaction.

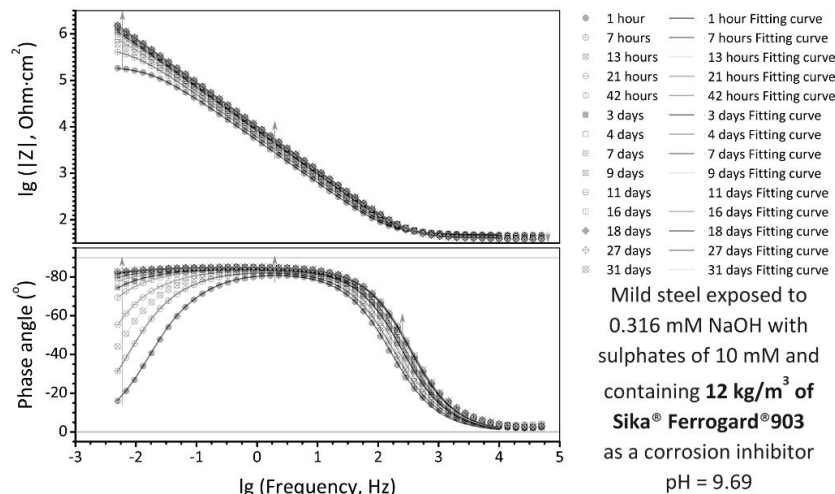


Figure 4: EIS spectra of mild steel exposed to sulphates in the presence of SF903

#### 4. Conclusions and Future work

In the current paper, the use of corrosion inhibitors to mitigate corrosion of plain carbon steel reinforcement in fresh calcium sulphoaluminate based materials, and consequently reduce the risk of the formation of concrete cracks was studied as a preventive method. Various amino-alcohols were assessed as corrosion inhibitors against the destructive action of sulphate ions in alkaline media, simulating a liquid phase of calcium sulphoaluminate binders at early stage of cement hydration. Among tested, 2-aminoethanol and Sika<sup>®</sup> FerroGard<sup>®</sup>903 have proven their high corrosion inhibition performance both in short- and long-term, providing cheap, robust, and elegant technological solution for the intrinsic incompatibility of carbon steel reinforcement with calcium sulphoaluminate binders. Nevertheless, these agents have to be comprehensively studied in the future to elucidate their optimum dosage with respect to the dissolved sulphate content, and to confirm their compatibility with binders to ensure that none of strength and service characteristics of calcium sulphoaluminate based mortars and concrete

were affected by their addition into the fresh mix. On top of that, other compounds will be evaluated in the future studies as corrosion inhibitors for the intended application.

### Acknowledgements

The authors acknowledge Fundação para a Ciência e Tecnologia for funding Centro de Química Estrutural (UID/QUI/00100/2013) and PhD grant SFRH/BD/88016/2012. In addition, the authors also acknowledge the CA15202 for financial support, and Sika Portugal - Produtos Construção e Indústria, SA. for materials provided.

### References

- [1] P.C. Aïtcin, Binders for Durable and Sustainable Concrete, Taylor & Francis, 2007.
- [2] F. Winnefeld, B. Lothenbach, Hydration of calcium sulfoaluminate cements - Experimental findings and thermodynamic modelling, *Cem. Concr. Res.*, 40 (2010) 1239-1247.
- [3] L. Zhang, F.P. Glasser, Hydration of calcium sulfoaluminate cement at less than 24 h, *Adv Cem Res*, 14 (2002) 141-155.
- [4] S. Ioannou, et al., Performance characteristics of concrete based on a ternary calcium sulfoaluminate-anhydrite-fly ash cement, *Cem. Concr. Compos.*, 55 (2015) 196-204.
- [5] G. Bernardo, et al., A porosimetric study of calcium sulfoaluminate cement pastes cured at early ages, *Cem. Concr. Res.*, 36 (2006) 1042-1047.
- [6] M. Andac, F.P. Glasser, Pore solution composition of calcium sulfoaluminate cement, *Adv Cem Res*, 11 (1999) 23-26.
- [7] L. Pelletier-Chaignat, et al., Influence of the calcium sulphate source on the hydration mechanism of Portland cement–calcium sulphoaluminate clinker–calcium sulphate binders, *Cem. Concr. Compos.*, 33 (2011) 551-561.
- [8] P. Chaunsali, Early-age hydration and volume change of calcium sulfoaluminate cement-based binders, Doctor of Philosophy in Civil Engineering Dissertation, University of Illinois, 2015
- [9] B. Elsener, et al., Migrating Corrosion Inhibitor Blend for Reinforced Concrete: Part 1 — Prevention of Corrosion, *Corrosion*, 55 (1999) 1155-1163.
- [10] H.E. Jamil, et al., An electrochemical and analytical approach to the inhibition mechanism of an amino-alcohol-based corrosion inhibitor for reinforced concrete, *Electrochim. Acta*, 48 (2003) 3509-3518.
- [11] P. Marcus, et al., Localized corrosion (pitting): A model of passivity breakdown including the role of the oxide layer nanostructure, *Corros. Sci.*, 50 (2008) 2698-2704.
- [12] M. Ormellese, et al., A study of organic substances as inhibitors for chloride-induced corrosion in concrete, *Corros. Sci.*, 51 (2009) 2959-2968.
- [13] Y. Morozov, et al., Alkanolamines as corrosion inhibitors against chloride-induced corrosion of mild steel in basic media, The European corrosion congress EUROCORR 2015, Graz, Austria, 2015.
- [14] K. Hladky, et al., Corrosion Rates from Impedance Measurements - an Introduction, *Br. Corros. J.*, 15 (1980) 20-25.
- [15] P. Marcus, F.B. Mansfeld, Analytical Methods In Corrosion Science and Engineering, CRC Press, 2005.

## **ASPECTS OF ACTIVATED FLY ASH: A COMPARATIVE STUDY OF DIFFERENT MECHANICAL TREATMENTS**

**Alexander Mezhov<sup>(1)</sup>, Ursula Pott<sup>(2)</sup>, Dietmar Stephan<sup>(2)</sup>, Konstantin Kovler<sup>(1)</sup>**

(1) National Building Research Institute, Technion – Israel Institute of Technology, Haifa, Israel

(2) Technische Universität Berlin, Berlin, Germany

### **Abstract**

The paper presents a new type of blended binder consisting of Ordinary Portland Cement and mechanochemically activated Fly Ash. The activation was performed by means of three different types of mill: vibratory ball mill, vibratory disc mill and planetary ball mill, in presence of anionic surfactant and without it. Activation was performed until the same surface area was achieved for all the samples regardless of the mill type. The structure of fly ash was characterized by X-ray diffraction and scanning electron microscopy. The properties of blended binder were examined by rheological measurements. It was found that introduction of surfactant in the mill allows to decrease yield stress and viscosity of blended binder up to 45% and 40%, respectively, in comparison to conventional introduction of surfactant. Hydration of blended binder was characterized by ultrasonic measurement and shows predictable retardation effect, that is commonly known for anionic surfactants. Blended binder prepared with fly ash interground with surfactant show higher strength than fly ash activated apart of surfactant.

### **1. Introduction**

Fly ash is a well-known and useful by-product that is being used in concrete technology for many years. When added to ordinary Portland cement (OPC) to create a blended binder, the amorphous silica in FA reacts with  $\text{Ca}(\text{OH})_2$  and forms C-S-H gel. The usage of FA as supplementary cementitious material (SCM) is limited since it accounts for retarded hydration, delayed setting times and reduced early strength [1]. To increase the benefits of FA usage, several types of activation are used nowadays: chemical activation (mostly by means

of alkaline activators); mechanical activation by its milling; thermal treatment and combined methods.

Mechanical activation of FA has several aspects: decrease in particle size – positively influencing the strength properties [2] due to higher reactivity, and therefore speed up the reaction with  $\text{Ca}(\text{OH})_2$ ; increasing the amount of amorphous phase [3].

Various types of mills are commonly used for mechanical activation: vibratory ball mills [4]; planetary ball mills [3], [5] vibratory disk mills [6], etc. In order to improve the efficiency of milling special additives can be used. In the cement production industry these additives are known as grinding aids, and they have been used at the stage of clinker grinding since the 1930s [7]. It has been suggested that in some cases the beneficial action of these modifiers is governed by mechano-chemical activation (MCA) [8]. This technology has already been in use for many years [9] and was also applied for FA activation [10],[11]. For MCA the type of additive plays a critical role. In this project, Polynaphthalene Sulfonate (PNS) was chosen as a surfactant. This choice is based on the past research related to obtaining so-called “Low water demand binders” [12] by milling the cement jointly with an anionic surfactant; in this case PNS.

This research is focused on the mechanical activation of FA by means of three types of milling, using vibratory disc mill (DM), vibratory ball mill (BM) and planetary ball mill (PBM). FA is activated jointly with the surfactant and without it in order to examine mechano-chemical theory as a method for FA activation.

## 2. Experimental

### 2.1 Materials

The fly ash is a low calcium fly ash class F, collected from “Orot Rabin” power station (Ashdod, Israel). Mineral compositions are presented in Table 1.

Table 1. Mineral composition of fly ash (by X-ray diffraction).

Phase	Quartz	Hematite	Mullite	Periclase	Lime
Weight, %	15.6	7.3	73.2	2.8	1.1

Cement is CEM I 52,5 R. Commercially available Polynaphthalene Sulfonate was used as a surfactant. Sand is standard according to DIN EN 196-1.

### 2.2 Methods

**2.2.1 Milling** protocols are presented below:

- Vibratory disk mill. Grinding media is two disks. Milling time: 1, 5, 15, 30 and 60 min. Milling regime: 5 min milling, 5 min break.
- Vibratory ball mill. Grinding media is stainless cylpebs. Milling time: 15, 30, 60 and 120 min.
- Planetary ball mill (PBM). Fritsch Pulverisette 5 classic line. Milling time: 15, 30, 60 and 120 min. Milling time regime: 5 min milling, 5 min break. The milling speed is 200 rpm.

**2.2.2 Specific surface area** is measurement according to DIN 1164 by Blaine.

**2.2.3 Particle Size Distribution** is measured by Malvern Mastersizer 2000.

**2.2.4 Casting and curing** is performed according to EN 196-1:2016 (E). Water to binder ratio is 0.5. Binder to sand ratio is 1:3. FA substitutes 10% wt. of cement in blended binder. Compressive strength was tested after 28 days of curing.

**2.2.5 Rheological measurements** are implemented without sand. Water to binder ratio was 0.5. Rheometer: Anton Paar Rotational Rheometer Rheolab QC incorporating a crossed-blade impeller stirrer. The samples for rheological measurements were equilibrated in three intervals: (1) A continuously increasing shear rate of 0 to 50 s<sup>-1</sup> at an acceleration of 1 s<sup>-2</sup>. (2) A constant shear rate of 50 s<sup>-1</sup> for 50 s. (3) The rheology measurement was performed with the shear rate being increased from 0 to 100 s<sup>-1</sup> at a rate of 1 s<sup>-2</sup>.

**2.2.6 Ultrasonic measurements** are performed by Ultrasonic Measuring Test System IP-8, UltraTest GmbH. The US frequency of 25 kHz of the transmitter was performed by the piezoelectric effect with an excitation voltage of 600 V. During the measurements, the development of the P-wave velocity was recorded over a period of 48 h each 60 s.

### 3. Results and Discussion

#### 3.1 Milling

FA is activated in three types of mill with subsequent measurement of specific surface area and finesses. Milling was performed until all the powders achieved the same specific surface by Blaine, around 770±10 m<sup>2</sup>/kg, while the initial specific surface area of FA was 360 m<sup>2</sup>/kg. The particle size and milling time are presented at Table 2. The samples were milled jointly with PNS (# 3; 5; 7) and a part of it (# 2; 4; 6).

Table 2. Median particle size and milling time of activated fly ash.

#	Samples	Median Particle Size, μm	Milling time, min
1	Fly Ash	31.1	0
2	DM FA	8.8	5
3	DM (FA+PNS)	7.6	5
4	BM FA	8.3	60
5	BM (FA+PNS)	7.2	60
6	PBM FA	8.4	120
7	PBM (FA+PNS)	6.9	120

The morphology of activated FA is presented in Fig. 1. It can be seen that morphology of FA is independent from presence of PNS during the activation.

#### 3.2 Rheology

Rheological curves of blended binders are presented in Fig. 2. Partial replacement of cement to non-activated FA leads to decreasing of viscosity.

All the curves were calculated by means of the standard Bingham model. The values of yield stress and viscosity are given in Tab.3. Interestingly, yield stress and viscosity are strongly related with type on introduction of PNS. The samples 4, 7 and 10 were prepared with

chemically introduced PNS (dissolved in water), while the samples 5, 8 and 11 - with mechano-chemically introduced PNS. The contrast between chemical and mechano-chemical introduction of PNS is clearly seen: yield stress and viscosity of the pastes dosed with mechano-chemical introduction of PNS decreased up to 45% and 40%, respectively.

It was also found that mechano-chemical introduction had a positive influence on strength (Tab. 3). FA activated in BM and PBM jointly with PNS had 10% higher strength (the samples 8 and 11), than the samples dosed with chemically introduced PNS. Nevertheless, all the samples regardless the way of PNS introduction had lower strength, than activated FA. This fact is related to retardation effect of PNS.

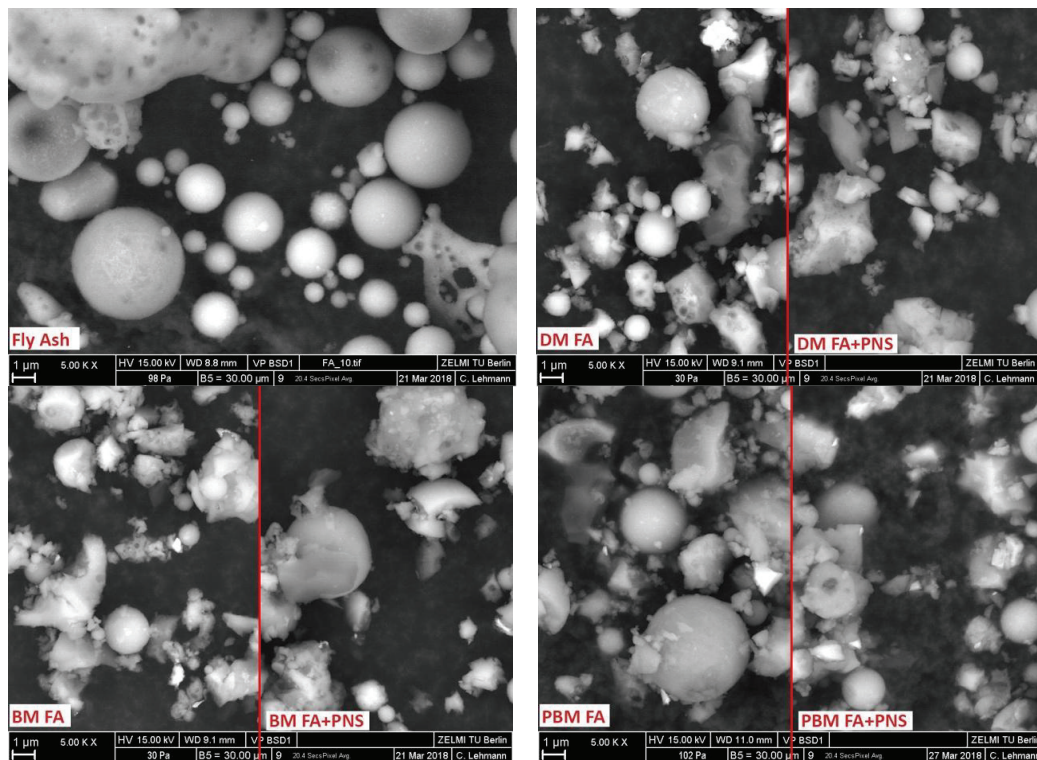


Figure 1: morphology of fly ash activated in different types of mills.

Table 3: Yield stress, viscosity and compressive strength of blended binders.

#	Samples	Yield Stress, Pa	Viscosity, mPa·s	Compressive Strength (28 days), MPa
1	Cement	430	2678	69.3
2	C + FA	400	2000	63.3
3	C + DM FA	475	2239	59.0
4	C + DM FA+PNS	191	1850	62.3
5	C + DM (FA+PNS)	98	1056	61.7
6	C + BM FA	466	2840	66.7
7	C + BM FA+PNS	261	1346	62.7
8	C + BM (FA+PNS)	145	1029	66.0
9	C + PBM FA	452	2477	67.3
10	C + PBM FA+PNS	159	1372	60.3
11	C + PBM (FA+PNS)	100	1031	63.7

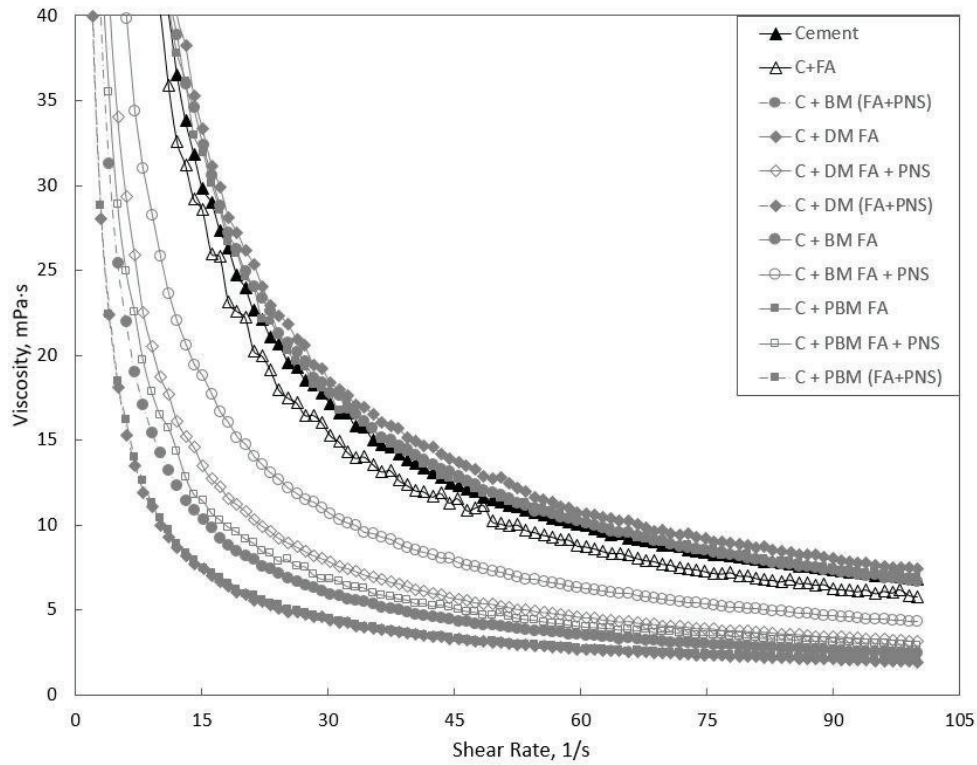


Figure 2: Viscosity of fly ash activated in different types of mills.

### 3.3 Ultrasonic measurements

Hydration of blended binders is characterised by ultrasonic velocity that is presented in Fig. 3. Cement without any surfactant and FA has the highest rate of hydration. Substitution of cement to FA has a retardation effect due to the pozzolanic reaction. Once the PNS is introduced in the blended binder, it exhibits the slowest hydration rate regardless the type of the mill and the method of PNS introduction. Apparently, this phenomenon occurs due to overlapping of the two retardation effects: one from the FA and another one from the PNS itself.

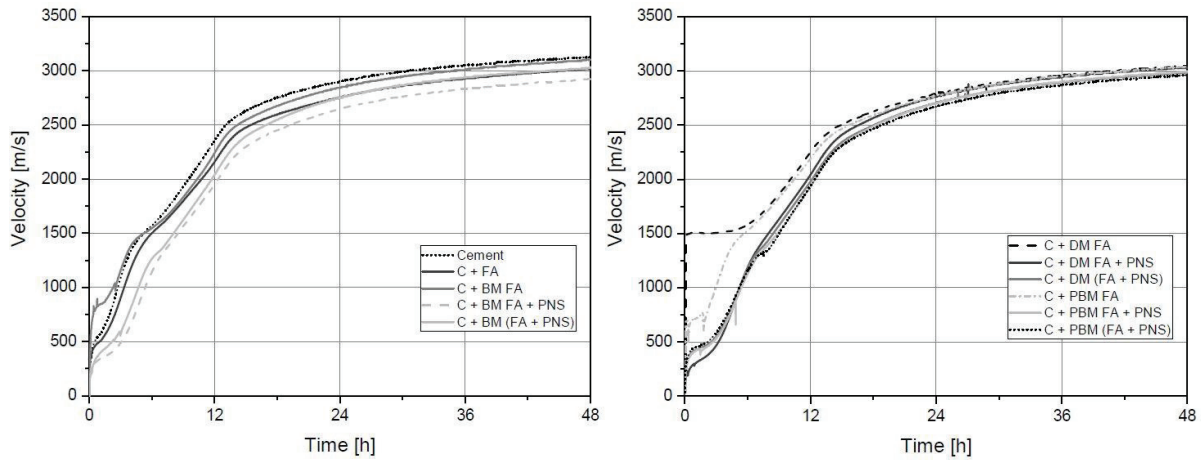


Figure 3: Ultrasonic velocity of blended binders.



#### 4. Conclusions

1. Changing of specific surface area is related with mill type and independent from the presence of PNS into the mill.
2. Introduction of PNS in the mill allows to decrease yield stress and viscosity of blended binder up to 45% and 40%, respectively, in comparison to conventional introduction of surfactant.
3. Blended binder prepared with fly ash interground with surfactant show higher strength than fly ash activated apart of surfactant.
4. Regardless of the type of introduction, presence of PNS diases the strength, due to retardation effect.

#### Acknowledgments

This research was accomplished in the framework of Short Term Scientific Mission sponsored by COST Action TU 1404 “Towards the next generation of standards for service life of cement-based materials and structures”.

#### References

- [1] D. P. Bentz and C. F. Ferraris, “Rheology and setting of high volume fly ash mixtures,” *Cem. Concr. Compos.*, vol. 32, no. 4, pp. 265–270, 2010.
- [2] G. Li and X. Wu, “Influence of fly ash and its mean particle size on certain engineering properties of cement composite mortars,” *Cem. Concr. Res.*, vol. 35, no. 6, pp. 1128–1134, 2005.
- [3] D. K. Rajak, A. Raj, C. Guria, and A. K. Pathak, “Grinding of Class-F fly ash using planetary ball mill: A simulation study to determine the breakage kinetics by direct- and back-calculation method,” *South African J. Chem. Eng.*, vol. 24, pp. 135–147, 2017.
- [4] S. Kumar and R. Kumar, “Mechanical activation of fly ash: Effect on reaction, structure and properties of resulting geopolymer,” *Ceram. Int.*, vol. 37, no. 2, pp. 533–541, 2011.
- [5] A. G. Patil and S. Anandhan, “Influence of planetary ball milling parameters on the mechano-chemical activation of fly ash,” *Powder Technol.*, vol. 281, pp. 151–158, 2015.
- [6] A. Terzić, N. Obradović, L. Andrić, J. Stojanović, and V. Pavlović, “Investigation of thermally induced processes in corundum refractory concretes with addition of fly ash,” *J. Therm. Anal. Calorim.*, vol. 119, no. 2, pp. 1339–1352, 2015.
- [7] Z. Sun et al., “Preparation of polycarboxylate-based grinding aid and its influence on cement properties under laboratory condition,” *Constr. Build. Mater.*, vol. 127, pp. 363–368, 2016.
- [8] K. Sobolev, “Mechano-chemical modification of cement with high volumes of blast furnace slag,” *Cem. Concr. Compos.*, vol. 27, no. 7–8, pp. 848–853, 2005.
- [9] P. Balaz, *Mechanochemistry in Nanoscience and Minerals Engineering*. Springer-Verlag, Berlin-Heidelberg, 2008.
- [10] G. Intini, L. Liberti, M. Notarnicola, and F. D. I. Canio, *Mechanochemical Activation of Coal Fly Ash for Production of High Strength Cement Conglomerates*, vol. 17, pp. 557–561, 2009.
- [11] M. Sadique, H. Al-Nageim, W. Atherton, L. Seton, and N. Dempster, “Mechano-chemical activation of high-Ca fly ash by cement free blending and gypsum aided grinding,” *Constr. Build. Mater.*, vol. 43, pp. 480–489, 2013.
- [12] V. R. Falikman, V.R., Bashlykov, “Low water demand binder technology for environmental friendly cements with low clinker content,” 2011, pp. 633–642.

## **ASSESSMENT OF INTERNAL RELATIVE HUMIDITY AND TEMPERATURE OF CEMENT-BASED MATERIALS – PARALLEL STUDY USING TWO SENSOR SYSTEMS**

**Martin Klun**<sup>(1)</sup>, **Violeta Bokan Bosiljkov**<sup>(1)</sup>, **Samo Beguš**<sup>(2)</sup>, **Slaven Ranogajec**<sup>(2)</sup>,  
**Zvonko Jagličić**<sup>(1),(3)</sup>

(1) University of Ljubljana, Faculty of Civil and Geodetic Engineering, Ljubljana, Slovenia

(2) University of Ljubljana, Faculty of Electrical Engineering, Ljubljana, Slovenia

(3) Institute of Mathematics, Physics and Mechanics, Ljubljana, Slovenia.

### **Abstract**

A custom made sensor system for measuring the temperature and relative humidity inside the cement-based materials (CBMs) was prepared and its functionality compared with a commercially available ConSensor 2.0 system. The obtained results show adequate functioning of the custom made sensor when measuring temperature inside the CBMs. Measurements of relative humidity were not yet compared to reference sensor measurements. However, continuous decrease of relative humidity at accelerated drying of CBM confirmed adequate protection of the sensor and thus its resistance to highly alkaline environment. Additionally, ConSensor 2.0 system was able to follow the cement hydration process through measurements of the CBMs' electrical conductivity ( $C$ ) in a similar way as the ultrasonic P-waves. Based on the obtained  $C(t)$  and  $dC/dt(t)$  profiles we were able to estimate initial and final setting times and the time of the most intensive development of the hydration products.

### **1. Introduction**

The sensor system for measuring the temperature and humidity within the cement-based materials currently in the process of development at the University of Ljubljana (UL) consists of a temperature and moisture sensor, the system for acquiring and processing signals, the power supply and the system for wireless data transfer. Since we would like to mix the sensor system into fresh cement-based material, before casting of the material into formwork, the system has to be wireless, of suitable dimension (size range of a few cm), with long-term

operation and resistance to environmental effects (water, alkaline environment). Denotation CM sensor system will be used for this product, where CM stands for “custom made”.

The first version of the CM sensor system is available for testing. We decided to carry out parallel tests using the CM sensor system and commercially accessible ConSensor 2.0 system [1], which measures temperature and conductivity of the cement-based materials (CBMs). Compositions of CBMs used for the testing are the same as those in the RRT+ programme of the COST TU1404 Action [2].

The paper presents and discusses results of obtained measurements. Temperature profile  $T(t)$  inside the CBMs, measured by using the CM sensor, is compared to the  $T(t)$  profile of the ConSensor 2.0 system. Relative humidity profile  $RH(t)$  of the CBMs is presented as measured by the CM sensor. It has not yet been compared to reference sensor measurements. Moreover, the development of electrical conductivity of the tested CBMs measured by the ConSensor 2.0 system is presented and analysed, in order to determine characteristic phases during setting and hardening of the CBMs.

## **2. Experimental Setup**

Two different CBM mixtures, namely, a modified ordinary mortar (MOM) and modified cement paste (MCP), were used to monitor the process of hydration.

### **2.1 Custom made sensors**

The multichannel measuring system was composed of eight combined temperature and relative humidity sensors and a main data logging unit (Raspberry Pi3). The sensing probes were capacitive sensors with digital I2C interface (SHT25 by Sensirion) enclosed in a filter cap for protection against dust, water immersion and against contamination by cement-based material, providing IP67 protection according to the European standard EN 62262 [3]. The built system had an operating range of 0 % to 100 % relative humidity (RH). In order to ensure the least possible structural intrusiveness, the sensor probes were assembled to be physically as small as possible (6 mm × 6 mm × 2 mm). The prototype sensor probes were connected to the main data logging unit by means of extremely thin wired connection leads (4 × 0.1 mm in diameter) to avoid any unwanted thermodynamic effects (air bubble lock, minimised heat flux, capillary action, etc.) from the surface of the material to the sensors.

Prior to immersion of the sensor into cement-based mixtures, the built system was calibrated by comparison in an accredited temperature laboratory at relative air humidity from 10 % to 95 %, while the temperatures were controlled at 20 °C and 40 °C. Maximal measuring errors of the sensors were below 2.5 % RH and standard uncertainties better than 2.2 % RH.

## 2.2 Specimens

Table 1: Shortcut for the combinations of the two mixtures and two sensors in each mixture.

ConSensor (CS) (temperature, conductivity)	Custom made sensor (CM) (temperature, RH)
MOM1-CS	MOM1-CM
MOM2-CS	MOM2-CM
MCP1-CS	MCP1-CM
MCP2-CS	MCP2-CM

Fig. 1 shows the position of sensors in a mould made of extruded polystyrene. Each specimen is of size 10 cm × 5 cm × 15 cm. For each mixture (MOM and MCP) two identical specimens were prepared, each with an inbuilt CS sensor and a CM sensor. Altogether four specimens were prepared. The short names assigned to each combination of particular mixture and sensor are collected in Tab. 1.

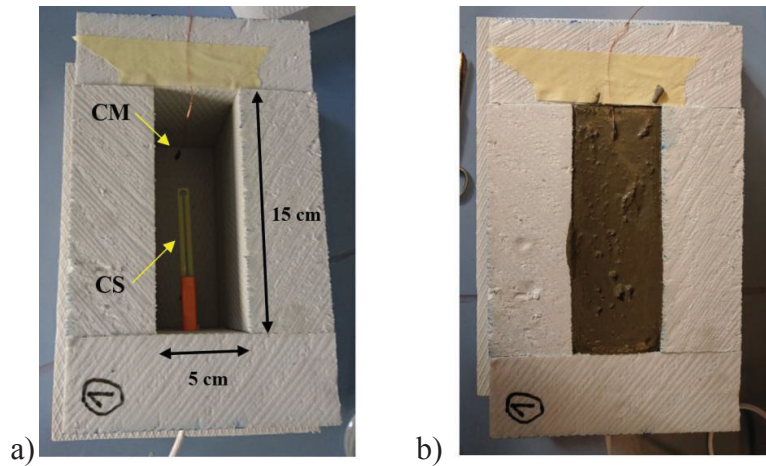


Figure 1: Positions of sensors in a specimen with a height of 10 cm (a), and an image after casting the mixture (MOM or MCP) (b).

## 3. Results and discussion

The time dependent temperatures of two MOM and two MCP specimens are shown in Fig. 2. Time  $t = 0$  is the time when casting of particular specimen was finished. The temperature profiles are almost identical for all four sensors in each CBM mixture, confirming correct functioning of the new CM sensors. The maximal temperature is higher when measured with the CM sensors, by about 5°C (7%) and up to 1°C (2.5%) for the MCP and MOM compositions, respectively. It results from the competition between the heat generated by the cement hydration and the heat transfer between the specimen and the environment. For the “massive” CS sensor the heat transfer to the environment is increased compared to the CM sensor, which results in a lower maximal temperature measured by the CS sensor. The CM sensors are connected to the main data logging unit with four tiny copper wires that provide only negligible heat flux.

The time dependent conductivity  $C(t)$ , measured by the CS sensor, and its time derivative  $dC/dt(t)$  are shown in Fig. 3 a), b), and c), for the MOM and MCP mixtures. Also temperature-time ( $T(t)$ ) profiles are presented, together with the  $dC/dt(t)$  diagrams. From the results given in Fig. 3 we can see excellent correlation between the  $dC/dt(t)$  and  $T(t)$  profiles.

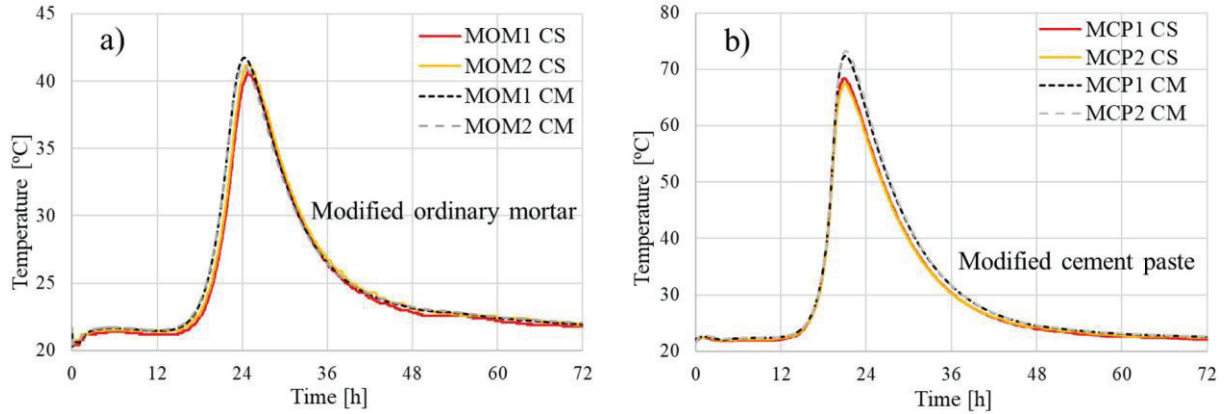


Figure 2: Temperatures of two MOM specimens (a) and two MCP specimens (b).

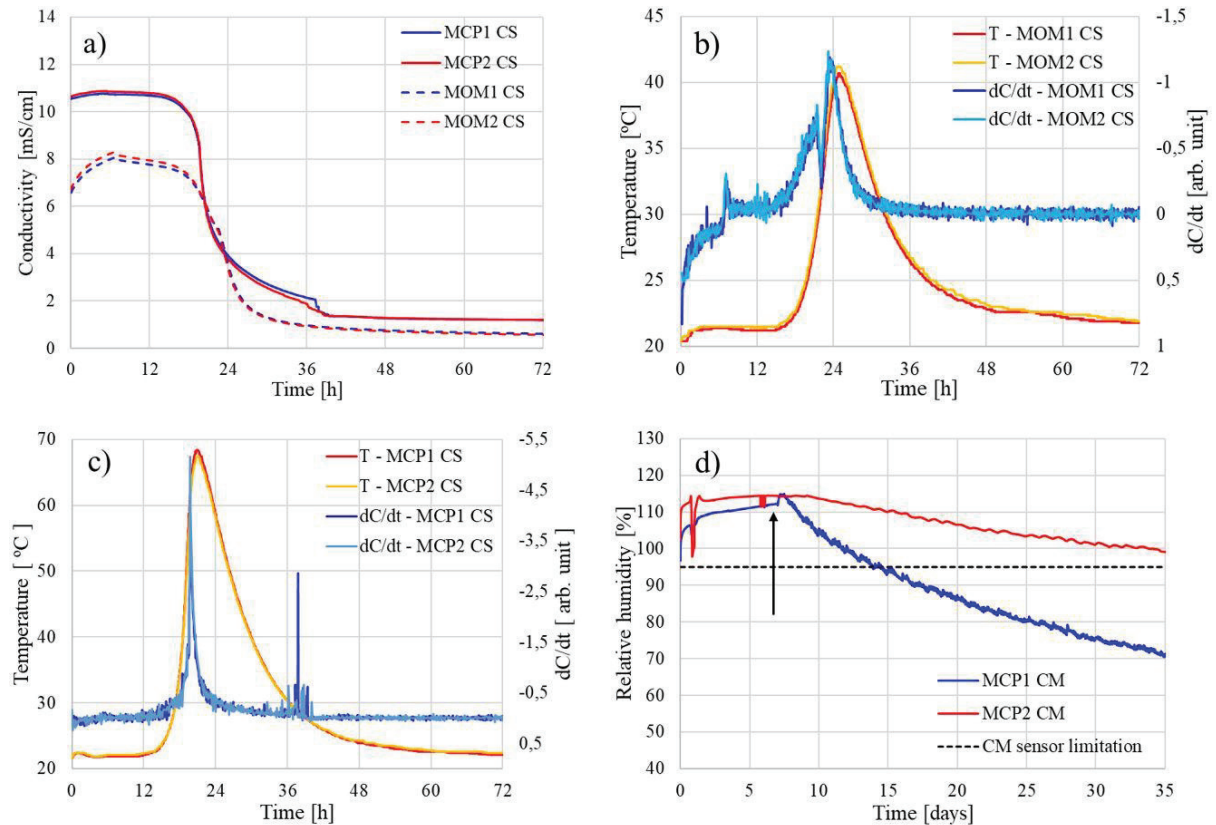


Figure 3: Time dependent conductivity (a), time dependent temperature (the same data as in Fig. 2 for CS sensors) and time derivative  $dC/dt$  for MOM specimens (b) and MCP specimens (c). Relative humidity of MCP specimens in a long term scale (d). The arrow denotes the time when the MCP1 specimen was put on the electric heater.

Vogrič et al. [4] show that five characteristic time periods of the cement hydration process, defined by different characteristic points (initial and final setting time, percolation of solid phases, de-percolation of water saturated pores, and the time of the most intensive solidification process) that appear on typical  $v_p(t)$  profile, where  $v_p$  presents velocity of US P-waves, also appear on the  $C(t)$  profile. By considering the correlation between these two profiles given in [4], we can estimate initial setting time ( $t_I$ ), final setting time ( $t_F$ ) and the most intensive development of the hydration products (CP4), from the  $C(t)$  and  $dC/dt(t)$  profiles in Fig. 3 b) and c). The CP4 time corresponds to the time at the minimum value of the  $dC/dt(t)$  profile. The obtained values are given in Tab. 2.

Table 2: Initial ( $t_I$ ) and final ( $t_F$ ) setting times and the time of the most intensive development of the hydration products (CP4).

	<b>MCP</b>	<b>MOM</b>
$t_I$ [hours]	12 - 13	15.5
$t_F$ [hours]	15 - 16	17.5
CP4 [hours]	19.5 – 20.5	23.2 – 24.4

Initial and final setting times of the MOM reported by Staquet and Serdar [5] are 13.15 and 14.82 hours, respectively. We can see that in our case the cement hydration process was slower, which can be due to two years older cement sample used for the tests by the UL. Moreover, the most intensive development of the hydration products was close to 20 and 24 hours for the MCP and MOM mixture, respectively.

Finally, long term functioning and stability of the CM sensors were examined by the measurements of relative humidity (Fig. 3 d). In all but one specimen the relative humidity was above 95 % during the first month of the measurements. Here we wish to point out again that the CM sensors were calibrated up to 95 % RH, at 20 °C and 40 °C. The reported values above 100 % RH in Fig. 3 d) are meaningless and mean only that the sensors were saturated. On day 7, after the casting (marked with an arrow in Fig. 3 d), specimen MCP2 was demolded and put on an electric heater that maintained temperature of the specimen, measured by the CM sensor, at  $35 \pm 1$  °C. This is the reason for accelerated drying of this specimen which was detected by the CM sensor. At time  $t = 14$  days the measured RH drops below 95 % and an exponential-like decrease of measured RH can be observed in Fig. 3 d). With this approach we were able to confirm the appropriate protection of the CM sensors against alkali environment in fresh mortar and cement paste. Moreover, obtained RH profiles in Fig. 3 d) are very similar to the internal RH development in cement paste specimens at 20 °C reported in [6]. However, further tests and comparison with the reference RH sensor are needed in order to confirm correct working of the CM sensor when measuring relative humidity inside the CBMs.

## 5. Conclusion

Test results presented in the paper show that custom made CM sensors were able to measure the development of the temperature inside particular CBM mixture correctly, since the temperature profiles measured by the CM sensors are almost identical to the same profiles measured by the commercial CS sensors. Moreover, by adopting accelerated drying of the selected MCP specimen we were able to follow also continuous decrease of the relative humidity with time inside the MCP specimen. In this way we confirmed that the used protection system of the CM sensor is adequate, since the sensor is resistant to high alkaline environment.

ConSensor 2.0 system was able to follow the early age evolution of the CBMs properties through measurements of the CBMs' electrical conductivity as function of time. The obtained results are in very good correlation with the measurements of P-wave propagation through the CBMs. Based on this correlation we were able to determine initial and final setting time and the time of the most intensive development of the hydration products, for MCP and MOM mixtures.

## Acknowledgements

This work was financially supported by the Slovenian Research Agency through Research Project J2-8194, Programme Group P2-0185, and PhD project of Martin Klun.

## References

- [1] Van Breek, A., Dielectric properties of young concrete, Non-destructive dielectric sensor for monitoring the strength development of young concrete, PhD thesis, Delft University (2000)
- [2] Staquet, S. et al., RRT+ Main phase of the Extended Round Robin Testing programme for TU1404, Testing protocols, Ver. 22<sup>th</sup> November 2016, (2016) 57p
- [3] EN 62262, Degrees of protection provided by enclosures for electrical equipment against external mechanical impacts (IK code), CEN, EU (2002)
- [4] Vogrič, N. et al., Experimental monitoring of early formation of cement paste structure, *Gradbeni vestnik* 66 (2017), 307-313 (in Slovenian language)
- [5] Staquet, S. and Serdar, M., Extended Round Robin Test RRT+ Main Phase, PPT presentation, COST TU 1404 Zagreb meeting, Croatia (2016)
- [6] Chen, H. et al., Prediction of self-desiccation in low water-to-cement ratio pastes based on pore structure evolution, *Cem Concr Res* 49 (2013), 38-47

## **CARBONATION RESISTANCE OF HIGH-VOLUME FLY ASH (HVFA) MORTAR: EFFECT OF APPLIED CO<sub>2</sub> CONCENTRATION**

**Philip Van den Heede<sup>(1)</sup>, Didier Snoeck<sup>(1)</sup>, Tim Van Mullem<sup>(1)</sup>, Nele De Belie<sup>(1)</sup>**

(1) Magnel Laboratory for Concrete Research, Ghent University, Belgium

### **Abstract**

To save time, the carbonation resistance of cementitious materials is usually assessed in an accelerated manner by exposing the material to CO<sub>2</sub> levels that highly exceed the atmospheric CO<sub>2</sub> concentration. However, a too high acceleration of the carbonation reaction could induce chemical, microstructural and mineralogical changes and excess production of the water reactant that are unrealistic. In this paper, it was evaluated whether the outcome of colorimetric carbonation experiments at 10% CO<sub>2</sub> for High-Volume Fly Ash (HVFA) mortar could still be used for calculating natural carbonation rates and to do an adequate service life assessment. This seems not true. The effect of full carbonation at 10% CO<sub>2</sub> on the capillary water uptake was also assessed gravimetrically and visually on neutron radiographs. This water uptake was found to be significantly lower than after full carbonation at only 1% CO<sub>2</sub>.

### **1. Introduction**

The carbonation resistance of cementitious materials is usually determined through accelerated laboratory experiments. Samples of a composition of interest are exposed to CO<sub>2</sub> levels that significantly exceed the around 0.04% CO<sub>2</sub> present in ambient air, at a given relative humidity (usually 60% RH) and temperature (usually 20°C). At regular time intervals, a number of samples is split and phenolphthalein is sprayed onto the fractured surfaces to visualize the front of the carbonation-induced pH drop. Depending on the test protocol, the applied CO<sub>2</sub> concentration can vary from 1 % up to 50 % CO<sub>2</sub> [1]. Today, there is more and more concern that exposure to CO<sub>2</sub> concentrations above 3 % CO<sub>2</sub> may modify the whole carbonation process too much [2]. Subsequent conversion of the result to a realistic natural carbonation rate using the often used calculation approach of Sisomphon and Franke [3] could highly underestimate the actual carbonation rate and the related service life in environments where carbonation-induced steel corrosion is a dominant mechanism, and this due to (i)



chemical, microstructural and mineralogical changes affecting the permeability, and (ii) excess water production during carbonation causing pore blocking [1, 4-7]. For now, it remains unclear which of these mechanisms is more dominant for potentially 'green' binder systems in which large cement portions are replaced by fly ash to lower cement related CO<sub>2</sub> emissions [1]. In this paper, it has been evaluated for High-Volume Fly Ash (HVFA) mortar to what extent natural carbonation rates estimated from experiments conducted at 10% CO<sub>2</sub> underestimate those estimated from tests conducted at 1% CO<sub>2</sub> and the atmospheric CO<sub>2</sub> concentration and how probabilistic service life predictions for carbonation-induced steel depassivation are affected by it. Moreover, 2 h neutron radiography monitored capillary sorption experiments cf. Snoeck et al. [8] were performed to study carbonation-induced changes in capillary water transport properties.

## 2. Materials and methods

### 2.1 Mortar mixtures

All tests were performed on HVFA mortar with a low carbonation resistance. The proportioning of the sand and binder for one batch of mortar was the same as for the standard mortar specified in NBN EN 196-1, and amounted to 1350 g and 450 g, respectively. The binder portion consisted for 50% of CEM I 52.5 N and for 50% of class F fly ash. The applied water-to-binder (W/B) ratio equalled 0.55, which is higher than the 0.50 value which is normally prescribed for a standard mortar. A high cement replacement level was used to make sure there was less carbonatable material, i.e. portlandite, available. This ensures a lower buffer capacity for the penetrating CO<sub>2</sub> and thus a faster inward movement of the carbonation front. Increasing the W/B ratio facilitated a higher porosity, and thus also a faster ingress of CO<sub>2</sub>.

### 2.2 Sample preconditioning and carbonation testing

For the colorimetric carbonation tests, a series of mortar cubes (side: 100 mm) were made. After 24 hours in a wet curing chamber at 20°C and 95% RH the cubes were demoulded, whereupon the cubes were stored again in the wet curing chamber until they reached 7 days of age. Then, they were dried in an oven at 40°C for 4 days to ensure a uniform moisture distribution in the cubes. Subsequently, the cubes were carefully wrapped in aluminium tape on all sides except for one exposure side. In this condition, they remained in a climate room at 20°C and 60% RH for 3 days. The next days, the cubes were equally divided among that same climate chamber, the carbonation chamber at 1% CO<sub>2</sub>, 20°C, 60% RH, and the carbonation chamber at 10% CO<sub>2</sub>, 20°C, 60% RH. At regular time intervals, three cubes were taken out of each chamber for colorimetric carbonation depth assessment using phenolphthalein. The neutron radiography monitored capillary sorption tests were performed on a series of 160×20×40 mm<sup>3</sup> prismatic mortar prisms. To make sure these experiments could be performed during an already scheduled measuring campaign at the Paul Scherrer Institute (PSI) in Switzerland, the preconditioning of those samples was somewhat different. Upon demoulding after 24 hours, the samples were immediately exposed to either 1% CO<sub>2</sub> (8 samples) or 10% CO<sub>2</sub> (8 samples) in the carbonation chambers that were mentioned before, and this for 21 days. During this period, CO<sub>2</sub> was able to penetrate the prisms from all sides. Given the fact that the prisms were quite thin, 21 days of exposure to 10% and also 1% CO<sub>2</sub> should normally be sufficient to have fully carbonated samples. Before taking the samples to PSI for testing, the samples were oven dried at 40°C for 4 days. After drying, 3 samples per

test series were split and sprayed with phenolphthalein to verify whether they were indeed fully carbonated. This was the case. The remaining 5 samples per test series were subjected to the neutron radiography monitored capillary sorption tests.

### 2.3 Probabilistic service life prediction

The time to carbonation-induced steel depassivation was estimated using a very basic limit state function representing the well-known square-root-time relation for carbonation (Eq. (1)).

$$g(d, x_c(t)) = d - A \cdot \sqrt{t} \quad (1)$$

with  $d$ , the concrete cover (lognormal,  $35 \pm 8$  mm),  $x_c(t)$ , the carbonation depth at time  $t$  (years), and  $A$ , the carbonation coefficient corresponding with the atmospheric  $\text{CO}_2$  concentration (normal, standard deviation (stdv):  $\pm 1$  mm/ $\sqrt{\text{years}}$ ). Three different values for this carbonation coefficient were to be considered, i.e. the value obtained directly from a natural non-accelerated carbonation test at around 0.04%  $\text{CO}_2$ , 20°C and 60% RH ( $A_{\text{atm}}$ ), and two estimates as calculated from accelerated carbonation experiments at 1% ( $A_{\text{atm est}_1\%}$ ) and 10%  $\text{CO}_2$  ( $A_{\text{atm est}_10\%}$ ) using Eq. (2) cf. [3].

$$A_{\text{atm est}} = A_{\text{acc}} \frac{\sqrt{c_{\text{atm}}}}{\sqrt{c_{\text{acc}}}} \quad (2)$$

with  $A_{\text{atm est}}$ , the estimated natural carbonation coefficient representing exposure to the atmospheric  $\text{CO}_2$  %, as estimated from accelerated carbonation tests at the same temperature and RH, yet at an elevated  $\text{CO}_2$  level (mm/ $\sqrt{\text{years}}$ ),  $A_{\text{acc}}$ , the carbonation coefficient measured during these accelerated carbonation experiments at elevated  $\text{CO}_2$  levels (mm/ $\sqrt{\text{years}}$ ),  $c_{\text{atm}}$ , the atmospheric  $\text{CO}_2$  concentration (around 0.04%  $\text{CO}_2$ ), and  $c_{\text{acc}}$ , the  $\text{CO}_2$  concentrations applied during the accelerated carbonation tests (1% or 10%  $\text{CO}_2$ ). Probabilities of failure ( $P_f$ ) as a function of time were calculated using the First Order Reliability Method (FORM) available in the probabilistic Comrel software. In accordance with *fib* Bulletin 34 [9],  $P_f$  for steel depassivation cannot exceed 0.10. As soon as it does, the end of service life has been reached.

### 2.4 Neutron radiography monitored capillary sorption tests after carbonation

As mentioned in Section 2.2, two times 5 prisms carbonated at 1% and 10%  $\text{CO}_2$ , respectively, were subjected to the neutron radiography monitored capillary sorption tests at the PSI. This experiment comprised gravimetric recordings of the water uptake and a visualization of the water penetration front. Just before the start of the test, the sides of the prisms were sealed with aluminium tape, to ensure unidirectional water uptake via the bottom surface. The bottom surface was partially taped so that water could only penetrate via the  $100 \times 20$  mm<sup>2</sup> central area of that surface. The top  $160 \times 20$  mm<sup>2</sup> surface of the prisms was not covered with aluminium tape. The initial mass of the prisms was recorded on a Sartorius 238 BP 3100 S balance (0.01 g accuracy). Next, the specimens were put on rods in small water basins. The water immersion depth amounted to  $\pm 3$  mm. After 2 hours, the prisms were removed from the water basins and their end mass was determined. To combine the gravimetric information with a visualization of the water penetration front during capillary water uptake, the sorption experiments were performed at the thermal neutron imaging facility NEUTRA. This facility is part of the spallation neutron source SINQ of the Paul

Scherrer Institute (PSI) in Switzerland. For more technical details on the beam line and the procedures followed for correction and post-processing of the raw neutron radiographs, we refer to Snoeck et al. [8].

### 3. Results and discussion

#### 3.1 Colorimetric carbonation assessment

Logically, exposing the studied HVFA mortar to CO<sub>2</sub> levels (10% and 1% CO<sub>2</sub>) that highly exceed the atmospheric CO<sub>2</sub> concentration of around 0.04%, results in significantly higher carbonation depths as a function of the square-root-of-time (Figure 1a). The corresponding carbonation coefficients amounted to 15.01 mm/√weeks (A<sub>10%</sub>), 7.79 mm/√weeks (A<sub>1%</sub>) and 2.21 mm/√weeks (A<sub>atm</sub>), respectively. The carbonation coefficient obtained for a CO<sub>2</sub> level of 1%, was estimated using Eq. (2) in which A<sub>acc</sub> and c<sub>acc</sub> equalled A<sub>10%</sub> and 10%, and A<sub>atm est</sub> and c<sub>atm</sub> were replaced with A<sub>1% est</sub> and 1%, respectively. This gives an estimated carbonation coefficient of 4.75 mm/√weeks (Figure 1b), which is only 61% of the value that was actually measured at 1% CO<sub>2</sub> (7.79 mm/√weeks). This is a first indication that Eq. (2) is not valid for CO<sub>2</sub> concentrations as high as 10%. Furthermore, both A<sub>1%</sub> and A<sub>10%</sub> were used once as input for the conversion formula (A<sub>acc</sub>, Eq. (2)). As such, two estimated carbonation coefficients for the atmospheric CO<sub>2</sub> concentration were obtained which could be compared with the actually measured one (Figure 1a: 2.21 mm/√weeks) during the non-accelerated carbonation experiment, i.e. 2.46 mm/√weeks and 0.95 mm/√weeks (Figure 1b). While the former estimated value is quite well in range with the actually measured natural carbonation coefficient of 2.21 mm/√weeks, the latter seems to be substantially lower. Clearly, conducting a carbonation experiment at 10% CO<sub>2</sub> and using Eq. (2) to obtain an estimate for the atmospheric carbonation rate, strongly underestimates the natural carbonation rate for the studied HVFA binder system.

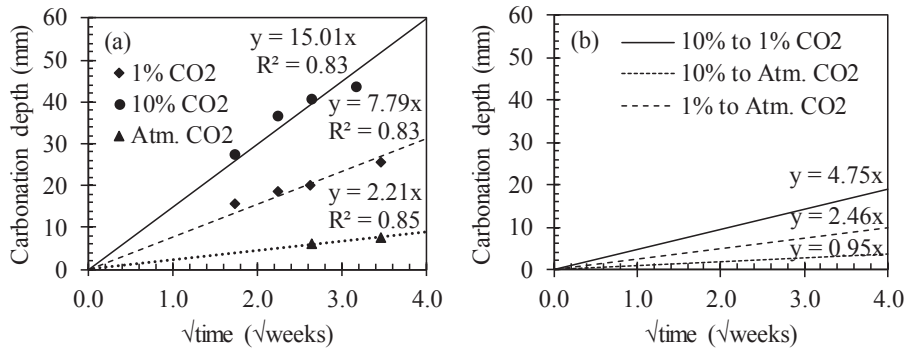


Figure 1: Measured (a) and estimated (b) carbonation coefficients for 1% and 10% CO<sub>2</sub> and the atmospheric CO<sub>2</sub> concentration.

#### 3.2 Service life assessment for carbonation-induced steel depassivation

When using the actually measured carbonation coefficient for the atmospheric CO<sub>2</sub> concentration in the prediction model (Eq. (1)), it would only take around 2.5 years before the carbonation front in the studied HVFA mortar reaches the location of the reinforcing steel at a typical cover depth of 35 mm. A very similar prediction outcome (2 years) was obtained with the estimated A<sub>atm est 1%</sub> value. For conversion of a carbonation coefficient obtained at 1% to a corresponding one for the atmospheric CO<sub>2</sub> concentration, Eq. (2) seems certainly valid. It

gives a reliable service life prediction. This can totally not be done for a carbonation coefficient measured at a CO<sub>2</sub> concentration of 10%. Estimated atmospheric carbonation coefficients calculated from this value underestimate the actual carbonation rate and thus overestimate the potential service life of the HVFA binder system. One would wrongfully assume that it would take about 12.5 years before the carbonation front reaches the reinforcing steel. Subsequent corrosion-induced damage prediction and adequate planning of future repair will for sure be compromised by adopting the latter approach.

### 3.3 Neutron radiography monitored capillary water uptake after carbonation

The total mass decrease ( $\Delta m \downarrow$ ) of the mortar prisms during the 4-day drying period at 40°C after carbonation was recorded. The same was done for the mass increase ( $\Delta m \uparrow$ ) during the subsequent capillary sorption experiment. The values obtained are presented in Table 1.

Table 1: Gravimetric measurements during pre-drying at 40°C and the 2h capillary sorption test

# Sample	$\Delta m \downarrow$ pre-drying	$\Delta m \uparrow$ capillary sorption	# Sample	$\Delta m \downarrow$ pre-drying	$\Delta m \uparrow$ capillary sorption
a_1%	1.48 g	13.07 g	a_10%	3.68 g	9.64 g
b_1%	1.56 g	12.73 g	b_10%	3.64 g	9.16 g
c_1%	1.57 g	12.77 g	c_10%	3.74 g	9.54 g
d_1%	1.61 g	13.82 g	d_10%	3.64 g	11.20 g
e_1%	1.62 g	14.60 g	e_10%	3.71 g	10.40 g
avg± stdv	1.57±0.06 g	13.40±0.80 g	avg±stdv	3.66±0.06 g	9.99±0.81 g

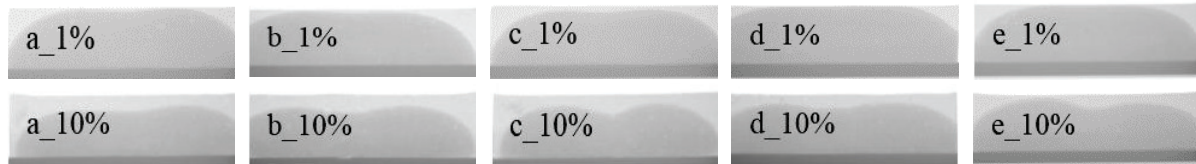


Figure 2: Neutron radiographs of HVFA mortar prisms after full carbonation at 1% or 10% CO<sub>2</sub> and a 2 h capillary sorption experiment.

For both  $\Delta m \downarrow$  and  $\Delta m \uparrow$ , a clear difference could be observed between the prisms that were carbonated at 1% and 10% CO<sub>2</sub>. Apparently, 4 days of drying at 40°C after full carbonation at 10% CO<sub>2</sub> results in a significantly higher mass loss (10% CO<sub>2</sub>: 3.66 ± 0.06 g versus 1% CO<sub>2</sub>: 1.57 ± 0.06 g). The reason for this behaviour remains unclear at the moment. Possibly, this is related to more abundant production of water – a key reactant of the carbonation process besides calcium carbonate – at higher CO<sub>2</sub> levels cf. [6,7]. This excess water should then also be removed during the subsequent drying step. However, this theory needs to be confirmed. Carbonation tests on samples with embedded humidity sensors are ongoing to monitor the excess water production. Another striking observation with regard to the gravimetric measurements relates to the clear difference in mass increase during the 2 h capillary sorption test between samples carbonated at 1% and 10% CO<sub>2</sub>. The substantially lower mass increase after full carbonation at 10% CO<sub>2</sub> (9.99 ± 0.81 g versus 13.40 ± 0.80 g at 1% CO<sub>2</sub>) implies less water uptake. The corresponding neutron radiographs showing the water penetration fronts not extending over the full height of the specimens further confirm this (Figure 2). From these results, it seems that a more dense and less permeable HVFA mortar is obtained

by carbonating them at 10% CO<sub>2</sub>. This finding was not immediately expected, since binder systems with high cement replacement levels, have less portlandite (CH) available which makes them more prone to carbonation of calcium–silicate–hydrates (C–S–H), causing a coarsening of the pore structure and not a densification [4]. Mercury intrusion porosimetry has been planned to see what has happened to the overall porosity and pore size distribution of these samples.

#### 4. Conclusions

- Atmospheric carbonation coefficients estimated from accelerated carbonation experiments at 10% CO<sub>2</sub> highly underestimate the actual values for HVFA binder systems and thus seriously overestimate the service life in environments where carbonation-induced corrosion is at risk. This was clearly observed from colorimetric carbonation experiments.
- HVFA mortar fully carbonated at 10% CO<sub>2</sub> is characterized by a significantly lower capillary water uptake than HVFA mortar fully carbonated at 1% CO<sub>2</sub>. Both gravimetric measurements and visual assessment of neutron radiographs confirmed this.

#### Acknowledgements

Philip Van den Heede is postdoctoral fellow of Research Foundation—Flanders (FWO) (project No. 3E013917) and acknowledges its support. The authors also would like to thank the PSI for granting beam time at the NEUTRA SINQ facility (proposal ID No. 20170327). They are also grateful to Mr. Hovind of PSI and Mr. Hillewaere of the Magnel laboratory for their help.

#### References

- [1] Van den Heede, P., Durability and sustainability of concrete with high volumes of fly ash, PhD thesis, Ghent University (2014)
- [2] Castellote, M. et al, Chemical changes and phase analysis of OPC pastes carbonated at different CO<sub>2</sub> concentrations, *Mater Struct* 42 (2009), 515-525
- [3] Sisomphon, K. and Franke, L., Carbonation rates of concretes containing high volume of pozzolanic materials. *Cem Concr Res* 37 (2007), 1647-1653
- [4] Borges, P.H.R. et al, Carbonation of CH and C–S–H in composite cement pastes containing high amounts of BFS, *Cem Concr Res* 40 (2010), 284-292
- [5] Thiéry, M., et al, Investigation of the carbonation front shape on cementitious materials: Effects of the chemical kinetics, *Cem Concr Res* 37 (2006), 1047-1058
- [6] da Silva, F.G. et al, Sources of variations when comparing concrete carbonation results, *J Mater Civ Eng* 21 (2009), 333-342
- [7] Saetta, A.V. and Vitaliani, R.V., Experimental Investigation and numerical modeling of carbonation process in reinforced concrete structures, Part I: Theoretical formulation, *Cem Concr Res* 34 (2004), 571-579.
- [8] Snoeck, D. et al, Water penetration through cracks in self-healing cementitious materials with superabsorbent polymers studied by neutron radiography, *CemConcrRes* (2018), und. review
- [9] *fib Bulletin* 34, Model code for service life design, fib, Switzerland (2006)

## CHARACTERISATION OF CONCRETE PUMPING BEHAVIOUR

Egor Secrieru<sup>(1)</sup>, Viktor Mechtcherine<sup>(1)</sup>

(1) Technische Universität Dresden, Institute of Construction Materials

### Abstract

Pumping is a widely and effectively used transportation and placing method for fresh cement-based materials. Despite the immense progress in the field of concrete technology in the last decades, including the application of additive manufacturing, so far there are still no official regulations to be used for the assessment and accurate prediction of concrete pumping behaviour. The design of a concrete pumping process becomes especially challenging when high performance concretes including highly viscous high-strength or self-compacting suspensions are involved.

In the present research, the pumping behaviour of concrete is characterised using state of the art rheological and numerical tools. The concrete mixtures under investigation exhibit various principal flow types which are already defined at low flow rates: partial bulk shear in a conventional vibrated concrete and pronounced bulk shear in the case of a self-compacting concrete (SCC). The obtained results are validated in full-scale pumping experiments. The pressure-flow rate curves serve as a reliable pumpability indicator for comparison between predicted results from experimental methods with tribometer/viscometer and Sliper devices, simulations with computational fluid dynamics (CFD) and actual results from full-scale tests.

### 1. General

Pumping of concrete plays a tremendous role in the contemporary construction industry. According to the European Ready Mixed Concrete Organisation, the amount of ready-mix concrete conveyed by pumping amounts 32 % and shows a rising trend worldwide [1].

In the context of concrete technology pumpability is a characteristic of the mixture describing its ability to be pumped easily and trouble-free through a conveying line. The flow behaviour of fresh concrete in a pipeline is related to the composition of the concrete and its ability to generate sufficient lubricating material to reduce the friction at the pipe wall-concrete interface [2].

The nature of concrete in its fresh and hardened states is perpetually evolving. The modern generation of concretes, e.g., high-performance concretes possess usually elevated viscosity in comparison to conventional vibrated concretes (CVC). The result is an increase in the effective pumping pressure needed to achieve a particular flow rate [3].

A series of practical guidelines for determination of pumping parameters in a concrete pumping operation has been used since the fifties of the last century [4] but are limited to CVC assuming the formation and full contribution of the lubricating layer to the concrete flow: The fresh material properties are accounted for slump or flow table test results, that by chance can be attributed to concrete yield stress parameter. Even so, such approaches fail in predicting pumpability of highly flowable or self-compacting concretes (SCC), for which the viscosity plays a crucial role during pumping [5]. Certainly, preliminary full-scale pumping tests are performed exclusively for large construction projects to ensure the suitability of the fresh material properties. With this respect, reliable tests to provide rapid means of concrete pumpability assessment are necessary [6].

## 2. Experimental investigation

### 2.1 Mixture and design parameters

The compositions of the two representative mixtures CVC and SCC are summarised in Tab. 1.

Table 1: Matrix composition of concrete mixtures under investigation.

Material	Density [kg/m <sup>3</sup> ]	Unit mass [kg/m <sup>3</sup> ]	
		CVC	SCC
CEM III/A 42.5 N	3075	360	360
Fly ash	2200	-	220
Sand 0/2	2650	781	667
Sand/gravel 2/8	2650	508	434
Gravel 8/16	2650	526	450
Water	1000	180	180
PCE HRWRA	1040	2.88	5.51
Water-to binder ratio [-]	-	0.50	0.31
Vol. aggregates [-]	-	0.69	0.59
Design strength [-]	-	C45/55	C55/67
Flow table <sup>1</sup> , slump flow <sup>2</sup> [mm]	-	530 <sup>1</sup>	673 <sup>2</sup>
Air content [%]	-	1.40	2.00
Density [kg/m <sup>3</sup> ]	-	2370	2270

The concrete mixtures were prepared at ready-mix station. The rheological tests were performed inside a warehouse on fresh concrete taken from the truck. The experimental circuit used for full-scale pumping experiments amounted ca. 154 m in length, cf. Fig. 1a. The entire circuit included three 180°, cf. Fig. 1b. The pipeline comprised two sections with

distinct diameters, Ø 125 and 100 mm, eight pressure sensors and a flow meter, cf. Figs. 1c and 1d.

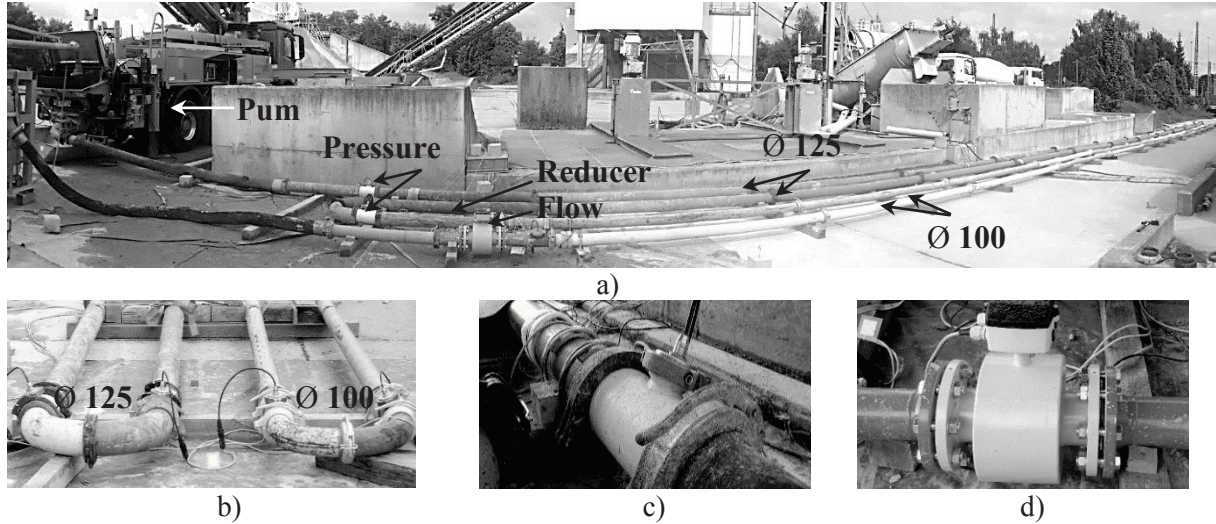


Figure. 1: a) Overview of the full-scale setup, b) 180° bends of two diameters, c) pressure sensor and d) flow meter.

## 2.2 Characterisation of concrete flow in pipeline

The pumping behaviour of fresh concrete can be well characterised applying the rheological and tribological properties of concrete bulk and the forming lubricating layer (LL). Based on Kaplan's approach [2] the pressure-flow rate relationship ( $P-Q$ ) is analytically estimated with Eq. (1), for concretes showing pure plug flow, and Eq. (2) in case of shear flow behaviour:

$$P = \frac{2L}{R} \left[ \tau_{0i} + \frac{Q \cdot \mu_i}{\pi \cdot R^2} \right] \quad (1), \quad P = \frac{2L}{R} \left[ \tau_{0i} + \frac{\frac{Q}{\pi \cdot R^2} - \frac{R}{4 \cdot \mu} \tau_{0i} + \frac{R}{3 \cdot \mu} \cdot \tau_0}{1 + \frac{R}{4 \cdot \mu} \cdot \mu_i} \cdot \mu_i \right] \quad (2)$$

where  $\tau_{0i}$  is the yield stress [Pa] and  $\mu_i$  the viscosity parameter [Pa·s/m] of the lubricating layer measured by tribometer;  $\tau_0$  is the yield stress [Pa] and  $\mu$  plastic viscosity [Pa·s] of the bulk concrete measured by viscometer, cf. Figs. 2a and 2b;  $R$  is the radius [m] and  $L$  the pipe length [m]. A further employed device was Sliper [7], that represents a novel approach to directly estimate the pumping pressure for a specific flow rate and pipe geometry, cf. Fig. 2c.

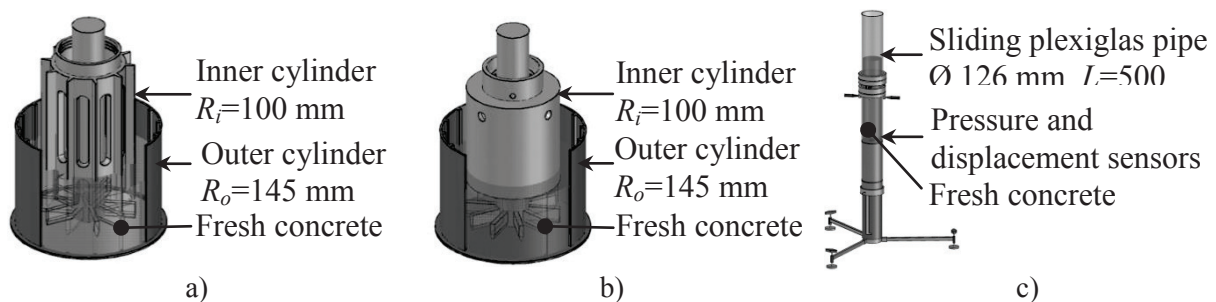


Figure 2: a) Viscometer and b) tribometer geometries, c) Sliper device.



The measured rheological parameters are shown in Tab. 2 and refer to the results obtained at the time of inserting the concrete into the pipeline. Further details are available in [8].

Table 2: Rheological parameters of concretes used in full-scale pumping tests [8].

Device	Parameter	CVC		SCC	
		Concrete bulk	LL	Concrete bulk	LL
Viscometer	Plastic viscosity $\mu$ [Pa·s]	30	-	36	-
	Yield stress $\tau_0$ [Pa]	112	-	18	-
Tribometer	Viscosity $\mu_i$ [Pa·s/m]	-	944	-	2349
	Yield stress $\tau_{0i}$ [Pa]	-	48	-	11
Sliper	Viscosity $b$ [Pa·s/m]	587	-	935	-
	Yield stress $a$ [Pa]	141	-	21	-

### 2.3 Numerical model

The numerical simulations were performed using computational fluid dynamics (CFD) in combination with the available commercial software ANSYS Fluent<sup>®</sup>. The single fluid approach was applied to model the flow of concrete in the pipeline following the approach presented in [9]. In addition to the no-slip condition at the concrete-pipe wall interface [10], the following assumptions were made:

- Concrete flow behaviour is approximated to that of a Bingham fluid and is considered continuous, laminar ( $Re < 1$ ) and time-independent;
- The model consists of lubricating layer (LL) and concrete bulk regions. The properties of each region are assigned in the form of parameters as obtained from rheological experiments, cf. Tab. 2;
- The thickness and rheological properties of LL are constant along the pipeline.

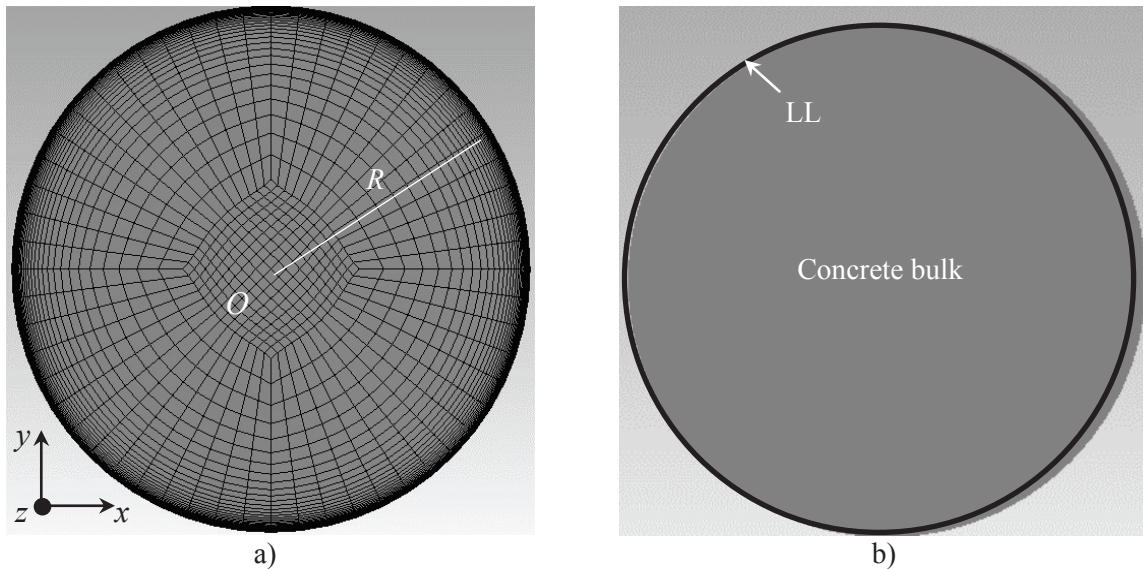


Figure 3: a) Generated mesh of pipe cross-section;  
b) boundaries between lubricating layer (LL) and concrete bulk.

### 3. Results and discussion

The experimental tools applied in this research to characterise the pumping behaviour and predict the necessary pumping pressure for the investigated concretes were successfully verified based on real results from full-scale pumping in terms of  $P$ - $Q$  relationship, cf. Figs. 4a and 4b.

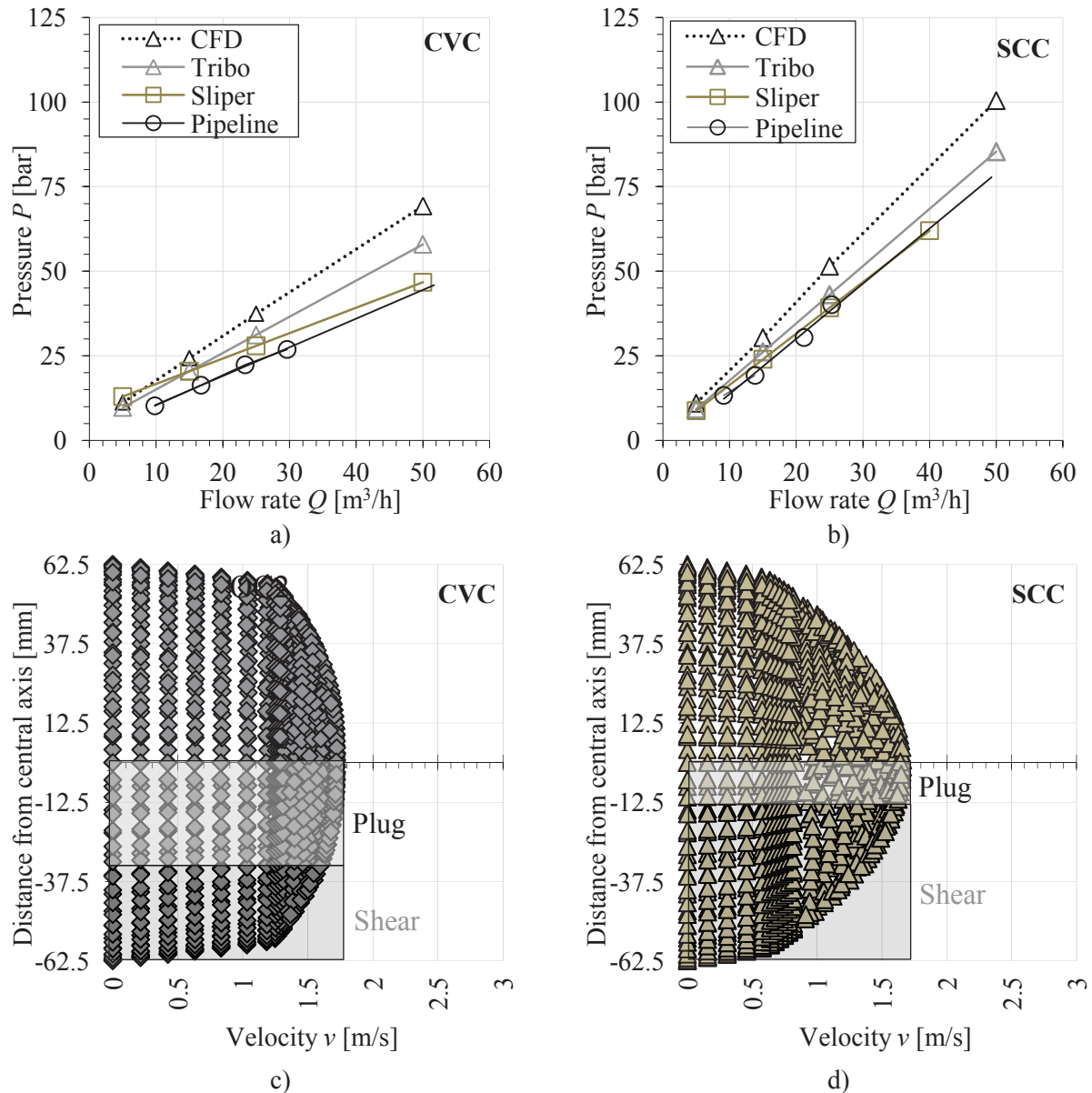


Figure 4: Comparison of  $P$ - $Q$  determined by experimental tools and full-scale pumping for the investigated concrete mixtures a) CVC and b) SCC; resulting velocity profiles in the pipeline cross-section for c) CVC and d) SCC obtained from CFD simulations for pipe diameter  $\text{\O} 125$ .

The used methods, i.e. viscometer/tribometer and Sliper slightly overestimate the pumping pressure. It seems that concrete undergoes structural breakdown corresponding to the elevated

shear rates in the pipes implying a lower needed pumping pressure than predicted based on tests at lower shear rates. Further, CVC mixture shows a shallower slope of the  $P-Q$  curve corresponding to “higher pumpability” in comparison to viscous SCC mixture.

The calculated velocity profiles are depicted in Figs. 4c and 4d; they correspond to a flow rate of  $Q = 30 \text{ m}^3/\text{h}$ . It can be seen that for all the mixtures the flow type is a combination of plug and shear. The regions of flow types, plug or shear, are represented schematically in order to illustrate and emphasise the considerable impact of pipe geometry on the material flow behaviour and high shear deformations at the pipe wall-concrete interface.

#### 4. Conclusions

The paper proposes easy-to-use methods for a reliable characterisation of concrete pumping behaviour. The methods discussed herein, i.e., viscometer/tribometer, Sliper and numerical simulations, were verified in full-scale pumping experiments on concretes showing different flow behaviour: predominantly plug for ordinary concrete CVC and shear type for SCC. The CFD model represents a powerful instrument to investigate the velocity profiles and pressure fields of the pumped concretes in the pipeline and can be applied for the prediction of material behaviour during pumping. The entire research study included an extended palette of concrete mixtures and it allows the authors to recommend the adoption and use of the methods under consideration of their limitations discussed in [8].

#### Acknowledgements

The present project was financially supported by the Federal Ministry for Economic Affairs and Energy and German Federation of Industrial Research Associations, grant number 18361 BR/1 „Zielsichere betontechnische Gestaltung des Pumpens von Frischbeton”.

#### References

- [1] ERMCO, Ready-Mixed Concrete Industry Statistics 2016, 2017.
- [2] D. Kaplan, F. de Larrard, T. Sedran, Design of concrete pumping circuit, *ACI Mater. J.* 102 (2005) 110–117.
- [3] D. Feys, G. De Schutter, R. Verhoeven, Parameters influencing pressure during pumping of self-compacting concrete, *Mater. Struct.* 46 (2013) 533–555.
- [4] Placing concrete by pumping methods, ACI 304.2R-96 (reapproved 2008), 1996.
- [5] D. Feys, G. De Schutter, K.H. Khayat, R. Verhoeven, Changes in rheology of self-consolidating concrete induced by pumping, *Mater. Struct.* 49 (2016) 4657–4677.
- [6] G. De Schutter, D. Feys, Pumping of fresh concrete: Insights and challenges, *RILEM Tech. Lett.* (2016) 76–80.
- [7] K. Kasten, Gleitrohr – Rheometer, Ein Verfahren zur Bestimmung der Fließeigenschaften von Dickstoffen in Rohrleitungen, PhD thesis, TU Dresden, 2010.
- [8] E. Secieru, Pumping behaviour of modern concretes - Characterisation and prediction, PhD thesis, TU Dresden, 2018.
- [9] M. Choi, N. Roussel, Y. Kim, J. Kim, Lubrication layer properties during concrete pumping, *Cem. Concr. Res.* 45 (2013) 69–78.
- [10] L.N. Thrane, Form Filling with Self-Compacting Concrete, PhD thesis, Technical University of Denmark, 2007.

## **CHLORIDE DIFFUSION RESISTANCE OF LIMESTONE CALCINED CLAY CEMENT (LC3) CONCRETE**

**Quang Dieu Nguyen<sup>(1)</sup>, M.S.H Khan<sup>(1)</sup>, Arnaud Castel<sup>(1)</sup>**

(1) Centre for Infrastructure Engineering and Safety, School of Civil and Environmental Engineering, The University of New South Wales, Sydney, Australia

### **Abstract**

This paper aims to evaluate the chloride diffusion resistance of limestone calcined clay cement (LC3) concrete by accelerated chloride migration and bulk chloride diffusion techniques. Three concrete mixes have been utilized: one mix using only General Purpose (GP) cement and two LC3 concretes with 15% and 20% GP cement replaced by a constant ratio 2:1 by mass of calcined clay and limestone. The mechanical and transport properties of three concretes were investigated. LC3 concrete with 15% substitution presented the higher compressive strength than reference concrete. Moreover, LC3 concretes showed the better performance in surface resistivity comparing with plain GP concrete. Rapid chloride penetration test (RCPT), chloride migration test and bulk diffusion tests were conducted. LC3 concretes containing 15% or 20% substitution of calcined clay and limestone increased significantly the chloride diffusion resistance comparing with the reference concrete in all diffusion tests.

### **1. Introduction**

Recently, limestone calcined clay cement (LC3) has received increasing worldwide attention due to its synergic advantage of calcined clay and limestone in ternary blended cement. Mechanical properties, crystalline analysis, rheological properties, carbonation and sulphate resistance of LC3 blends were reported in numerous studies [1-7]. Specifically, Shi et al. [4, 5] investigated the chloride binding capacity of LC3 mortars and revealed that cement-metakaolin-limestone blends produced higher Friedel's salt formation, which presents the higher binding capacity of LC3 mortars.

Tuutti [8] proposed a service life model of chloride-induced corrosion including two stages: the initiation stage and propagation stage. In the first stage, chloride ingress penetrates into

steel bars inside concrete and triggers the reinforcement corrosion. Critical chloride content known as the sufficient amount of chloride to promote active corrosion is a decisive input parameter in service life model of reinforced concrete structures [9]. Therefore, corrosion resistance against chloride diffusion into concrete is critical importance for the durability of reinforced concrete in chloride bearing-environment. Due to the current literature, this work aims to evaluate the impact of calcined clay and limestone in LC3 concrete on the chloride resistance, which facilitates the utilization of LC3 concrete in practical purpose.

## 2. Experimental program

### 2.1 Materials

The limestone calcined clay cement concrete used in the study is a ternary blend of General Purpose (GP) cement, calcined clay and limestone. The GP cement complies with the Australia Standard AS 3792-2010 and is similar to ASTM Type I cement (ASTM C150/C150M). The limestone branded as Stone Dust was supplied by Boral Construction Materials Limited in New South Wales, Australia. The calcined clay used was made using a flash calcination process and supplied by Argeco, France. Table 1 shows the chemical composition of all cementitious materials determined by X-ray fluorescence (XRF).

Fine aggregate is Sydney sand with specific gravity of 2.65 and water absorption of 3.5%. Crushed basalt supplied from Dunmore quarry in New South Wales, Australia was utilized as coarse aggregate. Its characteristics comprised specific gravity of 2.8, maximal nominal size of 10mm and water absorption of 1.6%.

Table 1: Chemical composition of cementitious materials.

Chemical composition	GP cement (wt. %)	Calcined clay (wt. %)	Limestone (wt. %)
SiO <sub>2</sub>	19.74	70.42	0.39
Al <sub>2</sub> O <sub>3</sub>	4.70	22.34	0.11
Fe <sub>2</sub> O <sub>3</sub>	2.98	2.34	0.1
CaO	64.62	0.49	57.51
MgO	1.48	0.16	0.29
Na <sub>2</sub> O	0.21	0.1	-
K <sub>2</sub> O	0.64	0.19	-
TiO <sub>2</sub>	0.31	1.1	-
SO <sub>3</sub>	2.24	0.02	-

### 2.2 Concrete mix design

Three concrete mixes were fabricated to investigate the properties of concrete with the high replacement of cement by calcined clay and limestone with the ratio 2:1 by mass in this study. The details of the mix designs are shown in the Table 2. After mixing, concrete was poured into cylinders with 100mm diameter and 200mm height in two layers and a vibrating table

was utilized to compact and remove entrapped air in concrete. After surface finishing, all moulds were covered by using lids to prevent the surface from moisture loss. All concrete specimens were removed from cylinder moulds after one day. All concretes were placed into a lime-saturated water bath continuously for 7 days. After immersion in lime water, the specimens were stored in the controlled room at a fixed temperature of  $23\pm 2^{\circ}\text{C}$  and relative humidity of 50% until the testing dates.

Table 2: Mix design details of concretes.

Materials ( $\text{kg}/\text{m}^3$ )	LC3-0	LC3-15	LC3-20
Coarse aggregate	1221	1221	1221
Fine aggregate	620.8	620.8	620.8
Total binder	388	388	388
GP cement	388	329.8	310.4
Calcined clay	0	38.8	50.4
Limestone	0	19.4	27.2
Water/binder ratio	0.45	0.45	0.45
Water	174.5	174.5	174.5

### 2.3 Mechanical and transport concrete properties tests:

The compressive strength, indirect tensile strength and surface resistivity were measured at 28 days in accordance with ASTM C39, ASTM C496 and AASHTO TP95, respectively.

### 2.4 Chloride diffusion tests:

At 28 days of curing,  $100\times 200\text{mm}$  cylinders were cut into discs with 50mm of height and 100mm of diameter with 25mm sections from the top and bottom of the cylinders being removed. The 50mm discs were utilized to conduct RCPT (ASTM C1202) and rapid migration test (NT Build 492).

The bulk diffusion test was carried out following ASTM C1556 protocol by using 75mm height discs cut from standard cylinders. The discs were immersed in 16.5% NaCl solution for 35 days. After the exposure duration, concrete powders were taken every 1mm from the exposure surface to 25mm using the Germanm Profile Grinder PF-1100. The apparent chloride diffusion coefficients ( $D_a$ ) of three types of concrete were calculated by using total chloride content profile measured by Metrohm 855 Robatic Titrosampler (a potentiometric titration machine).

## 3. Results and discussion

### 3.1 Mechanical and transport properties

Table 3 presented compressive strength, indirect tensile strength and surface resistivity of three different types of concrete at 28 days. LC3-15 concrete obtained the highest compressive strength, followed by LC3-0 and LC3-20 concrete. The average compressive strength of LC3-20 concrete was approximately 94% of LC3 concrete, which indicates 20% replacement rate of calcined clay and limestone in binder was only marginally decreased the

compressive strength. The highest indirect tensile strength was 4.6MPa achieved by LC3-0 concrete whilst LC3-20 concrete reported the lowest indirect tensile strength of 4.4MPa. The substitution of calcined clay and limestone in LC3 concrete increased significantly in surface resistivity comparing with plain OPC concrete. LC3-0 concrete showed the lowest surface resistivity at 19.4kΩ-cm while LC3-15 obtained the highest value at 27.3 kΩ-cm.

Table 3: Mechanical and transport properties of LC3 concretes at 28 days.

Concrete type	Compressive strength (MPa)	Indirect tensile strength (MPa)	Surface resistivity (kΩ-cm)
LC3-0	52.3	4.6	19.4
LC3-15	58.0	4.3	27.3
LC3-20	49.3	4.4	23.3

### 3.2 Chloride diffusion tests

The results of RCPT, chloride migration test and bulk diffusion test were shown in Table 4. Fig. 1 illustrates the total chloride profiles after 35 days immersion in 16.5% NaCl solution. In all tests, LC3-15 and LC3-20 concretes outperformed significantly in comparison with LC3-0 reference concrete. Over 4500 Coulombs passed through the LC3-0 concrete in RCPT, which classifies plain OPC concrete as high chloride ion penetrability following ASTM C1202 recommendation. By contrast, LC3-15 and LC3-20 concretes reduced remarkably the total charge passed to over 50% comparing with LC3-0 concrete. Regarding rapid migration test, LC3-0 obtained the highest magnitude of non-steady-state migration coefficient at  $21.7 \times 10^{-12} \text{ m}^2/\text{s}$  whilst 15% and 20% combination of calcined clay and limestone in binder reduced the amplitude to  $12.9 \times 10^{-12} \text{ m}^2/\text{s}$  and  $11.9 \times 10^{-12} \text{ m}^2/\text{s}$ , respectively. Similarly, after 35 days of exposing in 16.5% NaCl solution, LC3-0 presented the highest amplitude of apparent chloride diffusion coefficient at  $34.4 \times 10^{-12} \text{ m}^2/\text{s}$  within three concretes while calcined clay and limestone reduced significantly the coefficient in LC3-15 and LC3-20 with the values of  $7.7 \times 10^{-12} \text{ m}^2/\text{s}$  and  $8.2 \times 10^{-12} \text{ m}^2/\text{s}$ . From figure 1, LC3-15 and LC3-20 concretes obtained the higher total chloride content to 8mm from the exposed surface than that of plain concrete. However, the total chloride content of LC3-15 and LC3-20 decrease significantly and the magnitude was lower total chloride content of LC3-0 concrete after 8mm of depth. Moreover, LC3-0 concrete manifested a continuous decrease until 25mm whilst both LC3-15 and LC3-20 concretes exhibited stable chloride content after 15mm of the exposure depth.

Table 4: Results of RCPT, rapid migration test and bulk diffusion test.

Concrete type	Charge passed (Coulombs) ASTM C1202	Non-steady-state migration coefficient ( $10^{-12} \text{ m}^2/\text{s}$ ) NT Build 492	Apparent chloride diffusion coefficient ( $10^{-12} \text{ m}^2/\text{s}$ ) ASTM C1556
LC3-0	4545	21.7	34.4
LC3-15	2104	12.9	7.7
LC3-20	2263	11.9	8.2

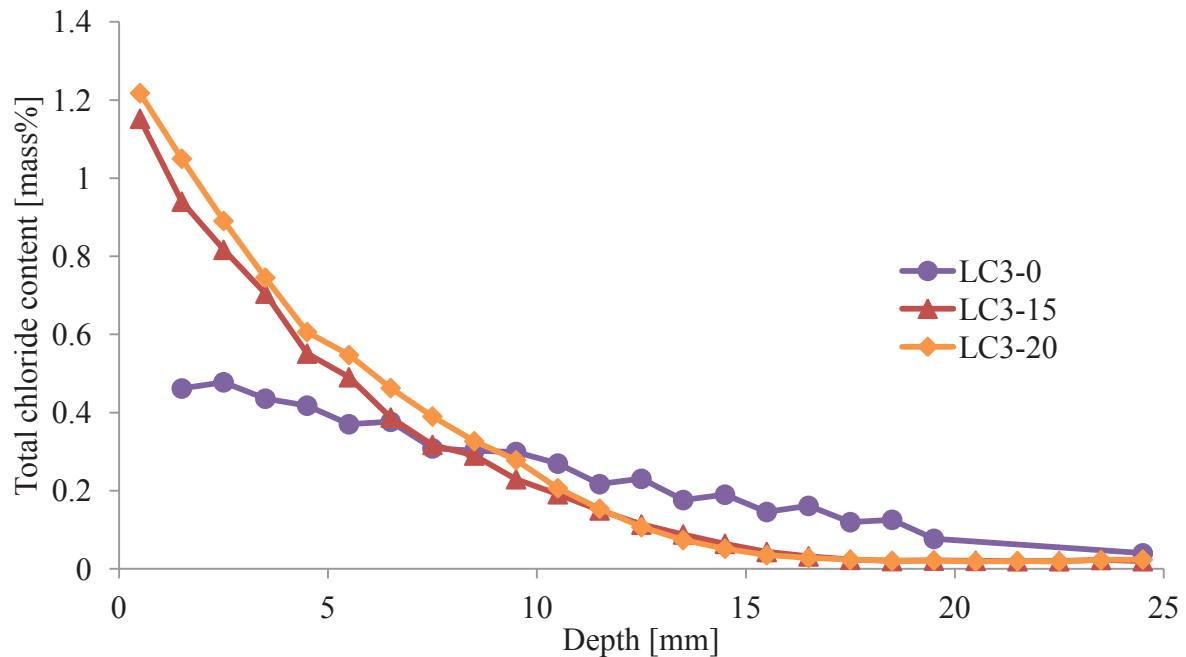


Figure 1: Total chloride content profile of LC3 concrete.

#### 4. Conclusion

The mechanical properties including compressive strength and indirect tensile strength of concrete containing calcined clay and limestone were compatible with plain concrete while the utilization of calcined clay and limestone increased the surface resistivity. Overall, three different test protocols including RCPT, chloride migration test and bulk diffusion test provided the similar results for the resistance of LC3 concretes against chloride ingress. The combination of calcined clay and limestone in binder increased significantly the chloride diffusion resistance in comparison with plain OPC concrete.

#### References

- [1] Antoni, M. et al, Cement substitution by a combination of metakaolin and limestone, *Cement and Concrete Research*, 42 (2012) 1579-1589
- [2] Tironi, A. et al, Blended Cements with Limestone Filler and Kaolinitic Calcined Clay: Filler and Pozzolanic Effects, *Journal of Materials in Civil Engineering*, 29 (2017) 1-8
- [3] Kunther, W. et al, Thermodynamic modeling of hydrated white Portland cement–metakaolin–limestone blends utilizing hydration kinetics from  $^{29}\text{Si}$  MAS NMR spectroscopy, *Cement and Concrete Research*, 86 (2016) 29-41
- [4] Shi, Z.G. et al, Role of calcium on chloride binding in hydrated Portland cement–metakaolin–limestone blends, *Cement and Concrete Research*, 95 (2017) 205-216
- [5] Shi, Z.G. et al, Friedel's salt profiles from thermogravimetric analysis and thermodynamic modelling of Portland cement-based mortars exposed to sodium chloride solution, *Cement Concrete Comp*, 78 (2017) 73-83



- [6] Vance, K. et al, Hydration and strength development in ternary portland cement blends containing limestone and fly ash or metakaolin, *Cement and Concrete Composites* 39 (2013) 93-103
- [7] Vance, K. et al, The rheological properties of ternary binders containing Portland cement, limestone, and metakaolin or fly ash, *Cement and Concrete Research* 52 (2013) 196-207
- [8] Tuutti, K. , Corrosion of steel in concrete, Swedish Cement and Concrete Research Institute, Stockholm, Sweden (1982)
- [9] Angst, U.M., Elsener, B., The size effect in corrosion greatly influences the predicted life span of concrete infrastructures, *Sci Adv* 3 (2017) 1-8

## **COMPARISON OF STANDARD CONCRETE AND ECO-CONCRETE IN RESPECT TO FUNCTIONAL, ENVIRONMENTAL AND DURABILITY PERFORMANCE**

**Joachim Juhart<sup>(1)</sup>, Rok Bregar<sup>(1)</sup>, Gheorghe Alexandru David<sup>(1)</sup>, Markus Krüger<sup>(1)</sup>**

(1) Graz University of Technology, Graz, Austria

### **Abstract**

In this study eco-concrete and in particular its paste is designed by a combined filler concept with the aim of optimizing its performance in respect to functionality, environmental impact and durability. Cement (PC) content is below the limits of traditional standards while w/c-ratio exceed such limits. The paste-mix development is based on a combination of particle packing optimization techniques, the reduction of water demand for certain flowability and designing an optimal mix of PC with properly selected, eco-friendly micro-fillers and “eco-fillers”. Subsequently the performance of the developed eco-concrete (ECO) in terms of workability, strength and durability indicators is evaluated versus a standard concrete (REF corresponding to normal concrete of RRT+ test of COST action 1404). While the functional performance of ECO in terms of workability (i.e. spread at flow-table) and strength is at least equivalent to REF, the eco-friendliness is substantially improved (global warming potential -36% and embodied energy -19%). Durability indicators, such as open porosity, water penetration depth and air permeability, show nearly equivalent performance of ECO and REF.

### **1. Introduction**

In times of climate change it is a desirable goal to reduce greenhouse gas emissions (CO<sub>2</sub>-equivalent, global warming potential, GWP) and embodied energy (primary energy demand, PE) of the worldwide most used construction material – normal concrete. Cement clinker, which represents 95% of Ordinary Portland cements (PC) and is also the main constituent of Portland composite cements, is mainly responsible for GWP and PE of normal concrete [1]. Thus enhancing the clinker-efficiency or cement efficiency in normal concrete is required to reduce GWP and PE while keeping a required performance.

Principles of “green concrete” or ecological concrete were pointed out by [1], [2], [3]. The general approach of this study is illustrated in Fig. 1. The key to success is to optimize the mix composition in terms of packing density and water demand especially of the powders that represent the paste (i.e. all granular materials with a maximum grain size  $< 125 \mu\text{m}$ ) taking into account their environmental impact. In an optimized paste PC with its high GWP and PE is partly substituted by properly selected very fine micro-fillers (MF, mean particle diameter  $d_{50} < 5 \mu\text{m}$ ) and coarser eco-fillers (EF,  $5 \mu\text{m} \leq d_{50} < 30 \mu\text{m}$ ) that have low water demand and environmental impact. In this study the fillers are properly selected limestone powders, but furthermore other stone-powders (dolomite, quartz, residuals etc.) or secondary cementitious materials, especially secondary raw materials (ground granulated blast furnace slag, fly ashes etc.) can be utilized according to the presented method if regional available. An optimized mix of PC/EF/MF requires less water for certain workability than the original granular mix (mainly PC). This is (i) due to packing optimization which corresponds to a physical filler effect of MFs placed into voids instead of interstitial water, and/or an optimized grain size distribution of all granular materials; (ii) due to a significant amount of EF which have a high sensitivity to water addition and therefore lower the water demand for certain flowability of a mix and (iii) water can be reduced by the addition of superplasticizers (SP). SP have to be used sparingly due to their high environmental impact, see Fig. 2. With such an optimized mix it would be possible to lower the w/c-ratio (water/cement) and achieve higher strength to design (ultra) high performance concrete. In our case of eco-concrete the paste-mix is ecologically optimized by substituting cement with eco-friendly fillers. Such eco-pastes typically have the same or an even higher w/c-ratio as pure PC-pastes, but have a decreased w/p-ratio (water/powder-ratio, “powder” = PC/EF/MF) at equal flowability.

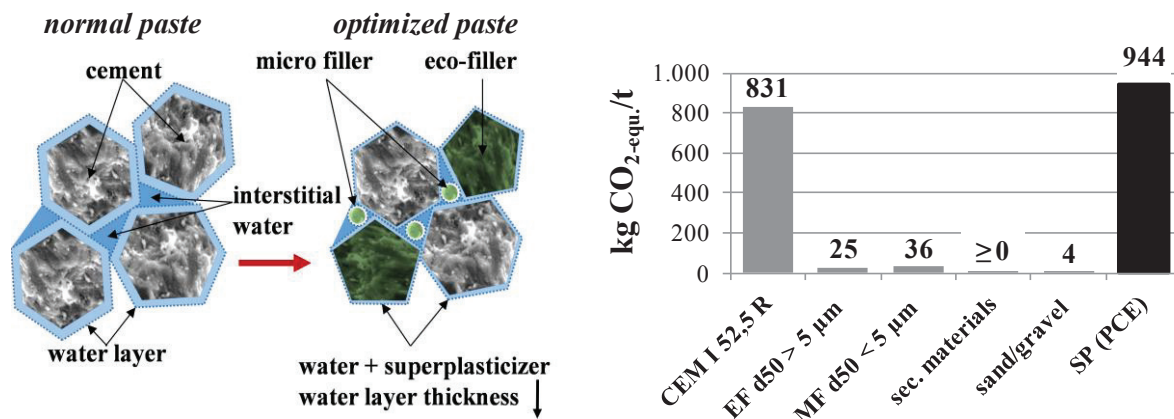


Figure 1: Optimizing paste by combined fillers. Figure 2: GWP of concrete constituents.

Traditional descriptive concepts of actual standards (e.g. EN 206-1:2014 and its national applications, e.g. ÖNORM B 4710-1:2018) prescribe a minimum cement content and maximum w/c of concrete, whereas innovative “eco-concretes” exaggerate these limits. Fortunately new, performance oriented approaches such as the “equivalent concrete performance concept” (ECPC) exist in the mentioned standards. It is shown in the outlined paper how to prove equivalent performance of a newly developed concrete (ECO) with reduced environmental impact to the reference concrete (REF) according to ECPC.

## 2. Materials and Mix Design

### 2.1 Materials and Design of the Paste

For the selection of the materials and mix-optimization of the paste the combined filler concept according to [4], [5] was applied to (i) experimentally characterize fine powders in terms of their packing density and water demand for certain flowability and (ii) to systematically optimize mix-ratios of PC, MF and EF of eco-pastes. Tab. 1 shows properties of source materials considered and of the eco-paste with a finally found mix ratio of OPC/EF/MF of 50/25/25 V.-%. Their significant properties are  $\rho$  (true density),  $d_{50}$ ,  $V_{ws}/V_p$  (water demand at the saturation point),  $\phi_{exp}$  (wet packing density) and  $V_{wf,100}/V_p$  (i.e. water demand at the onset of flow) as well as  $E_p$  (sensitivity of an individual material or mix to water addition). The parameters and the optimum mix-ratio were determined by a new combination of methods described in detail in [4], [5].  $V_{ws}/V_p$  is defined as water saturation point that is determined by the maximum power consumption of a mixer and indicative for the maximum reachable wet packing density  $\phi_{exp}$ . The flowability of mixes is tested subsequently by performing spread flow tests with increased  $V_w/V_p$ -ratios (volumetric w/p-ratios) with a Hägermann cone on a dry glas plate according to [6].  $V_{wf,100}/V_p$  represents the water demand at the onset of flow (where the spread flow  $f_{100}$  is identical to the base diameter of the lifted cone, i.e. 100 mm) and  $E_p$  is the sensitivity of the mix to water addition. By  $E_p$  different powders can be compared with respect to flowability. The lower  $E_p$ , the easier a material flows by adding a certain increment of water. Subsequently the strength of hardened pastes with different mixes of PC/EF/MF at constant spread flow is determined by compressive test according to EN 196-6. This additional information can be used for selecting a suitable mix-ratio of an eco-paste with equal strength to a pure OPC reference paste.

The data for the environmental indicators GWP and PE are shown in Tab. 2 and Fig. 2. They were taken from equivalent materials published in [4], [5] calculated by the method of Life Cycle Assessment (LCA) according to ISO EN 14044:2006 using SimaPro software (v. 7.3) and the ecoinvent database [7]. Fig. 2 shows that PC exceeds the environmental impact of finely milled stones, aggregates and secondary raw materials (GGBS, FA) by far. Superplasticizers possess very high GWP and PE due to the energy demand of the production according to [8].

Table 1: Properties of granular source materials of the paste and its optimum mix.

Type	$\rho$ (g/cm <sup>3</sup> )	$d_{50}$ (μm)	$V_{ws}/V_p$ (-)	$\phi_{exp}$ (-)	$V_{wf,100}/V_p$ (-)	$E_p$ (-)
CEM I 52.5 N SR3	3.17	10.5	0.75	0.57	0.99	0.102
EF (limestone)	2.70	6.9	0.68	0.60	0.79	0.047
MF (limestone)	2.73	2.2	0.61	0.62	0.63	0.013
Paste Mix (PC/EF/MF=50/25/25)	2.94	7.5	0.61	0.62	0.61	0.011

### 2.2 Concrete Mix Design

Concrete mixes REF and ECO were designed with the same volume of paste, same sieve line of aggregates as well as maximum grain size of 16 mm with mix-ratios according to Tab. 2. Equal SP-type and low SP-content was used for ECO and REF to minimize SP environmental impact. However, ECO had a significantly lower PC content and w/p-ratio but higher packing density than REF. Despite a significantly higher w/c-ratio of ECO than REF, flowability and

strength were nearly the same. REF corresponds to the concrete used in the extended round robin test program of COST action 1404 “Towards the next generation of standards for service life of cement based materials and structures”. The aggregates used had a not neglectable water adsorption (WA<sub>24</sub>-coefficient of sand 0/4 is 0.77 wt.%, of gravel 4/11 is 2.61 wt.%, of gravel 8/16 is 2.25 wt.%) which had to be considered as follows. The gravel was added fully water-saturated to the mix, but the sand was added in dry state. Effective water was assumed to correspond to the added water minus adsorbed water of the sand plus water content of SP, which leads to an effective w/c of 0.52 for REF and 0.58 for ECO.

Table 2: GWP, PE of concrete constituents as well as concrete mix-composition.

type	GWP (kg CO <sub>2</sub> -equ./t)	PE (MJ/t)	REF (kg/m <sup>3</sup> )	ECO (kg/m <sup>3</sup> )
CEM I 52.5 N SR3	831	4030	320.0	208.3
EF limestone	25	717	-	104.2
MF limestone	35	1005	-	104.2
sand 0/4 mm, dry	4	58	830.0	827.1
gravel 4/11 mm, fully saturated	4	58	449.0	447.4
gravel 8/16 mm, fully saturated	4	58	564.0	562.0
SP (80% water content)	944	29150	1.4	1.4
added water	0	0	172.4	126.4
effective water	0	0	167.1	121.2
w <sub>eff</sub> /c	-	-	0.52	0.58

### 3. Testing and Evaluation Methods

The performance of the produced concrete mixes was tested in terms of workability, strength and durability indicators and of environmental impact was evaluated. The flow-table spread (i.e. spread diameter on the flow-table after defined compaction according to EN 12350-5:2009) of the mix 10 min after water addition (spread<sub>10</sub>) was tested as well as the value 30 min after water addition (spread<sub>30</sub>). The compressive strength was tested on concrete cubes (150 mm, n = 3) according to EN 12390-3:2009 - stored under water until testing - at an age of 1 day (f<sub>cm, 1d</sub>) and 28 days (f<sub>cm, 28d</sub>). Open porosity was determined in accordance to EN 1936:2007 (water uptake of cubes ~50 mm after complete drying under partial vacuum related to the volume of specimen). The depth of water-penetration was tested according to EN 12390-8:2009 with specifications according to ONR 23303:2010 on water cured concrete prisms (200\*200\*120 mm<sup>3</sup>) at the age of 28d. Pressured water was applied to one surface in 2 steps of 1.75 and 7.0 bar up to 3 and 14 days, respectively. Afterwards each specimen was split, and the water penetration depth was measured. Air permeability was tested with two different testing procedures. First testing procedure was carried out in accordance to Swiss Standard SIA 262/1:2013 “air permeability on site” with a “PermeaTORR” device [9] on concrete cubes (150 mm). Specimen were stored under water to an age of 28d, then dried at 50°C for 8d, then stored at 65% r.h. and 20°C until testing at an age of 62 d. The rate of increase of pressure in the inner chamber due to unidirectional air-flow through the cover concrete was measured and directly linked to the calculated coefficient of air-permeability

$K_{SIA}$  [9]. For the second procedure a “Testing” bubble counter [11] was used and air permeability was tested in principle according to a RILEM specification [10]. Cylindrical specimen were casted ( $d=150$  mm, cut to  $h=50$  mm,  $n=2$ ), stored under water to an age of 28d, then dried at  $50^{\circ}\text{C}$  until 56d, then stored at 65% r.h. and  $20^{\circ}\text{C}$  until testing at an age of 91 d. Specimen were sealed on their sides. An overpressure was applied on the bottom of the specimen, so that a certain volume of inert gas (in our case air was used) migrated through the whole concrete disk. It was measured by the rate of ascent of a soap bubble at different pressure steps (2.5, 3.0, 3.5 bars). Corresponding coefficient of permeability  $K_{RIL}$  was calculated as the mean coefficient of the three pressure steps [10], [11]. The ecological impact of  $1\text{ m}^3$  fresh concrete was calculated according to the values for GWP and PE of the source materials and their content in fresh concrete to compare REF and ECO.

#### 4. Results and Discussion

Tab. 3 shows tested fresh- and hardened concrete properties as well as durability indicators. The aim of improving ecological performance while keeping workability and strength at the level of the reference concrete was reached. GWP of ECO was reduced up to 36% and PE up to 19% compared to REF. Very soft consistency of the fresh concrete just after mixing was achieved (spread\_10 equal to  $52\pm 2$  cm). However ECO loses its consistency faster than REF, as it can be read from the values spread\_30 in relation to spread\_10 of both mixes. The reason may be the lower w/p-ratio and the selected SP-type. Changing it from a highly liquefying type to a more consistency-keeping type could compensate the effect. The 1d-strength of ECO is significantly higher than that of REF, whereas the 28d-strength is equal, which means low w/p and a high content of MF accelerate strength development. This can be seen as an advantage, for example for precast applications, but may be disadvantageous for applications to massive construction elements regarding temperature rise and early shrinkage.

Table 3: Tested concrete properties with their standard deviation and calculated GWP and PE.

	unit	REF	ECO
flow-table spread_10	cm	54.3±0.3	50.5±1.3
flow-table spread_30	cm	43.5±0.5	37.0±0.0
1-day strength $f_{cm, 1d}$	N/mm <sup>2</sup>	11.3±1.1	17.5±0.4
28-day strength $f_{cm, 28d}$	N/mm <sup>2</sup>	55.4±2.2	56.2±3.5
open porosity	%	13.4±0.5	11.5±0.5
water penetration depth	mm	15.0±1.67	17.8±0.3
air permeability coefficient $K_{RIL}$	$10^{-16}\text{ m}^2$	1.03±0.19	0.26±0.01
air permeability coefficient $K_{SIA}$	$10^{-16}\text{ m}^2$	0.02±0.01	0.03±0.00
GWP	kg/m <sup>3</sup>	282	180
PE	MJ/t	1715	1400

Regarding durability performance, a differentiated view is necessary. ECO's open porosity and gas permeability coefficient  $K_{RIL}$  is lower than REF's. It is the other way round regarding air permeability coefficient  $K_{SIA}$  and water penetration depth. However, water penetration depth of REF and ECO are below limits of the Austrian Standard ÖNORM B 4710-1:2018

(class XW1 limits 50 mm, XW2 25 mm). Regarding air permeability, Torrent [9] classifies REF and ECO to “low permeability” ( $K_{SIA} 0.1-1.0 \text{ E-6 m}^2$ ). Further durability measures as carbonation depth (not tested explicitly) only correlate to limited extent to tested permeability indicators, as additional aspects (as for example the  $\text{Ca}(\text{OH}_2)$  puffer capacity) have to be considered.

## 5. Conclusions and Outlook

In this study eco-concrete and in particular its paste is designed by a combined filler concept with the aim of optimizing its performance in respect to functionality, environmental impact and durability. PC content is below the limits of traditional descriptive standards while w/c-ratio exaggerates such limits. The performance of the developed eco-concrete (ECO) in terms of workability, strength and durability indicators is evaluated versus a standard reference concrete (REF). While the functional performance of ECO in terms of workability (i.e. spread at flow-table) and strength (i.e. early age and 28d strength) is at least equivalent to REF, the eco-friendliness is substantially improved (GWP -36% and PE -19%). Durability indicators – open porosity, water penetration depth and air permeability – overall show nearly equivalent performance. In detail, water penetration and air permeability tested according to RILEM are lower of ECO than of REF while for water penetration and air permeability according to SIA it is the opposite. Further investigations on a larger number of specimen, mix variations as well as durability aspects are pending to derive clear relationships between mix-parameters and durability indicators and to clarify the significance of indicators and their testing methods.

## References

- [1] Glavind, M. et al, Guidelines for green concrete structures, International Federation for Structural Concrete (2012)
- [2] Fennis-Huijben, S.A.A.M., Design of ecological concrete by particle packing optimization” PhD thesis, Delft University of Technology (2010)
- [3] Proske, T et al, Eco-friendly concretes with reduced water and cement contents — Mix design principles and laboratory tests, *Cem Concr Res* 51 (2013), 38–46
- [4] Juhart J et al, Durable Eco-Crete in Austria: Materials and Mix Design Methods, *Proc. International Symposium - Environmental Friendly Concrete - Eco-Crete* (2014), 311–8
- [5] Juhart, J et al, A new combined filler concept for eco-concrete, *Proc. of 14th International Congress on the Chemistry of Cement (ICCC 2015)* (2015)
- [6] Okamura, H. and Ozawa, K., Mix design for self-compacting concrete, *Concrete library of JSCE* (1995)
- [7] EcoinventCenter, ecoinvent database v2.2: Swiss Center for LCA (2010)
- [8] Schiessl, P. and Stengel T., Nachhaltige Kreislaufführung mineralischer Baustoffe (2006), in: Haist, M. et al, „Entwicklungsprinzipien und technische Grenzen der Herstellung zementarmer Betone“, *Beton- und Stahlbetonbau* 3 (2014), 202–215
- [9] Materials Advanced Services Ltd, Torrent, R., User manual PermeATORR, <http://www.m-a-s.com.ar>, 22.05.2018
- [10] RILEM TC 116-PCD, Permeability of Concrete as a Criterion of its Durability. *Materials and Structures* 32 (1999)
- [11] TESTING Bluhm & Feuerherdt GmbH, Betriebsanleitung Prüfeinrichtung zur Messung der Luftpermeabilität, <https://testing.de/de/2.0331>, 22.05.2018

## **COMPRESSIVE STRENGTH DEVELOPMENT OF FLY ASH CONCRETES CURED UNDER DIFFERENT CONDITIONS**

**T. Altuğ Söylev<sup>(1)</sup>, Turan Özturan<sup>(2)</sup>**

(1) Gebze Technical University, Kocaeli, Turkey

(2) Boğaziçi University, Istanbul, Turkey

### **Abstract**

The use of fly ash as a cement replacement material brings economic, environmental advantages to concrete technology as well as some improvements in the properties of concrete. However, fly ash concrete may not reach specified strength values because of slower pozzolanic reaction and consequently its use in concrete is limited. Effective curing can lead to higher use of fly ash in concrete, by enabling higher strength at earlier ages. In the present study, the effect of three different curing regimes on the compressive strength (3, 7, 28, 56 and 91 days) of concretes with 0, 15, 30 and 45% fly ash replacement ratios. The ratios represent fly ash percentages with respect to the total binder content. The curing regimes were 1) air curing; 2) one week 30°C water curing + air curing; 3) one week 20°C water curing + air curing. Specimens with hot water curing (no 2) yielded higher results until 28 days when compared to those with mild water curing (no 3). The air curing caused lowest results with significant differences compared to water curing regimes. Water curing was effective in closing the gap between concretes with and without fly ash. However, beyond 15% cement replacement ratio, fly ash concretes had lower strength, even at 91 days.

### **1. Introduction**

The use of fly ash as a cement replacement material provides important advantages in many applications, beside the economic and environmental effect, by reducing the heat evolution, by improving durability etc. However, cement replacement ratio by fly ash has limitations due to the slower strength development of fly ash compared to Portland cement, which causes lower strength, particularly at early-ages. This effect was shown in the study of Gopalan et al. with the concretes containing up to 80% fly ash [1]. The prediction of compressive strength at different ages can be successfully made by using the maturity method. However, the



parameters used in this method are well applied to the Portland cement concrete exposed to water curing of different temperatures. For different binders under different curing conditions, the method may not be so straightforward. Xu et al. [2] who used the activation energy and equivalent time for maturity calculation, indicate that for high volume fly ash concrete they should be modified. Maturity approach worked better after applying different constants for different mineral additions in the study of Boubekeur et al [3]. Eren [4] calculated the parameters of the maturity method for concretes with 30% and 50% cement replacement by fly ash cured at five different curing temperatures and tested at five different ages. The results show that the parameters are different in each mix and condition, therefore they may be considered as material properties. The present study presents the effect of different curing conditions on the compressive strength development of concretes with and without fly ash and a detailed combination of temperature-age. The results trends were analyzed by interpreting the principles of the maturity method.

## 2. Experimental study

Three cubes of 150 mm were used to test the compressive strength of four different concrete mixes (Table 1) (0, 15, 30, 45% fly ash by mass of total binder) at three different curing conditions (Twelve concretes in total). Curing Condition 1 was air curing in hot and very humid laboratory conditions. Curing 2 and Curing 3 consist of 7-days water curing (30°C and 20°C respectively) and air curing until testing. CEM I 52.5 Portland cement and Class C fly, 5mm river sand, 10mm and 20mm basaltic crushed stones, naphthalene sulphonate based superplasticizer were the materials of concrete. The target slump of 22 cm was obtained by slightly adjusting the superplasticizer content. Compressive strength was tested at 3, 7, 28, 56 and 91 days after casting. The letters and the first digits in Table 1 indicate the replacement ratio by mass of total binder content and the third digit in Table 2 shows the curing condition.

Table 1: Concrete mixes.

kg/m <sup>3</sup>	FA00	FA15	FA30	FA45
Cement	430	365	300	235
Fly ash	0	65	130	195
Water	215	215	215	215
C agg (20mm)	564	557	550	540
C agg (10mm)	562	553	548	539
Sand	669	658	652	640
Superplasticizer	2.15	2.17	2.11	2.12

## 3. Results and Discussion

As expected, water cured specimens had significantly higher strength development and strength decreased with the increase of fly ash content (Figs. 1-4). The 7-days strength was equalized in 3 days and the 28-days strength was equalized in 7 days when hot water curing was applied instead of air curing in concretes with and without fly ash. The strength of FA451

was only 41% of the highest strength at 28 days (FA002). There was partial strength recovery at 91 days and the ratio of the strength recovery was a function of fly ash content in concrete.

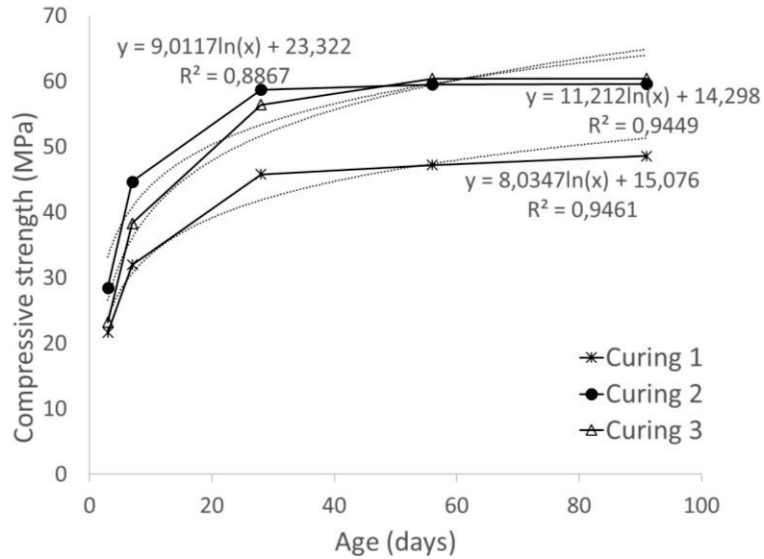


Figure 1: Strength development of FA00 at different curing conditions.

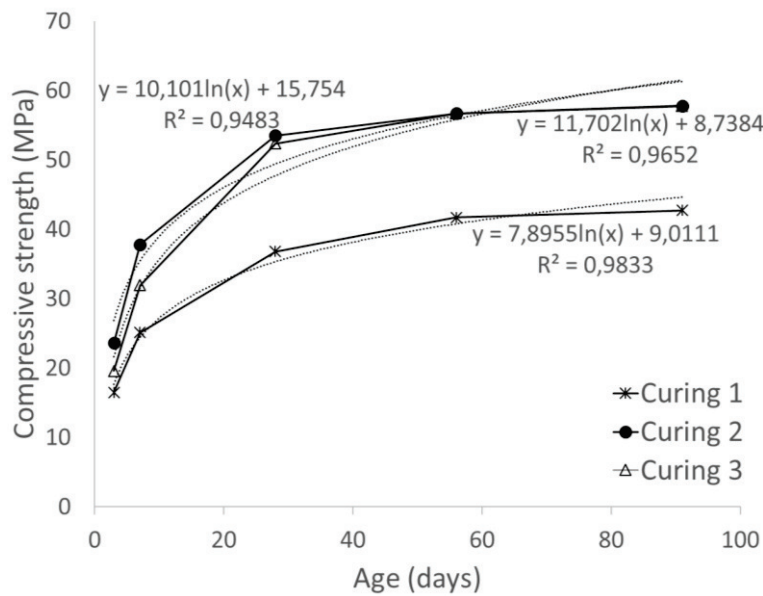


Figure 2: Strength development of FA15 at different curing conditions.

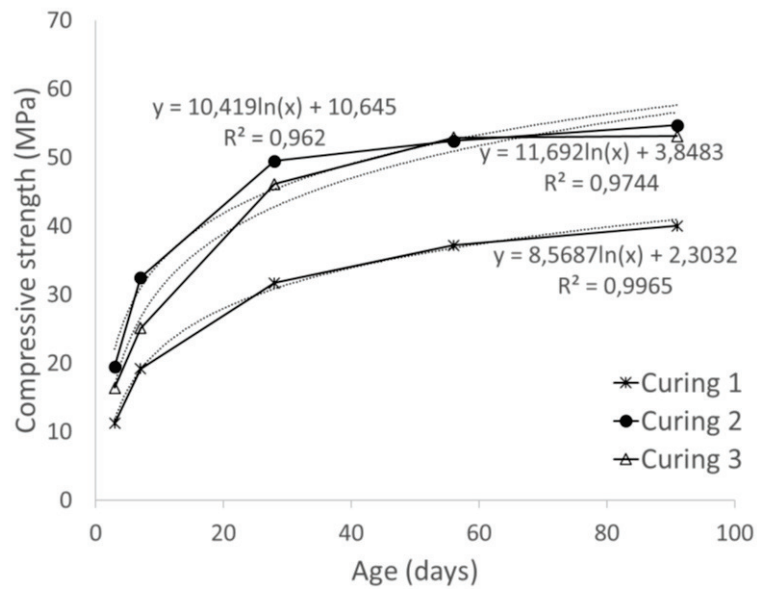


Figure 3: Strength development of FA30 at different curing conditions.

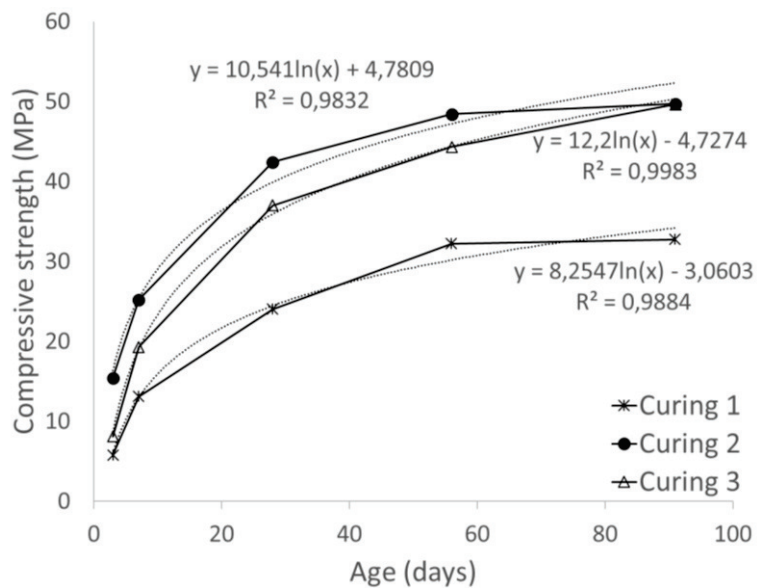


Figure 4: Strength development of FA45 at different curing conditions.

Control concretes exposed to Curing 3 had lower strength at early ages but they crossed over the strength of control concretes exposed to Curing 2, towards 56 days (Fig. 1). This behavior supports the well-known crossover effect for concretes cured at lower temperature at early ages. However, the crossover effect decreased (Fig. 2) and then disappeared (Figs. 3 and 4) with the increase of fly ash content, which emphasizes the importance of hot water curing for fly ash concrete.

Water curing led to higher rate of strength gain up to 28 days for fly ash concretes with and without fly ash (Figs. 1-4). However, the rate of strength gain up to 28 days decreased with increasing fly ash content (Figs. 2-4). In order to quantify this behavior, logarithmic trend lines with equation and R-square value were added to the strength development curves. For concretes without fly ash, the increase up to 28 days is sharp but very low after 28 days and the strength is almost constant until 91. Therefore, the strength development graph appears like the combination of two separate lines with different slopes rather than a continuous curve (Fig. 1). As a result of this, the strength development of concretes without fly ash does not fit well the logarithmic curve as indicated by the low R-square values. With an increase in fly ash content, the strength development becomes more continuous up to 91 days and it starts to fit better to the logarithmic curve (Figs. 2-4). On the other hand, the difference in R-square values between different curing conditions is insignificant at higher cement replacement ratios as the strength development becomes more and more slower even in Curing 2 and 3 (Figs. 3-4).

The ratio of the strength to 91-days strength as a percentage,  $S/S_{91}$ , for concretes without fly ash is given in Table 2. It is interesting to note that the rates of strength gain of concretes exposed to Curing 1 and Curing 3 are very close at almost all ages. The strength at Curing 3 was higher due to the higher availability of water which can react with a higher amount of Portland cement. On the other hand, as the mechanism of hydration is the same, the increase of  $S/S_{91}$  with age was similar despite the difference in the amount of hydrated cement. However, in fly ash concretes the mechanism of hydration is different. As pozzolanic reaction depends on the availability of  $\text{Ca(OH)}_2$ , when more Portland cement is reacted, the rate of the pozzolanic reaction will be higher. Consequently, the rate of strength gain at Curing 3 is higher than that at Curing 1.

This behavior can be explained with the principles of the maturity method. The maturity function, which is simply the product of temperature and age, is given by the following equation (Eq. 1) for the isothermal conditions:

$$S = S_{\infty} \frac{k_T(t-t_0)}{1+k_T(t-t_0)} \quad (1)$$

where  $S$  is strength at any age,  $S_{\infty}$  is the limiting strength at infinite age,  $k_T$  is the rate constant,  $t$  is time and  $t_0$  is the initial time below which there is no strength development. The rate constant increases with increasing curing temperature. The maturity method is based on the calculation of a relative strength rather than strength, which is given by the ratio  $S/S_{\infty}$ .

The limiting strength can be assumed to be theoretically independent of the curing temperature. However, this generalization cannot be directly applied in the present study for two reasons. First, concretes cured in air curing can practically never reach the same strength as that of water cured specimens. It is well known that the water/cement ratio does not affect the rate constant significantly. The air cured specimens can be considered as different concrete mixes compared to the water cured specimens since the cement available for hydration is lower as in the case of a concrete with low water/cement ratio. Consequently, the rate constant can be similar for Curing 1 and 3 but the limiting strength is different. Second, high volume fly ash concretes need hot water curing to complete their hydrations so fly ash

concretes cured in mild and hot water can also be considered as different mixes in the evaluation of maturity. As the mechanism of hydration and the effect of curing are different, the rate constants and the limiting strengths are different for concretes with and without fly ash. Therefore, the approach used to evaluate the rate of strength gain by taking the ratio  $S/S_{91}$  for each concrete mix individually at different ages looks appropriate for evaluating the rate of strength gain (Table 2 and Figs. 1-4).

Table 2:  $S/S_{91}$  (%) at different ages for concretes exposed to different curing conditions.

Age (days)	<b>3</b>	<b>7</b>	<b>28</b>	<b>56</b>	<b>91</b>
FA001	44	66	94	97	100
FA002	48	75	98	100	100
FA003	38	63	93	100	100

#### 4. Conclusion

The rate of strength gain with respect to 91 days strength was similar in the concrete mixes without fly ash at Curing 1 and Curing 3. In hot water curing (Curing 3), the rate was higher. Similar trend was observed for fly ash concretes, but water cured specimens had higher rate. The lower rate of strength gain was reflected to the shape of the logarithmic trendline and the more continuous strength development before and after 28 days resulted in better fitting to the trendline. The strength of specimens cured in mild water crossed over the strength of the specimens cured in hot water after 28 days. For fly ash concretes, the crossover effect was not observed. Hot water curing looks necessary to compensate low strength development of fly ash concretes. The rate of strength gain was related to the curing type, curing temperature and fly ash content. The findings can be useful in the application the maturity method, particularly for high volume concretes exposed to different curing conditions.

#### References

- [1] Gopalan, M. K. and Haque, M. N., Strength development of fly ash concretes, *Mater Struc* 19 (1986), 33-37
- [2] Xu, G., Tian, Q., Miao, J., Liu, J., Early-age hydration and mechanical properties of high volume slag and fly ash concrete at different curing temperatures *Constr Build Mater* 149 (2017) 367-377
- [3] Boubekeur, T., Ezziane, K., Kadri, E.H., Estimation of mortars compressive strength at different curing temperature by the maturity method, *Constr Build Mater* 71 (2014) 299-307
- [4] Eren, Ö., Strength development of concretes with ordinary Portland cement, slag or fly ash cured at different temperature, *Mater Struc* 35 (2002) 536-540.

## **DEVELOPMENT OF A HEATING MORTAR BLOCK SYSTEM FOR SNOW MELTING THROUGH QUASI MICROWAVES**

**Yosuke Ito<sup>(1)</sup>, Shinji Kawabe<sup>(1)</sup>**

(1) Nagoya Institute of Technology, Aichi, Japan

### **Abstract**

Snow shoveling requires effort in regions of snowfall. There are various types of snow removal systems that do not depend on manpower; however, they exhibit some problems. We can solve these problems by developing a snow melting system containing heating mortar blocks that convert electromagnetic waves into thermal energy. This system utilizes the electric arc furnace oxidizing slag, which is aggregated as an electromagnetic absorption material. Thus, this system can be expected to reduce the environmental load. Moreover, this system can melt snow more quickly as compared to that observed using the conventional methods. This study exhibits the snow melting performance of the heating mortar block system.

### **1. Introduction**

Snow shoveling requires considerable effort in regions of snowfall. Some elderly people living in such areas cannot remove snow on their own. There are various types of snow removal systems that do not depend on manpower; however, they exhibit some problems. A snow melting system with electric heating cables requires its heat source cables to be buried deep inside the ground to avoid being cut by the load. Therefore, it requires a longer time to melt the snow and makes the running cost high. A snow melting system by groundwater sprinkling pollutes the road with contained minerals in the groundwater. The system also causes ground subsidence by overusing the groundwater. The snow-melting agent contained chloride that causes the rusting of iron structures. Therefore, a new system is expected to be invented that can cause the snow to melt more quickly as compared to that observed in the other existing systems.

We are able to solve these problems by developing a snow melting system containing heating mortar blocks that convert electromagnetic waves into thermal energy. Fig. 1 depicts the

overview of the heating mortar block system to melt snow. This system utilizes a microwave of a frequency of 2.45 GHz. Oscillators with 2.45-GHz frequency are extensively available at a reasonable price because they are produced in bulk as components of microwave ovens in Japan. Moreover, as compared to the conventional methods, this system can melt snow more quickly. This system obtains the heat that is required to melt snow in the following three steps. (1) The oscillator generates the electromagnetic waves of 2.45-GHz frequency. (2) The electromagnetic waves are leaked from the slot on the leaky waveguide. (3) This microwave is irradiated by heating the mortar blocks.

Fig. 2 exhibits the structure of the heating mortar block, which comprises the following three layers: (1) a base layer (without electromagnetic absorption ability) using sand as an aggregate, (2) an electromagnetic absorption material layer using electric arc furnace oxidizing slag as an aggregate, and (3) an electromagnetic shielding material layer using the arranged steel fibers. The electromagnetic waves are transmitted through the base layer and are absorbed by the electromagnetic absorption material layer and are further converted into heat. The electromagnetic waves that are not absorbed are reflected by the electromagnetic shielding material layer and are prevented from leaking outside.

The proposed system melts snow using the heating mortar blocks that generates heat from electromagnetic absorption. In contrast, the conventional snow melting system melts snow using the heat generated from the electric heating cables. The electric heating cables that are used as heat sources are buried deep inside the ground to avoid disconnection. However, electromagnetic absorption materials, used as heat sources, and leaky waveguides, which transmit electromagnetic waves, exhibit only a minor risk of disconnection. Therefore, because the heat source of a heating mortar block can be placed near to the ground surface, the proposed system can cause the snow to efficiently melt in a short time.

As depicted in Fig. 2, (1) the base layer is mortar with sand as an aggregate, which exhibits almost no electromagnetic absorption ability. Hereinafter, “mortar with sand as an aggregate” is referred to as “the sand mortar.” (2) The electromagnetic absorption material layer exhibits an ability to absorb electromagnetic waves due to the presence of electric arc furnace oxidizing slag as an aggregate. Hereinafter “mortar with electric arc furnace oxidizing slag as an aggregate” is referred to as “the slag mortar.” (3) The electromagnetic shielding material layer is a mortar that contains steel fibers that are arranged to exhibit an electromagnetic shielding ability. This study exhibits the snow melting performance of the heating mortar block system.

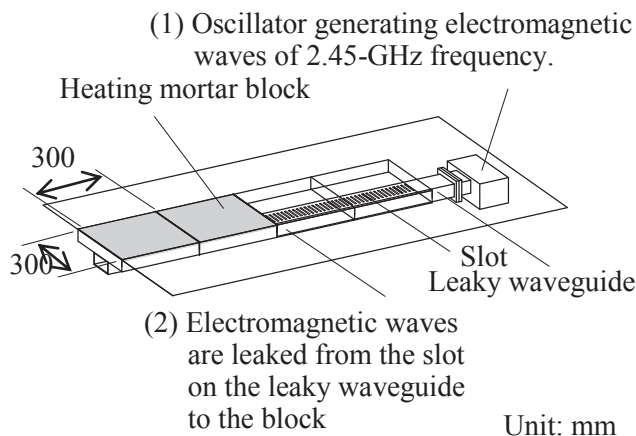


Figure 1: The heating mortar block system

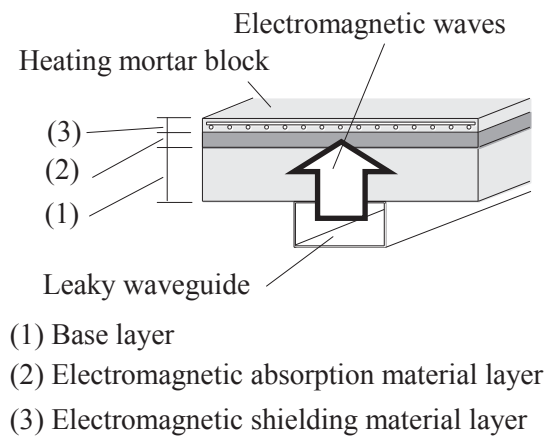


Figure 2: Heating mortar block

## 2. Design theory

If the absorbed power coefficient by the sample is  $S_0$ , the input power is  $P$  (W), irradiating time is  $t$  (s), and heating value is  $Q$  (J:W·s), Eq. (1).

$$Q = |S_0|^2 P \cdot t \quad (1)$$

Eq. (1) depicts the relation between the absorbed power coefficient and the heating value, and it can be observed that the heating value,  $Q$ , increases when the absorbed power coefficient increases. Therefore, an electromagnetic wave absorber can be utilized as a heating material.

## 3. Sample

### 3.1 Heating mortar block

Slag mortar contains electric furnace oxidizing slag as an aggregate. The electric furnace oxidizing slag is an industrial by-product that is generated when the recycled iron is produced. Hereinafter, “electric furnace oxidizing slag” is referred to as “slag.” The composition of the slag is presented in Tab. 1. Because the slag exhibits a crystal structure containing iron oxide, it depicts a characteristic of magnetic loss (absorption) of the electromagnetic waves [1].

Slag and sand mortar are manufactured using the optimum mix proportion and thickness [2] to enhance the electromagnetic absorption ability. The mix proportion of the slag and sand mortar is presented in Tab. 2. The cement that has been used is the ordinary Portland cement. The thickness of the slag mortar is 8 mm, and the thickness of the sand mortar is 29 mm, considering that the mortar contains water. A waterproofing agent is added to the cement to prevent frost damage and change in the electromagnetic absorption ability due to the large amount of water absorption. The composition of the waterproofing agent is presented in Tab. 3. The cut wire netting [3] for shielding the electromagnetic waves is installed on the slag mortar, and a mortar having a thickness of 8 mm is coated on the cut wire netting to form a shielding material layer. The sample is dried for 1 day in air and is cured underwater for more than 5 days. Further, the sample is dried until it reaches an absolute dry state in a thermo-hygrostat at 100 °C. The heating mortar block is a square having a side of 300 mm.

### 3.2 Leaky waveguide

The leaky waveguide [4] is depicted in Fig. 1. There are slots on the top surface of the leaky waveguide. The width of the slot is 1.6 mm, and the length is 30 mm; the interval is 10 mm.

### 3.3 The Snow melting system using the heat generated from the electric heating cables

The concrete to bury the electric heating cables exhibits a width of 300 mm, a length of 2400 mm, and a thickness of 150 mm. Four electric heating cables were buried at intervals of 70 mm in the length direction at a depth of 50 mm from the upper surface of the concrete. The mix proportion of the concrete is presented in Tab. 4.



#### 4. Measurement

The snow melting performance is clarified by performing the melting snow measurement. This experiment is performed using both the heating mortar block system (Fig. 1) and the electric heating cable system to melt the snow. The experimental setup is depicted in Fig. 3. To prevent the heating mortar block from affecting the electromagnetic wave leakage performance of the slot, as depicted in Fig. 4, the heating mortar blocks are installed upward at approximately 60 mm from the leaky waveguide using the U-shaped groove.

Each area that is capable of snow melting is approximately  $0.3 \times 2.4$  m. Eight heating mortar blocks are installed one row above the leaky waveguide.

The snow melting performance is evaluated by the area at which the snow was melted and the amount of melted snow. To confirm the area at which the snow was melted, photographs of the snow melting condition were captured at an interval of 30 minutes, as depicted in Fig. 5, and were binarized; further, the area of the road surface that was exposed by melting the snow is detected. The amount of melted snow is calculated based on the amount of remaining snow. As depicted in Fig. 6, in the cross section and a direction perpendicular to the leaky waveguide, the heating mortar block and concrete with electric heating cable are divided into six, and the amount of snowfall at the division boundary is measured at an interval of every 30 minutes. We calculate the sum of decreases of the snow cover at the boundary of each division and assume this to be the “snow melt amount.”

The electric power consumed in each area that capable of snow melting by the heating mortar block system and the electric heating cable system is 200 W. The measurement time is 330 minutes. The conditions to perform the snow melting measurement are presented in Tab. 5.

#### 5. Results and consideration of measurement

Fig. 7 depicts the relation between the ratio of the snow melting area and the measurement time. Snow melts quickly due to stirring effect caused by walking on snow. Therefore, the measurement time until walking becomes possible is compared. A person can walk easily if the width of the road surface is about 150 mm or more. Thus, comparing the time required to melt the snow accumulated on 50% of the total area can help us to judge the superiority and

Table 1: Chemical components of the slag (Weight %)

CaO	SiO <sub>2</sub>	MnO	MgO	FeO	Fe <sub>2</sub> O <sub>3</sub>	Al <sub>2</sub> O <sub>3</sub>	Cr <sub>2</sub> O <sub>3</sub>	TiO <sub>2</sub>	P <sub>2</sub> O <sub>5</sub>	Total
19.53	12.92	5.66	4.57	19.67	24.13	8.40	1.97	0.42	0.332	97.60

Table 2: Mix proportion of mortar (Weight ratio)

	Cement	Slag	Sand	Water	Waterproof agent
Slag mortar	100	150	-	45	0.3
Sand mortar	100	-	300	45	0.3

Table 3: Mix proportion of waterproof agent (Weight ratio)

Mixture such as higher fatty acid salt	Poly(oxyethylene) nonylphenyl ether	Water
30–35	< 2.0	64–69

Table 4: Mix proportion of concrete (Weight ratio)

Cement	Sand	Gravel	Water	air-entraining and water-reducing admixture	air-entraining admixture
100	163	108	54	1.0	0.5

inferiority of the snow melting performance. In the heating mortar block system, the road surface is exposed in 90 minutes, and the snow melting area is observed to become more than 50% of the total area in approximately 170 minutes. However, the electric heating cable system requires approximately 205 minutes because the snow melting area exceeds 50% of the total area. Because the power consumption is proportional to the measurement duration, the heating mortar block system can reduce the electric energy by approximately 17% as compared with that observed in the electric heating cable system.

Fig. 8 depicts the relation between the snow melting amount and the measurement duration. Throughout the measurement, the heating mortar block system exhibits more snow melting and better snow melting performance than those exhibited by the electric heating cable system. Fig. 9 depicts the photograph that was captured 150 minutes after initiating the measurement,

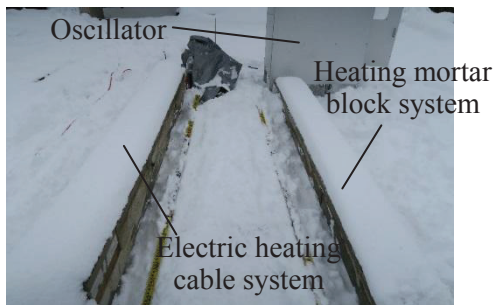


Figure 3: Snow melting experiment equipment

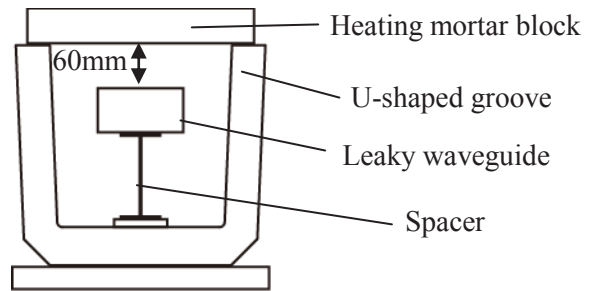


Figure 4: Cross sectional view of the heating mortar block system for melting snow

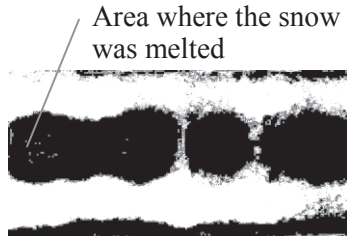


Figure 5: Binarized photograph

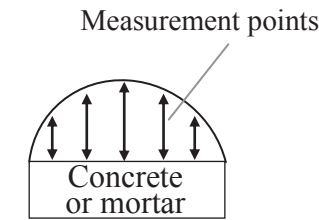


Figure 6: Measurement points

Table 5: The conditions of snow melting measurement

Place	Fukui Prefecture in Japan
Measuring date	Jan. 16, 2018
Temperature	0 °C
Snow depth	100 mm

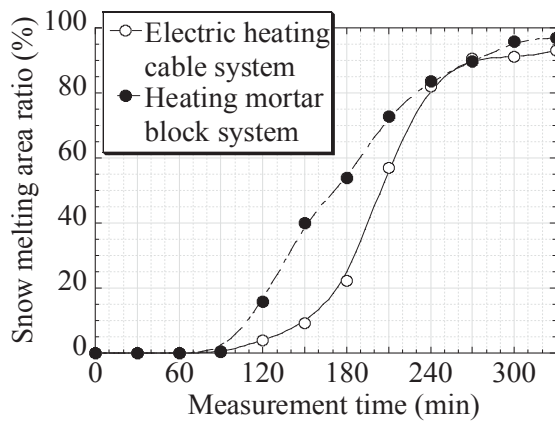


Figure 7: Relation between the ratio of snow melting area and measurement duration

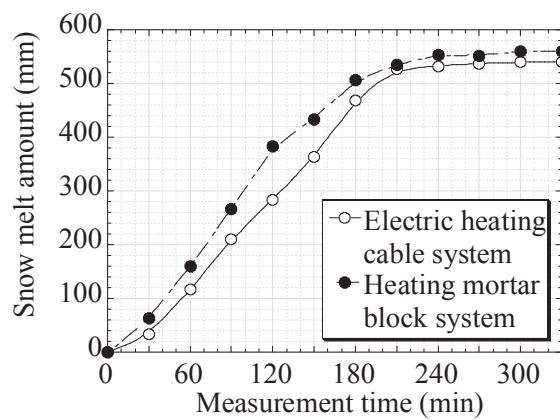


Figure 8: Relation between the snow melting amount and measurement duration



Figure 9: After 150 minutes



Figure 10: After 330 minutes

whereas Fig. 10 depicts the photograph that was captured after 330 minutes. The melting snow conditions of the heating mortar block system and the electric heating cable system exhibit the maximum difference after 150 minutes of initiating the measurement. After 330 minutes from the start of the measurement, there was no snow left in both the systems.

## 6. Conclusion

By conducting the experiment, the following points were clarified.

- (1) The heating mortar block system can reduce the electric energy by approximately 17% as compared to that observed in the electric heating cable system.
- (2) Throughout the measurement, the heating mortar block system exhibits more snow melting and improved snow melting performance as compared to those exhibited by the electric heating cable system.

## Acknowledgments

This work was partially supported by the JSPS KAKENHI Grant Number JP16K18183 and JP16K06569. Some suggestions were provided by the Honorary Professor of the Nagoya Institute of Technology, Tetsuo Ikeda, and Ten corporation. The experiment was conducted with the help of Haruki Taguchi and Hideyuki Yasui, who are both students of Nagoya Institute of Technology. We gratefully acknowledge their supports and contributions to the research that has been reported in this study.

## References

- [1] Kawabe, S., Ikeda, T., Ito, Y., Development of the Heating Mortar Block to Melt Snow by the Quasi Microwave, *Journal of Structural and Construction Engineering* 69 (586), Japan (2004), 1-5
- [2] Ito, Y., Ohba, S., Kawabe, S., Effects of thickness of the base layer on electromagnetic absorption in heating mortar blocks for snow melting through quasi microwave, *Journal of Advanced Concrete Technology* 16, Japan (2018), 170-178
- [3] Ito, Y., Kawabe, S. and Ohba, S., Study of Electromagnetic shielding material on heating mortar blocks for melting snow through quasi microwaves, *Journal of Structural and Construction Engineering* 82 (731), Japan (2017), 1-10
- [4] Ito, Y., Kawabe, S. Ohba, S. and ANZAI, H., Study of A Leaky Waveguide on Heating Mortar Blocks for Melting Snow through Quasi Microwaves, *Journal of Structural and Construction Engineering* 82 (737), Japan (2017), 969-978

## **DURABILITY PROPERTIES OF AUTOCLAVED AERATED AND HIGH PERFORMANCE FOAMED CONCRETE**

**Genadijs Sahmenko<sup>(1)</sup>, Aleksandrs Korjakins<sup>(1)</sup>, Eva Namsone<sup>(1)</sup>**

(1) Riga Technical University, Riga, Latvia

### **Abstract**

Autoclaved Aerated Concrete (AAC) and Foam Concrete (FC) are sustainable lightweight intelligent materials for the modern building industry. FC is a more universal material and it may be applied both for monolithic and prefabricated constructive elements. Flexible technology of FC allows achieving a wide range of properties (density 200 – 1800 kg/m<sup>3</sup> and compressive strength 0.2 – 40 MPa). The range of properties of a typical AAC includes density 250 – 800 kg/m<sup>3</sup> and compressive strength 0.5 – 10 MPa, but normal weight ready-mixed concrete is characterized by density > 2000 kg/m<sup>3</sup> and compressive strength 30 – 50 MPa.

In comparison with ACC, FC is more durable, at the same time, FC has lower strength at the same density, comparing to the aerated autoclaved concrete. The aim of this study is to elaborate high performance foam concrete, characterized by high durability properties and competitive compressive strength.

In the framework of this study, foam concrete compositions were elaborated, using intensive mixing technology and micro admixtures in order to improve their physical and mechanical properties. Properties of the elaborated compositions, such as density, compressive strength, capillary water absorption and frost resistance, were compared with the properties of commercially used AAC. The obtained FC compositions are characterized by low water absorption, high frost resistance and strength – density relation comparable with AAC.

### **1. Introduction**

Autoclaved Aerated Concrete (AAC) and Foam Concrete (FC) are two types of cellular concrete that are traditionally used in modern civil engineering. Its positive properties include simple technology, utilisation of local raw materials and by-products, as well as low embedded energy and carbon dioxide emission and economic benefits to transport [1].

Ecological benefits of cellular concrete are determined by its composition, because air cells take up to 80% from the total volume of the material. AAC technology provides chemical aeration of lime-silicate mix and thermal treatment in special steam pressure chamber, which saves a lot of energy. AAC technology allows producing only prefabricated elements. Production technology of FC provides mechanical aeration of cement mortar using foaming agents [2]. Therefore, FC is a more universal material and it may be applied both for monolithic and prefabricated constructive elements. Controlling the ratios of components and technological parameters, a wide range of FC properties may be achieved: density 200 – 1800 kg/m<sup>3</sup> and compressive strength 0.2 – 40 MPa. The range of properties of a typical AAC includes density 250 – 800 kg/m<sup>3</sup> and compressive strength 0.5 – 10 MPa, but normal weight ready-mixed concrete is characterized by density > 2000 kg/m<sup>3</sup> and compressive strength 30 – 50 MPa. Both FC and AAC have advantages and disadvantages. [1] High specific strength (strength – density ratio) is an advantage of AAC, at the same time, AAC is characterized by high water uptake and hygroscopicity. Lower strength at the same density is a disadvantage of FC compared to the aerated autoclaved concrete. Drying and carbonation shrinkage also increases the risk of cracking and loss of durability. Both materials are intended for use on wall constructions, there is a risk of material water saturation during construction process. In the conditions of wet and cold climate, negative effect of moisture is aggravated by freezing-thawing cycles. Thus, the following factors of FC durability should be taken into account: mechanical strength, water absorption, frost resistance, carbonation, and shrinkage.

Two FC preparation methods may be mentioned; the method of pre-foaming consists in mixing together of specially generated foam and prepared cement mortar. The other one, mixed-foaming method, implies mixing and foam generation in one mixing tank.

Previous investigations [3] demonstrated that highly intensive mixing has a lot of advantages: it provides homogenous mix, promotes accelerated hydration and effective use of cement, and keeps together fine aggregate and the agglomerated cement. Intensity of mixing depends on speed of mixing elements. Traditional low speed mixers are characterized by speed about 2 m/s, turbulence 2 – 10 m/s, and effect of cavitation may be achieved at the speed >15 m/s. FC compositions prepared in a turbulence mixer with the effect of cavitation have been evaluated in this study.

The aim of this study is to elaborate high performance foam concrete, characterized by high durability properties and competitive compressive strength. In the framework of this research, foam concrete compositions were elaborated using intensive mixing technology. Micro admixtures, porous aggregates and superplasticizers were applied in order to improve their physical and mechanical properties.

## 2. Materials and methods

Basic components of FC mixes are normal type Portland cement CEM I 42.5 N and natural washed sand (fraction size 0/0.5 mm), it was used as a filling component. A synthetic foaming agent (PB-Lux) was mixed with water and added during the mixing.

Lightweight filling materials (foamed glass grains and microspheres, or cenospheres) were used as filling, density reducing and internal curing component. Silica-alumina microspheres is a by-product from the combustion of coal in the thermal power plants [4]. Micro spheres

have a very hard shell, but they have density in the range of 600 to 900 kg/m<sup>3</sup> due to their hollow structure [5].

Pulverized silica fume and metakaolin were added as supplementary cementitious materials and an effective pozzolanic admixture [6]. These also decrease a potential risk of alkali – silica reactions in case of using foamed glass aggregate [7].

Eight experimental FC mixes were elaborated and produced using mixed-foaming technology. Composition I may be considered a reference mix. Compositions II, IIP, III and IIIP contain cenospheres, but Compositions III and IIIP are produced with superplasticizer, which allows decreasing water cement ratio. Compositions IP, IIP and IIIP contain lightweight filler – foamed glass granules, 4/8 mm.

First six mixes were produced in the laboratory mixed-foaming turbulence mixer providing mixing intensity up to 1,000 min<sup>-1</sup>. Mixes SF and SF/C were produced in Warmhouse Ltd. industrial turbulence mixer with the cavitation effect. Mix compositions (in mass proportions) are presented in Table 1.

The samples, 100x100x100mm cubes, were prepared and cured in normal hardening conditions (20±2°C, RH>90%). The samples of commercially available AAC with the same dimensions were used as reference AAC samples (GB400 with density 400 kg/m<sup>3</sup> and GB550 with density 550 kg/m<sup>3</sup>).

Compressive strength and density were determined in accordance with EN 772-1.

Capillary water absorption of the exposed concrete surface was determined immersing one side of the samples in water according to LVS EN 772 – 11. The values of the capillary surface water absorption (g/dm<sup>2</sup>) were evaluated as mass difference of the saturated and dry sample (g) related to the exposed surface area (dm<sup>2</sup>). After capillary water absorption test, the same specimens were subjected to frost resistance test by freezing to -20°C and thawing at +20°C (according to LVS CEN/TS 12390-9). After being exposed to freeze-thaw cycles, the specimens were visually inspected and the quantity of the crumbled particles (g/m<sup>2</sup>) was determined.

Table 1: Mix compositions.

	I (REF)	IP	II	IIP	III	IIIP	SF	CF/C
Portland cement CEM I 42.5 N	1.00	1.00	1.00	1.00	1.00	1.00	1.00	1.00
Sand	0.63	0.63	–	–	–	–	0.57	0.57
Water	0.61	0.61	0.75	0.75	0.63	0.63	0.80	0.80
Foaming agent	0.006	0.006	0.004	0.004	0.006	0.006	0.002	0.002
Cenospheres	–	–	0.50	0.50	0.50	0.50	–	–
Metakaolin	0.05	0.05	0.05	0.05	0.15	0.15	–	–
Silica Fume	0.04	0.04	0.04	0.04	0.04	0.04	0.03	0.03
Foamed glass granules, 4/8 mm	–	0.70	–	0.80	–	0.60	–	–
Plastic fibres	0.002	0.002	0.002	0.002	0.002	0.002	0.001	0.001
Carbon fibres	–	–	–	–	–	–	–	0.001
Superplasticizer	–	–	–	–	0.01	0.01	–	–

### 3. Results and discussion

Testing results of FC and AAC compositions are summarized in Table 2. Very low frost resistance of commercially produced AAC concrete may be recognized: after 10 – 16 cycles, the samples were almost totally destroyed (see Fig. 1). Comparing a FC sample (IP) and the same density AAC sample (GB550), at least twice lower strength of the FC sample was observed. The use of light weight fillers allows decreasing the density of FC samples (Compositions IP, IIP and IIIP). Combining cenospheres with foamed glass provides a more effective mix composition: FC sample IIP has the same strength as AAC sample GB550 with the same density. The best result was achieved by complex use of foamed glass, cenospheres and superplasticizer, which provides lower water cement ratio: strength of sample IIIP exceeds the strength of AAC sample GB550 of the same density 1.5 times. FC compositions with cenospheres and foamed glass showed much less surface scaling after freeze-thaw cycles ( $<60 \text{ g/m}^2$ ) compared to AAC samples ( $>1500 \text{ g/m}^2$ ).

The highest compressive strength, density and frost resistance were achieved for high density FC samples (SF and SF/C) produced in the industrial mixer with cavitation effect. No damages were observed after 76 (see Fig. 1) and 100 cycles and moderate surface scaling  $<100 \text{ g/m}^2$  after 130 cycles, thereby frost resistance can be evaluated as F100, which is comparable with normal concrete. Strength values of these compositions (13 – 18 MPa) also are comparable with the strength of normal weight concrete.

Table 2: Results summary.

Designation	Density (kg/m <sup>3</sup> )	28 d. compressive strength (MPa)	Freeze-thaw cycles	Weight loss (g/m <sup>2</sup> )	Capillary water absorption 1 h (g/dm <sup>2</sup> )
I (REF)	736	2.5	14	5	43.9
IP	565	1.4	14	60	17.6
II	769	6.3	14	130	28.3
IIP	445	2.5	14	50	14.0
III	952	14.4	14	110	7.9
IIIP	589	5.7	14	30	4.8
SF	1210	13.7	100	<100	12.2
SF/C	1360	18.2	100	<100	10.0
GB400	400	2.4	10	>1500	46.0
GB550	550	3.6	10	>1500	63.0

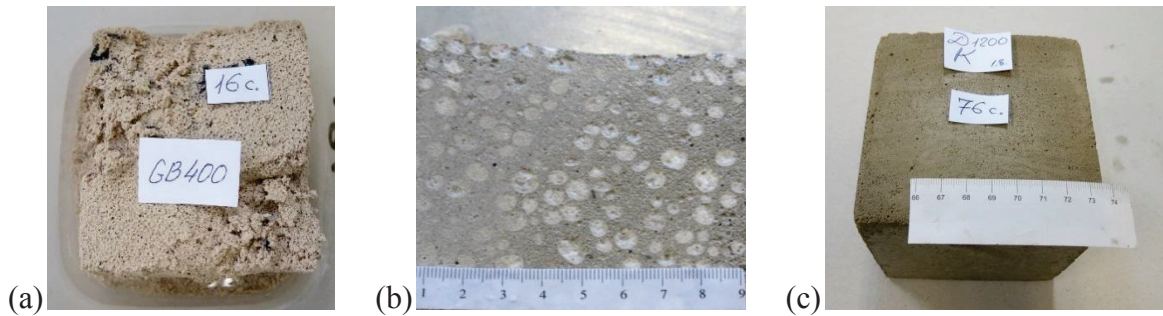


Figure 1: (a) AAC (GB400) after 16 cycles: material is destroyed; (b) IIP after 14 cycles: scaling 30 g/m<sup>2</sup>; (c) SF/C (D1200) after 76 cycles: scaling <100 g/m<sup>2</sup>.

The highest values of capillary water absorption (>40 g/dm<sup>2</sup>) were demonstrated by the samples of AAC (GB400 and GB600) and FC without light weight fillers and superplasticizer (Composition I). Adding foamed glass grains twice decreases water absorption (comparing Compositions I and IP, II and IIP, III and IIIP). Complex use of foamed glass, cenospheres and superplasticizer makes it possible to decrease water uptake up to nine times compared to the reference mix I. Previous studies [8] proved that the use of light weight fillers allows decreasing drying shrinkage up to six times.

Correlation diagram between strength and density is built for different FC compositions produced in the industry and in the laboratory (see Fig. 2). The relation close to parabolic is obtained. The authors suggest considering compositions situated above the averaged curves as effective, and compositions situated below the averaged curves as non-effective. Consequently, mix compositions SF, SF/C, IIP, IIIP may be considered effective (high performance), but composition above the curve – non-effective.

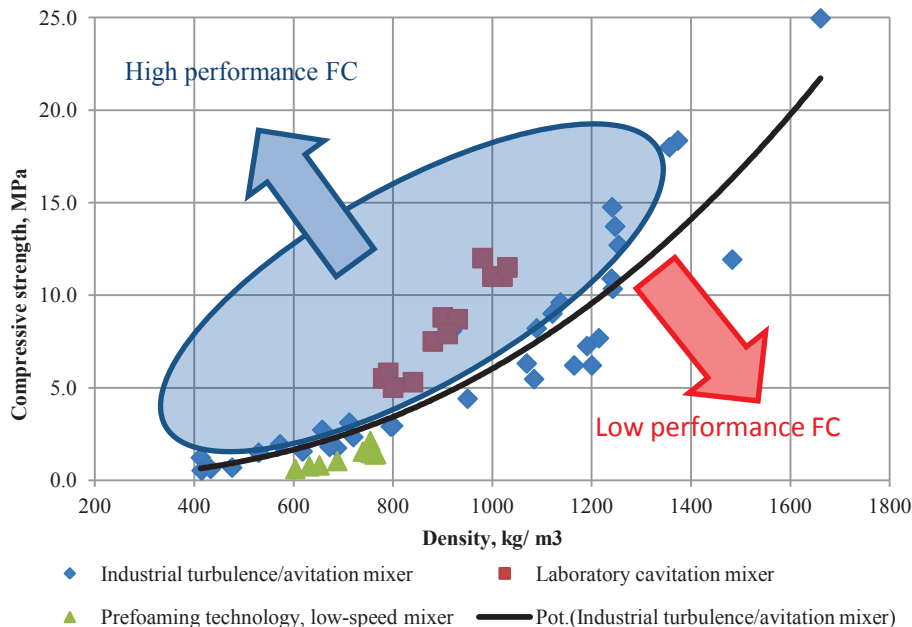


Figure 2: Correlation density – compressive strength.



#### 4. Conclusions

- Compared to the traditional autoclaved aerated concrete (AAC), foam concrete (FC) allows obtaining a more durable material in terms of improved water resistance, frost resistance and durability.
- Traditional autoclaved aerated concrete (AAC) has higher strength comparing to traditional foam concrete in the range of densities 400 – 600 kg/m<sup>3</sup>. The use of turbulence and cavitation mixing technologies combined with lightweight fillers and modifying admixtures is a way to obtain high performance foam concrete with higher strength compared to the traditional pre-foaming foam concrete and AAC.
- Complex use of foamed glass, cenospheres and superplasticizer allows reducing capillary water absorption up to eight times and reducing drying shrinkage up to six times due to the effects of self-curing and formation of the skeletal material.

#### Acknowledgement

The financial support of the European Regional Development Fund project Nr.1.1.1.1/16/A/007 “A New Concept for Sustainable and Nearly Zero-Energy Buildings” is acknowledged.

#### References

- [1] M. Kavita and C. Tarjani, “Comparison on Auto Aerated Concrete to Normal Concrete,” no. March, pp. 90–94, 2016.
- [2] K. Ramamurthy, E. K. Kunhanandan Nambiar, and G. Indu Siva Ranjani, “A classification of studies on properties of foam concrete,” *Cem. Concr. Compos.*, vol. 31, no. 6, pp. 388–396, 2009.
- [3] G. Sahmenko, A. Korjakins, and E. Namsone, “High Performance Foam Concrete Produced in Turbulence Mixers,” in *SBE 16 Malta Europe and the Mediterranean Towards a Sustainable Built Environment*, 2016, pp. 71–78.
- [4] N. Ranjbar and C. Kuenzel, “Cenospheres : A review,” *Fuel*, vol. 207, pp. 1–12, 2017.
- [5] K. S. Chia, M. H. Zhang, and J. Y. R. Liew, “High-strength high-performance lightweight concrete : a review,” *9th Int. Symp. high Perform. Concr. Verif. Util.*, no. August, pp. 9–11, 2011.
- [6] O. Poznyak and A. Melnyk, “Non-autoclaved aerated concrete made of modified binding composition containing supplementary cementitious materials,” *Bud. i Archit.*, vol. 13, no. 2, pp. 127–134, 2014.
- [7] E. Namsone, G. Sahmenko, E. Namsone, and A. Korjakins, “Reduction of the capillary water absorption of foamed concrete by using the porous aggregate,” *IOP Conf. Ser. Mater. Sci. Eng.*, vol. 251, no. 1, 2017.
- [8] E. Namsone, G. Šahmenko, A. Korjakins, and E. Namsone, “Influence of Porous Aggregate on the Properties of Foamed Concrete,” *Constr. Sci.*, vol. 19, no. 1, pp. 13–20, 2016.

## **EFFECT OF INITIAL CURING ON CORROSION BEHAVIOR OF STEEL BARS IN FA CONCRETE UNDER DRY AND WET ACTIONS**

**Wakako Sugino<sup>(1)</sup>, Keiyuu Kawaai<sup>(1)</sup>, Isao Ujike<sup>(1)</sup>**

(1) Ehime University, Ehime, Japan

### **Abstract**

This study reports on the effect of initial curing on the corrosion behavior in Fly ash (FA) concrete, which was examined through chloride-induced corrosion tests induced by dry and wet cycles. After 182 days of the corrosion tests, corrosion properties in the specimens cured under dry or wet conditions including (sealed moist curing and water curing) were examined based on cathodic polarization properties, half-cell potential, and microcell and macrocell corrosion current density. In particular, detailed analysis was carried out on the resistance against ingress of corrosive substances such as moisture and dissolved oxygen via cathodic polarization measurements in determining the rate of oxygen permeability on embedded steel bars. It is noted that segmented steel bars comprising two steel elements (steel element-I closer to the exposed surface; steel element-II far from the exposed surface) was embedded in the specimens. Based on the results obtained in this study, the results suggest that the macrocell corrosion observed in water cured specimens could be triggered by oxygen concentration cell actions.

### **1. Introduction**

When corrosion of steel bars occurs in concrete, anodic reactions in which iron ionizes and cathodic reactions in which oxygen is reduced progress on the surface of the steel bar. And a corrosion cell between the electro-chemical reactions is formed. It is reported that oxygen permeability is one of the significant factors that greatly affect the corrosion processes of steel bars in concrete [1]. In addition, corrosion of steel bars in concrete is classified into microcell corrosion and macrocell corrosion [2]. Generally, when anodic and cathodic reactions occur at the same or extremely close positions, they are referred to as microcell corrosion. On the other hand, macrocell corrosion occurs at positions where anodic reactions and cathodic reactions are separated from each other and the corrosion progresses locally. Factors

contributing to the macrocell corrosion formation include heterogeneity in the concrete, uneven distribution of chloride content, ambient environment, and, variations in dissolved oxygen concentrations. In addition, especially in Fly ash (FA) concrete, initial curing is a significant factor affecting durability and corrosion. This study examines the effect of initial curing on the corrosion behavior in fly ash (FA) concrete subjected to dry and wet actions.

## 2. Experimental program

### 2.1 Materials and mix proportion

In this study, water to binder ratio (W/B) was selected as 50% for both OPC and FA mixtures. FA (JIS A 6201 type-II) was used as partial replacement of cement with a replacement ratio of 30%. Fig. 1 shows the schematic of the reinforced concrete specimens. The specimens are of cross section, 100×150 mm and 200 mm long. And segmented steel bars comprising round steel bar ( $\phi 22$ ) and length of 100 mm, were embedded at the depth of 20 mm from the exposed surface. The steel bars were divided into two elements in the perpendicular direction of the section which was connected by epoxy resin with a thickness of 1 mm. It is noted that the segmented steel bars comprising two steel elements (steel element-I closer to the exposed surface; steel element-II far from the exposed surface) was embedded in the specimens. Tab. 1 shows the mix proportions of concrete mixtures and Tab. 2 shows the materials properties of the aggregate used in this study. The specimens were demolded and cured under different conditions as summarized in Tab. 3. After cured, 5 surfaces except for the exposed surface were covered with epoxy resin.

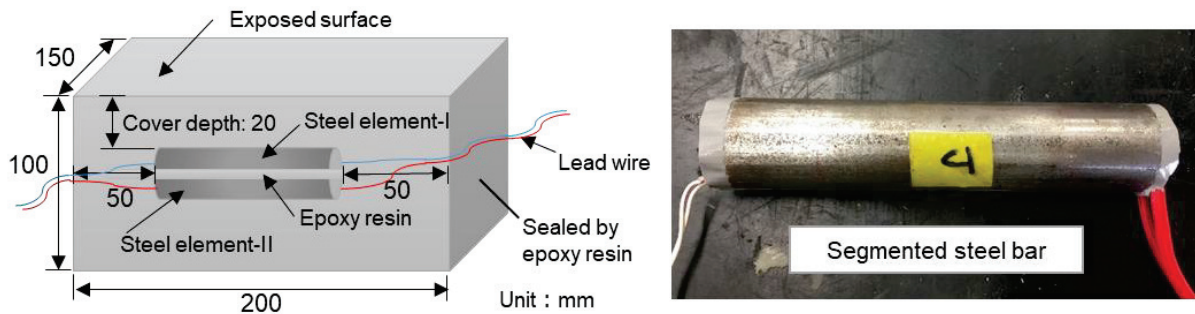


Figure 1: Schematic of the reinforced concrete specimens.

Table 1: Mix proportion

Mixtures	W/B (%)	Unit weight ( $\text{kg/m}^3$ )					( $\text{g/m}^3$ )	
		W	C	FA	S	G	AEA-WRA	AEA
OPC	50	175	350	-	845	922	5597	1400
FA	50	175	245	105	829	905	2099	700

Table 2: Properties of aggregate

Fine aggregate (S) Coarse aggregate (G)	Types	Specific gravity (SSD)	Absorption capacity	Fineness modulus
S	Crushed sand obtained from sandstone	2.61	0.88	2.87
G	Crushed sandstone G <sub>max</sub> : 20 mm	2.63	1.15	-

Table 3: Cases of initial curing condition

Mixtures	Age of demolding	Curing	CASE
OPC	1 day	Water (28 days)	A
	3 days	Air (28 days)	B
FA	1 day	Water (28 days)	D
	1 day	Sealed moist (7 days)	E
	1 day	Sealed moist (14 days)	G
	3 days	Air (28 days)	J

## 2.2 Electro-chemical measurements

Chloride-induced corrosion tests using salt water at a concentration of 10% NaCl was carried out through dry and wet cycles. The specimens were left under room conditions controlled at 20°C (4 days for the dry conditions and 3 days for the wet conditions). Half-cell potential (ASTM C876), and cathodic and anodic polarization curves were measured at the end of each wet period. In addition, the macrocell corrosion current density was measured using a zero-resistance ammeter connected between each steel element [2]. The rate of oxygen permeability was estimated based on the result of the cathodic polarization curve in which limiting current density is assumed according to past research [3].

## 3. Results and discussion

### 3.1 Half-cell potential

Fig. 2 shows the half-cell potentials of steel elements-I and II measured in the OPC and FA specimens up to 22 cycles of the dry and wet exposure tests. Fig. 3 shows differences in the half-cell potentials measured between the steel elements-I and II up to 22 cycles. It is noted that the positive value indicates the potential on the steel element-I is more negative. As can be seen in Fig. 2, the half-cell potential for both steel elements-I and II was the most positive in the case of the water cured FA specimens (D) until the age of 28 days. And, the results show that initiation time of the corrosion was dependent on the initial curing conditions. As shown in Fig. 3, in the cases of sealed moist cured FA specimens until the age of 7 days and 14 days and air cured FA specimens until the age of 28 days, the half-cell potential on the steel element-I close to the exposed surface is more negative and the steel element-II is relatively positive compared to those of the steel element-I. In contrast to the results, in the case of water cured FA specimens until the age of 28 days, the half-cell potential observed between the steel element-I and II draws a distinction in that the potential on the steel element-II was likely to be more negative. Thus, clear differences in the corrosion properties taking place on the steel elements were observed especially in the water cured FA specimens.

Based on the observations made in the potentials, it is assumed that the potential differences observed between the steel element-I and II could contribute to macrocell corrosion formation, which is discussed in Section 3.2.

### 3.2 Macrocell corrosion current density

Fig. 4 shows the results of the macrocell corrosion current density measured using a zero-resistance ammeter in each specimen for 1 week from the age of 175 days to 182 days. From these figures, in the cases of water cured OPC and FA specimens until the age of 28 days, element-I is observed to form cathodic region in the corrosion cell. On the other hand, the steel element-II in the other FA specimens is like to form cathodic region. Thus, the anodic and cathodic regions specified based on the current flows via macrocell corrosion are observed to be varied depending on the initial curing conditions. The results obtained in the macrocell corrosion current density are consistent with the electromotive force caused by the potential differences observed in Section 3.1. Generally, the steel element-I closer to the exposed surface could form anodic region owing to increased concentration of chloride ions through the dry and wet cycles. However, such corrosion behavior was not observed in the case of water cured specimens of OPC and FA until the age of 28 days.

As mentioned in introduction, apart from the electromotive force caused by the potential

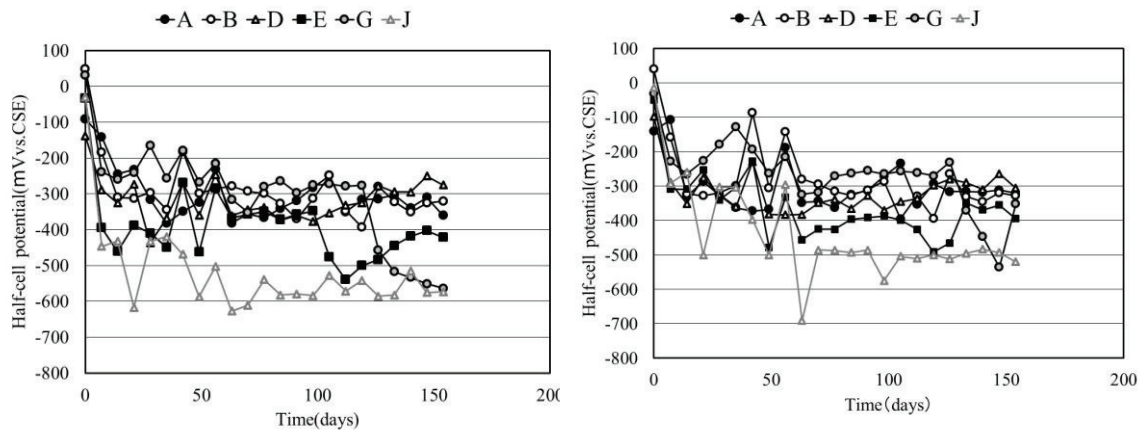


Figure 2: Half-cell potential (left: element-I, right: element-II).

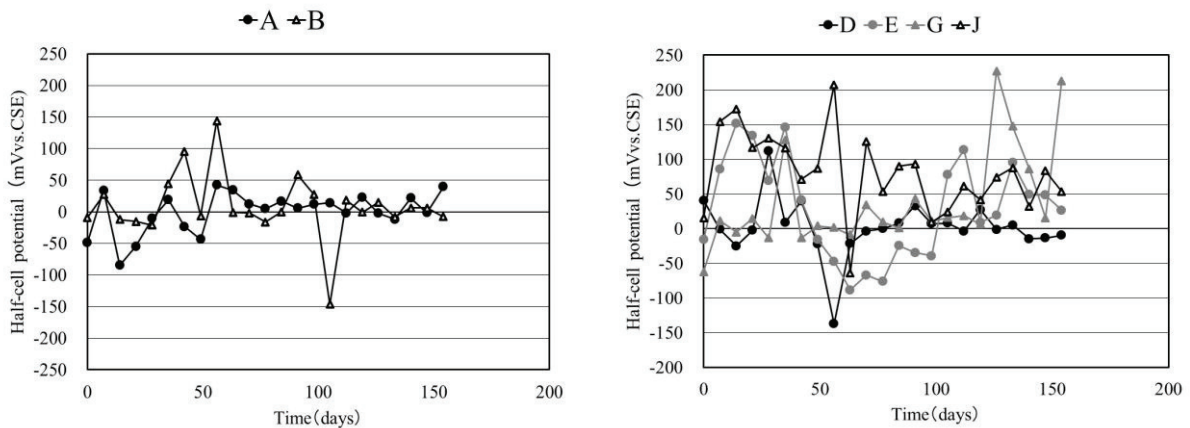


Figure 3: Differences in the half-cell potential measured on the steel element-I and II (left: OPC, right: FA).

difference, the oxygen concentration cell could be a significant factor contributing to the macrocell action on the steel bar in concrete. The regions on steel bars with lowered dissolved oxygen concentration tend to become the anode, and the regions on steel bars with relatively higher concentrations serve as the cathode, thus forming the concentration cell in promoting the corrosion in the anodic region. It has been pointed out that it plays a major role in corrosion of steel bars in concrete [4].

In the case of air cured specimens, the permeation front could penetrate up to the deeper zones of the cover concrete, and the steel element-II could be exposed to the water containing dissolved oxygen for longer periods compared to the water cured specimen [5]. However, the permeation front gradually becomes shallower for both cases, and then it was found to be slightly deeper in the case of water cured specimen. This is expected to reach the steel element-I. In addition, in the case of water cured specimen, the difference in the dissolved oxygen concentration could be possibly larger owing to the denser pore structure formed which has higher resistance against the water ingress. Based on the results obtained in this experiment, there is a good possibility that the steel element-II of the steel bar with lower dissolved oxygen concentration became the anode, and the steel element-I of the steel bar served as the cathode, thus forming the concentration cell. The results are consistent with the potential difference observed between the steel element-I and II. The rate of oxygen permeability on the steel elements is further discussed in Section 3.3.

### 3.3 Oxygen Permeability (Cathodic Polarization)

Fig. 5 shows the rate of oxygen permeability measured on the steel element-I and II at the age of 28 days. As can be seen in the cases of water cured OPC and FA specimens, the results show that the rate of oxygen permeability is clearly higher in the steel element-I of the segmented steel bar compared to those observed in the steel element-II. This led to the largest differences in rate of oxygen permeability measured between element-I and element-II. The rate of oxygen permeability is relatively lower in the steel element-II of the segmented steel bars and the oxygen permeability is found to be higher in the steel element-I in the case of water cured until the age of 28 days. In the FA specimens, the rate of oxygen permeability is gradually expected to change due to the pozzolanic reactions and the dry and wet cycles from the age of 28 days to 91 days. However, in the case of water cured specimens, the permeation front could reach deeper zones of cover concrete i.e. embedded steel bar element- I when steady state is assumed to reach. The results suggest that in the case of water cured specimens until the age of 28 days, the oxygen concentration cell action could be triggered via difference

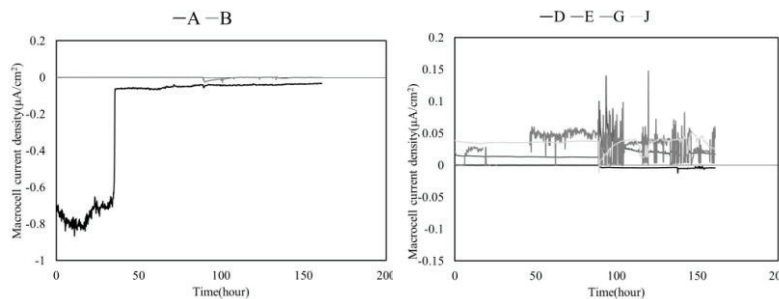


Figure 4: Macrocell corrosion current density (left: OPC, right: FA).

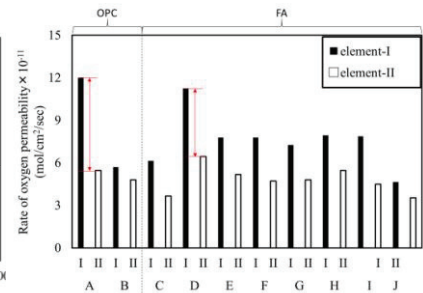


Figure 5: Rate of oxygen permeability.

of the rate of oxygen permeability observed in the steel bar located closer to and far away from the exposed surface. This agrees with the results of the anodic and the cathodic region specified based on the current flows of the macrocell corrosion formed in the segmented steel bars.

#### 4. Conclusion

Especially in FA concrete, initial curing is a significant factor contributing to the corrosion resistance. This study examined the effect of initial curing on the corrosion behavior and properties in FA concrete, which was conducted via chloride-induced corrosion tests. In particular, this study aimed at examining the effect of initial curing on the macrocell corrosion formation under dry and wet actions.

In the cases of water cured OPC and FA specimens until the age of 28 days, the difference in the rate of oxygen permeability between steel element-I (closer to the exposed surface) and II (far away from the exposed surface) at age of 28 days was found to be the largest compared to those observed in the specimens with other curing conditions. The results indicate that the difference in the macrocell corrosion properties observed up to the age of 182 days can be adequately explained by the differences observed in the rate of oxygen permeability between the element-I and II of the segmented steel bars, which was measured at the age of 28 days immediately after the initial curing was carried out. Based on the results obtained in this study, it is suggested that the macrocell corrosion observed in water cured specimens could be triggered by oxygen concentration cell actions.

#### References

- [1] Mohammed, T.U., Otsuki, N. and Hamada, H., Oxygen permeability in cracked concrete reinforced with plain and deformed bars, *Cem Concr Res*, 31 (2001), 829-834.
- [2] Miyazato, S. & Otsuki, N., The estimation of macrocell corrosion rate of rebar in existing concrete using non-destructive tests, *Concr Res Tech*, 12 (2001), 93-103. (in Japanese)
- [3] Nagataki, S. Otsuki, N. Moriwake, A. & Miyazato, S. 1996. The experimental study on Corrosion Mechanism of Reinforced Concrete at Local Repair Part. *Journal of Materials, Concrete Structures and Pavements, JSCE*, 544(32), 109-119. (in Japanese)
- [4] Gouda, V.K. & Mourad, H.M., *Corrosion Science*, 14 (1974) p. 681.
- [5] Kawai, K. & Ujike, I., Effect of Initial Curing on Ingress of Corrosive Substances and Corrosion Resistance in Fly Ash Concrete, *Journal of the Society of Materials Science*, 66 (2017), 608-614. (in Japanese)

## **EFFECT OF MARBLE POWDER WASTE ON THE PROPERTIES OF SELF COMPACTING CONCRETE**

**Ali M. Mansor<sup>(1)</sup>, Asaad A. Elshab<sup>(1)</sup>, Ruben P. Borg<sup>(2)</sup>, Ahmed M. M. Hamed<sup>(2)</sup>**

(1) Department of Civil Engineering, University of Tripoli, Libya

(2) Faculty of the Built Environment, University of Malta, Malta

### **Abstract**

The marble production industry generates a considerable amount of waste materials in Libya. Waste is generated in the mining, processing and polishing stages. The processing wastes are dumped, with a negative impact on the environment. However there is potential in the reuse of marble waste, particularly in the manufacture of concrete products. This study was conducted to investigate the influence of marble powder (MP), as a partial cement replacement in self-compacting concrete (SCC). Several SCC mixes were prepared with varying replacement of cement with MP. The properties of fresh SCC were determined through the slump flow, + T50 time, V-funnel, J-ring and L-box tests. In addition, hardened concrete properties including compressive strength, density, Young's modulus, stress-strain curve and Poison's ratio after 28 and 90-days were assessed. Results show that the fresh properties of SCC with MP cement replacement of up to 50% were in good agreement with specifications. As expected the compressive strength decreases with an increase in MP. The study confirmed that waste generated in marble manufacture has a great potential in SCC.

### **1. Introduction**

Waste materials can be exploited in the production of Self-Compacting Concrete (SCC). SCC is characterized by an increased powder content when compared to conventional vibrated concrete. The recycling of waste from different industrial sectors leads to environmental and economic benefits. Significant quantities of waste marble powder are generated in the processing of marble with negative impacts on the environment. Marble powder (MP) is increasingly seen as a valuable resource if transformed into an engineering material for the construction industry. Several studies have been conducted on SCC produced with marble powder. İlker Bekir Topçu et al. [1] reported that the workability of fresh SCC is not affected



with a marble dust content of up to  $200 \text{ kg/m}^3$ , while the mechanical properties decreased. Valeria Corinaldes et al. [2] concluded that 10% substitution of sand with marble powder resulted in maximum compressive strength at about the same workability. Amit Kumar Tomar, et al. [3] reported that waste MP can be utilized in concrete as a filler contributing to a reduction in the total void content while affecting strength. Anuj et al. [4] compared MP in SCC to SCC mixes based on fly ash and sand. Ulubeylia et al [5] concluded that the use of waste marble in conventional concrete as a fine/coarse aggregate improved hardened concrete properties. The increase in waste marble replacement ratios in self-compacting concrete, resulted in a decrease in the mechanical properties of concrete.

The objective of this research was to investigate the fresh and hardened properties of SCC, produced using waste MP, as a partially cement replacement (0% to 50%) by weight of cement. The investigation included the assessment of the rheological and hardened properties.

## 2. Experimental methodology

### 2.1 Materials

The marble powder used for this work was collected from marble production plants in Tripoli, Libya, for a consistent marble type. The waste was crushed and ground to a fineness of  $125\mu\text{m}$ . Ordinary Portland cement (OPC) type 42.5N conforming to the Libyan standards 340-2009 was used as the binder. Two different sizes of coarse aggregate were used, 10 mm and 14 mm, together with two types of fine aggregate; local natural sand and ground sand. Clean tap water was used as the mixing water and Sika Viscocrete Tempo 12 was used as a water reducer and superplasticizer. SCC mixes with MP replacement levels by weight of cement, ranging from, 0% to 50%, were prepared. The mixes are presented in Table 1.

Table 1: Details of constituents of the SCC mixes.

Mix No.	Total Powder $\text{kg/m}^3$	Cement $\text{kg/m}^3$	MP $\text{kg/m}^3$	MP %	Water lt	w/p	w/c	Total CA (10+14mm) $\text{kg/m}^3$	Total FA $\text{kg/m}^3$	Viscocrete liter
1	500	500	0	0	179.2	0.36	0.36	911.6	808.4	7.5
2	500	475	25	5	179.2	0.36	0.38	911.6	808.4	7.5
3	500	450	50	10	179.2	0.36	0.40	911.6	808.4	7.5
4	500	425	75	15	179.2	0.36	0.42	911.6	808.4	7.5
5	500	400	100	20	179.2	0.36	0.45	911.6	808.4	7.5
6	500	375	125	25	179.2	0.36	0.48	911.6	808.4	7.5
7	500	350	150	30	179.2	0.36	0.51	911.6	808.4	7.5
8	500	325	175	35	179.2	0.36	0.55	911.6	808.4	7.5
9	500	300	200	40	179.2	0.36	0.60	911.6	808.4	7.5
10	500	275	225	45	179.2	0.36	0.65	911.6	808.4	7.5
11	500	250	250	50	179.2	0.36	0.72	911.6	808.4	7.5

### 2.2 Mix design and concrete testing

Several trial mixes were produced intended to optimize the mix in view of rheological requirements. Ingredients were first mixed in dry conditions in the mixer for one minute. The water was added gradually to the dry mix and the material was mixed for another minute. The chemical admixture was added to the mix and the concrete was mixed for a further three minutes. After the mixing procedure was completed, the fresh concrete properties were determined through the measurement of slump flow time and diameter, J-Ring, L-Box and V-

funnel flow time tests. Minor adjustments to the mix water were considered for mixes with MP in view of the water absorption of the MP. The tests were carried out according to the EFNARC guidelines. Specimens were cured in a laboratory environment until the time of testing for hardened properties at 28 and 90 days.

### 3. Results and discussion

#### 3.1 Fresh properties

Fresh SCC is required to be flowable, stable and segregation resistant. Results show that SCC with MP had a satisfactory performance with regards to workability and homogeneity requirements. Slump-flow, V-funnel and L-box test results were, in general, in a good agreement with the limits presented in the European Guidelines for Self-Compacting Concrete (EFNARC). As shown in table 1, the content of the superplasticizer was kept constant with a constant water / powder (w/p) ratio and varying water / cement (w/c) ratio. Details of the fresh properties of SCC mixes are given in Table 2.

Table 2: Fresh Properties of SCC mixes.

Mix No	MP Content (kg)	w/p ratio	w/c ratio	Slump flow (mm)	T50 (sec)	J-Ring (mm)	L-Box (H2/H1)	V-funnel (sec)
1	0	0.36	0.36	800	2	10	0.88	8
2	25	0.36	0.38	715	4.3	7	0.824	10.3
3	50	0.36	0.40	720	3.1	15	0.875	9.1
4	75	0.36	0.42	680	4.5	20	0.83	10.5
5	100	0.36	0.45	740	2.8	10	0.85	8.8
6	125	0.36	0.48	760	3	10	0.878	9
7	150	0.36	0.51	800	2	12	0.918	8
8	175	0.36	0.55	800	2	2	0.87	8
9	200	0.36	0.60	730	4	2.5	0.81	10
10	225	0.36	0.65	710	2.8	3	0.78	8.8
11	250	0.36	0.72	730	2.6	5	0.877	8.6
EFNARC Spec.	---	---	---	650 - 800	2 - 5s	0 - 10	0.8 - 1.0	6 - 12s

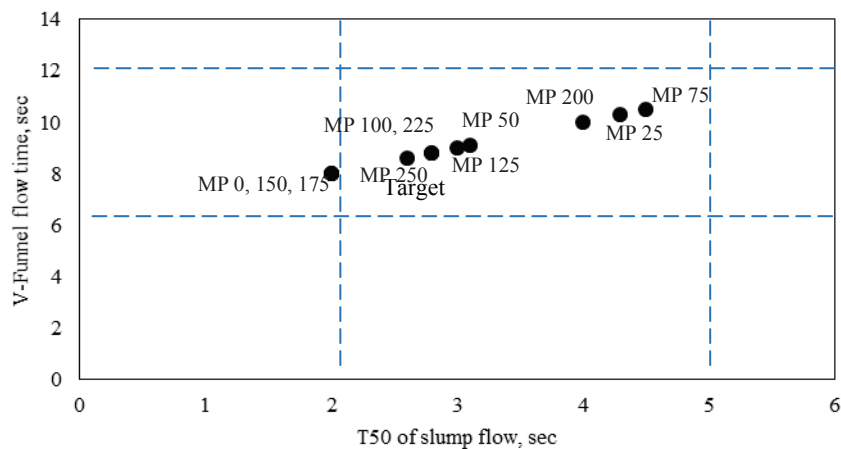


Figure 1: Relationship between V-Funnel time and T50 slump flow.

The relationship between the required time to reach 500 mm slump-flow and time of flow through the V-funnel, to determine the segregation resistance is shown in Fig. 1. The results are within the targeted limits and no segregation was observed.

### 3.2 Hardened concrete properties

The 28-day and 90-day compressive strength results are presented in table 3 and figure 2. It is clear that the compressive strength of SCC samples with MP as cement replacement is less than the strength of the control mix. This behavior was expected since MP is considered to act as an inert filler material rather than a reactive material. While the water / powder ratio was maintained constant for the mixes, the water / cement ratio increased resulting in a reduction in strength.

Table 3: Compressive strength of SCC mixes.

Sample	1	2	3	4	5	6	7	8	9	10	11
28 d Comp. Strength (MPa)	54.9	46.9	43.4	43.4	39.2	36.7	34.3	32.4	29.9	25.3	20.1
90 d Comp. Strength (MPa)	57.3	48.4	44.6	49.9	47.6	39.6	35.5	33.5	36.9	29.6	22.1

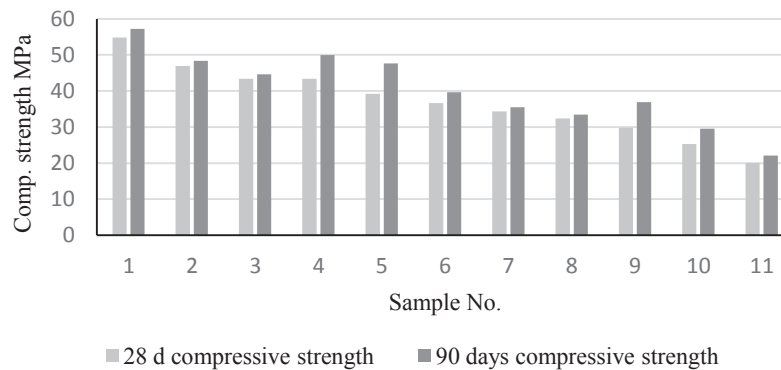


Figure 2: Compressive strength for different MP percentages.

The results reported in table 4 for hardened SCC indicate that the density is not significantly affected with the introduction of MP. The MP acted as a fine aggregate filling the voids in the concrete matrix.

Table 4: Density of SCC.

Sample	1	2	3	4	5	6	7	8	9	10	11
Density (kg/m <sup>3</sup> )	2400	2405	2402	2367	2385	2364	2349	2357	2365	2347	2331

The stress - strain relationships for SCC with MP are presented in Figures 3 to 8. Large strains are registered for higher replacement levels of MP, associated with a decrease in the compressive strength. This may be attributed to the micro-cracks generated at the paste - MP interface. Still the strain at the ultimate stress is around 0.003.

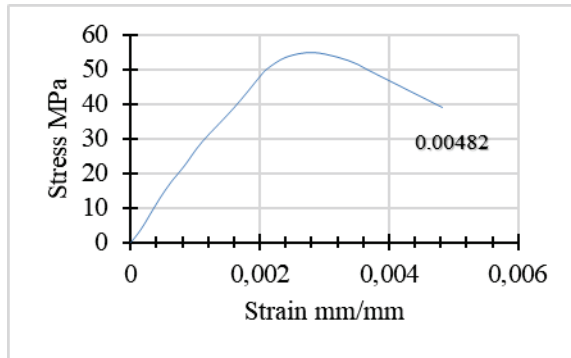


Figure 3: Stress-strain curve, Mix 1 at 28d

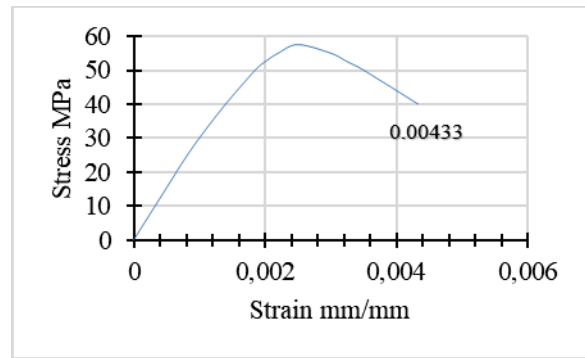


Figure 4: Stress-strain curve, Mix 1 at 90d.

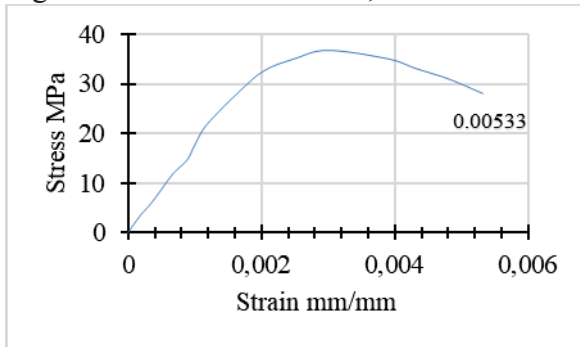


Figure 5: Stress-strain curve, Mix 6 at 28d.

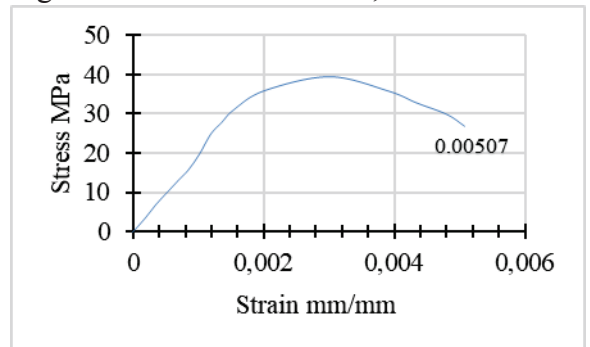


Figure 6: Stress-strain curve, Mix 6 at 90d.

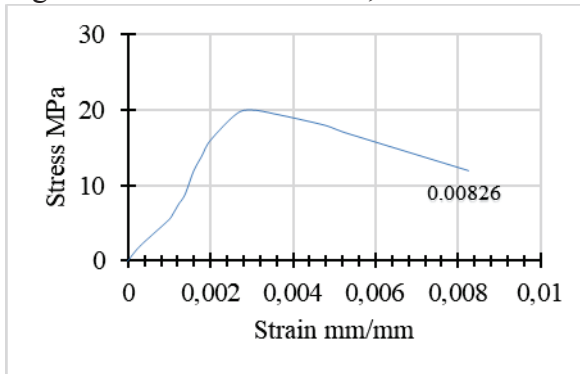


Figure 7: Stress-strain curve, Mix 11 at 28d.

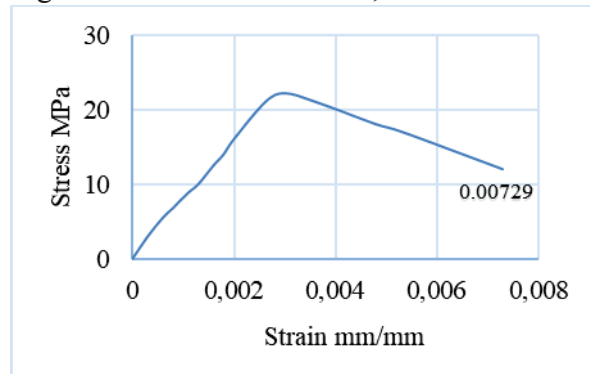


Figure 8: Stress-strain curve, Mix 11 at 90d.

The results presented in table 5 indicate that the efficiency of the cement (strength achieved for a certain amount of cement content, in MPa/kg) was about 0.1 MPa/ kg of cement. This has not been significantly affected by the different percentage replacement levels of cement with MP and can be interpreted as the MP not contributing in the hydration process. Figures 9, 10 present the modulus of elasticity at 28 days and 90 days respectively.

Table 5: Efficiency of cement (MPa/kg).

Sample	1	2	3	4	5	6	7	8	9	10	11
28d Effici.	0.11	0.10	0.10	0.10	0.10	0.10	0.10	0.10	0.10	0.09	0.08
90d Effici.	0.11	0.10	0.10	0.12	0.12	0.11	0.10	0.10	0.12	0.11	0.09

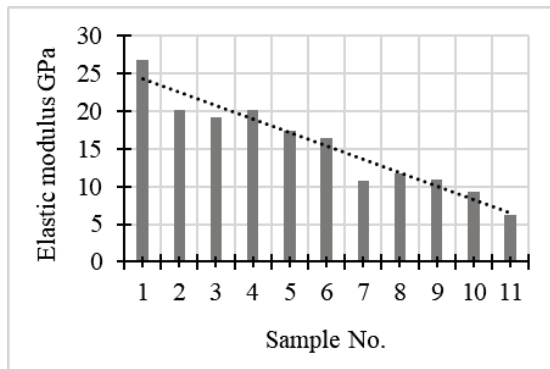


Figure 9: Modulus of elasticity at 28d.

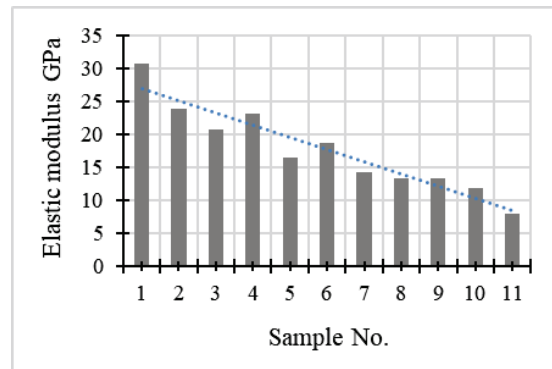


Figure 10: Modulus of elasticity at 90d.

## 5. Conclusion

On the basis of the experimental investigation conducted on the application of marble powder in self compacting concrete, the following conclusions can be drawn:

1. Marble powder MP can be recycled and used in the production of SCC as a partial replacement of cement.
2. The MP in the mixes affected the fresh properties of the SCC when compared to the control mix. However in general, the different fresh properties of SCC for the different mixes with MP were within the EFNARC limits.
3. MP did not present any improvement in the mechanical properties of SCC at 28 and 90 days. High replacement levels of cement result in significant reductions in compressive strength, at equal water / powder ratios.
4. The density of SCC was not significantly affected with varying MP in the mixes.
5. The efficiency of the cement has not been significantly affected by the different percentage replacement levels of cement with MP.
6. The disposal of waste MP from the intensive marble production industry in some regions has a negative impact on the environment. However MP has the potential to be used in Self compacting concrete, reducing its environmental impact.

## References

- [1] Topçu, İ.B. et al, Effect of waste marble dust content as filler on properties of self-compacting concrete, *Construction and Building Materials* 23(5) (2009), 1947-1953
- [2] Corinaldes, V. et al, Characterization of marble powder for its use in mortar and concrete, *Construction and Building Materials* 24(1) (2009), 113-117
- [3] Tomar, A.K. et al, Review on utilization of waste marble powder in self-compacting concrete, *Intern. Journal of Engineering Trends and Technology* 37(2) (2016), 122-124
- [4] Anuj, et al, Rheology of Self Compacting concrete with Marble Powder mixes in comparison to Fly ash and Sand Based Mixes, (2016)
- [5] Ulubeylia, G.C. and Artirb, R., Properties of Hardened Concrete Produced by Waste Marble Powder, *World Conference on Technology, Innovation and Entrepreneurship, Procedia Social and Behavioral Sciences* 195 (2015), 2181-90
- [6] Standard Test Methods for unit weight and voids in aggregates – American Society for Testing and Materials, ASTM C29/M129 (2007)

## **ESTIMATING THE STRESS DEVELOPMENT IN EARLY AGE CONCRETE WITH MINERAL ADDITIONS FROM COUPLED MEASUREMENTS**

**Jérôme Carette<sup>(1)</sup>, Brice Delsaute<sup>(1)</sup>, Stéphanie Staquet<sup>(1)</sup>**

(1) BATir department, Université libre de Bruxelles (ULB), Brussels, Belgium

### **Abstract**

In order to evaluate the efficiency of a given supplementary cementitious material, its mechanical behaviour has to be thoroughly investigated. In particular, early-age micro-cracking might occur at a time when all concrete properties evolve, while the rate of evolution of autogenous and thermal deformations is still very high. If these deformations are restrained, stresses are induced as the concrete hardens. These stresses are both homogeneously distributed and localized, depending on the scale considered, and may lead to localized cracking if the stress overpasses the strength of the material. The aim of this study is twofold. First, prediction models are presented. These models are specifically designed for the very early age description of in terms of strength, elastic properties, autogenous deformation as well as creep development of concrete with high content of mineral additions. Secondly, newly developed modelling strategies are confronted to experimental measurement of the stress development in restrained deformation conditions with a TSTM device. This study highlights the limits of the viscoelastic modelling approach using the superposition principle for modelling the early age behaviour of concrete with mineral additions.

### **1. Introduction**

Most supplementary cementitious materials (SCM) have a large impact on the chemical processes at the origin of the mechanical properties of concrete. In order to evaluate the efficiency of a SCM, its mechanical behaviour thus has to be thoroughly investigated. In particular, the early age behaviour of concrete is at the origin of an initial stress state, which might induce the development of micro-cracking. Indeed, early-age cracking occurs at a time when all concrete properties evolve, while the rate of evolution of autogenous and thermal deformations is still very high. If these deformations are restrained, stresses are induced as the

concrete hardens. These stresses may lead to localized cracking if the stress overpasses the strength of the material. The parameters that should be considered for crack prediction in restrained deformations are : the amplitude of the deformation, the viscoelastic behavior of the concrete, the strength of the material, and in particular its tensile strength, and the amount of restraint applied to these deformations. In previous studies, experimental assessment of the early age evolution of these above properties were presented. In parallel, models were successfully proposed, allowing proper consideration both of the early age behaviour and of the presence of SCM. The properties that were assessed from the setting time [1] include elastic properties as well as compressive and tensile strength [2], the autogenous deformation [3] and the creep behaviour [4]. These models as well as their corresponding empirical models are presented in this paper. They are used for computing the stress development in the case of fully restrained autogenous deformations from the setting time. The autogenous deformation includes the early age swelling deformation (supposedly originating from ettringite formation [3]) and the self-desiccation deformation. The results of this empirically-optimized model are confronted to experiments of the stress development in fully restrained conditions. As a result, situations in which the superposition principle cannot be easily applied are identified.

## 2. Materials and method

### 2.1 Concrete mix designs

Two binder types are studied (Tab. 1). They contain various combinations of CEM I 52.5 N, blast-furnace slag (BFS) and gypsum. The latter is added in order to keep the sulfate content constant between compositions. The water/binder ratio (w/b) is 0.4 for all compositions. Additional information related to the chemical composition of each binder component as well as the mechanical behavior of these compositions are available in [1-3].

Table 1. General composition of the tested concretes

[kg/m <sup>3</sup> ]	C1	C2
Aggregate 10/14	873	873
Aggregate 6/10	210	210
Sand 0/4	853	853
CEM I 52.5	432	104
Blast furnace slag	-	291
Gypsum	-	22
Water	173	167

### 2.2 Test setup

The stress development in fully restrained deformations conditions is measured for two tested compositions C1 and C2. This is performed through a dedicated Temperature Stress Testing Machine (TSTM) [5-8]. This test is used to cancel step-wise the deformations in a horizontal concrete sample. In order to do so, compensation cycles are applied with a jack attached to the mobile head of the mould. These cycles consist in applying a force to the concrete sample

every time the measured displacements exceeds a given threshold. Once this threshold (corresponding to 6  $\mu\text{m/m}$  deformation) is overpassed, the sample is loaded until the displacements come back to zero. Once this is achieved, the tensile (or compressive) stress is kept constant up to the next threshold is exceeded. These cycles continue until a major cracking occurs. The compensation cycles are started as soon as concrete reaches its final setting  $t_0$ , determined based on the combined measurement of ultrasonic compression and shear wave transmission velocity [1]. Tensile strength is obtained from  $t_0$  based on tensile splitting strength test [2]. The elastic modulus is also measured from  $t_0$  through a cyclic methodology using the TSTM device [2,9]. Finally, the autogenous deformation is measured with the BTJADE device [10]. This continuous measurement ensures fully isothermal and sealed conditions from the mixing to several weeks. Therefore, the autogenous deformation (including the early age swelling deformation) is determined from as soon as  $t_0$  [3].

### 3. Modelling of the early age properties

The models that are presented in this section are not necessarily obtained from standard codes. They are carefully chosen, for each considered property, based on three main criteria:

- Its ability to represent correctly the property evolution from the setting time
- Its number of material parameters to be determined experimentally
- Its ability to be applied to any of the tested materials, with and without SCM

The following equations Eq. (1-3) result from these considerations. All materials parameters for the expressions of compressive strength  $f_c$ , tensile strength  $f_t$  and elastic modulus  $E$  are identified from experiments.

$$f_c(t) = f_{c,28} \cdot e^{-\frac{s_c}{t}} \quad (1)$$

$$f_t(t) = f_{t,28} \cdot e^{-\frac{s_t}{t}} \quad (2)$$

$$E(t) = E_{28} \cdot e^{-\left(\frac{s_E}{t}\right)^r} \quad (3)$$

A new model was previously developed for representing the autogenous deformation  $\varepsilon_{au}$  of concrete with and without SCM at early age [3]. This model explicitly considers the contribution of the self-desiccation phenomenon  $\varepsilon_{sd}$  (Eq. (5)) but also the early age swelling deformation  $\varepsilon_{sw}$  (6). This expansion is assumed to be resulting from the ettringite formation, especially in presence of blast furnace slag [3]. The overall equation that is used is shown in Eq. (6-7), where  $\alpha$  is the degree of hydration,  $\alpha_0$  is the degree of hydration at final setting,  $A_{sd}$  and  $A_{sw}$  are amplitude parameters for the self-desiccation and swelling deformations respectively. The swelling deformation increases with a kinetic factor which includes two parameters  $a_{sw}$  and  $b_{sw}$ , which depend mostly on the cement type.

$$\varepsilon_{au} = \varepsilon_{sw} + \varepsilon_{sd} \quad (4)$$

$$\varepsilon_{sd}(t) = A_{sd} \cdot \tilde{\alpha}(t) \quad (5)$$

$$\varepsilon_{sw}(t) = A_{sw} \cdot \left(1 - e^{-a_{sw} \tilde{\alpha}(t)^{b_{sw}}}\right) \quad (6)$$

$$\tilde{\alpha}(t) = \frac{\alpha(t) - \alpha_0}{1 - \alpha_0} \quad (7)$$



The creep behaviour is modelled according to a modified version of the model code 2010 expression [11]. This expression is shown in Eq. (8). The parameter  $\tau$  is computed in Eq. (9) as a function of the time derivative of the elastic modulus. The material parameters  $p$  and  $q$  depend on the tested composition. The relaxation is deduced analytically from the creep coefficient according to the effective modulus method (Eq. (10)), which provides acceptable results in comparison with a more accurate numerical computation [12].

$$\varphi_c(t, t') = \frac{E(t')}{C} + \ln\left(1 + \frac{t - t'}{\tau(t')}\right) \quad (8)$$

$$\tau(t') = \text{minimum} \begin{cases} q \left(\frac{dE(t')}{dt}\right)^p \\ .088 \left(\frac{dE(t')}{dt}\right)^{-1} \end{cases} \quad (9)$$

$$\varphi_r(t, t') = \frac{1}{1 + \varphi_c(t, t')} \quad (10)$$

From all the above equations, the following equation must be verified in order to avoid cracking:

$$-f_c < \sum_{t'=t_0}^t \Delta(\varepsilon_{au} + \varepsilon_{th}) \cdot E(t') \cdot \varphi_r(t, t') < f_t \quad (11)$$

#### 4. Results and discussion

The results of the TSTM experiments performed at 20°C as well as the modelled stress build up in fully restrained conditions are shown in Fig. 2. The grey zones in these figures represent zones where stress is higher than the compressive / tensile strength. The C2 composition presents a significant amount of computed compressive stress due to the large amplitude of the swelling deformation in the presence of blast-furnace slag. The composition C1 presents significant tensile stress development in the first days after mixing, ultimately leading to its cracking at 48h, as shown by the sudden drop in the experimental stress value. The C2 composition did not show this cracking tendency, even after more than 2 weeks of testing.

The modelling strategy is based on the visco-elastic stress computation, considering the effect of creep, and by applying the superposition principle. The values of elastic modulus, autogenous deformation and creep are deduced from experimental measurements. However, there are very large differences between the predicted and experimental values. Two main issues can be observed. First, in the presence of Portland cement only, the model is very accurate until the tensile behaviour is reached. After this point, the model progressively underestimates the stress in the material. At the time of cracking of the sample, the computed stress is only 50% of what is obtained experimentally. Secondly, the early age expansion of C2 is not observed to generate compressive stress in the experiment, while the model

estimates up to 2.5 MPa of compressive stress after 48h. In this same experiment, the rate of tensile stress increase seems to be accurately predicted with the model, while the actual values are not correct.

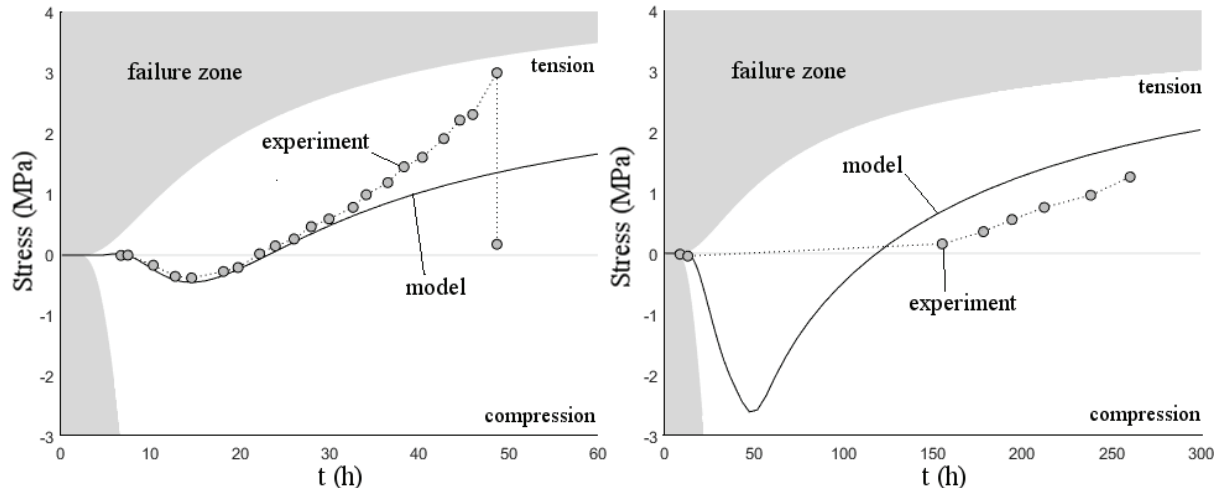


Figure 2. Comparison between modelled and experimental stress development in restrained autogenous deformations conditions (left) for concrete C1 and (right) for concrete C2.

These observations are expected to be the result of the combination of the following mechanisms, which are not included in the model:

- the creep function is deduced from experiments in compression. However, short term creep in tension is actually much lower than creep in compression [5]. The longer term creep is similar in tension and in compression. This explains why the C2 estimation of the rate of stress increase in tension is acceptable, since the loading in that latter case occur in a much longer amount of time than C1 (approximately 7 times slower),
- the principle of superposition can hardly be applied for stresses higher than 50% of the strength [9]. This explains why there is so large differences at high tensile stresses in the C1 mix,
- the linear principle of superposition is not verified in the case of strain reversals [9], which are observed in this study, especially in the case of C2. This explains why the absolute value of the modelled stresses in C2 is far from the experiment after 150h even if the rate of increase is plausible,
- the large swelling observed in the free autogenous deformation of C2 does not generate significant stress in the experiments in contrast with the predicted values. This cannot be explained by any of the above considerations. A possible mechanism for this observation is related to the ettringite formation. Indeed, if the swelling is caused by this ettringite production, it is possible that under confined compressive conditions, the ettringite does not form as an expansive hydrate (either by smaller sized needles or by lower production rate). In this case, the lack of compressive stress in the experiments would be due not to an issue regarding the estimation of creep, but rather to the feedback effect of stress on the formation of expansive hydration products such as ettringite.

#### 4. Conclusions

To conclude, it can be expected that the build-up of stress inside concrete samples under restrained deformations can be very difficult to predict, even in simple uniform 1-D situations. In addition to the well-known limits of applying the superposition principle (such as for high stress/strength ratio on when strain reversals are considered), coupled with the difficulty to assess the early age tensile creep, these computations are challenged by possible feedback mechanisms between the microstructural build-up and the stress state of the material. This issue might be particularly relevant in the case of early ettringite expansion.

#### References

- [1] Carette J & Staquet S., Monitoring the setting process of eco-binders by ultrasonic P-wave and S-wave transmission velocity measurement: Mortar vs concrete, *Construction and Building Materials*, 2016, 110, 32-41
- [2] Carette J. & Staquet S., Monitoring and modelling the early age and hardening behaviour of eco-concrete through continuous non-destructive measurements: Part II. Mechanical behaviour, *Cement and Concrete Composites*, 73, pp. 1-9, 2016
- [3] Carette, J., Joseph S., Cizer Ö, Staquet S., Decoupling the autogenous swelling from the self-desiccation deformation in early age concrete with mineral additions: micro-macro observations and unified modelling, *Cement and Concrete Composites*, 85, pp. 122-132, 2018
- [4] Brice Delsaute, Jean-Michel Torrenti, Stéphanie Staquet, Is the Model Code 2010 able to reproduce the basic creep of concrete with high substitution of Portland cement by mineral additions?, Under review in *Structural Concrete*, 2018.
- [5] B. Delsaute, New approach for monitoring and modelling for the creep and shrinkage behaviour of cement pastes, mortars and concretes since setting time, PhD thesis, Université libre de Bruxelles (ULB), 2016.
- [6] A. Klausen, T. Kanstad, Ø. Bjøntegaard, E. Sellevold, Comparison of tensile and compressive creep of fly ash concretes in the hardening phase, *Cement and Concrete Research*, 95, 2017, pp. 188-194
- [7] P. Lura, K. van Breugel, I. Maruyama, Effect of curing temperature and type of cement on early-age shrinkage of high-performance concrete, *Cement and Concrete Research*, 31, 2001, pp. 1867-1872
- [8] G. M. Ji, T. Kanstad, and Ø. Bjøntegaard, Calibration of Material Models against TSTM Test for Crack Risk Assessment of Early-Age Concrete Containing Fly Ash, *Advances in Materials Science and Engineering*, 2018
- [9] Delsaute B, Boulay C, Granja J, Carette J, Azenha M, Dumoulin C, Karaiskos G, Deraemaeker A, Staquet S., Testing Concrete E- modulus at Very Early Ages Through Several Techniques: An Inter- laboratory Comparison, *Strain*, 2016
- [10] Boulay, C., 2012. Test rig for early age measurements of the autogenous shrinkage of a concrete, *Concrack 3*, RILEM Publications, 111-122.
- [11] B.Delsaute, J.-M.Torrenti, S.Staquet, Modeling basic creep of concrete since setting time, *Cement and Concrete Composites*, 83, pp. 239-250, 2017
- [12] Z. P. Bažant, Numerical determination of long-range stress history from strain history in concrete, *Matériaux et Construction*, 5 (3), pp 135–141, 1972

## **EVALUATION OF STRENGTH OF REINFORCED CONCRETE SLABS OPERATING UNDER THE CHANGING WATER LEVEL**

**Raimondas Šadzevičius<sup>(1)</sup>, Rosita Norvaišienė<sup>(1)</sup> Edita Smetonaitė<sup>(2)</sup>**

(1) Kaunas University of Applied Engineering Sciences, Kaunas, Lithuania

(2) Kaunas University of Technology, Kaunas, Lithuania

### **Abstract**

Reinforced concrete slabs for ponds slope protection are under the impacts of various loads (ice, swimming solids or sediments, etc.) and aggressive environment; therefore they deteriorate and lose their durability especially in the zone of changing water level. The compressive strength of functioning concrete structures of hydraulic structures can be evaluated by testing the samples cut out from the investigated structures or by non-destructive methods (using rebound hammer).

During the investigation it was noticed, that all the investigated surfaces of reinforced concrete slabs for strengthening slopes of ponds in the zone of changeable water level are more or less deteriorated in form of pitting. Schmidt hammer rebound number and compressive strength of irregular samples taken from the reinforced concrete slabs were used for evaluation of whole upstream slope of pond. It is known, that the rebound hammer test shows only the state of the surface of concrete, therefore the result of compressive strength obtained by examining the core samples is more reliable, as it shows the strength of concrete in deeper layers. The irregular samples were taken from more deteriorated slabs, made from weaker concrete, compared with less deteriorated slabs tested by Schmidt hammer.

### **1. Introduction**

The surface protective layer of concrete and the joints of the slabs are damaged due to the processes of degradation (corrosion of concrete and reinforcement, erosion, biological decomposition) and due to the environment (cold cycles, ice, shock waves, mosses, grasses, shrubbery, periodic impregnation, etc.). The most destructive processes violates the protective layer of low-quality concrete (low strength and frost resistance), which crumbles when is influenced by cold cycles, its physical-mechanical properties are changing, the damage-

pittings- are formed. The pittings form and develop for a number of reasons [1, 2], among which, as one of the most important, are mentioned the destructive effects of cold cycles. The surface of concrete layer is broken in the following order: the expanding ice front displaces water from cementitious stone capillaries and pores under pressure, which exceeds the limit of tensile concrete strength; the surface of concrete layer degrades. Also, the structure degradation is caused by the accumulation of technological errors (inadequate composition of concrete, poor workmanship, concrete delamination), and specific service conditions [3]. The pond of Grauzė III with the earth dam (hereinafter –ED), built in 1973 was chosen for the research which is a typical example of Lithuanian small ponds (whose area is < 5 ha). The upper pool slope is covered with reinforced concrete slabs (175 × 100 cm), which are arranged in four rows with 138. Under water there are two rows of slabs, the third row of slabs is at the level of the changeable water level, the fourth is above the normal water level (NWL). These rows of slabs are divided into zones [4] (Fig.1).

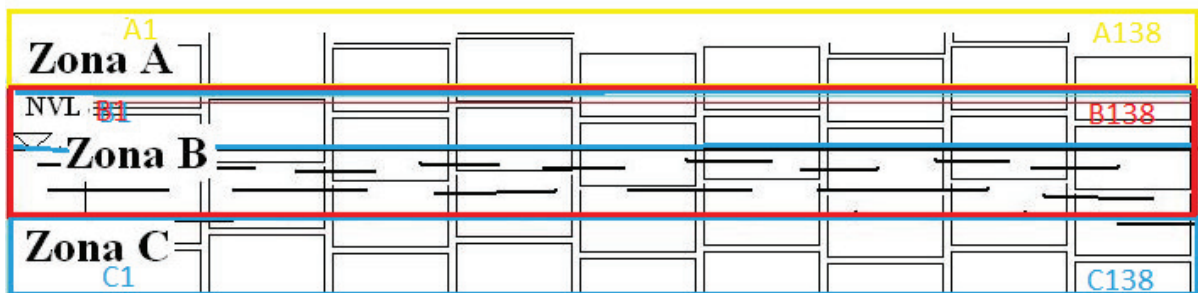


Figure 1: Zoning of slabs (in vertical direction): zone A – above the changeable water level; zone B – at changeable water level (above or below NWL); zone C – zone under water (below NWL).

The slabs of the dams A and B are horizontally divided into 12 sectors every 10 meters. The test area Zone A (in the vertical direction) is chosen 1.10 m above the NWL, and in the Zone B (in the vertical direction) it is selected 0.10 m above the NWL. The concrete strength of each section is determined.

## 2. Methodology

The actual compressive strength of reinforced concrete slabs for the earth dam slope protection (hereinafter SDP) was determined by the non-destructive method using E. Schmidt system device according to standard methods [1, 5; 6] and destructive methods according to the non-standard [7, 8] methodology. The macrostructure of the outer (hereinafter - protective) layer of SDP concrete, as well as of any other building materials of mineral origin, is not homogeneous, therefore the dispersion of its physical-mechanical properties is estimated by variance, coefficient of variation, average square deviation, and other statistical indicators.

Using the non-destructive method with a rebound hammer of concrete Cat.58–CO181/N (Schmidt's system), an actual compressive strength of concrete was measured. The non-destructive testing of compression strength was performed in accordance with the Standard EN 12504-2:2012, using the Schmidt Hammer. Before and after every examination, the

device was calibrated using the standard anvil. Research results were statistically evaluated: the average compressive strength of concrete  $f_c$ , the variation coefficient  $v$  and the root-mean-square deviation  $\sigma$  were calculated using “Microsoft Excel” macros.

The compressive strength of concrete was determined by destructive methods when testing non-dangerous places of the structures when taking out irregularly shaped concrete pieces on non-aligned surfaces. This method is more suitable for the determination of the compressive strength of weaker concrete (up to 10 MPa), which is especially relevant for determining the strength of SDP of ponds. The reliability of the method has been demonstrated by comparing the results obtained when testing samples of the same strength according to the standard methodology. Concrete pieces for testing were taken out from reinforced concrete structures by cutting.



Figure 1: Destroyed slabs for ponds slope protection in zone B.

The concrete pieces were placed in sealed polyethylene bags. Samples were measured with a slider, with an accuracy of 1.0 mm. Before the test, concrete pieces were carefully inspected. Cracked, layered and hollow samples were rejected.

The specimens, whose diameter corresponded to the diameter of the standard specimens, and samples with a smaller diameter than the standard, were compressed with available stamps. Dimensions of concave stamps are indicated in Table 1. The pit of the stamp is 10 mm.

Table 1: Dimensions of the stamps.

<b>n</b>	<b>Diameter d, mm</b>	<b>Area <math>A_n</math>, mm<sup>2</sup></b>
1	35.7	1000
2	50.5	2000
3	71.4	4000
4	100.0	7850

Remark:  $n$  – number of stamps.

The size of most of the concrete pieces was appropriate to test with stamps of maximum diameter ( $d = 100$  mm). Before the test, the pits of the selected stamps were filled with a levelling mortar with a compressive strength close to that of the concrete to be tested. The specimens were prepared in accordance with the requirements of standard [8] with hydraulic press MC-1000 (Fig. 2). The compression load was evenly increased to  $(0.6 \pm 0.4)$  (N/mm<sup>2</sup>)/s intensity. During the test, large concrete pieces, tested with stamps of 100 mm diameter, broke into smaller parts. The pieces of the broken concrete piece, if they were not damaged, were tested with a stamp of a smaller diameter by using compression machine – hydraulic press. After the test, the character of the destruction of the samples was evaluated, measured the largest particle size of the concrete filling.



Figure 2: The sample in hydraulic press MC-1000

### 3. Discussion

The compressive strength of SDP was determined by E. Schmidt device in April of 2012. In the same year, SDP concrete investigations were carried out using destructive methods according to the research methodology for the evaluation of the compressive strength of concrete in an attempt to test irregularly shaped specimens. The tests using destructive methods were repeated in October of 2014. The results of the tests are presented in Table 2. Mostly, the concrete is damaged in the area of ice and waves (changeable water level - zone B - see Figure 1), pittings are developing most in this area. In the case of improperly installed protective reinforcement concrete layer and its damage favourable conditions for reinforcement corrosion are created.

As it can be seen from the results of Table 2, the values of the average compressive strength of concrete used in the level of the changeable water level (zone B - see Figure 1)  $-f_{ck}=7,11$  MPa are smaller than in zone A above the water (Fig. 1)  $-f_{ck}=7,20$  MPa. The highest destructive effect of frost is expected in Zone B.

The destructive effect of cold is increasing with increasing humidity and negative temperatures (freezing water expands, its volume increases by about 9% and destroys concrete). Maximum moisture and the lowest temperature during cold cycles are foreseen in Zone B. In Zone C, the construction is heated by the water, and in the Zone A the water absorbability of the concrete decreases. In the case study, it was observed that slabs of Zone B are more affected by environmental factors and pittings are often formed in this area.

Table 2: Data of reinforced concrete slabs tests of Graužė III ED.

Research area	2012 (zone A)		2012 (zone B)		2012 (zone B) (non-destructive)			2014 (zone B)	
	$f_{ck}$ , MPa	$S$ , MPa	$f_{ck}$ , MPa	$S$ , MPa	$f_{ck}$ , MPa	$S$ , MPa	$v$ , %	$f_{ck}$ , MPa	$S$ , MPa
Sectors									
0-10m	8.19	2.98	7.3	1.28	13.9	2.13	15	6.48	0.93
10-20m	5.78	0.64	7.19	1.48	13.4	1.96	14	8.28	1.91
20-30m	6.57	1.07	6.48	1.34	17.8	3.85	22	7.22	2.86
30-40m	6.51	1.52	6.22	1.01	22.4	6.54	28	6.53	1.29
40-50m	6.17	1.15	8.07	6.11	16.9	2.33	13	6.13	0.82
50-60m	5.29	0.59	5.34	0.57	11.3	1.42	13	5.69	0.5
60-70m	9.73	5.3	6.44	1.14	14.2	3.11	22	5.69	1.25
70-80m	6.44	0.82	10.5	4.47	26.8	4.98	18	9.33	4.55
80-90m	6.75	0.93	6.42	1.51	17.6	2.5	14	6.09	1.16
90-100m	9.51	4.56	5.82	1.16	22.9	2.85	12	7.69	4.63
100-110m	9.14	2.39	8.14	2.08	20.4	2.27	11	6.64	1.53
110-120m	6.26	1.36	7.41	0.68	29.1	1.79	6	7.06	1.8
Whole slope	<b>7.20</b>	2.03	<b>7.11</b>	1.90	<b>18.9</b>	2.98	15.67	<b>6.90</b>	1.94

*Remark.* Markings in the table: average compressive strength of concrete  $f_{ck}$ , MPa; average square deviation  $S$ , MPa; coefficient of variation  $v$ , %.

Analysing the results of 2012 presented in Table 2, it was found that the strength of the SDP without damage to structures, determined by E. Schmidt system device, was bigger than the strength determined by the destructive method. This is explained by the fact that undisturbed (non-destroyed slabs) were tested by a non-destructive method, while irregularly shaped specimens, the samples taken out from reinforced concrete structures (from the reinforced concrete slabs of the ED) were tested using the destructive test methods according to the evaluation of the compressive concrete strength. It is also known that using a non-destructive method, with E. Schmidt system device, results higher values due to the environmental impact of the carbonisation of the surface protective concrete layer [9].

#### 4. Conclusions

The selected examples of hydraulic structures were presented and the durability problems occurring in concrete structures were revealed. In most cases, concrete is damaged in the impact zones of ice and waves - pittings is most evident in this area.



As it can be seen from the results, using non-destructive method (E. Schmidt system) the values of compressive concrete strength were 2-4 times higher than using the destructive method. These differences are possible due to the aforementioned reasons – non-destroyed slabs were tested using the non-destructive method and due to carbonization, the surface strength of the slabs is higher.

The compressive strength of concrete was determined by destructive methods when testing non-dangerous places of the structures when taking out irregularly shaped concrete pieces on non-aligned surfaces. The reliability of the method has been demonstrated by comparing the results obtained when testing samples of the same strength according to the standard methodology. The rebound hammer test shows only the state of the surface of concrete, therefore the result of compressive strength obtained by examining the drilled cores is more reliable, because tested concrete is not effected by carbonization, but in some cases, it is necessary to use the non-destructive methods, when it is impossible to drill the cores due to weak concrete or thin structures as slabs.

### References

- [1] ACI Manual of Concrete Practice Part3–2001, Strength Evaluation of Existing Concrete Buildings. American Concrete institute, Farmington hills (2001), 24
- [2] Venckevičius V. and Žilinskas R., Reconstruction and repair of buildings (in Lithuanian). Kaunas (2000)
- [3] Berkowskia, P. and Kosior-Kazberukb, M., Material and structural destruction of concrete elements in the industrial environment. Modern Building Materials, Structures and Techniques, MBMST 2016. Procedia Engineering 172 (2017), 96 – 103
- [4] Webber, D. et al, Design of Small Dams. Manual US Department of the Interior Bureau of Reclamation. Washington: A Water Resources Technical Publication, (1987)
- [5] EN 12504-2:2012 Testing concrete in structures - Part 2: Non-destructive testing - Determination of rebound number
- [6] Hannachim, S. and Guetteche, M. N., Review of the Rebound Hammer Method Estimating Concrete Compressive Strength on Site. Proceedings of International Conference on Architecture And Civil Engineering (ICAACE'14) (2014), 118-127
- [7] Vaišvila, K. A. and Lindišas, L., The research of the compression strength of concrete on reinforced concrete structures of functioning water engineering constructions. The 7th International Conference „Modern building materials. Structures and techniques“ (2001)
- [8] EN 12504-1:2009 Testing concrete in structures - Part 1: Cored specimens - Taking, examining and testing in compression
- [9] Šadzevičius, R. et al, Comparison of concrete compressive strength values obtained using rebound hammer and drilled core specimens // Rural Development 2015: Towards the Transfer of Knowledge, Innovations and Social Progress: Proceedings of the 7th International Scientific Conference (2015)

## **EXPERIMENTAL INVESTIGATION OF ACCELERATORS IN FLOOR CONCRETE MIXTURE UNDER COLD CLIMATIC CONDITIONS**

**Themistoklis Tsalkatidis <sup>(1)</sup>, Even Solbraa <sup>(1)</sup>**

(1) Norwegian University of Life Sciences, Ås, Norway

### **Abstract**

Cold climatic conditions are challenging when casting concrete since they significantly increase both the setting and the finishing time of concrete. The use of accelerators is known to counteract this retardation but it has mostly been examined under laboratory-controlled environment. This paper investigates the effect of admixtures, used in a typical concrete floor mixture, during cold weather exposure conditions, with temperatures ranging from +3 to -5<sup>0</sup>C, by performing three tests. The concrete mixture is first tested without the presence of additives and then with hardening, setting and combinations of hardening and setting accelerators. A total number of eleven case studies are examined. In each test, five specimens of slabs with dimensions of 1 by 1 by 0.1 m are constructed. The setting and finishing times of concrete are evaluated empirically. The compressive strengths of the concrete mixtures after 18, 24 and 30 hours are defined by testing cubic specimens. The experimental results verify that the presence of hardening and setting additives in concrete reduce the time for the finishing phase of a floor under cold climatic conditions. This reduction is close to 50% whilst at the same time the early strength of the concrete increases up to eleven times.

### **1. Introduction**

Concrete is a construction material that is affected by environmental conditions. Under cold climatic conditions, the hydration of cement becomes slower thus increasing the transition period from the initial plastic to the final rigid concrete state. In order to control the setting and finishing time of concrete, the use of admixtures such as set accelerators is highly recommended [1-4]. This paper examines the behaviour of a typical concrete floor mixture, with and without additives, during winter conditions in southern Norway [5]. An experimental analysis consisting of three tests is performed. Different additives are added to the reference

mixture resulting in eleven case studies. The workability and the development of early strength of concrete mixture are also considered.

## 2. Experimental program

### 2.1 Concrete

The reference floor mixture is concrete B30M60 standard FA without accelerating additives, a typical mixture used in Norwegian structures [5]. This is equivalent to C30/37.

### 2.2 Admixtures

Mapectast hardening accelerator (HA), Mapectast set accelerator (SA), Mapetard retarder (R), Mapectast Ultra N (HA) and Master X-Seed 100 (HA) are used as admixtures. Hardening, set accelerators and retarders are added in order to examine different case studies [5].

### 2.3 Methodology

The experimental procedure consists of three tests performed in temperatures ranging from +3 to -5°C [6-8]. The specimens used in the tests are concrete slabs with dimensions of 1 by 1 by 0.1 m. Five slabs for each test and eight cubes from each slab are constructed, resulting in a total number of 15 slabs and 120 cubes. The overview of the concrete mixtures is presented in Tab.1.

Table 1: Concrete mixtures examined.

Test Number	Mixture 1	Mixture 2	Mixture 3	Mixture 4	Mixture 5
Test 1	Reference	Reference+2% Mapectast HA+1% Mapectast SA	Reference+2% Mapectast HA+ 0.2% Mapetard R+1% Mapectast SA	Reference+1.5% Mapectast SA	Reference+ 3% Mapectast HA
Test 2	Reference	Reference+2% Mapectast Ultra N +1% Mapectast SA	Reference+2% Mapectast Ultra N+ 0.2% Mapetard R +1% Mapectast SA	Reference+1.5% Mapectast SA	Reference+ 3% Mapectast Ultra N
Test 3	Reference	Reference+2% Master X-Seed +1% Mapectast SA	Reference+2% BASF X-Seed + 0.2% Mapetard R +1% Mapectast SA	Reference+1.5% Mapectast SA	Reference+ 3% Master X- Seed

The main aims of the tests are to determine the setting and finishing times of concrete floor mixtures with or without the presence of admixtures. For the measurement of the setting time a cube of each concrete mixture is temperature logged. The setting time of the mixture is determined when the temperature of the cube has an increase of 2°C [9]. Finishing time is determined by the penetration length of a M10 bolt in the specimen. When the penetration is measured below 1cm then the specimen is ready to be brushed. The concrete has been cured using a curing membrane.

The workability and the strength of the concrete are also measured. For the determination of the compressive strength of the concrete at early stages, cubic specimens are tested after 18, 24 and 30 hours. Half of the cubes tested are placed indoor whereas the other half is placed outdoor. Regarding the workability of concrete, slump measurements are taken from the time of the addition of admixtures until the slump is measured below 200 mm. The flow is also measured and it has been found above the 340 mm limit for 200 mm of slump [10]. The used methods are presented in Tab. 2.

Table 2: Methods used.

Measurement	Method used
Setting time	Temperature logging
Finishing time	Bolt penetration
Strength	Compressive testing of cubes
Workability	Slump and flow calculations

### 3. Results and discussion

#### 3.1 Setting time

The setting time is defined when the temperature of the cube has increased 2°C [9]. The setting times of the mixtures are presented in Tab. 3.

Table 3: Setting times of tests 1 and 3.

Mixture	Setting time (hours):
<b>Test 1</b>	
Reference	29.5
HA+SA	21.5
HA+R+SA	30
SA	23
HA	26
<b>Test 3</b>	
Reference	>30
X-Seed+SA	Undetermined
X-Seed+R+SA	28.5
SA	24.5
X-Seed	17.5

In test 2, as shown in Fig. 1, the temperature development in the logged concrete cubes was not satisfactory, therefore only tests 1 and 3 are taken into consideration.

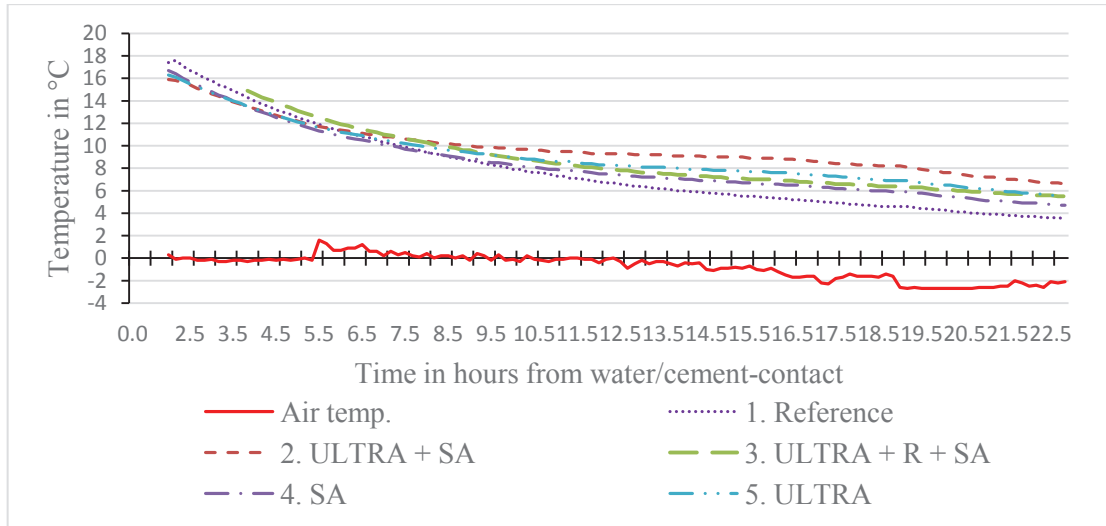


Figure 1: Temperature development in test 2.

### 3.2 Finishing time

The finishing time is achieved when the M10 bolt has a penetration equal to 10 mm. The following Fig. 2 depicts the finishing times for all tests. Mixtures 2 and 4 proved to be the most efficient. The difference in setting time between the reference mixtures of the tests must be related to a different water-to-cement ratio, concrete production temperature and weather conditions in each test.

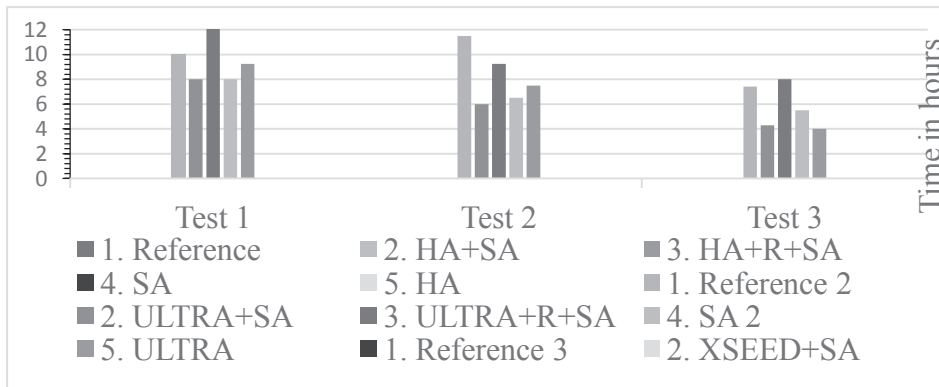


Figure 2: Finishing times.

### 3.3 Strength and workability

In Fig. 3 the compressive strength of the cubes measured after 18 hours is shown. The use of additives is proven to boost the early strength increase significantly, in all time measurements. Regarding workability, the use of both the hardening accelerators and the retarder has enhanced the workability of the reference mixture, as shown in Fig. 4. The average flow measurement is 342.5 mm, above the limit of 340 mm [10], when the slump is 200 mm.

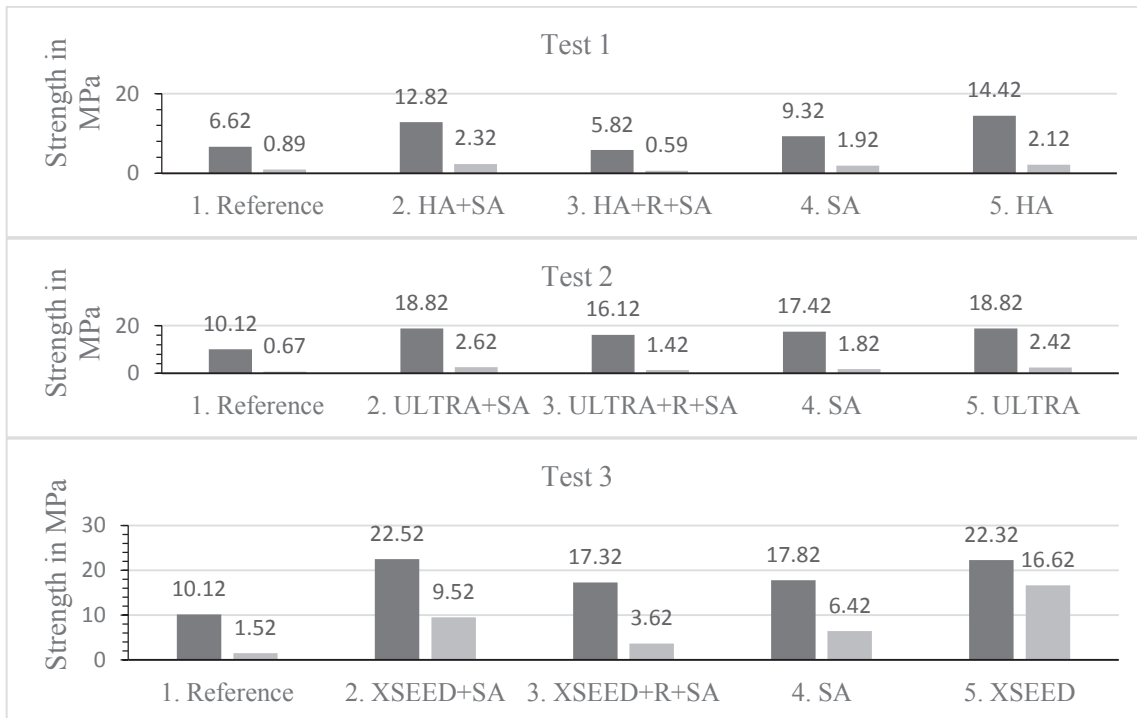


Figure 3: Compressive strengths of cubes after 18 hours inside (left) and outside (right).

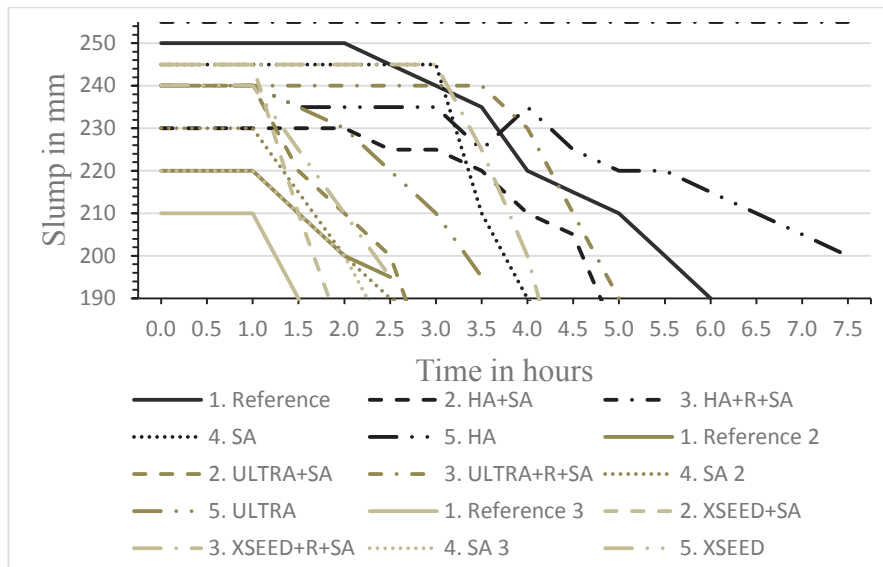


Figure 4: Slump measurements.

#### 4. Conclusions

The main conclusions of the experimental investigation are the following:

- The use of admixtures in a typical floor concrete under cold climatic conditions mixture significantly accelerates the setting and finishing times. The setting time can be decreased by up to 42% and the finishing time by up to 48% compared to the reference concrete

mixture where no additives are used. This is particularly important for countries that experience long winters such as Norway.

- The early compressive strength accumulation rate increases by adding a combination of hardening and setting accelerators in the reference mixture. The use of a single hardening accelerator can in some cases produce the same results, depending of the characteristics of the additive.
- The workability of concrete is best controlled when a combination of hardening accelerator and retarder is added to the reference mixture. Hardening accelerators are proven to enhance the workability of concrete.
- The combinations of Mapefast Ultra N or Master X-Seed 100 with Mapefast R have found to be the most effective in order to control the consistency of concrete.
- The use of single or combinations of admixtures is recommended provided that it is done in a monitored manner. A misuse of additives can result in unwanted effects.
- The temperature development of concrete in test 2 was very small, probably due to the lower temperature of concrete of 24.1<sup>0</sup>C from production in comparison to tests 1 (26.1<sup>0</sup>C) and 3 (26.7<sup>0</sup>C). Nevertheless, setting is still present in test 2 specimens.

## References

- [1] Bost, P. et al, Comparison of the accelerating effect of various additions on the early hydration of Portland cement, *Con and Build Mat* 113 (2016), 290-296
- [2] Fatma, K. et al, Behavior of fresh and hardened concretes with antifreeze admixtures in deep-freeze low temperatures and exterior winter conditions, *Con and Build Mat* 76 (2015), 388-395
- [3] Riza, P., The effect of antifreeze additives on fresh concrete subjected to freezing and thawing cycles, *Cold Reg Sc and Tech* 127 (2016), 10-17
- [4] Ryou, J.-S. and Lee, Y.-S., Properties of early-stage concrete with setting-accelerating tablet in cold weather, *Mat Sc and Eng A* 532 (2012), 84-90
- [5] Solbraa, E., Eksperimentell undersøkelse av akseleratorer i gulvbetong under kaldt klima, MSc thesis, Norwegian University of Life Sciences (2018) (In Norwegian)
- [6] NS-EN12350-2:2009, Testing fresh concrete- Part 2: Slump-test, Standard Norge, Norway (2009)
- [7] NS-EN12390-2:2009, Testing hardened concrete- Part 2: Making and curing specimens for strength tests, Standard Norge, Norway (2009)
- [8] NS-EN13670-2:2009+NA:2010, Execution of concrete structures, Standard Norge, Norway (2010)
- [9] Road standards, section 14.623 Avbinding, The Norwegian Public Roads Administration, Norway (1997) (In Norwegian)
- [10] Publication nr15, Betonggulv- gulv på grunn og påstøp, Norwegian Concrete Association, Norway (2017) (In Norwegian)

## **EXPERIMENTAL INVESTIGATION OF NEW CEMENT COMPOSITES LONG-TERM PROPERTIES**

**Andina Sprince<sup>(1)</sup>, Leonids Pakrastins<sup>(1)</sup>, Liga Radina<sup>(1)</sup>**

(1) Riga Technical University, Latvia

### **Abstract**

The purpose of this research is to experimentally determine the long-term properties of several new cement composites with unconventional additives - borosilicate lamp glass filler, montmorillonite mineral additive, and polyvinyl alcohol (PVA) fibres. Test specimens were prepared and subjected to constant compression load in a permanent temperature and level of moisture. The investigated laboratory determined properties included the compressive strength values, shrinkage strain, uniaxial compressive creep strain values and then the following parameters were calculated – creep coefficient, specific creep, creep modulus. The obtained experimental results showed that for the various mixes of new cement composites the creep coefficient was the same as for normal strength cement composite, ranging from 0.2 to 3; specific creep values were 10-85 microstrain /MPa; creep modulus was 15-105 GPa. The experimental study proves that new elaborated mixes can be successfully used in the production of concrete, thus potentially decreasing the use of cement, which would lead to a reduction of carbon dioxide released into the atmosphere.

### **1. Introduction**

Nowadays the construction material industry is developing rapidly, with an ever-increasing tendency towards the use of new materials. Since the beginning of the 20th century, scientists and cement composite technologists are working on developing new, various types of structural multi-component cement composites, the solutions ranging from mixtures with a reduced quantity of cement and smaller aggregate dimensions, to fibers being used as disperse reinforcement, introduction of various chemical additives and a lowered cement-water ratio, as well as substituting some of the cement with recycled materials, etc. [1, 2, 3, 4]. The newly developed cement composite matrixes, in general, have improved physical properties, e.g., their microstructure — cement paste accounts for a larger part of the volume, and the porosity



is reduced, leading to cement composites with smaller water absorption and better frost resistance properties [5, 6, 7]. Although the effect on these properties has been conscious, there are still several obstacles that prevent a more widespread use of these newly developed cement composites in construction. One of the main problems is insufficient information about the long-term properties, which are essential in ensuring safe and prolonged exploitation of structures.

## 2. Materials and Methods

One of the goals of the experiments was to find out whether the new cement composites can be competitive and whether their long-term properties are equivalent to those of normal strength cement composite (the compressive strength of normal concrete has a value ranging between 20 and 40 MPa and the high strength concrete will have strength above 40 MPa). During the research following cement composites were made and tested (graphs show designation and transcription of various cement composites):

- 20% S; 40% S; Ref S – high strength cement composite that has 20%; 40% borosilicate lamp glass micro size part powder obtained from reused lamp glass and used as an additive replacing a part of cement amount and reference composition for cement composite with borosilicate lamp glass additive. Cubic compressive strength at 28-day age appropriately ~60MPa; ~55MPa; ~63 MPa. Long-term test specimen dimensions 40×40×160 mm; at the beginning of experimental tests the age of cement composite specimen 51 days; loading level in long-term load tests 40% of ultimate stresses; in the long-term properties' tests the specimens were placed under constant static (permanent) load for 90 days; air-dry.
- ECC PVA – engineered cement composites with PVA (2%) fibres. Cubic compressive strength at 28-day age 47 MPa. Long-term test specimen dimensions Ø40×160 mm; at the beginning of experimental tests the age of cement composite specimen 28 days; loading level in long-term load tests 25% of ultimate stresses; in the long-term properties' tests the specimens were placed under constant static load for 100 days; air-dry;
- PS M – high strength cement composite with 1% montmorillonite mineral nano-size particles that in their essence is a powder of very fine, especially processed clay particles as an additive replacing a part of cement amount and Ref M – high strength cement composite (reference composition for cement composite with montmorillonite mineral nano additive). Cubic compressive strength at 28-day age appropriately ~55 MPa; ~78 MPa. Long-term test specimen dimensions 40×40×160 mm; at the beginning of experimental tests the age of cement composite specimen 57 days; loading level in long-term load tests 40% of ultimate stresses; in the long-term properties' tests the specimens were placed under constant static load for 90 days; air-dry;

The cement composite mixtures were prepared using a double shaft laboratory mixer (BHS, 3 kW, 20–100 rpm). The compressive strength of the specimens was determined in the compression machine “Controls”, model No. C56G2, with an accuracy of  $\pm 1\%$  and a measurement range of 0-3 kN; the loading speed was 0.8 MPa/s.

All the creep specimens were loaded with a constant static load, regularly performing strain readings. The specimen does not encounter bending. For determination of the correct creep amount, shrinkage strains determined in parallel to geometry specimens and in equivalent

environmental conditions, only without the load, were subtracted from the total strains (because of the paper's limited pages amount, there have not be shown the detailed creep and shrinkage result graphs). The basic and drying creep components haven't been determined separately. It has been assumed that the difference of specimen's age - 28, 51, 57 days, does not significantly influence the test results (because typically, it is expected that a concrete mix will reach 100% of its design strength in 28 day). During the tests all specimens were kept in a dry atmosphere of controlled conditions: temperature  $23\pm 1^\circ\text{C}$  and relative humidity  $35\pm 3\%$  [8, 9].

For all the creep specimens before placing into creep lever test stand, strain gauges were attached to the side surfaces. The strains were measured using Aistov electrical strain gauges with a scale interval of  $1\ \mu\text{m}$  and maximum range of  $\pm 5\ \text{mm}$ . Creep lever test stand (see Fig.1) allows using specimens ( $\leq 70\ \text{mm}$ ) more characteristic to the dimensions of high and ultra-high strength cement composite structures. With these stands, it is possible to apply constant loading on the specimens and to keep it uniform over a long period of time. In addition, it is not necessary to adjust the stress level during the experiments, the calibration curves are linear, no energy resources are consumed, and it is possible to test cement composites with the maximum aggregate dimension  $\leq 5\ \text{mm}$ , simultaneously ensuring economic use of materials. The lever arm ratio of the creep testing stand was 1:40. The accuracy of the counterweights was  $1/100\ \text{kg}$  or  $0.01\%$ . Therefore, the accuracy of creep levers is  $0.01 \times 40 = \pm 0.4\ \text{kg}$ .

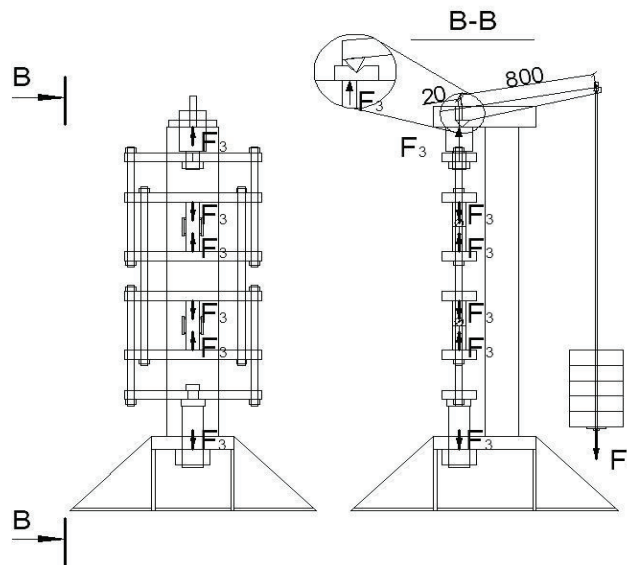


Figure 1: Creep lever test stand for determination of uniaxial compression creep strains ( $F_3 = F_4 \times \text{lever arm}$ ).

### 3. Results and Discussion

During the experiments, the values of strength, deformability and long-term properties of various new cement composites were found and parameters for designing of safe structures were determined, which have not been found out up until now.

Figure 2. shows the cubic compressive strength of various cement composites and values were from 32 to 60 MPa at the beginning of the tests and from 48 to 80 MPa at the end of tests. The largest cubic compressive strength was determined for cement composite without unconventional additives.

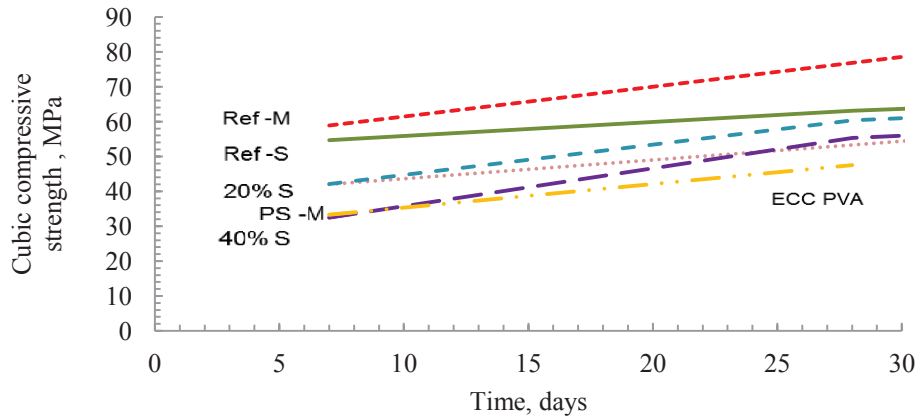


Fig. 2. Cubic compression strength of different kind of new cement composites

Creep coefficient shows the proportion of creep strain and elastic strain. Experimental data for the various mixes of cement composites show that for cement composite creep coefficient were the same as for normal strength cement composite and were within margins of 0.2 to 3 (see Fig.3), which does not comply with data of literary sources which predict a significant decrease of this coefficient [10]. The obtained results show that the proportion of elastic and creep strain for normal and high strength cement composites maintain similar proportions.

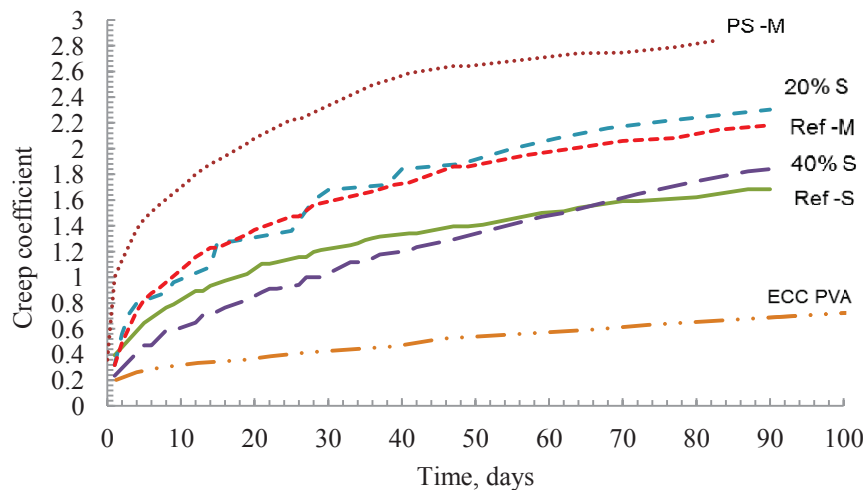


Figure 3: Creep coefficient in compression of different kind of new cement composites.

Specific creep is the most objective parameter of long-term loading as it excludes stress effect on long-term strains. Figure 4. shows specific creep of various cement composites and values

were from 10 to 85 microstrain /MPa. The largest specific creep was determined for cement composite with montmorillonite additive.

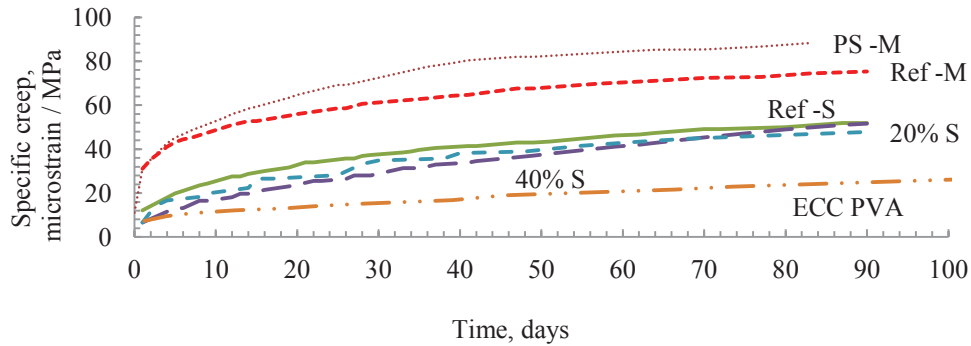


Figure 4: Specific creep in compression of different kind of new cement composites.

Creep modulus is the proportion of applied stress and creeps strain. This long-term parameter can be used for determining the displacement of long-term loaded structures after a long time period. Figure 5. shows the creep modulus of various new cement composites. As it can be seen, creep modulus has the tendency to decrease in time which can be explained by the increase of creep strain and total strain. The lower the creep modulus is, the less is creep in the material. Displacement amount rapidly increases in the first week, then the displacement speed in time decreases and approximately after 60 days significant changes in displacement cannot be observed anymore.

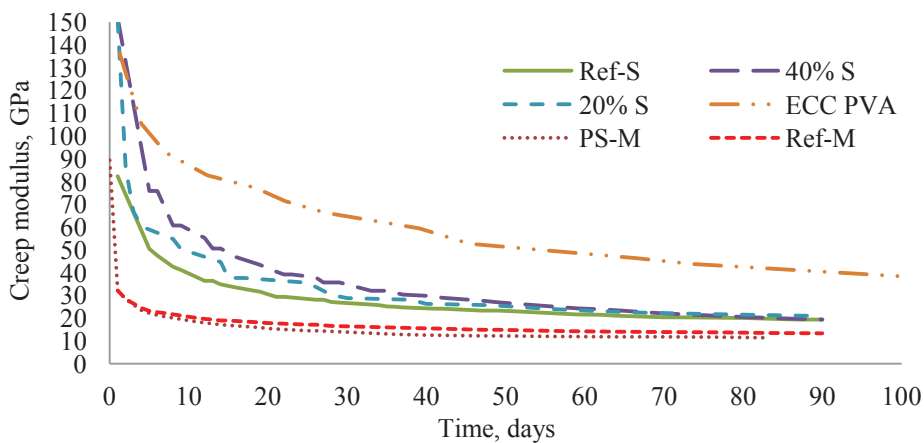


Figure 5: Creep modulus in compression of different kind of new cement composites.

It was experimentally determined that montmorillonite and borosilicate lamp glass added to cement composites neither significantly improves nor decreases the mechanical and deformability properties. The difference of the provided results reaches up to 20% to the reference cement composite results; therefore, it must be concluded that the use of such new cement composite made with alternative, more ecologic, nature-friendly mineral additive of recycled material in construction is permissible.

Similarly, it can be seen from the experimental results that PVA fibres improve long-term and durability properties of normal strength cement composites.

#### 4. Conclusions

Experimentally obtained results for various cement composite tests confirm the hypothesis raised by various leading researchers (Neville, Brooks, Bazant, Gardner, Lockman, Fanourakis, Gilbert, Ranzi, Wittmann, Rusch and others) - the higher is the density of cement composite, the stronger it is and strain is lesser. Similarly, it has been experimentally proved that cement composite final strength increases with cement composite age and it is not substantially affected by its subjection to loading.

The obtained experimental results showed that for the various new cement composites the creep coefficient was the same as for normal strength cement composite. After approximately 90 days of loading creep coefficients values of new cement composites were 0.2-3; specific creep values were 10-85 microstrain /MPa; creep modulus was 15-105 GPa.

The use of new additives will also give an indirect positive effect on the global environment, as, by increasing the use of new unconventional cement compositions and by reducing the dimensions of the cross-sections of structures, the total amount of cement consumption will decrease and, by substituting part of the cement with recycled mineral fillers, the use of non-renewable resources and non-biodegradable waste will also be reduced.

#### References

- [1] Fathifazl G., Razaqpur A.G., Isgor B., Abbas A., Fournier B., Somon F. Creep and drying shrinkage characteristic of concrete produced with coarse recycled concrete aggregate. *Cement and Concrete Composites* vol. 74 (2011), 1026-1037
- [2] Fehling E., Schmidt M., Walraven J., Leutbecher T., Frolich S. *Ultra-High Performance Concrete UHPC*. Ernst&Sohn, Berlin (2014)
- [3] Naaman A. E., Reinhardt H. W. *High Performance Fiber Reinforced Cement Composites*. RILEM Publications S.A.R.L., Proceedings PRO6, France (2003)
- [4] Prisco M., Plizzari G., Vandewalle L. Fibre reinforced concrete: new design perspectives. *Materials and Structures* Vol. 42 (2009), 1261-1281
- [5] Gilbert R. I., Ranzi G. *Time-Dependent Behaviour of Concrete Structures*. London and New York: Spon Press (2011) 3, 5, 9-11, 25-30, 26, 27, 33
- [6] Neville A. M., *Creep of Concrete and Behaviour of Structures*. *Concrete International* No.5 (2002)
- [7] Lu J., Poon C.S., Improvement of early age properties for glass-cement mortar by adding nanosilica. *Cement and Concrete Composites* Vol. 89 (2018), 18-30
- [8] Rilem TC 107 - CSP: Creep and Shrinkage Prediction Models: Principles of Their Formation. *Measurement of Time-Dependent Strains of Concrete*, *Materials and Structure*, Vol. 31 France (1998)
- [9] ACI 209.2R-08. *Guide for Modeling and Calculating Shrinkage and Creep in Hardened Concrete*, ACI Committee 209, USA (2008)
- [10] BS EN 1992-1-1:2004. *Eurocode 2: Design of concrete structures - Part 1-1: General rules and rules for buildings*, CEN (2004)

## **EXPERIMENTAL PROCEDURES FOR DETERMINING THE LEVEL OF SEGREGATION OF LIGHTWEIGHT AGGREGATE CONCRETES**

**Afonso Miguel Solak** <sup>(1,2)</sup>, **Antonio José Tenza-Abril** <sup>(1)</sup>, **Francisco Baeza-Brotons** <sup>(1)</sup>  
**Victoria Eugenia García-Vera** <sup>(3)</sup>, **Marcos Lanzón** <sup>(3)</sup>

(1) Department of Civil Engineering, University of Alicante, Alicante, Spain

(2) CYPE Ingenieros S.A., Alicante, Spain

(3) Department of Architecture and Building Technology, Technical University of Cartagena, Cartagena, Spain

### **Abstract**

In this work, four different segregation indexes were applied to evaluate the segregation phenomenon in lightweight aggregate concretes (LWAC). LWAC permits greater design flexibilities, positively impact the energy consumption of the buildings and may mean a substantial cost saving. However, LWACs are susceptible to present aggregate segregation during mixing, transport, placement and dormant periods, due to density differences between components. Segregation causes a non-uniform distribution of aggregates in the mixture and may strongly affect the strength and durability of the material. These facts justify the use of indexes to properly quantify this phenomenon. Just a few segregation indexes that permit an evaluation of hardened concrete samples were found in the bibliography. The non-destructive ultrasonic pulse velocity method has been widely applied to the investigation of concrete materials and its results can be easily related to the physical properties of the materials, such as the concrete density. In this study, four experimental segregation indexes were tested applying two different types of experimental data: classic methods of density measurement and through ultrasonic velocities. The results prove the effectiveness and precision of the methods proposed and compare their advantages and disadvantages within another method found in the literature.

### **1. Introduction**

Vibration is an industrial practice to compact fresh concrete in a formwork and around reinforcement. During this process, the yield stress of concrete is reduced or cancelled so the

concrete flows by its weight [1] for releasing air bubbles and producing concrete with higher density, strength and durability [2]. During the mixing of lightweight aggregate concrete (LWAC), due to the low density of the aggregates and the longer mixing times LWAC is susceptible to segregation of the aggregates as a result of the differences between the densities of their components [3]. Segregation, the tendency for coarse aggregate to separate from mortar, remains one of the major problems in fresh concrete [4]. In LWAC the tendency to the floatation of the lightweight aggregate (LWA) grows with the increase of the vibration energy and therefore the concrete must present an adequate cohesion to avoid the phenomenon of segregation [5]. The consequences of segregation are numerous and may affect the strength and durability of structures [4]. Visual inspection is insufficient to evaluate the degree of concrete segregation [6] and just a few segregation indexes that permit an evaluation of hardened concrete samples were found in the bibliography. Ke [7] estimated a segregation index ( $SI_{Ke}$ ) dividing the specimens into four equal sections and using the densities obtained from the upper ( $\rho_{top}$ ) and lower ( $\rho_{bottom}$ ) slices of a cylinder. A possible segregation tends to reduce the density in the upper section because the lightweight aggregates tend to float in the mortar matrix. The index is calculated according to the Eq (1). If  $SI_{Ke}=1$ , it can be considered that the sample shows perfect uniformity. An index of less than 0.95 indicates a start of segregation [7].

$$SI_{Ke} = \frac{\rho_{top}}{\rho_{bottom}} \quad (1)$$

The non-destructive ultrasonic pulse velocity (UPV) method has been widely applied to the investigation of concrete. These measurements are able to predict different properties of the materials. Solak [5] found empirical correlations between p-wave UPVs and densities of LWAC sections. The main objective of this study is to test four experimental segregation indexes applying classical density measurement methods and UPV measurements methods.

## 2. Experimental program

### 2.1 Materials

Four different concretes were manufactured considering different types of LWA, different modes of vibration (one or two layers) and different theoretical densities. The experimental campaign involved the production of a concrete made with LWAs using the Fanjul method [8], in order to produce LWAC with a target density of 1700 kg/m<sup>3</sup> and 1900 kg/m<sup>3</sup>. Tab. 1 presents the manufacturing characteristics of these concrete and includes their mix proportions. All samples were manufactured with the same water to cement ratio of 0.6, resulting in 350 kg/m<sup>3</sup> of cement and 210 kg/m<sup>3</sup> of water to produce 1 m<sup>3</sup> of concrete. CEM I 52.5 R cement with an absolute density of 3176 kg/m<sup>3</sup> was used for all the concretes; 2 types of expanded clay were used as lightweight aggregate; its physical properties are described in Tab. 2. The bulk density of the LWAs was obtained according to the procedure described in the standard UNE EN 1097-3. In addition, the density of the particles in the dry state was determined by the methodology proposed by Fernández-Fanjul et al [9], the absorption of water at 24 hours according to the UNE EN 1097-6 (pre-dried particles soaked in distilled water). The methods/standards used for testing are also presented in Tab. 2. Before mixing,

and to avoid the loss of water from kneading by absorption, the LWAs were presaturated. During the mixing, the water content of the LWA and the surface water content were determined, to make the appropriate corrections and maintain a constant effective water to cement ratio of 0.6.

Table 1: Manufacturing characteristics and mix proportions to produce 1 m<sup>3</sup> of concrete.

Concrete	Samples	Theoretical		Type of LWA	Fine Coarse (kg/m <sup>3</sup> )	LWA (kg/m <sup>3</sup> )
		Densities	Vibration			
LWAC1	20 uds	1700 kg/m <sup>3</sup>	two layers	Arlita Leca HS	723.9	416.2
LWAC2	20 uds	1900 kg/m <sup>3</sup>	two layers	Arlita Leca HS	1046.0	294.0
LWAC3	20 uds	1700 kg/m <sup>3</sup>	one layer	Arlita Leca M	991.1	148.9
LWAC4	20 uds	1900 kg/m <sup>3</sup>	one layer	Arlita Leca M	1234.8	105.2

Table 2: Characteristics of aggregates and the methods/standards used for testing

Property	Method	Arlita Leca M	Arlita Leca HS	Fine Aggregate
Dry particle density (kg/ m <sup>3</sup> )	According to [9]	482	1019	2688
Bulk density (kg/ m <sup>3</sup> )	UNE EN 1097-3	269	610	1610
24 h Water absorption (%)	UNE EN 1097-6	36.6	12.2	0.12

## 2.2 Experimental procedures

In the present study, four experimental segregation indexes were tested applying two different types of experimental data: the first type, using classic methods of density measurements and the second, through UPV measurements. The experimental procedures are presented in Fig.1.

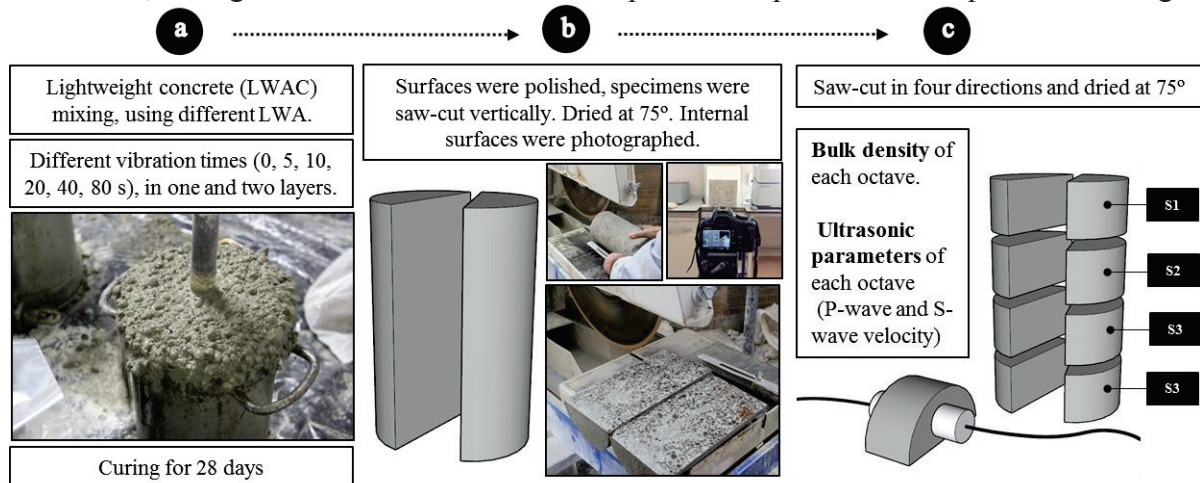


Figure 1: Flowchart of the methodology used in this study.

Cylindrical samples (Ø150mm and 300mm height) were compacted using an electric Ø25mm needle vibrator of 18000 rpm/min. Specimens were vibrated during 6 different times (0-5-10-20-40-80 seconds), in one and two layers (Tab. 1) in order to stimulate different behaviors and create different scenarios. These procedures were repeated 4 times, considering different times between mixing and molding of 15, 30, 60 and 90 min). After being made and cured in water at a temperature of  $20 \pm 1^\circ\text{C}$  for 28 days, the specimens were saw-cut through



longitudinal axis and their sections were photographed for visual analyses. Subsequently the specimen halves were then saw-cut into four equal parts, resulting in octaves, which had their bulk densities determined. Ultrasonic pulse velocity tests were further applied for each octave. Compressional (p-wave) and shear (s-wave) wave velocities were obtained using the direct transmission configuration using polarized Panametric transducers (250 KHz). Visco-elastic couplants were used to achieve good contact between the transducer and the samples.

### 2.3 Segregation indexes

In this work three new experimental segregations indexes were tested and compared with the methodology proposed by Ke [7] as a validation criteria. The first index ( $SI_A$ ), based on density measures, estimate a quantification for the segregation phenomenon considering the densities of the upper section of the sample ( $\rho_{top}$ ) and the average between the densities of the four sections ( $\rho_{average}$ ). Similarly to  $SI_{Ke}$ , a possible segregation tends to reduce the density in the upper section because the lightweight aggregates tend to float in the mortar matrix. The more intense is the phenomenon, the higher is the difference between  $\rho_{top}$  and  $\rho_{average}$ . If  $SI_A=1$ , it can be considered that the sample shows perfect uniformity. The index is calculated according to the Eq. (2).

$$SI_A = \frac{\rho_{top}}{\rho_{average}} \quad (2)$$

The second and the third indexes tested in this work,  $SI_B$  and  $SI_C$  respectively, are based on UPV measurements. These measurements are a non-destructive technique and when the ultrasonic pulse is applied to concrete it enables to predict different properties of the material. Solak [5] found empirical correlations between p-wave UPVs and densities of LWAC sections.  $SI_B$  estimates the segregation considering the UPVs obtained from the upper ( $UPV_{top}$ ) and lower ( $UPV_{bottom}$ ) slices of the samples. In LWAC a possible segregation tends to reduce the density in the upper section and as consequence, a reduction of the UPVs. The index is calculated according to the Eq. (3) and as described to the other indexes, if  $SI_B=1$ , it can be considered that the sample shows perfect uniformity.

$$SI_B = \frac{UPV_{top}}{UPV_{bottom}} \quad (3)$$

The third index,  $SI_C$ , estimates the segregation phenomenon considering the UPVs of the upper section of the sample ( $UPV_{top}$ ) and the average between the UPVs of the four sections of the sample ( $UPV_{average}$ ). The index is calculated according to the Eq. (4) and  $SI_C=1$ , it can be also considered that the sample shows perfect uniformity.

$$SI_C = \frac{UPV_{top}}{UPV_{average}} \quad (4)$$

### 3. Results and Discussion

Scatter diagrams were plotted to identify the possible correlation between  $SI_{Ke}$  and the new segregation indexes.  $SI_{Ke}$  and  $SI_A$  (Fig. 2a) presented the higher coefficient of determination

( $R^2$ ), reaching 0,9463. The same behavior was observed comparing the graphs of Fig. 3a and Fig 3b. Correlations between  $SI_{Ke}$  and  $SI_B$  (Fig. 2b) and  $SI_{Ke}$  and  $SI_C$  (Fig. 2c) are not as high as the first method tested, but the curves maintain the same ascendant slope tendency, presenting more dispersion on SIs near 1 (homogeneity).

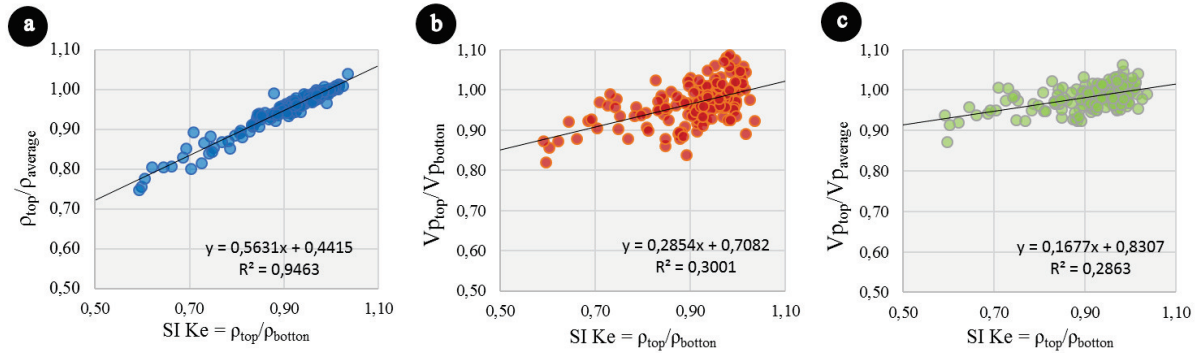


Figure 2: Scatter diagrams:  $SI_{Ke}$  vs  $SI_A$  (a),  $SI_{Ke}$  vs  $SI_B$  (b) and  $SI_{Ke}$  vs  $SI_C$  (c).

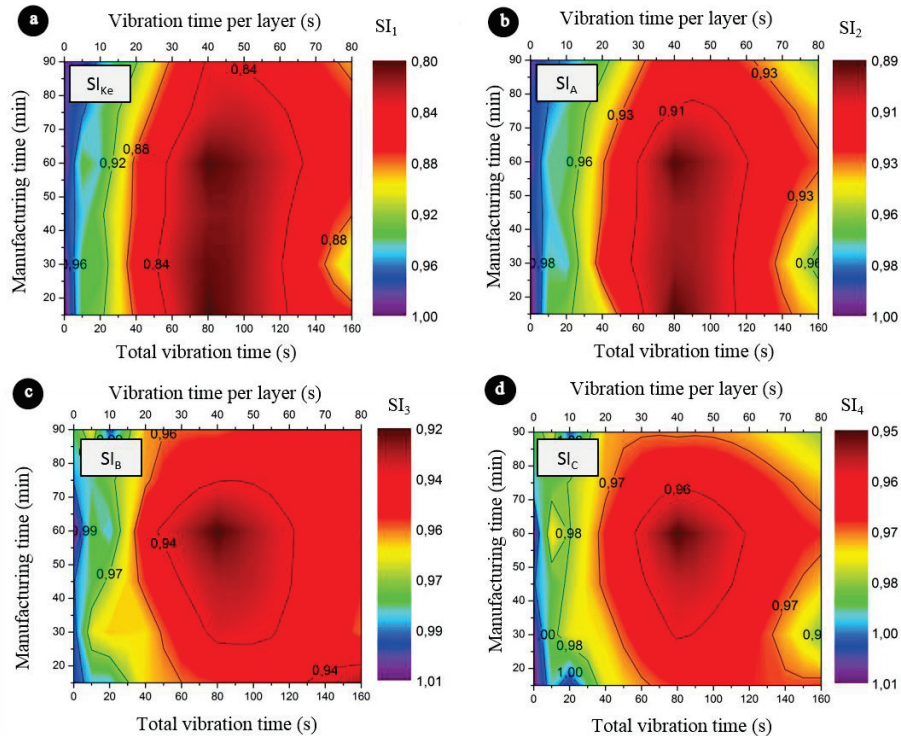


Figure 3: Segregation indexes for the concretes studied in this work

All SIs presented similar behaviors for the concretes studied (Fig. 3). However, some differences between SIs based on density and SIs based on UPVs were identified for manufacturing times of less than 30 minutes and more than 80 minutes. These differences can be identified comparing the central dark area of Fig. 3a and Fig. 3b, which have a shape of a “horseshoe” and the central dark area of Fig. 3c and Fig. 3d, which have “circular” shape. The scales of each index are also different.  $SI_{Ke}$  presented the highest difference between its minimum and maximum values (0.80 to 1.00) while  $SI_C$  presented the lowest variation (0.95 to 1.01).

#### 4. Conclusion

This study presents an experimental study on segregation in lightweight aggregate concretes (LWAC) presenting different ways to quantify this phenomenon. From the results presented in this study the following conclusions are drawn:

- A new segregation index applying density measurements was presented in this study.
- Based on the clear relation between ultrasonic waves and concrete densities, ultrasonic waves measurements could be used to evaluate the concrete segregation in hardened samples. Two new non-destructive methods to obtain a segregation index based on UPV measurements were presented.
- Although UPV methods are less accurate and may not detect certain heterogeneities, they are non-destructive and easy to apply methods.

#### Acknowledgements

This research was funded by the University of Alicante (GRE13-03) and (VIGROB-256). The authors wish to express their gratitude to Phd program in Materials, Structures and Soil Engineering of the University of Alicante.

#### References

- [1] Tattersall G, Baker P. The effect of vibration on the rheological properties of fresh concrete. *Mag Concr Res* 1988;40:79–89. doi:10.1680/macr.1988.40.143.79.
- [2] Banfill PFG, Teixeira MAOM, Craik RJM. Rheology and vibration of fresh concrete: Predicting the radius of action of poker vibrators from wave propagation. *Cem Concr Res* 2011;41:932–41. doi:10.1016/j.cemconres.2011.04.011.
- [3] Yu QL, Spiesz P, Brouwers HJH. Ultra-lightweight concrete: Conceptual design and performance evaluation. *Cem Concr Compos* 2015;61:18–28. doi:10.1016/j.cemconcomp.2015.04.012.
- [4] ACI Committee 238. Report on Measurements of Workability and Rheology of Fresh Concrete. Farmington Hills: 2008.
- [5] Solak AM. El fenómeno de la segregación en hormigones ligeros. Análisis mediante procesamiento de imágenes y estudio ultrasónico. Universidad de Alicante, 2017. doi:10.13140/RG.2.2.23798.29763.
- [6] ACI Committee 213. Guide for Structural Lightweight-Aggregate Concrete. Reported by ACI Committee 213; 2003.
- [7] Ke Y. Caractérisation du Comportement mécanique des bétons de granulats légers : expérience et modélisation. Université de Cergy-Pontoise, 2008.
- [8] Fernández-Fanjul A, Tenza-Abril AJ. Méthode FANJUL: Dosage pondéral des bétons légers et lourds. *Ann Du Bâtiment Des Trav Publics* 2012;5:32–50.
- [9] Fernández-Fanjul A, Tenza-Abril AJ, Baeza-Brotons F. A new methodology for determining particle density and absorption of lightweight, normal-weight and heavy weight aggregates in aqueous medium. *Constr Build Mater* 2017;146:630–43. doi:10.1016/j.conbuildmat.2017.04.052.

## **EXPOSITION TO ACID ATTACK OF MORTARS WITH NANOSILICA, ZINC STEARATE AND ETHYL SILICATE COATING**

**Victoria Eugenia García-Vera<sup>(1)</sup>, Antonio José Tenza-Abril<sup>(2)</sup>, Marcos Lanzón<sup>(1)</sup>, Afonso Miguel Solak<sup>(2)(3)</sup>**

(1) Department of Architecture and Building Technology, Technical University of Cartagena, Murcia, Spain

(2) Department of Civil Engineering, University of Alicante, Alicante, Spain

(3) CYPE Ingenieros S.A., Alicante, Spain

### **Abstract**

The demand for durable cementitious materials for applications where they are subjected to aggressive chemical environments is growing. As an example, some infrastructures can be affected by acid attacks, such as sanitation networks, foundations, infrastructures in contact with groundwater or in agricultural and farm facilities. Acid attacks are one of the most severe mechanisms in the deterioration of cementitious materials. The main objective of this study is to compare the physical and mechanical changes of four different mortars subjected to an acid attack (3% w/w of H<sub>2</sub>SO<sub>4</sub> solution). The mortars produced were: i) control mortar; ii) mortar with nanosilica; iii) mortar with zinc stearate; and iv) mortar with an ethyl silicate coating. After 28 days of hardening, the samples were exposed to an acid attack by immersing the specimens in a H<sub>2</sub>SO<sub>4</sub> solution. Physical changes (mass loss, ultrasonic impulse velocity and water absorption) and mechanical changes (compressive strength) were determined after the acid attack exposure. The results show that the lowest mass loss after 90 days of acid attack was observed in the zinc stearate mortar. Moreover, the zinc stearate mortar was also the one that had a lower percentage of strength loss after the acid attack.

### **1. Introduction**

External sources of sulfates have a detrimental impact on cementitious materials, such as concretes and mortars. External sulfate attack is a slow process originated from the outside and it can take years to manifest itself causing internal changes of the microstructure. These changes are manifested in physical and mechanical alterations such as strength loss, mass

variation, cracking, softening, decohesion, etc. [1-2]. There are two types of sulfate attacks, which can be classified as either chemical or physical. Chemical attacks are common in buried concretes exposed to sulfate waters existing in groundwater, where the sulfates react with aluminate hydrates to produce ettringite and gypsum. When a concrete is submerged in sulfate water a physical attack can occur due to the crystallisation of sulfate salts inside the pores of the concrete when it dries, this attack mechanism is usual in tidal zones where there are cycles of wetting and drying [3].

To obtain durable mortars and concretes against sulfate attacks is important to control the materials used during the manufacturing process, low w/c ratio (w/c ratio lower than 0.45 is considered safe), curing conditions, etc. [1]. In addition, it is possible to use additions (e.g. fly ash) or additives to extend the durability of cementitious materials. Mortars containing nanosilica have been studied in acid environments and its effectiveness has been proven in reducing the loss of both mass and compressive strength after an acid attack. This is because the nanosilica refines the pore structure creating a more compact microstructure, which reduces porosity and absorptivity [4]. Zinc stearate is one of the most frequently used materials to achieve hydrophobic mixtures [5]. It is used with different types of binders, such as cements, clays and limes. Lanzón et al. [6] proved its effectiveness on adobe materials exposed to an acid-rain attack. However, this material has not been extensively studied in cementitious mixtures exposed to acid attacks. Ethyl silicate is a liquid solution that is applied in the form of a coating and its use has been widely utilized for the stone consolidation. The ethyl silicate reacts with the substrate where is applied on, and after curing, it has a pozzolanic effect. Moreover, ethyl silicate decreases the capillary suction [7]. However, this material, like zinc stearate, has not been widely studied on cementitious materials exposed to chemical attacks.

The aim of this study is to analyze the behavior of four different mortars exposed to acid attack: an untreated mortar, a mortar with nanosilica, a mortar with zinc stearate and a mortar with an ethyl silicate coating.

## **2. Materials**

Four types of mortars were studied: i) control mortar; ii) mortar with nanosilica; iii) mortar with zinc stearate; and iv) mortar with an ethyl silicate coating. The dosage used for the mortars was one part cement (CEM I / 52.5R), 0.45 parts water and three parts of fine limestone aggregate. For adequate workability of the mortars, 1.5 % w/w on the amount of cement of superplasticizer (Sika ViscoCrete-5980) was added to the mixtures. The nanosilica mortar was manufactured adding 2% w/w of nanosilica (MasterRoc MS 685) on the cement amount. The zinc stearate mortar was made adding 2% w/w of zinc stearate (Alfa Aesar, 33238 ZnO) on the cement quantity. Finally, the ethyl silicate coating was carefully sprayed at a controlled distance (10 cm) using a small airbrush (Fig. 1, left).

## **3. Methods**

### **3.1 Manufacturing and curing process of the mortars and acid attack simulation**

Six prismatic specimens (40 x 40 x 160 mm) per each type of mortar were manufactured following the procedure of the standard EN 196-1 [8]. All the specimens were cured in a

humidity chamber for 28 days. The ethyl silicate coating was applied in the midst of the curing process, that is, after two weeks the specimens were taken out from the humidity chamber the time necessary to apply the coating. After applying the coating, the specimens were returned into the humidity chamber. After 28 days of curing, all the specimens were taken out from the humidity chamber. Half of the 24 specimens were exposed to an acid attack and the other half were used as a reference. The reference specimens were maintained in standard laboratory conditions, and the acid attack was performed by immersing the specimens into a  $H_2SO_4$  solution (3% w/w) (Fig. 1, centre). The  $H_2SO_4$  solution was changed weekly so that the concentration of acid sulphuric did not have an excessive variation. The change of the solution was made as follows: i) the specimens were extracted from the solution, and were gently brushed under a weak flow of tap water to eliminate rests of material weakly adhered to the surface; ii) the acid solution used was changed by a new solution; and iii) the specimens were reintroduced into the new solution.

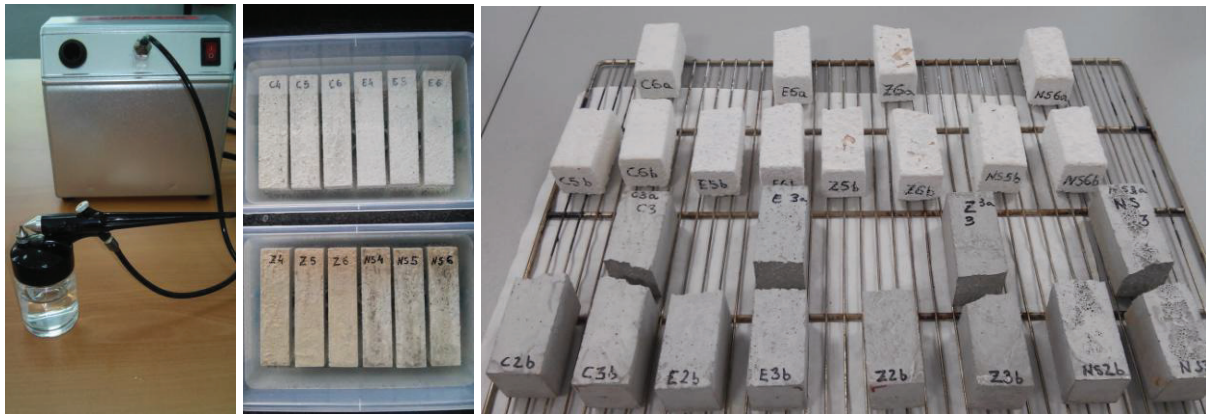


Figure 1. Left: airbrush used to spray the specimens. Centre: specimens submerged in the sulphuric solution (C = control; E = ethyl silicate coating; Z = zinc stearate; NS = nanosilica). Right: specimens before being broken in the testing machine at  $t_{118(90)}$ . The white specimens are those subjected to the acid attack, and the grey specimens are the reference ones.

### 3.2 Study of the physical and mechanical properties of the mortars

To study the mass variation, the specimens were weighed six times: 28 days after the manufacture and before starting the simulation (0 days of acid exposure) [ $t_{28(0)}$ ]; at 7 days [ $t_{35(7)}$ ]; 14 days [ $t_{42(14)}$ ]; 21 days [ $t_{49(21)}$ ]; 28 days [ $t_{56(28)}$ ] and 90 days [ $t_{118(90)}$ ] of acid attack exposure. The percentage of mass loss were calculated taken into account the initial weights [ $t_{28(0)}$ ].

The ultrasonic pulse velocity test was performed following the EN 12504-4 standard [9]. The test consisted in measuring the propagation time of the ultrasonic waves along the longest dimension of the specimen (160 mm). Contact transducers emitting ultrasonic pulses at 54 kHz were coupled to the end sides of the specimens. Three determinations were made per sample, the wave velocity was computed as quotient of the specimen length divided by the propagation time. The test was performed for all the specimens, both for the specimens that had been subjected to the acid attack simulation and for those that did not. The ultrasonic test was carried out at 28 days [ $t_{56(28)}$ ] of the acid attack simulation.

The compressive strength test was conducted according to the EN 196-1 standard [10]. A conventional mortars/bricks testing machine was utilized, at speed of 2.4 kN/s until failure

with a strain gauge load cell of 20 T capacity. For all the specimens, the test was carried out at 28 [ $t_{56(28)}$ ] and 90 [ $t_{118(90)}$ ] days of acid attack exposure (56 and 118 days from their manufacture).

The capillary water absorption test was performed at 90 days [ $t_{118(90)}$ ] of exposure to the acid attack following the standard EN-1015-18 [11]. According to the standard, the water absorption coefficient is the line slope that joins the points corresponding to 10 minutes and 90 minutes in the curve that represents the mass variation of water absorbed per unit area as a function of the square root of time, i.e. the coefficient was computed using the formula:

$$C = (M_2 - M_1) / (A \cdot (t_2^{0.5} - t_1^{0.5}))$$

where:

$C$  = capillary water absorption coefficient,  $k/(m^2 \cdot \text{min}^{0.5})$

$M_1$  = specimen mass after the immersion for 10 minutes, k

$M_2$  = specimen mass after the immersion for 90 minutes, k

$A$  = surface of the specimen face submerged in the water,  $m^2$

$t_2$  = 90 minutes

$t_1$  = 10 minutes

## 4. Results

### 4.1 Compressive strength

All the specimens not subjected to the acid attack increased their strength at  $t_{118(90)}$  in comparison with that at  $t_{56(28)}$  (Fig. 2, left), this strength increase is common in mortars curing under standard conditions. The specimens with the ethyl silicate coating had the highest strength for  $t_{56(28)}$  and  $t_{118(90)}$ , and the zinc stearate specimens had the lowest strength, having lower strength at  $t_{56(28)}$  than the control specimens, although at  $t_{118(90)}$  they slightly exceed them. In the time interval from  $t_{56(28)}$  to  $t_{118(90)}$  all the specimens treated increased their strength more than the control ones. The zinc stearate specimens increased approximately twice (8.5%) than the other two (4% - 4.6%) (Fig. 3, left).

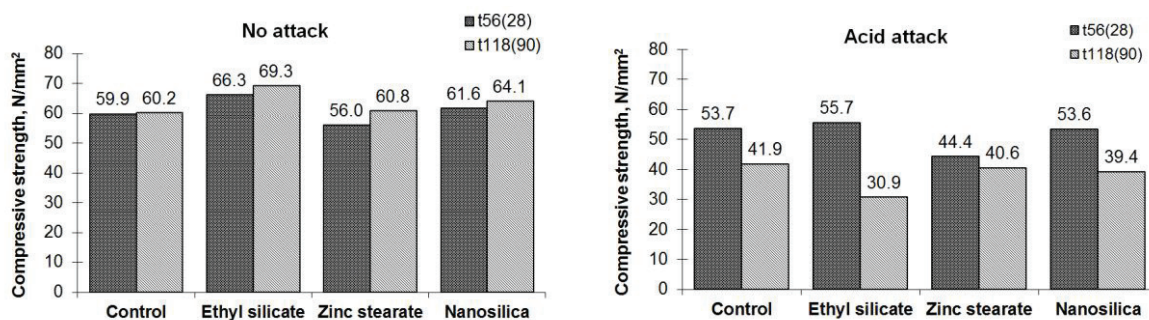


Figure 2. Compressive strength evolution, without acid attack (left) and with acid attack (right) at  $t_{56(28)}$  and  $t_{118(90)}$ .

The compressive strength for the mortars exposed to the acid attack was lower than the compressive strength of the non-attacked mortars, this strength decrease occurred at  $t_{56(28)}$  and  $t_{118(90)}$  (Fig. 2, left vs right). For all the attacked mortars, the strength at  $t_{56(28)}$  was lower than

the strength at  $t_{118(90)}$  (Fig. 2, right). The zinc stearate mortar had the lowest compressive strength decrease (8.4 %) compared to the rest of mortars (22% - 44.6%) (Fig. 3, left).

#### 4.2 Mass loss

The analysis of the mass loss as a function of the exposure time to the acid attack (Fig. 3, right) showed that the resistance to the attack of the nanosilica mortar and the mortar treated with an ethyl silicate coating was similar to the control mortar. However, the zinc stearate mortar was the one that best resisted the attack, its mass loss (22.9%) at  $t_{118(90)}$  was lower than for the other mortars (37.3% for the nanosilica mortar, and 39.2% for the mortar treated with ethyl silicate).

#### 4.3 Ultrasonic impulse velocity

The ultrasonic propagation velocity obtained for all the mortars studied was similar except for the zinc stearate mortar that was the lowest. As occurred with the compressive strength, when the mortars were exposed to acid attack, the ultrasonic pulse velocity was reduced (Fig. 4, left). The results demonstrate that the ultrasonic technique reflects the deterioration caused by acid attack in the mortars studied.

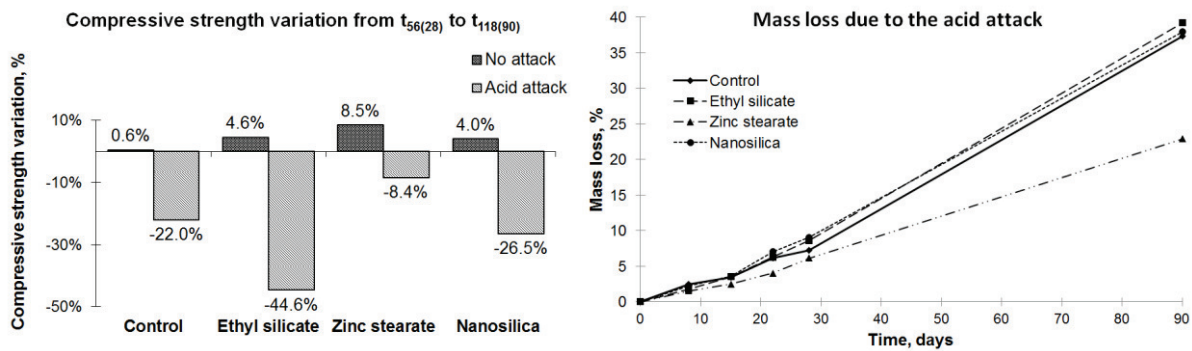


Figure 3. Left: variation percentage of the compressive strength from  $t_{56(28)}$  to  $t_{118(90)}$ . Right: mass loss as a function of the exposure time to the acid attack.

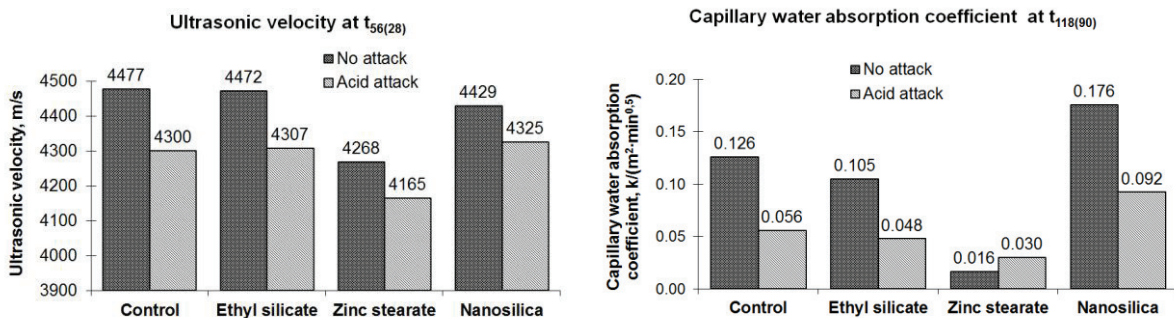


Figure 4. Left, ultrasonic velocity at  $t_{56(28)}$ . Right, coefficient water absorption at  $t_{118(90)}$ .

#### 4.4 Capillarity water absorption

The study of capillarity water absorption (Fig. 4, right) showed that the absorption coefficient of the mortars decreased when they were exposed to the acid attack, except the zinc stearate mortar that increased its coefficient from 0.016 before to 0.030 after the acid attack. This



finding may be due to the effect of the gypsum layer created on the surface of the mortar (Fig. 1, right) during the acid attack. In the mortars with zinc stearate, the layer of gypsum absorbs more water than the interior of the specimen in which the gypsum layer does not exist. Notwithstanding, mortars with zinc stearate have demonstrated its hydrophobic effect.

## 5. Conclusions

In this work, the effects of acid attack on physical and mechanical properties of four different mortars were analyzed (control mortar, nanosilica mortar, zinc stearate mortar and a mortar with an ethyl silicate coating). From the results presented in this study the following conclusions are drawn:

- After the acid attack, all the mortars presented a reduction of their mass and lower compressive strength. Greater impact in the reduction with longer periods of acid attack.
- Mortars with zinc stearate in the dosage exhibited the lowest mass loss and lowest reduction in compressive strength after 90 days of acid attack exposure.
- Mortars with zinc stearate have demonstrated its hydrophobic effect with the lowest coefficient of capillary water absorption (attacked and non-attacked by acid).

## References

- [1] Monteiro, P.J. and Kurtis, K.E., Time to failure for concrete exposed to severe sulfate attack, *Cem and Concr Res* 33(7) (2003), 987–993
- [2] Zhihong, Z. W. and Xiaomeng, X. S., Deterioration of fracture toughness of concrete under acid rain environment, *Eng Fail Anal*, 77 (2017), 76-84
- [3] Whittaker, M. and Black, L., Current knowledge of external sulfate attack. *Advances in Cement Research*. ICE Publishing, (2015), 1-14
- [4] Deb, P., Sarker, P. K. and Barbhuiya, S., Sorptivity and acid resistance of ambient-cured geopolymer mortars containing nano-silica, *Cem & Conc Comp*, 72 (2016), 235-245
- [5] Falchi, L., Zendri, E., Müller, U. and Fontana, P., The influence of water-repellent admixture on the behavior and the effectiveness of Portland limestone cement mortars, *Cem & Conc Comp*, 59 (2015), 107-118
- [6] Lanzón, M. Martínez, E., Mestre, M. and Madrid, J.A, Use of zinc stearate to produce highly-hydrophobic adobe materials with extended durability to water and acid-rain, *Cons & Buil Mat*, 139 (2017), 114-122
- [7] Pigino, B, Leemann, A. and Lura, P., Ethyl silicate for surface treatment of concrete – Part II: characteristics and performance, *Cem & Conc Com*, 34 (2012), 313-321
- [8] EN 196-1:2005, Methods of testing cement - Part 1: Determination of strength, CEN, (2005)
- [9] EN 12504-4:2006, Testing concrete - Part 4: Determination of ultrasonic pulse velocity, CEN, (2006)
- [10] EN 196-1:2005, Methods of testing cement - Part 1: Determination of strength, CEN, (2005)
- [11] EN-1015-18, Methods of test for mortar for masonry - Part 18: Determination of water absorption coefficient due to capillary action of hardened mortar (2002)

## **GAS DIFFUSION IN CEMENTITIOUS MATERIALS: TEST METHODS REVIEW**

**Fabien Gendron<sup>(1)</sup>, Mouna Boumaaza<sup>(2)</sup>, Philippe Turcry<sup>(1)</sup>, Bruno Huet<sup>(2)</sup>, Abdelkarim Aït-Mokhtar<sup>(1)</sup>**

(1) University of La Rochelle, LaSIE UMR CNRS 7356, La Rochelle, France

(2) LafargeHolcim Research Center, Saint Quentin Fallavier, France

### **Abstract**

The durability of reinforced concrete structures is strongly related to phenomena controlled by gas or liquid diffusion. Thus, gas diffusivity of concrete is a relevant durability indicator especially for carbonation induced corrosion. However, there is so far no standard procedure for the determination of this property. In the present paper, the main existing procedures for gas diffusion are first described. Two newly developed test methods are then presented. These procedures, which involve either CO<sub>2</sub> or O<sub>2</sub>, consist in assessing the gas diffusivity from an unsteady state diffusion. These diffusion tests are compared through results from a campaign carried out on oven-dried cement pastes made with OPC and a mix of blast furnace slag and OPC. All the so-determined diffusivities are finally compared to data from literature. The main challenge of such a comparison is to find diffusivity values obtained for the same type of materials at equal hydric state. It is concluded that round robin tests would be of great interest for the future development of gas diffusion tests.

### **1. Introduction**

The durability of reinforced concrete structures is strongly related to reactive transport phenomena such as carbonation. The latter involves the diffusion of atmospheric carbon dioxide within the material porous network. The corrosion rate of reinforcing bars itself is partly controlled by the diffusion of gaseous dioxygen in concrete. Therefore, gas diffusivity of concrete is undoubtedly an appropriate indicator for long term durability issues. Such an indicator could be used in performance based approaches of concrete structures design, for instance through the equivalent performance concept. Moreover, gas diffusivity is a key-property in the modelling of transport phenomena for the prediction of the structure service life. If ongoing efforts are invested in the design of testing procedures, there is so far no

standard procedure for the determination of gas diffusivity. The existing procedures that can be found in literature are based on quite different principles [1]. Furthermore, in performance based approach, other material properties (e.g. porosity, gas permeability, chloride diffusivity) or performance tests (e.g. accelerated carbonation test) are still preferred to gas diffusivity. It should be noted that there are relatively few studies on gas diffusion in concrete, compared to investigations on other transport phenomena such as permeation or ion diffusion.

In the present paper, the main existing techniques for gas diffusion tests are firstly described. Two newly developed tests are then presented. These experimental procedures, which involve diffusion of carbon dioxide and oxygen, respectively, consist in assessing the gas diffusivity from a non-steady state. In both procedures, the time-evolution of the gas concentration in a downstream chamber due to the diffusion through the tested sample is measured by means of local gas probes. Results of two testing laboratories using these diffusion tests are compared through an experimental campaign carried out on oven-dried cement pastes specimens. The tested pastes were made with an ordinary Portland cement (OPC) and a mix of OPC and blast furnace slag. Finally, all the so-determined diffusivities are compared to data from literature.

## 2. Principles of gas diffusion tests from literature

Figure 1 illustrates the principles of the main gas diffusion tests found in literature. In the procedure type 1, the specimen, placed between two chambers, is exposed to two pure gases or gas mixes. The time-evolution of gas 1 concentration in the lower chamber is measured, while its concentration is kept constant in the upper one. From this data, Fick's laws are used to calculate the effective diffusion coefficient. This kind of procedure is performed either in the transient state or in the steady state. In the latter case, the concentration gradient of gas 1 is kept almost constant by renewing the gas in the lower chamber after each measurement. Since the gas 1 concentration remains low, a very accurate gas analyzer has to be used [3].

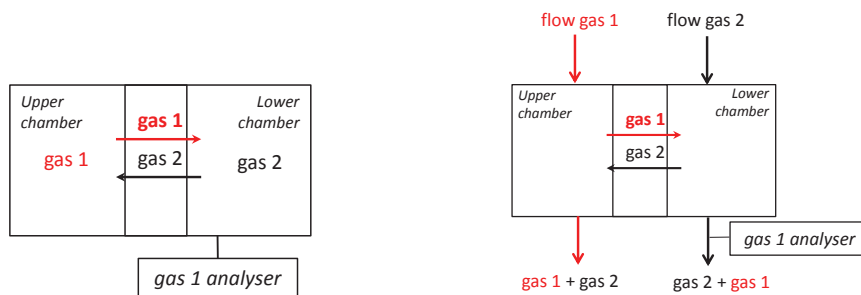


Figure 1: Classical procedures for gas diffusion: type 1 (left) and type 2 (right) [1].

Previously developed by Lawrence [2], the procedure type 2 consists in exposing both opposite faces of the specimen to streams of gas 1 and gas 2. While these gases flows are maintained constant, the increasing concentration of gas 1 in the outing gas from the lower chamber is determined by an analyzer. When the steady state is reached, gas 1 concentration becomes constant and its value can be used to calculate the diffusion coefficient knowing the gas flow rate using Fick's first law of diffusion.

Diffusion tests are currently done with pure gases, such as hydrogen or oxygen, which are somewhat inert for cementitious matrices [3-7]. Some authors presented also results from CO<sub>2</sub> diffusion tests [1, 8-10].

### 3. New proposed diffusion tests

#### 3.1 Experimental set-ups

Two diffusion tests were recently proposed, one for CO<sub>2</sub> diffusion [8] and the second one for atmospheric O<sub>2</sub> diffusion [6]. They are based on the procedure type 1 described previously taking into account the transient state. Fig. 2 gives an overview of the set-ups (chambers, specimen and seals). In both procedures, the concentration of the considered gas, CO<sub>2</sub> or O<sub>2</sub>, is measured continuously by means of a gas sensor located in the downstream chamber. Apart from the gas nature, the main difference between the two tests lies in the upstream system. In the CO<sub>2</sub> diffusion set-up, the upstream chamber is connected to a CO<sub>2</sub> bottle and is filled by a mix of air and CO<sub>2</sub> with a controlled CO<sub>2</sub> concentration (for instance 10% by volume). In the O<sub>2</sub> diffusion setup, there is no upstream chamber: one face of the specimen is in contact with the ambient air, i.e. at a O<sub>2</sub> concentration of around 20% by volume. The absence of O<sub>2</sub> bottle makes the great relevance of this setup from a practical point of view. At the beginning of O<sub>2</sub> diffusion test, the downstream chamber is flushed with nitrogen during maximum 20s to reach an O<sub>2</sub> concentration lower than 0.3%. Before CO<sub>2</sub> diffusion test, such a flushing of the downstream chamber is not required: the CO<sub>2</sub> concentration is assumed to be negligible. For both tests, tested specimens are discs of cement paste or mortar (40 to 70mm in diameter, 5 to 30mm in thickness for CO<sub>2</sub>; 40mm in diameter and 2 to 15mm in thickness for O<sub>2</sub>). Note that a second version of the O<sub>2</sub> diffusion test was also developed for concrete.



Figure 2: Overview of CO<sub>2</sub> (left) and O<sub>2</sub> (right) diffusion set-ups.

The result of both tests is an accumulation curve of the considered gas in the downstream chamber. The effective diffusion coefficient is computed by minimizing the difference between experimental data and concentration time-evolution calculated with the Fick's second law.

#### 3.2 Round robin tests

The previously described tests were compared through a round-robin testing campaign carried out on seven specimens of hardened cement pastes. The latter contained either an OPC or a mix of OPC and blast furnace slag (BFS) [6]. The pastes were made with two volumetric water/binder ratios, namely 1.6 and 1.9 (i.e. w/b mass ratios of around 0.5 and 0.6 respectively). The tested specimens were discs with a diameter of 40 mm and a thickness between 3 and 4mm. Before testing, all specimens were cured during 6 months, water-saturated under vacuum in order to determine porosity and then dried at 80°C until constant mass. After oven-drying, O<sub>2</sub> diffusion tests were carried out first. The specimens were then

sent by post to the second laboratory. Before CO<sub>2</sub> diffusion tests, the specimens were re-dried at 80°C to obtain as much as possible the same hydric state than before O<sub>2</sub> diffusion. Tab.1 gives composition, porosity and effective diffusion coefficient of each specimen.

Table 1: Composition, porosity and diffusivities of the tested specimens.

Binder (% in mass)	w/b in vol. (-)	Porosity (-)	D <sub>O<sub>2</sub></sub> (10 <sup>-8</sup> m <sup>2</sup> /s)	D <sub>CO<sub>2</sub></sub> (10 <sup>-8</sup> m <sup>2</sup> /s)
OPC (100%)	1.6	0.43	9.1	16.8
OPC (100%)	1.9	0.48	10.6	26.0
OPC (100%)	1.9	0.48	15.5	28.0
OPC+BFS (50%+50%)	1.6	0.46	3.8	8.0
OPC+BFS (50%+50%)	1.6	0.46	4.0	6.6
OPC+BFS (50%+50%)	1.9	0.51	8.5	15.2
OPC+BFS (50%+50%)	1.9	0.51	4.7	13.0

For a given binder type, the effective diffusion coefficient increases with porosity, whatever the considered gas. At equal w/b volume ratio, OPC specimens are more diffusive than BFS specimens although the latter are more porous. This is usually explained by the finer pore structure of pastes containing BFS [6].

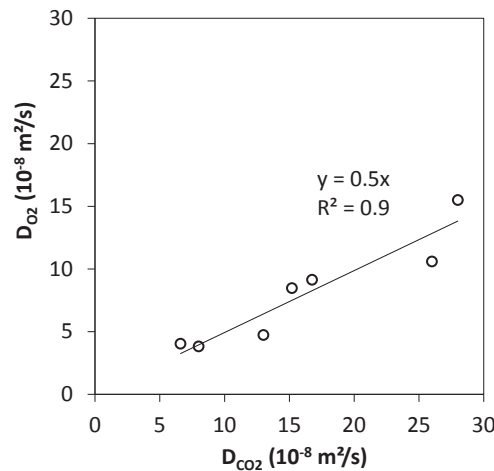


Figure 3: O<sub>2</sub> effective diffusion coefficient versus CO<sub>2</sub> effective diffusion coefficient.

Figure 3 compares O<sub>2</sub> diffusivities (D<sub>O<sub>2</sub></sub>) and CO<sub>2</sub> diffusivities (D<sub>CO<sub>2</sub></sub>). A rather good correlation is observed. However, the obtained ratio D<sub>O<sub>2</sub></sub>/D<sub>CO<sub>2</sub></sub> (=0.5) is not expected. By assuming that Knudsen diffusion is the dominant phenomenon, this ratio should be equal to 1.17, i.e. the squared ratio of molar masses (M<sub>CO<sub>2</sub></sub>/M<sub>O<sub>2</sub></sub>)<sup>1/2</sup> [11]. Apart from differences due to the setups, an explanation of the difference between theoretical ratio and experimental one is a possible damage of the specimens due to the re-drying at 80°C before the second diffusion tests series with CO<sub>2</sub>. At least, this emphasizes the care which has to be taken in the handling of specimens used for round-robin tests.

#### 4. Comparison with literature data

The main characteristics of the rare data on gas diffusion through dried hardened cement pastes used for comparison are the followings.

- Diffusivities from [3-5] were determined with the same setup using the procedure type 1 with H<sub>2</sub>. The tested pastes were made with CEMI (OPC) or CEMV type cements with w/c mass ratios from 0.3 to 0.5 and were dried at 3% RH and 20°C before testing.
- Diffusivities from [7] were determined using the procedure type 2 with O<sub>2</sub>. The paste contained CEMI type cement with w/c mass ratios from 0.3 to 0.5, oven-dried at 105°C.
- Diffusivity from [9] were determined using procedure type 2 with CO<sub>2</sub> diffusion carried out on OPC paste with w/c mass ratio of 0.5 dried at 10% RH and 20°C.
- Diffusivities from [1] were determined with procedure type 1 with CO<sub>2</sub>. The pastes were made of CEMI cement or a mix of CEMI and BFS (25-75% in mass) with w/b mass ratios from 0.3 to 0.5. Before diffusion, the specimens were oven-dried at 105°C.
- Diffusivities from [10] were extrapolated from a function fit by the authors on results of CO<sub>2</sub> diffusion tests carried out on OPC carbonated pastes with w/c from 0.4 to 0.8 conserved at different RH between 40 and 90%.

According to Graham's law, an "equivalent" CO<sub>2</sub> diffusivity was calculated by multiplying the diffusivity of the gas used for diffusion test by the ratio  $(M_g/M_{CO_2})^{1/2}$  where  $M_g$  is the molar mass of the diffusing gas species. In Fig. 5, the so-obtained coefficients were plotted versus porosity for ease of comparison. In addition, values calculated from the model in [12] giving the diffusivity as a function of the porosity were also plotted.

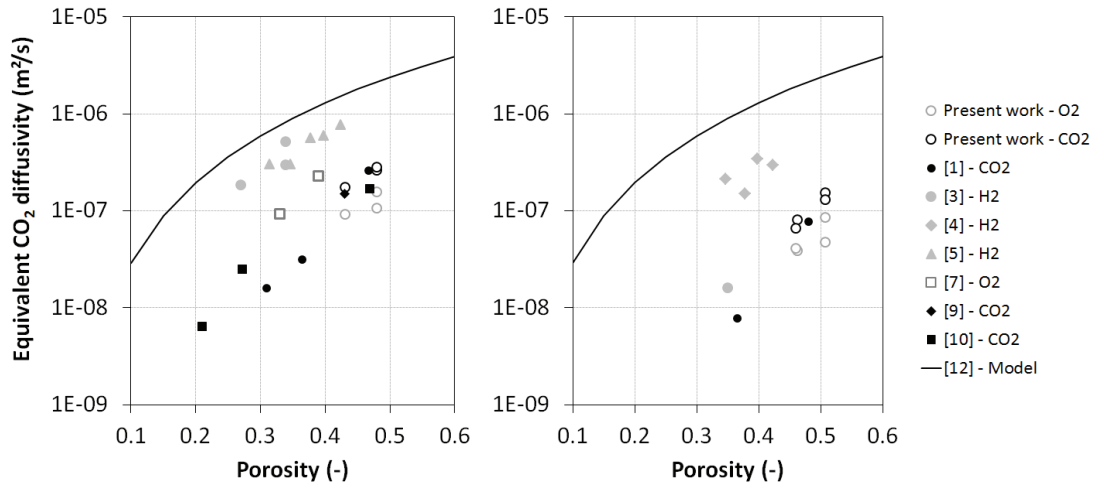


Figure 4: CO<sub>2</sub> effective diffusion coefficient deduced from literature data compared to data from the present round-robin tests, for OPC pastes (left) and pastes containing BFS (right).

Whatever the used test, diffusivity of OPC pastes is higher than diffusivity of pastes containing BFS, at equal porosity. Diffusivity depends on other characteristics of the porous network such as tortuosity. Thus, the proposed model [12] could not assess the gas diffusivity for blended cement pastes. Moreover, the plotted values in Fig. 4 are clearly scattered. Especially, a high difference is observed between diffusivities deduced from [3-5] and diffusivities from the setups presented here and from other literature data [1, 7-10]. This could

question the assumption of Knudsen diffusion mechanism. Above all, these results highlight the need of a broad round robin testing campaign.

## 5. Conclusion

Gas diffusivity of concrete is undoubtedly a relevant durability indicator of reinforced concrete structures. Effort has to be done to develop simple and reliable diffusion tests. In the present paper, newly developed tests were presented and compared with literature data. The main challenge of such a comparison is to find diffusivities determined for the same type of material (w/b ratio, binder type, porosity, curing age, etc.) at equal hydric state. Round robin tests carried out with various setups and procedures would be of great interest for the future development of gas diffusion tests. Mortars could be suitable materials for such a campaign since literature data on mortars are more numerous than data on cement pastes.

## References

- [1] Namouniara, K. et al, Measurement of CO<sub>2</sub> effective diffusion coefficient of cementitious materials, EJECE 20 (2016), 1183-1196
- [2] Lawrence, C.D., Transport of oxygen through concrete, Br Ceram Proc 35 (1984), 277-293
- [3] Sercombe, J. et al, Experimental study of gas diffusion in cement paste, Cem Concr Res 37 (2007), 579-588
- [4] Boher, C. et al, Influence of the pore network on hydrogen diffusion through blended cement pastes, Cem Concr Comp 37 (2013), 30-36
- [5] Vu, T.H., Caractérisation de la phase solide et transferts de gaz dans les milieux poreux insaturés. Etude expérimentale et modélisation appliquées à la diffusion de l'hydrogène dans les matériaux cimentaires, PhD Thesis, Université de Toulouse (2009)
- [6] Boumaaza, M. et al, A new test method to determine the gaseous oxygen diffusion coefficient of cement pastes as a function of hydration duration, microstructure, and relative humidity, Mater Struct 51 (2018)
- [7] Wong, H.S. et al, Influence of the interfacial transition zone and microcracking on the diffusivity, permeability and sorptivity of cement-based materials after drying, Mag Concr Res 61 (2009), 571-589
- [8] Turcry, Ph. Et al, CO<sub>2</sub> diffusion in cementitious materials: experimental investigation, 2nd International RILEM/COST Conference on Early Age Cracking and Serviceability in Cement-based Materials and Structures, Belgium (2017)
- [9] Jung, S.H. et al, Measurement device and characteristics of diffusion coefficient of carbon dioxide in concrete, ACI Mat Journal 108 (2011), 589-595
- [10] Houst, Y.F, and Wittmann, F.H., Influence of porosity and water content on the diffusivity of CO<sub>2</sub> and O<sub>2</sub> through hydrated cement pastes, Cem Concr Res 24 (1994), 1165-1176
- [11] Leemann, A. et al, Steady-state O<sub>2</sub> and CO<sub>2</sub> diffusion in carbonated mortars produced with blended cements, Mat Struct (2017)
- [12] Thiéry, M. et al, Investigation of the carbonation front shape on cementitious materials: Effects of the chemical kinetics. Cem Concr Res 37 (2007), 1047-1058

## HEAT OF HYDRATION OF TERNARY-, QUATERNARY- BLENDED CEMENTS

Arnaud Delaplace<sup>(1)</sup>, Denis Garcia<sup>(1)</sup>, Marie Bayle<sup>(1)</sup>, Quentin Favre-Victoire<sup>(1)</sup>

(1) LCR LafargeHolcim, Saint-Quentin-Fallavier, France

### Abstract

The heat release of seven different binders (Portland cement+two or three cementitious materials) during hydration process are evaluated. Two experimental protocols are compared: the first one is a standard quasi-adiabatic test performed at two different temperatures, the second one is an industrial test performed at a single temperature. The use of cementitious materials allows as expected to reduce the heat release during hydration process. The heat release normalized by the binder content is given for the different blended binders.

### 1. Introduction

Predicting temperature evolution into massive structures is mandatory in many projects in order to be sure that the maximum temperature and the gradient temperature will not exceed a prescribed value specified in the project specifications. This prediction can be achieved starting from an experimental characterization of the binder (using for example a calorimeter), then using a numerical solver that takes into account the relevant boundary conditions of the structure.

Limiting heat of hydration of cement can be done by using cementitious materials. These mineral additions can also be used to improve mechanical performance of the concrete. It leads to blended cements, with one, two or even three additional components. Chemical hydration reactions of the different species are strongly coupled and change the heat release of the binder.

We propose in this study to characterize heat of hydration of high performance concretes based on a Portland cement blended with silica fume and/or fly ash and/or slag. Two apparatus are used, an industrial non-calibrated calorimeter and a calibrated one. We focus the analysis on comparing the heat of hydration of the different binders. The mechanical



performance of the concretes will be also evaluated in order to get the optimized strength/heat release ratio for the blended binders.

## 2. Experimental characterization of the binder thermal fingerprint

The following analysis is based on the assumption that the hydration rate of the binder can be represented by the Arrhenius law:

$$\frac{\partial \xi(T)}{\partial t} = A(\xi) \exp\left(\frac{-E_a}{RT}\right) \quad (1)$$

in which  $T$  is the temperature,  $\xi$  is the hydration degree ranging between 0 to 1,  $A$  is the affinity function [ $s^{-1}$ ],  $E_a$  is the activation energy [ $J/mol$ ],  $R$  is the ideal gas constant [ $8,314 J/mol/K$ ].

### 2.1 Experimental apparatus

Two apparatus are used in this study:

- The first apparatus (QAB test) is a quasi-adiabatic test realized in a calibrated calorimeter on  $16 \times 32$ cm-concrete cylinders at two different temperatures (Fig. 1-left). One test lasts around 7 days and allows evaluating both the heat release and the activation energy [1].
- The second test (MeTooHeat test) is performed on small  $7 \times 12$ cm cylinders into a non-calibrated calorimeter (Fig.1-right). The test lasts around 48h [2]. Due to the small size of the specimen, this test is usually performed on mortar samples, with a mixdesign corresponding to the concrete one without the coarse aggregates [3]. It leads to a high proportion of binder, allowing a more accurate determination of the heat release. In this study and because the binder content is important, we use the same concrete mixdesign tested in the QAB box in order to evaluate the capability of the MeTooHeat device to determine the heat release directly on the target concrete mixdesign.

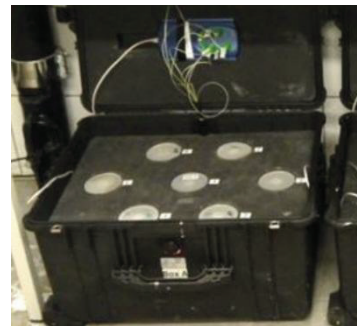


Figure 1: the QAB calibrated calorimeter used on concrete (left) and the non-calibrated calorimeter used on small sample (right).

## 2.2 Binders description

Seven binders are studied, based on four raw materials: a Portland cement (CEM I 52.5N), a silica fume, a fly ash and a slag. The weight percentages of oxides of the raw materials are given in Tab 1.

Table 1: weight percentage of oxides for the binder components

	SiO <sub>2</sub>	Al <sub>2</sub> O <sub>3</sub>	Fe <sub>2</sub> O <sub>3</sub>	CaO	MgO	K <sub>2</sub> O	Na <sub>2</sub> O	SO <sub>3</sub>
Cement	20,46	4,91	2,79	64,38	0,97	0,85	0,16	3,13
Fly Ash	57,51	24,74	6,4	2,41	1,46	2,2	1,77	0,26
Slag	37,95	10,19	0,38	42,93	6,63	0,35	0,23	1,61
Silica fume	>95							

The proportion of the binder and the free water used in the concrete mixdesigns are given in Tab 2. The type of these concretes corresponds to high performance concretes.

Table 2: binders proportion

	C1	C2	C3	C4	C5	C6	C7
Cement [kg/m <sup>3</sup> ]	365	272	336	240	256	328	199
FA [kg/m <sup>3</sup> ]	0	204	201	204	224	131	0
Slag [kg/m <sup>3</sup> ]	225	140	67	145	140	131	378
SF [kg/m <sup>3</sup> ]	65	66	67	60	60	65	65
<b>Total [kg/m<sup>3</sup>]</b>	<b>655</b>	<b>682</b>	<b>671</b>	<b>649</b>	<b>680</b>	<b>655</b>	<b>642</b>
Free Water [kg/m <sup>3</sup> ]	197	182	179	195	190	196	184
Water/binder	0,30	0,27	0,27	0,30	0,28	0,30	0,29

## 3. Results and on-going work

- QAB calibrated calorimeter

The analysis of the test is based on the evaluation of the heat released by the binder,  $q$ , considering the heat loss parameters  $a$  and  $b$  of the calorimeter:

$$q(t) = C_{tot}(\theta(t) - \theta(0)) + \int_0^t (a + b\theta(u))\theta(u)du \quad (2)$$

in which  $\theta$  is the temperature difference between the hydrating sample and a reference temperature (usually measured in a reference concrete sample),  $C_{tot}$  is the total heat capacity

of the concrete sample and of the calorimeter. The hydration degree is assumed to be proportional to the heat release. For each concrete, the first test has been performed with a reference temperature of 10°C (lab temperature and initial concrete temperature), the second one at 20°C. Then, the activation energy can be identified from the two temperature evolution curves, using the so-called “superposition method” [4]. The main assumption of this method is that a single constant activation energy is considered for the global binder (cement+cementitious materials). The evolutions of temperature corrected by the heat loss are plotted in Fig. 2 for the 7 binders.

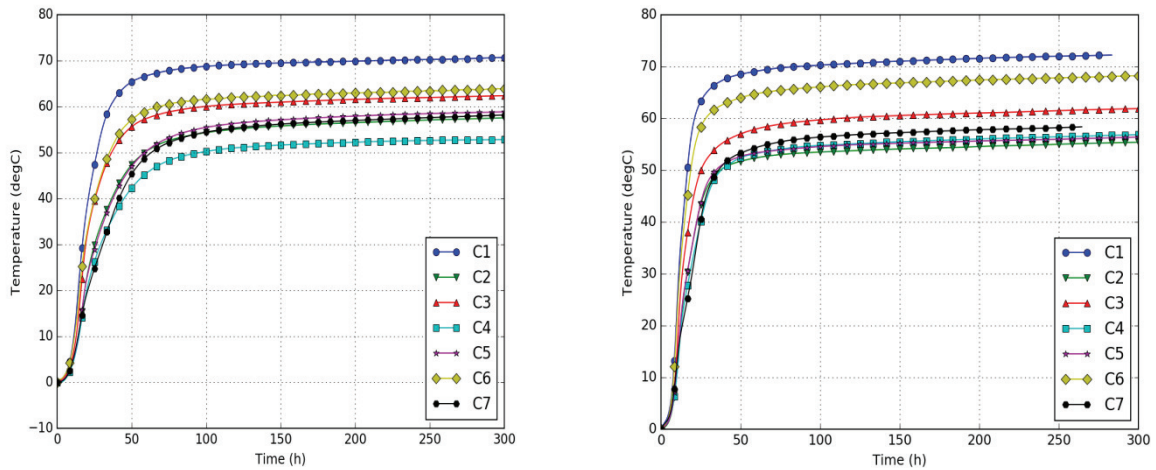


Figure 2: evolution of the temperature difference ( $T(t)-T(0)$ ) corrected by the heat loss of the calorimeter: -left-: reference temperature of 10°C, -right-: reference temperature of 20°C

- Industrial non calibrated calorimeter

This test is performed at a single temperature. An activation energy  $E_a=45000$  J/mol is assumed for the identification. Fig. 3 shows the results for the seven concretes. As mentioned above, the use of the concrete mix design is not optimal, and the increase of temperature (lower than 5°C for concretes 5 and 7) is not enough to have a fine evaluation of the heat release.

From these temperature evolutions, the heat release per gram of binder are computed for both tests (Tabs. 3 and 4), and the activation energy is computed for the QAB tests (Tab. 3). The activation energy ranges between 40000 and 48500 J/mol, except for concrete 3. There is no specific reason to have a different value for this concrete and the experiment should be repeated to verify the value. Although the assumption of having a single constant value of activation energy for these coupling hydration reactions is strong, the identified values are in agreement with values provided in literature [5, 6].

Fig. 4 gives the comparison of the heat release computed for the different binders. The MeTooHeat measurements on the small concrete samples are not satisfactory: a mortar must be used in this apparatus to limit result variability and to increase temperature range during the test. The low values of heat release can be explained by the low water/cement ratio for the considered high-performance concrete mix designs.

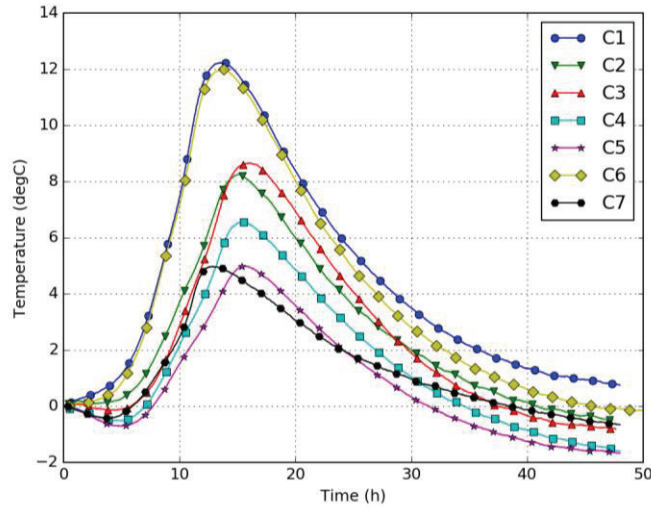


Figure 3: evolution of temperature difference ( $T(t)-T(0)$ ) for the industrial apparatus

Table 3: Results of QAB analysis

	<b>C1</b>	<b>C2</b>	<b>C3</b>	<b>C4</b>	<b>C5</b>	<b>C6</b>	<b>C7</b>
Q [J/g binder]	254	192	209	203	191	240	208
Ea [J/mol]	48452	40702	32716	45053	42702	45580	47823

Table 4: Results of MeTooHeat analysis

	<b>C1</b>	<b>C2</b>	<b>C3</b>	<b>C4</b>	<b>C5</b>	<b>C6</b>	<b>C7</b>
Q [J/g binder]	314	226	277	219	194	282	206

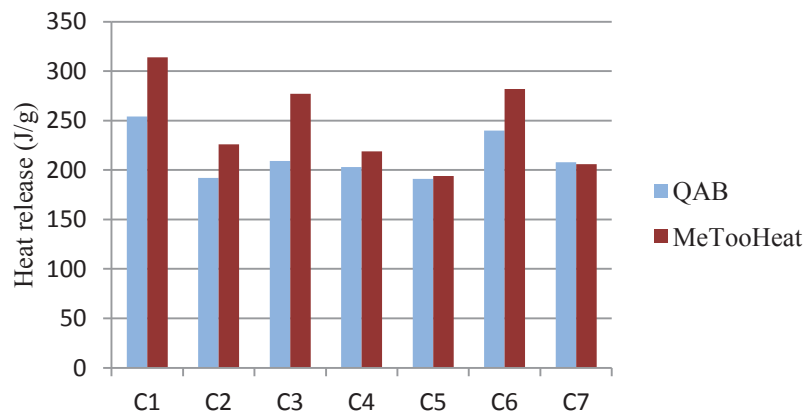


Figure 4: Comparison of the heat release for the different binders identified with the calibrated calorimeter (QAB) and with the industrial apparatus (MeTooHeat).

Additionally to these thermal tests, the compressive strength of the concretes will be characterized in order to evaluate the best strength/heat release ratio of the blended binders. Although the tests are still under progress, the first results show that the better ratios are obtained for the binders with a limited amount of Portland cements. The final results will be provided during the conference.

## References

- [1] Boulay, C., Torrenti, J.M., Andre, J.L., Saintilan, R.: Quasi-adiabatic calorimetry for concretes: Influential factors, *Bulletin des laboratoires des ponts et chaussées* 278 (2010), 19-36
- [2] Šmilauer, V., Baquerizo, L., Matschei, T., Havlásek, P., Ricardo Leal da Silva, W. Hájková, K.: Contemp - a virtual thermo-mechanical simulator for hydrating reinforced concrete blocks with extension to service life. *Proceedings of the International RILEM Conference Materials, Systems and Structures in Civil Engineering Segment on Service Life of Cement-Based Materials and Structures* (2016)
- [3] Lacarrière, L., Delaplace, A., Benhamouda, A.: Influence of the experimental apparatus on the prediction of temperature evolution in massive structure. *Proceedings of the 2nd International RILEM/COST Conference on Early Age Cracking and Serviceability in Cement-based Materials and Structures - EAC2* (2017)
- [4] National Project CALIBE, 'Operation of Civil Engineering Plan', *Recommandations. Résistance du béton dans l'ouvrage : la maturométrie* (2001)
- [5] D'Aloia, L., Chanvillard, G. Determining the "apparent" activation energy of concrete  $E_a$ —numerical simulations of the heat of hydration of cement. *Cem Concr Res* 32 (2002), 1277-1289.
- [6] Broda. M, Wirquin. E, Duthoit. B. Conception of an isothermal calorimeter for concrete – determination of the apparent activation energy. *Mater Struct* 35 (2002), 389-94.

## HYDRATION PROCESS OF NATURAL HYDRAULIC LIME BLENDED CEMENT MORTARS

Reda Jaafri<sup>(1)</sup>, Emmanuel Rozière<sup>(1)</sup>, Syed-Yasir Alam<sup>(1)</sup>, Ahmed Loukili<sup>(1)</sup>

(1) Ecole Centrale de Nantes, Institut de Recherche en Génie Civil et Mécanique (GeM),  
Nantes, France

### Abstract

This paper presents the influence of natural hydraulic lime (NHL) on setting and early-age hydration of cement-based materials. A reference mortar was designed with a water-to-cement ratio of 0.6. At a constant paste volume, cement was replaced with increasing mass proportions of 12.5%, 25% and 50% of NHL. The freshly mixed mortars were tested for hydration process and setting properties. Thermogravimetry and differential scanning calorimetry measurements were also carried out. The undertaken experimental approach shows that the nucleation on NHL particles leads to an acceleration of early-age hydration and a reduction of initial setting time. Thermal analyses also show faster production of portlandite and ettringite during the acceleration period of hydration. This rapid formation of hydration products at early age could provide a considerable benefit in shrinkage mitigation.

### 1. Introduction

The mix-design of a self-leveling mortar is a compromise between the fluidity and the stability required to avoid phase separation problems. The stability of self-compacting mortar can be improved through the use of mineral additions with water retention properties, such as lime. In addition to their beneficial effect on mortars' stability, mineral additions allow decreasing the cement content, which leads to a significant decrease in the cost of production, in the ecologic impact and in other negative effects (increased thermal constraints and shrinkage). In the past few years, lime has been increasingly used in the production of self-leveling screeds thanks to its stabilizing power and the workability provided to mixtures [1].

Two types of lime exist: aerial lime and natural hydraulic lime. They differ in their properties and in their hardening process. Natural hydraulic lime (NHL) is preferred to aerial lime for screeds' production since it hardens in water following a chemical reaction between the active particles of calcium silicate  $C_2S$  and water. It provides additional strengths, higher

permeability and deformability, and better resistance to moisture, frost and salt attack. However, there are very few publications to date on blended mortars of cement and NHL.

Cement-based structures with large exchange surfaces are subjected to significant drying effects, particularly to plastic and drying shrinkage. It should be noted that if the shrinkage takes place while the material has begun to harden, strong internal restraint stresses develop and thus increase the risk of cracking. In addition, the initial setting time is also important as it should allow the transport and the placement of the mortar without affecting its workability. Setting time and shrinkage are therefore properties that are of major interest for mortars.

This study focuses on the effect of cement substitution by natural hydraulic lime (NHL) on the setting and the hydration of cement-based materials. In addition to these two properties, thermal analyzes are performed to understand the effect of lime on the production rate of ettringite and portlandite.

## 2. Experimental investigation

### 2.1 Mortars mix-design

The aim of this study is to determine the influence of NHL on setting and hydration of fresh mortars. Preliminary tests allowed to set the reference mortar mix-design with a water-to-cement ratio of 0.6. It is composed of Portland cement (CEM I 52.5 N), siliceous sand 0/4mm, and water. The chemical and physical properties of cement and NHL are summarized in Tab.1. The amount of cement in the reference mortar was then substituted by mass, but at a constant paste volume, with 12.5%, 25% and 50% of NHL (Tab. 2).

Table 1 : Cement and NHL properties

	Cement	NHL
C <sub>3</sub> S (%)	68	-
C <sub>2</sub> S (%)	11	35
C <sub>3</sub> A (%)	8	0.5
C <sub>4</sub> AF (%)	7	0.5
CaCO <sub>3</sub> Unburnt (%)	-	25
Free Ca(OH) <sub>2</sub> (%)	-	26.2
BET (m <sup>2</sup> /g)	0.77	3.6
d50 (μm)	15	10.5
Density (g/cm <sup>3</sup> )	3.12	2.68

Table 2 : Compositions of studied mortars

	Ref.	12.5% NHL	25% NHL	50% NHL	100% NHL
Cement (kg/m <sup>3</sup> )	467	401	337	216	0
NHL (kg/m <sup>3</sup> )	0	57	112	216	401
Sand (kg/m <sup>3</sup> )	1389	1389	1389	1389	1389
Water (kg/m <sup>3</sup> )	280	280	280	280	280
Initial setting time (h)	5.6	4.4	4.1	3.6	-
S <sub>tot</sub> (m <sup>2</sup> /g)	0	0.51	1.2	3.8	-

## 2.2 Methods

According to the European standard EN 196-3, the Vicat test was used to monitor initial setting times for all the mixtures. The test was conducted on samples stored in water at 20 °C in order to avoid the drying of the upper surfaces.

A TamAir isothermal calorimeter was used to determine the heat flow of mortar samples during hydration. Tests were conducted at a temperature of 20 °C. The samples were 100 g in mass and cement was replaced with sand for the reference ampoule.

Thermal analyses were also conducted in order to determine the chemical activity of NHL and its effect on the nature and evolution of the hydration products. The evolution of portlandite and ettringite was monitored using different techniques: differential thermal analysis (DTA), thermogravimetric analysis (TGA), and differential scanning calorimetry (DSC). The tests were performed on the paste fractions of the reference and the 50% NHL mortars (Tab. 2) at 3, 8 and 12 hours. About 150 mg of finely ground samples were heated from 20 °C to 1100 °C under nitrogen atmosphere, with a heating rate of 10 °C/ min.

## 3. Experimental results and discussion

Setting time is an engineering property that is of major interest for cementitious materials. Initial setting time must allow for easier transport and placement of the mortar without its workability being impacted. The effect of NHL on setting was studied by measuring the initial setting time for mortars with increasing NHL content. Tab. 2 shows for each of the studied mortars the initial setting time and the total surface of contact defined as the total specific surface area available per mass of cement  $S_{tot}$  (calculated by Eq. (1)). It shows that, compared to the reference mixture, the replacement of cement by NHL leads to a significant acceleration of initial setting.

$$S_{tot} = \frac{S_{LF} \cdot m_{LF} + S_{NHL} \cdot m_{NHL}}{m_C} \quad (1)$$

Where  $S_{LF}$  and  $S_{NHL}$  are the specific surface areas from BET analyses respectively of LF and NHL, and  $m_{LF}$ ,  $m_{NHL}$  and  $m_C$  are the masses of LF, NHL and cement respectively in the mixtures.

On initial consideration, the amount of clinker in the mixture decreases with increasing cement substitution rate, resulting in a delay in setting. Nevertheless, the greater specific surface area generated by the NHL grains contributes to the creation of new CSH seeds [2], which accelerates hydration and setting. The accelerating effect of the specific surface area provided by the NHL is substantial until an optimal surface is reached. Beyond this surface, the incorporation of the powder no longer has an accelerating effect; percolation - which is defined here as the formation of a continuous solid skeleton, requires in fact more time to reach [3].

To understand the effect of NHL on the hydration of cementitious materials, the heat flow during hydration was monitored for the studied mortars. With the exception of the first exothermic peak, no significant heat flow was measured for the 100% NHL mortar. It can therefore be considered that the hydration of NHL had no influence on calorimetry



measurements from 1h. Thus, for all the studied mortars, the heat flow is normalized by the amount of cement in the sample (Fig. 1).

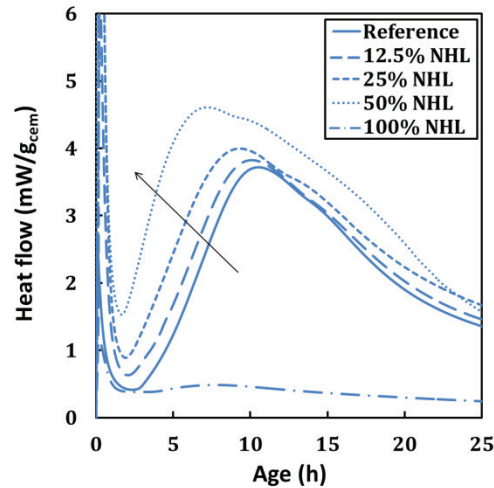


Figure 1: Heat flow curves for mortars with increasing NHL proportions

The curves represent the four characteristic periods of cement hydration, namely the initial reactions, the dormant, the acceleration and the deceleration periods. The last two periods correspond mainly to the hydration of alite ( $C_3S$ ) which is the main phase of cement clinker. Another peak corresponding to the "sulfate depletion peak" may appear as a shoulder on the decreasing part of the main peak [4]. This aluminate peak corresponds to an acceleration of  $C_3A$  dissolution as soon as the sulphate carrier is completely dissolved. The aluminates actually react with the sulphate to form ettringite. However, it has been reported that a significant quantity of ettringite is produced before this aluminate peak.

The progressive leftward shifts and the earlier apparition of the hydration peak as well as the induced shorter induction periods (Fig. 1) indicate the acceleration of the mortars' hydration when cement is substituted by NHL. Since, apart from the first exothermal peak, no significant hydration reaction of NHL is observed during the first hours, the NHL accelerating effect can be considered similar to that of aerial lime which has been reported in the literature [5]. The acceleration could be attributed to nucleation on lime particle surfaces or to homogeneous nucleation within pores rather than to a supersaturation of pore solution. Indeed, the influence of the amount of NHL is observed while the concentration of the pore solution is supposed to be the same for all samples after the first dissolution peak [5].

It appears from Fig. 1 that the sulfate depletion peak becomes visible on the isothermal calorimetry curves after 9 hours for the 50% NHL paste and after 13 hours for the reference paste. This suggests a faster formation of ettringite in NHL mortars.

The evolution of ettringite in the system was monitored using DSC by measuring the consumption of the setting regulator (gypsum for example) by the mineral phases of clinker  $C_3A$  and  $C_4AF$  to produce ettringite. Indeed, the evolution of the endothermic peak located between 120 and 160 °C is inversely correlated with the production of ettringite [6]. This peak disappears after 12h and 8h respectively for the reference and the 50% NHL pastes (Fig. 2), suggesting that ettringite is more rapidly produced in NHL mixtures. This confirms the earlier apparition of the sulfate depletion peak observed in Fig. 1.

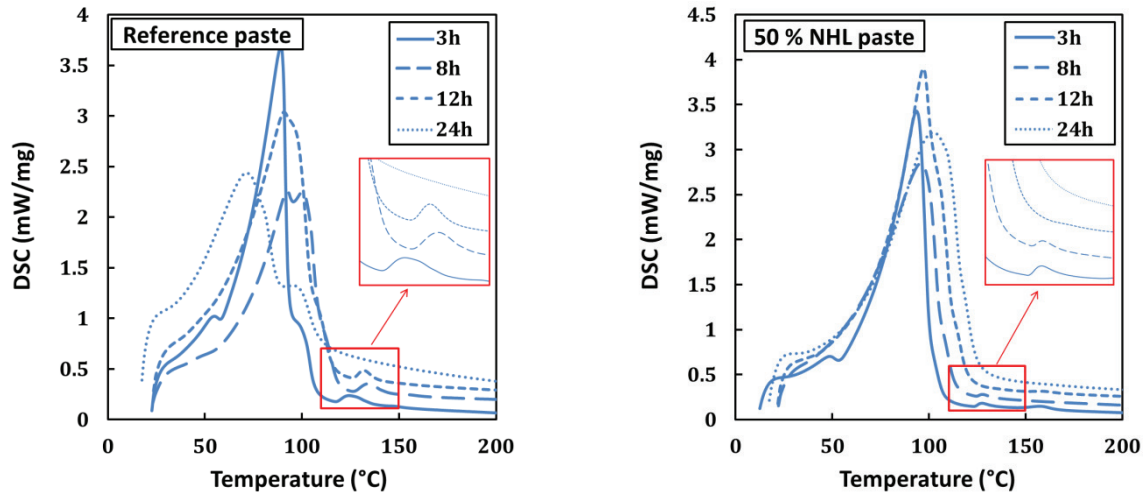


Figure 2: DSC for reference and 50% NHL pastes

TGA measurements were also performed on the reference and the 50% NHL pastes in order to examine the influence of NHL on the production rate of portlandite. It is well known that portlandite crystals decompose between 400 and 500 °C. The measured mass loss due to the evaporation of water is used to calculate the amount of portlandite in the mixture.

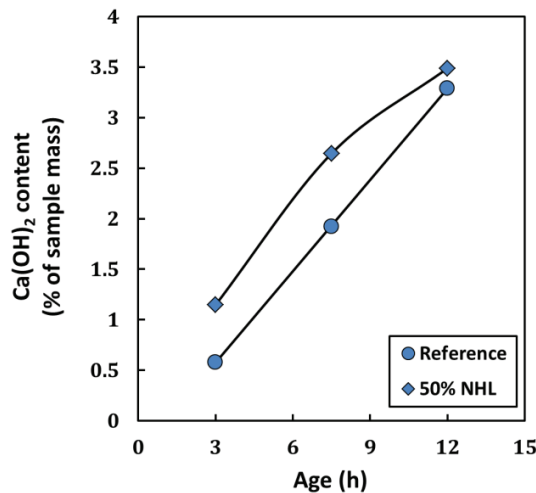


Figure 3: Evolution of the portlandite content for reference and 50% NHL pastes

The evolution over time in  $\text{Ca(OH)}_2$  content in the two pastes are shown in Fig. 3. Note that the values shown for the 50% NHL paste are corrected by removing the proportion of  $\text{Ca(OH)}_2$  initially brought by NHL powder. This fraction of portlandite was determined through TGA measurements conducted on NHL dry powder. This ensures that only the portlandite produced following the hydration of cement is considered.

It can be observed that during the acceleration period, the production rate of  $\text{Ca(OH)}_2$  is higher for the 50% NHL paste. This confirms that NHL does indeed have an influence on the dissolution-precipitation processes related to the hydration of  $\text{C}_3\text{S}$ .

If this rapide formation of hydration products (particularly ettringite and portlandite) take place while the stiffness of the material is relatively low, it can result in an expansion period at early age. Compressive stresses are thus induced in the system and could provide a considerable benefit in plastic shrinkage mitigation.

#### 4. Conclusions

In the present paper the effect of natural hydraulic lime/cement substitution on the setting and early hydration of cement-based mortars was investigated. The substitution of cement by natural hydraulic lime was observed to have the following effects:

- An acceleration of the early-age hydration and a reduction of initial setting times. This accelerating effect is due to nucleation on the lime particle surfaces rather than to a supersaturation of the interstitial solution.
- The accelerating effect of the surface area provided by the NHL is substantial until an optimal surface is reached. Beyond this surface, the incorporation of the NHL no longer has an accelerating effect since percolation requires more time to reach.
- Thermal analyzes show that the acceleration of hydration is accompanied by a higher production rate of ettringite and portlandite, which can cause crystalline pressures that could compensate for plastic shrinkage strain at a early-age.

#### References

- [1] H. Güllü, "On the viscous behavior of cement mixtures with clay, sand, lime and bottom ash for jet grouting," *Constr. Build. Mater.*, vol. 93, pp. 891–910, 2015.
- [2] E. Berodier and K. Scrivener, "Understanding the Filler Effect on the Nucleation and Growth of C-S-H," *J. Am. Ceram. Soc.*, vol. 97, no. 12, pp. 3764–3773, Dec. 2014.
- [3] L. Stefan, F. Benboudjema, J. M. Torrenti, and B. Bissonnette, "Prediction of elastic properties of cement pastes at early ages," *Comput. Mater. Sci.*, vol. 47, no. 3, pp. 775–784, 2010.
- [4] W. Lerch, "The influence of gypsum on the hydration and properties of Portland cement pastes," *Am. Soc. Test. Mater.*, vol. 46, pp. 1252–1297, 1946.
- [5] M. Fourmentin *et al.*, "Porous structure and mechanical strength of cement-lime pastes during setting," *Cem. Concr. Res.*, vol. 77, pp. 1–8, 2015.
- [6] A. Darquennes, S. Staquet, M.-P. Delplancke-Ogletree, and B. Espion, "Effect of autogenous deformation on the cracking risk of slag cement concretes," *Cem. Concr. Compos.*, vol. 33, no. 3, pp. 368–379, Mar. 2011.

## IMPROVEMENT OF THE MICROWAVE ABSORPTION CHARACTERISTICS BY SINTERING SLAG AS AGGREGATE

Haruki Taguchi <sup>(1)</sup>, Yosuke Ito <sup>(1)</sup>, Shinji Kawabe <sup>(1)</sup>

(1) Nagoya Institute of Technology (NIT), Aichi, Japan

### Abstract

In regions of heavy snowfall, removing snow requires considerable effort. The heating mortar block system that uses an oscillator with a frequency of 2.45 GHz has been investigated for melting snow. Using this system, snow can be quickly and easily melted. The electric arc furnace oxidizing slag (hereinafter referred to as “slag”) can convert the electromagnetic (EM) waves into heat. Utilizing this property, an EM absorption material used in the heating mortar is mortar mixed with slag as an aggregate (hereinafter referred to as “slag mortar”). The components of the slag vary based on the plant that is being produced. It has been clarified by previous studies that both components and particle sizes of slag affect the EM wave absorption ability of the slag mortar. Therefore, this study attempts to improve the EM wave absorption ability of slag mortar by sintering slag.

### 1. Introduction

In regions of heavy snowfall, removing snow requires considerable effort. It is particularly difficult for the elderly to go out. As depicted in Fig. 1, the snow on the public roads are removed using snow removal vehicles; however, snow removal, especially from the entrance of house to the front road, is often manually performed.

The heating mortar block system that uses an oscillator with a frequency of 2.45 GHz has been studied to melt snow [1], [2]. Conventional systems with electric heating cables exhibit a disadvantage that it requires time to warm up because the heating cables are buried deep inside the ground to avoid being cut. Using the heating mortar block system ensures that the snow will melt in a quicker and easier manner as compared to that observed in the systems using electric heating cables. As depicted in Fig. 2, the heating mortar block comprises the following three layers: (1) a base layer, (2) an electromagnetic (EM) absorption material layer, and (3) an EM shielding material layer. The electric arc furnace oxidizing slag can convert the

EM waves into heat. Hereinafter, “the electric arc furnace oxidizing slag” will be referred to as “slag.” Utilizing this property, an EM absorption material is used and is mortar mixed with slag as an aggregate. Hereinafter, “mortar mixed with slag as an aggregate” will be referred to as “slag mortar.” An EM absorption material layer is placed near the surface to ensure that the heating mortar block can melt snow efficiently.

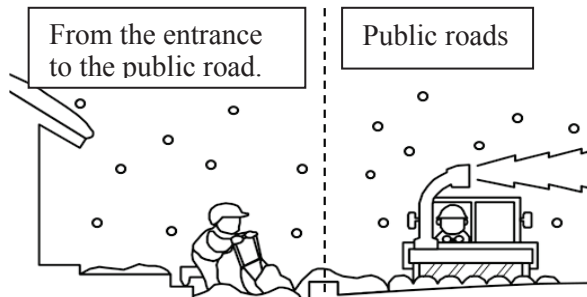


Figure 1: The state of the snowfall regions.

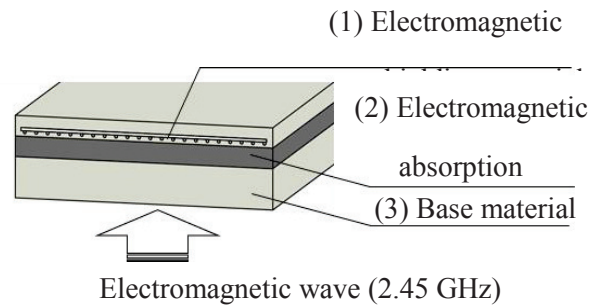


Figure 2: The heating mortar block.

The components of slag vary based on the plant that is being produced. It has been clarified by previous studies [3] that both components and particle sizes of slag affect the EM wave absorption ability of the slag mortar. This study attempts to improve the EM wave absorption ability of slag mortar by sintering slag, which exhibits low EM wave absorption ability, and by changing the crystal structure of slag.

## 2. The complex permittivity and permeability

The EM wave absorption ability is evaluated by return loss (RL). RL is calculated using the complex permittivity and permeability. Because the slag contains a magnetic oxide that depicts ferrimagnetism, it is classified as a magnetic loss material. The permittivity and permeability of the magnetic loss material are represented by complex numbers, and the complex permittivity,  $\hat{\epsilon}$ , and permeability,  $\hat{\mu}$ , are defined in Eqs. (1) and (2), respectively.

$$\hat{\epsilon} = \epsilon' - j\epsilon'' \quad (1)$$

$$\hat{\mu} = \mu' - j\mu'' \quad (2)$$

where  $\epsilon'$  and  $\epsilon''$ ,  $\mu'$  and  $\mu''$  are the real and imaginary parts of complex permittivity and permeability, respectively, and  $j$  is an imaginary number.

## 3. Materials

### 3.1 Electric arc furnace oxidizing slag

Two types of slags, slags A and B, which are industrial by-products generated while producing recycled iron using an electric furnace, are used. The slags A and B differ in components, production process, and grain shape. The mass ratio of the components of slags A and B obtained by the qualitative analysis of inorganic elements using X-ray fluorescence

are presented in Tab. 1 in terms of oxides. The particle size of slags A and B is 0.3–0.6 mm, and the absolute dry densities of slags A and B are 3.59 and 3.73 g/cm<sup>3</sup>, respectively.

Table 1: Chemical components of the slag (Weight %).

Components	CaO	SiO <sub>2</sub>	MnO	MgO	FeO	Fe <sub>2</sub> O <sub>3</sub>	Al <sub>2</sub> O <sub>3</sub>	Cr <sub>2</sub> O <sub>3</sub>	TiO <sub>2</sub>	P <sub>2</sub> O <sub>5</sub>	Total
Slag A	22.93	18.09	9.84	5.20	29.20	6.24	15.57	3.53	1.71	0.17	99.23
Slag B	20.69	13.63	7.97	3.34	30.79	5.67	10.32	3.55	0.47	0.43	96.86

### 3.2 Slag mortar

The mix proportion of the slag mortar is presented in Tab. 2. The cement used in the slag mortar is an ordinary Portland cement. The specimen is manufactured by filling the waveguide with slag mortar. The specimen is exposed to air for 1 day and is cured underwater for 5 days. Further, the specimen is dried until it reaches an absolute dry state.

Table 2: Mix proportion of the slag mortar (Weight ratio).

Cement	Slag	Water	Waterproofing agent
100	150	45.0	0.30

## 4. Measuring method

### 4.1 The complex permittivity and permeability

The complex permittivity and permeability of slag mortar are measured using the S parameter measurement method and the Nicolson–Ross method. The measuring equipment is depicted in Fig. 3. The EM waves are transmitted from Port 1 of a vector network analyzer and are irradiated to the specimens of slag mortar via a coaxial cable and a coaxial waveguide converter. The EM waves are reflected, transmitted, or absorbed by slag mortar. The reflected EM waves are received again at Port 1, and the reflection coefficient is calculated. The transmitted EM waves are received at Port 2, and the transmission coefficient is calculated. The complex permittivity and permeability of slag mortar are calculated using the reflection coefficient and transmission coefficient that were obtained by the Nicolson–Ross method.

### 4.2 Sintering method

Slag is sintered by an electric muffle furnace depicted in Fig. 4. Insert the slag into a heat-resistant container, as depicted in Fig. 5; further, place it in an electric muffle furnace, and sinter it at different temperatures as will be specified in section 5.1.

## 5. Measurement of the complex permittivity and permeability of slag mortar

### 5.1 Measurement conditions

This section intends to clarify the changing condition of the EM wave absorption ability by confirming the effect that was caused by the change in the sintering temperature on the

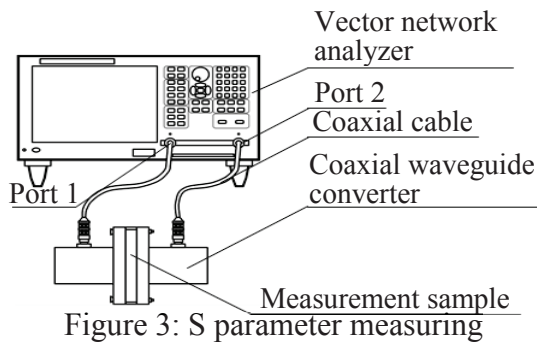


Figure 3: S parameter measuring device.



Figure 4: Electric muffle furnace.

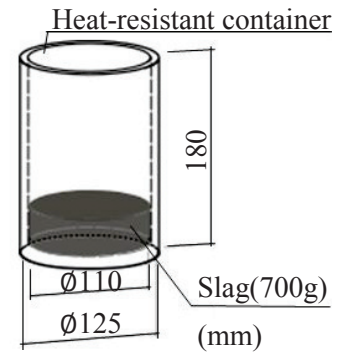


Figure 5: Condition of the sintering slag test.

complex permittivity and permeability of slag mortar. The sintering temperature of the slag is set to 200°C, 400°C, 600°C, 800°C, and 1,000°C, and the sintering time is 8 hours each. When the slags A and B are sintered at 1,100°C and 900°C, respectively, a part of the minerals that are contained in the slag melts and solidifies, and the slag cannot be treated as an aggregate. Therefore, by considering practicality, sintering is performed at 1,000°C and 800°C in case of slags A and B, respectively.

## 5.2 The complex permittivity and permeability as a function of frequency

For the slag mortar that uses slag A as an aggregate, the real part,  $\epsilon'$ , and the imaginary part,  $\epsilon''$ , of complex permittivity along with the imaginary part,  $\mu''$ , of complex permeability as a function of frequency are depicted in Figs. 6 to 8, respectively. Similarly, for the slag mortar that uses slag B as an aggregate are depicted in Figs. 9 to 11, respectively. Because the real part,  $\mu'$ , of complex permeability is approximately 1 within the measurement range, the data exhibiting the relation between  $\mu'$  and frequency are omitted. The complex permittivity and permeability of the slag mortar was altered by sintering the slag. The changing range of  $\epsilon'$  is extensive for slag A than for slag B throughout the frequency, and  $\epsilon''$  decreases when slag A is sintered at 1,000°C. In case of  $\mu''$ , the value becomes larger when slags A and B are sintered at 1,000°C and 800°C, respectively.

## 5.3 The complex permittivity and permeability of slag mortar at 2.45 GHz

The relation between  $\epsilon'$  at 2.45 GHz of the slag mortar using slags A and B and the sintering temperature is depicted in Fig. 12. The relation between  $\mu''$  and the sintering temperature is presented in Fig. 13.  $\epsilon'$  changes several times in slag A that was sintered at 800 °C or more, whereas slag B exhibits relatively few changes. This is because the chemical components are different and because the mineral structure produced by sintering is different in slags A and B.  $\mu''$  increases at 800°C or more in case of both slags A and B, and it is expected that the EM wave absorption ability of the slag mortar will be altered by sintering the slag.

## 6. Calculated return loss of slag mortar

Using the measurement results of the complex permittivity and permeability of slag mortar that were obtained in chapter 5, RL is calculated at a frequency of 2.45 GHz and the EM wave

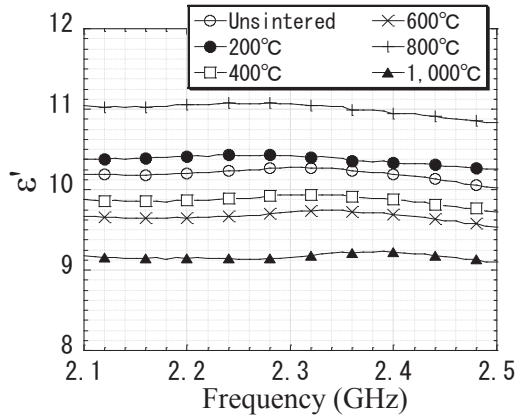


Figure 6: Real part of complex permittivity (slagA aggregate).

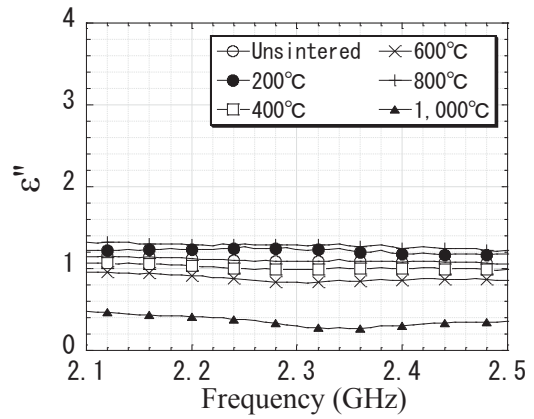


Figure 7: Imaginary part of complex permittivity (slagA aggregate).

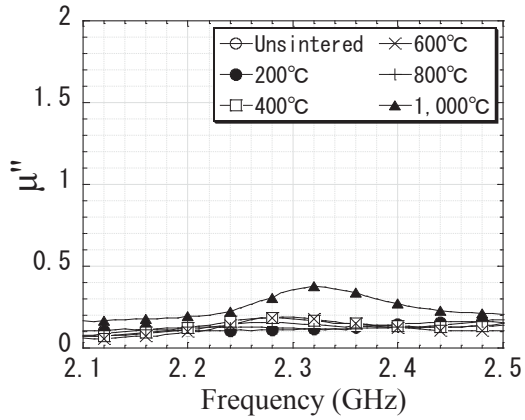


Figure 8: Imaginary part of complex permeability (slagA aggregate).

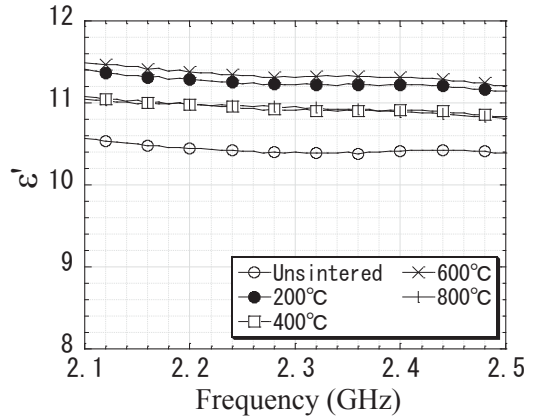


Figure 9: Real part of complex permittivity (slagB aggregate).

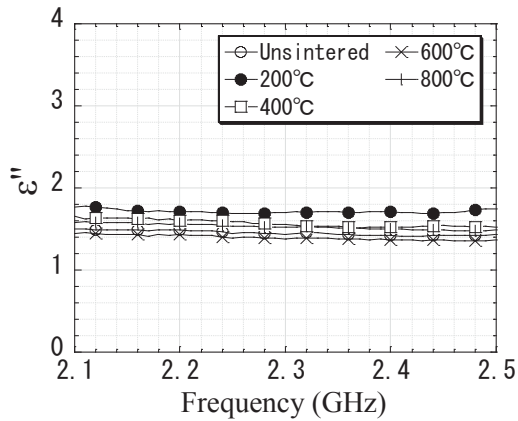


Figure 10: Imaginary part of complex permittivity (slagB aggregate).

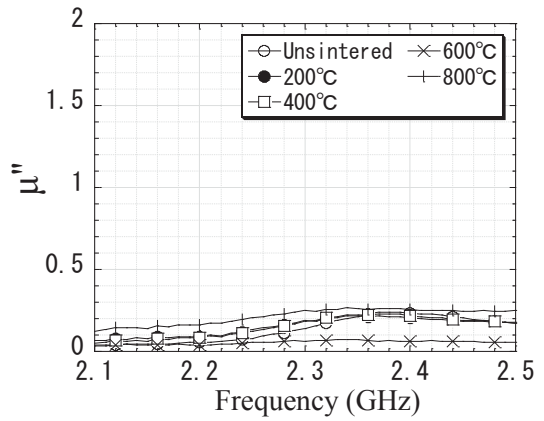


Figure 11: Imaginary part of complex permeability (slagB aggregate).



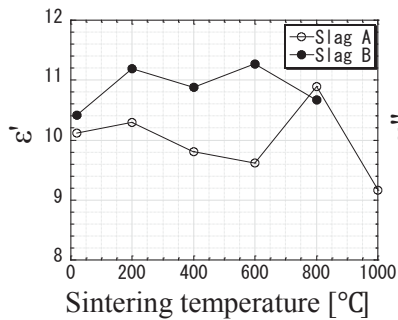


Figure 12:  $\epsilon'$  and sintering temperature.

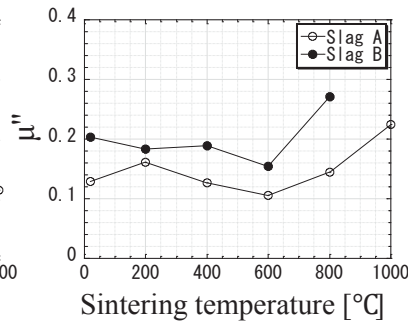


Figure 13:  $\mu''$  and sintering temperature.

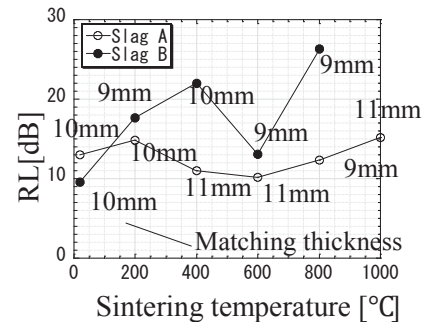


Figure 14: RL and sintering temperature.

absorption ability of the slag mortar is evaluated. The relation between RL of the slag mortar and the sintering temperature of the slag at a matching thickness is depicted in Fig. 14. RL of the slag mortar using unsintered slag A is 13.0 dB at a matching thickness of 10 mm, whereas that of the slag mortar using slag A that was sintered at 1,000 °C is 15.2 dB at a matching thickness of 11 mm. On the other hand, RL of the slag mortar using unsintered slag B is 9.6 dB at a matching thickness of 10 mm, whereas that of the slag mortar using slag B that was sintered at 800 °C is 26.3 dB at a matching thickness of 9 mm. Therefore, it is expected that the EM wave absorption ability of the slag mortar will be improved by sintering the slag. This makes it possible to produce slag mortar that depicts the EM wave absorption ability at a desired level, regardless of the type of slag.

## 7. Conclusions

- (1) The complex permittivity and permeability of the slag mortar was altered by sintering the slag.
- (2) It was assumed that the EM wave absorption ability of the slag mortar will be improved by sintering the slag.

## Acknowledgments

This research was partially supported by the Matching Planner Program from Japan Science and Technology Agency (JST) and the JSPS KAKENHI Grant Number JP16K18183 and JP16K06569. Some suggestions were provided by the Honorary Professor of the Nagoya Institute of Technology, Ikeda Tetsuo, and Ten corporation. We gratefully acknowledge their supports and contributions to the research reported in this study.

## References

- [1] Kawabe, S., et al, Development of the heating mortar block to melt snow by the quasi microwave, *Journal of Structural and Construction Engineering* 69(586) (2004), 1-5
- [2] Ito, Y. et al, Effects of thickness of the base layer on electromagnetic absorption in heating mortar blocks for snow melting through quasi microwave, *Journal of Advanced Concrete Technology* 16 (2018), 170-178

## **INFLUENCE OF RECYCLED AGGREGATE AND RECYCLED SAND ON THE DEVELOPMENT OF THE EARLY AGE PROPERTIES OF CONCRETE SINCE SETTING**

**Brice Delsaute<sup>(1)</sup>, Stéphanie Staquet<sup>(1)</sup>**

(1) Université Libre de Bruxelles, Brussel, Belgium

### **Abstract**

This paper aims at identifying the effect of the substitution of natural coarse aggregate and sand by recycled aggregate and sand on the early age development of the free deformation and the mechanical properties since setting. For this purpose, a new experimental testing protocol for the characterization of cementitious materials at early age is used. This new approach is based on the repeated application of thermal variation and loading using a newly developed testing device. The high porosity and absorption of the recycled aggregate and sand induces a strong reduction of the autogenous deformations, the modulus of elasticity and the strength during the hardening process. An elastic calculation of the restraint of the free deformations shows that the use of recycled aggregate and sand decreases the risk of cracking.

### **1. Introduction**

Aggregates, which are the backbone of concrete, are inequitably distributed resources and far from inexhaustible. Their transport is very energy intensive and it is therefore necessary to use local resources to reduce the environmental impact of the very huge production of concrete in the world. One solution to this problem is the use of recycled aggregate instead of natural aggregate. For structural applications, the use of these "green" materials requires a complete characterization of the evolution of the physical and mechanical properties which are quite different from those of standard concretes. At early age, the autogenous strain and the coefficient of thermal expansion (CTE) are two of the most important concrete properties that are responsible of volume changes of cement based materials. The restraint of the autogenous and thermal strain can induce early age cracking in concrete structures (especially for massive structures). To determine the risk of cracking, it is also necessary to define other concrete properties such as the heat release by the cement, the strength and the elastic

modulus. This paper aims to identify the effect of the substitution of natural aggregate and sand by recycled aggregate and sand on the development of concrete properties at early age and to estimate their impact on the risk of cracking induced by the restrained of the free deformation in sealed conditions.

## 2. Materials and methods

### 2.1 Concrete compositions

The substitution of natural aggregate by recycled one is studied on four concretes for which mix proportions are given in Table 1. Each composition was defined in the frame of the French National project RECYBETON. For each composition, the effective water to equivalent binder ratio (0.65) and the volume fraction of aggregate and sand are the same. The content of cement, limestone filler and superplasticizer is slightly adapted to obtain the same workability. Concrete are referred by 'X'RS'Y'RA where 'X' and 'Y' are the percentage of replacement of natural sand and natural aggregate by recycled sand (RS) and recycled aggregate (RA) in volume respectively. The first composition, called 0RS0RA, is a reference concrete without recycled aggregate and sand. For the second and third composition, 30 and 100% of the natural aggregate are replaced by recycled aggregate in volume. For the last composition 30RS0RA, 30% of the natural sand is replaced by recycled sand in volume. An ordinary Portland cement of type CEMII/A-L 42.5 N was used. Gravels and sand were used in saturated-surface-dry conditions.

Table 1: Mixture proportions in kg/m<sup>3</sup> and materials properties [1].

	0RS0RA	0RS30RA	0RS100RA	30RS0RA
<b>Natural gravel 6,3/20</b>	820	462	-	829
<b>Recycled gravel 10/20</b>	-	296	701	-
<b>Natural gravel 4/10</b>	267	228	-	190
<b>Recycled gravel 4/10</b>	-	-	163	-
<b>Natural sand 0/4</b>	780	813	806	549
<b>Recycled sand 0/4</b>	-	-	-	235
<b>CEM II/A-L 42.5, C</b>	270	276	282	276
<b>Limestone filler, L</b>	45	31	31	31
<b>Superplasticizer, SP</b>	0.747	0.861	0.798	0.798

For consideration of the ageing and the main temperature effects, concrete properties are expressed in function of the equivalent time  $t_{eq}$  (Eq. 1) which is based on the Arrhenius law and is function of the age of the material  $t$ , the evolution of the temperature  $T$  (°C), a reference temperature  $T_r$  (here 20°C), the universal gas constant  $R$  (=8.314 J/mol/K) and the apparent activation energy  $E_a$  (J/mol). The apparent activation energy was determined according to isothermal calorimetry results obtained in [2] and is equal to 35.15 kJ/mol.

$$t_{eq}(t, T) = \int_0^t \exp\left(\frac{E_a}{R} \cdot \left(\frac{1}{273 + T(s)} - \frac{1}{273 + T_r}\right)\right) \cdot ds \quad (1)$$

## 2.2 Methods

### *Assessment of the temperature in quasi-adiabatic conditions*

Quasi-adiabatic calorimetry (QAB) allows a continuous measurement of the temperature in quasi-adiabatic conditions which is similar to the evolution of the temperature in case of massive concrete structures. The testing device so-called QAB box was developed at the LCPC laboratory (now IFSTTAR) for the monitoring of the heat release [3]. During the test, the temperature inside the concrete sample is recorded as well as the temperature of the room. Tests were performed on  $\pm 15.5$  kg concrete samples.

### *Assessment of the elastic properties*

For the monitoring of the elastic properties, cylindrical specimens with a diameter of 97 mm and a height of 550 mm are produced. A dummy specimen with exactly the same dimensions is also produced. Samples are surrounded by 2 self-adhesive aluminum sheets in order to keep the sample in sealed conditions. An electromechanical testing setup with an extensometer in Invar<sup>®</sup> designed at ULB is used for the monitoring of the E-modulus by means of repeated loadings. The equipment is located in an air-conditioned room with a control system of the temperature and the relative humidity. The longitudinal displacement is measured with an extensometer composed by two rings spaced of 350 mm and three rods on which the 3 displacement sensors placed at 120° are pressed. Three anchorages with elastic blades are used for each ring to assure a good link between the concrete displacement and the sensor.

### *Assessment of the autogenous strain and the coefficient of thermal expansion*

The free strain of the studied concretes is measured from casting using the BTJADE device. The test rig is composed of a vertical flexible corrugated PVC mould to monitor the free strain and fixed metallic parts. The whole frame is placed in a temperature controlled bath. In addition, repeated thermal variations are applied during the test in order to define the evolution of the CTE. Complete details about the device and the test protocol are given in [4].

## 3. Experimental results

### 3.1 Temperature evolution in quasi-adiabatic conditions

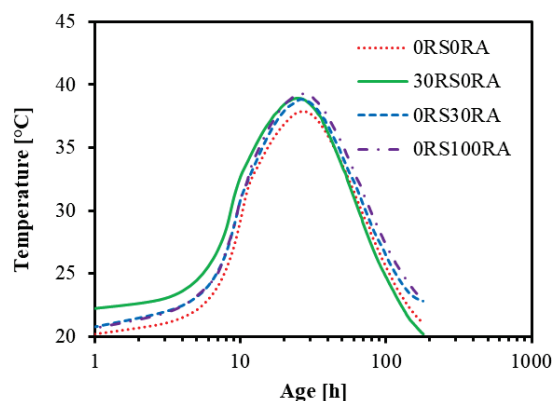


Figure 1 : Evolution of the temperature inside the cylindrical concrete sample.

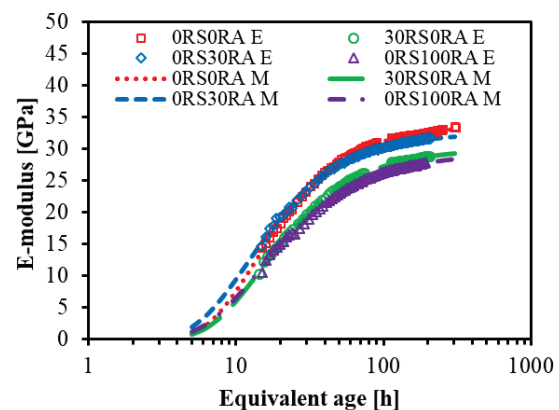


Figure 2 : Evolution of the E-modulus (E – Experimental data and M – Model) since 4 hours after setting

Each minute, the temperature of the sample and the one of the testing room is recorded. Measurements start around 30 minutes after the first contact between water and cement till a concrete age of 180 hours. In Figure 1, the recording of the concrete temperature is presented. For each composition, the temperature of the sample increases significantly between an age of 5 and 11 hours. The temperature peak is reached between an age of 23 and 26 hours and has a magnitude between 38 and 40°C. The evolution of the temperature is very similar between each composition.

### 3.2 Elastic modulus

Measurements on the samples have started 4 hours after setting. The whole test duration is 1 week. The temperature of the sample is set to 20°C and is recorded since the casting. For each repeated loading, the E-modulus is calculated from the set of recordings (load and displacement in the central section) between 30% and 80% of loading [5,6]. Results are given according to the equivalent time in Figure 2. The substitution of 30% of natural aggregate by recycled one does not change significantly the evolution of the E-modulus while a rate of substitution of 100% induce a decrease of the E-modulus by 5 GPa at an age of 1 week. The substitution of 30% of natural sand by recycled sand induces a decrease of the E-modulus by 4 GPa at an age of 1 week. The modeling of the E-modulus is carried out with Eq. 2 [7] where  $t_{eq}$  is expressed in hour,  $p_E$  and  $r_E$  are material parameters which are related to the kinetic evolution of the elastic modulus,  $E(t_{eq} = \infty)$  is expressed in GPa and corresponds to the value of the elastic modulus at an infinite time. Values of all parameters are given in Table 2.

$$E(t_{eq}) = E(t_{eq} = \infty) \cdot \exp\left(-\left(\frac{p_E}{t_{eq}}\right)^{r_E}\right) \quad (2)$$

Table 2 - E-modulus coefficient for Equation 2

Composition	$E(t_{eq} = \infty)$ [GPa]	$p_E$ [h]	$r_E$ [/]
0RS0RA	33.6	13.6	1.28
30RS0RA	29.9	14.7	1.22
0RS30RA	32.6	11.9	1.21
0RS100RA	29.3	14.4	1.11

### 3.3 Autogenous strain and coefficient of thermal expansion (CTE)

Autogenous strains are set to zero at the final setting time. The measurements of the autogenous strain are shown in Figure 3. A similar evolution is observed after the final setting (between 10 and 12 hours according to the composition) and goes on till an equivalent age of 24 hours. During this period, shrinkage is observed and evolves very similarly for each composition and is associated to the self-desiccation of the cement paste. Then a divergence takes place between the evolutions of the different compositions. The high porosity of the recycled aggregate and sand is at the origin of these differences between the three compositions. When self-desiccation occurs, relative humidity decreases inside the cement paste. In such case, recycled aggregate plays the role of water storage agent that refills capillarity pores during the hardening process and avoids or reduces the self-desiccation mechanism with the continuous release of water. Results of the CTE are given in Figure 4. During setting, a strong and quasi instantaneous decrease of the CTE takes place during the

same limited time slot for each composition (between an equivalent age of 6 and 8 hours). Then a low decrease or increase of the CTE is observed for each composition till and equivalent age of 24 hours. Then, the CTE does not evolve significantly anymore. For the composition with the highest rate of substitution of natural aggregate by recycled one, the value of the CTE is globally higher and a limited increase of the CTE is observed after several days of age (because of the internal curing effect induced by the high porosity of the recycled aggregate).

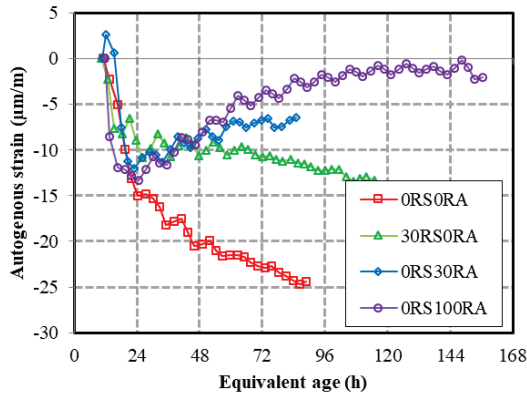


Figure 3 : Evolution of the autogenous strain

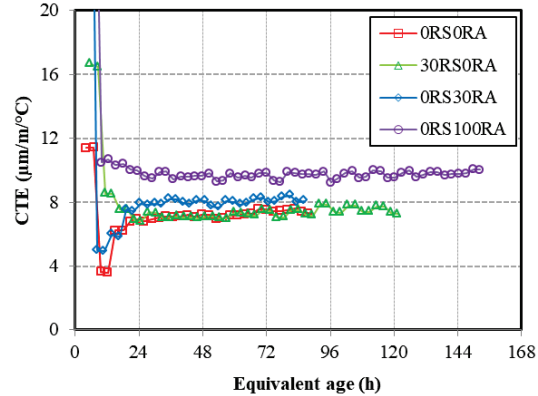


Figure 4 : Evolution of the coefficient of thermal expansion

#### 4. Evaluation of the stress under restrained condition

In order to evaluate the influence of recycled aggregate and sand on the risk of cracking, an elastic calculation of the full restraint of the free deformations is performed according to Eq. 3 where  $\varepsilon_r$  is the restrained strain. Basic creep was not considered for the calculation.

$$\sigma = - \sum_{t'=t_0}^t \Delta\varepsilon_r \cdot E(t') \quad (3)$$

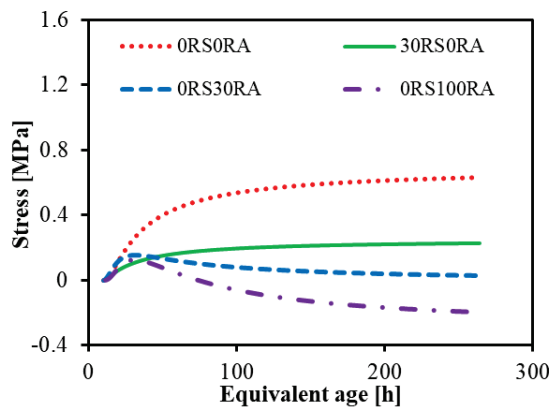


Figure 5 : Stress development in case of full restrained of the autogenous strain

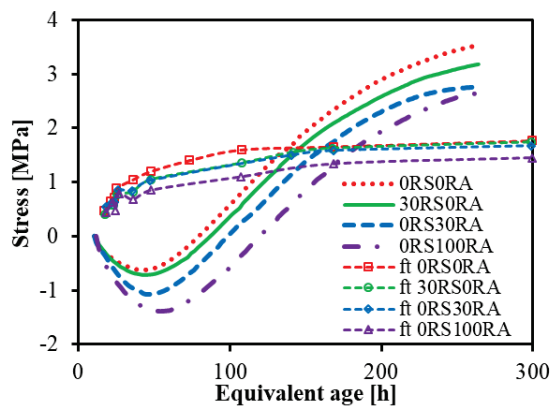


Figure 6 : Stress development in case of full restrained of the autogenous and thermal strain

Two scenarios were investigated. First, only the full restrained situation of the autogenous strain was considered (Figure 5). In this scenario, the decrease of the E-modulus and the autogenous shrinkage induced by the presence of recycled aggregate/sand leads to a significant decrease of the stress. At an equivalent age of 260 hours, the elastic stresses computed for the composition without recycled aggregate are equal to 0.6 MPa while compressive stresses of -0.2 MPa were computed for the composition 0RS100RA. Secondly, both autogenous and thermal strain were fully restrained (Figure 6). The thermal strain were computed by considering the evolution of the CTE and the evolution of the temperature recorded in the QAB. As in the first scenario, the substitution of natural aggregate/sand by recycled aggregate/sand leads to a decrease of the stress induced by the restraint strain. This is explained by the lower E-modulus and the lower increase of the CTE in the composition with recycled aggregate/sand. In addition, the evolution of the stress are compared to the evolution of the tensile strength obtained in [1].

## 5. Conclusion

A new experimental methodology based on repeated testing method is presented for the characterization of the early age behavior of concrete composed of recycled aggregate and sand in sealed conditions. The presence of recycled aggregates and sand induces a strong reduction of the autogenous shrinkage, the modulus of elasticity and the strength during the hardening process. An elastic calculation of the restraint of the free deformations shows that the use of recycled aggregate and sand decreases the risk of cracking of concrete structure (especially with recycled aggregate) which highlights the interest of the use of recycled aggregate for mass concrete. For further study, the internal curing effect of recycled aggregate could be studied on cement based materials with lower effective water-to-binder ratio (composition for which the self-desiccation phenomenon is very significant).

## References

- [1] A.Z. Bendimerad, E. Rozière, A. Loukili, Plastic shrinkage and cracking risk of recycled aggregates concrete, *Constr. Build. Mater.* 121 (2016) 733–745.
- [2] H. Kada-Benameur, E. Wirquin, B. Duthoit, Determination of apparent activation energy of concrete by isothermal calorimetry, *Cem. Concr. Res.* 30 (2000) 301–305.
- [3] C. Boulay, J.M. Torrenti, J. Andre, R. Saintilan, Quasi-adiabatic calorimetry for concretes : Influential factors, *Bull. Des Lab. Des Ponts Chauss Ees.* (2010) 19–36.
- [4] B. Delsaute, S. Staquet, Decoupling Thermal and Autogenous Strain of Concretes with different water/cement ratios during the hardening process, *Adv. Civ. Eng. Mater.* 6 (2017) 22.
- [5] B. Delsaute, C. Boulay, J. Granja, J. Carette, M. Azenha, C. Dumoulin, G. Karaiskos, A. Deraemaeker, S. Staquet, Testing Concrete E-modulus at Very Early Ages Through Several Techniques: An Inter-laboratory Comparison, *Strain.* 52 (2016) 91–109.
- [6] B. Delsaute, C. Boulay, S. Staquet, Creep testing of concrete since setting time by means of permanent and repeated minute-long loadings, *Cem. Concr. Compos.* 73 (2016) 75–88.
- [7] B. Delsaute, J.-M. Torrenti, S. Staquet, Monitoring and modeling of the early age properties of the Vercors Concrete, in: *TINCE 2016, Paris, 2016*: p. 12.

## **INFLUENCE OF SELECTED FACTORS ON UNCERTAINTY OF RHEOLOGICAL MEASUREMENT OF FRESH MORTARS**

**Jacek Gołaszewski<sup>(1)</sup>, Grzegorz Cygan<sup>(1)</sup>, Małgorzata Gołaszewska<sup>(1)</sup>**

(1) Silesian University of Technology, Gliwice, Poland

### **Abstract**

The paper presents the results of research carried out to determine the uncertainty, repeatability and reproducibility of rheological measurements of mortars in variable conditions. Obtained results allow to assess the repeatability of rheological measurements as good and show the good resistance of the rheometer and test procedure used to the time and operator's influence. It was confirmed that variations in mortar constituents may significantly affect the repeatability and reproducibility of the measurements.

### **1. Introduction**

The measurement uncertainty of set of measurements is usually expressed as the standard deviation or confidence level. Attributes of the measurement method related to uncertainty are: accuracy, precision, repeatability and reproducibility. Accuracy is the closeness of the mean of a set of measurement results to the true value of measuring quantity. Precision is the degree of closeness between results of repeated measurements of the same quantity. Repeatability and reproducibility are the degree of compliance of successive measurement results of the same measured quantity, carried out under the same measurement conditions or in changed measurement conditions respectively. In general, the available literature lacks the information on the attributes of rheometer made measurements of mortars and concretes. This makes it difficult the analysis of results of research into rheological properties of mortars or concretes, including the aspect of the significance of the influence of various material and technological factors. The paper presents the results of research on uncertainty, repeatability and reproducibility of rheological measurements of mortars performed using Viskomat NT rheometer. Although the research refers to the specific rheometer and procedure, it may be useful in the analysis of rheological measurements and its uncertainty in general.



## 2. Experimental

The influence of following factors on uncertainty and precision (repeatability and reproducibility) of measurements of rheological parameters of mortars was investigated:

- Time of testing intervals - 6 series of tests - the first 3 series were made during first week, and next 3 after respectively 1, 2 and 3 months;
- Operator - measurements of rheological parameters were made under the same conditions by four operators with different experience during one week;
- Variations in mortar constituents:
  - (1) type of sand - standard sand acc. [4] or ordinary sand were used for mortars, ordinary sand portion was prepared without or by quartering;
  - (2) batch of cement - batches of cement delivered over a period of 2 months from one cement plant (on average 1 per week, 7 batches were tested);
  - (3) batch of superplasticizer SP- batches of the SP of the same trade name delivered over period of 3 months (on average 1 per month, 3 batches were tested). Cements CEM I different in C<sub>3</sub>A content (C1 - 2%, C2 - 7%, C3 - 12%) were used in this part of research.

Uncertainty and precision of the measurements of rheological parameters was expressed using the coefficient of variation  $V$ , given in percent. It is calculated as quotient of the absolute measure of the variability of a given characteristics during the measurements (defined as a standard deviation  $\sigma$ ) and the average value of this characteristic. For study the effects of factors ANOVA was also used. Analysis was performed in the Statistica 13.1 program.

Rheological properties of fresh mortars and concretes are characterized by the Bingham model parameters: yield stress  $\tau_0$  [Pa] and plastic viscosity  $\eta_{pl}$  [Pas]. The yield stress  $\tau_0$  determines the stress above which the material becomes a fluid. The plastic viscosity  $\eta_{pl}$  is a measure of how easily the material will flow, once the yield stress is overcome. The principles of rheology and rheological measurements are presented in existing literature i.e. [1,2]. Rotational Viskomat NT rheometer was used, its construction and operating principles are presented in [3]. For this rheometer the Bingham equation is used in conventional form:

$$M = g + h N \quad (1)$$

Measurement of rheological parameters of the mortar consists of determination of torque  $M$  [Nmm] on stationary probe mounted concentrically in a rotating with different speeds  $N$  [1/s] cylindrical container with sample. On this basis it is possible to determine, using the method of least squares, an equation of  $M - N$  curve, and thus the rheological parameters  $g$  [Nmm] and  $h$  [Nmms] of the mortar corresponding to yield value  $\tau_0$  plastic viscosity  $\eta_{pl}$  respectively.

The composition of the mortars was based on the composition of standard mortars according to [4] (cement - 450g, sand 1350g). Mortars with  $w/c = 0.55$  or  $0.45$  (mortars without or with SP respectively) of fluidity adequate for measuring range of Viskomat NT were used. Different cements CEM I were used in the individual parts of the research. Cements were stored in plastic bags during the research period. Standard sand according to [4] was used and ordinary

sand was used in the part where the influence of the sand type and the method of preparation of ordinary sand were investigated. Mortars with ordinary sand were too stiff to be measured and 0.3% of plasticizer was used for obtain its adequate flowability. All mortars were prepared according to [4] procedure. Mortars were prepared and measurements were performed in an air-conditioned room at temperature  $20^{\circ}\text{C} \pm 1^{\circ}\text{C}$ , mortars temperature during measurement was maintained  $20^{\circ}\text{C} \pm 1^{\circ}\text{C}$  using thermostatic device. The measurements was carried out after 5 and 60 minutes from the end of mixing.

### 3. Test results and discussion

#### 3.1. General remarks

Tested mortars were characterized by yield value  $g$  values in the range from 11 to 61 Nmm and plastic viscosity  $h$  in the range from 6 to 21 Nmms. Mortars were stable and showed no tendency to segregation and sedimentation. The average  $R^2$  for individual rheological measurements which is a statistical measure of how well the regression line approximates the real data points and provides information about the goodness of a Bingham model for characterize rheological properties of mortars, was 0.990 (with  $R^2_{\min} = 0.982$ ). This confirms a very good fit of the Bingham model as a model characterizing the rheological properties of the tested mortars. Taking into account all series of measurements of mortars with standard sand, the average coefficients of variation are for the yield value  $g$  is  $V_g = 4.3\%$  and for plastic viscosity  $h$   $V_h = 4.1\%$ . The coefficients of variation  $V_g$  and  $V_h$  for a series carried out under the same measurement conditions are always less than 10%, which makes it possible to consider the repeatability of measurements using Viskomat NT to be good.

#### 3.2. Influence of time of testing intervals

As shown in Tab. 1 the coefficient of variation for average rheological parameters on particular days is less than 2 %. This indicates no impact of the time of testing intervals on the results of rheological parameters measurement. This is confirmed by the ANOVA (Fig. 1), which shows that differences in rheological parameters of mortars measured in different time are statistically insignificant.

Table 1: Average yield stress  $g$  [Nmm], plastic viscosity  $h$  [Nmms], coefficients of variation  $V_g$   $V_h$  [%] of mortars measured in different time days.

Time/number of repetitions	after 10 min				after 60 min			
	$g$	$h$	$V_g$	$V_h$	$g$	$h$	$V_g$	$V_h$
Time 1 (day 1, week 1)/3	34	12.2	3.6	3.2	39	8.8	4.5	3.2
Time 2 (day 2, week 1)/4	34	12.4	4.5	2.6	38	8.7	2.3	1.8
Time 3 (day 3, week 1)/4	33	12.1	5.2	6.5	37	8.7	5.7	1.7
Time 4 (day 4, month 1)/4	33	11.9	4.6	5.0	38	8.9	5.5	4.8
Time 5 (day 5, month 2)/3	34	12.5	2.9	2.4	38	9.0	5.5	3.5
Time 6 (day 6, month 3)/3	33	12.4	4.9	8.1	38	8.9	6.5	3.7
Average	34	12.3	4.3	4.6	38	8.8	5.0	3.1
Coef. of variation $V$ of average [%]	1.4	1.9			1.5	1.5		

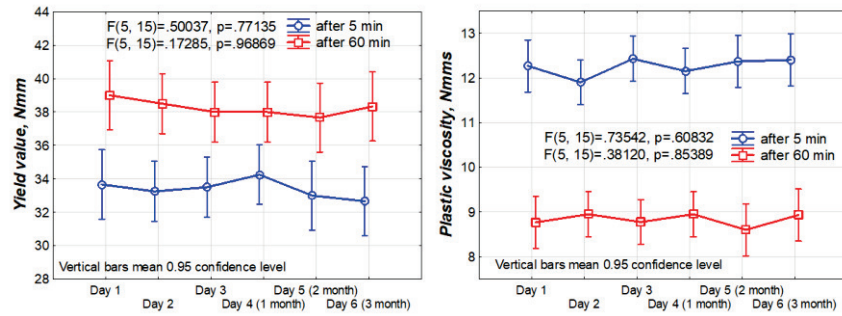


Figure 1: ANOVA of the influence of time (day) on rheological parameters of mortars.

### 3.3. Influence of operator

As Tab. 2 indicates, the coefficient of variation  $V$  of average rheological parameters measured by individual operators does not exceed 2.1%. It means the lack of influence of the operator on the measurements of rheological parameters. This is confirmed by the ANOVA (Fig. 2), which shows that influence of operator is statistically insignificant.

Table 2: Average yield stress  $g$  [Nmm], plastic viscosity  $h$  [Nmms], coefficients of variation  $V_g$  and  $V_h$  [%] of mortars measured by different operators.

Operator /number of repetitions	after 10 min				after 60 min			
	$g$	$h$	$V_g$	$V_h$	$g$	$h$	$V_g$	$V_h$
Operator 1/5	24.3	12.6	5.5	3.7	41.3	9.5	4.4	4.8
Operator 2/5	25.0	12.4	3.4	4.3	42.1	9.8	3.6	2.0
Operator 3/5	24.8	12.1	4.5	6.1	41.9	10.0	5.2	7.2
Operator 4/6	24.8	12.4	4.7	3.4	41.6	9.6	6.5	4.4
Average	24.7	12.4	4.5	4.4	41.7	9.7	4.9	4.6
Coef. of variation $V$ of average [%]	1.2	1.6			0.8	2.1		

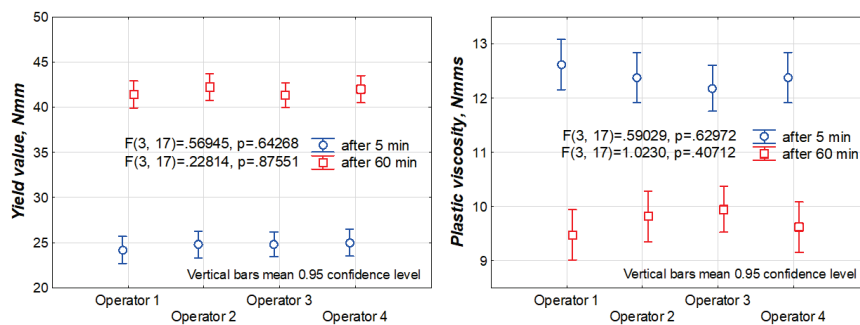


Figure 2: ANOVA of the influence of operator on rheological parameters of mortars.

### 3.4. The influence of variations in mortar constituents

**3.4.1. Influence of cement and SP batch.** As Fig. 3 - 4 and Tab. 3 indicate, that the change of cement or SP batch may significantly influence the rheological properties of mortars. It is worth to notice that tested mortars with different CEM I batches differ from each other in particular by the effect of the workability loss (Fig. 3) and effect of SP batch is the greater the higher the amount of  $C_3A$  in the cement.

Table 3: Average yield stress  $g$  [Nmm], plastic viscosity  $h$  [Nmms], coefficients of variation  $V_g$  and  $V_h$  [%] of mortars made of cement CEM I from different batches.

Batch/number of repetitions	after 10 min				after 60 min			
	$g$	$V_g$	$h$	$V_h$	$g$	$V_g$	$h$	$V_h$
Batch 1/3	24	4.0	10.3	4.2	53	4.4	7.5	6.7
Batch 2/3	28	4.1	8.5	4.3	42	4.7	6.7	6.1
Batch 3/3	25	4.2	8.9	3.3	35	4.6	6.5	6.1
Batch 4/3	25	3.9	11.5	3.7	37	4.3	8.4	6.1
Batch 5/3	23	4.5	9.6	1.1	41	5.5	7.6	3.0
Batch 6/3	22	3.5	12.4	2.3	37	4.2	9.8	4.0
Batch 7/3	25	4.2	12.6	4.5	46	3.5	9.6	1.5
Average	24	4.0	10.5	3.3	42	4.4	8.0	4.8
Coef. of variation $V$ of average [%]	7.7		15.7		15.1		16.3	

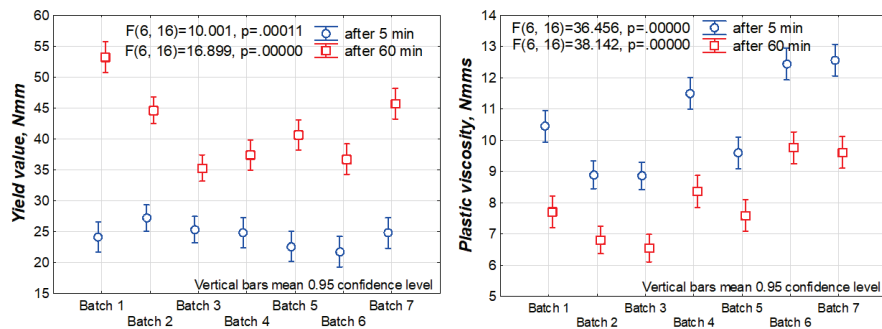


Figure 3: ANOVA of the influence of a CEM I batch on rheological parameters of mortars.

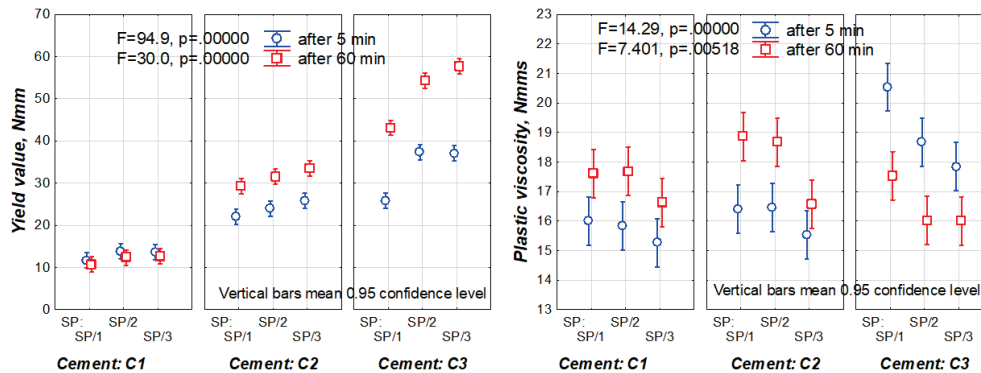


Figure 4: ANOVA of the influence of a SP batch on rheological parameters of mortars.

Table 4: Average yield stress  $g$  [Nmm], plastic viscosity  $h$  [Nmms], coefficients of variation  $V_g$  and  $V_h$  [%] of mortars made of different sand and in a different way prepared.

Sand type/ number of repetitions	after 10 min				after 60 min			
	$g$	$V_g$	$h$	$V_h$	$g$	$V_g$	$h$	$V_h$
Standard sand/10	24	4.2	11.5	3.3	38	4.3	11.2	4.3
Ordinary sand quartered/10	26	6.8	17.0	5.5	25	6.2	16.0	5.8
Ordinary sand non quartered/10	26	10.6	16.9	6.8	26	11.3	15.8	8.1

**3.4.2. The influence of the type and method of sand sample preparation.** As Tab. 4 indicates, coefficients of variability of measurements of rheological parameters of standard sand mortar do not differ from the coefficients obtained in other stages of research. The coefficients of variation of rheological parameters for mortars with ordinary sand are much higher than in the case of mortars with standard sand. A particularly large coefficient of variations was obtained for mortar with non-quartered ordinary sand, in case of the yield value  $g$  they are over 10%. Quartering of the ordinary sand reduces the dispersion of results, however, it is still higher than in the case of mortars with standard sand. It is also worth to note, that in the case of mortars with ordinary sand prepared by quartering or without quartering the same mean rheological parameters were obtained. This means that applying quartering improves precision without affecting accuracy of rheological measurements.

#### 4. Conclusions

The Bingham model describes well the rheological properties of the tested mortars. The coefficients of variation for all individual series of rheological measurements performed under the same conditions were always clearly smaller than 10%. It allows to assess the repeatability of performed rheometer measurements as good. Taking the number of measurements as significant and assuming the repeatability  $r$  as 2.8  $V$ , it can be calculated that the limits of repeatability for rheometer measurement performed using Visomat NT under conditions presented in p. 2 are for the yield value is  $r_g = 13\%$   $g$ , and similarly for plastic viscosity  $r_h = 13\%$   $h$ .

Under given conditions, the results of the measurement of the rheological parameters and their variability coefficient are not affected by the long intervals in mortar testing time (up to 3 months) and the operator. This indicates good reproducibility of measurements performed on different dates and by different operators.

In general, lack of control of the batch of cement or superplasticizer may significantly affects the repeatability and reproducibility of the test results. It is recommended to plan the research in order to perform it with the same batch of materials. The sand type and the method of its preparation significantly affect the repeatability and reproducibility of test results for mortars. It is beneficial to use standard sand, because its grading is strictly defined and controlled during production.

#### References

- [1] Tattarsall, G H, Banfill, P F G., The Rheology of Fresh Concrete, Pitman Books Limited, Boston, USA, (1983)
- [2] N. Roussel, Understanding the Rheology of Concrete, Woodhead Publishing Ltd, (2012)
- [3] [http://www.schleibinger.com/cmsimple/en/?Rheometers:Viskomat\\_NT\\_Rheometer\\_f\\_Mortar\\_and\\_Paste](http://www.schleibinger.com/cmsimple/en/?Rheometers:Viskomat_NT_Rheometer_f_Mortar_and_Paste), 30.06.2018
- [4] PN EN 196-1: Methods of testing cement - Part 1: Determination of strength (2006)

## **INFLUENCE OF THE MIXTURE COMPOSITION OF CEMENTITIOUS PASTES WITH OPTIMIZED PACKING DENSITY ON SETTING AND HARDENING STUDIED BY ULTRASOUND INVESTIGATION**

**Markus Krüger <sup>(1)</sup>, Rok Bregar <sup>(1)</sup>, Gheorghe Alexandru David <sup>(1)</sup>, Joachim Juhart <sup>(1)</sup>**

(1) Graz University of Technology, Graz, Austria

### **Abstract**

Ultrasonic methods have been developed in the past to study properties of cement based materials in the fresh and hardening period. Especially by combined shear and compressional wave measurements, several possibilities exist for better describing the changing properties of cementitious materials at very early age. Within the paper test results (Vicat and Ultrasound) from different cementitious pastes with optimized packing density (use of inert micro and eco fillers as replacement of Portland cement clinker) are presented and discussed. Dynamic elastic properties at early age like the dynamic shear modulus and the dynamic elastic modulus are calculated from the ultrasound investigations and correlated with standard test methods. Based on the experimental investigations it is discussed that the setting and hardening of cementitious mixes can be strongly influenced by just optimizing packing density. The concept of optimizing packing density results in a decreased water demand and thus reduced water film thickness between the particles that can be calculated analytically. It is shown that the calculated water film thickness is a good indicator not only for initial and final setting, but also for workability and strength development.

### **1. Introduction**

The properties of cement based materials in the fresh and hardening period are currently measured with rather conventional methods. Ultrasonic methods have been developed in the past using through-transmission techniques and analysing the whole waveform. Today ultrasound is accepted as a very useful tool to continuously investigate the setting and hardening process of cementitious materials [1-4]. Although many different concepts for the mix design of concrete with optimized performance are developed already, design still

strongly relies on trial mixing and testing. The reason for this is the complexity of the hydration of cementitious materials and the evolvement of the microstructure.

With respect to new concrete mixture concepts that especially focus on the optimization of the binder composition by using a well-defined amount of supplementary cementitious materials, many traditional concrete mix design methods to predict workability, setting and hardening as well as strength development fail. This is especially true for mixes, at which clinker is partly substituted by a filler [5]. In the current study, properly selected limestone powders of different size are selected as fillers in order to reduce the water demand while keeping the workability constant. However, it is also the setting and hardening behaviour as well as the strength development, which is strongly influenced.

## 2. Materials and Mix Design

Powder materials referred to in this study are classified into a group of micro-filler (MF) and eco-filler (EF) according to their mean particle diameter  $d_{50}$ .

The used micro-filler has a  $d_{50} < 3 \mu\text{m}$  that is significantly smaller than that of OPC. The eco-filler shows slightly smaller mean particle size but similar Blaine value like the cement. Details on the particle size distribution of the materials and the corresponding mixes determined by laser diffraction (HELOS) are presented in [5].

Table 1: Characteristic properties of the used materials.

Type	$\rho$ (g/cm <sup>3</sup> )	$d_{50}$ ( $\mu\text{m}$ )	Blaine (cm <sup>2</sup> /g)	$V_{w,s}/V_p$ (-)	$\phi_{\text{exp}}$ (-)	$V_{w,170}/V_p$ (-)
CEM I 52.5 N SR3	3.17	10.5	3744	0.75	0.57	1.13
EF (limestone)	2.70	6.9	4032	0.68	0.60	0.68
MF (limestone)	2.73	2.2	9314	0.61	0.62	0.65

Table 2: Composition and selected properties of the investigated mixtures.

		REF A1	ECO B1	ECO C1	REF A2	ECO B2	ECO C2	REF A3	ECO B3	ECO C3
flowability		standard consistency EN 196-3			$\phi = 190 \text{ mm}$			$\phi = 275 \text{ mm}$		
Cem I 52,5 N		100	40	50	100	40	50	100	40	50
LIME <sub>ECO</sub> (EF)	[V.-%]	0	60	25	0	60	25	0	60	25
LIME <sub>MICRO</sub> (MF)		0	0	25	0	0	25	0	0	25
w/c		0.28	0.59	0.38	0.40	0.85	0.42	0.48	1.03	0.43
$V_w/V_p$	[-]	0.90	0.74	0.61	1.27	1.09	0.66	1.53	1.31	0.68
$V_w/V_c$		0.90	1.86	1.21	1.27	2.72	1.32	1.53	3.27	1.35
$V_{w,s}/V_p$ (MEM-ST)		0.72	0.69	0.61	0.72	0.69	0.61	0.72	0.72	0.61
$f_{\text{cm},1\text{d}}$		47.9	19.5	42.8	30	7.7	42.7	19.7	4	37.1
$f_{\text{cm},7\text{d}}$	[N/mm <sup>2</sup> ]	91.3	46.1	80.5	57.3	21.9	74.6	37.5	12.7	73.8
$f_{\text{cm},28\text{d}}$		107	58.1	100.1	82.9	29.1	84.8	53.2	19.7	82.3
density	[kg/m <sup>3</sup> ]	2114	2023	2111	1949	1916	2136	1860	1841	2110

As the amount of water to achieve a certain workability of a water/powder-mix plays a major role, Table 1 show also the values for water demand  $V_{w,s}/V_p$ , which is the volume of water at saturation point and  $V_{w,fi}/V_p$ , which is the volume of water for a certain flowability (spread flow  $fi=170$  mm) and  $V_p$  which is the volume of powder in the mix. These values were determined by a method (MEM-ST) presented by Juhart et al. [5].

### 3. Experimental setup and laboratory tests

For the ultrasound measurements the FreshCon-system was used. The test setup of the FresCo-system is similar to that proposed by a RILEM recommendation worked out by RILEM TC 218-SFC [3]. However, besides the usage of a container equipped with p-wave transducers with a center frequency of 500 kHz an additional container with two broadband s-wave transducers with a center frequency of 250 kHz are used. To study the setting and hardening time at very early age in the following a test time of 24 hours was considered with a test interval of 5 minutes. In a post processing procedure the measurements were analysed and dynamic elastic parameters were calculated according to Krueger et al. [4]. Additionally Vicat needle test was conducted to determine initial setting time and final setting time of each given mixture.

### 4. Test results and evaluation of the mixes

Figure 1 shows the evolution of the dynamic shear modulus calculated from the ultrasound measurements for the first 24 h of hydration of the reference mix *REF A* and the packing density optimized mix *ECO C* for different workability resp. water content.

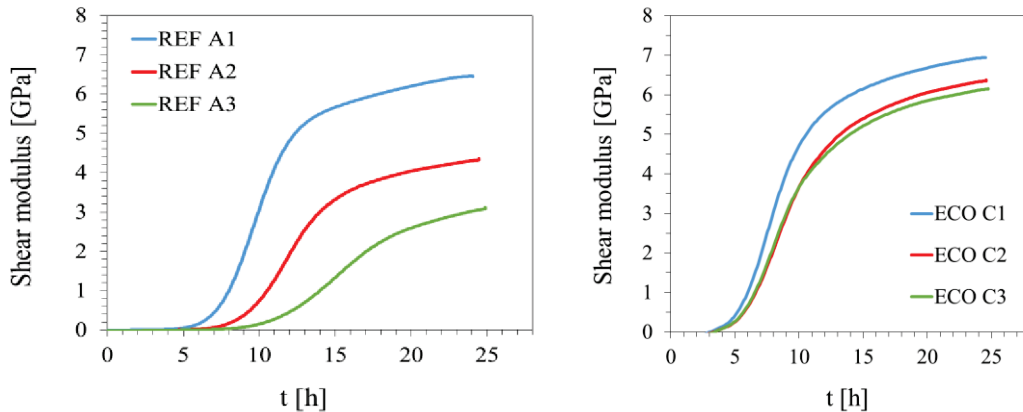


Figure 1: Evolution of dynamic shear modulus calculated from US testing.

Table 3 lists the results from the Vicat tests and also a certain time for which a specific dyn. elastic modulus (@ 0.1 GPa) resp. a specific shear modulus (@ 0.1 GPa and 0.2 GPa) was determined by the ultrasound testing. In addition to that, a water film thickness (WFT) was calculated. For the calculation one can use, among others, a relatively simple model like that of Krell, which is a mass-related method [6]. For the following calculation a modified equation (1), which is based on volumetric data as presented by Teichmann, is used [7]. With this model, an average water film thickness (WFT) can be calculated around each particle.



Here it is assumed that in the cementitious paste each particle is surrounded by a water film of the same thickness and where all cavities are filled with water and all particles are dispersed in the system. The water film thickness is determined as a function of the experimental packing density  $\phi_{exp}$ , the powder content  $V_P$ , the water demand or the pore volume at saturation point  $V_{w,s}$ , the resulting specific surface area  $s_{vf}$  (Blaine value of the total mix, neglecting uncertainty for Blaine > 5000 cm<sup>2</sup>/g) and the total water content  $V_{w,fi}$ . Although the WFT is obviously directly related to the  $V_w/V_p$  ratio, the influence of the specific surface is dominating factor.

$$\text{WFT} = \frac{V_{w,fi} - V_{w,s} \cdot \frac{1 - \phi_{exp}}{\phi_{exp}}}{s_{vf} \cdot V_P} \quad (1)$$

Table 3: Water film thickness and dynamic elastic properties of the investigated mixtures.

		REF A1	ECO B1	ECO C1	REF A2	ECO B2	ECO C2	REF A3	ECO B3	ECO C3
flowability		standard consistency acc. EN 196-3			$\phi = 190$ mm			$\phi = 275$ mm		
Water film thickness (WFT)	( $\mu\text{m}$ )	0.15	0.04	0.00	0.47	0.35	0.03	0.69	0.54	0.05
t ( $E_{dyn}=0,1$ GPa)	[h]	5.00	3.92	3.50	6.78	5.50	4.00	8.28	5.83	3.90
t ( $G_{dyn}=0,1$ GPa)	[h]	5.90	4.66	4.22	7.78	6.93	4.58	9.60	7.75	4.50
$G_{dyn}$ (initial Vicat)	[GPa]	0.05	0.02	0.01	0.13	0.07	0.016	0.16	0.2	0.03
Vicat initial set	[h]	5.35	3.68	3.05	7.97	6.43	3.47	10.25	9.32	3.90
Vicat final set	[h]	6.87	4.50	4.22	8.97	8.06	4.42	10.92	10.28	5.53

## 5. Discussion

From Tab. 3 and Fig. 1 one can see that the initial setting determined by the Vicat test strongly correlates with the increase of  $G_{dyn}$  calculated from the ultrasound testing. If the Vicat initial setting time is compared to  $G_{dyn}$  at the time of initial setting according to Vicat (see Fig. 2, left),  $G_{dyn}$  is higher for mixes that show later setting time. Taking into account that the Vicat needle test is a kind of a shear test one may postulate that values for Vicat initial setting should be obtained at a constant  $G_{dyn}$ . As this is not the case for the tested mixtures and if we neglect the influence of different air content, the main reason for that can be found in the WFT. From Fig. 2 (right) it can be seen that the WFT is the governing factor influencing the initial setting of the mixtures and not the composition of the cementitious matrix or the w/c ratio. However, the dominant role of the WFT at the very early stage decrease with increasing hydration time, although a general trend to higher strength at lower WFT can be observed.

Similar results have already been published by Berodier and Scrivener [8]. It was shown that independent from the nature of the particles the WFT resp. a smaller particle distance lead to an accelerated hydration rate. Several interpretations of the relation of WFT and early age hydration have been proposed by different researchers, among which are chemical effects, mechanical effects (esp. increased shearing during mixing [8, 9]) or just the geometrical effects, i.e. smaller particle distance allows the hydration products to earlier bridge the opposite particles. However, these effects do not explain why the replacement of cement

clinker with an inert material like limestone powder accelerates the hydration rate, if the calculated particle distance is considered as constant. One reason can be found in the fact that nucleation of the C-S-H is increased by increased particle surface. But it was also shown that nucleation of C-S-H preferably can be – if compared with other supplementary materials like quartz powder etc. – observed on limestone surface [8, 9]. Thus, surface area and type of surface resp. material are important factors driving the early age hydration.

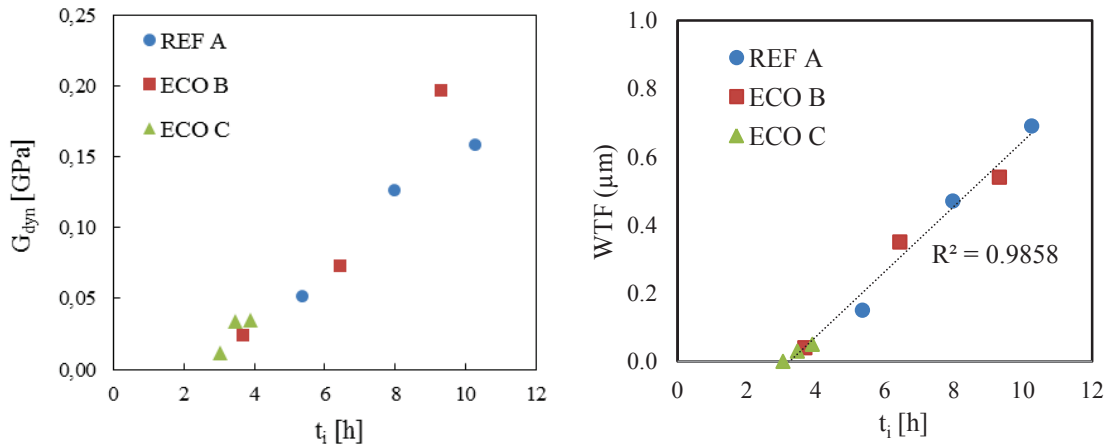


Figure 2: Dyn. shear modulus (left) and water film thickness (right) versus setting time according to Vicat needle test.

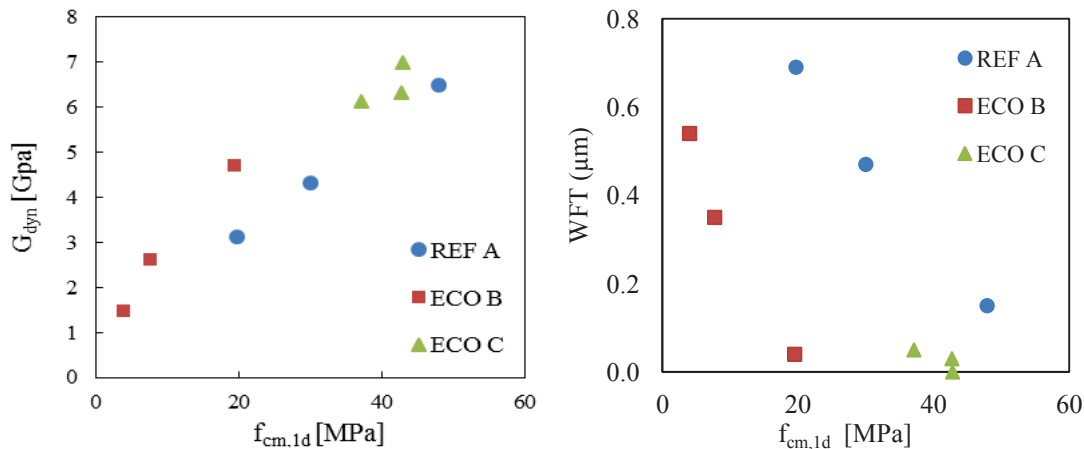


Figure 3: Dyn. shear modulus (left) and water film thickness (right) versus one day strength.

From the tests on workability it can also be confirmed that the particle interaction (esp. electrical double layer) is not negligible, either with respect to the workability but also to early age hydration and strength development [10, 11]. In this context it has to be noted that also the assumption that each particle is surrounded by a water film of the same thickness will not correspond with the reality.

Figure 3 shows the early age strength at one day vs. dyn. shear modulus after 24 h and vs. WFT. As expected dyn. shear modulus (and also dyn. elastic modulus, which is not shown here) correlates quite well with the strength for all the mixes. However, if WFT is plotted versus one day compressive strength a mix independent correlation between these two values

cannot be found. Although a clear trend of increasing strength with decreasing WFT is visible, the different mixture proportions and here the packing density and the W/C ratio have a strong influence on the early age strength, as it is known from traditional mix design experience.

## 6. Conclusions

From the test series and the results presented in this paper some conclusions can be drawn:

- The dynamic elastic properties derived from the US testing show good correlation with the strength development independently from the mixture composition.
- The initial setting time of a cementitious material can be estimated from WFT as well as from dyn. shear modulus calculated from ultrasound testing; If initial setting should be determined by an absolute value of dyn. shear modulus, the aspect of WFT has to be considered, i.e. lower WFT results in lower dyn. shear modulus at initial setting.
- From the conducted experiments it can be postulated that there is a linear relationship between WFT and initial setting, which is independent from the matrix composition. Thus, initial setting can be adjusted by the WFT quite easily. However, this aspect has to be further investigated if it holds true for different mixtures.

## References

- [1] Robeyst, N. et al, Monitoring the setting of concrete containing blast-furnace slag by measuring the ultrasonic p-wave velocity. *Cem. Concr. Res.* 38(10) (2008), 1169-1176
- [2] Carette, J., Staquet, S., Monitoring the setting process of eco-binders by ultrasonic P-wave and S-wave transmission velocity measurement: Mortar vs. concrete, *Constr. Build. Mater.* 110 (2016), 32-41
- [3] Reinhardt, H.-W. et al, Recommendation of RILEM TC 218-SFC: Sonic methods for quality control of fresh cementitious materials. Testing of fresh concrete by ultrasound transmission. RILEM TC 218-SFC, *Materials and Structures* 44 (2011), 1047-1062
- [4] Krüger, M. et al, Non-destructive evaluation of eco-friendly cementitious materials by ultrasound. International RILEM Conference on Materials, Systems and Structures in Civil Engineering, Denmark (2016), Vol. 2 503-512
- [5] Juhart, J. et al, A new combined filler concept for eco-concrete, Proc. of 14th International Congress on the Chemistry of Cement (ICCC 2015), Beijing (2015)
- [6] Krell, J., Die Konsistenz von Zementleim, Mörtel und Beton und ihre zeitliche Veränderung (in German), PhD thesis, RWTH Aachen (1985)
- [7] Teichmann, T., Einfluss der Granulometrie und des Wassergehaltes auf die Festigkeit und Gefügedichtigkeit von Zementstein (in German), PhD thesis, University of Kassel (2007)
- [8] Berodier, E., Scrivener, K., Understanding the filler effect on the nucleation and growth of C-S-H. *J Am Ceram Soc* 97(12) (2014), 3764-3773
- [9] Berodier, E., Impact of the supplementary cementitious materials on the kinetics and microstructural development of cement hydration, PhD thesis, Switzerland (2015)
- [10] Kwan, A.K.H., Li, L.G., Combined effects of water film thickness and paste film thickness on rheology of mortar, *Mater Struct* 45(9) (2012), 1359-1374
- [11] Kwan, A.K.H., Wong, H.H.C., Effects of packing density, excess water and solid surface area on flowability of cement paste, *Advances in Cement research*, 20(1) (2008), 1-11

## INFLUENCE OF UGANDAN VOLCANIC SCORIA AS AGGREGATES IN CONCRETE

Stephen O. Ekolu<sup>(1)</sup>, Kgashane T. Moila<sup>(1)</sup>, Mikaash Bhagwager<sup>(1)</sup>, Harry Quainoo<sup>(1)</sup>

(1) Department of Civil Engineering Science, University of Johannesburg, South Africa

### Abstract

This paper presents an investigation conducted on potential use of volcanic scoria as fine and coarse aggregates in concrete. In some developing countries, volcanic scoria is a widely available natural pozzolan which is presently not fully exploited for construction applications. In the present study, mortar mixtures of 3.0 aggregate/cement ratio and 0.5 water/cement ratio (w/c) or concretes of 0.6 w/c were used. Mortar samples of 50 mm cubes and 25 x 25 x 285 mm prisms containing 100% volcanic scoria aggregate (VAG) were prepared then used to determine compressive strength and drying shrinkage. In addition, concretes of 0.6 w/c containing 0, 50 or 100% VAG were used to prepare 70 dia x 140 mm height cylinders for measurement of elastic modulus. It was found that VAG mixtures gave slightly higher drying shrinkage than the control, while compressive strength and elastic modulus decreased significantly as the proportion of VAG aggregate content increased.

### 1. Introduction

Both scoria and pumice are vesicular igneous rocks typically emanating from volcanic eruptions, but their characteristics are quite different. Pumice is generally white or grey in colour, highly vesicular and exhibits a froth-like appearance. It forms from pyroclastic flow of hot gases and lava that was generally fluid during the process of effusion. Scoria, however, forms from iron-rich hot lava. It is typically darker and more dense than pumice [1]. A study was conducted by [2] in which the normal weight coarse aggregates in concrete were replaced with pumice aggregates in different proportions ranging from 0 to 100% pumice. Mixtures of 1:2:3 and 1:2:4 cement to fine aggregate to coarse aggregate were used to prepare samples at a water/cement (w/c) ratio of 0.45. The pumice aggregates had an oven-dry density of 763 kg/m<sup>3</sup> and a high water absorption of 37%, which were quite different compared to 2470 kg/m<sup>3</sup> and 2.86% for normal aggregate, respectively. It was reported that the 28-day

compressive strength, tensile strength, and Young's modulus, all decreased whereas the drying shrinkage and water absorption significantly increased, owing to the use of pumice in concrete. The 100% pumice aggregate mixture gave a 28-day tensile and compressive strength of 2.6 MPa and 22 MPa respectively, relative to 3.7 MPa and 35 MPa of the control. The oven-dry density for 100% pumice mixture was 1852 kg/m<sup>3</sup> compared to 2415 kg/m<sup>3</sup> for the control mix. Investigation by [3] found that water absorption was as high as 32.1% for pumice concrete compared to 1.6% for normal aggregate concrete. This result was attributed to the characteristically high porosity of pumice. They reported up to 50% increase in drying shrinkage for the pumice concretes. Saturating the pumice aggregate before batching was suggested to be capable of minimizing the effects of high water absorption by pumice. In an earlier investigation by [4], Ugandan volcanic scoria was studied for potential use as a pozzolanic material and found to be of Class N pozzolan. The present study focused on potential use of the scoria as aggregates in concrete. The mixtures with or without scoria aggregates were tested for compressive strength, drying shrinkage and modulus of elasticity.

## 2. Experimental work

### 2.1 Volcanic scoria aggregate

The volcanic scoria used in this investigation was obtained from the Rwenzori mountain range at the Western branch of the East African rift valley located at the border between Uganda and the Democratic Republic of Congo. Volcanic scoria is abundantly found in the region and could provide a cost-effective source as a cementitious material [4,5] which could be employed for low cost housing, among other uses. The scoria is a characteristically dark vesicular rock, easily broken into large chunks. Figure 1 shows samples of the crushed coarse and fine volcanic scoria aggregates (VAG). Samples of the scoria were finely ground into a powder finer than 45 µm size, and used for chemical analysis which was conducted using X-ray fluorescence (XRF). Table 1 gives the chemical compositions of scoria and of CEM 52.5 N cement used in this study. Microanalysis using X-ray diffraction (XRD) was also done to determine the mineralogical composition of scoria.

Table 1: Chemical compositions of cement and volcanic scoria ash.

Sample	SiO <sub>2</sub>	Al <sub>2</sub> O <sub>3</sub>	Fe <sub>2</sub> O <sub>3</sub>	CaO	MgO	SO <sub>3</sub>	K <sub>2</sub> O	Na <sub>2</sub> O
CEM1 52.5N (%)	17.8	3.45	3.86	68.5	1.37	3.41	0.27	0.24
Scoria (%)	42.8	14.6	13.5	10.4	6.95	0.22	3.21	3.3

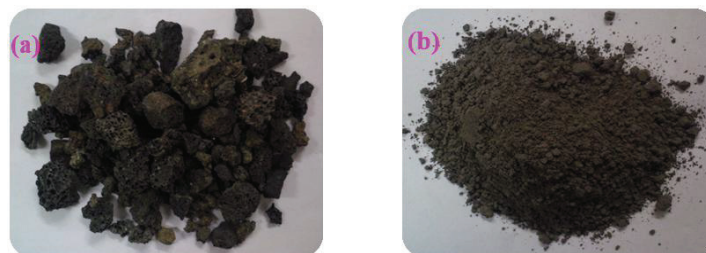


Figure 1: Volcanic scoria aggregate (a) 19 mm coarse aggregate, (b) fine aggregate.

## 2.2 Mixtures

Portland cement CEM I 52.5 N supplied by Pretoria Portland Cement (pty) Ltd was used to prepare mortar and concrete mixtures, shown in Table 2. Crushed granite (fine and coarse) aggregates were used as control. Mortars of 3.0 aggregate/cement ratio and 0.55 or 0.60 water/cement (w/c) were prepared, in which standard silica sand was replaced by 100% volcanic scoria as fine aggregate. Mortar cubes of size 50 mm were prepared for compressive strength testing. Also, mortar prisms of size 25 x 25 x 285 mm were made for drying shrinkage measurement. Mortar compressive strengths were tested at 3, 7, 14, 28 days while drying shrinkage was monitored under a laboratory environment of 23°C and 40 to 55%RH. Concrete mixtures of 0.60 w/c were prepared incorporating 0, 50, 100% coarse VAG and used to cast cylindrical samples of size 70 dia x 140 mm height. Electrical strain gauges were attached at curved sides of the cylinders and used to monitor changes in strain during monotonic loading. These results were used to determine the modulus of elasticity and compressive strength of the VAG concretes.

Table 2: Mortar and concrete mixtures used in the experiments.

Ingredients	Mortar				Concrete		
	50 mm cubes		25 x 25 x 285 mm prisms		70 dia x 140 mm cylinders		
Samples	0	100	0	100	0	50	100
VAG*(%)	0	100	0	100	0	50	100
CEM I 52.5N (g)	1172	1172	586	586	1800	1500	1500
Granite sand (g)	3316		1320		4400	1800	
Granite stone (g)					4400	1800	
Scoria sand (g)		3316		1320		1800	3600
Scoria stone (g)						1800	3600
Water (g)	646	636	360	360	1100	900	900

\*VAG – volcanic scoria aggregates

## 3. Results and discussion

### 3.1 Fineness, density, and the pozzolan classification

Scoria was ground to a fine powder of Blaine fineness 372.8 m<sup>2</sup>/kg which was at a similar level as that of CEM 52.5 N whose fineness was 378 m<sup>2</sup>/kg. The scoria powder had a density of 2930 kg/m<sup>3</sup> which is lower than 3150 kg/m<sup>3</sup> of CEM I 52.5 N. From the chemical composition given in Table 1, the natural pozzolan had a low CaO but rich in SiO<sub>2</sub> as expected. Its combined SiO<sub>2</sub>+Al<sub>2</sub>O<sub>3</sub>+Fe<sub>2</sub>O<sub>3</sub> is 70.9%, which meets the minimum requirement of 70% stipulated in ASTM C 618-03 [5]. The SO<sub>3</sub> content and moisture content were determined to be 0.22% and 1.0%, which are also lower than the maximum requirements of 4.0% and 3.0%, respectively. These results affirm the findings of an earlier study [3] in which a full range of the classification parameters for the natural pozzolan were determined in accordance with ASTM C 618-03 [5]. Recent researches indicate that the volcanic scoria pozzolans may also be suitable for producing geopolymer cementitious systems [7,8].

### 3.2 Water absorption and drying shrinkage

The water absorption of VAG aggregates was determined to be 13.9% and 19.2% for coarse and fine aggregates, which are much higher than the corresponding 1.66% and 4.3% for the control (granite) aggregates. Figure 2 gives results of mortar shrinkage containing 100% VAG fine aggregate. The VAG mortars show higher drying shrinkage over the control, which is consistent with reports in the literature [2,9]. It can be seen that use of the VAG led to an increase of up to 6% in drying shrinkage. This increase in drying shrinkage may be partly attributed to the higher water absorption and vesicular structure of scoria, whose mixtures tend to exhibit a more porous matrix that allows greater loss of water during evaporation. In addition, the relatively lower elastic modulus of VAG (Section 3.3), provides less restraint on the movement of paste due to shrinkage, in turn giving higher shrinkage behaviour for VAG relative to control.

### 3.3 Compressive strength and modulus of elasticity

The strength effect of using VAG was investigated using both mortars and concrete mixtures. Mortars were prepared using 100% VAG fine aggregate as replacement for the control. Figure 3(a) shows the change in compressive strength results for ages of up to 28 days. It can be seen that use of 100% VAG sand led to a reduction in compressive strength at all the ages. At later ages, however, there was progressive gain in strength of VAG mortars over the strength of control. At ages of 3 to 7 days, the strength of VAG mortars was 30 to 40% lower than that of control. At later ages of 14 to 28 days, the strength loss had decreased to about 21%, as seen in Figure 3(b). The higher strength gain at later ages is indicative of the pozzolanic reaction of VAG that must have occurred. In a pozzolanic reaction, the  $\text{Ca}(\text{OH})_2$  produced from hydraulic reaction of Portland cement with water, reacts with the amorphous silica of the pozzolan, leading to secondary formation of calcium silicate hydrate (CSH) product which is responsible for strength gain. Accordingly, the effects of a pozzolanic reaction in cementitious systems occur at later ages. It is interesting that pozzolanic behaviour occurs even in VAG aggregates that are much coarser than the fine powder which typically gives more pronounced pozzolanic effects [4]. The density of VAG mortar was 2211 to 2216  $\text{kg/m}^3$ , which is 5 to 8% lower than 2339 to 2395  $\text{kg/m}^3$  for control.

The effects of scoria on compressive strength and elastic modulus were also determined using concrete mixtures of 0.6 w/c containing 0, 50, 100% VAG coarse aggregates. Figure 4 gives the stress-strain behaviour of VAG concrete obtained using 70 dia x 140 mm cylinders. It is clear in Figure 4(a) that there was a significant decrease in stress resistance as the proportion of VAG in the mixture increased. The strength (in MPa) and elastic modulus (in GPa) of control granite concrete were of similar levels. However, VAG concrete showed a distinct difference between the two properties, with its elastic modulus being always significantly lower than the corresponding strength, as seen in Figure 4(b). Indeed, the elastic modulus of VAG concrete in GPa was 55 to 65% of concrete strength in MPa. A replacement of 50% coarse granite aggregates using VAG gave a 27.5% and 55.5% decrease in strength and elastic modulus, relative to control. The 100% VAG concrete showed over 70 to 80% decrease in strength or elastic modulus.

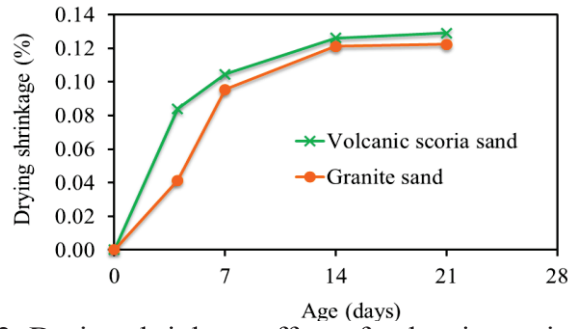


Figure 2: Drying shrinkage effect of volcanic scoria mortar.

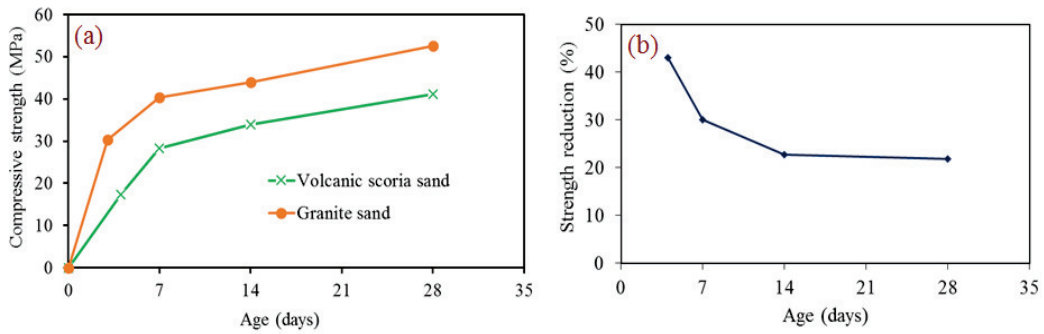


Figure 3: Effect of scoria aggregates on compressive strength of mortars (a) strength development, (b) strength gain at later ages due to pozzolanic reaction.

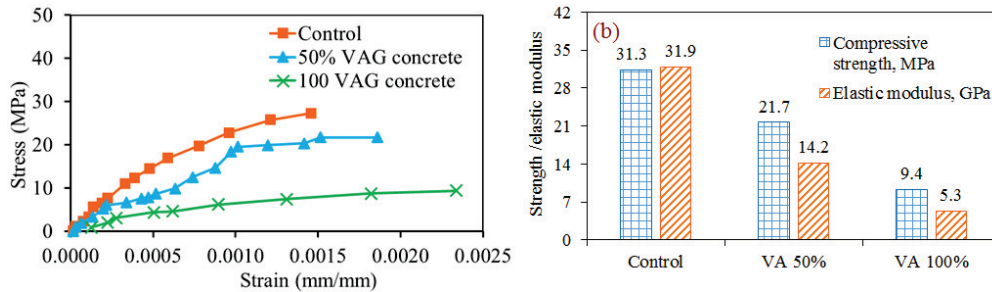


Figure 4: Volcanic scoria concrete (a) stress-strain behaviour, (b) strength and elastic modulus.

### 3.4 Mineralogy

Figure 5 gives XRD results showing the mineralogical composition of volcanic scoria ash passing 45  $\mu\text{m}$ . It can be seen that the main minerals of the scoria comprised mullite (aluminosilicate), quartz ( $\text{SiO}_2$ ) and haematite ( $\text{Fe}_2\text{O}_3$ ). These observations are consistent with the XRF results (Table 1) which show these oxides to be the main constituents of the volcanic scoria. It should, however, be noted that while XRF gives the total amount of constituents that are both amorphous and crystalline, XRD only detects the crystalline minerals present. Pozzolanic behaviour depends on amorphous silica which is usually not detectable by XRD.



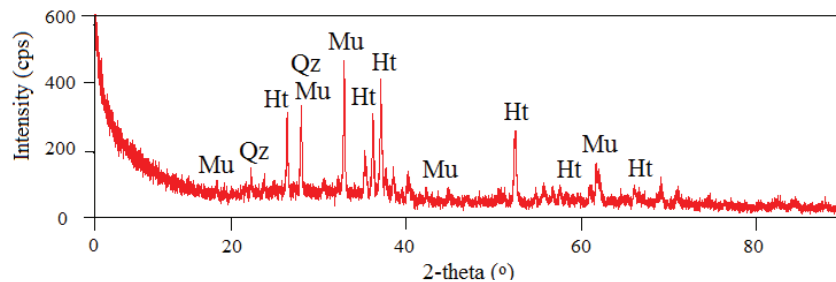


Figure 5: X-ray diffraction pattern of volcanic scoria, Mu – mullite, Ht – haematite, Qz – quartz.

#### 4. Conclusions

Upon evaluation of the volcanic scoria for potential use as aggregate in concrete, it was found that the scoria fine aggregate exhibits a pozzolanic reaction leading to increase in late strength development relative to that of control. The scoria consisted mainly of mullite, and phases of haematite and quartz. When used as aggregate, the volcanic scoria aggregate gave higher water absorption and higher shrinkage than the normal crushed aggregates. There is a decrease in compressive strength and elastic modulus in proportion with the amount of scoria aggregate incorporated into concrete.

#### Acknowledgements

This research was financially supported by the National Research Foundation (NRF) of South Africa, IPRR Grant No. 96800. The authors are grateful for the support given by NRF.

#### References

- [1] Evans, E.J, Inglethorpe, S.J.D, and Wetton, P.D, Evaluation of pumice and scoria samples from East Africa as lightweight aggregates, Mineralogy and Petrology, Technical Report, WG/99/15, NERC (1999), British Geological Survey, Keyworth, Nottingham, UK
- [2] Hossain, K.M.A., Properties of volcanic pumice based cement and lightweight concrete, *Cem Concr Res* 34 (2004), 283–291
- [3] Hossain, K.M.A., and Lachemi M., Mixture design, strength, durability, and fire resistance of lightweight pumice concrete, *ACI Mater J*, 104(5), 2007, 449-457
- [4] Ekolu, S.O., Thomas, M.D.A., and Hooton, R.D., Studies on Ugandan volcanic ash and tuff, *Proc. 1<sup>st</sup> Intl. Conf. on Adv. in Eng. and Tech.*, Entebbe, Uganda, July 2006, 75-83
- [5] Day, R.L., Pozzolans for use in low-cost housing, A state-of-the-art report, International Development Research Centre, Ottawa, Canada, September 1990
- [6] ASTM C 618-03, Standard specification for coal fly ash and raw or calcined natural pozzolan for use in concrete, ASTM Intl, West Conshohocken, PA, 2003, [www.astm.org](http://www.astm.org)
- [7] Naghizadeh, A., and Ekolu, S.O., Pozzolanic materials and waste products for formulation of geopolymer cements in developing countries: a Review, *Concrete Beton, Jour Concr Soc S Africa*, 151 (2017), 22-31
- [8] Tchadjie, L.N., and Ekolu, S.O., Enhancing the reactivity of aluminosilicate materials toward geopolymer synthesis, *Jour Mat Sci* 53 (2018), 4709–4733
- [9] Neville, A.M., Properties of concrete, 4<sup>th</sup> Edition, 1996, New York, John Wiley and Sons Inc

## **INVESTIGATION, ASSESSMENT AND REALTIME READJUSTMENT OF THE RHEOLOGICAL PROPERTIES OF SELF COMPACTING CONCRETE**

**Ivan Parić<sup>(1)</sup>, Wolfgang Kusterle<sup>(1)</sup>**

OTH Regensburg, Regensburg, Germany

### **Abstract**

This paper discusses a new fresh concrete control system with the following structure: a rheometer measures the fresh concrete directly after the mixing process, during a short break. The viscosity and the dynamic yield point are determined by a ball rheometer. The rheological parameters viscosity and dynamic yield point describe the consistency and thus the pouring ability and consequently the quality of Self Compacting Concrete (SCC). Data collected from the measurement are the basis for an expert system which will help to readjust mixes with deviating rheology.

Firstly, investigations were carried out during the development of different SCC mixtures in the COST TU 1404 Action. Secondly, investigations were done in two precast plants. A ball rheometer was installed in the respective mixers. The SCC for premium precast products was tested then during ongoing production. In addition, several test series were carried out in the laboratory of the OTH with the respective constitutive materials.

During the test series, the mix designs of the well working SCC's were modified by using a deviating water content. Subsequently, using the rheological data, water, superplasticizer or stabilizing agents were added to the mix, trying to reach proper workability again. The graphs for the changing rheological properties as a function of the respective amount of start water content and additional water dosage or admixture dosage were generated and analyzed for the mixes of the two precast plants. With this information and experience, an expert system for the mix readjustment is currently under development.

## 1. Introduction

Fresh concrete testing, including workability testing, is one of the important quality tests for concrete structures. Maintaining the workability within given numbers for a defined time is essential for a fast and effective casting process.

Concrete workability is a complex phenomenon, which is difficult to define with a few parameters or by a single testing procedure [1]. Rheological tests of SCC may be performed using one-point tests, as given in EN 12350-9, which will not give exact rheological numbers, or by using costly stationary concrete rheometers.

Rheological measurements will give more reliable data regarding workability than one-point tests [1]. The following figure 1 shows a way, how the physically data from rheological measurements can be used to reach an ongoing proper workability of SCC.

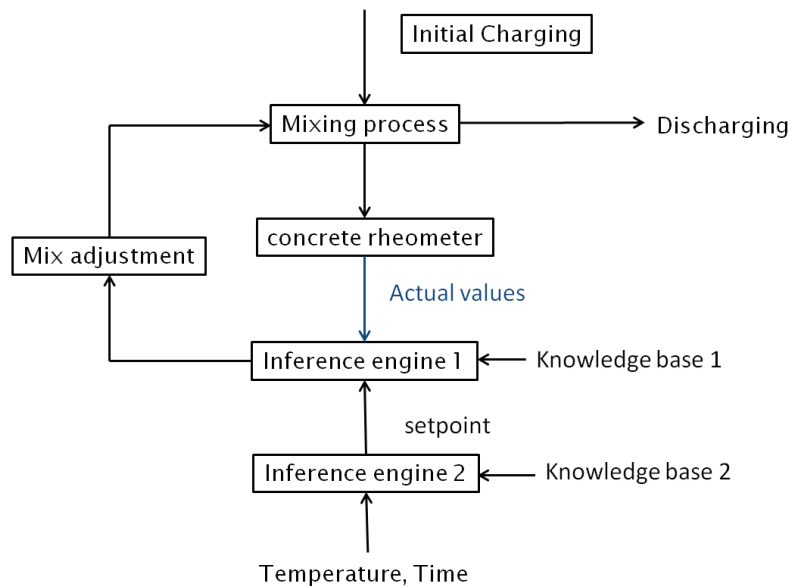


Figure 1: Principle of an expert system for SCC production [2].

## 2. COST TU 1404 Development procedure of some SCC recipes [3]

### 2.1 Tests

Based on the reference concrete mix of the initial experimental phase given by COST TU 1404, the development of Self Compacting Concrete (SCC) mix-design was realized with both of the cements available in the TU 1404.

Tested cements which are produced by Ciments Calcia in Gaurain-Ramecroix, Belgium:

- CEM I 52.5 N CP 2
- CEM I 52.5 N – SR 3 PM-CP2

Hard coal pulverised fly ash (PFA) according to EN 450 used:

- Rofament from Rohrdorfer Zement, Germany

The aim was a robust SCC mix-design. The development, according to the approach of Okamura, was divided into investigations on cement paste, mortar and in a final step the testing of the concrete with a ball rheometer.

For demonstrating the robustness of the developed SCC with a cement-fly ash-ratio of 65/35 the water content was raised stepwise by 7.82 l/m<sup>3</sup>. This equals a stepwise water/cement ratio increase of 0.02.

Table 1: Concrete mix-design for both cements

	Gravel 4/11	Gravel8/16	Sand 0/4	CEM	PFA	Water	SP	Unit
Initial weight 1 m <sup>3</sup>	357	436	794	392	156	144	7.825	kg

Rheological measurements were performed using a Ball rheometer and profiles described in [4]. The rising water amount in the mixture changes the rheological properties as shown in table 2, figures 2 and 3. The Dynamic yield stress, Bingham yield stress, viscosity and V-funnel time are decreasing while the slump flow is increasing.

Table 2: Rheological properties versus increasing water amount.

Water [l/m <sup>3</sup> ]	Dynamic yield stress g <sub>D</sub> [N mm]	Bingham yield stress g <sub>B</sub> [N mm]	Slump flow [mm]	V-funnel time [s]	Viscosity [-]
183	212.17	88.58	597.5	16.6	85.78
192	134.72	49.35	675.0	9.13	52.53
200	66.71	19.68	762.5	7.46	36.31
207	51.24	12.72	-	3.43	25.91

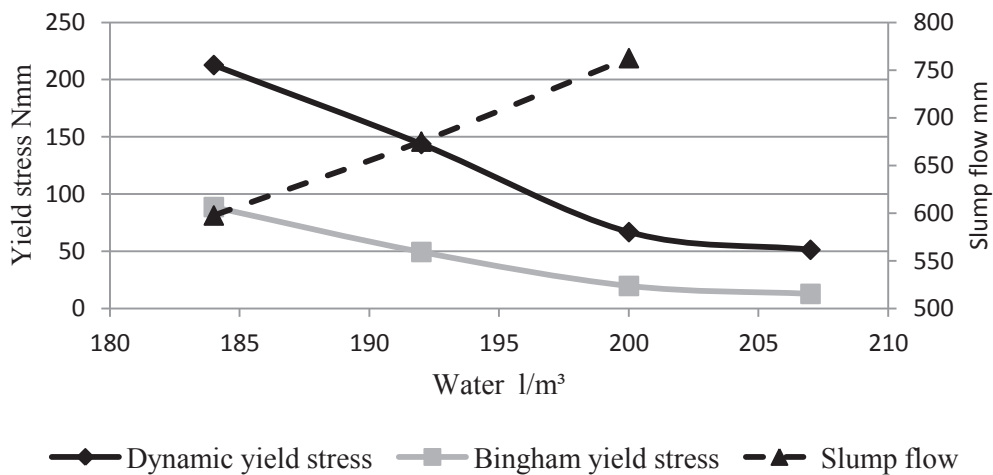


Figure 2: Yield stress and slump flow versus water content.

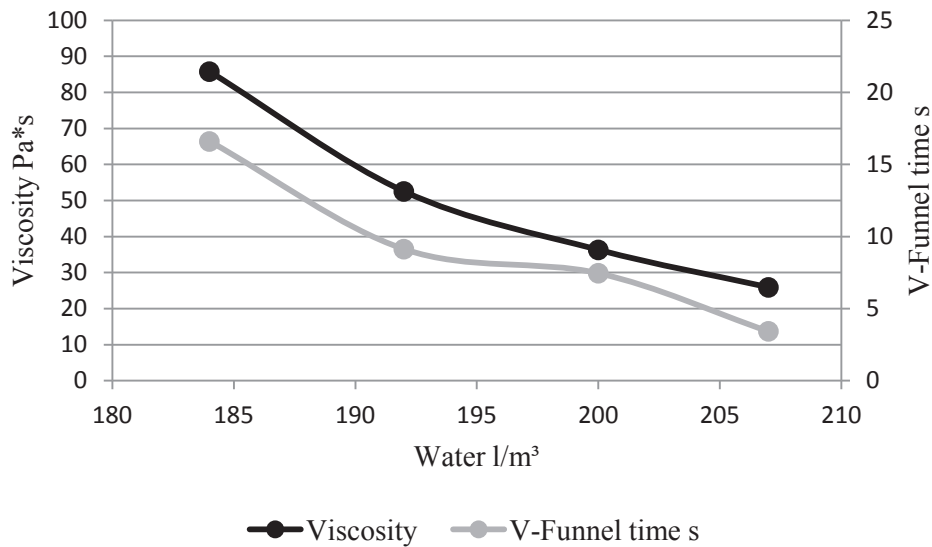


Figure 3: Viscosity and V-funnel time versus water content.

The tested mix designs showed both a well-fitting slump flow and V-funnel time over a range of mixing water, which indicates that these mixtures form a solid basis for a robust SCC mix-design. Furthermore the rheological results are in line with results from classic one point tests. The experience gained during the investigations in the COST Action TU 1404 were an important fundament for further developments regarding an expert system.

### 3. Self-compacting concrete with real-time readjustment of the mix-design in the concrete mixer

The results presented in this section were investigated during a Bavarian research project. The aim of the presented investigations was to predict which quantity of water should be added to obtain a correct rheology. Investigations were done in two precast plants and in parallel with the two different SCC mixes in the laboratory of the OTH Regensburg. This was the way to build up the knowledge base 1 (shown in figure 1) for both mixes. Thereby it was possible to define different areas of workability. The knowledge base was tested in some manual readjustment tests. An example for the data obtained for the knowledge base 1, is given for one specific mix in figure 4. It demonstrates the changes in consistency with a rising water amount in one single test. Other investigations were done with superplasticizer and different stabilizer. These values are also part of the data for the knowledge base 1. The configuration of the measuring system is different to the tests in the COST action. The speed of rotation is chosen lower, the ball is smaller. This leads to lower absolute values in the respective results. An optimum of workability for the here presented mix and test set-up is given by the value 20 for the dynamic yield stress and the viscosity.

In this test the water content was raised stepwise by  $5.2 \text{ l/m}^3$ . This equals a w/c ratio of 0.01 [5].

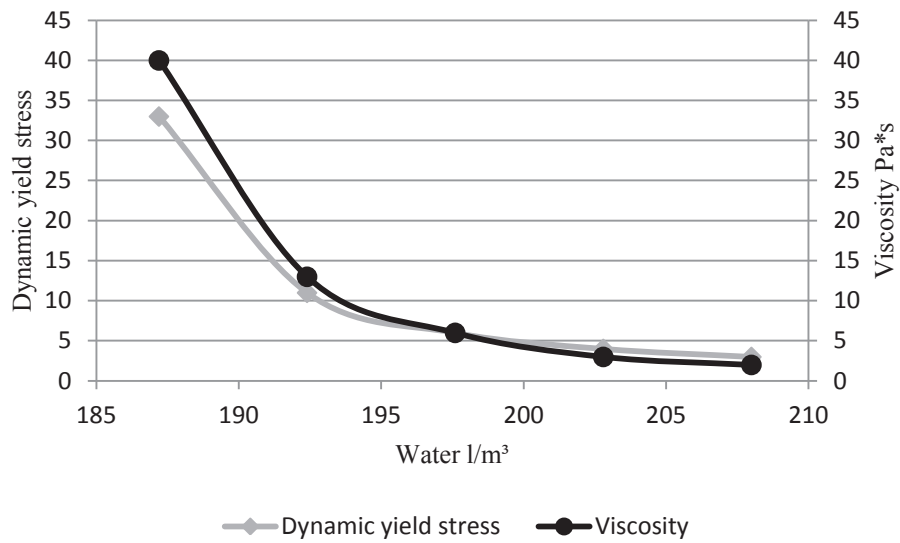


Figure 4: Viscosity and dynamic yield stress versus rising amount of water.

### 3.1 Tests for readjustments

The test results in figure 5 show the manual use of the knowledgebase 1 for this blend. This mixture was produced too stiff, with a lack of water. In this case 182 l/m<sup>3</sup> of water (equivalent to a w/c of 0.35) was the starting point. With the information from the expert system a readjustment with a defined amount of water in one step and within short time was possible [4]. The data of the knowledge base was still used without Inference engine. The amount of water was calculated manually.

Similar readjustments have been done with superplasticizer and stabilizer. In the last test series, a new programmed Inference (app) engine was tested. First automated readjustments using an app show promising results.

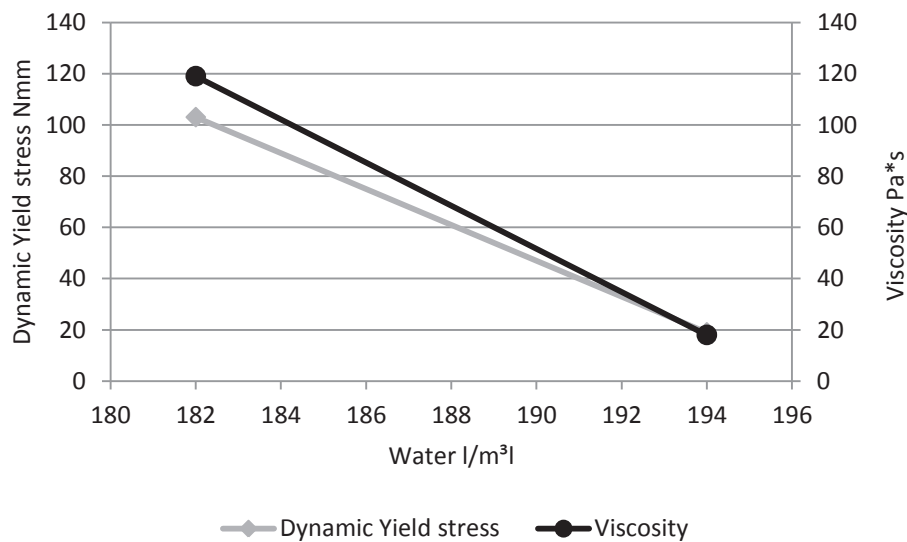


Figure 5: Readjustment with water in one step.

#### 4. Conclusions and outlook

During tests with varying water content, it was clearly demonstrated that results of the one-point tests coincided with rheology. When the slump flow increased, the V-funnel time and the yield stress decreased. This is an important finding for the future, because time-consuming one-point tests, such as slump flow and V-funnel time, can be replaced by inserting a rheometer into the concrete mixer for a fast test. In our tests, a ball rheometer delivered accurate and comparable data within a short time.

Ball rheometers with low shear rate are very effective in assessing rheological properties of SCC. The necessary short testing time allows the measurement as a final part of the mixing process.

Tests with different mixtures, distinguished only in small quantities of water content, show accurate and reliable results. With the help of stabilizers, it is possible to readjust a mix which is too soft and tends to segregation. With superplasticizer or, if possible with small amount of water, too stiff mixes may be adjusted. The development of an automated process using the detected data for a mix adaption is the topic of an ongoing research program.

#### Acknowledgement

We want to thank the Bavarian Research Foundation for funding these investigations.

#### References

- [1] Khrapko, M., Aufrechterhaltung der erforderlichen Verarbeitbarkeit von SVB, (Maintaining the required workability of SCC) BetonWerk international, Vol. 2, Nr. 2/2012 (2012).
- [2] Paric, I. and Kusterle, W., Selbstverdichtender Beton mit zeitnahe Aussteuerung der Mischungszusammensetzung im Betonmischer. (Self-compacting concrete with real-time control of the mix composition in a concrete mixer), research proposal, OTH Regensburg, Regensburg (2015).
- [3] Glashauser, J. and Feuerer, F., Entwicklung einer robusten SVB-Rezeptur nach Okamura fuer den Ringversuch "COST TU 1404 Action" und rheologischer Untersuchungen, (Development of a robust SCC-mix design according to Okamura for the Round Robin test "COST TU 1404 Action" and additional rheological tests), Bachelor thesis: OTH Regensburg (2016).
- [4] Paric, I. and Kusterle, W., The realtime assessment of the rheological parameters of SCC. In: Thrane, L.N., Proc. Of the international RILEM conference Materials, Systems and Structures in Civil Engineering 2016, Segment on Fresh Concrete. Proceedings PRO 115, ISBN 978-2-35158-184-1 Paris (2016).
- [5] Reuter, C., Stepper, H., Zeitnahe Aussteuerung der rheologischen Frischbetoneigenschaften von selbstverdichtendem Beton durch Betonzusatzmittel und Wasser, (Realtime modulation of the rheological fresh concrete properties of self-compacting concrete by concrete admixtures and water) Bachelor thesis: OTH Regensburg (2017).

## **MACRO- AND MICRO-STRUCTURE EVALUATIONS OF RECYCLED POST-CONSUMER GLASS CEMENTITIOUS MATERIAL FOR CONCRETE**

**Marija Krstic <sup>(1)</sup>, Julio F. Davalos <sup>(1)</sup>**

(1) Department of Civil Engineering, The City College of New York, New York, USA

### **Abstract**

Concrete is the most used material in the world, second only to water. The production of cement is energy intensive and has raised significant environmental concerns since one ton of cement produces an equal ton of CO<sub>2</sub>. In the USA, about 90 million tons of cement are used annually, with three million tons used in New York. The concrete industry is facing critical challenges with availability of essential Supplementary Cementitious Materials (SCMs), which are commonly used to partially replace cement for the production of concrete mixes. Recently and particularly in the Northeastern USA, there is a scarcity of fly-ash —as most widely used SCM in concrete . Recycled mixed-color post-consumer glass has a good potential to become one of the leading SCMs for concrete. With the goal of contributing to the implementation of sustainable concrete, this paper focuses on the development and characterization of mix designs with different percentages of cement replacement by a new SCM from recycled post-consumer glass, known commercially as Pozzotive. Concrete formulations with Pozzotive were evaluated at macro- and micro-level, showcasing significant strength and durability performances. This research has been successfully applied in field projects for sidewalk and high-rise building constructions and is contributing to the development of ASTM standard specifications for Glass-SCM.

### **1. Introduction**

The recycling operations of glass are problematic, costly, and often subsidized due to lack of profitable value-added product markets, particularly for color glass. At the same time, the concrete industry is facing a critical scarcity of essential cementitious materials which are commonly used to partially replace cement for the production of concrete mixes in construction. SCMs are fine powders of micro particles that when combined with cement produce high-performance concrete mixes with enhanced strength and durability properties.



Due to these benefits, SCMs, or pozzolans, are used in nearly all concrete mix designs for major buildings, sidewalks, roadways, bridges, and other infrastructure applications. In particular, fly-ash is the most widely used SCM produced as a byproduct from the residue of coal-burning plants [1]. But due to environmental concerns and costs a significant percentage of coal power plants is shutting down or converting to cheaper natural gas, resulting in shortage and price increase of fly-ash particularly in the North Eastern region of the USA. These two challenges, the lack of a major market for recycled glass and dwindling supply of fly-ash, present a unique and transformative opportunity for benefiting both the glass recycling industry and concrete production industry, through the development and implementation of glass SCM for concrete.

**Challenges for Glass Recycling:** In the USA, about 12.5 million tons of post-consumer glass (or 80 lbs per person) is generated annually, with only about 23% being recycled. In NY City, 140,000 tons are generated and about 50% is recycled. Worldwide, glass represents 6% of about 2 billion tons per year of solid waste. The recycling of glass in the USA has increased more than 4 times in the last 20 years. But most recyclers faced significant challenges and economic hardships processing glass, particularly color glass which has no real market and is generally used as low-cost granulated filler material. Glass is heavy (about 20% of total solid-waste weight), harsh on processing equipment, and costly to recycle. The research described in this paper offers the potential for post-consumer recycled glass to become a highly sought after material for producing cementitious pozzolan for concrete.

**Challenges for the Concrete Industry with Decreased Availability of SCMs:** The production of cement is energy intensive (~ 5% of total global energy) and results in one ton of CO<sub>2</sub> per one ton of cement [2]. In the USA about 90 million tons of cement are used annually (CO<sub>2</sub> emissions equivalent to 300 million cars) [2]. To produce *green* high-performance concretes, SCMs such as fly-ash and slag are used to partially replace cement content [3]. Fly-ash has been the most popular pozzolan, but recently its availability has decreased due to 25% of coal-fired power plants shutting down or converting to cleaner natural gas [4], [5]. Compounding this problem, granulated blast-furnace slag, is produced mainly outside the USA (Canada 35%, Japan 32%, Spain 12%, Italy, Brazil and others [6]). Thus, there is a pressing need for an alternate SCM to fly-ash, and post-consumer glass can be effectively and economically transformed into value-added pozzolanic material for concrete [7], [8], [9].

In 2013, a research was performed to study the effect waste glass powder in concrete. The workability, compressive strength, and density of concrete with used waste glass powder were evaluated in the lab. They concluded that using waste glass powder increased the workability and compressive strength of concrete, while reducing the density in comparison to standard mixture of concrete [8]. Another study in 2017 proposed the use of high volume glass powder as cement replacement in concrete. The microstructures, mechanical and durability properties of such concretes in the long term were investigated. Their results showed better mechanical behaviors, and higher durability performance [10].

## 2. Research Significance and Contributions

With the goal of contributing significantly to the implementation of sustainable High Performance Concrete, this study focuses on the development, evaluations, and field

implementations of mix designs with different percentages of cement replacement by a new SCM from recycled post-consumer glass, known commercially as Pozzotive. In addition to conventional macroscale tests, micro-level experiments were performed in the laboratory to study the microstructural interactions. This research also included full-scale field applications for sidewalks and high-rise building in New York City. This is the first large scale high-rise building application of Glass-SCM in the USA. The results of this study are being used on collaborative efforts to develop ASTM specifications for post-consumer Glass-SCM, which can benefit both the concrete and the solid waste management industries worldwide.

## 2.1 Macro-Scale Evaluations

**Materials:** The cementitious materials used for this study included Portland cement type I; post-consumer Glass-SCM Pozzotive, with an average particle size of 13  $\mu\text{m}$ ; Class F fly ash, and slag. The aggregates conformed to standard specification ASTM C33. The coarse aggregate was Nova Scotia crushed granite with a maximum nominal size of 3/4" (19 mm), specific gravity of 2.69, and absorption of 0.7. The fine aggregate was Roanoke sand with specific gravity of 2.63, and absorption of 0.4. The chemical admixtures as per ASTM C494 were surfactants for water reduction and air entraining. Six concrete mix designs were produced according to ASTM C192 and C511. For the six mix designs described next, the testing was performed for fresh and hardened concrete as per ASTM standard specifications. For compressive strength as per ASTM C39, the cylinders were tested at ages of 7, 28, 56 and 90 days. For flexural strength as per ASTM C78, the beams were tested at ages of 14, 28 and 56 days. For durability evaluations, rapid chloride permeability (RCP) test was performed on cylindrical disks as per ASTM C1202.

**Mix Designs and Methods:** The evaluations were based on ASTM standard specifications, and they were divided into two categories, strength/stiffness and durability. Only some of the most important evaluations are presented in this paper. The mix designs developed in the lab were based on specifications for sidewalk construction by the NY City Department of Design and Construction (NYC-DDT). Based on literature review and experience, six mix designs were selected: One with a 100% Portland cement as a control; three with percent replacements of cement by 20, 30 and 40% with glass SCM; and for correlation purposes with glass-SCM, one mix with 30% fly ash, and one with 40% slag. The last two mix designs were included because concrete mixes with fly ash and slag are the most commonly used; hence, concretes with Glass-SCM can be directly compared with them. The testing methods for strength/stiffness evaluations included compression, split tensile, flexure, static modulus, and dynamic modulus. In addition, free-shrinkage was also evaluated. The early compressive strength of concrete with slag is expected to be higher than with fly ash, because slag is a more cementitious material and hydration reactions occur early. Compressive strengths of concrete with Glass-SCM are expected to achieve or exceed the values obtained for the other mixes. In general, results for flexural strength are expected to be higher than for split tensile (both are indirect measures of tensile strength). As is generally the case, the dynamic modulus of elasticity is expected to be higher than the static modulus of elasticity. Concretes with SCMs are expected to have less shrinkage than straight cement concrete. The durability methods selected included RCP, and freeze-thaw cycling. For RCP results, the concretes with SCMs are expected to have lower permeability values than the mix with straight cement. This is primarily a diffusivity test used as an indirect method to evaluate the permeability of concrete when exposed to chloride ions from deicing salts during wintry

season or from exposure to ocean water. The freeze-thaw cycling test is design to simulate seasonal weather changes causing distress in concrete, for up to 400 accelerated cycles in a programmable environmental chamber. Once again, the mixes with SCM are typically known to outperform concretes with straight cement.

**Compressive Strength:** We evaluated compressive strength at different ages to monitor the strength development with time. The compressive strength test results for up to 90 days enabled to compare the relative strength developments of the six mix designs. It is generally accepted that the early high strength is due to the hydration reactions while the strength at later stages is driven by the pozzolanic reactions [11]. When using SCM materials in concrete the strength continues to increase in later ages because of pozzolanic activity [12], [13]. The compressive strength results are shown in Figure 1 for the six mix designs. At 7 days, the highest value was for the concrete with 100% cement (CM) and the lowest for 40% glass (G-40). This is due to the dominant cementitious hydraulic nature of cement. Consequently, the higher content of SCM for G-40 possibly slowed the early rate of hydration. At the age of 28 days, the concrete with 40% slag (S-40) showed the highest strength, because after cement, slag has the most cementitious content [14]. At 56 days, the tests for the mix designs with Glass-SCM showed significant increases in strength, with G-40 and S-40 at about the same level. At the age of 90 days, G-40 still showed increase in strength above the other mixes. Among all the mixes, G-40 had the overall highest strength gain of 105 % between 7 and 90 days.

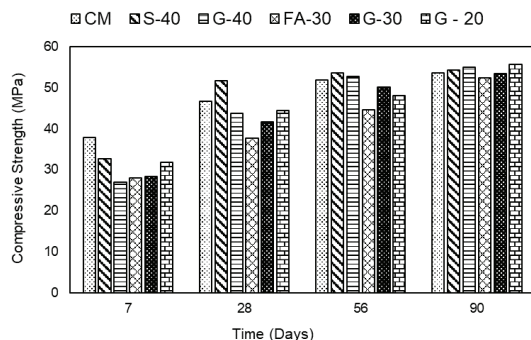


Figure 1: Comp. strength of 6 mix designs.

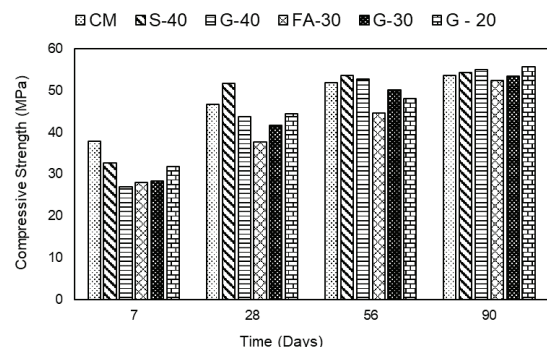


Figure 2: Flex. strength of 6 mix designs.

**Flexural strength:** This test induces primarily flexural stress, but can serve to evaluate tensile strength, since the test specimen is unreinforced and collapses due to critical tensile stresses at the bottom of the beam specimen. Most studies showed that flexural strength is higher (within ~10%) than the indirect Split-Tensile strength, due to differences in specimen geometry, loading, and state of internal stresses in the test samples. Three specimens per mix design were tested at 14, 28 and 56 days [15]. The results in Figure 2 show that all three Glass-SCM mixes outperformed the Slag and fly-ash counterparts.

**Permeability:** The resistance of concrete to chloride penetration is one of the most important concerns regarding the durability of concrete structures. The Rapid Chloride Permeability (RCP) test method consists of relating the electric charge through the specimen to the resistance to chloride ion penetration. In general, most concretes become progressively less permeable with time. In general, the addition of pozzolanic SCM materials improves the resistance to chloride penetration and reduces the chloride-induced corrosion initiation of steel reinforcement [16]. In Figure 3 the lowest permeability values were obtained for Glass-SCM

mixes. The notable improvement in resistance to chloride infiltration is the result of partial blocking of pores in hydrated cement paste with the products of pozzolanic reactions provided by Glass-SCM [17]. At 90 days, the slag samples tested at about 1100 Coulombs, which is considered low, while the G-40 specimens showed outstanding results with less than 300 Coulombs, which is an exceptional low value.

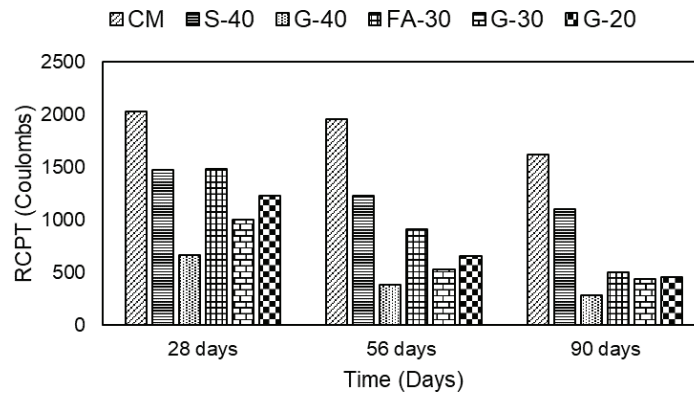


Figure 3: Rapid Chloride Permeability

## 2.2 Micro-scale Evaluations

**Overview of research in progress:** The research in progress includes microstructure evaluations of cement pastes focused on chemical and physical characterizations. Pastes will follow the same percentages of cement replacements as the six mix designs described above, to establish correlations between Micro- and Macro-levels. The results will be used to better understand and explain the macroscopic behavior of Glass-SCM concretes and recommend their effective implementations in practice. Methods have been selected to show how Glass-SCM influences the formation of binding compounds due to hydration reactions when water is added to the mix, such as Calcium-Silicate-Hydroxide (C-S-H gel), which for cement forms as 50-60% of total hydration products and beneficially influences the strength and durability characteristics. The glass pozzolan is very rich in silica dioxide  $\text{SiO}_2$  (about 70%) and its addition as SCM to concrete generates secondary or pozzolanic reactions. These pozzolanic reactions are slower than hydraulic reactions; however, they contribute to additional formation of C-S-H gel that leads to higher strength and lower permeability. The particle size distribution will be determined by laser diffraction method. The scanning electron microscopy (SEM) with Energy Dispersive X-ray Spectroscopy (EDX) will be used to determine the morphology and chemical composition of the non-hydrated cementitious materials and hydrated pastes and their hydration products, either combined with the X-ray Diffraction method (XRD) or with gas adsorption method (BET) for identifying the specific surface area (SSA). These characterization methods will provide valuable insights into the chemical interactions of the SCMs, cement and the natural aggregates, to better explain macroscopic results.

## 2.3 Field Applications

This project has contributed to field application projects for sidewalks and high-rise building construction. The first sidewalk project was completed in South Jamaica, Queens, New York, in May 2016. Three different mix designs were used: 20% and 40 % Glass and a typical

sidewalk concrete with 30% fly ash Class F. The in-situ and lab test results for glass mixes showed close correlations, and the field performance of these concrete mixes had been evaluated for over a year under exposure to traffic and weather conditions, with no visible signs of distress. More recently (April, June, and September 2017), two higher strength mixes were implemented in components of a 23-story building in Halletts Point, Queens, NY. The mixes for this application were produced with 30% Glass as self-consolidating concretes. Two mix designs were used: One with 55 MPa (8,000 psi) for a slab and several columns on the 5<sup>th</sup> floor, and the other with 70 MPa (10,000 psi) for a parapet wall on the 8<sup>th</sup> floor and also for the bulkhead roof. The test results so far indicate that the target strengths and performances were successfully achieved and actually surpassed significantly. Glass-SCM has also been used on sidewalk projects elsewhere: (1) in Montreal, Canada as 10% replacement, and this province has made a commitment to use glass pozzolan in all future sidewalk construction [18]; (2) in Mountain View, California using a mix with 50% cement, 30% slag, and 20% Glass-SCM. Their mix design followed the guidelines and glass material described in this paper, and they obtained very good results.

## References

- [1] Wilson, M. L. and Kosmatka, S. H., Design and Control of Concrete Mixtures, 15th ed., Portland Cement Association (2014)
- [2] "Concrete." <http://minerals.usgs.gov/minerals/pubs/commodity/cement/>
- [3] Davalos, J. F. et al, Advanced materials program – High performance concrete mixes for cast-in-place bridge decks in West Virginia; WVDOT/DOH Res. Proj. No. T699-AMP-1.00 (2006)
- [4] <http://www.bloomberg.com/graphics/2015-coal-plants/>
- [5] <http://www.eia.gov/todayinenergy/detail.cfm?id=21232>
- [6] [http://atlas.media.mit.edu/en/visualize/tree\\_map/hs92/import/show/all/2618/2013/](http://atlas.media.mit.edu/en/visualize/tree_map/hs92/import/show/all/2618/2013/)
- [7] Kamali, M. and Ghahremaninezhad, A., Effect of glass powders on the mechanical and durability properties of cementitious materials, *Constr Build Mater* 98 (2015), 407-416
- [8] Vasudevan, G. and Pillay, S.G.K., Performance of using waste glass powder in concrete as replacement of cement, *Am J Eng Res* 2(12) (2013) 157-181
- [9] Shi, C. et al, Characteristics and pozzolanic reactivity of glass powders, *Cem Concr Res* 35(5) (2005), 987-993
- [10] Du, H., and Tan, K.H., Properties of high volume glass powder concrete, *Cement and Concrete Composites* 75 (2017), 22-29
- [11] Mehta, P. K. and Monteiro, P. J. M., *Concrete, Microstructure, Properties, and Materials*, 4th ed., Mc Graw Hill Education (2014)
- [12] Omran, A. and Tagnit-hamou, A., Performance of glass-powder concrete in field applications, *Constr Build Mater* 109 (2016), 84-95
- [13] Shao, Y. et al, Studies on concrete containing ground waste glass, *Cem Concr Res* 30(1) (2000), 91-100
- [14] Khatib, J. M. and Hibbert, J. J., Selected engineering properties of concrete incorporating slag and metakaolin, *Constr Build Mater* 19 (2005), 460-472
- [15] Siddique, R., Performance characteristics of high-volume class F fly ash concrete, *Cem Concr Res* 34 (2003), 487-493
- [16] Chindaprasirt, P., Resistance to chloride penetration of blended Portland cement mortar containing palm oil fuel ash, rice husk ash and fly ash, *Constr Build Mater* 22 (2008), 932-938
- [17] Nassar, R. and Soroushian, P., Field investigation of concrete incorporating milled waste glass, *Journal of Solid Waste Technology and Management* 37(4) (2011), 307-319
- [18] <https://healthymaterialslab.org/news/glass-in-concrete>

## **MONITORING FRESH CEMENTITIOUS MATERIAL BY DIGITAL IMAGE CORRELATION (DIC)**

**Evin Dildar Dzaye**<sup>(1),(2)</sup>, **Geert De Schutter**<sup>(2)</sup>, **Dimitrios Aggelis**<sup>(1)</sup>

(1) Vrije Universiteit Brussel, Brussels, Belgium

(2) Ghent University, Magnel Laboratory for Concrete Research, Ghent, Belgium

### **Abstract**

Concrete undergoes strong displacements due to different processes at very early state, like shrinkage. This early state of concrete affects the long-term concrete performance. The concrete deformation cannot be directly attributed to a single process, due to the complexity of different processes such as, evaporation, water migration, settlement, formation of hydrates, shrinkage, early age cracking. Monitoring concrete properties at a very fresh state is essential to understand the different ongoing processes. Digital image correlation (DIC) has proven very useful as an optical and contactless method for surface monitoring of several materials. In the present paper the displacement distribution of fresh cementitious material from plastic state up to hardened state is studied by means of DIC. Moreover, an innovative technique of speckle pattern creation is presented, since creation of a pattern on fresh (and hence viscous) cementitious materials is not straightforward. The specimen surface is covered with a speckle pattern that deforms together with the specimen. The principle of DIC realizes a 3D continuous monitoring by recording the images at different time steps and comparing it to the reference or undeformed image. The experimental results confirmed the effectiveness and correctness of the new technique giving a global overview much more representative than point measurements with traditional displacement meters.

### **1. Introduction**

After casting, concrete stiffens with age that leads to concrete volume reduction (shrinkage). Properties of concrete are affected by its volume reduction caused by the loss of moisture due to evaporation process. Furthermore, there are several factors leading to concrete displacement such as the hydration reaction [1] between water and cement, drying process due to changes of pore water and thermal properties. The displacement of concrete has

detrimental effect on concrete quality. For this reason, it is essential to understand the evolution of concrete displacement. Recently several studies on concrete displacement are performed by means of DIC. The technique of DIC was very useful as an optical and contactless method for surface monitoring of several materials. Maurouc et al. [2] applied DIC to study cracking of coating mortar due to drying and DIC proved the ability to show the pattern and width of cracks. In another study, strain and crack distribution in concrete due to drying process was monitored by means of DIC [3]. Lagier et al. [4] evaluated cracking due to drying process by 2D-DIC. Yang et. al. [5] applied 3D-DIC to study the effect of aggregate size and volume on the drying process of concrete and mortar. The non-uniform strain distribution increased with increased drying time of concrete.

This study focuses on the vertical deformation (settlement) of fresh mortar in fresh stage (few minutes after casting) to understand concrete drying process. The experimental results will be compared to classical point measurement methods. DIC mapping can evaluate the settlement distribution on the surface that decrease the final material properties. Consequently, concrete drying process can be adjusted to reduce shrinkage formation, similar to the work of Slowik et al. [6].

## **2. Overview of DIC principle**

Digital image correlation (DIC) is a non-contact optical- numerical technique that offers the possibility to measure complex displacement and deformation of different materials. This system consists of a pair of high resolution cameras that build a stereoscopic vision to measure the surface deformation. The cameras are synchronized to record simultaneously images of the sample at a constant time interval. The sample surface is covered with randomly distributed white and black speckles. DIC software identifies the white and black speckles then measures the grey intensity of local zones. Displacement in space translated to movement of the speckle pattern is perceived as change on the grey intensity level compared to a reference stage [7]. The correlation between a reference and a 'deformed' image is built on the degree of grey level similarity [8]. The accuracy of DIC measurement depends on the speckle pattern quality. There are several techniques to create black-white speckle patterns. Researchers performed different ways to create patterns, such as marked pen [8], spray paint and airbrush guns [9]. The pattern should have clear contrast between black and white colour. Pixels are grouped and analysed in subset areas. Subset should be optimally chosen to keep measuring even in the case of great size movements. The creation of the speckles on fresh cementitious material is challengeable since speckles move or get absorbed on wet surface. In the present study, an innovative method of speckle pattern is analysed that allows understanding the drying process of fresh concrete. The specimen surface is covered by a powder speckle pattern (Aluminium oxide and carbon) immediately after casting the mortar into the mold.

## **3. Materials and experimental setup**

### **3.1 Material**

Cement mortar specimen were performed with ordinary portland cement (cement CEM I 52.5N and water). The mix design was prepared with 1 part of cement, 2 parts of sand, see

Tab. 1. The cement mortar was mixed in a laboratory concrete mixer for 3 min at low speed. Afterwards, the material was poured into metallic mold of size 150x150x150 mm (internal dimensions).

Table 1: Cement mortar mix design.

Cement [g]	Sand [g]	Water [g]	Water to binder ratio
2618.3	5236.6	1178.2	0.45

### 3.2 Experimental setup

Above the sample surface a pair of digital cameras (AVT Stingray) were installed, see Fig.1(a). The resolution of the cameras are 2504 by 2056 pixels. White light was installed above the sample surface to provide lighting to the monitoring area during the measurement. On the specimen surface white-black speckle pattern was created as shown in Fig.1(b). Firstly, a layer of white aluminium oxide powder covered the half sample surface. Later, well-distributed black dots of carbon powder are applied on the surface. Only the half of the sample surface is covered with speckle pattern since in the other half the vertical LVDT is placed. Consequently, DIC can visualize an area at which the left, right and bottom sides as shown in Fig.1(b) are attached to the metallic mold and the top side stands in the middle area of the sample. The boundary conditions are not identical for all four sides of the analysis area. The total area observed by DIC is equal to 135x63 mm<sup>2</sup>. DIC analysis were performed with 61x61 subsets with a step size of 10 between subset centres.

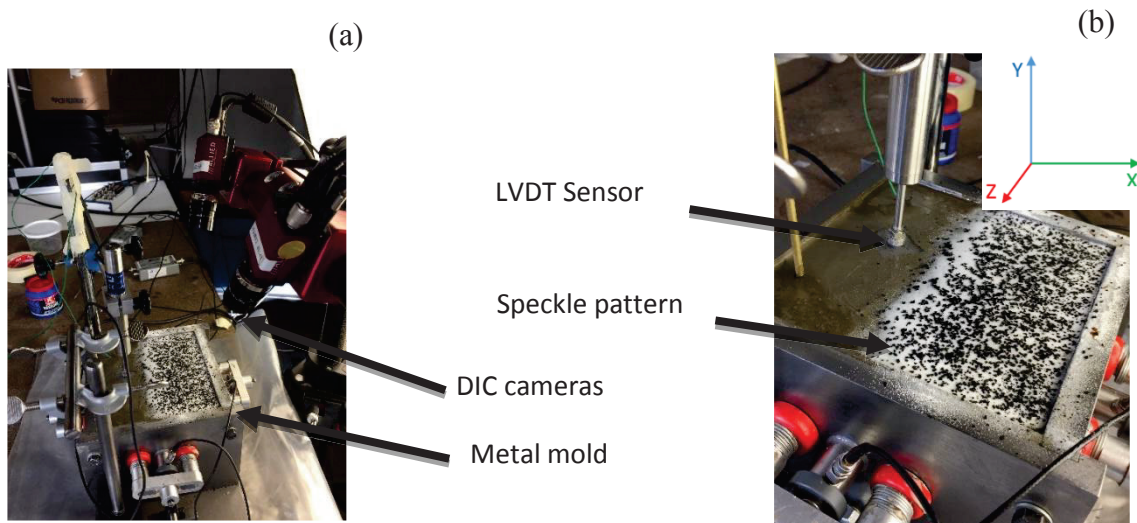


Figure 1: (a) overview of experimental setup including DIC; (b) sample surface covered with speckle pattern including LVDT sensor and DIC coordinate.

The measurement and the post-processing analysis was conducted using VIC-Snap and VIC-3D software respectively. The analysis is done considering an axis system shown in Fig.1(b). The displacement vectors  $U$ ,  $V$ ,  $W$  in mm are calculated at  $X$ ,  $Y$ ,  $Z$  directions respectively. DIC monitoring started up to 20 min after casting. Reference starting point (Time 0) is considered the time of casting and the duration of the experiment was approximately 3 days. Furthermore, one Linear Variable Differential Transformer (LVDT) was installed vertically



on the sample surface to measure the settlement. The vertically arranged LVDT tip touched a 20×20 mm metallic wire lattice that was applied on the specimen top surface Fig. 1(b). Consequently, the sensor tip was prevented from penetration as well as floating on the surface.

#### 4. Results and discussions

In the fresh state, water accumulate on mortar top surface (known as 'bleed water'). The accumulated water evaporates with time that causes mortar shrinkage in the early periods. This way, volume loss and displacement triggers plastic shrinkage.

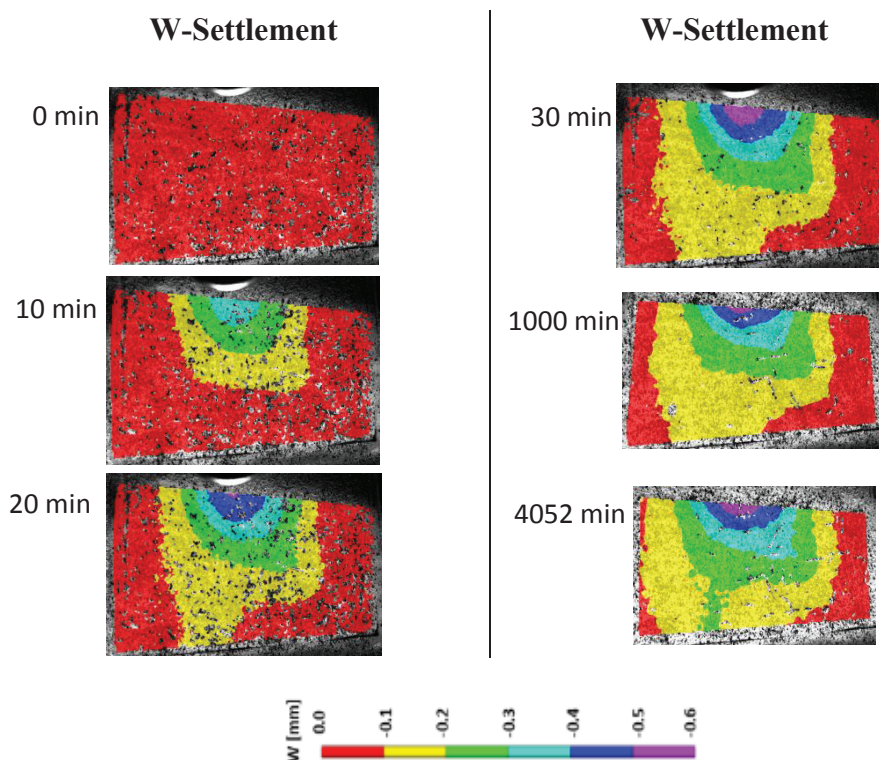


Figure 2: DIC surface settlement at discrete monitoring stages.

DIC allows monitoring settlement (vertical displacement) at different curing stages as shown in Fig. 2. The images visualize the evolution of settlement (W) at different monitoring stages. Time 0 stands for the start of monitoring and in this period mortar is in plastic state. The speckle pattern was fast applied after casting, therefore DIC monitoring starts as soon as 20 minutes after casting. An increased displacement in z direction at the surface takes place 10 minutes after monitoring. W displacement standing for surface settlement exhibits its highest value in the specimen top centre standing for specimen centre. At fresh state (representatively in 10, 20 and 30 minutes), settlement effect extends further. The pink regions exhibit the highest settlement evolution at the centre of the surface. It is visible that displacement is not uniformly distributed on the surface. The evolution of the settlement starts from the centre to the edges. It is possible that bleed water movement controls the settlement evolution. The

hardening process of the particle structure decreases the settlement rate at later stages. At hardening state (1000 and 4052 minutes) the evolution of the settlement rate decreases. DIC compared to traditional contact sensors, measures the settlement in contactless mode, therefore the sensor cannot affect the measurement process. Based on the observed DIC maps, it is evident that a point measurement of settlement is not sufficient to describe settlement. Settlement of a point at the surface is influenced by its elevation compared to the surrounding areas.

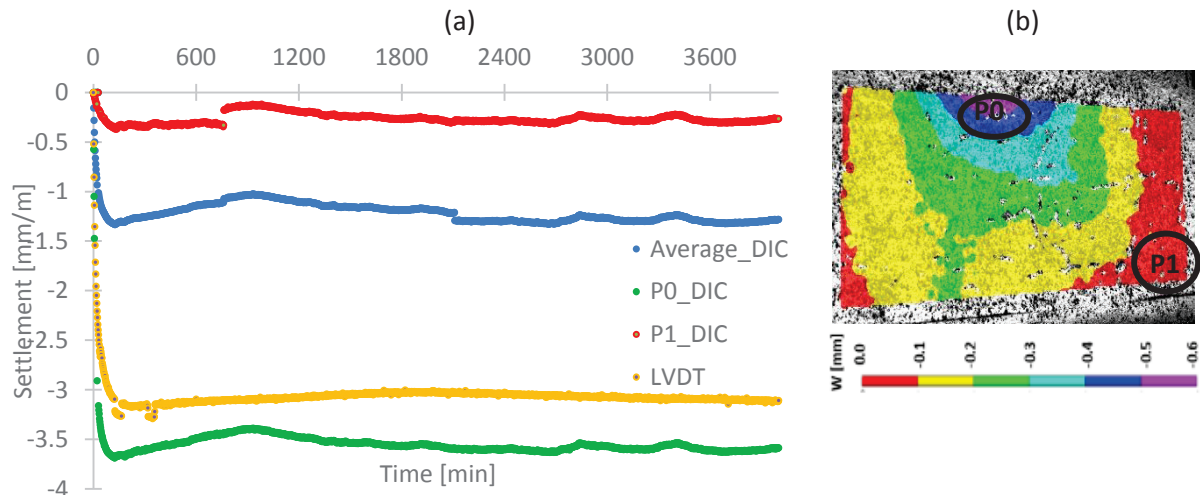


Figure 3: (a) DIC settlement and LVDT at different locations; (b) representative for the points (P0, P1 and total average area) of DIC measurement.

Settlement monitored by DIC the points with the highest settlement (P0), the lowest settlement (P1) and total average area are compared to classical LVDT point measurement as shown in Fig. 3(a). The locations of the points (P0, P1) and the total average area measured by DIC is presented in Fig. 3(b). The settlement reaches its maximum value 140 minutes after monitoring in all four curves. Beyond this time, the range is significantly wide between point P0 (-3.6 mm/m) and P1 (-0.3 mm/m). While the point measurement of LVDT presents a settlement of -3.1 mm/m and the average DIC measurement presents a settlement -1.3 mm/m after 140 min, see Fig. 3(a).

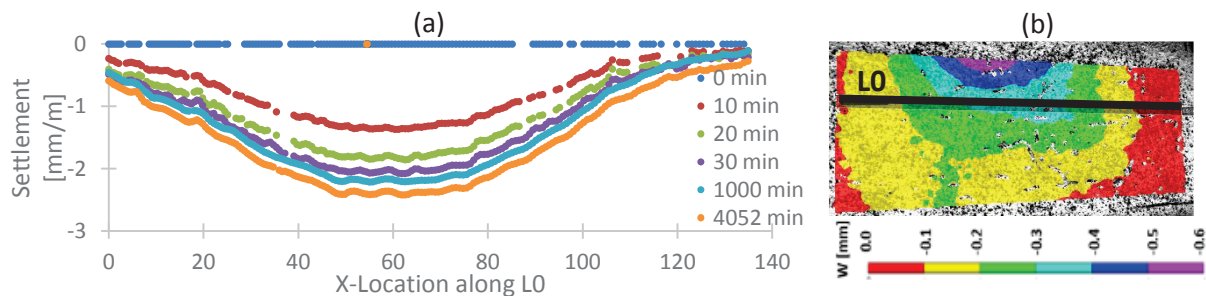


Figure 4: (a) Settlement distribution for mortar at discrete curing stages along Line L0; (b) the location of line L0 on the sample surface.

The difference in settlement between LVDT and DIC measurement in the absolute value is related to the circumstance that DIC considers the total surface area and LVDT monitors the

settlement at a point of the surface. It is clear that no robust conclusion can be attained when considering only point analysis. This is an evident for the significant drawback of the point analysis. In Fig. 4(a-b), the Settlement of points standing along line (L0) crossing the sample is presented at discrete stages of curing. It is revealed that as soon as 10 minutes after casting, the settlement progresses differently at different positions exhibiting the highest value of settlement close to the centre of the specimen and confirms the relatively “axisymmetric” profile.

## 5. Conclusions

This paper focuses on an effective technique of DIC to evaluate the displacement distribution of mortar in fresh state (few minutes after casting). DIC allows monitoring the non-uniform displacement distribution at different locations on sample surface. This approach realizes a deeper understanding of concrete hardening process and offering data for the whole surface that is not possible with the classical LVDT point measurement. Further study should be done regarding the accuracy of the speckle pattern that is affected by the bleed water in the first hours after casting.

## References

- [1] Wieslaw, K., *Cement and Concrete Chemistry*, Springer (2014)
- [2] Mauroux, T. et al, Study of cracking due to drying in coating mortars by digital image correlation, *Cement and Concrete Research* 42(7) (2012), 1014-1023
- [3] Maruyama, I. and Sasano, H., Strain and crack distribution in concrete during drying, *Materials and Structures* 47(3) (2014), 517-532
- [4] Lagier, F. et al, Numerical strategies for prediction of drying cracks in heterogeneous materials: Comparison upon experimental results, *Engineering Structures* 33 (2011), 920-931
- [5] Chen, Y. et al, Application of 3D-DIC to characterize the effect of aggregate size and volume on non-uniform shrinkage strain distribution in concrete, *Cement and Concrete Composites* 86 (2018), 178-189
- [6] Slowik, V. et al, Capillary pressure in fresh cement-based materials and identification of the air entry value, *Cement and Concrete Composites* 30(7) (2008), 557-565
- [7] Lecompte, D. et al, Quality assessment of speckle patterns for digital image correlation, *Optics and Lasers in Engineering* 44 (2006), 1132-1145
- [8] Sutton, M.A. et al, *Image Correlation for Shape, Motion and Deformation Measurements, Basic Concepts, Theory and Applications*, Springer, New York, USA (2009)
- [9] Barranger, Y. et al, Digital Image Correlation accuracy : influence of kind of speckle and recording setup, *EPJ Web of Conferences* 6, 31002 (2010)

## **NEW INSIGHTS ON THE SEGREGATION DUE TO MANUFACTURE CONDITIONS OF LIGHTWEIGHT AGGREGATE CONCRETES**

**Afonso Miguel Solak<sup>(1,2)</sup>, Antonio José Tenza-Abril<sup>(1)</sup>, Francisco Baeza-Brotons<sup>(1)</sup>,  
Victoria Eugenia García-Vera<sup>(3)</sup>, Marcos Lanzón<sup>(3)</sup>**

(1) Department of Civil Engineering, University of Alicante, Alicante, Spain

(2) CYPE Ingenieros S.A., Alicante, Spain

(3) Department of Architecture and Building Technology, Technical University of Cartagena,  
Cartagena, Spain

### **Abstract**

Lightweight aggregate concrete (LWAC) is susceptible to segregation because of the differences between the densities of lightweight aggregates and mortar, influencing the strength and durability of concrete. Besides that, due to high workability and low viscosity, LWAC is susceptible to segregation during mixing process, transporting, placement and dormant period. In the present study, three variables related to the manufacturing process of LWAC samples were studied. Six different LWACs were manufactured considering different times of vibration, in one and two layers. To verify the influence of the initial hydration of Portland cement and consequently loss of workability in the segregation, the same LWACs were manufactured considering different times between mixing and molding. A statistical analysis was applied for establishing the structure of the variable dependence in segregated concretes. The results contribute to a better understanding of the segregation in lightweight concrete concluding that the vibration time per layer and the type of vibration of LWAC have a significant influence on the segregation of the samples.

### **1. Introduction**

In recent years, more attention has been paid to the development of lightweight aggregate concrete (LWAC) [1]. LWAC substantially reduces building cost, eases construction, allows greater design flexibility and in some cases it may be considered a relatively 'green' building material, as the reduction in the concrete density results in superior thermal, acoustic and fire resistance and leads to a positive impact on the energy consumption of a building [1]. LWAC

compaction remains one of the major problems in fresh concrete because excess vibration time can easily produce the segregation phenomenon [2]. When lightweight aggregate (LWA) is used with a considerable lower density compared to that of the paste, an upward segregation of the coarse aggregate might be experienced [3]. The ability of fresh concrete to remain homogeneous during consolidation is a critical issue in the mixture design [2]. A homogeneous randomly-oriented-aggregate distribution improves the mechanical properties, durability, stability and impermeability of concrete [4]. In lightweight aggregate concrete, the constituent LWAs may have a lower strength and elastic modulus than the mortar matrix [1] and a region presenting high aggregates concentration may also lead to local concrete pathologies when a long time period is considered [5]. Besides that, due to high workability, commonly found in LWACs, this material is susceptible to segregation during mixing, transporting, placement and dormant periods. In the present study, three variables related to the manufacturing conditions of LWACs samples were analyzed focusing on their influence on the segregation phenomenon. Therefore, several authors have proposed different methodologies to quantify the phenomenon of segregation proposing segregation indexes involving the volumetric fraction of aggregates at different heights of a concrete specimen [2]; image-processing-based techniques [6] and the densities of different sections of a concrete specimen [7]. The last one, selected for the present work and proposed by Ke [7], estimate a segregation index ( $SI_{Ke}$ ) dividing the specimens into four equal sections and using the densities obtained from the upper ( $\rho_{top}$ ) and lower ( $\rho_{bottom}$ ) slices of a cylinder. A possible segregation tends to reduce the density in the upper section because the lightweight aggregates tend to float in the mortar matrix [7].

## 2. Experimental program

### 2.1 Materials

The experimental campaign involved the production of a concrete made with LWAs using the Fanjul method [8], in order to produce LWAC with a target density of 1700 kg/m<sup>3</sup> and 1900 kg/m<sup>3</sup>. Six different concretes were manufactured considering different types of LWA, different modes of vibration (one or two layers) and different theoretical densities. Table 1 presents the manufacturing characteristics of these concrete and includes their mix proportions. All samples were manufactured with the same water/cement ratio (w/c) of 0.6, resulting in 350 kg/m<sup>3</sup> of cement and 210 kg/m<sup>3</sup> of water to produce 1 m<sup>3</sup> of concrete. CEM I 52.5 R cement with an absolute density of 3176 kg/m<sup>3</sup> was used for all the concretes; 2 types of expanded clay were used as lightweight aggregate; its physical properties are described in the Table 2. The bulk density of the LWAs was obtained according to the procedure described in the standard UNE EN 1097-3. In addition, the density of the particles in the dry state was determined by the methodology proposed by Fernández-Fanjul et al [9], the absorption of water at 24 hours according to the UNE EN 1097-6 (pre-dried particles and in distilled water). The methods/standards used for testing are also presented in the Table 2. Before mixing, and to avoid the loss of water from kneading by absorption, the LWAs were presaturated. During the mixing, the water content of the LWA and the surface water content were determined, to make the appropriate corrections and maintain a constant effective a/c ratio of 0.6.

Table 1: Manufacturing characteristics and mix proportions to produce 1 m<sup>3</sup> of concrete.

Concrete	Samples	Theoretical Densities	Vibration	Type of LWA	Fine Aggregate (kg/m <sup>3</sup> )	LWA (kg/m <sup>3</sup> )
LWAC1	20 uds	1700 kg/m <sup>3</sup>	two layers	Arlita Leca HS	723.9	416.2
LWAC2	20 uds	1900 kg/m <sup>3</sup>	two layers	Arlita Leca HS	1046.0	294.0
LWAC3	20 uds	1700 kg/m <sup>3</sup>	one layer	Arlita Leca M	991.1	148.9
LWAC4	20 uds	1900 kg/m <sup>3</sup>	one layer	Arlita Leca M	1234.8	105.2
LWAC5	5 uds	1700 kg/m <sup>3</sup>	one layer	Arlita Leca M	991.1	148.9
LWAC6	5 uds	1700 kg/m <sup>3</sup>	one layer	Arlita Leca HS	723.9	416.2

Table 2: Characteristics of aggregates and the methods/standards used for testing

Property	Method	Arlita Leca M	Arlita Leca HS	Fine Aggregate
Dry particle density (kg/ m <sup>3</sup> )	According to [9]	482	1019	2688
Bulk density (kg/ m <sup>3</sup> )	UNE EN 1097-3	269	610	1610
24 h Water absorption (%)	UNE EN 1097-6	36.6	12.2	0.12

## 2.2 Experimental Procedures

In the present study, three variables related to the manufacturing process of LWAC samples were studied. The cylindrical samples (Ø150mm and 300mm height) were compacted using an electric needle vibrator of 18000 rpm/min and a Ø25mm needle. The specimens were vibrated with 6 different times (0-5-10-20-40-80 seconds), in one and two layers (Table 1) to evaluate the variables “vibration time per layer (VTL)” and “manufacturing type (MTy)”, respectively. These procedures were repeated 4 times, considering different times between mixing and molding (variable “manufacturing time (MTi)” of 15, 30, 60 and 90 min), to verify differences on the consistency of the concretes. The flowchart of the Fig 1 represents these procedures.

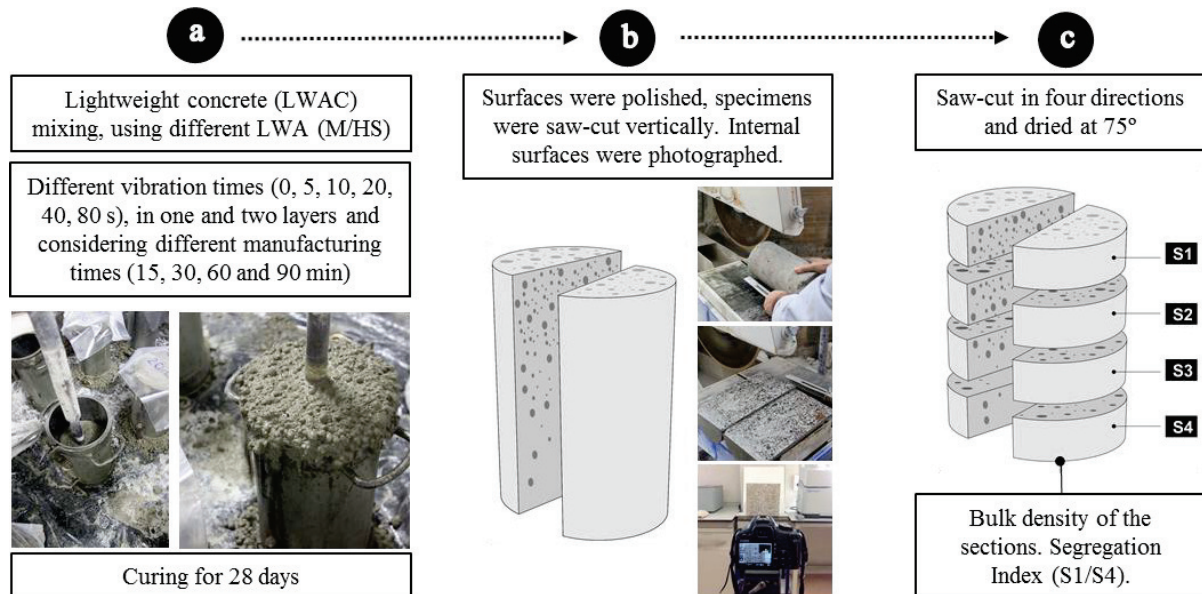


Figure 1: Flowchart of the methodology used in this study.

After being made and cured in the water at a temperature of  $20 \pm 1^\circ\text{C}$  for 28 days, the specimens were saw-cut through its longitudinal axis and their sections were photographed for visual analyses. Subsequently the specimen's halves were then saw-cut into four equal parts, resulting in octaves, which had their bulk densities determined. Using the density values of the upper and lower sections, the segregation index was obtained according to the methodology indicated by Ke ( $SI_{Ke}$ ) [7].

### 2.3 Statistical data analysis

A statistical analysis was applied for establishing the structure of the variable dependence and their interrelationship using XLSTAT® by Addinsoft®. First, a Shapiro-Wilk test was performed to verify the normality of the data. Second, scatter diagrams and Pearson's correlation coefficients were performed to identify existing patterns and quantify the linear association between two variables. Third, the analysis of variance (ANOVA) established the effect of each factor on the studied parameters and the possible interaction between the factors. Moreover, the statistically different groups were determined using Tukey's HSD test ( $P < 95\%$ ).

## 3. Results and discussion

The results of the Shapiro-Wilk test confirmed the normal distribution of the analyzed data. The scatter diagrams confirmed the linear correlation between VTL and  $SI_{Ke}$  (Figure 2a). In the LWAC production with strong vibration stages in which LWA tends to float, Fig 2 displays that longer vibration time causes more pronounced displacement of the LWA to the upper part of the concrete specimen due to prolonged yield stress reduction. Given the p-value of the F statistic computed in the ANOVA, and given the significance level of 5%, the information brought by the explanatory variable (VTL) is significantly better than what a basic mean would bring. According to the Tukey's HSD test a 95 % level of confidence, the variable VTL should be classified in different groups or subsets: Group A for  $VTL \leq 10\text{s}$ ; Group B for  $10\text{s} < VTL \leq 20\text{s}$ ; Group C for  $20\text{s} < VTL \leq 40\text{s}$  and Group D for  $VTL > 40\text{s}$ .

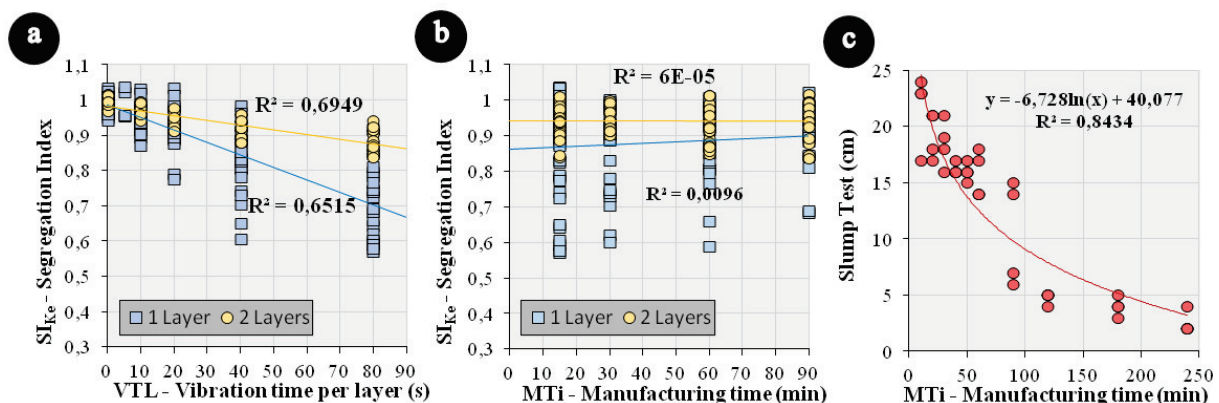


Figure 2: Scatter diagrams:  $SI_{Ke}$  vs VTL (a),  $SI_{Ke}$  vs MTi (b) and Slump Test vs MTi (c).

Focusing on the “manufacturing type” (MTy), the values presented important differences between the vibration in one or two layers. Fig. 2a shows that for the same vibration time per

layer, concretes vibrated in one layer presented more segregation. The same results are visible comparing Fig. 3a (1 layer) and Fig. 3b (2 layers), where the red areas indicate higher levels of segregation. As described by Ke [7], if  $SI_{Ke}=1$ , it can be considered that the sample shows perfect uniformity, and an index of less than 0.95 indicates a start of segregation. Manufacturing the samples in two layers resulted in more homogenized concretes and samples more resistant to the segregation phenomenon. The start of segregation for samples manufactured in one layer was observed in earlier periods than in samples manufactured in two layers. For those vibrated in one layer, the segregation starts between 10 and 20 seconds of total vibration (Fig 3a) and for those vibrated in two layers between 40 and 60 seconds of total vibration (Fig 3b). Given the p-value of the F statistic computed in the ANOVA, and given the significance level of 5%, the information brought by the explanatory variable (MTy) is significantly better than what a basic mean would bring. According to the Tukey's HSD test a 95 % level of confidence, the variable "manufacturing type" should be classified in two different groups: Group A for one layer and Group B for two layers.

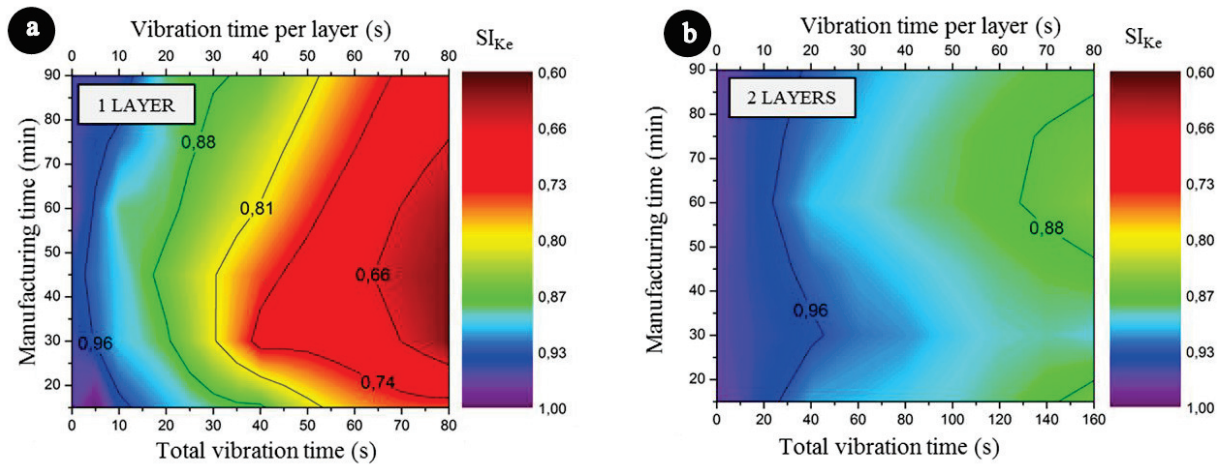


Figure 3: Behavior of the samples considering the variables evaluated in this study: manufacturing type (MTy), manufacturing time (MTi) and vibration time per layer (VTL).

However, the consistency of fresh concrete, directly related to the manufacturing time (Fig. 2c) does not present a clear correlation with  $SI_{Ke}$ , and the scatter diagrams of Fig 2b confirmed that there are no linear correlations between the variables MTi and  $SI_{Ke}$ . In this case, given the p-value of the F statistic computed in the ANOVA, and given the significance level of 5%, the information brought by the explanatory variable (MTi) is not significantly better than what a basic mean would bring. The fact that this variable does not bring significant information to the model may be interpreted in two different ways: either the variable does not contribute to the model, or some covariates that would help explaining the variability are missing and must be included in the study. According to the Tukey's HSD test a 95 % level of confidence, the variable "manufacturing time" should be classified in just one group of analysis.



#### 4. Conclusions

This study presents an experimental study on segregation in lightweight aggregate concretes (LWAC) considering different variables related to the manufacturing process of LWAC samples. From the results presented in this study the following conclusions are drawn:

- The statistical analysis revealed that the manufacturing type (vibration in one or two layers) and the vibration time per layer are parameters that affect the segregation of concrete. However, regarding consistency of fresh concrete and manufacturing time, for the concretes studied in this research the results of the statistical analysis do not allow an obvious conclusion.
- Concretes vibrated in two layers presented lower segregation than concretes vibrated in one layer, indicating the importance of this parameter during the manufacturing of lightweight aggregate concrete samples. Different sample sizes and different vibration frequencies should be analyzed for more accurate results on this behavior.

#### Acknowledgements

This research was funded by the University of Alicante (GRE13-03) and (VIGROB-256). The authors wish to express their gratitude to Phd program in Materials, Structures and Soil Engineering of the University of Alicante.

#### References

- [1] Cui HZ, Lo TY, Memon SA, Xing F, Shi X. Analytical model for compressive strength, elastic modulus and peak strain of structural lightweight aggregate concrete. *Constr Build Mater* 2012;36:1036–43. doi:10.1016/J.CONBUILDMAT.2012.06.034.
- [2] Navarrete I, Lopez M. Estimating the segregation of concrete based on mixture design and vibratory energy. *Constr Build Mater* 2016;122:384–90. doi:10.1016/j.conbuildmat.2016.06.066.
- [3] European Union – Brite EuRam III. EuroLightCon 1998, LWAC Material Properties - State of the Art. 1998.
- [4] Han J, Wang K, Wang X, Monteiro PJM. 2D image analysis method for evaluating coarse aggregate characteristic and distribution in concrete. *Constr Build Mater* 2016;127:30–42. doi:10.1016/j.conbuildmat.2016.09.120.
- [5] Ke Y, Ortola S, Beaucour A, Cabrillac R, Dumontet H. Influence of aggregates on mechanical behavior of lightweight aggregate concrete: experimental characterization and modeling. *First Euro-Mediterranean Adv. geomaterials Struct.*, Hammamet: 2006.
- [6] Barbosa FS, Beaucour AL, Farage MCR, Ortola S. Image processing applied to the analysis of segregation in lightweight aggregate concretes. *Constr Build Mater* 2011;25:3375–81. doi:10.1016/j.conbuildmat.2011.03.028.
- [7] Ke Y. Caractérisation du Comportement mécanique des bétons de granulats légers : expérience et modélisation. Université de Cergy-Pontoise, 2008.
- [8] Fernández-Fanjul A, Tenza-Abril AJ. Méthode FANJUL: Dosage pondéral des bétons légers et lourds. *Ann Du Bâtiment Des Trav Publics* 2012;5:32–50.
- [9] Fernández-Fanjul A, Tenza-Abril AJ, Baeza-Brotons F. A new methodology for determining particle density and absorption of lightweight, normal-weight and heavy weight aggregates in aqueous medium. *Constr Build Mater* 2017;146:630–43. doi:10.1016/j.conbuildmat.2017.04.052.

## **PARTICLE-MATRIX PROPORTIONING OF HIGH STRENGTH LIGHTWEIGHT AGGREGATE CONCRETE**

**Elisabeth Leite Skare** <sup>(1),(2),(3)</sup>, **Jelena Zivkovic** <sup>(1)</sup>, **Stefan Jacobsen** <sup>(1)</sup>, **Jan Arve Øverli** <sup>(1)</sup>

(1) Department of Structural Engineering, Norwegian University of Science and Technology (NTNU), NO-7491 Trondheim, Norway

(2) NorBetong AS (HeidelbergCementGroup), Heggstadmyra 6, NO-7080 Heimdal, Norway

(3) Department of Mechanical Engineering, Technical University of Denmark, 2800 Lyngby, Denmark

### **Abstract**

Production of lightweight aggregate concretes (LWAC) requires specific knowledge and processes in order to achieve good workability of paste and concrete. A particularly demanding case is high strength lightweight aggregate concrete, i.e. having 28-day characteristic compressive strength in the range 60-80 N/mm<sup>2</sup> with oven dry density equal or less than 2000 kg/m<sup>3</sup>. Coarse manufactured lightweight aggregates themselves often lack particles smaller than 2 mm, which together with open aggregate porosity causes a certain loss of workability during the first minutes after mixing. An efficient way of improving this is by particle-matrix proportioning. The desired concrete workability can be obtained by combining the filler modified paste with a suitable amount of coarse aggregate particles. In order to investigate this, several different LWAC mixes have been tested with the lightweight aggregate Stalite, an argillite slate from the US. We found that the particle-matrix proportioning approach can give desired workability of the LWAC mixes. This methodology is economical since no increase in cement and admixtures dosage is needed.

### **1. Introduction**

The material properties of lightweight aggregate concrete (LWAC) are mainly depending on the properties of the used lightweight aggregate (LWA). LWA has different water absorption properties, geometry, surface, shape, rigidity, porosity and density compared to normal density aggregate, which all together have impact on LWAC [1]. One of the main challenges in preparation of LWAC is to achieve good workability and stability of the mix. Two main

challenges encountered when making the LWAC are different density of the LWA and the paste that may cause LWA segregation by floating, and estimation of mix water absorption of LWA that can cause very unstable concrete and lack of control of effective mass ratio. Most of the lightweight aggregates are split to several fractions. Coarser fractions of the lightweight aggregates are often very precisely fractioned and do not contain fines. One more challenge is to provide good packing of aggregate and paste, which might be difficult when using just one specific fraction of prefabricated LWA. Porosity of the LWA is in the range from 2 till 30% of volume, which in a mix, if not presaturated, absorbs a large amount of mix water from the fresh paste [2,3]. The most demanding case is preparation of high strength lightweight aggregate concrete. In order to achieve desired strength of LWAC, larger sizes of LWA,  $\geq 8\text{mm}$ , are required, which often are in lack of particles smaller than 2 mm. Together with open porosity and high absorption, this causes a certain loss of workability during the first minutes after mixing. A previous investigation has found that when pre-wetted LWA is used, the workability is influenced little by the LWA type [5]. The aggregate used in this investigation was Stalite, fraction 1/2". The dry aggregate density is  $805\text{ kg/m}^3$  and the saturated surface dry density is  $833\text{ kg/m}^3$ . This paper investigates how the desired concrete workability can be obtained by combining lightweight coarse aggregate particles with a suitable amount of crushed fines, by using the method of particle-matrix proportioning. Several different mixes have been prepared where the amount of the fines were varied, and the workability has been measured according to the well-known slump procedure [4]. In addition, the total amount of water in the mixes have been controlled by measuring the moisture of the aggregate itself.

## 2. Methodology and results

The workability of the fresh concrete was measured, as well as visual inspection of the stability, in a series of LWAC mixes. The main idea when designing the LWAC mixes was using the particle-matrix proportioning method to obtain necessary workability (slump and stability against LWA floating) in high-strength LWAC mixes, by using a suitable paste. The 1/2 " fraction Stalite, an argillite slate-based LWA, was used in all the mixes, see sieve curves in Fig. 2. The experimental program was made up of four different batches of LWA. For determination of workability the slump test method was used [4], see Fig.1. The stability has been controlled by visual inspection.



Figure 1: Slump method

## 2.1 Grading

Structural-grade Stalite LWA is made from various raw materials, including suitable slates, fly ashes, or blast furnace slags. The Stalite used in this investigation is first mined from naturally deposits of argillite slate and later pyroprocessed in a rotary kiln process. After manufacturing the material is divided into proper sizes (3/4", 1/2" and 3/8" with respectively maximum aggregate sizes 18, 12.5 and 9.5 mm, and then their moisture contents is adjusted to a predetermined level. The fraction 1/2" is used in this investigation. Figure 2 shows particle size distributions from 4 different batches used in this study showing good agreement with each other, even though the batches were purchased and transported from different localizations and at different times. Fig 2 also shows that the Stalite has a low content of fines.

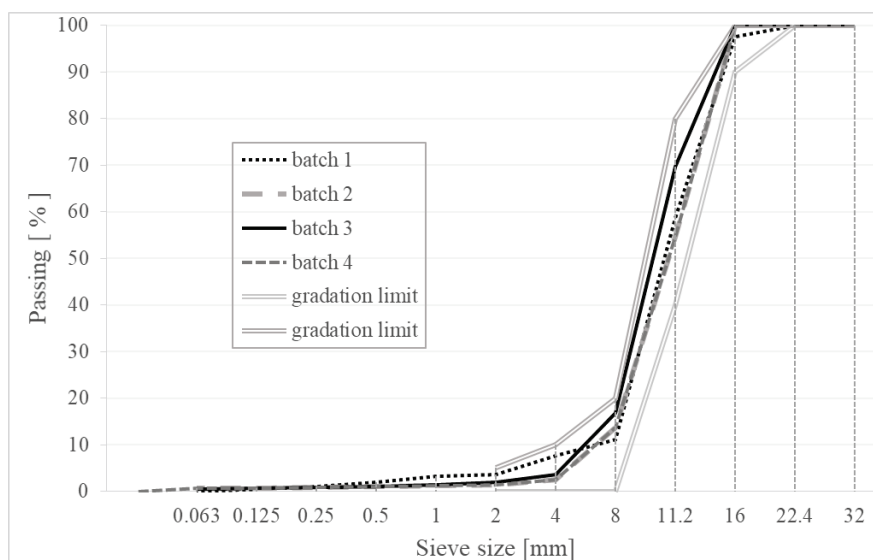


Figure 2: Sieve curves for aggregate Stalite fraction 1/2", batches 1-4,

## 2.2 Particle-matrix proportioning

Particle-matrix proportioning is a model that is dividing concrete into two phases: a matrix phase and a particle phase. The matrix phase consists of all solid particles less than 125 microns, as well as water and additives. The particle phase consists of all solid particles larger than 125 microns. In the particle-matrix model, the matrix phase fills all voids between the aggregate particles. Workability and consistency of the LWAC follow from the ratio between the phases [4]. This tool, particle-matrix proportioning, is making concrete production more sustainable and economical, optimizing concrete properties by controlling the composition of the particles and the matrix. By adjusting the amount and grading of the fines in the paste and varying volume fraction of the paste, the concrete workability can be controlled and improved substantially [6]. In addition, when using particle-matrix proportioning the stability of LWAC mixes can be improved. When increasing the amount of fines, the internal cohesion increases and that prevents bleeding, paste separation and segregation of LWAC [4]. In this investigation, LWA Stalite is used in all the mixes. Due to the splitting process, the Stalite is in lack of fine particles. A 0-2 mm sand was added to some of the mixes, in order to avoiding gap-graded aggregate and hence reduce the volume fraction of paste needed to obtain workable concrete.

Table 1: Proportioned concrete mix compositions (kg/m<sup>3</sup>)

Mix No.	Cement Norcem Anlegg FA [kg]	Microsilica Elkem [kg]	Free Water [kg]	Batch No.	Aggregate Stalite 1/2" [kg]	Sand Årdal 0-8 mm [kg]	Sand Ramlo 0-2 mm [kg]	Absor bed water Stalite +sand	Superplas. Mapei Dyn. SR-N [m.% of cem.]
M1	399.5	19.8	167.7	1	571.9	720.3		40.1	0.64
M2	420.7	21.9	193.5	2	537.1	543.0	232.4	49.2	1.23
M3	420.8	22.2	195.7	2	521.8	543.6	232.9	48.0	1.21
M4	431.8	20.4	176.4	2	566.9	730.1		51.0	1.33
M5	424.4	22.3	174.2	2	575.6	507.6	190.4	41.3	1.06
M6	423.8	22.3	174.0	2	585.1	516.0	193.5	52.5	1.19
M7	427.7	22.5	200.4	2	564.6	560.1	124.5	50.6	1.13
M8	431.8	20.3	176.5	2	581.4	705.0		52.1	1.25
M9	427.5	22.5	203.7	4	514.0	535.5	229.4	47.2	0.73
M10	442.2	23.3	146.0	4	515.4	536.8	230.0	6.1	0.75
M11	440.3	23.2	180.8	3	517.5	539.0	231.0	38.8	0.89

Table 2: Fresh concrete mix parameters

Mix No.	Matrix volume [l/m <sup>3</sup> ]	w/b	w/p	$\rho_{\text{theoretical}}/\rho_{\text{measured}}$	Slump test [mm]	Stalite Moisture [% of dry aggregate]	Stability: Floating of LWA*	Stability: Bleeding/Halo*
M1	350	0.40	0.33	1920 / 1993	140	8.2	Yes	Yes
M2	375	0.44	0.39	1967 / 2013	230	11.43	No	No
M3	375	0.44	0.39	1967 / -	240	11.43	No	No
M4	365	0.39	0.33	1968 / -	210	8.5	Yes	Yes
M5	360	0.39	0.33	1943 / -	200	6.2	No	Yes
M6	360	0.39	0.33	1921 / -	250	8.5	No	Yes
M7	376	0.44	0.40	1930 / -	230	11.43	No	No
M8	365	0.39	0.33	1922 / -	210	8.5	Yes	Yes
M9	378	0.45	0.41	1967 / 1927	250	12.5	No	No
M10	326	0.31	0.28	1929 / 1989	170	0.1	Yes	No
M11	360	0.39	0.35	1967 / 2015	190	6.3	No	No

\* Visual qualitative assessment

### 2.3 Experimental program and results

The experimental program consists of eleven different LWAC mixes, see Tab. 1 and Tab. 2. Tab. 1 shows nominal, uncorrected proportions. In Tab. 2 are given properties of fresh concrete.

The main parameters varied in the mixes were the amount of fines, incorporated in the sand Ramlo 0-2mm, SP-dosage, as well as the moisture content of the LWA Stalite. Pre-wetted LWA Stalite was used in all the mixes, except in mix M10, where Stalite was very dry with a moisture content of 0.1%, see Tab. 2. Aggregate absorbed water was not considered as free water. Measured workability was in the range from 140 mm to 250 mm. This workability experiment has been done in combination with a casting experiment, and mixers with different capacities have been used, depending on the necessary concrete amount. Mix M1 has been mixed in an 800 litres capacity mixer, while mixes M9-M11 has been produced in a 250 litres capacity mixer, both with vertical pedals. The mortar in mix M3 has been produced at a concrete plant, and mixed together with the Stalite in the concrete truck mixer. The remaining mixes are trial mixes, performed in a mixer with a capacity of 10 litres with vertical pedals.

In addition, stability of LWAC was controlled, by visual qualitative assessment. In the mixes M1, M4, M8 and M10 it was noted coarse aggregate separation, when LWA particles float on the paste [4]. In the mixes M1, M4, M5, M6 and M8 it was observed slight bleeding as a sheen on the concrete mass and presence of the Mortar Halo [7], see Tab. 2.

### 3. Discussion

The particle-matrix proportioning method resulted in good workability in terms of stability and slump of the LWACs, by increased matrix volume and content of fines. From Tab.1 and Tab. 2 we see that matrix volumes and admixture dosages seem to explain the observed slump values, since the proportioned w/b- and w/p- ratios not are varying to a large extent among the mixes, as respectively from 0.31-0.45 and 0.28-0.41. The low slump of M1 relates to its low matrix volume and SP dosage. The higher slump of M4 and M8 correspond to high matrix volume and SP dosages. Finally, for M2, M3, M7 and M9 a higher slump is measured due to higher matrix volumes. For M5, M6 and M11 the matrix volumes are all the same but for the mix with lower slump, M11, the SP dosage were lower than for M5 and M6. Mix M10 has the lowest matrix volume due to lower water content in the LWA, i.e absorption of mix water.

For the mixes without fine sand from 0-2 mm, mixes M1, M4 and M8 floating of the LWA and slight bleeding as a water sheen at the edges of the concrete mass and poor paste viscosity were observed. Floating of the LWA was also observed for mix M10 where the Stalite was dry. Floating of the LWA on the paste might be caused by the density differences between the paste and the aggregate. From tab. 2 it is obvious the difference between the theoretical and measured density and they are often offset by 40-50 kg/m<sup>3</sup>. This huge difference is due to the releasing of water from aggregate during the drying process.

From all mentioned above it is obvious that by using the particle-matrix method, workability and stability may be improved significantly. When controlling the amount of fine sand in the mix it is possible to achieve desired workability, without increasing amount of cement and silica, and particle-matrix proportioning is hence more economical and practice.

#### 4. Conclusions

Desired workability and stability was achieved in almost all LWAC mixes, except for the mixes without any fine sand. The mix with the dry aggregate obtained desired workability as a result of additional fines. By adding fines, it is possible to reduce the amount of water in the mix significantly, and still maintain good workability. Mixes without fine sand from 0-2 mm did not achieve enough stability, it is observed floating of the LWA and slight bleeding as a water sheen at the edges of the concrete mass. In general, particle-matrix proportioning by increasing the matrix volume by addition of sand is an economical and practical method, since sand is a more widespread and cheaper ingredient than cement and silica. In addition, methodology is not fully developed and future research have to be carried out.

#### Acknowledgements

The work presented in this paper is part of an ongoing PhD studies in the DACS project (Durable Advanced Concrete Solutions) and in the MiKS project (Microproportioning with Crushed Sand). The DACS partners are Kværner AS (project owner), Norwegian Research Council, Axion AS (Stalite), AF Gruppen Norge AS, Concrete Structures AS, Mapei AS, Multiconsult AS, NorBetong AS, Norcem AS, NPRA (Statens Vegvesen), Norwegian University of Science and Technology (NTNU), SINTEF Byggforsk, Skanska Norge AS, Unicon AS and Veidekke Entreprenør AS. The MiKS partners are Norcem AS, Norstone AS, Norbetong AS, Feiring Bruk AS, Skanska, SINTEF, National Institute of Standards and Technology (NIST), Norwegian University of Science and Technology (NTNU) and Technical University of Denmark (DTU).

#### References

- [1] ACI Committee 213, 2003, "Guide for Structural Lightweight-Aggregate Concrete (ACI 213R-03)", American Concrete Institute, Farmington Hills, MI, United States.
- [2] Punkki J. and Gjørsv O.E., Effect of water absorption by aggregate on properties of high-strength lightweight concrete, Proceedings from the International Symposium on Structural Lightweight Aggregate Concrete, Sandefjord, Norway (1995), 604-616.
- [3] ACI 211.2-98, 1998, (Reapproved 2004) "Standard Practice for Selecting Proportions for Structural Lightweight", ACI Manual of concrete practice, Part1, PP. 211.2-1-17.
- [4] S. Jacobsen et al, Concrete Technology 1. TKT 4215. Kompendium. Norwegian University of Science and Technology (2016), Chap. 3, 3-6 and 13-14; and Chap. 4, 12-22.
- [5] Hammer T.A. and Smeplass S., The influence of the lightweight aggregate properties on material properties of the concrete, Proceedings from the International Symposium on Structural Lightweight Aggregate Concrete, Sandefjord, Norway (1995), 517-532.
- [6] R.Cepuritis, Development of crushed sand for concrete production with microproportioning, PhD thesis, Norwegian University of Science and Technology (2016)
- [7] A. El hassan et al, The Impacts of Visual Stability Index on Flowability and Segregation 1 Properties of Self – Consolidating Concrete, Proceedings from the Transportation Research Board 94th Annual Meeting , Washington DC, United States (2015).

## **PHOTOCATALYTIC NOVEL CONCRETE MATERIAL APPLICATION AND ITS LIFE TIME STANDARD TESTING**

**František Peterka** <sup>(1)</sup>

(1) Nanotec System, Praha, Institute of Nanomaterials of TUL, Liberec, Czech Republic

### **Abstract**

Photocatalytic cementitious building materials, mainly with incorporation of  $\text{TiO}_2$  are being advertised as the promising technique to keep surface clean just thanks to illumination by light. This light-induced phenomenon can be applied for self-cleaning and disinfecting surfaces as building façades, decorative mortars, culture monuments etc. In addition, concentration of air pollutants such as  $\text{NO}_x$  and VOC's, frequently encountered in trafficked areas and the urban environment can also be reduced. However, there are still doubts and questions about the durability of the photocatalytic activities. To answer the logic question about the photocatalytic products service life, standardized testing methods have to be set up to give more reliable answers to the potential end users. First attempts have been made by Czech Republic and Belgian research groups within the European normalization efforts of CEN/TC386 "Photocatalysis". The testing method based on several years' studies incl. photocatalytic concrete manufactures was proposed for vertical as well as horizontal surfaces.

This presentation presents examples of results of these investigations as the first step towards the evaluation of the life time of these photo-active air purifying products.

### **1. Photoactive coating systems for environmental cleaning - new solutions**

Photocatalytic technologies offer new ecological technical solutions. The so-called solar self-cleaning allows the destruction of microorganisms on the façades of houses and the surfaces of other objects, including historical monuments. In the Czech Republic there are tens of thousands of insulated panel houses affected by the growth of algae and mold.





Figure 1: Light cleaning effect of BALCLEAN after 1 year of application on different cement containing surfaces.

Historical buildings are subjected to destruction in the polluted environment of large cities. The newly developed transparent nanocomposite system BALCLEAN with solar photocatalytic self-cleaning and disinfecting function is used to prevent the growth of algae on insulated objects and historical buildings.

The origin of the BALCLEAN coating system and its introduction to the market preceded many years of development and testing of photocatalytic applications, with several research teams from the Institutes of the Academy of Sciences of the Czech Republic and the Technical University of Liberec. NANOTEC SYSTEM was founded for the rapid application of photoactive nanomaterials, with the participation of leading Czech scientists in the field. At present, this company has the know-how for the following applications:

- Prevention of growth of microorganisms on façades of apartment buildings
- Protection of concrete constructions and structures
- Protection of historical objects

The BALCLEAN painting system is produced by the leading Czech manufacturer of coatings Barvy a Laký Teluria a.s., which concluded an exclusive agreement for its application to apartment buildings with the Pragothem servis fasád, s.r.o..

## **2. Application the BALCLEAN on shaded houses - Pragothem servis fasád, s.r.o.**

Pragothem servis fasád, s.r.o. focuses on the treatment of insulated buildings, including façades affected by algal and mold growth. The traditional use of long-term inefficient biocidal chemicals is replaced by a new photocatalytic technology that demonstrated beneficial effects on the environment (removing harmful micro-organisms and removing gaseous pollutants). New ecological technology has a long-term activity against the growth of all microorganisms on façades. Pragothem servis fasád, s.r.o. performs a two-year nationwide monitoring of algae-covered objects in all towns and municipalities in the Czech Republic. In the 23 000 apartment buildings, the algae and mold will be removed during the next two to three years, and then a protective photocatalytic coating will be applied to the refurbished façades. In 2017, 40,000 square meters were treated, in 2018 expected to grow to 100,000 square meters.

## **3. Understanding the type of biological pollution to assess the limits of photocatalysis**

Pragothem servis fasád, s.r.o. in cooperation with the Technical University of Liberec is doing microbiological sampling on façades covered with algae. In addition to the results of

microbiological analyzes, it collects other relevant data on the state of the insulated façades. Home owners get information about the types of micro-organisms growing on façades, what causes their growth, how the algae and molds affect the insulation system, and also the possible health risks for the residents of the house. Protocols also include a proposal for a technical solution, including recommendations for gardening of surrounding bio zone. For the period 2016 to 2017, Pragotherm sevis fasád, s.r.o. processed a total of 267 microbiological protocols of residential houses affected by algae. We expect that by the end of 2019, a total of 2,000 objects will be monitored and processed.. This project is unique in its scope and focus in Europe. The aim of this research is to find out the causes and consequences of the massive presence of microorganisms in most of the insulated objects in Central Europe.

#### **4. Application to Sights - Gallery of the Capital City of Prague**

The Gallery of the City of Prague has a number of monuments under management, which need to be quickly repaired and then protected. Deteriorating the environment has prompted the need to develop new technologies for their protection, and photoactive paint systems appear to be very promising.

Czech experts on the application of modern technologies to monuments developed the MONDIS (Monument Damage Information System), designed to preserve and transfer knowledge about the state, the causes of damage, and the course and results of repairs of immovable monuments. The MONDIS system provides a basis for mapping and cataloging historical objects suitable for treatment with a photoactive nanocomposite system. In cooperation with the Prague City Gallery, a test room of the first 10 plasters suitable for new technology treatment was selected, starting in the spring of 2018. This pilot experiment was preceded by a number of laboratory tests and applications on identical materials used in listed buildings. As well as fulfilling the necessary legislation was the rule. That is why it can be assumed that the evaluation of the results of this pilot experiment with the new technology will be successful and will be followed by applications to hundreds of other monumental objects that need to be repaired and protected in the capital city of Prague and worldwide.

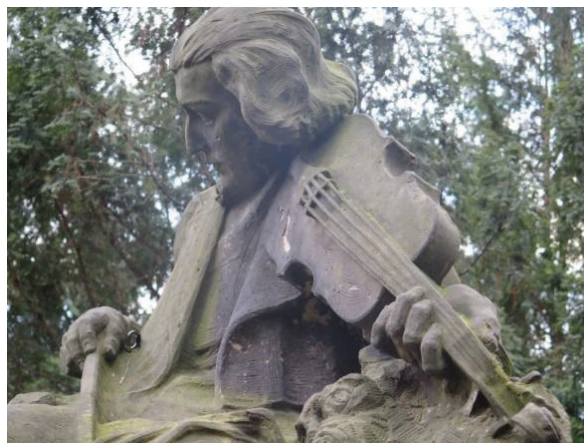


Figure 1: Example of a statute suitable for protection using modified BALCLEAN system

## 5. Photocatalytic products service life time

Standardized method to evaluate material ageing giving answer to photocatalytic surface life time is still missing. Czech Republic already proposed the photocatalytic life time evaluation as the possible new CEN standard within CEN/TC 386. The basic idea is to specify the accelerated aging conditions for a variety of photocatalytic materials like cement-based materials, paints, thin films, etc. for different applications (e.g. horizontally on a road surface or vertically on a building façade), based on already existing durability tests in the field of application and with a possibility to define different photocatalytic durability classes.

Research teams at the Institute for Nanomaterials, Advanced Technologies and Innovations of Technical University Liberec (TUL) together with Italcementi co. as well as from the Belgian Road Research Centre prepared the concept of the evaluation of the reduction in photocatalytic performance caused by different degradation processes encountered in practice such as abrasion or weathering of the photocatalytic surface (Figure 2).

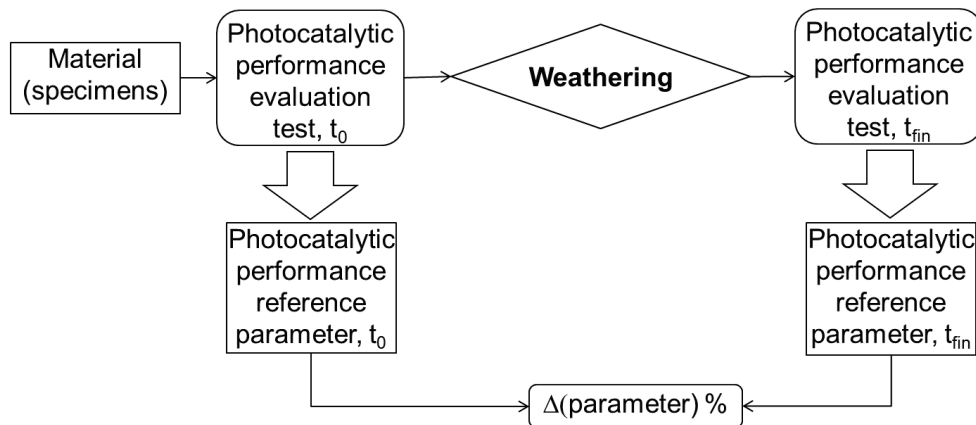


Figure 2: Concept of evaluation of photocatalytic performance reduction due to weathering.

Weathering for instance, is the adverse response of a material or product to the environmental conditions it is exposed to, often causing unwanted and premature product failures, where the main contributing factors are sunlight, temperature, moisture, and possible contamination by intermediate products formed during the photocatalytic process. In the case of photocatalytic materials, sunlight is needed to initiate the degradation process and drives it forward, but also leads to transformation of reaction products that can poison the  $\text{TiO}_2$  catalyst embedded in the building material. In addition, temperature and humidity (RH) together with UV ageing can also change the catalyst texture and/or the matrix material, and cause adverse effects as well [1, 2].

The objective of artificial weathering or the ageing test in general, is thus to reproduce the degradation processes and resulting damage that occurs naturally, in a laboratory under accelerated and reproducible conditions. Furthermore, the photocatalytic performance should be evaluated according to standard methods already accepted or to draft methods which are under development on international (ISO) and/or European (CEN) level, see e.g. [3].

The Institute of Nanomaterials at TUL and researchers from Czech academic Institutes were involved in development of novel nano composite photoactive coatings to be applied for self-

cleaning activity of building façades or industrial cementitious materials commercially named BALCLEAN and recently being also working on photocatalytic materials applied in the bulk or at the surface where abrasion might also play a significant role.

## 6. Photoactive materials and testing methods

NANOTEC SYSTEM with research teams from TUL, Czech Academy of Sciences and closely collaborating with industrial partners on the application of BALCLEAN are testing service life based on the standard tests for self-cleaning, antimicrobial properties and air purification effect. The air purification effect of the coated surface area is in this case considered to be a beneficial side effect.

### Photocatalytic activity testing

First of all, the photocatalytic self-cleaning activity of the coatings was determined on the one hand according to the ISO 10678:2010 standard method based on methylene blue decomposition [4]. Methylene blue (MB) is degraded upon contact with the photoactive surface under UV illumination. An aqueous solution of MB is used for these tests.

On the other hand, BALCLEAN was also applied on the outer concrete facade of a building (Fig. 3). The effect of the photocatalytic coating on the wall was followed by visual change surface analysis. For the analysis the Flip-Pal plus mobile scanner and the DoSa software application were used to describe the colour intensity changes of the surface. This analysis was performed more than one year after the coating application.

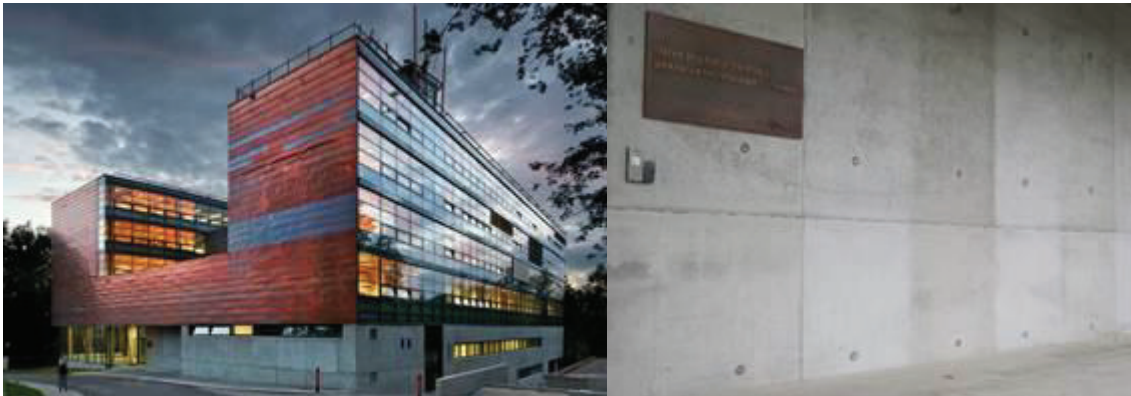


Figure 3: Photos of the entrance of Institute for Nanomaterials at TUL consisting of concrete panels which were protected by the BALCLEAN coating. To observe the self-cleaning function, only each second stream was coated, as illustrated in the picture on the right.

### Weathering test applied to coated cementitious samples

As an example, a combined weathering cycle used for testing of coating systems for exterior use according to the standard method CSN – EN 927-6 was applied:

- 24 h condensation of water at  $T = 45^{\circ}\text{C}$
- 2,5 h UV-A irradiation at  $1 \text{ W/m}^2$  and  $T = 60^{\circ}\text{C}$ , followed by 0.5 h water spraying at 6-7 l/min.

The BALCLEAN coating was applied on mortar samples of 5x5 cm with an upper layer of acrylate, silicate or silicone paint. In addition, the BALCLEAN coating was prepared with different amounts of photoactive nanomaterial (3% and 5%). Measurements of the photocatalytic activity were made on these samples before and after applying the artificial weathering test described above by all available ISO and CEN standard methods. The corresponding changes in photocatalytic material performance were evaluated.

## 7. Discussion and conclusion

The reduction in photocatalytic air purifying activity of coated and painted cement based materials is significant, but regarding self-cleaning performance the material can still keep its expected function after more than one year of outdoor exposure. However to approve the final version of CEN standard proposal for durability, accelerated weathering must be modified accordingly. In addition, the correlation between the conditions of the artificial weathering test and the expected life time (5, 10 years or even less) of the photocatalytic activity needs to be further investigated.

To guarantee the life time of advertised photocatalytic function to potential investors is important. To design broadly accepted CEN standard concerning accelerated ageing of photocatalytic cement based building materials the expertise of more experts from different fields is needed.

## Acknowledgements

These topical activities of the Institute for Nanomaterials of Technical University Liberec (TUL) were supported by the Czech Ministry of Education, Youth and Sports in the framework of COST program and by Technological Agency

## References

- [1] Fujishima, A., Zhang, X. & Tryk, D.A., TiO<sub>2</sub> photocatalysis and related surface phenomena, *Surf Sci Rep* 63 (2008), 515–582.
- [2] Peterka, F, Cleaning by photoactive nanosurfaces. *Public Service Review: European Science & Technology*, Issue 11, pp. 68-69 (2011)
- [3] CEN Technical Committee 386 “Photocatalysis” Business Plan—(internet) Draft BUSINESS PLAN CEN/TC386 PHOTOCATALYSIS. Available online: <https://standards.cen.eu/BP/653744.pdf> (accessed on 16th of June 2016).
- [4] ISO 10678:2010, Fine ceramics (advanced ceramics, advanced technical ceramics) - Determination of photocatalytic activity of surfaces in an aqueous medium by degradation of methylene blue, International Standards Organization, (2010).

## PHYSICAL EVOLUTION OF THE INTERFACE OF FRESH CONCRETE/FORMWORK FROM PLACEMENT TO SETTING TIME

Typhanie Craipeau <sup>(1)(2)</sup>, Arnaud Perrot <sup>(1)</sup>, Fabrice Toussaint <sup>(2)</sup>, Thibaut Lecompte <sup>(1)</sup>

(1) Institut de Recherche Dupuy De Lôme, Centre de recherche Christian Huygens, Lorient, France

(2) LafargeHolcim Research Center, Lyon, France

### Abstract

Cement hydration induces water consumption which induces a reduction of the capillary pressure in the concrete. The equilibrium of pressure implies an increase of the granular stress which is able to transmit shear stress to any support. Slipforming process is characterized by a continuous moving of the formwork, which creates adhesion phenomena and potential damages which have to be assessed and ideally reduced.

Experimental devices have been designed in order to evaluate the friction at this interface during the first hydration period. The role of pore water pressure is investigated and controlled in order to separate the influence of pore water pressure and hydrates formation.

### 1. Introduction

Concrete is a very versatile material whose rheological properties have to be adjusted, depending on the application and the process. The interface between the concrete and its support may also be critical at different states of its maturity.

The present study aims to characterize the evolution of the concrete interface with a support as a function of its level of hydration at very early age.

For example, in a slipforming process, concrete is continuously poured and the formwork is very frequently raised in order for the concrete to stand by itself at the bottom, after a few hours of hydration. This technique [1], see **Figure 1**, is a widely used construction methodology for high rise structures such as skyscrapers, pylons, silos or marine foundations that benefits from its high construction speed and the absence of cold joint that may affect the durability of the structure. The concrete is directly in contact with the formwork from its fresh

state to a set state without any demolding agent. During sliding, possible micro-cracking/lump formation can happen on the wall surface. These defects are most probably related with the concrete adhesion on the formwork. These issues should be solved and prevented to avoid a reduction of the durability of the structures that could turn into strong damages if not properly treated.

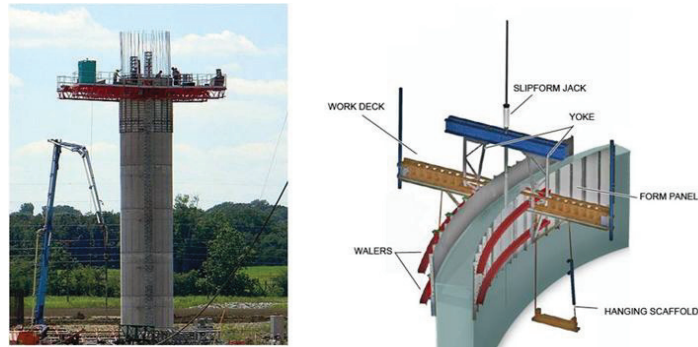


Figure 1. Slipforming illustration.

Usually, the industrial formworks are about 1.2 meters height and the average lifting speed is around 15 - 25 centimeters per hour.

The aim of the study is to determine the physical phenomena which govern friction and adhesion of concrete to the metallic surface. It has been shown that friction between the concrete and the formwork is mainly influenced by pore water pressure: water consumption caused by cement hydration will induce capillary suction which is assumed to play a major role on the interface [2]. Pore water depression can increase granular stresses acting on the particles assembly as described by Terzaghi equation [3].

This study aims to design tools studying the influence of pore water pressure on the shear stress of cement based materials/formwork interface.

## 2. Pore water pressure and granular stress (Terzaghi equation)

Thanks to Terzaghi equation, suction can be related to the normal force in case of saturated conditions. Terzaghi [1] describes that the total stress,  $\sigma$  (kPa) is equal to the sum of the effective stress  $\sigma'$  (granular stress, kPa) and the pore water pressure,  $u_w$  (kPa):

$$\sigma = \sigma' + u_w \quad (1)$$

The total stress of the concrete is considered in this study as almost constant. Therefore, the effective stress of the concrete only varies with concrete pore water pressure [4]. Terzaghi equation is illustrated in **Figure 2**. At constant total stress, negative pore water pressure increases the stress  $\sigma'$  acting on the granular skeleton (which is the case in the early stage of hydration). Unlike water pressure, the granular effective stress is able to transmit shear stress to the concrete itself, or to any support, depending on the friction level.

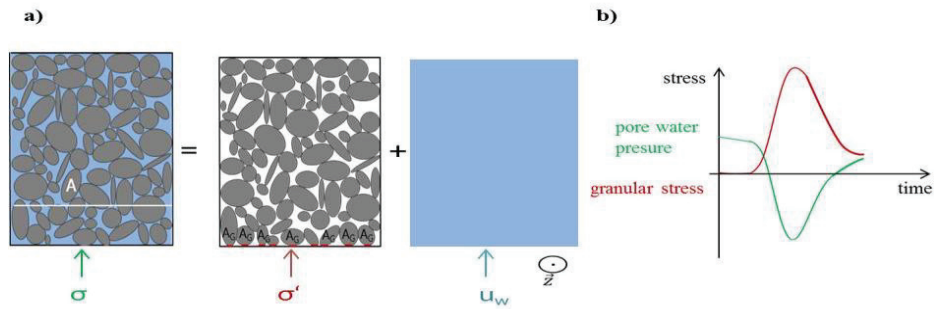


Figure 2. Terzaghi equation illustration.

### 3. Experimental procedures

#### 3.1 Materials and mixing procedure

The aim of the study is to understand the physical phenomena involved in the lifting resistance exerted by the concrete during the slipforming; therefore we chose usual materials: a Portland cement (CEM I 52.5N PM-ES CP2 NF), with 37v% of a fine sand (PE2LS 0/0.315 $\mu$ m) to help the mixing (also to reduce heating during mixing). A low Water/Cement ratio (W/C=0.3) is used to reduce strongly the pore water pressure. In order to obtain a low W/C ratio and a good rheology, a common polycarboxylate plasticiser admixture was used: Glenium 27 from BASF (0.063wt%/cement).

In the fresh state, the mortar is fluid (slump ASTM is 260 mm), and its air volume fraction is 2.7%.

The designed mortar was prepared with a Perrier mixer with the same mixing protocol in order to ensure tests reproducibility. The sand was first mixed with part of the water at low speed (140 rpm) during 1 minute. Then, after a waiting period of 4 minutes, cement is introduced and mixed at low speed during 1 minute. The rest of water is introduced during 30 seconds at low speed. Finally, the material is mixed at high speed (180 rpm) during 2 minutes.

#### 3.2 Devices and procedures

Two devices are used for the experiments. The first one gathers multiple physical phenomena as it is more representative of the real process. The second one aims at piloting and observing specific phenomena in order to isolate physical phenomena and understand the origin of the friction.

The first device consists of a parallelepiped box, filled with mortar. One face of the box, attached on a traction machine, can be moved and is made of the material that represents the formwork interface. A load cell permits to measure the global interfacial shear load (Figure 3). It is also fitted with pore pressure sensors [5] and force transducers to estimate those critical physical parameters. It allows to improve the understanding of the impact of suction on granular/interfacial friction and to assess its relative influence on the total stress. The advantage of this apparatus is to benefit from a total lifting run of 380 mm. For each lifting step, the lifting speed is 1 mm.s<sup>-1</sup> for a move of 5 mm. The time at rest is 565 seconds between each step. The average lifting speed is then 0.5mm.min<sup>-1</sup>. The total test lasts around 12 hours.



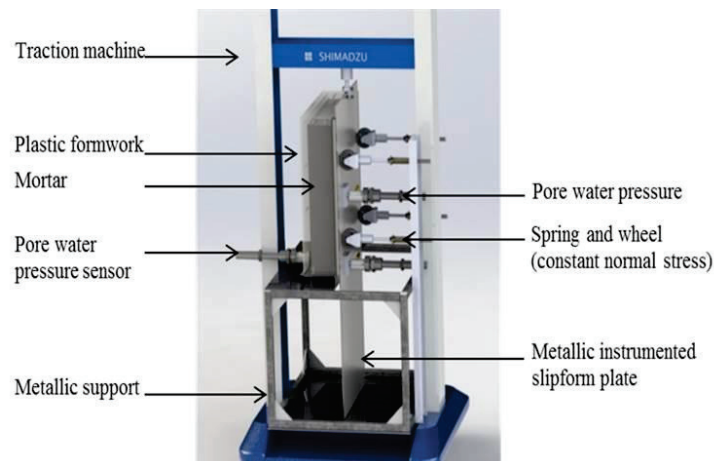


Figure 3. Vertical shear stress device developed to study slipforming operations.

The second device is composed of a small cylindrical box where the material is under controlled depressure. The objective is to measure shear stress evolution of the material under pore water depressure. The measuring cell is placed on a rheometer with a vane tool to observe rheological evolution (essentially yield stress) and a cylindrical tool to characterize tribology properties. The system is equipped with pore water pressure sensor and a system creating a depressure by removing water inside the material. The measuring cell is 50 mm high and 50 mm diameter to ensure the homogeneity of the material. This device is complementary to the vertical shear stress device because it will permit to separate the adhesion phenomena created by pore water pressure and the hydrates physical bonds to the metallic surface [6]. It will also allow comparing the material cohesion (yield stress) with its adhesion to a given support. We are not presenting results with this device in this paper.

## 4. Experimental results and discussions

### 4.1 Degree of hydration

Hydration degree over time was determined using calorimetry measurements: it is defined as the ratio between the cumulated heat flow (which is the surfaces under the curve of the evolution of the heat flow per gram of cement over time) and the total theoretical enthalpy of the hydrates ( $\Delta rH=353$  J/g for  $C_3S$  hydration which is the major hydrate); see **Figure 4**.

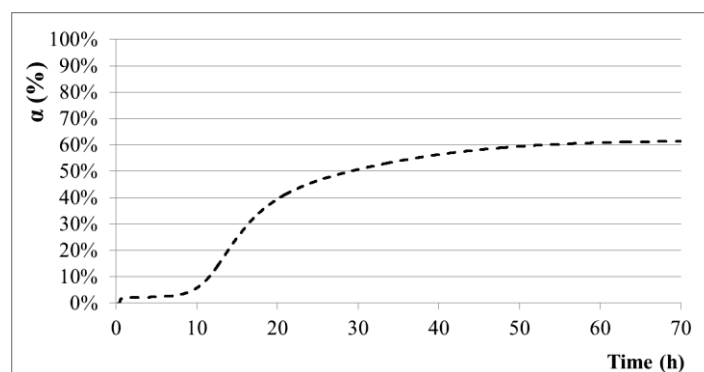


Figure 4. Degree of hydration in function of time (after cement/water contact).

Cement kinetic hydration is slow until 10 hours, then it is really fast until 20 hours, reaching 40 % of the state of hydration. After this transition period, the hydration is slower and reaches 60 % at 70 hours.

The degree of hydration is essential for the study because it shows where the maximum of water consumption is. It shows that only little water consumption, thus few hydrates created, induces suction.

In addition to hydration degree measurements, it should be noticed that it is *isothermal* calorimetry, this means that if temperature is not control in other experiment for example, the hydration development will be different.

#### 4.2 Friction evolution

The time evolution of the effective stress and tangential shear stress are plotted in Figure 5. (obtained with the vertical shear stress device presented above in Figure 3). We observe that the order of magnitude of the effective stress (dotted line) is really higher than the tangential shear stress (continuous line).

It seems that there is proportionality between tangential shear stress and the pore water pressure until 7 hours of hydration. Considering a constant total shear stress, as proposed by Terzaghi theory (saturated conditions), the granular stress should fluctuate with the opposite of the pore water pressure. This is in agreement with our measurements until 7 hours when the water network becomes discontinuous (thus Terzaghi equation cannot be applied because we are not in saturated condition). Thus, comparing the two different y-scales of Figure 5, a friction coefficient of about 0.4 can be determined. After the simultaneous evolution there is a separation, this occurs when the water network is not continuous anymore and the air network is linked, this is called air entry value [7]. Those first results have to be confirmed.

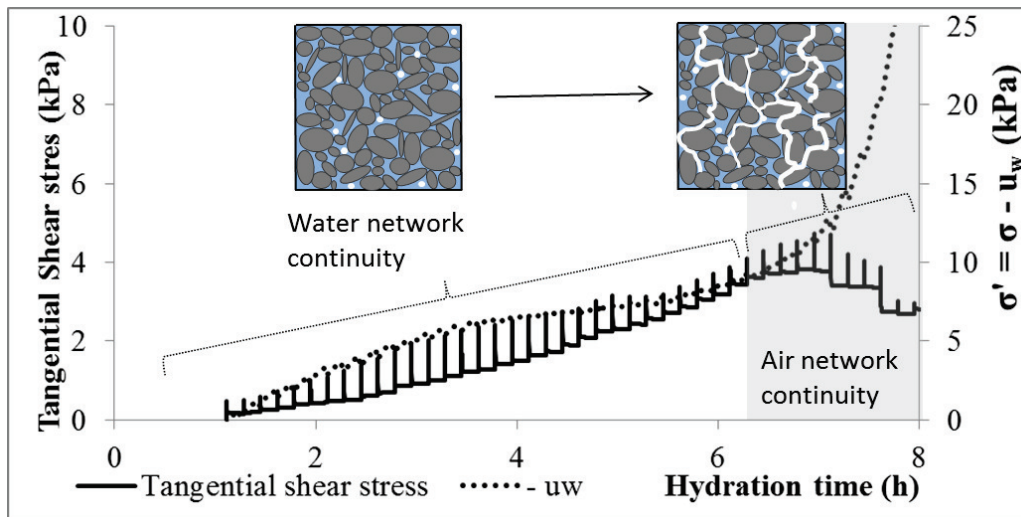


Figure 5. Calibrated pore water pressure and shear stress evolution measured with the experimental device.

This increase of the interfacial stress can be due to mortar stiffening. The granular stress increases due to water suction and hydrates formation at the interface.

Results on the second device are expected to demonstrate the influence of pore water pressure on the shear stress properties of the material using rheology and tribology data. The small device presents the advantages to control the influences of physical phenomena.

## 5. Conclusion and perspectives

A first estimation of the frictional coefficient between concrete and a metallic formwork has been evaluated thanks to a design device. Terzaghi equation was used under saturated condition. Nonetheless, pore water pressure was measured inside the material and the future objective is to measure it at the interface.

A new device has been described in order to appreciate the shear stress evolution properties under controlled pore water pressure which seems to be mainly at the origin of friction on concrete/formwork interface.

## Acknowledgements

The authors also wish to thank Alexandre Menguy who made the drawings of the experimental device.

## References

- [1] Fossa, K. T. Slipforming of Vertical Concrete Structures. Friction between Concrete and Slipform Panel. (Fakultet for ingeniørvitenskap og teknologi, 2001).
- [2] Hammer, T. A., «The use of pore water pressure to follow the evolution from fresh to hardened concrete », 2006 (e-ISBN: 2351580028) RILEM Publications SARL.
- [3] L. K. Mettler, F. K. Wittel, R. J. Flatt, et H. J. Herrmann, « Evolution of strength and failure of SCC during early hydration », *Cem. Concr. Res.*, vol. 89, p. 288-296, nov. 2016.
- [4] S. Ghourchian, M. Wyrzykowski, et P. Lura, « A poromechanics model for plastic shrinkage of fresh cementitious materials », *Cem. Concr. Res.*, vol. 109, p. 120-132, juill. 2018.
- [5] T. Lecompte, A. Perrot, V. Picandet, H. Bellegou, et S. Amziane, « Cement-based mixes: Shearing properties and pore pressure », *Cem. Concr. Res.*, vol. 42, no 1, p. 139-147, janv. 2012.
- [6] N. Roussel, G. Ovarlez, S. Garrault, et C. Brumaud, « The origins of thixotropy of fresh cement pastes », *Cem. Concr. Res.*, vol. 42, n° 1, p. 148-157, janv. 2012.
- [7] V. Slowik, M. Schmidt, et R. Fritsch, « Capillary pressure in fresh cement-based materials and identification of the air entry value », *Cem. Concr. Compos.*, vol. 30, n° 7, p. 557-565, août 2008

## PROPERTIES OF CEMENT WITH INCREASED LITHIUM CONTENT

Theodor Staněk <sup>(1)</sup>, Alexandra Rybová <sup>(1)</sup>, Anežka Zezulová <sup>(1)</sup>, Martin Boháč <sup>(1)</sup>

(1) Research Institute for Building Materials, Brno, Czech Republic

### Abstract

Lithium consumption in the production of batteries and accumulators for energy storage is increasing. It can be foreseen that the amount of waste with higher content of this metal will grow. Cement industry is one of the major consumers of several types of waste and secondary raw materials, therefore it is desirable to study the impact of lithium on the properties of clinker and cement. Under laboratory conditions, it has been found that lithium has a significant impact on clinker melt formation and on formation of main clinker phases. Moreover, cements with sufficient technological parameters were prepared from clinkers burned at 1350 °C with Li<sub>2</sub>O up to 1 wt.%. The research was conducted by means of XRD, DTA, optical and electron microscopy.

### 1. Introduction

The influence of LiO<sub>2</sub> on the properties of Portland clinker and cement has not been properly studied yet. It is desirable to look at this issue deeper due to the possibility of use of lithium-containing raw materials in cement production.

Lithium behaves differently from sodium and potassium. It forms non-volatile Li<sub>2</sub>O at higher temperatures and mainly it decreases the temperature of melt formation. The presence of Li<sub>2</sub>O changes the course of the burning process during which lime dissolves in the liquid phase and results in higher reactivity. The negative effect is that Li<sub>2</sub>O inhibits the conversion of C<sub>2</sub>S to C<sub>3</sub>S. The effects of Li<sub>2</sub>O are more intense compared to Na<sub>2</sub>O and K<sub>2</sub>O [1]. According to [2], these effects takes place when Li<sub>2</sub>O addition is higher than 1 %.

Saraswat et al [3] stated that Li<sub>2</sub>CO<sub>3</sub> addition lowers the decomposition temperature of CaCO<sub>3</sub> and the process takes place in two steps. When the addition of dopant is 1 %, CaO formed at low temperature reacts with SiO<sub>2</sub> to form the β-C<sub>2</sub>S even at 750 °C. The reaction is completed at 1350 °C, with formation of β-C<sub>2</sub>S and small amounts of γ-C<sub>2</sub>S. Addition of 5 % dopant

lowers the final reaction temperature down to 1290 °C, the reaction products are  $\beta$ -C<sub>2</sub>S and small amounts of C<sub>3</sub>S.

Kolovos et al [4] examined addition of 2.5 % Li<sub>2</sub>O into clinker raw meal. After sintering at 1450 °C, the samples were examined using SEM. Distinct differences compared to reference clinker were observed, concerning specifically the size and shape of belite grains. The alite crystals were coarse (size of 80-200 μm), prismatic and deposited in an idiomorphic underlay of belite. Belite distribution around alite grains was in a shape of fish bone composed of mix of elongated and roundish grains. Li oxides easily form eutectic mixtures with SiO<sub>2</sub>. According to the authors, Li effect on crystallization and development of silicates in clinker causes very unique belite configuration.

As an admixture (in adequate amount), Li can reduce the alkali-silica reaction in concrete, mainly in form of salts like LiOH or Li carbonates. It can be possible that Li in clinker has similar effect. [1]

Taylor [5] stated that lithium salts are strong accelerators of hydration process.

## 2. Materials and methods

Raw meals were prepared from chemically pure phases so that the effect of Li<sub>2</sub>O addition on temperature of clinker melt formation and phase composition can be observed. As Li<sub>2</sub>O source Li<sub>2</sub>CO<sub>3</sub> was used. All together 7 raw meals were prepared with different Li<sub>2</sub>O content in burned clinkers (0, 0.5, 1, 2, 3, 4 and 5 wt.%). The addition of Li<sub>2</sub>O replaced a part of CaO. Reference raw meal composition was 78.07 % CaCO<sub>3</sub>, 15.85 % SiO<sub>2</sub>, 3.71 % Al<sub>2</sub>O<sub>3</sub> and 2.36 % Fe<sub>2</sub>O<sub>3</sub>.

Raw meals were examined by DTA Netzsch Perseus STA 449 apparatus with temperature increase 10 °C/min up to 1450 °C.

Raw meals were burned in forms of tablets with temperature increase was 10 °C/min up to 1450 °C with 4 hours hold. Cooling was done in 2 different ways. Fast cooling – immediate pulling out of furnace and cooling by water. Slow cooling – clinker remains in furnace till 1400 °C then it is pulled out and cooled down in laboratory conditions.

Phase analyses of clinkers were done by X-ray diffraction method on the Bruker D8 Advance apparatus with Cu anode ( $\lambda K\alpha = 1.54184 \text{ \AA}$ ) and variable divergence slits at  $\Theta$ - $\Theta$  Bragg-Brentano reflective geometry. Quantitative phase analyses were done by Rietveld method using Topas software.

Clinker microstructure was observed on the surface of polished section etched by acetic acid [6] in reflective light of polarization microscope Nikon Eclipse LV100. Some phases were also observed by SEM by back scattered electrons (BSE) on apparatus JEOL JSM-7600F.

Another experiments were done using industrial raw meal which is not chemically pure. The raw meal was doped with 0.5 and 1 wt. % of Li<sub>2</sub>O in form of Li<sub>2</sub>CO<sub>3</sub>. Basic chemical parameters of the raw meal are LSF = 96, SR = 2.53 and AR = 0.74 (LSF – Lime saturation factor, SR – Silica ratio, AR – Alumina-iron ratio). Residuum on 0.09 mm sieve is 12 wt. %.

Reference industrial raw meal was burned up to 1450 °C. Meals with Li<sub>2</sub>CO<sub>3</sub> addition were burned up to 1350 °C. Clinker was cooled at laboratory condition.

Quantitative phase composition of these clinkers was evaluated by microscopic point counting method on polished section etched by acetic acid. The following specific weights of

clinker phases were used for vol. % to wt. % recalculation:  $C_3S - 3.15$ ;  $C_2S - 3.28$ ;  $C_3A - 3.03$ ;  $C_4AF - 3.77$ ; free  $CaO - 3.35 \text{ g.cm}^{-3}$ .

Clinkers with addition of gypsum as a setting regulator were ground in laboratory ball mill to the same specific surface ( $400 \text{ m}^2/\text{kg}$ ). Specific surface was determined by Lea and Nurse permeability method according to British standard BS 12:1958. Standard mortar bars were prepared according to EN 196. Strength development (EN 196-1) and heat of hydration (EN 196-8) were determined after 2, 7, 28 days.

### 3. Results and discussion

#### 3.1 Thermal processes in raw meal

DTA measurement shows endotherm of  $Li_2CO_3$  decomposition even in the raw meal with the lowest  $Li_2O$  content – the minimum of the endotherm is at  $643 \text{ }^\circ\text{C}$ . In the raw meal with the highest  $Li_2O$  content, the peak of  $Li_2CO_3$  decomposition is at  $662 \text{ }^\circ\text{C}$ .  $CaCO_3$  decomposes at  $875 \text{ }^\circ\text{C}$  in the reference raw meal. In raw meals with higher  $Li_2CO_3$  content, the endotherm is split as stated in [2,3]. Raw meal with the highest  $Li_2O$  content has two minimums of this double endotherm at  $820$  and  $860 \text{ }^\circ\text{C}$ . Temperature of melt formation decreases rapidly with  $Li_2O$  content in raw meal (see Tab. 1).

Table 1: DTA results of raw meals in  $^\circ\text{C}$ .

Raw meal	RM-0Li	RM-0.5Li	RM-1Li	RM-3Li	RM-5Li
Temperature of melt formation onset	1333	1252	1218	1174	1157
Temperature of minimum of melt formation endotherm	1404	1365	1352	1325	1320

#### 3.2 The influence of $Li_2O$ on the clinker phase composition

The burned clinkers show that  $Li_2O$  significantly lowers viscosity of melt. Clinkers with 1 and 2 wt.%  $Li_2O$  were considerably more sintered than clinker without  $Li_2O$  or with 0.5 wt.%  $Li_2O$ . Clinkers with higher  $Li_2O$  content were greatly melted and coloured by lithium to brown-pink.

The phase composition of individual clinkers burned from pure raw meals with graded  $Li_2O$  contents is given in Tab. 2. The number in clinker designation shows theoretical  $Li_2O$  content in clinker if there is no partial evaporation during burning.

The results have shown decrease of alite amount and increase of belite and free lime in clinkers with  $Li_2O$  that were cooled slowly. As can be seen by microscope, alite crystals decompose to submicroscopic mixture of belite and free lime even in clinkers with the lowest  $Li_2O$  addition. Almost all of the alite is decomposed in clinkers with more than 3 wt.% of  $Li_2O$ . In case of fast cooling this phenomenon is nearly suppressed. Therefore, there is no inhibition of conversion  $C_2S$  to  $C_3S$  as stated in [1] but the decomposition of formatted  $C_3S$  to  $C_2S$  and  $C$  takes place.

This phenomenon, which is connected to burning conditions and cooling of clinker, will be the subject of following research. Fig. 1 and 2 show examples of microstructure of burned clinkers. Due to lower viscosity of burned clinkers nucleation decreases and alite crystals

grow faster. The crystals are very big – more than 200  $\mu\text{m}$  and their outer lines are imperfect. For example, addition of  $\text{SO}_3$  has similar effect [7].

Table 2: Quantitative phase composition of clinkers in wt.% evaluated by X-ray diffraction analysis (amount of phase during fast cooling / slow cooling) -  $\text{C}_3\text{S}$  (alite) –  $3\text{CaO}\cdot\text{SiO}_2$ ,  $\text{C}_2\text{S}$  (belite) –  $2\text{CaO}\cdot\text{SiO}_2$ ,  $\text{C}_3\text{A}$  –  $3\text{CaO}\cdot\text{Al}_2\text{O}_3$ ,  $\text{C}_4\text{AF}$  –  $4\text{CaO}\cdot\text{Al}_2\text{O}_3\cdot\text{Fe}_2\text{O}_3$ , C (lime) – free  $\text{CaO}$ .

Clinker designation	$\text{C}_3\text{S}$	$\text{C}_2\text{S}$	$\text{C}_3\text{A}$	$\text{C}_4\text{AF}$	C
C-0Li	73.1/70.6	9.2/11.5	11.4/12.2	5.9/5.4	0.4/0.3
C-0.5Li	70.6/69.4	12.6/14.0	7.6/7.0	8.3/8.9	0.9/0.7
C-1Li	72.3/27.9	11.4/48.4	5.9/1.6	6.7/9.3	2.8/12.8
C-2Li	76.9/33.7	8.8/48.5	7.0/2.1	2.7/2.9	4.6/12.8
C-3Li	77.3/2.8	13.2/67.1	1.3/2.6	1.8/0.6	6.4/26.9
C-4Li	67.8/1.6	21.2/61.8	2.2/2.2	1.5/1.7	7.3/32.7
C-5Li	50.3/0.0	38.7/56.7	2.3/2.1	0.9/4.0	7.8/37.2

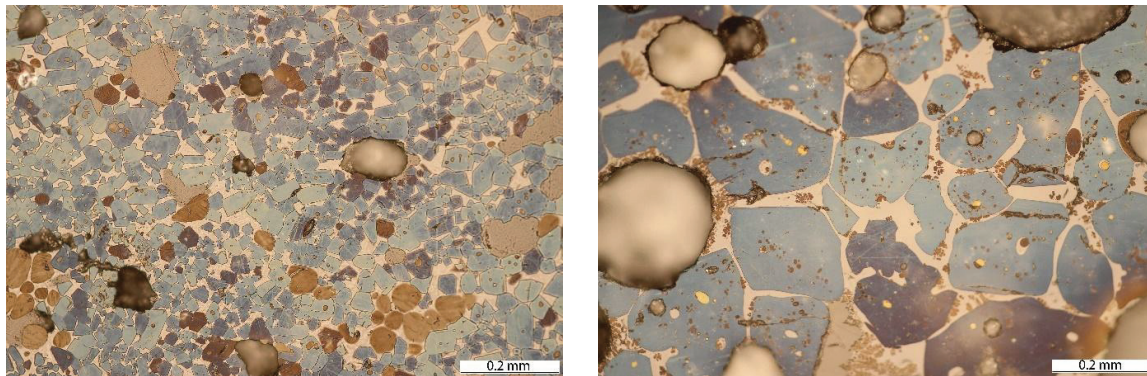


Figure 1: Microstructure of burned clinkers. Left – clinker C-0Li (fine blue alite crystals, nests of brown round belite grains in the right bottom corner). Right – clinker C-2Li with fast cooling (big alite crystal, small belite grains in white ground mass).

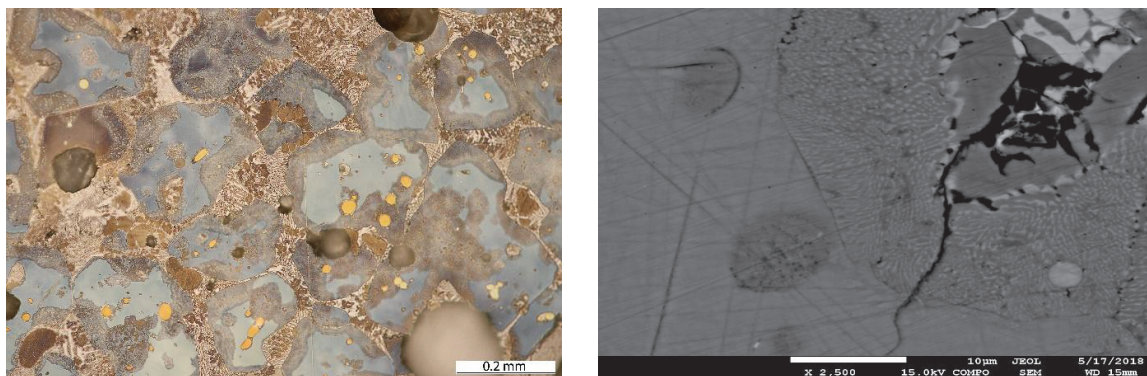


Figure 2: Left – microstructure of clinker C-2Li with slow cooling (big alite crystals with obvious zones of decomposition, fine dendritic belite can be seen in ground mass). Right – a part of alite with decomposition zone taken by BSE.

### 3.3 The influence of $\text{Li}_2\text{O}$ on the properties of cement

Microscopical determination of quantitative phase composition of clinkers for cement preparations can be seen in Tab. 3. The basic parameters of these cements are given in Tab. 4. Phase composition of these clinkers confirms results from chapter 3.2 – increase of  $\text{Li}_2\text{O}$  results in decrease of alite content which decomposes to submicroscopic belite and free lime. This phenomenon is also evident in scanning electron microscopy (see Fig. 2).

The results in Tab. 4 shows that higher degree of sintering and greater content of belite in clinkers containing  $\text{Li}_2\text{O}$  cause worse grinding ability by up to 18% – expressed as grinding time on the same specific surface. Setting of the cement prepared from clinker containing  $\text{Li}_2\text{O}$  is a little faster than reference cement CEM-0Li/P.

Table 3: Quantitative phase composition of clinkers in wt. % determined by X-ray diffraction analysis.

<b>Clinker designation</b>	<b>C<sub>3</sub>S</b>	<b>C<sub>2</sub>S</b>	<b>C<sub>3</sub>A</b>	<b>C<sub>4</sub>AF</b>	<b>C</b>	<b>C<sub>3</sub>S decomposed</b>
C-0Li/P	69.2	14.1	2.8	13.9	0.0	0.0
C-0.5Li/P	51.5	20.6	6.0	13.7	0.7	6.9
C-0.5Li/P*	51.8	25.9	6.1	13.8	2.5	*
C-1Li/P	52.6	23.8	5.2	7.3	0.9	9.4
C-1Li/P*	53.0	31.1	5.3	7.4	3.3	*

\* Composition with recalculation of decomposed  $\text{C}_3\text{S}$  to  $\text{C}_2\text{S}$  and C.

Table 4: Basic parameters of prepared cements.

<b>Cement designation</b>	<b>Specific surface [m<sup>2</sup>/kg]</b>	<b>Grinding time [mins]</b>	<b>Normal consistency [%]</b>	<b>Initial setting time [hours : mins]</b>	<b>Final setting time [hours : mins]</b>
CEM-0Li/P	400	195	28.0	3 : 40	4 : 40
CEM-0.5Li/P	399	220	27.7	3 : 20	4 : 00
CEM-1Li/P	400	230	27.7	2 : 30	3 : 10

The most important properties of cements are their compressive strengths, which are mentioned in Fig. 3. Short-term strengths after two days are approximately the same for all cements. In later stages of hydration, the strengths of the  $\text{Li}_2\text{O}$ -containing cements are lower by about 28% after 7 days and by about 20% after 28 days compared to cements without  $\text{Li}_2\text{O}$ . However, it should be noted that  $\text{Li}_2\text{O}$ -containing clinkers were burned at a lower temperature by 100 °C than the clinker for reference cement. From this perspective, the cements can be classified as low-energy with very high strength and they fulfil requirements for the 42.5R strength class according to EN 197-1. In addition, the cements have a favourably reduced hydration heat as can be seen in Fig. 3.



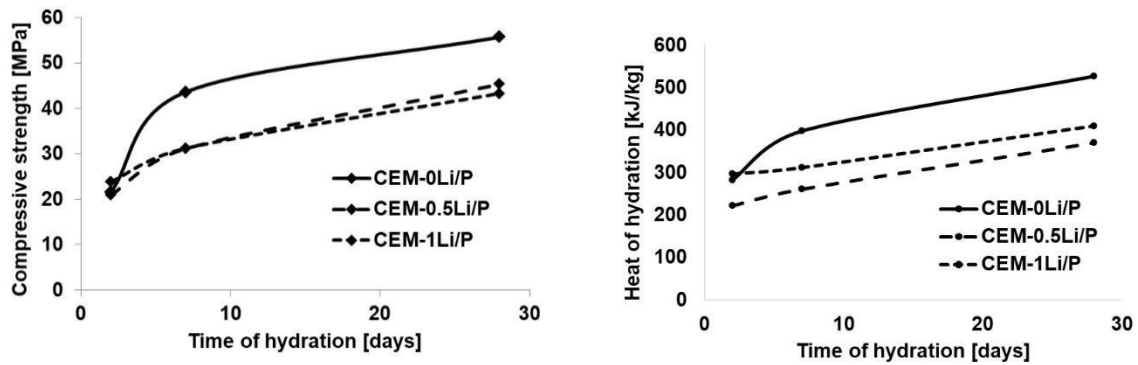


Figure 3: Left – development of compressive strength according to EN 196-1. Right – heat of hydration determined by dissolution method according to EN 196-8.

#### 4. Conclusions

The presence of lithium in raw meal has a significant mineralization effect on the formation of clinker. It causes a significant decrease of melt formation temperature and decreases the viscosity of melt. This enables burning of clinker at lower temperatures with sufficient alite content. Lowering the viscosity causes a reduction in nucleation and an increase in the growth rate of alite crystals. Therefore, less alite crystals of large dimensions are formed.

Higher additions of  $\text{Li}_2\text{O}$  have a significant negative effect during slow cooling and cause decomposition of alite to a submicroscopic mixture of belite and free lime.

It has been found that clinkers with 1 wt. % addition of  $\text{Li}_2\text{O}$  can be burned at temperature lower by 100 °C with similar properties as conventional clinker. Cements prepared from these clinkers have parameters of CEM I 42.5 R when grinded to the standard fineness.

#### Acknowledgement

This research was done within the project No. 16-08959J financed by the Czech Science Foundation.

#### References

- [1] Role of Minor Elements in Cement: Manufacture and Use. Javed I. Bhatti (Ed.), PC Association, Skokie (1995)
- [2] Kolovos, K. et al, The effect of foreign ions on the reactivity of the  $\text{CaO-SiO}_2\text{-Al}_2\text{O}_3\text{-Fe}_2\text{O}_3$  system. Part II: Cations, *Cem Concr Res* 32 (2002), 463-469
- [3] Saraswat, P. et al, Thermal studies of the  $\text{CaCO}_3\text{:SiO}_2$  (2:1) system containing lithium as dopant. *Termochim Acta* 97 (1986) 313-320
- [4] Kolovos, K. et al, SEM examination of clinkers containing foreign elements. *Cem Concr Comp* 27 (2005) 163-170
- [5] Cement chemistry. H. F. W. Taylor (Ed.), Academic press, London (1990)
- [6] Chromý, S., Anfärben des freiem  $\text{CaO}$  und Silikate in anschliffen von Portlandklinker. *Z-K-G*, 27(1974), 79-84
- [7] Maki, I. and Goto, K., Factors influencing the phase constitution of alite in Portland cement clinker. *Cem Concr Res* 12 (1982), 301-308

## **PROPOSAL OF A TEST SET UP FOR SIMULTANEOUS APPLICATION OF AXIAL RESTRAINT AND VERTICAL LOADS TO SLAB-LIKE SPECIMENS: SIZING PRINCIPLES AND APPLICATION**

**José Gomes<sup>(1)</sup>, Miguel Azenha<sup>(1)</sup>, José Granja<sup>(1)</sup>, Rui Faria<sup>(2)</sup>, Carlos Sousa<sup>(2)</sup>, Behzad Zahabizadeh<sup>(1)</sup>, Ali Edalat-Behbahani<sup>(1)</sup>, Dirk Schlicke<sup>(3)</sup>**

(1) University of Minho, School of Engineering, ISISE, Guimarães, Portugal

(2) Faculty of Engineering of the University of Porto, CONSTRUCT, Porto, Portugal

(3) Institute of Structural Concrete, Graz University of Technology, Graz, Austria

### **Abstract**

Cracking control in reinforced concrete (RC) is a key factor to ensure proper service life behaviour. However, current design recommendations are unable to provide straightforward methodologies for crack width prediction in RC structures subjected to the combined effects of applied loads and restrained deformations, which is a common situation in civil engineering. This is motivated by the lack of knowledge about the complex interactions that take place between self-imposed deformations, viscoelasticity and the effects of applied loads in the process of crack development.

A major challenge in studying these combined effects is the validation of numerical simulations with real scale experimental data. For that purpose, an experimental system for testing real scale RC slabs subjected to the above-mentioned conditions was developed. This system is capable of inducing a prescribed axial restraint to the slab, in correspondence to a high restraint degree that induces cracking in view of expectable shrinkage. At the same time, the setup enables the application of vertical loads. The experimental results obtained in this work allowed for the validation of the test setup, as well as the suitability of the slab geometry and reinforcement.

### **1. Introduction**

Cracking in RC structures is an acceptable phenomenon when controlled, but it is one of the main factors that affect structural durability when crack width exceeds the recommended limits. The design of RC structures that meet safety, functionality and aesthetic requirements

during their lifespan, without additional maintenance costs, depends also on adequate design practices that allow engineers to properly predict expectable crack widths.

Even though there is a wide body of design codes and recommendations providing practices for predicting the crack width due to applied loads or imposed deformations, they do not provide unambiguous rules for estimation of crack width under the combined effects of applied loads and restrained shrinkage. Different simplified approaches based on the application of CIRIA C660 [1], simplified combinations of the Eurocode framework, deformation-based methods [2] and explicit crack width calculations in composed bending with a percentage of the cracking axial force [3] may lead to differences in reinforcement for controlling crack width as large as 50% [4]. In view of such challenges, several authors have used the finite element method (FEM) to perform nonlinear numerical analyses in RC structures subjected to the combined effect of applied loads and restrained shrinkage, to quantify the stresses and forces which occur due to these effects [5-8]. These works, although very important to better understand the stress/crack development mechanism of such structures, are still lacking the experimental validation of long-term real scale tests.

This paper intends to show the development of an experimental system for testing real scale RC slabs under the above-mentioned effects. The paper starts by explaining the principles behind the design of the test specimens and the system requirements. After describing the test setup and procedures, the results of the preliminary test are discussed, and the suitability of the test setup and necessary improvements are addressed. This paper is a short version of the report of the research project IntegraCrete on the same matter [9].

## 2. Sizing and requirements

The main requirement of the developed testing system is the ability to provide an axial controlled restraint to a slab-type specimen, while simultaneously allowing it to be loaded with sustained bending/shear. It was intended to simulate a stretch of slab on a highly restrained condition, whilst monitoring the restraining forces, the in-plane and out-of-plane deformations and the reinforcement strain.

The design of the tested specimen corresponded to the simulation of a real-case one-way slab supported by transverse beams, under high axial restraint. Spans of 4.0m were considered for the slab, and a sizing considering permanent loads of  $2\text{kN/m}^2$  (acting together with the self-weight) and variable loads corresponding to class A of EN1991-1-1 [10] ( $2\text{kN/m}^2$  plus  $1.2\text{kN/m}^2$  relative to movable partitions) was performed. The slab was designed for the ultimate and service limit states according to EN1992-1-1 [11], which resulted in a 0.10m thick slab, reinforced for bending with  $\phi 8/0.10$  in the bottom face. This provides adequate behaviour without direct consideration of restraint, which was considered a design start point.

As the experimental setup was devised to test the slab under simply supported conditions, the 4.0m span was corrected to match the distance in between zero bending moments, which corresponds to approximately  $3/5$  of the span. Therefore, the test setup has a free span of 2.4m. The slab is supported by a perpendicular rod at each extremity (Fig. 1), and even though cracking is expected in such region due to stress concentration, the control region for restraint will be limited to 1.4m in the mid-span. The specimen is 0.50m wide, as to ensure a width-to-height ratio of  $1/5$ , and therefore have a standard slab-type behaviour.

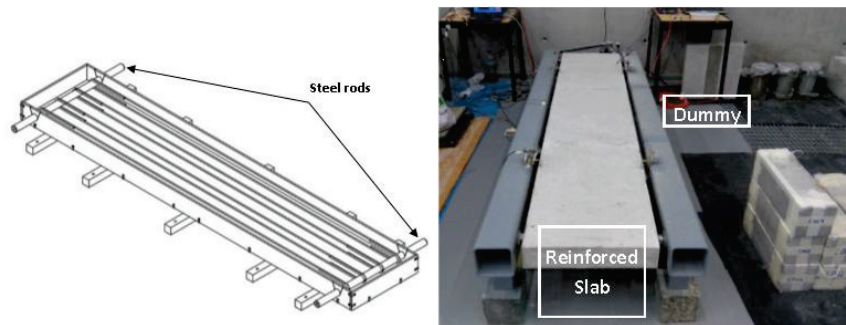


Figure 1: Slab formwork and steel rods (left); test setup (right).

### 3. Test set up and procedures

The long-term experiment that simultaneously combine the effect of self-induced deformations together with applied loads is conducted through the instrumentation of two specimens: a RC slab tested on the restraint frame and an unrestrained complementary plain concrete specimen (dummy) (Fig. 1). Furthermore, nine cubes (15cm edge) and three cylinders (15cm diameter; 30cm length) of the same batch were used for characterization of the concrete at different ages (compressive strength according to EN12390-3 [12] and E-modulus according to LNEC E397 [13]). The above-mentioned test setup, designed according to Section 2 to ensure the necessary performance requirements, is described next.

#### 3.1 Geometry and materials

The slab, made of a C20/25 concrete strength-grade class, is 2.6m long and has a transversal cross-section of  $0.5 \times 0.1 \text{ m}^2$ . A free span of 2.4m is assured by two 40mm steel rods embedded in the slab at mid-height and connected to the restraint frame (see Fig 1).

Even though the design of the slab reinforcement that has been addressed in Section 2 foresees a solution of 8mm rebars spaced by 100mm, for this prototype slab both top and bottom flexural reinforcement are materialized with 8mm rebars transversely spaced by 125mm (larger than 100mm as initially planned due to a placement mistake, which was however considered acceptable for the sake of this prototype testing stage). A secondary transverse reinforcement of 6mm rebars spaced by 300mm was applied, to fulfil the rule of 20% of the principal reinforcement, as recommended by EN1992-1-1 [11]. The described reinforcement has a concrete cover of 22mm. The complementary specimen is made of plain concrete of the same batch of the slab, has the same cross section ( $0.1 \times 0.5 \text{ m}^2$ ) and is 0.5m long. This specimen is not restrained, being simply placed vertically next to the restrained slab.

The slab was cast and tested in an experiment room without specific control of temperature or humidity. Recorded temperatures during test indicate variations between 20-28°C. Environmental humidity ranged 50-70%. Concrete was kept from drying before demoulding of the slab and dummy (at 7 days) using a plastic foil. From 7 days onwards, the slab was subjected to drying at all surfaces.

#### 3.2 Restraining device

The slab is simply supported and its axial deformation is restrained by controlling the axial force of the slab using hydraulic actuators, placed inside a metallic frame and connected to the

steel rod embedded in the slab. This frame is constituted by two 2.65m long rectangular hollow section (RHS) steel profiles with outer dimensions of  $140 \times 140 \text{mm}^2$  and an inner hollow region of  $124 \times 124 \text{mm}^2$ , supported by two 0.15m long RHS with outer dimensions of  $80 \times 80 \text{mm}^2$  and an inner hollow region of  $72 \times 72 \text{mm}^2$  (Fig. 2).

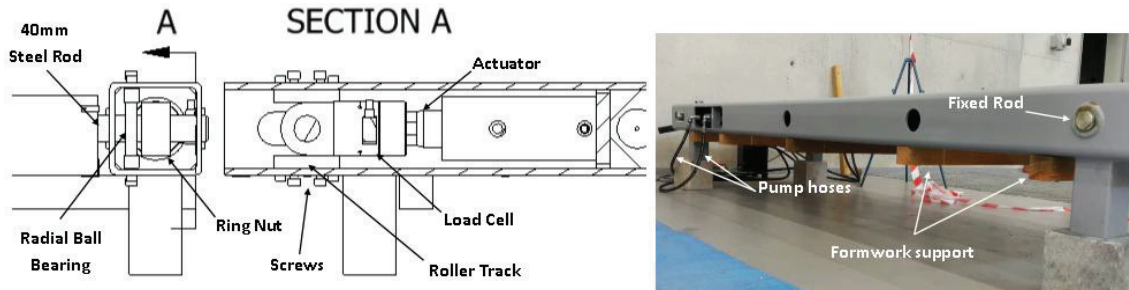


Figure 2: Restraining device: inside the metallic frame (left) and overview (right).

Each longitudinal RHS has five drills on the bottom to enable the fixation of the formwork in the frame with wooden slats. On the lateral side there are two 40mm diameter holes to insert both fixed and moving steel rods. The positioning of the moving rod is done with a radial ball bearing between two roller tracks, whose position is adjusted with 4 socket head cap screws (Fig. 2). For application of the axial load to the slab, two double effect hydraulic actuators supplied by a manual hydraulic pump are used, each with a 100kN capacity in compression and a 50kN capacity in traction, connected to the moving steel rod embedded in the slab.

Information about self-induced deformations of the slab are given by the dummy, and in both specimens the temperature and deformations are measured by means of electrical resistance strain gauges for rebar stress/strain assessment, a vibrating wire strain gauge (VWSG) acquiring the dummy deformation, linear variable displacement transformers (LVDT's) for slab deflection and longitudinal strains measurement and resistance temperature detectors (RTD's). The axial force applied by the actuators is measured by two load cells connected to the 40mm steel rod through a ring nut (Fig. 2).

On each side of the slab, one LVDT is fixed to a bracket, partially embedded in the concrete with a metallic clamp, and the concrete deformation in the central region of the slab is measured using a steel cable in tension, fixed between the other bracket and a steel plate in contact with the LVDT, as the steel plate is connected to the LVDT bracket with two springs (Fig. 3). With this spring system it was possible to measure the longitudinal strains of the slab during the application of the axial load.

#### 4. Results

The test specimens were cast and left undisturbed for 7 days, with the actuators fully inactive (and free to move). At the age of 7 days (~174h), both the slab and dummy were demoulded and a tensile axial load of approximately 16kN was applied. The result of such load application in both load cells and longitudinal LVDTs is shown in Fig. 4. The longitudinal strain of  $10\text{-}15 \mu\epsilon$  measured by the LVDTs was consistent with the corresponding calculated value, taking into consideration the geometry of the slab and the modulus of elasticity of the rebars and concrete [14] (200GPa and 26.3GPa, respectively):  $\sim 12 \mu\epsilon$ , although a more

precise concrete strain measuring device must be devised for next experiments in order to minimize the noise-to-signal ratio of the system.

At the age of 59 days the slab was loaded with 14 concrete blocks adequately spaced to avoid arch effects, and to simulate a quasi-permanent load combination (live load of  $2.96\text{kN/m}^2$ ). The blocks were placed sequentially from the mid-span towards the supports, leading to the formation of a single crack at mid-span, with a width of approximately  $0.2\text{mm}$ , as shown in Fig. 4. As it was expected, the measured crack was wider than what is predicted from the EN1992-1-1 [11] formulation ( $\sim 0.07\text{mm}$ ), since the combined effect of restrained shrinkage and applied loads has to be taken into account.

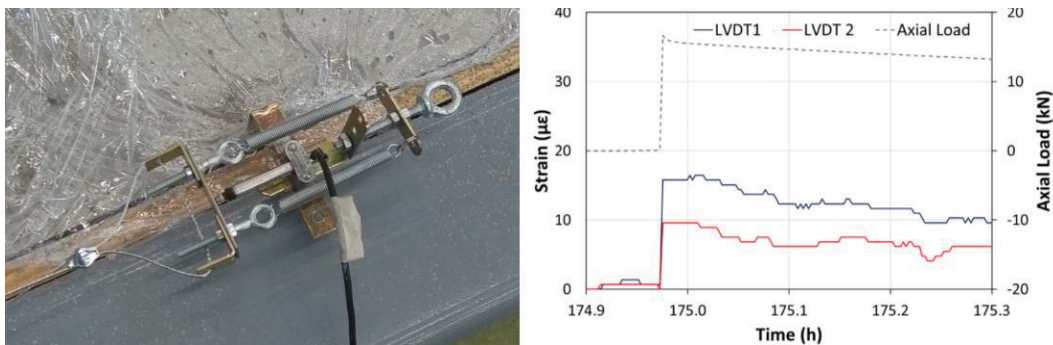


Figure 3: Concrete strain measurement setup (left) and results after axial loading (right).



Figure 4: Load blocks (left) and crack at midspan after application of the load blocks (right).

## 5. Conclusions

The current work describes the arrangement and preparation of the experimental setup designed for conducting long-term tests with real scale slabs subjected to the combined effect of applied loads and restrained shrinkage deformations.

The formwork support solution proved to be adequate, in the sense that it was possible to easily mount it and demould it in the restraining frame. The geometry of the specimens was accurate and therefore viable.

So far, the monitoring devices showed satisfying results at past key moments. Although there is some oscillation on the strain measurements, this was mostly caused by the fact that the experiment was not conducted in a controlled temperature chamber. This will be overcome in the next setup application. Even though the LVDT measurement system shown performed well, there are still operational drawbacks that can jeopardize reliability and thus deserve improvement in order to minimize the noise and the influence of the curvature of the slab in

the measurement. The loading frame/setup has demonstrated capacity to impose and keep/control of the axial load, with an example application being demonstrated herein.

In general, it can be claimed that the trial experiment has shown to be successful and that relevant hints for improvement were obtained. The production of a second setup is envisaged for a wider program to be conducted on long term.

### Acknowledgements

This work was financially supported by: Project POCI-01-0145-FEDER-007457 (CONSTRUCT - Institute of R&D in Structures and Construction) and by project POCI-01-0145-FEDER-007633 (ISISE), funded by FEDER funds through COMPETE2020 - Programa Operacional Competitividade e Internacionalização (POCI), and by national funds through FCT - Fundação para a Ciência e a Tecnologia. FCT and FEDER (COMPETE2020) are also acknowledged for the funding of the research project IntegraCrete PTDC/ECM-EST/1056/2014 (POCI-01-0145-FEDER-016841). The financial support of COST Action TU1404 through its several networking instruments is also gratefully acknowledged.

### References

- [1] Bamforth, P.B., C660: Early-age thermal crack control in concrete, in CIRIA, UK (2007)
- [2] Schlicke, D. and Tue, N.V., Crack width control–verification of the deformation compatibility vs. covering the cracking force, Proc. MSSCE2016/Service Life Segment, Denmark (2016)
- [3] Camara, J. and Luís, R., Structural Response and Design Criteria for Imposed Deformations Superimposed to Vertical Loads, Proc. *fib* Congress, Italy (2006)
- [4] Azenha, M. and Granja, J., Seminar: Design of reinforcement for RC elements under the combined effect of applied loads and restrained shrinkage. E-book of presentations. 2017: Zenodo. <http://doi.org/10.5281/zenodo.800693>
- [5] Luis, R., Análise e dimensionamento de estruturas de betão com sobreposição de cargas e deformações impostas, MSc thesis; Universidade Técnica de Lisboa (2005)
- [6] Carvalho, J.F., Estudo da fendilhação em lajes restringidas devido ao efeito conjunto da retração e das ações distribuídas no piso, MSc thesis, Universidade do Porto (2013)
- [7] Felisberto, E.A.d.O., Análise de lajes maciças de edifícios atendendo aos efeitos da retração restringida e às ações gravíticas, MSc thesis, Universidade do Porto (2015)
- [8] Carvalho, R., Rumo à análise 3D pelo método dos elementos finitos do efeito combinado de ações diretas e da retração impedida em lajes de betão armado, MSc thesis, Universidade do Minho (2017).
- [9] Gomes, J. et al, Task 4 – Setting up for long term experimental framework, IntegraCrete Report, Universidade do Minho (2017)
- [10] CEN, Eurocode 1 EN 1991-1-1 Actions on structures - Part 1-1: General actions -Densities, self-weight, imposed loads for buildings, CEN: Brussels (2004)
- [11] CEN, Eurocode 2 EN 1992-1-1 Design of concrete structures Part 1-1 General rules and rules for buildings, CEN: Brussels (2004)
- [12] IPQ, Ensaios do betão endurecido: Parte 3 - resistência à compressão de provetes NP EN 12390-3, IPQ: Caparica (2011)
- [13] LNEC, Especificação LNEC E397: Betões. Determinação do Módulo de Elasticidade em Betões. Lisboa (1993)
- [14] Beer, F. P. and Johnston Jr., E.R., Mechanics of materials. 3<sup>rd</sup> ed., McGraw Hill, USA (2001)

## **RESISTANCE TO SULFATE AND ACID ATTACK OF SELF-COMPACTING CONCRETE WITH RECYCLED AGGREGATES**

**Said Kenai <sup>(1)</sup>, Mohamed Omrane <sup>(1,2)</sup>**

(1) University of Blida 1, Algeria

(2) University of Djelfa, Algeria

### **Abstract**

Natural aggregates are sometimes lacking around big cities but construction and demolition waste debris are available to manufacture recycled aggregates. The durability performance of SCC with natural aggregates is well investigated. However, the durability of SCC with recycled aggregates under aggressive environments such as sulfate and acid attacks that could be encountered in structures near the sea, in aggressive soils or sewage treatment plants needs to be elucidated. In this paper, SCC mixes with only natural aggregates (SCCN) or 50% natural aggregates and 50% recycled coarse and aggregates (SCCR) were immersed in 3% hydrochloric acid (HCl) and 5% sodium sulfate ( $\text{Na}_2\text{SO}_4$ ) and the weight loss measured as well as visual inspection and XRD tests. The experimental results indicate that recycled aggregated reduced the resistance to aggressive environment. The addition of 15% to 20% of natural pozzolan mitigated this negative effect.

### **1. Introduction**

Recycled aggregates from construction and demolition waste (CDW) production worldwide is important. In 2014, the total waste generated in the EU-28 by all economic activities and households amounted to 2 503 million tons; of which 34.7% comes from CDW activities (Eurostat, 2017) [1]. The performance of concrete with recycled aggregates from CDW has been investigated extensively [2]. However, their incorporation in self-compacting concrete is less investigated especially under the effect of aggressive environments. Self-compacting concrete is highly flowable concrete with high paste content and hence cement replacement materials such as slag, natural pozzolan, limestone fillers and metakaolin are used. SCC with both recycled aggregates and mineral additions could be considered as an eco-concrete as it reduces the  $\text{CO}_2$  emission by reducing the cement content and reduces the consumption of



natural aggregates and hence help reducing the depletion of natural resources. The addition of mineral admixtures also mitigates some of the drawbacks of recycled aggregates addition such as reduction of compressive and tensile strength, increase of water and air permeability, a decrease in chloride penetration resistance and a decrease in sulfate attack [2-4]. In this paper, the resistance of SCC with recycled aggregates and natural pozzolan under acid and sulfate attack is investigated. These aggressive environments could be encountered in many structures like foundations on aggressive soils and slabs in industrial sites.

## 2. Materials and experimental program

CEM II/A-L 42.5R with a fineness of 300 m<sup>2</sup>/kg was used. A local natural pozzolan (PZ) from volcanic sediments in Beni-Saf quarry in the west of Algeria was crushed in a laboratory mill to a fineness of 400 m<sup>2</sup>/kg was used to partially replace cement. The chemical composition of cement and natural pozzolan is shown in Table 1. Concrete slabs (25 MPa grade) of 1m x 1m x 0.1m were manufactured in the laboratory and crushed at the age of 28 days. The crushed material was sieved to obtain the various recycled aggregate fractions. 50% substitution by weight of both fine and coarse natural aggregates by fine and coarse recycled aggregates was adapted. The ratio of replacement for natural pozzolan were (5%, 10% and 15%) for natural self-compacting concrete (NSCC) and (5%, 10%, 15% and 20% for recycled self-compacting concrete (RSCC) by mass of cement. The water/binder ratio was kept constant at 0.42 and an Ether polycarboxylates super-plasticizer (SP) that complies with EN 934-2 was used. The concrete mix proportions are summarized in Tables 2 and 3.

The resistance to aggressive environments was evaluated by the measurement of the loss in mass after immersion in sulfate solutions (5% sodium Na<sub>2</sub>SO<sub>4</sub>) or in 3% acid solutions (hydrochloric acid (HCl)), was measured after 1, 7, 14, 21, 28, 90 days and 180 days of immersion. The solutions were renewed after each weighing. Specimens were examined visually for any sign of deterioration and XRD analysis were performed on the outer face in contact with the aggressive solutions after immersion for 180 days.

Table.1: Chemical composition of cement and natural pozzolan

Compound (%)	CaO	SiO <sub>2</sub>	Al <sub>2</sub> O <sub>3</sub>	Fe <sub>2</sub> O <sub>3</sub>	MgO	Na <sub>2</sub> O	K <sub>2</sub> O	SO <sub>3</sub>	L.O.I
Pozzolan	12.4	43	19	9.5	4	3.0	1.4	--	6.5
Cement	63.6	20.5	5.8	2.6	0.9	0.4	0.9	3.3	--

Table 2: Mixes of SCC with natural aggregates (SCCN)

	SCCN0	SCCN5	SCCN10	SCCN15
Cement (kg)	468	447	425	404
Water (l)	197	196	195	194
Pouzzolane (kg)	0	19	39	59
Sand (kg)	907	907	907	907
Gravel 3/8 (kg)	265	265	265	265
Gravel 8/15(kg)	530	530	530	530
SP (kg)	5.14	5.13	5.11	5.09
W/B ratio	0.42	0.42	0.42	0.42

Table 3: Mixes of SCC with recycled aggregates (SCCR)

	SCCR0	SCCR5	SCCR10	SCCR15	SCCR20
Cement (kg)	458	438	416	396	374
Water (l)	192	192	191	190	190
Pouzzolane (kg)	0	19	38	58	77
Sand * (kg)	841	841	841	841	841
Gravel* 3/8 (kg)	265	265	265	265	265
Gravel*8/15(kg)	530	530	530	530	530
SP (kg)	3.67	3.65	3.64	3.63	3.61
W/B ratio	0.42	0.42	0.42	0.42	0.42

\*50% natural and 50% recycled.

### 3. Results and discussion

The rheological performance and mechanical test results are reported elsewhere [5]. SCC with recycled aggregates with good rheological properties was obtained when the recycled aggregates content was limited to 50%. The SCCN and SCCR mixtures containing PZ develop a comparable compressive strength to mixtures without PZ at 120 days of age.

#### 3.1 Resistance to sulfates

Figures 1 and 2 shows the variation of mass loss with immersion duration in the sulfate solution for both SCCN and SCCR specimens. For short term immersion (less than 4 weeks), the level of degradation for both types of concrete (SCCN and SCCR) were comparable. However, after 90 days, a slight difference is noticed. SCCN mixes showed a lower mass loss by 18.82% as compared to SCCR mixes. The addition of natural pozzolan enhances the resistance to sulfate attack for both SCCN and SCCR mixes. The loss of mass at 180 days as compared to reference concrete was reduced by 12.2%, 13.7 and 22.62% for SCCN mixes with 5%, 10% and 15% of PZ, respectively. The loss of mass after 180 days of immersion for SCCR mixes with 5%, 10%, 15% and 20% of PZ was 1%, 2.28%, 2.28% and 6.1%, respectively. The XRD analysis showed the presence of large quantity of gypsum (g) and ettringite (E) (Fig. 3). The intensity of gypsum does not show a significant difference between the two types of concrete with and without recycled aggregates. The portlandite is consumed by the sulfate attack. The attack by  $\text{Na}_2\text{SO}_4$  forms the gypsum which in its turn participates to the formation of secondary ettringite from  $\text{C}_3\text{A}$  and monosulfoaluminates. The incorporation of natural pozzolan increases the resistance to sulfate attack as it reacts with the portlandite of the hydrated cement to form C-S-H, reduces the capillary pores and reduces the diffusion of sulfate ions into concrete. The beneficial effect of using natural pozzolan is clearly seen on Figs.4 & 5 where the visual deterioration is reduced.

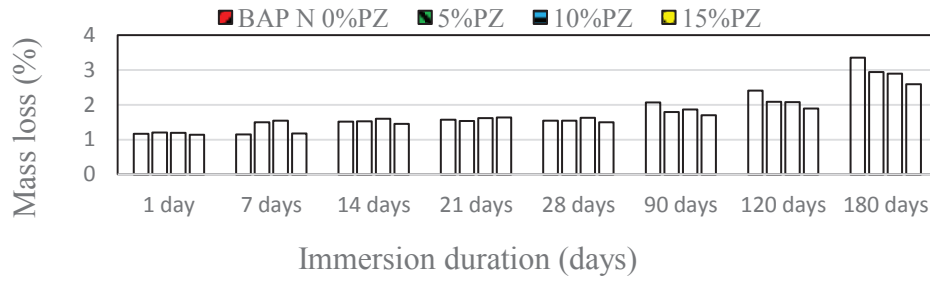


Figure 1: Mass loss of SCCN mixes after immersion in 5% Na<sub>2</sub>SO<sub>4</sub> solution.

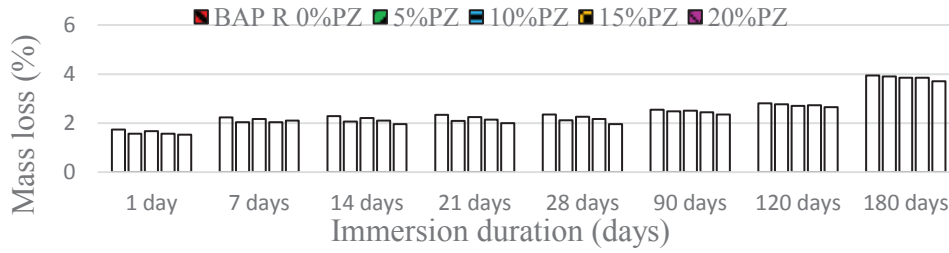


Figure 2: Mass loss of SCCR mixes after immersion in 5% Na<sub>2</sub>SO<sub>4</sub> solution.

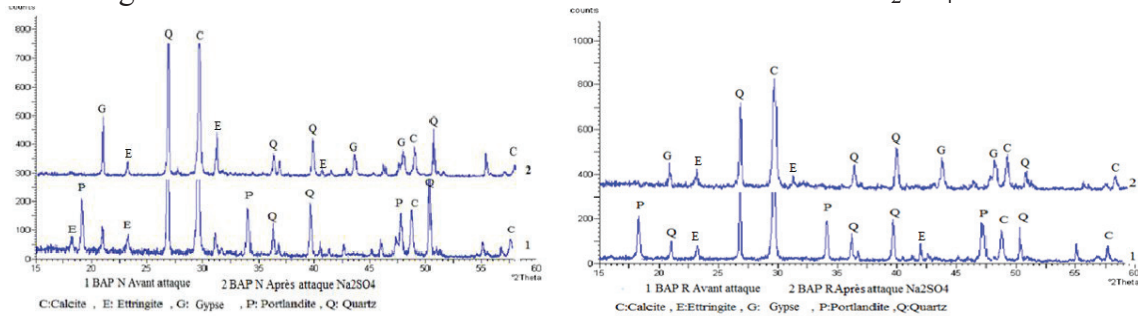


Figure 3: XRD spectrum of (a) SCCN and (b) SCCR mixes before and after immersion in 5%Na<sub>2</sub>SO<sub>4</sub>.



Figure 4: SCCN specimens degradation before and after immersion in 5%Na<sub>2</sub>SO<sub>4</sub> solution.

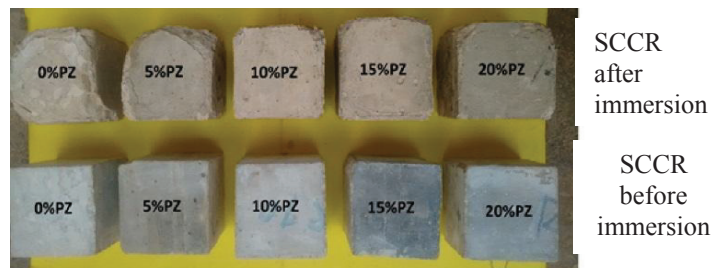


Figure 5: SCCR specimens degradation before and after immersion in 5%Na<sub>2</sub>SO<sub>4</sub> solution.

### 3.2 Resistance to acids

Figures 6 and 7 summarized the variation of mass loss with the increase of period of immersion in HCl solution. Similarly to sulfate attack, the performance under acid attack for up to 4 weeks of immersion was comparable. For both SCC with natural and recycled aggregates, a slight difference is noticed after 12 weeks. The loss of mass was more important for SCCR mixes (24.63%) than SCCN mixes. This shows the low performance of recycled aggregates under HCl acid attack contrary to the beneficial effect on the resistance to the more aggressive 5% sulfuric acid (H<sub>2</sub>SO<sub>4</sub>) solution reported elsewhere [5]. However, the addition of natural pozzolan enhances the resistance to acid. After 180 days of immersion, the reduction in mass loss was 1.38% and 8.77% for SCCN with 5% and 15% of PZ respectively. The reduction in mass loss was comparable for SCCR mixes with 3.16%, 4.81 and 20% for 5%, 15% and 20% PZ, respectively. The XRD spectrum shows the disappearance of the portlandite after HCl attack (Fig.8 ). When acid is in contact with cement hydration products, it will react with calcium hydroxide (Ca(OH)<sub>2</sub>) to form a highly soluble chloride calcium salt. The beneficial effect of adding natural pozzolan is also demonstrated as PZ reacts with portlandite to form C-S-H, fills the pores and reduce the lixiviation. The visual inspection of the specimens also conformed the beneficial effect of natural pozzolan.

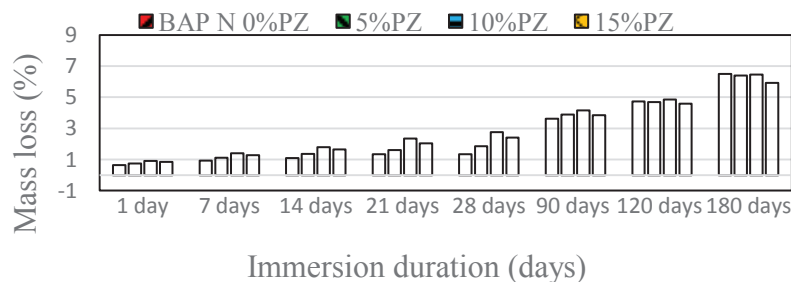


Figure 6. Mass loss for SCCN specimens after immersion 3% HCl solution.

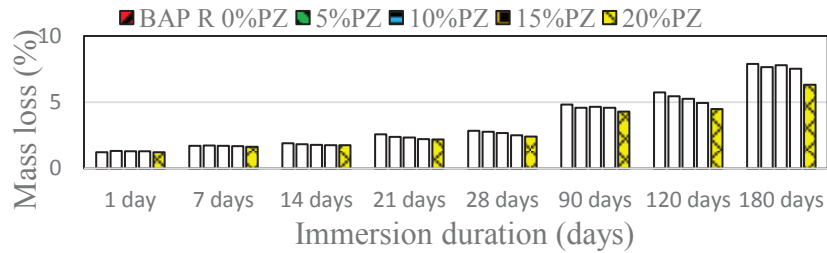


Figure 7: Mass loss for SCCR specimens after immersion 3% HCl solution.

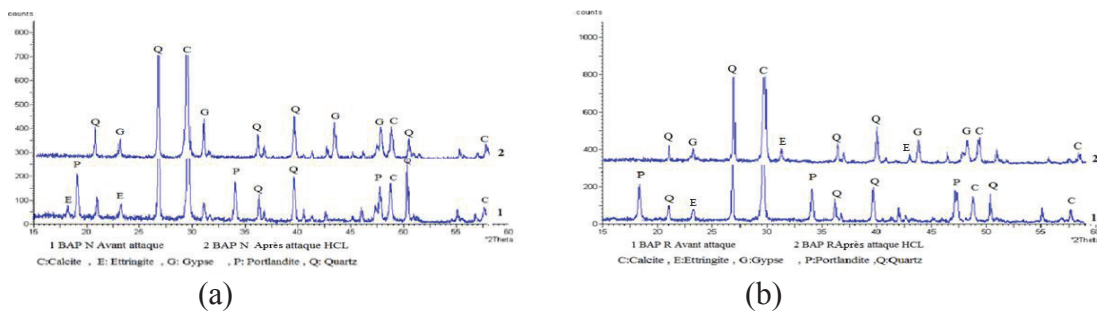


Figure 8: XRD spectrum of (a) SCCN and (b) SCCR mixes before and after immersion in 3% HCl.

#### 4. Conclusion

The replacement of natural aggregates with recycled aggregates in SCC mixes produced mixes with acceptable rheological and mechanical performance when the substitution level was limited. The resistance to sulfate and acid attacks of mixes with recycled aggregates was lower than that of mixes with natural aggregates as higher mass losses were observed. However, the incorporation of 15% to 20% natural pozzolan increased the resistance to both sulfate and acid attack and compensated partially the detrimental effect of recycled aggregates.

#### References

- [1] Eurostat (2017). Waste statistics in Europe.
- [2] Kenai, S. Recycled aggregates, chapter 3 in Waste and supplementary cementitious materials in concrete, edited by Siddique, R. and Cachim, P., Elsevier, 2018, pp. 81-121.
- [3] Dodds, W., Goodier, C., Christodoulou, C., Austin, S., Dunne, D. (2017). Durability performance of sustainable structural concrete: Effect of coarse crushed concrete aggregate on microstructure and water ingress. *Construction and Building Materials* 145, pp. 183–195.
- [4] Kapoor, K., Singh, S.P., Singh, B. (2017). Permeability of self-compacting concrete made with recycled concrete aggregates and metakaolin. *Journal of Sustainable Cement-Based Materials*, 6(5), pp. 293-313.
- [5] Omrane, M., Kenai, S., Kadri, E.H, Ait-Mokhtar, A Performance and durability of self-compacting concrete using recycled concrete aggregates and natural pozzolan. *Journal of Cleaner Production* 165 (2017) 415-430.

## **SELF-COMPACTING CONCRETE WITH RECYCLED CONCRETE AGGREGATE AS ECOLOGICAL MATERIAL**

**Iva Despotović<sup>(1)</sup>, Ksenija Janković<sup>(2)</sup>, Dragan Bojović<sup>(2)</sup>, Marko Stojanović<sup>(2)</sup>**

(1) Belgrade University College of Applied Studies in Civil Engineering and Geodesy, Serbia

(2) IMS Institute, Belgrade, Serbia

### **Abstract**

The concept of sustainable development, which in addition to social and economic aspects, includes energy saving, environmental protection and the conservation of exhaustible natural resources, is a strategic goal of many economic sectors including the particular contribution expected from the construction. Self-compacting concrete contains a certain amount of powdered materials – fillers. There are various possibilities of selecting this component. If we used any of the industrial by-products, such as fly ash or silica fume, we would solve the problem of depositing these materials, and thus made concrete ecological material. The research subject presented in this paper are the properties and technology of self-compacting concrete in the fresh and hardened state, made with various mineral additives: lime, fly ash, and silica fume, wherein the aggregates used, are both natural and recycled aggregates.

### **1. Introduction**

Construction industry uses vast amounts of natural resources, simultaneously producing significant amounts of construction waste, so that it has a great impact on the environment. Annual production of concrete in the world has reached 10 billion tons, classifying concrete in the most widely used building material. Having in mind the fact that 70 % of concrete is aggregate, it is clear what the quantity of natural and crushed aggregates requires. Uncontrolled exploitation of aggregates from rivers seriously disrupts aquatic ecosystems and habitats, while the production of crushed natural aggregates increases harmful gas emissions, primarily of CO<sub>2</sub>, which are responsible for the greenhouse effect. These gases are formed during blasting rocks and during the transportation of aggregates to the usually distant urban areas. On the other hand, the amount of construction waste generated during the construction and demolition of buildings is growing rapidly, deepening the problem of disposing this

waste, which is usually solved by making planned landfills (which occupy large areas of land and disposal is costly) or illegal dumps.

One of the solutions of the mentioned problems is recycling deposited building materials, primarily concrete. This idea is not new and developed countries, like Japan, the Netherlands, Belgium and Denmark achieve a high percentage of recycling of construction waste. Recycled concrete aggregates are mostly used in road engineering, for different fillings and making non-structural elements (curbs, fences, etc). Because of the uneven quality, the possibility of various impurities to rest during recycling, larger water absorption and lower bulk density, compared to natural aggregates, recycled aggregates require a series of tests and special technology of concrete making.

Self-compacting concrete contains a certain amount of powdered materials – fillers. There are various possibilities of selecting this component. If we used any of the industrial by-products, such as fly ash or silica fume, we would solve the problem of depositing these materials, and thus made concrete ecological material.

## 2. Materials

Self – compacting concrete (SCC), according to many authors “the most revolutionary discovery of concrete industry of the 20<sup>th</sup> century”, does not need vibrating when placing and compacting. It is estimated that when using self–compacting concrete instead of vibrated concrete, the need for workers is reduced by about 10 %; when using prefabricated elements, construction time is shorter by about 5 %, and demand for workers decreased by about 20 %; when applying sandwich elements ( steel – concrete) time saving is 20%, and savings in the labour force 50%. The main disadvantages of the use of self – compacting concrete are higher material prices, stricter quality requirements and increasing pressure on the formwork compared to vibrated concrete [1].

The initiators of the idea of applying **fly ash**, resulted from coal burning, in concrete were McMillan and Powers (1934). At the end of 40s the experiments carried out in the UK (Fulton and Marshal) led to the construction of dams Lednock, Clatworthy and Lubreoch, with fly ash as a cement additive. All these structures are after 60 years in excellent condition [2].

**Silica fume** is formed during melting quartz at high temperature in an electric arc furnace, wherein silicon or ferrosilicon occurs. Due to its nature, even a small addition of silica fume significantly changes physical and chemical properties of concrete. The customary dosage of 8- 10% by weight of cement means between 50 000 and 100 000 microspheres of dust per cement grain, which directly increases the cohesion of concrete. Because of higher specific area and higher content of silicon dioxide, silica fume is much more reactive than fly ash or granulated slag. This increased reactivity initially increases hydration rate of C<sub>3</sub>S cement mineral, but after two days the process becomes normal.

**Lime** is more widely used as a cement additive than a concrete additive. The presence of lime causes the acceleration of the hydration process and hydration shrinkage of concrete in the first few hours, because the particles of lime are used as additional cores for hydration.

The use of **recycled aggregates** in structures is not new. Buck (1977) defines its beginning in the period immediately after the Second World War, when there was a tremendous need for building new facilities and infrastructure and at the same time, clearing the existing ruins. After that, the use of recycled aggregates stopped but during 70s the US started to re-use

recycled aggregates in non-construction purposes, mainly as fill material and different fillings in road engineering [3]. Due to the above mentioned reasons, testing of recycled aggregates (not just concrete) and their application are more relevant today than ever, because the need for aggregates globally reached 26.8 billion tons per year [4]. For example, the US annually recycles about 149 million tons of concrete waste. According to the data from the annual report of the European Association for aggregates (2010), recycled aggregates make 5% of the total production of aggregates in the European Union, where Germany is the largest producer, followed by Great Britain (49 million tons), the Netherlands (20 million tons) and France (17 million tons). In Australia, around 50% of the concrete waste is recycled, while in Japan, the impressive 98% of concrete waste is turned into recycled aggregate [5]. It is estimated that in the Republic of Serbia, about 1 million tons of construction waste and demolition waste is annually produced. This waste ends up in landfills of municipal waste, and is also used as inert material for coverage of waste at landfills. Recycling construction waste actually does not exist [6].

### 3. Experimental research

For the purposes of the experimental work, nine three-fraction concrete mixes have been made. Cement PC 42.5 has been used as well as mineral additives: lime (120 kg/m<sup>3</sup>), fly ash (from the power plant, 120 kg/m<sup>3</sup>), and silica fume (52 kg/m<sup>3</sup>); natural aggregate, recycled aggregate obtained by crushing demolished retaining wall. Control concrete was made with each of the additives and a natural aggregate; in mixes K50, P50 and S50, fraction 8/16mm was replaced by the recycled aggregate, and in mixes K100, P100 and S100, both coarse fractions (4/8 and 8/16) were replaced by recycled fractions. In all the mixes, superplasticizer ViscoCrete 5380 (manufacturer SIKA) has been used. The criterion in the designing mixes was to achieve the same consistency of concrete, i.e. slump-flow class SF2, which includes the usual uses of concrete and involves spreading from 66 to 75cm. When used recycled aggregate, the amount of water which was absorbed by the aggregate in 30 minutes (II fraction 2.22%, III fraction 1.5%) was added, although this principle could not be consistently applied.

#### 3.1 Test results

The test results for concrete in the fresh state are shown in Table 1.

Table 1: Test results for concrete in the fresh state

Concrete mix	Density kg/m <sup>3</sup>	Slump-flow cm	T500 s	L-box H1/H2	Sieve segregation %
EK	2418	73	4	1	12.4
EP	2288	70	4	0.94	11
ES	2416	66	6	0.91	6.8
K50	2362	70	5	0.96	12
P50	2279	70	5	0.95	7.8
S50	2324	67	5	0.94	5.2
K100	2347	69	5	1	10
P100	2298	66	6	0.91	5.5
S100	2359	66	6	0.92	7.5



Testing compressive strength was carried out on the cubes with edges of 15cm. The test results for compressive strength after 2, 7 and 28 days are shown in Chart 1.

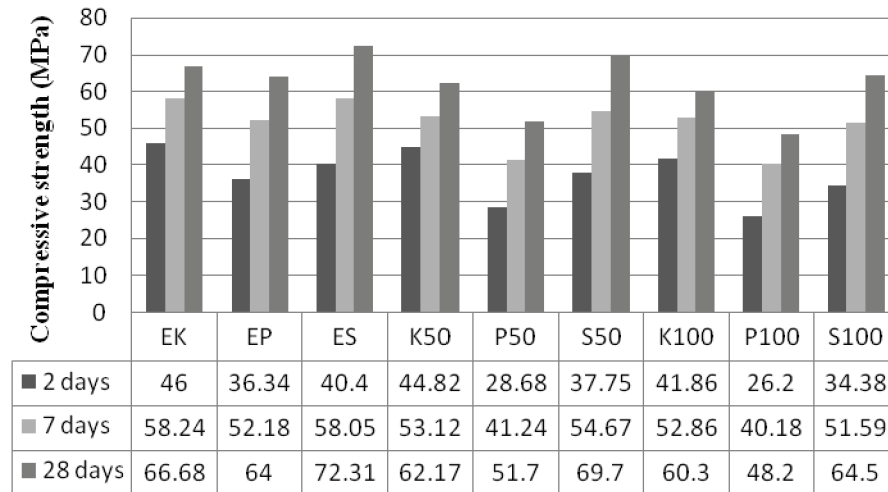


Figure 1: Compressive strength.

Shrinkage test was done on the samples of dimensions 12x12x36cm. 72 hours after the samples are made they are taken out from the water and exposed to thermo hygrometric conditions. We chose it to be  $70 \pm 5$  % air humidity and a constant temperature of  $20 \pm 4$  °C. First measurement was done  $72 \pm 0.5$  h hours after the samples were made, and then after 4 and 7 days. After this, further measurements were done after every seven days, until the process stabilized. The results of shrinkage tests after 4, 7, 14, 21, 28, and 35 days, are shown in Chart 2.

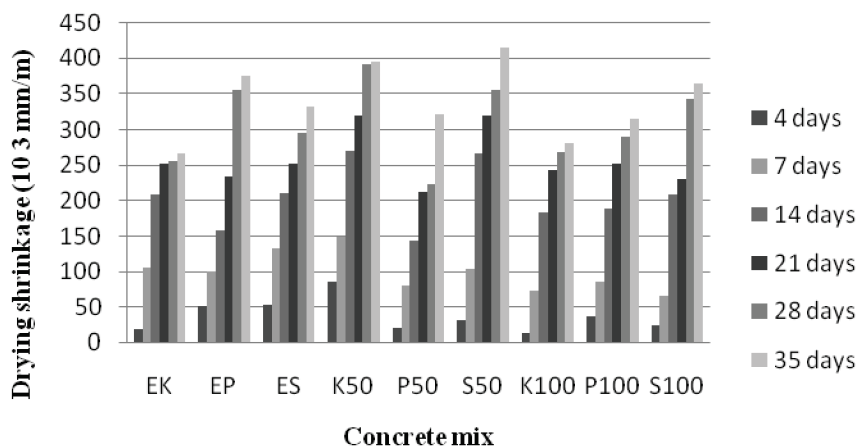


Figure 2: Shrinkage.

Scanning electron microscopy (SEM analysis) enables to “look into” the structure of concrete made and to better explain the results obtained by testing (Figure 1). Water absorption test was done on the samples of dimensions 12x12x36cm, by the method of gradual immersion. The results are in the range of 0.85% (mix S50) to 2.12% (mix EP). The highest water absorption was recorded in the mixes with fly ash, and the lowest in the mixes with silica fume, which is absolutely in accordance with the achieved concrete structure, which was,

according to SEM analyses, the most porous in concrete mixes with fly ash. Average water absorption in mixes with silica fume was 0.9%, in mixes with lime 1%, and in mixes with fly ash 2%.

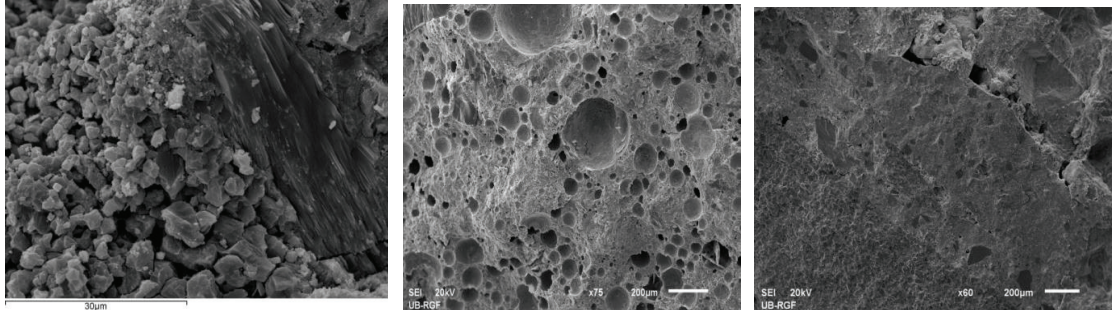


Figure3: Structure of concrete with lime, fly ash and silica fume

#### 4. Discussion

Properties of self-compacting concrete are affected both by a kind of mineral additive and a kind of the applied aggregate. Best properties of self-compacting are achieved by using lime. These concrete mixes had the best fluidity and viscosity, after passing through reinforcement they were absolutely horizontal, but because of the largest spreading, they had minimum segregation resistance. Mixes with fly ash had the best ratio of diameter of spreading (fluidity) and segregation resistance. Since they are very small and have very large area of grain ( $15\ 000$  to  $20\ 000\ \text{m}^2/\text{kg}$ ), particles of silica fume significantly increase concrete cohesion and adversely affect the fresh concrete self-compacting. Use of recycled aggregates, due to a sharp-edged shape of grains which increases adhesion, also adversely affects the properties of self-compacting concrete, so it was necessary to intervene in the sense of reducing III or increasing I fraction by 5%, in order to achieve the desired consistency.

Effect of silica fume: as concrete starts to bind and harden, pozzolanic activity of silica fume becomes the dominant reaction. Due to the high specific area and higher content of silicon dioxide, silica fume is much more reactive than fly ash. This increased reactivity will initially significantly intensify hydration rate of  $\text{C}_3\text{S}$  cement fraction, but after two days the process becomes normal. As silica fume reacts and forms calcium silicate hydrates, voids and pores in the concrete are filled, wherein crystals formed connect the space between cement particles and aggregate grains. If this effect is added by the physical presence of silica fume in the mix, it is clear that the concrete matrix will be very homogenous and dense, resulting in improved strength and impermeability, which is clearly seen in SEM pictures.

When fly ash is added to concrete, there is pozzolanic reaction between the silicon dioxide ( $\text{SiO}_2$ ) and calcium hydroxide ( $\text{Ca}(\text{OH})_2$ ) or lime, which is a by-product of hydration of Portland cement. Weak pozzolanic reaction occurs during the first 24 hours at a temperature of  $20^\circ\text{C}$ . That is why, for a given amount of cement, with increasing fly ash content, lower early compressive strength is achieved. The presence of fly ash slows the reaction of alite in Portland cement at an early stage. Slower early strengths of concrete with fly ash prevent its application where high early strength is expected, which can be solved by using accelerator.

The effect of lime: SEM analyses show the presence of lime particles in concrete even after 28 days, and on the other hand, two day increment of strength confirms that these particles

constitute the core for hydration  $C_3S$  and  $C_2S$ , so that they accelerate the reactions of hydration, which supports the thesis that lime is chemically inert. Available data from the literature, like own previous researches [7] show that it is difficult to predict or find regularities when shrinkage of concrete is in question. The measurements done show that the largest shrinkage was found in the concrete mix with silica fume and III recycled fraction, S50, and the smallest in the control concrete with lime EK, wherein the difference is 56%. No regularities can be drawn from these results. The main problem of using recycled aggregate is its increased porosity, caused by the remained old cement paste on aggregate grains. The amount of recycled aggregate affects the absorption of water in the sense that with increasing the amounts of recycled aggregates, the percentage of water absorption is also increased, as a consequence of greater porosity.

## 5. Conclusion

Using all three tested mineral additives, high performance self-compacting concretes can be obtained. Silica fume is ahead, but having in mind economic and ecological component of fly ash, as well as relatively small difference in the obtained results, fly ash should necessarily be taken into account. Besides, the use of recycled aggregates (with increased testing) makes these concretes ecological rightly considered. Insufficient research in this area opens up a wide range of options for further testing, in terms of variations in the amount of cement, combining different additives, etc.

## Acknowledgements

The work reported in this paper is a part of the investigation within the research project TR 36017 "Utilization of by-products and recycled waste materials in concrete composites in the scope of sustainable construction development in Serbia: investigation and environmental assessment of possible applications", supported by the Ministry for Education, Science and Technological Development, Republic of Serbia. This support is gratefully acknowledged.

## References

- [1] Corinaldesi V., Moriconi G., Influence of mineral additions on the performance of 100% recycled aggregate concrete, *Construction and Building Materials*, 23 (2009) 2869–2876.
- [2] Newman J., Chao B.S., *Advanced concrete Technology*, Elsevier, 2003, 280.
- [3] Meyer C., The greening of the concrete industry, *Cement & Concrete Composites* 31 (2009), 601-605.
- [4] [www.waste-environment.vin.bg.ac.rs](http://www.waste-environment.vin.bg.ac.rs)
- [5] Janssen G., Hendrik C.F., Sustainable use of recycled materials in building construction, *Advances in Building Technology*, Volume 2 (2002), 1399 – 1407.
- [6] Trumić M., Trumić M., Uloga pripreme u reciklaži otpada i održivom razvoju Srbije, Stanje i perspektive pripreme mineralnih sirovina u Srbiji, Izdavač: Inženjerska Akademija Srbije, Beograd, (2011), 73-93.
- [7] Despotović I., Uticaj različitih mineralnih dodataka na osobine samougrađujućeg betona, PhD thesis, Građevinsko- arhitektonski fakultet, Niš 2015.

## STANDARD AND INNOVATIVE CHARACTERIZATION OF STRENGTH, STIFFNESS, AND NON-AGING CREEP OF CONCRETE AT EARLY AGES

Mario Ausweger <sup>(1)</sup>, Eva Binder <sup>(1)</sup>, Olaf Lahayne <sup>(1)</sup>, Roland Reihnsner <sup>(1)</sup>, Gerald Meier <sup>(2)</sup>, Martin Peyerl <sup>(2)</sup>, Bernhard Pichler <sup>(1)</sup>

(1) TU Wien – Vienna University of Technology, Austria

(2) Smart Minerals GmbH, Vienna, Austria

### Abstract

Quantitative knowledge regarding the early-age evolutions of strength, stiffness, and creep properties of concrete are important for structures that are loaded already a few days after production. This was the motivation to characterize six concretes at early ages. The concretes were made of three types of cements (CEM II / A-M (S-L) 42.5N, CEM II/A-S 42.5R, and CEM I 52.5 R) and two types of aggregates (quartzite and limestone). The content of entrained air ranged from 2 % to 6 %. The standard tests included nondestructive loading-unloading experiments and destructive cube compression tests, performed 1, 3, 7, 14, and 28 days after production. The innovative experiments were performed according to the test protocol by Irfan-ul-Hassan et al. [1]. Three-minutes-long compression tests were performed once every hour, starting 24 hours after production and ending at material ages amounting to 8 days. Thus, each specimen was subjected to a series of 168 ultra-short creep experiments. Three minutes are *long* enough such that significant creep deformation is measured, and *short* enough such that the microstructure is virtually constant, i.e. that the chemical reaction between the cementitious binder and water does not progress significantly. Thus, each test provides access to the *non-aging* creep behavior of a specific material microstructure. Test evaluation is based on linear viscoelasticity, under explicit consideration that significant creep strains develop already during the short loading phase. Evaluation of more than 1000 three-minutes-long compression tests provided access to the hydration-induced evolutions of the elastic Young's modulus and the creep modulus of the tested concretes [2].

## 1. Introduction

For concrete structures which are loaded a few days after production, the strength, stiffness, and creep properties are of interest at the time of loading. The focus of this paper is to experimentally characterize six concretes within the first 28 days after production. Standard tests are performed according to the Austrian standard [3]. As for non-standard test methods, regularly-repeated short-term testing at early ages has become popular, see [3] as well as [4-6]. The individual tests are so short that the chemical reaction between the binder and the water does not progress significantly. Thus, each individual test provides access to the macroscopic properties of one specific material microstructure. The strategy for evaluation of ultra-short creep tests by Irfan-ul-Hassan et al. [1] is mechanically appealing, because it distinguishes rigorously between time-independent *elastic* and time-dependent *creep* deformation. In this context, it is considered that significant creep deformation develops not only during periods of constant loading, but also *during* short loading and unloading events. The availability of hundreds of ultra-short creep tests on cement pastes [1] was the motivation to perform top-down identification of creep constants of microscopic hydrate needles [7]. The latter represent the products of the chemical reaction between the binder and the water. Based on one and only one set of power-law creep *constants* of the hydrates, a multiscale model allowed for reproducing hundreds of ultra-short creep tests on cement pastes [7]. In addition, the identified creep constants of hydrates also allowed for predicting the evolution of deformation of a 30 years old cement paste subjected to a 30 days long creep test [7]. This success was the motivation to upscale the creep behavior from the scale of cement paste to the scales of mortars and concretes [8]. Thereby, it was shown that oven-dried sand and aggregates take up water during mixing of the raw materials, and that this water migrates back from the open porosity of the sand grains and the aggregates to the cement paste matrix during the hydration process [8]. Thus, the evolution of non-aging creep properties of cementitious materials at early ages could be deciphered based on the combination of repeated ultra-short creep testing with a careful test evaluation protocol and modern multiscale modeling. This was the motivation, to apply the same combined experimental-modeling strategy also to polymer modified cement pastes [9,10].

The present contribution combines standard and innovative test methods in order to gain quantitative insight into the early-age evolutions of strength, stiffness, and creep properties of six modern concretes with variable contents of entrained air. This way, a rich database of experimental results is produced supporting follow-up multiscale modeling activities in the future.

## 2. Materials

The experimental campaign involves six concrete mixes, see Table 1. They are made of three types of cement and two types of aggregates. The mass density of the quartzite and limestone aggregates is  $2.65 \text{ g/cm}^3$  and  $2.72 \text{ g/cm}^3$ , respectively. An air entrainment agent was used to arrive at an air content between 2% and 6%.

Table 1: Composition of the six concretes.

Concrete type	cement	w/c	aggregates
C30/37	CEM II / A-M (S-L) 42.5 N	0.48	quartzite / limestone
C35/45	CEM II / A-S / 42.5 R	0.45	quartzite / limestone
C40/50	CEM I / 52.5R	0.42	quartzite / limestone

### 3. Standard testing of strength and stiffness

In order to quantify the compressive strength and the unloading modulus at material ages amounting to 1, 3, 7, 14, and 28 days after production, standard tests were carried out according to the European standards, see the Austrian application document [3]:

- The compressive strength is quantified by means of cube compression test. Dividing the cube compressive strength by the factor 1.2 delivers the cylinder compressive strength.
- The unloading modulus is quantified as the average of at least three unloading cycles on a cylindrical specimen, whereby the unloading modulus is the quotient of the stress and strain differences observed during unloading from  $1/3$  to  $1/30$  of the compressive strength.

In order to study the effect of curing conditions, two types of strategies for storage of specimens were used. Both of them referred to quasi-isothermal curing at  $20^{\circ}\text{C}$ :

- Standard storage: The specimens remained in the mold for at least 16 hours and a maximum of three days. After demolding, the specimens were stored under water up to a material age of seven days. After that, specimens for compressive strength tests were exposed to the ambient air, while specimens used for quantification of the unloading modulus were stored always under water.
- Sealed storage: The specimen remains in the mold for about 24 hours. After demolding, the specimens were sealed by several layers of food preservation foil, in order to avoid significant drying.

For the standard testing methods, each concrete mixture was produced with an air content of either 2% or 6%. Exemplary experimental results are shown in Fig. 1.

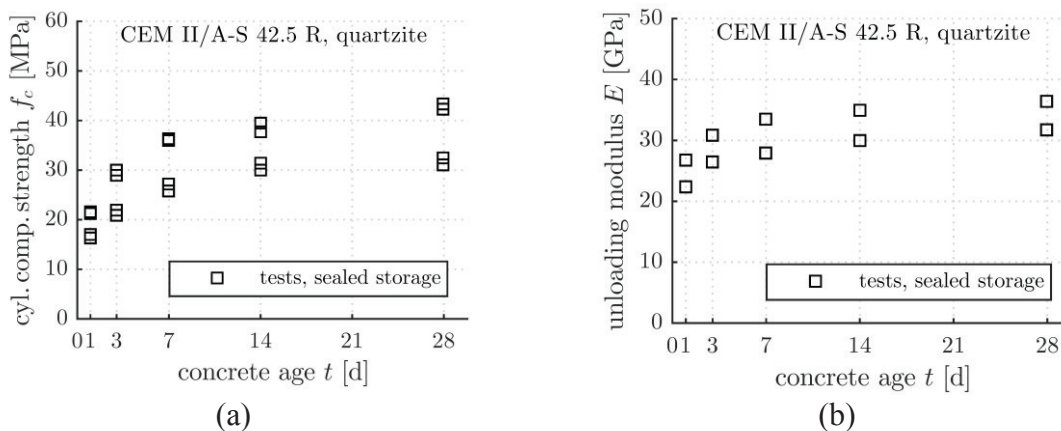


Figure 1: Experimental results of the standardized tests for the C35/45 concrete with quartzite and air contents of 2% and 6%, see the larger and the smaller values, respectively.

#### 4. Innovative testing of stiffness and creep properties

In order to characterize the early-age development of stiffness and creep properties, the experimental protocol of Irfan-ul-Hassan et al. [1] is used. This test protocol includes hourly repeated three-minutes-long creep tests under uniaxial compression. The test setup consists of a serial arrangement of one specimen (diameter = 7 cm, height = 30 cm) and two metal cylinders, for achieving a central load application [1]. Five linear variable differential transducers (LVDTs, type Hottinger Baldwin) are used for the quantification of the deformation. The first three-minutes-long creep test on the sealed specimens is carried out 24 hours after their production. Hourly testing is repeated until the tested specimens reach an age of eight days. Each specimen undergoes 168 loading-unloading cycles during the first week after production. In order to ensure that the specimens remain undamaged, the maximum forces are selected such that the loading does not exceed 20% of the strength of the specimen at the time of testing. The Young's modulus and the creep modulus of the microstructure present at the time of testing can be quantified based on the force readings and the averaged LVDT readings.

Concretes respond to any applied stress in a viscoelastic fashion, i.e. with a spontaneous *elastic* and a time-dependent *creep* deformation response. The viscoelastic behavior of concrete can be described by a power-law creep function, see also [11]:

$$J(t - \tau) = \frac{1}{E} + \frac{1}{E_c} \left( \frac{t - \tau}{t_{ref}} \right)^\beta, \quad (1)$$

where  $E$  denotes the Young's modulus,  $E_c$  the creep modulus,  $t - \tau$  the time elapsed since sudden loading,  $t_{ref} = 1$  day a constant reference time, and  $\beta$  a dimensionless creep exponent. Macroscopic creep of cementitious materials results from the viscoelastic behavior of microscopic hydrate needles which are reaction products of cement and water. Micromechanical investigations have shown that the hydrate needles have constant creep properties. Thus, also their creep exponent is a time-independent material constant:  $\beta = 0.25$  [7]. Furthermore, Königsberger et al. [7] showed that the same exponent also applies at the much larger scale of cement paste. This is the motivation to set the creep exponent  $\beta$  for concrete also equal to 0.25. Thus, only the elastic modulus and the creep modulus need to be identified from the measured data of each three-minutes-long creep test. Given that significant creep deformation already develops during the short loading period, it is necessary to calculate the viscoelastic strain response for a variable stress history. Since the examined specimens are loaded with a maximum of 20% of the compressive strength, there is a linear relationship between stresses and strains. Thus, Boltzmann's superposition principle can be used:

$$\varepsilon_{mod}(t) = \sum_{i=1}^n J(t - \tau_i) \Delta\sigma(\tau_i), \quad (2)$$

where the modeled strain  $\varepsilon_{mod}(t)$  results from the sum of the individual strains due to sudden stress jumps  $\Delta\sigma$ . In an ideal creep test, in which the load is applied infinitely fast, the sum in Eq. (2) would reduce to one single term. In a real experiment, however, the loading cannot be

applied infinitely fast. Thus, the loading process is subdivided into a sequence of many small stress jumps, see [1] for further details.

The Young's modulus  $E$  and the creep modulus  $E_c$  are identified for each individual creep test. This is done by minimizing the sum of squared error,  $E_{srss}$ , between the experimentally determined strains  $\varepsilon_{exp}(t_i)$  and the modeled strains  $\varepsilon_{mod}(t_i)$ :

$$E_{srss}(E, E_c) = \sqrt{\frac{1}{N} \sum_{i=1}^N [\varepsilon_{exp}(t_i) - \varepsilon_{mod}(t_i)]^2} \rightarrow \min. \quad (3)$$

Therein,  $N$  is the total number of experimental readings considered for test evaluation during the load application phase *and* the subsequent load holding phase. The optimization problem in Eq. (3) is solved iteratively. At first, search intervals for the Young's modulus and the creep modulus are defined and subdivided in seven equidistant values. For all  $7 \cdot 7 = 49$  parameter combinations, representing a search grid, the error function in Eq. (3) is evaluated. The combination of values for  $E$  and  $E_c$ , which results in the smallest error value, is treated as an initial estimate of the optimum solution. Depending on the position of this estimate within the search grid, the grid is shifted and/or refined, in order to define a new search grid. Thus, a sequence of progressively refined search grids is used, until both the Young's modulus and the creep modulus are identified up to an accuracy of 0.001GPa.

The optimization procedure was applied to each individual three-minutes-long creep test. As a result, the evaluation of the test data allows for a quasi-continuous quantification of the early-age development of Young's modulus and creep modulus. Covering air contents from 2% to 6%, the specimens exhibit similar evolutions of their stiffness and creep properties. Exemplary experimental results referring to the C35/45 concretes with quartzite are shown in Fig. 2.

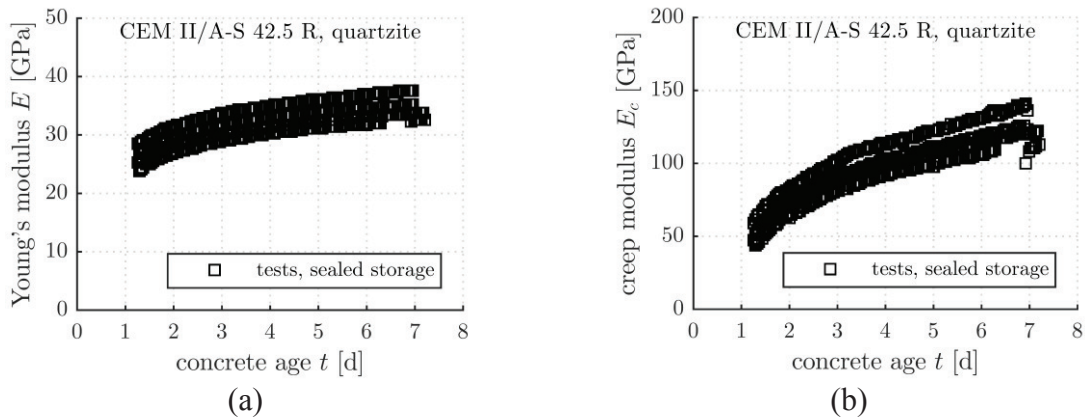


Figure 2: Exemplary experimental results of the innovative tests for the C35/45 concrete with quartzite and air pore contents in the range from 2% to 6%; information on the exact value of the air content is not available; due to the page-limit not all results are shown.



## 5. Summary and conclusions

Standard and innovative testing methods were combined for the experimental characterization of six concretes within the first 28 days after production. The standard tests provide quantitative insight into the evolution of strength and stiffness. The innovative short-time creep tests provide access to the stiffness and the non-aging creep properties at early ages. The stiffness evolutions from both testing methods are in good agreement, see Fig. 1(b) and 2(a). The testing campaign comprises some 120 strength tests, 60 stiffness tests, and more than 1000 short-time creep tests. The resulting database will be used for the development and validation of future multiscale models.

## Acknowledgment

Financial support by the Austrian Research Promotion Agency (FFG), provided within VIF-project 850554 "ÖBB – Österreichischer Betonbenchmark zur Steigerung der Vorhersagequalität mechanischer Eigenschaften moderner Betone" is gratefully acknowledged.

## References

- [1] M. Irfan-ul-Hassan, B. Pichler, R. Reihnsner, Ch. Hellmich: Elastic and creep properties of young cement paste, as determined from hourly repeated minute-long quasi-static tests, *Cement and Concrete Research*, 82, 36-49 (2016).
- [2] M. Ausweger: Quantification and prognosis of early-age development of strength, stiffness, and creep properties of modern Austrian concretes, Master Thesis, TU Wien – Vienna University of Technology, Austria (2017).
- [3] ONR 23303: Prüfverfahren Beton (PVB) – Nationale Anwendung der Prüfnormen für Beton und seine Ausgangsstoffe (2010).
- [4] P. Karte, M. Hlobil, R. Reihnsner, W. Dörner, O. Lahayne, J. Eberhardsteiner, B. Pichler: Unloading-based stiffness characterisation of cement pastes during the second, third and fourth day after production, *Strain*, 51 (2015), 156-169.
- [5] B. Delsaute, C. Boulay, J. Granja, J. Carette, M. Azenha, C. Dumoulin, G. Karaiskos, A. Deraemaeker, S. Staquet: Testing concrete E-modulus at very early ages through several techniques: An inter-laboratory comparison, *Strain*, 52 (2016), 91-109.
- [6] B. Delsaute, C. Boulay, S. Staquet: Creep testing of concrete since setting time by means of permanent and repeated minute-long loadings. *Cement and Concrete Composites*, 73, 75–88, (2016).
- [7] M. Königsberger, M. Irfan-ul-Hassan, B. Pichler, Ch. Hellmich: Downscaling based identification of nonaging power-law creep of cement hydrates, *Journal of Engineering Mechanics (ASCE)*, 142, 04016106 (2016).
- [8] M. Irfan-ul-Hassan, M. Königsberger, R. Reihnsner, Ch. Hellmich, B. Pichler: How water-aggregate interactions affect concrete creep: A multiscale analysis, *Journal of Nanomechanics and Micromechanics (ASCE)*, 7(4), 04017019 (2017).
- [9] L. Göbel, A. Osburg, B. Pichler: The mechanical performance of polymer-modified cement pastes at early ages: ultra-short non-aging compression tests and multiscale homogenization, *Construction and Building Materials*, 173 (2018) 495-507.
- [10] L. Göbel, M. Königsberger, A. Osburg, B. Pichler: Viscoelastic behavior of polymer-modified cement pastes: Insight from downscaling short-term macroscopic creep tests by means of multiscale modeling, *Applied Sciences*, 8(4), 487 (2018).

## **STRESS DISTRIBUTION IN RESTRAINED RING TEST DUE TO DRYING AND AUTOGENOUS SHRINKAGE**

**Semion Zhutovsky** <sup>(1)</sup>

(1) National Building Research Institute – Faculty of Civil and Environmental Engineering  
Technion – Israel Institute of Technology, Haifa 32000, Israel

### **Abstract**

Cracking of concrete is crucial from point of view of both durability and mechanical properties. With the extensive use of high-performance concretes that have low water to cement ratios, cracking sensitivity of concrete becomes even more important concern. Testing of concrete shrinkage restrained by steel ring turned into a standard for evaluation of the concrete potential for cracking. The stress at cracking in concretes with w/c ratios of 0.7, 0.45, 0.33, 0.25 and 0.21 was determined by means of restrained ring test and compared with the splitting tensile strength. The results show the significant change of stress to strength ratio at cracking with the change of water to cement ratio. Analysis of stresses was performed considering two types of shrinkage: drying shrinkage and autogenous shrinkage. Because drying shrinkage is driven by external drying that causes moisture gradient across the specimen and autogenous shrinkage is driven by internal drying – self-desiccation – that is uniformly distributed, stress distribution caused by these two types of shrinkage is significantly different. The analysis of the distribution of stresses in the restrained concrete ring due to autogenous and drying shrinkage provides a good explanation of the observed experimental data.

### **1. Introduction**

Cracking of concrete is an important issue for both durability and mechanical performance of concrete structures[1]. The extended use of high performance concretes (HPC) which are more sensitive to cracking has generated renewed interest in the early age cracking of concretes [2,3]. It has become clear that the cracking potential of concrete cannot be estimated just by the shrinkage [4,5]. Although shrinkage of concrete is the driving force for cracking, it is not the only parameter which needs to be considered. This understanding is especially

important in the view of the development of special technologies to control cracking, such as internal curing and shrinkage reducing admixtures [6–8]. As the result, new testing techniques have been developed to assess directly the cracking based on set-ups which can provide quantitative information beyond the time to cracking [9–13].

Testing of concrete shrinkage restrained by steel ring turned into a standard for evaluation of the concrete potential for cracking [13]. The ASTM C1581 test is one example [14]. The potential for cracking in such test is determined using either criterion of the net time to cracking or average stress rate. In addition to the thermal strains, two types of shrinkage need to be considered in evaluating cracking potential: drying shrinkage and autogenous shrinkage [15]. Drying shrinkage is driven by external drying from the concrete surface. Such drying causes moisture gradient across the specimen. Accordingly, drying shrinkage strain, at the early ages, is distributed from the maximum at the surface to the minimum at the inner core of the concrete. Autogenous shrinkage, on the other hand, is driven by internal drying called self-desiccation. For this reason, autogenous shrinkage strain in sealed concrete is uniformly distributed. In case of restrained shrinkage, due to the difference in the driving forces stresses distribution caused by these two types of shrinkage is significantly different. However, in the restrained shrinkage ring test, the stress is estimated as an average based on the measurements of the strain gages that are bonded to the inner surface of the restraining steel ring. Thus, the test results do not consider the distribution of stresses in the concrete sample.

Restrained ring test was performed on concretes with w/c ratios of 0.7, 0.45, 0.33, 0.25, and 0.21 and stress at cracking was compared with the splitting tensile strength. Experimental results show that in the case of the concretes with high water to cement (w/c) ratio, cracking takes place at a stress which is 37 to 56% higher than the splitting tensile strength, while the concretes with low water to cement ratio, the stress at cracking can be about 21% lower than the splitting tensile strength. This can be explained by the fact that the ratio of drying to autogenous shrinkage changes significantly with the reduction of water to cement ratio [16]. To support this assumption, analysis of stress distribution in restrained ring sample due to drying and autogenous shrinkage was performed. The results of stresses distribution provide a good explanation to the observed phenomena.

## **2. Materials and methods**

### **2.1 Mixture composition**

The mix composition is given in Table 1. The mix notation designate w/c ratio, so that 21, 25, 33, 45 and 70 stand for w/c ratios of 0.21, 0.25, 0.33, 0.45, and 0.70, respectively. In all mixes Portland cement CEM I 52.5 N was used. The mix compositions were adjusted with superplasticizing admixture to keep the workability similar. The superplasticizer was Rheobuild 2000 admixture produced by WR Grace, USA. The concretes were made with 14 mm maximum size dolomite as a coarse aggregate and sea sand as a fine aggregate.

### **2.2 Testing procedure**

The potential for cracking was determined by restrained shrinkage ring test following the standard procedure of ASTM C1581-04, 2004 [14]. Concrete was cast into the ring mold with 330 mm and 406 mm inner and outer diameters, respectively, and 150 mm height. The specimens were demolded and exposed to drying at one day in a controlled environment of

50±4% RH and 20±2°C. The measurements included continuous monitoring of the strain developed in the steel ring. The results of the ring tests were obtained in terms of strain-time curves. Cracking was identified by a sharp sudden decline in the strain. Cracking sensitivity was quantified according to the ASTM C 1581 in terms of the time to cracking and stress rate to cracking, determined at the time of cracking. Splitting tensile strengths were tested on cube specimens of 50 mm size at 1, 7, 28, and 90 days. The specimens for strength tests were demolded after 1 day and cured at conditions identical to those of the rings.

Table 1 Concrete composition (kg/m<sup>3</sup>)

Mix Notation	Cement	Mix Water	Sand	Gravel
21	667	140	532	1145
25	600	150	562	1145
33	506	167	572	1145
45	450	203	504	1191
70	291	213	652	1191

### 3. Results and discussion

#### 3.1 Cracking potential and stress to strength ratio at cracking

The strain that was measured in the restraining steel was used to evaluate the stress in the concrete according to equation proposed by See et al. [9]:

$$\sigma_t(t) = E_s \varepsilon_s(t) \frac{r_{ic} h_s}{r_{is} h_c} \quad (1)$$

where  $\varepsilon_s(t)$  is an elastic strain in steel ring at a time  $t$ ,  $E_s$  is the modulus of elasticity of steel ring,  $r_{is}$  and  $r_{ic}$  are internal radii of steel ring and of the concrete ring, respectively,  $h_s$  and  $h_c$  are thicknesses of steel ring and of the concrete ring, respectively.

In Figure 1, the stresses calculated according to the equation (1) for all concrete mixes are given. The data for sensitivity to cracking is presented in Figure 2 for both criteria, time to cracking and stress rate to cracking. The Figure 2 presents also the classification as outlined in the ASTM standard. Since the classification according to each of these criteria do not always coincide with each other, the integrated criterion suggested by Kovler and Bentur [13] was used, which is obtained by dividing the stress rate by the net time to cracking. The effect of w/c ratio on the integrated cracking potential criterion is presented in Figure 3. The data in this figure clearly shows the effect of reduction of w/c ratio on the increase of cracking sensitivity, as well as a demarcation line between the HPC and NSC which can be identified in the proximity to w/c ratio of 0.4. Figure 2 demonstrates that for HPC the tendency for increased cracking sensitivity rises steeply with the reduction of w/c ratio, while for NSC the reduction of w/c ratio results in an only modest increase in cracking potential. The increased cracking sensitivity of HPC should be emphasized in the view of the logarithmic base of the cracking criteria scale.

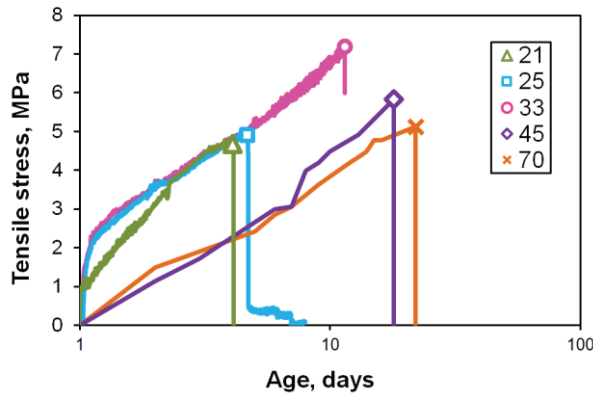


Figure 1: Stress build-up in concretes during the ring test

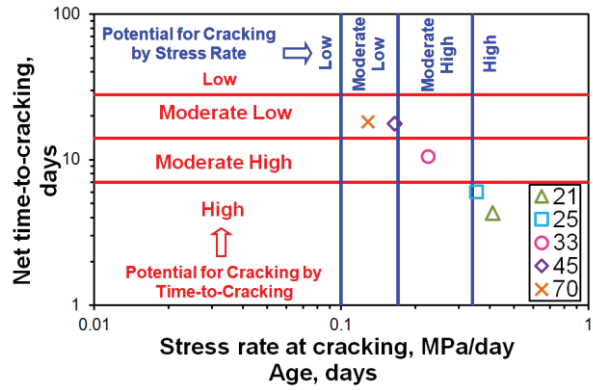


Figure 2: Cracking sensitivity of concretes by the standard cracking potential criteria

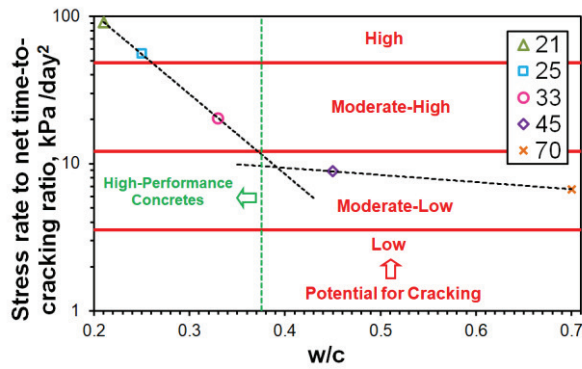


Figure 3: Cracking sensitivity of concrete by the integrated cracking potential criterion

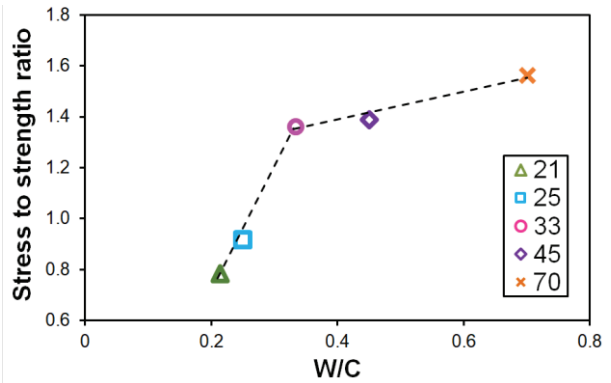


Figure 4: Stress to strength ratio at of concrete at cracking

In Figure 1, it can be clearly seen that the stress build-up rate is very high in the first few days in the concretes with  $w/c$  ratio of 0.33 and lower. This is consistent with the demarcation boundary in Figure 2. The obvious explanation for the big difference between the higher and lower  $w/c$  ratio concretes is in the autogenous shrinkage which takes place mainly within the first day or two. The occurrence of cracking can be expected to take place when the tensile strength and stress curves intersect. This is indeed roughly the case, but there are some variations which have significance. The ratio of the stress at cracking to is splitting tensile strength shown in Figure 4. In the case of the higher  $w/c$  ratio, cracking takes place at a stress which is about 56, 39 and 37% higher than the strength, for  $w/c$  ratios of 0.70, 0.45, and 0.33, respectively. While at the lower  $w/c$  ratios of 0.25 and 0.21 concrete cracks at a stress which is 8 and 21% lower than the splitting tensile strength, respectively. This difference in trends might be explained on the basis of the nature of shrinkage in the ring test. In the higher  $w/c$  ratio concretes, shrinkage is induced by external drying and the result is stress distribution in the ring due to the fact that the outer surface is shrinking first, leading to a stress gradient resulting in cracking which starts at the outer surface and gradually penetrates inwards. In the lower  $w/c$  ratio concretes, the shrinkage is largely due to internal drying, which is uniform, and it is therefore expected that cracking will start at the inner surface of the ring in these concretes.

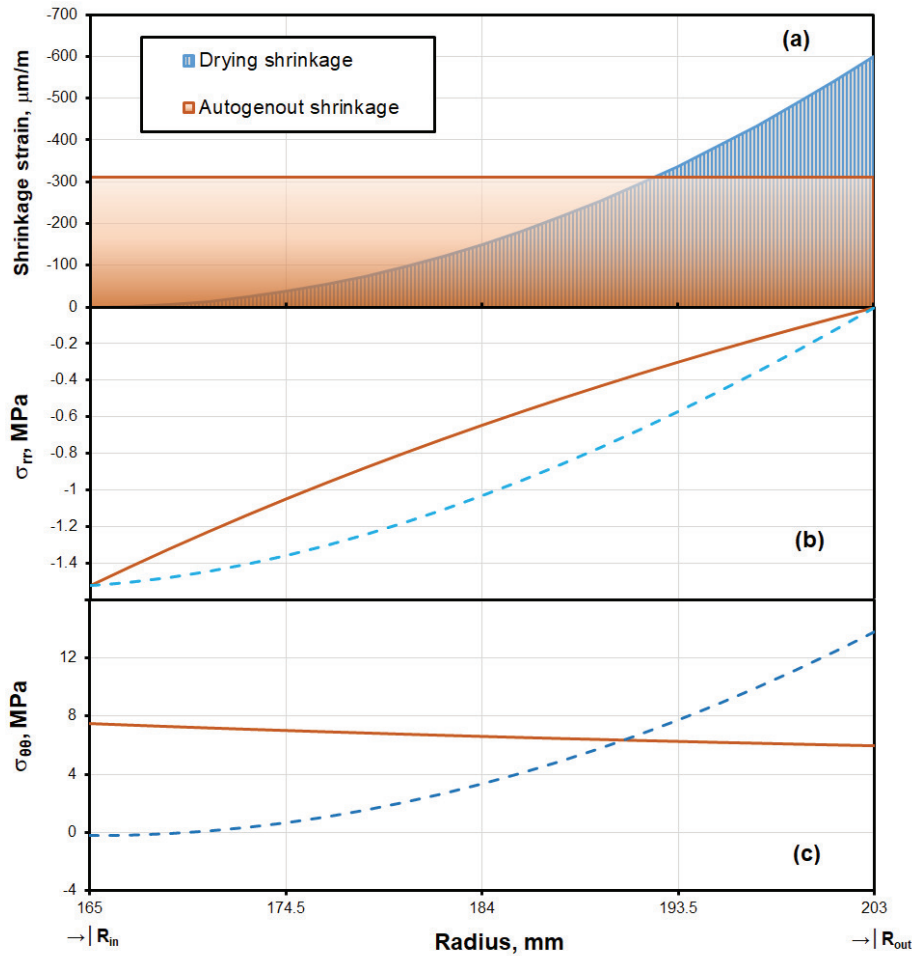


Figure 5: Stresses distribution induced by autogenous (solid lines) and drying (dotted line) shrinkage

### 3.2 Analysis of strains

Let us consider two distributions of shrinkage strains as shown in Figure 5a: (i) uniform strain distribution caused by autogenous shrinkage and (ii) parabolic strain distribution (for the sake of simplicity) caused by drying shrinkage. Solving equilibrium equation for plain stresses in the concrete ring with boundary conditions of zero radial displacement at the inner radius and zero radial stress at the outer radius we obtain the stress distributions as shown in Figure 5 b and Figure 5 c. Note that the relative magnitude of autogenous and drying shrinkage was adjusted to give the same normal radial pressure on the steel ring, i.e. the strain gages on the steel ring will measure the same strain, which will result in the same average stress in the concrete ring calculated according to the equation (1). However, as can be seen in Figure 5 c, the distribution of tangential stresses in the concrete ring is significantly different for the cases of autogenous and drying shrinkage. When shrinkage is induced by external drying, the outer surface is shrinking first, leading to a stress gradient resulting in cracking which starts at the outer surface and gradually penetrates inwards. The crack can be arrested in its propagation, especially when considering that the higher w/c ratio concretes are somewhat ductile. As a result, the mode of failure resembles more flexural type behavior, where the calculated

flexural strength is higher than the "pure" tensile one. In the case of autogenous shrinkage is the tensile stress distribution is uniform and the volume of concrete subjected to tensile stress is larger. Thus, the probability of cracking is higher and the cracking occurs when the tangent stress at the inner ring surface reaches tensile strength, and perhaps lower, considering the more brittle nature of these concretes. In this way, the difference in stresses distribution in concrete ring caused by autogenous versus drying shrinkage can satisfactorily explain the phenomena of strength to stress ratio change with the change of w/c ratio observed in Fig. 4.

## References

- [1] A. Bentur, S. Igarashi, K. Kovler, Prevention of Autogenous Shrinkage in High- Strength Concrete by Internal Curing Using Wet Lightweight Aggregates., *Cem. Concr. Res.* 31 (2001) 1587–1591.
- [2] E. Holt, M. Leivo, Cracking risks associated with early age shrinkage, *Cem. Concr. Compos.* 26 (2004) 521–530.
- [3] A. Bentur, K. Kovler, Evaluation of early age cracking characteristics in cementitious systems, *Mater. Struct.* 36 (2003) 183–190.
- [4] S.A. Altoubat, D.A. Lange, Creep, shrinkage, and cracking of restrained concrete at early age, *ACI Mater. J.* 98 (2001) 323–331.
- [5] S.A. Altoubat, D.A. Lange, The Pickett effect at early age and experiment separating its mechanisms in tension, *Mater. Struct. Constr.* 35 (2002) 211–218.
- [6] S. Weber, H.W. Reinhardt, A New Generation of High Performance Concrete: Concrete with Autogenous Curing, *Adv. Cem. Based Mater.* 6 (1997) 59–68.
- [7] O.M. Jensen, P.F. Hansen, Water-Entrained Cement-Based Materials II: Experimental Observations, *Cem. Concr. Res.* 32 (2002) 973–978.
- [8] S. Zhutovsky, K. Kovler, A. Bentur, Effect of hybrid curing on cracking potential of high-performance concrete, *Cem. Concr. Res.* 54 (2013).
- [9] H.T. See, E.K. Attiogbe, M.A. Miltenberger, Shrinkage Cracking Characteristics of Concrete Using Ring Specimens, *ACI Mater. J.* 100 (2003) 239–245.
- [10] E.K. Attiogbe, H.T. See, M.A. Miltenberger, Cracking Potential of Concrete under Restrained Shrinkage, in: *Adv. Cem. Concr. Vol. Chang. Cracking, Durab., Engineering Conferences International*, Copper Mountain, CO, USA, 2003: pp. 191–200.
- [11] K. Kovler, J. Sikuler, A. Bentur, Restrained shrinkage tests of fibre-reinforced concrete ring specimens: effect of core thermal expansion, *Mater. Struct.* 26 (1993) 231–237.
- [12] K. Kovler, Testing System for Determining the Mechanic Behavior of early age concrete under restrained and free uniaxial shrinkage, *Mater. Struct.* 27 (1994) 324–330.
- [13] K. Kovler, A. Bentur, Cracking Sensitivity of Normal- and High-Strength Concretes, *ACI Mater. J.* 106 (2009) 537–542.
- [14] ASTM C1581-04, Standard Test Method for Determining Age at Cracking and Induced Tensile Stress Characteristics of Mortar and Concrete under Restrained Shrinkage, American Society for Testing and Materials, 2004.
- [15] K. Kovler, S. Zhutovsky, Overview and future trends of shrinkage research, *Mater. Struct. Constr.* 39 (2006).
- [16] E. ichi Tazawa, S. Miyazawa, Experimental Study on Mechanism of Autogenous Shrinkage of Concrete, *Cem. Concr. Res.* 25 (1995) 1633–1638.

## **STUDY ON CHARACTERISTICS OF TENSILE STRENGTH OF CONCRETE CONSIDERING TEMPERATURE DEPENDENCE IN MASS CONCRETE STRUCTURES**

**Hiroki Izumi<sup>(1)</sup>, Jun-ichi Arai<sup>(1)</sup>, Toshiaki Mizobuchi<sup>(1)</sup>**

(1) Department of Civil and Environmental Engineering, Hosei University, Japan

### **Abstract**

It is important to grasp mechanical and thermal properties in order to verify the possibility of thermal cracking. In this study, for the purpose of improving the accuracy of analysis in prediction of cracking caused by thermal stress, it was investigated that the direct tensile strength and thermal properties considering temperature history inside concrete member may be applied as a design values for the analysis of prediction of cracking caused by thermal stress. From results of these experiments, in early age, the direct tensile strength under mass curing which is considered temperature history inside concrete member is higher than the splitting tensile strength under standard curing. However, the direct tensile strength under mass curing is lower than the splitting tensile strength under standard curing after 7 days. At 28 days, the strength of former was about 20% lower than that of latter. And the thermal expansion coefficient was estimated using measured values of strain and temperature. In this paper, it was reported that the test method of direct tensile strength considering temperature history inside concrete member was proposed and that the accuracy of analysis for the prediction of thermal cracking by using this method would be improved.

### **1. Introduction**

It is necessary to grasp mechanical and thermal properties of concrete exactly for improving of precision of the prediction for thermal cracking. Since thermal cracking occur when the tensile stress of concrete exceeds the tensile strength, it is particularly important to estimate the tensile stress and tensile strength definitely. Currently the tensile strength is required by the splitting tensile test. However, there is problem that the tensile stress does not occurs uniformly as a constraint stress is generated in the neighbourhood of loading point in the splitting tensile test. Further since specimens of standard curing under water of 20°C are used,



it cannot consider effects of temperature inside mass concrete member. Therefore, the tensile strength should be required by the direct tensile test using specimen considering the temperature history. In this study, the test method of direct tensile strength under mass curing which was conveniently obtained in site was proposed.

## 2. Outline of Experiment

### 2.1 Case studied

In this study, since the subject of investigation is mass concrete structure, six types of cement described in Guidelines for Control of Cracking of Mass Concrete 2016 published by Japan Concrete Institute (hereinafter referred to as JCI2016). For each cement, water to cement ratio was set to three levels of 45%,50% and 60%. In this experiment, the target slump was  $8\pm 1.5$ cm and the target air content was  $4.5\pm 1.0$ %. For each cement, unit content of water to satisfy the required quality of these fresh concrete was selected. Table 1 shows case studied.

### 2.2 Experimental method

**Method of investigation of mechanical properties.** The test device to evaluate thermal and mechanical properties using insulation container is shown in Fig. 1. The specimens of the both side in the device were used for the direct tensile test to investigate the tensile properties considering influence of temperature history inside mass concrete member. The direct tensile test was carried out at age of 3 days, 7 days, 14 days, 28 days using three specimens for each age. Loading rate is 0.05 N/sec by using oil pressure type universal testing machine. Further the compressive test and the splitting tensile test were carried out at age same as the direct tensile test.

**Method of investigation of thermal properties.** The temperature history measured by the specimen, which is  $\varnothing 300$  mm  $\times$  400 mm high, in the middle of the insulation container was used for the identification analysis by the temperature analysis to investigate insulation temperature rise properties. The formula described in JCI2016 were refed to estimate adiabatic temperature rise characteristics. And the relationship between the temperature amount of change and the strain amount of change used to calculate coefficient of thermal expansion.

Table 1: Concrete mixes investigated in this study.

kinds of cement	mark	water cement ratio W/C (%)	unit quantity (kg/m <sup>3</sup> )	
			water W	cement C
Normal Portland cement	N45	45	157	349
	N50	50	158	316
	N60	60	154	257
Moderate Portland cement	M45	45	157	349
	M50	50	157	314
	M60	60	157	262
Low-heat Portland cement	L45	45	157	349
	L50	50	157	314
	L60	60	157	262
High-early-strength Portland cement	H45	45	157	349
	H50	50	157	314
	H60	60	157	262
Portland blast-furnace cement B class	BB45	45	157	349
	BB50	50	154	308
	BB50	60	154	257
Fly ash cement B class	FB45	45	157	349
	FB50	50	157	314
	FB60	60	157	262

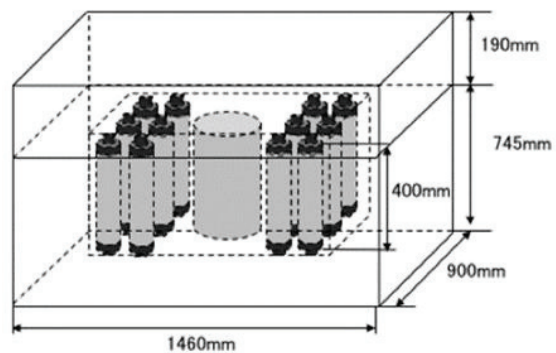


Figure 1: Layout of insulation container to evaluate thermal and mechanical properties conveniently.

### 3. Results of experiment

#### 3.1 Mechanical properties

**Tensile strength.** Figure 2 shows one case of the result of comparison between the direct tensile strength development considering influence of temperature history inside mass concrete member and the splitting tensile strength development under water of 20°C (BB50). The direct tensile strength is higher than the splitting tensile strength by the effect of temperature rise until age of 7 days. However the splitting tensile strength is higher than the direct tensile strength after age of 7 days. Though it is different by a kind of the cement, the splitting tensile strength is higher the direct tensile strength at age of 28 days in most cases. There is 20% of differences between the splitting tensile strength under water of 20°C and the direct tensile strength considering influence of temperature history inside mass concrete member at age of 28 days. Figure 3 shows example of the relationship between the splitting tensile strength under standard curing and the direct tensile strength considering influence of temperature history inside mass concrete member in all cases. The direct tensile strength considering influence of temperature history inside mass concrete member is lower than the splitting tensile strength under water of 20°C in area of that the splitting tensile strength under water of 20°C is beyond 2 N/mm<sup>2</sup>. And the direct tensile strength considering influence of temperature history inside mass concrete member is higher than the splitting tensile strength under standard curing in area of that the splitting tensile strength under water of 20°C is within 2 N/mm<sup>2</sup>. This is because the direct tensile strength development given a temperature history is early. Considering the mentioned above point, if the direct tensile strength considering influence of temperature history inside mass concrete member is near to structure body strength, it is evaluated the safe side for occurring cracking in area of that the tensile strength is within 2 N/mm<sup>2</sup> and the danger side for occurring cracking in area of that the tensile strength is beyond 2 N/mm<sup>2</sup>.

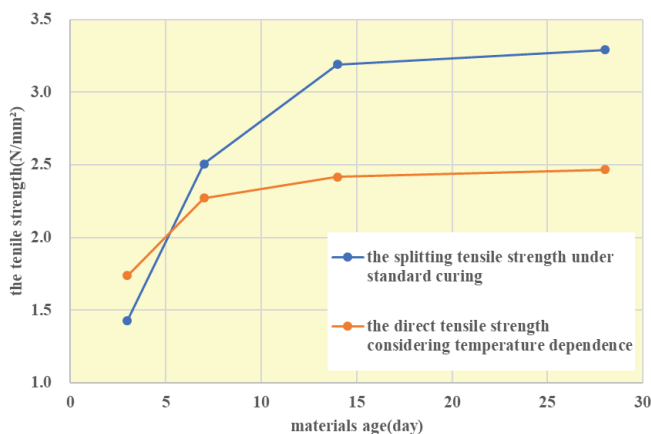


Figure 2: Tensile strength development considering influence of temperature history (BB50).

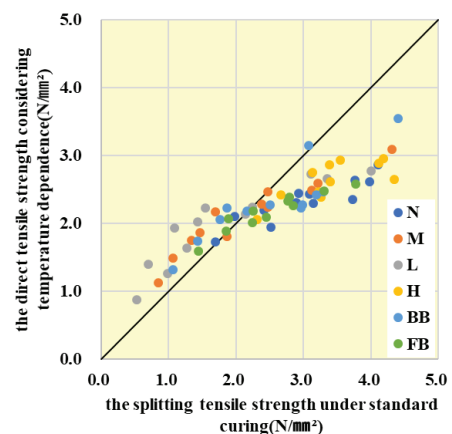


Figure 3: The relationship between the splitting tensile strength and the direct tensile strength.

**The estimated formula on the strength development of direct tensile strength.** The direct tensile strength development coefficient Eq. (1) and the direct tensile strength development

equation in management materials age 28 days considering influence of temperature history inside mass concrete member and a kind of cement are made based on the compressive strength development equation described in JCI2016 using the result of the direct tensile test.

$$f_s(t_e) = ((t_e - S_f)/(A+B(t_e - S_f)) \times f_t(t_n) \quad (1)$$

where :

$t_e$ : effective material age(day)

$t_n$ : manegement materials age of cocrete under standard curing(day)

$f_t(t_e)$ : the direct tensile strength at effective materials age  $t_e$

$A, B$ : coefficient expressed the tensile strength supported a kind of cement

$S_f$ : effective materials age expressed the hardening origin supported a kind of cement

$f_t(t_n)$ : the direct tensile strength at manegement materials age  $t_n$

Table 2 shows each coefficient of the estimated formula on the strength development of the direct tensile strength and the estimated formula on the strength development of the direct tensile strength considering a kind of cement at manegement materials age 28 days made using result of the direct tensile test. The tensile strength of structure can be estimated directly by using the estimated formula on the strength development of the direct tensile strength.

Figure 4 shows one case of the result of comparison between the tensile strength calculated using the estimated formula on the strength development of the direct tensile strength shown in Table 2 and using the estimated equation described in JCI2016(N50). the estimated formula on the strength development of the direct tensile strength made from the test result is nearer to the experimental value than that described in JCI2016.

Table 2 : Coefficients determined for strength development formula.

	A= $\alpha_1 + \beta_1 (C/W)$		B= $\alpha_2 + \beta_2 (C/W)$		$S_f$	$f_t = P_1 + P_2 (C/W)$	
	$\alpha_1$	$\beta_1$	$\alpha_2$	$\beta_2$		P1	P2
N	6.27	-1.49	0.64	0.19	0.37	1.17	0.75
M	11.2	-2.25	0.11	0.70	0.42	-0.13	1.42
L	16.5	-4.87	0.47	0.17	0.50	0.23	1.17
H	16.6	-6.52	0.96	0.00	0.30	2.62	0.14
BB	4.58	0.74	0.27	0.32	0.42	-1.66	2.24
FB	8.40	-2.30	0.75	0.10	0.47	1.85	0.32

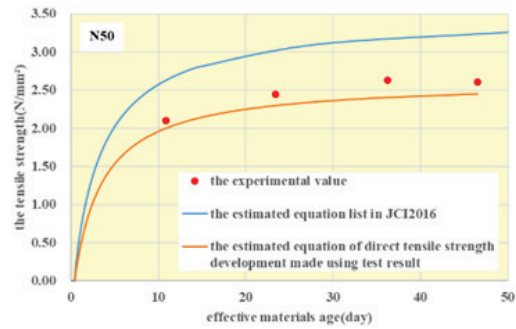


Figure 4: The result of comparison of tensile strength calculated using the estimated formula

### 3.2 Thermal properties

**Insulation temperature rise properties.** Properties of Adiabatic temperature rise are estimated by the identification analysis by the temperature analysis using the results of temperature history. Figure 5 shows comparison between the quantity of end insulation temperature rise calculated by using the estimated equation described in JCI2016 and that of the experimental value in all case. The quantity of end insulation temperature rise calculated by using the estimated equation described in JCI2016 is about 20% lower than that of the experimental value of insulation container regardless of a kind of cement and water cement ratio.

**Coefficient of thermal expansion.** In this study, it is examined that coefficient of thermal expansion calculated by the experimental value is the apparent coefficient of thermal expansion included a self-shrinkage strain, because the experimental strain of test to evaluate thermal properties is including self-shrinkage strain. In this study, the apparent coefficient of thermal expansion is calculated by dividing part about the same an incline in temperature rise area and descent area into four sections which is temperature rise section ①, ② and temperature descent section ①, ②. Table 3 shows the apparent coefficient of thermal expansion in each case. Although there is unevenness by a few water cement ratio, the apparent coefficient of thermal expansion is organized every a kind of cement.

Table 3: Apparent coefficient of thermal expansion.

a kind of cement	unit cement content (kg/m <sup>3</sup> )	the coefficient of thermal expansion ( $\mu/\text{C}$ )							
		temperature rise area①		temperature rise area②		temperature descent area①		temperature descent area②	
		experimental value	average	experimental value	average	experimental value	average	experimental value	average
N	349	18.19		7.13		23.54		10.76	
	316	20.31	19.88	7.16	7.18	20.98	20.45	9.63	11.07
	257	21.14		7.26		16.84		12.83	
M	349	7.70		6.43		15.52		10.85	
	314	10.48	10.31	5.96	6.63	16.21	14.68	12.56	11.64
	262	12.76		7.49		12.32		11.52	
L	349	5.51		4.17		16.50		16.40	
	314	9.79	10.03	5.44	5.06	13.84	13.61	13.98	14.22
	262	14.79		5.55		10.50		12.27	
H	349	12.93		3.90		9.66		11.53	
	314	13.99	12.97	5.31	5.14	3.12	5.04	10.72	11.05
	262	12.00		6.21		2.34		10.89	
BB	349	14.62		6.82		6.68		14.98	
	308	14.52	14.09	7.94	7.36	4.08	5.58	13.69	13.60
	257	13.14		7.34		5.98		12.13	
FB	349	11.16		6.88		4.56		12.23	
	314	10.63	11.68	6.86	6.93	23.88	13.09	12.29	12.29
	262	13.25		7.06		10.82		12.35	

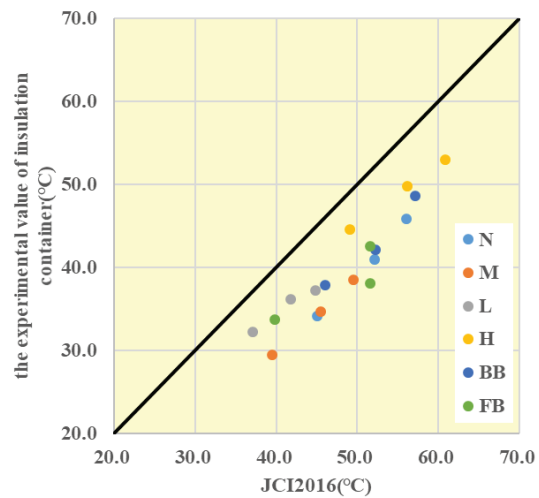


Figure 5: Comparison of ultimate adiabatic temperature rise.

#### 4. Thermal stress analysis

Thermal stress analysis was performed by using the experimental value. The analysis model of Box Calvert. The analysis model is 10 meters in height, 10 meters in width, 1 meters of wall-thicknesses, 10 meters in construction length.

The comparison between the case of using the experimental values as the design value and the case of using the value of JCI2016 was shown below. Figure 6 shows comparison between the cracking index described in JCI2016 and the cracking index of the result of the direct tensile test in all case. The cracking index of the result of the direct tensile test is great less in comparison with that described in JCI2016 in a kind of cement in a case of Moderate Portland cement and Low-heat Portland cement. In the area that is less than it of smallest cracking index to considered as a boundary line about having cracking outbreak or not 1.0, the cracking index of the result of the direct tensile test is less than that described in JCI2016 around 0.1 in case of a kind of cement of Normal Portland cement, High-early-strength Portland cement, Portland blast-furnace cement B class and Fly ash cement B class.

From results mentioned above, when it is supposed that the direct tensile strength considering influence of temperature history inside mass concrete member is near to structure body

strength, there is possibility to evaluate outbreking cracking in the danger side by using the splitting tensile strength under water of 20°C. It is necessary to examine the modulus of elasticity having the need to distinguish the tensile strength and the compressive strength and the creep greatly influencing generation stress in early age which are value for design of thermal stress analysis to express structure body strength.

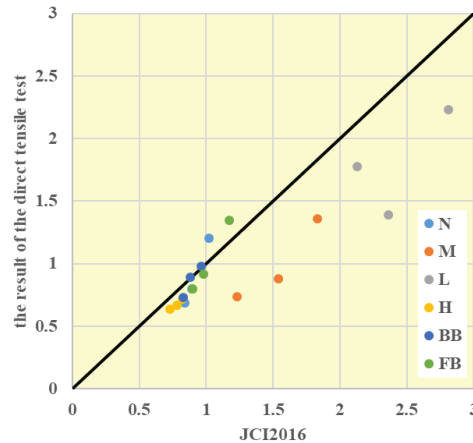


Figure 6: Comparison between the cracking index described in JCI2016 and the cracking index of the result of the direct tensile test in all case.

## 5. Conclusion

In this study, the direct tensile test using insulation container was conducted to investigate mechanical and thermal properties in mass concrete structure. The results are shown below.

1. In early age, the direct tensile strength under mass curing considering temperature history inside concrete member is higher than the splitting tensile strength under water of 20°C. However, at 28 days, the strength of former was about 20% lower than that of latter.
2. There is possibility to evaluate the tensile strength in the danger side for occurring cracking in area of that the tensile strength is beyond 2 N/mm<sup>2</sup>.
3. The estimated formula on the strength development of the direct tensile strength was proposed made it possible to estimate tensile strength inside concrete member directly.
4. If the direct tensile strength considering influence of temperature history inside mass concrete member is near to structure body strength, there is possibility to evaluate outbreking cracking in the danger side caused by result of the thermal analysis described in JCI2016 and that used experimental results.

## References

- [1] Tunashima, T. et al, The tensile properties of the concrete using various cement, Concrete Engineering Annual Memoirs 32(1) (2010)
- [2] Takeuchi, N. et al, Basic study on properties of evaluation of concrete using insulation container, Concrete Engineering Annual Memoirs 33(1) (2011)
- [3] Senba, R. et al, Examination about critical limit of concrete cracks using various cement, Concrete Engineering Annual Memoirs 37(1) (2015)

## **SULPHATE-INDUCED CORROSION OF STEEL REINFORCEMENT IN FRESH CALCIUM SULPHOALUMINATE BINDERS: PRELIMINARY STUDIES**

**Yegor Morozov**<sup>(1)</sup>, **Simone Pellegrini**<sup>(2)</sup>, **Sergio Lorenzi**<sup>(3)</sup>, **Fátima Montemor**<sup>(1)</sup>

(1) Centro de Química Estrutural, Instituto Superior Técnico, Universidade de Lisboa,  
Lisbon, Portugal

(2) Security Building Service S.R.L., Via Santi Filippo e Giacomo, Covo (Bergamo), Italy

(3) Department of Engineering, University of Bergamo, Bergamo, Italy

### **Abstract**

Ordinary Portland cement (OPC) production is the largest contributor to global emissions. Main strategies to reduce the environmental impact include optimization of clinker production and grinding, usage of alternative fuels and raw materials, and, finally, shift to blended cements. Nevertheless, such measures can shorten emissions just for 30-40 %, thus, alternative binders and their mixtures with OPC are recently in focus. Among those, calcium sulphoaluminate cements (CSA) are attractive for emissions minimization, and show unique properties, but they lack durability studies and the understanding of embedded steel reinforcement behaviour.

The corrosion behaviour of steel was tentatively tested in solutions that simulate liquid phase at various stages of binder hydration. In static tests, steel samples were immersed in solutions of constant composition, while in dynamic tests it was changed to mimic the evolution of key parameters, i.e. pH and sulphates, in a way it happens during binder hydration. The preliminary results suggested that the corrosion of plain mild steel reinforcement would start instantly in CSA binders upon water addition, due to simultaneously low pH and high sulphate concentration, and, despite favourable conditions in hydrated state, corrosion would proceed further, since no long-term repassivation was observed.

### **1. Introduction**

The construction sector is one of the greatest sources of carbon dioxide emissions, and the production of ordinary Portland cement (OPC) alone accounts for 6-8 % of its global output.

Today around 900 kg of CO<sub>2</sub> is released per each tonne of Portland clinker, which hardly can be lowered below 800 kg [1, 2]. The main strategies to reduce environmental impact target optimization of clinker production and grinding, the usage of alternative fuels and raw materials, and a shift to blended cements [2-4]. The intensive introduction of high performance concrete and concrete composites into construction practice reduced the amount of concrete required to support the same load [2, 5], improved durability and increased the service life of structures [2], decreasing the demand for cement both in short- and long-term respectively. Nevertheless, these measures are limited, thus alternative binders are in focus [3, 6]. Calcium sulphoaluminate cement (CSA) is particularly attractive. CSA clinker is produced at about 1250 °C, which is 200 °C lower compared to OPC [2, 7-12], need just 800 kJ/kg, and it is accompanied by the release of just ca. 340 kg of CO<sub>2</sub> per tonne of clinker [6, 9-13], which together with better grindability [13] make it discernibly advantageous in terms of energy conservation and emissions reduction. Besides, various industrial by-products can be used as raw materials, enhancing the sustainability of CSA production [13]. They are perfect for pre-cast construction due to high early strength and rapid hardening [2, 10], which together with high frost resistance of fresh mixes is valuable in cold weather. CSA is used in shrinkage-compensating formulations, or for self-stressing concrete [2, 6, 7, 14]. However, fresh CSA concretes have lower workability, as they require more water, but it is higher, when compared to OPC-slag blended concretes [11]. Nevertheless, self-consolidating CSA formulations, such as for self-levelling floors, can be easily obtained using proper admixtures. CSA binders are less alkaline compared to OPC, being safer against alkali-aggregate reactions and are suitable for glass-fibre composites [2, 15]. But the principal difference to OPC is the intrinsic immunity of CSA materials against sulphate attack [10, 11], which together with lower porosity [16], should result in higher durability and performance. On the other hand, lacking portlandite in the composition, CSA concretes could be susceptible to carbonation with an adverse effect on the passivation of steel reinforcement, as it has been proven for blended cements [17]. Long-term durability of CSA in terms of steel reinforcement corrosion is not well studied [2, 15].

Regardless of lower porosity and lower chloride ingress, compared to OPC [16, 18], high corrosion rates of embedded carbon steel rebars were previously observed since early beginning of testing [18], but no viable explanation was given. Thus, we assumed that the composition of CSA binder and pore solution, is the cause for the corrosion of carbon steel reinforcement.

The principal components of CSA binders are ye'elinite –  $3\text{CaO}\cdot 3\text{Al}_2\text{O}_3\cdot \text{CaSO}_4$ , calcium sulphate and belite, with their variable ratio to determine controlled shrinkage or expansion. Thus, CSA contain significant amount of sulphate-rich phases (17 wt. % of SO<sub>3</sub> vs 2.6 wt. % in OPC [2, 6, 7, 13, 19, 20]) that may release sulphate ions into pore solution. Previously, a combined action of sulphate and chloride ions on steel rebars was studied [21], but the behaviour of steel in the presence of sulphates alone has not been studied yet.

Pore solution composition for CSA and OPC binders at various stages of hydration was previously reported [7, 19, 22-24]. Though dissolved sulphate values are similar in the end of hydration – 10 mM and 4.5 mM respectively for OPC and CSA, in the beginning of hydration (0.5 h), OPC binders have in average more dissolved sulphates with respect to CSA analogues – 110 vs 20 mM. On the opposite, hydroxide concentration in the beginning of CSA hydration is 2.3 orders lower compared to OPC, evidenced by pH of 10.5 vs 12.8 respectively. However, after 8 hours of CSA cement hydration pH increases, reaching 12.5 in

average vs 13.6 for OPC. Therefore, regardless lower absolute value of dissolved sulphates, CSA binders are characterized by significantly lower pH, thus higher sulphate-to-hydroxide ratio.

Based on intensive analysis of the state-of-the-art, it has been assumed that the corrosion of mild steel reinforcement in fresh CSA binders is caused by the combination of low pH and relatively high concentration of sulphates in pore solution of CSA mortars and concretes. We believe that sulphate ions adsorb on the steel surface followed by the formation of soluble species, causing thinning and destruction of passive oxide film followed by the formation of corrosion pits in a similar manner as chlorides do [17, 25]. Since hydroxides stabilize passive oxide film, it is assumed, that the deleterious action of sulphate ions is inversely proportional to the concentration of hydroxides in pore solution, and a critical ratio between sulphate and hydroxide ions should exist, which separates corrosion and non-corrosion regions. The determination of that threshold is a fundamental task to confirm or disprove the assumptions made above over the mechanism of steel corrosion in CSA-based mortars and concrete.

Since the corrosion of steel is the main culprit for reduced durability of reinforced concrete structures due to cracking caused by expansive corrosion products, to find a scientific solution of the problem, or at least to propose a preventive repair methodology, the origin of mild steel reinforcement corrosion in fresh CSA-based cementitious materials must be comprehensively understood. Mild steel rebars were tentatively tested in simulating solutions to mimic conditions encountered in binders at various stages of CSA hydration. While in static corrosion tests steel samples continuously immersed in the solutions of constant composition, in dynamic corrosion tests the composition was changed in programmed way to reflect the evolution of key corrosion parameters, i.e. pH and dissolved sulphates, as it occurs during hydration of CSA. This paper overviews only preliminary findings of electrochemical tests, such as circuit potential (OCP) monitoring and electrochemical impedance spectroscopy (EIS) [26-28].

## 2. Materials and experimental procedures

Low carbon steel CK45K reinforcement rebar (in wt.%: C 0.4, Mn 0.7, Si 0.2, S max. 0.05, P max. 0.05, balance – Fe) of 1.2 cm in diameter was cut perpendicularly to the axis with a water-cooled circular sand saw. Copper wire was attached to the inner side of steel piece with a silver paint, and the pieces were embedded into epoxy resin. Samples were polished under water using SiC papers up to 1000 grit at 500 rpm, rinsed with deionized water and ethanol, dried with compressed air. Finally, 3M™ Scotchrap™ 50 tape was applied over polished surface, defining the exposed area of 0.24 cm<sup>2</sup>. At least three identical samples were prepared for all the tests and conditions.

Corrosion tests were performed in air at 25°C in 0.316, 3.16 and 31.6 mM NaOH solutions, containing or not 1.00, 10.0 and 200 mM of K<sub>2</sub>SO<sub>4</sub>. Electrochemical tests, – OCP and EIS, were performed in three-electrode arrangement (Pt wire as counter electrode - CE, saturated calomel electrode as a reference electrode, and steel sample as a working electrode - WE) using Autolab PGSTAT302N. OCP were recalculated vs standard hydrogen electrode (SHE) potential. For EIS single sinusoidal potential perturbations of 10 mV (rms) amplitude were applied vs OCP within the frequency range 50 kHz to 5 mHz. The impedance data were fitted with ZView.



### 3. Results and discussion

The results of OCP monitoring of exposed steel rebars in 0.316 mM NaOH suggested that corrosion immediately started even in the presence of just 1 mM of sulphates. OCP declined gradually till final values of -420 – -460 mV, suggesting severe corrosion. On the other hand, in the absence of sulphates, initial OCP values were 100-160 mV higher, and increased with time till 8.3 mV, indicating the passive state. EIS spectra, obtained after 7 hours of immersion, showed notable differences. In high frequency region (2-50 kHz), where the response from solution dominates,  $|Z|$  decreased with sulphates addition. In middle frequency range (1-10 Hz), where the response mainly comes from oxide film, impedance modulus values declined, as the number and size of corrosion pits increased –  $|Z|_{3.15\text{Hz}}$  were 3630, 700, 168 and 105  $\text{Ohm}\cdot\text{cm}^2$  for 0, 1, 10 and 200 mM  $\text{K}_2\text{SO}_4$  respectively, accompanied by lessening of the capacitive response of oxide film, evidenced from phase angle Bode plot. The greatest difference was seen for  $|Z|_{5\text{mHz}}$ , proportional to polarization resistance,  $R_p$ . Steel exposed to sulphate-free solution evidenced high value of 670  $\text{kOhm}\cdot\text{cm}^2$  in the opposite to the samples in solutions containing sulphates, in which the values were 2.5 - 3.5 orders lower – 4.2, 2.9 and 1.2  $\text{kOhm}\cdot\text{cm}^2$ , indicating active corrosion of steel reinforcement, intensified with the increase of sulphates.

While the corrosion tests carried out in 0.316 mM were designed to mimic the liquid phase of CSA binders at very beginning of cement hydration, testing in 3.16 mM NaOH solutions simulated the conditions encountered between 2 and 64 hours of hydration. Tenfold increase in hydroxide concentration improved the corrosion resistance of steel, and not only in sulphate-free, but also in 1 mM  $\text{K}_2\text{SO}_4$  a gradual OCP growth was found. In the latter case, mild steel depassivation occurred and corrosion initiated between 52.4 and 53.0 hours, evidenced by a drop from 66.5 to -331 mV, finally reaching -396 mV (64 hours) vs 90.2 mV (66 hours) for the reference. The samples immersed in 10 and 200 mM  $\text{K}_2\text{SO}_4$  since early beginning showed gradual decrease in OCP, reaching values of -471 and -501 mV in the end of the test.

These results fully corroborated with EIS findings.  $|Z|_{5\text{mHz}}$ , measured for mild steel in pure 3.16 mM NaOH, increased with time and reached 1.36  $\text{MOhm}\cdot\text{cm}^2$  after 2 days, being a bit higher, when compared to 1.27  $\text{MOhm}\cdot\text{cm}^2$  for the sample in 1 mM  $\text{K}_2\text{SO}_4$  solution, in which a sharp three-order drop was observed after 53 hours, reaching similar values for 10 and 200 mM sulphate solutions – 1.9, 1.4 and 1.3  $\text{kOhm}\cdot\text{cm}^2$  respectively. The middle frequency range EIS response followed the trend at low frequencies: high impedance values and phase angle close to  $90^\circ$ , were observed for steel in passive state, while corroding samples showed both low impedance and phase angle values, due to the progressive damage of the oxide film. Finally, corrosion studies were performed in 31.6 mM NaOH (pH 12.5) solutions containing sulphates to simulate pore media encountered in CSA and OPC mortars and concretes in the end of cement hydration. According to cumulative electrochemical results in 31.6 mM NaOH, mild steel could tolerate small amount of dissolved sulphates. In fact, the passive state of steel was observed in all 31.6 mM NaOH solutions, evidenced by gradual increase of OCP since the beginning of corrosion tests, until passive film breakdown occurred after 18-22<sup>nd</sup> and 5-6<sup>th</sup> days of immersion respectively for steel samples in solutions of 10 and 200 mM  $\text{K}_2\text{SO}_4$ , evidenced the drop in OCP due to aggressive action of sulphates as sulphate-hydroxide ratio increased. On the other hand, in the presence of 1 mM  $\text{K}_2\text{SO}_4$  mild steel reinforcement

remained passive until the end of corrosion test (30<sup>th</sup> day), confirmed by high OCP, by far exceeding 115 mV (SHE), similar to the reference sample in sulphates-free solution.

The results of corrosion tests suggested that in order to ensure persistent passivation of steel, the concentration of hydroxide ions should exceed that of sulphates about 18 times, serving a guide for the critical ratio. The combined findings suggested that sulphate-induced corrosion of common mild steel reinforcement would start instantly in CSA-based materials at early stages of hydration due to high sulphate-to-hydroxide ratio, well above proposed safe threshold, although the conditions in hydrated state are favourable for steel passivation (Fig. 1).

To understand whether re-passivation of steel would occur, as the environment becomes less aggressive, passing from the region of severe corrosion to no corrosion region (Fig. 1), dynamic corrosion testing in solutions of variable composition was performed, and they suggested that regardless of the perfect conditions for the passivation of steel in hydrated matrix, CSA binders fail to provide chemical protection of rebars, since due to corrosion emerged at early stages of hydration,

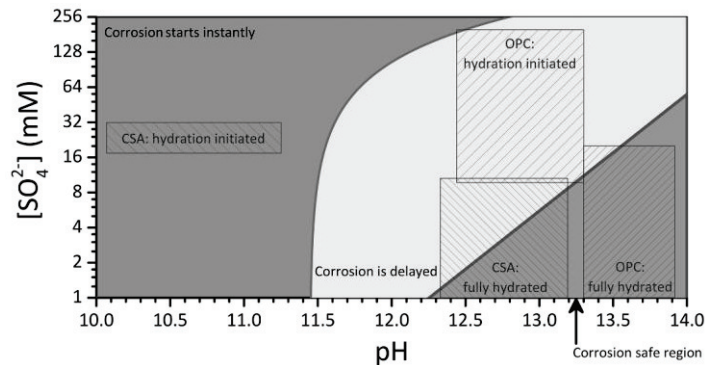


Figure 1: Sulphate-induced corrosion diagram of mild steel

caused simultaneously by elevated amount of dissolved sulphates and low pH, the corrosion of the reinforcement will likely progress, despite short-term re-passivation observed.

#### 4. Conclusions and Future work

The corrosion behaviour of plain carbon steel reinforcement was studied in solutions that simulate liquid phase of calcium sulphotoaluminate cement at various stages of hydration. Two types of tests were carried out. In static corrosion tests steel rebars were studied in solutions of constant fixed composition, while in dynamic corrosion tests their composition was changed with time to mimic the evolution of pH and sulphates as it occurs during hydration of calcium sulphotoaluminate cement. The deleterious role of sulphate ions on the passivity of steel has been proven. To guarantee a persistent protection of steel, the concentration of hydroxide ions should exceed that of sulphates about 18 times. The results suggested that the corrosion of steel would start instantly, stipulated by low pH and high concentration of dissolved sulphates, exceeding threshold, and, despite favourable conditions for passivation in the hydrated state of calcium sulphotoaluminate cement based materials, corrosion of the reinforcement would proceed further, since no long-term re-passivation was observed.

Therefore, the corrosion of steel reinforcement in calcium sulphotoaluminate cement based materials is their greatest single limitation, and its elimination is the most crucial, indispensable requirement for wide market acceptance and successful application in construction practice. Therefore, in our future research, we aim to search for viable scientific and technologic solutions or preventive repair methodologies to minimize the risk of reinforcement corrosion to meet the life expectancy level of conventional OPC-based concretes.

## Acknowledgements

The authors acknowledge Fundação para a Ciência e Tecnologia for funding PhD grant SFRH/BD/88016/2012 and Centro de Química Estrutural (UID/QUI/00100/2013), as well as acknowledge CA15202 for financial support.

## References

- [1] J.G.J. Olivier, G. Janssens-Maenhout, M. Muntean, J.A.H.W. Peters, Trends in global CO<sub>2</sub> emissions: 2015 Report, Institute for Environment and Sustainability of the European Commission's Joint Research Centre, 2015.
- [2] P.C. Aitcin, Binders for Durable and Sustainable Concrete, Taylor & Francis, 2007.
- [3] M. Schneider, M. Romer, M. Tschudin, H. Bolio, Sustainable cement production — present and future, *Cem. Concr. Res.*, 41 (2011) 642-650.
- [4] J.S. Damtoft, J. Lukasik, D. Herfort, D. Sorrentino, E.M. Gartner, Sustainable development and climate change initiatives, *Cem. Concr. Res.*, 38 (2008) 115-127.
- [5] V.S. Ramachandran, Concrete Admixtures Handbook: Properties, Science, and Technology, Noyes Publications, 1995.
- [6] P. Barnes, J. Bensted, Structure and Performance of Cements, Second Edition, Taylor & Francis, 2002.
- [7] F. Winnefeld, B. Lothenbach, Hydration of calcium sulfoaluminate cements - Experimental findings and thermodynamic modelling, *Cem. Concr. Res.*, 40 (2010) 1239-1247.
- [8] F.P. Glasser, L. Zhang, High-performance cement matrices based on calcium sulfoaluminate–belite compositions, *Cem. Concr. Res.*, 31 (2001) 1881-1886.
- [9] P. Arjunan, M.R. Silsbee, M.R. Della, Sulfoaluminate-belite cement from low-calcium fly ash and sulfur-rich and other industrial by-products, *Cem. Concr. Res.*, 29 (1999) 1305-1311.
- [10] K. Quillin, Performance of belite–sulfoaluminate cements, *Cem. Concr. Res.*, 31 (2001) 1341-1349.
- [11] S. Ioannou, K. Paine, L. Reig, K. Quillin, Performance characteristics of concrete based on a ternary calcium sulfoaluminate-anhydrite-fly ash cement, *Cem. Concr. Compos.*, 55 (2015) 196-204.
- [12] Y.S. Liao, X.S. Wei, G.W. Li, Early hydration of calcium sulfoaluminate cement through electrical resistivity measurement and microstructure investigations, *Construction and Building Materials*, 25 (2011) 1572-1579.
- [13] M.C. Gonçalves, F. Margarido, Materials for Construction and Civil Engineering: Science, Processing, and Design, Springer International Publishing, 2015.
- [14] L. Zhang, F.P. Glasser, Hydration of calcium sulfoaluminate cement at less than 24 h, *Adv Cem Res*, 14 (2002) 141-155.
- [15] M.C.G. Juenger, F. Winnefeld, J.L. Provis, J.H. Ideker, Advances in alternative cementitious binders, *Cem. Concr. Res.*, 41 (2011) 1232-1243.
- [16] G. Bernardo, A. Telesca, G.L. Valenti, A porosimetric study of calcium sulfoaluminate cement pastes cured at early ages, *Cem. Concr. Res.*, 36 (2006) 1042-1047.
- [17] L. Bertolini, B. Elsener, P. Pedferri, Corrosion of Steel in Concrete: Prevention, Diagnosis, Repair, Wiley, 2004.
- [18] D. Kalogridis, G.C. Kostogloudis, C. Ftikos, C. Malami, A quantitative study of the influence of non-expansive sulfoaluminate cement on the corrosion of steel reinforcement, *Cem. Concr. Res.*, 30 (2000) 1731-1740.
- [19] B. Lothenbach, F. Winnefeld, Thermodynamic modelling of the hydration of Portland cement, *Cem. Concr. Res.*, 36 (2006) 209-226.
- [20] B. Lothenbach, F. Winnefeld, C. Alder, E. Wieland, P. Lunk, Effect of temperature on the pore solution, microstructure and hydration products of Portland cement pastes, *Cem. Concr. Res.*, 37 (2007) 483-491.
- [21] V.K. Gouda, W.Y. Halaka, Corrosion and Corrosion Inhibition of Reinforcing Steel: II. Embedded In Concrete, *Br. Corros. J.*, 5 (1970) 204-208.
- [22] A. Vollpracht, B. Lothenbach, R. Snellings, J. Haufe, The pore solution of blended cements: a review, *Mater. Struct.*, 49 (2016) 3341-3367.
- [23] P. Chaunsali, Early-age hydration and volume change of calcium sulfoaluminate cement-based binders, Doctor of Philosophy in Civil Engineering Dissertation, University of Illinois, 2015
- [24] M. Andac, F.P. Glasser, Pore solution composition of calcium sulfoaluminate cement, *Adv Cem Res*, 11 (1999) 23-26.
- [25] P. Marcus, V. Maurice, H.-H. Strehblow, Localized corrosion (pitting): A model of passivity breakdown including the role of the oxide layer nanostructure, *Corros. Sci.*, 50 (2008) 2698-2704.
- [26] K. Hladky, L.M. Callow, J.L. Dawson, Corrosion Rates from Impedance Measurements - an Introduction, *Br. Corros. J.*, 15 (1980) 20-25.
- [27] M.F. Montemor, Estudo da deterioração por corrosão de estruturas de betão armado, PhD Dissertation, Instituto Superior Técnico, Universidade Técnica de Lisboa, 1995
- [28] P. Marcus, F.B. Mansfeld, Analytical Methods In Corrosion Science and Engineering, CRC Press, 2005.

## THE DEVELOPMENT OF THE EARLY-AGE ELASTIC MODULUS IN CEMENT-MATERIALS WITH DIFFERENT WATER COEFFICIENT

**Romana Halamová<sup>(1)</sup>, Dalibor Kocáb<sup>(1)</sup>, Barbara Kucharczyková<sup>(1)</sup>, Petr Daněk<sup>(1)</sup>**

(1) Brno University of Technology, Brno, Czech Republic

### **Abstract**

The effect of the composition of cementitious materials on the resulting value of the modulus of elasticity is a matter of common knowledge. However, the issue of what factors affect it during early age is still not well understood. The paper deals with the development of the modulus of elasticity in cement composites at an early age. The measurements were performed on cement pastes with varying water-cement ratio. The influence of plasticizer content was also investigated. Prism-shaped specimens with the dimensions of 40×40×160 mm and Vicat ring-shaped specimens were manufactured for the purposes of the experiment. The modulus of elasticity was determined based on a continuous measurement of the ultrasonic transit time during the first 24 hours of ageing. The measurement was started immediately after filling the measurement cell with the fresh material and took 24 hours. The internal temperature of the specimens was measured simultaneously, which provided information about the hydration process of the material. All the prismatic test specimens were removed from moulds at an age of 24 hours and tested for the dynamic modulus of elasticity by the ultrasonic pulse velocity test at the age of 24, 48 and 72 hours. The measurement of the dynamic modulus of elasticity was supplemented with a static test performed on the prismatic test specimens at the age of 24 and 72 hours.

### **1. Introduction**

Concrete is a common construction material which possesses great compressive strength. In the beginning of its existence, it consisted of cement, aggregate, and water, and only later did it start to be enhanced by various additives and admixtures, resulting in considerable advancement in concrete technology [1]. However, the composition of concrete was not the only thing that saw marked development; approaches to designing concrete structures have also undergone substantial changes. The trend of the past few years has been the construction

of (in some aspects) unorthodox, revolutionary, or at times even megalomaniac land structures and long-span bridges, which combine an emphasis on a low environmental impact and pleasant aesthetics. Modern concrete structures are increasingly taller, longer and slenderer [2]. It so happens that, aside from compressive strength, other properties enter the foreground of attention, e.g., durability, shrinkage, and especially deformation resistance, which is typically represented by the modulus of elasticity [3, 4, 5]. This property has recently become the subject of examination at research centres as well as in general construction practice. There are also a number of factors that affect the value of the modulus of elasticity, which can be divided into two basic groups [6]. The first group of factors includes the composition of the fresh mixture (mainly the type, amount, fraction, and quality of aggregate) and the conditions in which the concrete matures (ambient temperatures, curing time and technique, etc.) [7]. The second group involves the influences of the test methods used to determine the value of the elastic modulus. These factors have impact especially on the results of measurements which values deviate more or less from the real material's characteristic. In terms of the testing principle, these methods can be divided into static and dynamic [8]. Most test methods measure hardened composites (a material of a specific strength). In many cases, such as early formwork removal, rapid construction, or the installation of pre-stressing cables, it is useful to know how the value of the elastic modulus develops in concrete which has not yet fully hardened. This can be tested using the ultrasonic pulse velocity test, which is also the focus of this paper.

## 2. Experiment

The goal of the experiment was to determine the influence of the w/c ratio and plasticiser content on the value of the modulus of elasticity in cement pastes younger than 72 hours.

### 2.1 Materials and specimens

Prior to the experiment six cement pastes were mixed for the purposes of testing using cement CEM I 52.5 R produced by cement plant Mokra (Czech Rep.). The first three pastes contained no plasticiser and had a w/c ratio of 0.33, 0.40, and 0.50. They were identified as CP33, CP40, and CP50. The lowest w/c ratio corresponded to the theoretical minimum of water required for the cement to hydrate fully. The other three pastes had the same w/c ratio as the first three; however, they also contained polycarboxylate-based plasticiser Sika ViscoCrete 4035 at an amount of 1 % of cement weight. They were designated as CPP33, CPP40, and CPP50.

Each paste was made into a one specimen in the shape of the Vicat ring, which were used for the continuous measurement of the dynamic modulus of elasticity (henceforth  $E_{cu}$ ) using the ultrasonic pulse velocity test over the first 24 hours, and eight prisms with the dimensions of  $40 \times 40 \times 160$  mm used for measuring the modulus of elasticity at ages from 24 to 72 hours. The first four prisms were used for determining the dynamic and static modulus of elasticity (henceforth  $E_c$ ) at an age of 24 hours. The other four then served for the determination of  $E_{cu}$  at an age of 48 hours. The same specimens were then used for  $E_{cu}$  and  $E_c$  at 72 hours of age counted from the moment the cement was mixed with water. The prism specimens were covered with a PE foil while they aged and were stored in standard laboratory conditions at a temperature of  $(22 \pm 2)$  °C and RH =  $(55 \pm 5)$  %.

## 2.2 Test methods

**Measuring the modulus of elasticity during the first 24 hours.** After each of the cement pastes has been mixed, a Vicat ring was filled with the fresh mixtures and placed in the measuring chamber of a Vikasonic ultrasonic apparatus produced by the company Schleibinger [9] (pictured in Fig. 1 left). This ring, having been filled with a cementitious material, is placed between two transducers operating at 54 kHz, one of which functions as the transmitter and the other as the receiver of an ultrasonic pulse. Following parameters of the ultrasonic pulse were set before the start of measurement: pulses transmission frequency of 60 impulses per minute, impulse voltage of 2000 V, reading frequency of 10 s. The transit time was determined as the time when the amplitude of the signal exceeds the pre-set threshold. The apparatus is primarily designed for measuring the setting time, but unlike the traditional Vicat apparatus, it can continuously and non-invasively measure setting while monitoring the material's internal temperature together with the ultrasonic transit time. Given the fact that the instrument is designed so that the distance of the measuring base does not change during use, the continuous measurement of ultrasonic transit times can be used to calculate the ultrasonic pulse velocity and subsequently determine the values of the dynamic modulus of elasticity over the set time period according to the following formula [9]:

$$E = \rho \cdot v^2, \quad (1)$$

where  $E$  is the dynamic modulus of elasticity in MPa,  $\rho$  is bulk density in  $\text{kg/m}^3$  and  $v$  is the ultrasonic pulse velocity in km/s. Changes in the internal temperature of the material well demonstrates the progress of cement hydration. The use of the Vikasonic is discussed in greater detail e.g. in [10].

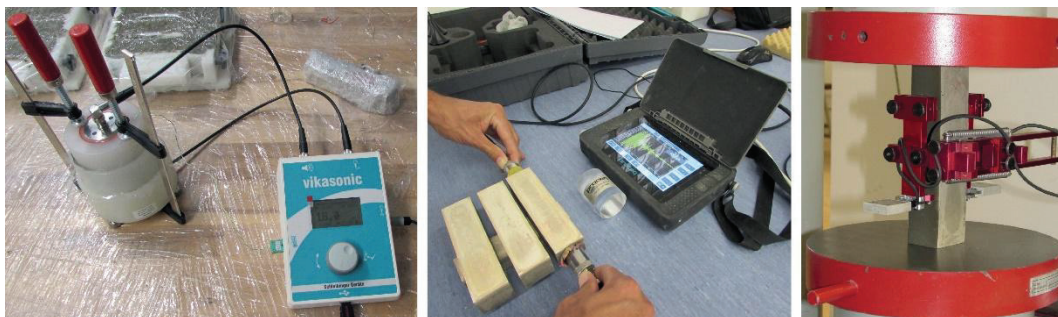


Figure 1: The Vikasonic ultrasonic device (left), ultrasonic pulse velocity test using Pundit PL-200 (middle) and static test (right).

**Measuring the modulus of elasticity at an age of 24 through 72 hours.** The measurements were performed on prism specimens with the dimensions of  $40 \times 40 \times 160$  mm, which were demoulded 24 hours after the cement was mixed with water. The first four specimens were measured for the modulus of elasticity at an age of 24 hours. The remaining four were wrapped in PE foil and left in standard laboratory conditions for later testing. The modulus of elasticity was determined by the ultrasonic pulse velocity test first – the measurements were made using the Pundit PL-200 apparatus manufactured by Proceq (see Fig. 1 middle) and the elastic modulus  $E_{cu}$  was calculated according to ČSN 73 1371 [11] using the formula:

$$E_{cu} = \rho \cdot v_L^2 \cdot \frac{(1+\mu) \cdot (1-2\mu)}{1-\mu}, \quad (1)$$

where  $E_{cu}$  is the dynamic modulus of elasticity in MPa,  $\rho$  is bulk density in  $\text{kg/m}^3$ ,  $v_L$  is the ultrasonic pulse velocity in  $\text{km/s}$  and  $\mu$  is the dynamic Poisson's ratio, which was estimated on the basis of a supplementary measurement of resonance frequencies using the same specimens. The second stage focused on determining the static modulus of elasticity  $E_c$ . The test was performed in accordance with ISO 1920-10 [12]. The specimens were loaded using the DELTA 6-300 press manufactured by FORM+TEST. The deformations were measured along a base of 80 mm using displacement transducers connected to a data logger (Fig. 1 right). The test of  $E_c$  was concluded by determining the compressive strength.

At the age of 48 hours, the remaining four prisms were tested for  $E_{cu}$ . Once the tests were finished, the prisms were again wrapped in a PE foil until the age of 72 hours when they were once again tested for both the static and dynamic modulus of elasticity.

### 3. Results and discussion

#### 3.1 Results of the dynamic modulus of elasticity in first 24 hours

The measurement results obtained using the Vikasonic are plotted in Fig. 2.

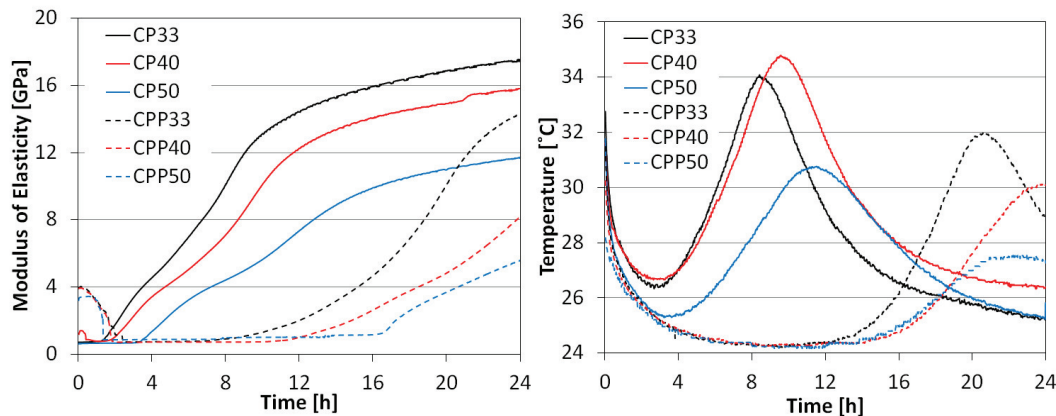


Figure 2: Progress of the dynamic modulus of elasticity of the cement pastes (left) and progress of the internal temperature (right) over the first 24 hours of age.

The diagrams show that as the w/c ratio rises, the values of the dynamic modulus of elasticity grow more slowly and the temperature peak also occurs at a later time. The cement pastes that contained plasticiser saw a significant delay in setting compared to pastes with no plasticiser content, which can be clearly seen in the development of internal temperature (Fig. 2 right). This was also visible in the markedly lower values of the dynamic modulus of elasticity during the monitored period (first 24 hours of age), see Fig. 2 left. The continuous measurement captured also the very early stage of hydration period (end of the first hydration peak) when the viscosity of the material was changing from the fluid to thixotropic state. This process was very well visible in the case of cement pastes with the plasticizer, when the initial value (at the start of measurement) of the modulus of elasticity corresponded to the ultrasonic

pulse velocity of approx. 1420 m/s which was close to the value of the ultrasonic pulse velocity of water. The subsequent changes in viscosity and formation of material's microstructure caused damping of the ultrasonic waves which was reflected in the decrease in the elastic modulus value. During the dormant period there were no changes in the value of elastic modulus. The subsequent growth of the elastic modulus started with the growth of the internal temperature (see Fig. 2).

### 3.2 Results of the dynamic modulus of elasticity from 24 to 72 hours after mixing

The average values of the measured elastic moduli  $E_{cu}$  and  $E_c$  taken from measurements performed on four test specimens are plotted as bar charts in Fig. 3; the error bars represent a sample standard deviation. The relative values of elastic modulus are summarized in Tab. 1.

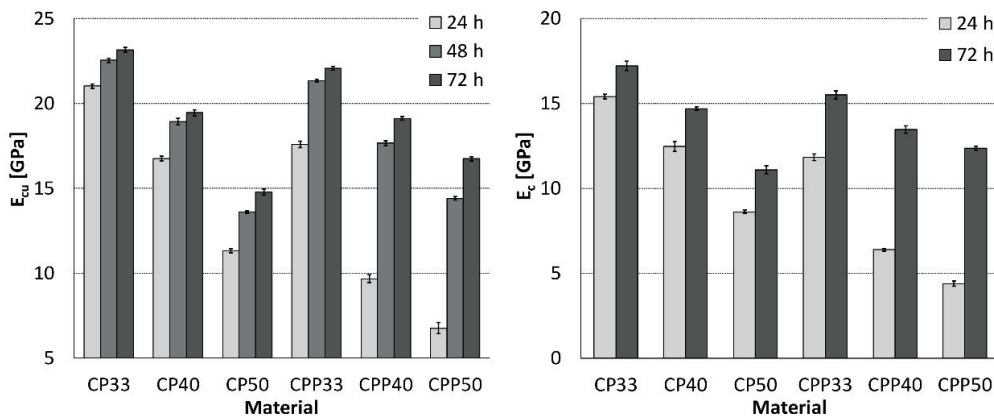


Figure 3: Results of the dynamic modulus of elasticity determined by the ultrasonic pulse velocity test and static modulus of elasticity (right).

Table 1: Relative values of elastic modulus: 100% is CP33 at the age of 24 hours.

Elastic Modulus	Age [h]	Material					
		CP33	CP40	CP50	CPP33	CPP40	CPP50
$E_{cu}$	24	100.0	79.7	53.9	83.6	46.0	32.1
	48	107.2	90.1	64.7	101.5	84.0	68.5
	72	110.2	92.5	70.3	104.9	90.9	79.7
$E_c$	24	100.0	81.0	56.0	76.7	41.4	28.5
	72	111.8	95.4	72.0	100.6	87.4	80.2

It can be said that the increasing trend of the elastic modulus was very similar in all the cement pastes without plasticiser (regardless of the w/c ratio); only their final absolute values differed – the lower the w/c ratio, the higher the values of elastic modulus. All the cement pastes with a content of plasticiser also exhibited a similar trend in the development of the modulus of elasticity (regardless of the w/c ratio), which, however, was markedly different from the development in pastes without plasticiser. During the first 24 hours the increase in pastes containing plasticiser was very slow, accelerating only over the second day of age. After that, the values of the elastic modulus increased much more rapidly.



#### 4. Conclusion

The experiment results showed the influence of w/c ratio and plasticiser on the development of the modulus of elasticity in young cement pastes. This case study showed that the pastes made from CEM I 52.5 R with plasticiser registered a significant retardation in the early growth of the modulus of elasticity compared to pastes without plasticiser, especially during the first 24 hours. However, only one kind of plasticiser has been used in the production of cement pastes. Other products may show different results.

It appears that the ultrasonic apparatus is well suited for determining the dynamic modulus of elasticity during the setting of cement composites. The question still remains, however, how to determine the Poisson's ratio, which influences the value of the elastic modulus  $E_{cu}$ . Hardened composites allow its value to be obtained e.g. by measuring resonance frequencies, as was done in the case of this paper.

#### Acknowledgements

This paper has been written as part of the project No. GA17-14302S “Experimental analysis of the early-age volume changes in cement-based composites”, supported by the GA0 - Czech Science Foundation and project No FAST-J-18-5516 “Determination of modulus of elasticity in the early phase of maturing of cement composites and their thermal expansion”.

#### References

- [1] Neville, A. M. and Brooks, J. J., Concrete technology, Prentice Hall, Harlow (2010)
- [2] Collepardi, M., The New Concrete, first ed., Grafiche Tintoretto, Treviso (2006)
- [3] Yldirim, H. and Sengul, O., Modulus of elasticity of substandard and normal concretes, Constr. Build. Mater. 25 (2011), 1645-1652
- [4] Zhou, Y. et al, A fundamental study on compressive strength, static and dynamic elastic moduli of young concrete, Constr. Build. Mater. 98 (2015), 137-145
- [5] Kucharczyková, B. et al, Experimental Analysis on Shrinkage and Swelling in Ordinary Concrete, Advances in Materials Science and Engineering (2017), ID 3027301
- [6] Huňka, P. et al, Test and technological influences on modulus of elasticity of concrete, Procedia Engineering 65 (2013), 266-272
- [7] Křížová, K. and Hela, R., Selected technological factors influencing the modulus of elasticity of concrete, World Academy of Science, Engineering and Technology, Turkey, 6 (2014), 557-559
- [8] Halamová, R. and Kocáb, D., Review of the Possibilities of Determining the Modulus of Elasticity and Poisson's Ratio in the Early Stage of Cement Composite Ageing, 10th Int. Scientific Conference of Civil and Environmental Engineering, Slovakia (2018), 1-7
- [9] Vikasonic – Measuring the Early Setting and Hardening with Ultrasonic Waves Measuring, [http://www.schleibinger.com/cmsimple/en/?Setting\\_and\\_Maturity:Ultrasonic\\_Setting\\_Measurement](http://www.schleibinger.com/cmsimple/en/?Setting_and_Maturity:Ultrasonic_Setting_Measurement)
- [10] Rozsypalová, I. et al, Monitoring of the Setting and Early Hardening with Ultrasonic Waves, to be published 2018
- [11] ČSN 73 1372 Non-destructive testing of concrete – Testing of concrete by resonance method, ČNI, Prague (2011) (in Czech)
- [12] ISO 1920-10 Testing of concrete – Part 10: Determination of static modulus of elasticity, ISO, Geneva (2010)

## **THE USE OF ACOUSTIC METHODS TO DESCRIBE THE BEHAVIOUR OF CEMENT PASTES IN THE EARLY STAGE OF AGEING**

**Michaela Hoduláková<sup>(1)</sup>, Libor Topolář<sup>(1)</sup>, Barbara Kucharczyková<sup>(1)</sup>, Dalibor Kocáb<sup>(1)</sup>**

(1) Brno University of Technology, Faculty of Civil Engineering, Brno, Czech Republic

### **Abstract**

Monitoring of properties of cement-based composites at an early age (approximately during the first 48 hours after mixing cement with water), understanding the hydration processes of the cement paste, and identifying various mechanisms, including potential formation of microcracks during hardening, are essential steps to ensure the quality of cement-based composites and to guarantee their long lifetime. The processes that occur at this early age significantly influence the resulting properties of cement-based composites. Various methods used today to expand the understanding of early hydration include, for example, non-contact complex resistivity, thermogravimetric X-ray computed tomography, scanning electron microscopy, ultrasound or the acoustic emission method. The paper deals with the use of the acoustic emission method to describe the behaviour of cement-based composites during the first 48 hours after mixing cement with water. The acoustic emission sensors allow the detection of elastic waves which may occur during the formation of hydration products, water cavitation, or during the formation and spreading of microcracks (e.g. as a result of plastic shrinkage). The acoustic emission method allows continuous monitoring of the hydration process throughout the experiment and by using the acoustic emission method, there is no need to stop the hydration process to allow its monitoring.

### **1. Introduction**

Monitoring the behaviour of composite building materials and structures is an important part of not only the production process (in course of their setting, hardening, and ageing), but also of the actual usage of the structure during its lifetime (compressive and bending stresses, cyclic loading, etc.). The description of the behaviour of composite building materials and

structures in laboratory, semi-laboratory, production, and practical use serves both research and development goals as well as practical purposes. To achieve this goal, the scope of current development and the use of the already existing methods should be expanded and non-standard methods and procedures should be employed. Non-destructive acoustic method, the acoustic emission method, is one of those non-standard methods which was utilized in the paper [1, 2].

The acoustic emission method (AE) belongs among the most advanced methods for material engineering and fatigue applications. The source of the AE signal can originate in many phenomena depending on the type of the material. For metals, the sources of the acoustic emissions can originate in dislocation movements, cracks, fractures, and even corrosion processes. In concrete, the AE signals can be generated by microscopic and macroscopic defects as well as by tearing or shifting of the reinforcement. In composites, the AE comes from matrix cracking, delamination, matrix separation from fibres, fibre tearing, and fibre pulling. Most acoustic emission sources are associated with defects. Detection and monitoring of these emissions is commonly used to predict material failure [1 – 4].

The AE event (Fig. 1) is emitted by irreversible dislocation and degradation processes in the microstructure and macrostructure of the material. The released energy is transformed into a mechanical stress impulse propagating throughout the material as an elastic longitudinal or transverse wave. A signal detected on the AE sensor and converted to an electrical signal is described as an AE signal [5].

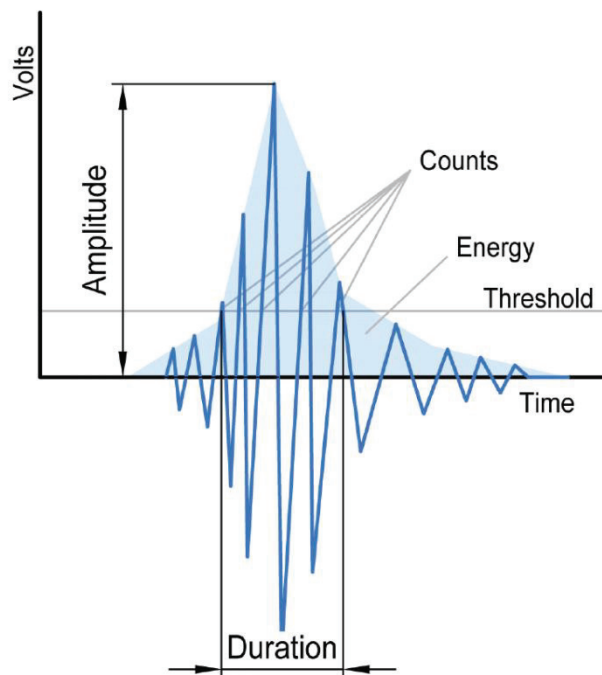


Fig. 1 AE events with measured parameters.

In parametric description of individual AE events, the aim is primarily to detect the emission source and to obtain as much information as possible about the progress of the AE signal. The

progress of the AE events is described in the basic parameters, the standard EN 1330-9 defines the following AE signal parameters [6]:

- hit - detection of one discrete signal (Fig. 1) on one AE channel;
- acoustic emission detection threshold - the voltage level that must be exceeded to detect a discrete signal;
- arrival time - time when the discrete signal first exceeds detection time;
- duration - time difference between the first and last exceeding of the detection threshold by the discrete signal;
- number of events - number of events of the discrete signal that exceeds the detection threshold in one polarity;
- maximum amplitude - maximum voltage deviation during the duration of the discrete signal;
- rise time - time difference between the first exceeding of the threshold and the maximum amplitude of the discrete signal;
- energy - the integral of the squared AE signal over the duration of the discrete signal.

In addition to these parameters, it is recommended to record the values of other significant parameters or physical quantities along with the individual AE events that correspond to the created internal stresses (e.g. force, temperature, etc.). Within the evaluation of experiments discussed in this paper, the focus was paid to the amplitudes of the AE signal [7].

## 2. Materials and experimental setup

For the purpose of the experiment, cement pastes were produced and placed into a Vicat ring. Individual specimens of the cement pastes were produced from two types of cement (CEM I 42.5 R and CEM I 52.5 R) with the water/cement coefficient of 0.40. Three test specimens were manufactured from each cement, i.e. there were six specimens manufactured in total. Two specimens from each set were submerged in a paraffin oil to prevent a water evaporation from the specimens' upper surface during the maturation. The upper surface of the remaining specimen of each set was exposed to free desiccation. All measurements started approx. 0.5 hours after the cement was mixed with water.

During recording and processing of the AE signals within the experiments, the Dakel system XEDO was used, which was developed by the company ZD Rpety-Dakel [8]. In general, the acoustic emission sensors are mostly attached directly on the surface of measured specimen or structure. This was, however, not possible in this particular case due to the fresh mixture of water with cement. In such cases, the acoustic waveguides are used as a support for the sensor. This configuration has a significant disadvantage – a loss of the signal on the sensor-waveguide interface [9, 10]. In the performed experiment, this disadvantage was eliminated by usage of specially constructed waveguides with an incorporated acoustic emission sensor, see Fig. 2. This approach led to the elimination of the signal attenuation and other possible disturbances of the signal at the interface of the waveguide and the sensor. The sensor-

waveguide was coated with a thin layer of beeswax before measurement, which enabled the safe extraction of the waveguide after the measurements were finished.



Fig. 2 Photo of placement of the AE sensors.

### 3. Results and discussions

The results are presented in figures where the curve shows the differential temperature inside the specimen ( $\Delta T$ ), which was calculated as the difference between the internal temperature measured in the specimen and the ambient temperature. Points show the AE amplitude ( $U_{AE}$ ). (Note: no comparison can be made between the specimens submerged in oil and the specimens exposed to free desiccation of one type of cement because different AE sensor sensitivity was set).

Generally, the higher the AE amplitude is, the larger changes in the inner structure of the specimen are in progress. In the case of a solid phase, a higher amplitude indicates the formation of a larger structural failure.

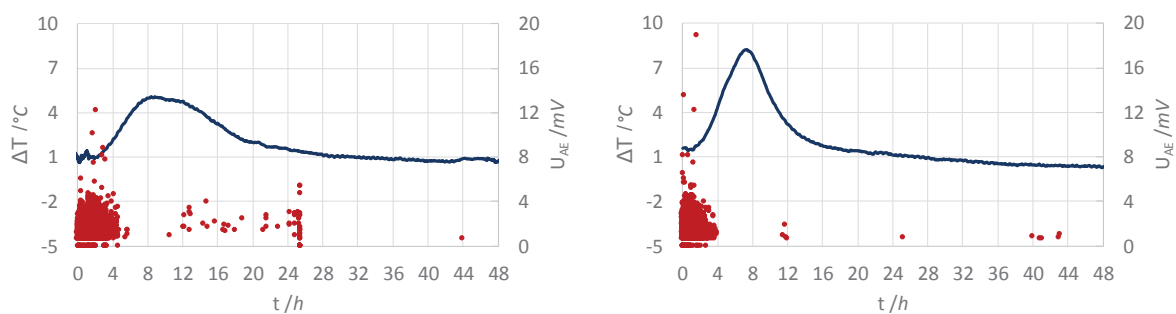


Fig. 3 Specimens submerged in oil (left CEM I 42.5 R; right CEM I 52.5 R).

Comparing the curves in Fig. 3 for the specimens submerged in oil, it can be seen that the specimens from CEM I 52.5 R exhibited higher inner temperature and also reached the relative setting time earlier. The relative setting time was estimated based on the measured curves as the time it takes to reach approximately half of the maximum of the temperature peak. The AE results show that the specimen from CEM I 42.5 R exhibits a higher number of

minor structural changes during the first 4.5 hours of mixing when compared to the specimen with the CEM I 52.5 R cement. This difference can be due to a faster creation of hydration products in the CEM I 52.5 R specimen, which also led to higher amplitudes. After reaching the maximum temperature, it can be seen that the acoustic activity of either specimen is much lower than the activity at the beginning of the measurement. Nevertheless, the results indicate that certain significant structural changes still occur after the maximum temperature was reached, particularly in the specimen with the CEM I 42.5 R cement.

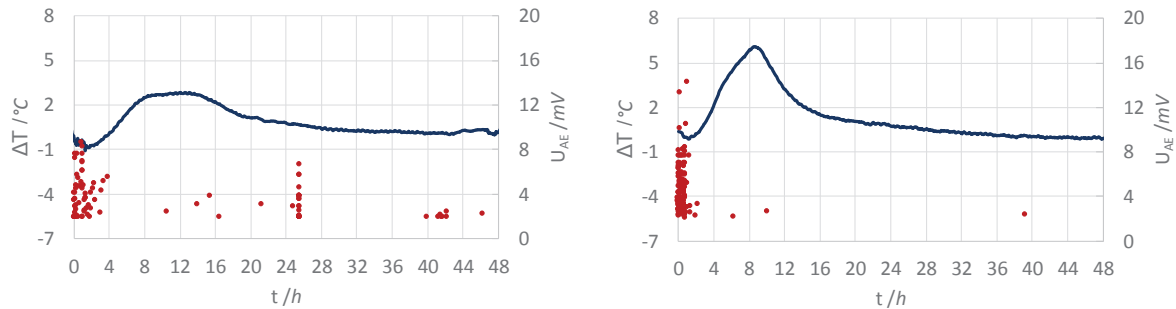


Fig. 4 Freely setting specimens (left CEM I 42.5 R; right CEM I 52.5 R)

The situation is different in the case of the specimens that were exposed to free desiccation (Fig. 4). Firstly, lower temperatures by almost two degrees were reached within the specimens. This was caused by cooling of the surface of the specimens due to evaporation of water. Secondly, the delay in the setting time of about 1.5 hours was recorded for CEM I 42.5 R and 0.5 hours for CEM I 52.5 R. The AE measurements show that the specimens made from CEM I 52.5 R exhibit higher amplitudes in a shorter time period than the specimens made from CEM I 42.5 R.

#### 4. Conclusions

The AE method appears to be an appropriate supplementary tool for determining the formation of new products and later even microcracks during maturation of cementitious composites. It can be said that the formation of more significant bonds in the cementitious matrix and later of microcracks generate higher AE signal amplitude values. The use of the AE method for continuous monitoring of cementitious composites can help to expand the understanding of structural changes in course of setting. The use of sensor-waveguides seems appropriate for monitoring the setting process of fresh mixtures. The sensor-waveguide allows the sensor to be placed in the early stage of the setting of cementitious composites while improving the sensitivity of the sensor, making the received waves more detectable.

Currently, supplemental measurements are performed, which focus on the strength and elastic modulus development expressed by the process of the ultrasonic pulse velocity measured during the maturation of the cement paste. As the next step, the degree of hydration will be determined for the times where the AE events are detected. It is expected that these results provide more details about the AE events which appear during material maturation.

### Acknowledgement

This outcome has been achieved with the financial support of the Czech Science Foundation under project no. 17-14302S “Experimental analysis of the early-age volume changes in cement-based composites”.

### References

- [1] Grosse, Ch.U. and Ohtsu, M., Acoustic emission testing. Springer, Berlin (2008)
- [2] Kopec, B. et al, Nondestructive testing of materials and constructions [in Czech]. CERM, Brno (2008)
- [3] Bentur, A. (Ed.), Report 25: Early Age Cracking in Cementitious Systems-Report of RILEM Technical committee TC 181-EAS: Early age cracking shrinkage induced stresses and cracking in cementitious systems (Vol. 25), Rilem Publications (2003)
- [4] Malhotra, V.M. and Carino, N.J., Handbook on Nondestructive Testing of Concrete Second Edition, CRC press (2003)
- [5] Miller, R.K. et al, Acoustic Emission Testing. Nondestructive testing handbook – 6, American Society for Nondestructive Testing (2005)
- [6] ČSN EN 1330- 9 (015005), Non-destructive testing - Terminology - Part 9: Terms used in acoustic emission testing, Úřad pro technickou normalizaci, metrologii a státní zkušebnictví, Praha (2001)
- [7] Sikorski, W., Acoustic emission – research and applications. InTech, Rijeka (2013)
- [8] Dakel - Systém XEDO. Dakel - O nás [online]. Copyright © [cit. 11.07.2018]. Available on: <http://www.dakel.cz/index.php?pg=prod/dev/xedo>
- [9] Topolář, L., Quantification of Micro-cracks by Acoustic Emission Method during Setting and Hardening of Concrete. In Ecology and New Building Materials and Products. Advanced Materials Research vol. 1000 (2014), 199-202
- [10] Topolář, L. et al, Using acoustic emission methods to monitor cement composites during setting and hardening. Applied Sciences - Basel, 7(5): 451, (2017), 1-11

## TIME DEPENDENT OF YOUNG'S MODULUS OF CONCRETE IN VERY EARLY AGE

Tatsuya Usui<sup>(1)</sup>, Hitoshi Takeda<sup>(2)</sup>, Hiroshi Murata<sup>(3)</sup>, Takuya Tani<sup>(1)</sup>

(1) Infrastructure Technology Research Department, Technology Center, Taisei Corporation, Japan

(2) Production Engineering Technology Department, Technology Center, Taisei Corporation, Japan

(3) Urban Engineering Research Department, Technology Center, Taisei Corporation, Japan

### Abstract

In the thermal stress analysis, the concrete stress is calculated from the early age. Therefore, it is considered that the influence on the concrete stress is great if the compressive strength and the Young's modulus in early age changes. However, these experimental data prior to 1 day of age have rarely been reported, because an appropriate measurement method has not been established. In this study, the Young's modulus of concrete was measured from very early age to 28 days material age based on JISA1149. The measurement was carried out with the ordinary cement concrete and the blast furnace cement concrete, and concrete temperatures were 20°C and 40°C to study the influence of cement types and concrete temperatures. As a result, it has been confirmed that the Young's modulus at 1.0N/mm<sup>2</sup> or less was smaller than the regression formula of JCI guidelines by 1/10-1/100 and clearly different from the regression equation of JCI guideline.

### 1. Introduction

The estimated equation of autogenous shrinkage of concrete which is used for thermal stress analysis has been formulated starting from the initial setting time in JCI mass concrete guideline[1]. On the other hand, the relationship between compressive strength and Young's modulus of concrete has been set based on experimental data of after 1 day of age which are the concrete compression strength 3 N/mm<sup>2</sup> or more and the Young's modulus 7 GPa or more. This is because the concrete strain can be continuously measured before the initial setting time is cured by using an embedded strain gauge, whereas in the case of the Young's modulus,



the method for preparing specimens, the measuring and calculating method which compressive strength is smaller than before 1 day of age have not been established. In the thermal stress analysis, it is thought that the effect of the temporal change of the compressive strength and the Young's modulus at the age of early ages is large, because the stress is calculated from the initial stage of concrete curing. However, almost no experimental data has been reported. In this study, the Young's modulus was measured from the very early age by improving the molding method based on the past research. The measurement of the Young's modulus was aimed at ordinary cement concrete and blast furnace cement concrete. In addition, the effect of cement types and concrete temperatures were investigated by measuring at concrete temperatures of 20 °C and 40 °C.

## 2. Method for measuring Young's modulus

### 2.1 Materials and Mix proportion of concrete

The mix proportion of the concrete is shown in Tab. 1 and the materials are shown in Tab. 2. As the binder, ordinary Portland cement and blast furnace slag fine powder were used. The mix proportion of the concrete was the ordinary cement concrete and the blast furnace cement concrete. The blast furnace cement concrete was replaced the blast furnace slag by 40% of the ordinary cement. In addition, the water binder ratio was 55%, the slump was  $15 \pm 2.5$  cm, and the air volume was  $4.5 \pm 1.5\%$ .

Table 1: Mix proportion of concrete

Binder	Slump (cm)	Air (%)	W/B (%)	s/a (%)	Unit weight [kg/m <sup>3</sup> ]					
					W	C	BFS	S	G	Ad
N	15	4.5	55	47.5	166	302		863	963	3.02
BB				47.5	164	179	119	861	961	2.98

Table 2: Properties of concrete materials

Symbol	Material	Property
C	Ordinary portland cement	Density 3.16g/m <sup>3</sup> Specific surface area 3300cm <sup>2</sup> /g
BFS	Blast-furnace slag	Density 2.83g/m <sup>3</sup> Specific surface area 4050cm <sup>2</sup> /g
S	Fine aggregate	Saturated surface-dry density 2.63g/m <sup>3</sup>
G	Coarse aggregate	Saturated surface-dry density 2.65g/m <sup>3</sup>
Ad	Air entraining and water reducing agent	Lignin acid binding agent

## 2.2 Test method for very early age

### (1) Test starting material age

In order to confirm the measurable start age of the Young's modulus, the initial set time of the condensation and the termination time were measured based on JIS A 1147 [2]. The concrete was used in two mix proportions, and curing temperatures were carried out at two conditions of 20°C and 40°C. In the test at the curing temperature of 20°C, the temperature of mixed concrete was set to 20°C. In the test at the curing temperature of 40°C, the temperature of mixed concrete was set from 35°C to 40°C by warming mixing water, cement and aggregate. After the concrete was mixed, slump, air volume, unit volume mass, and temperatures were measured. After that, mortar was screened from the concrete, and the penetration resistance value was measured under curing temperatures of 20°C and 40°C.

The test results are shown in Fig. 1. Under the curing temperature of 20°C, the ordinary Portland cement concrete had a slightly shorter termination time than the blast furnace cement concrete, but at the curing temperature of 40°C, there was almost no difference in two mix proportions. On the basis of the obtained test results, the Young's modulus was measured from aging for 7 hours at the curing temperature of 20 °C and 4 hours at the curing temperature of 40°C.

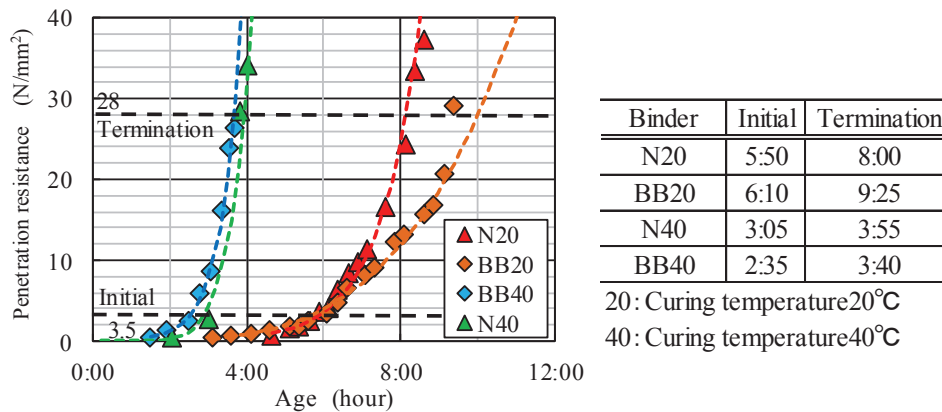


Figure 1: The penetration resistance value

## (2) Preparation of concrete specimen and loading speed

The age of the test material and the number of specimens are shown in Tab. 3. Specimens were cylindrical shapes with a diameter of 100 mm and a height of 200 mm, and steel molds were used. For the specimens with a the curing temperature of 20°C, the mixed concrete which temperatures were of 20°C was driven into the steel mold. After driving, the upper surface was covered with Teflon sheets to seal the specimens until the material age of demolding tests starting, and the curing was performed in a thermo-hygrostat chamber at the temperature of 20°C and the humidity of 80%.

Table 3: Age of test material and number of specimens

Age	Temp 20°C		Age	Temp 40°C	
	Loading method			Loading method	
	0.1mm/min	0.6 N/mm <sup>2</sup> /sec		0.1mm/min	0.6 N/mm <sup>2</sup> /sec
7hr	1		4hr	1	
8hr	1		6hr	1	
9hr	1		8hr	1	
10hr	1		10hr	1	
12hr	1		12hr		1
14hr	1		14hr		1
16hr	1		16hr		1
24hr		3	24hr		1
2d		3	2d		3
3d		3	3d		3
28d		3	28d		3

For the specimens with the curing temperature of 40°C, the mixed concrete which temperatures were from 35 to 40°C was driven into the mold, and the top surface was covered with Teflon sheets and sealed until the starting age of the test. Thereafter, it was cured in a

thermo-hygrostat chamber at the temperature of 40°C and the humidity of 80%. As devised at demolding, in the case of the specimens up to 10 hours at the curing temperature of 20°C and 40°C (hereinafter, referred to as "very early age"), Teflon sheets were affixed to the inside of the steel formwork to prevent the concrete from adhering to the steel mold when demolding. At the time of the loading test, the side Teflon sheets were removed, and the test was carried out. (Fig. 2(c)) Finishing of the upper surface of the specimens before covering with the Teflon sheets, the parallelism between upper and lower surfaces of the specimen was ensured by pressing the steel lid after the completion of water generation was confirmed. (Fig. 2(b))

In the measurement of very early age, it is difficult to conduct a test at a loading speed of  $0.6 \pm 0.2 \text{ N/mm}^2/\text{sec}$  according to JIS A 1149, because the compression strength is very small and the amount until the maximum load is large. From this reason, displacement was controlled and the displacement speed was set to 0.10 mm/min based on the previous research [3]. The measurement of the Young's modulus other than the very early age was carried out based on JIS A 1149, because compressive strength of concrete is sufficiently high. The Young's modulus was calculated according to JIS A 1149.

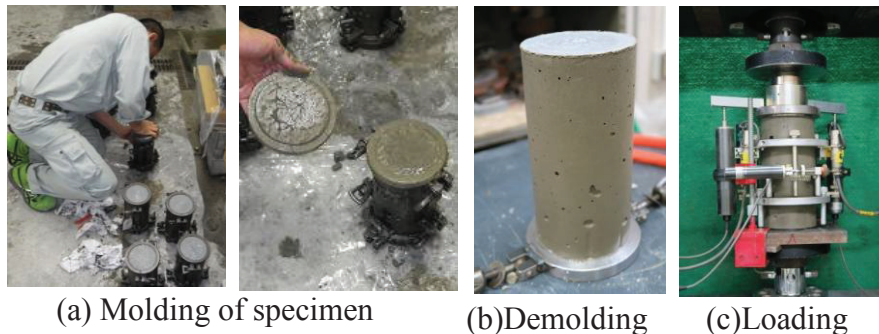


Figure2: Examination at the very early age

### 3. Results and discussions

The relationship between compressive stress and strain obtained from the measurement test of the Young's modulus of the very early age is shown in Fig. 3, and the relationship between compressive strength and strain obtained in JIS A1149 at the curing temperature of 20°C is shown in Fig. 4. From these results, it can be confirmed that the strain is more distorted until the compressive stress becomes maximum at the concrete of the very early age, and it is distinctly different from concrete of a general compressive strength. For the Young's modulus, the secant Young's modulus was calculated.

The relationship between the compressive strength and the Young's modulus is shown in Fig. 5 and Fig.6. In the figure, the regression equation obtained from the test results of the Young's modulus after 1 day of age using the concrete of the same mix proportion as this test in the past study[4] is shown. It can be confirmed that there is one correlation between the compressive strength and the Young's modulus regardless of the formulation, the cement type and the curing temperature. Also, since one correlation is shown, it can be confirmed that the difference between the displacement speed control and the load speed control measurement method is very small. According to Fig.5(a), the relationship between the compressive strength and the Young's modulus seems to be in good agreement with the regression equation[4], but in the range of the compressive strength 0 to  $3.0 \text{ N/mm}^2$  (Fig.5(b)), The

Young's modulus obtained by the test shows a value slightly smaller than the regression equation. In particular, it can be seen that when the compressive strength is  $1.0 \text{ N/mm}^2$  or less, it differs greatly. In the case where the vertical axis (Young's modulus) is taken as a logarithm (Fig.6(b)), it can be confirmed that the Young's modulus at  $1.0 \text{ N/mm}^2$  or less is smaller by 1/10-1/100 than the regression equation. This is because the regression equation is calculated based on the test results after 1 day of age. Also, paying attention to the compressive strength of 0 to  $0.75 \text{ N/mm}^2$ , the Young's modulus in this range increases exponentially. It clearly shows a different tendency from the expression characteristics of the Young's modulus at the compressive strength of  $1.0 \text{ N/mm}^2$  or more, suggesting that the Young's modulus development greatly changes around  $0.75$  to  $1.0 \text{ N/mm}^2$  of the compressive strength. Since the recommended formula in the JCI guidelines is set based on the test data after 1 day of age, it is considered that it is important to set an estimation formula that considers the test data of very early age.

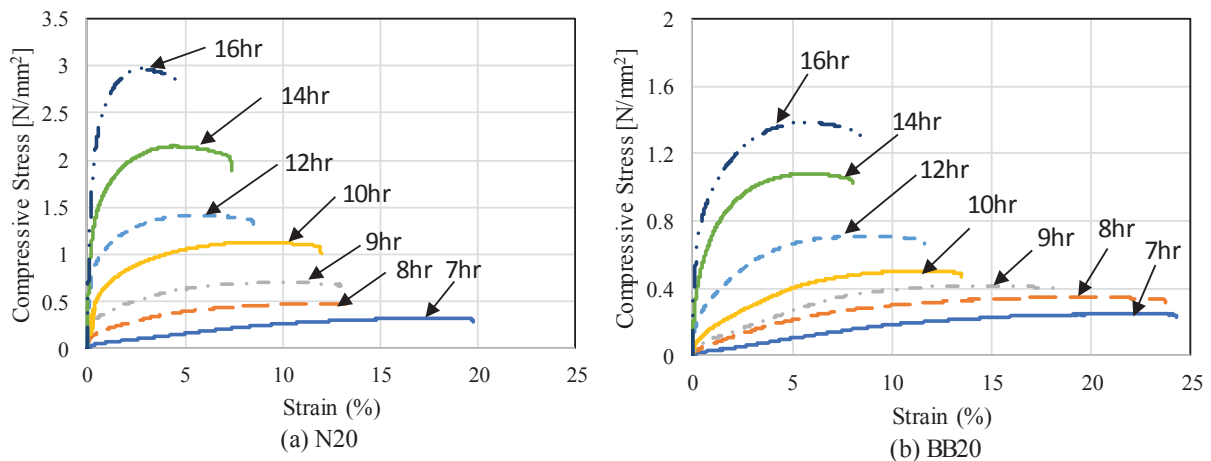


Figure 3: Relationship between compressive stress and strain (very early age)

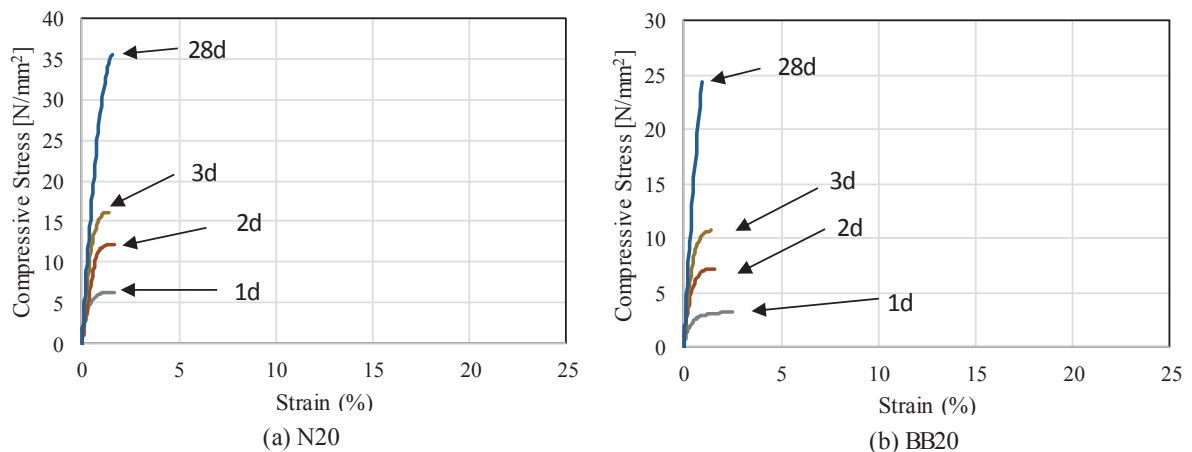


Figure 4: Relationship between compressive stress and strain ( JIS A1149 )

#### 4. Conclusions

From the test results in this study, it was clarified that the relationship between the compressive strength and the Young's modulus greatly differ in the Young's modulus

expression characteristics at very early age. Especially in the region where the compressive strength is  $0.75 \text{ N/mm}^2$  or less, the increase in the Young's modulus increases exponentially as it is the curing process of concrete. It is thought that it is important to consider the difference in the Young's modulus expression in order to improve the accuracy of temperature stress analysis at very early age.

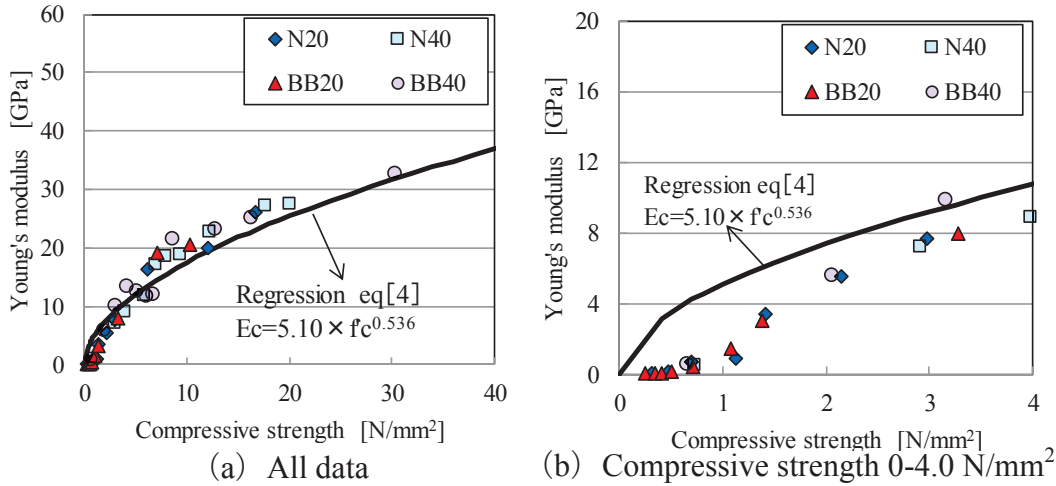


Figure 5: The relationship between compressive strength and Young's modulus

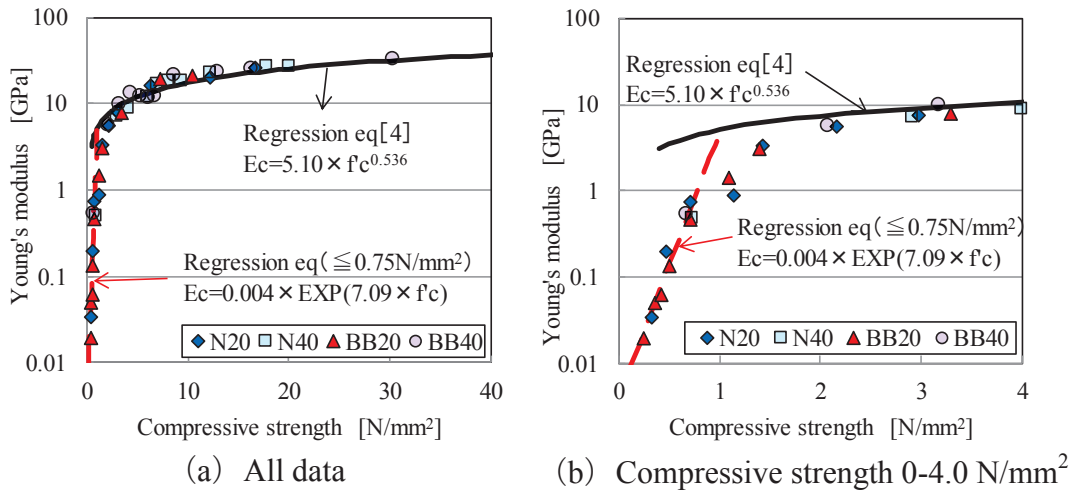


Figure 6: The relationship compressive strength and Young's modulus (Logarithmic display)

## References

- [1] JCI : Guidelines for Control of Cracking of Mass Concrete 2016, 2017.4
- [2] JISA1147 : Method of test for time of setting of concrete mixtures by penetration resistance
- [3] Takuya TANI, Tomoyuki AOKI, Toyokazu OGAWA, Hitoshi TAKEDA, Yoshiaki FUJII: Study on Deformation Characteristics of Young-Age Tunnel Shotcrete, Journal of MMIS Vol.128,p.113-120
- [4] Tatsuya USUI, Shigeyoshi MIYAHARA, Tsuyoshi MARUYA, Takeshi OTOMO: Study on Autogeneous Shrinkage and shrinkage Stress of Concrete using Ground Granulated Blast-Furnace Slag under Different Curing Temperature Conditions, Journal of Japan Society of Civil EngineersE2, vol.70, No.1, pp92-103, 2014.3

## UTILISING EXCAVATED ROCK MATERIAL FROM TUNNEL BORING MACHINES (TBMS) FOR CONCRETE

Torjus Berdal <sup>(1)</sup>, Pål Drevland Jakobsen <sup>(1)</sup>, Stefan Jacobsen <sup>(1)</sup>

(1) The Norwegian University of Science and Technology (NTNU), Norway

### Abstract

There are more than 2000 completed road, railroad and hydropower tunnels in Norway, with a current annual production of more than 7 million solid cubic metres excavated rock. The road and railroad tunnels are consumers of concrete, which is utilised for rock support, water- and frost protection. A small portion of the excavated rock affiliated with Norwegian tunnelling is used as concrete aggregate, while the major part of the rock is used for landfill. This paper reviews the potential of utilising excavated rock obtained by tunnel boring machines (TBM) as concrete aggregates, including results from recent European TBM projects that have utilised the excavated rock for concrete aggregates. Finally we present test results from excavated rock material from two new (including one ongoing) Norwegian TBM projects. Particle Size Distribution (PSD) of the filler / fines fraction and effect of the fines fraction (< 0.125mm) of the rock material on flow of fresh filler modified cement paste were measured. The reuse in concrete of excavated rock from 8 different recent European TBM projects varied from zero to 100 %. Reviewed PSDs and own PSD measurements show that TBM PSDs vary within wide ranges. Content of fines < 0.1 mm content can be more than 20 % of the total TBM and even higher when the coarsest material is used as feed in production of crushed aggregate. The newest project reviewed, the Norwegian Follo line, is generating the finest material with 50 % < 4 mm indicating the importance of rock quality in addition to TBM-technology for fines generation. The flow results of filler modified paste show that the TBM fines from the two projects with size 0-0.125 microns have very similar effect on fresh cement paste flow properties as a replica limestone filler with similar PSD composed from 3 different filler fractions.

## 1. Introduction

Most of the tunnels in Norway are excavated by the conventional drill and blast method. Furthermore, they are mostly less than 1000 m and the excavated rock has mainly been used for landfill, or even dumped in the sea. Around 30 of the tunnels in Norway were excavated by tunnel boring machines (TBMs) [1]. Hydropower tunnels are the main user of TBMs, as the TBM enables a smooth tunnel cross-section with reduced head-loss in comparison with drill and blast tunneling. Figure 1a) shows a typical TBM cutterhead. Currently the Norwegian Railroad Authorities are utilizing 4 TBMs for a major railroad project from Oslo towards the suburb Ski. Last year the same client achieved the breakthrough of the new Ulriken TBM railroad tunnel project in the city of Bergen. Thus, infrastructure owners in Norway are starting to utilize TBM more commonly for tunneling. One central question is how are the possibilities to utilize excavated rock material locally, for example as aggregate for the tunnel's permanent concrete rock support and linings.

The aims of this paper are 1) to give an overview of the potential of utilising excavated rock material obtained from TBMs for use as concrete aggregates. Knowing the magnitude of the challenge is important to assess the societal impact. 2) Present how various recent TBM projects have utilised the excavated rock for concrete aggregates as input to discuss technical prospects for future reuse of the residues also including fines and not just the coarse parts that are presently used as feed for crushed rock processing plants. 3) Discuss how local aggregates can be exploited more in connection with tunnel projects. The results of the paper are based on a literature review, collection of laboratory data from old, recent and ongoing TBM projects, own laboratory studies of PSD of fines, sand and coarser fractions, as well as laboratory measurements of the effect of filler from TBM debris on flow of fresh filler modified paste. The quality of fines have a proportionally much larger influence than the quality of coarse aggregate on rheology of concrete [2] and therefore we start with the fines in this work. The work is entirely based on the MSc thesis of Torjus Berdal [3]. The key question, which is, whether this reuse can be done within economic benefits is not addressed.

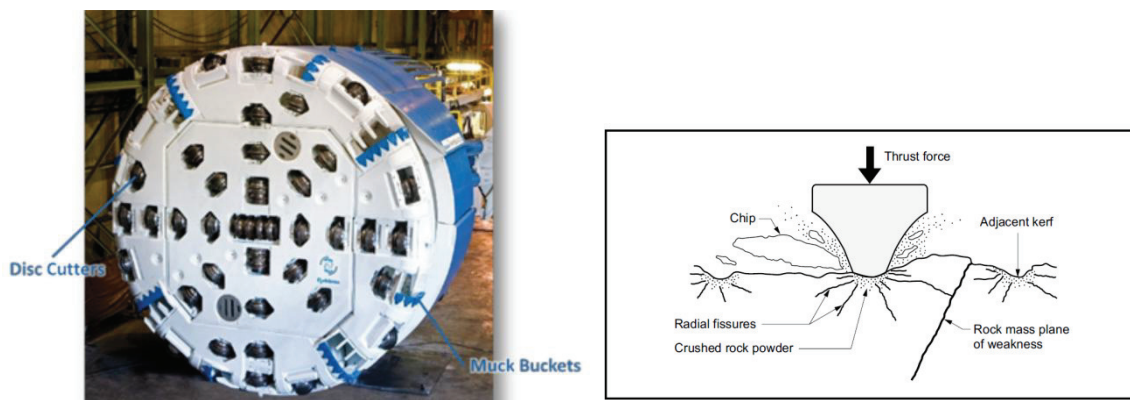


Figure 1: a) TBM cutterhead designed for hard rock excavation. Courtesy of the Robbins company [1], b) Idealised rock breaking principle under disc cutters after Bruland [1]

## 2. Generation of debris, utilization and PSD

The rock breaking of hard rock TBMs is done by rotating the cutterhead equipped with disc cutters and applying high axial forces (200 – 315 kN per disc cutter) while the cutterhead is rotating. The axial force enables a crushing zone between the disc cutter and the rock face as well as inducing radial fractures into the rock mass. When the radial fissures range to a natural plane of weakness or a mechanical induced fissure from another disc cutter, chipping occurs, see Figure 1b.

TBM debris, when intended used for concrete aggregates, needs to be handled similarly in quality control as ordinary concrete aggregate. Particle size distribution (PSD) of fines, sand and coarser fractions is hence one of the most important aggregate quality parameters. PSDs were therefore reviewed and measured with dry and wet sieving on various TBM debris materials and with X-ray sedigraph on fines, or filler which is the terminology used in concrete technology. Nine different newer TBM projects (Railway- and Hydropower tunnels) in 5 European countries were reviewed as well as 30 older TBM projects (25 Norwegian, 5 Swiss). Regarding the other continents, no data on TBM-debris were found in Asia, Oceania or America in this study [3]. Table 1 shows an overview of 8 different TBM projects with varying degrees of reuse in concrete from almost zero to 100 %. So in practice the variation in reuse is large.

Table 1: TBM projects with confirmed utilisation of TBM excavated rock in concrete [3]

Project name	Duration (year)	Minimum utilization fraction (mm)	Utilization of excavated rock (%)
Zugwald	N/A-1998	16	16
Gotthard base tunnel	1999-2016	0	23
Lötschberg	1999-2007	0	29.1
Linthal	2010-2015	0	100
Nanth de Drance	2008-2016	0	25
Breheimen	1986-1989	10	N/A
Follo Line	2016-2021	20	10*
Koralm KAT2	2013-2023	16	17

\* The utilisation of excavated rock for concrete purposes has stopped at the Follo line due to sulphur content  $\approx 0.1$  %

A literature review from various sources has compared PSDs from hard rock TBM projects between 1977 and 2018 from Switzerland or Norway. The number of projects and time span of the projects enables high reliability, in terms of varying geology, TBM operation and TBM development. Figure 2 shows an overview of PSDs from the major Norwegian and Swiss TBM projects. Fines contents vary from  $< 5\%$  to  $> 20\%$  and maximum particle size vary from  $< 10$  to  $> 100$  mm so these are clearly very variable materials. In addition, it is important to remember that use of coarse debris particles as feed in rock crushing plants will further increase the amount of fines. Careful selection of process technology for reuse of TBM debris is very important to limit the problem of fines generation and optimize particle shape.



Although particle shape was not investigated in this study it needs to be addressed in concrete aggregate production. An interesting observation from figure 2 is that the Follo line, which is a new project, is generating the finest sieve curve (50% < 4 mm). The reason for this could be related to the TBM operation (relative low load per disc cutter), the brittleness of the rock mass and/or the TBM cutterhead design. Anyway, this project shows how a modern TBM with carefully distanced cutter discs and a high thrust force for maximum penetration rates is not enough to generate coarser sieve curves. The geology and petrography seem to influence the outcome of TBM debris quality to a large extent.

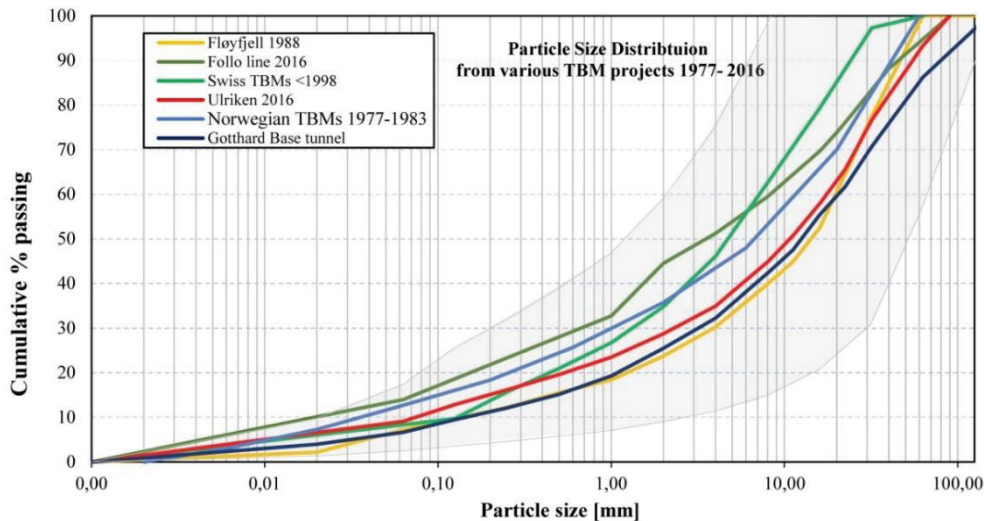


Figure 2: PSD from various hard rock TBM projects showing mean curves. Grey area represents possible variation for a single sieve curve

Observations in optical microscope of debris from Ulriken revealed that fines could adhere to the surfaces of larger (sand) particles to various extents, possibly due to the TBM process itself. This may cause negative effects on concrete properties (bond etc) as well as affect the measured PSDs. Therefore, both wet and dry sieving were done on 1 kg samples. These showed a +2.46% increase on the 0.125 mm sieve and +5.79% increase on the 0.063 mm sieve when wet sieving compared to when dry sieving. This seems to verify the visual observations of fines adhering to the surfaces of larger particles.

### 3. TBM filler vs limestone filler – PSD measurements and cement paste

TBM filler from Ulriken TBM project was collected on site in October 2017. The fraction <0.125mm was sieved out. Then the PSD was investigated with X-ray sedimentation using Micromeritics SediGraph III PLUS. With the known PSD of the TBM filler, the same PSD curve was composed with three different fractions of a crushed limestone filler. The reference limestone filler had been produced prior to the TBM material and separated through air classification and divided into coarse (40/250 $\mu$ m), medium (20/60 $\mu$ m) and fine (0/20 $\mu$ m) fractions. Figure 3 (left) shows the PSD of the TBM filler that was replicated with limestone filler with the method presented in [4]. A filler modified cement paste which would resemble that in a B45M40 concrete was designed for the purpose of measuring effect of TBM filler on

flow properties in terms of mini-slump flow value and flow resistance [5]. The mini cone had bottom diameter: 89 mm, top diameter: 39 mm, height 70 mm. The cement content in the mix would resemble a cement content of 360 kg/m<sup>3</sup> in a 1 m<sup>3</sup> concrete mix. Table 2 shows composition with mass ratios water/cement = 0.40 and filler/cement = 0.36.

Table 2: Cement paste composition used with TBM filler and limestone filler

Constituents	Kg	Density(kg/m3)
Norcem CEM II/A-V	2.288	3020
Water	0.915	1000
Superplastizer (0.9%)	0.021	1050
Filler (TBM/Limestone)	0.818	2700

2 litre cement paste mixes were prepared in the lab according to the procedure [6]. The slump-flow measurements were performed on a transparent plexiglass plate and assured no leakages between matrix and cone. In addition FlowCyl values were measured [5]. The latter method is similar to the Marsh cone and the resulting flow resistance number  $\lambda_Q$  (0 - 1) correlates well to plastic viscosity whereas slump flow correlates to yield stress [2,6]. Table 3 gives average results of 2 parallel mixes for each of the 5 studied fillers: 4 TBM fillers and 1 reference limestone filler. The results show marginal differences between the mixes. The slightly better workability of the replica limestone filler with similar PSD is in line with previous findings that limestone filler can have a favourable effect on workability compared to other minerals [6].

Table 3:  $\lambda_Q$  and Mini-slump results, each value is average of two parallel mixes

Constituents	$\lambda_Q$	Mini-slump(cm)
Limestone	0.745	27.2
TBM Ulriken 1	0.807	23.4
TBM Ulriken 2	0.808	22.8
TBM Ulriken 3	0.806	21.3
TBM Follo	0.817	21.3

Figure 3 also shows that the replica lime stone filler has slightly lower content of the very finest particles which also contributes to the slightly higher mini slump flow and lower flow resistance number  $\lambda_Q$  seen in Table 3. The photos in Figure 3 show very stable edges on the slump flow samples.

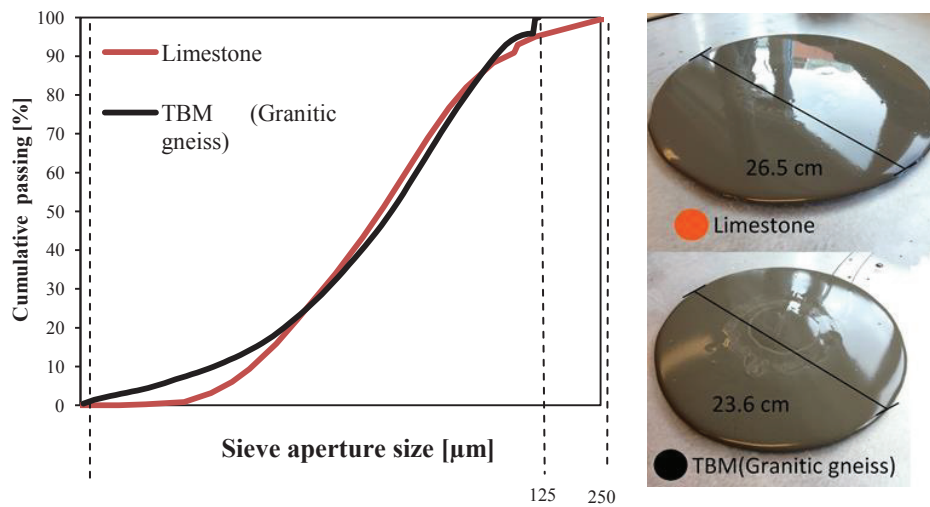


Figure 3: PSD of the filler from TBM debris and replica limestone (left) Mini slump measurements with stable edges (right)

#### 4. Conclusive remarks

This paper presents early findings associated with the potential of using excavated rock material obtained by TBM for concrete aggregates, as well as summarising the potential of recent TBM projects in Norway related to concrete aggregates. The authors believe that further research and development with the civil construction industry, as well as contractual incentives can increase the use of excavated rock, and reduce the waste-problems that are associated with tunnelling.

#### References

- [1] Jakobsen, P.D., Log, S., Skjeggedal, T., Hansen, A.M., Palm, A., Short introduction to the use of TBM. Kort innføring i bruk av TBM (in Norwegian only). NFF. (2015)
- [2] Cepuritis, R., Development of crushed sand for concrete production with microproportioning, PhD thesis, Norwegian University of Science and Technology (2016)
- [3] Berdal, T., Use of excavated rock material from TBM tunnelling for concrete Proportioning, Master thesis, Norwegian University of Science and Technology (2017)
- [4] Cepuritis R., Jacobsen S. and Onnela T., Sand production with VSI crushing and air classification: Optimising fines grading for concrete production with micro-proportioning, Minerals Engineering Vol 78 (2015) 1-14
- [5] Mørtzell E., Modelling the effect of concrete part materials on concrete consistency. PhD thesis, Norwegian University of Science and Technology (1996)
- [6] Cepuritis, R., Jacobsen, S., Smeplass, S., Mørtzell, E., Wigum, B. & Ng, S. Influence of crushed aggregate fines with micro-proportioned particle size distributions on rheology of cement paste. Cement and Concrete Composites Vol 80 (2017), 64-79

## **WATER ABSORPTION CHANGES IN MORTARS WITH CRYSTALLINE ADMIXTURE EXPOSED TO ACID ENVIRONMENT**

**Victoria Eugenia García-Vera<sup>(1)</sup>, Antonio José Tenza-Abril<sup>(2)</sup>, Marcos Lanzón<sup>(1)</sup>, Afonso Miguel Solak<sup>(2,3)</sup>, Concepción Pla<sup>(2)</sup>, David Benavente<sup>(4)</sup>**

(1) Department of Architecture and Building Technology, Technical University of Cartagena, Murcia, Spain

(2) Department of Civil Engineering, University of Alicante, Alicante, Spain

(3) CYPE Ingenieros S.A., Alicante, Spain

(4) Department of Earth and Environmental Science, University of Alicante, Alicante, Spain

### **Abstract**

In industrial cities, a common attack in concrete is sulfuric acid attack. Sulfuric acid is particularly corrosive due to the sulfate ion in addition to the dissolution caused by the hydrogen ion causing the deterioration of the cementitious materials. To improve acid attack resistance in those materials, the matrix must be dense, with low permeability, use in the production a sulfate resistant cement or high alumina cement, etc. Crystalline admixtures are used as a waterproofing product because they improve the protection of the cementitious materials filling the capillaries preventing the penetration of liquid by crystals formation that fill the capillary pores and micro-cracks, blocking the water entrance. The main objective of this work is to study the behaviour of mortars produced with the same quantity of cement, water, fine aggregate and including different percentages of crystalline admixture (1%, 1.5% and 2%) in an aggressive environment (sulfuric acid solution - 3% w/w). Changes in the mass, density, porosity and capillary absorption coefficient after 28 and 56 days of fully submerged in H<sub>2</sub>SO<sub>4</sub> solution. From the results obtained, we can observe a noticeable better performance of the mortars with crystalline admixtures.

### **1. Introduction**

Nowadays, cementitious materials are in contact to acids because of the environmental pollution —soils, seawater or treatment plants [1, 2]. In industrial cities, a common attack in concrete is sulfuric acid attack. Sulfuric acid is particularly corrosive due to the sulfate ion in

addition to the dissolution caused by the hydrogen ion causing the deterioration of the cementitious materials. There are numerous studies about acid attack in concrete; however, already is a challenge to find high durability performance mortars in aggressive environments. To improve acid attack resistance in those materials, the matrix must be dense, with low permeability, use in the production a sulfate resistant cement or high alumina cement, etc [3-5]. There are strategies aimed at extending the durability of cementitious materials against acid attacks, and try to increase the impermeability of these materials by introducing water-repellent admixture. Some of the most commonly investigated hydrophobic admixtures for mortars include metallic soaps, e.g. calcium stearate, zinc stearate, sodium oleate, and silanes [6]. Crystalline admixtures are commonly used as a waterproofing product to improve the protection of the concrete. The crystals formed grow and fill the capillary pores and micro-cracks, blocking the water entrance preventing the penetration of liquid.

The main objective of this work is to study the behaviour of mortars produced with the same quantity of cement, water, fine aggregate and including different percentages of crystalline admixture (1%, 1.5% and 2%) in an aggressive acid environment (sulfuric acid solution - 3% w/w). Changes in the mass, density, porosity and capillary absorption coefficient after 28 and 56 days of fully submerged in H<sub>2</sub>SO<sub>4</sub> solution.

## 2. Materials

Four types of mortars were studied: i) control mortar; ii) mortar with 1% xypex by cement weight (Xypex Admix C-100 NF); iii) mortar with 1.5% xypex by cement weight; and iv) mortar with 2% xypex by cement weight. The dosage used for the mortars was one part cement (CEM I / 52.5R), 0.45 parts water and three parts of fine limestone aggregate. For adequate workability of the mortars, 1.2 % of superplasticizer (Sika ViscoCrete-5980) by cement weight was added.

## 3 Methods

### 3.1 Manufacturing, curing process and acid sulfuric attack simulation

Twelve normalized specimens (40 x 40 x 160 mm) were prepared per each type of mortar. First, the water-repellent admixtures were added to the dry mass (cement and sand) and were well mixed for 1 minute with an automatic mortar mixer. Then, water was added and mixed for another 4 minutes respecting the velocities and times of the standard EN 196-1 [7]. Mortars were kept in laboratory conditions for 24 hours and then they were demoulded. All the samples were cured for 28 days in a temperature and humidity controlled chamber at 20 °C and 95% RH. When the curing period had finished, all specimens were exposed to two different media. The first one was a H<sub>2</sub>SO<sub>4</sub> solution (3% w/w) to study the behaviour of mortars regarding the attack of this aggressive. The second medium consisted in submerging the samples in distilled water until the testing age. This last condition has been used as a reference for comparing the effects of aggressive attack to an optimum hardening condition. Solution was renewed in periods of 7 days.

To change the acid sulfuric solution i) the specimens were extracted from aggressive medium, and were gently brushed with tap water to eliminate rests of material weakly adhered to the

surface; ii) the acid sulfuric solution was renewed; and iii) the specimens were reintroduced into the new solution. The temperature of the aggressive medium and the distilled water were kept constant at 20°C.

The test time has been coded as follows:  $t_{m(e)}$ . Where  $m$  is the age of the mortar and  $e$  the exposure time to aggressive medium (28 days after the manufacture corresponds to 0 days of acid exposure). The tests were conducted in two periods at 28 days [ $t_{56(28)}$ ] and 56 days [ $t_{84(56)}$ ] days of exposure.

### 3.2 Mass variation

To study the mass variation of the mortars exposed to acid, the specimens were weighed weekly up to 49 days after. The mass of the specimen was obtained after complete drying in an oven at 105 °C for 24 h. The following masses were obtained: 28 days after the manufacture and before starting the simulation (0 days of acid exposure) [ $t_{28(0)}$ ]; at 7 days [ $t_{35(7)}$ ]; 14 days [ $t_{42(14)}$ ]; 21 days [ $t_{49(21)}$ ]; 28 days [ $t_{56(28)}$ ] and 49 days [ $t_{77(49)}$ ] of acid attack exposure. The percentage of mass loss were calculated taken into account the initial weights [ $t_{28(0)}$ ] as:

$$M_c = [(m_e - m_0) / m_0] \cdot 100$$

Where  $M_c$  is the mass change;  $m_0$  is the initial mass of the specimen before being exposed to the chemical solution;  $m_e$  is the mass of specimen after exposure time  $e$ .

### 3.3 Study of the capillary water absorption of the mortars

The capillary absorption test was performed according to the standard EN-1015-18 [8]. Before the test, samples were subjected to a pre-conditioning procedure, which firstly consisted of a complete drying in an oven at 105 °C for 24 h, and from then to the start of the test they were saved in a hermetically sealed recipient with silica gel.

The lateral sides of the specimens were sealed to restrict the water flow along the longitudinal axis. The water flux through the sample was measured by partial immersion of the specimens at a depth of  $5 \pm 1$  mm. Throughout the test, water level was kept constant and the container was hermetically closed. The capillary absorption coefficient was calculated using the measurements for 10 and 90 min. The test was performed at 28 [ $t_{56(28)}$ ] and 56 [ $t_{84(56)}$ ] days of exposure to the aggressive medium. According to the standard, the water absorption coefficient is the line slope that joins the points corresponding to 10 minutes and 90 minutes in the curve that represents the mass variation of water absorbed per unit area as a function of the square root of time, i.e. the coefficient was computed using the formula:

$$C = (M_2 - M_1) / (A \cdot (t_2^{0.5} - t_1^{0.5}))$$

where:  $C$  is the capillary water absorption coefficient,  $k/(m^2 \cdot \text{min}^{0.5})$ ;  $M_1$  is the specimen mass after the immersion for 10 minutes;  $M_2$  is the specimen mass after the immersion for 90 minutes;  $A$  is the surface of the specimen face submerged in the water in  $m^2$ ;  $t_2$  corresponds to 90 minutes and  $t_1$  to 10 minutes.

## 4. Results

### 4.1 Mass variation

Fig. 1 plots the mass variation rates of the specimens soaked in  $H_2SO_4$  solution compared with the mass before the immersion up to 56 days. It can be seen that the percentage of mass

loss in the mortars is similar in all the samples (-22%, -24 and -26% in mortar with 1%, 1.5% and 2% of crystalline admixture in its composition respectively).

#### 4.2 Density and porosity

Fig 2a) and b) plot the density and porosity percentage variation due to the exposure of the mortar to the acid attack during 28 days and 56 days compared with mortars immersed in water (actual values are listed in Tab. 1). As can be seen in Fig.2a, the reduction in the density of the mortar at 28 days is similar in all the mortars.

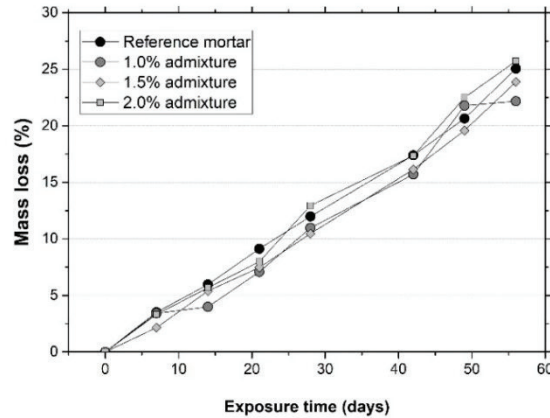


Figure 1: Percentage of mass loss in the mortars.

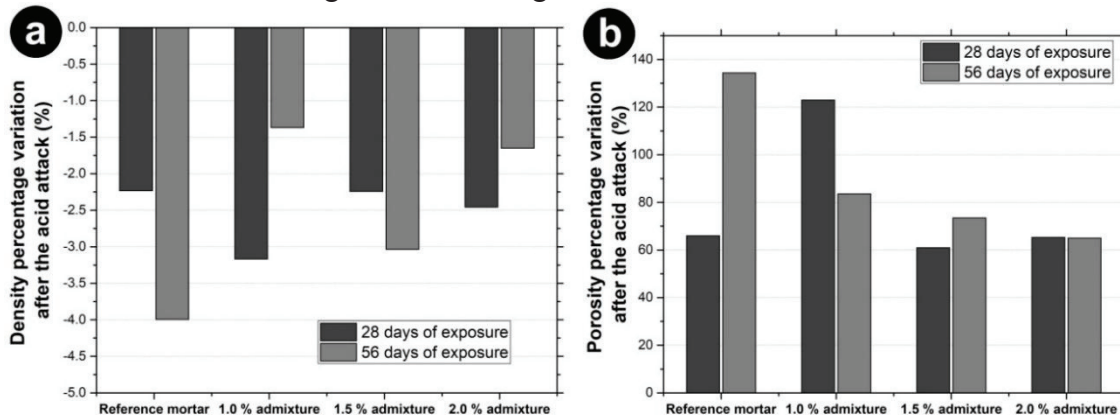


Figure 2: a) Density percentage variation and b) porosity percentage variation after the acid attack after 28 and 56 days of exposure. The bars are normalised to the values obtained in the same mortar immersed in water at the same age.

Table 1. Results obtained in the tests.

Days of immersion	% Mass loss		Dry density (kg/m <sup>3</sup> )				Porosity (%)			
			H <sub>2</sub> SO <sub>4</sub>		Water		H <sub>2</sub> SO <sub>4</sub>		Water	H <sub>2</sub> SO <sub>4</sub>
	28	56	28	28	56	56	28	28	56	56
Reference mortar	12,0%	25,0%	2301	2247	2348	2261	8,3%	13,8%	5,4%	12,1%
Admix. (1%)	11,0%	22,2%	2302	2223	2288	2246	6,2%	13,9%	6,3%	11,8%
Admix. (1,5%)	10,5%	23,9%	2307	2273	2345	2292	8,2%	12,5%	5,7%	8,8%
Admix. (2%)	13,0%	25,7%	2339	2285	2351	2319	7,0%	11,4%	5,0%	8,2%

However, after 56 days of exposure, the mortars that contains crystalline admixtures the impact of the reduction of the density is less compared with the reference mortar without admixture. The porosity of the mortars exposed to acid solution increased (Fig. 2b). As observed with density, the increase in porosity in mortars with crystalline additions is much less at 56 days than at 28 days and lower than the reference mortar probably due to the formation of crystals throughout the pores and capillary.

### 4.3 Capillary absorption

Fig. 3 shows the capillary water absorption coefficient of the mortars at 28 days (exposed and non-exposed to acid solution). As can be observed, the mortars with crystalline admixture exhibited less capillary absorption than the reference mortar in both conditions (immersed in water and immersed in acid solution).

Again, the crystalline formation throughout the capillary prevents the penetration of water. They usually consist in a certain dispersion of the complex chemical active substances that dissolve in water interacting with the products of hydration of Portland cement to form sparingly soluble compounds and filling the pore space [9]. Small newly formed needles are mostly located in the walls of capillaries and cavities, making it narrower. The composition of needle-like calcium hydrosilicates [9]. Figure 4 shows the X-ray diffraction pattern of the mineral admixture used to produce the mortars. No peaks attributed to any crystallised compound can be identified except a broad diffraction halo (amorphism of between 20° and 30°). Further research is needed to understand the mechanism that could be associated to the crystal formation (X-Ray diffraction, SEM imaging, and pore size distribution) that influences the reduction of water absorption in mortars exposed to acid environment.

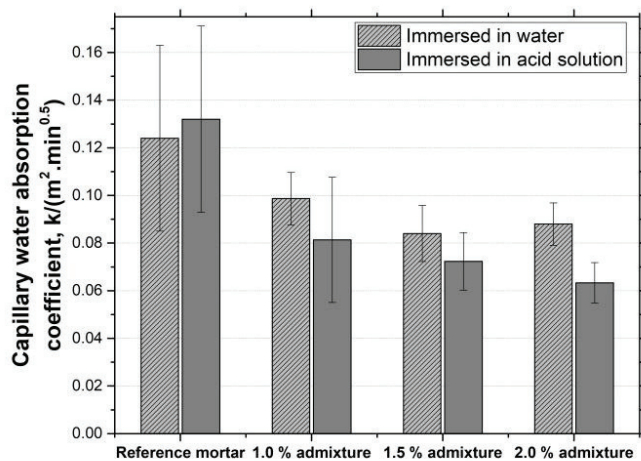


Figure 3: Capillary water absorption coefficient at 28 days [ $t_{56(28)}$ ].

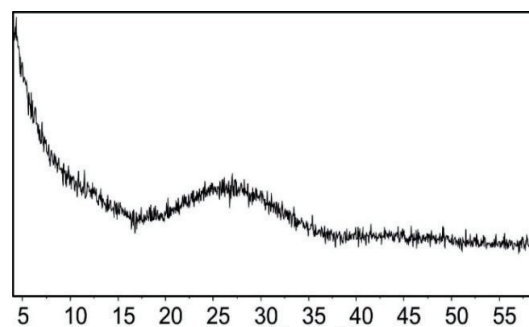


Figure 4: XRD pattern of the mineral admixture.



## 5. Conclusions

In this work, the effects of acid attack on physical properties of containing crystalline admixtures mortars were analysed. From the results presented in this study the following conclusions are drawn:

- Accordingly mass loss in H<sub>2</sub>SO<sub>4</sub> solution, the effect of crystalline admixtures on sulfate attack is small because it is similar in all the mortars.
- However, after 56 days of acid exposure, the mortars with crystalline admixture in its composition presented less reduction of the density and lower increase of the porosity. In addition, the capillary water absorption coefficient were lower in the mortars with crystalline admixture compared with the reference mortar after the acid attack.

## Acknowledgements

This research was funded by the University of Alicante (GRE13-03) and (VIGROB-256).

## References

- [1] Santhanam, M., Cohen, M.D. and Olek, J., Sulfate attack research — whither now?, *Cem Concr Res* 31,6 (2001), 845-851
- [2] RILEM TC 211 – PAE, Performance of Cement-based materials in aggressive aqueous environments, *State-of-the-Art*, 10 (2013)
- [3] Irassar, E.F., Di Maio, A. and Batic, O.R., Sulfate attack on concrete with mineral admixtures, *Cem Concr Res* 26, 1 (1996), 113-123
- [4] González, M.A. and Irassar, E.F., Ettringite formation in low C3A Portland cement exposed to sodium sulfate solution, *Cem Concr Res* 27,7 (1997), 1061-1072
- [5] Irassar, E.F., Sulfate attack on cementitious materials containing limestone filler – a review, *Cem Concr Res* 39,3 (2009), 241-254
- [6] Nunes, C. and Slízková, Z., Freezing and thawing resistance of aerial lime mortar with metakaolin and a traditional water-repellent admixture, *Constr Build Mater* 114 (2016)
- [7] EN 196-1:2005, Methods of testing cement - Part 1: Determination of strength, CEN, (2005)
- [8] EN-1015-18, Methods of test for mortar for masonry - Part 18: Determination of water absorption coefficient due to capillary action of hardened mortar (2002)
- [9] Kapustin, F., Pomazkin, E., Spiridonova, A. and Oleinik, V., Impact of Waterproofing Permeable Capillary Mixtures on Cement Stone. In book: *Progress in Materials Science and Engineering*, (2018), 99-106.

## **X-RAY MICROTOMOGRAPHIC IMAGES OF FIBRE CONCRETE COMPOSITES FABRICATED USING DIFFERENT METHODS**

**Zbigniew Ranachowski<sup>(1)</sup>, Marcin Lewandowski<sup>(1)</sup>, Krzysztof Schabowicz<sup>(2)</sup>, Tomasz Gorzelańczyk<sup>(2)</sup>, Stanislav Kudela Jr<sup>(3)</sup>, Tomas Dvorak<sup>(3)</sup>**

- (1) Institute of Fundamental Technological Research, Polish Academy of Sciences, Pawińskiego 5B, 02-106 Warsaw, Poland
- (2) Faculty of Civil Engineering, Wrocław University of Science and Technology, Wybrzeże Wyspiańskiego 27, 50-370 Wrocław, Poland
- (3) Institute of Materials and Machine Mechanics, Slovak Academy of Sciences, Dubravská Cesta 9, P.O. Box 95, 830-08 Bratislava, Slovakia

### **Abstract**

The fibres constituting the reinforcement of the fibre cement composites are of small diameter and colourless and thus difficult to recognize inside the cementitious matrix applying the optical or electron microscopy. Seven fibre cement composite specimens fabricated applying different methods were object of investigation. The X-ray microtomography enabled the authors to perform the following research applying the X-ray microtomographic technique. The length and shape of the fibres could be assessed on specimens' cross-sections. Applying the 3D visualization it was possible to present the fabrication errors resulting in the non-homogenous distribution of fibres within the specimen volume.

### **1. Introduction**

In the paper the microstructure of different kinds of fibre cement composites was investigated using the X-ray microtomographic (micro-CT) technique. Organic fibre cement composites are widely implemented despite of the complexity of its fabrication process. The cellulose fiber cement board (FCB) siding is commonly used as a replacement for wood siding, as it is less expensive and more durable, and has lower maintenance costs [1]. The FCB also referred to as precast fabrication, are becoming more and more important in the entire construction sector. Common applied fibers are of 2.5 to 3 mm of length and of 30 – 50 µm in diameter [2]. In some FCB of lower quality short fibres derived from recycled cellulose of ca. 1 mm

long are used. The methods of fabrication, mechanical properties, durability and microstructure of the standard fibre cement composites are described in [3–5].

## 2. X-ray microtomography

X-ray microtomography (micro-CT) offers the ability to create different modes of microstructure imaging of investigated specimens with a resolution of ca. 1 – 5  $\mu\text{m}$  per voxel (volumetric pixel). The early study of pore size distribution and of pore connectivity in concrete samples using this method was performed by Lu et al. in 2005 and presented in [6]. Several papers concern the application of micro-CT technique in testing the properties of concrete. Garboczi [7] reconstructed the aggregate shapes in concrete with voxel resolution of 0.4 mm<sup>3</sup>. This enabled the author to approximate the real shapes by its mathematical models to built the stereological model of entire population of aggregates. Schabowicz et. al. [8] applied the microtomography to assess the quality of fabricated cellulose fibre-cement boards. Lanzón et al. [9] used the micro-CT method to test the specimens made of concrete with low-density additions: expanded perlite, expanded glass and cenospheres (hollow microspheres). Stock et. al. [10] analysed the progression of sulfate attack within the cement paste by examining the microtomograms. It was found that recognized damage levels in specimens exposed to a Na<sub>2</sub>SO<sub>4</sub> solution in different conditions varied from 0 (no damage) to 4 (extreme damage).

The equipment for insight into specimens' microstructure with micro-CT technique is produced at present by a few firms and these apparatus are capable to perform tests on the small pieces of few millimetres size or on large elements of a few meters. They include the microfocal source of X-ray radiation, the movable table to place a specimen and the flat panel with a radiation detector, which resolution usually equals 2000 × 2000 pixels. The microstructure of is visualized on the cross-sections (tomograms) of the investigated specimen using grey scale convention related directly to the amount of local radiation absorption of the material. The grey scale covers several tens of grey levels and is ordered from white related to maximum of absorption to black related to the minimum, respectively. Unhydrated cement particles and aggregate grains are objects of the greatest absorption. The hydration products that cover major part of the cement matrix present slightly lower absorption ability. The next in the line are hydrated calcinates and at the end of the scale are the organic fibres (if present) and the regions of high porosity. The advantage of micro-CT technique is a possibility of reconstruction of 3-dimensional image of investigated objects and to determine the volumetric part of the material occupied by bulk matrix, aggregates, voids, cracks, fibres etc.

## 3. Experimental

The authors analysed five specimens made of different FCB compositions. According to the determined micro-CT scanning procedure, i.e. 50 X magnification, cylindrical cores 7 mm in diameter and 7 mm in height were cut from the larger blocks. Prior to analysis, the fibre cement composite specimens were tested using the additional procedures to evaluate their performance.

Materials 'A' – 'D' were the fabricated façade boards made using accumulative rolling

technology, known as the Hatscheck process [3]. Material 'A' was characterized by low moisture absorbability (8–10%) and the bending strength of boards was 11–13 MPa. The concentration of fibres cellulose fibres by weight in that was 6 % (wt.) of good quality 3 mm long cellulose fibres. Material 'B' was made using the same technology as material 'A', but contained 6 % (wt.) recycled cellulose short fibres ca. 1 mm long and thus the bending strength of boards was lower: 8,5–10 MPa. Material 'C' was of fabricated using the similar technology as of 'A' type but by another producer using the other type of fibres. Material 'C' was coloured in the volume that increased its density. Material 'D' was obtained by the accelerated production technology applying the Hatscheck process and autoclaving. The research presented below has revealed non-uniform, laminar distribution of fibers in it. Material 'E' was fabricated using another technology, i.e. extrusion what caused the increased tendency of agglomerating of the fibres.

The microstructure of all the specimens were tested using Nanotom 30 microtomograph by General Electric at the Institute of Materials and Machine Mechanics in Bratislava. The following parameters were set: lamp voltage - 115 kV, lamp current – 95 microamps, shot exposition time – 750 ms. Scanning performed by the authors resulted in a large set of tomograms (specimen cross-sections), performed every 5  $\mu\text{m}$  of the specimen height. This set of tomograms consisted of 1200 cross-sections,  $1200 \times 1200$  pixels each. The recorded data allows presenting a greater number of cross-sections within the single graph using a quasi 3D projection. However, the total number of bytes related to the consecutive voxels in such a dataset would be  $1.5 \times 10^9$  bytes, and would require additional lengthy processing. Therefore, a specific subset was taken from the entire dataset, preferably cube-shaped for further processing. The resulting subset is referred to as a ROI (Region Of Interest). Cracked areas in the proximity of the specimen surface, usually damaged by a drilling tool were left outside of that area. The study included ROIs 9003 (729,000,000) voxels each, representing  $4 \times 4 \times 4$  mm cubes and virtually extracted from the analysed specimens. 800 scans constituting the single ROI occupied the equivalent surface of  $128 \text{ cm}^2$ . The equipment and the dedicated software was capable of producing the data sets defining the microstructure of the specimen in the form of: a) three-dimensional projections of the specimens showing  $4 \times 4 \times 4$  mm cubes of the tested specimen and b) digital specimen images (i.e. BMP files), representing cross-sections of tested object in transverse or lengthwise direction to the mean axis of the cylindrical specimen. Example three-dimensional projections of  $4 \times 4 \times 4$  mm cubes virtually cut from specimens 'B' and 'D' are presented in Figures 1 and 2.

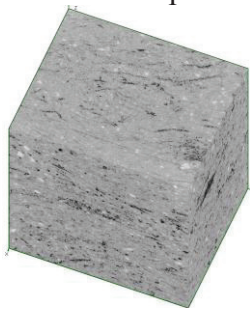


Figure 1. Three-dimensional projection of the  $4 \times 4 \times 4$  mm piece of specimen 'B'. Some ca. 1 mm long fibres are visible in the bulk of the material.

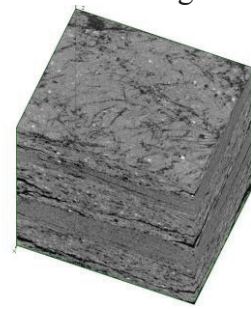


Figure 2. Three-dimensional projection of the  $4 \times 4 \times 4$  mm piece of specimen 'D'. Its layered structure was a result of autoclaving after completing of combining of layers in the fabrication sequence after Hatscheck process.

One can determine several 1 mm short cellulose fibres in the former of the Figures and in the latter –specific layered structure of material ‘D’, being a result of autoclaving after completing of combining of layers in the fabrication sequence.

Cross-sections of the specimens of type ‘A’ and ‘C’ are depicted in Figures 3, 4. Long fibres of ca. 3 mm are visible in Fig. 3. The fibre diameter and length seems to be lower in specimen ‘C’ than that determined in specimen ‘A’. The cross-section of the FCB specimen coded ‘E’ is shown in Figure 5. The fibres form distinct agglomerates (curls) here, what was caused by extrusion used during the fabrication process.

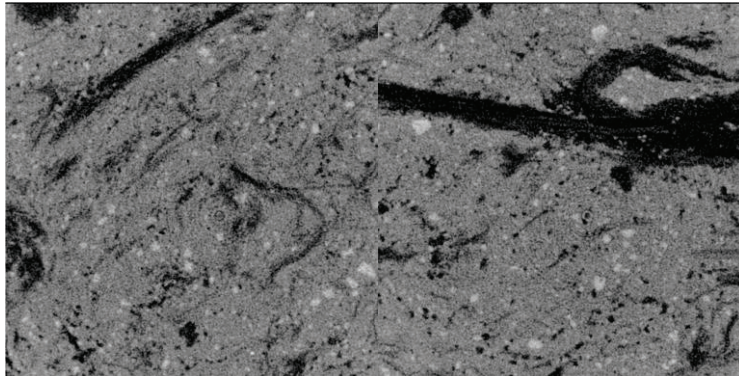


Figure 3. Examples of ca.3 mm long cellulose fibres depicted in micro-CT cross-sections elaborated in specimen ‘A’.

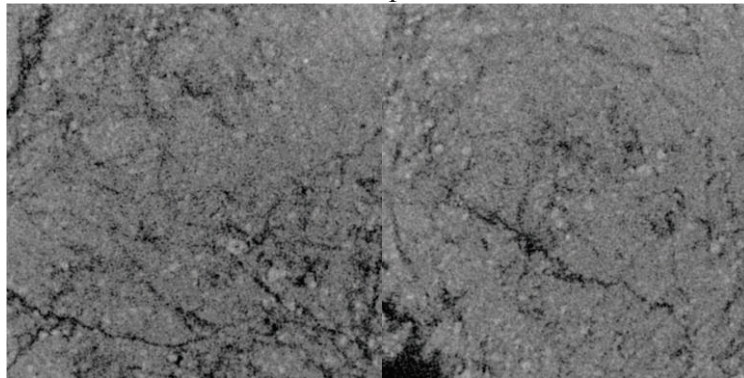


Figure 4. The cross-section of the FCB specimen coded ‘C’. The fiber diameter and length seems to be lower than that presented in Fig. 3.

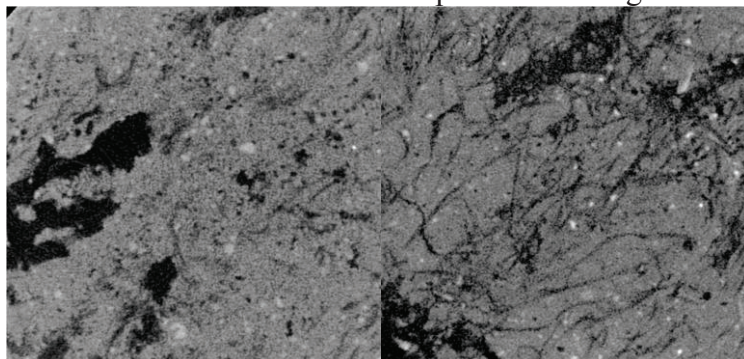


Figure 5. The cross-section of the FCB specimen coded ‘E’. The fibres form agglomerates (curls), what is caused by extrusion used during the fabrication process.

The other way to present the information included in the specimens' ROIs described above is to perform the brightness distribution of all voxels, i.e. (729,000,000) constituting the ROI ensembles. It was found experimentally that the magnitudes of brightness in different regions were included in the following ranges: the area of voids and fibres: 0 - 50 [arbitrary units, a.u.], fillers: 50 - 140 [a.u.], dense phases (unhydrated cement and fine aggregate grains: 140 - 170 [a.u.]. The greyscale brightness distribution (GBD) of all voxels belonging to the investigated ROIs are shown in Figures 6 and 7 to demonstrate the ability of GBD to determine the different microstructure differences among the investigated compositions. It is worth noting that the presence of dense phases (and their amount) can be observed as the peaks on the right side of the distributions mentioned above. By contrast, the potential presence of voids and cracks can be observed as the narrow peaks on the left end of GBD dependence.

It can be concluded that GBD dependencies constructed for the compositions fabricated applying standard Hatscheck method and extrusion techniques (specimen 'C' and 'E') are of similar shape however extrusion resulted in the more tight composition (the curve 'E' is shifted to the right) and probably the large fibre agglomerates are the reason of the remarkable peak at the left part of the graph. The composition 'D', presented in Fig. 2., which underwent the autoclaving process is characterised by different type of GBD curve.

Types of dark coloured and thus of low brightness (0-50 a.u.) fibres can be traced in Figure 7. Specimen 'A' containing 6 % of good quality ca. 3 mm long cellulose fibres (see Fig.3) is represented by GBD curve moved to the left comparing to that representing specimen 'B' containing 6% recycled cellulose short fibres ca. 1 mm long (see Fig. 1). Both specimens were fabricated applying the similar, standard Hatscheck technique what resulted in similar shape of curves depicted in Fig. 7.

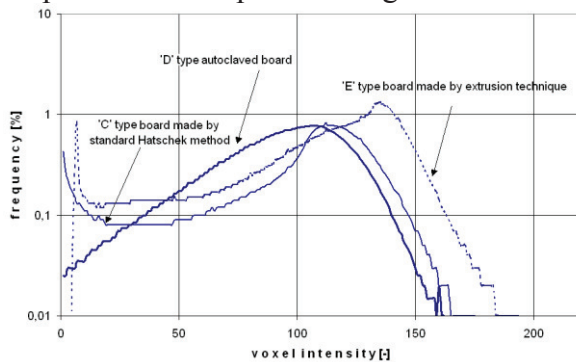


Figure 6. The dependence of greyscale brightness distribution determined for specimens fabricated applying different methods whose micro-CT scans of the microstructure were presented in previous Figures.

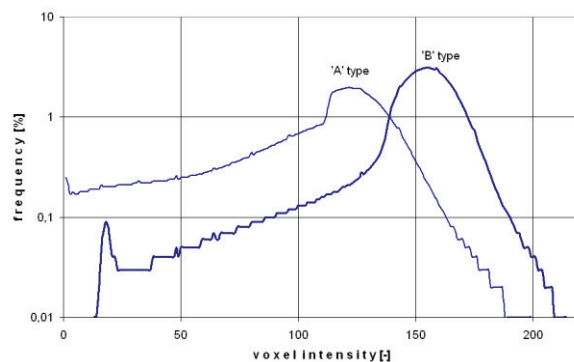


Figure 7. The dependence of greyscale brightness distribution determined for specimens compositions fabricated applying standard Hatscheck method and different fibre types.

#### 4. Conclusions

The micro-CT method applied in the research delivered the large amount of digital data enabling various schemes of it processing. The methods of data presentation include: three-

dimensional projections of the internal specimens microstructure, planar cross-sections at chosen specimen depth or comparative greyscale brightness distribution graphs. The technique presented in the paper appeared to be effective for determining of the certain micro structural properties of tested material, i.e.: microstructure compactness, volume homogeneity, and types of fabrication processes. The presented method can be then recommended as the efficient means for investigation and design of different fibre cement compositions.

## References

- [1] BS EN 12467:2004, Fibre-cement flat sheets. Product specification and test methods (2013)
- [2] Ardanuy M., Claramunt J., Toledo Filho R. D., Cellulosic fiber reinforced cement-based composites: A review of recent research, *Construction and Building Materials* 79 (2015), 115–128, doi.org/ 10.1016/j.conbuildmat.2015.01. 035
- [3] Cooke T., Formation of Films on Hatschek Machines. Bondelwood and Fibre Composites Conference, Idaho (2002), <http://www.fibreconsulting.com/publications/publications.htm>.
- [4] Cooke A. M., Durability of Autoclaved Cellulose Fiber Cement Composites. Conference on Inorganic Bonded Wood and Fibre Composites, Idaho (2000), <http://www.fibreconsulting.com/publications/publications.htm>
- [5] Akhavan A., Catchmark J., Rajabipour F., Ductility enhancement of autoclaved cellulose fiber reinforced cement boards manufactured using a laboratory method simulating the Hatschek process, *Construction and Building Materials* 135, (2017), 251–259
- [6] Lu S., Landis E. N., Keane D. T., X-ray microtomographic studies of pore structure and permeability in Portland cement concrete, *Materials and structures*. 39 (2006), 611-620, doi.org/ 10.1617/s11527-006-9099-1
- [7] Garboczi E. J., Three-dimensional mathematical analysis of particle shape using X-ray tomography and spherical harmonics: Application to aggregates used in concrete, *Cement & Concrete Research* 32 (2002), 1621-1638
- [8] Schabowicz K., Ranachowski Z., Józwiak-Niedźwiedzka D., Radzik Ł., Kúdela Jr. S., Dvorak T., Application of X-ray microtomography to quality assessment of fibre cement boards, *Construction and Building Materials* 110 (2016), 182-188
- [9] Lanzon M., Cnudde V., de Kock T., Dewanckele J., X-ray microtomography ( $\mu$ -CT) to evaluate microstructure of mortars containing low density additions, *Cement & Concrete Composites* 34 (2012), 993-1000
- [10] Stock S. R., Naik N. K., Wilkinson A. P., Kurtis K. E., X-ray microtomography (micro-CT) of the progression of sulfate attack of cement paste, *Cement & Concrete Research* 32 (2001), 1673-1675
- [12] Nakashima Y., Kamia S., Mathematica Programs for the Analysis of Three-Dimensional Pore Connectivity and Anisotropic Tortuosity of Porous Rocks using X-ray Computed Tomography Image data, *Journal of Nuclear Science and Technology* 44 (2012), 1233-1247
- [13] Provis, J. L., Myers R. J., White C. E., X-ray microtomography shows pore structure and tortuosity in alkali-activated binders, *Cement & Concrete Research* 42 (2012); 855-864

# **GEOPOLYMERS AND ALKALI-ACTIVATED MATERIALS**



## ACOUSTIC EMISSION PARAMETERS OF ALKALI ACTIVATED FLY ASH SPECIMENS WITH HEMP FIBRES UNDER STATIC LOADING

Libor Topolář <sup>(1)</sup>, Hana Šimonová <sup>(1)</sup>, Barbara Kucharczyková <sup>(1)</sup>

(1) The Brno University of Technology, Faculty of Civil Engineering, Brno, Czech Republic

### Abstract

This paper deals with the effect of the different amount of hemp fibres added to fine-grained composite based on alkali activated fly ash matrix on the values of acoustic emission signals parameters obtained during the fracture tests. The prisms specimens with nominal dimension  $40 \times 40 \times 160$  mm and initial central edge notch were subjected to tests in three-point bending configuration. The four magnetic sensors were placed on each specimen and acoustic emission signals were recorded during the loading. The obtained results indicate that the specimens with hemp fibres exhibit a larger number of acoustic emission events than reference specimens without the fibres. It can be most likely connected to pull-out or break of the hemp fibres. The addition of hemp fibres causes the attenuation of the AE signals and the reduction of the amplitude values.

### 1. Introduction

Currently, environmental aspects are much more pursued, therefore there is the increased effort to develop new environmentally friendly innovative building materials as an alternative to ordinary Portland cement-based concrete. The alkali activated materials (AAMs) belongs to a promising alternative to traditional cement [1, 2]. The manufacture of AAMs is more effective in reducing CO<sub>2</sub> emissions and energy consumption in comparison to the ordinary cement [3, 4], because of the industrial by-products like as blast furnace slag or fly ash is used. The major disadvantage of AAMs is an increased shrinkage during hardening period, which finally results in a decrease in values of tensile and bending properties/strengths [5, 6]. The addition of different types of fibres into alkali activated matrix might lead to the reduction of the cracking tendency and improvement of tensile properties of these materials, likewise as it is in the case of the fibre-reinforced ordinary Portland cement-based materials [7–9].

The above mentioned environmental friendly trend of research induces the use of a sustainable alternative to steel and synthetic fibres. Natural fibres produced from different types of plants (e.g. hemp, flax) belong to a relatively cheap alternative [10–12]. The main advantages of natural fibres are their biodegradability, their resources are renewable, neutral toward CO<sub>2</sub> emissions. On the other hand, natural fibres still have several drawbacks that limit their wider use. One of the most important is the dependence on their physical and mechanical properties on growing, harvesting and processing methods. Moreover, the use of natural fibres reinforced composites for civil engineering applications requires additional information about the damage mechanisms within these materials [13]. Therefore, in this paper, authors pay their attention to the effect of the different amount of hemp fibres added to fine-grained composites based on the alkali activated fly ash matrix on their behaviour during the fracture test. While the effect of fibres is expressed by the values of acoustic emission signals parameters obtained during the loading tests.

The acoustic emission method belongs to non-destructive methods which can be used to monitoring of active defects that occur inside the monitored structure. The inactive defects and the shape of the investigated structure do not have a decisive influence on the creation of AE signals. One of the AE measurement advantages is the capability to observe the damage propagation in real time during the specimens loading [14]. For the purpose of the AE measurements evaluation, it is necessary to analyse several parameters of an AE waveform, such as a number of events, counts, duration, amplitude and energy of AE signals. Counts refer to the number of pulses emitted by the measurement circuitry if the signal amplitude is greater than the threshold. Depending on the magnitude of the AE event and the characteristics of the material, one hit may produce one or many counts. The duration of AE signal is the time between the first and last overstepping of the threshold value. The amplitude is the greatest measured voltage of the signal which determines the detectability of the AE signal. The signals with amplitudes below the operator-defined minimum threshold value will not be recorded. The energy of AE signals is directly proportional to the area under the AE waveform [14].

## 2. Materials and methods

The prism specimens with nominal dimensions 40 × 40 × 160 mm made of alkali activated fly ash mortars were studied. In total three set of specimens were tested. The first one was a reference set, designated as AAFAM, another two sets contained different volume percentage of hemp fibres (0.5 and 1.0 %), designated as AAFAM\_0.5 and AAFAM\_1.0, respectively. The power plant fly ash (450 g), sodium silicate solution as alkali activator (306 g), river sand (1350 g) with a maximum grain size of 8 mm, water (70 g) and hemp fibres (6.25 and 12.5 g) with a length of 10 mm were used to produce the test specimens. The specimens were provided with a central edge notch with the depth of approximately one-third of the prism height and subsequently tested in the three-point bending fracture test configuration. The loading procedure was performed with the requirement of a constant increment of displacement which was set to 0.02 mm/min. In this way, the diagram of loading force  $F$  in

relation to the crack mouth opening displacement  $CMOD$  during the fracture test was recorded. The recorded  $F-CMOD$  diagrams for all specimens are shown in Fig. 1; three specimens were tested from each set.

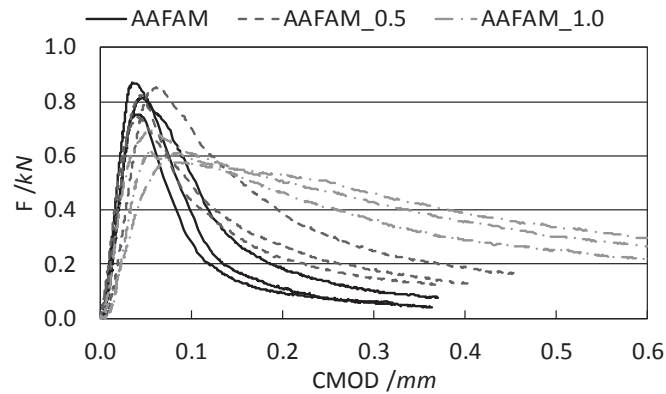


Figure 1:  $F-CMOD$  diagrams for all specimens

The acoustic emission (AE) signals (during the fracture tests) were detected using four magnetic sensors (MDK-13) which were placed for all specimens at the same positions, see Fig. 2. The AE sensors were magnetically attached to the pre-prepared metal strips glued onto the surface of the individual specimens. Moreover, AE signals were amplified by a 35 dB amplifier and transmitted to the universal measuring and diagnostic system DAKEL-XEDO which was developed by the Czech company ZD Rpety-Dakel. DAKEL-XEDO equipment allows record and digital processing of AE signals as well as measurement of additional physical parameters e.g. temperature, resistance, force etc.

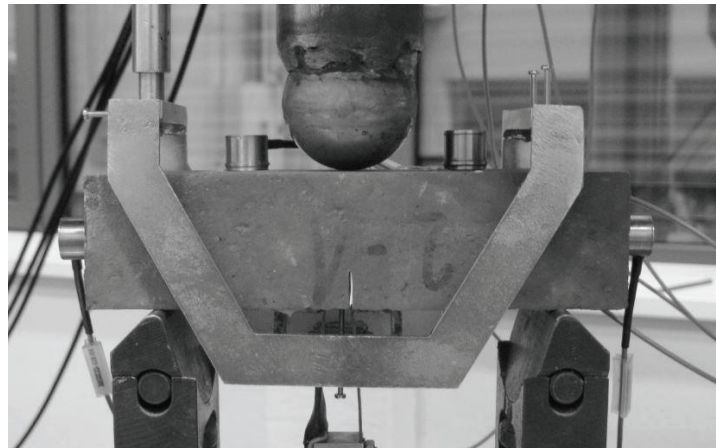


Figure 2: Fracture test configuration and positions of AE sensors.

### 3. Results and discussion

In this paper, the number of AE events, the duration of the AE signal, and the AE signal amplitude were selected to describe the effect of the different amount of hemp fibres in the fine-grained AAFAM composites on the values of AE signals parameters obtained during the

fracture tests. The results are shown in Figs. 3–5 in the form of bar charts representing mean values with error bars representing standard deviations values. The charts on the left always present the results obtained during the loading process from the start up to the maximum load (peak of the load-deflection diagram see Fig. 2) and the charts on the right the results obtained from the whole measurement, i.e. from the start or loading until the specimen's fracture.

The Fig. 3 shows the number of AE events for the individual sets. The number of AE events represents the approximate amount of defects (microcracks, cracks, etc.) formed in the material inner-structure. In the initial part of loading (up to the maximum load, Fig. 3, left), a decrease of a number of AE events was observed with the increasing amount of hemp fibres. The results obtained from the whole measurements exhibit a many-times higher number of AE events for specimens with the hemp fibres in comparison to the reference one. Furthermore, it is evident that the number of AE events increases with the increasing amount of hemp fibres. This is probably associated with a gradual rupture of the hemp fibres or they're pulling out from the matrix, therefore the higher amount of fibres produces the higher number of AE events.

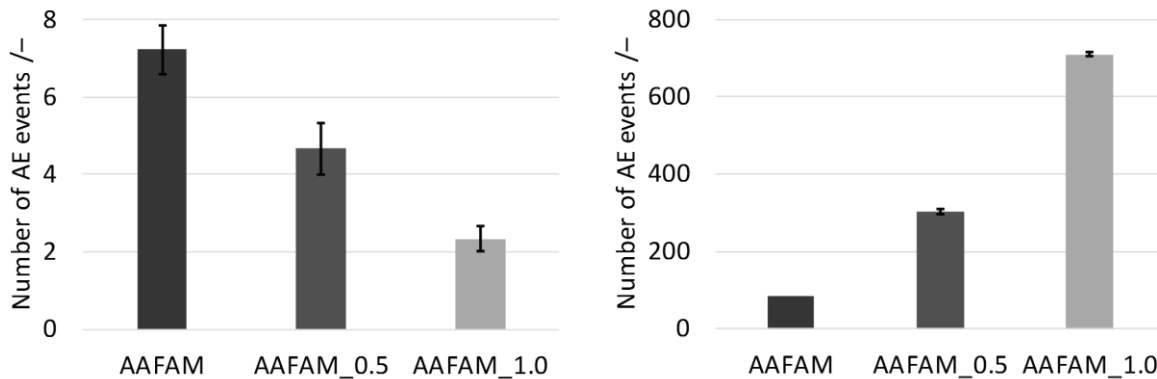


Figure 3: Number of AE events for individual specimen sets (up to maximum load (left) and from the whole measurement).

The Fig. 4 demonstrates that the duration of the AE signals is reduced by the addition of hemp fibres. The addition of hemp fibres causes the attenuation of the AE signals, therefore the AE signals are shorter. For the reference specimens (AAFAM) without hemp fibres, the AE signals propagate more easily and therefore produces higher AE signal duration values. The results also show that the AE signals attenuation was essentially the same for both amounts of fibres.

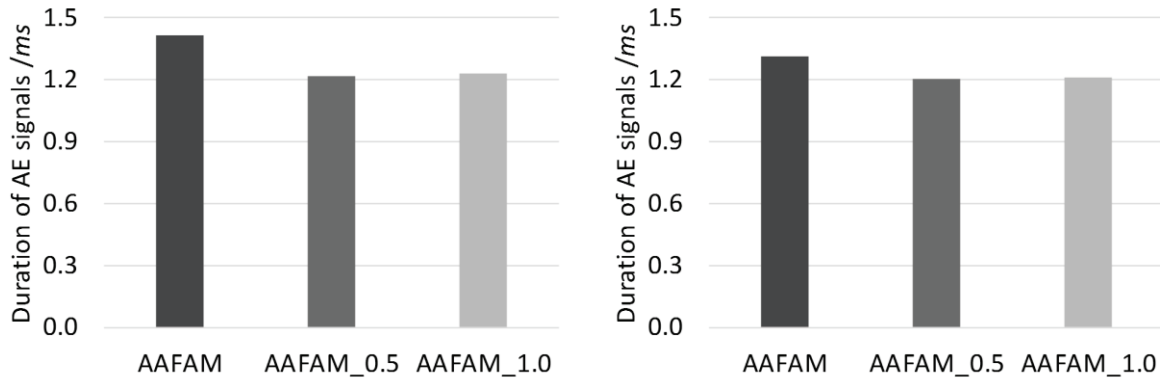


Figure 4: Duration of AE signals for individual sets (up to maximum load (left) and from the whole measurement).

The Fig. 5 shows the effect of hemp fibres addition on the values of AE signals amplitudes. The obtained trend is similar as in the case of the duration of AE signals. The higher amount of hemp fibres in the mixture causes attenuation of the AE signal which resulted in the reduction of the amplitude values.

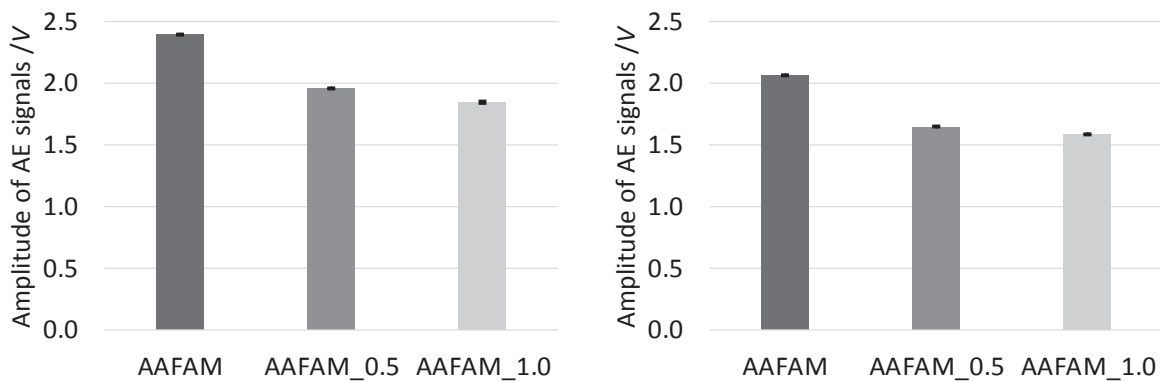


Figure 5: Amplitude of AE signals for individual sets (up to maximum load (left) and from the whole measurement).

#### 4. Conclusions

This paper presented evaluation of the experimental tests focused on the analysis of selected parameters of AE signals recorded during the three-point bending fracture test of alkali activated fly ash composites reinforced with hemp fibres. The AE method seems to be an effective tool for the detection of the disturbances in the inner-structure of the alkali activated composites during the fracture test. The selected parameters of the AE signals show the different behaviour of the individual sets of specimens depending on the amount of hemp fibres in the mortar.

The conclusions of this article can be summarized as follows:

- The addition of hemp fibres reduces the number of AE events before the maximum load is reached. In the case of whole measurement evaluation, it can be suggested that the

hemp fibres addition causes the increase in the number of AE events, which is associated with the gradual rupture of the fibres and their pulling out from the matrix.

- The addition of hemp fibres reduces the duration of the AE signals due to a greater signal attenuation.
- The addition of hemp fibres also causes a decrease in the values of AE signals amplitude.

### **Acknowledgement**

This outcome has been achieved with the financial support of the Czech Science Foundation, project No. 18-12289Y “Advanced characterization of crack propagation in composites based on alkali activated matrix”.

### **References**

- [1] Provis, J. L. and van Denventer, J. S. (eds), Alkali activated materials: state-of-the-art report, RILEM TC 224-AAM, Springer, Dordrecht (2014).
- [2] Shi, C. et al, Alkali-activated cements and concretes, Taylor & Francis, London (2006).
- [3] Keun-Hyeok, Y. et al, Assessment of CO<sub>2</sub> reduction of alkali-activated concrete, J Cleaner Production 39 (2013), 265–272.
- [4] McLellan, B. C., et al, Costs and carbon emissions for geopolymer pastes in comparison to ordinary Portland cement, J Cleaner Production 19 (2011), 1080–1090.
- [5] Cincotto, M. A. et al, Effect of different activators type and dosages and relation with autogenous shrinkage of activated blast furnace slag cement, Proc. of the 11<sup>th</sup> International Congress on the Chemistry of Cement, Durban, South Africa (2003)1878–1888.
- [6] Ye, H. et al, Understanding the drying shrinkage performance of alkali-activated slag mortars, Cement and Concrete Composites 76 (2017), 13–24.
- [7] Li, B. et al, The Mechanical Properties of Polypropylene Fiber Reinforced Concrete, Journal of Wuhan University of Technology-Mater. Sci. Ed. 19 (2004), No. 3, 68–71.
- [8] Ravikumar, C. S. et al, Effect of Fibres in Concrete Composites, International Journal of Applied Engineering Research 10 (2015), No. 1., 419–430.
- [9] Nedeljkovic, M. et al, Development and application of an environmentally friendly ductile alkali-activated composite, J Cleaner Production 180 (2018), 524–538.
- [10] Schwarzova, I. et al, Sustainable hemp-based composites for the building industry application, AIP Conference Proceedings, Vol. 1866, No. 1, 040036 (2017).
- [11] Zhou, X. and Kastiukas, G., Engineering Properties of Treated Natural Hemp Fiber-Reinforced Concrete, Frontiers in Building Environment 3 (2017), Article 33, 1–9.
- [12] Merta, I. and Tschegg, E. K., Fracture energy of natural fibre reinforced concrete, Construction and Building Materials 40 (2013), 991–997.
- [13] Lau, K. T. et al, Properties of natural fibre composites for structural engineering applications. Composites Part B: Engineering, 136 (2018), 222-233.
- [14] Ohtsu, M., Acoustic emission and related non-destructive evaluation techniques in the fracture mechanics of concrete: fundamentals and applications, Woodhead Publishing (2015).

## **ALKALI ACTIVATED MATERIALS: REVIEW OF CURRENT PROBLEMS AND POSSIBLE SOLUTIONS**

**Adeyemi Adesina**<sup>(1)</sup>

(1) Concordia University, Montreal, Canada

### **Abstract**

Focus on alkali-activated materials (AAMs) have increased in recent years due to its possibility to be a substitute for the ordinary Portland cement (OPC). However, the development of AAM that would be a viable substitute for OPC is still impeded due to several problems faced during its production, and properties of the resulting AAMs. Finding a substitute for OPC is imminent as a result of its contribution of about 7% to the world's human-induced carbon dioxide emission. The amount of emission is expected to increase in the coming years due to increase in development all over the world. Therefore, it is necessary to develop alternative green binder that would contribute less emission to the environment while conserving natural resources deposit.

This review explored the current problems hindering the universal acceptance and large-scale application of AAMs. It was concluded that with more research and development on user-friendly activators with low embodied energy and carbon, AAMs will be able to compete as a viable substitute for OPC.

### **1. Introduction**

Alkali-activated materials (AAMs) have gained huge attention recently in the concrete industry due to its viability to be used as a replacement for the conventional ordinary Portland cement (OPC). AAMs are obtained by activating an aluminosilicate precursor with an alkaline activator. The need for replacement of OPC in concrete is imminent due to its high embodied carbon and energy [1]. Approximately 1 tonne of carbon dioxide is emitted with an equivalent amount of OPC produced [2]. The carbon dioxide emission is from the calcination of raw materials and high amount of energy used during OPC's production. As OPC is the main binder in concrete, and billions of tonnes of concrete produced annually; OPC's production contributes between 5 – 10% of the total world anthropogenic greenhouse gases emission [3].

Higher strength and durability properties of AAMs compared to OPC concrete has made it attract huge research from the concrete industry. And majorly, AAMs has shown the possibility of having a huge reduction in carbon dioxide emissions between 55 – 75% of conventional OPC concrete [4]. In addition, AAMs conserves the natural deposits of raw materials such as limestone, as the aluminosilicate materials used for AAMs are by-products of other industrial processes. However, this green advantage is posed with several limitations. Some of the major limitations are quick setting times and high drying shrinkage. These limitations have inhibited the universal acceptance and commercial use of AAMs. Depending on the aluminosilicate materials used, AAMs can be further divided. For example, alkali-activated slag (AAS) is a type of AAMs which uses slag as the aluminosilicate precursor. As the component in AAMs is different from that of OPC, its chemical composition and process differ also [5, 6].

This review is aimed at exploring the major limitations of AAMs, and possible solutions for the limitations. It is anticipated that this review will be a great reference for researchers, construction managers and engineers in the field of construction in general.

## **2. Current AAMs problems**

The problems currently faced by AAMs are evident in the fresh and hardened properties of AAM. Some of the fresh properties limitations are short set times and extremely low flowability. While some of the hardened properties limitations are high drying shrinkage and low volume stability. Some of the major limitations are further explained as follows;

### **2.1 Short setting time**

Two major factors have been identified to affect the setting time of AAMs. These factors are the type of activator and the activator content [7]. Short setting time in AAMs is observed when sodium silicate is used as an activator. Earlier studies [8, 9] reported flash setting of AAMs when activated with sodium silicate. However, the quick setting of AAMs is more pronounced in those activated with sodium silicate compared to sodium hydroxide. The setting times of AAMs activated with a combination of sodium silicate and sodium hydroxide is longer than when activated with only sodium silicate [10]. Short set time caused by sodium silicate activation has been attributed to the initial formation of calcium silicate hydrate. Whereas, the extended setting time observed in AAS activated with sodium hydroxide and sodium carbonate is as a result of the formation of polysilicates hydrates and calcium carbonate respectively [11, 12]. Increase in the ambient temperature has been recorded to shorten the setting time of AAS [4]. However, no significant effect was found on the setting time of AAS when sodium silicate and sodium hydroxide was used to activate AAS. The difference in the effect of ambient temperature on the setting time of different AAS activated with various activator has been attributed to the difference in the chemical composition of the activator [4].

### **2.2 Elevated curing temperature**

AAMs with low calcium aluminosilicate precursors such as class F Fly ash fly ash requires an elevated temperature to accelerate the dissolution of the monomers. In order to achieve a similar strength of AAM made with fly ash compared to that of OPC, an elevated temperature



between 60 to 80<sup>0</sup> C is required [7, 13]. Though the elevated temperature is not required for high calcium aluminosilicate precursors such as slag. However, it has been reported that curing AAMs made with slag reduces the high drying shrinkage associated with it [10]. This elevated temperature requirement has limited the practical large-scale application of AAMs for different applications. However, elevated curing is reasonable in applications such as precast concrete, where the concrete is made in the plants, and it is easier to control the variables during production. Use of elevated temperature curing however consumed huge amount of energy and release more carbon dioxide to the environment thereby increasing the overall embodied energy and carbon of AAMs.

### **2.3 High drying shrinkage**

Shrinkage in AAMs has been found to be higher than that of OPC, especially those with slag as aluminosilicate precursors, and activated with sodium silicate [14, 15]. Formation of gel that is rich in silica has been attributed to the high shrinkage in slag activated with sodium silicate [16, 17]. As the rich silica gel loses moisture during drying, it causes microcracks within the AAS paste. Also, higher shrinkage in AAMs has been attributed to its high quantity of mesopores compared to that of OPC [18].

### **2.4 Non-user friendly activator**

Based on open literature, sodium silicate and sodium hydroxide are the most used activators for AAMs [1-5]. These common activators are expensive, corrosive and the highest contributor of embodied energy and carbon to AAMs. The high cost associated with AAMs activated with these activators have discouraged contractors in embracing this sustainable material. In addition, the high embodied energy and carbon of some of the common activators (i.e. sodium silicate and sodium hydroxide) have eliminated the advantage of using AAMs as a sustainable building material. Also, the corrosiveness of these activators will prevent its large-scale transportation and application as special handling will be required.

### **2.5 Unknown long-term durability and performance**

Most durability properties of concrete are associated with its permeability, which can be measured through its water absorption. Generally, AAMs has been reported in most studies to be more resistant to several detrimental forces in the environment that affects its durability. However, to date, there's no consensus on the water absorption of AAMs due to limited data availability and variation in the available data. For example, Bernal et al [19] and Yang et al [20] concluded that the water absorption of slag activated with sodium silicate is higher than that of OPC. However, some other studies [21, 22] recorded a contradicting observation in which the water permeability was lower than that of OPC. Albitar et al [23] also reported a lower water absorption for AAMs. These contrasting results and lack of extensive long-term results have discouraged project managers and contractors to embrace this innovative sustainable material (i.e. AAMs). Another durability aspect that there's no consensus yet is the alkali-aggregate reaction (AAR). Though the aluminosilicate precursors used for AAMs are used to curb AAR in conventional concrete, contradicting results exists in the open literature. Several studies reported lower AAR expansion in AAM when reactive aggregates are used. However, Bakharev et al. [24] reported that higher expansion when reactive aggregates were used. It should be noted that AAMs usually contain higher amount alkali due to activator used, therefore the probability of AAR to occur is higher. There exist

specifications to limit the equivalent sodium oxide in OPC to 0.8% to prevent the occurrence of AAR, however, AAMs contain a higher amount of sodium oxide equivalent. Resistance to AAR in AAMs reported in some studies might be as a result of the high alkali present in AAMs been bounded to the hydration products formed, thereby reducing the overall alkalinity in the pore solution [25, 26]. However, the practical proof exists of the quantity of alkali bounded to formed products [27].

## **2.6 Supply market for raw materials**

Compared to limestone which is the main raw material for OPC, the aluminosilicate materials use of AAMs are not readily available everywhere, and the type available varies from different geological location. For examples, rice husk ash is readily available in India, whereas its production is limited in Canada, and slag and fly ash is more readily available. This variation in large quantity availability limits the universal use of AAMs compared to that of OPC.

## **2.7 Lack of universal specification and standard for AAMs**

Most construction and research involving AAMs currently use the specifications and standards available for OPC, and OPC concrete. However, it has been found that some of these standards/ tests give false results as the chemistry of AAMs are different from that of OPC. Byfors et al [28], Bakharev [10], and Deja [29] observed that the carbonation rate of alkali-activated slag (AAS) concrete is faster than that of OPC using accelerated carbonation test. However, it concluded that this accelerated test used for OPC is not suitable for AAMs as it overestimates the carbonation of AAMs [30, 31].

## **2.8 Efflorescence**

Efflorescence is the whitish product that is formed on the surface of the concrete. The formation of this whitish products in AAMs has been associated with the use of high concentration of sodium hydroxide as an activator for AAMs [58] The whitish product is bicarbonate crystals formed as a result of the reaction of alkali that leached with the carbon dioxide in the environment. Ideally, low amount of bicarbonate formation on the surface of AAMs does not pose any danger to its durability and mechanical properties [58]. But the high formation of this whitish product might be detrimental to the hardened properties of the AAM. Also, high amount of bicarbonate crystals on the surface of AAM would affect its aesthetics. Use of sodium sulphate as activator might also lead to the formation of alkali sulphates on the surface of AAMs. This formation of alkali sulphate is as a result of the low solubility of sodium sulphate [32].

## **3. Possible solutions to AAMs problems**

Use of retarding admixtures employed for OPC concrete can be used to extend the setting time of AAS as there exists currently retarding admixtures made specifically for AAMs. As using sodium silicate is mainly responsible for most quick set times in AAMs, use of alternative activators such as sodium carbonate which produces similar set times similar to that of OPC will be a viable option. Shrinkage in AAMs can be controlled by the use of alternative activators instead of the conventional sodium silicate. For example, the use of sodium carbonate to activate slag has been found to reduce the shrinkage of AAS to give

shrinkage similar to that of OPC [14]. Other possible ways to reduce the shrinkage in AAMs includes the use of shrinkage reducing admixtures (SRAs) [33, 34], internal curing [33], heat curing [16, 35]. Use of supplementary cementitious materials (SCMs) [35, 36] can also reduce the shrinkage of AAMS. Also, air entrainers used for OPC concrete has been found to reduce the shrinkage in AAS [37]. Use of OPC by 10% by mass of the aluminosilicate material used has also been reported to reduce the shrinkage of AAMs [38]. Also, moist curing of AAMs has been found to reduce shrinkage significantly as it prevents rapid loss of moisture from the AAM matrix [18]. Other shrinkage mitigation techniques include fibre reinforcement [39], use of lightweight aggregates, high aggregate content, etc. Proper moist curing and use of activators with lower concentrations would prevent the formation of high amount of bicarbonate crystals (i.e. efflorescence) on the surface of AAM concrete. Curing of AAMs at relative humidity higher than 95% has been found to prevent the formation of efflorescence [32].

#### 4. Conclusions

This review showed that AAMs is a good substitute for OPC if all its limitations can be overcome. Based on this review, the following conclusions can be drawn;

- Use of alternative green activators will go a long way in eliminating most of the challenges faced by the fresh and hardened properties of AAMs
- Shrinkage in AAMs can be controlled with proper moist curing, use of shrinkage reducing admixture, and good mix design which employs the use of high coarse aggregate content
- Involvement of different stakeholders in the concrete industry will propel more acceptance of AAMs as an alternative sustainable building material.

#### References

- [1] Flower, D., and Sanjayan, J. Greenhouse gas emissions due to concrete manufacture," 26 International Journal of Life Cycle Assessment, (2007) 282- 288
- [2] Cabeza, F et al, Low carbon and low embodied energy materials in buildings: a review Renew. Sustain. Energy Rev., 23 (2013), 536-542
- [3] Scrivener, K.L and Kirkpatrick, R. J., Innovation in use and research on cementitious material Cem. Concr. Res., 38 (2008), p.128-136
- [4] Zivicz, V., Effects of type and dosage of alkaline activator and temperature on the properties of alkali-activated slag mixtures Construction and Building Materials Vol. 21, 7, 2007, 1463-1469
- [5] Pacheco-Torgal, F., et al Alkali-activated binders: A review: Part 1 Historical background, terminology, reaction mechanisms and hydration products Constr. Build. Mater.(2008), 1305-1314
- [6] Zhang, et al. Compositional, microstructural and mechanical properties of ambient condition cured alkali-activated cement Constr. Build. Mater., 113 (2016), 237-245
- [7] Duxson, P et al. Geopolymer technology: the current state of the art J Mater Sci, 42 (2007),
- [8] Cheng, Q.H., and Shondeep L. S., A study of rheological and mechanical properties of mixed alkali activated slag pastes. Advn Cem Bas Mat (1994), 178–84.
- [9] Gifford P. M., and Gillot, J. E., ASR and alkali carbonate reaction in activated blast furnace cement concrete. Cem Concr Res (1996) 21–6.
- [10] Bakharev, T. Resistance of alkali-activated slag concrete to carbonation Cem. Concr. Res., (2001),1277-1283
- [11] Hong S. Y. et al. Studies on the hydration of alkali activated slag. In: Proceedings of the third Beijing international symposium on cement and concrete, vol. 2. Beijing; (1993.)1059–1042.

- [12] Brylicky W et al. Alkali activated slag cementitious material for drilling operation. In: Proceedings of the ninth international congress on the chemistry of cement, v. 3. New Delhi; (1992). 312–318.
- [13] Palomo, A. et al. Alkali-activated fly ashes, a cement for the future, CCR, 29 (8) (1999), 1323-1329
- [14] Cartwright, C. et al Shrinkage characteristics of alkaliactivated 2slag cements, J. Mater. Civ. Eng. (2014), 401-407
- [15] Ye, H., and Radlinska, A. Shrinkage mechanisms of alkali-activated slag, Cement and Concrete Research, (2016), 126-135
- [16] Shi, C. et al Alkali-activated Cements and Concretes Taylor and Francis, London a. New York (2006)
- [17] Wu, C. Properties and application of alkali-slag cement,” Journal of Chinese Ceramic Society, (1993).
- [18] Collins F, Sanjayan J. G. Microcracking and strength development of alkali-activated slag concrete. Cem Concr Compos (2001), 345–52.
- [19] Bernal, S. et al Performance of an alkali-activated slag concrete reinforced with steel fibers Constr. Build. Mater., (2010), 208-214.
- [20] Yang, K., et al. Establishment of a preconditioning regime for air permeability and sorptivity of alkali-activated slag concrete Cem. Concr. Compos., 73 (2016), pp. 19-28.
- [21] Mithun, B.M. and Narasimhan, M.C. Performance of alkali activated slag concrete mixes incorporating copper slag as fine aggregate J. Cleaner Prod., (2016), 837-844
- [22] Bernal, S. et al Performance of an alkali-activated slag concrete reinforced with steel fibers Constr. Build. Mater., (2010), 208-214
- [23] Albitar, M. et al Durability evaluation of geopolymer and conventional concretes Constr. Build. Mater., 136 (2017), 374-385
- [24] Bakharev T. et al Resistance of alkali-activated slag concrete to alkali-aggregate reaction. Cem Concr Res (2001), 331–4
- [25] Krivenko, P. Sodium sulphate based slag alkaline cements, Proceedings of 3rd Beijing International Symposium on Cement and Concrete, Beijing, (1993). 1032-1037
- [26] Tailing, B., and Brandstetr, J. Present state and future of alkali activated slag concrete, Proceeding of 3rd International Conference on Fly ash, Silica Fume, Slag and Natural Pozzolanas in Concrete, Trondheim, (1989) 1519-1546.
- [27] Mesto, J. Alkali reaction of alkali activated Finish blast furnace slag, Silic. Indus. (1982), 123 -127.
- [28] Byfors, K. et al Durability of concrete made with alkali-activated slag, Third International Conference Proceedings. Fly Ash, Silica Fume, Slag, and Natural Pozzolans in Concrete (1989), 1429–1466.
- [29] Deja, J. Carbonation aspects of alkali activated slag mortars and conc. Silic Ind., (2002), 37-42.
- [30] Bernal, S. A et al. Accelerated carbonation testing of alkali-activated slag/metakaolin blended concretes: effect of exposure conditions Mater. Struct., (2014), 653-669.
- [31] Bernal, S.A. et al. Gel nanostructure in alkali-activated binders based on slag and fly ash, and effects of accelerated carbonation Cem. Concr. Res., (2013), 127-144.
- [32] Wang S. D, et al Factors affecting the strength of alkali-activated slag. Cem Concr Res (1994).
- [33] Saliba J. et al. Influence of shrinkage-reducing admixtures on plastic and long-term shrinkage. Cem. Concr. Compos. (2011), 209–217.
- [34] Rajabipour F. et al Interactions between shrinkage reducing admixtures (sra) and cement paste's pore solution. Cem. Concr. Res. (2008), 38:606–615.
- [35] Aydin S., and Baradan B. Mechanical and microstructural properties of heat cured alkali-activated slag mortars. Mater. Des. (2012), 374–383.
- [36] Rajabipour F. et al Interactions between shrinkage reducing admixtures (sra) and cement paste's pore solution. Cem. Concr. Res. (2008), 38:606–615.
- [37] Bakharev et al. Effect of admixtures on properties of alkali-activated slag concrete. Cem Concr Res (2000) 367–74.
- [38] Fu-seng W et al Study on modification of the high-strength slag cement material. Cem Concr Res (2005), 1344–8.
- [39] Mangat, P.S., and Bordeian, S. Shrinkage of fibre reinforced alkali activated composites. Cem. Concr. Compos., in press

## **ALKALI-ACTIVATED BLEND OF CALCINED LATERITIC SOIL AND WASTE MARBLE SLURRY**

**Luca Valentini<sup>(1)</sup>, Ludovico Mascarin<sup>(1)</sup>, Enrico Garbin<sup>(1)</sup>, Maria Chiara Dalconi<sup>(1)</sup>**

(1) Department of Geosciences, University of Padova, Italy

### **Abstract**

This contribution illustrates some preliminary results of a project focussed on the use of alkali-activated materials obtained from clays of different mineralogical composition, sampled in different localities in non-commercially exploited outcrops. Tests performed by alkali activation (using sodium silicate with added sodium citrate) of a calcined clay, consisting of 66% smectite, 22% volcanic glass and accessory phases gave encouraging results, showing that alkali activated materials with excellent mechanical properties can be produced from cheap, widely distributed raw materials, without previous beneficiation. The results also showed that both mechanical properties and workability could be enhanced by the use of marble slurry, a waste material from marble quarrying and cutting, which adds environmental value to the designed mix.

Here, we focus on the use of lateritic soils sampled in Yaoundé, Cameroon, as a raw material for the production of alkali-activated binders. This choice is motivated by the need of investigating the feasibility of producing robust, low-CO<sub>2</sub> cements from raw materials that are widely available across Africa, with the aim of boosting the sustainable development of this continent, in line with recent actions for the collaboration between African Union and European Union.

Some preliminary results of the microstructural and mechanical characterization of these materials as well as their kinetic and thermodynamic modelling will be illustrated.

### **1. Introduction**

The scientific literature on sustainable binders, alternative to Portland cement, has become consolidated. The two main lines of research being pursued comprise zero-clinker to low-clinker binders. The first group mostly encompasses the use of alkali-activated aluminosilicates, the main ones being fly ash, ground granulated blast furnace slag and

metakaolin [1]. The second group of binders is obtained by blending the same aluminosilicates with different amounts of OPC [2]. Given the lack of geographically homogeneous availability (fly ash, slag) or economic viability (metakaolin), in the last few years the use of calcined clays blended with OPC has been explored [3]. In such a scenario, research into the alkali activation of calcined clays still represents a niche.

In this contribution, we investigate the potential use, as sustainable binders, of alkali activated calcined clays of different chemical and mineralogical composition. Clay is an economically viable raw material and is homogeneously distributed geographically. Moreover, clay materials are particularly abundant in soils in many developing countries (Fig. 1) and represent, therefore, an important resource for the growing economies. In this context, we explore the performance of lateritic clays sampled in Cameroon as raw materials for the production of alkali activated cement, relying on previous findings that showed the possibility of obtaining an excellent mechanical performance by alkali activation of calcined smectites, blended with calcium carbonate slurry, a waste material deriving from marble quarrying and cutting [5].

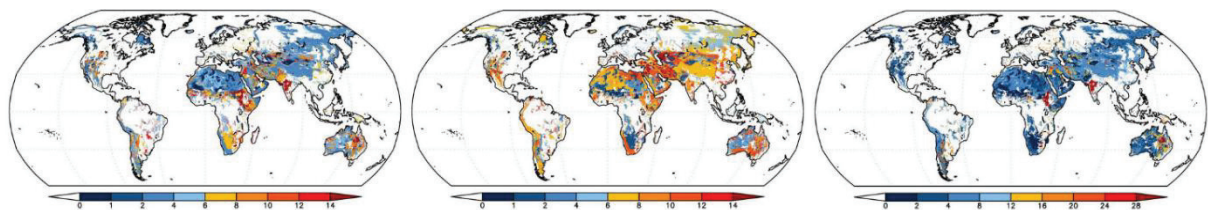


Figure 1: Concentration of clay minerals in soils (left to right: kaolinite, illite, smectite). Data from [4].

## 2. Material and methods

XRF compositions of the lateritic clay and marble slurry (oven dried at 60 °C) used are reported in Tab. 1. The XRD composition of the clay is: 60% kaolinite, 30% quartz, 8% goethite, 1% anatase, 1% calcite. Recalculating the chemical composition from this phase assemblage leads to an underestimation of Fe > 2%, suggesting that part of the iron might be incorporated in an amorphous phase or adsorbed to kaolinite surfaces. The high amount of iron yields an intense reddish coloration to the clay.

Table 1: XRF composition.

	SiO <sub>2</sub>	TiO <sub>2</sub>	Al <sub>2</sub> O <sub>3</sub>	Fe <sub>2</sub> O <sub>3</sub>	MnO	MgO	CaO	Na <sub>2</sub> O	K <sub>2</sub> O	P <sub>2</sub> O <sub>5</sub>
Clay	62.1	1.8	24.6	10.1	0.0	0.2	0.1	0.0	0.2	0.1
Slurry	0.0	0.0	0.1	0.0	0.0	0.6	55.9	0.0	0.0	0.0

Clay calcination was performed at 800 °C for 5 hours, with a heating rate of 10 °C/min. Dehydroxylation of goethite induced the formation of hematite.

The dried marble slurry consists of 100% calcite with some Mg impurities and was pre-mixed in different amounts with clay and a fixed amount of sodium silicate pentahydrate

( $\text{Na}_2\text{SiO}_3 \cdot 5\text{H}_2\text{O}$ ) used as an alkaline activator. The addition of dry sodium silicate rather than a previously prepared alkaline solution was preferred, in order to facilitate mixing and enhancing workability. The water-to-solid ratio was 0.5. The different mixes are summarized in Tab. 2.

Additional samples were prepared by blending a commercial metakaolin with an amount of finely ground quartz corresponding to that measured by XRD for the lateritic clay, with the aim of decoupling the effect of quartz from that of Fe-bearing phases.

Table 2: Mix composition (wt%).

	Clay	Marble slurry	Sodium silicate	Water
Sample 1	44.44	0	22.22	33.33
Sample 2	37.78	6.67	22.22	33.33
Sample 3	31.11	13.33	22.22	33.33

The fresh pastes were kept in teflon moulds for two days at ambient temperature and 95% relative humidity. After demoulding, the samples were cured at the same temperature and humidity conditions. One day before compressive strength testing, the samples were kept at ambient humidity. Powder XRD was performed to study the phase assemblage of the reacted materials and polished thin sections were prepared for SEM-EDS analyses. Simulations of the phase assemblage at thermodynamic equilibrium were performed using the software GEMS (<http://gems.web.psi.ch/>) and the database provided in [6].

### 3. Results

Samples obtained using the above mix compositions displayed low values of the 7 days compressive strength (4.3 – 4.5 MPa). The samples presented severe fracturing that may be ascribed to the presence of excess sodium silicate (the Na/Al of the three mixes varies between 0.98 and 1.4). It has to be noted, however, that the samples prepared by blending commercial metakaolin and quartz displayed values of the compressive strength up to 11.3 MPa, suggesting a detrimental effect of iron. Also, by reducing the amount of sodium silicate added to the lateritic clay, from 22.22 wt% to 11.11 wt% (Na/Al = 0.49 – 0.70), the 7 days compressive strength increased up to 13.0 MPa.

The EDS spot chemical composition of the matrix is reported in the Na-Al-Si system in Fig. 2 and compared to the N-A-S-H chemical composition predicted by the thermodynamic model. A good level of agreement exists for the systems with additions of marble slurry, whereas a slightly higher Na/Si is predicted by the thermodynamic model for the system in the absence of marble slurry.

Precipitation of up to 3% trona ( $\text{Na}_2\text{CO}_3 \cdot \text{NaHCO}_3 \cdot 2\text{H}_2\text{O}$ ), formed by carbonation of the alkaline pore solution, is observed by means of powder XRD at 28 days.

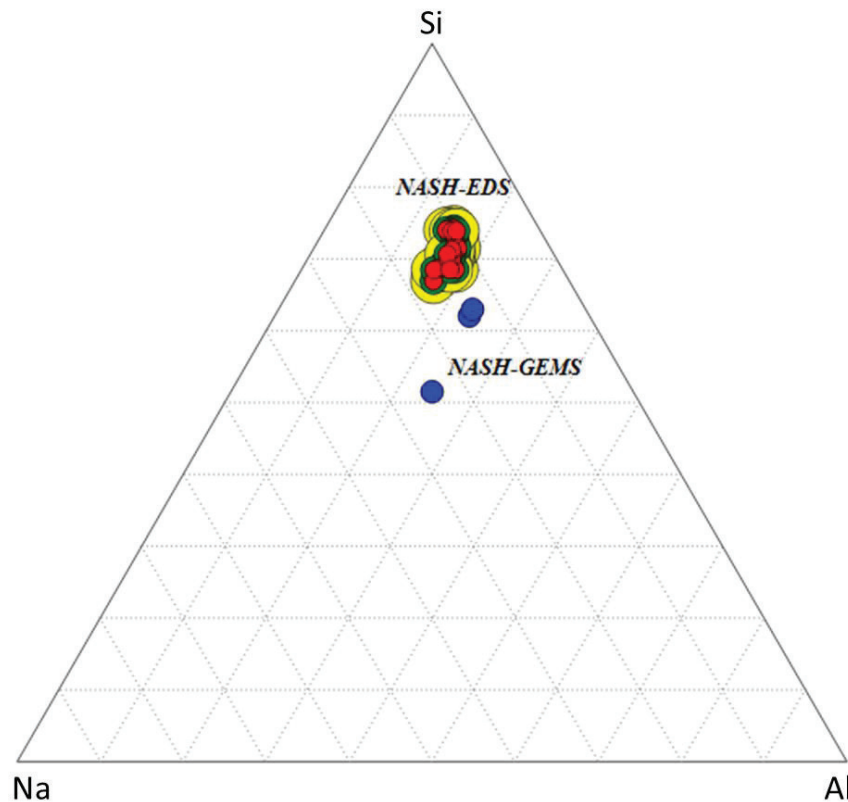


Figure 2: Chemical composition of the matrix, as measured by SEM-EDS and of the N-A-S-H product, as predicted by the GEMS thermodynamic model (blue circles, black in greyscale print).

#### 4. Conclusions and perspectives

This research draws on previous experience on the alkali activation of locally sampled smectitic clays to test the performance of calcined lateritic clay soils from Cameroon as raw materials for the production of sustainable binders. Although preliminary results gave low compressive strengths at one week, it could be observed that the mechanical performance could be significantly improved by adjusting the Na/Al ratio of the mix. Moreover, comparison with samples prepared by alkali activation of a blend of commercial metakaolin and quartz, in the same proportion of that of the lateritic clays, suggests that the presence of iron in clay soils may hinder the development of compressive strength.

It will be worth exploring further the possible role of calcined clays of different mineralogical and chemical composition for the production of alkali activated binders. We are currently testing the properties of alkali-activated calcined clays from Tunisia, consisting of kaolinite-illite mixtures and other additional phases. Preliminary tests using a blend of calcined clay and marble slurry gave a compressive strength of 24 MPa at one week.

This results show that a careful consideration of the chemical and mineralogical composition of such impure systems and subsequent adjustment of the mix proportion is mandatory.



The possibility of exploiting locally available raw materials for the African market is intriguing, and in line with current strategies of scientific collaboration between African Union and European Union [7].

## References

- [1] Siddique, R. and Khan, M. I., *Supplementary Cementing Materials*, Springer, Berlin, Germany (2011)
- [2] Provis, J. L. and van Deventer, J. S. J., *Alkali Activated Materials, State-of-the-Art Report*, RILEM TC 224-AAM, Springer, Berlin, Germany (2014)
- [3] Scrivener, K. L.; Favier, A., *Calcined Clays for Sustainable Concrete*. Proceedings of the 1st international conference on calcined clays for sustainable concrete. Springer, Berlin, Germany (2015)
- [4] Nickovic, S. et al., Mineral composition in arid soils: A global distribution. AGU Fall Meeting, abstract no NH53A-1254 (2010)
- [5] Valentini, L. et al., Alkali-activated calcined smectite clay blended with waste calcium carbonate as a low-carbon binder, *J Cleaner Prod* 184 (2018) 41-49
- [6] Myers, R. J. et al., Thermodynamic modelling of alkali-activated slag cements, *Appl Geochem* 61 (2015) 233-247
- [7] European Commission, *Science for the AU-EU Partnership: building knowledge for sustainable development* (2017)

## **CHARACTERIZATION OF THE SELF-HEALING EFFECT THROUGH PORE STRUCTURE AND DURABILITY OF ALKALI-ACTIVATED CEMENT CONCRETE**

**Pavel Krivenko <sup>(1)</sup>, Igor Rudenko <sup>(1)</sup>, Oleh Petropavlovskiy <sup>(1)</sup>, Oles' Lastivka <sup>(1)</sup>**

(1) Kyiv National University of Construction and Architecture, Scientific Research Institute for Binders and Materials, Povitroflotskyi prospect 31, Kyiv 03037 Ukraine

### **Abstract**

The paper considers the effect of constituents of alkali-activated cements (AAC) and the chemical admixtures on formation of effective porosity of concrete as a criterion for the AAC matrix to self-heal. The durability of concrete is performed by its frost resistance. Minimization of open capillary porosity was considered as the determining factor for reducing amount of ice in pores and predetermining a corresponding decrease in stresses. The influence of the anionic part of AAC's alkaline component on the features of pore structure of concrete is shown. Thus, sodium carbonate causes greater open capillary porosity of compared to sodium silicates. An increase of granulated blast-furnace slag in AAC from 50 to 100 % and adequate increase alkaline component determine decrease in the volume of open capillary pores with higher volume of micro- and conditionally closed pores. This phenomenon determines increasing AAC concrete's ability to self-heal under the cyclic action of freezing and thawing. It was determined negative changes in the pore structure of AAC concretes modified with polyesters. It has been proposed to use alternative admixtures of the polyether type.

### **1. Introduction**

One of the ways to avoid disadvantages of cements with high slag contents is to add alkali metal compounds in order to produce alkali-activated cement (further, AAC) [1, 2, 3].

A key factor which determines performance properties and durability of concrete is its porosity. However, if strength of concrete depends on a total porosity, freeze/thaw resistance and durability are determined chiefly by capillary porosity [4]. The tendency to simplify concrete technologies causes the use of plasticizers, which application is problematic with

AAC because of high alkaline medium [5]. The basis for designation of the main active ingredient of plasticizers for AAC concretes was proposed [6].

It is known the natural ability of cement materials to eliminate cracks, i.e. (improved) autogenous self-healing mainly due to hydration of unhydrated cement and carbonization of  $\text{Ca(OH)}_2$  [7]. The peculiarity of AAC in comparison with OPC is the tendency to higher volume of micropores (gel pores) and to reduce capillary porosity due to gradual formation in porous space of alkaline and alkaline-alkali-earth hydroaluminosilicates, which causes self-healing [8]. An important aspect is to ensure self-healing of AAC concrete with its modification by plasticizers, i.e. providing high frost resistance.

The purpose of this paper is to investigate the features of pore structure which determine autogenous self-healing of plasticized AAC concrete under the action of cyclic freezing and thawing.

## 2. Raw materials and testing techniques

The AACs varying in contents of ground granulated blast furnace slag (further, slag) between 50 and 100 % as per national standard of Ukraine were used [9].

Slag (basicity modulus  $M_b = 1.1$ , content of glass phase 56 %) and portland cement clinker were used as aluminosilicate components of the AACs, their chemical compositions are shown in Tab. 1. Soda ash ( $\text{Na}_2\text{CO}_3$ ) and sodium metasilicate pentahydrate ( $\text{Na}_2\text{SiO}_3 \cdot 5\text{H}_2\text{O}$ ) were used as alkaline components of the AACs. It is required to use sodium lignosulfonate (further, LST) in order to provide the required setting times and strength of AAC.

Table 1: Chemical composition of AACs components.

Component	Oxides, % by mass								
	$\text{SiO}_2$	$\text{Al}_2\text{O}_3$	$\text{Fe}_2\text{O}_3$	MnO	MgO	CaO	$\text{Na}_2\text{O}$	$\text{SO}_3$	LOI
Clinker	21,3	5,7	4,62	-	1,2	64,9	0,3	0,86	0,12
Slag	39,0	5,9	0,3	0,5	5,82	47,3	-	1,54	-

The AAC compositions are shown in Tab. 2. Fineness of the AACs (by Blaine) was  $4500 \text{ cm}^2/\text{g}$ .

In order to change a consistency of the AAC concrete mixtures from class S1 (that of the reference composition) to class S4 at  $t = 20 \pm 2 \text{ }^\circ\text{C}$  the chemical admixtures were used (% by AAC): type 1 – surfactant based on polyacrylate esters ("Dynamon SR 2", Mapei) – 1.2 %; type 2 - surfactant based on polyether (polyethylene glycol "PEG-400", JSC "Barva") – 1.3 %; type 3 - surfactant based on sodium gluconate ("Mapetard SD 2000", Mapei) – 1.0 %.

The mentioned surfactants are compatible with LST as components of complex admixtures (further, CA), used to ensure low water consumption of concrete mixtures with decrease in the surface tension of porous fluid. It is known that the latter circumstance facilitates migration of porous fluid, respectively, reducing the capillary stress that causes shrinkage [10].

The standard composition of the AAC concrete was taken in accordance with [11],  $\text{kg/m}^3$ : cement - 350; silica sand - 740; granite gravel: 350 (5/10) and 810 (10/20); water - 165.

Porosity (P) of AAC concretes was studied in accordance with methodology of the national standard of Ukraine [12]. The concrete cubes (100 mm) after 28 days of hardening ( $t = 20 \pm 2$

°C, RH= 95±5 %) were dried up to a constant weight at  $t= 105\pm5$  °C. Then, the concrete specimens were saturated with water until a constant weight at  $t= 20\pm2$  °C. The values of porosity, i.e. volumes of open capillary pores ( $P_o$ ) and conditionally closed pores ( $P_c$ ), were calculated from the values of average density and water absorption of the concrete specimens.

Table 2: Compositions of AAC.

# of composition	Basic composition
1	50 % slag, 50 % clinker, 2 % Na <sub>2</sub> CO <sub>3</sub> , 1 % LST
2	50 % slag, 50 % clinker, 3 % Na <sub>2</sub> SiO <sub>3</sub> ·5H <sub>2</sub> O, 1 % LST
3	69 % slag, 31 % clinker, 2,5 % Na <sub>2</sub> CO <sub>3</sub> , 1 % LST
4	69 % slag, 31 % clinker, 3,5 % Na <sub>2</sub> SiO <sub>3</sub> ·5H <sub>2</sub> O, 1 % LST
5	88 % slag, 12 % clinker, 3 % Na <sub>2</sub> CO <sub>3</sub> , 1 % LST
6	100 % slag, 4,7 % Na <sub>2</sub> CO <sub>3</sub> , 0,8 % LST

Freeze/thaw resistance was studied in accordance with the third test method prescribed by the national standard of Ukraine [13]. The concrete cubes (100 mm) after 28 days ( $t= 20\pm2$  °C, RH= 95±5 %) were saturated with 5 % solution of NaCl at  $t= 18\pm2$  °C and after that were subjected to freezing at  $t= -50\pm5$  °C. Thawing was also done in 5 % solution of NaCl. Class of concrete in freeze/thaw resistance was designated as a number of alternate freezing and thawing at which a mean compressive strength decreased by no more than 5 %. The freeze/thaw resistance of concrete was assessed by the correspondence between permissible number of freezing-thawing cycles on the used accelerated method and on first (basic) method prescribed in mentioned standard. The differences of the first method are specimens saturation medium (water), the medium and the freezing temperature (air,  $t= -18\pm2$  °C), the thawing medium (water).

### 3. Results and discussions

The use of polyester-based CA in the AAC concretes containing 50 % of slag lead to slight increase of  $P_o$  in comparison with the reference composition – for example, from 8.1 up to 8.8 % using soda ash (Fig. 1). With increase of slag content in AACs up to 88 % the effectiveness of this CA in concrete tended to significantly decrease and was accompanied by increase of  $P_o$  up to 11 %.

At the same time, there was observed general tendency to increasing effectiveness of pore structure of the concrete, i.e. to decrease  $P_o$  with increase in slag content and, accordingly, with increase in the required content of alkaline component in AACs (Fig. 1). In this case, the increasing  $P_c$  determines formation of more dense structure with advanced self-healing.

Modification of the AAC concretes by polyester-based admixtures in case of AAC with 50 % of slag (compositions #1 and #2) provided class F200 in freeze/thaw resistance (Fig. 2), i.e. highest class for the most demanding concrete structures in unheated buildings undergoing alternate freezing-thawing and operating at ambient temperature (-20 to -40) °C (exposure class XF4). However, with increase in slag contents up to 69 % the efficiency of this type of admixture tended to decrease. This was accompanied by lack in self-healing of the structure,  $P_o$  increased (up to 9.6 %) and freeze/thaw resistance declined (class F150).

Polyethylene glycol did not significantly affect pore structure of concrete in case of AACs containing 88 % of slag (Fig. 1). Significant self-healing function of concrete structure defined class F200 in freeze/thaw resistance. With an increase of slag up to 100 %, the structural parameters did not significantly change:  $P_o$  increases from 7.3 % to 7.7 % and  $P_c$  from 2.4 % to 2.6 % respectively. Due to additional volume of artificial air micropores this fact caused increasing self-healing of concrete and provided class F200 (Fig. 2).

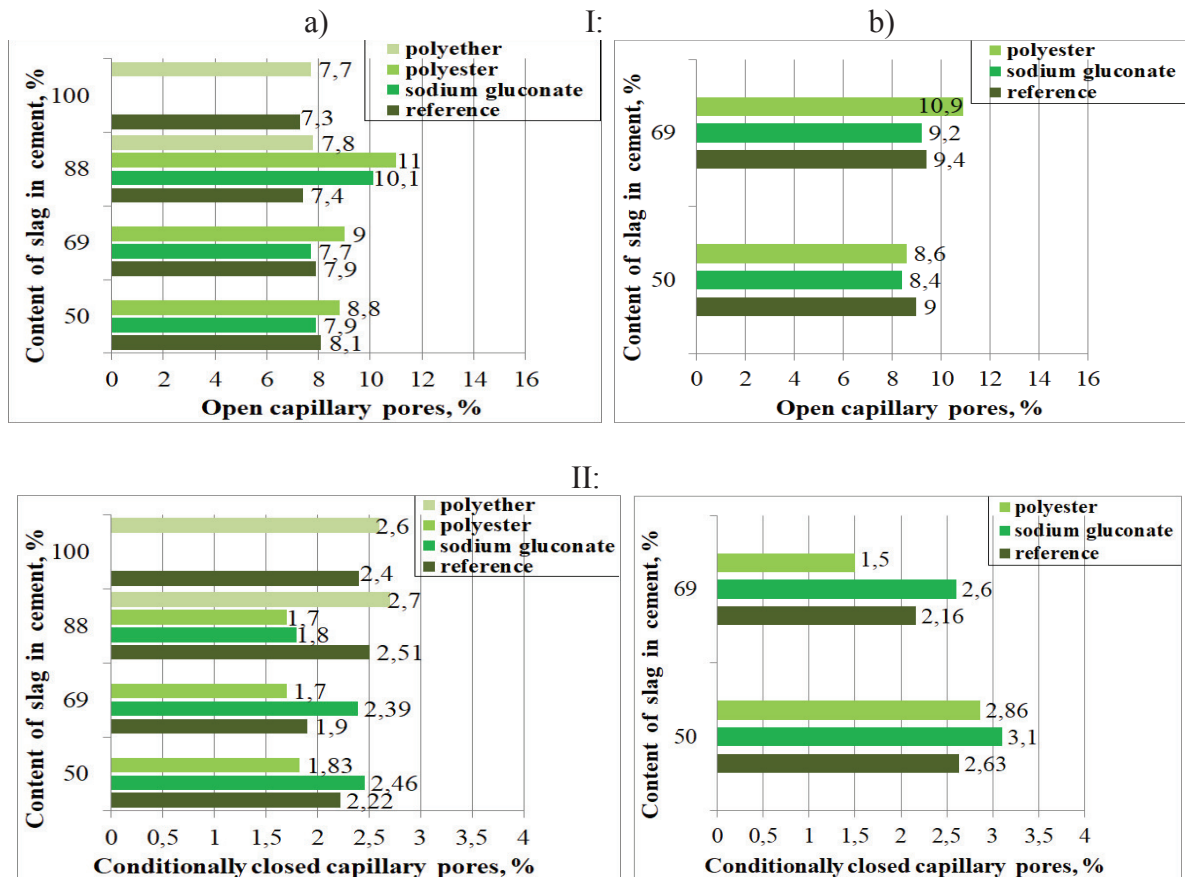


Figure 1: Volumes of open capillary pores (I) and conditionally closed capillary pores (II) of the AAC concrete vs. type of surfactant as ingredient of CA and slag contents in the AACs, % (see Tab. 2): a) #1, #3,#5, #6; b) #2, #4.

Sodium gluconate as ingredient of CA did not change the pore structure of concrete with 50 – 69 % slag in AAC essentially (Fig. 1). Thus, with 50 % slag in AAC  $P_o = 8.1$  % for the reference composition and  $P_o = 7.9$  % with the admixture. With an increase in the amount of slag up to 69 %, there was even some decrease in the volume of these pores. As a result, provided class for frost resistance of concrete was F200 (Fig. 3). However, this type of admixture in concretes with 88 % of slag in AAC deteriorated pore structure and  $P_o$  increased up to 10 % with reducing the frost resistance to class F150.

The replacement of the anion in AACs alkaline component from carbonate to silicate caused higher porosity of concrete both the reference composition and the modified ones by the mentioned surfactants (Fig. 1). This fact caused minor ability of concrete to self-healing and lack in frost resistance of concrete with high volume of slag in AAC (Fig. 3).

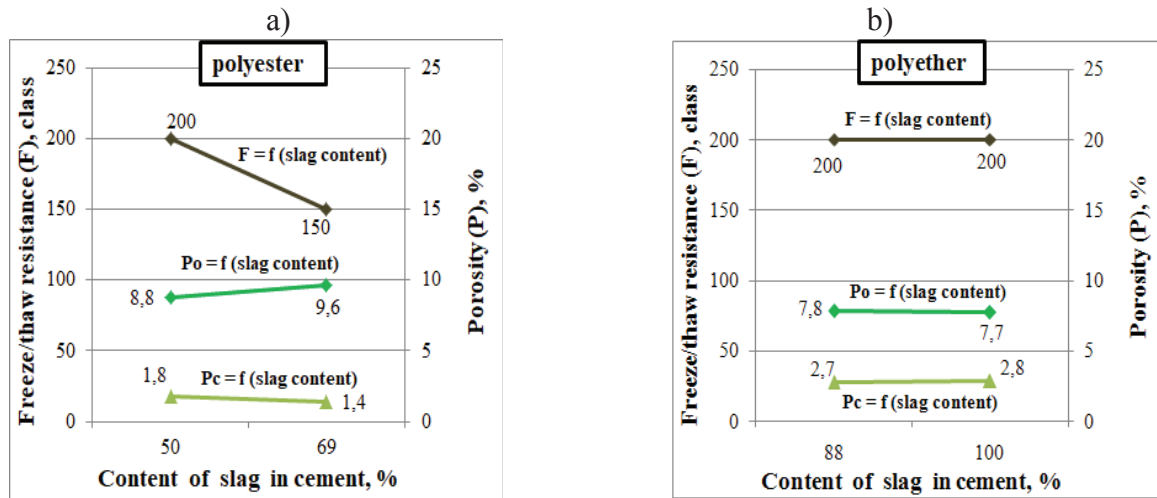


Figure 2: Open capillary porosity ( $P_o$ ), conditionally closed porosity ( $P_c$ ) and freeze/thaw resistance (F) of the AAC concretes vs. main active substance of plasticizing admixture as ingredient of CA and slag content in AAC (see Tab. 2): a) #1, #3; b) #5, #6.

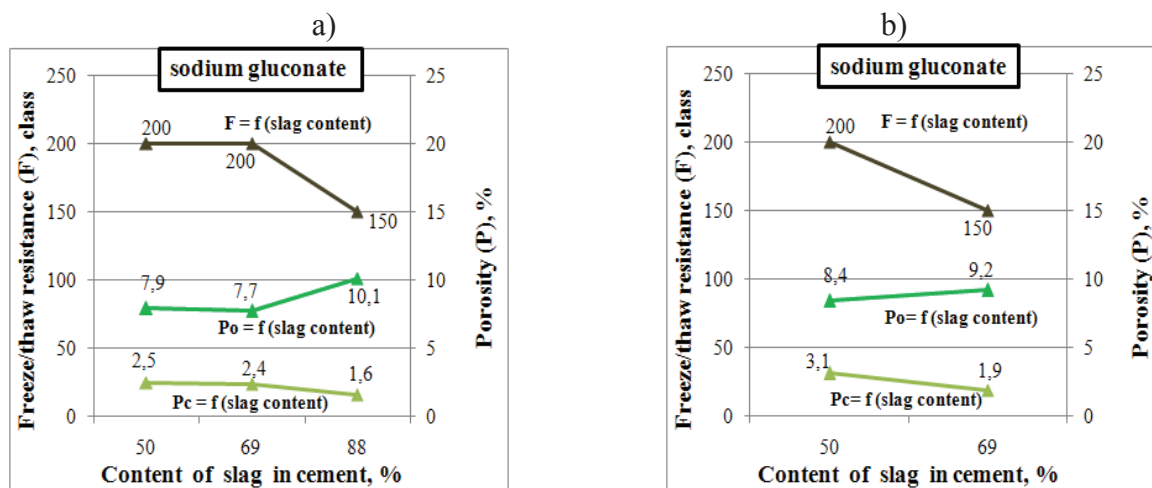


Figure 3: Open capillary porosity ( $P_o$ ), conditionally closed porosity ( $P_c$ ) and freeze/thaw resistance (F) of the AAC concretes plasticized by sodium gluconate vs. slag content in AAC (see Tab. 2): a) #1, #3, #5; b) #2, #4.

#### 4. Summary

It was found out that the ability of plasticized AAC concrete to (improved) autogenous self-healing, also under the cyclic freezing and thawing, can be provided by the features of pore structure, namely by minor volume of open pores and correspondingly high volume of conditionally closed capillary pores. In general, this phenomenon is observed with an increase in volume of slag in AAC with consequently maintenance in the required dosage of alkaline component. In this case, the polyesters become ineffective as plasticizers while the admixtures based on polyethers or alkaline salts of carboxylic acid in presence of sodium

lignosulfonate positively affect the formation of additional volume of micropores in the structure of concrete. This creates a reserve for the self-healing function of concrete, i.e. formation of air space for migration of water during cyclic freezing/thawing.

### Acknowledgements

The authors would like to acknowledge the contribution of the COST Action CA15202.  
<http://www.sarcos.enq.cam.ac.uk>

### References

- [1] Glukhovskiy, V.D. et al, Fine Alkali-Activated Slag Cement Concretes, Vysscha Shkola Publishing, Ukraine (1981)
- [2] Krivenko, P.V., Alkali-activated aluminosilicates: past, present and future, Proceed. the 4-th Meeting on Chemistry and Life, Brno University of Technology, Brno (2008), 1-5
- [3] Krivenko, P.V. et al, Features of Alkali-Activated Slag Portland Cement, Proceed. 1-st Int. Conf. on the Chemistry of Construction Materials, October 7-9, Berlin, Germany (2013), 453-456
- [4] Stark, J. Wicht, B., Dauerhaftigkeit von Beton, Weimar: Hochschule für Architektur u. Bauwesen, Weimar, Schriften 100 (1995)
- [5] Krivenko, P. et al, Plasticizing alkaline cements: state-of-the-art and solutions, Proceed. the 14-th Int. Congress on the Chemistry of Cement, China (2015)
- [6] Krivenko, P., Runova, R., Rudenko, I., Skoryk, V., Omelchuk, V., Analysis of plasticizer effectiveness during alkaline cement structure formation, EasternEuropean journal of Enterprise Technologies 4(6-88) (2017), 35-41
- [7] Tittelboom, K. V. et al, Most recent advances in the field of self-healing cementitious materials, 4th International conference on Self-Healing Materials (ICSHM 2013), Belgium (2013), 406-413
- [8] Krivenko, P., Physico-chemical bases of alkali-activated slag cement durability, Cement 11 (1990), 2-5
- [9] National standard of Ukraine DSTU B V.2.7-181:2009 Alkaline cements. Specification
- [10] Palacios, M., Puertas, F., Effect of shrinkage-reducing admixtures on the properties of alkali-activated slag mortars and pastes, Cem Concr Res 37 (2007) 691–702
- [11] National standard of Ukraine DSTU B V.2.7-171:2008 (EN 934-2:2001. NEQ). Admixtures for concretes and mortars. General specification (that meets EN 934-2:2001 “Admixtures for concrete. mortar and grout – Part 2: Concrete admixtures – Definitions. requirements. Conformity, marking and labelling”)
- [12] National standard of Ukraine DSTU B. V.2.7-170:2008 Building materials. Concretes. Methods for determining of average density, humidity, water absorption, porosity and water resistance
- [13] National standard of Ukraine DSTU B V.2.7-47-96 Building materials. Concretes. Method for determination of freeze/thaw resistance

## **DURABILITY OF CALCIUM SULFOALUMINATE – PORTLAND CEMENT BLENDS**

**Gultekin Ozan Ucal**<sup>(1)</sup>, **Mehmet Kemal Ardogan**<sup>(1)</sup>, **Melike Sucu**<sup>(2)</sup>, **Tughan Delibas**<sup>(2)</sup>,  
**Ismail Ozgur Yaman**<sup>(1)</sup>

(1) Middle East Technical University, Ankara, Turkey

(2) Cimsa Cement Co., Mersin, Turkey

### **Abstract**

Calcium sulfoaluminate cement (CSAC) is a low-energy cement with lower carbon footprint than ordinary portland cement (PC), and it may be a better alternative in certain applications where rapid setting or shrinkage compensating properties are desired. In this study, performance of PC-CSAC blends were investigated by preparing eight sets of mortar and concrete blends with CSAC/PC ratios of 0/100, 5/95, 10/90, 20/80, 30/70, 40/60, 50/50, 100/0. Their alkali-silica reactivity was determined on mortar specimens, and drying shrinkage, compressive strength development, rapid chloride ion permeability, and porosity were investigated on concrete specimens. As a result of the experimental investigation, 100% CSAC showed properties superior to both 100% PC and blended mixtures in most of the determined properties. It was observed that although blending CSAC with PC increases the 1-Day strength of concrete, its later-age performance was adversely affected. It appeared that the blend with 30% CSAC had the lowest performance.

### **1. Introduction**

Cement industry is responsible for around 5% of global humanmade CO<sub>2</sub> emissions [1]. Production of one ton of PC results in 0.87 ton of CO<sub>2</sub> emission on average [2]. PC production is also an energy-intensive process, with PC clinker consuming around 3.8 GJ/t of energy [3].

Main phases in calcium sulfoaluminate cement (CSAC) clinker are tetracalcium trialuminate sulfate (C<sub>4</sub>A<sub>3</sub>S) and belite (C<sub>2</sub>S), and principal hydration product is ettringite, which results in a relatively low pH final product due to the absence of calcium hydroxide [4]. CSAC can be produced by calcination of limestone, clay, bauxite and gypsum [4,5]. Due to a reduction in



production temperature from 1450 °C to 1250 °C and lower limestone content in raw mixture, ~1 GJ/t of energy saving in clinker production, and 25-35% lower CO<sub>2</sub> emission would be achievable by utilizing CSAC instead of PC [6].

Past studies had shown that blending CSAC with PC may increase the hardening rate [7], early strength [8], and reduce drying shrinkage [8,9], relative to using PC only. This study aims to contribute to the literature by investigating several performance characteristics of various CSAC/PC blends in mortar and concrete.

## 2. Experimental Program

This was an experimental study that investigated the effects of CSAC content in CSAC/PC blended mortar and concrete on several performance characteristics, by examining the results of 8 different mixtures containing CSAC/PC ratios of 0/100, 5/95, 10/90, 20/80, 30/70, 40/60, 50/50, 100/0. For ease of display, each mixture will be denoted with its CSAC/cementitious material ratio in the following sections.

For concrete batches, cement dosage of 400 kg/m<sup>3</sup> was selected and consistency was kept constant by changing water content to attain a slump of 21.5±1.5 cm.

### 2.1 Materials

Commercially available CSAC and CEM I/42.5R (PC) were used in this study. The chemical composition and the compound composition of the cements are provided in Tab.1 and 2. Properties of 0-4mm limestone fine aggregate (FA), 5-12mm limestone coarse aggregate (CA1), and 12-25mm limestone coarse aggregate (CA2) are shown in Tab. 3. 810 kg/m<sup>3</sup> of FA, 405 kg/m<sup>3</sup> of CA1, and 405 kg/m<sup>3</sup> of CA2 were used in all batches.

Table 1: Chemical composition of cements

Cement	SiO <sub>2</sub>	Al <sub>2</sub> O <sub>3</sub>	Fe <sub>2</sub> O <sub>3</sub>	CaO	MgO	K <sub>2</sub> O	Na <sub>2</sub> O	SO <sub>3</sub>	LOI	Cr <sub>2</sub> O <sub>3</sub>	Mn <sub>2</sub> O <sub>3</sub>
CSAC	7.53	27.51	0.73	39.06	2.39	0.44	0.8	19.62	0.76	0.06	0.19
PC	19.17	5.2	2.606	63.3	2.4	0.84	0.29	3.2	0.0292	0.06	3.28

Table 2: Compound composition of CSAC

C <sub>4</sub> A <sub>3</sub> S		C <sub>2</sub> S	C <sub>3</sub> S	MgO
Orthorhombic	Cubic			
44.3	11.9	22.8	19.8	1.1

Table 3: Properties of aggregates

	Fine Aggregate	Coarse Aggregate	
		(5-12 mm)	(12-25 mm)
Specific gravity (SSD)	2.67	2.69	2.71
Absorption capacity (%)	1.2	0.3	0.2
Moisture content (%)	0.2	0.2	0.2

Reactive fine aggregate complying with ASTM C1260 grading requirements was used to determine the alkali-silica reactivity of mortar mixtures [10].

## **2.2 Methods Employed during the Experimental Investigation**

Alkali-silica reactivity of mortar mixtures was determined in accordance with ASTM C1260 [10] by using three 25x25x285 mm mortar bars for each mixture.

To observe the effect of CSAC content on drying shrinkage, 75x75x320 mm concrete prisms were allowed to cure at 100% RH for 30 days, then stored at 35±5% RH for the next 28 days unrestricted. Length of each prism was measured initially, at the end of curing, and 28 days after the curing. The average reading of three prisms was reported as the result for each mixture.

To monitor compressive strength development, 100x200 mm concrete cylinder specimens were tested at 1, 3, 7, and 28 days in accordance with ASTM C39 [11]. The average reading of three cylinders was reported as the result for each mixture.

Rapid chloride permeability test was employed to determine the ion permeability of specimens [12]. 28 and 90 days conductivity values were measured by using four 100x50 mm concrete disc specimens for each test.

Permeable porosity was calculated by using three 100x50 mm concrete disc specimens in accordance with ASTM C642 [13], except only cold water-saturated and immersed masses were used to determine apparent density.

## **3. Results and Discussion**

Slump, water-to-cement ratio, air content, and fresh density values of concrete mixtures are shown in Tab. 4. Rapid setting property of CSAC started affecting workability of concrete after 20% CSAC. Therefore, use of set retarder admixture is advised with CSAC replacement ratios over 20%.

### **3.1 Drying shrinkage**

Specimen length after demolding is recorded as initial length. Length change after 30 days of curing, after concrete prisms were taken out of the 100% RH condition is shown in Tab. 5. It was seen that addition of CSAC to concrete resulted in expansive behavior during curing, with maximum expansion recorded for 30% and 100% CSAC specimens. However, this situation was reversed upon drying. All blends except 5% CSAC undergone a larger final shrinkage than PC concrete (0% CSAC). Only 100% CSAC concrete specimens were longer than their initial length after drying. This test confirmed that CSAC by itself shows shrinkage compensating properties, however, blending CSAC and PC actually increased drying shrinkage of concrete.

### **3.2 Alkali-silica reactivity**

Length change of mortar specimens at the end of the 16<sup>th</sup> day is shown in Tab. 6. It was observed that all blends expanded more than PC mortar, with an increasing trend up to 30% CSAC. Even though the aggregate was known to be reactive, expansion of 100% CSAC mortar was well below ASTM's safety limit of 0.1%, which was believed to be caused by the lower pH of the product upon hydration due to the absence of calcium hydroxide.

Table 4: Fresh concrete properties

	Slump (cm)	Water-to-cement ratio	Air content (%)	Density (kg/m <sup>3</sup> )
0% CSAC	21.0	0.60	2.5	2318
5% CSAC	20.5	0.60	2.0	2341
10% CSAC	23.0	0.60	2.5	2337
20% CSAC	21.0	0.60	2.4	2313
30% CSAC	21.0	0.56	2.7	2297
40% CSAC	21.5	0.57	2.3	2327
50% CSAC	20.5	0.61	2.5	2293
100% CSAC	21.5	0.58	2.1	2298

Table 5: Length change of concrete prisms after curing and drying

	0% CSAC	5% CSAC	10% CSAC	20% CSAC	30% CSAC	40% CSAC	50% CSAC	100% CSAC
After 30 days curing (%)	-0.004	0.012	0.014	0.026	0.034	0.026	0.014	0.034
28 days of drying after 30 days of curing (%)	-0.030	-0.022	-0.038	-0.076	-0.126	-0.085	-0.040	0.008

Table 6: Length change of mortar specimens at the end of ASR test

	0% CSAC	5% CSAC	10% CSAC	20% CSAC	30% CSAC	40% CSAC	50% CSAC	100% CSAC
Length change (%)	0.67	0.74	0.81	1.12	1.25	1.16	0.85	0.04

### 3.3 Compressive strength

1, 3, 7, and 28 days compressive strength of concrete cylinder specimens are shown in Tab. 7 along with standard deviations for each set. Although CSAC addition enhanced the 1-Day strength of concrete at all ratios, only 40% and 100% CSAC specimens yielded higher compressive strength than PC specimens after 28 days. Overall, blending CSAC and PC did not improve the later-age compressive strength of concrete.

Table 7: 1, 3, 7, and 28 days compressive strength of concrete specimens

Strength (MPa)	0% CSAC	5% CSAC	10% CSAC	20% CSAC	30% CSAC	40% CSAC	50% CSAC	100% CSAC
1-Day	7.8[1.1]	10.5[0.5]	9.8[1.2]	13.7[0.3]	11.4[0.2]	9.6[0.6]	12.2[0.9]	29.4[2.5]
3-Day	20.9[1.6]	24.1[1.6]	23.7[0.6]	18.5[0.5]	18.6[0.6]	21.9[1.0]	17.8[0.3]	36.9[1.1]
7-Day	26.4[2.4]	29.9[1.4]	26.7[1.6]	23.0[1.6]	27.5[0.5]	30.3[0.3]	24.3[2.8]	43.3[0.2]
28-Day	40.5[0.6]	38.9[0.2]	34.6[1.2]	27.8[1.2]	31.3[1.6]	42.6[0.6]	34.8[4.1]	44.9[2.4]

\* Numbers in brackets are the standard deviation of 6 specimens

### 3.4 Ion permeability

As an indication of chloride ion permeability, the electrical conductivity of concrete specimens was tested. Passing charge values at 28 and 90 days are shown in Tab. 8. It was observed that CSAC had a reduction effect on electrical conductivity when the replacement level is at least 40%. On the other hand, it was noted that 30% CSAC performed the worst at both ages. Thus, the replacement ratio is an important factor that affects ion permeability in CSAC-PC blends.

Table 8: Electrical conductivity of concrete specimens

Charges Passed (Coulomb)	0% CSAC	5% CSAC	10% CSAC	20% CSAC	30% CSAC	40% CSAC	50% CSAC	100% CSAC
28-Day	5741	6118	5732	5339	8138	4328	2644	4149
90-Day	4374	4831	4431	5257	5610	3776	1744	2687

### 3.5 Porosity

The permeable porosity of concrete specimens is shown in Tab. 9. While CSAC concrete had lower permeable porosity than the rest of the mixtures, blending PC and CSAC did not result in a notable trend on porosity relative to PC concrete.

Table 9: Permeable porosity of concrete specimens

	0% CSAC	5% CSAC	10% CSAC	20% CSAC	30% CSAC	40% CSAC	50% CSAC	100% CSAC
Permeable porosity (%)	15.4	16.8	17.8	18.3	15.1	14.7	17.9	10.4

## 4. Conclusion

At the end of this study, it was observed that CSAC appeared to be a superior alternative to PC consistently performing better than both PC and CSAC-PC blends. However, blending PC and CSAC did not improve the overall performance of the final product at any replacement amount. 30% replacement of PC with CSAC resulted in the worst performance. Hydration characteristics and microstructure will be further investigated, to reveal the underlying reasons for the behavioral change of the cement blends. Moreover, the following conclusions were drawn within the scope of this experimental program:

- Although CSAC-PC blends showed expansive behavior during curing, they experienced higher shrinkage after drying relative to PC.
- Blending CSAC with PC increases alkali-silica reactivity of mortar relative to PC.
- CSAC addition to PC increased the 1-Day compressive strength of concrete at all replacement ratios, however, later-age strength was negatively affected by blending, with only 40% CSAC having a higher 28-Day compressive strength than PC.
- Replacing at least 40% of PC with CSAC resulted in a decrease of concrete's electrical conductivity.

- Blending CSAC with PC did not yield a notable trend in permeable porosity of concrete.

## References

- [1] Hendriks, C.A. et al, Emission reduction of greenhouse gases from the cement industry, Proceedings of the 4th International Conference on Greenhouse Gas Control Technologies, Interlaken, Austria, IEA GHG R&D Programme, UK, (1998)
- [2] Damtoft, J.S., Lukasik, J., Herfort, D., Sorrentino, D., Gartner, E.M., Sustainable development and climate change initiatives, *Cem Concr Res* 38 (2008), 115-127
- [3] Tokyay, M., *Cement and Concrete Mineral Admixtures*, CRC Press, Boca Raton, (2000)
- [4] Odler, I., *Special Inorganic Cements*, first ed., Taylor and Francis Group, New York, (2000)
- [5] Chen, I.A., Juenger M.C.G., Incorporation of coal combustion residuals into calcium sulfoaluminate-belite cement clinkers, *Cem Concr Compos* 34 (2012), 893–902
- [6] Hanein, T., Galvez-Martos, J.L., Bannerman, M.N., Carbon footprint of calcium sulfoaluminate clinker production, *J Clean Prod* 172 (2018), 2278-2287
- [7] Trauchessec, R., Mechling, J.-M., Lecomte, A., Roux, A., Le Rolland, B., Hydration of ordinary portland cement and calcium sulfoaluminate cement blends, *Cem Concr Compos* 56 (2015), 106-114
- [8] Gastaldi, D. et al, Hydraulic behaviour of calcium sulfoaluminate cement alone and in mixture with Portland cement, Proc. 13th Int. Congr. Chem. Cem., Spain (2011)
- [9] Chaunsali, P., Mondal, P., Influence of calcium sulfoaluminate (CSA) cement content on expansion and hydration behavior of various ordinary portland cement- CSA blends, *J Am Ceram Soc* 98 (2015), 2617-2624
- [10] ASTM C1260, Standard Test Method for Potential Alkali Reactivity of Aggregates (Mortar-Bar Method), American Society for Testing and Materials, USA (2014)
- [11] ASTM C39, Standard Test Method for Compressive Strength of Cylindrical Concrete Specimens, American Society for Testing and Materials, USA (2017)
- [12] ASTM C1202, Standard Test Method for Electrical Indication of Concrete's Ability to Resist Chloride Ion Penetration, American Society for Testing and Materials, USA (2017)
- [13] ASTM C642, Standard Test Method for Density, Absorption, and Voids in Hardened Concrete, American Society for Testing and Materials, USA (2013)

## EARLY-AGE CRACKING TENDENCY OF ALKALI-ACTIVATED SLAG BINDERS COMPARED TO ORDINARY PORTLAND CEMENT

Farah Rifai <sup>(1,2)</sup>, Aveline Darquennes <sup>(3)</sup>, Benoist Muzeau <sup>(1)</sup>, Lavinia Stefan <sup>(4)</sup>, Farid Benboudjema <sup>(2)</sup>

(1) SECR, CEA, Université Paris-Saclay, Gif-sur-Yvette, France

(2) LMT Cachan – ENS Cachan – Paris-Saclay University, Cachan, France

(3) INSA Rennes, 20 Avenue des Buttes de Coesmes, Rennes

(4) Orano, NWM, Technical Department, Paris La Défense, France

### Abstract

Alkali-activated binders are increasingly used in civil engineering for different structural applications. Their thermo-chemo-mechanical behaviour (activation process, hydration reactions and mechanical properties' evolution) is investigated in the literature. However, few studies addressing their cracking tendency can be found. This paper focuses on the cracking risks induced by thermal and delayed strains' restriction, at materials' early age. First, the results of an experimental campaign comparing the early-age behaviour of an alkali-activated slag mortar to that of an OPC based mortar are discussed. Second, a simplified approach allowing comparing the cracking tendency of both materials is proposed. The alkali-activated mortar undergoes autogenous shrinkage strains higher than OPC mortar and showing an increase even at long term. However, its basic creep strains are more important than OPC mortar, tested in the same conditions. This implies a higher capacity of stress relaxation for the alkali-activated slag mortar. Regarding the evolution of mechanical properties, Young modulus and tensile strengths of the alkali-activated mortar are lower of those of OPC based mortar at all ages. A simplified cracking index comparison applied at this stage of study shows comparable cracking risks of both materials at 7 days, higher risks for alkali-activated slag mortar at 28 days.

### 1. Introduction

Ground granulated blast furnace slag (GGBFS) is a by-product of steel manufacturing, used as an alkali-activated hydraulic binder. The substitution of Ordinary Portland Cement (OPC)

binders by this type of material represents essentially an ecological advantage due to the reduction in CO<sub>2</sub> emissions. Additionally, these materials constitute relevant alternative of OPC binders in some specific industrial applications [1]. The advancement of Hydration reactions and the evolution of micro-structural properties of alkali-activated slag materials have been extensively studied in the literature. A large dependency both on the chemical and physical properties of the activated GGBFS, and the type and concentration of the alkaline activator used can be observed [2], [3]. Additionally, high autogenous shrinkage was demonstrated comparing to OPC [4], [5]. Nevertheless, few studies have addressed the creep behaviour of this type of binders [6]. Thus cracking tendency, related to the eventual restriction of the volumetric changes of the hydraulic binders (especially at early-ages when these changes are the most important), needs to be investigated. This is essential in order to study the durability of any structural application.

## 2. Experimental campaign

The experimental comparison presented here covers hydration heat release, delayed strains' evolution and mechanical properties' (mechanical strengths and Young's modulus) evolution of the mortars. The described experiments and measurements are conducted on samples kept in autogenous conditions, in a controlled room at 23±1°C.

The hydration heat determined in the same conditions allows comparing cracking tendency related to self-restriction of thermal strains in massive structures. A higher temperature gradient between the core and the surface leads to higher cracking risks. Autogenous shrinkage strains are considered as driving factor for cracking in restrained conditions, whereas basic creep is related to stress relaxation and thus decreasing cracking risks). Finally, the mechanical properties allow to evaluate the forces generated in the binders in restrained conditions and then to determine the subsequent cracking risks.

### 2.1 Materials

The tested hydraulic binders are prepared with the same water to binder (w/b) and sand to binder (s/b) ratios of 0.5 and 2 respectively. The alkali-activated mortar consists of a ground granulated blast furnace slag (GGBFS) – LA – activated with NaOH solution (2.5 M). 0.3% of setting retarder by mass of slag are added. Ordinary Portland Cement (OPC) mortar – SR0 – consists of a sulphates free formulation (CEM I 52.5 N-SR0 CE PM-CP2 NF). The choice of the latter OPC-based mortar is based on the relatively low hydration heat. Siliceous fine aggregate sand (0.1/1.2) is used.

### 2.1 Early-age hydration heat release

An isothermal micro-calorimetric test is performed using a “Tam Air Isothermal Calorimeter” with a precision of 20 μW at 22°C. The reference samples used for heat measurements consist of sand and distilled water. Mix proportions are calculated to have the same heat capacity of the binders.

The results obtained for both binders are shown in Fig.1 and Fig.2. The alkali-activated slag mortar presents shorter induction period implying faster formation of hydration products with respect to OPC-based mortar. This affects the advancement of hydration reactions, as the larger amount of hydration products formed can slow down water diffusion and therefore the

hydration process of anhydrous grains. This explains the earlier settlement of reactions heat flux of alkali-activated slag mortars.

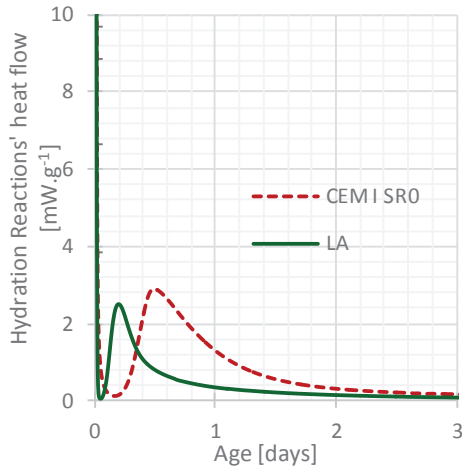


Figure 1: Comparison of hydration reactions' heat flow of studied mortars

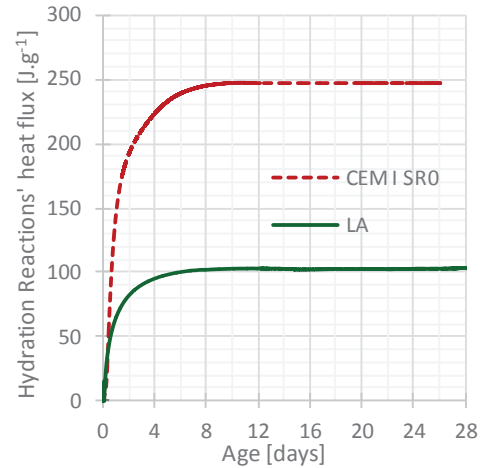


Figure 2: Comparison of hydration reactions' heat flux of studied mortars

Concerning the amount of heat released during the hydration process, the alkali-activated slag mortar show an important advantage with respect to OPC-based mortar. The total amount of heat measured at 28 days is around 100 and 250  $J.g^{-1}$  respectively. The lower amount of heat implies lower temperature gradient in massive structures and thus lower cracking tendency due to thermal self-restriction.

## 2.2 Time evolution of mechanical properties

Three-point flexural test are performed according to NF-EN-196-1 (2006), on three different 4x4x16 cm specimens, in order to compare the binders' tensile strength at 3, 7 and 28 days. Additionally, compression tests are conducted according to NF-EN-1015-11 (2000), on three different 11x22 cm cylindrical samples, at 3, 7 and 28 days. Three extensometers fixed to the samples allow the measurement of compressive strains in the elastic phase and the subsequent calculation of the binders' static Young modulus. Results are illustrated in Fig. 3 and Fig.4.

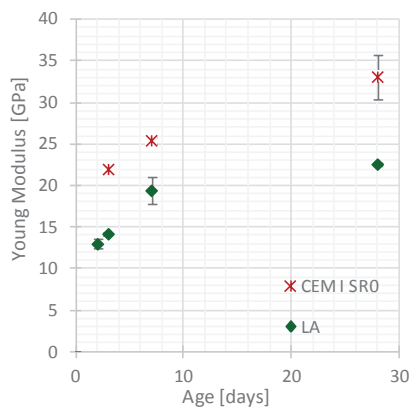


Figure 3: Comparison of the evolution of Young modulus of studied mortars

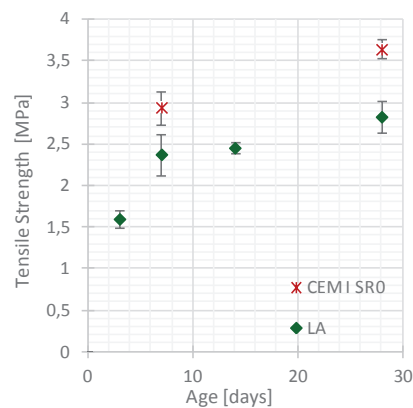


Figure 4: Comparison of the evolution of tensile strengths of studied mortars



OPC-based mortar shows higher stiffness and strength than alkali-activated slag mortar at all tested ages. Even though the lower stiffness represents an advantage with respect to the value of restriction-generated stress, the lower tensile strength of alkali-activated slag mortar can indicate higher cracking tendency of the material.

### 2.3 Time evolution of delayed strains

The autogenous shrinkage strains of tested mortars are continuously measured on three different 4x4x16 cm specimens, using linear variable differential transformer (LVDT) sensors. The basic creep is determined under compressive stress. 7x7x28 cm specimens kept in autogenous conditions. Two samples are loaded, at the age of 7 and 28 days, at 30% of their compressive strength at the respective ages, during 30 days. Both delayed strain measurements are performed in the controlled room at  $23\pm 1^\circ\text{C}$ .

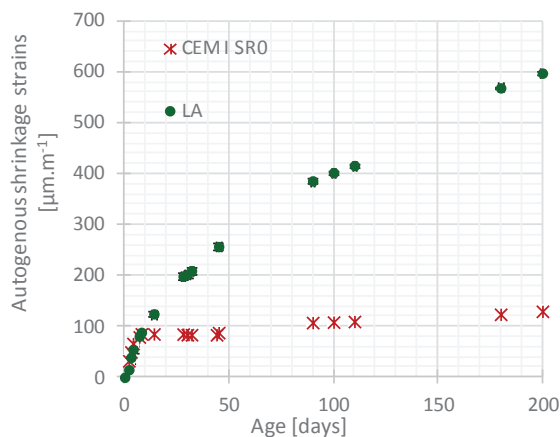


Figure 5: Comparison of autogenous shrinkage strains' measurements of studied mortars

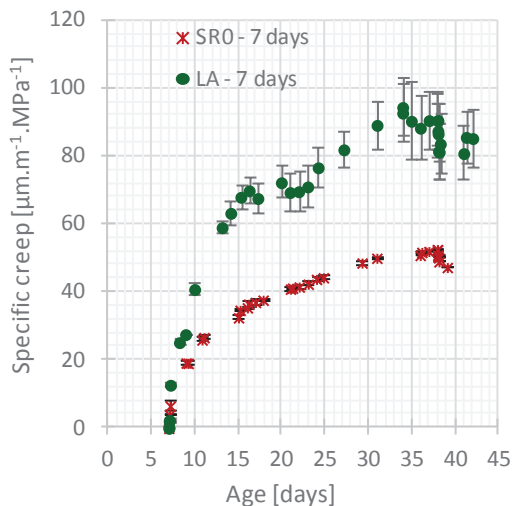


Figure 6: Comparison of creep compliance of studied mortars at 7 days (value of creep strains by MPa compressive force)

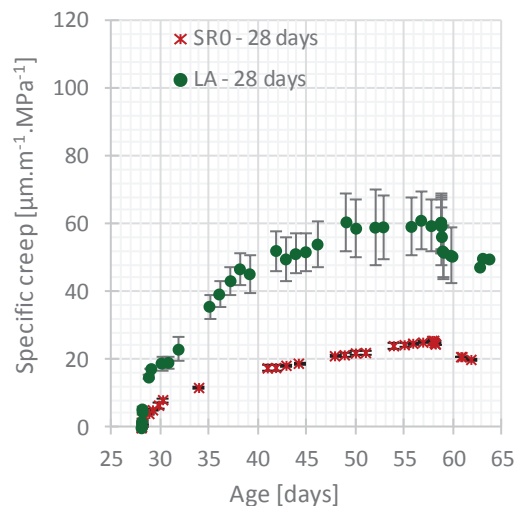


Figure 7: Comparison of creep compliance of studied mortars at 28 days (value of creep strains by MPa compressive force)

The mean values of measurements of autogenous shrinkage are illustrated in Fig.5. Similar behaviour can be detected at early-age for both mortars (up to 14 days of hydration).

Afterward, OPC-based mortar show stabilization in the shrinkage strains while alkali-activated slag mortar continues to shrink significantly. This was also observed in the literature in the case of drying shrinkage and is still being investigated [5], [7].

Specific creep is shown in Fig.6 and Fig.7 instead of basic creep strains, for the specimens loaded at 7 and 28 days respectively. It consists of basic creep strains (by deducing autogenous shrinkage and elastic strains from total measured strains, then dividing by the applied compressive load). The results show significantly higher creep capacity for the alkali-activated slag mortar, at both ages. This could be explained, by the higher amount of C-S-H forming the alkali-activated slag systems especially that the long term part of basic creep is usually explained by the mechanical sliding of C-S-H [8]. The decrease in creep capacity with the advancement of hydration (with time) is observed for the alkali-activated slag as well as for OPC-based mortar.

### 3. Evaluation of early-age cracking tendency (CI)

Based on the experimental results discussed in the previous section, a cracking index approach is applied to compare the cracking tendency of the binders. It considers a fully restrained configuration with constant materials' properties [9]. The thermal strains are not taken into account.

The restriction is expressed in terms of elastic  $\epsilon^e(t)$  [ $\mu\text{m.m}^{-1}$ ], autogenous shrinkage  $\epsilon^{\text{sh}}(t)$  [ $\mu\text{m.m}^{-1}$ ] and basic creep  $\epsilon^{\text{bc}}(t)$  [ $\mu\text{m.m}^{-1}$ ] strains as in Eq. (1).

$$\epsilon(t) = \epsilon^e(t) + \epsilon^{\text{sh}}(t) + \epsilon^{\text{bc}}(t) = 0 \quad (1)$$

Where  $\epsilon(t)$  [ $\mu\text{m.m}^{-1}$ ], is the total strain tensor at the age  $t$  [days]. By introducing the creep coefficient  $\phi$  defined as in Eq. (2), in 1D:

$$\phi(t) = \frac{\epsilon^{\text{bc}}(t)}{\epsilon^e(t)} \quad (2)$$

The relationship between elastic and shrinkage strains reads Eq. (3):

$$\epsilon^e(t) = \frac{-\epsilon^{\text{sh}}(t)}{1 + \phi(t)} \quad (3)$$

Applying Hooke Law in 1D, Eq. (4) can be obtained:

$$\sigma(t) = -1e^{-3} \times E(t) \times \epsilon^e(t) = \frac{E(t) \times \epsilon^{\text{sh}}(t)}{1 + \phi(t)} \quad (4)$$

Where  $\sigma(t)$  [MPa] is the generated stress tensor and  $E(t)$  [GPa] the material's Young modulus. The cracking index  $CI(t)$  comparing the generated tensile stress to the tensile strength  $f_t$  [MPa] of the material can then be expressed as in Eq. (5):

$$CI(t) = \frac{\sigma(t)}{f_t} = \frac{E(t) \times \epsilon^{\text{sh}}(t)}{f_t \times (1 + \phi(t))} \quad (5)$$

The results of calculations are reported in Tab.1, where the creep coefficient and the cracking index are exposed (creep coefficient is calculated according to creep measurements at 7 days). They show lower cracking tendency of alkali-activated slag mortar at early-age (7days), higher tendency at later ages (28 days). The high autogenous shrinkage of alkali-activated material is responsible of these observations.

Table 1: Comparison of cracking index of studied mortars at 7 and 28 days

	Age [days]	$\phi(t)$ (-)	$CI(t)$ (MPa)
LA r	7	1.02	0.33
	28	1.45	0.65
CEM I SR0	7	0.57	0.44
	28	0.81	0.43

#### 4. Conclusions and perspectives

The study presented here discussed essentially an experimental comparison of early-age behaviour between an alkali-activated slag mortar and an OPC-based mortar, including the compressive basic creep strains. The alkali-activated material showed lower hydration heat, fast evolution of the system at early ages and quick settlement of mechanical properties. However, the autogenous shrinkage strains continue to grow even at the long term. The creep capacity of OPC-based mortar is shown to be lower than alkali-activated slag mortar. At early-ages, the latter binder seems to be subjected to lower cracking the risks. At later ages, the high autogenous shrinkage strains increase these risks despite the material's great creep capacity.

#### Acknowledgments

The authors would like to thank Miss Ginger El Tabbal for contributing in the experimental campaign during her Master Research final project.

#### References

- [1] Bai, Y., Collier, N., Milestone, N. B., and Yang, C. H., The potential for using slags activated with near neutral salts as immobilisation matrices for nuclear wastes containing reactive metals, *J. Nuclear Materials* 413 (2011), 647-654.
- [2] Wang, S., Scrivener, K., and Pratt, P., Factors affecting the strength of alkali-activated slag, *Cem Concr Res* 24 (1994), 1033-1043.
- [3] Fernández-jiménez, A., Palomo, J. G., Puertas, F., Alkali-activated slag mortars Mechanical strength behaviour, *Cem Concr Res* 29 (1999), 1313-1321.
- [4] Cartwright, C., Rajabipour, F., Radli, A., Shrinkage Characteristics of Alkali-Activated Slag Cements, *J. Mat. Civ. Eng.* 27 (2014), 1-7.
- [5] Melo Neto, A. A., Cincotto, M. A., Repette, W., Drying and autogenous shrinkage of pastes and mortars with activated slag cement, *Cem Concr Res* 38 (2008), 565-574.
- [6] Collins, F.G., Sanjayan, J.G., Workability and mechanical properties of alkali activated slag concrete, *Cem Concr Res* 29 (1999), 455-458.
- [7] Ye, H., Cartwright, C., Rajabipour, F., Radlińska, A., Understanding the drying shrinkage performance of alkali-activated slag mortars, *Cem Concr Comp.* 76 (2017), 13-24.
- [8] Ulm, F., Acker, P., Le point sur le fluage et la recouvrance des bétons, *Bulletin des Laboratoires des Ponts et Chaussées* (1998), 73-82.
- [9] Darquennes, A.; Benboudjema F., Behavior of activated ternary binders under autogenous condition, 2nd International Workshop on Durability and Sustainability of Concrete Structures, 6-7 June 2018, Izmailovo Congress Centre.

## **EFFECT OF BAUXITE CONTENT AND FINENESS ON COMPRESSIVE STRENGTH OF VOLCANIC ASH-BASED GEOPOLYMER MORTARS**

**Léonel N. Tchadjé<sup>(1)</sup>, Stephen O. Ekolu<sup>(1)</sup>**

(1) Department of Civil Engineering Science, University of Johannesburg, South Africa

### **Abstract**

The particle size, mineralogical and chemical composition of starting materials are important factors affecting their geopolymeric reactivity. This study investigated the effect of bauxite fineness and content on the early compressive strength of volcanic ash-based geopolymers. Geopolymer mortars were prepared using volcanic ash with or without 5 to 20 wt% bauxite as a partial replacement. The bauxite used in the study was of three fineness levels comprising 0, 5 and 29 % retained on 45 µm sieve. Bauxite provided the source of alumina while sodium silicate solution was used as the alkaline activator. The results revealed that incorporation of bauxite decreased the overall SiO<sub>2</sub>/Al<sub>2</sub>O<sub>3</sub> molar ratio in the geopolymer products. The 7-day compressive strength of 50 mm cube mortars varied between 30.3 and 44.5 MPa. A strength increase of up to 46.9 % was attained with 15 wt% bauxite content of fineness level 0 to 5 % retained on 45 µm sieve.

### **1. Introduction**

Portland cement is a hydraulic binder mostly used in civil engineering construction. The production of this binder requires much energy and leads to significant release of CO<sub>2</sub> to the atmosphere. The production of one ton of Portland cement releases about 0.85 tons of CO<sub>2</sub>. Up to 8% of the world's CO<sub>2</sub> emission is attributed to the cement industry [1]. To reduce the environmental footprint linked to this industry, the development of alternative sustainable, low-CO<sub>2</sub> construction materials is essential. Geopolymers are the foremost alternative binders currently being developed with a view of promoting environmental benefits in the construction industry [2]. They offer attractive possibilities for commercial applications due to their impressive properties such as fast hardening, high early compressive strengths, high acid resistance, long-term durability and low cost [3]. Also, the optimal production of these

materials requires less energy, reducing the CO<sub>2</sub> resulting from Portland cement production by 80% [2]. According to previous works, the properties of geopolymers are affected by several factors such as the nature of starting materials including their mineralogical and chemical composition, the amorphous content, particle size, curing temperature, composition of alkaline solution and the liquid to solid ratio [4, 5].

In recent years, there has been a growing trend to use raw materials of volcanic origin in geopolymer synthesis, due to their abundant availability in some regions. Volcanic scoria are igneous rock deposits formed during volcanic eruptions and are widely available in various regions such as in the Rift valley region of East Africa, Cameroon in West Africa, etc. [6–8]. These materials are generally of low cost and of low environmental impact. However, geopolymers obtained from volcanic scoria exhibit relatively long setting times, high shrinkage, efflorescence and low compressive strength [9]. This characteristically low reactivity of these materials is related to their low amount of alumina (Al<sub>2</sub>O<sub>3</sub>) and low amorphous phase content [10]. It is well-known that availability of Al<sub>2</sub>O<sub>3</sub> significantly affects the properties of geopolymers. Greater availability of Al<sub>2</sub>O<sub>3</sub> during the reaction influences the gel homogeneity, contributing to the formation of a more homogeneous gel and better strength development [11]. Previous work has shown that bauxite can be used as a source of Al<sub>2</sub>O<sub>3</sub> to modify the SiO<sub>2</sub>/Al<sub>2</sub>O<sub>3</sub> ratio in the raw material, during geopolymer synthesis [12, 13]. However, bauxite in its natural state tends to exhibit low geopolymeric reactivity. For instance, Djobo et al. [12] investigated the effects of partial replacement of volcanic ash by 10 to 30 wt% bauxite. They found that bauxite addition of up to 10 wt% reduced the initial setting time, lowered the efflorescence and led to a 5 % increase in the 28-day compressive strength of paste specimens. Further increase of bauxite replacement beyond 10 % was found to be detrimental to compressive strength. As such, enhancing the reactivity of bauxite before using it as a source of Al<sub>2</sub>O<sub>3</sub> in geopolymerization should be of interest. This purpose can be achieved by employing various methods such as mechanical grinding, thermal treatment, physical separation, and chemical activation [4], of which mechanical activation by grinding is the most commonly employed technique [14].

The primary objective of this study was to determine the effect of bauxite fineness and content on the early compressive strength of volcanic ash-based geopolymers. Different levels of bauxite fineness were prepared by grinding the material in a ball mill.

## 2. Experimental details

### 2.1 Materials

Volcanic ash (VA) was used as the aluminosilicate raw material while bauxite (BX) was used to increase the availability of Al<sub>2</sub>O<sub>3</sub> during geopolymer synthesis. BX and VA were oven-dried at 105°C for 24 h then crushed and ground. BX was ground in a ball mill to three fineness levels of 0, 5 and 29 % retained on 45 µm (No. 325) sieve. The same procedure was followed for VA. The chemical compositions of these raw materials are presented in Table 1. Silica sand of fineness modulus 2.5 was used as fine aggregate for preparing mortar samples. The alkaline activator solution used was a mixture of 12 M sodium hydroxide and sodium silicate solutions, prepared to achieve a silicate modulus (SiO<sub>2</sub>/Na<sub>2</sub>O) of 1.4. After mixing,

the activator solution was kept for at least 24 h to allow equilibration and the depolymerization of sodium silicate species. The sodium hydroxide solution was obtained by dissolving technical grade sodium hydroxide pellets in distilled water. The sodium silicate used was a commercial product obtained from PQ Silicas South Africa (pty) Ltd. Its physico-chemical characteristics were 29.05% SiO<sub>2</sub>, 8.81% Na<sub>2</sub>O, 62.14% H<sub>2</sub>O, pH of 11.73, viscosity of 378 cP, specific gravity of 1.40 at 20°C, and SiO<sub>2</sub>/Na<sub>2</sub>O weight ratio of 3.3.

Table 1: Chemical composition of raw materials: VA-volcanic ash, BX-bauxite

Oxides (wt%)	SiO <sub>2</sub>	Al <sub>2</sub> O <sub>3</sub>	Fe <sub>2</sub> O <sub>3</sub>	CaO	TiO <sub>2</sub>	MgO	K <sub>2</sub> O	Na <sub>2</sub> O	P <sub>2</sub> O <sub>5</sub>	LOI
VA	45.94	15.58	13.68	9.00	2.86	7.10	1.43	3.75	0.60	-0.52
BX	2.31	39.56	28.09	0.07	6.68	0.23	-	-	0.23	21.60

## 2.2 Preparation of geopolymer mortars

To prepare the geopolymer mortars, bauxite was initially dry-mixed with VA for 3 mins using a laboratory mortar mixer, to homogenize the mixture. The alkaline activator solution was then gradually added and mixing continued for another 2 mins. Thereafter, silica sand was added and further mixing done for 3 mins. A liquid to powder ratio of 0.6 and sand to powder ratio of 2.25 were used in preparing all the mortar mixtures. Details of the mixtures are presented in Table 2. After mixing, the mortar slurry was rapidly poured into 50 × 50 × 50 mm moulds and tamped by hand in accordance with ASTM C 109. To prevent water evaporation, the freshly cast cubes in their moulds were sealed into polyethylene bags and cured at 80 °C for 7 days in an oven. Afterwards, the specimens were demoulded, cooled to room temperature and tested for compressive strength.

Table 2: Mix proportions of geopolymer mortars

Mix -ID	BX fineness (retained on 45 µm sieve)	BX(wt%)	BX(g)	VA(g)	SiO <sub>2</sub> /Al <sub>2</sub> O <sub>3</sub>	Liquid/Powder	Silica Sand (g)
Mix 1	0	0	0	310.0	5.0	0.6	698
		5	15.5	294.5	4.4	0.6	698
		10	31.0	279.0	3.9	0.6	698
		15	46.5	263.5	3.5	0.6	698
		20	62.0	248.0	3.1	0.6	698
Mix 2	5	0	0	310.0	5.0	0.6	698
		5	15.5	294.5	4.4	0.6	698
		10	31.0	279.0	3.9	0.6	698
		15	46.5	263.5	3.5	0.6	698
		20	62.0	248.0	3.1	0.6	698
Mix 3	29	0	0	310.0	5.0	0.6	698
		5	15.5	294.5	4.4	0.6	698
		10	31.0	279.0	3.9	0.6	698
		15	46.5	263.5	3.5	0.6	698
		20	62.0	248.0	3.1	0.6	698

### 3. Results and discussion

The 7-day compressive strength results of geopolymer mortars containing varied bauxite content with different levels of fineness, are shown in Figure 1. Also included in Figure 1 are error bars from data of replicate tests. It is evident that there was increase in compressive strength for all fineness levels, at 5 wt% bauxite content. At higher bauxite contents exceeding 5 wt%, the finer bauxite gave the highest compressive strength gain. The fineness levels of 0 and 5 % retained on 45  $\mu\text{m}$  sieve, showed compressive strength increase for all bauxite contents of up to 20 wt%. In the converse, the low fineness of 29 % retained on 45  $\mu\text{m}$ , had a negative effect leading to strength reduction at high bauxite contents exceeding 5 wt%. The highest compressive strength of 44.5 MPa was obtained at a bauxite fineness level of 0 % retained on 45  $\mu\text{m}$ , with 15 wt% bauxite content. This value corresponds to 46.9 % strength increase over that of the control.

The incorporation of bauxite to VA changes the bulk chemical composition of the geopolymer products. The overall  $\text{SiO}_2/\text{Al}_2\text{O}_3$  molar ratio varied from 5.0 in the control sample to 3.1 in the mixtures containing 20 wt% bauxite (Table 2). Furthermore, it is well known that the  $\text{SiO}_2/\text{Al}_2\text{O}_3$  molar ratio has a major impact on strength development in geopolymers. Also, the particle size distribution of raw materials affects their geopolymeric reactivity. So, the observed increase in compressive strength due to incorporation of bauxite (Figure 1), can be attributed to reduction of the  $\text{SiO}_2/\text{Al}_2\text{O}_3$  molar ratio in the system, thereby allowing greater dissolution of bauxite particles with increase in its fineness. These two factors induced greater geopolymerization and formation of a more compact microstructure. The observed results in the present study agree with those obtained by Tchakoute et al.[15] who claimed that addition of  $\text{Al}_2\text{O}_3$  to VA promoted the dissolution of aluminosilicate species, thereby forming higher amounts of geopolymeric gel, in turn leading to increase in compressive strength of the geopolymers. The relatively lower compressive strength observed at the fineness of 29 % retained on 45  $\mu\text{m}$ , is likely due to an increase in the proportion of less reactive bauxite particles in the system. It may be noted that the presence of excessively high amounts of  $\text{Al}_2\text{O}_3$  species at early stages of the geopolymerization reaction, may hinder the dissolution of silica particles from VA, while favouring the participation of the  $\text{Al}_2\text{O}_3$  in formation of the geopolymer network. This process leads to low strength development [16].

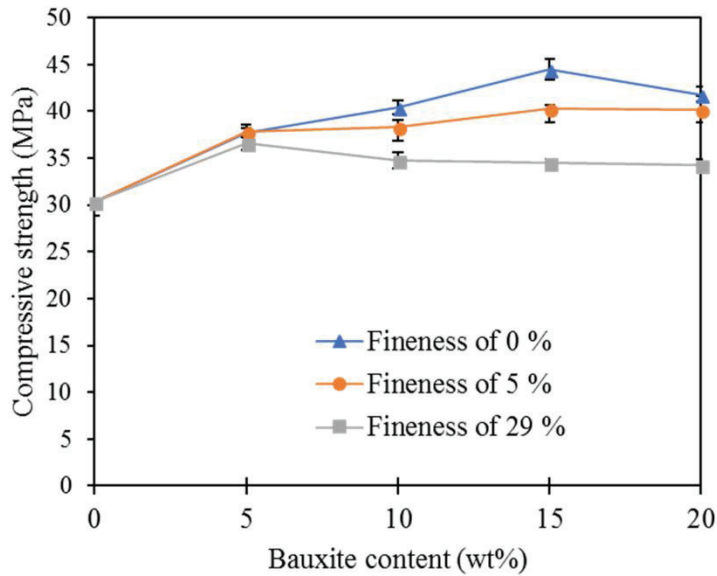


Figure 1: Compressive strengths of volcanic ash-based geopolymer mortars of various bauxite contents and fineness levels.

#### 4. Conclusion

In this work, the effects of bauxite content and fineness on compressive strength of volcanic ash-based geopolymer mortars were studied. It has been observed that incorporation of bauxite to volcanic ash, leads to a significant enhancement in geopolymeric reactivity, depending on the level of bauxite fineness. As the fineness level of bauxite increased, greater compressive strength gain was observed up to a certain amount of bauxite content. The highest improvement in strength development was obtained with 10 to 15 wt% bauxite content at fineness levels of 0 to 5 % retained on 45  $\mu\text{m}$  sieve. The combined effect of  $\text{SiO}_2/\text{Al}_2\text{O}_3$  molar ratio and particle size influenced the observed strength development. Further studies involving characterization of the geopolymer samples using X-ray diffraction (XRD) and Fourier Transform Infrared Spectroscopy (FTIR) are being undertaken so as to explain the microstructural changes that occurred during geopolymerisation.

#### Acknowledgements

This paper is part of the PhD study of Leonel Noubissie Tchadjie, conducted under the NRF-TWAS Doctoral Scholarship grant no. 99993. The candidate thanks the National Research Foundation (NRF) of South Africa for offering him this grant and study opportunity. The authors are grateful to Professor Paul Tematio of the Department of Earth Sciences of University of Dschang for providing bauxite samples.



## References

- [1] Mclellan, B. C., Williams, R. P., Lay, J., Van Riessen, A., and Corder, G. D., Costs and carbon emissions for geopolymer pastes in comparison to ordinary portland cement, *J. Clean. Prod.* 19 (2011), 1080–1090.
- [2] Davidovits, J., *Geopolymer Chemistry and Applications* 3<sup>rd</sup> edition, France (2011).
- [3] Provis, J. L., and Bernal, S. A., Geopolymers and related alkali-activated materials, *Annu. Rev. Mater. Res.* 44 (2014), 299–327.
- [4] Tchadjie, L. N., and Ekolu, S. O., Enhancing the reactivity of aluminosilicate materials toward geopolymer synthesis, *J. Mater. Sci.* 53 (2018), 4709–4733.
- [5] Naghizadeh, A., and Ekolu, S. O., Investigation of mixture factors influencing alkali-silica reaction in fly ash-based geopolymer mortars, *International Conference on Advances in Construction Materials and Systems*, India (2017), 395–400.
- [6] Ekolu, S. O., Thomas, M. D. A., and Hooton, R. D., Studies on Ugandan volcanic ash and tuff, *Proceedings of the First International Conference on Advances in Engineering and Technology*, Uganda (2006), 75–83.
- [7] Kamseu, E., Leonelli, C., Perera, D. S., Melo, U. C., and Lemougna, P. N., Investigation of volcanic ash based geopolymers as potential building materials, *InterCeram Int. Ceram. Rev.* 58 (2009), 136–140.
- [8] Naghizadeh, A., and Ekolu, S. O., Pozzolanic materials and waste products for formulation of geopolymer cements in developing countries : a Review, *Concr. Bet.* 151 (2017), 22–31.
- [9] Tchakoute, H. K., Elimbi, A., Yanne, E., and Djangang, C. N., Utilization of volcanic ashes for the production of geopolymers cured at ambient temperature, *Cem. Concr. Compos.* 38 (2013), 75–81.
- [10] Lemougna, P. N., Melo, U. F. C., Delplancke, M., and Rahier, H., Influence of the chemical and mineralogical composition on the reactivity of volcanic ashes during alkali activation, *Ceram. Int.* 40 (2014), 811–820.
- [11] Weng, L., Sagoe-Crentsil, K., Brown, T., and Song, S., Effects of aluminates on the formation of geopolymers, *Mater. Sci. Eng. B* 117 (2005), 163–168.
- [12] Djobo, J. N. Y., Elimbi, A., Manga, J. D., and Li, I. B. D., Partial replacement of volcanic ash by bauxite and calcined oyster shell in the synthesis of volcanic ash-based geopolymers, *Constr. Build. Mater.* 113 (2016), 673–681.
- [13] Martin, A., Pastor, J. Y., Palomo, A., and Fernández, A., Mechanical behaviour at high temperature of alkali-activated aluminosilicates (geopolymers ), *Constr. Build. Mater.* 93 (2015), 1188–1196.
- [14] Wei, B., Zhang, Y., and Bao, S., Preparation of geopolymers from vanadium tailings by mechanical activation, *Constr. Build. Mater.* 145 (2017), 236–242.
- [15] Tchakoute, H. K., Elimbi, A., Mbey, J. A., Sabouang, C. J. N., and Njopwouo, D., The effect of adding alumina-oxide to metakaolin and volcanic ash on geopolymer products : A comparative study, *Constr. Build. Mater.* 35 (2012), 960–969.
- [16] Hajimohammadi, A., Provis, J. L., and Van Deventer, J. S. J., Effect of alumina release rate on the mechanism of geopolymer gel formation, *Chem. Mater.* 22 (2010), 5199–5208.

## **EFFECT OF COMPACTING PRESSURE AND CARBONATION DURATION ON CARBON DIOXIDE ACTIVATED BINDERS**

**Pedro Humbert <sup>(1)</sup>, João Castro Gomes <sup>(1)</sup>**

(1) University of Beira Interior, Covilhã, Portugal

### **Abstract**

Alternative binders and hardening reactions are methods to reduce greenhouse gases emissions, energy and water consumption. Waste-based carbon dioxide activated binder represents a potential solution as an environmental friendly construction material. To achieve efficient mechanical properties and optimal mixture design, a preliminary comparison about the effect of compacting pressure and carbonation duration on carbon dioxide activated binders was studied. An electric arc furnace slag from the national steel industry in Portugal and a Portland cement CP-I were used as binders. This work shows the compressive strength development of a slag-based and Portland cement-based binders under different compacting pressures and carbonation durations. Compressive strength present stronger development due higher compacting pressures and longer carbonation duration however, its development ratio was decreasing after two hours under carbon dioxide atmosphere. The carbon dioxide activation has highly dependence on both studied factors, compacting pressure and carbonation duration, which enhance the compressive strength development.

### **1. Introduction**

Europe has adopted the Circular Economy Package which aims to close the loop of product lifecycles by improving recycling and re-use efficiency supporting the sustainable development with advantages for the environment and the economy [1]. The steel industry has great role in economy but, produce a huge amount of waste, the main one is the steel slag which has an annual production worldwide around 130 million tons [2]. Construction industry already reuse the steel slag as aggregate on few construction purposes such as concrete, asphalt, road bases and surfaces [3]. However, the amount of steel slag disposed in landfills is not reducing overtime.

Solutions for reduce and eliminate wastes' landfills have been investigated worldwide [4]. Alternative binders such as geopolymers, alkali-activated and carbon dioxide activated, follow sustainable development and Circular Economy guidelines as these binders use mainly wastes as raw material, less water and energy on its production, and sometimes store carbon dioxide in its matrix [5,6]. Carbon dioxide activated binder is a construction material made by calcium and magnesium rich wastes mixed with water (10%) and activated under carbon dioxide atmosphere, besides of its environmental qualities, its mechanical properties evidence the Portland cement replacement potential for structural applications [7].

Carbon dioxide activated binder have been investigated by some researchers which studied its synthesis and properties [8], mechanical performance [9], pore structure [10] and flexural fracture [11] under specified conditions. This experimental program aims to improve the steel slag carbonation kinetics and efficiency by moulding the samples under different compacting pressures and carbonating the samples for different durations. The effect of the sample compactness on the compressive strength development and the compressive strength development rate will be analysed. Optimal condition was used with Portland cement for comparison purpose.

## 2. Experimental program

### 2.1 Materials and procedures

An electric arc furnace slag was received from the national steel industry at Maia and Aldeia de Paio Pires, Seixal, Portugal. A Portland cement CEM II/B-L 32.5 N was also used. The as-received slag was left to dry at 60°C for 24 hours in an oven then, crushed into a mal size using a crusher mill and finally, pulverised into powder using a ball mill. The slag powder was sieved through a sieve of 45µm and subjected to density and Blaine tests which showed a result of 3.7712 g/cm<sup>3</sup> and 529 m<sup>2</sup>/kg respectively. Portland cement was also subjected to density and Blaine tests which showed a result of 2.977 g/cm<sup>3</sup> and 382 m<sup>2</sup>/kg.

The sieved powder and the Portland cement were subjected to an energy dispersive spectroscopy (EDS) analysis to determine its chemical composition where evidenced that the steel slag is rich in calcium (CaO), iron (Fe<sub>2</sub>O<sub>3</sub>) and silica (SiO<sub>2</sub>) with some other minor oxides on its composition, the Portland cement is also rich in calcium (CaO) and silica (SiO<sub>2</sub>) with some other minor oxides. Density, Blaine number and chemical composition of both powders are shown in Tab. 1.

Table 1: Powders characterisation.

Material	Oxides						Density (g/cm <sup>3</sup> )	Blaine number (m <sup>2</sup> /kg)
	CaO	SiO <sub>2</sub>	Al <sub>2</sub> O <sub>3</sub>	MgO	SO <sub>3</sub>	Fe <sub>2</sub> O <sub>3</sub>		
Steel slag	30.21	14.18	12	5.58		29.51	3.771	529
OPC	62.2	12.31	3.08	1.27	4.33	2.42	2.977	382

Twenty-one steel slag cylindrical samples were moulded and tested under seven different conditions, three different compacting pressures and five different carbonation durations. Three Portland cement cylindrical samples were moulded and tested under the optimal condition. The samples were compacted with 10, 20 and 30 MPa of compacting pressure into

a mould of 20mm of diameter and 40mm of height with a water to solid ratio of 0.1. The samples were subjected to carbonation curing right after casting with a concentration of 100% of CO<sub>2</sub> inside the chamber with 0.5 bar of partial pressure. The carbon dioxide used had 99.9% of purity and was injected to the chamber for 2, 4, 8, 12 and 24 hours being replenished as it was being consumed by the samples. The chamber was inside an oven at 40°C of temperature. After curing, the samples were taken from the chamber to dry inside an oven for 20 hours at 40°C of temperature and then subjected to compressive strength test in a rate of 0.05 kN/second. Table 2 shows the different used carbonation conditions with their respective labels.

Table 2: Carbonation conditions.

Carbonation conditions	Identification and carbonation condition									
	ID	CC	ID	CC	ID	CC	ID	CC	ID	CC
Compacting pressure (MPa)	c1	10	c2	20	c3	30				
Duration (hours)	t1	2	t2	4	t3	8	t4	12	t5	24

EDS analysis was done to compare the carbon dioxide uptake between steel slag and Portland cement binders. Non-carbonated and carbonated powders from Portland cement and steel slag were analysed and had their atomic mass of carbon compared to measure the carbon dioxide uptake.

### 3. Results and discussion

Compressive strength results evidenced that compacting pressure and carbonation duration has strong influence on the carbon dioxide activated binder's compressive strength development. Compacting the sample with 30 MPa showed a compressive strength of 72.1 MPa, 58.1% higher than compacting with 10 MPa which achieved 45.6 MPa however, the compressive strength development between 20 to 30 MPa was only 1.98% higher showing that after 20 MPa of compacting pressure the gain in compressive strength is minimal. The compactness of the sample influences on the compressive strength development once the binder will have its porosity reduced as much pressure is applied during compaction however, after certain point is hard to reduce the porosity or there will be less water to diffuse the carbon dioxide through the binder.

Table 3: Compressive strength.

Carbonation parameters	Identification and compressive strength (MPa)									
	ID	CS	ID	CS	ID	CS	ID	CS	ID	CS
Compacting pressure	c1	45.6	c2	70.7	c3	72.1				
Duration	t1	26.7	t2	37.5	t3	55.8	t4	60.8	t5	72.1
Optimal conditions	os	72.1	opc	63.4						

The carbonation duration analysis showed that during the first two hours the compressive strength development rate was 13.35 MPa/hour reducing to 0.9 MPa/hour during the last

twelve hours. After eight hours of carbonation the carbon dioxide activated binder already achieved 55.8 MPa. Table 3 present all compressive strength results and the compressive strength development rate correlated with the carbonation duration.

The optimal condition was under 30MPa of compacting pressure and with 24 hours of carbonation. Under the same conditions the Portland cement showed 63.4MPa of compressive strength which was 12.07% lower than the steel slag compressive strength. This result evidence that the steel slag has higher reactivity under the carbon dioxide environment than the Portland cement.

The carbon dioxide uptake was calculated considering the atomic weights of the elements [12] and the carbon weight found by the EDS analysis on the Portland cement and steel slag powders before and after the carbonation curing. The carbonated samples were under the optimal conditions. The steel slag sample reached a carbon dioxide uptake of 6.89% while the Portland cement sample reached 6.34% which was 7.98% lower than the steel slag CO<sub>2</sub> uptake. Tab. 4 shows the carbon weight before and after carbonation and the carbon dioxide uptake of the carbonated samples.

Table 4: Carbon dioxide uptake.

Sample	Carbon weight (%)	CO <sub>2</sub> uptake (%)
Steel slag	3.1	
Portland cement	6.3	
Os	4.98	6.89
Opc	8.03	6.34

#### 4. Conclusions

This study has reported experimental results and analysis about the influence of compacting pressure and carbonation duration on cement-free steel slag carbon dioxide activated binders compressive strength development. The following conclusions can be drawn from this investigation:

- Compacting pressure up to 20 MPa has strong effect on compressive strength development of the carbon dioxide activated binders. Higher compacting pressure does not represent sensible compressive strength increase.
- The carbon dioxide activated binder continuously develops its compressive strength within time. However, the compressive strength development rate decrease overtime after eight hours the development is less than 1.5 MPa/hour.
- The steel slag CO<sub>2</sub> activated binder showed good potential to be used as Portland cement replacer for construction materials applications due its mechanical properties. Moreover, the binder has great role on the sustainable production, besides the industrial waste valorisation, this construction material stores steel slag and uptake up to 6.89% of carbon dioxide.
- Further investigation is necessary to develop proper applications and analyse the size effect of the carbonation on the inner part.

## References

- [1] European Commission, Press release - Closing the loop: Commission adopts ambitious new Circular Economy Package to boost competitiveness, create jobs and generate sustainable growth, *NewEurope* (2015), 13-15. <http://neurope.eu/wires/closing-the-loop-commission-adopts-ambitious-new-circular-economy-package-to-boost-competitiveness-create-jobs-and-generate-sustainable-growth/>.
- [2] van Zomeren, A. et al, Changes in mineralogical and leaching properties of converter steel slag resulting from accelerated carbonation at low CO<sub>2</sub> pressure, *Waste Manag.* 31 (2011), 2236–2244
- [3] Piatak, N.M. et al, Characteristics and environmental aspects of slag: A review, *Applied Geochemistry* 57 (2015), 236-266
- [4] Kajaste, R. and Hurme, M., Cement industry greenhouse gas emissions - Management options and abatement cost, *J. Clean. Prod.* 112 (2016), 4041-4052
- [5] Sedira, N. et al, A review on mineral waste for chemical-activated binders: mineralogical and chemical characteristics, *Min. Sci.* 24 (2017), 29-58
- [6] Zhang, D. et al, Review on carbonation curing of cement-based materials, *J. CO<sub>2</sub> Util.* 21 (2017), 119-131
- [7] Humbert, P.S. et al, Cement-Free Binder Activated by Carbon Dioxide: Potential and Challenges, 3o Congr. Luso Bras. Mater. Constr. Sustentaveis, Portugal (2018)
- [8] Das, S. et al, Synthesis and Properties of a Novel Structural Binder Utilizing the Chemistry of Iron Carbonation, *ACS Appl. Mater. Interfaces.* 6 (2014), 8295-8304
- [9] Mo L. et al, Mechanical performance and microstructure of the calcium carbonate binders produced by carbonating steel slag paste under CO<sub>2</sub> curing, *Cem. Concr. Res.* 88 (2016), 217-226
- [10] Das, S. et al, Pore- and micro-structural characterization of a novel structural binder based on iron carbonation, *Mater. Charact.* 98 (2014), 168-179
- [11] Das, S. et al, Flexural fracture response of a novel iron carbonate matrix - Glass fiber composite and its comparison to Portland cement-based composites, *Constr. Build. Mater.* 93 (2015), 360-370
- [12] Meija, J. et al, Atomic weights of the elements 2013 (IUPAC Technical Report), *Pure Appl. Chem.* 88 (2016), 265-291

## **EFFECT OF GREEN ACTIVATORS ON THE PROPERTIES OF ALKALI ACTIVATED MATERIALS: A REVIEW**

**Adeyemi Adesina** <sup>(1)</sup>

(1) Concordia University, Montreal, Canada

### **Abstract**

The most common types of activators used for alkali activated materials (AAMs) are sodium hydroxide and sodium silicate. These activators have been found to be corrosive, viscous, expensive, and with high embodied energy and carbon. In addition, the properties of these activators have made the large-scale applications of AAMs possible as a result of the special handling and side effects it has on the properties of the resulting AAM.

Therefore, this review explored the use of alternative green activator used for AAMs, and the effects it has on its properties. A green activator herein is classified as an activator that has a less embodied energy and carbon compared to sodium silicate and sodium hydroxide. This study shows the possibility of producing a greener AAM with enhanced strength and durability properties. In addition, it was observed that there's a considerable cost reduction with the use of the green activators compared to the conventional ones.

### **1. Introduction**

The high emission of carbon dioxide due to production of ordinary Portland cement (OPC) has opened way for various sustainable initiatives that can be used to reduce these high emission. These initiatives vary from partial and total replacement of OPC, to use of alternative fuels and optimization of OPC's production processes. However, the one with the most promising possibility of reducing a significant amount of carbon dioxide are alkali activated materials (AAMs). Alkali activated materials creates an avenue for 100% replacement of OPC in concrete, and uses waste materials as one of the major components. AAMs are achieved by alkali activation of aluminosilicate precursors with an alkali source. Examples of aluminosilicate precursor used for AAMs are slag, fly ask, metakaolin, rice husk

ash, etc. The alkali activation results in dissolution of aluminate and silicate monomers from the precursor, and a gel which hardens is formed. The common types of alkali activators commonly used for AAMs eliminates the sustainable advantage of AAMs over OPC, as they are its major contributor of carbon dioxide.

The most commonly used activators used are sodium silicate and sodium hydroxide. These activators are mostly used due to its resulting high strength. However, these activators produce poor fresh and hardened properties that has limited the universal acceptance and large scale application of AAMs. The major poor properties ensued from the use of sodium silicate and sodium hydroxide are quick setting and high drying shrinkage. Quick setting of alkali activated slag (AAS) which is a type of AAM has been found to result in low workability and flowability of the AAM [12, 13]. In addition, these activators are expensive, corrosive, and are the highest contributor of embodied energy in AAM preventing the advantage of using AAM as binder in concrete [2,5].

As there exists no review in open literature that focuses on the use of green activators in AAMs, this review explores the use of activators that can be classified as green activators, and the effects they have on the resulting properties of the AAMs. AAMs used herein refers to different types of AAMs which use different types of aluminosilicate precursors. Where significant, the type of AAMs is mentioned. It is anticipated that this review will open a pathway for more application and research on the use of green activators.

## **2. Green activators**

Activators classified as green in this article have a significant lower embodied carbon and energy compared to that of sodium silicate and sodium hydroxide. Also, these green activators are more user friendly (i.e. less corrosive), and cheaper. Some types of green activators are further explored, alongside with their effect on the properties of the resulting AAMs.

### **2.1 Sodium carbonate**

Compared to sodium silicate and sodium hydroxide, sodium carbonate exists naturally in the environment, and can be extracted from sodium carbonate and trona mines [19]. Also, it can be obtained through a chemical procedure (i.e. Solvay) [18]. In addition, it is approximately 3 times cheaper than sodium silicate and sodium hydroxide [9].

However, activating aluminosilicate precursors with sodium carbonate results in lower early age strength compared to those activated with common activators (i.e. sodium silicate and sodium hydroxide). This lower early strength has been attributed to initial formation of sodium calcium carbonate which delays the activation reaction [4]. Sodium carbonate also results in lower drying shrinkage of AAM compared to those activated with sodium silicate.

AAMs activated with sodium carbonate shows a more practical set time compared to those activated with sodium silicate [4]. The extended set time has been attributed to the initial formation of calcium carbonate, which also results in lower early age strength as mentioned earlier. Also, sodium carbonate lower pH (i.e. 12.6) compared to that of sodium silicate (i.e. 13.4) and sodium hydroxide (i.e. 13.8) is responsible for the extended setting time. Wang et al [22] also attributed the lower early strength of slag activated with sodium carbonate to the activator's lower pH. Slag activated with sodium carbonate has been able to result in higher



strength at later ages (i.e. 28 days) which makes it a great alternative for sodium silicate and sodium hydroxide where high early strength is not required [4]. The later higher strength has been attributed to the formation of carbonated compounds which results in a more densified microstructure [4]. Other studies also recorded late higher strength of up to 60MPa at 28 days when sodium carbonate was used to activate slag.

## 2.2 Magnesium oxide

Slag activated by 10 - 20% of magnesium oxide has been found to have strength about four times that of those activated with calcium hydroxide [16]. However, between 5 – 10% magnesium oxide, the 28 days of the resulting AAM was found to be lower than those activated with calcium hydroxide. Use of magnesium oxide to activate slag has been found to reduce shrinkage and cracking capability of the resulting AAM [16].

Despite the great potential of using magnesium oxide as a green alternative activator for AAMs, it should be noted that the chemical composition of magnesium oxide varies considerably from different locations [1]. Birchall et al. [1] and Mo et al. [11] recorded variations in AAMs properties when different types of magnesium oxide was used. Therefore, proper initial tests should be carried out to determine the optimum proportions for a specific magnesium oxide before a large-scale production is carried out

Though high energy is consumed, and carbon dioxide is emitted during the manufacture of magnesium oxide, the very low amount (i.e. about 10% the mass of the binder) required to activate AAMs still makes the resulting AAM more sustainable compared to OPC [22].

## 2.3 Sodium sulphate

The common activators used for AAMs (i.e. sodium silicate and sodium hydroxide) cannot be mined directly from the environment, therefore they required several industrial processes that are energy intensive and emit large amount of carbon dioxide into the environment. On the other hand, sodium sulphate can be obtained from natural resources, which eliminates the negative impact production of the common activators have on the environment [14]. Similar to sodium carbonate, AAMs activated with sodium sulphate show low early age strength [23]. This is due to the low alkalinity of the sodium sulphate [14]. Increasing the sodium oxide equivalent of sodium sulphate from 1 to 3% resulted in a significant increase in the early age strength of AAMs [14, 15]. However, at 28 days, there's no significance difference between samples activated with 1% and 3% sodium oxide equivalent. Using 1% sodium oxide equivalent to activate slag, Douglas and Brandstetr [3] obtained a 24 hours strength similar to that of OPC

AAMs activated with sodium sulphate exhibited longer setting times compared to those activated with sodium silicate and sodium hydroxide. In addition, AAMs activated with sodium sulphate show excellent workability similar to that of OPC [14], and higher fire resistance [15]. This shows to use sodium sulphate as activator for large scale AAMs applications. However, AAMs activated with sodium sulphate exhibited higher drying shrinkage compared to that of OPC, but lower than those activated with sodium hydroxide and sodium silicate [14]. Use of shrinkage reducing admixtures (SRA), OPC, hydrated lime, or fly ash can be used to control the drying shrinkage in AAMs activated with sodium sulphate. A reduction of 43.64% and 58.73% in drying shrinkage was recorded when hydrated lime and OPC was used respectively [14]. Sodium sulphate is also more economical in terms of cost and availability compared to the common activators

## 2.4 Calcium hydroxide

Calcium hydroxide has a lower alkalinity compared to that of sodium silicate, sodium hydroxide and sodium carbonate. This lower pH has resulted to lower strength gain of AAMs activated with calcium hydroxide due to slower dissolution of silicate and aluminate monomers from aluminosilicate precursors [8, 24]. When calcium hydroxide is used as AAMs activator, an optimum activator level has to be determined as this type of activators does not behave like other activators where increasing the concentration leads to higher strength. This is as a result of the low solubility of calcium hydroxide in water, which results in an insignificant change in alkalinity when higher amount is dissolved in water as observed in Figure 1 [10]. These results are also similar to Jeonung et al. [7] study where they observed no significant gain in strength when the concentration of the calcium hydroxide was increased

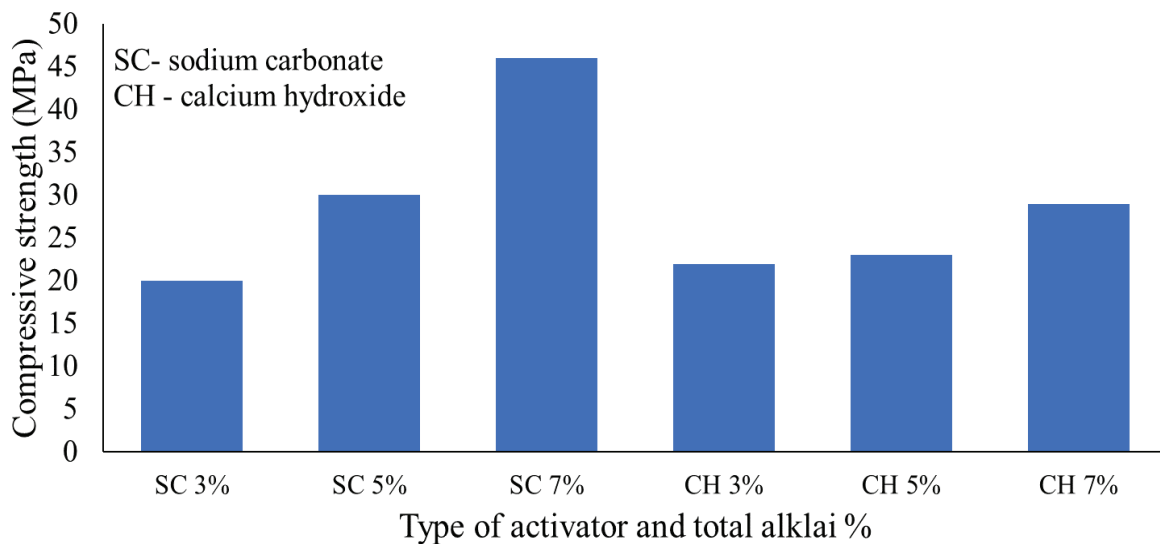


Figure 1: 28 days compressive strength of different types of activator and total alkali percentage (data from [10])

Calcium hydroxide is a more user-friendly activator as it safe to handle, less expensive, and readily available for purchase in household stores. Calcium hydroxide is approximately 6 times cheaper than sodium hydroxide [6]. Use of sodium sulphate with calcium hydroxide as AAM activator has been reported to improve the strength of the AAM significantly [17]. The improved strength has been attributed to the formation of ettringite which densify the microstructure, thereby leading to higher strength [17]. A study carried out by Jeong et al. [7] showed that the early strength of AAMs activated with calcium hydroxide can be improved by addition of supplementary activators. The supplementary activators used were gypsum, sodium hydroxide, sodium carbonate and sodium sulphate. However, the later age strength was not improved with the addition of supplementary activators. Yang et al [24] used longer curing duration to improve the later age strength of AAM which employs slag as the aluminosilicate precursor. The improved later age strength can be attributed to a more stabilized calcium silicate hydrate

### 3. Conclusions

Based on the short review on the effect of green activators on the properties of AAMs, the following conclusion can be made;

- Use of sodium hydroxide and sodium silicate as activators for AAMs is not a sustainable option, as these common activators cannot be obtained from natural resources, and their production process is energy intensive, and emits carbon dioxide to the environment
- In cases where high early strength is not required, activating AAMs with sodium carbonate is a greener alternative, as it results in similar strength at later ages compared to those activated with sodium silicate and sodium hydroxide
- Binary and ternary application of green activators will result in practical early age and later age strength. In addition, the combination of the green activators at right percentages will help to improve the overall durability of AAMs
- More research in the field of green activators is still required as very limited research is available, majority of all the studies in AAMs employs the use of sodium silicate and sodium hydroxide as activators

### References

- [1] Birchal, V. et al effect of magnesite calcination conditions on magnesia hydration Miner Eng, (2000), 1629-1633
- [2] Deventer, J.S.J. et al Chemical research and climate change as drivers in the commercial adoption of alkali activated materials Waste Biomass Valoriz., (2010), 145-155
- [3] Douglas E, Brandstetr J. A preliminary study on the alkali activation of ground granulated blast-furnace slag. Cem Concr Res, (1990), 746–56
- [4] Fernández-Jiménez, A. et al. Alkali-activated slag mortars: mechanical strength behavior Cem. Concr. Res., (1999), 1313-1321
- [5] Habert, G et al. An environmental evaluation of geopolymers based concrete production: reviewing current research trends J. Clean. Prod., (2011), 1229-1238
- [6] ICIS Indicative Chemical Prices A–Z (2015) <http://www.icis.com/chemicals/channel-info-chemicals-a-z>
- [7] Jeong, Y. et al Influence of four additional activators on hydrated-lime [Ca(OH)<sub>2</sub>] activated ground granulated blast-furnace slag Cement and Concrete Composites (2016) 1-10
- [8] Kim, M. S. et al Use of CaO as an activator for producing a price-competitive non-cement structural binder using ground granulated blast furnace slag Cem. Concr. Res., (2013), 208-214
- [9] Kostick D. S. Soda Ash: Statistics and Information U.S. Geological Survey (2013)
- [10] Maghsoodloorad, H. et al Recycling phosphorus slag as a precursor for alkali-activated binder; Impact of type and dosage of activator, Journal Ceramics-Silikáty, (2014), 227 - 236
- [11] Mo, L et al. Effects of calcination condition on expansion property of MgO-type expansive agent used in cement-based materials Cem Concr Res, (2010), 437-446

- [12] Pacheco-Torgal, F. et al Alkali-activated binders: a review. Part 2. About materials and binders manufacture *Constr Build Mater*, (2008), 1315-1322
- [13] Palacios, M and Puertas, F Effect of superplasticizer and shrinkage reducing admixtures on alkali-activated slag pastes and mortars, *Cem. Concr. Res.* (2005), 1358-1367
- [14] Rashad, A. M. Influence of different additives on the properties of sodium sulfate activated slag *Const and Buil Mat*, (2015), 379–389
- [15] Rashad, A. M. et al Chemical and mechanical stability of sodium sulfate activated slag after exposure to elevated temperature. *Cem Concr Res*, (2012), 333–43.
- [16] Shen W. et al Magnesia modification of alkali-activated slag fly ash cement. *J Wuhan Univ Technol Sci Ed*, (2011), 121–5.
- [17] Shi, C and Day, R Chemical activation of lime-slag blends V.M. Malhotra (Ed.), *Fly Ash, Silica Fume, Slag, and Natural Pozzolans in Concrete – Proceedings, Fifth International Conference*, vols. 1 and 2, American Concrete Institute, Detroit (1995), pp. 1165-1177
- [18] Shi, C. et al, D. *Alkali-activated Cements and Concretes* Taylor & Francis, Oxon (2006)
- [19] U.S. Geological Survey *Mineral Commodity Summaries: Soda Ash* (2013)
- [20] Wang, J et al Influence of the combination of calcium oxide and sodium carbonate on the hydration reactivity of alkali-activated slag binders. *Journal of Cleaner Production*, (2018), 622-629
- [21] Rashad Alaa M. An exploratory study on sodium sulfate-activated slag blended with Portland cement under the effect of thermal loads. *J Therm Anal Calorim*, (2014), 4345-4347
- [22] Wang S. D, et al Factors affecting the strength of alkali-activated slag. *Cem Concr Res* (1994), 1033–43.
- [23] Xueqan, W. et al. Early activation and properties of slag cement. *Cem Concr Res* (1990), 961–974.
- [24] Yang, K. H. et al Hydration products and strength development of calcium hydroxide-based alkali-activated slag mortars *Constr. Build. Mater.*, (2012), 410-419

## **EFFECT OF TEMPERATURE ON RHEOLOGICAL PROPERTIES OF ALKALI ACTIVATED BRICK POWDER BASED PASTES**

**Martin Vyšvařil<sup>(1)</sup>, Pavla Rovnaníková<sup>(1)</sup>**

(1) Brno University of Technology, Faculty of Civil Engineering, Brno, Czech Republic

### **Abstract**

The effect of temperature on flow properties and viscoelastic properties of brick powder based pastes prepared by alkaline activation of red clay brick waste is monitored in this paper. A different effect of temperature with respect to its classic rheological influence was ascertained. Elevated temperature has a considerable impact on the yield stress, viscosity and thixotropy of brick pastes, which turn to be more pseudoplastic and rheopectic. Raising temperature accelerates the geopolymer curing kinetics and contributes to the more rigid structure of the resulting geopolymeric gel.

### **1. Introduction**

Alkali activated materials are formed by alkaline activation of suitable aluminosilicate precursors (e.g metakaolin, blast furnace slag, fly ash). Ceramic and red clay brick wastes are considered to be efficacious aluminosilicate materials, which can be used as alternative to metakaolin and fly ash [1-4]. Bricks waste is usually rich in glass and burned clays, consisting in dehydrated aluminosilicates not only in crystalline phase but also in amorphous state which is important for alkaline reaction. In recent years, large volumes of brick dust have been produced with the development of building elements for the construction of low-energy houses. As activators, a wide range of alkaline solutions can be applied: NaOH, Na<sub>2</sub>CO<sub>3</sub>, sodium silicate (water glass), sodium aluminate, or their potassic equivalents. The elevated temperature promotes the alkali reaction, the temperature of 60 to 90 °C is mostly used, although even at ambient temperature an aluminosilicate gel is formed by brick powder activation [3]. In order to develop a building material that could be used as a cement replacement for specific applications, the understanding of its rheological behaviour at fresh state is fundamental. Some studies on alkali activated materials based metakaolin, fly ashes or blast furnace slags showed that similarly to cement pastes, these materials display viscoelastic

behaviour with thixotropic properties [5-8]. In spite of the common alkali activation of aluminosilicates at elevated temperatures, very few studies have been conducted regarding the effect of temperature on rheological properties of alkali activated materials. In metakaolin based geopolymers, increasing the temperature also produces an increase of viscosity and yield stress [9].

In this study, the effect of temperature on the rheological properties of brick powder based pastes prepared by alkaline activation of red clay brick waste is monitored. The influence of the composition of activation solution (varied silicate modulus) on the flow properties and the viscoelastic properties of pastes has been also studied.

## 2. Materials

A brick powder from the grinding of calibrated thermal insulating brick elements from the HELUZ Brickworks factory, v.o.s., plant in Hevlín, was used to prepare test specimens. The powder was used as-received, just the particles larger than 1 mm were removed by sieving. The chemical and phase composition of the brick powder as well as the particle size distribution and fundamental physical parameters were presented in the previous study (ceramic powder H) [10]. Fresh brick pastes were prepared from the brick powder with three dosages of activating solutions (potassium silicate, supplied by Vodní sklo, a.s., Czech Republic, and KOH p. a., by Penta Chemicals, a.s.). The silicate modulus ( $M_s$ ) of the activator varied from 1.0 to 1.4; the water content – sum of dosed water and water present in potassium silicate solution – was equal in all mixes. The recipes were based on preliminary experiments performed with varying activator composition and dosage. The varying dosage of liquid activator means varying Si/Al and K/Al ratio in the prepared materials. The testing specimens were prepared by mixing of brick powder and alkaline activator prearranged from potassium silicate solution, KOH and tap water (Tab. 1). The mixtures were homogenized by hand stirring for 1 minute.

Table 1: Composition of mixtures.

Mixture	Brick powder (g)	Potassium silicate (g) $M_s = 3.0$	KOH (g)	H <sub>2</sub> O (ml)	$M_s$ (-)
BP-K-1.0	50	20	6.3	5	1.0
BP-K-1.2	50	20	4.6	5	1.2
BP-K-1.4	50	20	3.5	5	1.4

## 3. Experimental methods

The rheological investigation including the characterization of flow properties and viscoelastic properties of pastes were carried out on the hybrid rheometer Discovery HR-1 (TA Instruments) in the Peltier Concentric Cylinder system with a DIN rotor with rough surface lowering the slippage and segregation of mixes during measurements. TRIOS 4.0.2.30774 software was used for a data evaluation [11]. The standard gap for DIN cylinder (5.917 mm) was adopted. The measurements were done at 20, 40 and 60 °C.

### 3.1 Flow properties

The brick suspension was placed into the measurement system at the end of the mixing cycle and the rheological measurements were started after a period of rest of 60 s. The testing routine was composed of a shear rate increase (from 0.1 to 100 s<sup>-1</sup>) applied through 30 steps with 15 s of measuring time at each shear rate followed by a decrease of shear rate on the same conditions. The results of flow measurements were expressed as shear rate vs. shear stress (flow curves) and the Herschel-Bulkley model Eq. (1) was applied to descending branches of the flow curves to fit the experimental data and to describe the pastes rheological behaviour [12]:

$$\tau = \tau_0 + k\dot{\gamma}^n \quad (1)$$

where  $\tau$  is the shear stress,  $\dot{\gamma}$  is the shear rate,  $\tau_0$  corresponds to the yield stress,  $k$  is the consistency coefficient, and  $n$  is the fluidity index which characterizes shear-thinning ( $n < 1$ ) or shear-thickening ( $n > 1$ ) behaviour of a material. Thixotropy or rheopexy of pastes were determined as an area between flow curves using TRIOS software.

### 3.2 Viscoelastic properties

Time evolution of the viscoelastic properties of pastes were evaluated by small amplitude (0.01%) oscillation tests measuring elastic ( $G'$ ) and viscous ( $G''$ ) modulus. If the elastic behaviour dominates the viscous one ( $G' > G''$ ), the sample exhibits a certain rigidity. Conversely, if  $G'' > G'$ , the sample shows the character of a liquid without a consistent chemical or physical network-of-forces [12]. Since one of the purposes of this study is to determine the variation over time of the viscoelastic parameters according to the geopolymer composition, it is important to determine the linear viscoelasticity region (LVR) in order to prevent structural decomposition of the geopolymerized network. The LVR is the region in which measurements are non-destructive to the microstructure of a material and it ends at a critical strain  $\gamma_c$ . The strain of 0.01% used in the oscillation tests is lower than the critical strain for all brick pastes studied. The rheological characterization was completed by frequency sweep tests with increasing the frequency from 0.1 Hz to 10 Hz. Experimental data were reported in terms of complex modulus ( $G^*$ ) and loss tangent ( $\tan \delta$ ) defined as follows Eqs. (2–3):

$$G^* = \sqrt{(G')^2 + (G'')^2} \quad (2)$$

$$\tan \delta = G''/G' \quad (3)$$

## 4. Results and discussion

### 4.1 Flow properties

The course of flow curves (Fig. 1) dramatically changed with increasing temperature indicating the change from thixotropic (time-dependent shear-thinning) to rheopectic (time-dependent shear-thickening) behaviour of brick powder pastes. Strong rheopexy can be revealed on the flow curve of BP-K-1.4 sample measured at 60 °C. Increasing  $M_s$  tended to the rheopectic character of brick powder pastes. This is also evident on the thixotropy values in Tab. 2. The shape of descending branches of the flow curves indicates continual conversion

from dilatant to pseudoplastic behaviour of the pastes with increasing temperature and  $M_s$ , respectively. The last-mentioned is confirmed by the downtrend of the flow index values,  $n$ , (Tab. 2). The yield stress and the consistency coefficient (which can be compared to plastic viscosity of the material) of pastes increased with increasing temperature and  $M_s$ ; this is in agreement with the metakaolin based geopolymers [9] and the generally known inverse dependence of alkali-activated paste workability on the increasing silicate modulus of alkali activator.

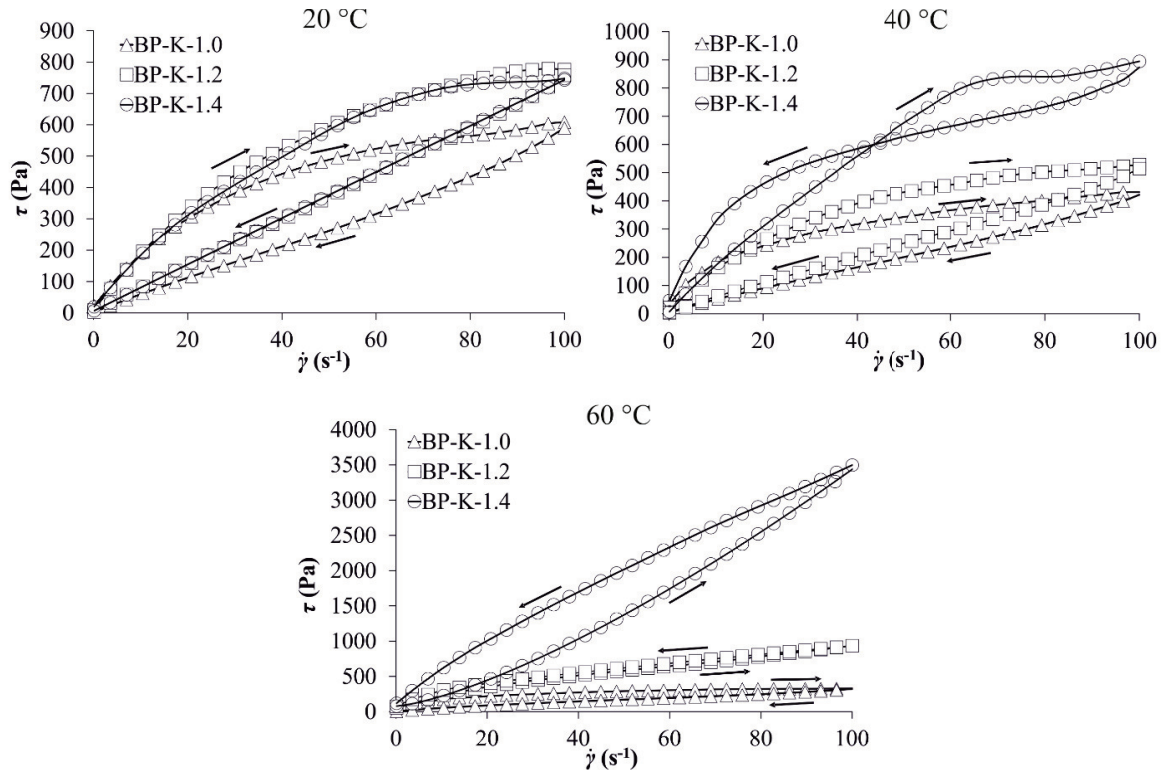


Figure 1: Flow curves of brick powder pastes measured at temperatures of 20, 40 and 60 °C.

Table 2: Rheological parameters of brick powder based pastes.

Mixture	$\tau_0$ (Pa)	$k$ (Pa s)	$n$ (-)	Thixotropy (Pa s)	$t_{SG}$ (s)	$G^*$ (Pa)	$\tan \delta$ (-)
BP-K-1.0 (20 °C)	6.03	2.55	1.17	16 233	1 060	300	1.07
BP-K-1.0 (40 °C)	13.96	2.92	1.06	13 084	921	356	1.05
BP-K-1.0 (60 °C)	19.79	5.21	0.88	9 951	826	4 936	0.69
BP-K-1.2 (20 °C)	7.98	3.35	1.03	16 200	591	399	0.99
BP-K-1.2 (40 °C)	14.75	4.13	1.01	11 565	432	816	0.98
BP-K-1.2 (60 °C)	74.93	51.08	0.61	-3 896	429	7 034	0.66
BP-K-1.4 (20 °C)	12.29	7.55	0.99	14 433	257	754	0.67
BP-K-1.4 (40 °C)	47.50	63.65	0.92	357	190	10 534	0.59
BP-K-1.4 (60 °C)	91.81	78.76	0.36	-45 705	119	222 939	0.31



#### 4.2 Viscoelastic properties

Fig. 2 shows the time evolution of the viscoelastic parameters ( $G'$  and  $G''$ ) during a small amplitude oscillation test. Geopolymer gel formation was monitored by a time point  $t_{SG}$  at the intersection of the curves of  $G'$  and  $G''$  (gel point). Before the gel point, samples show the behaviour of a liquid with  $G'' > G'$ , after the gel point, the samples show gel-like or solid behaviour with the existence of interactions between the constituents [12]. The results (Tab. 2) confirmed that elevated temperature accelerates the geopolymer curing kinetics and that the gel point was observed at earlier times. In addition, it has been found that the increasing silicate modulus results in faster gel formation and more rigid structure (the elastic component ( $G'$ ) varies rapidly than the viscous component ( $G''$ )).

The results of frequency sweep tests (Tab. 2) proved the relationship between elevated temperature and the stiffness of brick pastes; the ratio between dissipation and elasticity increased (growing  $G^*$ ) with increasing temperature and the pastes became more rigid and more viscous. Since the  $\tan \delta$  of the pastes decreased, the brick paste showed higher and higher proportion of the elastic component ( $G'$ ) with increasing temperature and  $M_s$ , suggesting that the pastes had a stronger structure more resistant to external interference.

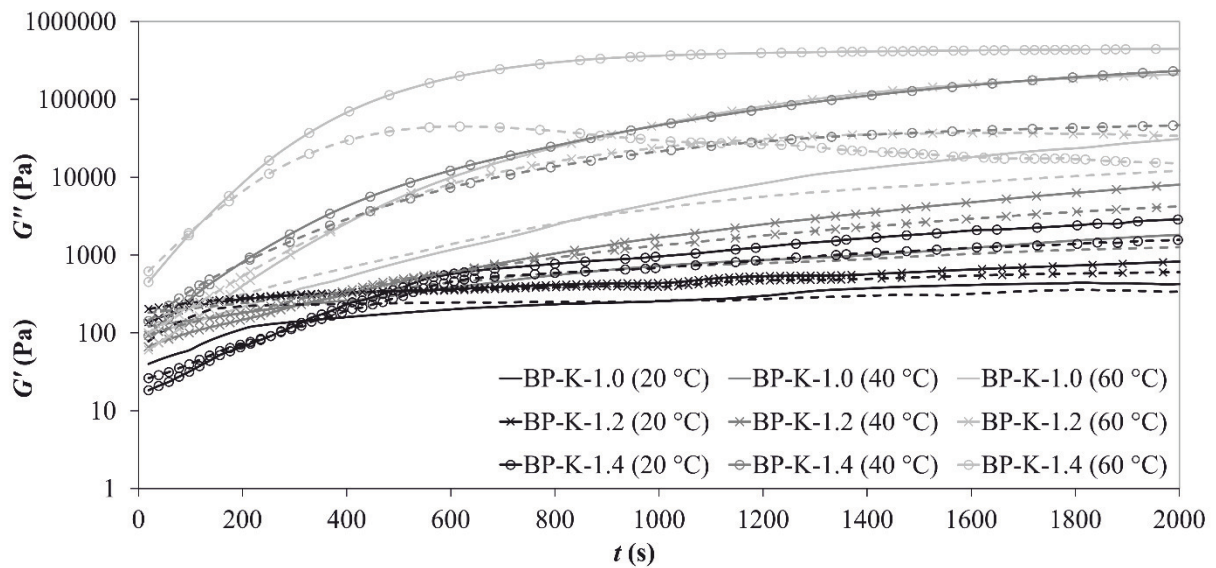


Figure 2: Time evolution of storage modulus ( $G'$ ; continuous curves) and loss modulus ( $G''$ ; dash curves) for the brick powder based pastes.

#### 5. Conclusions

In this study, it is shown that:

- Brick powder based pastes prepared at ambient temperature by alkaline activation of red clay brick waste are highly thixotropic fluids with relatively low yield stresses and viscosities.
- Elevated temperature has a considerable impact on the yield stress, viscosity and thixotropy of brick pastes, which turn to be more pseudoplastic and rheopectic. Raising

temperature accelerates the geopolymer curing kinetics and contributes to the more rigid structure of the resulting geopolymeric gel; this is a different effect of temperature with respect to its classic rheological influence.

- Increasing silicate modulus of alkali activator tends to the rheopectic character of brick powder pastes; the pastes become more rigid and more viscous. The increasing viscosity of the activator solution at rising  $M_s$  is the main reason for it. This also leads to the acceleration of gel formation in brick pastes.
- The effect of temperature and silicate modulus of alkali activator is similar as on metakaolin geopolymerization.

### Acknowledgments

This outcome has been achieved with the financial support of the GA ĀR research project 16-02862S and due to the Ministry of Education, Youth and Sports under the „National Sustainability Programme I“ – the project No. LO1408 „AdMaS UP – Advanced Materials, Structures and Technologies“.

### References

- [1] Reig, L. et al, Alkaline activation of ceramic waste materials, *Waste Biomass. Valoriz.* 4 (2013) 729-736
- [2] Reig, L. et al, Properties and microstructure of alkali-activated red clay brick waste, *Constr. Buil. Mater.* 43 (2013) 98-106
- [3] Bignozzi, M.C. et al, Ceramic waste as new precursors for geopolymerization, *Adv. Sci. Tech.*, 92 (2014) 26-31
- [4] El-Fadaly, E. et al, Eco-friendly cement from ceramic waste geopolymerization, *Natur. Soc. Sci.*, 2 (2014) 195-210
- [5] Palacios, P. et al, Rheology and setting of alkali-activated slag pastes and mortars: Effect of organic admixture, *ACI Materials Journal*, 105 (2008) 140-148
- [6] Palomo, A. et al, Properties of alkali-activated fly ashes determined from rheological measurements, *Adv. Cem. Res.* 17 (2005) 143-151
- [7] Abdalqader, A. and Al-Tabbaa, A., Rheological Properties of Sodium Carbonate - Activated Fly Ash/Slag Pastes with Different Superplasticisers, 27<sup>th</sup> Biennial National Conference of the Concrete Institute of Australia in conjunction with the 69<sup>th</sup> RILEM Week, Australia (2015), 1105-1115
- [8] Poulesquen, A. et al, Rheological behavior of alkali-activated metakaolin during geopolymerization, *J. Non-Cryst. Solids.* 357 (2011) 3565-3571
- [9] Romagnoli, M. et al, Rheology of geopolymer by DOE approach, *Constr. Build. Mater.* 36 (2012) 251–258
- [10] Keppert, M. et al, Red-clay ceramic powders as geopolymer precursors: Consideration of amorphous portion and CaO content, *Appl. Clay Sci.* 161 (2018) 82-89
- [11] <http://www.tainstruments.com/trios-software/>
- [12] Mezger, T.G., *The Rheology Handbook*, 4<sup>th</sup> ed., Vincentz Network, Germany (2014)

## **EXPERIMENTAL STUDY OF THE CHEMICAL DEFORMATION OF METAKAOLIN BASED GEOPOLYMER**

**Zhenming Li <sup>(1)</sup>, Guang Ye <sup>(1)</sup>**

(1) Section Materials and Environment, Faculty of Civil Engineering and Geosciences, Delft University of Technology, Delft, the Netherlands

### **Abstract**

Chemical deformation is an important material property which influences the autogenous deformation of the materials. While geopolymer is emerging as an eco-friendly alternative to ordinary Portland cement (OPC), few studies have been conducted on the chemical deformation of this material. In this paper, the chemical deformation of a metakaolin (MK) based geopolymer is studied. Unlike OPC paste which exhibits monotonous chemical shrinkage, metakaolin-based geopolymers can show chemical shrinkage and chemical expansion at different stages of curing. X-ray diffraction (XRD) and Fourier transform Infrared Spectrophotometer (FTIR) tests were conducted to characterize the geopolymer paste cured at different ages in order to explain the mechanisms of different chemical deformation behaviors. It was confirmed that the early age chemical shrinkage was mainly due to the dissolving of MK, where the density of MK plays an important role. The chemical expansion taking place in the second stage was mainly associated with the formation of Al-rich products. The chemical shrinkage in the late age was related to the formation of Si-rich products in literature, but this finding was not confirmed in this study. The understanding of chemical deformation of geopolymers is helpful to explain the autogenous deformation of geopolymers.

### **1. Introduction**

Geopolymer has emerged as an eco-friendly alternative to OPC. OPC has been widely utilized in construction for many centuries with stable properties but the CO<sub>2</sub> emission produced by cement industry is becoming a serious issue hindering the application of this material. Geopolymer, in contrast, can be made from industrial by-products or other inexpensive aluminosilicate materials, to which little or no CO<sub>2</sub> footprint is usually attributed. To serve as a qualified binder in construction, geopolymer needs to have good volume stabilities.

However, the autogenous deformation property of geopolymers remains an unsolved issue. To better understand the autogenous deformation of geopolymers, research attention needs to be paid on the chemical deformation, since it essentially influences the driving force of autogenous deformation [1]. Li et al. [2] have studied the chemical deformation evolution and mechanism of a geopolymer made from a highly reactive MK with a typical Si/Al ratio around 1. They found that the metakaolin based geopolymer (MKG) experiences three stages of chemical deformation, i.e. chemical shrinkage in the first stage which was mainly due to dissolution of the precursor, chemical expansion in the second stage which was strongly associated with the formation of Al-rich (nano-) zeolites and chemical shrinkage again in the final stage due to the reorganization and polymerization of the Al-rich products to form Si-rich gels. To verify the applicability of their theories in explaining geopolymers synthesized from different precursors, this paper concentrates on the chemical deformation of a geopolymer made of MK with different reactivity and a different Si/Al ratio. The reaction products of the MKG paste are characterized.

## 2. Materials and experiments

### 2.1 Materials

The MK used as precursor was from Argeco (France), with a particle size range of 0.15-142  $\mu\text{m}$  and a  $d_{50}$  of 69.4  $\mu\text{m}$ . The chemical compositions of MK determined by X-ray fluorescence spectrometry (XRF) are shown in Tab. 1. The reactive  $\text{SiO}_2$  and  $\text{Al}_2\text{O}_3$  contents in MK were determined by chemical dissolution treatment. The MK was dissolved in dilute hydrochloric acid solution and were afterwards treated with boiling solution of sodium carbonate. The obtained residue was rinsed, heated up to 950  $^\circ\text{C}$  and then was cooled to room temperature in a desiccator before subject to XRF test. The dissolved fraction corresponding to the mass loss after chemical dissolution treatment is determined as the amorphous phase content. The amount of reactive  $\text{SiO}_2$  and  $\text{Al}_2\text{O}_3$  was shown in Tab. 2. The mole ratio of  $\text{SiO}_2/\text{Al}_2\text{O}_3$  in the reactive part of MK is 0.65.

The activator was prepared by mixing solid NaOH and liquids (sodium silicate and distilled water) in a closed plastic bottle to prevent evaporation. The solution was then allowed to cool for 24 hours before mixing with MK. The mixture proportions of the MKG paste are presented in Tab. 3.

Table 1: Chemical compositions of MK and insoluble residue.

Oxide weight (%)	$\text{SiO}_2$	$\text{Al}_2\text{O}_3$	CaO	$\text{Fe}_2\text{O}_3$	$\text{K}_2\text{O}$	$\text{TiO}_2$	$\text{ZrO}_2$
MK	55.14	38.43	0.55	2.60	0.17	1.12	0.05
Insoluble residue	83.65	12.61	0.12	0.79	0.23	2.43	0.11

Table 2: Reactivity of MK (wt%).

Components (%)	I.R.	Reactive content	Total $\text{SiO}_2$	Reactive $\text{SiO}_2$	Total $\text{Al}_2\text{O}_3$	Reactive $\text{Al}_2\text{O}_3$
MK	51.23	48.77	55.14	12.29	38.43	31.97

Table 3: Mixture proportions of MKG paste.

	SiO <sub>2</sub> (mol)	Al <sub>2</sub> O <sub>3</sub> (mol)	Na <sub>2</sub> O (mol)	H <sub>2</sub> O (g)
MK	1.23	1.88	--	--
Activator	1	--	1.5	350
MKG	2.23	1.88	1.5	350

## 2.2 Experiments

The densities of MK and the insoluble residue were measured by pycnometer. The chemical deformation of the paste was measured from casting till 2 weeks according to gravimetry method, with the detailed procedure described elsewhere [2]. The chemical deformation value was described as the absolute volume change of the paste per gram of the reactive part of the precursor. XRD was conducted by using a Philips PW 1830 powder X-ray diffractometer, with Cu K $\alpha$  (1.5406 Å) radiation, tube setting to be 40 kV and 40 mA, a step size of 0.030°, and a 2 $\theta$  range of 5–70°. FTIR was performed by using a Spectrum TM 100 Optical ATR-FTIR spectrometer over the wavelength range of 600 to 4000 cm<sup>-1</sup> with a resolution of 4 cm<sup>-1</sup>.

## 3. Results and discussion

### 3.1 Chemical deformation evolution

The evolution of chemical deformation of MKG is shown in Fig.1 (a). For the convenience of comparison, the chemical deformation of the geopolymer synthesized from another kind of MK (denoted as MKG2) studied in [2] is shown in Fig.1 (b). It can be seen that the chemical deformations of the two MKGs both experience three stages of evolutions, i.e. chemical shrinkage in the first few hours, chemical expansion in the subsequent stage and chemical shrinkage again in the third and final stage. No evident change was observed after 2 weeks of curing. These results indicate that the three-stage evolution of chemical deformation seems an intrinsic behavior of MKGs rather than a phenomenon dependent on the properties of precursors. The development of chemical deformation of geopolymers is essentially different from that of OPC, where OPC always exhibits a monotonous chemical shrinkage in the whole age of curing. The absolute volume change of OPC is called chemical shrinkage, but the one of geopolymers can only be called chemical deformation due to the expansion observed.

Despite of the same trend followed by the chemical deformations of the two MKGs, the magnitudes of the first-stage chemical shrinkages of these two mixtures differ a lot. This difference will be emphasized in next section.

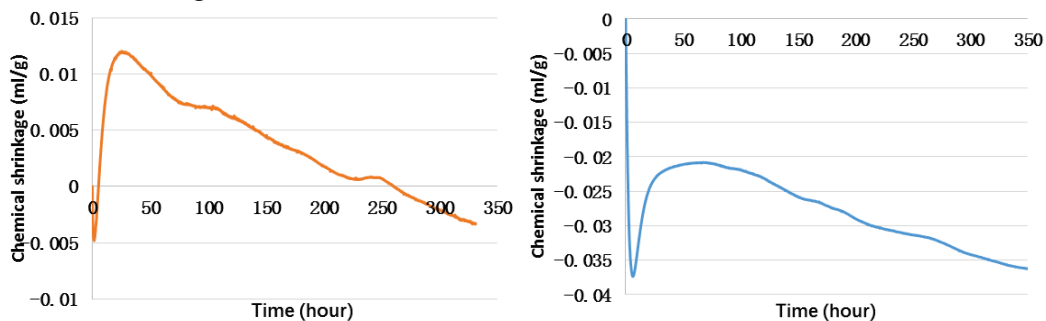


Figure 1: Comparison of chemical deformations of MKG from this study (a) and MKG2 from [2] (b).

### 3.2 Explanation of the chemical deformations in different stages

#### 3.2.1 Chemical shrinkage in the first stage (the first few hours after casting)

According to [2], the first stage chemical shrinkage of MKG was mainly due to the dissolution of the precursor. To verify this hypothesis, 120g of MK was mixed with 1200g of alkali activator with continuous stirring. The volume change of the suspension during mixing was measured according to Le Chatelier method. The volume change (ml) divided by the mass (g) of the reactive part of MK is shown in Fig.2.

It can be seen that the volume of the suspension decreased in the first half an hour of mixing. Due to the low concentration of MK in the solution, the dissolution of MK should be the dominant reaction in this period. After half an hour of mixing, the volume of the suspension began to increase, indicating that the concentrations of the dissolved species reached a threshold and the polymerization among them began to occur. Therefore, the volume reduction of 0.0044 ml/g at the time 0.5 hour can be considered as an approximation of the chemical shrinkage caused by dissolution of MK. In fact, the value of 0.0044 ml/g is quite close to the chemical shrinkage of MKG in the first stage which is 0.0048 ml/g as shown in Fig.1 (a). This result supports the hypothesis proposed in [2] that the early age chemical shrinkage of MKGs is mainly due to the dissolution of MK.

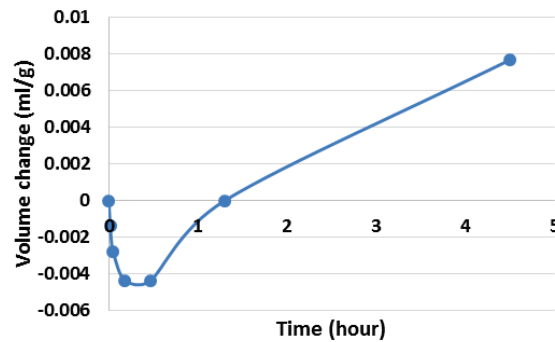
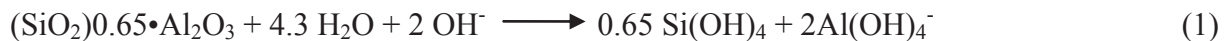


Figure 2: Volume change during dissolution of MK.

Moreover, the chemical shrinkage due to dissolution of MK can also be approximated by calculation. If we assume the reaction products after dissolving of MK are simply monomers,  $\text{Si}(\text{OH})_4$  and  $\text{Al}(\text{OH})_3$ , without considering the ionization or the polymerization of these species, the dissolution of MK can be described as Eq. (1). The chemical formula of MK is expressed as  $(\text{SiO}_2)_{0.65} \cdot \text{Al}_2\text{O}_3$  because the  $\text{SiO}_2/\text{Al}_2\text{O}_3$  ratio of the reactive part of MK is 0.65.



The chemical deformation associated with Eq.(1) can be calculated based on the density of reactive MK and the molar volumes of  $\text{H}_2\text{O}$ ,  $\text{OH}^-$ ,  $\text{Si}(\text{OH})_4$  and  $\text{Al}(\text{OH})_3$ . Based on the densities of MK and insoluble residue measured by pycnometer method, the density of the reactive part of MK can be calculated to be 2.37 g/ml. The molar volumes of  $\text{Si}(\text{OH})_4$  and  $\text{Al}(\text{OH})_3$  are assigned as 58.68 ml/mol and 42.3 ml/mol, respectively, according to the data in literatures [3–5]. The chemical deformation associated with Eq. (1) is calculated to be -0.034 ml/g, i.e. chemical shrinkage of 0.034ml/g. This is qualitatively consistent with the experiment results which also show chemical shrinkage in the first stage. However, the value 0.034ml/g is much higher than the measured chemical shrinkage of MKG in the first stage

which is 0.0048 ml/g. This is because the calculation above assumes the precursor was 100% dissolved while in real alkali activation only a part of the MK was dissolved in the first hours. Even though the dissolution of MK proceeded with elapse of time, the chemical shrinkage induced by later dissolution was compensated by the chemical expansion which occurred in the second stage, hence the experimentally measured chemical shrinkage in the first stage reached only 0.004 - 0.005 ml/g.

The calculation also indicates that a key parameter influencing the early age chemical shrinkage of MKG is the density of the reactive part of the precursor, which determines the volume of the reactants before reaction. The big difference between the densities of the precursors used in this study and in [2], which are 2.37 g/ml and 2.09 g/ml, respectively, explains the big difference between the first-stage chemical shrinkages of the two MKGs shown in Fig.1.

### 3.2.2 Chemical expansion in the second stage (from 3 to 50 hours curing)

The FTIR spectra of the MKG pastes at different curing times are shown in Fig.3. The main band of the spectrum of raw MK located at around  $1045\text{ cm}^{-1}$  is assigned to the asymmetric stretching vibration of Si-O-T bonds (T= tetrahedral Si or Al). After 4 hours of activation, the main band shifts to around  $940\text{ cm}^{-1}$ , which is attributed to the formation of NASH gels [6], indicating that the MK was largely dissolved and the reaction products began to form in this period. At the curing age of 16 hours and 30 hours, the humps at  $680\text{ cm}^{-1}$ ,  $740\text{ cm}^{-1}$  and  $860\text{ cm}^{-1}$ , which represent the vibrations of Al-O bonds in  $\text{AlO}_4$  tetrahedral groups, become apparent, indicating that a large amount of Al was incorporated into the polymerized structures. These reaction products are normally denoted as “Al-rich” products [7]. The formation of Al-rich products corresponds to the chemical expansion occurring in this stage, indicating that the finding proposed in [2] that the chemical expansion occurring in the second stage of geopolymerization is associated with the formation of Al-rich products is also applicable to the present MKG.

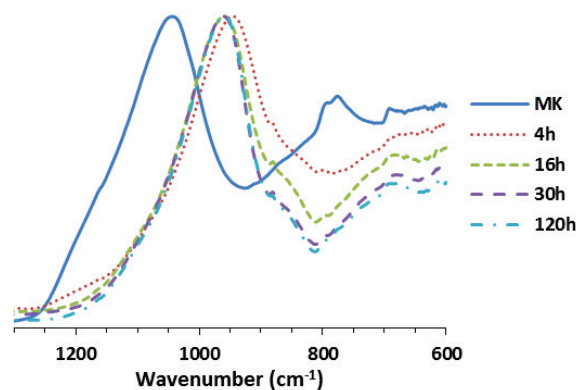


Figure 3: FTIR spectra of MK and MKG pastes cured for 4 hours, 16 hours, 30 hours and 120 hours.

### 3.2.3 Chemical shrinkage in the final stage (after about 50 hours curing)

The formation of Si-rich gels was reported to be responsible on the chemical shrinkage happening in the final stage of geopolymerization [2]. However, this hypothesis cannot be confirmed in this study by only the FTIR results. As shown in Fig.3 (a), the spectra of 30h and 120h are indistinguishable, although the reactions were ongoing and the chemical

shrinkage was continuously developing in this period. It is suggested that techniques like nuclear magnetic resonance (NMR) need to be utilized to detect the Si coordination environments of the MKG pastes cured at different ages.

### 3.3 Perspective

In [8], the autogenous deformation of the MKG paste with the same mixture design as in this study was investigated. Autogenous expansion after final setting time (2.3 hours after mixing) and subsequent autogenous shrinkage after 1 day of curing were observed, but the mechanisms behind these behaviors were not clearly understood. The chemical expansion and the chemical shrinkage observed in this study may help to explain the autogenous expansion and autogenous shrinkage of MKG, respectively.

## 4. Conclusions

The MKG experienced three stages of chemical deformation regardless of the reactivity of the precursor. The chemical shrinkage in the first stage was mainly due to the dissolving of precursor. MK with higher density of the reactive part was supposed to have lower chemical shrinkage in this period. The chemical expansion occurred subsequently was associated with the formation of Al-rich products, which may consist of nano-zeolites that cannot be detected by X-ray. The chemical shrinkage in the late age may be due to the reorganization and polymerization of the previously formed entities, where further research is needed.

## References

- [1] O.M. Jensen, P.F. Hansen, Autogenous deformation and RH-change in perspective, *Cem. Concr. Res.* 31 (2001) 1859–1865. doi:10.1016/S0008-8846(01)00501-4.
- [2] Z. Li, S. Zhang, Y. Zuo, W. Chen, G. Ye, Chemical deformation of metakaolin based geopolymer, *Cem. Concr. Res.* (2018) (Submitted).
- [3] J.G. Reynolds, The Density of Aqueous Sodium Hydroxide- Sodium Aluminate Solutions : Data Review and Model Development, in: *WM'06 Conf.*, 2006.
- [4] T. Ikkatai, N. Okada, K.K. Showa, Viscosity, specific gravity, and equilibrium concentration of sodium aluminate solutions, *Extr. Metall. Alum.* 1 (1963) 159–173.
- [5] J. Li, C.A. Prestidge, J. Addai-Mensah, Viscosity, density, and refractive index of aqueous sodium and potassium aluminate solutions, *J. Chem. Eng. Data.* 45 (2000) 665–671. doi:10.1021/je000025d.
- [6] W.K.W. Lee, J.S.J. van Deventer, Use of infrared spectroscopy to study geopolymerization of heterogeneous amorphous aluminosilicates, *Langmuir.* 19 (2003) 8726–8734. doi:Doi 10.1021/La026127e.
- [7] P. Duxson, A. Fernández-Jiménez, J.L. Provis, G.C. Lukey, A. Palomo, J.S.J. van Deventer, Geopolymer technology: the current state of the art, *J. Mater. Sci.* 42 (2007) 2917–2933. doi:10.1007/s10853-006-0637-z.
- [8] Z. Li, P. Gao, G. Ye, Experimental study on autogenous deformation of metakaolin based geopolymer, in: *2nd Int. RILEM/COST Conf. Early Age Crack. Serv. Cem. Mater. Struct.*, Brussels, 2017: pp. 209–214.



## **FLEXURAL BEHAVIOR AND STRENGTHENING OF GEOPOLYMER CONCRETE BEAMS REINFORCED WITH GFRP BARS USING CFRP SHEETS**

**Abdalla Elbana <sup>(1)</sup>, M. Talha Junaid <sup>(1)</sup>, Salah Altoubat <sup>(1)</sup>**

(1) Department of Civil and Environmental Engineering, University of Sharjah, UAE

### **Abstract**

Fiber Reinforced Polymers (FRP) are a relatively new material, and some behavioral aspects are not yet studied, especially pertaining to flexural and serviceability behavior in structural members. On the other hand, researchers have found that Geopolymer concrete has significantly high mechanical properties making it suitable for structural applications. A combination of FRP and Geopolymer should result in a durable, sustainable, and environment-friendly. This paper has two main aims. Firstly, to study the flexural behavior and serviceability of geopolymer concrete beams reinforced with Glass Fiber Reinforced Polymer (GFRP) bars. Secondly, to investigate the applicability of carbon fiber reinforced polymer (CFRP) as a strengthening regime for such systems. A total of six 2.1meter beams were tested under quasi-static four-point flexural tests for this purpose. Two identical beams were tested to failure. The remaining 4 beams were partially damaged and then repaired and strengthened with CFRP sheets using four different strengthening regimes. The CFRP strengthening system restored the capacity of the damaged beams, however, the contribution of GFRP rebars and CFRP sheet in load carrying capacity is not as efficient as in beams with conventional reinforcement strengthened with CFRP. This could be attributed to the stress-strain relationship of CFRP and GFRP that is distinctly different from each other.

### **1. Introduction**

Geopolymers are formed when an alumina and silica-rich source material is activated with a strong metallic alkaline. The source material is usually fly-ash (class F or C), naturally occurring clays, and furnace slag from the production of metals. Generally, sodium, potassium and calcium hydroxides or silicates, or a combination of these is used as activator solutions. Geopolymer concrete is highly sustainable and cost-effective since it is

manufactured from industrial waste materials. Researchers have found that Geopolymers could be a possible replacement of conventional concrete [1-9]. Conventional steel reinforcement is prone to corrosion thus leading to non-durable concrete structures. Recently, glass fiber-reinforced polymer (GFRP) reinforcement bars have become an alternative to the traditional rebars. GFRP has superior durability properties being a noncorrosive material and superior mechanical properties, such as high tensile strength and low self-weight [10]. A combination between GFRP and GPC should result in a durable, sustainable, and cost-effective system. Moreover, externally bonded Carbon fiber reinforced polymers (CFRP) are used for strengthening or repairing of existing concrete members to improve load-resistance as well as serviceability. The current research aims at studying the behavior of flexural members composed of the different materials described above, and their interaction with each other. To this end, six (6) beams made with GPC and reinforced with GFRP bars in flexure and shear were tested. Two beams were tested to failure and served as reference beams for the remaining testing. The other 4 beams were loaded to induce substantial damage and repaired by CFRP sheets using different strengthening regimes and then tested to failure. The results of this testing program help in understanding the flexural behavior of such a composite system and the interaction of these materials with each other.

## 2. Materials

Commercially available fly ash class-F and ground granular blast furnace slag (GGBFS) was used as a binder for making geopolymer concrete. 12 molar sodium hydroxide solution was prepared by dissolving sodium hydroxide pallets with tap water 24 hours prior using. An extra pure sodium silicate solution was used with chemical compositions of 27.2%  $\text{SiO}_2$ , 8%  $\text{Na}_2\text{O}$ , and 64.8% water. The sodium hydroxide to sodium silicate ratio is 1.8 and the GGBFS content of the total binder is 20%. Geopolymer concrete mix proportions are summarized in Tab. 1. The 28 days average compressive strength of geopolymer concrete is 34.1 MPa.

GFRP bars under the product name MateenBar provided by Pultron Composites UAE were used in this study. The nominal diameters used were 16 mm for moment reinforcement ( $f_{fu}^* = 690$  MPa  $\epsilon_{fu}^* = 0.0135$  and  $E_f = 51 \pm 2.5$ ) and bar size 10 mm for shear stirrups reinforcement. All beams are equipped with two 10 mm bars in the compression zone. Straight GFRP bars without anchor head with a deformed surface were used.

Table 1: Geopolymer concrete mix proportions

Component	20 mm C.A.	10 mm C.A.	5 mm F.A.	Dune Sand	NaOH (12M)	FA	$\text{Na}_2\text{SiO}_3$	GGBFS	Water	Superplasti cizer
Quantity ( $\text{Kg/m}^3$ )	540.8	302.5	582.2	289.4	55.1	99.2	340	85	47	4

A high strength, high elastic modulus, and uni-directional carbon fiber reinforced polymer sheet provided by CONMIX LTD was used for strengthening the damaged beams. The carbon fiber sheets were externally bonded to the soffit of the beam as per ACI 440.R2-08 [11] guideline for installation. CFRP material has a tensile strength of 4000 MPa and a tensile modulus of 230 GPa with an ultimate elongation of 1.80% as specified by the supplier. Grout

and injection resin as provided and installed by CONMIX LTD under the brand name Recon FCE and Recon LVE was used to repair damaged beams.

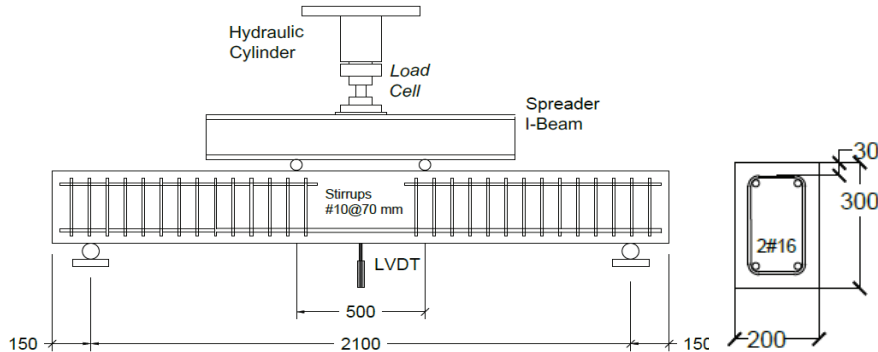
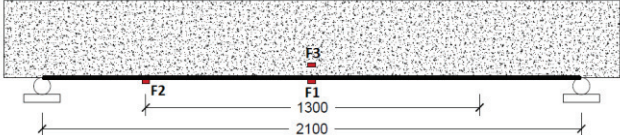
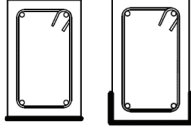
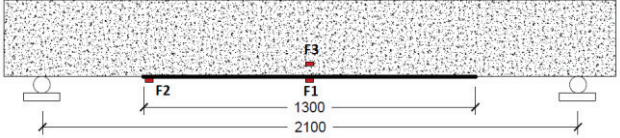
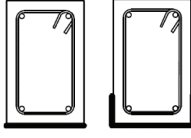


Figure 1: Schematic diagram of test set up and reinforcement details (dimensions are in mm)

### 3. Methodology

All beam specimens were tested under four-point bending static test. The load was applied through a spreader beam (Fig. 1) by a 1500 KN capacity hydraulic jack. The beams were simply supported with a clear span and shear span of 2100 mm and 800 mm, respectively. Displacement controlled load was applied at 0.01 mm/sec rate. The distance between the two loads was 500 mm. Two beams were loaded to failure. The remaining four beams are loaded to 50% of the experimental ultimate moment to substantially damage them. The damaged beams were repaired by injecting the cracks with epoxy and strengthened with different schemes using CFRP sheets as explained in the next section. A total of six GPC beams reinforced with GFRP bars were tested in this program. Each beam is 2.4m long and a simply supported span of 2.1m with a section of 200mm by 300mm. The beams were reinforced with 2#16 bars in flexure and #10@70mm in shear and designed to fail in flexure. In the constant moment zone, no stirrups or compression bars were provided, so as not to affect the strain and crack development on the pure bending zone. Fig. 1 summarizes the test setup and reinforcement details of the beams. Two such beams were tested to failure and their results were used as a reference for the other 4 beams, which were initially loaded to 50% of the moment capacity. This loading caused substantial damage to the test specimens. These four beams were then repaired and strengthened using two layers of CFRP sheets and the schemes summarized in Tab. 2. A linear variable differential transformer (LVDT) was placed at the midspan section, to measure the incremental midspan deflection. Two strain gauges were installed at the center of the flexural GFRP reinforcement (M). The CFRP sheet were instrumented with four strain gauges, two in the midspan F1, and one at the half shear span F2, and one at the U-wrap side F3 depth (at the same depth of the longitudinal reinforcement).

Table 2: beam specimens and Strengthening Schemes

Ref	Strengthening length	Strengthening profile
GPC-LF and GPC-LU		
GPC-SF and GPC-SU		

\*F3 is placed at CFRP only for U-shape

#### 4. Results and Discussion

Tab. 3 summarizes the observed experimental failure modes of each specimens. All beams were designed to be under-reinforced in flexure, however, the beams experimentally behaved as over-reinforced and failed due to concrete crushing because the GFRP properties reported by the manufacturer were conservative. For the reference beams GPC-R1 and GPC-R2 the strain values of the strain gauges (M2 and M3) installed in the middle of the two flexural GFRP bars (2#16) exceeded the guaranteed rupture strain ( $\epsilon_{fu}^* = 0.0135$ ) provided by the manufacturer at these applied loads before concrete crushing. However, the GFRP bars did not physically rupture at this strain values and contributed to the load carrying capacity of the beams until concrete crushing. Long flat and long U-wrap strengthened beams GPC-LF and GPC-LU failed due to CFRP sheet rupture at the constant moment zone. While beams that has short strengthening system (GPC-SF and GPC SU) failed due to concrete cover delamination which initiated at either end of the CFRP sheet. This failure is due to the short development length (less than that recommended by ACI 440.R2-08 [11] which failed to develop an effective CFRP stress. After CFRP failure, all the strengthened beams continued to resist the applied load until the GFRPs'  $\epsilon_{fu}^*$  was reached, shortly followed by concrete crushing.

Tab. 3 summarizes the experimental flexural capacities at CFRP ( $M_{n,CFRP}$ ), GFRP ( $M_{n,GFRP}$ ), and concrete crushing ( $M_{n,CC}$ ) failure. The experimental flexural capacity  $M_{n,GFRP}$  for each specimen is obtained when the strain of GFRP exceeds  $\epsilon_{fu}^*$  provided by the manufacturer. The Flexural capacity of the strengthened beams changed by -18.4, -5.5%, -63.8%, -60% for GPC-LF, GPC-LU, GPC-SF, GPC-SU from the reference beams respectively. The U-wrapped beams in GPC-LU and GPC-SU experienced 15.7% and 8% improvement in flexural capacities over GPC-LF and GPC-SF respectively. This may be due to the transfer of some of the tensile stresses to the sides by the strengthening system. The flexural capacity of GPC-SU and GPC-SF is dramatically lower than the reference beams because of the early cover delamination failure caused insufficient development length. Nevertheless, the strengthened beams continued to resist loads after CFRP failure until the GFRP reaches its  $\epsilon_{fu}^*$  followed by concrete crushing failure. This may be attributed to the substantial difference in the CFRP and GFRP modulus of elasticity values, therefore, CFRP carries a substantially higher amount of load, while GFRP bars are not strained to a similar extent. It is only after CFRP sheet fails that the GRRP bars contribute significantly towards the tensile load carrying function.

Table 3: Experimental failure mode and load level at CFRP, GFRP, and concrete crushing.

Sample	$M_{n,CFRP}$	$M_{n,GFRP}$	$M_{n,CC}$	Failure Mode
GPC-R1	-	53.9	63.9	Concrete Crushing
GPC-R2	-	58.9	66.4	Concrete Crushing
GPC-LF	53.2	56.8	73.6	CFRP Rupture
GPC-LU	61.6	56.4	62.4	CFRP Rupture
GPC-SF	23.6	58.8	62.0	Cover Delamination
GPC-SU	25.6	50.8	78.4	Cover Delamination

Fig. 2 presents the relationship between the applied load and mid-span deflection. The first loading phase of all 6 beams represents the elastic behavior which corresponds to the beam's uncracked condition. After cracking the load-deflection curve shows a slight nonlinearity with a reduced slope up to a load at concrete crushing for control beams or at CFRP sheet failure for the strengthened beams. The strengthened beams have steeper load-deflection curve because of the enhanced stiffness that is provided the CFRP strengthening system. GPC-LF and GPC-LU experienced an abrupt drop in the applied load resistance after CFRP rupture failure this is due to the sudden change in stiffness of the system. While GPC-SF and GPC-SU showed a slight drop in load due to the peeling of the concrete cover. All the 4 strengthened beams continued to resist additional load as the GFRP continues to strain after CFRP failure. This continued up to the load at which the  $\epsilon_{fu}^*$  of GFRP bars was achieved followed by concrete crushing at the absolute peak load.

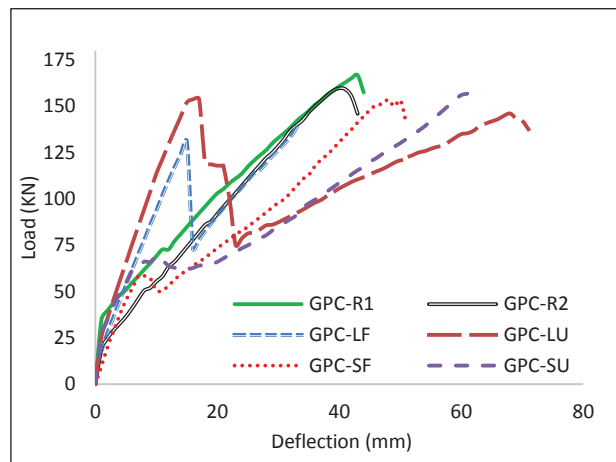


Figure 2: Load-Deflection relationship

## 5. Summary and Conclusion

This paper studied the performance of concrete beams reinforced with GFRP rebars and strengthened with CFRP sheet under four points quasi-static loading. Failure modes, flexural capacities, and load-deflection relationship were determined. The findings of this experimental program are summarized as below:

- The observed failure mode of the control beams is concrete crushing. However, the strain at GFRP bars exceeded its  $\epsilon_{fu}^*$  before crushing failure indicating that the specified  $\epsilon_{fu}^*$  is conservative.

- Externally bonded CFRP sheet in a GFRP-CFRP system works very differently from that of CFRP-steel system. In conventional cases after steel yielding the bars will exhibit plastic behavior and will continue to contribute to load carrying capacity side by side with CFRP sheets. However, in case of GFRP reinforced beams which are CFRP strengthened, the moment carrying capacity of the beams did not change significantly from the reference beams because the GFRP bars have a much lower modulus value than the CFRP sheets. However, for such systems, the original capacity of the beams is restored, provided sufficient development length is ensured for the CFRP sheets.
- For long strengthening schemes, both flat and U-shaped, the failure happens due to CFRP rupture. This shows the effectiveness of the long strengthening schemes in utilizing the strain capacity of the CFRP sheets. In case of short strengthening schemes, premature failure was experienced.
- The long strengthening schemes, both flat and U-wrap, restored the load carrying capacity of the damaged beams because proper development length was provided.
- For the short flat and short U strengthened beams experienced a decrease in moment resisting capacity. This indicates that such schemes are detrimental to the section capacity and must not be used.
- The CFRP strengthening system provided a stiffer member and reduced the ultimate deflection at CFRP failure to almost half of the ultimate deflection of the reference beams.

## References

- [1] Elbana, A., Evaluation of flexural behavior of reinforced concrete beams with glass fiber reinforced polymer (GFRP) bars, in Department of Civil and Environmental Engineering. 2018, University of Sharjah. p. 108.
- [2] Junaid, M.T., et al., Aspects of the deformational behaviour of alkali activated fly ash concrete at elevated temperatures. *Cement and Concrete Research*, 2014. 60: p. 24-29.
- [3] Junaid, M.T., et al., A mix design procedure for low calcium alkali activated fly ash-based concretes. *Construction and Building Materials*, 2015. 79: p. 301-310.
- [4] Davidovits, J. and J.L. Sawyer, Early high-strength mineral polymer. 1985, Google Patents.
- [5] Davidovits, J., Geopolymer cement. A review. Geopolymer Institute, Technical papers, 2013. 21: p. 1-11.
- [6] Provis, J. and J. van Deventer, Alkali Activated Materials State-of-the-Art Report, J. Provis and J.S.J. van Deventer, Editors. 2014, RILEM.
- [7] Junaid, M.T., A. Khennane, and O. Kayali, Stress-Strain Behaviour of Alkali Activated Fly Ash Concrete at Elevated Temperatures, in 2nd International Conference on Advances in Cement and Concrete Technology in Africa. 2016: Tanzania. p. 301-308.
- [8] Rangan, B., Fly ash-based geopolymer concrete. *Your Building Administrator*, 2008. 2.
- [9] Junaid, M.T., O. Kayali, and A. Khennane, Response of alkali activated low calcium fly-ash based geopolymer concrete under compressive load at elevated temperatures. *Materials and Structures*, 2017. 50(1): p. 50.
- [10] 440, A.C. Guide for the design and construction of structural concrete reinforced with FRP bars. 2007. American Concrete Institute.
- [11] Institute, A.C., Guide for the Design and Construction of Externally Bonded FRP Systems for Strengthening Concrete Structures, in ACI 440.2R-08. July, 2008, ACI Committee 440.

## HYBRID ALKALI-ACTIVATED PORTLAND CEMENTS

Lukáš Kalina<sup>(1)</sup>, Vlastimil Bílek Jr.<sup>(1)</sup>, Lada Bradová<sup>(1)</sup>, Radoslav Novotný<sup>(1)</sup>,  
Tomáš Opravil<sup>(1)</sup>, František Šoukal<sup>(1)</sup>

(1) Brno University of Technology, Materials Research Centre, Brno, Czech Republic

### Abstract

The most promising way to improve the sustainability of cement is to produce blended Portland cements with supplementary cementitious materials. Blast furnace slag (BFS) is one of significant pozzolan sources used worldwide in blended cements which contributes to lowering the environmental impact of cement industry. On the other hand, the replacement of Portland clinker is connected with undesirable effects such as the reduction of early strength development. In order to overcome this disadvantage, the study deals with the development of hybrid cements in which the utilization of solid waste alkaline activator quickly awakens the pozzolanic properties of BFS. New types of blended alkali activated cements were designed to meet the European standard EN 197-1 and classified to the Blastfurnace CEM III cements in accordance with the mechanical, physical and chemical requirements. The alkali activation caused an increase of early compressive strength in comparison with reference cement and at the same time the initial setting time was delayed which is also interesting from the point of view of concrete production. Moreover, this non-traditional hybrid alkali-activated Blastfurnace cement provides considerable ecological and economical potential.

### 1. Introduction

The cement industry is one of the most carbon-intensive industries required to produce Portland clinker which is the key component of ordinary Portland cement (OPC). The industry predicts that the global cement production will reach 5.9 billion tons by 2020 which represents more than 4.8 Gt of CO<sub>2</sub> emissions [1]. The global approach to reducing the carbon footprint of cement includes several options. Firstly, the alternative fuels and/or raw materials should be used. Further the replacement of Portland clinker with supplementary cementitious materials (SCMs) is suggested. The development of alternative binders not based on Portland clinker represents the third option and finally the capture of CO<sub>2</sub> emitted by cement plants

could be another solution [2]. In most parts of the world, the utilization of SCM is particularly advantageous, especially if the “low-carbon” materials such as industrial waste products are used. Blast furnace slag (BFS), a by-product from pig iron production, or fly ash from coal combustion provide a viable way to substitute Portland clinker [3]. On the other hand, blended cements with high content of SCMs can slow down the early strength development which represents considerable drawback in practical applications [4]. Apart from low clinker content, one of the potential solutions is the production of new cement binders, like hybrid alkaline cements. Hybrid alkali-activated Portland cements aim at combining the positive characteristics of traditional OPC materials with those of alkali-activated materials (AAMs), generating materials with enhanced durability and mechanical properties [5]. These facts were also confirmed in the study of Gelevera and Munzer [6] who focused on alkali-activated Portland clinker/BFS blends in which the increase of BFS content in conjunction with alkali silicate solution led to higher compressive strength and frost resistance as well.

The production of hybrid binders can be achieved in two different approaches. The first option is the activation of aluminosilicate materials (mixture of OPC and SCM) with high alkaline solution which is the conventional procedure for AAMs preparation. Whereas the second possibility consists in the production of special type of cement with incorporated alkaline activator mixed in solid form with other cement components. The binder formed in this way provides two major benefits. It can be activated only with water and subjected to certain criteria it can be classified to Blastfurnace CEM III/C cements in accordance with European standard EN 197-1 [7]. Moreover, such developed non-traditional hybrid cement fulfils the ecological and economical aspects due to the utilization of waste alkaline activator. The verification of mechanical, physical and chemical properties of the new type of hybrid alkali-activated Portland cement is the main purpose of this study.

## 2. Experiment

### 2.1 Materials and sample preparation

The hybrid alkali-activated Portland cements were composed of Portland clinker (HeidelbergCement Czech Republic, Ltd.), blast furnace slag (ArcellorMittal Ostrava, Ltd.) and dried, milled technological waste from waterglass production (Vodní sklo, Ltd.). The chemical compositions of raw materials are summarized in Tab. 1.

Table 1: Chemical composition (wt. %) of used raw materials as determined using XRF.

	CaO	SiO <sub>2</sub>	Al <sub>2</sub> O <sub>3</sub>	Na <sub>2</sub> O	K <sub>2</sub> O	MgO	SO <sub>3</sub>	Fe <sub>2</sub> O <sub>3</sub>	TiO <sub>2</sub>	MnO
Portland clinker	64.9	20.7	5.4	0.3	0.6	1.3	3.0	3.3	0.3	0.2
BFS	41.1	34.7	9.1	0.4	0.9	10.5	1.4	0.3	1.0	0.6
WG-waste*	0.1	84.2	0.4	14.2	0.2	–	–	0.6	0.3	–

\*The waterglass waste (WG-waste) contains 7.89 wt. % of Na<sub>2</sub>O and 16.03 wt. % of SiO<sub>2</sub> in soluble fraction determined according to conductometry titration.

The cement samples were designed according to the EN 197-1 standard for Blastfurnace CEM III/C cements. The content of Portland clinker was lowered to the minimum required



quantity (5 wt. %). The rest of binder was formed by BFS, WG-waste and minor additional constituents as shown in Tab. 2. The WG-waste was added to the hybrid cement with given Na<sub>2</sub>O/BFS ratio (0.3; 0.6; 0.9 and 1.2), therefore the tested samples were named according to that.

Table 2: Designed compositions of reference and hybrid cements (wt. %).

	REF.	H-0.3	H-0.6	H-0.9	H-1.2
Portland clinker	5.00	5.00	5.00	5.00	5.00
BFS	94.34	89.92	86.74	83.78	81.02
WG-waste (additive)	–	4.42	7.60	10.56	13.32
additional constituents	0.66	0.66	0.66	0.66	0.66

## 2.2 Testing methods

The compressive strengths of cement mortars were determined in accordance with EN 196-1 [8] at 7 and 28 days with w/c = 0.5. The standard siliceous sand was used in the amount of three times higher than the weight of cement. After 24 h of moist curing, the specimens were demolded and cured at 25 °C in water conditions. The initial setting time as well as the expansion were tested in accordance with EN 196-3 [9]. The total content of sulfate, recalculated to SO<sub>3</sub>, was obtained using the combustion analyzer (G4 ICARUS HF). The amount of chlorides was measured according to EN 196-21 [10]. Sulfate as well as chloride contents are the chemical requirements for the appropriate type of cement (CEM III). The loss on ignition and insoluble residue were determined according to EN 196-2. The process of hydration mechanism was explained by means of TAM Air isothermal calorimeter (TA instruments) at the temperature of 20 °C.

## 3. Results and Discussion

### 3.1 Chemical and physical properties of hybrid cements

Table 3 shows the chemical as well as physical properties of hybrid cements. With respect to the EN 197-1 standard, all hybrid cements meet the requirements for CEM III cement types. The loss on ignition and insoluble residue increased with higher content of alkaline activator mainly due to the siliceous sand present in WG-waste. The amount of insoluble residue with higher WG-waste (samples H-0.9; H-1.2) does not meet the EN 197-1 standard, which could be solved by the addition of effective ingredients in the form of fully soluble solid sodium silicate leading to lower the contribution of WG-waste with insoluble siliceous sand. Conversely, the sulfate and chloride content decreased with higher Na<sub>2</sub>O/BFS ratio which is related to lower amount of BFS containing these elements. The interesting results could be observed in case of initial setting time. Hybrid cements exhibited significant differences compared to reference sample. It was determined that lower content of alkalis contributed to the acceleration of setting time, however higher content (samples H-0.9; H-1.2) delayed it significantly. This behaviour is closely associated with different hydration mechanism discussed further. The expansion measurements did not show any substantial changes.

Table 3: Chemical and physical characteristics of reference and hybrid cements.

sample	Loss on ignition ( $\leq 5\%$ )	Insoluble residue ( $\leq 5\%$ )	Sulfate content as $\text{SO}_3$ ( $\leq 4\%$ )	Chloride content ( $\leq 0.1\%$ )	Initial setting time ( $\geq 75$ min)	Expansion ( $\leq 10$ mm)
REF.	0.96	–	0.61	0.031	162	0.9
H-0.3	1.25	2.27	0.58	0.028	158	0.4
H-0.6	1.57	4.74	0.56	0.022	142	0.3
H-0.9	1.68	7.31	0.55	0.022	187	0.2
H-1.2	1.70	8.97	0.53	0.015	324	0.5

The values in italics are the requirements for CEM III cement type according to EN 197-1 standard [7].

### 3.2 Mechanical properties of hybrid cements

The amount of WG-waste addition plays the key role not only in chemical and physical properties of hybrid cements but also affects the compressive strength development significantly. The percentage comparison of compressive strength between hybrid cements and reference sample is shown in Fig. 1. The results were obtained after 7 and 28 days with regards to prescribed values for early and standard strength as defined in the EN 197-1 standard [7]. It is obvious that the small amount of alkaline activator decreased the compressive strength down to certain limit. Nevertheless, if the  $\text{Na}_2\text{O}/\text{BFS}$  ratio rose to 0.9 (sample H-0.9), the compressive strength approached the reference sample. Moreover, the sample H-1.2 exhibited better results in comparison with the reference sample after 7 and 28 days.

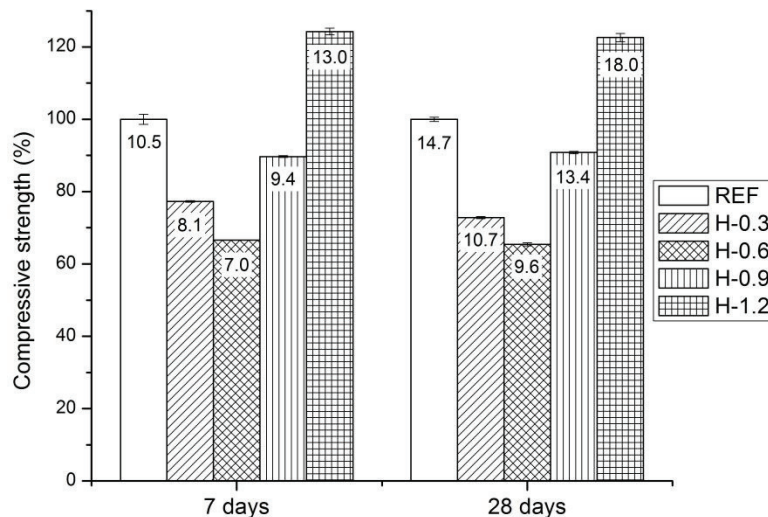


Figure 1: Compressive strength comparison of hybrid cements with reference sample without alkaline activator (values in columns represent the compressive strength in MPa).

### 3.3 Hydration process of hybrid cements

The hydration process which is closely related to the mechanical properties of cements, is shown in Fig. 2. The calorimetric curves characterizing the heat flow can be observed in Fig. 2A. The first peak (zoomed area) occurring during the first 30 minutes is associated with the wetting and dissolution of BFS and Portland clinker grains. The results suggest that higher content of alkaline activator leads to better dissolution of cementitious particles. Thereafter, the induction period took place. It is well observed that small amount of alkaline activator contained in samples H-0.3 and H-0.6 shortens the induction period. Contrary, higher  $\text{Na}_2\text{O}/\text{BFS}$  ratio (H-0.9; H-1.2) delays the C-S-H gel creation in comparison with the reference sample. The total amount of heat evolution (Fig. 2B) is particularly associated with the quantity of C-S-H gel formation. Higher addition of WG-waste resulted in higher amount of C-S-H gel but only in early stages of hydration process. Whereas, the evolution of hydration heat very quickly slowed down in case of hybrid cements, the reference sample exhibited almost linear increase of heat. In other words, it can be expected that the amount of binder phase will be higher in reference sample compared to hybrid cements with lower content of alkaline activator after a long time. These results correspond to compressive strength development after 7 and 28 days when only the sample with the highest WG-waste addition exceeded the values of early and standard strengths of reference sample.

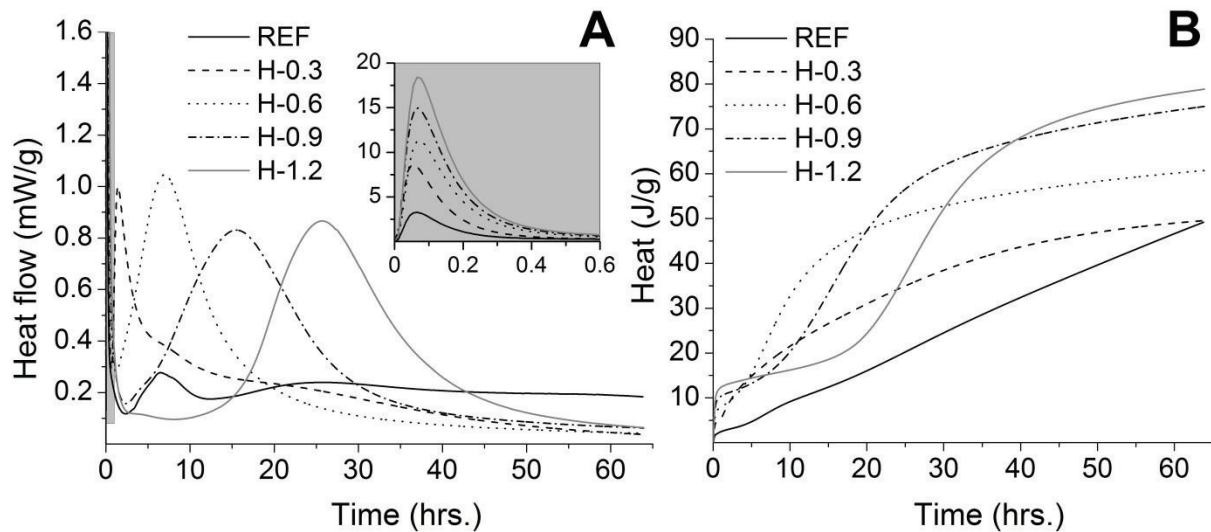


Figure 2: Evolution of heat flow (A) and total heat (B) of hybrid cements and reference sample without alkaline activator.

### 4. Conclusion

The results show that hybrid cements with alkaline activator in the form of WG-waste are a promising option to reduce the Portland clinker content in cements which contributes to the production of more ecological as well as economical type of cements belonging to CEM III/C class. Especially, the hybrid cements with the weight ratio  $\text{Na}_2\text{O}/\text{BFS} = 1.2$  achieved better mechanical properties in early and long-term ages compared to standard CEM III/C cement.

### **Acknowledgments**

This outcome has been achieved with the financial support by the project: Materials Research Centre at FCH BUT- Sustainability and Development, REG LO1211, with financial support from the National Programme for Sustainability I (Ministry of Education, Youth and Sports) and GA17-03670S “Development of shrinkage reducing agents designed for alkali activated systems”, with financial support from the Czech Science Foundation.

### **References**

- [1] Gupta, A., Cement Primer Report, Carbon War Room (2011)
- [2] Gartner, E. and Hirao, H., A review of alternative approaches to the reduction of CO<sub>2</sub> emissions associated with the manufacture of binder phase in concrete, *Cem Concr Res* 78 (2015), 126-142
- [3] Lothenbach, B. et al, Supplementary cementitious materials, *Cem Concr Res* 41 (2011), 1244-1256
- [4] Donatello, S. et al, The early age hydration reactions of hybrid cement containing a very high content of coal bottom ash, *J Am Ceram Soc* 97 (2014), 929-937
- [5] Rivera, J.F. et al, Hybrid cement based on the alkali activation of by-products of coal, *J Construction* 13 (2014), 31-39
- [6] Gelevera, A.G., and Munzer, K., Alkaline Portland and slag Portland cements. Krivenko, P.V. (ed.) *Proceedings of the First International Conference on Alkaline Cements and Concretes, Ukraine (1994)*, 173-179
- [7] EN 197-1:2005, Cement – Part 1: Composition, specifications and conformity criteria for common cements, European committee for standardization, EU (2005)
- [8] EN 196-1:2016, Methods of testing cement – Part 1: Determination of strength, European committee for standardization, EU (2015)
- [9] EN 196-3:2016, Methods of testing cement – Part 3: Determination of setting times and soundness, European committee for standardization, EU (2016)
- [10] EN 196-21:1992, Methods of testing cement. Determination of the chloride, carbon dioxide and alkali content of cement, European committee for standardization, EU (1992)
- [11] EN 196-2:2013, Methods of testing cement. Chemical analysis of cement, European committee for standardization, EU (2013)

## **INFLUENCE OF SODIUM HYDROXIDE CONCENTRATION ON MECHANICAL PARAMETERS OF FLY ASH-BASED GEOPOLYMER**

**Natalia Paszek <sup>(1)</sup>, Marcin Górski <sup>(1)</sup>**

(1) Silesian University of Technology, Gliwice, Poland

### **Abstract**

Geopolymer is considered to be the new alternative to the ordinary Portland cement concrete. Some of its characteristics surpass OPC concrete parameters. Additionally, it should be emphasised that geopolymer is an environmentally friendly material since it is based mainly on wastes and the CO<sub>2</sub> emission during its production is limited because of lack of the cement in the composition. Geopolymer parameters can be influenced by many factors. In the paper, the influence of NaOH concentration on the compressive and flexural strength of fly-ash based geopolymer is considered. Tests were carried out on right rectangular prism samples made from five mixtures containing fly ash, sodium silicate and sodium hydroxide of varying concentrations: 6, 8, 10, 12 and 14 mol/L. Compressive and flexural strength tests were performed after 7 days. Tests showed that compressive strength generally increases with the increase of NaOH concentration. No obvious dependence between flexural strength and NaOH concentration was found.

### **1. Introduction**

Geopolymer is an aluminosilicate material formed during geopolymerization process by activation of oxides of aluminium and silicon minerals or aluminosilicate minerals by alkalis [1]. The term "geopolymer" was applied firstly by a French material scientist Joseph Davidovits in the early 1980s [2]. According to Davidovits, geopolymeric materials can be treated as "polymers" because of the ability to polycondensate and to adopt the final shape rapidly in the low temperatures. The prefix "geo" stands for the fact that they are hard and resistant materials able to withstand high temperatures [3]. Regularly, when talking about geopolymer, the ecological aspect of the matter is brought up. Geopolymer is considered to be a new alternative binder without cement in the composition which allows for energy and greenhouse gases emission savings. According to different estimations, the CO<sub>2</sub> emission

during geopolymer production can be lowered in comparison to the concrete production by 9% to 80% [4,5]. The gross disparity between estimations results mainly from the different scientific approach to the calculations, different basic assumptions and finally, different meaning of keywords "geopolymer" and "concrete" which hide the versatile range of materials having various compositions. The next reason why geopolymer is considered to be environmental friendly material is the fact that it can be based on industrial and mining wastes. It means that geopolymer production not only does not consume raw materials like limestone, marl or chalk which are used for cement production [6] but also allows for wastes utilisation. Almost every country produces wastes which can state the main component of geopolymer. It means that in nearly each country geopolymer can be a response to the problem of wastes utilisation. Furthermore, production of geopolymer is possible almost everywhere without transport of wastes for long distances what would be senseless from the ecological point of view. Some kinds of wastes are specific for particular parts of the world and cannot be easily found in the others. Portuguese scientists found out that residues which are by-products of the Panasqueira tungsten mine can be effectively used as a precursor in geopolymer concrete [7]. Geopolymer is likewise believed to be the solution for the excess of the oil sand wastes in Canada [1]. In some cases, geopolymer is not only the way of economic and ecological wastes utilisation but also gives a possibility to immobilise toxic substances present in wastes [3,8]. According to this, the necessity of toxic red mud waste utilisation was one of the main reasons why scientists tried to add it to the geopolymer concrete [9].

Fly ash is one of the most popular industrial by-products used as a precursor in geopolymer. Fly ash is produced all over the world and consists mainly of silicon and aluminium oxides what makes it an excellent material for geopolymeric reaction. Nonetheless, it should be emphasised that properties and chemical composition of fly ash can differ in dependence on its source [10]. Consequently, there is no one optimal composition for all fly ash-based geopolymers. Exact parameters of geopolymer containing fly ash from the new source cannot be predicted on the base of literature examples either. Additionally, mechanical characteristics of geopolymer are affected by many factors starting from the choice of exact composition and ending with the curing conditions [10].

The primary goal of the paper is to present the influence of NaOH concentration on the compressive and flexural strength and density of the fly ash-based geopolymer. Fly ash used in the experiment comes from the Polish power plant and is a by-product of the black coal combustion.

### **1.1 Influence of NaOH concentration on the geopolymer strength – State of Art**

Many scientists investigated the influence of sodium hydroxide concentration on the geopolymer strength. Tests results presented in the scientific literature show that impact of NaOH concentration on geopolymer strength cannot be easily predicted since it depends on many factors, mainly on the kind of the precursor.

According to the Wang et al. [11], both compressive and flexural strength of metakaolin-based geopolymer increase with the increase of NaOH concentration. Prepared mixtures contained metakaolin, sodium silicate and sodium hydroxide in concentrations: 4, 6, 8, 10 and 12 mol/L. The most significant increase in compressive strength was noticed between samples activated by NaOH of 8 and 10 mol/L. The increase in flexural strength was approximately monotonic. The similar dependence was also noticed by Stevenson 2005 [12]. In that experiment differences between results of samples containing NaOH of different

concentrations were more significant. The compressive strength of samples made of mixture activated with NaOH of concentration 10 mol/L was over 5 times greater than of concentration 7 mol/L. The compressive strength of samples containing NaOH of concentration 12 mol/L increased once more about 1,5 times.

As it was proved by tests, the influence of NaOH concentration on the compressive strength of fly ash-based geopolymers is depended on the sodium silicate to NaOH ratio. Sathonsaowaphak et al. 2009 [13] compared results obtained on samples activated by sodium silicate and NaOH mixed in ratios 1,5 and 0,67. Concentrations of NaOH were equal to: 5; 7,5; 10; 12,5 and 15 mol/L. In the first case (sodium silicate to NaOH ratio equal to 1,5), the monotonic increase of compressive strength from about 18 MPa to 35 MPa was registered. All samples activated by sodium silicate and NaOH in ratio 0,67 obtained higher compressive strengths, but the influence of NaOH concentration was not monotonic this time. Firstly, there was registered a significant increase in compressive strength between samples activated with NaOH of concentration 5 and 7,5 mol/L. Then, the compressive strength decreased slightly for samples activated with NaOH of concentration 10 mol/L, increased for next part (NaOH concentration 12,5 mol/L) and decreased again.

The similar experiment was conducted by Chindaprasirt et al. 2007 [14]. The lignite fly ash-based geopolymer was activated by a mixture of sodium silicate and sodium hydroxide at concentrations 10, 15 and 20 mol/L. In case of samples containing sodium silicate and sodium hydroxide mixed in ratios 1,0 and 3,0, the compressive strength increased with the increase of NaOH concentration. Samples activated with sodium silicate mixed with NaOH in ratio 0,67 obtained the same compressive strength for NaOH concentrations 10 and 20 mol/L and higher strength for NaOH concentration 15 mol/L. Almost opposite dependence was registered for samples containing 1,5 times more sodium silicate than NaOH.

Another experiment performed on fly ash-based geopolymer activated only by sodium silicate this time was presented by Alvarez-Ayso et al. 2008 [15]. During the test, fly ash was mixed with NaOH of concentrations 5, 8 and 12 mol/L. The experiment showed that compressive strength increases significantly with the increase of NaOH concentration.

On the contrary to examples showed above, geopolymer based on the waste glass powder from crushed glass bottles achieves higher compressive strength for smaller NaOH concentrations [16].

## **2. Laboratory tests**

The main goal of the laboratory tests was to establish the influence of NaOH concentration on flexural and compressive strength and the density of fly ash-based geopolymer. The flexural strength test was conducted on right rectangular prism samples of dimensions 4x4x16cm. Compressive strength test was carried out on halves of samples broken during the flexural strength test according to the European standard EN 196-1:2016 [17].

### **2.1 Mixture composition**

Each mixture contained the same components used in the same quantity. The exact mixture composition is presented in Tab. 1. Fly ash was the only one precursor. Sodium silicate and sodium hydroxide were used in a role of activators. The only variable was the NaOH

concentration. There were prepared five mixtures containing NaOH of concentrations 6, 8, 10, 12 and 14 mol/L.

Table 1: Mixture composition.

	Fly ash	Sodium silicate	Sodium hydroxide
Quantity [kg/m <sup>3</sup> ]	1133	664	219
Contribution [%]	56,2	32,9	10,9

## 2.2 Samples preparation

Mixtures activated by NaOH of different concentration were prepared separately. Sodium hydroxide solution was prepared 24 hours before mixtures preparation by dissolving sodium hydroxide in solid form in demineralized water. The procedure for samples preparation was the same for all mixtures. Sodium hydroxide was mixed with sodium silicate by 5 minutes and then poured into the vessel with the fly ash. All components were mixed with a mechanical mixer. The mixture was placed into forms, covered and kept in the climatic chamber for 24 hours in the temperature of 60°C and humidity of 40%. After 24 hours samples were demoulded and kept at the room temperature for the next 6 days.

Curing regime was chosen on the base of experience taken from literature. Both curing time and curing temperature has an influence on mechanical properties of geopolymer. Many scientists believe that 60°C is the optimal curing temperature [18,10].

## 2.3 Test results

Compressive and flexural strength test results are presented respectively in Fig. 1 and Fig. 2.

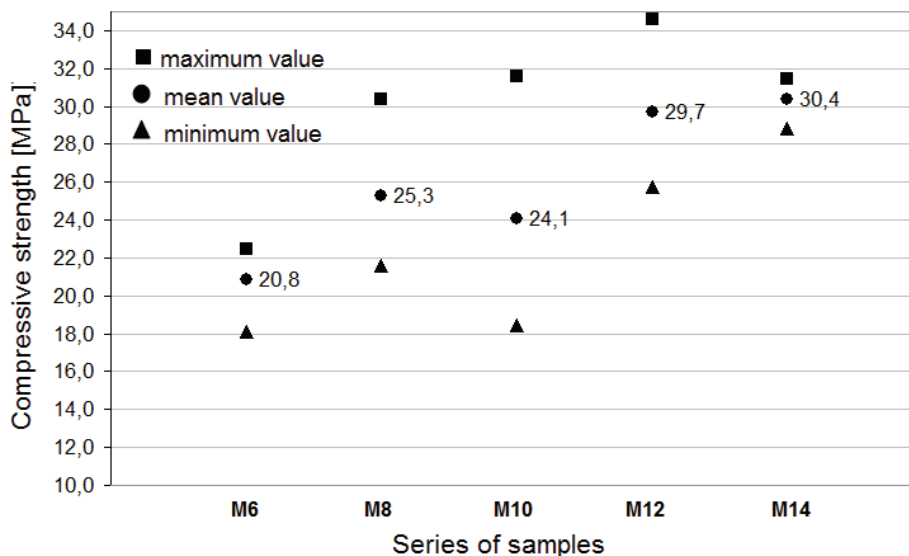


Figure 1: Compressive strength of geopolymer samples after 7 days.

The conducted test showed that compressive strength of fly ash-based geopolymer increase with the increase of NaOH concentration. The only exception is the compressive strength of samples containing NaOH of concentration 10 mol/L which average value is slightly smaller than the average compressive strength of samples activated with NaOH of concentration



8 mol/L. Additionally, results of samples activated with NaOH of concentration 10 mol/L had the most significant standard deviation. The highest compressive strength was obtained by samples activated with NaOH of concentration 14 mol/L. The standard deviation of these results was smallest.

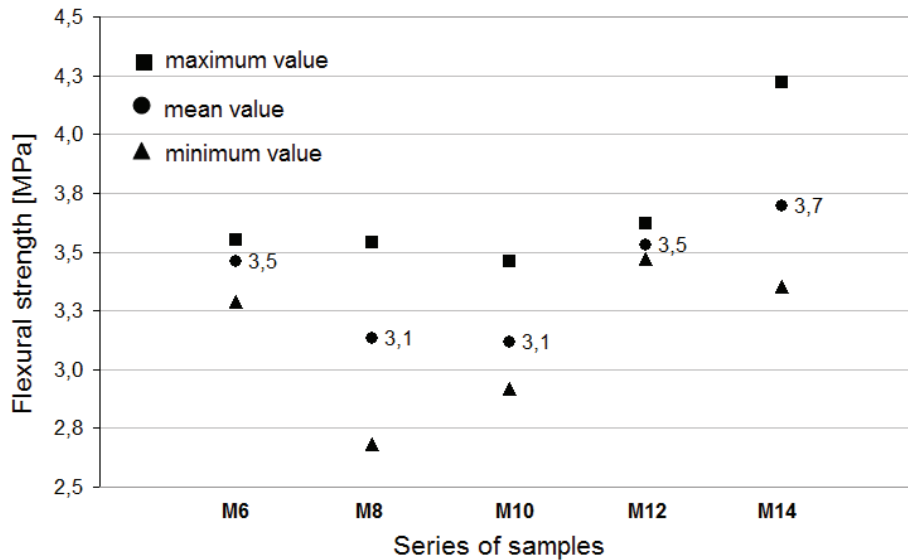


Figure 2: Flexural strength of geopolymers samples after 7 days.

No obvious connection between NaOH concentration and flexural strength was registered. The highest flexural strength was observed for series of samples M14 but also the most significant standard deviation for these results was registered.

No dependence between NaOH concentration and density of fly ash-based geopolymer samples were registered either. Differences between densities of samples from different series were small. Average value of all densities was equal to  $1720 \text{ kg/m}^3$ . This is relatively low value in comparison to the density of cement mortar.

### 3. Summary

During the experiment, the influence of NaOH concentration on flexural and compressive strength and density of geopolymer was investigated. Test results showed that compressive strength of examined fly ash-based geopolymer generally increases with the increase of NaOH concentration. The highest compressive strength was obtained by samples containing NaOH of concentration 14 mol/L and the smallest by samples containing NaOH of concentration 6 mol/L. No straight dependence between flexural strength and NaOH concentration was registered. Similarly, due to the test results, the density of geopolymer is not connected with NaOH concentration.

### Acknowledgements

REMINE H2020-MSCA-RISE, support of the Polish Ministry of Science and Higher Education for Department of Structural Engineering, Silesian University of Technology (Grant No. BK-237/RB6/2018) and project 341284/PnH /2016

## References

- [1] Rao, F. and Liu, Q., Geopolymerization and its Potential Application in Mine Tailings Consolidation: A review, *Min Proc Ext Met Rev* 36 (2015), 6
- [2] Provis J. L. and van Deventer J. S. J., *Alkali Activated Materials. State-of-the-Art Report*, RILEM TC 224-AAM, London (2014)
- [3] Davidovits, J., Geopolymers: Inorganic polymeric new materials, *J Therm Anal Calorim* 37 (1991), 1633-1656
- [4] Tuner, L. and Collins, F., Carbon dioxide equivalent (CO<sub>2</sub>-e) emissions: A comparison between geopolymer and OPC cement concrete, *Constr Build Mater* 43 (2013), 125-130.
- [5] von Weizsacker, E., Hargroves, K., Smith, M. H., Desha, C. and Stasinopoulos, P., *Factor Five: Transforming the Global Economy Through 80% Improvements in Resource Productivity*, Earthscan, London (2009)
- [6] Neville, A., *Właściwości betonu*, Kraków (2000)
- [7] Pacheco-Torgal, F., Castro-Gomes, J. and Jalali, S., Tungsten mine waste geopolymeric binder: Preliminary hydration products investigations, *Constr Build Mater* 23 (2009), 200-209
- [8] Boca Santa, R. A. A., Soares, C. and Riella, H. G., Geopolymers with a high percentage of bottom ash for solidification/immobilization of different toxic metals, *J Hazard Mater* 318 (2016), 145-153
- [9] Toniolo, N., Rincon, A., Avadhut, Y. S., Hartmann, M., Bernardo, E. and Boccaccini, A. R., Novel geopolymers incorporating red mud and waste glass cullet, *Mater Lett* 219 (2018), 152-154
- [10] Hardjito, D. and Rangan, B. V., Development and properties of low-calcium fly ash-based geopolymer concrete. Research Report GC 1 Faculty of Engineering Curtin University of Technology, Perth (2005)
- [11] Wang, H., Li, H. and Yan, F., Synthesis and mechanical properties of metakaolinite-based geopolymer, *Colloids Surf, A Physicochem Eng Asp* 268 (2005), 1-6, 2005
- [12] Steveson, M., Relationships between composition, structure and strength of inorganic polymers. Part I: Metakaolin-derived inorganic polymers, *J Mater Sci* 40 (2005), 2023-2036
- [13] Sathonsaowaphak, A., Chindaprasirt, P. and Pimraksa, K., Workability and strength of lignite bottom ash geopolymer mortar, *J Hazard Mater* 168 (2009), 44-50
- [14] Chindaprasirt, P., Chareerat, T. and Sirivivatnanon, V., Workability and strength of coarse high calcium fly ash geopolymer, *Cement Concrete Comp* 29 (2007), 224-229
- [15] Alvarez-Ayso, E., Querol, X., Plana, F., Alastuey, A., Moreno, N., Izquierdo, M., Font O., Moreno, T., Diez, S., Vazquez, E. and Barra, M., Environmental, physical and structural characterization of geopolymer matrixes synthesised from coal (co-)combustion fly ashes, *J Hazard Mater* 154 (2008), 175-183
- [16] Pascual, A. B., Tognonvi, M. T. and Tagnit-Hamou, A., Waste glass powder-based alkali-activated mortar, *Int J Res Eng Technol* 3 (2014), 15-19
- [17] EN 196-1:2016, *Method of testing cement – Part 1: Determination of strength*, Brussels (2016)
- [18] Bing-hui, M., Zhu, H., Cui, X. M., He, Y. and Gong, S. Y., Effect of curing temperature on geopolymerization of metakaolin-based geopolymers”, *Appl Clay Sci*, 99 (2014), 144-148

## INVESTIGATION ON STRENGTH DEVELOPMENT IN GEOPOLYMER MADE OF POWER PLANT FLY ASH SUSPENSION

Szymon Dawczyński <sup>(1)</sup>, Anita Kajzer <sup>(1)</sup>, Marcin Górski <sup>(1)</sup>

(1) Silesian University of Technology, Gliwice, Poland

### Abstract

In general, the geopolymers have potential to compete with cement-based materials because of their good mechanical parameters as well as because they are considered as environmentally friendly materials. It is not only because of the reduction of carbon dioxide during the production process (which reduces greenhouse effect) but also because of a large amount of industrial wastes (like fly ashes, mine tailings or metallurgical slags) which are consumed. Paper presents laboratory investigation on geopolymeric binder made of fly ash suspension, metakaolin, and recycled ground glass. The geopolymerisation reaction was activated with the use of a 10M solution of sodium hydroxide mixed with sodium silicate. The researches were focused on strength development in the first two weeks just after the day when samples were prepared. The curing time in the climatic chamber was 24 hours in a temperature of 60°C and humidity 40%. The prism samples 40x40x160 mm were used for flexural strength tests and halves of broken prisms were used for compression strength tests. These tests were performed after 1, 3, 7 and 14 days after samples preparation. In both cases, it was noted that the strength was increased with the increasing of curing time (in case of flexural strength from 1.29 to 2.58 MPa, and in case of compressive strength from 19.05 to 21.99 MPa).

### 1. Introduction

Nowadays, concrete is the most frequently used structural material all over the World. This is obvious due to its very good strength parameters, good performance, and durability, as well as the relatively low cost of production. From the ecological point of view, the most significant disadvantage of concrete is the fact that during the production process of cement (a key ingredient of concrete), a significant amount of carbon dioxide is released to the atmosphere. This is the result of two issues: first one is related to decomposition of  $\text{CaCO}_3$  (limestone) into

CaO (lime) and CO<sub>2</sub> by providing the heat, and the second one is associated with the combusting of fossil fuels in order to obtain the energy necessary to ensure the correct course of the clinker burning process (the required temperature may reach even up to 1500°C) [1]. Unfortunately, every percent of this harmful gas released into the atmosphere contributes to poisoning the environment and climate change, which affects our lives directly. More detailed information about CO<sub>2</sub> emission from cement production can be found in [2], and in general about global emission in [3, 4]. Taking into consideration the carbon dioxide emission, as well as the need for natural resources, the possibility of replacing concrete with other, more environmentally friendly material is very attractive. Such an alternative may be geopolymers or in general alkali-activated materials (AAM). From the mechanical point of view, geopolymers have similar strength properties as ordinary concrete has [5]. However, interesting is that they also have other features that far outweigh cement-based materials. One of them is high-temperature resistance. Davidovits tests [6] showed that geopolymers composed of metakaolin, sodium, and potassium silicate were able to withstand the temperature even up to 1400°C. They are also more heat-stable than concrete – the binding water which builds up vapour pressure in the event of fire results in spalling or cracking. Depending on the mix composition, a temperature that can withstand varies between 800-1400°C. Also, another interesting fact – geopolymers are highly resistant to chemicals like acids, chlorides, and sulphates. Ready products that contain metakaolin or fly ash exhibit high resistance to sulphuric acid, nitric and hydrochloric acids in comparison to OPC concrete. The tests [7] indicated that geopolymers activated with sodium hydroxides had better resistance than those activated with a solution of sodium silicate.

Even though the geopolymers are known for several dozen years, still there are no standards or formal regulations regarding their structural use as well as designing and testing procedures. This paper presents laboratory tests focused on strength development in time, as a contribution to the complex description of these materials.

## **2. Mixture and samples preparation**

Geopolymers are obtained as a product of the chemical reaction between aluminosilicate material (precursor) and alkaline solution (activator). Some additions are often added to the mixture to improve the geopolymer properties. There are many possibilities in proportioning of components in dependence on what result we expect or what is our primary aim.

### **2.1 Precursor**

The precursor used in this mixture is a carbon suspension. It is fly ash obtained from Bełchatów Power Plant – the largest brown coal power plant in the world. The power plant is located in the central part of Poland, and it is the largest emitter of carbon dioxide in this country. The fly ash suspension is an ash/dust depositing on electrofilters in huge boilers which is a product of burning brown coal. This fly ash is extremely fine material, what makes that it has higher reactivity. This feature is essential to the geopolymerization process.

The fuel that is used for energy production is brown coal from a nearby open-cast mine. The most important effect of the power plant's operation is the emission of a large amount of pollutants like: sulphur dioxide, nitrous oxide, carbon monoxide and ashes. For this reason, four-chamber electrofilters were installed in every block. The ash is captured by electrofilters,

then it is transmitted through the pipeline system into the reservoir, and finally, it is transmitted to special humidifiers. In the next step, it is served to the mine excavation by conveyor belt.

Because of the volume of produced wastes, the fly ash from those electrofilters was chosen to be the primary product of the mix to prepare geopolymer samples. An additional advantage is the fact that if more fly ash is used in the mixture, the volume of metakaolin can be reduced. A large amount of metakaolin in the mix results in higher energy consumption which is another problem of this type of mixtures.

The exact composition of fly ash suspension from Belchatów Power Plant is shown in Tab. 1.

Table 1: Oxide composition of fly ash suspension.

Oxides	Mass (%)
SiO <sub>2</sub>	39.56
CaO	23.45
Al <sub>2</sub> O <sub>3</sub>	20.05
SO <sub>3</sub>	7.27
Fe <sub>2</sub> O <sub>3</sub>	5.72
TiO <sub>2</sub>	1.83
MgO	1.54
Na <sub>2</sub> O	0.42
K <sub>2</sub> O	0.17

## 2.2 Activator

The combination of sodium hydroxide and sodium silicate was used as a chemical activator of the geopolymerisation reaction. Pellets for preparation of the NaOH solution had 99.5% of purity and molar mass equal to 40 g/mol. As a combination of these pellets and demineralized water, it was obtained a solution with the concentration of 10M. The sodium silicate was the R-145 type with the purity higher than 99%. The molar ratio was between 1.6 and 2.6, while the density was about 1.45 g/cm<sup>3</sup>. The ratio of sodium silicate to sodium hydroxide was equal to 2.0.

## 2.3 Additives

The carbon fly ash suspension was combined with recycled ground glass and metakaolin. The ground glass in powder form was obtained as a result of crushing glass bottles in Los Angeles machine. The percentage share of the solid precursor in the mixture was about: carbon fly ash suspension 80%, recycled ground glass 10% and metakaolin 10%.

## 2.4 Mixture

The exact mass of all components was weighed with a laboratory scale with the accuracy of 1.0 mg. All dry components were mixed, and then the precursor and activator were combined

and mixed. The ratio of precursor to activator was equal to 1.0, while the ratio of precursor to sodium silicate was equal 1.5.

The fresh geopolymeric mixture was cast in a mould made of Plexiglas (PMMA) because it is characterized by high alkaline reaction so it might react with steel. All the samples were tightly covered because previous studies [8] have shown that it may influence the strength properties and it prevents the shrinkage cracking in the top layer of the samples. In the next step, the mould was placed in the climatic chamber with a constant temperature of 60°C and humidity 40%. The higher temperature of curing usually influences positively on final mechanical properties (both flexural and compression strength) [9] because it accelerates the geopolymerisation reaction. The exact curing temperature which has the most favourable consequences on the final strength of geopolymers was checked during the laboratory investigation [8]. All samples were prepared exactly in the same way and from the same mixture and then put into the climatic chamber for 24 hours. After the first day of heat curing, samples were put in the ambient temperature (20°C) up to the day of testing.

### 3. Test results

In case of cement-based materials, the tests are usually carried out 28 days after the samples preparation. However, because there are no geopolymer standards and test procedures at the moment, it cannot be explicitly stated what the optimal time for testing the strength properties is. For this reason, the impact of time (from the moment of samples preparation to the time of conducting test) on strength parameters, was examined in this paper. The tests have been made on the basis of the standard procedures described in [10]. The flexural strength, as well as the compression strength, were investigated after 1, 3, 7 and 14 days from the moment when the samples were made.

#### 3.1 Flexural strength test

It was the regular three-point flexural test with the span length between the supports equal to 100mm. The load was applied on the upper surface of the sample, in the middle of the span length. An example of the failure of the geopolymer sample is shown in the Fig. 1 left. While in Fig. 2 there are presented average values of bending strength for each set of samples.



Figure 1: Left: an example of the flexural failure, Right: an example of compression failure.

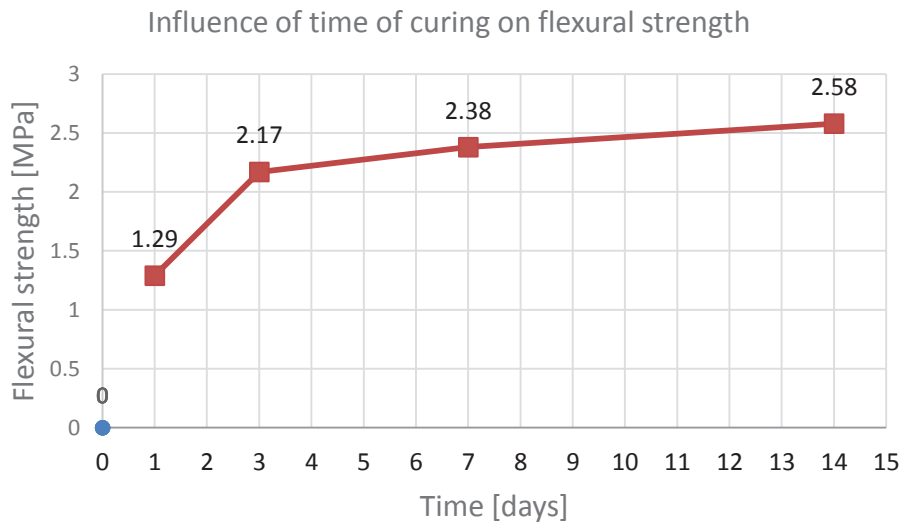


Figure 2: Results of three-point bending test.

### 3.2 Compression strength test

An example of the compression failure of the geopolymer sample is shown in the Fig. 1 right. The values of compression strength were determined from the destructive forces magnitudes. The results of those tests are presented in Fig. 3.

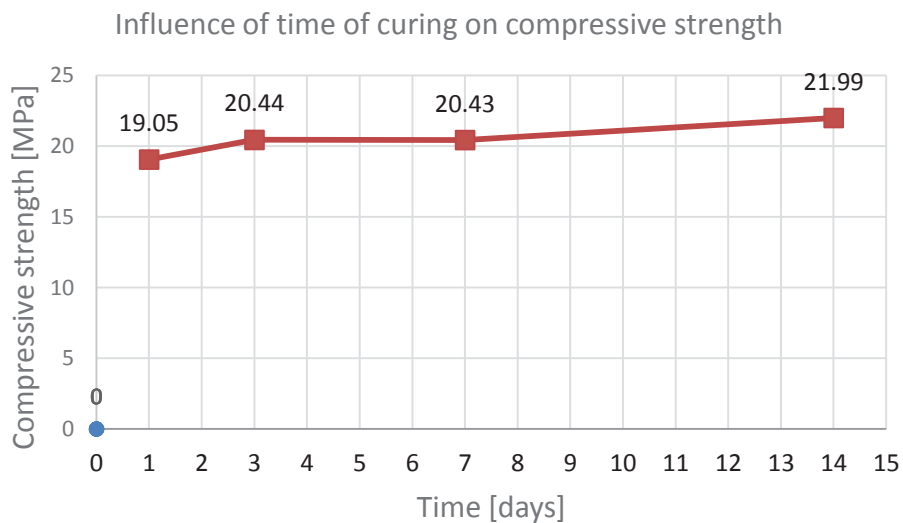


Figure 3: Results of the compression test.

## 4. Final remarks

Geopolymers are a broad group of materials with good mechanical properties. In case of flexural strength, it could be observed that with the increasing of curing time also the strength

increased. The most significant increase was observed between 1<sup>st</sup> and 3<sup>rd</sup> day – the growth has reached over 68%. Between 3<sup>rd</sup> and 7<sup>th</sup> day (the period was twice larger), the growth was equal to 9.7%. While in the last period – between 7<sup>th</sup> and 14<sup>th</sup> day – the flexural strength growth was only 8.4%. Of course, also it would be interesting to know the strength value after 28 days (like in the case of cement-based materials), but these tests are still ongoing.

In case of compressive strength results, it can be observed that in two periods – between 1<sup>st</sup> and 3<sup>rd</sup> day and between 7<sup>th</sup> and 14<sup>th</sup> day – the strength increase in relative terms was equal 7.3% and 7.6%, but in absolute values, it was only 1.39 MPa and 1.56 MPa respectively.

The presented results indicate that structural behaviour of geopolymers is different from the structural behaviour of any other cement-based materials.

Cement is still the most - known and used material in the world. Especially in the construction industry. However, geopolymers have the potential to compete with those products due to their good mechanical, psychical and chemical properties. The most important feature of this material is the possibility of using the industrial wastes as well as the reduction of CO<sub>2</sub> emission. Its environmentally friendly performance is very much needed nowadays.

### Acknowledgement

This paper has been prepared with the financial support of the Silesian University of Technology (BK-235/RB6/2017); European Union's Horizon 2020 Research and Innovation Staff Exchange (RISE) programme (Marie Skłodowska-Curie Actions) under grant agreement no. 645696, project REMINE (Reuse of Mining Waste into Innovative Geopolymeric-based Structural Panels, Precast, Ready Mixes and Insitu Applications) and Polish Ministry of Science and Higher Education project no. 341284/PnH /2016.

### References

- [1] Crow, J.M., The concrete conundrum, Chem. World March (2008), 62-66
- [2] Andrew, R. M., Global CO<sub>2</sub> emissions from cement production, Earth Syst. Sci. Data 10 (2018), 195-217
- [3] Le Quéré, C. et al., Global Carbon Budget 2016, Earth Syst. Sci. Data 8 (2016), 605-649
- [4] Le Quéré, C. et al., Global Carbon Budget 2017, Earth Syst. Sci. Data 10 (2018), 405-448, in review
- [5] Dawczyński, S., Górski, M., Krzywoń, R., Geopolymers as an alternative ecological material for buildings, Proceedings of the 14<sup>th</sup> International Conference on New Trends in Statics and Dynamics of Buildings, Slovakia (2016), 374-378
- [6] Davidovits, J., Geopolymers – Inorganic polymeric new materials, Jour. of Therm. Anal. 37 (1991), 1633-1656
- [7] Provis, J.L., van Deventer, J.S.J., Alkali Activated Materials, Springer (2014)
- [8] Dawczyński, S., Soczyński, M., Górski, M., Feasibility and strength properties of the geopolymeric binder made of fly ash suspension, 64 Scientific Conference Krynica Zdrój, Poland (2018), in review
- [9] Adam, A.A., Horianto, The effect of temperature and duration of curing on strength of fly ash based geopolymer mortar, Proc. Engin. 95 (2014), 410-414
- [10] PN-EN 1015-11:2001: Methods of test for mortar for masonry – Part 11: Determination of flexural and compressive strength of hardened mortar, Poland (2001)



## **SELF-SENSING PROPERTIES OF ALKALI-ACTIVATED SLAG COMPOSITE WITH CARBON NANOTUBES**

**Pavel Rovnaník<sup>(1)</sup>, Maria Míková<sup>(1)</sup>, Ivo Kusák<sup>(1)</sup>, Pavel Schmid<sup>(1)</sup>, Libor Topolář<sup>(1)</sup>**

(1) Brno University of Technology, Brno, Czech Republic

### **Abstract**

Conductive concrete is produced by addition of conductive filler to ordinary concrete. Electrically conductive concrete allows analysing stress and strain variation in structures by means of resistivity measurements. The study of self-sensing properties of conductive concrete is now of great importance to its application in civil engineering. Since there is very limited information about electrical properties of alkali-activated materials as alternative binders to Portland cement, this paper presents the study on basic electrical and self-sensing properties in compression of alkali-activated slag composite with carbon nanotubes as conductive filler. The results showed that addition of carbon nanotubes reduced the electrical resistance of alkali-activated slag, however, it did not improve its sensing properties.

### **1. Introduction**

Development of multifunctional materials is within the scope of many researchers in order to fulfil the demand for smart structures. Among these functionalities, strain and damage sensing, heating control, absorption of electromagnetic waves or weight control of moving objects can be mentioned. A certain level of conductivity is necessary in order to achieve these functional properties of structural composites, and for this reason, conductive admixtures are usually added [1]. Despite the fact that much effort was already devoted to design, observations and utilization of electrically enhanced cement-based materials that can be used as smart materials, there does not exist any complex research focused on alkali-activated materials enhanced in such way.

The present study aims to investigate the self-sensing properties of alkali-activated slag (AAS) mortars with multi-walled carbon nanotubes (MWCNTs) as conductive admixtures under compressive loading. The results are compared to reference AAS mortar without MWCNTs treated under the same conditions. This work relates to our previous study that

analysed the influence of MWCNTs on the electrical properties of AAS without mechanical loading [2].

## 2. Experimental part

### 2.1 Materials

The alkali-activated slag was composed of granulated blast furnace slag supported by Kotouč, s.r.o. (CZ) finely ground to the specific surface of  $383 \text{ m}^2/\text{kg}$  with the mean particle size of  $15.5 \text{ }\mu\text{m}$  and solid sodium silicate Susil MP 2.0 (Vodní sklo, CZ) as an activator. Quartz sand with a maximum grain size of  $2.5 \text{ mm}$  was used as aggregate. MWCNTs were added in the form of well-dispersed aqueous dispersion containing 1 wt.% of MWCNTs (Graphistrengths CW 2-45, Arkema, France). In order to prepare the aqueous dispersions, the procedure prescribed by the producer was followed. MWCNT pellets were dissolved in hot water and dispersed bundles of MWCNTs were further disintegrated by a mechanical homogenizer (3 h at 14000 rpm).

Alkali-activated slag was prepared according to the following procedure. Sodium silicate activator was suspended and partially dissolved in water. Since no additional water is used in case of CNT 0.4 mixture, sodium silicate was dissolved directly in the dispersion of MWCNTs. Then, slag and quartz aggregate were added and the mixture was stirred in a planetary mixer for about 5 min to prepare a fresh mortar. Finally, additional water or dispersion of MWCNTs was mixed into fresh alkali-activated slag mortar. The composition of mixtures is presented in Tab. 1.

Table 1: Mixture proportions

	REF	CNT 0.1	CNT 0.4
Slag (g)	600	600	600
Susil (g)	120	120	120
Sand (g)	1800	1800	1800
1% MWCNTs (g)	0	60	240
Water (mL)	240	180	0

Investigation of self-sensing properties was performed on  $100 \times 100 \times 100 \text{ mm}$  cubes with embedded gauze electrodes. The electrodes were made of copper having the wire thickness of  $1 \text{ mm}$  and the mesh size of  $2.5 \text{ mm}$ . The size of the electrodes was  $80 \times 120 \text{ mm}$  and the span between electrodes was  $40 \text{ mm}$ .

After 24 h the hardened specimens were immersed in a water bath at  $20 \text{ }^\circ\text{C}$  for another 27 days. The cubes for the measurement of sensing properties were stored at ambient conditions for 30 days before testing in order to reach moisture equilibrium.

### 2.2 Methods

Prepared prismatic samples were characterized by impedance spectroscopy in the range of 40 Hz to 1 MHz using sinusoidal signal generator Agilent 33220A and dual-channel oscilloscope

Agilent 54645A [3]. The output voltage of the signal generator was 5.5 V. Input values of electrical capacity and resistance of oscilloscope were 13 pF and 1 M $\Omega$ , respectively. These instruments were assembled for fully automated measurement. In order to perform impedance analysis, the prismatic specimens were placed between parallel brass electrodes (30  $\times$  100 mm) with the distance of 40 mm.

Measurement of sensing properties during compressive load was carried out on a FORM+TEST Prüfsysteme hydraulic testing machine with the measuring range 0–3000 N. The cubic specimens were loaded perpendicular to the plane of the Cu-electrodes (Fig 1). In the experiment, cyclic loading and releasing of the samples was performed linearly with loading rate 400 N s<sup>-1</sup> and in the range 5–50 kN which corresponds to approx. 8% of the maximum compressive stress. Finally, in the last experiment, these cubes were loaded linearly with loading rate 200 N s<sup>-1</sup> up to failure.

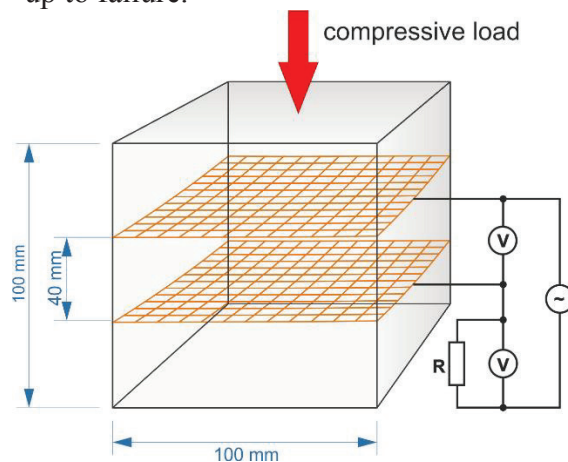


Figure 1: Experimental configuration during the compressive loading tests

For the measurement of electrical resistance of loaded samples in AC field, a sinusoidal signal generator Agilent 33220A and two multimeters Agilent 34410A were used. These appliances were arranged according to the scheme (Fig. 1) and connected via USB hub to the computer for fully automated measurement. The frequency of AC field was 1 kHz and voltage of the sinusoidal generator was 5 V. The electrical current was calculated from the voltage measured on one of the voltmeters and the reference resistance R which was exactly 6796  $\Omega$ . The electrical resistance of the measured sample was computed from the electric current flowing through the exact resistance R and the voltage that was measured separately on the test sample using Ohm's law and taking into account the internal resistance of the voltmeter.

The universal measurement and diagnostic system DAKEL-XEDO<sup>®</sup> (ZD Rpety-Dakel company) was used for the acoustic emission (AE) measurements. The guard sensors eliminated noise that is generated from outside the area of interest. In this work, three acoustic MIDI emission sensors (type IDK-09) were used, all having identical frequency range and being attached to the surface by beeswax.

### 3. Results and discussion

Self-sensing properties of building materials stem from the change of conductive network inside composites, so the change in resistivity is able to characterize the sensing behaviour.

For this purposes, the fractional change in resistivity (FCR) is used as a relative measure to describe self-sensing properties under different loading conditions. It can be calculated as follows:

$$FCR (\%) = \frac{R - R_0}{R_0} \cdot 100 \quad (1)$$

where  $R$  is electrical resistance and  $R_0$  is the initial electrical resistance. The initial resistance of AAS composite decreased with increasing content of MWCNTs (Tab. 2), which is in accordance with previously reported work [2].

Table 2: Initial electrical resistance of AAS composites

	REF	CNT 0.1	CNT 0.4
$R_0$ ( $\Omega$ )	18700	12880	8800

In order to compare the self-sensing properties of alkali-activated slag and cement mortars, cubic specimens with embedded Cu-electrodes were subjected to repeated compressive loading at a fixed maximum of 5 MPa. This range fits into the elastic part of loading and does not cause any irreversible changes in microstructure. Totally ten loading cycles were accomplished in order to collect enough data of electrical resistance. The curves drawn in Fig. 2a show the response of electrical properties, which are expressed as fractional change in resistivity, to the applied compressive load. As the compressive stress increases the electrical resistance decreases, which is in accordance with other studies reported for the cement based composites with conductive filler [4, 5–7]. During compressive loading, the resistance decreased due to the healing of microcracks and defects formed by drying shrinkage. During unloading, it increased due to defect aggravation. Alkali-activated slag shows the fractional change in resistivity of 2.1% during repeated loading with the amplitude of 45 kN and the baseline signal is very stable for selected conditions. Although MWCNTs decrease resistivity of AAS matrix, self-sensing properties of AAS composites with MWCNTs appeared to be similar to those observed for the reference AAS mortar. The fractional change in resistivity was only 1.2% for the composite with 0.1% of MWCNTs and 2.6% for the composite with 0.4% of MWCNTs. The baseline signal of these two composites continuously increased, which was more obvious for the mixture with higher nanotubes content. This effect was reported also for a cement mortar during repeated loading and is attributed to its irreversible damage [5].

Fig. 2b shows the fractional change in resistivity during compressive loading till failure. The FCR of reference AAS mortar is quite extraordinary because it has a local maximum. At first, the resistance linearly decreased up to 6 MPa but then it increased again and reached its maximum at 24 MPa. In the range 14–35 MPa the resistance even exceeded the reference value but with higher compression, it gradually decreased up to failure, at which it increased abruptly. Sudden increase in resistance is caused by interruption of conductive routes at the failure point and this behaviour has already been reported for conductive cement composites [4]. Such behaviour is probably caused by the formation of some preliminary defects under compression causing an opening of microcracks and partial destruction of conductive routes which results in the increase of electrical resistance. When the monotonous compression

proceeds the conductive routes are reconstructed due to defect healing and the electrical resistance decreases again till failure. There is no significant difference between curves recorded for the reference AAS mortar and AAS composites with MWCNTs. However, the increase in FCR starts at lower compressive stress and the local maximum is higher and closer to the beginning compared to reference mortar.

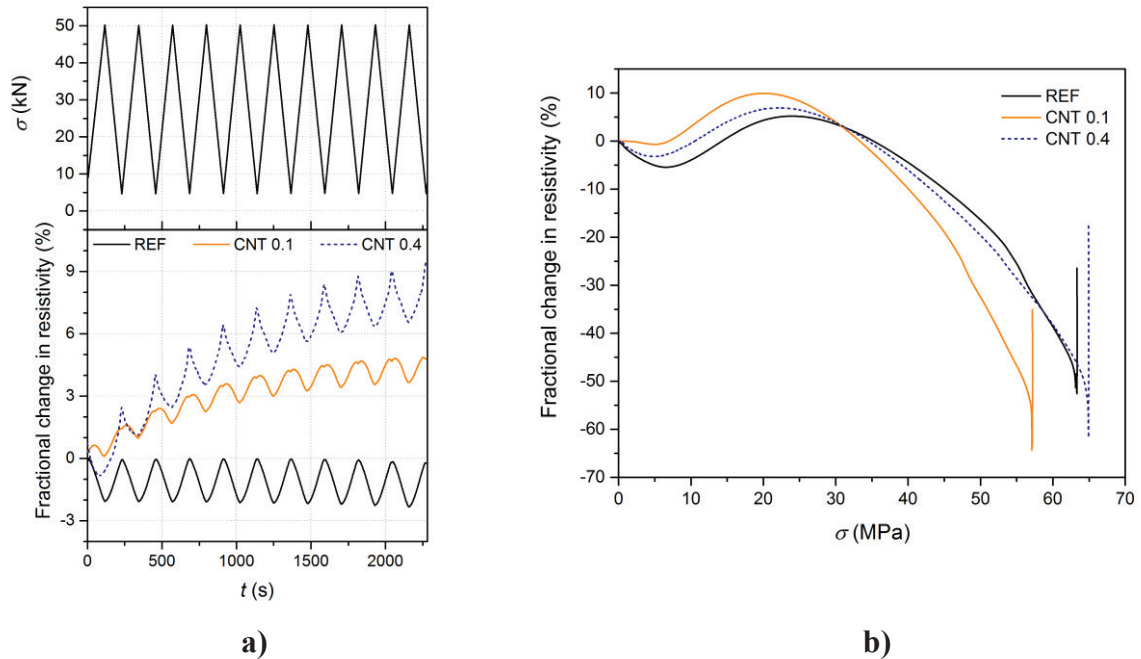


Figure 2: Fractional change in resistivity of alkali-activated slag composites: a) during repeated compressive loading; b) during compressive loading till failure

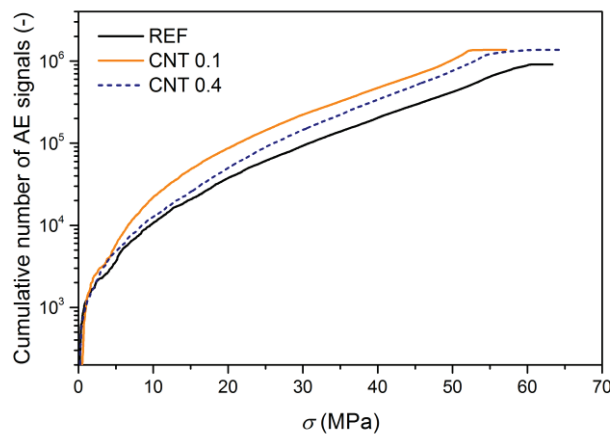


Figure 3: Cumulative number of recorded AE signals versus compressive stress

The acoustic emission (AE) method is considered to be a “passive” non-destructive technique because it identifies defects while they are being developed during the test. This technique has quite unique ability to detect crack formation and propagation occurring not only on the surface but also deep inside the material. To detect defects formation, we focused on a number of signals overshooting a pre-set threshold level. The cumulative number of AE

signals versus compressive stress is presented in Fig. 3. All three curves are quite similar, however, the total number of AE signals of AAS composites with MWCNTs is higher by  $5 \cdot 10^5$ . The increase in AE signals recorded for CNT 0.1 sample at compressive stress higher than 5 MPa corresponds to the increase in fractional change in resistivity. This also supports a presumption that the local maximum on FCR curves is caused by the microcrack formation and partial deterioration of the mechanical properties.

#### 4. Conclusions

In this paper, self-sensing properties of alkali-activated slag composites with two different amounts of MWCNTs under compressive loading were investigated. The properties were compared with reference AAS mortar without MWCNTs. The experimental and analytical results have led to the following conclusions:

- Addition of carbon nanotubes to AAS mixture led to a significant decrease in electrical resistance of AAS mortars.
- Self-sensing properties under repeated compressive loading can be observed for all three mixtures, however, the addition of MWCNTs does not improve sensing properties of AAS mortar.
- The composites with MWCNTs showed a permanent damage during repeated loading, which is reflected in a gradual increase in basic FCR.
- FCR decreased during compression till failure, however, it showed a local maximum, which is associated with microcrack formation. This conclusion is also supported by AE measurements.

#### Acknowledgements

This outcome has been achieved with the financial support of the Czech Science Foundation, project No. 16-00567S, and the MEYS CR under the “National Sustainability Programme I”, project No. LO1408 (AdMaS UP).

#### References

- [1] Han, B., Yu, X., Ou, J., Self-sensing concrete in smart structures, Butterworth-Heinemann (2014)
- [2] Kusák, I., Luňák, M. and Rovnaník, P., Electric conductivity changes in geopolymer samples with added carbon nanotubes, *Procedia Eng* 151 (2016) 157-161
- [3] Kusák, I., Luňák, M. and Schauer, P., Tracing of concrete hydration by means of impedance spectroscopy (New tool for building elements testing), *Appl Mech Mater* 248 (2013) 370-378
- [4] Wen, S. and Chung, D. D. L., Pressure-sensitive properties and microstructure of carbon nanotube reinforced cement composites, *Cem. Concr. Compos.* 29 (2007) 377-382
- [5] Cao, J., Wen, S. and Chung, D. D. L., Defect dynamics and damage of cement-based materials, studied by electrical resistance measurement, *J Mater Sci* 36 (2001) 4351-4360
- [6] Li, G. Y., Wang, P. M. and Zhao, X. H., Pressure-sensitive properties and microstructure of carbon nanotube reinforced cement composites, *CemConcrCompos* 29 (2007) 377-382
- [7] Wen, S. and Chung, D. D. L., Electric polarization in carbon fibre-reinforced cement, *Cem Concr Res* 31 (2001) 141-147

## **SOLIDIFICATION/STABILIZATION OF PORT SEDIMENTS CONTAMINATED BY HEAVY METALS AND TBT USING SLAG- BASED BINDERS**

**Tanya Gutsalenko<sup>(1)</sup>, Alexandra Bourdot<sup>(1)</sup>, Peter Seymour<sup>(2)</sup>, Laurent Frouin<sup>(2)</sup>,  
Mohend Chaouche<sup>(1)</sup>**

(1) LMT, CNRS/ENS-Cachan/Paris-Saclay University, Cachan, France

(2) Ecocem Ltd. F1, Dublin, Ireland

### **Abstract**

Dredge sediments from marine basins represent an environmental issue. Indeed, they are often contaminated with heavy metals and/or organic pollutants. Thus, they are considered as hazardous waste and must undergo treatments to stabilize them and if possible to valorize them. The Dublin Port sediments are contaminated with heavy metals and TBT (Tributyltin) related to port activities (paintings used for boats). In this study, the Solidification/Stabilization method is used because of its technical, environmental and economic benefits. Compression tests were performed on the composites of sediments-OPC-GGBS. The results are correlated with XRD analyses and micro-tomography observations. Regarding the plain OPC based samples, the degradation of the strength can be attributed to the decrease of the amount of some hydration products, may be attributed to internal carbonation resulting from eventual decomposition of organic matter at high pH. This led then porosity increase in comparison to the GGBS-based binder, which microstructure is denser. The stability of contaminant compounds solidified in hydraulic binders was considered through leaching tests. The leachates were analyzed using ICP-MS technique for HM and GC-MS analyses to follow the evolution of TBT and its derivatives throw. The results show a positive effect of GGBS based binder in stabilizing contaminated sediments.

### **1. Introduction**

The port activities induce sediment accumulation in basins. In order to maintain a viable navigation within the port structures, it is essential to carry out dredging operations to evacuate the sediments accumulating in their basins. Much of this sediment is once again

dumped at sea. Nevertheless, marine basins are polluted due to mining, chemical, mechanical industry, agriculture industry emissions, port activities (paintings used for boats). Therefore some of sediments are polluted with heavy metals (HM) and/or organic pollutants (PCBs, PAHs, TBT). Thus, they are considered as hazardous waste and are regulated in Europe by the Decree of August 9, 2006 which defines threshold values N1 and N2 for heavy metals, PCB, HAP, and TBT. They must undergo treatments to stabilize them and if possible to valorize them.

In this study, the Solidification/Stabilization method using a hydraulic binder for sediments valorization is considered because of technical, environmental and economic benefits. On this way, Granulated ground blast furnace slag (GGBS) based binders is used for their effectiveness in immobilizing various heavy metals [1]. GGBS is expected to impact immobilization through several mechanisms: the porosity of the binder is finer (due in particular to its pozzolanic activity), presence of hydrotalcite like phases that are characterized by high immobilization capacity, etc.

Three different hydraulic binders of Portland cement-Granulated ground blast furnace slag (GGBS) were used for the Dublin port sediments valorization: Portland cement (OPC) and Portland cement-Granulated ground blast furnace slag (GGBS) at two different GGBS contents. Compression tests were performed on the composites of sediments- OPC-GGBS at 28 and 90 days. The results are correlated with XRD analyzes and micro-tomography observations. The Dublin Port sediments are contaminated with heavy metals (As, Cu, Ni, Zn, Pb, Cr) and TBT (Tributyltin) related to port activities (paintings used for boats). The stability of heavy metal compounds contained in the sediments solidified in hydraulic binders was considered through leaching tests. Each mixture was analyzed using ICP-MS technique. In the same way, the paper presents preliminary results from leaching tests carried out to follow the evolution of TBT and its derivatives. The organic compounds were analyzed by GC-MS.

## 2. Materials

Sediment sampling took place at Alexandra basin (Dublin Port) at around 1.5 m depth. The sediment comprises mainly very fine fractions with the average diameter of about 40  $\mu\text{m}$ . The sediment consisted of both organic and inorganic components. The main inorganic crystalline components observed by X-ray diffraction (Co  $K\alpha$ ,  $\lambda = 1.79^\circ$ ) were mainly Quartz, Calcite, Muscovite, and clays. The clays are composed mainly of Illite (59%) associated with chlorite (25%) and kaolinite (14%). Smectite is present as trace (2%). The average value of the organic carbon (TOC) in the Dublin sediment is 35.3 g/kg. The sediment is characterized by the presence of several heavy metals as Zn, Cu, Ni, Cr, Pb and As. The initial TBT, DBT and MBT contents in the sediment were 205, 78.9 and 34.3  $\mu\text{(Sn)/kg/sec}$ , respectively (according to [2]). The TBT concentration in the Dublin port sediment is superior to the first threshold level N1 of 100  $\mu\text{g/kg/sec}$  defined by the Decree of August 9, 2006. Consequently, its reimmersion is in question, therefore, the stabilization is proposed using cement-GGBS binders. The cation exchange capacity (CEC) for the exchangeable ions  $\text{Al}^{3+}$ ,  $\text{Ca}^{2+}$ ,  $\text{Fe}^{2+}$ ,  $\text{K}^+$ ,  $\text{Mg}^{2+}$ ,  $\text{Mn}^{2+}$ ,  $\text{Na}^+$ , determined according to [3] is 21.3 cmol/kg.

The sediment, noted F0 in the paper, was first sieved to remove the aggregates larger than 4 mm. Then, the sediment sample was let to settle over 24 hours and the bleeding water was



removed. All the samples were prepared with sediments having water content of  $45\pm 1.5\%$ wt and density of  $1400\pm 70$  kg/m<sup>3</sup>.

The hydraulic binders considered consisted of mixtures of Portland cement (OPC) and slag (GGBS) from ECOCEM Ireland. Three different hydraulic binders were mixed with sediments. The mixtures are reported in Table 1. F1 correspond to Portland cement (OPC) binder, F2 and F3 are Portland cement-Granulated ground blast furnace slag (GGBS) mixtures at two different GGBS contents. Initially, the binder is mixed with water with a w/b ratio 0.5. Samples F1 to F3 are obtained by mixing 150 kg of total binder with 1 m<sup>3</sup> of sediment.

Table 1: Sediment-Binder mixtures and compressive strength Rc at 28 and 90 days

Mixture	Binder content (%)		Rc (MPa)	
	Cement	GGBS	28 days	90 days
F1	100	0	1.90±0.14	0.77±0.08
F2	50	50	1.90±0.14	2.53±0.22
F3	15	85	1.10±0.07	2.00±0.13

### 3. Methods

The compressive strength of the sediment–binder samples was determined at both 28 and 90 days. X-Ray microtomography imaging (voxel size  $7.5 \times 7.5 \times 7.5$  μm) was performed to observe the microstructure.

The leaching tests of heavy metals were performed according to compliance test from NF EN 12457-2 standard [4]. This consisted in dispersing  $90\pm 5$ g of solid particles of sediment-binder in 900 ml of demineralized water (pH=5-7.5 and conductivity  $<0.5$  mS/m) for 24 hours at 10 rpm (horizontal rotation) in a room at controlled temperature  $24^{\circ}\text{C}\pm 1^{\circ}\text{C}$ . For each mixture three samples were prepared and analyzed using ICP-MS technique.

The semi-dynamic leaching tests of TBT and its derivatives were performed for monolithic waste according to NEN 7375 [5]. The cylindrical specimen of  $\varnothing 40 \times 40$  mm is immersed in a leachant (demineralized water ( $5 < \text{pH} < 7.5$ ) with a conductivity  $<0.1$  mS/m) that is renewed after specified intervals. The leachant volume (in cm<sup>3</sup>) used for each interval was  $8 \times$  the surface area of the specimen (in cm<sup>2</sup>). The water solution was analyzed after each exchange using GC-MS according to XP T 90-250 [2].

### 4. Results and discussion

#### 4.1 Mechanical strength

The compressive strength of the samples is reported in Table 1. At 28 days the strength is not modified when replacing 50% of OPC with GGBS. Increasing the replacement level of OPC by GGBS leads to a significant decrease of the strength at 28 days. On the other hand, at longer term (90 days) the strength of the samples with GGBS exceeds that of cement-based mixtures. In addition, the strength of the GGBS-based materials increases between 28 and 90 days while that of the OPC-based samples decreases. This phenomenon can be explain by examining the XRD results (Fig. 1). The greatest amount of Portlandite is formed between 7

and 30 days, but then the peaks decreased significantly. The Ettringite phase completely disappeared after 60 days of storage.  $C_4AH_x$  phase reached its maximum at 45 days and then decreased. The decrease of the amount of these hydration products may be attributed to internal carbonation resulting from eventual decomposition of organic matter at high pH. This led then porosity increase (Fig. 2) and degradation of the strength.

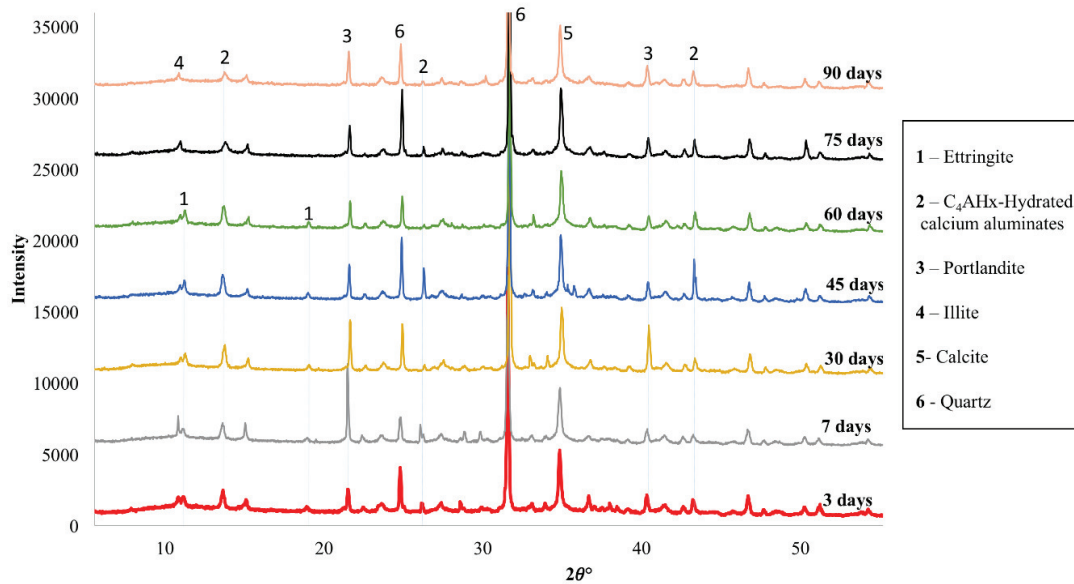


Figure 1: XRD of F1 mixture over time

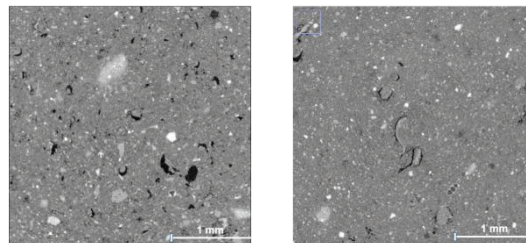


Figure 2: Microstructure of F1 (left) and F3 (right) mixtures from X-ray micro-tomography

#### 4.2 Heavy metals leaching tests

The leaching test results for the HMs are reported in Fig. 3. Surprisingly the leachability of the HMs from the plain sediment (F0) is quite low. This suggests that they should be present in rather stable compounds. The effect of the binder depends on the HM considered. For instance As, Cr, Pb and Zn are quite efficiently immobilized with all the binders. On the other hand, Cu and Ni are rather destabilized in the presence of the binder. It can be noticed that the destabilizing effect decreases when the level of OPC substitution with GGBS increases. These trends seem to be related to the pH of the samples (Fig. 3). The highest pH is obtained with the OPC based sample F1 (around 12.5). Overall the pH decreases when increasing the fraction of GGBS. The lowest pH is obtained with F3. As already observed in other studies [6], the dissolution of metal species is highly pH dependent. Most metal species are soluble at very low pH. Nevertheless, actually, solubility of metals such as Cu significantly increases also at high pH [7]. This may be a primary explanation for the significant increase of leachability of this metal in a cementitious environment.

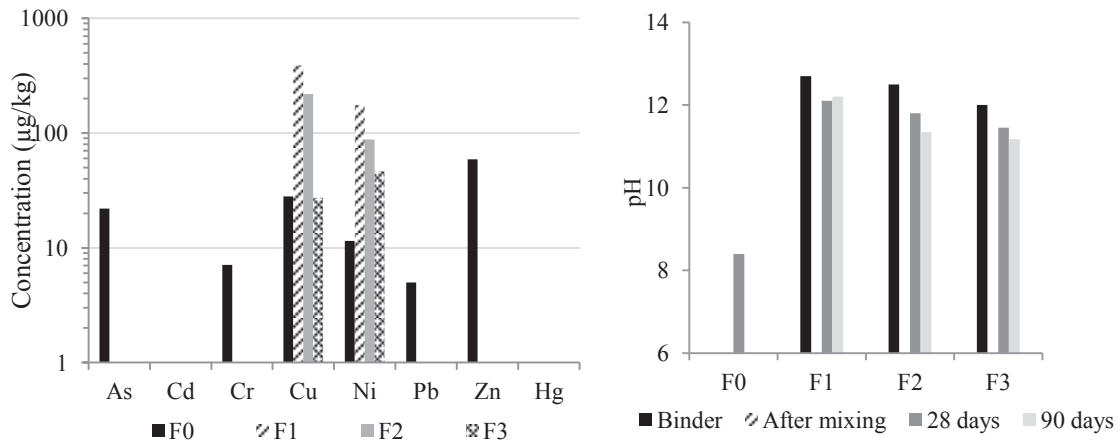


Figure 3: Amount of leached heavy metals and pH for the different mixes.

#### 4.3 TBT leaching tests

The TBT leaching test for 3 months were conducted on sediment-binder mixes, the results are presented in Fig. 4. TBT, MBT and DBT are quite efficiently immobilized with all the binders.

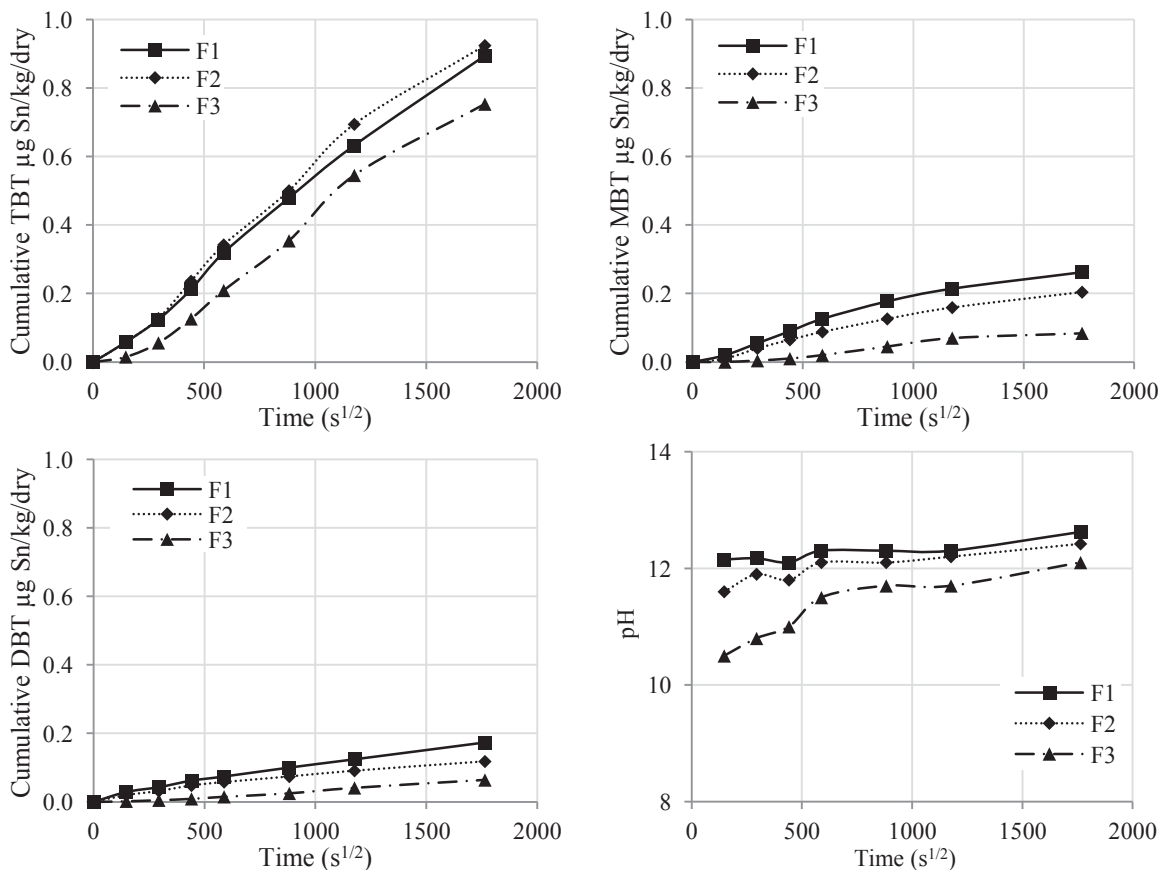


Figure 4: Leaching measurement of TBT, MBT and DBT and pH for the different mixes.

The compounds could stay strongly adsorbed to clays minerals, oxides and hydroxides, and organic material. It can be noticed that the destabilizing effect decreases when the level of OPC substitution with GGBS increases. These trends seem to be related to the pH of the samples (Fig. 4). The highest pH is obtained with the OPC based sample F1 (around 12.5). Overall the pH decreases when increasing the fraction of GGBS. The lowest pH is obtained with F3. The effect of pH on TBT or DBT adsorption was already studied by [8,9] and showed a destabilization at low and high pH. However the gap between pHs for the different mixes is decreasing with time whereas the concentration gap of pollutant is increasing. Therefore, pH does not seem to be the only parameter influencing the leachability of TBT and its derivatives.

## 5. Conclusion

The study proposed the valorization of polluted sediment by solidification in cement-GGBS binder. Mechanical strength values are quite interesting as soil application using GGBS. Leaching tests were performed on Dublin port sediment embedded in binders with different contents of GGBS. It was found that the leachability of most heavy metals contained in the sediment under initially neutral pH conditions is quite low. Regarding the leachability of TBT and its derivatives with time, the values are very weak. The values are the lowest using high percentage of GGBS in binder. Consequently, the results indicated that the heavy metals and TBT within the sediment are embedded in stable compounds using high level of GGBS.

## References

- [1] Deja J., Immobilization of  $\text{Cr}^{6+}$ ,  $\text{Cd}^{2+}$ ,  $\text{Zn}^{2+}$  and  $\text{Pb}^{2+}$  in alkali-activated slag binders, *Cem Concr Res* 32 (2002), 1971–1979
- [2] AFNOR XP T90-250, Water quality - Determination of selected organo-tin compounds in sediments - Gas chromatography method, Association Française de Normalisation, France (2006)
- [3] AFNOR NF EN ISO 23470, Soil quality — Determination of effective cation exchange capacity (CEC) and exchangeable cations using a hexamminecobalt trichloride solution, Association Française de Normalisation, France (2011)
- [4] NF EN 12457-2, Characterization of waste — Leaching — Compliance test for leaching of granular waste materials and sludges — Part 2: One stage batch test at a liquid to solid ratio of 10 l/kg for materials with particle size below 4 mm (without or with size reduction), Association Française de Normalisation, France (2002)
- [5] EA NEN 7375, Leaching characteristics of moulded or monolithic granular building and waste materials 'The tank test', Environment Agency, UK (2004)
- [6] Spence R. D. and Shi C., Stabilization and solidification of hazardous, radioactive and mixed wastes, Boca Raton, CRC Press (2004), 382pp
- [7] Chatain V., Blanc D., Borschneck D., and Delolme C., Determining the experimental leachability of copper, lead, and zinc in a harbor sediment and modeling, *Environ Sci Pollut Res* 20 (2013), 66–74
- [8] Burton E. D., Phillips I. R., and Hawker D. W., Sorption and Desorption Behavior of Tributyltin with Natural Sediments, *Environ Sci Technol* 38 (2004), 6694–6700
- [9] Hoch M., Alonso-Azcarate J., and Lischick M., Assessment of adsorption behavior of dibutyltin (DBT) to clay-rich sediments in comparison to the highly toxic tributyltin (TBT), *Environ Pollut* 123 (2003), 217–227

# **BIO-BASED MATERIALS**

## **ALGINATE-BACILLUS SUBTILIS BASED REPAIR MATERIALS FOR SEALING CRACKS IN CONCRETE**

**Masahiko Ide<sup>(1)</sup>, Keiyuu Kawaai<sup>(1)</sup>, Isao Ujike<sup>(1)</sup>**

(1) Ehime University, Ehime, Japan

### **Abstract**

Recently, repair materials associated with microbial induced calcium carbonate precipitation (MICP) have been intensively studied in the field of self-healing concrete. We have proposed a liquid-based repair system comprising microorganism and organic carbon sources mixed with alkali buffering solution. This study examined crack repair methods using alginate gel films (1.0-1.5 wt%) mixed with healing agents under wet and dry actions. The healing agents consist of bacillus subtilis as aerobic microorganism and glucose as an organic carbon source, thereby producing insoluble calcium carbonate precipitation in the gel films in the presence of calcium ions. The results showed that water permeability was significantly lowered for the cases of alginate gel films with MICP, thus suggesting that the precipitates could enhance the resistance against water pressure of the gel films formed on the cracked surface.

### **1. Introduction**

In recent years, bio-based materials for repairing cracks in concrete through the metabolic processes of microorganisms and enzymes have been intensively studied [1-3]. According to past research reported by Kawaai et al., 2017 [4], precipitation of calcium carbonate in alkaline environment has been confirmed by precipitation test using aerobic *Bacillus subtilis* (natto) encapsulated in calcium alginate capsules. Sodium alginate extracted from brown seaweed could provide viscosity in aqueous solution, which varies depending on the concentrations. When sodium alginate dissolved in a liquid is used for repairing cracks in concrete, there is a strong possibility that the alginate reacts with calcium ions available on the cracked surface, thus forming a polymer comprising calcium alginate via ion-link on the cracked surface. This could result in in-situ encapsulation for the microorganism and nutrients in the cracks. Generally, there are two types of microorganisms, anaerobic and aerobic microorganisms. The former can metabolize an organic carbon sources in an oxygen-free

environment. On the other hand, the latter requires oxygen for the metabolic activity. In this study, we selected *Bacillus subtilis* (natto) as an aerobic microorganism. The liquid-based mixture is supposed to be applied to concrete structures in tidal zones under marine environment. Dissolved oxygen is expected to be available during the dry and wet cycles. Based on the above background, this study examines the effect of crack repair using the viscosity modified mixture containing the *Bacillus subtilis* (natto) and nutrients via liquid-based approach under dry and wet conditions

## 2. Experimental program

### 2.1 Materials

First, culture solution of *Bacillus subtilis* (natto) containing sodium alginate is stirred using a stirrer for 30 minutes until the sodium alginate dissolves. Subsequently, Tris buffer solution or glucose is added. The concentrations of each constituent of the mixtures are shown in Tab. 1. The experimental parameters include the presence (N1 mixtures) and absence (W mixture) of *Bacillus subtilis* (natto), the concentration of sodium alginate ranging from 1.0 to 1.5 wt%. The use of Tris buffer solution with concentrations of 0.1 mol/L is also considered as testing parameters. In this study, 4 mixtures were totally prepared.

Table 1: Concentrations of each constituent of mixtures.

Mixtures	Sodium Alginate (%)	Glucose (mol/L)	Tris buffering solution (mol/L)
1.0-N1-G1-T0	1.0	0.4	-
N1 1.5-N1-G1-T0	1.5	0.4	-
1.5-N1-G1-T1	1.5	0.4	0.10
W 1.5-W-G0-T0	1.5	-	-

### 2.2 Cultivation of bacillus subtilis (natto)

In this study, *Bacillus subtilis* (natto) was cultivated using culture media mainly comprising  $\text{NH}_4\text{Cl}$ ,  $\text{NH}_4\text{NO}_3$ ,  $\text{Na}_2\text{SO}_4$ ,  $\text{MgSO}_4$ ,  $\text{CaCl}_2$ ,  $\text{K}_2\text{HPO}_4$ ,  $\text{KH}_2\text{PO}_4$  in this study. The round rod shape of *Bacillus subtilis* (natto) forms one spore per one bacterial cell in the bacterial body. Spores are formed when it becomes an environment not suitable for growth such as oxygen, water and nutrient sources. And then, they become dormant and inactive. However, if the environment is set, the spore dormancy state ends, and germination begins. And then it becomes vegetative cell and the activity starts. Therefore, the *Bacillus subtilis* (natto) has higher resistance to environmental fluctuation compared to other microorganisms. Also, the metabolic activity of the *Bacillus subtilis* (natto) in a highly alkaline environment of pH 12 has been confirmed [4]. In this study, the culture solution of the *Bacillus subtilis* (natto) after 24 hours was used as repair mixtures. Before preparing the mixtures, the dissolved oxygen concentration in the culture solution was measured to confirm the metabolic activity of *Bacillus subtilis* (natto).

### **2.3 Specimen preparation and exposure tests via dry and wet cycles**

In this study, a mortar specimen with a water cement ratio of 50% and unit water content of  $316 \text{ kg/m}^3$  and unit weight of crushed sand  $1264 \text{ kg/m}^3$  was prepared using a cylindrical mold of  $\phi 50 \times 100 \text{ mm}$ . Specimens were demolded in 24 hours after casting and sealed curing was carried out until the age of 28 days. In order to simulate the cracks generated in the concrete member, split cracks were induced using a loading machine. The experimental set-up is similar to tensile strength test. The crack width was targeted from 0.2 to 0.4 mm. The dry and wet exposure test was carried out through dry conditions (12 hours) and wet conditions (12 hours). Dry and wet cycles were repeated using either distilled water or distilled water containing NaCl (3%).

### **2.4 Observations by microscope, FE-SEM and FT-IR analysis**

Cracked surface including crack width, distribution of calcium carbonate precipitates and the presence of *Bacillus subtilis* (natto) was observed via microscope and FE-SEM. Three pictures were taken in each specimen, and the maximum and average crack widths of each image were measured. And the precipitates produced by the metabolic activity of *Bacillus subtilis* (natto) were analyzed by a Fourier transform infrared spectrophotometer (hereinafter referred to as FT-IR).

### **2.5 Water permeability tests**

Water permeability test was carried out using specimens subjected to dry and wet exposure tests using distilled water containing NaCl. It was tested before and after the specimens were repaired. The water pressure was set as high as 25 kPa and the amount of water flowing through the crack is measured by weighing machine for 10 minutes.

## **3. Experimental results and discussion**

### **3.1 Exposure tests via dry and wet cycles using distilled water**

For the mortar specimens repaired with each mixture, the materials formed on the cracked surface were firstly observed by microscope. The observations were made before repaired, 1 week later before the specimens were exposed to the dry and wet cycles. As shown in Fig. 1, precipitates in a white colour were clearly observed by microscope on the specimens repaired with the mixture of 1.5-N1-G1-T0. The specimens were exposed to the room conditions controlled at  $20^\circ\text{C}$  for a week. They were also visually confirmed after the dry and wet exposure tests. In contrast to the results, such precipitates were not observed on the specimens repaired with the mixture of 1.5-W-G0-T0 without the *Bacillus subtilis* (natto) for a week after the mixture was poured onto the cracked surface. They were not visually observed even after the dry and wet exposure tests. Therefore, the results suggest that the white precipitate can be produced through the metabolic processes of the *Bacillus subtilis* (natto) in the gel films formed on the cracked surface. It is noted that the addition of glucose in the mixtures is essential for the metabolic processes and MICP in the gel films.

### **3.2 Exposure tests via dry and wet cycles using distilled water containing NaCl**

As shown in Fig. 1, precipitates in a white color were clearly observed by microscope on the specimens repaired with the mixture of 1.5-N1-G1-T0. The specimens were exposed to the dry and wet exposure tests for a week. In contrast to the result, such precipitates were not



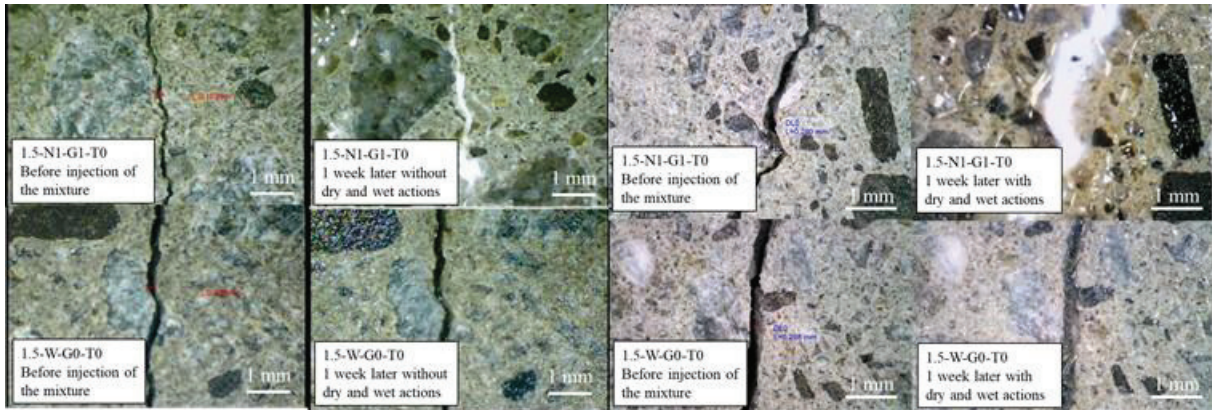


Figure 1: Cracked surface repaired with the liquid-based mixtures.  
(Left: distilled water, Right: distilled water containing NaCl)

observed on the specimens repaired with the mixture of 1.5-W-G0-T0 without the *Bacillus subtilis* (natto) for a week after the mixture was poured onto the cracked surface. They were not visually observed even after the dry and wet exposure tests. Therefore, the results suggest that the white precipitate can be formed in the gel films through the metabolic processes of the *Bacillus subtilis* (natto) under the saline environment.

### 3.3 FT-IR analysis

Fig. 2 shows the results of FT-IR measurements using samples containing white precipitates taken from the cracked surface repaired with the mixtures (1.0-N1-G1-T0 and 1.5-N1-G1-T0) which were exposed to dry and wet cycles using either distilled water or distilled water containing NaCl. Also shown is a spectrum obtained by calcium carbonate for the reference. In the case of the reference spectrum of calcium carbonate, one of the peak is prominent at the wavenumbers of  $872\text{ cm}^{-1}$ . Based on the results obtained by the samples tested in this study, similar peaks exist in the samples tested in the experiments. Thus, the results indicate the presence of calcium carbonate in/on the gel films formed on the cracked surface during the testing periods irrespective of the mixtures formulated in this study.

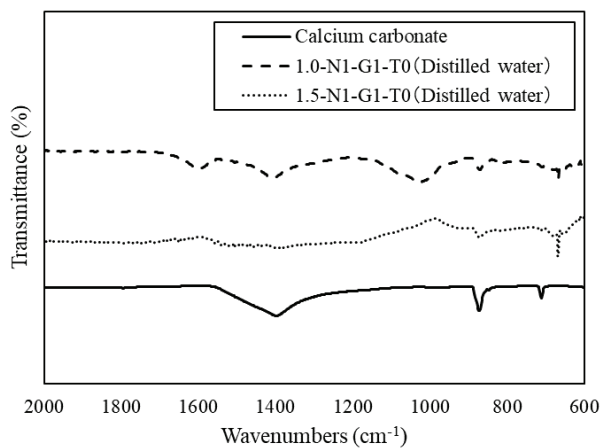


Figure 2: Results of FT-IR.

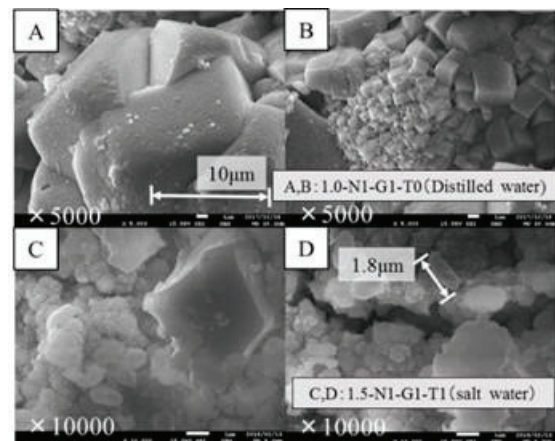


Figure 3: FE-SEM observations.

### 3.4 FE-SEM observations

In order to confirm the precipitates comprising calcium carbonate formed in/on the gel films, samples including white precipitates were collected from the materials in the vicinity of cracks. Some pictures observed by FE-SEM for 1.0-N1-G1-T0 and 1.5-N1-G1-T1 are shown in Fig. 3. It is noted that FE-SEM images show the materials exposed to the dry and wet cycles for 2 weeks. As can be seen in Fig. 3 (A) and (B), the size of crystals reached about 10  $\mu\text{m}$  at maximum for the testing periods. In addition to this, Fig. 3 (C) and (D) show the presence of the *Bacillus subtilis* (natto) of about 1.8  $\mu\text{m}$  long in the vicinity of those crystals. Based on the observations made on the samples, it is certain that the calcium carbonate precipitates through the microbial metabolic processes taking place in/on the gel films formed on the cracked surface under the dry and wet environment.

### 3.5 Water permeability tests

Three specimens for each case were tested for the water permeability to confirm the consistency of the results. The amount of water flowing through the cracked parts of the specimens was weighed for 10 minutes, and average values were calculated. Fig. 4 shows the results of water permeability measured after repaired and average crack width of the specimens. As can be seen, the sealing effect is found to be obtained in the cases of specimens with the crack width ranging from about 0.2 to 0.4 mm. Of the total 8 specimens (1 specimen for 1.5-W-G0-T0 was omitted), the water permeability of 6 specimens was observed to be negligible, thus indicating that the resistance against ingress of water and water pressure was significantly improved by the repair. In particular, the specimens repaired with the mixtures mixed with *Bacillus subtilis* (natto) resulted in a significant decrease in the water permeability. The results suggest that the calcium carbonate precipitated in/on the alginate gel films formed on the cracked surface is highly effective in improving the water permeability. In addition, even in the specimens repaired with 1.5-W-G0-T0 without *Bacillus subtilis* (natto), the water permeability was decreased by about 70% on average. The results indicate the gel films of calcium alginate formed on the cracked surface could solely contribute to the improvement of water permeability possibly by absorbing moisture and swelling. Although the sealing effect for the long-term was unclear in this study, which could be dependent on the

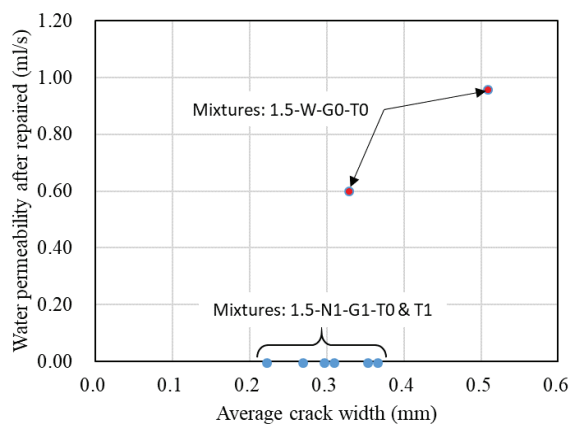


Figure 4: Results of water permeability test.

concentrations of glucose and Tris buffer solution. Therefore, we will continue to examine long-term effect for sealing cracks under dry and wet actions for future research.

#### 4. Conclusion

(1) Based on the observations made by microscope and FE-SEM, calcium carbonate precipitates through the metabolic activity of *Bacillus subtilis* (natto) cultivated in this study in/on the gel films of calcium alginate formed on the cracked surfaces with cracking width ranging from 0.2 to 0.4 mm under dry and wet actions.

(2) Water permeability test was carried out using specimens repaired with mixtures mixed with and without *Bacillus subtilis* (natto). Calcium carbonate precipitated in/on the gel films of calcium alginate formed on the cracked surface is found to show beneficial effect in sealing cracks and decreasing water permeability. Although the sealing effect was observed to some extent in the cases of specimens repaired with only gel films of calcium alginate without *Bacillus subtilis* (natto), the results suggest that precipitation of calcium carbonate by the microbial metabolism further enhances the sealing effect of cracks in concrete.

#### Acknowledgement

This study is financially supported by JSPS KAKENHI Grant-in-Aid for Young Scientists (A), Grant numbers JP17H04933.

#### References

- [1] H. Jonkers et al., Application of bacteria as self-healing agent for the development of sustainable concrete, *Ecological Engineering*, 36 (2010), 230-235.
- [2] P.Y. Putri et al., Effect of Temperature on Precipitation Rate of Calcium Carbonate Produced through Microbial Metabolic Process of Bio Materials, *Civil Engineering Dimension*, 18 (2016), 103-108.
- [3] J. Wang, D. Snoeck, S. Van Vlierberghe, W. Verstraete, N. De Belie, Application of hydrogel encapsulated carbonate precipitating bacteria for approaching a realistic self-healing in concrete, *Construction and Building Materials*, 68 (2014), 110-119.
- [4] K. Kawaai et al., Alginate capsules encapsulating aerobic and anaerobic microorganism for repairing cracks in concrete, 6th International Conference on Self-Healing Materials, web (2017).

## **EFFECT OF ANISOTROPY ON THERMAL AND HYGRIC PREPERTIES OF HEMP COMPOSITE.**

**Florence Collet<sup>(1)</sup>, Sylvie Prétot<sup>(1)</sup>, Brahim Mazhoud<sup>(1)</sup>, Christophe Lanos<sup>(1)</sup>**

(1) Université de Rennes, LGCGM, Rennes, France

### **Abstract**

This study investigates the effect of anisotropy on thermal and hygric properties of hemp - clay composite.

The clay based binder is made of fines from aggregate washing mud. It is stabilized with 5% of Portland cement and 5% of lime based binder (Thermo®). The aggregates are CAVAC Biofibat® hemp shiv. The hemp to binder mass ratio is 0.5, representative of wall formulation. The specimens are produced by casting with successive layers, compacted at 0.1 MPa. The density of hemp-clay composites is about 445 kg/m<sup>3</sup> after stabilization at (23°C, 50%RH).

The thermal conductivity is measured with a hot wire at dry state. The measurements are performed placing the wire in planes perpendicular to or parallel to the compaction direction. The anisotropy induces 16.8 % of discrepancy between the two measurement directions.

The moisture buffer value (MBV) is measured following the Nordtest protocol. After stabilization at 23°C, 50 %RH, the specimens are exposed to daily cyclic variations (8 hours at 75 %RH , 16 hours at 33 %RH). The MBV is calculated from the mass variation through the exposed surface under relative humidity step. The anisotropy induces 27 % of discrepancy between moisture flux parallel and perpendicular to the compaction direction.

### **1. Introduction**

In order to meet the requirements of sustainable development, hemp composites are developed to be used as non load bearing material in building envelop. They show low density, low thermal conductivity and high moisture buffering capacity [1]. Such materials can be precast (building blocks or elements) or implemented on site by casting or spraying. All these implementation techniques lead to anisotropy of materials which is both due to the shape of aggregates and to the successive layers (compacted or not). William et al. [2]

demonstrate a significant anisotropy within hemp concrete thanks to image analysis method. This anisotropy impacts all multi-physical properties of materials. It was investigated on thermal conductivity of hemp concrete and on mechanical properties of hemp concrete [3-7] but not on hygric properties, to our knowledge. So, this study investigates the effect of anisotropy on thermal conductivity and moisture buffer value of washing fine – hemp.

## 2. Material and methods

### 2.1 Material

The studied material is a hemp - clay composite. The clay based binder is made of fines from aggregate washing mud taken from a gravels production site. After decanting, the mud is dried in an oven at 100°C. After drying, the material is milled with a knife mill. The powder is then sieved with a square mesh of 2 mm side to remove the larger particles. The fines are stabilized with 5% of Portland cement and 5% of lime based binder (Thermo®), following the stabilisation study performed in [8][9].

The bio-sourced aggregates are CAVAC Biofibat® hemp shiv. They were characterised following the Rilem protocol [10]. The particle size distribution is given Fig. 1. Their width ranges from 0.14 to 6.8 mm, and their length from 0.6 to 40.6 mm. Their elongation (width/length) ranges from 0.09 to 0.90 with a medium value of 0.26.

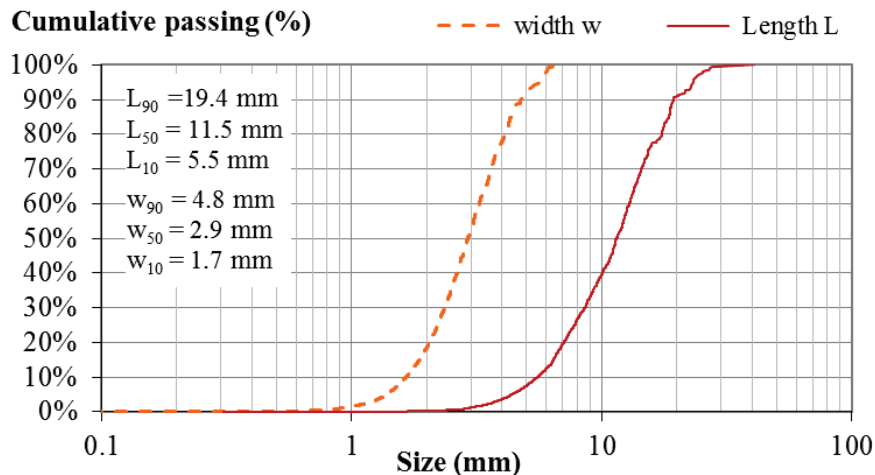


Figure 1: Particle size distribution of hemp shiv

The hemp to binder mass ratio is 0.5, representative of wall formulation.

For the production, the hemp shiv is weighed and mixed by hand for about 2 min in a container with water to hemp mass ratio of 0.4. At the same time, binder powder and water are mixed with the mixer to form a binder paste. The cubic specimens (10\*10\*10 cm<sup>3</sup>) are produced by casting with successive 5 cm thick layers. Each layer is compacted at 0.1 MPa. The specimens are demoulded after 6 days and are stabilised in a climate room at (23°C, 50%RH).

The average bulk density after stabilisation is 443 kg.m<sup>-3</sup>, with a variation coefficient of 2.45 % between the 9 specimens. This value is close to the one found in previous work [8]. This underlines the reproducibility of the washing fine – hemp composite production.

## 2.2 Measurement of thermal conductivity

The thermal conductivity is measured at dry state. After drying in an oven at 60°C, the specimens are stabilized in a desiccator where the measurements are performed at ambient temperature. The measurements are performed with a 5 centimetres long hot wire. This transient method consists in analysing the temperature rise versus heating time (Eq. 1).

$$\Delta T = \frac{q}{4\pi\lambda} (\ln(t) + C) \quad (1)$$

Where  $\Delta T$  is the temperature rise (°C),  $q$  is the heat flow per meter ( $\text{W}\cdot\text{m}^{-1}$ ) and  $\lambda$  is the thermal conductivity ( $\text{W}\cdot\text{m}^{-1}\cdot\text{K}^{-1}$ ),  $t$  is the heating time (s) and  $C$  is a constant including the thermal diffusivity of the material.

The measurement is performed with the sensor sandwiched between two specimens. To investigate the effect of anisotropy, the measurements are performed placing the wire in planes perpendicular to or parallel to the compaction direction (Fig. 2). The heat flow (212 mW) and heating time (120 s) are chosen to reach high enough temperature rise (>10°C) and high correlation coefficient ( $R^2$ ) between experimental data and fitting curve. These settings meet the requirements of the manufacturer, the expected accuracy is thus better than 5%. For each sensor position, the measurements are performed on two pairs of specimens. The thermal conductivity of a pair of specimens is the average of five values with a coefficient of variation lower than 5%. The thermal conductivity is the average value of the two pairs of specimens.

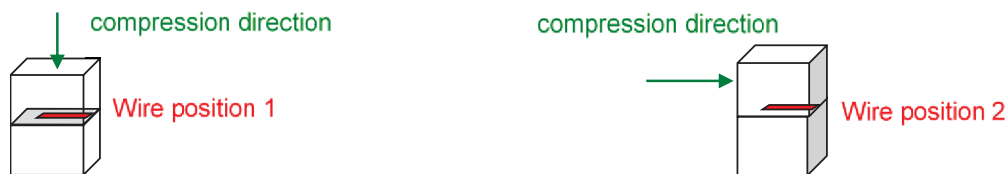


Figure 2: Measurement of thermal conductivity – wire position :  
 $\lambda_1$  wire perpendicular to the compaction direction,  $\lambda_2$  wire parallel to the compaction direction

## 2.3 Measurement of Moisture Buffer Value (MBV)

The moisture buffer value (MBV) is measured following the Nordtest protocol [11]. Specimens are sealed on all but one surfaces. In order to investigate the effect of anisotropy, the open surface allows moisture flux to be parallel or perpendicular to compaction direction. The open surface area is measured by image analysis (Fig. 3).

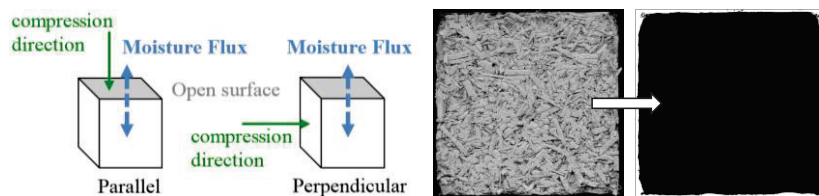


Figure 3: Measurement of moisture buffer value -  
left : moisture flux direction versus compaction direction, right : image treatment

The specimens are firstly dried at 60°C and then stabilised at 23°C, 50%RH to begin the test from the adsorption curve. After stabilization, specimens are exposed to daily cyclic variation

of ambient relative humidity (8 hours at 75%RH and 16 hours at 33 %RH) in a climate chamber (Vötsch VC4060). The moisture buffer value is then calculated from their moisture uptake and release with:

$$MBV = \frac{\Delta m}{A \times (RH_{high} - RH_{low})} \quad (2)$$

Where MBV is the moisture buffer value ( $\text{g}/(\text{m}^2 \cdot \%RH)$ ),  $\Delta m$  is the moisture uptake/release during the period (g), A is the open surface area ( $\text{m}^2$ ),  $RH_{high/low}$  is the high/low relative humidity level (%).

Temperature and relative humidity are measured continuously with sensor SHT75; the average air velocity in the surroundings of the specimens is 0.13 m/s with standard deviation of 0.06 m/s for the horizontal velocity and is 0.04 m/s with standard deviation of 0.02 m/s for the vertical one. The specimens are weighed out of the climatic chamber five times during absorption period and two times during desorption one. The readability of the balance is 0.01 g, and its linearity is 0.01 g. The accuracy of the moisture buffer value is thus about 5%. The measurement is performed on five specimen for perpendicular configuration and on four specimens four parallel one. The MBV is the mean value of all specimen on the three stable cycles.

### 3. Results and discussion

#### 3.1 Thermal conductivity

Fig; 4 gives the thermal conductivity of washing fines – hemp composites versus wire position.

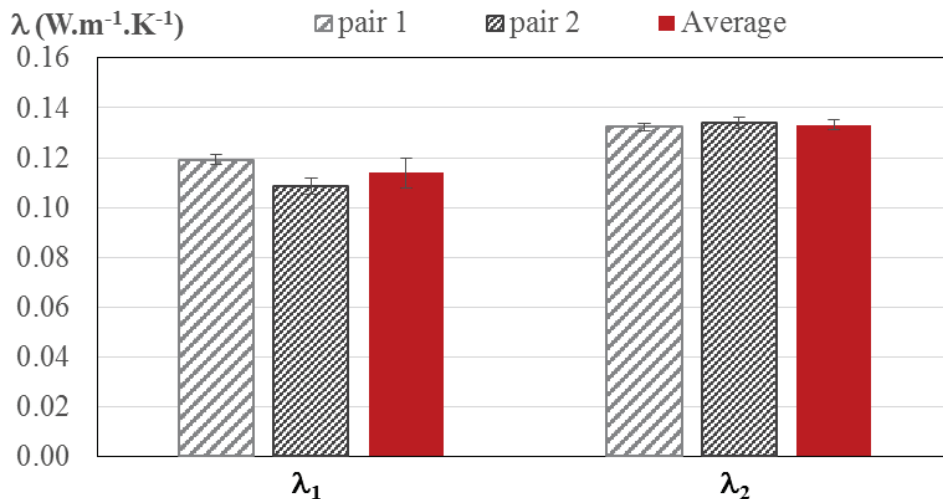


Figure 4: Thermal conductivity of washing fines-hemp composites versus anisotropy -  $\lambda_1$  wire perpendicular to the compaction direction,  $\lambda_2$  wire parallel to the compaction direction

For the two directions of measurement, the results obtained on the two pairs of specimens are close. When the wire is perpendicular to the compaction direction, the average thermal

conductivity is  $0.114 \text{ W.m}^{-1}.\text{K}^{-1}$ . This value is the same as the one found in previous work [8]. It underlines the reproducibility of the material and its thermal performances. When the wire is parallel to the compaction direction, the average thermal conductivity is  $0.133 \text{ W.m}^{-1}.\text{K}^{-1}$ . This value is 1.168 times higher than the previous one and underlines the effect of anisotropy on the thermal conductivity of washing fine – hemp composite. Such results are also observed on hemp composites by several authors. The effect of anisotropy is more or less important with ratios between thermal conductivities ranging from 1.01 to 1.10 in [3], from 1.13 to 1.33 in [4, 5] and from 1.20 to 1.30 in [6], in link with different formulations and productions.

Finally, on thermal point of view, such composite shows lower performances when its implementation leads to heat flux perpendicular to the compaction direction. So, the best way to implement it is to induce compaction direction parallel to heat flux. This can be reach by implementing it by spraying [7] or by precasting.

### 3.2 Moisture Buffer Value

The moisture buffer value of washing fine – hemp versus moisture flux direction is given in Fig. 5.

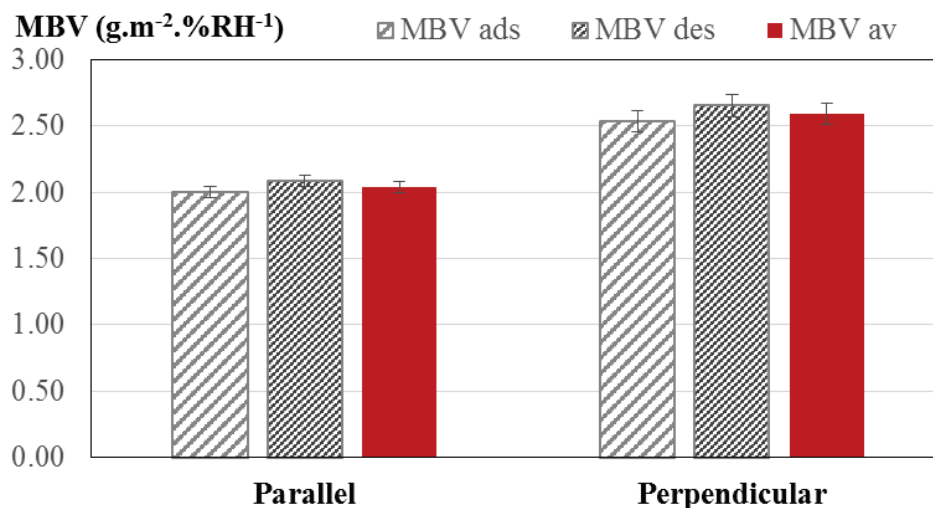


Figure 5 : Moisture Buffer Value of washing fines-hemp composites versus anisotropy – moisture flux parallel or perpendicular to the compaction direction

When the moisture flux is parallel to the compaction direction, the average moisture buffer value is  $2.04 \text{ g.m}^{-2}.\text{RH}^{-1}$ . This value is lower than the value found in previous study where the specimen were not firstly dried ( $2.24 \text{ g.m}^{-2}.\text{RH}^{-1}$  in [8]). This difference is probably due to different initial water content of the material. Actually, as shown in [12], the hygric history impacts the hygric behaviour of materials. When the moisture flux is perpendicular to the compaction direction, the MBV is 27 % higher ( $2.59 \text{ g.m}^{-2}.\text{RH}^{-1}$ ). So, the best way to take advantage from this material is to implement it in order to have moisture flux perpendicular to the compaction direction. This can be reached with framing technique where the composite is poured and more or less compacted.



#### 4. Conclusion

This study underlines the effect of anisotropy on thermal conductivity and moisture buffer value of washing fine – hemp composite produced by moulding and compacting successive layers.

The thermal conductivity exhibits 16.8 % of discrepancy between the two measurement directions. For moisture buffer value, the discrepancy reaches 27 %.

So, implementation way can be recommended. However, the best performance is not obtained for the same orientation of the material on hygric and on thermal point of view.

#### References

- [1] S. Amziane, F. Collet, M. Lawrence, V. Picandet, C. Lanos, S. Marceau, S. Pavia, Bio-aggregates Based Building Materials, Springer Netherlands, Amziane Sofiane and Collet Florence, (2017).
- [2] J. Williams, M. Lawrence, P. Walker, A method for the assessment of the internal structure of bio-aggregate concretes, *Construction and Building Materials*. 116 (2016) 45–51.
- [3] C. Niyigena, Variabilité des performances de bétons de chanvre en fonction des caractéristiques de la chènevotte produite en Auvergne, phdthesis, Université Blaise Pascal - Clermont-Ferrand II, (2016).
- [4] Dinh, T.M., Magniont, C., Coutand, M., and Escadeillas, G.. Hemp concrete using innovative pozzolanic binder. In ICBBM, (Clermont-Ferrand, France), (2015) 265-270.
- [5] V. Nozahic, S. Amziane, G. Torrent, K. Saïdi, H. De Baynast, Design of green concrete made of plant-derived aggregates and a pumice–lime binder, *Cement and Concrete Composites*. 34 (2012) 231–241.
- [6] T.T. Nguyen, V. Picandet, P. Carre, T. Lecompte, S. Amziane, C. Baley, Effect of compaction on mechanical and thermal properties of hemp concrete, *Eur. J. Environ. Civ. Eng.* 14 (5) (2010) 545–560.
- [7] S. Elfordy, F. Lucas, F. Tancret, Y. Scudeller, L. Goudet, Mechanical and thermal properties of lime and hemp concrete (“hempcrete”) manufactured by a projection process, *Construction and Building Materials*. 22 (2008) 2116–2123.
- [8] B. Mazhoud, Elaboration et caractérisation mécanique, hygrique et thermique de composites bio-sourcés, PhD Thesis, INSA de Rennes (2017).
- [9] B. Mazhoud, F. Collet, S. Prétot, et C. Lanos, « Characterization and comparison of thermal and hygric properties of hemp-clay composite and hemp-lime concrete », International Conference On Materials and Energy, ICOMÉ 2016, La Rochelle, France, (2016).
- [10] S. Amziane, F. Collet, M. Lawrence, C. Magniont, V. Picandet, M. Sonebi, Recommendation of the RILEM TC 236-BBM: characterisation testing of hemp shiv to determine the initial water content, water absorption, dry density, particle size distribution and thermal conductivity, *Materials and Structures*. (2017) 50:167.
- [11] Rode, C., Peuhkuri, R.H., Mortensen, L.H., Hansen, K.K., Time, B., Gustavsen, A., Ojanen, T., Ahonen, J., Svennberg, K., and Arfvidsson, J. Moisture buffering of building materials - BYG-DTU R-126, (2005).
- [12] Y. Aït Oumeziane, Evaluation des performances hygrothermiques d’une paroi par simulation numérique : application aux parois en béton de chanvre, PhD Thesis, INSA de Rennes (2013).

## **EVALUATION OF THE POTENTIAL OF CORN AND SUNFLOWER BARK PARTICLES AS BIO-AGGREGATES FOR LIGHTWEIGHT CONCRETE**

**Alexandra Bourdot<sup>(1)</sup>, Camille Magniont<sup>(1)</sup>, Méryl Lagouin<sup>(1)</sup>, Guillaume Lambaré<sup>(1)</sup>, Laurent Labonne<sup>(2)</sup>, Philippe Evon<sup>(2)</sup>**

(1) LMDC, Université de Toulouse, INSAT, UPS, Toulouse, France

(2) LCA, Université de Toulouse, INP-ENSIACET, Toulouse, France

### **Abstract**

Biomaterials are an alternative to non-renewable materials. Hemp shives allowed developing an industrial sector favorable to sustainable development. Hence, hemp concrete is currently used as filling material in a timber frame (cast onsite, sprayed or precast). Nevertheless, hemp shiv, the reference biobased aggregate, has a limited availability. It is thus necessary to consider other bio-aggregates largely and locally available. Sunflower and corn stalks were selected for their large availability in south-west of France. The objective of this paper is to evaluate the potential of these two agricultural by-products as alternative bio-aggregates for vegetal lightweight concrete through the determination of aggregate properties and the study of chemical interactions between plant particles water-soluble compounds and a pozzolanic binder. The results revealed a strong deleterious effect of corn water-soluble compounds on the setting and the hardening mechanisms of the pozzolanic binder. A 24 hours long setting delay was not only observed but an almost complete inhibition of the hardening was also highlighted by the mineralogical analysis and the evolution of the mechanical performances. Sunflower particles could be a good candidate for hemp shives substitution, since their characteristics are similar and their impact on the binder setting and hardening is moderate.

### **1. Introduction**

The building sector is responsible for major environmental impacts (consumption of non-renewable raw materials, emission of greenhouse gases and waste production). As a consequence, the design and characterization of innovative eco-friendly building materials has become a priority. The incorporation of bio-based raw materials could be a response to this

environmental challenge since they are renewable, are mainly by-products of local crops, and are carbon neutral. Over the last fifteen years, these environmental benefits have contributed to the development of a specific building material called hemp concrete. This composite combines a mineral binder and a plant aggregate: hemp shiv, i.e. the ligneous by-product resulting from the mechanical extraction of technical fibers from hemp stalk. Nevertheless, although hemp has been considered as the reference agro-resource for bio-aggregates based building materials, its availability is limited. Therefore, it is necessary to consider other bio-aggregates largely and locally available.

The present study aims to evaluate the potential of two agricultural by-products (corn and sunflower bark particles) as alternative bio-aggregates for vegetal lightweight concrete. Sunflower and corn stalks were selected for their large availability in south-west of France. Corn is the second most cultivated cereal in France, generating large quantities of by-products: 5.2 Mt of stalks in 2015. Sunflower is grown for its seeds to produce vegetal oil with about 614,000 ha cultivated nationwide. 230,000 tons of by-products were produced each year due to this agricultural crop. In comparison, only 17,000 t/year of hemp by-products are available [1].

The first part of the study focused on the plant particles characterization. According to the recommendations of RILEM TC 236-BBM [2], bulk density, particles size distribution and water absorption capacity were determined on hemp shives and on bark particles extracted from corn and sunflower stalks. In a second part, the impact of the water-soluble components extracted from the different bio-aggregates on the setting and hardening mechanisms of the lime-metakaolin binder was investigated.

## 2. Materials and methods

### 2.1 Bio-aggregates

Two bio-aggregates are evaluated : corn and sunflower bark particles compared to hemp shives. The samples are presented in Fig.1.

Alternative aggregates result from the combination of a preliminary stage of grinding of the entire stalk and a second phase of separation of the pith from the bark using a tilted conveyor belt and a blowing system. The bark particles under 1 mm were then eliminated by sieving.

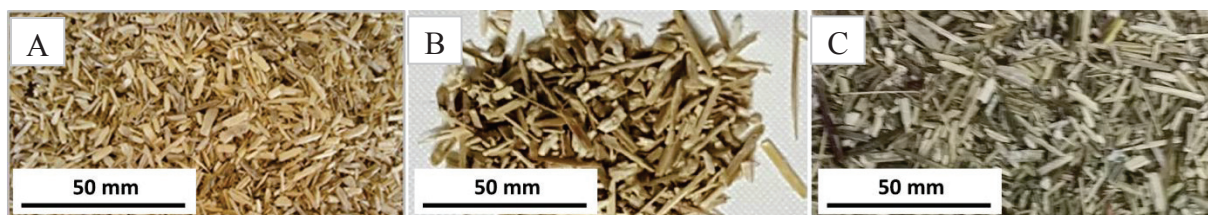


Figure 1: Photographs of the three studied bio-aggregates: hemp shives (A), corn (B) and sunflower (C) bark particles

### 2.2 Mineral binder

The binder is composed of 70 %wt of metakaolin and 30 %wt of aerial lime. Metakaolin, a pozzolanic admixture, is mainly composed of quartz, silicon and aluminium oxides with an

amorphous silicoaluminate mineralogical form. The aerial lime is around 92%  $\text{Ca}(\text{OH})_2$ . Potassium sulfate and a superplasticizer glycerol carbonate (GC) were added.

### 2.3 Aggregate characterization

The physical characterization of plant particles (bulk density, water absorption and particle size distribution) was realized according to RILEM Technical-Committee 236 – BBM (Bio Based Building Materials) recommendations [2].

### 2.4 Experimental methods on binder pastes

Four different mixtures were tested and differed by the nature of the mixing solution: a control paste was made with demineralized water, and the other three pastes were mixed with the filtrate of bio-aggregates. The filtrates were obtained after immersion of crushed particles (under 1 mm) in demineralized water for 48h with a water to particles ratio 15. The distilled water or filtrate to binder ratio was 0.55. The potassium sulfate to binder ratio was 0.03 and the superplasticizer to binder ratio was 0.016.

After mixing, the binder paste was cast in  $40 \times 40 \times 160 \text{ mm}^3$  moulds complying with NF-EN 196-3 [3]. The samples were then demolded at 3 days, cut in three samples and continuously cured in a room at  $20^\circ\text{C}$  and  $\text{RH} > 95\%$  until the date of the test. The pastes are noted Hemp\_P, Corn\_P, and Sunflower\_P. Compressive strength tests were conducted after 3, 14 and 150 days with a constant loading speed of 2.4 kN/s according to NF-EN 196-1 [4].

The setting process of the pastes was studied by isothermal calorimetry using TAM AIR 3116 microcalorimeter. The paste was elaborated manually with components at  $20^\circ\text{C}$  outside the calorimeter. Heat flow due to the setting reactions was recorded during 6 days.

The mineralogical evolution was carried out by X-ray diffraction and thermogravimetric analyses. The measuring system was a Bruker D8 Advance diffractometer using  $\text{K}\alpha$  ( $\lambda=1.542 \text{ \AA}$ ) copper anticathode. The 2-Theta values ranged from  $4^\circ$  to  $70^\circ$  and were recorded at a  $0.02^\circ$  step with an acquisition time of 0.25 s per step. Thermogravimetric analyses were performed on a thermal analyser NETZSCH STA 449 F3 Jupiter® operating at a heating rate of  $10^\circ\text{C}/\text{min}$  up to  $1000^\circ\text{C}$ . For each age, the hydration is stopped by immersion in liquid nitrogen and freeze-drying.

## 3. Results and discussion

### 3.1 Bio-aggregates properties

The bulk densities of bio-aggregates are  $154.2 \pm 0.6 \text{ kg/m}^3$ ,  $120.2 \pm 1.0 \text{ kg/m}^3$ ,  $168.2 \pm 4.5 \text{ kg/m}^3$ , for hemp, corn and sunflower particles, respectively.

The fitted curves and histograms of particle size distribution are presented in Fig. 2.

Fig. 2 reveals that hemp shives present a very narrow particle size distribution in comparison with corn or sunflower bark particles. This could be corrected by a more adequate calibration process for these alternative aggregates in order to eliminate the longer particles. Their circularity is also lower than for hemp particles in particular for corn particles. This result is consistent with bulk density measurement. Corn particles are more elongated and consequently induce a larger interparticular porosity responsible for a lower bulk density.

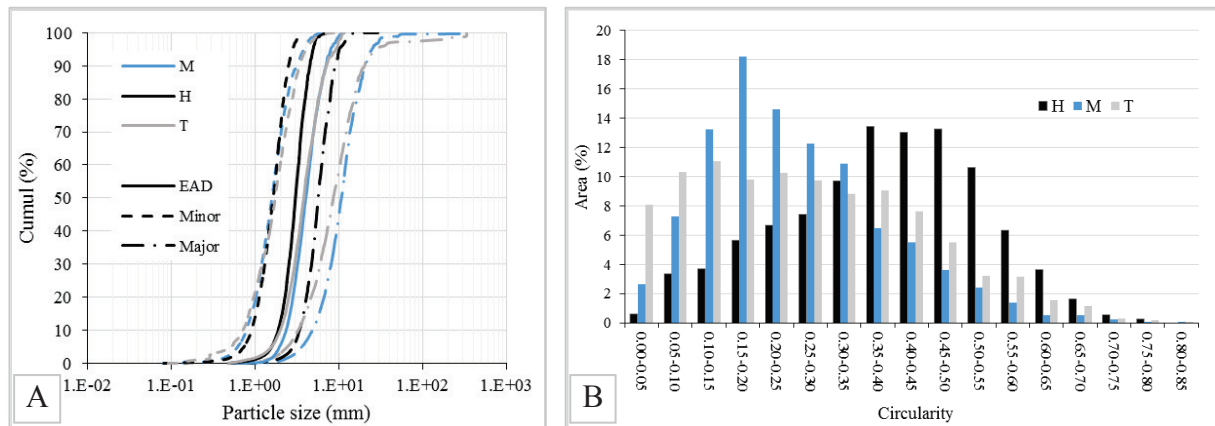


Figure 2: Particle size distribution (A) and circularity (B) of hemp, corn and sunflower particles

The kinetics of water absorption of the three plant particles have been assessed and are plotted in Fig. 3. The figure presents the evolution of the water content of plant particles with the time of immersion and as a logarithmic function of time. The three bio-aggregates present high water absorption capacity, from 250 to 300 %wt after 48h immersion. Fig. 3B evidences distinct initial rate of absorption (IRA) between the particles. After 1 minute, hemp and sunflower aggregates already retain more than 150 %wt while corn particles only absorb 100 %wt. This could be a benefit for corn particles at the time of mixing with the mineral binder.

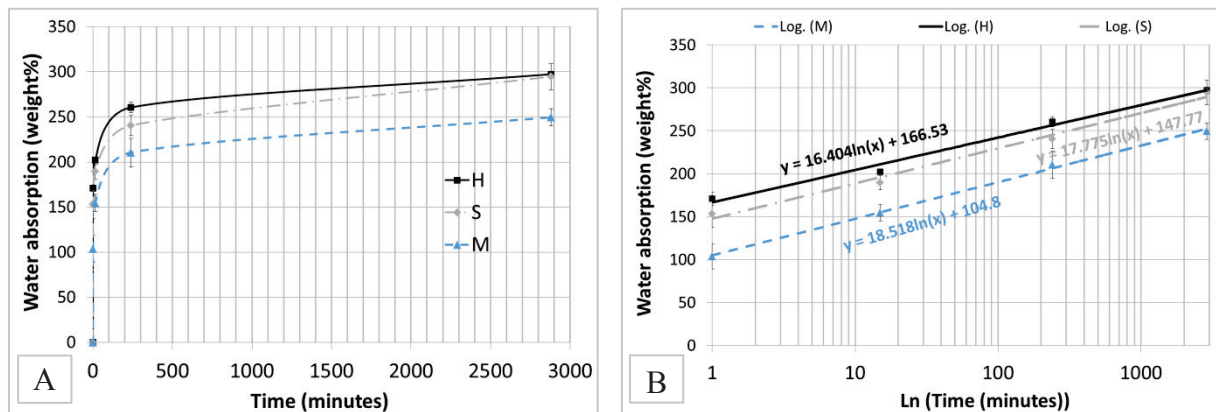


Figure 3: Water absorption curves as a function of time: linear (A) and logarithmic (B) scale

### 3.2 Interactions between bio aggregates extractives and pozzolanic binder

#### 3.2.1 Composite setting study

The isothermal calorimetry tests results are presented in Fig. 4. The heat flow curves highlight the impact of bio-aggregate extractives on the setting mechanisms of the pozzolanic matrix. Two phases are noted. The first ① corresponds to the exothermic reaction between potassium sulphate and calcium ions forming ettringite. The second ② is attributed to the pozzolanic reaction. Regarding hemp and sunflower pastes, a slight delay is observed. In addition, the heat flow intensity related to the reaction is reduced. However, the setting reaction takes place. The corn extractives induce the highest impact by a delay of 27 hours and a significant reduction of the heat flow intensity related to the reaction implying partial inhibition of the setting and hardening mechanisms of the pozzolanic binder. This effect was previously reported in the literature during the hydration of Portland cement in the presence of wood, hemp or lavender.

### 3.2.2 Mechanical performance of pastes

The compressive strengths of pastes are presented in Fig. 5. The results show that the filtrates of bio-aggregates can strongly influence binder pastes strengths. The effect of extractives can be observed from 3 days with a compressive strength value for control paste (CP) of 15.2 MPa while for the other pastes made with extractives the values are lower. Hemp and sunflower filtrates moderately impact the 3 days strength (11.7 Mpa). On the contrary, the model pastes with corn filtrate only reach 1.0°MPa. This decrease noticed at 3 days is still observed after 150 days of curing. At that age, the reduction of compressive strength in comparison with control paste is about 27, 14 and 88 % for hemp, sunflower and corn based pastes, respectively.

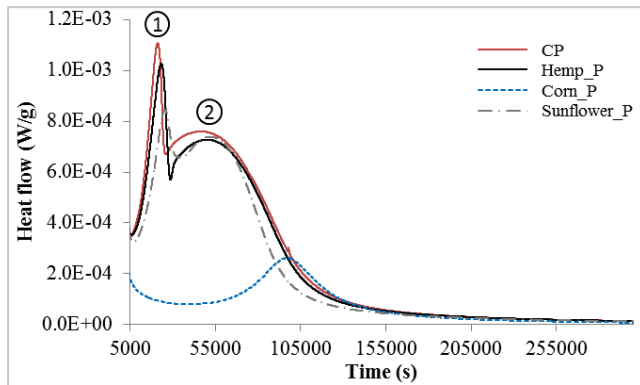


Figure 4: Heat flow by isothermal calorimetry of model pastes.

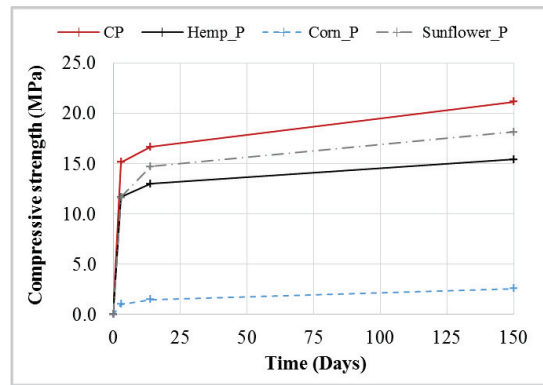


Figure 5: Compressive strength of model pastes at 3, 14 and 150 days.

### 3.2.3 Mineralogical evolution

The short term effect of bio-aggregate extractives was studied by XRD and TGA in order to explore the hardening mechanisms of model pastes. Differential TGA curves realized 24 hours after mixing are plotted in Fig. 6A.

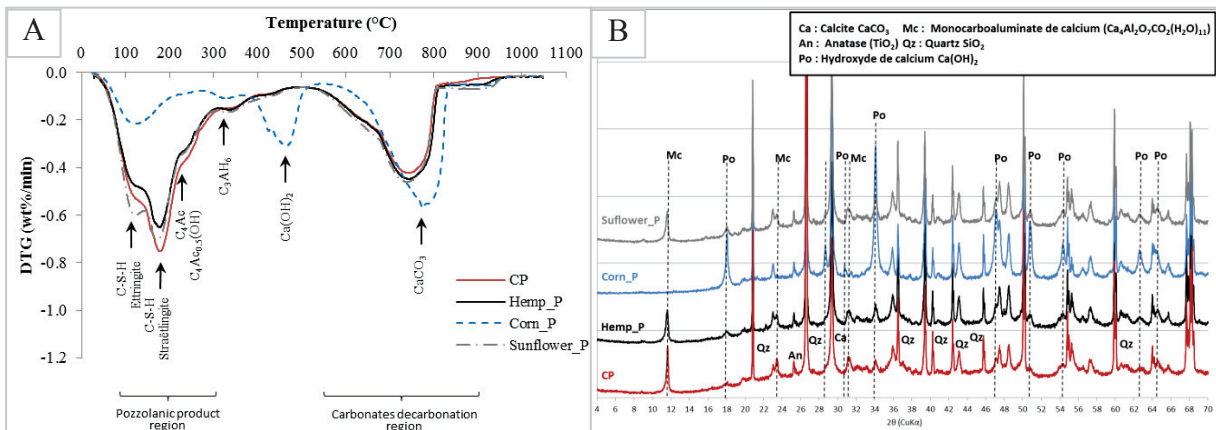


Figure 6: Differential TGA curves (A) and XRD analyses (B) of model pastes after 24h.

Extractives have a significant impact on the pozzolanic reaction development by reducing the amount of reaction products. The difference between the pastes based on hemp and sunflower extractives, and the control paste is mainly related to the peaks in a temperature range of 100-250°C. These peaks are attributed to the dehydration of C-S-H, ettringite and straetlingite.

The small peak at 250°C is attributed to calcium carboaluminates phases: calcium aluminium oxide carbonate hydrate,  $\text{Ca}_4\text{Al}_2\text{O}_6\text{CO}_3(\text{H}_2\text{O})_{11}$  (noted  $\text{C}_4\text{Ac}$ ) and calcium aluminium oxide hemi-carbonate hydroxide hydrate,  $(\text{Ca}_4\text{Al}_2\text{O}_6(\text{CO}_3)_{0.5}(\text{OH})(\text{H}_2\text{O}))_{11.5}$  (noted  $\text{C}_4\text{Ac}_{0.5}(\text{OH})$ ) [5]. No significant delay is observed in the consumption of portlandite (430°C) in these pastes. On the contrary, in the paste based on corn extractives, a large amount of residual portlandite is observed after 24 hours. A deficit in the formation of C-S-H and straelingite phases is also evidenced. These phenomena may be responsible for the decrease in mechanical performances. Finally, the increased presence of carbonates could be related to the release of carbon dioxide induced by the alkaline degradation of corn particles, which was responsible for the carbonation of portlandite [6]. These results are consistent with XRD analyses (Fig. 6B) that show similar crystallised compounds between control, hemp and sunflower pastes while corn paste is distinguished by the absence of calcium carboaluminates and the presence of portlandite.

#### 4. Conclusion

This study aims to evaluate the potential of bark particles of sunflower and corn as bio-aggregates for lightweight concrete. It has been shown that:

- Particle size distribution of sunflower and corn particles could be corrected through a calibration process, notably based on the elimination of the longer particles.
- Corn particles present a limited water absorption capacity. This could be valorized in association with a clay matrix for example. On the contrary, the deleterious effect of corn extractives on the setting and hardening mechanisms of the pozzolanic binder would largely reduce the mechanical performances of vegetal concrete designed with these two components.
- Sunflower bark particles appear to be a good candidate for hemp shives substitution since their characteristics are close and their impact on the setting mechanisms of the pozzolanic binder negligible.

#### References

- [1] Laborel-Préneron A., Magniont C., and Aubert J.-E., Characterization of Barley Straw, Hemp Shiv and Corn Cob as Resources for Bioaggregate Based Building Materials, *Waste Biomass Valor* (2017), 1–18
- [2] Amziane S., Collet F., Lawrence M., Magniont C., Picandet V., and Sonebi M., Recommendation of the RILEM TC 236-BBM: characterisation testing of hemp shiv to determine the initial water content, water absorption, dry density, particle size distribution and thermal conductivity, *Mater Struct Constr* 50 (2017), 1-11
- [3] AFNOR NF EN 196-3, Methods of testing cement – Part 3 : Determination of setting times and soundness, Association Française de Normalisation, France (2017)
- [4] AFNOR NF EN 196-1, Methods of testing cement – Part 1: Determination of strength, Association Française de Normalisation, France (2006)
- [5] Magniont C., Escadeillas G., Oms-Multon C., and De Caro P., The benefits of incorporating glycerol carbonate into an innovative pozzolanic matrix, *Cem Concr Res* 40 (2010), 1072–1080
- [6] Govin A., Peschard A., and Guyonnet R., Modification of cement hydration at early ages by natural and heated wood, *Cem Concr Compos* 28, (2006), 12–20

## **EVOLUTION OF HEMP CONCRETE PROPERTIES EXPOSED TO DIFFERENT TYPES OF ENVIRONMENTS**

**Guillaume Delannoy<sup>(1)</sup>, Sandrine Marceau<sup>(1)</sup>, Philippe Glé<sup>(2)</sup>, Etienne Gourlay<sup>(2)</sup>,  
Marielle Guéguen-Minerbe<sup>(1)</sup>, Sofiane Amziane<sup>(3)</sup>, Fabienne Farcas<sup>(1)</sup>**

(1) Université Paris-Est, MAST, CPDM, IFSTTAR, Marne-la-Vallée, France

(2) Cerema, Laboratory of Strasbourg, Strasbourg Cedex 2, France

(3) Université Clermont Auvergne, Institut Pascal, Clermont-Ferrand Cedex 1, France

### **Abstract**

Vegetal aggregates-based materials, as hemp concrete, are used to improve thermal insulation, acoustical and hygrothermal performances for a better living comfort in buildings, by using renewable resources. Hemp concrete is frequently used. However, the lack of knowledge about its long-term performances is a limitation to the development of the material. Therefore, the objective of this study of durability is to identify the ageing mechanisms of hemp concrete by using a pluridisciplinary and multiscale approach. Hemp concrete is aged for two years under two different environmental conditions, the factors of ageing used are temperature and variations of relative humidity. The evolution of functional properties (thermal, acoustical and mechanical) is followed and related to the evolution of microstructure and chemistry of the different components. The results show that under static laboratory conditions, the properties of hemp concrete are stable with time. The accelerated ageing allows changes in the functional properties with time, due to modifications of the binder chemistry and of the microstructure of vegetal aggregates, with an action of microorganisms.

### **1. Introduction**

Hemp concrete is an insulating material used for its thermal, hygrothermal and acoustic properties [1]. It is composed of plant aggregates, called hemp shiv, which are coated and bound by a thin layer of mineral binder, whose thickness is less than 0.5 mm. The microstructure, and in particular the high porosity of shiv, brings the functional properties of the material [2].

Feedbacks on real constructions [3] made it possible to identify problems of implementation in the first constructions, which have since been largely corrected, in particular after the publication of building codes [4]. Therefore, the question of the evolution of the long-term performances of the material arises. Former studies focused on the durability of hemp concretes. In order to observe changes in functional properties or microstructure, accelerated aging is used with variations of relative humidity [5, 6], immersion in water [7] or freeze-



thaw cycles [8, 9]. The presence of water is indeed a risk factor for the durability of hemp concrete. Indeed, the hydrophilic nature of hemp shiv induces a swelling of the particles, and thus constraints at the interface between the vegetal components and the binder [10]. Moreover, in the presence of water and mineral binders, a high pH value can be achieved within the material, leading to alkaline degradation [11] as well as mineralization of plants [12]. The relative humidity value applied also has an impact on the evolution of the binder, and in particular on the kinetics of carbonation [13].

Too short aging periods (<75 days) explain the small variations in properties observed in the durability studies that set hygrometry as an aging factor [14]. Nevertheless, this type of aging is closer to the real conditions of use of the materials, and does not modify their integrity. Indeed, a leaching of organic or mineral materials is observed during the immersion cycles, which correspond rather to accidental conditions such as water damage in a building. It is for this reason that the study presented in this article uses accelerated aging consisting of humidification and drying cycles, by applying relative humidity variations, at a temperature favourable to the potential development of microorganisms. A multi-scale and multi-disciplinary approach makes it possible to highlight and link possible evolutions of functional properties (thermal, acoustic and mechanical performances) with the evolution of the microstructural and physicochemical properties of hemp concretes. In order to study the impact of the formulation on all long-term properties, two binders, with a different chemical composition and commonly used on worksites are chosen.

Firstly, the characterization of the functional, microstructural and chemical properties is presented as a function of time, depending on the type of aging. Then, these results are discussed by making the link between characterizations at different scales

## 2. Materials and methods

### 2.1 Materials and manufacturing

A commercial hemp shiv sold for insulation applications is selected for this study. A: commercially formulated binder (FL), based on natural lime (70%) and hydraulic and pozzolanic binders (30%), is selected.

Formulation of hemp concretes is set according to the building codes of hemp construction for a wall formulation [4]. The binder/shiv ratio is 2, and the total water/binder ratio is 1. The fresh density of hemp concretes is set to  $530 \text{ kg.m}^{-3}$ . Samples are demoulded after 7 days, and after 83 days of drying at 65% RH and  $20^\circ\text{C}$ , the dried density is about  $350 \text{ kg.m}^{-3}$ . Hemp concretes containing the formulated binder based on lime are called HC-FL.

### 2.2 Aging protocols

After curing, the test pieces are divided into two lots and are placed under two different environments for 2 years, defined from the results of the Marceau et al. [6]

- The first batch is used as reference (REF) and is stored in a room at 50% RH and  $20^\circ\text{C}$ .
- The second batch is submitted to accelerated aging ( $A_{\text{WD}}$ ), corresponding to cycles of relative humidity from 40 to 98% at a constant temperature of  $30^\circ\text{C}$  in a climatic chamber.

The properties of the material are measured before aging ( $A_0$ ) and then regularly over a period of 2 years (3, 6, 12, 18 and 24 months) on samples previously dried 48h at  $40^\circ\text{C}$ .

### 2.3 Aging protocols

Thermal conductivity measurements are conducted using a transient measurement technique (Hot Disk method) at 24 °C on five specimens for each formulation (measurement time 80 s, power 0.1 W).

The sound absorption coefficient  $\alpha$  is measured using a Kundt tube (Acoustitube AFD) over a frequency range of 250 to 2000 Hz on five specimens.  $\alpha$  (f) is between 0 (no absorption) and 1 (total absorption).

Concrete samples are mechanically tested in compression (10 cm in diameter and 20 cm in height) using a Zwick press with controlled displacement at 3 mm/min.

An analysis of the mineral phases is carried out by thermogravimetric analysis.

Open air porosity is measured using a porosimeter as described in [2] on 4 specimens.

Microstructural analysis is performed using a Quanta 400 FEI scanning electron microscope in SE and BSE mode.

## 3. Results

### 3.1 Functional properties

The evolution of thermal conductivity of hemp concrete for both types of aging is shown in Fig. 1. For the reference aging, no change in thermal conductivity is observed. In contrast with  $A_{WD}$  aging, an increase in thermal conductivity is visible.

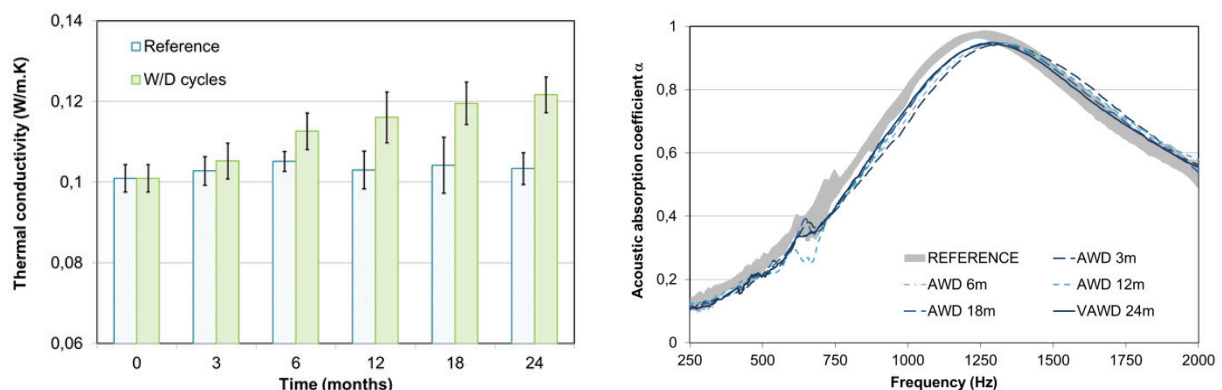


Figure 1: Evolution of the thermal conductivity and of the acoustic absorption coefficient in both environments.

Similarly, no significant evolution of the acoustic absorption coefficient is observed for the reference samples (Fig. 1). The results are therefore represented as an area representing the spindle of all measurements between 0 and 24 months. For aging  $A_{WD}$ , we observe a shift of the curve towards the higher frequencies, with a decrease of the maximum value. This stall occurs between 0 and 3 months, the other curves do not vary significantly.

The compressive strength results of hemp concrete specimens are shown in Fig. 2. In view of the results and of their dispersion, no change in the mechanical behaviour is observed. The weak mechanical resistance observed comes from a poor hydration of binder which is inhibited by extractible molecules of hemp, such as sugars [2].

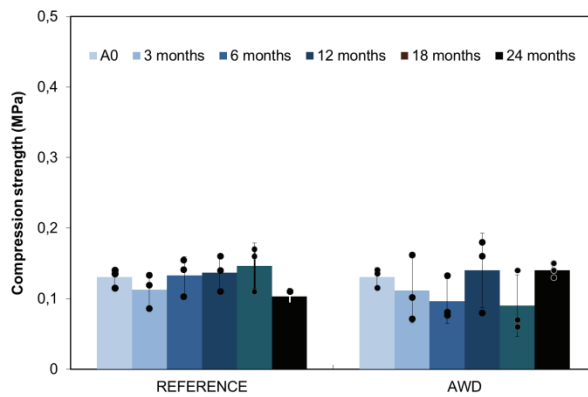


Figure 2: Evolution of the compression strengths in both environments

### 3.2 Physical properties

The mass variation of the test pieces is shown in fig. 3. Due to the low mechanical strength of the samples, some vegetal particles are released during their handling. In the reference environment, this induces an initial mass loss of around 3%. In spite of this, during the  $A_{WD}$  cycles, an increase in mass is visible over time. This increase occurs up to 18 months, then the mass seems to stabilize until 24 months. Considering an equivalent mass loss as observed for the reference specimens, the weight gain of samples stored in  $A_{WD}$  environment can be estimated at 10%.

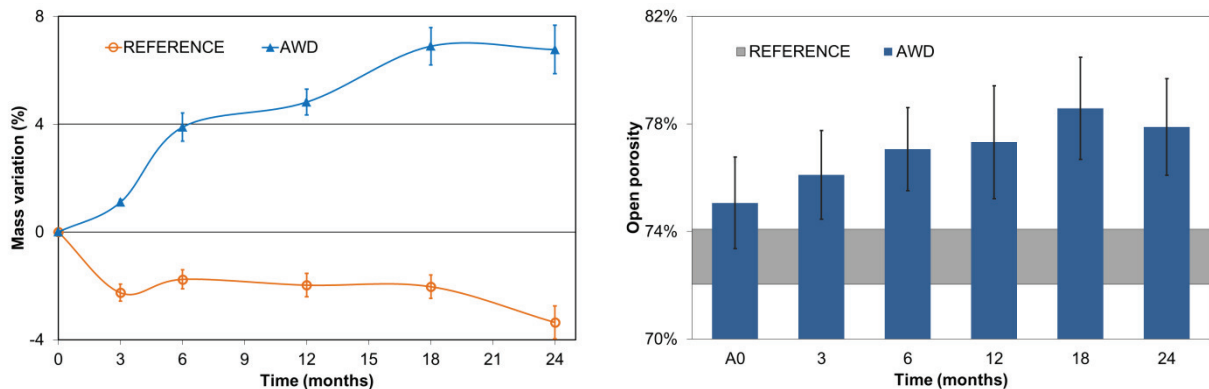


Figure 3: Evolutions of the mass and of the open porosity as a function of time

The open porosity accessible to the air is stable for the reference environment (Fig. 3). On the other hand, the value of open porosity increases of 4% in  $A_{WD}$  aging until 18 months then seems to have reached its maximum.

The observations with a scanning electron microscope were carried out on longitudinal and cross sections (Fig. 4). Perforations are visible in the plant walls (Fig. 4c), as well as hyphae (Fig. 4a) and penetration of the binder into the porosity of the aggregates (Fig. 4b and d).

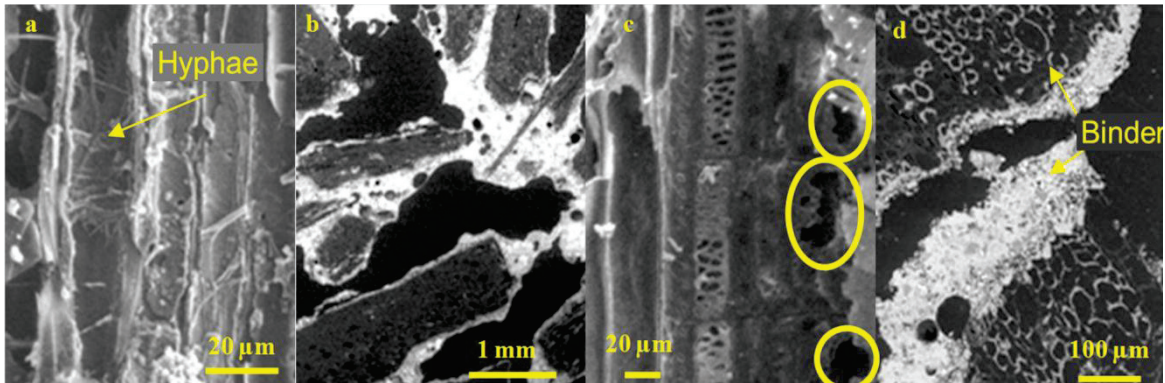


Figure 4: Observation of concrete microstructure by scanning electron microscopy

### 3.3 Chemical properties

The synthesis of the results of the thermogravimetric analyses on the mineral part is presented in Fig. 5 on the binder powder, at  $A_0$  and during aging  $A_{WD}$ . It is observed that between the binder powder and the results at  $A_0$ , the hydration is not complete, as observed previously [2]. For this concrete, hydration is low at  $A_0$  and most of the initial portlandite has carbonated. During aging  $A_{WD}$ , the hydration and carbonation of the binder slowly resume.

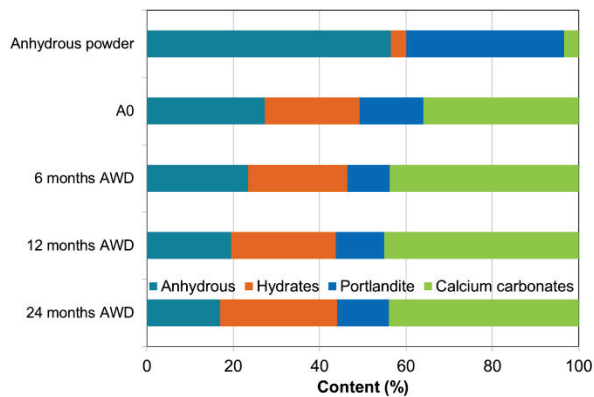


Figure 5: Evolution of the chemical composition on the binder during  $A_{WD}$  aging

## 4. Conclusion

The first conclusion of this study is that under reference conditions, no change in functional, microstructural or chemical properties is observed for 2 years. The material remains stable over time under these conditions.

The application of an accelerated aging protocol to hemp concrete under hygric stress has made it possible to highlight changes in functional, microstructural and chemical properties. Two major mechanisms seem to operate simultaneously: a densification of the mineral part by hydration and carbonation of binders during aging, as well as a degradation of the shiv by microorganisms. The densification of the mineral part leads to an increase in the mass of concretes, but also in their thermal conductivity. The attack of the vegetal particles is visible by an increase of the open porosity, the degradation of the plant wall allowing the access to an intraparticulate porosity initially closed.

The presence of lime in the binder causes the modification of the mineral part by carbonation and by mineralization of the shiv porosity. These changes affect functional properties, such as acoustic behaviour, portlandite being water soluble and subject to migration under water stress. This binder is also sensitive to carbonation, which leads to a build-up and therefore an increase in thermal conductivity.

Finally, no evolution of the mechanical properties is observed, the effects of the hydration and carbonation recovery being counterbalanced by a weakening of the plant.

## References

- [1] Amziane, S. and Collet, F., Bio-aggregates Based Building Materials, RILEM State-of-the-Art reports, Vol. 23, Springer, Dordrecht (2017)
- [2] Delannoy, G. et al, Influence of binder on the multiscale properties of hemp concretes, European Journal of Environmental and Civil Engineering (2018), 1-17
- [3] Agence Qualité Construction, Isolants biosourcés: points de vigilance (2016)
- [4] Construire en chanvre, Règles professionnelles d'exécution, SEBTP, Paris (2012)
- [5] Arizzi, A. et al., Predicting the long-term durability of hemp-lime renders in inland and coastal areas using Mediterranean, Tropical and Semi-arid climatic simulations, Science of Total Environment 542 (2016), 757-770
- [6] Marceau, S. et al., Influence of accelerated aging on the properties of hemp concretes, Construction and Building Materials 139 (2017), 524-530
- [7] Sentenac, C. et al., Investigation on the performance and durability of treated hemp concrete with water repellent, Proceedings of the 2nd International Conference on Bio-based Building Materials, Clermont-Ferrand, France (2017), 20-28
- [8] Walker, R. et al., Mechanical properties and durability of hemp-lime concretes, Construction and Buildings Materials 61 (2014), 340-348
- [9] Sassoni, E. et al., Experimental study on the physical-mechanical durability of innovative hemp-based composites for the building industry, Energy and Building 104 (2015), 316-322
- [10] Nozahic, V., Vers une nouvelle démarche de conception des bétons de végétaux lignocellulosiques basée sur la compréhension et l'amélioration de l'interface liant / végétal, PhD Thesis, Université de Clermont-Ferrand (2012)
- [11] Wei, J. and Meyer, C., Degradation mechanisms of natural fiber in the matrix of cement composites, Cement and Concrete Research 73 (2015), 1-16
- [12] Chabannes, M., Studying the hardening and mechanical performances of rice husk and hemp-based building materials cured under natural and accelerated carbonation, Construction and Building Materials 94 (2015), 105-115
- [13] Marceau, S. and Delannoy, G., Durability of Bio-based concretes in Bio-aggregates Based Building Materials, RILEM State-of-the-Art reports 23, Eds. Amziane, S. and Collet, F., Springer, Dordrecht (2017), 167-187
- [14] Gourlay, E., Caractérisation expérimentale des propriétés mécaniques et hygrothermiques du béton de chanvre, PhD Thesis, Université de Lyon (2014)

## **INFLUENCE OF FILLER EFFECT AND POZZOLANIC REACTION OF BIOMASS ASHES ON MECHANICAL PROPERTIES OF CEMENT MORTARS**

**Vlastimir Radonjanin<sup>(1)</sup>, Mirjana Malešev<sup>(1)</sup>, Slobodan Šupić<sup>(1)</sup>, Miroslava Radeka<sup>(1)</sup>**

(1) Faculty of technical sciences, University of Novi Sad, Serbia

### **Abstract**

The contribution of pozzolana in cement-based materials (concrete and mortar) can be categorized into: (i) physical or filler effect which is attributed by the fineness of the particles and (ii) chemical or pozzolanic effect which is attributed by the pozzolanic reaction. Various types of biomass, from agro-industrial processes, generate ashes through their combustion. These ashes, under certain conditions (chemical configuration, level of fineness), can have pozzolanic and/or filler activity in cementitious composites. In this study, the influence of filler effect and pozzolanic reaction of wheat straw ash (WSA), soya straw ash (SSA) and mixed soya and wheat straw ash (WSSA) was analysed. In the first phase pozzolanic activity and activity index of these ashes were tested and results have shown that SSA and WSSA have lower pozzolanic activity and activity index compared to wheat straw ash. That is why authors of this paper have tried to improve their filler effects by additional grinding in a lab ball mill. Filler effect was checked by testing of compressive strength of mortars in which 10 and 25% of cement was replaced with grinded ashes. Additional grinding had a positive impact on the activity index of WSSA, but in the case of SSA, it was close below the required value.

### **1. Introduction**

Cement is the principal raw material for the concrete production, by which manufacturing leads to severe environmental problems, primarily caused by CO<sub>2</sub> emission. The emission of CO<sub>2</sub> is estimated as 1 tonne of CO<sub>2</sub>/1 tonne of cement produced which makes 8% of the total global emission. In addition, production of cement requires high energy and generates considerable costs; hence cement nowadays becomes unsuitable for the sustainable development in civil engineering [1].

Several research has been conducted on finding alternative materials that can be used as cement replacement, such as the disposable and less valuable wastes from industry and agriculture, whose potential benefits can be realized through recycling, reuse and renewing regimes [2]. Some studies showed that certain agro-waste materials could be utilised as a cement replacement in cement based materials. The utilization of agricultural waste can provide the alternative needed to make the industry more environmentally friendly and sustainable.

In Autonomous Province (AP) Vojvodina, in a northern part of Republic of Serbia, biomass is commonly utilized through combustion for heat generation. Wheat straw, soya straw and sunflower husk are major energy biosources and, by their combustion, large quantities of biomass ash are generated. This ash represents a potential source for the production of alternative mineral binders with cementitious properties.

The activity of these ashes, used as a binder in cement-based composites, is mainly influenced by amorphous silica content and fineness. In this study, the influence of filler effect and pozzolanic reaction of biomass ashes (wheat straw ash, soya straw ash and mixed soya and wheat straw ash) on mechanical properties of cement mortars was investigated.

## 2. Experimental research - Phase 1

Biomass ashes, used in this experimental study, were collected from three producers of biomass ash in Vojvodina. In the first phase of the experiment, following properties of ashes were tested:

- Basic physical properties (density, specific surface area),
- Chemical composition,
- Pozzolanic activity,
- Activity index.

The following materials were used in the study:

- Portland cement CEM I 42,5R (Lafarge-BFC Serbia),
- Wheat straw ash (WSA), "Mitrosrem", Sremska Mitrovica, Serbia, Fig. 1,
- Mixed wheat and soya straw ash, the ratio 50:50, (WSSA), "Soya Protein", Bečej, Serbia, Fig. 2,
- Soya straw ash (SSA), "Hipol", Odžaci, Serbia, Fig. 3,
- CEN Standard sand in accordance with EN 196-1,
- Distilled water.



Figure 1: View of biomass ashes after grinding, a) WSA, b) WSSA, c) SSA

## 2.1 Physical properties and chemical composition

After grinding for 6 hours, all types of biomass ashes had densities cca 2.400 kg/m<sup>3</sup>, while specific surface area (Blaine) exceeded 5.000cm<sup>2</sup>/g. Physical properties of tested biomass ashes are shown in Tab. 1.

Table 1: Physical properties of tested biomass ashes.

	Density (kg/m <sup>3</sup> )	Specific surface (Blaine) (cm <sup>2</sup> /g)
WSA	2.380	5.800
WSSA	2.370	5.500
SSA	2.400	5.200

The chemical composition of tested biomass ashes is given in Tab. 2. Ashes WSA and WSSA have relatively high silica content, exceeding 50%, while soya straw ash is characterized with lower silica content (13.8%), which should reflect on its pozzolanic activity.

Table 2: Chemical composition of biomass ashes (wt% of ash) [3].

	SiO <sub>2</sub>	Al <sub>2</sub> O <sub>3</sub>	Fe <sub>2</sub> O <sub>3</sub>	CaO	MgO	Na <sub>2</sub> O	K <sub>2</sub> O	LOI
WSA	53.21	4.00	2.69	13.45	1.90	0.41	12.05	10.19
WSSA	51.93	0.19	1.39	14.28	2.07	0.43	18.43	9.27
SSA	13.80	1.76	1.45	47.53	7.76	0.07	5.23	18.60

With respect to the chemical composition, higher amorphous silica content results in the higher pozzolanic reactivity of ashes. Materials with very high silica content and large surface area intensively react with the water and the calcium hydroxide, generated during the hydration of cement, to produce additional C-S-H, which is the main strength contributing compound in cement-based composite. C-S-H gel makes denser microstructure of biomass ashes containing cement-based material.

## 2.2 Pozzolanic activity

The pozzolanic activity was tested on specimens prepared according to the procedure given in SRPS B.C1.017-2001. Results are given in Tab. 3. The class of pozzolanic activity was determined based on 7 day compressive (fp) and flexural (fzs) strength of standard mortar prisms (SRPS B.C1. 018-2001). Mortars were prepared with biomass ash, slaked lime and standard sand, (Figure 18), with following mass proportions: msl:mbash:mqs=1:2:9 and water/binder ratio 0,6 (where: msl – mass of slaked lime; mbash – mass of biomass ash; mqs – mass of CEN standard sand). After compacting, specimens were hermetically packed and cured 24h on 20°C, then 5 days on 55°C. After cooling of specimens in next 24h up to 20°C, compressive and flexural strength were tested.



Table 3: Pozzolanic activity of biomass ashes.

	$f_{zs,mean}$ [MPa]	$S_{dev}$	$f_{zs,min}$ [MPa]	$f_{p,mean}$ [MPa]	$S_{dev}$	$f_{p,min}$ [MPa]	CLASS
WSA	3.4	0.22	3.3	11.0	0.49	10.3	<b>10</b>
WSSA	3.6	0.05	3.3	9.3	0.30	8.75	<b>5</b>
SSA	1.6	0.17	1.45	4.06	0.08	3.84	/

Testing of pozzolanic properties showed that wheat straw ash has medium pozzolanic activity of Class 10, mixed soya and wheat straw ash has lower pozzolanic activity - Class 5, while soya straw ash has low pozzolanic activity that is not sufficient to express through Class. These classes are used to measure pozzolanic activity based on the strength of cementitious mixtures containing the pozzolan with lime. They are one of the parameters in the selection and classification of pozzolans. Higher Class of pozzolanic activity will probably lead to the better reactivity of these materials in cementitious systems.

### 2.3 Activity index

Activity index was studied on specimens prepared according to the standard EN 450-1. Results are given in Tab. 4. Activity index is a ratio of the compressive strength of standard mortar prisms, prepared with 75%wt cement and 25%wt fly ash by mass, to the compressive strength of standard mortar prisms prepared with 100% cement, when tested at the same age. According to the criteria, activity index at 28 days and at 90 days shall not be less than 75% and 85%, respectively. Wheat straw ash exhibited even higher compressive strength in relation to the reference mortar's strength, which can be attributed to the filler effect of small particles of wheat straw ash. Ashes WSSA and SSA didn't fulfil criteria, as their activity indexes were below required value. This is due to the insufficient pozzolanic activity of soya-based biomass ashes.

Table 4: Activity index of biomass ashes.

	$f_{p,28d}$ [MPa]	Index, 28d (%)	$f_{p,90d}$ [MPa]	Index, 90d (%)
C	50.26	-	54.53	-
WSA	52.39	<b>104.24</b>	58.96	<b>108.12</b>
WSSA	32.65	64.90	41.80	76.60
SSA	28.3	56.3	test in progress	

The results indicate that SSA and WSSA have lower pozzolanic activity and insufficient activity index compared to WSA. As pozzolanic reactivity depends heavily on the size of the material particles, the next stage in the experimental research was an attempt to improve filler effects of these biomass ashes by additional grinding in a lab ball mill.

### 3. Experimental research - Phase 2

Ashes WSSA and SSA were additionally grinded for 18 hours (total of 24 hours) in a lab ball-mill, thereby achieving Blaine fineness:  $15.000\text{cm}^2/\text{g}$ . The ashes were further used for activity index test, by testing of compressive strength of mortars, in which 10 and 25% of cement was replaced with grinded ashes. This approach enabled recording the pure effect of fineness on soya straw ash reactivity (filler effect).

Additional grinding of biomass ashes had a positive impact on activity index of WSSA ash, by both replacement levels (10 and 25%). Activity indexes were 91.7% and 94.3% for replacement levels 10% and 25%, respectively. Within this process, activity index of WSSA ash at the replacement level of 25%, was increased by 29% (from 64,9 to 91,7%), hence the criterion for activity index at the age of 28 days, according to EN 450-1, was satisfied ( $>75\%$ ) – Fig. 4.

Activity index of SSA was over 75% at the replacement level of 10%, whereas additional grinding increased index by 7%. At the replacement level of 25%, additional grinding increased index by 19% (from 56,3 to 69,9%); however, it was still below the required value ( $69.6 < 75\%$ ) – Fig. 5.

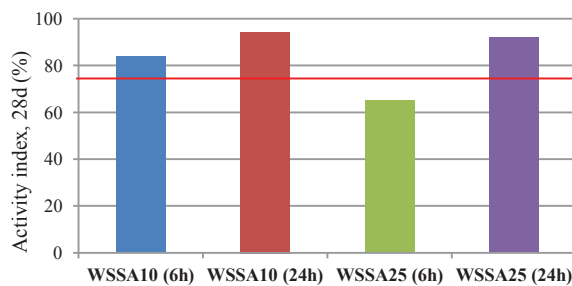


Figure 4: Activity index of WSSA.

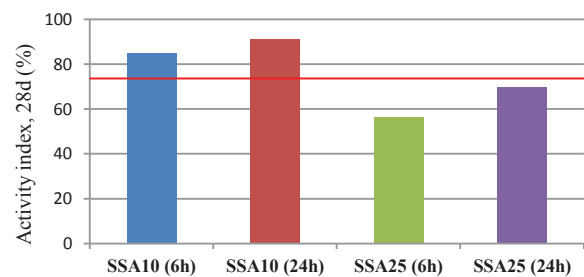


Figure 5: Activity index of SSA.

### 4. Conclusions

In this study, pozzolanic properties and activity index of agro-waste materials, originating from AP Vojvodina: wheat straw ash, soya straw ash and mixed soya and wheat straw ash were tested in order to investigate the possibility of their application in cement based composites.

Results show that wheat straw ash has high pozzolanic activity of Class 10 and high activity index, while soya straw ash and mixed soya and wheat straw ash have lower pozzolanic activity and activity index. In order to define possible use of soya-based biomass ashes, authors of the paper tried to improve filler effect of these types of ashes by additional grinding in a lab ball mill. Additional grinding had a positive impact on the activity index of WSSA, as it was increased by 29%, satisfying criterion at the age of 28 days. In the case of SSA, activity index was increased by 19%; however, it was close below the required value.

Main reason of low pozzolanic activity of soya-based biomass ash lies in its low silica content (13,8%). Therefore, in the third phase, an attempt to stimulate pozzolanic activity of soya straw ash and improve its activity index will be performed by using mineral admixture with

high amount of amorphous silica – silica fume, as a substitute for part of biomass ash. This research should provide reasons for use of inert biomass ashes in cement composites.

### **Acknowledgements**

The paper presents the part of research realized within the project “Theoretical and experimental research and improvement of educational process in civil engineering” conducted by the Department of Civil Engineering and Geodesy, Faculty of Technical Sciences, University of Novi Sad.

### **References**

- [1] Josephin A. et al, Experimental investigation on rice husk ash as cement replacement on concrete production, *Construction and Building Materials* 127 (2016), 353–362
- [2] Aprianti E. et al, Supplementary cementitious materials origin from agricultural wastes – A review, *Construction and Building Materials* 74 (2015), 176–187
- [3] Malešev M. et al, Physical and mechanical properties of cement mortars with biomass ashes as SCM, *International RILEM Conference on Materials, Systems and Structures in Civil Engineering - Conference segment on Concrete with Supplementary Cementitious Materials*, Technical University of Denmark, Lyngby, Denmark (2016), 223-233.
- [4] SRPS EN 196-6: Methods of testing cement - Determination of fineness
- [5] SRPS EN 196-1: Methods of testing cement - Determination of strength
- [6] SRPS B.C1.018.2001 - Non-metal mineral raw material: Testing of pozzolanic activity
- [7] EN 450-1:2012: Fly ash for concrete. Definition, specifications and conformity criteria

## IN-PLANE RACKING STRENGTH OF TIMBER WALLS FILLED WITH HEMP CONCRETE

Husam Wadi<sup>(1,2)</sup>, Sofiane Amziane<sup>(1,2)</sup>, Evelyne Toussaint<sup>(1,2)</sup>, Mustapha Taazount<sup>(1,2)</sup>

(1) Université Clermont Auvergne, Institut Pascal, Clermont-Ferrand, France

(2) CNRS, Aubière, France

### Abstract

The use of low carbon material in structures improves the insulation level and sound absorption and also decreases the weight of building. In response to this need, the use of bio-aggregate such as hemp shives is increasing in Europe and especially in France. Hemp concrete is now used in construction as a sustainable and carbon neutral infill wall material around timber-framed construction. This study focuses on the effect of wall dimensions on the in-plane racking strength of timber frame walls filled with hemp concrete. Two wooden geometrical configurations were used as wall units, the first was diagonal bracing walls under compression, and the second was vertical stud walls. These two types of timber walls are most widely used as structural elements in construction subjected to lateral loads. In this research, an experimental investigation of large-scale timber walls both with and without hemp concrete was carried out to investigate the contribution of this filling material against the lateral loads. The hemp walls then compared to empty frames to determine the real contribution of hemp concrete in the lateral strength of the timber wall. Based on the results obtained from the experimental tests, this study confirms, firstly, that hemp concrete has a small participation against lateral loads with wall dimensions 2.5 m height and 1.2 length. However, several studies found that hemp concrete has a high racking strength. In fact it cannot be generalized that hemp concrete has always a significant strength in timber wall. The filling material could not work mechanically against lateral load without a complete form of compression diagonal zone which make the material loaded under shear forces. This zone is related to the dimensions of the wall and is present when the ratio between the height and the length of the wall ( $L/h$ )  $\geq 1$ . Within this limit, the material mechanically works, otherwise, the results are totally different.

## 1. Introduction

Construction and public projects nowadays are facing a significant challenges of reducing energy consumption due to the large amount of using daily services such as heating, electricity and hot water in the residential and commercial buildings especially in Europe. For this purpose, many buildings regulations try to use now bio-base materials with a high quality of physical properties in construction sectors. The use of low carbon material in structures will firstly, improve the insulation level and sound absorption and secondly, will decrease the weight of building because this natural material considered as a lightweight aggregate. In response to this need, the use of bio-aggregate such as hemp, flax and sunflower is increasing in Europe and especially in France [1]. Wood is one of the most widely used building materials in many countries in the world, because it has a good physical properties and environmentally friendly [2]. Timber walls are frequently used as a structural system in the buildings designed to withstand lateral loads and transfer these forces to the foundations with ductile behaviour [3]. Timber shear wall consists of timber frame and sheathing board, connected by fasteners. The sheathing board may be made of a variety of materials, such as Oriented Strand Board [4-7]. Hemp particles are a natural low carbon material used to reduce energy consumption in buildings [5]. Nowadays this natural material is used in construction as infill wall material within timber framed construction in Europe and especially in France [5].

## 2. Theoretical approach

Two different shapes of timber walls were considered in this study, vertical stud and diagonal bracing walls (see Fig. 1 & 2). A linear elastic behaviour of the wall-unit were assumed in this approach, also the deformations are caused by only external force. By applying the virtual work transformation by unit-load theorem ( $F$ ), the total top displacement of the wall unit ( $\Delta$ ) can be calculated as:

$$\Delta = \frac{\partial W}{\partial F} \quad (1)$$

where  $W$  is the elastic strain energy stored in the wall and provided by an external horizontal load  $F$  applied on the top of the wall unit. In the present case, the total strain energy consists of three internal forces: a normal force  $N$ , shear force  $V$  and an internal moment  $M$  as illustrated in Eq. (2). By taking the material characteristics into account, then the total horizontal displacement ( $\Delta_1$ ) in vertical stud wall can be calculated as a function of the internal forces by Eq. (3), also the total horizontal displacement ( $\Delta_2$ ) in the diagonal bracing wall can be calculated by Eq. (4) using the same principle.

- For vertical stud timber frame:  $F(\text{kN}) = 0.0083 \times \Delta_1 (\text{mm})$
- For diagonal bracing element:  $F(\text{kN}) = 2.7 \times \Delta_2 (\text{mm})$

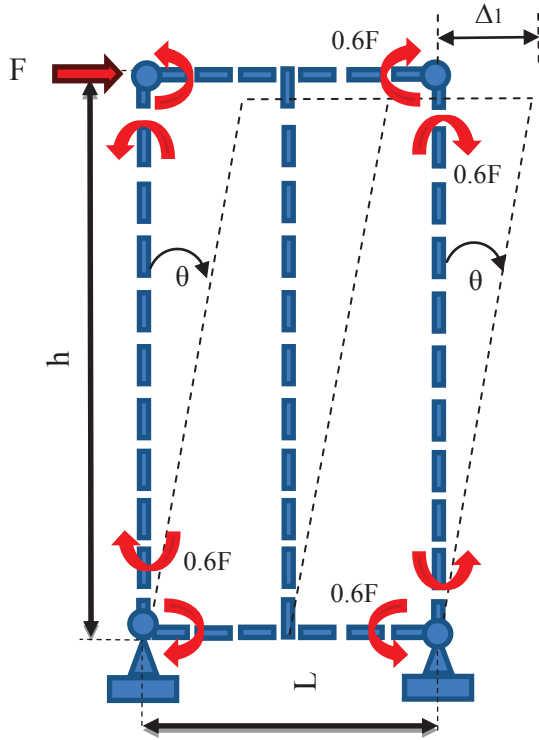


Figure 1: Loaded and unloaded state of vertical stud wall unit.

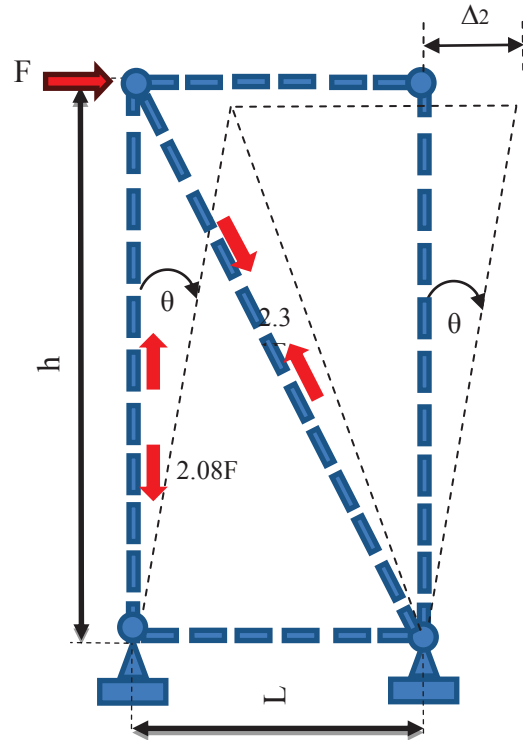


Figure 2: Loaded and unloaded state of diagonal bracing wall unit.

$$W = \frac{1}{2} \left[ \frac{1}{E_{0,05} I} \int M^2(x) dx + \frac{1}{E_{0,mean} A} \int N^2(x) dx + \frac{1}{G_{mean} A'} \int V^2(x) dx \right] \quad (2)$$

$$\Delta_1(m) = \left[ \left( \frac{0.964}{E_{0,05} I} \right) + \left( \frac{5.72}{E_{0,mean} A} \right) + \left( \frac{3.85}{G_{mean} A'} \right) \right] F(N); \quad A' = \frac{2}{3} A \quad (3)$$

$$\Delta_2(m) = \left[ \left( \frac{1.26 \times 10^{-5}}{E_{0,05} I} \right) + \left( \frac{25.5}{E_{0,mean} A} \right) + \left( \frac{1.0 \times 10^{-4}}{G_{mean} A'} \right) \right] F(N) \quad (4)$$

$$\Delta_i(m) = (a_M + a_V + a_N)F(N) \quad (5)$$

It was obvious that on the first hand, normal and shear forces in the vertical stud walls are negligible compared to the value of internal moments ( $1.2 \times 10^{-4}$ ). On the second hand, shear forces and internal moments are negligible in the diagonal bracing case compared to the value of normal forces ( $3.5 \times 10^{-7}$ ) as presented in previous Figures (Fig. 1 & 2).

### 3. Experimental Results

#### 3.1 Vertical stud wall

The empty vertical stud wall was considered as a control frame for comparing with hemp walls (see Fig. 3). The maximum load bearing capacity of the empty frame was around 0.18 kN (Fig. 4). It was obvious that the theoretical approach describe the elastic behaviour of the wall and matches the initial experimental behaviour experimental results. Vertical stud hemp walls (V-H) were tested with the same set up and method as illustrated in Fig. 5. The average load bearing capacity of the vertical stud hemp wall was around 2 kN (Fig. 6).

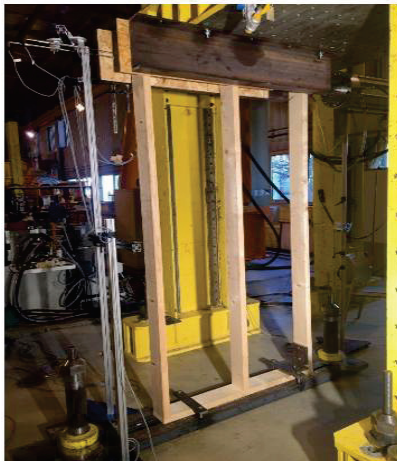


Figure 3: Empty vertical stud frame in test.

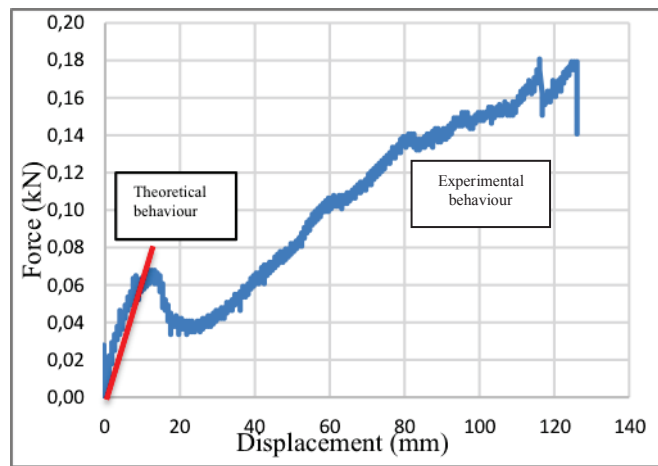


Figure 4: Force-Displacement behaviour for frame only.



Figure 5: Vertical stud hemp wall in test.

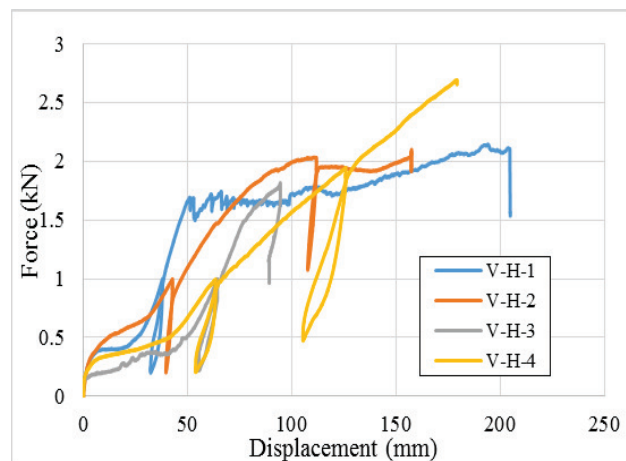


Figure 6: Force-Displacement behaviour for vertical stud hemp wall.

#### 4.2 Diagonal bracing walls

The load bearing capacity of empty diagonal bracing walls was presented below in Fig. 8 by force-displacement plots. The average maximum load bearing capacity of diagonal bracing wall was 10.78 kN. The theoretical behaviour of diagonal bracing wall did not show the same behaviour of the experimental results (Fig. 8), this difference is related to the joint consideration. It is clear from the results that the experimental behaviour of the wall is less rigidity than the mathematical approach. Figure 10 presents the lateral strength of diagonal bracing walls filled with hemp concrete (D-H) and obviously, the hemp concrete did not contribute in the lateral strength with the diagonal bracing wall and no clear contribution of the hemp concrete in both cases in the lateral resistance as infill material in the diagonal configuration.



Figure 7: Diagonal bracing walls in test.

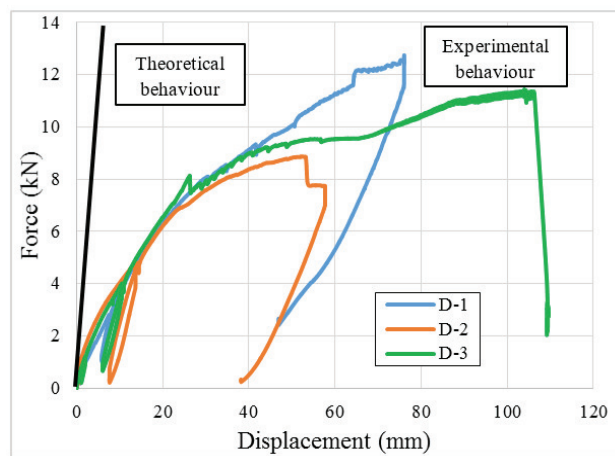


Figure 8: Force-Displacement behaviour for diagonal bracing walls.



Figure 9: Diagonal bracing hemp walls in test.

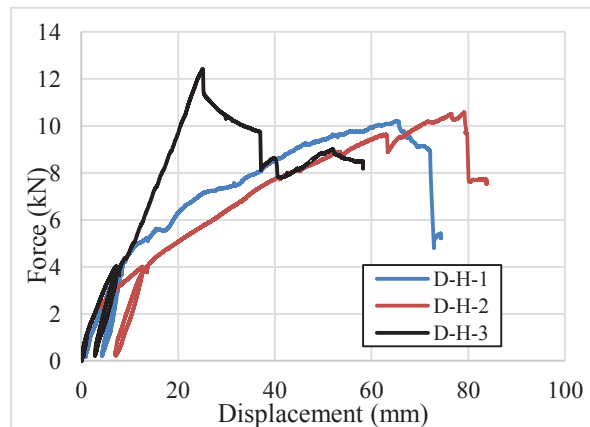


Figure 10: Force-Displacement behaviour for diagonal bracing hemp walls.



## 5. Analysis and conclusion

Obviously, the two shapes have a completely different behaviour with the filling material. On the first hand, the participation of hemp concrete has more than ten times in vertical stud wall comparing to the empty frame, on the other hand, the participation of hemp concrete is around zero in the diagonal bracing. Simply, the forces did not transmit to the filling material in the diagonal bracing due to the high rigidity of the whole system. However, in case of vertical stud wall which is less rigidity, the forces easily transmit to the filling material and make it participate in the lateral strength. Despite the contribution of hemp concrete with vertical stud wall, still this contribution is insufficient. In fact, the dimensions of the timber wall (L/h) play a main role to make the filling material load under shear forces. Several studies found that hemp concrete has a high racking strength. This study confirms that the contribution of hemp concrete in the lateral strength of the timber wall depends significantly on the length of the wall as the height is constant. Also installing hemp concrete in a very high rigid system will prevent transmitting forces to the filling materials and decrease its participation in the lateral resistance, the more rigid the wall is, the less resistant hemp is.

## References

- [1] Amziane, S. and Arnaud, L. Eds., Bio-aggregate-based building materials: applications to hemp concretes, Holboken: ISTE Ltd., London, UK (2013)
- [2] Premrov, M. and Kuhta M., Influence of fasteners disposition on behavior of timber-framed walls with single fibre-plaster sheathing boards, *Constr Build Mater* 23 (2009), 2688-2693
- [3] Loo, W.Y. et al, A numerical study of the seismic behavior of timber shear walls with slips-friction connectors, *Engineering Structures* 34 (2012), 233-243
- [4] Vessby, J. et al, Coupled and uncoupled nonlinear elastic finite element models for monotonically loaded sheathing-to-framing joints in timber based shear walls. *Engineering Structures* 32 (2010), 3433-3442
- [5] Gross, C. and Walker P., Racking performance of timber studwork and hemp-lime walling, *Constr Build Mater* 66 (2014), 429-435
- [6] Bevan, R. et al, Hemp lime construction: a guide to building with hemp lime composites. IHS BRE Press (2008)
- [7] Wadi, H. and Amziane S., Mechanical behaviour of unclassified timber walls against horizontal forces, 35èmes Rencontres universitaires de génie civil de l'AUGC, Nantes, France (2017)
- [8] Christopher, G. and Pete, W., Racking performance of timber studwork and hemp-lime walling. *Constr Build Mater* 66 (2014), 429-435
- [9] Hans, S. et al, Mechanical behaviour of wooden framework buildings with sprayed hemp concrete, Proc. ICBBM: 2nd International Conference on Bio-based Building Materials (3BM), Clermont-Ferrand, France (2017)

## **LIFE CYCLE ASSESSMENT OF BIO-BASED CONSTRUCTION PANELS WITH MAGNESIUM BINDER**

**Maris Sinka<sup>(1)</sup>, Aleksandrs Korjamins<sup>(1)</sup>, Diana Bajare<sup>(1)</sup>, Genadijs Sahmenko<sup>(1)</sup>**

(1) Riga Technical University, Riga, Latvia

### **Abstract**

The hemp-lime concrete as a self-bearing thermal insulation material has a low thermal conductivity and neutral CO<sub>2</sub> emissions. However, the strength limitation of lime binder is an issue to use this material as a load-bearing material. Magnesium oxychloride binders are of considerably higher strength level and better bio-compatibility compared to the lime-based binders. In this study, magnesium oxychloride binders were used in combination with hemp shives as a filler to produce composite materials to be used in production of construction panels on industrial scale. These panels consist of an outer and inner border layer and a middle thermal insulation layer. The life cycle assessment of such panels was performed, analysing various impacts on the environment in the production process and comparing it to usual materials with similar thermal transmittance properties. Results of the research showcase that the magnesium-hemp concrete can be used in production of bio-based construction panels because the strength of their outer layers can reach more than 1.0 MPa at 450 kg/m<sup>3</sup> density and thermal conductivity for inner layer – 0.062 W/m·K at 210 kg/m<sup>3</sup> density. It was proved in the research that the magnesium-hemp panel represents reduced impact on environment by CO<sub>2</sub> emissions 6 times less compared to usual construction materials.

### **1. Introduction**

The construction industry is one of the largest emitters of CO<sub>2</sub> [1] mainly because of the production of traditional construction materials and insufficient building insulation with resulting energy demand [2]. It also contributes negatively to other environmental impact categories [3].

To reduce this negative impact materials with low thermal conductivity and reduced impact on environment are necessary. One group of such materials is bio-based insulation composites

that uses agricultural waste products as the primary filler, hemp concrete is one of the most studied materials in this group. It is a mixture of hemp shives and usually hydraulic lime, it is a self-bearing thermal insulation material with low thermal conductivity (lower than  $0.064 \text{ W/m}\cdot\text{K}$ ) [4] and neutral or negative  $\text{CO}_2$  emissions [5]. However, the hydraulic lime binder used in this material is of limited strength because of compatibility issues with bio-based filler, so to ensure broader use of the bio-based materials, a binder of higher strength and better bio-compatibility is required.

Magnesium oxychloride cement (MOC) is a binder that can be used to produce bio-based materials with higher mechanical strength compared to lime binder. This is because magnesium oxychloride cement has better compatibility with organic fillers [6] compared to lime based binders creating highly alkaline environment that enables organic substances, such as lignin, to be released from filler. The MOC is usually used for production of sheeting boards containing wood fibres and perlite [7] or to create various bio-composites with wood [6].

Magnesium oxychloride cement is produced by combining magnesium oxide with magnesium chloride brine solution; it forms  $\text{MgO-MgCl}_2\text{-H}_2\text{O}$  ternary system [8] respectively. Magnesium oxychloride cement can also reach higher mechanical strength than lime: 120 [9] to 140 MPa [8]. Magnesium carbonate decomposes at lower temperatures than calcium carbonate, about  $700 \text{ }^\circ\text{C}$ , which releases less  $\text{CO}_2$ . However, no  $\text{CO}_2$  is sequestered when magnesium oxide reacts with magnesium chloride as opposed to lime binders.

## 2. Materials and Methods

In this study multi layered bio-based construction panel is proposed as a solution to optimally use material properties using less dense middle layer for insulation and denser outer layers for envelope purposes (Fig. 1.). The panels can be used as a load-bearing panels with structural timber frame. Magnesium binder is used for bio-based composites with varying ratio of shives:binder, to control density. Mixtures are created in laboratory conditions (Fig. 1.) and tested, the results acquired are used for conducting Life cycle assessment of the panel and comparing it to traditional building materials.

Mechanical properties of biocomposites were tested with Zwick Z100 universal testing machine, pressure was applied with  $10 \text{ mm/min}$  speed, compressive strength was recorded at 10% relative deformations (according to LVS EN 826). Thermal conductivity was measured with LaserComp FOX600 heat flow meter.

Hemp shives used in this research are manufactured by local producers, their granulometry has been optimized for hemp concrete in previous research [10]. Caustic magnesium oxide CCM RKMH-F from Austrian company "RHI AG Ltd" is used with 76%  $\text{MgO}$  purity. Hardener magnesium chloride hexahydrate containing 47%  $\text{MgCl}_2$  is used in this research.

A forced action mixer was used to produce the test samples. At the beginning of production process, the hemp shives are blended with water at a ratio 1:1.25 of volume, to hydrate the hemp shives ensuring that the water would not be eventually reduced from the binder. After adding magnesium oxide and magnesium chloride it is mixed for three minutes, after which samples are placed for two days into molds, and after demolding they are dried in laboratory conditions -  $20\pm 2 \text{ }^\circ\text{C}$  and  $40\pm 10 \text{ \% RH}$  – until constant volume is reached.



Figure 1: Proposed panel prototype with three different density layers (left), experimental panel scaled model (right)

Table 1: Composition and properties of different panel layers

	Shives, kg	Binder, kg	Average density, kg/m <sup>3</sup>	Thickness, mm	Thermal conductivity, W/m·K	Target compressive strength, MPa
Outer layer	3.77	9.64	452.2	30	0.112	1.00
Middle-insulation layer	36.42	28.65	210.1	290	0.062	0.15
Inner layer	6.28	10.50	332.5	50	0.077	0.35

### 3. Results and Life cycle assessment

In the scope of this research Life cycle assessment was carried out according to ISO 14040/44 guidelines which consist of the following steps: 1. Definition of goal and scope; 2. Inventory analysis; 3. Impact analysis; 4. Interpretation.

#### 3.1. Definition of goal and scope

Goal of this research is to assess the life cycle of a multi-layer construction panel produced of experimental magnesium-hemp concrete, by evaluating impact of material on the greenhouse gas emissions and comparing it with the traditionally used construction materials.

The LCA calculation programme SimaPro 8 and the Ecoinvent 3.0 data base that have been used for most of the related processes, was used for assessment. Calculations were performed according to the CML-IA baseline method.

To compare the life cycle of magnesium-hemp material with that of other materials there must be a comparable functional units of alternative materials. As thermal insulation is the primary function of the material, functional unit is defined with U value – 0.18 W/m<sup>2</sup>·K. Dimensions of the panel are based on experimental results in Tab. 1., outer layer is 30mm, middle-insulation layer is 290 mm, inner layer is 50 mm.

Alternative materials with similar U values were chosen to be the 500 mm 300 kg/m<sup>3</sup> blocks of aerated concrete without additional thermal insulation, 300 mm 375kg/m<sup>3</sup> blocks of aerated concrete with 100 mm 120kg/m<sup>3</sup> rock wool insulation, and 440 mm thick ceramic blocks with 100 mm 120kg/m<sup>3</sup> of rock wool insulation. Transportation for all the materials was set at 100 km.

None of the materials created specific additional emissions in the usage phase so they are not considered in this research, thus “Cradle-to-gate” system is used for analysis [10].

### 3.2. Inventory analysis

When possible, the data was used from the Ecoinvent database, as well as the required data from the previous researches about life cycle assessment of the hemp construction materials [10] and other related papers [11], [12].

### 3.3. Life cycle impact assessment and interpretation

After life cycle impact assessment, it is possible to analyse separately emissions created by the magnesium-hemp functional unit and its separate processes. It can be seen that impact of different major components of the panel (such as different density layers and wooden frame) is similar, with exception of Global warming potential (GWP) where middle layer has negative CO<sub>2</sub> emissions due to highest shives:binder ratio (Tab. 2.). Compared by thickness, outer and inner layers have proportionally greater impact in all categories as middle layer due to the elevated levels of binder. The binder is responsible for 70-75% of all impacts of middle layer and 80-90% of inner and outer layer impacts, due to highly energy intensive binder production.

Even though the hemp shives absorb more CO<sub>2</sub> than is produced during the cultivation and processing period, these processes also release carbon dioxide in atmosphere that could be reduced. The largest part of emissions (around 45%) from hemp cultivation comes from mineral fertilisers, both in their production and in use, so their reduction would be necessary - for example, by using covering crops, complementing the nitrogen fertiliser after braiding of plants, broader use of tests to determine optimal nitrogen level in the ground, etc., as agriculture already is second largest GHG emitting industry in Latvia with 24% of total emissions [13].

Compared to all alternative materials bio-based panel emit 6 times lower amounts of CO<sub>2</sub>, only 12.6 kg/CO<sub>2</sub> eq. per m<sup>2</sup> of wall (Fig. 2., Tab. 2.). This is mainly due to absorbed CO<sub>2</sub> amounts by hemp shives in the growth process and because of considerable amount of energy used in production of construction blocks [14] that makes up the largest part of functional unit of alternative materials.

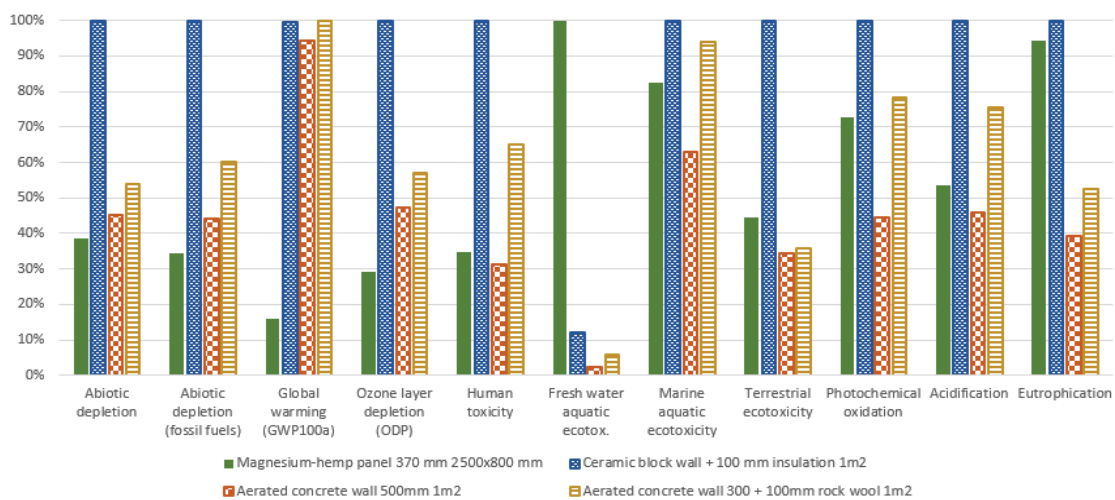


Figure 2: CML-IA baseline environmental impact results of magnesium-hemp panel and alternative materials

Considering other impact categories, panel has lower or similar impact in all categories except Fresh water aquatic ecotoxicity and Eutrophication (Fig. 2.). Eutrophication is due to the fertilizer use and could be reduced by lowering amount of fertilizer applied by using techniques described above. Fresh water aquatic ecotoxicity impact comes from magnesium oxide production that has high amounts of emissions to water oxide in Ecoinvent database, as it is based on iron mining. The impact of magnesium oxide is around 200 times higher than for similar binders as cement or lime according to the database, but no sources in literature indicate such difference, so it should be viewed with caution.

#### 4. Conclusions

To answer the growing need for construction materials with lowered environmental impact a new type of material is needed. Bio-based construction materials can answer this need, as their environmental impact is low, due to usage of large volumes of agricultural waste as filler and due to their thermal properties, that allows to provide optimal building insulation. In the paper it was proposed to use these materials in wall insulation panels with constructive wooden frame, hemp shives as a filler and an alternative binder – magnesium oxychloride cement.

Properties of various density magnesium-hemp material were tested experimentally. Material has compressive strength of around 0.15 MPa at low densities of 210 kg/m<sup>3</sup> that allow to achieve thermal conductivity of 0.062 W/m·K. To achieve 1 MPa compressive strength a 450 kg/m<sup>3</sup> density is needed with  $\lambda$  value 0.112 W/m·K. These properties can allow for material to be used in wall insulation panels in three layers – outer envelope layers and middle thermal insulation layer, and to achieve U value of 0.18 W/m<sup>2</sup>·K at 370 mm panel thickness.

LCA for magnesium-hemp panel were done and environmental impact compared with alternative materials. In most categories panel shows lower impact than alternative construction block materials, in GWP it has the largest advantage, as hemp shives absorbs CO<sub>2</sub> in the growing process, thus having 6 times lower emissions - only 12.6 kg/CO<sub>2</sub> eq. per 1 m<sup>2</sup> panel. Highest impact of the panel is in the Fresh water aquatic ecotoxicity and Eutrophication. The former is due to high amounts of emissions to water for magnesium oxide in Ecoinvent database, as it is based on iron mining. Compared to similar binders as cement or lime, these emissions are about 200 times higher and should be interpreted with consideration. Eutrophication is due to fertilizer used for hemp production, impact is 95% of ceramic block impact and 2 times higher than aerated concrete impact.

Table 2: CO<sub>2</sub> emissions in detail for studied and other materials 1 m<sup>2</sup> (upper), emissions in detail for each part of studied material (lower)

Proposed materials	Magnesium-hemp panel	Ceramic block	Aerated concrete	Aerated concrete with insul.	-
kg CO <sub>2</sub> eq	12.62	78.66	74.55	79.05	-
Components of the studied material	Outer layer	Middle layer	Inner layer	Wooden frame	Transport
kg CO <sub>2</sub> eq	5.06	-6.28	3.68	9.39	0.77

## Acknowledgements

The financial support of European Regional Development Fund project Nr.1.1.1.1/16/A/007 "A New Concept for Sustainable and Nearly Zero-Energy Buildings" is acknowledged.

## References

- [1] Kylili, A., M. Ilic, and P. A. Fokaides, Whole-building Life Cycle Assessment (LCA) of a passive house of the sub-tropical climatic zone, *Resour. Conserv. Recycl.* 116 (2017), 169–177
- [2] Li, H. X., L. Zhang, D. Mah, and H. Yu, An integrated simulation and optimization approach for reducing CO<sub>2</sub> emissions from on-site construction process in cold regions, *Energy Build.* 138 (2017), 666–675
- [3] Hossain, M. U., C. S. Poon, Y. H. Dong, and D. Xuan, Evaluation of environmental impact distribution methods for supplementary cementitious materials, *Renew. Sustain. Energy Rev.* 82 (2018), 597–608
- [4] Walker, R., S. Pavia, and R. Mitchell, Mechanical properties and durability of hemp-lime concretes, *Constr. Build. Mater.*, 61 (2014), 340–348
- [5] Arrigoni, A., R. Pelosato, P. Meli, G. Ruggieri, S. Sabbadini, and G. Dotelli, Life cycle assessment of natural building materials: the role of carbonation, mixture components and transport in the environmental impacts of hempcrete blocks, *J. Clean. Prod.* 149 (2017), 1051–1061
- [6] Zhou, X. and Z. Li, Light-weight wood-magnesium oxychloride cement composite building products made by extrusion, *Constr. Build. Mater.* 27 (2012), 382–389
- [7] Manalo, A., Structural behaviour of a prefabricated composite wall system made from rigid polyurethane foam and Magnesium Oxide board, *Constr. Build. Mater.* 41 (2013), 642–653
- [8] Xu, B., H. Ma, C. Hu, S. Yang, and Z. Li, Influence of curing regimes on mechanical properties of magnesium oxychloride cement-based composites, *Constr. Build. Mater.* 102 (2016), 613–619
- [9] Li, Y., H. Yu, L. Zheng, J. Wen, C. Wu, and Y. Tan, Compressive strength of fly ash magnesium oxychloride cement containing granite wastes, *Constr. Build. Mater.* 38 (2013), 1–7
- [10] Sinka, M., P. Van Den Heede, N. De Belie, D. Bajare, G. Sahmenko, and A. Korjakins, Comparative life cycle assessment of magnesium binders as an alternative for hemp concrete, *Resour. Conserv. Recycl.* 133C (2018), 288–299
- [11] Stramkale, V., Multipurpose hemp for bioproducts and biomass. Latgale Agriculture Research Centre. Latgale Agriculture Research Centre, Vilani, Latvia (2015)
- [12] Turunen, L. and H. M. G. van der Werf, Life Cycle Analysis of Hemp Textile Yarn, Comparison of Three Hemp Fiber Processing Scenarios and a Flax Scenario, INRA-French Natl. Inst. Agron. (2006)
- [13] Gancone, A., J. Pubule, M. Rosa, and D. Blumberga, Evaluation of agriculture eco-efficiency in Latvia, *Energy Procedia* 128 (2017), 309–315
- [14] Yang, D., L. Fan, F. Shi, Q. Liu, and Y. Wang, Comparative study of cement manufacturing with different strength grades using the coupled LCA and partial LCC methods—A case study in China, *Resour. Conserv. Recycl.* 119 (2017), 60–68

## **MARKET POTENTIAL OF WOOD BIOMASS ASH UTILISATION IN CEMENT COMPOSITES - CROATIAN CASE STUDY**

**Nina Štirmer<sup>(1)</sup>, Ivana Carević<sup>(1)</sup>, Bojan Milovanović<sup>(1)</sup>, Ana Baričević<sup>(1)</sup>**

(1) University of Zagreb, Faculty of Civil Engineering, Zagreb, Croatia

### **Abstract**

The growing trend of using biomass as a renewable energy source (RES) results in a growth of the wood biomass ash (WBA) as a by-product. Considering the increasing amount of WBA as well as the costs of its disposal, it is necessary to establish its sustainable management.

The WBA quality varies depending on the biomass used in power plants, combustion technology and the location where collection of WBA is done. One of the possible solutions of the WBA's disposal problem is an application in cement composites. Since WBA differs from the coal fly ash and does not satisfy the existing regulation for use of fly ash in cement, determination of the potential and adequacy of WBA as a cement replacement and/or mineral admixture in cement composites is needed.

This paper presents detailed analysis of market conditions in Croatia regarding possible use of WBA in cement composites. Estimation of the WBA production in Croatia has been made based on data gathered from energy power plants. A survey for assessing current demands of the cement and concrete industry has been carried out and the extent to which the market is ready to accept WBA is evaluated.

### **1. Introduction**

To achieve a sustainable future, the European Union (EU) has committed to the targets set in the EU's Renewable Energy Directive, meaning that a 20 % of the total energy required will come from renewable sources by 2020. For a period beyond 2020, the Revised Renewable Energy Directive [1] is already introduced and activities are proposed to cut emissions in the Union by at least 40% below 1990 levels by 2030. As the most significant renewable energy source in the EU, solid and gaseous biomass fuelled power plants are expected to contribute in achieving the set goals [2].



Croatia belongs among the countries of large biomass potential and part of biomass could be used for production of energy. The Energy Strategy of the Republic of Croatia [3] was adopted to define the development of Croatian Energy sector by 2020 and with a goal to build, under the conditions of uncertainty in the global energy market and scarce local energy resources, a sustainable energy system. Within the Energy Strategy, it was defined that a part of the available biomass shall be used as feedstock in biomass combustion power plants, preferably cogeneration plants, to assure the total power of 85 MW by 2020 (Figure 1).

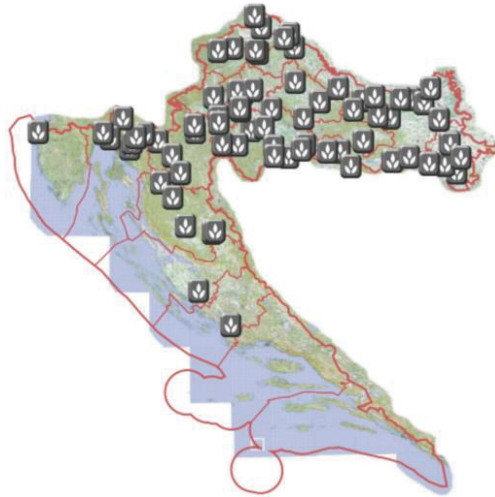


Figure 1: Locations of the biomass plants planned by 2020 in Croatia [4]

Based on the official data from the Croatian Energy Market Operator (CEMO), currently in the Republic of Croatia there are 14 plants with the total installed capacity of 28.955 MWe. However, the CEMO database contains only data for plants connected to the public power network. The plants that produce the energy for their own production needs (such as wood industry drying ovens, etc.) or district heating plants that produce only thermal energy and are not included in the CEMO database. Therefore, the database of CEMO was supplemented by the review of published papers where in total 22 biomass plants were confirmed running at the time of writing this paper. Additional data was collected through survey conducted within 13 biomass plants and 11 concrete producers.

The aim of the research was to determine the available quantities of wood biomass ash (WBA) in Croatia and their potential for the future application in the construction industry. Research is carried out as part of the research project *Transformation of Wood Biomass Ash into Resilient Construction Composites (TAREC<sup>2</sup>)*. TAREC<sup>2</sup> involves a detailed characterization of available WBA in the Republic of Croatia (biomass origin, combustion technology, ash type) with the aim of detecting wood biomass plants whose WBA has potential for application in the construction sector.

## 2. Types & quantities of wood biomass ash

Croatia has a large wood industry, and therefore the potential of using biomass as fuel. A total of 48% of the territory of the Republic of Croatia is covered by forests. Biomass is mainly

obtained from sawdust, wood and paperboard industry. As the biomass, the following types of wood are often used: beech and oak, then hornbeam, and to a lesser extent poplar and mixed woods, spruce, willow and fir.

This research and survey concentrated to wood biomass ash (WBA) which is obtained by combustion of forest biomass and non-contaminated waste wood. Different types of combustors are being used in Croatian biomass plants, but grate combustors are most often (69.2 %), then fluidized bed combustors (23.1 %) and pulverized fuel combustors (7.7 %). Combustion temperature ranges from 500 to 1000°C, with an average value of 800°C. The biomass plants are in operation for an average of 7580 hours or approximately 316 days per year with the average biomass consumption of 5 t/h.

The greatest influence on the quality and the quantity of WBA produced has the type of biomass feedstock used. Respondents stated that 15 % of surveyed biomass plants use pure wood chips, while 85 % use other types of wood biomass as well, such as wood chips with impurities like soil, etc. None of the respondents uses residues from agriculture, herbaceous plants or wood pellets and briquettes.

Surveyed biomass plants produce in total 15,190 tons of WBA per year. Consumption of wood biomass in the representative biomass plant can easily be calculated based on the acquired data. If the representative biomass plant is in the operation 7580 hours per year and the consumption of wood biomass is 5 t/h, then 37,900 tons of wood biomass is averagely consumed per one biomass plant. This means that the combustion of 1 t of the wood biomass on average produces 3.1% of WBA.

Based on the data available from the survey, a projection of the total wood biomass consumption and the WBA production in Croatia was performed. Proportionally to the installed power in biomass plants, it is estimated that the consumption of wood biomass is 676,786 tons per year and that the total amount of WBA in the existing biomass plants is 20,890 tons.

### **3. Cement consumption and concrete production**

The conducted surveys show that approximately 35,000 tons per year of mineral admixtures are used for cement production; mostly slag, limestone and fly ash. Most commonly used cement types are: CEM I – 18 %, CEM II – 64 % and CEM III – 18 %. According to the survey results, concrete is mainly produced with the following compressive strength classes: C25/30 and C30/37 (each represented with 91%), then C20/25, C35/45 and C40/50 all represented with 64 % within surveyed producers. As additional concrete properties, producers mainly specify water permeability, freeze-thaw resistance, abrasion and resistance to chemicals. To assure improved concrete properties, 27% of the respondents use mineral additives such as silica fume, fly ash and metakaolin.

### **4. Application of WBA in concrete production**

Today's commercially available cements typically contain about 20% of supplementary cementitious materials – such as fine-milled limestone, granulated slag and fly ash from coal-combustion thermal power plants. European standard EN 450-1:2013 [5] and US standard

ASTM C618 [6] prevent the use of fly ashes that are not obtained by combustion of coal, i.e. limit the use of WBA as a mineral additive in the production of cement. Nevertheless, the standard EN 450-1:2013 [5] allows the use of fly ash produced by parallel co-combustion. Following, many studies have been focused on the use of ash obtained by combining coal and wood [7]. Given that the chemical composition of the WBA is different from fly ash obtained from the combustion of coal and does not meet the existing regulations, a detailed characterization of WBA is required to determine the potential and appropriateness of WBA in cement composites.

State of the art review on the application of WBA in the construction industry concludes that WBA contains higher amounts of CaO, K<sub>2</sub>O, P<sub>2</sub>O<sub>5</sub> and MgO compared to fly ash from coal. According to [8], WBA has irregular particles while other types of ash (fly ash from coal, milled ash obtained from coal and wood biomass) show approximately spherical shapes (Figure 2). WBA particles are coarser than cement particles and are more porous and irregular in shape [9]. In addition, increasing the WBA share in concrete showed increase of the initial and final setting time as well as postponed hardening [10,11,12]. This may be desirable when postponed setting is required [7] or for use in massive concrete [12]. However, results vary depending on the type of WBA used [9].

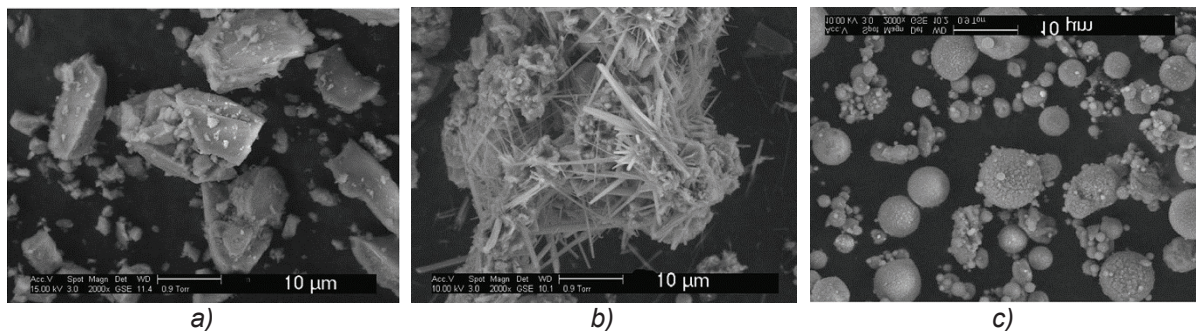


Figure 2: SEM analysis: a) cement, b) WBA i c) 80 % of coal fly ash (class C) mixed with 20 % of WBA [13]

Maximum recommended cement replacement with WBA is 20 %, as further increase of WBA has negative influence on the properties of cement composites. Based on significant degradation of properties, some authors recommend a maximum replacement up to 10%. Especially, if durability properties are considered. Namely, analysis of the durability properties shows that the optimal proportion of cement substitution by WBA is 5%. Substitution in larger shares (up to 10% of cement) causes an increased water absorption. Carevic et al. [14] suggest that mixtures with WBA content below 10 % have satisfying behaviour when exposed to the aggressive environment XF4 (56 cycles) [15]. Others, state that WBA has no adverse effects on freezing and thaw resistance [9,10,16]. Similar conclusions were obtained for the influence of WBA on the chloride diffusion. According to [17], the chloride diffusion coefficient decreases with the increase in WBA content. On contrary, according to [9] the WBA does not have an adversely effect on the chloride resistance of the concrete. Using WBA as a swelling admixture, due to the large share of free CaO and MgO, is yet to be research. However, swelling that occurs due to the WBA incorporation in concrete can be used to alleviate the problem of autogenous shrinkage

occurring in cement composites with a very low water-cement ratio. Flexural and compressive strength of cement composites is reduced as the WBA content increases.

Further research is needed to assure distinguished understanding of the WBA influence on both, mechanical and durability properties of cementitious composites. Nevertheless, following the conducted literature review, it can be concluded that based on its characteristics WBA can be used as: (a) alternative raw material for the production of clinker; (b) mineral admixture in cement production and (c) a mineral admixture in the manufacture of cement composites (as a partial cement replacement).

## 5. Conclusions

Based on the conducted surveys and proportionally to the installed power in biomass plants in Croatia, an annual consumption of wood biomass is estimated to approximately 680,000 tons. Furthermore, total amount of WBA produced in the active biomass plants is 20,890 tons per year. This quantity could be used to satisfy the needs of approximately 20 concrete productions plants with an average production of 50,000 m<sup>3</sup> of concrete per year. For example, in only 1 concrete plant by replacing 10% of cement, 1500 t of WBA can be used annually. The inert particles of WBA can be used as a substitute for a fine aggregate fraction (sand). However, such implementation in the construction industry must be followed by the strict and regular quality control due to the variable quality of WBA.

## References

- [1] European Commission, Proposal for a Directive of the European Parliament and of the Council on the promotion of the use of energy from renewable sources (recast) (2017)
- [2] European Commission, State of play on the sustainability of solid and gaseous biomass used for electricity, heating and cooling in the EU, SWD (2014) 259 final, Comm. Staff Work. Doc. (2014)
- [3] Croatian Council, Energy Strategy of the Republic of Croatia, Official Gazette 130 (2009)
- [4] Ministry of Economy, Labour and Entrepreneurship of the Republic of Croatia, Renewable Energy Sources – review – Interactive map 62 (2012). [Online]. Available: <http://oie-aplikacije.mingo.hr/InteraktivnaKarta/>. [Accessed: 01-Jan-2016].
- [5] HRN EN 450-1, Fly ash for concrete -- Part 1: Definition, specifications and conformity criteria, Croatian Standards Institute, Croatia (2013)
- [6] ASTM C 618, Standard Specification for Coal Fly Ash and Raw or Calcined Natural Pozzolan for Use, American Society for Testing and Materials, USA (2010)
- [7] M. Berra, T. Mangialardi, and A. E. Paolini, Reuse of woody biomass fly ash in cement-based materials, *Constr. Build. Mater.* 76 (2015), 286–296
- [8] J. Rosales, M. Cabrera, M. G. Beltrán, M. López, and F. Agrela, “Effects of treatments on biomass bottom ash applied to the manufacture of cement mortars,” *J. Clean. Prod.*, vol. 154, pp. 424–435, 2017
- [9] S. Chowdhury, M. Mishra, and O. Suganya, The incorporation of wood waste ash as a partial cement replacement material for making structural grade concrete: An overview, *Ain Shams Eng. J.* 6 (2) (2015), 429–437

- [10] C. B. Cheah and M. Ramli, The implementation of wood waste ash as a partial cement replacement material in the production of structural grade concrete and mortar: An overview, *Resour. Conserv. Recycl.* 55 (7) (2011), 669–685
- [11] A. U. Elinwa and Y. A. Mahmood, Ash from timber waste as cement replacement material, *Cem. Concr. Compos.* 24 (2) (2002), 219–222
- [12] F. F. Udoeyo and P. U. Dashibil, Sawdust Ash as Concrete Material, *J. Mater. Civ. Eng.* 14 (2) (2002), 173–176
- [13] S. Wang, L. Baxter, and F. Fonseca, Biomass fly ash in concrete: SEM, EDX and ESEM analysis, *Fuel* 87(3) (2008), 372–379
- [14] I. Carević, I. Banjad Pecur, and N. Stirmer, Utilization of Wood Biomass Ash (WBA) in the Cement Composites, in *ICBBM 2017 - Proceedings of the 2nd International Conference on Bio-based Building Materials* (2017), 196–201
- [15] HRS CEN/TS 12390-9 Testing hardened concrete -- Part 9: Freeze-thaw resistance with de-icing salts – Scaling, Croatian Standards Institute, Croatia (2016)
- [16] S. Wang, E. Llamazos, L. Baxter, and F. Fonseca, Durability of biomass fly ash concrete: Freezing and thawing and rapid chloride permeability tests, *Fuel* 87 (3) (2008), 359–364.
- [17] M. D. L. Garcia and J. Sousa-Coutinho, Strength and durability of cement with forest waste bottom ash,” *Constr. Build. Mater.* 41 (2013), 897–910

## **MECHANICAL PERFORMANCE, SHRINKAGE AND WEATHERING OF TREATED HEMP CONCRETE**

**Mohammed Sonebi<sup>(1)</sup>, C. Sentenac<sup>(1)</sup>, Sofiane Amziane<sup>(2)</sup>**

(1) Queen's University Belfast, Belfast, UK

(2) University Clermont Auvergne, Polytech Clermont-Ferrand, France

### **Abstract**

This paper investigated the effects of aggregate treated with linseed oil and two types of binders (calcic lime and Prompt Natural Cement binder-Vicat). The particle distribution, the absorption of particles, the capillarity absorption of hemp concrete and the compressive strength at 7, 14 and 28 days were determined. The results showed that with higher density treated samples get a higher compressive strength. In addition, hydraulic performance was tested with the capillarity test and highlighted the great decrease of sorption coefficient on treated samples. Concerning the autogenous shrinkage, the results of treated samples shrinkage were higher than no-treated ones. Finally, the durability performance test included the full water immersion showed that treated samples with linseed oil are better compared to none-treated. These treated samples absorbed less water, therefore less degradation and softening of the specimens.

### **1. Introduction**

Hemp concrete principal weakness point is the strength in compression but the lack of information concerning the durability performance of this material can also be an explanation for the professional's reluctance to use bio-based concrete [1-3]. These ten last years have conducted several studies on hemp concrete to improve its properties this included the binders effect on mechanical strength but also the compaction effects [1, 2]. Matrix additions and aggregates treatments were also conducted to improve hemp concrete performances [1, 2]. The durability and cure conditions stay the less studying properties [7, 8] but this lack of information can be an explanation for the professional's reluctance to use bio-based concrete. In this study, the effect of linseed oil (LO) as treatment of aggregates was investigated. Few studies have already been conducted on this treatment [1, 2] but in our case hemp concrete

has been made with two different binders: Cement Vicat (V) and a composite binder based on calcic lime (C). The mix composition for this study was similar for all mixes and each treated aggregates type was compared to a normal hemp (NH) concrete sample for every performance. In total, four mixes were investigated:

- LOV : Vicat binder with linseed oil treatment on hemp shiv
- NHV : Vicat binder with normal hemp shiv
- LOC : Calcic lime binder and additions with linseed oil treatment on hemp shiv
- NHC : Calcic lime binder and additions with normal hemp shiv.

## **2. Materials, mix compositions and test methods**

Hemp shiv was used for this work. Hemp shiv used in the experimental program was Yorkshire hemp in UK. The first binder used in this study was Vicat Cement. Linseed oil is yellow oil obtained from the dried, ripened seeds of the flax plant. Linseed oil is a drying oil; meaning it can polymerize into a solid form. Because of polymerisation it took time to drying process, therefore after mixing the oil with the aggregates, they were left for 20 days to be dry. The linseed oil (LO) amount was evaluated by 0.5 mass ratios with aggregates. The sample was homogenised every day to ensure the homogenous of drying process.

According to the French professional rules for hemp concrete structures [9], shuttered wall mix composition was tested in this investigation with water/aggregates = 3, Binder to aggregates = 2 and water to binder = 1.5.

The water absorption and bulk density were measured according the protocols to RILEM TC 236 [2]. Water absorption test is particularly interested in this study to compare treatments effects on particles water absorption.

The compressive strength was determined on cubes of 50 mm size tested with a displacement of loading rate of 3 mm/min.

The capillary absorption was measured of cube 100 mm at 14 and 28 days after manufacture. During this curing time samples are placed in a control room at 20°C of temperature and e relative humidity of 55%.

Basically, this test is used to measure the volume and weight change of the hemp concrete under several drying and wetting cycles. It enables to simulate the weather conditions, at the end of all the cycles the influence of these cycles on the strength in compression is measured. Samples used in this case are 100mm cubes, four samples for each mixed are needed: two in the air and two for weathering cycles. The autogenous shrinkage was measured on prism of 50x50x200 mm<sup>3</sup> to measure the variation of length of the samples at different ages.

## **3. Results and discussion**

### **3.1 Water absorption and bulk density**

In this part the water absorption was measured on normal hemp shiv (NH) and treated hemp shiv with linseed oil (LO). Fig. 1 presents the variation of water absorption.

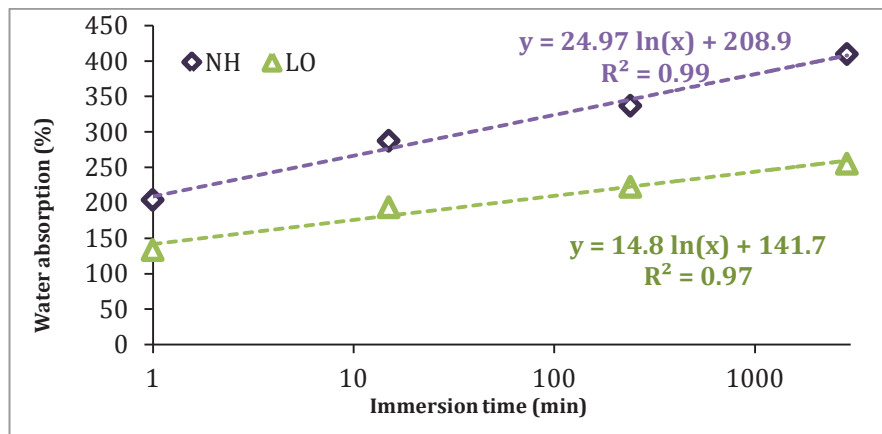


Figure 1: Water absorption of particles in function of time of treated and none-treated hemp shiv

After 1 min of immersion the LO treatment is effective with 133% of water absorption compare to NH aggregates with 204%. After 48 hours the result is the same LO is less absorbent than NH with respectively 255% and 410%.

Water absorption of bio-aggregates is a recurrent problem. The water absorbed by the particles is not available for the binder hydration this is the reason why this investigation is based on aggregates treatments. LO treatment is not just a coating, the treatment infiltrate with polymerisation into the particle and, with this mass addition it blocks particles pore, which avoid water to enter inside the particle.

The bulk density on treated hemp shiv and normal hemp shiv were measured to compare the weight added or not on our samples. Following the process described on previous chapter we have measured the bulk density of three samples for each type of hemp. An average can enable us at the end to obtain the bulk density.

The bulk density obtained for normal hemp (NH) was around  $100.9 \pm 4.1 \text{ kg/m}^3$ . This value is lower than the usual value about  $110 \text{ kg/m}^3$ . This resulted can be explained by the important quantity of fibres contained in the hemp shiv used in this investigation. The bulk density of LO aggregates is almost double of NH one of  $186.4 \pm 9.1 \text{ kg/m}^3$ .

### 3.2 Autogenous shrinkage

NHV results of autogenous shrinkage of hemp shiv mixes were the lowest one (Fig. 2). The treated mixes with linseed oil for both binder seems to led a high autogenous shrinkage and this can be attributed that there was more water in mix (not absorb by hemp shiv) which hydrated and therefore, led to more autogenous shrinkage. At 50 days, the autogenous shrinkage treated Vicat mix was 5 times higher than none treated and it was almost the same with calcic lime for both mixes NHC and LOC.



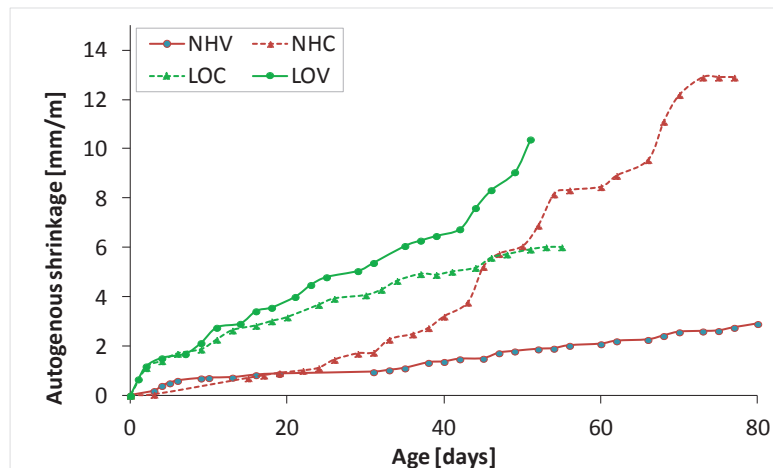


Figure 2: Autogenous shrinkage all mixes

### 3.3 Effect of treatment with linseed oil on compressive strength

The density has been reduced with age due to the drying of samples in air. The lower reduction is observed for NHC mix with:  $374 \text{ kg/m}^3$  at 7d and  $335 \text{ kg/m}^3$  at 28d ( $39 \text{ kg/m}^3$  of loss). It can be observed the fact that all mixes with Vicat exhibited the highest densities than those mixes with calcic lime. For example at 28d the difference in percentage represents 9% for NH and 13% for LO between Calcic mix and Vicat mix. LO mixes have the higher density at any age of samples compared to NH mixes, which are quite similar.

Fig. 3 presents the compression strength at 5% of deformation (2.5mm in case of 50mm cubes). At 7 d, LO mixes have the higher compressive strength. However, at 28 d, it is NHV mix which had the highest compressive strength about 0.21 MPa and the  $f'_c$  of LOV and LOC were 0.17 MPa and 0.20 MPa, respectively. The lowest  $f'_c$  at 28 d was for NHC (0.14 MPa). Fig. 3 highlights the fact that at 5% of deformation, NHV has the highest compressive strength following by LO mixes. On the other hand, LO treatment enables hemp concrete to be stronger in case of mixed lime, however in average, the compressive values at 14d and 28d of Vicat cement LOV were lower by 5% than NHV.

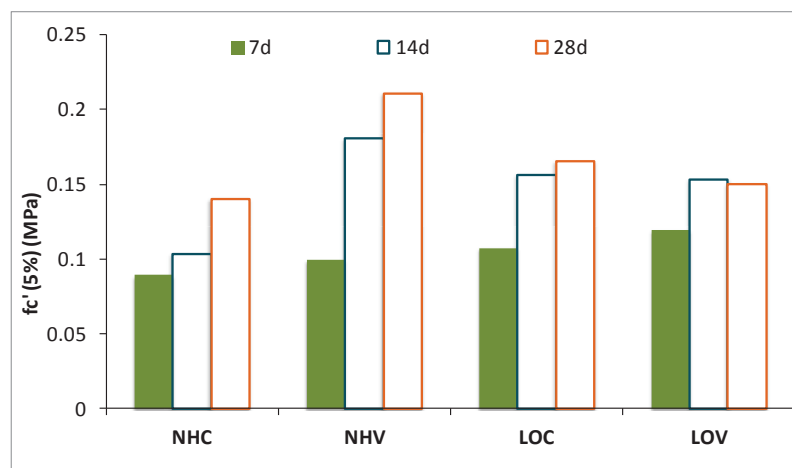


Figure 3: Compressive strength at 5% deformation of all mixes

### 3.4 Effect of treatment with linseed oil on weathering

Figure 4 represents the water absorption evolution during weathering cycles. It highlights the fact that NH mixes were the most absorbent with a water absorption average included between 60% and 90%. Fig. 5 shows only the wetting cycles and the significant rate increased after the first immersion 60% for NH mixes. After 3 cycles the NHV mix absorbed an average of 80%, NHC is more around 70%, these rates were higher than treated mixes ones. LO mixes were no more than 11% as water absorption during the partial immersion test.

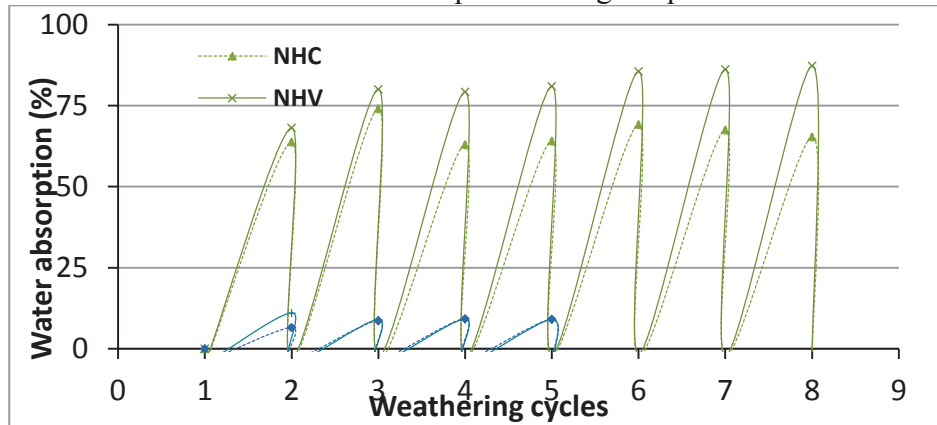


Figure 4: Water absorption rate evolution during partial immersion test

A comparison of partial and full immersion tests are presented in Fig. 5. As expected, it can be observed that the water absorptions of the all mixes in partial immersion were lower than those placed in full immersion. This has been proved to be more efficient for concrete treated with LO for both type of binders.

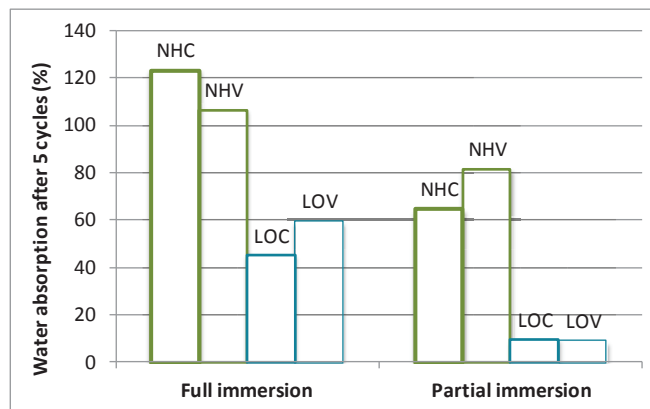


Figure 5: Comparison of water absorption for partial and full immersion test after 5 cycles

Figure 6 highlights the difference of compressive strength between mixes submitted to full immersion and partial immersion. The compressive strength dropped significantly when the samples were subjected to full weathering cycles. Similarly, the compressive strengths were reduced for mixes subjected to partial immersion. As it can be observed, the compressive strength of mixes submitted of full weather are lower than none weathering and when the aggregates were treated, the dropped on compressive is much lower than none-treated. In case of partial immersion, the reduction of compressive strength after 5 cycles of weathering

was lower compared to those full immersions. The full water immersion showed that treated samples with linseed oil are better compared to none-treated. It can be concluded that the treated samples absorbed less water, therefore less degradation and softening of the specimens.

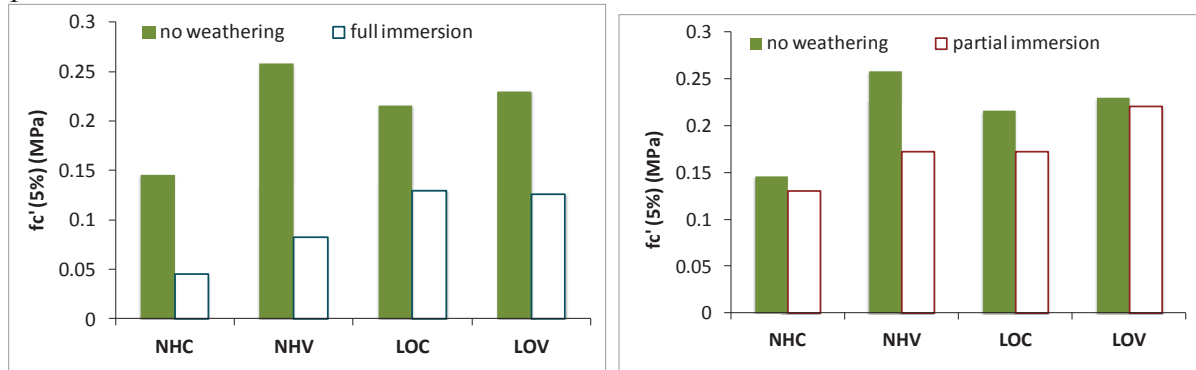


Figure 6: Compressive strength of full and partial immersions

#### 4. Conclusions

Based on the results of this paper, the following conclusions can be drawn:

- The characterisation of hemp shiv particles has highlighted the fact that the LO treatment doubled the density of the aggregates. LO demonstrated a significant decrease by twice of the water absorption of particles. In general, the compressive strength of hemp concrete made with LO has been improved compared to the no-treated concrete.
- Additionally, the sorption coefficient of hemp concrete has been divided by two when LO treatment was used for hemp shiv aggregates.
- Full immersion has shown that treatments significantly decreased the water absorption during cycles. Treatments led to a smaller difference in compressive strength between weathering and no weathering samples.
- Partial immersion demonstrated lower absorption compared to full absorption and it reduced slightly the compressive strength compared to those of full immersion.
- The treated mixes with LO seems to have the highest autogenous shrinkage particularly with Vicat mixes.

#### References

- [1] Amziane, S., Sonebi, M., K. Charlet, Proceedings of the Second International Conference on Bio-Based Building Materials, ICBBM-2017, Proceedings PRO 119, Ed. Amziane, S., Sonebi, M., Clermont-Ferrand (France), RILEM Publications s.a.r.l. (2017)
- [2] RILEM STAR of RILEM TC 236-BBM., Bio-aggregates based Building materials, Springer Publisher, (2017)
- [3] Amziane, S., Sonebi, M., Proceedings of the First International Conference on Bio-Based Building Materials, ICBBM-2015, Proceedings PRO 99, Ed. Amziane, S., Sonebi, M., Clermont-Ferrand (France), RILEM Publications s.a.r.l. (2015)

## **MECHANICAL PREDICTION OF W.C.C. PROPERTIES: EXPERIMENTAL STUDY AND ANALYTICAL MODELING**

**Jean Gérard Ndong Engone<sup>(1)</sup>, Ahmed El-Moumen<sup>(2)</sup>, Chafika Djelal<sup>(3)</sup>, Abdellatif Imad<sup>(2)</sup>, Yannick Vanhove<sup>(3)</sup>**

(1) Laboratoire Matériaux, Géoscan-Structure & Réhabilitation Ingénierie, 26 rue ampère, F-91430 Igny France

(2) Laboratoire de Mécanique de Lille FRE 3723, Université Lille, F-59655 Villeneuve d'Ascq, France

(3) Univ. Artois, EA 4515, Laboratoire de Génie Civil et géo-Environnement (LGCgE), 62408 Béthune, France

### **Abstract**

The wood industry generates some 12 million tons of waste in France. The reuse of this waste in the most common construction materials (e.g. concrete) may offer a sustainable solution. In this work, an experimental study was performed in order to develop wood cement composite (WCC) based on poplar sawdust by vibrocompaction process and used in concrete masonry blocks. The volume fraction of wood particles in the mixes varies from 23% to 46%. The mechanical properties in compression of these composites are characterized experimentally to determine the breaking stress and the Young's moduli. Thereafter, these Young's moduli are estimated in compression using both analytical homogenization models in order to predict the effective elastic properties of cement-wood composites. The obtained results show a good agreement between the experimental data and analytical calculations up to a 40% volume fraction. The poor models estimation for large volume fractions could be attributed to the experimental sample size, which is no longer representative for large volume fractions. Aside from the effect of specimen size, the physico-chemical phenomena (inhibition of the cement, WP percolation) could be the cause of poor models estimation for large volume fractions.

### **1. Introduction**

Various works have focused on using wood byproducts like sawdust [1], wood chips [2], wood fibers [3] and even wood ash [4] as reinforcement in manufacturing wood-cement composites (WCC). These byproducts originate from deciduous [5] as well as evergreen species [3]. Despite considerable research devoted to WCC, their use in the field of construction remains confined to partition walls and acoustic insulation. This limitation is due

to the drop in mechanical characteristics and the lower durability of these WCC. In the literature, the optimization of WCC generally focuses on experimental studies regardless of mechanical behaviour prediction. The few number of studies actually dedicated to predict the mechanical behaviour of WCC are based on statistical studies of experimental results [6]. This work is focus on the predicting of mechanical behaviour of WCC using the analytical modeling. In this paper, an experimental study has achieved to develop a wood cement composite based on cementitious matrix and sawdust by the vibrocompaction process. The mechanical properties in compression of these composites are characterized experimentally to determine the Young's moduli. Thereafter, these Young's moduli are estimated in compression using an analytical homogenization technique. The experimental and analytical data are compared.

## 2. Materials

The wood particle (WP) using are wood waste from sawmill. These particles originate from the poplar species. These WP have been used and described by Ndong et al [7]. The mass densities of these WP were determined in accordance with standard NF EN 1097-6. This bulk density is equal to  $178 \text{ kg.m}^{-3}$ . Wood is renowned for its high sensitivity to water; in fact, this material absorbs a quantity of water often exceeding twice its weight. Such water sensitivity has a negative consequence on material properties in both the fresh and hardened states of the composites incorporating these WP. In fact, the water absorption of WP were determined, she is equal to 174%. In this study, the sand with a 0/4 particle grading were used. The cement tested is a CEM I 52.5 N EC CP2 NF.

## 3. Methods

### 3.1 Experimental studies

In this work, 7 mix designs were studied (see Tab. 1 for details). These formulations have been studied by Ndong et al [7]. The sand was subsequently replaced by WP. This substitution corresponds to a wood particle volume in the mix varying from 23% (WCC<sub>23</sub>) to 46% (WCC<sub>46</sub>). All mix designs are characterized by a cement paste volume of 40%.

Table 1: Various concentrations of wood mortars,  $\delta_{(C+W)}$ ,  $\delta_{(Sa)}$  and  $\delta_{(Sw)}$  being, the volume ratio of paste (cement+ water), sand and sawdust and the mixture.

	WCC <sub>0</sub>	WCC <sub>23</sub>	WCC <sub>26</sub>	WCC <sub>32</sub>	WCC <sub>35</sub>	WCC <sub>40</sub>	WCC <sub>46</sub>
$\delta_{(C+W)}$	40%	40%	40%	40%	40%	60%	0%
$\delta_{(Sa)}$	60%	37%	34%	28%	25%	20%	14%
$\delta_{(Sw)}$	0%	14%	26%	32%	35%	40%	46%

One design composed solely of sand, cement is use as the reference design (WCC<sub>0</sub>). The WCC are shaped by vibrocompaction as defined by Xing et al [8]. The samples are cylindrical in shape of 10 cm diameter. They have a height of 20 cm. The vibrocompaction step was carried out with a compactor installed in a temperature-controlled room ( $T = 20 \pm 2^\circ\text{C}$ ). The

specimens were stored in a chamber at a temperature of  $20 \pm 2^\circ\text{C}$  and a relative humidity of 65%. The compression test was conducted using according to standard NF EN 772-1.

### 3.2 Analytical evaluation

The main objective of this part of study is to analytically simulate the effective's elastic properties of WCC. We have focused on the multiscale analysis of the macroscopic elastic behavior through the knowledge acquired of the mechanical behavior of each phase. Multiscale analysis is based on both of analytical homogenization models. A comparison between experimental data and results of analytical homogenization steps has been drawn. Analytical evaluations of the effective elastic properties of cement-wood composites can be obtained by means of several analytical methods. The proposed estimation typically depends on the inclusion shape and its distribution. These models obviously converge whenever the volume fraction of particles or the contrast between the properties of both phases is too small. Several of analytical homogenization methods can be found and presented in the literature. The following popular approaches will be assessed in the isotropic case namely: the Mori and Tanaka (MT) model [9], the first-order bounds of Voigt [10] and Reuss [11] (VR), and the optimal bounds of Hashin and Shtrikman (HS) [12]. According to these models, elastic properties of composites are determined by knowing those of each phase, "m: matrix" and "i: inclusion", and wood volume fraction "p". Analytical expressions of each model are expressed and given by Equations (1), (2), (3), (4), (5), (8), (9) and (10) as:

- Upper and lower HS bounds,  $H^{S^+}$  and  $H^{S^-}$

$$\begin{cases} K^{HS^-} = k_m + \frac{p}{1/(k_i - k_m) + 3(1-p)/(3k_m + 4\mu_m)} \\ K^{HS^+} = k_i + \frac{(1-p)}{1/(k_m - k_i) + 3p/(3k_i + 4\mu_i)} \end{cases} \quad (1)$$

$$\begin{cases} \mu^{HS^-} = \mu_m + \frac{p}{1/(\mu_i - \mu_m) + 6(1-p)(k_m + 2\mu_m)/5\mu_m(3k_m + 4\mu_m)} \\ \mu^{HS^+} = \mu_i + \frac{(1-p)}{1/(\mu_m - \mu_i) + 6p(k_i + 2\mu_i)/5\mu_i(3k_i + 4\mu_i)} \end{cases} \quad (2)$$

HS analytical models obviously propose to calculate the bulk "k" and shear "μ" moduli. It should be pointed out that to derive Young's modulus "E", Equation (5) links all of these elastic properties. Where  $E^{HS^+}$  and  $E^{HS^-}$  represent upper and lower Young's modulus, respectively.

$$E^{HS^\pm} = \frac{9k^{HS^\pm}\mu^{HS^\pm}}{(3k^{HS^\pm} + \mu^{HS^\pm})} \quad (3)$$

- Mori-Tanaka model

$$k^{MT} = k_m \left( 1 + \frac{p(k_i - k_m)}{k_m + \alpha(1-p)(k_i - k_m)} \right) \quad (4)$$

$$\mu^{MT} = \mu_m \left( 1 + \frac{p(\mu_i - \mu_m)}{\mu_m + \beta(1-p)(\mu_i - \mu_m)} \right) \quad (5)$$

$$\alpha = 3k_m / (3k_m + 4\mu_m) \quad (6)$$

$$\beta = (6(k_m + 2\mu_m)) / (5(3k_m + 4\mu_m)) \quad (7)$$

Mori-Tanaka Young's modulus,  $E^{MT}$ , is calculated using the following equation:

$$E^{MT} = \frac{9k^{MT}\mu^{MT}}{(3k^{MT} + \mu^{MT})} \quad (8)$$

- VR bounds

$$E^{Voigt} = pE_i + (1 - p)E_m \quad (9)$$

$$E^{Reuss} = \frac{E_i E_m}{(1 - p)E_i + pE_m} \quad (10)$$

#### 4. Results and discussions

Figure 1 shows the Young's modulus variation as function of wood volume present in the mix at 14 days. The presence of two behavioral fields can be distinguished. In the first field, the decline in Young's modulus is nearly linear until reaching 35% of WP in the mix, at which point its value equals 6.02 GPa (a drop of 51%). This lower Young's modulus in the first field can be attributed to various parameters, including inhibition of the hydration reaction, the mix porosity, the lack of WP stiffness, and distribution of the WP in the mixture. The inhibition of the cement hydration reaction occurs in the fluid state during cement paste / wood particle contact. The alkaline materials stemming from cement dissolution interact with the sugars contained in wood particles [3]. The impact of the wood particles used in this study on the hydration reactions has been demonstrated by several studies [8]. This inhibition plays an even greater role at a greater WP volume in the matrix. The porous WP structure raises the level of composite porosity [8]. During the compression test, this porosity triggers microcracking, which in turn weakens the composite. The effect of these parameters on the composite's mechanical behavior depends on the WP volume in the composite. The WP are arranged randomly, which creates areas of fragility located at different areas in the composite structure. Once the wood volume has reached 35%, another more pronounced decrease is noticed, displaying a value of 1.40 GPa, for a loss of 89%. This rate corresponds to a threshold volume beyond which WP percolates extensively into the composite. This leads to the saturation percolation thereof. This percolation effect modifies the composites' mechanical response. During percolation, the WP are basically entangled, leading to higher composite porosity and creating a vast zone of minimal stiffness. When conducting mechanical tests, these zones behave like pores due to the relatively non-rigid WP; such behavior significantly reduces composite ductility. After WP percolation in the mix, the higher WP volume exerts very little influence on the composite microstructure, hence with only a minimal influence on mechanical behaviour. The analytical results have been compared with experimental data provided by the compression test on specimens. Figure 2 illustrates these results. In the case of a low proportion of aggregates, it appears that the experimental Young's modulus values of WCC systematically lie between the HS bounds, which is in agreement with homogenization theory. It also appears that, both of the MT models and upper HS bounds closely match the experimental results. Beyond a proportion of 35%, the experimental values remain below those of the Reuss model; this limit corresponds to the percolation threshold, as highlighted in figure 1.

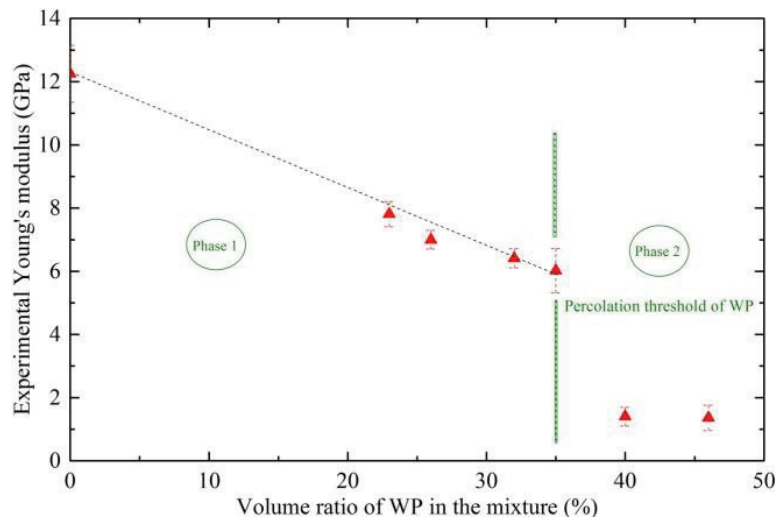


Figure 1: Experimental data of WCC at 14 days.

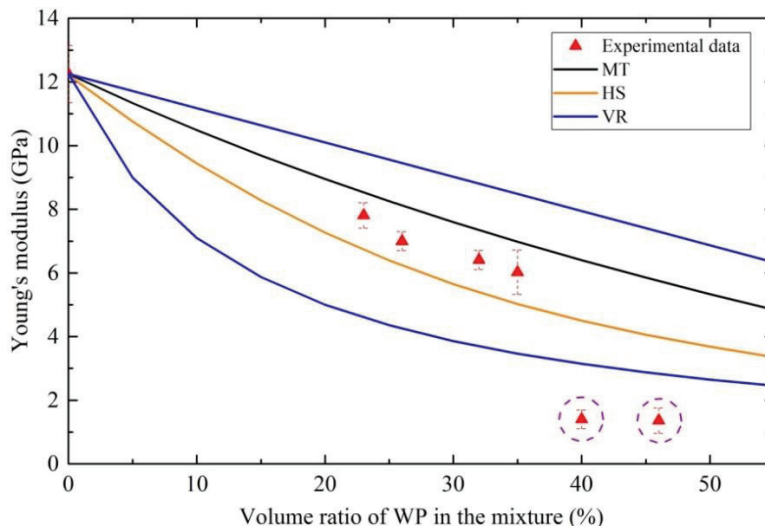


Figure 2: Confrontation between experimental and analytical results

The homogenization models not to have a good estimation of mechanical properties. Methods for estimating effective properties are based on the micromechanics interaction of composite components. In the case of composites of wood, there is a chemical interaction between the WP and the cementitious matrix. This interaction varies depending on the proportion of WP in the mix. For low proportion, the effective properties in the elastic range are weakly impacted. In this study, low impact provides a good estimate of the elastic properties. In the case of high wood proportion, the chemical interaction is high, which could justify the wrong estimation of the actual properties. The mechanical characteristics of the matrix are no longer that of the initial matrix. Homogenization models does not take into account the change in properties of the matrix. Other parts of the percolation phenomenon observed in figure 3 could also be the cause of poor estimation of actual properties. The homogenization theory requires the assumption of inclusion perfectly coated with the matrix. WP percolation invalidates this assumption, which could explain disability the bounds of homogenization. For



the future, numerical modeling based on the homogenization technique will be carried out. The impact of cement phase inhibition will be taken into account.

## 5. Conclusions

In this study, tests have been conducted to estimate effective properties of WCC by using analytical models. The following conclusions can be drawn; The Young's modulus of wood-cement composites drops with an increase in WP volume. This decline comprises two behavioral fields, one of which remains quasi linear up to a 35% threshold volume, which corresponds to a percolation threshold for WP in the mix; The prediction of Young's modulus by the homogenization analytical method shows that in the case of low proportion of wood particles in the mixture, the Mori-Tanaka model (MT) and upper Hashin and Shtrikman bounds (HS) allow having a good approximation of mechanical properties. Beyond 35% of WP volume in the mixture, conventional homogenization models cannot make a good approximation of mechanical properties. Percolation of WP and significant inhibition of the cement results in poor approximation of mechanical properties.

## References

- [1] Almir S, Rodrigues de Souza F, and al. Mechanical properties of concrete produced with a composite of water treatment sludge and sawdust. *Constr. Build. Mater* 25(2001), 2793–2798.
- [2] Mohammed B, Abdullahi M, Hoong CK. Statistical models for concrete containing wood chipping as partial replacement to fine aggregate. *Constr. Build. Mater* 55(2014), 13–19.
- [3] Wei YM, Tomita B, Hiramats Y, Fujii T. Study of hydration behaviors of wood-cement mixtures: compatibility of cement mixed with wood fiber strand obtained by the water-vapor explosion process. *J. Wood. Sci* 48(2002), 365–373.
- [4] F. Udoeyop, H. Inyang, DT. Young, EE Oparadu. Potential of wood waste ash as an additive in concrete. *J. Mat. Civ. Eng.* 18 (2006), 605–611.
- [5] Yasuda ES, Ima K, Matsushita Y. Manufacture of wood-cement boards VII: cement-hardening inhibitory compounds of hannoki. *J. Wood. Sci* 48(2002):242–244.
- [6] Chowdhury S, Maniar A, Suganya OM. Strength development in concrete with wood ash blended cement and use of soft computing models to predict strength parameters. *J. Adv. Res.* 6(2014), 907–1013.
- [7] Ndong Engone, J.G., Vanhove, Y., Djelal, C. et al. Optimizing mortar extrusion using poplar wood sawdust for masonry building block. *Int J Adv Manuf Technol* 95(2018), 3769-3780.
- [8] Xing Z, Kada H, Djelal C, Vanhove Y. Wood Waste in Concrete Blocks Made by Vibrocompression. *Environ. Process.* (2015) 2(Suppl 1), 223-232.
- [9] T. Mori and K. Tanaka. Average stress in the matrix and average elastic energy of materials with misfitting inclusions. *Acta Metall.* 21(1973), 571–574.
- [10] Voigt W. Über die beziehung zwischen den beiden elastizitatskonstanten isotroper korper. *Wied. Ann* 38(1889), 573–587.
- [11] Reuss A. Berechnung der fließgrenz von mischkristellen auf grund der plastizitatsbedingung für einkristalle. *ZAMM* 9 (1929), 49–58.
- [12] Hashin Z, Shtrikman S. A variational approach to the theory of the elastic behavior of multiphase materials. *J. Mech. Phys. Sol.* 11(1963), 127–140.

## **RISK ASSESSMENT OF MOLD GROWTH IN HEMP CONCRETE**

**Dmytro Kosiachevskyi<sup>(1)</sup>, Kamilia Abahri<sup>(1)</sup>, Mohend Chaouche<sup>(1)</sup>, Evelyne Prat<sup>(2)</sup>,  
Anne Daubresse<sup>(2)</sup>, Cécile Bousquet<sup>(2)</sup>**

(1) LMT, ENS Cachan, CNRS, Université Paris-Saclay, 94235 Cachan, France

(2) Centre d'Innovation Parexgroup, St Quentin Fallavier, France

### **Abstract**

The use of the hemp concrete in the construction sector is interesting due to its hygro-thermal performances, economic and environmental benefits. Nevertheless, these performances can be affected as the hemp aggregate is a perfect substrate for a fungi proliferation. This paper focuses on the evaluation of the risk of mold contamination of the hemp concrete. The main objective is, first, to determine the risks of mold growth in the hemp concrete for durability, and, second, to verify the interconnection between the contamination by the mold of the hemp shiv and of the hemp concrete. Experimentally, a mold identification procedure was used for both samples of hemp shiv and hemp concrete, after being cultured in a Sabouraud culture medium at different conditions in desiccators. In addition, Scanning Electronic Microscope (SEM) observations have been conducted on different contaminated samples to investigate the material degradation and the interaction between the hemp fibers and the concrete. The obtained results have revealed that the fungi from the *Aspergillus* family are the most common mushrooms present in the material. Their impact on human health has been presented in the paper.

### **1. Introduction**

The use of bio-based building materials is hampered by the lack of a database relating to their intrinsic properties and durability. Nevertheless, the question of their sensibility to several characteristics is still open. The mold growth is one of the most important criterion when assessing the degradation of bio-based materials [1,2,3]. Besides the effect of the degradation of substrate, an exposition to fungi could provoke several adverse health effects as allergic reactions, aggravated rhinitis and asthma [4]. Fungal components, such as spores and hyphal fragments and others volatile particles, may have effects on the health of an exposed

individual because of their size and characteristics [5, 6, 7]. Spores are emitted in the result of the fungal growth that depends on several parameters such as temperature, relative humidity, light, etc.

The fungi are eukaryotic, heterotrophic with septate or siphoned filamentous thallus [8]. They are classified into 5 groups: Chytridiomycota, Zygomycota, Basidiomycota, Ascomycota and Deuteromycota. Unfortunately, there are still a lack of knowledge on the effects of molds on durability of bio-based structures such as the hemp concrete. Particularly, literature presents few works in the field of civil engineering that consider the mold risk on material durability of the building and health of people living there.

That's why, the main objective is, first, to observe and to characterize the mold growth for two different hemp concrete formulations, and, then, to determine the strains and the risk of the mold growth for durability and human health. Since, there is a difference between the samples of two formulations, the results could not be compared. Experimentally, a morphological analysis and interface observation of the mold structures on the contaminated samples have been conducted. Then an identification procedure, that consist to identify them, has been investigated. Overall, the correlation between the contamination of the hemp shiv and the hemp concrete has been studied.

## 2. Materials and methods

In this part the material formulation and the experimental protocol are presented. For this study one sample of each of two different hemp concrete formulations with two different types of hemp has been used. The HC-B formulation sample was made according to the professional rules of execution of hemp concrete works [9]. It is used as wall insulation. The shiv has the apparent density of about 100 to 110 kg/m<sup>3</sup>. The binder is based on the lime. It is called Batichanvre, produced by French lime producers St. Astier. This binder is a mixture of natural lime from Saint-Astier (Hydraulic lime: NHL and aerial one: CL), cement CEM I 52.5, and different adjuvants to improve rheology and permeability of hemp concretes. Its density is of 500 kg/m<sup>3</sup>. The HC-P formulation (produced by ParexGROUP) is made to let an application as a shotcrete. The binder is based on calcic lime, specific binder and specific admixtures. The hemp, used for HC-P, was harvested in the same year in the same region by different farmers, stocked differently but grinded in the same way at different days. Four different types of this hemp have been studied but just one of them (type 4) has been used for a HC-P sample. The two formulations are presented in Tab. 1. The sample of the HC-B formulation of the dimensions of 20,48x20,06x6,29 mm<sup>3</sup> has been produced on 31 January 2016. They were conditioned at 23°C and 50% of relative humidity for letting the carbonatation of the binder to diminish the pH level and favour the fungi development. After that, in March 2017 the specimen was put in a desiccator at 94% of relative humidity which is a favourable condition to provoke the mold growth. After one year this sample has been observed using the numerical microscope Keyence VHX-2000. In the case of the HC-P formulation the sample has been taken from real construction site after the mold growth has been visible (after one month, on 28 November 2017). The same numerical microscope observation has been used for the HC-P formulation. The interface and the morphology of the mold structures have been also studied for both formulations using the Hitachi S3400 Scanning Electronical Microscope. The acceleration voltage of 10 kV, the pressure of 50 Pa

for the sample of the HC-B formulation and of 70 Pa for the sample of the HC-P have been chosen for all the observations.

Table 1: Formulation of the studied hemp concretes.

Material	HC-B	HC-P
Hemp shiv (kg)	10 kg	10 kg
Binder (kg)	25 kg	20 kg
Water (kg)	35 kg	50 kg
Water / binder (-)	1.4	2.5
Binder / hemp shiv (-)	2.5	2

After having observed the mold proliferation the mold types have been determined. It could let us to analyse the risks of such contamination. In this case the experimental protocol consists firstly in sowing contaminated particles separately in Petri dishes to let the mold grow. In order to analyse the mold types present in the hemp concrete, hemp concretes of two formulations have been studied. In order to verify relations between molds from the hemp concrete and the hemp and the dispersion of the contamination four samples of hemp, used for HC-P, have been studied. In this context, the microbiological identification protocol has been used. Electrical burner has been used to protect our samples of bacteria and prevent a possible contamination from outside. The question of repeatability has been studied by seeding contaminated particles twice to be sure in the repeatability. After seeding the particles, Petri dishes were packed with parafilm and put in the closed desiccator to prevent external contamination by the air stream. The temperature of 23 ° C and the relative humidity of 50% was controlled. After 8 days we observed the sampled parts of the mold from these dishes between a microscope slides and cover glasses on the adhesive tape. The identification of mold species was made using the numerical microscope Keyence VHX-2000 based on the morphological characteristics.

### 3. Results and discussion

#### 3.1 Morphology analysis and interface observation

As expected previously, in this chapter the results of optical and SEM microscopes observation are presented. Hemp concrete has been observed in different scales. So, firstly, we have analysed the numerical microscope images of the hemp concrete before and after the mold contamination (Fig. 1 a and b respectively). They showed that both materials are heterogeneous, porous and represent a big quantity of micro cracks (Fig.1a) in the interface between hemp shives (1) and the cementitious part (2). Additionally, these images give us a better understanding of the procedure of the contamination and the mold growth. On the Fig. 1b we can see the mold on the surface of the contaminated sample (3). As for SEM images Fig. 2 (a and b) represents the photos of one sample of the HC-B formulation. Mold structures such as the filamentous thallus (1) and vesicles (2) are visible on the Fig.2a. Figure 2b shows that the cementitious part (3) covers and protects the hemp shiv (4). The mold net (1) is also visible. The images of the SEM observation of the contaminated sample of the HC-P formulation are presented on the Fig. 3 (a and b).

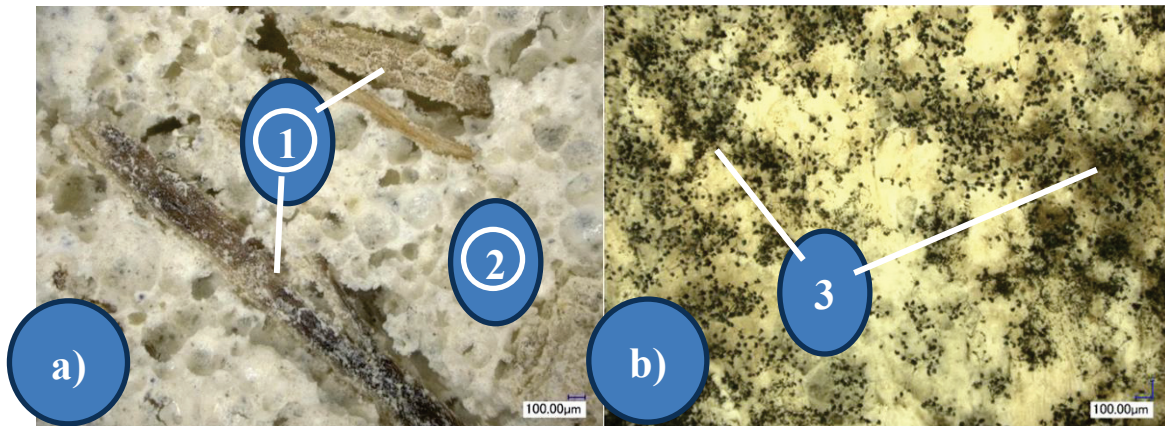


Figure 1: Example of numerical microscope photos of the hemp concrete before (a) and after (b) mold growth: 1 – hemp shiv, 2 - cementitious part, 3 – mold contamination

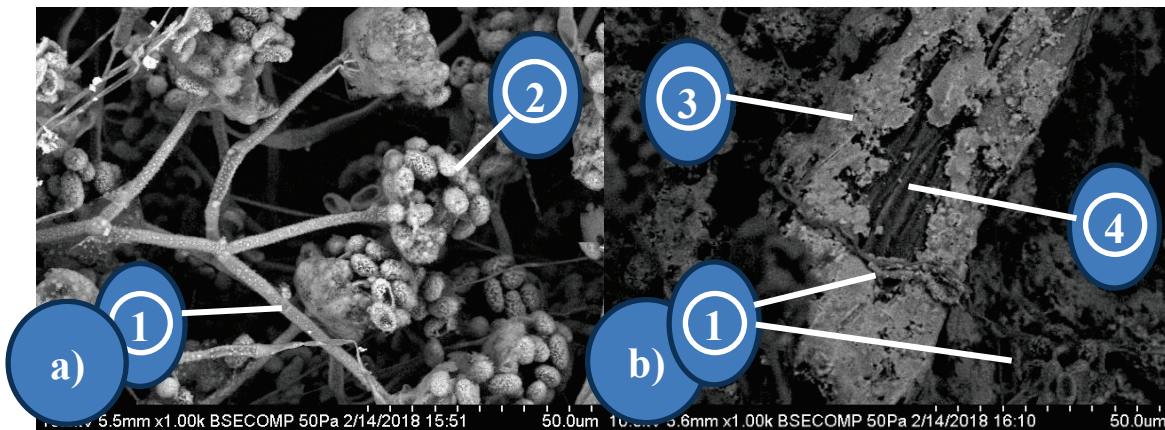


Figure 2: SEM images of the morphological structures of the mold present on the hemp concrete of the HC-B formulation (a and b): 1 - filamentous thallus, 2 – vesicles, 3 - cementitious part, 4 – hemp shiv

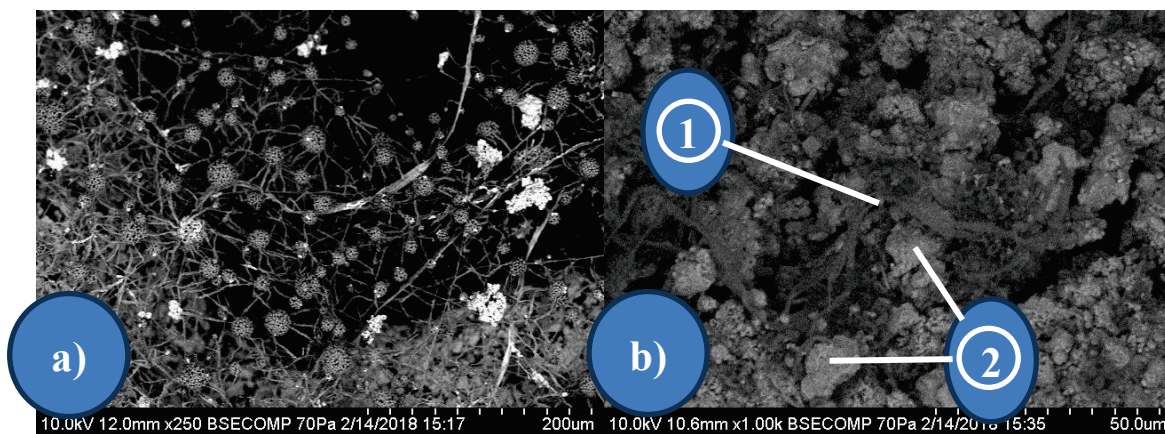


Figure 3: SEM images of the morphological structures of the mold present on the hemp concrete of the HC-P formulation (a and b): 1 - filamentous thallus, 2 - cementitious part

Analogically to the first case, we can see the mold structures with a huge number of the vesicles (Fig. 3a). The mold net (1), that is on the surface of the cementitious part (2) of our sample, is presented on the Fig. 3b. Then we proceeded with the mold identification.

### 3.2 Mold identification and risk assessment

After cultivating twice molds from two studied formulations of the hemp concrete and four types of the hemp, several types of fungi were identified. Tab. 2 represents all the identified types during this test. Hemp shives could be contaminated at different stage of their life cycle (harvest, storage or implementation). Indeed, all types of hemp particles with the different storage conditions have the similar fungi samples. At the same time, we can see that despite the presence of the dispersion of the contamination there is the consistent pattern of the fungi contamination. Also, we can see that two formulations represent different mold samples that can be explained by the difference of hemp shiv (the main source of fungi spores).

Table 2: Results of the determination of the fungi strains for each type of material.

Type of material		Mold strains
Hemp	Hemp type #1	Rhizopus sp, Aspergillus niger
	Hemp type #2	Rhizopus sp, Aspergillus niger
	Hemp type #3	Rhizopus sp, Aspergillus niger
	Hemp type #4	Rhizopus sp.
Hemp concrete	#1 Batichanvre	Aspergillus niger, Aspergillus nidulans
	#2 ParexGroup (hemp type #4)	Rhizopus sp, Aspergillus niger

According to the literature, the toxicity of *Aspergillus niger* comes from their production of oxalic acid, flavaspérone and aflatoxins [10]. *Aspergillus nidulans* is toxic through its production of sterigmatocystin, and molecules such as oxalic acid, nidulotoxin or kojic acid. *Rhizopus sp.* is one of the most isolated species in cerebral and rhinofacial mucormycosis injuries. Patients are often diabetic patients with ketoacidosis, but also leukemic patients, sometimes AIDS patients. More, *Rhizopus sp.* is dangerous for transplant surgery because of the great risk of the transplant rejection [11].

## 4. Conclusion

This research lays to examine the risk of mold growth for two different formulations of the hemp concrete. Firstly, optical and SEM microscopic observations of both non-contaminated and contaminated samples have been conducted. Then the mold identification protocol has been used to identify the fungi present in our samples. The favorable microstructure for the mold growth of the hemp concrete has been noticed. Studied hemp concrete represents the difficult heterogeneous microstructure with a high number of micro cracks and pores that facilitate the mold proliferation. Mold growth depends on the contamination of the

components before, during and after the production of a hemp concrete. Several mold strains were determined using the phenotypic method - microscopic observation. At the same time, these tests have demonstrated defects of microscopic identification of strains: (1) under certain conditions certain mold strains do not form structures that make it possible to determine the family of a strain; (2) there is a high possibility of contamination of Petri dishes, which distorts results; (3) due to the effect of synergy some strains may not proliferate which is not representative for the real case; (4) there are some microorganisms in a hemp mortar or hemp itself that probably cannot be identified by this method.

### Acknowledgments

The authors acknowledge ParexGroup for financing this project.

### References

- [1] Arizzi A., Brümmer M., Martín-Sánchez I., Cultrone G. and Viles H. The influence of the type of lime on the hygric behaviour and bio-receptivity of hemp lime composites used for rendering applications in sustainable new construction and repair works, PLoS ONE 10(5): e0125520. doi:10.1371/journal.pone.0125520, 2015
- [2] Vereecken E., Roels S. Review of mould prediction models and their influence on mould risk evaluation, Building and Environment 51, 296 -310, 2011
- [3] Crawford, B., Pakpour, S., Kazemian, N., Klironomos, J., Stoeffler, K., Rho, D., Denault, J., Milani, A.S. Effect of Fungal Deterioration on Physical and Mechanical Properties of Hemp and Flax Natural Fiber Composites, Materials 2017, Vol. 10, Issue 11, 1252, 2017
- [4] Mazur, L.J. and Kim, J., Spectrum of noninfectious health effects from molds. Pediatrics 118(6) (2006), 1909-1926
- [5] Górný, R.L., Filamentous microorganisms and their fragments in indoor air - a review. Annals of Agricultural and Environmental Medicine 11(2) (2004), 185-197
- [6] Eduard W., Fungal spores: a critical review of the toxicological and epidemiological evidence as a basis for occupational exposure limit setting. Crit Rev Toxicol 39(10) (2009), 799-864
- [7] Fischer, G. and Dott, W., Relevance of airborne fungi and their secondary metabolites for environmental, occupational and indoor hygiene. Archives of Microbiology 179(2) (2003), 75-82
- [8] Djossou O., Post-harvest Robusta mycoflora and the use of lactic acid bacteria for the control of mycotoxinogenic molds and ochratoxin A, PhD thesis, Paul Cézanne University (2011)
- [9] SEBTP. 2012. Professional rules for the execution of hemp concrete works: research development metier, France (2012)
- [10] Botton B. et al, Mold, useful and harmful, industrial importance, Collection Biotechnologies, Masson Edition (1990)
- [11] Almyroudis N.G., Sutton D.A., Linden P., et al, Zygomycosis in solid organ transplant recipients in a tertiary transplant center and review of the literature. Am J Transplant 6(10) (2006)

**MULTI-PHYSICS SIMULATION  
AND  
STRUCTURAL DESIGN**



## CONCRETE CASTING AND LIFETIME CONDITIONS IMPACT ON HIGH TEMPERATURE RESISTANCE

Giuseppe Sciumè <sup>(1)</sup>, Stefano Dal Pont <sup>(2)</sup>, Dorjan Dauti <sup>(2)</sup>

(1) I2M – Institut de Mécanique et d'Ingénierie, Université de Bordeaux, France

(2) 3SR – Laboratoire Sols, Solides, Structures, Risques, Université Grenoble Alpes, France

### Abstract

In this paper the impact of early age and service-life conditions on high temperature behaviour is analysed and shown for a 60-cm heated wall. Numerical experiments are performed using a porous media model, coupling dependencies of material parameters on hydration advancement degree. Concrete hydration at early age and dehydration/degradation due to high temperature exposure are here treated by means of an original unified approach. The mathematical model is based on general conservation equations of mass, energy and linear momentum. The explicit introduction of the stoichiometric model of Powers allows deriving some of the needed closure relationship. A new constitutive model is also proposed for the desorption isotherms.

### 1. Introduction

Despite two thousand years of history, concrete is yet among the most complex materials to be understood and modelled. Advances in concrete mixtures (current concretes may include non-conventional binders, additives, low weight aggregates, polymer fibres, etc.) are certainly one cause of such complexity. However the main reason resides in the mesoscale and microscopic structure of concrete: the connection between coarse aggregates and cement paste strongly affects the material behaviour and often constitutes the “weak link” where failure initiates. Furthermore cement paste has a porous and chemically active nature with capillary and adsorbed water strongly affecting its global behaviour (shrinkage, creep, etc.).

The presence of water and moisture transport within the pores give to the time dimension a critical importance for prediction of concrete performance; hence, the knowledge of casting and environmental conditions during service-life of the structure is needed for a predictive

simulation of concrete response when submitted to extreme loads and/or hard environmental conditions.

While the awareness of early age and curing conditions is often not important, it becomes critical point for massive structures. Cement hydration is a thermo-activated reaction and therefore the rise of temperature, not well dissipated in mass concrete, increases the rate of reaction which may become very important inducing a temperature gradient up to 40-60 °C (see [1]). The positive thermal strain associated with heating is very often restrained by an existing substrate, or self-restrained due to the cast geometry, leading to compressive stresses. Then, during the subsequent cooling phase the volume of concrete decreases progressively and also this compressive stress decreases. However, due to the increased stiffness of the material with hydration, the stress in certain parts of the structure is transformed to traction and may induce diffuse cracking or traversing localized cracks. These phenomena are well known and concern civil engineering structures of safety and strategical relevance such as concrete dams, reactor's containments in nuclear power plants and tunnels.

In this work, it is shown that state-of-the-art models ([2,3]), can be further formally improved introducing stoichiometric relations of Powers and treating hydration and high-temperature degradation in a unified way. The resulting mathematical model has been implemented in the finite element software Cast3M (<http://www-cast3m.cea.fr>) and allows to naturally compute solutions about high temperature resistance accounting for concrete history: early age and aging.

## 2. The multiphase model

Concrete is here modelled as a multiphase material consisting of the solid phase,  $s$ , the liquid phase,  $l$ , and the gaseous phase,  $g$ . The solid phase consists of fine and coarse aggregates and cement paste, the liquid phase is liquid water whereas the gaseous phase is a binary mixture of water vapour and dry air.

At each macroscopic point the three phases coexist and their volume fractions, indicated as  $\phi^\alpha$  ( $\alpha = s, l, g$ ) have to satisfy the following constraint:

$$\phi^s + \phi^l + \phi^g = 1 \quad (1)$$

### 2.1 The unified hydration de-hydration model

Cement hydration is a thermo-activated process. In other words, hydration's rate of reaction increases as temperature increases during concrete hardening. On the other hand, during a fire accident when temperature increases over a certain threshold, hydrated products release the chemically bound water and the cement paste loses gradually mechanical properties attained with hydration. Such process is concrete dehydration induced by high temperature exposure. To take into account the effect of high temperature an internal variable, here indicated as  $F$  (for fire dehydration), is considered. The equivalent degree of reaction, is then given as:

$$\tilde{\Gamma} = \Gamma(1 - F) \quad (2)$$

where  $\Gamma$  is the advancement of hydration degree. Most of parameters of the computational model (porosity, permeability, Young's modulus, etc.) depends on  $\tilde{\Gamma}$ .  $F(T)$  is a continuous function growing from 0 to 1 with temperature [2]. Deriving Eq. (2) with time gives:

$$\frac{D^s \tilde{\Gamma}}{Dt} = (1 - F) \frac{D^s \Gamma}{Dt} - \Gamma \frac{D^s F}{Dt} \quad (3)$$

Considering that fire damaging is irreversible, a non-negative increment of  $F(T)$  is imposed.

## 2.2 Concrete stoichiometry

The adoption of Powers model allows estimating the amount of water chemically combined after the complete hydration of cement in the mix. In particular simple calculations give:

$$m_\infty = 0.228c\xi_\infty \quad (4)$$

where  $c$  is the cement content in the mix, and  $\xi_\infty$  is the fraction of cement hydrated when at the end ( $\xi_\infty$  depends on the water-to-cement ratio) [4].

Powers model allows also obtaining the evolution of porosity,  $\phi$ , which reads:

$$\phi = \phi_\infty + a_\phi(1 - \tilde{\Gamma}) \quad (5)$$

with  $\phi_\infty$  the final porosity, and  $a_\phi$  a constant coefficient; both parameters can be calculated from data about the concrete mix as explained in [1].

## 2.3 Conservation equations

The mathematical model is governed by mass, momentum and energy conservation equations of considered phases and gas species. From these, introducing some assumptions as detailed in [2] a system of four independent equations is derived and then solved numerically:

- the mass conservation equation of dry air;
- the mass conservation equation of water species (liquid water + water vapour);
- the enthalpy conservation equation;
- the momentum conservation equation for the multiphase system.

It can be shown that Eq. (4) and (5) allow deriving naturally and explicitly some of terms of the reference formulation [2]; these terms must otherwise be identified experimentally or assumed from literature.

## 2.4 The pressure-saturation relationship

A new equation is also proposed for the desorption isotherm. This equation accounts for modifications of concrete microstructure and evolution of water surface tension due to temperature. Differently from equation proposed in [2], this law is less intricate, and allows describing in a unified way effect of hydration/dehydration. Furthermore, effect of fire-induced dehydration on retention curve is properly accounted as irreversible since depending on  $\tilde{\Gamma}$  (and not on  $T$  as in [2]). The developed relationship is an extension to high temperature of the constitutive model proposed in [1, 5] by the first author for young concrete.

### 3. Low rate heating (2 K/min) for a 60-cm wall

A 1-dimensional case is simulated numerically to analyse and quantify the impact of age on the computed results. A 60-cm wall exposed from both sides to heating is modelled. Due to symmetry only one half of the wall is considered and discretized in the FE code. The concrete is the OC adopted for the COST Action TU1404 benchmark [6], its water to cement ratio is of 0.45 (other details about the composition are available in [6]). Data provided by benchmark organisers are assumed to identify most of model parameters; the remaining ones are assumed from literature [2] and author previous works on similar concretes [3, 5, 7].

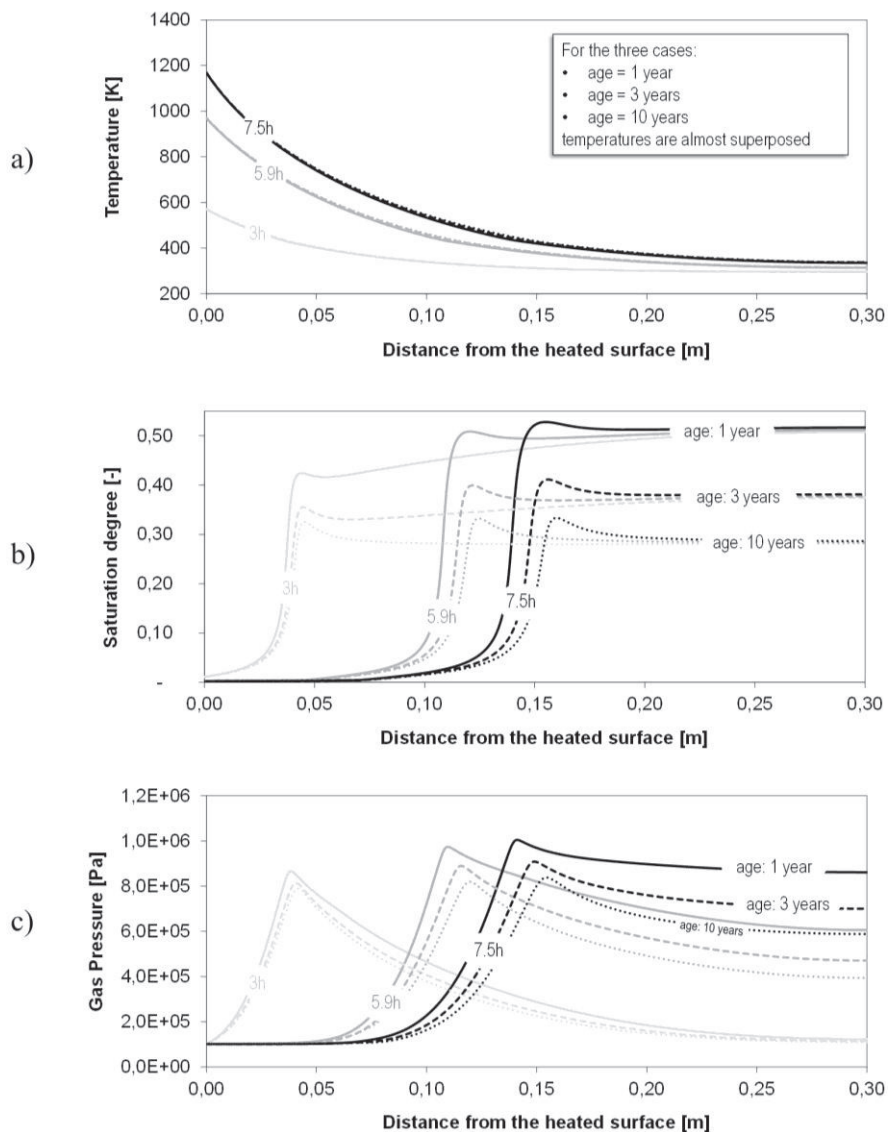


Figure 1: a) Temperature, b) saturation and c) gas pressure in a concrete wall for 3 different heat exposure times (3h, 5.9h, 7.5h) highlighting the impact of the concrete age (1 year, 3 years, 10 years).

### 3.1 Test description and assumed boundary conditions

The assumed heating conditions are the same as in [2]. However this time the test is more complex as the wall history, early age and aging, is also considered.

Three phases are modelled:

- Phase 1, very early age – from casting to 3 days: the adiabatic calorimetry test provided in [6] is used to identify hydration parameters. The wall is assumed sealed (no mass exchange) while a convective model is assumed for thermal exchange ( $h_t = 10 \text{ W}/(\text{m}^2\text{K})$ ). Initial and external temperatures are assumed of  $22^\circ\text{C}$ .
- Phase 2, drying-aging – from 3 days to considered “age time”: at 3 days the wall starts drying (e.g. due to formwork removing) assuming the following convective model:

$$\mathbf{q}^l = \beta_c (\rho_{surf}^{wg} - \rho_{ext}^{wg}) \mathbf{n} \quad (6)$$

with  $\rho_{surf}^{wg}$  and  $\rho_{ext}^{wg}$  surface and external density of the water vapour respectively, and  $\beta_c = 0.002 \text{ m/s}$ ; the external relative humidity is assumed constant and equal to 50%. Thermal exchange is also convective with the same convective coefficient of phase 1. Three aging times are considered: case-1) one year; case-2) three years; case-3) 10 years.

- Phase 3, fire accident – 8 hours of heating from “age time”: results of the three cases of phase 2 (“age time” = 1, 3 and 10 years), are assumed as starting condition for simulation of high temperature heating. External temperature is imposed as a linear function of time with a heating rate of  $2 \text{ K/min}$ : so external temperature change from  $295.15 \text{ K}$  ( $22^\circ\text{C}$ ) to  $1255.15 \text{ K}$  ( $982^\circ\text{C}$ ) after 8 hours of heating. Surface thermal exchange is convective-radiative with convection coefficient equal to  $h_t = 20 \text{ W}/(\text{m}^2\text{K})$  and emissivity  $\varepsilon = 0.9$ . Moisture exchange at the heated surface is assumed convective as in phase 2 but this time the convection coefficient is ten times higher ( $\beta_c = 0.02 \text{ m/s}$ ), and the partial pressure of vapour is imposed,  $p^{sw} = 1300 \text{ Pa}$ , instead of prescribing the relative humidity.

### 3.2 Numerical results

Results for temperature, saturation degree and gas pressure are plotted in Fig. 1 for the three modelled cases: the graphs represent spatial evolution of such variables after 3 hours, 5.9 hours and 7.5 hours of heating. The chosen time stations are the same as in the numerical analyses of [2]; indeed their numerical results have been compared with the shown ones. Actually, such comparison is only qualitative due to the fact the simulations deal with different concrete mixes. Nevertheless, it has been useful to assess the impact of the modification introduced in the constitutive laws.

As one can observe in Fig. 1.a, age has no impact on temperature in the wall, i.e. the lines corresponding to the three cases are almost superposed. Nevertheless, age has a significant impact on the saturation profiles and desaturation fronts, as shown in Fig. 1.b. When heating starts, initial condition in term of saturation degree is very different depending on the concrete

age: after 10 years of drying the hygral equilibrium is reached while at 1 year the saturation degree varies from 0.5 (in the centre) to 0.28 (at the drying surface) following a typical parabolic drying profile. Even if initial pressure field is the same, gas pressure results are different for the three considered concrete ages (see Fig. 1.c). In particular it is observed that the “younger” the concrete, the higher will be gas pressure peaks. This is due to previous commented differences on saturation degree which influence gas permeability and gas pressure. A difference of almost 20% can be observed after 7.5 hours between peaks obtained for the 1-year concrete and the 10-year one.

#### 4. Conclusions

A thermo-hydro-mechanical model describing concrete behaviour from casting until accident conditions has been implemented and used in this study for the investigation of the impact of concrete age on the high temperature behaviour of the material. A novel approach expressing the constitutive laws at high temperature such as porosity, permeability and sorption isotherms with respect to the hydration degree is presented. The results have shown that different concrete age induces different conditions, notably a different saturation field, when the high temperature load is initiated. This has a direct influence on the saturation and gas pressure fields developing during the fire incident. The combined “early age – high temperature” model is a powerful tool for investigating and shedding light on the often-random behaviour of concrete samples at high temperature observed experimentally. Such behaviour could be linked with the varying saturation field when concrete is exposed to heat.

#### References

- [1] Sciumè, G., Thermo-hygro-chemo-mechanical model of concrete at early ages and its extension to tumor growth numerical analysis, PhD Thesis, École normale supérieure de Cachan - ENS Cachan (2013)
- [2] Gawin, D. et al, What physical phenomena can be neglected when modelling concrete at high temperature? A comparative study. Part 1: Physical phenomena and mathematical model, *International Journal of Solids and Structures*, 48 (2011), 1927-1944
- [3] Dal Pont, S. et al, A multiphase thermo-hydro-mechanical model for concrete at high temperatures - finite element implementation and validation under LOCA load. *Nuclear Eng. and Design* 237(20) (2007), 2137-2150
- [4] Mills, R.H., Factors Influencing Cessation of Hydration in Water Cured Cement Pastes, (1966), 406-424
- [5] Sciumè, G. et al, A multiphysics model for concrete at early age applied to repairs problems, *Engineering Structures* 57 (2013), 374-387
- [6] Jędrzejewska, A. et al, COST TU1404 benchmark on macroscopic modelling of concrete and concrete structures at early age: Proof-of-concept stage, *Constr Build Mater* 174 (2018) 173-189
- [7] Dauti, D. et al, Modelling Concrete Exposed to High Temperature: Impact of Dehydration and Retention Curves on Moisture Migration, *International Journal for Numerical and Analytical Methods in Geomechanics* 42(13) (2018) 1516-1530

## **DAMAGE INVESTIGATION AND ANALYTICAL INVESTIGATION OF PILOTIS-TYPE RC BUILDING IN THE 2016 KUMAMOTO EARTHQUAKE**

**Masaru Shimazu** <sup>(1)</sup>

(1) Sojo University, Kumamoto, Japan

### **Abstract**

This research carried out a static elastoplastic analysis of a Pilotis-type reinforced concrete building that collapsed in the 2016 Kumamoto earthquake. It examined the usability of these types of analyses. Also, it conducted a damage survey and executed a static three-dimensional frame analysis with the aim of unravelling the collapse mechanism of the damaged building. It turned out that the analysis is actually effective.

### **1. Introduction**

The Pilotis structure is widespread as a way to utilize space effectively. This type of structure is expected to be used for a number of buildings also in the future. But the Pilotis floor has a low inter-story stiffness since it is made of independent columns. In the event of a severe earthquake, therefore, the damage is likely to concentrate on this type of building, causing it to fall apart. Many RC-made Pilotis structures are reported to have fallen to pieces or been devastated in the wake of the 2016 Mw 7.0 Kumamoto earthquake [1]. These reports effectively warned against the danger of RC-made Pilotis structures.

This research reports on the results of a survey of Pilotis-type RC-made structures that sustained damage in the 2016 Kumamoto earthquake. The research also carries out an elastoplastic analysis of destroyed buildings and compares the damage status with the analysis results. It examines the usability of a static three-dimensional frame analysis as a way to evaluate the seismic capacity of conventional buildings and check the mechanism of damaged buildings falling down.

## 2. The overview and damage of buildings

### 2.1 The overview and buildings

The main target of the survey in this research was the Pilotis-type 7-story RC-made building that served as a middle scale dwelling complex in Kumamoto, which collapsed to pieces in the Kumamoto earthquake during the early hours of April 16, 2016. By the way, the building was constructed in 1974.

Figure 1 shows the first-floor plan view while Fig. 2 gives the second-floor plan view. The third to sixth floors carry the same plan views as the second floor. The seventh-floor plan view is unknown. Hereafter, the column and beam positions are shown by codes as in respective floor plans. For example, the No.4 column on aisle C on the first floor is described as 1C4. The height of the second floor is 3,000 millimeters while that of the third to seventh floor is 2,700 millimeters. The building takes on a planar shape that looks like the alphabetic character L. The first floor includes the staircase, retail stores, and parking lots. The second to seventh floors are used for dwelling.

Figure 3 shows cross-sectional views of the first-floor columns and the second-floor beams. The column bar is 8-D29 and the column stirrup is  $\phi 12@100\text{mm}$ . The section size and the location of the reinforcement in the column are measured by convex rule. Since the measurement is taken from damaged components, they differ from the figures taken in the perfect status before the earthquake.

**Concrete strength.** The concrete strength of the 1C4 column, photo 5, is measured with the use of a rebound hammer. The concrete compressive strength is determined to be  $27.3 \text{ N/mm}^2$ , which is the average of 25 measured data. The measurement took place in June 2016, two months after the earthquake. No cracks were found on the measurement point.

**Mechanical property of the reinforcing bar.** Tensile tests show the yield strength of the D29 column rebar to be  $357 \text{ N/mm}^2$  and its elastic modulus to be  $207 \text{ kN/mm}^2$ . The yield strength of the  $\phi 12$  stirrup is identified to be  $206 \text{ kN/mm}^2$ . The rebars used as test pieces were free of any deformation from buckling and squeezing. Chances are, however, that the test pieces actually yielded.

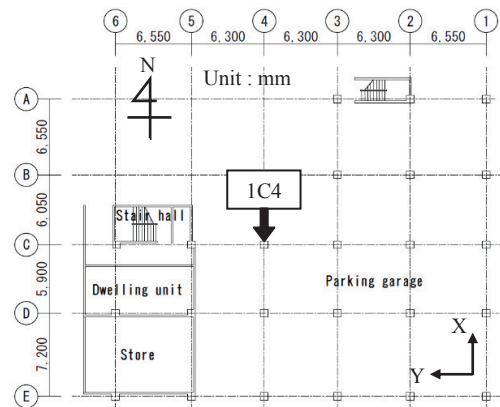


Figure 1: 1F.

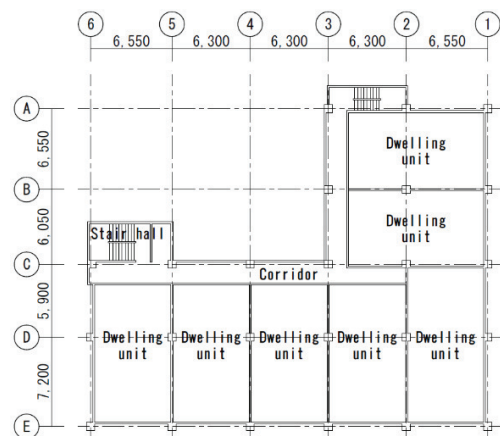


Figure 2: 2F.

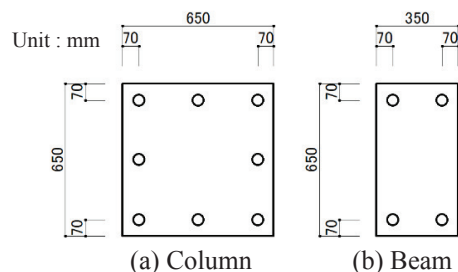


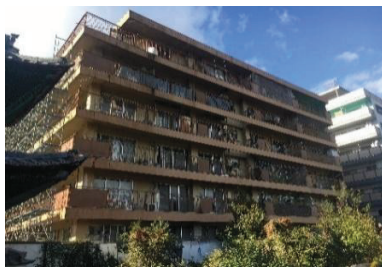
Figure 3: Cross section of member.



## 2.2 The overview of the damage

Photo 1 shows the building after the earthquake from respective directions. Photo 2 to 4 respectively show the 1A1, 1A3, and 1C3 columns. Many of these Pilotis columns show severe damage. By comparison, photo 2 and 3 confirms severe damage on the columns whose heads slipped off to the east face. The fracture pattern is unknown, however. Photo 5 shows the 1C4 column. It is presumed that flexural fracture first occurred on its head and base, causing the rebar to bend severely in vibrations. As a result, the swelling of the rebar probably drove the head concrete to a fall. The shear-margin  $Q_{su}/Q_{mu}$  is calculated from the measurement results to be 1.53. The calculations of the ultimate shear strength  $Q_{su}$  and the ultimate bending-moment strength  $Q_{mu}$  are based on the Arakawa mean method [2] and the AIJ standard formula [3]. The member length is defined to be 2,350 millimeters in the inner measurement.

Figure 4 shows side views of the 3A to 3C axes and the C3 to C5 axes. The post-quake beam positions on the respective floors are marked by red lines in respective charts. It is obvious from the illustration that the 3A to 3C aisle beams sank deep into the south face while the C34 beam deformed deep into the east face. The 1C34 beam, in particular, sank by a maximum 2,050 millimeters. In this research, a measurement survey of the building was carried out in October 2017. So, the results of measurement include deformity in aftershocks.



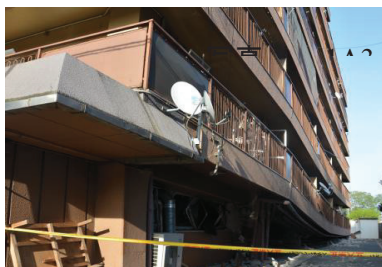
(a) East face



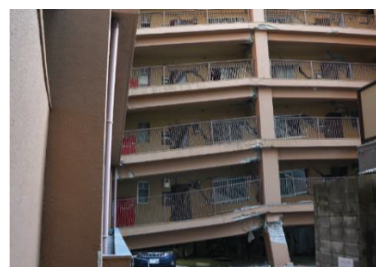
(b) West face



Photo 4: 1C3 column.



(c) South face



(d) North face



Photo 5: 1C4 column.

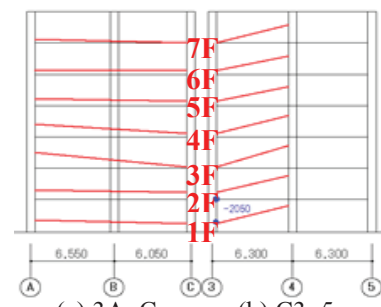
Photo 1: Full view.



Photo 2: 1A1 column.



Photo 3: 1A3 column.



(a) 3A~C (b) C3~5  
Figure 4: Side view.

### 3. The elastoplastic analysis

#### 3.1 The analysis method

Figure 5 shows the analysis model. The static elastoplastic analysis uses the finite element analysis program, FPHM v4.01 [4]. This analysis method is a one-dimensional complex non-linear finite element method that can evaluate the load-bearing capacity at high accuracy in the collapse analysis of reinforced concrete one-story frame [5]. The model is generated with beam elements. The model is constructed on the basis of one element per member. Walls and floors constitute an elastic structure subject to brace replacement. In the brace replacement method, the walls are replaced with braces with equivalent shear stiffness. Walls containing openings and the terrace are not modeled. Based on the actual measurement, the compression strength, tensile strength, and elastic modulus of concrete are set to be  $27.3 \text{ N/mm}^2$ ,  $2.73 \text{ kN/mm}^2$ ,  $24 \text{ kN/mm}^2$  respectively. Also, the yield strength and elastic modulus of the column rebar are set at the standard values of  $300 \text{ N/mm}^2$  and  $206 \text{ kN/mm}^2$  respectively. The elastic modulus of the brace members used for the modeling of walls and floors are  $20 \text{ kN/mm}^2$  and  $1,000 \text{ kN/mm}^2$  respectively. The configuration rule on the reinforcing bar is the bilinear type with the strain hardening exponent of 0.01. The constitutive law on the compression stress of the concrete is to be elastic-perfectly plastic and that on the tension stress is to become zero after the tensile strength is achieved.

Table 1 shows the values of  $W_i$ ,  $\Sigma W_i$  and  $A_i$ . In the table,  $W_i$  is defined as the sum of the fixed and movable loads on the respective floors, and  $\Sigma W_i$  is the sum of the loads on the top to the  $i$  floors. Used in the calculation are the reinforced concrete unit weight of  $24 \text{ kN/m}^3$  and the movable weight on the residential zone. The column weight is calculated separately for the upper and lower floors. In the analysis, the horizontal force is increased on the respective floors under the influence of the vertical load, or the sum of the fixed and movable loads, on the floor center in the incremental load displacement control method following the  $A_i$  distribution [6]. The analysis ends when the maximum strength point is reached. Vibrations were three-dimensional in the real earthquake. So, this analysis examines the mechanical properties of the building faced with the in-plane loading.

Table 1 shows the values of  $W_i$ ,  $\Sigma W_i$  and  $A_i$ . In the table,  $W_i$  is defined as the sum of the fixed and movable loads on the respective floors, and  $\Sigma W_i$  is the sum of the loads on the top to the  $i$  floors. Used in the calculation are the reinforced concrete unit weight of  $24 \text{ kN/m}^3$  and the movable weight on the residential zone. The column weight is calculated separately for the upper and lower floors. In the analysis, the horizontal force is increased on the respective floors under the influence of the vertical load, or the sum of the fixed and movable loads, on the floor center in the incremental load displacement control method following the  $A_i$  distribution [6]. The analysis ends when the maximum strength point is reached. Vibrations were three-dimensional in the real earthquake. So, this analysis examines the mechanical properties of the building faced with the in-plane loading.

#### 3.2 The analysis results

Figure 6 shows the relationship between the shear force coefficient and the inter-story drift angle. The downward triangle in the illustration shows the maximum strength point on the first floor and the figure gives the shear force coefficient at those points. The inter-story drift angle is expressed as the value at the representative point. Also, the dashed line in Fig. 6 (b) shows the data on the south-face first-floor load in the event of the brace stiffness being reduced by half. Figure 6 (b) shows a rapid increase in the first-floor inter-story drift angle both on the east- and south-face loading. Comparison between the maximum story-shearing

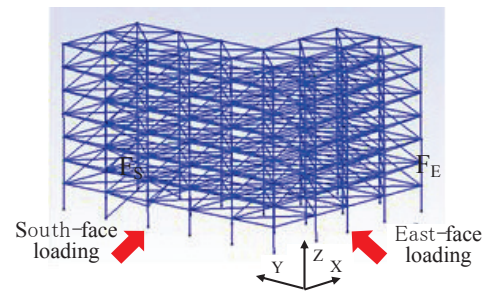


Figure 5: 3D analysis model.

Table 1: Values of  $W_i$ ,  $\Sigma W_i$  and  $A_i$

Story i	$W_i$ [kN]	$\Sigma W_i$ [kN]	$A_i$
7	5180	5180	1.92
6	5502	10682	1.58
5	5502	16184	1.40
4	5502	21686	1.27
3	5502	27188	1.17
2	5502	32690	1.08
1	5538	38228	1.00

force coefficients on both faces shows a greater coefficient on the south face. This is because the first-floor wall resists the south to north directional horizontal force with its in-plane force. In addition, data on the south-face loading as in Fig. 6 (b) shows no major disparity in the results in the event that there is a change in the stiffness of the bracing member used for the wall modeling.

Figure 7 shows the fracture status of column members on the first and second floors. In this analysis, the column is found to have yielded at the time part of the column cross-section fractures, in other words, at the moment part of the concrete reaches compression strength or tensile strength or a reinforcement bar reaches yield strength. No. 1 to 10 in the illustration shows the order of the occurrence of the yield. The point of the 10th yield is marked by a red dot in Fig. 6. At the time the 10th yield occurs, no yield is underway in the beam member.

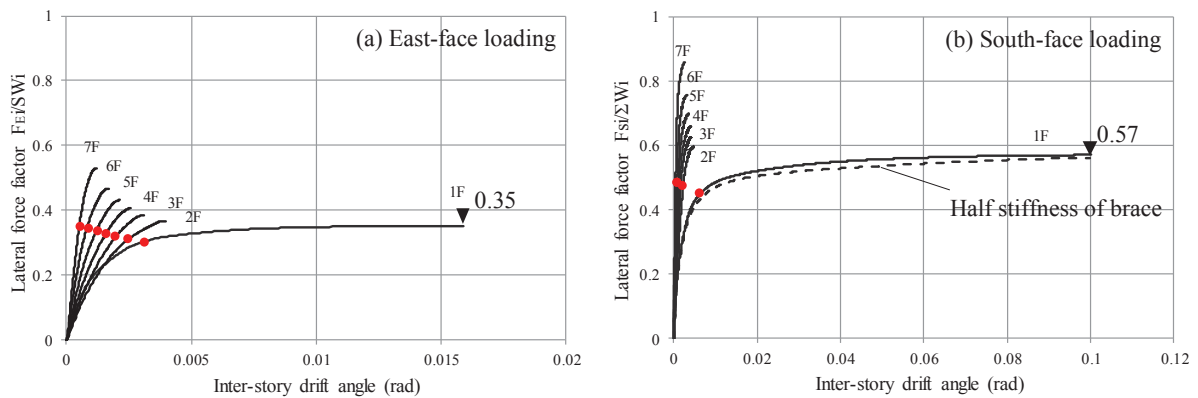


Figure 6: Relationship between lateral force factor and inter-story drift angle.

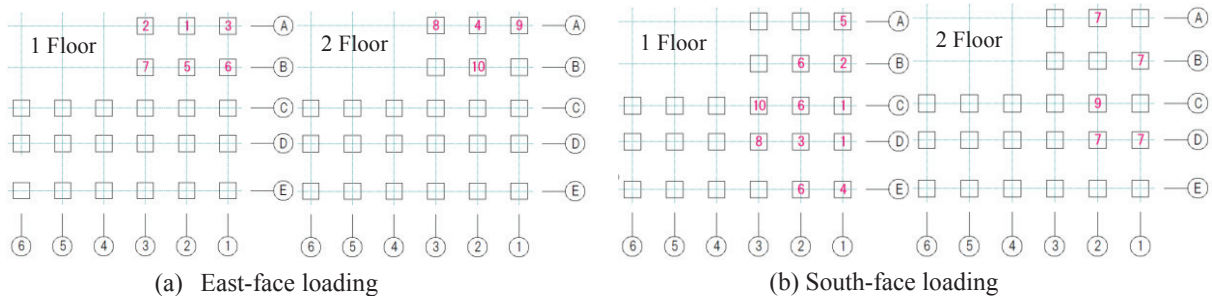


Figure 7: Fracture status of column members.

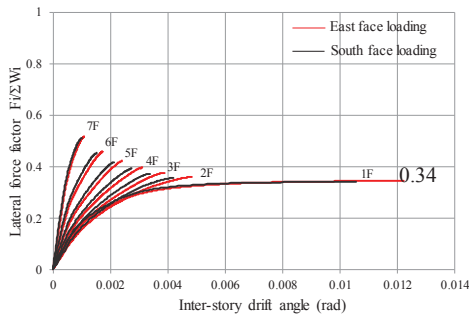


Figure 8: Relationship between lateral force factor and inter-story drift angle.

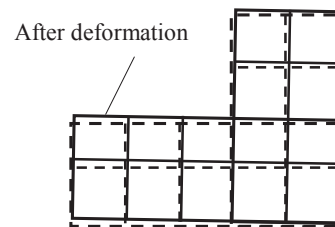


Figure 9: Deformation diagram.

In all loading directions, Fig. 7 shows, first-floor columns yielded in their bases first, followed by surrounding columns. It also shows that damage spreads onto the second floor. Also indicated is the fact that the yield strength reaches about 80 percent of the maximum level at the time the 10th column yields. This means damage does not spread onto the entire building, but that the frame collapses because the damage concentrates on the first-floor columns. Since the beam ends do not yield, this type of collapse can be said to be triggered by fractured columns.

For comparison, Fig. 8 shows the relationship between the lateral force factor and the inter-story drift angle in the modeled case in which all walls are disregarded. Fig. 9 shows the deformation diagram of the second floor with a load on the south surface at a red dot in Fig. 6.

### 3.3 Comparison between the damage status of the real building and the analysis results

The maximum acceleration measured at a location in Ohe, Chuo Ward, Kumamoto, about 3 kilometers away from the building was 298.8gal in the east to west direction and 363.5gal in the north to south direction on April 14, 2016, and 478.2gal in the east to west direction and 626.8gal in the north to south direction on April 16, 2016 [7]. These values were not measured at the building in question. Therefore, they are likely to differ from the maximum acceleration actually inputted into that affected building. Since there is no other indicator for comparison, however, these values are used as the benchmark for the examination.

The building in question collapsed to pieces in the April 16 earthquake. It is presumed to have been destroyed by a seismic force equivalent to about 0.48 in the east to west direction and 0.63 in the north to south direction in the lateral force factor. Based on this assumption, the actual damage status of the real building is compared with the analysis results.

## 4. Conclusion

An elastoplastic analysis using the results of actual measurement can generally help figure out the fracture mode of construction components and the horizontal load-bearing capacity of the frame. It should be noted, however, that the exclusion of walls in the process of modeling can lead to an underestimated load-bearing capacity.

## References

- [1] Hideo, A., Kumamoto Earthquake damage survey report, <http://saigai.aij.or.jp/> (in Japanese)
- [2] Arakawa, T., Ultimate shear strength and transvers reinforcement of reinforced concrete beams, Transactions of the Japan Concrete Institute 8 (1970), 11-20 (in Japanese)
- [3] AIJ Standard for Structural Calculation of Reinforced Concrete Structures, Architectural Institute of Japan, (1991), 615-616 (in Japanese)
- [4] FPHM v.4.01., <http://naosite.lb.nagasaki-u.ac.jp/dspace/handle/10069/37150>
- [5] Shimazu, M., Elastoplastic analysis of reinforced concrete frames by the fibered plastic hinge model, Proceedings of the Japan Concrete Institute 31 (2009) (in Japanese)
- [6] Enforcement Ordinance of Construction Standard Law, the 88 amendment (in Japanese)
- [7] Japan Meteorological Agency, Strong-motion earthquake record, Ohe, Kumamoto, Japan <http://www.data.jma.go.jp/svd/eqev/data/kyoshin/jishin> (in Japanese)

## **EFFECT OF HUMIDITY AND ELEVATED TEMPERATURE ON THE MECHANICAL BEHAVIOR OF CONCRETE**

**Laurie Lacarrière<sup>(1)</sup>, Ponleu Chhun<sup>(1)</sup>, Alain Sellier<sup>(1)</sup>**

(1) Université de Toulouse, UPS, INSA, LMDC (Laboratoire Matériaux et Durabilité des Constructions), 135, avenue de Rangueil, 31 077 Toulouse Cedex 04, France

### **Abstract**

This paper deals with the prediction of the evolution of mechanical behaviour of concrete when it is subjected to high humidity and temperatures. a non linear creep-damage model to assess the mechanical response of the concrete to such solicitations. This model was previously developed for the prediction of concrete behaviour at ambient or moderate temperature. But the effect of combined high humidity and elevated temperature was not investigated up to now.

In this paper, laws are proposed to reproduce the evolution of strengths according to the saturation degree and temperature of concrete. A thermal damage is also introduced in addition to the thermo-activation of creep by temperature. The complete THCM model is validated using tests performed, at different temperatures and relative humidity, on lab specimens and on structural members.

### **1. Introduction**

In French nuclear power plants, the prestressed reinforced concrete containment vessel plays a major role to limit the radionuclide dispersion in the environment in case of failure of the first two barriers (the fuel cladding and the primary cooling system). It is thus of primary importance to master the containment building tightness during all the duration of a severe accident. In the scenario of a severe accident, the internal pressure (0.5 MPa) and temperature (180 °C) on the inner face of the concrete containment structure are maintained constant during two weeks.

During this accident scenario, the high temperature level, the high relative humidity and the loading duration are going to affect the mechanical behaviour of concrete and steel. The aim of the work done in the framework of the program MACENA (Tightness assessment of

confinement vessels during an accident) was thus to assess the behaviour of concrete when it is subjected to high humidity and temperature. Based on results obtained by some partners in the project [1], the evolution of mechanical behaviour of concrete in such environmental conditions is modelled.

## 2. General principle of non-linear mechanical model for concrete

The mechanical model used and adapted to carry out the couplings with the physico-chemical evolutions presented here is the result of work carried out at the LMDC in the recent years. It is based on a non-linear behaviour law taking into account concrete damage, plasticity and delayed behaviour [2,3]. The total stress is defined from the effective stress on the sound material by considering two kinds of damages (more details in [2]) (Eq. (1)):

- Isotropic damages due to microcracks: This is the case of the compressive damage  $D^{\text{shear}}$  induced by the compressive loadings (shear damage at microlevel which induced isotropic distribution) and of the thermal damage  $D^{\text{TH}}$  which is induced (as it will be explained in section 3) by the incompatibilities of strains at the mesoscale.
- Anisotropic damages characterizing an oriented cracking: This is the case of the post-tensile damage  $D^t$  that is evaluated from the opening of oriented cracks under the effect of tensile stresses and of the crack closure damage  $D^r$  applied to compressive stresses to reproduce the transmission loss of compressive stresses when the previously opened crack is not closed.

For both damages, an energetic regularisation based on Hillerborg theory is made [2].

$$\sigma_{ij} = (1 - D^{\text{TH}}) \cdot (1 - D^{\text{shear}}) \cdot [(1 - D^t)_{ijkl} \cdot \tilde{\sigma}_{kl}^+ + (1 - D^r)_{ijkl} \cdot \tilde{\sigma}_{kl}^-] \quad (1)$$

The effective stress (in terms of damage) is calculated from a rheological model reproducing the delayed behaviour of concrete as the sum of the elastic stress applied to the solid skeleton and the stress induced by capillary depression  $\sigma^W$  (Eq. (2)). The following creep model has been validated on several tests under constant temperature in [3].

$$\begin{aligned} \tilde{\sigma}_{kl} &= S_{klmn} \cdot \varepsilon_{mn}^{\text{el}} - \sigma_{kl}^W \\ \varepsilon_{mn}^{\text{el}} &= \varepsilon_{mn} - \varepsilon_{mn}^{\text{pl}} - \varepsilon_{mn}^{\text{th}} - \varepsilon_{mn}^{\text{KV}} - \varepsilon_{mn}^{\text{M}} \end{aligned} \quad (2)$$

- $S_{klmn}$  is the material stiffness tensor (fct° of E and  $\nu$ );
- $\varepsilon_{mn}$  is the total strain;
- $\varepsilon_{mn}^{\text{el}}$  is the elastic strain and  $\varepsilon_{mn}^{\text{th}}$  is the thermal strain;
- $\varepsilon_{mn}^{\text{pl}}$  is the plastic strain (resulting from the application of the plastic criteria [2]);
- $\varepsilon_{mn}^{\text{KV}}$  and  $\varepsilon_{mn}^{\text{M}}$  are the strain of Kelvin-Voigt reversible viscoelastic creep modulus and Maxwell consolidating viscous creep level (more details in [3]).

## 3. Effect of saturation degree on concrete mechanical behaviour

The degree of saturation first influences the creep rate. Indeed, at the microscopic scale, creep is linked to water movements or to variations in disjunction pressure, and it will be affected by a decrease of saturation of the material (leading to a lower creep rate). For simplification it

is assumed that the characteristic time of both Kelvin and Maxwell levels in the creep model are both affected by the variation of water content:

$$\tau^K = \frac{\tau_{ref}^K}{Sr} \cdot f^K(T) \text{ and } \tau^M = \frac{\tau_{ref}^M}{Sr} \cdot f^M(T) \quad (3)$$

In this equation the functions  $f^K(T)$  and  $f^M(T)$  reproduce the effect of temperature on creep rate and will be presented in the next section (Eq. (7)).

The preponderant effect of the saturation state of a concrete on its mechanical behaviour is of course the application of a capillary pressure on the solid skeleton leading to a strain.

In the modelling approach adopted here, this effect is directly taken into account by introducing the effect of capillary pressure in the law of behaviour (through  $\sigma^W$  in Eq. (2)).

In addition to this poro-mechanical effect, the capillary depression also has indirect effects on the mechanical properties. As in the case of thermal strains, the shrinkage of the paste can lead to a micro-cracking by incompatibility of paste-aggregates strain. However, recent results, obtained by tests performed at LMDC in the framework of Mosaic project [4], show an increase in tensile strength when the degree of saturation decreases (Fig. 1). This increase is explained by the fact that the application of capillary depression on the skeleton prestresses the paste [5], and this effect is greater than the micro-cracking effect. On Fig. 1 it can also be noticed that the tests conducted at SIAME within the framework of Macena [1], on concretes subjected to varying (but controlled) temperatures and degrees of saturation, confirm this increase in resistance but with a decreasing effect with temperature.

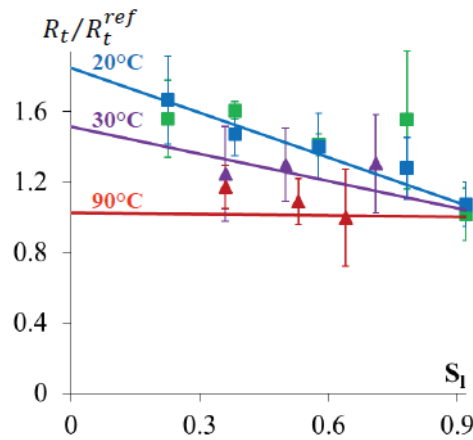


Figure 1: Evolution of tensile strength according to temperature and saturation degree (experimental results issued from [4,1] and proposed law for  $R_t$ )

As these tests also showed that the effect of the degree of saturation on the Young's modulus (macroscopic indicator of damage) was rather limited [1], it seems consistent to neglect the effect at the macroscopic level of micro-cracking induced by aggregates. The consolidation effect of the material by the degree of saturation is therefore only considered, by proposing a law of tensile strength evolution as a function of the degree of saturation (Eq. (4)). The decrease of the effect of  $Sr$  when the temperature increases is attributed to the effect of temperature on the desorption isotherm [6]. Indeed if the temperature increases the capillary depression will be reduced for the same degree of saturation. This effect is therefore modelled by the exponential term of Eq. (4).

$$\frac{Rt}{Rt_{ref}} = 1 - K^W \cdot \exp\left(-\frac{T - T_{ref}}{T_{kW} - T_{ref}}\right) \cdot (Sr - Sr_{ref}) \quad (4)$$

- $Rt_{ref}$  is the reference resistance measured at  $T_{ref}$  and  $Sr_{ref}$ ;
- $K^W$  is a material parameter identified at  $T_{ref}$  (0.85 if  $T_{ref} = 20^\circ C$ ).

#### 4. Effect of temperature on concrete mechanical behaviour

First of all, temperature variations within the material can lead to concrete damage. Our approach decouples the effect on the mechanical properties of very high temperatures (leading to dehydration of the paste) from the more moderate temperature effect for which variations in mechanical properties are attributable more to the consequences of incompatibility strains at the material scale (leading to micro-cracking or to the creation of micro-defects). This effect is thus reproduced by the introduction of an isotropic damage variable  $D^{TH}$  in the equation (1). This damage is determined with the equation (5) from the coefficient  $C^{T,D}$ . The function presented in Eq. (5) has been developed and validated for saturated concrete in [7] and has been adapted to other saturation states in this study by introducing a calibration function  $A^{TH}$  to control the level of damage at a given temperature that depends on saturation degree. Indeed, as the incompatibilities of thermal strains are related to the differences of thermal expansion coefficient, a dry paste will have a lower expansion coefficient and thus a potential of incompatibility of strains lower.

$$D^{TH} = 1 - \frac{1}{A^{TH}(C^{T,D} - 1) + 1} \text{ and } C^{T,D} = \exp\left(-\frac{E_a^W}{R}\left(\frac{1}{T} - \frac{1}{T_{thr}}\right)^+\right) \quad (5)$$

- $E_a^W/R$  is the associated activation energy (approx.  $3000K^{-1}$  according to [7]);
- $T_{thr}$  is the threshold temperature at which thermal damage occurs ( $45^\circ C$  [7]).

$$A^{TH} = \frac{1}{C^{T,D}(80^\circ C) - 1} \cdot \frac{Sr \cdot D_{80}^{TH}}{1 - Sr \cdot D_{80}^{TH}} \quad (6)$$

- $E_a^W/R$  is the associated activation energy (approx.  $3000K^{-1}$  according to [7]);
- $T_{thr}$  is the threshold temperature at which thermal damage occurs ( $45^\circ C$  [7]);
- $C^{T,D}(80^\circ C)$  is calculated for  $T=80^\circ C$ ;
- $D_{80}^{TH}$  is the thermal damage determined experimentally at  $80^\circ C$  for  $Sr=1$ .

This parameter is identified using the experimental results from [7] and it can be noticed in Fig. 2 that the identified value (0.15) allows reproducing the damage obtained in [1] for a higher temperature (without refitting of the law). Fig. 2 also gives the evolution of  $D^{TH}$  as a function of temperature for several degrees of saturation to illustrate the decrease of thermal damage with drying.

Temperature has also a physical effect on the creep rate because it changes the viscosity of the water. The creep rate of the Kelvin and Maxwell levels are therefore both affected by this effect modelled by an exponential function depending on  $T$  (Eq. (7)). For the viscous level (linked to consolidation and to C-S-H behaviour) the thermal damage identified previously will lead to an increase in the non-linear creep rate. This effect is modelled by also affecting the characteristic time of the Maxwell viscous creep level by the  $C^{T,D}$  coefficient defined in Eq. (6).



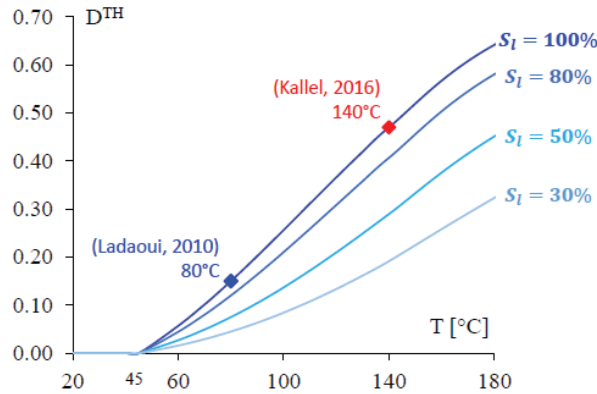


Figure 2: Evolution of thermal damage according to temperature and saturation degree

$$\begin{cases} f^K(T) = \exp\left(-\frac{E_a^W}{R}\left(\frac{1}{T} - \frac{1}{T_{ref}}\right)\right) \\ f^M(T) = \exp\left(-\frac{E_a^W}{R}\left(\frac{1}{T} - \frac{1}{T_{ref}}\right)\right) \times C^{T,D} \end{cases} \quad (7)$$

## 5. Validation of the proposed laws on lab tests

The laws of evolution of mechanical properties and damage as a function of temperature and humidity have been tested on the tests performed under the ANR Macena at SIAME [8] for instantaneous tests and at CERIB [9] for creep tests (Fig. 3).

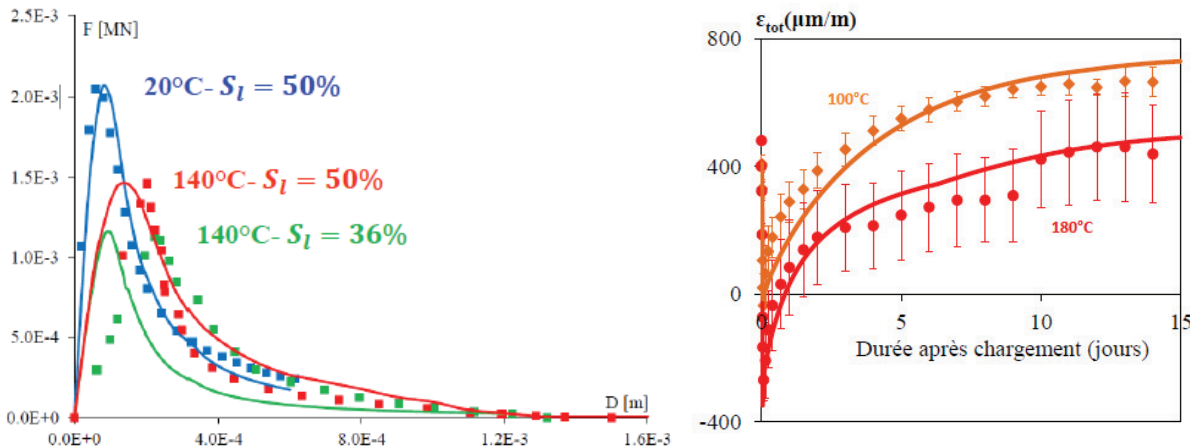


Figure 3: Modelling of DCT tensile test (left) and compressive creep test (right) at different temperature and saturation degree (experimental results from [8,9]).

The DCT tests were developed at SIAME laboratory to maintain both temperature and relative humidity constant in the sample during the test and are therefore performed on small notched discs (15 cm diameter, 5 cm thickness and 5.5 cm long notch) (see [8] for details). The possible uncertainty on the control of the displacements, of the real relative humidity at the bottom of notch led us to consider that the model could be considered as valid even if it

does not reproduce perfectly the pre-pic part for the tests at high temperature. For creep tests (see [9] for more details), the relative humidity was not controlled so the specimens were subjected to drying concomitantly with temperature rise and loading. This effect was taken into account in by modelling the drying and the associated desiccation creep strains which allows a good reproduction of the strains during the test.

## 6. Conclusions

The paper dealt with the prediction of the mechanical behaviour on concrete in severe environmental conditions corresponding to high temperature (up to 200°C) and high variation of humidity. In these conditions the non-linear behaviour of concrete is affected, creep rate are increased and a diffuse damage is induced by the temperature evolution (and the associated incompatibilities of paste and aggregate strains). The originality of the work was to proposed a way to model these effects that take into account the concomitant effects of temperature and saturation. Indeed, it was shown that the temperature effect is reduced by a decrease of saturation degree. The proposed evolution laws, implemented in a non-linear mechanical model for concrete were successfully applied to the simulation of mechanical tests performed at high temperature and for different saturation degrees.

## Acknowledgements

The investigations and results reported here were supported by the French National Research Agency (ANR-PIA) under the MACENA research program 11-RSNR-0012 (Control of nuclear vessel in accident conditions). We are also grateful to CEA/DEN/DM2S/SEMT for providing the finite element code CASTEM.

## References

- [1] Kallel H., Carré H., Laborderie C., Masson B., Tran NC., (2016) Effect of temperature and moisture on the instantaneous behaviour of concrete, *Cem. Concr. Compos.* 80, 326-332
- [2] Sellier A., Cazaux-Ginestet G., Buffo-Lacarrière L., Bourbon X. (2013) Orthotropic damage coupled with localised crack reclosure processing. Part I: Constitutive laws. *Engineering Fracture Mechanics* 97(1), 148-167
- [3] Sellier A., Multon S., Buffo-Lacarrière L., Vidal T., Bourbon X., Camps G. (2016) Concrete creep modelling for structural applications: non-linearity, multi-axiality, hydration, temperature and drying effects. *Cem. Concr. Research*, 79(1); 301-315
- [4] Bucher, R., Vidal, T., Sellier, A., and Verdier, J. (2017). Effet du séchage sur les propriétés mécaniques des matériaux cimentaires, Rapport intermédiaire ANR Mosaic (LMDC), *in French*
- [5] Burlion, N., Bourgeois, F., and Shao, J.-F. (2005). Effects of desiccation on mechanical behaviour of concrete. *Cem. Concr. Compos.* 27, 367–379
- [6] Chhun P. (2017). Modélisation du comportement thermo-hydro-chemomécanique des enceintes de confinement nucléaire en béton armé-précontraint. phd. Université de Toulouse, Université Toulouse III - Paul Sabatier, *in French*
- [7] Ladaoui, W., Vidal, T., Sellier, A., Bourbon, X. (2013). Analysis of interactions between damage and basic creep of HPC and HPFRC heated between 20 and 80 °C. *Mater. Struct.* 46, 13–23
- [8] Kallel H., Carré H., Laborderie C., Masson B., Tran NC., (2016) Effects of the Hygrothermal Conditions on the Fracture Energy of the Concrete, *Key Engineering Materials* 711, 397-403
- [9] Daval C., 2016, Rapport intermédiaire ANR Macena: Compression et module élastique à 20°C, 100°C et 180°C – Fluage à 100°C (CERIB), *in French*

## **EFFECT OF PARTIAL RESTRAINING CONDITIONS AND POISSON'S RATIO IN BOTTOM-RESTRAINED WALLS**

**Dirk Schlicke**<sup>(1)</sup>, **Lýdia Matiašková**<sup>(2)</sup>, **Július Šoltész**<sup>(2)</sup>

(1) Institute of Structural Concrete, Graz University of Technology, Graz, Austria

(2) Department of Concrete Structures and Bridges, Slovak University of Technology in Bratislava, Bratislava, Slovakia

### **Abstract**

The stress distribution in bottom-restrained walls is a desired information for an efficient design of wall-like concrete members which are eccentrically restrained at the bottom. Practical examples are retaining walls or bridge abutment walls where the results were used in order to assess the risk and intensity of harmful separating cracks over the wall height. The stress distributions of common design tasks are usually estimated with graphical solutions in form of diagrams or determined on basis of analytical solutions. In general, all these solutions provide straightforward results, whereby effort and complexity is usually limited by generally approved simplifications within these solutions. This contribution provides detailed background on the effect of common simplifications, namely (i) assuming complete restraint at the wall bottom, or respectively, (ii) separate determination of axial and bending restraint in order to consider partial restraining conditions, and (iii) neglect of Poisson's effect. The significance of these simplifications is outlined by comparative studies with an illustrative shell model. Overall, recommendations for the consideration of the outlined effects in practical design were given on basis of these results.

### **1. Introduction**

Bottom-restrained walls are wall-like concrete members whose deformation behavior is eccentrically restrained at the wall bottom. This contribution defines a wall-like concrete member as any concrete member with a height of at least five times the width ( $H/B > 5$ ) and a length of at least 2 times the height ( $L/H > 2$ ). As soon as the deformation behavior of such wall-like members is restrained at the bottom, e.g. because they are cast on a foundation or slab, a distinct stress distribution from imposed thermal and moisture induced deformations occurs over the width, length and height of the wall. Main parameters on the size and shape of

these stress distributions are the imposed deformation in the wall, stiffness ratios between wall and foundation (axial and bending stiffness) as well as length to height-ratio of the wall ( $L/H$ ). Neglecting at first the stress distribution over the width, the resulting stresses can be estimated at the decisive center section by the product of the imposed strain  $\bar{\epsilon}$ , the effective modulus of elasticity  $E_{c,eff}$  and the degree of restraint over the height  $a(x)$ . Various solutions for the estimation of the degree of restraint can be found in the literature, e.g. [1] - [6]. Fig. 1 exemplarily shows two engineering solutions which are often used in practice. The diagram in Fig. 1a) is a simplified graphical solution derived from shell models with complete axial and bending restraint at the wall bottom but taking into account the effect of  $L/H$ , whereas Fig. 1b) presents a combined solution with regard to the influence of  $L/H$  by the factor  $K_R(x)$  as well as the influence of decreasing restraint due to the real axial stiffness ratio between the wall and restraining foundation by the factor  $K_F = [1 + (A_W E_W)/(A_F E_F)]^{-1}$ .

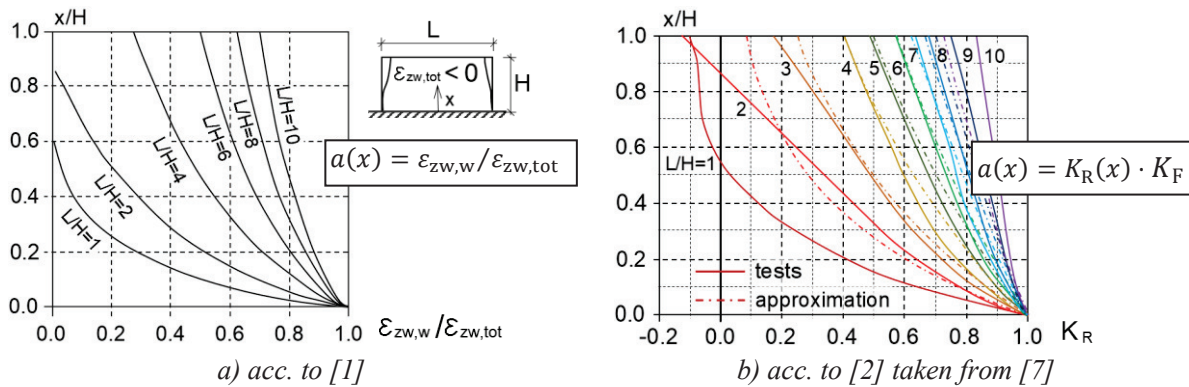


Figure 1: Diagrams for the degree of restraint in the center section of walls

Besides the shown solutions in Fig. 1, solutions of different nature are available in the literature, e.g. empirical restraint factors of [3] and [4], restraint factors derived from a comprehensive 3D-FEM study [5] or other simplified methods according to [6]. These may allow the consideration of additional effects such as slip at the free wall corner, asymmetric location of the wall on the foundation, etc., but they are not further described in this paper. Another possibility for stress calculation in walls is the analytical solution given in [8] and [9]. Hereby, the restraint stresses due to an imposed strain  $\bar{\epsilon}$  were determined by superposition of stress resultants due to cross section compatibility and additional bending due to uplift of the whole wall-foundation-system according to  $L/H$ , (see Fig. 2). A general overview and further details of all these solutions can be found in [10].

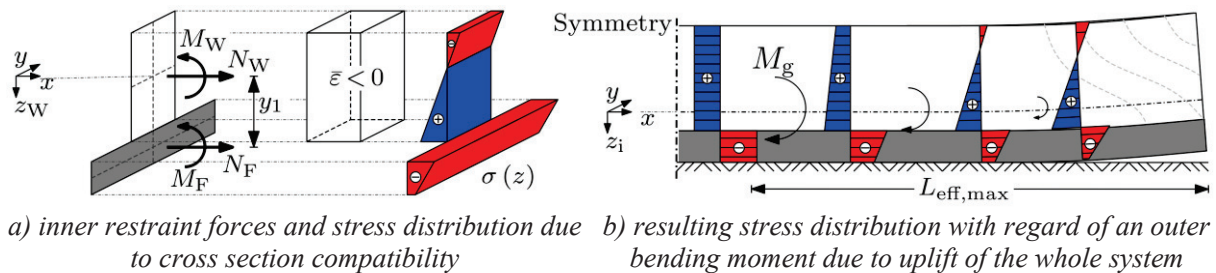


Figure 2: Stress distribution in bottom-restrained walls acc. to [8] and [9]

The stress distribution can also be determined by thermo-(chemo)-mechanical Finite Element Analysis, see e.g. [6], [7], [8], [10] or [11]. Although, numerical models enable a significantly better consideration of the real temperature distribution, shrinkage, the effect of maturity and viscoelasticity, implicit consideration of the restraining condition, etc., these solutions require also expertise and experience, see e.g. [12]. On the contrary, engineering solutions are gaining more importance in practical design. Although as outlined before, the available graphical and analytical solutions come along with some simplifications, which are expected to provide results on the safe side. With the aim of optimized design, the significance of these simplifications is discussed in the following by means of a parametric study.

## 2. Parametric study

### 2.1. Calculation Model

The study was conducted with the deliberately simple linear-elastic FE shell models of a wall on a foundation shown in Fig. 3. The models use symmetry in length direction and enable the consideration of two axial restraining conditions at the bottom of the wall (fully and partially restrained) as well as two restraining conditions of the uplift (fully and partially restrained according to the self-weight activation).

In case of full bottom restraint (Fig. 3a), the shell model comprises only the wall with bottom support conditions fully constraining displacements in horizontal and vertical directions. In case of partial axial restraint but full restraint of uplift (Fig. 3b), a foundation was included at the wall bottom with shell elements. The supports were kept at the wall bottom but set for only constraining vertical displacements. Thus, contribution of the stiffness ratio between the wall and the adjacent foundation as well as the full vertical restraint to the enforced uplift from the shortening of the wall could be examined. In case of partial restraint of both (axial deformation and uplift (Fig. 3c), springs with very high stiffness in vertical compression ( $k = 10^6 \text{ kN/m}^3$ ) that fail in tension were introduced at the bottom of the wall, allowing for uplift of edges with the subsequent activation of self-weight.

In these models, the wall was imposed with a uniformly distributed unit deformation of  $\Delta T = -10 \text{ }^\circ\text{C}$  and the degree of restraint over the height in the center section of the wall was determined from the resulting course of calculated stresses in length direction with  $a(x) = -\sigma_{\text{calc}} / (E_W \times \alpha_T \times \Delta T)$ . Thus, the result of this study is independent from the entering values of thermal loading  $\Delta T$ , thermal expansion  $\alpha_T$  and the elastic modulus  $E_W$ . Moreover, an uncracked cross section of the walls was assumed, hence Poisson's effect on stresses was taken into account with the Poisson's ratio of  $\mu = 0.2$ .

### 2.2. Studied scenarios

The parametric study covers eight different  $L/H$  ratios starting from 2 until 10 with steps of 1 which were all considered with full and partial axial restraint at the wall bottom as well as full and partial restraining of the uplift due to self-weight activation.

Presuming that the resulting stresses are determined from the inner forces of the ideal cross section including both the wall and foundation, the changing position of the center of gravity (CoG) was of interest as well. For this reason, the study was conducted for two types of wall and foundation cross-section geometries with CoG located above and below the wall bottom. Geometrical data for the analyzed walls is summarized in the Tab. 1 and illustrated in Fig. 3.

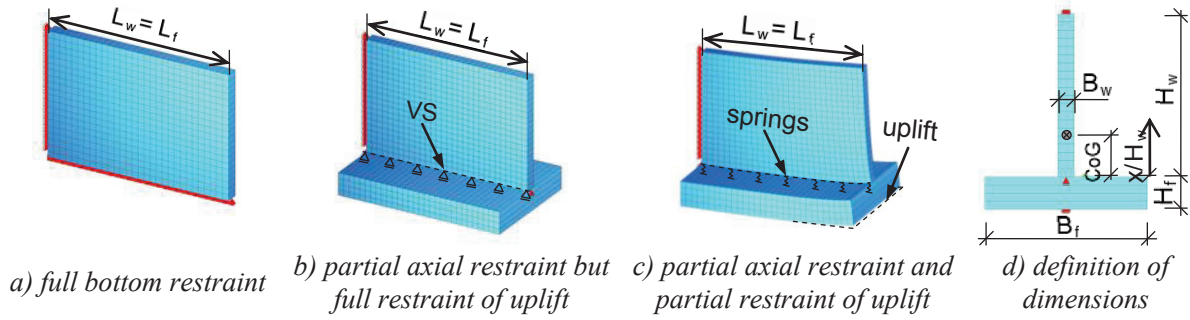


Figure 3: Models of the parametric study

Table 1: Geometrical data of the analysis

Wall					Foundation					$\frac{EA_w}{EA_f}$
$L/H$	$L_w=L_f$ (m)	$B_w$ (m)	$H_w$ (m)	$A_w$ (m <sup>2</sup> )	No.	CoG (m)	$B_f$ (m)	$H_f$ (m)	$A_f$ (m <sup>2</sup> )	
2 - 10	8 - 32, 40	0.4	4	1.6	1	0.4	4	0.8	3.2	0.5
					(incr. 4)	2	-0.4	1	3.2	3.2

### 2.3. Results

The following figures, Fig. 4 – Fig. 6, depict the distribution of the degree of restraint over the height of analyzed walls for the different restraining conditions. Hereby, the proportional height above base complies with  $x/H$  as in Fig. 1. At first, Fig. 4 gives the results of the full bottom restraint with regard to the consideration, or respectively, the neglect of Poisson's ratio. In general, the results agree with the expectation that the degree of restraint gradually decreases over the height and increases with higher  $L/H$  ratios.

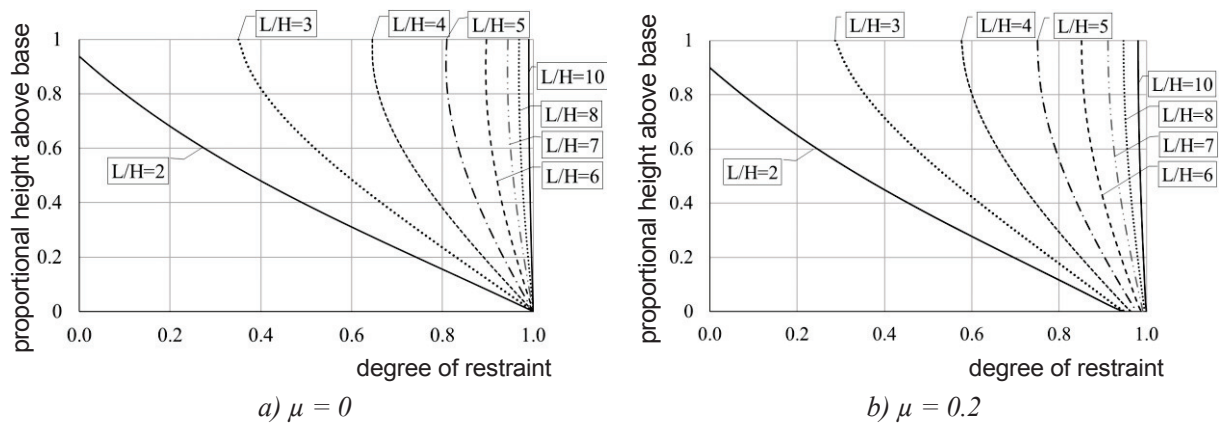


Figure 4: Degree of restraint for full bottom restraint

It can further be seen in Fig. 4 that the consideration of Poisson's effect in the present FE model decreases the degree of restraint for shorter walls by 5 - 10%. This is most obvious at the wall bottom, where the determined values approach 100 % restraint only in case of  $\mu = 0$ . The reason can be found by abstracting the stress distribution in the wall with a strut and tie model. In such model, the restraint force in the center section is in equilibrium with a diagonal tie starting at the bottom of the free edge and progressing to half height of the wall with increasing distance from the free edge. And this diagonal tie is in turn in equilibrium with a

vertical strut at the end of the introduction length which causes beneficial compressive stresses in horizontal direction in case of  $\mu \neq 0$ .

In contrast, consideration of a partial axial restraint causes an overall decrease of restraint, as shown in Fig. 5. However, the degree of restraint is also significantly influenced by the location of the CoG of the ideal wall-foundation cross section. In case CoG is placed above the wall bottom (Fig. 5a), short walls show higher degree of restraint at the bottom as long walls, whereas cases with CoG below the wall bottom (Fig. 5b) show an obvious decrease of this effect as well as a slight decrease of restraint over the whole height. The reason can be found in the positive global bending moment caused by vertically restrained uplift of edges, as illustrated in Fig. 2. As already shown in [8], this global bending moment creates beneficial compression at the wall bottom in case the CoG is located above the wall bottom. However, resulting compressive stresses in short walls gain lower values due to the lower activation of self-weight compared to longer walls. Hence, tensile stresses, and accordingly the degrees of restraint, at the bottom of short walls increase compared to long walls.

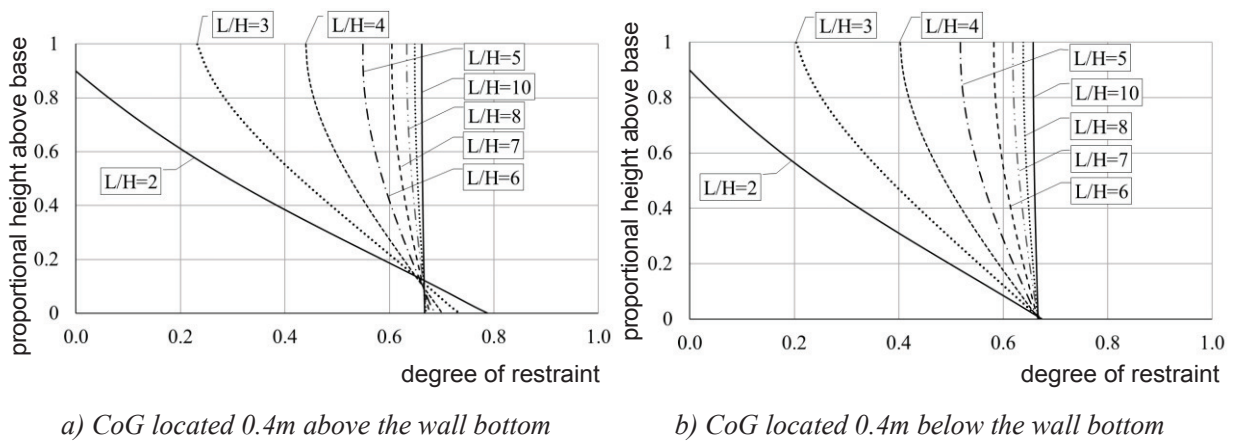


Figure 5: Degree of restraint for partial axial restraint but full restraint of uplift,  $\mu = 0.2$

Another important effect is the realistic consideration of uplift of edges shown in Fig. 6.

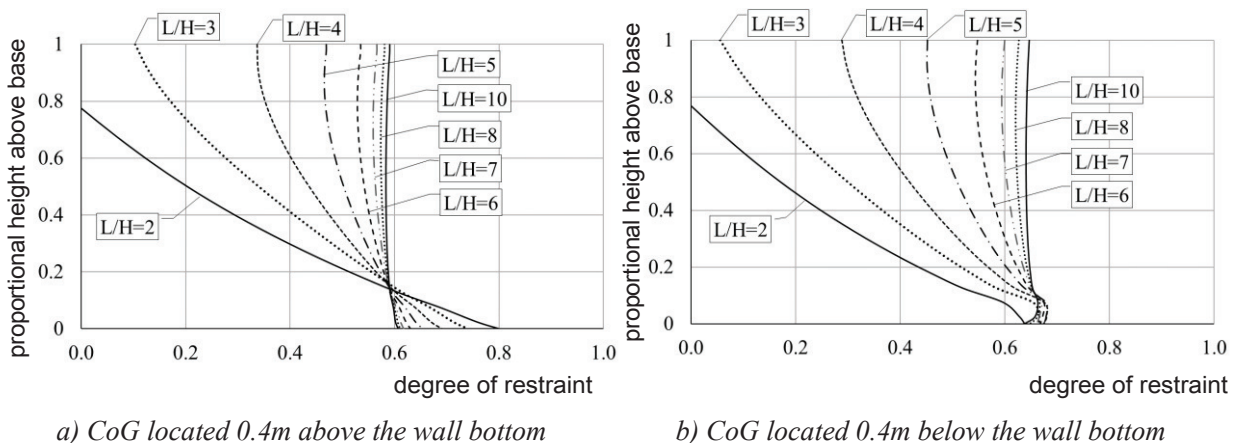


Figure 6: Degree of restraint for partial axial restraint and partial restraint of uplift,  $\mu = 0.2$

The uplift of edges generally shows a stress releasing effect over the height of the wall. However, in short walls with CoG located above the wall bottom (Fig. 6a), the degrees of

restraint exceed even the ones from the previous case. The reason can again be found in the effect of the global bending moment due to self-weight activation. This positive effect was overestimated in the previous case since more beneficial compressive stresses were induced due to the full restraint of uplift.

### 3. Conclusion

Restraint stresses in bottom-restrained walls are determined on the safe side when presuming full restraint at the wall bottom and  $\mu = 0$ . Consideration of partial restraint results in lower stresses, however, this numerical study indicates in accordance with the analytical solution of [8] that a representative consideration of the CoG of the whole cross section is required. In fact, a simple reduction of the degree of restraint on basis of the axial stiffness ratio, as proposed by [2] or [4], can only be seen as a pragmatic solution without a mechanically consistent background. In short walls with CoG located above the foundation, this approach would even give results on the unsafe side. Altogether, it is recommended to determine the degree of restraint in bottom-restrained walls with an explicit consideration of the bending stiffness ratio as well as the real restraining condition of uplift due to self-weight activation.

### Acknowledgements

This contribution was completed with the support of COST Action TU1404 together with the support of the Scientific Grant Agency VEGA under the contract No. VEGA 1/0456/17.

### References

- [1] König, G. and Tue, N.V.: Grundlagen und Bemessungshilfen für die Rissbreitenbeschränkung im Stahlbeton und Spannbeton. DAFStb Heft 466. Beuth-Verlag, (1996)
- [2] ACI 207.2R-07: Report on thermal and volume change effects on cracking of mass concrete (2007)
- [3] EN 1992-3: Design of concrete structures, Part 3: Liquid retaining and containment structures (2006)
- [4] CIRIA C766: Control of Cracking caused by restrained deformation in concrete (2017)
- [5] JSCE: Guidelines for concrete, 15: Standard specifications for concrete structures. Design (2007)
- [6] COIN Project report 31, Basis for and practical approaches to stress calculations and crack risk estimation in hardening concrete structures (2011)
- [7] Knoppik-Wróbel, A.: Analysis of early-age thermal–shrinkage stresses in reinforced concrete walls. Ph.D. Thesis. Silesian University of Technology, Gliwice, Poland (2015)
- [8] Schlicke, D., Minimum reinforcement for restrained concrete, PhD thesis, Graz University of Technology, Austria (2014), ISBN: 978-3-85125-473-0 (revised edition)
- [9] ÖBV Bulletin: Analytical design of watertight structures with optimized concrete (in German), Austrian society for construction technology, Vienna, Austria (2018)
- [10] Fairbairn, E. M.R. and Azenha, M.: Thermal Cracking of Massive Concrete Structures. State of the Art Report of the RILEM TC 254-CMS, Springer (2018), DOI: 10.1007/978-3-319-76617-1
- [11] Matiašková, L. and Šoltész, J.: Macroscopic calculation model for simulating early age behavior of concrete members. In: Early Age Cracking and Serviceability in Cement-based Materials and Structures. Vol. 2, RILEM Publications, Brussels, Belgium (2017)
- [12] Jędrzejewska, A. et.al: COST TU1404 benchmark on macroscopic modelling of concrete and concrete structures at early age: Proof-of-concept stage, Construction and Building Materials, Volume 174 (2018), ISSN 0950-0618



## **GAMMA AND X RADIATION ABSORPTION CHARACTERISTICS OF SPECIALLY SELECTED TYPES OF CONCRETE**

**Srboljub Stankovic <sup>(1)</sup>, Ksenija Jankovic <sup>(2)</sup>**

(1) Institute of nuclear sciences VINCA, Belgrade, Serbia

(2) IMS Institute, Belgrade, Serbia

### **Abstract**

Medical institutions with linear accelerators, cyclotrons as installations for particles acceleration, nuclear facilities as nuclear power stations and nuclear research reactors using concrete in building construction. In cost-benefit analysis the question is what are the radiation characteristics of different types of concrete, which could be used to protect against gamma and X rays. In this paper, computer code XCOM was used for the calculation of the total mass attenuation coefficients, which is an important factor for determination of the photon attenuation, as well as during research and testing of radiation protection properties for concrete with components of different type materials. Thereby, the basic absorption radiation characteristics of ordinary and barite concretes, as well as specially selected type of concrete with magnetite and steel and concrete UHPC with barite and nanosilica as specific material composition, were considered. The results of this research point to the conclusion that before the concrete production of certain mechanical properties is approached, it is reasonable to apply the appropriate methodology with the numerical calculation of the basic absorption characteristic of the concrete for protection against gamma and X radiation.

### **1. Introduction**

Medical institutions with linear accelerators, cyclotrons as installations for particles acceleration, nuclear facilities as nuclear power stations and nuclear research reactors using concrete in building construction. Barite aggregate is used to produce heavyweight concrete which application concerns radiation shielding in hospitals and nuclear facilities. The basic characteristics of ordinary concrete and heavy-weight concrete with barite were studied for the case of their use for shielding from gamma radiation [1, 5, 6]. In cost-benefit analysis the question is what are the radiation characteristics of different types of concrete, which could be

used to protect against gamma and X rays [2, 3, 4]. The energy deposited the transmission factor and the mass attenuation coefficients in ordinary and barite concretes have been calculated with the photon transport Monte Carlo software. The numerical simulations results show that using barite as an aggregate in the concrete is one of the solutions for gamma ray shielding. Thereat, it is shown non-destructive method for determining the gamma radiation absorption characteristics of concrete [9]. In references [10, 11], one of the goals is to implement appropriate numerical calculations for obtaining the value of the total mass attenuation coefficient in the energy range 10 keV - 150 MeV of gamma and X radiation, and their dependence in the content of barite and nano-silica in UHPC concrete with specially defined mechanical properties. Nanosilica has a dominant influence on the improvement of the mechanical properties, and barite has a dominant influence on the characteristics that increase the absorption of ionizing radiation, i.e., improves the characteristics for protection against ionizing radiation. Investigations in these references [10, 11] is designed to, by simultaneously using different portions of the two materials, nano-silica and barite, in the composition of various types of concrete conduct tests on the ability to improve the mechanical properties and properties for the radiation protection of concrete.

In this paper, computer code XCOM [8] was used for the calculation of the total mass attenuation coefficients  $(\mu/\rho)_{tot}$ , which is an important factor for determination of the photon attenuation, as well as during research and testing of radiation protection properties [1-6] for different content of aggregates in concrete. Computer code XCOM operates on a method of combining the values of the existing database for effective cross section of physical processes accompanying the transport of photons through different materials. This means that there is a possibility to use data bases for coherent and incoherent scattering, photoelectric absorption, and pair production cross-sections for the different chemical structure of materials which enter into the composition of the concrete.

## 2. Numerical methods

One of the most important characteristics of the concrete for protection against gamma and X radiation is its Total Mass Attenuation Coefficient  $(\mu/\rho)_{tot}$ .

Basic relations for engineering calculations the attenuation of exposure dose rate of ionizing radiation, which passes through the wall of concrete, can be displayed as:

$$X = X_0 \cdot \exp \left[ - \left( \frac{\mu}{\rho} \right)_{tot} \cdot \rho d \right] \quad (1)$$

where  $X$  (C/kg s) and  $X_0$  are intensity exposure rates behind and in front of the wall, where the wall thickness is  $d$  (m) and the density is  $\rho$  (kg/m<sup>3</sup>). This Eq. (1) is consistent with the application of Bouguer-Lambert-Beer law for attenuation of the intensity of mono energetic photon radiation for the cases of penetration of the narrow beam of radiation through a concrete wall as a protective barrier.

The definition of Total Mass Attenuation Coefficient for mixture or compound is given by:

$$\left(\frac{\mu}{\rho}\right)_{tot} = \sum_j w_j \cdot \left(\frac{\mu}{\rho}\right)_j \quad (2)$$

where  $w_j$  and  $(\mu/\rho)_j$  are the weight fraction and mass attenuation coefficient of the constituent element  $j$ .

The numerical calculations included two steps: 1. For each type of concrete from Tab. 1 its composition was determined in accordance with the nomenclature of chemical elements and chemical compounds, 2. Interactive use of the program XCOM [8], where the known composition of individual types of concrete determines the total mass attenuation coefficient depending on the change of energy photon radiation.

XCOM program enables to calculate interaction coefficients for the following processes: Compton (incoherent) and Rayleigh (coherent) scattering, photoelectric absorption, and pair production in the field of the atomic nucleus and in the field of the atomic electrons. The mean free paths between scatterings, between photo-electric absorption events, or between pair production events are the reciprocals of partial interaction coefficients. The total attenuation coefficient is equal to the sum of the interaction coefficients for the individual processes.

### 3. Results and discussion

In our work, computer code XCOM was used for the calculation of the total mass attenuation coefficients for four different concrete types, which is specified in Table 1.

Table 1: Types of concrete for numerical calculations of the total mass attenuation coefficients with software code XCOM [8].

Mark	Type of concrete	Density (g cm <sup>-3</sup> )	Material composition data in [reference]
CB	Concrete, Barite (Type BA)	3.350	[7]
CMS	Concrete, Magnetite and Steel	4.640	[7]
COR	Concrete, Ordinary (NBS 04)	2.350	[7]
B5n	Concrete, UHPC barite nanosilica 5%	2.830	[11]

The dependence of values total mass attenuation coefficients on energy photon radiation is shown in the figure Fig. 1.

On the graphs Fig. 1, one can see, that total mass attenuation coefficients  $(\mu/\rho)_{tot}$  has dependence of the photon energy ( $E$ ): a) in three ranges for concrete types CMS and COR,

decreasing sharply at low energies ( $E < 0.15$  MeV), decreasing slightly in the middle range ( $0.15 \text{ MeV} < E < 6$  MeV) and increasing slightly at high energies ( $E > 6$  MeV); b) in three ranges for concrete types CB and B5n, decreasing sharply in bottom range ( $10 \text{ keV} < E < 400 \text{ keV}$ ) with the sharp discontinuity around 30 keV, decreasing slightly in the middle range ( $0.4 \text{ MeV} < E < 6$  MeV) and increasing slightly at high energies ( $E > 6$  MeV); c) in the energy range of 400 keV to 6 MeV values for the total mass attenuation coefficients are approximately the same for four different types of concrete. The results, which we have pointed out, are tied to different photon absorption mechanism for different energy range. The sharp discontinuities in energy dependence for total mass absorption coefficient are connected with the processes of the photoelectric absorption.

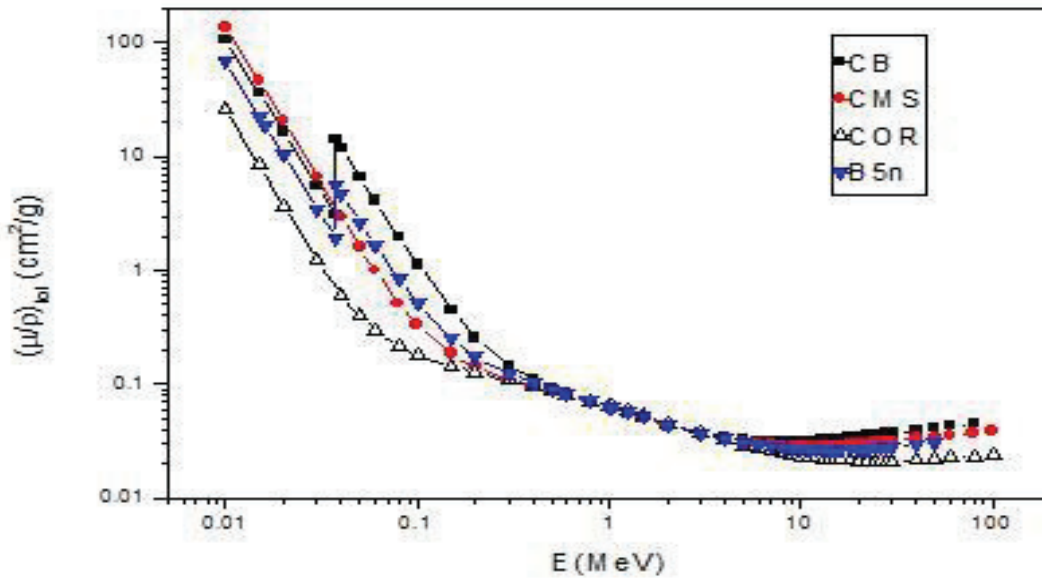


Figure 1: Total mass attenuation coefficients for four different concrete types.

#### 4. Conclusion

In this investigation, based on the results of the corresponding graphs for Total Mass Attenuation Coefficient  $(\mu/\rho)_{tot}$  it can be concluded that in the range of energy of gamma and X radiation from 30 keV to 300 keV, concrete types CB and B5n with barite sand has greater protective power than concrete types CMS or COR. Concrete type CMS with magnetite and steel has greater protective power than other three concrete types for the energy of gamma and X radiation  $E < 30$  keV, while the concrete type CB is with better characteristics than other types of concrete for the attenuation of the radiation beam for photon energies greater than 30 keV. The results of this research point to the conclusion that before the concrete production of certain mechanical properties is approached, it is reasonable to apply the appropriate

methodology with the numerical calculation of the basic absorption characteristic of the concrete for protection against gamma and X radiation.

### **Acknowledgements**

The work presented in this paper is a part of the investigation conducted within the research projects TR 36017 and III 43009 supported by the Ministry of Education, Science and Technological Development, Republic of Serbia. This support is gratefully acknowledged.

### **References**

- [1] Yilmaz, E. et al, Gamma ray and neutron shielding properties of some concrete materials, *Annals of Nuclear Energy* 38 (2011), 2204–2212
- [2] Ling, T.C. et al, X-ray radiation shielding properties of cement mortar prepared with different types of aggregate, *Materials and Structures* (2013), DOI 10.1617/s11527-012-9959-2
- [3] Bashter, I.I. et al, Magnetite ores with steel or basalt for concrete radiation shielding, *Jpn. J. Appl. Phys. Vol. 36, Part 1, No.6A* (1997), 3692-3696
- [4] Sarkawi, M.S. et al, Radiation shielding properties of ferro-boron concrete, *IOP Conf. Series: Materials Science and Engineering* 298 (2018), doi:10.1088/1757-899X/298/1/012037
- [5] Juniora, T.A.A. et al, Mass attenuation coefficients of X-rays in different barite concrete used in radiation protection as shielding against ionizing radiation, *Radiation Physics and Chemistry* 140 (2017), 349-354
- [6] Ouda, A.S., Development of high-performance heavy density concrete using different aggregate for gamma-ray shielding, *Progress in Nuclear Energy* 79 (2015), 48-55
- [7] Shultis J.K. and Faw, R.E., *Radiation Shielding*, Prentice Hall, Englewood Cliffs, New Jersey, (1996)
- [8] Berger, M.J. et al, XCOM: Photon Cross Section Database (version 3.1). <http://www.nist.gov/pml/data/xcom/index.cfm>, NBSIR 87-3597. National Institute of Standards and Technology, Gaithersburg, MD (2010)
- [9] Stankovic et al, Gamma Radiation Absorption Characteristics of Concrete with Components of Different Type Materials, *Acta Physica Polonica A*, Vol. 117, (2010), 812-816
- [10] Jankovic et al, Effect of nano-silica and aggregate type on properties of ultra high performance concrete, *Proceedings of the 9<sup>th</sup> International Concrete Conference 2016 “Environment, Efficiency and Economic Challenges Challenges for Concrete”*, Dundee, Scotland, UK (2016), 839-846
- [11] Jankovic et al, The influence of nano-silica and barite aggregate on properties of ultra high performance concrete, *Construction and Building Materials* 126 (2016), 147-156

## **HYDRO-MECHANICAL MODELLING OF SELF INDUCED STRESSES: IMPACT OF DRYING GRADIENTS ON DAMAGE**

**François Soleilhet<sup>(1)</sup>, Farid Benboudjema<sup>(1)</sup>, Xavier Jourdain<sup>(1)</sup>, Fabrice Gatuingt<sup>(1)</sup>**

(1) LMT, ENS Cachan, CNRS, University Paris-Saclay, 94230 Cachan, France

### **Abstract**

The prediction of the concrete structure durability is closely linked to the prediction of cracking in the long-term. Initially saturated cementitious materials are the seat of water movements that are responsible for mechanisms such as drying shrinkage, creep or changes in mechanical properties. For instance, the differential drying between the surface and the core of the structure leads to a heterogeneous state of stresses and can induce significant micro-cracking at the surface [1]. Those micro-cracks will impact not only the mechanical properties but also the permeability of the structure [2]. In this study, a sequential analysis is proposed to represent the drying evolution and the corresponding cracking pattern. First, calculations are performed to model the drying process and drying gradients. Then relative shrinkage strains are computed through shrinkage model proportional to water content. The impact of the initially determined water fields is investigated both in terms of drying shrinkage and damage generated by the different drying shrinkage models. The influence on the damage fields of the initial drying gradients is thus highlighted. Depending on the hydric fields determined, the damage is not similar. This finding illustrates the importance of precise characterization of drying gradients.

### **1. Introduction**

Cementitious materials are the most widely used in civil engineering works. They are heavily used to face a various or aggressive environments in the fields of housing, transport or energy. Today, the durability of buildings is a major challenge. To address this problem it is necessary, among other things, to predict the long-term behaviour of the structures. Nevertheless, this task remains difficult. The great heterogeneity of the material combined with multiple origins of stresses (thermal, chemical, drying, mechanical) make the work complex.

The objective of the work presented is to study the impact of the determination of hydric fields resulting from concrete drying on the prediction of drying shrinkage and induced damage. To answer this question a sequential analysis integrating the prediction of the drying of 7x7x28 cm concrete test pieces and the development of the drying shrinkage is studied. The mechanical model used is based on a damage model. The state of induced damage is then determined. The impact of hydric prediction is thus studied by comparing two hydric modelling with the same macroscopic results (same relative mass variation).

## 2. Hydro-mechanical modelling

As part of the proposed work, some simplifying assumptions were made. The material is considered mature (final material properties) and hydration is not taken into account. All the mechanisms are considered in a decoupled way [3] which makes it possible to consider them one after the other.

### 2.1 Drying modelling

The drying of cement-based materials is a complex phenomenon. Several, more-or-less coupled, mechanisms are involved: permeation, diffusion, adsorption-desorption and condensation-evaporation. Drying can be analysed through the resolution of liquid water, vapour and dry air mass balance equations. The use of several hypotheses [4,5] allows for considering only the mass balance equation of liquid water:

$$\frac{dS_l}{dP_c} \frac{dP_c}{dt} = \text{div} \left( k_{rl}(S_l) \frac{K}{\mu_l \phi} \text{grad}(P_c) \right) \quad (1)$$

where  $S_l$ ,  $P_c$ ,  $\phi$ ,  $K$ ,  $k_{rl}$  and  $\mu_l$  are, respectively, the saturation degree, the capillary pressure, the porosity, the intrinsic permeability, the relative permeability and the viscosity of the liquid water. It is shown [6,7] that this equation is sufficient for an accurate prediction of the drying of ordinary and high-performance concretes at 20°C with a relative humidity greater than 50%. The capillary pressure and the relative permeability are related to the degree of saturation through van Genuchten's relations [8]:

$$S_l = \left( 1 + \frac{P_c}{P_0} \right)^{1-\gamma} \quad (2)$$

$$k_{rl}(S_l) = S_l^{n_k} \left( 1 - \left( 1 - S_l^{\frac{1}{\beta}} \right)^\beta \right)^2 \quad (3)$$

where  $n_k$ ,  $P_0$  and  $\beta$  are materials parameters. Drying at surfaces was modelled using a convection-type approach with a convection coefficient equal to 50 (m<sup>3</sup>.s).

### 2.2 Shrinkage modelling

There are different ways to model drying shrinkage. Some of these are based on the theory of porous media mechanics. The development of this kind of modelling could be easily found in literature [6]. Other models are based on phenomenological observations. Indeed, following experimental results [7,9] it was found a proportional relation between water content variation and drying shrinkage rate. These observations lead to the equation (5).

$$\underline{\dot{\epsilon}}_{ds} = k_{ds} \dot{w} \underline{\underline{1}} \quad (5)$$

where  $k_{ds}$  is a constant hydrous compressibility factor and  $\underline{\underline{1}}$  is the unit matrix. It is possible to find alternative approaches but in this present work this modelling approach was chosen. It is easy to implement and gives satisfactory results.

### 2.3 Mechanical Modelling

This study is based on 3D modelling. It involves non-explicit modelling of concrete cracking using a damage theory. The variable  $D$ , a scalar damage variable ranging from 0 to 1, is considered in the stress-strain relation:

$$\sigma_{ij} = (1 - D)C_{ijkl}\epsilon_{kl}^{elas} \quad (6)$$

where  $\sigma_{ij}$ ,  $C_{ijkl}$ ,  $\epsilon_{kl}^{elas}$ , are respectively stress, elastic stiffness and elastic strains. The evolution of the damage relies on an equivalent strain criterion, calculated from the equivalent strain  $\epsilon_{eq}$  introduced by Mazars [10]. It was shown [11] that the evolution of damage in tension could be taken as an exponentially decreasing:

$$D = 1 - \frac{\epsilon_{d0}}{\epsilon_{eq}} \cdot \exp\left(-B_t(\epsilon_{eq} - \epsilon_{d0})\right) \quad (7)$$

where  $\epsilon_{d0} = f_t/E_c$ , with  $f_t$  the tensile strength,  $E_c$  the Young modulus and  $B_t$  a parameter controlling the softening behaviour of the concrete.

Softening behaviour of concrete may lead to non-unicity of solutions and mesh dependency. Energetic regularization prevents these difficulties [12]. Regularization is then based on the parameter  $B_t$ , which is a function of  $h$ , the characteristic size of the finite element,  $f_t$  the tensile strength,  $G_f$  the fracture energy and a parameter for the initiation of the damage  $\epsilon_{d0}$  as described above.

$$B_t = \frac{h \cdot f_t}{G_f - \frac{h \cdot \epsilon_{d0} \cdot f_t}{2}} \quad (8)$$

## 3. Results

In this section, the numerical results of the different studies are presented. These are based on experimental results of standard concretes carried out within the LMT Cachan over a period of 440 days and which has been kept under conditions of 45% relative humidity and 21.5°C. The experimental results will not be detailed; only the relative mass variation and drying shrinkage curves will serve as a basis for numerical tests.

### 3.1 Hydric fields

The various simulations are carried out using three-dimensional modelling of one eighth of the total section. The elements, numbering of 2187, are linear. The specimens are subjected on their exposed sides to storage conditions. After identifying the model parameters presented in Tab. 1, the hydric fields are simulated. The reader will notice that at time “0” on Figure 1 and 2 the concrete had already 28 days of age.



Table 1: Water solutions.

Set of parameters	$\beta$ [-]	$P_0$ [MPa]	$n_k$ [-]	$K$ [m <sup>2</sup> ]	$\Phi$ [-]	$\rho$ [kg.m <sup>-3</sup> ]
1	0.45	11.4	-1.42	$5.81 \cdot 10^{-21}$	0.16	2400
2	0.48	24.2	-0.46	$4.35 \cdot 10^{-21}$	0.17	2366

The comparison with the evolution of the experimental relative mass variation presented in Figure 1, shows a good similarity of the numerical results with both sets of parameters.

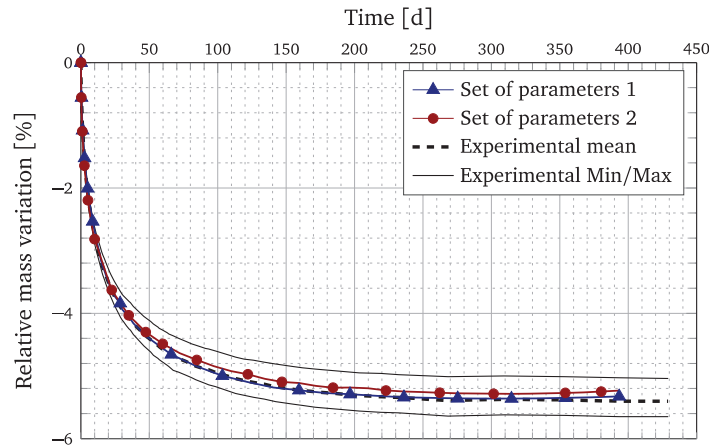


Figure 1: Evolution of relative mass variation after 440 days of drying

Although the evolution of relative mass variation is the same for both modelling, we notice that the hydric fields are not equal. Figure 2 shows major difference between both simulations. First of all, after 440 days of drying, the two profiles are not yet in equilibrium with the environment. Moreover, the field from the first parameter set is much less dry than the second. The drying is more concentrated on the first centimetres of the sample while the second model shows a drying that seems more homogeneous. This difference is mainly explained by different isotherms.

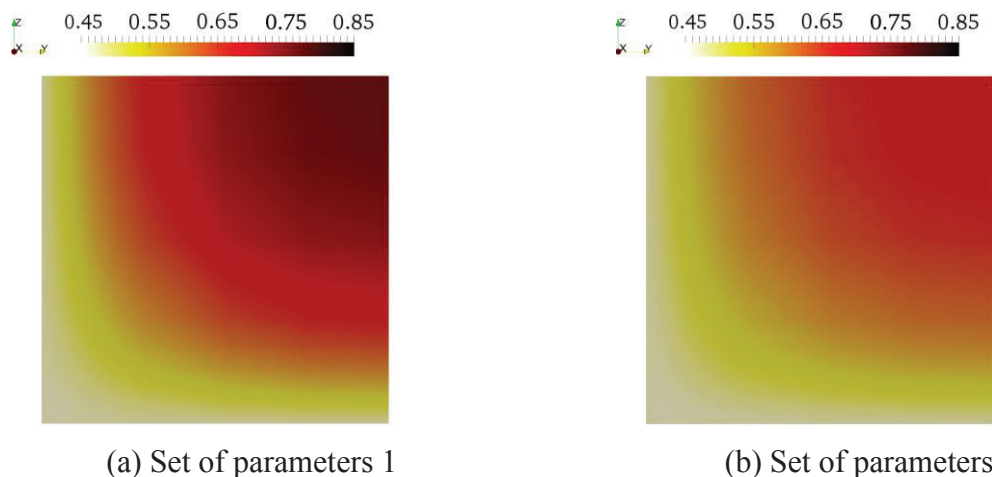


Figure 2: Relative humidity fields within the sample in the mid-section (eighth of section)

### 3.2 Damage induced by shrinkage

Once the hydric state is set, it is then possible to simulate the evolution of the drying shrinkage using equation (5). The mesh size data are similar to the previous hydric problem. Figure 3 shows the drying shrinkage trend after 440 days of drying. It can be seen that by adapting the  $k_{ds}$  coefficient it is possible to represent the shrinkage over this period of time in almost the same way. Moreover, the coefficients are close to each other.

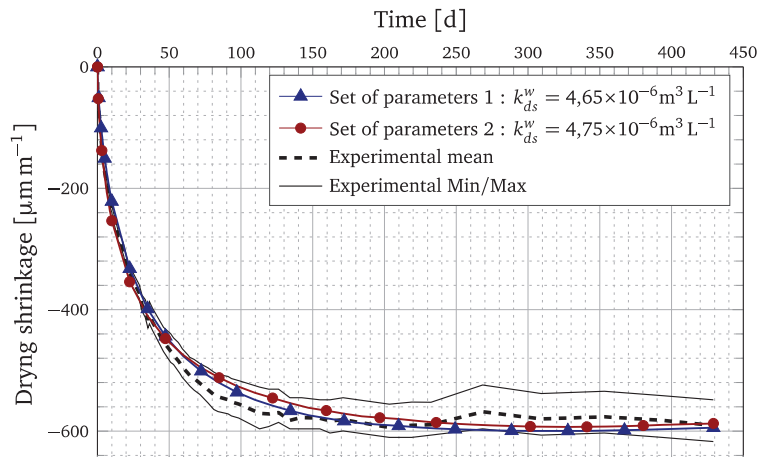
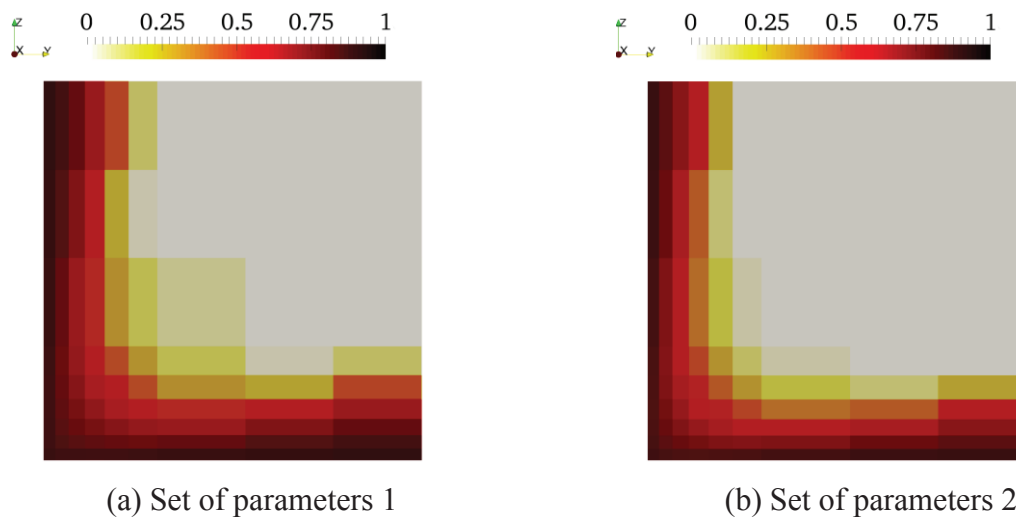


Figure 3: Evolution of drying shrinkage after 440 days

Although a good similarity is observed at the macroscopic level if we now place ourselves at the cracking scale when the shrinkage reaches a plateau, which is here around 220 days, we see in Figure 4 that the damage profiles differ. With almost similar shrinkage, the damage to profile 1 is greater than the second. This observation seems logical at the sight of the model used; the first hydric profile is the one which presents the strongest gradients which generates a more important damage. All this suggests that it is necessary to define the hydric state and more particularly the saturation degree precisely.



(a) Set of parameters 1

(b) Set of parameters 2

Figure 4: Comparison of damage fields between the two sets of parameters after 220 days

#### 4. Conclusion

In this communication, the impact of the determination of hydric fields was investigated. After defining hydric state, drying shrinkage was simulated using a phenomenological model proportional to water content. We note:

- Macroscopically the relative mass variation is similar but we notice that at the cracking scale the hydric fields are very different. This difference is mainly explained by the difference in desorption isotherms.
- It can be seen that by adapting the proportionality coefficient, the two hydric fields make it possible to determine the apparent drying shrinkage; nevertheless the corresponding damage fields are not similar. This observation leads the modeller to define precisely the hydric state of the material so as not to over- or underestimate the cracking of the material.

#### References

- [1] Bisschop, J. and van Mier, JGM., How to study drying shrinkage microcracking in cement-based materials using optical and scanning electron microscopy. *Cement and Concrete Res*, 32 (2002), 279–287.
- [2] Yurtdas, I., Peng, H., Burlion, N. and Skoczylas, F., Influences of water by cement ratio on mechanical properties of mortars submitted to drying. *Materials and Structures*, 36 (2006), 1286–1293.
- [3] Granger L. Comportement différé du béton dans les enceintes de centrales nucléaires : analyse et modélisation, PhD Thesis from Ecole Nationale des Ponts et Chaussées (1995).
- [4] Bazant ZP, Sener S, Kim JK, Effect of cracking on drying permeability and diffusivity of concrete. *ACI Materials Journal* 84 (1986), 351-357
- [5] Hansen TC, Creep of concrete: the influence of variations in the humidity of ambient atmosphere, *Proceedings 6th Congress of the International Association of Bridge and Structural Engineering*, Stockholm (1960), 57-65
- [6] Thiery M, Baroghel-Bouny V, Bourneton N, Villain G, Stefani C, Modélisation du séchage des bétons : analyse des différents modes de transfert hydrique, *Revue Européenne de Génie Civil* 11(5) (2007), 541-577
- [7] Goltermann P, Mechanical predictions of concrete deterioration – Part 2: classification of crack patterns, *ACI Materials Journals* 92(1) (1995), 58-63
- [8] Lassabatère T, Torrenti J-M, Granger L, Sur le couplage entre séchage du béton et contrainte appliqué, *Proceedings Actes du Symposium Saint-Venant*, Paris (1997), 331-338
- [9] Baroghel-Bouny V and al., Characterization and identification of equilibrium and transfer moisture properties for ordinary and high-performance cementitious materials, *Cement and Concrete Research* 29 (1999), 1225-1238
- [10] Mazars J. A description of micro-and macro scale damage of concrete structures. *Eng Fract Mech* 25(5) (1986), 729–37
- [11] Feenstra PH. Computational aspects of biaxial stress in plain and reinforced concrete, PhD thesis Technical University of Delft (1993)
- [12] Hillerborg A, Modéer M, Petersson P-E. Analysis of crack formation and crack growth in concrete by means of fracture mechanics and finite elements. *Cem Concr Res* 6(6) (1976), 773–81

## **NUMERICAL MODELING OF POROUS MEDIA FREEZING PROCESS BY MEANS OF A NON-EQUILIBRIUM APPROACH**

**Dariusz Gawin**<sup>(1)</sup>, **Francesco Pesavento**<sup>(2)</sup>

(1) Lodz University of Technology, Lodz, Poland

(2) University of Padova, Padova, Italy

### **Abstract**

Freezing-thawing cycles are one of the most significant causes of durability problems for concrete structures in cold climate countries. Water freezing in a porous material is a very complex physicochemical process, difficult to model numerically due to the interactions between different phases/components, the inner microstructure of the material and phase changes taking place in a confined environment, what leads to an alteration of the standard freezing and fusion points of water.

In this work, we present a coupled model for the numerical modelling of heat and mass transport and their mechanical effects in partially saturated porous media, exposed to freezing – thawing processes. Phase changes are modelled by means of a kinetic, non-equilibrium approach derived from the Thermodynamics of porous media. It is able to reproduce the cryosuction, supercooling and undercooling phenomena considering in such a way the hysteresis of ice content vs. temperature during the phase change, what results also in hysteresis of material strains. The latter ones are calculated here by means of appropriately formulated effective stress principle considering crystallization pressure in partially saturated materials. Some relevant numerical cases will be presented to show the effectiveness of the formulated model in the simulation of freezing-thawing process.

### **1. Introduction**

In this work we present a new numerical model for the simulation of the behaviour of porous materials under cooling, with particular regard to cementitious materials. The latter ones are characterized by a fine inner microstructure, formed of C–S–H gels, mineral crystals of various compositions and pores of different sizes which can be fully or partially saturated with water. Due to this complex microstructure and the mutual interactions between various

phases/components at micro level, the formulation of a mathematical/numerical model able to take into account all the most important phenomena is particularly difficult, especially in the case of partially saturated states, i.e. when all the phases of water (solid, liquid and vapour) are simultaneously present.

Unlike most of the models in literature, which are based on an approach at equilibrium (see [1] for example), here the water freezing/melting processes for the porous material are modelled far from equilibrium. Their kinetics are governed by a first order evolution law, obtained from the second law of Thermodynamics with capillary pressure as main physical variable used for the definition of the thermodynamic imbalance during the process evolution. Pore water freezing is initiated by heterogeneous nucleation and then followed by a progressive penetration of the ice front from larger to smaller pores. With the formulation here proposed, it is possible to observe the so-called supercooling phenomenon, i.e. the delayed first freezing of water at temperature below zero, due to the uncertainties of nucleation. The liquid water can flow through a thin film of physically adsorbed water between the skeleton and ice crystal, hence water pressure does not increase during freezing in a partially saturated material.

The model takes also into consideration the freezing point depression due to the confinement of the water phases in the pores' network and their mutual interactions. This phenomenon is known as undercooling process and leads to a sort of hysteresis between the freezing and the melting stages (because of the different curvatures of the ice-water interface we can observe during freezing and melting [2]).

The model defined in this way, is able to take into account several phenomena leading to the deformation of the porous material and to the internal microcracking: (i) the expulsion of unfrozen water from the freezing sites towards the airvoids, which is usually related to the 9% expansion of water upon freezing, (ii) the crystallization process which is strictly related to the formation of ice crystals and their growth; (iii) the transfer of liquid water from the unfrozen pores to already frozen sites (i.e. cryo-suction process); (iv) the thermo-mechanical interactions between the solid skeleton and the water in its various forms (liquid, gaseous, solid).

A comparison between experimental results (obtained from a DSC test) and numerical ones, are shown for the validation of the model proposed. Furthermore, some additional numerical examples are presented to show its effectiveness.

## 2. Kinetics of water freezing in porous materials

Here the water freezing/melting in a capillary-porous material is modelled as a non-equilibrium process, the kinetics of which is governed by a linear evolution law, obtained from the second law of Thermodynamics in the following form [3],

$$\dot{s}_i = A_{fr} \dot{\Gamma}_{fr} \quad (1)$$

where  $\dot{s}_i$  is the rate of internal production of molar entropy due to the freezing,  $\dot{\Gamma}_{fr}$  the rate of freezing, and the process affinity is  $A_{fr} = \mu_w(T, p^w) - \mu_{ice}(T, p^{ice})$ , with  $\mu_w$  and  $\mu_{ice}$  being chemical potentials of liquid water and ice (solid water), respectively.

By considering:

- i) the definition of the chemical potentials and equilibrium condition for the transition of bulk phases at temperature  $T_0$  and pressure  $p_0$ ;
- ii) that in porous materials, due to curved interfaces between the phases and interaction of pore walls, the water and ice pressures are different;
- iii) a simplified form of the affinity  $A_{fr}$ ;
- iv) the relationships at equilibrium;

it is possible to formulate the equations describing the kinetics of the freezing/melting processes taking place in the pores of the material (see [3] for further details). These evolution equations have the form described in the following.

### **Water freezing process**

The evolution equation of the ice mass source due to freezing of liquid water,  $\dot{m}_{fr/w}$ , can be described through the following law ( $T_m^*$  is the melting temperature):

$$\text{if } p_{fr}^c < p_{fr,eq}^c(T) \text{ and } T < T_m^*: \quad \dot{m}_{fr/w} = -n\rho^w S_w \frac{v_w}{RT} \frac{p_{fr}^c - p_{fr,eq}^c}{\tau_{fr}}; \quad (2)$$

otherwise :  $\dot{m}_{fr/w} = 0$ .

where  $n$  is the porosity of the material,  $\rho^w$  and  $v_w$  are the density and the molar volume of the water respectively,  $R$  is the universal gas constant and, finally,  $\tau_{fr}$  is the characteristic time of freezing which is related to the affinity of the process and to its reaction rate. Moreover in eq. (3)  $p_{fr}^c$  is the actual value of the capillary pressure during freezing process (far from equilibrium) and  $p_{fr,eq}^c$  is the corresponding value of capillary pressure under equilibrium. From eq. (3) it is clear that it is possible to have freezing of liquid water only if the current value of capillary pressure is lower than the value of the same quantity at equilibrium.

### **Ice melting process**

Ice melting can be treated in a similar manner. In such a case, it is needed to consider the different shape of the liquid water-ice interface respect to the case of freezing. At this aim, a parameter  $\bar{\lambda}(S_w)$  is introduced in the evolution model. This parameter is the ratio of the curvature of the meniscus during freezing and melting. Thus, the ice mass source during melting process can be expressed as follows:

$$\text{if } p_{fr}^c > p_{m,eq}^c(T) \text{ and } \dot{T} > 0: \quad \dot{m}_{fr/w} = -n\rho^w S_w \bar{\lambda}(S_w) \frac{v_w}{RT} \frac{p_{fr}^c - p_{m,eq}^c}{\tau_m}; \quad (3)$$

otherwise :  $\dot{m}_{fr/w} = 0$ .

where  $\tau_m$  is the characteristic time of melting, and  $p_{m,eq}^c(T)$  is the capillary pressure at equilibrium during the melting process (different than the one during freezing). One can observe melting only if the actual value of capillary pressure  $p_{fr}^c$  is higher than the value

under equilibrium conditions  $p_{m,eq}^c(T)$ . The latter one, is related to the capillary pressure at equilibrium during the freezing process according to the following relationship:

$$p_{m,eq}^c = p_{fr,eq}^c / \bar{\lambda}(S_w).$$

The constitutive law for  $\bar{\lambda}(S_w)$  can be identified by means of experimental tests conducted with a calorimeter or by supposing a spherical and a cylindrical shape for the water-ice interface during freezing and melting respectively. In such a case  $\bar{\lambda}(S_w)$  assumes a constant value equal to 0.5.

This evolution model for freezing was introduced in a more general model which treats concrete as multiphase porous material. It takes into account the bulk phases, the interfaces and their thermo-chemical and mechanical interactions, as well as, phase changes and chemical reactions for the components/species considered. The reader can refer to [4] for further details.

### 3. Validation of the model

In the following some results of a DSC (Differential Scanning Calorimetry) test, are compared with the numerical ones in order to validate the model proposed in this work. The material is a silicate whose main properties are depicted in Table 1.

Table 1: Main properties of the material used in DSC test.

Property	Value
Density	1792 kg/m <sup>3</sup>
Young's Modulus	9 GPa
Compressive Strength	26 MPa
Thermal Conductivity	0.78 W/mK
Specific Heat	880 J/kgK
Porosity	30.1 %

For the identification of the suction curve (i.e. the main isotherm of the porous material) some results of a MIP (Mercury Intrusion Porosimetry) test have been used in order to characterize the inner microstructure. Fig. 1 shows a comparison between the MIP experimental results and the theoretical isotherm adopted in the range of interest for the capillary pressure. The initial saturation of the material was 35% corresponding to a relative humidity of 96.4%. For the sake of simplicity, the coefficient  $\bar{\lambda}(S_w)$  was assumed constant equal to 0.5 in the numerical simulation of the DSC test, while the same value of the characteristic time for freezing and melting processes was adopted (15 sec). The temperature history during the DSC test is shown in Fig. 2. In Fig. 3 one can observe a comparison between experimental and numerical results in terms of ice saturation degree (in the domain of temperature). We can identify a maximum level of ice content corresponding to the instants at which the

temperature reaches the lowest value and then increase, and an intermediate level corresponding to the central part of the temperature evolution. The overall agreement is good: the differences are mainly due to the form of the isotherm adopted, which represents the hygral behavior of the material only in a short (central) range of capillary pressure. Furthermore, we can notice as the peculiar approach adopted here (i.e. far from equilibrium) helps in capturing the first-freezing phase which is often characterized by a sudden release of energy.

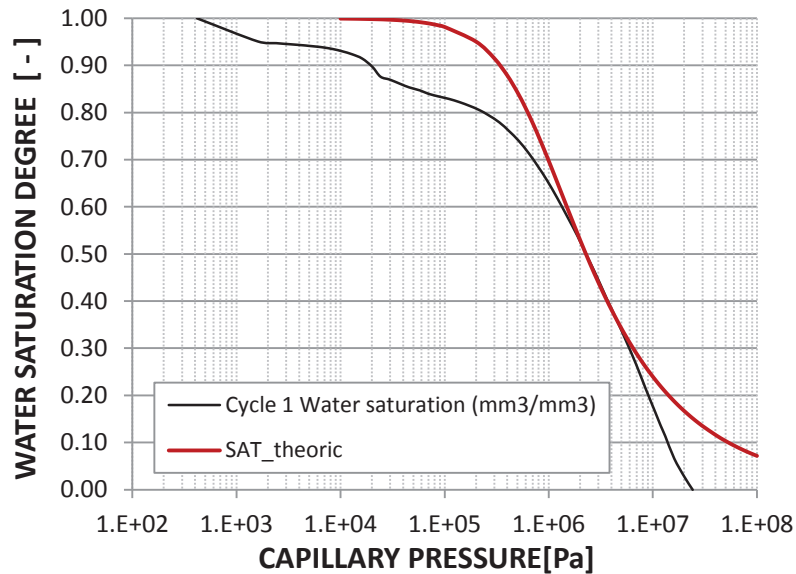


Figure 1: Isotherm of the silicate used for the validation: comparison between MIP test results and the theoretical formulation used in the model.

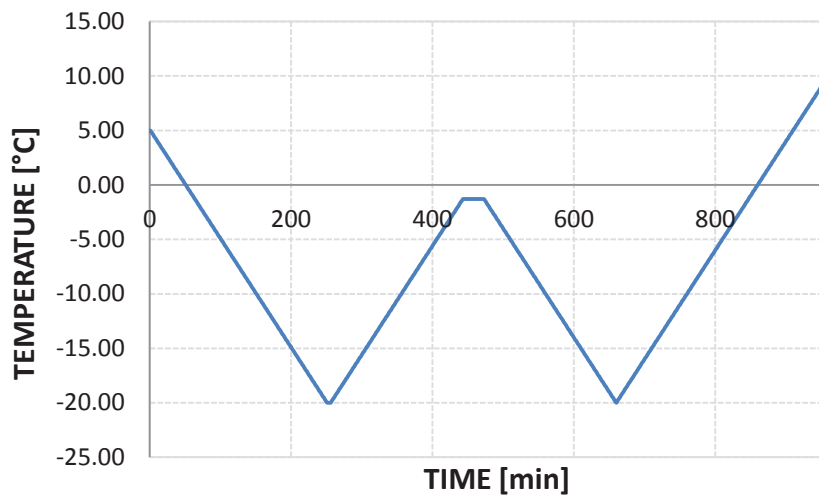


Figure 2: Thermal cycle applied to the specimen during the experimental tests.



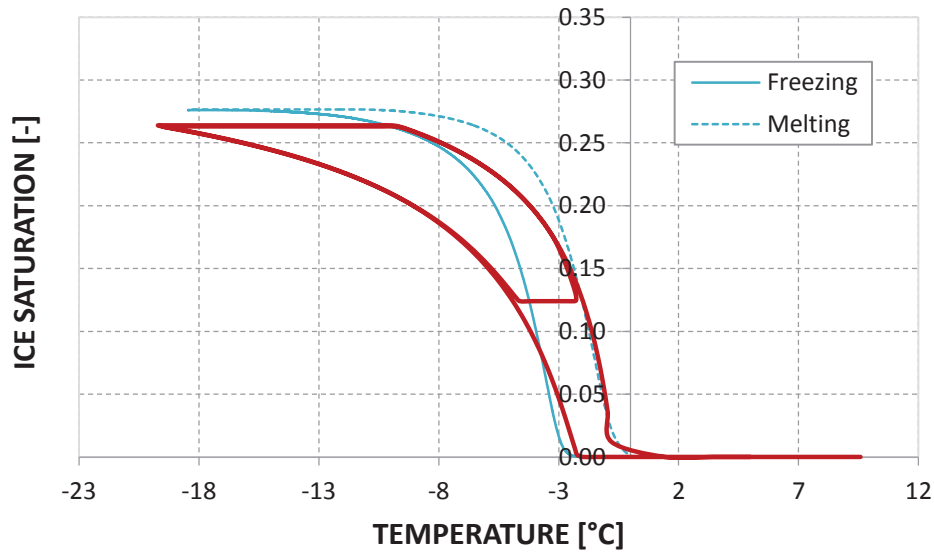


Figure 3: Comparison between experimental (thin lines) and numerical (bold line) results in terms of ice saturation degree  $S_{ice}$ .

#### 4. Conclusions

In this work, we have shown a coupled model for the numerical simulation of freezing-melting processes in partially saturated porous media. The model is able to catch the heat and mass transfer phenomena taking place in the material and also the related mechanical effects. It is based on a non-equilibrium approach derived from the Thermodynamics of Phase Changes (considering all the phases of water simultaneously present in the pores of the material). By means of such a kind of approach, it is possible to reproduce numerically the cryo-suction, supercooling and undercooling phenomena as well as the associated hysteresis in the ice content and material strains evolution.

#### References

- [1] Coussy, O and Monteiro, P.J.M., Poroelastic model for concrete exposed to freezing temperatures, *Cem Concr Res* 38 (2008), 40-48
- [2] Sun, Z. and Scherer, G.W., Measurement and simulation of dendritic growth of ice in cement paste, *Cem Concr Res* 40 (2010), 1393-1402
- [3] Gawin, D., Pesavento, F., Schrefler, B.A., Non-equilibrium modeling of water freezing-thawing with hysteresis in partially saturated porous media., submitted to *Transport in Porous Media*
- [4] Gawin, D., Pesavento, F., Schrefler, B.A., Hygro-thermo-chemo-mechanical modelling of concrete at early ages and beyond. Part I. Hydration and hygro-thermal phenomena, *Int J for Num Meth in Eng* 67(3) (2006), 299-331

## NUMERICAL SIMULATION OF EARLY-AGE CONCRETE BEHAVIOUR OF AN ARCH DAM

Noemi Schclar Leitão <sup>(1)</sup>, Eloísa Castilho <sup>(1)</sup>

(1) Laboratório Nacional de Engenharia Civil, Lisbon, Portugal

### Abstract

This paper reports a case study of the chemo-thermal-mechanical analysis of a concrete arch dam during its construction and first reservoir filling phases. The hydration kinetics model is formulated in the framework of thermodynamics of chemically reactive porous media based in the model presented by Ulm and Coussy. The structural response of the dam is assessed by a viscoelastic model. The parameters of the normalized affinity and the double power creep law are defined based on laboratory tests performed on samples extracted during construction. The predicted temperatures and stresses are compared with the monitoring system values.

### 1. Introduction

In dam engineering, the analysis of the observed behaviour and assessment of security conditions is performed by comparing the values measured by the monitoring system installed in the dam with the values predicted by mathematical models representing the structural behaviour, the material properties and the loads. Instrumentation provides data for monitoring the safe performance during the various phases of the dam's life including design, construction, first filling of the reservoir, evaluation of long-term, in service performance (normal operation), and to manage or predict unsatisfactory performance. Installation of instrumentation typically occurs 1) during constructions, and 2) during the life of the dam to address new or changing conditions [1].

The purpose of this paper is to describe the main issues concerning the chemo-thermal-mechanical modelling necessary to obtain a representative simulation of early-age concrete behaviour of an arch dam. The general description of the dam as well as the finite element mesh, material properties and loads adopted to simulate the first filling of the reservoir can be

seen in [2]. This paper will be focused on the definition of the hydration kinetics and the viscoelastic models which allow the simulation of the dam behaviour since its construction.

## 2. Determination of the normalized affinity

The hydration kinetics model is formulated in the framework of thermodynamics of chemically reactive porous media based in the model presented by Ulm and Coussy [3]. Among the different empirical relationships used to represent the normalized affinity  $\tilde{A}(\xi)$  [4] [5] [6], the one presented by Cervera *et al.* [6] is used:

$$\tilde{A}(\xi) = \frac{k_{\xi}}{\eta_{\xi_0}} \left( \frac{A_{\xi_0}}{k_{\xi} \xi_{\infty}} + \xi \right) (\xi_{\infty} - \xi) \exp\left(-\bar{\eta} \frac{\xi}{\xi_{\infty}}\right) \quad (1)$$

where  $\xi$  is the hydration degree,  $\xi_{\infty}$  is the asymptotic degree of hydration and  $k_{\xi}$ ,  $A_{\xi_0}$ ,  $\eta_{\xi_0}$  and  $\bar{\eta}$  are material properties. According to [6] the material properties involved in expression (1) can be determined experimentally, by an adiabatic calorimetric test, considering:

$$\tilde{A}(\xi) = \frac{\xi_{\infty} \dot{T}^{ad}}{T_{\infty}^{ad} - T_0} \exp\left(\frac{E_a}{RT}\right) \quad \text{and} \quad \xi = \xi_{\infty} \frac{T^{ad} - T_0}{T_{\infty}^{ad} - T_0} \quad (2)$$

where  $T^{ad}$  is the measured temperature of concrete during the experiment,  $\dot{T}^{ad}$  is the measured temperature rate,  $T_{\infty}^{ad}$  is the final reached temperature,  $T_0$  is the initial temperature,  $E_a$  is the activation energy of the reaction and  $R$  is the ideal gas constant. In many cases, however, the available data of heat of hydration is restricted to a few points. Thus, in order to represent the whole course of the adiabatic hydration process, an analytical expression has to be fitted to the data points. For example, adopting an S-shape function of the form [7]:

$$Q = Q_{\infty} \exp\left(-(\tau/t)^{\beta}\right) \quad (3)$$

where  $Q_{\infty}$  is the liberated heat when hydration has practically ceased,  $t$  is the time and  $\tau$  and  $\beta$  model the shape of the function. Adopting  $\beta = 1$  and taking into account that  $T^{ad} = Q/(\rho c)$ , where  $\rho c$  is the volumetric specific heat of concrete, the normalized affinity function (2) is as follows:

$$\tilde{A}(\xi) = \frac{\xi_{\infty}}{T_{\infty}^{ad} - T_0} \exp\left(\frac{E_a}{RT}\right) \frac{Q_{\infty} \tau}{\rho c t^2} \exp(-(\tau/t)) \quad (4)$$

Finally, the analytical expression (1) is determined by calibrating the three material properties  $k_{\xi}/\eta_{\xi_0}$ ,  $A_{\xi_0}/k_{\xi}$  and  $\bar{\eta}$  with expression (4). Although the analytical expression (4) can be used directly to model the affinity, it was decided to approximate it to the Cervera *et al.* [6] function form, in order to preserve the meaning of the different terms involved in the empirical relationship, as described in [8]. In the case under analysis, as part of the *Concrete Quality Assurance*, three samples of cement were tested to determine the heat of hydration at the ages of 3, 7 and 28 days. These results and the best fitting curve (3) adopting  $\beta = 1$  are presented in Fig. 1.

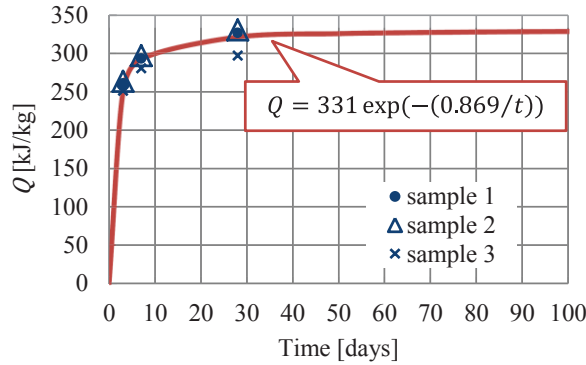


Figure 1: Cement heat of hydration development.

To consider the reduction in the total heat of hydration produced by the replacement of a portion of the Portland cement with fly ash, the results obtained by EDP [9] for the mass concrete of the Portuguese dams was taken into account. This study shows that for 50% of fly ash, the decrease in heat of hydration is of approximately one third.

To the composition of the concrete used in the body of the dam characterized by a cementitious content of  $260 \text{ kg/m}^3$  with 55% of fly ash and a ratio  $w/c = 0.55$  and considering a decrease in heat of hydration is approximately of  $1/3$  [9], the following parameters (to be used in Eq. (1)) were determined  $\xi_{\infty} = 0.77$ ;  $k_{\xi}/\eta_{\xi_0} = 4 \times 10^5 \text{ h}^{-1}$ ;  $A_{\xi_0}/k_{\xi} = 1.04 \times 10^{-2}$  and  $\bar{\eta} = 5.59$ . The adiabatic temperature rise and the normalized affinity obtained are illustrated in Fig. 2. Fig. 2 (b) shows the comparison of the estimated normalized affinity of Eq. (4) and the Cervera *et al.* analytical expression (1) evaluated with the parameters defined above.

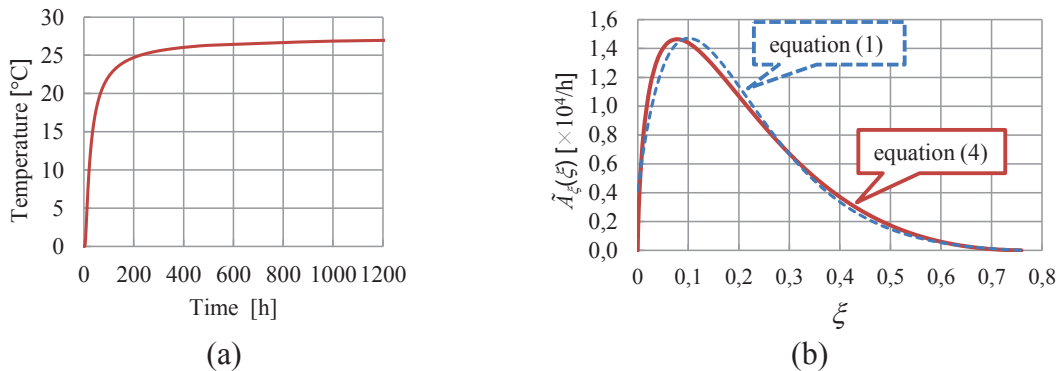


Figure 2: (a) Adiabatic temperature rise, (b) normalized affinity

### 3. Concrete creep law

Following the normal procedure utilized by the National Laboratory for Civil Engineering for the monitoring of the Portuguese dams, the double power law [10] was adopted as the concrete creep prediction model:

$$J(t - t') = \frac{1}{E_o} + \frac{\varphi_1}{E_o} (t'^{-m} + \alpha)(t - t')^n \quad (5)$$

in which  $J(t - t')$  is the compliance function (or the creep function), *i.e.* the strain at age  $t$  caused by a unit uniaxial constant stress acting since age  $t'$ ;  $E_o$  is the asymptotic modulus;  $n$ ,  $m$ ,  $\alpha$  and  $\varphi_1$  are material parameters. The static modulus as function of age may be expressed also from the double power law, setting  $t - t' = 0.1$  day in Eq. (5):

$$\frac{1}{E(t')} = \frac{1}{E_o} + \frac{\varphi_1}{E_o} 10^{-n}(t'^{-m} + \alpha) \quad (6)$$

Figure 3 shows the fit of Eq. (5) and (6) to the results obtained in laboratory for creep in samples at ages 28 and 32 days and for the modulus of elasticity at ages 28, 32, 90 and 365 days for  $E_o = 35$  GPa,  $n = 0.12$ ,  $m = 0.51$ ,  $\alpha = 0.043$  and  $\varphi_1 = 4$ .

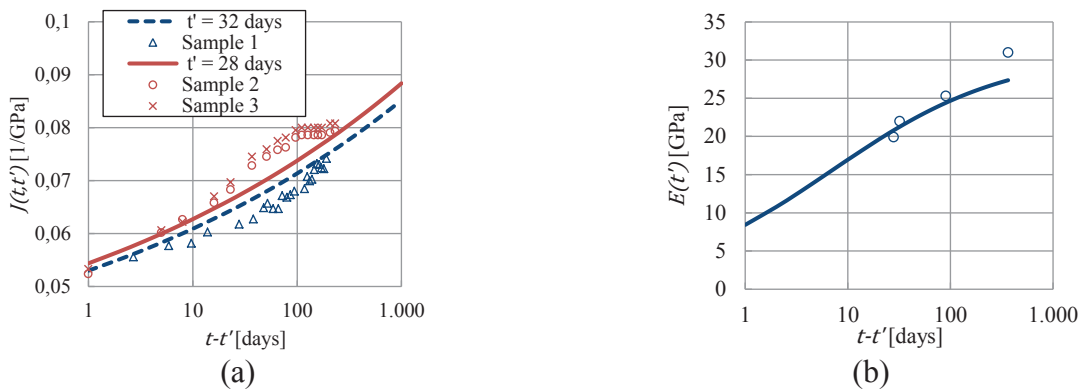


Figure 3: (a) Fits of creep test, (b) fits of modulus of elasticity

#### 4. Results and discussion

The analysed dam is a concrete double curvature arch dam with artificial gravity abutments. The total height above the foundation is 41 m, the crest length is 100 m, and the crest elevation is 668.50 m. Its shape definition is based on parabolic arches, which increase in thickness towards the abutments; the central cross section has a theoretical thickness of 2 m at the crest and 5.5 m at the base. The dam is divided in six blocks along its axes, the two central blocks have 16 m in width and the laterals blocks have 17 m in width.

The simulation starts with the beginning of the construction on June 22, 2011. The finite element model of the dam was updated for every construction stage by applying the birth and death methods. At this stage, all the contraction joints, simulated by zero thickness interface elements, were considered open, *i.e.* no interaction between blocks was allowed. On May 1, 2013 the interface elements were activated in order to simulate the grouting of the contraction joints. The first filling of the reservoir began on June 28, 2013 and by July 8 the water level reached the first stage at elevation 642.00 m and was maintained during the summer. At the end of September the hold point at elevation 649.00 m was achieved and it was maintained for several weeks. Finally, the period of severe rainstorms that occurred during late 2013 and early 2014 led to an uncontrollable rising of the reservoir, being reached the second stage at elevation 658.50 m on January 9, the third stage at elevation 664.00 m on February 4 and the last stage at elevation 665.40 m on February 11, 2014.

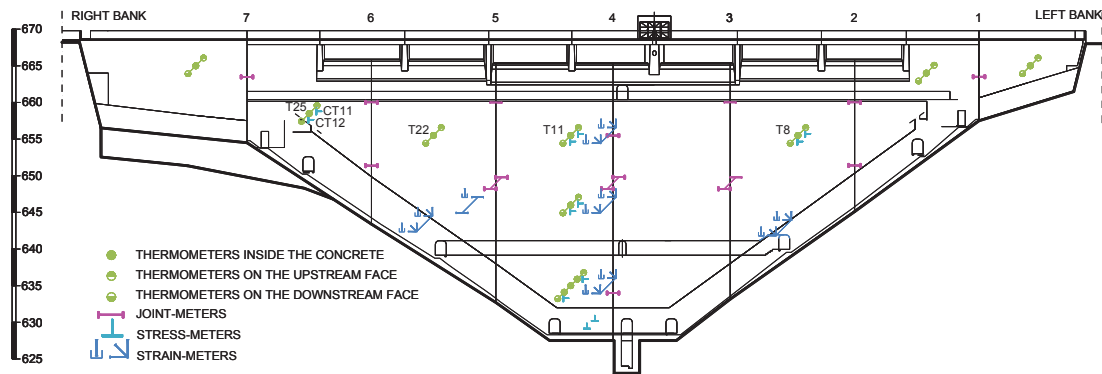


Figure 4: Monitoring electrical devices embedded into the concrete

Fig.4 shows the instrumentation embedded into the concrete based on electrical devices: strain-meters, stress-meters, joint-meters and thermometers. This figure also includes the name of the electrical devices mentioned in Fig. 5.

Fig.5 shows the comparison between the recorded and calculated values of temperatures at elevation 655.50 m (thermometers T8, T11 and T22) and temperatures and arch stresses at elevation 658.50 m (thermometer T25 and stress-meters CT11 and CT12). Considering the uncertainties associated with air and water temperatures and solar radiation, the variability in concrete composition and the approximation involved in the finite element mesh, mainly during the construction stage, the results obtained in the chemo-thermal-mechanical analysis are very encouraging. Additional work remains to be done on modelling the concrete properties evolution as result of cement hydration.

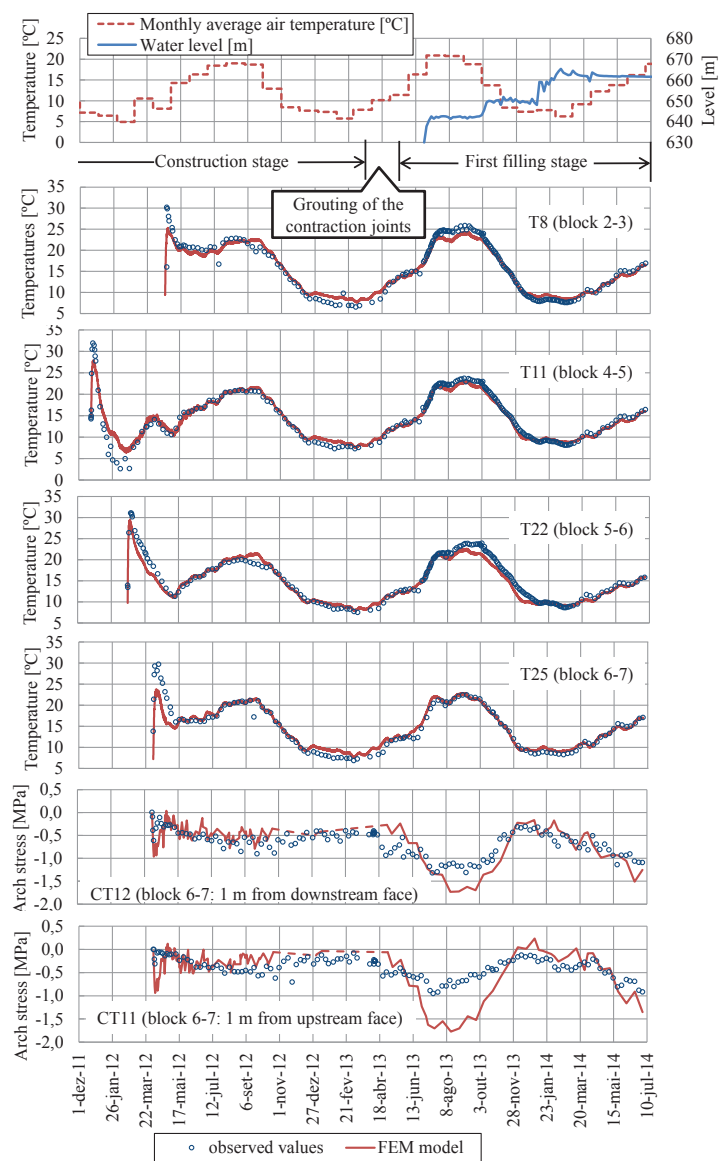


Figure 5: Comparison of monitored and numerical results

## References

- [1] Leitão, N.S. et al, Analysis of the observed behavior of Alto Ceira II dam during the first filling of the reservoir, Second International Dam World Conference, Portugal (2015)
- [2] USSD, Development of a dam safety instrumentation program, United States Society of Dams (2013)
- [3] Ulm, F.J. and Coussy, O., Modeling of thermochemomechanical couplings of concrete at early ages, *J. Engrg. Mech., ASCE*, 121(7) (1995), 185-794
- [4] Hellmich, C. et al, Consistent linearization in Finite Element analysis of coupled chemo-thermal problems with exo- or endothermal reactions, *Computational Mechanics* 24 (1999), 238-244
- [5] Lackner, R. and Mang, H., Chemoplastic material model for the simulation of early-age cracking: From the constitutive law to numerical analyses of massive concrete structures, *Cement & Concrete Composites* 26 (2004), 551-562
- [6] Cervera, M. et al, Thermo-chemo-mechanical model for concrete. Part I: Hydration and aging, *Journal of Engineering Mechanics* 125(9) (1999), 1018-1027
- [7] Van Breugel, K., Prediction of temperature development in hardening concrete, Prevention of thermal cracking in concrete at early ages, RILEM Report 15 (1998)
- [8] Cervera, M. et al, Numerical modelling of concrete curing, regarding hydration and temperature phenomena, *Computer & Structures* 80 (2002), 1511-1521
- [9] Camelo, A., Durabilidade e vida útil das estruturas hidráulicas de betão e de betão armado, JMC2011 Proceedings from 1<sup>as</sup> Jornadas de materiais na construção, Portugal (2011), 149-169
- [10] Bazant, Z.P. and Panula, L., Practical Prediction of Time-Dependent Deformation of Concrete, *Materials and Structures*, Part I and II: 11(65) (1978), 307-328; Parts III and IV: 11,(66) (1978), 415-434; Parts V and VI: 12(69) (1979), 169-173

## **NUMERICAL STUDY OF CHLORIDE INGRESS IN CONCRETE: EFFECT OF EXPOSURE CONCENTRATION**

**Mohamad Achour<sup>(1,2)</sup>, Ouali Amiri<sup>(2)</sup>, François Bignonnet<sup>(2)</sup>, Emmanuel Rozière<sup>(1)</sup>,  
Mahdi Haidar<sup>(2)</sup>**

(1) Centrale Nantes, Nantes, France

(2) University of Nantes, Nantes, France

### **Abstract**

The corrosion process is usually described into two periods that model the service life of the reinforced concrete structures such as bridges and other structures exposed to marine environments: 1) the initiation period and 2) the propagation period. The initiation period is the time required for aggressive substances (e.g., carbon dioxide, chlorides, etc.) to penetrate from the environment into the cover concrete until critical chloride ion concentration is reached at the bar reinforcement to initiate the corrosion process. In the present paper, a numerical model is developed to study the effect of the exposed concentration of chloride on the initiation period of the corrosion. This initiation period is modelled by considering physico-chemical interactions between the ions and the solid components of the concrete. Several examples of application of the model are presented to show the interest of studying the influence of the exposure concentration of chloride ions on the penetration depth in the concrete. The effects of chloride binding, chemical activity of the pore solution and electrostatic interactions are also presented.

### **1. Introduction**

The corrosion of reinforcement concrete structures due to the penetration of chloride ions is an important problem in civil engineering. When the concentration of chloride ions is critical, the corrosion of the steel will start and the service life of the concrete structure will reduce. In United Kingdom, this pathology of concrete is the first cause of degradation of bridges. This degradation depends on the exhibition class [1]. According to the norm NF EN 206-1 there are 18 exhibition classes. These classes depend on the exposure weather and on the concentration of chloride ions which penetrate in the concrete structure such as sea water



attack (XS class) and de-icing salt (XD class). When concrete is submerged totally in water, chloride ions will penetrate by diffusion only such as in the submerged bridge pier. When concrete is partially saturated and exposed to wetting and drying cycles chloride ions will penetrate by diffusion and convection.

The transport of chloride ions is well studied in the literature and many models are available for the simulation of chloride ions in saturated [2-3] and unsaturated concrete [4-5]. The ingress of chloride ions is significant in a marine environment and also when using salt spray. For this reason, this paper aim to enhance the signification of the penetration depth of chloride ions taking into account the exposure weather and the exposure concentration of chloride ions. This study will show us the effect of the initial concentration of chloride ions on the service life of concrete structure and on the initiation of corrosion of reinforced concrete. In order to study the unsaturated case, this work could be considered as an extension or a continuation of the Benchmark WG2.4 “Macroscopic model to predict chloride content in saturated concrete” carried out in the framework of Cost action.

After this introduction, the used numerical model is presented in section 2. It considers the physico-chemical mechanisms of the penetration of chloride ions. The influence of the exposure concentration of chloride ions on the service life of concrete and on the penetration depth of chloride ions are shown in section 3. The conclusion of this work follows in section 4.

## 2. Model of chloride transport in unsaturated concrete

The chloride penetration is a complex physical and chemical process. In our model, this process is divided into four parts: transport of chloride by 1) diffusion, 2) convection, 3) ions interaction and 4) chemical activity of ions. The flowchart of the model is illustrated in Fig.1. The governing equations can be given by:

$$J_i = -D_i \left[ \text{grad}C_i + \frac{z_i F}{RT} C_i \text{grad}\Psi + C_i \text{grad}(\ln Y_i) \right] + C_i V \quad (1)$$

Where  $D_i$ ,  $C_i$ ,  $z_i$  and  $Y_i$  are respectively the effective coefficient of diffusion ( $\text{m}^2/\text{s}$ ), the concentration ( $\text{mol} \cdot \text{m}^{-3}$ ), the valence and the coefficient of activity of the ion  $i$ .  $F$  the Faraday constant ( $96485,309 \text{ C} \cdot \text{mol}^{-1}$ ),  $R$  the ideal gas constant ( $8,3143 \text{ J} \cdot \text{mol}^{-1} \cdot \text{K}^{-1}$ ),  $T$  the temperature (K),  $\Psi$  the electrostatic potential (V) and  $V$  the velocity of water (m/s).

To take into account the effect of water content, the coefficient of diffusion of ions is assessed by Buchwald's work [6] for the ions in the pore solution.  $D_i$  depends on the evolution of the porosity  $\varepsilon$  and on the saturation degree  $S_e$  which is linked to water content volume  $W$ . The equation is expressed as follows:

$$D_i = D_i^{\text{sat}} \left( \frac{W}{\varepsilon} \right)^\lambda \quad (2)$$

Where  $D_i^{\text{sat}}$  is the coefficient of diffusion of ions in saturated concrete ( $\text{m}^2/\text{s}$ ) and  $\lambda = 6$ .

The model adopted for the humidity transport can be derived as follows:

$$\frac{\partial S_e}{\partial t} = - \frac{K_e K_{re}}{\varepsilon \mu_e} \frac{\partial P_c}{\partial S_e} \text{grad}S_e + \frac{R_a D_{va}}{\rho_e} \frac{\partial \rho_v}{\partial S_e} \text{grad}S_e - \frac{M_{H_2O}}{\rho_e} \frac{\partial S_{CaOH_2}}{\partial t} \quad (3)$$

Where  $D_{va}$ ,  $\mu_e$ ,  $M_{H_2O}$  and  $\rho_e$  are, respectively, the coefficient of diffusion of water vapor, the viscosity, the molar mass and the density of water.  $S_{CaOH_2}$  is the solid content of Portlandite during the transport of chloride ions.  $P_c$  is the capillary pressure (atm) calculated from  $\varphi(W)$ , which describes sorption and desorption isotherms which relate the water content to the humidity. The isotherms can be derived from experimental results depending on the type of concrete and on wetting-drying cycles

$$P_c = -\rho_e \frac{RT}{M_v} \ln \varphi(W) \quad (4)$$

$K_e$  is the intrinsic permeability ( $m^2$ ). It depends on the microstructure of concrete and it was assessed from its initial porosity  $\varepsilon_0$  through Genuchten's equation [7] and  $K_{re}$  is the relative permeability ( $m^2$ ) [8].  $R_a$  is the resistance to the air (Thiery's work [9] based on Millington's study [10])

$$K_e = K_e^0 \left(\frac{\varepsilon}{\varepsilon_0}\right)^2 \left(\frac{1-\varepsilon_0}{1-\varepsilon}\right)^2 \quad (5)$$

$$K_{re} = (S_e)^{0.5} [1 - (1 - (S_e)^{1/0.34})^{0.34}]^2 \quad (6)$$

$$R_a = (\varepsilon)^{2.74} (1 - S_e)^{4.8} \quad (7)$$

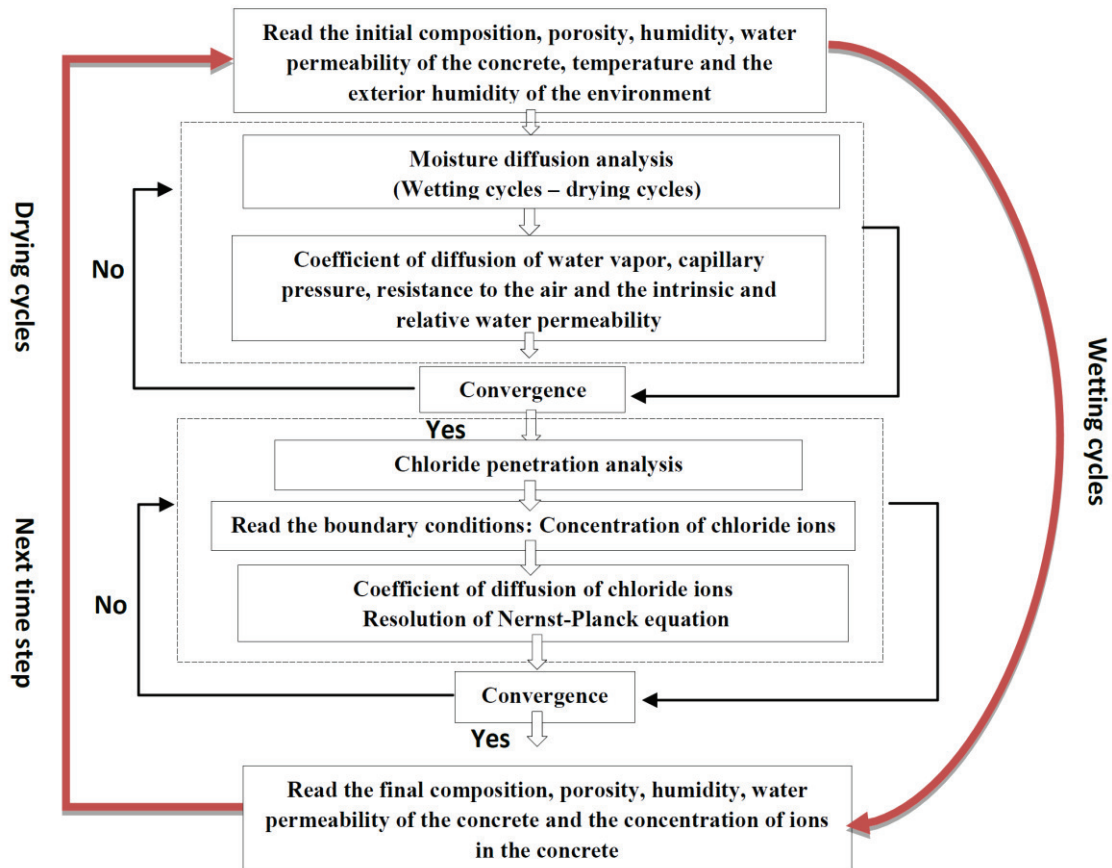


Figure 1: Flowchart of the numerical model.

### 3. Results and discussion

The discretization approach for 1D domain had been to model the ionic transport process of concrete. The finite difference method is used to solve the above equations (1-7).

#### 3.1 Concrete composition, input data and boundary conditions

The concrete mixture used in this study has the composition described in Tab.1 [11].

Table 1: Composition of the concrete specimen.

Concrete M30CV	Value
Gravel 5/12.5	565 Kg/m <sup>3</sup>
Sand 0/5	864 Kg/m <sup>3</sup>
Cement	436 Kg/m <sup>3</sup>
Fly Ash	223 Kg/m <sup>3</sup>
Silica fume	95 Kg/m <sup>3</sup>
Water/Binder	0.74

This concrete is selected from the literature because the input data and the parameters needed in the model are available. The concrete properties and the input data needed for the model are listed in Tab.2. The sorption and desorption isotherms are presented in the Bouny's works [11].

Table 2: Input data of the numerical model.

	Value
Water porosity	0.128
Density of concrete	2349 Kg/m <sup>3</sup>
Effective coefficient of diffusion of chloride ions	2.17 E-13 m <sup>2</sup> /s
Water permeability	4 E-21 m <sup>2</sup>

In order to take into consideration the interaction between chloride ions and the cement paste of the concrete, binding isotherms were measured. The results show that a Langmuir isotherm can be used to link free and bound chlorides:

$$C_{cl,b} \text{ (mol/m}^3\text{)} = \frac{0.000025C_{cl,f}}{1+0.0006C_{cl,f}} \quad (8)$$

The concrete specimen (50 mm) is initially partially saturated ( $S_e^0 = 80\%$ ) and then exposed to chloride attack (0.5 mol/L) under 6h/6h of wetting and drying cycles ( $S_e^{t>0} = 92\%$  wetting,  $S_e^{t>0} = 60\%$  drying,  $T=23^\circ\text{C}$ ).

### 3.2 Chloride transport validation in concrete under cyclic drying-wetting conditions

Fig. 2 shows the profile of chloride ions after an exposure period of 10 years with 6h/6h of wetting and drying conditions. It is clear from the results that the model can predict well the penetration of chloride ions obtained experimentally. We can also note the convection zone is identified. This profile is the result of eq.1 considering chloride ions.

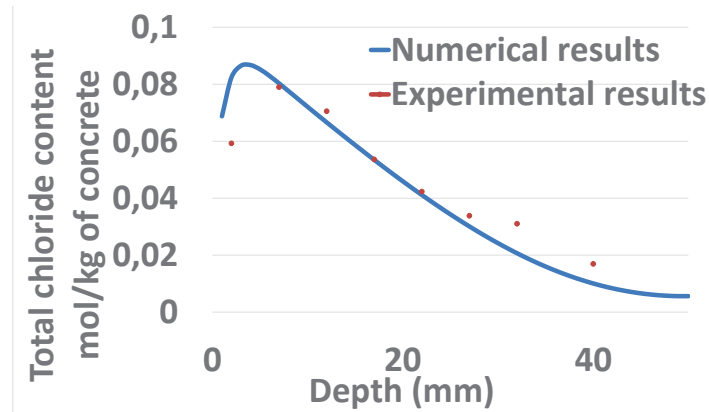


Figure 2: Validation of the model to predict the penetration of chloride ions in the concrete.

### 3.3 Influence of the exposure concentration on the chloride penetration and on the service life of concrete

In order to show the influence of the exposure concentration (0.5-1-2-3 mol/L) on total chloride concentration, a number of simulations are presented in Fig.3 and Fig.4. The numerical model simulates the profile of chloride ions fixing all the parameters and changing only the exposure concentration. These figures show clearly that when the concentration of chloride ions on the surface increases, the penetration depth of chloride increases also due to the high amount of chloride ions. We have to note that the convection zone occurs whatever the chloride concentration. This is due to the convection effect which accelerates the penetration of chloride ions.

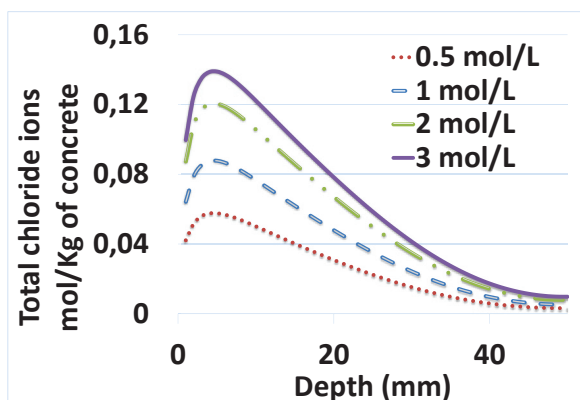


Figure 3: Influence of the exposure concentration on the chloride penetration into concrete.

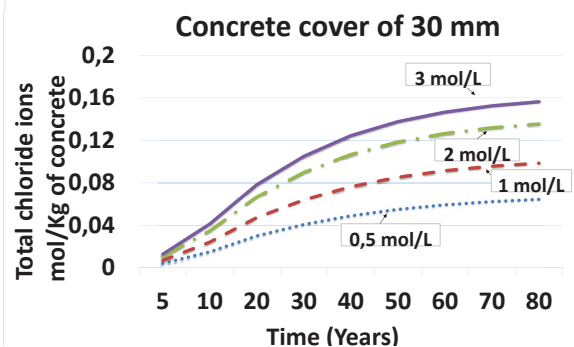


Figure 4: Influence of the exposure concentration on the initiation stage of corrosion.

The numerical model simulates the profile of chloride ions after 80 years of time exposure. For every 10 years the concentration of chloride ions at  $x=30$  mm is plotted in Fig.4 shows clearly that for a concrete cover of 30 mm and after 50-80 years, the initiation stage of corrosion is accelerated when the exposure concentration increases. Finally, as expected, when the chloride content is important (de-icing salt) the corrosion initiation is accelerated.

#### 4. Conclusion

This study is focussed on the study of the effect of exposure concentration on chloride ingress in concrete. The main conclusions that can we drawn are;

- 1- To highlight the convection zone, the coupling of chloride and humidity ingress is required.
- 2- When the concentration of chloride ions is more important on the surface, the initiation time of corrosion is increased.
- 3- The numerical predictions of the penetration of chloride ions are compared with a set of experimental results for unsaturated concrete. It was clear that the experimental results support the validity of the model.

#### References

- [1] NF EN 197-1 Ciment-Partie 1: Composition, spécification et critères de conformité des ciments courants. 2001.
- [2] Tang, L., Lindvall, A., Validation of models for prediction of chloride ingress in concrete exposed in de-icing salt road environment, *Int. J. of Structural Engineering* 4 (2013), 86-99.
- [3] Li, L., Page, C., Finite element modelling of chloride removal from concrete by an electrochemical method, *Corrosion Science* 42 (2000), 2145–2165.
- [4] Achour M., Amiri O., Bignonnet F., Rozière E., Influence of carbonation on ionic transport in unsaturated concrete: evolution of porosity and prediction of service life. *European Journal of Environmental and Civil Engineering* 0 (2018), 1–16.
- [5] Nguyen P., Amiri O., Study of the chloride transport in unsaturated concrete: Highlighting of electrical double layer, temperature and hysteresis effects. *Constr. Build. Mater* 122 (2016), 284–293.
- [6] Buchwald, A.: Determination of the Ion Diffusion Coefficient in Moisture and Salt Loaded Masonry Materials by Impedance Spectroscopy. In 3rd International Symposium Vienna (2000), 475–482.
- [7] Van Genuchten, M. T., A Closed-form Equation for Predicting the Hydraulic Conductivity of Unsaturated Soils1. *Soil Science Society of America Journal* 44 (1980), 892-897.
- [8] Mualem, Y., A new model for predicting the hydraulic conductivity of unsaturated porous media. *Water Resour. Res.* 12 (1976), 513–522.
- [9] Thiery, M., Dangla, P., Villain, G., Platret, G. : Modélisation du processus physico-chimique de carbonatation des bétons. *Acte des Journées des Sci. L'Ingénieur du réseau des LPC* (2003), 403–408.
- [10] Millington, R., Gas diffusion in porous media. *In Science* 130 (1959), 100–102.
- [11] Baroghel-Bouny, V., Dierkens, M., Wang, X., Soive, A., Saillio, M., Thiery, M., Thauvin, B.: Ageing and durability of concrete in lab and in field conditions: investigation of chloride penetration. *Journal of Sustainable Cement-Based Materials.* 2 (2014), 67-110.

## **PARAMETRIC STUDY OF THE MINIMUM REQUIRED REINFORCEMENT FOR CRACKING CONTROL IN THICK RESTRAINED RC MEMBERS BASED ON THERMO-HYGRO-MECHANICAL FE ANALYSES**

**Carlos Sousa <sup>(1)</sup>, Miguel Azenha <sup>(2)</sup>, Cláudio Ferreira <sup>(1)</sup>, Rui Faria <sup>(1)</sup>**

(1) CONSTRUCT, University of Porto, Porto, Portugal

(2) ISISE, University of Minho, Guimarães, Portugal

### **Abstract**

This paper discusses the structural behaviour of walls or slab-like reinforced concrete (RC) elements fully restrained at their ends, considering the effects of self-induced deformations due to the heat of hydration and concrete shrinkage. It focuses on the formation and propagation of cracks in thick ties. The analysed thicknesses are 500 mm and 1000 mm. The ultimate objective of the analyses presented in the paper is the rational calculation of the minimum required area of reinforcement to control cracking. For that purpose, thermo-hygro-mechanical analyses are conducted, so that the non-uniform cross-sectional distribution of self-induced deformations is conveniently simulated, and the crack propagation process can be studied. A staggered analysis approach is followed: an uncoupled thermo-hygral analysis is firstly conducted to calculate the self-induced deformation, in each location throughout the structure thickness, for each instant of time. Then, this deformation field is used as input for the mechanical analysis, where the relevant features of the mechanical concrete behaviour are simulated: maturity; creep; softening behaviour after cracking; and nonlinear bond stress-slip relationship at the steel-concrete interface. The results are discussed in view of the regulatory framework of Eurocode 2 for minimum reinforcement for adequate crack width control.

### **1. Introduction**

The definition of the reinforcement for thick RC slabs or walls is frequently governed by cracking control criteria, particularly in situations where the deformation of such members is externally restrained. Design codes, such as the Eurocode 2 [1], provide simple design procedures for calculation of the required reinforcement. These procedures are simple to use,

but involve very important simplifications of the actual structural and material behaviour. One of the most important is the adoption of a simple correction factor,  $k$ , to take into account the effect of self-induced stresses which vary nonlinearly throughout the member thickness. This factor is set as a function of a single variable, the member thickness. This simplification is very convenient for a rapid estimate of the required reinforcement. However, the simplicity comes with a price: the calculated amount of reinforcement may give rise to crack openings significantly higher or smaller than the specified crack limit (to meet durability, water tightness or other conditions). In view of these limitations of the design rules, alternative methodologies have been proposed for crack width control, namely the deformation compatibility approach [2].

In this context, this paper shows the experience gained with the application of a thermo-hygro-mechanical framework to the calculation of minimum required reinforcement in thick restrained RC members (slabs or walls). The temperature and shrinkage deformations of concrete are completely hindered at the member extremities, thus creating a case of full end restraint. No additional action is considered.

An uncoupled analysis strategy is followed. The local concrete deformations due to temperature variations during the cement hydration and drying shrinkage are calculated for unidirectional fluxes of temperature and humidity (perpendicular to the middle plane of the studied member). The evolution along time of the temperature and humidity fields, as well as the relationship between humidity and local shrinkage, are determined for a concrete mix and exposure conditions previously characterized in laboratory. Thermo-hygral analyses are carried out using the modelling framework described in [3, 4]. Their output is used as input for the mechanical model. In the mechanical analyses, concrete is discretized using plane stress finite elements (FEs). The constitutive model for concrete is based on a total strain approach with rotating cracks. A Kelvin chain approach is used to simulate creep and the time variation of the concrete modulus of elasticity. The reinforcement is discretized using truss elements. The bond action between steel and concrete is explicitly modelled. The mechanical analyses are made with recourse to the FE package DIANA [5].

The discussion of the analysis results focuses on the mechanical response of the structure in terms of crack propagation, crack openings and steel stresses.

## 2. Structures under analysis

### 2.1 Geometry and loading

The analysed structures are RC tie elements, 500 mm and 1000 mm thick. The longitudinal deformation of each tie is fully restrained at its extremities, since the instant of casting. The ties are assumed to be moulded and cured for a period of 7 days after casting. No additional load is considered besides the self-induced deformations due to the heat of hydration and the shrinkage of concrete.

The concrete cover to the longitudinal reinforcement is 50 mm (measured from the concrete surface to the reinforcement axis). For each concrete geometry, two different amounts of reinforcement are considered in the analyses shown in this paper:

- The minimum amount of reinforcement which, according to the Eurocode 2 [1] is required to avoid yielding of the reinforcement, herein labelled as  $a_{s,min}$ . It is equal to 24.9 cm<sup>2</sup>/m for the 0.5 m thick slab and 37.3 cm<sup>2</sup>/m for the one with a thickness of

1 m. Note that this is, according to the code, the minimum amount to avoid yielding. The reinforcement which ensures, according to the code, that a certain limit crack opening (e.g. 0.3 mm) is not exceeded is much higher.

- An amount of reinforcement 30% higher than  $a_{s,min}$ , labelled as  $1.3 a_{s,min}$ .

The bar diameter is determined, for all of the analysed geometries, by considering that the bar spacing is equal to 100 mm. The diameter is, therefore, 13.4 mm and 15.4 mm for the 500 mm structure reinforced with  $a_{s,min}$  and  $1.3 a_{s,min}$ , respectively. For the 1000 mm thick member, the diameters are 16.7 mm and 19.3 mm. The fact that these diameters are not available in the reality does not impair the validity of this study.

## 2.2 Finite element modelling

Eight-node plane stress quadrilateral FEs, with 25 mm edges, are adopted to discretize the concrete elements. The plane stress FE thickness is taken as 1 m. Compatible interface FEs and truss FEs were used to model the bond action and the steel behaviour, respectively. The model length, ( $L$  in Fig. 1) is 4 m for the 1 m thick slab. For the 0.5 m thick one, different  $L$  values were considered (4 m and 2 m), in order to assess the influence of this variable. Only half of the thickness was discretized owing to symmetry.

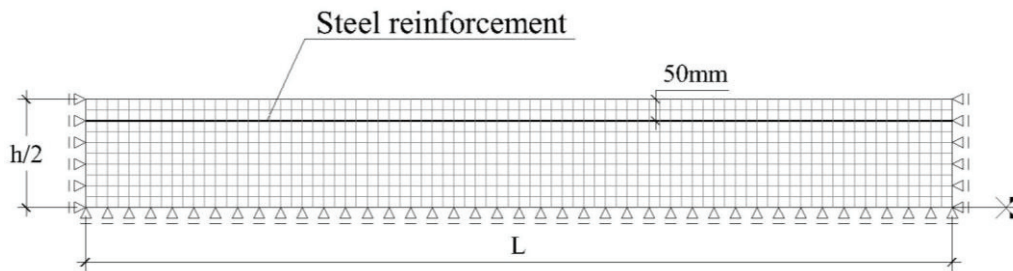


Figure 1: FE mesh for 500 mm thick RC ties

## 2.3 Material and boundary properties

The parameters to define the concrete properties, the environment and the boundaries take the values previously characterized and experimentally validated [6]. The most relevant parameters are shown in Tab. 1. A full characterization can be found in reference [6]. Note that, to make it concise, no information about the heat generation function is shown in Tab. 1. The adopted concrete mix can be considered as a relatively typical mixture for applications with normal strength requirements. It includes  $280 \text{ kg/m}^3$  of CEM II 42.5R,  $40 \text{ kg/m}^3$  of fly ash,  $143 \text{ kg/m}^3$  of water,  $6 \text{ kg/m}^3$  of water reducing admixture and granitic aggregates. The local relationship between the relative humidity in concrete and the local concrete shrinkage strain is given by the equation proposed by Kwak [7], with a shrinkage strain of  $539 \mu$  when the concrete humidity reaches 60%. The kelvin chain model to describe the viscoelastic concrete behaviour is fitted to the fib Model Code [8] creep and modulus of elasticity models, considering that the mechanical properties start developing in concrete at the end of the dormant period. The tension softening model adopted for concrete is the one proposed by the fib Model Code [8].

A linear elastic-perfectly plastic behaviour is assumed for steel, with a modulus of elasticity of 200 GPa and a yield stress equal to 500 MPa. The steel-concrete interface behaviour is



modelled according to the cubic function by Dörr [9] up to a slip value of 0.06 mm. For higher slip values, the bond-stress is kept constant and equal to 1.9 times the concrete tensile strength ( $1.9 \times 2.9 = 5.51$  MPa).

Table 1: Material and boundary properties.

Analysis	Property	Value
Thermal	volumetric specific heat	2400 kJm <sup>-3</sup> K <sup>-1</sup>
	thermal conductivity	2.6 Wm <sup>-1</sup> K <sup>-1</sup>
	convection/radiation coefficient for free surfaces	10.0 Wm <sup>-2</sup> K <sup>-1</sup>
	convection/radiation coefficient before demoulding	5.0 Wm <sup>-2</sup> K <sup>-1</sup>
	environmental temperature	20 °C
Hygral	diffusivity for H=1, $D_1$	$3.08 \times 10^{-10}$ m <sup>2</sup> s <sup>-1</sup>
	diffusivity for H=0, $D_0$	0.0967 $D_1$
	H for $D_H = 0.5 D_1$	0.8
	material parameter $n$	2
	moisture emissivity coefficient	$4.81 \times 10^{-8}$ ms <sup>-1</sup>
	environmental relative humidity	60 %.
Mechanical	average tensile strength	2.9 MPa
	average compressive strength	38 MPa
	fracture energy	0.140 kNm/m <sup>2</sup>
	thermal dilation coefficient	10 <sup>-5</sup> °C <sup>-1</sup>

### 3. Results and discussion

As mentioned before, the discussion focuses on the results of the mechanical analyses. It was found that the adopted analysis strategy to model cracking and bond action is robust. Converged results were always reached. Preliminary parametric analyses (considering linear or, alternatively, bilinear tension softening models; different structure lengths; and one or, alternatively, three structure spots with 5% lower tensile strength to induce the first crack localizations) showed that the most significant analysis variables (maximum crack openings and steel stresses) are not significantly affected by these variations. This conclusion shows that the analysis results are meaningful.

Figs. 2 and 3 show the deformed meshes, for the two concrete thicknesses, for two instants of time: before the formation of the second crack, which is the instant when the highest steel stresses and crack openings are reached; at the end of the analysis. The crack propagation sequence followed the expected behaviour for thick RC elements: initially, micro-cracks were formed throughout all the surface region of the member; then, closely spaced cracks were formed from the surface; later, through cracks were formed, gradually along time. The time

variation of steel stresses at the location of the first through crack (the position where the highest stresses occur) is shown in Fig. 4.

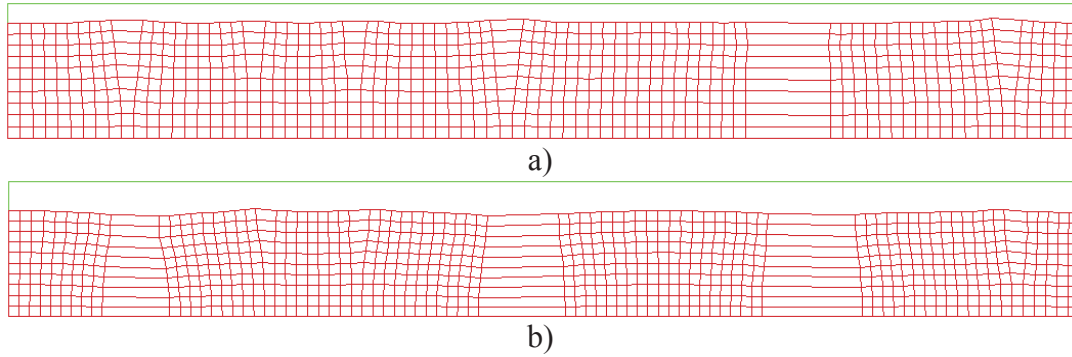


Figure 2: Deformed mesh for 500 mm thick RC ties with reinforcement  $a_{s,min}$ :  
a) 3 years after casting; b) at 50 years

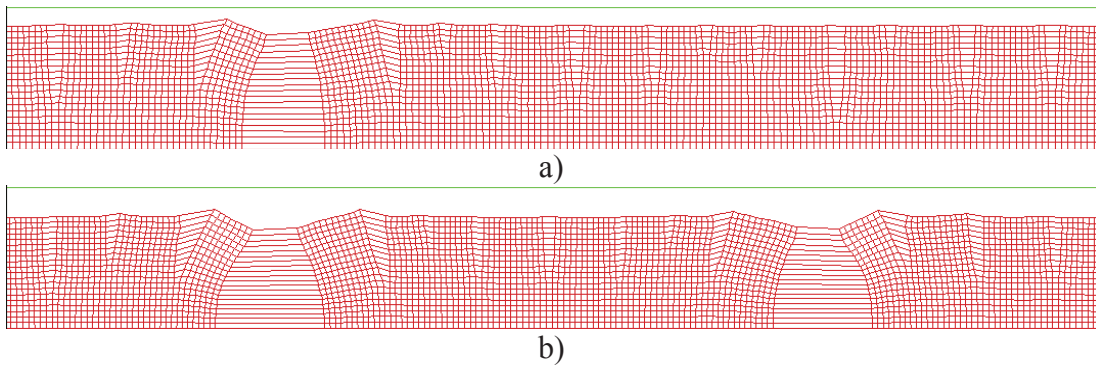


Figure 3: Deformed mesh for 1000 mm thick RC ties with reinforcement  $a_{s,min}$ :  
a) 10 years after casting; b) at 50 years

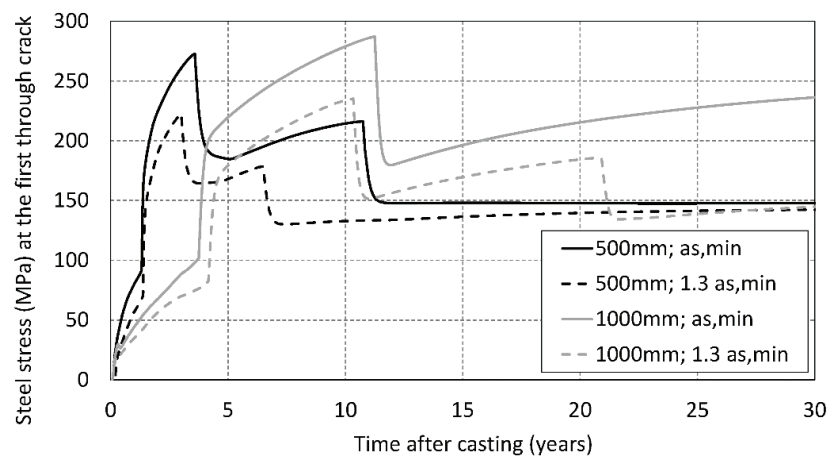


Figure 4: Steel stresses at the most critical position

#### 4. Final remarks

Three relevant conclusions are summarized: (i) The analysis results revealed, for the studied cases, that the rules in Eurocode 2 for calculation of the minimum reinforcement to avoid yielding are conservative. The maximum steel stress in the analysed ties was always lower than 300 MPa, a value considerably inferior to the yield limit (500 MPa in this case); (ii) In the studied cases, by adopting an amount of reinforcement 30% higher than  $a_{s,min}$ , the maximum crack opening was approximately equal to 0.30 mm. According to the Eurocode 2, the required area of reinforcement to reach such limit crack opening is much higher (~ twice  $a_{s,min}$ ); (iii) the adopted analysis strategy can be a useful tool to study the cracking behaviour of thick RC members, however, further analyses and validations are required to confirm the applicability of the reached conclusions.

#### Acknowledgements

This work was financially supported by: Project POCI-01-0145-FEDER-007457 (CONSTRUCT - Institute of R&D in Structures and Construction) and by project POCI-01-0145-FEDER-007633 (ISISE), funded by FEDER funds through COMPETE2020 - Programa Operacional Competitividade e Internacionalização (POCI), and by national funds through FCT - Fundação para a Ciência e a Tecnologia. FCT and FEDER (COMPETE2020) are also acknowledged for the funding of the research project IntegraCrete PTDC/ECM-EST/1056/2014 (POCI-01-0145-FEDER-016841). The financial support of COST Action TU1404 through its several networking instruments is also gratefully acknowledged.

#### References

- [1] EN 1992-1-1, Eurocode 2: Design of Concrete Structures – Part 1-1: General Rules and Rules for Buildings, CEN (2004)
- [2] Schlicke, D. and Vie Tue, N., Minimum reinforcement for crack width control in restrained concrete members considering the deformation compatibility, Structural Concrete 2 (2015), 221-232
- [3] Azenha, M., Numerical Simulation of the Structural Behaviour of Concrete since its Early Ages, PhD thesis, University of Porto – Faculty of Engineering (2009)
- [4] Azenha, M., Sousa, C., Faria, R. and Neves, A., Thermo-hygro-mechanical modelling of self-induced stresses during the service life of RC structures, Eng Struct 33 (2011), 3442-3453
- [5] DIANA, Finite Element Analysis, release 10.2, DIANA FEA BV, Delft (2017)
- [6] Azenha, M., Leitão, L., Granja, J., Sousa, C., Faria, R. and Barros, J., Experimental validation of a framework for hygro-mechanical simulation of self-induced stresses in concrete, Cem Concr Compos 80 (2017), 41-54
- [7] Kwak, H., Ha, S. and Kim, J., Non-structural cracking in RC walls: Part 1, finite element formulation, Cem Concr Res 36 (2006), 749-760
- [8] fib, Model Code for Concrete Structures 2010, Ernst & Sohn (2013)
- [9] Dörr, K., Ein Beitrag zur Berechnung von Stahlbetonscheiben unter besonderer Berücksichtigung des Verbundverhaltens, PhD thesis, University of Darmstadt (1980)

## **PARAMETRIC STUDY ON DAMAGES AND STRENGTH BEHAVIOUR OF POST-TENSIONED GIRDERS IN DECHATIWONG BRIDGES**

**Nat Hanwiboonwat<sup>(1)</sup>, Tidarut Jirawattanasomkul<sup>(1)</sup>, Songpol Charuvisit<sup>(1)</sup>, Nattamet Wuttiwannasak<sup>(1)</sup>, Nuttapon Kongwang<sup>(1)</sup>, Chinapat Banluelap<sup>(1)</sup>, Tawan Norsakul<sup>(1)</sup>**

(1) Kasetsart University, Department of Civil Engineering, Faculty of Engineering, Thailand

### **Abstract**

The Dechatiwong bridges located on Nakhon Sawan province, Thailand, are in the part of national highways as well as Asian Highways, connecting between Bangkok and the northern part of the country. To date, horizontal cracks have been observed at the ledge's corner of the end girders in these bridges. This research, therefore, aims to indicate causes of such cracks and investigate their behaviour using 2D non-linear finite element method by ATENA program. The vehicle loads and load patterns were evaluated based on AASHTO LRFD-2012 standards. The analysed Post-tensioned Concrete (PC) girder is 11.75 m long with a cantilever fixed-end support. The analysis is focused on influences of prestressing sequences and losses in prestress which are varied from 0-50%. From the analytical results, severe cracks at the end of girders are caused by the losses in prestress.

### **1. Introduction**

The Dechatiwong Bridges are located in the national highways no.1 as well as Asian Highways (AH1). Therefore, this research is essential for Asian transportation and can contribute to Thailand's economic growth. This research focuses on investigation of the horizontal crack at re-entrant corner of Post-tensioned Concrete (PC) girders in the extension part of Dechatiwong Bridge No.2 and No.3 (see Fig. 1). This project is aimed to evaluate behavior of bridge's superstructure using Finite Element Method (FEM) by 2D ATENA program. The vehicle loads and load patterns were followed AASHTO LRFD-2012 standard. The analysed Post-tensioned Concrete (PC) girder has 11.75 meters long with a cantilever fixed-end support at pier. The models could simulate I-girders in 2D which material properties of the girders were based on the previous researches [1-5]. In this research, there are two possible assumptions for causes of the horizontal cracks which are prestressing

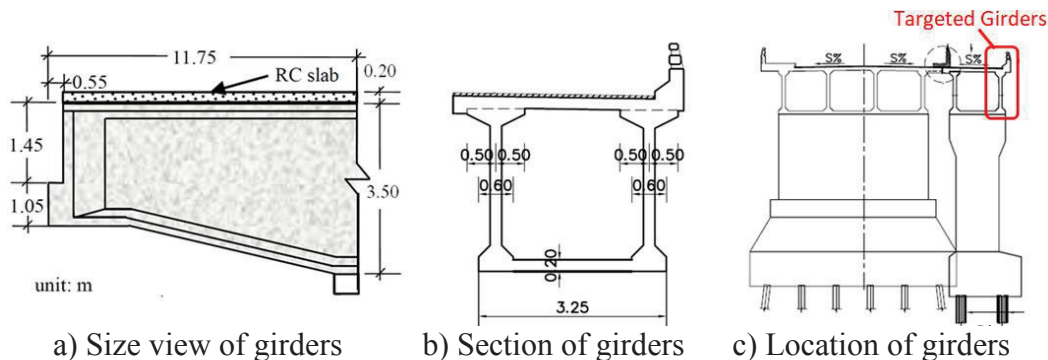
sequences and losses in prestress. From the analytical results, prestressing sequences may not be a cause of the cracks since crack did not occur. When losses in prestress are reached to 20%, cracks appeared in the analysis. Therefore, this may be one of the most possible causes for the current horizontal cracks.



a) Cracks at Dechatiwong Bridge No.2      b) Cracks at Dechatiwong Bridge No.3  
Figure 1: Ledge girders and horizontal crack at reentrant corner in Dechatiwong Bridge.

## 2. Detail of girders

The extension girders of Dechatiwong Bridge No.2 and No.3 were designed as the Prestressed Concrete (PC) girders in box-shape section based on AASHTO LRFD standards. However, only exterior I-girders were analysed because cracks were observed. In this research, cantilever girders have a span length of 11.75 m and the maximum height of 3.50 m. The effective width of flange is 1.72 m. Details of targeted cantilever girders are shown in Fig 2.



a) Size view of girders      b) Section of girders      c) Location of girders  
Figure 2: Details of targeted cantilever girders.

## 3. Finite Element Analysis

The 2D Finite Element Method (2D-FEM) by ATENA program is used to analyse crack patterns and behaviours at the re-entrant corner of ledge girders in Dechatiwong Bridge. In the analysis, the material properties and models were followed previous researchers [1-5].

### 3.1 Materials

**Concrete.** The compressive strength of concrete is 30 MPa for PC girder. In compression, the stress-strain relationship of concrete is based on the uniaxial behaviour of concrete proposed by CEB-FIB Model Code 2010 [5], as shown in Fig. 3a. In tension, the stress-strain

relationship of concrete is based on the bilinear softening behaviour of concrete proposed by Hordijk [3], as shown in Fig. 3b.

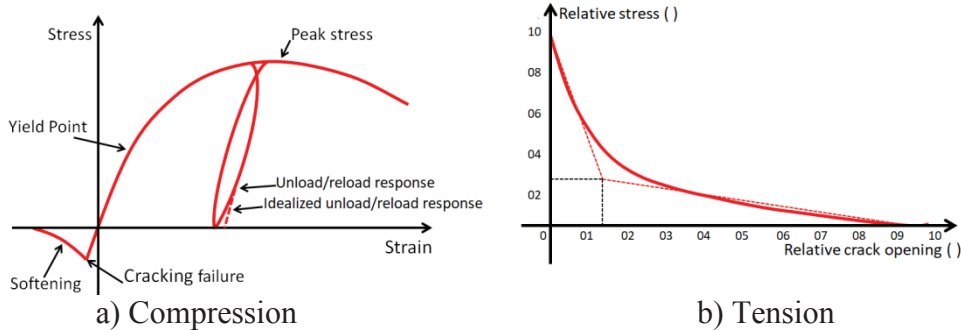


Figure 3: Uniaxial behaviour of concrete.

**Reinforcement and Prestressed Tendon.** There are 10 post-tensioned tendons in the girder with profiles as shown in Fig. 4a and sectional area of each tendon is  $416.8 \text{ mm}^2$  with a yield strength of 1,356 MPa and an ultimate strength of 1,600 MPa. For the steel reinforcement, the deformed bar with a diameter of 12 mm and spacing of 200 mm is used to prevent shear crack and lateral buckling with details as shown in Fig. 4b. A yield strength of steel reinforcement is 400 MPa and an ultimate strength is 435 MPa. The modulus of elasticity of tendons and reinforcement are  $2.0 \times 10^5 \text{ MPa}$  with poisson ratio of 0.3.

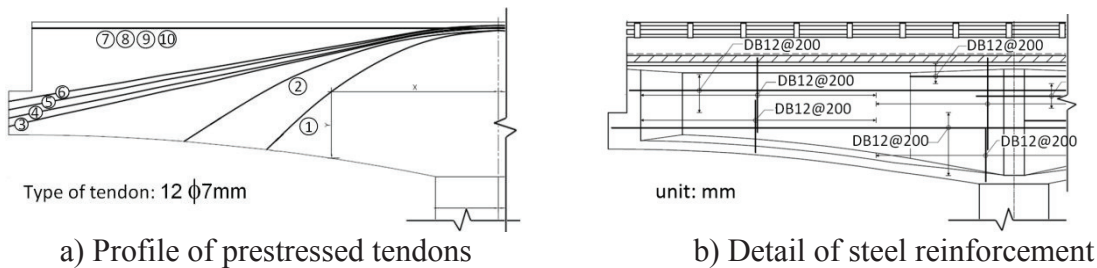


Figure 4: Detail of prestressed tendons and steel reinforcement.

**Connection and Element Type.** In analytical models, the connections in steel reinforcement-concrete and prestressed tendons-concrete are assumed as the perfect connections and defined as a discrete reinforcement. Therefore, prestressing forces are constant along the tendons length. The concrete element is modelled as 4-node quadrilateral plane. The element size at free-ended ledge is 50 mm based on a maximum aggregate size of concrete. For the other parts of model, the element is defined with a size of 100 mm as shown in Fig. 5.

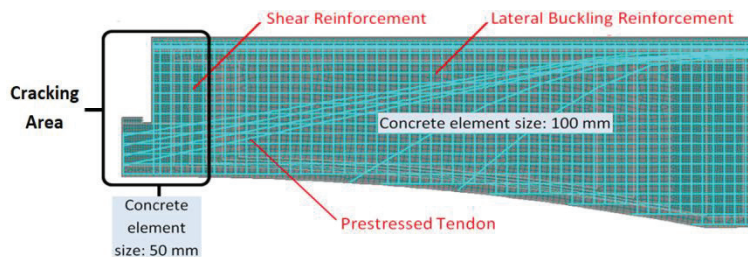


Figure 5: Detail of discrete reinforcement in analytical model and element size of concrete.

### 3.2 Boundary condition

From the designed detail, the support of extension-cantilevered girders is designed as a fixed support as shown in Fig. 6a. Therefore, at the pier-end, the support of girder's models was assumed as a fixed support. At the free end, the displacement control is applied to increase 0.25 mm in each step as shown in Fig. 6b. Types and locations of monitoring points in the models are also shown in Fig. 6b.

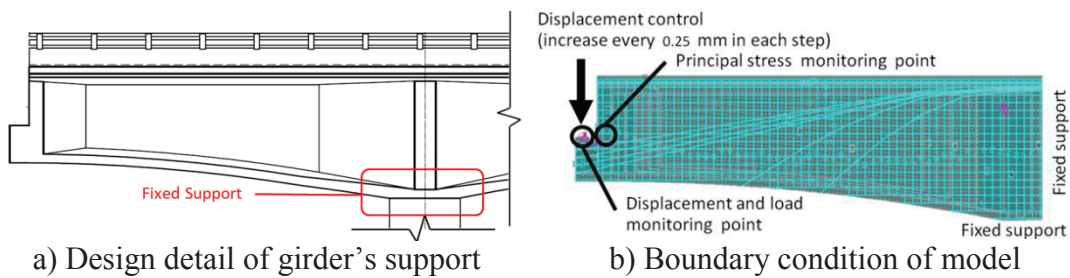


Figure 6: Design detail of girder's support and boundary condition of model.

### 3.3 Analytical cases

In this research, there are 2 assumptions of the causes of horizontal cracks at re-entrant corner which are 1) prestressing sequences and 2) losses in prestress. Therefore, analytical models were created in 2 types; 1) Type 1-analysis of horizontal cracks caused by different prestressing sequences, and 2) Type 2-analysis of horizontal cracks caused by losses in prestress.

**Effect of prestressing sequences.** Initial prestressing or bursting forces at anchorage zones were defined as forces from the design details. The size of steel plate is 200×200 mm and prestressing sequences of analytical models are assumed into 3 pulled out steps as shown in Fig. 7. Note that Steps 1–3 are prestressing sequences in the analytical models, whereas tendon No. (1) – (10) are prestressing forces in the actual design details. As a result, prestressing sequences in the actual construction were different from that in the design details.

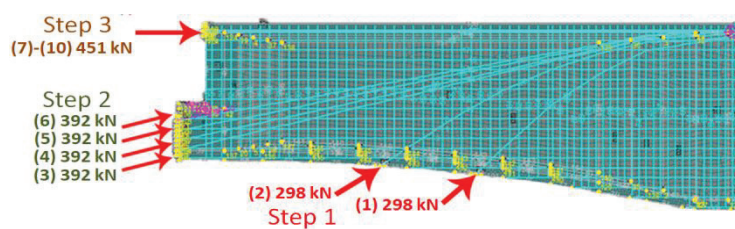


Figure 7: Sequences of prestressing in analytical models and prestressed forces defined in actual design details.

**Effect of losses in prestress.** From calculation based on ACI-423, the actual immediate losses are between 5 - 25% and time dependent losses are between 15 - 25%. Therefore, to analyse the cracks caused by losses in prestress, losses in prestress are assumed as 0, 10, 20, 25, 30, 40, and 50% of prestressed force as stated in design details.

## 4. Analytical results

### 4.1 Effect of prestressing sequences

From the analytical models, the horizontal cracks do not occur at re-entrant corner after all of tendons are pulled out as assumed steps. This is because the principal stress at that re-entrant corner is still in compression after pulling out all of tendons. The contour of the principal stress is shown in Fig. 8.

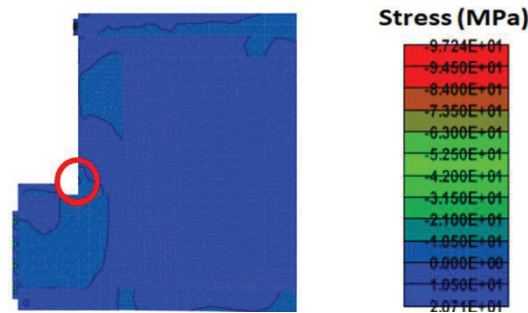


Figure 8: Principal stress for analytical model of girder after analysis.

### 4.2 Effect of losses in prestress

From the analysis, the first cracking load at re-entrant corner of ledge is significantly depended on the losses in prestress as shown in Table 1. It can be seen that the higher losses in prestress are applied, the less girder's first cracking load is observed. If losses in prestress are increased more than 20% of the designed prestressed forces, the analytical first cracking load is less than 809 kN which is a minimum required load based on AASHTO LRFD 2012 standard. In summary, the predicted cracks may occur when losses are more than 20%.

Table 1: Analytical results and cracks prediction by 2D-FEM analysis.

Losses in prestress (%)	Analytical first cracking load (kN)	Minimum required load AASHTO LRFD (kN)	Predicted crack
0	865	809	Not occur
10	835	809	Not occur
20	772	809	Occur
25	741	809	Occur
30	710	809	Occur
40	678	809	Occur
50	615	809	Occur

The graphics of crack patterns from 2D-FEM are shown in Fig. 9a. In addition, the cracks analysed by 2D-FEM model show the same direction and pattern as the cracks observed in visual inspection. In Fig.9b, the stress at re-entrant corner and the load is shown with varied losses in prestress from 0 to 50%. The tensile stress at re-entrant corner depends on vertical compressive force. If the vertical force is increased, the tensile stress is also increased. From the analysis, this area is subjected to tensile stress which is increased step by step until



reaching the tensile strength of concrete (+2.4 MPa). After that the horizontal cracks occur at the re-entrant corner of the ledge. In addition, the curves indicate that the stress is depended on the losses in prestress. If the losses in prestress are increased, the tensile stress is higher and reaches to tensile strength of concrete earlier, leading to the horizontal cracks in this area.

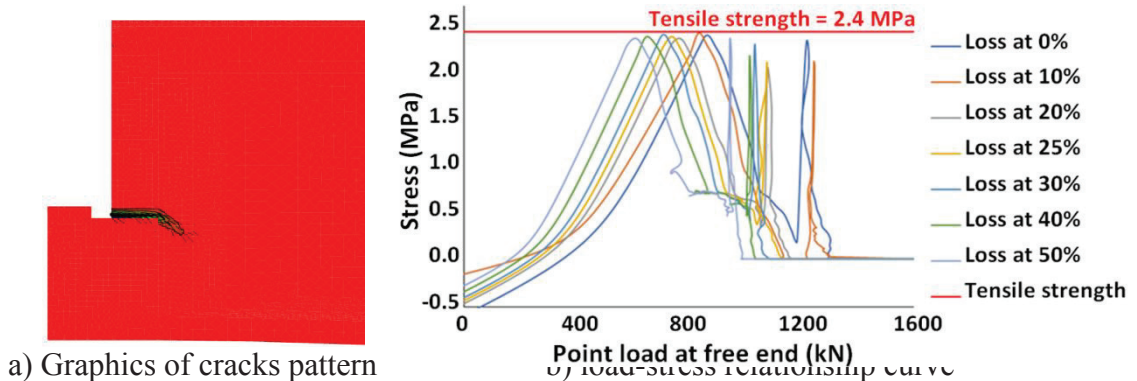


Figure 9: Graphics of cracks pattern at re-entrant corner and load-stress relationship curve.

## 5. Conclusions

- 1) From the analytical models, the horizontal crack occurred at the re-entrant corner of PC ledge girders agrees well with the cracks observed by visual inspection.
- 2) From the analytical models, the cracks may be caused by the tensile stress at that re-entrant corner which is a result from perpendicular compressive force.
- 3) In the analysis, losses in prestress significantly affect to first cracking load of girders.
- 4) The horizontal cracks occur at re-entrant corner when the prestressed losses are increased more than 20% of designed prestressed forces. This is because girders cannot carry the loads which are required by AASHTO LRFD 2012 standards (809 kN).

## Acknowledgement

The authors would like to acknowledge Dr. Rajwanlop Kumppong and Dr. Sukit Yindeesuk from Department of Highway, Ministry of Transport, Thailand, for providing information of the Dechatiwong Bridge and invaluable guidance. The authors would also like to acknowledge AUN-Seed Net for research funding under project titles “Development of Upgrade Systems for Structural Performances of Existing Concrete Bridges in Thailand”.

## References

- [1] Wu, X.-H. et al, Tendon Model for Nonlinear Analysis of Prestressed Concrete Structures, J Struct Eng 127(4) (2001) 398-405
- [2] Hognestad, E., Study of combined bending and axial load in reinforced concrete members. University of Illinois at Urbana Champaign, USA (1951)
- [3] Hordijk, D.A., Local approach to fatigue of concrete. PhD Thesis, Delft University of Technology, The Netherlands (1991)
- [4] Timoshenko S.P., Strength of materials, 3rd Ed, Van Nostrand, Princeton, USA (1956)
- [5] FIB Bulletin 55, CEB-FIB Model Code 2010

## **PARAMETRIC STUDY ON DAPPED-END OF PRESTRESSED CONCRETE GIRDER IN DECHATIWONG BRIDGE USING FINITE ELEMENT ANALYSIS**

**Nuttapong Kongwang<sup>(1)</sup>, Tidarut Jirawattanasomkul<sup>(1)</sup>, Wanakorn Prayoonwet<sup>(2)</sup>,  
Songpol Charuvisit<sup>(1)</sup>**

(1) Department of Civil Engineering, Kasetsart University, Bangkok, Thailand

(2) Division of Engineering and Policy for Sustainable Environment, Hokkaido University,  
Sapporo, Japan

### **Abstract**

End parts of concrete bridge girders in Thailand are usually dapped-end connections, particularly in a suspended span of bridges. However, the diagonal cracks in the dapped-end zone were found in a 40-meter suspended span in Dechatiwong Bridge due to insufficient reinforcement in the dapped-end region compared to that in PCI Design 2010. Hence, the aim of this research is to analyze the influence of different dapped reinforcement and effect of the tendon in the nib portion of the dapped-end on the failure modes and strength of dapped-end girders using 2D nonlinear finite element modeling in ATENA program. The result of nonlinear finite element analysis indicated that the hanger reinforcement is significant because it can change the failure mode from shear compression at the nib region to flexure shear in the full-depth section, and the models with tendon in nib portion can significantly increase the structural strength compared to that without tendon in the nib portion model. It was also found that the strength of the dapped-end girder predicted by the PCI design agrees well with that of girders without prestressing in nib portion. Therefore, the design equations proposed by PCI is still reliable and accurate for the structure without prestressing in the nib portion.

### **1. Introduction**

Currently, precast girder is widely used, especially in bridge structures with long span, because of its convenience for quality control and construction. Girder's lateral stability is increased when its depth at end support, a dapped-end connection, is reduced. When placed it on to supporting structures, this can help to decrease the overall height of bridges. Nevertheless, this part is characterized by a high concentration of stress at the end of the beam

due to discontinuity. The dapped-end connection is also implemented in Dechatiwong Bridge, Nakornsawan, Thailand. This bridge consists of 40 meters suspended span of post-tensioned Prestressed Concrete (PC) girder; however, the dapped-end region is very sensitive to loads if dapped-end reinforcement is insufficiently used or improperly placed. These may cause severe cracks, leading to a sudden failure [1]. It is also evident that the cracks have already occurred at the dapped-end of Dechatiwong Bridge. Thus, this research focuses on the behavior and characteristics or failure patterns of dapped-end PC girder using the non-linear Finite Element Method (FEM) by 2D ATENA program to construct analytical models for that bridge under static loading.

## 2. Bridge's Details

This research focuses on Dechatiwong Bridge No.3 in which the cracks were observed at the dapped-end region. Only 40 meters suspended span post-tensioned PC girder with an I-shape cross section is studied which is supported by cantilever beams with lower nibs at both sides.

### 2.1 Details of a 40 meters Suspended Span

The 40 meters suspended span girder has an I cross-section with depth 2.50 m (Fig. 1b); the cast-in-place Reinforced Concrete (RC) top flange slab of thickness ( $t$ ) 0.18 m; the effective flange width ( $b_e$ ) of 2.75 m; a dapped-end connection of girder with a nib depth of 1.40 m, and recession length of 0.55 m (Fig. 1a).

### 2.2 Material Properties

According to the as-built drawing of the bridge, the compressive strength of concrete cylinder is 35 MPa and 25 MPa for the PC girder and the RC slab, respectively.

The PC girder had 17 tendons, the end region of the girder had 11 tendons (Fig. 1a), and the position of tendons as shown in Fig. 1b. Each tendon contained 12 wires with a diameter of 7 mm. In addition, the tensile strength ( $f_{py}$ ) and the ultimate tensile strength ( $f_{pu}$ ) of the wires were 1,377 MPa and 1,632 MPa respectively. The prestressing forces were assumed to apply with 25% prestress losses [2], in all case of the analysis. In the dapped-end area, the deformed bar of 10 mm (DB10) with SD40 grade was placed with a spacing of 150 mm. The DB10 had the tensile strength ( $f_y$ ) of 400 MPa and the ultimate tensile strength ( $f_u$ ) of 435.4 MPa.

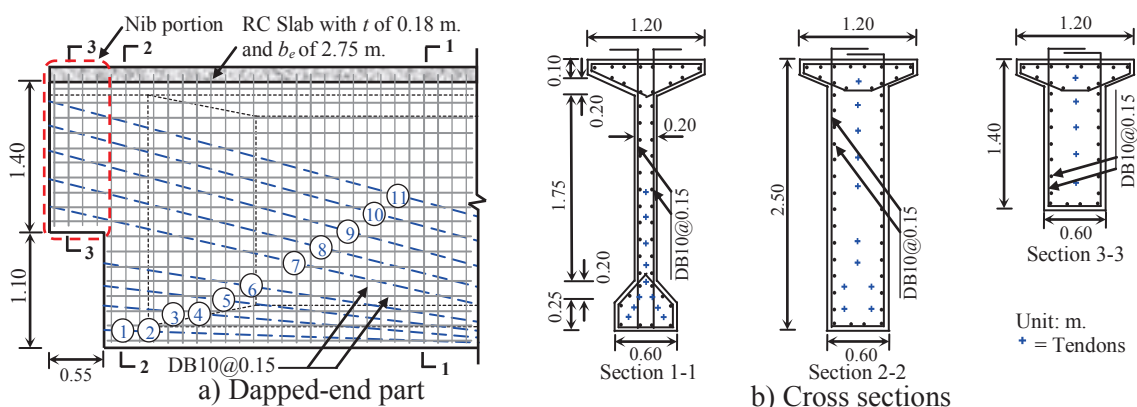


Figure 1: Dapped-end details of a 40 meter suspended span girder

### 3. Design Code for Dapped-End Connection

Dapped-end connection can be designed based on the Precast/Prestressed Concrete Institute (PCI) Design Handbook [3] in which five potential modes of failure are proposed (Fig. 2a). Each mode of failure are prevented by dapped reinforcement as shown in Fig. 2b. The amount of dapped reinforcement can be calculated with equations proposed in PCI 2010 [3].

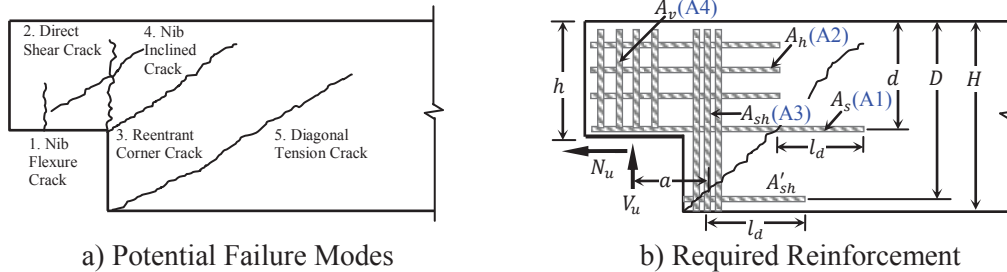


Figure 2: Failure modes and required reinforcement in dapped-end connection

#### 3.1 Dapped-End Reinforcement in Actual Girder

The actual amount of dapped-end reinforcement in Dechatiwong's PC girder was compared with the design equations recommended in the PCI design; the applied load is calculated based on a factored load combination with HL-93 truck [4], which is approximately 1,896 kN. These reinforcement are summarized in Table 1. It can be seen that all of the actual dapped-end reinforcement is less than the calculated from the PCI equations.

Table 1: Reinforcement in dapped-end

Type of Reinforcement	Reinforcement Area (mm <sup>2</sup> )		% Ratio Actual/PCI
	Actual	PCI Requirement	
Flexure Reinforcement, $A_s$	314	2,935	11%
Shear Friction Reinforcement, $A_h$	628	1,233	51%
Hanger Reinforcement, $A_{sh}$	471	6,320	7%
Vertical Reinforcement, $A_v$	628	2,255	28%

\* % Ratio between Actual and PCI is calculated from  $(Area_{actual}/Area_{PCI}) \times 100$ .

### 4. Finite Element Analysis

The 2D-FEM in this study were constructed using the ATENA program to analyze the behavior and failure modes of the dapped-end of the 40 meters suspended span.

#### 4.1 Material Models

The concrete models can be classified into compression and tension. The former—is recommended by the CEB-FIP Model Code 90 [5], with compressive strain at peak ( $\epsilon_c$ ) of 0.002 and a Poisson's ratio of 0.2; whereas, the latter, assumed linear elastic, the tension behavior after cracking is an exponential function, experimentally derived by Hordijk [6], with fracture energy of 71.6 N/m.

For reinforcing steel, the bilinear stress-strain curve with an elastic-perfectly plastic behavior is used. For tendon, the stress-strain curve proposed by Ramberg and Osgood [7] is used. Additionally, the modulus of elasticity ( $E_{ps}$ ) is  $2.0 \times 10^5$  MPa and a Poisson's ratio of 0.3 is used in both curves.

#### 4.2 Boundary Conditions and Element types

In 2D-FE modeling, the load was applied at 6 m from the end support with simple support boundary condition. The displacement was monitored under the loading point, as shown in Fig. 4a. Two element types (Fig. 4b): 1) a 2-node truss element for reinforcing and prestressing steels, and 2) a plane quadrilateral element for concrete are used and are bonded perfectly.

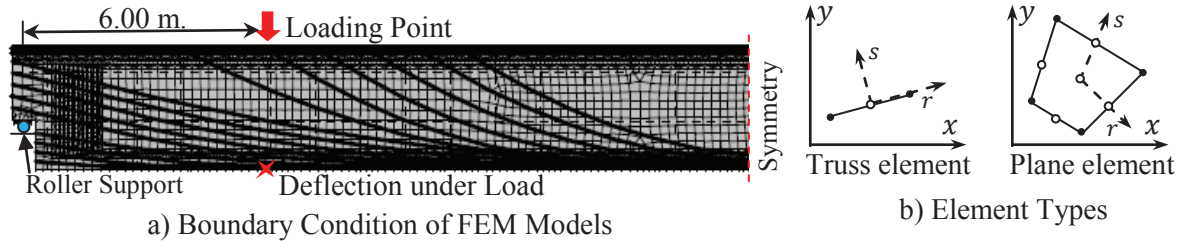


Figure 4: Boundary condition and element types in FEM

#### 4.3 Analytical Cases

In this research, the analytical cases are categorized into 2 cases, and the summary is presented in Table 2. In Case 1, in order to evaluate the effect of different types of the dapped-end reinforcement, 5 analytical models were performed with varied reinforcement details ( $A_s$ ,  $A_{sh}$ ,  $A_h$ , and  $A_v$ ), denoted as A0-A4. A0 represents the actual girder with actual reinforcement from the existing drawing, whereas A1-A4, only one reinforcement detail such as  $A_s$ ,  $A_{sh}$ ,  $A_h$ , and  $A_v$  changes based on the PCI design. The rest of the reinforcement details such as the number of tendons (T) and spacing of the hanger reinforcement (S) are based on the actual drawing. In Case 2, in order to evaluate the effect of the prestressing steel in the nib portion, 6 analytical models were analyzed with different number of tendons, denoted as T0-T5. T0 represents a model without tendon, and T5, the most prestressing steel of 5 tendons. In this case, A3 with  $A_{sh}$  of 12-DB28 from PCI design and the spacing of hanger reinforcement 50 mm (S50) was used to prevent cracks at a re-entrant corner.

Table 2: Summary of analytical cases

Case No.	Models	Dapped-End Reinforcement (mm <sup>2</sup> )				No. of Tendon, T	Spacing of Hanger Bars, S (mm)
		$A_s$	$A_h$	$A_{sh}$	$A_v$		
1	A0-T5-S150	314	628	471	628	5	150
	A1-T5-S150	3,142	628	471	628	5	150
	A2-T5-S150	314	1,257	471	628	5	150
	A3-T5-S50	314	628	7,389	628	5	50
	A4-T5-S150	314	628	471	2,513	5	150
2	A3-T0-S50	314	628	7,389	628	No	50
	A3-T1-S50	314	628	7,389	628	1	50
	A3-T2-S50	314	628	7,389	628	2	50
	A3-T3-S50	314	628	7,389	628	3	50
	A3-T4-S50	314	628	7,389	628	4	50
	A3-T5-S50	314	628	7,389	628	5	50

**Note:** A0 = Actual dapped-end reinforcement, A1 = Flexure reinforcement ( $A_s$ ), A2 = Shear friction reinforcement ( $A_h$ ), A3 = Hanger Reinforcement ( $A_{sh}$ ), A4 = Vertical reinforcement ( $A_v$ ), T = Number of tendon in a nib portion, S = Spacing of hanger reinforcement.

## 5. Analytical results

In both cases, the first crack width of all models are less than limited crack width which is 0.43 mm. [4], so PC dapped-end girders can be used in the crucial condition. However, the crack propagation increasing when the vertical compressive force was increased.

### 5.1 Sensitivity of Dapped-End Reinforcement in Case 1

From FEM results, A3-T5-S50 show the highest load capacity with the increase in the amount of hanger reinforcement based on PCI code (Fig. 5a). This is because the mode of failure changes from compression shear (Fig. 6a) to flexure-shear (Fig. 6b). In the grey zone, compressive strain is greater than 0.002 resulting the concrete failure. This criterion was used by Hassan et al. [8]. However, the Dechatwong's PC girder remains safely operated under HL-93 according to the ASSHTO LRFD 2012, because the actual girder's strength from FEM (A0-T5-S150) is 2,784kN, whereas  $V_u$  is 1,896 kN.

### 5.2 Effect of Prestressing Steel in Nib Portion for Case 2

Most of the failures in the 2D-FEM of case 2 are flexure shear (Fig. 6b), except that A3-T0-S50 showing direct shear combined with flexure shear (Fig. 6c). This failure is attributed by the absence of tendon in the nib portion. Therefore, it indicates that the prestressing steel can impact the dapped-end structural behavior. In addition, the strength predicted by PCI agrees well with case A3-T0-S50 as shown in Fig. 5b, illustrating the accurate prediction of PCI design.

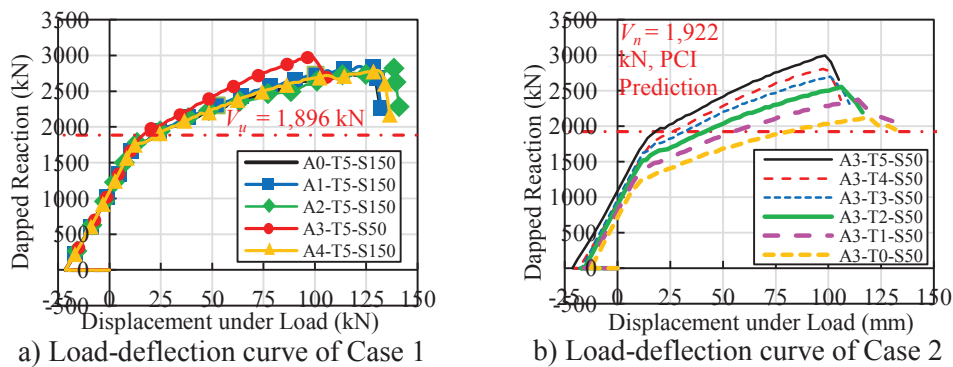


Figure 5: Load-deflection curves

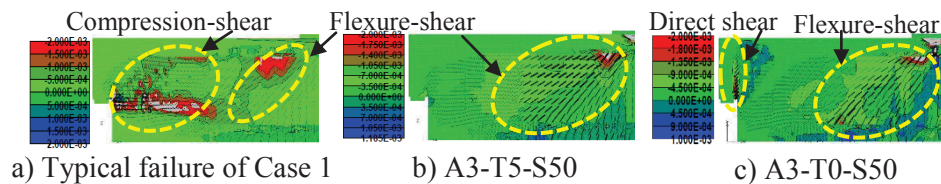


Figure 6: Failure modes

## 6. Conclusions

- 1) The sensitivity study of dapped-end reinforcement in each type shows that hanger reinforcement is significant because it can change the failure mode from shear compression at the nib region to flexure shear in the full-depth section.
- 2) The Dechatwong's PC girder remains safely operated because the actual girder's strength from FEM is 2,784 kN while the ultimate load calculated by ASSHTO is only 1,896 kN.
- 3) Predicted strength from PCI design agrees well with girders without prestressing in nib portion, so PCI equations are suitable for structures without prestressing steel in nib portion.

## Acknowledgement

The authors would like to acknowledge Dr. Rajwanlop Kumppong and Dr. Sukit Yindeesuk from Department of Highway, Ministry of Transport, Thailand, for guidance and information of the Dechatiwong Bridge, and AUN-Seed Net for research funding under the project title "Development of Upgrade Systems for Structural Performances of Existing Concrete Bridges in Thailand". The last author is thankful for the Master's scholarship granted by Faculty of Engineering, Kasetsart University, Thailand.

## References

- [1] Mitchell, D. et al, Concorde overpass collapse: structural aspects, *Journal of Performance of Constructed Facilities* (2011), 545-553
- [2] Branson, D.E. and Kripanarayanan, K.M., Loss of prestress, camber and deflection of non-composite and composite prestressed concrete structures. *PCI Journal* (1970), 22-52
- [3] Precast/Prestressed Concrete Institute, *PCI Design Handbook* 7th ed, Chicago (2010).
- [4] AASHTO, LRFD., *Bridge design specifications 2012* Washington, DC, USA American Association of State Highway and Transportation Officials (2012)
- [5] CEB-FIP Model Code 1990, First Draft, Committee Euro-International du Beton, Bulletin information No. 195,196, Mars (1990)
- [6] Hordijk, D.A., *Local Approach to Fatigue of Concrete*, Doctor Dissertation, Delft University of Technology, the Netherlands (1991)
- [7] Ramberg, W. and Osgood, W.R, *Description of stress-strain curves by three parameters*, (1943)
- [8] Hassan, T. et al., Modeling of L-shaped, precast, prestressed concrete spandrels, *PCI journal* (2007), 78

## **PREDICTION OF THE IMPACT OF SHRINKAGE ON CONCRETE STRENGTH WITH THE BEAM-PARTICLE APPROACH**

**Nicolas Chan <sup>(1)</sup>, Cécile Oliver-Leblond <sup>(1)</sup>, Farid Benboudjema <sup>(1)</sup>, Frédéric Ragueneau <sup>(1)</sup>, François Soleilhet <sup>(1)</sup>**

(1) LMT, ENS Cachan, CNRS, Université Paris-Saclay, Cachan, France

### **Abstract**

Durability is a relevant criterion for preserving a safe structure and avoiding the renewal of costs. However, several phenomena – such as delayed deformation, corrosion, leading to cracking – can severely affect the service life. Not only cracks opening have an influence on concrete performance, but also the crack pattern. In the case of drying shrinkage, due to the low rate of gas and water transfers, stress that may lead to a network of micro-cracks. Mechanical and hydric properties are directly impacted by those cracks.

Therefore, it seems essential to consider shrinkage when studying cracking of cementitious materials. This study focuses on a beam-particle model in order to investigate the formation and impact of drying shrinkage cracks. The cohesion of the material is obtained with a lattice of Euler-Bernoulli brittle beams. When a crack occurs, cohesion disappears. To capture the crack closure, a contact law with friction is considered between the polygonal particles. 2D simulations on three points bending test with or without considering drying shrinkage are performed. The finite element method is used to obtain the drying shrinkage strain field. Then, a reanalysis method – inspired from [1]– is used to obtain the cracking patterns caused by drying. The parameters of the numerical models are identified on the results of an experimental campaign carried out by Soleilhet [2]. This same campaign is then used to validate the pertinence of an explicit representation of cracking.

### **1. Introduction**

In this paper, the beam particle model and the hydric transport model are presented. Then, three points bending modelling is achieved in two cases: with and without considering previous drying.



Moreover, the beam-particle model generates a random mesh which represents material's heterogeneity. It reproduces the experiment variability.

## 2. Beam-particle model

This model is constituted by a set of polygons. It is generated in four steps [3] with a Voronoi's tessellation and Delaunay's triangulation. Each rigid particle has a centroid which is randomly placed, to represent the material's heterogeneity. They are connected to each neighbour with Euler-Bernoulli brittle beam to represent cohesion between particles (Figure 1).  $E, \alpha, A_b, l_b$  respectively represent beam young modulus, the inertia, the cross-section area and the length.  $\vec{U}_i, \vec{U}_j, \theta$  are the three degrees of freedom: 2 translations, 1 rotation. Otherwise, a contact law with friction is introduced to represent particles interaction such as cracks closure.

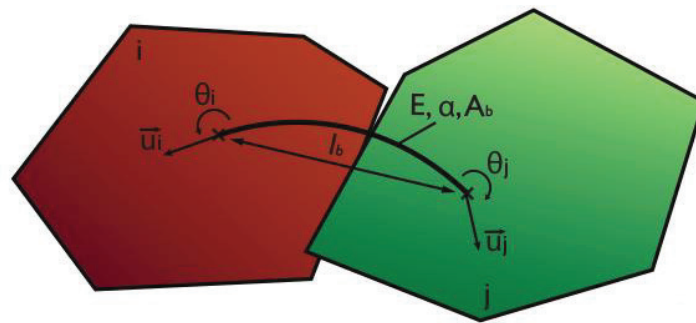


Figure 1: Linked particles [3].

These mechanisms permit to capture the elastic and softening behaviour. Indeed, for a mechanical or a hydric loading, a breaking criterion based on Mohr Coulomb is considered [3] with deformation and beam's rotation, which represent particles displacement. When the criterion threshold is reached the beam is deleted. The link between two particles disappears and it permits to obtain an explicit crack opening.

Furthermore, due to random mesh, each simulation gives different results. Experiment variability is represented. Contrary to an experiment campaign, virtual testing permit to generated more than 3 specimens which is generally considered in an experiment campaign. A statistic model is taken account with the normal distribution. Properties such as flexural strength average seem to convert with more than 20 tests.

## 2. Hydric transport model

In this study, two steps are needed to obtain a hydric strain field. A simulation is realised on Cast3m which is a finite element program. Then a reanalysed method is used [1]. This method acts as a bridge between continuum and discrete models.

The hydric transport model is based on a non-stationary transport equation with Eq. (1). It is supervised with initial intern and extern moisture. In this equation, liquid transfer is supposed.

$$\phi \frac{\partial S}{\partial P_c} \frac{\partial P_c}{\partial t} = \left( \frac{K \cdot k_r}{\mu} \text{grad}(P_c) \right) \quad (1)$$

$\phi$  is material's porosity,  $S$  the degree of saturation,  $P_c$  the capillarity suction,  $k_r$  the relative permeability,  $K$  the permeability and  $\mu$  the water viscosity. These parameters are identified with van Genuchten model which is basically developed for soil [4] It is also supposed that liquid moisture transport is predominant compared to gas transport in a considered interval of moisture [5]. Otherwise, relative permeability is determined with Eq. (2), with the parameter  $m$ .

$$k_r = \sqrt{S} \left( 1 - \left( 1 - S^{\frac{1}{m}} \right)^m \right)^2 \quad (2)$$

Degree of saturation is obtained with Eq. (3). Then, Kelvin-Laplace equation Eq. (4) permits to create a link between capillarity suction and relative humidity with ideal gas hypothesis.

$$S(P_c) = \left( 1 + \left( \frac{|P_c|}{a} \right)^{\frac{1}{1-m}} \right)^{-m} \quad (3)$$

$\rho$  bulk weight,  $R = 8.314 \text{ Jmol}^{-1}\text{K}^{-1}$ ,  $T$  temperature,  $M$  molar mass,  $HR$  relative humidity.

$$P_c = \frac{\rho RT}{M} \ln (HR) \quad (4)$$

Once the finite element analysis is realised, a hydric strain field is obtained. The reanalysis method [1] permits to project nodes or gauss points of this strain field on the beam-particle discretisation. The shrinkage induces a force which is locally estimated on each beam. Then, the discrete model converges to a steady state which induces cracks due to the breaking criterion. Results represent explicit cracks' expansion and trajectory [6].

### 3. Three points bending modelling

In this part, 2D three points bending simulations are performed to determine the impact of drying shrinkage on an 84x10cm specimen Figure 2. 21 000 nodes are generated in the random mesh, which is equivalent to 63 000 degrees of freedom. Concerning boundary conditions, an isostatic case is considered. The mechanical and hydric parameters correspond to Soleilhet [5] concrete. Then, beam-particle model's parameters are identified. 26 simulations are performed with or without modelling shrinkage. Experimentally [5], drying specimens are conserved in a controlled room at temperature 25°C ( $\pm 1^\circ\text{C}$ ) and 36% RH ( $\pm 5$ ). Beam-particle parameters permit to characterise quasi-brittle material's behaviour. Then, drying simulations are realised with the same set of parameters to predict the drying impact on strength resistance.

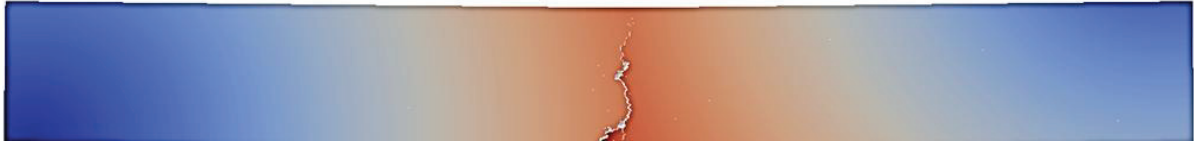


Figure 2: Cracking pattern.

In Figure 3 numerical and experimental forces-displacements curves are represented. The identification reveals a difference of 2.7%.

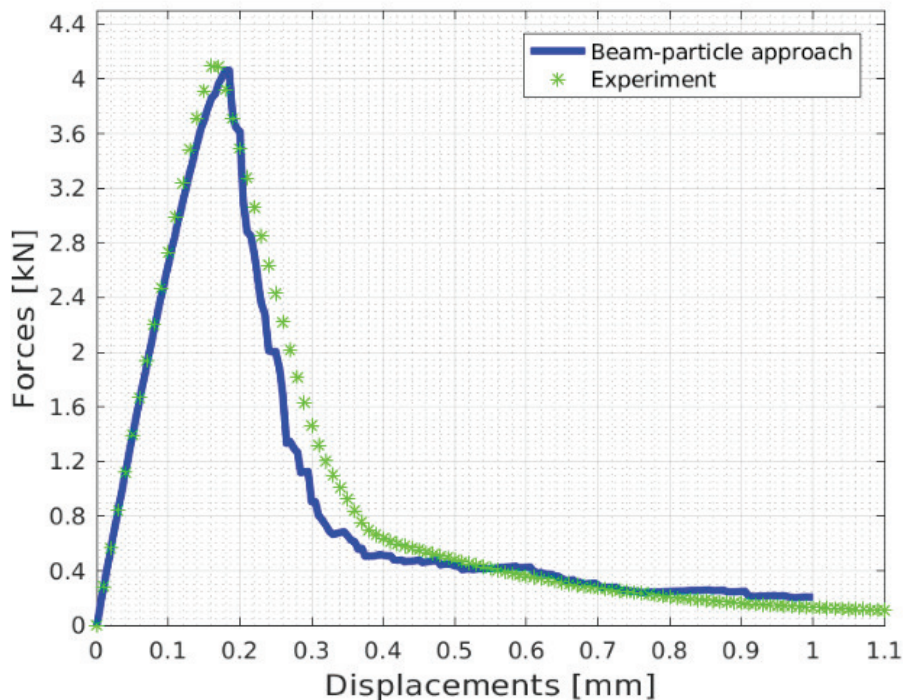


Figure 3: Three points bending forces-displacements average curves without shrinkage.

For non-drying case, the results are given in Figure 3 and for drying case results are given in Figure 4. It demonstrates a reduction of 12% of the maximum flexural strength due to initial strains at the peak, in the numerical model. Furthermore, in the elastic part, Young modulus decreases slightly due to previous micro-cracks formed during shrinkage. The cracks opening is in the order of 10  $\mu\text{m}$ .

In drying case, because of three points bending, the upper part of the beam is compressed, previous shrinkage cracks are closed, and particles are interacted to model the unilateral effect and the stiffness' recovering, whereas on the down side, the beam is in tensile state and cracks are still opened.

Otherwise, contact law, between particles, has an impact on post peak behaviour. Indeed, with contact law between each particle the drop is less significant because cracks closure is considered.

In Figure 4 the beam-particle model's prediction underestimates the experimental curves. Indeed, it has to consider complementary phenomena. The comparison between numerical and experimental results reveals a difference of 12% at the peak. The average of 26 virtual

testing drying specimen is represented on the force-displacement curve. Standard deviation reveals that the maximal and minimal strength force is respectively included between 20% and 14% of the average value.

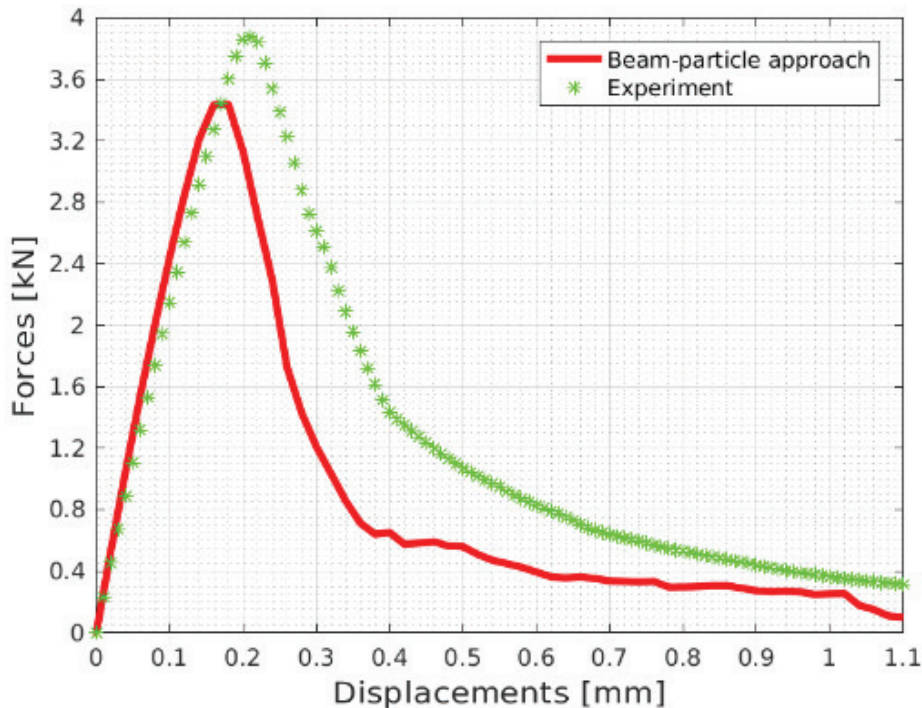


Figure 4 : Three points bending forces-displacements average curves with shrinkage.

It is important to emphasize that experimentally, there's generally not enough considered specimens to represent reality with certainty.

It is noticed that the main crack caused by mechanical loading is often initiated on a shrinkage crack. It is not possible to claim that shrinkage cracks directly impact the specimen force-strain, with certainty. Indeed, in Euler-Bernoulli beam's theory, three points bending test induces a maximal moment at the middle of the beam. However, numerical crack appears around this zone.

So therefore, to examine only the macroscopic crack openings without forcing the initiation in the middle of the beam, four points bending tests are achieved. As a matter of fact, moment is both maximal and constant between the two points of loading.

Besides, the prediction of decrease of flexural strength and Young modulus are lower (and thus closer to experimental values) than the ones obtained with a macroscopic damage approach [2]. This may be due to the explicit considered cracking and cracks closure. The consideration of additional phenomenon such as creep should also improve the numerical results.

## 5. Conclusion

In this study, the impact of shrinkage on concrete's strength is examined with a beam-particle approach. It indicates that natural shrinkage due to a gradient of moisture, induces a decrease of concrete's strength. Then, this decrease depends on crack initiation. Indeed, in case of mechanical crack initiation on a previous shrinkage crack, a drop of 12% of the flexural strength is observed.

Variability is also highlighted. Maximal force strength depends on material heterogeneity, which is represented by Voronoi polygons' mesh. The model's confidence interval seems to be excessive to represent the reality.

## References

- [1] Oliver-Leblond, C. et al, 3D Global/Local Analysis of Cracking of Reinforced Concrete. The third International Conference on Computational Modeling of Fracture and Failure of Materials and Structures (CFRAC2013), Prague, Czech Republic (2013)
- [2] Soleilhet, F. et al, Hygro-mechanical modelling of self-induced stresses during the service life of concrete, 2nd International RILEM/COST Conference on Early Age Cracking and Serviceability in Cement-based Materials and Structures – EAC02, Vol. 2, Brussels, Belgium (2017)
- [3] Vassaux, V. et al, Beam-particle approach to model cracking and energy dissipation in concrete: Identification strategy and validation, *Cement and Concrete Composites* 70 (2016), 1-14
- [4] Van Genuchten, M.Th., A closed form equation for predicting the hydraulic conductivity of unsaturated soils, *Soil Sci Soc Am J* 44(5) (1980), 892-898
- [5] Soleilhet, F., Experimental and numerical investigations of cementitious materials under hydro-mechanical loadings, PhD thesis, Ecole normale superieure Paris-Saclay (2018)
- [6] Oliver-Leblond. C., Two scale description of local mechanisms: application to reinforced concrete, PhD thesis, Ecole normale superieure Paris-Saclay (2013)

## **THERMOMECHANICAL MODELLING FOR THE ESTABLISHMENT OF A NEW BUILDING METHOD FOR BASEMENTS OF CONVENTIONAL HOUSINGS**

**Dirk Schlicke<sup>(1)</sup>, Thomas Hochgatterer<sup>(2)</sup>, Martin Zabern<sup>(2)</sup>, Alexander Glebe<sup>(2)</sup>,  
Alexander Reinisch<sup>(2)</sup>**

(1) Institute of Structural Concrete, Graz University of Technology, Graz, Austria

(2) Doka GmbH, Amstetten, Austria

### **Abstract**

This paper presents an interdisciplinary cooperation between structural engineering, concrete technology and formwork technology aiming at the establishment of an innovative building method for basements of conventional housings, named *DokaBase*. Its innovation consists of an integrative application of the external insulation as formwork already with the main benefits of (i) an simplified and accelerated construction process; (ii) a defined and precise mounting of the insulation; and (iii) the achievement of enhanced concrete quality at the outer surface of the concrete members providing watertightness without additional measures.

However, the establishment of this solution in practice requires also targeted investigations on the effect of the presence of the insulation during the hydration and hardening of the concrete. In detail, the one-sided insulation is expected to cause higher temperature increases in the members as well as temperature gradients over the thickness of the slab and the wall. Therefore, detailed thermomechanical modelling was conducted on macroscopic level. This contribution presents this thermomechanical modelling with special regard to interdisciplinary aspects of this cooperation in order to achieve best possible acceptance of the results and conclusions for practical application.

### **1. Introduction**

*DokaBase* is a new building method for basements of conventional housings. In this solution, the external insulation of the basement serves already as formwork, as illustrated in Fig. 1. The insulation itself is XPS with a ca. 5 mm thick cement-based coating of the surface in order to enable a durable bond between XPS and fresh concrete without additional measures.

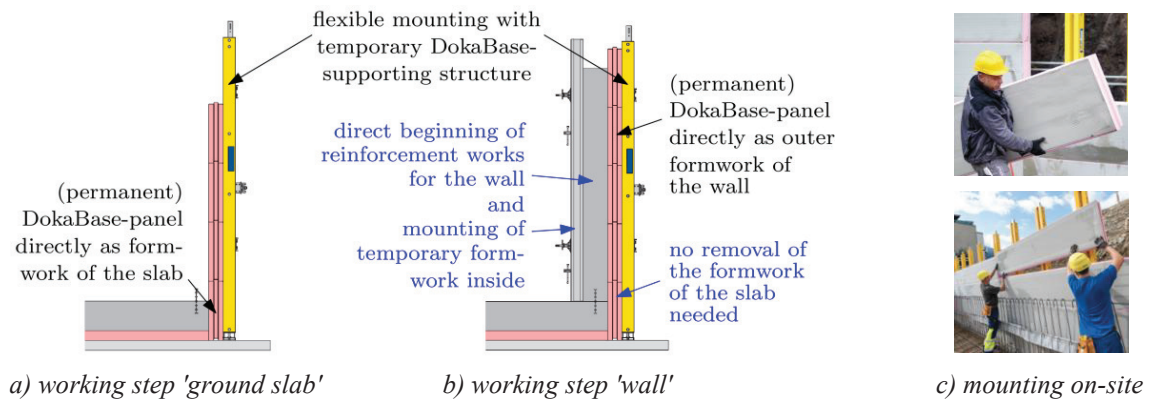


Figure 1: *DokaBase* system taken from [1].

On the one hand, this solution simplifies and accelerates the construction process; and on the other hand, the continuous treatment with XPS ( $\lambda = 0.036 \text{ W/m}^\circ\text{C}$ , closed-cell content  $\geq 95 \%$ ) reduces temperature and moist gradients at the outer surface with a beneficial effect on the concrete quality. As outlined in [1], detailed investigations on material level showed that the finally achieved concrete quality will limit the water penetration to a depth  $< 25 \text{ mm}$  for high water pressure up to 10 m water pressure height. Thus, adequate watertightness can be provided without additional measures in the present basements.

Nevertheless, using insulation material as formwork reduces the outflow of hydration heat. And even if the thicknesses of the present members are rather small and the insulation exists only on one side, higher temperature increases in the member as well as higher temperature gradients between the outer surface with insulation and the inner surface without insulation are to be expected. Aiming at a profound understanding of the temperature field and stress development in one-sided insulated members as well as for a quantification of this effect in the present case, detailed thermomechanical modelling was conducted on macroscopic level. Altogether, a comprehensive parametric study was accomplished with regard to the influence of different concretes, changing areal dimensions, fresh concrete temperature and climatic conditions, seasonal climatic conditions, different stripping times and treatments at the inner surface as well as delays in the construction process.

This contribution presents this thermomechanical modelling on basis of the reference case with special regard to interdisciplinary aspects of this cooperation in order to achieve best possible acceptance of the results and conclusions for practical application.

## 2. Reference case

### 2.1 Geometry and dimensions

The reference case was defined by a basement with a room height of 2.7 m and areal dimensions at the inside of  $13 \times 13 \text{ m}$ . The dimensions of the basement at the outside amount  $13.8 \times 13.8 \text{ m}$  taking into account  $2 \times 15 \text{ cm}$  insulation and  $2 \times 25 \text{ cm}$  wall thickness. The overall height of this basement is 3.15 m taking into account a 10 cm subbase concrete layer, 10 cm insulation layer, 25 cm concrete ground slab and 2.7 m high walls. Fig. 2 illustrates this reference case in detail. The  $L/H$ -ratio of the wall is 5.0.

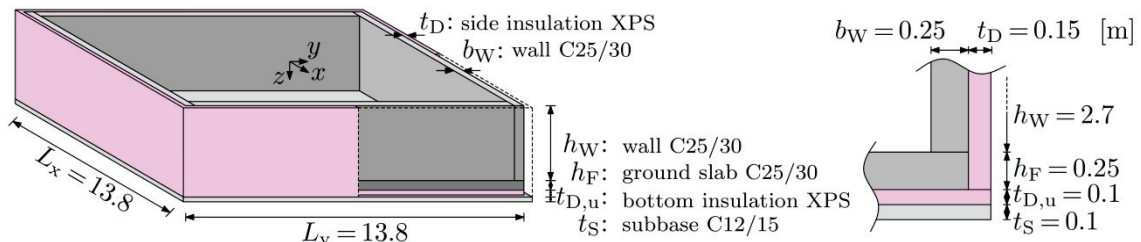


Figure 2: Dimensions of the reference case.

## 2.2 Concrete used

The concrete mix for the reference case in the investigations is shown in Tab. 1. This mix is based on a conventional Austrian concrete with strength class C25/30 and durability requirements of XC3/XD2/XF1/XA1 according to [2]. Further information on the hydration heat development as well as evolution of mechanical properties was determined with targeted material testing according to [2]. The results are given in Tab. 2.

Table 1: Mix properties for the reference concrete.

	specification	Amount
aggregates	0-4 / 4-8 / 8-16 / 16-32	1092 / 356 / 559 / 544 kg/m <sup>3</sup>
cement	CEM II/A-M (S-L) 42,5 N Kirchdorfer	330 kg / m <sup>3</sup>
superplasticizer	Master Glenium Sky676MONO BASF	2,8 kg / m <sup>3</sup> (0,6 %)
water	[-]	180 kg / m <sup>3</sup>

Table 2: Evolution of hydration heat and mechanical properties.

effective age [h]	Hydration heat [J/g]	Elastic modulus [N/mm <sup>2</sup> ]	Tensile strength [N/mm <sup>2</sup> ]
24 h	160	[-]	[-]
48 h	250	23 062	1.44
72 h	283	[-]	[-]
672 h	340	31 000	2.60
Activation energy:		33 500 J/mol	

## 2.3 Initial temperatures and climatic conditions

The reference case represents a moderate summer scenario. Initial temperatures were set with 15 °C for the ground, 17.5 °C for the subbase, 20 °C for the insulation and 25 °C for fresh concrete. And the ambient air was considered with an average temperature of 20 °C and a daily sinusoidal variation of ± 10 °C. In this scenario the effect of solar radiation and radiation losses was not considered explicitly.

## 3. Calculation Model

### 3.1 Geometric idealization

The basement was idealized with a 3D Finite Element calculation model using volumetric elements for the hardening concrete members, but also for insulation elements, the subbase and the soil in order to represent their heat storage effect, as shown in Fig. 3 with additional information on the used symmetry for minimization of computational efforts.



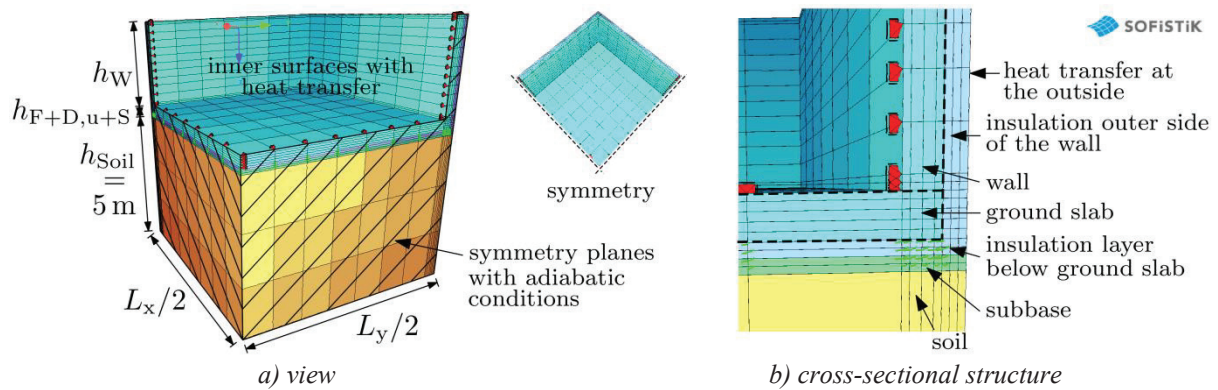
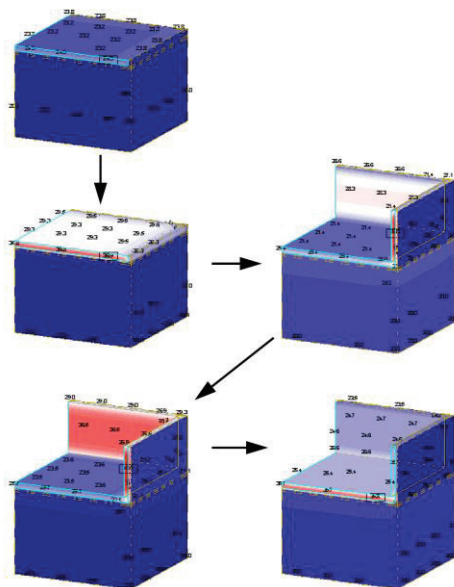


Figure 3: Calculation model.

Apart from that, the model is generated according to the modelling assumptions presented in [3] with special regard to realistic horizontal restraint and self-weight activation due to uplift.



- $t = 0$  h (1<sup>st</sup> day; 4:00 pm):
  - casting ground slab
  - no thermal treatment at the top surface of the slab; heat transfer  $\alpha = 20 \text{ W / } ^\circ\text{Cm}^2$
- $t = 24$  h (2<sup>nd</sup> day; 4:00 pm):
  - casting wall
    - » safe side assumption of casting "all in once", formwork  $\alpha = 5.5 \text{ W / } ^\circ\text{Cm}^2$
  - no thermal treatment at the top surface of the wall,  $\alpha = 20 \text{ W / } ^\circ\text{Cm}^2$
- $t = 40$  h (3<sup>rd</sup> day; 8:00 am):
  - one-sided removal of the formwork at the inner surface of the wall
  - no thermal treatment at the inner side of the wall,  $\alpha = 20 \text{ W / } ^\circ\text{Cm}^2$

Figure 4: Considered stages to represent the construction process.

### 3.2 Material model

The hydration was simulated with a thermo-mechanically coupled material model for aging concrete with regard to heat release and heat flow under transient conditions, maturity, evolution of elastic modulus, shrinkage and viscoelasticity. The model was implemented for each element independently enabling a time- and localization-discrete consideration of the several thermal and mechanical properties. Special attention was hereby given to the viscoelastic behaviour with regard to each elements own stress history. Further information can be found in [3] and [4].

### 3.3 Time control of the calculation with special regard to the construction process

The model represents the construction process with the considered stages shown in Fig. 4. It is on the safe side assumed, that the wall is casted all in once around the corner.

## 4. Typical results and expected insights

### 4.1 Temperature and stress history in slab and wall

The temperature and stress history in the slab and in the wall was analysed on basis of the timely development of temperature and stresses in selected points with extreme values. Fig. 5 shows the results for the slab of the reference case (areal location of the analysed points is at  $L_x/2$  and  $L_y/2$ ); and Fig. 6 shows the results for the wall (areal location of the analysed points is in the symmetry of the wall in length direction).

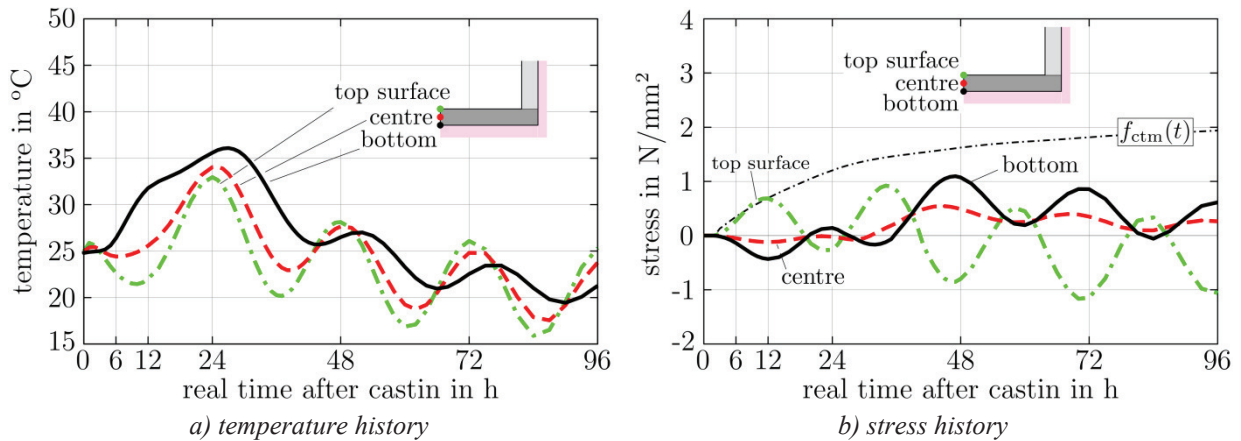


Figure 5: Typical nodal results for the ground slab exemplified for the reference case.

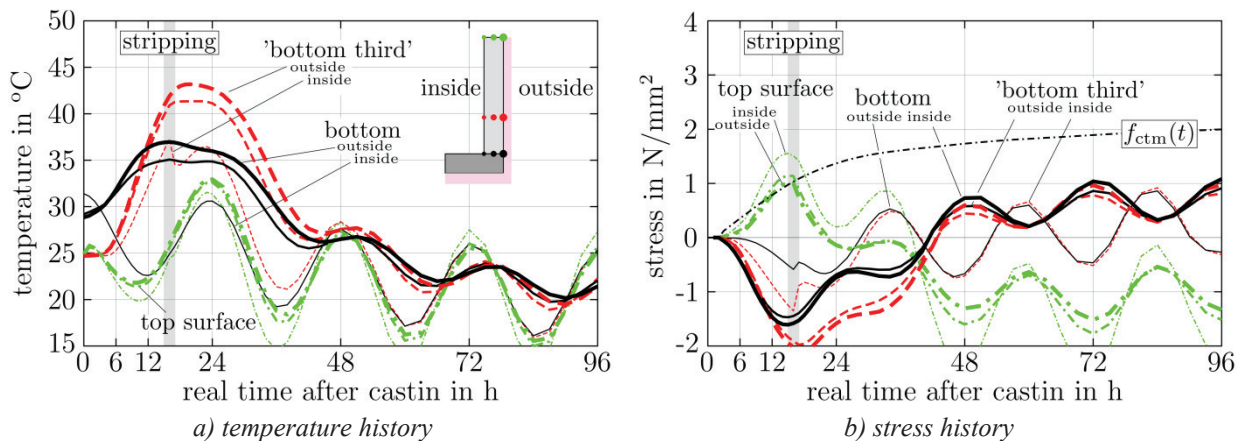


Figure 6: Typical nodal results for the wall exemplified for the reference case.

In addition to the nodal results, the stress field was further analysed regarding uniformly and linearly distributed parts corresponding with a restraint force and restraint moments. This was done by removal of the self-balanced non-linear part of the stress distribution, see Fig. 7.

### 4.2 Assessment of cracking risk

The cracking risk was assessed by the two-stage procedure proposed in [3]: Firstly, the general risk of cracking is assessed by a comparison of maximum stresses in the material point or element with 80 % of  $f_{ctk;0.05}(t)$ . If this is fulfilled, cracking can be safely excluded at

all. If not, micro-cracking with reduction of Eigenstresses is to be expected, so that the uniformly and linearly distributed parts have to be assessed in the second step. These stresses correspond with restraint forces and moments and will cause macrocracks when the cracking forces and moments are exceeded. Thus, the stresses were now compared with the mean-value  $f_{ctm}(t)$  of the actual tensile-strength; see also [5]. Fig. 7 illustrates this procedure.

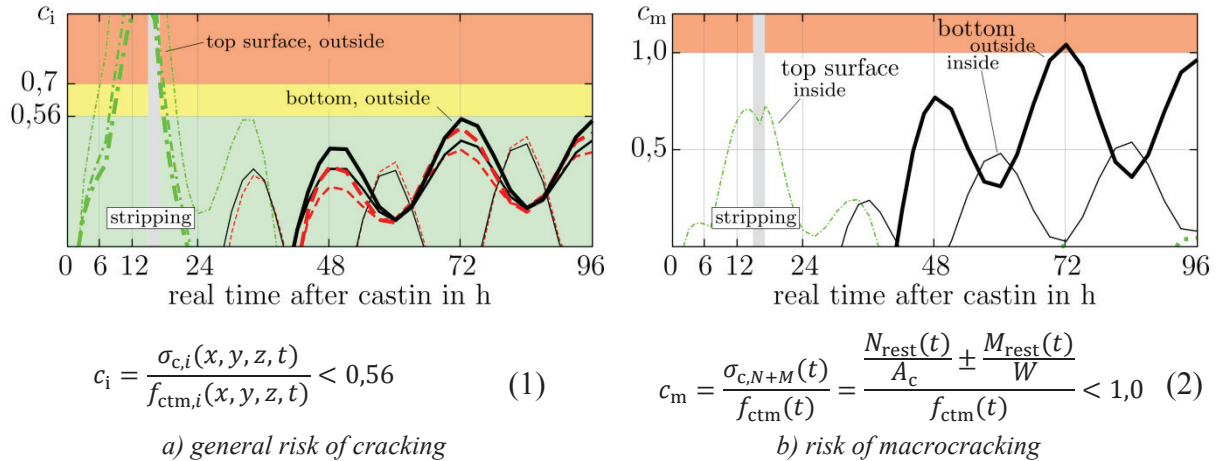


Figure 7: Crack assessment exemplified for the wall of the reference case.

## 5. Conclusion

This contribution presents the thermomechanical modelling for the establishment of the building method *DokaBase* aiming at a simplified and fastened construction for watertight basements of conventional housings. In fact, it exemplifies an interdisciplinary cooperation between structural engineering, concrete technology and formwork technology, whereby all the different aspects and demands of the three stakeholders were adequately addressed and suitably combined. The result is a robust tool for comprehensive analysis of the building method with regard to the influences of different concretes, changing areal dimensions, fresh concrete temperature and climatic conditions, seasonal climatic conditions, different stripping times and treatments at the inner surface as well as delays in the construction process.

## References

- [1] DokaBase, application information 999810001 - 07/2017, Doka GmbH (in German)
- [2] EN 206-1:2017 + AC:2018 (ÖNORM B 4710-1): Concrete – Part 1: Specification, performance, production and conformity
- [3] Schlicke, D. and Tue, N.V., Minimum reinforcement for crack width control in restrained concrete members, *Structural Concrete* 16 (2014), 221-232
- [4] Schlicke, D., Minimum reinforcement for restrained concrete, PhD thesis (revised edition), Graz University of Technology (2014)
- [5] ÖBV Bulletin, Analytical design of watertight structures with optimized concrete (in German), Austrian society for Construction Technology, Vienna, Austria (2018).

**MULTI-SCALE IN TIME AND SPACE  
MODELLING  
AND  
EXPERIMENTS**

## **A NEW CREEP TEST METHOD FOR REINFORCED CONCRETE TENSION MEMBERS UNDER CONSTANT LOADING**

**Eugenijus Gudonis <sup>(1\*)</sup>, Pui-Lam Ng <sup>(1,2)</sup>, Shao-Hua Chu <sup>(2)</sup>, Aleksandr Sokolov <sup>(1)</sup>**

(1) Vilnius Gediminas Technical University, Vilnius, Lithuania

(2) The University of Hong Kong, Hong Kong, China

### **Abstract**

This paper reports the experimental study on creep behaviour of reinforced concrete (RC) tension members subjected to long-term constant loading. An innovative testing rig was designed and four replicates were fabricated for concurrent testing of multiple specimens under the same temperature and humidity conditions. Four direct tension specimens were produced and tested under sustained loading up to beyond 300 days. The test results indicated the augmentation of deformation due to concrete creep in RC member. The creep strain of specimens became practically steady after 300 days, and the creep half-time was obtained as approximately two weeks.

### **1. Introduction**

Creep of concrete is a major component of time-dependent deformation that affects the serviceability of concrete structures. Experimental investigation of concrete creep behaviour has been attempted by many researchers [1-5]. From previous research findings, when the sustained tensile or compressive load does not exceed approximately 40% of the respective concrete tensile or compressive strength, the creep can be treated as linear creep, where the creep strain is linearly dependent on the sustained stress, and the principle of superposition is applicable for evaluating the creep strain subject to variable stress history [6,7].

There are issues in connection with concrete creep experiment that require particular attention. First is the environmental condition: The experiment normally would span over prolonged durations. There might be difficulty in maintaining constant environmental conditions even in laboratories with controlled indoor environment. This might introduce errors and undulations in the measured creep deformations. Second is presence of embedded reinforcement: Whilst the creep of plain concrete is regarded as a fundamental property of

concrete, the creep deformation of reinforced concrete is subject to the influence by reinforcement. The interaction between creeping concrete and reinforcing bars is complicated and cannot be reflected in the creep test of plain concrete [8].

To tackle the first issue, the fluctuations of environmental condition can be minimised by providing active control of the indoor temperature and relative humidity. On the other hand, to tackle the second issue, creep test of reinforced concrete that requires tailored loading mechanism is necessary. This calls for a new concept of experiment design. A bespoke testing rig for creep test of RC tension members has been innovated in this research. The long-term tension loading was constantly exerted via a double lever system with adjustable fixities to ensure verticality, which is an improved version of lever type testing rig described in the literature [8]. Four RC direct tension specimens were tested under constant loading up to beyond 300 days using the new test set-up.

## 2. Test set-up of creep test

The scheme design of the double lever system test set-up is shown in Fig. 1. It has double tiers of lever mechanisms. The external load is applied by placing pre-defined weights in the tray container. The gross weight of the loaded container would be transmitted via the first-tier lever of ratio close to 4:1 (the actual measured ratio is 3.93:1, with respect to the projected length of loaded lever arm), to become a downward load on the second lever. This downward load would be transmitted via the second-tier lever of ratio 4:1, to become an upward load at the opposite side of the pivot. Through the double lever mechanism, the resulting upward load would be magnified to approximately 16 times the gravity loading at the tray container, and it would act on the upper end of the vertically oriented direct tension specimen. The lower end of the specimen is connected to the ground beam of the testing rig and restrained from any vertical movement. To ensure verticality of the specimen, the connection from the lower end of specimen to the ground beam is adjustable with a horizontal slot. By this arrangement, the testing rig would be self-equilibrating and the specimen would be subjected to pure axial tension loading.

The overall height of the testing rig is close to 2.35 m, and its internal headroom has been designed to accommodate 1.5 m long vertically-placed specimen, with sufficient vertical clearance allowed for the connection components and instrumentation. Four replicated testing rigs have been fabricated for concurrent testing in the same environment. Before usage, each testing rig has been calibrated by placing standard weights in the tray container and recording the resultant force transmitted through the double lever system. To conduct the creep test, initially, the designated load should be applied to the test specimen in a sequential manner. Standard weight blocks are placed into the tray container one by one. This process is done manually and gently to maintain the balanced position of the container hung from the hanging point using metal chains. A short pause should be given after placing each weight block to stabilise the load and to record the load and deformation readings. After the load addition, the weight blocks are undisturbed as sustained loading.

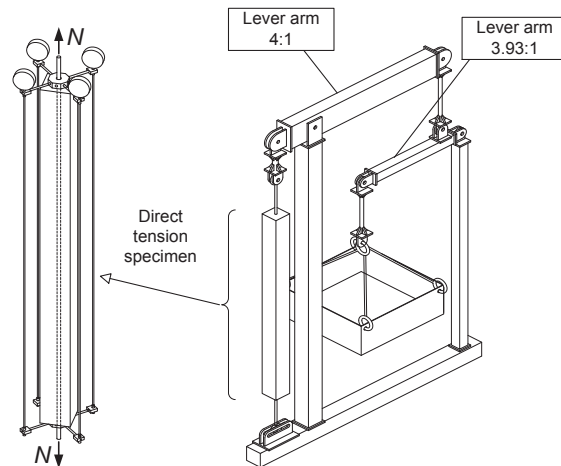


Figure 1: Schematic diagram of test set-up.

The RC tension specimen has uniform 100 mm square cross-section and is of 1500 mm long. A steel bar is embedded at the centre, and protruded 50 mm from each of the two ends. The protruded parts of steel bar were connected to the testing rig via hexagonal coupling bolts and steel rods. The long-term deformation of the specimen was measured using 4 mechanical gauges installed at diagonal positions of the specimen. The gauges have resolution of 0.001 mm and the gauge length of measurement is 1520 mm. The measured values from the 4 mechanical gauges can be averaged for better reliability of experimental results. Fig. 2 depicts a photograph of the creep test.



Figure 2: Photograph of ongoing creep test.

### 3. Testing programme

Four RC tension specimens (labelled DT-12, DT-13, DT-14 and DT-15) have been fabricated and tested. Each specimen was reinforced with 12 mm diameter high-strength deformed steel bar. The corresponding reinforcement ratio  $p$  was 1.1%. The specimens were cast from the same concrete mix, with water/cement ratio of 0.45 and fine to total aggregate ratio of 0.49 by mass. The 28-day mean cylinder compressive strength  $f_{cm}$  was 33.6 MPa and the elastic

modulus  $E_{cm}$  was 35.9 GPa. Subsequent to casting, the specimens were demoulded at 2 days and cured under moist condition until loading at age  $t_0$  of 52 days. Regarding reinforcing bar, the nominal yield stress  $f_y$  and the elastic modulus  $E_s$  averaged from test samples were 945 MPa and 190 GPa, respectively.

With regard to the determination of loading magnitude, the ultimate capacity of specimen  $N_{ult}$  is taken as the nominal yield stress of reinforcement  $f_y$  multiplied by the area of reinforcement  $A_s$ . Then, for specimens DT-12 and DT-13, the applied tension load was designated as 38% of the ultimate capacity of specimen (load magnitude of 40 kN); whereas for specimens DT-14 and DT-15, the applied tension load was designated as 33% of the ultimate capacity of specimen (load magnitude of 35 kN). The test was conducted in a laboratory room with controlled temperature and humidity without natural ventilation. The creep test was conducted over a period of 315 days (concrete age of 367 days). Throughout the test duration, the average temperature and average relative humidity were respectively 19°C and 64%.

#### 4. Test results and discussion

At any time, the deformation measurement can be converted to strain with respect to the specimen length. Theoretically, the long-term deformation comprises of the short-term deformation in response to the load application and the time-dependent creep deformation. To reveal the creep behaviour, the instantaneous deformation recorded upon the completion of load application prior to the creep effect can be deducted from the measured time-dependent deformation. In other words, the creep strain  $\Delta\varepsilon_m(t, t_0)$  can be obtained by subtracting the instantaneous strain  $\varepsilon_m(t_0)$  from the total strain  $\varepsilon_m(t, t_0)$ . Fig. 3 presents the variation of creep strain results with time in days. It can be seen that the creep strain increased more rapidly initially and then at a gradually diminishing rate. Beyond 300 days, the creep strains became approximately steady. Therefore, the strain values subsequent to 300-day duration of constant loading can be regarded as the final creep strain.

The respective strain values of the specimens are tabulated in second to fourth columns of Tab. 1. Among the specimens, the total strains were ranging from 1620 to 1920  $\mu\varepsilon$ , whereas the instantaneous strains were ranging from 1290 to 1680  $\mu\varepsilon$ . As expected, the more heavily-loaded specimens DT-12 and DT-13 exhibited larger total and instantaneous strains than specimens DT-14 and DT-15. To indicate the proportional augmentation of deformation under sustained loading, the ratio of creep strain to instantaneous strain is computed, which is found to be ranging from 0.145 to 0.257 as listed in the fifth column of Tab. 1. It can be seen that under the restraining effect of reinforcement, the creep of concrete would increase the deformation by approximately 15% to more than 25%. This is not small and should be properly considered in designing concrete structures.

From the experimental results, the creep half-time  $t_{0.5}$  (which means the time required for half of the ultimate creep strain to take place) is evaluated. The creep half-time is useful information for construction planning and control. It allows engineers to assess the time to compensate certain amount of creep deformation and anticipate the remaining creep deformation during construction [9,10]. In the present study, as the creep strain was practically steady beyond 300 days, the final creep strain is treated as the ultimate creep strain. For the 4 specimens, the creep half-time was ranging from 13.8 to 14.8 days as reported in the last column of Tab. 1. Therefore, although creep is a long-term process, half of



the ultimate creep deformation would occur approximately in the first two weeks after loading.

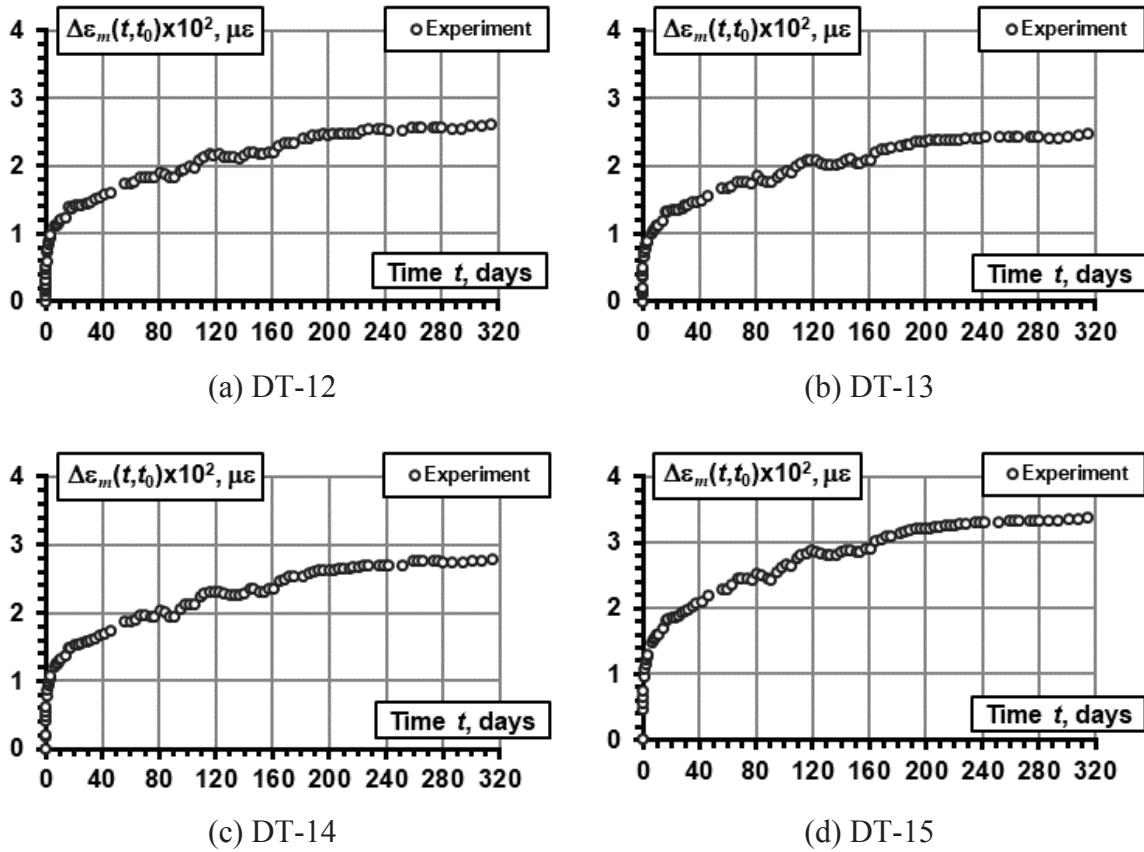


Figure 3: Variations of creep strain with time.

Table 1: Results of creep test.

Specimen	Total strain, $\varepsilon_m(t, t_0) \times 10^{-6}$	Instantaneous strain, $\varepsilon_m(t_0) \times 10^{-6}$	Creep strain, $\Delta\varepsilon_m(t, t_0) \times 10^{-6}$	Ratio of creep strain to instantaneous strain	Creep half-time, $t_{0.5}$ (days)
DT-12	1740	1480	255	0.172	14.8
DT-13	1920	1680	243	0.145	14.7
DT-14	1690	1420	271	0.191	14.2
DT-15	1620	1290	332	0.257	13.8

## 5. Conclusions

A new test method of the creep behaviour of reinforced concrete (RC) tension members has been developed. A bespoke testing rig with double-tier lever system for load application was innovated. In this paper, the principles and details of the test set-up have been explicated. Four RC direct tension specimens were fabricated for undergoing the creep test up to beyond 300 days. The test results have revealed approximately 15% to more than 25% augmentation of short-term deformation in RC member due to long-term creep effect. The creep half-time (the time for half of the ultimate creep to take place) of specimens has been found as equal to approximately two weeks.

## Acknowledgements

The authors gratefully acknowledge the financial support provided by the Research Council of Lithuania (Project No. MIP-093/2015). The second author wishes to express his gratitude for the support provided by the European Commission Research Executive Agency under the Marie Skłodowska-Curie Actions (Project no.: 751461).

## References

- [1] L'Hermite, R., Déformation du béton, *Bâtir* 27 (1952), 18-22
- [2] Troxell, G. E., Raphael, J. M. and Davis, R. E., Long-time creep and shrinkage tests of plain and reinforced concrete, *ASTM Proc* 58 (1958), 1101-1120
- [3] Neville, A. M., The influence of cement on creep of concrete and mortar, *PCI J* 2(1) (1958), 12-18
- [4] Tamtsia, B. T. and Beaudoin, J. J., Basic creep of hardened cement paste: a re-examination of the role of water, *Cem Concr Res* 30(9) (2000), 1465-1475
- [5] Persson, B., Correlating laboratory and field tests of creep in high-performance concrete, *Cem Concr Res* 31(3) (2001), 389-395
- [6] Comité Euro-International du Béton, Structural effects of time-dependent behaviour of concrete, *CEB Bulletin* 142, Lausanne (1984)
- [7] Balevicius, R. and Marciukaitis, G., Linear and non-linear creep models for a multi-layered concrete composite, *Archives Civ Mech Engin* 13(4) (2013), 472-490
- [8] Scott, R. H. and Beeby, A. W., Test rigs for long-term tension tests, *Strain* 41 (2005), 151-155
- [9] Ng, P. L., Lam, J. Y. K. and Kwan, A. K. H., Multi-layer visco-elastic creep model for time-dependent analysis of concrete structures, *Proceedings of the Eleventh International Conference on Civil, Structural and Environmental Engineering Computing*, Malta (2007)
- [10] Ng, P. L., Kwan, A. K. H., Fung, W. W. S. and Du, J. S., Prediction of concrete creep by multi-layer visco-elastic model, *Proceedings of the 7th International Conference on Tall Buildings*, Hong Kong (2009), 677-688

## **AN EXPERIMENT-BASED FE APPROACH TO ANALYZE EARLY-AGE TEMPERATURE AND STRAIN DISTRIBUTION IN LARGE-DIMENSION CONCRETE WALL**

**Yan Geng**<sup>(1)</sup>, **Suduo Xue**<sup>(1)</sup>, **Xiongyan Li**<sup>(1)</sup>, **Jinguang Li**<sup>(2)</sup>

(1) Beijing University of Technology, Beijing, China

(2) China Huanqiu Contracting and Engineering Co. Ltd., Beijing, China

### **Abstract**

Hydration heat and thermal cracking is a main concern for large-dimension concrete structures. In order to investigate the early-age properties of concrete under research, a set of time-varying experiments were conducted, namely the hydration experiment, standard thermal and mechanical tests. Then a finite-element (FE) method based on the material experiments was proposed with User Subroutine UMATHT, USDFLD and UEXPAN. In order to verify the accuracy of the proposed FE method and investigate the temperature distribution and strain development of large-dimension concrete structures, an experimental wall of 3.6m×0.8m×3.6m in dimension was constructed. According to the temperature measurement, the highest temperature reached a maximum of 52.3°C at the central point after 36 hours of pouring. The maximum temperature difference between the core and ambient environment was 41.5°C, with a maximum cooling rate of 9.0°C per day. Compared with the FE analysis results, the average temperature difference at the peak was only 3.6%. As for the strain results, the computed curves reflected the trend of measured strain development with a maximum difference of 9.5% despite some local deviations. Overall, the computed results agreed well with test data, indicating the effectiveness of the proposed FE approach.

### **1. Introduction**

Hydration heat and thermal cracking is a main concern for large-dimension concrete structures, which experience rapid temperature rise in the core and manifest distinct temperature difference between centre and surface at very early age [1]. Micro thermal cracks may consequently occur [2] and gradually develop into obvious cracking through structures, severely reducing the service life of structures or even resulting in structure failures.

Therefore, it is significant to make accurate prediction of structural thermal stress and strain development and to take appropriate measurements to prevent concrete cracking.

Thermo-mechanical analysis has been applied to concrete structures for decades. Zreiki *et al.* [3] developed a thermo-chemo-mechanical model based on a set of mechanical characterization experiments. Xiang *et al.* [4] presented a thermal-mechanical sequential coupling analysis of a newly cast concrete wall in the construction of a subway station structure and provided suggestions for prediction and control of early age concrete cracking. De Schutter [5] performed a finite element simulation on temperature fields and the resulting stresses at any time during hardening of a non-reinforced massive concrete wall. However, some complexities still exist particularly in the current reinforced concrete structure embedded with corrugated pipes.

In this research, a FE approach was proposed with User Subroutine UMATHT, USDFLD and UEXPAN on the basis of complete time-dependant material experiments, namely hydration heat test, standard thermal tests of thermal conductivity, thermal expansion and specific heat, and standard mechanical tests for  $E$ -modulus, compressive strength and shrinkage. Moreover, an experimental wall of 3.6m×0.8m×3.6m in dimension was constructed to investigate temperature distribution and strain development and validate the accuracy of the proposed FE method.

## 2. Material and method

Adiabatic temperature rise experiment and standard thermal and mechanical tests at totally thirteen sets of casting ages (namely 1day(d), 2d, 3d, 5d, 7d, 10d, 14d, 20d, 28d, 45d, 60d, 90d and 120d) were carried out with the designed concrete mix proportion (as listed in Tab.1). The adiabatic temperature rise experiment was performed using a concrete adiabatic temperature measuring instrument with an accuracy of 0.02°C. A hydration model based on hydration degree  $\alpha(t_e)$  (see Eq.1) was utilized in this study. The cumulative heat of hydration  $Q_c(t_e)$  with  $\alpha(t_e)$  was expressed as Eq.2 based on the improved exponential function formula proposed by Zhu B.F.[6]. Equivalent time  $t_e$  (in day) was expressed according to Arrhenius equation as Eq.3. The hydration degree-dependant equation was then written in the subroutine UMATHT to define heat generation of the concrete.

$$\alpha(t_e) = (1 - e^{-0.75t_e^{0.87}}) \quad (1)$$

$$Q_c(t_e) = 1.72 \times 10^5 \times \alpha(t_e) \quad (2)$$

$$t_e = \int_0^t \exp\left[\frac{E_A}{R}\left(\frac{1}{T_r} - \frac{1}{T}\right)\right] dt \quad (3)$$

Table 1: Mix proportion of concrete (mass in kg/m<sup>3</sup>).

Water	Cement	Slag powder	Fine aggregate	Coarse aggregate	Super-plasticiser	W/B
140	310	142	759	1006	9.04	0.31

As for thermal tests, thermal conductivity  $\lambda$  and specific heat  $c$  were obtained according to Code GB/T 10294-2008 and SL 352-2006, respectively, and the results of  $\lambda$  and  $c$  are shown in Fig.1. In general, the values of  $c$  remained within empirical value range, while the values of  $\lambda$  were slightly smaller, considering the component of slag in the concrete proportion and relative humidity conditions of the test samples. Since the values of  $\lambda$  and  $c$  both varied relatively greatly during the first 7days, they were directly written into Subroutine UMATHT.

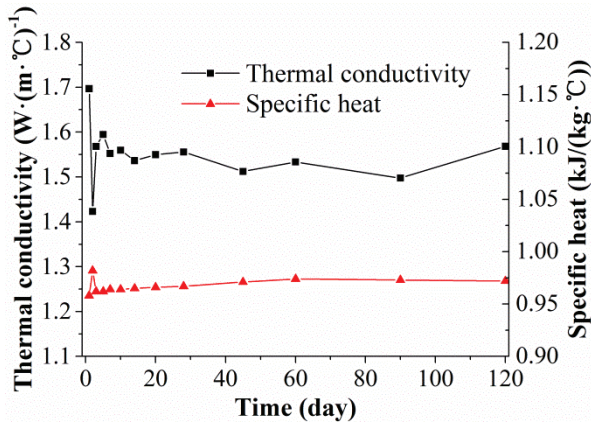


Figure 1: Test results of  $\lambda$  and  $c$ .

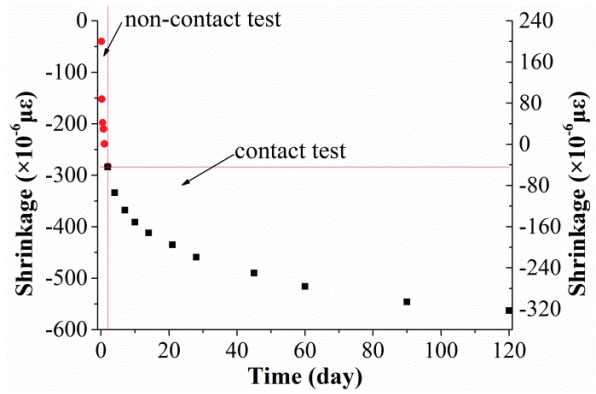


Figure 2: Measured shrinkage.

Besides, mechanical characterization of compressive strength  $f_c$ , tensile splitting strength  $f_{ts}$  and elastic modulus  $E_c$  were also conducted and the results are fitted to Eq.4, Eq.5 and Eq.6,

$$f_c(t_e) = 64.3 \times (1 - (1 - \alpha(t_e))^{0.47}) \text{ MPa} \quad (4)$$

$$f_{ts}(t_e) = 0.075 \times f_c(t_e) \text{ MPa} \quad (5)$$

$$E_c(t_e) = 39.5 \times (1 - e^{-0.9 \times \ln^{0.64}(1 - \alpha(t_e))}) \text{ GPa} \quad (6)$$

Moreover, free shrinkage tests were carried out with non-contact method at 20°C and RH=68% for the first two days and with contact method from the third day till the 120d after demoulding according to GB/T 50082-2009. The results of the tested shrinkage were depicted in Fig.2. The results of non-contact test were mainly autogenous shrinkage for high performance concrete, while those of contact test were mainly drying shrinkage [7]. The contact shrinkage results were in accordance with the values calculated with CEB/FIP 2010 Model, while the non-contact shrinkage results was much larger, which may be accounted for slag replacement and low water to binder ratio(w/b) of the concrete. Based on the tests illustrated above, subroutine USDFLD and UEXPAN was developed to describe the hydration degree-dependent mechanical and shrinkage properties.

### 3. Case study

#### 3.1 General description

In order to validate the effectiveness of the proposed FE approach, four experimental walls of 3.6m×0.8m×3.6m in dimension was constructed, the original design of which derived from a practical project to be constructed in China. A reinforced concrete base of 10.8m×7m×1m and

columns of 1.5m×1.2m×4m were previously constructed to provide fixed boundaries to the wall. Six PT100 temperature sensors and four vibration wire(VW) sensors were appropriately fixed onto rebars and embedded in each concrete wall to obtain the temperature and strain variations at the specified test points, as shown in Fig.3(a). Meanwhile, a FE model was established to perform a thermo-mechanical coupling analysis, as shown in Fig.3(b). The convection coefficients for wall surfaces was estimated to be 6.8 W/(m<sup>2</sup>·K) and 23W/(m<sup>2</sup>·K) before and after formwork removal (at 5th day after casting), respectively, abiding by the third type of boundary condition. Ambient temperature was taken from in situ record.

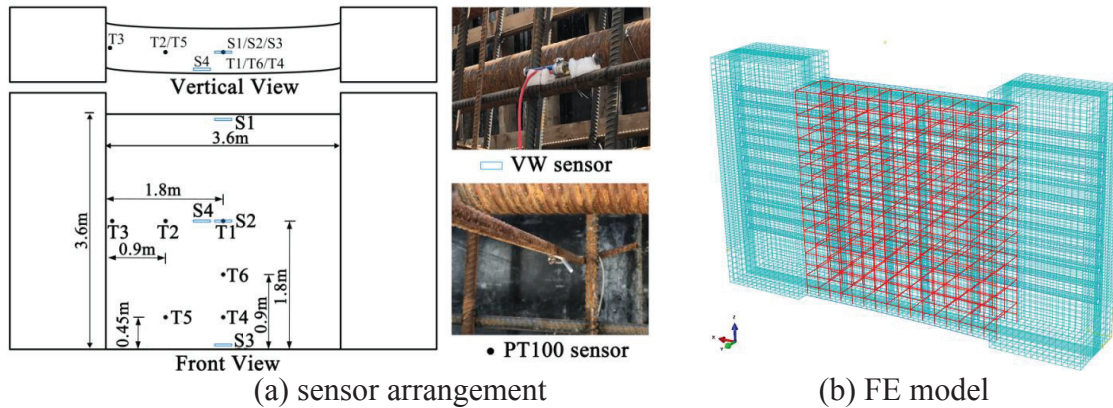


Figure 3 : Sensor arrangement and FE model.

### 3.2 Temperature comparison

The first 14 days of temperature data are shown in Fig.4. It is noticed that the highest temperature reached a maximum of 52.3°C at the central point (Point T1) after 36 hours of pouring. The maximum temperature difference between the core and ambient environment was 41.5°C, with a maximum cooling rate of 9.0°C per day. Compared with the calculated results, the average temperature difference at the temperature peak of all the 6 test points was only 3.6%, among which the minimum deviation occurred in the central part of the wall (Point T1 and T6) and the maximum deviation (1.2°C) occurred in the boundary part adjacent to the column (Point T3). It may be accounted for the heat conduction between the wall and column.

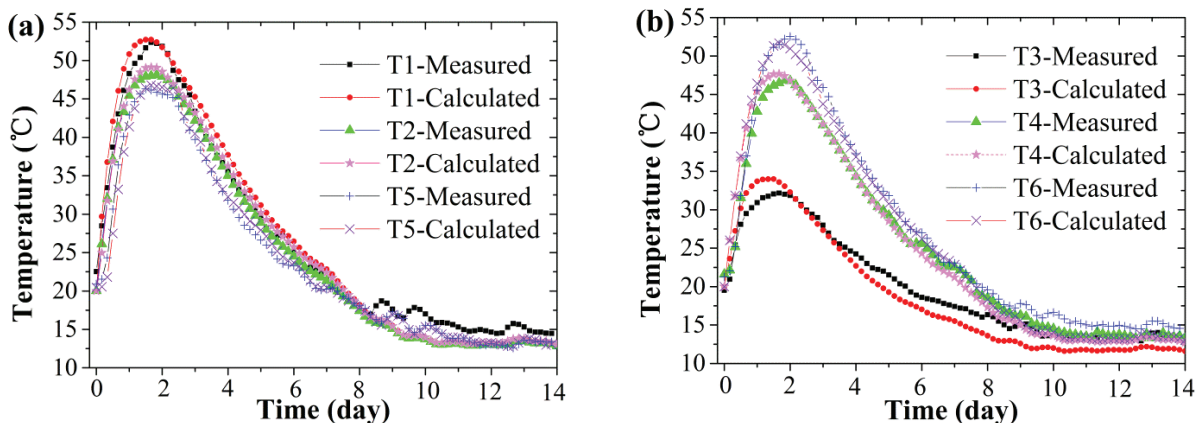


Figure 4: Temperature comparison between calculated and tested data.

### 3.3 Strain comparison

Internal strain variations of concrete were monitored and compared with the results obtained from thermo-mechanical coupling analysis, as shown in Fig.5. It is observed that the core concrete firstly experienced a sharp rise of tensile strain due to hydration heat and thermal expansion. With concrete hardening and temperature decline, tensile strain instantly decreased and turned to compressive strain, reaching a maximum of  $-369\mu\epsilon$  after 800hours. Besides, both the tensile and the compressive strain were larger on the upper surface than those on the lower surface, owing to the stronger constraint at the bottom. Compared with the test strain results, the computed curves reflected the overall trend of strain development with a maximum difference of 9.5% despite some local deviations.

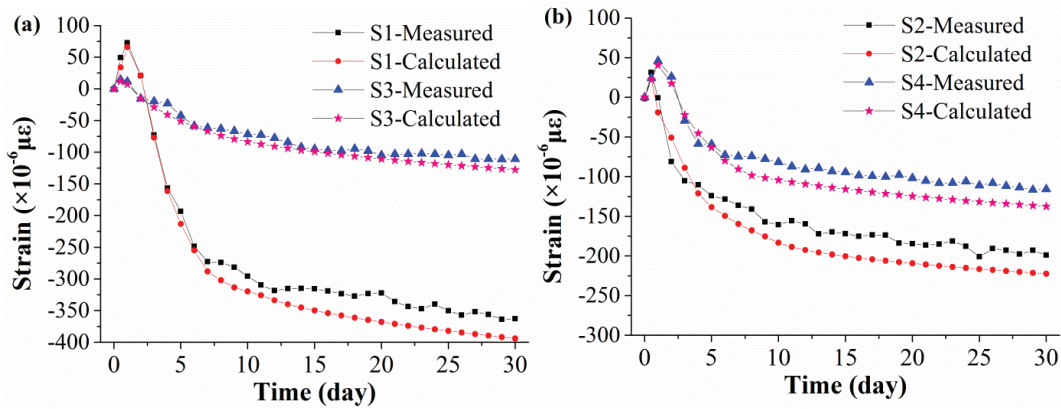


Figure 5: Strain developments at specified points.

### 3.4 Cracking risk

The first principle thermal stress  $\sigma_1$  was obtained from coupled simulation considering variation of  $E_c$  with time and compared with tensile strength, as is shown in Fig.6. It is noticed that the stress was compressive during the first 5 days till tensile stress occurred then and remained stable after the 8th day. The ratio of  $\sigma_1$  to  $f_{ts}$  was 0.637 at the 8th day, indicating that the cracking risk is relatively high according to the cracking criterion proposed by Sule [8]. In fact, one surface crack did occur at the 7th day after concrete pouring, which belonged to the type of base-restrained crack, as is shown in Fig.7. Therefore, it implies that the proposed FE subroutine can effectively predict the occurrence of surface cracking.

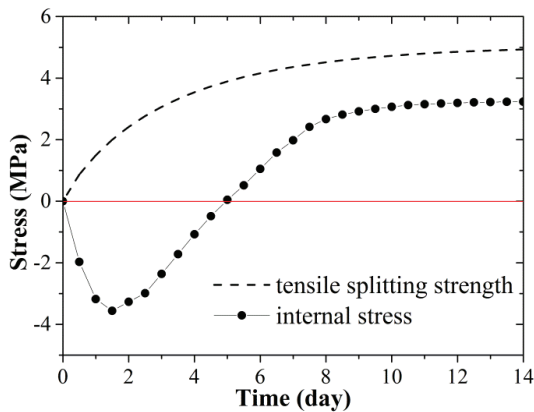


Figure 6: First principle stress of internal concrete.



Figure 7: Surface cracking.

#### 4. Conclusion

An experimented-based FE method was proposed for early-age thermo-mechanical analysis with redevelopment of user subroutine UMATHT, USDFLD and UEXPAN, based on complete thermal and mechanical characterization of concrete. Moreover, an experimental wall was constructed to validate the effectiveness of the proposed FE approach. According to the comparison results, the calculated results in temperature and strain field both agreed well with test data, indicating the effectiveness of the proposed FE approach. Moreover, the occurrence of surface cracking can be effectively predicted with the proposed method by considering the cracking risk index. It can provide a sufficient way to perform more parametric analysis of the experiment wall under different ambient conditions and air cooling through corrugated pipes, as well as to predict temperature and strain development of similar massive reinforced concrete structures.

#### References

- [1] Geng, Y. et al, Early-age thermal analysis and strain monitoring of massive concrete structures, *Comp Concr* 21(3) (2018), 279-289
- [2] Knoppik, A. et al, Cracking risk and regulations, in: Eduardo M R Fairbairn, Miguel Azenha (Eds), *Thermal cracking of massive concrete structure*, Springer International Publishing, Cham, Switzerland (2019), 257-304
- [3] Zreiki, J. et al, Early-age behaviour of concrete in massive structures, experimentation and modelling, *Nucl Eng Des* 240 (2010), 2643-2654
- [4] Xiang, Y.Y. et al, Thermal–mechanical analysis of a newly cast concrete wall of a subway structure, *Tunn Undergr Space Technol* 20 (2005), 442-451
- [5] De Schutter, G., Vuylsteke, M., Minimisation of early age thermal cracking in a J-shaped non-reinforced massive concrete quay wall, *Eng Struct* 26 (2004), 801-808
- [6] Zhu B.F., *Thermal Stresses and Temperature Control of Mass Concrete*. Butterworth-Heinemann: Waltham (2014)
- [7] Wu L.M. et al, Autogenous shrinkage of high performance concrete: A review, *Constr Build Mater* 149 (2017), 62-75
- [8] Sule M. S., *Effect of reinforcement on early-age cracking in high strength concrete*, Ph.D. Thesis, Delft University of Technology (2003)



## ASSESSING THE CO<sub>2</sub>-BINDING OF CONCRETE DURING ITS SERVICE LIFE

Andreas Leemann<sup>(1)</sup>, Fritz Hunkeler<sup>(2)</sup>, Heiner Widmer<sup>(3)</sup>

(1) Empa, Dübendorf, Switzerland

(2) TFB AG, Wildegg, Switzerland

(3) cemsuisse, Bern, Switzerland

### Abstract

In order to assess the impact of cement production on the atmospheric CO<sub>2</sub> concentration and with it on the global warming, not only the CO<sub>2</sub> emissions but also the CO<sub>2</sub> capture by carbonation of cementitious products during their service life needs to be considered. The key parameter for a reasonably accurate estimation is the carbonation coefficient that allows to calculate the temporal evolution of carbonation depth and the CO<sub>2</sub> adsorption by the cement hydrates. Current approaches use a strength-based concept linking carbonation coefficient and compressive strength. This approach has proven to be valid for Portland cement-based concrete, but appears to be questionable in the case of concrete produced with blended cements, which are prevalent nowadays. Based on recent scientific findings showing an excellent correlation between the CO<sub>2</sub> binding capacity of concrete and the carbonation coefficient, an alternative approach is proposed.

### 1. Introduction

The increasing CO<sub>2</sub> concentration in the atmosphere is regarded as a governing factor for the observed global temperature increase. The important contribution of cement production to anthropogenic CO<sub>2</sub> emission with 5-6 % is indisputable [1]. However, due to carbonation of cement hydrates, part of the emitted CO<sub>2</sub> is recaptured. Calcium-silicate-hydrate (C-S-H) is decalcified, leading to the formation of a phase with a lower Ca/Si-ratio and CaCO<sub>3</sub> and portlandite is transformed into CaCO<sub>3</sub>. [2]. Only if CO<sub>2</sub> binding by carbonation of cementitious products during their service life is considered as well, the environmental impact of cement can thoroughly be assessed.

Carbonation starts at the surface of mortar or concrete components. The carbonation depth as a function of the square root of time is described by the carbonation coefficient  $K_N$ . It depends on various parameters like water-to-cement-ratio (w/c) of the mortar or concrete and relative humidity (RH) [3]. Therefore, an assessment of the carbonation coefficient  $K_N$  is mandatory to calculate CO<sub>2</sub> uptake by cementitious materials during their service life. This has been the subject of several studies, in which the carbonation coefficient  $K_N$  was assessed based on concrete strength [4-7]. In addition to CO<sub>2</sub> adsorption during its service life, a substantial amount of CO<sub>2</sub> is bound during the recycling phase of concrete [4-7]. This aspect is not considered in this study, as it solely focuses on service life.

A major drawback of the majority of studies dealing with CO<sub>2</sub> adsorption of cementitious materials is that the assessment of the carbonation coefficient  $K_N$  is based on concrete strength or that attempts are made to link the obtained experimental values only with strength-based concepts. Currently, CEN TC 229 WG 5 is following this path. However, mortar and concrete produced with blended cements do not show the same relation between carbonation coefficient  $K_N$  and compressive strength as mortar and concrete produced with Portland cement [8-10]. The share of blended cement used worldwide is steadily increasing in an attempt to decrease CO<sub>2</sub> emissions. Therefore, alternative approaches to assess the carbonation coefficient of mortar and concrete should be considered. In this paper, the CO<sub>2</sub> binding capacity of mortar and concrete as a tool to assess carbonation coefficient  $K_N$  of mortar and concrete is explored.

## 2. CO<sub>2</sub> binding capacity of mortar and concrete

The scientific background of the presented approach was published in Leemann et al. [9] and Leemann and Moro [10]. In these studies mortar and concrete mixtures containing various mineral additions were exposed both to accelerated and natural carbonation in sheltered and unsheltered conditions. They showed that it is possible to assess carbonation coefficient  $K_N$  based on the water-to-CaO-ratio ( $w/CaO$ ) in concrete (Fig. 1). Hereby, only CaO present in clinker and reactive mineral additions like fly ash or slag but not in unreactive ones like limestone powder are taken into account. The  $w/CaO$  can easily be calculated, if the cement composition is known. It expresses the CO<sub>2</sub> binding capacity per volume of cement paste and, as it is a mass ratio between water and solid, it additionally contains information about porosity and microstructure. It shows a considerably better correlation with the carbonation coefficient  $K_N$  determined in sheltered ( $R^2 = 0.90$ ) and unsheltered ( $R^2 = 0.83$ ) outdoor exposure (Fig. 1) than the compressive strength. Based on these findings, the following empirical equations can be approximated for sheltered and unsheltered exposure [21]:

$$K_{N,S} = C \cdot (8.3 \cdot w/CaO - 4.7) \quad C = 1.00 \quad (1)$$

$$K_{N,US} = C \cdot (8.3 \cdot w/CaO - 4.7) \quad C = 0.47 \quad (2)$$

Of course, these equations are representative for the environmental conditions at the specific exposure site. In this case, yearly averages of temperature, RH and precipitation were 11.4 °C, 78 % and 1200 l/m<sup>2</sup>, respectively. The slope of the linear regression is mainly dependent on the moisture state of the concrete. The value of  $C$  can be adapted to different humidity conditions dependent on the exposure site. Assessing carbonation coefficient  $K_N$  and

carbonation depth  $d_c$  based on the  $w/CaO$  is advantageous compared to a strength-based concept, because it is chemistry-based and as such takes into account cement composition and with it the cement-specific carbonation resistance.

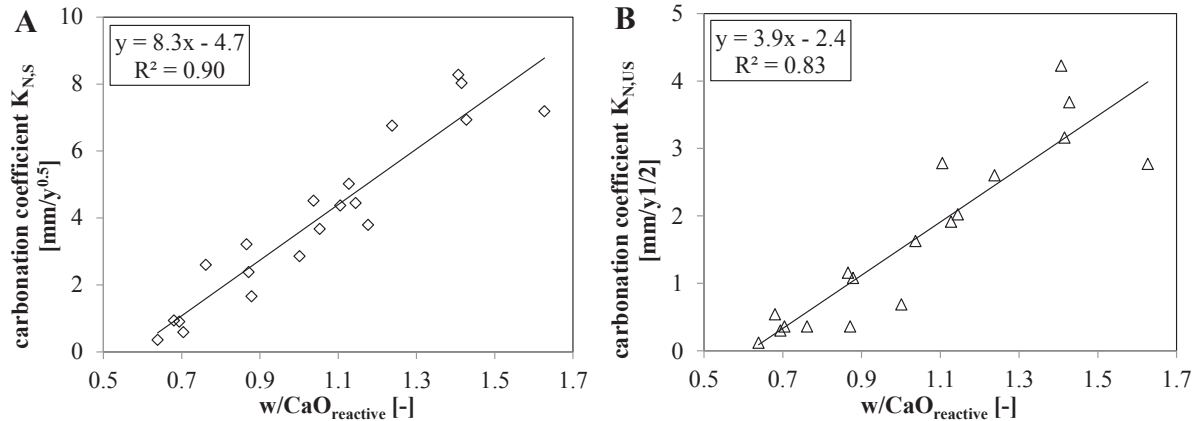


Figure 1: Carbonation coefficient  $K_{N,S}$  in sheltered (A) and carbonation coefficient  $K_{N,US}$  in unsheltered (B) outdoor exposure as a function of the  $w/CaO_{reactive}$  according to [10].

### 3. Calculation of CO<sub>2</sub>-binding

As calculation examples, Swiss cements as described in Environmental Product Declarations (EPD) [11] are used, representing the average composition of the specific cement types (CEM I, CEM II/A, CEM II/B, CH-total). The key figures for the model calculation assumed typical Swiss concrete compositions used for house building. This type of concrete represents about 35 % of the concrete produced in Switzerland. For other types of concrete used for different types of structures, the input parameters like cement type and w/c leading to different values of  $w/CaO$  can easily be adapted using software as basic as an excel spreadsheet. The following comments provide additional information on some of the parameters used in the exemplified calculation shown in Table 1:

- The empirical value for the degree of carbonation  $a_c$  corresponds to the relative amount of carbonated CaO in concrete under natural conditions (1= CaO fully carbonated, 0= no CaO carbonated). It has been reported to be about 0.50 in [12].
- The content of the reactive CaO in Swiss cements has been determined in [9]. Only the CaO reacting during cement hydration is taken into account. Limestone powder for example is not included.
- Carbonation coefficients in sheltered ( $K_{N,S}$ ) and unsheltered ( $K_{N,US}$ ) conditions have been calculated according to Eq. 1 and Eq. 2, respectively. In the exemplified calculation, the ratio of sheltered to unsheltered surfaces has been assumed to be 1. This ratio has to be adapted for individual cases. The sum of sheltered and unsheltered carbonation depth is finally represented by  $d_{c,tot}$ .
- A service life of 100 years is used for this calculation corresponding to EN 16757 [13].
- The implications of carbonation on reinforcement corrosion are not elaborated in this publication, as it is focusing on CO<sub>2</sub>-binding. Possible implications between carbonation and corrosion have to be considered in the structural design.

- The thickness of the concrete element is assumed to be 200 mm. This value refers to 1 m<sup>3</sup> of concrete, allowing to derive the surface area exposed to carbonation.
- The ratio of CO<sub>2</sub>-uptake to emission of concrete ( $U/E_{conc}$ ) is calculated using the carbonation depth  $d_{c,tot}$ , the degree of carbonation  $a_c$  and the thickness of the concrete  $x$ .
- The CO<sub>2</sub> emission resulting from calcination (kg CO<sub>2</sub>/kg cement) was published in the EPD for Swiss cements (www.cemsuisse.ch) following SN EN 15804+A1 [14].
- The final CO<sub>2</sub> uptake by concrete is calculated in kg CO<sub>2</sub>/t of concrete.

Table 1: Exemplified calculation of CO<sub>2</sub>-binding in concrete used for housing during its service life applied for Swiss cements (average composition corresponding to [11]).

parameter	abbr.	units	CEM I	CEM II/A	CEM II/B	CH-total	source / calculation
degree of carbonation (abs)	$a_c$	%	0.50	0.50	0.50	0.50	Thiery et al., 2013
water-cement ratio	$w/c$	-	0.60	0.60	0.60	0.60	typical Swiss value
cement content	$c$	kg/m <sup>3</sup>	280	280	280	280	typical Swiss value
water content	$w$	kg/m <sup>3</sup>	168	168	168	168	typical Swiss value
CaO content of cement	$CaO_{reactive}$	mass-%	0.61	0.53	0.44	0.53	Leemann et al., 2015
CaO content of concrete	$CaO_{reactive}$	kg/m <sup>3</sup>	171	147	123	149	$CaO_{reactive} \cdot c$
water/CaO-ratio	$w/CaO_{reactive}$	-	0.98	1.14	1.36	1.13	$w/CaO_{reactive}$
carbonation coefficient sheltered	$K_{N,S}$	mm/y <sup>0.5</sup>	3.46	4.77	6.63	4.66	Eq. 1
carbonation coefficient unsheltered	$K_{N,US}$	mm/y <sup>0.5</sup>	1.63	2.24	3.12	2.19	Eq. 2
reference service life	$RSL$	y	100	100	100	100	see EN 16757 [25]
carbonation depth sheltered at end of service life	$d_{c,S}$	mm	34.6	47.7	66.3	46.6	$K_{N,S} \cdot y^{0.5}$
carbonation depth unsheltered at end of service life	$d_{c,US}$	mm	16.3	22.4	31.2	21.9	$K_{N,US} \cdot y^{0.5}$
sum of carbonation depth	$d_{c,tot}$	mm	50.9	70.1	97.4	68.5	$d_{c,S} + d_{c,US}$
thickness of concrete element	$x$	mm	200	200	200	200	related to 1 m <sup>3</sup> of concrete
CO <sub>2</sub> emission from calcination of cement	$E_{cem}$	kg CO <sub>2</sub> /kg of cement	0.474	0.413	0.357	0.422	EPD cemsuisse, 2015
ratio of CO <sub>2</sub> uptake-to-emission of concrete	$U/E_{conc}$	-	<b>0.127</b>	<b>0.175</b>	<b>0.244</b>	<b>0.171</b>	$d_{c,tot} \cdot a_c / x$ (Eq. 3)
density of concrete	$\rho_{conc}$	t/m <sup>3</sup>	2.4	2.4	2.4	2.4	
CO <sub>2</sub> -uptake per volume of concrete	$U$	kg/m <sup>3</sup>	16.9	20.3	24.3	20.2	$c \cdot E_{cem} \cdot (U/E_{conc})$
<b>CO<sub>2</sub>-uptake per mass of concrete</b>	<b><math>U</math></b>	<b>kg CO<sub>2</sub>/t of concrete</b>	<b>7.0</b>	<b>8.4</b>	<b>10.1</b>	<b>8.4</b>	$U/\rho_{conc}$

As shown in Table 1, the ratio of CO<sub>2</sub> uptake to CO<sub>2</sub> emission ( $U/E_{conc}$ ) per volume of concrete can be calculated according to Eq. 3:

$$U/E_{conc} = (\text{CO}_2 \text{ uptake})/(\text{CO}_2 \text{ emission}) = (d_{c,tot} \cdot a_c)/x \quad (3)$$

The ratio  $U/E_{conc}$  increases with decreasing thickness of the concrete element as its surface-to-volume-ratio increases (Fig. 2). The higher  $d_{c,tot}$  and  $a_c$  are, the higher is the ratio  $U/E_{conc}$ . The ratio  $U/E_{conc}$  was calculated for the three different cement types and the average of cement

types used in Switzerland as presented in Table 1 using Eq. 3. Concrete mix design (cement type, cement content, w/c) and dimensions of the concrete elements can easily be adapted in the model calculation. Fig. 2 shows how the ratio  $U/E_{conc}$  changes as a function of the thickness of a given concrete element.

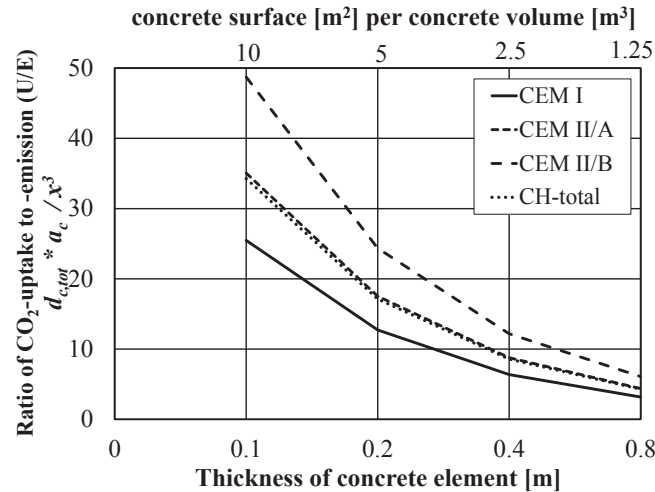


Fig. 2: Ratio of CO<sub>2</sub> uptake to CO<sub>2</sub> emission of concrete ( $U/E_{conc}$ ) as a function of thickness of concrete element.

#### 4. Limitations of assessing CO<sub>2</sub>-binding

Any calculation of CO<sub>2</sub>-binding has its limitations, as simplifications have to be made in order to achieve a manageable degree of complexity. This applies on the approach presented in this paper, as it does for strength-based concepts as well. One key question is the role of RH. Progress of carbonation shows a non-linear response to changes in RH [3,10]. Moreover, both porosity and RH change with concrete depth [15,16]. This point has to be studied further, because the carbonation depth as calculated in this study may be overestimated and therefore, an adaptation of the carbonation coefficients  $K_{N,US}$  and  $K_{N,S}$  used to calculate long-term CO<sub>2</sub>-binding may be required.

#### 5. Summary

CO<sub>2</sub>-binding of concrete during its service life is an important point to be taken into account, when the impact of cement production on atmospheric CO<sub>2</sub> concentration and global warming is considered. It can be calculated by assessing the carbonation coefficient  $K_N$  and the carbonation depth  $d_c$ . This paper presents an approach based on the  $w/CaO$  of concrete, as this parameter governs the carbonation coefficient  $K_N$ . Examples for the implementation of this approach are given using boundary conditions of cement and concrete as used for housing in Switzerland. The two key parameters for the  $w/CaO$  are cement composition and w/c. They can easily be adapted for specific concrete compositions, climatic conditions and service life. The presented approach seems to be especially advantageous when the increasing use of blended cements is considered. In this scenario, the strength-based concept has clear limitations. Therefore, it is proposed that the presented approach is used instead of or in addition to existing strength-based concepts. This approach was not incorporated into EN

16757 [25], but it is currently under consideration to be included into the Technical Report “Carbonation” by CEN TC 104 SC1 TG20.

As shown in this paper, the amount of CO<sub>2</sub> bound by concrete during its service life is substantial compared to the emission of geogenic CO<sub>2</sub> during cement production. A comprehensible assessment of recaptured CO<sub>2</sub> is paramount for a realistic life cycle assessment.

## References

- [1] Le Quéré, C., Andrew, R. M., Canadell, J. G., Sitch, S., ... and Keeling, R. F., Global carbon budget 2016. *Earth System Science Data*, 8(2) (2016), 605-649
- [2] Groves, G.W., Brough, A., ... and Dobson, C.M., Progressive changes in the structure of hardened C<sub>3</sub>S cement pastes due to carbonation, *J Am Ceram Soc* 74 (1991), 2891-2896
- [3] Wierig, H.J., Longtime studies on the carbonation of concrete under normal outdoor exposure. In: *Proceedings of the RILEM Seminar on the Durability of Concrete Structures under Normal Outdoor Exposure* (1984), 239-249
- [4] Lagerblad, B., Carbon dioxide uptake during concrete life cycle—state of the art. Swedish Cement and Concrete Research Institute CBI, Stockholm (2005)
- [5] Pade, C. and Guimaraes, M., The CO<sub>2</sub> uptake of concrete in a 100 year perspective, *Cem Conc Res* 37(9) (2007), 1348-1356
- [6] Nygaard, P. and Leemann A., Kohlendioxidaufnahme von Stahlbeton durch Karbonatisierung, *Cemsuisse Projekt 201106*, Bern (in German) (2012)
- [7] Andersson, R., Fridh, K., Stripple, H. and Häglund, M., Calculating CO<sub>2</sub> uptake for existing concrete structures during and after service life, *Envir Sc Tech*, 47(20) (2013), 11625-11633
- [8] Papadakis, V. G., Effect of supplementary cementing materials on concrete resistance against carbonation and chloride ingress, *Cem Conc Res* 30(2) (2000), 291-299
- [9] Leemann, A., Nygaard, P., Kaufmann, J. and Loser, R., Relation between carbonation resistance, mix design and exposure of mortar and concrete, *Cem Conc Comp* 62 (2015), 33-43
- [10] Leemann, A., Moro, F., Carbonation of concrete: the role of CO<sub>2</sub> concentration, relative humidity and CO<sub>2</sub> buffer capacity, *Mat Struct* 50 (2017), 30.
- [11] cemsuisse, EPD for four types of Swiss cements. <http://www.cemsuisse.ch/cemsuisse/ueberuns/publikationen/epd/index.html?lang=de> (2016)
- [12] Thiery, M., Dangla, P., Belin, P., Habert, G., Roussel, N., Carbonation kinetics of a bed of recycled concrete aggregates: A laboratory study on model materials, *Cem Conc Res* 46 (2013), 50-65
- [13] EN 16757, Sustainability of construction works - Environmental product declarations - Product Category Rules for concrete and concrete elements (2017)
- [14] EN 15804+A1, Sustainability of construction works - Environmental product declarations - Core rules for the product category of construction products, 2013.
- [15] Parrott, L.J., Influence of cement type and curing on the drying and air permeability of cover concrete, *Mag Concr Res* 47 (1995), 103-111
- [16] Parrot L.J., Factors influencing relative humidity in concrete, *Mag Concr Res* 43 (1991), 45-52

## **CREEP PROPERTIES OF POLYMER PARTICLES IN POLYMER-MODIFIED CEMENT PASTES, QUANTIFIED BY MEANS OF MULTISCALE MODELING**

**Luise Göbel<sup>(1,2)</sup>, Markus Königsberger<sup>(2,3)</sup>, Andrea Osburg<sup>(1)</sup>, Bernhard Pichler<sup>(2)</sup>**

- (1) Bauhaus-Universität Weimar, F.A. Finger-Institute for Building Material Engineering, Germany
- (2) TU Wien – Vienna University of Technology, Institute for Mechanics of Materials and Structures, Austria
- (3) Université libre de Bruxelles (ULB), BATir Department, Belgium

### **Abstract**

Polymer-modified mortars and concretes are more creep active than conventional cement-based materials. The present contribution studies the effects of the polymer particles at microscopic observation scales and quantifies their viscoelastic properties during cement hydration. To this end, two different polymer-modified cement pastes were characterized in the context of a comprehensive early-age creep testing campaign. Experimental results are exploited by means of multiscale modeling, carried out using methods of continuum micromechanics. Scale-transition relations are used for downscaling macroscopic experimental results, referring to the material scale of cement pastes, to the microscopic creep behavior of the cementitious hydrates and the polymer particles. In order to study the creep-magnifying effect of the polymers, three different modeling approaches are investigated. The microscopic polymer particles are considered as (i) pores, exhibiting vanishing elastic stiffness, (ii) an elastic phase without creep activity, or (iii) a viscoelastic material phase. The modeled creep curves obtained from the latter approach agree well with the experimental results. This corroborates that polymers act as viscoelastic phases in the cement microstructure and, thus, magnify the macroscopic creep behavior of polymer-modified cement-based materials.

### **1. Introduction**

Polymer-modified mortars and concretes (PCC) have been successfully used for repair and overlays [1,2]. The materials are used to extend the service life of structures and bridge decks

by providing increased adhesion strength, improved chemical resistance, and reduced permeability. However, the polymer modification entails a lowered elastic stiffness of the mortars and concretes, accompanied by a larger creep activity [3,4]. The present contribution investigates whether or not the more pronounced creep behavior of PCC can be explained by considering that both the cementitious hydration products *and* the polymers contribute to the creep strains. Thereby, three different modeling approaches are used: (i) polymers are considered as pores, without viscoelastic stiffness; (ii) polymers are considered as an elastic material phase, without creep activity; (iii) polymers are considered as a viscoelastic material phase, whereby an isochoric power-law creep function is considered and the creep parameters are obtained from downscaling the aforementioned macroscopic creep tests.

The homogenized (upscaled) creep behavior is compared with experimental results from an early-age creep testing campaign on two different polymer-modified cement pastes [3]. As for the required scale transitions (creep up- and downscaling), we rely on a recently proposed continuum micromechanics model for polymer-modified cement-based materials [3–5]. This provides the relation between the micromechanical properties of the polymer particles and the hydration products, on the one hand, and the macroscopic creep strains of polymer-modified cement pastes subjected to short-term compressive loads, on the other hand.

The paper is structured as follows. In Section 2, the continuum micromechanics model for homogenization of the viscoelastic properties of polymer-modified cement pastes is presented. Then, the predictive capability of the multiscale model is assessed by comparing the modeling results to the measured creep strains (Section 3). This comparison allows for conclusions on the role of the polymers in hydrating cement pastes (Section 4).

## 2. Modeling of the non-aging creep properties of polymer-modified cement pastes

### 2.1 Micromechanical representation and viscoelastic phase behavior

The hierarchically organized microstructure of polymer-modified cement pastes can be represented by two scale-separated representative volume elements (RVEs) [3–5]. The RVE of cement paste is envisaged as a matrix-inclusion type composite of a polycrystalline hydrate foam matrix [6,7], spherical clinker inclusions, and entrapped air voids. The latter result from polymer-cement interactions during the mixing of the raw materials [8]. The hydrate foam is resolved at the scale of a few microns and consists of spherical polymer particles, capillary pores, and isotropically oriented needle-shaped hydrates [6,7], see Fig. 1.

During the hydration process, the phase volume fractions can be described by means of the Powers hydration model [9], as functions of the hydration degree and the initial water-to-cement mass ratio. This was extended to include the volume fractions of the polymers and the entrapped air porosity at the scales of the hydrate foam and the cement paste, respectively [3].

As for the mechanical phase properties, the bulk and shear moduli of the purely elastic clinker phase amount to 116.7 GPa and 53.8 GPa. The water- and air-filled pores exhibit vanishing elastic stiffness. Ultrasonic tests on solid polymer specimens provided access to their elastic bulk and shear modulus as 4.0 GPa and 0.9 GPa [3], their creep behavior is identified from macroscopic experiments in Section 3. The hydrate creep function  $J_{hyd}$  is isochoric [10]:

$$J_{hyd}(t - \tau) = \frac{1}{3k_{hyd}} \mathbf{I}^{vol} + \frac{1}{2} \left[ \frac{1}{\mu_{hyd}} + \frac{1}{\mu_{c,hyd}} \left( \frac{t - \tau}{t_{ref}} \right)^{\beta_{hyd}} \right] \mathbf{I}^{dev} \quad (1)$$



$I^{vol}$  and  $I^{dev}$  are the volumetric and deviatoric parts of the symmetric fourth-order identity tensor  $I$ .  $t$  and  $\tau$ , respectively, are the chronological time and the time instant of loading.  $t_{ref} = 86400$  s is a fixed reference time. In Eq. (1),  $k_{hyd} = 18.7$  GPa and  $\mu_{hyd} = 11.8$  GPa [7], and  $\mu_{c,hyd}$  and  $\beta_{hyd}$  denote the shear creep modulus and the power-law creep exponent of the hydrates. Based on 500 early-age short-term creep tests, they were identified as [10]  $\mu_{c,hyd} = 20.93$  GPa and  $\beta_{hyd} = 0.251$ .

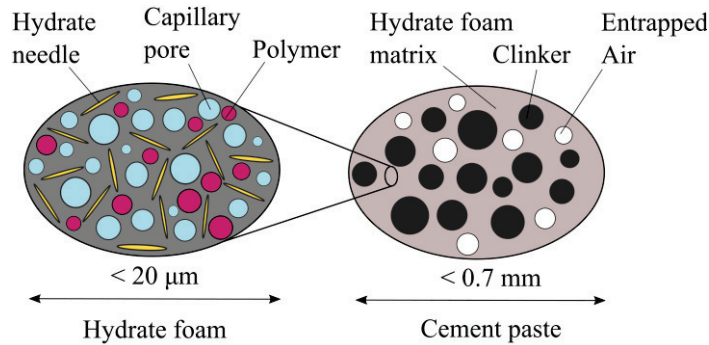


Figure 1: Two-scale representation of polymer-modified cement pastes: material organogram according to [4]. The 2D sketches illustrate qualitative properties of 3D RVEs.

## 2.2 Homogenization of the viscoelastic behavior of polymer-modified cement pastes

Homogenization of the viscoelastic properties is carried out based on the correspondence principle [11]. Accordingly, the elastic and viscoelastic behavior of the material phases is transformed from the time domain to the Laplace-Carson (LC) domain. There, upscaling of the creep behavior of the microscopic phases, via the scale of the hydrate foam, up to the cement paste scale can be performed as quasi-elastic homogenization. As for the polycrystalline RVE of hydrate foam, the self-consistent scheme is employed [12]. As for the matrix-inclusion RVE of cement paste, homogenization is performed by means of the Mori-Tanaka scheme. Computational details about the upscaling procedure and the analytical formulae for the LC-transformed creep properties of the cement pastes are given in [4,10]. The obtained creep tensor function of cement paste in the LC domain is numerically back-transformed to the time domain, applying the Gaver-Wynn-Rho algorithm [13].

## 3. Top-down identification of the viscoelastic polymer behavior

In the following, it is investigated whether or not the polymer phase contributes to the viscoelastic behavior of polymer-modified cement pastes. To this end, the mechanical properties of the polymers are introduced according to the three different approaches described in Section 1. The performance of the model is checked by comparing the modeled creep strains to experiments which are described next.

### 3.1 Early-age creep testing of polymer-modified cement pastes

Hourly repeated ultra-short creep tests were performed to characterize the creep behavior of one ordinary Portland cement paste and two different polymer-modified pastes, see [3] for details. Polymer-modified paste P1 was mixed with a polymer dispersion containing styrene

acrylate copolymers. Paste P2, in turn, contained a dispersion with styrene butadiene copolymers. The initial water-to-cement mass ratio for all pastes amounted to 0.40 and the initial polymer-to-cement mass ratio to 0.10.

A series of 168 uniaxial compressive creep tests was performed on every specimen during ongoing hydration of the pastes, whereby each individual test lasted for three minutes. The material ages ranged from 21 hours up to eight days. The load levels were restricted to 7.5 % of the estimated uniaxial compressive strength at the time instant of loading, in order to avoid damage of the specimens and to get access to the linear creep behavior.

It was observed that the neat reference paste exhibits a creep activity which is approximately three times smaller than that of the polymer-modified specimens. Paste P2 shows a smaller elastic stiffness and a slightly more pronounced creep activity than paste P1. This is particularly related to the entrapped air porosity of paste P2, amounting to 4.8 %. Paste P1, in turn, does not contain entrapped air porosity [3].

### 3.2 Modeling results and comparison with experimental data

The goodness-of-fit between modeled and experimentally determined viscous part of the uniaxial creep functions  $J_{v,cp}$  is assessed via the mean error, which is defined as  $\epsilon = \frac{1}{n_{\zeta} n_t} \sum_{i=1}^{n_{\zeta}} \sum_{j=1}^{n_t} |J_{v,cp}^{mod}(t_j) - J_{v,cp}^{exp}(t_j)|$ . The sum over  $n_{\zeta}$  refers to the 168 varying material ages of the cement pastes,  $n_t$  refers to a temporal resolution of the individual three-minutes-long creep tests in 180 steps. For details concerning the determination of  $J_{v,cp}^{mod}$  and  $J_{v,cp}^{exp}$ , see [4,10]. Scenario 1 envisages that the polymers act as pores, without any stiffness. The resulting model underestimates the experimentally observed creep strains, see Fig. 2 (a) and (d). The mean errors amount to  $3.59 \times 10^{-6}$ /MPa for paste P1 and to  $1.53 \times 10^{-6}$ /MPa for paste P2. Scenario 2 envisages that the polymers act as elastic phases with (non-zero) experimentally determined stiffness properties given in [3]. The resulting model underestimates the experimental creep strains considerably, see Fig. 2 (b) and (e). The mean errors amount to  $5.78 \times 10^{-6}$ /MPa for paste P1 and to  $4.74 \times 10^{-6}$ /MPa for paste P2.

Scenario 3 envisages that the polymers act as a viscoelastic phase. An isochoric creep tensor function is used to model the polymers. As for quantification of the related creep properties, a top-down identification process is carried out, starting with results from ultra-short creep tests on polymer-modified cement pastes, see [4] for all details. It was found that the creep activity of the polymer particles decreases significantly as a function of the material age of the cement pastes. The shear creep modulus increases rapidly within the first 40 h. It is almost constant between 40 h and 110 h and amounts to 80 MPa for paste P1 and to 110 MPa for paste P2. Afterwards, it increases rapidly again up to values of 600 MPa and 400 MPa, respectively. The related creep strain evolutions, obtained from the multiscale model, re-produce the experimental observation very reliably, see Fig. 2 (c) and (f). The residual mean errors are as small as  $1.98 \times 10^{-7}$ /MPa for paste P1 and  $2.23 \times 10^{-7}$ /MPa for paste P2.

### 3.3 Discussion of the results shown in Fig. 2

The micromechanical origin of the macrostrain differences between the three modeled scenarios is discussed next. Notably, the strains depicted in Fig. 2 are the time-dependent viscous macrostrains, obtained from subtracting the instantaneous elastic macrostrains from the total macrostrains. When considering the polymers as pores, the hydrates are the only solid constituent of the hydrate foam, see Fig. 1. Thus, they take over significant stresses upon

macroscopic loading. Their viscous behavior results in a stress-transfer to the cement grains, but this is not very effective, because the hydrates and the cement grains refer to *different* scales of observation (Fig. 1). When considering the polymers as a purely elastic solid phase, they do also take over stresses upon macroscopic loading. Thus, the hydrates experience smaller stresses as in the previously discussed scenario. In addition, the viscous behavior of the hydrates results in a stress-transfer both to the polymer particles and the cement grains. The stress transfer to the polymers is quite effective, because the hydrates and the polymers refer to the *same* scale of observation. Thus, modeling polymers as elastic solid phases results in smaller stress levels in the hydrates and, thus, in smaller viscous macrostrains compared to the case where polymers are considered as pores. When considering the polymers as a viscoelastic solid phase, the initial microstress distribution is the same as in the previously discussed scenario. Given that both the hydrates and the polymers are viscous, the stress transfer from the hydrates to the polymers and vice versa is not very effective. Also, the stress transfer to the cement grains is not very effective, see above. Thus, the largest macroscopic creep activity is obtained, provided that polymers are modeled as a viscoelastic solid phase. Finally, it is worth mentioning that modeling the polymers as pores results in a significantly larger spontaneous elastic deformation of cement paste compared to the alternative of modeling polymers as solids, but this is not shown in Fig. 2, see above.

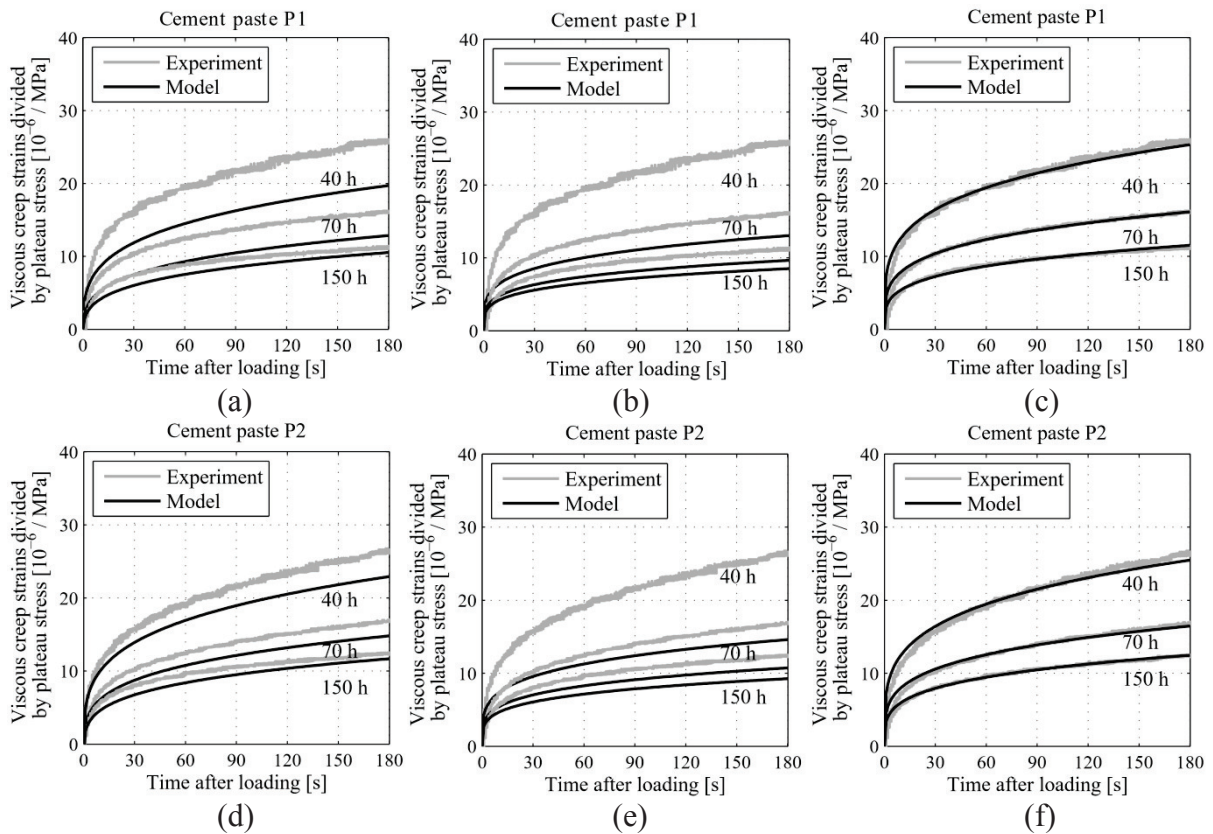


Figure 2: Measured vs. modeled evolutions of viscous strains: (a) and (d) refer to polymers acting as pores; (b) and (e) refer to polymers acting as elastic phases; (c) and (f) refer to polymers acting as viscoelastic phases; see also the discussion in Section 3.3.

## 5. Conclusions

The present contribution studied the viscoelastic characteristics of polymer particles at microscopic scales. Based on an early-age creep testing campaign and multiscale modeling, the following conclusions can be drawn:

- Considering polymer particles as elastic phases without creep activity considerably underestimates the creep activity of polymer-modified cement pastes.
- The situation can be significantly improved provided that modeling accounts for the viscoelastic behavior of the polymer particles. Their creep properties were identified by means of a top-down identification approach, based on results of an early-age creep testing campaign on polymer-modified cement pastes.

## References

- [1] R. Wang, Z. Yang (Eds.), *Progress in Polymers in Concrete*, Trans Tech Publications, Zürich, 2013.
- [2] Y. Ohama, D. van Gemert, M. Ota, Introducing process technology and applications of polymer-modified mortar and concrete in construction, *International Journal for Restoration of Buildings and Monuments* 19 (2013) 369–392.
- [3] L. Göbel, B. Pichler, A. Osburg, The mechanical performance of polymer-modified cement pastes at early ages: ultra-short non-aging creep tests and multiscale homogenization, *Construction and Building Materials* 173 (2018) 495–507.
- [4] L. Göbel, M. Königsberger, A. Osburg, B. Pichler, Viscoelastic Behavior of Polymer-modified Cement Pastes: Insight From Downscaling Short-term Macroscopic Creep Tests by Means of Multiscale Modeling, *Applied Sciences* 8 (2018) 487.
- [5] L. Göbel, C. Bos, R. Schwaiger, A. Flohr, A. Osburg, Micromechanics-based prediction of the elastic properties of polymer-modified cementitious materials using nanoindentation and semi-analytical modeling, *Cement and Concrete Composites* 88 (2018) 100–114.
- [6] B. Pichler, C. Hellmich, J. Eberhardsteiner, Spherical and acicular representation of hydrates in a micromechanical model for cement paste: prediction of early-age elasticity and strength, *Acta Mech* 203 (2009) 137–162.
- [7] B. Pichler, C. Hellmich, Upscaling quasi-brittle strength of cement paste and mortar: A multi-scale engineering mechanics model, *Cement and Concrete Research* 41 (2011) 467–476.
- [8] D.A. Silva, John, V.M., Ribeiro, J.L.D., H.R. Roman, Pore size distribution of hydrated cement pastes modified with polymers, *Cement and Concrete Research* 31 (2001) 1177–1184.
- [9] T.C. Powers, T.L. Brownyard, Studies of the Physical Properties of Hardened Portland Cement Paste, *Research Laboratories of the Portland Cement Association Bulletin* 43 (1948) 101–132.
- [10] M. Königsberger, M. Irfan-ul-Hassan, B. Pichler, C. Hellmich, Downscaling Based Identification of Nonaging Power-Law Creep of Cement Hydrates, *Journal of Engineering Mechanics* 142 (2016) 4016106.
- [11] N. Laws, R. McLaughlin, Self-Consistent Estimates for the Viscoelastic Creep Compliances of Composite Materials, *Proceedings of the Royal Society of London A: Mathematical, Physical and Engineering Sciences* 359 (1978) 251–273.
- [12] A.V. Hershey, The elasticity of an isotropic aggregate of anisotropic cubic crystals, *Journal of Applied Mechanics* 21 (1954) 236.
- [13] J. Abate, P.P. Valkó, Multi-precision Laplace transform inversion, *International Journal for Numerical Methods in Engineering* 60 (2004) 979–993.

## **DEVELOPMENT OF PORE-SCALE MODEL FOR INGRESS OF CO<sub>2</sub> BRINE THROUGH CEMENT PASTE**

**Ravi A. Patel**<sup>(1)</sup>, **Nikolaos I. Prasianakis**<sup>(1)</sup>

(1) Laboratory for waste management (LES), Paul Scherrer institute, Villigen CH 5232, Switzerland

### **Abstract**

Carbonation of cementitious materials is of relevance for a wide range of practical applications. It leads to dissolution of calcium bearing phases in cementitious materials and subsequent precipitation of calcite. This process alters the properties of the material itself. The progression of carbonation and its effect on the microstructure of cementitious materials depends on a variety of parameters. Therefore, a pore-scale modelling approach capable of capturing changes in microstructure under external boundary conditions, can be a useful tool in developing mechanistic understanding. With this aim, a pore-scale modelling approach is presented for carbonation under saturated conditions, and is applied to a stylized pore structure consisting solely of portlandite and open pores. Evolution of this pore structure under different boundary conditions is investigated. Preliminary simulations illustrate that the model is able to capture qualitatively the main trends that are reported in the literature. These simulations also effectively demonstrate that a very small volume fraction of precipitating mineral can have a large effect on transport pathways, inhibiting or slowing down the dissolution.

### **1. Introduction**

Carbonation of cementitious materials refers to the interaction of cement with CO<sub>2</sub>. CO<sub>2</sub> as a gas, dissolves in the pore water of cement paste forming carbonic acid (H<sub>2</sub>CO<sub>3</sub>) which further reacts with calcium bearing cement paste chemical phases leading to calcite precipitation. Carbonation is of practical relevance in the context of several practical applications such as service life predictions of reinforced concrete structures, improving recycled aggregates quality, capturing CO<sub>2</sub> in cementitious materials, self-healing of concrete structures through carbonation, long-term integrity of geological nuclear waste disposal system, etc [1].

Therefore, it is important to understand the underlying mechanisms and to be able to model changes in cement paste micro structure due to carbonation. This eventually allows to also predict the progression of carbonation.

Carbonation models developed at continuum scale, require as input a wide range of parameters. The evolution of these parameters due to microstructural changes during carbonation are difficult if not impossible to measure directly [2]. Therefore, such models can only provide qualitative understanding, and can be hardly used for predictive purposes. Similarly, most of the service life models for carbonation, are based on the square root time approach and are highly empirical [3,4]. A “bottom up” approach in which the pore-scale model which simulates changes in the pore-space due to carbonation can be used for upscaling can prove to be a valuable tool. With this aim, a pore-scale model is developed to simulate changes in a saturated cement paste micro-structure due to ingress of CO<sub>2</sub> brine. While, in reality natural carbonation occurs under unsaturated conditions, this model setup is relevant within the context of clay rock-concrete interfaces which is of significant for deep geological disposal of nuclear waste [5,6] and well-bore cement interaction with CO<sub>2</sub> brine in context of CO<sub>2</sub> sequestration [7]. Further details on modelling approach for carbonation is given in section 2. In section 3 we discuss the simulation results for different boundary composition of CO<sub>2</sub> brine ingress through a stylized portlandite pore-structure. Finally, conclusions are presented in section 4.

## 2. Pore-scale modelling approach

A lattice Boltzmann method (LBM) based pore scale reactive transport modelling tool, *Yantra*, is used for the modelling and simulations [8,9]. It also has a special implementation for multilevel porous systems where continuum media and pores co-exist. Such treatment is essential for cementitious systems which has wide range of pore size distribution. In *Yantra*, the LBM solver for simulating mass transport, has been coupled with the geochemical solver *IPhreeqC*, to account for complex reaction networks using appropriate thermodynamic databases [10]. Its reactive transport solver can track microstructure evolution which occurs due to dissolution, and precipitation process. For further details on algorithms implemented in readers are referred to [8]. Previously, the application of this scheme has been successfully demonstrated to simulate calcium leaching through cementitious systems [11,12].

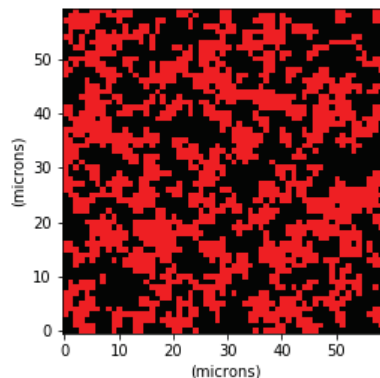


Figure 1: Stylized porous media used for simulation. Portlandite is represented in red and pores in black.

In this preliminary study, a simplified porous system consisting of portlandite and pores, is considered as shown in Figure 1. The volume fraction of portlandite is 45% and correspondingly, the initial porosity of the domain is 0.55. The simulation domain consists of  $60 \mu\text{m} \times 60 \mu\text{m}$  with  $1 \mu\text{m}$  discretization. The diffusion coefficient of all primary species is taken as  $2.2 \times 10^{-9} \text{ m}^2/\text{s}$  corresponding to diffusion of calcium ions [11]. Simulations are carried out using different boundary solutions at left hand boundary as summarized in Table 1, and all other boundaries are set as zero flux boundary. Case 1 refers to the system subject to left-boundary concentration of primary carbon species (C) 0.01 M and primary sodium species (Na) 0.082 M with pH maintained at 7. For Case 2, the concentration is reduced to 0.001 M and pH is maintained at 7 by reducing Na concentration to 0.00081 M. For Case 3, Na is not added to system with C concentration 0.01 M, which correspond to a pH= 4.192. Finally, for Case 4, instead of Na, the primary calcium species (Ca) concentration is equal to 0.00414 and is added in order to keep the pH of the solution at the boundary equal to 7. For all the cases, the boundary solution is undersaturated with respect to portlandite which leads to its dissolution. Moreover, for Cases 1-3, the boundary solution is undersaturated with respect to calcite which might lead to dissolution of precipitated calcite whereas for Case 4 boundary solution is oversaturated with respect to calcite. These different cases have been inspired from the experimental observations reported by Schwotzer et al. [13]. They reported that in case calcium is supplied from pore-water for calcite precipitation it triggers chemical degradation of solid phases in cement paste. However, if calcium is supplied from external boundary a dense protective layer of calcite can build up. The developed simulation example aims to reproduce this observation. The dissolution of portlandite and precipitation of calcite is modelled under the assumption of thermodynamic equilibrium. For simplification, it is assumed that calcite only nucleates heterogeneously on the surface of portlandite phase. The results of the simulations are discussed in next section.

Table 1: Boundary solution composition used for different cases in simulation.

	Ca [M]	Na [M]	C[M]	pH
Case 1	-	0.00821	0.01	7
Case 2	-	0.00081	0.001	7
Case 3	-	-	0.01	4.192
Case 4	0.00414	-	0.01	7

### 3. Results

Figure 2 shows the evolution of microstructure at different times for the four cases described in previous section. For Case 1 and Case 3 the calcite precipitation front is dynamic, with its location varying with time. This is due to fact that boundary solution is unsaturated with respect to calcite. However, for Case 2 precipitation of calcite only occurs near the boundary during the time span of simulation, and the calcite front does not penetrate into the portlandite structure. For Case 4 calcite is precipitating in a fast pace, initially clogging the surface, while only slight dissolution of portlandite is observed near the surface. Evolution of average volume fractions of portlandite and calcite with respect to time are plotted in Figure 3. It shows that for case 3, the portlandite dissolution is fastest, followed by case 2 and case 1. For case 4 after initial clogging at the boundary portlandite dissolution is stopped. In case 3, a

continuous dissolution and reprecipitation occurs whereas in case 1 the precipitation of calcite slows down dissolution of portlandite and further dissolution of calcite reinitiates dissolution of portlandite. As a result, dissolution of portlandite for case 3 is much slower.

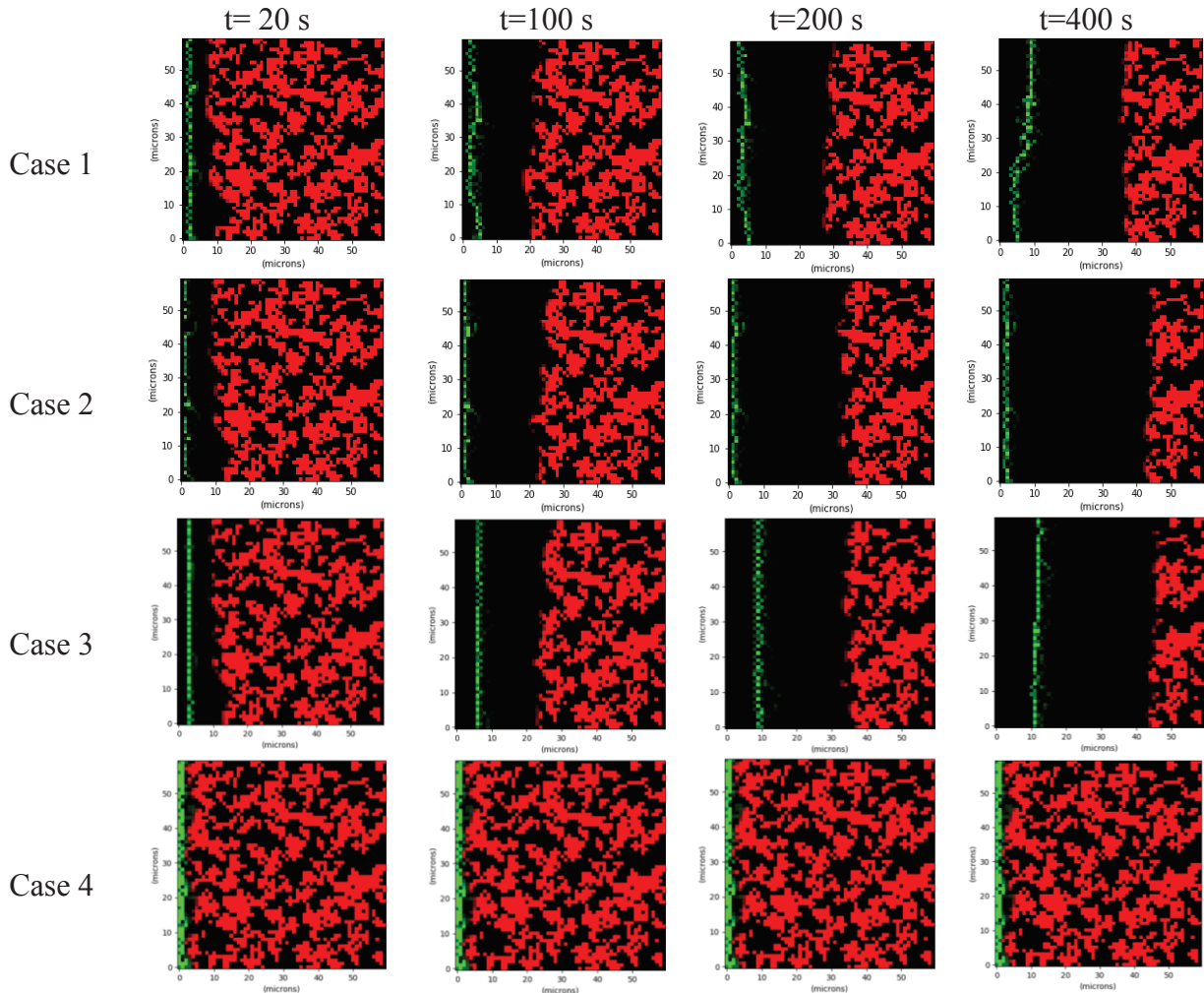


Figure 2: Evolution of pore-structure at different timesteps. Calcite, portlandite and pores are represented in green, red and black respectively (for colour figure refer to the online version). Shading of colour is proportional to the volume fraction of the phase.

In case 2, due to low carbon species concentration at the boundary, the precipitation of calcite is slower and initially less compared to case 3 and case 1. These simulations reveal the rich physics and complexity of the effect of chemical concentrations on the pore structure evolution. The simulations are able to capture the essence of the observations reported by Schwotzer et al [13] and as summarized in previous section. It should be noted the total volume of solid phases in the domain is less than one and the volume fraction of precipitating mineral ranges from 1 to 3% at the end of simulation. It demonstrates that the process of clogging (case 4) can occur much earlier, compared to the standard assumption of continuum scale models, which stipulates that clogging occurs when the control volume is filled



completely with solid. Similarly, a small volume of precipitating mineral can have a large effect on dissolution process. Therefore, it is important to understand how the precipitating mineral affects transport pathways at lower scales, which can be readily captured by pore-scale modelling. This example highlights the importance of pore-scale modelling in context of carbonation of cementitious materials.

#### 4. Conclusions

A pore-scale reactive transport model has been developed, to simulate carbonation under saturated conditions in a cementitious system. Preliminary simulations on stylized pore-structure, illustrate the distinct evolution paths due to carbonation, which strongly depend on the solution concentrations. The simulation reveals the complexity as well as the effect of different boundary conditions, and their influence on pore structure evolution. The simulations are able to qualitatively capture the observations reported in literature. We also stress and demonstrate that even a small volume fraction of precipitating mineral can affect transport pathways inhibiting or slow down the dissolution pores, highlighting the need for pore-scale modelling. In the future, simulations considering realistic cement pore-structure and more detailed precipitation mechanisms [14] are planned, which will provide new insights into the process of carbonation.

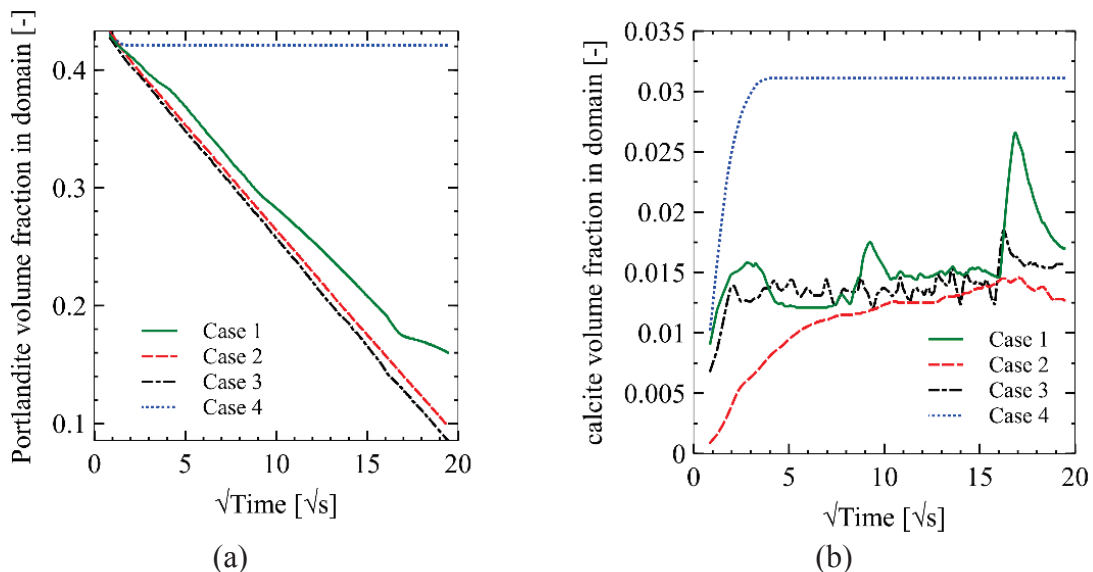


Figure 3: Time evolution of (a) portlandite and (b) calcite volume fraction (averaged over simulation domain).

#### Acknowledgements

This project has received funding from the European union's Horizon 2020 research and innovation programme under the Marie Skłodowska-Curie grant agreement No 701647.

## References

- [1] B. Šavija, M. Luković, Carbonation of cement paste: Understanding, challenges, and opportunities, *Constr. Build. Mater.* 117 (2016) 285–301.
- [2] Q.T. Phung, N. Maes, D. Jacques, G. De Schutter, G. Ye, J. Perko, Modelling the carbonation of cement pastes under a CO<sub>2</sub> pressure gradient considering both diffusive and convective transport, *Constr. Build. Mater.* 114 (2016) 333–351.
- [3] S.O. Ekolu, Model for practical prediction of natural carbonation in reinforced concrete: Part 1-formulation, *Cem. Concr. Compos.* 86 (2018) 40–56.
- [4] V.-L. Ta, S. Bonnet, T. Senga Kiese, A. Ventura, A new meta-model to calculate carbonation front depth within concrete structures, *Constr. Build. Mater.* 129 (2016) 172–181.
- [5] E.C. Gaucher, P. Blanc, Cement/clay interactions – A review: Experiments, natural analogues, and modeling, *Waste Manag.* 26 (2006) 776–788.
- [6] U. Mäder, A. Jenni, C. Lerouge, S. Gaboreau, S. Miyoshi, Y. Kimura, V. Cloet, M. Fukaya, F. Claret, T. Otake, M. Shibata, B. Lothenbach, 5-year chemico-physical evolution of concrete–claystone interfaces, Mont Terri rock laboratory (Switzerland), *Swiss J. Geosci.* 110 (2017) 307–327.
- [7] B.G. Kutchko, B.R. Strazisar, D.A. Dzombak, G. V. Lowry, N. Thuiow, Degradation of well cement by CO<sub>2</sub> under geologic sequestration conditions, *Environ. Sci. Technol.* 41 (2007) 4787–4792.
- [8] R. Patel, Lattice Boltzmann Method Based Framework for Simulating Physico-Chemical Processes in Heterogeneous Porous Media and Its Application to Cement Paste, Ghent university, 2016.
- [9] R.A. Patel, <https://bitbucket.org/yantralbm/yantra>, (2016).
- [10] R.A. Patel, J. Perko, D. Jacques, G. De Schutter, K. Van Breugel, G. Ye, A versatile pore-scale multicomponent reactive transport approach based on lattice Boltzmann method: Application to portlandite dissolution, *Phys. Chem. Earth.* 70–71 (2014) 127–137.
- [11] R.A. Patel, J. Perko, D. Jacques, G. De Schutter, G. Ye, K. Van Breugel, A three-dimensional lattice Boltzmann method based reactive transport model to simulate changes in cement paste microstructure due to calcium leaching, *Constr. Build. Mater.* 166 (2018).
- [12] S.C. Seetharam, R.A. Patel, J. Perko, D. Jacques, Quantification of leaching kinetics in OPC mortars via a mesoscale model, *Constr. Build. Mater.* 180 (2018) 614–628.
- [13] M. Schwotzer, T. Scherer, A. Gerdes, Protective or damage promoting effect of calcium carbonate layers on the surface of cement based materials in aqueous environments, *Cem. Concr. Res.* 40 (2010) 1410–1418.
- [14] N.I. Prasianakis, E. Curti, G. Kosakowski, J. Poonoosamy, S. V. Churakov, Deciphering pore-level precipitation mechanisms, *Sci. Rep.* 7 (2017) 13765.

## **EARLY AGE MECHANICAL PROPERTIES AND SHRINKAGE OF BLENDED CEMENT CONCRETE CONTAINING SLAG**

**Tahsin Alper Yikici<sup>(1)</sup>, Egemen Kesler<sup>(2)</sup>, Yilmaz Akkaya<sup>(2)</sup>**

(1) MEF University, Istanbul, Turkey

(2) Istanbul Technical University, Istanbul, Turkey

### **Abstract**

Slag cement concrete is usually preferred for the design of mass concrete structures exposed to the marine environment, due to chloride binding capacity and low heat of hydration properties. However, the early age property development of slag cement concrete is comparatively slower than Portland cement concrete (PCC). Therefore, longer curing might be essential to prevent early age cracks. In general, early age cracking potential of concrete mixtures depend on the stresses induced by shrinkage strains caused by hydration of cement, drying, and thermal contraction. Depending on the development of rigidity and modulus of elasticity of the concrete, such strains cause stresses that result in cracking when they exceed the tensile strength capacity of concrete. Thus, early-age shrinkage, mechanical strength and elasticity modulus development of slag cement concrete are essential parameters in early age cracking risk calculations. This study investigates the adiabatic heat development of slag cement concrete and its relation to the development of compressive strength, tensile strength, modulus of elasticity, and early-age shrinkage. Concrete mixtures containing 380-440 kg/m<sup>3</sup> CEMIII B 32.5N were cast with water to cement ratio of 0.32-0.40. Additionally, the effect of aggregate size and aggregate type was investigated by using limestone aggregates, and sandstone. The microstructure of the cement paste, investigated by thin sections, provided valuable information to distinguish the relationship between adiabatic heat, early-age shrinkage, and mechanical properties. The distance between particles and differences in particle size distribution of binders and aggregates were essential parameters in understanding the differences in performance of the concrete mixtures.

### **1. Introduction**

Blast-furnace slag (BFS) is being used as a cement substitute to produce high performance concrete for structural applications such as anchorage blocks and caissons of bridges due to

slower rate of heat generation and chloride ingress. Additionally, when used in higher levels (>70%) it provides more economic and environmental friendly solution compared with PCC [1]. However, BFS concrete with low water to cement ratio (<0.40) and relatively fine pore structure exhibits larger early-age shrinkage. If not properly accounted for, such rapid deformations may cause cracking under restrained conditions since concrete has very low strain capacity thereby very sensitive to internal stresses at early ages [2,3,4,5].

In this study early-age shrinkage behavior of high early strength BFS concrete was investigated in accordance with development of degree of hydration. Early-age shrinkage was measured as the length change occurring from the time of concrete solidification to the age of 28 days. Degree of hydration of the concrete mixtures was calculated from the heat development obtained experimentally from semi-adiabatic calorimeter tests [6,7]. Moreover, development of compressive strength, tensile strength and modulus of elasticity of concrete specimens was determined. The relationship between early-age shrinkage, mechanical properties and degree of hydration was presented by means of mix design parameters.

## 2. Experimental Study

For this study eight different concrete mixtures were investigated with different types of cement and cementitious materials, and equivalent water to cement ratios ranging from 0.32 to 0.40. Compressive strength class and the workability class of all mixtures were C50/70 and S5, respectively. Each concrete mixture design was specifically developed to satisfy structural service life requirement of minimum 100 years, by using CEM III B cement or combining CEM I cement with Class F fly ash, (FA) micro silica (MS) and BFS as mineral admixtures. Natural sand and crushed sand were used as fine aggregates, and two crushed aggregates with nominal maximum sizes of 12.5 mm (No1) and 22 mm (No2) were used as coarse aggregates. Concrete mixture design proportions are given in Table 1.

Table 1: Concrete Mix Designs per m<sup>3</sup>.

Mix design	Mix 1*	Mix 2*	Mix 3*	Mix 4*	Mix 5 <sup>+</sup>	Mix 6 <sup>+</sup>	Mix 7*	Mix 8*
w/c	0.37	0.37	0.40	0.37	0.37	0.37	0.38	0.32
D <sub>max</sub> , mm	22.0	12.5	12.5	22.0	22.0	22.0	22.0	22.0
CEM IIIB, kg	390	380	380	390	390	390		
CEM I, kg	-	-	-	-	-	-	285	146
GGBS, kg	-	-	-	-	-	-	-	294
Class F FA, kg	-	-	-	-	-	-	50	-
MS, kg	-	-	-	-	-	-	12	-
Water, kg	144	141	152	144	144	144	123	141
Natural Sand, kg	508	486	479	458	540	540	386	470
Crushed Sand, kg	414	398	392	434	415	415	456	373
No1, kg	472	910	897	493	440	450	498	542
No2, kg	401	-	-	423	380	385	479	469

\*Limestone aggregate +Sandstone aggregate

Ready-mix concrete was delivered to the laboratory from the plant. Fresh concrete properties including slump, flow diameter and air content were tested and results are given in Table 2. Specimens were prepared for compressive strength, tensile strength, modulus of elasticity,

shrinkage and microstructural evaluations. The evaluation of the early-age shrinkage and mechanical properties will be discussed by means of degree of hydration. Moreover, semi-adiabatic calorimetry tests were conducted in accordance with NT BUILT 388 [7].

Table 2: Fresh concrete properties.

Mix design	Slump [cm]	Flow [cm]	Air Content [%]	Unit Weight [kg/m <sup>3</sup> ]	Ambient Temp [°C]	Concrete Temp [°C]
Mix1	20	50	6.5	2350	16.7	21.2
Mix2	24	-	3.0	2450	21.0	25.0
Mix3	20	47	4.7	2450	14.5	19.7
Mix4	19	48	4.0	2400	19.2	25.1
Mix5	18	50	5.4	2350	19.0	24.8
Mix6	18	41	4.6	2400	9.7	16.5
Mix7	21	-	-	2450	20.4	22.2
Mix8	23	50	1.3	2500	13.2	11.0

### 2.1 Semi-Adiabatic Calorimetry

The concrete for semi-adiabatic calorimetry was mixed in the laboratory and samples were immediately placed in heat insulated drums. The temperature increase in the sample was measured during hydration. The total heat produced from the hydration and the rate of heat of hydration of the concrete mixtures were calculated based on the heat capacity and activation energy of the sample in addition to the heat losses through the insulated drum [7]. The results of semi-adiabatic calorimeter test are given in Figure 1.

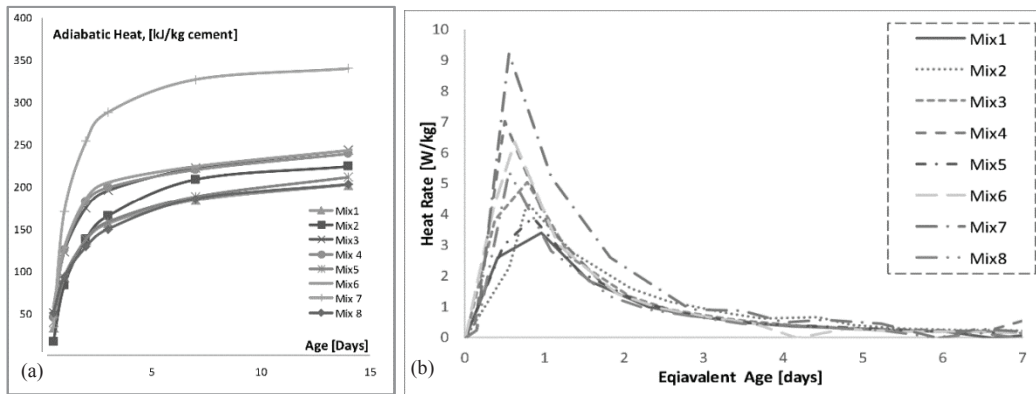


Figure 1: Semi-adiabatic test results (a) Total heat generated (b) Rate of heat generation.

### 3. Results and Discussion

Early-age shrinkage and mechanical properties of the hardening concrete was evaluated as a function of degree of hydration ( $\alpha$ ). Consequently, degree of hydration  $\alpha(t)$  was calculated as the ratio of the heat generated by the mixture  $Q(t)$  to the total heat available in the mixture referred to as  $Q_{ult}$  [6].

$$\alpha(t) = \frac{Q(t)}{Q_{ult}} \quad (1)$$

### 3.1 Evaluation of Mechanical Properties

Compressive strength, tensile strength and modulus of elasticity of the samples were determined testing three 150 by 300 mm cylinder specimens at 12 hours, 1, 2, 3, 7, 14 and 28 days of age. Average test results are presented in Figure 3a, 3b and 3c, respectively. The mechanical properties increase as a function of hydration degree.

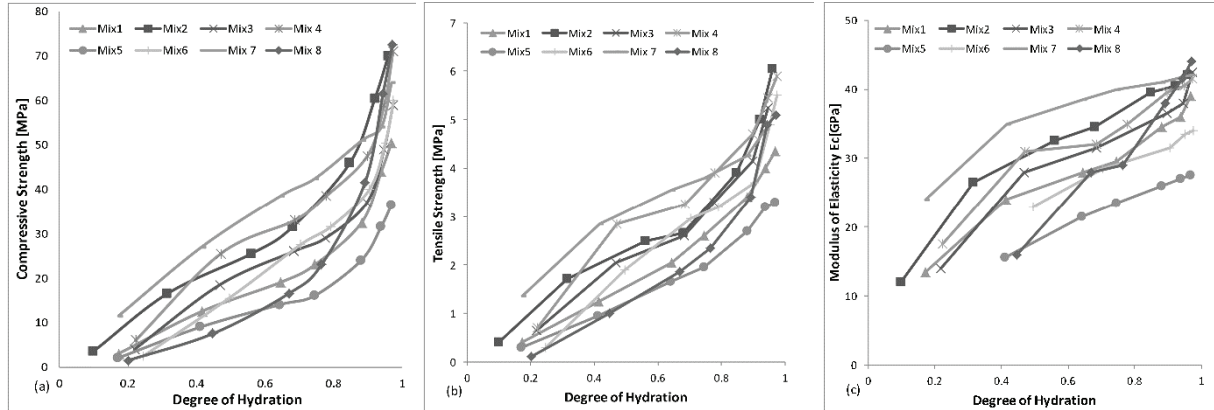


Figure 2: Evolution of (a) compressive strength (b) tensile strength (c) modulus of elasticity.

It can be observed from Figure 2, the relative rate of development of compressive and tensile strength is much lower compared to the relative rate of development of modulus of elasticity. Similar behavior of low water to cement ratio and high early age strength concrete was demonstrated in earlier studies as well [8].

Table 3: Development of mechanical properties, %

Mix#	$\sigma_{c,2d/28d}$	$\sigma_{t,2d/28d}$	$E_{2d/28d}$
Mix1	38	47	72
Mix2	36	41	77
Mix4	44	50	74
Mix5	36	45	73
Mix6	46	54	84
Mix7	60	74	92
Mix8	23	36	64

In general mixtures containing CEMIII B cement show slower mechanical property development compared to CEMI cement mixtures. Especially, development of modulus of elasticity of Mix5 and Mix6 is much slower. This can be related to the use of sand stone aggregates instead of limestone (Figure 2c). Furthermore, the effect of maximum nominal size of aggregates is observed between Mix1 and Mix2. Eventually, use of smaller size of aggregates resulted in higher mechanical properties. Table 3 represents the percentage of the achieved mechanical properties of the concrete mixtures at two days. According to the results, Mix7 containing large amount of CEMI cement with fly ash and micro silica gains its mechanical properties much faster than the mixtures containing GGBS.

### 3.2 Evaluation of Early-Age Shrinkage

Early age shrinkage deformations are determined using two 130 by 700 mm cylinder specimens as a function of the age of the concrete starting after final set for a period of 28 days [9]. Specimens are kept in a temperature controlled environment under sealed conditions. Figure 3 shows shrinkage strains up to 28 days.

The shrinkage strain  $\varepsilon_s$  is determined as the measured concrete strain in the specimen corrected for contributions from the temperature deformations of the concrete:

$$\varepsilon_s = \varepsilon_{m,s} + \alpha_c(T_c - T_{c0}) \quad (2)$$

where  $\varepsilon_{m,s}$  is the concrete strain,  $\alpha_c$  is the thermal expansion coefficient,  $T_c$  and  $T_{c0}$  are two consecutive temperature readings from the specimens.

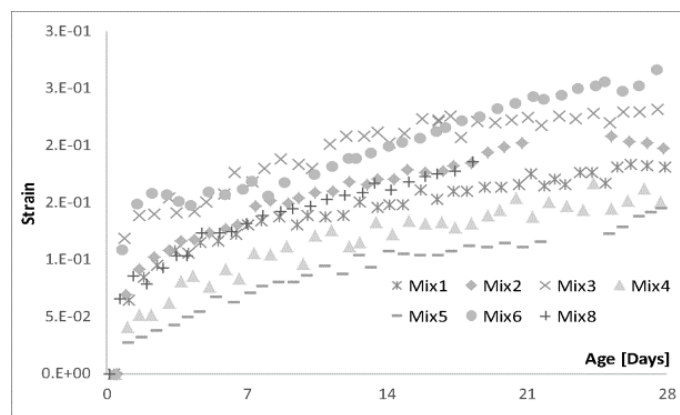


Figure 3: Early-age shrinkage deformations.

Mix2 and Mix3 has relatively higher early-age shrinkage deformation which can be related to the smaller maximum nominal size of aggregate. Although Mix4, 5 and 6 have similar concrete compositions, Mix6 shows the largest shrinkage strain development (Figure 3). In order to investigate this behavior microstructural analysis on thin sections were performed.

### 3.3. Evaluation of Microstructure

Concrete microstructure, was investigated via fluorescent optical microscopy. Thin sections of approximately 30 microns thickness were produced according to DS.423.4 [10] and images were taken by a UV-light polarization microscope where aggregate particles appear in dark, voids and cracks appear in light color, and cement paste can be observed in between, depending on the volume of capillary porosity. The smaller white spots which can be recognized on the images are the GBFS particles. Thin section images of Mix1, Mix4, Mix5 and Mix6 are presented in Figure 4a, 4b, 4c and 4d, respectively.

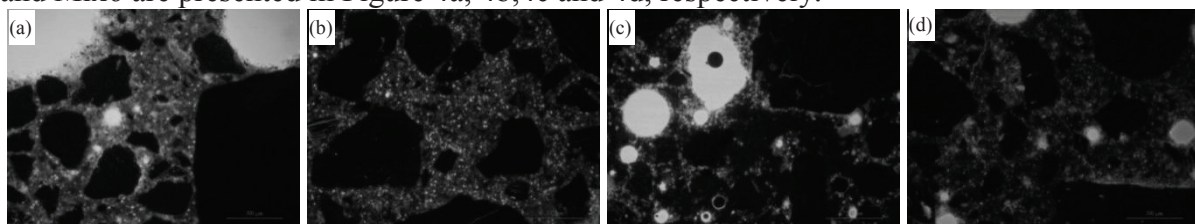


Figure 4: Microstructure of concrete samples (a) Mix1 (b) Mix4 (c) Mix5 (d) Mix6

#### 4. Summary and Conclusion

Adiabatic heat development of slag cement concrete and its relation to development of compressive strength, tensile strength, modulus of elasticity, and early-age shrinkage. Concrete mixtures with CEMIII/B 32,5N were cast with water to cement ratios of 0,32 to 0,40. The maximum size of the aggregates varied from 12,5 mm to 22 mm. Effect of aggregate type was investigated by using limestone aggregates, and sand stone. Results showed that the early age property development of CEMIII/B cement concrete is comparatively slower than CEM I cement concrete. In an attempt to analyze this matter further, microstructure of the cement paste was investigated by thin section analysis and results provided valuable information to distinguish the development of mechanical properties, adiabatic heat and early-age shrinkage deformations of different concrete mixtures. In conclusion, differences in particle size distribution of binders and aggregates as well as the homogeneity of the cement paste and cement-aggregate interface needs to be investigated to identify the differences in performance of the concrete mixtures.

#### References

- [1] Osborne, G. J., Durability of Portland blast-furnace slag cement concrete, *Cem Concr Comp* 21 (1) (1999), 11-21
- [2] Lura P., Van Breugel K. and Maruyama I., Effect of curing temperature and type of cement on early-age shrinkage of high-performance concrete, *Cem Concr Res*, 31 (2001), 1867-1872
- [3] Lee, K. M., H. K. Lee, S. H. Lee, and G. Y. Kim, Autogenous shrinkage of concrete containing granulated blast-furnace slag, *Cem Concr Res*, 36 (7) (2006), 1279-1285
- [4] Bentz D. P., and Jensen O. M., Mitigation strategies for autogenous shrinkage cracking, *Cem Concr Comp*, 26(6) (2004), 677-685
- [5] Darquennes, A., Staquet, S., Delplancke-Ogletree and M.P. and Espion, B., Effect of autogenous deformation on the cracking risk of slag cement concretes. *Cem Concr Comp*, 33(3) (2011), 368-379
- [6] De Schutter, G., Hydration and temperature development of concrete made with blast-furnace slag cement. *Cem Conc Res* 29.1 (1999), 143-149
- [7] NT BUILD 388, Concrete: Heat Development. Nordtest, Finland, (1992)
- [8] Bisschop, J., Evolution of solid behavior, RILEM REPORT (2003), 27-36
- [9] TI-B 102 (15), Testing and Sampling Method Concrete: Stress from Shrinkage and Contraction at an Early Age, Danish Technological Institute, Denmark (2015)
- [10] DS 423.40 Testing of concrete - Hardened concrete - Producing fluorescence impregnated thin sections, Danish Standard, Denmark, (2002)



## **EARLY-AGE EVOLUTION OF ELASTIC STIFFNESS AND COMPRESSIVE STRENGTH OF RECYCLED CONCRETE: INSIGHTS FROM MULTISCALE MICROMECHANICS MODELING**

**Markus Königsberger<sup>(1)</sup>, Stéphanie Staquet<sup>(1)</sup>**

(1) Université libre de Bruxelles, Belgium

### **Abstract**

Recycled concrete, i.e. concrete which contains aggregates that are obtained from crushing waste concrete, typically exhibits a smaller elastic stiffness and a smaller compressive strength than conventional concretes. Based on a continuum micromechanics multiscale model, the mechanical origin and the extent of the reduction are studied herein. Therefore, recycled aggregates are considered as a mix of old cement paste and old aggregates, and they are considered to be embedded in a cement paste matrix at the scale of centimeters. Both, the old and the new cement paste are resolved at micrometer-sized observation scales. The multiscale representation allows for stiffness homogenization (micro-to-macro upscaling) as well as stress concentration (macro-to-micro downscaling), and the latter allows for strength predictions by considering that failure in most unfavorably loaded cement hydrates triggers macroscopic failure. The model suggests that the stiffness of recycled concrete significantly decreases with increasing replacement of natural by recycled aggregates. The strength reduction is less pronounced, in particular at early age, except if the old source concrete is significantly weaker than the targeted new concrete.

### **1. Introduction**

Recycled concrete, i.e. concrete which contains aggregates that are obtained from crushing waste concrete, typically exhibits a smaller elastic stiffness and a smaller compressive strength than conventional concretes [1, 2]. The reduction of the mechanical properties originates from the (old) cement paste which typically comprises 20-40% of the volume of recycled aggregates. Recycled aggregates are less stiff than their natural counterparts, given that the old cement paste is typically less stiff than the natural aggregates. Moreover, recycled aggregates induce additional potential “weak links” in the microstructural interfaces. Such

weaknesses occur, by analogy to conventional concrete, between aggregates and the (new) cement paste, but also between the old and the new cement paste and even "within" the recycled aggregate, i.e. between the old aggregate and the old cement paste. Failure of recycled concrete is triggered by failure of either of the interfaces [3].

Herein, we aim for quantifying the extend of the reduction of elastic stiffness and uniaxial compressive strength at early and late material ages by means of micromechanics-based modeling. Therefore, we use a recently developed multiscale model [3]. Recycled concrete is represented across four scales of observation ranging from micrometer-sized hydration products to centimeter-sized natural aggregates, see Section 2 for details. Combining homogenization techniques with a quasi-brittle failure criterion for the hydration products, we upscale the intrinsic stiffness and failure behavior of the constituents of concrete (such as hydrates, clinker, and aggregates) to predict the macroscopic stiffness and strength of recycled concrete. The model is evaluated for different composition and different maturity states of both old and new cement paste (Section 3). This paper is closed by micromechanics-inspired conclusions on extend and origin of the stiffness and strength reduction as compared to conventional concrete (Section 4).

## 2. Multiscale Modelling

### 2.1 Multiscale representation of recycled concrete including ITZs

Recycled aggregates are separated into three classes to capture their morphology [4]: (I) plain aggregates without attached old mortar or paste, (II) old mortar aggregates which consist – at a smaller observation scale – of aggregates embedded in an old cement paste matrix, and (III) old aggregates covered by a layer of old cement paste, see Fig. 1. The microstructural features of old/new cement paste, both for the bulk material and for the ITZs are millimeter-to-micrometer scales, and are built up by elongated hydration products, capillary pores, and unhydrated clinker grains, following the extensively validated model of Pichler and Hellmich [5].

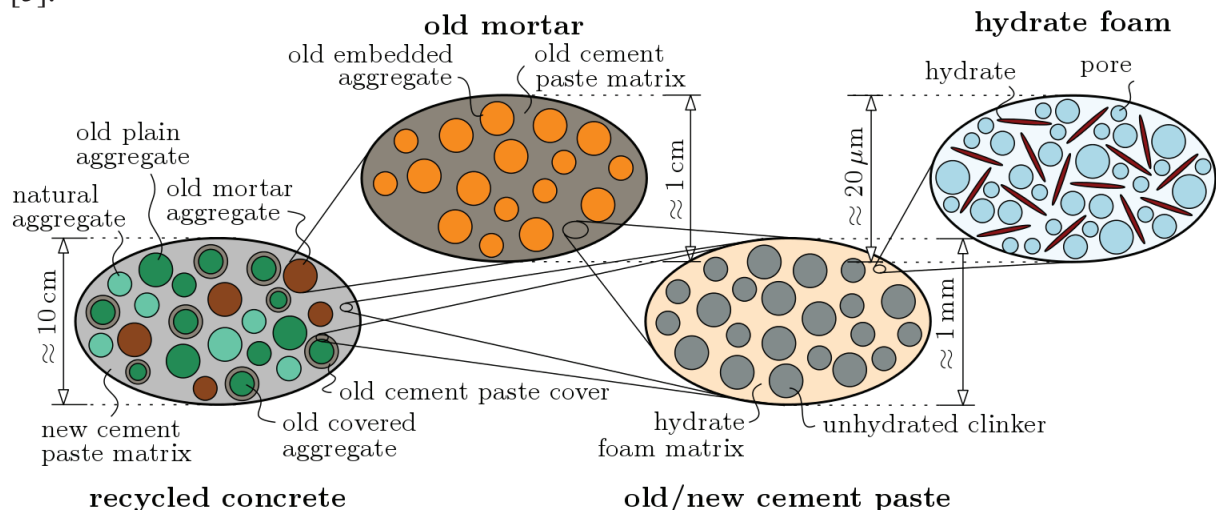


Figure 1: Hierarchical micromechanical representation of recycled concrete across four observation scales from [3].

Interfacial transition zones (ITZs) occur between old aggregates and old cement paste, old aggregates and new cement paste, new aggregates and new cement paste, as well as between old and new cement pastes. We consider that the ITZs are thin enough to be represented as two-dimensional, perfectly bonded interfaces at the scale of concrete and mortar, but that the three-dimensional nature of their microstructure is resolved only at scales which are one order of magnitude smaller than the concrete and mortar scales. The ITZ microstructure is considered to be identical to the microstructure of the adjacent cement paste matrix, either the old or the new one.

## 2.2 Model input: elastic phase constants and volume evolution

We consider that all constituents exhibit isotropic elastic phase constants. The Young's moduli for aggregates (old and new ones), clinker and hydrates amount to 70.0, 139.9, 29.2 GPa and the Poisson's ratio amount to 0.17, 0.3, 0.24, respectively; by analogy to the [6].

While we consider that all constituents exhibit invariant mechanical properties, their volume dosage changes (i) according to the initial composition and (ii) during the hydration of cement with water. We apply Powers' model [6] to get access to the volume fraction of hydrates in new and old pastes with respect to their water-to-cement ratios  $(w/c)_{ocp}$  and  $(w/c)_{ncp}$  and their hydration degrees  $\xi_{ncp}$  and  $\xi_{ocp}$ . Moreover, we consider that all three recycled aggregate classes are equally represented, that the old cement paste content in recycled aggregates as well as the new cement paste content in the recycled concrete amount to 35%, and that the old cement paste is fully hydrated, see [4] for corresponding expressions of the scale-specific volume fractions.

## 2.3 Stiffness and strength homogenization

In order to obtain the macroscopic stiffness of recycled concrete, we apply mean-field homogenization techniques to upscale the phase stiffness constituents to the macroscopic ("homogenized") stiffness of concrete. Thereby, we consider the self-consistent scheme for homogenization of the polycrystalline hydrate foam, and the Mori-Tanaka scheme for homogenization of the other three matrix-inclusion-type volume elements.

As for strength predictions, we apply a brittle failure upscaling approach, which has been successfully validated for cement paste [5] as well as for mortar/concrete [7]. Failure of the most unfavorably loaded hydration product, located in the most unfavorable ITZs, is considered to trigger concrete failure. The macro-to-micro stress concentration is realized stepwise:

- i. First, the volume averages of aggregate stresses are derived by applying mean field-based micromechanics stress concentration laws as function of the macroscopic loads at the concrete level.
- ii. Next, ITZ stress states prevailing in the immediate vicinity of the aggregate-to-cement paste interface follow from stress and strain compatibility relations at the aggregate-to-cement paste interface.
- iii. Finally, we derive second-order stress averages of the volumetric and the deviatoric stress scalars of the needle-shaped hydrates, which qualify as stress measures to determine microscopic failure.

Failure of micrometer-sized hydrates is considered by means of a Drucker-Prager failure criterion [4], with intrinsic strength properties obtain from limit state analysis of nanoindentation data [8].

### 3. Results and discussion

The model is first exploited in order to predict the reduction of the mechanical properties of recycled concrete with respect to conventional concrete. Therefore, the sensitivity of the elastic modulus and of the compressive strength of recycled concrete, respectively, is studied regarding changes of the aggregate replacement ratios  $\Gamma$  in the interval from zero (only natural aggregates) to one (only recycled aggregates). We focus on recycled concrete with  $(w/c)_{ocp} = (w/c)_{ncp} = 0.5$ . The Young's modulus and the compressive strength naturally decrease with increasing replacement ratio, see Fig. 2. The decrease at early ages is much less pronounced than at late ages, because the "weakness" of the recycled aggregate due to the attached old paste is less critical as long as the new cement paste matrix is still very soft. In other words, at early ages, the potential of the stiff natural aggregates can be less exploited. The model also shows that the stiffness reduction is much larger (approximately 25% at full hydration) than the strength reduction (approximately 12% at full hydration), which is also in line with related experimental findings [2]. Notably, the presented stiffness reduction refers to similar elastic properties of old and new aggregates. In case of old aggregates being softer than the new aggregates, the resulting reduction would be even more pronounced. The amount of strength reduction, in turn, crucially depends on the ITZ properties, as discussed in [4]. Interestingly, there is a discontinuity (a change in slope) in the strength evolution of fully hydrated recycled concrete at  $\Gamma = 0.8$ , see Fig. 2(b), resulting from a change in the failure mode from ITZ failure around plain or natural aggregates to ITZ failure around old embedded aggregates, see [4] for more in-depth discussions on the critical ITZ for various compositions.

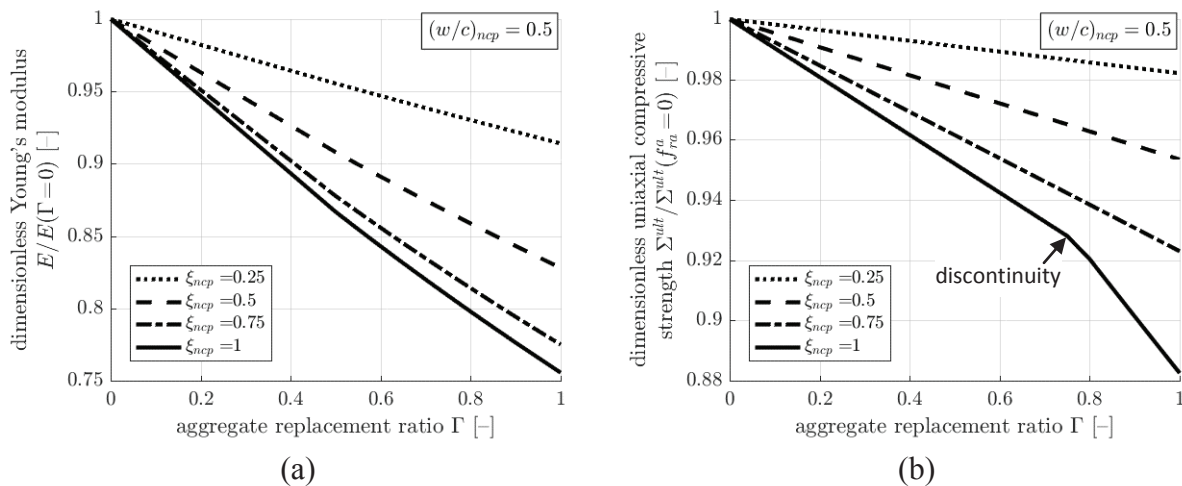


Figure 2: Model-predicted (normalized) Young's moduli and (normalized) uniaxial compressive strength as function of the aggregate replacement ratio for  $(w/c)_{ocp} = (w/c)_{ncp} = 0.5$ ;  $\xi_{ncp} = \{0.25, 0.5, 0.75, 1\}$ ;  $\xi_{ocp} = 1$

Next, we study the evolution of the elastic properties with respect to the hydration degree of the new cement paste. The model is evaluated for a recycled concrete with recycled aggregates only ( $\Gamma = 1$ ), but several combinations of water-to-cement ratios of the old and new cement paste are studied. The stiffness is higher if water-to-cement ratio (of both old and new paste) is smaller and if the hydration degree is higher, see Fig. 3(a). The stiffness loss by using a less quality (high-w/c-ratio) old paste is less significant at early age, but more significant at late ages.

The strength for recycled concrete progressively increases with increasing hydration degree (of the new cement paste) and increasing w/c ratio (of the new cement paste), see Fig. 3(b). However, the sensitivity towards varying w/c ratios of the old paste is quite remarkable. The model suggests that for high-w/c-new pastes, the strength is virtually independent on the w/c ratio of the old cement paste. For low-w/c-new pastes, the strength evolution is virtually identical up to a certain hydration degree. Thereafter, however, the strength does not significantly increase, even when hydration proceeds, if the old cement paste is not strong enough. The weakest link in the microstructure then becomes the ITZ around old cement paste. This shows that a high strength recycled concrete requires the use of a high strength recycled aggregate (obtained from crushing low w/c ratio parent concretes). This demonstrates the importance of quality control when selecting recycled aggregates.

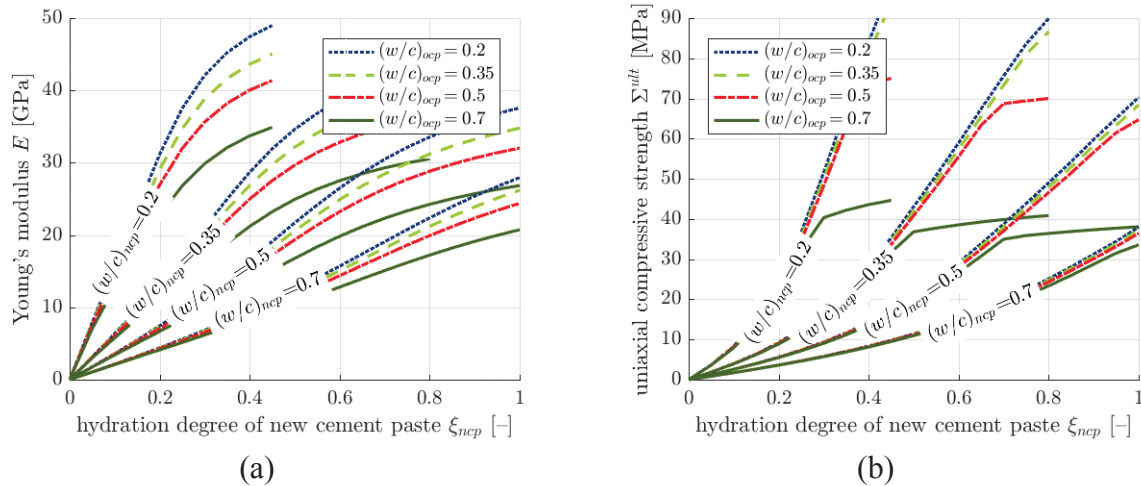


Figure 3: Model-predicted Young's moduli and uniaxial compressive stresses as function of the degree of hydration of the new paste for  $(w/c)_{ocp} = \{0.2, 0.35, 0.5, 0.7\}$ ;  $(w/c)_{ncp} = \{0.2, 0.35, 0.5, 0.7\}$ ;  $\xi_{ocp} = \min\{(w/c)_{ocp}/0.42, 1\}$ ; and 100% recycled aggregates.

#### 4. Conclusions

This micromechanics approach provides some unique insights into the origin of the reduction of the mechanical properties when recycled aggregates are used instead of natural aggregates. It allows to quantify the reduction for any combination of mixture parameters, and therefore might be very helpful for the design of recycled concrete compositions. The model suggests that the stiffness of recycled concrete significantly decreases with increasing replacement of natural by recycled aggregates. The strength reduction is less pronounced, in particular at

early age. Furthermore, the model also shows that if high-strength recycled concretes are targeted, the old source concrete must exhibit a high strength, otherwise the ITZs between old aggregate and old cement paste are prone to failure and the potential of a high-quality new cement paste cannot be exploited.

## References

- [1] Poon, C. S., Shui, Z. H. and Lam, L. Effect of microstructure of ITZ on compressive strength of concrete prepared with recycled aggregates. *Construction and Building Materials*, 18(6),461-468, 2004.
- [2] Omary, S., Ghorbel, E., Wardeh, G. and Nguyen, M. D. Mix Design and Recycled Aggregates Effects on the Concrete's Properties. *International Journal of Civil Engineering*, DOI 10.1007/s40999-017-0247-y, 2017.
- [3] Otsuki, N., Miyazato, S. and Yodsudjai, W. Influence of recycled aggregate on interfacial transition zone, strength, chloride penetration and carbonation of concrete. *Journal of Materials in Civil Engineering*, 15(5),443-451, 2003.
- [4] Königsberger, M. and Staquet, S. Micromechanical Multiscale Modeling of ITZ-driven Failure of Recycled Concrete: Effects of Composition and Maturity on the Material Strength. *Applied Sciences*, 8(6), 976, 2018.
- [5] Pichler, B. and Hellmich, C. Upscaling quasi-brittle strength of cement paste and mortar: A multi-scale engineering mechanics model, *Cement and Concrete Research*, 41(5),467-476, 2011.
- [6] Königsberger, M., Hlobil, M., Delsaute, B., Staquet, S., Hellmich, C. and Pichler, B. Hydrate failure in ITZ governs concrete strength: A micro-to-macro validated engineering mechanics model. *Cement and Concrete Research*, 103,77-94, 2018.
- [7] Powers, T. C. and Brownyard, T. L. Studies of the physical properties of hardened Portland cement paste. *American Concrete Institute Journal Proceedings*, 18(2-8),101-992, 1946-1947.
- [8] Sarris, E. and Constantinides, G. Finite element modeling of nanoindentation on C-S-H: Effect of pile-up and contact friction. *Cement and Concrete Composites*, 36,78-84, 2013.

## **EFFECT OF HIGH TEMPERATURE AT EARLY AGE ON INTERFACIAL TRANSITION ZONE AND MATERIAL PROPERTIES OF CONCRETE**

**Shingo Asamoto <sup>(1)</sup>, Ryosuke Yuguchi <sup>(1)</sup>, Isao Kurashige <sup>(2)</sup>, Pang-Jo Chun <sup>(3)</sup>**

(1) Saitama University, Saitama, Japan

(2) Central Research Institute of Electric Power Industry (CRIEPI), Abiko, Japan

(3) Ehime University, Matsuyama, Japan

### **Abstract**

In this study, we investigated the damage risk at interfacial transition zone of concrete exposed to 65°C at early age assuming steam curing and the influence of the damage on material properties of concrete such as dynamic elastic modulus, permeability and shrinkage. When the concrete was exposed to the high temperature at early age, the dynamic elastic modulus was reduced and air permeability was increased comparing to concrete without high temperature history. The modulus reduction and permeability increase of the concrete subjected to 65°C with ground granulated blast furnace slag were larger than those of the concrete without the slag. It can be attributed to larger coefficient of thermal expansion and larger shrinkage of cement paste with the slag to form microcracks around the aggregate. The impregnated fluorescent resin also indicated more microcracks in concrete having the slag when 65°C was induced at early age. Although it is reported that the drying shrinkage was generally reduced after curing at high temperature, the drying shrinkage of concrete with the slag was increased when the concrete was cured in water after 65°C exposure and then dried.

### **1. Introduction**

In Japan, the application of precast concrete to members of civil infrastructures is expected to increase in order to improve the productivity and quality of concrete structures. The precast concrete is generally subjected to the steam curing with high temperature to achieve earlier strength development than the concrete cured at normal ambient temperature. The maximum temperature of steam curing should be less than 65°C according to JSCE specification [1] but it was reported that the high curing temperature can increase volume of coarse pores to

increase the permeability [2]. In addition, the previous studies [3] suggested that the high-temperature history at early age can cause microcracking between mortar and coarse aggregate during temperature decline period due to the different coefficient of thermal expansion between the cement paste and the aggregate. It is important to comprehend the damage the risk at interfacial transition zone due to the high temperature history leading to material properties change for precast concrete.

In this paper, the influence of high temperature at early age on the material properties of concrete such as dynamic elastic modulus, air permeability and drying shrinkage was studied. The damage at interfacial transition zone due to the high temperature was also examined using the florescent resin to discuss the relation to the properties. Two types of cements were used to investigate the different coefficients of thermal expansion.

Table 1: Mix proportion of concrete

Cement type	W/C	Water [kg/m <sup>3</sup> ]	Cement [kg/m <sup>3</sup> ]	Fine aggregate [kg/m <sup>3</sup> ]	Coarse aggregate [kg/m <sup>3</sup> ]	AE agent [kg/m <sup>3</sup> ]	AE water reducing agent [ml/m <sup>3</sup> ]	Air	Slump
OPC	0.50	175	350	831	959	0.021	875	5.3%	16 cm
BB	0.50	175	350	825	953	0.021	875	4.6%	19 cm

## 2. Experimental program

### 2.1 Materials and specimens

The concrete with W/C = 0.5 was used for all tests. Two types of cement were studied to compare the different coefficients of thermal expansion: Ordinary Portland cement (OPC) and blast furnace slag cement type B (BB). The fine and coarse aggregates are river sand and limestone, respectively. The maximum coarse aggregate size was 20 mm. AE agent and AE water reducing agent are the alkyl ether type surface acting agent and the mix of lignosulfonic acids compound and polyol, respectively. The mix proportion, air content and slump values are given in Tab. 1.

ø100 x 200 mm cylinder specimens were used for dynamic elastic modulus and cut to be slices when air permeability and fluorescent impregnation tests were carried out while drying shrinkage was measured using 100 × 100 × 400 mm prismatic specimens. Three initial curing temperature conditions for 24 hours after casting were set up under sealed conditions to investigate the temperature effect at early age: keeping constant 20°C (20°C curing) and 65°C (65°C curing) and simulating steam curing temperature (steam temp. curing) based on JSCE specification even though it was sealed condition as shown in Fig .1. The accumulated temperature of 65°C curing was set to be the same as that of steam temp. curing to investigate the effect of temperature rise and drop rates on concrete properties. After the initial curing for 24 hours, all specimens were submerged into water at 20°C till an age of 7 days to be saturated with water regardless of curing conditions. Then, the prismatic specimens were dried to measure drying shrinkage while the cylinder specimens were cured under sealed curing until air permeability and fluorescent impregnation tests at about 50 days age.

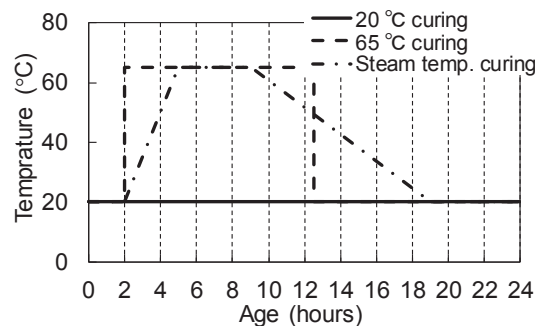


Figure 1: Initial curing temperature



## 2.2 Dynamic elastic modulus, drying shrinkage and air permeability tests

The first resonance frequency was measured at an age of 7 days after water curing and at about 50 days age using cylinder and dried prismatic specimens to calculate the dynamic elastic modulus based on Japan industrial standard (JIS). The frequency was measured twice for the same specimens and three specimens for each condition were used. The dynamic elastic modulus was obtained by averaging total 6 values of three specimens.

The cylinder specimens under sealed condition were cut to be slices with 40 mm thickness for air permeability test at about 50 days of age. Before the test, the sliced specimens were dried at 50°C for 48 hours to remove water in capillary pores. The air pressure of 0.5 MPa by nitrogen was applied to the specimen sealed by rubber in the air flow cell for about 1 hour to be steady by checking air flow amount several times. Then, air flow amount was measured per a minute for three minutes. The results were obtained by averaging values for three specimens. The permeability was calculated as below:

$$K = \frac{2LP_2\gamma_N}{P_1^2 - P_2^2} \times \frac{Q}{A} \quad (1)$$

where,  $K$  is air permeability,  $L$  is thickness of specimen,  $P_1$  and  $P_2$  are air pressure and pressure at vent (atmospheric pressure),  $\gamma_N$  is unit volume weight of nitrogen,  $Q$  is air flow amount and  $A$  is cross section area of specimen.

The longitudinal length change of about 200 mm spans in the drying shrinkage specimens was measured under drying at a relative humidity of 60±10% and 20±1°C from 7 days of age by using a contact strain gauge with an accuracy of 0.001mm. The weights of specimens were also measured with a resolution of 10 g.

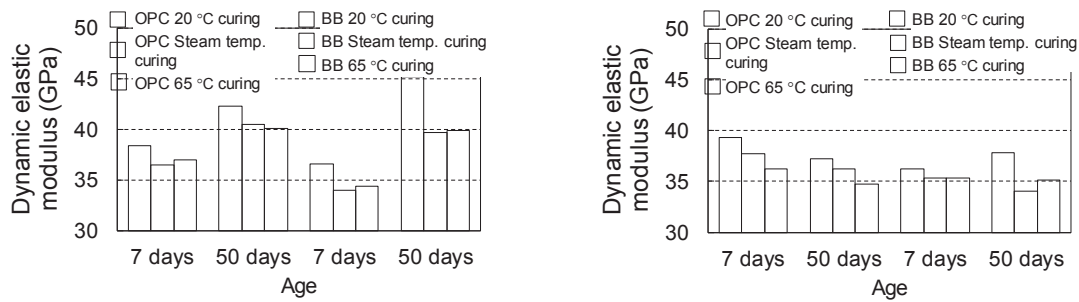
## 2.3 Fluorescent impregnation method by epoxy resin

The both sides of the sliced specimens with 40 mm thickness for the air permeability test were cut into two 10 mm sliced samples to be used for fluorescent impregnation. The both surfaces were polished with water to remove the damage by concrete cutter. After polishing, the samples were dried at 50°C for 24 hours to remove the water near surface. Then, they were impregnated by fluorescent epoxy resin under vacuum condition. The fluorescent resin impregnated in the microcracks was observed by ultraviolet light. The impregnated area was distinguished by the image analysis. The brightness in the image can be approximately classified into 4 parts: air, the mortar area impregnated by the resin, mortar without impregnation and coarse aggregate. In order to distinguish the 4 parts, the threshold selection method proposed by Otsu et al. [4] was applied. One pixel corresponds to about 3 μm.

## 3. Results and discussion

### 3.1 Dynamic elastic modulus

The dynamic elastic modulus of longitudinal and flexural oscillation is shown in Fig. 2. At an age of 7 days after water curing, the dynamic elastic modulus of concrete subjected to 65°C at early age for both longitudinal and flexural oscillations of OPC and BB was reduced comparing to that of the concrete cured at 20 °C. It is suggested that the different coefficient



Cylinder specimen (under water by 7 days age and sealing by about 50 days age) Prismatic specimen (under water by 7 days age and drying by about 50 days age)

Figure 2: Dynamic elastic modulus (longitudinal and flexural oscillation for cylinder and prismatic specimens).

of thermal expansion between cement paste and aggregate can cause the damage in concrete during high temperature exposure to reduce the modulus as reported in the previous study [3]. In addition, large autogenous shrinkage of concrete with the slag during heating may also induce cracking. The modulus reduction of flexural oscillation for BB concrete with high temperature after drying at about 50 days of age was greater than that at an age of 7 days. It may be ascribed to the shrinkage of cement paste during curing and drying as discussed later. The effect of temperature rise and drop rates was not clarified in this experiment as the dynamic elastic modulus between steam temp. curing and 65°C curing was not so different.

### 3.2 Air permeability

The result of air permeability test was shown in Fig. 3. The air permeability of BB concrete with high temperature at early age was much larger than that of BB concrete cured at 20°C while the air permeability of OPC concrete with high temperature is slightly increased comparing to that of OPC concrete without high temperature. The dynamic modulus of longitudinal oscillation was greatly reduced at about 50 days age when BB concrete was exposed to high temperature as shown in Fig. 2. It is deduced that the air permeability was increased because the damage at interfacial transition zone arising from larger coefficient of thermal expansion and larger autogenous shrinkage of BB cement paste may be more significant with aging under sealing condition comparing to that in OPC concrete with smaller coefficient of the cement paste.

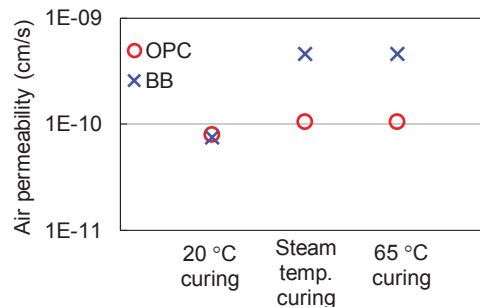


Figure 3: Air permeability at about 50 days age

### 3.3 Image analysis of fluorescent impregnation

The examples of image analysis for 20°C and steam temp. curing are given in Fig. 4. The red colour in the images represents the bright part in mortar by ultraviolet light to indicate the microcracks where the fluorescent resin was impregnated. The results of concrete cured at 65°C show similar tendency to those of both OPC and BB concrete with steam temp. curing. As shown in Fig. 4, the red area of BB concrete with high temperature is likely to be more significant especially around the coarse aggregate than that of BB concrete cured at 20°C. It is suggested that microcracks arising from the large coefficient of expansion of BB cement paste

as discussed above were severely formed in the BB concrete with high temperature to make air permeability larger. It is also possible that larger shrinkage of BB cement paste was confined by aggregate to cause microcracks around aggregate. The microcracks around the coarse aggregate were also visually confirmed by digital microscope. On the other hand, the difference between curing at 20 °C and with high temperature was small in the case of OPC concrete. It is speculated that the microcracks during the temperature rise and drop may be too small in the OPC concrete to be impregnated by the resin but slightly reduce the dynamic elastic modulus. The brightness of the samples, however, was not stable even though the camera and light were fixed at the same position and the calculated area by the analysis was scattered for the same condition although the tendency of all samples is the same as discussed above. Hence, further improvement of fluorescent impregnation method is necessary for more quantitative discussion.

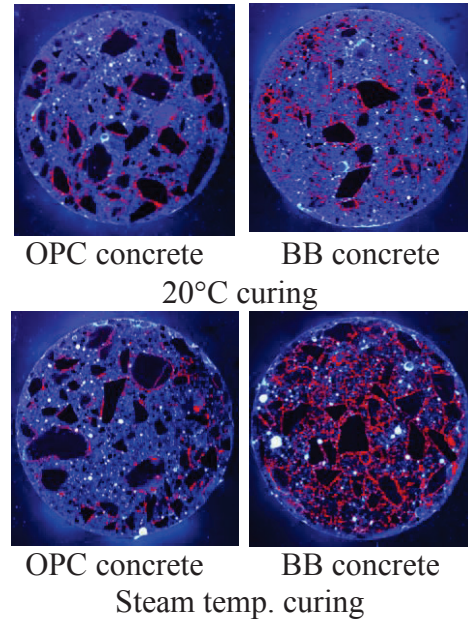


Figure 4: Results of image analysis

### 3.4 Drying shrinkage

Mass loss and drying shrinkage of concrete dried at an age of 7 days is represented in Fig. 5. The mass loss of OPC concrete with high temperature increased while the drying shrinkage is smaller comparing to the concrete cured at 20°C. Thomas and Jennings reported the same tendency using cement paste and explained that the coarsened capillary pores due to the densification of the C-S-H gel phase by high temperature increase the mass loss and reduce

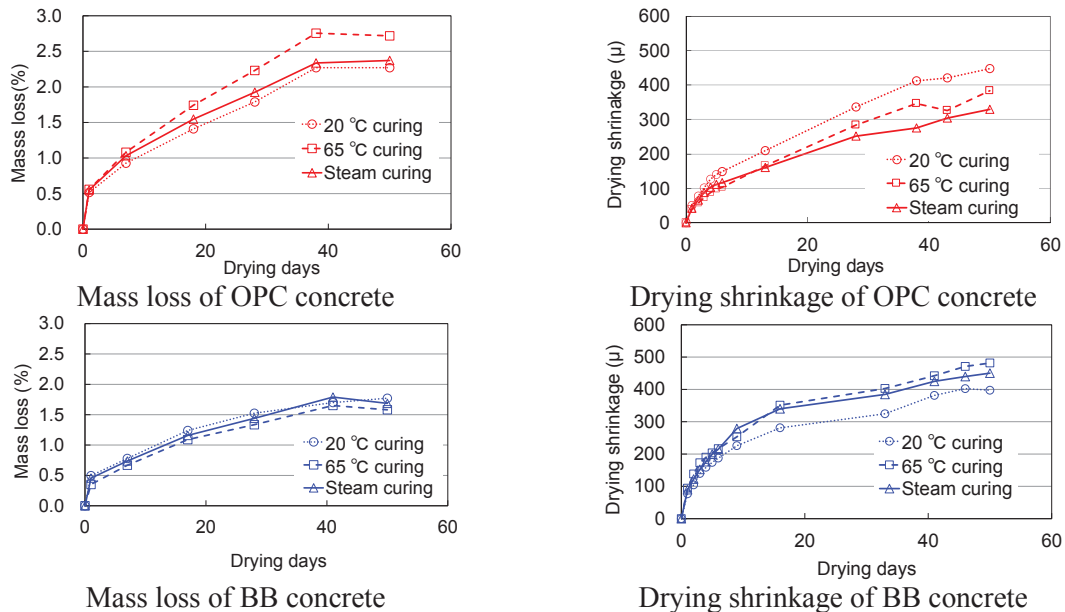


Figure 5: Mass loss and drying shrinkage of concrete dried at 7 days of age.

the shrinkage [5]. In this experiment, it is suggested that the effect of the coarsened pore structure in the cement paste is dominant even in concrete with OPC. On the other hand, in the case of BB concrete, the mass loss was almost independent of curing temperature while the shrinkage of concrete with high temperature is larger than that of concrete cured at 20 °C. It is reported that Portland cement with blast furnace slag can precipitate hydration products with different morphology from OPC [6]. It is speculated that the larger shrinkage of BB cement paste with different amorphous phase can promote the microcracks around the aggregate leading to larger dynamic elastic modulus reduction after 50 days of drying than OPC concrete as shown in Fig 2.

#### 4. Conclusion

The findings in the paper are summarized below.

- The dynamic elastic modulus was reduced and the air permeability increased when the concrete was cured at 20 °C by about 50 days age after exposing to 65 °C at early age, especially using the slag, comparing to the concrete cured at constant 20 °C.
- The image analysis of the impregnated florescent resin in concrete suggests that more microcracks around the coarse aggregate can be formed in the concrete with the slag subjected to 65 °C.
- The drying shrinkage of concrete with the slag was increased when the concrete was submerged in water after 65 °C exposure and then dried comparing to the concrete cured at 20 °C. The large shrinkage may promote microcracks around aggregate.

#### Acknowledgement

This study was supported by the JSPS Grant-in-Aid for Scientific Research (B) No. 17H03285 and by JSPS Core-to-Core Program B. Asia-Africa Science Platforms.

#### References

- [1] Japan Society of Civil Engineering, Standard Specifications for Concrete Structures 2007, Materials and Construction, No. 16 (2007), 484-485
- [2] Goto, S. and Roy, D.M., The effect of w/c ratio and curing temperature on the permeability of hardened cement paste, *Cem Concr Res* 11 (1981), 575-579
- [3] Son, H. N. and Hosoda, A., Detection of microcracking in concrete subjected to elevated temperature at very early age by acoustic emission, *J Adv Concr Tech* 8 (2010), 201-211
- [4] Otsu, N., A threshold selection method from gray-level histograms, *IEEE transactions on systems, man, and cybernetics* 9(1) (1979), 62-66
- [5] Thomas, J.J. and Jennings, H.M., Effect of heat treatment on the pore structure and drying shrinkage behavior of hydrated cement paste, *J Am Ceram Soc* 85 (2002) 2293-98
- [6] Richardson, I. G., Tobermorite/jennite- and tobermorite/calcium hydroxide-based models for the structure of C-S-H: applicability to hardened pastes of tricalcium silicate, h-dicalcium silicate, Portland cement, and blends of Portland cement with blast-furnace slag, metakaolin, or silica fume, *Cem Concr Res* 34 (2004), 1733-1777

## **EFFECT OF THE MATURATION PRESSURE ON MECHANICAL AND HYDRAULIC PROPERTIES OF OILWELL CEMENT PASTE**

**Issam Takla <sup>(1)</sup>, Nicolas Burlion <sup>(1)</sup>, Jian-Fu Shao <sup>(1)</sup>, Thomas Rougelot <sup>(1)</sup>**

(1) University of Lille, LaMcube, F-59000 Lille, France

### **Abstract**

Oilwell cement (G class) is commonly used for the cementing works in the boring operations. The cementing aims to place a ring of cement paste between the wall of the drilled hole and the tubing.

The maturation of oilwell cement takes place at high temperatures and under pressures higher than the pressure at the surface. Within the framework of a general project for the sequestration of CO<sub>2</sub> in oil reservoirs developed by Total Exploration and Production (E&P), this study aims to investigate the effects of pressure during the maturation of G class cement on its mechanical and hydraulic properties.

All tests were performed at a temperature of 90°C (real temperature of the well) for two different maturations of the cement paste: under atmospheric pressure or under a pressure of 3000 psi (20.7 MPa) usually reached in oilwells. Porosity, permeability and mechanical strength were measured and analysed. A very slight difference between the two types of maturation was observed: the kinetic effect of curing pressure at early age seems to be concealed on the long term if a sufficient hydration time is guaranteed.

### **1. Introduction**

The curing pressure is an important factor when studying oilwell cement since maturation of the cement paste takes place usually under a pressure higher than atmospheric pressure.

In literature, most studies were dedicated to the effect of curing pressure on hydration products and on the microstructure of hardened cement. According to Le Saout et al [1] the increase in pressure and temperature of oilwell cement paste leads to more polymerised C-S-H. Scherer et al [2], by treating the hydration of H class cement as a simply activated process, found that the increase in pressure and temperature only change the rate of hydration but not

the nature of the process. Le Saout et al [3] found also that the effect of temperature and pressure on the hydration of cement paste seems to be only kinetic.

The effect of the pressure on the hydration kinetic could be explained by an increase in the amount of water passing into the gel coating and thus an increase in the hydrolysis at the clinker grain surface [4]. More recently, Zhou and Beaudoin [5] found by using SEM examination that micro-cracking only appears on samples hydrated under pressure which in turn facilitates the migration of water into the protective layers around cement grains and thus accelerating the reaction with the unreacted cores of the particles.

Most studies on the effect of curing pressure on mechanical properties were often performed on concrete (autoclaved concrete); it would be important now to verify the effect of curing pressure on mechanical and hydraulic properties of G class cement paste.

The value of this pressure is variable according to the depth and the location of the cement paste in the well. The cement paste is subjected also to an additional pressure coming from its self-weight.

In order to study the possible effect of curing pressure on mechanical and hydraulic behaviour of oilwell cement G class, two groups of samples were prepared:

- first group: samples matured under atmospheric pressure at a temperature of 90°C in the Laboratory of Mechanics, Multi-physics, Multi-scale (LaMcube).
- second group: samples matured under a pressure of 3000 psi (20.7 MPa) at a temperature of 90°C. The pressure value of 3000 psi was adopted by Total to match the requirements of API (American Petroleum Institute) as a maximal value which might be found in the well for the G class cement paste. These samples were prepared by Total and a part of them were transmitted to LaMcube to perform the mechanical and hydraulic tests.

## 2. Fabrication protocol

The present study was performed with classic cement "G class" used in the petroleum domain. The composition of the cement paste is detailed in Tab. 1.

Table 1: Composition of the cement paste

<b>Component</b>	<b>Quantity (kg/m<sup>3</sup>)</b>
Cement G class	1308.3
Water	578.5
D175 (antifoaming)	5.2
D 80 (dispersant)	8.1
Water/Cement ratio	0.44

Two additives, an antifoaming and a dispersant (supplied by Total) were added when preparing the cement paste.

Samples (Ø36, H = 100 mm) were obtained by using stainless steel moulds, from which other samples (Ø20, H = 22 mm) were later derived to perform the tests.

The cement paste was mixed at ambient temperature, then the moulds were kept for 72 h in lime saturated water at 90°C. This temperature was adopted to simulate the real conditions in the wells. Samples were kept after demoulding in lime saturated water at 90°C for one month.

The mass evolution during this period was monitored and shows a stabilization before the age of one month, ensuring a quasi-complete hydration of samples and that mechanical properties of sample may only slightly evolve after this age. The same protocol has been adopted for the fabrication of the second type of samples. These ones have been kept immediately after mixing in a pressurized oven regulated at a temperature of 90°C and a pressure of 3000 psi.

### 3. Porosity

The test of water porosity was performed on sound samples of G class cement paste matured under atmospheric pressure or under a pressure of 3000 psi at a temperature of 90°C (one sample for each type of maturation). The porosity was measured at 90°C then at 105°C for both cases (Tab. 2). Saturated samples (kept in lime saturated water during maturation) were first dried in an oven at 90°C until the mass stabilization. Then, the temperature was raised to 105°C and the porosity was measured once more in the same manner. This rise of temperature up to 105°C aims to quantify the change of porosity due to the partial removal of water (mainly from C-S-H and ettringite), which could slightly modify the microstructure of these hydrates.

Table 2: Values of the porosity obtained for sound samples of G class cement paste matured under atmospheric pressure and under a pressure of 3000 psi.

	Porosity 90°C (%)	Porosity 105°C (%)
Atmospheric pressure	35.4	36.3
Pressure of 3000 psi	35.1	36

No real change in porosity was detected, the curing pressure seems not to have an influence on the void ratio.

After one month of maturation at 90°C, the two types of samples in this study might have the same hydration products and nearly the same pore size distribution, although some difference could have existed at a very early age.

The results of the porosity show a priori that the microstructure of the cement paste was not changed by raising the curing pressure when a sufficient period of hydration is guaranteed. This conclusion has to be confirmed according to the results of permeability and triaxial tests.

## 4. Triaxial tests and permeability measurement

### 4.1 Experimental devices

A triaxial cell has been used and was placed in an oven in order to perform the tests at 90°C. Three Gilson® pumps connected to the cell were necessary to apply confining and deviatoric pressure and also for the injection of interstitial fluid (distilled water). A data acquisition system has been used to record axial strain measured by two displacement transducers (LVDTs) and lateral deformation measured by a circumferential collar.

#### 4.2 Water permeability at 90°C

The test of permeability was performed at 90°C on samples of G class cement paste matured under atmospheric pressure or under a pressure of 3000 psi for a confining pressure of 3MPa and an interstitial pressure of 2.5 MPa.

Results of the permeability for the two types of samples are presented in Tab. 3.

Table 3: Values of the permeability obtained for sound samples of G class cement paste matured under atmospheric pressure and under a pressure of 3000 psi for a confining pressure of 3MPa and an interstitial pressure of 2.5 MPa.

	<b>Pc=3MPa</b>
Atmospheric pressure	K=3.7 E-18 m <sup>2</sup>
Pressure of 3000 psi	K=1E-18 m <sup>2</sup>

The permeability slightly changes between the two cases. The curing pressure does not affect the connectivity rate of the pores which is in accordance with the results of the porosity. In fact, the permeability of a cement paste is influenced by the development of hydration ratio; the permeability decreases rapidly along with the progress of the hydration because the volume of the gel becomes bigger, so that it fills gradually a part of the space which was occupied initially by mixing water [6]. Although the curing pressure affects the hydration ratio at early ages, this effect is still less significant than the effect of the temperature in this study, as all tests were realized at 90°C. Curing temperature has a much stronger effect on cement hydration rate than curing pressure [7].

#### 4.3 Triaxial tests at 90°C

For the two types of samples (matured under atmospheric pressure and under a pressure of 3000 psi), four triaxial tests were performed at a temperature of 90°C. The confining pressure for the four tests was Pc= 0, 3, 10 and 20 MPa and the interstitial pressure was Pi=2.5 MPa when Pc≠0.

Fig. 1 shows a comparison of triaxial results between the two types of samples under different confining pressures. For the four values of confining pressure, the two types of cement paste have nearly the same stress-strain behaviour. The post-peak behaviour is widely dependent on the confining pressure; the material is rather brittle when confining pressure is low, the post-peak behaviour becomes more and more ductile with the increase of the confining pressure, the failure of the two types of samples takes places nearly at the same ratio of strain for each value of confining pressure. The tests at Pc= 20 MPa have been stopped when the axial strain reaches a value of about 7%, in order to avoid to damage the two LVDTs. The real peak was not reached in this case.

Fig. 2 recapitulates the evolution of failure strength in function of the confining pressure. Mechanical tests for the four values of confining pressure show very close results between the two types of samples. The curing pressure does not have a significant influence on mechanical behaviour of studied cement paste. This seems somehow logical and in accordance with the previous tests as the two types of sample have nearly the same values of porosity and permeability.

In general, the development of the strength of cementitious materials depends on the duration of maturation even when cured under a pressure higher than the atmospheric pressure.



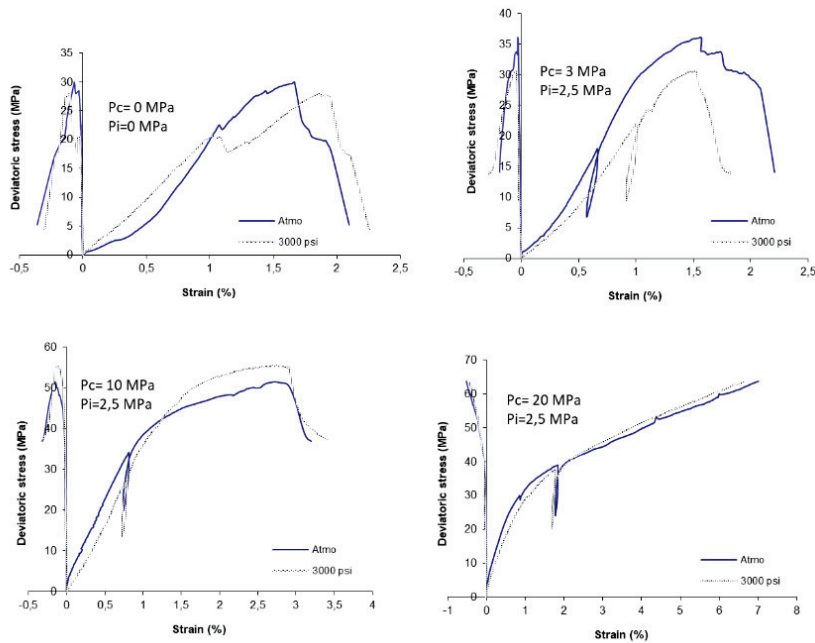


Figure 1: Evolution of axial and lateral deformations at 90°C of samples matured under atmospheric pressure and under a pressure of 3000 psi for  $P_c=(0,3, 10, 20)$  MPa and  $P_i=2.5$  MPa

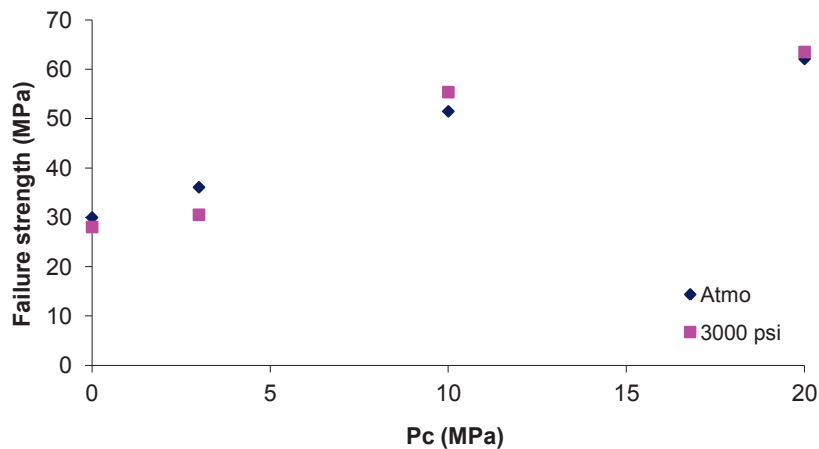


Figure 2: Failure strength obtained at 90°C of samples matured under atmospheric pressure and under a pressure of 3000 psi in function of confining pressure

The acceleration of the chemical reactions of hydration process due to the curing temperature of 90°C has positively affected the mechanical strength at early age, as the duration of dormant (induction) has been reduced because of this hot curing, thus the global structure of hydrated cement paste was established very soon. At the age of one month, the two types of samples have mostly the same hydration rate, regardless of the curing pressure. Hence a similar mechanical behaviour has been obtained.

## 5. Conclusions

This study has been realized on two types of samples of G class cement paste: the first one was matured under atmospheric pressure at a temperature of 90°C and the second one was matured under a pressure of 3000 psi (20.7 MPa) at the same temperature.

After one month of maturation the two types of sample have nearly the same pore size distribution and the same pore connectivity, values of porosity and permeability being very close.

Triaxial mechanical tests show that the two types of samples have a similar stress-strain behaviour for the four values of confining pressure and that the failure strength slightly varies between these two types.

The obtained results prove that the effect of curing pressure was only kinetic; microstructure and hydration products might be the same when a sufficient period of maturation is guaranteed.

This conclusion has enabled us to perform all other tests in this project, in term of carbonation and leaching, on samples cured under atmospheric pressure, which is simpler for laboratory work conditions, and thus to extrapolate the results of these tests to cement paste in the oilwell for minimum error rate.

## Acknowledgments

The authors gratefully acknowledge Total for entrusting this study to the Couplages Thermo-Hydro-Mechanical-Chemical (THMC) team of the Laboratory of Mechanics, Multi-physics, Multi-scale (LaMcube), Lille - France, and for the permission to publish these results.

## References

- [1] Gwenn Le Saout, Eric Lécolier, Alain Rivereau, Hélène Zanni. Study of oilwell cements by solid-state NMR. *C. R. Chimie* 7 (2004) 383–388.
- [2] George W. Scherer, Gary P. Funkhouser, S. Peethamparan. Effect of pressure on early hydration of class H and white cement. *Cement and Concrete Research* 40 (2010) 845–850.
- [3] Gwenn Le Saout, Eric Lécolier, Alain Rivereau, Hélène Zanni. Chemical structure of cement aged at normal and elevated temperatures and pressures Part I. Class G oilwell cement. *Cement and Concrete Research* 36 (2006) 71–78.
- [4] A.A. Rahman and D.D Double. Dilatation of Portland cement grains during early hydration and the effect of applied hydrostatic pressure on hydration. *Cement and Concrete Research* 12 (1982) 33–38.
- [5] Zhou, Q.; Beaudoin, J.J. Effect of Applied Hydrostatic Stress on the Hydration of Portland Cement and C3S. *Advances in Cement Research* 15 (2003) 9–16.
- [6] Adam M.Neville (2000). "*Propriétés des bétons*" CRIB, Sherbrooke- Laval pp. 12-57, 345-358.
- [7] Pang X, Meyer C, Darbe R, Funkhouser GP. Modeling the effect of curing temperature and pressure on cement hydration kinetics. *ACI Mater J* 110 (2013)137–48.

## **ESTIMATION OF SETTING TIME IN CONCRETE THROUGH MODELLING OF ULTRASONIC PARAMETERS**

**Ivan Gabrijel <sup>(1)</sup>, Mario Pintar <sup>(1)</sup>**

(1) University of Zagreb, Faculty of Civil Engineering, Zagreb, Croatia

### **Abstract**

In a standardized procedure initial and final setting in mortar or concrete is determined from penetration resistance test. A wide variety of different test methods has been explored which are sensitive to the transformation of cement composites from a fluid to solid state. Different suggestions on how to determine initial and final setting from these measurements were given by their authors but up today there is no method which would be generally accepted and which would serve as a new standard for setting time measurement. In this paper a methodology of estimating setting time from ultrasonic measurements is given. Ultrasonic data for two concrete mixtures is modelled with exponential model using a curve fitting procedure. Model parameters representing time/age are compared with setting time determined by penetration resistance test.

### **1. Introduction**

The point at which initial setting occurs represents a beginning of the transformation process of cement based material from fluid-like to a solid material. Initial setting indicates that the connectivity between particles has started to develop. From a practical point of view all activities involving placing of concrete should finish before initial setting. The point at which final set occurs in concrete is important since it provides an estimate when the development of concrete strength and stiffness starts.

Standardized method for measuring setting time of concrete (ASTM C403/C403M-16) gives the procedure for initial and final setting determination on mortar sieved from the concrete mixture by measuring resistance (in MPa) to penetration of needles with specified bearing areas. The purpose of penetration resistance test is to optimize concrete mixtures with respect to setting. The drawback of standard method is that measurements are limited to small

number of discrete points in time, measurement is semi-destructive and sample is disturbed each time a new penetration is made and penetration resistance is not measured directly on concrete material itself but on mortar obtained by sieving concrete.

To improve understanding of the relationship between hydration process and setting times alternative methods are investigated. Ultrasonic transmission [1, 2] and reflection [3, 4] methods can provide a finer representation of the fluid-solid transformation process. However, ultrasonic measurement results do not show distinct points in time which could be unambiguously recognized as initial and final setting. This lead to different criterions for setting times that have been proposed based on measurement of ultrasonic parameters. It has been reported that final setting of cement paste determined according to standard EN 196-3 arise at the longitudinal wave velocity of about 1500 m/s [2, 5]. Initial setting of mortar and concrete determined according to standard ASTM C 403 appears in the vicinity of the first inflection point of the curve which describes changes in the wave velocity over time [6, 7]. Making parallel measurements of P-wave (Primary wave) and S-wave (Secondary wave, shear wave) it was found that in mortar the peak of the S-wave velocity derivative corresponds to the initial setting time and the peak of the dynamic elastic modulus derivative occurs at the final setting time [8]. Trtnik and Gams successfully applied frequency spectrum analysis of the waveform transmitted through the specimen for setting time evaluation [9]

In this paper a methodology of estimating setting time from transmission measurements of ultrasonic P-waves is given. Curve fitting procedure is applied to the ultrasonic pulse velocity (UPV) and frequency centroid (FC) obtained during first few days of hydration in concrete. Model parameters representing time/age are compared with setting time determined by penetration resistance test according to ASTM C403/C403M-16.

## 2. Experimental work

Experimental work is made on two concrete mixtures. Each mixture is prepared two times and measurement was repeated. Mix composition is presented in Table 1. All components were preconditioned at a temperature of  $20\pm 2^{\circ}\text{C}$  before mixing. From 1 batch for each mixture initial and final setting time was determined by standardized penetration method

Table 1: Mix composition.

Material	Type of the material	OC	MOC
Cement [kg]	CEM I 52.5 N N-SR3 CE PM-CP2 NF HRC	320	439
Sand [kg]	0-4 mm	830	772
Gravel [kg]	4-11mm (rounded silicate and limestone)	449	525
	8-16 mm (rounded silicate and limestone)	564	424
Admix. [kg]	Plasticizer SIKAPLAST Techno 80	1.44	3.73
Water [kg]		166.4	175.6
w/c		0.52	0.40

Ultrasonic measurements started when mixture was in the fresh state. Dimension of the concrete specimens in the mould are 15×15×10 cm. The distance between sending and receiving sensors was 10 cm. Compaction of specimens was made by hand and specimens were stored in a temperature controlled room with temperature  $19 \pm 2^\circ\text{C}$ . In the specimen under test type K thermocouple was embedded and temperature was recorded at an interval of 5 minutes. From each batch 3 samples for ultrasonic measurements were made and tested simultaneously. UPV was measured on 1 specimen and acousto-ultrasonic (AU) measurement was made on 2 samples (Fig. 1a). UPV was measured using Pundit instrument from CNS Farnell with 54 kHz transducers. UPV was recorded every 120 seconds during measurement. Equipment for AU measurements consisted of Physical Acoustics Corporation (PAC) components: PAC 1220 preamplifiers with selectable gain of 0/20/40 dB, 16 bit PCI-8 data acquisition system and piezoelectric transducers type R6 which are sensitive in the range 20-120 kHz. Waveforms were recorded at a sampling rate of 1 MHz. Arbitrary waveform generator was used to pulse R6 sensors with repetition frequency of 0,01 Hz.

Frequency centroid (FC) is parameter calculated from the frequency domain of a waveform recorded by receiving sensor. It is also known as a first moment of inertia calculated from Eq. 1. In Fig. 1b magnitude of frequency spectrum is plotted for two waveforms recorded at concrete age of 10 h and 72 h. Position of FC for these two waveforms is also plotted.

$$FC = \frac{\sum(\text{magnitude} \times \text{frequency})}{\sum \text{magnitude}} \quad (1)$$

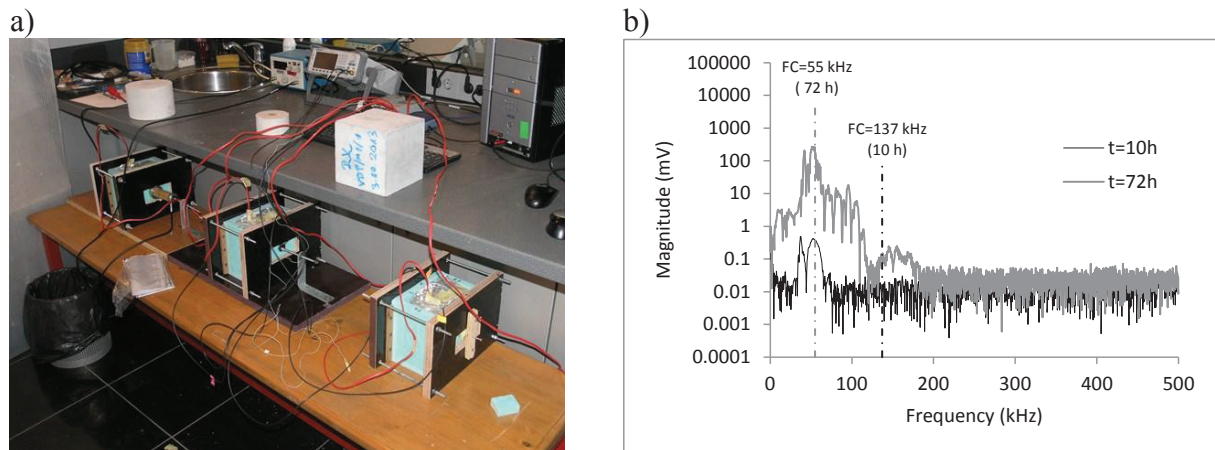


Figure 1: a) Samples during ultrasonic test; b) comparison of magnitude of the frequency spectrum and FC for waveforms recorded at 10 h and 72 h after mixing (from OC mix)

### 3. Results

In Fig. 2 development of UPV (Fig. 2a) and FC (Fig. 2b) during first 72 hours is presented. In Fig. 2 numbers 1 and 2 represent batch from which sample was taken and letters a and b represent two samples from one batch tested with AU method.

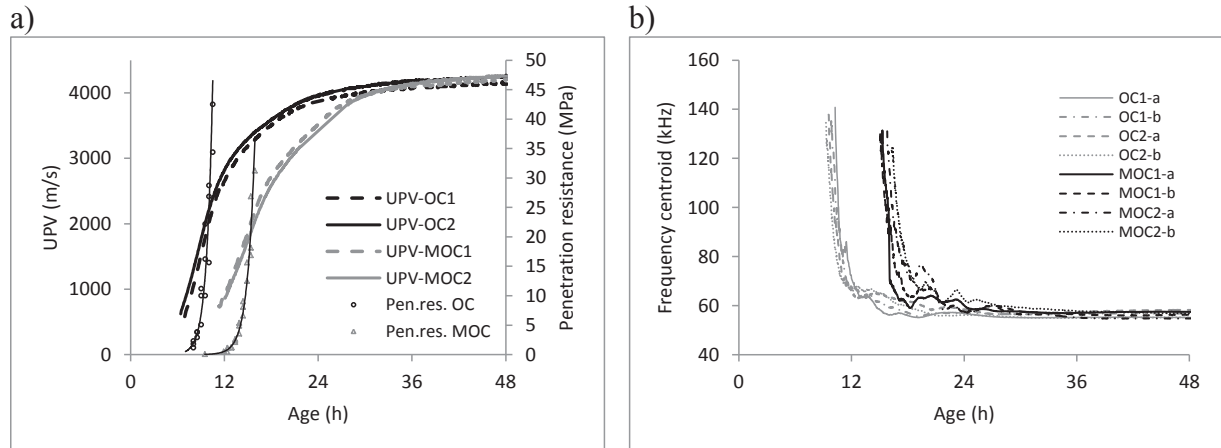


Figure 2: Ultrasonic data on samples from mixtures OC and MOC: a) UPV and penetration resistance; b) FC

Changes in UPV and FC can be accurately described by 3-parameter exponential model (Fig. 3). Model for UPV data is presented in Eq. 2. In this model  $V_u$  is ultimate velocity,  $\tau V$  is time parameter and  $\beta V$  is shape parameter. Since FC has a decreasing trend it is modelled with exponential model given in Eq. 3. In this model  $F_u$  is ultimate frequency,  $\tau F$  is time parameter and  $\beta F$  is shape parameter.

$$UPV(t) = V_u \cdot e^{-\left(\frac{\tau V}{t}\right)^{\beta V}} \quad (2)$$

$$FC(t) = F_u \cdot e^{-\left(\frac{\tau F}{t}\right)^{\beta F}} \quad (3)$$

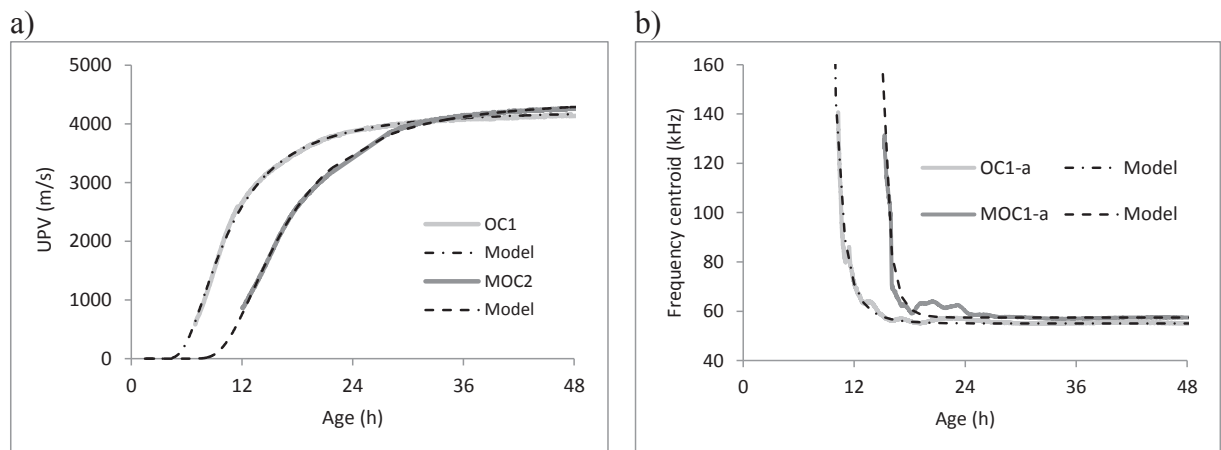


Figure 3: Modelling of measured ultrasonic parameters: a) UPV; b) FC

Model parameters calculated by a curve fitting procedure are given in tables 2 and 3. Values of time parameter  $\tau V$  and  $\tau F$  are close to initial and final setting time value obtained by penetration resistance test.

Table 2: Curve fitting parameters for UPV measurements and setting time determined by penetration test

Measurement	Parameter				Penetration resistance test	
	$V_u$ (m/s)	$\tau V$ (h)	$\beta V$	$R^2$	Initial setting (h)	Final setting (h)
OC1	4233	9,0	2,5	0,998	8,6 ( $\pm 0,4$ )	10,2 ( $\pm 0,4$ )
OC2	4316	8,5	2,4	0,999	average ( $\pm$ st.dev.)	average ( $\pm$ st.dev.)
MOC1	4332	14,1	3,0	0,999	13,8 ( $\pm 0,1$ )	15,6 ( $\pm 0,3$ )
MOC2	4418	14,6	2,9	0,999		

Table 3: Curve fitting parameters for FC measurement results

Measurement	Parameter				Average value of $\tau F$ (h)
	$F_u$ (m/s)	$\tau F$ (h)	$\beta F$	$R^2$	
OC1-a	55	10,0	7,3	0,967	9,5 ( $\pm 0,5$ ) average ( $\pm$ st.dev.)
OC1-b	56	9,7	7,2	0,982	
OC2-a	58	9,3	7,7	0,960	
OC2-b	56	8,9	5,1	0,944	
MOC1-a	57	15,1	15,8	0,902	15,1 ( $\pm 0,4$ ) average ( $\pm$ st.dev.)
MOC1-b	57	14,6	8,2	0,960	
MOC2-a	55	15,0	5,9	0,951	
MOC2-b	57	15,6	7,3	0,950	

Additional calculation is made where all parameters are expressed as a function of maturity. Maturity is calculated from the measured temperature history in the samples. Evaluation of maturity is made through *temperature-time factor* maturity function defined in the standard ASTM C1074-04. In evaluation of maturity assumption was made that datum temperature is 0°C. Comparison of initial and final setting time obtained by penetration resistance test with time parameters calculated from UPV and FC measurements are presented in Fig. 4. From Fig. 4 it can be noticed that values of time parameters are better related to the values of initial setting time. For two mixtures analysed average value of  $\tau F$  gave a better estimate of initial setting time than average value of  $\tau V$ .

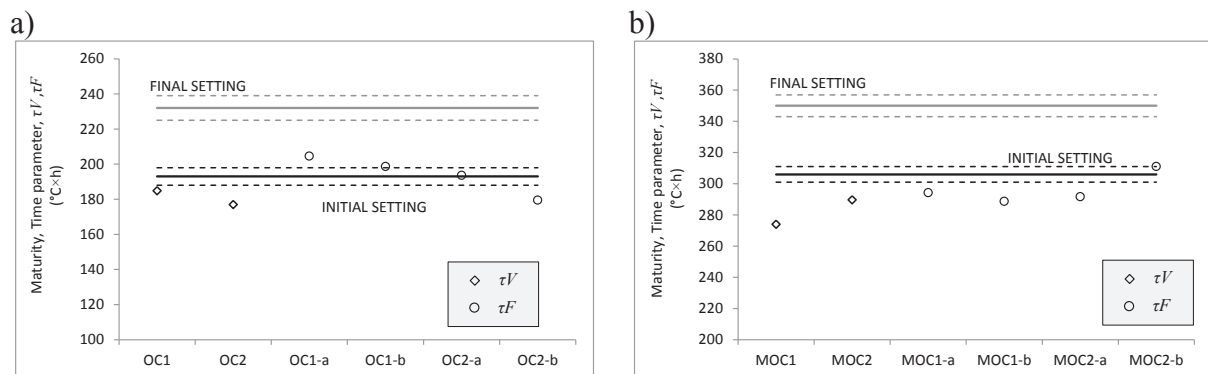


Figure 4: Comparison of initial and final setting time with time parameters  $\tau V$  and  $\tau F$  for a) OC mixture; b) MOC mixture (all parameters expressed as a function of maturity)

#### 4. Conclusion

Ability of concrete to support transmission of acoustic waves of different frequencies is highly dependent on the connectivity of the structure. Parameter called frequency centroid which can be calculated from the frequency spectrum shows a rapid decrease during the transformation of concrete from fluid to solid state. Changes of the frequency centroid during hydration can be accurately described by 3-parameter exponential model. For two mixtures analysed in this work average value of time parameter  $\tau^F$  was closely related to initial setting time obtained by penetration resistance test.

#### References

- [1] Reinhardt, H.W. and Grosse, C.U. Continuous monitoring of setting and hardening of mortar and concrete, *Construction and building materials*, Vol. 18, (2004), pp 145-154.
- [2] Trtnik, G., Turk, G., Kavčič, F., Bokan Bosiljkov, V. Possibilities of using the ultrasonic wave transmission method to estimate initial setting time of cement paste, *Cement and Concrete Research* V. 38 (2008), pp 1336–1342
- [3] Valič, M. I. Hydration of cementitious materials by pulse echo USWR: Method, apparatus and application examples, *Cement and Concrete Research*, Vol. 30, Issue 10, (2000), pp 1633-1640
- [4] Voigt, T. and Shah, S.P. Properties of early age Portland cement mortar monitored with shear wave reflection method, *ACI Materials Journal*, Vol.101, No. 6, (2004), pp 473-482
- [5] Kamada, T., Uchida, S., Rokugo, K. Non-destructive evaluation of Setting and Hardening of Cement Paste Based on Ultrasonic Propagation Characteristics, *Journal of Advanced Concrete Technology*, V. 3(3) (2005), pp 343-353
- [6] Grosse, C. U., Reinhardt, H. W., Krüger, M. Beutel, R. Ultrasound trough-transmission techniques for quality control of concrete during setting and hardening // *Workshop: Advanced testing of fresh cementitious materials / ed. Reinhardt, H. W, Stuttgart, Germany, 2006. pp 1-11*
- [7] Mikulić, D., Sekulić, D., Štirmer, N., Bjegović, D. Application of ultrasonic methods for early age concrete characterisation. // *International Journal of Microstructure and Materials Properties* V. 1(3/4) (2006), pp 297-309
- [8] Carette, J., Staquet, S. Monitoring the setting process of mortars by ultrasonic P and S-wave transmission velocity measurement, *Construction and Building Materials* 94(2015), pp 196-208
- [9] Trtnik, G., Gams, M. The use of frequency spectrum of ultrasonic P-waves to monitor the setting process of cement pastes, *Cement and Concrete Research* 43 (2013) pp 1–11



## **EULERIAN TWO-PHASE COMPUTATIONAL FLUID DYNAMICS MODEL OF A CONCRETE SCREW MIXER**

**Nicolò Beccati <sup>(1)</sup>, Cristian Ferrari <sup>(1)</sup>**

(1) Institute for Agricultural and Earthmoving Machinery of the Italian National Research Council (CNR - IMAMOTER), Ferrara, Italy

### **Abstract**

The state-of-art in computational fluid dynamics (CFD) simulations of fresh concrete mostly focuses on gravitational based physics, like Abrams cone test or L-box test. Focus of this work is the Eulerian-Eulerian two-phase CFD model of the working cycle of a continuous concrete screw mixer, useful for a simulation of the machine and a characterization of its performances. Screw mixers are used in the concrete industry to produce and convey fresh concrete directly in the moulds, starting from segregated materials put directly into the machine. The work focuses mainly on the calibration of the numerical fresh concrete fluid model, simplified as a homogenous and continuous liquid as mainly reported in scientific literature. Another task is the review of the critical in applying this simplified fluid model into a real industrial machine cycle, with centrifugal based physics applied. The calibration of the fresh concrete behaviour is obtained through a parameterization of the viscosity models. The results show how the numerical rheology of the fluid has to be corrected as a function of the simulated physics applied, and how the CFD model can be used to study the performances or compare a new design of the studied machine.

### **1. Introduction**

From scientific literature, the CFD applied on fresh concrete flow is mainly used for simple geometries, such as Slump test or L-box test, for a correct calibration of physical and rheological properties of the material [1][2]. The correction of the numerical viscosity model applied to the material is the main parameter to calibrate, so the hypothesis of the fresh concrete described as an homogeneous fluid is applied in the screw simulations, as found for a mixer drum [3], a Slump test [4][5][6] or a L-box test [5][7]. This simplification permits to reduce the physical uncertainty only to a rheological calibration. In previous works of the

authors, a study of the working process of a self-loading mixer drum was performed using a CFD model, in which the discharge process and the Slump test have been calibrated using different viscosity models for the fresh concrete simulated as an homogeneous and Newtonian fluid. The same model for the fluid will be applied in the screw simulations for a calibration of the dynamic viscosity value, related to the experimental tests realized.

## 2. Geometry Analysed

The screw mixer is a machine capable to mix and convey in short time fresh concrete from the feeding to the moulds. The helicoid screw auger is welded to a centre shaft and inserted into a U-shape trough with a wear-resistant rubber bottom. The trough has an outlet spout at one end and two end plates at each through end, while the inlet spot is larger in order to gather the segregated components. The production cycle starts with the feeding of the segregated materials, water, cement and solid aggregates, into the conveyor. The auger is designed to fulfil a satisfying mixing in the first envelope of the screw and, at the same time, to convey the material in the last development towards the discharge, without any change in its speed direction. The analysed mixer (Fig. 1) can be inclined up to  $35^\circ$  from the horizontal plane and the auger can reach a rotational speed up to 200 rpm. The machine is employed directly in the building site, but the following considerations can be made also for simple screw conveyors. The geometry is then prepared from 3D CAD to a finite element discretization. The volume is split into two defined regions, a stationary and a rotating domain. The stationary domain collects the inlet hopper, the trough and the discharge tank, while the rotating domain includes the screw auger and the shaft; between the two domains a rotor-stator interface is set, in order to define the separation of the finite volumes that are rotating or not. The final mesh adopted after a grid sensibility analysis is a hybrid unstructured mesh, made of prismatic, hexahedral and tetrahedral elements, of globally  $2.5 \cdot 10^6$  elements (Fig. 2).

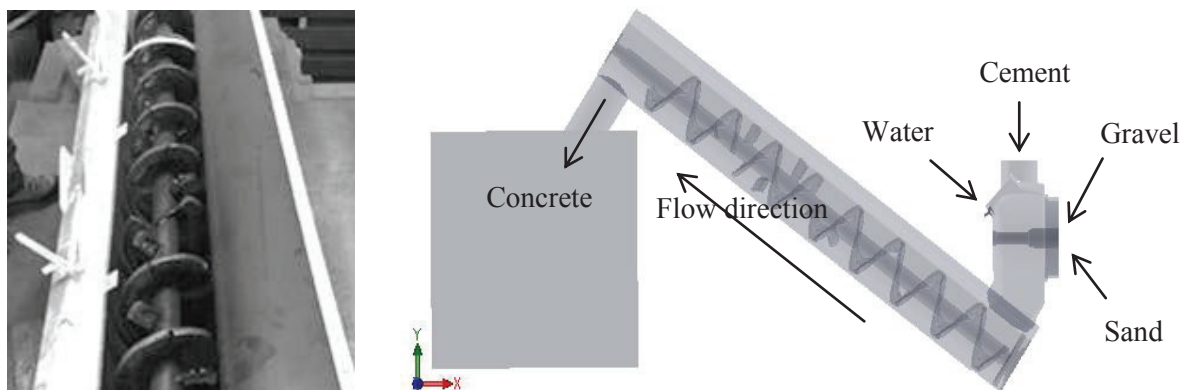


Figure 1: Screw mixer analysed, real geometry (left) and 3D CAD geometry (right).

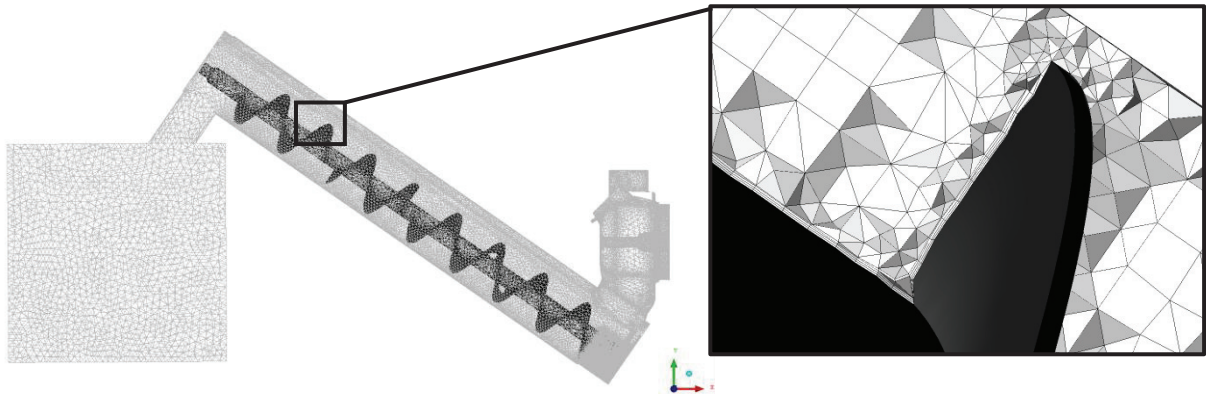


Figure 2: Finite element mesh used for simulations.  
The different colours identify the stationary (light) and the rotating (dark) walls.

### 3. Numerical Model

The numerical simulations are carried out with the commercial CFD code ANSYS CFX, Release 17. The code solves the 3D Reynolds averaged form of the Navier–Stokes equations by using a finite element based finite-volume method. The Eulerian-Eulerian approach, based on the principle of interpenetrating continua, is the most generally used to solve a multiphase flow [8]. The phases, which are each described by its physical properties and its own velocity, pressure, concentration and temperature field, share the same volume and penetrate each other in space exchanging mass, momentum and energy. Two distinct models are available for Eulerian-Eulerian multiphase flow: homogeneous model and inhomogeneous model. In the homogeneous model, the fluids share common fields for flow, temperature and turbulence. In the inhomogeneous model each fluid possesses its own flow field and the fluids interact via interphase transfer terms. This last model is chosen for the following work because of the expected differences between the flows of air and concrete. The main equations in fluid mechanics, for a generic phase  $\alpha$ , are derived from conservation of mass (Eq. 1), momentum (Eq. 2) and energy, not simulated for the isothermal hypothesis applied. For every volume element simulated, the sum of the volume fractions of the phases ( $\alpha$ ,  $\beta$ ) has to equal 1 (Eq. 3). The numerical computation involves a discretization in both space and time of the properties of the fluid. The calculated variables are related to the velocity and pressure fields and the materials volume fractions for every discrete element [9].

$$\frac{\partial}{\partial t} \rho_i + \text{div}(\rho_i \mathbf{u}_i) = 0 \quad (1)$$

$$\frac{\partial}{\partial t} (\rho_i \mathbf{u}_i) + \mathbf{u}_i \cdot \text{div}(\rho_i \mathbf{u}_i) = -\nabla p_i + \nabla \bar{\tau}_i + \mathbf{F}_i \quad (2)$$

$$\sum_{i=\alpha, \beta} r_i = 1 \quad (3)$$

The gravitational field is set, with a buoyancy model based on density difference between air and concrete. For the transient simulation of 45 s total time, a discretization for time stepping

occurs. The time step is set as an adaptive iteration in order to maintain the RMS Courant number below 1 [10]. With these settings, the time step sets around  $2.5 \cdot 10^{-3}$  s, resulting in circa  $2 \cdot 10^4$  time iterations. The following tables (Tab. 1, 2, 3) resume the material properties and the numerical settings implemented as boundary conditions in the simulation. For an analysis of the screw performances, three different inlet flow rates of concrete are simulated: 14, 18 and 22 m<sup>3</sup>/h. The inlet flow of the fresh concrete is divided into the surfaces that simulate the real inlets of the different components, water, cement, sand and gravel, into the machine. On the upper surface of the inlet hopper it has been placed an opening, named degassing condition surface. The degassing condition permits the out flow only to the air phase, in order to avoid a pressurization of the domain. The calculation of the Reynolds number gives the laminar flow regime, in which the viscous forces are dominant.

Table 1: Materials properties.

	$\rho$ (kg/m <sup>3</sup> )	$\mu$ (Pa s)	Thermodynamic State
Air (Standard)	1.185	$1.831 \cdot 10^{-5}$	Gas
Fresh concrete	2403	150	Liquid

Table 2: Numerical schemes adopted.

Setting	Value	Setting	Value
Advection scheme	High Resolution	Transient scheme	Second Order Backward Euler
Turbulence model	Laminar	Interphase transfer	Mixture Model
Convergence max. coefficient loops	10	Convergence criteria	$5 \cdot 10^{-4}$

Table 3: Constant parameters implemented.

Setting	Value	Setting	Value
Screw rotational speed	200 rpm	Surface tension coefficient	66 mN/m [11]

#### 4. Conclusions and perspectives

The constitutive equation for the simulated fresh concrete is calibrated in relation to the experimental tests of the machine. The tested screw, with a constant inlet bulk flow rate of 18 m<sup>3</sup>/h, starts to discharge fresh concrete after approximately 20 s from the insertion of the raw materials. The first result was the correction of the viscosity parameter for the simulated concrete, by measuring the discharge starting time. The model adopted for the concrete viscosity is the Newtonian model. The calibration of the viscosity for the fresh gives satisfying results with a viscosity value of 150 Pa s concrete (Fig. 3). With the calibrated material, the numerical model can simulate the machine performances at different flow rates

of concrete inserted. The following Fig. 4 shows the performances of the machine, by plotting the volume of concrete discharged versus time.

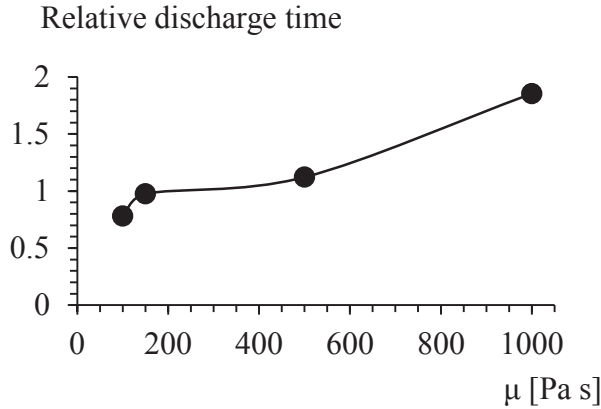


Figure 3: Correction of the viscosity with the starting discharge time, related to the experimental.

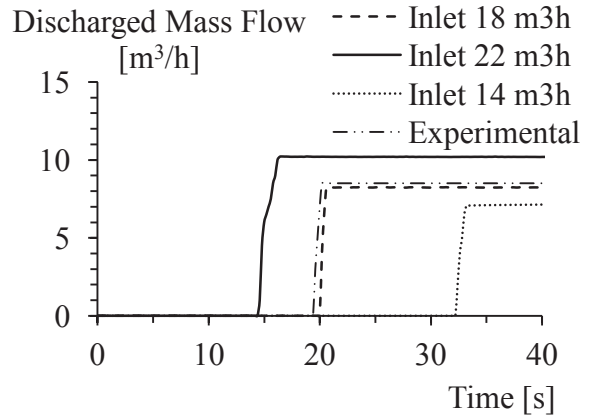


Figure 4: Concrete discharge flow rate versus time.

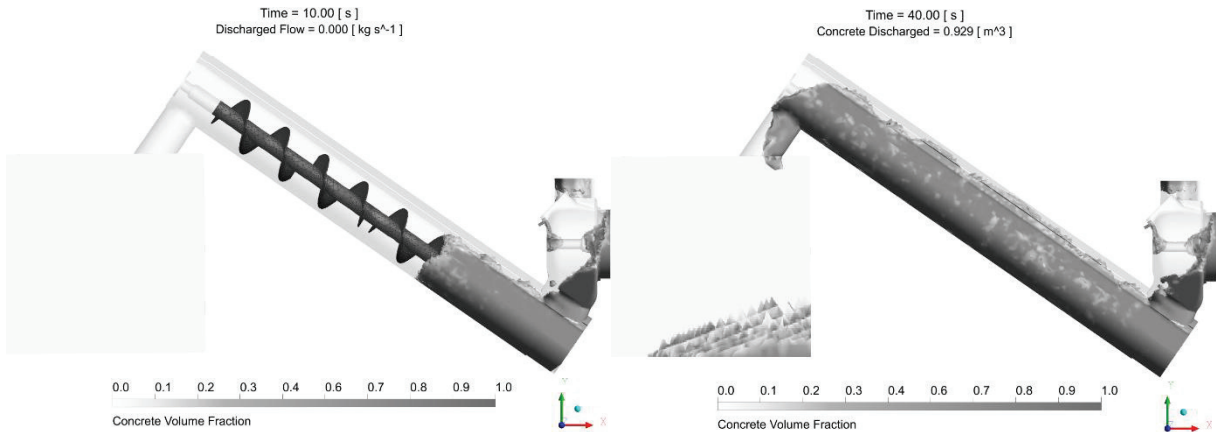


Figure 5: 3D plot of the elaborated concrete in different time steps.

A further improvement of the numerical model will regard the application of a Non-Newtonian Bingham's viscosity model (Eq. 4) to the simulated fluid, as mainly related to the fresh concrete behaviour in the listed references.

$$\tau = \tau_0 + K\dot{\gamma} \quad (4)$$

The difficulties in applying the model is the two-parameter calibration that has to be made with more experimental data available, different from the classical Slump test results, with an iterative calibration on both the yield stress and the plastic viscosity values. For this reason, there is the need to develop a new experimental test method for the characterization of the fresh concrete. The new method should take in account at the same time the centrifugal and the gravitational forces applied on the material, in order to better calibrate the numerical

properties and apply the Bingham's model for future applications of the CFD on industrial machinery for fresh concrete production.

### List of symbols

Variable	Description	Variable	Description
$\alpha, \beta$	Analysed phase	$r_i$	Phase volume fraction
$\rho_i$	Phase density	$\mu$	Newtonian viscosity
$\mathbf{u}_i$	Flow velocity	$\tau$	Shear stress
$p_i$	Pressure	$\tau_0$	Yield stress
$\bar{\tau}_i$	Deviatoric stress tensor	$K$	Bingham plastic viscosity
$F_i$	Total specific energy	$\dot{\gamma}$	Shear rate

### References

- [1] Patzak, B. et al, Modeling of fresh concrete flow, *Computers and Structures* 87 (2009), 962-969
- [2] Roussel, N. et al, Simulation of fresh concrete flow, *RILEM State-of-the-Art Reports* 15, Springer (2014)
- [3] Wallewik, J. E. et al, Analysis of shear rate inside a concrete truck mixer, *Cement and Concrete Research* 95 (2017), 9-17
- [4] Saak, A. W. et al, A generalized approach for the determination of yield stress by slump and slump flow, *Cement and Concrete Research* 34 (2004), 363-371
- [5] Dufour, F. et al, Numerical modelling of concrete flow: homogeneous approach, *Int. J. Numer. Anal. Meth. Geomech.* 29 (2005), 395-416
- [6] Roussel, N., Correlation between yield stress and slump: Comparison between numerical simulations and concrete rheometers results, *Materials and Structures* 39 (2006), 501-509
- [7] Cremonesi, M. et al, Simulation of the flow of fresh cement suspensions by a Lagrangian finite element approach, *J. Non-Newtonian Fluid Mech.* 165 (2010), 1555-1563
- [8] Enwald, H. et al, Eulerian Two-Phase Flow Theory Applied to Fluidization, *Int. J. Multiphase Flow* 22 (1996), 21-66
- [9] Hiltunen, K. et al, *Multiphase Flow Dynamics Theory and Numerics*, VTT Publications 722, Edita Prima Oy, Helsinki (2009)
- [10] Courant, R. et al, On the Partial Difference Equations of Mathematical Physics, *IBM Journal of Research and Development* 11 (1967), 215-234
- [11] Sahin, Y. et al, Characterization of air entraining admixtures in concrete using surface tension measurements, *Cement and Concrete Composites* 82 (2017), 95-104

## FROM DISORDERED TO ORDERED PACKINGS: A NEW PACKING MODEL FOR UHPC?

Gerard Roquier<sup>(1)</sup>

(1) Laboratoire Navier, France

### Abstract

A high efficiency packing model constitutes a key concept in a wide range of concrete. In a binary mixture, the peak shape at the optimum of a packing fraction curve represented as a function of the volume fraction of the fine class does not really exist, due to the compaction which is not optimal: the Compressible Packing Model (CPM) was developed with the introduction of a compaction index  $K$ . The latter is representative of the packing process efficiency and is one of the three parameters which are taken into account in the original CPM. The two other parameters are the wall effect parameter and the loosening effect parameter. Concerning this last geometrical effect, the cavity size ratio at which the loosening effect appears significantly depends of the coarse particle shape and of their surface roughness. By the introduction of a critical cavity size ratio as the fourth parameter, the CPM has evolved into the 4-parameter CPM. Herein, this model is validated both for application to disordered ternary mixtures of spherical, round aggregate and crushed aggregate particles (from  $K=4.7$  to  $K=15$ ) and for application to binary crystalline structures of alloys ( $K=100$ ). The 4-parameter CPM appears to be a useful tool for predicting the packing fraction of the granular skeleton in all circumstances. The microstructure of UHPC could be thus optimized by precise gradation of all particles in the mix to yield minimum void ratio.

### 1. Introduction

Particle packings of many different sizes are often used as structural models for a wide range of concrete. These models usually generalize the case of binary particle packings. Herein, the 4-parameter Compressible Packing Model (CPM), originally developed for predicting the packing fraction of binary mixtures, is validated for ternary mixtures from literature test results for different shape of particles. However, the efficient arrangement of particles inside a packing concerns many sectors in science and industry. One of them is the crystallography. In

this experimental science, many efforts have been made to identify the densest binary sphere packings. In the quest of the highest performance concrete, we wanted to know if the 4-parameter CPM was also efficient in the field of high packing fractions by applying it on binary crystalline structures of alloys.

## 2. The 4-parameter for binary mixtures

The 4-parameter CPM was originally developed for binary mixtures of spherical particles [1] and crushed aggregate particles [2]. Firstly, the packing fraction is calculated in a virtual reference frame where each particle is placed in its ideal location: this is the virtual packing fraction that characterizes the material. Secondly, the real packing fraction is determined by involving the compaction index  $K$  that characterizes the packing process efficiency. Let us consider a binary mixture composed of two monosized classes: size classes 1, 2 with diameters  $d_1, d_2$  ( $d_1 \geq d_2$ ). Their volume fractions by reference of the total solid volume are denoted by  $y_1, y_2$  ( $y_1 + y_2 = 1$ ), their real and virtual packing fractions are respectively denoted by  $\alpha_1, \alpha_2$  and  $\beta_1, \beta_2$ . Let us consider  $x$  as the size ratio  $d_2/d_1$ . The virtual packing fraction of the binary mixture when size classes 1, 2 are dominant are given by:

$$\gamma_1 = \frac{\beta_1}{1 - \left(1 - \frac{\beta_1}{\beta_2} a_{12}\right) y_2} ; \gamma_2 = \frac{\beta_2}{1 - \left(1 - \beta_2 + b_{21} \beta_2 \left(1 - \frac{1}{\beta_1}\right)\right) y_1} \quad (1)$$

where  $b_{21}$  is the wall effect parameter and  $a_{12}$  the loosening effect parameter.

### 2.1 Theory about wall effect and loosening effect for spheres

In the virtual reference frame, the wall effect and the loosening effect theory [1] is elaborated on the basis of a coarse or a fine spherical particle belonging to the dominated class and surrounded by dominant class neighbours (Figure 1). A spherical reference cell concentric to the central spherical particle is used for quantifying the two geometrical interactions.

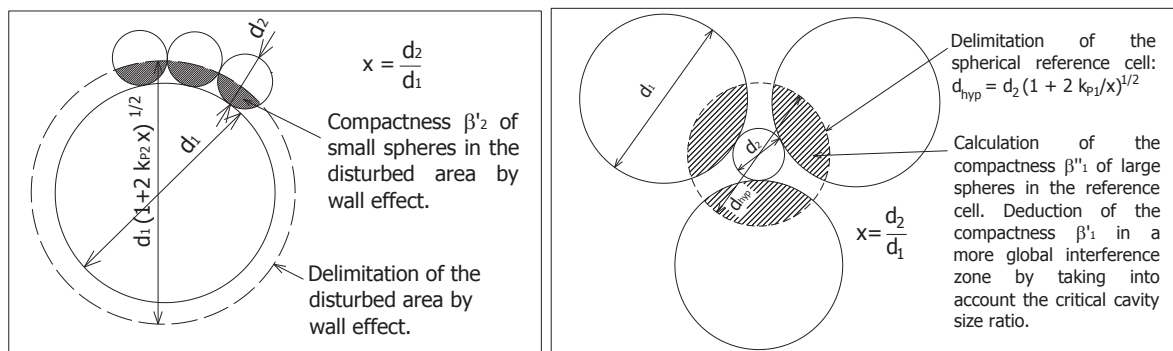


Figure 1: Definition of the spherical reference cells for studying the wall effect (left) and the loosening effect (right)

The packing fraction of the fine particles inside the disturbed volume by the wall effect  $\beta'_2(x)$  and the packing fraction of the coarse particles inside the reference cell affected by the loosening effect  $\beta''_1(x)$  are calculated on the basis of geometrical considerations by calling



upon the coordination number. The latter is determined by an original method. As part of the dense virtual packings [1], the Spherical Square Model (SSM) highlights two remarkable achievements in the field of crystalline packings of spherical particles. Indeed, for the loosening effect theory, the number of coarse spherical particles against a small one is deduced from the following mathematical expression:

$$N_{21,SSM}^{dense}(x) = \frac{\pi(1+x)}{\arcsin\left(\frac{1}{(1+x)}\right)} \quad (2)$$

Firstly,  $N_{21,SSM}^{dense}(1) = 12$ : it means that 12 spherical particles can touch a central spherical particle with the same diameter. It corresponds to the answer of the famous kissing number problem in three dimensions. Secondly,  $N_{21,SSM}^{dense}(0.222) = 4$ : it means that 4 coarse spherical particles, whose centers constitute the vertex corners of a regular tetrahedron, can be in contact with a small central particle with a size ratio of 0.222. This value is in very close agreement with the tetrahedral cavern theory ( $x_0 = \frac{(\sqrt{3}-\sqrt{2})}{\sqrt{2}} \approx 0.2247$ ) [2]. The critical cavity size ratio  $x_0$  has been introduced as the fourth parameter in the present theory to study all types of aggregate particles. When  $x \leq x_0$ : the loosening effect does not occur. When  $x > x_0$ , the loosening effect occurs.

## 2.2 Influence of the compaction index $K$

The real packing fraction  $\phi^*$  of aggregate particles directly depends of the packing process. In the 4-parameter CPM, to reach the maximum packing fraction value, each particle should be placed one by one in a determined manner: it corresponds to the virtual packing fraction. The latter takes into account the intrinsic characteristics of the material: state of particle surfaces and morphology. The link between the virtual packing fraction and the real packing fraction of the mixture is provided through the compaction index  $K$ . This scalar value is of the following form to guarantee the self-consistency of the model:

$$K = \frac{\frac{\gamma_1}{\beta_1}}{\frac{1}{\phi^*} - \frac{1}{\gamma_1}} + \frac{\frac{\gamma_2}{\beta_2}}{\frac{1}{\phi^*} - \frac{1}{\gamma_2}} \quad (3)$$

$K$  has been calibrated from the analysis of 654 packing fractions [1,2] measured on binary mixtures under different packing process conditions (Table 1).

Table 1: Compaction index  $K$

Packing process	Pouring	Vibration or compaction	Vibration + compression	Optimized filling + vibration + compression	Crystalline structures
<b>K</b>	<b>4.7</b>	<b>5.6</b>	<b>9</b>	<b>15</b>	<b>100</b>

Let us consider a monodisperse system with  $\alpha_1 = \alpha_2 = \alpha = 0.64$ . The influence of  $K$  on the packing fraction of a binary mixture is represented in Figure 2 for a size ratio  $x = 0.2$  and, for example, for a critical cavity size ratio  $x_0 = 0.1$ . When  $K$  tends to infinity, the representative

curve reveals a peak shape at the optimum. In contrast, the peak shape reduces significantly as the packing process becomes less efficient.

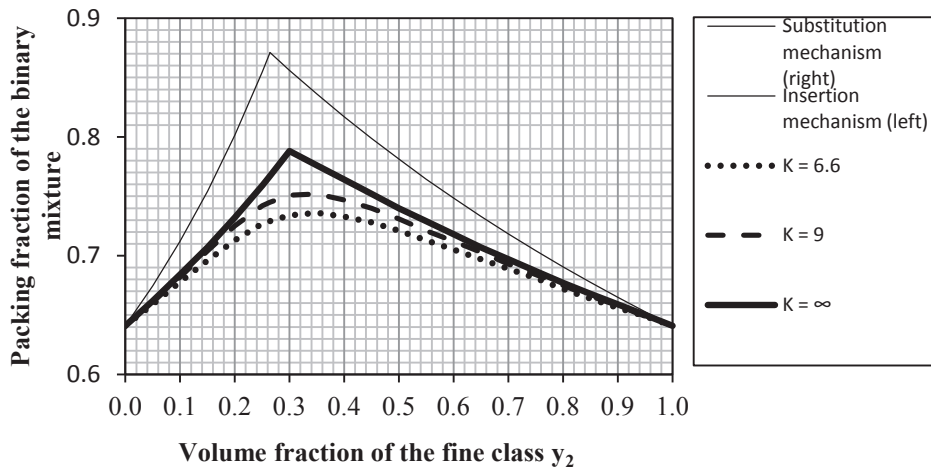


Figure 2: 4-parameter CPM – Influence of the compaction index  $K$  on the packing fraction -  $\alpha_1=\alpha_2=0.64 - x = 0.2 - x_0 = 0.1$

### 2.3 Influence of the critical cavity size ratio $x_0$

Experimental results show that the cavity size ratio at which the loosening effect occurs depends of the coarse particle shape and of their surface roughness [2]. The chosen way consists in calibrating only one parameter, the critical cavity size ratio  $x_0$ : from  $x_0 = 0$  for irregular particles with strong surface roughness to  $x_0 = 0.2$  for frictionless spherical particles. In Figure 3, the theoretical influence of  $x_0$  on the packing fraction of binary mixtures is represented for a size ratio  $x = 0.2$ .

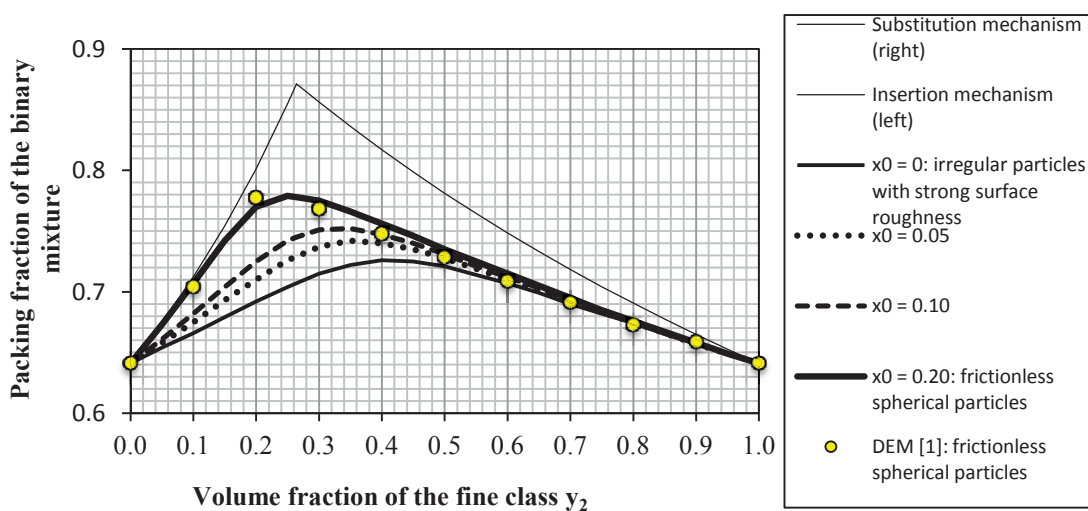


Figure 3: 4-parameter CPM – Influence of the critical cavity size ratio  $x_0$  on the packing fraction -  $\alpha_1=\alpha_2=0.64 - x = 0.2 - K = 9$

### 3. Packing fraction: from non-crystalline to crystalline binary structures

In the 4-parameter CPM, ordered and very packed piles of spherical particles are used as the virtual reference frame. This suggests the opportunity of studying various particle structures thanks to the compaction index  $K$ : from non-crystalline to crystalline ones. For a high value of  $K$ , the 4-parameter CPM is expected to be valid for the structures of alloys: the densest binary sphere packings, as A.B. Hopkins *et al.* called them [3]. Let us examine the predictions of the 4-parameter CPM for  $K = 100$  and  $\beta = 0.711$  at the optimum of each packing fraction curve for a wide range of size ratios: from 0.217 to 0.497, including 0.225 which corresponds to the tetrahedral cavern theory.

Table 2: Comparison between the 4-parameter CPM predictions for  $\beta=0.711$ ,  $K=100$  and the selected densest binary alloy packing fractions (AAPE: Average Absolute Prediction Error)

Binary Alloy	(11-1)	(10-1)	(6-1) <sub>10</sub>	(6-1) <sub>4,6,8</sub>	(6-6)	(7-3)	(5-2)	(4-2)	(2-2)	Overall
Size ratio $x$	0.217 to 0.220	0.225 to 0.270	0.264 to 0.292	0.295 to 0.352	0.414 to 0.457	0.468 to 0.480	0.480 to 0.483	0.480 to 0.488	0.480 to 0.497	
Number of values	2	14	11	21	16	5	2	4	7	82
AAPE	0.93%	2.03%	1.89%	0.72%	1.42%	0.15%	0.60%	0.45%	0.46%	1.17%

Let us compare them with those of [3] (Table 2): the agreement is good, the Average Absolute Prediction Error (AAPE) being 1.17% for 82 packing fraction values. Further validations are required but the field of binary sphere packings is so complex that the development of a packing fraction model able to provide accurate predictions for both disordered assemblies of particles and crystalline structures appears to be well launched.

### 4. Packing fraction for ternary mixtures

Table 3: Average Prediction Error (APE) and Average Absolute Prediction Error (AAPE) characterizing the three models tested on packing fractions obtained on ternary mixtures

Types of particles	Packing fractions data	Statistical indicators	PAL model	3PPM	4-parameter CPM
Spherical particles (117 data)	Ridgway, Tarbuck [4]: 30 data	APE	-0.38%	-1.62%	<b>-0.10%</b>
		AAPE	<b>0.52%</b>	1.62%	<b>0.52%</b>
	Jeschar et al. [5]: 66 data	APE	1.73%	-0.63%	<b>-0.11%</b>
		AAPE	2.27%	0.78%	<b>0.73%</b>
	Standish, Borger [6]: 21 data	APE	-3.32%	-4.34%	<b>-1.17%</b>
		AAPE	3.32%	4.34%	<b>1.22%</b>
Round aggregate particles (66 data)	Westman, Hugill [7]: 66 data	APE	5.58%	-0.34%	<b>0.19%</b>
		AAPE	5.60%	1.05%	<b>1.03%</b>
Crushed aggregate particles (66 data)	Goltermann et al. [8]: 66 data	APE		-1.13%	<b>-0.07%</b>
		AAPE		1.51%	<b>1.16%</b>

The 4-parameter CPM is now going to be evaluated from 249 packing fraction results obtained on ternary mixtures. The compaction index  $K$  has been adjusted to the different packing processes involved. The critical size ratio  $x_0$  has been optimized for each set of aggregate data. The 4-parameter CPM predictions are compared with those of the 3-parameter Particle Packing Model (3PPM) elaborated by V. Wong, A.K.H. Kwan [9] and those of the PAL (J.M.V. Prior, I. Almeida, J.M. Loureiro) model [10]. The 4-parameter CPM provides the most consistent predictions ( $APE$  range from  $-1.17\%$  to  $-0.10\%$ ) for the spherical particles with a single value of the critical cavity size ratio  $x_0$  ( $x_0 = 0.2$ ), is really accurate for the round aggregate particles ( $APE = 0.19\%$ ), and is very efficient for the tested crushed aggregate particles ( $APE = -0.07\%$ ).

## 5. Conclusion

With the incorporation of the compaction index and the critical cavity size ratio, it is found that the 4-parameter CPM can predict the packing fraction of both binary crystalline structures and ternary mixtures of mono-sized spherical particles, round and crushed aggregate particles. The open way in the field of high packing fractions and in the field of ternary mixtures suggests the possibility of studying the high packing fraction polydisperse mixtures. Thus, the 4-parameter CPM could be employed in optimization algorithms for the design of UHPC.

## References

- [1] Roquier, G., The 4-parameter Compressible Packing Model (CPM) including a new theory about wall effect and loosening effect for spheres, *Powder Technol.* 302 (2016) 247-253
- [2] Roquier, G., The 4-parameter Compressible Packing Model (CPM) for crushed aggregate particles, *Powder Technol.* 320 (2017) 133-142
- [3] Hopkins, A.B., Stillinger, F.H., Torquato, S., Densest binary sphere packings, *Phys. Rev. E*, 85(2) (2012) 021130
- [4] Ridgway, K., Tarbuck, K.J., Particulate mixture bulk densities, *Chem. Process Eng.* , 49(2) (1968) 103
- [5] Jeschar, R., Potke, W., Petersen, V., Polthier, K., Blast Furnace Aerodynamics, In: *Proceedings of the symposium on blast furnace aerodynamics* (1975) 25-27
- [6] Standish, N., Borger, D.E., The porosity of particulate mixtures, *Powder Technol.* 22(1) (1979) 121-125
- [7] Westman, A.E.R., Hugill, H.R., The packing of particles, *J. Am. Ceram. Soc.* 13.10 (1930) 767-779
- [8] Goltermann, P., Johansen, V., Palbøl, L., Packing of aggregates: an alternative tool to determine the optimal aggregate mix, *Materials Journal* 94(5) (1997) 435-443
- [9] Wong, V., Kwan, A.K.H., A 3-parameter model for packing density prediction of ternary mixes of spherical particles, *Powder Technol.* 268 (2014) 357-367
- [10] Prior, J.M.V., Almeida, I., Loureiro, J.M., Prediction of the packing porosity of mixtures of spherical and non-spherical particles with a geometric model, *Powder Technol.* 249 (2013) 482-496

## HOW DOES THE SIZE OF AGGREGATES AFFECT PERMEABILITY OF DAMAGED CONCRETE?

**Marta Choinska**<sup>(1)</sup>, **Stéphanie Bonnet**<sup>(1)</sup>, **Aurélié Fabien**<sup>(1,2)</sup>, **Hayder Al-Khazraji**<sup>(1,3)</sup>,  
**Abdelhafid Khelidj**<sup>(1)</sup>

- (1) Institut de Recherche en Génie Civil et Mécanique GeM, Université Bretagne Loire, Université de Nantes, Saint-Nazaire, France
- (2) ESITC Caen, Épron, France
- (3) Missan University, Engineering College, Iraq

### Abstract

This experimental study concerns impact of aggregate size on mechanical behavior and gas permeability of concrete. The work has been carried out using three types of materials: a microconcrete, a concrete and a macroconcrete, all with the same water-to-cement ratio, as well as the same aggregate volume fraction. Specimens of the formulated materials have been submitted to controlled uniaxial compression cycles or to indirect tensile in the Brazilian splitting test, till certain damage levels. Gas permeability have then been measured on damaged specimens, after unloading for specimens loaded in compression, and during loading for specimens loaded in indirect tension. For the latter, a special lab-made device has been developed to control tensile loading in the pre-peak and the post-peak phases and to measure gas transfer during loading. For all the tested materials, the results emphasize that compressive and tensile strengths decrease and gas permeability increases, when aggregate size increases, independently on the cement type, CEM I or CEM III. Moreover, the obtained results highlight that the effects of tensile or compressive damage on permeability may be separated from the effects of aggregate size by two distinct functions. This behaviour, independent on cement type, represents a strong advantage for concrete modelling.

### 1. Introduction

In quasi-brittle materials, like concrete, fracture exhibits a finite size process zone. The size of this zone is not dependent on the structural size, but is controlled by local heterogeneity parameter (aggregate size) and concrete behaviour yields therefore size effects [1, 2]. It is

important to characterise these effects in order to correlate laboratory test results with structural behaviour. In fact, two approaches may be employed to investigate this issue: the first one, based on the change of the specimen size for the same material, and the second one, based on the change of the aggregate size for the same specimen size. The authors of this work propose to study the effects of the aggregate size on concrete mechanical and mass transfer behaviour, as far as the literature review presents important scatter concerning this issue. Indeed, the remark of Wolinski et al. [3] is still relevant: « Obviously, the test data with respect to the influence of the aggregate size on the tensile behaviour of concrete are conflicting ». Let's mention, for example, the work of Hillerborg [4] who concluded that there is a tendency for fracture energy to increase, while the maximum aggregate size increases. The same tendency was noticed by Bazant and Oh [5]. However, Petersson [6] reported that the fracture energy does not seem to be affected by the maximum particle size. Bisschop and van Mier [7] observed drying shrinkage microcracking increase in cement-based composites with spherical glass aggregates size and with volume percentage increases. Szczesniak et al. [8] noticed a great correlation between spherical glass aggregate diameter and compressive strength: the latter decreases when aggregate size increases. However, Rao and Prasad [9] observed the opposite effect for tensile behavior. Currently, opinions still differ on outcomes because many parameters must be taken into account. Besides, there are very few results in the literature review regarding the effects of the aggregate size on the concrete mass transfer. Grassl et al. [10] pointed out that the concrete permeability increases with the increasing of crack width and with the aggregate diameter. Moreover, permeability increase with cracking appears to be amplified under loading [11].

In view of these results, this work has therefore two main objectives: the first one concerns the effects of aggregate size on mechanical behavior and permeability and the second one is focused on the evolution of permeability with mechanical compressive and tensile loading. The authors use experimental methods to investigate these issues.

## **2. Experimental program**

### **2.1 Materials**

For the sake of simplicity, experimental study has been restricted to dry materials with mix proportions given in Tab. 1. All the materials have the same water-to-cement ratio, equal to 0,48, as well as the same aggregate volume fraction, equal to 66% of the total volume. All the aggregates are crushed limestone. In order to investigate aggregate size effect on mechanical and transport properties, three types of formulations have been proposed: microconcrete, concrete and macroconcrete. Microconcrete contains sand and medium size aggregates, two concretes contain sand, medium and coarse size aggregates and macroconcrete contains sand and coarse size aggregates only, following to the grading curves of aggregate mixes presented by Fabien et al. [12].

Cylindrical specimens (diameter of 11 cm, length of 22 cm) of microconcrete, concrete and macroconcrete have been prepared from single batches and cast in PVC rigid moulds. 24 h after casting, they have been stored in a room maintained at 20°C with a 95% relative humidity, and then cured in water at 20°C for at least 4 weeks for the CEM I materials and 3 months for the CEM III ones, what permit to stabilise mechanical strengths. After the storage in water, a part of the cylinders have been damaged in compressive tests, then all the cylinders

have been cut using a diamond blade saw in order to obtain “disc” specimens (diameter of 11 cm, length of 5 cm) within each cylinder. “Disc” specimens have been dried at 80°C over 2 weeks, then at 105°C down to constant mass to permit permeability tests. The latter have been performed on the sound and on the compressive-damaged materials, as well as at the tensile-damaged materials under loading, using a specially developed set-up.

Table 1: Microconcrete, concrete and macroconcrete constituents and mix proportions.

Ingredients	Quantity (kg/m <sup>3</sup> )		
	Microconcrete	Concrete	Macroconcrete
Cement CEM I 52.5 PM ES or CEM III/A 52.5 PM ES	350	350	350
Sand 0-4mm	868	868	868
Medium aggregate 4-12mm	1009	432	-
Coarse aggregate 12-20m	-	561	981
Water	168	168	168
Superplasticizer (solid content 20%)	1.71	1.71	1.71

## 2.2 Compressive damage and permeability test methods

A part of the specimens have been loaded using cyclic uniaxial compression test. This method permits to generate uniform damage as already shown by other researchers [13]. The tests were performed under load control with a hydraulic loading frame. The loading and unloading rate was kept constant and equal to 2 kN/s. The specimens have been instrumented using three axial and one circumferential extensometers. Three levels of loading, corresponding to 30%, 60% and 80% of the compressive strength have been applied to the specimens. At 30 and 60%, six loading-unloading cycles were applied to the specimen, and at 80%, only three cycles were applied in order to avoid any damage of extensometer equipment.

In order to evaluate the intrinsic permeability of a concrete specimen, a gas permeability device was used. It was equipped with a permeability cell based on the Cembureau one [12]. The tests have been performed using an inert gas (dry nitrogen, N<sub>2</sub>). In order to ensure a uniaxial flow of the gas and to prevent any gas leakage, the lateral face of each cylindrical specimen has been protected by an aluminum film and a specimen is placed in a fitted collar and then confined during the tests (0,5 MPa). A gas was injected at the lower surface of a specimen at a pressure ranging between 0,3 and 0,1 MPa (relative values), the upper side of a specimen being at the atmospheric pressure. The injection pressure has been applied and maintained until gas flow stabilization. Apparent permeability value for each injection pressure was determined following to French standards XP P18-463 and the intrinsic permeability was calculated using Klinkenberg’s regression of the apparent permeabilities.

## 2.3 Tensile loading-permeability test method

For many years, our lab (GeM) has been working and developing coupled mechanical and permeability tests. The authors developed [14] a tensile loading - gas permeability set-up, based on indirect tension in the Brazilian splitting test (compression in the diameter plane). The principle of this test is to perform gas permeability measurements during loading, for different levels of controlled cracking in the pre-peak and post-peak phases, using a “disc”

specimen loaded in the Brazilian splitting test. This test presents the advantage of forming a single crack, parallel to the loading direction, where openings may be measured at one or two sides of a specimen, using f.ex. a CMOD sensor (crack-mouth opening displacement) as a feedback signal during the test. The new modified “double” device is presented in Fig. 1. It includes two aluminium cells: one placed on the up-stream side and the second one on the down-stream side, each one fitted with a CMOD sensor, called COD 1 and COD 2. The 250 kN MTS loading cell is employed within a hydraulic loading frame CFM / MTS 1000 kN. Gas pressure and flow rates are measured at the up-stream and at the down-stream and the feedback signal of the tensile test corresponds to the mean COD value between COD 1 and COD 2, in the pre-peak and in the post-peak phases.

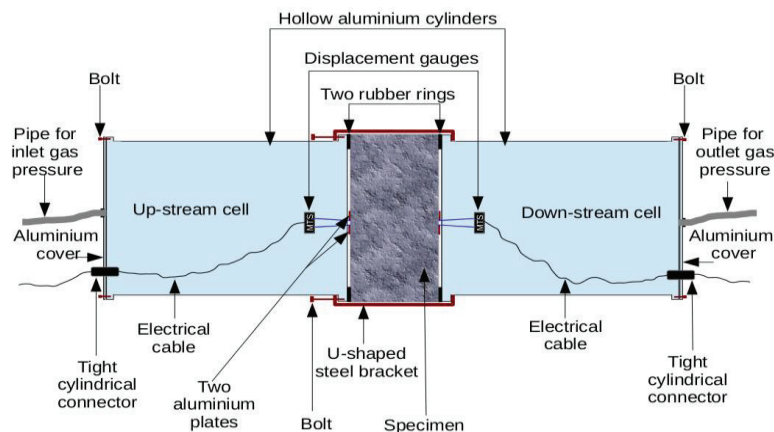


Figure 1. Upper section view of the “double” loading-permeability device (GeM).

### 3. Results and discussion

Results emphasized a general tendency: compressive and tensile strengths slightly decrease with aggregate size increase. The opposite is noticed for the permeabilities of the sound materials. The competition between the specific surface effects and the restrained shrinkage effects, acting in the opposite ways, lead to the observed tendencies, independent on the cement type, CEM I or CEM III.

Following the analysis proposed by Picandet et al. [15], it is more consistent, in the pre-peak phase, to record the evolution of the permeability with compressive damage instead of the strain or stress. We follow here this procedure and compressive damage is determined as an initial elastic modulus loss for each loading level. The obtained results highlight higher damage for the both macroconcretes (CEM I and CEM III) in comparison to the microconcretes and concretes (see Fig. 2 (a)). The evolution of a relative permeability (the measured permeability divided by the initial permeability of the sound material) versus compressive damage of the specimens, presented in Fig. 2 (b), exhibits a non-linear increase, common to all the specimens tested. One may therefore imagine that the contributions of the damage on concrete permeability evolution may be therefore separated from the effects of the aggregate size.

Concerning the tensile loading-permeability tests, the study was restricted to 4 materials: the microconcrete, the concrete and the macroconcrete CEM I and the concrete CEM III. Fig. 3



(a) plots the experimental results obtained on the CEM I materials during tensile cracking. Here, permeabilities are reported to the permeability of the CEM I concrete (equal to  $3,6 \cdot 10^{-17} \text{m}^2$ ). Moreover, one may observe that permeability increase with cracking is amplified by the aggregate size. Fig. 3 (b) plots a relative permeability evolution for all the tested specimens and materials (with 2 different cements) during tensile cracking. Once again, one may observe that all the results fall on the same master curve, function of the permeability reported to the initial one of each material, and to the COD reported to the peak COD at the failure side. These results assume that a relative permeability evolution follows a single sigmoid law, independently to other parameters. Therefore, one may say that the permeability increase due to tensile cracking may be separated from the aggregate size effect.

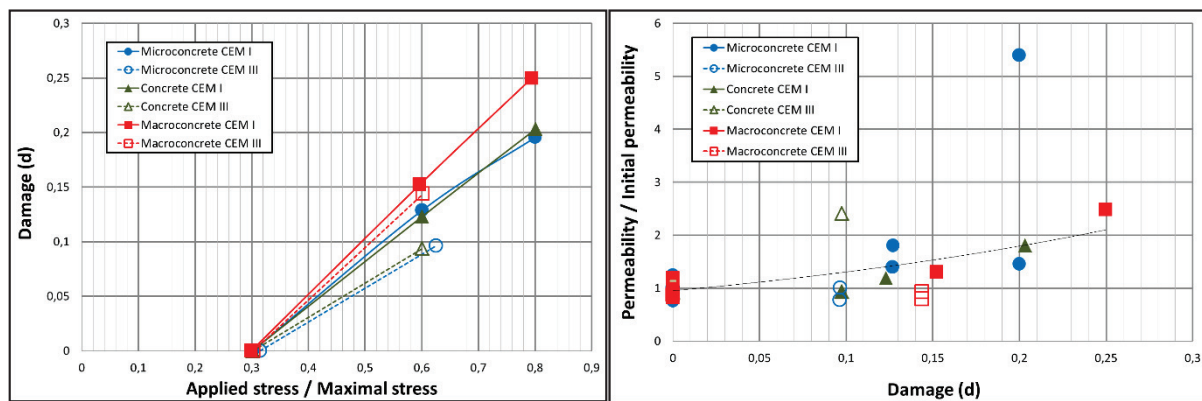


Figure 2: (a) Compressive damage evolution with loading level. (b) Relative permeability evolution with compressive damage.

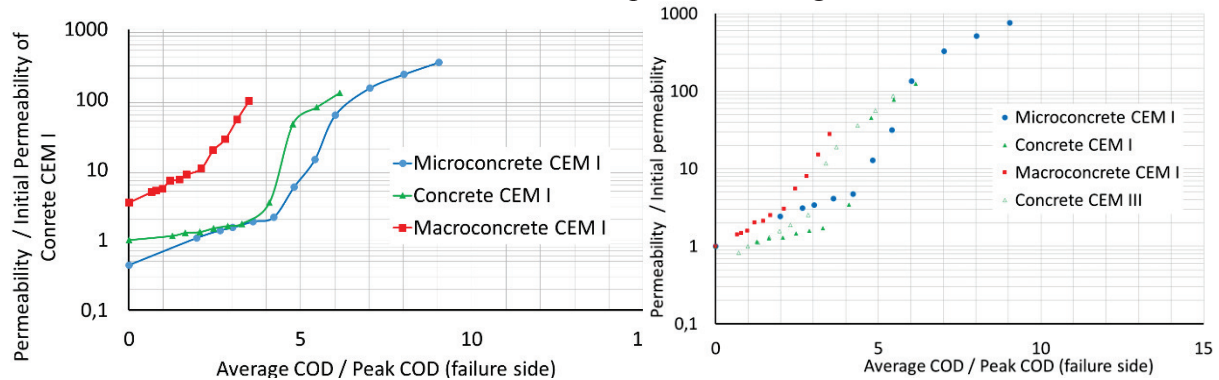


Figure 3: (a) Relative permeability evolution versus tensile cracking and aggregate size. (b) Another relative permeability evolution versus tensile cracking.

#### 4. Concluding Remarks

The results reported in this study can be summarised as follows:

- The developed testing methods and materials permit to highlight the effects of aggregate size on concrete mechanical behaviour and its gas permeability. An original device has been developed to evaluate crack opening simultaneously to gas permeability.
- Permeability increases not only with the compressive or tensile damage, but also with the aggregate size, independently on the cement nature.

- Permeability increase versus tensile cracking, represented by a crack-mouth opening displacement, follows a sigmoid curve, already observed for the compressive tests [11]. Three regimes with different rates may be distinguished for this sigmoidal evolution, depending on crack connectivity and geometry.
- Results highlight that the overall evolution of a relative permeability versus compressive or tensile damage follows a single law for all the materials tested. The effects of cracking and of aggregate size may therefore be separated by two distinct functions.

## References

- [1] Bazant, Z., Introduction aux effets d'échelle sur la résistance des structures, Lavoisier, Paris (2004)
- [2] Pijaudier-Cabot, G. et al, Non local damage models with evolving internal length: motivations and applications to coupled problems, *FraMCoS 5* (2004), 531-538
- [3] Wolinski, S. et al, Influence of aggregate size on fracture mechanics parameters of concrete, *Int. J. of Cem. Comp. and Lightweight Concrete* 9(2) (1987), 95-103
- [4] Hillerborg, A. A., Results of three comparative test series for determining the fracture energy  $G_f$  of concrete, *Materials and Structures* 18 (1985), 33-39
- [5] Bazant, Z. P. and Oh, B. H., Crack Band theory for fracture of concrete, *Materials and Structures* 16 (1983), 155-177
- [6] Petersson, P.E., Fracture energy of concrete: practical performance and experimental result, *Cem. Concr. Res.* 10 (1980), 91-101
- [7] Bisschop, J. and Van Mier, J.G.M., Effect of aggregates on drying shrinkage microcracking in cement-based composites, *Materials and Structures* 35 (2002), 453-461
- [8] Szczesniak, M. et al, Compressive strength of cement-based composites: Roles of aggregate diameter and water saturation degree, *Cem. Concr. Compos.* 37 (2013), 249-258
- [9] Rao, G. A. and Prasad, B. R., Fracture energy and softening behavior of high-strength concrete, *Cem Concr Res.* 32 (2002), 247-252
- [10] Grassl, P. et al, Influence of aggregate size and volume fraction on shrinkage induced micro-cracking of concrete and mortar, *Cem. Concr. Res.* 40(1) (2010), 85-93
- [11] Choinska M. et al, Effects and interactions of temperature and stress-level related damage on permeability of concrete, *Cem. Concr. Res.* 37 (2007), 79-88
- [12] Fabien, A. et al, Experimental Study of Aggregates Size Effect on Strain, Damage and Permeability of Concrete, *Key Engineering Materials* 729 (2017), 115-121
- [13] Saito, M. and Ishimori, H., Chloride permeability of concrete under static and repeated compressive loading, *Cem. Concr. Res.* 25(4) (1995), 803-808
- [14] Choinska, M. et al, How to extract a crack opening from a continuous damage finite element computation? Application for the estimation of permeability, *ISTE – Wiley, GeoProc 2008, Lille, France* (2008)
- [15] Picandet, V. et al, Effect of axial compressive damage on gas permeability of ordinary and high-performance concrete, *Cem. Concr. Res.* 31(11) (2001), 1525-1532

## IMPACT OF DRYING RATE ON DELAYED STRAINS IN CEMENT-BASED MATERIALS

Justin Kinda<sup>(1,2)</sup>, Laurent Charpin<sup>(1)</sup>, Jean-Luc Adia<sup>(1)</sup>, Farid Benboudjema<sup>(2)</sup>, Sylvie Michel-Ponnelle<sup>(3)</sup>

(1) EDF R&D MMC, France

(2) LMT, ENS Paris-Saclay, France

(3) EDF R&D ERMES, France

### Abstract

A part of the concrete containment buildings (CBB) in French nuclear power plants operated by EDF are double-walled CBBs. The concrete of the post-tensioned inner containment building plays a major role as a barrier against radiological release during a hypothetical accident. The leak-tightness of the inner CCB depends vastly on the pre-stress. If it is too low due to pre-stressing cable relaxation or concrete creep and shrinkage, some parts of the concrete might experience tension during the integrated leak rate test (performed every 10 years) or an accident, inducing cracking and an increased leakage.

Therefore, EDF builds simulation tools dedicated to the prediction of strains in CCBs, which requires properly calibrated models.

Most of the time models are calibrated on laboratory test on rather small samples, while CCBs are very large structures. These different concrete thicknesses induce vastly different drying kinetics. Thus, the concrete constitutive laws should be able to correctly take into account the effect of the rate of drying on the delayed strains (creep, shrinkage) of concrete.

As an introduction to this subject, it has been decided to work on the experimental data provided by literature.

The set of experimental data is first simulated with a delayed strains law used at EDF R&D [2]. Second, the microprestress-solidification law [3] (which was implemented for this purpose) is used.

It is shown that both these constitutive laws can reproduce the main features of the shrinkage and creep tests, but also that the experimental program lacks some information to be truly discriminant. This motivates further experimental developments which will be undergone in the future.

## 1. Introduction

In the present paper, two delayed strain models are used to simulate the experimental data by Day [1], in which mass loss, shrinkage and creep strains were measured on thin cement paste samples for two drying rates.- The final goal is to verify if those models are able to reproduce the creep and shrinkage for these different experimental conditions. -

To do so, for each model, we used the same set of parameters to reproduce the experimental curves, regardless of the rate of drying.

First the models are briefly presented. Then, the experimental set up is explained. Finally the simulation results are shown and conclusions are drawn.

## 2. Delayed strain model description

### 2.1 EDF model

The model was originally developed for EDF R&D by F. Benboudjema [4]. It was later modified to better reproduce basic creep in long term following ideas from [5] and [6]. The material was assumed to be viscoelastic. Under such assumption, the total strain is considered as the sum of four main contributions: elastic strain, drying shrinkage, basic creep and drying creep. A detailed description of the model can be found in [2]. The basic creep compliance is based on a Burgers unit as show on Figure 1, left.

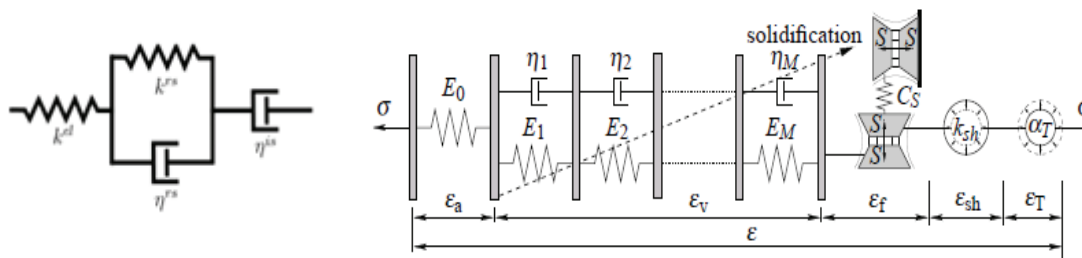


Figure 1– Left: Burgers unit of EDF model (spherical part)[2]. Right: Rheological scheme of the complete hygro-thermo-mechanical MPS model [3].

### 2.2 Microprestress-solidification (MPS) model

The second model (Figure 1 right) was published in [3]. The model was formulated within the framework of viscoelasticity, hence the principle of superposition is applied and the behavior of is captured by compliance function  $J$  (strain under unit stress). The model is based on three main phenomena: aging of concrete (short term chemical aging, long term aging), drying creep effect and transitional thermal creep. For more details, refer to [3].

The model was recently implemented in MFront (tfe.sourceforge.net), and coupled with Code\_aster, the finite element simulation tool used developed at EDF R&D (www.code-aster.org).

### 3. Experimental Data

Results from tests performed by Day [1], on thin cement paste specimen are used here. The experiments were conducted on S-shaped thin specimens, to avoid cracking induced by drying. The S-shaped specimens are 1.9 mm thick (see Figure 2).

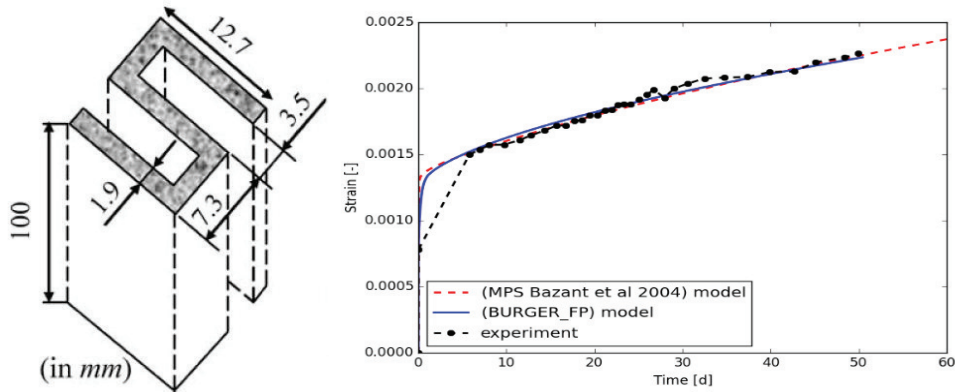


Figure 2: Left: S-shaped specimen [1], Right: Basic creep.

The specimens were loaded by means of miniature, hydraulically controlled, creep rigs. A compressive load of 11.6 MPa was applied, 75 days after casting. The specimens were exposed to two different drying rate. The humidity reduction starts 7 days after loading; it was made between 100% and 53% RH (See Figure. 3). by using saturated magnesium nitrate. For more details, refer to [1].

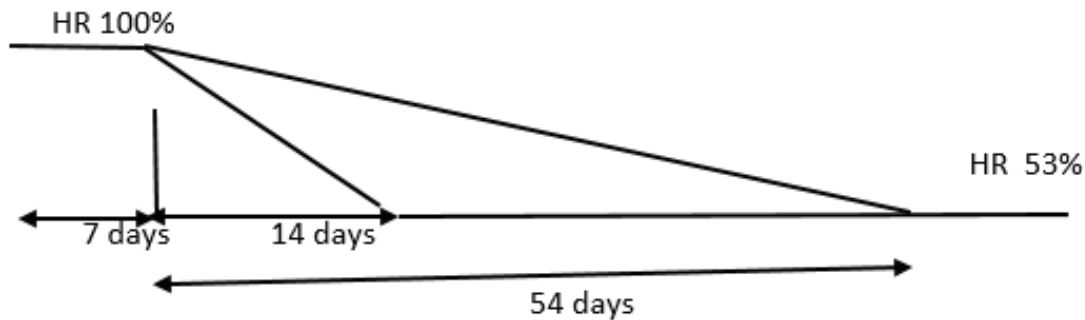


Figure 3: Humidity control, two rates of drying.

### 4. Simulations

The basic creep parameters have been identified first. In the case of drying, a full water transport analysis is necessary. In this study, the water content evolution was supposed to be homogenous in the specimen, due to lack of sufficient information on the imposed relative humidity and on the desorption isotherm of the material. Under this assumption, which will be

discussed later, the parameters identification have been performed by a least square method implemented thanks to the Python function `scipy.optimize.fmin`.

The parameters associated to the identification using the EDF model on the slow rate test are: for basic creep,  $\kappa^{rd} = 1.946 \cdot 10^{10}$  Pa,  $\eta^{id} = 1.050 \cdot 10^{14}$  (Pa.s),  $\eta^{rd} = 3.677 \cdot 10^{14}$  (Pa.s),  $\alpha = 0.423$ ,  $\kappa^{shr} = 1.617 \cdot 10^{-5}$  m<sup>3</sup>/Kg for drying shrinkage and  $\eta^{fdd} = 1.071 \cdot 10^9$  (Pa.s) for drying creep. For MPS model, fits have been obtained using the following optimum values of the parameters:  $q_1 = 9.482998 \cdot 10^{-5}$  /MPa,  $q_2 = 2.747752 \cdot 10^{-4}$  /MPa,  $\alpha = 1.601378 \cdot 10^{-3}$ ,  $c = 1.164680 \cdot 10^{-9}$  / (MPa.day).

The simulation results are presented below for both models, first for basic creep, secondly for drying shrinkage (slow and fast rate) and finally for drying creep. The parameters calibration for basic creep went well (see Figure 2), but in case of drying, the parameters calibrated on slow drying rate, could not be used to fit fast rate drying experimental data (see Figures 4,5). Was the assumption on homogenous water content in the specimen valid? Apparently not. The difference between the experimental and calculated results might come from this assumption.

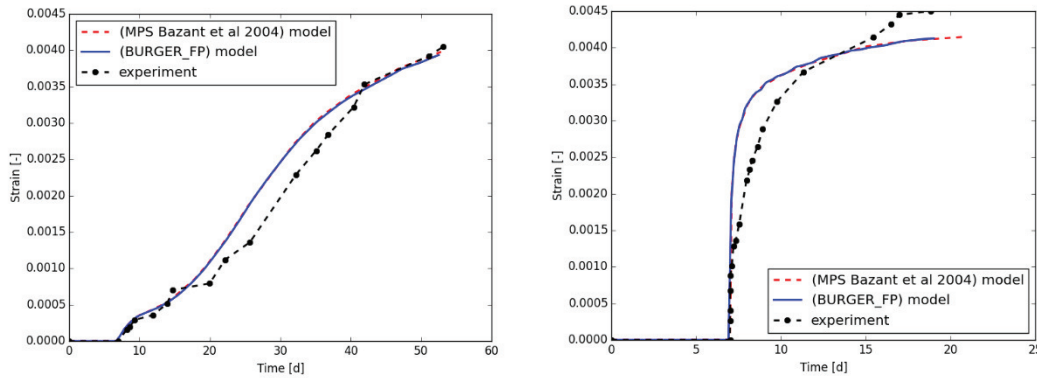


Figure 3 - Left: slow drying shrinkage calibration, Right: Fast drying shrinkage simulation.

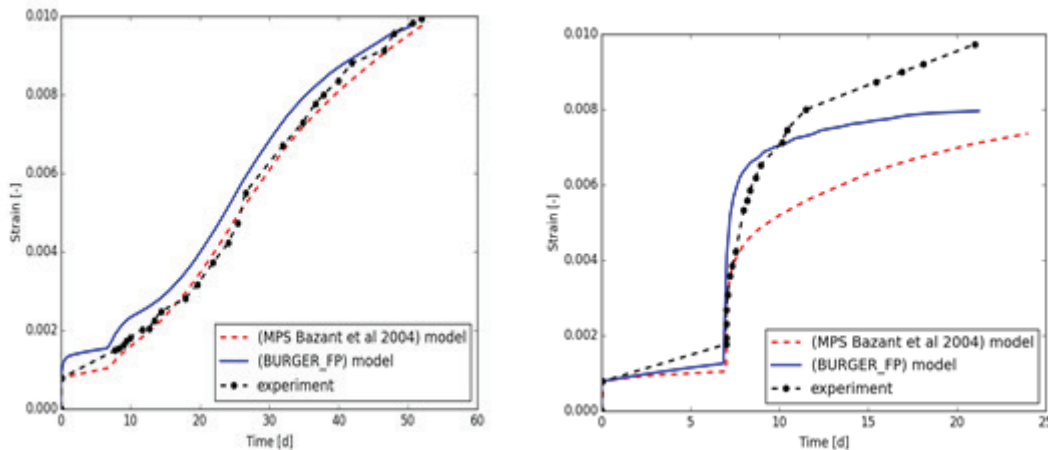


Figure 4- Left: slow drying creep calibration, Right: fast drying creep simulation.

Figures 4, 5 show how strongly, the rate of drying affects the delayed response of the material, but does the final value of drying creep still the same regardless of the rate of drying? That still is an open question.

## 5. Conclusions

The prediction of delayed strains in large structures such as CCB, requires models that correctly take into account the rate of drying. In this work, It is shown that both constitutive laws can reproduce the main features of the shrinkage and creep tests. The MPS model seems to underestimate drying creep in the case of fast drying. The experimental program is also shown to lack some information to be truly discriminant. This motivates further experimental developments which will be undergone in the future. Then, more calculations combining different RH/water content related to creep coefficient, shrinkage and cracking would be performed, to understand this phenomenon.

## Acknowledgements

This work has been funded by EDF R&D, France

## References

- [1] Day, R.L., Cuffaro, P., and Illston, J.M., The effect of rate of drying on the drying creep of hardened cement paste. *Cement and Concrete Research*, 14(3): 329–338, 1984.
- [2] Charpin, L., Sow, T.O., d'Estève de Pradel, X.; Hamon, F., and Mathieu, J.-P., Numerical simulation of 12 years long biaxial creep tests. Efficiency of assuming a constant Poisson's ratio, *Proceedings of the VI<sup>th</sup> Biot conference on poromechanics*, Champs-sur-Marne, France, 2017
- [3] Bažant, Z.P., Cusatis, G., and Cedolin, L., Temperature effect on concrete creep modeled by microprestress-solidification theory. *Journal of engineering mechanics*, 130(6): 691–699, 2004
- [4] Benboudjema, F. (2002). Modélisation des déformations différées du béton sous sollicitations biaxiales. Application aux enceintes de confinement de bâtiments réacteurs des centrales nucléaires (Doctoral dissertation, Université de Marne la Vallée).
- [5] Sellier, A., & Buffo-Lacarrière, L. (2009). Vers une modélisation simple et unifiée du fluage propre, du retrait et du fluage en dessiccation du béton. *European Journal of Environmental and Civil Engineering*, 13(10), 1161-1182.
- [6] Foucault, S. Michel-Ponnelle, E. Galenne. A new creep model for NPP containment behavior prediction. *Proceedings of the 1st SSCS (Strategies for Sustainable Concrete Strategies) Conference*, Aix-en-Provence, France, May 29th – June 1st, 2012.

## **INFLUENCE OF THE FLEXIBILITY OF CALCIUM SILICATE HYDRATES LAYERS ON THE MESOTEXTURE: COARSE GRAINED SIMULATIONS ACCOUNTING FOR THREE-BODY INTERACTIONS**

**Tulio Honorio** <sup>(1,2)</sup>

(1) Laboratoire Modélisation et Simulation Multi Echelle, Université Paris-Est Créteil,  
Créteil, France

(2) *Present address:* LMT-Cachan/ENS-Cachan/CNRS/Université Paris Saclay, Cachan,  
France

### **Abstract**

Calcium silicate hydrates exhibit various mesotextures, composed of fundamental pieces presenting with different morphologies. The structuration of nanolayer (2D) and nanofibrillar (1D) materials is a result of the interplay between intermolecular forces involving the fundamental pieces (layers or fibrils) and the pore fluid as well as the flexibility of each piece. In this paper, coarse-grained simulations are performed to simulate the differences in the mesotexture of crystalline calcium silicate hydrate with a fibril morphology taking into account the flexibility of these fibrils. The resulting pore size distributions of the gel are computed and exhibit a dependence on the size of the fibril. These results are a contribution to a better understating of C-S-H nanostructuration.

### **1. Introduction**

Calcium silicate hydrates exhibit a variety of morphologies, such as isotropic grains, 1D fibrils and 2D foils as well as in-plane dimensions, ranging from few tens of nanometers up to several micrometers [1]. For layers with large aspect ratio, the flexibility of the layers might play a role in the structuration of the material with important repercussion in the hygro-mechanical response of the material [2]. However, the effects of flexibility (or three body interactions) are not generally taken into account in simulations of the mesotexture of calcium silicate hydrates [3–5]. The structuration of nanolayered or nanofibrillar materials is a result of the interplay between intermolecular forces involving the fundamental “pieces” (layers of fibrils) and the pore fluid as well as the flexibility of piece. These intermolecular forces, or



potential of mean force, can be computed by means of grand canonical simulations (c.f. the paper “Interactions between crystalline calcium silicate hydrates: grand canonical simulation of pressure and temperature effects” presented by the author also in this conference). The flexibility of single layers of tobermorite (Hamid’s 11 Å tobermorite with Ca/Si=1 [6]) have been previously computed by the author [2]. The bending moduli in each orthogonal in-plane direction of the pseudo-orthorhombic cell are, respectively  $(4.68 \pm 1.74) \times 10^{-17}$  J and  $(1.42 \pm 0.91) \times 10^{-17}$  J [2]. These values are few orders of magnitude larger than (flexible) polymeric layers ( $\sim \times 10^{-20}$  J) and on the same order than other phyllosilicates such as clays [7]. With this bending modulus, tobermorite layers with more than few nanometers in one of the in-plane dimensions may potentially exhibit a bent configuration [2].

The flexibility of clays layers is recognized to play a major role on the structuration of the nanolayered materials. The reasoning can be, of course extended to nanofibrillar materials. Two limit cases can be compared [8]: (a) flexible or long layers or fibrils that are not prone to stack leads to entangled or spaghetti-like mesotextures, whilst (b) rigid or short layers or fibrils that are prone to stack leads to brick-like mesotextures. The resulting microstructure in (a) presents smaller pores (less permeable, therefore) and cohesion due to entanglement of a layer in different ordered domains, which may lead to a more ductile macroscopic behaviour. The resulting microstructure in (b) presents larger pores (more permeable) and granular behaviour, which may translate in a brittle macroscopic behaviour.

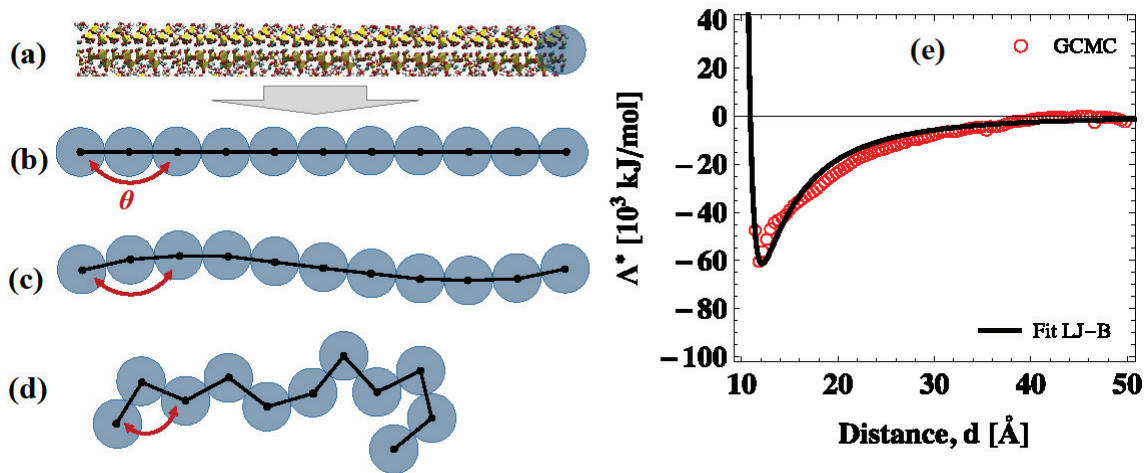


Figure 1. *At left*, Representation of a solid layer by a chain of spherical grains: (a) snapshot of the atomic structure of Hamid’s [6] 11 Å tobermorite with Ca/Si = 1; fibril representation with (b) large bending modulus (c) intermediary bending modulus (persistence length larger than the grain sizes) and (d) small bending modulus (the persistence length smaller than the grain size). *At right*, (e) potential of mean force obtained from grand canonical Monte Carlo simulation [9] and fitted LJ-B potential from a previous study.

In this paper, coarse-grained simulations are performed to simulate these differences in the mesotexture of calcium silicate hydrates. The potential of mean force and flexibility of a crystalline calcium silicate hydrate are considered. Three fibrils sizes and their propensity to stack are explicitly taken into account. The resulting pore size distributions for each scenario

are compared. These results are a contribution to a better understating of C-S-H nanostructuration.

## 2. Models and simulations

The atomic structure of Hamid's 11 Å tobermorite [6] with molar Ca/Si ratio of 1 is considered ( $\text{Ca}_6[\text{Si}_6\text{O}_{18}]\cdot 2\text{H}_2\text{O}$ ). This same structure was also studied by other authors interests in the meso-structuration of calcium silicates (e.g. [10, 11]). Figure 1 (a) shows the replicated monoclinic cell ( $a = 6.69 \text{ \AA}$ ,  $b = 7.39 \text{ \AA}$ ,  $c = 22.77 \text{ \AA}$  and  $\gamma = 123.49^\circ$ ) along a-axis, as proposed by Hamid [6]. The atoms in tobermorite are interacting via CSHFF [12], which is a force field based only in non-bonded Lennard-Jones interactions for metal and metalloids while harmonic bonds are only defined for water molecules and hydroxyls. This force field has been extensively used in the computation mechanical, thermal and interfacial properties of crystalline and disordered calcium silicates [13]. The surface charge density of the tobermorite layer is  $-0.55 \text{ C}\cdot\text{m}^{-2}$ , which is close to the experimental value of  $-0.5 \text{ C}\cdot\text{m}^{-2}$  [14].

### 2.2 Coarse-grained simulations accounting for two- and three-body interactions

The tobermorite solid layer is represented by a chain of spherical grain interacting *via* non-bonded forces (derived from the potential of mean force), two-body forces (derived from the in-plane elasticity of the solid layer) and three-body forces (derived from the bending modulus of the solid layer). The interaction between solid tobermorite layers and the fluid in drained conditions are detailed in another study [9]. These interactions are fitted by a generalized Lennard-Jones (LJ) potential combined with the Buckingham potential, as reported in Fig. 2, for all distances smaller than the cut-off distance  $d_c = 50 \text{ \AA}$ :

$$U_{LJ-B}(d) = 4\epsilon \left[ \left( \frac{\sigma}{d} \right)^{2\alpha} - \left( \frac{\sigma}{d} \right)^\alpha \right] + A \exp\left(-\frac{d}{\beta}\right) - \frac{C}{d^6} \quad \forall d < d_c \quad (1)$$

with  $\sigma = 5.907 \text{ \AA}$ ,  $\epsilon = 151.85 \times 10^3 \text{ kJ/mol}$  and  $\alpha = 2.85$ , for the LJ potential and  $A = 1.213 \times 10^{12} \text{ kJ/mol}$ ,  $\beta = 0.4670 \text{ \AA}$  and  $C = 0$ , for the Buckingham potential.

Bonds or two-body interaction are described by an harmonic bond:

$$U_{2-b}(d) = k_{2-b}(d - d_0)^2 \quad (2)$$

with force constant  $k_{2-b} = 939 \text{ kJ}/(\text{mol } \text{\AA}^2)$  computed from the elastic moduli according to the in-plane direction of the solid layer; and the equilibrium bond length distance  $d_0$ , corresponding to the effective thickness of the solid layer. In this study, the in-plane elastic moduli computed by first principles simulations [15], in Hamid 11 Å tobermorite with Ca/Si = 1, are used (i.e. 148.25 and 138.35 GPa). The equilibrium bond length adopted is  $d_0 = 11.81 \text{ \AA}$ .

Angles or three-body interaction described by a harmonic bond:

$$U_{3-b}(d) = k_{3-b}(\theta - \theta_0)^2 \quad (2)$$

where  $k_{3-b} = 11.44 \text{ kJ}/(\text{mol rad}^2)$ , is the bending modulus of the solid fibril and  $\theta_0$  is the equilibrium angle ( $180^\circ$  for a flat solid fibril). According to their flexibility and persistence length (parameter depending on the bending modulus), the fibril can assume different configurations (Fig. 1 right): from a flat surface (large bending modulus) to a crumpled configuration (small bending modulus).

The molecular dynamics simulations are performed with LAMMPS [16]. The fibrils are generated in a grid with a dilute concentration so that the distance between the fibrils is much larger than the cut-off of the non-bonded interactions. Circa 40000 grain are considered in each scenario. A velocity corresponding to 5000 K is randomly attributed to each individual grain. A 0.5 ns run in NVT ensemble is performed so that the fibril may assume random orientations. Then, the temperature is decreased to 300 K during 0.1 ns and equilibrated in this temperature during 0.2 ns. Next, the system is subjected to a pressure of 1 atm; an equilibration run of 0.5 ns is followed by the sampling of the configurations to be considered in pore size distribution analysis. The pore size distribution of the resulting mesotexture is assessed by means of the method developed by Bhattacharya et al. [17]. Three fibril size are considered  $N = 5, 10,$  and  $20$  grains, where  $N = L/d_0$  is the ratio between the largest dimension  $L$  of the fibril divided by the diameter of the grain  $d_g = d_0$ .

### 3. Results and discussion

Figure 2 displays the mesotextures obtained for the three fibril sizes considered. It is possible to identify only slightly bent configurations in all cases. In the cases treated here, the fibrils can be fairly approximated by rigid rods. This aspect highlights the importance of considering bending rigidity in modelling C-S-H.

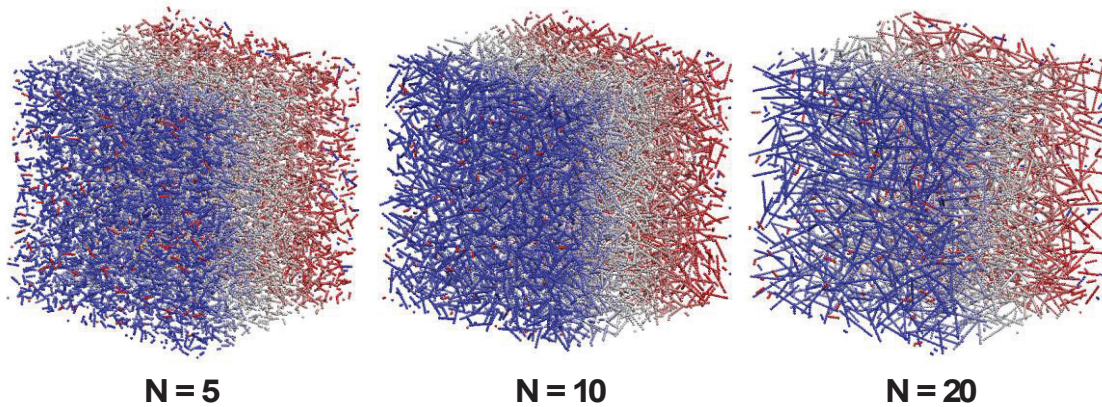


Figure 2. Mesotexture according to the size of the fibril: systems with 8000 ( $N = 5$ ), 4096 ( $N = 10$ ) and 1728 ( $N = 20$ ) fibrils, respectively (i.e. circa 40000 grains in each case).

The corresponding pore size distributions of the mesotextures are compared in Fig. 3. The range of pore sizes covered by the numerical samples corresponds to gel pores (0.5-10 nm) and medium capillary pores (10-50 nm). The probability density function follows a normal

distribution with average ( $\pm$  standard deviation) pore diameter of  $7.6 \pm 1.8$  nm ( $N = 5$ ),  $9.0 \pm 1.9$  nm ( $N = 10$ ) and  $9.1 \pm 2.2$  nm ( $N = 20$ ), respectively. For moderately flexible fibrils as tobermorite, increasing the fibril size leads to an increase in the average pore size and the standard deviation of the pore size distribution.

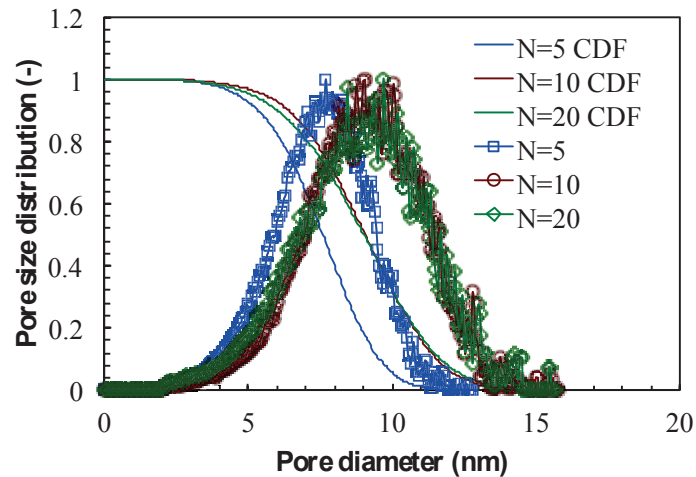


Figure 3 Differential and cumulative pore size distributions according to the size of the fibril (considering the bending modulus of tobermorite layer).

#### 4. Conclusion

In this paper, the effect of considering the flexibility (or three-body interaction) of solid fibrils on the mesotexture of calcium silicate hydrates is studied. Fibrils of tobermorite are moderately flexible in the sense that they can show some bent configurations for moderate loads on the order of the kPa up to the MPa [2], which can easily be found in cement-based materials [18]. The increase of fibril size translates in the increase of the probability of finding bent fibrils in the equilibrium configurations. In this study, only slightly bent configurations were observed even for the scenarios with the longest fibril ( $N = 20$ ). An increase in the fibril size, for a fixed bending modulus, leads to changes in the meso-structuration of calcium silicate hydrates: both the average pore size and the standard deviation of the pore size distribution increase with the size of the fibril. Future investigations will tackle with the structuration of 2D layers as well as combination of fibrils of different sizes.

#### References

- [1] Richardson IG. Tobermorite/jennite- and tobermorite/calcium hydroxide-based models for the structure of C-S-H: applicability to hardened pastes of tricalcium silicate,  $\beta$ -dicalcium silicate, Portland cement, and blends of Portland cement with blast-furnace slag, metakaolin, or silica fume. *Cem Concr Res* 34 (2004), 1733–1777
- [2] Honorio T, Brochard L. Flexibility of C-S-H sheets and stacks from molecular simulations. Second International RILEM/COST Conferene on Early Age Cracking and Serviceability in Cement-Based Materials and Structures, Belgium (2017)
- [3] Masoero E, Del Gado E, Pellenq RJ-M, et al. Nanostructure and Nanomechanics of

- Cement: Polydisperse Colloidal Packing. *Phys Rev Lett* 109 (2012), 155503
- [4] Ioannidou K, Krakowiak KJ, Bauchy M, et al. Mesoscale texture of cement hydrates. *Proc Natl Acad Sci* (2016) 201520487
- [5] Yu Z, Zhou A, Lau D Mesoscopic packing of disk-like building blocks in calcium silicate hydrate. *Sci Rep* 6 (2016)
- [6] Hamid SA. The crystal structure of the 11 Å natural tobermorite  $\text{Ca}_{2.25}[\text{Si}_3\text{O}_7.5(\text{OH})_{1.5}] \cdot \text{H}_2\text{O}$ . *Z Für Krist - Cryst Mater* 154 (1981), 189–198
- [7] Suter JL, Coveney PV, Greenwell HC, Thyveetil M-A. Large-Scale Molecular Dynamics Study of Montmorillonite Clay: Emergence of Undulatory Fluctuations and Determination of Material Properties. *J Phys Chem C* 111 (2007), 8248–8259
- [8] Zabat M, Vayer-Besançon M, Harba R, et al. Surface topography and mechanical properties of smectite films. In: Rosenholm JB, Lindman B, Stenius P (eds) *Trends in Colloid and Interface Science XI*. Steinkopff, (1997) pp 96–102
- [9] Honorio T. Interactions between crystalline calcium silicate hydrates: grand canonical simulation of pressure and temperature effects. Funchal, Madeira Island, Portugal (2018)
- [10] Masoumi S, Valipour H, Abdolhosseini Qomi MJ. Intermolecular Forces between Nanolayers of Crystalline Calcium-Silicate-Hydrates in Aqueous Medium. *J Phys Chem C* 121 (2017), 5565–5572
- [11] Masoumi S, Valipour H, Abdolhosseini Qomi MJ. Interparticle Interactions in Colloidal Systems: Toward a Comprehensive Mesoscale Model. *ACS Appl Mater Interfaces* 9 (2017), 27338–27349
- [12] Shahsavari R, Pellenq RJ-M, Ulm F-J. Empirical force fields for complex hydrated calcio-silicate layered materials. *Phys Chem Chem Phys* 13 (2010), 1002–1011
- [13] Mishra R, Kunhi A, Geissbühler D, et al. cemff: A force field database for cementitious materials including validations, applications and opportunities. *Cem Concr Res.* (2017)
- [14] Allen AJ, Thomas JJ, Jennings HM. Composition and density of nanoscale calcium–silicate–hydrate in cement. *Nat Mater* 6 (2007), 311–316
- [15] Shahsavari R, Buehler MJ, Pellenq RJ-M, Ulm F-J. First-Principles Study of Elastic Constants and Interlayer Interactions of Complex Hydrated Oxides: Case Study of Tobermorite and Jennite. *J Am Ceram Soc* 92 (2009), 2323–2330
- [16] Plimpton S. Fast Parallel Algorithms for Short-Range Molecular Dynamics. *J Comput Phys* 117 (1995), 1–19
- [17] Bhattacharya S, Gubbins KE. Fast Method for Computing Pore Size Distributions of Model Materials. *Langmuir* 22 (2006) 7726–7731
- [18] Honorio, T, Brochard, L, Bary, B. Statistical variability of mechanical fields in thermo-poro-elasticity: multiscale analytical estimations applied to cement-based materials at early-age. *Cem. Concr. Res* 110 (2018) 24-41

## **INTERACTIONS BETWEEN CRYSTALLINE CALCIUM SILICATE HYDRATES: GRAND CANONICAL SIMULATION OF PRESSURE AND TEMPERATURE EFFECTS**

**Tulio Honorio** <sup>(1,2)</sup>

(1) Laboratoire Modélisation et Simulation Multi Echelle, Université Paris-Est Créteil,  
Créteil, France

(2) *Present address:* LMT-Cachan/ENS-Cachan/CNRS/Université Paris Saclay, Cachan,  
France

### **Abstract**

The interactions between calcium silicate hydrates and pore solution at the nanoscale are crucial in physical phenomena related to the thermo-hydro-mechanical behaviour of cement-based materials. In this paper, these interactions are studied using grand canonical Monte Carlo simulations according to various temperatures and pressures. A nanocrystalline structure of calcium silicate hydrate (tobermorite) is considered. Micro-instabilities of snap-through type are identified. The corresponding potential of mean force, accounting for the interactions of the solid layers in drained conditions, is provided, which leaves rooms to upscale the behaviour of calcium silicate hydrates to the mesoscale.

### **1. Introduction**

Adsorption related phenomena is reported to be at the heart of important features of cement-based materials behaviour such as drying shrinkage and hysteresis [1], creep [2], thermal expansion [3] and transmission of stresses between solid and liquids phases [4]. Adsorption takes place at the molecular scale and is recognized to be pressure and temperature dependent. The main product of cement hydration processes is calcium silicate hydrates, a microporous adsorbing material. Cement-based materials are generally subjected to variations of temperatures during their service life. Under temperature rise, fluid molecules are expected to desorb whereas the entire system is expected to show thermal expansion.

Simulations at the molecular scale are well suited to investigate adsorption phenomena in details. These simulations allow assessing water structuration as a function of confinement

and the presence of ions in microporous materials [5]. Such approach have been use to evaluate the intermolecular forces between solids layers of calcium silicate hydrates in drained conditions [6, 7]. Even if a macroscopically a nanoporous material, as calcium silicate hydrates, is not under drained conditions, at the nanoscale, due to the exchange of fluids between interlayer pores and gel pores the former class of pores can be seen as in drained conditions with respect to the fluid reservoir in gel pores. Experimental evidence [8] showing instantaneous changes in water population in these pores under temperature change corroborates this assumption regarding the internal migration of water. In this context, the thermodynamic ensemble adapted to study adsorption phenomenon is the grand canonical ensemble for the fluid combined with canonical ensemble for the solid layers: the total volume  $V$  and temperature  $T$  are fixed (while the total pressure  $P$  and entropy fluctuate), the chemical potential of the fluid  $\mu_w$  is fixed (while the number of fluid molecules  $N_w$  fluctuates) and the number of atoms in the solid as well as counterions are fixed. This ensemble minimises the mixed thermodynamic potential  $\Lambda(V, T, \mu_w)$ . For a layered materials, the confinement pressure (in the direction orthogonal to the basal plane)  $P = -\left.\frac{\partial \lambda}{\partial d}\right|_{T, \mu_w}$  can be defined in terms of  $\Lambda$  per unit area  $\lambda(d, T, \mu_w) \equiv \Lambda(V, T, \mu_w)/A$ , where  $d$  is the basal spacing. The energy profile for a system controlled by the volume is  $\lambda = \lambda_0(d_0, T, \mu_w) - \int_{d_0}^d P d(d)$ . The convex hull of  $\lambda$ , resulting from the integration of  $\lambda$  over a Representative Volume Element (RVE) represents the energy associated with all stable states of stacks under displacement control. The corresponding energy profile for a system controlled by the confining pressure is the Legendre transform of  $\lambda$ :

$$\lambda^* = \lambda + P d = \Lambda^*(P, T, \mu_w)/A \quad (2)$$

This is what is called the free energy of swelling in clay science [5, 9]. This energy profile informs on the prevalence and stability of specific basal spacings.

In this paper, the dependence of adsorption, disjoining pressure isotherms and free energy of swelling on temperature and pressure is investigated by means of grand canonical Monte Carlo molecular simulations (GCMC).

## 2. Molecular simulation of crystalline calcium silicate hydrates

Classical Monte Carlo simulations in grand canonical ensemble are run as a function of the confinement (i.e. for different centre-to-centre or basal distance with respect to solid layers) and temperature. Interactions between the species are described by CSHFF force field [10] and SPC water model. The chemical potential of SPC water as a function of the temperature is obtained by means of thermodynamic integration of Gibbs-Duhem equation. Calcium counterions are added to the interlayer space in order to ensure the electroneutrality of the system. For each temperature and basal spacing, a simulation is run with Towhee [11] package using configuration bias methods. Each simulation is run during 30 million Monte Carlo steps (10 million steps for equilibration and 20 million for sampling). The convergence criterion adopted is a stable energy system (with the standard deviation of the total energy

below 0.02 % of the mean value). The atomic structure of calcium silicate hydrate is derived from Hamid's [12] structure of tobermorite 11 Å with molar Ca/Si ratio of 1:  $\text{Ca}_6[\text{Si}_6\text{O}_{18}]\cdot 2\text{H}_2\text{O}$ . The cell parameters of the resulting monoclinic cell are  $a = 6.69 \text{ \AA}$ ,  $b = 7.39 \text{ \AA}$ ,  $c = 22.77 \text{ \AA}$  and  $\gamma = 123.49^\circ$  [12]. Figure 1 shows snapshots of configurations at equilibrium associated to three basal spacings.

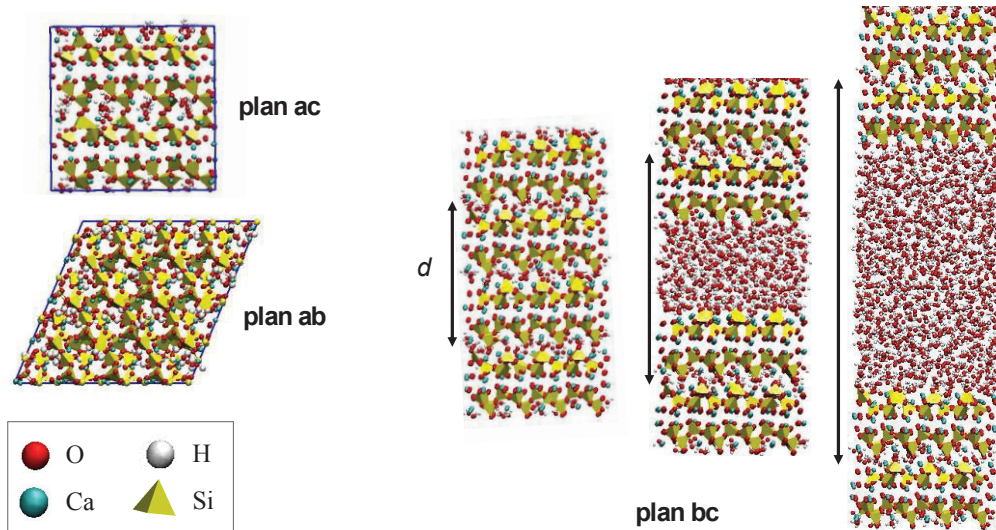


Figure 1: Snapshots of the (monoclinic) structure of Hamid's 11 Å tobermorite with Ca/Si = 1 and equilibrium configurations at three basal spacings  $d$ .

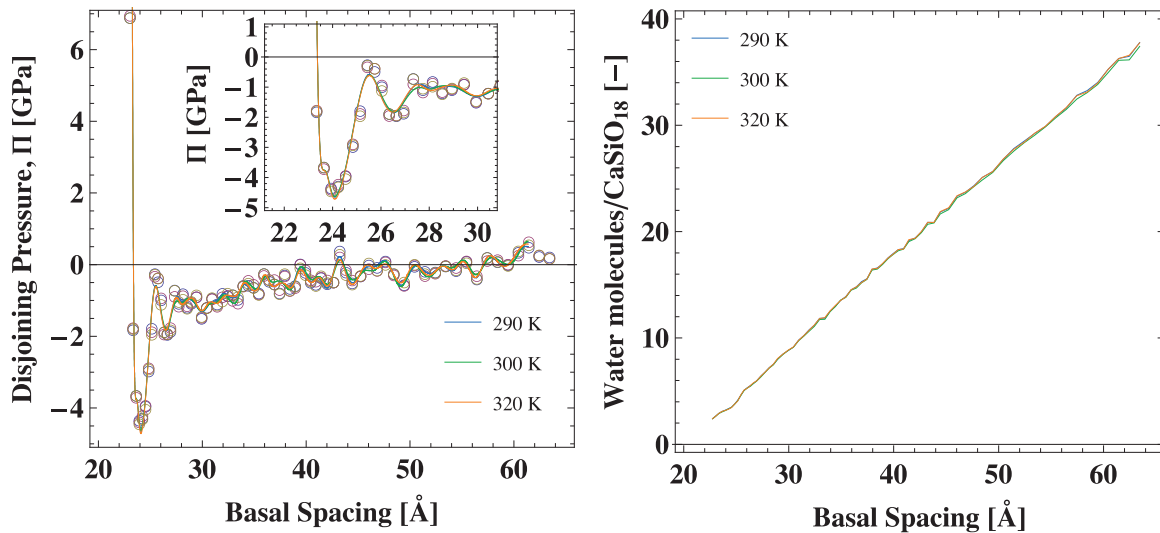


Figure 2: *At left*, disjoining pressure isotherms as a function of basal spacing for three temperatures. The inset shows the details of oscillation corresponding to the first hydration states. *At right*, adsorption isotherms as a function of basal spacing for the same temperatures.



#### 4. Results and discussion

Figure 2 (left) shows the disjoining pressure isotherms according to the three temperatures. The disjoining pressure is the difference between the confining pressure and the fluid pressure  $\Pi = P - P_w$ . The effects of the temperature, in the temperature range considered, is not very pronounced. The confining pressure isotherms at 300 K are in agreement with other pressure isotherms reported in the literature [6, 7]. For small basal spacings, it is possible to identify the quasi-dehydrated (some water molecules remains trapped in the calcium silicate pores even for small basal spacings), in which the confining pressure strongly increases with the decrease in  $d$  as a result of the steric repulsion between the solid layers, counterions and the remaining water molecules. The oscillations corresponds to the various possible hydration states  $nW$  with water structuring in discrete  $n$  layers up to the state of pore water  $\infty W$ . The  $1W$  hydration state can be clearly distinguished, as can be seen in the inset of Fig. 2. The distance between the oscillations (taking, for example, the minimum values in the inset of Fig. 2 as reference) is circa  $3 \text{ \AA}$ , which roughly corresponds to the Lennard-Jones diameter of the oxygen in SPC water model. The portions of the curve in which the pressure increases with the basal spacing are instable. Therefore, the system is subjected to micro- or snap-through instabilities [13], which are reported to be at the heart of important phenomena in nanoporous materials such as shrinkage and creep. Figure 2 (right) reports the adsorption isotherms for the three temperatures. Again, the effect of the temperature in the range considered is not very pronounced.

Some key physical properties can be computed from the pressure isotherms. This information can be used to validate the output of the simulation [6]. Table 1 shows the out-of-plane elastic modulus  $E_{zz} = -d_{eq} \left. \frac{\partial \lambda}{\partial d} \right|_{d_{eq}}$ , surface energy  $\gamma_s = -\frac{1}{2} \int_{d_{eq}}^{\infty} \lambda d(d)$  and cohesive pressure  $P_{cohesive}$  (i.e. the pressure needed to disjoin two solid layers, which corresponds to the minimum in the pressure isotherms) computed at different temperatures. The estimates are compared against results from experiments and simulations reported in the literature and a fair agreement is observed.

Table 1: Physical properties computed from the confining pressure isotherms: validation against experimental and simulation results from the literature.

	<b>Out-of Plane elastic modulus, <math>E_{zz}</math> (GPa)</b>	<b>Surface energy, <math>\gamma_s</math> (<math>\text{J/m}^2</math>)</b>	<b>Cohesive pressure, <math>P_{cohesive}</math> (GPa)</b>
This work:	79.7 (290 K) 77.7 (300 K) 79.9 (310 K)	1.07 (290 K) 1.07 (300 K) 1.05 (310 K)	4.18 (290 K) 4.16 (300 K) 4.22 (310 K)
Others	77.6 [6]; 61 [14] 89 [15]; 68.4 [16]	0.67 [6]; 1.15 [19] 0.32-0.4 [17, 18]	6.5 [6] 5.0 [20]

Figure 3 shows the free energy of swelling as a function of the basal spacing: according to the temperature (left) and control pressure (right). The effect of temperature, in the range considered, is minor. The control pressure affects the depth of the potential well, or the total

surface energy. The energy barriers associated with hydrate state transitions can be measured directly on these energy profiles. The energy profile concerning the system at 300 K was fitted using the of generalized Lennard-Jones potential:  $U_i(d) = 4\epsilon \left[ \left( \frac{\sigma}{d} \right)^{2\alpha} - \left( \frac{\sigma}{d} \right)^\alpha \right]$ , with  $\sigma = 21.81 \text{ \AA}$ ,  $\epsilon = 60.1 \times 10^3 \text{ kJ/mol}$  and  $\alpha = 7.01$ . This potential can be used to upscale calcium silicate hydrates behaviour at the mesoscale.

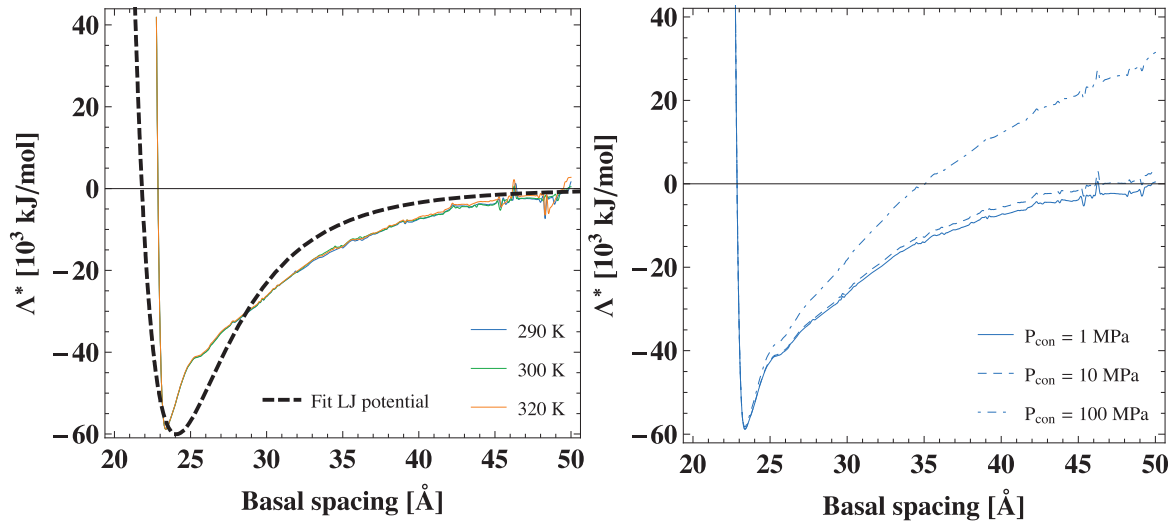


Figure 3: Free energy of swelling as a function of the basal spacing: according to the temperature (*left*) and control pressure (*right*). At left, the energy profile at 300K is fitted using the generalized Lennard-Jones potential.

#### 4. Conclusion

In this article, the intermolecular interactions between crystalline calcium silicate hydrates were reported. These interactions result from the interplay between steric repulsion, attractive forces and depletion forces or entropic solvation, which lead to an oscillatory (non-convex) energy profile susceptible to manifest (snap-through) micro-instabilities. Here, these interactions were presented in terms of disjoining pressure isotherms and free energy of swelling. The convexification of the energy profile leads to the mesoscopic energy profile of a stack of solid layers in drained conditions. These results leave room to a better understating of the nature of water confined in calcium silicate hydrates nanopores (i.e. interlayer and gel pores). The derived energy profiles can be used to compute the interparticle interactions at a mesoscale (gel scale).

#### References

- [1] Pinson MB, Masoero E, Bonnaud PA, et al. Hysteresis from Multiscale Porosity: Modeling Water Sorption and Shrinkage in Cement Paste. *Phys Rev Appl* 3 (2015), 064
- [2] Acker P Swelling, shrinkage and creep: a mechanical approach to cement hydration. *Mater Struct* 37 (2004), 237–243

- [3] Sellevold EJ, Bjøntegaard Ø. Coefficient of thermal expansion of cement paste and concrete: Mechanisms of moisture interaction. *Mater Struct* 39 (2006), 809–815
- [4] Honorio T, Brochard L, Vandamme M. Effective stresses and estimations of the apparent Biot coefficient in stacked clay nanolayers. *Géotechnique Lett* (2018)
- [5] Honorio T, Brochard L, Vandamme M (2017) Hydration Phase Diagram of Clay Particles from Molecular Simulations. *Langmuir* 33 (2017), 12766–12776
- [6] Masoumi S, Valipour H, Abdolhosseini Qomi MJ. Intermolecular Forces between Nanolayers of Crystalline Calcium-Silicate-Hydrates in Aqueous Medium. *J Phys Chem C* 121 (2017), 5565–5572
- [7] Bonnaud PA, Labbez C, Miura R, et al. Interaction grand potential between calcium–silicate–hydrate nanoparticles at the molecular level. *Nanoscale* 8 (2016), 4160–4172
- [8] Wyrzykowski M, McDonald PJ, Scrivener K, Lura P. Water Redistribution within the Microstructure of Cementitious Materials Due to Temperature Changes Studied with <sup>1</sup>H NMR. *J Phys Chem C* (2017)
- [9] Tambach TJ, Bolhuis PG, Hensen EJM, Smit B. Hysteresis in Clay Swelling Induced by Hydrogen Bonding: Accurate Prediction of Swelling States. *Langmuir* 22(2006), 1223–1234
- [10] Shahsavari R, Pellenq RJ-M, Ulm F-J. Empirical force fields for complex hydrated calcio-silicate layered materials. *Phys Chem Chem Phys* 13 (2010), 1002–1011
- [11] Martin MG. MCCCSTowhee: a tool for Monte Carlo molecular simulation. *Mol Simul* 39 (2013), 1212–1222
- [12] Hamid SA. The crystal structure of the 11 Å natural tobermorite Ca<sub>2.25</sub>[Si<sub>3</sub>O<sub>7.5</sub>(OH)<sub>1.5</sub>]·1H<sub>2</sub>O. *Z Für Krist - Cryst Mater* 154 (1981), 189–198
- [13] Bazant ZP, Bazant MZ. Theory of sorption hysteresis in nanoporous solids: Part I. Snap-through instabilities. *J Mech Phys Solids* 60 (2012), 1644–1659
- [14] Oh JE, Clark SM, Monteiro PJM. Does the Al substitution in C–S–H(I) change its mechanical property? *Cem Concr Res* 41 (2011), 102–106
- [15] Oh JE, Clark SM, Wenk H-R, Monteiro PJM. Experimental determination of bulk modulus of 14 Å tobermorite using high pressure synchrotron X-ray diffraction. *Cem Concr Res* 42 (2012), 397–403
- [16] Shahsavari R, Buehler MJ, Pellenq RJ-M, Ulm F-J. First-Principles Study of Elastic Constants and Interlayer Interactions of Complex Hydrated Oxides: Case Study of Tobermorite and Jennite. *J Am Ceram Soc* 92 (2009), 2323–2330
- [17] Brunauer S. Surfaces of solids. *Pure Appl Chem* 10 (1965), 293–308
- [18] Brunauer S, Kantro DL, Weise CH. The Surface Energy of Tobermorite. *Can J Chem* 37 (1959), 714–724
- [19] Bauchy M, Laubie H, Qomi MJA, et al. Fracture toughness of calcium–silicate–hydrate from molecular dynamics simulations. *J Non-Cryst Solids* 419 (2015), 58–64
- [20] Pellenq RJ-M, Lequeux N, van Damme H. Engineering the bonding scheme in C–S–H: The ionic-covalent framework. *Cem Concr Res* 38 (2008), 159–174

## **MICROSTRUCTURAL CHARACTERISATION OF CEMENT-BASED MATERIALS (CBM) USING THE NUMERICAL SIMULATION OF ULTRASONIC PROPAGATION**

**José Vicente Fuente <sup>(1)</sup>, Sreejith Nanukuttan <sup>(2)</sup>, Jorge Gosálbez <sup>(3)</sup>, Neil Campbell <sup>(4)</sup>**

(1) Geozone Asesores SL, Paterna, Valencia, Spain

(2) Queens University of Belfast, Northern Ireland, United Kingdom.

(3) iTEAM, Universitat Politècnica de València, Valencia, Spain

(4) Amphora NDT, Northern Ireland, United Kingdom, United Kingdom

### **Abstract**

This article reports the developments made during a short term scientific mission (STSM) funded by COST Action TU1404. The aim was to develop a refined methodology for the microstructural characterisation of cement-based materials (CBM) using the numerical simulation of ultrasonic propagation. Images that represent the microstructure of cement paste and mortars were created using the uniform and gaussian functions.

Further the attenuation-dependence of the ultrasonic pulse for the wide range of microstructures has been tested since from a set of Images of Microstructure (IoM) as an output of the image generation process. This IoM were the input for the ultrasonic modelling to obtain some ultrasonic parameters that they characterise each microstructure. This theoretical procedure has been used to simulation a wide range of CBM microstructures. The microstructural parameters considered in the analysis were the porosity (two size ranges), grain number and size and interfacial zone modelling.

Finally, it is planned to integrate the findings from the previous objectives to develop a refined methodology for microstructural characterization of CBM using ultrasonic pulse. This study has been funded by COST Action through a Scientific Short Time Mission (STSM), numbered by 38439, being supported the main author of this paper for the Congress and being part of the dissemination activities of this STSM.

## 1. Introduction

It is well-known the phenomena (scattering, absorption, reflection ...) of the ultrasonic pulse along a porous media and including the cement microstructures [1]. For the conventional tests at the concrete technology, the ultrasonic testing is commonly used. Most authors have worked in an extended model for the strength behaviour using combined NDT as ultrasounds and sclerometer (Schmidt hammer). Ultrasonic velocity [2] and its amplitude [3] in some cases reveal as some good estimation parameters in certain conditions. Many efforts and contribution have been performed in the experimental research side, with large testing campaign and intensive ultrasonic measurements [4].

One of the weak points that we have detected is the limited control of the microstructure that it can be generated in the manufacturing process at real scale (on-site) mainly for concrete mixtures. In other words, there are some restrictions in the process of production the cement matrix and the final microstructure with specific microstructural parameters by using the standard raw materials and mixing methods. It is very difficult to maintain porosity and move in a wide range their sizes, tortuosity and the distribution of aggregates. Definitively, you cannot vary a single parameter remaining constant others. This effect can be reduced and overcome with numerical simulation. Therefore, we have focused in the theoretical side of this research and using simulation tools for developing a wide range of microstructure building a set of images where test the simulation procedure.

The objectives of this research were the following: a) to generate microstructure of cement paste and mortars by simulation tools using Matlab<sup>®</sup> uniform and gaussian functions. The output was some IoM., b) to develop a set of the numerical simulation using different kinds of ultrasonic pulse to analysis the attenuation-dependence of the pulse for the wide range of microstructures, c) to analysis the most relevant parameters in time and spectral domain and d) to integrate the findings from the previous objectives to develop a refined methodology for microstructural characterization of CBM using ultrasonic pulse.

## 2. Research workplan

The work plan was implemented by 4 different tasks which were repeated for cement pastes as well as for mortar. Results of cement pastes matrix were used as an input in the numerical simulation of mortars.

### 2.1 Microstructure generation

It was implemented to different matlab script to generate the cement paste matrix as a 2-phases grey-scale image reproducing the capillary porosity and small air bubbles that it simulates the real situation during the mix performing. The porosity under 1 micron was not generated in this procedure due to the required high cost computation and it was considered as part of the elastic cement matrix. The matlab scripts consist of some brief instructions to set the desirable amount of the circular porous with gaussian diameter size distribution, uniformed distributed in a 2000 x 2001 pixelated image. Each pixel corresponds to a 1 nm therefore the representative IoM were 2 mm-sized. A total of 12 cement paste microstructures were generated by using the above scripts from 16.7% until 39.0%. The IoM were a composition of two images, first one for capillary porosity from 1 to 10 microns and the

second for macropores from 10 to 100 microns. Next figure shows images and pore values of the IoM.

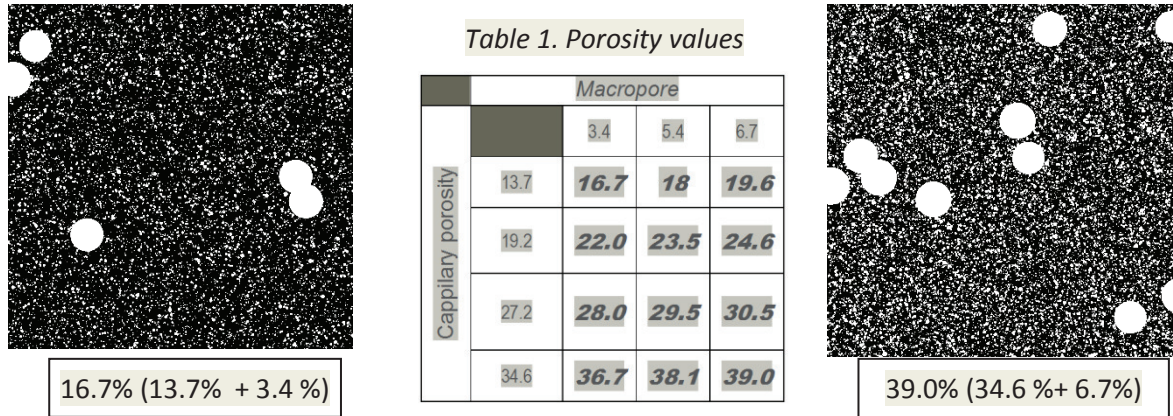


Figure 1. Images of porous cement matrix by using gaussian and uniform functions.

The mortar image generation has obtained by using 2D-concrete builder programme (developed by IZPF Fraunhofer of Dresden). The input parameters allow to generate an output image with specific features that can be varied to range were the following:

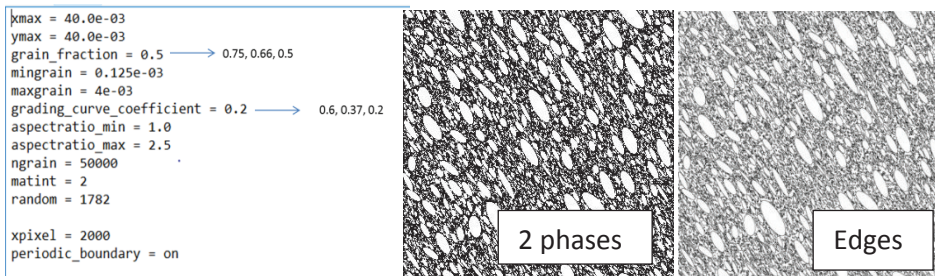


Figure 2. Input parameters, specification ranges and intermediate mortar images.

In order to reproduce the Interfacial Zone (ITZ) it was performed a digital image processing algorithm to select edges of the white scatters that represents the sand grains while cement matrix (including capillary porous and macropores) remains in a black colour. The n-index reflect the grading curve of the particle distribution of scatters (sand particles) and it is considered the different values, the considered values were 0.2 (German DIN grading curve B); 0.37 (optimal compacity factor) and the binder an the 0.7 value (DIN grading curve A), all above following the grading curve that it can be mathematically described by:

$$A_{d_{min}/d} = \frac{100}{1 - \left(\frac{d_{min}}{D}\right)^n} \cdot \left[ \left(\frac{d}{D}\right)^n - \left(\frac{d_{min}}{D}\right)^n \right] \quad (1)$$

It gives the volume fraction (in %) of grains with diameters between  $d_{min}$  (fixed to 0.125 mm) and  $d$  as a function of the maximum grain size  $D$  (fixed to 4 mm), the minimum grain size  $d_{min}$  and the grading curve coefficient  $n$ . After that, adding both images it can be obtained the 9 different microstructures for CP. Higher values of  $n$ -index represent lower sand filler contain. The task is completed using intermediate images capillary and macropore 2D-phases (sand and cement matrix) and edges images for mortars.

## 2.2 Ultrasonic simulations

This task concerns with the ultrasonic propagation through the above images. It was used the Wave2000-Plus software from Cyberlogic© where output image can be loaded as basis media where a range of ultrasonic pulse were propagated. Following Tab.2 shows the different frequencies applied to the IoM.

Table 2: Set of numerical simulation for cement pastes and mortars.

Cement Pastes Simulations							Mortar Simulations						
Frec. (MHz)	0.35	1	3.5	5	10	20	Cement Porosity	Matrix	Frec. (MHz)	0.35	1	3.5	5
16.7	X	X	X	X	X	X			1/1-0.20	X	X	X	X
18.4	X	X	X	X	X	X			1/1-0.37	X	X	X	X
19.6	X	X	X	X	X	X			1/1-0.70	X	X	X	X
22.0	X	X	X	X	X	X			2/1-0.20	X	X	X	X
23.5	X	X	X	X	X	X	24.6		2/1-0.37	X	X	X	X
24.6	X	X	X	X	X	X			2/1-0.70	X	X	X	X
28.0	X	X	X	X	X	X			3/1-0.20	X	X	X	X
29.5	X	X	X	X	X	X			3/1-0.37	X	X	X	X
30.5	X	X	X	X	X	X			3/1-0.70	X	X	X	X
36.9	X	X	X	X	X	X			1/1-0.2	X	X	X	X
38.1	X	X	X	X	X	X			1/1-0.37	X	X	X	X
39.0	X	X	X	X	X	X			1/1-0.70	X	X	X	X
							39.0		2/1-0.20	X	X	X	X
									2/1-0.37	X	X	X	X
									2/1-0.70	X	X	X	X
									3/1-0.20	X	X	X	X
									3/1-0.37	X	X	X	X
									3/1-0.70	X	X	X	X

An amount of 144 numerical simulations for the cement pastes and mortars have been performed. Also, it is considering 140 as valid regarding the acquired waveforms from the P-wave and S-Wave velocity. The instability reasons can occur in the process of solving the differential wave propagation equation in every matrix. Each time the discrete wave propagation equation must be solved for each matrix cell and boundary conditions but in certain cases the solving algorithms cannot converge to concrete solutions. In order to manage a reasonable number of simulations it was selected low different range of the cement pastes porosity matrix to perform since from them the mortar simulations.

## 3. Signal processing and ultrasonic parameters

Reference values for the different phases are shown in the Tab. 3. The parameters were:  $V_p/V_s$  longitudinal/ shear wave velocities,  $\lambda/\mu$  were the lame constants,  $\rho$  the apparent

density,  $\nu$  (Poisson ratio),  $E$  (Young Modulus),  $\alpha$  (attenuation) and  $\eta/\phi$  that were the scattering parameters.

Table 3. Ultrasonic parameters and elastic constants.

	Vp (m/s)	Vs (m/s)	$\lambda$ (MPa)	$\mu$ (MPa)	$\rho$ (kg/m <sup>3</sup> )	$\sigma$ [0-0.5] Poisson ratio	E (Mpa) Young Modulus	$\alpha$ (dB/cm) - Long Wave	$\alpha$ (dB/cm) - Shear wave	$\eta$ (Pa s) at 1 Mhz	$\phi$ (Pa s) at 1 MHz
<b>Sand</b>	5044	3018	15900	20040	2200	0.22	49.98	0.0318	0.106	3.75	0.25
<b>IZT</b>	2835	1823	2270	5482	1650	0.15	12.50	4.72	1.71	10	90
<b>Cement Paste</b>											
<b>39.0</b>	2867	1307	3429	9636	2007	0.36	9.45	3.5	2.18	5.70	89.00
<b>24.6</b>	3455	1835	16657	9636	2244	0.32	19.97	0.39	0.14	1.64	30.55
<b>0.0</b>	4004	2606	6500	18000	2650	0.13	40.03	0.00	0.00	0.00	0.00

The blue values have been changed for the different used frequencies in order to reflect the changes on the attenuation coefficient for both cement pastes matrix (including porosity effect 24.6/39.0 %). Digital signal processing involves the output parameters estimation. After that, it was performed the correlation with the microstructural features controlled by the IoM. Ultrasonic parameters were the P-wave and S-wave velocity, attenuation coefficient for full wave and P and S independent waves, centroid frequency calculated at transmitted and reflected signal. These parameters are selected to characterize the viscoelastic and the scattering effect of ultrasonic energy on each IoM and the subsequent matching with the ranged microstructural features involved in this theoretical study. Last stage involves the relationship of the extracted parameters and the analysis of them in the range of microstructures will provide relevant information to assess the referred microstructures (respect of the IoM) using frequency-variation of ultrasonic testing.

#### 4. Results

Regarding the simulations on the CP-Matrix, it can be extracted the following results:

- The different evolution of the attenuation coefficient from the pulse frequencies allows establishing some kind of estimation of porosity typology and range. Some missed points in the Figure 3 are related to unstable simulation and the scattered relationship could be observed in some porous range caused by the reduced size of IoM and the limited portion interaction between the propagation inside the considered IoM.
- Higher porosity range (35%-39%) show a rapid increasing of attenuation and a saturation effect from 5 MHz of central frequency.
- Lower (16%-20%) and intermediate (22%-31%) porosity ranges show linear increasing with different slopes. For the lower porosity range it is shown slopes lower than 1.5 dB/MHz, intermediate porosity ranges show slopes higher than 2 dB/MHz.

Regarding the simulations on the Mortar matrix, it can be extracted the following results:

Finding edges of the IoM at the 2-phases images, it can be simulated the interfacial zone of 50  $\mu$ m of width by using 1000x1000 pixels (6% of total area will be assigned to ITZ). This new phase represents a better approach to the real microstructural composition. The ITZ has been simulated as a higher porosity CP-matrix, so that low density and elastic values are assigned (Tab. 3). This is a novel contribution of the STSM of the Cost Action TU1404.



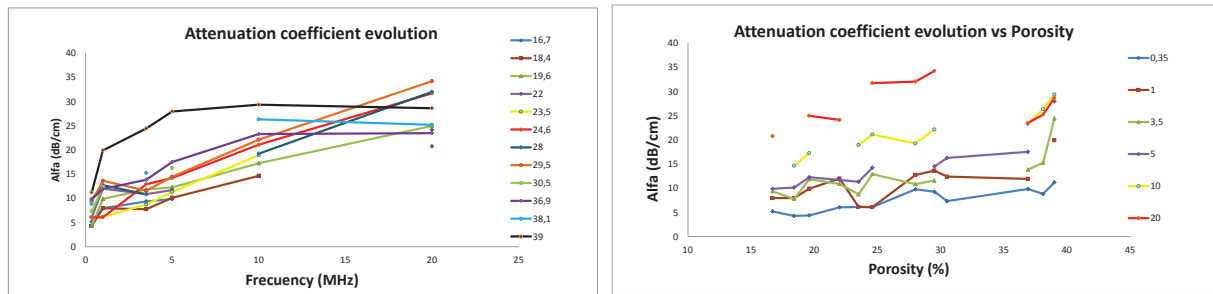


Figure 3. Correlation attenuation, porosity and ultrasonic frequencies (cement pastes).

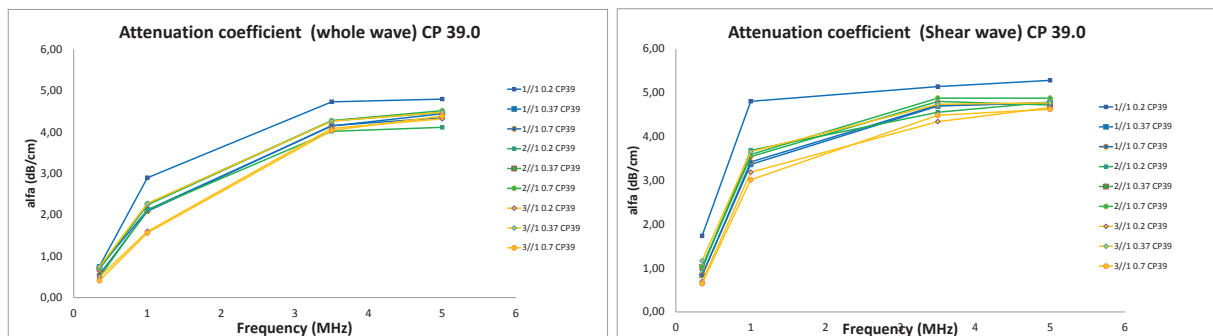


Figure 4. Correlation ultrasonic attenuation, porosity and ultrasonic frequencies (mortars).

## 5. Conclusions

This study explores the feasibility of using the frequency-attenuation dependence of the ultrasonic attenuation for a wide range of microstructures. A limited set of images has been obtained in this research. Some reasonable matching of expected trends for ultrasonic parameters has been obtained for the low elastic constant of the interfacial zone or region in the mortar simulation regarding the output values for IZT in the Tab 3.

## Acknowledgements

The Spanish Ministry of Economy, Industry and Competitiveness supported this research under grants numbers BIA-2014-55311 OndaTest.

## References

- [1] Jens Becker; Laurence J. Jacobs and J. Qu. Characterization of cement-based materials using diffuse ultrasound, *Journal of Engineering Mechanics* 129 (2013), 1478-1484.
- [2] M. Molero, I. Segura, S. Aparicio, J.V. Fuente, Influence of aggregates and air voids on ultrasonic, velocity and attenuation in cementitious materials, *European Journal of Environmental and Civil Engineering*, Vol. 15, Issue 4 (2011), 501-517.
- [3] Ivan Gabrijel, Dunja Mikulić and Bojan Milovanović, Application of Ultrasonic Measurements for Determination of Setting and Hardening in Cement Paste, *Journal of Civil Engineering and Architecture* Volume 5, No. 3 (2011), 278-283.
- [4] G. Ye, K. van Breugel, A.L.A. Fraaij, Experimental study on ultrasonic pulse velocity evaluation of the microstructure of cementitious material at early age, *Delft University of Technology, HERON*, vol. 46, n° 3, (2001).

## **MICROSTRUCTURE-BASED PREDICTION OF THERMAL PROPERTIES OF CEMENT PASTE AT EARLY AGES**

**Hadi Mazaheripour<sup>(1)</sup>, Amin Abrishambaf<sup>(1)</sup>, Rui Faria<sup>(1)</sup>, Miguel Azenha<sup>(2)</sup>, Guang Ye<sup>(3)</sup>**

(1) Faculty of Engineering, University of Porto (FEUP), Porto, Portugal

(2) School of Engineering, University of Minho, Guimarães, Portugal

(3) Microlab, Delft University of Technology, Delft, The Netherlands

### **Abstract**

The time-dependent process of cement hydration affects many physical and mechanical properties of the cement-based materials, particularly at early ages. To estimate the thermomechanical response of cementitious composites, such as concrete, determination of thermal properties, including heat capacity, thermal conductivity and coefficient of thermal expansion, are necessary. An effort is made in the present study to predict the thermal behaviour of cement pastes by simulating the development of the microstructure during the hydration progress. The model deals with the thermal properties of main cement hydration products, Calcium-Silicate-Hydrate (C-S-H) and Calcium Hydroxide CH, and the change in their volume fraction in the microstructure. The paper discusses the results of thermal conductivity and the specific heat capacity from the model, and they are compared to some recent experimental data from the literature.

### **1. Introduction**

The prediction of the thermomechanical behaviour of concrete depends on adequate knowledge of its thermal properties. Heat capacity, thermal conductivity and coefficient of thermal expansion are the properties that play important roles in the structural behaviour of concrete structures (RC) at early ages, especially the massive ones [1], which are particularly prone to significant thermal stress development. At early ages, these thermal properties evolve with the changes in the microstructure due to cement hydration processes. Therefore, an understanding of the thermal properties of cement paste can contribute to the prediction of such properties for concrete. The evolution of thermal properties in cement paste during hydration is mainly due to the difference between the thermal properties of the hydration product (i.e. Calcium-Silicate-Hydrate (C-S-H)) and those of the corresponding reactants. In

this paper, a microstructural modelling strategy is proposed to estimate the thermal properties of cement paste at early age in respect with the change in the volume fraction of the cement paste components in the microstructure. The thermal properties of cement paste are simulated by modelling its microstructure on a cubic representative elementary volume (REV) with a periodic boundary condition. The REV is obtained through application of the HYMOSTRUC3D hydration model. The method and some primary results in terms of the effective thermal conductivity and the specific heat capacity per unit mass are presented in the present herein.

## 2. Cement paste: properties and simulations of nano-micro structural features

This study focuses on CEM II 42.5R, as marketed in Portugal. The mineral composition of this cement, expressed in mass percentage, is: 63.2% C3S, 2.6% C2S, 7.6% C3A, 11.6% C4AF, and 11.3% limestone. The cumulative particle distribution size (PSD) of cement was measured by using Laser Diffraction Spectrometry (LDS). The PSD curves can be fairly defined as a Rosin-Rammler function, i.e.  $f(D)=1-e^{-bD^n}$ , where  $D$  is the diameter of the cement particle, and  $b$  and  $n$  are coefficients. By employing a curve fitting analysis, the values of 0.052 and 1.00 were calculated for, respectively,  $b$  and  $n$ . The thermal properties of individual components of cement clinker and limestone, as well as the hydration product adopted from the literature, and written in Table 1.

Table 1: Some thermal properties of cement paste components used for the simulation.

Compound	Thermal conductivity		Specific heat capacity		Density	
		W/m.K		J/(kg.K)		g/cm <sup>3</sup>
Clinker phases	C3S	3.45 [2]		0.69 [2]		3.13 [2]
	C2S	3.35 [2]		0.68 [2]		3.31 [2]
	Average	3.29		0.73		3.15
Limestone (saturated)		2.95 [3]		0.92 [3]		2.50 [3]
CH		1.32 [2]		1.15 [2]		2.17 [2]
C-S-H globules (Ca/Si=1.75)		0.98 [2]		0.84 [2]		2.6 [2]
Inner C-S-H – saturated *		0.870 [2] (0.883)		0.86-0.97 [2] (0.88)		2.18
Outer C-S-H – saturated *		0.825 [2] (0.830)		0.86-0.97 [2] (0.90)		1.99
Water in gel pores		0.607 [4]		1.13 [5]		1.0
Water in capillary pores		0.607 [4]		4.18		1.0

\* the values in the parenthesis obtained from the nanostructure model in the present study.

### 2.1 Simulation of the nanostructure of C-S-H

The thermal conductivity and the specific heat capacity of the inner and outer C-S-H is estimated by simulating the nanostructure of these products. The nanostructure of outer C-S-H is constructed by assuming the random close packing of mono-sized (5 nm) C-S-H sphere globules (Figure 1a). The random close packing of mono-sized is equivalent to “*the maximum density that a large, random collection of spheres can attain and this density is a universal quantity*” [6]. This packing density of mono-sized sphere is about 0.64, which is very close to the packing density reported for the outer C-S-H globules [2]. In this study, the code from Skoge *et al.* [7] is used to generate the nanostructure of outer C-S-H, which is based on molecular dynamics mechanism. The nanostructure of the inner C-S-H is also simulated by

the close packing of mono-sized (5 nm) C-S-H globules (Figure 1b). For the case of the inner C-S-H, the close packing of mono-sized spheres is arranged in a lattice, and not as a random form. The packing density is approximate 0.74, which is higher than that of the random close packing, and it is very close to the density reported for the inner C-S-H in the literature [2].

## 2.2 Simulation of the microstructure of cement paste

The latest version of HYMOSTRUC3D software [8] is used for constructing the cement paste microstructure during hydration. This simulation is implemented in a cubic REV volume of the cement paste where the cement particles are modelled as spheres randomly distributed. The initial number and diameter of the particles are built in accordance with PSD curve. The main cement hydration products are the Calcium-Silicate-Hydrate (C-S-H) and the Calcium Hydroxide (CH). C-S-H is formed as two layers of inner and outer products, which are the result of the inward and outward radial growing of the cement spheres. The important parameters to be defined in HYMOSTRUC3D for modelling cement hydration are minimum and maximum size of the cement particles, REV size, temperature,  $w/c$ , and two reaction factors that control the speed and progress of hydration. For further details on fundamental aspects of the model parameters, the reader is addressed to the studies in [8, 9]. The hydration analysis was performed for  $w/c = 0.3, 0.4, 0.5$  and  $0.6$ . The curing temperature was set at  $20^{\circ}\text{C}$ . An image of the microstructure can be seen in Fig. 1c.

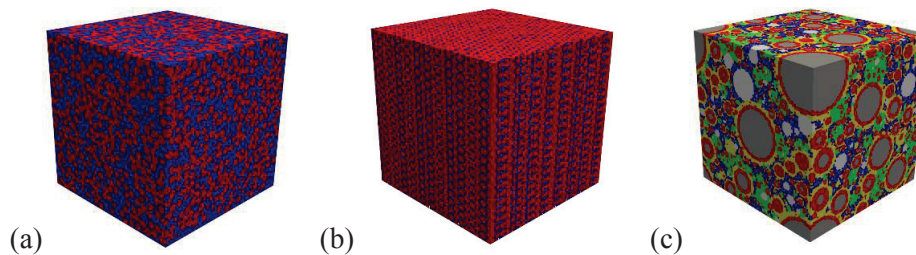


Figure 1: The nanostructure of (a) the outer CSH, and (b) the inner CSH (blue: gel water, red: CSH globules); (c) the microstructure of a hydrated cement paste (grey: unreacted cement, red: inner CSH, yellow: outer CSH, white: limestone, blue: capillary water, green: CH).

## 3. Estimation of the effective thermal properties

The REV microstructure obtained from HYMOSTRUC3D is digitalized by means of voxels of  $1.0 \times 1.0 \times 1.0 \mu\text{m}^3$ . A single material phase is assigned for each voxel based on the greatest volume fraction of the material that the voxel is representing. For example, if the voxel is in the boundary of two material phases (e.g. inner and outer C-S-H), the voxel represents the material with the higher volume fraction. The whole REV is totally discretized to  $10^6$  voxels of six different material phases including: unreacted cement, inner and outer C-S-H, CH, limestone, and pore/water phases. The simulations assume saturated conditions (simplifying assumption at the present stage), hence the pore phases are filled by water, and they are simulated as solid-like behaviour elements with the relevant thermal conductivity. The simplification of solely considering thermal conduction effects for water is backed by previous studies, which have shown that the other contributions such as thermal convection and radiative conductivity in the pore phases (both capillary and gel pores) can be neglected at the microstructural scale [10]. The size of the pores is an effective parameter to address the

thermal properties of water. Two types of water phases are assumed: 1) water in gel pores (being presented only in gel porosity in the nanostructure of C-S-H), and 2) water in capillary pores (being presented in the microstructure of cement paste. The thermal properties of these two types of confined water are given in the last rows in Table 1, based on [2, 4]. The same strategy is followed for discretization of the nanostructure of the inner and outer C-S-H. In this case, the nanostructure includes only two material phases: 1) C-S-H globules; 2) gel pores.

**The thermal conductivity:** the thermal conductivity of C-S-H is estimated by simulating the discretised REV nanostructure of the outer and inner C-S-H under a steady state condition of temperature field. By imposing unit degree of temperature difference at two sides of the REV, the effective thermal conductivity simply is

$$\lambda_{eff} = -\langle q_z^r \rangle \Delta z = -\langle q_z^r \rangle L \quad (1)$$

where  $q_z^r$  is the heat flux of phase  $r$  flowing through the REV in  $z$  direction from the outer surface with higher temperature to another surface with lower temperature. The operator  $\langle \cdot \rangle$  denotes volume averaging.  $L$  is the length of the REV, in correspondence to the distance between the two surfaces with a unit degree of temperature difference. The discretised REV is imported to DIANA FEA software. The voxels are considered as eight-node isoparametric solid elements for general three-dimensional potential flow analysis.

**The specific heat capacity:** according to the thermoelasticity, the elastic properties, the heat capacity, and thermal expansion coefficient are correlated [10]. However, for C-S-H hydration product, the contribution of heat energy to its elastic behaviour can be neglected, meaning that the specific heat at constant volume ( $C_v$ ) can be assumed equal to the specific heat capacity per unit volume ( $C_p$ ) [2, 10]. Therefore, the effective heat capacity per unit volume ( $C_p^{eff}$ ) can be derived by

$$C_p^{eff} = \langle C_p^r \rangle \approx C_v^{eff} \quad (2)$$

where  $C_p^r$  is the specific heat capacity of phase  $r$  in the nanostructure of the C-S-H. The calculated results of the effective thermal conductivity and specific heat capacity of the inner and outer C-S-H are also given in Table 1 (values in the parenthesis). The results are in good agreement with the previous results reported in [2]. Eqs. (1) and (2) can be also used for calculation of the effective thermal properties of the cement paste microstructure. The thermal properties of C-S-H phases (inner and outer) are taken from the analysis on the nanostructure of C-S-H as described earlier. The thermal properties of other phases are written in Table 1.

#### 4. Experimental vs numerical results

An example of the results from the model for  $w/c = 0.3$  at 0.65 degree of reaction in terms of temperature gradient and the heat flux gradient is shown, respectively, in Figure 2a and b. In Figure 3, the obtained results in terms of the effective thermal conductivity are compared to

the results from recent studies in the literature [11-15] for  $w/c$  ratios of 0.3 and 0.4 at different hydration time. It should be noted that the experimental results are collected only for saturated cement paste samples, and that the data is not necessarily correspondent to the same type of cement. Despite the observable scatter in the data obtained from the literature, the simulation lies within acceptable margins in regard to experimental data. In the same figure, a comparison is also made between the simulation results and some few data in the literature [12, 13, 16] in terms of the specific heat capacity per mass unit of cement paste. The specific heat capacity per unit mass is calculated in accordance with the calculated density by the model using the discretized REV microstructure. The measurement of thermal properties of the exact cement type simulated in the present paper is still an ongoing process, and cannot yet be communicated herein.

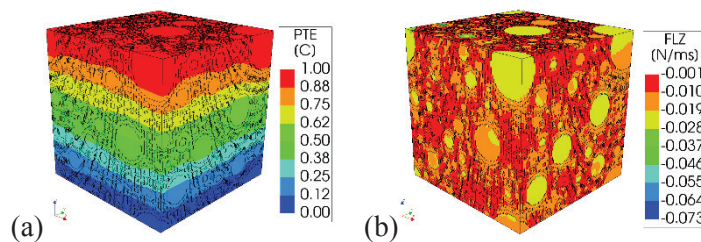


Figure 2: (a) nodal temperature gradient (PTE), (b) heat flux gradient in z direction (FLZ).

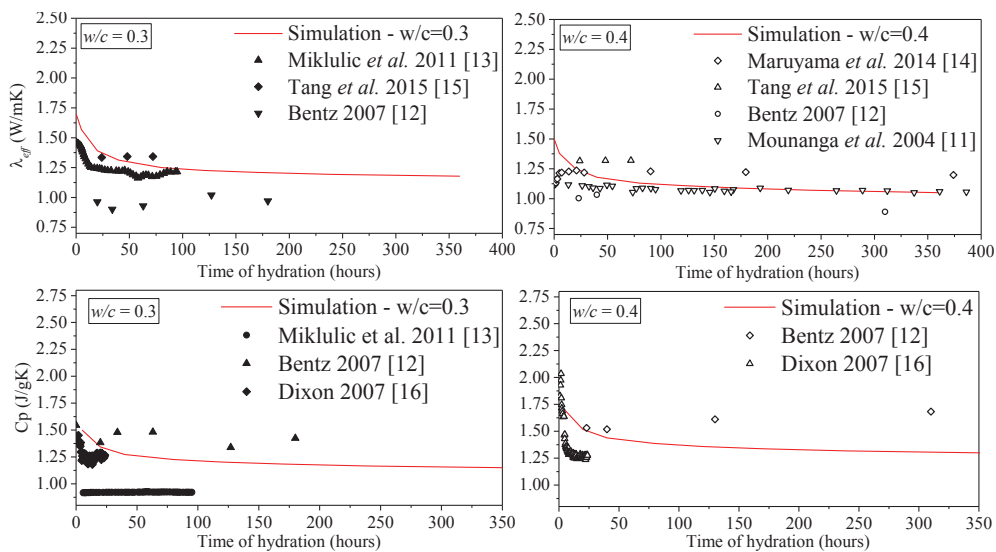


Figure 3: Comparison between the experimental and numerical results.

## 5. Conclusion

The primary focus was on the evolution of the thermal conductivity and the specific heat capacity. The thermal properties obtained based on the nanostructure of C-S-H (both inner and outer) are in good agreement with the results in the literature. Despite the experimental results from the literature for cement paste being highly scattered, the obtained results are in an acceptable margin, providing grounds to the feasibility of the proposed methodology.

### Acknowledgements

This work was financially supported by: Project POCI-01-0145-FEDER-007457 (CONSTRUCT - Institute of R&D in Structures and Construction) and by project POCI-01-0145-FEDER-007633 (ISISE), funded by FEDER funds through COMPETE2020 - Programa Operacional Competitividade e Internacionalização (POCI), and by national funds through FCT - Fundação para a Ciência e a Tecnologia. FCT and FEDER (COMPETE2020) are also acknowledged for the funding of the research project IntegraCrete PTDC/ECM-EST/1056/2014 (POCI-01-0145-FEDER-016841). The financial support of COST Action TU1404 through its several networking instruments is also gratefully acknowledged.

### References

- [1] Azenha, M. et al, Application of air cooled pipes for reduction of early age cracking risk in a massive RC wall. *Engineering Structures* 62-63 (2014), 148-163
- [2] Abdolhosseini Qomi, M.J. et al, Physical Origins of Thermal Properties of Cement Paste. *Physical Review Applied* 3(6) (2015), 064010
- [3] Thomas Jr, J. et al, Thermal conductivity of carbonate rocks. *Engineering Geology* 7(1) (1973), 3-12
- [4] Etzler, F.M. and White, P.J., The heat capacity of water in silica pores. *Journal of Colloid and Interface Science* 120(1) (1987), 94-99
- [5] Bonnaud, P.A. et al, Temperature dependence of nanoconfined water properties: application to cementitious materials. *The Journal of Physical Chemistry C* 120(21) (2016), 11465-11480
- [6] Torquato, S. et al, Is random close packing of spheres well defined? *Physical review letters* 84(10) (2000), 2064
- [7] Skoge, M. et al, Packing hyperspheres in high-dimensional Euclidean spaces. *Physical Review E* 74(4) (2006), 041127
- [8] Ye, G., Experimental study and numerical simulation of the development of the microstructure and permeability of cementitious materials, PhD Thesis, Delft University of Technology (2003)
- [9] Van Breugel, K., Simulation of hydration and formation of structure in hardening cement-based materials, PhD Thesis, Delft University of Technology (1991)
- [10] Honorio, T. et al, Thermal properties of cement-based materials: Multiscale estimations at early-age. *Cement and Concrete Composites* 87 (2018), 205-219
- [11] Mounanga, P. et al, Experimental study and modelling approaches for the thermal conductivity evolution of hydrating cement paste. *Advances in Cement Research* 16(3) (2004), 95-103
- [12] Bentz, D.P., Transient plane source measurements of the thermal properties of hydrating cement pastes. *Materials and Structures* 40(10) (2007), 1073
- [13] Mikulić, D. et al, Analysis of thermal properties of cement paste during setting and hardening, *Nondestructive Testing of Materials and Structures*, Springer (2013), 465-471
- [14] Maruyama, I. and Igarashi, G. Cement reaction and resultant physical properties of cement paste. *Journal of Advanced Concrete Technology* 12(6) (2014), 200-213
- [15] Tang, S.W. et al, A fractal approach to determine thermal conductivity in cement pastes. *Construction and Building Materials* 74 (2015), 73-82
- [16] Dixon, J.C., *The shock absorber handbook*, John Wiley & Sons (2008)

## **MULTI-SCALE MODELING AND NON DESTRUCTIVE TESTING: ASSESSING WATER CONTENT OF CONCRETE**

**Vincent Guihard**<sup>(1,2)</sup>, **Jean-Luc Adia**<sup>(3)</sup>, **Julien Sanahuja**<sup>(3)</sup>

(1) LMDC, Toulouse, France

(2) EDF lab PRISME department, Chatou, France

(3) EDF lab MMC department, Moret sur Loing, France

### **Abstract**

Concrete delayed behavior (shrinkage, creep, etc...) prediction can be significantly improved by monitoring the amount and spatial distribution of water within a concrete structure over time. Electromagnetic properties, such as dielectric permittivity, of heterogeneous and porous materials are closely linked to water content. Measurement of these properties is thus a common non destructive technique to assess the moisture content. A calibration curve is then required to relate the measured permittivity to the saturation degree. This curve can be classically determined experimentally, or from empirical models. However, the first approach is tedious and time consuming, and the second one is not tailored to the specific concrete at stake. This contribution thus proposes an alternative route, relying on an explicit description of liquid and gas phases in the pore domain, and on upscaling techniques. This approach is presented and validated on unsaturated sand for the sake of simplicity. Then, an application to cement pastes is described.

### **1. Introduction: industrial context**

Both concrete delayed mechanical behavior and durability properties depend on its moisture content. Assessing the latter is thus of paramount importance for long term operation of civil engineering structures. While direct measurements are possible, they are by nature destructive, which may not be feasible depending on the structure of interest. Non destructive testing procedures are thus of great importance. These techniques take advantage of the sensitivity to water content of an easily measurable physical property. Due to the relative contrast between liquid (around 80), gas (1) and solids (about 3-10) properties, dielectric permittivity represents an appealing property. It is straightforward to measure, either from



embedded sensors or from the surface using a hand-held probe [1]. A calibration curve is then required to relate permittivity to moisture content.

Such a calibration curve is often obtained experimentally, point per point [2, 3]. This requires to successively equilibrate a concrete sample with various relative humidities. At each step, once equilibrium has been reached, permittivity is measured. A large enough sample must be considered, to be representative of concrete, but the larger the sample, the longer the moisture equilibration process. Obtaining such an experimental calibration curve can thus be tedious and time consuming, and this process has to be repeated for each different concrete. On the other hand, classical empirical relations tend to lack accuracy as they are not tailored to the uniqueness of each concrete. Multi-scale modeling then represents an interesting alternative, as it could allow to break down concrete into individual phases whose elementary permittivity is expected to be a unique property from one concrete to another.

The main originality of this contribution lies in the proposed multidisciplinary approach, combining signal processing, multi-scale microstructure representation, fluids repartition modeling in pore domain, and permittivity homogenization. The process is first validated on a model material: unsaturated sand. Then, a multiscale morphological model of mature cement paste is designed, going down to elementary solid phases, liquid, and gas. Finally, a first validation is performed with respect to several cement pastes.

## **2. Dielectric constant measurement with an open-ended coaxial probe**

Dielectric constant of materials can be derived from the analysis of transmission and reflection of electromagnetic waves through a sample inserted into a coaxial structure [4] or placed at the end of this structure in the case of reflection-only based devices. In this particular case, reflection phenomena are induced by the impedance discontinuity caused by the sample located at the end of the coaxial structure. Open-ended coaxial probes are one of these methods. They present simple implementation and a broad frequency range driven by the network analyzer used to synthesize the RF signal. The non-destructive and non-invasive characteristics of such tools have enabled investigations of various kinds of media, including soils [2] and stems of mature trees [3]. Measurements have also been performed to validate models for coupled heat and moisture transport in building materials [5].

In the present contribution, a specially designed large probe (figure 1 left) was built in order to investigate heterogeneous materials. Appropriate signal processing yields the complex permittivity of the material as a function of frequency.

## **3. Relating permittivity to saturation degree: principle and validation on sand**

A model material is first considered: unsaturated sand. Indeed, the solid phase (sand grains) can be considered as homogeneous. From density measurements on the dry sand in a natural state and on the bulk rock (characteristic of the solid phase), porosity is estimated as  $\phi = 37 \pm 0.2 \%$ . For each target saturation degree  $S_r$ , the volume of water to be added is deduced. After mixing this water with dry sand, the sample is compressed to reach the reference volume of dry sand. Porosity is thus maintained equal for each saturation degree. Permittivity measurement is then performed over the frequency range 200 - 800 MHz

(figure 1 right). The average over this range will be considered for subsequent comparisons. The modeling process is first briefly described in the next three subsections.

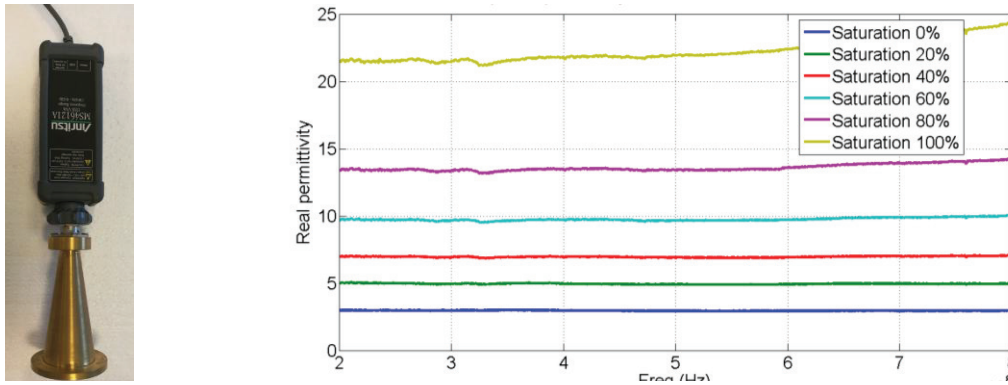


Figure 1: Left: coaxial probe and vector network analyser (VNA) used in this contribution. Right: real part of permittivity of sand for saturation degrees  $S_r = 0, 20, 40, 60, 80, 100$  %.

### 3.1 Microstructure generation

First, a representative elementary volume (REV) of dry sand has to be generated. In the pore domain (complementary to the solid grains), liquid and gas phases are not yet distinguished. To later optimize convergence with respect to the REV size, microstructure is built as periodic. Sand grains are obviously non overlapping, and represented as spheres. The size distribution is assumed to be monodisperse. The diameter of particles is 2 mm while the REV size is 10 mm. The solid volume fraction, 63 %, being around the random close packing of monodisperse spheres, the Random Sequential Adsorption algorithm cannot be used as it is far from being able to reach such a high volume fraction. The Lubachevsky and Stillinger algorithm [6] is more suitable, as it considers particles growing up to the required volume fraction.

The microstructure generation process is more detailed in [7]. The geometrical representation of the microstructure is obtained as a list of spheres. For subsequent operations, a sampled version is generated, as a 3D image made up of voxels (figure 2 left).

### 3.2 Liquid and gas repartition

Second, a realistic repartition of liquid and gas at equilibrium in the pore domain of the sand REV has to be generated. It can be derived from multiphase fluid flow modeling. The macroscopic approach, using computational fluid dynamics, can be tedious due to the specific treatments required to track the interfaces between liquid and gas phases. The microscopic approach, based on molecular dynamics, is highly time and memory consuming: current computers cannot cope with large volumes such as realistic pore domains. Therefore, a mesoscopic description based on kinetic theory is considered as a compromise. The Lattice Boltzmann Method (LBM) [8] is indeed an appealing numerical tool, particularly for multiphase flows. Liquid and gas interfaces emerge from the physical nature of the interactions between fluid molecules at the microscopic level, which are described by a mean-field interaction potential.

For the interested reader, more details about theory, implementation and validation of the LBM method used in this contribution can be found in [9]. Sample repartitions of liquid and gas in pore domain of sand are represented on figure 2 right.

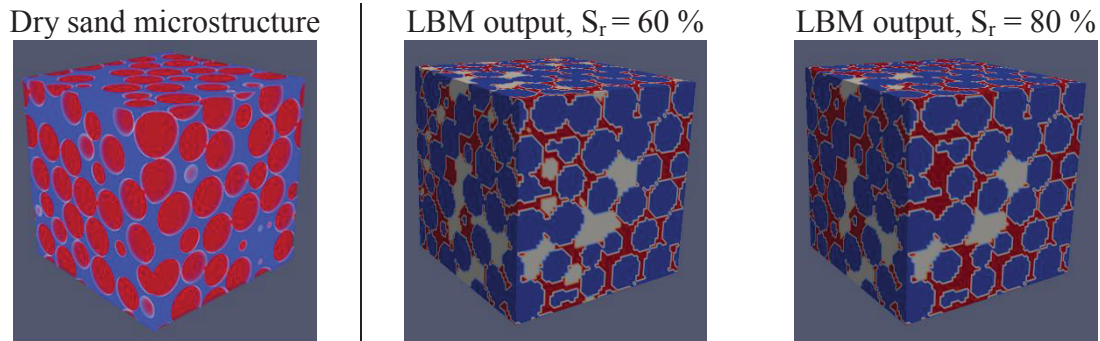


Figure 2: Generated periodic microstructure of dry sand (red: sand grains; blue: pore domain), and liquid/gas repartitions from LBM computations (blue: sand grains; red: liquid; gray: gas).

### 3.3 Numerical homogenization of permittivity

Third, the effective permittivity of a 3D image of unsaturated porous material is estimated using numerical homogenization. Taking advantage of the equivalence between an electrostatics boundary value problem and a heat conduction one, a numerical code initially developed for heat transfer [10] is reused. The latter is based on finite differences and implements a multigrid solver, relying on the PETSc library [11]. Periodic boundary conditions are considered to optimize convergence with respect to the REV size [12]. The permittivities of elementary phases are respectively 4.5, 1 and 80 for sand grains, gas and liquid. Once the boundary value problem is solved, the effective permittivity is computed from volume averages of local fields.

### 3.4 Comparison to experimental measurements and alternative analytical estimates

For each saturation degree, calculation processes are repeated from five different random geometries, in order to investigate results deviation. A very good agreement between experimental and numerical permittivities is observed (figure 3).

As computation time may prevent the broad use of numerical homogenization processes, analytical estimates can be appealing. Both the empirical Topp equation [2] and the symmetric Bruggeman upscaling model [13] (also known as the self-consistent scheme in the elasticity framework) provide a reasonable estimate of the effective permittivity, see figure 3.

## 4. Application to cement paste

This first application to cementitious materials uses mean-field homogenization, as microstructure is highly complex to describe comprehensively. A morphological model of mature cement paste is proposed (figure 4), going down to elementary solid phases, liquid and gas. It is inspired by the morphologies designed to upscale mechanical behavior, such as [14, 15]. The main differences rely in the pore space representation and liquid/gas repartition in the latter. A specific procedure is conducted to identify the permittivity of the elementary solid phases.

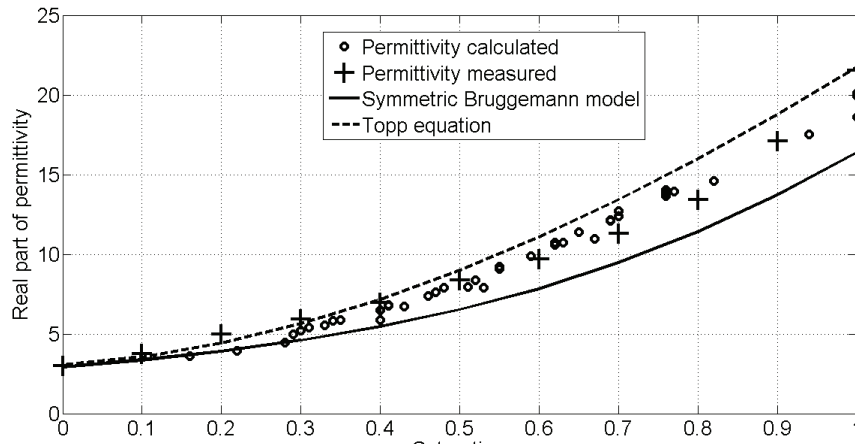


Figure 3: Comparison between measured and numerically or analytically estimated effective permittivity of unsaturated sand.

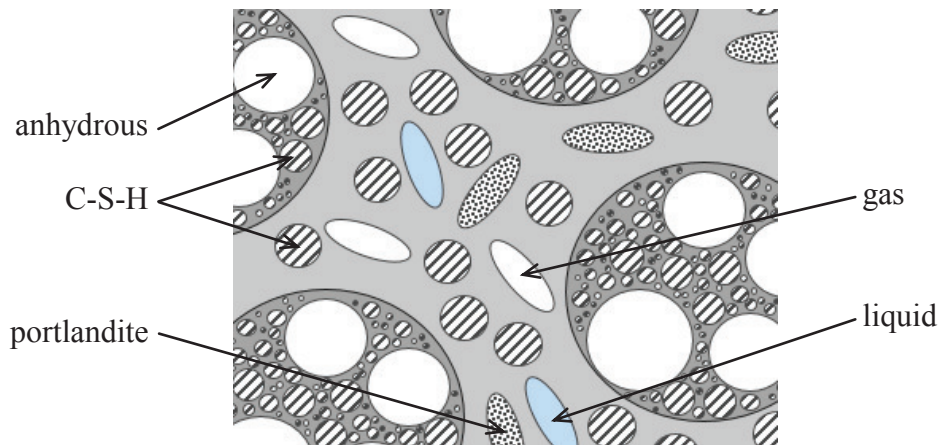


Figure 4: Simplified morphological model of cement paste.

The global approach is then validated on two different cement pastes. The saturation degree dependence of permittivity is reasonably predicted (figure 5).

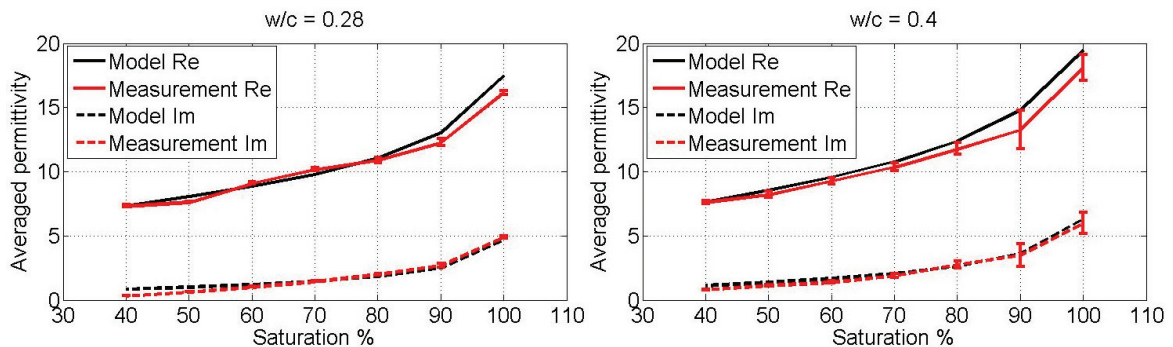


Figure 5: Average (over 750 - 1000 MHz range) real and imaginary permittivities, measured and modeled for cement pastes at  $w/c = 0.28$  and  $0.4$ .

Prospects include refinements of the morphological model and extensions to concrete. Direct application to drying structures would yield an average moisture content, over a depth roughly equivalent to the probe diameter. Measuring the moisture profile requires further investigations. Moreover, classical homogenization techniques consider a homogeneous moisture content across the REV, so that structures with high moisture gradients need more developments.

## References

- [1] Guihard, V., Taillade, F., Balayssac, J.-P., Steck, B., Sanahuja, J., and Deby, F. Modelling the behaviour of an open-ended coaxial probe to assess the permittivity of heterogeneous dielectrics solids. In Progress In Electromagnetics Research Symposium, St. Petersburg, Russia, may 2017.
- [2] Topp, G., Davis, J., and Annan, A. Electromagnetic determination of soil water content: Measurements in coaxial transmission lines. *Water Resources Res.*, 16(3):574-582, 1980.
- [3] Irvine, J. and Grace, J. Non-destructive measurement of stem water content by time domain reflectometry using short probes. *Journal of Experimental Botany*, 48(308):813-818, 1997.
- [4] Chen, L. F., Ong, C. K., Neo, C. P., Varadan, V. V., and Varadan, V. K. *Microwave Electronics Measurement and Materials Characterization*. Chapter 3, Reflection Methods. Johan Wiley and Sons, Inc., 2004.
- [5] Gawin, D. and Klemm, P. Coupled heat and moisture transfer with phase changes in porous building materials. *Archives of Civil Engineering*, 40:89-103, 1994.
- [6] Lubachevsky, B. and Stillinger, F. Geometric properties of random disk packings. *J. Stat. Phys.*, 60:561-583, 1990.
- [7] Lavergne, F., Sab, K., Sanahuja, J., Bornert, M., and Toulemonde, C. Investigation of the effect of aggregates' morphology on concrete creep properties by numerical simulations. *Cement and Concrete Research*, 71(0):14-28, 2015.
- [8] Shan, X. and Chen, H. Lattice Boltzmann model for simulating flows with multiple phases and components. *Physical Review E*, 47(3):1815-1819, 1993.
- [9] Adia, J.-L. Multi-scale modelling of the shrinkage and creep phenomena of cementitious materials: a combined Finite Elements-Lattice Boltzmann-numerical approach. PhD, 2017.
- [10] Sanahuja, J. and Toulemonde, C. Numerical homogenization of concrete microstructures without explicit meshes. *Cement and Concrete Research*, 41(12):1320-1329, 2011.
- [11] Balay, S., Abhyankar, S., Adams, M. F., Brown, J., Brune, P., Buschelman, K., Dalcin, L., Eijkhout, V., Gropp, W. D., Kaushik, D., Knepley, M. G., May, D. A., McInnes, L. C., Mills, R. T., Munson, T., Rupp, K., Sanan, P., Smith, B. F., Zampini, S., Zhang, H., and Zhang, H. PETSc Web page. <http://www.mcs.anl.gov/petsc>, 2018.
- [12] Kanit, T., Forest, S., Galliet, I., Mounoury, V., and Jeulin, D. Determination of the size of the representative volume element for random composites: statistical and numerical approach. *International Journal of Solids and Structures*, 40:3647-3679, 2003.
- [13] Bruggeman, D. A. G. Berechnung verschiedener physikalischer konstanten von heterogenen substanzen. i. dielektrizitätskonstanten und leitfähigkeitigkeiten der mischkörper aus isotropen substanzen. *Annalen der Physik*, 416(7):636-664, 1935.
- [14] Bernard, O., Ulm, F.-J., and Lemarchand, E. A multiscale micromechanics-hydration model for the early-age elastic properties of cement-based materials. *Cement and Concrete Research*, 33(9):1293-1309, 2003.
- [15] Sanahuja, J., Dormieux, L., and Chanvillard, G. Modelling elasticity of a hydrating cement paste. *Cement and Concrete Research*, 37(10):1427-1439, 2007.

## **NUMERICAL ANALYSIS OF THE DRYING KINETICS IN 3D CONCRETE SPECIMENS OF DIFFERENT SIZE**

**Benoit Bary<sup>(1)</sup>, Stéphane Poyet<sup>(1)</sup>**

(1) Den-Service d'Etude du Comportement des Radionucléides (SECR), CEA, Université Paris-Saclay, F-91191, Gif-sur-Yvette, France

### **Abstract**

We propose in this study to investigate numerically the variability of water permeability in unsaturated conditions through the simulation of drying on concrete specimens of different size. Numerical simulations on 3D reconstructed cylindrical concrete samples are performed and analyzed so as to investigate the effects of their thickness on the overall drying kinetics. Water transfer is modelled via a classical approach involving a single mass balance equation associated with the matrix phase corresponding to mortar. Besides the 'structural' variability related to the random process of aggregate placement, another source of variability is introduced through a distribution on the porosity. The results obtained in terms of drying kinetics and saturation degree profiles are analyzed and discussed, with a special regard to the effects of the thickness of the concrete specimens. Comparisons with simulations on the same specimens with homogeneous parameters for the drying model are made macroscopically.

### **1. Introduction**

An accurate description of water exchange between concrete material and its surrounding environment is of major importance for durability assessment of concrete structures. In this regard, permeability is a key parameter as it characterizes the ability of a fluid to transport through concrete porosity due to pressure gradients. As such, permeability is generally viewed as a relevant durability index for service-life prediction. Its experimental characterization is usually performed using specimens prepared in laboratory conditions. However this procedure may not appear totally satisfactory since the obtained properties often differ from the ones of concrete prepared onsite. Indeed, while 'labcrete' specimens are commonly prepared carefully with batches of limited volume in controlled environmental conditions, 'fieldcrete' is prepared in much larger batches in concrete plants with variable conditions,

before being cast onsite. In this context it has been shown recently that fieldcretes exhibit lower general performance and more variability regarding permeability properties than labcretes [1].

In this study we investigate numerically the water permeability and its variability in unsaturated conditions via the simplified simulation of drying on concrete specimens of different sizes. Computations on 3D reconstructed cylindrical concrete samples are then performed and analyzed to examine the effects of their thickness on the overall drying kinetics. The specimens are generated by randomly dispersing polyhedral aggregates of various shapes and sizes in a cube, from which cylinders of specified diameter and various thicknesses are cored. Water transport is modelled via a standard approach involving a single mass balance equation for the matrix phase corresponding to mortar. Besides the 'structural' variability related to the random process of aggregate placement, another source of variability consisting in a spatial distribution on the porosity is introduced in the simulations. The results obtained in terms of drying kinetics, overall saturation degree and mass loss profiles are analyzed and discussed, with a special regard to the effects of the thickness of the concrete specimens. Comparisons between simulations on the same specimens with homogeneous parameters for the drying model are also made macroscopically.

## 2. Model

Water transport in unsaturated concrete is described here via a simplified approach accounting only for liquid water permeation. The contribution of overall gas permeation and vapor diffusion is assumed as negligible with respect to the liquid transport [2]. The problem is then formulated with a single equation in the form:

$$\phi \left( \frac{\partial S}{\partial P} \right) \frac{\partial P}{\partial t} = \text{div} \left[ \frac{K k_r}{\eta} \text{grad}(P) \right] \quad (1)$$

with  $\phi$  the concrete porosity,  $S$  the saturation degree,  $P$  the water pressure,  $\eta$  the water viscosity,  $K$  the intrinsic permeability and  $k_r$  the relative permeability to water. The intrinsic permeability of the concrete was evaluated previously using classical inverse analysis [2]. The classical relation proposed by van Genuchten [3] is further used to describe the water retention curve:

$$S = \left[ 1 + \left( \frac{P}{P_0} \right)^{\frac{1}{1-m}} \right]^{-m} \quad (2)$$

where  $m$  and  $P_0$  are two positive parameters that have been identified in [1] to the following values corresponding to a fieldcrete:  $m = 0.532$  and  $P_0 = 59.05 \text{ MPa}$ . Finally, Mualem's model [4] is used to express the relative permeability to water  $k_r$ :

$$k_r = \left[ 1 + \left( \frac{P}{P_0} \right)^{\frac{1}{1-m}} \right]^{-m\alpha} \left\{ 1 - \left( \frac{P}{P_0} \right)^{-\frac{m}{1-m}} \left[ 1 + \left( \frac{P}{P_0} \right)^{\frac{1}{1-m}} \right]^{-m} \right\}^2 \quad (3)$$

where  $\alpha$  is the pore-interaction factor that characterizes the connectivity and tortuosity of the pore network, and is set to the value -1.2 (see [1] for details). Eq. (1) is solved by means of the finite element code Cast3m (<http://www-cast3m.cea.fr/>).

### 3. Numerical procedure

#### 3.1 Specimens generation

The procedure for generating the numerical specimens is described in e.g. [1], [5]. It takes advantage of the functionalities of the CAD code Salome ([www.salome-platform.org](http://www.salome-platform.org)), and consists in constructed samples by randomly distributing inclusions of given shape and size in a parallelepipedic box. In this study, mesoscopic numerical samples of concrete material are obtained from cubic volumes with dimensions  $15 \times 15 \times 15$  cm, from which cylindrical samples of diameter 60 mm and different heights ranging from 8 to 110 mm are extracted. The aggregate dimensions are set to conform to an actual grading curve. They consist of convex polyhedrons obtained by a Voronoi space decomposition, further modified to comply with an aspect ratio selected between 1 and 4, so as to resemble real shapes as closely as possible. Note that the actual aggregate volume fraction calculated in the specimens ranges between 0.354 and 0.383, which is higher than the value 0.35 imposed in the initial cubic volumes, see [1]. Figure 1 presents the matrix of 3 generated specimens with thickness of 8, 20 and 55 mm. In this preliminary study, the number of generated specimens is 4, 4, 9 and 15 for the thicknesses of 110, 55, 20 and 8 mm, respectively, which is deemed to be sufficient to get basic statistical information.



Figure 1: examples of specimens with thickness of 8 (left), 20 (middle) and 55 (right) mm.

#### 3.2 Porosity variability

As mentioned above, in this paper we are concerned with the effects of the porosity variability on the drying kinetics and permeability properties. To this aim, simulations are performed with porosity field randomly generated conforming to a Gaussian distribution with mean 0.2 and standard deviation 0.04. Such probability distribution is considered to be close to that of the mortar tested in [6].

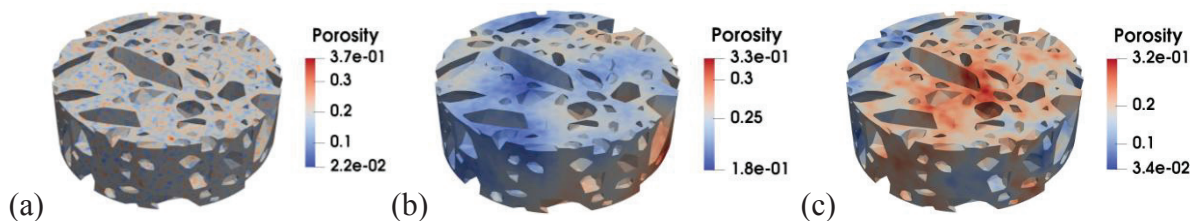


Figure 2: randomly generated porosity field in a 20 mm-thick specimen: uncorrelated (a), correlation length of 10 mm (b) and of 50 mm (c).

To further analyze the impact of the porosity variability, spatially uncorrelated field and spatially correlated ones with 2 different correlation lengths are generated and the results are compared with constant porosity. Figure 2 illustrates the obtained random fields in the case of a 20 mm-thick specimen for uncorrelated distribution (a), correlated one with correlation



length of 10 mm (b) and of 50 mm (c). Due to the lack of experimental data, the chosen values for these lengths are somewhat arbitrary; this point would deserve further investigations. We observe important differences between the porosity fields obtained with uncorrelated and correlated distributions; the extrema values may be as high as 0.37 and as low as 0.022 in the case of the uncorrelated distribution. Note that, besides being explicitly involved in Eq. (1), the porosity also enters in the expression of the intrinsic permeability through the following Kozeny-Carman relation [7]:

$$K = K_0 \left( \frac{\phi}{\phi_0} \right)^3 \left( \frac{1 - \phi_0}{1 - \phi} \right)^2 \quad (4)$$

where  $K_0$  is the mean permeability value set to  $2.1 \times 10^{-22} \text{ m}^2$ , and  $\phi_0$  is the corresponding mean porosity of 0.2.

#### 4. Results: drying simulations

The drying simulations consist in imposing a relative humidity of 55% at the lateral surfaces of the initially saturated specimens. Figure 3 presents the numerical results in terms of mass loss and average saturation degree evolutions with time, for the 110 (left) and 55 (right) mm-thick specimens, for the different considered porosity distributions.

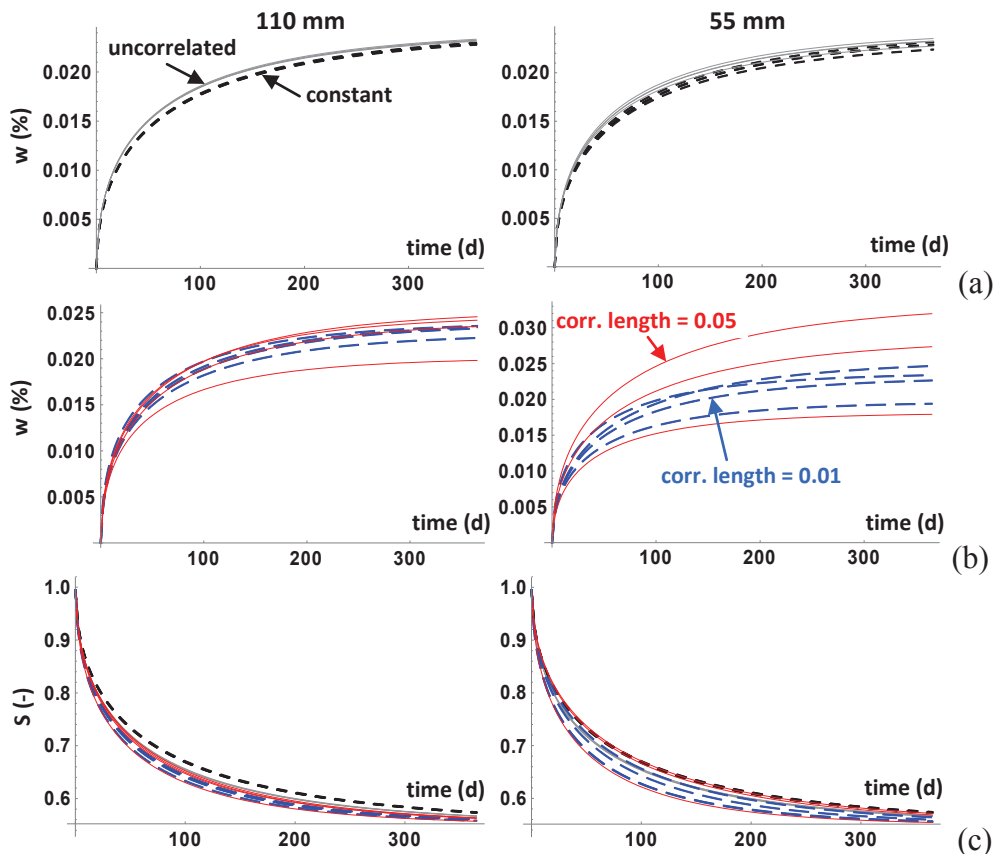


Figure 3: mass loss for the 110 mm (left) and 55 mm-thick specimens (right), for constant and uncorrelated (a), and correlated distributions (b); corresponding saturation evolution (c).

Figure 4 shows the same curves for the 20 (left) and 8 (right) mm-thick specimens. The water mass loss is determined assuming a solid phase density estimated to 2.37 and accounting for the local variable porosity. Note that the isotherm sorption curve is kept constant in the simulations, which is likely an oversimplifying assumption in the case of varying porosity.

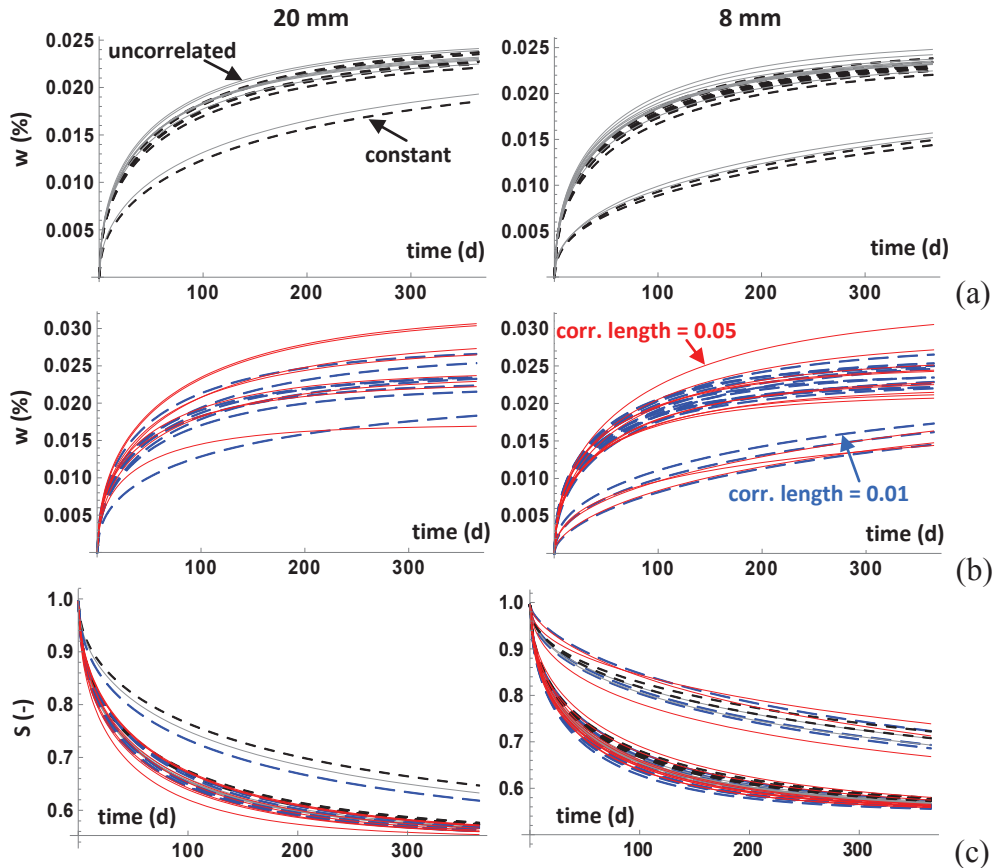


Figure 4: mass loss for the 20 mm (left) and 8 mm-thick specimens (right), for constant and uncorrelated (a), and correlated distributions (b); corresponding saturation evolution (c).

The legend of curves is as follows: black lines and black dashed curves correspond to uncorrelated and constant porosity, blue long-dashed curves and red lines to a correlation length of 10 and 50 mm, respectively. From these curves, we observe that, as expected, reducing the specimen thickness leads to increase the results dispersion. This is particularly visible when comparing the results with constant porosity for 110 and 8 (or 20) mm-thick specimens. Thus, for a sufficiently important specimen size, the variability related to random aggregate size and placement does not appear to explain the dispersion observed experimentally. Another aspect is the moderate effect of the uncorrelated Gaussian distribution on the results, which are very close to the ones obtained with constant porosity. By contrast, introducing correlation lengths in the distribution results in greater dispersion, all the more than the length is high. As mentioned, this aspect would deserve to be more thoroughly examined, as it appears to be very influential. We also note that the results in terms of macroscopic saturation degree evolutions are much less dispersed than their counterparts expressed in mass loss. This is because the saturation degree is defined through a pore volume ratio and does not explicitly integrate the (local) porosity value, contrary to the

mass loss. Finally, we observe on the 20 mm and 8 mm-thick curves that some specimens exhibit a different response, corresponding to a slower drying kinetics. It may be explained by a significantly lower surface exposed to drying.

## 5. Conclusion

This paper presents first simulation results regarding drying of cylindrical concrete samples of different thicknesses. The 3D specimens are generated numerically by randomly distributing polyhedral aggregates of various shape and size. Water transport is modelled classically via a single mass balance equation involving only liquid water permeation. A variability is introduced in the porosity through uncorrelated and correlated Gaussian distributions. The results are analyzed in terms of time evolutions of mass loss and saturation degree. The main conclusions are that as expected the greater the thickness of the specimens, the lower the dispersion in the mass loss, independently of the porosity variability. The results with constant porosity report a negligible dispersion for the 110 mm-thick specimens, while they exhibit a slight scatter for the 55 mm-thick ones, which signifies that the size of a representative volume may range between these 2 values. Further, the curves obtained with the uncorrelated distribution are close to the ones with constant porosity, indicating that such distributions have very limited effects. By contrast, distributions with correlation lengths may affect significantly the results, depending on the length value. It is then important that this parameter be accurately identified and characterized experimentally.

Among the aspects that would deserve further investigations in the future, besides the characterization of the porosity variability, its links with the isotherm desorption curve dispersion would also be of importance as this curve is known to have a great impact on drying. Confrontation of drying simulation results with experimental data obtained on specimens of same microgeometry (characterized for instance by tomography and numerically reconstructed for the simulations) would be helpful to validate the whole procedure. Finally, possible microcracking, which affects considerably the drying kinetics, should also be accurately described and characterized.

## References

- [1] S. Poyet and B. Bary, "Analysis of water transport in unsaturated conditions: comparison between labcrete and fieldcrete," *Submitted in Constr. Build. Mater.*, 2018.
- [2] M. Mainguy, O. Coussy, and V. Baroghel-Bouny, "Role of air pressure in drying of weakly permeable materials," *J. Eng. Mech. ASCE*, vol. 127, no. 6, pp. 592–592, 2001.
- [3] M. T. van Genuchten, "A Closed-form Equation for Predicting the Hydraulic Conductivity of Unsaturated Soils," *Soil Sci. Soc. Am. J.*, vol. 44, no. 5, pp. 892–898, 1980.
- [4] Y. Mualem, "A new model for predicting the hydraulic conductivity of unsaturated porous media," *Water Resour. Res.*, vol. 12, no. 3, pp. 513–522, 1976.
- [5] T. de Larrard, B. Bary, E. Adam, and F. Kloss, "Influence of aggregate shapes on drying and carbonation phenomena in 3D concrete numerical samples," *Comput. Mater. Sci.*, vol. 72, 2013.
- [6] J. Jeong, P. Sardini, H. Ramézani, M. Siitari-Kauppi, and H. Steeb, "Modeling of the induced chemo-mechanical stress through porous cement mortar subjected to CO<sub>2</sub>: Enhanced micro-dilatation theory and 14C-PMMA method," *Comput. Mater. Sci.*, vol. 69, pp. 466–480, Mar. 2013.
- [7] W. D. Carrier III, "Goodbye, hazen; hello, kozeny-carman," *J. Geotech. Geoenvironmental Eng.*, vol. 129, no. 11, pp. 1054–1056, 2003.

## NUMERICALLY ACCELERATED CHEMICAL EVOLUTION IN CEMENTITIOUS SYSTEMS

Janez Perko<sup>(1)</sup>, Diederik Jacques<sup>(1)</sup>

(1) Belgian Nuclear Research Centre SCK·CEN

### Abstract

This paper describes the approach for numerical acceleration of reactive transport pore-scale models where transport dominates dissolution/precipitation processes. Chemical changes in cementitious systems are typically transport dominated because of slow chemical reaction rates. The conditions under which the acceleration is possible and the level of acceleration are analysed. For this purpose we derive a new dimensionless number. On this basis the applicability of the approach is demonstrated on a simple system as well as on complex systems and applied to dissolution processes. The result demonstrate that, in the case of calcium leaching from hardened cement paste the dissolution can be accelerated for 50 times.

### 1. Introduction

Cement-based materials are known as materials with large resistance to some chemical detrimental processes such as calcium leaching because it combines slow transport processes with high buffer properties in a high solid-to-liquid ratio. This high resistance of cementitious materials poses challenges to experimental studies aiming to understand cement behaviour or to optimize cement compositions to increase durability; chemical alterations take a lot of time under natural conditions. To alleviate the problems of slow chemical processes, experimental approaches use so-called accelerated conditions where the chemical processes are accelerated, for example by increasing the solubility of Ca. The shortcoming of accelerated conditions is that the resulting chemical evolution may differ chemically from the evolution obtained under natural conditions. Another approach to alleviate long chemical processes is by numerical modelling. In numerical modelling, the processes are represented by a conceptual and numerical model that are solve by computers which is believed to be faster. When modelling complex problems also numerical models face practical limitations linked to computational resources. In recent years, pore-scale approaches became an attractive method to simulate

durability [1]. However, in order to capture the critical features at that scale, such as the presence of capillary pores or heterogeneity in mineral phases, geometrically information with high resolution is needed in a sufficiently large volume to assure a representative elementary volume (REV). This leads to a very high number of unknowns with substantial memory and computational costs, especially in three-dimensional simulations. Moreover, in diffusion-controlled systems any numerical method should obey Neumann criteria to correctly assess the chemical degradation. This inevitably leads to a huge amount of time steps and cannot be treated with parallelization of computational processes. In this work, we present a new approach, which allows for considerable accelerations of the simulation of the chemical evolutions of cementitious systems. The idea is that the number of iterations can be reduced if the chemical buffering is sufficient to bring transport to a steady state. If this condition is satisfied, then it is possible to reduce physical (and thus also computational) time by adjusting the chemical system appropriately. The process is in fact similar to chemically accelerated experiments, but without the risk of influencing the chemical evolutionary path.

In this paper we first define the theoretical background and reasoning for the acceleration. The derivation is based on the diffusive transport process, because this process is usually the main transport process in cementitious materials. The theoretical assumptions are tested on a simple regular material and on a real cementitious system. The analysis shows that the pore structure resulting from the dissolution process remains invariant with respect to certain ratio between solid and equilibrium concentration.

## 2. Theoretical background

Consider a chemical system which involves a dissolution of solid. For the purpose of presentation we define the concentration in solid  $C_{solid}$  and the equilibrium concentration  $C_{eq}$  in solute. We further assume that diffusive transport defines the rate of dissolution. When solid mass at the solid surface decreases below the equilibrium concentration, this solid becomes liquid and solid geometry changes. Every time the geometry changes, there is some time required to establish new equilibrium. We can distinguish between two different situations depicted in Fig. 1. The situation (a) represents the system when the geometry changes before the transport equilibrium is established (i.e. when the diffusion process is not in steady-state). This means that fluxes at time  $t_1$  and time  $t_2$  ( $t_2 > t_1$ ) are not the same. In other words, this system is not buffered enough to be accelerated. On the other hand, Figure 1b represents the situation where there is a steady state at  $t_3$  achieved without the change of geometry. Any time larger than  $t_3$  the specie flux remains constant until  $t_4$  when the geometry changes. The time between  $t_4$  and  $t_3$  is the time which could be accelerated.

In order to determine whether the buffering is sufficient or not, we define the reference distance between the boundaries between two solids (or between a solid and the boundary as shown in Fig. 1)  $L$ . The time during which the aqueous solution is close to a steady-state can be determined from the amount of mass which is distributed within the length  $L$ , the so-called length patch or root-mean-square displacement [ $L$ ]. For pure diffusion processes, the amount of mass that is distributed within the interval  $L$  at time  $t$  can be expressed in terms of standard deviation of mass in the domain  $\sigma = \sqrt{2 D t}$ . The length of mass patch at time  $t$  is then defined by the confidence interval  $\psi \times \sigma$  or

$$L = \psi \sqrt{2Dt} \quad (1)$$

where  $\psi$  is an arbitrary constant defining how many  $\sigma$  of mass is in the patch of length  $L$  and  $D$  is diffusion coefficients.

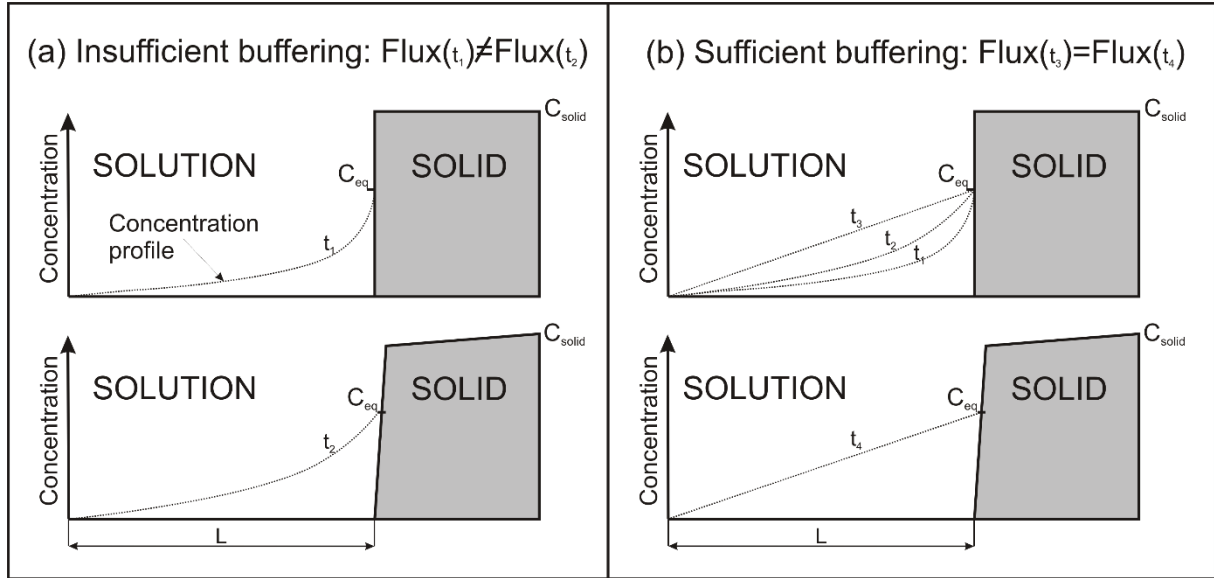


Figure 1: Graphical representation of sufficiently buffered system.

At time  $t$  the concentration is distributed as a function from the distance from the solid as

$$C(x,t) = C_{eq} \left[ 1 + \operatorname{erf} \frac{x}{\sqrt{4Dt}} \right] \quad (2)$$

From these two relations we can define the minimal time until the steady-state is achieved. Further derivation [2] leads to a final dimensionless number, which we call *Buffering number* which is denoted as *Bu* number. *Bu* number obtains a simple form in Eq.(3)

$$Bu = \frac{V_{total} C_{eq}}{V_{solid} C_{solid}}, \quad (3)$$

where  $V_{total}$  and  $V_{solid}$  are a total volume and volume of solid, respectively. The volumes represent initial volumes in this case. The ratio between  $V_{total}$  and  $V_{solid}$  does not change considerably with time as long as REV is respected (e.g. that the volume is large enough) because  $V_{total}$  also reduces with time in completely leached domain. Hence we assume that *Bu* number remains constant during calculations.

We demonstrated that the physical time, and thus the number of iterations, required to dissolve the solid can be scaled by *Bu*. For example, if time  $t_1$  is required to fully dissolve a solid phase in a system with  $Bu_1$  number, the time can be, according to Eq.(3), reduced by reducing either  $V_{solid}$ ,  $C_{solid}$  or increasing  $C_{eq}$ . In a real chemical system only  $V_{solid}$  can be changed. However the intention of this numerical analysis is to leave the pore geometry

( $V_{solid}$ ) intact and change either  $C_{solid}$  (solid grain density) or  $C_{eq}$  in order to numerically accelerate dissolution.

the time  $t_2$  to dissolve the same volume of solid with other  $C_{solid}$  or  $C_{eq}$  (other  $Bu$  number –  $Bu_2$ ) would be

$$t_2 = t_1 \frac{Bu_2}{Bu_1} \quad (4)$$

Expanding this relation with Eq. (3) we get

$$t_2 = t_1 \frac{C_{eq,2} \times C_{solid,1}}{C_{solid,2} \times C_{eq,1}} \quad (5)$$

This means that in order to reduce the final time  $t_2$  at given original solid concentration  $C_{solid,1}$  and given equilibrium concentration  $C_{eq,1}$  we can either decrease solid concentration  $C_{solid,2}$  or increase the equilibrium concentration  $C_{eq,1}$ . The latter is typically done in accelerated experiments where the solubility is increased in order to accelerate the dissolution [3].

### 3. Numerical examples

To support our assumptions described in the previous section the dissolution will be made on a regular configuration of solid within a solute. The pattern tested here is made out of solid blocks of size 3 voxels which is surrounded by 3 voxels space (3×3 space block configuration). The ratio  $V_{solid}/V_{total}$  for this configuration is 11%. By changing either  $C_{solid}$  or  $C_{eq}$  we can adapt the  $Bu$  number.

The dissolution profile at the final time for different  $Bu$  numbers for the 3x3 configuration is shown in Fig. 2 The dissolution front progresses faster with higher  $Bu$  numbers because the solute concentration profiles are not in equilibrium and mass fluxes from the solid are higher. Visually, there is only a small difference between  $Bu=0.9$  and  $Bu=0.2$ , which indicates that even with  $Bu$  around 1 the results are within the order of few percent difference if  $Bu$  doubles. With  $Bu$  around 0.2-0.5 the system has less than 1% difference and even less when the  $V_{solid}/V_{total}$  is larger than in this system

A cementitious system is a typically examples of a system for which a significant numerical acceleration can be obtained;  $V_{solid}/V_{total}$  and  $C_{solid}/C_{eq}$  are high. Therefore, Ca-leaching is therefore a slow process which requires a lot of time steps to simulate. To illustrate the gain in numerical application, we take an example from [4] which describes leaching of a mortar. The model consists of random spherical particles (i.e. cement clinkers) between two hypothetical aggregate surfaces, respecting initial water-to-cement (W/C) ratio of mortar as well as particle size distribution of the cement type. Particle size distribution represents CEM I 42.5 N cement with Blaine fineness of 430 cm<sup>2</sup>/g with W/C=0.35. The domain is of size 2.5×5×5 mm<sup>3</sup>. Volume fraction of aggregates in the presented case is  $V_{agg}=0.2$ . Volumetric fraction of portlandite (CH) is  $V_{CH}=0.154$  and of C-S-H is  $V_{CSH}=0.476$ . Diffusion coefficient in cement paste is  $2.22 \times 10^{-12} \text{ m}^2/\text{s}$ .

The initial  $Bu$  numbers for CH, Ca in C-S-H and Si in C-S-H are  $1.05 \times 10^{-2}$ ,  $6.63 \times 10^{-3}$  and  $1.73 \times 10^{-5}$ , respectively. According to our previous discussion the acceleration of dissolution process can be at least 20-50 times without any visible difference in a dissolution front. The limiting phase is portlandite (CH) because  $Bu$  number is the highest. Other phases and species are even less limited and could be accelerated more than that.

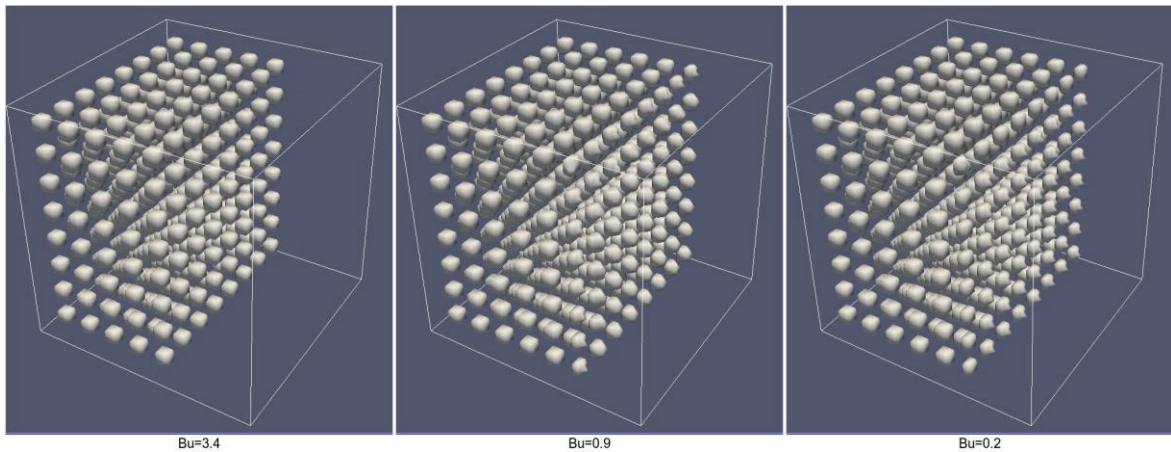


Figure 2: Final position of dissolution front at the same time for the example of  $3 \times 3$  configurations for  $Bu=3.4$  left,  $Bu=0.9$  middle, and  $Bu=0.02$  right.

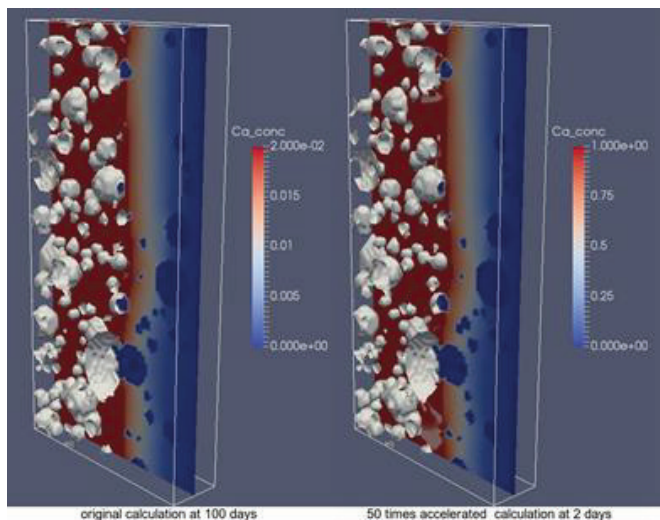


Figure 3: Dissolution front in mortar at 100 days for the original system (left and at 2 days for system with 50 times higher  $Bu$  number (right). Dissolved Ca concentration is given in  $\text{mol/dm}^3$ . Dark blue spots are aggregates (zero concentration).

The acceleration solved the problem in a few hours which is significantly faster than without acceleration requiring a simulation time of about. This enables analysis of larger systems or to perform a parameter sensitivity or uncertainty analysis in the same time. The figure below shows that the dissolution front (white represents portlandite) obtained with the proposed



approach is virtually the same at the original system and at 50 times accelerated system (right). For this particular example, we shortened the real calculation time from one month to less than a half day on desktop workstation.

#### 4. Conclusions

In this text we summarized and illustrated an approach to reduce calculation time when dealing with equilibrium geochemical systems. The approach is based on the evaluation of real chemical system in terms of  $Bu$  number and reduction of time steps by the increase of  $Bu$  number to the critical value either by the decrease of  $C_{solid}$  or increase of  $C_{eq}$ . The latter approach is similar to the experimental techniques where solubility is increased which in fact increases  $Bu$  number in a similar way as we showed in this work. A significant advantage of numerical approach compared to the experimental one; in experiments the reaction rate might change because of higher ion strength while in numerical approach the same chemistry and activity correction approach can be used when  $C_{solid}$  is decreased. In other words, the acceleration can represent natural conditions with high fidelity. For the difference in remaining solid mass to be below 1% if the concentration in solid doubles  $Bu$  number is around 0.2, but can be higher when  $V_{solid}/V_{total}$  is high. The analysis showed that for mortar the acceleration can be until  $Bu=0.5$  which resulted in 50 times acceleration.

#### References

- [1] Patel, R.A., Perko, J., Jacques, D., Schutter, G.D., Ye, G., Breugel, K.V.: A three-dimensional lattice Boltzmann method based reactive transport model to simulate changes in cement paste microstructure due to calcium leaching. *Construction & Building Materials* 166, 158–170 (2018)
- [2] Perko, J., Jacques, D.: Numerically accelerated pore-scale equilibrium dissolution, In preparation
- [3] Phung, Q.T., Maes, N., Jacques, D., Perko, J., Schutter, G.D., Ye, G.: Modelling the evolution of microstructure and transport properties of cement pastes under conditions of accelerated leaching. *Construction and Building Materials* 115, 179 – 192 (2016).
- [4] Seetharam, S., Patel, R.A., Perko, J., Jacques, D.: Quantification of leaching kinetics in OPC mortars via a mesoscale model. *Construction & Building Materials* Accepted, n/a–n/a (2018)

## **PARTICLE MODEL FOR THE PREDICTION OF LONG-TERM DEFORMABILITY PROPERTIES OF DAM CONCRETE**

**Carlos Serra <sup>(1)</sup>, Nuno Monteiro Azevedo <sup>(1)</sup>, António Lopes Batista <sup>(1)</sup>**

(1) National Laboratory for Civil Engineering, Lisboa, Portugal

### **Abstract**

This paper presents a methodology for the prediction of dam concrete instantaneous and long-term deformability properties using discrete element method (DEM) based on particle models (PM). The concrete mix, namely the content, size and distribution of the aggregates is explicitly taken into account. This type of concrete has large aggregate size and fraction volume. Due to the computational cost of the analysis of a large number of particles, dam concrete specimen is represented by an arrangement of mortar particles and of coarse aggregates particles. The overall behaviour is determined by the micro properties at each contact type, i.e., mortar-mortar, aggregate-aggregate, and aggregate-mortar which defines the interfacial transition zone (ITZ).

The proposed approach is to characterize and model both the mortar and the coarse aggregates separately and study their interaction in the heterogeneous model of concrete. For the mortar, a long-term analysis is required for modelling the aging viscoelastic properties. For the aggregates, an elastic analysis defines the contact micro properties in order to obtain the macro properties of the intact rock. The numerical results obtained from the dam concrete particle model using DEM show a good agreement with the available experimental results for several loading ages.

### **1. Introduction**

Mesoscale analyses are being used to study of the behaviour of concrete focusing on the interactions between coarse or fine aggregates and the maturing mortar or cement paste in order to evaluate the main mechanical properties and their evolution over time [1], [2].

The discrete or distinct element method (DEM) is especially suited for the analysis of quasi-brittle behaviour of some heterogeneous materials, such as concrete, since it is easier to consider the material microstructure and the randomness of material heterogeneity [3].

For modelling of concrete, main heterogeneity is due to the aggregates, mainly because the rock used for the aggregates and the cement paste have very different mechanical properties and due to the weaker properties of the interfacial transition zone (ITZ). The long-term behaviour of cementitious materials has an important role on the development of stresses inside concrete and it should be taken into account for the prediction of the behaviour over time, including complex deterioration scenarios that can occur relatively slow over a large period of time.

This paper presents the methodology for the prediction of dam concrete mechanical properties using particle models. The contact micro properties are calibrated using small homogeneous numerical specimens.

## 2. Discrete element method based on particle models

### 2.1 General aspects

The discrete element method (DEM) can be described as a numerical method for solving structural systems of individual elements, blocks (polygons) or particles (circular or spherical) interacting with each other at contact points or interfaces. The Newton's second law of motion defines the differential equation that governs the kinematics of the elements, which is solved using explicit methods. The interaction law determines the interaction forces between elements at the contact point, according with their relative displacement. In the DEM particle model, the elements interacting with each other are circular rigid particles defined by a position in space and a given radius. The normal and shear contact force increments,  $\Delta F_n^C$  and  $\Delta F_s^C$ , are obtained from an incremental linear constitutive law of the contact,

$$\Delta F_n^C = -k_n \Delta x_n^C, \quad \Delta F_s^C = -k_s \Delta x_s^C \quad (1)$$

where  $\Delta x_n^C$  and  $\Delta x_s^C$  are the normal and shear contact displacement increments, respectively, and  $k_n$  and  $k_s$  are the normal and shear contact stiffnesses.

The mechanical critical time step, related to the maximum frequency and required for explicit time integration schemes, is usually very small, which can be time consuming and computationally demanding. In order to avoid overshooting of the solution, an adaptive dynamic relaxation algorithm (ADR) can be used in which the global damping coefficient is updated at each time increment [4]. At each step, the scaled masses and inertias need to be updated for stability purposes whenever there is an increase in the model stiffness, for example due to the constitutive law or if new contacts are found to occur during numerical simulation.

### 2.2 Aging viscoelastic contact model based on the solidification theory

The aging viscoelastic model used is based on Bažant's solidification theory [5]. The model considers viscoelastic strain,  $\varepsilon^v$ , a consequence of the volume fraction growth associated to the viscoelastic behaviour,  $v(t)$ , and viscous strain,  $\varepsilon^f$ , a consequence of the volume fraction growth associated with the viscous behaviour,  $h(t)$ , and has a consistent mathematical formulation [5].

One can write the quasi-elastic incremental contact normal force,  $\Delta F_n$ ,

$$\Delta F_n = k_n'' (\Delta x_n - \Delta x_n'') \quad (2)$$

$$\frac{1}{k_n''} = q_{1,n} + \frac{1}{v_n(t_i^*)} \sum_{\mu=0}^N \left( \frac{1 - \lambda_{\mu,n}}{k_{\mu,n}} \right), \Delta x_n'' = \frac{\Delta \gamma_n''}{v_n(t_i^*)} + \frac{q_{4,n} F_n(t_i^*) \Delta t_i}{t_i^*} \quad (3)$$

$$v_n(t) = \left( \frac{1}{t} \right)^m + \frac{q_{3,n}}{q_{2,n}} \quad (4)$$

The shear contact behaviour follows the same formulation as the one previously described for normal direction.

To simulate creep behaviour of structural systems, such as rock or concrete, total calculation time can be expensive. A fast numerical procedure for the long-term behaviour was adapted from [6] for cementitious materials and makes use of both the adaptive dynamic relaxation method to obtain a fast equilibrium without overshooting and the aging viscoelastic contact model [7]. The effect of temperature can be taken into account by converting both the loading age and the time under loading into equivalent values, based on the measured temperature and maturity concepts. Higher temperatures increases the mechanical property rate of development, decreasing the creep rate and it increases the movement of water inside the cement structure and the rate of bond breakage and, therefore, increasing the creep strains [8].

### 3. Prediction of dam concrete deformability properties using particle models

#### 3.1 Definition of particle model properties

The goal of this type of analysis is to explicitly take into account the deformability and strength properties of each component of concrete. Therefore, the particle model definitions should reflect, as much as possible, the internal structure of the different types of concrete. Table 1 presents the macro parameters used for the behaviour simulation of each type of contact: aggregate, mortar and ITZ. The modulus of elasticity of the aggregate was obtained directly from experimental testing of the rock used in the production. The aging viscoelastic parameters of the mortar were calculated using the available experimental results of concrete, a calibrated composite model and B3 model fitting [9]. The behaviour of ITZ is taken into account using a serial model of the elastic properties of the aggregate ( $E_{agg}$ ) and the aging viscoelastic properties of the ITZ ( $q_{i,ITZ}$ ). Since the aggregates only have elastic behaviour, the asymptotic elastic part of the aging viscoelastic model of ITZ,  $q_{1,ITZ}$ , is affected by the aggregate's stiffness and the other aging coefficients,  $q_{2,ITZ}$ ,  $q_{3,ITZ}$  and  $q_{4,ITZ}$ , remain equal to the ones considered for the mortar properties.

The size of the particles has to take into consideration the size of the smallest coarse aggregate. On the other hand, the model refinement is constraint to the computational costs, especially when testing large specimens of dam concrete. In order to reproduce the testing conditions, the particle model includes two rigid boundary walls, at the top and bottom of the specimen, which represent the rigid platens of the testing equipment and sets the same loading conditions for each boundary particle (Fig. 1).

### 3.2 Model validation using wet-screened concrete test results obtained in creep cells

The *in situ* characterization of dam concrete relies, among others, on a specific experimental setup based on creep cells [10], in which compressive creep tests can be done. The creep cells are subjected to the same thermohygro-metric conditions as the structural concrete since its top face is connected to the dam concrete and are cast and completely covered with the surrounding lift. A typical temperature profile includes a sharp temperature increase in the first days, followed by a slow decrease which can last several months.

Table 1: Macro deformability properties of each concrete component.

Type of contacts	E (GPa)	$q_1$ ( $1 \times 10^{-6}$ /MPa)	$q_2$ ( $1 \times 10^{-6}$ /MPa)	$q_3$ ( $1 \times 10^{-6}$ /MPa)	$q_4$ ( $1 \times 10^{-6}$ /MPa)
Aggregate	46.3	-	-	-	-
Mortar	-	27.2	164.7	26.0	11.6
ITZ	-	13.6	164.7	26.0	11.6

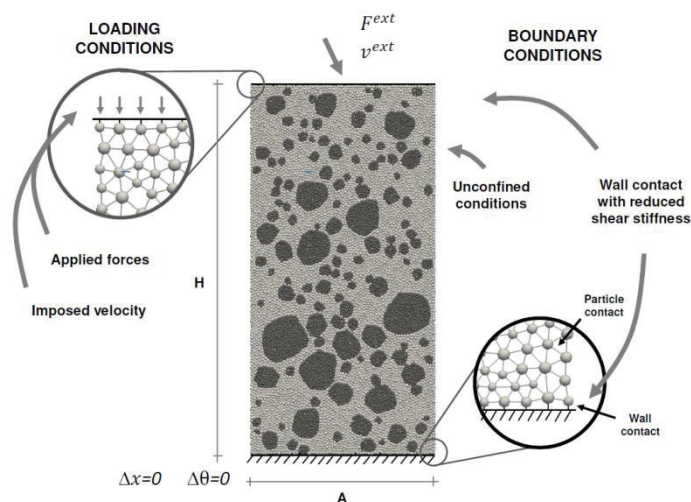


Figure 1: Representation of the loading conditions and the boundary conditions.

As it would be expected, the high initial temperatures accelerate the hydration processes and yield an increase of the modulus of elasticity. The grey area in the left plot of Fig. 2 is the particle model prediction which is in agreement with the measured modulus of elasticity in creep cells (diamond points). This effect is also present in the development of the creep strains, since its initial values are lower mainly due to higher modulus of elasticity at loading age (right plot in Fig. 2). The creep strain development over time has a misfit for the younger ages after loading, especially for the loading age of 28 days. The results show that this type of model is capable of accurately simulate the concrete deformability including not only the internal mesostructure of concrete but also the effect of temperature. The typical high temperatures in the early ages and rapid temperature variations, besides introducing differential imposed strains are known to increase the concrete stiffness and, therefore, influence the development of stresses over time.

### 3.3 Prediction of dam concrete test results obtained in creep cells

Using the same contact micro properties as the ones used for the wet-screened prediction, the dam concrete particle model gives a prediction for the experimental *in situ* results obtained *in situ* in dam concrete creep cells. As previously stated, the prediction of dam concrete deformability properties is greatly related to the aggregate's modulus of elasticity. Due to its large scatter, the presented numerical results include three scenarios, considering the mean value of the aggregate's modulus of elasticity, an upper bound value of the aggregate's modulus of elasticity and, a lower bound value of the aggregate's modulus of elasticity.

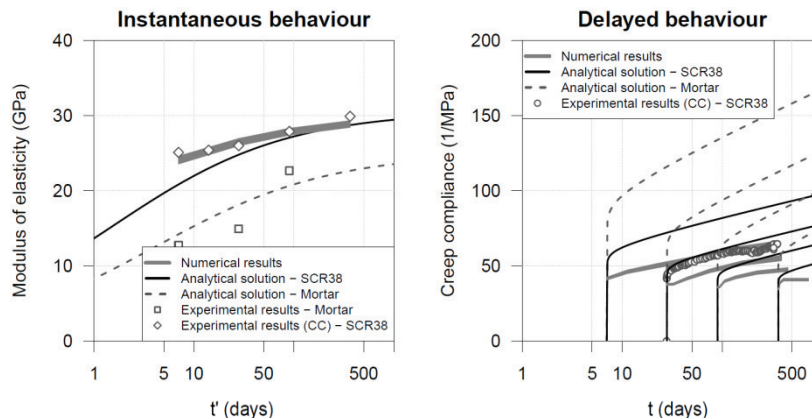


Figure 2: Results of wet-screened concrete (SCR38) particle model and comparison with creep cell results.

The difference between the prediction of the composite model at reference constant temperature (continuous black line in Fig. 3) is partially due to the acceleration of hydration processes, which is very significant at the younger ages. For the latter ages, the deviation between the numerical results and the experimental results can be due to the variability of the aggregate's modulus of elasticity. The large percentage deviation of the creep strain for the loading age of 28 days can be due to the difficulty of the maturity concepts under heating and cooling conditions applied to the creep rate. Some studies indicate that creep increases under cooling while other show the opposite effect [8].

## 4. Conclusions

This paper presents an aging viscoelastic contact model based on the solidification theory and a DEM particle model for the prediction of long-term dam concrete behaviour, considering the different types of contacts between each material, namely the mortar, the aggregates and the ITZ. The effect of temperature on the strain development is also considered in the model. Firstly, the model is validated for instantaneous and long-term properties of wet-screened concrete and, then, a prediction of dam concrete behaviour is obtained using the same contact micro properties. The model results show that the large stiffness of dam concrete, obtained *in situ*, can be partially explained by the elevated temperatures at early age and by the large scatter of the aggregate. The effect of temperature on creep development is well captured with the DEM particle model.

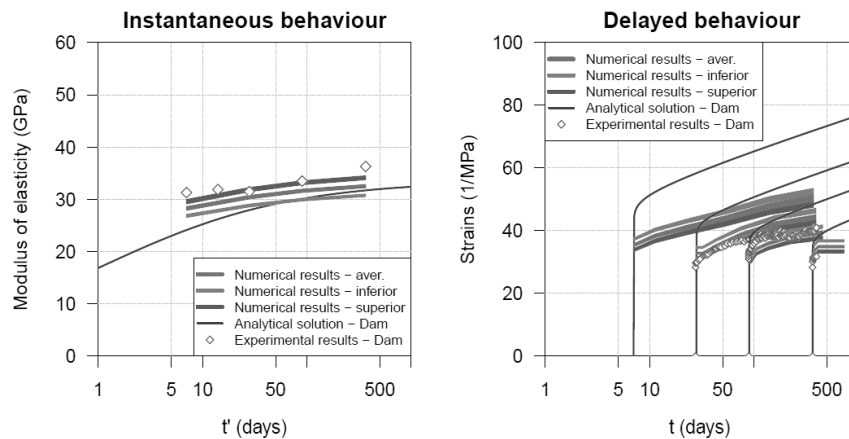


Figure 3: Results of dam concrete particle model and comparison with creep cell results.

### Acknowledgements

Thanks to EDP for permission to publish data related to monitoring of Baixo Sabor dam.

### References

- [1] M. Alnaggar, G. Cusatis, and G. Di Luzio, “Lattice Discrete Particle Modeling (LDPM) of Alkali Silica Reaction (ASR) deterioration of concrete structures” *Cem. Concr. Compos.*, vol. 41, August, pp. 45–59, Aug. 2013.
- [2] Y. Pan, A. Prado, R. Porras, O. Hafez, and J. Bolander, “Lattice Modeling of Early-Age Behavior of Structural Concrete” *Materials (Basel)*, vol. 10, no. 3, p. 231, Feb. 2017.
- [3] N. Monteiro Azevedo, J. Vieira de Lemos, and J. R. de Almeida, “Influence of aggregate deformation and contact behaviour on discrete particle modelling of fracture of concrete” *Eng. Fract. Mech.*, vol. 75, no. 6, pp. 1569–1586, Apr. 2008.
- [4] P. Underwood, “Dynamic Relaxation” in *Computational Methods for Transient Analysis*, Oxford, United Kingdom: Elsevier Science Publishers B.V., 1983, pp. 245–265.
- [5] Z. P. Bažant and S. Prasanna, “Solidification theory for concrete creep. I: Formulation” *J. Eng. Mech.*, vol. 115, no. 8, pp. 1691–1703, Aug. 1989.
- [6] J. Feng, Z. Chuhan, W. Gang, and W. Guanglun, “Creep Modeling in Excavation Analysis of a High Rock Slope” *J. Geotech. Geoenvironmental Eng.*, vol. 129, no. 9, pp. 849–857, 2003.
- [7] C. Serra, N. Monteiro Azevedo, A. L. Batista, and N. Schlar, “Discrete Element Method for Modeling the Long-Term Aging Viscoelastic Behavior of Concrete Considering Its Mesostructure” *J. Eng. Mech.*, vol. 144, no. 5, May 2018.
- [8] Z. P. Bažant and S. Baweja, “Creep and shrinkage prediction model for analysis and design of concrete structures - model B3” in *Adam Neville Symposium: Creep and Shrinkage - Structural Design Effects*, 2000, vol. 28, no. 6, pp. 1–83.
- [9] C. Serra, “Prediction of dam concrete structural properties based on wet-screened test results and mesoscale modelling”, PhD. Thesis, Universidade Nova de Lisboa, 2018.
- [10] C. Serra, A. L. Batista, and N. Monteiro Azevedo, “Dam and wet-screened concrete creep in compression: in situ experimental results and creep strains prediction using model B3 and composite models” *Mater. Struct.*, vol. 49, no. 11, pp. 4831–4851, Nov. 2016.

## SCALE EFFECT ON ALKALI-SILICA REACTION

**Jacques Jabbour** <sup>(1) (2) (3)</sup>, **Aveline Darquennes** <sup>(2)</sup>, **Loic Divet** <sup>(3)</sup>, **Rachid Bennacer** <sup>(2)</sup>,  
**Jean-Michel Torrenti** <sup>(3)</sup>, **Georges Nahas** <sup>(1)</sup>

(1) IRSN, Fontenay-aux-Roses, France

(2) LMT ENS-Paris-Saclay, CNRS, University Paris-Saclay, Cachan, France

(3) University Paris-Est, Materials and Structures Department, IFSTTAR, Marne la Vallée,  
France

### Abstract

Many laboratory studies of internal swelling reactions are realized on relatively small size samples. Those laboratory samples do not allow to reproduce real conditions to which is submitted the real concrete in its environment, in terms of kinetics, volume/surface ratio, thermal and mechanical conditions especially in massive structures. Therefore, an experimental protocol to accelerate internal swelling reactions of concrete on a structural scale has been developed to allow better observation and understanding of swelling reactions at structure scale. A representative massive concrete structure (2.4 x 1.4 x 1 m<sup>3</sup>) was realized under controlled and optimized conditions for the development of alkali silica reaction (ASR). The scale effect on swelling kinetics is demonstrated by an experimental study comparing the evolution of swelling reaction in the massive sample with the evolution in reconstituted concrete laboratory specimens as well as coring specimens. Results show different swelling kinetics and amplitude in function of sample type, size and boundary conditions.

### 1. Introduction

Alkali-silica reaction (ASR) is a chemical reaction between amorphous silica mineral from the aggregates and the alkali hydroxides (Na, K – OH) dissolved in the concrete pore solution [1]. This reaction generates a secondary alkali-silica gel which expands and induces overpressure within the reacting aggregate material and the adjacent cement paste upon moisture uptake from its surrounding environment, thus causing micro-cracking, loss of material's integrity (mechanical/durability). It's known that swelling pathologies act at different scales: microscopic, mesoscopic and macroscopic. Thus, multi-scale approaches are



necessary in order to fill the gap between conventional laboratory samples and the behavior of real scale massive structures.

The experimental laboratory investigations about the scale effect on swelling reactions have been carried out on concrete specimens, using cement with a high alkali-content combined with reactive aggregates. It aims to quantify the expansion magnitudes and kinetics in different specimen types and sizes. Three sample geometries are considered: first, the massive structure mock-up ( $2.4 \times 1.4 \times 1 \text{ m}^3$ ). The second and third specimens geometry studied are concrete cylinders cast in the laboratory and subjected to conservation conditions equivalent to those of the mock-up. The concrete cylinders dimensions are 16 cm (diameter)/32 cm (height), and 11 cm (diameter)/22 cm (height) respectively. In addition to that, three cores were extracted from the massive structure and subjected to conventional test procedures in order to determine the structure's residual swelling. The cores dimensions are equally 11 cm (diameter)/22 cm (height). This article, presents the results of expansion for the different concrete samples. The swelling behaviour of the massive structure and the impact of boundary conditions are discussed. Then the swelling characteristics (magnitude and kinetics) of the different concrete specimens are quantified using a mathematical relation. The impact of conservation conditions is thus demonstrated. Finally, the impact of specimen's size on the swelling magnitude and kinetic parameters is discussed.

## 2. Materials

The concrete used in this study is made with calcareous non-reactive sand (0/5), reactive siliceous coarse aggregates (5/12.5 – 12.5/20), and a W/C=0.57. This combination was chosen based on the works of Guedon-Dubied [2], hence the same quarry provides the reactive aggregates. These aggregates are rich in carbonals which, from a mineralogical point of view, is a microcrystalline silica deemed to have a significant alkali reactivity [2]. Furthermore, Monnin showed that the kinetics of alkali consumption increases when the aggregate diameter decreases [3]. This causes a rapid drop in the alkali concentration of the interstitial solution which may limit the final swelling of the concrete. Therefore, by opting for non-reactive sand, the final swelling due to the alkali-granulate reaction is maximized. The binder used is a Portland cement CEM II/A-LL 42.5 R. It contains 1.06% of  $\text{Na}_2\text{eq}$  (by mass), hence providing a total of  $4.24 \text{ Kg/m}^3$  of alkalis in the mix. As a result, this concrete mix is highly ASR-prone.

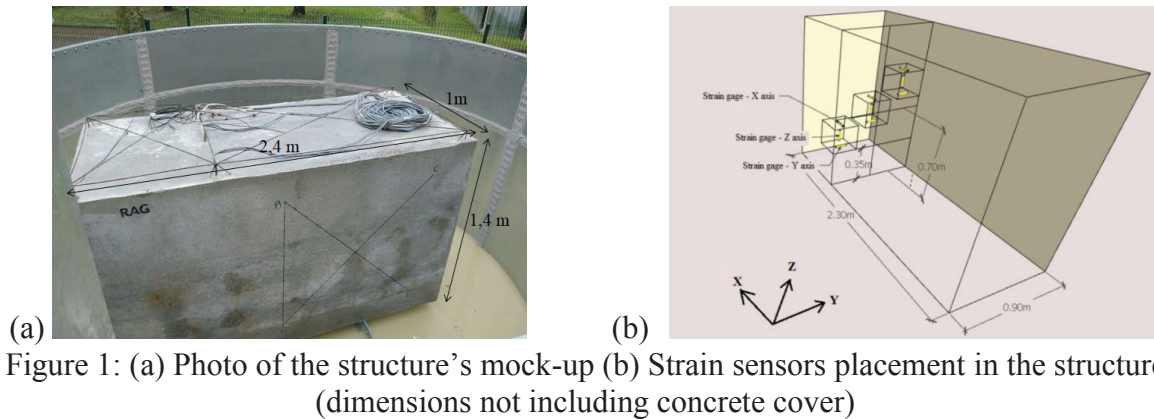
## 3. Multi-scale experimental study

### 3.1 Structural scale

The monitoring of swelling in the structure is ensured by 9 vibrating wire extensometers embedded within the concrete at three levels (Fig. 1b): 0.25 H, 0.5 H and 0.75 H, where H is the mock-up height (140 cm). At each level, three strain sensors are oriented in the three directions (X, Y, Z) respectively making it possible to continuously follow the deformations over time with an accuracy of the order of  $2 \mu\text{m/m}$ .

Special measures were taken in order to keep the concrete temperature at the early age below  $65^\circ\text{C}$  in order to avoid delayed ettringite formation. The mock-up is conserved fully

submerged in a pool constantly maintained at 38°C (Fig 1a). The pool is emptied monthly in order to perform a follow up of the structure's surface. Tap water is used to fill the pools.



### 3.2 Specimen scale

Six cylindrical concrete specimens (three Ø11H22 and three Ø16H32) were prepared according to the standards NF P 18-400 and NF P 18-422. After casting, the concrete specimens were heat treated. The heat treatment applied is identical to the temperature profile measured in the structure mock-up at the early age. It was performed in a climatic chamber regulated at 100% relative humidity. The maximum temperature reaches a value of 62°C. Afterwards, the specimens are stored in 20°C water until 28 days age, then they are placed at 38°C in a volume of water respecting the same ratio (Water Volume)/(Exposed Surface) as the structure in the pool and respecting the same renewal cycles as well. Therefore, the specimens have an identical heat profile and an equivalent conservation environment.

In addition to that, three Ø11H22 core samples were extracted from the structure at 0.25 H along the Y axis. They are subjected to the *LPC N44 test method*, in which the cores are conserved at 38°C and 100% relative humidity [4]. For each sample, the length variation is measured along three longitudinal lines located at 120° from each other in the circumference using an extensometer. The length base used for strain measures is 10 cm for Ø11H22 specimens (cast and coring) and 20 cm for Ø16H32 specimens.

## 4. Results

Results show different expansion behaviour in the massive structure in comparison with unrestrained laboratory specimens.

### 4.1 The effect of boundary conditions on swelling mechanism in massive structures

Fig. 2 shows the swelling in the mock-up as recorded by the strain sensors. Until the time 235 days, the massive structure is conserved in water at ambient temperature. This phase corresponds to the time required to finalize the construction of the experimental platform and install the temperature regulation system. There's hardly no swelling at this stage. Once the temperature rose to 38°C, swelling in the mock-up started increasing in a similar manner to accelerated tests on laboratory specimens. Fig. 2 shows the swelling in the structure and that thermo-activation is a valid method to accelerate ASR on a massive scale.

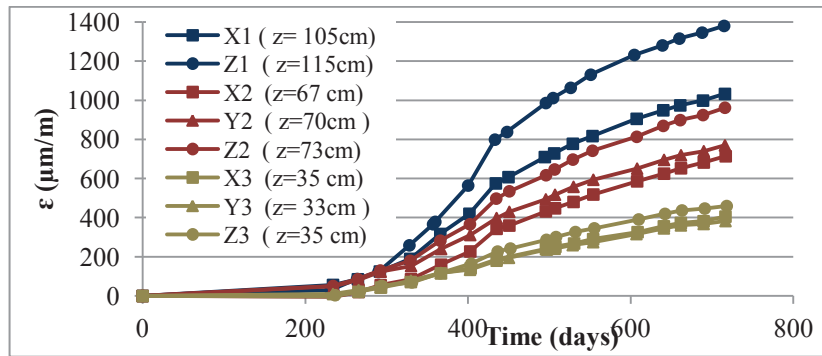


Figure 2: Swelling evolution in the massive structure mock-up.

After 700 days of follow-up, swelling in the structure seems to reach the second inflection point. The maximum amplitude recorded at this stage is about 1400  $\mu\text{m/m}$ . However this value varies according to the position of the sensor and its orientation. As a general rule, the swelling decreases as we approach the base of the structure regardless of the orientation of the sensor. Thus, a  $\Delta\epsilon$  of approximately 900  $\mu\text{m/m}$  is measured between the sensors Z1 ( $z = 115$  cm) and Z3 ( $z = 35$  cm). Simulations showed that this behavior is actually due to the stress generated by the restraint effect due to the metal support on which the structure was cast. The upper part of the mock-up can expand freely whereas the lower part is hindered by the boundary conditions. However, at lower heights, the swellings measured in the horizontal plane parallel to the support (along X and Y) are hindered more than the swelling measured vertically (along Z). Another approach to analyze this behavior would be to consider that the expansion, which is prevented along the directions of the metal support, is compensated by a greater expansion in the unstressed direction (Z). This effect decrease as we approach the upper part of the mock-up. As a matter of fact, the experimental campaign conducted by Larive, has shown that the mean volume swelling remains generally constant when the value of the uni-axial stress applied to the specimens remains below 10 Mpa [1].

#### 4.2 Scale-effect on swelling kinetics and magnitude

Fig. 3 shows the swelling in the small scale concrete specimens in comparison to that of the structure. A correction was applied to the expansion results of the mock-up taking into account the temperature shift at 235 day and the difference in maturity conditions.

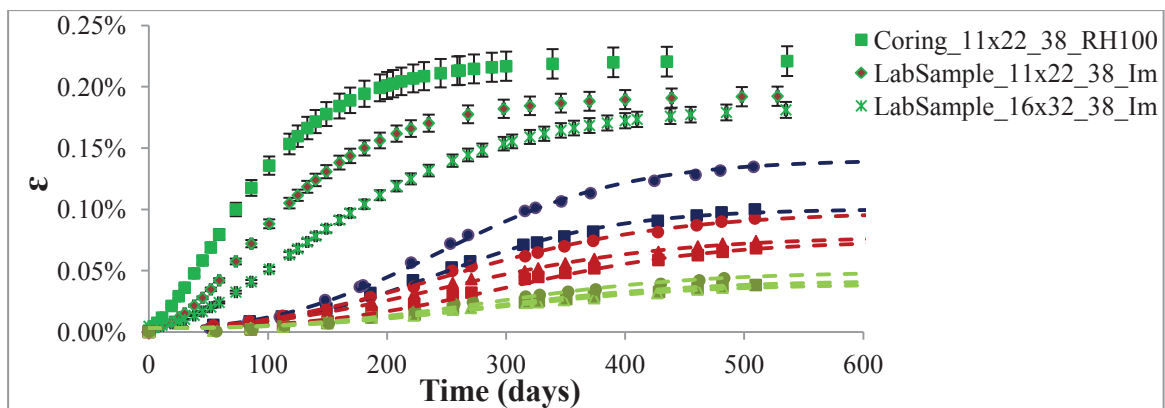


Figure 3: Comparison of the swelling evolution between the laboratory scale specimens and the massive structure behavior

The cores subjected to the *LPC N°44 test method* (Coring\_11x22\_38\_RH100) yield a residual swelling of 0.22% whereas the cast concrete specimens of the same dimensions (LabSample\_11x22\_38\_Im) yield a swelling of 0.19%. This difference is most probably due to the conservation environment: the immersed specimens are subject to a higher alkali-leaching than the cores conserved at 100% relative humidity. This reduces the final volume of gel formed. Similar results were obtained by Martin [5].

However, if we consider the series LabSample\_11x22\_38\_Im, LabSample\_16x32\_38\_Im and the mock-up, we notice different swelling behaviours knowing that we have the same concrete composition and conservation environment but different sample sizes. Hence, the swelling characteristics (magnitude and kinetics) are quantified using Kchakech's law (a mathematical relation). Tab. 2 recapitulates Kchakech's swelling parameters obtained for the different specimens' series by minimizing the differences between the curve and the experimental points using the least squares method where  $\epsilon^\infty$  is the final magnitude of expansion,  $\tau_L$  and  $\tau_C$  are respectively the latency and the characteristic times [6].

Sensors in the upper part of the mock-up are considered for this comparison knowing that this part of the structure expands "freely".

Table 2: Parameters of Kchakech's model.

	<b>Coring</b>	<b>LabSample 11x22</b>	<b>LabSample 16x32</b>	<b>Z1 (z= 115cm)</b>	<b>X1 (z= 105 cm)</b>
$\epsilon^\infty$	0.22%	0.19%	0.18%	0.1375%	0.0975%
$\tau_L$	0	18	32	240	240
$\tau_C$	55	53	105	80	75

We notice that the latency and characteristic times increase and that the final swelling decrease as the sample size increase. By assuming that the swelling in the concrete generates a tensile solicitation, then the decrease in the final swelling can be explained by the Weibull's effect [7]. Rossi's research in scale effects on the mechanical behavior of concrete suggests that tensile strength of the concrete decreases as the volume of the specimen increase [7]. From another perspective, given that the ASR kinetics can be assimilated to a diffusive phenomenon, Fig. 4 shows a normalized evolution of the swelling in the different specimens function of  $(\sqrt{t})/r$ , where t stands for time (days) and r is the radius of the specimen (m). An equivalent radius was computed for the massive structure taking into account the shape factor (parallelepiped vs cylinder) and yielding the same cross-section area ( $r_{\text{mock-up}} = 0.668$  m).

Fig. 4 reveals different swelling slopes in the normalized graph. This suggests different reaction kinetics and swelling mechanisms. If we consider that we have the same chemical advancement in the three specimen sizes (same pore distribution, same aggregate-cement paste interface...); then a possible explanation is the following: as the sample size increase, crack occurrence increase hence creating stress release points and additional space for gel permutation thus slowing down the over-all expansion mechanism. However this point ought to be clarified by further research considering additional intermediate geometries and microscopic observations.

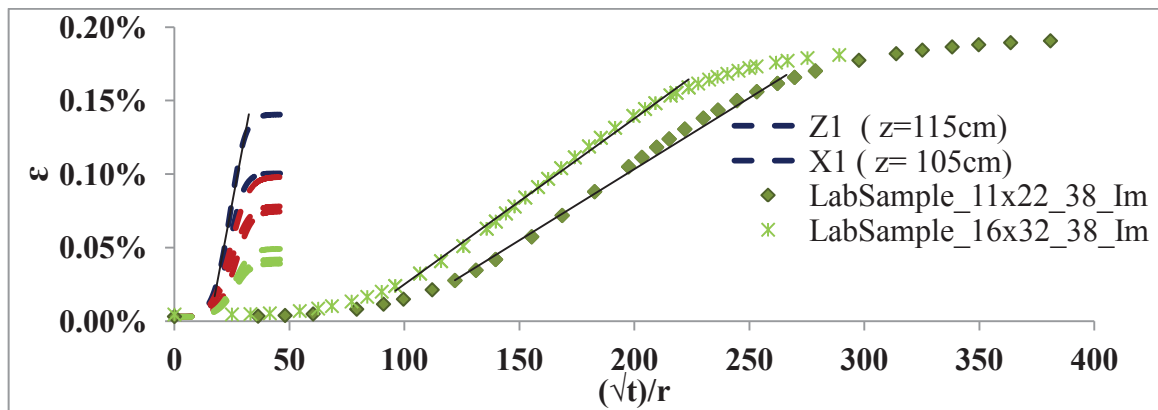


Figure 4: Normalized evolution of the swelling in the different specimens sizes

## 5. Conclusions

We show in this paper that thermo-activation can be used to accelerate ASR in a massive structure. However, expansion in massive structures varies greatly from analogous laboratory samples. Boundary conditions could hinder expansion along certain directions thus compensated by a higher expansion along unstressed directions which leads to an anisotropic behaviour in the material. The most important observation is that we identified the existence of a scale effect on internal swelling reactions. By comparing the strain evolution in different samples sizes subject to analogous concrete composition, thermal history and conservation environment, we found that the final swelling amplitude and the swelling kinetics are reduced by increasing the specimen's size.

It ought to be mentioned that similar results were obtained in a parallel study investigating two similar pathologies: Delayed Ettringite Formation (DEF) and the concomitance of ASR and DEF.

## References

- [1] Larive, C., Apports combinés de l'expérimentation et de la modélisation à la compréhension de l'alcali-réaction et de ses effets mécaniques. PhD thesis, Ecole Nationale des Ponts et Chaussées. (1997).
- [2] Guédon-Dubied, J-S., Etude du calcaire tournaisien de la carrière Cimescaut à Antoing (Belgique). Bulletin des Laboratoires des Ponts et Chaussées 226 (2000), 57-66.
- [3] Monnin, Y., Méthodologie pour décrire le gonflement multi-échelle de calcaires siliceux soumis à la réaction alcali-silice dans le matériau béton. PhD thesis, Université de l'Artois, (2005).
- [4] Fasseu, P., Alkali-réaction du béton : Essai d'expansion résiduelle sur béton durci. Méthode d'essai LPC n° 44, Techniques et méthodes des laboratoires des ponts et chaussées, 1997.
- [5] Martin, R-P., Analyse sur structures modèles des effets mécaniques de la réaction sulfatique interne du béton. PhD thesis, Université Paris-Est, (2010).
- [6] Kchakech, B., Etude de l'influence de l'échauffement subi par un beton sur le risque d'expansions associées à la Réaction Sulfatique Interne. PhD thesis, Université Paris-Est, (2015).
- [7] Rossi, P. et al., Scale effect on concrete in tension, Materials and Structures 27 (1994), 437-444

## **SMALL SCALE FRACTURE PROPERTIES OF CEMENT PASTE AND ALKALI-ACTIVATED FLY ASH**

**J. Němeček<sup>(1)</sup>, J. Němečková<sup>(1)</sup>, J. Němeček<sup>(1)</sup>, J. Maňák<sup>(2)</sup>**

(1) Czech Technical University in Prague, Faculty of Civil Engineering, Prague, Czech Republic

(2) Institute of Physics, Academy of Sciences, Prague, Czech Republic

### **Abstract**

The paper shows novel methodology and quantitative results of small scale elastic and fracture properties of cement paste and alkali-activated fly ash constituents at the level of micrometers. Local Young's moduli, tensile strengths and fracture energies are derived from nanoindentation and micro-beam bending on microscale specimens prepared with focused ion beam milling. It is shown that the main cement hydration products (inner and outer products) that are rich of C-S-H gel reach tensile strength of 260-700 MPa. N-A-S-H gel in alkali-activated fly ash is characterized with the mean strength of 340 MPa. The values are several orders of magnitude higher compared to their macroscopic counterparts. Supremum fracture energies were found in the range 4-20 J/m<sup>2</sup> on individual microstructural components.

### **1. Introduction**

Composites based on cement of alkali-activated fly ash matrix are highly heterogeneous multi-scale materials. Usual engineering properties vary with the level of observation as the representative volume element contains different amount of heterogeneities or inclusions at individual scales. Among others, tensile strength and fracture energy are crucial material properties that vary significantly starting from C-S-H globules in cement paste [1] to concrete level [2]. Mutual similarities between C-S-H in cement paste and N-A-S-H gels in alkali-activated fly ash (AAFA) exist [3,4]. In this paper, we introduce a unique experimental method that allows cutting out a micrometer sized cantilever beams using the Focused Ion Beam (FIB) milling technique [5] from a heterogeneous composition of hydrated cement or alkali-activated fly ash pastes. High precision geometry of the beams is reached with FIB at micrometer scale. The beam is loaded in bending with the help of a nanoindenter and

mechanical response is determined. Careful selection of homogeneous-like regions allows assigning results to dominant micro-mechanical phases, particularly C-S-H rich inner and outer products and Portlandite regions in cement paste and N-A-S-H gel areas in AAFA. From these tests, it is possible to determine tensile strengths of the individual phases in micrometer scale and, in some extent, fracture energy needed to break the cantilever.

## 2. Experiments

In order to study small scale material properties on individual phases of cement pastes and AAFA several micro-machined samples were prepared by FIB milling in the form of cantilever beams laying in a specific material phase. Samples were scanned in electron microscope (SEM) to assess local beam positions based on the morphology of individual phases. The morphologically detectable and mechanically significant phases have been selected. The beams were subsequently loaded by the nanoindenter and local elastic and fracture properties deduced.

### 2.1 Cement paste samples

Samples were prepared from Portland cement CEM-I 42.5R with water to binder ratio 0.4 and cast into small plastic moulds. After 24 hours, samples were stored in water for a long period of 8 years, thus fully hydrated. Then, samples were taken out of water, cut into ~5 mm thick slices and prepared with a metallographic procedure [3,5] to get a flat and smooth surface with small roughness of several tens of nm suitable for microscopy and micromechanical testing.

Microstructure of cement paste composes mainly of C-S-H rich phases [6]. Two morphologies are distinguished. Inner product surrounding unhydrated clinkers is described with higher density and forms less portion of the sample volume (~28%) while more porous outer product forms majority of the sample volume (~50%). Large Portlandite crystals (CH) appear in the microstructure (~10%). The rest of the volume is occupied by unhydrated clinkers (3%) and capillary porosity (12%), see [5] for details. The situation is illustrated in Fig. 1a.

### 2.2 Alkali activated fly ash samples

Raw fly ash from brown coal power plant Opatovice (Czech Republic) was used as a binder precursor for preparation of AAFA samples. The fly ash was mixed with an alkali-activator which was prepared by dissolving NaOH pellets in tap water and by adding sodium silicate (water glass). Resulting mixture was characterized by mass oxide ratio of an activator and activator-to-solid mass ratio as:  $\text{Na}_2\text{O}/\text{SiO}_2=0.881$ ,  $\text{H}_2\text{O}/\text{Na}_2\text{O}=3.068$ ,  $\text{activator}/\text{solid}=0.456$ . After mixing, samples were cured at 80°C for 12 h and then stored in laboratory conditions (~22°C) until testing. Before SEM and nanoindentation samples were mechanically polished with equal polishing procedure as cement paste samples.

Microstructure of AAFA samples is more complex. It consists of the main reaction product, the N-A-S-H gels, non-reacted and partly reacted slag grains, non-reacted glass particles and multi-level porosity [4]. Typical microstructure with a N-A-S-H region used for preparation of micro-beams is shown in Fig. 1b.

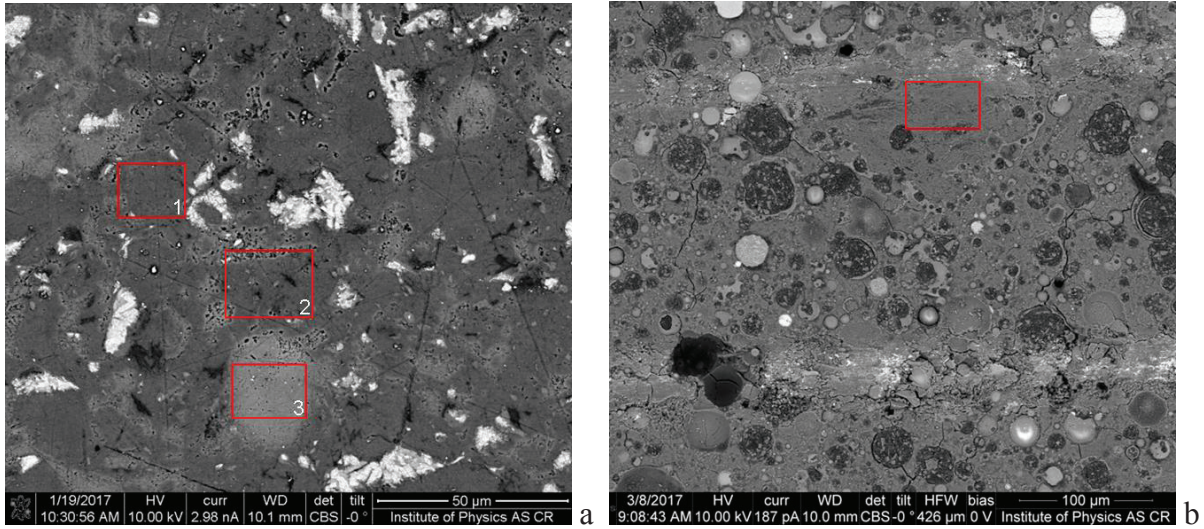


Figure 1: Examples of (a) cement paste (1=inner product, 2=outer product, 3=CH) and (b) AAFA (rectangle shows a N-A-S-H gel region).

### 2.3 FIB

Micro-beams were prepared with FEI Quanta 3D FEG dual beam instrument combining SEM and FIB was used for fabrication of all samples. The FIB technique uses a finely focused beam of gallium ions for precise milling of microscopic samples. The sample geometry was chosen to be a cantilever beam of 15-20 μm length and triangular cross-section with approximate dimensions of 3-4 μm in height and width. FIB works similar to scanning electron microscope (SEM) with working conditions of accelerating voltage between 10 and 50 kV and current in the interval between 1 pA and 30 nA. FIB milling procedure was optimized to suppress the redeposition of sputtered material on the micro-beam surface and the final milling step was done at an accelerating voltage of 30 kV and low current of 1 nA [5] on cement samples and 0.1 nA on AAFA samples. Milling of a single beam takes a few hours. After FIB milling, the micro-beams were observed by SEM to scan their actual dimensions and position in a particular microscopic phase. An example of the milled beam is shown in Fig. 2.

### 2.4 Nanoindentation

Nanoindentation was employed to derive elastic properties of a specific material phase measured with standard indentation technique [7] and as a loading tool for bending micro-beams [5]. Force-deflection diagrams were recorded in the displacement controlled regime and tensile strength,  $f_t$ , and fracture energy,  $G_f$ , calculated using beam theory as

$$f_t = \frac{F_{\max} L}{W_h}, \quad (1)$$

$$G_f^{\text{sup}} = \frac{1}{A_f} \int_0^{w_{\max}} F dw, \quad (2)$$



where  $F_{max}$  is the maximum measured force,  $L$  is the beam length and  $W_h$  is the section modulus,  $w_{max}$  is the peak deflection and  $A_f$  is the nominal fracture area (i.e.  $A_f = \frac{1}{2}bd$  for the triangle  $b \times d$ ). Note that the fracture energy was computed as the supremum estimate based on the assumption that the micro-beam behavior shows neither snap-back nor softening and that the maximum force corresponds to the maximum energy release rate with a limiting stable crack propagation. Such assumption is not fully correct since some of the loading diagrams show stable softening. Unfortunately, stable softening can be captured only in very limited cases with the current instrument even in depth controlled regime. Therefore, only supremum energies are calculated here.

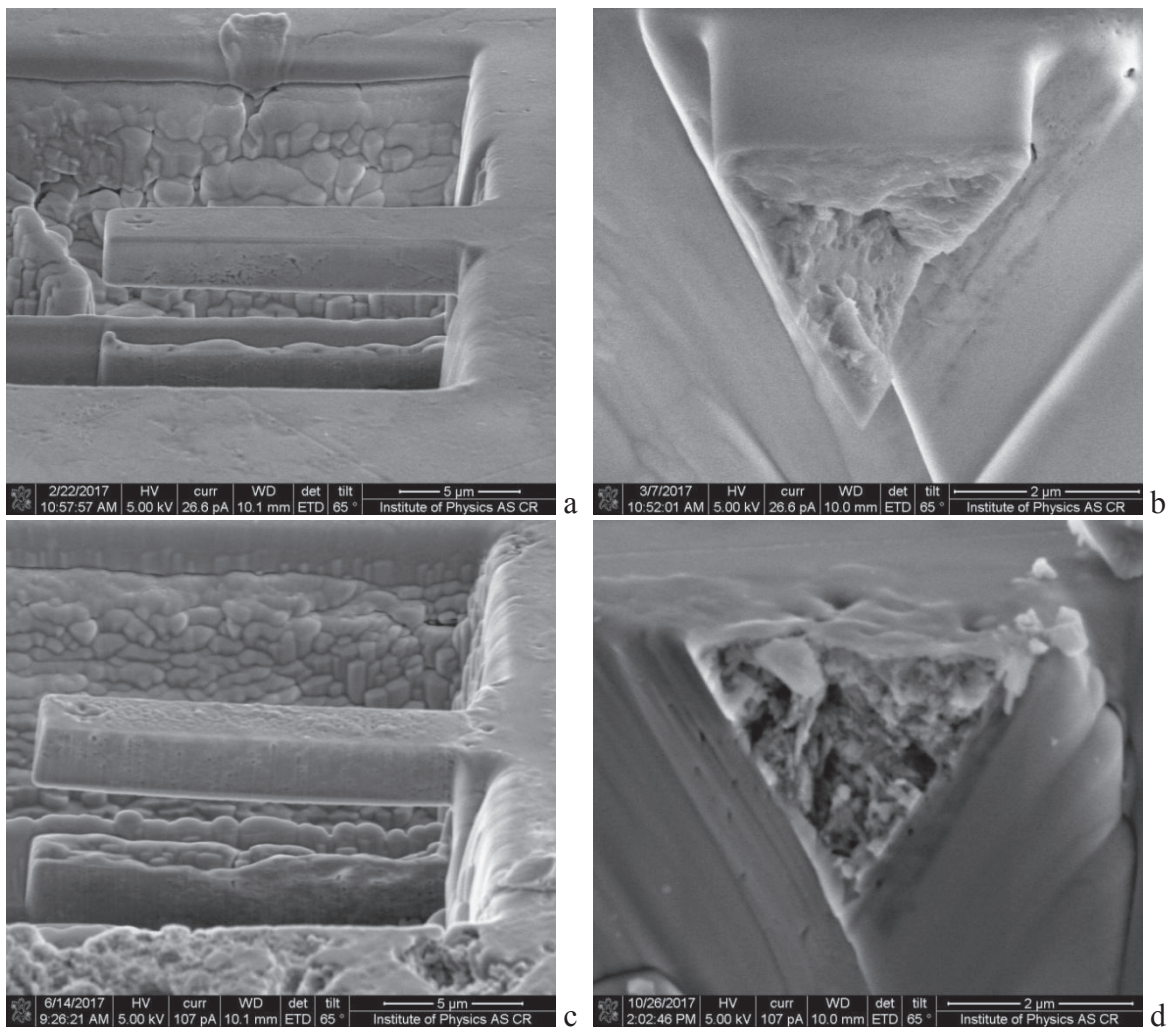


Figure 2: Examples of micro-beam geometry before and after fracture (a,b=outer product in cement paste; c,d=AAFA).

### 3. Results and discussion

Results of material parameters collected from bending of about 10 beams for each phase is summarized in Tab. 1. Typical load-deflection curves normalized with respect to the

microbeam length are shown in Fig. 1. The micro-beams in bending behave approximately linearly up to the break which suggests that no or small microcracking appears before the rupture. Then, sudden failure characterized with steep brittle fracture on unloading branch is a demonstration of release of elastic energy stored in the beam. Although, in some cases also stable descending (softening) branch has been recorded (as seen in Fig. 1 for AAFA sample), usually unstable behavior was encountered (most cement samples). Thus, the post-peak is not well maintained even in the depth controlled regime in the nanoindenter and must be treated only as approximate.

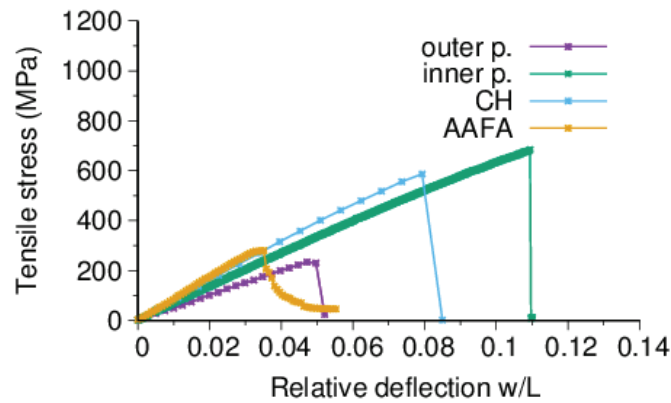


Figure 1: Examples of micro-beam stress vs. relative deflection curves.

Table 1: Results of nanoindentation and micro-beam bending.

	Outer product	Inner product	CH	N-A-S-H
$E$ (GPa)	$24.9 \pm 1.3$	$33.6 \pm 2.0$	$39.0 \pm 7.1$	$25.5 \pm 4.24$
$f_i$ (MPa)	$264.1 \pm 73.4$	$700.2 \pm 198.5$	$655.1 \pm 258.3$	$340.8 \pm 124.1$
$G_f^{sup}$ (J/m <sup>2</sup> )	$4.4 \pm 1.9$	$19.7 \pm 3.8$	$19.9 \pm 14.4$	$4.5 \pm 1.8$

The results of strengths in Tab. 1 are several orders of magnitude higher compared to macroscopically obtained characteristics where the tensile strengths on mm/cm sized samples are a few MPa. The reason lies in the defects that are present on higher composite scales and lead to strength reduction [8].

The results are in good agreement with previously obtained results of elastic and strength properties of individual cement paste constituents [3,5] and AAFA [4]. Strength calculation at C-S-H level are provided e.g. by molecular dynamics models which yield tensile strength for low density and high density C-S-H as 550-720 MPa [9], AFM measurements as 930 MPa [10]. Those values are comparable with microbending tests in Tab. 1. MD simulations give fracture energies in the range of 0.4-3 J/m<sup>2</sup> [11,12] which is slightly less than our results suggesting that our supremum energies are slightly above the real values.

So far, no particular data on strength and fracture energy were known for N-A-S-H gel at micrometer scale. This measurement gives first experimental estimates (Tab. 1). It seems that the values are mechanically comparable with outer product of cement paste which also has similar density [4,5].

#### 4. Conclusions

The paper provides quantitative results of low level micromechanical properties (strength and fracture energy) of individual components of hydrated cement paste and AAFA with the aid on FIB and nanoindentation. It was found that the strength in micrometer scale is in the order of hundreds of MPa and the specific fracture energy lies in the range of units of J/m<sup>2</sup>. N-A-S-H gel mechanical response was found to be similar to outer product in cement paste.

#### Acknowledgement

Financial support of the Czech Science Foundation (project 17-18652S) is gratefully acknowledged.

#### References

- [1] Jennings, H. M., A model for the microstructure of calcium silicate hydrate in cement paste, *Cement and Concrete Research* 30 (1) (2000), 101-116
- [2] Bažant, Z. P., *Scaling of Structural Strength*, 2nd ed., Elsevier Ltd. (2005)
- [3] Němeček, J. et al, Micromechanical analysis of heterogeneous structural materials. *Cement and Concrete Composites* 36 (2013), 85-92
- [4] Němeček, J. et al, Nanoindentation characteristics of alkali-activated aluminosilicate materials, *Cem Concr Comp* 33 (2011) 163-170
- [5] Němeček, J. et al, Tensile strength of hydrated cement paste phases assessed by microbending tests and nanoindentation, *Cem Concr Comp* 73 (2016), 164-173
- [6] Scrivener, K.L., Backscattered electron imaging of cementitious microstructures: understanding and quantification. *Cem Concr Comp* 26(8) (2004), 935-945
- [7] Oliver, W. and Pharr, G., An Improved Technique for Determining Hardness and Elastic-Modulus using Load and Displacement Sensing Indentation Experiments, *J. Mater. Res.* 7 (1992), 1564-1583
- [8] Němeček, J. et al, Fracture properties of cement hydrates determined from microbending tests and multiscale modeling, *Proceedings of EURO-C 2018*
- [9] Davie, C. and Masoero, E., Modelling damage from the nano-scale up. In *10th International Conference on Mechanics and Physics of Creep, Shrinkage, and Durability of Concrete and Concrete Structures (2015)*
- [10] Plassard, C. et al, Nanoscale experimental investigation of particle interactions at the origin of the cohesion of cement. *Langmuir* 21(16) (2005), 7263–7270
- [11] Ghebrab, T. and Soroushian, P. Mechanical properties of hydrated cement paste: development of structure-property relationships, *J. Concr. Struct. Mater.* 7(4) (2010), 37-43
- [12] Bauchy, M. et al, Fracture toughness of calcium-silicate-hydrate from molecular dynamics simulations, *J. Non Cryst. Solids* 419 (2015), 58-64

## **STRUCTURAL PERFORMANCE OF REINFORCED CONCRETE SLAB SUBJECTED TO FIRE AND EXPLOSION**

**Jiangpeng Shu<sup>(1)</sup>, Terje Kanstad<sup>(1)</sup>, Max Hendriks<sup>(1)(2)</sup>, Jan A. Øverli<sup>(1)</sup>, Assis Barenys<sup>(1)</sup>**

(1) NTNU Norwegian University of Science and Technology, Trondheim, Norway

(2) Delft University of Technology, Delft, the Netherlands

### **Abstract**

This study was conducted as part of the submerged floating tunnel (SFT) for the “Ferry-free coastal route E39” project by the Norwegian Public Roads Administration (NPRA). The aim of the project is to represent the condition, the concrete shell of SFT under a combination of fire and explosive loads, and for the calibration of the developed numerical model for the analysis of SFT. A laboratory experiment was designed by using shock tube to apply blast load to a series of RC slabs, after heated in a burner according to ISO 834 fire curve. A numerical simulation was conducted to develop modelling strategy for RC structures under such extreme loading condition and calibrated by the laboratory experiment. The influence of high temperature on material properties of concrete, reinforcing steel as well as the stiffness and strength of slab structures were investigated.

### **1. Introduction**

“Ferry-free coastal route E39” is a project by the Norwegian Public Roads Administration (NPRA) that aims at designing a coastal route between Kristiansand and Trondheim (1100 km) without ferry connections [1]. The feasibility of submerged floating tunnels (SFT) is being evaluated, see Figure 1. In the unfortunate situation of accidental events, such as an earthquake, the explosion of oil tank truck, the submerged floating tunnel (SFT) reinforced concrete (RC) structure may become damaged by high temperature and blast loads. The present study focuses on the structural performance and risk analysis of the SFT structure.



Figure 1: Proposed submerged floating tunnels (SFT) for the E39 fjord crossing [1].

RC slabs can be a representative component of the concrete structure of SFT and it is important to study if the RC shells can carry the combination of fire and blast load if an accidental explosion occurs. Shock tube can be a helpful equipment for the experiment. Concrete panels could be experimentally tested at the Polytech University of Milan. The shock tube is equipped with a fire burner that can heat the specimen according to different standard fire curves. Once the desired fire exposure time has been reached, the shock test is performed under “hot” conditions.

## 2. Design of Experiments

Figure 2 shows a sketch of the shock tube, with the driver section on the left and the driven section, which makes up most of the length of the shock tube, in the middle. Several pressure sensors are mounted on the right, close to where the slabs are mounted. A detailed description of the shock tube can be found in the work by Colomb et al. [2].

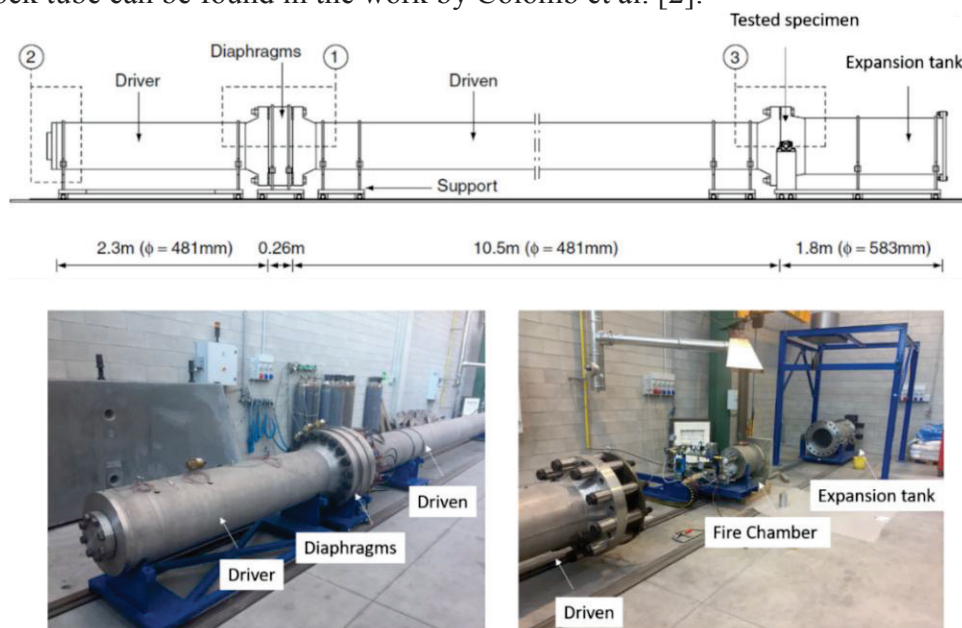


Figure 2: Schematic view of the shock tube including the Fire Chamber [2].

One of the main problems in tunnel accidents is the explosion of a vehicle after a fire exposure; for this reason, proper burner chamber has been designed to simulate fire conditions in the investigated specimen. Different fire curves can be applied, such as hydrocarbon or ISO 834 temperature curves. Once the desired fire exposure time for the specimen is reached, the burner is turned off, the specimen section is connected to the driven chamber and the test is performed. To fasten the slabs to the shock tube-mounting flange, a metal plate is placed on the outside of the concrete slabs.

### 3. Numerical Prediction

#### 3.1 Numerical simulation approach and solution schemes

According to the experiment scheme, the numerical simulation can be divided into to three phases: (1) Transient heat transfer analysis; (2) Coupled thermal-stress analysis (3) Transient dynamic analysis. Phase (1) aims to simulate the temperature distribution in the RC slab. Phase (2) aims to analysis the performance of RC slab under fire load, including material property and structural deformation. Phase (3) aims to predict the dynamic responses of fire-damaged RC slabs subjected to an explosive load. The influence of high temperature effect on the concrete and steel material is emphasized.

#### 3.2 Finite element model

A finite element model of the tested RC slabs was developed in the commercial software TNO DIANA according to the designed dimension and the solution scheme. Since the slab is axisymmetric, only a quarter of the slab was modelled with 16-node quadratic brick elements, see Figure 3. The average element size is 20 mm. The yellow color area was applied with fire load and following with blast impulse load. The remaining part of the slab was applied with an ambient temperature of 20°C. The temperature time history suggested by ISO 834 was uniformly applied to the exposed area of the slab as flow boundary conditions.

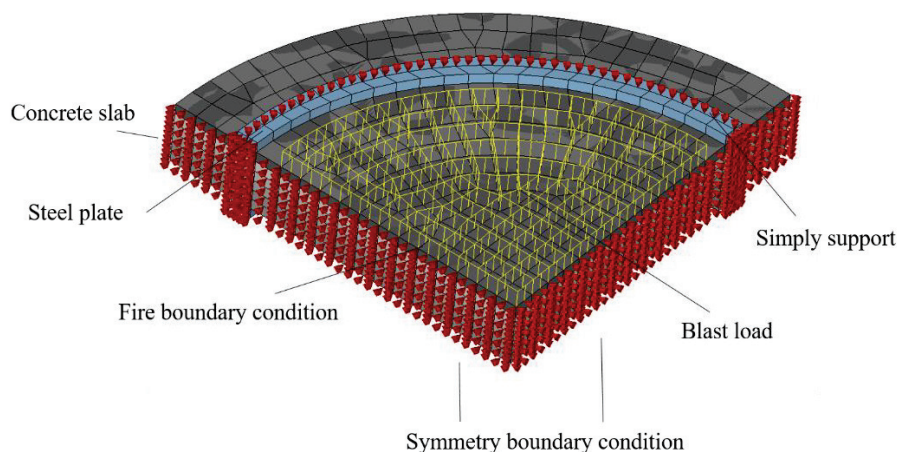


Figure 3: Finite element model of the tested slab, in the TNO DIANA environment.

### 3.3 Material model and input parameters

Regarding the material model of concrete, the Total Strain rotating crack model with a crack band width approach was used. More information of the material properties for the FE analysis can be found in Shu et al. [5]. The calculated parameters for concrete, steel and boundary interface are listed in Table 1.

Table 1: Calculated input parameters for concrete, steel and boundary interface

	Concrete	Reinforcing steel	Boundary interface
Conduction coefficient	1.32 W/m°C		48 W/m°C
Thermal capacity	7.5×10 <sup>-6</sup> 1/°C		
Density	2400 kg/m <sup>3</sup>	7800 kg/m <sup>3</sup>	
Poisson's ratio	0.2	0.3	
Heat capacity	2.3×10 <sup>6</sup> J/m <sup>3</sup> °C		
Mode I Fracture Energy	65 Nm/m <sup>2</sup>		

The material mechanical properties of concrete after fire can be calculated according to EN 1992-1-2; see Figure 4, where  $f_{c,\theta}$ ,  $f_{ct,\theta}$  and  $E_{c,\theta}$  denote the compressive strength, tensile strength and Young's modulus of concrete after fire exposure, respectively.

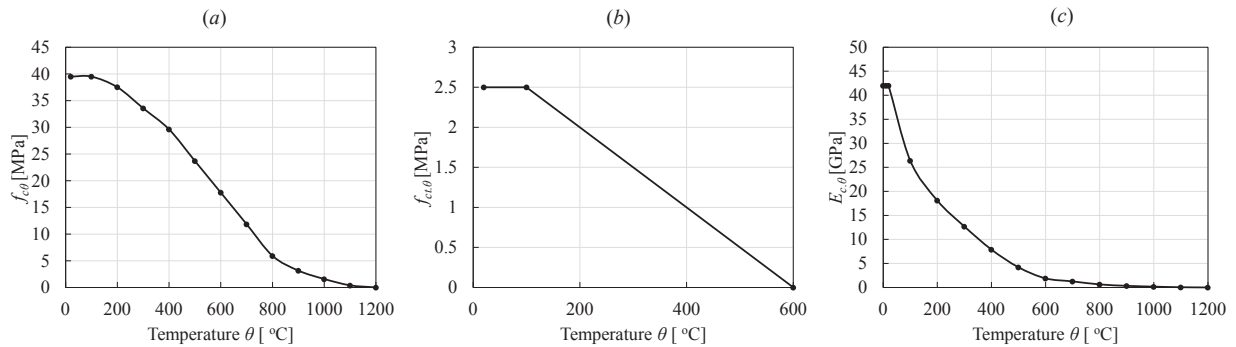


Figure 4: Material properties of concrete after exposed to fire (a) Compressive strength (b) Tensile strength (c) Young's modulus.

## 4. Numerical Results and Discussion

The fire load was applied to the exposed surface of the slab as the boundary conditions, and a total heat transfer process of 15, 30 and 60 minutes were calculated with a step length of 2 minutes. Figure 5 (a) (b) (c) and (d) show the simulation results of the slab under the fire duration of 15 minutes, 30 minutes and 60 minutes, plus the cooling phase of 30 minutes. It is observed that the temperature distribution was different between the heating phase (before 60 min) and cooling phase (after 60 min). During the heating phase, the heat transferred from the boundary to the inner part. On the contrary, the heat emanates from the inner part during the cooling phase. Figure 5 (e) presents the temperature-time histories at different depth of the slab. It indicates the variation of the temperature inside the slab model is reasonable.

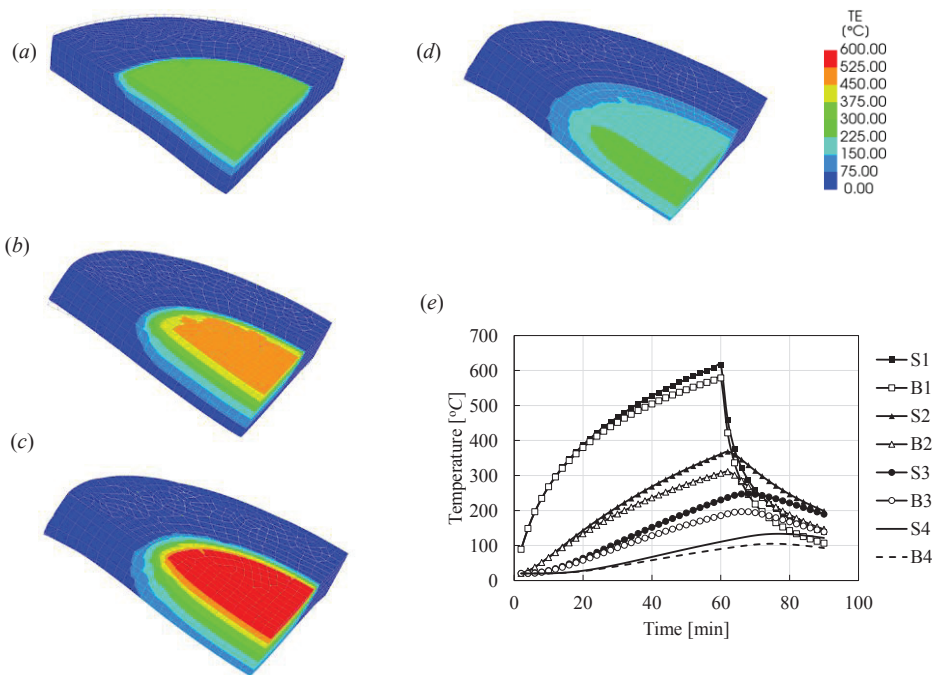


Figure 5: The temperature distribution under the fire duration of (a) 15 minutes (b) 30 minutes and (c) 60 minutes, (d) 90 minutes; (e) Temperature-time histories at different depth of the slab.

Figure 6 (a) presents the deflection-time history after the blast load was added to the surface of the RC slab. When the exposure time increased from 0 minute to 30 minutes and 60 minutes, the deflection was largely increased. It indicates that the mechanical property of the concrete and reinforcement was degraded due to the high temperature. However, one interesting observation is for the case of 15 minutes of exposure time, the average deflection was not influenced but the oscillation was largely decreased. However, the decrease of the oscillation shows the possibility of an increase of the damping, which needs to be studied further. Figure 6 (b) presents the total strain based crack pattern of the slab. It shows the crack pattern was extensively distributed at the surface. However, the discrete crack was not shown here because the element size is not small enough.

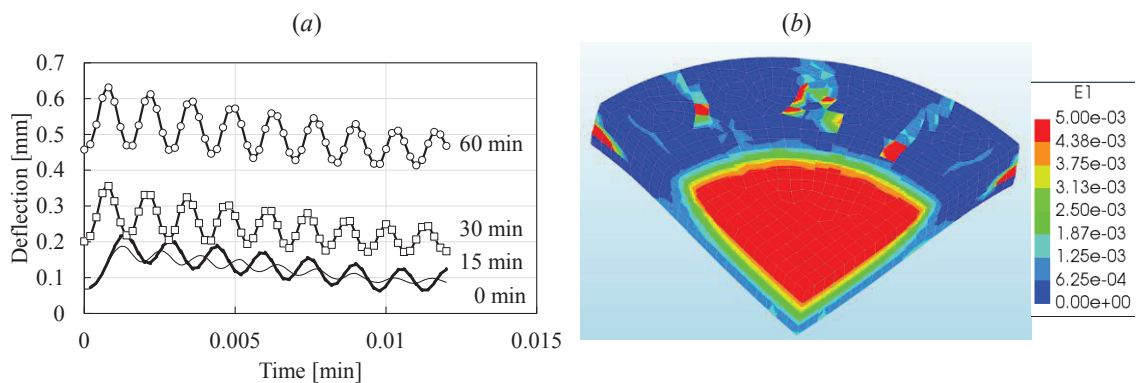


Figure 6: (a) Deflection-time history after the blast load (b) Strain based crack pattern after the blast load.



## 5. Summary and Conclusions

Through the study, the following conclusions can be drawn: (a) The mechanical property of concrete, reinforcing steel and the structural behaviour of the RC slab under variable extreme temperature environment can be modelled accurately using the developed modelling strategy. (b) The stiffness of the RC slab can be decreased considerably by the accumulative fire exposure time. (c) A short exposure time may not decrease the stiffness of the slab, but instead, increase the damping related property of the structure. The achievement of this study would help the engineers to have a better understanding of the structural behaviour, and validate the structural safety of the submerged floating tunnel (SFT) considering fire and explosion accidents occur inside the tunnel.

## Acknowledgments

This project is funded by NTNU, Department of structural engineering and the Norwegian Public Roads Administration as a part of the Ferry-free coastal route E39 project. The authors would like to express his outmost gratitude to the financers and colleagues at NTNU.

## References

- [1] Statens Vegvesen, Overview of the E39 Coastal Highway Route, Norway (2016)
- [2] Colombo, M. et al, A New Shock Tube Facility for Tunnel Safety, *Exp. Mech.* 51(7), (2011) 1143-1154
- [3] Cornelissen, H. W. et al, Experimental Determination of Crack Softening Characteristics of Normalweight and Lightweight Concrete, *Heron* 31(2), (1985) 45-56
- [4] Thorenfeldt, E. et al, Mechanical properties of high-strength concrete and applications in design, In *Proc. Symp. Utilization of High-Strength Concrete*, Norway (1987)
- [5] Shu, J. et al, Numerical prediction of punching behavior of RC bridge deck slabs using 3D continuum non-linear FE analysis, *Maintenance, Monitoring, Safety, Risk and Resilience of Bridges and Bridge Networks - Proc. 8th International Conference on Bridge Maintenance, Safety and Management*, Brazil (2016), 1607-1611

## THE IMPACT OF C-S-H NANOSTRUCTURE ON AUTOGENOUS SHRINKAGE AND SORPTION ISOTHERMS

Enrico Masoero <sup>(1)</sup>, Giovanni Di Luzio <sup>(2)</sup>, Gianluca Cusatis <sup>(3)</sup>

(1) Newcastle University, Newcastle upon Tyne, United Kingdom

(2) Politecnico di Milano, Milano, Italy

(3) Northwestern University, Evanston, IL, United States of America

### Abstract

The hydration and durability of cementitious materials are largely determined by the interaction between solid hydration products and water in the pores. This paper shows that drying shrinkage and sorption isotherms during early hydration can be explained by a progressive densification of the cement hydrates at sub-micrometre length scales. A simple conceptual model is presented to support this statement. The model predicts the evolution of self-desiccation during early hydration. The model predictions also align with recent results on C-S-H densification from proton nuclear magnetic resonance experiments. Overall, this indicates how nanoscale modelling can inform the current macroscopic models of concrete hygro-mechanics. This goes beyond the current state of the art, in that self-desiccation and sorption isotherms can now be predicted from the mix design, without other empirical inputs.

### 1. Introduction

Autogenous shrinkage is the volume contraction of a cement paste hydrating in sealed conditions. It can be explained as the results of a decrease of internal humidity ( $h$ ), experimentally measured with a humidity sensor placed inside a cavity that is created and kept within a hydrating sample. The decrease of  $h$  typically starts after *ca.* 1 day of hydration, when the degree of hydration  $\alpha$  is 0.4-0.5 [1,2], and is the combined result of: (i) a progressive desaturation of the pores, due to the consumption of water during the precipitation of hydration products (*e.g.* calcium-silicate-hydrate C-S-H gel and calcium hydroxide CH), (ii) chemical shrinkage, *i.e.* the negative difference in molar volumes between products (C-S-H, CH, etc.) and reactants (dry cement powder and water), and (iii) filling of pore space by hydration product. Three main humidity-dependent mechanisms are usually invoked to

explain autogenous shrinkage [3,4]: (i) capillary pressure due to curved vapour-liquid interfaces, (ii) changes in pore-vapour interfacial energy as a function of the thickness of the layer of adsorbed water, and (iii) disjoining pressure due to hindered adsorption of water in sub-nanometric pores. The internal pressures generated by each of these mechanisms can be expressed as direct (logarithmic) functions of  $h$ .

Predicting the autogenous shrinkage of a hydrating cement paste is a current challenge for continuum-based models of chemo-mechanics at the macroscale. Their typical approach is the following [5]: (i) autogenous shrinkage is computed from poromechanics, considering the above-mentioned  $h$ -dependent pressures; (ii)  $h$  is obtained from the saturation degree,  $S$ , using a sorption isotherm function  $S(h)$  which is an empirical input that depends on the chemical composition of the cement paste and on the degree of hydration  $\alpha$ ; (iii) the saturation degree  $S$  is a function of the cement paste composition and of  $\alpha$ , whose temporal evolution  $\alpha(t)$  is usually expressed as a differential equation (in the so-called “affinity” approach) with empirical parameters that depend on the composition of the cement paste.

The just-described macroscopic modelling approach has limited predictive ability, because  $S(h)$  and  $\alpha(t)$  rely on empirical parameters to be obtained experimentally. Recent work has shown that  $\alpha(t)$  can instead be parametrised using state-of-the-art simulations of the chemical and microstructural evolution of a cement paste during hydration, *e.g.* CEMHYD3D [2,6]. In principle, the same could be done for  $S(h)$ , because simulators such as CEMHYD3D also predict the temporal evolution of  $S(t)$  and of the 3D evolution pore structure, and these two are in principle sufficient to compute the corresponding  $h$ . However, such a bottom-up prediction of  $S(h)$  has not been achieved yet. The reason is that a drop of  $h$  below 99% (autogenous shrinkage typically entails  $h$  between 75% and 92%) requires the liquid-vapour interface to sit in pores with diameter  $\leq 100$  nm. This is at least one order of magnitude below the resolution of the above-mentioned microstructural simulators. Therefore, to predict the evolution of  $S(h)$ , simulators such as CEMHYD3D must be complemented with information about the chemistry-dependent evolution of the pore structure below the micrometre scale. In typical portland cement pastes, this nanoscale porosity is intrinsic to the C-S-H gel phase.

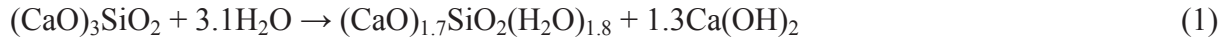
This manuscript presents a simple conceptual model of the co-evolution of hydration degree  $\alpha$  and C-S-H gel nanopore structure. This is a simplified version of another recently published model [7], whose key feature is to allow for the C-S-H to: (i) initially precipitate as a low-density high-porosity phase, with pores in the 10-100 nm range, and (ii) subsequently get denser with a progressive reduction of pore sizes towards 1-10 nm. The results shows that the nanopore structure of the C-S-H gel and its densification are essential to predict the onset of self-desiccation (decrease of  $h$  during hydration) and a realistic evolution of the sorption isotherm  $S(h)$ . This model provides a starting point to complement the current simulators of microstructure development, such as CEMHYD3D, and eventually to enable continuum-based macroscopic models that can predict autogenous shrinkage starting directly from the chemical composition and curing conditions of the cement paste.

## 2. Conceptual model

The aims of the conceptual model presented here are to highlight the importance of nanostructure on self-desiccation and sorption isotherms, and to indicate a possible approach

to include information about nanostructure in chemo-mechanical models of cement hydration. A more detailed development of the same concept has recently been published recently [7].

The model considers the hydration of pure tricalcium silicate,  $C_3S$ , to produce C-S-H and CH:



The C-S-H in Eq. (1) refers to the solid part of it only, *i.e.* it does not consider the amount and size of nanopores in the C-S-H gel phase. Considering the molar volumes of the various elements in Eq. (1) [8], one can express the evolutions of  $C_3S$ , C-S-H, CH, and water volumes as a function of the degree of hydration  $\alpha$  and per unit volume or original paste at  $\alpha = 0$ . This leads to the plots of volume fractions *vs.*  $\alpha$  in the next section of this manuscript. Furthermore, the balance of molar volumes associated to Eq. (1) indicates *ca.* 8.1% of chemical shrinkage [8], *i.e.* a negative difference in volume between products and reactants.

Most of the models of cement hydration to date assume that the C-S-H gel forms immediately with a nanostructure that is similar to the one observed in mature paste. This means an average volume fraction of solid C-S-H per unit volume of gel of  $\eta \approx 0.655$ , *i.e.* a 34.5% volume fraction of nanopores [8]. Water sorption experiments and computer simulations estimate the average nanopore width in this dense C-S-H gel to be about 3 nm [9, 10]. However, recent results from  $^1H$  nuclear magnetic resonance [1] confirmed the already widespread idea that the C-S-H gel initially forms as a low-density phase and significantly larger nanopores. A simple way to model this is to assume a low initial  $\eta_0$  of the gel, here  $\eta_0 = 0.22$  [7], and a linear increase of  $\eta$  with hydration time towards the final above-mentioned  $\eta_f = 0.655$ . During early hydration (first day or two, with  $\alpha$  reaching 0.4 to 0.7 depending on the cement type and curing conditions) one can reasonably approximate  $\alpha(t)$  as proportional to  $t^{1/2}$ , therefore the linear evolution of  $\eta(t)$  can be replaced by  $\eta(\alpha) = \eta_0 + (\eta_f - \eta_0) \alpha^2$ . Parallel to this densification, the model should incorporate some information about the evolution of nanopore sizes. A possibility, consistent with nanoparticle models of cement hydrates [10], is to assume an initial average nanopore size  $D_0 = 45$  nm at  $\alpha = 0$  which decreases linearly with  $\eta$  until a final  $D_f = 3$  nm. A similar, but more thorough, model of C-S-H densification is available in the literature.

At equilibrium, the Kelvin equation relates the internal humidity  $h$  to the diameter  $D$  of the largest saturated pore (for water in cylindrical pores with perfectly hydrophilic surface):

$$D = -4 \frac{\gamma_w MV_w}{RT \ln h} \quad (2)$$

In Eq. (2),  $\gamma_w = 0.073$  N/m and  $MV_w = 18.02 \times 10^{-6}$  m<sup>3</sup>/mol are the liquid-vapour interfacial energy and the molar volume of water. In the next section, Eq. (2) will be used to predict self-desiccation and to discuss implications of the presented model for sorption isotherms.

### 3. Results

Fig. 1 shows the evolution of volume fractions of different phases during the hydration of a pure  $C_3S$  paste, as per Eq. (1). The paste has  $w/c = 0.42$ , which is the value that, when  $\alpha = 1$  and if the gel has  $\eta_f = 0.655$ , leads to the complete consumption of  $C_3S$  and filling of capillary pores by C-S-H gel, while the nanopores inside the gel remain fully saturated with water. This is shown in both Fig. 1a and Fig. 1b at  $\alpha = 1$ . Both the subfigures also display the same amount of solid phases ( $C_3S$ , CH, solid part of the C-S-H) and of chemical shrinkage (the white-coloured complement to volume fraction = 1): this is expected because all these quantities are directly controlled by Eq. (1), which is the same for both the subfigures.

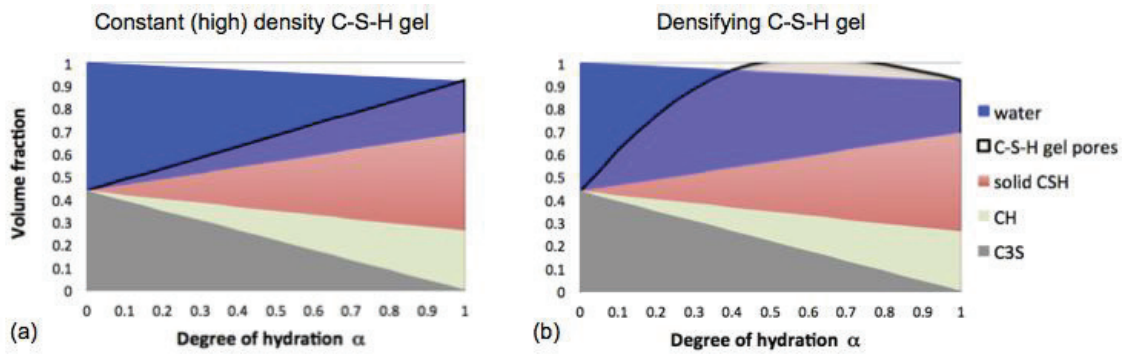


Figure 1: Model results for the evolution of volume fractions of various phases in a  $C_3S$  paste during hydration. (a) assumes C-S-H gel with constant volume fraction of pores 0.345 independent of  $\alpha$ . (b) assumes a C-S-H gel that gets denser with  $\alpha^2$ .

The difference between Fig. 1a and b is in the evolution of the nanoporosity and solid fraction  $\eta$  of the C-S-H gel with  $\alpha$ . Fig. 1a considers a constant  $\eta_f = 0.655$ , independent of  $\alpha$ , which is the common assumption in current microstructural simulators of cement hydration, such as CEMHYD3D. Under such an assumption, until  $\alpha = 1$ , there will always be more water than is necessary to fill all the C-S-H gel nanopores. This water will sit in leftover spaces between the hydration products and the still anhydrous  $C_3S$ , and these spaces are typically in the micrometre range. In such a scenario, where the largest saturate pore diameter  $D$  is in the micrometre range, Eq. (2) always predicts internal humidity  $h > 99\%$ , only except for  $\alpha = 1$ . This clearly contrasts with the experimental observation of self-desiccation starting already at  $\alpha = 0.4-0.5$ , as shown in Fig. 2 (the impact of considering  $w/c = 0.4$ , as in the experiment, instead of 0.42, as in the simulation, is very limited, simply reducing the  $\alpha$  triggering the humidity drop from 1 to *ca.* 0.9, which is still far from the experiment). Fig. 1b considers a progressive densification of the C-S-H gel with  $\eta$  scaling as  $\alpha^2$  (see rationale in the previous section). This implies that the volume fraction of gel pores increases rapidly at low  $\alpha$  and soon, already at  $\alpha = 0.4$ , all the remaining water in the paste is within the gel (nano)pores. Any further reaction causes the gel nanopores to partially desaturate, leading to a decrease of  $h$  predicted by Eq. (2). This is reflected by the drop of  $h$  in Fig. 2 starting already at  $\alpha = 0.4$ , in agreement with the experiment.

Fig. 1b and Fig. 2 display two unphysical features that are due to the strong approximations in the presented conceptual model: these limitations have been already overcome in a more detailed version of a similar model that has been recently published [7]. The first problematic

feature is that the sum of solid phases and gel porosity in Fig. 1b, at some point during hydration ( $0.4 < \alpha < 1$ ) is greater than one. This means that the paste, overall, should swell in that range of  $\alpha$ . This unphysical prediction can be (and has been) overcome considering that the precipitation of new C-S-H gel is only possible within capillary pores that contain water (some of them instead empty out during hydration) [7]. The second problematic feature is that the internal humidity in Fig. 2 shows a sudden drop at  $\alpha = 0.4$  for the case of a densifying gel, whereas the experiments show a continuous trend of progressively decreasing  $h$  with  $\alpha$  starting from  $\alpha = 0.4$ . The reason for the unphysical discontinuity is that the model considers only one single characteristic width for all the pores in the C-S-H gel. In reality, the gel has a wider distribution of nanopore sizes. It has been shown that the discontinuity in Fig. 2 indeed disappears if one takes nanopore size distributions from nanoparticle models of the C-S-H gel, and expresses these pore distributions as functions of the gel solid fraction  $\eta$  [7,10].

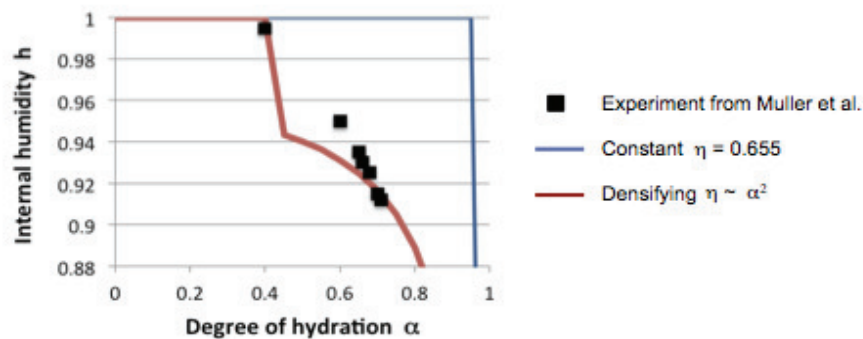


Figure 2: Model and experimental results of self-desiccation (decrease of  $h$ ) as a function of degree of hydration. The experiment from Muller et al. (cite) refer to a low-alkali cement paste with  $w/c = 0.4$ . The model results correspond to the two cases in Fig. 1.

#### 4. Conclusion

The simple model presented here has shown that the prediction of self-desiccation in a hydrating cement paste relies on two key features that a model must incorporate:

- (i) A progressive densification of the C-S-H gel, which forms initially with a very low density. This is critical in order for the gel to fill the pore volume in the paste and enable the desaturation of nanopores already at low degrees of hydration ( $\alpha = 0.4-0.5$ , as shown by the experiments). Only when the nanopores starts to desaturate, the Kelvin equation predicts a drop of internal humidity (self desiccation);
- (ii) A progressive reduction of the average nanopore size as the gel gets progressively denser. This is necessary in order to predict the progressive decrease of  $h$  with  $\alpha$  once the nanopores have started to desaturate.

Incorporating these two features in the current model of microstructure development during cement hydration and then, in turn, in the macroscopic models of cement hygro-mechanics, is the way forward to obtain genuine predictions of self-desiccation and autogenous shrinkage based only on the chemical composition, degree of hydration, and curing conditions of the cement paste. This would remove the current reliance of macroscopic models on empirical

sorption isotherms  $S(h)$ ; indeed, coupling the presented model with a more detailed description of the nanopore gel size distribution, has been shown to yield realistic predictions of the sorption isotherms too [7]. To this end, a detailed description of how the nanostructure of the gel evolves, as a function of the chemical composition of the cement and on the curing time and conditions, is needed. This level of detail can be obtained from state-of-the-art nanoparticle simulations of cement hydration [11]. This opens to a truly multi-scale predictive modelling approach of self-desiccation, sorption isotherm, and autogenous shrinkage, in line with the vision of a simulation-guided design of future nano-engineered cements.

## References

- [1] Muller, S. et al, Use of bench-top NMR to measure the density, composition and desorption isotherm of C—S—H in cement paste, *Microporous Mesoporous Mater*, 178 (2013), 99 – 103
- [2] Pathirage, M. et al, A Multiscale Framework for the Prediction of Concrete Self-Desiccation, *Proceedings of the EURO-C 2018 Conference - Computational Modelling of Concrete and Concrete*, Austria (2018)
- [3] Jennings, H.M., et al, Water isotherms, shrinkage and creep of cement paste: hypotheses, models and experiments. In *Mechanics and Physics of Creep, Shrinkage, and Durability of Concrete: A Tribute to Zdeňk P. Bažant* (2013), 134-141
- [4] Bažant, Z.P., Interaction of concrete creep, shrinkage and swelling with water, hydration, and damage: Nano-Macro-Chemo. *Proceedings of the 10th International Conference on Mechanics and Physics of Creep, Shrinkage, and Durability of Concrete and Concrete Structures* (2015), 1-12
- [5] Di Luzio, G. and Cusatis, G., Hygro-thermo-chemical modeling of high performance concrete. I: Theory. *Cem Concr Res* 31 (2009), 301-308
- [6] Bentz, D.P., CEMHYD3D: A three-dimensional cement hydration and microstructure development modelling package. Version 2.0. US Department of Commerce, National Institute of Standards and Technology (2000)
- [7] Masoero, E., et al, C—S—H gel densification: The impact of the nanoscale on self-desiccation and sorption isotherms, *Cem Concr Res* 109 (2018), 103-119
- [8] Masoero, E., et al, A Reaction Zone Hypothesis for the Effects of Particle Size and Water- to- Cement Ratio on the Early Hydration Kinetics of C3S. *J Am Ceram Soc* 97 (2014), 967-975
- [9] Baroghel-Bouny, V., Water vapour sorption experiments on hardened cementitious materials: Part I: Essential tool for analysis of hygral behaviour and its relation to pore structure, *Cem Concr Res* 37 (2007), 414-437.
- [10] Ioannidou, K., et al, Mesoscale texture of cement hydrates. *Proc Natl Acad Sci* 113 (2016), 2029-2034
- [11] Shvab, I., et al, Precipitation Mechanisms of Mesoporous Nanoparticle Aggregates: Off-Lattice, Coarse-Grained, Kinetic Simulations. *Cryst Growth Des* 17 (2017), 1316-1327

# **BIM AND STRUCTURAL CONCRETE**



## **BIM FOR PRECAST**

**Peter Karlsson** <sup>(1)</sup>

(1) StruSoft AB, Malmö, Sweden

### **Abstract**

The precast process is divided into three sub-processes; design, erection and production. Design is giving birth to the precast process with a rough 3D model. When planning the process is reversed so that it starts with the planning of the erection on site and step backwards to the time for production and the time for delivery of detailed shop- drawings.

By doing this planning in a shared Building Information Modelling (BIM) platform in real time all three sub-processes get the correct priority for the main process the project on site.

The site project planners use the 3D model when they make the rough planning on the design structure. They start by setting the planned erection date and then step backwards through the planned delivery date, planned storage date, planned production date and planned drawing delivery date.

The planned production date gives production the time frames when they need to deliver the manufactured elements and the planned drawing date gives design the information when the shop-drawings needs to be ready so that the production can produce the elements in time.

### **1. Introduction**

Building Information Modelling (BIM) means different things for different people. I will not try to define BIM in this article as too much time has been spent on that already, but we prefer to think that there is a silent M after “BIM(M)” that is read out as “Management”. Because BIM is about managing multi-disciplinary processes (companies/people), that connect and sometimes overlap, and share data on a high level.

When discussing BIM, it's of course hard to narrow down and focus on precast but I think that's the first step to a successful implementation of BIM for a precast company (“Precaster”). To look at “what's in it for me”? The precast structure is of course only a part delivery of the whole building project. But if you see that as a process that you bring data into and at the end delivers more high level out from, you can start to make the Precast process

fully BIM so that within in that process, which sometimes is controlled by one company (different departments) or several companies, all the people share their data in a real time environment. Maybe the parties involved have different interfaces or applications, but they are all having the same source of information.

## 2. The precast process and BIM

BIM is a way of working not a software. That's why the software should support the way of working and not the other way around. To get to a high implementation of BIM you absolutely need to adopt to a new way of working and have a software that supports that new path.

We think that the precast process (once the project is won by a precast company) has three main legs/sub processes. The three legs of precast is design, production and erection. The different legs have different priorities and needs. If you can expose the information of those sub processes for all the other parties involved (in the precast process), in real time, so that for instance the production can see the planning of the erection and vice versa there is a lot of time and effort to save.

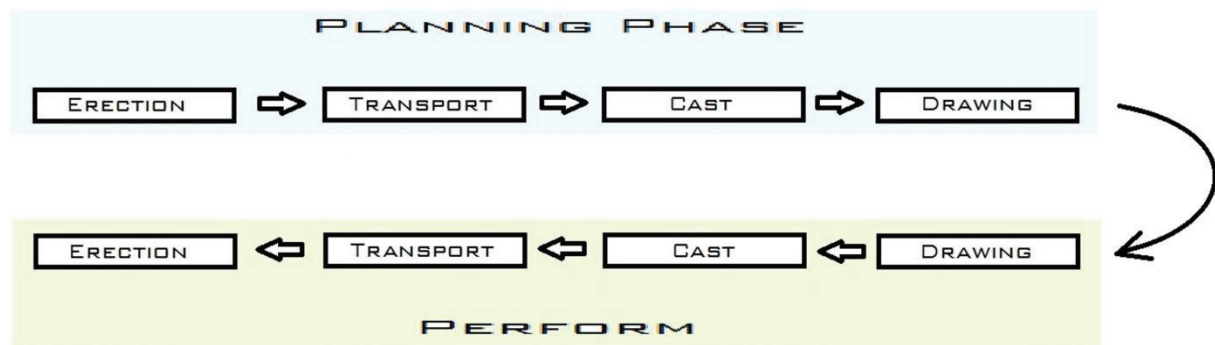


Figure 1: The planning and perform process of precast.

The design is giving birth to the structure of the precast process with the 3D model. First on a rough level and later on a more detailed one. by reversing the process so that we start with the planning of the erection on site and step backwards to the time for production and the time for delivery of detailed shop drawing all three legs get the correct priority for the main process the project on site. By doing this you can setup your production to “just in time delivery” and then the design to deliver precast detailed design (finalizing production drawings) in time to fulfil the needs from production. To come to this doesn't require the same mindset for all legs of precast; it does however require “BIM for precast”.

The input for the “Precasters” today (if it's digital) comes from many different formats produced in software packages like ArchiCAD, AutoCAD, Revit, Tekla etc. Industrial Foundation Classes (IFC) is a great format for the exchange of BIM data. But there is one weakness by using it as the only technical format for the contract of the building: the object information in it needs to be converted to objects of the software it shall be represented in. When doing that there is a great risk that this conversion will make something different with the data than it was originally. To be able to take that type of data in at a high level with less

risk of conversion problems it's better to make plugins into the different software where the information was initially created and then with user control import the data from the origin platform to the BIM database. This is the only reasonable way to deal with the problem today. The Precast process could be illustrated like a relay race with parallel teams that run towards a common goal (the completed structure of the building on site). Handover of the stick (information) is done within the teams as well as between the different teams. The information provided with the stick changes constantly. Good logistics is the key to success and if things are not in the right place in the right time, the work becomes more complicated not only within the own team but for all the other teams as well.

In the light of that, we see a common storing of data and exchange in real time as the base of BIM for Precast. The change of data happens so frequently during the precast process and if manual (snapshot) exchange of data should be the way of communicating you will lose time and quality. The precast process is iterative: that's why you need to have all the corresponding data updated all the time to make the right decisions.

In the precast world outsourcing has come to stay. In that view the need of a common language between the different stakeholders in the project, whether they are in the homeland of the project or abroad, is the key to success for the "Precasters". The base structure in that language is the 3D model. We can then bind all information needed to the model throughout the process. Then you can sit on the other side of the planet and understand the priorities of the project.

Another important thing when we talk about BIM is that the output is relevant and present for each person involved ("right information at the right time") in the process. That, for instance, means that the production picks the material take off data directly from the BIM database based on their own selection (maybe the planned molds of the week) not based on what design pass on in their offline Excel report delivery. To have the production and design to operate on the same data (real time BIM database) is essential for a successful BIM integration for Precast.

### **3. Building Information Modelling platform**

Our customers today use a mix of taking the information in as reference AutoCAD or on a higher level through our Revit and Tekla interfaces. We have AutoCAD, BricsCAD, Revit and Tekla plugins that interact in real time with our BIM database.

Inside the precast process our customers interact between their departments by using different interfaces to our BIM database.

Design starts by making a rough 3D model in AutoCAD, BricsCAD, Revit or Tekla with our plugins. Rough means that not all element connections are solved (yet) and no shop drawings are produced.

The erection planners then continue to make the rough planning on the design structure. They start by setting the planned erection date (erection sequence) and then steps backwards through the planned delivery date, planned storage date, planned production date and planned drawing date. They have functionality to simulate time and check against cranes. This they do on a model-based software (Project Manager) that interacts directly with the BIM database. The Project Manager is a common platform for both design, erection and production.

The planned production date gives Production the time frames they need to deliver the manufactured elements and the planned drawing date gives the Design the information when the drawings need to be ready so that the Production can produce in time.

Production then starts the detailed planning based on the erection planning data. They plan their molds and beds to be as effective as possible and coordinate this with storage and transportation. As a support they use both the Project Manager (Project focus) and the Resource Manager (Factory focus). Throughout the whole process the status chain on the elements gives an instant visible feedback for all the stakeholders in the project of the current situation.

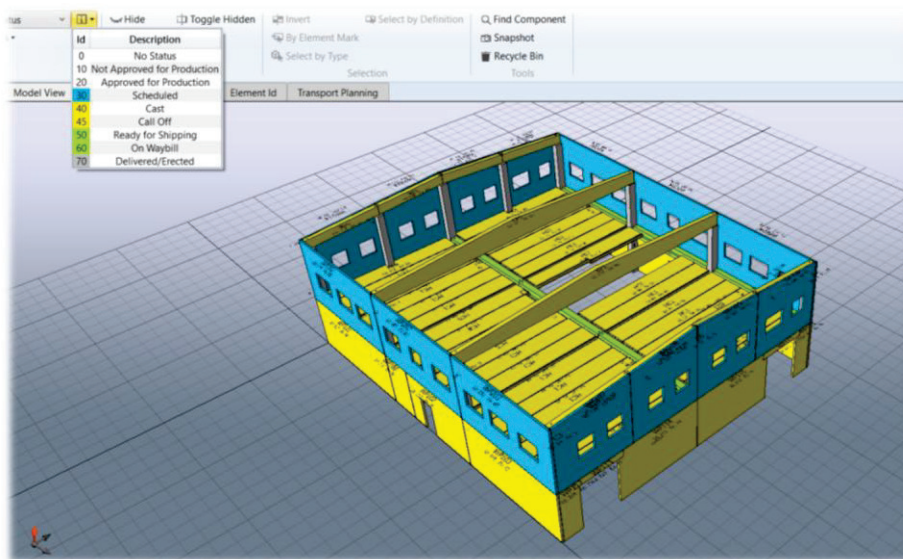


Figure 2: The real time status of the project.

Mobile apps (also connected to the BIM database) gives a remote connection to the BIM database for people working out in the storage or at the erection site. With that application in their phones they can, in real time, add information to the database such as storage location, transport information etc.

The most common output from our customers today to parties in the bigger outer process of the project is IFC models for clash control (clashes in space).

#### 4. Future and the precast process

Different perspectives need different interfaces/apps. We see a future where an extended toolbox of apps for different needs will be joined together with multi-linked cloud-based databases. “The internet of precast” if you like.

With that online functionality the designer that makes the detailed design can for instance directly communicate with the mesh welding machinery (like the Progress Group PTS service application) and check the producibility for the reinforcement mesh and then in real time receive the response in his 3D model for correction.

Talking about clash control the obvious thing is to detect clashes in space, but the future is to use BIM to see clashes in time as well. Sharing time information between different systems will be possible by communicating cloud databases. The IMPACT BIM Cloud database directly communicates with real time interfaces to the main process time schedule.

The Precast manufactures can outsource and let their consultants connect directly to their data (manufacture) in an environment controlled by the precast manufacturer in the cloud. With this the precast manufacturer will be able to check the progress of their consultants and let them see the data needed for making the right decisions.

With environmental data connected to the BIM model the footprint of the precast concrete structure will be visual for everybody in the project. The customer (of the precast manufacturer) will be able to see the result, follow the progress and see the planning ahead in a cloud-based BIM environment.



Figure 3: Real time environmental IMPACT of the Precast structure.

Ask the reinforcement vendor for price and time to deliver reinforcement stirrups or reinforcement mesh for the whole project (or parts of a project) by online communication with the vendor cloud-based system (like the Celsa Steel Service application QR). Instantly let your vendors system give you the expected delivery time and check the producibility of your data. If the vendor fulfils your expectations (including price), accept and place the order directly. Ask the vendor of steel plates in the same way.

Mixed reality where the real environment co-exist with the virtual reality creates a platform for better understanding and implementation of the engineered solutions in the real world. Microsoft HoloLens glasses projection in the mould combined with “naked eyes” can be used to place and control the cast in items in the mould. Mixed reality has already successfully been used in the aerospace and car industry and it will for sure create advantages for the building industry as well. By using mixed reality in the precast production, we will speed up and increase the quality of the manufacturing process and make the production paperless. We can combine the design element model with step by step procedures (data displayed in sequence not all at once) on how to manufacture and assemble an item like for instance a reinforcement cage. This will make it easier to produce advanced components with a less

experienced workforce. When more of the workforce can do complicated task, it will be easier to remove bottlenecks in the production. The data used in the mixed reality environment collect the data in real time from the BIM database information and is always updated and the risk for producing on an outdated paper drawing will be avoided.



Figure 4: Digital element in the mould at SCF Betongelement AB factory in Strömsund Sweden picture from Information Experience.

## 5. Conclusions

In the future the process at building sites will be more an assembly process than a manufacture process. This will make advance logistics even more important for success. Exchange and visibility of real time data that describes all dimensions (3D, time, cost and environmental impact) to all the stakeholders of the process will reduce the cost and delivery times for the building industry and make the work more attractive for the new generations.

## **COST-OPTIMAL ANALYSIS OF CONCRETE SOLUTIONS FOR SINGLE-FAMILY NZEBs APPLYING AN OPEN BIM WORKFLOW**

**Afonso Miguel Solak**<sup>(1,2)</sup>, **Javier Pereiro-Barceló**<sup>(2)</sup>

(1) University of Alicante, Alicante, Spain

(2) CYPE Ingenieros S.A., Alicante, Spain

### **Abstract**

In this study, Building Energy Simulations (BES) have been performed to check the impact of concrete-based building materials as part of the building envelope on the primary energy consumption of a single-family nearly Zero Energy Building (nZEB) to be built in Spain. The aim of this study is to evaluate different concrete solutions and determine which configurations combine the lowest primary energy consumption and the lowest cost by analyzing the building's energy performance throughout its life cycle. An Open BIM workflow, proposed by CYPE Software, was used for the achievement of these objectives. An architectural model was developed using the freeware application IFC Builder and synchronized through the online platform, BIMserver.center, where its project data was available for the energy simulations performed later in CYPETHERM HE Plus. Although the results refer to a Spanish-Mediterranean residential reference, the methodology applied in this study is applicable in other cases and can be useful to support nZEBs design and decision making.

### **1. Introduction**

Cement-based products must play a key role in the transition towards a more sustainable construction, replacing traditional forms of construction with more advantageous, economic and durable ones. In Spain, in 2016, 11.08 million tons of cement were used, with 46% destined to the buildings construction sector [1]. Concrete buildings can provide substantial energy savings during their lifetime. The high level of thermal mass in concrete constructions means that indoor temperatures remain stable, regardless of external fluctuations [1]. In the following years, across the European Union, every new building must fulfill the requirements of the nearly Zero Energy Buildings (nZEB) concept, as it is stated by the Directive 31/2010 -

Energy Performance of Buildings Directive (EPBD) [2]. The deadline, 2020 targets the reduction of the primary energy consumption, but there are no general requirements for the application of the nZEB concept in all countries. In Spain, the basic document outlining Energy Savings, part of the national construction normative "Technical Building Code (CTE-DB-HE)", published in 2013, will be updated during 2018 as the Directive 31/2010 establishes in its Article 4 that "minimum energy performance requirements shall be reviewed at regular intervals which shall not be longer than five years". Cost optimal levels can be seen as a first step towards the achievement of the nZEB target. They refer to the energy performance in terms of primary energy leading to the minimum life cycle cost, and according to the EPBD Guidelines, must include the initial investment and running, replacement and disposal costs.

Building Information Modeling (BIM) can be a useful tool to evaluate the economical and technical viability of a project. In the past decade, BIM has become widely used in the Architecture, Engineering and Construction (AEC) sector [3]. The use of BIM and its visual programming interface has become an integral tool for building design, not only for the conceptual design stage, but also for optimizing the design for thermal performance [4]. It is a remarkable improvement in terms of cooperation and management of the documentation, since it establishes a common platform between the different subjects involved in a project [5]. The term "Open BIM" appears when we take advantage of this protocol to implement an open collaboration system that does not depend on a specific application. The main property of Open BIM technology is that it is based on the use of IFC standard interchange formats. By using this format, which is also public and not linked to a specific developer, the durability of the work that has been carried out is guaranteed [5].

This study focused on the evaluation of different concrete solutions and configurations which combine the lowest total energy consumption of primary energy of non-renewable origin (Ct,nr) and the lowest cost. This was done by analyzing the building's energy performance throughout its life cycle, including the Costs of Construction (CC), Maintenance/Replacement (CM) and Operation (CO), in the Open BIM Workflow proposed by CYPE Software.

## 2. Methodology

### 2.1 The Reference Building

The selected reference building consisted of a two-story, single-family house with a net floor area of 164.97 m<sup>2</sup>, a net floor height of 2.70 m and a net volume of 573.15 m<sup>3</sup>. The aspect ratio was 1.29:1 and the window-to-wall ratio was 16%. Technical drawings and an isometric view of the building are provided in Fig.1. Since the building is located in Colmenar Viejo (Madrid, Spain), it was designed in compliance with the maximum values of energy consumption required by national regulation (CTE DB-HE). Air permeability of the envelope, considering a reference pressure of 100 Pa, was 16 m<sup>3</sup>/(h.m<sup>2</sup>) for façades and roofs, 60 m<sup>3</sup>/(h.m<sup>2</sup>) for doors and 10 m<sup>3</sup>/(h.m<sup>2</sup>) for the other openings.

The demand for sanitary hot water was 112.0 l/day and the set point temperatures established in CTE DB-HE (17 °C to 28 °C) were conditions of operation and internal comfort, considering a residential profile of use. The efficiency of the heat recovery system of the mechanical ventilation system was 87.1%. The values of infiltrations were obtained the calculation method of Enhanced Model (ASHARAE), with a calculated flow coefficient,



without admission openings and considering that the operational conditions were constant. The total ventilation of the habitable enclosures was 0.63 ren/h. The solution adopted for the air-conditioning-heating system consisted of a set of low temperature under floor radiant system complemented by fan coils of low silhouette ducts, associated with an arothermal system with air/water heat pump and reversible cycle (total cooling power of 10000 W, energy efficiency ratio of 2.78, total heating power of 11200 W and a coefficient of performance of 4.55).

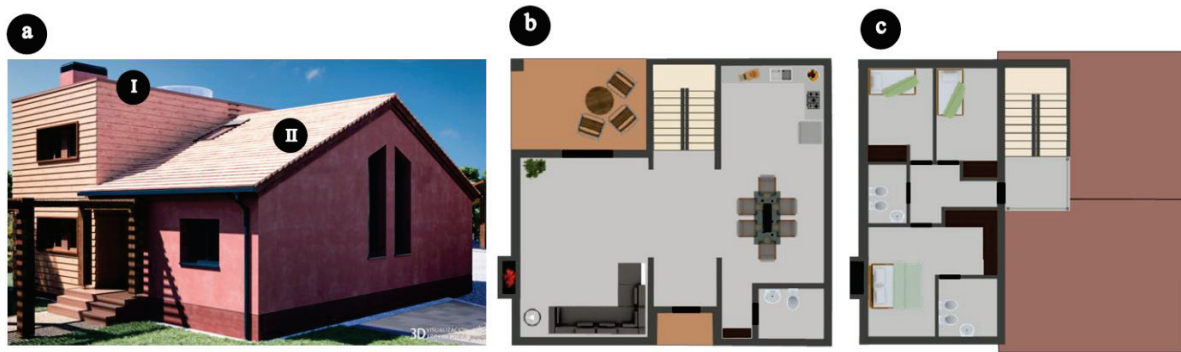


Figure 1: Technical Drawings and Isometric View of the Case Study.

Reinforced concrete slabs (thickness of 15 cm) were used for the horizontal structural system. Its resultant thermal transmittance ( $U$ ), associated with its insulation layers, were  $0.19 \text{ W}/(\text{m}^2 \cdot \text{K})$  for the ground floor slab,  $0.22 \text{ W}/(\text{m}^2 \cdot \text{K})$  for the flat roof slab (I in Fig. 1a) and  $0.31 \text{ W}/(\text{m}^2 \cdot \text{K})$  for the sloped roof slab (II in Fig. 2a). Windows were composed wood frames (thermal conductivity ( $\lambda$ ) of  $1.10 \text{ W}/(\text{m}^2 \cdot \text{K})$  and solar factor of 0.61) and double low emissivity glass with argon cavity and aluminum spacers ( $\lambda = 1.43 \text{ W}/(\text{m}^2 \cdot \text{K})$ ), resulting in a frame-glass ratio of 22%. Eight additional photovoltaic panels, with a total area of  $12.78 \text{ m}^2$ , provide  $16.92 \text{ kWh}/\text{m}^2$  yearly.

## 2.2 Concrete Solutions Studied

The vertical surfaces (Fig.2) were the main elements evaluated in this work. In all cases, the walls have structural and enclosing function. An External Thermal Insulation Cladding System (ETICS) was considered for the external surface of the façades in order to reduce the losses caused by thermal bridges. ETICS was formed by one layer of a 60 mm rigid expanded polystyrene panel ( $\lambda = 0.04 \text{ W}/(\text{m} \cdot \text{K})$ ) and four layers, of 4 mm each, of mortar as part of the system, but with no relevant thermal properties. Internal surfaces of the façades were covered by 10 mm plasterboards ( $\lambda=0.25 \text{ W}/(\text{m} \cdot \text{K})$ ) spaced 10 mm from the structural core.

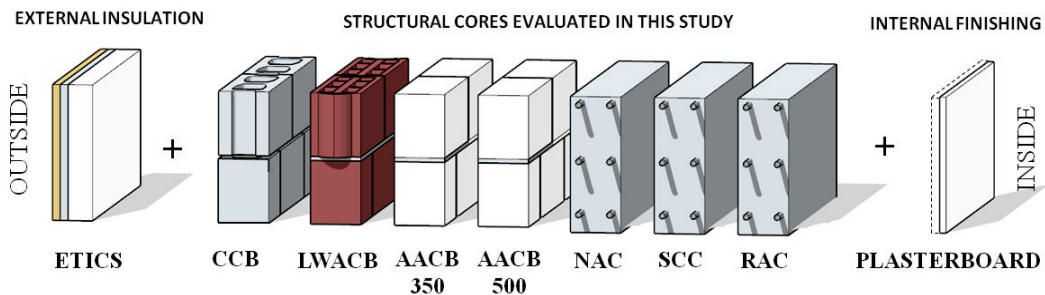


Figure 2: External walls evaluated in this study.

Six different solutions were evaluated as wall-core materials. Three types of cast-in-place concretes were included in the simulations as reinforced concrete walls with materials commonly used in Spain: Natural Aggregate Concrete (NAC), Recycled Aggregate Concrete (RAC) and Self-Compacting Concrete (SCC). In the same way, the structural masonry walls are formed by Conventional Concrete Blocks (CCB), Lightweight Aggregate Concrete Blocks (LWACB) and two different types of Autoclaved Aerated Concrete Blocks (AACB). The thicknesses considered in this study are dimensions commonly used and commercialized by manufactures in Spain (Table 1).

Table 1: Thermal Properties of the Concrete Wall-Cores Evaluated in this Study

Material		Thickness (cm)											
		10.0	12.0	15.0	20.0	22.5	25.0	30.0	34.0	35.0	36.5	40.0	42.0
CCB	$\lambda$	0.605	0.670	0.759	0.891	-	1.009	1.117	-	-	-	-	-
	$\rho$	1337	1247	1201	1112	-	1048	998	-	-	-	-	-
LWACB	$\lambda$	-	0.202	0.224	0.256	-	0.285	0.310	-	-	-	-	-
	$\rho$	-	1066	1001	924	-	868	824	-	-	-	-	-
AACB 350	$\lambda$	-	-	-	-	0.090	0.090	0.090	0.090	-	0.090	-	0.090
	$\rho$	-	-	-	-	350	350	350	350	-	350	-	350
AACB 500	$\lambda$	-	-	-	0.125	-	0.125	0.125	-	-	-	-	-
	$\rho$	-	-	-	500	-	500	500	-	-	-	-	-
NAC	$\lambda$	2.300	2.300	2.300	2.300	-	2.300	2.300	-	2.300	-	2.300	2.300
	$\rho$	2400	2400	2400	2400	-	2400	2400	-	2400	-	2400	2400
SCC	$\lambda$	2.300	2.300	2.300	2.300	-	2.300	2.300	-	2.300	-	2.300	2.300
	$\rho$	2400	2400	2400	2400	-	2400	2400	-	2400	-	2400	2400
RAC	$\lambda$	2.300	2.300	2.300	2.300	-	2.300	2.300	-	2.300	-	2.300	2.300
	$\rho$	2400	2400	2400	2400	-	2400	2400	-	2400	-	2400	2400

$\lambda$  – Thermal conductivity (W/(m.K)).  $\rho$  – density (kg/m<sup>3</sup>)

### 2.3 Open BIM Workflow

The Open BIM Workflow proposed by CYPE Software was employed for the achievement of the objectives (Fig 3).

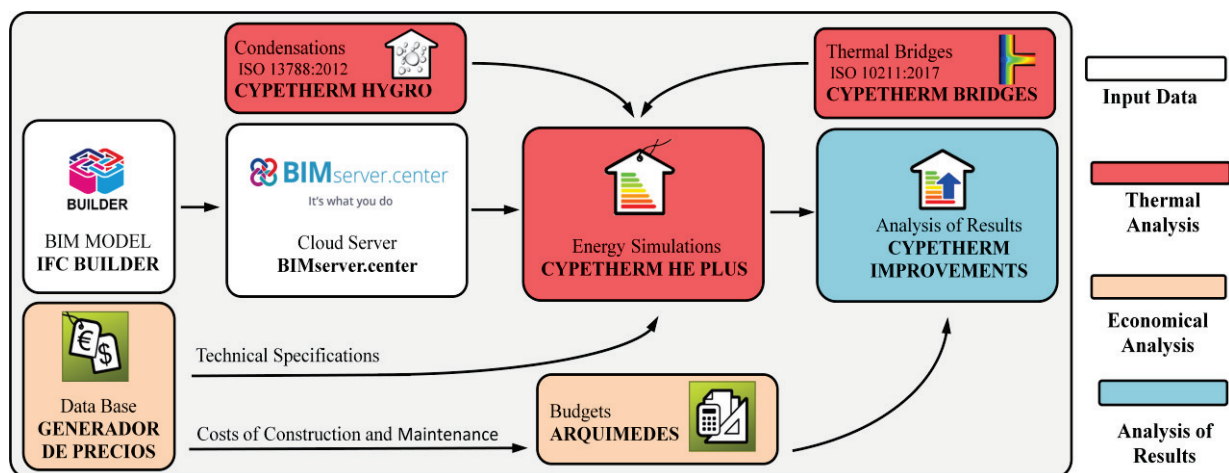


Figure 3: Flowchart of the Methodology Adopted in this Study

First, an architectural model was developed using the freeware application IFC Builder (IFC4 format), where the spaces, orientation and other aspects of the building's geometry were described. Subsequently, the model was synchronized through the online platform BIMserver.center, where its project data became available for the following steps of the workflow. Forty-four energy simulations were performed in CYPETHERM HE Plus employing technical data from CYPE's data base (Generador de Precios) to characterize the building's envelope, thickness detail, materials and thermal characteristics of each element. In the same way, the thermal transmittances in linear thermal bridges were evaluated, solving and processing a heat transfer finite element model based on the EN ISO 10211 using CYPETHERM Bridges. The results of each energy simulation were exported to CYPETHERM Improvements, where the budget information related to each hypothesis was also included. Construction and maintenance costs considered were also obtained from CYPE's data base. The global costs method described by Signes-Orovay et al [6] was adopted considering a 50 year building life-cycle.

### 3. Results and Discussion

$C_{t,nr}$  was assessed in terms of delivered primary energy, including energy use for heating, cooling and domestic hot water. Primary energy values were calculated using the Spanish primary energy factor (2.368 for electricity). The results for the energy consumption ( $\text{kWh/m}^2\cdot\text{y}$ ) versus global cost ( $\text{€}/\text{m}^2$ ) were reported for all scenarios in Fig. 4a.

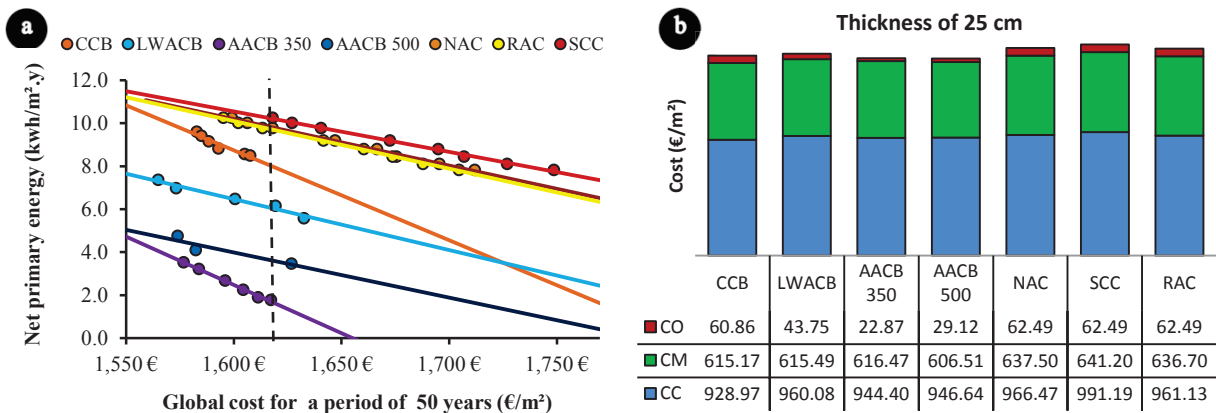


Figure 4: a) Global Costs versus Net Primary Energy b) Costs Breakdown Analysis for Examples with Thickness of 25 cm

The minimum  $C_{t,nr}$  was achieved by the scenario considering AACB350/42cm ( $1.78 \text{ kWh/m}^2\cdot\text{y}$ ). For comparative purposes (indicated by the vertical dashed line in Fig. 4a) and considering linear interpolated data, the same global cost necessary to implement this solution ( $1617.19 \text{ €/m}^2$ ) would increment the  $C_{t,nr}$  from 106% to 450% if AACB500 or NAC solutions were respectively employed in substitution of AACB350. Global cost (50 years) ranges from  $1564.82 \text{ €/m}^2$  (LWACB/12cm) to  $1748.59 \text{ €/m}^2$  (SCC/40cm). Construction Costs (CC) are the most relevant cost, ranging from 57% to 61% of the global cost. Although the initial investments for CCB solutions are lower compared with other solutions, the best results for the whole life cycle of the building were found in AACB solutions, which had their

operational costs reduced due the optimization of the thermal performance of the envelope. The Cost of Operation (CO), related to energy consumptions, could be reduced from 5% (cast in place solutions) to 1% (AACB solutions) of the total overall cost if AACB solutions were employed. Costs of Maintenance/Replacements (CM) are important during construction. The same HVAC and photovoltaic systems were employed for all combinations, and since the calculation period was set to 50 years, replacements occurred twice during the building life cycle. All combinations presented similar results for the Costs of Maintenance/Replacement (CM), ranging from 37 to 39% of the total cost. Fig 4b shows the costs breakdown analysis for examples with thickness of 25 cm.

#### 4. Conclusion

In this study, energy simulations have been performed to check the impact of concrete-based building materials as part of the building envelope on the primary energy consumption of a single-family nZEB. From the results presented, the following conclusions are drawn:

- Since just one architectural model was developed and all scenarios were simulated in specialized applications linked to the workflow, applying the Open BIM method proposed by CYPE led to a compact, but complete, final consolidation of the project.
- Since both masonry and cast-in-place concrete walls can be employed as the building structure, results presented in this work suggest that concrete masonry walls are possible solutions to be used in projects of single-family nZEBs once it presents better energy and economical performances.
- The results also indicate higher energy-economical performances of Autoclaved Aerated Concrete Blocks (AACB), when compared to other structural masonry wall solutions.

#### References

- [1] OFICEMEN - Agrupación de fabricantes de cemento de España. Anuario del sector cementero español - 2016. Madrid: 2016.
- [2] EU, European Union. Directive 2010/31/EU of the European Parliament and of the Council of 19 May 2010 on the energy performance of buildings. Off J Eur Union 2010;53:13–35. doi:doi:10.3000/17252555.L\_2010.153.eng.
- [3] Ma Z, Liu Z. Ontology- and freeware-based platform for rapid development of BIM applications with reasoning support. Autom Constr 2018;90:1–8. doi:10.1016/J.AUTCON.2018.02.004.
- [4] Natephra W, Yabuki N, Fukuda T. Optimizing the evaluation of building envelope design for thermal performance using a BIM-based overall thermal transfer value calculation. Build Environ 2018;136:128–45. doi:10.1016/J.BUILDENV.2018.03.032.
- [5] Díez Montenegro V. Herramientas de análisis acústico dentro de un flujo de trabajo BIM. 48o Congr. Español Acústica - Encuentro Ibérico Acústica, A Coruña: 2017.
- [6] Signes-Orovay J, Miñana-Giner V, Solak AM, García-Hermosa JL, Martínez de los Mozos J, Gilabert-Boronat P, et al. Anexo 6: Análisis Económico y Energético. Proyecto. Cypewood., Alicante: CYPE Ingenieros S.A.; 2018, p. 41.

## **INTEGRATED APPLICATION OF ADVANCED SURVEYING TECHNIQUES AND BIM FOR INSPECTION AND ASSET MANAGEMENT OF REINFORCED CONCRETE BRIDGES**

**Miguel Azenha <sup>(1)</sup>, Gabriel Sousa <sup>(1)</sup>, José Matos <sup>(1)</sup>, José Sena-Cruz <sup>(1)</sup>, Vitor Brito <sup>(2)</sup>**

(1) ISISE, University of Minho, Guimarães, Portugal

(2) Betar Consultores, Lisbon, Portugal

### **Abstract**

The aim of the work reported herein was to explore the possibilities of integrating new ways of surveying into RC bridge inspection activities and evaluating the possibility of integrating data into a BIM model, as to allow quick overviews to be obtained after each inspection. Efforts were made in regard to modelling strategies, not only of the RC bridge elements, but also of 'damage' information that required special attention, as to allow non-graphic information to be easily retrievable. Special tools (add-ins to the BIM platform) were also developed in order to allow quick introduction of inspection data into the BIM model through Excel spreadsheets. The concepts/methods proposed were put to test in an extensive inspection to a bridge located in the north of Portugal. This work results from a collaboration of the University of Minho with Betar, a consulting office with more than 20 years of experience in Bridge inspection, which has authored a managing system for road infrastructure and actively applies it.

### **1. Introduction**

Bridges and viaducts are very important and fundamental assets for road/railway infrastructure managers, who need to manage the information of each structure in an organized manner as to perform timely reactions and maintenance activities to ensure safety, adequate service levels and durability. Most countries in the world have national infrastructure strategies for inspection, with Portugal having issued their latest inspection manual in 2015 [1]. Several types of inspection are envisaged (as well as their timing), from the simplest routine ones, to the most complex, the special inspections that intend to gather extensive information on the entire asset or specific aspects of it. In spite of the well-structured activities in such manuals, they are still lacking explicit references to the

integration of the inspection information into Building Information Modelling (BIM) frameworks, particularly taking into account the opportunities brought about by new/emerging surveying inspecting techniques (e.g. laser scanning, GPR, thermography, 360 photography). This is not necessarily a ground-breaking activity in view of the extensive recent developments occurring in BIM at the '*facilities management*' discipline (BIM-FM) [2]. However, very little has been done in applied discussion of the challenges and opportunities brought about by BIM-FM in the particular scope of reinforced concrete bridges that incorporate a set of specificities. This was therefore the main aim of the present work, that focused in the application of BIM methodologies to the extensive survey/inspection of a reinforced concrete bridge located in the North of Portugal. The work carried out was closely monitored and supported by the company Betar, which has authored a widely-used system for infrastructure management in Portugal, named GOA (focus on bridges/viaducts) [3], but does not incorporate yet BIM-based technology in their inspection/management processes. It is also noted that the work reported herein is more extensively described in the MSc dissertation of the second author [4].

This paper is structured in two main parts in Sections 2 and 3: Section 2 presents the case study of the Saltadouro Bridge and a global overview of the survey/inspection actions that were carried out. Section 3, in turn discusses the processes and methods for producing the corresponding BIM model, with adequate incorporation of the inspection data. Final conclusions of the work are presented in Section 4.

## 2. Saltadouro Bridge: the case study

### 2.1 Description of Saltadouro Bridge

The Saltadouro Bridge is located in the North of Portugal, within the Natural Park of Gerês (Ruivães). It has been built in the 1950's, but the owner did not have any drawings or written records of the bridge design. The bridge, whose recent photo is shown in Figure 1, has two free spans of approximately 16.8m each, supported in a central column and two lateral abutments. The cross-section of the bridge is a double "T", with two longitudinal ribs supporting the top slab (all monolithically connected to each other). As seen in Figure 1, the water height is different in both spans of the bridge. For that reason, and taking into account the similar apparently similar state of both spans, the detailed inspection has been focused on the leftmost span according to Figure 1 (South side), which was made accessible by a specifically assembled scaffolding.



Figure 1: Overall view of Saltadouro Bridge (left side: North abutment; right side: South abutment).

## 2.2 Surveying and inspection actions

The surveying and inspection actions needed to be rather extensive in view of the total lack of information about the bridge. In terms of geometry, both manual processes (handheld laser distance meter, measuring tape) and laser scanning techniques were applied for mutual validation. The laser scanning was carried out with a Leica ScanStation P40 with the following main features: survey of 1.000.000 points per second, range of 240m, 1.2mm precision ( $\pm 10$  ppm) and integrated digital camera. The equipment was placed at 8 different measuring stations in order to cover the entire structure, as identified in Figure 2a. The resulting global point cloud has more than 170 million points. One view of such point cloud is shown in Figure 2b. From a structural point of view, it was interesting to note that the accuracy of the obtained point cloud, allowed to compare the actual shape of the bottom surface of the beams, to the hypothetical straight line that connects the supports, and therefore infer the deformation. As shown in Figure 2c, a deformation of 2.6cm could be assessed in regard to the fictitious straight line, and the noise level of the point cloud is compatible with the 1.2mm precision mentioned above. This level of accuracy brings laser scanning to a great degree of usefulness in accompanying the deformational behaviour of structures, indeed. It is also remarked that, as expected, all tape measurements have validated the measurements that could be made directly on the point cloud.

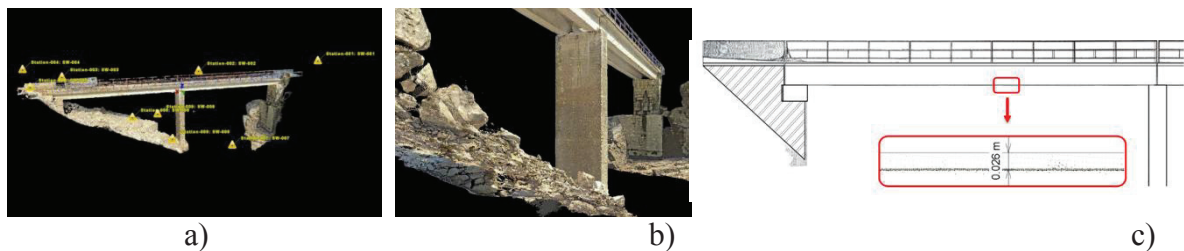


Figure 2: Laser scanning: a) location of stations; b) view of the point cloud; c) deformed shape in comparison to reference line.

The inspection has also involved several inspection techniques that are briefly addressed here. Visual inspection (together with photographic record) allowed the traditional identification of biological colonization, corrosion, surface delamination and suchlike (e.g. corrosion and delamination in Figure 3a). Infrared thermography was also applied with a FLIR E50bx camera, that allowed recording several barely perceptible delamination processes to the naked eye (Figure 3b). In order to assess the rebar diameter, position and type, several minor destructive inspection activities were made, by opening cavities up to the reinforcement (here termed as inspection windows), and even gathering a few rebar samples for lab testing. Two steel rebar detectors were used together in order to get a global picture of all reinforcement distribution within the ribs and the deck: a Hilti PS200 detector and a Hilti PS1000 GPR based scanner. An example of the GPR imaging obtained can be seen in Figure 3c. Seven concrete cores (with  $\sim 10$ cm diameter) were obtained from the bridge and tested in laboratory (Figure 4a). Schmidt hammer assessment of compressive strength was also assessed at 24 distinct locations. Cracks were marked with a felt pen and photographed, whereas a set of representative crack widths were measured with a handheld USB Microscope VEHO VMS-004D, that could accurately pinpoint widths to the hundredth of millimetre (Figure 4b).

The photographic record of the bridge was also taken through 360° photography at 7 locations with a Ricoh Theta camera. An example of a flattened spherical panorama can be seen in

Figure 4c. These spherical photos can be of great utility due to the quickness in which they are obtained and the embedded richness of context.

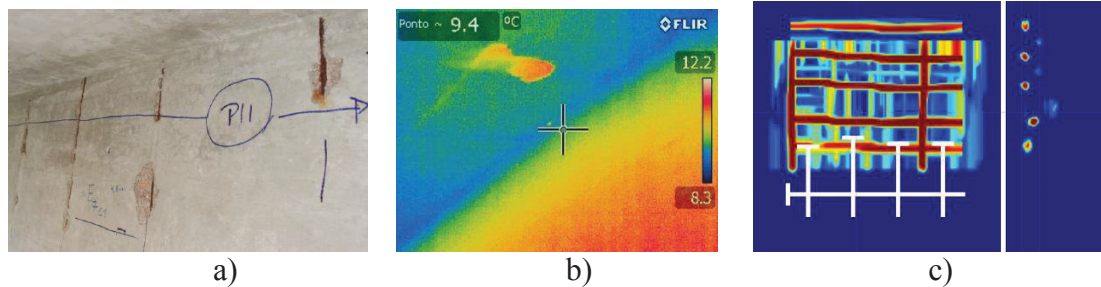


Figure 3: Inspection techniques: a) photography record of corrosion and delamination; b) infrared thermography image; c) GPR image obtained with a steel rebar detector.



Figure 4: Inspection techniques: a) core extraction; b) crack width; c) 360° photography.

### 3. BIM Model and data organization

The selected application for modelling was Autodesk REVIT, following a structural template that encompasses native object classes for such purpose. The point cloud was embedded as a reference in the BIM model and used to support the geometry definition throughout the entire process. In regard to the level of information/detail/development to be included in the model, it was decided to follow similar prescriptions to those provided by BIMFORUM/AIA for LOD400 [5], which means that reinforcement was explicitly modelled. Warping/deformations of the structure's geometry were not explicitly modelled, with the idealized undeformed geometry being considered sufficient for the intended use of the model. The final BIM model is shown in Figure 5a, with a specific comparison of the idealised geometry of the model with the point cloud being shown in half cross-section in Figure 5b. A view of the modelled reinforcement is shown in Figure 5c.

The modelling of inspection information can be made either explicitly, as shown for the cores exemplified in Figure 6a (which incorporate core objects that embed the relevant information of compressive strength, laboratory test sheets, carbonation depth, etc.) or in an implicit manner through 'patch' objects, such as the green patches shown in Figure 6b, which stand for the observed biological colonization. The mentioned patches are BIM objects themselves with relevant fields that characterize the information considered relevant (e.g. type of colonization, extent, link to photo, etc.) in such a way that it remains interoperable and exportable in a specific IFC 'property set'. The authors consider that, for the sake of BIM-FM purposes, damages and inspection information (including cores, cracks, inspection windows, etc.) are well represented through the 'patch' strategy, that allows embedding all the necessary



information in an easy to systematize/query manner, and indexed to the relevant date of inspection. Furthermore, scripts have been developed within Autodesk REVIT (Dynamo-Python) that allow that inspection data can be inputted or analysed directly in Microsoft Excel, under a natural interface for people that have no expertise in BIM (e.g. an inspector). More details on these contexts can be found in [4].

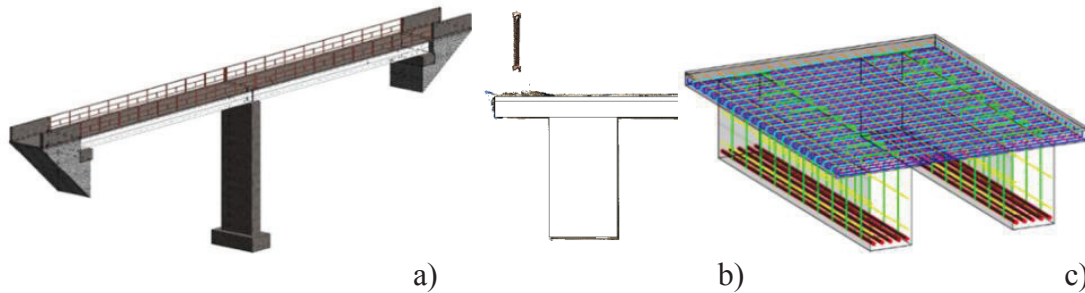


Figure 5: BIM Modelling: a) global overview of the model; b) comparison of BIM model and laser scanning at cross-sectional level; c) part of modelled reinforcement.

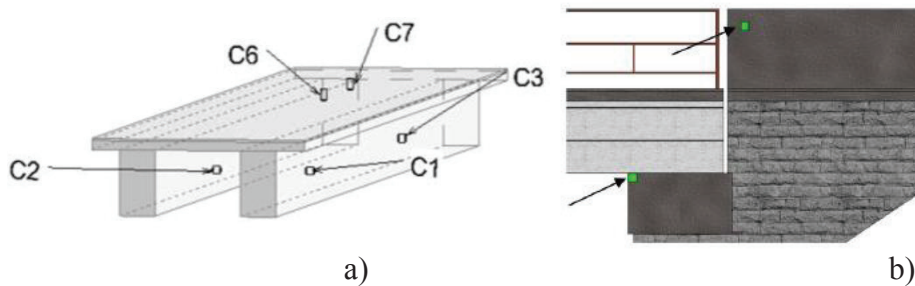


Figure 6: BIM Modelling: a) explicit modelling approach for cores; b) patch modelling approach for biological colonization.

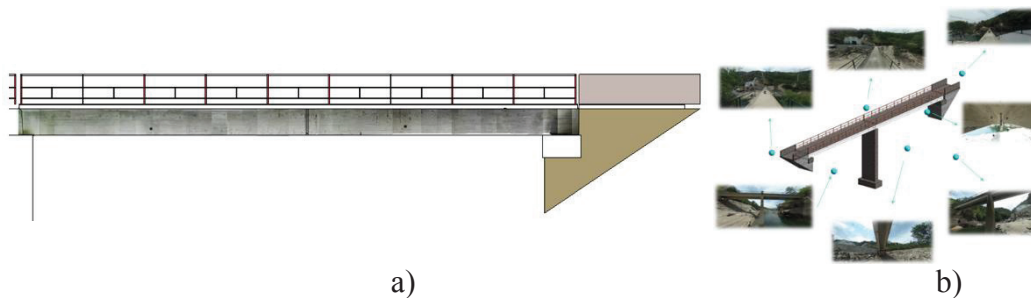


Figure 7: BIM Modelling: a) photogrammetry stitching on the surfaces of objects; b) sphere objects to host spherical panoramas.

Another important aspect to preserve is the visualization of inspection/damage data. Not only is the point cloud of each inspection preserved in the BIM model, but also photogrammetry-composed images of beam surfaces can be embedded into the model's surfaces (see Figure 7a), and spherical panoramas can be embedded into specific 'sphere' objects located at the exact spot where each 360 photo was taken in the inspections, as shown in Figure 7b. This has important benefits in the perception of evolution of damages by an experienced user that wants to navigate the model and observe the evolution of surface damages/aspect. Finally, the work reported herein has also tackled with success aspects related to semi-automatic

inspection report generation (drawings) and exporting the model to BIM viewers (including through the use of the open IFC format) that allow the observation of the model and all its data to be made by stakeholders that might not hold licensing for BIM Software.

#### 4. Conclusions

This paper addressed a proposed methodology to gather/register information pertaining operation and maintenance in reinforced concrete bridges, based on BIM modelling. The proposed methodology has been presented and discussed with support on the inspection of a Bridge located in the North of Portugal, for which no data was available before inspection. An extensive surveying inspection has been carried out including: classical measuring tape techniques; laser scanning; standard photography/photogrammetry; spherical panoramas; concrete core extraction; obtaining reinforcement samples; magnetic/GPR reinforcement detection; thermography; crack width measurement, among others. A BIM model has been established with specific action being taken in order to incorporate data that is not normally taken into account in design or 'facilities management' context, due to its specificity for structural inspection of reinforced concrete bridges. A proposal for simplified 'patch' representation of damage objects has been forwarded, and the layout of information in the model (including exporting to other stakeholders) has been address.

Based on the case study reported herein, it is considered that the proposed framework and corresponding workflow are feasible for implementation of bridge management systems.

#### Acknowledgements

This work was financially supported by: project POCI-01-0145-FEDER-007633 (ISISE), funded by FEDER funds through COMPETE2020 - Programa Operacional Competitividade e Internacionalização (POCI), and by national funds through FCT - Fundação para a Ciência e a Tecnologia. FCT and FEDER (COMPETE2020) are also acknowledged for the funding of the research project IntegraCrete PTDC/ECM-EST/1056/2014 (POCI-01-0145-FEDER-016841). The financial support of COST Action TU1404 through its several networking instruments is also gratefully acknowledged. The collaboration of Eng. Luís Santos from Leica GeoSystems Portugal is gratefully acknowledged, in view of his participation by carrying out the laser scanning survey of the bridge. The participation of the former MSc student of UMinho, João Rodrigues, in the inspection and early BIM modelling activities is also acknowledged.

#### References

- [1] EP, Manual de Inventário, Rotina, Principal, Especificações Técnicas, Estradas de Portugal, S.A. (2015)
- [2] Pärn, E. et al, The building information modelling trajectory in facilities management, *Automation in Construction* (2017), 45-55
- [3] Mendonça, T. Et al, *Aplicação de Gestão de Obras de Arte - GOA - Nova Geração*, BETAR Consultores Lda. (2010), 1-10
- [4] Sousa, G., 'Implementação BIM no contexto de inspeção e gestão da manutenção de Obras de Arte em betão armado: proposta de metodologia e aplicação piloto, MSc Thesis, Universidade do Minho (2017)
- [5] BIMForum, Level of Development Specification, Available: <http://bimforum.org/wp-content/uploads/2017/11/LOD-Spec-2017-Part-I-2017-11-07-1.pdf> (2017)

## **STRUCTURAL DESIGN WITH OPENBIM: FROM THE ARCHITECTURAL MODEL TO THE STRUCTURAL ANALYSIS WITH A STATE-OF-THE-ART CALCULATION ENGINE**

**Javier Pereiro-Barceló<sup>(1)</sup>, Afonso Miguel Solak<sup>(1,2)</sup>**

(1) CYPE Ingenieros S.A., Alicante, Spain

(2) University of Alicante, Alicante, Spain

### **Abstract**

OpenBIM is a universal approach to collaborative design, construction and maintenance of buildings. This technology allows a transparent and open workflow, facilitating the participation of all intervening technicians in a coordinated and simultaneous way, regardless of the software tools they use. The process of calculation and structural design can be integrated into the OpenBIM workflow without complicating or modifying the way of working that has traditionally been carried out. To this end, CYPE has recently created applications integrated in the OpenBIM flow to analyze and design structures such as StruBIM Analysis, in addition to adapt the existing ones. StruBIM Analysis is a new software to calculate the structure, that is to say, it obtains nodal displacements, sectional forces of one-dimensional elements and shell forces by means of FEM analysis. StruBIM Analysis integrates OpenSees as its calculation engine. OpenSees is a well-known framework developed by University of California: Berkeley, which performs complex calculations efficiently. This calculation engine has the data entry through code and the result output without graphical interface. However, thanks to the integration of OpenSees in an OpenBIM workflow, calculating non-linearly building structures with a dynamic analysis with integration over time will be possible in a user-friendly and reliable way.

### **1. Introduction**

Open BIM is a global proposal to achieve user collaboration in the design, execution and maintenance of buildings, based on an exchange of information using standard formats (IFC) and an open workflow. By using IFC format, which is standard and public, and not linked to a specific developer, the durability of the work that has been carried out is guaranteed, since it

does not depend on the applications that have been used. Even the own data files of these applications, from a durability point of view of the project, are set aside as auxiliary files, because the generated IFC provides the final information of the project. At the same time, it allows real and efficient communication amongst users, since these formats can be read and generated by the vast majority of applications used in project development.

Cype has recently integrated OpenSees [1] within Open BIM workflow. OpenSees [1] is a well-known framework to perform linear or non-linear analysis, developed at University of California, Berkeley. Its use is widespread all over the world mainly to simulate seismic behavior in structures. Cype has integrated OpenSees [1] as calculation engine for StruBIM Analysis, StruBIM Design and StruBIM Foundations. These programs are in charge of analyzing, designing and checking structures, including their foundations. To fulfill this, Cype has extended OpenSees [1] in some ways and one of them is creating two new finite elements, which will be explained in the following sections.

## **2. Open BIM workflow**

The phases of Open BIM workflow are displayed in Figure 1. A BIM Project starts with an IFC file which must be generated based on a 3D geometrical model produced by any architectural modelling software. This geometrical model is uploaded to a web platform called BIMserver.center which allows direct communication between all the users and applications that participate in a project. Next, all the applications that are compatible with the Open BIM workflow import the IFC model. All intervening agents receive the same geometry and architecture. Each specialized application imports the geometrical model and exports an IFC file with the results. This way, the BIM project is enriched and completed. Thus information of the BIM model increases using the IFC files generated by all the applications and defines the complete BIM project. This process is called consolidation of the BIM project. This information consolidation allows for the complete project to be generated, as a whole, and therefore detect, any possible interferences between the solutions that have been adopted. Besides, during the whole process, if any changes are made to the initial model, all the applications can undergo an updating process. This guarantees that no information is lost. The IFC format files do not include specific information that makes up the project; all the data is generated and stored in the specialized applications. In other words, each member only shares the results and adopted solutions, whilst the data that has been introduced, the work methodology and intermediate results remain in the private domain of the specialist. By working in this way, the size of the files is significantly reduced, since each member is only in charge of the part of the project which he/she is responsible for. The information in IFC format, which forms the project, exclusively defines the project, and therefore, the specific tools and programs used to create it are auxiliary elements that can be changed or eliminated during the life span of the project.

When the project designer is faced with a design problem, he/she usually has to evaluate different solutions or proposals. As alternative options are rejected and decisions are made, more detailed work is carried out on them, to achieve greater definition. In the Open BIM flow, each analysis model is independent from the rest, so different solutions for the same field can be proposed and defined, since the other models are not affected no matter what decision is made.

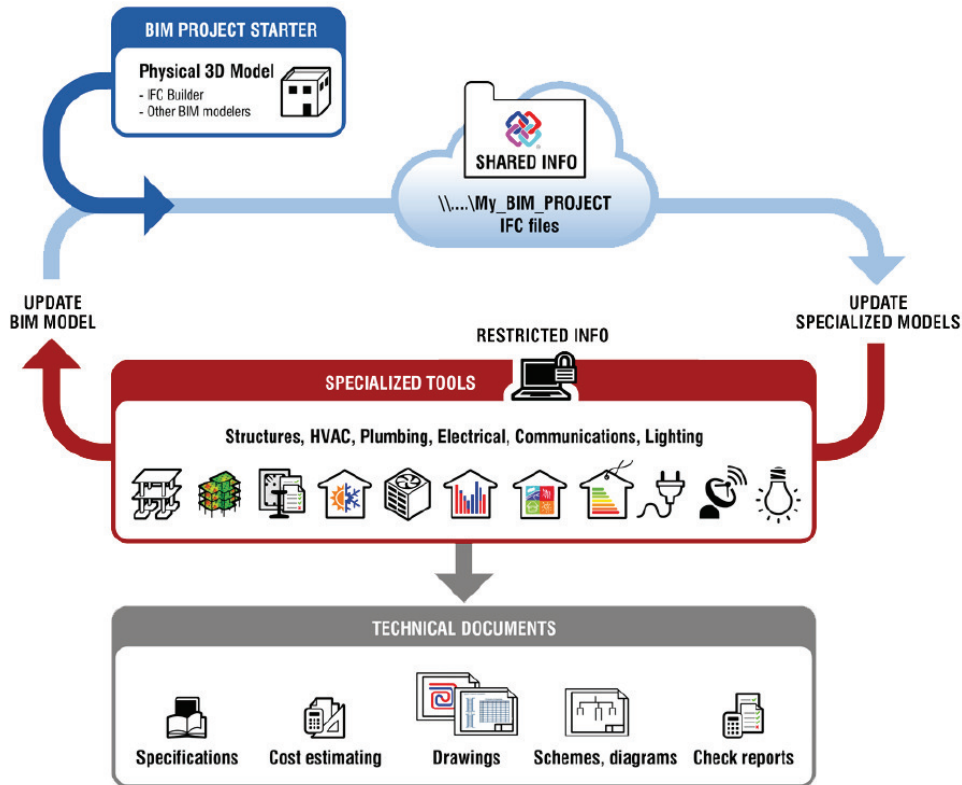


Figure 1: Open BIM workflow.

### 3. Structural analysis and design in open BIM flow

The stages to carry out the analysis and design of structures are perfectly delimited (Figure 2): (1) create the structural model (based on the architectural or geometrical model); (2) generate the analytical model based on the structural model; (3) solve the analytical model; (4) design and check of structural elements; (5) generate layouts and reports.

#### 3.1 Generation, edition and analysis of analytical model

Cype has developed a program to generate, edit and perform structural analysis: StruBIM Analysis. This program forms part of StruBIM suite, which is a group of structural programs, each one related to one stage of structural design. Sequential version of OpenSees [1] has been used as calculation engine in StruBIM analysis (Figure 3). For this purpose several extensions have been implemented in OpenSees [1]: two new finite elements (one-dimensional and shell) [2-4], a new constraint manager, a new solver called MUMPS (Multifrontal Massively Parallel Sparse Direct Solver) [5], etc. Besides, multiple instances of sequential OpenSees [1] are used to solve several load cases at the same time.

Regarding the generation of the analytical model based on the structural model, StruBIM Analysis transforms automatically entities such as columns, beams or slabs, into one dimensional and two dimensional elements. Problems with this conversion may come up, for instance, when structural elements with different depths are connected. In this case, axes of the structural elements do not coincide and, consequently, neither the finite element nodes of

the analytical model. In order to solve these problems, kinematic constraints are added to assure analytical model behaves as the structural model.

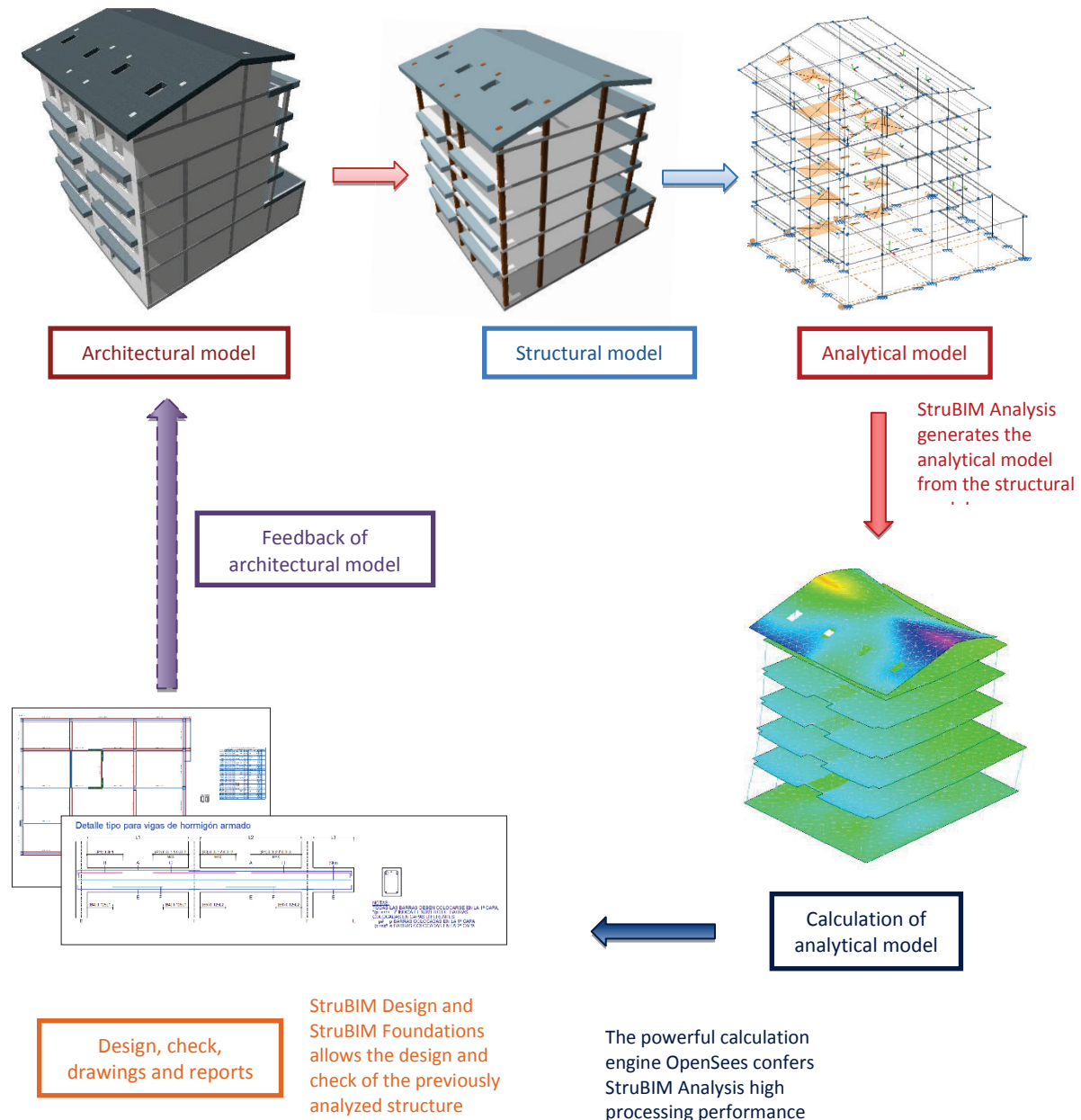


Figure 2: Structural analysis and design integrated in an Open BIM workflow.

The main benefits that users can take from the workflow displayed in Figure 2 is that they will be able to use all the functionality of OpenSees [1] just importing the structural model into StruBIM. The structural model which derives from the architectural model can be made with any modelling commercial tool available on the market. User will be able to perform a

complex non-linear analysis of an actual structure with OpenSees [1] with a minimum effort. This is unthinkable by coding the data input as OpenSees [1] itself requires.

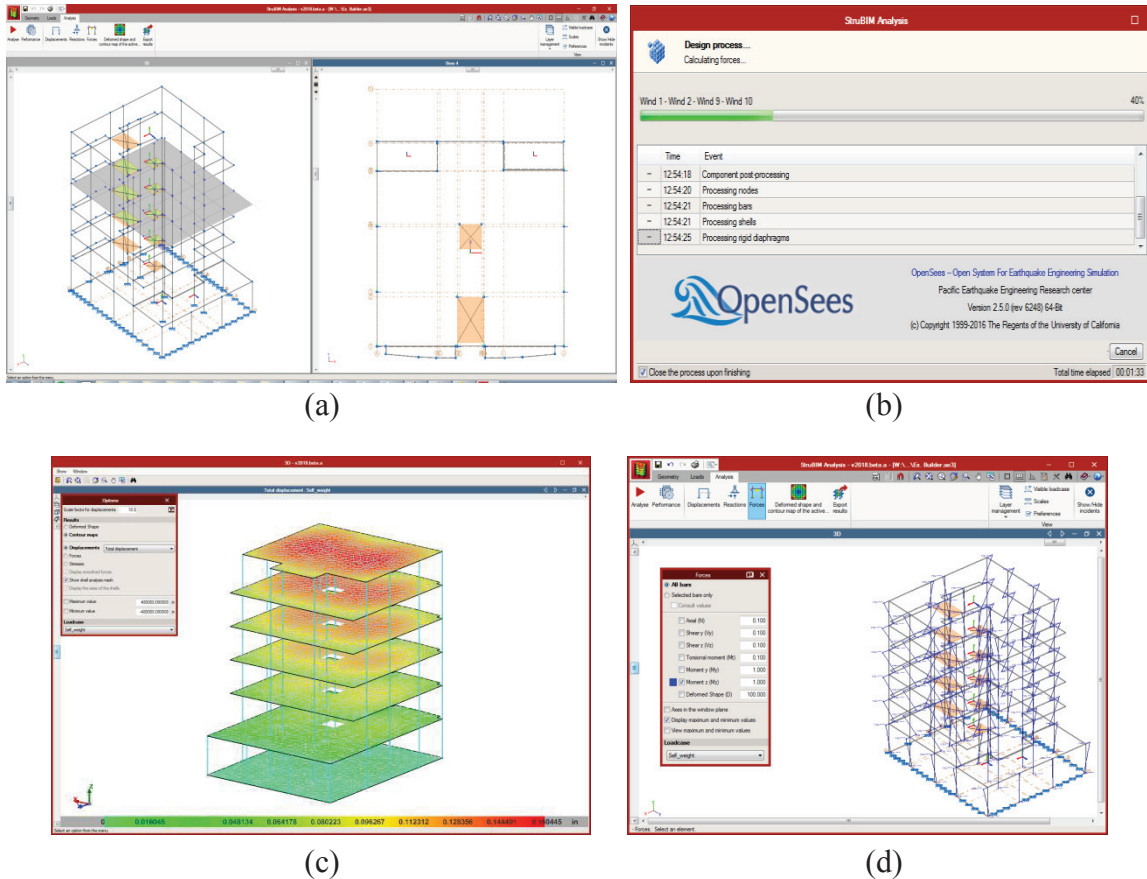


Figure 3: Structural analysis with StruBIM analysis plus OpenSees [1]: (a) Analytical model, (b) Calculating with OpenSees [1], (c) Deflections results, (d)  $M_z$  moments in columns.

### 3.2 Design and check of structural elements

StruBIM Design is responsible for designing and checking columns, beams, slabs and walls according to ACI Codes. It imports the analytical model results from StruBIM Analysis or from an xml file with a specific format. Besides, it is able to manage a local analytical model of each floor to design tendons, slabs and beams. Analogously to StruBIM Design, Cype has created StruBIM Foundations to design foundation elements.

## 4. Conclusions

The following conclusions are drawn:

- In the Open BIM flow, users work with specific and highly specialized applications to solve each aspect of the project in detail. The relationship and interaction amongst all

the applications is solved via including and integrating the BIM model composed of all the solutions adopted for each project area (consolidation process).

- Using open format interchange files, the applications are capable of reading all the information of the project and show it in an integrated way. Furthermore, with the consolidation process, users are able to detect any possible interferences between the adopted solutions.
- In the Open BIM flow, open formats are used at all times, which implies that any tool of any manufacturer can be part of the workflow in a simple way and, therefore, does not oblige users to have to modify their current working habits,
- Cype has recently integrated OpenSees [1] as calculation engine in its new suite StruBIM which is part of an Open BIM workflow. To fulfill this, Cype has extended OpenSees [1] in some ways and one of them is creating two new finite elements.
- OpenSees [1] itself requires the data input by coding. The main benefits that users can take from the integration of OpenSees [1] in an Open BIM workflow is that they will be able to use all the functionality of OpenSees [1] just importing the structural model into StruBIM. The structural model which derives from the architectural model can be made with any modelling commercial tool available on the market. User will be able to perform a complex non-linear analysis of an actual structure with OpenSees [1] with a minimum effort.

## References

- [1] McKenna F, Fenves GL, Filippou FC. OpenSees. University of California, Berkeley.
- [2] E. Oñate, *Cálculo de Estructuras por el Método de Elementos Finitos, 1th Edition*, Centro internacional de Métodos Numéricos en Ingeniería, Universitat Politècnica de Catalunya, Barcelona, 1992.
- [3] C.A. Felippa *Introduction to Finite Element Methods*, Department of Aerospace Engineering Sciences and enter for Aerospace Structures, University of Colorado, USA, 2004.
- [4] C.A. Felippa *Finite Element Methods in Dynamics*, Department of Aerospace Engineering Sciences and enter for Aerospace Structures, University of Colorado, USA, 2004.
- [5] Multifrontal Massively Parallel Solver (MUMPS), *Users's guide*, March 21, 2017.



## THE ROAD TO SENSOR-DRIVEN CLOUD-BASED INFRASTRUCTURE MANAGEMENT

Carlos G. Berrocal <sup>(1,2)</sup>, Ignasi Fernandez <sup>(1)</sup>, Rasmus Rempling <sup>(1,3)</sup>

(1) Chalmers University of Technology, Gothenburg, Sweden

(2) Thomas Concrete Group AB, Gothenburg, Sweden

(3) NCC AB, Gothenburg, Sweden

### Abstract

Today, the accelerated degradation of many concrete structures poses a major challenge for the proper maintenance of the transport infrastructure. Therefore, inspection and maintenance operations constitute an important part of the recurrent costs of infrastructure. Furthermore, the increasing migration of population to urban areas has made sustainable development an imperative need. This need has become a driving force for innovation and new challenges such as the concept of smart cities and infrastructure. The successful utilization of newly available technologies will enable a whole new range of possibilities such as sensor driven cloud-based strategies for infrastructure management, which will promote an upgrade of the current infrastructure network to a new generation of safer, more efficient and more sustainable smart infrastructure: the infrastructure 2.0. The aim of this paper is to review the state-of-the-art of the different key technologies comprising a smart monitoring system, focusing on the aspects that are required to ensure a successful implementation of such system. The main result of the study is a scientific roadmap that can serve as a guide for traffic administrations and academic institutions in their task to develop and create a new infrastructure management strategy based on emerging technologies and innovative processes.

### 1. Introduction

Infrastructures are the fundamental facilities and systems required to support societal activity within a certain region. In particular, the transport infrastructure consisting of mainly roads, bridges and tunnels, is one of the oldest and most crucial elements for society as it embodies the physical platform for the transportation of passengers and goods [1]. Since deterioration of the transport infrastructure poses a serious public safety issue and has a negative impact on

the nation's economy, to effectively maintain the performance of the transport infrastructure is of utmost importance. Nevertheless, the accelerated degradation of structures caused by prolonged exposure to harsh environments added to the advanced age of many structures and the ever-increasing level of demands in terms of traffic loads, volume and vehicle speeds [2], represents an enormous challenge for the effective management of the transport infrastructure, which is often translated into an increased frequency of inspections and maintenance operations. Due to the conservative nature of the construction industry relying on traditional methods and lagging behind in innovation compared to other sectors, these inspections are today very inefficient and, together with maintenance operations, constitute a major part of the recurrent costs of infrastructure, which represent a significant share of the annual budget in developed countries [3].

New management methodologies must, therefore, be developed based on newly available technologies and new ways of thinking, to deliver smart systems that could minimize the number of interventions in the transport infrastructure as well as their extent and duration. Along these lines, current technological development is taking society to a new era where an unprecedented type of knowledge will be accessible through the combination of: (i) extensive wireless sensor networks; (ii) ubiquitous and remote access to cloud-stored data and services; (iii) constantly increasing computational power and more efficient calculation algorithms; and (iv) novel tools to visualize digital information. The successful utilization of the aforementioned technologies will enable a whole new range of possibilities such as a sensor-driven cloud-based strategy for infrastructure management. The main aim of this paper is to investigate the feasibility of combining emerging technologies to create an integrated system that enables an upgrade of the current infrastructure network through a new generation of smart structures. The study focuses on the aspects that are required to ensure that such a system could be successfully implemented in practice.

## **2. Review of emerging technologies**

In order to create a system that minimizes the need for structural inspections, some sort of Structural Health Monitoring (SHM) system must be implemented. A SHM system is a technology based on the continuous condition assessment of a structure through the analysis of data acquired on-site by a distributed network of sensors [4]. If properly implemented, SHM systems could extend the service life of structures by ensuring the early identification of deterioration and/or damage, thereby allowing relatively minor corrective actions to be taken before the damage grows to a state where major actions are required [5]. For a SHM to be effective a streamline of data must undergo four different steps: acquisition; management; analysis; and visualization. In the following section, a review of the different existing technologies enabling these four steps is presented.

### **2.1 Data acquisition – Sensor networks**

Sensors are critical elements in SHM systems, which must be chosen adequately to serve the intended purpose under the expected conditions and for a certain time span. Sensors can be subdivided according to various features, e.g. wired/wireless, embedded/external or active/passive. Each type of sensor possesses its own advantages and drawbacks, which must

be considered with care. Regarding the measured properties, the most commonly used sensors in SHM applications include sensors measuring kinematic parameters, such as displacements, strains and accelerations, dynamic quantities, such as vibrations and forces and environmental factors, such as temperature or relative humidity (RH), some of which are commercially available for concrete applications, see e.g. [6]–[8]. Conventional sensors often present difficulties to perform stable and reliable readings in the long term. Many sensors can be easily affected by changes in temperature, humidity, cable length, magnetic or electric fields, etc, whereas other sensors need to be powered, which requires the use of batteries, thus limiting the service life of the sensors [9]. Nevertheless, the common problems that are often encountered with conventional sensors today will most likely be overcome in the future as new sensing technologies are developed for bridge monitoring and other large structure applications. Two examples of novel sensor applications, currently under development, which possess great potential for the long-term monitoring of reinforced concrete structures are smart cement-based sensor [10] and polymeric optic fibre [11].

## **2.2 Data management – Cloud services**

In large infrastructures with distributed sensor networks containing tens or hundreds of sensors measuring continuously, the amount of generated data can easily surpass the storage capacity of any modern computer. To manage such data volumes and enhance accessibility to the content, a series of cloud-based platforms exists, which provide a wide range of services for users with the only requirement of an internet connection. These platforms are referred to as PaaS (Platform as a Service) and can be defined as a cloud computing model in which a third-party provider delivers hardware and software tools (usually those needed for application development) which can be accessed anywhere via a web browser. One of the main advantages of a PaaS providers is that they host the hardware and software on its own infrastructure, thereby freeing users from having to install in-house hardware and software to develop or run new applications. Some of the best-known PaaS include Microsoft Azure, Google App Engine or Amazon Web Services.

## **2.3 Data analysis – Machine learning**

Another of the key steps towards the implementation of an effective SHM system is the analysis of the measured data. Individual data values by themselves are meaningless. They need to be situated in a context, relativized to other parameters and combined with a certain set of assumptions to extract relevant information. This information must be placed within a theoretical background and used in conjunction with a model to obtain knowledge. Lastly, this knowledge can eventually be turned into expertise, i.e. the required parameters for decision making, through experience and training. The first two steps are relatively easy to automate but for the last one, an experienced and trained operator is still required. This could change in the near future through the implementation of artificial intelligence, i.e. machine learning algorithms, which could not just become a decision support tool for engineers but also unlock the path towards predictive structural assessment.

Machine Learning is currently being used in many existing fields of research to develop countless applications, some of which are fully operational in everyday situations such as spam filters or face recognition systems. For structural health monitoring applications, two main anomaly detection approaches, which may classify as precursors of today's machine

learning, have been previously used for damage identification: model-driven methods and data-driven methods. The former rely on high-fidelity physical models to detect deviations of the measured data whereas the latter usually adopt a statistical representation of the system where data appearing in regions of very low density may indicate deviation from normality [12]. In civil engineering, the application of machine learning has been also attempted, particularly for vibration-based damage assessment of steel bridges, see e.g. [13]–[16]. However, owing to the large size and one-of-a-kind nature of the transport infrastructure elements, the development of effective and generic machine learning algorithms for structural health monitoring have not yet been developed.

#### **2.4 Data visualization – BIM**

Effective data visualization is another crucial aspect for the successful implementation of an integrated SHM system. The information, whether it is raw measured data or a sophisticated damage index, needs to be conveyed in a clear, efficient and intuitive way to the operator. Building Information Modelling (BIM), combining 3D computer-aided design visualization with integrated data, is a process originally intended to improve the performance of building projects during their construction phase and service life. Due to the high complexity of the transport infrastructure elements, BIM stands out as a very promising alternative for its integration within a SHM system. Today, a variety of BIM software is available, including both more user-friendly and intuitive commercial packages and more flexible, free open-source programmes. Perhaps, one of the major technical challenges is to find a suitable interface that enables the effective integration of real-time measured data with a 3D design model. A very promising solution to this technical challenge is provided by Autodesk FORGE [17], a connected cloud platform comprised of web services, and technical resources that allows for the development of customized and scalable solutions.

Augmented Reality (AR) also possesses a great potential for the visualization of data on-site, which could represent a giant leap in the efficiency of structural inspections. By visualizing information regarding the real condition of the structure as an overlay displayed on the actual structure, inspection operators could easily spot the location of deficient elements and focus on critical elements, notably reducing the time and extent of the inspection and subsequently minimizing the cost and disruption to the infrastructure users.

### **3. A scientific roadmap to sensor-driven cloud-based infrastructure management**

Based on the four steps constituting a SHM system and the different reviewed technologies, a roadmap towards sensor-driven cloud-based infrastructure management has been drafted. This roadmap, referred to as SensIT and presented in Fig. 1 as an infographic, identifies the critical areas where further research is required and how these areas are interrelated.

- **Sensor technology:** the first obstacle to overcome in the creation of an integrated SHM system is the deployment of a sensor network that measures different kinematic and physicochemical parameters to form the basis for remaining steps. Ideally, robust and stable sensors which are not affected by external stimuli and can surpass the service life of the parent structure should be developed. This data should be then combined with

environmental information as well as previous damage report in the case of existing structures to offer a holistic view of the structural condition.

- **Cloud-based services:** the integration of existing cloud platforms is a key aspect to ensure the efficiency, flexibility and scalability of the system. Cloud platforms play multiple roles as: a means to obtain the necessary storage; a platform to carry out remote calculations; and a tool to manage, share and access data from virtually any place in the world.
- **Machine Learning:** with the steady gain in computational power, these types of algorithms have shown their immense potential for pattern recognition and anomaly detection in multiple areas. Novel algorithms need to be developed focused specifically in the needs of the construction industry and particularly for structural health monitoring of concrete structures. Moreover, these algorithms might benefit from reciprocal data retrofitting with detailed finite element analyses.
- **Real-time BIM:** a digital twin of the physical structure created through BIM can become a very suitable channel to convey the information related to the structure condition of the transport infrastructure. Interactive BIM applications with an intuitive, user-friendly and cross-platform interface should be developed to offer an effective and versatile decision support tool for the owner/manager/operator of the structure.

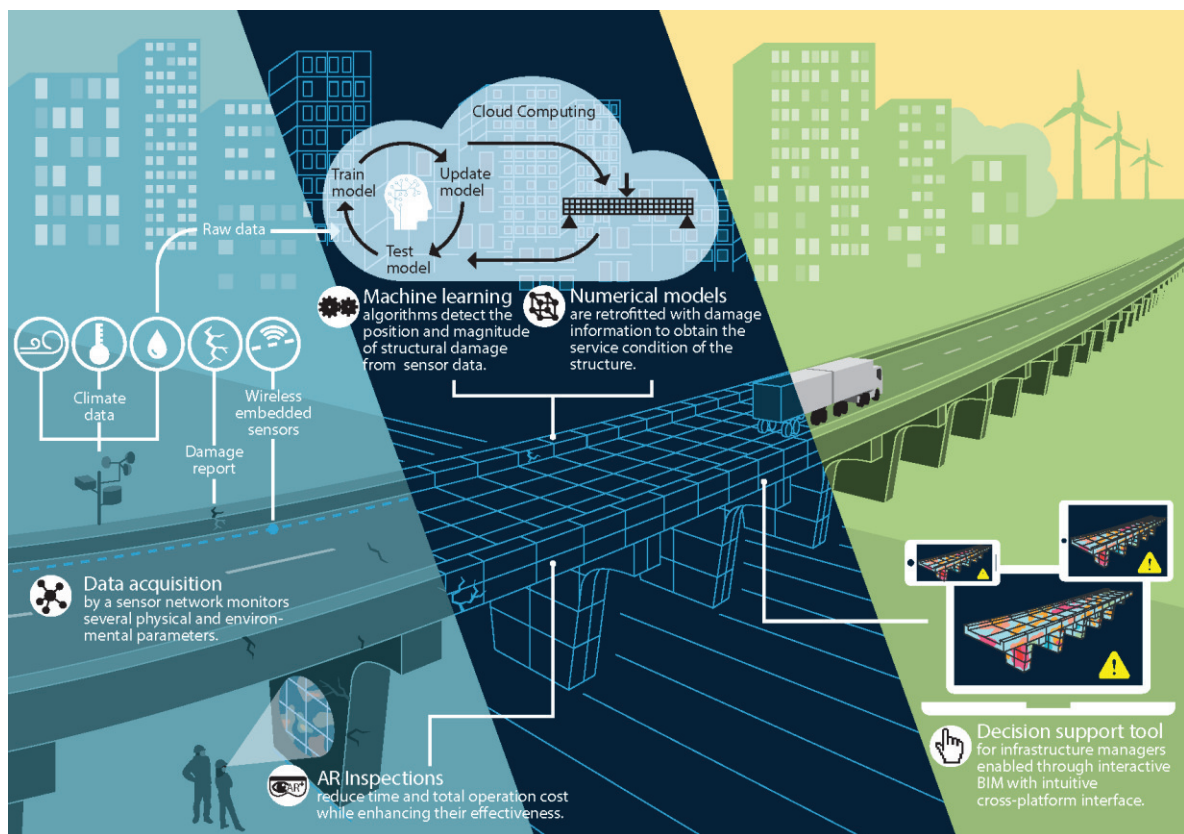


Figure 1: Schematic representation of the SensIT monitoring system.

It is worthwhile mentioning that the approach discussed in this paper presents two main limitations that hinder its full applicability as of today. The first limitation is the absence of sensors specifically developed for concrete applications, which can provide accurate, stable

and reliable measurements during the entire service life of the infrastructure. The second is the lack of advanced numerical models that can describe the various multi-physics phenomena involved in the deterioration mechanisms of concrete, including corrosion of reinforcement, alkali-silica reaction, etc. to support the development of machine learning algorithms.

## References

- [1] J. Fulmer, "What in the world is infrastructure?," *PEI Infrastruct. Invest.*, vol. July/Augus, pp. 30–32, 2009.
- [2] J. Leander, A. Andersson, and R. Karoumi, "Monitoring and enhanced fatigue evaluation of a steel railway bridge," *Eng. Struct.*, vol. 32, no. 3, pp. 854–863, 2010.
- [3] OECD - Organization for Economic Co-operation and Development, "Infrastructure investment (indicator) - [Accessed on 18 October 2017]." 2017.
- [4] J. M. W. Brownjohn, "Structural health monitoring of civil infrastructure," *Philos. Trans. R. Soc. A Math. Phys. Eng. Sci.*, vol. 365, no. 1851, pp. 589–622, Feb. 2007.
- [5] B. M. Phares, T. J. Wipf, L. F. Greimann, and Y.-S. Lee, "Health Monitoring of Bridge Structures and Components Using Smart Structure Technology - Vol. 1," Center of Transportation Research and Education, Iowa State University, 2005.
- [6] Giatec, "SmartRock2," 2017. [Online]. Available: <https://www.giatecscientific.com/concrete-sensors/smartrock2/>.
- [7] Electrotech, "Themisto," 2017. [Online]. Available: <http://www.electrotech.se/Produkter/BetongsensorThemisto/tabid/1768/Default.aspx>.
- [8] H. Arup, O. Klinghoffer, and J. Mietz, "Long term performance of MnO<sub>2</sub>-reference electrodes in concrete," in *Corrosion97*, 1997, no. 243, p. Paper 243.
- [9] H. Ceylan, K. Gopalakrishnan, P. Taylor, P. Shrotriya, S. Kim, M. Prokudin, S. Wang, A. F. Buss, and J. Zhang, "A Feasibility Study on Embedded Micro-Electromechanical Sensors and Systems (MEMS) for Monitoring Highway Structures," 2011.
- [10] F. Azhari and N. Banthia, "Cement-based sensors with carbon fibers and carbon nanotubes for piezoresistive sensing," *Cem. Concr. Compos.*, vol. 34, no. 7, pp. 866–873, Aug. 2012.
- [11] Shute, "Optical Fibre Sensor System," 2017. [Online]. Available: [http://shute.dk/?page\\_id=107](http://shute.dk/?page_id=107).
- [12] C. R. Farrar and K. Worden, *Structural Health Monitoring - A Machine Learning Perspective*. 2013.
- [13] H. Hao and Y. Xia, "Vibration-based Damage Detection of Structures by Genetic Algorithm," *J. Comput. Civ. Eng.*, vol. 16, no. 3, pp. 222–229, Jul. 2002.
- [14] K. Worden and G. Manson, "The application of machine learning to structural health monitoring," *Philos. Trans. R. Soc. A Math. Phys. Eng. Sci.*, vol. 365, no. 1851, pp. 515–537, Feb. 2007.
- [15] S. Soyoz and M. Q. Feng, "Long-Term Monitoring and Identification of Bridge Structural Parameters," *Comput. Civ. Infrastruct. Eng.*, vol. 24, no. 2, pp. 82–92, Feb. 2009.
- [16] A. C. Neves, I. González, J. Leander, and R. Karoumi, "Structural health monitoring of bridges: a model-free ANN-based approach to damage detection," *J. Civ. Struct. Heal. Monit.*, vol. 7, no. 5, pp. 689–702, Nov. 2017.
- [17] Autodesk, "Autodesk Forge," 2017. [Online]. Available: <https://forge.autodesk.com/>.

**DIGITAL FABRICATION  
AND  
ROBOTICS**

## **A 3D PRINTER OF CEMENT MORTARS BASED ON INITIAL DEPOSITION OF DRY MATERIALS**

**Miguel Azenha <sup>(1)</sup>, Caetano Monteiro <sup>(2)</sup>, Ricardo Morais <sup>(1)</sup>**

(1) ISISE, University of Minho, Guimarães, Portugal

(2) Dep. Mechanical Engineering, University of Minho, Guimarães, Portugal

### **Abstract**

The paper presents the studies of implementation of an equipment for producing mortar elements through a 3D printing process, aiming to demonstrate feasibility and challenges, with the intent of a future upscaling to actual concrete production. The technique for 3D printing is based on the additive method, with an innovative approach in regard to the deposition of materials. Indeed, the cement/sand are deposited by layers into their final positions. After the deposition of each layer, water is sprayed in a controlled manner. When a given set of layers is deposited, compaction is applied to the entire part. This technique has the interesting feature of allowing to differentiate mortar composition at different regions of the produced elements, with possibility of structural optimization of the spatial use of cement. The feasibility of the developed equipment and produced parts is demonstrated, and discussions are held in regard to challenges and future developments.

### **1. Introduction**

The term Construction 4.0, in direct connection with Industry 4.0 concepts, has gained significant attention and momentum in recent years. Amongst the former, one of the most promising fields seems to be the use of 3D printing techniques for digital fabrication of construction elements, or even for entire constructions. An extensive and very up to date recent literature review has been made by Ghafar *et al.* [1], with particular focus on the use of additive manufacturing (AM) technologies, which are defined in such review *as procedures that form layers to create three-dimensional (3D) solid objects from digital models, allowing creatives, engineers, architects and designers to make customised designs in one-step process.*



Several processes have been devised for construction with AM techniques based on extrusion of pre-mixed cement based blends, such as the contour crafting [2], the 'concrete printing' method by the team at Loughborough University [3], amongst other initiatives based on similar principles and applied at laboratory and construction scale by the industry (review in [1]). Even though this is a very interesting idea, the fact that the mix is 'wet' at the stage of deposition, brings many challenges regarding the fresh state material problems, and concerns about printable shapes without the need for specifically tailored support material. However, much less research has been focused on 'dry' deposition of binders, with very few works known on the subject, except for a conceptual discussion by Pegna [4], and the efforts initiated by Enrico Dini with the D-Shape method that relies on such principle with use of binders that require activators [5]. Except for a brief reference at the website of D-Shape [6], and an alternative method based on extrusion of pastes to sand packings [7], no scientific works written in English were found to focus on dry deposition of cement-based materials for 3D printing efforts, which seems to be an important research gap. However, the research team at the Civil Engineering Department at UMinho has dedicated attention to this matter since 2012, with a line of research based on a 3D printer of cement based materials through the dry method. A MSc thesis has been initially developed by Sepúlveda in late 2012 [8], followed by a national conference paper, written in Portuguese [9]. The work has then been continued in a further MSc thesis by Morais [10], which delved further within the acknowledged limitations and challenges. In view of such efforts, the present paper aims to provide an integrated view of the developments achieved, identifying opportunities and challenges.

## **2. The concept and implementation**

### **2.1 Concept**

The concept behind the proposed printing process is relatively straightforward. It relies on the principle that the element to be printed can have an absolutely arbitrary geometry within the printing bounds, and the mixing proportions of the cement-based material can be changed at any given position of the element under construction. In order to materialize these two important performance requirements, the concept is based on mortar printing (cement, graded sand and water) through a dry method. The explanation of the printing method can be understood by observation of the schemes in Figure 1. Three separate containers are attached to the movable printing head: one for cement, one for graded sand, and another for water. The containers of cement and graded sand have their bottom extremity controlled by a computer controlled valve, that allows continuous feed at known rates of sand and cement, which are in turn gathered in a mixing funnel and deposition head. The principle is that this movable deposition head can deposit controlled quantities of each material, allowing to create regions of different mixing proportions in the printed element, according to performance requirements (e.g. structural, tightness or any other). In the regions that are to become hollow, or merely support the printed layers to be placed above (e.g. cantilevered portions), deposition of sand alone is made, so that it can be washed away and reused after the printing process is finished. On the right side of Figure 1, it is possible to see a layer of deposited materials, surrounded by a confining boundary, having respectively: sand deposited in the vicinity of the confining boundary, mortar 1 in the outer regions of the solid to be printed, and mortar 2 (potentially less rich in cement) in the core region. At the present stage of the description, mortars 1 and 2

are not yet watered, so they are mere blends of cement/sand. The controlled watering of these mixtures is then done through an additional printing head, as shown in the left part of Figure 1, which allows finishing the mixing proportions defined by the user, by judiciously spraying water in a potentially differentiated manner throughout the entire layer of dry materials that had previously been deposited. Afterwards, the conceptual principle includes the application of a controlled static compaction weight over the entire recently watered layer, as to promote better final density and material properties.

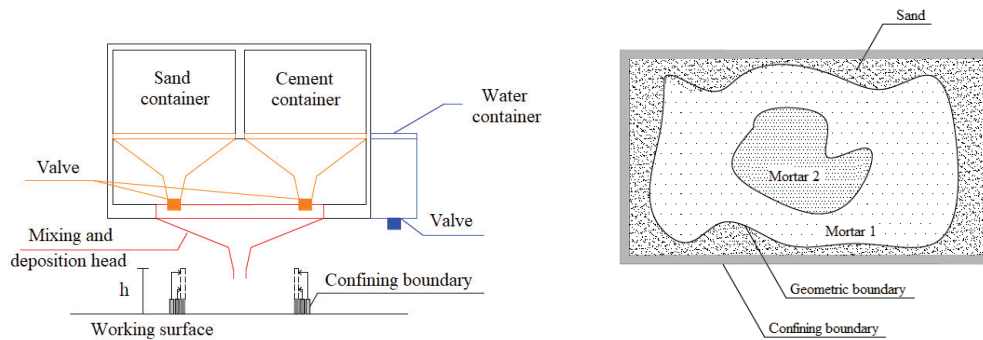


Figure 1: The basic concept of the proposed 3D printing process: cross-sectional view (left); plan view of resulting printing (right). Adapted from [9].

## 2.2 Implementation

In order to prepare a prototype, the requirements stated above were mostly satisfied, except for the fact that the sand and cement containers were not separated. Instead of that, a single reservoir containing a predefined blend of sand and dry cement was considered. The prototype printer that was developed has a potential field for printing of  $1.2 \text{ m} \times 0.6 \text{ m}$  in plan, and maximum potential printing height of  $0.3 \text{ m}$ . The frame is depicted in Figure 2a, where the necessary linear guides for the 3 active axes ( $x$ ,  $y$ ,  $z$ ) and corresponding computer controlled step motors can be seen. The dry material dispenser is shown in Figure 2b: it basically consists of a funnel with bottom dispensing diameter of  $9 \text{ mm}$ , which in turn is filled up to its bottom by a threaded bar. The dry mix for printing (sand and cement) is placed in the funnel, and the threaded bar is acted by a rotary engine (seen in the top part of Figure 2b) that allows controlled deposition of the mix (Archimedes screw principle). The water spraying is made through a standard aerograph, as show in Figure 2c, which is controlled by the central processing unit of the system. For more details on the mechanics and electronics of the system, the reader is directed to [8].

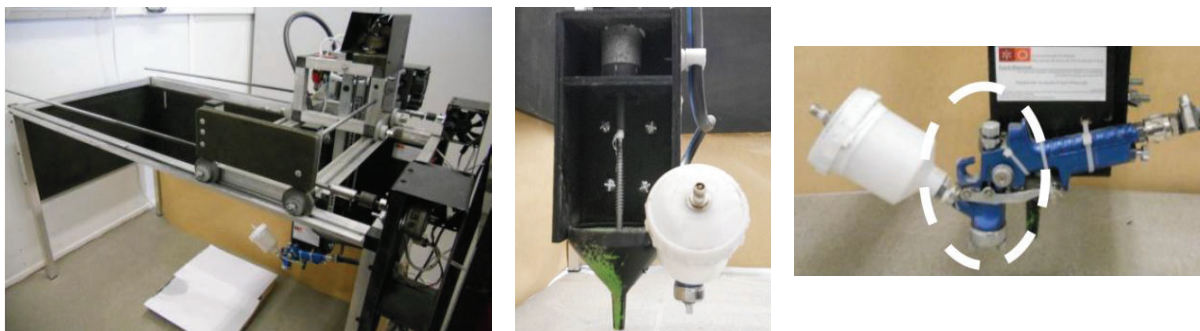


Figure 2: a) The printing frame; b) The dry material dispenser; c) The water dispenser [8].

### 3. Use of prototype printer and results

#### 3.1 Procedure in effect

The setup described above has been put under test in a small confined region of 5 cm × 5 cm, which in turn was used to produce test cubes of 5 cm edge. At this point, it was also decided to solely print a single proportion of cement/sand, whereas not allowing the possibility of depositing sand only. This means that the single deposit description of Section 2.2 above also applies here. The lateral confinement for pressure application was guaranteed by wooden moulds of 1.25 cm height, that were cumulatively added to the system as needed for lateral confinement of subsequent printing layers. The process is described with support of Figure 3.

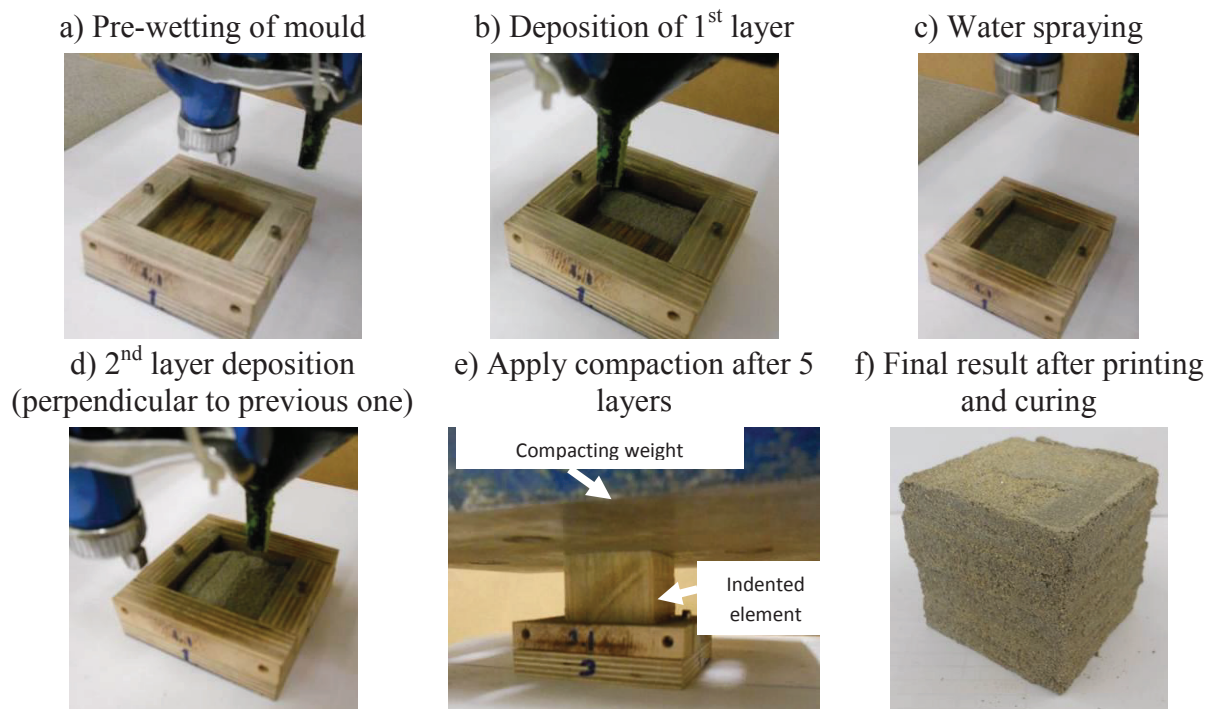


Figure 3: The procedure adopted for printing test mortar cubes.

Initially, the mould is pre-wetted with water spraying (Fig. 3a), followed by the deposition of the 1<sup>st</sup> layer in a sequence of parallel lines of deposition (Fig. 3b). Immediately afterwards the 1<sup>st</sup> layer is finished, controlled water spraying is started, as to attain the desired water-to-cement ratio (pre-calibrated timings of valve opening of water – Fig. 3c). The process is then continued in a similar fashion for the subsequent layers (Fig. 3d). However, every subsequent layer that is deposited, is placed on a perpendicular direction of deposition, as compared to the previous one (attempt to avoid excessive accumulation of fragilities in the interfaces of deposition). The process is followed by water spraying, as done for the 1<sup>st</sup> layer and sequentially repeated up to the 5<sup>th</sup> layer. At every five layers, a compacting weight is placed on top of a compacting interface which comes into contact with the specimen (Fig. 3e). This compacting interface is slightly indented at its bottom, as to improve connection between this layer after compaction and the layers that follow. As mentioned before, the lateral confinement parts are added as needed, and the final result of the process described is shown in Figure 3f.

### 3.2 Systematic experimental program and results

A systematic program of testing has been applied to test both the robustness of the mechanical and electrical parts, as well as the feasibility of the obtained specimens in terms of density and compressive strength. CEM II/B-L 32.5 N was used for the test mortars with fine river sand (maximum grain size ~1 mm). In terms of weight, the following mixing proportions were selected: sand/cement=2:1 and water/cement=0.23. A total of 9 specimens have been prepared with the 3D printing process, with the nomenclature and information provided in Tab.1: 3 specimens compacted with 25 kg weight and tested perpendicularly to the plan of layer deposition; 6 specimens compacted with 50 kg and tested both in parallel (3) and perpendicular direction (3) to the plan of layer deposition. Additionally, 3 more specimens have been prepared and mixed in a Hobart mixer with the same raw materials and mix proportions (except for the addition of superplasticizer to ensure adequate workability).

All specimens were cured at 20 °C (sealed conditions) up to the age of testing, at 7 days, in which density and compressive strength were assessed sequentially.

The 3D printer was able to produce all specimens without malfunctioning and exhibiting an apparently robust capacity for repetition of the test procedure.

The results are cumulatively shown in Table 1. It was noticed that the density of specimens made with standard mixing had an average of 2069 kg/m<sup>3</sup>, as opposed to the average density of 1720 kg/m<sup>3</sup> for printed specimens compacted with 50 kg and 1660 kg/m<sup>3</sup> for printed specimens compacted with 25 kg. These are significant reductions of ~20% with impact on the average compressive strength. In fact, not only is the  $f_c$  of 3D printed specimens significantly lower than the traditionally mixed ones, but it also exhibits a significant dispersion, as shown in Tab.1. This is an indication that the process needs improvements, as to allow, at least a better consistency of the quality of produced specimens. Additionally, to the results shown below, more experiments have been made further to try to increase strength and decrease dispersion [10]. In spite of such efforts, no significant improvements were attained yet. Further studies with potentially better performing mixes (e.g. higher w/c ratio) might pave the way for new developments.

Table 1: Systematic experimental programme.

Name	Size [mm]	Compacting weight [kg]	Test direction	Density [kg/m <sup>3</sup> ]	Compressive strength [MPa]
P1 25 PER	50×50×50	25	Perpendicular to the plan of the layers	1632.24	4.15
P2 25 PER		25		1682.24	***
P3 25 PER		25		1680.22	6.50
P4 50 PER		50		1725.63	7.66
P5 50 PER		50		1730.86	4.80
P6 50 PER		50		1698.47	8.64
P7 50 PAR	50×50×50	50	Parallel to the plan of the layers	1756.57	3.39
P8 50 PAR		50		1721.83	7.44
P9 50 PAR		50		1733.34	4.05
P10 Standard	50×50×50	-	-	2091.28	11.32
P11 Standard		-	-	2074.48	12.25
P12 Standard		-	-	2041.89	10.75

\*\*\* Invalid test result.

### 3. Conclusions

This paper has presented the underlying concept and development of a fully working prototype of a 3D printer for mortars (additive manufacturing), based on the deposition of dry material (sand and cement) and subsequent spraying of water, followed by compaction. The concept may extend further to allow differentiated mixture deposition and creating arbitrary geometry, without having problems of material support of overhangs (satisfied by printing sand to be removed after printing). The working prototype has demonstrated robustness of its mechanical and electronic parts, but the quality of the produced mortar is still inferior to that which can be obtained with the same raw materials through traditional mixing of constituents. The attained results have demonstrated viability to justify further works following the same line of thought of dry-material deposition in 3D printing of cement-based materials.

### Acknowledgements

This work was financially supported by: project POCI-01-0145-FEDER-007633 (ISISE), funded by FEDER funds through COMPETE2020 - Programa Operacional Competitividade e Internacionalização (POCI), and by national funds through FCT - Fundação para a Ciência e a Tecnologia. FCT and FEDER (COMPETE2020) are also acknowledged for the funding of the research project IntegraCrete PTDC/ECM-EST/1056/2014 (POCI-01-0145-FEDER-016841). It is also fundamental to acknowledge the fundamental contribution of João Marcelo Sepúlveda and João Rodrigues, who were fundamental for the initial devising and testing of the 3D printer reported herein during their MSc theses development, but were unfortunately unavailable to assist in the preparation of the present draft.

### References

- [1] Ghaffara S. et al, Additive manufacturing technology and its implementation in construction as an eco-innovative solution. *Aut. Const.* 93 (2018), 1-11
- [2] Khoshnevis B. et al, Mega-scale fabrication by contour crafting, *Int. J. Ind. Syst. Eng.* 1 (2006), 301–320,
- [3] Lim S. et al, Developments in construction-scale additive manufacturing processes, *Autom. Constr.* 21 (2012), 262–268
- [4] Pegna, J., Exploratory investigation of solid freeform construction. *Automation in Construction* 5 (1997)
- [5] Cesaretti G. et al, Building components for an outpost on the lunar soil by means of a novel 3D printing technology, *Acta Astronaut.* 93 (2014), 430–450
- [6] <https://d-shape.com/materials/d-shape-materials/> Accessed in June 2018
- [7] Pierre, A. et al, Penetration of cement pastes into sand packings during 3D printing: analytical and experimental study. *Materials and Structures* 51(1) (2018), 22
- [8] Sepúlveda, J., Bio-inspiração aplicada a estruturas de betão: desafios e possibilidades associados às técnicas de impressão 3D, MSc Dissertation, University of Minho (2012)
- [9] Sepúlveda, J., et al, Bio-inspiração aplicada a estruturas de betão: desafios e possibilidades associados às técnicas de impressão 3D, *Proc. BE2012, FEUP, Porto, Portugal* (2012)
- [10] Morais, R., Desenvolvimento de técnica de impressão 3D para produção de peças de matriz cimentícia, MSc Dissertation, University of Minho (2014)

## **RESEARCH AND DEVELOPMENT OF INFRASTRUCTURE DIAGNOSTIC ROBOT SYSTEM (ALP) BY CONCRETE WALL MOVING MECHANISM USING VACUUM SUCTION PAD**

**Junichiro Nojima**<sup>(1)</sup>, **Toshiaki Mizobuchi**<sup>(2)</sup>

(1) J-POWER DESIGN (JPD), Kanagawa, Japan

(2) HOSEI University, Tokyo, Japan

### **Abstract**

In this paper, the authors describe the construction of an inspection diagnostic system applying robot technology in detailed investigation of infrastructure such as concrete walls at high places. ALP uses a vacuum suction pad improved by testing with a real structure as a moving mechanism at a high place. In addition, a measurement mechanism uses a high-definition camera, an electromagnetic wave radar, a hammering sound diagnostic device.

### **1. Introduction**

Damage due to aged deterioration of infrastructure has a big influence on safety and security of people's living. In order to prevent such an accident, it is necessary to conduct an appropriate inspection in the maintenance and management of infrastructure. However, in high places where it is difficult for people to access, there are problems such as time and expense are required by using scaffolding etc., danger is involved in inspection works. Therefore, in recent years, various infrastructure diagnosis robots are being developed.

Inspection at high positions on the walls are made by investigations by people applying climbing technology and UAV (Unmanned Aerial Vehicle). (Fig. 1 shows) However, these methods have problems such as human error problems and difficulty in obtaining detailed data. Therefore, as shown in Tab. 1, the authors carried out research and development of infrastructure diagnostic robot system (ALP) which stably adsorbs on the wall surface and can conduct detailed investigation. The ALP can be moved while adsorbing to the wall with a vacuum suction pad installed in the movement mechanism unit. In addition, by acquiring data near the surface of the wall, it is possible to safely conduct surveys of the same accuracy as human inspections. The ALP is composed of two mechanisms. The first is a moving

mechanism that moves the vacuum suction pads. The second is a measurement mechanism that acquires data by horizontally moving various measuring machines.

In this paper, the excellent functions possessed by ALP are introduced and the possibility of investigating the deterioration of concrete in place where measurement is difficult such as downstream surface of structure of dam is reported by using ALP.



Figure 1: (Left photo) Climbing survey, (Right photo) UAV.

Table 1: Comparison of inspection methods at high places.

	<b>Climbing survey</b>	<b>UAV</b>	<b>ALP</b>
Nearness survey	◎: It is possible	×: It is impossible	◎: It is possible
Inspection item	◎: Something which can be carried	▲: Only picture Photography	○: Something which can be installed
Accuracy of result	○: Depending on the skill of the person	▲: It's bad because an object distance is far	◎: High accuracy, and no human error
Carrying power	○: Basically the lightest one	▲: Very light one	○: About 10 kg can be installed
Reaction force for wall	▲: The reaction force is small	×: It isn't possible to touch	○: It's possible to get the reaction force in plenty
Safety	×: There is a danger of people falling	▲: There is fear of a fall	○: It's possible to secure safety
Cost of inspection	▲: A considerable cost are needed	◎: Very cheap.	○: The cost performance can be expected
Proficiency in operation	×: Lack of experienced technicians	▲: Lack of skilled pilots	○: Easy to use

## 2. Moving mechanism

The size of ALP is 1.8 m in length  $\times$  1.75 m in width  $\times$  0.75 m in thickness, the weight is 80 kg. This size is determined by a measurement mechanism that can continuously measure in the lateral direction 1 m. As a moving mechanism of ALP, 3 units are installed on the upper side of the measurement mechanism, and 2 units are installed on the lower side. This unit possesses an improved vacuum suction pad for concrete walls and can be stabilized against shear force of 60 kg per unit. When moving the robot, first a vacuum suction pad remove from concrete surface, move and suction each unit one by one in the moving direction (up, down, left and right), and then move the all robot frame. Fig. 2 shows the outline of ALP and Fig. 3 shows the outline of vacuum suction pad.

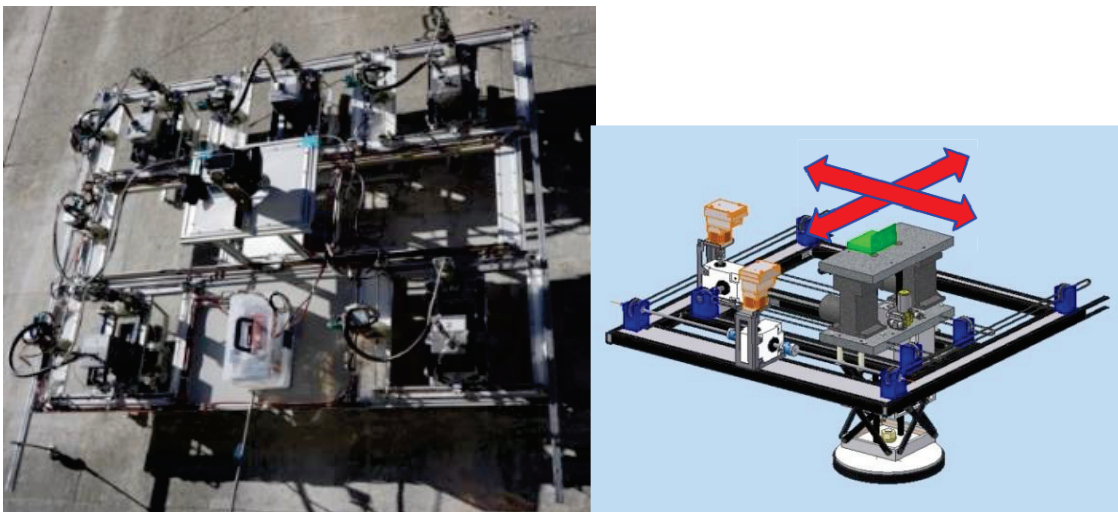


Figure 2: ALP and movement mechanism unit.

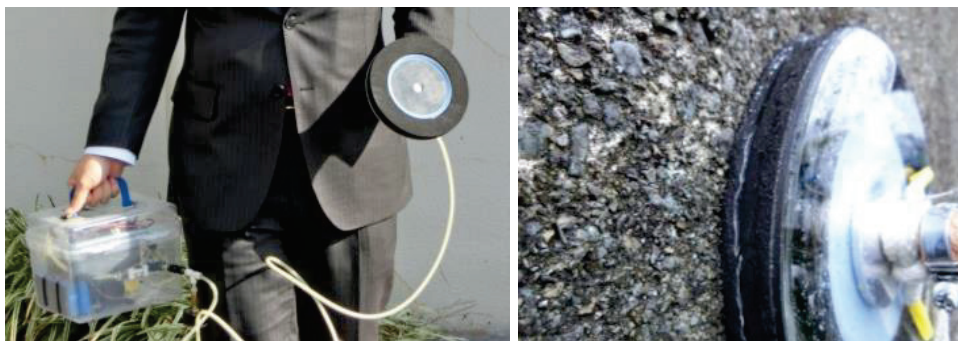


Figure 3: Vacuum suction pad for ALP.

## 3. Measurement mechanism

The measuring mechanism is possible to move the measuring machine in the horizontal direction 1 m and to press the measuring device against the wall surface. At the time of measurement, it is possible to acquire data in a state of being stably adsorbed on the wall surface.



As shown in Fig. 4, the measurement mechanism is equipped with "high-definition camera", "hammering device" and "electromagnetic wave radar". "High-definition camera" mounted a camera with 51.5 million pixels so that cracks of 0.2 mm in width can be judged. Moreover, it is possible to create a highly accurate three-dimensional model by SfM (Structure from Motion). [1] "Hammering device" [2] uses a solenoid magnet to hit the wall surface, acquires the sound generated by the striking with a microphone, and judges the concrete flaking. "Electromagnetic wave radar" can estimate the position of the re-bar and the depth of cover concrete. Moreover, it is possible to estimate the chloride contents in the cover concrete by using the attenuation rate of the electromagnetic wave from re-bar. [3]

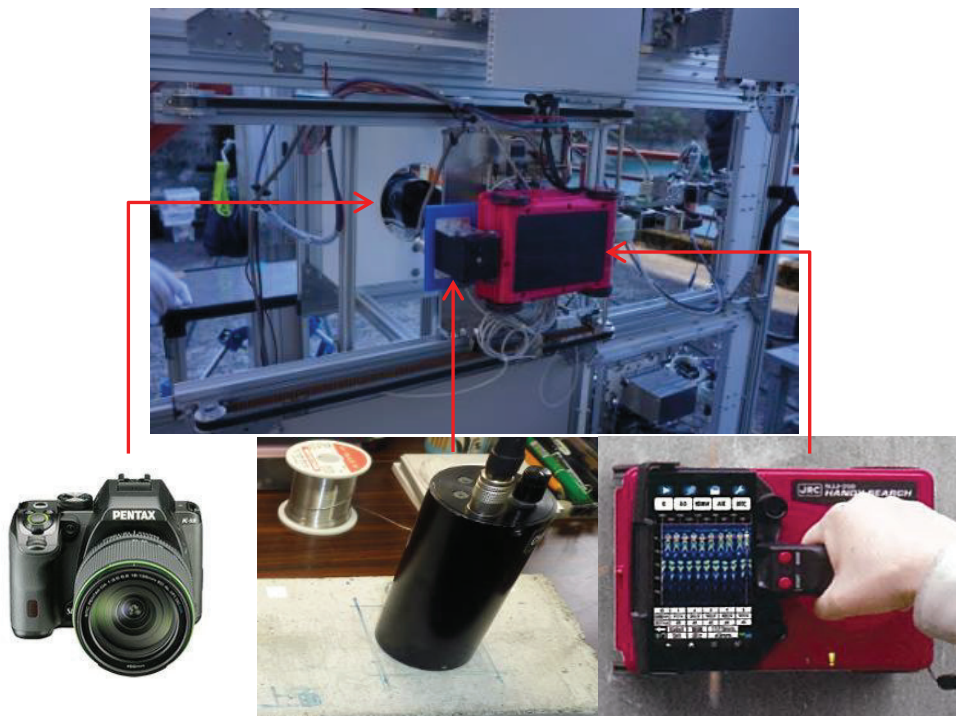


Figure 4: ALP registered measuring instruments.

#### 4. Experimental results on actual structure

The ALP demonstration experiment was carried out on the side wall of the intake gate concrete pier of the arch type dam. Because the ALP is heavy, it moved from the vehicle to the wall of the target using a lifter. Thereafter, the ALP self-moved the wall and acquired data by remote control. The power supply to the ALP was supplied by the power cable, and it was able to drive sufficiently with 0.9 kVA supply by the gas cylinder type small generator. In the demonstration experiment, data was acquired over five hours, and then a three-dimensional model was generated by analysis by SfM. Fig. 5 shows the high-resolution three-dimensional model acquired by the ALP, data by hammering device and electromagnetic wave radar. In addition, the measurement and movement time to acquire the data of fig.5 (about 1 m<sup>2</sup>) was 2 hours.

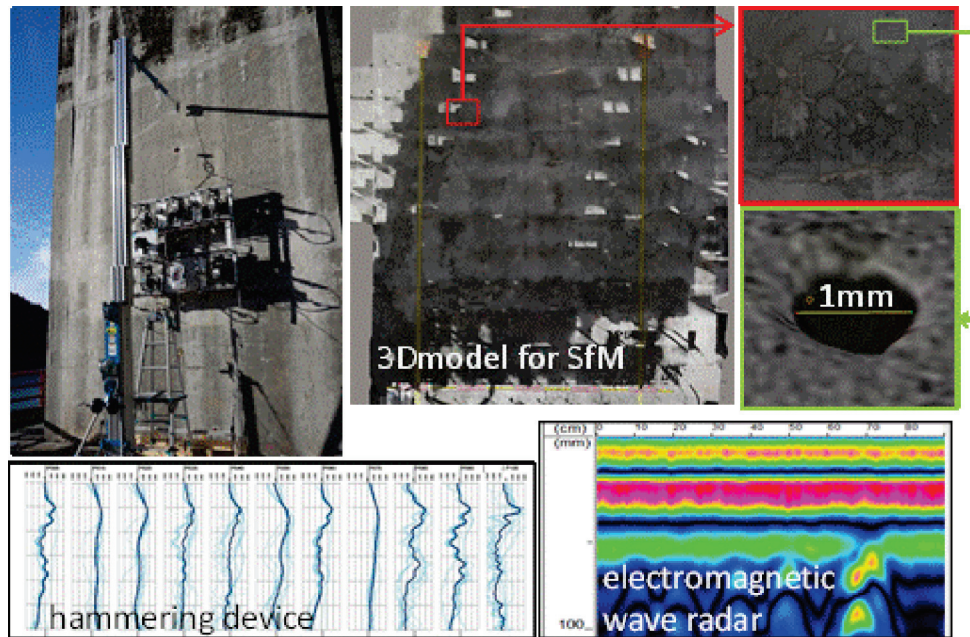


Figure 5: ALP registered measuring instruments.

## 5. Conclusions

ALP has inferior access function compared with UAV, stable contact investigation is possible, construction of precise three-dimensional model and non-destructive inspection for confirming the progress of deformation etc. are possible. In addition, since diagnosis by a plurality of measurement devices also includes information other than images, it can be expected that the accuracy of judgment of deformation and progressiveness will be higher when AI is applied.

Main issues confirmed in demonstration experiments of actual structures are as follows.

- Moving speed on the wall is slow
- Reflection of shadows on images
- Difference in data acquired by hitting devices when conducted by people

The authors plan to solve these problems and to put ALP in practical use.

Finally, This ALP practical development project was obtained by the subsidy of New Energy and Industrial Technology Development Organization (NEDO).

## References

- [1] Nishiyama, S. et al, A study on photogrammetric algorithm for crack width measurement, Computer Methods and Recent Advances in Geomechanics - Oka, Taylor & Francis Group (2014)
- [2] <http://nihonites.co.jp/product/doc/CHES%EF%BC%8DPEA%E2%85%A1.pdf>
- [3] Nojima, J., Study on Accuracy Improvement and Practical Application for Estimation of Chloride Content in Concrete Structures Using Electromagnetic Wave Method, PhD thesis, Hosei University of Japan (2014)

## THE ROLE OF VARIOUS AGGREGATES ON RHEOLOGY OF FRESH 3D PRINTING CONCRETE

Martin Boháč<sup>(1)</sup>, Bohdan Nešpor<sup>(1)</sup>, Theodor Staněk<sup>(1)</sup>

(1) Research Institute for Building Materials, Brno, Czech Republic

### Abstract

The improvement of rheological properties of fresh 3D printing concrete by partial replacement of fine aggregate by fine recycled concrete was studied. The fineness and shape of the aggregate and sand content affects the rheological parameters of fresh mixture. Testing on rotational rheometer was carried out using coaxial cylinders. Testing was carried out in flow regime to evaluate shear and time-dependent rheological properties of fresh printing concrete. The role of packing density of various printing concrete mix designs on rheological parameters were discussed. Small addition of recycled concrete can improve rheological parameters of fresh printing concrete. The proper combination of recycled concrete and sand is the key in optimization of flow properties of 3D concrete.

### 1. Introduction

The rheology of fresh 3D printing concrete is crucial in terms of print quality, shape stability and printability window [1]. Mix design of the concrete, using right proportions of sand and cement blended with admixtures together with proper dosage of superplasticizer, should be balanced to achieve a material with relatively high yield stress and low plastic viscosity to meet the requirements for both pumpability and buildability [2]. The particle shape of aggregate strongly affected the plastic viscosity than the yield stress [3,4]. The type of aggregate influences the workability of concrete by packing density and surface morphology [5-9]. The smooth surface of rounded aggregates or natural aggregates reduces the inter-particle friction and results in an increase in the flowability. The flat and elongated particles can increase the particle collision due to their shape leading to a significant increase in plastic viscosity and yield stress [9]. Recycled aggregates are characterized by the higher water absorption due to the higher porosity of the adhering mortar. Kenai et al. [10] stated that the substitution of natural aggregates by recycled concrete aggregates gave SCC excellent

rheological properties comparable to that of the reference SCC. Güneyisi et al. [11] revealed that the rheological properties and fresh properties of SCC were remarkably improved by the replacement levels of fine recycled concrete aggregates due to their smoother surface. The larger the maximum particle size is, the smaller the specific surface area is and the less the amount of mortar requirement is needed, thus the lower the values of rheological parameters of concrete [12], the weaker the shear thickening behavior [8].

## 2. Materials and Methods

### 2.1 Materials

The binder of the printing concrete consists of Portland cement (PC) CEM I 52.5 R (cement Hranice, CZE), silica fume (SF) ELKEM 971 and fly ash (FA) (Dětmarovice, CZE) in proportions 40:40:20 wt. %. Two combinations of fine aggregate - quartz sand Bzenec (B) and Střeleč (S) with fine recycled concrete (R) (fraction below 0.355 mm) were tested. In the mix design, the fine aggregate was replaced by 0% (ref), 2%, 4% and 6% of recycled concrete. Water to solids (PC+SF+FA) ratio was 0.4 for B mixtures and 0.44 for S mixtures. The ratio of binder to aggregates was 1:1.7.

Table 1: Printing concrete mix design.

Sample	Binder	Aggregate			Water	SP
		B	S	R		
Weight (g, ml)						
<b>B ref</b>	100	170	-	0	40	1
<b>B 2% R</b>	100	166.6	-	3.4	40	1
<b>B 4% R</b>	100	163.2	-	6.8	40	1
<b>B 6% R</b>	100	159.8	-	10.2	40	1
<b>S ref</b>	100	-	170	0	40	1
<b>S 2% R</b>	100	-	166.6	3.4	40	1
<b>S 4% R</b>	100	-	163.2	6.8	40	1
<b>S 6% R</b>	100	-	159.8	10.2	40	1

Superplasticizer (SP) based on PCE (Glenium ACE 40) was used in amount of 1 wt.% (binder). The mix designs are given in Tab. 1. The binder was homogenized for 30 min and then the mixture with aggregates was homogenized again for 1 min in mixer. Liquid SP was added to water and stirred and then the water with SP was added to dry mixture which was then mixed for 3 min.

### 2.2 Methods

Measurement of particle size distribution (PSD) was carried out by a laser diffraction method using CILAS 920L laser particle size analyzer. In laser diffraction particle size analysis, a representative cloud or ensemble of particles passes through a broadened beam of laser light which scatters the light onto Fourier lens. This lens focuses the scattered light onto a detector array and, using an inversion algorithm, a particle size distribution is inferred from the

collected diffracted light data. Size range of particle size analyzer is 0.3 – 400  $\mu\text{m}$ , dispersing medium was isopropyl alcohol. Before the measurement, every sample was treated with ultrasound (60 s). The particles of sands and recycled concrete were studied in reflected light on an optical microscope. Samples were mounted in epoxy resin and then ground and polished to prepare cross sections.

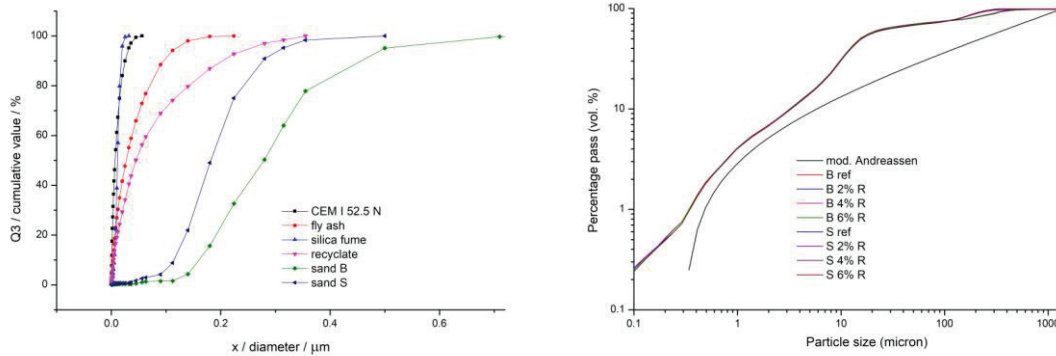


Figure 1: PSD of constituents (right) and cumulative curves (left)

Rheological parameters of printing concrete were determined by means of rotational rheometry (rheometer DHR1). All rheological tests were done at 25 °C. The coaxial cylinders (DIN) geometry. Flow curves were monitored in range of 1-150 1/s using standard DIN coaxial cylinders geometry. Before each measurement of flow properties, the sample was pre-sheared for 10s with 10 rad/s. To achieve equilibrium conditions at each shear rate, the sweep regime (stepwise measurement) was chosen for flow tests. Yield stress and plastic viscosity were calculated as a linear approximation of descending branch of flow curves using Bingham model eq. (1). Where  $\tau_0$  is yield stress,  $\mu$  is plastic viscosity and  $\dot{\gamma}$  is shear rate.

$$\tau = \tau_0 + \mu\dot{\gamma} \quad (1)$$

To quantify the thixotropy (Pa/s), the area between ascending and descending curve was calculated by TRIOS software.

### 3. Results and Discussion

Cumulative particle size distribution was evaluated and curves of all samples were correlated to modified Andreassen model for ideal packing density with q-value 0.35. Cumulative curves of 3D printing mortar binder show only slight difference among mixtures that vary in the content of fine recycled concrete with fraction below 0.355 mm (Fig. 1). The hump around 10-100 microns resulting in gap-gradation is caused by large amount of silica fume with more uniform gradation in the mix (Fig. 1). With increasing content of recycled concrete, the cumulative curve gradation becomes more continuous both in the region of tenths and hundreds of microns. Previous study [2] confirmed positive role of continuous sand gradation on rheological properties, especially on high yield stress and low plastic viscosity. Light microscopy examination showed that particles of recycled concrete compared to B and S sand are often non-spherical or irregularly shaped showing variety of shapes including rectangle, ellipse or random shapes with sharp edges. B sand shows broader distribution of quartz

particles compared to narrower distribution of S sand. Lower circularity of particles of recycled concrete should influence the flow properties and stability of fresh mixtures.

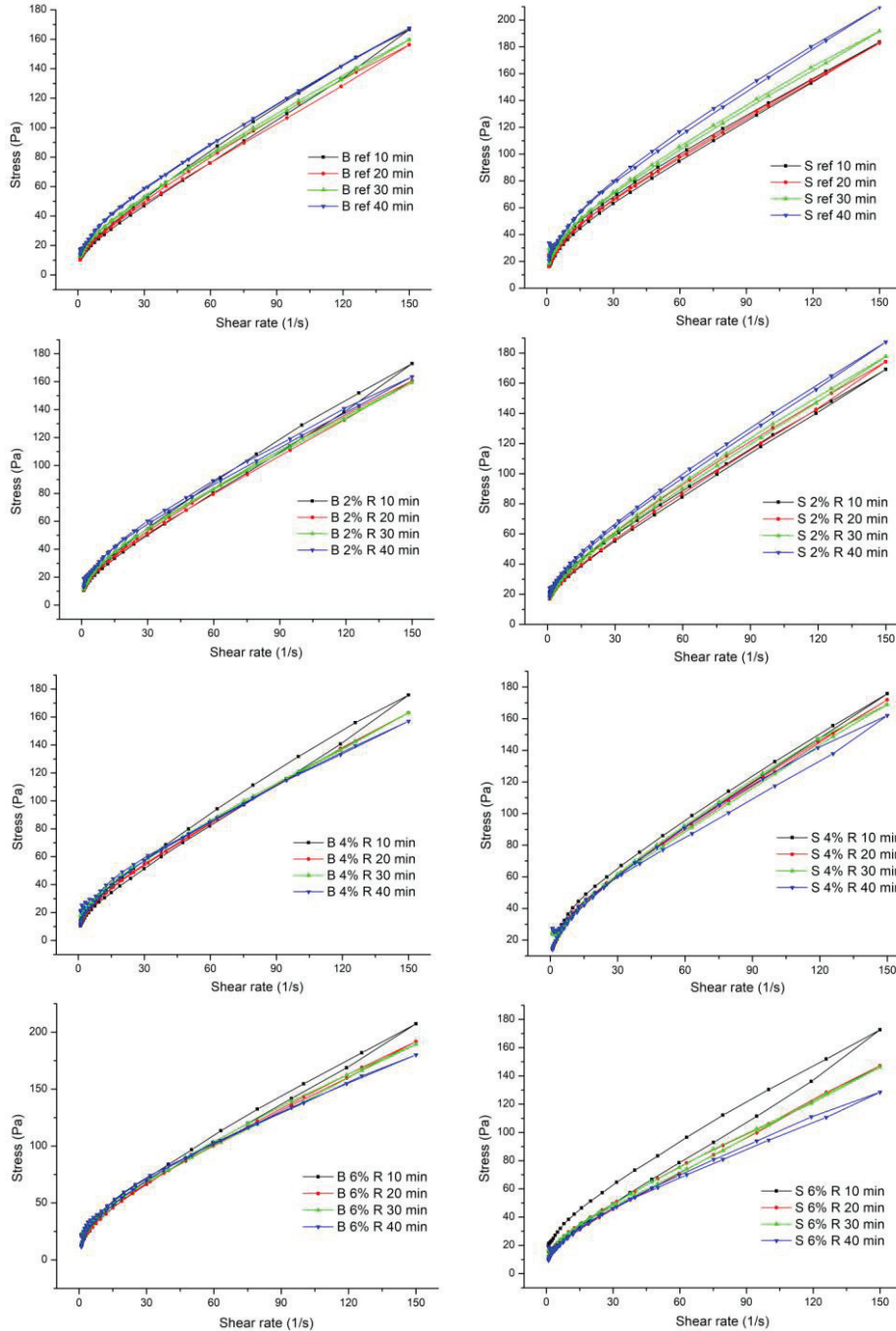


Figure 2: Flow curves of fresh printing concrete with recycled concrete

The role of various content of recycled concrete (R) with quartz sand B or S on rheological parameters was studied. Yield stress and plastic viscosity of fresh mixtures after 10, 20, 30 and 40 min of hydration were calculated from descending branches of flow curves (Fig. 2) using Bingham model (Fig. 3).

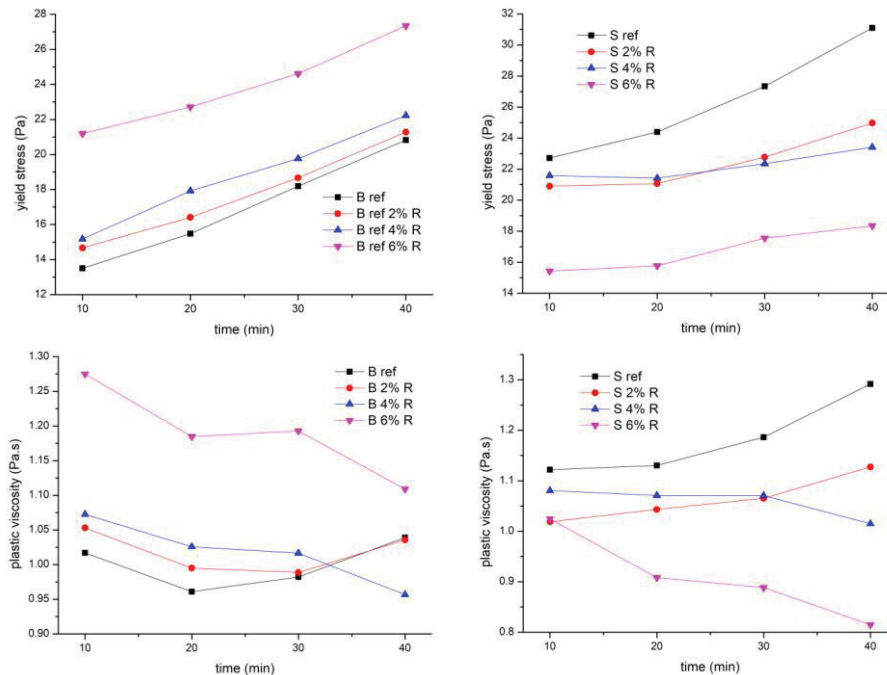


Figure 3: Rheological parameters: yield stress and plastic viscosity of fresh printing concrete

The goal was to find fresh mixture with high yield stress and low plastic viscosity that are needed for good buildability and pumpability. Yield stress increases with increasing content of R in B samples but opposite trend was found for S samples. Plastic viscosity is low up to 4 % of R for B samples and comparable with reference sample. 6% of R considerably increases both yield stress and plastic viscosity in mix with B sand. Addition of R in S samples caused the decrease of values of both yield stress and plastic viscosity. During dormant period, linear increase of the yield stress was confirmed. The increase of yield stress within first 40 minutes is slow showing no signs of initial setting [13,14]. Thixotropy decreases with time of hydration but no clear trend was found between thixotropy and content of recycled concrete. The reason of this fact may be related to combination of thixotropy as a reversible build-up and workability loss as permanent change in rheological properties of the material [15]. An alternative technique of thixotropic build-up quantification calculating critical shear strain measured at low shear rates was proposed by Perrot et al. and Wangler et al. [16,17] giving more insight in what happens when material builds-up after its deposition during printing and defining open time between two deposits.

#### 4. Conclusions

The role of recycled concrete on rheology of fresh 3D printing concrete was studied. Flow parameters of printing concrete can be improved by addition of small amount of fine recycled concrete with irregular shape of particles and proper grading. Replacement of sand by fine recycled concrete up to 4 wt.% can improve rheological parameters related to pumpability and buildability of fresh printing concrete. When using recycled concrete for 3D printing concrete, not only the replacement level of recycled concrete but also the combination with proper sand is crucial.

## Acknowledgements

This paper was elaborated with the institutional support for the long-term development of research organizations by the Ministry of Industry and Trade of the Czech Republic.

## References

- [1] Kazemian, A., Yuan, X., Cochran, E., Khoshnevis, B., Cementitious materials for construction-scale 3D printing: Laboratory testing of fresh printing mixture *Construction and Building Materials* 145 (2017), 639-647
- [2] Weng, Y., Li, M., Tan, M.J., Qian, S., Design 3D printing cementitious materials via Fuller Thompson theory and Marson-Percy model, *Construction and Building Materials* 163 (2018), 600-610
- [3] Westerholm, M., Lagerblad, B., Silfwerbrand, J. et al., Influence of fine aggregate characteristics on the rheological properties of mortars, *Cem. Concr. Compos* 30 (4) (2008) 274-282
- [4] Tattersall, G.H., *Workability and Quality Control of Concrete*, E & F N Spon, London, 1991.
- [5] Hu, J., Wang, K., Effects of size and uncompacted voids of aggregate on mortar flow ability, *J. Adv. Concr. Technol.* 5 (1) (2007) 75-85
- [6] Harini, M., Shaalini, G., Dhinakaran, G., Effect of size and type of fine aggregates on flowability of mortar, *KSCE Civ. Eng.* 16 (1) (2012) 163-168
- [7] Hu, J., *A Study of Effects of Aggregate on Concrete Rheology*, Iowa State University, Iowa, 2005
- [8] Feys, D., Verhoeven, R., De Schutter, G., Why is fresh self-compacting concrete shear thickening, *Cem. Concr. Res.* 39 (6) (2009) 510-523
- [9] Aïssoun, B.M., Hwang, S., Khayat, K.H., Influence of aggregate characteristics on workability of superworkable concrete, *Mater Struct.* 49 (1-2) (2016) 597-609
- [10] Kenai, S., Menadi, B., Debbih, A., et al., Effect of recycled concrete aggregates and natural pozzolana on rheology of self-compacting concrete, *Key Eng. Mater* 600 (2014) 256-263
- [11] Güneyisi, E., Gesoglu, M., Algin, Z., et al., Rheological and fresh properties of self-compacting concretes containing coarse and fine recycled concrete aggregates, *Constr. Build. Mater* 113 (2016) 622-630
- [12] Ba, H., Zhang, W., Influence of aggregate on the rheological parameters of high-performance concrete, *Concr* (06) (2003) 7-8 (In Chinese).
- [13] Struble, L.J., Lei, W.-G., Rheological changes associated with setting of cement paste, *Adv. Cem. Based Mater.* 2 (1995) 224-230
- [14] Lei, W.G., Struble, L.J., Microstructure and flow behavior of fresh cement paste, *J. Am. Ceram. Soc.* 80 (1997) 2021-2028
- [15] Feys, D., Cepuritis, R., Jacobsen, S., Lesage, K., Secrieru, E., Yahia, A., Measuring rheological properties of cement pastes: most commontechniques, procedures and challenges, *RILEM Technical Letters* (2017) 2: 129- 135
- [16] Perrot, A., Rängeard, D., Pierre, A., Structural built-up of cement-based materials used for 3D-printing extrusion techniques, *Materials and Structures* (2016) 49:1213-1220
- [17] Wangler, T., Lloret, E., Reiter, L., Hack, N., Gramazio, F., Kohler, M., Bernhard, M., Dillenburger, B., Buchli, J., Roussel, N., Flatt, R., *Digital Concrete: Opportunities and Challenges*. RILEM Technical Letters 2016 1:67-75



**ON-SITE MONITORING  
AND  
STRUCTURAL CONDITION ASSESSMENT**

## **AN INVESTIGATION ON APPROPRIATE CURING REGIMES FOR PRECAST CONCRETE STRUCTURAL ELEMENTS WITH GGBS USING MATURITY FUNCTIONS**

**Fragkoulis Kanavaris<sup>(1)\*</sup>, Marios Soutsos<sup>(2)</sup>, Jian-Fei Chen<sup>(2)</sup>, Sreejith Nanukuttan<sup>(2)</sup>**

(1) Formerly at Queen's University Belfast, currently at Advanced Technology & Research,  
Arup, London, UK

(2) School of Natural and Built Environment, Queen's University Belfast, Belfast, UK

### **Abstract**

Nowadays, it has been an increasing demand for reducing the carbon footprint of concrete. In several construction projects, new, blended cements are required; not only for being more environmental friendly compared to neat Portland cement but also due to their enhanced durability performance. Precast concrete manufacturers have been traditionally using concretes with high cement content to achieve early compressive strength in order to safely lift structural elements as early as 16 hours after casting and maintain a particular production schedule. However, and regardless of the urge for environmental friendlier construction materials, precast concrete manufacturers are still sceptical with respect to using supplementary cementitious materials, such as ground granulated blast-furnace slag (GGBS), in their concretes due to a potentially slower strength gain of concrete of blended cements compared to conventional ones; which in return causes difficulties to the manufacturer if such cements are specified. In this study, it is demonstrated that using maturity functions for the estimation of the expected compressive strength of concrete is an effective tool towards deriving appropriate curing regimes for precast structural elements containing GGBS without necessarily affecting the production schedule and consequently promoting environmentally friendlier concretes.

### **1. Introduction**

Concrete is arguably the most widely used material worldwide mainly due to its versatility, durability and relatively low production and construction costs. Although it has been used in “countless” projects, from residential buildings to marine and high security structures, the

primary drawback of the material is that its production contributes 5% of total annual anthropogenic global CO<sub>2</sub> production [1]. With Portland cement production being responsible for the higher carbon footprint of concrete, over the past decades the incorporation of cement additions, also known as replacement materials (CRMs) is encouraged, such as ground granulated blast-furnace slag (GGBS).

The need to reduce the carbon footprint of concrete together with the required blended cements for durability performance (CEM II, CEM III, CEM IV and particularly CEM III/B which contains 66-80% GGBS based on EC2 and BS8500) has led to increased demand for innovative and environmental friendlier cement-based materials to be used in the construction industry, including major railway and tunnelling projects. However, precast concrete contractors are faced with barriers regarding the adoption of such cements, especially with high replacement levels of GGBS and they may subsequently fail to comply with the project's regulations or the environmental impact of the project is compromised. These barriers are mostly related with the traditionally preferred CEM I from precast concrete manufacturers and have a direct impact on major construction projects' carbon footprint when precast elements such as structural walls, slabs and tunnelling segments are involved.

One of the main reasons that GGBS has not gained popularity in precast concrete applications, regardless of the need to reduce the carbon footprint of modern concrete, is the fact that the strength development of GGBS concretes at room temperature is slower compared to that of neat Portland cement. A precast concrete contractor is interested in achieving high early age compressive strength in order to enable safe lifting of structural elements within few hours after casting, as this will result in accelerated construction schedules; hence CEM I concrete is generally preferred. However, it has been demonstrated elsewhere that high curing temperature results in greater early age strength enhancement for GGBS rather than for CEM I concrete [2-5]. It is therefore necessary to investigate and optimise curing regimes for GGBS concretes so that early strength lifting criterion of 15 MPa, as specified by PD CEN/TR 15728:2016, is met within a specific time frame. Usually, based on the desired production schedule of precast concrete manufacturers, this time frame lies between 16 and 18 hours after casting (as shown in Figure 1), which enables sequential casting, curing and lifting of precast elements.

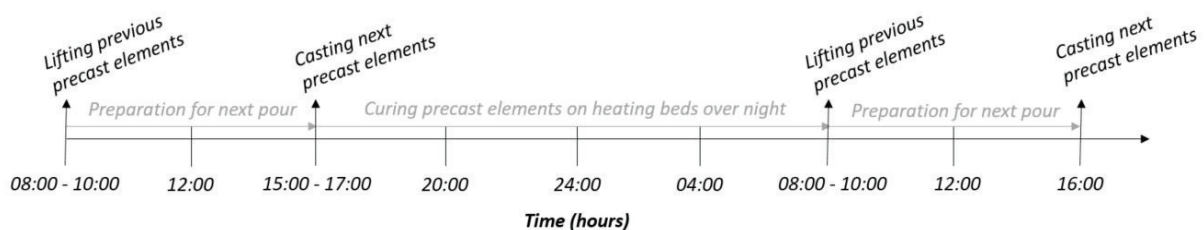


Figure 1: Preferred construction/production schedule of precast concrete manufacturers.

To the authors' best knowledge, such investigation has not been previously evaluated, either experimentally or analytically. However, it is a common in the construction industry which impacts the production efficiency of precast concrete manufacturers, but most importantly, a problem which contributes to ongoing relatively high CO<sub>2</sub> emissions. A solution to this problem will be attempted herein through the use of maturity functions, whilst a brief description of the latter will be provided in the following section. Furthermore, through

combining the curing temperature profile and time required to meet the lifting strength criterion, an indication of the energy consumption required is derived.

## 2. Maturity functions for concrete

Maturity functions for concrete, initially developed by Nurse and Saul in the early 1950s [5], aim to account for the combined effect of temperature and time on concrete strength. Although several maturity functions exist, as outlined in [5], the most frequently used are the Nurse-Saul and the Arrhenius [5] ones, also due to their inclusion in ASTM C1074-11. While the Nurse-Saul function considers that strength varies linearly with temperature, the Arrhenius function implies an exponential variation of strength with temperature. This, together the temperature sensitivity factor (known as activation energy) inherent in the Arrhenius function, resulted the latter to be deemed as more appropriate for mixes containing CRMs, such as GGBS:

$$t_e = \sum_0^t e^{-\frac{E_a}{R} \left[ \frac{1}{273+T} - \frac{1}{273+T_r} \right]} \Delta t \quad (1)$$

Where,  $t_e$  is the equivalent age of concrete (hours),  $E_a$  is the activation energy (kJ/mol),  $R$  is the universal gas constant (J/mol·°K),  $T$  is the average concrete temperature (°K) at time interval  $\Delta t$  (hours) and  $T_r$  is the reference concrete temperature (°K) which is most frequently taken to be equal to 20 °C. Apart from the maturity function to be used, strength-maturity (or strength-age) is also required in order to relate maturity to compressive strength development. A frequently used one is that developed by Carino [2-5] which is also recommended by the ASTM C1074-11 standard:

$$S = S_u * \frac{k * (t - t_0)}{1 + k * (t - t_0)} \quad (2)$$

Where,  $S$  is the concrete strength (MPa),  $k$  is the rate constant (hours<sup>-1</sup>),  $t$  is the concrete age (hours) and  $t_0$  is the age at which the strength development is assumed to begin (hours). Although there are several maturity functions, as mentioned before, for this particular investigation, the combination of Equations (1) and (2) produced the most reliable results, hence used herein (detailed information can be extracted from [7]; however, it is thought that further elaboration on the accuracy of different maturity functions does not fall within the scope of this study).

## 3. Materials and experimental procedures

The materials and experimental methods implemented in this study are briefly explained in the following sections and in detail in [5].

### 3.1 Materials, mix proportions and number of mixes considered

In order to elucidate the potential of using GGBS in precast concrete applications for structural concrete, appropriate curing regimes for three medium to high replacement levels of cement with GGBS were considered. The mixes were designed to have a 47 MPa target mean

cube compressive strength at 28 days, whilst the GGBS replacement levels (by weight) were 35, 50 and 70% of total binder [5].

### 3.2 On-site temperature monitoring of precast concrete walls

The temperature evolution in various locations within a precast concrete wall (at Creagh Concrete Products Ltd.) was monitored with the use of thermocouples. The  $4.86 \times 2.47 \times 0.150$  m, precast concrete wall was cast (CEM I concrete mix with  $420 \text{ kg/m}^3$  cement content) on the so called “heating beds” and prescribed heat was supplied to concrete through the bottom surface (Figure 2). Temperatures were recorded at various locations in the slab and the monitoring was subsequently terminated few hours after lifting.



Figure 2: From left to right – Thermocouples attached on the reinforcement bars, temperature logging system, concrete wall casting on heating bed, wall lifted [photographs: F. Kanavaris].

## 4. Results and discussion

### 4.1 Parametric study on appropriate curing regimes for precast concrete

The recorded temperature histories of the investigated precast concrete wall in various locations are shown in Figure 3(a). As it can be seen, the temperature reached up to approximately  $37^\circ\text{C}$  at the heating bed and bottom of slab; however, due to heat dissipation through the lateral and top boundaries the temperature achieved was lower in these regions. However, as the original precast mix contained solely CEM I, such temperatures were ample for the wall to achieve the required strength at 16-18 hours. Therefore, this temperature profile, together with modified ones for GGBS concrete should be investigated and proposed, as shown in Figure 3(a). The “original” curing regime (“CR-org” in Figure 3(b)) is taken as the simplified version of “long side/lifting anchor” in Figure 3(a) as this location is considered to be the critical one for safe lifting, i.e. the concrete region around the lifting anchor.

The predicted strength development for precast concrete walls containing different levels of GGBS and based on the hypothetical temperature histories in Figure 3(b) are shown in Figure 4. The parameters needed for Equations 2 and 3 ( $E_a$ ,  $S_u$ ,  $k$ , and  $t_0$ ) to enable a strength prediction were previously determined and shown in detail in [5]. It is rather evident that as the GGBS content increases and the temperature remains relatively low, then the early age strength gain is penalised and the required curing time to enable safe lifting is prolonged to a considerable extent. However, due to the temperature sensitivity of GGBS mixes, in the cases where high curing temperature is applied at early ages, strength develops much faster and the lifting criterion can be met as soon as 9 hours after casting, as also shown in Table 2. In this case, the effect of temperature becomes more pronounced as the percentage of GGBS in the mix increases; a behaviour that is particularly beneficial and can be exploited in precast

concrete manufacturing for the production of greener structural elements. It is therefore suggested that the barriers in the adaptation of GGBS from the precast concrete industry could be potentially overcome if appropriate curing is applied, which includes high temperature curing starting from very early ages.

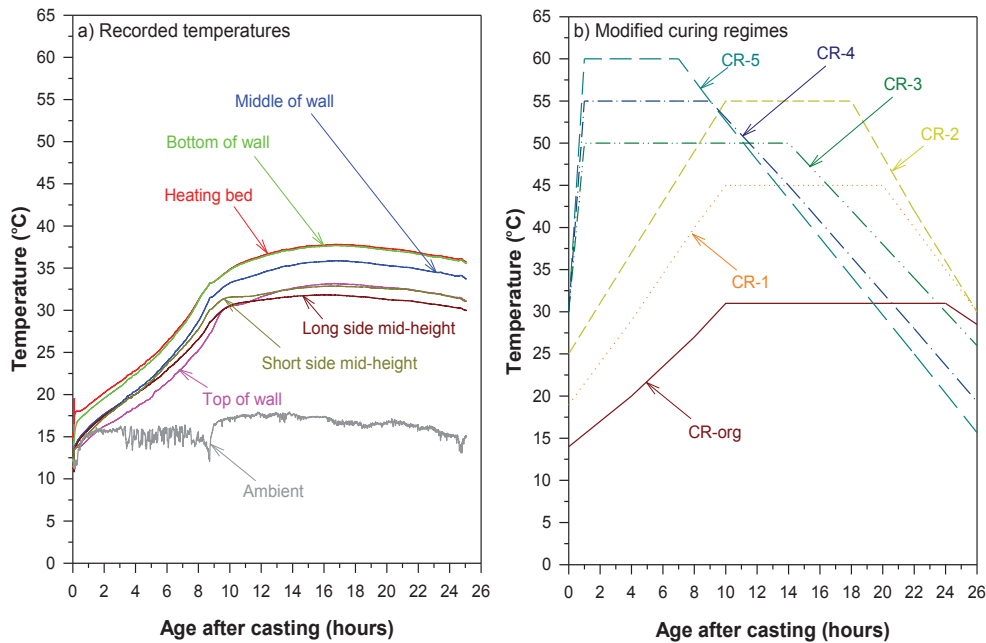


Figure 3: Recorded (a) and investigated (b) temperature profiles

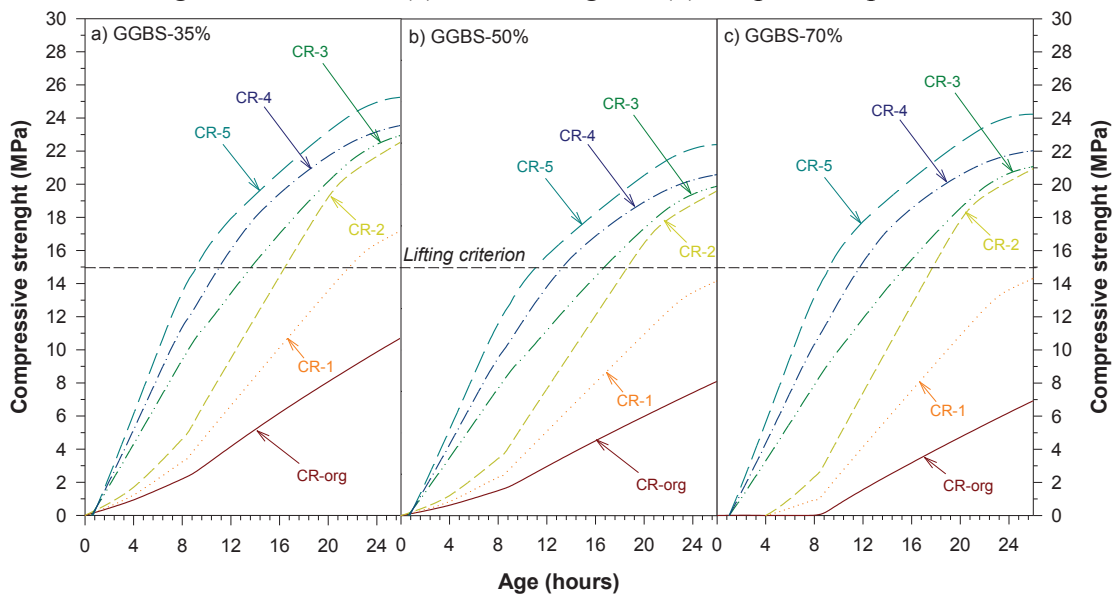


Figure 4: Predicted strength development for mixes containing GGBS based on the temperature histories in Figure 3(b).

#### 4.2 Indication of energy demand

Another issue that should be taken into consideration whenever accelerated curing is investigated is the energy demand of the curing process. Although its accurate calculation in this case may not be possible, it is proposed that indication of energy demand could be

roughly provided through an energy consumption factor (ECF), as shown in Table 2. This ECF can be easily calculated from Figure 3(b) as the area under each curing regime graph whilst the end of curing age is taken to be equal to the time at which the lifting criterion is met. As it can be seen, there is an increase in energy demand for all hypothetical curing regimes when compared to the original ones; however, it may be more environmental friendly to cure GGBS concrete at high temperature for a relatively short period of time rather than at a lower temperature for prolonged periods of time.

Table 2: Calculated potential lifting times and energy consumption factors for the investigated curing regimes and GGBS mixes.

Material	GGBS-35%		GGBS-50%		GGBS-70%	
	Lifting time [hours]	ECF [C·hours <sup>2</sup> ]	Lifting time [hours]	ECF [C·hours <sup>2</sup> ]	Lifting time [hours]	ECF [C·hours <sup>2</sup> ]
CR-org	36	275	42	315	54	380
CR-1	22	565	28	621	27	616
CR-2	17	530	19	605	18	587
CR-3	14	480	16	530	15	503
CR-4	11	429	13	479	12	454
CR-5	9	454	10	499	9	454

## 5. Summary and outlook

In this study a preliminary investigation of appropriate curing regimes for precast concrete structural elements containing GGBS was conducted. It was found that it is possible to obtain similar to PC concrete strengths when concretes with GGBS are considered, however, higher curing temperature must be applied to satisfy the lifting criterion at 16 hours after casting, whilst to obtain an indication of the energy demand based on the curing regime applied and mix considered, an energy consumption factor (ECF) may be implemented.

## References

- [1] Crow, J. M., The concrete conundrum, Chemistry World (2008), 62-66.
- [2] Soutsos, M., Hatzitheodorou, A., Kwasny, J. and Kanavaris, F., Effect of in-situ temperature on the early age strength development of concrete with supplementary cementitious materials, Con Build Mat (2016), 103, 106-116.
- [3] Soutsos, M., Hatzitheodorou, A., Kanavaris, F. and Kwasny, J., Effect of temperature on the strength development of mortar mixes with GGBS and fly ash, Mag Con Res (2017), 69(15), 787-801.
- [4] Barnett, S.J., Soutsos, M., Millard, S.G. and Bungey, J.H., Strength development of mortars containing ground granulated blast-furnace slag: Effect of curing temperature and determination of apparent activation energies, Cem Con Res (2006), 36(3), 434-440.
- [5] Kanavaris, F. Early age behaviour and cracking risk of concretes containing GGBS, Ph.D. Thesis, Queen's University of Belfast, UK (2017).

## **DETECTION, ASSESSMENT AND MONITORING OF COMMON ANOMALIES IN CONCRETE DAMS**

**João Conde Silva** <sup>(1)</sup>

(1) National Laboratory for Civil Engineering (LNEC), Lisbon, Portugal

### **Abstract**

The current document compiles some of the most relevant information concerning the symptoms and respective causes of common anomalies observed in concrete dam bodies. These include physical degradation phenomena, like abrasion, cavitation and freeze-thaw cycles, and chemical reactions, such as expansive reactions and leaching. The methodologies available to detect, assess and monitor these are addressed as well, with a special focus on cracking.

### **1. Introduction**

Portland cement is an inherently durable material. Nonetheless, even the most well designed and built concrete structures have a life time limited by the cement itself. The degradation of a concrete structure is always a concern, with the situation becoming even more serious when the risk of failure jeopardizes people's lives and properties, which is the case of dams with populations downstream [1, 2]. Given the importance of this topic, some of the most frequently observed anomalies in concrete dam bodies, along with their respective causes as well as procedures developed to identify and evaluate them, are presented here.

### **2. Most common anomalies**

Some of the most common symptoms of pathologies observed in concrete dams are cracking, unexpected displacements, water seepages and degradation of the exposed concrete, mainly in upstream and downstream faces as well as around spillways and outlets [2].

The causes of these anomaly signs can be divided into two main categories, the ones with origin in physical phenomena and the ones caused by chemical reactions. The first ones include abrasion, cavitation, shrinkage, mechanical and thermal loads and freeze-thaw cycles.



In what concerns to the chemical reactions, the most frequent ones in concrete dams are leaching of the cement matrix by seepage water, alkali silica reactions (ASR) and internal sulfate attack (ISA). The dam design, concrete manufacture and construction process are also within the main reasons for the appearance of anomalies in concrete dams [1, 3, 4].

Despite being a symptom, cracking is addressed separately due to its remarkable relevance.

## 2.1 Physical phenomena

### 2.1.1 Abrasion

Mirza *et al.* [2] define abrasion in concrete dams as the wear of the concrete surface due to the flowing water carrying solid particles (e.g. sand, gravel and even larger particles), resulting in a smooth surface (smoother than the one produced by cavitation). The extension of the damage is dependent on the speed and turbulence of the water transporting the abrasive material, the hardness of this material as well as the quality of the surface submitted to the abrasion action. Stilling basins (Fig. 1a)) and bottom outlets are particularly susceptible to abrasion and the most effective way to detect it is through visual inspection [5].

### 2.1.2 Cavitation

The erosion by cavitation is one of the most common causes of deterioration in high head spillways and outlet works. It occurs due to a sharp reduction of water pressure during the flow, which may change the state of the water from liquid to vapor. When the pressure drops under a certain limit, the vapor cavities formed inside the liquid become unstable and blow up, which may produce damage to the concrete structure. The damaged surface is more likely to be eroded by cavitation, which often result in a snow ball effect. In hydraulic structures, with high-speed flows, this reduced pressure is typically due to irregularities in the flowing concrete surface, with the most vulnerable zone being the one where the water changes to free flow, e.g. the spillway surfaces, immediately downstream of a floodgate or a valve. The most efficient way to detect damage by cavitation is also through visual inspection [2, 5].

### 2.1.3 Freeze-thaw cycles

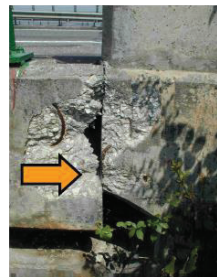
Once saturated, the concrete cracks when exposed to freezing temperatures. The saturation degree is a function of its capillarity and amount of air in its pores. The water expands around 9% from the liquid to the solid state and this volume increase cannot be absorbed by the saturated concrete without damage, normally resulting in cracking or scaling. When there are dissolved salts in the water, the potential damage is even higher. The greater the difference between the thermal expansion coefficients between the aggregates and the cement paste, the higher is the chance of damage due to the freeze-thaw cycles. It can also be easily detected by visual inspection and is mostly observed in the downstream face and in the crest of dams [6].



a) Abrasion in stilling basin



b) Map cracking [8]



c) Crushed joints [8]



d) Relative displacements [8]

Figure 1 - Common anomalies in concrete dams.

## 2.2 Chemical reactions

The anomalies caused by chemical reactions are also very recurrent in concrete dams, with the expansive reactions (ASR and ISA, which may appear in a combined form) standing out. The ASR needs three ingredients to occur: reactive aggregates, alkalis and external water. The reaction product is a gel, which gradually absorbs external water, resulting in an expansion of concrete and, consequently, introducing internal stresses. Concerning the ISA, the sulfates, soluble in water or in the aggregate, may react with the aluminates in the cement paste. The product, ettringite, absorbs water, which may eventually cause expansion and cracking of the concrete. This reaction is relatively common in massive structures like dams, due to the high temperatures achieved at early ages (over 70°C), which delay the formation of ettringite. This mineral also expands by water absorption, hence this late reaction results in swelling of concrete after hardening, with similar consequences as for the ASR [6, 7, 8].

The current state-of-the-art regarding these swelling reactions is already sufficient to avoid its occurrence in new dams, as long as appropriate measures are taken. The methods to prevent the manifestation of ASR and ISA in new constructions are mostly based on controlling and minimizing the variables that contribute to the development of these chemical reactions. Concerning the ASR, the reaction potential of the aggregates may be assessed by a petrologist, whereas the alkalis present in the cement can be controlled. Regarding the ISA, the recommended procedures are to limit the maximum temperature achieved during the hydration reaction of the binders (e.g. replacing part of the cement by pozzolanic materials) and limiting the amount of aluminates and sulfates in the binder (e.g. using high sulfate resistant cements). Accelerated tests are usually efficient in detecting the concrete potential for developing ISA. Keeping the concrete relatively dry is another relatively common solution to mitigate these expansive reactions (e.g. waterproofing the upstream face), although this solution is mostly used in existing dams [4, 6, 7, 9].

When dealing with operating dams, there are several ways to detect the symptoms resulting from ASR and ISA in concrete dams. The most direct one is through visual inspection, with cracking (Fig. 1b)) and ASR gel being among the most frequent manifestations. Further information on crack assessment can be found in 2.3.1. The other key signs are abnormally closed contraction joints (which may eventually start crushing against one another) (Fig. 1c)), relative displacements between adjacent blocks (Fig. 1d)), elevation of the dam height (crest rising) and horizontal permanent displacements (often upstream drift). The dam apertures may also be affected, e.g. ovalization of the ducts and warping of the floodgates. The most effective way for detecting most of these manifestations is through surveillance instrumentation installed in the structure, whose complexity depends on the dimension and safety risk of the dam [6, 8, 10].

The surveillance methods that can be used to monitor the dam behavior and consequently assess the above mentioned symptoms are: a) internally embedded and external joint meters (axial/radial, planar or 3D measurement) for measuring the joint displacements; b) mechanically isolated extensometers embedded in the concrete, to assess the stress-independent extensions, such as the ones resulting from ASR and ISA; c) geometric levelling, for measurement of vertical displacements of the dam crest; d) plumb lines, global navigation satellite systems (GNSS) or geodetic planar system, for measuring the horizontal displacements. However, the interpretation of the data obtained by most of the above mentioned surveillance methods should include a statistical analysis, in order to estimate the weight that distinct variables have on the dam behavior. Thus, statistical models to

quantitatively interpret the collected data are usually utilized. One of the most used methods is the separation of the effects caused by the variables hydrostatic pressure (which is proportional to the reservoir level), temperature (air and reservoir water) and ageing (such as creep or swelling caused by expansive reactions). The first two variables are usually known (by direct measurement) and their effects are assumed to be reversible, whereas ageing effect is presumed to be a non-elastic phenomenon solely time dependent [6, 10, 11, 12].

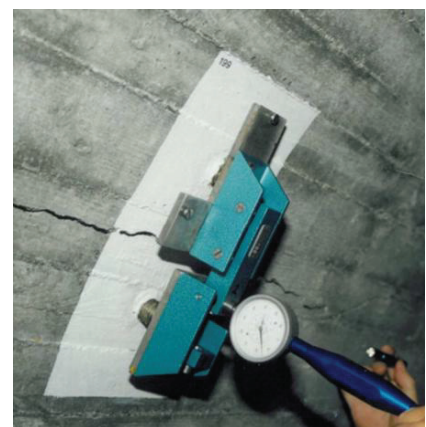
The other frequently occurring chemical reaction in concrete dams, i.e. leaching, consists on the dissolution of material from the cement matrix (calcium and magnesium hydroxide crystals) by reservoir water, with the dissolving potential being enhanced by the pureness of the water. This often leads to formation of crystalline salt deposits known as efflorescence (Fig. 2a)). This loss of solids from the cement matrix reduces the strength and the permeability, which will eventually facilitate the penetration of harmful substances into the concrete, namely water. Hydrochemical analyses of the reservoir water, such as temperature, pH, electrical conductivity, redox potential and total dissolved solids are undertaken to evaluate the water aggressiveness [1, 5].

### 2.3 Cracking

Cracking may have origin on loads (e.g. hydrostatic pressure, self-weight) or on volumetric changes (e.g. thermal, shrinkage, expansion, creep) and should be faced as a potential deficit which needs to be evaluated. The most common causes of cracking in concrete dams are drying shrinkage, temperature changes, expansive reactions (namely ASR and ISA), design or construction defects, ageing, freeze-thaw cycles, foundation settlement and occasional mechanical loads. Understanding the cause of cracking is indispensable for the repair to have effective and long lasting effects. For instance, if cracking is due to drying shrinkage, it will stabilize, so crack repair is more likely to be successful. On the other hand, for the progressive phenomena, such as differential foundation settlements, the treatment of the cracks have more limited effects. Cracking may be the first symptom indicating other issues in concrete. Thus, the structure evaluation, including a detailed crack assessment, should be undertaken when a crack is detected [1, 6, 13].



a) UAV (drone) visual inspection of dam with efflorescence ( $\text{CaCO}_3$ )



b) Crack meter in gallery [10]

Figure 2 - Crack assessment in concrete dams.

### 2.3.1 Assessment of cracking

The surveying of cracks is one of the main tasks involved in the monitoring plan of a concrete dam. It includes a general structure inspection, identifying and describing the cracks as well as, eventually, deducing their origin. Crack meters may also be used to monitor their movement (see Fig. 2b)). If, by chance, the reservoir is emptied, a detailed visual inspection should be undertaken in upstream face, even if no crack signs have been detected. Differential settlements, spalling, seepage and leaching deposits (see Fig. 2a)) are common consequences of cracking [6].

New technologies based on digital image processing are very useful for visual inspections (Aided Visual Inspections) of cracking and its consequences (see Fig. 3). Unmanned Aerial Vehicles (UAV) (see Fig. 2a)) are also extremely convenient for visual inspections [14].

The surface cracking might be mapped using the detailed surveying, photos and pathology maps (see Fig. 3). If necessary, underwater inspections may be undertaken by divers. All the openings (such as tunnels) related to the structure should be inspected as well. When possible, the external signs of cracking should be correlated with internal cracks. The internal cracks may be detected through soft hammering, as a hollow sound usually indicates the presence of unsound concrete, e.g. internal cracks. Several tests to identify the internal cracking degree are at one's disposal, such as lab tests on concrete core extracted from the dam. Non-destructive tests (NDT) are also available for this purpose, namely sonic and ultrasonic waves, geo-radar (based on the changes of magnetic permeability and dielectric constant), video cameras, optic fibers, permeability tests and controlled injection of fluids [6, 15].

Numerical damage models, such as finite element models (FEM) and discrete element models (DEM), are often used as a supplement to the above mentioned methods. These models are very helpful at predicting the locations where cracking is probably occurring. FEM and DEM may even indicate the directions in which cracks are most likely to develop.

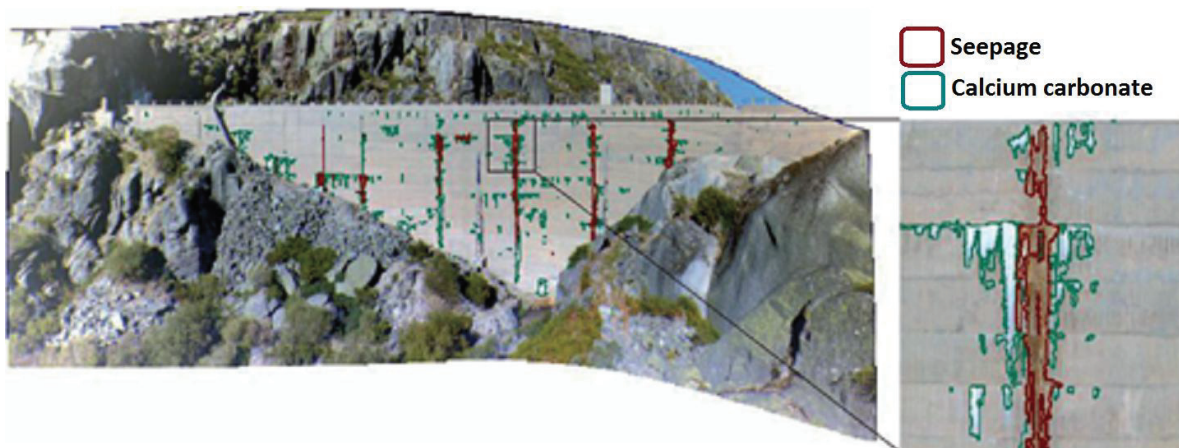


Figure 3 - Pathologies map obtained in the sequence of Aided Visual Inspection [14].

The methods utilized for surface mapping of cracks are relatively simple and relatively inexpensive. On the other hand, the methods to assess the internal cracking degree are usually sophisticated and need specialized workers with adequate training, namely for the processing and interpretation of data [6].

#### 4. Final remarks

The most frequent anomalies in concrete dams may be divided in two main groups, as function of their origin: physical and chemical phenomena. The first ones include abrasion, cavitation and freeze-thaw cycles, and the most adequate way to detect these is through visual inspections. The most relevant chemical reactions are the expansive ones (ASR and ISA) and leaching of the cement matrix. The swelling due to the expansive reactions has numerous typical symptoms, such as abnormally closed contraction joints, distinct displacements and cracking. Instrumentation along with visual observation play a key role in providing early warnings for these unusual behaviors, hence contributing to avoid any subsequent incidents.

Cracking is a common symptom for different causes, so it should be thoroughly evaluated, as an accurate diagnosis is crucial for a successful repair. Several methods for assessing surface and internal cracking have been developed, with their own advantages and limitations.

#### References

- [1] Corns, C.F. et al, Advanced dam engineering for design, construction and rehabilitation, Van Nostrand Reinhold Company (1988)
- [2] Mirza, J. et al, Influence of structural parameters on abrasion-erosion resistance of various repairing mortars, Canadian Journal of Civil Engineering 17(1) (1990), 12-18
- [3] Sims, G.P., The rehabilitation of dams and reservoirs. In Water Storage, Transport and distribution - Vol 1. Encyclopedia of Life Support Systems, Japan (2009), 126-153
- [4] Custódio, J. et al, Concrete structures affected by internal expansive reactions, 3<sup>rd</sup> National Congress on Safety and Conservation of Bridges (2013)
- [5] ICOLD bulletin 119: Rehabilitation of Dams and Appurtenant Works (2000)
- [6] ICOLD bulletin 107: Control and Treatment of Cracks (1997)
- [7] Taylor, H.F.W., Cement Chemistry, London: Academic Press (1997)
- [8] Santos Silva, A., Degradation of concrete due to alkali-silica reaction. The use of fly ash and metakaolin for its prevention (in Portuguese), PhD thesis, University of Minho (2006)
- [9] Divet L. et al, Optimization of the choice of binder to reduce the expansion of concrete due to the delayed formation of ettringite (in French), Proceedings 7<sup>th</sup> CANMET/ACI International Conference on Durability of Concrete, Montreal, Canada (2006), 331-342
- [10] Amberg, F., Performance of dams affected by expanding concrete, V-0009401EN/1021-R-237, Switzerland (2011)
- [11] Batista, A.L. et al, Models for safety control of concrete dams, Proceedings 3<sup>rd</sup> International Conference on Dam Engineering, Singapore (2002)
- [12] Gomes, J.P. et al, Evaluation of the effects of the deterioration process of Fagilde concrete dam: Analysis of observed behavior and mitigation recommendations (in Portuguese). Proceedings 2<sup>nd</sup> Encontro Luso-Brasileiro de Degradação de Estruturas de Betão, LNEC, Portugal (2016)
- [13] Delatte, N., Failure, distress and repair of concrete structures, CRC Press (2009)
- [14] Fonseca, A.M. et al; Visual inspection automation with image processing, Proceedings 7<sup>th</sup> International Conference on Engineering Surveying (INGEO), LNEC, Portugal (2017)
- [15] McDonald J.E. and Curtis N.F., Repair and rehabilitation of dams: case studies, Technical Report REMR-CS-63 US Army Engineer Research and Development Center (1999)

## **DETERIORATION DIAGNOSIS TECHNIQUE OF POLYMER CEMENT WATERPROOFING MEMBRANES BY DIFFERENCE IN THERMAL CHARACTERISTICS OF CONSTITUENT MATERIALS USING ACTIVE THERMOGRAPHY**

**Masayuki Tsukagoshi <sup>(1)</sup>, Hiroki Toyoda <sup>(1)</sup>, Takao Ueda <sup>(1)</sup>, Masashi Ishikawa <sup>(1)</sup>**

(1) Tokushima University, Tokushima, Japan

### **Abstract**

An accelerated degradation test of polymer modified cement waterproofing membrane was carried out. The change in mechanical properties and gloss of the surface was measured. Polymer modified cement waterproofing membranes were prepared according to set polymer to cement ratio parameters, and then applied on concrete surface. These specimens were exposed to 3 types of accelerated deterioration conditions: light irradiation in a quantity of 18.2 W/m<sup>2</sup> by UV lamp; ambient conditions of a temperature of 70 °C and 50 %R.H.; and 70 °C hot water. After exposure test, the surface of the test pieces were heated by a halogen lamp for about 20 seconds and cooled at room temperature. The temperature change during same period was observed with an infrared camera.

For all the test pieces exposed under deterioration conditions the elongation rate tended to gradually decrease as the exposure period increased and the tensile strength increased. And the surface temperature increased as P/C was higher. As the polymer deterioration progressed the lower the observed increases in temperature became. The decrease of the elongation rate due to degradation and the rate of increase in temperature showed a relatively good correlation, but the tensile strength varied greatly.

### **1. Introduction**

Waterproofing materials, of course, must provide waterproof performance and must be able to resist fracturing even when they receive crack bridging tension. Therefore, the polymer cement modified waterproofing membrane is made by polymer-rich formulation, and mixing amount of polymer to cement ratio is 100 to 200 %. Generally, organic materials are degraded by things such as ultraviolet rays, water, oxygen, heat or a combination of these effects during

service period. The organic material is inferior in durability and resistance to weather when compared to the concrete, which is an inorganic material, and because of this it is repaired or modified in a cycle of 10 to 20 years [1]. Generally, in order to evaluate the degree of deterioration of waterproofing materials, the following tests are normally carried out: surface observation, elongation performance test, and component analysis. Any of these existing methods though, require a certain degree of knowledge and high cost. Especially then, when the waterproofing membranes are applied to a large area, there is a need for evaluation methods that can be easily conducted and are non-destructive.

In the field of construction, the active thermography method is a non-destructive and non-contact inspection technique utilized for detection of defects such as peeling of tiles on wall and cavities in concrete. At this point, polymer modified cement is a composite material composed of organic material and cement as an inorganic material, and the thermal characteristics of both materials are greatly different. To this purpose, the degradation condition of the polymer modified cement waterproofing membrane was examined using active thermography method in this study.

## 2. Experimental program

### 2.1 Test pieces

For polymer modified cement materials, ordinary Portland cement (Density: 3.16 g/cm<sup>3</sup>), crushed sand (Density: 2.56 g/cm<sup>3</sup>, Grain diameter <200 µm) acrylic acid ester copolymer (Density: 1.0 g/cm<sup>3</sup>, Re-emulsifiable resin powder) were used. The aqueous emulsion was prepared by mixing re-emulsified resin with water in advance. The emulsion, cement, and sand were mixed to produce the test pieces. The preparation of the test pieces largely followed the Guideline for polymer-modified cement waterproofing membrane work [2] and specification. The coating thickness was adjusted to 1.0 mm by controlling the applied weight. These test pieces were cured for 7 days in an environment of 20 ± 2 °C, 60 ± 6 %R.H.. After the polymer cement was fabricating into a film, it was punched out into a dumbbell shape and used as a tensile test piece. The tensile test was carried out at 500 mm/min in the environment of 20 °C and 60 %R.H. according to JIS K 6251. The mix proportion of the test pieces is shown in Tab. 1. The number of test pieces was 3, and the test results showed the average. The test condition and the shape of the dumbbell test piece are shown in Fig. 1.

Table 1 : Mix proportion of polymer cement.

W/B (%)	P/C (%)	S/C (%)	W (kg/m <sup>3</sup> )	B (kg/m <sup>3</sup> )		S (kg/m <sup>3</sup> )
				P	C	
70	100	200	401	572		572
				286	286	
	150		403	575		460
				345	230	
	200		405	405		385
				365	193	

For the thermography test pieces, a polymer modified cement waterproofing membrane was applied on one surface of the substrate concrete (100×100×100 mm) of W/C = 55 %. These were sealed with epoxy resin except for the surface where the polymer modified cement waterproofing membrane was applied.

## 2.2 Accelerated weathering test

The three main factors of degradation to polymer materials in the outdoors (ultraviolet, heat and moisture) were tested. The distance from the test piece to UV lamp was adjusted so that the irradiation intensity was  $18.2 \text{ W/m}^2$  in ultraviolet degradation test. The test pieces were exposed under the atmosphere of  $70 \text{ }^\circ\text{C}$  and 50 %R.H. in the thermal degradation test, and the test pieces were immersed in hot water at  $70 \text{ }^\circ\text{C}$  for heat and water degradation test. The accelerated degradation test time was 500 and 1,000 hours. After exposure, the test pieces were placed in the laboratory for more than 48 hours ( $20 \pm 2 \text{ }^\circ\text{C}$ ,  $60 \pm 6 \text{ \%R.H.}$ ), then the temperature and moisture content were adjusted for estimating degree of degradation.

## 2.3 Active thermography test

The test condition of the active thermography test is shown in Fig. 2. Active thermography test method is composed of 1,000 W halogen lamp, thermography camera, and PC for image display and data processing [3]. The temperature resolution of the camera was  $0.05 \text{ }^\circ\text{C}$ , resolution of the picture was  $640 \times 480 \text{ pix}$ , and the sampling frequency was 3.75 Hz. The resolution of 1 pix image is approximately  $0.8 \times 0.8 \text{ mm}$ , due to the size of the specimen, the camera installation position and resolution. The surface of the specimen was naturally cooled for 40 seconds after 20 second irradiation with the lamp.

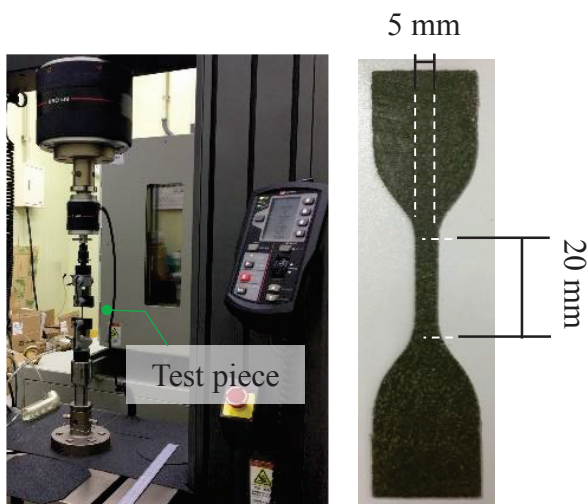


Figure 1 : Tensile test

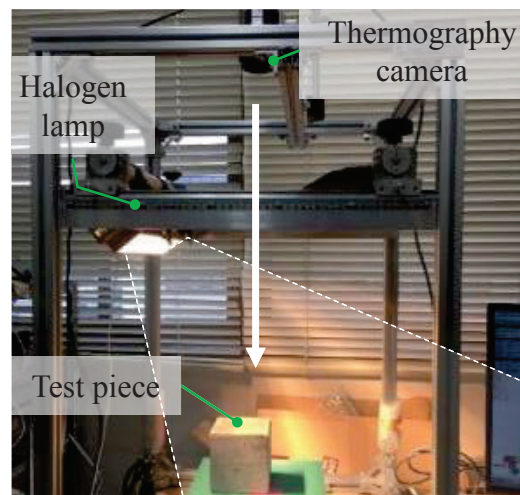


Figure 2 : Active thermography test

## 3. Test results and discussion

### 3.1 Mechanical properties

Fig. 3 shows the rate of change in tensile strength and elongation rate for each deterioration condition. With the test pieces made with the materials used in this experiment in sound



condition, the higher the P/C ratio the higher tensile strength and elongation. Tensile strength tended to increase and elongation rate decreased due to weathering degradation, and the mechanical property of polymer modified cement gradually became brittle. In all the test pieces, after the accelerated deterioration tests the rate of change in tensile strength and elongation tended to increase as P/C was higher. Among all these test conditions, the change of mechanical properties of the test piece exposed under hot water degradation was especially remarkable. The strength of the test piece exposed to the hot water degradation test appeared to be due to the increased promotion of the hydration of cement. This, it seems, led to the formation of a cement material with an especially brittle mechanical property.

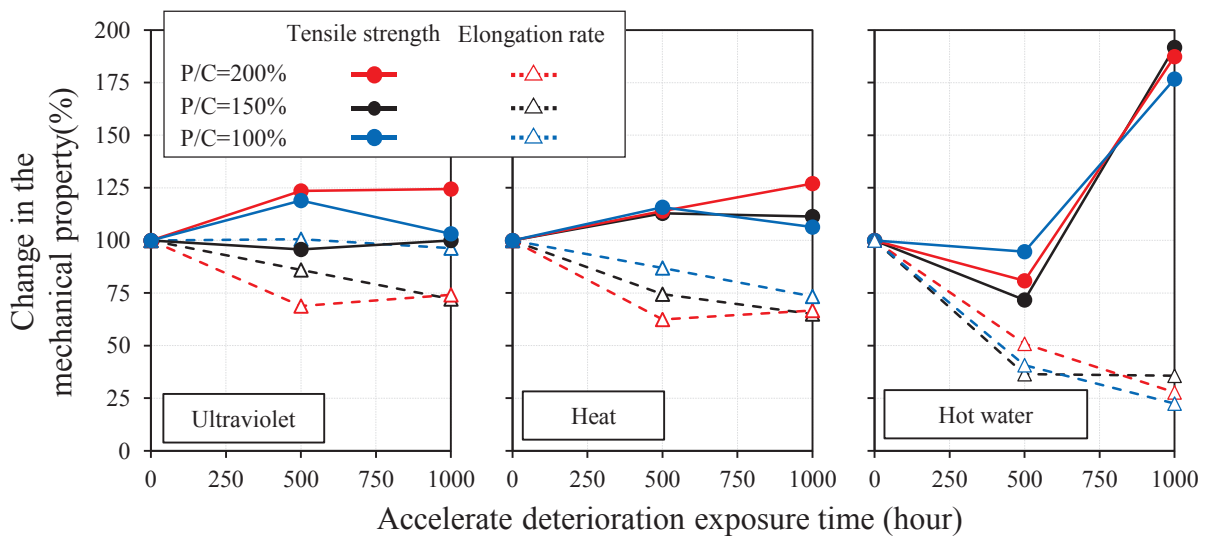


Figure 3 : Change in the mechanical properties of the polymer modified cement due to the accelerated deterioration test

### 3.2 Active thermography test result

Fig. 4 shows the active thermography test results of the test pieces of P/C = 150 %. The rate of changes in surface temperature during heating decreased as the degradation period increased under all accelerated degradation conditions. Here, the difference of the rate of increase in surface temperature before and after the deterioration test was defined as  $\Delta T$ .

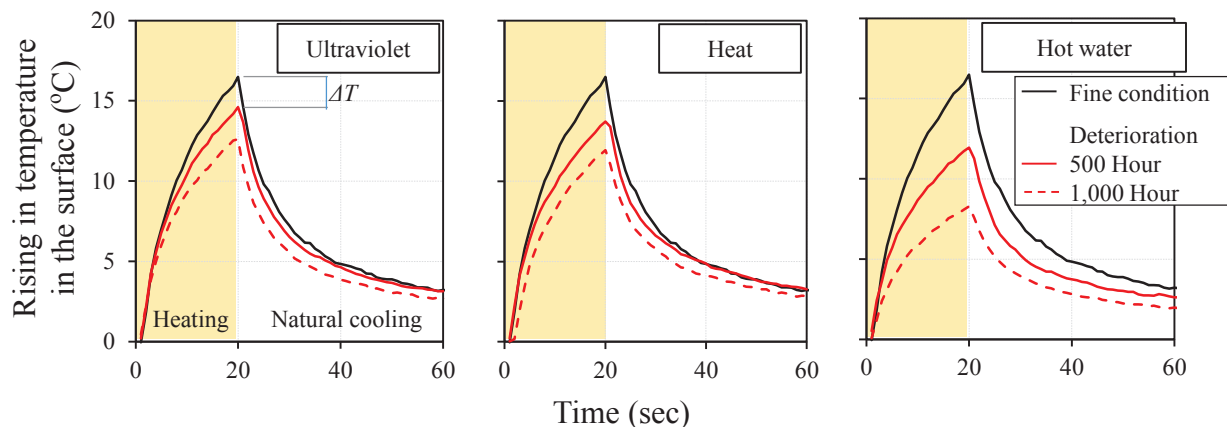


Figure 4 : Changes in surface temperature during heating of specimens exposed to accelerate deterioration condition (P/C=150 %)

Fig. 5 shows the value of  $\Delta T$  for each degradation test condition. The changes in surface temperature during heating decreased with the progress of deterioration, and the higher the P/C, the lower the temperature and the lower the value of  $\Delta T$ . In general, dark-color with low reflectance tend to absorb heat and become high temperature. However, the rate of change in temperature during heating decreased despite of the decrease in the reflectivity of the test pieces with deterioration test. It is assumed that the effect of the exposure of cement and aggregate, whose thermal conductivity is much higher than the polymer, is greater than the effect of changes in reflectivity. This result suggests that the measured changes of thermal characteristics recorded by thermography, are not merely the effect of the discoloration of the polymer modified cement waterproofing membrane, but rather a measure of the deterioration of the components constituting the polymer cement.

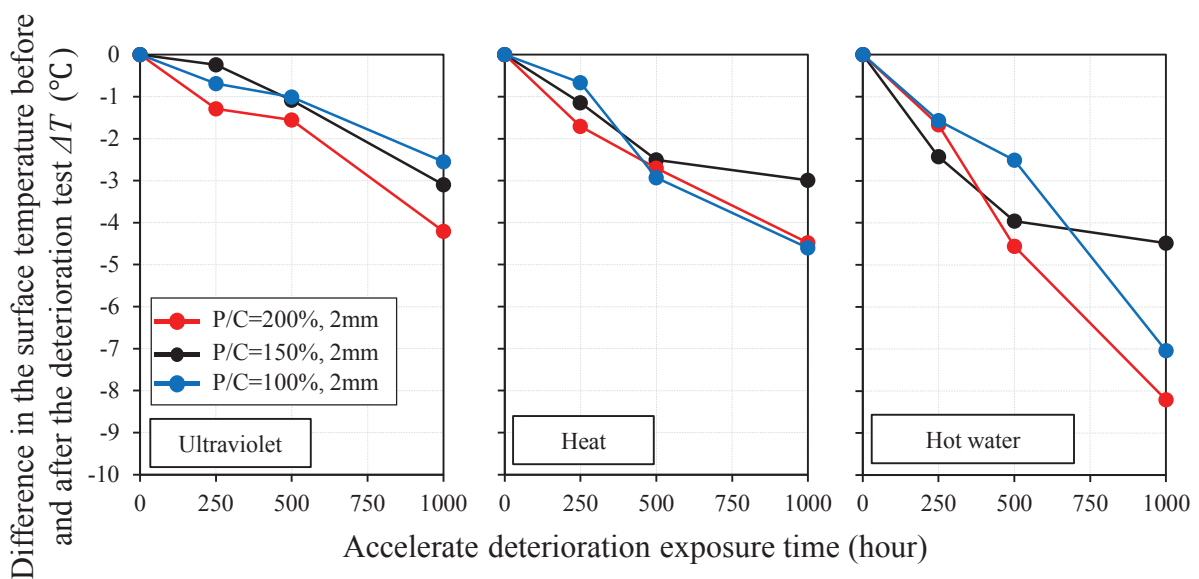


Figure 5 : Difference in the surface temperature before and after the deterioration test

The relationship between the change in the mechanical properties and the value of  $\Delta T$  is shown in Fig. 6. Although the relationship between elongation rate and  $\Delta T$  is relatively good, there is great variations in the tensile strength and  $\Delta T$ . In particular, the greatest deviated value was found in the most deteriorated test pieces subjected to the heat and motion condition. In the deterioration condition of heat and moisture, the deviation seems due to the effect of the promotion of the hydration of cement components in addition to the degradation of polymer components. In addition, the loss of polymer components and numerous small cracks are also observed. This seems to indicate a brittle fracture behaviour similar to cement material caused by the progress of hydration of cement. However, the effect of progress of the hydration of cement is negligible on the thermal properties of polymer cement. As mentioned earlier, the effect of deterioration of the glossiness of the surface due to degradation on  $\Delta T$  is smaller than the effect of deterioration of the polymer component for changing of thermal conductivity. All this suggests the possibility of estimating the rate of degradation of polymer cement by active thermography.

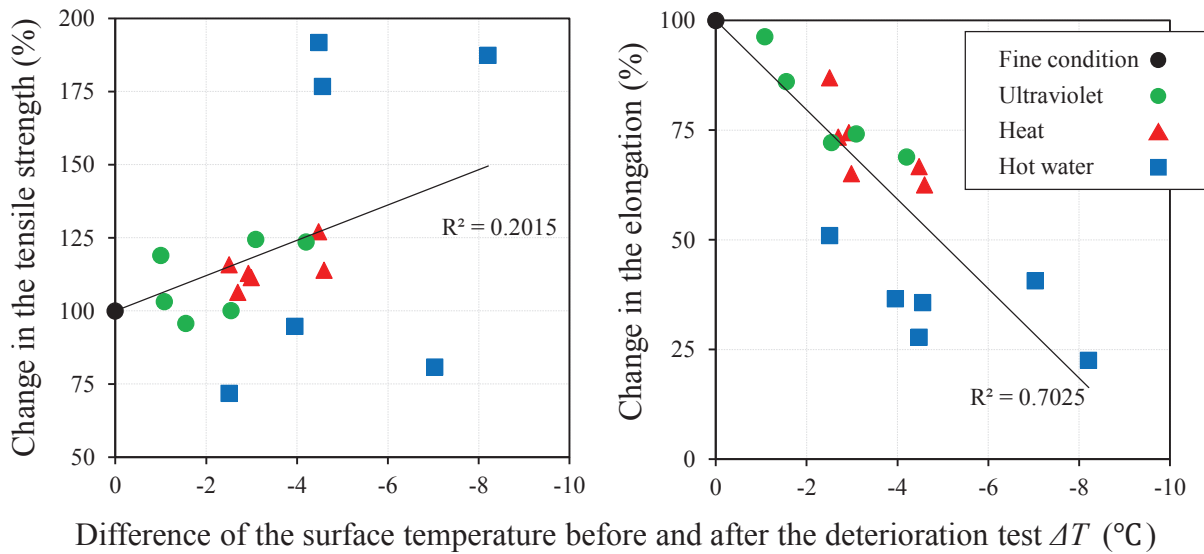


Figure 6 : The relationship between the elongation rate and the difference of surface temperature of  $\Delta T$

#### 4. Conclusion

As the degradation of the polymer modified cement test pieces progressed, the elongation rate decreased gradually, and the tensile strength tended to increase.

The higher the P/C test piece, the higher the temperature of the surface during heating. Degradation caused decomposition and discoloration of polymer components. And, the glossiness of the surface was lowered because the cement or aggregate were exposed and the surface became uneven. However, the rate of increase in surface temperature of the deteriorated test piece with weathering became smaller. This result implies that the change in thermal properties due to deterioration of polymer modified cement is more significant than the effect of merely the changes on the surface.

The active thermography method can possibly be used to estimate the reduction of the elongation performance of polymer modified cement waterproofing membrane caused by weathering of polymer component.

#### References

- [1] Naoki Matsuno, Follow-up capability for the substrate cracking and fatigue test results of Polymer-modified cement waterproofing membrane after accelerated deterioration, Summaries of technical papers of Annual Meeting Architectural Institute of Japan, pp863-864, 2005
- [2] Architectural Institute of Japan, Guideline for Polymer-modified Cement Waterproofing Membrane Work, Vol.1, 20064
- [3] Masashi Ishikawa, Hatta Hiroshi, Habuka Yoshio, Fukui Ryo and Utsunomiya Shin, Detecting deeper defects using pulse phase thermography, Infrared Physics & Technology, Vol.61, pp.216-223, 2013

## EVALUATION OF THE MATERIAL EMBEDDED IN CONCRETE BY ULTRASONIC AND GPR IMAGES

**Sofia Aparicio<sup>(1)</sup>, José Vicente Fuente<sup>(2)</sup>, Dalmay Lluveras<sup>(1)</sup>, Miguel A.G. Izquierdo<sup>(3)</sup>,  
Margarita Gonzáles Hernández<sup>(1)</sup>, José Javier Anaya Velayos<sup>(1)</sup>**

(1) Instituto de Tecnologías Físicas y de la Información “Leonardo Torres Quevedo”, ITEFI  
(CSIC), Madrid, Spain

(2) Geozone Asesores SL, Paterna, Valencia, Spain

(3) ETSI de Telecomunicación (UPM), Madrid, Spain

### **Abstract**

The evaluation of cementitious materials by images from non-destructive techniques has gained prominence during the last years. Ultrasonic Tomography and Ground Penetrating Radar are two non-destructive techniques that are particularly well suited for the inspection of cementitious structures and materials using ultrasonic and electromagnetic waves, respectively. In this paper, these two techniques were used to generate images for the identification of embedded objects in concrete specimens.

A set of concrete specimens were manufactured in which cylindrical bars and pipes of different materials have been embedded, covering a wide range of acoustic and electromagnetic impedances representative of the most common materials found in concrete. For that purpose, three different types of inclusions were inserted in the concrete specimens: PVC tubes, and aluminium and steel tendons.

The experimental ultrasonic images have been obtained using a portable tomographic inspection system, which has the advantage of needing only two ultrasonic transducers to carry out the inspections. The same mechanical system was used with a commercial GPR using a 2 GHz antenna to generate the GPR images. The positions and diameters of the inclusions have been visualized using tomographic images and the results are discussed.

### **1. Introduction**

In recent years, ultrasonic imaging, and tomographic imaging in particular, has gained increasing prominence in the evaluation of cementitious materials by using different

techniques, equipment, frequencies, and wave types [1]. Tomographic images allow the visualization of the cross section of structures, thus enabling better detection of defects, cracks or discontinuities in the material [2-3]. A tomographic image is obtained from projections through the object. These projections consist of velocity or attenuation measurements of ultrasonic pulses transmitted through the specimen. The most popular methods of tomographic reconstruction are the algebraic techniques, such as the algebraic reconstruction technique (ART) and the simultaneous iteration technique (SIRT), which are based on the resolution of the system of linear equations generated by the projections [4].

The techniques based on the use of the georadar, also known as GPR (Ground Penetrating Radar) are based on the use of the pulse-echo technique using electromagnetic waves. The potential of this technique to generate maps of fractures and discontinuities is well known in the literature [5-6]. These maps can allow early detection of internal fractures and other defects such as inclusions or make a detailed map of the extent and orientation of the fracture in the structure, [7-8].

This study presents the results of ultrasonic tomographic and GPR images used to identify embedded objects in concrete specimens. Several concrete specimens were manufactured in which cylindrical bars and pipes of different materials have been embedded: PVC tubes, and aluminium and steel bars. The results of ultrasonic tomographic reconstruction are based on attenuation measures to obtain information about the positions and sizes of inclusions in concrete specimens. The tomographic images are obtained by an immersion ultrasonic tomography system that operates in transmission mode [9], which has the advantage of needing only two ultrasonic sensors. The same system was used to obtain the radargrams of concrete specimens coupling the antenna to the mechanical system of ultrasound tomography.

## 2. Experimental setup

The main objective of this work is by means of tomographic and GPR images identify embedded objects in concrete specimens. In the following sections, both inspection systems are presented as well as the set of concrete specimens used in the inspections.

### 2.1 Ultrasonic tomography

A portable inspection system for immersion ultrasonic tomography was developed by the authors [9]. The system is easy to transport and allows in situ ultrasonic inspections in transmission for specimens with cylindrical symmetry or cores, see Fig. 1. A detailed description can be found in [10].

The procedure used to generate tomographic images consists of three movements. The first movement is a vertical displacement along the height of the specimen, carried out with a step 2 mm in height. The second movement establishes the relative position between the emitter and the receiver. In this case, the inspection angle is  $220^\circ$  and, accordingly, the restriction angle is  $70^\circ$ . The last movement is the rotation of the specimen, which is equivalent to the motion of the emitter transducer. The programmed movement is equivalent to having 100 emission positions. Therefore, each revolution of the specimen generates A-scans coming from 100 emitter positions times 220 receiver positions, resulting in 100 B-scan images of 220 signals taken at 2 mm each, or 22000 A-scans. The diameter between the transducers is 242 mm.

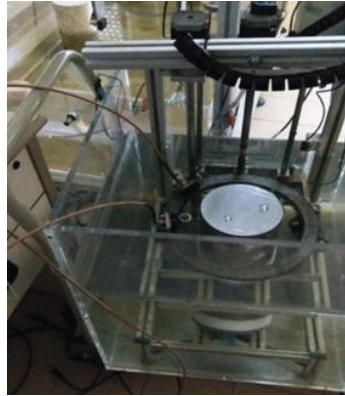


Figure 1: Portable inspection system for immersion ultrasonic tomography.

SENDAS equipment system (CSIC; Madrid, Spain) is used for the emission, amplification, and reception of signals [11]. Two v413 500 kHz wideband transducers (Panametrics, Waltham, MA, USA) are used. A 1  $\mu$ s and 400 V rectangular pulse is applied as excitation signal, and a variable gain receiver amplifier of between 20 and 60 dB is used. The sampling frequency is 10 MHz. The reconstruction algorithm used to generate the tomographic images is SIRT. This algorithm allows to obtain better solutions at the expense of a lower convergence speed [10].

## 2.2 GPR

For the GPR measurement the Subsurface Interface Radar SIR 3000 device, of GSSI, was used with the GSSI PALM antenna of 2GHz that reaches tightly spaces as corners and rounded objects. The tests were made using antenna configurations in reflection mode. The GPR techniques measures the time of flight of electromagnetic waves which are reflected and backscattered at interfaces with different dielectric permittivity. The antenna was placed in the mechanical structure of the ultrasonic inspection system. The inspections were made in three different zones of concrete specimens, inferior, medium and upper that corresponds to 0, 1 and 3 inclusions, Fig. 2.

## 2.3 Concrete specimens

Concrete specimens with different sizes and inclusion materials (aluminium, steel tendon, and PVC tubes) were made. Three inclusions of same diameter ( $\varnothing$ 20 mm), except the tendons ( $\varnothing$ 14 mm), and different heights, 200mm, 150mm and 100mm, were placed in each mold before fabrication (Fig 2). The PVC tubes were sealed to prevent their being filled with concrete during the manufacturing process. Three cylindrical specimens ( $\varnothing$ 150 mm x 300 mm) were moulded according to the UNE 12390-2 and were kept in a laboratory environment for 1 day. After that, the specimens were removed from the molds and stored in water over a 28 days curing process until the inspections were carried out.

Table 1: Concrete mix proportion.

Material	Cement (kg/m <sup>3</sup> )	Sand (kg/m <sup>3</sup> )	Aggregates (kg/m <sup>3</sup> )	Water (kg/m <sup>3</sup> )	Superplasticizers (% of cement weight)
amount	433	983	1000	177.53	1

The materials used to make the concrete specimens were Portland white cement type CEM I 52.5R, normal sand, crushed limestone aggregates, and ViscoCrete 5980 superplasticizer to improve workability. Table 1 shows the mix proportion.

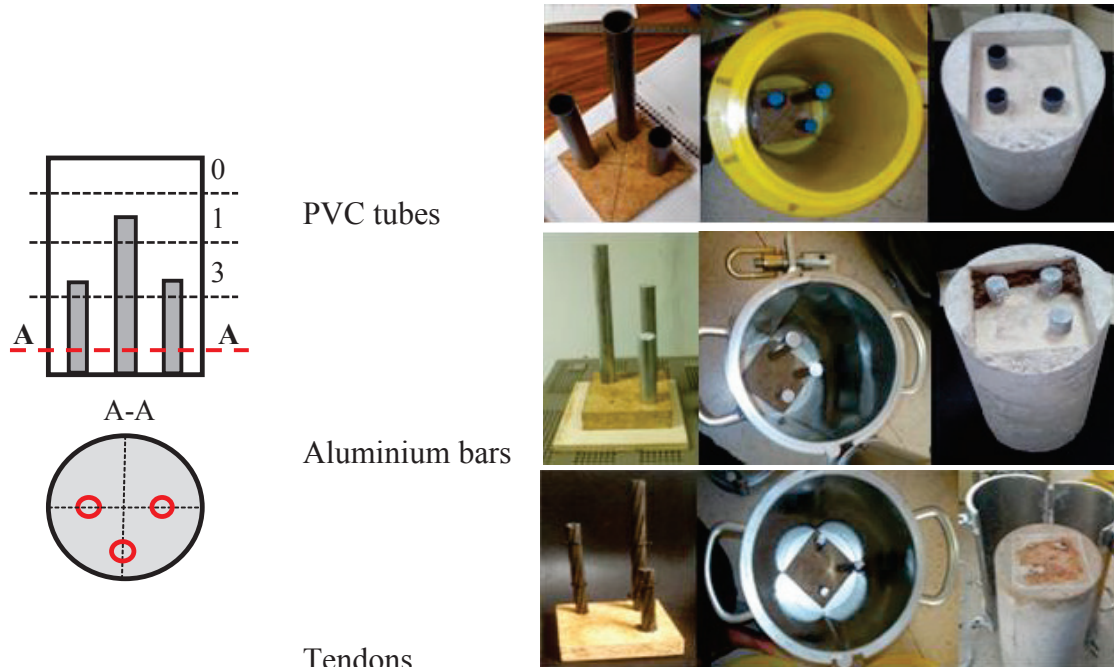


Figure 2: Cylindrical concrete specimens to inspect.

### 3. Experimental Results

Figure 3 shows the experimental ultrasonic tomography reconstruction images of the concrete specimens. All the images are  $80 \times 80$  pixels in size. Each side of the image is physically equivalent to the external diameter of the ring of the inspection system, which means that each pixel represents a 3 mm length. Thus, the concrete specimens, as shown in the reconstructed tomographic images, are 50 pixels in diameter. A blue external ring can also be observed in the experimental reconstruction images. This ring is composed by the multiple echoes produced in the aluminium ring of the inspection system. The bars/tubes inserted in concrete modify the ultrasonic image in different ways depending on the material; in all cases it is possible to correctly locate different inclusions from the reconstruction tomographic images. Since the material of the inclusions was known it is possible to determine their size [10].

From the radargrams we have built three tomograms using the usual geometric transformation than correspond to three zones previously mentioned of each concrete specimen, Fig. 4. The inclusions at each zone are identified for all embedded materials. The PVC tubes show lower contrast than aluminium and steel tendons. Therefore, metallic objects are very well identified using GPR techniques, but other materials are not so well detected.

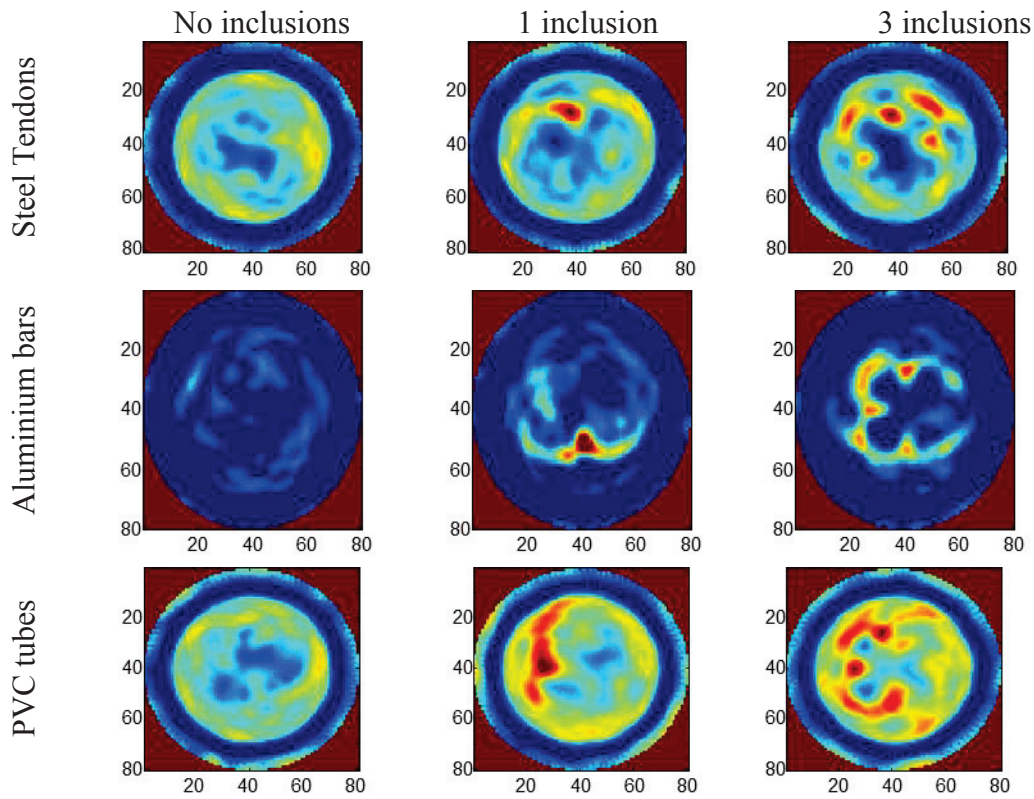


Figure 3: Ultrasonic tomographic reconstruction images of the concrete specimens.

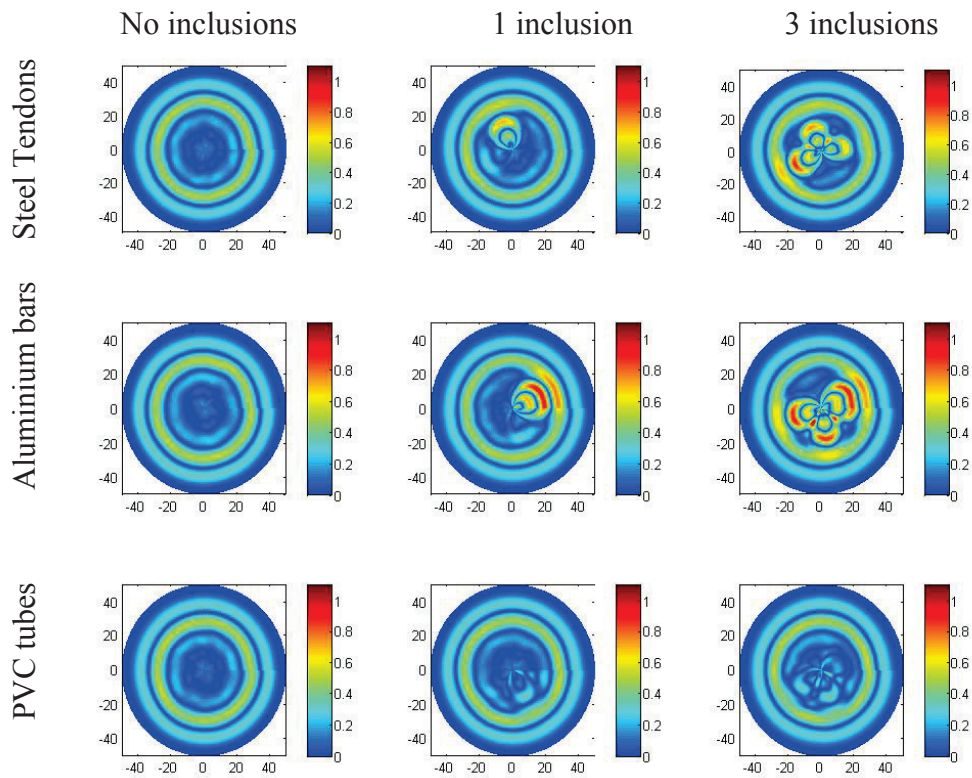


Figure 4: Tomographic images from GPR of the concrete specimens.



#### 4. Conclusions

This study explores the feasibility of using ultrasonic tomographic and georadar images to detect and estimate the most common materials that are embedded in concrete, reinforcements and natural and artificial voids. A limited set of concrete specimens has been made in which bars/tubes of steel, PVC and aluminium have been embedded to analyse the effect of size, material and multiplicity of the inclusions.

The embedded inclusions of different materials have been identified by tomographic and GPR images. Both techniques are complementary. Ultrasonic tomography is better to detect discontinuities of the material. Knowing previously the position and material of the inclusion, the ultrasonic tomography allowed to determine its size very well. GPR technique is better to detect metallic inclusions but it is not well suited to detect their size. The fusion of GPR and ultrasonic tomographic images could to identify material, size and position of the inclusions.

#### Acknowledgements

The Spanish Ministry of Economy, Industry and Competitiveness supported this research under grants numbers BIA2016-77992-R (AEI/FEDER, UE) and RTC-2015-3185-4 (MAPMIT), co-funded by the European Union through FEDER funds under the objective of promoting the technological development, innovation and high quality research.

#### References

- [1] Schabowicz, K., Ultrasonic tomography – The latest non-destructive technique for testing concrete members – Description, test methodology, application example, Arch Civil Mech Eng 14 (2014), 295-303
- [2] Haach, V. G., Ramirez, F. C., Qualitative assessment of concrete by ultrasound tomography, Constr Build Mater 119 (2016), 61-70
- [3] Choi, H. et al, NDE Application of Ultrasonic Tomography to a Full-Scale Concrete Structure, Ultrason Ferroelectrics Freq Control IEEE Trans 62 (2015), 1076-1085
- [4] Kaks, A. C., Slaney, M. G., Principles of Computerized Tomographic Imaging, New York: Society of Industrial and Applied Mathematics, 2001
- [5] Loperte, A. et al, Ground Penetrating Radar in Dam Monitoring: The Test Case of Acerenza (Southern Italy), Int J Geophys 2011 (2011), 1-9
- [6] Yehia, S. et al, Investigation of concrete mix variations and environmental conditions on defect detection ability using GPR, NDT & E Int 65 (2014), 35-46
- [7] Arosio, D. et al, Quality control of stone blocks during quarrying activities. 14th International Conference on Ground Penetrating Radar (2012), 822-816
- [8] Deparis, J. et al, On the potential of ground penetrating radar to help rock fall hazard assessment: A case study of a limestone slab, Gorges de la Bourne (French Alps), Eng Geol 94 (2007), 89-102
- [9] Molero, M. et al, Portable non-destructive testing system for cementitious samples with axial symmetry by using ultrasonic imaging and associated procedure. Patent PCT/ES2011/070499
- [10] Lluveras, D. et al, Ultrasound transmission tomography for detecting and measuring cylindrical objects embedded in concrete, Sensors 17 (2017), 1085
- [11] Fritsch, C. et al, SENDAS: An approach to modular digital processing for automated NDE, Proc. of 2nd Conference on NDE Applied to Process Control on Composite Fabrication, St. Louis, USA (1996)

## **INCREASE CONCRETE QUALITY DURING DESIGN AND EXECUTION PHASE**

**Stefan Scheuchelbauer <sup>(1)</sup>, Massimo Maffezzoli <sup>(1)</sup>, Alexander Reinisch <sup>(1)</sup>**

(1) Doka GmbH, Amstetten, Austria

### **Abstract**

Amidst the different options in concrete construction, there is one goal at the top of the list: producing a concrete structure faster/better/cheaper. Although the objective is formulated with utmost simplicity, the solutions for getting there are no less challenging.

The combination of formwork experience and concrete expertise of Doka allows the customer a 'scenario gaming' in the design phase of a construction project. During execution phase the 'Concremote Value Engineering Methodology' offers the possibility to use the most economic concrete mixture and to monitor the evolution of the temperature gradients in the concrete. The resulting benefits are a higher productivity during construction, higher concrete quality and financial savings during execution and the service life of a concrete structure.

### **1. Introduction**

The durability and service life of a concrete structure is designed in an early stage of the planning phase. In order to achieve the planned target of concrete quality, monitoring during execution is one of the keys of quality management. For instance, in case of mass concrete structures one of the most important aspects is the monitoring of the temperature gradient and appropriate actions on site to avoid cracking and simply guarantee the concrete quality already during construction.

The ambition is to emphasize the importance how to optimize the combination of formwork expertise with superior material technology enabling a well-defined construction sequence between all relevant parties resulting in increased quality management and enhanced durability of the designated concrete structure.

## 2. Understanding the building material concrete

Already in the project tendering and work preparation phase, the early strength development of individual concrete mixtures with different performance will be simulated with respective calibration and temperature assumptions. Therefore, the maturity method (e. g. De Vree [1] or Saul [2]) will be applied. Maturity methods are described in different standards (such as ASTM C1074 [3]) and the topic of various research papers ([4] [5]). Necessarily, the intended concrete formulations can be re-adjusted.

For this purpose, the early strength development of the intended concrete type is used as a performance indicator that can be planned, measured and controlled with Concremote (= real-time concrete monitoring system). Doka Concremote is used as a method to optimize the construction process and thus significantly increase productivity on the job site resulting in secured cycle time and optimized concrete costs in the execution phase (= 'Concremote Value Engineering Methodology', Fig. 1).

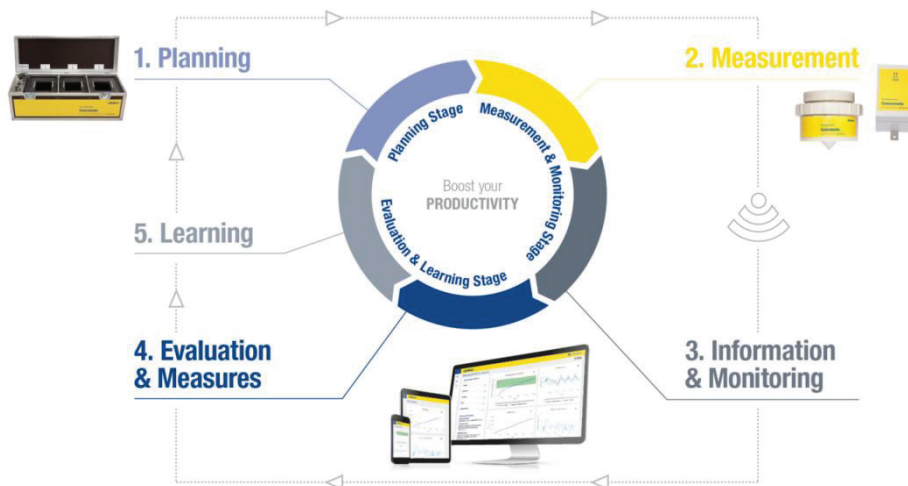


Figure 1: The Concremote Value Engineering Methodology.

Ideally a construction company defines a concrete mix portfolio for example to consider ambient temperature changes (e.g. winter, summer, ...) and other influences already before construction. In order to be able to create a portfolio of concrete mix designs a final design strength of specific structure member has to be defined by design engineers. To meet the requirements a wide set of scenarios for possible concrete mix designs are proposed for specific concrete structure ('scenario gaming').

Once the optimized concrete mix portfolio is defined the project can go into the execution phase (transfer to real-time). Before the start of the construction phase each concrete mix design has to be calibrated in order to define correlation between compressive strength and maturity.

In the construction phase, the monitoring of the temperature and strength development by Concremote takes place in each critical concreting section. The reusable devices will be installed before pouring and the result will be monitored with the Concremote web portal (Fig. 2).

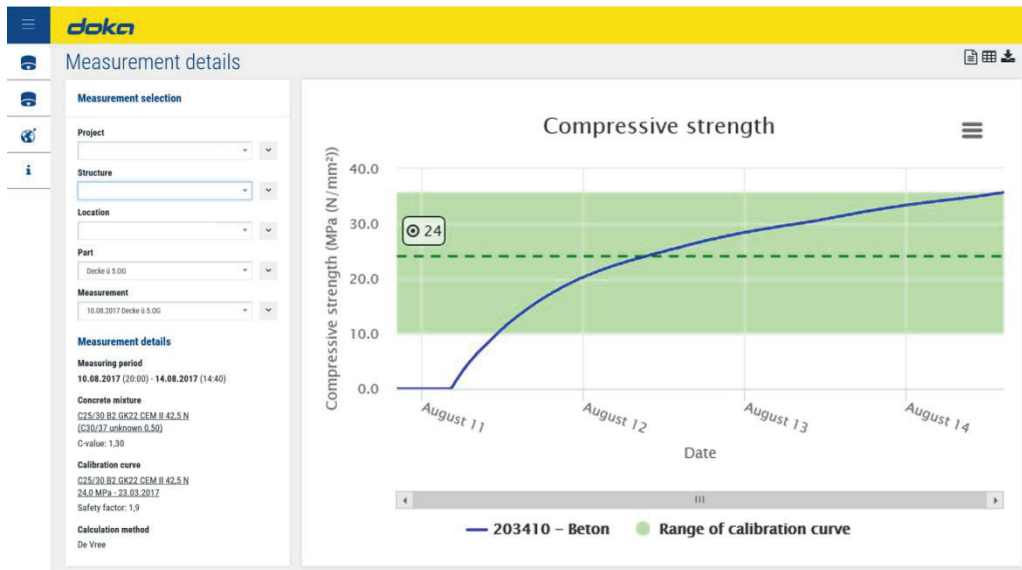


Figure 2: Concremote web portal – Real-time information (e. g. strength).

To enhance the quality of the concrete the curing is monitored and documented. As soon as a certain target value of compressive strength is reached formwork removal takes place. According to that, cycle times and commissioning quantities are reduced and the most optimized curing is obtained at the same time.

Beside the benefits during design and construction phase, Concremote provides easy access for all stakeholders to the measurement data and a digital backup of all measured data.

In addition to the benefits of the Concremote Value Engineering Methodology, the combination with Doka's formwork expertise will positively impact the durability and the service life of the designated concrete construction.

### 3. Understanding the formwork design

Understanding, the building and job site requirements as well as the clients' intention of the construction method, is one of the main subjects to discuss before talking about an optimized formwork solution. Different to the common procedure on standard projects, the construction method and the corresponding formwork solution for concrete constructions shall be defined already in the design phase of a project in order to optimize the processes during execution phase.

The optimized formwork solution – for example at a dam construction – can be influenced by the geology, the geometry of the structure, the construction method as well as the construction schedule (Fig. 3). Vice versa an optimized formwork design can influence the geometry of the structure (e.g. increased block size resulting in less construction and block joints), improve the construction method and speed up the construction schedule resulting in increased productivity and ideally reduced construction costs.



Figure 3: Bykle Dam, Norway – influence of geology and geometry.

#### 4. Understanding jobsite requirements and construction methods

At the beginning of a planning phase of a project we need to understand two main subjects:

- What is being built?
- How is it being built?

##### 4.1 Understanding – What is being built?

Already in the project tendering and work preparation phase, the early strength development of individual concrete mixtures with different performance will be simulated with respective calibration and temperature assumptions with the real-time monitoring system Concremote (= ‘Concremote Value Engineering Methodology’). A temperature simulation of the critical structural members shows the temperature gradient of various points in the current pouring section and also the influence to the following building parts (= ‘scenario gaming’).

In the construction phase, the monitoring of the temperature and strength development by Concremote sensors takes place in each critical concreting section. A systematic analysis shows whether the selected concrete mixture matches the requirements or any adjustments has to be made. This ensures compliance with the desired cycle time and concrete costs.

Based on the project’s unique requirements (“what is being built”, Fig. 4) a tailor-made formwork solution in combination with an optimized construction method between all main structures (e.g. dams) shall be the target of the communication between ‘formwork solution provider’ and the ‘contractor’.

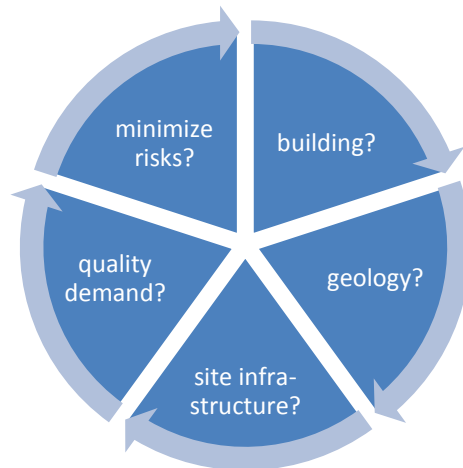


Figure 4: Influencers for optimized formwork solution (what is being built?).

#### 4.2 Understand – How is it being built?

Understanding the building and job site requirements (Fig. 5) is the basis to achieve an optimized working solution. A formwork solution can be influenced by the geometry of the structure, the construction method as well as the construction schedule. Vice versa a formwork design can influence the geometry of the structure (increased block size) resulting in less construction and block joints, improve the construction method and construction schedule to increase productivity and reduce the construction costs.

Just the 'big picture', considering the impact from the formwork and the superior material technology, is providing the possibility to optimize the construction method resulting in increased concrete quality in concrete constructions.

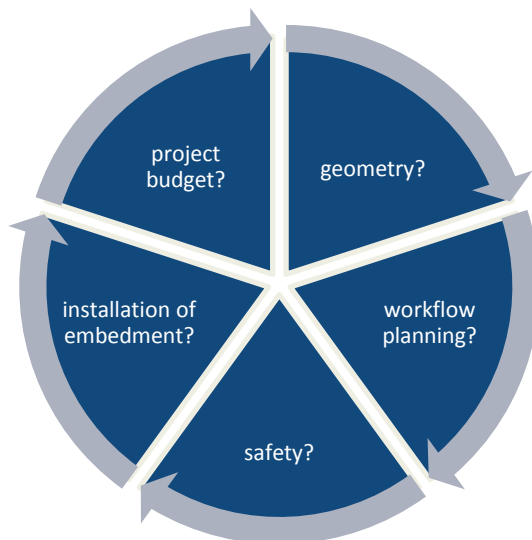


Figure 5: Influencers for optimized formwork solution (how is being built?).

## 5. What does it mean in practice? (project procedure)

The project success does not only depend on selecting the right material. Guidance for the 'big picture' (= products, concrete, logistics and on-site services) from an expert (consultant) can help to enable target oriented processes and assure to meet the demanded result. Consultancy from the very beginning produces a comprehensive solution for the entire production cycle of the concrete structure.

Professional coordination (Project Management) in all involved processes and along the entire project – for example at ESO Supernova (Fig. 6) – is the foundation of having an influence on the concrete result. Just the sum of all involved processes and the learning of the monitoring is creating and assuring the final concrete result.

To sum up, the 'big picture', considering the influences from the concrete and concrete temperature & strength development in combination with an effective and efficient formwork solution, is providing the possibility to optimize the construction method resulting in increased concrete quality in constructions.



Figure 6: ESO Supernova, Germany.

### References

- [1] De Vree, R.T. and Tegelaar, R.A., Gewichtete Reife des Betons – Kontinuierliche, zerstörungsfreie Ermittlung der Betondruckfestigkeit, *Beton* 48(11) (1998), 674-678
- [2] Saul, A., Principles underlying the steam curing of concrete at atmospheric pressure, *Magazine of Concrete Research* 6 (1951), 127-140
- [3] ASTM C1074-17, Standard Practice for Estimating Concrete Strength by the Maturity Method, ASTM International, West Conshohocken, USA, 2017
- [4] Reinisch, A. et al, Confirmation of real time concrete strength in construction projects, *Tagungsband 11th CCC Congress Hainburg* (2015)
- [5] Zitzenbacher, A. et al, Increase concrete quality in dam construction during design and execution phase, *ICOLD 2018 Vienna* (2018)

## **INSPECTION AND MAINTENANCE OF CONCRETE BRIDGES: INVESTIGATION OF MOST SIGNIFICANT DAMAGE MECHANISMS VS. LOCATIONS**

**R.M. Chandima Ratnayake<sup>(1)</sup>, Yousef Saad<sup>(1)</sup>, Kamshan Karunaharan<sup>(1)</sup>, Samindi M.K. Samarakoon<sup>(1)</sup>**

(1) Department of Mechanical Structural and Material Sciences, University of Stavanger, Stavanger, Norway

### **Abstract**

This manuscript demonstrates a methodology that has been developed to support bridge inspection planning. The methodology has been demonstrated using a case study performed to investigate significant damage mechanisms and locations on concrete bridges. The case study and analysis have been carried out using the concrete bridge inspection data available in the Norwegian Public Roads Administration (NPRA) database. This manuscript presents the significant damage mechanisms that were identified, the frequency of occurrence of the identified major damage mechanisms, and the typical locations of each type of damage. The developed guideline has been verified using the actual inspection data of a randomly selected reinforced concrete bridge.

### **1. Introduction**

Reinforced concrete bridges are inspected to detect harmful deterioration and other types of deficiencies, as well as to reduce unnecessary maintenance costs. In general, inspection and maintenance procedures are not consistent [1] (e.g. the Norwegian Public Roads Administration (NPRA) handbook [2] provides guidelines and methods for the inspection and maintenance activities of bridges in Norway). Hence, it is important to develop consistent approaches, to perform optimal inspection and maintenance.

Visual inspection is the starting point of any inspection procedure, which enables the prioritization of areas for detailed inspection. In this context, identification of the potential damage mechanisms in a structure vs. locations is vital for developing optimal inspection procedures/guidelines [3]. The damage in concrete bridges is mainly due to discoloring,



scaling, spalling (i.e. because of steel corrosion) and surface cracks. This damage occurs at different locations (i.e. the structural members/joints) of a concrete bridge. Therefore, it is important to figure out the most vulnerable locations prone to damage. Hence, the classification of concrete bridges into different groups that have similar characteristics is essential to enhance the inspection program. This paper discusses how to enhance the existing inspection NPRA guidelines by applying the group technology (GT) concept to bridges, to group those with similar characteristics and prioritize the damage locations.

## 2. Methodology

It is essential to have inspection guidelines to support inspection planners in developing an optimal inspection program. To develop inspection guidelines, it is vital to identify locations that experience the main degradation mechanisms. For a selected geographical region, it is possible to use the GT concept to group concrete bridges (i.e. bridges with similar characteristics) into families [4], based on type of supports (i.e. continuous, cantilever, simply supported), function and construction

methodology (e.g. pre-stressed, in-situ, pre-cast, etc.). This study has selected 30% of the highest damage frequency of a particular damage mechanism (Note: this percentage shall be based on the inspection philosophy) as the cutoff level. Locations with a greater damage frequency than the cutoff frequency are recommended as locations that need to be prioritized in the inspection planning (i.e. as guidelines to support inspection-planning activities). A case study has been carried out to investigate the damage mechanisms vs. where they occur, using the historical inspection data available in the bridge inspection database (BIDB) at the NPRA. Fig. 1 illustrates the overall methodology that has been used to develop the inspection guidelines.

### 2.1 Development of inspection guidelines

It is important to identify the most common damage mechanisms, as well as damage mechanism vs. location, in order to develop inspection guidelines. The aforementioned enables damage mechanisms vs. most vulnerable locations to be investigated, in order to

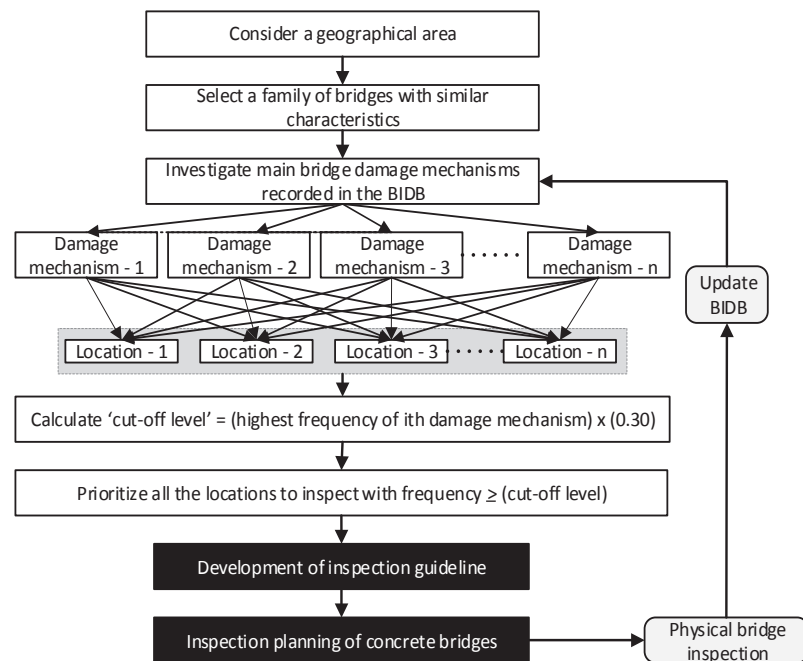


Figure 1: Development of an inspection guideline.

prioritize inspection that will optimize inspection planning and the utilization of inspection task-related resources.

### 2.1.1 Damage analysis

Using the BIDB at the Norwegian Public Road Authority in Norway (NPRA) (i.e. *Staten Vegvesen*, in Norwegian), 34 bridges with similar characteristics (i.e. bridge family BFX) located in a particular geographical area (i.e. region code RGXA1) have been selected to investigate the most common damage mechanisms and the frequency and locations of the damage. Fig. 2 illustrates the bridge element details of a representative bridge in the selected bridge family [2].

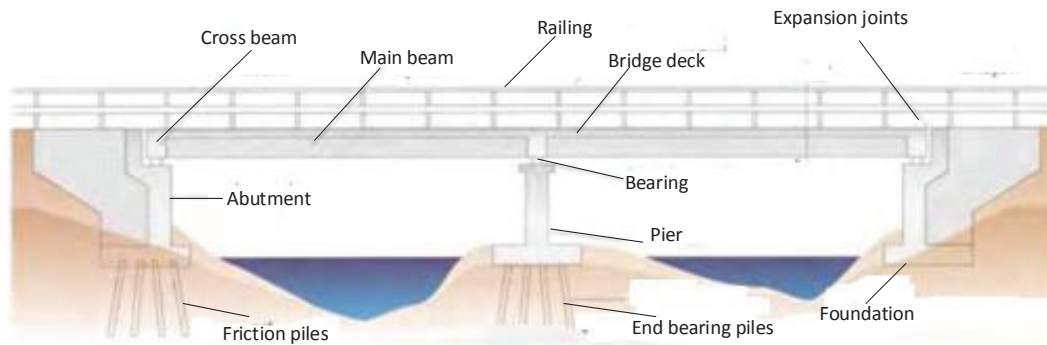
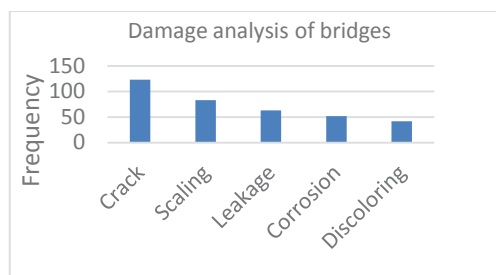


Figure 2: The typical elements of a bridge [2].

The results of the damage analysis of 34 bridges revealed 133 cracks; 53 areas of corrosions; 42 instances of discoloring; 85 incidences of scaling; and 67 leakages. Fig. 3a illustrates damage mechanism vs. frequency plot and Fig. 3b illustrates discoloring damage on concrete, which has not been taken into further analysis (i.e. due to less seriousness in relation to the structural damage) for developing inspection guidelines to carry out inspection prioritizations.



a. Damage vs. frequency



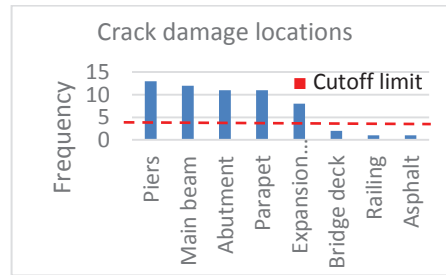
b. Discoloring

Figure 3: Damage mechanism analysis.

Fig. 4a illustrates an example of cracks appearing on a bridge element, while Fig. 4b illustrates the frequency of cracks vs. location. In this case, the cutoff limit is calculated as  $13 \times 0.3 \approx 4$ . Fig. 4b reveals that most of the cracks have appeared (i.e. in relation to the cutoff limit 4) in piers, the main beam, abutments, parapet systems and expansion joints. Hence, it is possible to develop a guideline for inspection planning as follows: bridge elements such as piers, main beam, abutments, parapet systems and expansion joints shall be inspected to examine whether there are any cracks.



a. Cracks



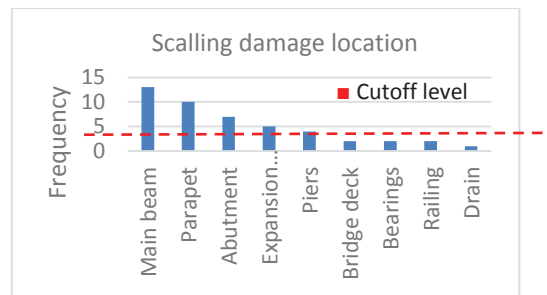
b. Crack location vs. frequency

Figure 4: Crack damage analysis.

Fig. 5a illustrates an example of scaling, and Fig. 5b illustrates the frequency of scaling damage vs. location. In this case, the cutoff limit is calculated as  $13 \times 0.3 \approx 4$ . Fig. 5b reveals that most of the scaling damage has appeared (i.e. in relation to the cutoff limit 4) in the main beam, parapets, abutments, expansion joints, and piers. Hence, it is possible to develop a guideline for inspection planning as follows: bridge elements such as the main beam, parapets, abutments, expansion joints and piers shall be inspected to examine whether there is any scaling damage.



a. Scaling



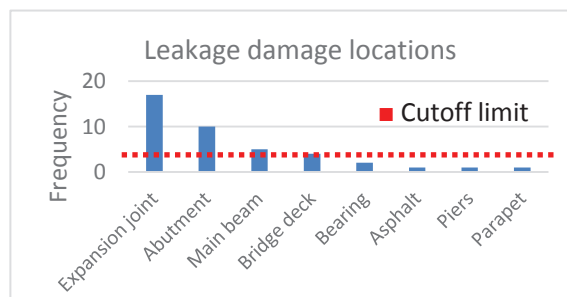
b. Location vs. scaling damage frequency

Figure 5: Scaling damage analysis.

Fig. 6a illustrates an example of leakage, while Fig. 6b illustrates the frequency of leakage damage vs. location. In this case, the cutoff limit is calculated as  $17 \times 0.3 \approx 5$ . Fig. 6b reveals that most leakages have appeared (i.e. in relation to the cutoff limit 5) in expansion joints, abutments, the main beam, and the bridge deck. Hence, it is possible to develop a guideline for inspection planning as follows: bridge elements such as expansion joints, abutments, main beam, and bridge deck shall be inspected to examine whether there is any leakage damage.



a. Leakage



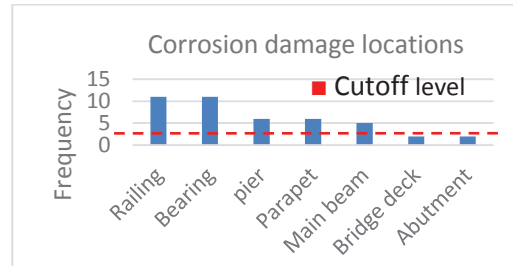
b. Location vs. leakage damage

Figure 6: Leakage damage analysis.

Fig. 7a illustrates an example of corrosion damage and Fig. 7b illustrates the frequency of corrosion damage vs. location. In this case, the cutoff limit is calculated as  $11 \times 0.3 \approx 3.3$ . Fig. 7b reveals that most of the corrosion has appeared (i.e. in relation to the cutoff limit 3.3) in railings, bearings, piers, parapets and the main beam. Hence, it is possible to develop a guideline for inspection planning as follows: bridge elements such as railings, bearings, piers, parapets and main beam shall be inspected to examine whether there is any corrosion damage



a. Corrosion



b. Location vs. corrosion damage

Figure 7: Corrosion damage analysis.

Tab. 1 illustrates the summary of the guidelines that have been developed, based on the damage analysis.

Table 1: Guidelines for concrete bridge inspection.

Region – RGXA; bridge family - BFx	
Damage mechanisms	Guidelines for inspection planning
Cracks	• Focus on piers, main beam, abutments, parapet systems and expansion joints
Scaling	• Focus on main beam, parapets, abutments, expansion joints, and piers
Leakage	• Focus on expansion joints, abutments, main beam, and bridge deck
Corrosion	• Focus on railings, bearings, piers, parapets and main beam

## 2.2. Verification study

In order to investigate the validity of the suggested guidelines, a verification study was performed, choosing a bridge at random. The chosen bridge is 207.1m long. It was built in 1967 with a remaining life of 49 years (i.e. built of reinforced concrete) and located over a fjord with seawater (i.e. exposed to chloride ingestion). Therefore, the focus was reinforcement corrosion and spalling. Furthermore, two other common types of damage, cracks and leakage, were taken into consideration. Based on the developed inspection planning guidelines, employing a 30% cutoff limit for corrosion, it is possible to conclude that bridge elements such as railings, bearings, piers, parapets and main beams should be inspected for corrosion. Similarly, bridge elements such as main beam, parapets, expansion joints and piers should be inspected for scaling. The focus locations for cracks should be on piers, main beam, abutments, parapet systems and expansion joints. Tab. 2 illustrates the results revealed by the actual inspections.

Table 2: Actual inspection results- H-0676 Hafrsfjord bridge.

Bridge	Damage type and frequency			
	Corrosion	Scaling	Cracks	Leakage
11-0676 - Hafrsfjord	8	8	5	0

Furthermore, we have established a bar chart that graphically illustrates the greatest occurrence of corrosion and scaling for 11-0676 Hafrsfjord.

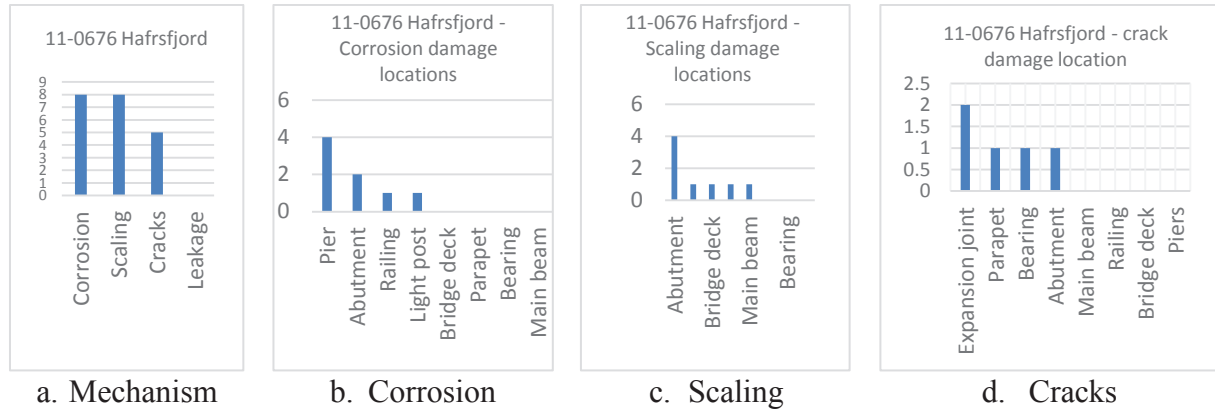


Figure 8: Actual inspection results of '11-0676 – Hafrsfjord' bridge.

Although there are differences, the results (see Fig. 8) reveal that inspection guidelines developed at the 30% cutoff limit provide significantly accurate results.

### 3. Conclusion

The methodology and resulting guidelines presented in this manuscript are important when a new engineer (or inspection planner) starts inspection planning. It is possible to follow the same methodology and develop a set of guidelines for all the possible groups of bridge families. It is also possible to use the output of the damage analysis to develop a comprehensive risk based inspection (RBI) planning approach.

Future research shall be carried out to investigate the optimal cutoff level and to group bridges into families using the GT approach. Then, these studies shall be continued to develop an RBI planning approach.

### References

- [1] Vogel, T. and Schellenberg, K., Design for inspection of concrete bridges, Mater Corros 63 (12) (2012)
- [2] SVV, Inspeksjonshåndbok for bruer, håndbook V441 (2014), [https://www.vegvesen.no/\\_attachment/69833/binary/964063?fast\\_title=H%C3%A5ndbok+V441+Inspeksjonsh%C3%A5ndbok+for+bruer+%2836+MB%29.pdf](https://www.vegvesen.no/_attachment/69833/binary/964063?fast_title=H%C3%A5ndbok+V441+Inspeksjonsh%C3%A5ndbok+for+bruer+%2836+MB%29.pdf), accessed on 16.05.2018
- [3] Samarakoon, S. M. S. M. K. and Ratnayake, R. M. C., Risk-based in-service inspection framework for offshore concrete wind turbine structures and application of Fuzzy Inference System, paper number: OMAE2018-78264, Proceedings of 37<sup>th</sup> Int. Conf. on Ocean, Offshore and Arctic Engineering (OMAE2018) in Madrid, Spain (2018)
- [4] Sacchetti, J. F. et al, A group technology based classification and coding system for reinforced concrete structures, Comput Aided Civ Inf 7 (4) (1992), 307-322

## OVERVIEW ON THE MULTI-DECADE DATABASE OF PORTUGUESE LARGE CONCRETE DAMS MONITORING DATA

António Tavares de Castro <sup>(1)</sup>, José Barateiro <sup>(1)</sup>, Carlos Serra <sup>(1)</sup>

(1) National Laboratory for Civil Engineering, Lisboa, Portugal

### Abstract

Monitoring is a key activity to ensure the structural safety of dams and is used for detection of deterioration, including local degradation issues and more extensive deterioration scenarios, such as the development of internal expansion reactions which, in the worst case scenario, can lead to severe cracking and even to the abandonment of the dam.

This paper presents an overview of an information system that includes a monitoring database, which includes the records of the main actions (water level, air and water temperatures and temperature inside the concrete) and of the main structural responses (radial and tangential displacements measured in inverted plumb-lines and using geodetic techniques, displacements measured in rod extensometers and by precision levellings in target points, joint displacements measured in joint meters, bi- and tridimensional strain fields measured in sets of strainmeters). The hydraulic behaviour of the foundation is also monitored, including the measurement of water discharges along the drainage gallery and the water pressure in the foundation (uplift). The database has monitoring data since the construction period of each dam until this date through periodic readings over the years.

Different measurements in some dams, with and without identified deterioration processes, are presented and compared in order to showcase the importance of monitoring activities over the structures lifetime.

### 1. Introduction

The Portuguese Regulation on the Safety of Dams (RSB) [1] determines that the National Laboratory for Civil Engineering (LNEC) must create and maintain updated a digital archive of the monitoring data of the higher risk Portuguese large dams during their lifetime. Based in this determination, LNEC developed an information system that includes the referred database as well as several tools for the numerical and graphical presentation and for processing of all the data. According to this regulation, large dams are considered dams with maximum height larger than 15.0 m or dams that create a large reservoir (with volume larger than 100 000 m<sup>3</sup>) [1].

The paper describes the main features of the information system and of the type of dams, devices and the multi-decade results available in the database. It also showcases two examples which represent an overview of the type of results and the comprehensiveness of the information system. The goal of this work is to present the importance of a comprehensive and systematic monitoring system for dam safety assessment, from the planning and installation of each device to the management and storage of the collected data over several decades.

## **2. Description of the information system and of the monitoring database**

### **2.1 Importance of monitoring**

In general, dam surveillance is the assessment of the performance, safety and operability of dam and reservoir [2], which includes monitoring of the dam, foundation and appurtenant structures, visual physical inspections and maintaining the operational facilities. Monitoring of the main actions and of the main structural effects is key for the safety assessment, not only in a short-term period but also for a long-term evaluation of, for example, deterioration scenarios [3]. Additionally, monitoring must result in the analysis and interpretation of the data and, in case of abnormal behaviour, in proper and timely decisions. According to [4], the main goals of monitoring are: i) checking the expected structural behaviour; ii) giving a warning of a potential problem ; iii) Aiding in the identification, definition and analysis of a problem ; and, iv) evaluating the proper remedial actions.

### **2.2 Type of monitoring devices and data and information system**

According to the RSB [1], the type and number of devices and measured quantities is related to the type and height of the dam. Small dams require just the measurement reservoir's water level, of water discharge rates and water pressure in the interface between dam and rock foundation. Large dams, with height larger than 100 m, must have a more complete monitoring system which includes the records of the main actions: water level, air and water temperatures and temperature inside the concrete; and of the main structural responses: radial and tangential displacements measured in plumb-lines and by geodetic methods; displacements measured in rod extensometers and by precision level surveys in target points; joint displacements measured in jointmeters; bi- and tridimensional strain fields measured in sets of strainmeters. The hydraulic behaviour of the foundation is also monitored, including the measurement of water discharges along the drainage gallery and the water pressure in the foundation. RSB also defines the reading frequency for each type of structure and for each stage of the dam: during construction; during the first filling of the reservoir; and during the dam's exploitation.

The Portuguese information system, Gestbarragens [5] includes the results obtained from concrete dams of all types, like double curvature arch and gravity structures, including dams with more than 50 years and structures under construction. In the last years the database has been extended to include also monitoring data of embankment dams and some concrete bridges. Fig. 1 presents the evolution of the number of results included in the database throughout the years obtained from manual and automated monitoring systems and presents an example of a time-series radial and tangential displacement in an inverted plumb-line base of Alto Rabagão dam. The use of automated monitoring systems since 2000 significantly increased the amount of data in the information system.

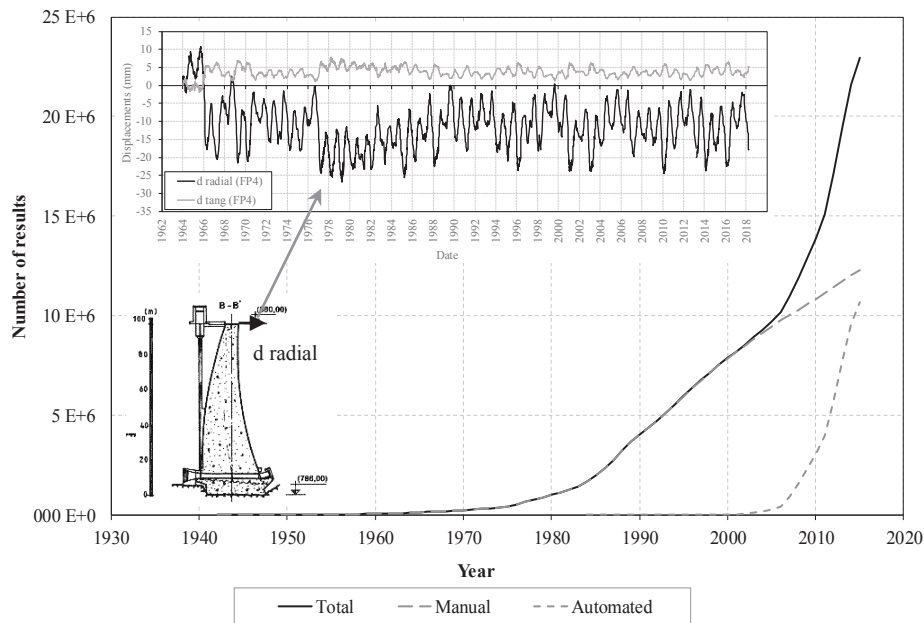


Figure 1: Evolution of the number of total results available in the database collected throughout the years obtained from manual and automated monitoring systems. Example of the development of a radial displacement ( $d_{\text{radial}}$ ) in Alto Rabagão dam.

### 3. Alto Lindoso and Alto Ceira dams

#### 3.1 Brief description of the dams

In order to illustrate the type of information provided by the monitoring systems, two examples are presented. The first example is the Alto Lindoso dam, a double curvature arch dam with an height of 110,0 m above the rock mass foundation, a crest development of 296,8 m and a crest thickness of 4,0 m [6]. The Alto Lindoso dam's body cast ended in July, 1990 and the first filling started in January, 1992 after the forced cooling and the grout of the vertical contraction joints. Fig. 2 shows the elevation and a central cross section of Alto Lindoso dam. The other example is the Alto Ceira dam which was abandoned and demolished due to severe damage as a results of alkali-silica reactions [7]. This dam was a double curvature arch dam with a height of 33,5,0 m above the rock mass foundation, a crest development of 85,0 m and a crest thickness of 1,5 m. The Alto Ceira dam's construction was completed in 1949.

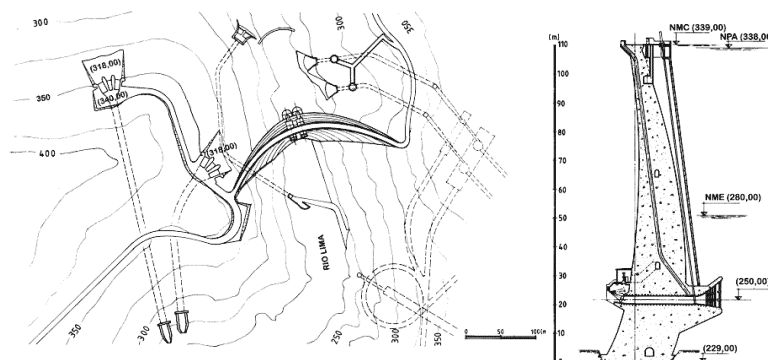


Figure 2: Elevation and cross section of Alto Lindoso dam.



### 3.2 Examples of dam monitoring data

Fig. 3 and 4 show a set of monitoring data regarding the structural behaviour of Alto Lindoso e Alto Ceira dams, respectively. Alto Lindoso dam has a complete monitoring system which includes the record of all quantities (actions and effects) mentioned before and large reading frequencies. Alto Lindoso dam presents a good behaviour throughout the years and it is possible to observe the influence of the annual temperature variations, which is the main action during the exploitation period. Fig. 3 show the comprehensiveness of the Alto Lindoso dam database, since casting (for temperatures inside the concrete) and since the beginning of the first filling.

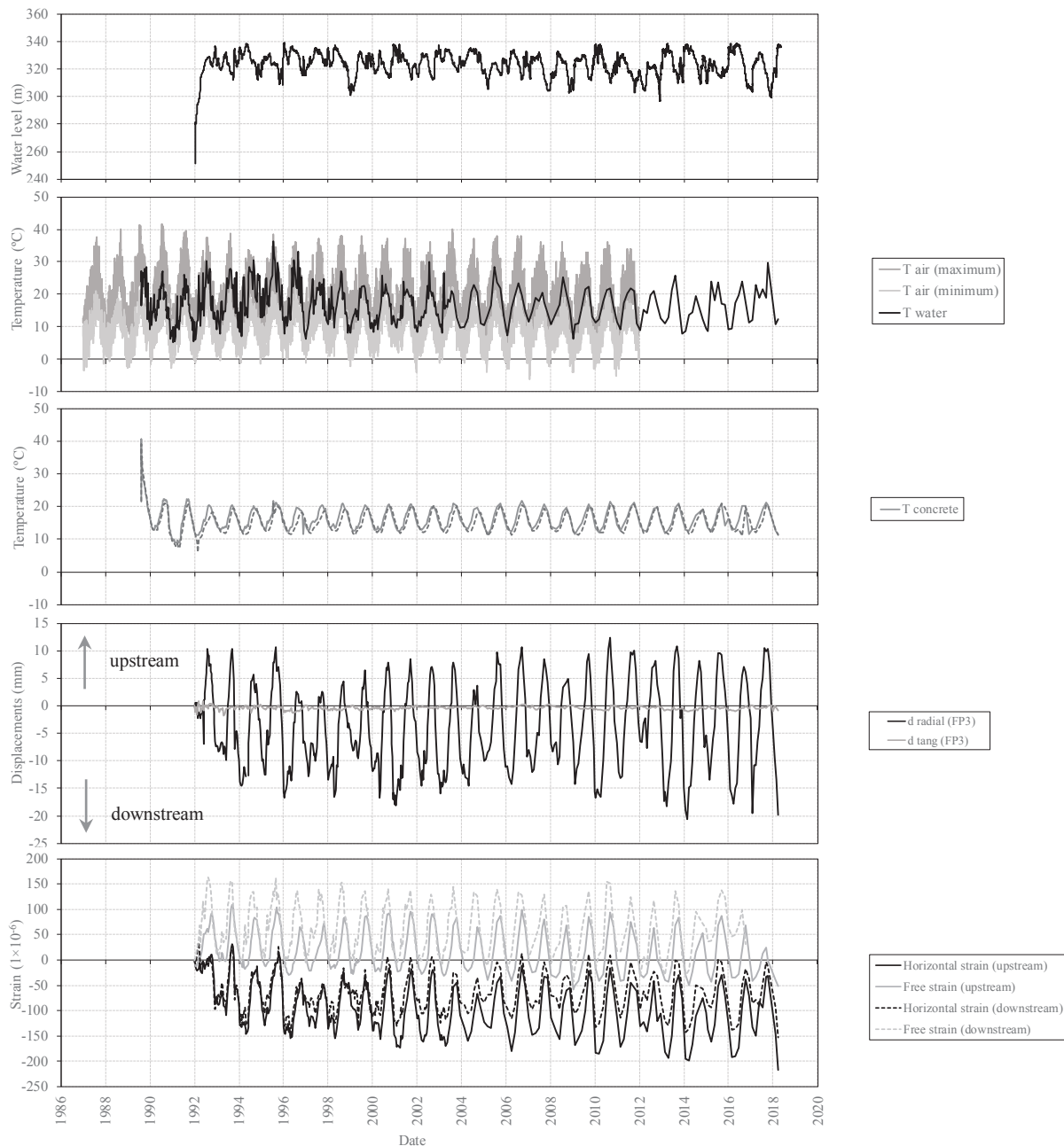


Figure 3: Set of monitoring data of Alto Lindoso dam.

The results show the effect of the upstream water pressure and of the annual temperature variations on the radial and tangential displacements in an inverted plumb-line, on the compressive strains measured in horizontal strainmeters placed in the central cantilever. The free strains are also measured in non-stress specimens in order to separate the effects of temperature and of the water level.

During several years, the behaviour of Alto Ceira dam was mainly monitored using geodetic techniques, namely precision level and triangulation surveys to evaluate the vertical and horizontal displacements, respectively (Fig. 4). Over the years a continuous significant upward displacement was detected, indicating the existence of expansive reactions.

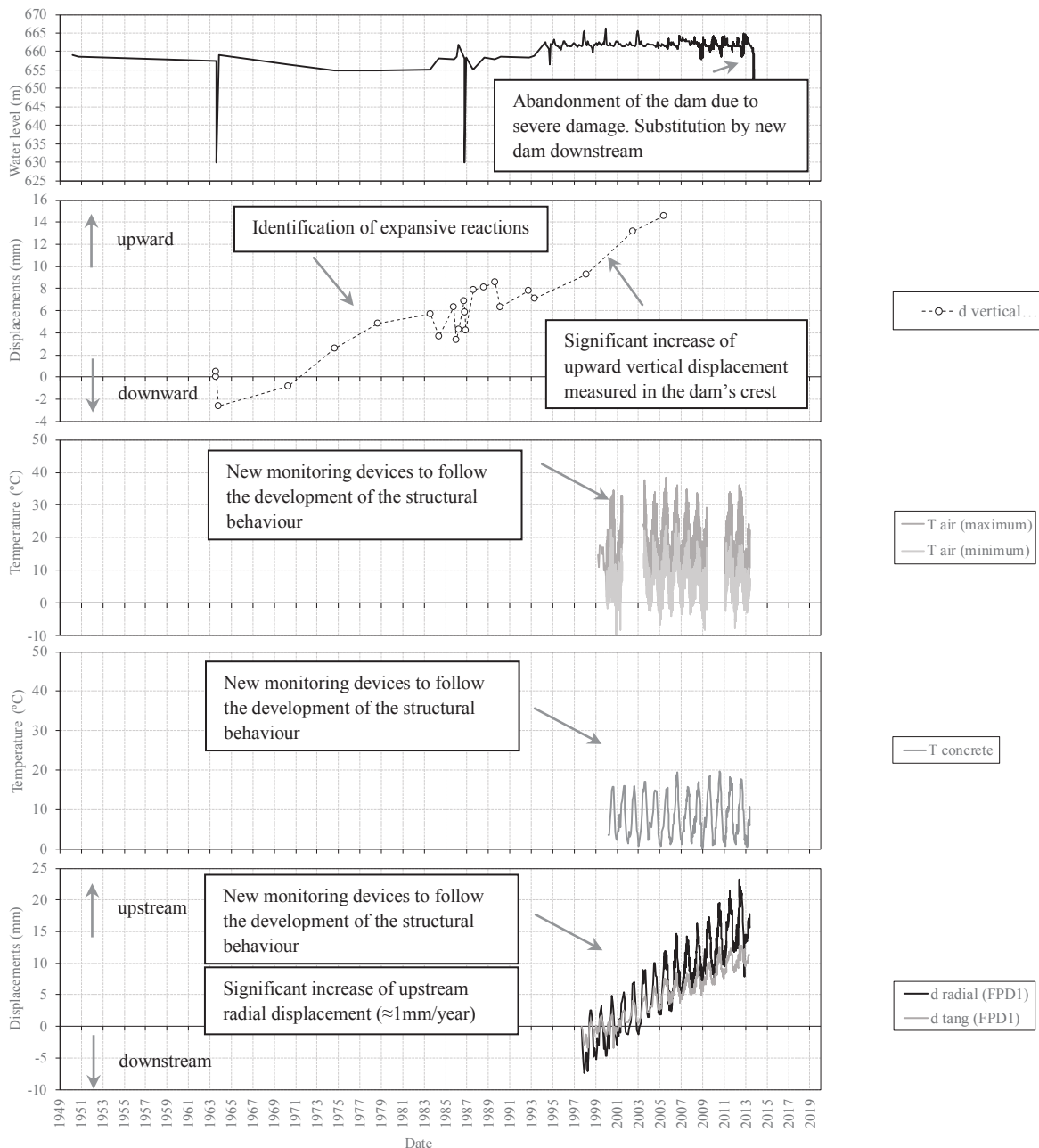


Figure 4: Set of monitoring data of Alto Ceira dam.

In the 1990's new monitoring devices were installed to follow the development of the structural behaviour. These new devices showed that the dam was moving upward and upstream compatible with a generalized increase of the dam's size, despite the main actions remained almost constant over several years. This behaviour was accompanied by severe structural damage in the dam's body which led to the its demolishing and substitution downstream in 2013.

#### **4. Conclusions**

The presented paper discusses the importance of dam monitoring system, including the planning, installation of instrumentation and collection and storage of data throughout several years. The National Laboratory for Civil Engineering (LNEC) has developed the GestBarragens system, which stores, organizes and maintains the multi-decade database of Portuguese large concrete dams.

Two examples are presented in order to showcase the type of dams, devices and comprehensiveness of the available data. The examples illustrate the importance of monitoring and of an operational monitoring system for evaluating the expected structural behaviour and for the assessment of deterioration scenarios.

#### **Acknowledgements**

Thanks are due to EDP for permission to publish data related to the monitoring of Alto Rabagão, Alto Lindoso and Alto Ceira dams.

#### **References**

- [1] RSB, "Regulation on Dam Safety". Decree-Law n.º 344/2007, Lisboa, 2007 (in Portuguese).
- [2] J. Mata, N. Schclar Leitão, A. Tavares de Castro, and J. Sá da Costa, "Construction of decision rules for early detection of a developing concrete arch dam failure scenario. A discriminant approach", *Comput. Struct.*, vol. 142, pp. 45–53, Sep. 2014.
- [3] ICOLD, "Monitoring of dams and their foundations - State of the art (Bulletin 068)", Paris, 1989.
- [4] E. Almog, P. Kelham, and R. King, "Delivering benefits through evidence. Modes of dam failure and monitoring and measuring techniques", Bristol, UK, 2011.
- [5] A. Tavares de Castro, J. Mata, J. Barateiro, and P. Miranda, "Information management systems for dam safety control. The Portuguese experience". in *Dam World*, 2012, p. 13.
- [6] LNEC, "Alto Lindoso dam. Behaviour analysis report", Lisboa, 2009 (in Portuguese).
- [7] A. L. Batista and J. Piteira Gomes, "Practical assessment of the structural effects of swelling processes and updated inventory of the affected Portuguese concrete dams", in *Dam World* 2012, 2012.

## **LOAD-BEARING PERFORMANCE SIMPLE EVALUATION SYSTEM OF RC BRIDGE DETERIORATED CAUSED BY SALT DAMAGE**

**Hitoshi Ito <sup>(1)</sup>, Toshiaki Mizobuchi <sup>(2)</sup>**

(1) Yachiyo Engineering Co., Ltd., Tokyo, Japan

(2) Hosei University, Tokyo, Japan

### **Abstract**

For small bridges managed by municipalities, in order to apply to a large number of bridges than precision, we construct the structural performance simple assessment system that emphasis is placed on simplicity. This system can evaluate the structural performance of bridges in a certain area by obtaining deterioration data from the representative bridge by non-destructive testing. This system does not require a lot of cost and time, because of the less amount workload of survey and analysis. As the structural performance, we evaluate load-bearing performance from the incubation period to the deteriorated period based on structural performance and deterioration factors. However structural performance and deterioration progression have uncertainly factors. Therefore we apply probability method to the system. Since the system of this research is a simple and doesn't require a lot of cost and time, it is possible to periodically update the assessment results. Therefore, we propose efficient maintenance method using this method, such as utilization of area maintenance method.

### **1. Purpose of the research**

In Japan, it is necessary to implement effective maintenance, in order to maintain the good condition of bridges, because the safety of bridges changes by structural performance degradation due to deterioration [1-3]. The structural performance (load-bearing performance) of RC road bridges descend by the deterioration of reinforcement bars. As the result, the traffic of some bridges are closed. In the future, as the number of the aging bridge increasing, the traffic restricted bridge number and the maintenance cost will increase [4]. In addition, human resources of maintenance work have been decreasing. Therefore, the shortage of budget and time are problems in bridge maintaince. As the result, it is required to reduce the maintenance cost and improve the efficiency [5]. Especially, municipalities in Japan have

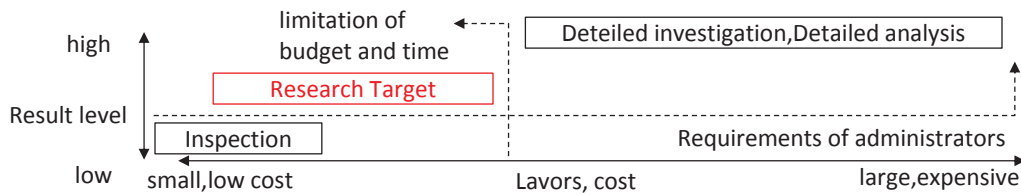


Figure 1: Labors, cost and the result level.

many bridges in need of maintenance, but budget and human resources are limited. However, accidents, caused by insufficient maintenance, are serious problem (safety level requirements are same as national roads). As the result, efficient maintenance is required (preventive maintenance, choice and concentration of maintenance work).

In the bridge maintenance, we evaluate the degree of the bridge safety as part of the structural condition assessment, prior to planning appropriate maintenance items. We collect the information about the degree of deterioration by surveying corrosion of rebars, salt damage. After that, we predict the current structural performance and structural performance degradation based on the obtained surveying results.

Municipalities do inspection for bridge maintenance, and municipalities are difficult to apply the data other than inspection results due to limitation of budget and time. However, we cannot evaluate the individual bridge situation and safety based on only inspection results. As a result, only inspection results are insufficient as evaluation results required by administrators (Fig. 1). Therefore, we propose the method (the structural performance assessment method without much cost and time), to compensate for the insufficient. In addition, the method does not require cost and time for data collection, analysis and update, for continuous implementation. We define it as the "simple" structural performance assessment system.

## 2. Performance simple assessment system

### 2.1 Outline of Performance simple assessment system

It is possible to assess the structural performance with high accuracy by carrying out enough

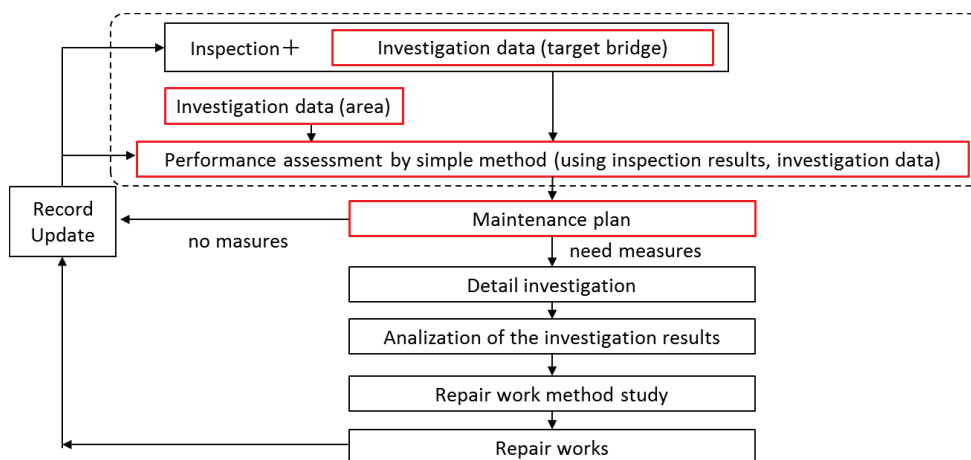


Figure 2: Flow of bridge maintenance.

Table 1: Comparison between conventional and purpose method, \*( ) shows example

Item	Conventional method	Proposed method
Investigatin	Detail (Chemical analysis, natural potential etc)	Simple (electromagnetic wave radar, fluorescent X-ray etc)
Analysis	Precise model (FEM etc)	Simple model (based on Specification)
Lavors, Cost	Large, expensive	Small, low cost

Table 2: Applicable condition

Item	Applicable condition
target	small reinforced concrete road bridges
structural type	slab bridge
deterioration factor	complex deterioration due to salt damage and carbonation
Structural performance	bending strength

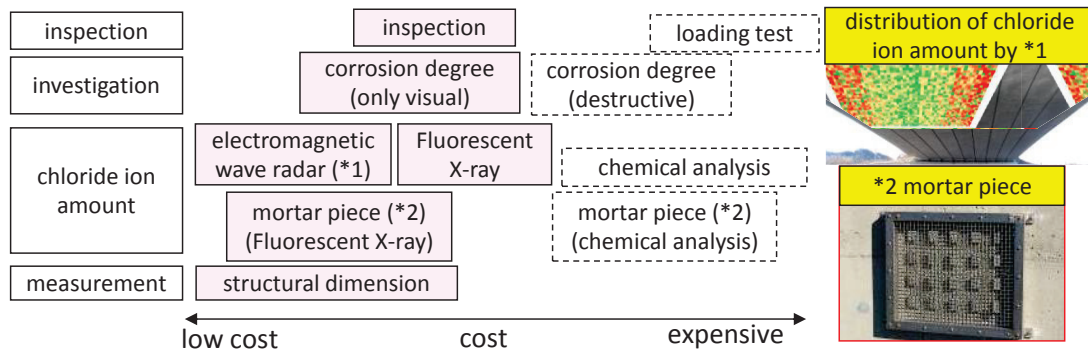


Figure 3: Cost of investigation.

surveys and analysing the condition using an elaborated model. However, that requires a lot of cost and time. Therefore, in this paper, for small bridges managed by municipalities, in order to apply to a large number of bridges than precision, we construct the structural condition simple evaluation system that emphasis is placed on simplicity. In the maintenance flow (Fig. 2), the system provides quantitative evaluation results, they are useful for the maintenance plan. Tab. 1 shows the comparison between the propose method and the conventional method. In this paper, applicable conditions to the system are limited (Tab. 2), and assumption values are applied to a part of data.

## 2.2 Data of the system requirements

Existing structural data (chloride ion amounts etc.) is necessary for assessment of structural performance. Cost is different for each investigation (Fig. 3). Our proposal system applies low cost investigation data (chloride ion amounts investigation by electromagnetic wave radar method [6], fluorescent X-ray method [7] etc.). These investigation are taken about 1 hour per place including preparation time. The distribution of deterioration can be assessment combining investigation result by these investigations. In addition, the investigation using mortar pieces can be assessment the tendency of salt damage in the area. These investigations are effective in municipality's bridges investigation, because a lot of cost and time is not required.

### 2.3 Method of performance assessment

The system can evaluate the structural condition of bridges by the deterioration condition. The evaluation is based on specification for highway bridges [8]. As the structural condition, we evaluate load-bearing performance from the incubation period to the performance deteriorated period based on structural condition and deterioration factors. However structural condition and deterioration progression have uncertainly factors. For example, initial performances of structures depend on the material performance, structural dimensions and reinforcement position. In addition, the deterioration progression is affected by various conditions, and also estimation results are depended on the way of evaluation. Furthermore, the thickness of covering concrete is not uniform, so progressions of deterioration depend on the location of the structure. Therefore we apply probability method (Monte Calro method) to the system. Tab. 5 shows specific procedures.

## 3. Trial assessment result about existing structure

### 3.1 Target structure

This chapter shows a trial calculation example using proposal system. The target area has a temperate climate with an average annual temperature of 16 ° C or more, and two sides of this area face the sea. Coastal roads are important, because many citizens live in the coastal area. Target structures are 2 bridges (Tab. 3) located in the coastal area. The deterioration condition of salt damage is set as shown in Tab. 4 from investigation results of the representative bridge in each area (3 samples). Nos.1 to 3 are the results of applying the equation of Fick's second law to investigation results. Nos. 4 to 6 are the results of applying the method considering complex deterioration [9]. As described before, the deterioration status depends on the part of the structure, so we varied deterioration conditions according to the distance from the outer surface. The limit value of the bending strength is calculated by the live load shown in Tab. 3. In this case, we set deterioration condition based on the representative investigation result of

Table 3: Bridges condition.

Bridge No	55 (area A)	62 (area B)
Years after construction	56	87
Width,Height,Span length (mm)	W=10000,H=500,S=5400	W=4000,H=300,S=4000
re-bar	D19,n=80	D16, n=32
Strength of concrete	21N/mm <sup>2</sup>	21N/mm <sup>2</sup>
Strength of re-bar	235	235
Live load	200kN*2	88kN*1

Table 4: Deterioration condition.

	No	No.1	No.2	No.3	No.4	No.5	No.6
the apparent diffusion coefficient(mm <sup>2</sup> /year)	Bridge 55	530.99	29.64	105.91	530.99	17.54	67.14
	Bridge 62	55.15	2.23	28.01	20.66	3.19	6.94
the values of surface concentration(kg/m <sup>3</sup> )	Bridge 55	9.91	22.35	9.83	9.91	27.44	11.85
	Bridge 62	7.57	2.02	3.97	9.14	1.26	10.50

Table 5: Evaluation procedure.

STEP	Implementation content
1	set parameters using random numbers (uniform, normal distribution etc) [10]
2	caluculate time of corrosion occuring, crack occuring, and caluculate reduction of rebar sectional area, based on parameters and data from investigation
3	predict rebar sectional area for trial (1,000 case)
4	based on predicted values, trial cases they match corrosion status are selected.
5	set parameters, for each rebar, to assess performance in assuming that selected trial cases uniformly occurs.
6	assess performance for trial 1,000 case of Monte Carlo method
7	before cracking occur : caluculate probability occur corrosion , cracking after cracking occur : calculate probability of risk index
8	aggregate in $t=1\sim 100$ year

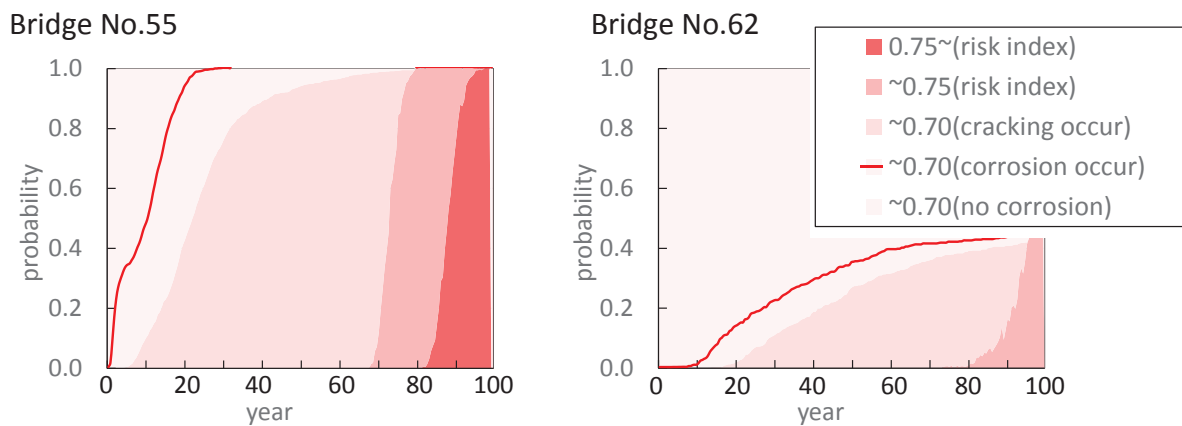


Figure 4: Probability

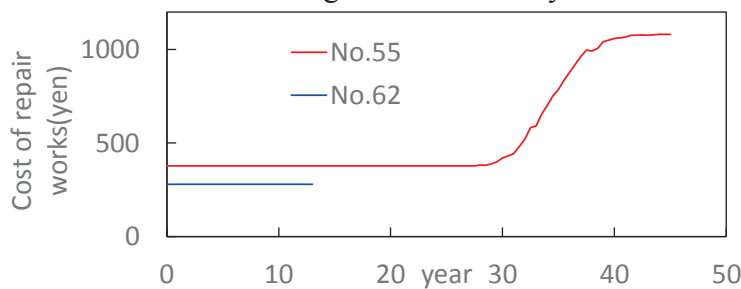


Figure 5: Cost prediction of repair works

each area. However, in the future, we plan to reflect the deterioration distribution assessment result based on investigation result of using mortar pieces, electromagnetic wave radar and X-ray fluorescence.

### 3.2 The result of the trial assessment

We assessed structural performance according to the procedure shown in Tab. 5. Next we calculate varies in the probability due to progression of deterioration. Fig. 4 shows the result. According to Fig. 4, bridge administrator can quantitatively grasp varies performance



degradation, for example, the risk index expresses safety degradation due to repair works delay, as probability increasing. Fig. 5 shows the repair cost estimation (using the probability by this system). As a result, it is possible to decide the timing and necessity of repair works, such as doing repair at No55 bridge within 30 years before the cost changes greatly.

#### 4. Conclusions

We constructed a framework of the system capable of assessing the current and future performance of structure, in limited budget and time. The results of this paper are below.

- It is possible to construct the system that can assess a series of processes from evaluation of deterioration to structural safety.
- Assessment results (bending strength) include structural characteristics and environmental conditions, in addition, assessment results include from incubation period to deteriorated period (difficult to assess by inspection results).
- The performance simple assessment system does not require significant increasing cost and time relative to the bridge inspection, as the result, updating is easy.
- The system is possible to apply investigation results by simple method (chloride ion amounts investigation using electromagnetic wave radar, mortar piece etc.), as the result, accuracy improvement will be expected.
- The risk index (limit value to structural performance) is effective to set due timing to repair works, and the risk index expresses safety degradation due to repair works delay, as probability increasing.
- The maintenance cost estimation (reflect the result of structural characteristics and deterioration progress assessment) using proposal system is effective as the decision-making basis for repair works timing and repair necessity.

#### References

- [1] Yuji, N., Decaying infrastructure, Nikkei publishing, Inc., (2011)
- [2] Toshiaki, M., Concrete collapse, PHP publishing, Inc., (2013)
- [3] Satoshi, F., Country resilience theory, Bungeishunju Ltd., (2011)
- [4] MLIT, Current status of road structure maintenance, [http://www.soumu.go.jp/main\\_content/000497036.pdf](http://www.soumu.go.jp/main_content/000497036.pdf) (2013)
- [5] MLIT, Measures of road aging, <http://www.mlit.go.jp/road/sisaku/yobohozen.html> (2016)
- [6] Junnichiro, N. et al, Future prediction method of salt damage progression using estimation of chloride ion amounts by electromagnetic wave, Concrete Research and Technology, Vol.35, No.1 (2013)
- [7] Ruiko, W. et al, Prediction of chloride ion amounts using fluorescence X-ray, 2017 JSCE annual meeting (2017)
- [8] Japan road association, Specification for highway bridges, part3 concrete bridges (2012)
- [9] Hitoshi, I. et al, Prediction of complex deterioration and evaluation of RC structural performance, fib symposium (2017)
- [10] Shinichi, K. et al, Degradation prediction method on bending strength of RC members in splash zone, Concrete Research and Technology, Vol.33, No.1 (2011)

**SCIENTIFIC INSIGHTS**  
**VS.**  
**STANDARDIZATION**

## **A COMPARISON OF TWO MAJOR APPROACHES USED FOR CONCRETE STRENGTH PREDICTION FOR DIFFERENT CONCRETE TYPES**

**Seda Yesilmen <sup>(1)</sup>, Sinan Kefeli <sup>(1)</sup>**

(1) Cankaya University, Ankara, Turkey

### **Abstract**

Predicting concrete strength has been a popular topic for the last decade and several methods were proposed by researchers each claiming to increase accuracy of predictions. Two methods were selected namely linear regression, and artificial neural networks and their predictive performances were compared using data for different concrete types. Data for high performance concrete (HPC), self-compacting concrete (SCC) and ordinary concrete (OC) were implemented in selected prediction models.

### **1. Introduction**

Compressive strength is arguably the most important mechanical property of concrete. Consequently, prediction of concrete compressive strength has been a popular area for a while. The major factor determining the compressive strength of concrete is mix design the components of which widely used in concrete compressive strength (CCS) prediction. There are lots of other contributing factors such as age, curing, and handling practices, etc. Most common methods predicting the strength of concrete are based on the linear and nonlinear regression methods [1,2] and artificial neural networks [3,4].

Although it was claimed that [5,6] regression analysis is usually less accurate than that Artificial Neural Networks (ANN) method, regression can be more advantageous because it is faster and more effective since it does not require model training. Additionally non-linear regression (NLR) models were proved to be more accurate than linear models [7].

### **2. Strength prediction methods**

Predicting CSS using mix design parameters is a widely researched topic [5,8]. When the popularity of the deep learning was renewed, CSS prediction methods evolved accordingly.

Although several hybrid methods were offered, ANN is still one of the most used methodologies for strength prediction mostly owing to very high accuracy of results.

Regression methods also maintained their popularity because of their simple implementation specifically nonlinear regression was reported to predict CSS with high accuracy [7]. Method of CSS prediction is also important for different concrete types, because concrete ingredients can profoundly affect prediction accuracy.

## 2.1 Nonlinear regression

Concrete compressive strength (CCS) can be predicted using linear or non-linear regression (NLR) methods. Eq. (1) is known as multivariable power equation and it is used in several studies [2,7,9,10] for CCS prediction. It was reported to be the regression model with the highest accuracy.

$$\ln Y_i = b + w_i \ln x_{ij} \quad (1)$$

where  $Y_i$  is predicted CCS for  $i^{\text{th}}$  mix design at a certain age,  $b$  and  $w_i$  are regression coefficients and  $x_{ij}$  is the  $j^{\text{th}}$  input parameter for the  $i^{\text{th}}$  mix design.

## 2.2 Artificial neural networks

Artificial neural networks (ANNs) are used to construct mapping functions for predicting CCS [11,12]. Notably, researchers have applied or evaluated the capability of ANNs to predict strength and other concrete behaviors [13-15]. The ANN is a powerful tool for solving very complex problems and it has been used commonly for CCS prediction [14,15]. Multilayer perception (MLP) neural networks are standard neural network models with an input layer representing concrete mix design components, hidden layers with computation neurons, and an output layer containing one neuron representing CCS.

Two hidden layers were used in the ANN model for this study. ANN model was implemented using Tensorflow library and python. Activation function was selected to be sigmoid for all layers except output layer. Adam Optimization algorithm was used since it became a popular algorithm recently which enables learning rate decay using exponential moving average of the gradient. Training and testing data were separated using train test split function of sklearn library. This function also shuffles the data before splitting which can be critical during training. Validation data was not used instead cross validation was performed for hyper parameter tuning.

## 3. Results

A total of 108 different mix designs for ordinary concrete (OC) mixtures are obtained from various sources [14,16-19]. Ordinary concrete mix design only included 5 parameters namely; cement content, water content, coarse aggregate content, fine aggregate content and superplasticizer content. All the parameters were defined in  $\text{kg}/\text{m}^3$  of concrete.

Self-compacting concrete mix design included an additional parameter of Fly Ash content with units of  $\text{kg}$  per  $\text{m}^3$  of concrete. Accordingly 6 features were considered in the ANN model. A total of 203 different mix designs were extracted from literature [14,20-27]. SCC

mixtures can contain different types of water reducers in addition to superplasticizers, in this study SCC mixtures with only one type of superplasticizers are included as input data (Fig. 3). High performance concrete (HPC) mix design included both blast furnace slag content, and Fly Ash content, so a total of 7 input parameters were included in the model. A total of 426 different mix designs were extracted from literature [14,16-19,28-32].

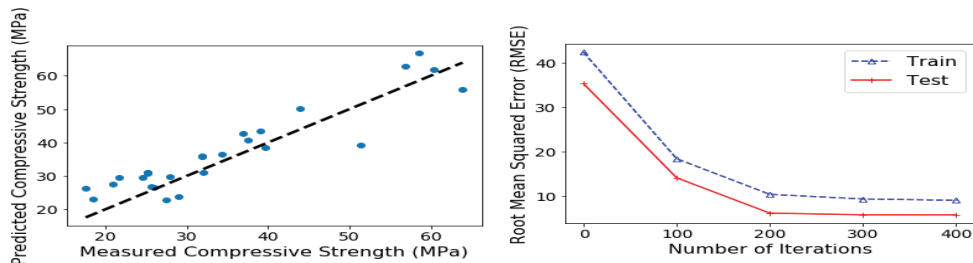


Fig. 1 Predicted strength versus actual strength values for test data and the reduction in RMSE during iterations for both training and test data in ANN model for OC.

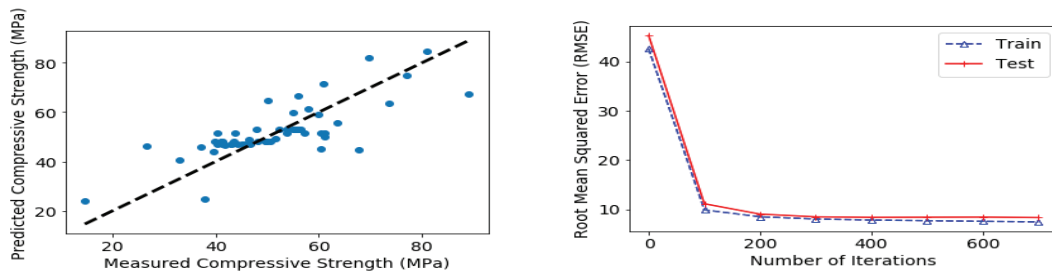


Fig. 2 Predicted strength versus actual strength values for test data and the reduction in RMSE during iterations for both training and test data in ANN model for SCC.

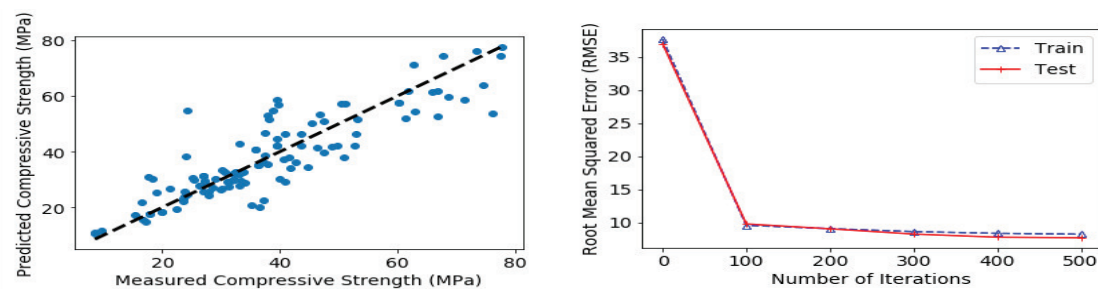


Fig. 3 Predicted strength versus actual strength values for test data and the reduction in RMSE during iterations for both training and test data in ANN model for SCC.

Regression coefficients for NLR and ANN modeling are shown in Tab 1 and Tab 2 respectively. For both analysis methods ordinary concrete has the highest correlation coefficient among other concrete types. However correlation coefficients are low and root mean squared error values are higher than acceptable ranges especially for self-compacting concrete (SCC). The same behavior can be observed from graphs illustrating the relationship between predicted and tested strength values in Fig 4.

Table 1: Nonlinear regression modeling results for test data.

	OC	SCC	HPC
MSE	39.06	46.79	123.31
RMSE	6.25	6.84	11.10
R <sup>2</sup>	0.84	0.53	0.70

Table 2: ANN modeling results for test data.

	OC	SCC	HPC
MSE	36.48	43.83	59.92
RMSE	6.04	6.62	7.74
R <sup>2</sup>	0.91	0.67	0.84

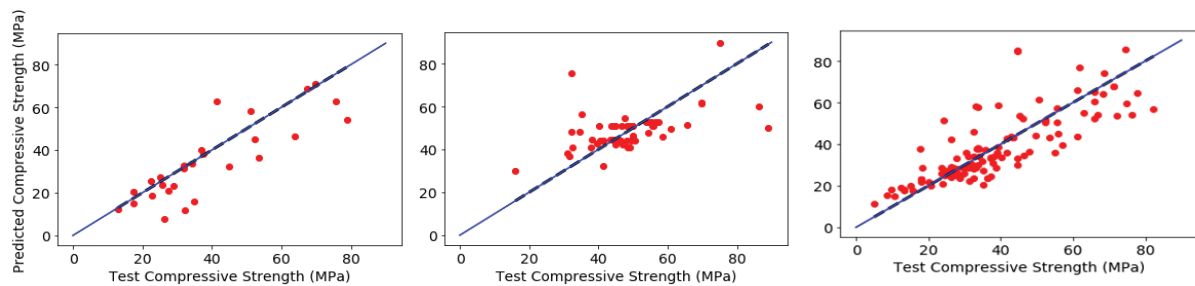


Fig. 4 Predicted strength versus actual strength values for test data in NLR model for OC, SCC and HPC respectively.

#### 4. Conclusion

High accuracy of Ordinary concrete can be attributed to the absence of pozzolans. Among the pozzolanic materials, properties of fly ash known to spread a very wide range and they are dependent on the properties of burned coal in thermal plants. A large percentage of SCC specimens contain fly ash which would be expected to increase the variance of the distribution.

Comparing the two methodologies accuracy of ANN models are slightly higher. Much higher correlation coefficients reported when ANN is used for CSS prediction but most of the literature on CSS prediction uses mix design data from the one or two batches of concrete. Data from several papers with very different sources for ingredients were used in this study which introduced a considerable variance. Addition of certain features such as calcium and silica content of pozzolanic materials should increase the accuracy of ANN predictions. It must be noted that an ANN model needs to be trained on more data and more features in order to claim high accuracies globally. However considering the implementation ease of regression, it might be acceptable to use nonlinear regression for CSS approximation.

Specifically for applications that does not need high accuracy nonlinear regression can stay as a viable option.

## References

- [1] Tsivilis, S. and Parissaki, G., A mathematical model for the prediction of cement strength, *Cem Concr Res* 25(1) (1995), 9–14.
- [2] Zain, M.F.M. and Abd, SM., Multiple regression model for compressive strength prediction of high performance concrete, *J Appl Sci* 9(1) (2009), 155–60.
- [3] Oztas, A., Pala, M., Ozbay, E., Kanca, E., Caglar, N. and Bhatti, M.A., Predicting the compressive strength and slump of high strength concrete using neural network, *Constr Build Mater* 20(9) (2006), 769–75.
- [4] Hong-Guang, N. and Ji-Zong, W., Prediction of compressive strength of concrete by neural networks, *Cem Concr Res* 30(8) (2000), 1245–50.
- [5] Atici, U., Prediction of the strength of mineral-addition concrete using regression analysis, In: *Concrete Research*. Thomas Telford Ltd. (2010), 585–92.
- [6] Chitra, S., Kumar, SRRS., Chinnaraju, K. and Ashmita F.A., A Comparative Study on the Compressive Strength Prediction models for High Performance concrete Containing Nano Silica and Copper Slag Using Regression Analysis and Artificial Neural Networks, *Const and Build Mat* 114 (2016), 528-535
- [7] Jin, R., Chen, Q. and Soboyejo, A.B.O., Non-Linear and Mixed Regression models in predicting sustainable concrete strength, *Const and Build Mat* 170 (2018), 142-152
- [8] Bhanja, S. and Sengupta, B., Investigations on the compressive strength of silica fume concrete using statistical methods, *Cem Concr Res* 32(9) (2002), 1391–4.
- [9] Kheder, G.F., Al-Gabban, A.M. and Suhad, M.A., Mathematical model for the prediction of cement compressive strength at the ages of 7 and 28 days within 24 hours, *Materials and Structures* 36 (2003), 693-701
- [10] Chopra, P., Sharma, R.K. and Kumar M., Predicting Compressive Strength of Concrete for Varying Workability Using Regression Models, *IJEAS* (2014)
- [11] Dantas, A.T.A., Batista Leite M., Nagahama, K.J., Prediction of compressive strength of concrete containing construction and demolition waste using artificial neural networks, *Constr Build Mater* 38 (2013), 717–22.
- [12] Uysal, M. and Tanyildizi, H., Predicting the core compressive strength of self compacting concrete (SCC) mixtures with mineral additives using artificial neural network, *Constr Build Mater* 25(11) (2011), 4105–11.
- [13] Yeh, I.C., Analysis of strength of concrete using design of experiments and neural networks, *J Mater Civ Eng* 18(4) (2006), 597–604.
- [14] Yeh, I.C., Modeling of strength of high-performance concrete using artificial neural networks, *Cem Concr Res* 28(12) (1998), 1797–808.
- [15] Ni, H.G. and Wang, J.Z., Prediction of compressive strength of concrete by neural networks, *Cem Concr Res* 30(8) (2000), 1245–50.
- [16] Jiang, L.H. and Malhotra, V.M., Reduction in water demand of non-air-entrained concrete incorporating large volumes of fly ash, *Cem. Concr. Res.*, 30(11) (2000), 1785–1789
- [17] Bouzoubaa, N. and Fournier, B., Optimization of fly ash content in concrete: Part I: Non-air-entrained concrete made without superplasticizer, *Cem. Concr. Res.*, 33(7) (2003), 1029–1037

- [18] Pala, M., Ozbay, E., Oztaş, A. and Yuce, M. I., Appraisal of long-term effects of fly ash and silica fume on compressive strength of concrete by neural networks, *Constr. Build. Mater.* 21(2) (2007), 384–394
- [19] Demirboga, R., Turkmen, I. and Karakoc, M.B., Relationship between ultrasonic velocity and compressive strength for high-volume mineral-admixed concrete, *Cem. Concr. Res.* 34(12), (2004), 2329–2336
- [20] Dinakar, P., Sethy, K.P. and Sahoo, U.C., Design of self-compacting concrete with ground granulated blast furnace slag *Mater. Des.* 43 (2013), 161–169, 2013.
- [21] Liu, M., Self-compacting concrete with different levels of pulverized fuel ash, *Constr. Build. Mater.* 24(7) (2010), 1245–1252
- [22] Almeida Filho, F.M., Barragán, B.E., Casas, J.R. and El Debs, A.L.H.C., Hardened properties of self-compacting concrete — A statistical approach, *Constr. Build. Mater.*, 24(9) (2010), 1608–1615
- [23] Abu Yaman, M., Abd Elaty, M. and Taman, M., Predicting the ingredients of self compacting concrete using artificial neural network, *Alexandria Eng. J.* 56(4) (2017), 523–532
- [24] Vivek, S.S. and Dhinakaran, G., Fresh and hardened properties of binary blend high strength self compacting concrete, *Eng. Sci. Technol. an Int. J.* 20( 3) (2017), 1173–1179
- [25] Mahalingasharma, S.J., Prakash, P., Vishwanath, K.N. and Jawali, V., Effect of mineral admixtures on kinetic property and compressive strength of self compacting concrete, *IOP Conf. Ser. Mater. Sci. Eng.* 216(1) (2017), 120-126
- [26] Ramanathan, B., Baskar, I., Muthupriya, P. and Venkatasubramani, R., Performance of self-compacting concrete containing different mineral admixtures, *KSCE J. Civ. Eng.* 17(2) (2013), 465–472
- [27] Gesoğlu M. and Özbay, E., Effects of mineral admixtures on fresh and hardened properties of self-compacting concretes: binary, ternary and quaternary systems *Mater. Struct.* 40(9) (2007), 923–937
- [28] Proske, T., Hainer, S., Rezvani, M. and Graubner, C.A., Eco-friendly concretes with reduced water and cement content – Mix design principles and application in practice, *Constr. Build. Mater.* 67 (2014), 413–421
- [29] Bharatkumar, B., Narayanan, R., Raghuprasad, B. and Ramachandramurthy, D.S., Mix proportioning of high performance concrete 23 (2001)
- [30] Oner, A. and Akyuz, S., An experimental study on optimum usage of GGBS for the compressive strength of concrete, *Cem. Concr. Compos.* 29(6) (2007). 505–514
- [31] Durán-Herrera, A., Juárez, C.A., Valdez, P. and Bentz, D. P., Evaluation of sustainable high-volume fly ash concretes, *Cem. Concr. Compos.* 33(1) (2011), 39–45
- [32] Bilim, C., Atis, C.D., Tanyildizi, H. and Karahan, O., Predicting the compressive strength of ground granulated blast furnace slag concrete using artificial neural network *Adv. Eng. Softw.*, 40(5) (2009), 334–340



## **A SIMPLIFIED 1D STRESS APPROACH FOR CRACKING RISK PREDICTION**

**Luis Ebensperger** <sup>(1)</sup>

(1) Construtechnik Ltda, Concrete Technology Consultant, Santiago, Chile

### **Abstract**

Cracks in concrete structures during early ages occur more often than expected. It affects adversely the concrete structure, especially serviceability and durability. The effect of internal concrete volume changes in absence of loads, such as the effect of temperature changes caused by heat of hydration and the chemical/drying shrinkage, is normally not included during design stages. This occurs despite specific recommendations in Codes for situations when these volume changes are significantly restrained.

This work addresses the development of a simple 1D assessment tool that considers the cement's heat of hydration, the thermal and viscous-elastic properties of young concrete, and the degree of external restraint. By performing an iterative calculation procedure for seven days, the model graphically shows the expected core and surface temperature, the corresponding stress development, and the Cracking Index for different heights of the concrete member. The tool allows to consider parameters, such as mix design, thermal properties including the heat transfer coefficient, placement conditions such temperature during pouring and curing, demoulding time, geometry of the member, and consideration of chemical and drying shrinkage. Its applicability is discussed for a cast-in-place beam with registered temperature measurements and for a high-cracked wall foundation system of a liquid containing structure.

### **1. Concrete Cracking at Early Ages**

The left side of Figure 1 shows schematically the global situation that occurs at an early age, including the effect of daily variations in temperature, identifying two periods of high risk of cracking [1]:

- From day 1 to 7 approximately, due to the effects of the heat of hydration
- After approximately 3 weeks, due to the effects of hydraulic shrinkage.

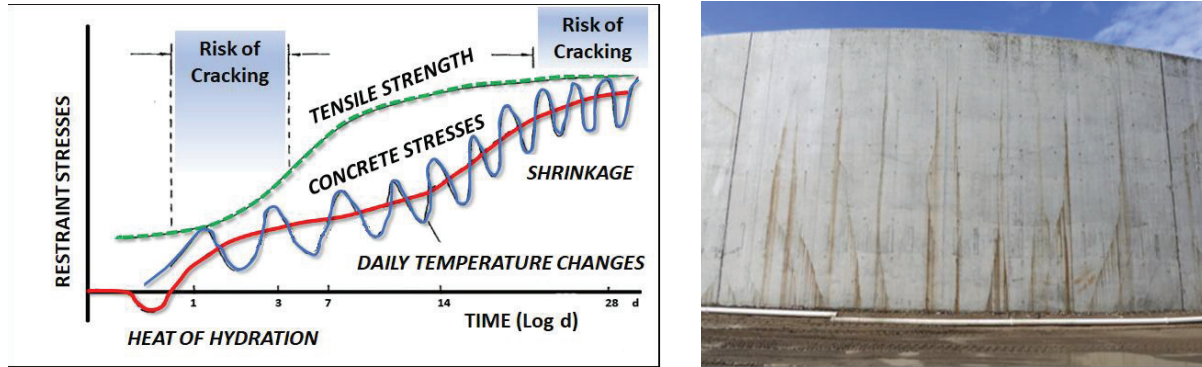


Figure 1: Periods of higher cracking risk and a typical thermal cracking pattern.

## 2. Modelling Concrete Properties

### 2.1 Temperature Development

Through the use of the semi-adiabatic Langavant method [2] the heat generation curve  $\Delta Q_{Hyd}(t)$  and the seven days value of  $Q_{Hyd}(7d)$  are determined. This allows to calculate the adiabatic development of temperature  $T_{ad}$  in concrete. The cement content  $cem$ , the specific heat  $C_{con}$ , and the density of the concrete  $\rho_{con}$  have to be known (Eq. (1)).

$$\Delta T_{Hyd}(t) = \frac{cem \cdot \Delta Q_{Hyd}(t)}{C_{con} \cdot \rho_{con}} \quad (1)$$

$$m = \frac{U \cdot S}{C_{con} \cdot \rho_{con} \cdot V} \quad (2)$$

Due the fact the concrete member stays under certain environmental conditions, usually at a lower temperature than the concrete, it will cool down to equilibrium with the ambient temperature. The speed will depend on the capacity or Cooling Index  $m$ , which depends on the Coefficient of Heat Transfer  $U$  on the concrete surface (insulation conditions), and on the relation between exposed surface  $S$  and volume of concrete  $V$  (Eq. (2)).

The following equation adopted from [3] allows to estimate the Core (Nucleus) Temperature  $T_{Nu}$  of the member, considering the Ambient Temperature  $T_a$  in each time interval  $\Delta t$ :

$$T_{Nu,i+1} = T_{a,i} + \Delta T_{Hyd,i} + (T_{Nu,i} - T_{a,i}) \cdot \exp(-m \cdot \Delta t) \quad (3)$$

To characterize the internal heat flow within the concrete, the Biot Number  $Bi$  is used (Eq. (4)), which is the ratio of the heat transfer resistances inside of (Thermal Conductivity  $\lambda$ ) and at the surface of a body (Coefficient of Heat Transfer  $U$ ). This ratio determines whether or not the temperatures inside a body will vary significantly, while the body heats up or cools down over time since a thermal gradient is applied in the surface. With this number it is possible to estimate the Surface Temperature  $T_{Su}$  (Eq. (5)).

$$Bi = \frac{U \cdot L}{\lambda} \quad (4)$$

$$\frac{T_{Nu} - T_{Su}}{T_{Nu} - T_a} = \frac{Bi}{Bi + 2} \quad (5)$$

With the information provided by the model, two temperature differentials may be calculated (Fig. 2):

- $\Delta T^\circ \text{ Section} = T_{Nu} - T_{Su}$  (temperature gradient  $\rightarrow$  Tensile stresses at the surface of the concrete, minor cracks that tend to close when the temperature equilibrium is reached).
- $\Delta T^\circ \text{ Axial} = T_{Max} - T^{7d}$  (contraction of the member  $\rightarrow$  Tensile stresses in the concrete due to the cooling of the whole member, through-cracks that cross the thickness).

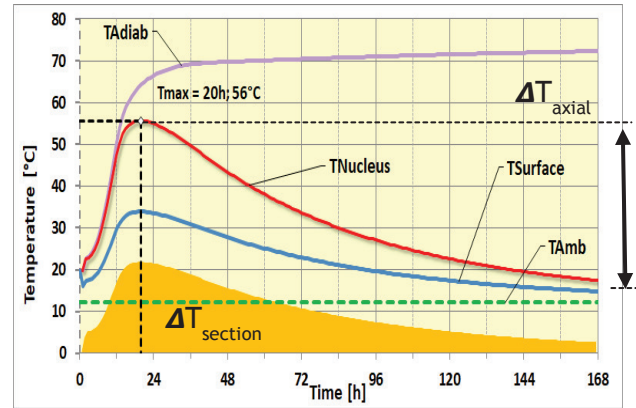


Figure 2: Temperature development in a concrete member.

The amount of heat of hydration lost from the core depends mainly on four factors:

- **Type of element and its dimensions:** the model recognizes the wall-type and the foundation-beam type element. The difference lies in the procedure to determine the L/H ratio (length / height) and the exposed surface. In the wall type, the heat loss occurs sideward of the wall, in both exposed sides, and upper surface. In the case of the foundation or beam, the heat loss occurs upwards and normally only in the exposed upper surface.
- **Placement conditions:** the time of placement and temperature of fresh concrete have a high effect in the expected temperature development in the concrete, as well as the ambient temperature and wind conditions. The latter can be incorporated in 3 ways:
  - Constant value during the seven days.
  - Sinusoidal curve, which requires the average temperature of the period, the daily variation and the time when the maximum daily temperature is reached.
  - Real ambient data measured on-site conditions.
- **Insulation conditions:** the model calculates according to type of material and wind conditions the  $U$ -value, while the concrete is in the formwork and after demoulding.
- **Steam Curing:** the model allows to enter the complete cycle, from start to end with time and temperature profile.

The temperature deformation is calculated using the CTE of concrete, according to:

$$\varepsilon_T = CTE \cdot \Delta T \quad (6)$$

## 2.2 Chemical and Drying Shrinkage Deformations

For the consideration of Chemical Shrinkage, the model uses the methodology of the European standard EN 1992-1-1 [4], which takes the characteristic resistance of the concrete to estimate the ultimate deformation  $\varepsilon_{asu}$ . The model considered the period of the 7 first days.

$$\varepsilon_{asu} = 2.5 \cdot (f'_c - 10) \quad (7) \quad \varepsilon_{as}(t) = \{1 - \exp(-0.20 \cdot t^{0.50})\} \cdot \varepsilon_{asu} \quad (8)$$

For the consideration of the Drying Shrinkage, the model uses the methodology of the Australian AS 5100.5 standard [5], according to the environmental humidity and the effective thickness subjected to the superficial drying conditions. The ultimate deformation  $\varepsilon_{su}$  is

defined and the shrinkage at any time  $\varepsilon_s$  is estimated according to the environmental condition (40% to 70% r.h.) by the factor  $k_1$ , which is calculated for the period of 7 days.

$$\varepsilon_{su} = 850\mu\text{s} \pm 30\% \quad (9) \quad \varepsilon_s = k_1 \cdot \varepsilon_{su} \quad (10)$$

### 2.3 Development of Mechanical Properties

The concrete begins its hardening about 8 hours, at which time it begins to take tensions. This period is known as "dormant phase". The model considers the existing experience in the current update work of Eurocode 2, Annex D [5].

The development of the mechanical properties depends directly on the temperature conditions of the concrete member. This effect is considered in the model by the concept of "Equivalent Age"  $t_{eq}$ , which includes the Activation Energy  $E_{AC}$  of the cement.

$$t_{eq} = \sum H(Ti) \cdot \Delta ti \quad (11) \quad H(Ti) = \exp \left[ \frac{E_{Ac}}{R} \cdot \left( \frac{1}{293} - \frac{1}{273 + Ti} \right) \right] \quad (12)$$

For the determination of the development of the mechanical properties referred to the Equivalent Age, the 28-day values of each property are considered with the factor  $\beta$ , which depends on the factor  $s$ , the dormant time, type of cement and class of concrete.

$$\beta = \exp \left[ s \cdot \left( 1 - \sqrt{\frac{28 - t_{dor}}{t_{eq} - t_{dor}}} \right) \right] \quad (13)$$

The corresponding development of the compressive strength  $f_c$ , the tensile strength  $f_t$  and of Elasticity Modulus  $E_c$  is considered as follows [6]:

$$f_c(t_{eq}) = \beta \cdot f_{c,28} \quad (14) \quad f_t(t_{eq}) = \beta^{0.5} \cdot f_{t,28} \quad (15) \quad E_c(t_{eq}) = \beta^{0.3} \cdot E_{c,28} \quad (16)$$

## 3. Stress Calculation

### 3.1 Degree of Restraint

The possibility of concrete members to deform freely due to the action of volumetric changes depends on the degree of restriction of this member. For most cases this condition is not known, which makes it difficult to estimate the generated stresses. The Degree of Restraint can vary from a totally free state  $\gamma_R = 0$ , in which the member moves freely, to a totally restricted state  $\gamma_R = 1.0$ , in which all the deformation turns to stresses. In the height of a wall the degree of restraint changes according to the geometry of the member (Fig. 3 left).

### 3.2 Stress Relaxation Function

As the deformations are generated and these are transformed into stresses, the stress relaxation begins, due to the viscous properties of concrete. The stresses relax in time, which is very strong in the early hours while the concrete is still fresh (Fig. 3 right). The above is represented through a Relaxation Function  $\psi$ , which depends mainly on the degree of hydration of the cement. The following function taken from the work of van Breugel [7]

allows precise modeling of this situation:

$$\psi(t, t') = \exp \left[ - \left\{ \left( \frac{E(t)}{E(t')} - 1 \right) + \nu \cdot t'^{-d} \cdot (t - t')^n \cdot \frac{E(t)}{E(t')} \right\} \right] \quad (17)$$

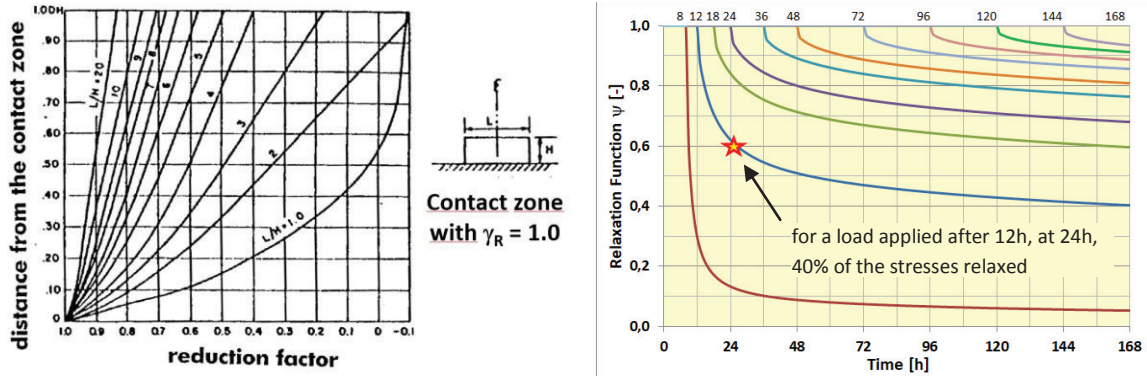


Figure 3: Effect of external restraint in the height and relaxation function.

### 3.3 Estimation of Stresses

The main difficulty in estimating stresses in concrete at early age, due to volumetric changes, lies in the impossibility of knowing precisely the development of the different properties of concrete. Through the following equations the model calculates, considering all the factors mentioned previously, in an hourly step by step procedure, the estimated stresses in the concrete member.

$$\Delta\sigma_t = (\varepsilon_{as,t} + \varepsilon_{T,t} + \varepsilon_{s,t}) \cdot E_t \cdot \psi_{t,t'} \cdot \gamma_R \quad (18) \quad \sigma_t = \sum \Delta\sigma(t, t') \quad (19)$$

### 3.4 Cracking Index

This index corresponds to the ratio between the concrete tensile stress  $\sigma_t$  and tensile strength  $f_t$ . It varies in the height of the concrete member, due to the fact of decrease of the internal restraint with height (Fig. 3 left). A value of 1.0 means a crack will occur.

$$I_{cr(t)} = \frac{\sigma_t(t)}{f_{t,t}(t)} \quad (20)$$

## 4. Case Studies

Case I Temperature measurements on-site:  
a 7.6 m long concrete beam, 4.9 m width, 0.9 m height. Input values:  $f_{c28} = 35$  [MPa] - Cement content:  $380$  [ $\text{kg}/\text{m}^3$ ] HE -  $Q_{7d} = 314$  [ $\text{kJ}/\text{kg}$ ] -  $U = 25$  [ $\text{kJ}/\text{m}^2\text{h}^\circ\text{K}$ ]. In Fig. 4 measured values (continuous lines) are compared to estimated values (dotted lines) for Core and Surface temperature. Ambient temperature is also plotted.

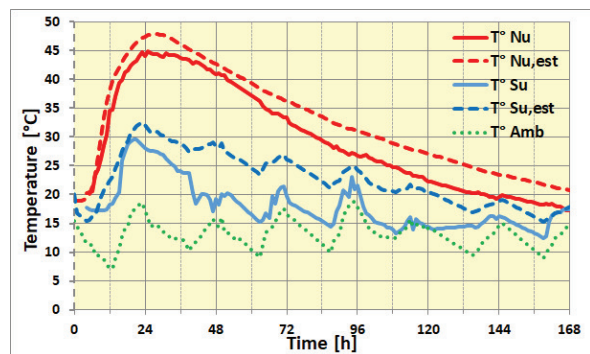


Figure 4: Case I: Concrete beam temperatures.

Case II Cracking observed at early age:

a cylindrical water tank, poured in 20 sectors, each 20 m long, 10 m height and 0.65 m width. Input values:  $f'_{c28} = 55$  [MPa] - Cement content = 425 [kg/m<sup>3</sup>] HE+8% SF -  $Q_{7d} = 300$  [kJ/kg] -  $E_a = 35,000$  [kJ/mol] - Conductivity = 5.12 [kJ/(mh°K)] -  $U = 20$  [kJ/m<sup>2</sup>h°K] Fresh Concrete  $T^\circ = 18$  [°C] / Mean Ambient  $T^\circ = 10$  [°C] / Degree of Restraint = 85 [%].

The predicted temperatures are shown in Fig. 5a, including the  $\Delta T^\circ$  Section in the shadow area. The dotted line correspond to the measured ambient temperature. Figure 5b shows the predicted stresses for a constant elastic, an elastic time dependent and a real elasto-plastic Young's Module, including the tensile strength development with the dotted line. Figure 5c shows the Cracking Index development for 5 different sections in the height of the wall. The real structure (Fig. 1 right) presented cracks till 1/3 of the height.

**5. Conclusions**

Despite its simplicity, the model predicts temperature and stress development together with a reliable crack assessment. Sensitivity analysis are easy to perform due to the consideration of technological, pouring, curing and ambient conditions.

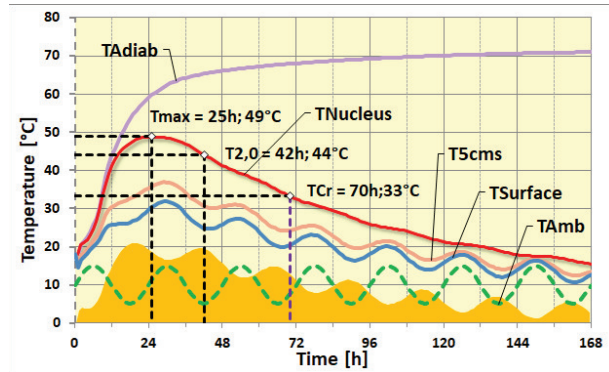


Figure 5a: Temperature Development.

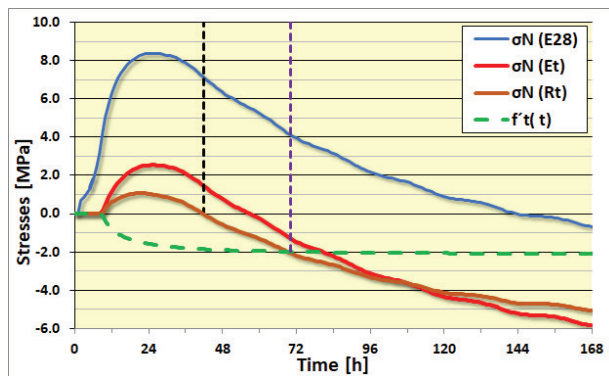


Figure 5b: Stress Development.

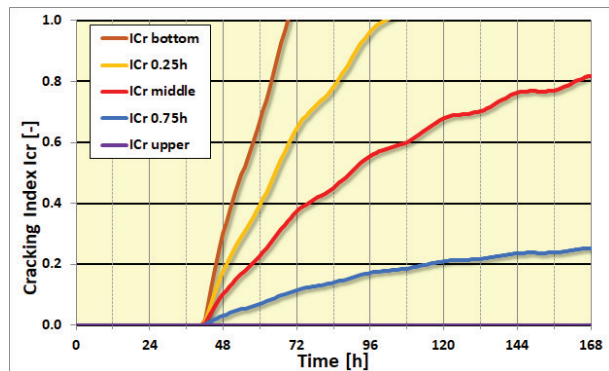


Figure 5c: Crack Development in the height.

**References**

- [1] Ebensperger, L., Wirksamkeit von Quellszusätzen im Beton zur Kompensation von Zwangsspannungen infolge Hydratationswärme, PhD Thesis, TU München (1991)
- [2] EN 196-9: Methods of testing cement. Part 9: Heat of hydration - Semi-adiabatic method (2010)
- [3] Informations Zentrum Beton, Zement-Merkblatt, Massige Bauteile aus Beton (2006)
- [4] EN 1992-1-1: Eurocode 2: Design of concrete structures. Part 1-1: General rules and rules for buildings (2004)
- [5] AS 5100.5: Australian Standard. Bridge Design – Concrete, Section 6.1.7 (2004)
- [6] Kanstad, T., Annex D for Eurocode 2 - 2020: Guidance to limit early age cracking (2017)
- [7] van Breugel, K, Development of Temperature and Properties of Concrete as a Function of the Degree of Hydration, RILEM Int. Conf. on Concrete at Early Ages, Paris (1982)

## EXPERIMENTAL SETUP FOR CHARACTERIZATION OF LONG TERM BOND AND CRACK WIDTHS IN RC TIES UNDER CONSTANT AXIAL FORCE

Carlos Sousa <sup>(1)</sup>, Mário Pimentel <sup>(1)</sup>, Amin Abrishambaf <sup>(1)</sup>, Rui Faria <sup>(1)</sup>, Miguel Azenha <sup>(2)</sup>

(1) CONSTRUCT, University of Porto, Porto, Portugal

(2) ISISE, University of Minho, Guimarães, Portugal

### Abstract

Crack openings in reinforced concrete (RC) ties are usually calculated as the integral of the relative strains between steel and concrete along the transfer length. The contribution of shrinkage strains (of concrete within the transfer length) to the long-term crack openings is, still today, an unsolved issue. In this context, this paper starts by summarizing common procedures for calculating crack openings in thin RC ties or tensile chords. Then, a short parametric analysis is shown to illustrate the relevance of shrinkage strains in crack openings calculations. Finally, a new test setup, developed for characterization of long-term crack widths and bond stresses between steel and concrete (taking into account the shrinkage influence), is presented.

### 1. Code formulas for crack width calculations

The procedure for calculation of crack openings, in European codes for RC concrete, is under discussion [1]. In previous Eurocode and Model Code versions, the formulas for determining the maximum crack width,  $w_{max}$ , are of the type:

$$w_{max} = 2 l_{s,max} (\varepsilon_{sm} - \varepsilon_{cm} - \eta_r \varepsilon_{sh}) \quad (1)$$

where  $l_{s,max}$  is the transfer length;  $\varepsilon_{sm}$  and  $\varepsilon_{cm}$  are the steel and concrete average strains along such length;  $\varepsilon_{sh}$  is the concrete shrinkage (therefore  $\varepsilon_{cm}$  does not include the shrinkage component);  $\eta_r$  is a coefficient to consider the shrinkage contribution. The coefficient  $\eta_r$  takes the value 1 in fib Model Codes (MCs) 1978 [2] and 1990 [3], and 0 in Eurocode 2 [4]. In fib MC 2010 [5],  $\eta_r$  is 1 for long-term loading of members in the stabilized cracking stage

and 0 in the remaining cases. From a theoretical point of view, considering different  $\eta_r$  values depending on the cracking stage (crack formation or stabilizing cracking) is not justified. The adoption of such  $\eta_r$  value seems to be the result of an effort to calibrate code expressions against experimental results. However, MC background documents do not discuss this important topic [6].

## 2. Crack width calculations based on the local bond stress-slip relationship

As an alternative to the use of Eq. (1), the maximum crack width can be calculated based on equilibrium and compatibility conditions applied to the transfer length and constitutive relationships for concrete, steel and for the steel-concrete interface (i.e, the local bond-slip relation). The crack opening is equal to twice the slip between steel and concrete at the crack mouth,  $s_{max}$ :

$$w_{max} = 2 s_{max} = 2 \int_0^{l_{s,max}} \varepsilon_s(x) - \varepsilon_c(x) dx \quad (2)$$

where  $\varepsilon_s(x)$  and  $\varepsilon_c(x)$  are the local steel and concrete strains. The coordinate  $x$  is the distance to the section of zero slip. The local bond-slip relation is paramount in this type of calculation. The one proposed by the fib MC 2010 [5], for good bond conditions, long-term loading and small slip values (range of values of interest for serviceability calculations), is:

$$\tau(s) = 2.5 \sqrt{f_{cm}} \left( \frac{s}{(1 + k_t) s_1} \right)^{0.4} \quad (3)$$

where  $\tau$  is the local bond stress in MPa,  $s$  is the local slip,  $s_1$  is a reference slip value (1mm),  $f_{cm}$  is the average concrete compressive strength and  $k_t$  is a coefficient to account for the influence of time. This problem can be solved analytically in particular cases (crack formation stage, neglecting the influence of shrinkage) [7]. In the remaining cases, the solution can be calculated using numerical methods, as explained in [8]. It becomes evident that, for long-term calculations, concrete shrinkage strain shall be included in  $\varepsilon_c(x)$ .

## 3. Parametric analysis to show the relevance of shrinkage in crack width calculations

Two rectangular RC ties were selected for illustration of the relevance of shrinkage strains in crack width calculation, covering a wide and recurrent range of bar diameters and effective reinforcement ratios. Each tie has a rectangular cross section with dimensions  $B=1$  m and  $H=5(c + \phi/2)$ , where  $c$  is the clear concrete cover (equal to 40 mm) and  $\phi$  is the bar diameter. The reinforcement consists of two layers of  $\phi 10 // 100$  mm in the first tie and  $\phi 20 // 100$  mm in the second one. The steel cross section,  $A_s$ , and the effective area of concrete,  $A_{c,eff}$ , are shown in Tab. 1. The transfer length, according to the MC 2010 [5] provisions for the stabilized cracking stage, is shown in the same table. The calculation was performed using the numerical framework described in [8], as outlined in §2. The concrete properties correspond



to the strength class C25:  $f_{cm} = 33$  Mpa and tensile strength  $f_{ctm} = 2.6$  Mpa. The effective modulus of concrete was taken as 12 GPa and the coefficient  $k_t$  is 1.8. Besides the amount of reinforcement, the following parameters were varied in the parametric analysis: steel stress at the crack (150 MPa or 250 MPa) and shrinkage strain (0 or 500  $\mu$ ). Tab. 2 shows representative analysis results, where  $\beta$  is the calculated ratio between the average value (along  $l_{s,max}$ ) of the normal stress in concrete and  $f_{ctm}$ ; and  $\tau_{bms}$  is the average bond stress along the same length. The calculated diagrams of local bond stresses are shown in Fig. 1 for the members reinforced with  $\phi 20 // 100$  mm.

Table 1: Characteristics of the analysed RC tensile chords.

	Reinforcement $\phi 10 // 100$ mm	Reinforcement $\phi 20 // 100$ mm
$A_s$ (cm <sup>2</sup> )	15.8	62.8
$A_{c,eff}$ (m <sup>2</sup> )	0.225	0.250
$l_{s,max}$ (mm)	238	150

Table 2: Results of the parametric analysis.

	$\phi 10 // 100$ mm				$\phi 20 // 100$ mm			
	$\sigma_s = 150$ MPa		$\sigma_s = 250$ MPa		$\sigma_s = 150$ MPa		$\sigma_s = 250$ MPa	
	$\varepsilon_{sh} = 0$	$\varepsilon_{sh} = 500\mu$	$\varepsilon_{sh} = 0$	$\varepsilon_{sh} = 500\mu$	$\varepsilon_{sh} = 0$	$\varepsilon_{sh} = 500\mu$	$\varepsilon_{sh} = 0$	$\varepsilon_{sh} = 500\mu$
$w_{max}$ (mm)	0.12	0.24	0.24	0.39	0.14	0.27	0.27	0.40
$\beta$	0.25	0.36	0.36	0.49	0.38	0.49	0.49	0.59
$\tau_{bms} / f_{ctm}$	0.54	0.85	0.85	1.09	0.82	1.09	1.09	1.29

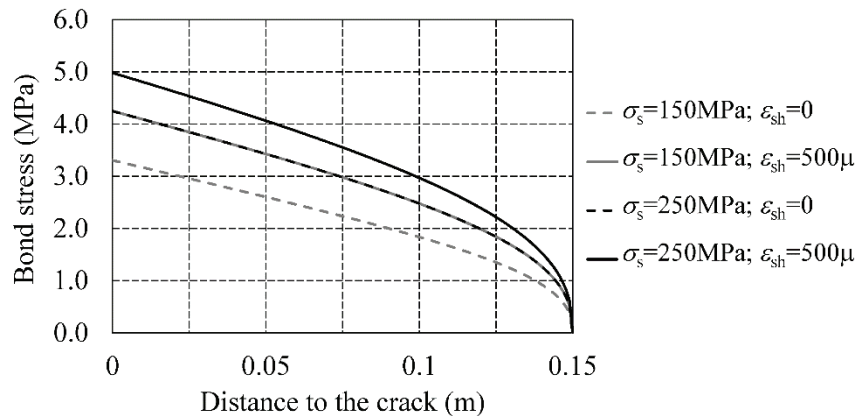


Figure 1. Calculated bond stresses along the transfer length, for the tensile chord reinforced with  $\phi 20 // 100$  mm.

Note that fib MC2010 [5], as well as the other codes mentioned before [2-4], propose specific values for the parameters  $\beta$  and  $\tau_{bms} / f_{ctm}$  (explicitly or implicitly, in the adopted formulas). The values shown in Tab. 2, on the other hand, are the result of the analytical calculations.

These results show that shrinkage strains are responsible for an important increase of crack width. Two effects are responsible for an equal crack width variation (because they give rise to the same average deformation): concrete shrinkage equal to  $500\mu$ ; and steel stress variation equal to 100 MPa. Local bond stresses undergo a moderate increase as a consequence of shrinkage.

This analytical approach provides a sound basis for the derivation of formulas for crack width calculation. However, the calibration of the bond-slip relation and the experimental validation of the analysis methodology is paramount.

#### **4. Tests to assess the bond-slip behaviour**

The standard tests to assess the bond behaviour of steel bars embedded in concrete, proposed by RILEM, are described in EN10080 [9]: the pull-out test and the beam test. Even though these tests provide important information regarding the bond behaviour, their results do not provide a true local bond stress-slip relationship to be used in crack width calculations, because: the concrete is loaded differently from what happens in tensile chords; the bond stress and the slip are not measured locally.

A different alternative has been used in the past to assess the bond behaviour [10, 11]: the so-called 'transfer type' test. It consists in a tensile test of an RC tie, with measurement of steel strains in various positions throughout the transfer length. These measurements provide the diagrams of steel strains and, based on that, the bond stresses can be indirectly determined. The main advantage of this test alternative is the fact that it replicates the steel-concrete interaction in a real RC tie or tensile chord. The main difficulty is the steel strain measurement without disturbing the bond action. In the past, electrical resistance strain gages were installed in channels. This technique was pioneered by Mains [10] and improved by Scott [11], among others. More recently, optical Fibre Bragg Grating (FBG) sensors have been used to measure steel strains in closely spaced positions, with a negligible interference in the steel bar and bond action [12, 13]. This technique offers new possibilities for the characterization of the long-term bond stress-slip relation.

#### **5. Developed test setup**

The proposed test system applies a tensile force, which can be adjusted to be kept constant throughout time. The test specimen is an RC tie with a single, centred, steel bar. Upon casting of the RC element, a crack is pre-induced, at mid-length, by using a 3 mm thick plate which covers all the concrete cross section. The plate is removed before loading the specimen, in order to create the crack. The initial ( $\sim 3$  mm thick) crack width ensures that the concrete stress in that cross section is zero, even if the system is not perfectly symmetric (small eccentricities are common in test systems to induce axial tension). The length of the concrete element is (in the performed tests) 120 cm. It has to be greater than four times a conservative estimate of the maximum transfer length, so that the transference of bond stresses, near the central crack, can be captured.

Bond stresses are indirectly quantified by measuring the steel strains in 13 positions along the bar length, at the vicinity of a crack (1 at the crack, 6 for each side). For this purpose, an array

of FBGs (made with through-the-coating technology, with a 155  $\mu\text{m}$  thick polyimide continuous coating) is installed in a thin groove (1 mm wide and 1 mm deep) milled in the rebar. The experimental characterization of the slip is carried out using the measured crack opening and transfer length values. In turn, the transfer length is assessed by analysing the diagram of steel strains measured through the FBGs.

Fig. 1 shows the proposed setup. The main components of the load application system are: a rigid frame, two adaptors (couplers), a load cell (capacity of 50 kN), and a hinge. The load is applied simply by tightening a loading nut. The average tie deformation is recorded by four LVDTs (one per lateral face of the RC member), with accuracy of 0.001 mm, held by an aluminium frame. The crack width evolution is measured by a USB digital microscope with a 2Mp camera. For this purpose, two SIM chips (phone SIM cards with known width engravings that act as relative scales) were glued on the pre-induced crack lips, in each of the four sides of the specimen. At some instants of time, the images are captured and processed to determine the crack opening variation.

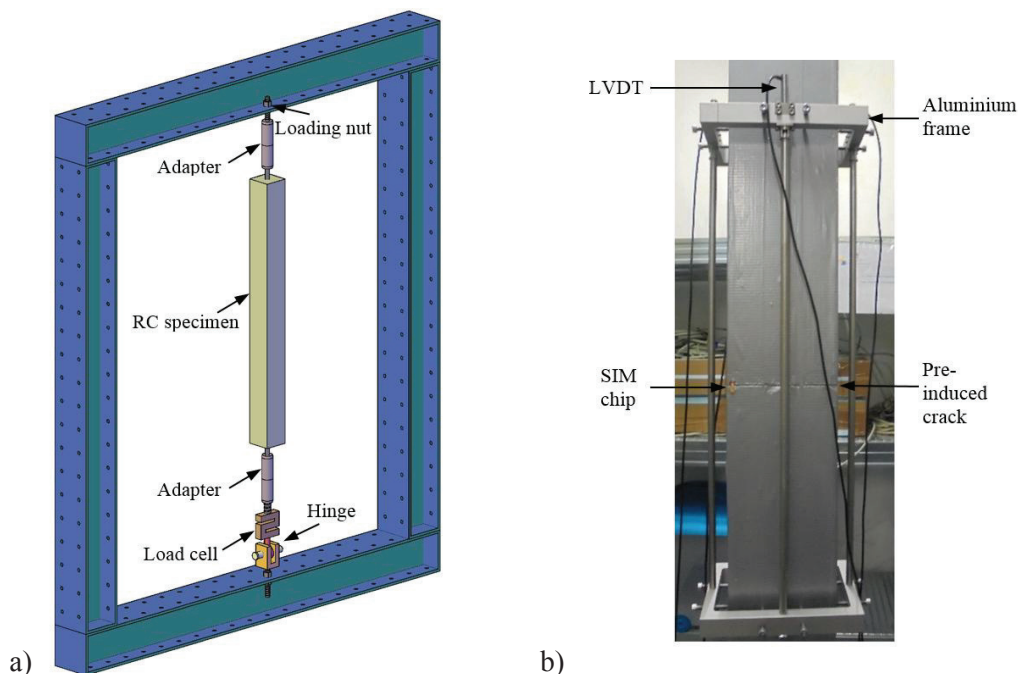


Figure 1. Developed setup: a) three-dimensional image and  
b) LVDTs to measure the average deformation.

In the ongoing test campaign, two series of tests are performed: a first series of tests on sealed specimens (a sealing membrane is used to prevent drying and, consequently, minimize drying); a second series, with identical specimens, but unsealed. In both series, companion concrete specimens, with the same cross section, are used to measure the free concrete shrinkage. Two bar diameters are tested: 8 and 12 mm. The concrete cross section is chosen so that it corresponds to a reinforcement ratio of 1,1%. FBG sensors are used only in the second series (the one where higher variation of bond stresses are expected throughout time). The results of the first series of tests revealed that the setup is able to record, with good resolution, the specimen long-term deformation and crack opening under a sustained tensile load.

## 6. Final remarks

The necessity of a new test setup for assessment of the influence of shrinkage on bond stresses and crack width in RC was justified. The developed setup was presented. The experimental results of the ongoing test campaign are expected to provide a contribution to: the understanding of the long-term evolution of crack openings, calibration of constitutive models for long-term finite element analyses; calibration of empirical formulations for calculating long-term crack widths.

## Acknowledgments

This work was financially supported by: Project POCI-01-0145-FEDER-007457 (CONSTRUCT) and by project POCI-01-0145-FEDER-007633 (ISISE), funded by FEDER funds through COMPETE2020 - Programa Operacional Competitividade e Internacionalização (POCI), and by national funds through FCT-Fundação para a Ciência e a Tecnologia. FCT and FEDER (COMPETE2020) are also acknowledged for the funding of the research project PTDC/ECM-EST/1056/2014 (POCI-01-0145-FEDER-016841). The financial support of COST Action TU1404 through its several networking instruments is also acknowledged.

## References

- [1] Caldentey, A., Proposal of new crack width formulas in the Eurocode 2, background, experiments, etc., Proceedings from the miniseminar Crack width calculation methods for large concrete structures, Norway (2017), 17-20
- [2] CEB-FIP, Model Code for concrete structures (1978)
- [3] CEB-FIP, Model Code 1990. Design code (1993)
- [4] CEN, EN 1992-1-1 - Eurocode 2: Design of concrete structures - Part 1-1: General rules and rules for buildings. (2004)
- [5] fib, Model Code for Concrete Structures 2010. Wilhelm Ernst & Sohn (2013)
- [6] Balázs, G.L. et al, Design for SLS according to fib Model Code 2010, Structural Concrete 14 (2013), 99-123
- [7] Balázs, G.L, Cracking analysis based on slip and bond stresses, ACI Materials Journal 90 (1993), 340-348
- [8] Sousa, C., Calçada, R. and Neves, A., Numerical evaluation of the non-linear behaviour of cracked RC members under variable-amplitude cyclic loading, Materials and Structures 48 (2015), 2815-2838
- [9] CEN, EN 10080 - Steel for the reinforcement of concrete - Weldable reinforcing steel - General (2005)
- [10] Mains, R.M., Measurement of the distribution of tensile and bond stresses along reinforcing bars, ACI Journal 23 (1951), 225-252
- [11] Scott, R.H., Intrinsic Mechanisms in Reinforced Concrete Beam-Column Connection Behavior, ACI Structural Journal 93 (1996), 1-11
- [12] Nellen et al, High strain and high strain gradients measured with fiber Bragg gratings in structural engineering applications, 15<sup>th</sup> Optical Fiber Sensors Conference TD (2002)
- [13] Kenel, A. et al, Reinforcing steel strains measured by Bragg grating sensors, Journal of Materials in Civil Engineering 17 (2005), 423-431

## INFLUENCE OF CARBONATION AND CONCRETE SPECIMEN SIZE ON GAS DIFFUSION COEFFICIENT

Mouna Boumaaza<sup>(1)</sup>, Bruno Huet<sup>(1)</sup>, Philippe Turcry<sup>(2)</sup>, Christoph Gehlen<sup>(3)</sup>, Abdelkarim Aït-Mokhtar<sup>(2)</sup>, Detlef Heinz<sup>(3)</sup>

(1) LafargeHolcim research center, 95 rue du Montmurier, 38291 Saint Quentin Fallavier, France

(2) Laboratoire des Sciences de l'Ingénieur pour l'Environnement (LaSIE), UMR 7356 CNRS, Université de La Rochelle, Avenue Michel Crépeau, 17042 La Rochelle, France

(3) Centre for building materials (cbm) Technical University of Munich, Arcisstraße 21, 80333 Munich, Germany

### Abstract

This paper investigates the effect of accelerated carbonation on the oxygen-effective diffusion coefficient ( $D_{e,O_2}$ ) of dry hardened cement pastes, non-carbonated and carbonated, at different hydration durations (for 1 day to 8 months); the influence of concrete specimen size (discs of 5, 10 and 50mm thickness) on  $D_{e,O_2}$  and compares  $D_{e,O_2}$  against oxygen permeability for 14 concrete mixes. The effect of concrete specimen size on oxygen diffusion coefficient is investigated on four concrete mixes hydrated for 90 days. Measurements are made after drying the specimens at 95%RH and 105°C. For each concrete mix: nine replicates of 5mm and 10mm thickness are tested at the dry state and after equilibration at 95%RH and three specimens of 50mm thickness are tested at the dry state only. Carbonation is found to influence  $D_{e,O_2}$  differently depending on the binder type.  $D_{e,O_2}$  varies slightly with the concrete specimen thickness, and no clear correlation is found between  $D_{e,O_2}$  and oxygen permeability.

### 1. Introduction

Experimental determination of concrete transport properties is required to understand the level of gas tightness of concrete structures in order to limit the ingress of gaseous aggressive species through cementitious materials. Furthermore, the gas diffusion coefficient is a key-parameter for service life prediction models of concrete structures in real environment [1]. In

the case of carbonation which is widely recognized as a significant cause of corrosion of reinforcement in concrete [2], atmospheric carbon dioxide ( $\text{CO}_2$ ) penetrates the concrete by means of a diffusion process through its porous network where it dissolves in the pore water and reacts with different calcium-based phases of the cement paste. Carbonation kinetics depend on how fast the carbon dioxide moves through the concrete carbonated and non-carbonated layers [3]. Thus, it is necessary to determine concrete transport parameters for both carbonated and non-carbonated states in order to model the phenomenon under site conditions. The carbonation reaction modifies the microstructure, changes the porosity of the concrete containing Portland cement [4] and, consequently, could affect the gas transport properties [5]. This brings up the reason why this paper investigates the influence of carbonation on the gaseous oxygen diffusion coefficient of cement paste mixes tested at three different ages, and cast at a volumetric W/C ratio of 1,6. This investigation is carried out at the dry state.

Usually, when concrete transport properties are experimentally determined, common practice is to test specimens of a thickness equal to at least three times the maximum size of the aggregate present in the sample. A major limit in testing these concrete specimens is the long time required to reach water equilibrium. In this work, an experimental campaign is carried out on 4 different concrete mixtures with a main focus on the influence of concrete specimen thickness on gas diffusivity. For each concrete mix, nine discs of 5mm and 10mm thickness are sawn and used to measure oxygen diffusivity at the dry state (oven at  $105^\circ\text{C}$ ) and after equilibration at 95%RH. Three discs of 50mm thickness that respect the criteria of a thickness 3 times the maximum aggregate size are also tested to oxygen diffusivity but only at the dry state. Finally, the oxygen diffusion coefficient is compared to the oxygen gas permeability for 14 concrete mixes and a correlation between the two transport properties is discussed, as gas permeability is the transport property commonly measured [6].

## **2. Materials and methods**

### **2.1 Cement pastes**

Three cement pastes are tested: Ordinary Portland Cement (OPC) and two paste mixtures prepared by replacing OPC with 50% slag and 10% silica fume (labelled OPC\_Slag and OPC\_SF, respectively). Additional information on the chemical composition, fineness and specific surface of these materials is given in [7]. These samples are cast at a constant volumetric water-per-cement ratio 1,6. All pastes are tested at three different hydration durations: two months, eight months, 1 day (only for OPC) and 7 days (OPC\_SF and OPC\_Slag). The latter is achieved by means of an organic solvent, i.e isopropanol. First, the cement pastes are oven dried at  $80^\circ\text{C}$  for a month until hydric equilibrium is reached, then they are stored under vacuum for 24h to cool down to laboratory temperature without any mass gain. Then, the diffusion tests are done at the dry non-carbonated state. The paste samples are water saturated under vacuum for 24h, equilibrated for 3 weeks in a relative humidity (RH) of 57%, placed in a storage chamber with a carbon dioxide concentration of 3% by volume for one month and finally oven dried at  $80^\circ\text{C}$  to be tested to oxygen diffusivity.

## 2.2 Concrete

In order to investigate the influence of concrete specimen size on oxygen diffusivity, four concrete mixes are prepared using three cement types as shown in Tab.1. The aggregate volume fraction of these concrete mixes is 70%, the air content 2% and the maximum aggregate size is 22mm. Water porosity of these specimens is determined following the French standard NF P18-459. The mixtures are cast into 11\*22cm moulds, demoulded after 24h and stored at 100% relative humidity for 90 days. For each concrete mix, nine replicates are sawn to 5 and 10mm thickness and three replicates to 50mm thickness. First, 5mm and 10mm thickness specimens are dried at 95%RH in a climate chamber. At this relative humidity the water equilibrium was reached after six months. The sides of the specimens are sealed using an epoxy resin to retain oxygen diffusion in one direction. After the determination of the oxygen diffusion coefficient of these samples at 95%RH, they are gradually dried: stored for a week at 60%RH, then at 30%RH, oven dried at 80°C to be finally dried at 105°C until mass equilibrium. This drying process takes around five weeks. Once the mass equilibrium is reached, the samples are placed in a vacuum desiccator 24 hours prior to the diffusion tests to prevent moisture gain when the temperature decreases. As for concrete samples intended to measurements of both oxygen diffusivity and oxygen permeability, 14 mixes are cast and cured for 90 days, then gradually dried at 105°C.

Table 1: Cement type, W/B mass ratio and total porosity of the tested concrete

Concrete label	Cement type	W/B	Water porosity (%)
C1	CEM I	0.65	14.1
C2	CEM III/A	0.4	11.2
C3	CEM III/A	0.65	14.1
C4	CEM IV/A	0.4	11.8

## 2.3 Transport properties test methods

The oxygen diffusion coefficient is measured using an experimental setup developed during our previous works [7,8]. The test method relies on the accumulation of gaseous oxygen inside the cell. Oxygen diffusion coefficient is determined by the numerical fitting of the accumulation curve to Fick's second law. For cement paste samples, the tested specimens are discs of 4cm diameter and 3mm thickness. Concrete specimens have a diameter of 11cm and a thickness that varies between 5 and 50mm. Oxygen permeability is determined for 14 concrete mixes following the French Standards XP P18-463. For each concrete, three replicates of 5cm thickness and 15cm diameter are tested after being dried at 105°C. These specimens are then cored into discs of 11cm diameter to be tested to oxygen diffusivity.

## 3. Results and discussion

### 3.1 Cement pastes

Fig.1 shows results of the oxygen diffusion coefficient of non-carbonated (NC) and fully carbonated cement pastes (C) at three hydration durations (early age = 1 day for OPC and 7

days for OPC\_SF and OPC\_Slag). These results show that carbonation seems to induce different effects on the three mixes. First, we note that the oxygen effective-diffusion coefficient ( $D_{e,O_2}$ ) decreases for OPC pastes by a factor of 9 at two months and 2 at eight months of hydration, and by a factor of 50 at early age. This strong decrease of  $D_{e,O_2}$  for OPC pastes hydrated only for 1 day could be explained by a possible restart of hydration of these samples during the 24h water saturation under vacuum, the conditioning at 57% RH or during the accelerated carbonation. Carbonation is known to lower the total porosity [4] which could affect the transport properties. However, the decrease of  $D_{e,O_2}$  with carbonation is not a consequence of the total porosity variation only, since previous works [8] showed that blended cement pastes have lower diffusivity than Portland pastes even though their total porosity was higher. These works also revealed that oxygen-effective diffusion coefficients display a somewhat linear trend with respect to the mean pore diameter. Meanwhile, carbonation impact on blended cements is less consistent:  $D_{e,O_2}$  decreases by a factor of 3 at the most at early age and slightly increases at two months hydration. Previous works showed that accelerated carbonation of hardened cement pastes containing slag increases gas diffusivity [9,5]. Still, further investigations including XRD/TGA and pore size distribution of the carbonated samples are required for a deeper interpretation of these results.

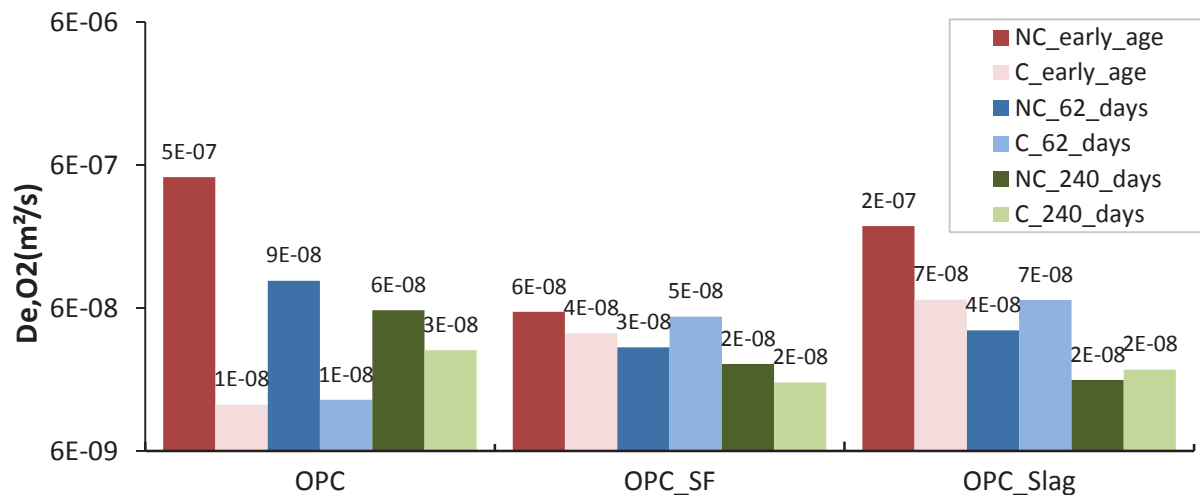


Figure 1: Oxygen diffusion coefficients for carbonated and non-carbonated cement pastes.

### 3.2 Concrete

Fig. 2 shows that the oxygen diffusivity increases slightly with the specimen thickness (by a factor of 3 at the most) for both dry samples and samples equilibrated at 95%RH (the water saturation degree of the latter samples is found to vary between 65% and 70%). It is suggested that this is a result of cracks induced by oven drying at 105°C. For thin samples, the thermal gradient leads to a lower thermal stress, hence less cracking would appear [10]. Note that  $D_{e,O_2}$  of specimens equilibrated at 95%RH (i.e high water saturation degree ~70%) is three orders of magnitude lower than  $D_{e,O_2}$  of dry specimens (example : concrete C4).

Fig.3 shows the oxygen permeability as a function of the oxygen diffusivity in log-scale. For each mix, values of  $D_{e,O_2}$  and oxygen permeability are computed as the average value of three replicates. Markers on Fig. 3 indicate the cement type used for the tested concrete and colours indicate the W/B ratio value. For example, a red circle is used for a CEMI concrete of a 0.4



W/B. Our results show a very poor correlation between the two transport properties. This could be explained by the fact that drying induced microcracks influence highly the oxygen permeability, while they only vary  $D_{e,O_2}$  by a factor of 2 at the most [11]. Note that previous works have found a rather good correlation between the two transport properties [11-12]. Nevertheless, their results were established only for few concretes (4 to 6 mixes).

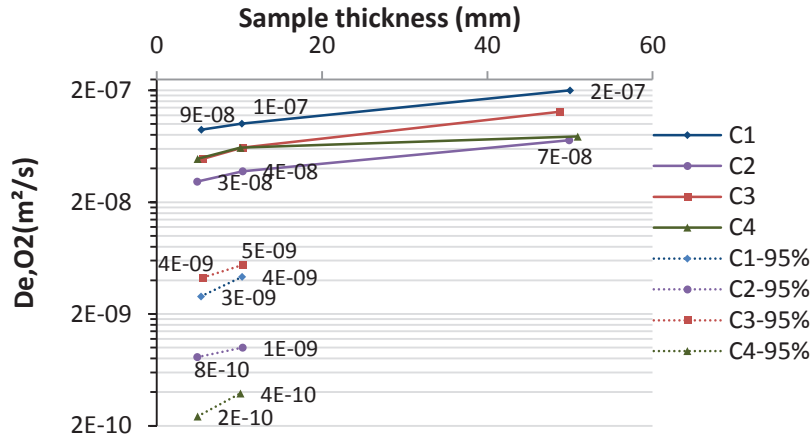


Figure 2: Oxygen-effective diffusion coefficient as a function of sample thickness for concretes at the dry or equilibrated at 95%RH.

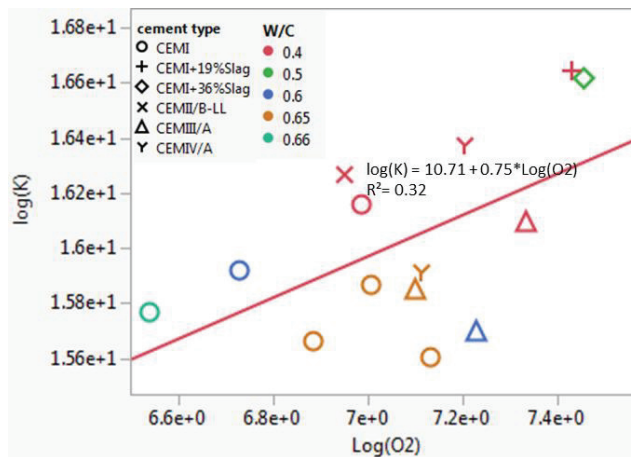


Figure 3: Average (n=3) oxygen effective diffusion coefficient vs oxygen permeability.

#### 4. Conclusion

Even though carbonation decreases highly the oxygen-effective diffusion coefficient ( $D_{e,O_2}$ ) of OPC pastes, it slightly varies  $D_{e,O_2}$  of blended cement pastes. We cannot presently assess these results and further research has to be carried out, especially on pore size distribution variation after carbonation. Using our diffusion test,  $D_{e,O_2}$  is found to vary by a factor of 3 at the most with the concrete specimen thickness. This is a rather encouraging result since

testing thin concrete samples is of a high convenience: water equilibrium and gas diffusion steady state are reached much faster for thinner concrete samples. Still, these results are only established for 4 concrete mixes and further tests are necessary. No clear correlation is found between  $D_{e,O_2}$  and oxygen permeability for 14 concrete mixes, oven-dried at 105°C.

## References

- [1] S. Von Greve-dierfeld, C. Gehlen, Performance based durability design , carbonation part 1 – Benchmarking of European present design rules, 17 (2016) 309–328.
- [2] B. Huet, V. L'hostis, G. Santarini, D. Feron, H. Idrissi, Steel corrosion in concrete: Determinist modeling of cathodic reaction as a function of water saturation degree, *Corros. Sci.* 49 (2007) 1918–1932.
- [3] W. Ashraf, Carbonation of cement-based materials: Challenges and opportunities, *Constr. Build. Mater.* 120 (2016) 558–570.
- [4] G. Villain, M. Thiery, Impact of carbonation on microstructure and transport properties of concrete, in: 10DBMC Int. Conférence Durab. Build. Mater. Components, Lyon , France, 2005.
- [5] M. Bertin, Impact du séchage au jeune âge sur la carbonatation des matériaux cimentaires avec additions minérales, PhD thesis, Université Paris-est marne la vallée, 2017.
- [6] J.S. Andrade, U.M.S. Costa, M.P. Almeida, H.A. Makse, H.E. Stanley, Inertial Effects on Fluid Flow through Disordered Porous Media, (1999) 5249–5252.
- [7] M. Boumaaza, B. Huet, G. Pham, P. Turcry, A. Ait-Mokhtar, C. Gehlen, A new test method to determine the gaseous oxygen diffusion coefficient of cement pastes as a function of hydration duration , microstructure , and relative humidity, *Mater. Struct.* 51 (2018).
- [8] M. Boumaaza, B. Huet, P. Turcry, C. Gehlen, A. Ait-Mokhtar, D. Heinz, Gas diffusion coefficient of cement paste and concrete : effect of water saturation degree and specimen thickness, in: 12th Fib Int. PhD-Symposium Civ. Eng., 2018: pp. 1–8.
- [9] P. Turcry, F. Gendron, A. Ait-Mokhtar, CO<sub>2</sub> diffusion in cementitious materials : experimental investigations, in: 2nd Int. RILEM/COST Conf. Early Age Crack. Serv. Cem. Mater. Struct. EAC2, ULB-VUB, Brussels , Belgium, (2017).
- [10] T. Gardner, Chloride transport through concrete and implications for rapid chloride testing, PhD thesis, University of Cape Town, 2006.
- [11] H.S. Wong, M. Zobel, N.R. Buenfeld, R.W. Zimmerman, Influence of the interfacial transition zone and microcracking on the diffusivity, permeability and sorptivity of cement-based materials after drying, *Mag. Concr. Res.* 61 (2009) 571–589.
- [12] C. Villani, R. Loser, M.J. West, C. Di Bella, P. Lura, W.J. Weiss, An inter lab comparison of gas transport testing procedures: Oxygen permeability and oxygen diffusivity, *Cem. Concr. Compos.* 53 (2014) 357–366.

## **INFLUENCE OF PRESTRESS LOSSES ON THE DYNAMIC OVER STATIC CAPACITY RATIOS OF RAILWAY CONCRETE SLEEPERS**

**Chayut Ngamkhanong<sup>(1),(2)</sup>, Sakdirat Kaewunruen<sup>(1),(2)</sup>**

(1) Department of Civil Engineering, School of Engineering, University of Birmingham,  
Birmingham B152TT, United Kingdom

(2) Birmingham Centre for Railway Research and Education, School of Engineering,  
University of Birmingham, Birmingham B152TT, United Kingdom

### **Abstract**

Railway sleeper, which is placed underneath the rail, is one of the main components of railway track. Railway sleepers can be made of timber, concrete, composite materials etc. Prestressed concrete sleeper is one of the most popular types which can be seen in railway track all over the world. However, loss of prestress is a significant concern as it can affect strength of member and its serviceability including stresses in concrete, cracking etc. In prestressed concrete applications, the most important variable is the prestressing force. It was observed that the prestressing force can be reduced with time because of several factors such as creep and shrinkage of concrete, steel relaxation, friction loss, anchorage slip etc. RESPONSE2000 was used to evaluate the static and dynamic capacities based on the modified compression field theory. The study results exhibit that the losses of prestress have significant effects on the overall strength of prestressed concrete sleepers. It is recommended to take into account the effect of prestress losses in standard design of prestressed concrete sleepers.

### **1. Introduction**

Railway sleepers are a main part of railway track structures. Railway sleepers embedded in ballasted railway tracks are laid to support the rails. The main functions of sleeper are to redistribute loads from the rails to the underlying ballast bed, to secure rail gauge and to enable safe passages of rolling stocks. It should be noted that railway sleepers are a structural and safety critical component in railway track systems [1-6]. The sleepers can be typically

made of timber, concrete, steel, composites etc. Remarkably, railway prestressed concrete sleepers have been used in railway industry for over 50 years [7, 8]. Prestressed concrete sleepers would have an improved structural capacity and/or serviceability as compared to conventional reinforced concrete sleepers. However, they are prone to deterioration issues as cracks may occur and expand during operation. Moreover, losses of prestress are a serious concern since it affects the strength of prestressed concrete member. In fact, the prestressing force in prestressed concrete can be reduced due to the initial losses and long-term losses [9, 10]. Initial prestress losses occur when the prestress is transmitted to the concrete, there is contraction due to prestress. This contraction causes a loss of stretch in the wire. Loss can be expressed as percentage or in terms of stress or in terms of total deformation or in terms of strain. According to the literature [11], it is interesting to note that prestrain in steel has a significant effect on the strength of steel. The strength increases with the increasing of pre-strain in steel but the elongation decreases.

Generally, railway track structures often experience impact loading conditions due to wheel/rail interactions associated with abnormalities [12] in either a wheel or a rail. Wheel/rail irregularities induce high dynamic impact forces along the rails that may greatly exceed the static wheel load. Although, the dynamic behaviour of railway sleepers has been studied [13-17], the considerations of its behaviour when the sleepers undergo prestress losses, have not been fully studied. This paper investigates and presents an advanced railway concrete sleeper modelling capable of parametric analysis into the effect of prestress loss on the dynamic behaviors of railway sleepers. This paper considers the wide range of prestress loss in order to cover all the possible behaviours as the railway sleeper may experience higher time dependent losses [18]. The dynamic factors are highlighted. The emphasis of this study has been placed on the impact capacity of the sleepers. The improved understanding in this paper will help update the practical maintenance issues in railway industry. The understanding of the dynamic capacity of railway concrete sleepers will also help improve technology for track condition monitoring [19].

## **2. Methodology**

### **2.1 Modified compression field theory**

The ultimate moment has been used to represent the capacity of prestressed concrete sleepers. In general, concrete sleepers would fail in bending or shear bending mode. The moment capacities are predicted by the adaptation of modified compression field theory using Response-2000 [20]. This software is a nonlinear sectional analysis for the analysis of concrete elements. The theory is capable of predicting the behaviour of reinforced concrete subjected to in-plane shear and normal stresses. The concrete stresses in principal directions along with prestressing steel are considered in only axial direction and uncracked portion will carry on to sustain a load in the analysis [21]. The assumptions of this theory are that the deformation plane section remains plane after loading and there is no transverse clamping stress across the depth of the section. It is also assumed that prestressing wires and concrete are bonded perfectly. The section can be failed in only pure bending or shear-bending modes. The dimension of prestressed concrete sleeper is shown in Figure 1. There are 4 layers with 22 tendons. The ultimate strength of 1860MPa and elastic modulus of 200000MPa are

considered. The high strength concrete with the cylinder compressive strength of 55MPa is taken into account.

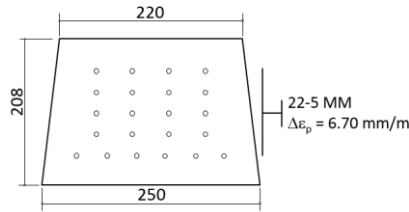


Figure 1: Prestressed concrete sleeper dimension.

## 2.2 Effect of strain and loading rates

In this study, it is assumed that prestressing wires and concrete are bonded perfectly. It should be noted that the strain rate plays a role in material strengths. The prediction of moment capacity has been carried out using the data obtained from the previous experiments [22, 23]. It should be noted that the average total duration of impact forces is about 4 ms. In this study, the strain rate of concrete used is  $2 \text{ s}^{-1}$  as recommended by previous studies. It is known that the dynamic ultimate strain of prestressing steel is about 0.02, and the total duration of impact force influencing the steel fibre is roughly from 6 ms. This is because the impact stress wave delays during the stress propagation and will be impeded through concrete [24]. Hence, the strain rates of prestressing wires are estimated to be  $6 \text{ s}^{-1}$ . The dynamic strength of materials can be obtained as the input for the sectional analysis using Eqs. (1) and (2) as follows.

Concrete:

$$\frac{f'_{c,dyn}}{f'_{c,st}} = 1.49 + 0.268 \log_{10} \dot{\epsilon} + 0.035 [\log_{10} \dot{\epsilon}]^2 \quad (1)$$

Prestressing wires:

$$\frac{f_{y,dyn}}{f_{y,st}} = 10^{0.38 \log_{10} \dot{\epsilon} - 0.258} + 0.993 \quad (2)$$

Where  $f_{y,dyn}$  is the dynamic upper yield point stress,  $f'_{c,st}$  is the static upper yield point stress of prestressing wires (about 0.84 times proof stress), and  $\dot{\epsilon}$  is the strain rate in tendon.

## 3. Results and Discussions

Figure 2 show the static moment capacities of prestress concrete sleepers with the consideration of prestress loss. It is clearly seen that prestress losses play a significant effect on prestressed concrete strength especially at first crack. The moment at first crack decreases with the increasing of prestress loss. They are observed as linear trends in both positive and negative directions. The trends of results are quiet similar to the strength of steel [11] with the consideration of pre-strain as it highly effects the moment at first crack rather than ultimate strength. It is also interesting to note that the difference between moment at first crack and ultimate strength of prestressed concrete sleepers slightly increase with the increase

percentage of prestress losses as prestress loss has a little effect in ultimate moment capacity. Dynamic capacities of prestressed concrete sleepers are shown in Figure 3.

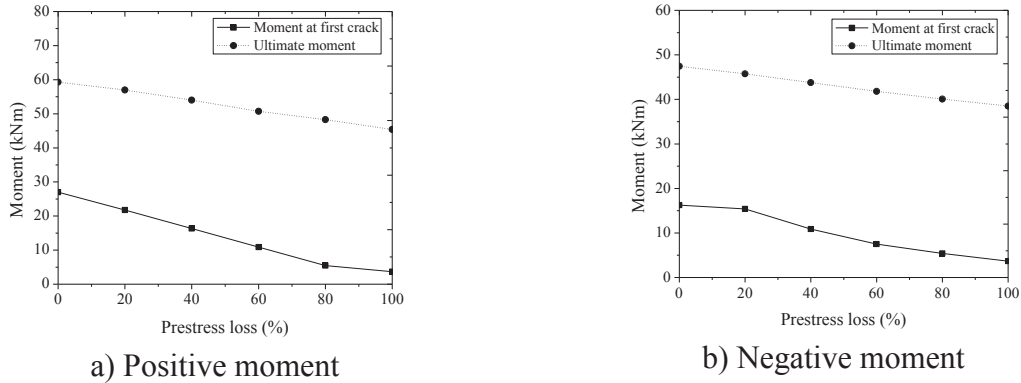


Figure 2: Static capacities of prestressed concrete sleepers at various prestress losses.

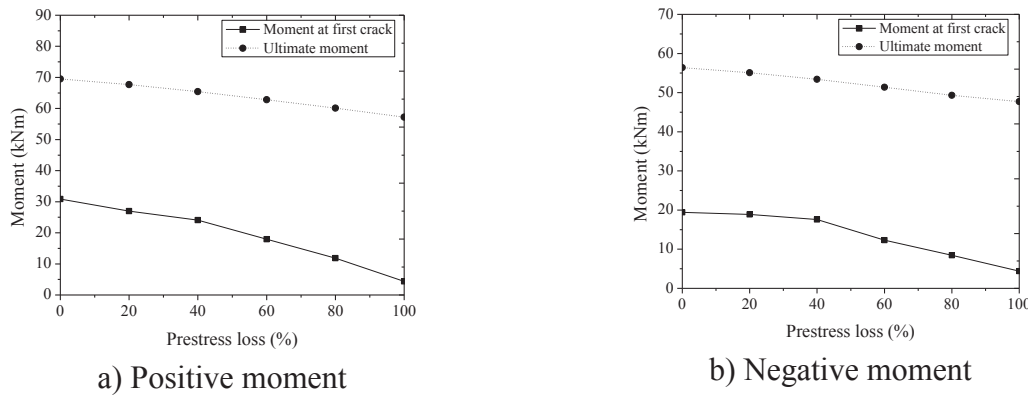


Figure 3: Dynamic capacities of prestressed concrete sleepers at various prestress losses.

Figure 4 shows dynamic over static ratios at various prestress losses. It can be seen that the dynamic factors of both positive and negative ultimate moment are in the range of 1.15-1.25. As for the dynamic factor of moment of first crack, it is observed that the dynamic factors of positive and negative moments are in the range of 1.15-2.17 and 1.19-2.26. However, it should be noted that when the huge losses of prestress are applied, the moment at first crack cannot be predicted accurately. This is because the moments observed are at very low range and software cannot provide the appropriate step of results.

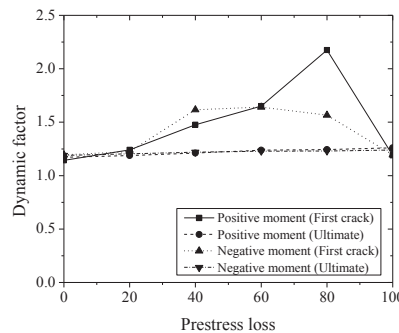


Figure 4: Dynamic factors

#### 4. Conclusions

This study presents the dynamic factor of railway concrete sleepers considering the effects of prestress losses. Dynamic factors are presented in term of the ratio between dynamic and static capacities. The results obtained show that the dynamic factors of ultimate moment are in the range of 1.15-1.25. Moreover, the ranges of 1.15-2.26 are also observed as the dynamic factor of moment at first crack. Nevertheless, it should be noted that the moment at first crack cannot be predicted precisely when the huge losses of prestress are considered. It is interesting to note that the prestress losses have more significant effects on moment at first crack rather than ultimate moment since it shows the variation of dynamic factors associated with prestress losses. The results show that the losses of prestress have crucial effects on the overall strength of prestressed concrete sleepers.

#### Acknowledgements

The authors are sincerely grateful to European Commission for the financial sponsorship of the H2020-MSCA-RISE Project No. 691135 “RISEN: Rail Infrastructure Systems Engineering Network,” which enables a global research network that tackles the grand challenge of railway infrastructure resilience and advanced sensing in extreme environments ([www.risen2rail.eu](http://www.risen2rail.eu)) [25].

#### References

- [1] Fryba, L., Dynamics of railway bridges, Thomas Telford Czech Republic (1996)
- [2] Gamage, E., Kaewunruen, S. and Remennikov, A.M., Design of holes and web openings in railway prestressed concrete sleepers, Railway Engineering Conference, Edinburgh, UK (2015)
- [3] Kaewunruen, S. and Remennikov, A.M., Structural safety of railway prestressed concrete sleepers, Aust. J. Struct. Eng 9(2) (2009), 129–140
- [4] Kaewunruen, S. and Remennikov, A.M., On the residual energy toughness of prestressed concrete sleepers in railway track structures subjected to repeated impact loads, Electronic Journal of Structural Engineering 13(1) (2013), 41-61
- [5] Remennikov, A.M., Murray, M.H. and S. Kaewunruen, S., Conversion of AS1085.14 for railway prestressed concrete sleeper to limit states design format, AusRAIL Plus 2 (Dec 2-6, Sydney, Australia) (2007)
- [6] Remennikov, A.M., Murray, M.H. and S. Kaewunruen, S., Reliability based conversion of a structural design code for prestressed concrete sleepers, Proceedings of the Institution of Mechanical Engineers: Part F Journal of Rail and Rapid Transit 226(2) (2012), 155-173
- [7] Kaewunruen, S. and Remennikov, A.M., Sensitivity analysis of free vibration characteristics of an in-situ railway concrete sleeper to variations of rail pad parameters, Journal of Sound and Vibration 298(1) (2006), 453-461
- [8] Kaewunruen, S. and Remennikov, A.M., Investigation of free vibrations of voided concrete sleepers in railway track system, Proceedings of the Institution of Mechanical Engineers Part F: Journal of Rail and Rapid Transit 221(4) (2007), 495-507

- [9] Li, D., C. Ngamkhanong, C. and Kaewunruen, S., Time-dependent topology of railway prestressed concrete sleepers, IOP Conference Series: Materials Science and Engineering 245 (3) (2017)
- [10] Li, D., C. Ngamkhanong, C. and Kaewunruen, S., Influence of Surface Abrasion on Creep and Shrinkage of Railway Prestressed Concrete Sleepers, IOP Conference Series: Materials Science and Engineering 245 (3) (2017)
- [11] Zulfi, F.R. and Korda, A.A., Effect of pre-strain on mechanical properties and deformation induced transformation of 304 stainless steel, J. Phys.: Conf. Ser, 739 (2016)
- [12] Remennikov, A.M. and Kaewunruen, S., A review on loading conditions for railway track structures due to wheel and rail vertical interactions, Structural Control and Health Monitoring 15(2) (2008), 207-234
- [13] Ngamkhanong, C., Li, D. and Kaewunruen, S., Impact capacity reduction in railway prestressed concrete sleepers with vertical holes, IOP Conference Series: Materials Science and Engineering 236(1) (2017)
- [14] Ngamkhanong, C., Kaewunruen, S. and Remennikov, A.M., Static and dynamic behaviours of railway prestressed concrete sleepers with longitudinal through hole, IOP Conference Series: Materials Science and Engineering 251(1) (2017)
- [15] Kaewunruen, S. and Remennikov, A.M., Dynamic flexural influence on a railway concrete sleeper in track system due to a single wheel impact, Engineering Failure Analysis 16(3) (2009), 705-712
- [16] Kaewunruen, S. and Remennikov, A.M., Dynamic properties of railway track and its components: recent findings and future research direction, Insight-Non-Destructive Testing and Condition Monitoring 52(1) (2010), 20-22(3)
- [17] Ngamkhanong, C., Li, D. and Kaewunruen, S., Impact capacity reduction in railway prestressed concrete sleepers with surface abrasions, IOP Conference Series: Materials Science and Engineering 245(3) (2017)
- [18] Ngamkhanong, C., Kaewunruen, S. and Costa, B.J.A., State-of-the-Art Review of Railway Track Resilience Monitoring, Infrastructures, 3(1) (2018), 3
- [19] Ngamkhanong, C., Li, D., Remennikov, A. and Kaewunruen, S., Dynamic capacity reduction of railway prestressed concrete sleepers due to surface abrasions considering the effects of strain rate and prestressing losses, International Journal of Structural Stability and Dynamics (2018), DOI: 10.1142/S0219455419400017
- [20] Bentz, E.C., Sectional analysis of reinforced concrete members, University of Toronto, Department of Civil Engineering (2000)
- [21] Remennikov, A.M. and Kaewunruen, S., Experimental load rating of aged railway concrete sleepers, Engineering Structures 76(1) (2014), 147-162
- [22] Kaewunruen, S. and Remennikov, A.M., Impact capacity of railway prestressed concrete sleepers, Engineering Failure Analysis 16(5) (2009), 1520-1532
- [23] Li, D., C. Ngamkhanong, C. and Kaewunruen, S., Influence of vertical holes on creep and shrinkage of railway prestressed concrete sleepers, IOP Conference Series: Materials Science and Engineering 236(1) (2017)
- [24] Wakui, H. and Okuda, H., A study on limit-state design for prestressed concrete sleepers, Concr Lib JSCE 33 (1999), 1-25
- [25] Kaewunruen, S., Sussman, J.M. and Matsumoto, A., Grand Challenges in Transportation and Transit Systems, Frontiers in Built Environment, 2(4) (2016)



## THE INFLUENCE OF SLAG CHEMISTRY ON BLENDED CEMENTS MADE WITH IRON-RICH SLAG

Vincent Hallet<sup>(1,2)</sup>, Jos Denissen<sup>(1)</sup>, Remus Ion Iacobescu<sup>(1)</sup>, Yiannis Pontikes<sup>(1)</sup>

(1) Department of Materials Engineering, KU Leuven, Leuven, Belgium

(2) Magnel Laboratory for Concrete Research, Faculty of Engineering & Architecture, Ghent University, Ghent, Belgium

### Abstract

Ordinary Portland cement is often substituted by ground granulated blast furnace slag (GGBFS) in order to adjust the properties and decrease the CO<sub>2</sub> emissions of the cement binder. GGBFS is rich in Ca and Si and poor in Fe. On the contrary, non-ferrous metallurgy slags are rich in Fe and Si and poor in Ca. Nonetheless, it is known that Fe<sup>3+</sup> could develop hydration products at the expense of Al<sup>3+</sup>. Therefore, this paper investigates the pozzolanic activity of 3 iron-rich slags with varying content of major oxides, as single components and in blended cements. Slag reactivity was assessed through dissolution tests in 0.1M NaOH solution and by thermogravimetric analysis. Additionally, blended cements with 30 wt% substitution of Portland cement were produced and investigated for the phase assemblage and mechanical strength using quantitative X-ray powder diffraction and compression tests, respectively. Following the characterisations, slags with low (CaO+MgO)/SiO<sub>2</sub> weight ratio showed pozzolanic activity, whereas the slag with high (CaO+MgO)/SiO<sub>2</sub> weight ratio exhibited more latent hydraulic behaviour. Furthermore, after 90 days of curing, all slag blend formulations had higher compressive strengths than those without slag. This work therefore shows that the Fe-rich slags used in this study are suitable candidates for OPC substitution.

### 1. Introduction

Currently, the only slag type specified in the European EN197-1 norm [1] is ground granulated blast furnace slag (GGBFS), originating from iron production. On the other hand, non-ferrous metallurgy produces high volumes of slags as well. If these slags would exhibit cementitious properties, they could be considered as supplementary cementitious materials (SCMs) in the future. In this way they may contribute to decreased CO<sub>2</sub> emissions for the

cement and concrete industry, although the environmental loads of the metallurgical processes should also be taken into account. These non-ferrous slags are nowadays only scarcely investigated as viable SCMs and are mostly considered for lower-value applications, such as aggregate. Research on typical non-ferrous slags, such as copper slags [2], ferronickel slags [3] and lead/zinc slags [4], has shown that the use of such slags as SCM often leads to lower compressive strengths with respect to pure ordinary Portland cement (OPC), especially at early age, thereby limiting the viable replacement volumes. These lower compressive strengths are a consequence of the chemistry of non-ferrous metallurgy slags. Since GGBFS originates from iron production, they have typically low iron and high calcia contents [5]. On the contrary, non-ferrous metallurgy slags usually have high iron and moderate/low calcia content. Iron is often reported to yield silicious hydrogarnets after hydration in typical OPC hydration environments [6], which do not lead to strength increases due to their low specific volume. Therefore, the high iron content appears to be non-beneficial to their use as SCMs. However, another factor might be the low dissolutions rates, leading to low iron release in the pore solution, also resulting from the high iron contents of these slags [7]. In this work, in order to improve the dissolution rates of the slags, and thus also their reactivity, the slags were water quenched to obtain a high amount of amorphous phase, as it has been shown that this increases the slag dissolution rates [8]. Moreover, the slags with either increased  $\text{Al}_2\text{O}_3/\text{SiO}_2$  or increased  $(\text{CaO}+\text{MgO})/\text{SiO}_2$  weight ratios with respect to a reference slag were produced, as it has been reported that these factors can increase the dissolution rate, the former due to weaker Al-O bonds with respect to Si-O bonds[9] and the latter by acting as additional network modifier [10].

## 2. Materials & methods

Slags used in this study were a reference slag (B-slag) and slags with either increased  $\text{Al}_2\text{O}_3/\text{SiO}_2$  weight ratio (A-slag) or  $(\text{CaO}+\text{MgO})/\text{SiO}_2$  weight ratio (M-slag) with respect to the reference slag. All slags were characterized by X-ray fluorescence (PW2400, Philips) to determine the chemical composition (Tab. 1) and by quantitative X-ray powder diffraction (QXRD;D2 PHASER, Bruker), for the phase assemblage (Tab. 2). The chemical composition of the amorphous phase was measured using electron probe microanalysis with wavelength dispersive spectroscopy (JXA-8530F, JEOL;Tab. 1). Slags, as well as the inert quartz filler used as a reference, were milled to a specific surface of  $4500 \pm 200 \text{ cm}^2/\text{g}$ , as determined using the Blaine method described in EN196-6 [11], for all experiments.

Reactivity was investigated by means of dissolution tests and a  $\text{Ca}(\text{OH})_2$  consumption test. Dissolution tests were conducted by immersion of slags in 0.1 M NaOH (pH = 13) solutions with a liquid-to-slag ratio of 100 to avoid precipitation. Stirring was not used in order to avoid particle abrasion. After filtration, elemental concentrations of Al, Ca and Si were measured at specific times over 7 days with inductively coupled plasma optical emission spectroscopy (ICP-OES). In the  $\text{Ca}(\text{OH})_2$  consumption test, pastes containing 20 wt%  $\text{Ca}(\text{OH})_2$  and 80 wt% slag or quartz (as inert material), with water in a water/solid (W/S) ratio of 0.4, were prepared and  $\text{Ca}(\text{OH})_2$  consumption was determined by thermogravimetric analysis (TGA). TGA was conducted from 20 to 900 °C, with a temperature step of 10 °C/min and under inert ( $\text{N}_2$ , 100 ml/min) atmosphere.

Finally, blended cements with 30 wt% slag, 70 wt% cement (CEM I 52.5N) and water over solid weight ratio (W/S) of 0.4 were prepared. Phase assemblage over time was investigated using QXRD and compression strength was determined in accordance with EN196-1 [12]. Before QXRD analysis, hydration was stopped by immersion of crushed paste in isopropanol, followed by shaking for 2 hours and finally drying at 40 °C for 1 hour. For QXRD, zincite (95% purity) was used as an internal standard, and quantification was done with normalized Rietveld analysis using TOPAS Academic V5 software.

Table 1: Composition of the slags, where A, B and M refer to the different slags. Subscripts “b” and “am” represent the bulk and amorphous content, respectively and ratios are weight ratios. Relative estimated error of 10% for bulk composition.

Element	B <sub>b</sub> (wt%)	A <sub>b</sub> (wt%)	M <sub>b</sub> (wt%)	B <sub>am</sub> (wt%)	A <sub>am</sub> (wt%)	M <sub>am</sub> (wt%)
FeO	40	38	30	37 ± 0.9	23 ± 0.9	25 ± 0.9
SiO <sub>2</sub>	27	24	24	26 ± 0.4	32 ± 0.7	25 ± 0.5
CaO	18	16	22	18 ± 0.2	21 ± 0.3	22 ± 0.6
Al <sub>2</sub> O <sub>3</sub>	7	13	8	7 ± 0.1	11 ± 0.3	7 ± 0.1
MgO	2	2	10	2 ± 0.0	2 ± 0.0	10 ± 0.1
Other	6	7	6			
Al <sub>2</sub> O <sub>3</sub> /SiO <sub>2</sub>	0.26	0.54	0.33	0.27	0.34	0.28
FeO/SiO <sub>2</sub>	1.48	1.58	1.25	1.42	0.72	1
(CaO+MgO)/SiO <sub>2</sub>	0.74	0.75	1.33	0.77	0.72	1.28

Table 2: Phase assemblage of the slags where A, B and C refer to the different slags.

Phases	Chemical formula	B (wt%)	A (wt%)	M (wt%)
Wüstite	FeO	8	4	0
Spinel	Mg <sub>x</sub> Al <sub>y</sub> Fe <sub>z</sub> O	3	9	8
Periclase	MgO	0	1	9
Trace phases (Quartz, Corundum)	(SiO <sub>2</sub> , Al <sub>2</sub> O <sub>3</sub> )	(<1, 0)	(1, 2)	(< 1, <1)
Others/Amorphous	/	89	83	82

### 3. Results & discussion

#### 3.1 Reactivity tests

The dissolution behaviour of slag B and A (Fig. 1) in the 0.1 M NaOH solution is very similar, with a slightly higher fraction of the A-slag dissolving after 7 days, most likely due to

the higher Al-content in combination with more easily broken Al-O bonds with respect to Si-O bonds [9]. Additionally, Fig. 1 (left) shows the % of the element dissolved with respect to the amorphous phase content, but taking into account the higher Al-content of the A-slag, the total absolute release difference is even higher. Similarly, total Si-release from slag A was higher as well, and both elements are crucial in pozzolanic reactions. Slag M on the other hand shows increased  $\text{Ca}^{2+}$  release, both in absolute amounts as well as relative to the amount in the amorphous phase. This is most likely related to the presence of additional  $\text{Mg}^{2+}$  and  $\text{Ca}^{2+}$  in the slag, both acting as a network modifier, increasing the dissolution rate [10].  $\text{Mg}^{2+}$  ions could not be detected, as they are probably precipitating. The enhanced release of  $\text{Ca}^{2+}$ , and most likely also  $\text{Mg}^{2+}$ , will lead to more latent hydraulic behaviour.

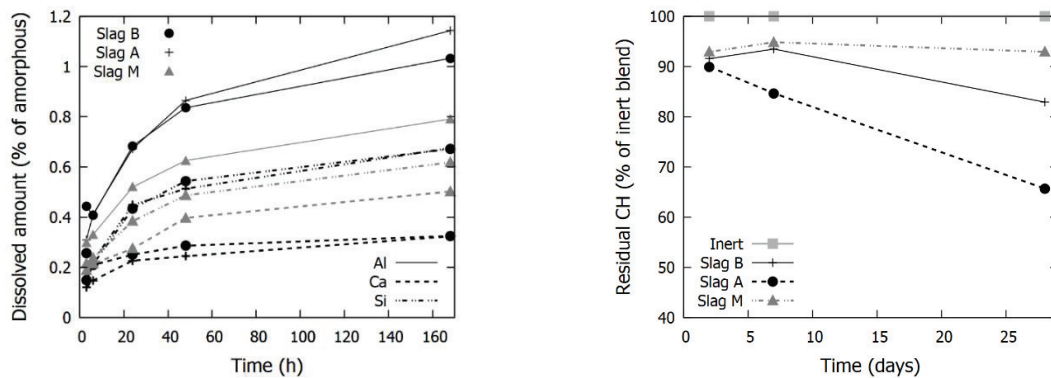


Figure 1: (left) Percentag of the amorphous content of the slags dissolved in 0.1 M NaOH solution over time. (right) CH ( $\text{Ca}(\text{OH})_2$ ) remaining as percentage of remaining CH in the inert-CH blend.

$\text{Ca}(\text{OH})_2$  consumption is used to determine whether the slags take part into pozzolanic reactions, and thus consume  $\text{Ca}(\text{OH})_2$ . However, since the experiment was carried out with distilled water rather than lime-saturated water, some dissolution of  $\text{Ca}(\text{OH})_2$  into the water will occur even if there is no pozzolanic reaction. This effect has been taken into account by normalizing to the remaining amount of  $\text{Ca}(\text{OH})_2$  in an inert- $\text{Ca}(\text{OH})_2$  blend (Fig. 1, right). Over time, the amount of consumed  $\text{Ca}(\text{OH})_2$  increases in the order  $\text{M} < \text{B} < \text{A}$ , with the ratio for the M-slag blend staying roughly constant over the entire time. This is a strong indication of either latent hydraulic or inert behaviour. However, considering the increased release of  $\text{Ca}^{2+}$  from the slag in the dissolution tests (Fig. 1, left), it is most likely that this slag exhibits latent hydraulic behaviour. Strong  $\text{Ca}(\text{OH})_2$  consumption for the A-slag probably results from pozzolanic reactions or reactions of  $\text{Ca}(\text{OH})_2$  with the  $\text{Al}^{3+}$  which is released to the solution to a high extent for this slag, as discussed before.

### 3.2 Blended cements

The compressive strengths of the slag-blended cements (Fig. 2) are lower than pure OPC at early curing times (2-28 days). However, after 90 days there is a strength increase of 2.5%, 4% and 11% with respect to pure OPC for blends with the B, A and M-slag, respectively. These increased strengths can be attributed to the pozzolanic and latent hydraulic behaviour of the slags. The more latent hydraulic behaviour of slag M yields slightly higher strength gain at late ages whereas the higher  $\text{Al}_2\text{O}_3/\text{SiO}_2$  weight ratio of the A-slag leads to faster strength gain

at early age. This is most likely due to higher Al- and Si-release seen in the dissolution tests, leading to faster pozzolanic reactions.

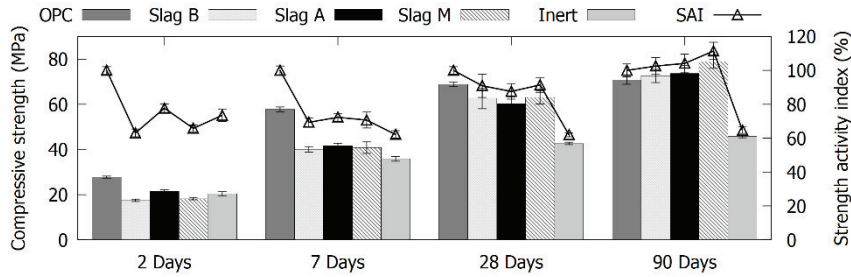


Figure 2: Compressive strength (bars) and corresponding strength activity index (lines) of the hydrated (blended) cements (70 wt% OPC + 30 wt% as indicated in the key). Error bars indicate the standard deviation.

The phase assemblage, as determined by QXRD, (Fig. 3) clearly shows the consumption of clinker phases, with more alite dissolution for slag- and inert-blended cements in comparison to pure OPC hydration at early age. The amount of unreacted alite after 28 days is higher for M-slag blended cement than for the other blends or even pure hydrated cement. This is most likely caused by higher release rate of  $\text{Ca}^{2+}$  from this slag at later times, leading to lower alite dissolution and is thus another indication of the more latent hydraulic behaviour of this slag. The main crystalline reaction products are ettringite, portlandite and, at later times, monocarboaluminate (Mc). It should be noted that in the M-slag blended cement there was also a presence of hydrotalcite, due to the higher Mg-content of the slag. However, brucite ( $\text{Mg}(\text{OH})_2$ ) was not detected, so even though a part of the periclase had reacted, as determined by XRD, no expansive effects were recorded. The amorphous reaction product, C-S-H, could not be investigated properly for the slag-blended cements as it is impossible to distinguish in XRD between amorphous C-S-H and unreacted slag. It is clear that all the slag-blended cements have a higher amount of Mc, most likely caused by aluminium release from the slag at later times as higher Al-availability has been shown to lead to enhanced calcite reactivity and subsequent carbonate-AFm formation [13]. However, it should be mentioned that the high  $\text{CaCO}_3$  contents indicate carbonation of the samples, thereby hindering the deduction of more definitive conclusions.

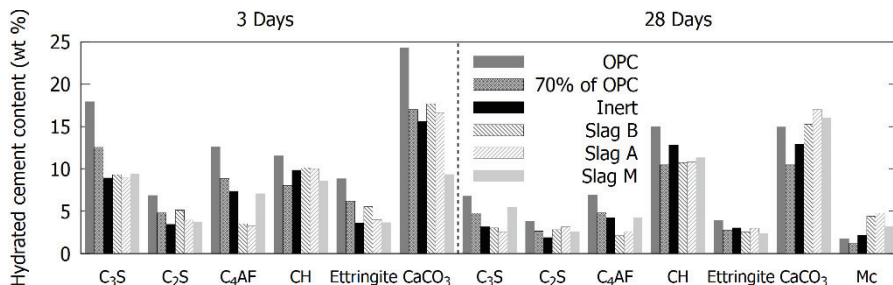


Figure 3: Phase assemblage of hydrated blended cements with different slags after 3 and 28 days, as determined by QXRD.  $\text{CaCO}_3$  includes both vaterite and calcite while Mc represents monocarboaluminate. Other phases are represented using typical cement chemistry notation.

#### 4. Conclusions

This work shows that iron-rich slags can be used as supplementary cementitious materials in blended cements, mainly contributing to late strength although all slags enhance alite dissolution at early age. Slag chemistry determines the type of behaviour, with high  $(\text{CaO}+\text{MgO})/\text{SiO}_2$  weight ratios leading to more latent hydraulic behaviour and low  $(\text{CaO}+\text{MgO})/\text{SiO}_2$  weight ratios yielding pozzolanic behaviour. Furthermore, early strength gain can be improved by a higher  $\text{Al}_2\text{O}_3/\text{SiO}_2$  weight ratio, whereas a higher  $(\text{CaO}+\text{MgO})/\text{SiO}_2$  weight ratio yields higher final strength, showing that slag chemistry engineering is an important tool in modifying the properties of blended cements with these slags, such as compressive strength.

#### References

- [1] EN197-1, Cement - Part 1: Composition, specifications and conformity criteria for common cements, European committee for standardization, Belgium (2011)
- [2] Shi, C. and Meyer, C. and Behnood A., Utilization of copper slag in cement and concrete, *Resour Conserv Recycl* 52 (2008), 1115-1120.
- [3] Rahman, M.A. and Sarker, P.K. and Shaikh, F.U.A. and Saha, A.K., Soundness and compressive strength of Portland cement blended with ground granulated ferronickel slag, *Constr Build Mater* 140 (2017), 194-202.
- [4] Benkendorff, P.N., Potential of lead/zinc slag for use in cemented mine backfill, *Miner Process Extr Metall (Trans Inst Min Metall C)* 115 (2006), 171-173.
- [5] Piatak, N.A. and Parsons, M.B. and Seal II, R.R., Characteristics and environmental aspects of slag: A review, *Appl Geochem* 57 (2015), 236-266
- [6] Dilnesa, B.Z. and Wieland, E. and Lothenbach, B. and Dähn, R. and Scrivener, K.L. Fe-containing phases in hydrated cements, *Cem Concr Res* 58 (2014), 45-55
- [7] Paul, A. and Youssefi, A., Alkaline durability of some silicate glasses containing CaO, FeO and MnO, *J Mater Sci* 13 (1978), 97-107.
- [8] Pontikes, Y. and Machiels, L. and Onisei, S. and Pandelaers, L. and Geysen, D. and Jones, P.T. and Blanpain, B., Slags with a high Al and Fe content as precursors for inorganic polymers, *Appl Clay Sci* 73 (2013), 93-102.
- [9] Oelkers, E.H. and Gislason, S.R., The mechanism, rates and consequences of basaltic glass dissolution: I. An experimental study of the dissolution rates of basaltic glass as a function of aqueous Al, Si and oxalic acid concentration at 25°C and pH = 3 and 11, *Geochim Cosmochim Acta* 65 (2001), 3671-3681.
- [10] Snellings, R. and Paulhiac, T. and Scrivener, K., The Effect of Mg on Slag Reactivity in Blended Cements, *Waste Biomass Valor* 5 (2014), 369-383.
- [11] EN196-6, Methods of testing cement - Part 6: Determination of fineness, European committee for standardization, Belgium (2010)
- [12] EN196-1, Methods of testing cement - Part 1: Determination of strength, European committee for standardization, Belgium (2016)
- [13] Steenberg, M. et al, Composite cement based on Portland cement clinker, limestone and calcined clay, XIII International Congress on the Chemistry of Cement, Spain (2011), 97-103

# **FIBRE-REINFORCED CONCRETE AND NON-METALLIC REINFORCEMENT**

## **A NUMERICAL MODEL FOR PREDICTING CRACKING OF FIBRE REINFORCED CONCRETE RINGS IN RESTRAINED SHRINKAGE TEST**

**Wei Dong<sup>(1)</sup>, Xiaoyu Zhao<sup>(2)</sup>, Xiangming Zhou<sup>(3)</sup>, Wenyan Yuan<sup>(4)</sup>**

(1) Dalian University of Technology, Dalian, China

(2) Dalian University of Technology, Dalian, China

(3) Brunel University London, Uxbridge, United Kingdom

(4) Dalian University of Technology, Dalian, China

### **Abstract**

In practice, short discrete fibres in concrete can effectively reduce the cracking potential of concrete caused by the restrained shrinkage. In the present study, a fracture mechanics-based numerical model was developed to predict the cracking of fibre reinforced concrete rings in restrained shrinkage test tailored for assessing cracking potential of fibre reinforced concrete. With the proposed model, some remarkable features on the shrinkage cracking such as the age of crack initiation and crack evolution process can be predicted accurately, as well as the crack width for plain and fibre-reinforced concretes. The findings are helpful to move forward the ring test from an index test to be more meaningful that potentially provides quantitative results for interpreting cracking of restrained concrete in the field.

### **1. Introduction**

Restrained shrinkage cracking is of critical concern in concrete elements with a large surface area-to-volume ratio such as highway pavements, industrial floors and slabs, bridge decks etc. Cracks enable the entrance of water and other corrosive ions into concrete, further leading to steel corrosion, which jeopardizes the serviceability and durability of concrete structures. One of the effective methods to reduce the adverse effects of cracking due to restrained shrinkage is the use of short discrete fibres as reinforcement for concrete [1]. Many researchers have conducted restrained ring test to evaluate the cracking resistance of fibre reinforced concrete [2-4]. In ring test, usually strain gauges are attached on the inner circumferential surface of the central restraining steel ring to continuously monitor its circumferential strain over



concrete shrinkage process. The age corresponding to the sudden drop in the measured steel strain is the cracking age of the ring, in which the crack would also propagate throughout the concrete ring cross-section. It is because that a crack once initiates, it can propagate throughout the whole cross-section of the ring in a short period (usually less than 1day). While for fibre reinforced concrete, the existence of fibres will bridge cracks and restrain them to open, which may cause several cracks occurring in the ring, delay the age of crack through-going, and cause significant drop in strain [2]. Thus it is difficult to determine the age of initial cracking and through-going cracking from the measured strain in the ring test in case of fibre reinforced concrete.

In this study, a fracture mechanics-based numerical model was developed, from which some remarkable features of the shrinkage cracking such as the ages of crack initiation and through-going can be determined accurately, as well as the crack width for plain and fibre-reinforced concretes. It is expected that such a fracture mechanics-based numerical model would be useful in exploring the cracking mechanism of plain and fibre reinforced concretes.

## 2. Experimental program

The mix proportion of the concrete was: 240:750:1150:186:60 (cement: sand: coarse aggregate: water: fly ash) by weight, which was similar to that investigated by Zhang et al. [5, 6]. The physical and mechanical properties of steel fibres for reinforcing concrete are as follows: length 25 mm; diameter 0.5 mm; tensile strength 1000 Mpa; and modulus of elasticity 210 GPa, respectively. The fibre volume fraction was 0.5% in concrete.

### 2.1 Mechanical and fracture properties of fibre reinforced concrete

Elastic modulus,  $E$  (in GPa), and splitting tensile strength,  $f_t$  (in MPa), of the concrete were measured from  $100 \times 100 \times 200$  mm<sup>3</sup> prisms and  $100 \times 100 \times 100$  mm<sup>3</sup> cubes, respectively. They can be represented by Eq. (1) and (2) by fitting the experimental data at various ages into a continuous expression as following:

$$f_t(t) = 0.487 + 0.314 \ln(t) \quad (t \leq 28) \quad (1)$$

$$E(t) = 10.017 + 5.161 \ln(t) \quad (t \leq 28) \quad (2)$$

Fracture properties of concrete, i.e. the initial fracture toughness,  $K_{IC}^{ini}$  (in MPa·mm<sup>1/2</sup>) and the fracture energy,  $G_f$  (in N/m), were determined from three-point bending test of prismatic concrete beams of  $100 \times 100 \times 500$  mm<sup>3</sup>, with a pre-crack length of 30 mm. The experimental results were curve-fitted leading to the following continuous equations:

$$G_f(t) = 39.219 + 12.622 \ln(t) \quad (t \leq 28) \quad (3)$$

$$K_{IC}^{ini}(t) = 6.180 + 2.657 \ln(t) \quad (t \leq 28) \quad (4)$$

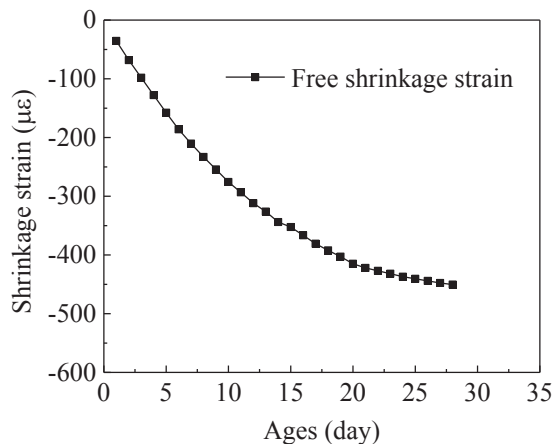
In all these equations,  $t$  is the age of the concrete (in days).

## 2.2 Free shrinkage

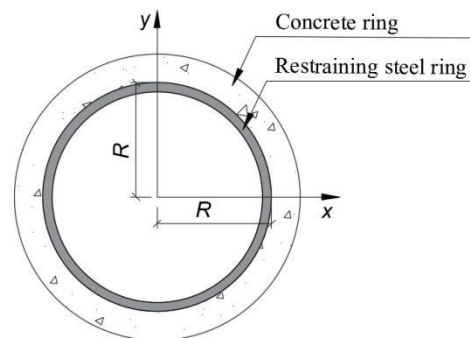
Free shrinkage tests were conducted using prisms with the dimensions of  $300 \times 75 \times 37.5 \text{ mm}^3$  but with only one  $300 \times 75 \text{ mm}^2$  surface was exposed to the environment and the other surfaces were sealed by two layers of aluminum tapes. The drying condition of the free shrinkage specimens was the same as that of the concrete rings in the test. The evolution of shrinkage strain with respect to concrete age from experiment is presented in Fig. 1(a).

## 2.3 Restrained ring test

The restrained circular ring test was performed conforming to ASTM C1581/C1581 M-09a to evaluate the cracking resistance of plain and fibre reinforced concretes subject to restrained shrinkage. The restrained ring test setup is illustrated in Fig. 1(b). The inner radius of the concrete ring  $R$  was 150 mm, and the wall thickness of the restraining steel ring and concrete ring were 12.5 mm and 37.5 mm, respectively. Four rings were prepared, including two plain concrete rings and two fibre reinforced concrete rings. In ring tests, concrete was cast directly around the steel ring, and after demoulding, these rings were sealed with double-layer aluminum tapes on their top and bottom surfaces immediately to allow drying from their outer circumferential surface only. They were then moved into an environment chamber of  $23 \text{ }^\circ\text{C}$  and 50% relative humidity (RH) for curing. The number and width of cracks occurring in rings were detected by a DJCK-2 Crevice Width Finder.



(a) Free shrinkage strains



(b) Restrained ring test setup

Figure 1: Free shrinkage strains and the schematic of restrained ring test setup

## 3. Numerical simulations

The numerical simulation was carried out using ANSYS FE code with a two-stage process: thermal analysis and structural analysis. In thermal analysis, the shrinkage of concrete was simulated by applying a fictitious temperature drop to the concrete. The shrinkage caused by the fictitious temperature drop was the same as the magnitude of shrinkage that measured in the free shrinkage test. In structural analysis, through introducing the fictitious crack model and the constitutive model of the bond between fibres and concrete, a fracture mechanics-based method was utilized to investigate the whole process of crack initiation and propagation with respect to the plain and fibre reinforced concretes in the restrained shrinkage ring test.

### 3.1 Moisture distribution and fictitious temperature field

In this research, an integrative model proposed by Zhang et al. [6, 7] was introduced to calculate the moisture distribution for the concrete ring under drying from outer circumferential surface, and the results are shown in Fig. 2(a). It has been verified that, in the case of  $RH > 50\%$ , the relationship between moisture distribution and shrinkage strain is linear. Applying a fictitious temperature field in the simulation which is the same as the moisture distribution of the concrete prismatic specimen to calculate the shrinkage strain, by comparing the shrinkage strain with those measured in the free shrinkage test, a fictitious temperature field can be determined, which is illustrated in Fig. 2(b).

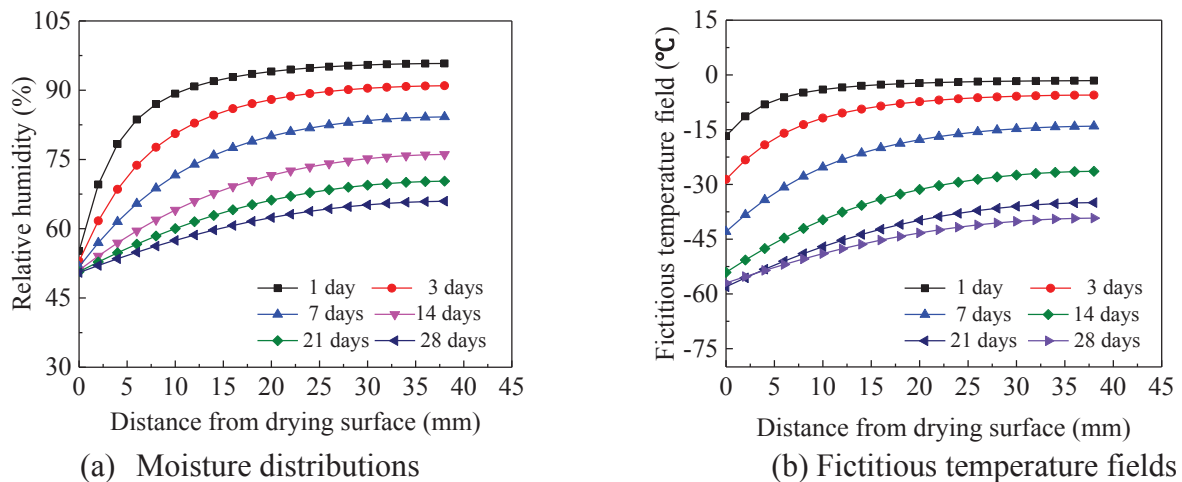


Figure 2: Moisture distributions and fictitious temperature fields in the concrete ring

### 3.2 Fictitious crack model and the constitutive modelling

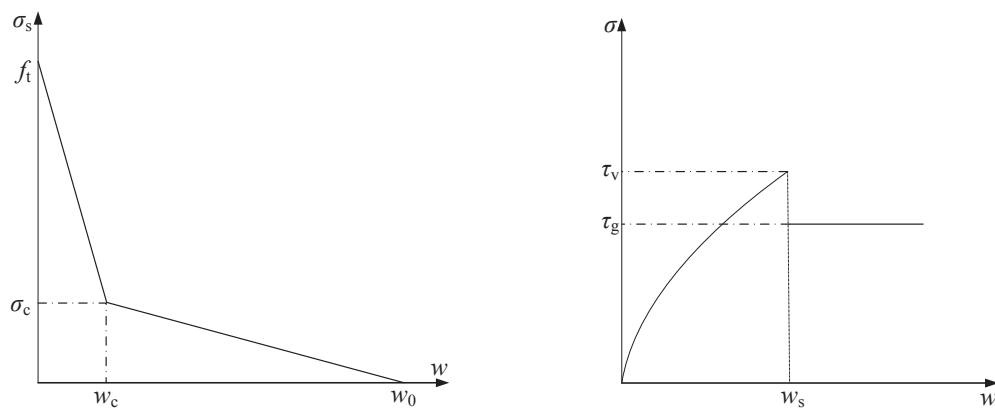


Figure 3: Bilinear softening curve of concrete and the constitutive law  $\sigma-w$  for fibres

The fictitious crack model [8] was introduced to characterize the softening behavior of concrete in micro-cracks, as represented by a relation between the softening stress ( $\sigma_s$ ) and the crack opening displacement ( $w$ ). A bilinear stress-crack opening displacement relation ( $\sigma_s-w$ ) was chosen and illustrated in Fig. 3(a). The interfacial bond behavior between the matrix and

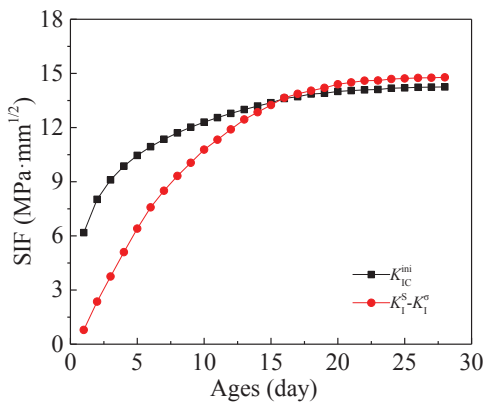
fibres can be featured from a pullout test of the fibre, and the constitutive law between the pullout force ( $\sigma$ ) of the fibre per unit area and crack width ( $w$ ) is schemed in Fig. 3(b).

### 3.3 Crack initiation and propagation

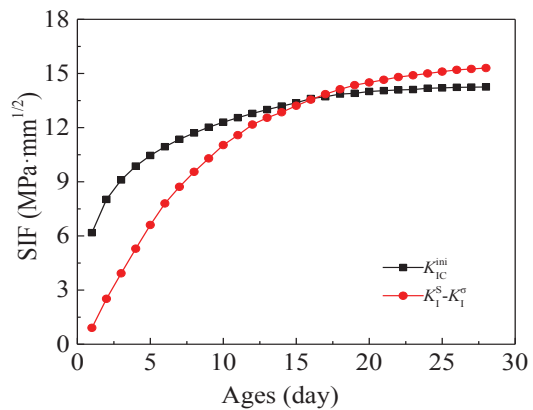
A crack propagation criterion [9, 10] based on initial fracture toughness was employed to analyze crack initiation and propagation, and predict the whole fracture process of concrete. The criterion can be described as: a crack would propagate if the value of the difference between  $K_I^F$  and  $K_I^\sigma$ , which are the stress intensity factor (SIF) caused by the applied fictitious temperature field and the cohesive stress, respectively, is greater than  $K_{IC}^{ini}$ .

## 4. Results and discussion

Through the above-mentioned simulation technique, the variation of  $K_I^F - K_I^\sigma$  and  $K_{IC}^{ini}$  at various ages for the plain concrete and fibre reinforced concrete are illustrated in Fig. 4(a) and (b), respectively. It can be seen that, from Fig. 4(a), the crack in plain concrete initiated at the age of 16 days while that in fibre reinforced concrete at the age of 17 days.



(a) SIF for plain concrete



(b) SIF of concrete with 0.5vol.% fibres

Figure 4: Evolution of  $K_I^F - K_I^\sigma$  and  $K_{IC}^{ini}$  under various concrete ages

Table 1: Comparison of the results from experimental and numerical

Concrete type	Experimental results				Simulation results			
	Num.	C-T (d)	T-T (d)	Width (mm)	Num.	C-T (d)	T-T (d)	Width (d)
Plain	1	18	18	0.17	1	16	16	0.19
With 0.5% fibre	1	19	-	0.04	1	17	17	0.085

\*Num. denotes the total number of crack at the age 28 days, C\_T denotes the age of initial cracking, and T\_T denotes the age of the through-going cracking.

In addition, the number of cracks and crack width, as well as cracking age and crack through-going age from experiment and simulation are listed in Table 1. It can be seen that the

addition of 0.5% by volume fibres can substantially reduce the width of cracks. Besides, the age of through-going cracking for the concrete reinforced with 0.5% by volume fibres was the same as that of cracking initiation, which were at the age of the 17<sup>th</sup> day because the amount of fibre was relatively low. Thus, if the addition of the amount of fibre in concrete is less than or equal to 0.5% by volume, once crack initiates, it will continue to propagate throughout the whole cross-section of the concrete ring.

## 5. Conclusions

Based on the experimental and numerical investigations in this study, the following conclusions can be drawn: (1) the addition of small amount of fibres (0.5% by volume in this study) can substantially reduce crack width in the restrained concrete rings; (2) Once the crack initiates in the concrete reinforced with less than or equal to 0.5% by volume fibres, it will continue to propagate throughout the whole cross-section of the concrete ring.

## References

- [1] Yousefieh, N., Joshaghani, A., Hajibandeh, E., Shekarchi, M., Influence of fibres on drying shrinkage in restrained concrete, *Construction and Building Materials* 148 (2017), 833-845.
- [2] Grzybowski, M., Shah, S. P., Shrinkage cracking of fibre reinforced concrete, *ACI Materials Journal* 87 (1990), 138-148.
- [3] Shah, S. P., Grzybowski, M., Model to predict cracking in fibre reinforced concrete due to restrained shrinkage, *Magazine of Concrete Research* 41 (1989), 125-135.
- [4] Seung, H. K., Shah, S. P., Prediction of early-age cracking of fibre-reinforced concrete due to restrained shrinkage, *Aci Materials Journal* 105 (2008), 381-389.
- [5] Zhang, J., Hou, D. W., Chen, H., Experimental and Theoretical Studies on Autogenous Shrinkage of Concrete at Early Ages, *Journal of Materials in Civil Engineering* 23 (2011), 312-320.
- [6] Zhang, J., Gao, Y., Han, Y. D., Evaluation of Shrinkage Induced Cracking in Early Age Concrete: From Ring Test to Circular Column, *International Journal of Damage Mechanics* 26 (2015), 771-797.
- [7] Zhang, J., Hou, D. W., Gao, Y., Sun, W., Determination of Moisture Diffusion Coefficient of Concrete at Early Age from Interior Humidity Measurements, *Drying Technology* 29 (2011), 689-696.
- [8] Hillerborg, A., Mod er, M., Petersson, P. E., Analysis of crack formation and crack growth in concrete by means of fracture mechanics and finite elements, *Cement & Concrete Research* 6 (1976), 773-781.
- [9] Dong, W., Wu, Z. M., Zhou, X. M., Calculating crack extension resistance of concrete based on a new crack propagation criterion, *Construction and Building Materials* 38 (2013), 879-889.
- [10] Dong, W., Zhou, X. M., Wu, Z. M., On fracture process zone and crack extension resistance of concrete based on initial fracture toughness, *Construction and Building Materials* 49 (2013), 352-363.

## **BRITTLINESS OF HIGH-STRENGTH LIGHTWEIGHT AGGREGATE CONCRETE**

**Jelena Zivkovic<sup>(1)</sup>, Mladena Lukovic<sup>(2)</sup>, Jan Arve Øverli<sup>(1)</sup>, Dick Hordijk<sup>(2)</sup>**

(1) Department of Structural Engineering, Norwegian University of Science and Technology (NTNU), NO-7491 Trondheim, Norway

(2) Department of Engineering Structures, Delft University of Technology (TU Delft), 2628 CN Delft, The Netherlands

### **Abstract**

Modern society and infrastructure are facing an increased demand for fast construction. A number of viaducts are aged and will need to be replaced in near future. When considering this replacement task, lightweight, slender bridge is the solution. Dead load reduction and high-strength to weight ratio are the main advantages when using the lightweight aggregate concrete (LWAC). Still, structural applications of LWAC are lacking. The main disadvantage of LWAC compared to regular concrete, which refrains its wider structural application, is its brittleness and uncontrolled crack propagation, especially when LWAC is exposed to compression. One of the ways to improve brittleness and increase the ductility of concrete is by addition of fibers. In this research, preliminary study is performed where fiber reinforced LWAC mixture was designed and tested. The mix consisted of lightweight aggregate Stalite, leading to high-strength LWAC and polyvinyl alcohol fibers (PVA) providing reduced brittleness and explosive failure. Results on fracture behavior and compressive strength with the increased amount of fibers were investigated and showed promising behavior. In future, structural tests (e.g. compression tests on prisms and beams) will be performed to further verify the benefits of combining aggregate Stalite with PVA fibers for structural applications of high-strength LWAC.

### **1. Introduction**

Nowadays, the demand for fast construction increases. A special task is that a majority of the bridges and viaducts are aged and will need to be replaced in the near future. Many countries worldwide face a similar problem and a solution for dealing with it is urgently needed. In this

context, new materials and techniques can provide cost-effective solutions thereby minimizing the construction time and reducing the traffic hinder. When considering replacement task high-strength lightweight, slender bridge can be an optimal solution [1].

Lightweight aggregate concrete (LWAC) has been used successfully for structural purposes for many years. The preferable structures are floating offshore platforms, marine structures and bridges [2,3]. The main advantage that classified lightweight concretes as a desired material for use is reduced dead weight of a structure, and in long-span bridges and high-rise buildings, dead load is a significant portion of the design load. By reducing the weight of the structure, lightweight concrete also reduces bearing, substructure and foundation design loads that may contribute to cost savings in the structure. For the projects where seismic events must be considered in design, reduction of weight is especially significant since it lead to reduction in seismic design load [4,5]. Another important application for the reduced density of lightweight concrete is its use for concrete elements that are prefabricated (precast) to facilitate easier handling and faster construction [2]. High strength lightweight aggregate concrete, i.e. having 28-day characteristic compressive strength in the range 60-80 N/mm<sup>2</sup> with oven dry density equal or less than 2000 kg/m<sup>3</sup>.

Apart from many foreseen benefits and advantages when using LWAC, structural applications is still lacking. The main reason for that compared to normal weight concrete (NWC) is its brittleness and uncontrolled crack propagation, especially faced when LWAC is exposed to compression. The brittleness of concrete is characterized by sensitivity to stress concentrations and a rapid crack/fracture development. This is attributed to the difference in fracture behaviour of two types of concretes: in regular concrete, cracks are formed around the aggregates, following aggregate-paste interface zone whereas in LWAC cracks propagate through the aggregate. As a result, more tortuous cracking route is made in regular concrete leading to more stable crack propagation and higher fracture energy. For structural analysis, it is essential to know the complete stress-strain curve under uniaxial compression including the descending branch. The main concern for designers when using LWAC is steep and short descending branch, since concrete behave in a brittle manner. Therefore, additional brittleness introduced by LWAC should be certainly avoided. In order to improve this disadvantage of the LWAC concrete, a case study on several LWAC mixes was performed, whereby lightweight aggregate Stalite was combined with polyvinyl alcohol fibers (PVA) [6].

## **2. Future replacement task**

In the past, many cast in-situ reinforced concrete plate bridges were built. The main advantage of this bridges were higher slenderness because of multiple intermediate supports over a single span bridge. At the time when cast in-situ plate bridges were built, the construction time and traffic hindrance was not a serious issue as today. Keeping in mind that many of these bridges and viaducts are constructed for a design service life of 50 years, the replacement is needed. Nowadays, with expansion of the road network and serious implications due to traffic hindrance, the main replacement requirements become more demanding. Rebuilding of cast in-situ plate bridges is due to its impact on traffic, undesirable solution and should be avoided. In this context, new materials and techniques can provide cost-effective solutions thereby minimizing the construction time and reducing the traffic hinder. The main requirements for the replacement of the existing structures are: to keep the

same traffic profile without additional ground work, to minimize the work on existing foundations and to ease transportation during the construction process and provide joining of separate elements of the bridge. Having in mind all aspects mentioned above, high-strength lightweight, slender bridge can be an optimal solution. With this type of bridge it is possible to keep or reduce bridge height, where traffic profile stays the same or increases. Using of the prefabricated LWAC box girders reduce the weight of concrete elements, making the use of precast elements more feasible by reducing requirements for shipping, handling and erection. In addition traffic impact is reduced to a minimum during construction time.

### **3. Case study - LWAC with fibres**

#### **3.1 Lightweight aggregate concrete (LWAC)**

Structural lightweight aggregate concrete is made when normal weight aggregate (NWA) is replaced with lightweight aggregate (LWA). That is simply lighter rock, produced using shale, clay or slate, so the same batching and admixtures are used for preparation of lightweight aggregate concrete like the same procedures and equipment as for conventional concrete. Typical LWAC mixtures that use coarse LWA and conventional sand have an oven-dry density of 1750 to 2000 kg/m<sup>3</sup>, followed by compressive strength up to 70 MPa (based on cylinder strength). Water absorption of LWA is higher than the absorption of NWA, in the range from 6% to 25%. Because LWA has a higher absorption, lightweight concrete typically loses mass with time as excess absorbed water migrates out of the concrete. The oven-dry density as the density achieved after moisture loss has occurred is used for design criteria. As a result of lower density of aggregate, density of LWAC is reduced in range from 25-30% compared with NWA. That is significant in areas where dead load is one of the largest determinative factors, especially in seismic areas. This feature allows the reduction of cross sections, improve structural efficiency and economy.

Density of the LWA is lower than density of the cementitious paste, which requires extra care during the production of LWAC. Control of absorption and moisture during production is necessary to produce concrete with consistent properties. LWAC generally requires more cementitious material and lower water-cement (w/c) ratio to achieve higher compressive strength. The porous nature of lightweight aggregate reduces its stiffness. In hardened LWAC, strength and rigidity of the aggregate is lower than that of the paste, leading to crack distribution through aggregate, lower strength development and lower ductility. As a result of that phenomena, fracture energy, tensile strength and E-modulus are lower for LWAC [2-5]. In addition, LWAC have brittle nature, uncontrolled crack/fracture development followed by an explosive failure. Together with the main stress-strain curve under uniaxial compression, where the descending branch is steep and short, this is a main concern for the designers when using LWAC as a preferable material. One of the advantages when using lightweight concrete is improved fire resistance. This feature is significant for building construction where structural elements are often required to provide a certain resistance to fire exposure. The insulating properties of lightweight concrete allow a smaller (and also lighter) thickness of concrete to provide the same resistance as for NWA [2,5]. The significant benefit with respect to durability when using the lightweight concrete is reduced shrinkage. This is provided due to internal curing from the water that is absorbed and stored in aggregate itself [5].



### **3.2 Tensile strength and shear capacity of LWAC with Stalite as aggregate**

Previous experimental investigation dealt with the tension behaviour of LWAC with Stalite as aggregate. Behaviour and ductility of beams with and without shear reinforcement were observed in 4-point bending test. The main test parameters that were varied in those tests were the shear span length to effective height ratio ( $a/d$ ) and amount of shear reinforcement. All the tested beams showed ductile behaviour because they were able to withstand significant increase of load after formation of shear splitting cracks. Crack formation in the tested beams were similar as for normal weight concrete. By qualitative visual inspection for all the tested beams without shear reinforcement it was observed explosive, loud and brittle failure [7]. When observing the cracked area, propagation of cracks goes through and around LWA, leading to higher tensile strength and fracture energy [5,7]. High-strength LWAC with Stalite as aggregate showed promising behaviour.

### **3.3 Polyvinyl alcohol fibres (PVA)**

Polyvinyl alcohol fibers (PVA) is mostly use to improve the inherent brittleness of cementitious materials and to control cracking. They have very little effect on the flexural strength and deflection capacity. The compressive capacity is slightly reduced while concrete surface of the elements become extremely ductile [8].

### **3.4 Experimental program, results and discussion**

Small experimental program have been created in order to create non brittle and ductile high-strength LWAC. The main concern was to deal with brittleness, explosive failure and to improve ductility of LWAC. Because of that PVA fibres was introduced in range 0.5 to 1 % at volume fractions. PVA was type "Kuralon RSC15", 8 mm long with E-modul of 36 MPa. All the concrete mixes have been prepared from the same batch of LWA Stalite, argillite slate from North Carolina.

Stalite was completely saturated to avoid water exhaustion from the paste and in addition have been controlled moisture and absorption of the aggregate just before the mix preparation. One concrete mix (LWAC 65) was prepared as a reference one without addition of the fibres, while three mixes contain fibres. Tab. 1 shows all the concrete mixes and fresh concrete characteristics. All the mixes have been prepared in laboratory controlled conditions, in a mixer with vertical pedals and capacity 25 liters. In order to provide good distribution of the fibres in FLWAC, first was prepared paste where were added fibres and later was introduced aggregate with continuous mixing. From the LWAC and FLWAC mixes have been casted several cubes and cylinders for the testing and following of compressive strength at 7, 14, 28, 38 and 46 days. At age of 28 days cylinders from all the prepared concretes were tested under compression to get E modulus [9]. From that test it was plotted stress-strain diagram, see Fig. 1. It can be noticed that LWAC65 showed brittle behaviour, when failure happened load immediately failed down, while all other mixes with fibres showed ductile behaviour with very smooth peak load where load goes slowly down and samples can sustain additional loading .

When testing lightweight aggregate concretes it was noticed that by adding the fibres, even in small amounts, workability of the concrete mix was significantly reduced. Concrete like this is very tough to cast, especially in sections that contain a lot of reinforcement is tough to embed this concrete. Mix FLWAC 65\* contain more fine sand, fraction 0-2mm, in order to provide more stable paste and concrete, but still workability was very low. That happens

because fibres arrest water which is wrapped around them. From the other side through qualitative visual inspection of the fracture, all three FLWAC concretes did not show any brittleness and explosive failure compared to LWAC 65. It was surprising that all the FLWAC cubes and cylinders kept together afterwards and can sustain additional loading. By adding the fibres in amount of 0.5% compressive strength is very slightly reduced while effect on the brittleness is the same like for mix with 1% of the fibres. For the FLWAC mix that contain 1% of the fibres compressive strength is significantly reduced, almost 18%.

Table 1: Concrete mix compositions (kg/m<sup>3</sup>) and fresh concrete properties.

Constituent	LWAC65	FLWAC65 with 0.5 % fibres	FLWAC65* with 0.5 % fibres	FLWAC65 with 1% fibres
Cement (Norcem Anlegg FA)	431.1	414.4	397.5	435.5
Silica fume (Elkem Microsilica)	22.7	21.8	20.9	22.9
Water (free)	177	170.1	163.2	206.3
Absorbed water *sand+aggregate	53.6	49.3	46.7	45.6
Sand (Ramlo 0-8 mm)	552.6	559.1	531	517.5
Sand (Ramlo 0-2 mm)	236.8	239.6	377.3	221.8
Aggregate (Stalite ½")	530.5	536.72	493	496.8
Superplasticizer	5.4	5.1	6.2	6
Synthetic fibres (% of volume)	-	6.5	6.5	13
<b>Fresh concrete properties</b>				
Matrix volume [l/m <sup>3</sup> ]	360	360	360	400
Slump [mm]	240	35	40	10
Fresh density [kg/m <sup>3</sup> ]	2013	1900	2011	1663

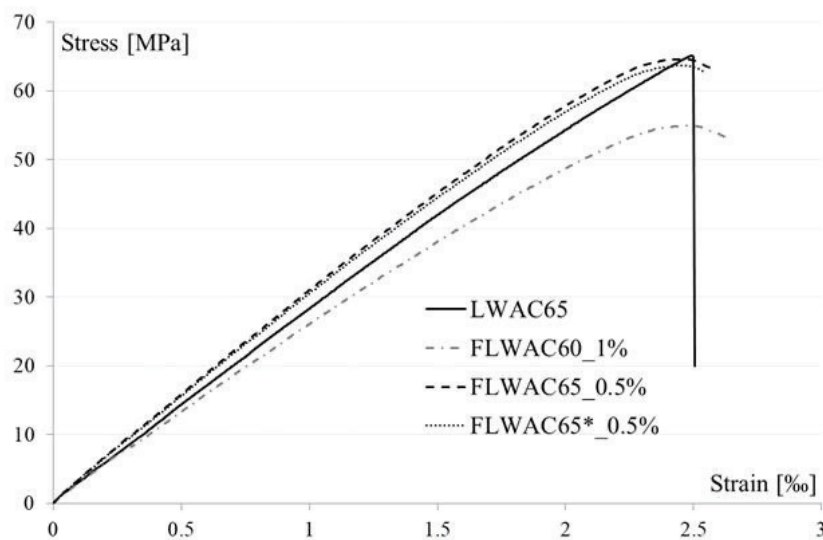


Figure 1: Stress-strain diagram for all the tested mixes at age 28 days

#### 4. Conclusions

When using the LWAC the weight of the structure can be reduced for the 25-30 %. Having this in mind, like all the other mentioned advantages, LAWAC seems to be a promising material for any structural applications, especially for the replacement bridge task. By introducing a small amount of PVA fibres, just 0.5%, the lightweight concrete became non brittle and without an explosive behaviour. In addition small amount of fibres did not influenced the compressive strength of concrete. In the future, structural tests (e.g. compression tests on prisms and beams) will be performed to further verify the benefits of combining aggregate Stalite with PVA fibers for structural applications of high-strength LWAC.

#### Acknowledgement

The work presented in this paper is part of an ongoing PhD studies in the DACS project (Durable Advanced Concrete Solutions). The DACS partners are Kværner AS (project owner), Norwegian Research Council, Axion AS (Stalite), AF Gruppen Norge AS, Concrete Structures AS, Mapei AS, Multiconsult AS, NorBetong AS, Norcem AS, NPRA (Statens Vegvesen), Norwegian University of Science and Technology (NTNU), SINTEF Byggforsk, Skanska Norge AS, Unicon AS and Veidekke Entreprenør AS.

#### References

- [1] A. Reitsema, M. Lukovic, D. Hordijk, Towards slender, innovative concrete structures for replacement of existing viaducts, fib Symposium 2016 Performance-based Approaches for Concrete Structures Cape Town (2016).
- [2] Castrodale, R. W. et al, High-performance lightweight concrete bridges and buildings, Eleventh High Performance Concrete (11th HPC) & the Second Concrete Innovation Conference (2nd CIC), Tromsø, Norway (2017).
- [3] Sandvik, M. and Hammer, T. A., The development and use of high performance lightweight concrete in Norway, International Symposium on Structural Lightweight Aggregate Concrete, Sandefjord, Norway (1995), 617-627
- [4] ACI 213R-03, Guide for Structural Lightweight Aggregate Concrete, American Concrete Institute, ACI Committee 213, Farmington Hills, MI, USA (2003).
- [5] Castrodale, R. W., Zivkovic, J. et al., Material properties of high performance structural lightweight concrete, Eleventh High Performance Concrete (11th HPC) & the Second Concrete Innovation Conference (2nd CIC), Tromsø, Norway (2017)
- [6] Kuraray Co, Characteristics of KURALON (PVA fibres), PVA fibres-application, available: <http://kuralon-frc.kuraray.com/product-application>
- [7] Zivkovic, J. and Øverli, J. A., Behavior and capacity of lightweight aggregate concrete beams with and without shear reinforcement. Nordic Concrete Research. Volume 57(2) (2017), 59-72
- [8] Savija, B. et al., Development of ductile cementitious composites incorporating microencapsulated phase change materials, International Journal of Advances in Engineering Sciences and Applied Mathematics, Volume 9, Issue 3, (2017), 169-180
- [9] NS 3676, Norwegian standard, Concrete testing-Hardened concrete-Modules of elasticity in compression. NSF, Oslo, Norway (1987)

## **COST-OPTIMAL DESIGN OF FLEXURAL CONCRETE BEAM REINFORCED WITH FRP REINFORCEMENTS**

**Sigbjørn Tveit<sup>(1)</sup>, Martin Wilhelmsen<sup>(1)</sup>, Vlad Aleksander Lundeland<sup>(1)</sup>, Mahdi  
Kioumarsi<sup>(1)</sup>**

(1) OsloMet – Oslo Metropolitan University, Oslo, Norway

### **Abstract**

Because of the non-ductile nature of FRP reinforcement, the convention of designing cross-sections with the flexure strength limited by reinforcement yield, as for steel, is not adequate. Although ACI 440.1R-15 gives easily fetched explanations on how to design FRP-reinforced concrete (FRPRC) sections for flexure, an understanding of the different parameters economic influence is required for FRP to be a competitive alternative to steel. In this paper, an analytical tool for cost-optimally analyzing and designing FRPRC-cross-sections according to ACI 440.1R-15 is presented. To this aim, by optimizing the functions for flexural strength and for the approximated price pr. meter of a cross-section – with respect to both fiber cross-section area and effective depth of concrete cross-section – a formula for the most economical ratio of these parameters in regard to flexural strength is presented. For a given FRP and concrete type, the optimal ratio proves to be the same for all desired flexural capacities, and can for rectangular cross-sections be presented as a function of the cross-section width.

### **1. Introduction**

Along with higher initial costs - the lack of experience, standards and guidelines may scare many engineers from entering the unknown landscapes of fiber reinforced polymer (FRP) reinforcement [1]. Despite providing durable concrete structures, free of deterioration caused by corrosion [2], FRP bars as reinforcement has not yet managed to become a major competitor to steel in Europe [3]. Chloride initiated corrosion on steel reinforcement is the number one cause of reinforced concrete (RC) bridges not being serviceable, making up 2/3 of all recorded failures on German bridge constructions [4]. Regardless - the low weight, high tensile strength, superior resistance to deterioration from aggressive environments [5] and

significantly smaller environmental impact [6] has not been sufficient to penetrate the European mainstream market.

Depending on the matrix, as well as the fiber type and their alignment, some important properties of FRP products are generally associated with a drawback in comparison to those for steel [4]. Considering design for flexural strength of rectangular FRP-reinforced concrete beams, the relatively low modulus of elasticity of the reinforcement and its lack of ductility in many cases sets limitations for the possibility to exploit its high tensile strength.

Because of FRPs resistance to electrochemical corrosion, the total life cycle cost of a non-metallic reinforced structure is nevertheless likely to be lower than those for steel-reinforced structures when situated in corrosion-aggressive environments [7], taking realistic costs of repairs and traffic delay in to consideration [3]. This long-term economical viewpoint is part of the reason for an increase in the use of non-metallic reinforcement for new bridge structures in North America. As of 2015 more than 200 Canadian concrete bridges have been designed and built using FRP in slabs, barriers or girders, without showing any signs of deterioration after 10 years [8]. Meanwhile the corresponding market in Europe is gradually growing importance, and the expanding and extensive construction of new concrete structures reinforced with FRP is motivating research on ways to design FRP structures more efficiently [10]. Because of this, the European Committee of Standardization (CEN) in 2016 published *Prospect for new guidance in the design of FRP: Support to the implementation, harmonization and further development of the Eurocodes* [9], as a step in the direction of a Eurocode governing guidelines for the design and construction of structural concrete reinforced with FRP.

With the industry's concerns of non-metallic reinforcements high first costs, the significance of developing ways to optimize costs is crucial to encourage further use for the future. According to authors' knowledge, there is no guiding to obtain cost-optimal FRP-reinforced concrete cross sections. In this paper, a method for determining the cost-optimal ratio of reinforcement to concrete area in a cross section is therefore presented.

## **2. Flexural design of FRP reinforced concrete (FRPRC) beams**

Designing traditional steel RC beams, it is desirable to take advantage of the ductile nature of the steel reinforcement to obtain a non-brittle failure of the RC element [10]. This is done by designing RC beams so that the strain level in the reinforcement is beyond what is the yield strain of steel, when concrete crushing occurs. This limits an engineer's needs and possibilities to experiment with different reinforcement ratios. FRP reinforcements on the other hand does not inherent this ductile behavior [10]. Instead, the stress/strain of FRP reinforcement bars develops linear elastically, with sudden termination by brittle failure [10].

### **2.1 Reinforcement ratio and reduction factor for flexural design**

Because of the non-ductile behavior of FRP, shown in Fig. 1, the conventional way of designing cross-sections with flexure strength limited by the reinforcement, as for steel, is not adequate [10]. ACI 440.1R-15 [10] refers to researches [11-12] proving failure by FRP-reinforcement rupture to be sudden and catastrophic, with compression-controlled cross-sections being marginally more desirable, exhibiting some inelastic behavior prior to failure.

To compensate for the lack of ductility using FRP, ACI [1] introduces a reduction factor to the nominal flexure strength,  $\phi$ , which is reliant on which limiting state is controlling.

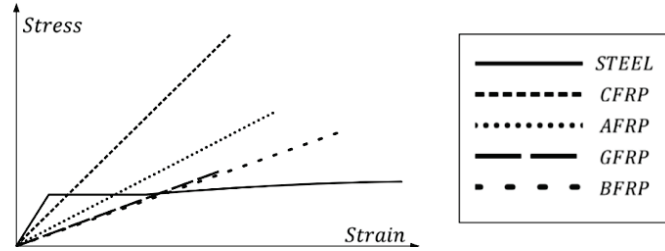


Figure 1: Stress-strain diagrams for steel, GFRP, CFRP, AFRP and BFRP, showing linear-elastic strain development with sudden failure for FRP reinforcement.

$$\phi M_n \geq M_u \quad (1)$$

where  $\phi$  is strength reduction factor,  $M_n$  is nominal flexural capacity (kNm) and  $M_u$  is factored moment at section (kNm). Comparing a beams reinforcement ratio to a balanced reinforcement ratio, one can determine whether its failure will be controlled by FRP-rupture or concrete crushing, giving a corresponding reduction factor.

$$\rho_f = \frac{A_f}{b \cdot d} \quad (2)$$

where  $\rho_f$  is FRP reinforcement ratio,  $A_f$  is area of FRP reinforcement ( $\text{mm}^2$ ),  $b$  is width of rectangular cross-section (mm) and  $d$  is effective depth of cross-section (mm). In ACI 440.1R-15 [10] is presented an equation for the balanced reinforcement ratio – the ratio where concrete crushing and FRP rupture will occur simultaneously. The equation does not include any geometric parameters and is along with Eq. (2) also valid for T sections as long as the depth of the compression zone is not larger than the thickness of the flange of the section. If the reinforcement ratio from Eq. (2) is greater than the value of the balanced reinforcement ratio,  $\rho_{fb}$ , the section will theoretically be controlled by the concrete crushing limit state. However, for a section with  $\rho_{fb} < \rho_f < 1.4\rho_{fb}$  a linearly reduced value of  $\phi$  is imposed in case the member as constructed does not fail accordingly, see Fig. 2.

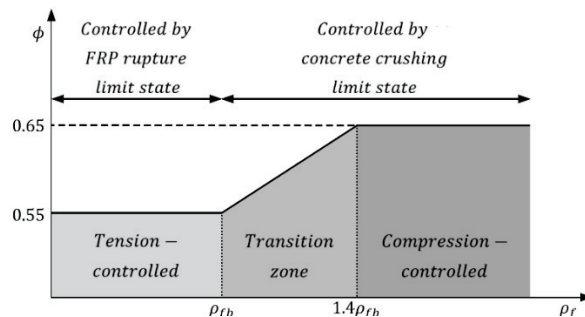


Figure 2: Strength reduction factor as function of reinforcement ratio, showing values for tension-controlled ( $\rho_f < \rho_{fb}$ ), compression-controlled ( $\rho_f > 1.4\rho_{fb}$ ) and a linear transition zone ( $\rho_{fb} < \rho_f < 1.4\rho_{fb}$ ) [10].

### 3. Cost-optimization method

Having the option to design a cross-section to be controlled by different limit states creates a demand for determining the most economically optimal design with respect to reinforcement ratio. Based on methods from ACI 440.1R-15 the factored nominal flexural strength of a FRP reinforced concrete cross-section can be presented as a function of FRP reinforcement area and effective depth. This is obtained by locking the width of the cross-section, looking at a specific type of FRP.

#### 3.1 Price of cross-section per meter

To consider the material costs of a rectangular FRP reinforced beam, a function of the same variables can be approximated based on the geometry of the cross-section. For the same specific width, the function representing price pr. meter beam can be presented as follows.

$$P(A_f, d) = P_{FRP}A_f + P_c(b(d + d_{c,m}) - A_f) \quad (3)$$

where  $P$  is price of cross-section per meter (price/m),  $P_{FRP}$  is average price of specific FRP type (price/mm<sup>2</sup>/m),  $P_c$  is price of concrete (price/mm<sup>2</sup>/m) and  $d_{c,m}$  is thickness of concrete cover measured from extreme tension fiber to collective center of reinforcement. Since the price of FRP bars varies within the different available diameters, the expression is based on an average price of the most current diameters. Not knowing how many lateral layers of reinforcement will be necessary, an approximated distance from extreme tension fiber to collective center of reinforcement is assumed.

#### 3.2 Minimizing by Lagrange multiplier

According to the method of Lagrange multipliers [13] the price function is minimized by analyzing the dot product of the two functions' associated gradients, when the factored nominal flexural capacity is constrained to a desired value. The pair of input values giving parallel gradients, is the most economically optimal.

$$\nabla\phi M_n(A_f, d) = \lambda \cdot \nabla P(A_f, d) \quad (4)$$

$$\phi M_n(A_f, d) = i \quad (5)$$

where  $\nabla$  is the del operator giving the functions gradients [14],  $\lambda$  is the Lagrange multiplier scalar [13], and  $i$  is the equality constraint which can be set to any current factored moment at section,  $M_u$  [1], or any desired flexural capacity.

Plotting the optimal pairs of input when varying the equality constraint,  $i$ , the nature of the two functions gives a straight line, proving a fixed ratio ( $A_f/d$ ) minimizing the price function for all flexural capacities, see Fig. 3.

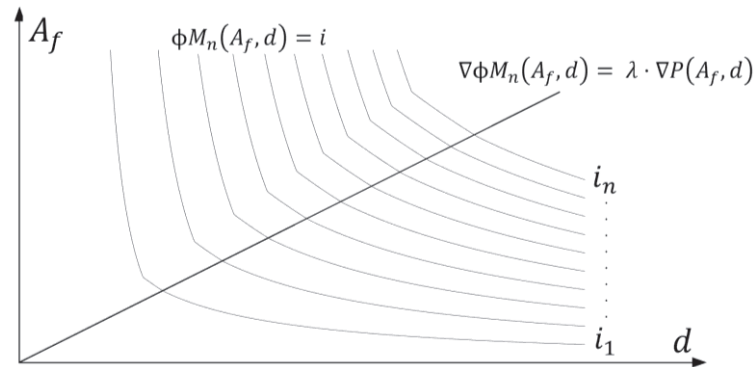


Figure 3: Price optimal combinations of  $A_f$  and  $d$  for a section reinforced with a specific FRP type, with fixed width. The straight line is obtained by plotting every optimal  $A_f$  and  $d$  pair which satisfies a flexural capacity  $M(A_f, d) = i$ , varying  $i$  continuously.

With a fixed cost-optimal reinforcement to effective depth ratio for a given width, we can easily generalize the concept to all cross-section widths. Repeating the operation of the optimization, varying the cross-section width discretely, the cost-optimal reinforcement to effective depth ratio as a function of the width,  $\Lambda_{FRP}(b)$ , is obtained by regression analysis.

$$\Lambda_{FRP}(b) = \frac{A_{f,opt}}{d_{opt}}(b) \quad (6)$$

where  $A_{f,opt}$  over  $d_{opt}$  represents the fixed relationship of values that together fulfills Eq. (4) and Eq. (5). Note that  $A_{f,opt}$  and  $d_{opt}$  does not exist independently.

In the case of a GFRP-reinforced cross-section of C45 concrete with the width  $b$ , the cost-optimal ratio of  $A_f$  over  $d$  is presented in Eq. (7). The specific GFRP reinforcement has a modulus of elasticity of 46 000 MPa, guaranteed tensile strength of 724 MPa and price of 0,03 Euro/mm<sup>2</sup>/m. The calculation is based on 142 Euro/m<sup>3</sup> as the price of C45 concrete.

$$\Lambda_{GFRP}(b) = 0,405b - 0,367 \quad (7)$$

#### 4. Conclusion

This paper presents an analytical method to minimize material costs of rectangular FRP reinforced concrete beams designed for flexural strength. Establishing a function for price per meter beam, the cost-optimal relationship between FRP reinforcement area and the cross-sections effective depth is derived. This function,  $\Lambda_{FRP}$ , proves to be invariant of demanded flexural capacity, and can for a specific FRP and concrete type be presented as a function of the cross-section width,  $b$ . The high first costs associated with FRP makes this method very useful - specifically when material costs in a project are significant.

Further research will be concerned around generalizing the results and looking into the possibility of an appliance to deflection limit state.



## References

- [1] Guadagnini, M. et al, FRP reinforcement for durable concrete structures, Proc. 11th annual International fib Symposium. Concrete: 21st Century Superhero: Building a sustainable future, London, UK (2009), 1-8
- [2] Erki, M.A. and Rizkalla S.H., FRP reinforcement for concrete structures. Concrete International 15 (1993), 48-53
- [3] Balafas, I. and Burgoyne, C.J., Economic viability of structures with FRP rebar and prestress, Magazine of Concrete Research 64(10) (2012), 885-898
- [4] Sonnenschein, R. et al, FRP Composites and their Using in the Construction of Bridges. Procedia Engineering 161 (2016), 477-482
- [5] International Federation for Structural Concrete (*fib*), FRP reinforcement in RC structures, Lausanne, Switzerland (2007)
- [6] Katz, A., Environmental Impact of Steel and Fiber-Reinforced Polymer Reinforced Pavements, Journal of Composites for Construction 8(6), (2004) 481-488
- [7] Pearson, C. et al, An Investigation into the Sustainability of FRP Reinforcement Bars, CDCC-11 4th International Conference on Durability and Sustainability of Fibre Composites for Construction and Rehabilitation, Quebec City, Canada (2011), 71-80
- [8] Mufti, A. et al, Field Study of Glass-Fibre-Reinforced Polymer Durability in Concrete, Canadian Journal of Civil Engineering 34(3) (2007), 355-366
- [9] Ascione, L. et al, Prospect for new guidance in the design of FRP: Support to the implementation, harmonization and further development of the Eurocodes, Publications Office of the European Union (2007)
- [10] American Concrete Institute, ACI 440.1R-15: Guide for the Design and Construction of Structural Concrete Reinforced with Fiber-Reinforced Polymer (FRP) Bars, Farmington Hills, USA (2015)
- [11] Nanni, A., Flexural behavior and design of RC members using FRP reinforcement. Journal of Structural Engineering 119(11) (1993), 3344-3359
- [12] Jaeger, L.G. et al, The concept of the overall performance factor in rectangular-section reinforced concrete members. Proc. 3rd International Symposium on Non-Metallic (FRP) Reinforcement for Concrete Structures, Sapporo, Japan (1997), Vol. 2, 551-559
- [13] Bertsekas, D.P., Constrained optimization and Lagrange multiplier methods, Academic press (1982)
- [14] Ghorpade, S. and Limaye, B.V., A course in multivariable calculus and analysis, Springer, New York, USA (2010), 346-361

## **DURABILITY OF HEMP FIBRE REINFORCED CEMENTITIOUS MORTARS BY MEANS OF FIBRE PROTECTION AND CEMENT SUBSTITUTION WITH METAKAOLIN**

**Bojan Poletanović<sup>(1)</sup>, Katalin Kopecskó<sup>(2)</sup>, Ildiko Merta<sup>(1)</sup>**

(1) TU Wien, Vienna, Austria

(2) Budapest University of Technology and Economics, Budapest, Hungary

### **Abstract**

The aim of this research was to investigate the influence of protection of hemp fibres (with linseed oil) and of partial substitution of cement in matrix with metakaolin (in mass ratio 10wt% and 15wt%) on the durability of hemp fibre mortars under severe environmental conditions of freeze/thaw cycles. Cementitious mortars reinforced with discrete short hemp fibres (*Cannabis sativa L*) were exposed to accelerated aging of 51 freeze/thaw cycles under laboratory conditions and by mean of the composites compression strength, flexural strength and energy absorption capacity in bending its durability assessed.

The results showed that the fibre protection with linseed oil effectively prevents the degradation of the composite after freeze/thaw cycles in term of its compression- and flexural strength, whereas still a significant loss in flexural toughness occur.

In case of partial substitution of cement with metakaolin the results are more promising, the degradation of the composites compression strength under freeze/thaw cycles was completely prevented. The loss in composites flexural strength was prevented only in case of higher substitution rate of cement with metakaolin (15wt%), whereas its flexural toughness still markedly decreased after freeze/thaw cycles.

### **1. Introduction**

Recently cellulose fibres have been widely used for cementitious materials as fibre reinforcement. Their worldwide availability, biodegradability, low density, favorable mechanical properties make them attractive alternatives to the traditional synthetic fibres [1]. Natural fibres such as hemp, flax, coir, sisal, jute, cotton, bamboo are already proved to positively affect the mechanical properties of cementitious composites, such as their tensile

strain capacity, post-cracking toughness, impact- and abrasion resistance, and crack resistance [2-3]. However, the main challenge in broader application of natural fibre composites is their long term durability. Natural fibres within the alkaline environment of cement matrix are found to undergo degradation caused by two main mechanisms, i.e. alkaline attack and fibre mineralization [4]. As a consequence, cementitious composites reinforced with natural fibres undergo significant reduction in mechanical properties – especially in composites toughness [5,6].

It has been found that matrix modification (decrease of the alkalinity of the matrix by adding pozzolanic materials) [7, 8] and impregnation of fibres prior to addition into the matrix [9, 10] are efficient methods in improving the durability of natural fibres in cementitious composites. The aim of this research was to investigate the influence of fibre protection with linseed oil [10] and of partial cement substitution in matrix with metakaolin (mass ratio of 10wt% and 15wt%) on the durability of hemp fibre mortars under severe environmental conditions of freeze/thaw cycles.

## 2. Materials and experimental procedure

### 2.1. Raw materials and specimens preparation

For fibre reinforcement primary bast hemp fibres (*Cannabis sativa L*) with a diameter of 16–50  $\mu\text{m}$  was used. The tensile strength of fibres is between 300-1100 N/mm<sup>2</sup> according to the literature [1] and their density is 1.5 g/cm<sup>3</sup>. In all fibre reinforced mortar mixtures the length of the fibres was 10 mm and the dosage 1% by volume.

The ratio of cement:sand:water in mortar mix designs was 1:2:0.5 by weight with the size of aggregate 0-4 mm and with cement CEM I 42,5 N. The first mixture referred as “plain mortar” contained no fibres. The second mixture referred as “non treated fibres” contained hemp fibres which were added in water saturated condition to the matrix. The third mixture referred as “oiled fibres” contained impregnated fibres. Prior to the addition of fibres into the matrix, the fibres were immersed in linseed oil for one hour, then slightly squeezed by hand and wiped. The last two mixtures contained hemp fibres and the cement was partially substituted with metakaolin by 10 wt% and 15 wt% respectively. These mixtures are referred as “10% metakaolin” and “15% metakaolin” respectively. The chemical composition of metakaolin used was SiO<sub>2</sub>, 52-54 wt%, Al<sub>2</sub>O<sub>3</sub>, 42-44 wt%, Fe<sub>2</sub>O<sub>3</sub>, < 1wt%, TiO<sub>2</sub>, < 2 wt%, K<sub>2</sub>O < 0.1 wt%.

The mortars were mixed in a laboratory drum-mixer. Specimens with dimensions of 40x40x160 mm<sup>3</sup> were cast and demolded after 24 hours.

### 2.2 Aging condition

The demolded specimens were cured in water for 28 days followed by storage of 3 months in a climate chamber (relative humidity 60% and temperature 20°C) in order to undergo self desiccation. The specimens were exposed to 51 freeze/thaw cycles (FTC) from -20°C to +20°C alternately. The individual freeze (and thaw) cycle lasted 4 hours, which resulted in 17 days of total aging.

### 2.3. Mechanical tests

Three point bending tests (3PBT) and compressive tests were conducted first on specimens at 28 days of age and second after FTC cycles according to the norm ÖNORM EN 1015-11

[11]. The bending tests were done on 6 identical prisms specimens of dimensions 40x40x160 mm<sup>3</sup>. The compressive tests were carried out on one half of the split specimens by applying the compressive force on 40x40 mm<sup>2</sup> area on 3 identical specimens.

The flexural toughness (absorbed energy) of the material was calculated from the force-mid span deflection curve of the 3PBT as the area under the curve till the deflection in post-peak part corresponding to 90% drop of the maximal force.

### 3. Results and Discussion

#### 3.1. Compressive strength

The specimens with oil impregnated fibres and cement substitution showed after FTC no decrease in strength when compared to their counterparts tested at the age of 28 days.

After FTC cycles the specimens with 10 wt% and 15 wt% cement substitution with metakaolin showed 30% and 36% higher compressive strength respectively compared to specimens without metakaolin substitution. The increase could be related to the fact that the fine metakaolin particles fill the pores within the specimens resulting in denser material with higher strength. However, in case if the fibres are impregnated with oil the compression strength of the composite after FTC decrease up to 23%.

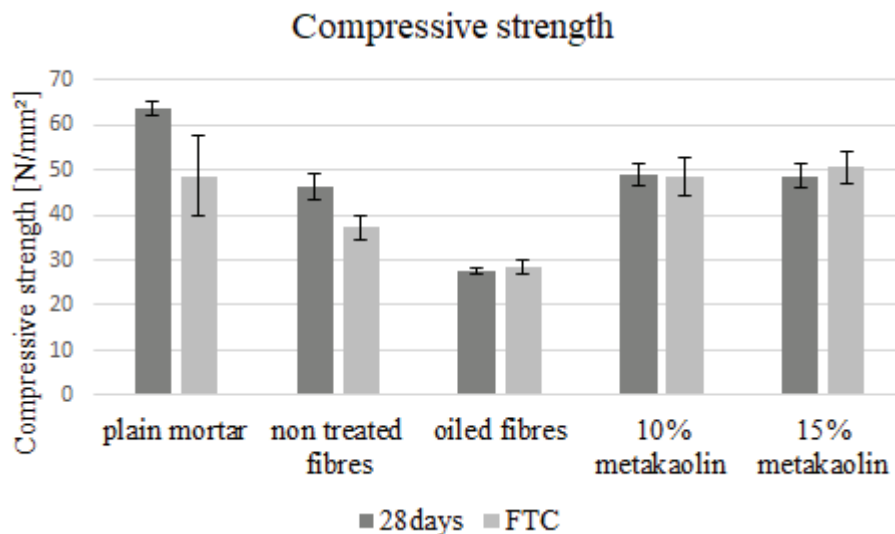


Figure 1. Compressive strength of specimens at the age of 28 days and after freeze-thaw cycles

#### 3.2. Flexural strength

Both the impregnation of fibres and the substitution of cement with 15 wt% metakaolin, efficiently prevented the decrease of the materials flexural strength after FTC when compared to their counterparts tested at the age of 28 days.

The fibres impregnation or cement substitution with metakaolin did not improve the specimens flexural strength after FTC when compared to the specimens with non treated fibres.

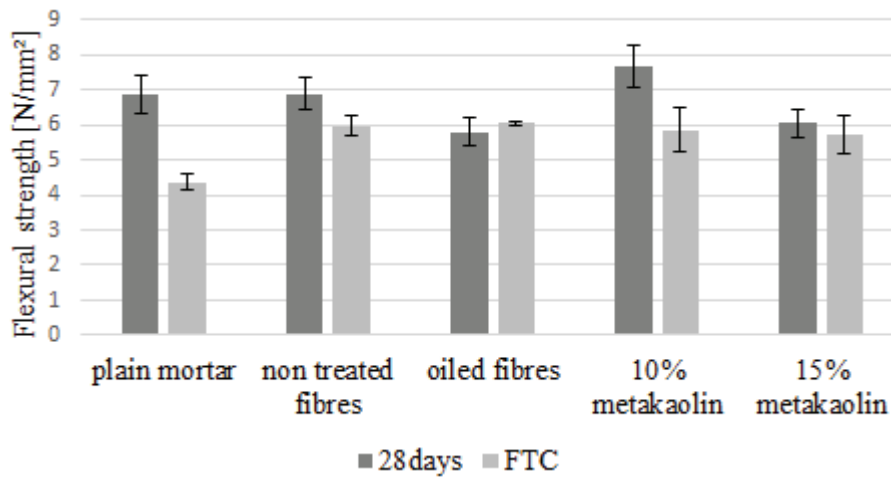


Figure 2. Flexural strength of specimens at the age of 28 days and after freeze-thaw cycles

### 3.3. Flexural toughness

All specimens after FTC showed decrease in flexural toughness compared to their counterparts tested at the age of 28 days. The most significant loss is observed in case of oiled impregnated fibres.

It seems that fibre impregnation with linseed oil is not so effective in preventing the toughness loss of the material after FTC. In contrary, cement substitution with metakaolin significantly improved the flexural toughness after FTC when compared to the specimens with non treated fibres. In case of 10 wt% and 15 wt% cement substitution with metakaolin, the toughness increased up to 61% and 50% respectively.

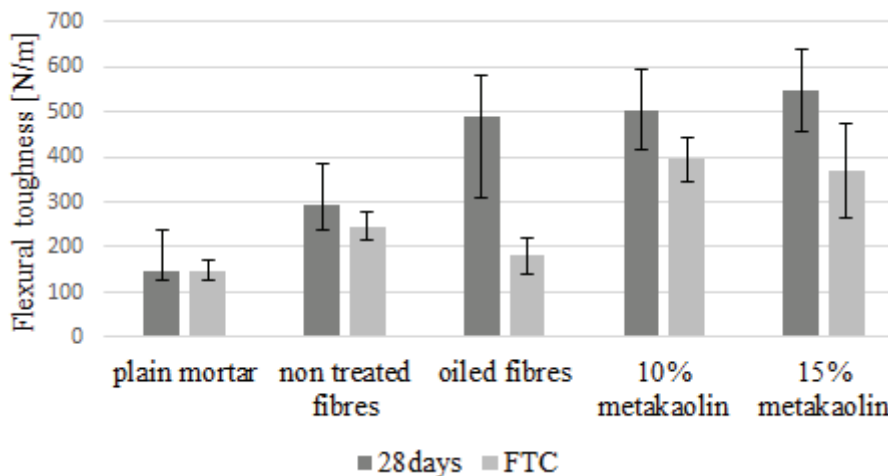


Figure 3. Flexural toughness of specimens at the age of 28 days and after freeze-thaw cycles

## 4. Conclusion

Based on this research it could be concluded that in term of flexural strength of the composite both applied method, the fibre protection with linseed oil and partial substitution of cement with metakaolin, are effective in preventing the degradation after freeze/thaw cycles. Besides,

the fibre protection with linseed oil proved to be effective also in term of compressive strength of the composite after freeze/thaw cycles, whereas in case of the cement substitution only higher substitution rate of cement with metakaolin (15wt%) was effective.

Neither the fibre protection with linseed oil nor partial substitution of cement with metakaolin proved to be effective in term of flexural toughness of the composites after freeze/thaw cycles.

### **Acknowledgement**

The research is supported by the Stiftung Aktion Österreich-Ungarn in the frame of a bilateral research cooperation project Nr. 95öu6, and in the framework of a visiting student fellowship of the first author at the Budapest University of Technology and Economics. Additionally, the second author acknowledges the support by the Hungarian Research Grant NVKP\_16-1-2016-0019 “Development of concrete products with improved resistance to chemical corrosion, fire or freeze-thaw”. The authors greatly acknowledge the support of Meselia Hungária Kft for providing metakaolin for the research.

### **References**

- [1] Yan, L. et al, A review of recent research on the use of cellulosic fibres, their fibre fabric reinforced cementitious, geo-polymer and polymer composites in civil engineering, *Composites Part B* (2016)
- [2] Merta, I. et al, Fracture energy of natural fibre reinforced concrete, *Original Research Article Construction and Building Materials* 40 (2013), 991-997
- [3] Merta I., et al, Fracture Mechanics of Concrete Reinforced With Hemp, Straw and Elephant Grass Fibres, *Composite Materials: Key to the Future, 18th International Conference on Composite Materials, Jeju Island, Korea* (2011)
- [4] Tolêdo Filho, R. et al, Durability of compression molded sisal fiber reinforced mortar laminates, *Constr. Build. Mater.* 23 (2009), 2409–2420
- [5] Merta, I. et al, Influence of natural fibres on mechanical properties and durability of cementitious mortars, *CoMS - 1st International Conference on Construction Materials for Sustainable Future* (2017), 1 - 8
- [6] Wei J., Meyer C., Degradation mechanisms of natural fiber in the matrix of cement composites, *Cement and Concrete Research* 73 (2015), 1-16
- [7] Merta, I. et al, Durability of natural fibres within cement-based materials - Review, *Concrete Structures, Journal of the Hungarian Group of fib* 18 (2017), 10-15
- [8] Silva F., A. et al, Physical and mechanical properties of durable sisal fiber–cement composites. *Constr Build Mater* 24 (2010), 777–785.
- [9] Ferreira S., R., et al, Effect of fiber treatments on the sisal fiber properties and fiber-matrix bond in cement based systems. *Construction and Building Materials* 101 (2015), 730-740
- [10] Merta, I., et al, Durability of hemp fibres in the alkaline environment of cement matrix, *BEFIB2012 - Fibre reinforced concrete* (2012)
- [11] ÖNORM EN 1015-11: 2018 01 01, Methods of test for mortar for masonry - Part 11: Determination of flexural and compressive strength of hardened mortar

## **INFLUENCE OF MICRO-CRACKING ON CAPILLARY WATER ABSORPTION OF AN UHPFRC**

**Ana Mafalda Matos <sup>(1)</sup>, Sandra Nunes <sup>(1)</sup>, José L. Barroso Aguiar <sup>(2)</sup>**

(1) CONSTRUCT-LABEST, Faculty of Engineering, University of Porto, Portugal

(2) University of Minho, School of Engineering, Guimarães, Portugal

### **Abstract**

The aim of this research was to investigate the influence of cracking on water transport by capillary suction in UHPFRC. Specimens were firstly pre-loaded under four-point bending up to a wide range of pre-defined crack open displacement. Crack pattern created was characterized (width, number of cracks) before capillarity testing. Test results showed that micro cracks induced by previous loading significantly increased the sorptivity comparing with non-cracked specimens. However, increasing the damage (COD of 200 up to 400  $\mu\text{m}$ ), did not significantly compromise the absorption capillary suction of UHPFRC, as compared to good quality conventional concrete or engineered cementitious composites (ECC).

### **1. Research Scope**

The emergence of Ultra-High Performance Fibre Reinforced Cement-based Composites (UHPFRC) provided the structural engineer with an unique combination of extremely low permeability and very high strength, namely, compressive strength higher than 150 MPa, tensile strength over 7 MPa and with considerable tensile strain-hardening behaviour (multiple micro-cracking formation stage). A promising field of application is the rehabilitation and/or strengthening of reinforced concrete structures, in which a new layer of UHPFRC replaces the deteriorated concrete (cracked, carbonated, chloride attack, etc.). The combination of the UHPFRC as protective layer, which can be reinforced, provides a simple and efficient way of increasing the durability (prolonging the service life), the stiffness and structural resistance capacity while keeping compact cross sections [1], [2], [3].

In those applications, UHPFRC is exposed to severe environmental conditions (as de-icing salts, marine environment, chemical attack) and/or high mechanical loading (e.g. concentrated forces, wear, fatigue, impact) for extended periods. Under applied loads in service conditions,

a progressive multiple micro-cracking is achieved in UHPFRC due to the addition of a significant amount of short steel fibres. Higher number and finer cracks generally characterize the crack pattern of UHPFRC, which might affect the transport mechanisms rates. The water transport through cracked UHPFRC is possibly driven by pressure gradient water permeation or capillary absorption. Very fine cracks can be quickly filled by water due to capillary action, thus the structural element is not protected against aggressive aqueous solutions. Since resistance to water penetration may be considered as a criterion for durability of cementitious-based materials, an investigation on the influence of cracking on transport properties of water is necessary.

In order to improve knowledge on water transport by capillary action in UHPFRC, a research was launched to study the absorption of UHPFRC submitted to pre-defined deformations. The objective was to assess admissible deformations for which the material presents satisfactory transport properties and to evaluate the existence of correlation between certain crack pattern parameters and water absorption by capillary.

## 2. Experimental program

### 2.1 UHPFRC tested mixtures

Materials used to prepare UHPFRC in this study were: Type I 42.5R Portland cement, dry micro silica fume, limestone filler, siliceous sand, a polycarboxylate type superplasticizer and short steel fibres ( $\phi_f=21\text{mm}$ ;  $l_f=13\text{mm}$ ;  $f_{yk}=2750\text{MPa}$ ). In addition, a waste generated by the Portuguese oil refinery industry, the spent equilibrium catalyst (ECat) was introduced in the matrix as partial aggregate replacement. UHPFRC mixture compositions, incorporating 1.5% and 3.0% of steel fibres (in volume), are presented in Figure 1. The UHPFRC self compactability was assessed using the mini-slump flow test [4] ( $D_{\text{flow}}$ ). After the fresh state test, several prismatic (40x40x160 mm) specimens were casted following the procedure prescribed by the standard NP EN 196-1 [5] except the compaction step. In addition, cube specimens (50mm) were casted to assess compressive strength. All specimens were demoulded in the following day and then wet cured in controlled environment chamber at  $20\pm 2$  °C and  $\text{HR}\geq 95\%$ . At 28 days, four-point bending and compressive strength were assessed, as well as, several cracking levels were induced in the prismatic specimens. Main fresh and hardened properties of UHPFRC mixtures are listed in Table 1.

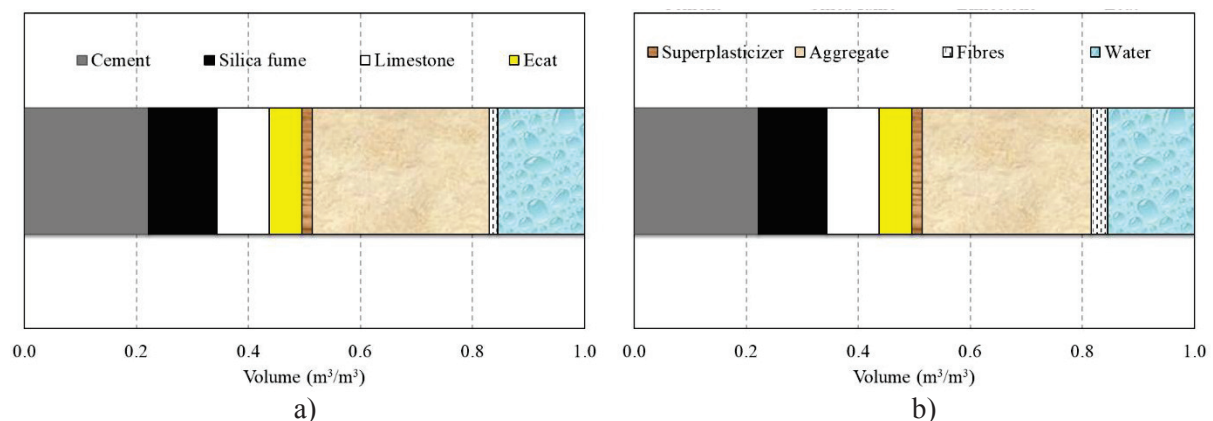


Figure 1 – Mixture composition of UHPFRC with a) 1.5% and b) 3.0% fibres content.



## 2.2 Specimens cracking methodology

UHPFRC specimens were pre-cracked by imposing different crack open displacements (COD) between 200 and 400 $\mu\text{m}$ , in steps of 50  $\mu\text{m}$ , to obtain different crack patterns. Predefined COD, were produced through four-point bending loading where the loading span is 1/3 of the support span. The test was performed as displacement-controlled (displacement rate = 0.003 mm/s) and carried out by means of a 300 kN Instron testing machine. Two LVDTs were fixed on each sides of the specimen, perpendicular to loading direction, to monitor the COD. When the target COD was achieved, the specimen was unloaded and the residual COD was recorded. Load-displacement curves obtained during cracking procedure are presented in Figure 2, along with the complete load-displacement curves obtained when the test was conducted until the end (grey lines). For each mixture, non-cracked prisms were also tested for control purposes. As it can be observed from Figure 2, some specimens reached the peak load, in which a macro crack develops (approximately between COD 300-400 micron).

Table 1 – Main fresh and hardened properties of tested UHPFRCs mixtures

		UHPFRC-1.5%	UHPFRC-3%
$D_{\text{flow}}$	[mm]	302	283
Final setting time (NP EN 196-3)	[hh:mm]	02:00	02:00
Compressive strength (ASTM C109/C109M)	7 days [MPa]	104 $\pm$ 5.1	118 $\pm$ 2.6
	28 days [MPa]	121 $\pm$ 4.4	147 $\pm$ 2.3
Flexure Strength (4-point bending) (prisms 40x40x160 mm)	28 days [MPa]	23 $\pm$ 2.5	36 $\pm$ 1.6

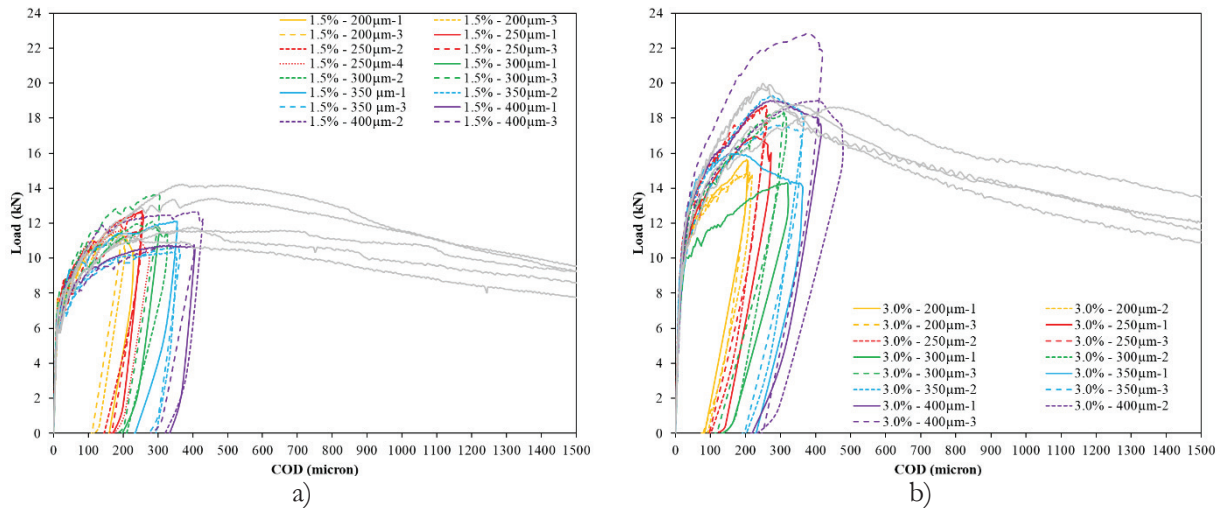


Figure 2 – Obtained load-displacement curves in four-point bending test: a) UHPFRC 1.5%; b) UHPFRC 3%.

## 2.3 Characterization of the crack pattern produced by bending

For each specimen a mesh was drawn in the zone of maximum tension strain (in between the two applied forces) (Fig. 3-a). After imposing the target COD, a 40 $\times$ 40 $\times$ 40 mm<sup>3</sup> cube was cut

from the central portion of each beam specimen. The widths of cracks observed in the tension face of each specimen were measured using a Microscope Multizoom Nikon AZ100 in the unloaded state. Measurements were taken from cracks crossing the three lines A, B and C, as shown in Figure 3.

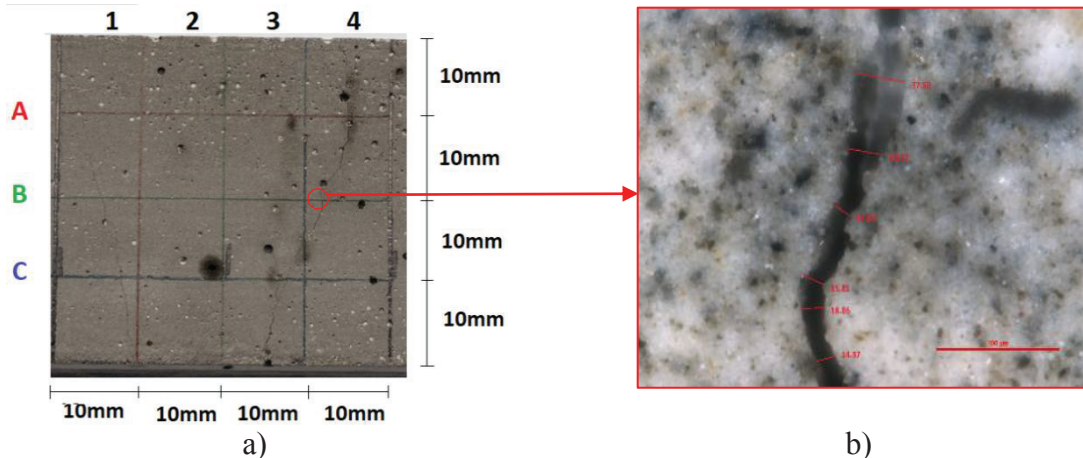


Figure 3 – a) Scheme for measuring of the crack number and widths; b) Typical photo made from a measurement.

### 2.3 Capillary water absorption test

The sorptivity test was carried out according to RILEM TC 116-PCD [6] and it was undertaken on cubic specimens (40 mm), after curing for 28 days plus 12 days drying in an oven at 40°C, until constant mass was achieved. The absorption of water under capillary action is dependent on the square-root of time and may be modelled [7] following Equation 1, where  $A$  ( $\text{mg}/\text{mm}^2$ ) is the water absorption by unit area of a specimen surface since the moment the specimen was dipped in water,  $S$  is the sorptivity of the material ( $\text{mg}/(\text{mm}^2 \cdot \text{min}^{0.5})$ ),  $t$  is the elapsed time (minutes) and  $A_0$  ( $\text{mg}/\text{mm}^2$ ) is the water absorbed initially by pores in contact with water. The slope of the obtained line defines the sorptivity of the specimen during the initial four hours of testing. For all specimens (cracked and uncracked), this slope is obtained by using linear regression analysis of the plot of the rate of absorption versus the square root of time. Equation (1) was found to provide a very good fit to the data with correlation coefficients of over 0.96.

$$A = A_0 + S \times t^{0.5} \quad (1)$$

## 3. Results and Discussion

Figure 4-a illustrates the relationships between the COD before unloading the specimen ( $\text{COD}_{\text{load}}$ ) and COD after unloading ( $\text{COD}_{\text{res}}$ ). The  $\text{COD}_{\text{res}}$  increases nearly linearly with the  $\text{COD}_{\text{load}}$ , representing the higher level of damage. Generally, the  $\text{COD}_{\text{res}}$  values decrease when the dosage of steel fibres increases under the equivalent damage, since the cracking severity is reduced by the higher dosage of steel fibres.

The relation between sorptivity values and  $\text{COD}_{\text{res}}$  is depicted in Figure 4-b, including non-cracked specimens. The sorptivity of control specimens was 17.8 and 7.6 ( $\text{mg}/(\text{mm}^2 \cdot \text{min}^{0.5}) \times 10^{-3}$ ) for 1.5% and 3% fibres content, respectively. These results are

corroborated with previous research works [8], [9], [10], [11] also illustrated in Figure 4-b. When compared to good quality conventional concrete ( $w/c=0.40$ ), exhibiting sorptivity above  $0.09 \text{ (mm/min}^{0.5}\text{)}$  [12], or even with sorptivity of engineered cementitious composite (ECC) with indicative values around  $0.028 \text{ (mm/min}^{0.5}\text{)}$  [13], UHPFRC presented a very low water absorption in a non-damage state. This may be attributed to the very low water content, the absence of coarse aggregates and the dense cementitious matrix that provide a significantly lower capillary porosity and thus capillary sorption capacity of UHPFRC.

The main mechanisms responsible for fluid transport during the absorption test are hydrostatic pressure due to the gravity effect and capillary suction. Since the test was performed at atmospheric pressure, the key mechanism in this study was the suction. The effect of crack width on capillary absorption is reversed compared to permeability under pressure gradients: finer cracks lead to higher capillary absorption. When the first target COD ( $200\mu\text{m}$ ) is achieved, it corresponds to a multiple cracking stage with cracks below  $80\mu\text{m}$  and  $10\mu\text{m}$  for 1.5% and 3% fibres content, respectively. For these cases, the sorptivity value increased 60% and 300% compared to non-cracked specimens. By increasing the damage, the number of cracks and the crack widths increased with no substantial effect on sorptivity, even when a macro crack develops for target CODs of  $350$  and  $400 \mu\text{m}$ . Therefore, the measured sorptivity for the cracked UHPFRC specimens ( $< 44 \times 10^{-3} \text{ mg}/(\text{mm}^2 \cdot \text{min}^{0.5})$ ) was not particularly high when compared to that of conventional concrete. Moreover, the sorptivity values of cracked UHPFRC specimens presented in Figure 4-b possibly represent an upper limit of sorptivity in actual structures or elements, since the effect of self-healing was not considered due to the short experiment duration. These features provide UHPFRC with distinct barrier qualities proving that even when cracked it can act as protective layer increasing the durability (and service life) in the rehabilitation of structures or elements.

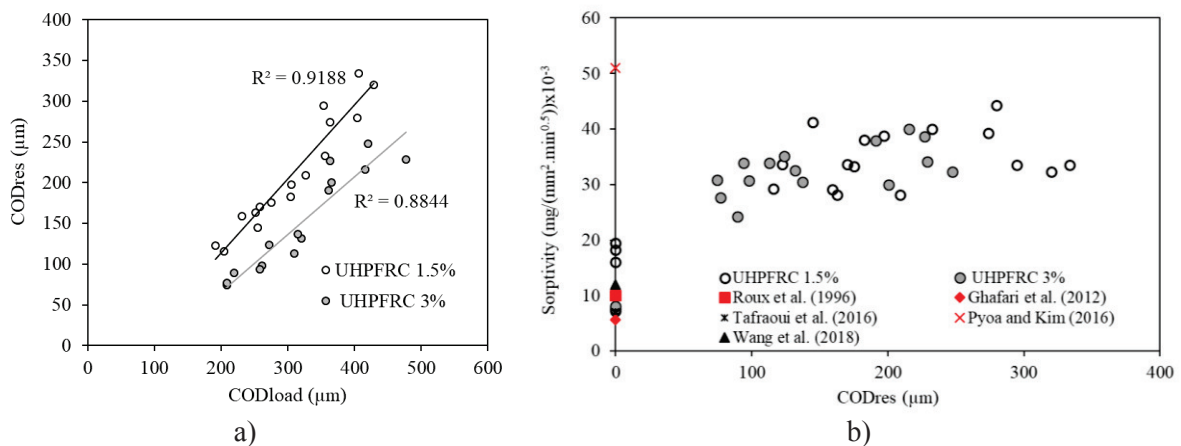


Figure 4 – a)  $\text{COD}_{\text{load}}$  and  $\text{COD}_{\text{res}}$ ; b) Sorptivity of UHPFRCs as a function of  $\text{COD}_{\text{res}}$ .

#### 4. Conclusion

The results revealed that the very low water content in addition with no coarse aggregate and a dense cementitious matrix provided extremely low sorptivity to non-cracked UHPFRC. Even though UHPFRC cracking increased the sorptivity results, the capillary absorption is still very low when compared to conventional concrete. This feature provides UHPFRC with distinct barrier qualities, which can be beneficial for rehabilitation applications, proving an

improved durability, as well as, increased service life of structures or elements. The influence of cracking patterns on other durability indicators, such as, resistance to chlorides ingress is also under evaluation within the current PhD project.

### Acknowledgments

This work was financially supported by: Project POCI-01-0145-FEDER-007457 - CONSTRUCT - Institute of R&D In Structures and Construction and by project POCI-01-0145-FEDER-007633 (ISISE) funded by FEDER funds through COMPETE2020 - Programa Operacional Competitividade e Internacionalização (POCI) – and by national funds through FCT - Fundação para a Ciência e a Tecnologia through the PhD scholarship PD/BD/113636/2015, attributed within the Doctoral Program in Eco-Efficient Construction and Rehabilitation (EcoCoRe). Acknowledgements are also due to Secil, EUROMODAL, Omya-Comital, Dramix and Sika for supplying constituent materials.

### References

- [1] B. A. Tayeh, B. H. A. Bakar, M. A. M. Johari, and Y. L. Voo, “Utilization of Ultra-high Performance Fibre Concrete (UHPFC) for Rehabilitation – A Review,” *Procedia Eng.*, vol. 54, pp. 525–538, 2013.
- [2] Emmanuel Denarié and Eugen Brühwiler, “Cast-on site UHPFRC for improvement of existing structures – achievements over the last 10 years in practice and research,” in *HPFRCC7: 7th workshop on High Performance Fiber Reinforced Cement Composites*, 2015.
- [3] M. Bastien-Masse and E. Brühwiler, “Ultra high performance fiber reinforced concrete for strengthening and protecting bridge deck slabs,” in *7th International Conference on Bridge Maintenance, Safety and Management (IABMAS)*, 2014, pp. 2176–2182.
- [4] H. Okamura, K. Ozawa, and M. Ouchi, “Self-compacting concrete,” *Struct. Concr.*, vol. 1, no. 1, pp. 3–17, Mar. 2000.
- [5] Instituto Português da Qualidade, “NP EN 196-1. Methods of testing cement. Part 1: Determination of strength.” IPQ, Lisbon, pp. 1–37, 2006.
- [6] RILEM, “RILEM TC 116-PCD: Permeability of concrete as a criterion of its durability,” *Mater. Struct.*, vol. April, pp. 174–179, 2008.
- [7] C. Hall, “Water sorptivity of mortars and concretes: a review,” *Mag. Concr. Res.*, vol. 41, no. 147, pp. 51–61, Jun. 1989.
- [8] N. Roux, C. Andrade, and M. A. Sanjuan, “Experimental study of durability of reactive powder concretes,” *J. Mater. Civ. Eng.*, vol. 8, no. 1, pp. 1–6, 1996.
- [9] A. Tafroui, G. Escadeillas, and T. Vidal, “Durability of the Ultra High Performances Concrete containing metakaolin,” *Constr. Build. Mater.*, vol. 112, pp. 980–987, Jun. 2016.
- [10] S. Pyo and H.-K. Kim, “Fresh and hardened properties of ultra-high performance concrete incorporating coal bottom ash and slag powder,” *Constr. Build. Mater.*, vol. 131, pp. 459–466, Jan. 2017.
- [11] Y. Chen, R. Yu, X. Wang, J. Chen, and Z. Shui, “Evaluation and optimization of Ultra-High Performance Concrete (UHPC) subjected to harsh ocean environment: Towards an application of Layered Double Hydroxides (LDHs),” *Constr. Build. Mater.*, vol. 177, pp. 51–62, Jul. 2018.
- [12] A. M. Neville, *Properties of concrete*, Fifth. Longman Group Limited, 2011.
- [13] H. Liu, Q. Zhang, C. Gu, H. Su, and V. C. Li, “Influence of micro-cracking on the permeability of engineered cementitious composites,” *Cem. Concr. Compos.*, vol. 72, pp. 104–113, 2016.

## **INFLUENCE OF THE ALKALINE TREATMENT ON THE TENSILE PROPERTIES OF JUTE FIBERS AND ON THE FIBER-MATRIX BONDING**

**Yasmim Gabriela dos Santos Mendonça <sup>(1)</sup>, Bartosz Zukowski <sup>(1)</sup>, Romildo Dias Toledo Filho <sup>(1)</sup>**

(1) Federal University of Rio de Janeiro, Brazil

### **Abstract**

This work presents the influence of alkaline treatment on the fiber tensile properties and cementitious matrix bond for jute fibers. The reference group of fibers was washed for 3 hours in water at 80 °C, then cooled at 40 °C for 5 hours. This process was applied to remove residues and impurities from the fiber's surface. The group of alkaline treated fibers, after washing and cooling, was additionally submerged in a saturated solution of calcium hydroxide, Ca(OH)<sub>2</sub> for 50 minutes. Both groups were dried for 24 hours at 40 °C. The tensile stress-strain behavior of the fibers was determined for the two groups at a microforce testing system using the gage length of 20 mm. The cross-sectional area of the fiber was measured using scanning electron microscope (SEM) micrographs and image analysis. The Young's modulus, force at rupture, maximum stress and strain were calculated from the collected data to evaluate the influence of alkaline treatment on fiber's tensile properties. Pullout tests for embedment length of 7 mm were realized to evaluate the effect of the alkaline treatment on the fiber-matrix bond. The alkaline treatment improved the mechanical behavior of the jute fibers and the fiber-matrix bond.

### **1. Introduction**

The mechanical properties of natural fibers present a lot of variation and depend on some factors: diameter of the fiber, the degree of polymerization, crystalline structure, origin (stem, leaf, fruit, and seed) and growth conditions [1]. The area of jute is smaller than the area of some other fibers as sisal or curauá. The tensile strength of the jute (249 MPa) is less than curauá (543 MPa) and sisal (484 MPa), but Young's modulus is not so distant from it, 43,9, 19,5 and 63,7 GPa to jute, sisal and curauá, respectively [2]. The physical and mechanical

properties of the fibers are influenced by their composition, mainly cellulose, hemicelluloses, and lignin. Fiber treatments can promote a better interaction between lignin, cellulose, and hemicellulose, resulting in a stronger fiber, with a higher crystallinity and modulus. The natural fibers tensile strength increase with the application of hornification treatments, because of the change in the cellulose crystallinity and possible bonds created between different polymer chains in the microfibrils. Alkaline treatment promotes changing in cellulose chemical bonds, as well as the reduction of fiber-water absorption capacity. The jute is the fiber that presents a higher interaction with the calcium hydroxide. Jute contains cellulose of high crystallinity, which collaborates well with  $\text{Ca}(\text{OH})_2$  [3]. It is reported in the literature that the alkaline treatment improved the interaction between jute fibers and cementitious matrix, providing a better frictional phase [3]. This work presents the results of the study of stress-strain behavior and the fiber-matrix bond of alkaline treated jute fibers.

## 2. Materials and methods

### 2.1 Jute fiber and treatment applied

The jute fiber is extracted from the plant stem in a process based on the following steps: cutting, hardening, crushing, drying and classification [2]. The jute from Amazon region is combed and then cut in a guillotine. The chemical composition of jute fiber was verified on two sets of samples at the COPPE/UFRJ by calorimetric determination of hexuronic acids. The percentage values showed the amount of cellulose 74.4%, hemicellulose 15.0%, lignin 8.4%. The fibers were first washed in water at 80 °C for 3 hours to remove residues and impurities. Then they were cooled at 40 °C for 5 hours. After the washing process, the fibers were separated into two groups, namely untreated and alkaline. The untreated group was not submitted for treatment and for this reason this group was considered the reference group. The alkaline group was submerged in a saturated solution of  $\text{Ca}(\text{OH})_2$  with water for 50 minutes, and then dried for 24 hours at the temperature of 40 °C.

### 2.2 Fiber microstructural analysis

The fiber's microstructure was investigated using a SEM (TM 3000) at 25kV of accelerating voltage. The images obtained were processed using the software package ImageJ for measuring the cross-section of each fiber.

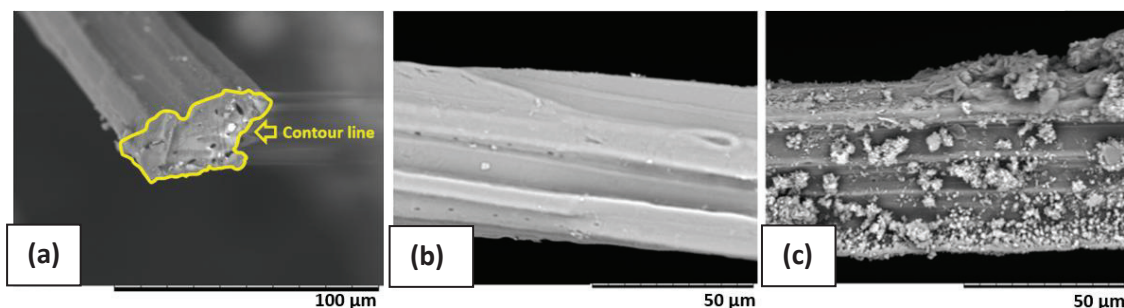


Figure 1: Micrographs of jute fibers at SEM: (a) area calculation using ImageJ, (b) surface of untreated jute fiber, (c) surface of alkaline treated jute fiber.

A contour line was interactively drawn to delineate the fiber's cross-section and then the area was measured, as illustrate the Fig.1. The visual analysis of fiber surface was carried at SEM. The fibers were covered with an approximately 20 nm layer of gold before the visual investigation under the microscope.

### 2.3 Fiber tensile test

The jute fibers were investigated at the gage length of 20 mm. The groups untreated and alkaline were tested. Before the test fibers were dried for 24 hours at 40 °C. The preparation of the test was performed according to ASTM C1557 [4]. The tensile tests were performed in a microforce testing machine Tytron 250 (Fig.2) at the strain rate of 0.4 mm/min.

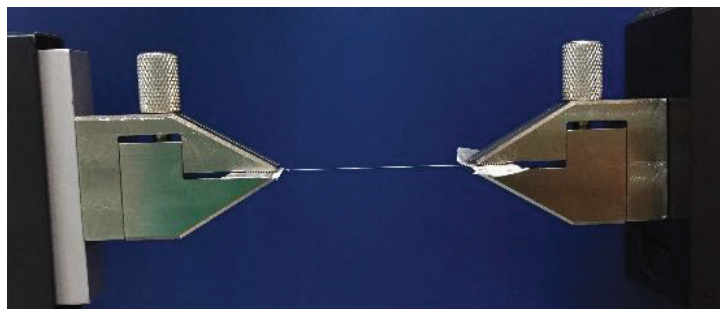


Figure 2: Setup of the tensile according to ASTM C1557 with the detail of clamps and specimen.

### 2.4 Cementitious matrix composition

The cement matrix was produced with 33% of cement Portland CPII F-32, 27% of metakaolin, 40% of fly ash, sand with maximum diameter of 250  $\mu\text{m}$ , water, superplasticiser Glenium 51, and viscosity agent, in a proportion of 1:0.5:0.4 (cementitious materials: sand: water/cementitious materials). The high dosage of fly ash is justified because of the mechanical behaviour and high deformation capacity [5].

### 2.5 Fiber-matrix bond

Verification of the fiber-matrix interface was performed through pull-out tests. To ensure an adequate coating of the fiber in the matrix, PVC molds were used. The PVC mold is a tube with a depth of 7 mm corresponding to the fiber embedment length and 25 mm of diameter. The Fig.3a shows the sequence of pull-out specimen preparation.

The matrix was poured inside the PVC mold, and the paper tape closed the specimen providing the straight and central position of the fiber in the mold. After 27 days of curing in a room of 100% RH and  $21^\circ\text{C} \pm 1^\circ\text{C}$  additional 1 day of drying at  $23^\circ\text{C} \pm 1^\circ\text{C}$ , to provide conditions similar to composite's curing, the fibers were tested to verify pull-out behavior in microforce machine Tytron 250 at the strain rate of 0.4 mm/min with 50 N load cell.

The pull-out test starts with the tube placed in the iron ring and clenched by screws to prevent specimen's movement during the test. The fiber is pulled out from the specimen and the data of force and displacement are collected by Tytron 250 (Fig.3b). Then the collected data was analyzed according to the modified model of Lin [6] adapted to the vegetal fiber using the perimeter and the area of the surface calculated in ImageJ. According to this model, the values

of chemical debonding energy ( $G_d$ ) and the maximum bond strength ( $\tau_{max}$ ) were calculated (Eq. (1) and Eq. (2)).

$$G_d = \frac{(P_a - P_b)^2}{2E_f A_f Perimeter} \quad (1)$$

$$\tau_{max} = \frac{P_{max}}{l_f Perimeter} \quad (2)$$

where  $P_a$  is the peak load of single fiber pullout curve,  $P_b$  is the load after sudden drop following  $P_a$ ,  $E_f$  is the fiber modulus of elasticity,  $A_f$  is the fiber area measured in ImageJ software,  $Perimeter$  is the perimeter measured in the same software,  $P_{max}$  is the maximum force in the frictional region, and  $l_f$  is the embedment length.

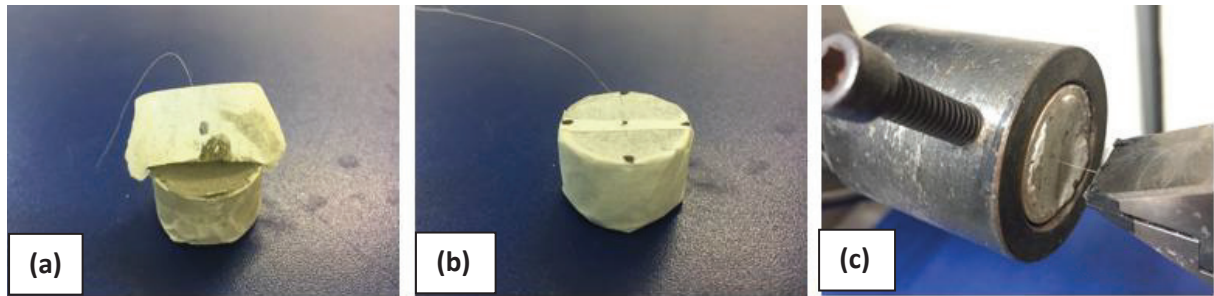


Figure 3: Pull-out test: (a), (b) specimens preparation, (c) completed test.

### 3. Results and discussion

In the Tab.1 and in the Fig. 4 are presented the results of the tensile test of jute fibers for the two groups (untreated and alkaline). It is possible to note that the alkaline treatment reduced the area of the fibers in comparison to the untreated group, and the treated fibers presented higher tensile strength values than untreated fibers. Moreover, the alkaline treatment increased the value of the elastic modulus. The untreated jute fiber ruptured at 0.89 N (0.35) when the alkaline treated fibers ruptured at 1.37 N (0.15). The higher value of force at rupture of treated fibers was followed by the higher tensile strength 689.77 MPa (74.80) versus 244.34 MPa (95.20) for untreated fiber. The increased value of strength was also a result of the area difference 3660  $\mu\text{m}^2$  (57) for untreated fibers versus 1990  $\mu\text{m}^2$  (50) for alkaline treated fibers. The pullout tests (Tab.2 and Fig.05) provided information on the fiber-matrix bond for untreated and alkaline treated jute fibers. The debonding force ( $P_a$ ), the force required to disconnect the fiber from the matrix and begin the frictional phase was higher after alkaline treatment 0.92 N (0.34) versus 0.85 N (0.08) for untreated fiber suggesting the higher chemical fiber-matrix bond. The latter is confirmed by the higher chemical bond energy needed to disconnect the fiber from the matrix ( $G_d$ ), 13.31  $\text{J/m}^2$  (3.45) for alkaline treated fiber versus 6.88  $\text{J/m}^2$  (0.56) for untreated fiber. The alkaline treatment improved the frictional phase of fiber-matrix interaction, which is visible by the maximum frictional bond strength 0.47 MPa (0.10) for treated fiber versus 0.44 MPa (0.05) for untreated fiber.



Table 1: Summary of average tensile test results and standard deviation for untreated jute fibers and alkaline jute fibers.

Jute fiber	N° of specimens	Area ( $\mu\text{m}^2$ )	Diameter ( $\mu\text{m}$ )		Strain to failure (%)	Force at rupture (N)	Tensile strength (MPa)	Young's modulus (GPa)
			Major	Minor				
Untreated	11	3660 (570)	95.32 (20.31)	50.01 (9.31)	1.06 (0.40)	0.89 (0.35)	244.34 (95.20)	22.17 (7.89)
Alkaline	7	1990 (500)	74.52 (14.72)	34.87 (10.97)	2.06 (0.77)	1.37 (0.15)	689.77 (74.80)	35.94 (10.83)

\*Parenthesis number: standard deviation.

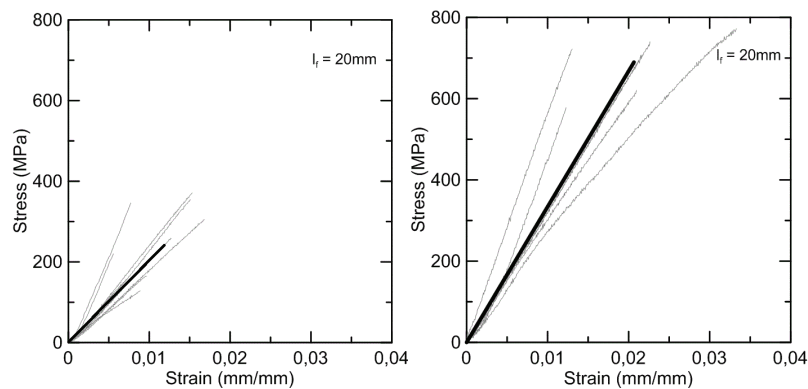


Figure 4: Tensile test results for untreated jute fibers (left) and for alkaline jute fibers (right).

Table 2: Summary of the results of pullout test for untreated jute fibers and alkaline jute fibers.

Jute fiber	$l_f$ (mm)	Area ( $\mu\text{m}^2$ )	Perimeter ( $\mu\text{m}$ )	$P_a$ (N)	$P_b$ (N)	$P_{m\acute{a}x}$ (N)	$G_d$ ( $\text{J}/\text{m}^2$ )	$\tau_{max}$ (MPa)
Untreated	7	4401 (248)	290 (35.61)	0.85 (0.08)	0.44 (0.10)	0.89 (0.05)	6.88 (0.56)	0.44 (0.05)
Alkaline	7	4391 (1067)	280 (46.92)	0.92 (0.34)	0.50 (0.17)	0.93 (0.33)	13.31 (3.45)	0.47 (0.45)

\*Parenthesis number: standard deviation.

The treatment applied to the jute fibers was effective to promote a better interaction between the fiber and the matrix, improving the frictional phase. After the treatment, the modified fiber surface promotes a better chemical and mechanical adhesion improving the interaction, giving it a frictional phase promoted by the surface products.

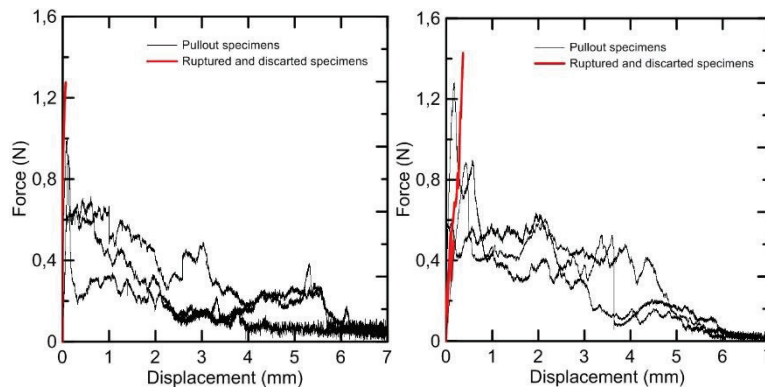


Figure 5: Pullout test results for untreated jute fibers (left) and for alkaline jute fibers (right).

#### 4. Main conclusions

From the results, the alkaline treatment improved the mechanical properties of the fibers, and this can be because of the removal of non-cellulosic materials and impurities that distributed in the interfibrillar region of the fibers. After treatment alkaline, as the fibers become more capable of rearranging over the tensile arrows, since the region is interfibrillar is less dense and all rigid due to removal of hemicellulose. The results presented in this work encouraging the application encouraging their application as a reinforcement in cement-based composites.

#### References

- [1] Thomas, S., Paul, S. A., Pothan, L. A., Deepa, B., "Natural Fibres: Structure, Properties and Applications", in *Cellulose Fibers: Bio and Nano Polymer Composites – Green Chemistry and Technology*. Springer-Verlag. Edited by Kalia, S., Kaith, B. S., Kaur, I, (2011).
- [2] Fidelis, M.E.A., *Desenvolvimento e Caracterização Mecânica de Compósitos Cimentícios Têxteis Reforçados com Fibras de Juta*. PhD thesis, Federal University of Rio de Janeiro, (2014).
- [3] Ferreira, S.R, *Effect of surface treatments on the structure, mechanical, durability and bond behavior of vegetable fibers for cementitious composites*. PhD thesis, Federal University of Rio de Janeiro, (2016).
- [4] ASTM.C1557 /2014 - Standard Test Method for Tensile Sntrength and Young's Modulus of Fibers. West Conshohocken, PA, USA: American Society for Testing and Materials.
- [5] Wang, S., Li, V. C., "Engineered Cementitious Composites with High-volume Fly Ash", *ACI Materials Journal*, Vol. 104, N° 3, pp. 233-241, 2007.
- [6] Lin, Z., T. Kanda, and Victor C. Li. "On Interface Property Characterization and Performance of Fiber Reinforced Cementitious Composites." *Concrete Science and Engineering 1*: (1999), 173–184.

## NUMERICAL SIMULATION OF REINFORCED CONCRETE CUT-OFF WALL WITH STEEL FIBERS UNDER DAM

Homa Kazemi <sup>(1)</sup>, Mohammad Mahdi Kioumarsi <sup>(2)</sup>, Mohsen Zarghani <sup>(3)</sup>, Hamed Sarkardeh <sup>(4)</sup>

(1) Taha Institute of Higher Education, Tehran, Iran

(2) Oslo Metropolitan University, Oslo, Norway

(3) Iran University of Science and Technology, Tehran, Iran

(4) Hakim Sabzevari University, Sabzevar, Iran

### Abstract

One of the main components of dams is the cut-off wall, which any damage to this concrete structure could encounter the dam with danger. Flexural behavior of concrete is an important factor in view of creating and growing cracks in the cut-off wall. Few researches have been done on properties and application of fibers in the cut-off walls, but the advantages of using this type of concrete in other hydraulic structures have been proved. In the present research, numerical simulation of a reinforced concrete cut-off wall with steel fibers was performed and its behavior under hydrostatic and earthquake loads were studied using Finite Element Method (FEM). Results showed that by increasing the volume of fibers, the fracture strain of the cut-off wall becomes larger and more energy was absorbed. It can be concluded that using fibers in the concrete cut-off wall improve its flexural behavior.

### 1. Introduction

The stored water behind the dam is always looking for a way to escape because of its high potential, and therefore penetrates into the porous mass of foundation and bodies of earth dams and leaks to the downstream [1]. One of the most important points in the design and construction of earth dams is the leakage of the body and foundation of the dam [2]. Therefore, evaluation of methods for controlling or reducing water leakage in earth dams is necessary [3]. In the recent years, the concrete cut-off wall, which is one of the anti-seepage structures, has been widely used in the reinforcement of dam projects. For the earth-rock dams where the covering layer of the dam foundation was not thick, the closed cut-off wall

was usually built in the dam, and directly embedded in the rock, usually extends deeply underground and affected by the surrounding formation and the construction process, so its own stress state is very complex [4,5]. Dopant performed tests on 28 beams with the actual size and examined the load-deflection values of the beam by changing the volumetric ratio of the fiber [6]. Pine et al. [7] also considered 1-2% volumetric percentage of fiber as the most suitable amount of fiber to achieve the best mechanical properties of concrete, which is almost confirmed by other researchers. Olivito and Zocarolo indicated that increasing the volumetric percentages and the length of the steel fibers increases the ductility and durability of the concrete [8]. Johnston and Zamap examined the effect of length to diameter ratio and fiber type on fatigue strength under flexural loading [9]. Researches on the concrete structures were recently focused on effect of using fibers and other additives [10-14]. In the present study, effect of using fibers in concrete cut-off wall on its behavior was compared the plain concrete cut-off wall in the dam using a numerical model.

## 2. Materials and Methods

The dimensions of this wall are 70×50×5 m in y, z and x directions, respectively. All simulations were performed in three dimensional (3D) and ductile form. The Abaqus software was used based on Finite Element Method (FEM). Geometry, mesh and boundary conditions of arches are shown in Figure 1. Cell size is considered cubic as 1×1×1 m in the model regarding the mesh sensitivity analysis. To assign boundary conditions, the cut-off wall bases were considered fixed with zero displacement in three directions.

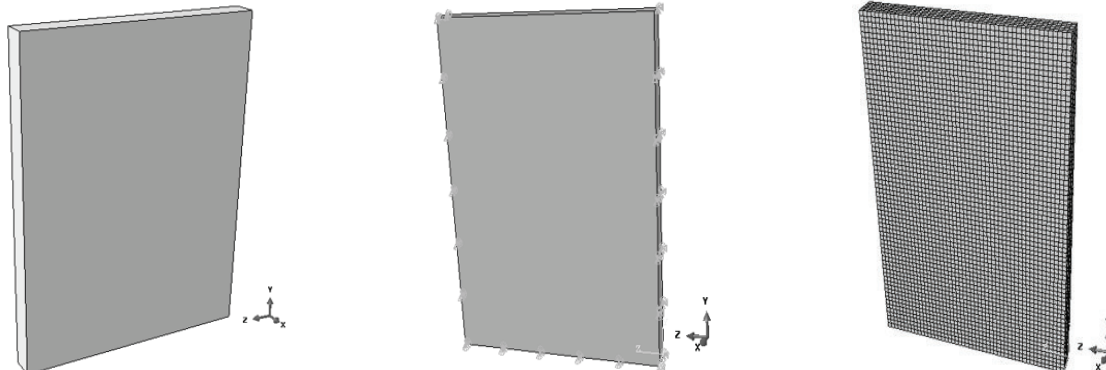


Figure 1: Geometry, mesh and boundary conditions.

To verify the numerical model, results of research by Ben Cardiou et al. on cylindrical and cubic samples of plain concrete and reinforced concrete with steel fibers and fiber content of 1%, 1.6% and 3% were used. Physical characterizes were used according Table 1 [15].

Table 1: Properties of steel fiber and concrete

	Portland cement of ASTM type I	aggregate	silica fume	superplasticizer	steel fibers (length of 22 mm)
Density (g/cm <sup>3</sup> )	3.15	2.65	2.2	1.15	7.85

The hydrostatic pressure load in collaboration with equal soil load on both sides of the cut-off wall which counterbalances each other were considered. The amount of applied load on the structure as a hydrostatic pressure is equivalent to a water pressure to an altitude of 50 m. Moreover, the cut-off wall with the same dimensions and the same volume of fiber was simulated under dynamic load of a recorded earthquake of Tabas as a significant earthquake. Using SAP software the 5% attenuation spectrum response was determined. After that, the response spectra were combined using a root sum square method. Moreover, a single combined spectrum was also constructed which was then compared at the next stage in the range of frequency times of 0.2T and 1.5T with the standardized design spectrum curve. The acceleration scale factor of the structure was found to be such that these mean values are by no less than 1.4 times the value of the standard spectrum. The terrain of Type II structure was assumed with a moderate relative risk and the main time of the fluctuations of the structure was considered to be equivalent to the structures with other systems [16].

$$T = 0.05H^{\frac{3}{4}}$$

$$B = 1 + S\left(\frac{T}{T_0}\right) \quad 0 \leq T \leq T_0$$

$$B = S + 1 \quad T_0 \leq T \leq T_s$$

$$B = (S + 1)\left(\frac{T_s}{T}\right)^{\frac{2}{3}} \quad T \geq T_s$$

where,  $B$  is the reflection coefficient of the structure represents the response of the structure to the motion of the earth,  $T$  is the time of the main frequency of the structure oscillation in seconds (s) and  $T_s$  and  $S$  are parameters that depend on the terrain and the seismicity of the region. The boundary conditions for this modeling are intended with the assumption that the wall at the bottom of its height  $Z = 0$  is immersed in impermeable soil layers and is thus considered to be completely stuck. Boundary conditions for earthquake loading are intended as wall conditions in hydrostatic loading, and the loading is in the horizontal direction of the earthquake in x direction. The type of analysis for hydrostatic loading was selected in one step as dynamical implicit for nonlinear analysis of the structure, and the type of analysis in dynamic loading is considered as dynamic explicit analysis. The aim of this research is to provide a preliminary result including stress-strain behavior and displacement in a cut-off wall under dam. Because the area under the curve of the concrete with fiber volume of 1.6% and 3% is approximately equal, results of 3% and 1% fibers concretes are compared with plain concrete.

### 3. Results and Discussions

#### 3.1 Under Hydrostatic Load

Since the loading conditions were symmetric in the y direction, evaluation of the results were conducted in the direction of the thickness and height of the cut-off wall (Figures 2 and 3). According to the Figure 2, it was observed that concrete with a 3% volume of fiber at the zero level, due to the greater length in the softening region, has the highest strain value in defining the materials and is 75% higher than that of plain concrete. Figure 3 shows that the total stress

in plain concrete and concrete with 1% volume of fiber at the level of 16.67 m is about 30% larger than concrete with 3% volume of fiber. Due to the smaller strength and modulus of elasticity, the materials behavior for 3% volume of fiber in concrete should have a smaller stress and a greater strain. Figures 4 and 5 show the stresses in x direction and deformations in z direction, respectively.

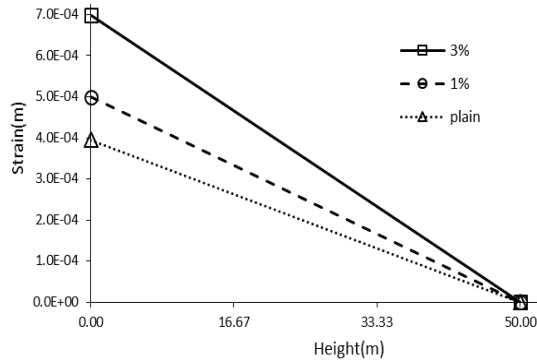


Figure 2: Comparison strains in z direction

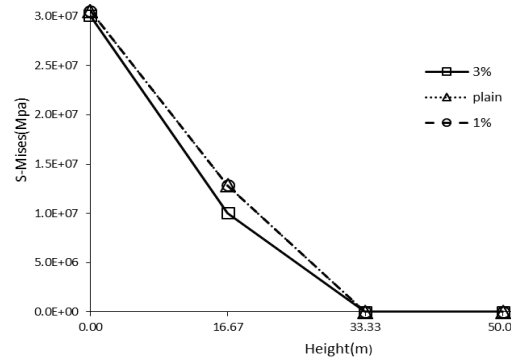


Figure 3: Comparison stresses in z direction

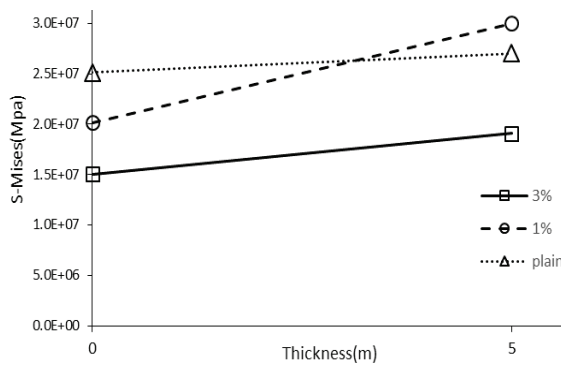


Figure 4: Comparison stresses in x direction

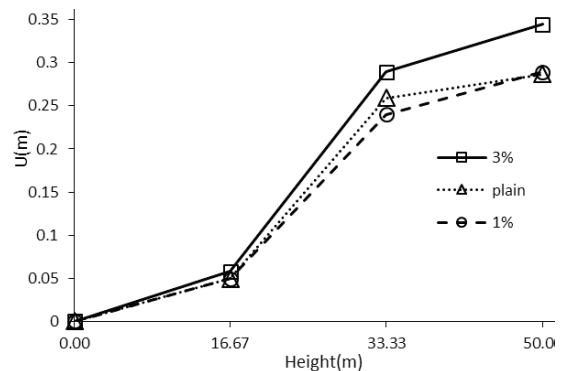


Figure 5: Comparison deformations in z

As can be seen from Figure 4, the minimum of stress is was occurred in concrete with 3% volume of fiber. In Figure 5 by comparing the deformations, concrete with 3% volume of fiber at the level of 50 m, had 19% more deformation compared to the plain concrete, which seems reasonable according to the small modulus of elasticity in concrete with 3% volume of fiber.

### 3.2 Under Earthquake Load

In the interpretation of the earthquake loading results, stress changes at height and in the direction of wall thickness were compared in Figures 6 and 7, respectively.

Figure 6 shows that the maximum stress in cut-off wall is related to the plain concrete at the level of 16.67 m, which is 66% more than the stress value in concrete with 1% volume of fiber. The behavior of the fiber concretes in the dynamic loading is softer than the plain concrete, and concrete with 1% volume of fiber, in spite of its compressive strength, is almost the same as the behavior of 3% concrete. Moreover, in direction of wall thickness, variations in stress are approximately equal. The strain and deformation changes are also compared to the height of the cut-off wall in Figures 8 and 9, respectively.

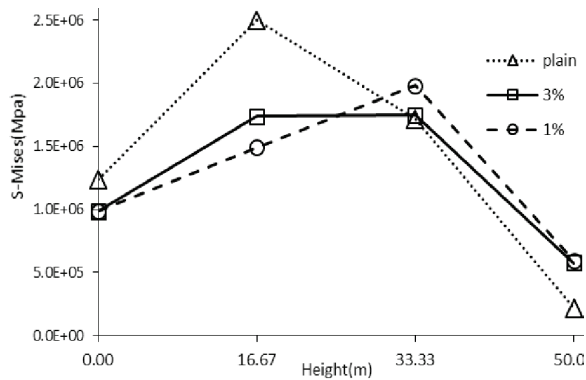


Figure 6: Comparison stresses in height

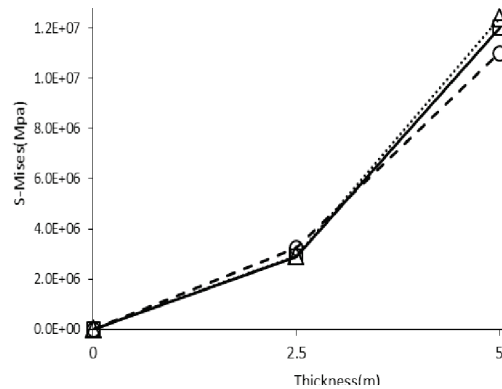


Figure 7: Comparison stresses in x direction

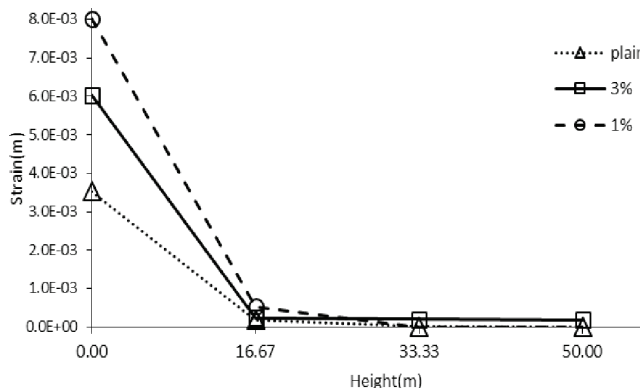


Figure 8: Comparison strains in z directions

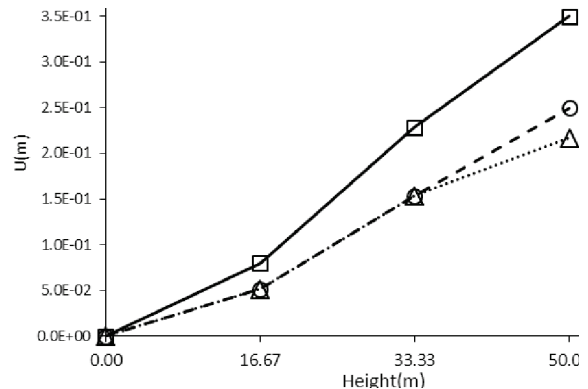


Figure 9: Comparison deformations in z

Figure 8 shows that the maximum value of the strain at the zero level is related to the concrete with 3% volume of fiber, which is different from the lowest value for the plain concrete of 128%. Figure 9 shows that concrete with 3% volume of fiber has the most deformation values, and only at the height of 50 m, the plain concrete has a deformation of 13% less than concrete with 1% volume of fiber.

Table 1: Amount of absorbed energy at the end of the analysis under earthquake loading.

Concrete type	Plain	1%	3%
The amount energy at the end of the analysis	0.1	0.25	0.5

The total energy related to the concrete cut-off wall with 3% volume of fiber is more in comparison with two other types and this means that the energy absorption to the structure in this type is larger than cut-off wall with plain concrete and 1% volume of fiber.

#### 4. Summery and Conclusions

In this study, the concrete behavior of concrete cut-off wall was examined by adding different percentages of fiber to the total volume of materials under hydrostatic and earthquake loads. To do so, simulations were performed using the stress-strain curve obtained from the experimental results of Ben Cardiou et al. [14] for verification. Results of simulations of concrete cut-off wall with 1% and 3% volume of fiber show that the zero level of the wall, the minimum stress created in the structure related to the concrete with 3% volume of fiber,

which is about 30% less than the concrete cut-off wall with 1% volume of fiber and plain concrete. In the direction of wall thickness, the minimum stress value is related to the concrete cut-off wall with 3% volume of fiber. Maximum deformation was for concrete cut-off wall with 3% volume of fibers and 19% with the other two other types. Moreover, the energy absorption at the end of the analysis time, absorption of the energy in concrete cut-off wall with 3% volume of fibers was more in comparison to the concrete cut-off wall with 1% volume of fibers and plain concrete. Strength of concrete against crack increased by adding steel fibers but effect of steel fibers decreased with increasing friction. Maximum deformation and strain under earthquake load was occurred in concrete cut-off with 3% volume of fibers.

## References

- [1] Hosainy, E., Siosemarde, M. (2015). Seepage analysis in body and foundation of Sang Siah Dam using the Seep/W. *Science Journal (CSJ)*, 36(4), 1697-1701.
- [2] Da Silva, J. (2006). Optimization of concrete gravity dams foundation systems. 22<sup>nd</sup> International congress on large dams-ICOLD, 18 June, Barcelona, Spain.
- [3] Soleymani, S., Akhtarapur, A. (2011). Seepage Analysis for Shurijeh Reservoir Dam Using Finite Element Method. *Geo-Frontiers*, 3227-3234.
- [4] Qingyou, W., Wangong, S., Huan, X. (2008). *Plastic Concrete Cutoff Wall*. China Water Power Press.
- [5] Nawy, G. (2000). *Fundamentals of high performance concrete*, New York: John wiley.
- [6] Dupont, V.L. (2002). Bending capacity of steel fiber reinforced concrete (SFRC) beams, *Proceeding of the international congress on challenges of concrete construction*. P.81-90.
- [7] Paine, KA., Elliott, KS., Peaston CH. (2002). Flexural toughness as a measure of shear stress strength and ductility of prestressed fiber reinforced concrete. *University of Dundee*.
- [8] Olivito, RS., Zuccarello, FA. (2010). An experimental study on the tensile strength of steel fiber reinforced concrete, *Composites Part B: Engineering*, 41(3): 246-255.
- [9] Johnston, C.D., Zemp, R.W. (1991). Flexural fatigue performance of steel fiber reinforced concrete-Influence of fiber content, aspect ratio, and type, *ACI Materials J.*, 88(4): 374-83.
- [10] Shahrabadi, H., Sayareh, S., Sarkardeh, H. (2017). Effect of natural zeolite-pozzolan on compressive strength of oil-polluted concrete marine structures, *Civil Engineering Journal*, 2(12): 623-636.
- [11] Barkhordari Bafghi, M.A., Amini, F., Safaye Nikoo, H., Sarkardeh, H. (2017). Effect of Steel Fiber and Different Environments on Flexural Behavior of Reinforced Concrete Beams, *Applied Sciences*, 7(10): 1011.
- [12] Shahrabadi, H., Sayareh, S., Sarkardeh, H. (2017). Effect of silica fume on compressive strength of oil-polluted concrete in different marine environments, *China Ocean Engineering*, 31(6): 716-723.
- [13] Sarabi, S., Bakhshi, H., Sarkardeh, H., Safaye Nikoo, H. (2017). Thermal stress control using waste steel fibers in massive concretes, *European Physical Journal Plus*, 132(11):491
- [14] Barkhordari Bafghi, M.A., Amini, F., Safaye Nikoo, H., Sarkardeh, H. (2018). Strength of Different Fiber Reinforced Concrete in Marine Environment, *Materials Science*, 24(2):204-211.
- [15] Bencardino, F., Rizzuti, L., Spadea, G. (2008). Stress-strain behavior of steel fiber-reinforced concrete in compression, *ASCE*.
- [16] Housing and Building Research Center (2010). *Regulation Building Designs Against Earthquakes*, Third Edition.



## **PERFORMANCE OF RECYCLED AND COMMERCIAL FIBRE REINFORCED CONCRETE BEAMS IN COMBINED ACTION WITH CONVENTIONAL REINFORCEMENT**

**Katerina Bernhoft<sup>(1)</sup>, Samindi Samarakoon<sup>(1)</sup>, Luis Evangelista<sup>(1)</sup>, Bjarne Mikalsen<sup>(1)</sup>**

(1) University of Stavanger, Stavanger, Norway

### **Abstract**

Reuse of recycled steel fibres recovered from tire recycling is a sustainable solution to contribute to the reduction of the waste disposal burden. In addition, commercially available steel fibres are widely used in the construction industry, especially mixed with concrete to enhance flexural strength, toughness, ductility and cracking resistance. Various researchers have found that there is an opportunity to replace commercially available steel fibres with recycled steel fibres from tire waste. However, there are few studies on the behavior of reinforced concrete beams with recycled fibres. Therefore, laboratory experiments have been carried out to study the behavior of reinforced concrete beams cast with recycled fibres and commercially available fibres, which comprise a fibre content of 0%, 0.5% and 1% by volume. The results indicate that the load versus the displacement behavior of the reinforced concrete beams with recycled fibres is similar to that for commercial fibres. Moreover, a numerical analysis was performed, using finite element tool, ATENA, to study the behavior of recycled fibre reinforced concrete, and to compare the performance with commercial steel fibre reinforced concrete. ATENA simulates real structural behavior, such as cracking, crushing and reinforcement yielding, by using non-linear finite element analysis. Moreover, the load-displacement diagrams computed in ATENA were compared to the experimental load-displacement diagrams.

### **1. Introduction**

Used tires are considered the most challenging type of waste to handle, due to the huge quantity of production and their non-biodegradability. Currently, there is a trend towards innovative material recycling and sustainable buildings. The recycling of the used tire is one of the attractive solutions which results in three by-products: crumb rubber/rubber powder,

steel wires and fibre. The aforementioned steel wires have irregular shapes and variable lengths and are further processed into steel fibres. Many studies in the literature have proposed the use, in concrete, of granulated rubber and steel fibres recovered from waste tires [1-2]. Moreover, the addition of recycled steel fibres, instead of their commercially available steel counterparts, gave good post-cracking behavior [3]. However, few studies have been carried out to study the behavior of concrete beams reinforced with recycled steel fibres.

The behavior of concrete beams reinforced with steel fibres can be studied experimentally, as well as numerically, using software like ATENA [4]. Moreover, the numerical models are widely used to simulate/verify the structural performance of the beams, which are observed during experiments. Hence, this study focuses on the development of finite element models of the tested beams with different fibre contents and compares them with the experimental behavior.

## 2. Experimental testing of beams

Concrete beams reinforced with recycled fibres (RFRC) and commercially available fibres (SFRC) (i.e. fibre content: 0%, 0.5% and 1% by volume) have been tested using the four-point bending test, set up as shown in Fig. 1. The RFRC was supplied by Ragn-Sells Dackåtervinning AB, Sweden. The load vs. displacement behaviors from the experimental study [5, 6] are shown in Fig. 2, and the results are given in Tab. 1.

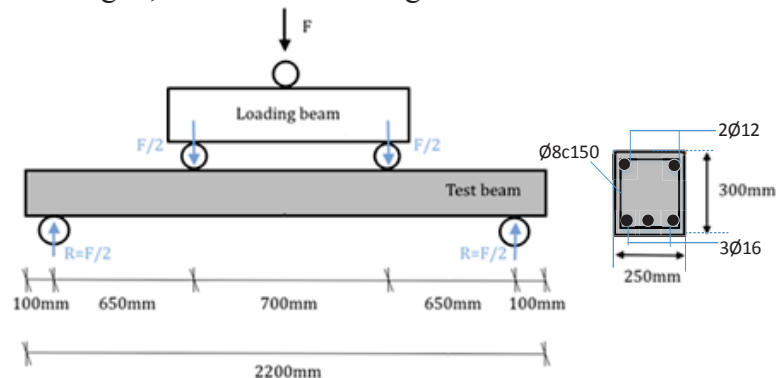


Figure 1: Test setup for four-point bending test [5].

Table 1: Results of the beam tests [6].

	0.0%	0.5% RFRC	1.0% RFRC	0.5% SFRC	1.0% SFRC
First peak load [kN]	236.1	228.0	237.8	248.4	243.4
Displacement at first peak load [mm]	10.1	11.7	11.3	11.4	12.7
Maximum load [kN]	251.20	245.3	238.4	259.6	251.5
Displacement at maximum load [mm]	29.6	36.6	13.3	21.8	20.3
Failure at displacement [mm]	≈54.7	≈84.8	≈91.6	76.9	97.7

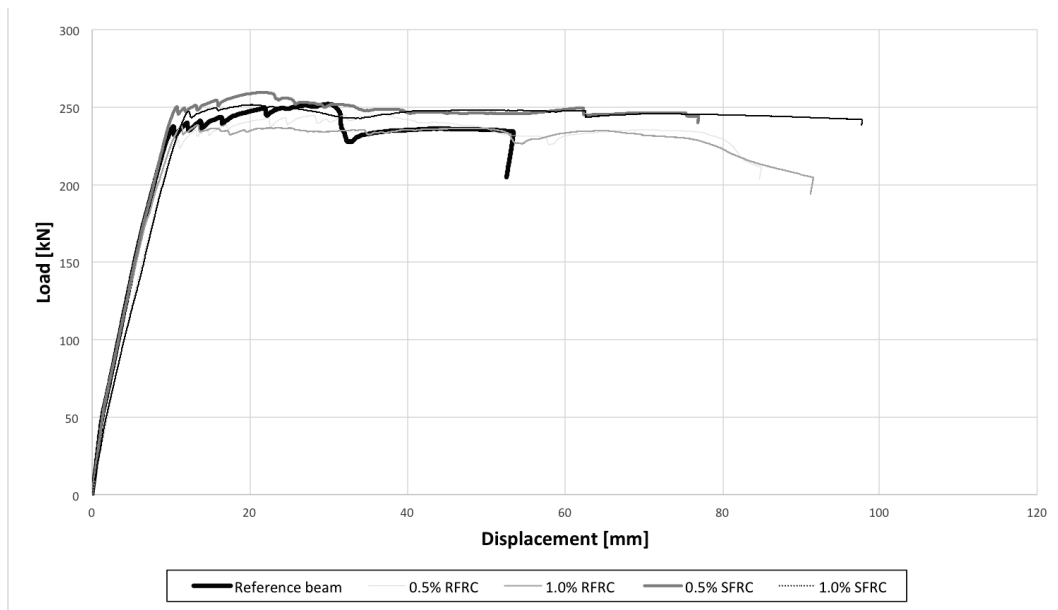


Figure 2: Load vs. displacement of reinforced concrete beams [6].

### 3. Numerical modeling of reinforced concrete beams with steel fibres

Numerical modeling and analysis were carried out using the software, ATENA and GiD. ATENA-GiD is a finite element-based software, specifically designed to analyze both plain and reinforced concrete structures. Basically, GiD is used for the data preparation and mesh generation, while ATENA is used for the analysis part itself. GiD is a general-purpose pre- and post-processing tool for a variety of numerical problems. ATENA can simulate real structural behavior, such as cracking, crushing and reinforcement yielding, by using non-linear finite element analysis (NFEA). Fracture mechanics and plasticity theories lay the foundation for the non-linear material models implemented in the software [4].

#### 3.1 Modeling of the four-point bending test in ATENA

GiD is used to develop models of the four-point bending test shown in Fig. 1. The model is derived from the software manuals and theory documentation developed by Cervenka Consulting [4]. Since the beam is symmetric about its mid-point, only half of the 3D concrete beam is modeled in GiD. The beam is simply supported by steel roller bearings, in the physical experiments. To avoid local concrete crushing, the load is applied through steel plates of square cross-section of 1.5mm·1.5mm. Steel bars (3Ø16 and 2Ø12) are modeled as discrete elements, and stirrups (Ø8) are modeled as smeared. Quadratic hexahedral isoparametric elements are used, as well as 0.025m mesh size. The Newton-Raphson method is used as a solution method. Fig. 3 shows a geometric model of the beam.

The top surface of the beam is assigned a fixed contact surface to the top steel plate, and the bottom beam surface is assigned a fixed contact surface to the bottom steel support. Displacement-controlled analysis is used, by applying a prescribed vertical displacement at the middle point on top of the loading plate in constant increments of 0.001m. From the

experimental results [5], it has been found that the beams failed at deflection between 0.06 and 0.08m, as given in Tab. 1. The predefined displacement therefore has be multiplied approximately 80 times, to reach failure.

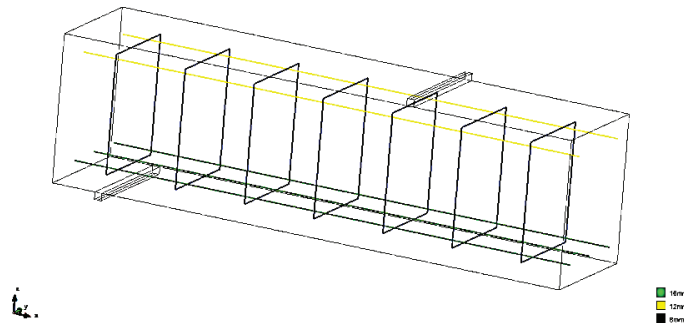


Figure 3: Geometric model of the beam.

### 3.2 Material models

The steel plates which are used as the support to the beam are modeled as an elastic and isotropic material, using SOLID Elastic material type given in ATENA, where Young's modulus is 200GPa and Poisson's ratio is 0.3. When modeling the reinforcement as discrete bars, the predefined material, Reinforcement from 1D Reinforcement, is selected. The characteristic yield strength of steel reinforcement and stirrups is taken as 500MPa, and  $E_s$  is 200GPa. Ultimate strain of steel is used as 7.5%. The bilinear material law is chosen for the steel bars. Moreover, there are several ATENA fracture-plastic constitutive models given in the manual for structural concrete. In this study, the material model, CC3DNonLinCementitious, is used. To input the properties of fibre-reinforced concrete to the material model given in ATENA, the mechanical properties were found experimentally. For example, the average value of compressive strength, modulus of elasticity, splitting tensile strength, and fracture energy (using the wedge splitting test) were found experimentally [5, 6] and are given in Tab. 2. Poisson's ratio of concrete is chosen as 0.2.

Table 2: Input values for the material model for concrete from experimental findings.

<b>Fibre content</b>	<b>0%</b>	<b>0.5% RFRC</b>	<b>1% RFRC</b>	<b>0.5% SFRC</b>	<b>1% SFRC</b>
Modulus of elasticity (GPa)	25.45	26.7	25	26.7	26.6
Compressive strength (MPa)	29.2	30.6	32.9	34.3	35.1
Splitting tensile strength (MPa)	2.18	2.58	2.49	2.87	2.97
Fracture energy (N/m)	132	592	1096	2616	1726

## 4. Comparison of results from ATENA and experimental testing

### 4.1 Reference beam (0% fibres)

To determine the best fit curve for the load vs. displacement behavior of the experimental results, variables, such as different methods of input of shrinkage strain and influence of

dowel action, are considered. In this study, the dowel effect of lower longitudinal reinforcement is taken into account, as well as shrinkage, which is applied as initial strain to the concrete volume by recommended value of  $-5.5 \cdot 10^{-5}$  [4]. Furthermore, the crack pattern and crack widths are also taken into consideration when determining the best fit curve. Moreover, the reinforcement is monitored to make sure no rupture occurs in the bars before failure is reached. Based on the best fit model, the first peak for the ATENA models is reached earlier than that of the experimental test for the both mesh size; 0.025m and 0.05m. There is a difference in the maximum loads of about 8% (232kN/252kN) for the mesh size; 0.025m.

#### 4.2 Reinforced concrete beams with different fibre contents

When modeling recycled fibres recovered from tire waste, Young's modulus is used as 200GPa, and average yield strength is estimated from laboratory testing as 870 MPa. According to the ATENA Theory manual, the fibres can be represented in the material model by simply increasing the fracture energy of the concrete or fibres is to define them as smeared reinforcement, pointing in six different directions, i.e. three in the principal axes and three in the middle of the octants.

In the case of increasing the fracture energy of the concrete, a higher peak load is predicted for the ATENA model, with 7.6% relative difference of peak loads for the beam with 0.5% RFRC. Moreover, when representing the fibres with smeared reinforcement, the ATENA model predicts a greater capacity of the beam, i.e. a 9.6% difference in maximum loads, as shown in Fig. 4. Similar analysis is performed for the beam with 1% RFRC, and the difference in maximum loads is found to be about 4%.

As regards the beams with 0.5 % SFRC, the difference between the maximum loads for the ATENA model and the experimental beam is about 1%. For the beams with 1% SFRC, the ATENA model with smeared fibres is somewhat overestimated, with the difference in maximum loads between the experimental results and the model with smeared fibres being about 5%.

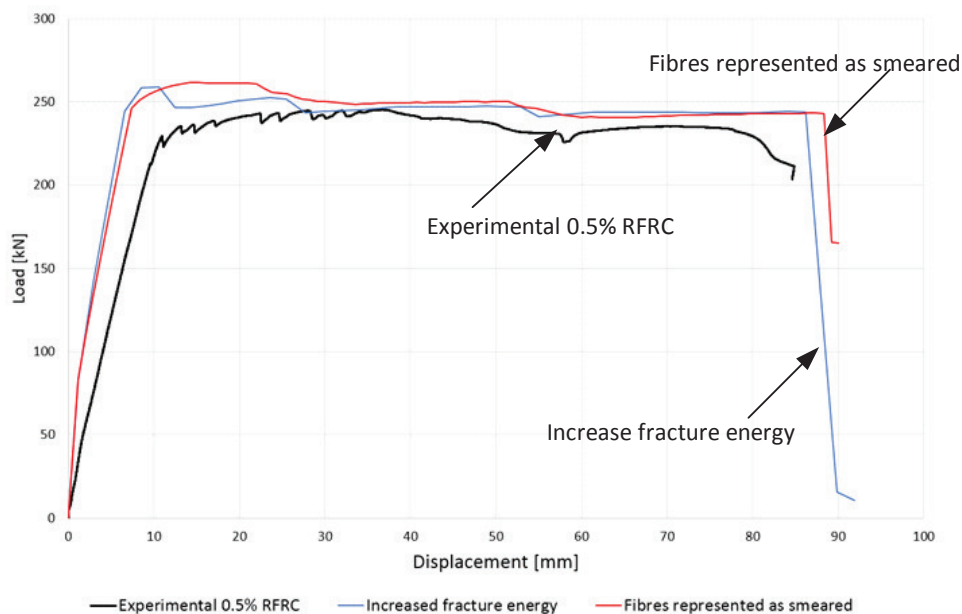


Figure 4: Load-displacement diagram for beam containing 0.5% recycled steel fibres.

## 5. Discussion and Conclusions

This paper studies the behavior of concrete reinforced with recycled fibre and compares the structural performance of concrete reinforced with commercial steel fibre. It mainly focuses on the load vs. displacement behavior of beams with different fibre content. During the study, the load vs. displacement diagrams using ATENA were compared to the experimental load-displacement diagrams. An equivalent performance of the recycled steel fibres compared to commercially available steel fibres can only be found in the loading phase before yielding of the conventional reinforcement. Moreover, a 1% – 9.6% difference in the maximum load in the load vs. displacement behavior has been found. However, the results were very dependent on the parameters adjusted to create load-displacement diagrams, e.g. representing the fibres as smeared or by simply increasing the specific fracture energy. It should also be noted that several simplifications and assumptions were made along the way, which may also have influenced the results.

## References

- [1] Aiello, et al, Use of steel fibres recovered from waste tyres as reinforcement in concrete: Pull-out behavior, compressive and flexural strength, *Waste Manage*, 29 (2009), 1960-1970
- [2] Bignozzi, M. C. and Sandrolini, F., Tyre rubber waste recycling in self-compacting concrete, *Cem Conc Res*, 36 (2006), 735-739
- [3] Centonze, M. L. and Aiello, M. A., Steel fibres from waste tires as reinforcement in concrete: A mechanical characterization, *Constr Build Mater*, 36 (2012), 46-57
- [4] Červenka, V., Jendele, L. and Červenka, J., (2016). ATENA Program Documentation Part 1: Theory. Retrieved from [http://www.cervenka.cz/assets/files/atena-pdf/ATENA\\_Theory.pdf](http://www.cervenka.cz/assets/files/atena-pdf/ATENA_Theory.pdf)
- [5] Bernhoft, K., Numerical modelling of recycled fibre reinforced concrete beams and comparison with experimental findings, Master thesis, University of Stavanger, Norway (2017)
- [6] Hovind, P. R., Pedersen, J. W. and Mikalsen, B., Behaviour of recycled tyre fibre reinforced concrete, Bachelor thesis, University of Stavanger, Norway (2107)

## **PROBABILISTIC NUMERICAL MODEL FOR DESIGNING STEEL FIBRE REINFORCED CONCRETE STRUCTURES**

**Pierre Rossi <sup>(1)</sup>, Jean-Louis Tailhan <sup>(1)</sup>**

(1) Paris-Est University, IFSTTAR/MAST, France

### **Abstract**

This paper enumerates the reasons that motivate the use of finite elements simulations for the design of SFRC structures for the analysis of their cracking behaviour. Those reasons are mainly the consequences of the irrelevancy of the actual design recommendation to take into account adequately some loading conditions of SFRC structures.

The mean criteria to be respected for a relevant numerical model of cracking behaviour of SFRC are also proposed.

Finally, an example of these relevant models is presented with its validation.

### **1. Introduction**

Steel fiber reinforced concrete (SFRC) is increasingly used in structural applications. One of the principal reasons of its gain in popularity is due to the existence of national and international recommendations for the design of structures using this type of material.

These recommendations are efficient for designing simply supported structural elements subjected to bending. However, they do not possess a sufficient physical base to propose relevant solutions for more complex structures such as statically indeterminate or for others types of failure modes such as beam shear and pushing-shear. In certain cases, the proposed methods are too conservative and lead to an over consumption of material, which is not good in the frame of sustainable development. In some other cases, the non-homogeneity of SFRC properties is not considered adequately which could lead to overestimate the strength provided by SFRC.

In addition, cracking control in serviceability limit state is one of the main interests of using SFRC. Crack control is very important for durability aspects, and is certainly an advantage of SFRC compared to structures using traditional reinforcement bars.

Nowadays, existing design recommendations are not able to give enough relevant information regarding cracking in serviceability limit state (cracks openings and spacing). Hence, the most efficient approach for designing structures with respect to both safety and sustainable development is to use finite element analysis.

IFSTTAR, formerly known as LCPC, has been developing and using numerical models in order to achieve this objective.

In order for SFRC to be fully accepted in industrial applications, a cracking model has to be relevant to:

- determine the cracks opening, especially in the service state situation;
- analyze the non-linear behaviour of concrete structures under loadings as shear and punching and of statically indeterminate concrete structures.

## 2. Numerical Modelling of the SFRC Tensile Cracking Process

IFSTTAR has been developing a probabilistic discrete cracking model to simulate the cracking process of concrete [1]. In this model, cracking is explicitly treated through the creation of random kinematic discontinuities, which provides access to quantitative information on the cracking state (number of cracks, opening and spacing). Numerically speaking, these cracks are represented by interface elements.

The criterion for the crack creation is very simple: the interface element opens when the normal tensile stress at the centre of the interface element reaches a critical value. This critical value is probabilized through a Weibull distribution function [2]. This means that the rigidity of the interface element becomes equal to zero (perfect brittle behaviour). The value of this critical value depends on the total volume of the two volumetric elements interfaced by the considered interface element.

After the crack creation, which only depends on the cement matrix, the influence of the fibres has to be taken into account. The following modelling approach is considered:

- Normal and tangential stresses in the interface element linearly increase with normal and tangential displacements when a “broken” interface element re-opens to take into account the elastic effect of the fibres inside the crack. Physically speaking, the rigidity of the fibres (inside the cracks) is more important in tension than in shear. Thus, the interface element rigidity is considered different for normal and tangential displacements. In 2D, normal and tangential rigidities of the interface element are  $K_n$  and  $K_t$  respectively. The post-cracking elastic behaviour exists until it reaches a limit,  $\delta_0$ , related to the normal displacement. Once this limit value is reached, the mechanical behaviour of the interface element changes. As a matter of fact, the normal stress is considered as **linearly decreasing** with the normal displacement in order to take into account the damage of the bond between the concrete and the fibre. The decreasing evolution is obtained by a damage model.

Finally, the interface element is considered definitively broken and its rigidity (normal and tangential rigidities) is equal to zero when the normal displacement occurring during the damage step reaches a critical value,  $\delta_c$ . This value corresponds to the state where the effect of fibres is considered negligible.



- The post-cracking total energy dissipated during the linear increase and followed by the linear decrease of the normal stress is considered randomly distributed on the mesh elements as for the material tensile strength. The random distribution is a log-normal distribution function with a mean value independent of the mesh elements size and a standard deviation increasing with the decrease in the mesh elements size, which is physically logical. In practice, to model a given structure, the distribution function is determined in the following manner:
  - The mean value is directly obtained by uniaxial tensile tests on notched specimens. It has been previously shown [3] that this mean value is not affected by scale effects.
  - The standard deviation, which depends on material volume tested and so of the mesh elements size, is determined by an inverse analysis approach that consists of simulating the uniaxial tests with different element mesh sizes.

#### Remark

It is also required to know the values related to  $\delta_0$  and  $\delta_c$  to perform numerical simulation with the above model.  $\delta_c$  is directly obtained by the uniaxial tensile tests and  $\delta_0$  is obtained by the inverse analysis approach assuming that it is a mesh independent parameter.

The numerical mechanical behaviour adopted for the post-cracking step is illustrated in Figure 1. Only the normal stress - normal displacement curve is considered in this figure.

To conclude this part about the adopted numerical modelling approach, it can be said that it is considered a deterministic approach with probabilized parameters. Hence, it is necessary to perform a large number of computations to statistically validate the results following a Monte Carlo method.

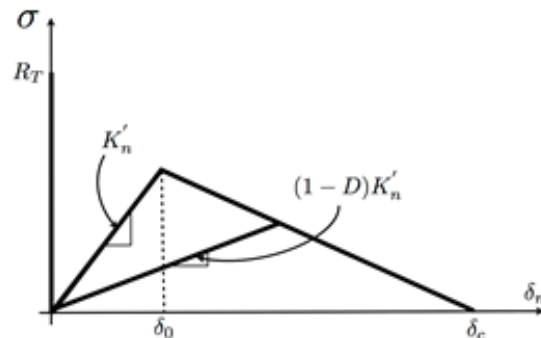


Figure 1: Modelling of the post-cracking behaviour

### 3. Numerical Simulations of the shear behaviour of a large SFRC beam

The shear behaviour of a large reinforced beam [4] was analyzed by using the above numerical model. This beam contained traditional rebars for the bending strength and only steel fibres as shear reinforcement. The beam was designed to fail in shear.

The beam geometry, its reinforcement, the boundary conditions, and the test apparatus are presented in Figure 2. A normal-strength SFRC containing  $100 \text{ kg/m}^3$  of steel fibres with a length of 30 mm and a diameter of 0.5 mm was used. Its compressive strength was 40 MPa.

Uniaxial tension tests on notched cylindrical specimens were performed to evaluate its tensile behaviour (and to determine all the values of the model parameters). These specimens had a diameter of 120 mm and a height of 100 mm, with a 2 mm width and a 20 mm depth circumferential notch.

Two types of measurement were recorded during the shear test:

- evolution of the beam deflection,
- shear crack openings and evolution by using stereophotogrammetry technique.

A single beam was tested during this experimental study.

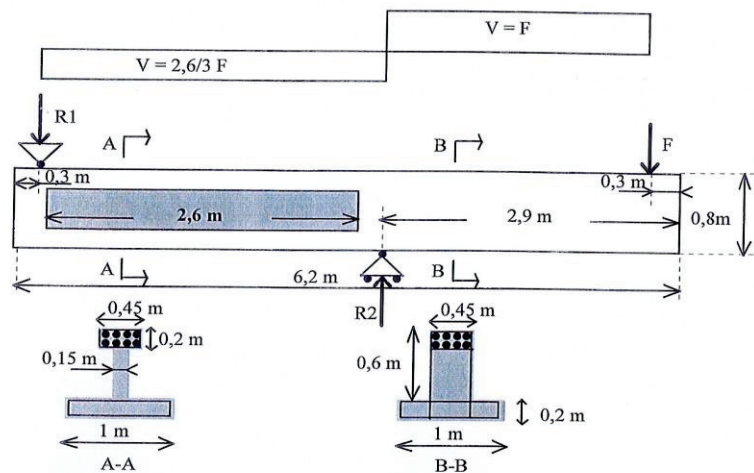


Figure 2: Beam geometry and test set-up

The finite element mesh and the boundary conditions are presented in Figure 3.

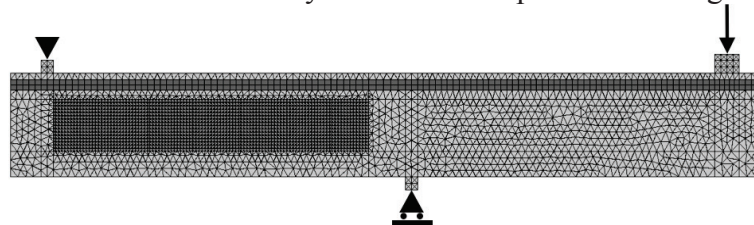


Figure 3: Mesh of the beam and boundary/loading conditions.

The values of the model parameters used in the numerical simulations of the beam behaviour were the followings:

- Means tensile strength: **4.5 MPa**
- Standard deviation: **0.7**
- Mean post-cracking energy: **3.25 MPa.mm**
- Standard deviation of the post-cracking energy: **1.18 MPa.mm**
- $\delta_0 = 100 \mu\text{m}$
- $\delta_C = 3 \text{ mm}$

Figure 4 shows the global responses (load - displacement) of the numerical simulations and the experimental test. It can be noticed that the numerical mean curve is very close to the experimental one. Moreover, the experimental response is clearly located in the scattering of the set of the numerical responses.

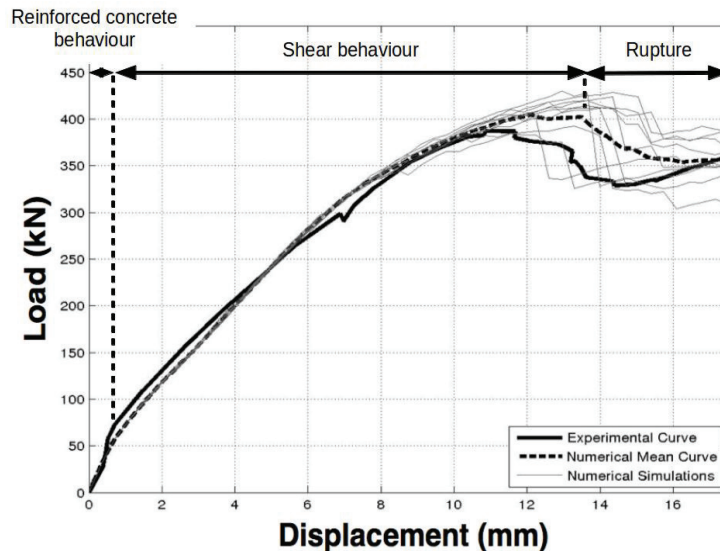


Figure 4: Comparison between simulations and experiment: load vs. deflection curve.

An example of a numerical crack pattern can be observed in Figure 5. On this same figure, the numerical crack pattern is compared to the experimental one at the peak load. Numerical values of crack openings were computed and were found to be comparable in magnitude with the experimental values. Furthermore, numerical and experimental cracks at a loading step just before the peak load exhibit openings of about 1 mm (see Figure 5).

#### 4. Conclusions

This paper enumerates the reasons that motivate the use of finite elements simulations for the design of SFRC structures for the analysis of their cracking behaviour.

These reasons are mainly the consequences of the irrelevancy of the actual design recommendation to take into account adequately some of the technical problems such as:

- the evaluation of the crack openings in SFRC structures under serviceability loads;
- the analysis of the non-linear behaviour of SFRC structures under complex loadings.

In this paper, the mean criteria to be respected for a relevant numerical model of cracking behaviour of SFRC, is also proposed.

Finally, an example of these relevant models with its validation in the frame of the shear behaviour of a large beam is presented.

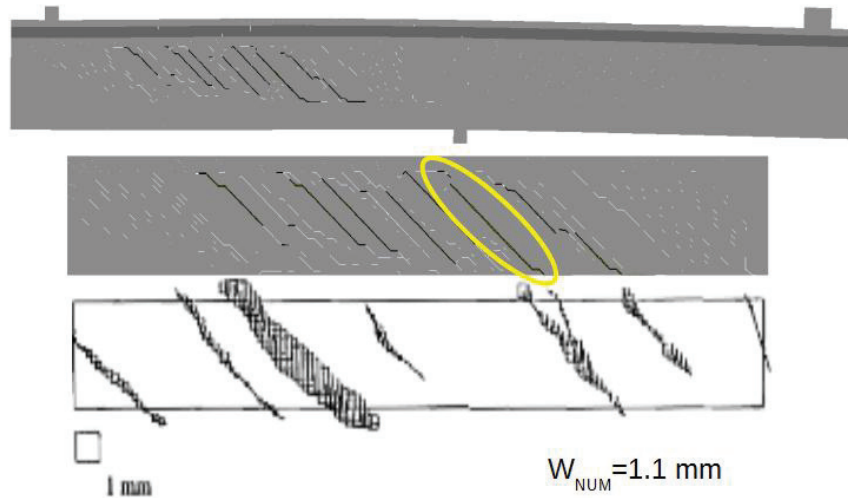


Figure 5: Example of crack pattern at the peak load

### References

- [1] Rossi, P. and Richer S., Numerical modelling of concrete cracking based on a stochastic approach, *Materials and Structures*, vol. 20 (1987), 334-337.
- [2] Tailhan J.L., Dal Pont S. and Rossi P., From local to global probabilistic modelling of concrete cracking, *Ann. Solid. Struct. Mech.*, vol. 1 (2010), 103-115.
- [3] Rossi, P., Experimental study of scaling effect related to post-cracking behaviours of Metal Fibres Reinforced Concretes, *European Journal of Environmental and Civil Engineering*, Vol.16(10) (2012), 1261-1268.
- [4] Casanova, P. and Rossi P., Can steel fibers replace transverse reinforcements in reinforced concrete beams, *ACI Materials Journal*, vol. 94, n°5 (1997), 341-354.

## **RHEOLOGICAL BEHAVIOUR OF FLEXIBLE FIBER-REINFORCED CEMENTITIOUS MATERIALS**

**Fariza Sultangaliyeva <sup>(1)</sup>, H el ene Carr e <sup>(1)</sup>, Christian La Borderie <sup>(1)</sup>, Nicolas Roussel <sup>(2)</sup>**

(1) Universit e de Pau et Pays de l'Adour, Anglet, France

(2) Navier Laboratory, IFSTTAR, Champs-sur-Marne, France

### **Abstract**

Polypropylene fibers are accepted in many studies as an effective preventative measure against concrete spalling due to fire exposure. A high dosage of the fibers enhances this effect but reduces the flowability of fresh concrete. Due to a lack of literature, it is hard to identify optimal fiber dosage and geometry. This paper is aimed at understanding the influence of polypropylene fibers on the rheology of fresh cementitious materials. Slump flow tests that ensure an isotropic flow of the material are conducted in order to assess the yield stress of cement pastes containing flexible fibers. The results present the influence of fiber dosage and geometry (fiber length and diameter) on the yield stress of fresh cementitious materials. Using predictive scheme for the yield stress of the cementitious materials with rigid fibers, it is seen that the rheology of cement pastes with flexible fibers is more complex compared to the rheology of paste with rigid fibers.

### **1. Introduction**

Numerous studies have been conducted by researchers presenting a positive effect of polypropylene fibers for a reduction of concrete spalling risk due to fire [1], [2]. Higher dosage reinforces this effect but leads to the loss of concrete's workability [3]. In order to reach a compromise between fire resistance and fluidity, it is essential to identify an optimal fiber dosage and geometry. Current state of knowledge concerning the influence of flexible fibers on the rheology of fresh cementitious materials is not sufficient to respond to this question. This paper is aimed at understanding the effect of flexible fibers on the rheology of fresh concrete. Initially, we study the influence of fiber dosage and geometry on the yield stress of cement paste. Then, using prediction for the yield stress of cementitious materials

with rigid fibers, we prove the complexity of the rheology of flexible fiber reinforced cementitious composite.

## 2. Influence of rigid inclusions on the yield stress

The biphasic approach used for describing the rheology of fresh concrete suggests that concrete is composed of a continuous phase of the suspending fluid (a cement paste assumed to be homogeneous) and a dispersed phase (the inclusions such as sand, gravel and fibers) [4]. Using the extrapolation for Krieger-Dougherty relation for apparent viscosity [5], the yield stress of concrete can be presented as the function of the yield stress of the suspending fluid and the function of the volume fraction of its inclusions [4]:

$$\tau_0^c \approx \tau_0^p f\left(\frac{\phi}{\phi_m}\right) \quad (1)$$

where  $\tau_0^c$  is the yield stress of concrete,  $\tau_0^p$  is the yield stress of cement paste,  $\phi$  is the volume fraction of the inclusions,  $\phi_m$  is the dense packing fraction of the inclusions. Packing regimes may influence the interactions of rigid inclusions in the suspending fluid. Change in the interactions, consequently, leads to the change in the yield stress of the material. We therefore need to define different packing regimes. A comprehensive explanation of various packing regimes based on spherical inclusions is given in [4]. It is important to note here that dense packing fraction is characterized by direct contacts between the inclusions. These contacts are a dominant force in the material flow.

## 3. Rheology of cementitious materials with rigid fibers

### 3.1 Distinction between flexible and rigid fibers

At high dosage of fibers, direct contacts between fibers provoke significant dissipation of the energy leading to the increase of the yield stress and the decrease of the workability of fresh cementitious material [4]. Since packing of the inclusions influences the interactions and, consequently, the yield stress, we should be able to define it for both rigid and flexible fibers. We expect different packing tendencies for flexible and rigid fibers. Rigid fibers are prone to change a granular skeleton thanks to their rigidity they can move the aggregates that are relatively large compared to fiber length and increase the void space. To compare, flexible fibers tend to bend around aggregates and to occupy the empty spaces between them [6].

In order to distinguish flexible fibers from rigid ones, the rigidity criterion for the fibers in cementitious materials was developed by Martinie et al. [4]. She has identified that the order of the deflection of fibers is estimated as:

$$\frac{f}{L} \cong \frac{\tau_0}{E} R^3 \quad (2)$$

where  $f$  is the deflection,  $L$  is the length of the fiber,  $\tau_0$  is the yield stress of the fresh cementitious material,  $E$  is Young's modulus of fiber,  $R$  is the aspect ratio (the ratio between

the length and the diameter of the fiber). Depending on the properties of the fiber and the nature of the suspending fluid, different flexure responses can be obtained. For example, in case of steel fibers with an aspect ratio of 50, the Young's modulus of 210 GPa in SCC mix (the yield stress of approximately 50 Pa) this value is around 0.003 %, whereas for carbon fibers of the aspect ratio of 500 and the Young's modulus of 190 GPa in regular concrete mix (the yield stress of 1000 Pa), the magnitude of deflection is around 66% [4].

### 3.2 Dense packing fraction of rigid fibers

We are interested in evaluating dense packing fraction of rigid fibers. Dense packing fraction of rigid fibers was determined experimentally in [4] from the measurements of the apparent volume occupied by fibers before vibration  $\Omega_{\text{before}}$  and after vibration  $\Omega_{\text{after}}$  of the known mass of fibers. Using Philipse's approach for slender bodies with a range of aspect ratios between 50 and 100 [7], a relation between dense packing fraction  $\phi_m$  and aspect ratio  $R$  for rigid fibers was determined as:

$$\phi_m = \frac{4}{R} \quad (3)$$

In case of rigid fibers, it is possible to measure dense packing fraction as their flexure in air is comparable to the flexure in cement paste (less than 1%). In case of flexible fibers, dense packing fraction cannot be measured directly due to the fact that their flexure depends on the nature of the suspending medium.

### 3.3 Yield stress prediction

Yield stress of rigid fiber reinforced cement paste can be predicted as a function of the relative packing fraction of fibers. The yield stress evolves as a function of  $\phi/\phi_m$  equal to  $\phi R/4$  [4]. This means that for the yield stress prediction in case of rigid fibers two parameters are sufficient: fiber volume fraction  $\phi$  and aspect ratio  $R$ . Returning back to flexible fibers, we have stated that dense packing fraction is impossible to measure experimentally. Nevertheless, we shall still verify whether the evolution of the yield stress of cementitious material with flexible fibers could be described using framework for rigid fibers, i.e. the yield stress should evolve a function of relative packing fraction  $\phi R$ .

## 4. Rheology of cementitious materials with flexible fibers

### 4.1 Materials and experimental procedure

All cement pastes for experiments were prepared using Portland cement CEM I 52.5 N Brest. Cement paste with  $w/c = 0.5$  is tested using nine different geometries of fibers at various fiber dosages (0 %, 0.25 %, 0.5 %, 1 %, 2 % and 3 % vol. of cement paste). Tested fiber geometries are presented in Table 1.

Cement is mixed with water by rotating mixer for 2 minutes. It is then left for rest during 20 minutes and remixed again for 2 minutes. The fibers are added and mixed by hand for 2 minutes. The sample is then tested using slump flow test described in [6]. For each dosage and geometry, a new sample is prepared. Samples that presented any signs of instability were not taken into account.

Table 1: Tested fiber geometries.

Aspect ratio, R	Length, L (mm)	Diameter, D ( $\mu\text{m}$ )
176	6	34
188	6	32
300	6	20
333	6	18
353	12	34
400	6	15
529	18	34
588	20	34
706	24	34

#### 4.2 Experimental results

The results were obtained from the slump flow test on cement pastes with nine various fiber geometries tested at different dosage. We present our experimental results in terms of the relative yield stress (a ratio of the yield stress of cement paste with fibers and cement paste without fibers) in order to study the influence of fibers as rigid inclusions.

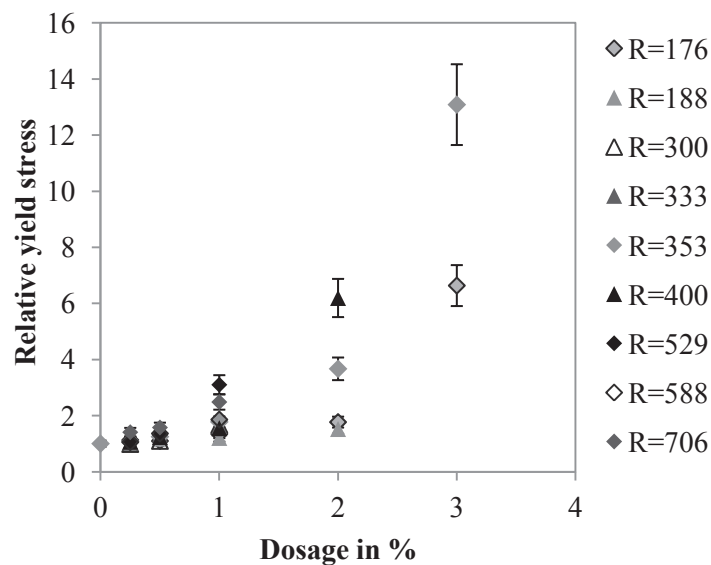


Figure 1: Relative yield stress as a function of fiber dosage. Triangles: fibers of the same length  $L = 6$  mm, rhombus: fibers of the same diameter  $D = 34$   $\mu\text{m}$ .

In Fig.1 the relative yield stress of fresh cement pastes with fibers is plotted as a function of the dosage of fibers. The error bar of 11% is found by repeating the experiment five times on the fibers with an aspect ratio  $R = 353$  ( $L = 12$  mm,  $D = 34$   $\mu\text{m}$ ) at 1 % vol. of fibers. This value is assumed as an error for all the results presented here.



### 4.3 Discussion

The relative yield stress is presented in Fig.1 as a function of fiber dosage for different fiber geometries. As expected, the relative yield stress increases with the increase of fiber dosage. It could be suggested that after a certain critical fiber concentration direct frictions appear and the relative yield stress increases rapidly as seen in Fig.1. In terms of geometry influence, it can be seen that the yield stress does not increase proportionally to aspect ratio of fibers. We plot Fig. 2.a and Fig 2.b in order to study the effect of the length and the diameter of fibers on the relative yield stress accordingly. We observe that the increase of the length of fibers appears to lead to the increase of the yield stress. Even though it seems that fibers with  $L = 12$  mm may have the highest yield stress values, there is insufficient data for longer fibers (18, 20 and 24 mm) due to the instability of the mix. In Fig 2.b we observe that fiber diameter increase, on the contrary, leads to the decrease of the yield stress.

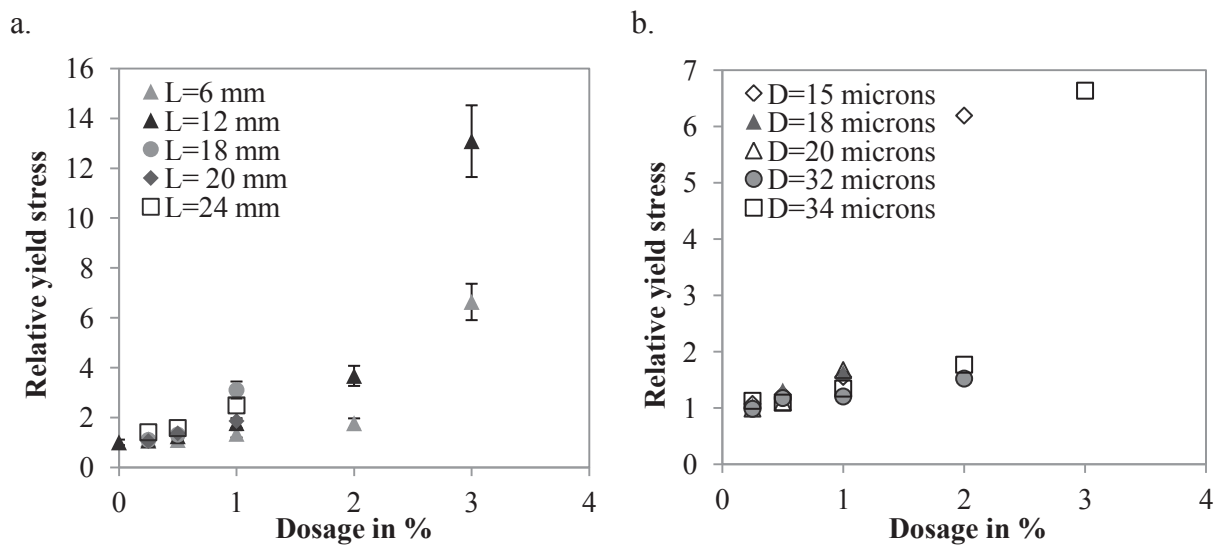


Figure 2: Relative yield stress as a function of fiber dosage. a. Fibers with  $D = 34 \mu\text{m}$  and  $L = 6, 12, 18, 20$  and  $24$  mm. b. Fibers with  $L = 6$  mm and  $D = 15, 18, 20, 32$  and  $34 \mu\text{m}$ .

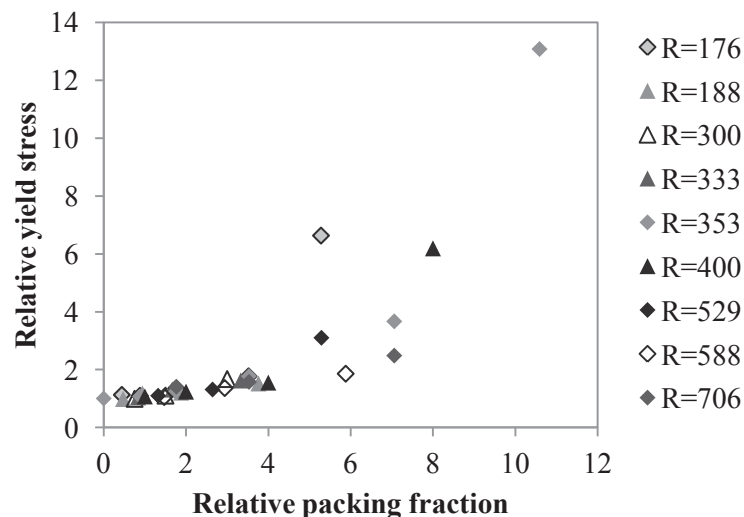


Figure 3: Relative yield stress as a function of relative packing fraction  $\phi R$  for rigid fibers.

In this part we verify whether we can predict the yield stress of the fresh cementitious materials with flexible fibers based on the existing scheme for material with rigid fibers. In Fig. 3 we have plotted our results of the Fig. 1 using the predictive scheme for rigid fibers described in Section 3.3. It can be seen that the scheme is valid at low dosages of fibers when the yield stress of the material with fibers is dictated by the yield stress of the cement paste. With an increase of fiber dosage, after formation of a connected network, direct frictional contacts start to be dominant in the system. Therefore, it is logical to observe that data is more scattered with an increase of fiber dosage. From the analysis using predictive scheme for the yield stress of rigid fiber reinforced materials we can conclude that the influence of the flexible fibers is far more complex than that of rigid fibers due to their bending.

## 5. Conclusions

The aim of this work was to study the impact of flexible fibers on the rheology of the fiber reinforced cementitious materials. In order to accomplish this, slump flow tests were conducted on fresh cement pastes containing polypropylene fibers of various geometries at different dosage. The influence of fiber dosage and geometry was presented and analyzed. From the results, it was possible to conclude that the rheology of flexible fiber reinforced material cannot be characterized the same way as the rheology of rigid fiber reinforced

## Acknowledgements

This work is carried out using the financial assistance from the program of the Investments for the Future of the French government managed by ANDRA.

## References

- [1] Shuttleworth, P., Fire protection of precast concrete tunnel linings on the Channel Tunnel Rail Link, *Concrete* 35(2001), 12-22
- [2] Bilodeau, A., Kodur, V.K.R. and Hoff, G.C., Optimization of the type and amount of polypropylene fibres for preventing the spalling of lightweight concrete subjected to hydrocarbon fire, *Cement and Concrete Composites* 26 (2004), 163-174
- [3] Szwabowski, J. and Ponikiewski, T., Rheological properties of fresh concrete with polypropylene fibres, *Proceedings from the 3rd International Conference on Concrete and Concrete Structures, Slovakia* (2002), 331-338
- [4] Martinie, L., Rossi, P. and Roussel, N., Rheology of fiber reinforced cementitious materials: classification and prediction, *Cem Concr Res* 40 (2010), 226-234
- [5] Krieger, I.M. and Dougherty, T.J., A mechanism for non-Newtonian flow in suspensions of rigid spheres, *Trans.Soc.Rheol.* 3(1959), 137-152
- [6] Roussel, N., *Understanding the rheology of concrete*, UK (2011)
- [7] Philipse, A.P., The random contact equation and its implication for (colloidal) rods in packings, suspensions and anisotropic powders, *Langmuir* 12 (1996), 1127-1133

## **STRAIN HARDENING CHARACTERISTICS OF BLENDED ALKALI ACTIVATED BINDERS CURED AT AMBIENT TEMPERATURES**

**M. Talha Junaid<sup>(1)</sup>, Mohamed Maalej<sup>(1)</sup>**

(1) Department of Civil and Environmental Engineering, University of Sharjah, UAE

### **Abstract**

Micro fibers are extensively used to reduce the brittle response of concrete and alkali activated matrix in tension and flexure. Such composites, if designed correctly, can offer strain hardening characteristics both in flexure and axial tension, which are characterized by large deformations, multiple cracking and high energy absorption during loading. This study looks at characterizing the strain hardening properties of ambient cured alkali activated binders during direct tension and flexural tests at 7 and 28 days. Three-point bending test was performed for flexural evaluation while direct tension test with dog-bone samples were performed to evaluate the axial tensile behavior. A combination of sodium silicate and sodium hydroxide is used to activate a blend of Fly ash and slag to form binders. A high aspect ratio polyethylene (PE) fiber was used in this study. Strength and ductility properties of all samples improved with age of the matrix. The results indicate that the introduction of fibers induced strain hardening response in all samples during flexure and direct tension tests. The load deflection response was significantly improved with high deformations and multiple cracking observed in all tested samples. A significant increase in the flexural toughness for all samples was also witnessed. The results indicate that highly ductile strain hardening alkali activated composites can be obtained at ambient temperatures without the need for heat curing, with properties comparable to both OPC based and heat cured alkali activated composites.

### **1. Introduction**

The brittle response of concrete is of major concern in structural engineering applications. One way of reducing this brittle behavior is the introduction of short discrete fibers, which may be metallic or non-metallic. Practical dosage of fibers varies by volume and has been reported to reduce the brittle response of such composites [1, 2]. Nevertheless, the use of macro fibers in case of fiber reinforced concrete (FRC) results in a quasi-brittle response with increased fracture toughness. More recently over the past few decades the use of micro fibers

has been reported for the development of cementitious composites commonly referred to as engineered cementitious composites (ECC). Such material is characterized by multiple cracking and strain hardening properties. Despite the advantages, such composites utilize a large amount of cement per unit volume thus are deemed unsustainable with a relatively large environmental footprint. To reduce the environmental footprint, alternate binders have been used in the recent past to develop strain hardening composites. Among these is the use of alkali activated binder or geopolymer, which have come to the forefront as an alternate binder to ordinary Portland cement. Alkali activated binders are formed when an alumina and silica-rich source material is activated with a strong metallic alkaline. The source material is usually fly-ash (class F or C), naturally occurring clays, and furnace slag from the production of metals. Generally, sodium, potassium and calcium hydroxides or silicates, or a combination of these is used as activator solutions. Such binders are highly sustainable and cost-effective, since they are manufactured from industrial waste materials. Researchers have found that such binders could be a possible replacement of conventional concrete [3-10]. Past studies [1, 11] on strain hardening alkali activated binders have used extrusion and/or heat curing methods resulting in limited practical applicability for such composites.

In the current work, the alkali activated binder was made using a combination of Class F Fly Ash (FA) and ground granular blast furnace slag (GGBFS) and activated with a combination of sodium hydroxide and sodium silicate solutions. A high aspect ratio polyethylene (PE) fiber in 1.5% by volume was used. The current research aims at studying the flexural and direct tensile behavior of ambient cured alkali activated engineered cementitious composites (AAECC). This works reports on the deflection hardening and multiple cracking behavior of such composites.

## 2. Materials

Commercially available fly ash class-F and ground granular blast furnace slag (GGBFS) was used in equal proportion as a binder for making the matrix. 10 molar sodium hydroxide solution was prepared by dissolving sodium hydroxide pallets with tap water 24 hours prior using. An extra pure sodium silicate solution was used with chemical compositions of 27.2%  $SiO_2$ , 8%  $Na_2O$ , and 64.8% water. The sodium hydroxide to sodium silicate ratio was kept constant at 1.0. The mix proportions of the composite are shown in Table 1. The Polyethylene (PE) Fiber had a dia of 38  $\mu m$  and length of 12.7mm with an elastic modulus of 120 GPa. The fiber tensile strength and density were 2700 MPa and 0.98  $g/cm^3$ , respectively.

Table 1: Mix proportions of the AAECC

<b>NaOH(10M/12M): Sodium Silicate</b>	<b>FA: GGBFS</b>	<b>Fiber Volume</b>
1:1	1:1	1.0%; 1.5% and 2.0%

## 3. Methodology

Rectangular beam samples were used for flexural testing, while dog-boned samples were used for direct tensile tests. Beam samples has a 25mm by 55mm cross-section and a length of

300mm and a clear span of 250mm. The dog bone sample dimension are shown in Figure 1. All beam specimens were tested under three-point bending static test at a loading rate of 1.5mm/min. The loading rate for the dog-bone sample was 1.5mm/min up to first cracking and then increased to 3mm/min thereafter up to failure. The test setup for the flexural and direct tension test are shown in Fig. 1.

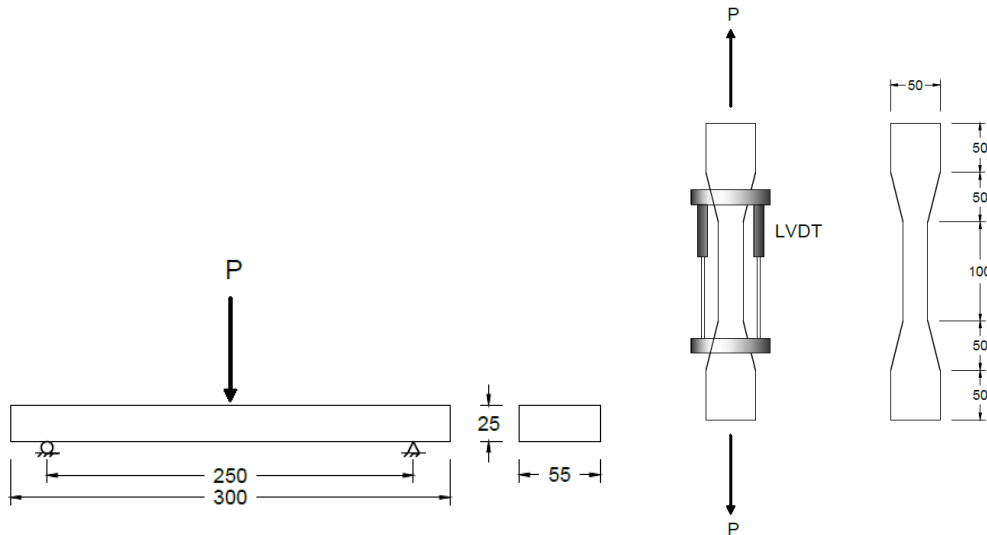


Figure 1: Test set up and sample details (dimensions are in mm)

#### 4. Results and Discussion

The flexural response of the samples made using 10 and 12 M sodium hydroxide solutions at 7 and 28 days is given in Figure 2, while the characteristic properties of these curves are given in Table 2. LOP is the limit of proportionality while, MOR is the modulus of rupture which is defined as the maximum stress after LOP. As per ASTM C1609 the point L/600 and L/150 are defined when the deflection is equal to these values. Since the span of the samples is 250mm these deflection values are 0.417mm and 1.667mm respectively. Other values are defined as; d5 when the deflection is 3 times deflection at LOP, d10 when the deflection is 5.5 times deflection at LOP and d20 when the deflection is 10.5 times deflection at LOP. The toughness, found using the area under the load-deflection curve, at all these key points is also calculated and tabulated in Table 2. As is evident from the results presented in Figure 2, the 7 day behavior for the 10 and 12M specimen is very similar with both samples exhibiting substantial strain hardening response. The toughness properties of these samples is also similar as can be seen from Table 2. At 28 days, the 10M sample gained slight strength as compared to the 7 day samples, while the post peak behavior of this sample exhibited lesser strain softening as compared to samples at 7 days. However, the 28 day response for the 12M sample is much different from all other samples. This sample not only showed increase in LOP and MOR values as well as substantial increase in the toughness at all points of interest, but also had a much better deflection hardening response. This can be attributed to the fact that with time the 12M hydroxide solution was able to form a much denser and stronger binder, resulting in better bond properties between the fibers and the matrix. This enhanced matrix and bond resulted in a more efficient composite.

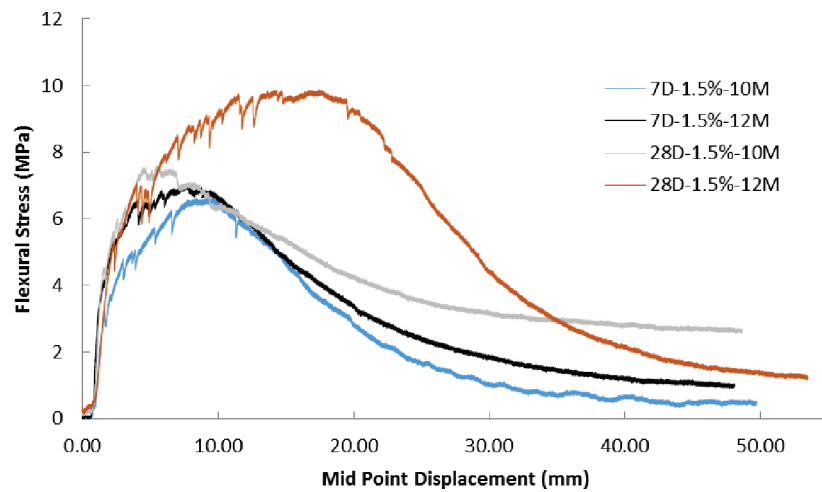


Figure 2: Flexural Response of AAEC with varying Hydroxide Molarity and Time

Figure 3 shows the flexural response of the samples with 1, 1.5 and 2% fiber content at 7 and 28 days for the AAEC with 12M hydroxide solution. As expected, the samples with higher fiber content exhibit better performance in terms of strength and deflection. Also the performance of the samples increased with age of the samples with samples with 2% fiber at 28 days exhibiting the highest strength and a very pronounced deflection hardening response.

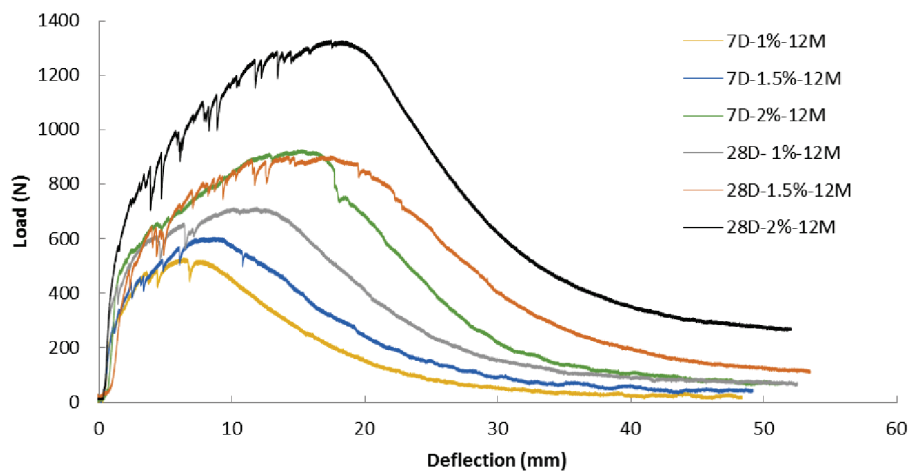


Figure 3: P-Delta curves for AAEC samples with varying fiber content at different age.

The direct tension test results for dog bone samples on 10M samples containing 1.5% fiber by volume at 7 and 28 days is presented in Figure 4. These samples exhibit multiple cracking with significant strain hardening response after first crack with the 28 day sample having a better performance due to increased strength of the matrix, which also positively effects the bond between the matrix and the fiber.

Table 2: Response Quantities of AAEECC

<b>Property</b>	<b>7D-1.5%-R1-10M</b>	<b>28D-1.5%-R1-10M</b>	<b>7D-1.5%-R1-12M</b>	<b>28D-1.5%-R1-12M</b>
$P_{LOP}$	286.2 N	409.8 N	328.2 N	459.9 N
$\delta_{LOP}$	1.58 mm	1.49 mm	1.28 mm	2.12 mm
$f_{LOP}$	3.12 MPa	4.4 MPa	3.58 MPa	5.04 MPa
$Tough_{LOP}$	0.09 N.m	0.215 N.m	0.121 N.m	0.36 N.m
$P_{d5}$	497.4 N	683.7 N	591.9 N	729.3 N
$\delta_{d5}$	4.74 mm	4.47 mm	3.84 mm	6.36 mm
$f_{d5}$	5.43 MPa	7.46 MPa	6.46 MPa	7.98 MPa
$Tough_{d5}$	1.38 N.m	1.87 N.m	1.37 N.m	2.92 N.m
$P_{d10}$	593.7 N	641.7 N	629.4 N	854.4 N
$\delta_{d10}$	8.69 mm	8.195 mm	7.04 mm	11.66 mm
$f_{d10}$	6.48 MPa	7.0 MPa	6.87 MPa	9.41 MPa
$Tough_{d10}$	3.58 N.m	4.35 N.m	3.28 N.m	7.22 N.m
$P_{d20}$	363.6 N	478.8 N	493.5 N	746.1 N
$\delta_{d20}$	16.59 mm	15.65 mm	13.44 mm	22.26 mm
$f_{d20}$	3.97 MPa	5.22 MPa	5.38 MPa	8.16 MPa
$Tough_{d20}$	7.55 N.m	8.45 N.m	7.04 N.m	16.38 N.m
$P_{L/600}$	8.4 N	18.9 N	6.3 N	35.4 N
$\delta_{L/600}$	0.417 mm	0.417 mm	0.417 mm	0.417 mm
$f_{L/600}$	0.1 MPa	0.21 MPa	0.07 MPa	0.39 MPa
$Tough_{L/600}$	0.02 N.m	0.05 N.m	0.01 N.m	0.02 N.m
$P_{MOR}$	606.3 N	694.2 N	644.1 N	904.8 N
$\delta_{MOR}$	8.4 mm	5.46 mm	7.34 mm	17.43 mm
$f_{MOR}$	6.61 MPa	7.57 MPa	7.03 MPa	9.8 MPa
$Tough_{MOR}$	3.41 N.m	2.53 N.m	3.47 N.m	12.29 N.m
$P_{L/150}$	259.2 N	388.8 N	393 N	338.1 N
$\delta_{L/150}$	1.667 mm	1.667 mm	1.667 mm	1.667 mm
$f_{L/150}$	2.83 MPa	4.24 MPa	4.29 MPa	3.76 MPa
$Tough_{L/150}$	0.12 N.m	0.29 N.m	0.27 N.m	0.18 N.m

## 5. Summary and Conclusion

An experimental program was conducted to report on the performance of ambient cured alkali activated engineered cementitious composites in flexure and direct tension. Different dosage of fibers, alkaline activator concentration and curing time were studied as variables and their effect on the response of AAEECC was studied. It was found that such composite undergo strain hardening and might be a feasible alternate to ordinary cement based ECC. Based on the current study the following conclusions can be drawn:

- Ambient cured alkali activated engineered cementitious composites offer a viable option for such composite materials and has properties comparable to OPC composites.
- Age of the sample and dosage of fiber have a positive effect on the strength and deformation characteristics of such composites.

- Increasing the molarity of the sodium hydroxide solution does not significantly affect the response at early age, but has a substantial affect at a later age of the sample.
- Bond between the matrix and fiber plays a very important role in the performance of such composites and increasing this bond can substantially enhance the strength and deflection response of AAEC.

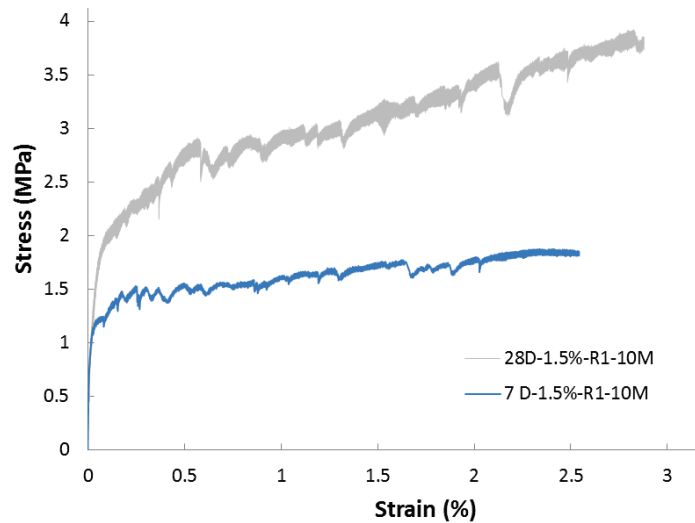


Figure 4: Direct Tensile Response of AAEC at 7 and 28 days

### Acknowledgement

The authors appreciate the support provided by the Sustainable Construction Materials and Structural Systems (SCMASS) group at the University of Sharjah. Help provided by Abdallah Elbana is also highly appreciated.

### References

- [1] SherifEl-Tawil, D.j.A.E.N., Comparative flexural behavior of four fiber reinforced cementitious composites. *Cement and Concrete Composites*, 2008. 30(10).
- [2] Li, M.M.V.C., Flexural/Tensile-Strength Ratio in Engineered Cementitious Composites. *Journal of Materials in Civil Engineering*, 1994. 6(4).
- [3] Elbana, A., Evaluation of flexural behavior of reinforced concrete beams with glass fiber reinforced polymer (GFRP) bars, in *Department of Civil and Environmental Engineering2018*, University of Sharjah: University of Sharjah. p. 108.
- [4] Junaid, M.T., et al., Aspects of the deformational behaviour of alkali activated fly ash concrete at elevated temperatures. *Cement and Concrete Research*, 2014. 60: p. 24-29.
- [5] Junaid, M.T., et al., A mix design procedure for low calcium alkali activated fly ash-based concretes. *Construction and Building Materials*, 2015. 79: p. 301-310.
- [6] Davidovits, J. and J.L. Sawyer, Early high-strength mineral polymer, 1985, Google Patents.
- [7] Davidovits, J., Geopolymer cement. A review. Geopolymer Institute, Technical papers, 2013.
- [8] Provis, J. and J. van Deventer, Alkali Activated Materials State-of-the-Art Report, J. Provis and J.S.J. van Deventer, Editors. 2014, RILEM.
- [9] Junaid, M.T., A. Khennane, and O. Kayali, Stress-Strain Behaviour of Alkali Activated Fly Ash Concrete at Elevated Temperatures, in *2nd International Conference on Advances in Cement and Concrete Technology in Africa2016: Tanzania*. p. 301-308.
- [10] Rangan, B., Fly ash-based geopolymer concrete. *Your Building Administrator*, 2008. 2.
- [11] F.U.A.Shaikh, Deflection hardening behaviour of short fibre reinforced fly ash based geopolymer composites. *Materials & Design*, 2013. 50.



## **STRAIN RATE EFFECT ON THE TENSILE BEHAVIOUR OF ULTRA-HIGH PERFORMANCE STEEL FIBER REINFORCED CONCRETE**

**Veronika Goglin<sup>(1)</sup>, Götz Hüsken<sup>(1)</sup>, Hans-Carsten Kühne<sup>(1)</sup>, H.J.H. Brouwers<sup>(2)</sup>**

(1) Bundesanstalt für Materialforschung und -prüfung (BAM), Berlin, Germany

(2) Eindhoven University of Technology, Eindhoven, The Netherlands

### **Abstract**

For the design and application of concrete structures exposed to high-dynamic loading scenarios, e.g. caused by vehicular impact or seismic events, profound knowledge on the rate sensitive changes in the material behaviour is necessary. Based on its ductile behaviour under tensile loading, ultra-high performance steel fiber reinforced concrete (UHPFC) is a suitable material when it comes to high-dynamic mechanical impacts. Therefore, this research investigated experimentally the strain rate effect on the mechanical behaviour of UHPFC under direct tensile loading. The uniaxial tensile tests were performed on small sized dumbbell shaped specimens at different strain rates, ranging from quasi-static to seismic loading conditions of up to 0.5 1/s. Material parameters of single and hybrid steel fiber reinforced UHPFCs were evaluated regarding first and post cracking stresses, strain capacity, as well as energy absorption capacity. The strain rate effect was expressed by the dynamic increase factor (DIF), describing the ratio between dynamic and quasi-static response.

### **1. Introduction**

The strain rate effect on the mechanical response of conventional concrete under tension has been investigated by numerous authors and methods [1-4]. It is assumed that the strain rate dependent increase of the ultimate stress, the elastic modulus, and the peak strain is caused by two different physical mechanisms [5]. These mechanisms comprise the dependence of the rate of crack opening during the fracture process, and the dependence of the viscoelastic deformation of the unfractured cement matrix, respectively [5]. Nevertheless, structures made of conventional concrete or high-strength concrete have a limited protective effect against high-dynamic loading due to its brittle material failure in tension. Based on its improved mechanical properties regarding strength, stiffness and energy absorption capacity, ultra-high

performance steel fiber reinforced concrete (UHPFC) represents an important material advance in the field of protective construction materials [6]. A summary of previously published studies on the influences of the volume fraction and shape of steel fibers on fiber reinforced concrete subjected to dynamic loading can be found in the review of Soufeiani, L. et al. [7]. They concluded that the behaviour of steel fiber reinforced concrete under blast and impact is still insufficient understood as a consequence of limited research in both numerical and experimental.

The objective of this study is to obtain further experimental information on the strain rate sensitive changes of the mechanical response of single and hybrid reinforced UHPFC mixtures under direct tensile loading. The strain rates considered ranged from 0.000025 1/s to 0.5 1/s, representing quasi-static and seismic loading rates, respectively. To compose a consistent experimental data-base, relevant material parameters, such as first and post-cracking stresses, strain capacity, energy absorption capacity, as well as the dynamic increase factor (DIF) were determined and will be discussed.

## 2. Experimental program

An experimental program was designed to investigate the stress-strain response of two UHPFC mixtures at three different strain rates. The following sections will give a brief description of the materials, mixtures and the test setup.

### 2.1 Materials and mixtures

The base mix proportions of the plain ultra-high performance concretes (UHPCs) are given in Tab. 1. Single and hybrid reinforcements of the UHPFCs were realized by the addition of normal and high-strength smooth steel fibers, respectively. Tab. 2 summarizes the fiber properties, including fiber diameter, fiber length, length-to-diameter ratio, as well as the tensile strength. The fiber volume fractions for both tested UHPFC mixtures F02\_Dx and F02\_BIDx were set to two percent, in which the total number of fiber per unit volume increases with a decrease in length-to-diameter ratio. The single reinforced F02\_Dx mixture incorporated 100 % Dx fibers, whereas the hybrid reinforced F02\_BIDx mixture was composed of 75 % Bl fibers and 25 % Dx fibers, respectively.

Table 1: UHPC base mix proportions in (kg/m<sup>3</sup>).

CEM I 42.5 R-HS/NA	CEM I 52.5 R LA SR	Micro- silica	Meta- kaolin	Basalt 0.125/2.0	Basalt 2.0/5.0	Water	Super- plasticizer
625	125	37.5	75	916.7	550	180	20.25

Table 2: Properties of steel fiber Bl and Dx.

Notation	Diameter $d_f$ (mm)	Length $l_f$ (mm)	$l_f/d_f$ (-)	Tensile strength (MPa)
Bl	0.30	20	67	> 1200
Dx	0.20	13	65	> 2600

## 2.2 Test-setup

The direct tensile tests were conducted displacement controlled using a servo hydraulic and a universal testing machine, respectively. The tests were performed on small sized dumbbell shaped specimens at an age of 56 days or older. The geometry of the specimens (cross-section 20x40 mm; gauge length 100 mm) was designed according to the suggestions of Mechtcherine, V. and Schulze, J. [8]. In order to facilitate stable and even crack growth throughout the cross-section, rigid specimen-to-machine connections were generated. For vertical displacement measurements, linear variable differential transformers (LVDTs) were used. A more detailed description of the test-setup can be found in [9]. Three nominal strain rates of 0.000025 1/s, 0.01 1/s, and 0.5 1/s were applied to the corresponding testing series. At least three specimens were tested for each strain rate and UHPFC mixture, resulting in a testing matrix of two mixtures, three specimens, and three loading rates.

## 3. Experimental outcomes

Four material parameters, including the first cracking stress  $\sigma_{cc}$ , the post cracking stress  $\sigma_{pc}$ , the strain capacity  $\epsilon_{pc}$  at post cracking stress, and the energy absorption capacity  $g_{tc}$  were evaluated in this study. The first cracking stress is defined as the turning point between elastic and plastic parts, whereas the post cracking stress represents the peak stress within the strain hardening phase. The energy absorption capacity is obtained by integrating the stress versus strain curve up to  $\epsilon_{tc}$ , with  $\epsilon_{tc}$  describing the point of transition to consistent softening behaviour (Eq. 1 and Eq. 2). Fig. 1 shows a typical interpretation of the generated test results.

$$\sigma(\epsilon_{tc}) = \sigma_{tc} = \frac{1}{10 - \epsilon_{pc}} \cdot \int_{\epsilon_{pc}}^{10} \sigma(\epsilon) d\epsilon \quad (1)$$

$$g_{tc} = \int_0^{\epsilon_{tc}} \sigma(\epsilon) d\epsilon \quad (2)$$

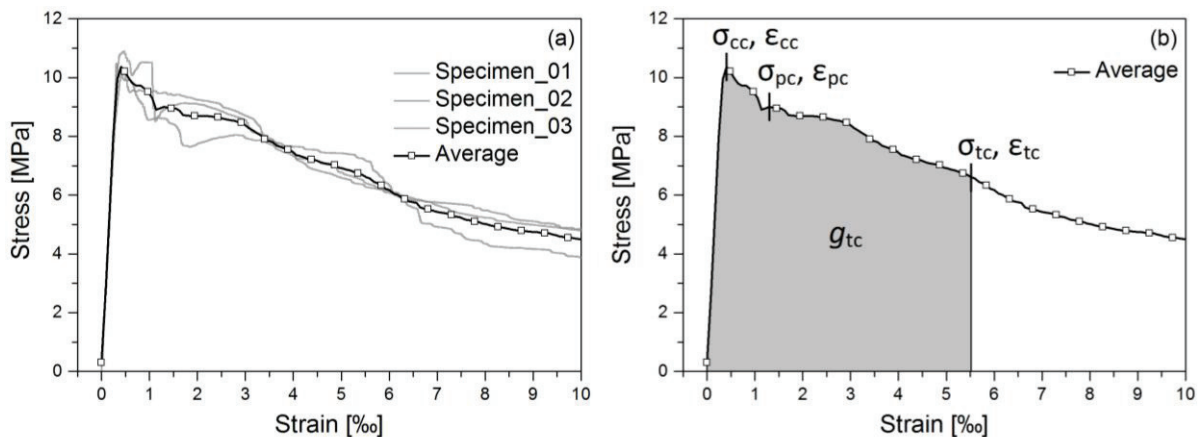


Figure 1: Interpretation of stress-strain results: (a) averaging of the stress-strain curves, (b) material parameters obtained from the averaged stress-strain curve.

### 3.1 Strain rate effect

Fig. 2 shows the average direct tensile stress versus strain relationship of a single and a hybrid steel fiber reinforced UHPFC subjected to nominal strain rate of 0.000025 1/s, 0.01 1/s, and 0.5 1/s. Corresponding material parameters are summarized in Tab. 3. All given values in Tab. 3 are averaged values from at least three specimens. In general, specimen-to-specimen variability within each tested strain rate was relatively low, although a slightly greater variability was registered at quasi-static testing conditions. The strain rate effect was expressed by the dynamic increase factor (DIF), describing the ratio between dynamic and quasi-static material response. The DIF values are also given in Tab. 3.

An increase in the strain rate led general to an increase of the first cracking stress and associated first cracking strain, although the hybrid fiber reinforced F02\_BIDx showed a higher rate sensitivity of first cracking stress than the single reinforced F02\_Dx mixture. The first cracking stress of mixture F02\_BIDx increased by 54 % at a strain rate of 0.01 1/s and 48 % at a strain rate of 0.5 1/s, whereas the first cracking stress of mixture F02\_Dx increased by 32 % for both applied dynamic strain rates. A consistent strain rate dependent increase in post cracking stress was only obtained by the hybrid fiber reinforced F02\_BIDx mixture, exhibiting a value of 9.52 MPa at a strain rate of 0.01 1/s and a value of 10.02 MPa at a strain rate of 0.5 1/s. The single fiber reinforced F02\_Dx mixture revealed a slight decrease in post cracking stress from 7.82 MPa to 7.01 MPa as the strain rate changed from 0.000025 1/s to 0.01 1/s, even though a value of 9.43 MPa was reached at a strain rate of 0.5 1/s. In contrast to the strain rate effect on the post cracking stress, mixture F02\_Dx exhibited a significant strain rate sensitive behaviour for strain capacity which in particular doubled when the strain rate was set to dynamic loading conditions. Mixture F02\_BIDx revealed a negligible strain rate effect on strain capacity. For both tested mixtures, not only first cracking stress generally increase as the strain rate increase from quasi-static to seismic loading conditions, but also the energy absorption capacity. The energy absorption capacity of mixture F02\_Dx increased from 29.83 kJ/m<sup>3</sup> to 34.20 kJ/m<sup>3</sup> to 49.01 kJ/m<sup>3</sup> as the strain rate increased, resulting in DIF values of 1.15 and 1.64, respectively. Mixture F02\_BIDx displayed an energy absorption capacity of 23.01 kJ/m<sup>3</sup> at 0.000025 1/s, 44.94 kJ/m<sup>3</sup> at 0.01 1/s, and 37.89 kJ/m<sup>3</sup> at 0.5 1/s, respectively. Corresponding DIFs were calculated to 1.95 at 0.01 1/s and 1.65 1/s at 0.5 1/s.

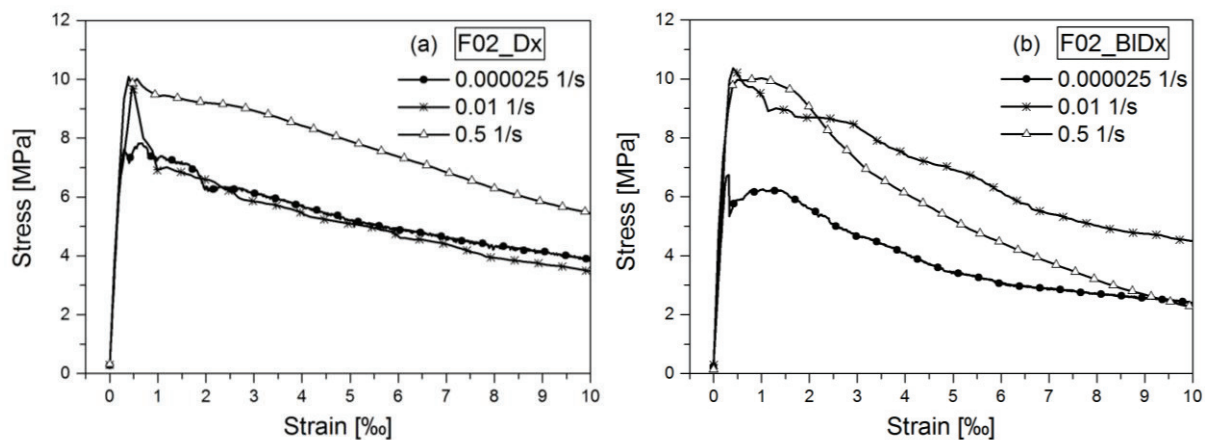


Figure 2: Strain rate effect on the tensile response of single and hybrid reinforced UHPFCs.

Table 3: Average tensile parameters of UHPFC mixtures tested at different strain rates.

Notation	Strain rate (1/s)	First cracking stress $\sigma_{cc}$ (MPa)	DIF (-)	Post cracking stress $\sigma_{cc}$ (MPa)	DIF (-)	Strain capacity $\varepsilon_{pc}$ (‰)	DIF (-)	Energy absorption capacity $g_{tc}$ (kJ/m <sup>3</sup> )	DIF (-)
F02_Dx	0.000025	7.62	1.00	7.82	1.00	0.60	1.00	29.83	1.00
	0.01	10.08	1.32	7.01	0.90	1.19	1.98	34.20	1.15
	0.5	10.02	1.32	9.43	1.21	1.22	2.03	49.01	1.64
F02_BIDx	0.000025	6.73	1.00	6.26	1.00	1.03	1.00	23.01	1.00
	0.01	10.36	1.54	9.52	1.44	1.29	1.25	44.94	1.95
	0.5	9.97	1.48	10.02	1.60	0.99	0.96	37.89	1.65

Overall, the single fiber reinforced mixture F02\_Dx showed typical strain rate affected behaviour, revealing a log-linear relationship of DIF values. Comparable DIF trends for UHPFC mixtures incorporating two volume percent of high-strength smooth steel fibers were reported by Xu, M. and Wille, K. [10] for moderate strain rates. However, the hybrid fiber reinforced mixture F02\_BIDx displayed relative high strain rate sensitivity for all obtained material parameters except the strain capacity, although the increase in DIF values was inconsistent. The high strain rate sensitivity of mixture F02\_BIDx might be attributed to the higher fiber-matrix bond of the incorporated long fibers. Furthermore, it can be generally assumed that the embedded fibers are primarily oriented in the longitudinal direction of the specimen, which enhances the mechanical properties of both mixtures under uniaxial tensile loading. The fiber alignment in the direction of the applied load is attributed to the small mold geometry (20 mm x 40 mm) relative to fiber length (13 mm and 20 mm), and hence to the casting method. In case of the hybrid reinforced mixture the incorporated long fibers serve as additional boundaries, which restrict the rotation of the short fibers, and thus maintain a more favorable fiber allegation in the direction of applied load. Nevertheless, for the same volumetric fiber content of two percent the single reinforced mixture F02\_Dx generally exhibited better mechanical performance than the hybrid reinforced mixture F02\_BIDx. This improvement can be explained by the more efficient fiber dispersion per unit volume, as well as by the effective higher tensile strength of the incorporated steel fibers.

#### 4. Conclusion

The strain rate sensitive changes in the mechanical response of single and hybrid reinforced UHPFCs were investigated experimentally at three different strain rates. Based on the obtained results, the following conclusions can be drawn:

- For both tested UHPFC mixtures first cracking stress and energy absorption capacity generally increased as the strain rate increased from quasi-static to seismic loading conditions. Among all tests, the single reinforced F02\_Dx mixture revealed the highest value for energy absorption capacity with 49.01 kJ/m<sup>3</sup> at a strain rate of 0.5 1/s.

- The hybrid fiber reinforced mixture F02\_BIDx displayed relative high strain rate sensitivity for first and post cracking stresses and energy absorption capacity. The high strain rate sensitivity of mixture F02\_BIDx might be attributed to the higher fiber-matrix bond of the incorporated long fibers.
- For the same volumetric fiber content of two percent the single reinforced mixture F02\_Dx generally exhibited better mechanical performance than the hybrid reinforced mixture F02\_BIDx. This improvement can be explained by the more efficient fiber dispersion per unit volume, as well as by the effective higher tensile strength of the incorporated steel fibers.
- Typical strain rate affected behaviour was only observed for the single reinforced F02\_Dx mixture, revealing a log-linear relationship of DIF values.

## References

- [1] Watstein, D., Effect of straining rate on the compressive strength and elastic properties of concrete, *J Am Concrete Inst* 49 (1953), 729-744
- [2] Mindess, S. and Bentur, A., A preliminary study of the fracture of concrete beams under impact loading, using high speed photography, *Cem Concr Res* 15 (1985), 474-484
- [3] Jawed, I., Childs, G., Ritter, A., Winzer, S., Johnson, T. and Barker, D., A., High-strain-rate behavior of hydrated cement pasts, *Cem Concr Res* 17 (1987), 433-440
- [4] You, J. H., Hawkins, N. M. and Kobayashi, A. S., Strain-rate sensitivity of concrete mechanical properties, *ACI Mat J* 89 (1992), 146-153
- [5] Cusatis, G., Strain-rate effects on concrete behavior, *Int J Impact Eng* 38 (2011), 162-170
- [6] Millon, O., Analyse und Beschreibung des dynamischen Zugtragverhaltens von ultrahochfestem Beton, PhD thesis, Technische Universität Dresden (2014)
- [7] Soufeiani, L., Raman, S. N., Jumaat, M.Z, Alengaram, U. J., Ghadyani, G. and Mendis, P., Influences of the volume fraction and shape of steel fibers on fiber-reinforced concrete subjected to dynamic loading – A review, *Eng Struct* 124 (2016), 405-417
- [8] Mechtcherine, V. and Schulze, J., Testing the behaviour of strain hardening cementitious composites in tension, Paper presented at the int. RILEM Workshop on HPCFRCC in Structural Applications, Honolulu (2005)
- [9] Goglin, V. et al, Tensile response of ultra-high performance steel fiber reinforced concrete under moderate strain rates, *Proc. of the 12th fib International PhD Symposium in Civil Engineering*, Prague (2018)
- [10] Xu, M. and Wille, K., Fracture energy of UHP-FRC under direct tensile loading applied at low strain rates, *Composites Part B* 80 (2015), 116-125

## **STRAIN RESILIENT CEMENTITIOUS COMPOSITES MADE WITH CALCAREOUS FLY ASH AND POLYPROPYLENE FIBERS: THE EFFECT OF TEMPERATURE AND FREEZE-THAW ON FLEXURAL TENSION**

**Souzana Tastani <sup>(1)</sup>, Ioannis Savvidis <sup>(2)</sup>**

(1) Assistant Professor, Dep. of Civil Engineering, Democritus University of Thrace, Greece

(2) Civil Engineer, Democritus University of Thrace, Xanthi, Greece

### **Abstract**

Strain Resilient Cementitious Composites (SRCC) made by Greek unclassified calcareous fly ash and polypropylene fibers are sustainable materials with adequate mechanical properties, appropriate for structural solutions. They are experimentally studied in the present study in regards to their flexural response with parameters in the composition the high fly ash and fibers contents. Prisms of different geometry were tested in three and four-point bending aiming to explore the effect of the static system on the tensile properties. Accompanied specimens were subjected to elevated temperature (above the fiber's melting point) and freeze-thaw cycling before testing aiming to assess the material tensile vulnerability under these conditions. The experimental results of load and deflection are inversely analyzed for the assessment of the tensile stress-strain law of these materials given the two static systems.

### **1. Introduction – Scope of the research**

Former studies [1,2] on Strain Resilient Cementitious Composites (SRCC) made with Greek unclassified calcareous fly ash and polypropylene fibers (PP) in regards to the compressive behavior (at 28 days, at later age and after being subjected to freeze-thaw conditioning) and to drying shrinkage (in terms of volumetric strain) showed that these materials have adequate strength and resistance against cracking and can be used as sustainable materials for conventional structures. In this accompanying paper, these SRCCs are examined in regards to their flexural tension with parameters in the composition the fly ash share (two and three times the cement weight) and the fibers content (0 as a reference composition, 1.5% and 2% per volume). Specimens of different geometry (prisms and beams) were tested in three and

four-point bending, respectively, aiming to study the effect of the static system on the material mechanical response. Accompanying specimens were subjected to elevated temperature and freeze-thaw cycling before flexural testing aiming to assess any deterioration in the mechanical properties, like as first cracking load, ultimate load, deformation resilience and fracture energy. Three tests were performed for each SRCC and static system. In the second part of the paper, reverse analysis on load – deflection measurements was implemented for both static systems aiming to extract milestone values of the direct tension response of the studied SRCCs. For this purpose the principle of virtual work and cross section analysis along with simplified constitutive relations for compression and tension were adopted.

## 2. Experimental Program

Cement CEM I 52.5N (C) was used to provide adequate compressive strength at 28 days (over 30MPa) given the later activation of the fly ash. Dried, fine silica sand (S) was also used (100% passed through a sieve with diameter of 0.5 mm). The Greek fly ash (FA) has low sum of pozzolanic components (in the order of 50%) and high content of CaO and CaO<sub>f</sub> (38% and 15% respectively). Polypropylene microfibers (PP) had the following characteristics: diameter  $d_f=25\mu\text{m}$ , length  $l_f=12\text{mm}$ , stress and strain at fracture  $f_{fu}=400\text{MPa}$ ,  $\varepsilon_{fu}=0.25$ , melting/ignition point 160/570°C (ThracePlastics, type TMIX-12). The effective water was kept constant for all mixes ( $w'$  is the water to binder ratio). The quantity of the HRWR super-plasticizer (SIKA Hellas, VISCOCRETE-ULTRA 200) was varied in each composite (in Table 1, it is given per binder weight). The composition of the four SRCC mixes is shown in Table 1; the code name FAi-PPj is interpreted as follows: FA2 or 3 denotes the fly ash share per cement weight and PP1.5 or 2 the fibers content per volume. The reference compositions (no fibers) had the same mixing ratios except of the required HRWR (1.33% and 1.5% for FA2 and FA3 respectively). A total of 78 specimens were constructed: 54 prisms of 40x40x160 (height x width x length, in mm) and 24 small beams of 70x60x370 were loaded in three and four point bending, respectively (Fig. 1a). In the case

of beams, the absence of shear in the region of constant moment, as opposed to a single cross section of maximum moment in the case of prisms, may mobilize more material in tension. All specimens were cured in chamber ( $\sim 20^\circ\text{C}$ , 95% RH) for a month from casting. For prisms, 18 specimens were tested in pristine condition (3 specimens x 4 composites + 3 specimens x 2 mixes without fibers, named as FA2 and FA3), 18 accompanied specimens were exposed to 200°C (pre-heated oven) for 2 hours before loading and the remaining 18 were subjected to 34 freeze/thaw cycles ( $\pm 20^\circ\text{C}$ , cycle duration 48 hours) before testing (simulating extreme winter conditions in Greece). For beams, 12 specimens were served as reference whereas the rest 12 were exposed to 200°C for 3 hours before loading. It is noted that no decaying or cracks were observed after heating or freeze/thaw. A displacement-control protocol was adopted for both tests (0.3mm/min); deflection was recorded by LVDT and digital monitoring (Fig.1a).

Table 1: Mixing ratios of four SRCC composites

Code Name	C	FA / C	S / C	$w'$	PP (%)	HRWR (%)
FA2-PP1.5					1.50	4.67
FA2-PP2	1.00	2.00	1.10	0.37	2.00	5.33
FA3-PP1.5					1.50	5.00
FA3-PP2		3.00			2.00	6.00



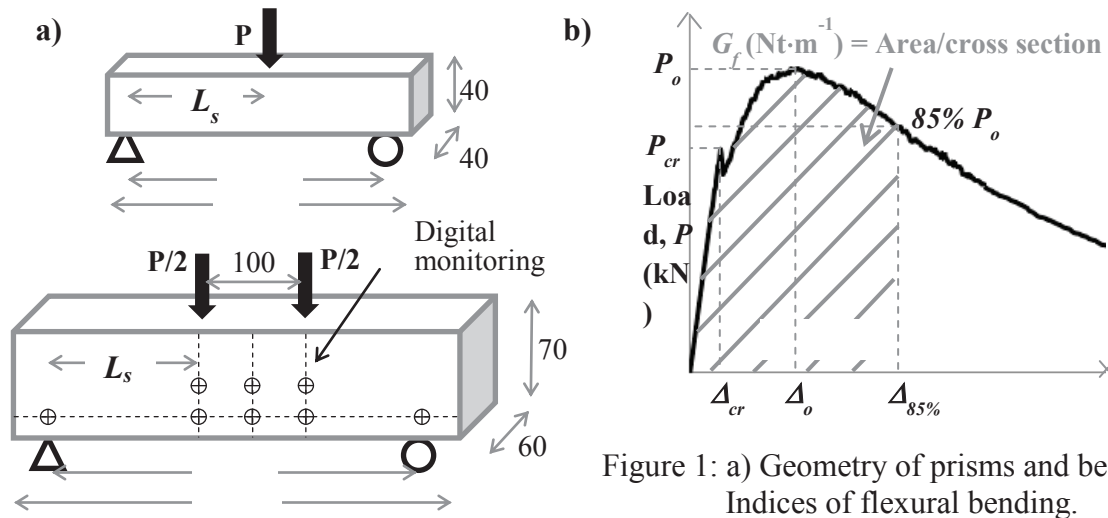


Figure 1: a) Geometry of prisms and beams. b) Indices of flexural bending.

### 3. Experimental results

The experimental results are presented as average load versus mid-deflection envelopes of three tests for each SRCC. With reference to Fig. 1b, important stages are a) the first cracking ( $\Delta_{cr}$ ,  $P_{cr}$ , where the flexural elastic strength  $f_{fl,cr}$  is calculated for each test, as  $f_{fl,cr} = 3P_{cr}L_s/(bh^2)$ , where  $L_{s,prism/beam} = 70/120\text{mm}$ ), at strength ( $\Delta_o$ ,  $P_o$ ) and at residual resistance ( $\Delta_{85\%}$ ,  $P_{85\%}$ , with deflection resilience,  $\mu_{85\%} = \Delta_{85\%}/\Delta_{cr}$ ) and b) the apparent fracture energy  $G_f$  (ratio of the grey-hatched area up to 85% of residual strength to the specimen cross-sectional area, Fig. 1b).

#### 3.1 Prisms

The reference prisms (denoted at “ref.” in Figs. 2, 3) developed only one crack near the point of maximum moment (critical cross section). On the other hand, prisms exposed either to elevated temperature or freeze/thaw cycles (denoted at “t” and “fr-th” respectively in Figs. 2, 3) developed more than two cracks, usually on either side of the critical cross-section. Figure

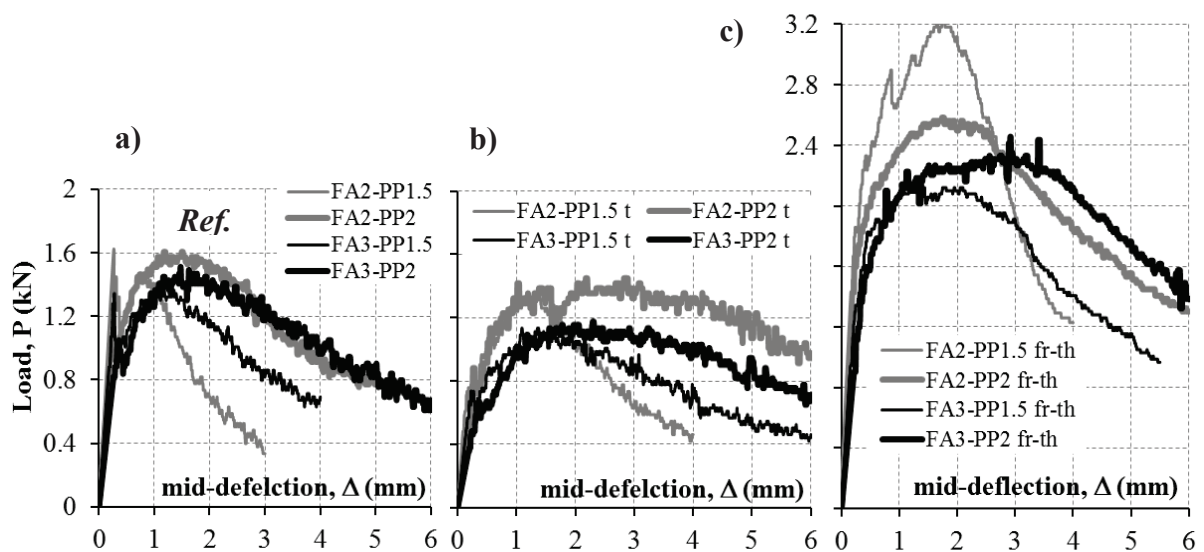


Figure 2: Comparative response of SRCC prisms under conditioning (ref., t, and fr-th).

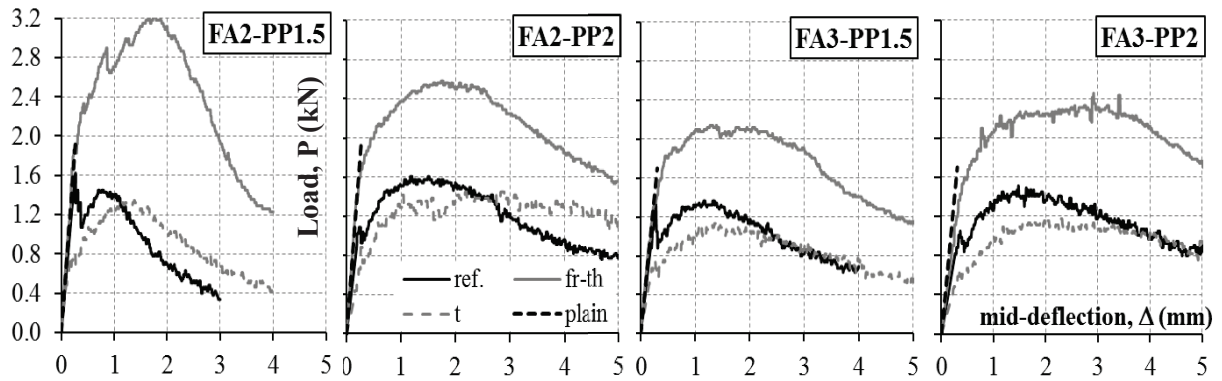


Figure 3: The impact of conditioning (temperature  $t$ , and freeze-thaw  $fr-th$ ) on each SRCC prism bending response. Also appeared is the elastic response of mixes without fibers (plain). 2 shows the average load-mid deflection curves of the three prism categories, where with grey and black color are denoted the mixes with two and three parts of fly ash respectively (the line thickness is related to the increase in PP content). From Fig. 2a it may be concluded that the most sustainable SRCC (i.e., FA3-PP2) behaved similarly to that of the highest cement content (i.e., FA2-PP2). The fibers' volumetric ratio affected the transition from elastic to post-elastic stage (see also in Fig. 3 the reference curves): in mixes with 1.5% PP, load  $P_{cr}$  was instantly reduced by near 35% and fully recovered at strength ( $P_{cr} \approx P_o$ ) whereas in mixes with 2% PP there was a mild transition and  $P_{cr} < P_o$ . Elevated temperature (Fig. 2b) affected the tensile behavior as follows: there is no distinct first cracking stage (absence of load jump), strength was reduced (it is more pronounced in FA3 compositions, see also Fig. 3), whereas the post-strength response is mildly descending as a consequence of multiple cracking thus attributing the characteristic of strain resilience (i.e., a wide parabolic response, that is stronger in case of FA2-PP2-t, Fig. 3b). Under freeze/thaw conditioning, all SRCCs showed a mild transition from elastic to un-elastic stage, they improved strength (even twice, Fig. 2c) as a result of ongoing saturation during conditioning (thus mobilizing the development of late CSH hydrants) as well as strain resilience due to multicracking. Comparing Figs. 2a-c, it is noted that the most sustainable FA3-PP2 is equivalent to the most cementitious FA2-PP2.

### 3.3 Beams

The reference specimens during loading developed a single crack in the constant moment region despite the fact that a region rather than a cross section is under maximum tension. This may be attributed to both the low fiber's stiffness and the strong fiber-to-matrix bond which favors fiber elongation rather than slippage in the cracked cross section resulting in the widening of the crack. Mix FA2-PP2 prevails as per strength, but FA3-PP2 seems to be more resilient demonstrating a broader load – deflection response (Fig. 4a). Heating of beams before loading had the same effect in

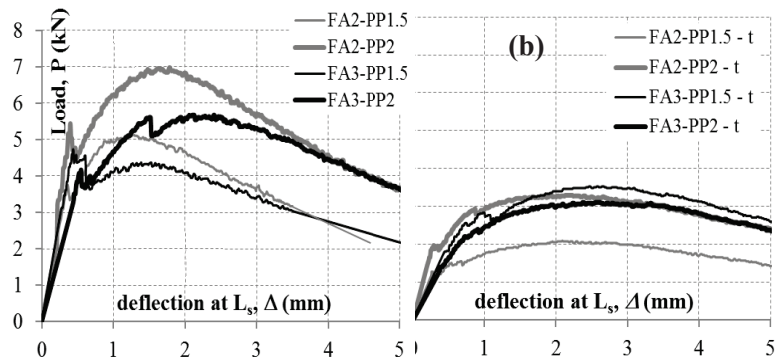


Figure 4: Comparative response of SRCC beams (ref. and t).

Figure 4a. Heating of beams before loading had the same effect in

respect to cracking and the associated shape of load-deflection response (Fig.4b). The increased duration of heating caused drop of strength about 40 to 60%; to this contributed the elimination of fibers near the outer surfaces of specimens (after inspection of cracked sections).

### 3.3 The effect of the static system on the flexural response

The comparison of behavioral indices between the two systems is discussed with reference to

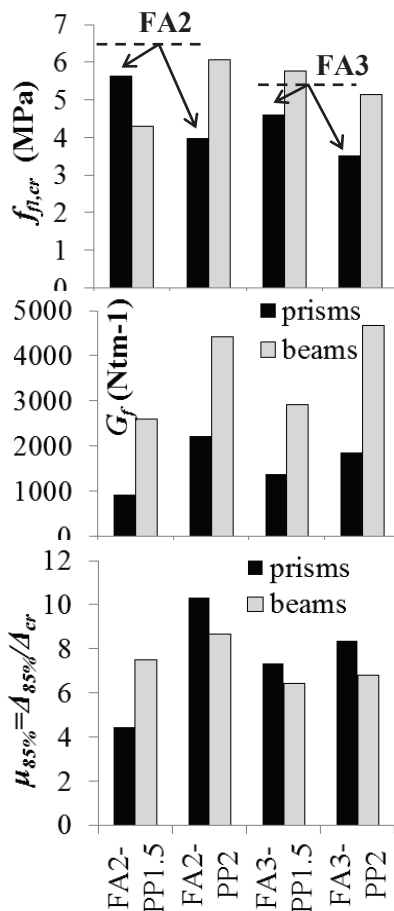


Figure 5: Indices  $f_{fl,cr}$ ,  $G_f$ ,  $\mu_{85\%}$  of reference specimens.

Fig.5: prisms in three-point bending are indicated in black color and beams in four-point bending in gray. The comparison only refers to the reference specimens:

- The elastic flexural strength,  $f_{fl,cr}$ , is greater in beams for the majority of SRCCs mainly due to the absence of shear in the constant moment area. The associated value for the plain mixes (without fibers) was measured only by prisms and is denoted by dashed lines.

- Apparent fracture energy,  $G_f$ , is greater in beams due to the fact that more material is activated in maximum tension (and not a single cross section in the case of prisms); SRCCs with 2% PP fibers (regardless the FA content) have the same magnitudes per static system (plain mixes,  $G_f \approx 1500 \text{ Nm}^{-1}$ ).

- Deflection resilience  $\mu_{85\%}$  at residual resistance of beams is somehow inferior of prisms. Lower bound values of indices  $f_{fl,cr}$ ,  $G_f$ , and  $\mu_{85\%}$  of SRCCs with PP2% can be considered 5.5MPa,  $4500 \text{ Nm}^{-1}$  and 7 respectively.

### 4. Analytical tensile stress-strain relation

The following algorithm [3] is implemented in both static systems aiming to determine the axial tensile stress - strain law of the SRCCs; here, only mixes with 2% PP fibers are analyzed (and only the reference tests):

a) First, from load versus deflection the moment - curvature diagram is assessed using the principle of virtual work.

b) Second, a cross-sectional analysis was performed based on force and moment equilibrium and Bernoulli's

hypothesis for plane cross section during bending. Necessary tools are the constitutive relations of axial compression and tension. The response in compression is shown in Fig. 6a and it was based on accompanying tests on cubes [1,2]. The response in axial tension is approximated as a tri-linear envelope, in where the stress and strain values are to be the output of the algorithm. The unknown values of the milestone points of the tension law are (Fig. 6b): first cracking (point 1:  $\varepsilon_{t,cr}$ ,  $f_{t,cr}$ ), strength (point 2:  $\varepsilon_{t,o}$ ,  $f_{t,o}$ ) and residual resistance (point 3:  $\varepsilon_{t,85\%}$ ,  $85\%f_{t,o}$ ). The analysis is performed under the conditions that the strains of the extreme fibers of the cross section do not exceed the limits imposed by the compression strain capacity of the SRCC (15% drop of strength, Fig. 6a) and the rupture strain of fiber,  $\varepsilon_{fu}=0.25$ . Any excess of strain denotes failure. Figure 6.b illustrates the resulting tensile stress-strain law of the considered SRCCs for both static systems. Prism (continuous lines) shows lower strength

but higher strain resilience whereas beam (dashed lines) demonstrates reverse behavior. As lower, safe values for these SRCCs may be considered: tensile strength (point 2),  $f_{t,o}=2.5\text{MPa}$  (average of two static systems) while the strain resilience at point 3 is conservatively set to 0.03 (from four-point bending).

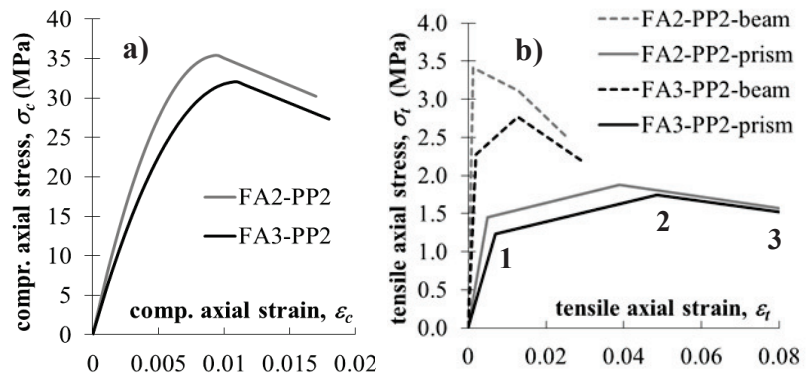


Figure 6: Laws of SRCCs in a) compression and b) tension.

## 5. Conclusions

Aiming to explore the influence of Greek, calcareous fly ash and the polypropylene fibers contents, as both materials are the list studied ingredients in SRCCs, flexural tests were conducted considering two static systems. Apart from reference specimens, associated coupons, before loading, were subjected to elevated temperature and to freeze/thaw cycling. In general, the experimental curves of load vs. deflection had a wide parabolic shape, with limited load jumps in the post elastic response as a result of the development of few cracks, in where all material's deformation was concentrated. This response is believed to be attributed to the low stiffness of the PP fibers in combination with strong bond at the fiber-matrix interface. The latter promotes fiber elongation rather than controlled slippage promoting the occurrence of early crack stabilization. Comparison between the four SRCCs revealed that the greenest composition (with the maximum fly ash share and 2% PP fibers, FA3-PP2) had equivalent behavior to the one with the higher cement dosage, both in pristine and after freeze-thaw conditioning, and somehow inferior due to heating. This new material is deemed as a sustainable material appropriate for structural use, with axial tensile strength 2.5MPa, strain resilience at least 0.03 and compressive strength over 30MPa.

## Acknowledgements

Materials grant: SIKKA HELLAS, Thrace Plastics Co S.A., DEI Ptolemais. Funding: SARF DUTH (Project ETAA, ID 81483).

## References

- [1] Tastani, S. Veneti M., Zapris V. Strain resilient cementitious composites: compressive response and volumetric stability, RILEM/COST PRO from 2<sup>nd</sup> Int. Conf. on Early Age Cracking and Serviceability in Cement-based Materials and Structures - EAC2, Belgium (2017)
- [2] Tastani, S. Ntampanli E., Savvidis I., Veneti M., Zapris V. Strain Resilient Cementitious Composites of unclassified calcareous fly ash and PP fibers: performance by also considering durability effects, RILEM PRO from 4<sup>th</sup> Int. Conf. SHCC, Germany (2017)
- [3] Georgiou, A.V. and Pantazopoulou, S.J., Effect of fiber length and surface characteristics on the mechanical properties of cementitious composites, *Constr Build Mat* 125 (2016), 1216–1228

## **STUDY ON TEMPERATURE DEPENDENCE OF PROPERTIES OF HIGH STRENGTH MORTAR USING HIGH ALITE CEMENT AND POZZOLANIC FINE POWDER**

**Hirokazu Kiriya<sup>(1)</sup>, Eiji Maruya<sup>(1)</sup>, Kenji Kawai<sup>(2)</sup>, Ryoichi Sato<sup>(2)</sup>**

(1) Technical Development Center, Construction Materials Co., UBE Industries, Ltd., Japan

(2) Department of Civil and Environmental Engineering, Hiroshima University, Japan

### **Abstract**

A new ultra-high-performance fibre-reinforced concrete (UHPFRC) with a high alite content cement and fine pozzolanic powder matrix, has recently been developed in Japan. This new UHPFRC does not require the heat treatment needed for conventional UHPFRC. The new UHPFRC includes a large quantity of highly reactive binders and fine pozzolanic powder. Moreover, its hydration generates remarkably large heat and the development of its compressive strength is difficult to be evaluated. The objective of this study was to establish a method of estimating the compressive strength of this new UHPFRC. Therefore, the apparent activation energy of the new UHPFRC was estimated to modify the temperature adjusted age. It was found that the temperature dependency of the compressive strength can also be evaluated with high accuracy by using the modified temperature adjusted age. Additionally, it is possible that the apparent activation energy may depend on the reaction of fine pozzolanic powder.

### **1. Introduction**

A new ultra-high-performance fibre-reinforced concrete (UHPFRC), with a high alite content cement and fine pozzolanic powder matrix, has recently been developed in Japan. This new UHPFRC does not require the heat treatment needed for a conventional UHPFRC; therefore, it can be casted on-site. The new UHPFRC has a large quantity of highly reactive binders, whose hydration generates remarkably large heat and results in higher member temperature. Additionally, the new UHPFRC has a low water/binder ratio, which produces high autogenous shrinkage and results in high risk of cracking at early ages.

To reasonably control early age cracking, it is important to properly evaluate the development of physical properties depending on the high temperature thermal history. UHPFRC has a

binders that reacts more actively at high temperatures. Therefore, it is difficult to estimate the properties of UHPFRC, since this depends on the thermal history of high temperatures.

From the abovementioned background, this study estimated the apparent activation energy based on the development of compressive strength, which was normalized by the ultimate strength as an index of the reaction rate, to establish a method of estimating the material properties of ultra-high-strength mortar comprising of high alite content cement and fine pozzolanic powder. Additionally, a modified temperature adjusted age is proposed based on the estimated apparent activation energy. Finally, in order to investigate the factor that the apparent activation is not constant, the relationship between the hydrations of binders and modified temperature adjusted age was studied.

## **2. Experimental programme**

### **2.1. Materials and proportions of high strength mortar and cement paste**

High alite content cement and fine pozzolanic powder were mixed with unreactive inorganic powders as a high strength mortar binder for UHPFRC. Crushed sand (dry density: 2.62 g/cm<sup>3</sup>, water absorption rate: 2.5%, fineness modulus: 2.59) was used as a fine aggregate, and a polycarboxylate based superplasticizer was also used. The mixed proportions of high strength mortar for UHPFRC consisted of 230 kg/m<sup>3</sup> of water, 1,830 kg/m<sup>3</sup> of premixed powder, 330 kg/m<sup>3</sup> of fine aggregate, and 31.2 kg/m<sup>3</sup> of superplasticizer content. The cement components were 57.6% C<sub>3</sub>S, 21.5% C<sub>2</sub>S, 1.1% C<sub>3</sub>A and 14.3% C<sub>4</sub>AF. The blain surface area was 3,180 cm<sup>2</sup>/g. The main component of fine pozzolanic powder was SiO<sub>2</sub>, the density was 2.2 g/cm<sup>3</sup>, and the BET specific surface area was 18.9 m<sup>2</sup>/g.

The mix ratio of cement paste with water/binder was 16%, the replacement ratio of fine pozzolanic powder to cement was 10%, and 1.4% of superplasticizer was used as the binder.

### **2.2. Specimen preparation and curing**

High strength mortar was mixed by mortar mixer for 10 minutes. The fresh mortar was casted into  $\phi 50 \times 100$  mm cylinder moulds, which were then sealed by plastic sheets and cured at the temperatures listed in Tab.1. The curing temperature exceeded 60 °C. First, the moulds were maintained at a temperature of 20 °C for 8 hours. Then, the heat increase to the set temperature/decrease to ambient temperature was controlled at 20 °C/h. Cement paste was conducted the same way.

### **2.3. Compressive strength**

The compressive strength was measured according to JIS A1108. The ages in the compressive strength experiment are listed in Tab. 1.

### **2.4. Hydration of cement and fine pozzolanic powder**

When the pastes hydrated at the curing temperature (Tab.2), the slices from the cylinders were placed in acetone to stop the hydration reaction, and were then measured hydrations.

The reaction rate of cement was calculated by estimating the area of the unreacted cement particles [1].The specimen was polished to mirror-finish. A scanning electron microscope (SEM) fitted with a backscatter electron detector (BSE) was used for imaging. The microscope was operated at an accelerating voltage of 15Kv, and images were collected per specimen at a magnification of 500 with 20 fields. Image processing was carried out based on

the mode method, such that a binarized image corresponding to the anhydrous particles could be obtained. Subsequently, we estimated the unhydrated area.

The amount of the unreacted fine pozzolanic powder was measured according to the HCl- $\text{Na}_2\text{CO}_3$  selective dissolution method [2].

Table 1: Curing temperature and measuring ages of mortar's compressive strength.

$T_k^{*1}$	Ages of measuring (h: hours, d: days)
80°C	12h, 16h, 18h, 21h, 3d, 7d, 28d
60°C	14h, 23h, 3d, 7d, 28d
40°C	1d, 2d, 3d, 7d, 14d, 21d, 28d
30°C	9.5h, 10.5h, 12h, 14h, 16.5h, 20h, 1d, 2d, 7d, 28d, 56d, 91d
20°C	11.3h, 15.5h, 18h, 20h, 21h, 22h, 1d, 2d, 3d, 6d, 7d, 14d, 21d, 28d, 42d, 56d, 70d, 91d
15°C	16h, 22h, 1.2h, 1.8h, 2.8h
10°C	20h, 1d, 1.2d, 1.3d, 1.4d, 1.9d, 7d, 14d, 21d, 28d, 42d, 56d, 70d, 91d, 182d, 300d

\*1: Curing temperature.

Table 2: Curing temperature and measuring age of pastes' compressive strength.

Curing Temperature	Ages of measuring (h: hours, d: days) Paste
80°C	2d, 5d
40°C	2d, 7d, 28d
30°C	2d, 7d, 28d
20°C	2d, 7d, 28d

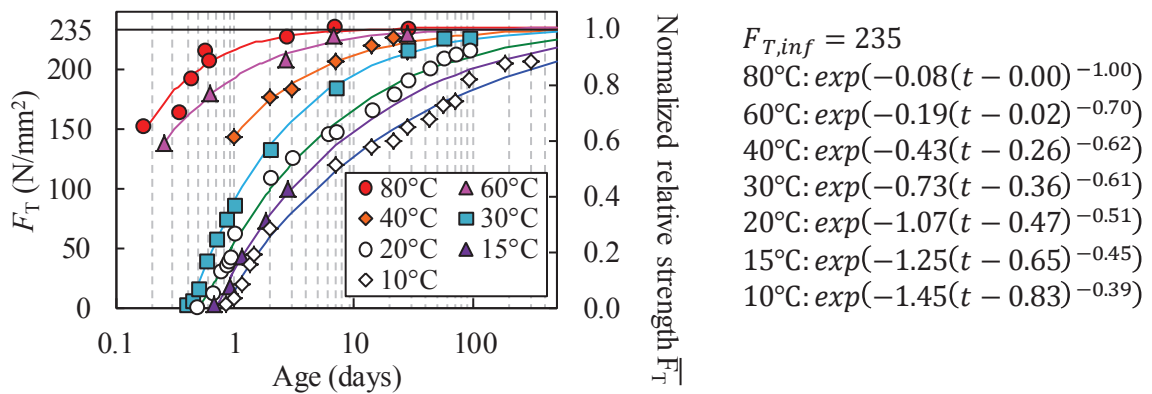


Figure 1: Compressive strength/normalized relative strength at each curing temperature.

### 3. Result and discussion

Figure 1 shows the compressive strength of mortar at each curing temperature. The compressive strength of the specimens cured at higher temperature was naturally higher. With regard to the specimens cured at 80 °C, their compressive strength peaked at approximately 235  $\text{N/mm}^2$  at the age of two days, which indicates that the compressive strength reached the

ultimate value. The compressive strength of the other specimens appeared to have gained the same ultimate strength, as shown in Fig. 1.

#### 4. Estimation of apparent activation energy

First, the function (Eq. (1)) was applied to estimate the compressive strength development obtained at each curing temperature by using the least-squares method under the assumption that the ultimate compressive strength is constant at 235 N/mm<sup>2</sup>, regardless of the curing temperature.

$$F_T = F_{T,\text{inf}} \cdot \exp(a \cdot (t - t_0)^b) \quad (1)$$

where  $F_T$  is the compressive strength at curing temperature  $T$ ,  $F_{T,\text{inf}}$  is 235 N/mm<sup>2</sup>, and  $a$  and  $b$  are constant. At all curing temperatures, the correlation coefficients between the estimated curves and the compressive strength measurements were higher than 0.90.

Eq. (2) was obtained by dividing both sides of Eq. (1) by the ultimate compressive strength. As the reaction rate index, the relative strength expressed by Eq. (2) was adopted.

$$\overline{F}_T = F_T / F_{T,\text{inf}} = \exp(a \cdot (t - t_0)^b) \quad (2)$$

Eq. (3) is the Arrhenius Equation, which represents the temperature dependency of the chemical reaction, as follows:

$$k_t = A \exp(-E_a / RT) \quad (3)$$

where  $k_t$  is the constant reaction rate,  $E_a$  is the apparent activation energy,  $R$  is a gas constant, and  $T$  is the curing temperature. By substituting Eq. (3) into the chemical reaction rate equation ( $d\alpha/dt = k_t f(\alpha)$ ), Eq. (4) is obtained, which is a reaction rate equation with temperature as an independent variable.

$$d\alpha/dt = k_t f(\alpha) = A \exp(-E_a / RT) f(\alpha) \quad (4)$$

where  $\alpha$  is the reaction degree,  $f(\alpha)$  is a function of  $\alpha$ , and  $A$  is constant. Taking the logarithm of both sides of Eq. (4) yields Eq. (5). When the curing temperature and rate of reaction are available, the Arrhenius plot graph is obtained, which indicates the relationship between the log of the reaction rate and  $1/T$ . The slope from the Arrhenius plot gives the activation energy. As the reaction rate index, the development of the compressive strength was adopted, which was normalized by the ultimate strength calculated by Eq. (2).

$$\ln(d\alpha/dt) = \ln(d\overline{F}_T/dt) = -E_a / RT + \ln(Af(\overline{F}_T)) \quad (5)$$

In Fig. 2(a), it can be seen that the Arrhenius plot is only partially plotted as a straight line within the entire range. However, the slope of the Arrhenius plot within the linearly plotted range in the vicinity of 30°C changes depending on the relative strength and curing temperature. Fig. 2(b) shows the apparent activation energy estimated from the linearly plotted range in the vicinity of 30°C. It can be clearly seen that the apparent activation energy increased depending on the development of the relative strength. Additionally, in the case



where the relative strength was more than 0.7, the apparent activation energy at curing temperatures over 30°C had lower values in comparison with the activation energy at temperatures lower than 30°C, which is different to previously reported results [3].

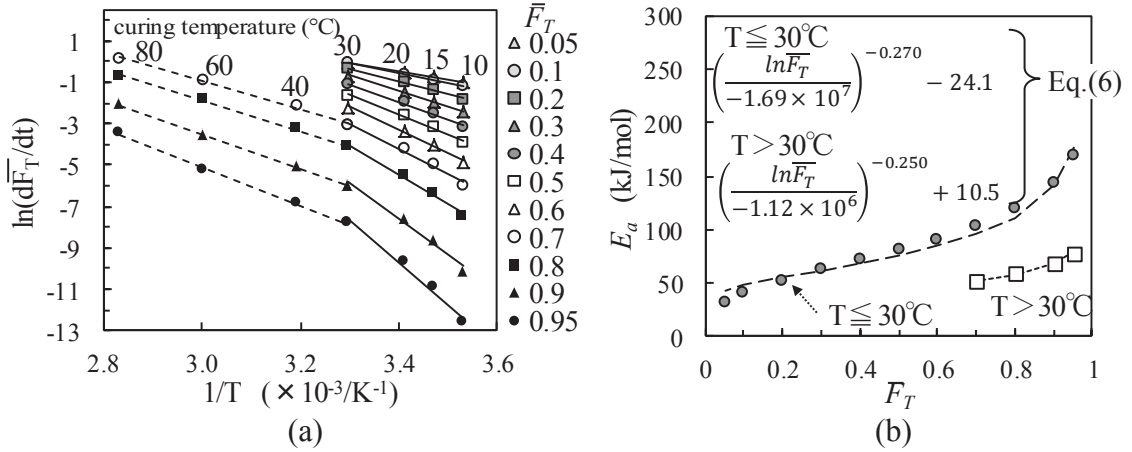


Figure 2: (a) Arrhenius plot and (b) relationship between normalized relative compressive strength  $\bar{F}_T$  and apparent activation energy  $E_a$ .

Eq. (6) in Fig. 2(b) is a function that expresses the apparent activation energy of the high strength mortar, which was obtained from fitting by the least squares method. Eq. (7) shows the temperature adjusted age [4]. The modified temperature adjusted age is derived by substituting the estimated activation energy into the  $E_a$  term of Eq. (7).

$$t_e = \sum \exp\{E_a/R (1/T_0 - 1/T_k)\} \Delta t \quad (7)$$

where  $t_e$  is the thermal equivalent age,  $T_0$  is the reference temperature,  $T_k$  is the curing temperature during time interval  $\Delta t$ , and  $t$  is the age of the concrete. Figure 3 shows the relative strength that was obtained based on the conventional thermally adjusted age (Fig. 3(a)), and that based on the new modified temperature applied to the adjusted age (Fig. 3(b)). Fig. 3(b) shows that the modified temperature adjusted age evaluated the dependency of the developing relative compressive strength at various curing temperatures more appropriately.

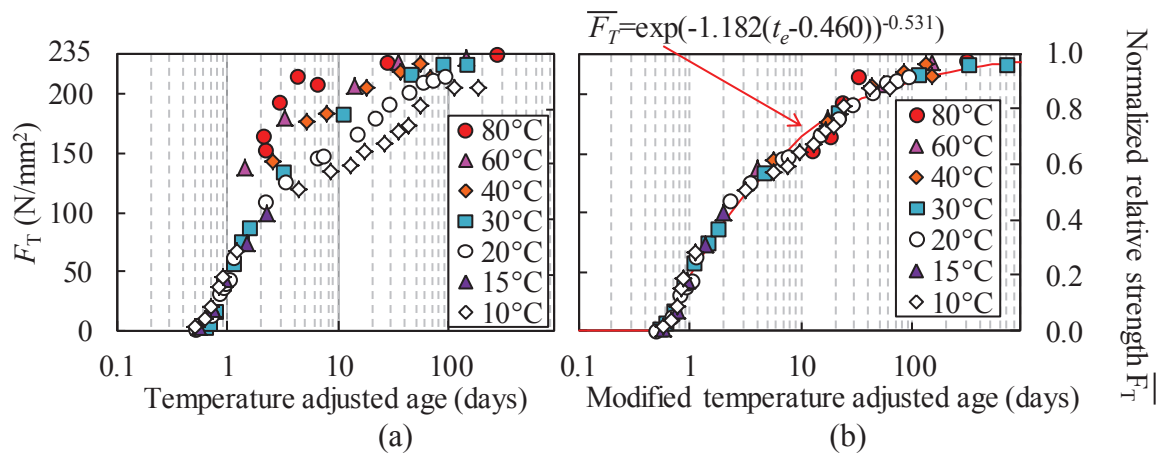


Figure 3: Compressive strength normalized by ultimate compressive strength.

Figure 4 shows the reaction degree of the high alite content cement and fine pozzolanic powder that was applied to the temperature adjusted age shown in Fig. 4(a), and the modified temperature adjusted age shown in Fig. 4(b). Moreover, Fig. 4(b) shows the good relationship between the modified temperature adjusted age and the reaction of the fine pozzolanic powder. Therefore, it is possible that the apparent activation energy was strongly influenced by the fine pozzolanic powder reaction.

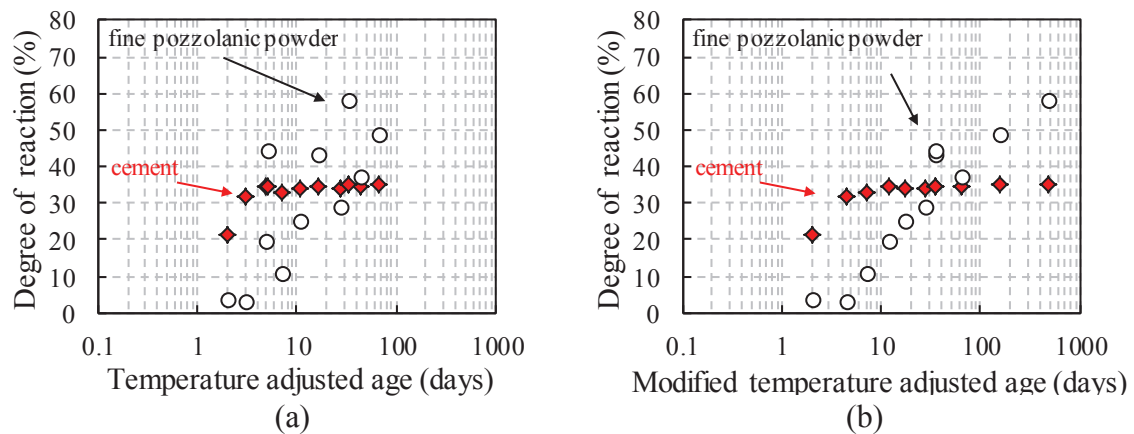


Figure. 4: reaction degree of high alite content cement and fine pozzolanic powder.

## 5. Conclusion

In this study, the apparent activation energy of a high strength mortar with high alite content cement and fine pozzolanic powder was investigated to establish a method of estimating the compressive strength. The results revealed that the apparent activation energy obtained from the relative strength as an index of the reaction rate was not constant, but rather developed depending on the relative strength and curing temperature. Additionally, the modified temperature adjusted age using the new apparent activation energy was estimated more appropriately in comparison with the conventional temperature adjusted age. Moreover, it was found that the apparent activation energy could have been strongly influenced by the reaction of the fine pozzolanic powder.

## References

- [1] Inoue, G. and Igarahi, S., Comparison of degree of hydration of cement obtained by several methods, Proceedings of the Japan Concrete Institute 27(1) (2005), 541-546
- [2] Asaga, K. et al, Determination of uncombined quartz in hydrothermal reaction of quartz and Portland cement, Journal of the Ceramic Society of Japan 90(1043) (1982), 397-400
- [3] Kjellsen, K.O. and Detwiler, R.J., Later-age strength prediction by a modified maturity model, ACI Materials Journal 90(3) (1993), 220-227
- [4] Hansen, P.F. and Pedersen, E.J., Maturity computer for controlled curing and hardening of concrete, Nordisk Betong 1(19) (1977), 21-25

## **TENSION STIFFENING MODEL FOR SERVICEABILITY ANALYSIS OF STEEL AND FRP REINFORCED CONCRETE BEAMS**

**Gintaris Kaklauskas**<sup>(1)</sup>, **Pui-Lam Ng**<sup>(1,2)</sup>, **Aleksandr Sokolov**<sup>(1)</sup>

(1) Vilnius Gediminas Technical University, Vilnius, Lithuania

(2) The University of Hong Kong, Hong Kong, China

### **Abstract**

An improved tension stiffening model is proposed for short-term deformational analysis of reinforced concrete flexural members. The model has been derived by utilising the direct and inverse analysis techniques with the use of layered approach of computation based on experimental moment-curvature relationships of concrete beam specimens. For ease of implementation by structural designers, a simple formulation of tensile stress block with dependence on the reinforcement ratio has been established. The proposal has been verified to have desirable accuracy. In addition to steel reinforced concrete beams, the analytical methodology has been applied to fibre-reinforced polymer (FRP) reinforced concrete beams.

### **1. Introduction**

When a reinforced concrete beam is loaded up to cracking, at the cracked section, the flexural tension is resisted entirely by the reinforcement. Between adjacent cracks, the intact concrete remains to be able to carry tensile stresses transferred via bond between reinforcement and concrete [1]. The tensile resistance of concrete effectively stiffens the member response and this phenomenon is known as tension stiffening. For serviceability analysis of concrete members, the use of a rational tension stiffening constitutive model is of crucial importance. To model tension stiffening, the tension stiffening stress may be attributed to the reinforcement or to the concrete. The latter allows comparative study of concrete stress-strain relations among smeared crack and discrete crack modelling, thus offering additional advantage for analysts. The tension stiffening stress-stress law reflects the interaction between concrete and reinforcement through bond in the tension zone of member, and is commonly referred to as tensile stress block. It forms a useful tool in combination with sectional analysis for deformational assessment of concrete members [2].

In the current study, an improved tension stiffening model is devised for concrete beams subjected to short-term load. The direct and inverse analysis techniques are employed in the derivation process, with the use of layered approach of computation [1]. A simple formulation of tensile stress block is proposed for practical use. Besides, fibre-reinforced polymer (FRP) has emerged as a corrosion-free reinforcement material. Though its tensile strength can be comparable to reinforcing steel, its elastic modulus is remarkably lower. The flexibility of FRP material would render FRP reinforced concrete members having distinct deformational characteristics from conventional steel reinforced counterparts. In view of this, the authors embark research on the tension stiffening behaviour of FRP reinforced concrete beams.

## 2. Tension stiffening effect in concrete beams

At the outset, doubly-reinforced concrete beam with uniform cross-section is considered. Plane sections are assumed to remain plane under flexure. The cracks are regarded as smeared over the sections along the longitudinal direction. To conduct analysis, the cross-section is sub-divided into multiple layers (i.e. the layered approach). Governing equations are set up from the force and moment equilibria, and are solved for the concrete stresses at extreme fibres. After establishing the extreme fibre strains, the strain levels of all other fibres can be obtained by linear interpolation, and the corresponding stresses are determined from the materials law. The stress-strain law and the moment-curvature diagram of concrete beam are inter-related. The direct technique enables determination of moment-curvature diagrams from given materials law, whereas the inverse technique enables determination of average stress-strain relationship from known moment-curvature diagrams [1].

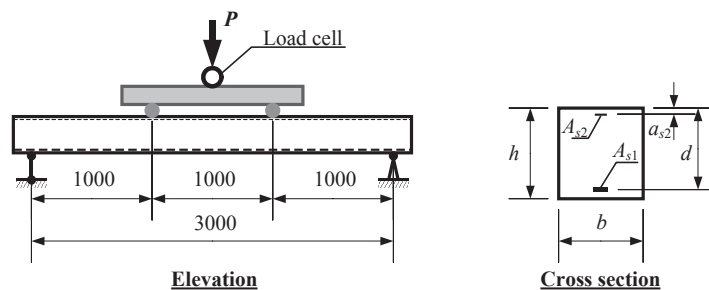


Figure 1: Elevation and cross-section of beam specimen.

The above analytical methodology is applied to a series of steel reinforced concrete beam specimens in the literature [3]. Fig. 1 depicts the elevation and cross-sectional views and Tab. 1 summarises the main characteristics of the specimens. The notations of quantities are graphically annotated in Fig. 1. The beams had uniform rectangular cross-section of 280 mm breadth by 300 mm depth. The reinforcement ratio  $p$  was varied among 0.3%, 0.6% and 1.0%. The beams had span length of 3.0 m and were subject to symmetrical four-point loading with pure bending zone of 1.0 m and shear span of 1.0 m.

Table 1: Main characteristics of steel reinforced concrete beams.

Beam	$d$ (mm)	$a_{s2}$ (mm)	$A_{s1}$ (mm <sup>2</sup> )	$A_{s2}$ (mm <sup>2</sup> )	$p$ (%)	$f_c$ (MPa)
S1-3	268	23	755	57	1.0	48.2
S2-3	272	29	466	57	0.6	48.1
S3-2-2	274	32	232	57	0.3	52.8
S3-2-3	271	32	232	57	0.3	50.9

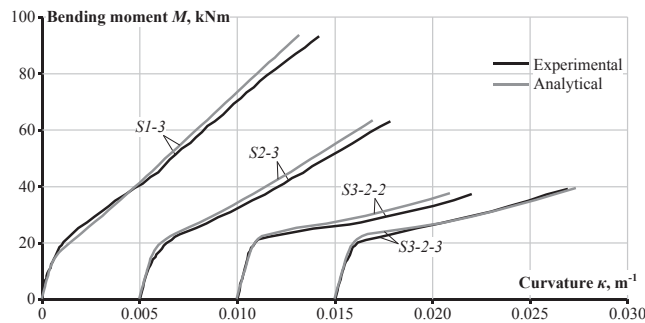


Figure 2: Experimental and analytical moment-curvature response.

The laboratory testing procedures were described in detail in the dedicated study [3]. The experimentally obtained moment-curvature diagrams of the specimens are presented in Fig. 2. By means of inverse analysis technique, the tension stiffening stress-strain curve was obtained from the moment-curvature diagram of each specimen. The stress  $\sigma_{ct}$  and strain  $\varepsilon_{ct}$  are normalised with respect to the tensile strength  $f_{ctm}$  and cracking strain  $\varepsilon_{cr}$  of concrete, respectively. Fig. 3 shows the resulting normalised stress-strain curves.

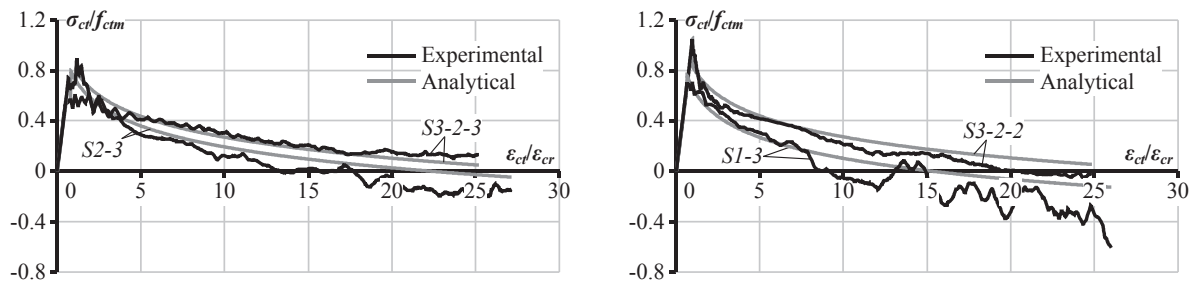


Figure 3: Normalised tension stiffening stress-strain curves.

From Fig. 3, it can be seen that the stress-strain curve typically comprises an ascending branch and a descending branch. Initially, the tensile stress varies linearly with the tensile strain from the origin up to the peak point, which is close to the tensile strength of concrete. Afterwards, the tensile stress decreases gradually with increasing tensile strain. A number of tension stiffening curves in Fig. 3 manifest negative stress portions at large strains, especially for the more heavily-reinforced beam specimens. This could be due to the idealisation of reinforcement-concrete bond as perfect bond, as well as the shrinkage of concrete that had effectively shifted the stress-strain curve towards the negative side. The computational methodology for shrinkage elimination had been studied in detail by the authors' team [4].

### 3. Derivation and verification of tensile stress block

On the basis of the tension stiffening stress-strain curves, an improved tension stiffening model is devised by curve fitting. The form of equation chosen is a compromise between accuracy and simplicity. In essence, the ascending branch is a straight line passing through the origin, and the descending branch is a logarithmic decay curve. The proposed tensile stress block is depicted in Fig. 4 and its ascending and descending branches are algebraically given by Eq. (1a) and Eq. (1b), respectively. In Eq. (1),  $p$  is expressed in percentage. It is apparent that for a more heavily-reinforced beam, the descending branch would be shorter, and vice versa. For cross-comparison, Eq. (1) is plotted for each specimen in Fig. 3 as analytical curve.

$$\sigma_{ct} = (0.9 - 0.25p)f_{ctm} \left( \frac{\varepsilon_{ct}}{\varepsilon_{cr}} \right) \quad \text{for} \quad \varepsilon_{ct} < \varepsilon_{cr} \quad (1a)$$

$$\sigma_{ct} = f_{ctm} \left[ 0.9 - 0.25p - 0.24 \ln \left( \frac{\varepsilon_{ct}}{\varepsilon_{cr}} \right) \right] \geq 0 \quad \text{for} \quad \varepsilon_{ct} \geq \varepsilon_{cr} \quad (1b)$$

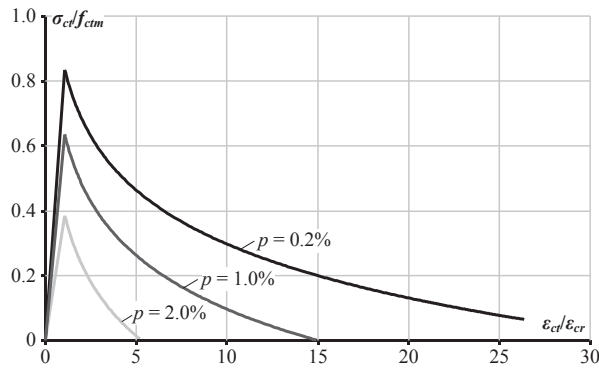


Figure 4: Proposed tensile stress block.

The proposed tensile stress block is verified in the following. By means of the direct analysis technique, the moment-curvature response of concrete beams is evaluated with the stress-strain law of reinforced concrete element taken as Eq. (1). For each specimen, the analytical moment-curvature response is plotted in Fig. 2 for comparison with the experimental data. It is evident that close agreement between the experimental and analytical results is achieved.

### 4. Tension stiffening behaviour of FRP reinforced concrete beams

To extend the proposed tension stiffening model to concrete beams reinforced with FRP bars, reference is made to the experimental data of five FRP reinforced concrete beam specimens reported in the literature [5-9]. The specimens are labelled F1 [5], FRP1A-HF [6], Group 3 [7], BC2HA [8] and Series 1 [9]. Tab. 2 summarises the main characteristics of the beams, which were all subjected to symmetrical four-point bending loading arrangement.

Table 2: Main characteristics of FRP reinforced concrete beams.

Beam	$b \times h$ (mm)	$d$ (mm)	$L$ (m)	$p$ (%)	$f_c$ (MPa)	$f_f$ (MPa)	$E_f$ (GPa)
F1	500×185	145	3.40	1.23	30.0	494	42.0
FRP1A-HF	254×184.2	138.2	2.89	1.12	74.3	690	40.3
Group 3	200×260	218	2.70	1.16	31.3	886	43.4
BC2HA	130×180	154	1.50	1.20	57.2	773	38.0
Series 1	200×300	260	3.00	1.10	43.0	690	45.0

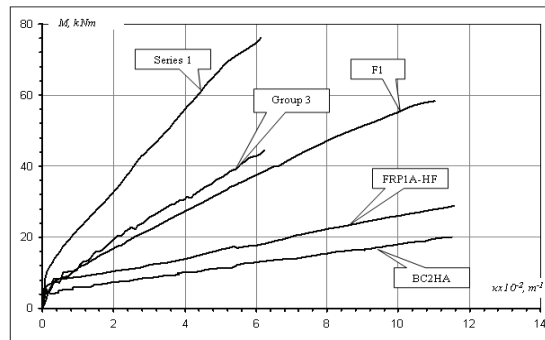


Figure 5: Experimental moment-curvature diagrams of FRP reinforced concrete beams.

The experimentally obtained moment-curvature diagrams for the beams are depicted in Fig. 5. Applying the inverse analysis technique, stress-strain relationship is determined for each specimen. The normalised tension stiffening stress-strain curves are presented in Fig. 6. In comparison with steel reinforced concrete beams, it can be observed that the descending branches in Fig. 6 are significantly longer for FRP reinforced concrete beams. Such difference would be due to the lower elastic modulus of FRP material, and could be reflected in the model by adjusting the coefficient values in Eq. (1). Nevertheless, further research with larger sample size of FRP reinforced concrete beams is necessary to confirm the mathematical formulation of the tensile stress block. From Fig. 6, it is noted that the ratio of ultimate tensile strain (at which the stress level of the descending branch is zero) to the cracking strain ranges from circa 50 to 135, with an average value of approximately 100.

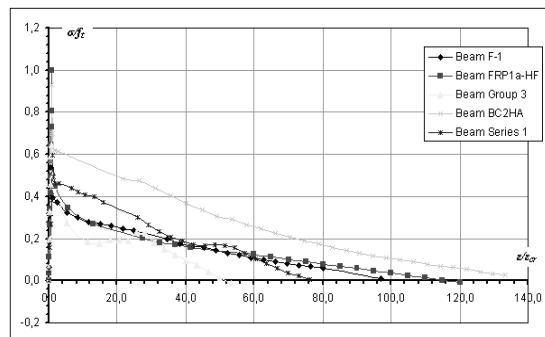


Figure 6: Tension stiffening stress-strain curves of FRP reinforced concrete beams.

## 5. Conclusions

The tension stiffening effect in steel and fibre-reinforced polymer (FRP) reinforced concrete beams has been studied. An improved tension stiffening model has been formulated with reference to experimental data of beam specimens. The mathematical formulation has accounted for the dependence of tensile stress block on the reinforcement ratio. Good agreement between experimental and analytical moment-curvature response has been attained. Application of the analytical methodology to FRP reinforced concrete beams has revealed longer descending branches. Further research is recommended to confirm the formulation of tensile stress block for FRP reinforced concrete beams.

## Acknowledgements

The authors gratefully acknowledge the financial support from the Research Council of Lithuania and the European Union Structural Fund (Project no.: 09.3.3-LMT-K-712-01-0145). The second author wishes to express his gratitude for the support provided by the European Commission Research Executive Agency under the Marie Skłodowska-Curie Actions (Project no.: 751461).

## References

- [1] Kaklauskas, G., Flexural layered deformational model of reinforced concrete members, *Mag Concr Res* 56(10) (2004), 575-584
- [2] Lam, J. Y. K. et al, Tension stiffening in concrete beams. Part 2: member analysis, *Proc ICE Struct Bldgs* 163(1) (2010), 29-39
- [3] Gribniak, V. et al, Experimental investigation of deformations of lightly reinforced concrete beams, *Proc. 9th International Conference Modern Building Materials, Structures and Techniques*, Vilnius (2007), 554-562
- [4] Kaklauskas, G. et al, Eliminating shrinkage in tension stiffening model of concrete beams by the hybrid approach, *Proc. 24th Australasian Conference on the Mechanics of Structures and Materials*, Perth (2016), 129-135
- [5] Pecce, M. et al, Experimental response and code models of GFRP RC beams in bending, *J Compos Constr ASCE* 4(4) (2000), 82-90
- [6] Yost, J. R. et al, Flexural stiffness of high strength concrete beams reinforced with GFRP bars, *ACI SP 210* (2003), 209-224
- [7] Almusallam, T. H., Analytical prediction of flexure behaviour of concrete beams reinforced by FRP bars, *J Compos Mater* 31(7) (1997), 640-657
- [8] Thériault, M. and Benmokrane, B., Effects of FRP reinforcement ratio and concrete strength on flexural behaviour of concrete beams, *J Compos Constr ASCE* 2(1) (1998), 7-16
- [9] Benmokrane, B. et al, Flexural response of concrete beams reinforced with FRP reinforcing bars, *ACI Struct J* 93(1) (1996), 46-55



## USING INTELLIGENT SYSTEM APPROACH FOR SHEAR STRENGTH FORECASTING OF STEEL FIBER-REINFORCED CONCRETE BEAMS

Ali Kheyroddin <sup>(1)</sup>, Masoud Ahmadi <sup>(1)</sup>, Mahdi Kioumarsi <sup>(2)</sup>

(1) Semnan University, Semnan, Iran

(2) OsloMet – Oslo Metropolitan University, Oslo, Norway

### Abstract

Previous studies have shown that brittle failure in reinforced concrete buildings caused huge losses, both in human and economic terms. The appropriate use of steel fibers to a reinforced concrete beam can change the brittle behavior to a ductile behavior and significantly increase the ductility ratio. The aim of this study is to develop an intelligent system approach for shear strength estimation of steel fiber-reinforced concrete (SFRC) beams without transversal reinforcement using a large number of existing experimental results. The main parameters in this investigation are the steel fiber-volume fraction, the aspect ratio and volume of fiber, compressive strength of concrete, longitudinal reinforcement, effective depth and shear span of beams. The precision of the proposed approach is compared with other existing models for estimating the shear capacity of SFRC beams based on experimental results which showed a reasonable agreement.

### 1. Introduction

In recent decades different types of fiber, including natural fiber (NF), steel fiber (SF), glass fiber (GF), and synthetic fiber (SNF), were used in various field of the civil engineering concrete construction [1–3]. It is well known that concrete as a material subjected to the tensile stress conditions is brittle. The findings of the previous studies revealed that fibers can significantly boost the post-cracking behavior, flexural toughness, spalling resistance, impact resistance, shear strength, thermal characteristics, and ductility of concrete members under various types of loading conditions [4–6]. SF delays crack propagation in the concrete and noticeably enhances the tensile performance. The brittle failure in reinforced concrete (RC) structures caused huge losses, both in human and economic terms. Thus, it is necessary to

prevent brittle failure and change it to ductile mode. The sufficient amount of SF in a RC beam can alter the brittle mode to a ductile behavior and enhance the ductility ratio. Up to now, many researchers have been studying the use of the steel fibers as replacement of the shear reinforcement, which will ultimately help to improve the behavior of RC beam. It is worth mentioning that the orientation, distribution, and resistance to pull out of fibers play a substantial role in the performance improvement of the steel fiber reinforced concrete (SFRC) beams [7]. Among the steel fibers types, hooked and crimped fibers have acceptable efficiency to prevent premature pull out which affects the load carrying ability. A SFRC beam with hooked/crimped fibers, when design appropriately, has superior ductility in comparison with common RC beams [8].

## 2. Shear capacity of SFRC beam

Several studies have been carried out to identify the effect of steel fibers on shear strength of SFRC beams without stirrups. Researchers based on the theoretical and experimental studies have been proposed several equations for determining shear strength of SFRC beams. These models are mainly categorized in two groups. In the first group, the independent contribution is assumed for steel fibers and its shear strength is added to the contribution of plain concrete and stirrups.

$$V_{SFRC-Beam} = V_c + V_S + V_{SF} \quad (1)$$

where,  $V_c$ ,  $V_S$  and  $V_{SF}$  are the shear strength contribution provided by the plain concrete, transverse reinforcement, and steel fibers. The second group assumes that steel fibers influence on the shear strength of concrete. Narayanan and Darwish (1987) [9] studied the effects the steel fibers on the behavior of RC beams under predominant shear. They proposed empirical formulation for design of SFRC beams without stirrups.

$$v_u = e \left[ 0.24f_{spfc} + 80\rho \frac{d}{a} \right] + v_b \quad (2)$$

where,  $e$  is arch action factor,  $f_{spfc}$  is split tensile strength of concrete,  $\rho$  is reinforcement ratio,  $\frac{d}{a}$  is effective depth-to-shear span ratio, and  $v_b$  is calculated based on average bond stress. The arch action factor is 1.0 for  $\frac{a}{d} > 2.8$  and  $2.8\frac{d}{a}$  for  $\frac{a}{d} \leq 2.8$ . Khuntia et al. (1999) [10] developed a design equation for calculating the ultimate shear strength of SFRC beams based on the basic shear transfer mechanisms and large number of experimental results. They proposed the following equation for determining shear capacity of SFRC beams without transverse reinforcement:

$$v_u = (0.167\alpha + 0.25\beta v_f \frac{l_f}{d_f}) \sqrt{f_c} \quad (3)$$

where,  $\alpha$  is arch action factor,  $v_f$  is fiber volume fraction,  $\beta$  related to fiber shape and concrete type,  $f_c$  is compressive strength of concrete, and  $\frac{l_f}{d_f}$  is fiber length-to-fiber diameter

ratio. Ultimate shear capacity of SFRC beams without stirrups can be determined according to Sharma (1986) [11] from the following equation:

$$v_u = \frac{2}{3} \hat{f}_t \left( \frac{d}{a} \right)^{0.25} \quad (4)$$

where,  $\hat{f}_t$  is split-cylinder tensile strength of concrete, and  $\frac{d}{a}$  is effective depth-to-shear span ratio.

### 3. Group method of data handling (GMDH)

GMDH neural network is a self-organizing black-box learning technique proposed by Ivakhnenko in 1971 [12]. Artificial neural networks is a superior tool in forecasting (any non-linear functions or features) and data mining [13–15]. The discrete form of the GMDH model is given in following equation:

$$\bar{y} = a_0 + \sum_{i=1}^n a_i f_i \quad (5)$$

where  $a$  is coefficient,  $f$  is the basic function based on different sets of inputs, and  $n$  is the number of the base function components. The Kolmogorov-Gabor (KG) polynomial is the most popular base function used in GMDH approach. The KG-form of equation 5 based on input vector  $X(x_1, x_2, x_3, \dots, x_n)$  can be expressed as following equation:

$$\bar{y} = a_0 + \sum_i^n a_i x_i + \sum_i^n \sum_i^n a_{ij} x_i x_j + \sum_i^n \sum_i^n \sum_i^n a_{ijk} x_i x_j x_k + \dots \quad (6)$$

where  $a_i$ ,  $a_j$ , and  $a_k$  are the weighting coefficients. The GMDH algorithm is considered as a feedforward multilayer network with low-degree polynomial activation function. The outcomes of the first layer is computed based on only two input variables using partial quadratic polynomial function as given in following:

$$z = z(x_i, x_j) = s_0 + s_1 x_i + s_2 x_j + s_3 x_i x_j + s_4 x_i^2 + s_5 x_j^5 \quad (7)$$

The coefficients of partial function are determined utilizing the least squares method to minimize the difference between real and estimated value for each pair of the input vectors.

### 4. Experimental database

In order to calculate the average shear stress of steel fiber-reinforced concrete beams without transversal reinforcement, 112 experimental results were gathered from the previous studies. A summary range of mechanical-geometric properties of beams is given in Table 1. The

considered parameters include: 1) Shear span-effective depth ratio ( $a/d$ ), 2) Effective depth of beams ( $d$ -mm), 3) Longitudinal reinforcement ratios ( $\rho$ ), 4) Compressive strength of concrete ( $f'_c$ -MPa), 5) Fiber ratio ( $F_{SF}$ ). Fiber ratio is determined as follows:

$$F_{SF} = V_{SF} L_{SF} / d_{SF} \quad (8)$$

where,  $d_{SF}$  and  $L_{SF}$  are diameter and length of steel fiber, and  $V_{SF}$  is volume percentage of fibers.

Table 1. Range of input parameters for network application

Reference	No. of test data	Parameter											
		d (mm)		a/d		$\rho$ (%)		f <sub>c</sub> (MPa)		F <sub>SF</sub>		$v_{exp}$ (MPa)	
		Min	Max.	Min	Max	Min	Max	Min.	Max.	Min.	Max.	Min.	Max.
[16]	12	197	197	2	3.6	1.3	2	20.6	33.4	30	60	1.5	3.11
[9]	31	126	130	2	3.5	2	5.72	31.9	63.6	25	200	1.94	7.15
[17]	8	215	215	2	4	2.8	4.58	75.0	79.2	37.5	112.	2.27	7.21
[18]	2	204	204	3	3	2.2	2.2	22.7	26	60	100	3.05	3.05
[19]	4	340	340	2	2.5	3.4	3.44	33	36	30	60	3.78	5.34
[20]	7	265	265	2	4.91	1.5	4.31	33.1	40.9	100	100	2.92	5.51
[21]	9	212	212	2	4	1.5	1.5	30.8	68.6	31.2	46.8	2	5.44
[22]	17	260	305	2.5	4	1.0	3.55	26.5	47.6	11.2	48.7	1.57	3.03
[23]	4	219	219	2	2.8	1.9	1.92	40.9	43.2	60	120	2.93	3.52
[24]	10	381	381	3.4	3.5	1.9	2.67	31	49.2	60	90	2.53	3.77
[25]	8	381	381	3.4	3.5	2	2.7	31	44.9	41.2	82.5	2.6	3.4

## 5. The GMDH-based equation

In order to construct GMDH network and preventing overfitting, the database was divided randomly in two sets. The overfitting occurs when the error on the training set is driven to a very small value, but when new data is presented to the network the error is large. 74 experimental data were considered for training state and remaining data for testing state. Shear span-effective depth ratio, effective depth of beams, longitudinal reinforcement ratios, concrete compressive strength of standard cylinder, and fiber ratio were utilized as the input variables of the model, and average shear stress of SFRC beam was chosen as the target variable. Shear stress can be obtained using the following equations:

$$v_{GMDH} = 2.273 + 4 * 10^{-6}d^2 - (1.92 + 0.26\rho + 0.013\hat{f}_c - 0.38 a/d) a/d + (0.84 + 0.00185F_{SF})\rho + 0.07\hat{f}_c + (0.025 - 0.0001F_{SF})F_{SF} \quad (9)$$

In order to verify and quantify the proposed relationship, the predicted values were compared with the three existing models introduced in Section 2 based on a broad range of experimental results. The simulated shear stress compared to the existing equations are plotted in Figure 1. It is found that, the proposed GMDH-based formulation demonstrated the most optimized result compared to all of the other existing formulations. The average absolute error of the GMDH formulation for determining the experimental results is equal to 10% while the

average error for the other three models including Narayanan and Darwish, Khuntia et al., and Sharma are 14.70%, 30.96%, and 22.34% respectively. It should be noted that the best performance of the proposed equation is addressed in the considered ranges of the input parameters.

## 6. Conclusion

In this paper, a new formulation is developed to determine average shear stress of SFRC beams without web reinforcement. Five input parameters representing shear span-effective depth ratio, effective depth of beams, longitudinal reinforcement ratios, compressive strength of concrete, and fiber ratio were considered as input vectors. In order to overcome overfitting issue, the database was divided randomly in training and testing sets. The results of comparative assessment between existing equations and proposed method reveal that the GMDH model has acceptable ability to determine average shear stress. Finally, it could be concluded that the GMDH-based formulation can be utilized as an alternative method in the pre-design of SFRC beams.

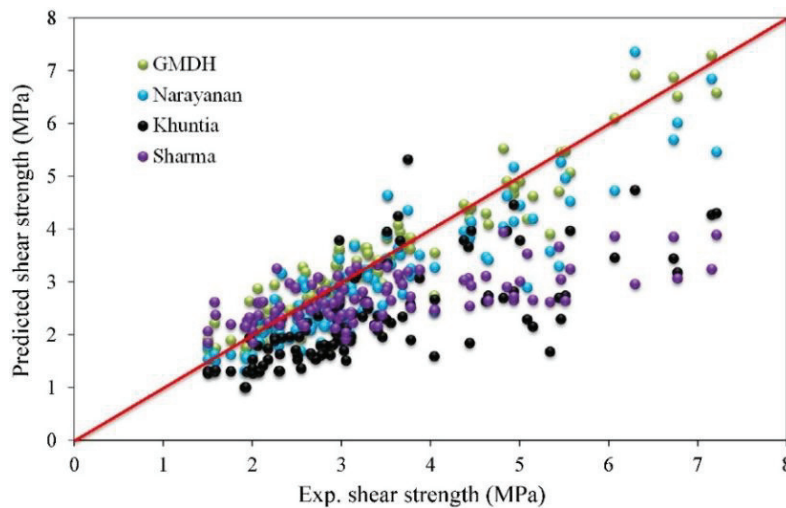


Figure 1. Experimental value against predicted shear strengths

## References

- [1] M. Shahnewaz, M.S. Alam, Improved shear equations for steel fiber-reinforced concrete deep and slender beams, *ACI Struct. J.* 111 (2014) 851.
- [2] F. Pacheco-Torgal, S. Jalali, Cementitious building materials reinforced with vegetable fibres: A review, *Constr. Build. Mater.* 25 (2011) 575–581.
- [3] C.-C. Chen, C.-Y. Li, Punching shear strength of reinforced concrete slabs strengthened with glass fiber-reinforced polymer laminates, *ACI Struct. J.* 102 (2005) 535.
- [4] E. Cuenca, J. Echeagaray, P. Serna, A. Pasetto, Ductility analysis on the post-peak behavior of self-compacting fiber reinforced concrete (SCFRC) beams subjected to shear, in: *8th RILEM Int. Symp. Fibre Reinf. Concr. Challenges Oppor. (BEFIB 2012)*, 2017.

- [5] A. Hemmati, A. Kheyroddin, M. Sharbatdar, Y. Park, A. Abolmaali, Ductile behavior of high performance fiber reinforced cementitious composite (HPFRCC) frames, *Constr. Build. Mater.* 115 (2016) 681–689.
- [6] A. Hemmati, A. Kheyroddin, M.K. Sharbatdar, Plastic hinge rotation capacity of reinforced HPFRCC beams, *J. Struct. Eng.* 141 (2013) 4014111.
- [7] H. Singh, *Steel Fiber Reinforced Concrete: Behavior, Modelling and Design*, Springer, 2016.
- [8] S.-H. Cho, Y.-I. Kim, Effects of steel fibers on short beams loaded in shear, *Struct. J.* 100 (2003) 765–774.
- [9] R. Narayanan, I.Y.S. Darwish, Use of steel fibers as shear reinforcement, *Struct. J.* 84 (1987) 216–227.
- [10] M. Khuntia, B. Stojadinovic, S.C. Goel, Shear strength of normal and high-strength fiber reinforced concrete beams without stirrups, *Struct. J.* 96 (1999) 282–289.
- [11] A.K. Sharma, Shear strength of steel fiber reinforced concrete beams, in: *J. Proc.*, 1986: pp. 624–628.
- [12] A.G. Ivakhnenko, Polynomial Theory of Complex Systems, *IEEE Trans. Syst. Man. Cybern. SMC-1* (1971) 364–378. doi:10.1109/TSMC.1971.4308320.
- [13] M. Ahmadi, H. Naderpour, A. Kheyroddin, Utilization of artificial neural networks to prediction of the capacity of CCFT short columns subject to short term axial load, *Arch. Civ. Mech. Eng.* 14 (2014) 510–517. doi:10.1016/j.acme.2014.01.006.
- [14] M. Ahmadi, H. Naderpour, A. Kheyroddin, ANN Model for Predicting the Compressive Strength of Circular Steel-Confined Concrete, *Int. J. Civ. Eng.* 15 (2017) 213–221. doi:10.1007/s40999-016-0096-0.
- [15] A. Kheyroddin, H. Naderpour, M. Ahmadi, Compressive strength of confined concrete in CCFST columns, *J. Rehabil. Civ. Eng.* 2 (2014) 106–113.
- [16] M.A. Mansur, K.C.G. Ong, P. Paramasivam, Shear strength of fibrous concrete beams without stirrups, *J. Struct. Eng.* 112 (1986) 2066–2079.
- [17] S.A. Ashour, G.S. Hasanain, F.F. Wafa, Shear behavior of high-strength fiber reinforced concrete beams, *Struct. J.* 89 (1992) 176–184.
- [18] V.C. Li, R. Ward, A.M. Hamza, Steel and synthetic fibers as shear reinforcement, *ACI Mater. J.* 89 (1992) 499–508.
- [19] K.H. Tan, K. Murugappan, P. Paramasivam, Shear behavior of steel fiber reinforced concrete beams, *Struct. J.* 90 (1993) 3–11.
- [20] R.N. Swamy, R. Jones, A.T.P. Chiam, Influence of steel fibers on the shear resistance of lightweight concrete I-beams, *Struct. J.* 90 (1993) 103–114.
- [21] Y.-K. Kwak, M.O. Eberhard, W.-S. Kim, J. Kim, Shear strength of steel fiber-reinforced concrete beams without stirrups, *ACI Struct. J.* 99 (2002) 530–538.
- [22] D. Dupont, L. Vandewalle, Shear capacity of concrete beams containing longitudinal reinforcement and steel fibers, *Spec. Publ.* 216 (2003) 79–94.
- [23] C. Cucchiara, L. La Mendola, M. Papia, Effectiveness of stirrups and steel fibres as shear reinforcement, *Cem. Concr. Compos.* 26 (2004) 777–786.
- [24] H.E. Yakoub, Shear stress prediction: Steel fiber-reinforced concrete beams without stirrups, *ACI Struct. J.* 108 (2011) 304.
- [25] H.H. Dinh, G.J. Parra-Montesinos, J.K. Wight, Shear Behavior of Steel Fiber-Reinforced Concrete Beams without Stirrup Reinforcement, *ACI Struct. J.* 107 (2010).

**SELF-HEALING AND REPAIR OF CONCRETE  
STRUCTURES  
(COST CA15202 - SARCOS)**

## **A METHOD FOR INDUCING CONTROLLED CRACKS IN CONCRETE AND MEASURING THE EFFICIENCY OF SELF- HEALING AGENTS**

**Amir Sidiq<sup>(1)</sup>, Syed Adil Amzar Bin Syed Amerruddin<sup>(1)</sup>, Rebecca Gravina<sup>(1)</sup>, Sujeeva Setunge<sup>(1)</sup>, Filippo Giustozzi<sup>(1)</sup>**

(1) Royal Melbourne Institute of Technology – RMIT University, 376-392 Swanston st.,  
Melbourne, VIC 3000, Australia

### **Abstract**

Durability and mechanical properties of concrete decreases with time due to cracking, resulting in contaminant ingress such as rapid chloride penetration and water particles transferred through these cracks to cause corrosion of the steel in reinforced concrete. The present research presents a method to induce cracking throughout the entire concrete sample's volume homogeneously. By placing a cylindrical concrete sample into an ad-hoc steel mould and applying a compressive loading, confined axial and circumferential pressure is generated that induces controlled cracks in the sample. This procedure is used to induce a specific amount of cracks in the concrete sample hence triggering the repairing action of the self-healing agent. This method overcomes common drawbacks of self-healing efficiency measurements where a single crack is usually being generated by a standard flexural test on beams. X-ray tomography analysis was adopted to calibrate the internal state of damage generated into the sample.

### **1. Introduction**

Cracking occurrence in concrete structures is expected at any stage during the life span of the structure typically under tension stresses due to limited tensile characteristics [1]. Due to cracking, the durability and structural capacity of concrete are compromised in an aggressive environment since chlorides and atmospheric water can infiltrates through the cracks and permeate the concrete matrix [2], which will lead to diffusion and enlargement of micro-cracks. Subsequently, corrosion in reinforcement may occur and the risk of failure of the structure increases [3]. To determine the efficiency of self-healing of concrete, research



studies tend to develop artificial cracks in cementitious materials. Conventionally, there are limited techniques available for developing cracks in concrete including four-point bending, three-point bending and split tensile testing. Researchers utilise these test methods to determine the onset of cracking and calculate the crack load capacity for a specific concrete material design and then use this experiment to obtain cracks based on their requirements for self-healing. A few studies utilised split test to generate single cracks in their specimens and further test healing efficiency of the mix [4]. Other studies used the three-point bending test to develop single cracks in the mid-span of a concrete beam [5]. However, the majority of studies on concrete healing use the four-point bending test to initiate cracks [6]. Several methodologies have also been applied to quantify the internal cracking of damaged concrete samples. Researchers utilized non-destructive test methods for crack detection and evaluation, such as ultrasonic methods [7], X-Ray tomography [8], acoustic emission [8] and ground penetrating radar [9]. In this paper an innovative method to induce controlled crack damage in the entire concrete sample was developed. The experiment was conducted by applying various percentage of maximum concrete compressive strength in a specifically-developed steel mould. Measurements before and after sample damaging were taken and comparison related to internal void content, recovery of compressive strength and stiffness were also conducted.

## **2. Materials and Methodology**

The concrete mix consisted of water to cement, sand to cement and aggregate to cement ratio of 0.54, 1.83 and 2.42, respectively. Target compressive strength of the mix was 30-40 MPa although mechanical resistance was not a main focus of the present study, which was instead intended to develop a procedure to generate controlled damage state inside the samples. Cylindrical samples were casted as per AS 1012.8.1-14 [10] with diameter of 100 mm and height of 200 mm. Samples were demoulded after 24 hours and wet cured for 28 days.

### **2.1 Steel mould fabrication and illustration**

A specific steel mould was developed to obtain a controlled internal damage. The designed mould consisted of two semi-circular sections with side plates connected through bolts. Finite Element analysis was used to determine the appropriate thickness of the mould and bolt strength depending on the concrete ultimate strength. The circumference of the mould was 1% larger than the cylindrical sample (with this value depending on the preliminary FE analysis of stresses and strain as well as to accommodate possible small asperities of the sample after demoulding); the height was designed as to accommodate samples of up to 250 mm. Depending on the height of the sample, circular steel plates could be placed at both ends of the mould to provide uniform compression.

### **2.2 Sample damaging**

Concrete cylindrical samples were removed from the water bath after 28 days and dried for two hours at ambient temperature. Samples were then labelled and measured, and Ultrasonic Velocity Pulse (UPV) test was conducted according to ASTM C597-16 [11] to identify the stiffness of concrete before damaging it. Three samples were tested without any confinement to measure the unconfined compressive strength at failure of concrete after 28 days of curing

(e.g. undamaged condition). The remaining samples were then put in the steel mould and incremental loads corresponding to 10%, 15%, 25%, 40%, 55%, 70% and 85% of the maximum strength (unconfined) were applied to generate internal cracking. Four samples were 'damaged' at each loading condition, with one of them being used to evaluate the internal cracking through X-ray testing. UPV measurements were taken after each loading step to obtain the samples' residual stiffness and compressive strength at damaged condition.

### 2.3 X-Ray Tomography - $\mu$ CT scan

In this experiment Bruker Skyscan 1275 X-Ray micro-tomograph was used to determine internal porosity and cracking. Concrete samples with diameter of 55 mm and height of 67 mm were placed on the micro-positioning stage. When the X-ray beam passes through the concrete sample, the intensity is attenuated due to the concrete absorption and the detector receives the residual intensity hence producing the 2D image. At 0.2 degree rotation around its axis and resolution of 1540x1540 a total of 1535 images with thickness of 35  $\mu$ m were obtained. Porosity and crack development were further investigated.

## 3. Analysis of Results

### 3.1 Internal Damage Evaluation

The X-ray tomography was used to determine the porosity induced in the concrete samples; due to differential compression loading and the ad-hoc fabricated mould, an internal damage state was developed. All samples were analysed by separating the internal air phase (e.g. voids and cracks) from the solid phase (e.g. aggregates and cement mortar) for each 2D image. Material with higher density was observed with lighter grey intensity whereas air pores were dark grey coloured due to less attenuation of the translated intensity [12]. To determine the porosity of various concrete samples and controlled cracks, the optimum of 44-255 grey level threshold was used throughout the entire experiment for consistency of results. Global thresholding algorithm to convert the image to binary from the grey-scale image followed by the application of Otsu's method [13] to further separate the pores and solid phases, were applied during post-processing of x-ray results. The results in Fig. 1 show the porosity of different crack-controlled damages in comparison to undamaged concrete sample (average of 8 undamaged samples). Fig. 2-4 depicts the frequency with respect to sphericity and volume of internal pores at 25% and 85% crack controlled damage in comparison to undamaged samples.

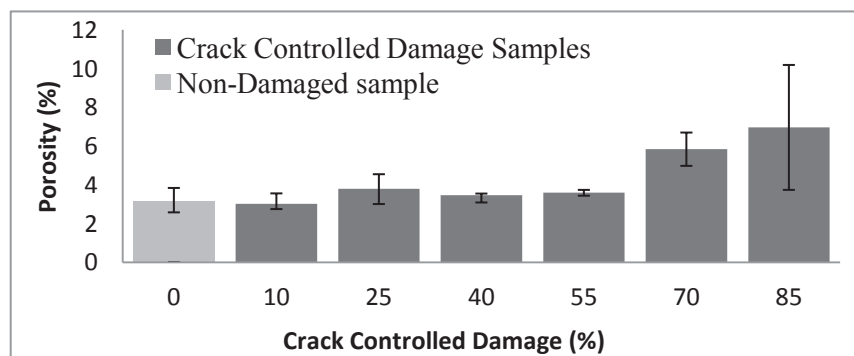


Figure 1: porosity of damaged samples

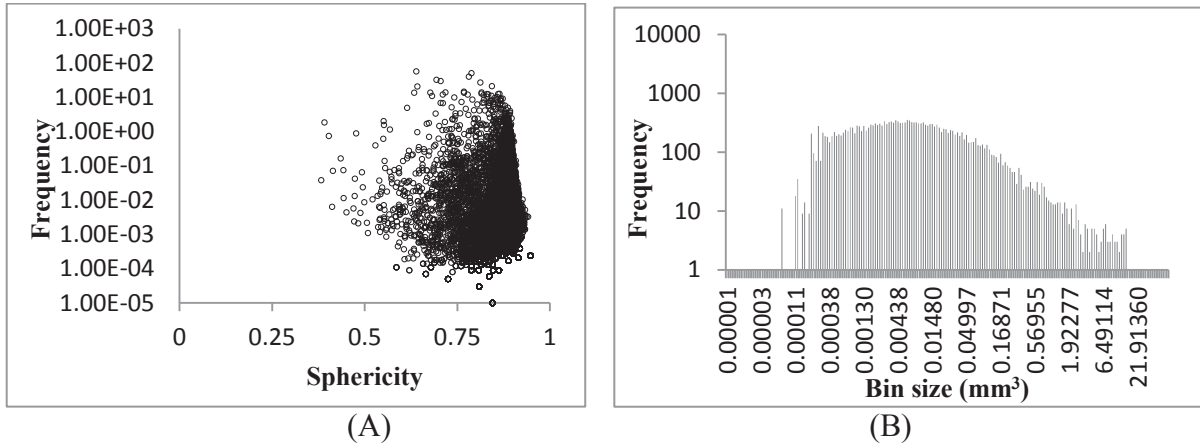


Figure 2: Frequency of sphericity (A) and bin size (B) of pores for undamaged sample

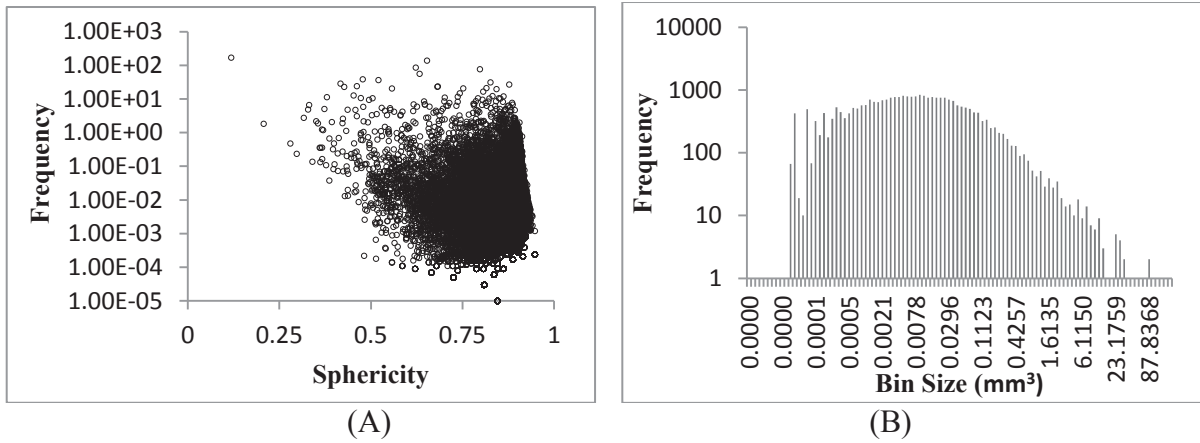


Figure 3: Frequency of sphericity (A) and bin size (B) of pores for 25% damage

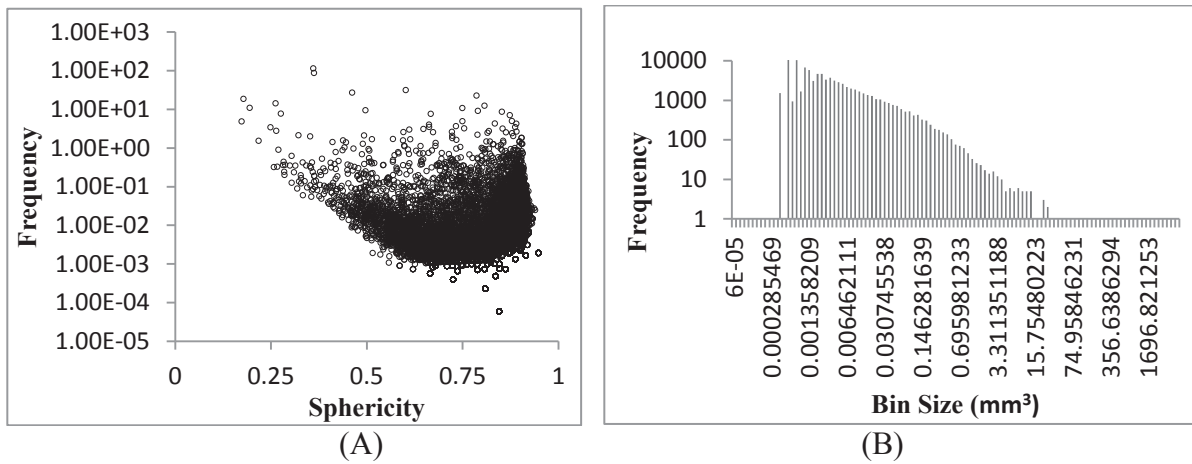


Figure 4: Frequency of sphericity (A) and bin size (B) of pores for 85% damage

### 3.2 Compressive strength and stiffness

MTS 1000 kN was used to induce cracks in concrete samples through the steel mould and compressive strength test. After cracks were being induced at different loading levels,

concrete samples were tested under ultimate compressive strength to obtain the residual compressive strength after damage. Fig. 5 shows the compressive strength and residual stiffness modulus at various damage levels in comparison to the control mix. Dynamic modulus of elasticity was measured before and after inducing cracks on the same sample through Ultrasonic Velocity Pulse test.

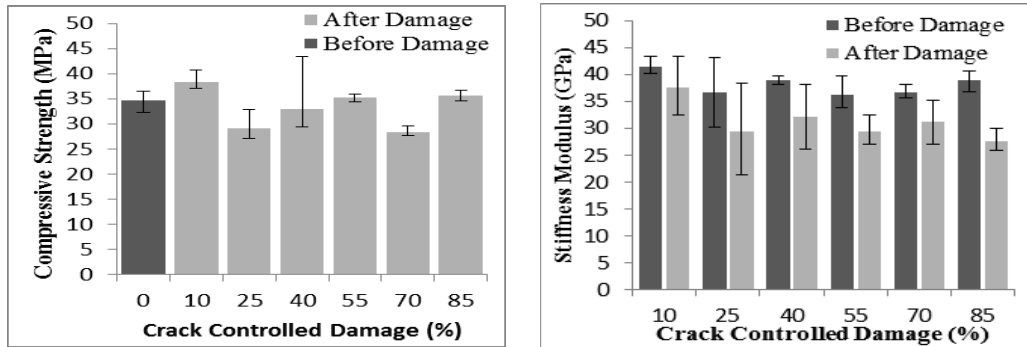


Figure 5: Compressive strength and residual stiffness of concrete after inducing cracking

#### 4. Discussion and conclusions

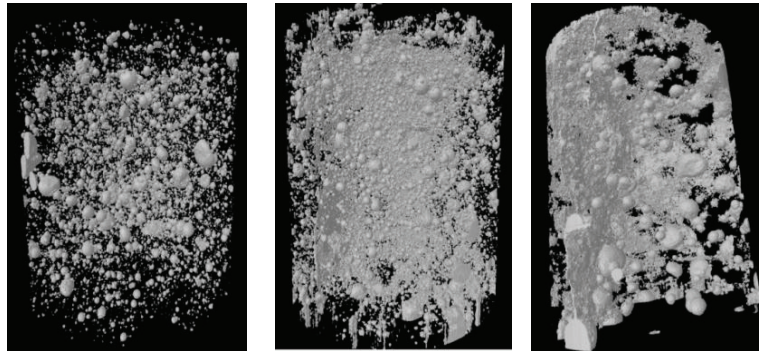
Compared to common methods that only trigger one single crack (or a few cracks in correspondence to the point of maximum stress), the present approach showed an early possibility to generate cracks of various size and shape inside the entire volume of the sample. The ad-hoc developed steel mould, coupled with X-ray analysis and non-destructive testing, could represent a viable alternative to study the efficiency of healing agents in cementitious materials. The evaluation of the internal damage only based on mechanical testing is in fact a not fully reliable method as depicted in Fig. 5; results showed great variability and very small differences were noticed among different damage levels. The application of loading rates between 10% and 55% proved to generate very small cracking patterns with these being not easy to capture by the X-ray machine; thin capillary cracking (e.g. less than 10-30  $\mu\text{m}$ ) can be overlooked due to the equipment resolution. UPV testing was able to capture small variations in stiffness (Fig. 5) before and after damage although variability was slightly high.

Internal porosity was evaluated according to its overall magnitude but also through the study of the distribution of shape and volume of the cracks. From Fig. 2-4, one can observe that the sphericity of the cracks is very close to 1 (perfect sphere) in undamaged samples – bottom right of the graph – and moves to the upper left area of the graph with increasing damage intensity. Sphericity tends to shift from a value of 1 to 0.5 (and lower) thus indicating the change in shape of internal voids due to the formation of the cracks and their geometrical inconsistency. The distribution of the volume of internal voids also follows a clear trend where a greater damage (e.g. 85%) corresponds to bigger voids and the shifting of the volume distribution towards the right side of the histogram scale.

As general representation of results, Fig. 6 shows the 3D visualization of three concrete samples under X-ray at undamaged, 25% and 85% damage conditions.

Based on the results, the fabricated steel mould for developing internal cracks in concrete cylindrical specimens showed to be a viable alternative to generate cracking patterns inside

the sample overcoming common approaches that only simulate single cracks, or a group of cracks in a small specific area of the sample. With proper calibration of the external load to be applied to the sample, the size, shape and volume of the cracks can be modified. Healing agents could achieve different results depending on size and density of the cracks to be filled.



(A) undamaged sample (B) 25% damage (C) 85% damage

Figure 6: 3D visualization of undamaged sample compared to 25% and 85% damage

## References

- [1] Chahal, N., R. Siddique, and A. Rajor, Influence of bacteria on the compressive strength, water absorption and rapid chloride permeability of fly ash concrete. *Construction and Building Materials*, 2012. 28(1): p. 351-356.
- [2] Picandet, V., A. Khelidj, and H. Bellegou, Crack effects on gas and water permeability of concretes. *Cement and Concrete Research*, 2009. 39(6): p. 537-547.
- [3] Van Tittelboom, K. and N. De Belie, Self-healing in cementitious materials—A review. *Materials*, 2013. 6(6): p. 2182-2217.
- [4] Van Tittelboom, K., et al., Self-healing efficiency of cementitious materials containing tubular capsules filled with healing agent. *Cem. Conc. Composites*, 2011. 33(4): p. 497-505.
- [5] Qureshi, T. and A. Al-Tabbaa. The effect of magnesia on the self-healing performance of Portland cement with increased curing time. in *1st International Conference on Ageing of Materials & Structures*. 2014.
- [6] Van Tittelboom, K., et al., The efficiency of self-healing concrete using alternative manufacturing procedures and more realistic crack patterns. *Cement Conc. Comp.*, 2015. 57.
- [7] Clayton, D.A., et al., *Evaluation of Ultrasonic Techniques on Concrete Structures*. 2013, Oak Ridge National Laboratory (ORNL).
- [8] Suzuki, T., et al., Use of acoustic emission and X-ray computed tomography for damage evaluation of freeze-thawed concrete. *Const. B. Materials*, 2010. 24(12): p. 2347-2352.
- [9] Eisenmann, D., et al. Inspection of a large concrete block containing embedded defects using ground penetrating radar. in *AIP Conference Proceedings*. 2016. AIP Publishing.
- [10] Method for making and curing concrete. Compression and indirect tensile test specimens. 2018.
- [11] ASTM C597 - 16 Standard Test Method for Pulse Velocity Through Concrete. 2018.
- [12] Fan, S. and M. Li, X-ray computed microtomography of three-dimensional microcracks and self-healing in engineered cementitious composites. *Smart Mat. Struc.*, 2014. 24(1).
- [13] Manahiloh, K.N., et al., X-ray computed tomography and nondestructive evaluation of clogging in porous concrete field samples. *J. Mat. Civil Eng.*, 2012. 24(8): p. 1103-1109.

## **A PRELIMINARY STUDY ON THE SELF-HEALING POTENTIAL OF BACTERIA-MODIFIED FIBERS IN CONCRETE**

**Kira Weise**<sup>(1)</sup>, **Henk Jonkers**<sup>(2)</sup>, **Eddie Koenders**<sup>(1)</sup>

(1) Institute of Construction and Building Materials, TU Darmstadt, Germany

(2) Microlab, Delft University of Technology, Delft, The Netherlands

### **Abstract**

Enhancing the self-healing potential of cementitious materials can be achieved in many different ways. An innovative method that gained a lot of attention is to add concrete compatible bacteria to a mixture that reacts when activated with oxygen and water, and produces limestone with the ability to fill up cracks. Most challenging is how to add the bacteria into a concrete so that they survive and are properly positioned with access to the nutrient (lactate). A common way is to add bacteria and precursor together in a porous clay particle, or more recently, adding them as a compressed pill. In this contribution, results of a preliminary study will be presented that show the potential of modifying polypropylene fibres with bacteria and its nutrient. In addition to the bacteria to produce limestone at the crack surfaces, limestone was also formed in the crack opening. This mechanism showed an accelerated self-healing process with the potential to close wider cracks. The study reports first results of various ways to modify the fibres with bacteria with emphasis of the adhesion between fibres and bacteria. The preliminary study showed interesting results and demonstrated the difficulties of getting the bacteria properly coated on fibre surfaces.

### **1. Introduction**

Using self-healing materials cannot only save a lot of maintenance costs but also has the potential to preserve resources and cut back CO<sub>2</sub> emissions. An innovative approach to use bacteria in the concrete mixtures that are activated by oxygen and water after crack occurrence enable to produce limestone as a repair agent for cementitious matrix. With present methods it is possible to heal cracks up to widths of 0.8 mm [1, 2]. However, it turned out that closing these crack sizes with healing agent goes along with a lot of uncertainty. This paper contributes to this issue and presents a preliminary study with the aim to make the healing process for larger crack width more reliable and even more efficient. The conceptual

idea is on the modification of polymer fibres by covering their surfaces by a thin layer of bacteria or blending them in a polymer melt, so that after cracking the limestone will not only be produced on the crack surfaces, but also on the fibres itself, enhancing the healing potential of wider cracks.

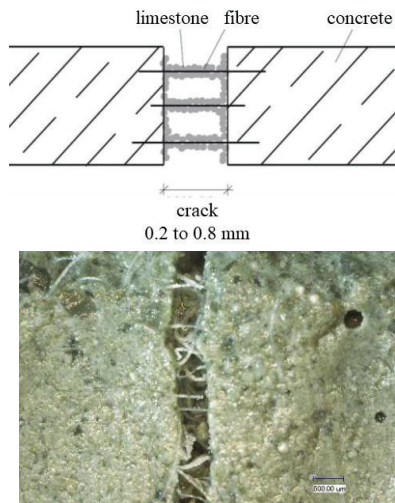


Figure 1: Crack bridging of bacteria-modified polymer fibres.

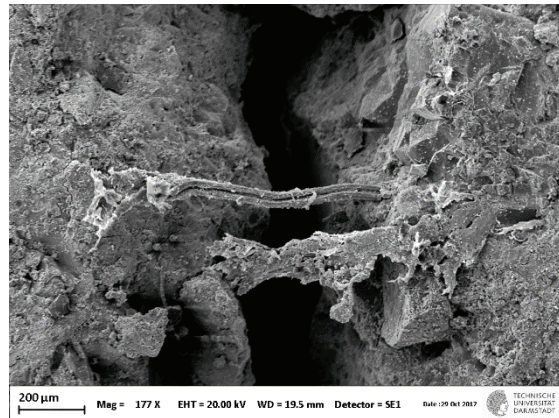


Figure 2: Limestone production on crack bridging polymer fibre.

Fig. 1 and 2 show the basic principles of the mechanism as addressed in this paper. Due to the formation of limestone on the fibres an acceleration of the bio-based self-healing mechanism and its potential to close wider cracks would be very likely. A first step in the development of this method would be on the modification of the fibres, or in this case, on the addition of bacteria on the fibre surfaces. In this paper, four different methods are presented to achieve this, and their performance is evaluated.

## 2. Materials and methods

The polymer fibres used in this study were received from the company Baumhueter extrusion GmbH [3]. The fibres are made of polypropylene, which is a thermoplastic synthetic polymer. While mixed in a cementitious system, polymer fibres have the potential to bridge micro cracks, reduce shrinkage and enhance the material's fire resistance. In this study, modifying the fibres with a bacteria-nutrient solution was done for a fibre length of 6 mm. In addition to this, uncut fibre strands were used for the modification process, with a liquid polyactide (PLA) granulate and a gluing method. Fig. 3 and 4 show a few grams and a detailed view of polymer fibres used. The bacteria applied for this specific purpose need to be able to produce spores that survive in the high alkalinity of a cementitious system. Researchers from TU Delft [4] found a bacteria type that fulfils these needed criteria. When a crack occurs the bacteria is activated by oxygen and water and produces limestone that fills the crack. For this process, nutrients like for example calcium lactate and yeast extract are required. An impression of the used raw materials are shown in Fig. 5 to 7. For easy handling, storing, transport and preparation, as well as to avoid inhalation of these ultra-fine particles, the bacteria spores were dried on limestone powder. From this, Green-Basilisk B.V. produces concrete resistant PLA granulate that was also used as the healing component in this study [5].



Figure 3: Polymer fibres.

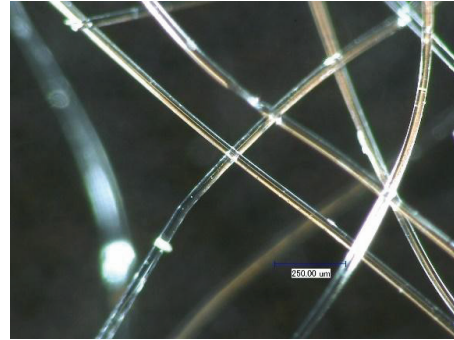


Figure 4: Magnified polymer fibres.



Figure 5: Bacteria spores.



Figure 6: Calcium lactate.



Figure 7: Yeast extract.



Figure 8: PLA granulate 0.25 to 0.5 mm (right) and 0.5 to 1.0 mm (left).

In general, the applied bio-based agent consists of polyactide (PLA), bacteria spores and yeast extract [6]. On one hand PLA protects the bacteria from water and mechanical abrasion, and on the other hand it acts as a nutrient. Fig. 8 gives an impression of the used PLA granulate in two different particle sizes. These materials were used for this study with the main aim to either modify the polymer fibres by producing a blend or to try to cover each individual fibre with a thin layer of it. This was the main difficulty of this approach, namely to find a robust procedure for getting the bacteria and nutrient properly blended in, or on the fibre surface [5]. In order to get an impression about ability to possibilities and their robustness, in this study the adhesion between four different combinations of polymer fibres and bacteria are investigated on their fibre modification potential and their performance. These methods are described in the next sections followed by a systematic evaluation.



#### a) Bacteria-nutrient solution

A bacteria-nutrient solution was made of water, bacteria spores, calcium lactate and yeast extract. Two different fibre types (multifil and splicing film fibres) with a length of 6 mm were wetted with this solution and dried in an oven afterwards.



Figure 9: a) Bacteria-nutrient solution.

#### b) Liquefied PLA granulate

For this modification method, PLA granulate was melted and uncut multifil fibre strands were pulled through it manually. A detailed impression of the final result is provided in Fig. 10, showing the irregularities in the coated fibres.



Figure 10: b) Liquefied PLA granulate.

#### c) Gluing method

Different types of commercial glues as well as wax and resin were spread over uncut multifil fibre strands. Subsequently, calcium lactate was attached to them.



Figure 11: c) Gluing method (wax).

#### d) Melted polymer and PLA granulate

Polymer fibres and PLA granulate were melted and stirred together. From this melt fibres were pulled manually. Fig. 12 shows the polymers in a melted situation.



Figure 12: d) Melted polymer and PLA granulate.

### 3. Results and discussion

All four techniques showed various difficulties in the bacteria-modification process, in particular the adhesion process. To enable an accelerated self-healing process with the potential to close wider cracks by bacteria-modified polymer fibres, the way of properly combining both components is of mayor importance. The bacteria modified polymer fibres need to fulfil various specifications. On one hand, to guarantee an adequate self-healing

process, meaning that the bacteria should to be distributed homogenously in the fibre or over its full surface. On the other hand is it necessary that both components act as a stable system in the cementitious matrix. The bacteria-modified polymer fibres need to be resistant against mechanical abrasion and water, especially with regard to the concrete mixing process, where both influences may occur simultaneously. When modifying the fibres with a bacteria-nutrient solution, agglomerations formed that lumped multiple fibres to an Igel-like configuration. As a result, the modified fibres were not resistant against mechanical abrasion and were soluble in water (Fig. 13). The same issue was observed when gluing the healing components on the fibres' surface (Fig. 15). Distributing the bacteria homogenously in or on the fibre was difficult to achieve for all modification techniques applied (Fig. 11, 13, 14 and 16). When modifying the fibres by adding them in a melt of PLA granulates, and successively pulling fibres from a melt of PLA and polypropylene, a reasonable resistance against mechanical abrasion and water was reached. A more detailed evaluation of the different techniques is outlined in Tab. 1.

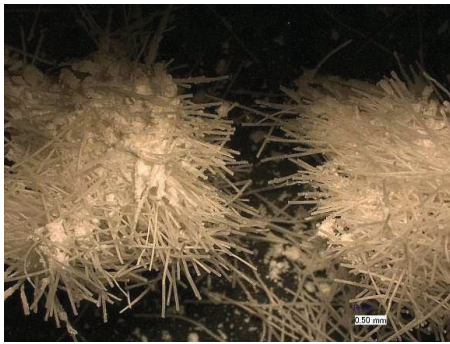


Figure 13: a) Broken agglomeration.



Figure 14: b) No homogenous distribution.



Figure 15: c) No resistance against mechanical abrasion.



Figure 16: d) No homogenous distribution.

It turned out that for the bacteria-modified polymer fibres the lack of resistance against mechanical abrasion and water was the main issue that could be improved by adding a coating on the fibre surface. From this, the highest potential was identified for the modification with melted PLA granulate and with pulling fibres from a melt of PLA and polypropylene. The fact that the components of the healing agent were not distributed homogenously in or on the fibre surface (Fig. 16) was mainly because of the manual application, as done in this study. This procedure could probably be improved with an automated modification process. In this way, a controlled modification of the fibre, consisting of polymers and the healing agent could be achieved.

Table 1: Evaluation of different modification techniques (- : 1 point, 0 : 2 points, + : 3 points).

	a) Bacteria-nutrient solution	b) Liquified PLA granulate	c) Gluing method	d) Melted polymer and PLA granulate
Homogenous distribution	0	-	0	-
Water resistance	-	+	0	+
Resistance against mechanical abrasion	-	+	-	+
<b>Total</b>	<b>4</b>	<b>7</b>	<b>5</b>	<b>7</b>

#### 4. Conclusion

A preliminary study has been conducted that showed conceptual results on modification techniques, and demonstrated the difficulties of getting the bacteria properly attached to the surface, or blended with the polymer fibre. The presented techniques provide a basis for further research by showing main influencing factors as well as potentials and problems whenever developing bacteria-modified fibres. Identified difficulties are on one hand, the lack of resistance against mechanical abrasion and solubility in water, which could be improved with an additional coating on top of the modified fibre. On the other hand, this study shows problems of distributing the bacteria homogeneously in or on the fibre surface. This issue could be due to the manual application methods applied. Possibly, this problem could be solved by modifying the fibres by automatic processing. Further research is needed to improve and expand the presented techniques of modifying polymer fibres with bacteria to reach a more efficient self-healing process in cementitious systems.

#### Acknowledgement

The authors acknowledge support from EU COST Action CA15202-SARCOS, and also from the EU H2020 SUPERCONCRETE Project (H2020-MSCA-RISE-2014 n 645704).

#### References

- [1] Zhang, J. et al., Immobilizing bacteria in expanded perlite for the crack self-healing in concrete, *Construction and Building Materials* (2017), 610-617
- [2] Luo, M. et al., Factors affecting crack repairing capacity of bacteria-based self-healing concrete, *Construction and Building Materials* (2015), 1-7
- [3] Baumhueter extrusion GmbH, <https://www.baumhueter-extrusion.de/produkte/pb-eurofiber/funktionsfasern-fuer-moertelmassen/>
- [4] Jonkers, H.M., *Self Healing Concrete: A Biological Approach*, Springer Series in Materials Science (2007), vol 100, Springer, Dordrecht
- [5] Backes, F., *Applikationstechnik, Wirkungsgrad und Mechanismus der Risschließung faserbewehrter selbstheilender Mörtel*, M.Sc. Thesis, TU Darmstadt (2017)
- [6] Green-Basilisk B.V., <http://www.basiliskconcrete.com/product-healing-agent/?lang=en>

## **ACTIVE MINERAL ADDITIVES AND THEIR CONTRIBUTION TO NATURAL SELF-HEALING ABILITY OF CONCRETE**

**Pavel Reiterman** <sup>(1)</sup>

(1) Czech Technical University in Prague, Prague, Czech Republic

### **Abstract**

Reducing of maintenance costs of concrete structures have got into increased professional concern. The protection of existing structures is determined by their primary resistance to the action of the environment, secondarily by additional performance. Concrete is effective material with sufficient structural properties, however the efficiency of its use is essentially dependent on the level of maintenance costs. Present paper is focused on the experimental study dealing with primary resistance of concrete, which is determined by its composition and selection of particular components. The great potential for durability increase of structural concrete have various types of supplementary cementitious materials (SCM), which have beneficial effect on the durability and environment quality. There was studied influence of fly ash, ceramic powder and metakaolin addition. The properties of concrete are evaluated in terms of freeze-thaw resistance and mechanical properties. The experimental program performed confirmed positive impact of active mineral additives on the frost resistance of concrete mixtures with SCMs addition. On the basis of results of residual mechanical properties during cycle freeze-thawing can be assumed, that cycle freeze-thawing could stimulate blended binding system to additional hydration, which led to the partial strengthening. This effect could create reserve leading to the increase of frost resistance.

### **1. Introduction**

Number of relatively new existing concrete structures exhibit significant deterioration due to progressive impact of external environment. It is caused by the limited primary resistance of used concrete, which is determined by its composition. That is why, the development of new concrete mixes is closely related to the assessment of final durability performance. There is also significant simultaneous need to reduce energy consumption, which is related to the production of concrete and Portland cement, respectively, by using various SCMs [1]. Besides positive environmental effect, they considerably contribute to the durability of concrete [2,3].

Increased durability performance of concrete has direct impact on final maintenance costs, which are invested to infrastructure to ensure its service. That is why, technologies able to ensure prolongation of service-life of current concrete structures are concerned through scientific community [4]. Present paper is focused on the assessment of autogenous self-healing ability of concrete exposed to freeze-thaw cycling. Studied technology is closely related to the application of various SCMs, which later hydration after freezing-thawing was monitored. Present work corresponds with focus of COST Action “Self-healing as preventive repair of concrete structures”.

## 2. Experimental program

Performed experimental program was focused on the determination of residual compressive strength of cement based mortars modified by various SCMs, ceramic powder, fly ash, blast furnace slag and metakaolin were used. Studied mineral additives were applied as 10.0% cement replacement by mass. Chemical composition of used additives and Portland cement is introduced in Tab. 1.

Table 1: Chemical composition of used binding components [%].

Component	Cement	Ceramic powder	Fly ash	Blast furnace slag	Metakaolin
SiO <sub>2</sub>	18.5	18.5	52.4	36.0	53.1
Al <sub>2</sub> O <sub>3</sub>	6.5	6.5	35.9	9.0	41.7
Fe <sub>2</sub> O <sub>3</sub>	2.4	2.4	4.9	0.3	1.08
CaO	64.9	64.9	1.2	43.5	0.13
MgO	1.0	1.0	0.8	8.3	0.18
K <sub>2</sub> O	1.2	1.2	1.4	0.5	-
Na <sub>2</sub> O	0.1	0.1	-	0.5	-
TiO <sub>2</sub>	-	-	2.4	0.3	1.8
SO <sub>3</sub>	4.9	4.9	0.2	0.5	0.7

Present binding components were mixed with natural siliceous sand of gradings 0-4mm in mass proportions 1:4, water to binder ratio was set to constant 0.55. Sets of prismatic samples 40×40×160 mm were produced from particular bathes. Samples were cured under standard laboratory conditions for 28 days.

Determination of flexural strength was carried out using three-point bending test with support span 100mm and axial loading. Compressive strength measurement was conducted using fragments left after bending test on loading area 40×40 mm. After 28 days started cyclic freezing-thawing in automatic chamber. Each cycle consisted on freezing phase lasting 4 hours and defrosting period performed by automatic flooding of testing chamber by water. Residual mechanical properties were determined after 25 cycles of freezing-thawing.

### 3. Results and discussion

Performed experimental program was focused on the determination of residual mechanical properties of cement based mortars modified by partial replacement by various SCMs after cyclic freezing-thawing. Conducted experiments confirmed previous observations during freezing-thawing, where initial increase of mechanical performance was monitored. Residual values of compressive strength after 25 cycles are shown in Fig. 1. It is necessary to note, that values of flexural strength were nearly similar after 25 cycles for all studied mixtures.

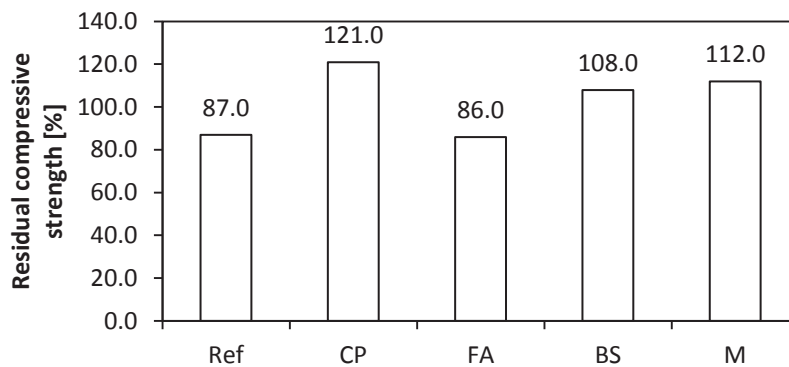


Figure 1: Residual compressive strength [%].

It is evident that 10% replacement by ceramic powder, blast furnace slag and metakaolin led to slight increase of compressive strength by 21%, 8% and 12%, respectively. On the other hand, control mixture as well as mixture with fly ash exhibited decay of mechanical performance by 13% and 14%, respectively. Gradual increase of mechanical performance of concrete mixes with mineral additives replacement during cyclic freezing-thawing was also in [5]. They confirmed additional hydration of binding components induced by action of frost. The positive effect of low temperatures on process of hydration of blended system was confirmed by number of experimental studies [6,7]. Because, the reduced hydration kinetic contributes to the long-term durability performance [8]. Observed mechanism lies in the ongoing hydration, which is positively supported by the presence of water and partial deterioration by micro-cracks propagation, which opens non-hydrated parts of used binding system. It is necessary to note, that present mechanism was observed only in case of mixtures with increased volume of the binder, so concretes with low content of binding components are not able to exhibit the above described self-healing effect. Increase of mechanical performance during freezing-thawing culminates in dependence on the loading regime and used composition, however after initial phases of cycling loading, studied mixtures exhibit gradual decay of mechanical properties. On the other hand, the initial increase create sufficient reserve before following loading induced by external environment.

### 4. Conclusions

Conducted experiments dealt with the influence of cyclic freezing-thawing on compressive strength of mortars with addition of various SCMs. Realized program confirmed previous

results and observation, that blended binding systems could exhibit increase of mechanical performance during cyclic freezing-thawing, especially in initial phases of loading. Such reached increase create sufficient reserve before additional loading. Laboratory testing related to the simulation of real condition is conducted by accelerated testing, however the effect of external environment is very slow. In Middle Europe the temperature drops below 0°C approximately 35-40 per year, what does not correspond with the kinetic of testing. In real conditions the effect of environment is cumulative, what contributes to the self-healing through stimulated by low temperatures. Controlling of the above described mechanism could significantly contribute the prolongation of service life of current concrete structures and infrastructure. Beneficial of this mechanism in the incorporation of waste materials such as waste ceramics, or materials related to reduced energy consumption such as fly ash, blast furnace slag and metakaolin, which can replace energy demanding Portland cement.

### Acknowledgement

This research was supported by project No. LTC18063.

### References

- [1] Kubissa, W., Jaskulski, R. and Reiterman, P., Ecological Concrete Based on Blast-Furnace Cement with Incorporated Coarse Recycled Concrete Aggregate and Fly Ash Addition, *J Renew Mater* 5(2017), 53-61
- [2] Khodabahshian, A., Ghalehnovi, M., de Brito, J. and Shamsabadi, A. E., Durability performance of structural concrete containing silica fume and marble industry waste powder, *J Clen Prod* 170 (2018), 42-60
- [3] Duan, P., Shui, Z., Chen, W. and Shen, C., Influence of metakaolin on pore structure-related properties and thermodynamic stability of hydrate phases of concrete in seawater environment, *Constr Build Mater* 36 (2012), 947-953
- [4] Ferrara, L., Van Mullen, T., Alonso, M. C., Antonaci, P., Borg, R. P., Cuenca, E., Jefferson, A., Ng, P. L., Peled, A., Roig-Flores, M., Sanches M., Schroefl, C., Serna, P., Snoeck, D., Tulliani, J. M. and De Belie, Experimental characterization of the self-healing capacity of cement based materials and its effects on the material performance: A state of the art report by COST Action SARCOS WG2, *Constr Build Mater* 167 (2018), 115-142.
- [5] Chung, C. W., Shon C. S. and Kim Y. S., Chloride ion diffusivity of fly ash and Silica fume concretes exposed to freeze-thaw cycles, *Contr Build Mater* 24 (2010), 1739-1745
- [6] Soriano, L., Monzó, J., Bonilla, M., Tashima, M. M., Payá, J. and Borrachero, M. V., Effect of pozzolans on the hydration process of Portland cement cured at low temperatures, *Cem Concr Comp* 42 (2013), 41-48
- [7] Hassan, A. A. A., Lachemi, M. and Hossain, K. M. A., Effect of metakaolin and silica fume on the durability of self-consolidating concrete, *Cem Concr Comp* 34 (2012), 801-807
- [8] da Silva W. R. L., Šmilauer, V. and Štemberk, P., Upscaling semi-adiabatic measurements for simulationg temperature evolution of mass concrete structures, *Mater Struc* 48 (2015), 1031-1041

## APPLICATION OF *LYSINIBACILLUS SPHAERICUS* FOR CONCRETE CRACK HEALING USING DIFFERENT CALCIUM SOURCES

Christine Farrugia <sup>(1)</sup>, Ruben Paul Borg <sup>(1)</sup>, Joseph Buhagiar <sup>(2)</sup>, Liberato Ferrara <sup>(3)</sup>

(1) Faculty for the Built Environment, University of Malta, Malta

(2) Department of Biology and Argotti Botanic Gardens & Resource Centre, University of Malta, Malta

(3) Dipartimento di Ingegneria Civile e Ambientale, Politecnico di Milano, Italy

### Abstract

Micro-cracks, which develop during the service life of reinforced concrete structures, reduce the durability of concrete through the penetration of fluids. Microbially-induced calcium carbonate precipitation occurs naturally in the presence of ureolytic bacteria which precipitate calcium carbonate ( $\text{CaCO}_3$ ) through urea hydrolysis. This deposition leads to the filling of micro-cracks and sealing of pores, reducing ingress of fluids into the concrete. The research aim was to assess the potential of *Lysinibacillus sphaericus* to precipitate  $\text{CaCO}_3$  on concrete through urea hydrolysis. *Lysinibacillus sphaericus* was cultivated *in vitro* and induction of MICP through urea hydrolysis was tested on cement paste with two different calcium sources. The calcium precipitates were characterised by light microscopy, Scanning Electron Microscopy, Energy Dispersive Spectroscopy and Fourier Transform Infrared Spectroscopy. The study confirmed that MICP is induced successfully on concrete using *Lysinibacillus sphaericus*. Samples exposed to repeated treatment cycles of *Lysinibacillus sphaericus* in the presence of a calcium source exhibited a more extensive and even coating of  $\text{CaCO}_3$  crystals on the surface confirming that repeated cycles of treatment are more effective in increasing the amount of  $\text{CaCO}_3$  deposition and therefore increasing crack healing capacity.

### 1. Introduction

The durability of concrete is greatly reduced by the presence of micro-cracks within the material [1]. Micro-cracks may develop due to various processes and can occur at any time during the service life of the material. They have a negative effect on the concrete as they allow ingress of fluids including liquids, gases and ions into the concrete matrix, causing corrosion of reinforcement and degradation of the cementitious matrix. Therefore crack



widths must be controlled and healing reduces the ingress of fluids. These micro-cracks can heal naturally through autogenous healing which also involves the precipitation of calcium carbonate ( $\text{CaCO}_3$ ) inside the crack in the presence of water. However, autogenous healing is only possible in small cracks and takes a long time to occur. Cracks may also heal through a natural microbial process known as microbial-induced calcium carbonate precipitation (MICP). This biological repair by bio-deposition occurs naturally in the presence of ureolytic bacteria which can precipitate  $\text{CaCO}_3$  in the presence of appropriate nutrients [2]. The process can be induced artificially in the laboratory by adding urea to the medium containing the bacteria. The  $\text{CaCO}_3$  precipitation allows rapid filling of cracks in concrete and plugging of pores to reduce absorption of fluids. As opposed to autogenous healing, this process can therefore seal cracks a lot quicker and avoid further damage occurring.

Bio-deposition methods as opposed to conventional surface treatments and crack repair methods with synthetic chemicals and formulations are alternative and eco-friendly techniques which merit further investigation. MICP is a natural, non-polluting process which has no damaging effects on the natural environment and therefore can be promoted as a viable alternative to conventional, polluting treatments on concrete. The aim of this research was to assess the potential of *Lysinibacillus sphaericus* to precipitate  $\text{CaCO}_3$  on concrete through urea hydrolysis in the presence of different calcium sources.

## 2. Materials and Methods

### 2.1 Preparation of Medium and Bacterial Inoculum for Bio-precipitation

The strain *L. sphaericus* (LMG 22257) was used in this study. This strain of bacteria is alkaliphilic and was seen to have a continuous formation of dense calcium carbonate crystals from previous studies [3]. Medium 295 agar was prepared using recommended protocol provided by the Belgian Co-ordinated Collections of Micro-organisms (BCCM). The autoclaved medium was poured into sterile petri dishes and later used for surface inoculation. Medium 295 broth was similarly prepared but the addition of agar was omitted. An ampoule of *Lysinibacillus sphaericus* (LMG 22257) was purchased from BCCM in lyophilized form and revived by using 0.5 ml of the recommended Medium 295 broth. The contents of the ampoule were allowed to re-hydrate for a few minutes before transferring onto a Medium 295 agar plate and streaked to obtain individual colonies after incubation. Two drops were also plated but were left untouched to preserve a concentrated inoculum at the centre of the plate. The remaining drops hydrated *L. sphaericus* were added to Medium 295 broth to prepare a liquid culture. The inoculated agar plates and the broth were incubated for 48-72 hours in an incubator (CERTOMAT BS-1, Sartorius) set at 30°C. The bacterial colonies were repeatedly sub-cultured over a period of time using the same procedure of spreading a colony over an agar plate and incubated for 48-72 hours at 30°C to increase the volume of bacterial inoculum required for bio-precipitation. Once substantial colony growth was reached, plates with were transferred to a refrigerator set at 4°C to prevent further multiplication of the bacteria. In order to induce sporulation, the same procedure of bacterial subculture was used but the agar medium was further modified by the addition of 10mg/L of  $\text{MnSO}_4$  to the Medium 295 agar. For the preparation of the bacterial inoculum for the bio-precipitation experiments, a 0.5 McFarland bacterial inoculum in Medium 295 broth was prepared by comparison to barium sulphate standard prepared using standard protocol. The solution was incubated for 24 hours

at 30°C to obtain a one-day old stock culture. This procedure was repeated using a plate containing *L. sphaericus* (LMG 22257) and Medium 295 agar with 10mg of MnSO<sub>4</sub>.

## 2.2 Preparation of Calcium Source Solutions

A solution of calcium chloride (CaCl<sub>2</sub>) was prepared by adding 6.25g of CaCl<sub>2</sub> to 250mL of distilled water. A solution of calcium acetate (Ca(CH<sub>3</sub>COO)<sub>2</sub>) was prepared by adding 6.5g of Ca(CH<sub>3</sub>COO)<sub>2</sub> to 250mL of distilled water. Both solutions were subsequently autoclaved at 121°C for 15 minutes.

## 2.3 Preparation of Cement Paste Samples

500g of CEM 1 42,5R cement and 140ml of distilled water were mixed for 2.5 minutes at 285r.p.m. in a 5 litre bowl. The cap of a 1mL Eppendorf flask was isolated from the flask so as to obtain a mould which could hold circa 0.15-0.2g of cement paste. The cement paste was placed in the moulds and vibrated on a vibrating table. They were then allowed to cure inside an enclosed container at 20°C±1°C and a relative humidity of 70%.

## 2.4 Treatment Procedure for Cement Paste Samples

The cement paste samples were placed under an ultraviolet light source at 254nm for 40 minutes so as to sterilize their upper surface. These samples were labelled and placed inside a sterilized container so as to avoid contamination. The other half of the samples were also labelled and placed inside a container. All treatments were applied on the upper surface of the sample as follows. The bacterial inoculum was applied to the surface of the samples using a Pasteur pipette until ponding was achieved on top of the sample. The samples were left to stand in an enclosed container for 24 hours. After this 24-hour period, any remaining bacterial inoculum on the surface of the samples was gently removed using a paper towel so that ureolytic activity would result primarily from bacteria inside the cement paste. The calcium source solution was then applied to the surface of the samples using a Pasteur pipette until ponding was achieved on top. The samples were left to stand in an enclosed container for 72 hours. After this 72-hour period, any remaining calcium solution on the surface of the samples was gently removed using a paper towel. For the set of samples requiring a second repetition of the treatment, this procedure was repeated at the end of the first treatment. The samples were observed using surface visual observation, stereoscopic microscopy, Fourier Transform Infrared Spectroscopy (FTIR), Scanning Electron Microscopy (SEM) and Energy Dispersive Spectroscopy (EDS).

All treatments were applied on the upper surface of the sample. The variables in the treatment procedures were sterilization of the sample, sporulating or active bacteria (with or without MnSO<sub>4</sub> respectively), the presence and type of calcium source, drying of the sample in an oven and the number of repetitions of the treatment procedure. All treatment procedures were carried out in duplicate.

## 3. Results and Discussion

### 3.1 Stereomicroscopy

The samples were observed under a stereomicroscope to confirm the presence of crystals on the surface. In Figure 1, the surface of a control sample with no treatment and a sample treated with *L. sphaericus* and CaCl<sub>2</sub> under a stereomicroscope can be seen. The control

sample on the left exhibits no precipitates while the treated sample on the right exhibits white precipitates on its surface.

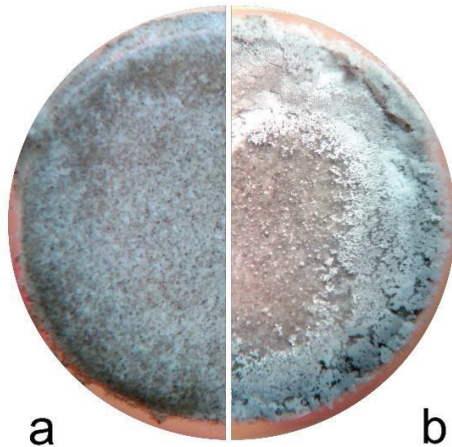


Figure 1: Stereoscopic microscopy images of the surface of cement paste specimens. (a) Control - no treatment (b) treated with *L. sphaericus* and  $\text{CaCl}_2$ .

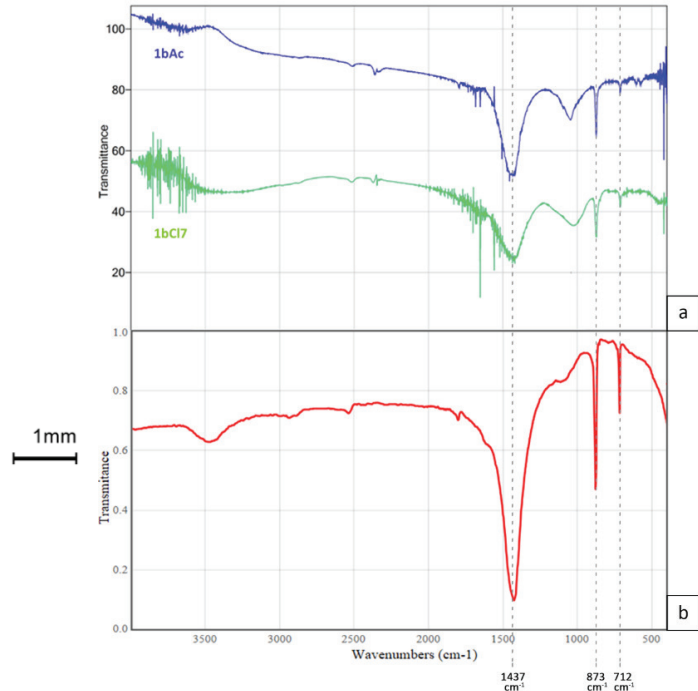


Figure 2: FTIR spectra for (a) scraping from surface of samples 1bCl7 treated with *L. sphaericus* and  $\text{CaCl}_2$  (bottom) and 1bAc7 treated with *L. sphaericus* and  $\text{Ca}(\text{CH}_3\text{COO})_2$  (top), (b) reference spectrum for calcite [4].

### 3.2 FTIR

The FTIR spectra in the range of 4000-500 $\text{cm}^{-1}$  for the scraping of crystals from the surface of sample 1bCl7 (treated with *L. sphaericus* and  $\text{CaCl}_2$ ) and 1bAc7 (treated with *L. sphaericus* and  $\text{Ca}(\text{CH}_3\text{COO})_2$ ) can be seen in Figure 2. The shape of the spectrum indicates the presence of  $\text{CaCO}_3$ . When compared to the typical FTIR spectrum for calcite (Figure 2b), major vibrational bands with peaks at 1437 $\text{cm}^{-1}$ , 873  $\text{cm}^{-1}$  and 712  $\text{cm}^{-1}$  are comparable. This confirms that the precipitate obtained on the surface of the cement paste samples is calcite ( $\text{CaCO}_3$ ).

### 3.3 SEM and EDS

Sample 1bAc7 treated with *L. sphaericus* and  $\text{Ca}(\text{CH}_3\text{COO})_2$  exhibited numerous clusters of crystals on its surface (Figure 3). At a magnification of 5,000X, the crystals were clearly observed to be rhombohedral with sharp edges and with a size ranging from 10 $\mu\text{m}$ -15 $\mu\text{m}$ . Within these rhombohedral crystals, bacterial cells were observed. This confirms that the crystals are a product of the bio-deposition process induced using *L. sphaericus* and a calcium source. Sample 2/1bCl7 treated with two rounds of treatment of *L. sphaericus* and  $\text{CaCl}_2$  also exhibited clusters of crystals on its surface similar to those precipitated on sample 1bAc7.

These crystals were also observed to be rhombohedral with sharp edges (calcite) and bacterial cells could be observed within the crystals (Figure 4).

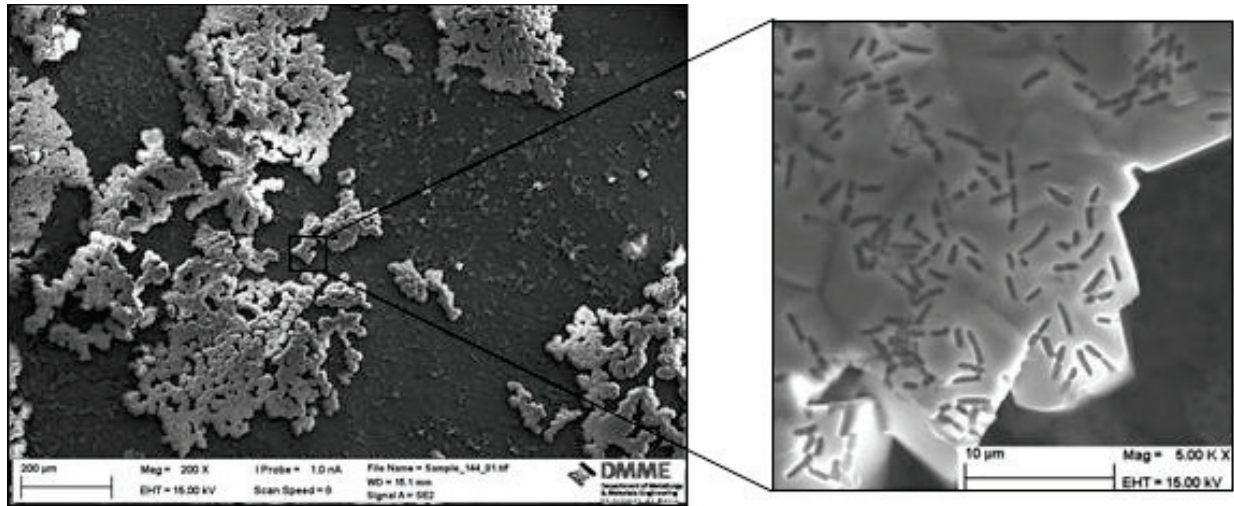


Figure 3: SEM image for sample 1bAc7 (treated with *L. sphaericus* and  $\text{Ca}(\text{CH}_3\text{COO})_2$ ) at 200X and 5000X magnification.

As opposed to the crystals precipitated on sample 1bAc7, the crystals precipitated on sample 2/1bCl7 covered the whole surface of the cement paste. This was confirmed through EDS analysis of the surface of the sample (Figure 5) as the EDS analysis did not show peaks for Mg, Si, Al and S, indicating that the surface of the cement paste was entirely covered in crystals produced through MICP. Also, various different sizes of crystals were observed on the surface. On average, the size of the crystals ranged from  $2\mu\text{m}$ - $50\mu\text{m}$ .

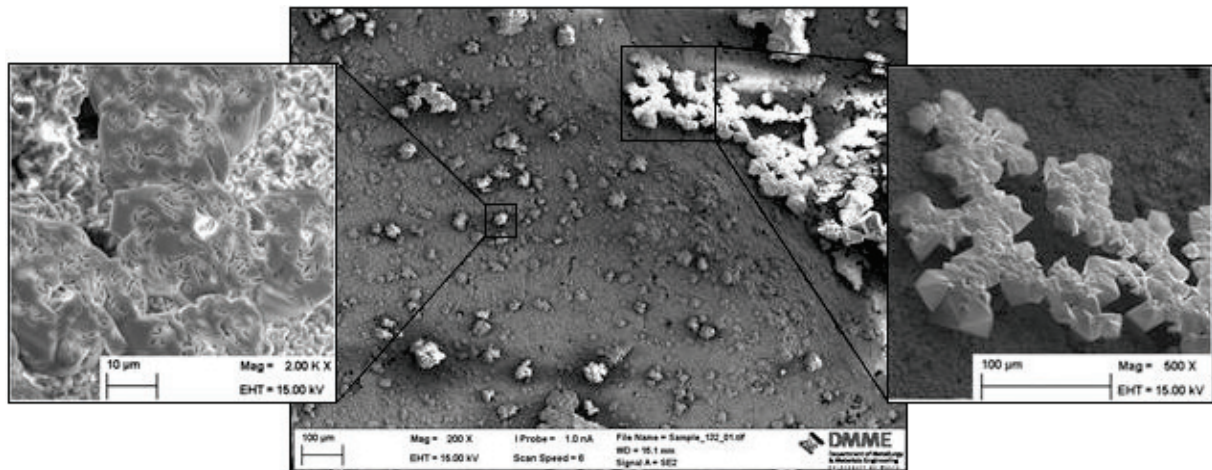


Figure 4: SEM image for sample 2/1bCl7 (two rounds of treatment of *L. sphaericus* and  $\text{CaCl}_2$ ). Image magnification: centre 200X, right enlargement 500X and left enlargement 2000X.

These differences between sample 1bAc7 and sample 2/1bCl7 were attributed to the fact that the latter received 2 rounds of treatment of *L. sphaericus* and a calcium source. This resulted in a more even coating on the surface and larger crystal depositions.

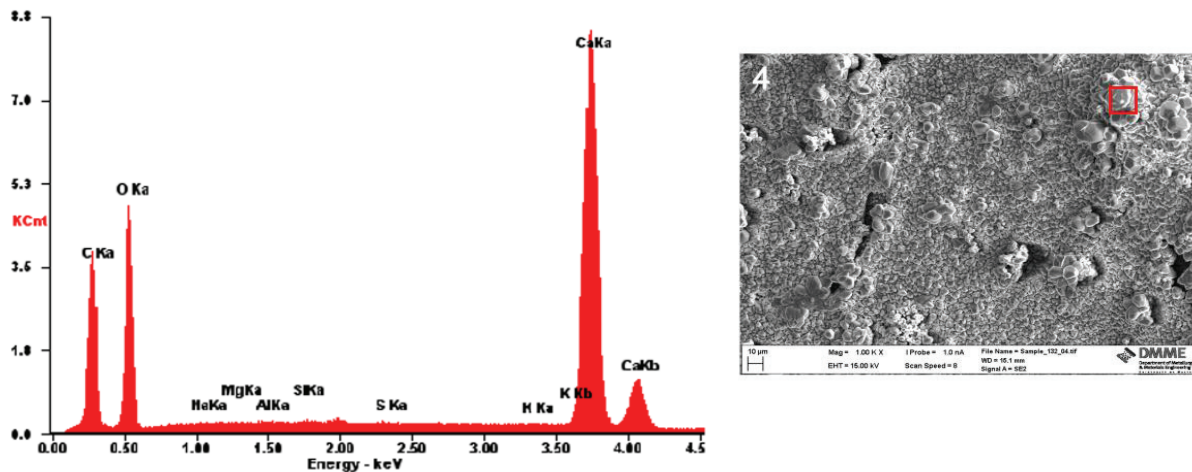


Figure 5: EDS for crystals on surface of sample 2/1bCl7.

#### 4. Conclusion

First and foremost, it was confirmed that MICP could be induced successfully on concrete using *L. sphaericus* and  $\text{CaCl}_2$  or *L. sphaericus* and  $(\text{Ca}(\text{CH}_3\text{COO})_2)$  in the presence of urea. Furthermore, the characterisation of the precipitates from the MICP process confirmed that the crystals precipitated on these samples were  $\text{CaCO}_3$  crystals. No difference in the amount of crystal precipitation was observed between samples treated with *L. sphaericus* and  $\text{CaCl}_2$  or *L. sphaericus* and  $(\text{Ca}(\text{CH}_3\text{COO})_2)$ . It was also noted that samples exposed to 2 rounds of treatment of *L. sphaericus* and a calcium source exhibited a greater and more even coating of crystals on the surface. This proves that repeated cycles of treatment are effective in increasing the amount of  $\text{CaCO}_3$  deposition.

#### Acknowledgements

ERDF (Malta) testing equipment: “Developing an Interdisciplinary Material Testing & Rapid Prototyping R&D Facility” (Ref. No. 012); Ing. J. Camilleri University of Malta for technical support.

#### References

- [1] Newman, J., and Seng Choo, B., Advanced Concrete Technology: Concrete Properties. Burlington: Elsevier Ltd. (2003)
- [2] De Belie, N., et al, Microbial carbonate precipitation in construction materials: A review. Ecological Engineering 36 (2010), 118-136
- [3] Chahal, N., and Siddique, R., Effect of ureolytic bacteria on concrete properties. Construction and Building Materials 25 (2011), 3791-3801.
- [4] Calcium carbonate (calcite) (2016). Retrieved from National Institute of Standards and Technology (NIST): <http://webbook.nist.gov/cgi/cbook.cgi?ID=B6004659&Mask=80>

## **BIOTREATED CONVENTIONAL CONCRETE AND CDW-CONCRETE BY USE OF MICROBIAL MIXED CULTURES BIOPRODUCTS**

**Julia García-González<sup>(1)</sup>, André Freches<sup>(2)</sup>, Pedro Vaz<sup>(3)</sup>, Paulo C. Lemos<sup>(2)</sup>, Alice S. Pereira<sup>(4)</sup>, Andrés Juan-Valdés<sup>(1)</sup>, Paulina Faria<sup>(5)</sup>**

(1) Escuela de Ingeniería Agraria y Forestal, University of Leon, León, Spain

(2) LAQV-REQUIMTE, Department of Chemistry, Faculdade de Ciências e Tecnologia, Universidade NOVA de Lisboa, Caparica, Portugal

(3) Department of Civil Engineering, Faculdade de Ciências e Tecnologia, Universidade NOVA de Lisboa, Caparica, Portugal

(4) UCIBIO-REQUIMTE, Department of Chemistry, Faculdade de Ciências e Tecnologia, Universidade NOVA de Lisboa, Caparica, Portugal

(5) CERIS and Department of Civil Engineering, Faculdade de Ciências e Tecnologia, Universidade NOVA de Lisboa, Caparica, Portugal

### **Abstract**

Cracks form in all concrete constructions shortening the life of concrete elements, particularly in exposed concrete. They provide a path for transport of moisture, chlorides, and various other deleterious substances. The aim of this study was to assess the protection and consolidation effect of eco-friendly healing biotreatments on water absorption of conventional and recycled concrete, with 50% substitution of natural coarse aggregate by CDW aggregate. Concrete were treated with bioproducts obtained using waste biomass from a microbial mixed culture process for polyhydroxyalkanoates production. Results showed that the reference samples, with application of tap water, presented an increase in water drop permeability, being the absorption time shorter than in the control (untreated) samples. The biotreatment with the non-sonicated bioproduct increased significantly the water absorption time, more evident in conventional concrete samples than in recycled ones. In the case of the sonicated bioproducts, the behaviour was similar for both types of concrete specimens, but the healing effect was higher. When the biotreatment was performed with three applications, the healing effect was not so effective. This observation may be associated with the formation of a hydrophobic film of organic material from the bioproduct, which detached from the concrete surface after outdoors exposure.

## 1. Introduction

The quality of concrete surface plays an important role in the concrete service life [1], particularly in exposed concrete. Its quality is impacted by the water/cement ratio of the fresh concrete [2] and affects spreading processes but also hardened concrete properties [3-6]. That is even more important in the case of concrete with recycled aggregates. Due to phenomena such as the wall effect [7], contact with formworks [8] or segregation [9], the exterior layer of exposed concrete often has a different composition from the internal one and its porosity is higher than in the core of the concrete element [10]. Several studies have tested the surface healing effect of organic and inorganic treatments on cement-based materials [11,12], showing improvements on permeability, resistance to moisture diffusion and filling of surface cracks and voids. Leung et al. [13] tested neat epoxy and neat silane as well as epoxy/organoclay and silane/organoclay nanocomposites and stated that the incorporation of organoclay into silane could improve its resistance to moisture diffusion. Pigino et al. [14] applied ethyl silicate by brushing onto the surface of concrete, penetrating up to a depth of about 3-5 mm into the concrete, induced a substantial decrease in water absorption, despite the low quantity of the absorbed product. Amidi and Wang [15] tested other types of surface treatments, using calcium carbonate deposition by hydrolysis of dimethyl carbonate (DMC) to fill the surface cracks and voids of concrete elements. A reduction in water absorption was achieved. Sodium silicate has also been used [16,17].

The search for a suitable bioproduct compatible with the existing cementitious substrate and able to improve the concrete surface quality by biotreatment of incipient cracks and porous structure may be an appropriate technique. Healing, helping the external repair, decreasing maintenance costs of aged concrete structures and increasing sustainability in the construction industry would be some of the advantages of this technology.

## 2. Materials and methods

Conventional and recycled concrete samples were prepared to assess the protection and consolidation effect of an eco-friendly healing biotreatments on water absorption. For the manufacture of the concrete mixtures, the following materials were employed. Commercially available Portland blended cement (CEM III/A 42.5 N/SR) was conformed to the Spanish [18-19] and European [20] standards. Natural aggregates presented a siliceous nature and complied with the requirements of the EHE-08 [21] and EN 12620+A1 [22]. Recycled mixed aggregates (RMA) were obtained through a mechanical treatment of construction and demolition wastes (CDW) in a recycling plant located in the Autonomous Community of Madrid (Spain). The composition of the RMA, determined according to EN 933-11 [23], is presented in Tab. 1. Physical and mechanical properties of RMA and natural aggregates such as D/d ratio [24], fines content [24], flakiness index [25], Los Angeles coefficient [26], were within the suitable parameters established by EHE-08 [21] for the concrete manufacture. Nevertheless, results obtained for RMA water absorption [27] showed a greater variation compared to the natural aggregates. The presence of attached mortar and ceramic materials in the recycled aggregates caused a significant water absorption, higher than the one of the natural aggregates. The use of aggregates with high water absorption could result in a workability drawback. Consequently, the RMA were pre-saturated: a technique that showed

to be a suitable method to manufacture inexpensive recycled concrete with low strength requirements and maintain a suitable workability [28]. Tab. 2 shows the detailed composition of the different raw components used in the manufacture of the conventional concrete (CC) and recycled concrete (RC). The w/c ratio and  $f_{ck}$  of both concretes is 0.5 and 25 MPa, respectively.

Table 1: Non-floating components of recycled aggregates.

Component	% (w/w)
Unbound aggregates (natural aggregates without cement mortar attached)	44.1
Ceramics (bricks, tiles, stoneware and sanitary ware, ...)	33.6
Concrete and mortar (natural aggregates with cement mortar attached)	17.5
Asphalt	0.4
Glass	0.8
Gypsum	3.5
Other impurities (wood, paper, metals, plastic, ...)	0.2

Table 2: Mix composition per cubic metre of conventional and recycled concrete.

Material	CC	RC
Water (l)	165	155
Cement (kg)	333	313
Sand 0/4 mm (kg)	103	97
Sand 0/5 mm (kg)	470	442
Gravel 4/10 mm (kg)	516	242
Gravel 6/12 mm (kg)	172	81
RMA 4/20 mm (kg)	0	323

The test samples were cubes cut from concrete specimens that were molded, and had a cut surface with 50 mm x 50 mm. The bioproducts used as healing agents were obtained using waste biomass from a microbial mixed culture (MMC) for polyhydroxyalkanoates production using pine wood bio-oil as substrate. MMC cell walls were disrupted by sonication (MMC-P\_S) or not (MMC-P). Samples were treated with 2 mL of each bioproduct suspensions by using a pipette, covering the top surface. Half of the samples were biotreated with a single application, whereas on the other half, three applications were made (one application every 24 h). The effect of each bioproduct on surface treatment was evaluated and compared with untreated samples (control) and treated with the same volume of tap water (reference).

For each biotreatment and concrete, three samples were tested. The test room conditions were  $20 \pm 2^\circ\text{C}$  and  $40 \pm 5\%$  relative humidity (RH). Two days after the last application, the bio-healing capacity was assessed by water-drop absorption test in the air, in order to simulate real conditions. This test allows evaluating the permeability variation of the biotreated surfaces by monitoring the time required to absorb a water drop under open air conditions. The test was video recorded and the absorption time was then defined for each concrete,



number of applications and treatment. After this test the samples were placed outdoors for natural aging.

### 3. Results and discussion

Figure 1 shows the treated samples. When the treatment included three applications, a layer of organic material from the bioproduct deposited on the surface of the concrete samples, changing its color, and the healing effect decreased. After 1 month in outdoors exposure the samples were visually observed, and the layer was no longer visualized: it was washed off or, in case of three applications of the bioproducts, it cracked and separated from the concrete surface without spotting (treated samples looked like control and reference samples, without the brownish layer).

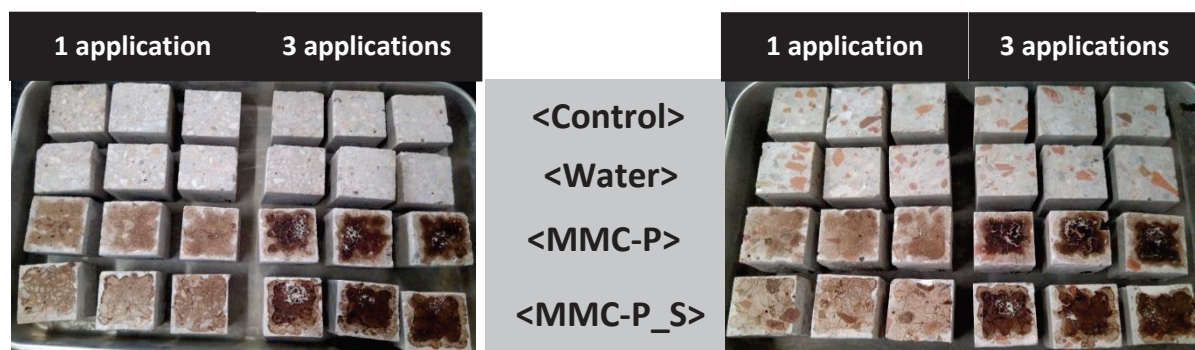


Figure 1: Conventional concrete (left) and recycled concrete (right) samples after treatment.

Figure 2 shows the time of water drop absorption for each biotreated concrete samples, the control (untreated) and the reference (with water application) samples.

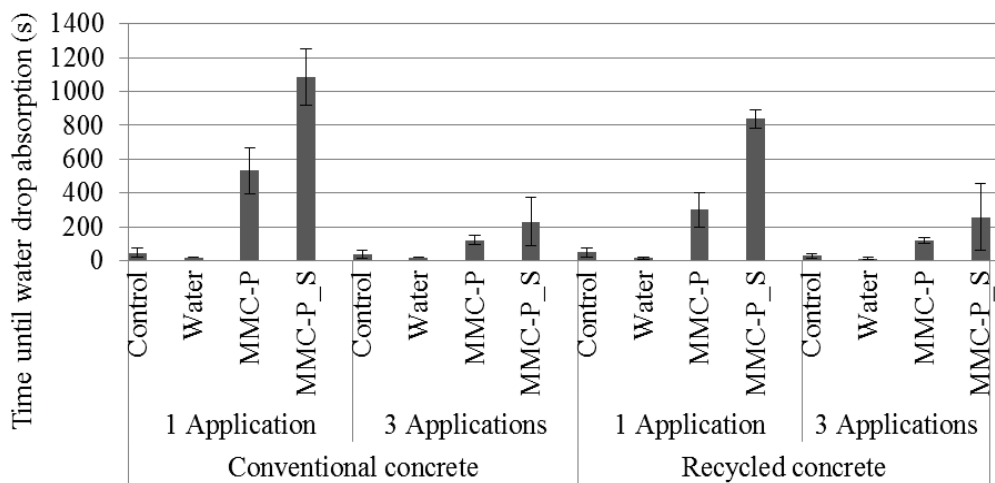


Figure 2: Results of water drop absorption test.

Results have shown that the reference concrete, with tap water, presented an increase in water drop permeability, being the absorption time shorter than in the control concrete in all cases. The biotreatment MMC-P increased the water absorption time significantly, more evident in

conventional concrete than in recycled one. In the case of the sonicated bioproducts (MMC-P\_S), the behavior was similar regarding the different kinds of concrete, but the healing effect was even higher.

A comparison of results of the biotreatments with studies from other researchers is presented in Tab. 3. In the short term, the good efficiency of the biotreatments tested in the present study is clearly evident. Further studies will allow to justify this effect and if it will be durable.

Table 3: Water ingress decrease due to concrete surface treatments.

Study	Type concrete	Treatment	Reduction (%)
Woo et al. [11] - permeability	With PVA Fibers	Neat silane and silane/clay nanocomposite	29-57
Chandra et al. [12] - water absorption	Portland	Extract of cactus	83
Present - water drop ingress in comparison with control	Portland	MMC-P - 1 application	996
		MMC-P_S - 1 application	2130
	With CDW	MMC-P - 1 application	521
		MMC-P_S - 1 application	1622

#### 4. Conclusion

The biotreatments with bioproducts from a microbial mixed culture for polyhydroxyalkanoates production process produced a decrease of the permeability on both conventional and recycled concrete. Besides, the sonicated bioproduct achieved a greater healing effect when compared with the non-sonicated MMC one. Multiple applications of biotreatment cause the formation of a hydrophobic film of organic material from the bioproduct, which detached from the concrete surface, cracking with time passed even between applications and decreasing the healing effect. Therefore, a single application of the sonicated MMC bioproduct was the most efficient tested biotreatment to increase concrete durability to water access.

#### Acknowledgements

This work was supported by a STSM Grant from the COST Action CA15202. (<http://www.sarcos.enq.cam.ac.uk>). This work was also supported by the Associate Laboratory for Green Chemistry-LAQV and Applied Molecular Biosciences Unit-UCIBIO which are financed by national funds from FCT/MCTES (UID/QUI/50006/2013; UID/Multi/04378/2013) and co-financed by the ERDF under the PT2020 Partnership Agreement (POCI-01-0145-FEDER – 007265; POCI-01-0145-FEDER-007728).

#### References

- [1] Gandhi, G. K., et al, Quantifying changes in surface characteristics of concrete due to progressive deterioration, *J Mater Civ Eng* 29 (2017), 1-10.
- [2] Rizzo, P. et al, Detecting the presence of high water-to-cement ratio in concrete surfaces using highly nonlinear solitary waves, *Appl Sci* 6(104) (2016), 1-16
- [3] Mors, R. and Jonkers, H., Effect on concrete surface water absorption upon addition of lactate derived agent, *Coatings* 7 (2017), 1-10

- [4] Huang, Y., Modeling moisture transport at the surface layer of fatigue-damaged concrete, *Constr Build Mater* 151 (2017), 196-207
- [5] Williams, M. et al, Non-destructive study of the microstructural effects of sodium and magnesium sulphate attack on mortars containing silica fume using impedance spectroscopy, *Appl Sci* 7 (2017), 1-21
- [6] Salvoldi, B. G., Oxygen permeability of concrete and its relation to carbonation, *Constr Build Mater* 85 (2015), 30-37
- [7] Zheng, J.J., Aggregate distribution in concrete with wall effect, *Mag Concrete Res* 55 (2003), 257-265
- [8] De Caro, P., Influence of the nature of the demoulding agent on the properties of the formwork-concrete, *Mag Concrete Res* 59 (2007), 141-149
- [9] Safawi, M. I., The segregation tendency in the vibration of high fluidity concrete, *Cem Concr Res* 34 (2004), 219-226
- [10] Weber, S. and Reinhardt H.W., A new generation of high performance concrete: concrete with autogenous curing, *Adv Cem Based Mater* 6 (1997), 59-68
- [11] Woo et al., Barrier performance of silane-clay nanocomposite coatings on concrete structure, *Compos Sci Technol* 68 (2008), 2828-2836
- [12] Chandra, S. et al., Use of cactus in mortars and concrete, *Cem Concr Res* 28 (1998), 41-51
- [13] Leung et al., Use of polymer/organoclay nanocomposite surface treatment as water/ion barrier for concrete, *J Mater Civ Eng* 20 (2008), 484-492
- [14] Pigino, B., Ethyl silicate for surface treatment of concrete – Part II: characteristics and performance, *Cement Concr Compos* 34 (2012), 313-321
- [15] Amidi, S. and Wang, J., Surface treatment of concrete bricks using calcium carbonate precipitation, *Constr Build Mater* 80 (2015), 273-278
- [16] Jia, L. et al., Effects of inorganic surface treatment on water permeability of cement-based materials, *Cement Concr Compos* 67 (2016), 85-92
- [17] Li, J., et al., Progress of silane impregnating surface treatment technology of concrete structure, *Mater Rev* 26 (2012), 120-125
- [18] Royal Decree 256, Cement Reception Instruction (RC-16) [In Spanish], Ministry of Public Works, Madrid, Spain (2016)
- [19] UNE 80303-1, Cements with additional characteristics. Part 1: Sulphate resisting cements [in Spanish], AENOR, Spain (2013)
- [20] EN 197-1, Cement. Part 1: Composition, specifications and conformity criteria for common cements, CEN, Spain (2011)
- [21] Permanent Commission on Concrete, Code on Structural Concrete (EHE-08) [in Spanish]. Spanish Ministry of Public Works, Spain (2008)
- [22] EN 12620+A1, Aggregates for concrete, CEN, Brussels (2008)
- [23] EN 933-11, Tests for geometrical properties of aggregates – Part 11: Classification test for the constituents of coarse recycled aggregate, CEN, Brussels (2009)
- [24] EN 933-1, Tests for geometrical properties of aggregates – Part 1: Determination of particle size distribution - Sieving method, CEN, Brussels (2012)
- [25] EN 933-3, Tests for geometrical properties of aggregates – Part 3: Determination of particle shape - Flakiness index, CEN, Brussels (2012)
- [26] EN 1097-2, Tests for mechanical and physical properties of aggregates – Part 2: Methods for the determination of resistance to fragmentation, CEN, Brussels (2010)
- [27] EN 1097-6, Tests for mechanical and physical properties of aggregates – Part 6: Determination of particle density and water absorption, CEN, Brussels (2013)
- [28] García-González, J. et al., Pre-saturation technique of the recycled aggregates: solution to the water absorption drawback in the recycled concrete manufacture, *Materials* 7 (2014), 6224-6236

## **CHARACTERIZATION AND MONITORING OF THE CRACK SELF-HEALING ABILITY OF BIO-MORTAR**

**Bojan Miljevic<sup>(1)</sup>, Francesco Lo Monte<sup>(2)</sup>, Snezana Vucetic<sup>(1)</sup>, Olja Sovljanski<sup>(1)</sup>, Ivan Ristic<sup>(1)</sup>, Branka Pilic<sup>(1)</sup>, Sinisa Markov<sup>(1)</sup>, Liberato Ferrara<sup>(2)</sup>, Jonjaua Ranogajec<sup>(1)</sup>**

(1) University of Novi Sad, Faculty of Technology, Novi Sad, Serbia

(2) Politecnico di Milano, Department of Civil and Environmental Engineering, Milan, Italy

### **Abstract**

It is known that bacteria can promote self-healing of the cracks in concrete structures, but the elevated pH value of the cement-based concrete matrix affects negatively the life span of bacteria and consequently, the self-healing effect. Therefore, a method for encapsulation of bacteria healing agent in a polymer hydrogel system has been successfully established to protect the bacteria from surrounding environment. In order to investigate the healing capacity of the employed bacterial colony and the effectiveness of the proposed encapsulation methods, three groups of mortar specimens were systematically prepared: standard reference samples, samples with hydrogel and bio-mortar samples (with bacteria species encapsulated in the hydrogel system surrounded with nutrition). Microstructure and texture analysis were performed before and after the healing treatment. The mortar specimens were notched at mid-span and pre-cracked by means of 3-point bending tests performed in CMOD-control mode. Water sorption tests were performed periodically in order to ascertain the effects of healing on the recovery of durability performance. The healing ability was also measured by crack opening displacement change by optical microscopy. The specimens were tested in 3-point bending up to failure, to assess the effect of the healing, if any. A cross-comparison analysis of the obtained results was provided.

### **1. Introduction**

Innovative and sustainable solutions for self-healing concrete structures are at the highest demand in these days as their repair and maintenance can reach very high costs [1]. It is known that bacteria promote a self-healing phenomenon in the existing cracks in a concrete structure [1,2]. However, an elevated pH value of the cement-based concrete matrix affects

negatively the life span of bacteria and consequently, the self-healing effect. Therefore, a method for encapsulation of bacteria healing agent in a polymer hydrogel system is needed in order to protect the bacteria from surrounding. The ureolytic bacteria especially *Sporosarcina pasteurii* have generated a lot of interest in the field of crack repair in concrete and calcareous materials, and have been studied extensively. The use of these bacteria leads to accumulation of insoluble  $\text{CaCO}_3$  in a calcium rich environment through the hydrolysis of urea; this produces dissolved ammonium, inorganic carbon and  $\text{CO}_2$ , and the ammonia released in the surroundings subsequently increases pH [3].

In order to investigate the healing capacity of the employed bacterial colony and the effectiveness of the proposed encapsulation methods, systematically varied mortar specimens were prepared. The prepared samples were characterized by X-ray diffraction (crystal phases revealed), X-ray fluorescence analysis (chemical content), mercury intrusion porosimetry (pore size distribution) as well as examined by scanning electron microscopy (surface morphology). Microstructure and textural analysis were performed.

The mortar specimens were notched at mid-span and then pre-cracked in 3-point bending in CMOD-control mode (Crack Mouth Opening Displacement). After unloading, the water sorptivity test was performed and then the specimens were kept in a moisture room (90% RH). Their healing ability was measured by crack opening displacement change examined by optical microscopy immediately after the crack formation and after two months of healing. Moreover, at the end of the scheduled exposure periods (one and two months) the water sorption test was performed and the specimens were finally tested in 3-point bending up to failure, in order to assess the effect of the healing. The obtained results were compared with those of the reference samples.

## 2. Experimental procedures

### 2.1 Polymer encapsulation of bacterial spores

The carbonate precipitating bacteria *Sporosarcina pasteurii* DSM 33 was used in this experiment. Living cells were cultured on Trypton Soya Agar (HiMedia, India) with the addition of 20% urea (Difco, USA). The culture was aerobically incubated at 30 °C for 5 days, in order to achieve a high yield of spores. The suspension of *S. pasteurii* spores was formed in sterile distilled water and was exposed to the thermal treatment at 80 °C for 10 minutes to remove vegetative cells. The number of spores was determined after the incubation at 30 °C for 48 h on TSA with the addition of 20% urea.

The hydrogel used in the experiment was synthesised by the method of microwave polymerisation. Acrylic acid and acryl amide, in molar ratio of 1: 1, were mixed with a curing agent (N,N'-methylene bisacrylamide) and polymerised in microwave reactor for 2 minutes. The resulting hydrogel was postpolymerised for 24 hours at room temperatures, and then dried to constant mass. The obtained xerogel (dried hydrogel) was mechanically ground and passed through a sieve <0.5 mm. The equilibrium swelling degrees of the xerogel was previously experimentally determined (22.7 g of liquid for 1 g of xerogel).

The obtained quantity of the xerogel particles was divided into three parts, in order to form: (1) hydrogel with nutrients, (2) hydrogel with spores and (3) pure xerogel. The first part of xerogel was hydrated with nutrients, a solution of urea (20 g/L) and calcium lactate (40 g/L). The second part of xerogel was hydrated with a suspension of spores ( $4.1 \cdot 10^8$  cfu/g of

xerogel). In both cases, the maximum amount of fluid for hydration was 80 % of the equilibrium degree of swelling (~18 ml). After drying, the both types of hydrogels (with nutrients and spores) were mechanically ground. The final concentration of bacterial spores after the complete procedure was  $1.1 \cdot 10^8$  cfu/g of xerogel.

The obtained xerogels (gel with nutrients and gel with spores) were encapsulated as follows. The xerogel particles were coated with an elastomer, dissolved in dichloromethane, at a solvent evaporation temperature (~40 °C). These particles were sprayed from both sides in order to achieve a uniform encapsulation.

## 2.2 Preparation of mortar specimens

The mortar specimens with the dimensions of (160×40×40) mm were prepared, according to the EN 196-1 standard. Three groups of specimens were made systematically as follows: S (standard reference mortar samples), B (bio-mortar samples based on standard mortar mixture with the addition of encapsulated bacterial culture and separately encapsulated nutrition in the hydrogel) and G (mortar samples with addition of hydrogel of the same amount and type as in bio-mortars). All specimens were cured in the same way: firstly kept in a climate chamber at  $t = 20$  °C and relative humidity (RH) of 90 % for 24 h, then demolded and for the next 3 days kept in a tap water ( $t = 20$  °C). The next 24 days of investigation they were kept in laboratory at room temperature and RH of 60 %.

## 2.3 Characterization

### CMOD-controlled 3-points bending tests

The mortar specimens were notched at mid-span (6.2 mm deep) by wet sawing, prepared for the test (gluing knife edges for clip-gauge over the gap with 10 mm spacing) and then pre-cracked in CMOD-controlled (Crack Mouth Opening Displacement) 3-points bending with the target value of 200  $\mu\text{m}$  for the crack opening. For the CMOD 3-points bending tests an *Instron 8562* machine was used with a clip COD gauge and *Instron 8800* control unit. The same set-up was used to monitor and to control the crack opening. The specimens were tested on a 100 mm span. The displacement rate used in the experiment was 0.3  $\mu\text{m/s}$ .

### Water sorption tests

The specimens were kept in water with a depth of 10 mm (at room temperature) and their weight was measured manually at time intervals of 10, 20, 30 minutes and 1-8 hours with the step of 0.5 h. The removal of water from the sample surface was done gently by wiping.

### Mercury intrusion porosimetry

Pore size distribution of the specimens aged 28 days was measured with a mercury porosimeter (AutoPore IV 9500, *Micromeritics*). Prior to the measurements, the samples were dried in oven at 105 °C for 2 h in order to remove the residual water contained in the samples. Maximal intrusion pressure used was 228 MPa.

### X-ray diffraction/ X-ray fluorescence

The X-ray diffraction measurements of the 28 days aged specimens were carried out using a *Philips PW 1710 XRD* instrument, with the  $\text{Cu K}\alpha_{1,2}$  radiation, and a step scan mode of  $0.02^\circ$  in the angular range  $2\theta = (5-60)^\circ$ . The exposition time at each point was 2 s. The X-ray fluorescence measurements were performed by a portable  $\mu\text{-XRF}$  spectrometer *ARTAX 200 (Bruker-Nano)* using the Rh source (25 kV, 1.5 mA) under the He atmosphere with the acquisition time of 100 s.

### Optical microscopy / Scanning electron microscopy

The crack mouth opening displacement of each pre-cracked specimen was monitored by optical microscopy using a mobile digital microscope Dino-Lite Pro AM-413ZT (*ANMO Electronics Co.*) at the magnification of  $\times 200$ . The obtained pictures were evaluated by the software *DinoCapture 2.0*. The study of localization of the used bacterial culture in the newly developed material (bio-mortar) was investigated by Low Vacuum Scanning Electron Microscopy (*JEOL*, JSM-5500LV) at the pressure of 18 Pa and the voltage of 20 kV. All systems had been previously frozen using a liquid nitrogen and subsequently fractured (fresh cross-sections were studied). The imaging was conducted in the first 15 minutes after the samples freezing.

## 3. Results and discussion

### 3.1 Microstructure and textural characteristics of the mortar specimens

The results of the XRF analysis of the standard mortar prism show a relatively high content of calcium (35.7 %), followed by the content of silicon (13.7 %), aluminium (2.3 %), sulphur, potassium, iron ( $\sim 1$  %) and the rest elements (Ti, Mn, Zn, Sr) in traces. Expectedly, the results of XRD analysis confirmed no difference between the different specimens. All of the measured mortar specimens consist of alite, belite, portlandite and calcite beside quartz from the sand aggregates. Different pore size distribution between the standard mortar specimen and the specimen with hydrogel can be seen in Fig. 1. The mortar with hydrogel features higher content of pores with a diameter between 32 nm and 64 nm.

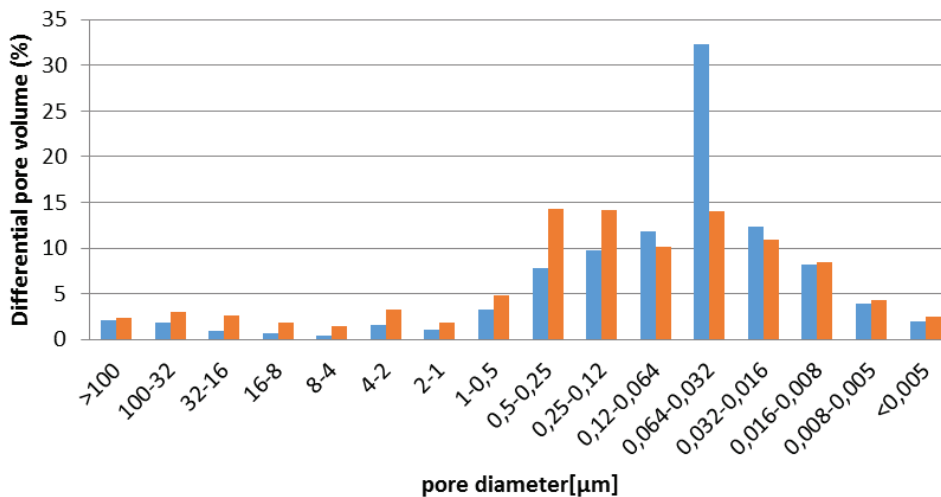


Figure 1: Pore size distribution of mortar specimen with hydrogel – G (blue) in comparison to the standard reference mortar specimen – S (orange)

### 3.2 CMOD-controlled pre-cracking

Fig. 2a) shows the load force as a function of crack mouth opening displacement measured for different specimens. There is a different relaxation between the samples. For the mortar specimens with hydrogel (G) and for bio-mortar specimens (B) the nature of fractures is less brittle, which is the characteristic of the standard reference specimens.

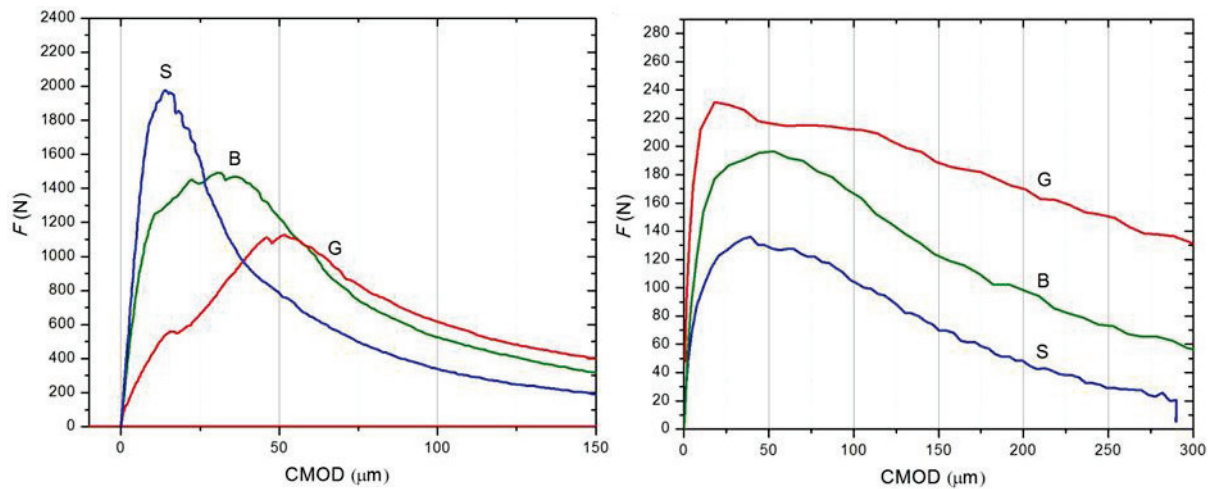


Figure 2: Load force  $F$  as a function of crack mouth opening displacement (CMOD) measured for different samples, a) during the crack formation b) after two months of curing

The maximum loading force was around 2000 N for the reference sample (S), less than 1500 N for the bio-mortar (B), while it was only about 1100 N for the specimen with hydrogel (G).

After the curing in the moisture room at 20 °C and RH 90 %, the specimens behaved differently. Partially healed specimens were again tested in 3-points bending test. Fig. 2b) showed a much lower maximum load force (between 120 N and 240 N) than the one that specimens could endure, in comparison to the load applied for the crack formation (1100 N – 2000 N, Fig. 2a). Also, the order of specimens regarding the maximum load force changed in the opposite direction. This fact could be attributed to different residual strength values obtained during the crack formation. However, the values of the maximum load force are considerably closer to each other in comparison to the crack formation values. The externally healed specimen unfortunately broke apart at very low load.

### 3.3 Water sorption

The difference between the weights of the sample kept in water and the dry sample was plot as a function of the square root of time. In fig. 3, the values, averaged over three samples of the same kind, of such a function were plot. The mortar specimens with hydrogel (G) absorb absolutely more water than other two, bio-mortar (B) and standard reference (S). This was expected as hydrogel uptakes water as much as it can and in bio-mortar there is about 30 % less hydrogel substituted with bacteria and nutrition. However, after the initial water uptake the increase of water sorption was steepest for the standard (S), than less steep for bio-mortars (B) and finally,

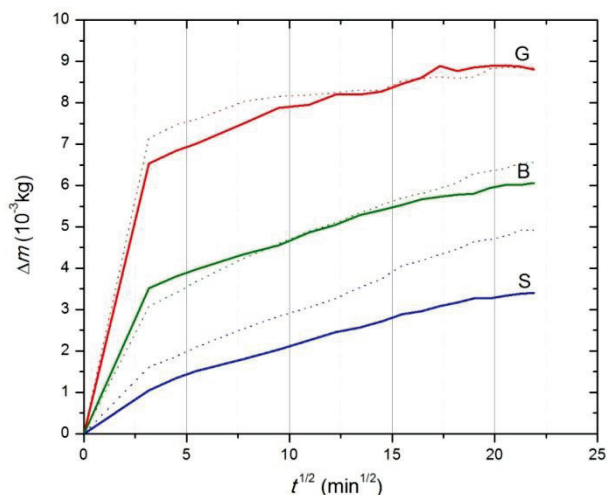


Figure 3: Water sorption of measured mortar specimens after pre-cracking (dashed lines) and after two months of curing (solid lines)



this function was the most flat for the mortars with hydrogel (G). After two months of healing process the water sorptivity of the measured specimens remained almost the same or a bit lower. However, the steepness became lower.

### 3.4 Scanning electron microscopy of bio-mortars

The results obtained by Low Vacuum SEM showed that the used bacterial culture was successfully encapsulated in the hydrogel (Fig. 4). The obtained results explained the behaviour of bio-mortars regarding textural and mechanical characteristics.

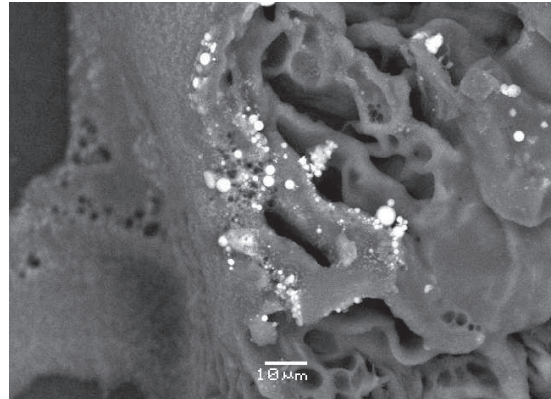


Figure 4: SEM micrograph of the encapsulated bacterial culture (white spheres) in the hydrogel

## 4. Conclusion

The presence of microorganisms encapsulated in hydrogel particles inserted in the cement matrix, proved by SEM investigation, shows a positive effect on mechanical characteristics and water sorption of the mortar specimens. The CMOD mechanical test of the fresh mortar specimens designed with hydrogel and the specimens with bio-mortar show less brittle behaviour in comparison to the standard ones. After two months of curing, the resistance to the maximum load force changed in favour of the specimens with hydrogel and bio-mortar. The mechanical characteristics of the two months cured specimens could be directly related to the water sorption values. Evidently, the hydrogel ability to retain water affects positively the self-healing phenomenon of the bio-mortar specimens.

## Acknowledgment

The authors are grateful for the support of the Ministry of Education, Science and Technological Development of the Republic of Serbia (project number: III 45008) and for the support of COST CA 15202 for the Short-term scientific mission (reference no. 39833) and for the Conference grant no. COST-ITCCG-CA15202-494. The authors would also like to thank Luca Brambilla and Isabella Fisogni, students at Politecnico di Milano for the help during the experiments.

## References

- [1] Van Tittelboom, K. and De Belie, N., Self-Healing in Cementitious Materials – A Review, *Materials* 6 (2013), 2182-2217; doi:10.3390/ma6062182
- [2] De Belie, N. et al, A Review of Self-Healing Concrete for Damage Management of Structures, *Adv Mater Interfaces* 5 (2018), 1800074; doi: 10.1002/admi.201800074
- [3] Okwanda, G.D.O. and Li, J., Optimum conditions for microbial carbonate precipitation, *Chemosphere* 81 (2010), 1143–1148; doi: 10.1016/j.chemosphere.2010.09.066

## **EFFECT OF FLY ASH AND SUPERABSORBENT POLYMER OPTIMIZATION ON SELF-HEALING CAPABILITY OF CONCRETE**

**Pattharaphon Chindasiriphan <sup>(1)</sup>, Hiroshi Yokota <sup>(1)</sup>, Paponpat Pimpakan <sup>(1)</sup>**

(1) Hokkaido University, Sapporo, Japan

### **Abstract**

Concrete with self-healing capability realizes sustainable structures by reducing life cycle cost and extending service life. Many self-healing techniques proposed so far are limited because of requiring prolonged water exposure. This paper investigates the potential of using fly ash and superabsorbent polymer (SAP) as concrete admixtures from the self-healing point of view. Fly ash concrete is characterized by pozzolanic reaction which results in a greater long-term strength. SAP contributes to water accumulation around damaged areas. The effect of both admixtures is examined with varying fly ash and SAP replacement ratios. Cylindrical cement mortar specimens were prepared and PVC jacketed. A uniaxial splitting pre-load was applied at the top edge to generate a crack in the range of 0.02 - 0.5 mm wide. The cracked specimens were water immersed for 28 days. The self-healing performance was evaluated based on crack width mitigation and water-flow through the crack.

### **1. Introduction**

Concrete is a well-known material that is widely used in construction industry. Due to its versatility, durability, and cost saving, the majority of national infrastructure is made of concrete. It is estimated that around US\$ 2.7 trillion is invested annually to build new infrastructure [1], but some of them are suffered from inevitable degradation of their performance, especially those exposed to severe environment conditions. Once a crack occurs in concrete, it accelerates transportation of harmful agents into concrete, such as chloride ion and carbon dioxide, and as a consequence, those agents accelerate steel corrosion. Structural maintenance is a time- and cost-intensive process. To prolong service life of concrete structures and overcome the limitation of maintenance budget, concrete with self-healing capability has been developed based on many techniques such as those integrate with calcite-

precipitating microorganism, expansive polymer including second hydration of cement and pozzolanic reactive admixture. This study investigates the potential of using fly ash and superabsorbent polymer (SAP) as concrete admixtures. The effect of both admixtures is examined with varying fly ash replacement ratios and SAP replacement ratios.

## 2. Methodology

### 2.1 Specimen preparation

The experiment was conducted by preparing cement mortar specimens that were divided into 2 groups. The first group was focused on optimization of self-healing capability by varying fly ash replacement ratios. The second group was investigated the effect of fly ash and SAP contents with 2 environmental exposure conditions. Table 1 lists the mix proportions of mortar. The mixing started with ordinary Portland cement (OPC), sand, fly ash along with a half of total SAP and lasted for 1 minute. The remaining SAP was mixed for another 1 minute to achieve a uniform distribution of materials. The dry-mix was conducted to minimize potential of adhesive effect and reduction of workability provoked by swollen SAP after exposed to water. Water was then gradually added and mixed with all powders for 3 minutes.

The fresh mortar was casted in cylinder mold that measures 100 mm in diameter and 200 mm in height. The specimens were demolded and cured in tap water for 28 days. Then, three of them were used for determining compressive strength conducted according to ASTM C39. The remaining specimens were spilt into 4 disks having 50 mm thick each. The top and the bottom most disks were disposed, and only the middle disks were fitted into a PVC pipe. A splitting crack was achieved by laid the specimen longitudinally on the concrete compression testing machine. The steel pins were placed on both sides of the specimen to keep it in place. One-point load was gradually applied along the steel plate which attached at the top of the specimen to create a concentrate point load. Under the splitting load, the PVC pipe deformed along with the specimen until the load reached its maximum. When the specimen started to crack, it was spontaneously confined with a lateral support. Crack widths were marked at 6 locations (three locations on the top surface and another three locations on the bottom surface), and were averaged to evaluate the crack closing ratio [2] that can be obtained by Eq. (1)

$$\text{Crack Closing Ratio} = 1 - \frac{\text{Final Crack width}}{\text{Initial Crack width}} = 1 - \frac{\omega_{28}}{\omega_0} \leq 0 \quad (1)$$

$\omega_0$  = Average initial crack width [mm] measured at pre-cracking

$\omega_{28}$  = Average final crack width [mm] measured at 28 days of healing period

### 2.2 Water-flow through crack

An initial water-flow rate after pre-cracking was measured by flow test apparatus. It is specifically designed to achieve a constant hydrostatic pressure adequate to inject water throughout the crack. The inflow was supplied by the tap water which has an inlet located at the top of the apparatus. The excess water was drained out at the overflow outlet which allows water head to be controlled at 320 mm from the top of the specimen. The water-flow through the crack was measured at the measurement outlet.

### 2.3 Exposure conditions

Once the initial water-flow was investigated, the specimens were cured in the separate water tank for 28 days with the following conditions:

- FXX (specimen with fly ash): continuously immersed in water at 40 °C.
- F45SX (specimen with fly ash and SAP): continuously immersed in water at 40 °C.
- F45SX\_WD (specimen with fly ash and SAP): immersed in water at 40 °C for 1 day and left in the air for 1 day. The procedure was done repeatedly.

Table 1: Mix proportion of mortar

Type	Cement (kg/m <sup>3</sup> )	Fly ash (kg/m <sup>3</sup> )	Water (kg/m <sup>3</sup> )	Sand (kg/m <sup>3</sup> )	SAP (% weight cement)
F00	525	0	237	1459	0
F15	466	79	237	1459	0
F25	394	131	237	1459	0
F35	341	184	237	1459	0
F45	289	236	237	1459	0
F45S4	289	236	237	1459	4
F45S6	289	236	237	1459	6
F45S8	289	236	237	1459	8

## 3. Results and Discussions

### 3.1 Effect of fly ash and SAP content on compressive strength

The compressive strengths are listed in Table 2. In the previous research, the authors investigated specimens with SAP replacement ratio between 0%-4%, and found that the SAP has a negligible effect on compressive strength of mortar specimen [3]. However, it is clearly noticeable that compressive strength fairly decreases when the SAP replacement ratio is higher than 4%. The reduction in compressive strength was also confirmed by Lee et al. [4] and Hasholt et al. [5]. They revealed that a sudden water exposure provokes SAP swelling and results in increase in porosity of specimens. At 28 days, the results showed that fly ash mortar encounters the reduction in compressive strength. The reduction is significant when fly ash content is increased. However, it is well known that pozzolanic activity in fly ash attributes to gradual development of strength and to greater final strength. It promotes self-healing behavior, which results in crack closure and mechanical properties recovery.

Table 2: Compressive strength at 28 days of curing

Type	Compressive Strength			
	Strength (MPa)	Standard deviation (MPa)	Coefficient of variation (%)	Strength reduction (%)
F00	55.36	0.35	0.63	0
F15	54.17	0.64	1.19	2.16
F25	54.79	1.52	2.78	1.03
F35	52.15	1.34	2.57	5.79
F45	49.11	1.23	2.50	21.28
F45S4	40.02	2.2	5.50	27.70
F45S6	35.26	2.62	7.42	36.31
F45S8	36.65	0.87	2.38	33.79

### 3.2 Effect of fly ash replacement ratio and SAP content on cracking behaviour and self-healing performance

Crack widths reductions of healed specimens and the load required to achieve crack widths range between 0.43-0.17 mm are presented in Table 3. Crack closure performance was determined by crack closure ratio. The calculation of crack closure was made via the method explained in equation (1). The results revealed that less load is necessary for mortar with higher fly ash content to achieve the designate crack widths.

Table 3: Cracking strength and crack closure ratio at 28 days

Type	Initial Crack width (mm)	Final Crack width (mm)	Cracking load (kN)	Crack closing ratio
F00	0.32	0.18	50.6	0.45
F15	0.26	0.07	50.9	0.73
F25	0.22	0.03	47.1	0.86
F35	0.2	0.04	48.8	0.80
F45	0.21	0.01	49.3	0.95
F45S4	0.2	0.03	37.1	0.84
F45S4_WD	0.18	0.06		0.67
F45S6	0.19	0.05	40.8	0.76
F45S6_WD	0.19	0.05		0.75
F45S8	0.18	0	40.3	1.00
F45S8_WD	0.19	0		0.98

On the other hand, a smaller crack width was achieved at higher fly ash content whereas the load was slightly lower. The crack widening was mitigated by newly form products generated by calcium carbonate crystallization [6]. The healing product is clearly noticed as carbonate-like white sediment which is primarily consolidated along the crack area. It was observed that, for the specimens subjected to wet-dry cycle (F45SX\_WD), the amount of calcite deposition and crack closing ratio was accountable at the lower average value. The facts confirmed that water and moisture are essential to promote the self-healing mechanism [2]. Narrower cracks have higher potential to be closed completely as they need less volume of calcite. Furthermore, other newly formed hydration products bridge an interconnecting surface. Specimens with the crack widths between 0.15-0.25 mm show the most satisfactory crack closure performance at 28 days of healing. However, the healed specimens show high dispersion in crack sealing performance particularly those exposed to the wet-dry condition. The higher SAP content slightly mitigated variations in crack sealing performance in all the mixes. The phenomenon was characterized by the extensive internal curing due to the discharge of water entrapped by SAP.

### 3.3 Effect of fly ash replacement ratio and SAP content on water-flow through crack.

Water-flow through crack is plotted in Figures 1 and 2. The SAP specimens show the significant initial water-flow reduction compared to the non-SAP having the same crack width. It was explained by Lee et al. [4] that the swollen SAP gel acts as flow barrier sealing an opening crack. In case of continuously immersed in water, the rate of water-flow gradually decreases as healing time increases due to the maximum expansion of SAP gel, whereas in the wet-dry exposure, specimens reviewed an inconsistent trend of water-flow reduction which caused by insufficient water supply during air curing and shrinkage of SAP. After 12 days healing in wet-dry exposure, the specimens showed a constantly decreasing in water-flow through the crack.

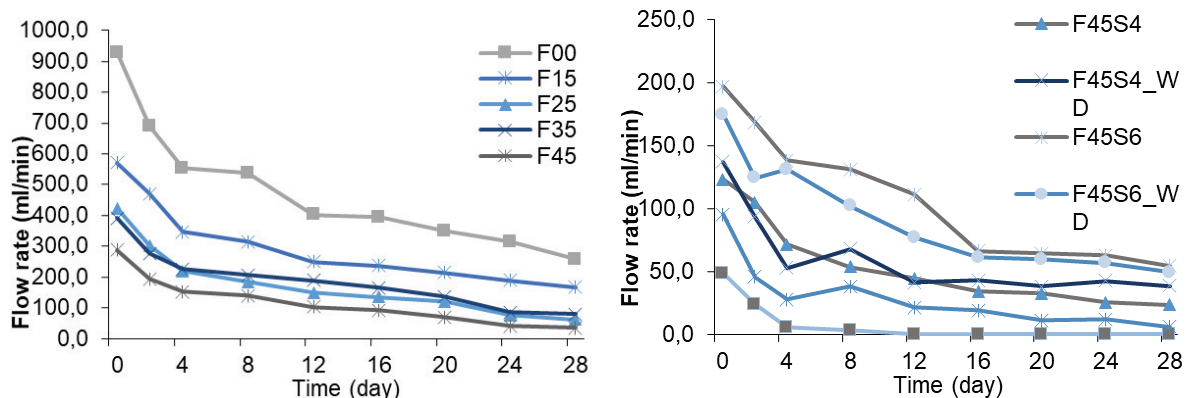


Figure 1: Waterflow through crack of F00-F45 Figure 2: Waterflow through crack of cast-in SAP

The non-SAP-containing specimen showed gradually decreasing in water-flow through the crack. Initial water-flow measurements indicate that the water-flow reduction of the following cases could be attributed from rehydration of cementitious materials and pozzolanic reaction. In the non-SAP-containing specimens, increase in fly ash replacement ratio shows better water-flow rate reduction. F45 achieved the most efficient water-flow reduction, while F45S8 yielded the completely watertight crack around 12 days of healing. The increase in SAP

content accounts for a better water-flow reduction despite of exposure conditions, whereas the effect of fly ash on the recovery of water tightness was not clearly observed. However, as mentioned earlier, higher replacement ratio of fly ash obtained a finer crack under the same pre-crack condition. The advantage of fly ash as damage prevention and self-healing performance were confirmed.

#### 4. Conclusions

This study investigated the effect of fly ash and SAP as concrete admixtures on the self-healing capability. The following conclusions can be drawn:

1. The compressive strength development is interfered by SAP and fly ash at 28 days.
2. Increasing the SAP replacement ratio enhances the efficiency of crack sealing performance which featured in higher crack closure and water-flow reduction. The contribution is attributed by an extensive moisture supply from SAP.
3. The presence of water and moisture is essential to provoke self-healing activity which is characterized by crack width mitigation of the swollen SAP and deposition of newly form cementitious materials.
4. The initial water-flow rate of SAP specimens is significantly decreased resulting from impermeable gel expanding to seal a crack patronized swollen SAP.
5. The continuous immersion in water at 40 °C promotes the best healing efficiency, which contributes to a rapid water-flow reduction and crack closure.
6. A significant impact on crack closure is found when the initial crack width is smaller than 0.25 mm. The development of calcium carbonate-like substance along the cracked area is generally found in healed specimens.

#### Acknowledgements

The authors wish to express our sincere gratitude and appreciation to Professor Minoru Kunieda of Gifu University and his team for all their support and collaboration. The SAP used in this study was sponsored by Nippon Shokubai, Co., Ltd.

#### Reference

- [1] "The Global Infrastructure Gap." Web. 2018 <http://reports.weforum.org/strategic-infrastructure-2014/introduction-the-operations-and-maintenance-om-imperative/the-global-infrastructure-gap/>
- [2] Roig-Flores, M. et al, Effect of crystalline admixtures on the self-healing capability of early-age concrete studied by means of permeability and crack closing tests, *Constr Build Mater* 114 (2016), 447-457
- [3] Chindasiriphan P. and Yokota H., Self-healing ability of concrete made with fly ash and superabsorbent polymer, *The 2nd ACF Symposium 2017 from Innovations for Sustainable Concrete Infrastructures, Thailand* (2017)
- [4] Lee, H. X. D. et al, Self-sealing of cracks in concrete using superabsorbent polymers, *Cem Concr Res* 79 (2016), 194-208
- [5] Hasholt M.T. et al, Mechanical properties of concrete with SAP Part 1: Development of compressive strength, *RILEM Proceedings PRO 74 from the International RILEM Conference on Use of Superabsorbent Polymers and Other New Additives, Denmark* (2010), 117–126
- [6] Snoeck, D. et al, The effects of superabsorbent polymers on the microstructure of cementitious materials studied by means of sorption experiments, *Cem Concr Res* 77 (2015), 26-35

## **EFFECTIVENESS OF SELF-HEALING TECHNOLOGIES IN CEMENT BASED MATERIALS: CONCEPT FOR AN INTER-LABORATORY EXPERIMENTAL EVALUATION BY MULTIPLE TEST METHODS. A PROPOSAL BY COST ACTION CA 15202 SARCOS**

**Liberato Ferrara <sup>(1)</sup>, Tim Van Mullem <sup>(2)</sup>, Estefania Cuenca <sup>(1)</sup>, Henk M. Jonkers <sup>(3)</sup>,  
Francesco Lo Monte <sup>(1)</sup>, Mercedes Sanchez <sup>(4)</sup>, Nele De Belie <sup>(2)</sup> and Antony Jefferson <sup>(5)</sup>**

(1) Politecnico di Milano, Italy

(2) Ghent University, Belgium

(3) Delft University of Technology

(4) University of Cordoba, Spain

(5) University of Cardiff, United Kingdom

### **Abstract**

The use of self-healing cement-based materials has been recognized as a viable pathway to enhance the durability of reinforced concrete structures and contribute to increase their service life. Research activities have provided enlightening contributions to understand the crack-healing mechanisms and have led to the blooming of stimulated and engineered self-healing technologies, whose effectiveness has been proven in the laboratory and, in a few cases, also scaled up to field applications, with ongoing performance monitoring. Nonetheless, the large variety of methodologies employed to assess the effectiveness of the developed self-healing technologies makes it necessary to provide a unified framework for their validation. This is also instrumental to pave the way towards a consistent incorporation of self-healing concepts into structural design and life-cycle analysis codified approaches and promote their diffusion into the construction market. COST Action CA15202 SARCOS ([www.sarcos.eng.cam.ac.uk](http://www.sarcos.eng.cam.ac.uk)) has revealed that a reliable assessment of a healing technology has to rely upon multiple measurements, encompassing all the issues recalled above and establishing correlation between the measured crack closure and recovery of the engineering properties of interest. In this paper the concept for a multi-laboratory evaluation of self-healing technologies is presented.



## 1. Introduction

The implementation in the construction industry of self-healing cement based materials has been recognized as a pathway worth being travelled with the aim of improving the durability and long-term performance of structures made of and/or retrofitted with the aforementioned category of construction materials, able to extend their lifespan, also through the incorporation of new advanced functionalities to traditional materials. The variety of materials and techniques to either stimulate the autogenous healing capacity of concrete or engineer it [1], also through the incorporation of advanced functionalities, has been validated, in a much needed effort to assess their efficiency, through a multi-fold set of experimental tests and methodologies [2].

As a matter of fact, the experimental characterization of the durability of construction materials in real structure scenarios is quite a challenging task, which requires “tailored” experimental capabilities and consists of several tasks. These range from creating a controlled “damage state” (a crack) in the material to the implementation of “healing conditions” suitably representing the intended functional and structural service scenario, to the evaluation of the sealing of the crack and of the related performance recovery, supported by the comprehension of the underlying mechanisms through the characterization of the healing products.

In this paper the proposal developed in the framework of the same COST Action for a multi-laboratory evaluation of self-healing technologies is presented. Besides the proposed types of tests, the most important experimental variables governing the healing phenomenon and also discriminating about its successful and physically sound experimental evaluation will be discussed, including, e.g., the method to produce the initial crack and control its width, the selection of exposure conditions replicating true structural service scenarios. The selection of experimental properties to be measured will be also discussed in a modelling-oriented framework, in which such properties play the role of model input parameters [3].

## 2. Experimental variables governing the healing of cement-based materials

In defining the tasks for the inter-laboratory testing activities the concept of the experimental plan has been based on a few fundamental governing variables, while leaving to each participating partner the choice of one or more healing methodologies of its own interest. These may include either autogenous healing stimulated by tailored additions, including, e.g., supplementary cementitious materials, crystalline admixtures, superabsorbent polymers, or autonomous healing, engineered by means of encapsulated minerals or polymers (micro- and macro-encapsulation) or through bacteria. In the planned activities all these techniques can be employed in combination with plain concrete and mortars as well as with high performance fibre reinforced cementitious composites (HPFRCCs).

Mortars can be employed both “per se”, as for example local repair materials [4], or be designed with a concrete equivalent composition, In the last case, with main reference to a preliminary validation of the potentials of a healing technology, the use of smaller material quantities than necessary with a conventional concrete would be feasible, even if a dilution effect in the quantity of the healing agent when scaling up to concrete has to be considered.

With reference to HPFRCCs, which are characterized by a mix composition highly conducive

to self-healing [5,6], it is extremely interesting to investigate the synergy between the aforementioned autogenous healing capacity and healing stimulating/engineering constituents. The choice of the material to be investigated has a twofold outcome. First of all it will affect the size of the specimen which has to be employed, with reference to the material heterogeneity scale. Moreover, it will govern the choice of the experimental methods to be employed for the creation of the “controlled state of damage”, i.e. a crack with a controlled width, which has to be healed. Additionally, the type of material and the specimen size will influence the test methods which can be used to evaluate the sealing/healing behaviour.

As a matter of fact, since plain mortar and concrete are inherently brittle, closed-loop crack-opening controlled tests are needed in order to produce a crack through bending, splitting tensile or direct tensile tests, in order of difficulty. A few authors [7,8] have proposed to “pre-damage” the specimens by means of compression tests, pre-loading them at a fraction of the compressive strength, either in the pre- or post-peak regime. Though this approach induces a diffused state of damage which can be, *e.g.*, quantified by means of comparative ultrasonic pulse velocity tests, it can hardly be employed to produce a crack whose controlled width has also to stand as a governing variable for the healing processes to be investigated.

In view of this the SARCOS group has recommended the use of prism specimens:

$L \times b \times h = 160 \times 40 \times 40 \text{ mm}$  in the case of mortars, and

$L \times b \times h = 500 \times 100 \times 100 \text{ mm}$  in the case of plain concrete.

The preferential pre-cracking technique would be in such cases the three-point bending test. In case, a notch could be prearranged through cast-in inserts at the specimen mid-span in order to pre-determine the crack-site formation and ease the crack opening measurement. In all cases, this would provide, *e.g.* through a clip-gauge suitably attached at the beam specimen tension side (Figure 1a), the opening of the crack at its mouth, the true tip opening in the case of notched specimens being even lower, with no information neither on the trend of the crack opening along its length nor on its internal structure. While the former information could be obtained by micro-imaging the crack and processing the images through suitable image analysis tools [9], the latter can only be obtained through advanced experimental techniques such as Computer Tomography [10,11], even if so far no quantitative information has been garnered on the topic.

In the case of HPFRCCs the same mix composition recognized as highly conducive to self-healing yields a signature tensile behaviour, characterized by an extended stable multiple cracking phase after the formation of the first crack and before the onset of unstable crack localization. This makes it possible to stably perform, even under displacement control, three- and four-point bending tests and even direct tension tests. Moreover, at least four-point bending tests need to be performed in order to usefully develop the aforementioned multiple cracking. For this reason, the SARCOS group has recommended for HPFRCCs prism specimens  $L \times b \times h = 500 \times 100 \times 20 \text{ mm}$  to be pre-cracked in four-point bending, *e.g.* under a third-point loading scheme.

It is anyway worth remarking that, through such a test, where multiple cracks are expected to develop in the central “between the loads” portion of the specimen, the deformation measured, *e.g.*, at the beam tension side through LVDTs across a gauge length (Figure 1b), represents the sum of the surface openings of all the cracks and is thus only representative of an overall damage level. The quantification of the opening of each single crack would require, *e.g.*, image analysis of crack micrographs as above.

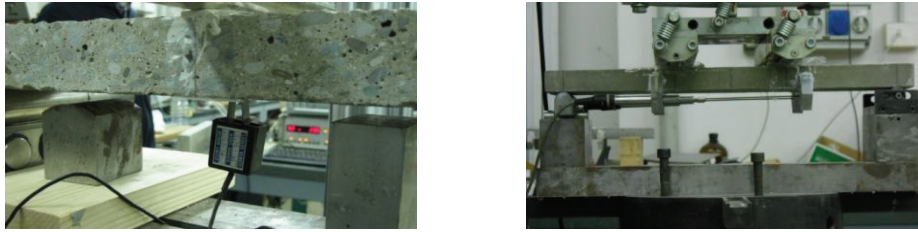


Figure 1: examples of crack measurement via a clip-gauge at specimen mid-span in a three-point bending test (left) and via LVDTs across gauge-length in a four-point bending test (right).

The three-point bending test, recommended for plain concrete and mortar, and the four-point bending test, selected as the most suitable for HPFRCCs, feature a common artefact as far as their use to “pre-crack a to-be healed specimen” is concerned. In most of the investigations, after being cracked the specimen has to be unloaded before being exposed to the healing conditions representative of the structural service scenario. This results in a partial back-closure of the crack, due to the elastic regain of the specimen, unless active crack control techniques are enforced. The amount of crack closure depends on the type of test and pattern of the crack(s), which makes it hardly predictable. This leaves the only option to perform the test up to a prescribed crack opening under load, accepting the elastic regain and anyway measuring the residual opening of the crack upon complete load removal, both through the employed measuring instruments as well as through micro-imaging of the cracks to be further processed. This implies that a range of residual crack openings can be obtained, which have to be duly taken into account when assessing the efficiency of different healing techniques. Crack opening ranges can be defined *e.g.* in accordance with current code prescriptions for serviceability and durability limit states.

The initial crack opening is surely one of the governing parameters which represent the structural service scenario under which the healing has to occur and which has to be replicated in the experiments. Such a scenario also encompasses, as expectable, the environmental exposure conditions but also the age of cracking. In the case of autogenous (stimulated) healing, the age of cracking will be first of all directly related to the amount of un-hydrated binder particles, and hence on the autogenous self-healing capacity, also discriminating between the prevalence between the autogenous mechanisms and the action of the stimulating agent. In the case of autonomous healing, *e.g.* engineered through encapsulated chemicals, the age of cracking is also likely to affect the efficiency of the mechanism, related as it is to the concrete fracture toughness. The formation of a crack at an earlier age is likely to be associated to a lower energy release rate, which is hence likely to be less effective in rupturing the intercepted capsules.

In view of this the SARCOS group has decided in the planned inter-laboratory activity to foresee two different ages of cracking: an earlier one ( $< 7$  days) which highlights the autogenous healing potential and a later one ( $> 28-56$  days, also depending on the presence of pozzolanic mineral additions) to highlight the effects of any stimulating agents. In the case of healing engineered through encapsulated polymers, for which generally quite large crack openings are studied, the combination with the very short healing duration ( $< 7$  days) allows only for a very limited autogenous healing and then may require only one age of cracking.

The reproduction of structural service scenario is then complemented with the exposure conditions. The availability of water being essential for stimulated autogenous and some engineered healing mechanisms to occur, the proposal is to investigate, besides a continuous

immersion condition also wet/dry cycles, in case in the presence of aggressive substances in the water to broaden the representativeness of the investigation (involved partners may select the aggressive scenario of interest).

### **3. Measuring the healing through the recovery of the material performance**

Once the experimental testing framework, representing the intended structural service scenario, has been defined as above, the healing evaluation methodology through the measurement of the crack sealing and of the recovery of the material durability and mechanical performance has to be specified. Tab. 1 presents the summary of the healing evaluation procedures currently available in the literature [2]. Healing related indices of performance reported in the table stand as the first step for the quantification of the healing efficiency. The inter-laboratory testing activity will consist of:

- the measurement of the crack closure at least by means of optical methods;
- the recovery of one durability related property and a (set of) mechanical properties;
- the assessment of the correlation among the aforesaid parameters, for consistency.

With reference to the connection between index of crack sealing and indices of performance recovery, it is worth remarking that the former, computed from visual measurements of crack closure, only does account for the crack sealing which is taking place on the surface of the specimen, whereas the recovery of any performance, mainly mechanical, is also the outcome of the internal through crack reconstruction of the matrix continuity. This, besides contributing to better understand the trend of the established correlation may also call for the concept and implementation of methods to indirectly estimate the amount of crack closure from the amount of recovered performance. Some attempts in this sense have been proposed in [6] from cross-wise comparison of pre-crack vs. post-healing load vs. crack-opening curves and from damage vs. crack opening curves as built from the evaluation of the stiffness recovery. This implies a modelling concept to be incorporated into the healing evaluation approach.

### **4. Modelling**

The experimental characterization of the self-healing capacity of any material requires the investigation to span along a time frame whose extension could hardly match with the needs of an effective and market oriented technology transfer. In this respect the availability of sound and reliable predictive modelling tools becomes of the utmost importance, since only they would allow to extrapolate the results of performed experimental characterization of the durability performance of cement-based materials to real structure service scenarios [4].

In this respect, the availability of test data from tests on companion undamaged specimens undergoing the same curing history as the cracked/healed ones, will provide the necessary calibration of the evolution of mechanical fracture parameters of the material allowing to discriminate between healing-induced recovery and aging evolution of the property of interest.

As a mere example, it may be worth remarking that, definition of damage evolution curves as a function of crack opening, healing time and exposure may be for example interpreted in this framework, whenever damage mechanics based models are going to be employed. Similarly,

the establishment and validation of correlation between permeability recovery and crack closure may be instrumental, in the case of smeared crack models, to establish a link between the mechanical part of the modelling, which has at least to describe the pre-cracking, and the transport one, the models being linked by a mutual input parameter feeding.

Microstructural models will require likewise microstructural related parameters to be experimentally identified also with the aim of deeper understanding the nature of the healing mechanisms as well as the intrinsic signature properties of the healing products, in a multiscale comprehension effort of the outcomes of the healing.

A survey recently published by the SARCOS consortium [4] has revealed that many papers do not review experimentally observed material behaviour in advance of presenting model theory.

There are probably a number of reasons for this state of affairs. One could be that there is a paucity of experimental data suitable for properly validating numerical models. Another reason might be that there has been insufficient interaction between relevant numerical and experimental research teams. The inter-laboratory activity planned by the SARCOs consortium would hence stand as a one-of-a-kind opportunity in this sense.

Table 1: healing index from recovery of durability related and mechanical properties

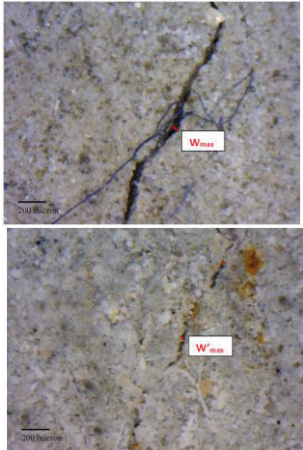
	Recovered property	Healing Index	Quantities of interest
	Crack closure	Index of Crack Sealing  $ICS = \frac{W_{pre-cracking} - W_{post-healing}}{W_{pre-cracking}}$ $= \frac{W_{pre-cracking} - W_{pre-cracking} \cdot \text{crack opening at pre-crack}}{W_{pre-cracking}}$ $= \frac{W_{post-healing} \cdot \text{crack opening after healing}}{W_{pre-cracking}}$	
Durability properties	Permeability	Index of permeability recovery  $ISH_{permeability,1} = \frac{W_{unhealed,t} - W_{healed,t}}{W_{unhealed,t}}$ $ISH_{permeability,2} = \frac{W_{initial} - W_{final}}{W_{initial}}$	$W_{unhealed,t}$ : amount of water passing through the specimen's unhealed crack at time $t$ $W_{healed,t}$ : amount of water passing through the specimen's healed crack at time $t$ $W_{initial}$ : amount of water passing through the target specimen before healing $W_{final}$ : amount of water passing through the target specimen after healing.

Table 1 (ctd.): healing index from recovery of durability related and mechanical properties

	Recovered property	Healing Index	Quantities of interest
Durability prop.	Sorptivity	Index of Sorptivity Recovery	$S_{unhealed}$ : sorptivity index for the cracked and unhealed specimen
		$ISH_{sorptivity} = \frac{S_{unhealed} - S_{healed}}{S_{unhealed} - S_{uncracked}}$	$S_{healed}$ : sorptivity index for the cracked and healed specimen $S_{uncracked}$ : sorptivity index for the uncracked specimen
Mechanical properties	Residual post-cracking strength	<p><b>Index of Strength Recovery</b></p> $ISR = \frac{f_{peak,post-conditioning} - \sigma_{unloading,pre-cracking}}{f_{peak,pre-cracking} - \sigma_{unloading,pre-cracking}}$	
	Stiffness	<p><b>Index of Damage Recovery</b></p> $IDR = \frac{K_{loading,post-conditioning} - K_{unloading,pre-cracking}}{K_{loading,pre-cracking} - K_{unloading,pre-cracking}}$	

## 5. Conclusions

In this paper the concept has been presented for an inter-laboratory experimental activity which is going to be performed by the consortium of the COST Action CA 15202 SARCOS. The activity will include both autogenous/stimulated and autonomous healing, investigating both plain concrete and mortar and HPRCCs. The action will be based on the assessment of the selected healing technique(s) under the exposure conditions of choice (common to all: immersion in water and wet/dry cycles; optional: one aggressive condition) through:

- measurement of the crack sealing through visual micro-imaging of the cracks
- measurement of the recovery of one durability property and mechanical performance with establishment of mutual correlation between the measurements garnered as above.

The choice of the material of interest will dictate the specimen geometry as well as the method of pre-cracking. This has anyway to take into account the experimental capabilities of the partners as well as the selected method of performance recovery assessment.

Particular care has to be dedicated to the measurement of the crack opening in the pre-cracking stage both because of experimental artefacts inborn in such a procedure (elastic regain upon unloading) but also in view of the representativeness of a “surface garnered”

measure of the crack opening to described a 3D structure such as a crack. In view of this, correlation between surface crack measurements and observation on the internal crack structure through advanced methods, though not mandatory, could be pursued.

The experimental activity as a whole will also be targeted to provide a broad enough database for the calibration and validation of numerical predictive models, thus standing as a one of a kind research also intended to pave the way towards incorporation of self-healing concepts and outcomes into durability-based design approaches.

### Acknowledgements

The authors acknowledge the support from EU COST Action CA 15202 “Self-healing as preventive repair of concrete structures – SARCOS” (<http://www.sarcos.enq.cam.ac.uk>).

### References

- [1] De Belie, N., Gruyaert, E., Al-Tabbaa, A., Antonaci, P., Baera, C., Bajare, D., Darquennes, A., Davies, R., Ferrara, L., Jefferson, T., Litina, C., Miljevic, B., Otlewska, A., Ranogajec, J., Roig-Flores, M., Pain, K., Lukowski, P., Serna, P., Tulliani, J.M., Vucetic, S., Wang, J., Jonkers, H.M., A review of self-healing concrete for damage management of structures, *Advanced Materials and Interfaces*, accepted (2018).
- [2] Ferrara, L., Van Mullem, T., Alonso, M.C., Antonaci, P., Borg, R.P., Cuenca, E., Jefferson, A., Ng, P.L., Peled, A., Roig, M., Sanchez, M., Schroefl, C., Serna, P., Snoeck D., Tulliani, J.M. and De Belie, N., Experimental characterization of the self-healing capacity of cement based materials and its effects on the material performance: a state of the art report by COST Action SARCOS WG2, *Construction and Building Materials*, 167 (2018), 115-142.
- [3] Jefferson, T., Javierre, E., Lee Freeman, B., Zaoui, A., Koenders, E. and Ferrara, L., Research progress on numerical models for self-healing cementitious materials, *Advanced Materials and Interfaces*, accepted (2018).
- [4] Sanchez, M., Faria, P., Ferrara, L., Horszczaruk, E., Jonkers, H.M., Kwiecien, A., Mosa, J., Peled, A., Pereira, A.S., Snoeck, D., Stefanidou, M. and Stryzewska, T., External treatments for the preventive repair of existing constructions: COST Action CA15202 framework”, *Construction and Building Materials*, submitted (2018).
- [5] Ferrara, L., Krelani, V., Moretti, F., Roig Flores, M. and Serna Ros, P., Effects of autogenous healing on the recovery of mechanical performance of HPFRCCs: part 1, *Cement and Concrete Composites*, 83 (2017), 76-100.
- [6] Ferrara, L., Krelani, V. and Moretti, F.: “Autogenous healing on the recovery of mechanical performance of HPFRCCs: part 2 – correlation between healing of mechanical performance and crack sealing, *Cement and Concrete Composites*, 73 (2016), 299-315.
- [7] De Nardi, C., Bullo, S., Ferrara, L., Ronchin, L. and Vavasori, A., Effectiveness of crystalline admixtures and lime/cement microcapsules in engineered self-healing capacity of lime mortars, *Materials and Structures*, 50(4) (2017), 191.1-191.12
- [8] De Nardi, C., Cecchi, A., Ferrara, L., Benedetti, A. and Cristofori, D., Effect of age and level of damage on the autogenous healing of lime mortars, *Composites-Part B: Engineering*, 124 (2017).
- [9] Snoeck, D., Dewanckele, J., Cnudde, V., and De Belie, N., X-ray computed microtomography to study autogenous healing of cementitious materials promoted by superabsorbent polymers, *Cement and Concrete Composites*, 65, (2016), 83-93.
- [10] Van Tittelboom, K., Wang, J., Araujo, M., Snoeck, D., Gruyaert, E., Debbaut, B., Derluyn, H., Cnudde, V., Tsangouri, E., Van Hemelrijk, D. and De Belie, N., Comparison of different approaches for self-healing concrete in large-scale lab tests, *Construction and Building Materials*, 107 (2016), 125-137.

## **EXTENDING THE SERVICE LIFE OF POLYMER INDUSTRIAL FLOOR COATINGS BY IMPROVING THEIR ADHESION TO CEMENT-BASED SUBSTRATES**

**Łukasz Sadowski <sup>(1)</sup>, Agnieszka Chowaniec <sup>(1)</sup>**

(1) Wrocław University of Science and Technology, Wrocław, Poland

### **Abstract**

The study focuses on extending the service life of polymer industrial floor coatings by improving their adhesion to cement-based substrates. The purpose of the study is to evaluate the possibility of using waste glass powder in polymer industrial floor coatings made with the use of epoxy resin. The chemical composition and particle size of waste glass powder make it an attractive additive for the durable and sustainable epoxy resins used in industrial floors systems. Waste glass powder is used in epoxy resin coating as a filler. Samples were stored in air curing conditions. Pull-off tests were performed in order to study the effect of adding waste glass powder on the adhesion between modified polymer industrial floors and cement-based substrates. The results were compared to reference samples without waste glass powder.

### **1. Introduction**

State-of-the-art epoxy resins are very popular in civil engineering for producing a full range of floor coatings [1]. These kinds of resins are more and more frequently playing a special role. They need to be, e.g. heavy-duty, conductive, decorative or chemically resistant. In civil engineering they are usually laid on cement-based substrates. It is required that these resins are characterized by high adhesion to the substrate [2, 3].

In order to obtain adequate adhesion of the epoxy resin to the substrate, two technological treatments must be carried out. First, the substrate is required to be processed by grinding, sand- or shot-blasting with thorough cleaning and vacuuming of the surface. There is then a need to apply a bonding agent on the previously treated substrate. After these two actions, the epoxy coating can be applied. It should be noted that there is a risk of making mistakes during the implementation of these technological actions. In addition, they are expensive and time-



consuming. Therefore, in recent times solutions have been sought to reduce or eliminate one of these drawbacks.

It was noted in [4] that recent innovations in civil engineering cannot be done without considering sustainable development. Thus, mineral industrial wastes have recently become more popular as the additives in cement-based composites [5]. To the best of our knowledge, there is no study related to the adhesive properties of epoxy resins modified using waste glass powder. The chemical composition and particle size of waste glass powder make it an attractive additive that can be used in the sustainable epoxy resins used in industrial floor systems. Bearing the above in mind, the paper presents studies on coatings made of epoxy resins modified with the addition of waste glass powder. The purpose of the tests was to check whether it is possible to obtain the required adhesion of the epoxy resin coating without the use of a bonding agent. According to the authors, this will be possible with the addition of glass powder, which is a by-product from the production of glass microspheres. The aim of the research is also to determine the optimal ratio between the base material and the additive.

## 2. Materials and methods

A coating containing an epoxy resin based on bisphenol A in an amount from 64.5 to 74.1% by weight, a glass powder filler with a proportion of at least 60% of a plurality of grains of less than 63  $\mu\text{m}$  in diameter and hardener based on aliphatic polyamines in the amount from 16.1 to 8.5% by weight was used. The resin contains bisphenol A with a molecular weight <700. The bisphenol A was mixed with the hardener in weight proportions of 100:25. The composition contains a quartz powder filler that has a mass composition of about 71%  $\text{SiO}_2$ , 1%  $\text{Al}_2\text{O}_3$ , 9%  $\text{CaO}$ , 4%  $\text{MgO}$ , 14%  $\text{Na}_2\text{O} + \text{K}_2\text{O}$  and a maximum of 0.1%  $\text{TiO}_2$  in an amount from 7.4 to 9.4% by weight. The glass powder used is a waste material from the production of glass microspheres. It is successfully used, among others, as a flux, conditioner and as a very good filler, e.g. for cement-based and ceramic materials.

The epoxy resin is ready for use after thorough mixing of the bisphenol A and the glass powder filler. After mixing, a fluid consistency is obtained, and the hardener is added immediately before applying the coating to the surface of the substrate. An indicator of a sufficiently thorough mixing of three components that have a different colour in their initial state is the obtaining of a uniform colour and consistency of the whole mass.

As a substrate for the coating, a cement substrate with a thickness of 40 mm was used. This substrate was made of a ready mix cement screed with self-levelling properties. A total of 11 cement substrates with a compressive strength ranging from 8.7 to 16.5 MPa and a tensile strength ranging from 1.4 to 3.0 MPa were prepared. The letter R indicates the control sample, which was coated with an epoxy resin without the addition of glass powder, and the numbers from 10 to 100 indicate the weight proportions of the content of glass powder X in a weight ratio to the coating components (100:25:X).

The surface of the substrate was cleaned, grinded and then vacuumed. As a result, a dry, (mass humidity of about 4%) hard and stable surface was obtained. The epoxy resin was then spread on the surface of the cement substrate by means of a serrated trowel and deaerated using a paint roller. The application and curing period of the coating took place at room temperature (about 20°C). Pull-off adhesion ( $f_b$ ) measurements were made after 7 days, after obtaining the full mechanical load capacity for the epoxy coating (Fig. 1a). The  $f_b$  of the

coating to the substrate was tested at three points for each sample using the pull-off method (Fig. 1b).

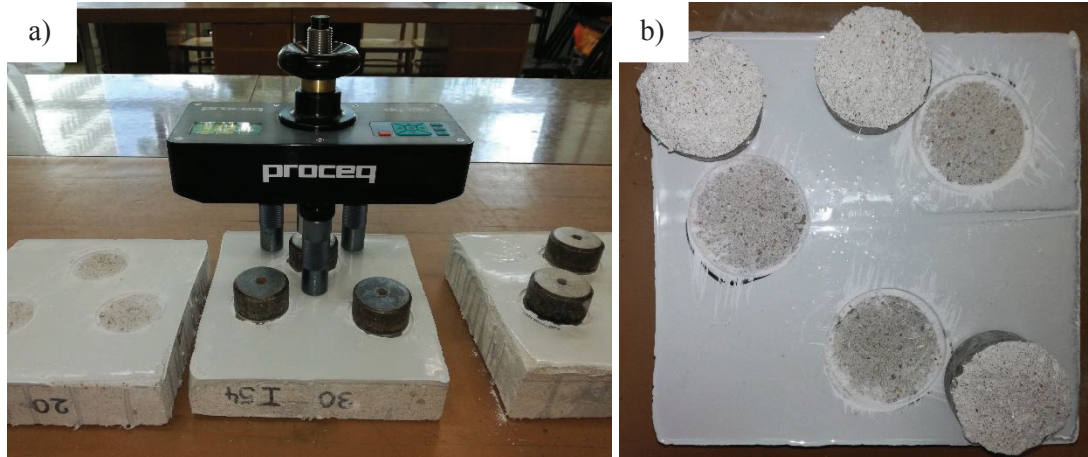


Figure 1: The view of: a) testing the pull-off adhesion using the pull-off method, b) the surface of the sample after the testing

### 3. Test results and analysis

The summary of the obtained research results is presented in Table 1. The results of the tests are also visualized in Fig. 2 in the form of graphs of functions of three variables.

During the research it was observed that along with the increase in the amount of added glass powder, it was also necessary to extend the mixing time and increase its diligence in order to obtain a uniform mass. A greater amount of powder caused an increase in the density of the mixture, and thus an increase in the force needed for mixing, especially for samples 80, 90 and 100. It was also observed that the absorptivity of the roller decreased with an increasing content of the waste glass mineral powder.

It was also observed that the increase in the content of glass powder resulted in a reduction in the self-levelling ability of the epoxy resin coating. For samples from 10 to 40, the resin still spread very well over the surface of the substrate and self-levelled. However, for subsequent samples, there was a gradual increase in surface irregularities. Even coverage of the undercoats with 80, 90 and 100 coatings was not feasible.

While testing the adhesion of the coating to the substrate using the pull-off method, the failure of the measuring disk was most often at the interface between the coating and the cement substrate (or partially in the substrate).

Table 1: Summary of the obtained research results.

Composition (100:25:X)	Average value of pull-off adhesion $f_b$ (MPa)	Average value of the compressive strength of the substrate $f_c$ (MPa)	Average value of the tensile strength of the substrate $f_t$ (MPa)
0	2.71	14.2	1.7
10	2.31	12.5	1.8
20	2.43	16.5	1.4
30	1.78	10.3	1.4
40	3.07	14.0	1.5
50	2.79	15.7	1.6
60	2.20	15.5	3.0
70	2.53	14.9	2.3
80	2.44	8.7	2.1
90	2.61	10.9	3.0
100	2.12	13.0	2.9

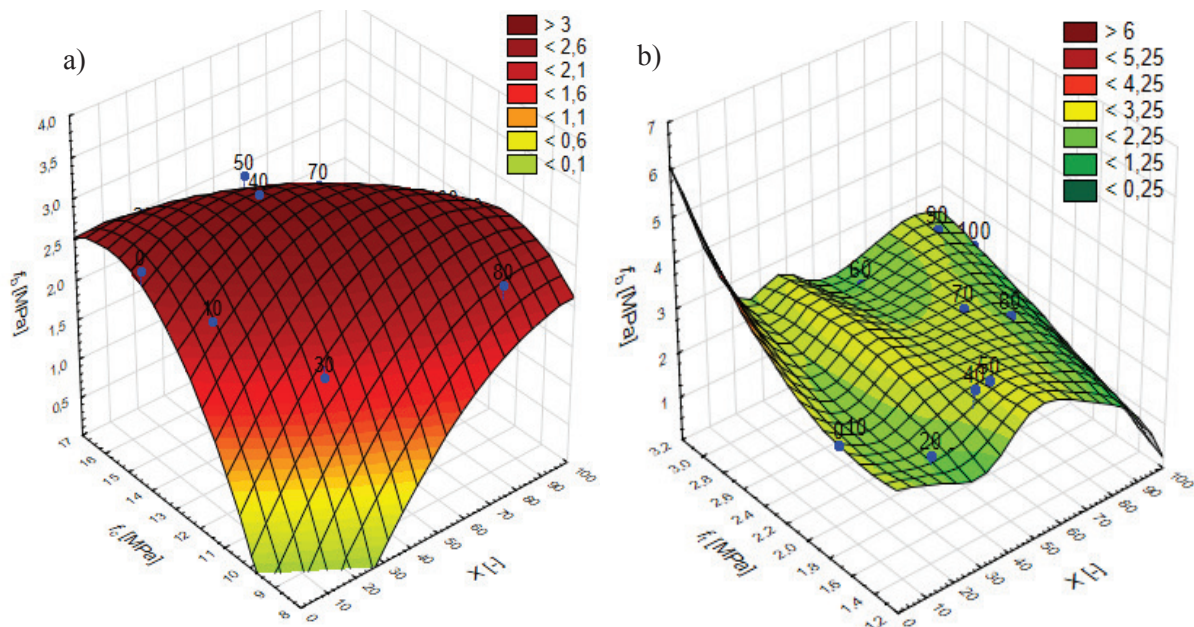


Figure 2: Graphs of functions of three variables for: a) the compressive strength of the substrate, b) the tensile strength of the substrate

In general, it can be seen from Figure 2 that the increase of the value of the pull-off adhesion corresponds with the increase of the compressive and tensile strength and also the amount of glass powder. It should be noted that the plane visible in Figure 2 was determined by the least squares method. It can be concluded from Figure 2a that for the substrates with a compressive strength  $f_c$  lower than 10 MPa and a very low value of the amount of waste glass powder, the delamination is expected ( $f_b = 0$ ). This could be due to the lack of mechanical compatibility of the material of the coating and the substrate [6]. This is caused by too high difference in compressive strength between epoxy resin and such a low-strength cement substrate.

#### 4. Conclusions and perspectives

The study was focused on extending the service life of polymer industrial floor coatings by improving their adhesion to cement-based substrates. The performed research results show that in some configurations the addition of glass powder improved the adhesion of the epoxy resin coating. This research proved that it is possible to obtain the required value of pull-off adhesion without prior application of the bonding agent. An additional advantage is the increase in the efficiency of the coating, which is caused by the decrease in the absorptiveness of the roller.

Based on the obtained results, it was found that the optimal weight ratio between the components of epoxy coating A and B, and the content of glass powder X, is A: B: X = 100: 25: 40. The higher content of the additive makes it difficult to obtain a smooth surface.

The presented epoxy resin is convenient to use and can be used in a very wide range of industrial conditions. It may be applied for the manufacturing of epoxy resin coatings. Thanks to the application of the developed coating, it is possible to obtain the required adhesion of the coating to the substrate without the need of applying the bonding agent.

#### References

- [1] Mays, G. C., Hutchinson, A.R., Adhesives in civil engineering, Cambridge University Press (2005)
- [1] Sadowski, Ł., Czarnecki, S., & Hoła, J., Evaluation of the height 3D roughness parameters of concrete substrate and the adhesion to epoxy resin. *International Journal of Adhesion and Adhesives*, 67 (2016) 3-13
- [3] Garcia, J., De Brito, J. Inspection and diagnosis of epoxy resin industrial floor coatings. *Journal of Materials in Civil Engineering*, 20-2 (2008), 128-136
- [4] Czarnecki, L., van Gemert D., Innovation in construction materials engineering versus sustainable development. *Bulletin of the Polish Academy of Sciences Technical Sciences* 65(6) (2017), 765-771
- [5] Nagrockienė, D., Girskas, G., & Skripkiūnas, G., Properties of concrete modified with mineral additives. *Construction and Building Materials* 135 (2017), 37-42
- [6] Bissonnette, B., Courard, L., & Garbacz, A., *Concrete surface engineering*. CRC Press (2015)

## **IMPROVEMENT OF SELF-HEALING EFFICIENCY IN ENGINEERED CEMENTITIOUS COMPOSITES BY ADDITION OF FOREST BIOMASS ASH**

**Gloria Perez <sup>(1)</sup>, José Luis García Calvo <sup>(1)</sup>, Pedro Carballosa <sup>(1)</sup>, Ana Guerrero <sup>(1)</sup>**

(1) Institute of Construction Science Eduardo Torroja (CSIC), Madrid, Spain

### **Abstract**

Self-healing efficiency of an Engineered Cementitious Composite (ECC) in which fly ash is partially substituted by a forest biomass ash was studied in the present work. Prismatic specimens were fabricated with a ratio of fly ash to biomass ash content of 70/30 (material A) and 30/70 (material B). After 28 days of curing in a humidity chamber, some specimens were cracked and left back in the same previous conditions for self-healing during more than 8 months. The results from capillary water absorption tests suggest a higher initial tightness for the uncracked material with a higher content of fly ash, while after the healing period, a higher healing efficiency is inferred for the ECC matrix with higher content of biomass ash. The study of the self-healing mechanism by electron microscopy with compositional analysis indicates that sealing is promoted by reaction products deposited on the fibres bridging the cracks and by crystalline phases incorporating sulphur. The higher content of this element in the composition of biomass ash, as compared to fly ash, explains the higher crack healing efficiency in material B.

### **1. Introduction**

Self-healing Engineered Cementitious Composite (ECC) is a special type of high performance fibre-reinforced cementitious composite designed on a micromechanics base to obtain a high tensile ductility and a tight crack width under mechanical loading [1]. The typical main components of these composites are type I Portland cement, fine silica sand, class F fly ash and poly-vinyl-alcohol (PVA) fibres [2,3], although some works have analysed ECCs incorporating other supplementary cementitious materials [4,5]. The present work studies the self-healing efficiency of an ECC material in which fly ash is partially substituted by a forest biomass ash from the combustion process of a paper Spanish company. The availability of

this by-product and the interest of its valorisation imply economic and environmental benefits from this substitution.

## 2. Materials and methods

Specimens of the ECC were produced with a composition similar to that described by other authors [2,4]. A CEM I 42,5R Ordinary Portland Cement (OPC), a mix of fly ash (FA) and biomass ash (BA) in a proportion of 1.2 relative to OPC content and siliceous aggregate in a proportion of 0.8 relative to OPC content were used. The water to binder ratio was 0.35 and a 1.5% of weight of superplasticizer, together with a 2% of weight of PVA fibres, were added to the solid.

The chemical composition of OPC, FA and BA used in this work is shown in Tab. 1 in terms of percentage of main oxides (percentage content higher than 0.3%), as obtained by X-ray fluorescence. It is important to indicate that, in addition to the oxides shown in Tab. 1, a 2.8% of Cl was measured in the composition of the biomass ash. In order to minimize the matrix fracture toughness, standard siliceous sand was sieved to establish a maximum aggregate size of 400  $\mu\text{m}$ . Finally, commercial PVA fibres incorporated to the matrix had a length of 8mm and a diameter of 39 $\mu\text{m}$ .

Table 1: Percent chemical composition of cement (OPC), fly ash (FA) and biomass ash (BA) used for the specimens preparation. L.I. stands for Loss on Ignition.

	CaO	SiO <sub>2</sub>	Al <sub>2</sub> O <sub>3</sub>	Fe <sub>2</sub> O <sub>3</sub>	MgO	SO <sub>3</sub>	K <sub>2</sub> O	Na <sub>2</sub> O	TiO <sub>2</sub>	P <sub>2</sub> O <sub>5</sub>	MnO	L.I.
<b>OPC</b>	59.6	20.0	6.0	2.6	1.6	4.6	1.5	0.6	< 0.3	< 0.3	< 0.3	3.3
<b>FA</b>	5.4	44.7	26.1	5.5	1.1	0.7	2.6	0.3	1.4	0.9	< 0.3	10.9
<b>BA</b>	39.9	18.0	6.0	4.5	3.4	3.0	6.2	0.8	0.7	1.2	1.3	11.7

Prismatic specimens of 4 cm x 4cm x 16 cm were fabricated with a ratio of fly ash to biomass ash content of 70/30 (material A) and 30/70 (material B). The solid materials (CEM I 42.5R, aggregate and mix of ashes) were first mixed for 2 min at low speed. Water and superplasticizer were then added and mixed at low speed for 1 min, followed by high speed mixing for 2 min. Finally, fibres were added at low speed and mixed at high speed for another 2 min.

The specimens were demoulded after 24 hours and cured for 28 days at 98 $\pm$ 2% RH and 20 $\pm$ 2 $^{\circ}$ C. At that age, one set of specimens were cracked by means of the three point bending test using an INSTRON 8801 universal testing machine with a loading velocity of 0.03 kN/s, up to a specified strength value (around 5kN). After the test, the presence of cracks on the specimens' surface was confirmed and the set was left back, together with the uncracked set, in the same previous conditions for more than 8 months for self-healing until the testing date.

In order to study the influence of the biomass ash addition on the self-healing efficiency of the ECC material, capillary water absorption test according to UNE 83892 was conducted in the two uncracked and three cracked specimens of each material previously dried at 50  $^{\circ}$ C for several days until constant weight. In addition, samples obtained from the cracked area of each specimen were analysed by backscattering electron microscopy with compositional

analysis to characterize the sealing mechanism with a scanning electron microscope Hitachi S-4800 equipped with an energy dispersive analyzer BRUKER 5030. The samples were embedded in resin and polished for the analysis.

### 3. Results and discussion

#### 3.1 Capillary water absorption

Fig. 1 shows the mean curves of mass increase of the specimens during the capillary water absorption test and Fig. 2 collects the values of the mean capillary water absorption coefficient with corresponding error bars. The uncracked specimens of material A showed a slower mass increase, with a lower final mass increase value during the test than those of material B. Accordingly, the mean capillary absorption coefficient (K) of  $0.061 \text{ kg/m}^2 \text{ min}^{0.5}$  was significantly lower than the value obtained for uncracked material B (K equal to  $0.085 \text{ kg/m}^2 \text{ min}^{0.5}$ ). This result suggests a higher initial tightness for the uncracked material with a lower content of biomass ash.

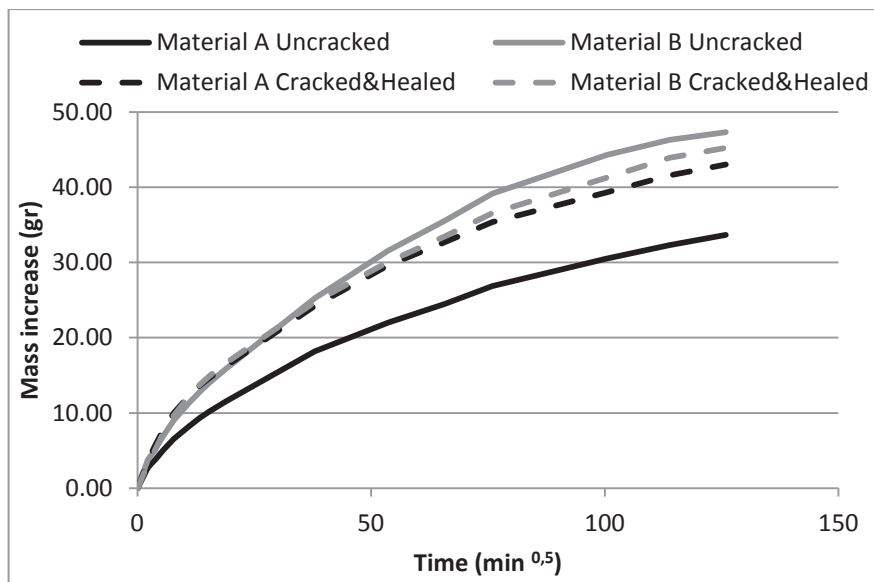


Figure 1: Mean mass increase of ECC specimens during the capillary water absorption test.

Regarding the results of cracked samples after the healing period, in the case of material A a higher water absorption was obtained in the test as compared to the uncracked samples, indicating that tightness recovery was not complete. On the contrary, in the case of material B the mean mass increase curve was very similar in the uncracked and the cracked and healed specimens. Moreover, the mean K value of cracked specimens after the healing period was almost equal to that of uncracked specimens, indicating a practically complete tightness recovery. Consequently, a higher healing efficiency may be inferred from the results for the ECC matrix with higher content of biomass ash.

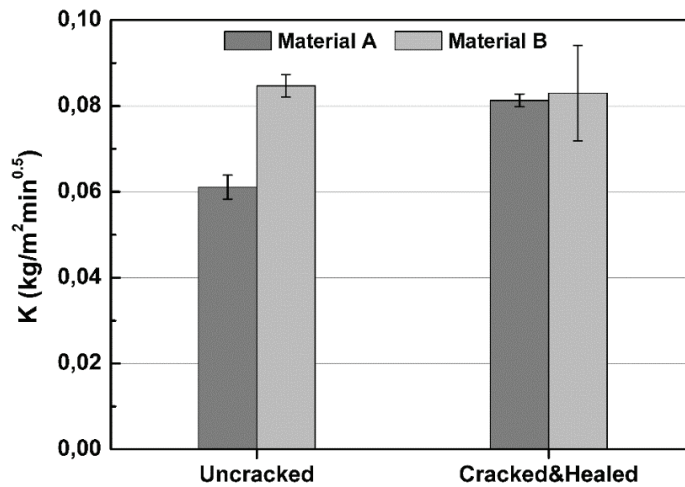


Figure 2: Capillary water absorption coefficient of the ECCs.

### 3.2 Crack sealing mechanism

The analysis by electron microscopy of the sample from the cracked area of material A, with lower content of BA, showed not sealed wide cracks that appeared filled with the resin used for sample preparation. This is the case of the representative crack in the left side of the top left image in Fig. 3, marked with a star symbol. Thinner cracks, like that in the right side of the top left image (marked with a triangle symbol and zoomed in the bottom left image) were also observed that were at least partially sealed by hydration products. On the contrary, no broad open cracks were observed along the surface of the sample of material B (right side images in Fig. 3). These results confirm the higher healing efficiency in the case of higher BA content within the matrix.

The detailed analysis of the representative crack in the case of ECC specimen prepared with higher content of BA showed healing products growing from both faces of the crack towards the middle, as previously observed by other authors [4]. A smooth surface was observed in areas more separated from the crack (point marked as 1 in Fig. 4) in which the composition was coherent with that expected for the cementitious matrix of the ECC. Silicon and calcium were the predominant elements, with significant contribution from C, Al and K and incorporation of Mg, Na, S and Cl as minor components. On top of the surface, separated cubic structures were clearly observed along the sample, as those surrounding number 1 in Fig. 4. The composition of these structures was coherent with calcium carbonate compound.

Approaching the remaining crack aperture, a less dense morphology was observed with structures clearly oriented perpendicular to the crack (point 3). In fact, perpendicular structures were seen to connect both sides of the remaining crack aperture that may be related to fibres bridging the crack sides on which hydration products precipitate. According to the results of compositional analysis, the precipitate in this case contained a clearly lower amount of silicon than the ECC matrix, with a higher content of aluminium and, especially, a significantly higher content of sulphur. The higher content and the availability of this element in the composition of BA, as compared to FA (see Tab. 1), may explain the higher crack healing efficiency in material B with a higher content of biomass ash.



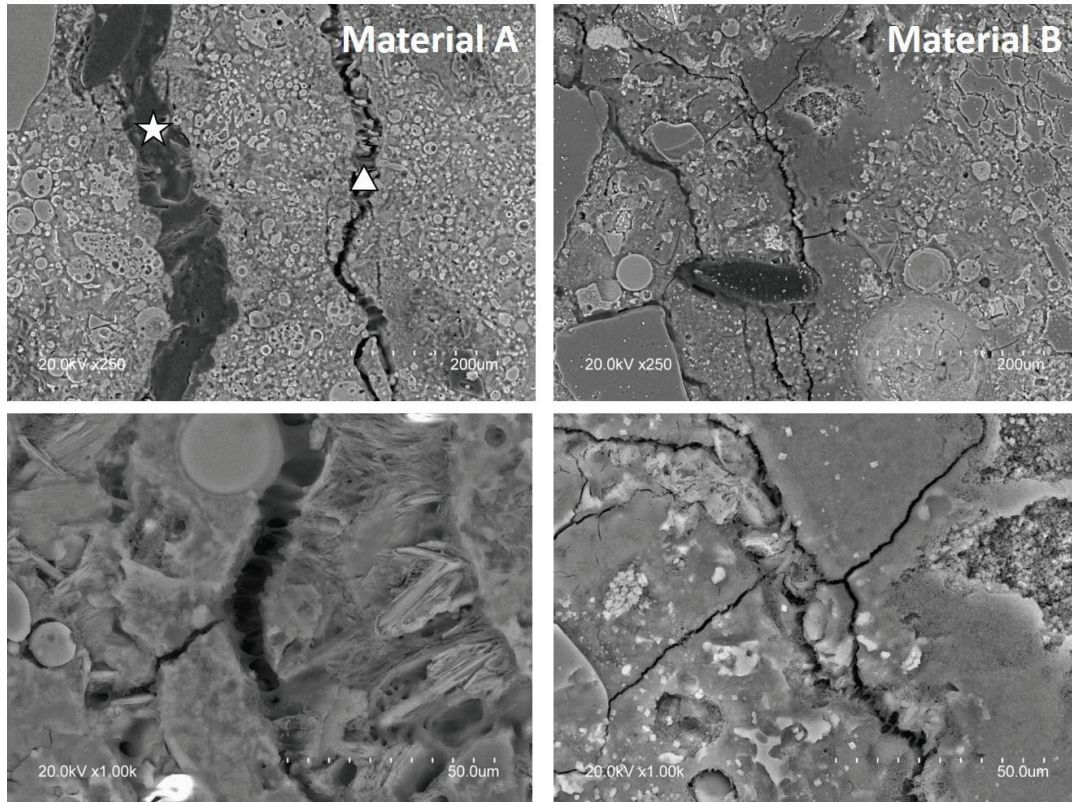


Figure 3: Backscattering electron microscopy images of representative cracks within the crack area of ECC specimens.

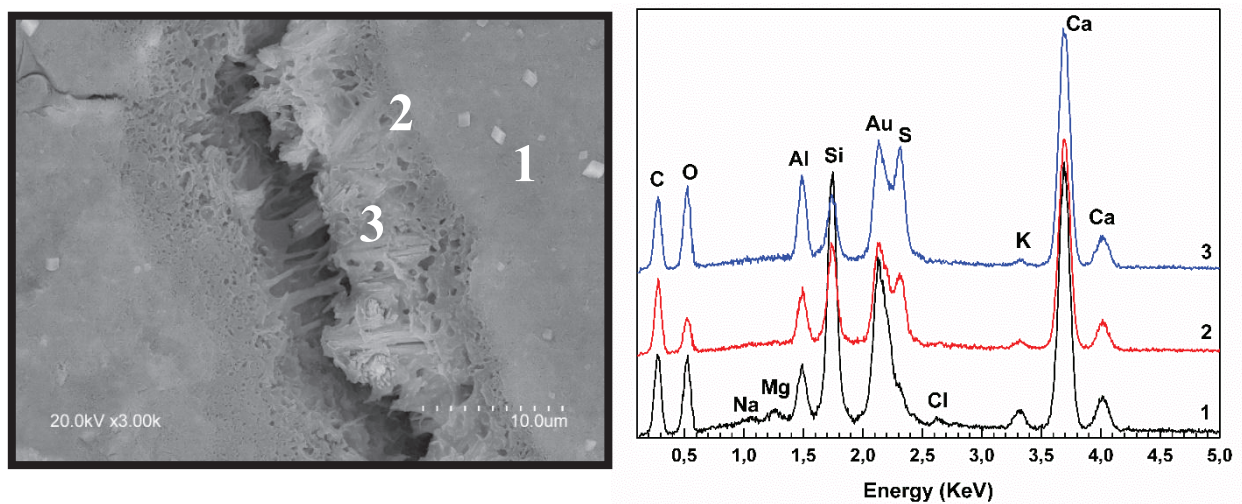


Figure 4: Zoomed backscattering electron microscopy image with compositional analysis of a representative crack within the cracked area of ECC specimen prepared with Material B.

#### **4. Conclusion**

The results of the present work confirmed an improvement of the self-healing efficiency of ECC specimens upon partial substitution of a conventional fly ash by a biomass ash. Sealing of cracks was promoted by reaction products deposited on fibres bridging the cracks and by crystalline phases incorporating sulphate ions from the biomass ash composition.

#### **Acknowledgements**

Thanks are due to Jose A. Sanchez and to the Physical-Chemical Analysis Unit of IETcc-CSIC for their help in experimental work.

#### **References**

- [1] Li, V.C., On Engineered Cementitious Composites (ECC). A review of the material and its applications, *J Adv Concr Technol* 1 (2003), 215-230
- [2] Sahmaran, M. and Li, V.C., Durability properties of micro-cracked ECC containing high volumes fly ash, *Cem Concr Res* 39 (2009), 1033-1043
- [3] Liu, H. et al, Influence of microcrack self-healing behaviour on the permeability of Engineered Cementitious Composites, *Cem Concr Com* 82 (2017), 14-22
- [4] Qian, S. et al, Self-healing behavior of strain hardening cementitious composites incorporating local waste materials, *Cem Concr Comp* 31 (2009), 613-621
- [5] Sahmaran, M. et al, Self-healing capability of cementitious Composites incorporating different supplementary cementitious materials, *Cem Concr Comp* 35 (2013), 89-101

## **NANO-SCALE TAILORING OF ENGINEERED CEMENTITIOUS COMPOSITES FOR SIMULTANEOUS ACHIEVEMENT OF ENHANCED SELF-HEALING AND SELF-SENSING ATTRIBUTES**

**Oğuzhan Öztürk<sup>(1)</sup>, Gürkan Yıldırım<sup>(2)</sup>, Anıl Kul<sup>(3)</sup>, Ülkü Sultan Keskin<sup>(1)</sup>, Mustafa Şahmaran<sup>(3)</sup>**

(1) Konya Technical University, Konya, Turkey

(2) Kırıkkale University, Kırıkkale, Turkey

(3) Hacettepe University, Ankara, Turkey

### **Abstract**

Autogenous self-healing can be a handy tool for concrete material to self-repair its own damage. On the other hand, to keep infrastructures in a serviceable state, it is also important to identify and assess any structural damage (cracks) as early as possible, before losing complete and/or sectional integrity. In this regard, efforts can be made to make concrete material work like a sensory material by making its nature electrically conductive (i.e. self-sensing) and responsive to any changes in applied strains. Engineered Cementitious Composites (ECCs) are new-generation ductile concretes capable of favouring autogenous self-healing through the formation of micron-size cracks upon straining. ECCs are also characterized by piezoresistive (self-sensing) response meaning that they exhibit strong dependence of electrical resistivity to the applied loading. Within this context, an attempt has been made here to further nourish both autogenous self-healing and self-sensing capabilities of ECCs by tailoring the matrix properties with different nanomaterials. With the purpose of improving self-healing and self-sensing attributes of ECC material, nano-silica and carbon nanotubes were simultaneously incorporated in mixture compositions, respectively. Tests were performed on sound and pre-loaded (almost-failed) prismatic ECC specimens under four-point bending loading. Both self-sensing and self-healing properties were evaluated before/after the introduction of microcracking and upon exposure to further curing. Results revealed that proposed nano-modification of ECC mixtures significantly improved the autogenous self-healing and self-sensing capabilities simultaneously. Outcomes of this study are believed to make a marked impact on true infrastructural sustainability by not only reducing the frequency of repair/maintenance applications but also making infrastructures much smarter to easily track their own damage.

## 1. Introduction

As an emerging material, Engineered Cementitious Composites (ECCs) with inherent tight microcracking behaviour under excessive tensile loading were introduced to the construction market by Li V.C [1]. ECCs-based studies have grown in number for the past 20 years. In addition to their superior mechanical/durability properties, ECCs were also tailored to possess additional structural and non-structural functionalities [2-3]. Many efforts were made on investigating the autogenous self-healing performance of ECCs under various conditions [4-5]. Although they are scarce, studies aiming at the self-sensing behaviour of ECCs can also be encountered in the current literature [6-7].

To multiply the benefits of ECC-material utilization in infrastructures, here, efforts were made to nourish autogenous self-healing and self-sensing ability of ECCs simultaneously by tailoring the mixture designs with different nano-materials. Characterization of self-sensing (piezo-resistive) behaviour was made via carbon nano tubes (CNTs) incorporated in ECC systems while intrinsic (autogenous) self-healing attribute was tried to be promoted by the inclusion of nano silica (NS) particles in ECC matrices. According to wide literature review, this study which aims at achieving self-healing and self-sensing functionalities concordantly in ECCs is the first of its kind and is believed to make a significant impact on sustainability of infrastructures not only by reducing the frequency of repair/maintenance applications but also making infrastructures much smarter to easily track their own damage.

## 2. Experimental Program

### 2.1 Materials and mixtures

The experimental studies were performed on four ECC mixtures produced with different nano materials. The mixtures were produced using Class-F fly ash (FA), CEM I 42.5 Portland cement (PC) silica sand (with maximum aggregate size of 0.4 mm), polyvinyl-alcohol (PVA) fibres, water and high range water reducing admixture (HRWRA). Carbon nano tubes (CNT, used by 0.55% of the total weight of cementitious materials) and nano silica (NS, used by 3% of the total weight of cementitious materials) were used to achieve self-sensing and self-healing attributes simultaneously.

Two different ECC mixtures were produced with a water to cementitious materials (CM=FA+PC) ratio (W/CM) of 0.27 and a pozzolanic material to Portland cement (PM/PC) ratio of 1.2. PVA fibres were used on a volumetric basis by 2%. HRWRA was used considering the reasonable fresh properties of ECC mixtures. The proportions for ECC mixtures were given in Table 1. Reference ECC mixture (ECC-Ref.) was produced as follows; i) raw materials were first mixed together at 100 rpm for a minute, ii) total water amount and HRWRA was then poured into the dry mixture and mixing was continued at 150 rpm for a minute and later at 300 rpm for additional 2 minutes, iii) PVA fibres were added into fresh mixture and mixing was continued 3 minutes more at 150 rpm for reference mixtures. Nano modified ECC mixture (ECC-CNT-NS) were produced as follows; i) CNTs were mixed with half of the total water and 75% of total HRWRA amount in another blender for 15 min at 3000 rpm [6]. During the preparation of the CNT solution, NS particles were mixed with another half of the mixing water and 25% of the total HRWRA amount for 5

minutes by using ultrasonic mixer [8]. Both nano solutions were added gradually into ongoing raw material mixing after a minute and rest of procedure was similar to ECC-Ref. mixing as mentioned earlier.

Table 1: Proportions of ECC mixtures.

Mix ID	PC/PC <sup>1</sup>	Sand/PC <sup>1</sup>	FA/PC <sup>1</sup>	W/CM <sup>1</sup>	HRWRA <sup>2</sup>	PVA <sup>2</sup>	NM/CM <sup>3</sup>
<i>ECC-Ref.</i>	1	0.36	1.2	0.27	5.1	26	-
<i>ECC-CNT-NS</i>	1	0.36	1.2	0.27	6.1	26	0.55-3

<sup>1</sup> by mass; <sup>2</sup> in kg/m<sup>3</sup>; <sup>3</sup>NM/CM stands for nano material to cementitious materials ratio, by mass (i.e. CNT/CM=0.55; NS/CM=3)

## 2.2 Experimental setup and methods for self-healing/self-sensing evaluation

For the main purpose of the study, prismatic ECC specimens (360x75x50 mm<sup>3</sup>) were produced and after one day in their molds, specimens were cured in plastic bags for six days at 95±5% RH, 23±2 °C. Additionally, 50 mm cubic specimens were fabricated for the determination of compressive strength at 7 and 28 days. Prismatic ECC specimens were preloaded up to 75% of their ultimate deformation capacities at the age of 7 days for crack generation. Preloaded specimens were cured in water and tested again after 7 and 28 days. Mechanical tests were conducted by using a loading machine with a computerized data recording system and loading points were insulated for accurate resistivity readings.

Electrical resistivity measurements were executed before and after crack formations by the use of a concrete electrical resistivity meter following procedures explained in [9]. The moisture states of the specimens were standardized by oven drying of specimens for 24 hours at 60 C° before electrical measurements to avoid any variations. ER (electrical resistivity) measurements were evaluated by the use of Eq. (1). Self-sensing of initial pre-loading was determined by calculating the fractional change in electrical resistivity (FCR) as demonstrated in Eq. (2). The self-healing degree was evaluated by comparing the ER values calculated at 7 and 28 days with the initial ER results recorded after pre-loading (Eq. 3). Cracks of all ECC specimens were also tracked by using a video microscope.

(1)  $ER = Z \cos(\theta) \times A/L$ , where ER is the electrical resistivity ( $\Omega \cdot m$ ), Z is the impedance measured by resistivity meter ( $\Omega$ ), A is the cross-sectional area of the specimen ( $m^2$ ), L is the length of the specimen (m) and  $\theta$  is the phase angle ( $^\circ$ ).

(2)  $FCR = ((ER_0 - ER)) / ER \times 100$ , where ER and ER<sub>0</sub> are electrical resistivity values of sound and preloaded ECC specimens at 7+0 days, before and after pre-loading, respectively.

(3) Self-healing rate in terms of ER =  $((ER_n - ER_0)/ER_0) \times 100$ , where ER<sub>n</sub> and ER<sub>0</sub> electrical resistivity measured at n<sub>th</sub> day and initial day of self-healing age, respectively.

## 3. Results and Discussion

### 3.1 Compressive strength

Table 2 presents the compressive strength results of 50 mm ECC cubes tested at 7 and 28 days. Incorporation of nano materials into ECCs increased the compressive strength both at 7

and 28 days. Compared to ECC-Ref., 7-day-old cubic specimens modified with nano materials exhibited 22.6% higher compressive strength on average. Similar increment was recorded as 21.4% for 28 days. In ECC-CNT-NS mixtures, NS particles may have acted as a media to improve the interaction between CNTs and C-S-H products so that denser interface could have formed. In addition, CNTs may have provided nucleation sites for additional C-S-H formation together with NS. For this reason, improved microstructure of nano modified ECC specimens resulted in higher compressive strength at 7 and 28 days.

Table 2: Compressive strength results of nano modified ECC specimens (results are in MPa).

Mix ID	7 days			28 days		
<i>ECC-Ref.</i>	28.96	29.95	30.66	53.84	58.08	59.91
<i>ECC-CNT-NS</i>	36.20	36.08	37.45	69.79	70.36	69.44

### 3.2 Self-healing and self-sensing performance

Table 3 presents the ER results of sound and preloaded specimens at 7+0, 7+7 and 7+28 days. According to Table 3, average of ER results of sound ECC-Ref specimens were 17% higher than the average of ER results of sound ECC-CNT-NS specimens which was attributed to the presence of CNTs in ECC-CNT-NS mixture creating more electrically conductive paths.

Table 3: ER results of nano modified prismatic ECC specimens ( $\Omega$  m), \*Sound, \*\*Preloaded.

Mix ID	7+0 days (S)*	7+0 days (PL)**	7+7 days (PL)**	7+28 days (PL)**
<i>ECC-Ref.</i>	21.34	22.68	32.20	36.80
	23.72	24.15	33.42	40.00
	22.40	25.48	33.39	40.80
	24.60	25.77	35.77	38.90
<i>ECC-CNT-NS</i>	19.87	26.84	45.60	61.50
	21.30	27.90	45.10	65.20
	22.12	28.00	43.40	65.40
	15.03	24.15	41.50	64.80

Fractional changes in electrical resistivity were 6.6% and 36.5% for ECC-Ref., and ECC-CNT-NS mixtures at 7+0 days, respectively. These results confirm the efficiency of CNT utilization to improve electrical conductivity, i.e. self-sensing capability. Nano-sized CNT particles provided continuous electrically conductive paths in ECC matrix and favoured the through movement of electrons. When pre-loaded, CNT particles may have debonded from the mixture and crack bridging mechanism of CNT could have been worsened so that increased fractional changes in ER results were recorded.

The further curing of preloaded specimens (7+7 and 7+28 days) caused ER results to increase irrespective of ECC mixture compared to ERs evaluated after preloading at 7+0 days. Self-healing rates (ER results compared to initial preloading at 7+0 days) were 37% and 56%, 59% and 140% for the ECC-Ref., and ECC-NS-CNT mixtures at 7+7 and 7+28 days, respectively. Increased ER results of both mixtures is due to high volume C-S-H reducing overall porosity and conductivity of pore solution leading to increase in ERs. However, increases of ER results were clearly more pronounced in ECC-NS-CNT specimens in both 7+7 and 7+28 days. This

finding is in line with the results of [10] which concluded that use of carbon-based materials increases the self-healing rate of ECCs. The faster and greater self-healing rates of CNT bearing specimens (ECC-CNT-NS) can be attributed to the tendency of CNTs to provide nucleation sites for additional C-S-H formation in self-healing reactions together with NS. This rate of increase indicates that self-healing products are probably the formation of C-S-H and  $\text{CaCO}_3$  through ongoing cement hydration and pozzolanic reaction. Moreover, only 0.55% of CNT incorporation by weight of total cementitious materials resulted in reduced crack widths in ECC-CNT-NS specimens which is indicative of enhanced self-healing ability. Since crack widths are more decisive than crack numbers on ER measurements [5], increased recovery rate of ECC-CNT-NS specimens can be explained by the reduced crack widths conforming [11]. Video microscope observations also support the above findings. Reductions in crack numbers and widths can be seen for ECC-Ref specimen in Figure 1. However, incorporation of CNT and NS into ECC-Ref. seems favour self-healing more. It can be seen that 100% self-healing of cracks can be achieved in a very limited time due to efficiency of CNTs to lower crack widths together with NS helping create denser C-S-H gels and triggering more stable self-healing products in tight microcracks.

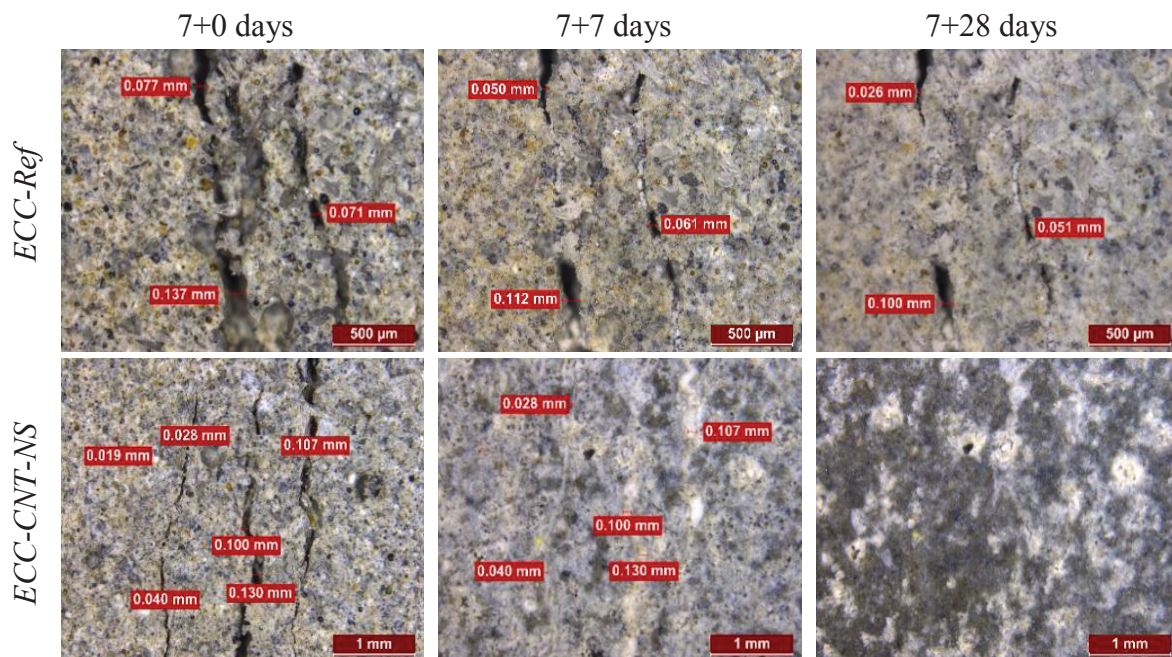


Figure 1: Self-healing of cracks in four different ECC specimens.

#### 4. Conclusions

This study investigated the development of multifunctional ECCs with self-sensing and self-healing efficiency. Below are the conclusions that can be drawn from this study;

- Incorporation of nano materials improved the compressive strength of ECC specimens. More than 20% of increment can be obtained in the presence of CNT and NS compared to reference ECCs after 7 and 28 days.

- After initial pre-cracking, ECC-CNT-NS specimens showed an increased number of cracks and reduced crack widths favouring enhanced self-healing.
- Greater self-healing rates (140%) were registered for ECC-CNT-NS specimens in comparison with ECC-Ref specimens (59%) in terms of ER measurements.
- Microanalysis indicated that ECC-CNT-NS specimens exhibited a full self-healing behaviour after 7 and 28 days of further curing. Moreover, 100% self-healing can be possible when multiple tight cracks form in ECC-CNT-NS specimens. Confirming the possibility to develop multifunctional ECCs having self-sensing and self-healing attributes simultaneously by the inclusion of 0.55% CNT and 3% NS in mixtures.

## References

- [1] Li, V.C. ECC-tailored composites through micromechanic modelling. In: Banthia N., editor. Proceeding fiber reinforced concrete: present and the future conference. Montreal: CSCE Press; (1998), 64-97.
- [2] Sakulich, A.R., Li, V.C., Nanoscale characterization of engineered cementitious composites (ECC), *Cement Concrete Research*, 41:2, (2011), 169-175.
- [3] Han, B., Sun, S., Ding, S., Zhang, L., Yu, X., Ou, J., Review of nanocarbon-engineered multifunctional cementitious composites, *Composite Part A: Applied Science* 31:70, (2015), 69-81.
- [4] Ferrara L., Krelani V., Moretti, F., Flores M.R., Ros, P.S., Effects of autogenous healing on the recovery of mechanical performance of HPFRCCs: Part 1, *Cem. Concr. Compos.*, 1:83, (2017). 76-100.
- [5] Sahmaran, M., Yıldırım, G., Aras, G.H., Keskin, S.B., Keskin, Ö.K., Lachemi M., Self-healing of cementitious composites to reduce high CO<sub>2</sub> emissions, *ACI Mater. J.* 1, (2017)-114.
- [6] Al-Dahawi, A., Öztürk, O., Emami, F., Yıldırım, G., Sahmaran, M., Effect of mixing methods on the electrical properties of cementitious composites incorporating different carbon-based materials, *Constr. Build. Mater.* 1. 104 (2016), 160–168.
- [7] Han B., Sun S., Ding, S., Zhang, L., Yu, X., Ou, J. Review of nano-carbon-engineered multifunctional cementitious composites, *Compos. Part A: Appl. Sci. Manuf.* 31 70, (2015) 69–81.
- [8] Yeşilmen, S., Al-Najjar, Y., Balav, M.H., Şahmaran, M., Yıldırım, G., Lachemi, M. Nano-modification to improve the ductility of cementitious composites, *Cem. Concr. Res.*; 76 (2015), 170-179.
- [9] Al-Dahawi, A., Öztürk, Ö., Emami, F., Yıldırım, G., Sahmaran, M. Assessment of self-sensing capability of Engineered Cementitious Composites within the elastic and plastic ranges of cyclic flexural loading. *Constr. Build. Mater.* (2017), 1-10.
- [10] Siad, H., Lachemi, M., Sahmaran, M., Mesbah, H.A., Hossain, K.A. Advanced engineered cementitious composites with combined self-sensing and self-healing functionalities. *Constr. Build. Mater.*, (2018), 313-322.
- [11] Yıldırım, G., Aras, G.H., Qais, S.B., Sahmaran, M., Lachemi M. Estimating the self-healing capability of cementitious composites through non-destructive electrical-based monitoring, *Ndt & E Int.*, 76 (2015) 26-37.



## **SELF-HEALING AND STRENGTH RECOVERY EVALUATION OF SUPER ABSORBENT POLYMERS CONCRETE MIXES UNDER CONTROLLED DAMAGE**

**Amir Sidiq<sup>(1)</sup>, Rebecca Gravina<sup>(1)</sup>, Sujeeva Setuge<sup>(1)</sup>, Filippo Giustozzi<sup>(1)</sup>**

(1) Royal Melbourne Institute of Technology – RMIT University, 376-392 Swanston st,  
Melbourne VIC 3000, Australia

### **Abstract**

The durability of concrete is invariably a challenge for engineers and material technologists due to the frequent maintenance and service required on concrete structures and infrastructures hence resulting in economical deficiency. Concrete healing innovations have been developed over the past decade; these various technologies for concrete self-healing include biotechnological, polymeric and chemical compounds. Super absorbent polymers are considered as a progressive method to deliver the water content into the cementitious matrix and stimulate hydration and in situ carbonation of cementitious materials. This study investigates the effect of super absorbent polymer addition into the cementitious materials and the efficiency of concrete crack healing and recovery of mechanical properties from cracks.

### **1. Introduction**

Concrete is the most favourable material used in the construction industry due its production process, raw material availability, affordability and recyclability [1]. Divergently, it is the tensile characteristics of concrete that causes cracking probability [2] which compromises the durability of concrete [3]. The development of micro-cracks in the cementitious matrix is the result of hydration and volumetric variation (i.e. thermal contraction, shrinkage in fresh and hardened concrete), environmental conditions (freezing and thawing) and mechanical loadings (static or dynamic). The formed micro-cracks are extremely difficult to be detected and can lead to the formation of macro-sized cracks [4]. In reinforced concrete, undesirable fluid and gas transport through these cracks can lead to corrosion of steel reinforcement and potential failure of concrete structures [5, 6]. Repairing micro-cracks in a cementitious matrix using the conventional methods could be extremely difficult and expensive. Concrete self-healing is one of the most promising methods for repairing these cracks, autonomously.

Super Absorbent Polymers (SAPs) is a technological material also utilized for concrete self-healing purposes. SAPs are cross-linked polymers and can absorb significant amounts of liquid in the surrounded environment and expand up to 500 times of their size [7]. This swelling capacity property proposes SAP as an additive in cementitious materials that carries water into the cementitious matrix and stimulates the cement hydration and in situ carbonation; however, during the release of the absorbed water, the dry SAP shrinks and reverses to its original dimension [4]. This mechanism of liquid provision and self-shrinkage of SAPs influences crack sealing and crack filling [8].

Researchers have used super absorbent polymers in various methods to propose crack healing and partial recovery of mechanical properties in cementitious materials. Kim and Schlangen [9] deployed SAPs with PVA-based ECC in the mortar mixture for crack width reduction and healing; SAPs content of 0.5% and 1.0% to the weight of cement were considered. After curing for 28 days, the four-point bending test was adopted to develop cracks and an average of 17.3  $\mu\text{m}$  and 15.67  $\mu\text{m}$  in crack width was obtained with respect to the SAP content (0.5 and 1%, respectively) compared to 22.3  $\mu\text{m}$  for the control mix. After additional 28 days, samples were tested to failure by using a four-point bending test and it was concluded that the healing samples developed additional flexural strength and less deflection compared to the control samples. Sneek et al. [8] used SAP (cross-linked Potassium salt polyacrylate, particle size of  $476.6 \pm 52.9 \mu\text{m}$ ) of 1%, 2% and 4% with respect to the cement weight and 2% by volume of PVA for all mixes. After 28 days, cracks were again developed by using the four-point bending method with crack width of 100-150  $\mu\text{m}$ . Samples were cured under wet and dry cycles for additional 28 days and a four-point bending test to failure was finally conducted. It was observed that cracks' width up to 138  $\mu\text{m}$  was healed for all SAP contents with 100% healing for SAP content of 2% and 4%; a strength reduction of 50% for 4% SAP and strength increment of 20% for 2% SAP was also observed. Gruraert et al. [10] added the in-house fabricated SAP with particle size less than 400  $\mu\text{m}$  and 0.5% and 1% content by weight of cement, and achieved an increment of flexural strength of 8% and 6%, respectively; a general reduction of compressive strength for all SAP mixes was also noticed.

The present study investigates the effect of Super Absorbent Polymers in the concrete mix without the addition of superplasticizer, micro-fibres and excessive water content. The analysis was carried out using X-Ray tomography for internal micro-porosity and cracking evaluation as well as standard mechanical tests and non-destructive tests for recovery assessment of mechanical properties.

## **2. Materials and Methodology**

### **2.1 Materials**

General purpose cement (equivalent to CEM-I-42.5R) and local aggregates with nominal size of 7.0 mm, 10.0 mm, sand and water were used for the mixing process. Super absorbent polymers (Floset<sup>TM</sup> 27CS) with particle size less than 500  $\mu\text{m}$  were purchased from SNF Pty Ltd Australia.

### **2.2 Sample preparation and curing**

Concrete specimens were fabricated with addition of SAPs; the concrete mix consisted of water to cement and sand to cement ratio of 0.54 and 1.83, respectively and nominal

aggregate size of 7 mm and 10 mm with ratio of 0.8 and 1.61 to the weight of cement (PC CEM-I-42.5R) with addition of 1% (by cement weight) of SAPs. Cylindrical samples were casted as per AS 1012.8.1-14 [11] with diameter of 100 mm and height of 200 mm and a vibrating table was used for concrete compaction at 50Hz. Sample were kept at controlled conditions for 24 hours before de-moulding; they were then immersed in water for 28 days. Later, samples were cured in water to the completion of the experiment.

### **2.3 Crack development**

After 28 days of wet curing, samples were removed and dried at ambient conditions for two hours. Three replicates were tested to obtain the maximum compression strength at 28 days. A self-synthesised steel mould was used to generate internal crack patterns; the mould consisted of two halved semi-circular sections with open ends at top and bottom sections. The semi-circular sections were connected by bolts and nuts. Cracks were developed by placing the concrete specimens into the self-synthesised mould and locating cylindrical steel plates at both opened ends. The steel mould with the concrete sample was positioned in the MTS-1000 kN machine between loading platens and an axial force was applied to induce axial circumferential pressure on the samples. Cracks were thus developed throughout the entire volume of the sample. Cracks were triggered by applying 40% and 70% of the maximum compressive strength as per initial measurement at 28 days.

### **2.4 Methods of testing**

Ultrasonic Velocity Pulse and compression tests were conducted on concrete samples with SAPs for mechanical properties recovery while X-ray micro-tomography was undertaken for healing efficiency and change in porosity due to cracking. The three test types were performed at various time intervals after damaging the sample, including the 0, 3, 7, 14 and 28 days post 28 days of curing. All samples were labelled and Ultrasonic Velocity Pulse (UVP) was used to determine the dynamic modulus of concrete before the damaging procedure occurred as well as for each individual time interval (e.g. after being damaged).

Bruker SkyScan 1275 X-Ray micro-tomograph was used to obtain the porosity variation due to the formed cracks as well as to evaluate cracks development during healing. Concrete samples with diameter of 55 mm and 67 mm in height were placed on the micro-positioning stage of the instrument. The X-ray micro-tomograph was set to its maximum capacity with X-ray source of 100 kV tube voltage and 100  $\mu$ A tube current; for a superior transmission of x-ray through concrete and to obtain minimum noise level, a 1 mm copper film was placed between the x-ray source and concrete sample. The intensity of the x-ray beam transferred through concrete sample is attenuated due to concrete density and the detector receives the residual intensity hence the 2D image is produced [12]. At 0.2-degree rotation around its axis and resolution of 1540x1540 a total of 1535 images with 35  $\mu$ m thickness were obtained. Based on the 2D images, a 3D object reconstruction was obtained and data on internal porosity and crack development were collected.

## **3. Results and analysis**

### **3.1 Dynamic Stiffness**

In this experiment, non-destructive tests were conducted to obtain the dynamic modulus of concrete. Ultrasonic Velocity Pulse was used to determine the pressure wave velocity passing

through concrete samples. Then, according to ASTM C597-16 [13], Poisson's ratio of 0.15 and obtained average density of  $1878.4 \text{ kg/m}^3$  the stiffness of concrete was calculated. In figure 1, the dynamic modulus of the concrete with SAPs is shown at different curing times in comparison to the dynamic modulus of the concrete before cracking development.

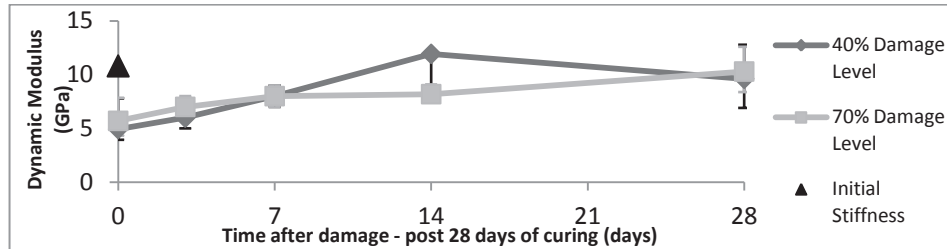


Figure 1: Dynamic modulus of samples after damage and healing effect with time.

### 3.2 Compressive strength

After internal micro-cracks were generated in all concrete samples, MTS-1000 kN compression machine was used to obtain the maximum axial force at failure; three replicates for each data set were measured. Figure 2 shows the compressive strength at each time interval after damage for 40% and 70% controlled crack development in comparison to the maximum compression strength prior to crack generation.

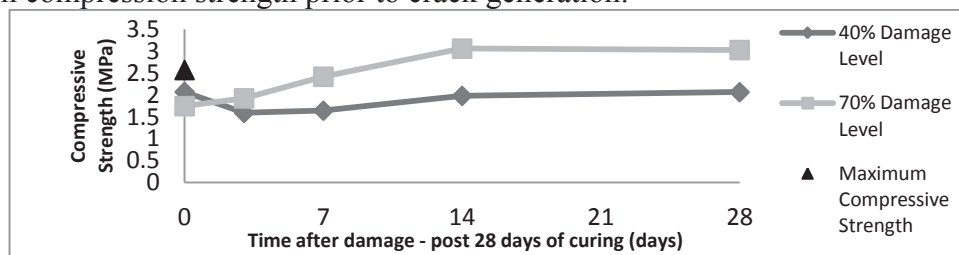


Figure 2: Residual and regain of compressive strength due to healing.

### 3.3 Micro CT-scan analysis

Micro CT scan tomography was used to analyse the induced porosity in the concrete samples due to damage. The operation involves analysing each 2D image based on the possible grey levels of intensity and the separation of air (voids and cracks) and solid phases. Air pores are dark grey due to lighter density hence less attenuation in translated intensity[14]. To determine the porosity of damaged samples by 40% and 70% in comparison to the control samples, the optimum of 44-255 grey level was applied throughout the entire campaign for consistency of results. Noise was reduced to the minimum level by applying global thresholding algorithm to convert the image to binary grey-scale image followed by the application of Otsu's method [14] to further separate the pore and solid phases. Also, black speckles smaller than 60 voxels were removed to obtain minimum noise level. Figure 3 shows the porosity at each time interval of 40% and 70% crack control damaged samples in comparison to control samples.

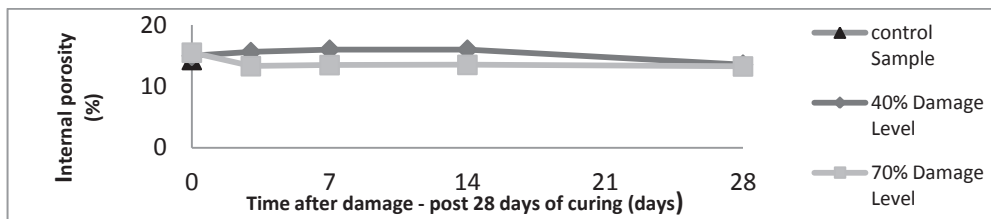


Figure 3: Porosity at various damage levels with respect to time.

#### 4. Discussion

The efficiency of the addition of SAPs solely in a concrete mix for the purpose of crack healing and mechanical properties recovery was evaluated by utilizing non-destructive test methods and standard mechanical testing. It should be noted that the overall mechanical performance of the mix itself was not of interest to this research but rather was the effect of SAP on triggering concrete healing. Figure 1 shows the trend in stiffness of the concrete with SAPs. Prior to damage (and after 28 days of curing), the dynamic modulus of concrete was 10.8 GPa while right after being damaged at 40% and 70% of the maximum compressive strength, samples showed reduced stiffness of 5.44 GPa and 5.87 GPa, respectively. A regain in stiffness, thus increase in the velocity of ultrasonic pulses, was observed in both cases with almost full recovery (10.3 GPa for 70%-damage specimens and 9.6 GPa for 40%-damaged specimens) as per UPV assessment.

In this experiment the compressive strength and dynamic modulus results are generally lower than the standard concrete due to the inclusion of SAPs – absorbing water - without any extra water in the mix; hence less hydration in the cementitious matrix. Though the analysis of compressive strength results has suggested a partial strength regain with greater variability was observed among replicates. Both damaged samples exhibited an upward trend in the capacity of regaining strength with time although the 40%-damage specimens were not capable of fully recover from damage to their initial strength. This may be due to the different crack size generated by the damaging procedure.

Porosity content determination and crack healing efficiency was also estimated by utilizing X-ray tomography. Prior to damage, internal void content was 14.3%, which is generally higher than standard concrete although this could have been expected since no extra water or superplasticiser were used at this stage. Their addition is part of an ongoing research.

After being damaged, samples experienced an initial increase in porosity up to 15% and 15.5% for 40% and 70% damage, respectively. However, in both cases, a reduction of the internal void content was found with time although this was more gradual in the 40%-damaged samples.

Generally, 40%-damaged specimens needed more time to recover after being damaged; this suggests that there could be a close relationship between the healing efficiency of SAP and the size of the crack, which deserves more investigation.

#### 5. Conclusion

The addition of super absorbent polymers in concrete proved to be beneficial in promoting healing phenomena; the efficiency of healing, though, followed different trends depending on

the internal damage being generated in the samples. Non-destructive methods, such as UPV and X-ray, showed to capture well the internal micro-structure before and after damage. Compared to other studies where healing efficiency is evaluated on a single crack generated by different form of flexural tests (or by a small group of cracks within a restricted area in the proximity of the maximum stress point), the present research developed a methodology to induce cracking patterns inside the entire volume of the sample. This approach, although still at an early stage, can prove to fit well in the assessment of healing. Finally, the swelling capacity of super absorbent polymers enable them to be used in cementitious materials for delivering stored water into cementitious matrix hence stimulating cement hydration and crack healing.

## References

- [1] Pelletier, M.M., et al., Self-healing concrete with a microencapsulated healing agent. *Cem. Concr. Res*, 2011.
- [2] Karaiskos, G., et al., Performance monitoring of large-scale autonomously healed concrete beams under four-point bending through multiple non-destructive testing methods. *Smart Materials and Structures*, 2016. 25(5): p. 055003.
- [3] Joseph, C., A. Jefferson, and M. Cantoni. Issues relating to the autonomic healing of cementitious materials. in *First international conference on self-healing materials*. 2007.
- [4] Yang, Z., et al., Laboratory assessment of a self-healing cementitious composite. *Transportation Research Record: Journal of the Transportation Research Board*, 2010(2142): p. 9-17.
- [5] Aldea, C.-M., S.P. Shah, and A. Karr, Permeability of cracked concrete. *Materials and structures*, 1999. 32(5): p. 370-376.
- [6] Mignon, A., et al., pH-sensitive superabsorbent polymers: a potential candidate material for self-healing concrete. *Journal of materials science*, 2015. 50(2): p. 970-979.
- [7] Snoeck, D., et al., Visualization of water penetration in cementitious materials with superabsorbent polymers by means of neutron radiography. *Cement and Concrete Research*, 2012. 42(8): p. 1113-1121.
- [8] Snoeck, D., et al., Self-healing cementitious materials by the combination of microfibres and superabsorbent polymers. *Journal of Intelligent Material Systems and Structures*, 2014. 25(1): p. 13-24.
- [9] Kim, J. and E. Schlangen. Super absorbent polymers to simulate self healing in ECC. in *2nd International Symposium on Service Life Design for Infrastructures*, RILEM Publications SARL, Delft. 2010.
- [10] Gruyaert, E., et al., Self-healing mortar with pH-sensitive superabsorbent polymers: testing of the sealing efficiency by water flow tests. *Smart Materials and Structures*, 2016. 25(8): p. 084007.
- [11] Method for making and curing concrete\_Compression and indirect tensile test specimens. 2018.
- [12] Fan, S. and M. Li, X-ray computed microtomography of three-dimensional microcracks and self-healing in engineered cementitious composites. *Smart materials and structures*, 2014. 24(1): p. 015021.
- [13] ASTM C597 - 16 Standard Test Method for Pulse Velocity Through Concrete. 2018.
- [14] Manahiloh, K.N., et al., X-ray computed tomography and nondestructive evaluation of clogging in porous concrete field samples. *Journal of Materials in Civil Engineering*, 2012. 24(8): p. 1103-1109.

## **SELF-HEALING OF CEMENT SLURRY FOR OIL WELLS CONTAINING CRYSTALLINE ADMIXTURE: EARLY RESULTS**

**Aline de Souza Oliveira <sup>(1)</sup>, Romildo Dias Toledo Filho <sup>(1)</sup>, Eduardo de Moraes Rego Fairbairn <sup>(1)</sup>, Otávio da Fonseca Martins Gomes <sup>(2)(3)</sup>**

(1) COPPE – The Graduate Institute of the Federal University of Rio de Janeiro, Brazil

(2) CETEM, Centre of Mineral Technology, Brazil

(3) National Museum, Federal University of Rio de Janeiro, Brazil

### **Abstract**

In this paper we present the early results of the self-healing analysis of an oil well cement slurry containing 1% by weight of cement of crystalline admixture. The specimens cured in a bath at 60°C were pre-cracked at 7 days by splitting test until crack width of 200 µm. The healing process lasted 66 days in a 60°C water bath to reproduce pre-salt temperature conditions. The effectiveness of the healing process was verified by the mechanical recovery of the specimens after reloading. The analysis indicated that self-healing can be useful to improve the performance of the cement sheaths in oil wells.

### **1. Introduction**

During the drilling of an oil well, primary cementing is the process of placing cement slurry in the annulus between the steel casing and the geological formation. After hardening, this hollow cylinder is called cement-sheath [1]. In Brazil, pre-salt oil and gas reserves have been discovered in 2006. In order to explore these reservoirs in ultra-deep water, many scientific and technological challenges had to be overcome. Total depth of the well can reach 7,000 meters. Layers are formed by water, followed by rocks and salt. The upper limit of pressure can reach around 90 MPa, while temperature range varies between 60-70°C [2], [3]. These extreme service conditions may result in crushing or cracking that may cause the lack of zonal isolation. This can lead to contamination of the crude oil or even catastrophic accidents if gas could escape from the well [4]. Therefore, considering the various factors that tend to damage the cement sheath, it would be worthy if the cement slurry had self-healing properties.

In view of the high environmental aggressiveness and loading conditions of the pre-salt, the crystalline admixture (*CA*) used in this research corresponded to those classified as PRAH (Permeability-reducing admixtures for concrete exposed to hydrostatic conditions) as described by the ACI [5].

According to Sisomphon et al. [6] the main healing mechanism on the external surface of the crack is the precipitation of calcium carbonate, since the presence of *CA* boosts the dissolution of ions ( $\text{Ca}^{2+}$ ) and increases the environmental alkalinity. Thus, the region close to the crack would have the optimal concentrations of the ions: (i)  $\text{Ca}^{2+}$  (released from the matrix); (ii) carbonate ( $\text{CO}_3^{2-}$ ); (iii) bicarbonate ( $\text{HCO}_3^-$ ). Kishi et al. [7] explain that the calcium carbonate is the product of the reaction between bicarbonate ions ( $\text{HCO}_3^-$ ) or carbonates ions ( $\text{CO}_3^{2-}$ ) solubilized in water, originating from the crystalline additives, and  $\text{Ca}^{2+}$  ions from the concrete.

From the perspective of internal healing, which results in increased mechanical properties, Sisomphon et al. [8] found that the predominant mechanisms are further hydration and the expansion of anhydrous grains. In view of this, the hydrates produced in greater quantity were  $\text{CaCO}_3$ , C-S-H and ettringite. Jiang et al. [9] classified the action of *CA* into three types: (i) crystallization-precipitation, in which the admixture can supply  $\text{CO}_3^{2-}$  (carbonate ions) and accelerate the reaction with  $\text{Ca}^{+2}$  originated from the cement system, forming  $\text{CaCO}_3$ ; (ii) expansive formation associated with the presence of new hydrates with higher volume, such as Aft due to hydration of the calcium sulfo-aluminate; (iii) pozzolanic reaction with the formation of C-S-H.

No reference can be found in the use of crystalline admixture as healing agent for oil well cement slurries. Ferrara *et al.*, [10] investigated the interaction between crystalline admixtures and disperse fiber reinforcement. They found that the material could have a better mechanical behavior after the self-healing process. De Nardi *et al.*, [11] realized that the presence of crystalline admixtures in lime mortars enhanced self-healing. They also found that the phenomenon is more evident for specimens exposed to open air. Roig-Flores *et al.*, [12], [13] used a high content of crystalline admixture in concretes, which reached different healing performances according to the exposure conditions. Sisomphon *et al.*, [8] reported how the mechanical recovery of mortars is related to the chemical properties of healing products. Ferrara *et al.*, [14] conclude that crystalline admixture accelerated the healing process and the recovery of mechanical properties. However, in accelerated exposure conditions, under high relative humidity and cycling temperature, the high dispersion of the results did not allow to draw any definitive conclusion. Jiang *et al.*, [15] reported that crystalline admixtures combined with chemical expansive agents can accelerate the healing process.

In this paper we investigated the use of crystalline admixture as healing agent in cement slurries for oil well applications. The effectiveness of the healing process was verified by the response of the specimens after reloading. The analysis indicated that self-healing can be useful to improve the performance of the cement sheaths in oil wells.

## 2. Experimental program and methodology

### 2.1 Materials and mixture proportions of cement slurries

Cement slurry was produced with crystalline admixture, in powder form, with content of 0% and 1% by weight of cement. The water/cement ratio was fixed in 0.44. The cement used was



high sulfate-resistant (HSR) class G well cement, with defoamer admixture at a dosage of 0.25% by weight of cement. Discontinuous polypropylene microfibers were added to the mixtures with 0.4% in fiber volume fraction ( $V_f$ ). This low fiber content was added to guarantee cohesion between the two sides of the samples after crack opening. Proportions are shown in Table, where DE stands for defoamer admixture, PP stands for polypropylene microfibers, and CA stands for crystalline admixture. The former is commercially known as Sika WT-200P and its purpose is to seal cracks up to 400  $\mu\text{m}$  and to reduce water penetration under hydrostatic pressure.

Table 1: Mixture proportions with 0.44 of w/c ratio.

Mix code	Cement (kg/m <sup>3</sup> )	Water (kg/m <sup>3</sup> )	DE (kg/m <sup>3</sup> )	PP (kg/m <sup>3</sup> )	CA (kg/m <sup>3</sup> )
0%CA	1330	585	3.3	4.0	0.0
1%CA	1307	575	3.3	3.9	13.1



Figure 1: Molds with notch.

## 2.2 Sample preparation

The mixing procedure was carried out in accordance to API-S-10A standard. The mixture passed the stability requirement of API-10B-2 standard. The slurry was poured in cylindrical moulds ( $\text{Ø}50 \times 100 \text{ mm}$ ) that had notches positioned in two opposite diametrical positions as showed in Figure 1. They were cured in water immersion at 60°C up to 7 days in such a way that the hydration is almost complete as reported by [16] for a similar slurry. The specimens were then cut on the top, middle and bottom resulting in 3 discs ( $\text{Ø}50 \times 25 \text{ mm}$ ), here called samples.

## 2.3 Pre-cracking by feedback-controlled splitting test

Pre-cracking corresponding to a single and localized crack was induced by a splitting tensile test based on ASTM C496M. The test is controlled in a twofold manner: (i) loading is controlled by the stroke displacement; (ii) a clip gage placed closed to the crack controls the end of the test for a given crack width ( $w$ ). The test was carried out in a Shimadzu press with load cell of 100 kN, in constant rate of 0.5  $\mu\text{m/s}$ . The preloading was automatically stopped until the crack width reached the imposed value of 200  $\mu\text{m}$ .

## 2.4 Exposure and evaluation of healing properties

After pre-cracking, the samples were left in continuous immersion in water at a temperature of 60°C for 66 days. For this early study, we decided to submit the samples only to the typical temperature of the pre-salt wells in order to separate the various effects of this application such as pressure and salt content. After the healing period, the samples were again submitted to the splitting tensile test. The clip gage was zeroed and the end of the test was set to  $w = 200 \mu\text{m}$ .

The following parameters were defined for the load-crack width curves, as displayed in Figure 2: the load at first crack ( $P_{fc}$ ); the load at a crack width of 200  $\mu\text{m}$  ( $P_{200}$ ); the residual crack width ( $w_r$ ); the load corresponding to the crack width of  $w_r + 200 \mu\text{m}$  ( $P'_{200}$ ). The self-healing capacity was computed by means of the Index of Load Recovery ( $ILR$ ) as defined in reference [14] and presented in (1).  $ILR=1$  corresponds to total healing and  $ILR=0$  indicates

that there was no healing. Besides these values,  $ILR < 1$  would indicate that the exposure could have further damaged the cracked region, while  $ILR > 1$  corresponds to an increase of the tensile strength of the healed crack.

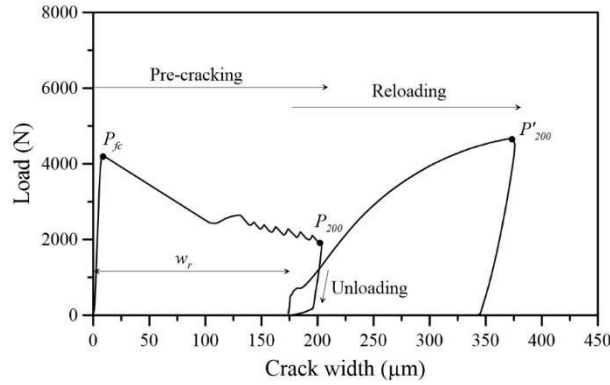


Figure 2: Typical load-crack width curve for self-healing analysis.

$$ILR = \frac{P'_{200} - P_{200}}{P_{fc} - P_{200}} \quad (1)$$

### 3. Results and discussion

The samples obtained from the top of the specimens were rejected because they presented discrepant  $P - w$  curves, with values of load much lower than the samples obtained from the medium and the bottom of the specimens. Considering that the specimens passed the stability test, a first interpretation of this phenomenon indicates that there was segregation of the PP fibers. Further investigation of the positioning and fiber content will be performed to confirm this hypothesis.

Figure 3 and Figure 4 present the  $P - w$  individual curves (with lower and upper limits) and average curves for both mixtures with 0% and 1%CA contents, respectively. For the pre-cracking branch of the curve, an initial softening region can be observed after the elastic range. It is followed by a sawtooth portion indicating that the fibers are bridging the two faces of the crack. For reloading, it appeared that the samples became much more compliant after healing. Since the clip gage measures the relative displacement in a very tight region close to the crack mouths, this seems to indicate that the healed crack has elastic properties quite different from the initial ones.

The samples with 0%CA had  $ILR$  equal to 0.8, it means that the mechanical strength was not completely recovered. In contrast, the mixtures with 1%CA had average  $ILR$  equal to 1.1, which corresponds to complete healing with a slight increase in strength.

To illustrate the evolution of the healing process, we show in Figure 5 a panoramic view of a crack before and after healing assembled from micrographs obtained by a stereo microscope.

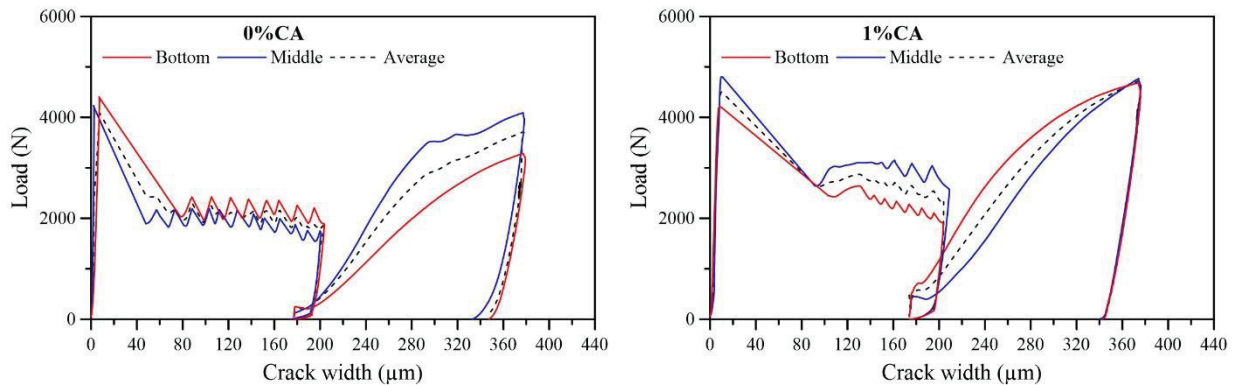


Figure 3: Load-crack width curves for specimens with 0% and 1%CA submitted to pre-cracking and post-conditioning splitting tensile test: bottom, middle and average.

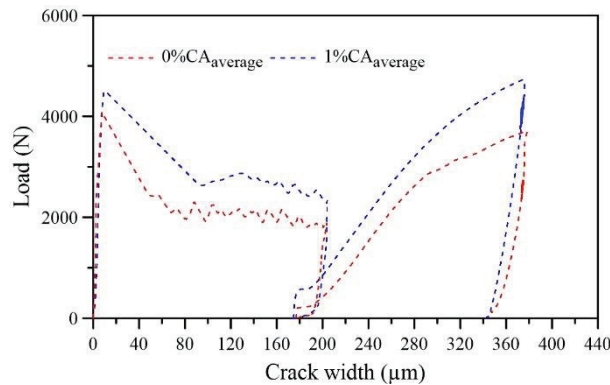


Figure 4: Load-crack width averages curves for specimens with 0% and 1%CA submitted to pre-cracking and post-conditioning splitting tensile test.

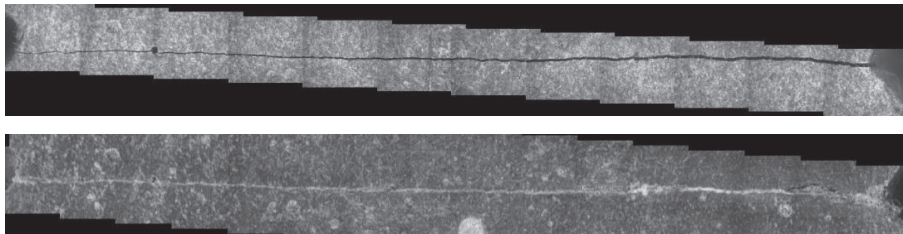


Figure 5: Panoramic view of a crack before and after self-healing.

#### 4. Concluding remarks

The early results for self-healing of the cement slurry for oil well with 1% CA studied in this paper, indicated better mechanical recovery than mixtures with 0% CA. It should be noted that the hydration of the samples was almost completed when they have been submitted to pre-cracking and exposure. Therefore, the healing process was not facilitated by the presence of unreacted anhydrous grains and it can be considered that the conditions for the onset of healing were not the most favorable.

We can then consider that these early results are very promising and that self-healing of oil well cement sheaths may become an important research topic in the coming years.

## References

- [1] J. D. Mangadlao, P. Cao, and R. C. Advincula, "Smart cements and cement additives for oil and gas operations," *J. Pet. Sci. Eng.*, vol. 129, no. April 2010, pp. 63–76, 2015.
- [2] J. Formigli Filho, A. Pinto, and A. Almeida, "Santos Basin's Pre-Salt Reservoirs Development—The Way Ahead," *Offshore Technol. Conf.*, no. May, pp. 4–7, 2009.
- [3] J. O. D. S. A. Pizarro and C. C. M. Branco, "Challenges in implementing an EOR project in the Pre-Salt province in deep offshore Brasil," *Soc. Pet. Eng. - SPE*, vol. 2, pp. 954–966, 2012.
- [4] A. L. Martins, P. E. Aranha, M. G. Folsta, C. A. Simão, N. A. Batalha, and G. H. V. P. Pinto, "Integrated cementing hydraulics design for massive salt zones," *SPE Lat. Am. Caribb. Pet. Eng. Conf. Proc.*, vol. 1, no. April, pp. 93–101, 2012.
- [5] A. 212.3R, "ACI 212.3R-10: Report on Chemical Admixtures for Concrete," 2010.
- [6] K. Sisomphon, O. Copuroglu, and E. Koenders, "Self-healing of surface cracks in mortars with expansive additive and crystalline additive," *Cem. Concr. Compos.*, vol. 34, pp. 566–574, 2012.
- [7] T. Kishi, T. Ahn, A. Hosoda, S. Suzuki, and H. Takaoka, "Self-Healing Behaviour By Cementitious Recrystallization of Cracked Concrete," *First Int. Conf. Self Heal. Mater.*, no. April, pp. 1–10, 2007.
- [8] K. Sisomphon, O. Copuroglu, and E. Koenders, "Effect of exposure conditions on self healing behavior of strain hardening cementitious composites incorporating various cementitious materials," *Constr. Build. Mater.*, vol. 42, pp. 217–224, 2013.
- [9] Z. Jiang, W. Li, Z. Yuan, and Z. Yang, "Self-healing of cracks in concrete with various crystalline mineral additives in underground environment," *J. Wuhan Univ. Technol. Sci. Ed.*, vol. 29, no. 5, pp. 938–944, 2014.
- [10] L. Ferrara, V. Krelani, and F. Moretti, "On the use of crystalline admixtures in cement based construction materials: From porosity reducers to promoters of self healing," *Smart Mater. Struct.*, vol. 25, no. 8, 2016.
- [11] C. De Nardi, S. Bullo, L. Ferrara, L. Ronchin, and A. Vavasori, "Effectiveness of crystalline admixtures and lime/cement coated granules in engineered self-healing capacity of lime mortars," *Mater. Struct.*, vol. 50, no. 4, p. 191, 2017.
- [12] M. Roig-Flores, S. Moscato, P. Serna, and L. Ferrara, "Self-healing capability of concrete with crystalline admixtures in different environments," *Constr. Build. Mater.*, vol. 86, pp. 1–11, Jul. 2015.
- [13] M. Roig-Flores, F. Pirritano, P. Serna, and L. Ferrara, "Effect of crystalline admixtures on the self-healing capability of early-age concrete studied by means of permeability and crack closing tests," *Constr. Build. Mater.*, vol. 114, pp. 447–457, 2016.
- [14] L. Ferrara, V. Krelani, and M. Carsana, "A 'fracture testing' based approach to assess crack healing of concrete with and without crystalline admixtures," *Constr. Build. Mater.*, vol. 68, pp. 535–551, 2014.
- [15] Z. Jiang, W. Li, and Z. Yuan, "Influence of mineral additives and environmental conditions on the self-healing capabilities of cementitious materials," *Cem. Concr. Compos.*, vol. 57, pp. 116–127, 2015.
- [16] C. A. A. Rocha, "Influência da pressão e temperatura de cura e da adição de NaCl e KCl no comportamento de pastas para cimentação de poços de petróleo," Universidade Federal do Rio de Janeiro (UFRJ), 2015.

## **STRESS REDISTRIBUTION MECHANISM IN CONCRETE ELEMENTS WITH POLYMER FLEXIBLE JOINT: EXPERIMENTAL RESULTS**

**Łukasz Zdanowicz <sup>(1)</sup>, Marcin Tekieli <sup>(1)</sup>, Arkadiusz Kwiecień <sup>(1)</sup>**

(1) Cracow University of Technology, Cracow, Poland

### **Abstract**

This paper describes the application of a Polymer Flexible Joint (PFJ) as a method of repairing concrete members. Prismatic specimens were concreted and tested in four-point bending up to failure to simulate damage. After failure they were repaired with PFJ with PT-type polymer and tested in flexure again. The aim of the research was to assess the repair effectiveness regarding load bearing capacity and strain capacity before and after repair and to show the stress redistribution phenomenon. Furthermore, during the tests two methods of measurements were applied – conventional measurements with extensometers and Digital Image Correlation (DIC) method. Results of load – crack mouth opening displacement (CMOD) and load – displacement obtained from both methods were compared and their compliance is presented. Moreover, it is shown that the DIC method is capable of presenting the developing crack pattern even before the maximum force is achieved. Failure mode can be thus better described and understood. Finally, the repair effectiveness was calculated as 87% in terms of load-bearing capacity and 278% in terms of strain capacity. The phenomenon of stress redistribution in concrete was explained and described.

### **1. Introduction**

Cracking of concrete is a common problem in civil engineering, which demands a lot of effort during repair [2, 8]. However, not all typical repair methods are effective in the long-term. In this paper we aim to present a method of repairing concrete members with Polymer Flexible Joint (PFJ), based on PT-type polyurethane polymer. Our research is focused on repair of prismatic concrete specimens subjected to flexure and assessing the repair effectiveness in terms of load-bearing and strain capacities. Furthermore, we compare two methods of

measurements – conventional measurements using extensometers and Digital Image Correlation (DIC) method. PFJ allows repairing such structures as concrete floors [5].

## 2. Experimental program

### 2.1 Materials

**CONCRETE.** Specimens were made from normal-weight concrete based on Portland cement with  $w/c = 0.45$  and a maximal aggregate size of 16 mm. The compressive strength of concrete, calculated from results of compressive test (AV – average value, CV – coefficient of variation - CV), is  $AV = 68.9$  MPa ( $CV = 5.2\%$ ; according to EN 12390-3) and tensile strength obtained from uniaxial tensile test described in [6] is  $AV = 3.76$  MPa ( $CV = 8.0\%$ ).

**POLYMER.** A two-component PT-type polyurethane polymer was used in the research programme. This polymer has elastic properties. According to EN ISO 527-1, tensile strength of the polymer was equal to  $AV = 18.8$  MPa ( $CV = 7.2\%$ ) [7]. Here only short-term investigation was conducted, nevertheless it should be noted that rheology of the polymer might influence the results. If the tests are performed under long-term or sustained loading, the deflections tend to increase [1].

### 2.2 Methods

The experimental program contains 63 four-point bending (4PB) tests, here only one series (3 specimens: S01 to S03) is presented.

Prismatic concrete beams with cross-section of 100 x 100 mm and total length of 400 mm were used in 4PB. Each specimen was cut with a 30 mm deep notch in the middle of its bottom surface. The plain concrete elements, before repair, were called “original specimens” and tested in flexure. After failure the specimens were repaired with PT-type polymer with joint thickness 10 mm. Such bonded elements were called “repaired specimens”. The repaired elements were tested in flexure about 16-20 hours after polymer application as after this time the full stiffness and strength of the polymer are achieved. All bonded concrete surfaces were cleaned and covered with a primer layer.

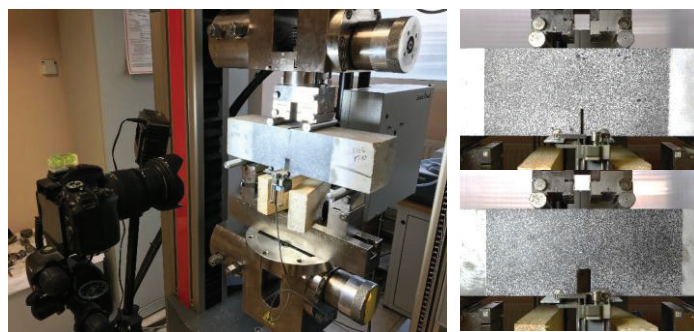


Figure 1: Test setup for four-point bending test (left) with DIC field of original (top right) and repaired specimen (bottom right).

Four-point bending tests were conducted using Zwick/Roell Z100 testing machine. The following test parameters were applied: initial force of 800 N, displacement rate of 0.10 mm/min, span length of 300 mm, distance between loading forces of 100 mm and temperature of 20°C (laboratory conditions). To measure selected values in 4PB tests, three

methods were used: (1) clip gauge with base of 50 mm (extensometer for the crack mouth opening displacement – CMOD), (2) extensometer for vertical displacement of the bottom surface, (3) DIC for measuring the strain field on side surfaces of the specimens (Fig. 1).

### 2.3 Digital Image Correlation

Optical measurements during the described test have been carried out using CivEng Vision system developed by Tekieli at Cracow University of Technology [3, 4]. System is based on DIC method with subpixel measurement resolution. The main procedure of the iterated measurements is based on the correlation of the digital images obtained during the test. Non-contact measurements during the tests have been conducted using digital single lens cameras equipped with 24 Mpx matrices and low-distortion zoom lenses. Barrel and tangential distortion have been corrected using calibration patterns.

## 3. Experimental results

### 3.1 Load response

The load response in 4PB tests using two methods (extensometer and DIC with the same base distance of 50 mm) is presented in Figure 2. Based on the load – CMOD curves, it can be observed that pre-critical phase (before cracking) for both types of specimens, i.e. original and repaired, is typically linear. After achieving  $F_{max}$ , a post-critical phase with softening was observed. Stiffness of the original specimens is higher in the linear-elastic phase than of the repaired ones, hence the CMOD values for the repaired specimens were higher than for plain concrete. The original elements showed usually higher load-bearing capacity ( $F_{max}$ ) than the repaired specimens in presented series (specimens S01 to S03). It was noticed that extensometer and DIC have a good compliance for deflection and CMOD results.

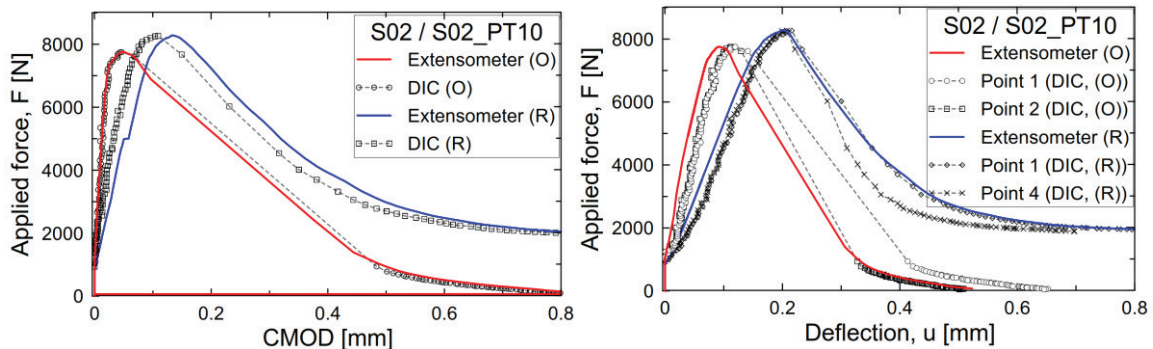


Figure 2: Load response of the notched beam in 4PB for specimen S02: applied load – CMOD (left) and load – deflection (right); (O) – original and (R) – repaired specimens.

### 3.2 Failure mode

Similar failure mode was observed for all specimens. A main crack ran through cement matrix and aggregates, from the notch up to top surface (Fig. 3). The main crack in the repaired elements ran also through concrete, at 1-3 mm distance from the crack of original specimen. It is considered to appear in the weak zone caused by previous crack.

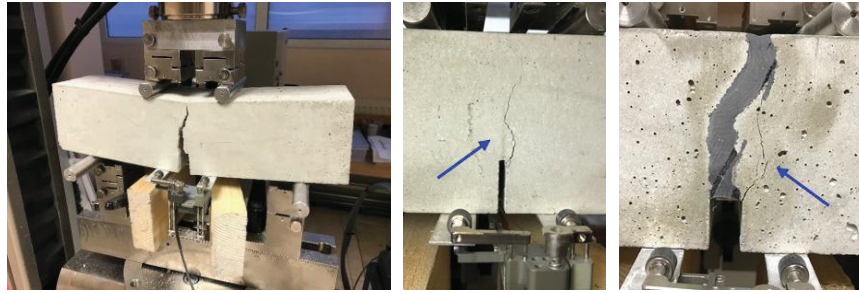


Figure 3: Failure of an original specimen (left), main crack in an original (middle) and a repaired specimen (right).

### 3.3 Results obtained from Digital Image Correlation

DIC allows to record the sequence of initial micro-cracks, before the peak load is achieved. Figure 4 shows the crack development, the colour-scale designates the horizontal strains. This method can present the whole cracking process in concrete. In original specimen (Fig. 4, top row) initial cracks occurred on the left side of the notch. These cracks developed up to the moment, when some of them linked into one main crack just before failure, and the rest were closed. The main crack selected the easiest path (the lowest energy requirements) through the micro-cracks in the cross-section and no more cracks were observed in DIC, because of micro-cracks closing in the damage area. Contrary to original elements, the failure mechanism of repaired specimens was slightly different (Fig. 4, bottom row). Due to previously damaged cross-section, the initial crack(s) occurred much earlier (at 32% of  $F_{max}$ ) in the same location.

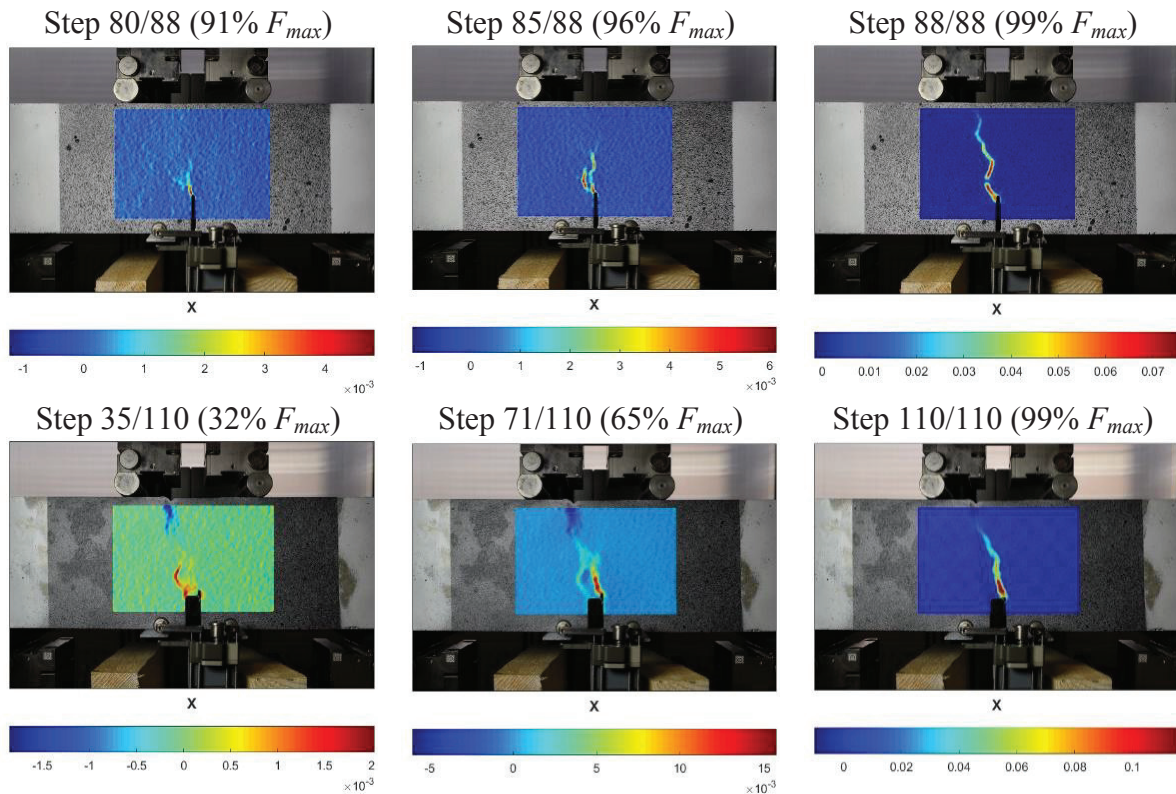


Figure 4: Crack development under applied load for the original specimen S02 (top) and the repaired one S02\_PT10 with PT-type polymer joint of 10 mm (bottom).



However, the presence of PFJ after repair allowed protecting the weak, previously damaged zone (surrounding the main crack) by reduction of stress concentrations (responsible for micro-cracks formation) and redistribution of them to larger area. This phenomenon is what is called stress redistribution. As the consequence, the micro-cracks in the weak zone were closed (mechanical healing of the concrete) and a new crack developed on the other side of the notch (at 65% of  $F_{max}$ ), where micro-cracks required the lowest energy for the main crack formation. From that moment, the previous cracks stopped developing and the new one on the right side caused failure. It was noticed that maximum strain values (DIC measure) of the repaired specimens were 1.5 to 3.0 times higher than of the original ones. Similarly, increase of maximum load and CMOD was observed for this specimen (Figure 2).

### 3.4 Results comparison

Table 1 presents the results obtained from 4PB tests for the specimens S01, S02 and S03. The average values of maximal load are 8.63 kN for original and 7.52 kN for repaired elements, and the average value of CMOD at failure is equal to 0.0477 mm and 0.1327 mm, respectively. Figure 5 presents a comparison of all tested original and repaired elements. The repair effectiveness is measured by ratios of load-bearing capacity and strain capacity of specimens after and before repair. The load capacity ratio was between 71-107% (AV = 87%). Anyway, in the post-critical phase (after  $F_{max}$ ) the load-bearing capacity of the repaired elements was significantly higher than of the original ones (Fig. 2). Regarding the deformability, the strain capacity ratio achieved value of 2.78.

Table 1: The results of four-point bending tests.

Specimen	$F_{max}$ [kN]		CMOD [mm]	
	Original specimen	Repaired specimen	Original specimen	Repaired specimen
S01 / S01_PT10	8.47	7.45	0.0481	0.1337
S02 / S02_PT10	7.76	8.28	0.0482	0.1328
S03 / S03_PT10	9.66	6.81	0.0469	0.1316
<b>AV (CV) of S01 – S03</b>	<b>8.63 (11.1%)</b>	<b>7.52 (9.8%)</b>	<b>0.0477 (1.5%)</b>	<b>0.1327 (0.8%)</b>

where: AV – average value, CV – coefficient of variation

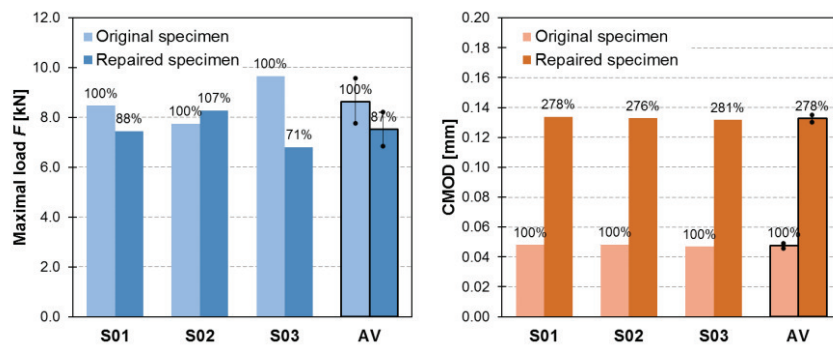


Figure 5: Comparison of the original and repaired specimens in terms of maximal load (left) and CMOD values (right).

#### 4. Summary and Conclusions

This paper presented the experimental results of four-point bending tests of original and repaired specimens. The possibility of using DIC system CivEng Vision was proven. On the basis of presented results, the following conclusions can be drawn:

- Load-bearing capacity of original specimens (100%) was usually higher than the repaired ones (87%); contrary, in post-critical phase the load-bearing capacity of repaired elements was higher than original ones,
- Deformation capacity of the repaired specimens was significantly higher than of the original ones,
- Contrary to the original specimen, the repaired specimen showed that the weak zone around the first main crack does not determine the path of failure (micro-cracks were mechanically healed), it is possible to rearrange failure path under applied load,
- Comparison of traditional equipment (extensometer) and the DIC method shows a good compliance of results of deformation and CMOD; when using DIC method it is possible to register original phenomenon which cannot be observed using ordinary methods,
- It is needed to conduct more research with various parameters and specimens' geometry to confirm the stress redistribution phenomena. Further, the behaviour of polymer at elevated temperatures needs to be investigated. Moreover, it is desirable later to adjust the geometry to real field application setups to confirm the practical application of PFJ method.

#### References

- [1] Kwiecień, A., Polymer Flexible Joints in Masonry and Concrete Structure, Monograph 414, Series: Civil Engineering. Wyd. PK, Cracow, Poland (2012), (in Polish)
- [2] Pröbster, M., Baudichtstoffe. Erfolgreich Fugen abdichten, Springer, Wiesbaden (2016)
- [3] Tekieli, M. et al., Application of Digital Image Correlation to composite reinforcements testing, *Compos. Struct.* 160 (2017), 670–688
- [4] Tekieli, M. and Słoński, M., Particle filtering for computer vision-based identification of frame model parameters. *Comput. Assist. Methods Eng. Sci.* (2014), 39–48
- [5] Zdanowicz, Ł. Et al, Stress redistribution in concrete floor on ground due to application of polymer flexible joint to fill expansion joint, *Procedia Eng.* 108 (2015), 467-474
- [6] Zdanowicz, Ł. et al, Interaction of polymer flexible joint with brittle materials in four-point bending tests, *Procedia Eng.* 193 (2017), 517-524
- [7] Zdanowicz Ł. et al, Interaction of Polymer Flexible Joint with Concrete Elements in an Uniaxial Tensile Test, *High TechConcrete: Where Technology and Engineering Meet*, Editors: D.A Hordijk, M. Lucović – Proc. fib Symposium, Maastricht (2017) 1049-1057
- [8] Zilch, K. et al, Experimental investigation of reinforced glued joints, Proc. Hipermat, Kassel University Press (2012)

## **SURFACE TREATMENTS AS REPAIR METHODS FOR PROTECTING REBARS FROM CORROSION**

**Mercedes Sánchez**<sup>(1),(2)</sup>, **Fabiano Tavares**<sup>(2)</sup>

(1) Institute of Construction Sciences “Eduardo Torroja”, Madrid, Spain

(2) University of Córdoba, Córdoba, Spain

### **Abstract**

In the present work two different solutions based on the application of electrochemical removal chloride treatments for the decontamination of the concrete cover are proposed for improving the treatment effectiveness. After a first stage of the electrochemical extraction of the chloride from the concrete cover until non-active corrosion current values are measured, two different methods are proposed:

1. Application of colloidal nanosilica treatment for sealing the concrete cover avoiding further chloride penetration.
2. Application of silane-based inhibitor for avoiding a further corrosion of the rebars.

The application of both types of treatments promote a significant increase in the resistivity of the treated concrete cover, while similar values of corrosion current density are registered, confirming that no further action of chloride is occurring within the treated samples. The visual analysis of the rebars showed the presence of a more extended corrosion damage on the non-treated samples, and almost no-presence of corrosion in the case of the electrochemical treatment with a further stage of sealing by colloidal nanosilica.

### **1. Introduction**

The electrochemical removal of chlorides has been reported as alternative for repairing reinforced concrete affected by corrosion. It is a highly interesting solution as the removal of the aggressive agent is proposed instead of the removal of the local area affected by the corrosion damage [1]. The application of protective solutions is also interesting for improving the service life of the reinforce concrete, using corrosion inhibitors for protecting the rebar against the action of corrosive agents such as chloride [2], or applying surface methods for sealing the concrete cover for avoiding the penetration of aggressive agents such as chloride.

During the last years the development of innovative corrosion inhibitors which are able to migrate to the rebar surface protecting appear as an alternative for protecting reinforced concrete [3], even considering the simultaneous application of the inhibitor during the electrochemical removal chloride treatment [4]. The penetration of nanoparticles by electrokinetic treatments has been also proposed as an efficient method for improving the durability of reinforced concrete [5-6].

Although different studies have been reported concerning the improvement of performance in reinforced concrete after these types of treatments, no studies have been found about the behaviour of the repaired concrete exposed to a further penetration of the aggressive agent. Thus, in the present work, a comparative study on the real effectiveness of repair treatments based on the electrochemical chloride removal and a further protective surface treatment has been carried out by assessing the electrochemical behaviour of the repair specimens against the action of chloride.

## 2. Experimental procedure

### 2.1 Materials

Prismatic concrete samples with a steel rebar (10 mm in diameter) in the centre were fabricated for the study, as shown in figure 1-left. Lime sand (0-4 mm) and aggregates (4-12 mm) were used to produce a low-quality concrete, with water/cement ratio 0.81 and 250 kg/m<sup>3</sup> of CEM I 42.5 R. The samples were cured for 28 days in controlled conditions of temperature (21°C) and relative humidity (95%) before testing. After curing, the prismatic samples were cut to decrease the concrete cover in the treatment side, as schemed in figure 1-right.

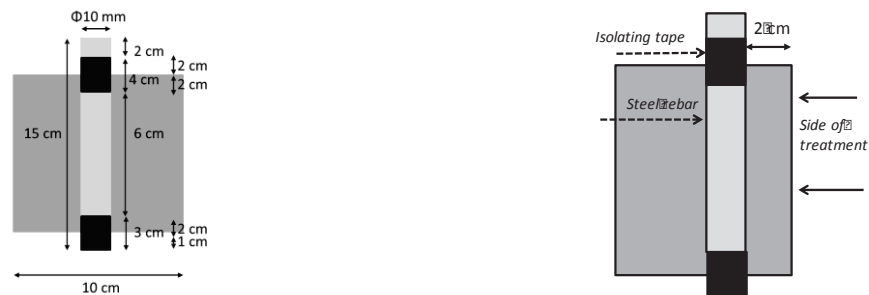


Figure 1: Left – Concrete sample dimensions after casting. Right – Concrete samples prepared for testing.

### 2.2 Corrosion initiation procedure

In order to promote an accelerated corrosion initiation, the reinforced samples, with an age of 30 days, were submitted to a pre-drying period in oven at 50°C until a constant weight was registered. Then, the dried samples were immersed in a 0.5 M NaCl solution to favour the entrance of chloride to the rebar level. The end parts of the rebar were isolated (Figure 1) for avoiding the exposure to chloride. During this immersion period, the corrosion potential ( $E_{\text{corr}}$ ) and the corrosion current density ( $i_{\text{corr}}$ ) were periodically measured to detect the corrosion initiation by a sharp drop of  $E_{\text{corr}}$  and/or a sharp increase of  $i_{\text{corr}}$ .

The part of the specimens without rebar obtained after the cut procedure were also immersed in the chloride solution and were used for analysing the chloride concentration at the same depth at the same time than the corrosion initiation in the reinforced samples was detected.

### 2.3 Electrochemical chloride removal treatment

Once the corrosion of the rebar was detected, an electric field was connected between the rebar and an external anode located on the concrete surface and consisting in a stainless steel mesh to promote the migration of the chloride ions from the concrete bulk to the surface. For the decontamination procedure the rebar was connected as cathode and a constant current of  $0.1 \mu\text{A}/\text{cm}^2$  was applied [7].

The corrosion current density was obtained at the end of each cycle of 5 days of electric field connection and 2 days with the electric field stopped for rebar depolarization. The polarization resistance technique [8] was used for obtaining the  $i_{\text{corr}}$  values by the Stern and Geary equation:  $I_{\text{corr}} = B/R_p \cdot A$ , where B is a constant,  $R_p$  is the polarization resistance and A is the exposed area. A compact potentiostat/galvanostat PGSTAT204 was used for the linear polarization measurements. Attending to the literature [8], a B value of 26 mV has been used for  $I_{\text{corr}}$  estimation. The cycles were repeated until corrosion current density values ( $i_{\text{corr}}$ ) below  $0.2 \mu\text{A}/\text{cm}^2$  were registered, associated to a low level of corrosion according to [9].

### 2.4 Protection methods after the chloride removal was finished

A second stage for the protection of the decontaminated samples was considered. Two different situations were studied:

- a) Application of colloidal nanosilica treatment for sealing the concrete cover avoiding further chloride penetration (P3).
- b) Application of silane-based inhibitor for avoiding a further corrosion of the rebars (P2).

After the surface treatment with the nanosilica or with the corrosion inhibitor, applied by fixing a ponding with the solution on the surface of treatment, a period of 7 days for curing in high humidity conditions was carried out to consolidate the formation of the silica layer. Before exposing the sealed samples to a further chloride penetration, the corrosion current density was measured to confirm that the rebars were not suffering from corrosion anymore. A reference case without further treatment (P1) was also tested as control situation.

### 2.5 Effectiveness of the treatments

At the end of the treatment, the reinforced samples were broken for confirming the treatment effectiveness through the visual inspection of the rebar with an optical microscope.

## 3. Results and discussion

### 3.1 Corrosion initiation

The evolution of the  $E_{\text{corr}}$  and  $i_{\text{corr}}$  values during the exposure of the reinforced concrete specimens to the chloride penetration is shown in figure 2. The electrochemical data registered the corrosion initiation after the 3<sup>rd</sup> day of exposure in two of the samples (P1 and P2) and after the 9<sup>th</sup> day of exposure in the other (P3).

The corrosion initiation is associated to a sharp drop of the  $E_{\text{corr}}$  (figure 1-left) reaching values below -400 mV vs SCE, and to a sharp increase of  $i_{\text{corr}}$  (figure 1-right), with values up to 0.5

$\mu\text{A}/\text{cm}^{-2}$ , reaching even  $1.5 \mu\text{A}/\text{cm}^{-2}$ , which are associated to a high loss of material due to the corrosion process.

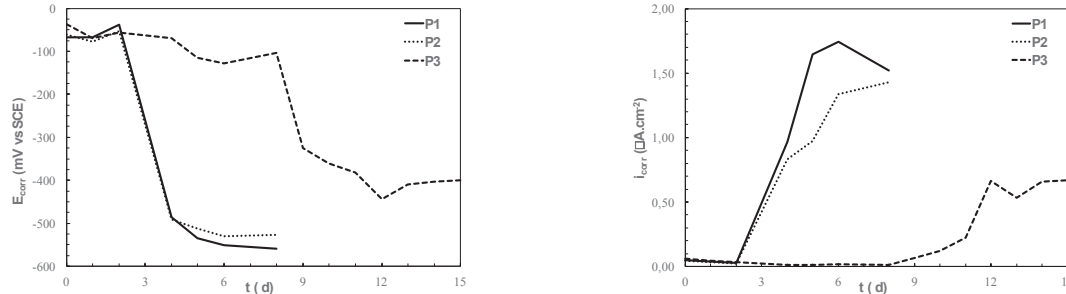


Figure 2: Evolution of  $E_{\text{corr}}$  (Left) and  $i_{\text{corr}}$  (Right) values during the chloride penetration for initiating the rebar corrosion.

The analysis of the total chloride content was made in the specimens without rebars but exposed to the same conditions following RILEM recommendations [10]. Three power samples were obtained in each specimen; the average value measured was  $1.32 \pm 0.20$  % total chloride per cement weight.

### 3.2 Electrochemical chloride removal treatment

During the electrochemical chloride removal treatment, the  $E_{\text{corr}}$  and the  $i_{\text{corr}}$  values were measured during the periods of disconnection of the electric field, as has been summarized in the experimental section of the present work. In Figure 3 the evolution of both parameters is shown for the three specimens treated. It can be observed from the figure that both parameters are indicating values of negligible corrosion at the end of the test, after 150 days of treatment.  $E_{\text{corr}}$  (figure 3-left) around -100 mV vs SCE, and  $i_{\text{corr}}$  (figure 3-right) below  $0.2 \mu\text{A}/\text{cm}^2$ .

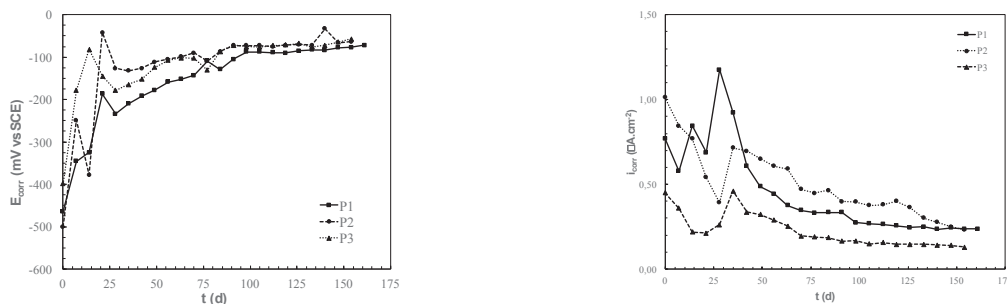


Figure 3: Evolution of  $E_{\text{corr}}$  (Left) and  $i_{\text{corr}}$  (Right) values during the electrochemical chloride removal treatment.

### 3.3 External surface treatment for improving the effectiveness of the repair

After finishing the treatment for the electrochemical removal of the chloride, a further treatment based on applying colloidal nanosilica (P3) or a corrosion inhibitor (P2) on the concrete surface was carried out. After a 7-days curing period in high humidity conditions, the treated samples were exposed to the penetration of chloride. A sample without further surface treatment has been used as control (P1). The evolution of the electrochemical parameters

appears represented in figure 4,  $E_{\text{corr}}$  (left) and  $i_{\text{corr}}$  (right). A quick depassivation of the non-treated sample (P1) is observed, as expected due to the chloride penetration.

In the case of the specimen after the treatment with the corrosion inhibitor, a slight decrease of  $E_{\text{corr}}$  and a slight increase of  $i_{\text{corr}}$  are detected during the exposure to chloride, while in the case of the treatment with colloidal nanosilica no change associated to the presence of chloride can be observed.

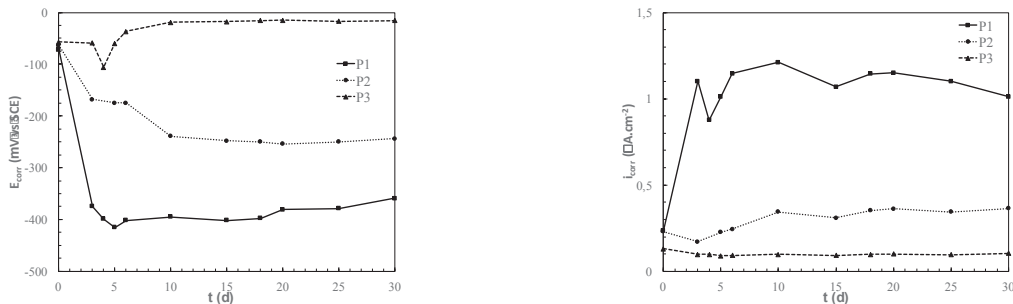


Figure 4: Evolution of  $E_{\text{corr}}$  (Left) and  $i_{\text{corr}}$  (Right) values of the treated samples exposed to chloride penetration.

As no sealing effect is expected by the corrosion inhibitor, the chloride in this case should be able to penetrate to the rebar where the competition with the inhibitor avoids the development of a fast corrosion process like in the case of the non-treated rebar. The sealing effect of the treatment with colloidal nanosilica avoids the chloride penetration through the concrete cover, and thus the  $i_{\text{corr}}$  values are not affected as the chloride is not present at the rebar level.  $E_{\text{corr}}$  values increase probably due to the extra ohmic drop associated to the presence of the sealing layer of silica.

### 3.4 Treatment effectiveness assessment

At the end of the test, the samples were broken for the visual observation of the rebar with the optical microscope. In figure 5 the surface of the non-treated rebar (figure 5-left) with an extended presence of corrosion products can be observed. The rebar treated with the corrosion inhibitor (P2) can be observed in figure 5-right. The presence of local spots of corrosion products was observed along the lateral area of the exposed rebar. No corrosion products were observed in the rebar after the treatment with colloidal nanosilica.



Figure 5: Images from the optical microscope of corrosion points at the end of the test. Left: sample without surface treatment after. Right: sample treated with the corrosion inhibitor.

#### 4. Conclusions

From the present study it can be concluded that the application of an electric field for the electrochemical removal of chloride allows repassivating the corroding rebars. However, the decontaminated specimens are susceptible of further penetration of chloride promoting fast processes of corrosion. It has been confirmed that a further treatment on the concrete cover surface is interesting in order to improve the protection of the rebar against chloride action. The most effective has shown to be the sealing of the surface with colloidal nanosilica, although the application of a corrosion inhibition on the concrete surface also improve the performance of the treated specimen against the corrosion due to the presence of chloride.

#### Acknowledgements

Authors acknowledge the financial support from COST Association (CA15202) and from the Spanish Ministry MEIC (BIA2014-56825 JIN and RYC-2016-21422).

#### References

- [1] Bertolini, L. et al, Electrochemical methods, Corrosion of Steel in Concrete: Prevention, Diagnosis, Repair, Wiley-VCH Verlag GmbH&Co, Weinheim (2004), 345-380.
- [2] Bertolini, L. et al, Corrosion Inhibitors, Corrosion of Steel in Concrete: Prevention, Diagnosis, Repair, Wiley-VCH Verlag GmbH&Co, Weinheim (2004), 217-230.
- [3] Zheng, H., Li, W., Ma, F. and Kong, Q., The effect of a surface-applied corrosion inhibitor on the durability of concrete, *Constr. Build. Mater.* 37 (2012) 36-40.
- [4] Sánchez, M. and Alonso, M.C., Electrochemical chloride removal in reinforced concrete structures: Improvement of effectiveness by simultaneous migration of calcium nitrite, *Constr. Build. Mater.* 25 (2011) 873-878.
- [5] Kupwade-Patil, K., Cárdenas, H.E., Gordon, K. and Lee, L.S., Corrosion mitigation in reinforced concrete beams via nanoparticle treatment, *ACI Mater. J.* 109 (2012) 617-626.
- [6] Sánchez, M., Alonso, M.C. and González, R., Preliminary attempt of hardened mortar sealing by colloidal nanosilica migration, *Constr. Build. Mater.* 66 (2014) 306-312.
- [7] Technical Specification CEN/TS 14038-2:2011. Electrochemical realkalization and chloride extraction treatments for reinforced concrete. Part 2: Chloride extraction (2011).
- [8] Andrade, C. and Alonso, C., Corrosion rate monitoring in the laboratory and on-site, *Construction and Building Materials* 10 (1996) 315-328.
- [9] COST 521. Corrosion of steel in reinforced concrete structures, final report. Cigna R., Andrade C., Nürnberger U., Polder R., Weydert R. and Seitz E., editors. European Communities. Luxembourg Publication (EUR) (2003) p. 20556.
- [10] Andrade, C. and Castellote, M., Recommendation of RILEM TC 178-TMC: "Testing and modelling chloride penetration in concrete: analysis of total chloride content in concrete", *Materials and Structures* 35(2002) 583-585.



## **THE EFFECTS OF CONTINUED HYDRATION OF UNDAMAGED MATERIAL ON APPARENT HEALING INDICES IN CEMENTITIOUS MATERIALS**

**Robert Davies**<sup>(1)</sup>, **Cristina De Nardi**<sup>(2)</sup>, **Anthony Jefferson**<sup>(1)</sup>

(1) Cardiff University, Cardiff, United Kingdom

(2) University IUAV of Venice, Venezia, Italy,

### **Abstract**

This paper addresses the effects of continuing hydration in undamaged material on reported healing for cementitious materials. Numerical simulations show how the increase of strength in self-healing test specimens can be due to a combination of ageing material properties and healing. A numerical model framework combines a hydration model, used to predict material property changes, and a damage mechanics approach, to simulate the cracking and then healing. An experimental study using natural hydraulic lime base mortars is used to illustrate the simulation capability and to examine the contribution to strength increase after healing. The lime mortar cube specimens have a first damage range of between 14 and 84 days old and then are healed for two different periods, 14 and 28 days, in water. The insight gained from this one dataset, on the composition of the strength increase due to either continued hydration or healing, will be useful to other researchers investigating self-healing behaviour in cementitious materials.

### **1. Introduction**

Self-healing materials are being developed in many fields of material science as an alternative to the traditional damage prevention methods. A material is classed as self-healing when there is an inbuilt mechanism for recovering one or more of its initial properties following an occurrence of damage [1]. In general, the measurement of recovery involves a comparison between an initial and a post-healed material property. When the material properties of a material do not change over time, it is relatively straightforward to evaluate the degree of recovery of a material property from a self-healing experiment. However, evaluating the degree of recovery in materials, such as cementitious composites or lime mortar, with

changing properties over time is altogether more complex. The difficulty is further compounded by the fact that the degree of change in any one property varies considerably with the type of cementitious material, the degree of damage, the age of the material when damage occurs, the duration of the healing period and the environmental conditions during healing [2].

## 2. Essential components of the micro-mechanical model

A cementitious material with aggregate particles and cement paste is represented using a two phase composite with inclusions ( $\Omega$ ) and a matrix (M) phase. A detailed description of the basic micromechanical model can be found in [3] and [4]. The essential components of the micro-mechanical model are shown in the following constitutive equation (1):

$$\bar{\boldsymbol{\sigma}} = \mathbf{D}_{M\Omega} : (\bar{\boldsymbol{\varepsilon}} - \boldsymbol{\varepsilon}_a) \quad (1)$$

$\bar{\boldsymbol{\sigma}}$  is the average stress and  $\bar{\boldsymbol{\varepsilon}}$  is the total strain in the composite.  $\mathbf{D}_{M\Omega}$  is the composite elastic tensor whose properties are computed using the classical Eshelby solution and the Mori-Tanaka homogenization scheme for non-dilute inclusions.  $\boldsymbol{\varepsilon}_a$  is the total additional strain resulting from anisotropic micro-cracking using the approach of Budiansky and O'Connell. A local stress-strain relationship for the micromechanical model is defined in equation (2), in which the added strain is taken to be the equivalent of a micro-cracked band in the material.

$$\mathbf{s}_L = (1 - \omega) \mathbf{D}_L \boldsymbol{\varepsilon}_L \quad (2)$$

$\mathbf{s}_L$  is the equivalent local stress tensor and  $\boldsymbol{\varepsilon}_L$  is the equivalent local strain tensor, both of which are expressed in a reduced vector form that considers only those components that are non-zero.  $\mathbf{D}_L$  is a 3x3 matrix containing the non-zero components of the local stiffness tensor.  $\omega$  is the micro-crack variable for each direction, taking the values between 0 for uncracked and 1 for the fully micro-cracked state. The elastic local strain can be subtracted from the local strain within the micro-crack band ( $\boldsymbol{\varepsilon}_L$ ) to give the additional strain resulting from the crack in one direction.

This micromechanical model is taken forward to establish a framework for instructing healing, as described in [5]. This work shows that the local constitutive relationship presents itself as a convenient form for including healing. The healing allows the stiffness of a proportion of the damaged component of material to be recovered. An offset or 'solidification' strain is included to ensure that the healing material solidifies in a stress-free state. The healed local stress is given in equation (3).

$$\mathbf{s}_{Lh} = (1 - \omega) \mathbf{D}_L \boldsymbol{\varepsilon}_{Lh} + (1 - \omega_h) h \omega_h \mathbf{D}_{Lh} (\boldsymbol{\varepsilon}_{Lh} - \boldsymbol{\varepsilon}_s) \quad (3)$$

The healing proportion is defined by the parameter  $h$ , which takes the values between 0 for no healing and 1 for fully healed. A subscript  $h$  is added to the terms to show the healing equivalent terms.  $\mathbf{s}_{Lh}$  is the equivalent local stress tensor after healing,  $\boldsymbol{\varepsilon}_{Lh}$  is the local

equivalent strain tensor after healing and  $\omega_h$  is the micro-cracking parameter at the time of healing.  $\mathbf{D}_{Lh}$  is the local stiffness of the healed material and  $\varepsilon_s$  is the ‘solidification’ strain. Since this newly healed material can also undergo micro-cracking, a term is also included to simulate this further micro-cracking, where  $\omega_h$  is the healed micro-cracking variable. The degree of micro-cracking is controlled by an effective strain parameter according to the following standard exponential relationship (4);

$$\omega = 1 - \frac{\varepsilon_t}{\zeta} e^{-c \left( \frac{\zeta - \varepsilon_t}{\varepsilon_0 - \varepsilon_t} \right)} \quad (4)$$

in which  $\zeta$  is the effective strain parameter,  $c$  is a constant equal to 5,  $\varepsilon_t = f_t/E$ , where  $f_t$  is the uniaxial tensile strength.  $\varepsilon_0$  is the strain at the effective end of the uniaxial softening curve.

A new thermodynamically consistent component is added to this model, which allows for the change in an effective strain parameter over a curing period in an undamaged component of material that undergoes no healing. This means that the effect of hydration on the undamaged ligament of the material can be evaluated and therefore the actual degree of healing can be evaluated. In this work the material is simulated using a model which shows the relative effect of strength recovery for different levels of initial damage and different healing periods.

### 3. Self-healing experiments on lime based mortar

Natural hydraulic lime-based mortars exhibit promising autogenous self-healing capabilities. The effect of age and damage level on the recovery performance of compression strength and ultrasonic pulse velocity in cube samples of natural hydraulic lime mortars have been investigated [6]. Specimens in this study were pre-cracked (loaded) at ages ranging between 14 and 84 days old and then cured in water, to promote healing, for two periods of 14 and 28 days. These experimental results are used to illustrate the simulation capability of the micromechanical model and to provide an insight into the composition of the continued hydration and autogenous healing.

### 4. Results

A parametric study was carried out on the lime mortar cube specimens [6]. The micromechanical model was calibrated using a limited number of mechanical parameters. An example is shown in Fig. 1, where the stress against strain response is plotted comparing the experimental data and the resulting output from the micromechanical model. This process was repeated for whole data set and it was found to have excellent correlation. The mechanical properties derived at different material ages were used to evaluate the change in the effective strain parameters. This meant that the undamaged component of the lime mortar can be evaluated over time.

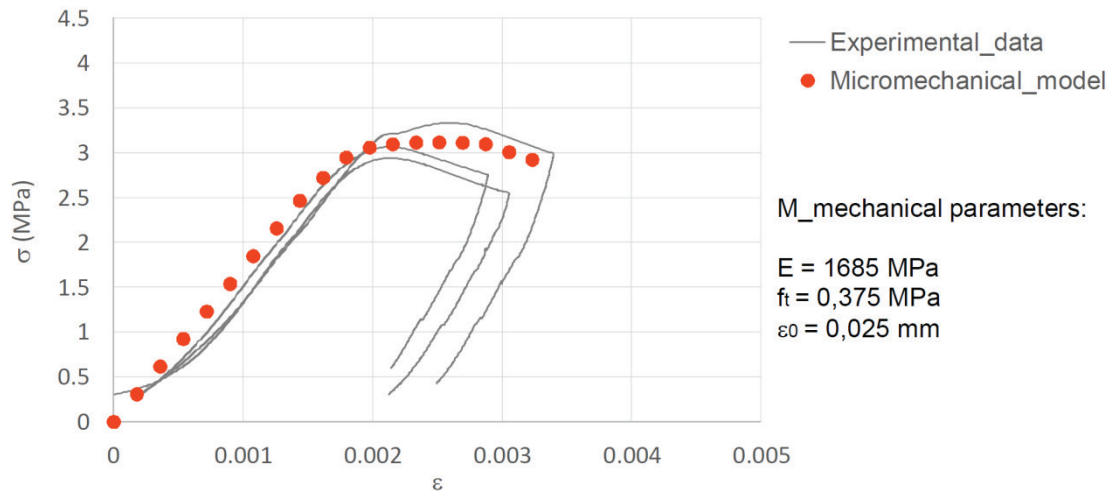


Figure 1: Comparison between experimental data and micromechanical model alongside the key mechanical properties chosen

The behaviours of the compressive strength (derived from the experimental data) and the tensile strength (derived from micromechanical model parameters) were evaluated. However, only the results of the compressive strength analysis is shown in Fig 2 below.

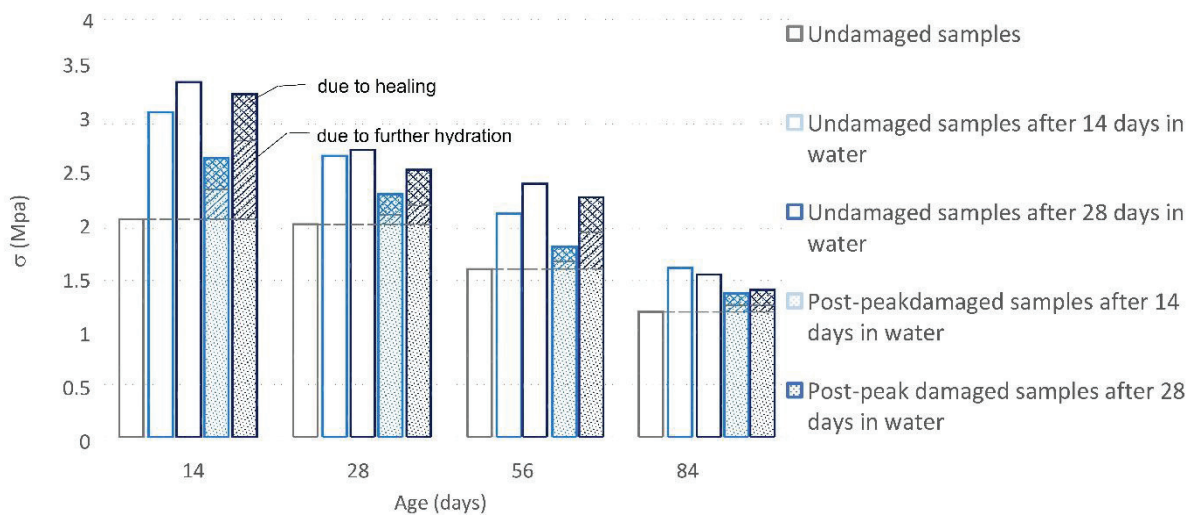


Figure 2: Variation in compressive strength after 14-28 days in water immersion, derived from experimental data, with contribution of strength increase attributed to further hydration and healing

In Fig. 2 the undamaged sample strength, at first test, is shown for an increasing age of sample. As the age of first test increases there is a decrease in strength, which is due ambient curing conditions of lime mortar. After placing undamaged samples in water for 14 and 28 days there is significant increase in strength. Specimen that were damaged into the post peak regime also exhibit an increase in strength after curing in water. The composition of this strength increase is estimated using the micromechanical model and the figure shows the contribution due to continued hydration and autogenous healing. Interestingly, it was found that the older the specimen on first damage the lower the contribution of strength recovery

due to the ageing of undamaged material. This means that healing is contributing more to the strength increase, than continued hydration, for older lime mortar specimens. This work shows that the micro-mechanical self-healing model can represent the characteristic mechanical response of self-healing cementitious materials and provide an insight into the composition of the strength increase.

## 5. Conclusion

A two-phase composite micro-mechanical constitutive model, that includes anisotropic micro-cracking, provides an excellent basis for the development of a model for cementitious materials, such as hydraulic lime-based mortars, that exhibit self-healing behaviour. The relative simplicity of this micromechanical healing model, combined with the fact that it requires a small number of physically meaningful parameters, shows that it can manage the complex time dependant processes. Numerical simulations have shown how the increase of strength in the self-healing test specimens can be due to a combination of ageing material properties and healing. This study showed that the older the specimen on first damage the higher the contribution of strength recovery is due to healing rather than the ageing of undamaged material.

## Acknowledgements

Thanks must go to the EPSRC for their funding of the Materials for Life (M4L) project (EP/K026631/1) and the follow on programme grant Resilient Materials for Life (EP/P02081X/1) <http://www.RM4L.com>. This conference contribution was supported by a STSM Grant from the COST Action CA15202. <http://www.sarcos.enq.cam.ac.uk>

## References

- [1] S. van der Zwaag, *Self Healing Materials - An Alternative Approach to 20 Centuries of Materials* | Springer. 2007.
- [2] K. Van Tittelboom and N. De Belie, 'Self-Healing in Cementitious Materials—A Review', *Materials*, vol. 6, no. 6, pp. 2182–2217, May 2013.
- [3] I. C. Mihai and A. D. Jefferson, 'A material model for cementitious composite materials with an exterior point Eshelby microcrack initiation criterion', *Int. J. Solids Struct.*, vol. 48, no. 24, pp. 3312–3325, Dec. 2011.
- [4] R. Davies and A. Jefferson, 'The simulation of inelastic matrix strains in cementitious materials using micromechanical solutions', *Eng. Fract. Mech.*, 2014.
- [5] Davies, R., Jefferson, A., 2017. Micromechanical modelling of self-healing cementitious materials. *International Journal of Solids and Structures* 113–114, 180–191. <https://doi.org/10.1016/j.ijsolstr.2017.02.008>
- [6] De Nardi, C., Cecchi, A., Ferrara, L., Benedetti, A., Cristofori, D., 2017. Effect of age and level of damage on the autogenous healing of lime mortars. *Composites Part B: Engineering* 124, 144–157. <https://doi.org/10.1016/j.compositesb.2017.05.041>

## THE ROLE OF NANO-PARTICLES IN SELF-HEALING PROCESS OF CEMENTITIOUS MATERIALS

Maria Stefanidou <sup>(1)</sup>, Eirini-Chrysanthi Tsardaka <sup>(1)</sup>, Evangelia Tsampali <sup>(1)</sup>

(1) Laboratory of Building Materials, School of Civil Engineering, Aristotle University of Thessaloniki, Greece

### Abstract

The importance of producing materials that can heal their flaws is easily understood as the performance of those materials is high in terms of durable structures with low maintenance cost. The construction section, the last decades, is characterized by efforts to produce high performance rather than high strength materials. To that direction, self-healed concrete has an important role.

On the other hand, the addition of nano-particles in cement-based materials has been proved beneficiary in terms of pozzolanic reaction and early strength gain. The possibility to explore the role of nano-particles to heal the cracks in cement pastes is presented in this article. For that purpose, nano-SiO<sub>2</sub> and nano-CaO were incorporated in cement pastes in different proportions. The produced pastes were tested in terms of mechanical, physical and microstructure properties. The formation of secondary crystals into the nano-modified structure resulted in: porosity refinement, strength increase and the most important, dense structure by the presence of fully compatible products that reinforce the material's structure.

### 1. Introduction

Despite its numerous advantages, cement is vulnerable to cracking, which limits both its potential uses as well as its structure service life [1]. In the case of concrete and other cementitious products, attention has been directed mainly at the development of composite materials capable of self-healing [2-7]. The advantages of using self-healing materials, on the one hand is the treatment of early-cracks, and on the other the reduction of penetration of harmful agents [5,6]. The research that has already been conducted on old-lime based mortars, which exhibit self-healing properties was very useful to understand the mechanism [8,9]. These studies have revealed that fine-grained lime has the inherent capacity to react with the

environment and produce secondary crystals deposited in empty spaces into the mortar's structure [10]. This results in a compact, continuous structure, which heals cracks and restricts the absorption capacity of damaging substances (i.e. moisture with diluted ions).

Drawing inspiration from this, different ways of healing approaches have been developed during the last decade focusing mainly on adding particles in the binding system generating autogenous healing [11-13]. The combination of this concept of autonomous self-healing and of nanotechnology, resulted in a new class of nano-modified cement, where nano-materials are selected as an alternative particle choice [14-16]. These efforts have produced mortars with upgraded properties such as increased durability and high mechanical stresses and improved performance at environmental conditions in which non-modified cement would degrade rapidly.

In this study, a self-healing system is proposed and evaluated. More specifically, the use of nano-SiO<sub>2</sub> and nano-CaO was investigated. Both of the two possible choices offer distinct advantages. Nano-silica particles contribute to an increased formation of calcium silicate (CSH) gel in cementitious systems due to the reaction of nano-silica with Ca(OH)<sub>2</sub> produced from the hydration of tricalcium silicate (C<sub>3</sub>S) [17,18].

## 2. Materials and methods

The Portland cement used for the needs of the experimental work was CEMII32.5N, classified by the EN 197-1. This is a blended pozzolanic cement with major constituents natural pozzolan, fly ash and limestone and it is commonly used in construction. Aerial lime CL90 (according to EN 459-1:2001) and the nanoparticles (commercially available by Sigma Aldrich) that were used are given in Table 1. The addition of superplasticizer (SP) was necessary in the nano-modified mixtures for keeping stable the consistency that was determined according to EN 196-3:2005. To evaluate the consistency, Vicat Needle tests (VNT) according to EN 196-3:2005 were conducted.

Pastes 2.5x2.5x5cm and 2.5x2.5x10cm were formed and cured in a humid environment (85-90% humidity and 20±2°C). Compressive strength and porosity were tested at 7 and 28 days of hydration, according to EN 1015-1 and RILEM CPC 11.3 under vacuum, respectively.

Capillary absorption coefficient tests were determined after 28 days of curing according to EN 1015-18:2002. The microstructure of the samples was characterized, using SEM (Jeol JSM-840A), 28 days. Simultaneous DTA-TG (Differential Thermal- Thermogravimetric Analysis), SDT 2960 TA Instruments, was used for the determination of calcium hydroxide (Ca(OH)<sub>2</sub>) and calcium carbonate (CaCO<sub>3</sub>), under N<sub>2</sub> atmosphere from 10<sup>0</sup> to 1000°C.

## 3. Results and Discussion

### 3.1 Physic-mechanical properties

Compressive strength of cement pastes is given in Fig. 1. The addition of NS is increasing compressive strength by 13.5% and 23.4% at 7 and 28 days respectively in R<sub>A</sub>. The NS doesn't improve the strength in the RL system as the hydration and the carbonation mechanism act in parallel. The addition on NCaO in R<sub>B</sub> is also assisting strength while the combination of nano-particles (R<sub>C</sub>) results in small strength reduction. The addition of NCaO does not significantly modify this property, either in R<sub>B</sub>, or in R<sub>C</sub> along with NS. The aerial

lime incorporation in cement affected the mechanical properties of the pastes, so as RL series have slightly reduced strength values in respect to the R series. Cement-lime systems present a similar behavior of the strength development in relation to the nanoparticle inclusion. The only differentiation relies on RL<sub>B</sub> strength increase at early age strength by 11.5% comparing to RL, which might be connected to the action mechanism of NCaO in the presence of lime.

Table 1: Content of cement based pastes.

	CEM II32,5N (g)	Aerial Lime (g)	H <sub>2</sub> O (mL)	Nano- Silica (NS) %	Nano- CaO (NCaO) %	SP %	Vicat (mm)
<b>R</b>	2000	-	650	-	-	-	6
<b>R<sub>A</sub></b>	2000	-	650	1.5	-	2	6
<b>R<sub>B</sub></b>	2000	-	650	-	1.5	2	0
<b>R<sub>C</sub></b>	2000	-	650	1	0.5	2	7
<b>RL</b>	1600	400	720	-	-	-	6
<b>RL<sub>A</sub></b>	1600	400	720	1.5	-	2	7
<b>RL<sub>B</sub></b>	1600	400	720	-	1.5	2	0
<b>RL<sub>C</sub></b>	1600	400	720	1	0.5	2	7

The comparison between the nano-modified systems and the reference samples at open porosity measurements are displayed in Fig. 2. At both, cement pastes and cement-lime pastes, the addition of NCaO influences impressively the open porosity. At early age, porosity reduction reaches 55% in R<sub>B</sub>. and 46% in RL<sub>B</sub>. NCaO contributes in porosity reduction and this advantage can be considered as a potential of healing factor. Also, it is worthy to annotate that the filling of porosity is not accompanied by simultaneous compressive strength increase. The latter is connected to the nature of crystals originated from NCaO, as at this early ages they are very small.

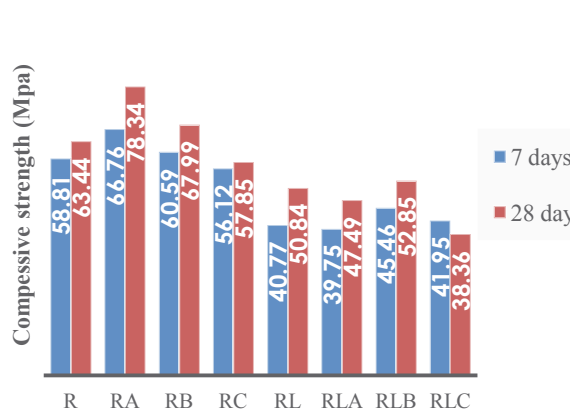


Figure 1: Compressive strength of cement pastes.

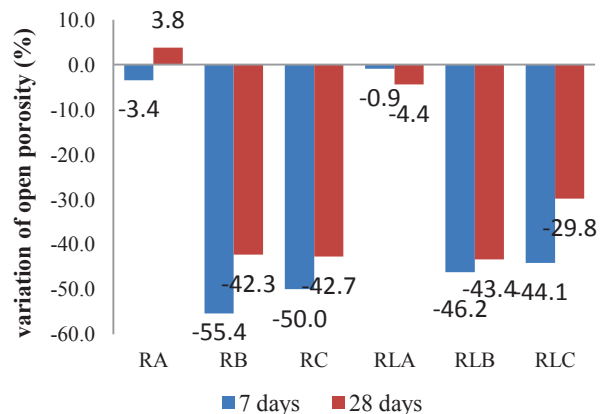


Figure 2: Variation of open porosity (%) of cement pastes, in respect to the reference paste.

Capillary water absorption is given in Fig. 3. The capillarity of nano-modified cement pastes was measured lesser than reference (R). In specific, sorptivity of R<sub>B</sub> is 40% smaller than R



and is in agreement to open porosity. The presence of lime in RL series affects capillary absorption but also the addition of NCaO favours capillarity of cement-lime pastes by reducing the water absorption capacity. The water absorption of RL<sub>A</sub>, RL<sub>B</sub> and RL<sub>C</sub> is alike and smaller than RL by approximately 25%.

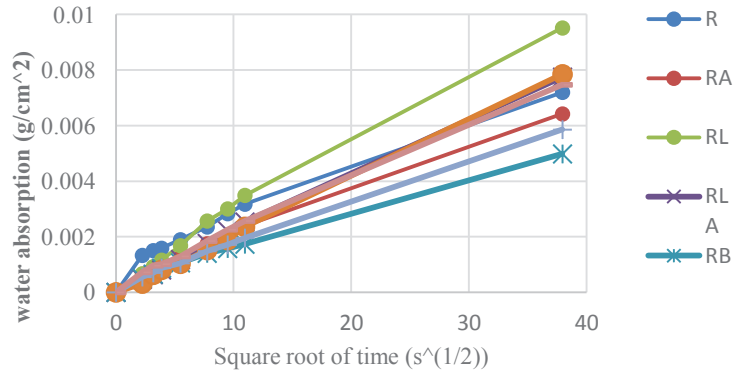


Figure 3: Capillarity of cement pastes at 28 days.

### 3.2. Differential Thermal and Thermogravimetric Analysis

DTA-TG analysis is used to quantify the portlandite and calcite content of the samples. As given in Fig. 4 and 5, the differentiation of each nano-modified sample from the reference displays the behavior due to NS and NCaO incorporation.

The addition of NS reduced the portlandite by 35% and 32% at 7 and 28 days, respectively. The action of NS initiated further consumption of portlandite in C-S-H compounds. On the other hand, the incorporation of NCaO, both in R<sub>B</sub> and R<sub>C</sub>, maintained portlandite quantity at early age. At 28 days, R<sub>B</sub> and R<sub>C</sub> present a smaller proportion of Ca(OH)<sub>2</sub>, probably due to calcite or C-S-H formations. In cement-lime pastes the addition of NCaO increases the portlandite content (RL<sub>B</sub>), as the hydration of nanoparticles contributes in Ca(OH)<sub>2</sub> content. On the contrary, NS conduces to the decrease of portlandite. Calcite content is approximately stable in R<sub>A</sub> samples, in comparison to R system at 7 and 28 days. The values of R<sub>B</sub> and R<sub>C</sub> though, indicate higher calcite precipitation from the early age. The acceleration of carbonation is related to NCaO presence. When NCaO particles carbonate, they turn to pure CaCO<sub>3</sub> and aid the precipitation of calcite. RL<sub>B</sub> and RL<sub>C</sub> calcite content at 7 days is higher than the reference and enforced by lime carbonation. RL<sub>A</sub> samples have the highest calcite content at 28 days.

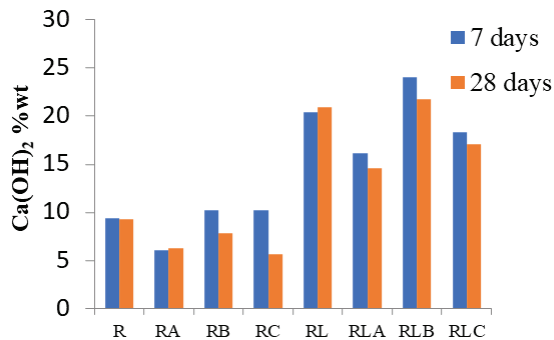


Figure 4: Portlandite content of samples as a percentage by mass, at 7 and 28 days.

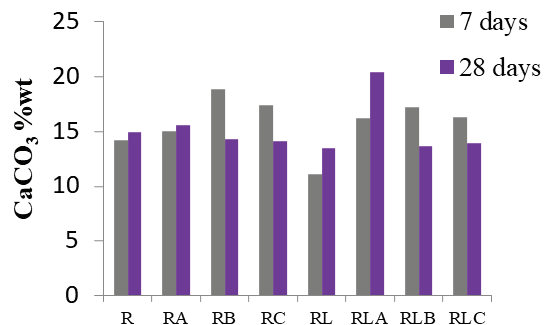


Figure 5: Calcite content of systems as a percentage by mass, at 7 and 28 days.

### 3.3. SEM observation

Observation of the microstructure by scanning electron microscope (SEM) verifies the efflorescing structure of pastes containing NCaO (Fig.6). The presence of nano-CaO was beneficiary in all cases studied as precipitation of small calcitic crystals was observed in openings in the structure, during the first 28 days of curing. Black arrows, in Fig. 6, highlight the flourished microstructure, calcite precipitation and healing “bridges” on cracks.

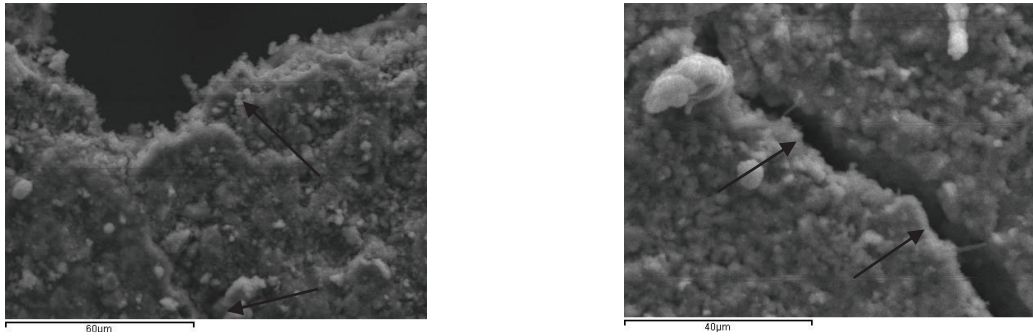


Figure 6: Microstructure of  $R_c$  (left) and  $RL_c$  (right), where development of secondary crystals filling small and bridging larger cracks have been observed, at 28 days.

## 4. Conclusions

Cement pastes with incorporated nanoparticles present dense structure and improved mechanical properties. A 13.5% and 23.45% increase in compressive strength was recorded at 7 and 28 days respectively when NS was added in cement pastes. In pastes where cement-lime was combined, NS had lower influence due to different mechanisms acting in parallel. NCaO on the other hand had a positive role in strength in both pastes as 7% and 4% in cement-lime pastes at 28 days was recorded. In  $R_B$  and  $RL_B$  pastes the porosity reduction was also impressive. The physical properties such as porosity and capillary absorption have been reduced. CaO nanoparticles not only benefit cement properties, but also the mechanism of their action favors calcite precipitation. Nano-CaO has a vital role in terms of healing through secondary calcite formation at very early ages, which even in low percentage (0.5%w/w of binder) is very active.

Lime-cement pastes with nanoparticles contain a considerable amount of available portlandite which at later ages can contribute to further calcite precipitation. Even at 28 days, healing crystals seem to be formed in wide cracks. Portlandite content increase and healing “bridges” on cracks enforce that claim.

Despite the encouraging results, the phenomena need to be further studied. The proportion of nanoparticles and the preferable curing environment are some of the issues that need further consideration.

## Acknowledgement

The authors would like to express their acknowledgments to the COST Action 15202 “Self-healing as preventive repair of concrete structure - SARCOS”

(<http://www.sarcos.eng.cam.ac.uk>) for the mobility support to present the research

## References

- [1] Ferrara L. et al, Experimental characterization of the self-healing capacity of cement based materials and its effects on the material performance: A state of the art report by COST Action SARCOS WG2, *Construction and Building Materials* 167 (2018), 115-142
- [2] Roig-Flores M. et al, Effect of crystalline admixtures on the self-healing capability of early-age concrete studied by means of permeability and crack closing tests, *Construction and Building Materials* 114 (2016), 447-457
- [3] Polat R. et al, Effects of nano and micro size of CaO and MgO, nano-clay and expanded perlite aggregate on the autogenous shrinkage of mortar, *Construction and Building Materials* 81 (2015), 268-275
- [4] Huang H. et al, Effect of blast furnace slag on self-healing of microcracks in cementitious materials, *Cement and Concrete Research* 60 (2014), 68-82
- [5] Min Wu et al, A review: Self-healing in cementitious materials and engineered cementitious composite as a self-healing material, *Construction and Building Materials* 28 no. 1 (2012), 571-583
- [6] Mihashi H. et al, Development of Engineered Self-Healing and Self-Repairing Concrete-State-of-the-Art Report, *Journal of Advanced Concrete Technology* 10 no. 5 (2012), 170-184
- [7] Perez Z. et al, Characterisation of cement pastes with innovative self-healing system based in epoxy-amine adhesive, *Cement & Concrete Composites* 60 (2015), 55-64
- [8] Papayianni I., Stefanidou M., Durability aspects of Ancient Mortars of the archeological site of Olynthos, *Journal of Cultural Heritage* 8 no. 2 (2007), 193-196
- [9] Papayianni I., Stefanidou M., The role of fines in lime-based mortar's technology, *Romanian Journal of Materials* 41 no. 1 (2011), 26-29
- [10] Papayianni I., Stefanidou M., Re-crystallization phases in ancient mortars, from the 9th Euroseminar on Microscopy Applied to Building Materials, Trondheim Norway (2003)
- [11] Termkhajornkit P. et al, Effect of fly ash on autogenous shrinkage, *Cem Concr Res* 3 (2005), 473-82
- [12] Mihashi H., Nishiwaki T., Development of engineered self-healing and self-repairing concrete-state-of-the-art report, *J. Adv. Concr. Technol.* 10 (2012), 170-184
- [13] Ferrara L., Albertini I., Gettu R., Krelani V., Moscato S., Pirritano F., Theeda S., Self-healing of cement based materials engineered through crystalline admixtures: experimental results form a multinational university network, *ACI Special Publication* 305 (2015), 13.1-13.10. ISBN 13:978-1-942727-44-6
- [14] Stefanidou M., Nano-modified lime-pozzolan pastes, *Romanian Journal of Materials* 43 no. 2 (2013), 223-226
- [15] Nunes C., Slížková Z., Stefanidou M. and Němeček J., Microstructure of lime and lime-pozzolan pastes with nanosilica, *Cement and Concrete Research* 83 (2016), 152-163
- [16] Stefanidou M., Modification of lime-based pastes by the addition of nano-SiO<sub>2</sub>, from the 4th International Symposium on Nanotechnology in Construction NICOM4, Crete (2012)
- [17] Stefanidou M. Papayianni I., Influence of nano-SiO<sub>2</sub> on the Portland cement pastes, *Composites: Part B* 43 (2012), 2706-2710
- [18] Sobolev K. Z. et al, Performance of Cement Systems with Nano- SiO<sub>2</sub> Particles Produced Using Sol-gel Method, *Advanced Structural Materials* 3 1276 (2010), 139-145

## UTILIZATION OF QUARTZ QUARRY DUST IN ENGINEERED CEMENTITIOUS COMPOSITES PRODUCTION

**Olkan İlter Taş<sup>(1)</sup>, Süleyman Bahadır Keskin<sup>(1)</sup>, Özlem Kasap Keskin<sup>(1)</sup>, Mustafa Şahmaran<sup>(2)</sup>**

(1) Muğla Sıtkı Koçman University, Muğla, Turkey

(2) Hacettepe University, Ankara, Turkey

### **Abstract**

Engineered Cementitious Composites (ECC) is a type of high performance fiber reinforced cementitious composites characterized by tight micro cracking under mechanical loading, high ductility, hence high durability. Moreover, ECC has been shown to exhibit intrinsic self-healing behaviour. ECC design requires the use of abundant supplementary binding materials especially fly ash together with Portland cement. As aggregate, only micron sized quartz sand is used in order to provide homogeneity and restrict the matrix fracture toughness. Polyvinyl alcohol type synthetic fibers, high range water reducing admixtures and water are the other ingredients of ECC. Tight micro cracks together with abundant binding materials bring about intrinsic self-healing as an important feature for ECC. In this study, a successful ECC mixture is produced with local available fly ash and quartz sand; mechanical and self-healing properties of this mixture are determined. In addition to this control mixture, another ECC mixture is also produced by using quartz quarry dust, which is a waste of a local quartz quarry, as aggregate. The effect of using quartz quarry dust as aggregate for ECC on mechanical and self-healing properties are investigated by comparing with the properties of control mixture.

### **1. Introduction**

Although conventional concrete is a widely used material, it has many disadvantages which shorten its service life and cause economic loss [1]. Engineered Cementitious Composites (ECC) which have similar mechanical properties to concrete under normal service conditions promote sustainability through enhanced tensile and self-healing behavior. Under excessive mechanical tensile and bending loads ECC exhibit strain hardening and deflection hardening

behaviors as a result of multiple tight micro cracking, respectively [2, 3]. ECC not only prevent sudden failure under impact loading such as earthquakes due to its ductile behavior, but also possess self-healing property in multiple micro cracks formed after loading due to abundant binding material content. Although initial cost of ECC is much higher than that of ordinary concrete, dimensional compatibility, low cracking and high self-healing potential put ECC forward as a class of sustainable construction materials [4, 5]. Self-healing property obtained due to controlled tight cracking together with high amount of binding materials is an intrinsic property of ECC. Through self-healing mechanism, the material can heal itself by filling the cracks and regain its properties over time. It is possible to design materials to provide the self-healing characteristics. This feature may avoid costly solutions such as maintenance and renewal and does not require any human intervention [1, 6, 7].

In this study, quartz quarry dust obtained as a waste material from quartz mines located in Muğla region was used for the production of ECC. The effects of utilizing this waste material on self-healing properties and mechanical properties of ECC were investigated. Quartz quarry dust is stacked in nature in wet and dry conditions. Both forms of waste storage lead to environmental pollution and health problems.

## 2. Experimental Study

### 2.1 Materials

The aim of this study is to produce ECC by using the fly ash obtained from Yatağan Thermal Power Plant in Muğla region and replacing the commercial quartz sand used in production with quartz quarry dust of a local mine. For this reason, keeping all other ingredients same, an ECC is produced with local fly ash (FA 1.2) with the same proportions reported in the literature which also serves as a control mixture. In addition, another mixture is also produced in which the silica sand is replaced with the quartz quarry dust (FA 1.2 W). The chemical compositions of quartz sand and quartz quarry dust are shown in Tab. 1 together with the chemical compositions of the other ingredients. Due to high SiO<sub>2</sub> content of quarry dust, potential alkali aggregate reactivity test was also conducted on mortar bars and the expansion was found to be innocuous 16 days after casting.

Table 1. Chemical composition and physical properties of powder materials

	Cement	Fly Ash	Quartz Sand	Quartz Quarry Dust
<b>Chemical Composition (%)</b>				
SiO <sub>2</sub>	18.69	50.04	99.37	91.98
CaO	61.87	11.21	0.14	0.12
Al <sub>2</sub> O <sub>3</sub>	4.74	22.85	0.16	4.94
Fe <sub>2</sub> O <sub>3</sub>	3.37	8.02	0.03	0.08
MgO	3.36	2.23	-	0.02
Na <sub>2</sub> O	0.19	0.27	0.03	2.77
K <sub>2</sub> O	0.63	2.50	0.03	0.04
SO <sub>3</sub>	2.93	0.78	-	-
<b>Physical Properties</b>				
Specific Gravity	3.15	2.28	2.60	2.60
Blaine fineness	3420	2845	-	-

Mixture proportions of ECC used in this study is also provided in Tab. 2.

Table 2. Proportioning of ingredients of ECC mixtures (kg/m<sup>3</sup>)

Ingredient	Cement	Fly ash	Water	Sand	HRWRA	PVA fiber
Amount (kg/m <sup>3</sup> )	560	672	333	442	8.4	26

## 2.2 Test Methods

Two sets of experiments were carried out on ECC specimens to determine the mechanical and self-healing properties. For mechanical properties, specimens were tested under compression and four-point bending at 7, 28 and 90 days after casting. Compressive strength was determined on 50 mm cubic specimens while for the determination of flexural strength and mid-point deflections 50x75x360 mm beam specimens were used. Flexural tests were carried out on deformation controlled universal testing machine.

For self-healing test specimens were preloaded to 60% of their deflection capacities at 28 days. Self-healing capabilities were tested in terms of four-point bending test, ultrasonic pulse velocity (UPV) test and rapid chloride permeability test (RCPT). UPV and bending tests were conducted on beam specimens while for RCPT tests 100 mm diameter and 50 mm thick puck specimens were cut from ECC cylinders as described in ASTM C 1202 [8]. Results obtained from the virgin specimens were compared with the preloaded specimens for self-healing assessment.

## 3. Test Results and Discussions

### 3.1 Mechanical Properties

The compressive strength, flexural strength and mid-point deflection capacities of the specimens determined as average of 3 specimens at ages of 7, 28 and 90 days are provided in Tab. 3.

Table 3. Mechanical Properties of ECC Mixtures

Age (Day)	Compressive Strength (MPa)		Flexural Strength (MPa)		Mid-Point Deflection (mm)	
	FA1.2	FA1.2W	FA1.2	FA1.2W	FA1.2	FA1.2W
7	39.3	40.0	8.84	11.28	5.16	5.58
28	63.3	64.9	11.10	11.49	3.84	4.88
90	75.2	78.6	11.97	12.33	3.32	3.41

Mixtures which contains fly ash obtained from Yatağan Thermal Power Plant shows similar mechanical properties to the mixtures given in the literature [9]. It is clear that it is possible to produce ECC with the locally available materials around Muğla region. Under bending loads, the specimens show high amounts of deflections as expected in ECC specimens. Test results also indicate the performance of quartz quarry dust as aggregate in ECC production. Mechanical properties observed in FA1.2W is slightly better than that observed in FA1.2. Compressive strength, flexural strength and deflections under four-point bending test are all

higher in case of quartz quarry waste usage. The improved mechanical properties may be attributed to the change in particle size distribution of the aggregates [10, 11] or activation potential of fly ash by higher alkali content of quartz quarry dust [12]. According to the mechanical test results, it is obviously clear that ECC can be produced by using quartz quarry dust waste as replacement of silica sand.

### 3.2 Self-Healing Properties

Self-healing capacities of ECC mixtures produced by locally available materials were investigated by three different test methods; four-point bending test, UPV test and RCPT test. At 28 days, preloading was applied on some specimens. Preloaded (PL) specimens were moisture cured until the test ages. The rest of the specimens were kept as sound specimens (S), and they were also tested at the same ages. The comparison of the test results for the PL and S specimens is expected to indicate the level of self-healing development in ECC mixtures. Flexural strength and mid-point deflection results are listed in Tab. 4.

Table 4. Flexural properties of the mixtures

Age (Day)	Property	FA 1.2 S	FA 1.2 PL	FA 1.2 W S	FA 1.2 W PL
<b>28+0</b>	Flexural Str. (MPa)	11.10	8.44	11.49	6.58
	Mid-Point Defl.(mm)	3.84	2.07	4.88	2.66
<b>28+30</b>	Flexural Str. (MPa)	11.88	10.5	12.41	8.42
	Mid-Point Defl.(mm)	3.35	3.30	4.58	3.78
<b>28+60</b>	Flexural Str. (MPa)	12.25	10.99	12.46	9.83
	Mid-Point Defl.(mm)	3.27	3.41	4.13	4.27
<b>28+90</b>	Flexural Str. (MPa)	12.56	11.27	12.49	11.52
	Mid-Point Defl.(mm)	3.05	3.69	3.92	4.58

As seen in Tab. 4, with the age of the specimen, flexural strength increased and the deflection capacity decreased as expected for both ECC mixtures. Preloading process caused a significant decrease both in the maximum flexural load carrying and mid-point deflection capacities. In PL specimens, the flexural properties improved with time which was an indication of self-healing of the cracks in the specimens. For both FA1.2 and FA1.2W mixtures, flexural strength of specimens reached the 28-day values of sound specimens in 90 days after preloading process.

UPV is a non-destructive test method which allows to observe the changes in the properties of the same specimens with time. Monitoring the changes in the UPV results provides information about the crack closure because in the presence of cracks. Cracks extend the path for the ultrasonic waves to travel and result in an overall decrease in UPV. The difference between the UPV values of sound and preloaded specimens are shown in Fig. 1. In both mixtures UPV increased with time which indicated the continuation of hydration process in sound specimens and development of self-healing in preloaded specimens. UPV values were decreased in ECC mixtures after the crack formation by preloading. However, as time passes the difference between the sound and pre-loaded specimens decreased. This reduction in the

difference between sound and preloaded specimens showed that the cracks were closed with time.

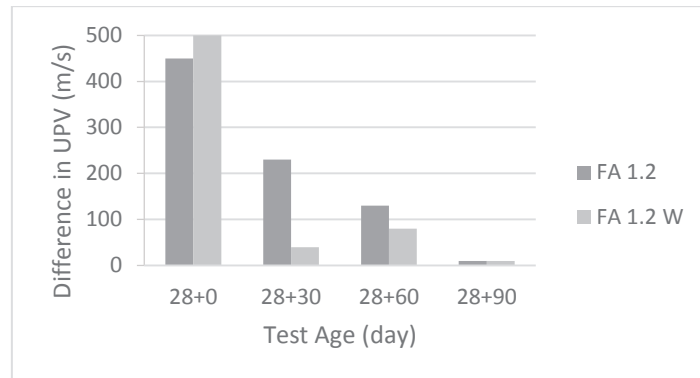


Figure 2. Difference in UPV test results

RCPT is also a non-destructive testing method which shows the transport properties of the specimens. Higher RCPT test result means higher permeability and hence higher pore content, especially in case of precracked specimens with larger or more cracks. Therefore, preloaded specimens are expected to show larger RCPT results. RCPT results decreased with time as hydration continued and the permeability decreased. Preloading application lead to an increase in RCPT results due to increase in permeability as a result of crack formation. However, as seen from Fig. 3 the difference in the results of sound and preloaded specimens decreased with time as in the case of UPV test. Reduction in difference is an evidence of crack closure which indicates that the preloaded specimens self-healed.

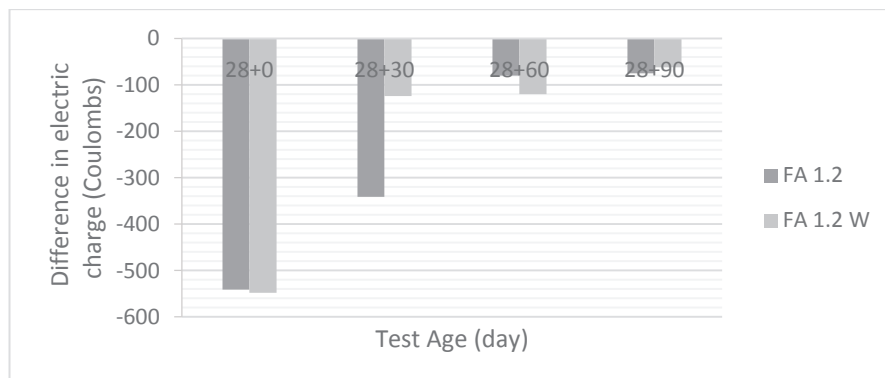


Figure 3. Difference in RCPT results

#### 4. Conclusion

This paper represents the results of an experimental study which aims to produce ECC with locally available waste materials around Muğla region in Turkey. The results revealed that it is possible to produce cementitious composites having high compressive strength, high deflection capacity under bending and self-healing capability by using the locally available



materials. Additionally, it is also possible to reduce the initial cost of ECC mixture by using waste quartz quarry dust as aggregate instead of quartz sand.

### **Acknowledgement**

This paper has been granted by the Mugla Sitki Kocman University Research Projects Coordination Office. Project Grant Number: 17/006 and title “Usability of Industrial Wastes of Muğla Region in Cementitious Composite Production”.

### **References**

- [1] Yıldırım, G., Kasap Keskin, Ö., Keskin, S.B., Sahmaran, M., Lachemi, M., A review of intrinsic self-healing capability of engineered cementitious composites: Recovery of transport and mechanical properties, *Construction and Building Materials* (2015), 101: 10–21.
- [2] Gohil, B.D. & Parikh, K.B., Study on engineered cementitious composites with different fibres: a critical review, *International Journal of Innovations in Engineering and Technology* (2016), 6:366-370.
- [3] Deshpande, U.L. & Murnal, P.B., Ductile concrete using engineered cementitious composites. *International Journal of Engineering Research* (2016), 5:756-760.
- [4] Sahmaran, M., Yıldırım, G., Erdem, T.K., Self-healing capability of cementitious composites incorporating different supplementary cementitious materials. *Cement and Concrete Composites* (2013) 35:89–101.
- [5] Keskin, S.B., Sahmaran, M., Yaman, I.O., Lachemi, M., Correlation between the viscoelastic properties and cracking potential of engineered cementitious composites. *Construction and Building Materials* (2014), 7: 375–383.
- [6] Schlangen, E., Jonkers, H., Qian, S., Garcia, A., Recent advances on self-healing of concrete. *Fracture Mechanics of Concrete and Concrete Structures* (2010), 291-298
- [7] Li, V.C., On engineered cementitious composites (ECC) - a review of the materials and its applications, *Journal of Advanced Concrete Technology* (2013), 1:215–230
- [8] ASTM C1202, Standard Test Method for Electrical Indication of Concrete’s Ability to Resist Chloride Ion Penetration, ASTM International (2017)
- [9] Keskin, S.B., Dimensional stability of engineered cementitious composites, PhD thesis, Middle East Technical University, Ankara, Turkey (2012)
- [10] Yang, Y.Z., Yao, Y., Zhu, Y., Effects of Gradation of Sand on the Mechanical Properties of Engineered Cementitious Composites, *Advanced Materials Research* (2011), 250-253: 374-378.
- [11] Tian, L., Chen, J.R., Zhao, T.J., Ding, Z., Influence of Aggregate Gradation on Mechanics Performance of Strain-Hardening Cement-Based Composites (SHCC), *Advanced Materials Research* (2009), 79-82: 207-210.
- [12] Fraay, A.L.A., Bijen, J.M., de Haan, Y.M., The reaction of fly ash in concrete a critical examination. *Cement and Concrete Research* (1989),19:235-246.



# Syner '18 Crete

RILEM Proceedings PRO 121 – Volume 1&2  
ISBN Vol. 1: 978-2-35158-211-4  
ISBN Vol. 2: 978-2-35158-212-1  
ISBN Vol. 1&2: 978-2-35158-202-2  
e-ISBN Vol. 1&2: 978-2-35158-203-9  
DOI: 10.5281/zenodo.1405563  
2018 Edition

RILEM Publications S.a.r.l.  
4 avenue du Recteur Poincaré  
75016 Paris  
FRANCE  
Tel: +33 1 42 24 64 46  
Fax: +33 9 70 29 51 20  
E-mail: [dg@rilem.net](mailto:dg@rilem.net)